

Jerzy Leszczynski

*Editor*

Anna Kaczmarek-Kędziera

Manthos G. Papadopoulos

Heribert Reis

Andrzej J. Sadlej

Manoj K. Shukla

*Co-Editors*

SPRINGER  
REFERENCE

# Handbook of Computational Chemistry

 Springer

# Handbook of Computational Chemistry





Jerzy Leszczynski (Ed.)

# Handbook of Computational Chemistry

With 415 Figures and 88 Tables

*Editor*

Jerzy Leszczynski  
Department of Chemistry and Biochemistry  
Jackson State University  
Jackson, MS 39217  
USA  
jerzy@icnanotox.org

ISBN 978-94-007-0710-8 e-ISBN 978-94-007-0711-5

DOI 10.1007/978-94-007-0711-5

ISBN Bundle 978-94-007-0712-2

Springer Dordrecht Heidelberg London New York

Library of Congress Control Number: 2011941760

© Springer Science+Business Media B.V. 2012

No part of this work may be reproduced, stored in a retrieval system, or transmitted in any form or by any means, electronic, mechanical, photocopying, microfilming, recording or otherwise, without written permission from the Publisher, with the exception of any material supplied specifically for the purpose of being entered and executed on a computer system, for exclusive use by the purchaser of the work.

Printed on acid-free paper

Springer is part of Springer Science+Business Media ([www.springer.com](http://www.springer.com))

# Preface

It has been an amazing experience to witness and comprehend transformation of chemistry during the twentieth century. Since its ancient beginnings, chemistry has been considered to be an experimental science. However, during the last 50 years it has been advancing through noticeable contributions of computational methods. This transformation has its roots in both theoretical breakthroughs (Heisenberg's 1925 and Schrodinger's 1926 first papers on quantum mechanics) as well as development of the first computer – Electronic Numerical Integrator and Computer (ENIAC) build in 1943 for the USA Department of the Army. However, it took about twenty years after creation of ENIAC computers to deliver computational chemistry techniques to scientific community. Such early methods being semi-empirical in nature rely on the number of parameters derived from experiments. Though such an approach unites experimental chemistry origins with new theoretical approaches, in some cases it also produced artificial computational results. Further, it also lacks reliable parameters for some elements. The next, successful chapter for computational chemistry started in the 1970s with applications of non-empirical *ab initio* methods. The first *ab initio* computer code popular among non-theoreticians – GAUSSIAN 70 – was developed in the 1970s by John A Pople's group. It initiated a computational chemistry revolution that fired up in the 1980s when supercomputers became accessible to the general scientific community. Also during this period, the Density Functional Theory approaches gained a prominent position among efficient computational methods. The vital role of computational chemistry in many research areas was convincingly acknowledged in 1998 when the chemical and physical community celebrated the Nobel Prize that was awarded to two leading computational experts. Walter Kohn and John A. Pople were recognized by the Nobel Committee for their contributions to the development of efficient computational methods for quantum chemistry.

Over the years, different methods of theoretical chemistry have been successfully transformed into useful tools that could be applied in diverse areas of scientific and technological research. Owing to the fundamental methodological developments and continued impressive progress in computational technologies in the last quarter of the twentieth century, several fast and user-friendly programs have been developed and made accessible to a wide community of scientists. These nearly automatic computer codes indicate how methods of theoretical chemistry could be applied as both diagnostic and predictive research tools which support efforts and even guide directions of traditional experimental approaches. The user-friendly features of commercial codes combined with efficient visualization methods make them accessible to researchers with practically any educational background. Generally, only a limited knowledge and a little formal experience in theoretical chemistry are required to use such programs and to obtain some numerical data. This might cause unexpected outcomes. Most of the methods of theoretical (quantum) chemistry have a limited range of applications and their use by an inexperienced amateur who performs computational studies without understanding such constraint may lead to serious problems and spurious results. Moreover, due to the availability of a variety of methods of different quality, a user without a good background in theoretical chemistry may feel lost given the choices from usually rich menus of available programs.

The three volume “Handbook of Computational Chemistry” is primarily intended as a guide that can help to navigate among different computational methods currently in use. In order to accomplish this goal, we collected 39 chapters that provide compact description of the basis of computational chemistry techniques along with vast examples of applications of these methods in various areas. The handbook is designed for researchers who are just being introduced to computational methods, as well as for those who are searching for the best choice for solution to specific problems involving theoretical approaches.

The first volume briefly describes different methods used in computational chemistry without going into exhaustive details of theory. Basic assumptions common to the majority of computational methods based on either quantum or statistical mechanics are outlined. Particular attention is paid to the limits of their applicability. Importantly, this volume also establishes definitions of a variety of acronyms and terminology used in the area of computational chemistry.

Since we assumed that the readers of this book are interested in applications of computational methods, a broad range of the most important applications of computational chemistry is provided in the second section of the first volume. The applications include descriptions of standard chemical calculations for model molecules under various conditions. The Handbook provides information on the prediction of various molecular properties as well as investigations of chemical reactions.

There are two classes of species: biomolecules and nanomaterials that are of a vital interest not only to chemists but also to physicists, biologists, and material scientists. Two volumes are devoted to a description of specific computational methods that are designed to investigate such species. Numerous examples of applications as well as descriptions of specific research problems and their solutions for various types of biomolecules and nanoparticles are given in the second and third volumes of the Handbook. The reviewed topics will attract the attention of all those who are already working or planning to start research involving computational approaches.

The idea of this handbook crystallized after numerous discussions with a dear friend and the leading Polish quantum chemists Andrzej J. Sadlej. Andrzej was also actively involved in selecting the potential contributors and editing the book. Unfortunately, he passed away before the book was published. Though he is no longer with us, he will always be remembered. Andrzej’s intellectual contributions will continue to live on and this Handbook, which is dedicated to him, is intended as a tribute to his memory for friends, colleagues and students to remember him.

The Editors

# Editorial Board

## **Theory and Methodology**

Anna Kaczmarek-Kędziera and Andrzej J. Sadlej

## **Applications of Computational Methods to Model Systems**

Anna Kaczmarek-Kędziera and Andrzej J. Sadlej

## **Solid States and Nanomaterials**

Manthos G. Papadopoulos and Heribert Reis

## **Biomolecules**

Manoj K. Shukla



# Table of Contents

<b>Preface</b> .....	<b>v</b>
<b>Editorial Board</b> .....	<b>vii</b>
<b>List of Contributors</b> .....	<b>xiii</b>

## Volume 1

<b>1 From Quantum Theory to Computational Chemistry. A Brief Account of Developments</b> .....	<b>1</b>
<i>Lucjan Piela</i>	
<b>2 The Position of the Clamped Nuclei Electronic Hamiltonian in Quantum Mechanics</b> .....	<b>13</b>
<i>Brian Sutcliffe · R. Guy Woolley</i>	
<b>3 Remarks on Wave Function Theory and Methods</b> .....	<b>55</b>
<i>Dariusz Kędziera · Anna Kaczmarek-Kędziera</i>	
<b>4 Directions for Use of Density Functional Theory: A Short Instruction Manual for Chemists</b> .....	<b>95</b>
<i>Heiko Jacobsen · Luigi Cavallo</i>	
<b>5 Introduction to Response Theory</b> .....	<b>135</b>
<i>Thomas Bondo Pedersen</i>	
<b>6 Intermolecular Interactions</b> .....	<b>157</b>
<i>Alston J. Misquitta</i>	
<b>7 Molecular Dynamics Simulation: From “Ab Initio” to “Coarse Grained”</b> .....	<b>195</b>
<i>Chris Lorenz · Nikos L. Doltsinis</i>	
<b>8 Statistical Mechanics of Force-Induced Transitions of Biopolymers</b> .....	<b>239</b>
<i>Sanjay Kumar</i>	
<b>9 Molecular Mechanics: Method and Applications</b> .....	<b>259</b>
<i>Valeri Poltev</i>	
<b>10 Molecular Structure and Vibrational Spectra</b> .....	<b>293</b>
<i>Jon Baker</i>	



<b>11</b>	<b>Molecular Electric, Magnetic, and Optical Properties .....</b>	<b>361</b>
	<i>Michał Jaszuński · Antonio Rizzo · Kenneth Ruud</i>	
<b>12</b>	<b>Weak Intermolecular Interactions: A Supermolecular Approach.....</b>	<b>443</b>
	<i>Mark Waller · Stefan Grimme</i>	
<b>13</b>	<b>Chemical Reactions: Thermochemical Calculations.....</b>	<b>467</b>
	<i>John D. Watts</i>	
<b>14</b>	<b>Calculation of Excited States: Molecular Photophysics and Photochemistry on Display .....</b>	<b>483</b>
	<i>Luis Serrano-Andrés · Juan José Serrano-Pérez</i>	
<b>15</b>	<b>Solvent Effects in Quantum Chemistry.....</b>	<b>561</b>
	<i>Gerald Monard · Jean-Louis Rivail</i>	
<b>16</b>	<b>Auxiliary Density Functional Theory: From Molecules to Nanostructures .....</b>	<b>573</b>
	<i>Patrizia Calaminici · Victor-Daniel Domínguez-Soria · Roberto Flores-Moreno · Gabriel Ulises Gamboa-Martínez · Gerald Geudtner · Annick Goursot · Dennis R. Salahub · Andreas M. Köster</i>	
<b>17</b>	<b>Guide to Programs for Non-relativistic Quantum Chemistry Calculations .....</b>	<b>611</b>
	<i>Tao Zeng · Mariusz Klobukowski</i>	

## Volume 2

<b>18</b>	<b>Functional Nanostructures and Nanocomposites – Numerical Modeling Approach and Experiment.....</b>	<b>631</b>
	<i>Malgorzata Makowska-Janusik · Abdel-Hadi Kassiba</i>	
<b>19</b>	<b>Structures and Stability of Fullerenes, Metallofullerenes, and Their Derivatives.....</b>	<b>667</b>
	<i>Alexey A. Popov</i>	
<b>20</b>	<b>Structures and Electric Properties of Semiconductor clusters.....</b>	<b>723</b>
	<i>Panaghiotis Karamanis</i>	
<b>21</b>	<b>Structures, Energetics, and Spectroscopic Fingerprints of Water Clusters <math>n = 2-24</math> .....</b>	<b>761</b>
	<i>Soohaeng Yoo · Sotiris S. Xantheas</i>	
<b>22</b>	<b>Fundamental Structural, Electronic, and Chemical Properties of Carbon Nanostructures: Graphene, Fullerenes, Carbon Nanotubes, and Their Derivatives.....</b>	<b>793</b>
	<i>Tandabany C. Dinadayalane · Jerzy Leszczynski</i>	

<b>23</b>	<b>Optical Properties of Quantum Dot Nano-composite Materials Studied by Solid-State Theory Calculations.....</b>	<b>869</b>
	<i>Ying Fu · Hans Ågren</i>	
<b>24</b>	<b>Modeling of Quasi-One-Dimensional Carbon Nanostructures with Density Functional Theory.....</b>	<b>901</b>
	<i>Veronica Barone · Oded Hod · Juan E. Peralta</i>	
<b>25</b>	<b>Variation of the Surface to Bulk Contribution to Cluster Properties.....</b>	<b>939</b>
	<i>Antonis N. Andriotis · Zacharias G. Fthenakis · Madhu Menon</i>	
<b>26</b>	<b>Theoretical Studies of Structural and Electronic Properties of Clusters.....</b>	<b>955</b>
	<i>Michael Springborg</i>	
<b>27</b>	<b>Modeling of Nanostructures.....</b>	<b>995</b>
	<i>Hande Toffoli · Sakir Erkoç · Daniele Toffoli</i>	

### Volume 3

<b>28</b>	<b>Quantum Cluster Theory for the Polarizable Continuum Model (PCM).....</b>	<b>1043</b>
	<i>Roberto Cammi · Jacopo Tomasi</i>	
<b>29</b>	<b>Spin-Orbit Coupling in Enzymatic Reactions and the Role of Spin in Biochemistry.....</b>	<b>1067</b>
	<i>B. F. Minaev · V. O. Minaeva · Hans Ågren</i>	
<b>30</b>	<b>Protein Modeling.....</b>	<b>1095</b>
	<i>G. N�ray-Szab� · A. Perczel · A. L�ng</i>	
<b>31</b>	<b>Applications of Computational Methods to Simulations of Proteins Dynamics.....</b>	<b>1127</b>
	<i>Wieslaw Nowak</i>	
<b>32</b>	<b>Molecular Dynamics and Advanced Sampling Simulations of Nucleic Acids.....</b>	<b>1155</b>
	<i>Jeremy Curuksu · Srinivasaraghavan Kannan · Martin Zacharias</i>	
<b>33</b>	<b>Model Systems for Dynamics of <math>\pi</math>-Conjugated Biomolecules in Excited States.....</b>	<b>1175</b>
	<i>Mario Barbatti · Matthias Ruckebauer · Jaroslaw J. Szymczak · Bernhard Sellner · Mario Vazdar · Ivana Antol · Mirjana Eckert-Maksić · Hans Lischka</i>	
<b>34</b>	<b>Low-Energy Electron (LEE)-Induced DNA Damage: Theoretical Approaches to Modeling Experiment.....</b>	<b>1215</b>
	<i>Anil Kumar · Michael D. Sevilla</i>	
<b>35</b>	<b>Computational Modeling of DNA and RNA Fragments.....</b>	<b>1257</b>
	<i>Jiří Sponer · Manoj K. Shukla · Jerzy Leszczynski</i>	

<b>36 Metal Interactions with Nucleobases, Base Pairs, and Oligomer Sequences; Computational Approach .....</b>	<b>1277</b>
<i>Jaroslav V. Burda · Jiří Šponer · Jerzy Leszczynski</i>	
<b>37 Predictive QSAR Modeling: Methods and Applications in Drug Discovery and Chemical Risk Assessment .....</b>	<b>1309</b>
<i>Alexander Golbraikh · Xiang Simon Wang · Hao Zhu · Alexander Tropsha</i>	
<b>38 Quantitative Structure–Activity Relationships of Antimicrobial Compounds .....</b>	<b>1343</b>
<i>F. P. Maguna · N. B. Okulik · Eduardo A. Castro</i>	
<b>39 Ab Initio Investigation of Photochemical Reaction Mechanisms: From Isolated Molecules to Complex Environments.....</b>	<b>1359</b>
<i>Igor Schapiro · Patrick Zakhia El-Khoury · Massimo Olivucci</i>	
<b>Index .....</b>	<b>1405</b>

# List of Contributors

## **Hans Ågren**

Division of Theoretical Chemistry and  
Biology  
School of Biotechnology  
Royal Institute of Technology  
Stockholm  
Sweden

## **Antonis N. Andriotis**

Institute of Electronic Structure and Laser  
FORTH  
Heraklio, Crete  
Greece

## **Ivana Antol**

Laboratory for Physical-Organic  
Chemistry – Division of Organic Chemistry  
and Biochemistry  
Rudjer Bošković Institute  
Zagreb  
Croatia

## **Jon Baker**

Parallel Quantum Solutions  
Fayetteville, AR  
USA

## **Mario Barbatti**

Institute for Theoretical Chemistry  
University of Vienna  
Vienna  
Austria  
and  
Max-Planck-Institut für Kohlenforschung  
Mülheim an der Ruhr  
Germany

## **Veronica Barone**

Department of Physics  
Central Michigan University  
Mount Pleasant, MI  
USA

## **Jaroslav V. Burda**

Charles University in Prague  
Prague 2  
Czech Republic

## **Patrizia Calaminici**

Departamento de Química  
CINVESTAV  
Avenida Instituto Politécnico  
México, DF  
Mexico

## **Roberto Cammi**

Dipartimento di Chimica G.I.A.F.  
Università di Parma  
Parma  
Italy

## **Eduardo A. Castro**

INIFTA  
División Química Teórica  
Departamento de Química  
Facultad de Ciencias Exactas  
UNLP Diag. 113 y 64  
La Plata  
Buenos Aires  
Argentina

## **Luigi Cavallo**

Department of Chemistry  
University of Salerno Via Ponte don Melillo  
Fisciano  
Italy

**Jeremy Curuksu**

Mathematics Department  
Swiss Federal Institute of Technology  
Lausanne (EPFL)  
Switzerland

**Tandabany C. Dinadayalane**

Interdisciplinary Center for Nanotoxicity  
Department of Chemistry and  
Biochemistry  
Jackson State University  
Jackson, MS  
USA

**Nikos L. Doltsinis**

Department of Physics  
King's College London  
London  
UK  
and  
Institute for Solid State Theory  
Department of Physics  
University of Münster  
Münster  
Germany

**Victor-Daniel Domínguez-Soria**

Departamento de Química  
CINVESTAV  
Avenida Instituto Politécnico  
México, DF  
Mexico

**Mirjana Eckert-Maksić**

Laboratory for Physical-Organic  
Chemistry – Division of Organic Chemistry  
and Biochemistry  
Rudjer Bošković Institute  
Zagreb  
Croatia

**Patrick Zakhia El-Khoury**

Chemistry Department  
Bowling Green State University  
Bowling Green, OH  
USA

**Sakir Erkoç**

Department of Physics  
Middle East Technical University  
Ankara  
Turkey

**Roberto Flores-Moreno**

Departamento de Química  
CUCEI  
Universidad de Guadalajara  
Guadalajara, Jalisco  
Mexico

**Zacharias G. Fthenakis**

Institute of Electronic Structure and Laser  
FORTH  
Heraklio, Crete  
Greece

**Ying Fu**

Division of Theoretical Chemistry and  
Biology  
School of Biotechnology  
Royal Institute of Technology  
Stockholm  
Sweden

**Gabriel Ulises Gamboa-Martínez**

Departamento de Química  
CINVESTAV  
Avenida Instituto Politécnico  
México, DF  
Mexico

**Gerald Geudtner**

Departamento de Química  
CINVESTAV  
Avenida Instituto Politécnico  
México, DF  
Mexico

**Alexander Golbraikh**

Laboratory for Molecular Modeling and  
Carolina Center for Exploratory  
Cheminformatics Research  
Division of Medicinal Chemistry and  
Natural Products  
UNC Eshelman School of Pharmacy  
University of North Carolina  
Chapel Hill, NC  
USA

**Annick Gourso**

Institut Charles Gerhardt  
UMR 5253 CNRS  
Ecole de Chimie de Montpellier  
Montpellier  
Cédex 5  
France

**Stefan Grimme**

Organisch-Chemisches Institut  
Westfälische Wilhelms-Universität Münster  
Münster  
Germany

**Oded Hod**

Department of Chemical Physics  
School of Chemistry  
The Sackler Faculty of Exact Sciences  
Tel Aviv University  
Tel Aviv  
Israel

**Heiko Jacobsen**

KemKom  
New Orleans, LA  
USA

**Michał Jaszucki**

Institute of Organic Chemistry  
Polish Academy of Sciences  
Warszawa  
Poland

**Anna Kaczmarek-Kędziera**

Department of Chemistry  
Nicolaus Copernicus University  
Toruń  
Poland

**Srinivasaraghavan Kannan**

Martin-Luther-Universität Halle-Wittenberg  
Institut für Pharmazie  
Halle  
Germany  
and  
School of Engineering and Science Jacobs  
University Bremen  
Bremen  
Germany

**Panaghiotis Karamanis**

Groupe de Chimie Théorique et  
Réactivité ECP  
IPREM UMR 5254  
Université de Pau et de Pays de l'Adour  
PAU Cedex  
France

**A. Kassiba**

Institut de Recherche en Ingénierie  
Moléculaire et Matériaux Fonctionnels FR  
CNRS 2575 – Laboratoire de Physique de  
l'Etat Condensé  
UMR CNRS 6087  
Université du Maine  
Le Mans Cedex 9  
France

**Dariusz Kędziera**

Department of Chemistry and  
Photochemistry of Polymers  
Nicolaus Copernicus University  
Toruń  
Poland

**Mariusz Klobukowski**

Department of Chemistry  
University of Alberta  
Edmonton, AB  
Canada

**Andreas M. Köster**

Departamento de Química  
CINVESTAV  
Avenida Instituto Politécnico  
México, DF  
Mexico

**Anil Kumar**

Department of Chemistry  
Oakland University  
Rochester, MI  
USA

**Sanjay Kumar**

Department of Physics  
Banaras Hindu University  
Varanasi  
India

**A. Láng**

Laboratory of Structural Chemistry and  
Biology and Protein Modelling Group  
HAS-ELTE  
Institute of Chemistry  
Eötvös Loránd University  
Budapest  
Hungary

**Jerzy Leszczynski**

Department of Chemistry and  
Biochemistry  
Interdisciplinary Center for Nanotoxicity  
Jackson State University  
Jackson, MS  
USA

**Hans Lischka**

Institute for Theoretical Chemistry  
University of Vienna  
Vienna  
Austria  
and  
Department of Chemistry and  
Biochemistry  
Texas Tech University  
Lubbock, TX  
USA

**Chris Lorenz**

Department of Physics  
King's College London  
London  
UK

**F. P. Maguna**

Facultad de Agroindustrias  
Universidad Nacional del Nordeste  
Chaco  
Argentina

**M. Makowska-Janusik**

Institute of Physics  
Jan Dlugosz University  
Czestochowa  
Poland

**Madhu Menon**

Department of Physics and Astronomy and  
Center for Computational Sciences  
University of Kentucky  
Lexington, KY  
USA

**B. F. Minaev**

Theoretical Chemistry  
School of Biotechnology  
Royal Institute of Technology  
Stockholm  
Sweden  
and  
Bogdam Khmel'nitskii National University  
Cherkassy  
Ukraine

**V. O. Minaeva**

Bogdam Khmel'nitskii National University  
Cherkassy  
Ukraine

**Alston J. Misquitta**

TCM Group  
Cambridge  
UK  
and  
School of Physics  
Queen Mary  
University of London  
London  
UK

**Gerald Monard**

Theoretical Chemistry and Biochemistry  
Group SRSMC  
Nancy-University CNRS Boulevard des  
Aiguillettes  
Vandoeuvre-les-Nancy  
France

**G. Náray-Szabó**

Laboratory of Structural Chemistry and  
Biology and Protein Modelling Group  
HAS-ELTE  
Institute of Chemistry  
Eötvös Loránd University  
Budapest  
Hungary

**Wieslaw Nowak**

Institute of Physics  
Nicholaus Copernicus University in Torun  
Torun  
Poland

**N. B. Okulik**

Facultad de Agroindustrias  
Universidad Nacional del Nordeste  
Chaco  
Argentina

**Massimo Olivucci**

Chemistry Department  
Bowling Green State University  
Bowling Green, OH  
USA  
and  
Dipartimento di Chimica  
Universita di Siena  
Italy

**Thomas Bondo Pedersen**

Centre for Theoretical and Computational  
Chemistry  
Department of Chemistry  
University of Oslo  
Oslo  
Norway

**Juan E. Peralta**

Department of Physics  
Central Michigan University  
Mount Pleasant, MI  
USA

**A. Perczel**

Laboratory of Structural Chemistry and  
Biology and Protein Modelling Group  
HAS-ELTE  
Institute of Chemistry  
Eötvös Loránd University  
Budapest  
Hungary

**Lucjan Piela**

Department of Chemistry  
University of Warsaw  
Poland

**Valeri Poltev**

Autonomous University of Puebla  
Mexico



**Alexey A. Popov**

Leibniz-Institute for Solid State and  
Materials Research (IFW Dresden)  
Dresden  
Germany  
and  
Chemistry Department  
Moscow State University  
Moscow  
Russia

**Jean-Louis Rivail**

Theoretical Chemistry and Biochemistry  
Group SRSMC  
Nancy-University CNRS Boulevard des  
Aiguillettes  
Vandoeuvre-les-Nancy  
France

**Antonio Rizzo**

Istituto per i Processi Chimico Fisici del  
Consiglio Nazionale delle Ricerche  
Pisa  
Italy

**Matthias Ruckebauer**

Institute for Theoretical Chemistry  
University of Vienna  
Vienna  
Austria  
and  
Research Lab Computational Technologies  
and Applications  
University of Vienna  
Vienna  
Austria

**Kenneth Ruud**

Centre for Theoretical and Computational  
Chemistry  
Department of Chemistry  
University of Tromsø  
Tromsø  
Norway

**Dennis R. Salahub**

Department of Chemistry  
IBI – Institute for Biocomplexity and  
Informatics  
ISEEE – Institute for Sustainable Energy  
Environment, Economy  
University of Calgary  
Calgary, AB  
Canada

**Igor Schapiro**

Chemistry Department  
Bowling Green State University  
Bowling Green, OH  
USA

**Bernhard Sellner**

Institute for Theoretical Chemistry  
University of Vienna  
Vienna  
Austria

**Luis Serrano-Andrés**

Instituto de Ciencia Molecular  
Universitat de València  
Valencia  
Spain

**Juan José Serrano-Pérez**

Instituto de Ciencia Molecular  
Universitat de València  
Valencia  
Spain  
and  
Department of Chemistry  
Imperial College London Computational &  
Structural Research Group  
London  
UK

**Michael D. Sevilla**

Department of Chemistry  
Oakland University  
Rochester, MI  
USA

**Manoj K. Shukla**

Department of Chemistry and  
Biochemistry  
Interdisciplinary Center for Nanotoxicity  
Jackson State University  
Jackson, MS  
USA  
and  
Environmental Laboratory  
US Army Engineer Research and  
Development Center  
Vicksburg, MS  
USA

**Jiří Šponer**

Institute of Biophysics  
Academy of Sciences of the Czech Republic  
Brno  
Czech Republic

**Michael Springborg**

Physical and Theoretical Chemistry  
University of Saarland  
Saarbrücken  
Germany

**Brian Sutcliffe**

Service de Chimie Quantique et  
Photophysique  
Université Libre de Bruxelles  
Bruxelles  
Belgium

**Jaroslav J. Szymczak**

Institute for Theoretical Chemistry  
University of Vienna  
Vienna  
Austria

**Daniele Toffoli**

Department of Chemistry  
Middle East Technical University  
Ankara  
Turkey

**Hande Toffoli**

Department of Physics  
Middle East Technical University  
Ankara  
Turkey

**Jacopo Tomasi**

Dipartimento di Chimica e Chimica  
Industriale  
Universita di Pisa  
Pisa  
Italy

**Alexander Tropsha**

Division of Medicinal Chemistry and  
Natural Products  
UNC Eshelman School of Pharmacy  
University of North Carolina  
Chapel Hill, NC  
USA

**Mario Vazdar**

Laboratory for Physical-Organic  
Chemistry – Division of Organic Chemistry  
and Biochemistry  
Rudjer Bošković Institute  
Zagreb  
Croatia

**Mark Waller**

Organisch-Chemisches Institut  
Westfälische Wilhelms-Universität Münster  
Münster  
Germany

**Xiang Simon Wang**

Laboratory for Molecular Modeling and  
Carolina Center for Exploratory  
Cheminformatics Research  
Division of Medicinal Chemistry and  
Natural Products  
UNC Eshelman School of Pharmacy  
University of North Carolina  
Chapel Hill, NC  
USA

**John D. Watts**

Department of Chemistry and  
Biochemistry  
Jackson State University  
Jackson, MS  
USA

**R. Guy Woolley**

School of Science and Technology  
Nottingham Trent University  
Nottingham  
UK

**Sotiris S. Xantheas**

Chemical & Material Sciences Division  
Pacific Northwest National Laboratory  
Richland, WA  
USA

**Soohaeng Yoo**

Chemical & Material Sciences Division  
Pacific Northwest National Laboratory  
Richland, WA  
USA

**Martin Zacharias**

Physik-Department T38  
Technische Universität München  
Garching  
Germany

**Tao Zeng**

Department of Chemistry  
University of Alberta  
Edmonton, AB  
Canada

**Hao Zhu**

Laboratory for Molecular Modeling and  
Carolina Center for Exploratory  
Cheminformatics Research  
Division of Medicinal Chemistry and  
Natural Products  
UNC Eshelman School of Pharmacy  
University of North Carolina  
Chapel Hill, NC  
USA

# 1 From Quantum Theory to Computational Chemistry. A Brief Account of Developments

*Lucjan Piela*

Department of Chemistry, University of Warsaw, Poland

<i>Introduction – Exceptional Status of Chemistry</i> .....	2
<i>A Hypothetical Perfect Computer</i> .....	5
<i>Does Predicting Mean Understanding?</i> .....	7
<i>Orbital Model</i> .....	9
<i>Power of Computer Experiments</i> .....	10
<i>Conclusions</i> .....	10
<i>Acknowledgments</i> .....	11
<i>References</i> .....	11

**Abstract:** Quantum chemical calculations rely on a few fortunate circumstances, like usually small relativistic and negligible electrodynamic (QED) corrections, and large nuclei-to-electrons mass ratio. Unprecedented progress in computer technology has revolutionized quantum chemistry, making it a valuable tool for experimenters. It is important for computational chemistry to elaborate methods that look at molecules in a multiscale way, provide its global and synthetic description, and compare this description with those for other molecules. Only such a picture can free researchers from seeing molecules as a series of case-by-case studies. Chemistry is a science of analogies and similarities, and computational chemistry should provide the tools for seeing this.

## Introduction – Exceptional Status of Chemistry

---

Contemporary science fails to explain the largest-scale phenomena taking place in the universe, such as the speeding up of the galaxies (supposedly due to the undefined “black energy”) and the nature of the lion’s share of the universe’s matter (and also unknown “dark matter”).

Quantum chemistry is in a far better position, which may be regarded even as exceptional in the sciences. The chemical phenomena are explainable down to individual molecules (which represent the subject of quantum chemistry) by current theories. It turned out, by comparing theory and experiment, that the solution to the Schrödinger equation (Schrödinger 1926a, b, c, d) offers in most cases a quantitatively correct picture. Only molecules with very heavy atoms, due to the relativistic effects becoming important, need to be treated in a special way based on the Dirac theory (Dirac 1928a, b). This involves an approximate Hamiltonian in the form of the sum of Dirac Hamiltonians for individual electrons, and the electron–electron interactions in the form of the (non-relativistic) Coulomb terms, a common and computationally successful practice ignoring, however, the resulting resonance character of all the eigenvalues (Brown and Ravenhall 1951; Pestka et al. 2008). When, very rarely, higher accuracy is needed, one may eventually include the quantum electrodynamics (QED) corrections, a procedure currently far from routine application, but still feasible for very small systems (Łach et al. 2004).

This success of computational quantum chemistry is based on a few quite fortunate circumstances (for references see, e.g., Piela 2007):

- Atoms and molecules are built of only two kinds of particles: nuclei and electrons.
- Although nuclei have non-zero size (electrons are regarded as point-like particles), the size is so small that its influence is below chemical accuracy (Łach et al. 2004). Therefore, all the constituents of atoms and molecules are treated routinely as point charges.
- The QED corrections are much smaller than energy changes in chemical phenomena (e.g., 1 : 10000000) and may be safely neglected in most applications (Łach et al. 2004).
- The nuclei are thousands times heavier than electrons and therefore, except in some special situations, they move thousands times slower than electrons. This makes it possible to solve the Schrödinger equation for electrons, assuming that the nuclei do not move, i.e., their positions are fixed in space (“clamped nuclei”). This concept is usually presented within the so called adiabatic approximation. In this approximation the motion of the nuclei is considered in the next step, in which the electronic energy (precalculated for any position of the nuclei), together with a usually small diagonal correction for coupling the nuclei-electrons motion, plays the role of the potential energy surface (PES). The total wave

function is assumed to be a product of the electronic wave function and of the function describing the motion of the nuclei. The commonly used Born–Oppenheimer (Born and Oppenheimer 1927) approximation (B-O) is less accurate than the adiabatic one, because it neglects the above-mentioned diagonal correction, making the PES independent of nuclear masses. Using the PES concept one may introduce the crucial idea of the spatial structure of a molecule, defined as those positions of the nuclei that assure a minimum of the PES. This concept may be traced back to Hund (1927a, b, c). Moreover, this structure corresponds to a certain ground-state electron density distribution that exhibits atomic cores, atom–atom bonds, and atomic lone pairs.

It is generally believed that the exact analytical solution to the Schrödinger equation for any atom (except the hydrogen-like atom) or molecule is not possible. Instead, some reasonable approximate solutions can be obtained, practically always involving calculation of a large number of molecular integrals, and some algebraic manipulations on matrices built of these integrals. The reason for this is efficiency of what is known as algebraic approximation (“algebraization”) of the Schrödinger equation. The algebraization is achieved by postulating a certain finite basis set  $\{\Phi_i\}_{i=1}^{i=M}$  and expanding the unknown wave function as a linear combination of the “known”  $\Phi_i$  with unknown expansion coefficients. Such an expansion can be encountered in the one-electron case (e.g., linear combination of atomic orbitals introduced by Bloch 1928), or/and in the many-electron case, e.g., the total wave function expansion in Slater determinants, related to configurations (Slater 1930), or in the explicitly correlated many-electron functions (Hylleraas 1929). It is assumed for good quality calculations (arguments are as a rule of numerical character only) that a finite  $M$  chosen is large enough to produce sufficient accuracy, with respect to what would be with  $M = \infty$  (exact solution). The above-mentioned integrals appear because, after the expansion is inserted into the Schrödinger equation, one makes the scalar products (they represent the integrals, which should be easy to calculate) of the expansion with  $\Phi_1, \Phi_2, \dots, \Phi_M$ , consecutively. In this way the task of finding the wave function by solving the Schrödinger equation is converted into an algebraic problem of finding the expansion coefficients, usually by solving some matrix equation. It remains to take care of the choice of the basis set  $\{\Phi_i\}_{i=1}^{i=M}$ . The choice represents a technical problem, but unfortunately it contains a lot of arbitrariness and, at the same time, is one of the most important factors influencing cost and quality of the computed solution. Application of functions  $\Phi_i$  based on the Gaussian-type one-electron orbitals (GTO) (Boys et al. 1956) provides a low cost/quality ratio and this fact is considered as one of the most important factors that has made computational chemistry so efficient.

Algebraization involves as a rule a large  $M$  and therefore the whole procedure requires fast computing facilities.<sup>1</sup> These facilities changed over time, from very modest manual mechanical calculators at the beginning of the twentieth century to what we consider *now* as powerful supercomputers. Almost immediately after formulation of quantum mechanics in 1926, Douglas Hartree published several papers (Hartree 1928) presenting his manual calculator-based solutions for atoms of rubidium and chlorine. However amazing it looks now, these were self-consistent *ab initio*<sup>2</sup> computations.

<sup>1</sup> Computational chemistry contributed significantly to applied mathematics, because new methods had to be invented in order to treat the algebraic problems of a previously unknown scale (like for  $M$  of the order of billions), see, e.g., Roos (1972).

<sup>2</sup> That is, derived from the first principles of (non-relativistic) quantum mechanics.

In 1927, Walter Heitler and Fritz Wolfgang London clarified the origin of the covalent chemical bond (Heitler and London 1927), the concept crucial for chemistry. In the paper the authors demonstrated, in numerical calculations, that the nature of the covalent chemical bond in  $H_2$  is of quantum character, because the (semiquantitatively) correct description of  $H_2$  emerged only after inclusion the exchange of electrons 1 and 2 between the nuclei in the formula  $a(1)b(2)$  ( $a, b$  are the 1s atomic orbitals centered on nucleus  $a$  and nucleus  $b$ , respectively) resulting in the wave function  $a(1)b(2)+a(2)b(1)$ . Thus, taking into account also the contribution of Hund (1927a, b, c), 1927 is therefore the year of birth of computational chemistry.

Perhaps the most outstanding manual calculator calculations were performed in 1933 by Hubert James and Albert Coolidge for the hydrogen molecule (James and Coolidge 1933). This variational result has been the best one in the literature over a period of 27 years.

The 1950s marked the beginning of a new era – the time of *programmable* computers. Apparently, just another tool for number crunching became available. In fact, however, the idea of programming made a revolution because it

- Liberated humans from tedious manual calculations.
- Offered large speed of computation, incomparable to any manual calculator. Also, the new data storage tools soon became of massive character.
- Resulted in more and more efficient programs, based on earlier versions (like staying “on the shoulders of the giants”), offering possibilities to calculate dozens of molecular properties.
- Allowed the dispersed, parallel and remote calculations.
- Resulted in the new branch of chemistry: computational chemistry.<sup>3</sup>
- Allowed performing calculations by anyone, even those not trained in chemistry, quantum chemistry, mathematics, etc.

The first ab initio Hartree–Fock calculations (based on ideas of Douglas Hartree (1928) and Vladimir Fock (1930a, b)) on programmable computers for diatomic molecules were performed at the Massachusetts Institute of Technology in 1956, using a basis set of Slater-type orbitals. The first calculations with Gaussian-type orbitals were carried out by Boys and coworkers, also in 1956 (Boys et al. 1956). An unprecedented spectroscopic accuracy was obtained for the hydrogen molecule in 1960 by Kołos and Roothaan (1960). In the early 1970s the era of gigantic programs<sup>4</sup> began with the possibility to compute many physical quantities at various levels of approximation. We currently live in an era with computational possibilities growing exponentially (the notorious “Moore law” of doubling the computer power every 2 years).<sup>5</sup> This enormous progress revolutionized our civilization in a very short time. The revolution in computational quantum chemistry changed chemistry in general, because computations became feasible for molecules of interest for experimental chemists. The progress has been accompanied by achievements in theory, however mainly of the character related to computational needs. Today, fairly accurate computations are possible for molecules composed

<sup>3</sup> It is difficult to define what computational chemistry is. Obviously, whatever involves calculations in chemistry might be treated as part of it. This, however, sounds like a pure banality. The same is true with the idea that computational chemistry means chemistry that uses computers. It is questionable whether this problem needs any solution at all. If yes, the author sticks to the opinion that computational chemistry means quantitative description of chemical phenomena at the molecular level.

<sup>4</sup> Perhaps the best known is GAUSSIAN, elaborated by a large team headed by John Pople.

<sup>5</sup> The speed as well as the capacity of computer, memory increased about 100 billion times over a period of 40 years. This means that what now takes an hour of computations, would require in 1960 about 10,000 years of computing.

of several hundreds of atoms, spectroscopic accuracy is achievable for molecules with a dozen atoms, while the QED calculations can be performed for the smallest molecules only (few atoms).

## A Hypothetical Perfect Computer

---

Suppose we have at our disposal a computer that is able to solve the Schrödinger equation exactly for any system and in negligible time.<sup>6</sup> Thus, we have free access to the absolute detailed picture of any molecule. This means we may predict with high accuracy and confidence the value of any property of any molecule. We might be tempted to say that being able to give such predictions is the ultimate goal of science: “*We know everything about our system. If you want to know more about the world, take other molecules and just compute, you will know.*”

Let us consider a system composed of 6 carbon nuclei, 6 protons and 42 electrons. Suppose we want to know the geometry of the system for the ground state. The computer answers that it does not know what we mean by the term “geometry”. We are more precise now and say that we are interested in the carbon–carbon (CC) and carbon–hydrogen (CH) distances. The computer answers that it is possible to compute only the *mean* distances, and provides them together with the proton–proton, carbon–electron, proton–electron and electron–electron distances, because it treats all the particles on an equal footing. We look at the CC and CH distances and see that they are much larger than we expected for the CC and CH bonds in benzene. The reason is that in our perfect wave function the permutational symmetry is correctly included. This means that the average carbon–proton distance takes into account *all* carbons and *all* protons. The same with other distances. To deduce more we may ask for computing other quantities like angles, involving three nuclei. Here, too, we will be confronted with numbers including averaging over identical particles. These difficulties do not necessarily mean that the molecule has no spatial structure at all, although this can also happen. The numbers produced would be extremely difficult to translate into a 3D picture even for quite small molecules, not to mention such a floppy molecule as a protein.

In many cases we would obtain a 3D picture we did not expect. This is because many molecular structures we are familiar with represent higher-energy metastable electronic states (isomers). This is the case in our example. When solving the time-dependent Schrödinger equation, we are confronted with this problem. Let us use as a starting wave function the one corresponding to the benzene molecule. In time-evolution we will stay probably with a similar geometry for a long time. However, there is a chance that after a long period the wave function changes to that corresponding to three interacting acetylene molecules (three times HCCH). The Born–Oppenheimer optimized ground electronic state corresponds to the benzene [–230.703 au in the Hartree–Fock approximation for the 6-311-G(d) basis set]. The three isolated acetylene molecules (in the same approximation) have the energy –230.453 au, and the molecule (also with the same formula  $C_6H_6$ )  $H_3C - C \equiv C - C \equiv CH_3$  – 230.592 au. Thus, the benzene molecule seems to be a stable ground-state, while the three acetylenes and the diacetylene are metastable states within the same ground electronic state of the system.

---

<sup>6</sup> In addition, we assume the computer is so clever, that it automatically rejects those solutions, which are not square-integrable or do not satisfy the requirements of symmetry for fermions and bosons. Thus, all non-physical solutions are rejected.



All the three physically observed realizations of the system  $6C + 6H$  are separated by barriers; this is the reason why they are observable.

What is, therefore, the most stable electronic ground state corresponding to the flask of benzene? This is a quite different question, which pertains to systems larger than a single molecule. If we multiply the number of atoms in a single molecule of benzene by a natural number  $N$ , we are confronted with new possibilities of combining atoms into molecules, not necessarily of the same kind and possibly larger than  $C_6H_6$ . For a large  $N$  we are practically unable to find all the possibilities. In some cases, when based on chemical intuition and limiting to simple molecules, we may guess particular solutions. For example, to lower the energy for the flask of benzene we may allow formation of the methane molecules and the graphite (the most stable form of carbon). Therefore, the flask of benzene represents a metastable state.

Suppose we wish to know the dipole moment of, say, the HCl molecule, the quantity that tells us important information about the charge distribution. We look up the output and we do not find anything about dipole moment. The reason is that all molecules have the same dipole moment in any of their stationary state  $\Psi$ , and this dipole moment equals to zero, see, e.g., Piela (2007) p. 630. Indeed, the dipole moment is calculated as the mean value of the dipole moment operator i.e.,  $\mu = \langle \Psi | \hat{\mu} | \Psi \rangle = \langle \Psi | (\sum_i q_i \mathbf{r}_i) | \Psi \rangle$ , index  $i$  runs over all electrons and nuclei. This integral can be calculated very easily: the integrand is antisymmetric with respect to inversion and therefore  $\mu = \mathbf{0}$ . Let us stress that our conclusion pertains to the *total* wave function, which has to reflect the space isotropy leading to the zero dipole moment, because all orientations in space are equally probable. If one applied the transformation  $\mathbf{r} \rightarrow -\mathbf{r}$  only to some particles in the molecule (e.g., electrons), and not to the other ones (e.g., the nuclei), then the wave function will show no parity (it would be neither symmetric nor antisymmetric). We do this in the adiabatic or Born–Oppenheimer approximation, where the electronic wave function depends on the electronic coordinates only. This explains why the integral  $\mu = \langle \Psi | \hat{\mu} | \Psi \rangle$  (the integration is over electronic coordinates only) does not equal zero for some molecules (which we call polar). Thus, to calculate the dipole moment we have to use the adiabatic or the Born–Oppenheimer approximation.

Now we decide to introduce the Born–Oppenheimer approximation (we resign from the absolute correct picture) and to focus on the most important features of the molecule. The first, most natural one, is the molecular geometry, this one that leads to a minimum of the electronic energy. The problem is that usually we have many such minima of different energy, each minimum corresponding to its own electronic density distribution. Each such distribution corresponds to some particular chemical bonds pattern.<sup>7</sup> In most cases the user of computers does not even think of these minima, because he or she performs the calculations for a predefined configuration of the nuclei and forces the system (usually not being aware of it) to stay in its vicinity. This is especially severe for large molecules, such as proteins. They have an astronomic number of stable conformations,<sup>8</sup> but often we take one of them and perform the calculations for this one. It is difficult to say why we select this one, because we rarely even consider the other conformations. In this situation we usually take as the starting point a crystal structure conformation (we *believe* in its relevance for a free molecule).

<sup>7</sup> Bond patterns are almost the same for different conformers.

<sup>8</sup> For a dipeptide one has something like ten energy minima, counting only the backbone conformations (and not counting the side chain conformations for simplicity). For a very small protein of, say, a hundred amino acids, the number of conformations is therefore of the order of  $10^{100}$ , a very large number exceeding the estimated number of atoms in the Universe.

Moreover, usually one starts calculations by setting a starting electronic density distribution. The choice of this density distribution may influence the final electronic density and the final geometry of the molecule. In routine computations one guesses the starting density according to the starting nuclear configuration chosen. This may seem to be a reasonable choice, except when small deformation of the nuclear framework leads to large changes in the electronic density.

*In conclusion, in practice the computer gives the solution which is close to what the computing person considers as “reasonable” and sets as the starting point.*

## Does Predicting Mean Understanding?

---

The existing commercial programs allow us to make calculations for molecules, treating each molecule as a new task, as if every molecule represented a new world, which has nothing to do with other molecules. We might not be satisfied with such a picture. We might be curious about the following:

- Living in the 3D space, does the system have a certain shape or not?
- If yes, why the shape is of this particular kind?
- Is the shape fairly rigid or rather flexible?
- Are there some characteristic substructures in the system?
- How do they interact?
- How do they influence the calculated global properties, etc?
- Are the same substructures present in other molecules?
- Does the presence of the same substructures determine similar properties?

*It is of fundamental importance for chemistry that we do not study particular cases, case by case, but derive some general rules.* Strictly speaking these rules are false because, due to approximations made, they are valid to some extent only. However, despite this, they enable chemists to operate, to understand, and to be efficient. If we relied uniquely on exact solutions of the Schrödinger equation, there would be no chemistry at all; people would lose the power of rationalizing chemistry, in particular to design syntheses of new molecules. Chemists rely on molecular spatial structure (nuclear framework), on the concepts of valence electrons, chemical bonds, electronic lone pairs, importance of HOMO and LUMO energies, etc. All these notions have no rigorous definition, but they still are of great importance in describing a *model* of molecule. A chemist predicts that two OH bonds have similar properties, wherever they are in molecule. Moreover, chemists are able to predict differences in the OH bonds by considering what the neighboring atoms are in each case. It is of fundamental importance in chemistry that a group of atoms with a certain bond pattern (functional group) represents an entity that behaves similarly, when present in different molecules.

We have at our disposal various scales at which we can look at details of the molecule under study. In the crudest approach we may treat the molecule as a point mass, which contributes to the gas pressure. Next we might become interested in the shape of the molecule, and we may approximate it first as a rigid rotator and get an estimation of rotational levels we can expect. Then we may leave the rigid body model and allow the atoms of the molecule to vibrate about their equilibrium positions. In such a case we need to know the corresponding force constants. This requires either choosing the structural formula (chemical bond pattern) of the molecule

together with taking the corresponding empirical force constants, or applying the normal mode analysis, first solving the Schrödinger equation in the Born–Oppenheimer approximation (we have a wide choice of the methods of solution). In the first case, we obtain an estimation of the vibrational levels, in the second, we get more reliable vibrational analysis, especially for larger atomic orbital expansions. If we wish we may consider anharmonicity of vibrations.<sup>9</sup>

At the same time we obtain the electronic density distribution from the wave function  $\Psi$  for  $N$  electrons<sup>10</sup>

$$\rho(\mathbf{r}) = N \sum_{\sigma_1=\frac{1}{2}}^{\frac{1}{2}} \int d\tau_2 d\tau_3 \dots d\tau_N |\Psi(\mathbf{r}, \sigma_1, \mathbf{r}_2, \sigma_2, \dots, \mathbf{r}_N, \sigma_N)|^2.$$

According to the Hellmann–Feynman theorem (Feynman 1939; Hellmann 1937),  $\rho$  is sufficient to compute the forces acting on the nuclei. We may compare the resulting  $\rho$  calculated at different levels of approximation, and even with the naive structural formula. The density distribution  $\rho$  can be analyzed in the way known as Bader analysis (Bader 1994). First, we find all the critical points, in which  $\nabla\rho = 0$ . Then, one analyzes the nature of each critical point by diagonalizing the Hessian matrix calculated at the point<sup>11</sup>:

- If the three eigenvalues are negative, the critical point corresponds to a maximum of  $\rho$ .
- If two are negative and one positive, the critical point corresponds to a covalent bond.
- If one is negative and two positive, the critical point corresponds to a center of an atomic ring.
- If all three are positive, the critical point corresponds to an atomic cavity.

The chemical bond critical points correspond to *some* pairs of atoms; there are other pairs of atoms, which do not form bonds. The Bader analysis enables chemists to see molecules in a synthetic way,<sup>12</sup> nearly independent of the level of theory that has been used to describe it, focusing on the ensemble of critical points. We may compare this density with the density of other molecules, similar to ours, to see whether one can note some local similarities. We may continue this, getting a more and more detailed picture down to the almost exact solution of the Schrödinger equation.

*It is important in chemistry to follow such a way, because at its beginning as well as at its end we know very little about chemistry. We learn chemistry on the way.*

<sup>9</sup> The low-frequency vibrations may be used as indicators to look at possible instabilities of the molecule, such as dissociation channels, formation of new bonds, etc. Moving all atoms, first according to a low-frequency normal mode vibration and continuing the atomic displacements according to the maximum gradient decrease, we may find the saddle point, and then, sliding down, detect the products of a reaction channel.

<sup>10</sup> The integration of  $|\Psi|^2$  is over the coordinates (*space and spin ones*) of all the electrons except one (in our case the electron 1 with the coordinates  $\mathbf{r}, \sigma_1$ ) and in addition the summation over its spin coordinate ( $\sigma_1$ ). As a result one obtains a function of the position of the electron 1 in space:  $\rho(\mathbf{r})$ . The wave function  $\Psi$  is antisymmetric with respect to exchange of the coordinates of any two electrons, and, therefore,  $|\Psi|^2$  is symmetric with respect to such an exchange. Hence, the definition of  $\rho$  is independent of the label of the electron we do not integrate over. According to this definition,  $\rho$  represents nothing else but the density of the electron cloud carrying  $N$  electrons, and is proportional to the probability density of finding an electron at position  $\mathbf{r}$ .

<sup>11</sup> Strictly speaking the nuclear attractors do not represent critical points, because of the cusp condition (Kato 1957).

<sup>12</sup> We may also analyze  $\rho$  using a “magnifying glass” represented by  $-\Delta\rho$ .

## Orbital Model

---

The wave function for identical fermions has to be antisymmetric with respect to exchange of coordinates (space and spin ones) of any two of them. This means that two electrons having the same spin coordinate cannot occupy the same position in space. Since wave functions are continuous this means that electrons of the same spin coordinate avoid each other (“Fermi hole” or “exchange hole” about each of them). This Pauli exclusion principle does not pertain to two electrons of opposite spin. However, electrons repel one another (Coulombic force) at any finite distance, i.e., have to avoid one another because of their charge (“Coulomb hole” or “correlation hole” around each of them). It turned out, references in Piela (2007) p. 605, that the Fermi hole is by far more important than the Coulomb hole. A high-quality wave function has to reflect the Fermi and the Coulomb holes. The corresponding mathematical expression should have the antisymmetrization operator in front, this will take care of the Pauli principle (and introduce a Fermi hole). Besides this, it should have some parameters or mathematical structure controlling somehow the distance between any pair of electrons (this will introduce the Coulomb repulsion). Since the Fermi hole is much more important, it is reasonable to consider first a wave function that takes care of the Fermi hole only. The simplest way to take the Fermi hole into account is the orbital model (approximation). Within the orbital model the most advanced is the Hartree–Fock method. In this method the Fermi hole is taken into account by construction (antisymmetrizer). The Coulomb hole is not present, because the Coulomb interaction is calculated through averaging the positions of the electrons.

The orbital model is wrong, because it neglects the Coulomb hole. Being wrong, it has however, enormous scientific power, because:

- It allows one to see the electronic structure as contributions of individual electrons, with their own “wave functions” i.e., orbitals with a definite mathematical form, symmetry, energy (“orbital levels”), etc.
- We take the Pauli exclusion principle into account by not allowing occupations of an orbital by more than two electrons (if two, then of the opposite spin coordinates). The occupation of all orbital levels is known as orbital diagram.
- The orbital energy may be interpreted as the energy needed to remove an electron from the orbital (assuming that all the orbitals do not change during the removing, Koopmans’ theorem, Koopmaans 1934).
- Molecular electron excitations may often be identified with changing the electron occupancy in the orbital diagram.
- We may even consider electron correlation (Coulomb hole), either by allowing different orbitals for electrons of different spin, or considering a wave function expansion composed of electron diagrams with various occupations.
- One may trace the molecular perturbations to changes in the orbital diagram.
- One may describe chemical reactions as a continuous change from a starting to a final molecular diagram. Theory and computational experience bring some rules, like that only those orbitals of the molecular constituents mix, which have similar orbital energies and have the same symmetry. This leads to important symmetry selection rules for chemical reactions (Fukui and Fujimoto 1968; Woodward and Hoffmann 1965) and for optical excitations (Cotton 1990).

- The orbital model provides a language to communicate among chemists (including quantum chemists). This language and the numerical experience supported by theory create a kind of quantum mechanical intuition coupled to experiment, which allows us to compare molecules, to classify them, and to predict their properties in a semiquantitative way. A majority of theoretical terms in quantum chemistry stem from the orbital theory.

## Power of Computer Experiments

---

In experiments we always see quantities averaged over all molecules in the specimen, all orientations allowed, all states available for a given temperature, etc. In some experiments we are able to specify the external conditions in such a way as to receive the signal from molecules in a given state. Even in such a case the results are averaged over molecular vibrations, which introduce (usually quite small) uncertainty for the positions of the nuclei, close to the minimum of the electronic energy (in the adiabatic or Born–Oppenheimer approximations).

This means that in almost all cases the experimenters investigate molecules close to the minimum of the electronic energy (minimum of PES). What happens to the electronic structure for other configurations of the nuclei is a natural question, sometimes of great importance (e.g., for chemical reactions). Only computational chemistry opens the way to see what would happen to the energy and to the electronic density distribution if

- Some internuclear distances increased, even to infinity (dissociation)
- Some internuclear distances shortened, and the shortening may correspond even to collapsing the nuclei into a united nucleus, or approaching two atoms which in the minimum of PES form or do not form a chemical bond. This allows us to investigate what happens to the molecule under a gigantic pressure, etc
- Some nuclei changed their mass or charge (beyond what one knows from experiment)
- We apply to the system an electric field, whose character is whatever we imagine as appropriate.<sup>13</sup> Sometimes such a field may approximate the influence of charge distributions in neighboring molecules

This makes out of computational chemistry a quite unique tool allowing to give the answer about the energy and electronic density distribution (bond pattern) for any system and for any deformation of the system we imagine. This powerful feature can be used not only to see what happens for a particular experimental situation, but also what would happen if we were able to set the conditions much beyond any imaginable experiment.

## Conclusions

---

What counts in computational chemistry is looking at molecules at various scales (using various models) and comparing the results for different molecules. If one could only obtain an exact picture of the molecule without comparing the results for other molecules, we would

---

<sup>13</sup> One has to be aware of a related mathematical trap. Applying even the smallest uniform electric field immediately transforms the problem into one with metastable energy (the global minimum corresponding to dissociation of the system, with the energy equal to  $-\infty$ ), see, e.g., Piela (2007), p. 642.

be left with no chemistry. The power of chemistry comes from analogies and similarities, as well as from trends rather than from the ability of predicting properties. Such ability is certainly important for being efficient in any particular case, but predicting by computation does not mean understanding. We need computers with their impressive speed, capacity, and possibility to give us precise predictions, but also we need a language to speak about the computations, a model that simplifies the reality, but allows us to understand what we are playing with in chemistry.

## Acknowledgments

---

The author is very grateful to his friends, Professor Andrzej J. Sadlej and Professor Leszek Z. Stolarczyk, for the joy of being with them, discussing all exciting aspects of chemistry, science and beyond; a part of them is included in the present chapter.

## References

---

- Bader, R. F. W. (1994). *Atoms in molecules. A quantum theory*. Oxford: Clarendon Press.
- Bloch, F. (1928). PhD Thesis. University of Leipzig.
- Born, M., & Oppenheimer, J. R. (1927). Zur Quantentheorie der Molekeln. *Annalen Physik*, 389, 457.
- Boys, S. F., Cook, G. B., Reeves, C. M., & Shavitt, I. (1956). Automatic fundamental calculations of molecular structure. *Nature*, 178, 1207.
- Brown, G. E., & Ravenhall, D. G. (1951). On the interaction of two electrons. *Proceedings of the Royal Society A*, 208, 552.
- Cotton, F. A. (1990). *Chemical applications of group theory* (3rd ed.). New York: Wiley.
- Dirac, P. A. M. (1928a). The quantum theory of the electron. *Proceedings of the Royal Society (London)*, A117, 610.
- Dirac, P. A. M. (1928b). The quantum theory of the electron. Part II. *Proceedings of the Royal Society (London)*, A118, 351.
- Feynman, R. P. (1939). Forces in molecules. *Physical Review*, 56, 340.
- Fock, V. (1930a). Näherungsmethode zur Lösung des quantenmechanischen Mehrkörperproblems. *Zeitschrift für Physik*, 61, 126.
- Fock, V. (1930b). "Selfconsistent field" mit Austausch für Natrium. *Zeitschrift für Physik*, 62, 795.
- Fukui, K., & Fujimoto, H. (1968). An MO-theoretical interpretation of nature of chemical reactions. I. Partitioning analysis of interaction energy. *Bulletin of the Chemical Society of Japan*, 41, 1989.
- Hartree, D. R. (1928). The wave mechanics of an atom with a non-coulomb central field. Part I. Theory and methods. *Proceedings of the Cambridge Philosophical Society*, 24, 89.
- Heitler, W., & London, F. W. (1927). Wechselwirkung neutraler Atome und homöopolare Bindung nach der Quantenmechanik. *Zeitschrift für Physik*, 44, 455.
- Hellmann, H. (1937). *Einführung in die quantenchemie*. Leipzig: Deuticke.
- Hund, F. (1927a). Zur Deutung der Molekelspektren. I. *Zeitschrift für Physik*, 40, 742.
- Hund, F. (1927b). Zur Deutung der Molekelspektren. II. *Zeitschrift für Physik*, 42, 93.
- Hund, F. (1927c). Zur Deutung der Molekelspektren. III. *Zeitschrift für Physik*, 43, 805.
- Hylleraas, E. A. (1929). Neue Berechnung der Energie des Heliums im Grundzustande, sowie des tiefsten Terms von Ortho-Helium. *Zeitschrift für Physik*, 54, 347.
- James, H. M., & Coolidge, A. S. (1933). The ground state of the hydrogen molecule. *Journal of Chemical Physics*, 1, 825.
- Kato, T. (1957). On the eigenfunctions of many-particle systems in quantum mechanics. *Communications on Pure and Applied Mathematics*, 10, 151.
- Koopmans, T. C. (1933/1934). Über die Zuordnung von Wellenfunktionen und Eigenwerten zu den Einzelnen Elektronen Eines Atoms. *Physica*, 1, 104.
- Kolos, W., & Roothaan, C. C. J. (1960). Accurate electronic wave functions for the H<sub>2</sub> molecule. *Reviews of Modern Physics*, 32, 219.

- Łach, G., Jeziorski, B., & Szalewicz, K. (2004). Radiative corrections to the polarizability of helium. *Physical Review Letters*, 92, 233001.
- Pestka, G., Bylicki, M., & Karwowski, J. (2008). Frontiers in quantum systems in chemistry and physics. In P. J. Grout, J. Maruani, G. Delgado-Barrio, & P. Piecuch (Eds.), *Dirac-Coulomb equation: Playing with artifacts* (pp. 215–238). Springer, New York/Heidelberg.
- Piela, L. (2007). *Ideas of quantum chemistry*. Amsterdam: Elsevier.
- Roos, B. O. (1972). A new method for large-scale CI calculations. *Chemical Physics Letters*, 15, 153.
- Schrödinger, E. (1926a). Quantisierung als Eigenwertproblem. *Annalen Physik*, 384, 361.
- Schrödinger, E. (1926b). Quantisierung als Eigenwertproblem. *Annalen Physik*, 384, 489.
- Schrödinger, E. (1926c). Quantisierung als Eigenwertproblem. *Annalen Physik*, 385, 437.
- Schrödinger, E. (1926d). Quantisierung als Eigenwertproblem. *Annalen Physik*, 386, 109.
- Slater, J. (1930). Cohesion in monovalent metals. *Physical Review*, 35, 509.
- Woodward, R. B., & Hoffmann, R. (1965). Selection rules for sigmatropic reactions. *Journal of the American Chemical Society*, 87, 2511.

# 2 The Position of the Clamped Nuclei Electronic Hamiltonian in Quantum Mechanics

Brian Sutcliffe<sup>1</sup> · R. Guy Woolley<sup>2</sup>

<sup>1</sup> Service de Chimie Quantique et Photophysique, Université Libre de Bruxelles, Bruxelles, Belgium

<sup>2</sup> School of Science and Technology, Nottingham Trent University, Nottingham, UK

<i>Introduction</i> .....	14
<i>The Clamped Nuclei Approximation</i> .....	14
The Separation of Translational Motion .....	17
Choosing Electronic and Nuclear Variables in the Translationally Invariant Hamiltonian .....	19
Atoms .....	21
Molecules .....	21
<i>Which Is the “Correct” Clamped Nuclei Hamiltonian?</i> .....	27
<i>The Symmetries of the Clamped Nuclei Electronic Hamiltonian</i> .....	30
Permutational Symmetry .....	32
Point Groups and Transformations .....	36
Spin and Point Group Symmetry .....	47
<i>The Construction of Approximate Eigenfunctions of the Clamped Nuclei Hamiltonian</i> .....	48
<i>Conclusions</i> .....	52
<i>References</i> .....	53



**Abstract:** Arguments are advanced to support the view that at present it is not possible to derive molecular structure from the full quantum mechanical Coulomb Hamiltonian associated with a given molecular formula that is customarily regarded as representing the molecule in terms of its constituent electrons and nuclei. However molecular structure may be identified provided that some additional chemically motivated assumptions that lead to the clamped nuclei Hamiltonian are added to the quantum mechanical account.

## Introduction

The traditional specification of a molecule in classical chemistry is in terms of atoms joined by bonds, and this accounts for the central fact of chemistry that the generic molecular formula is associated with the occurrence of isomers. Such an approach does not provide a useful basis for a physical theory since we do not know the general laws of interaction between atoms. Instead a more abstract description in terms of the particle constituents of a molecule, electrons and nuclei, is employed. We shall confine the discussion to the nonrelativistic level of theory; with this proviso the interactions between electrons and nuclei are assumed to be fully specified by Coulomb's law, and this makes possible the explicit formulation of a molecular Hamiltonian. This so-called Coulomb Hamiltonian will be given explicitly (► Eq. 2.1) in the next section; it forms the starting point of the chapter.

We concentrate on two broad themes. It is obvious that the whole collection of isomers supported by a given molecular formula share the same Coulomb Hamiltonian. The first part of the chapter is concerned with how this fundamental fact has been treated in quantum chemistry through the introduction of the *clamped nuclei Hamiltonian*. This involves two crucial assumptions: (1) the nuclei can be treated as fixed ("clamped") classical particles that merely provide a classical external potential for the electrons and (2) formally identical nuclei can be treated as distinguishable. The second part of the chapter discusses in a general way the basic quantum mechanical theory of the clamped nuclei Hamiltonian, concentrating particularly on its symmetry properties.

## The Clamped Nuclei Approximation

The conventional nonrelativistic Hamiltonian for a system of  $N$  electrons with position variables,  $\mathbf{x}_i^e$ , and a set of  $A$  nuclei with position variables  $\mathbf{x}_i^n$  may be written as

$$\begin{aligned} H(\mathbf{x}^n, \mathbf{x}^e) = & -\frac{\hbar^2}{2m} \sum_{i=1}^N \nabla^2(\mathbf{x}_i^e) + \frac{e^2}{8\pi\epsilon_0} \sum_{i,j=1}^N \frac{1}{|\mathbf{x}_i^e - \mathbf{x}_j^e|} - \frac{e^2}{4\pi\epsilon_0} \sum_{i=1}^A \sum_{j=1}^N \frac{Z_i}{|\mathbf{x}_j^e - \mathbf{x}_i^n|} \\ & - \frac{\hbar^2}{2} \sum_{k=1}^A \frac{\nabla^2(\mathbf{x}_k^n)}{m_k} + \frac{e^2}{8\pi\epsilon_0} \sum_{i,j=1}^A \frac{Z_i Z_j}{|\mathbf{x}_i^n - \mathbf{x}_j^n|}. \end{aligned} \quad (2.1)$$

This is the *Coulomb Hamiltonian* for the electrons and nuclei specified by a given molecular formula. We use a Schrödinger representation in which the operators are simple time-independent

multiplicative operators acting on functions of the coordinate variables (“wavefunctions”). Kato (1951) established that the Coulomb Hamiltonian,  $H$ , is essentially self-adjoint.<sup>1</sup> This property, which is stronger than Hermiticity, guarantees that the time evolution

$$\Psi(t) = \exp\left(\frac{-iHt}{\hbar}\right)\Psi(0)$$

of a Schrödinger wavefunction is unitary, and so conserves probability. Furthermore the eigenvalues of  $H$  are associated with a complete set of eigenfunctions. This is not necessarily true for operators that are Hermitian but not self-adjoint.<sup>2</sup> It was pretty obvious to applied mathematicians that the kinetic energy operator alone is indeed self-adjoint because of their classical mechanical experience. It was shown by Stone in the 1930s that multiplicative operators of the kind specified above are also self-adjoint but it was entirely unobvious that the sum of the operators would be self-adjoint because the sum of the operators is defined only on the intersection of their domains.

What Kato showed was that for a range of potentials including Coulomb ones, and for any function  $f$  in the domain  $\mathcal{D}_0$  of the full kinetic energy operator  $T_0$ , the domain of the full problem  $\mathcal{D}_V$  contains  $\mathcal{D}_0$  and there are two constants  $a$  and  $b$  such that

$$\|Vf\| \leq a\|T_0f\| + b\|f\|,$$

where  $a$  can be taken as small as is liked. This result is often summarized by saying that the Coulomb potential is small compared to the kinetic energy. Given this result he then proved that the usual operator is indeed, for all practical purposes, self-adjoint and is bounded from below. Why worry about this? Well if the operator is not self-adjoint it could support solutions interpretable as a particle falling into a singularity or getting to infinity in a finite time and these are unacceptable as physical solutions. Such pathologies occur in, for example, the classical mechanics of three bodies in a Coulomb field. The practical significance of Kato’s proof is the guarantee that such unphysical solutions will not arise from solving the quantum mechanical eigenvalue problem for the Coulomb Hamiltonian.

It is easily established that the Coulomb Hamiltonian is invariant under the coordinate transformations that correspond to uniform translations, rotation-reflections, and permutations of particles with identical masses and charges. Because of the symmetry of the Coulomb Hamiltonian its eigenfunctions will be basis functions for irreducible representations (irreps) of the translation group in three dimensions, the orthogonal group in three dimensions, and for the various symmetric groups corresponding to the sets of identical particles.

Quantum mechanical molecular structure calculations are most commonly attempted by first clamping the nuclei at fixed positions and then performing electronic structure calculations treating the clamped nuclei as providing a potential field for the electronic motion. With the

<sup>1</sup>The work was completed in 1944 and was actually received by the journal in October 1948.

<sup>2</sup>An elementary example is afforded by the momentum operator  $\hat{p} = -i\hbar d/dq$ , which is Hermitian on an appropriately defined class of  $L^2$  functions  $\phi(q)$ ; for these functions it is self-adjoint on  $-\infty \leq q \leq +\infty$  but this property is lost if either of the  $\infty$  limits is replaced by any finite value  $a$  – see, for example, Thirring (1981).

nuclei clamped at a particular fixed geometry specified by the constant vectors  $\mathbf{x}_i^n = \mathbf{a}_i$ ,  $i = 1, 2, \dots, A$ , this modified Hamiltonian takes the form

$$\begin{aligned} H^{\text{cn}}(\mathbf{a}, \mathbf{x}^e) = & -\frac{\hbar^2}{2m} \sum_{i=1}^N \nabla^2(\mathbf{x}_i^e) - \frac{e^2}{4\pi\epsilon_0} \sum_{i=1}^A \sum_{j=1}^N \frac{Z_i}{|\mathbf{x}_j^e - \mathbf{a}_i|} + \frac{e^2}{8\pi\epsilon_0} \sum_{i,j=1}^N \frac{1}{|\mathbf{x}_i^e - \mathbf{x}_j^e|} \\ & + \frac{e^2}{8\pi\epsilon_0} \sum_{i,j=1}^A \frac{Z_i Z_j}{|\mathbf{a}_i - \mathbf{a}_j|}. \end{aligned} \quad (2.2)$$

It is customary to incorporate the nuclear repulsion energy into  $\blacktriangleright$  Eq. 2.2; the nuclear repulsion term is merely an additive constant and so does not affect the form of the electronic wavefunctions. Its inclusion modifies the spectrum of the clamped nuclei Hamiltonian only trivially by changing the origin of the energy. The eigenvalue equation for the clamped nuclei Hamiltonian is then

$$H^{\text{cn}}(\mathbf{a}, \mathbf{x}^e) \psi_p^{\text{cn}}(\mathbf{a}, \mathbf{x}^e) = E_p^{\text{cn}}(\mathbf{a}) \psi_p^{\text{cn}}(\mathbf{a}, \mathbf{x}^e), \quad (2.3)$$

in which the eigenvalues (“electronic energies”) have a parametric dependence on the constant nuclear position vectors  $\{\mathbf{a}_i\}$ .

It is sometimes asserted that the clamped nuclei Hamiltonian can be obtained from the Coulomb Hamiltonian by letting the nuclear masses increase without limit. The Hamiltonian that would result if this were done would be

$$\begin{aligned} H^{\text{nn}}(\mathbf{x}^n, \mathbf{x}^e) = & -\frac{\hbar^2}{2m} \sum_{i=1}^N \nabla^2(\mathbf{x}_i^e) - \frac{e^2}{4\pi\epsilon_0} \sum_{i=1}^A \sum_{j=1}^N \frac{Z_i}{|\mathbf{x}_j^e - \mathbf{x}_i^n|} + \frac{e^2}{8\pi\epsilon_0} \sum_{i,j=1}^N \frac{1}{|\mathbf{x}_i^e - \mathbf{x}_j^e|} \\ & + \frac{e^2}{8\pi\epsilon_0} \sum_{i,j=1}^A \frac{Z_i Z_j}{|\mathbf{x}_i^n - \mathbf{x}_j^n|}, \end{aligned} \quad (2.4)$$

with the formal Schrödinger equation, by analogy with  $\blacktriangleright$  Eq. 2.3,

$$H^{\text{nn}}(\mathbf{x}^n, \mathbf{x}^e) \psi_p^{\text{nn}}(\mathbf{x}^n, \mathbf{x}^e) = E_p^{\text{nn}}(\mathbf{x}^n) \psi_p^{\text{nn}}(\mathbf{x}^n, \mathbf{x}^e). \quad (2.5)$$

Given that the Coulomb Hamiltonian has eigenstates such that

$$H(\mathbf{x}^n, \mathbf{x}^e) \psi(\mathbf{x}^n, \mathbf{x}^e) = E \psi(\mathbf{x}^n, \mathbf{x}^e), \quad (2.6)$$

if the solutions of  $\blacktriangleright$  Eq. 2.5 were well defined, it would seem that the eigenstates in  $\blacktriangleright$  Eq. 2.6 could be expanded as a sum of products of the form

$$\psi(\mathbf{x}^n, \mathbf{x}^e) = \sum_p \Phi_p(\mathbf{x}^n) \psi_p^{\text{nn}}(\mathbf{x}^n, \mathbf{x}^e), \quad (2.7)$$

where the  $\{\Phi\}$  play the role of “nuclear wavefunctions.”

In the Hamiltonian  $\blacktriangleright$  Eq. 2.4, the nuclear variables are free and not constant and there are no nuclear kinetic energy operators to dominate the potential operators involving these free nuclear variables. The Hamiltonian thus specified cannot be self-adjoint in the Kato sense. The Hamiltonian can be made self-adjoint by clamping the nuclei because the electronic kinetic energy operators can dominate the potential operators which involve only electronic variables. The Hamiltonian  $\blacktriangleright$  Eq. 2.2 is thus a proper one and the solutions  $\blacktriangleright$  Eq. 2.3 are a complete set. But since the Hamiltonian  $\blacktriangleright$  Eq. 2.4 is not self-adjoint it is not at all clear that the hoped for eigensolutions of  $\blacktriangleright$  Eq. 2.5 form a complete set suitable for the expansion  $\blacktriangleright$  Eq. 2.7.

However that may be, it was observed more than 30 years ago (Woolley and Sutcliffe 1977) that the arguments for an expansion (► Eq. 2.7) are quite formal because the Coulomb Hamiltonian has a completely continuous spectrum arising from the possibility of uniform translational motion and so its solutions cannot be properly approximated by a sum of this kind. This means too that the arguments of Born and Oppenheimer (1927), and of Born and Huang (1955) for their later approach to representations of this kind, are also quite formal.

As a basis for the Born–Oppenheimer and the Born approach, it is commonly assumed that it is possible to construct an analytic potential function  $V(\mathbf{x}^n)$  such that

$$E_p^{\text{cn}}(\mathbf{a}) = V(\mathbf{a}), \text{ for some } p \text{ and for all } \mathbf{a}, \quad (2.8)$$

and that this potential forms an adequate starting point for a discussion of the nuclear motion part of the full problem. Examination of the form of ► Eq. 2.2 makes it clear, however, that  $E_p^{\text{cn}}(\mathbf{a})$  takes the same value for all choices of  $\mathbf{a}$  that differs from a given choice merely by a uniform translation. Similarly it remains unchanged if the  $\mathbf{a}$  differ only by a constant orthogonal transformation. Thus any potential formed according to ► Eq. 2.8 will have some variables under any change of which no change in the potential will be described. In the context of calculations of molecular spectra, these variables are often referred to as *redundant* ones. It is also the case that  $E_p^{\text{cn}}(\mathbf{a})$  is invariant under the permutation of any nuclei with the same charge (nuclear mass does not enter into ► Eq. 2.3). This means that the potential in ► Eq. 2.8 will have the same value for all geometries that can be obtained from a given geometry by means of a permutation of nuclei with the same charge. Should the potential have any minima at all, it always has as many as there are permutations of the nuclei with the same charge. This would seem to make the assumption of a single isolated minimum in the potential, which is essential to the usual account of the Born–Oppenheimer approximation, a rather too restrictive one for comfort, except perhaps in the case of the diatomic system.

It is thus not at all clear to precisely which question the clamped nuclei Hamiltonian provides the answer and a further discussion of the properties of the Coulomb Hamiltonian is required before the clamped nuclei problem can be put into an appropriate form for yielding a potential. There are two main ways in which such a discussion can be attempted. If it is desired to stay with the Coulomb Hamiltonian in its laboratory-fixed form then the solutions must be expressed in coherent state (wave-packet) form to allow for their continuum nature. If the solutions are required as  $L^2$ -normalizable wavefunctions, then the translational motion must be separated from the Coulomb Hamiltonian and the solutions of the remaining translationally invariant part must be sought. It is in this second approach that it is easiest to make contact with the standard arguments and this will be considered in the following section.

## The Separation of Translational Motion

All that is needed to remove the center-of-mass motion from the molecular Coulomb Hamiltonian is a linear point transformation symbolized by

$$(\mathbf{t} \xi) = \mathbf{x} \mathbf{V}. \quad (2.9)$$

In ► Eq. 2.9,  $\mathbf{t}$  is a  $3 \times N_T - 1$  matrix ( $N_T = N + A$ ) and  $\xi$  is a  $3 \times 1$  matrix, so that the combined (bracketed) matrix on the left of ► Eq. 2.9 is  $3 \times N_T$ .  $\mathbf{V}$  is an  $N_T \times N_T$  matrix which, from the

structure of the left side of  $\blacklozenge$  Eq. 2.9, has a special last column whose elements are

$$V_{iN_T} = M_T^{-1} m_i, \quad M_T = \sum_{i=1}^{N_T} m_i. \quad (2.10)$$

Hence  $\xi$  is the standard center-of-mass coordinate

$$\xi = M_T^{-1} \sum_{i=1}^{N_T} m_i \mathbf{x}_i. \quad (2.11)$$

As the coordinates  $\mathbf{t}_j, j = 1, 2, \dots, N_T - 1$  are to be translationally invariant we require the condition,

$$\sum_{i=1}^{N_T} V_{ij} = 0, \quad j = 1, 2, \dots, N_T - 1 \quad (2.12)$$

on each remaining column of  $\mathbf{V}$  and it is easy to see that  $\blacklozenge$  Eq. 2.12 forces  $\mathbf{t}_j \rightarrow \mathbf{t}_j$  as  $\mathbf{x}_i \rightarrow \mathbf{x}_i + \mathbf{a}$ , all  $i$ .

The  $\mathbf{t}_i$  are independent if the inverse transformation

$$\mathbf{x} = (\mathbf{t} \xi) \mathbf{V}^{-1} \quad (2.13)$$

exists. The structure of the right side of  $\blacklozenge$  Eq. 2.13 shows that the bottom row of  $\mathbf{V}^{-1}$  is special and, without loss of generality, its elements may be required to be

$$(\mathbf{V}^{-1})_{N_T i} = 1, \quad i = 1, 2, \dots, N_T. \quad (2.14)$$

The inverse requirement on the remainder of  $\mathbf{V}^{-1}$  implies that

$$\sum_{i=1}^{N_T} (\mathbf{V}^{-1})_{ji} m_i = 0, \quad j = 1, 2, \dots, N_T - 1. \quad (2.15)$$

The Coulomb Hamiltonian ( $\blacklozenge$  Eq. 2.1) in the new coordinates becomes

$$\begin{aligned} \mathbf{H}(\mathbf{t}, \xi) &= -\frac{\hbar^2}{2} \sum_{i=1}^{N_T-1} \frac{1}{\mu_{ii}} \nabla^2(\mathbf{t}_i) - \frac{\hbar^2}{2} \sum_{i,j=1}^{N_T-1} \frac{1}{\mu_{ij}} \vec{\nabla}(\mathbf{t}_i) \cdot \vec{\nabla}(\mathbf{t}_j) + \frac{e^2}{8\pi\epsilon_0} \sum_{i,j=1}^{N_T} \frac{Z_i Z_j}{r_{ij}(\mathbf{t})} \\ &\quad - \frac{\hbar^2}{2M_T} \nabla^2(\xi) \\ &= \mathbf{H}'(\mathbf{t}) - \frac{\hbar^2}{2M_T} \nabla^2(\xi). \end{aligned} \quad (2.16)$$

Here the positive constants  $1/\mu_{ij}$  are given by:

$$\frac{1}{\mu_{ij}} = \sum_{k=1}^{N_T} m_k^{-1} V_{ki} V_{kj}, \quad i, j = 1, 2, \dots, N_T - 1. \quad (2.17)$$

The operator  $r_{ij}$  is the interparticle distance operator expressed as a function of the  $\mathbf{t}_i$ . Thus

$$r_{ij}(\mathbf{t}) = \left( \sum_{\alpha} \left( \sum_{k=1}^{N_T-1} ((\mathbf{V}^{-1})_{kj} - (\mathbf{V}^{-1})_{ki}) t_{\alpha k} \right)^2 \right)^{1/2}. \quad (2.18)$$

In  $\blacktriangleright$  Eq. 2.16, the  $\vec{\nabla}(\mathbf{t}_i)$  are gradient operators expressed in the Cartesian components of the  $\mathbf{t}_i$  and the last term represents the center-of-mass kinetic energy operator. Since the center-of-mass coordinate does not enter the potential energy term, the center-of-mass motion may be separated off completely so that the eigenfunctions of  $H$  are of the form

$$T(\xi)\Psi(\mathbf{t}), \quad (2.19)$$

where  $\Psi(\mathbf{t})$  is a wavefunction for the Hamiltonian  $H'(\mathbf{t})$ ,  $\blacktriangleright$  Eq. 2.16, which will be referred to as the *translationally invariant* Hamiltonian. The eigenfunctions of this Hamiltonian will be basis functions for irreps of the orthogonal group in three dimensions and for the various symmetric groups of the sets of identical particles.

It should be emphasized that different choices of  $\mathbf{V}$  are unitarily equivalent so that the spectrum of the translationally invariant Hamiltonian is independent of the particular form chosen for  $\mathbf{V}$ , provided that it is consistent with  $\blacktriangleright$  Eqs. 2.10 and  $\blacktriangleright$  2.12. In particular it is perfectly possible to put the kinetic energy operator into diagonal form by choosing an orthogonal matrix  $\mathbf{U}$  that diagonalizes the positive definite symmetric matrix of dimension  $N_T - 1$  formed from the  $1/\mu_{ij}$  and then replacing elements of the originally chosen  $\mathbf{V}$  according to

$$V_{ij} \rightarrow \sum_{k=1}^{N_T-1} V_{ik} U_{kj}, \quad j = 1, 2, \dots, N_T-1.$$

As can be seen from  $\blacktriangleright$  Eq. 2.18, the practical problem with any choice of  $\mathbf{V}$  is the complicated form given to the potential operator.

## Choosing Electronic and Nuclear Variables in the Translationally Invariant Hamiltonian

In order to identify the electrons, let the translationally invariant electronic coordinates be chosen with respect to the center-of-nuclear mass

$$\mathbf{t}_i^e = \mathbf{x}_i^e - \mathbf{X}, \quad \mathbf{X} = M^{-1} \sum_{i=1}^A m_i \mathbf{x}_i^n, \quad M = \sum_{i=1}^A m_i.$$

In the case of the atom  $A = 1$  and the origin is the nucleus. Other coordinate choices are possible, but this is the only choice that avoids a term in the kinetic energy operator coupling the electronic and nuclear variables and which allows the electronic part of the potential to be written in terms of the electronic variables and the clamped nuclei positions (see Mohallem and Tostes 2002; Sutcliffe 2000).

There is no need to specify the proposed  $A - 1$  translationally invariant nuclear variables  $\mathbf{t}^n$  other than to say that they are expressed entirely in terms of the laboratory nuclear coordinates by means of a matrix  $\mathbf{V}^n$  exactly like  $\mathbf{V}$  in  $\blacktriangleright$  Eq. 2.9, but with side  $A$  and with  $M$  in place of  $M_T$  and  $\mathbf{X}$  in place of  $\xi$ . It is also sometimes useful to define a set of redundant Cartesian coordinates

$$\bar{\mathbf{x}}_i^n = \mathbf{x}_i^n - \mathbf{X}, \quad i = 1, 2, \dots, A, \quad \text{so that} \quad \sum_{i=1}^A m_i \bar{\mathbf{x}}_i^n = 0. \quad (2.20)$$

Of course the laboratory nuclear variable  $\mathbf{x}_i^n$  cannot be completely written in terms of the  $A - 1$  translationally invariant coordinates arising from the nuclei, but in the electron-nucleus

attraction and in the nuclear repulsion terms the center-of-nuclear mass  $\mathbf{X}$  cancels out. For ease of writing  $\mathbf{x}_i^n$  will continue to be used in those terms but it should be remembered that the nuclear potentials are functions of the translationally invariant coordinates defined by the nuclear coordinates.

On making this choice of electronic coordinates the electronic part of  $\blacklozenge$  Eq. 2.16 is

$$\begin{aligned} H'^e(\mathbf{x}^n, \mathbf{t}^e) = & -\frac{\hbar^2}{2m} \sum_{i=1}^N \nabla^2(\mathbf{t}_i^e) - \frac{\hbar^2}{2M} \sum_{i,j=1}^N \bar{\nabla}(\mathbf{t}_i^e) \cdot \bar{\nabla}(\mathbf{t}_j^e) - \frac{e^2}{4\pi\epsilon_0} \sum_{i=1}^A \sum_{j=1}^N \frac{Z_i}{|\mathbf{t}_j^e - \bar{\mathbf{x}}_i^n|} \\ & + \frac{e^2}{8\pi\epsilon_0} \sum_{i,j=1}^N \frac{1}{|\mathbf{t}_i^e - \mathbf{t}_j^e|} + \sum_{i,j=1}^A \frac{Z_i Z_j}{|\mathbf{x}_i^n - \mathbf{x}_j^n|}. \end{aligned} \quad (2.21)$$

This electronic Hamiltonian is translationally invariant and would yield the usual form were the nuclear masses to increase without limit. It has been noted (Kutzelnigg 2007) that to take  $\blacklozenge$  Eq. 2.21 as the electronic Hamiltonian is inconsistent with a consideration of the solution to the full problem being expressed in a series in terms of powers of the inverse total nuclear mass, since this Hamiltonian already contains a term involving the inverse of this mass to the first power. There is, however, no need to consider this term at the first stage of development of a solution to the full problem and it can be included at the point where terms of similar magnitude are considered. The remaining part of  $\blacklozenge$  Eq. 2.21 is then exactly the same as the clamped nuclei form. The clamped nuclei form can be deployed consistently in an account of solutions to the full problem only if a uniform translational factor is included in the full solution. In the work of Nakai et al. (2005) (see also Sutcliffe 2005) the translational motion of the center-of-mass is subtracted to yield a Schrödinger eigenvalue problem from which the translational part of any continuous spectrum has been removed. Of course the spectrum of the resulting operator can have a continuous spectral range, as can the translationally invariant form itself, for reasons quite other than translational motion.

The nuclear part of  $\blacklozenge$  Eq. 2.16 involves only kinetic energy operators and has the form:

$$K^n(\mathbf{t}^n) = -\frac{\hbar^2}{2} \sum_{i,j=1}^{A-1} \frac{1}{\mu_{ij}^n} \bar{\nabla}(\mathbf{t}_i^n) \cdot \bar{\nabla}(\mathbf{t}_j^n), \quad (2.22)$$

with the inverse mass matrix defined as a special case of  $\blacklozenge$  Eq. 2.17 involving only the original nuclear variables.

Both  $\blacklozenge$  Eqs. 2.21 and  $\blacklozenge$  2.22 are invariant under any orthogonal transformation of both the electronic and nuclear variables. If the nuclei are clamped in  $\blacklozenge$  Eq. 2.21 then invariance remains only under those orthogonal transformations of the electronic variables that can be reexpressed as changes in the positions of nuclei with identical charges while maintaining the same nuclear geometry. The form  $\blacklozenge$  Eq. 2.21 remains invariant under all permutations of the electronic variables and is invariant under permutations of the variables of those nuclei with the same charge. Thus if an electronic energy minimum is found at some clamped nuclei geometry there will be as many minima as there are permutations of identically charged nuclei. The kinetic energy operator  $\blacklozenge$  Eq. 2.22 is invariant under all orthogonal transformations of the nuclear variables and under all permutations of the variables of nuclei with the same mass.

The splitting of the translationally invariant Hamiltonian  $H'(\mathbf{t})$  into two parts breaks its symmetry, since each part exhibits only a sub-symmetry of the full problem. If wavefunctions derived from approximate solutions to  $\blacklozenge$  Eq. 2.21 are to be used to construct solutions to the full problem  $\blacklozenge$  Eq. 2.6 utilizing  $\blacklozenge$  Eq. 2.22 care will be needed to couple the sub-symmetries to yield solutions with full symmetry.

## Atoms

For the atom there is no nuclear kinetic energy part and, denoting the nuclear mass by  $m_n$ , the full Hamiltonian is simply the electronic Hamiltonian

$$\begin{aligned} H^e(\mathbf{t}^e) = & -\frac{\hbar^2}{2m} \sum_{i=1}^N \nabla^2(\mathbf{t}_i^e) - \frac{\hbar^2}{2m_n} \sum_{i,j=1}^N \vec{\nabla}(\mathbf{t}_i^e) \cdot \vec{\nabla}(\mathbf{t}_j^e) - \frac{e^2}{4\pi\epsilon_0} \sum_{j=1}^N \frac{Z_j}{|\mathbf{t}_j^e|} \\ & + \frac{e^2}{8\pi\epsilon_0} \sum_{i,j=1}^N \frac{1}{|\mathbf{t}_i^e - \mathbf{t}_j^e|}. \end{aligned} \quad (2.23)$$

The electronic problem for the atom (Eq. 2.23) has exactly the same form and symmetry as the full problem and meets the requirements for Kato self-adjointness, for there is a kinetic energy operator in all of the variables that are used to specify the potential terms. This would continue to be the case were the nuclear mass to increase without limit.

The atom is sometimes used as an illustration when considering the original form of the Born–Oppenheimer approximation (as in Deshpande and Mahanty 1969), but the only aspect of the approximation that can be thus illustrated is the translational motion part and that is easily considered in first order by treating the second term in Eq. 2.23 as a perturbation to the solution obtained using an infinite nuclear mass. The inclusion of this term in this way is analogous to making the usual *diagonal Born–Oppenheimer* correction and it can be made exactly in the case of any one-electron atom (see Handy and Lee 1996). As noted in Hinze et al. (1998) it is usually made approximately simply by including the diagonal part of the mass polarization term (the second term in Eq. 2.23 above) to produce an electronic reduced mass

$$\frac{1}{\mu_e} = \frac{1}{m_n} + \frac{1}{m}$$

in place of  $1/m$ .

The Hamiltonian (Eq. 2.23) maintains full symmetry and is invariant under electronic permutations and under rotation-reflections of the electronic coordinates. Trial functions are usually constructed from atomic orbitals and from their spin-orbitals. Permutational antisymmetry is achieved by forming Slater determinants from the spin-orbitals. Rotational symmetry is usually realized by vector coupling of orbitals that form bases for representations of the rotation group  $SO(3)$ . Spin-eigenfunctions too are achieved by vector coupling.<sup>3</sup>

## Molecules

Even after separating the translational motion, for a molecule there is always at least one nuclear variable in the kinetic energy part of the operator, and self-adjointness cannot be achieved if such terms are neglected while the potential terms involving the nuclear variables are included except by clamping the nuclei. The treatment of molecules is, thus, technically much more difficult than is the treatment of atoms.

Although the discussion that follows is, for the most part, quite general, explicit consideration is confined to the diatomic case in order to avoid overburdening the exposition with

<sup>3</sup>Some specifics of the implementation of permutational and rotational symmetry in quantum mechanics are discussed in section “The Symmetries of the Clamped Nuclei Electronic Hamiltonian.”



details. However here too, there are certain technical features which simplify the diatomic case and which cannot be transferred to the polyatomic case so care will be taken in the following discussion not to make the diatomic the general case. For a system with two nuclei the natural nuclear coordinate is the internuclear vector which will be denoted here simply as  $\mathbf{t}$ . When needed to express the electron-nuclei attraction terms,  $\mathbf{x}_i^n$  is simply of the form  $\alpha_i \mathbf{t}$  where  $\alpha_i$  is a signed ratio of the nuclear mass to the total nuclear mass. In the case of a homonuclear system  $\alpha_i = \pm \frac{1}{2}$ . The di-nuclear electronic Hamiltonian is

$$\begin{aligned} H'^e(\mathbf{t}^e) = & -\frac{\hbar^2}{2m} \sum_{i=1}^N \nabla^2(\mathbf{t}_i^e) - \frac{\hbar^2}{2(m_1 + m_2)} \sum_{i,j=1}^N \bar{\nabla}(\mathbf{t}_i^e) \cdot \bar{\nabla}(\mathbf{t}_j^e) \\ & - \frac{e^2}{4\pi\epsilon_0} \sum_{j=1}^N \left( \frac{Z_1}{|\mathbf{t}_j^e + \alpha_1 \mathbf{t}|} + \frac{Z_2}{|\mathbf{t}_j^e + \alpha_2 \mathbf{t}|} \right) \\ & + \frac{e^2}{8\pi\epsilon_0} \sum_{i,j=1}^N \frac{1}{|\mathbf{t}_i^e - \mathbf{t}_j^e|} + \frac{Z_1 Z_2}{R}, \quad R = |\mathbf{t}|, \end{aligned} \quad (2.24)$$

while the nuclear kinetic energy part is:

$$-\frac{\hbar^2}{2} \left( \frac{1}{m_1} + \frac{1}{m_2} \right) \nabla^2(\mathbf{t}) \equiv -\frac{\hbar^2}{2\mu} \nabla^2(\mathbf{t}). \quad (2.25)$$

The electronic part is not self-adjoint in the manner prescribed by Kato because it contains no kinetic energy terms involving the nuclear variable which would dominate the potential energy terms. The full Hamiltonian would not be Kato self-adjoint if both nuclear masses were to increase without limit either. It is seen from  $\blacktriangleright$  Eq. 2.25, however, that if only one nuclear mass increases without limit then the kinetic energy term in the nuclear variable remains in the full problem and so the Hamiltonian remains self-adjoint in the Kato sense.

The di-nuclear case has been considered numerically by Frolov (1999) in a study of the hydrogen molecular ion. In extremely accurate calculations on the discrete states of this system, he investigated what happened when first one and then two nuclear masses are increased without limit. He showed that when one mass increased without limit, any discrete spectrum persisted but when two masses were allowed to increase without limit, the Hamiltonian ceased to be well-defined and this failure led to what he called *adiabatic divergence* in attempts to compute discrete eigenstates. This sort of behavior would certainly be anticipated from the present discussion.

Irrespective of any choices made for the nuclear masses, the electronic Hamiltonian ( $\blacktriangleright$  Eq. 2.24) becomes self-adjoint in the Kato sense if the nuclei are clamped for then the nuclear variables in the potential terms become constants and the only variables are the electronic ones. So the clamped nuclei potential is dominated by the electronic kinetic energy. Thus the usual practice of clamped nuclei electronic structure calculations is a consistent one.

Writing the variable  $\mathbf{t}$  in spherical polar coordinates,  $R$ ,  $\beta$ , and  $\alpha$  where  $t_z = R \cos \beta$ , were the clamped nuclei Hamiltonian to be used to define a potential it is easily seen that for  $\mathbf{t} = \mathbf{a}$ ,  $R = a$  then

$$E^{\text{cn}}(\mathbf{a}) = V(a), \quad (2.26)$$

so that the potential would have the form  $V(R)$ . But the potential is not just a curve, it is a series of spherical shells of rotation swept out by the curve by all choices of  $\beta$  and  $\alpha$ . It is thus a genuine central-field potential. If the internuclear distance is fixed but  $\mathbf{a}$  allowed to rotate or invert, then  $E^{\text{cn}}(\mathbf{a})$  is a sphere of constant energy as swept out by the variables  $\beta$  and  $\alpha$

at radius  $a$ . If  $\mathbf{a}$  is oriented so as to define a  $z$ -axis then  $E^{\text{cn}}(\mathbf{a})$  will take the same value at  $+a_z$  and  $-a_z$  so that if there is a minimum at  $+a_z$  there will be another at  $-a_z$ . The electronic Hamiltonian is not invariant under inversion of the nuclear variables alone unless the two nuclei have identical charges in which case inversion and permutation will have identical effects. In differential geometry terms, the potential is homeomorphic to  $S^2$ .

The Hamiltonian (Eq. 2.24) is invariant under all rotations of the electronic coordinates about the internuclear axis and all reflections in a plane containing the internuclear axis. The electronic states can be labeled by a quantum number  $m$  which takes the values  $0, \pm 1, \pm 2, \dots$  corresponding to the eigenvalues of the  $z$ -component of the electronic angular momentum about the internuclear axis.

It is easily seen that the potential will tend to increase without limit as  $R \rightarrow 0$  but the behavior as  $R \rightarrow \infty$  presents a problem. To see this consider the asymptotic behavior of the electron-nucleus potential terms in the case of the one-electron homonuclear di-hydrogen molecule ion. The electronic coordinate is

$$\mathbf{t}^e = \mathbf{x} - \frac{1}{2}(\mathbf{x}_1^n + \mathbf{x}_2^n), \quad (2.27)$$

where  $\mathbf{x}$  is the laboratory coordinate of the electron. As the internuclear distance becomes very large, the nuclear repulsion term becomes very small and one would expect the trial wavefunction to approach the wavefunction for a one-electron ion corresponding to one of the atoms. Thus one might expect the lowest energy wavefunction to be of the form

$$N e^{-cr}, \quad \mathbf{r} = \mathbf{x} - \mathbf{x}_1^n, \quad r = |\mathbf{r}|,$$

for instance. However working in the chosen coordinate set

$$\mathbf{r} = \mathbf{t}^e - \frac{1}{2}\mathbf{t},$$

so that the expected asymptotic electronic solution could be expressed only in terms of both the electronic and nuclear variables. This does not, of course, mean that the potential cannot approach the required value. It simply means that it cannot do so in any calculation in which the trial functions are confined to electronic functions whose variable origin is at the center-of-nuclear mass.

This sort of difficulty is a general one and obviously not confined simply to one-electron diatomic molecules. It would clearly be unwise to attempt to approximate solutions for molecules at energies close to their dissociation limits in terms of electronic coordinates with the origin at the center-of-nuclear mass. A trial function for the general case of the Born–Huang form

$$\psi(\mathbf{t}^n, \mathbf{t}^e) = \sum_p \Phi_p(\mathbf{t}^n) \psi_p^{\text{nn}}(\mathbf{t}^n, \mathbf{t}^e), \quad (2.28)$$

where the  $\mathbf{t}^e$  have an origin at the center-of-nuclear mass, could, therefore, approximate only a limited region of the spectrum of the full problem.

This difficulty cannot be got round by working in the laboratory frame. The solution to the full problem would be defined in terms of a three-dimensional subspace expressed in terms of a translation variable and a  $3(N_T - 1)$ -dimensional subspace expressible in terms of translationally invariant variables. Translationally invariant variables must involve at least a pair of variables and so there must be at least one such variable which involves a laboratory frame electron and a laboratory frame nuclear variable. All this can be easily illustrated by considering the exact ground-state wavefunction of the hydrogen atom, as is seen in Kutzelnigg (2007).

This point is developed in more detail by Hunter (1981) in a paper considering to what extent a separation of electronic and nuclear motion would be possible if the exact solution to the Schrödinger equation for the Coulomb Hamiltonian was actually known. Were the exact solution known Hunter argues (1975) that it could be written in the form

$$\psi(\mathbf{t}^n, \mathbf{t}^e) = \chi(\mathbf{t}^n)\phi(\mathbf{t}^n, \mathbf{t}^e), \quad (2.29)$$

with a nuclear wavefunction defined by means of

$$|\chi(\mathbf{t}^n)|^2 = \int \psi(\mathbf{t}^n, \mathbf{t}^e)^* \psi(\mathbf{t}^n, \mathbf{t}^e) d\mathbf{t}^e.$$

Then, providing this function has no nodes,<sup>4</sup> an “exact” electronic wavefunction could be constructed as

$$\phi(\mathbf{t}^n, \mathbf{t}^e) = \frac{\psi(\mathbf{t}^n, \mathbf{t}^e)}{\chi(\mathbf{t}^n)}, \quad (2.30)$$

if the normalization choice

$$\int \phi(\mathbf{t}^n, \mathbf{t}^e)^* \phi(\mathbf{t}^n, \mathbf{t}^e) d\mathbf{t}^e = 1$$

is made. In fact it is possible (Hunter 1981) to show that  $\chi$  must be nodeless even though the usual approximate nuclear wavefunctions for vibrationally excited states do have nodes. The electronic wavefunction (Eq. 2.30) is, therefore, properly defined and a potential energy surface could be defined in terms of it as

$$U(\mathbf{t}^n) = \int \phi(\mathbf{t}^n, \mathbf{t}^e)^* H'(\mathbf{t}^n, \mathbf{t}^e) \phi(\mathbf{t}^n, \mathbf{t}^e) d\mathbf{t}^e. \quad (2.31)$$

Although no exact solutions to the full problem are known for a molecule, some extremely good approximate solutions for excited vibrational states of  $\text{H}_2$  have been computed and Czub and Wolniewicz (1978) took such an accurate approximation for an excited vibrational state in the  $J = 0$  rotational state of  $\text{H}_2$  and computed  $U(R)$ . They found strong spikes in the potential at close to two positions at which the usual wavefunction would have nodes. To quote Czub and Wolniewicz (1978):

- This destroys completely the concept of a single internuclear potential in diatomic molecules because it is not possible to introduce on the basis of non-adiabatic potentials a single, approximate, mean potential that would describe well more than one vibrational level.

It is obvious that in the case of rotations the situation is even more complex.

Bright Wilson suggested (1979) that using the clamped nuclei Hamiltonian instead of the full one in Eq. 2.31 to define the potential might avoid the spikes but Hunter (1981) showed why this was unlikely to be the case and Cassam-Chenai (2006) repeated the work of Czub and Wolniewicz using an electronic Hamiltonian and showed that exactly the same spiky behavior occurred. However Cassam-Chenai showed, as Hunter had anticipated, that if one simply ignored the spikes, the potential was almost exactly the same as would be obtained by deploying the electronic Hamiltonian in the usual way.

Although the spiky nature of an “exact” potential has been demonstrated explicitly only for  $J = 0$  states of a small diatomic molecule, there is no reason to suppose that its occurrence is

<sup>4</sup>A similar requirement must be placed on the denominator in Eq. 12 of Kutzelnigg (2007) for the equation to provide a secure definition.

not general. Matters would be further complicated by rotational motion. Thus the demonstrably smooth potentials generated by solving an electronic problem cannot be approximations to any exact form but are simply computationally useful intermediates in a solution to the full problem. It would therefore seem unwise to assign too much weight to them in explaining chemical structure.

In the standard approach to solving the nuclear motion part of the diatomic problem, the potential  $V(R)$  is specified and the nuclear motion Hamiltonian becomes

$$-\frac{\hbar^2}{2\mu}\nabla^2(\mathbf{t}) + V(R). \quad (2.32)$$

Expressing this Hamiltonian in spherical polar coordinates one obtains the usual form

$$-\frac{\hbar^2}{2\mu}\left(\frac{1}{R^2}\frac{\partial}{\partial R}R^2\frac{\partial}{\partial R}\right) + \frac{1}{2\mu R^2}L^2 + V(R), \quad (2.33)$$

where  $L$  is the operator for the angular momentum of the nuclear motion. The angular part of the solution is known analytically and the solution of the nuclear motion problem can be reduced to one in the single variable  $R$ .

The eigensolutions to this problem are quite naturally eigenfunctions of the nuclear angular momentum and can easily be chosen with the required permutational symmetry. But things are not quite so clear for the electronic part of the problem because one does not in practice have a form which is explicit in the nuclear variables as it is computed only at fixed nuclear geometries. It is easy to achieve the correct permutational symmetry for the electronic part of the function at each and every nuclear geometry, but it would be not at all easy to make each function an eigenfunction of the electronic angular momentum.

To try to deal with the rotational motion it is possible to reformulate the diatomic problem to exhibit explicitly the angular symmetry of the Hamiltonian. As shown in Kołos and Wolniewicz (1963) and, in a somewhat more general way in Sutcliffe (2007), it is possible to define an internal coordinate system by a transformation that makes the internuclear vector  $\mathbf{t}$  the  $z$ -axis in a right-handed coordinate system and in this system the electronic Hamiltonian (Eq. 2.24) becomes

$$-\frac{\hbar^2}{2m}\sum_{i=1}^N\nabla^2(\mathbf{r}_i) - \frac{\hbar^2}{2(m_1 + m_2)}\sum_{i,j=1}^N\vec{\nabla}(\mathbf{r}_i)\cdot\vec{\nabla}(\mathbf{r}_j) + V(R, \mathbf{r}), \quad (2.34)$$

with

$$V(R, \mathbf{r}) = \frac{e^2}{8\pi\epsilon_0}\sum_{i,j=1}^N\frac{1}{r_{ij}} + \frac{e^2}{4\pi\epsilon_0}\frac{Z_1Z_2}{R} - \frac{e^2}{4\pi\epsilon_0}\sum_{j=1}^N\left(\frac{Z_1}{r_{i1}(R)} + \frac{Z_2}{r_{i2}(R)}\right), \quad (2.35)$$

where the  $\mathbf{r}_i$  are the electronic variables expressed in the transformed system. In this formulation the vector  $\mathbf{t}$  orients freely and “clamping the nuclei” comes down to simply choosing  $R = a$ . A clamped nuclei solution of Eq. 2.34 would lead to a clamped nuclei energy

$$E^{\text{cn}}(a) = V(a), \quad (2.36)$$

rather than the form given by Eq. 2.26. Thus any minima in  $V(a)$  would not be duplicated by the requirement of rotational invariance. Inversion is achieved by means of

$$\beta \rightarrow \pi - \beta, \quad \alpha \rightarrow \pi + \alpha,$$

and thus involves just the angular part of the formulation. An identical operation achieves the nuclear permutation. The electronic Hamiltonian is invariant under neither operation unless the nuclei have identical charge.

The nuclear kinetic energy operator (Eq. 2.25) becomes

$$-\frac{\hbar^2}{2\mu R^2} \frac{\partial}{\partial R} R^2 \frac{\partial}{\partial R} + \frac{1}{2\mu R^2} D_1(\alpha, \beta, \mathbf{r}), \quad (2.37)$$

with

$$D_1(\alpha, \beta, \mathbf{r}) = \left[ (J_x - l_x)^2 + (J_y - l_y)^2 + \frac{\hbar}{i} \cot \beta (J_y - l_y) \right],$$

where the electronic angular momentum is

$$l = \sum_{i=1}^N l(i) = \frac{\hbar}{i} \sum_{i=1}^N \mathbf{r}_i \times \frac{\partial}{\partial \mathbf{r}_i}, \quad (2.38)$$

and the total angular momentum operator is denoted  $J$  and involves both the electronic and nuclear variables in such a way that  $J_z = l_z$ . The Jacobian for this transformation is

$$R^2 \sin \beta.$$

It is seen that in this formulation any solution of the clamped nuclei form of the electronic Hamiltonian (Eq. 2.34) will give rise to a potential which is simply a curve and not a surface of rotation. However the angular part of the nuclear kinetic energy operator now involves the electronic angular momentum so that the electronic motion and the overall rotational motion are coupled.

The electronic wavefunction in this case has the same axial symmetry as in the previous case and is characterized by the quantum number  $m$ . However the states can no longer be regarded as occurring in degenerate pairs for  $m > 0$  since  $l_z$  is the  $z$ -component of the total angular momentum so  $m$  can take integer values lying between  $J$  and  $-J$ , where  $J$  is the total angular momentum. The coupling of the electronic and nuclear angular momenta lifts the  $m$  degeneracy as the Hamiltonian becomes a system of  $2J + 1$  coupled partial differential equations.

In the first of the two possible ways of looking at the diatomic, one remains in the Cartesian product space  $R^3 \times R^{3N}$  and it is thus necessary to give some explicit consideration to the angular properties of solutions to the electronic part of the problem. If the usual approach were taken to approximating solutions to the nuclear motion Hamiltonian using sums of products of electronic and nuclear parts, a typical term in the sum used as trial function for the form (Eq. 2.33) would be

$$\phi_{pm}(\mathbf{r}, R)^L \Phi_{pm}(R) \Theta_{Lm}(\beta, \alpha), \quad (2.39)$$

where  $p$  denotes an electronic state and  $L$  the nuclear angular momentum quantum number. There are no operators in the nuclear motion part of the problem which explicitly couple the electronic and nuclear motions. It is thus possible to represent for any electronic state, any number of rotational states specified by values of  $L$ , without considering any coupling.  $L$  in Eq. 2.24 is not the total angular momentum operator and so a description of rotational motion given in these terms yields only an approximate quantum number.

If one transforms to the manifold  $R_+ \times S^2 \times R^{3N}$  then one can consider explicitly the rotational coupling of electronic and angular motions. The fact that the transformation is to a manifold rather than a vector space means that any operator built using coordinates defined on the manifold will be well defined only where the Jacobian for the transformation does not vanish. This does not cause great problems here because the only places where the Jacobian vanishes are when  $R = 0$  and where  $\beta = 0$  and  $\beta = \pi$ . The region around  $R = 0$  is inaccessible because of the nuclear repulsion term and the exact angular wavefunctions take care of the problem with  $\beta$ .

It would not be consistent to use only a single term in a product approximation for a trial for the form (Eq. 2.37) with a potential  $V(R)$  except in considering a  $J = 0$  state. Here the minimum consistent product approximation is

$$\sum_{m=-J}^J \phi_{pm}(\mathbf{r}, R)^J \Phi_{pm}(R) \Theta_{Jm}(\beta, \alpha). \quad (2.40)$$

It is only for  $J = 0$  states that the forms (Eqs. 2.39 and 2.40) are the same.

Of course the angular momentum coupling in Eq. 2.40 implies a coupling of different electronic states, between  $\Sigma$  and  $\Pi$  states or  $\Sigma$  and  $\Delta$  states, for example. To allow explicitly for that possibility (Eq. 2.40) should really be extended to

$$\sum_{m=-J}^J \sum_{pm}^J \phi_{pm}(\mathbf{r}, R)^J \Phi_{pm}(R) \Theta_{Jm}(\beta, \alpha), \quad (2.41)$$

where the electronic state is denoted  $pm$  to indicate that the state must have quantum number  $m$ . Thus for  $J = 2$  one would need at least five electronic states.

## Which Is the “Correct” Clamped Nuclei Hamiltonian?

There is clearly a choice between the form (Eqs. 2.24 and 2.34) and although in the clamped nuclei approximation both would yield the same energies for any chosen internuclear separation  $a$ , the resulting energy would be a potential for two quite different situations.

To generalize from the diatomic case, if the usual approach were taken to approximating solutions to the nuclear motion Hamiltonian using sums of products of electronic and nuclear parts a typical term in the sum used as trial function for the form (Eq. 2.33) would be

$$\phi_p(\mathbf{t}^e, \mathbf{t}^n) \Phi_p(\mathbf{t}^n), \quad (2.42)$$

where  $p$  denotes an electronic state. The solutions are on the Cartesian product space  $R^{3A-3} \times R^{3N}$ . There is again no explicit coupling of the nuclear motion and electronic motions and it is thus possible to represent for any electronic state, any number of rotational states. It is only in the diatomic case that the nuclear angular momentum can be realized explicitly as part of the nuclear kinetic energy so it is not generally possible to choose  $\Phi$  directly as an eigenfunction of the nuclear angular momentum, neither is it possible to choose  $\phi$  directly as an eigenfunction of the electronic angular momentum.  $\phi$  as usually computed belongs to the totally symmetric representation of the symmetric group of each set of nuclei with identical charges.  $\Phi$  could then be a basis function for an irreducible representation of the symmetric group for each set of particles with identical masses if the permutational symmetry were properly considered in solving the nuclear motion problem.

Clamped nuclei calculations are usually undertaken so as to yield a potential that involves no redundant coordinates. Thus a translationally invariant electronic Hamiltonian like (Eq. 2.24) would actually generate a more general potential than this. A clamped nuclei potential is, therefore, more properly associated with the electronic Hamiltonian after the separation of rotational motion like (Eq. 2.34) than with the merely translationally invariant one. With this choice again, the minimum consistent product approximation is

$$\sum_{m=-J}^J \phi_{pm}(\mathbf{r}, \mathbf{R})^J \Phi_{pm}(\mathbf{R}) |JMm\rangle, \quad (2.43)$$

where  $\mathbf{R}$  represents the  $3A - 6$  internal coordinates invariant under all orthogonal transformations of the  $\mathbf{t}^n$  and  $|J M m\rangle$  is an angular momentum eigenfunction. The general solutions are on the manifold  $R^{3A-6} \times S^3 \times R^{3N}$  though for triatomic molecules the internal coordinate part of the manifold is confined to  $R_+ \times R^2$  because the three nuclear positions define a plane. It is only in the diatomic case that the electronic variables play a direct part in the specification of the angular momentum eigenfunctions and where there is therefore only one internal coordinate. However the Coriolis coupling terms in the angular part of the Hamiltonian contain terms in the electronic angular momentum so coupling of the electronic motion to the angular motion would still be anticipated, see Sections V and VI of Sutcliffe (2000). Although the angular momentum coupling could imply a coupling of different electronic states, as it certainly does in a diatomic, it is not obviously implied in the general case. To achieve permutational symmetry in the nuclear motion part of the wavefunction would in the general case be very tricky. The nuclei are identified in the process of defining a body-fixed frame to describe the rotational motion, even if they are identical. If only a subset of a set of identical nuclei were used in such a definition, some permutation of the nuclear variables would induce a change in the definition of the body-fixed frame and thus spoil the rotational separation. Thus permutations of identical nuclei are considered usually only if such permutations correspond to point group operations which leave the body-fixing choices invariant.

If one considers the clamped nuclei Hamiltonian as providing input for the full Hamiltonian in which the rotational motion is made explicit, the basic nuclear motion problem should be treated as a  $2J + 1$  dimensional problem. If this is done then the translational and rotational symmetries of the full problem are properly dealt with. However the solutions are not generally basis functions for irreps of the symmetric groups of sets of identical nuclei except for such subgroups as constitute the point groups used in frame fixing. This restriction of the permutations is usually assumed justified by appealing to the properties of the potential surface. The idea here was introduced by Longuet-Higgins (1963) and is widely used in interpreting molecular spectra.

As noted earlier, the original attempts to justify the Born–Oppenheimer and the Born approaches from the full Coulomb Hamiltonian lack rigorous mathematical foundations. So far there have been no attempts to make the foundations of the Born approach mathematically secure. However the coherent states approach has been used to give mathematically rigorous accounts of surface crossings and a review of this work can be found in Hagedorn and Joye (2007). It seems very unlikely that it would be possible to provide a secure foundation for the Born approach in anything like the manner in which it is usually presented.

The Born–Oppenheimer approximation, whose validity depends on there being a deep enough localized potential well in the electronic energy, has, however, been extensively treated. The mathematical approaches depend upon the theory of fiber bundles and the electronic Hamiltonian in these approaches is defined in terms of a fiber bundle. It is central to these approaches, however, that the fiber bundle should be trivial, that is that the base manifold and the basis for the fibers be describable as a direct product of Cartesian spaces. This is obviously possible with the decomposition choice made for  $\blacktriangleright$  Eq. 2.42 but not obviously so in the choice made for  $\blacktriangleright$  Eq. 2.43.

The Born–Oppenheimer approach has been put on a rigorous foundation for diatomics with solutions of the form ( $\blacktriangleright$  Eq. 2.39) in work which is described in a helpful context in Combes and Seiler (1980). For solutions like ( $\blacktriangleright$  Eq. 2.40), it is possible that more than one vector (coordinate) space can be constructed on it because the transformation is to a manifold. In fact two coordinate spaces are possible on  $S^2$  a trivial one and a twisted one, the latter associated with

the possibility of an electronic wavefunction with a Berry phase and the “twisted” solutions are accounted for in Herrin and Howland (1997).

A mathematically satisfactory account of the Born–Oppenheimer approximation for polyatomics in an approach based on  $\blacklozenge$  Eq. 2.43 has not yet been provided but it has proved possible to provide one based on  $\blacklozenge$  Eq. 2.42 (see Klein et al. 1992). Because the nuclear kinetic energy operator in the space  $R^{3A-3}$  cannot be expressed in terms of the nuclear angular momentum, it is not possible in this formulation to separate the rotational motion from the other internal motions. This work also considers the possibility that there are two minima in the potential as indeed there would be because of inversion symmetry if the potential minimum were at other than a planar geometry. It does not, however, consider the possibility of such multiple minima as might be induced by permutational symmetry. It might be possible to extend the two minima arguments to the multiple minima case and perhaps provide a mathematically secure account of the Longuet-Higgins approach to ignoring some of the inconvenient permutations. This has not so far been attempted.

For a secure account to be given in terms of the separation ( $\blacklozenge$  Eq. 2.43), which is what is really required if one is to use the clamped nuclei electronic Hamiltonian, it would be necessary to consider more than one coordinate space. On the manifold  $S^3$  at least two coordinate spaces are required to span the whole manifold. The internal coordinates within any coordinate space are such that it is possible to construct two distinct molecular geometries at the same internal coordinate specification, so that a potential expressed in the internal coordinates cannot be analytic everywhere (Collins and Parsons 1993). It would therefore seem to be a very tricky job. But even if it were to be accomplished it seems very unlikely that a multiple minima argument could be constructed to account for point group symmetry in this context. It is possible to show (see Section IV of Sutcliffe (2000)) that in the usual Eckart form of the Hamiltonian for nuclear motion, permutations can be such as to cause the body-fixed frame definition to fail completely.

If it is wished to perform a clamped nuclei calculation on a molecule containing three or more nuclei, avoiding translations and rigid rotations, it is necessary to fix the values of six of the  $3A$  nuclear variables. In practice this is usually done by choosing one nucleus,  $\mathbf{x}_1^n$ , at the origin, one nucleus,  $\mathbf{x}_2^n$ , defining an axis and a third,  $\mathbf{x}_3^n$ , defining a plane. Every possible geometry of the molecule, except where the three particles become collinear, can be specified with this choice but not every component of the  $3A$  variables will appear in the clamped nuclei electronic energy as six of them have been chosen to be zero. This means that even though the clamped nuclei electronic energy can be specified in terms of a molecular geometry in which the positions of  $A$  points can be given, the energy itself is a function of only the relative positions of a subset of the nuclei. Thus performing clamped nuclei calculations will not make possible the expression of the electronic energy in anything other than internal coordinates and the electronic energy when expressed in any set of internal coordinates cannot be analytic everywhere. Thus there cannot really be a “global” potential energy surface. In any case, as has been seen, the potential, even locally, cannot be regarded as an approximation to anything in particular and thus should be treated simply as a convenient peg on which to hang further calculations. From this perspective, the further calculations should properly be ones in which the electronic Hamiltonian results from the full Hamiltonian in which the rotational motion has been made explicit. Such Hamiltonians have only a local validity and can be defined only where the Jacobian for the transformation to the rotational variables does not vanish. However at present there is no satisfactory account of how nuclear permutational symmetry should be treated from this perspective, neither is there any secure mathematical justification of the Born–Oppenheimer approximation or of the Born approach.



Naturally any extension of the trial wavefunction for the full Coulomb Hamiltonian problem from a single term to a many term form must be welcomed as an advance; it is, however, simply a technical advance and it might prove premature to load that technical advance with too much physical import.

At present it is not possible to place properly the clamped nuclei electronic Hamiltonian in the context of the full problem, including nuclear motion. However if the nuclei were treated as distinguishable particles, even when formally identical, then some of difficulties that arise from the consideration of nuclear permutations would not occur. But it would still be necessary to be able to justify the choice of subsets of permutations among identical particles when such seem to be required to explain experimental results. A particular difficulty arises here for it is not possible to distinguish between isomers nor is it possible to specify a molecular geometry, unless it is possible to distinguish between formally identical particles.

But regarding the nuclei as distinguishable would not avoid the difficulty of constructing total angular momentum eigenfunctions from the nuclear and electronic parts. Such treatment of the nuclei would not make the traditional demonstrations of the Born–Oppenheimer or the Born approximations mathematically sound either. However it would ensure that the mathematically sound presentations of the Born–Oppenheimer approximation mentioned earlier need no further extension to include permutations of identical nuclei. There is, unfortunately, little good to be said, from a mathematical point of view, of the traditional Born argument. This is troubling because the Born approach is assumed to provide the basis for the consideration of chemical reactions on and between potential energy surfaces. However it is clear that the clamped nuclei electronic Hamiltonian can be usefully deployed in nuclear motion calculations if the nuclei are considered identifiable and in the next sections this Hamiltonian will be considered in detail.

## The Symmetries of the Clamped Nuclei Electronic Hamiltonian

Before considering the symmetry under permutations of identical particles it is necessary first to say a little about the spin of particles. Each particle is specified not only by space variables but also by spin variables. These have not been considered so far because there are no spin operators in the Hamiltonians discussed in the previous sections. Nevertheless spin is, indirectly, very important in the construction of approximate wavefunctions.

Spin ideas are usually developed in terms of a vector operator  $S$  with three components  $S_\alpha$ ,  $\alpha = x, y, z$  and functions  $\Theta_{S, M_s, k}^N$  such that

$$S^2 \Theta_{S, M_s, k}^N = \hbar^2 S(S+1) \Theta_{S, M_s, k}^N, \quad S^2 = S_x^2 + S_y^2 + S_z^2,$$

and

$$S_z \Theta_{S, M_s, k}^N = \hbar M_s \Theta_{S, M_s, k}^N,$$

with,

$$S = 0, 1, 2, \dots, \quad -S \leq M_s \leq S. \quad (2.44)$$

The  $\Theta_{S, M_s, k}^N$  are called spin eigenfunctions and the  $k$  index denotes a particular member of a possible set. In the simple case of a single electron,  $S = \frac{1}{2}$ ,  $M_s = \pm \frac{1}{2}$ , and  $k = 1$  so usually  $\Theta_{\frac{1}{2}, \frac{1}{2}, 1}^1$  is written as  $\alpha$  and  $\Theta_{\frac{1}{2}, -\frac{1}{2}, 1}^1$  as  $\beta$ .

It can be shown that under the operations of the full rotation-reflection group in three dimensions,  $O(3)$ :

$$(S_x S_y S_z) \rightarrow (S_x S_y S_z) |\mathbf{R}| \mathbf{R}, \quad (2.45)$$

where  $\mathbf{R}$  is the matrix representation of the rotation inversion and is thus an orthogonal matrix with determinant  $|\mathbf{R}|$  which is  $+1$  for a rotation and  $-1$  for a reflection. Clearly  $S^2$  is an invariant operator. Thus, its eigenfunctions provide a basis for irreducible representations of  $O(3)$  and in general we label these representations by the  $S$  value to which they correspond, using  $k$  to distinguish between different basis functions for the same representation. Obviously the dimension of these is  $2S + 1$  since the  $2S + 1$  functions with  $M_s = S, S - 1, \dots, -S$  are degenerate in the sense of having the same  $S$  eigenvalue.

It is useful to treat the spin functions as having variables  $s_i$  though these can take only discrete values and from now on to label the Cartesian space variables as  $\mathbf{r}_i$  so that  $\mathbf{x}_i$  can be used to denote the totality of variables. To construct a many-particle function to describe space and spin for a collection of  $N$  identical particles it is apparently simply necessary to form the products:

$$\Psi_n(\mathbf{x}_1, \mathbf{x}_2, \dots, \mathbf{x}_N) = \Psi_n(\mathbf{r}_1, \mathbf{r}_2, \dots, \mathbf{r}_N) \Theta_{S, M_s, k}^N(s_1, s_2, \dots, s_N) \quad (2.46)$$

at will, and the generalization to groups of sets of identical particles is obvious. However there is a snag. It turns out that there is an extra rule that must be obeyed. The Hamiltonian is invariant under the operators that permute the variable designations (space and spin) of sets of identical particles. For any one set, these operators form a group and the full invariance group of  $H$  is the direct product of the groups for all the sets of identical particles. This means that the eigenfunctions of  $H$  are a basis for the irreps of this group. The extra rule is related to what irreps can actually occur and it is usually called the *Pauli principle*. If the set of identical particles individually have spin  $S = 0, 1, 2, 3$ , etc., then the only irreps that can arise are the totally symmetric ones. Thus every wavefunction must be invariant under permutations that interchange the variable designations of particles with integer spins (*bosons*). If the particles individually have spin  $S = \frac{1}{2}, \frac{3}{2}, \frac{5}{2}, \dots$  etc., then the only irreps are the antisymmetric ones. Thus every wavefunction must change sign if the permutation is odd or be invariant if the permutation is even for permutations that interchange the variable designations of particles with odd half-integer spin (*fermions*).

What this means is that not every function of the form (◆ Eq. 2.46) actually corresponds to a physical state, but it can be shown that in any given problem there are enough eigenfunctions of  $S^2$  with any given  $M_s$  value (i.e.,  $k$  is sufficiently large) to form a basis for irreps of the permutation group of  $N$  particles. Similarly it can be shown that there are enough space functions to provide irreps of the same group. It is then possible to derive rules for combinations of the space and spin functions such that the resulting function obeys the Pauli principle.

Since in this and the following sections only the clamped nuclei Hamiltonian will be considered, it will be convenient to simplify the notation somewhat and to drop the superscripts on the electronic variables because, from now on, these will be the only variables to be considered. Thus ◆ Eq. 2.2 is rewritten as

$$\begin{aligned} H(\mathbf{a}, \mathbf{r}) = & -\frac{\hbar^2}{2m} \sum_{i=1}^N \nabla^2(\mathbf{r}_i) - \frac{e^2}{4\pi\epsilon_0} \sum_{j=1}^A \sum_{i=1}^N \frac{Z_j}{|\mathbf{r}_i - \mathbf{a}_j|} + \frac{e^2}{8\pi\epsilon_0} \sum_{i,j=1}^N \frac{1}{|\mathbf{r}_i - \mathbf{r}_j|} \\ & + \frac{e^2}{8\pi\epsilon_0} \sum_{i,j=1}^A \frac{Z_i Z_j}{|\mathbf{a}_i - \mathbf{a}_j|}, \end{aligned} \quad (2.47)$$

while  $\blacktriangleright$  Eq. 2.3 is rewritten as

$$\mathbf{H}(\mathbf{a}, \mathbf{r})\psi_p(\mathbf{a}, \mathbf{r}) = E_p(\mathbf{a})\psi_p(\mathbf{a}, \mathbf{r}). \quad (2.48)$$

For later purposes it is useful to group the first two terms by writing

$$h(i) = -\frac{\hbar^2}{2m}\nabla^2(\mathbf{r}_i) - \frac{e^2}{4\pi\epsilon_0}\sum_{j=1}^A\frac{Z_j}{|\mathbf{r}_i - \mathbf{a}_j|} \equiv k(i) + V(i), \quad (2.49)$$

and to express the third term with

$$g(i, j) = \frac{e^2}{4\pi\epsilon_0}\frac{1}{|\mathbf{r}_i - \mathbf{r}_j|}. \quad (2.50)$$

The electronic part of the Hamiltonian for any given set of nuclear positions may then be written as

$$\mathbf{H} = \sum_{i=1}^N h(i) + \frac{1}{2}\sum_{i,j=1}^N{}' g(i, j). \quad (2.51)$$

The operator  $h$  is self-adjoint and a mathematically simple extension of the hydrogen atom operator. It therefore has some discrete one-particle eigenfunctions

$$h(i)\phi(\mathbf{r}_i) = \epsilon\phi(\mathbf{r}_i). \quad (2.52)$$

Such one-particle functions are called *orbitals* and the associated energies  $\epsilon$  are *orbital energies*. If there is only one nucleus, they are called *atomic orbitals* (AOs) and in the many nuclei case, *molecular orbitals* (MOs). The orbitals may be extended to become *spin-orbitals* by multiplying them with an  $\alpha$  or  $\beta$  spin function and the resulting spin-orbitals are therefore denoted as  $\phi(\mathbf{x}_i)$  to indicate the inclusion of spin. Clearly every orbital can generate two spin-orbitals.

It is usual in the case of electrons to work with functions that obey the Pauli principle from the start. This is possible when using an orbital basis through the use of Slater determinants of spin-orbitals which, by definition, change sign under odd permutations but are invariant under even permutations as is required for fermions. These will be explicitly considered later; first the permutational symmetry will be considered more generally.

## Permutational Symmetry

The clamped nuclei Hamiltonian is invariant under the permutation of electrons so that its eigenfunctions must be basis functions for irreducible representations (irreps) of the symmetric group of degree  $N$ . However, because of the Pauli principle, not all irreducible representations of this group are allowed.

As noted above for electrons there are only two kinds of spin functions so that in any product of spin functions for  $N$  spin variables, only a limited set of permutations of the spin variables will lead to distinct product functions. Since there are no spin terms in the electronic Hamiltonian, the operators for total spin commute with the Hamiltonian and so its eigenfunctions must be spin eigenfunctions as well as basis functions for an irrep of the symmetric group. To see how these two requirements can be combined consider permutations rather generally.

The abstract permutation operator on  $N$  objects  $1, 2, 3, \dots, N$  is always denoted by

$$P = \begin{pmatrix} 1 & 2 & 3 & \dots & N \\ i_1 & i_2 & i_3 & \dots & i_N \end{pmatrix}, \tag{2.53}$$

where the  $i_r$  are the set of objects  $1, 2, 3, \dots, N$  at most in some new order. The effect of the operator on the original set of objects is

$$P(1, 2, 3, \dots, N) = (i_1 i_2 \dots i_N). \tag{2.54}$$

Clearly the product of any two permutations is a permutation, the products are associative, and there is an identity permutation, and every permutation possesses a unique inverse so the permutations form a group as required. The order of the group is obviously  $N!$ , because there are  $N!$  distinct permutations of  $N$  objects. This is the symmetric group of degree  $N$ , usually denoted as  $S_N$ .

A permutation like

$$\begin{pmatrix} 1 & 2 & 3 \\ 2 & 3 & 1 \end{pmatrix} \text{ is often written as } (123), \tag{2.55}$$

on the interpretation that 2 replaces 1, 3 replaces 2, and 1 replaces 3. The right-hand expression in  $\blacktriangleright$  Eq. 2.55 is said to be in a *cycle* form and is a cycle of *length* 3. Any permutation can be decomposed uniquely into cycles of disjoint elements, thus for example:

$$\begin{pmatrix} 1 & 2 & 3 & 4 & 5 & 6 \\ 2 & 4 & 5 & 1 & 3 & 6 \end{pmatrix} = (1\ 2\ 4)(3\ 5)(6), \tag{2.56}$$

where the order in which the individual cycles are written down does not matter and where, of course, each cycle is invariant under cyclic permutations of its elements. A cycle of length two is called a *transposition* and is an involutory operation, that is:

$$(i_1 i_2) = (i_1 i_2)^{-1}. \tag{2.57}$$

A cycle can always be written as a product of transpositions, thus

$$(1\ 2\ 3) = (1\ 2)(2\ 3), \tag{2.58}$$

where the transposition on the right operates first, but the decomposition is obviously not unique nor are the transpositions always of disjoint elements. However the *number* of transpositions into which a cycle can be decomposed is obviously unique and this number is said to be the *parity* of the permutation, *even* if the number is even and *odd* if the number is odd. It follows, therefore, that we can classify the permutation operators themselves as either even or odd. Parity is usually indicated as  $(-1)^p$  where  $p$  is the number of transpositions. The product of two even permutations is an even permutation so that the even permutations constitute a subgroup (counting the identity permutation as even) of the symmetric group of order  $N!$ . This subgroup is called the *alternating* group. It is obvious then that the set of all distinct transpositions are the generators of the symmetric group.

It is reasonably easy to show that all permutations in the same class have the same cycle structure.<sup>5</sup> Thus if the possible cycle structures are known, then the number of classes and

---

<sup>5</sup>This means that the permutation and its inverse are always in the same class. A group with this property is said to be an *ambivalent* group.

hence the number of irreducible representations is known. But the number of cycle structures is obviously the number of possible ways that there is of dividing  $N$  objects in integer partitions. Thus for four objects the possible cycle structures are

$$\begin{aligned}
 & (i_1 i_2 i_3 i_4), \\
 & (i_1 i_2 i_3)(i_4), \\
 & (i_1 i_2)(i_3 i_4), \\
 & (i_1 i_2)(i_3)(i_4), \\
 & (i_1)(i_2)(i_3)(i_4).
 \end{aligned} \tag{2.59}$$

If there are  $m$  cycles in any partition, the cycle lengths are usually written symbolically as  $\lambda_i$ , where

$$\lambda_1 + \lambda_2 + \lambda_3 + \dots + \lambda_m = N, \tag{2.60}$$

and by convention

$$\lambda_1 \geq \lambda_2 \geq \lambda_3 \geq \dots \geq \lambda_m \geq 0. \tag{2.61}$$

Thus in  $\blacklozenge$  Eq. 2.59 above in the first decomposition there is only one cycle and  $\lambda_1 = 4$ , in the second there are only two cycles  $\lambda_1 = 3$  and  $\lambda_2 = 1$ . It is a custom to denote the totality of  $\lambda$  for any partition by the vector  $[\lambda] \equiv [\lambda_1, \lambda_2, \dots, \lambda_m]$  and to indicate  $r$  repeats of a cycle of given length  $\lambda$  by  $\lambda^r$ . Thus in  $\blacklozenge$  Eq. 2.59 above the partitions should be denoted as  $[4]$ ,  $[3\ 1]$ ,  $[2^2]$ ,  $[2\ 1^2]$ , and  $[1^4]$ .

The notation ( $\blacklozenge$  Eq. 2.59) is not especially well adapted for present purposes and instead a notation invented by Young, the so-called Young diagram, is used. The Young diagrams equivalent to  $\blacklozenge$  Eq. 2.59 are

$$\begin{array}{ccccc}
 \begin{array}{|c|c|c|c|} \hline \square & \square & \square & \square \\ \hline \end{array} & 
 \begin{array}{|c|c|c|} \hline \square & \square & \square \\ \hline \square & & \\ \hline \end{array} & 
 \begin{array}{|c|c|} \hline \square & \square \\ \hline \square & \square \\ \hline \end{array} & 
 \begin{array}{|c|} \hline \square & \\ \hline \square & \\ \hline \square & \\ \hline \square & \\ \hline \end{array} & 
 \begin{array}{|c|} \hline \square \\ \hline \square \\ \hline \square \\ \hline \square \\ \hline \end{array} \\
 [4] & [3\ 1] & [2^2] & [2\ 1^2] & [1^4]
 \end{array} \tag{2.62}$$

where the boxes in each row stand for a cycle and different cycles form different rows in the diagram.

Since there are as many irreducible representations of a group as it has classes and there is one Young diagram for each class, Young diagrams can obviously be used to label each of the different irreducible representations. The dimensionality of the irreducible representation must pretty clearly be associated with the number of ways it is possible to put the objects  $1, 2, \dots, N$  into the boxes in the Young diagram, in a unique way. In fact it turns out that if the numbers  $1, 2, \dots, N$  are put into the boxes in a diagram so that when they are read across any row they are increasing and when they are read down any column they are also increasing, the totality of all such assignments is the dimension of the irreducible representation.

Thus the first diagram in  $\blacklozenge$  Eq. 2.62 can only yield

$$\begin{array}{|c|c|c|c|} \hline 1 & 2 & 3 & 4 \\ \hline \end{array} \tag{2.63}$$

A Young diagram with numbers in it like (Eq. 2.63) is called a *Young tableau* and it is seen at once that there is only one tableau for the last Young diagram in Eq. 2.62, namely:

$$\begin{array}{|c|} \hline 1 \\ \hline 2 \\ \hline 3 \\ \hline 4 \\ \hline \end{array} \tag{2.64}$$

so that both [4] and [1<sup>4</sup>] correspond to one-dimensional irreducible representations.

The representation [3 1] yields

$$\begin{array}{|c|c|c|} \hline 1 & 3 & 4 \\ \hline 2 & & \\ \hline \end{array} \quad \begin{array}{|c|c|c|} \hline 1 & 2 & 4 \\ \hline 3 & & \\ \hline \end{array} \quad \begin{array}{|c|c|c|} \hline 1 & 2 & 3 \\ \hline 4 & & \\ \hline \end{array} \tag{2.65}$$

and in these circumstances it is clearly nice to have some sort of standard order; the one often adopted is to read the tableau across each row as if it were an ordinary number and then to arrange the tableaux in ascending order of these numbers, but other orders are used. Thus the numbers in Eq. 2.65 are

$$1342 \quad 1243 \quad 1234 \tag{2.66}$$

so that the standard order for the tableaux would be

$$\begin{array}{|c|c|c|} \hline 1 & 2 & 3 \\ \hline 4 & & \\ \hline \end{array} \quad \begin{array}{|c|c|c|} \hline 1 & 2 & 4 \\ \hline 3 & & \\ \hline \end{array} \quad \begin{array}{|c|c|c|} \hline 1 & 3 & 4 \\ \hline 2 & & \\ \hline \end{array} \tag{2.67}$$

This representation is therefore three-dimensional.

One can obviously get the tableaux for [2 1<sup>2</sup>] simply by transposing the tableaux for [3 1] and a little reflection will show that this is generally the case, simply because of the structure of the Young diagrams. The representations [2 1<sup>2</sup>] and [3 1] are said to be *conjugate* representations (or sometimes *adjoint*, or *dual* or *associated*). In the present case the representation [2<sup>2</sup>] is self-conjugate. Generally if the representation is denoted by [λ] then the conjugate representation is denoted by [λ̃], and of course both representations are of the same dimension.

Since there is obviously freedom in which is associated with which, the choice is made in the two one-dimensional cases that [N] is associated with the symmetric representation and [1<sup>N</sup>] with the antisymmetric representation. Thus if one has a representation [λ], then the conjugate representation [λ̃] is just [λ] × [1<sup>N</sup>].

The [λ] symbols are also used to denote classes from time to time and in that context the correspondences established between Eqs. 2.62 and 2.59 are appropriate. Thus [1<sup>4</sup>] represents the last partition in Eq. 2.59 which is clearly the class that just contains the unit operator, [2 1<sup>2</sup>] stands for the class containing all operators involving only one transposition and so on.

Now it can be shown that if one can find a basis for a representation [λ] for the symmetric group and another basis which is a representation for [λ̃] then the direct product of these two bases is a basis for the antisymmetric representation [1<sup>N</sup>]. So to construct antisymmetric wavefunctions from space-spin products, as in constructing electronic wavefunctions, one can do so as

$$\Psi^{[1^N]} = \sum_i \Phi_i^{[\tilde{\lambda}]}(\mathbf{r}) \Theta_{S, M_S, i}^{[\lambda]}(\mathbf{s}), \tag{2.68}$$

where the sum goes over all functions in the basis for the irrep and N identical particles are assumed involved. They can have any spins at all and although in the expression above they are

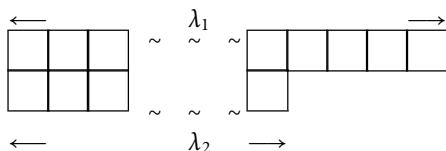
assumed to be spin eigenfunctions this is obviously not necessary just as long as a suitable set of spin products is used. However if they are spin- $\frac{1}{2}$  particles then the only possible representations that can be constructed in the spin space are of the form  $[\lambda_1, \lambda_2]$ . No other irreps are possible. Furthermore in the case of  $N$  electrons properly coupled to a spin state  $S$  then

$$\lambda_1 + \lambda_2 = N, \quad \lambda_1 - \lambda_2 = 2S, \quad (2.69)$$

so that

$$\lambda_1 = \frac{N}{2} + S, \quad \lambda_2 = \frac{N}{2} - S, \quad (2.70)$$

where



Thus any allowed space wavefunctions, such as those formed from orbital products, must form a basis for  $[\tilde{\lambda}]$ .

This result arises basically because there are only *two* kinds of spin functions for spin- $\frac{1}{2}$  particles. Thus lots of permutations that *could* arise do not arise in practice because they are the same if they involve only, say,  $\alpha$  spin particles. However it can also be shown that if the spin basis consists of spin eigenfunctions then the reps provided of  $S_N$  are actually irreps and that they are the same irreps for any value of  $M_S$ . That is, there are *exactly* as many spin eigenfunctions with the same  $S$  value as the dimension of the irrep  $[\lambda_1, \lambda_2]$  of  $S_N$ . This is an enormous blessing and makes life much easier in electronic structure calculations than it might otherwise be. For fermions of spin greater than  $\frac{1}{2}$  it is not the case and it makes, for example, the problem of calculating statistical weights in molecular spectroscopy, or nuclear spin states in nuclear physics, much more complicated.

## Point Groups and Transformations

In the Cartesian coordinate system, the Laplacian operator for the  $i$ th electron is written as

$$\nabla^2(i) = \frac{\partial^2}{\partial r_{xi}^2} + \frac{\partial^2}{\partial r_{yi}^2} + \frac{\partial^2}{\partial r_{zi}^2}, \quad (2.71)$$

and the inter-electron distance as

$$r_{ij} = \left( \sum_{\alpha} (r_{\alpha j} - r_{\alpha i})^2 \right)^{1/2}, \quad (2.72)$$

where here and hereafter sums over  $\alpha$  run over  $x$ ,  $y$ , and  $z$ . The electron-nucleus distance will be written as

$$r_{ai} = \left( \sum_{\alpha} (r_{\alpha i} - a_{\alpha})^2 \right)^{1/2}, \quad (2.73)$$

where the  $\alpha$ th coordinate of the nucleus  $a$  is written as  $a_{\alpha}$  to emphasize that it is a pure number and not a variable, since the nuclear positions are assumed to be fixed.

It is easy to show that

$$r_{ij}^2 = (\mathbf{r}_j - \mathbf{r}_i)^T (\mathbf{r}_j - \mathbf{r}_i), \quad (2.74)$$

and

$$r_{ai}^2 = (\mathbf{r}_i - \mathbf{a})^T (\mathbf{r}_i - \mathbf{a}), \quad (2.75)$$

where the superscript  $T$  denotes the matrix transpose.

Now let it be supposed that  $\mathbf{r}$  is subject to positive rotation about the  $z$ -axis through an angle  $\phi$  to yield the vector  $\mathbf{r}'$ . Positive rotations are in the direction of a right-handed screw-twist when the point of the screw is moving in the axis direction. It is then easy to show that the new and old vectors are related by an orthogonal matrix

$$\mathbf{r}' = \mathbf{R}(\phi) \mathbf{r}, \quad (2.76)$$

with

$$\mathbf{R}(\phi) = \begin{pmatrix} \cos \phi & -\sin \phi & 0 \\ \sin \phi & \cos \phi & 0 \\ 0 & 0 & 1 \end{pmatrix}. \quad (2.77)$$

In this section we shall be concerned only with transformations like (Eq. 2.77), that is, with *point transformations* and, in the case of the clamped nuclei Hamiltonian, consideration may be confined to *finite point groups*, specifically the crystallographic point groups. However from time to time it will be convenient to think a bit more generally and to recognize, for example, that the full rotation-reflection group in three dimensions is a point group, though an *infinite* one, and that some Hamiltonians are invariant under the operators of this group.

Now it should be understood quite clearly as to what happens in a transformation of variables in a fixed basis. It is supposed that *every* point in space goes over into its *image* according to the appropriate transformation rule

$$\mathbf{r}' = \mathbf{R}\mathbf{r}, \quad (2.78)$$

where  $\mathbf{R}$  is a constant orthogonal matrix.<sup>6</sup>

Thus imagining the situation appropriate to the Schrödinger equation with Hamiltonian (Eq. 2.47), the assertion of a transformation of variables realized by  $\mathbf{R}$  would imply

$$\mathbf{r}'_i = \mathbf{R}\mathbf{r}_i, \quad i = 1, 2, \dots, N. \quad (2.79)$$

However, in the fixed nuclei approximation, it would *not* imply that

$$\mathbf{a}' = \mathbf{R}\mathbf{a}, \quad \mathbf{a} = \text{any nucleus}. \quad (2.80)$$

This is not for any sinister reason but simply because of the definition chosen of the clamped nuclei approximation. In this approximation the nuclear positions are triplets of numbers which take particular but fixed values once a particular basis is chosen.<sup>7</sup>

It is now very easy to show that the Laplacian and the inter-electronic distance are invariant under any constant orthogonal transformation of variables but that in general the electron-nucleus distances are not invariant. It is perhaps sensible to show how this comes about for it illustrates one or two points and makes the idea of *invariance* a bit clearer.

<sup>6</sup>By “constant” here is meant simply that the elements of the matrix are not themselves dependent on the variables.

<sup>7</sup>It is sometimes convenient to think of the nuclear positions as *defining* a particular embedding for the basis vectors or coordinate frame.



First the Laplacian. Using the chain rule for differentiation

$$\frac{\partial}{\partial r_{\alpha i}} = \sum_{\beta} \frac{\partial r'_{\beta i}}{\partial r_{\alpha i}} \frac{\partial}{\partial r'_{\beta i}}, \quad (2.81)$$

since the transformation does not “mix”  $\mathbf{r}_i$  and  $\mathbf{r}_j$  so that

$$\frac{\partial}{\partial r_{\alpha i}} = \sum_{\beta} R_{\beta\alpha} \frac{\partial}{\partial r'_{\beta i}}, \quad (2.82)$$

and hence

$$\frac{\partial^2}{\partial r_{\alpha i}^2} = \sum_{\gamma\beta} R_{\gamma\beta} R_{\beta\alpha} \frac{\partial^2}{\partial r'_{\gamma i} \partial r'_{\beta i}}, \quad (2.83)$$

but

$$\nabla^2(i) = \sum_{\alpha} \frac{\partial^2}{\partial r_{\alpha i}^2},$$

and

$$\sum_{\alpha} R_{\gamma\alpha} R_{\beta\alpha} = \delta_{\gamma\beta} \quad (\mathbf{R}^T \mathbf{R} = E_3), \quad (2.84)$$

therefore

$$\nabla^2(i) = \sum_{\gamma\beta} \delta_{\gamma\beta} \frac{\partial^2}{\partial r'_{\gamma i} \partial r'_{\beta i}} = \sum_{\beta} \frac{\partial^2}{\partial r'_{\beta i}^2} = \nabla^2(i'). \quad (2.85)$$

But clearly if

$$\nabla^2(i) f(\mathbf{r}_i) = g(\mathbf{r}_i), \quad (2.86)$$

then

$$\nabla^2(i') f(\mathbf{r}'_i) = g(\mathbf{r}'_i), \quad (2.87)$$

so that  $\nabla^2(i)$  is an invariant operator under the transformation since its effect on an arbitrary function is unchanged (except for the variable names which, in this context, are irrelevant). Notice that if  $\nabla^2$  had been set up in the primed system as  $\nabla^2(i')$  the same argument would have shown that  $\nabla^2(i') = \nabla^2(i)$ , as required.

Next  $r_{ij}$ . From  $\blacktriangleright$  Eq. 2.78 it follows that

$$\mathbf{r}'_i = \mathbf{R} \mathbf{r}_i \quad \text{and} \quad \mathbf{r}_i = \mathbf{R}^T \mathbf{r}'_i. \quad (2.88)$$

Combining the form ( $\blacktriangleright$  Eqs. 2.74 with  $\blacktriangleright$  2.88) we get

$$\begin{aligned} r_{ij}^2 &= (\mathbf{R}^T (\mathbf{r}'_j - \mathbf{r}'_i))^T (\mathbf{R}^T (\mathbf{r}'_j - \mathbf{r}'_i)) \\ &= (\mathbf{r}'_j - \mathbf{r}'_i)^T \mathbf{R} \mathbf{R}^T (\mathbf{r}'_j - \mathbf{r}'_i) \\ &= (\mathbf{r}'_j - \mathbf{r}'_i)^T (\mathbf{r}'_j - \mathbf{r}'_i), \end{aligned}$$

so that

$$r_{ij}^2 = r'^2_{ij}, \quad (2.89)$$

showing that  $r_{ij}^2$  and hence  $r_{ij}$  is invariant in the same sense as above.

For the electron-nucleus distance one gets

$$\begin{aligned} r_{ai}^2 &= (\mathbf{R}^T \mathbf{r}'_i - \mathbf{a})^T (\mathbf{R}^T \mathbf{r}'_i - \mathbf{a}) \\ &= (\mathbf{R}^T (\mathbf{r}'_i - \mathbf{R} \mathbf{a}))^T (\mathbf{R}^T (\mathbf{r}'_i - \mathbf{R} \mathbf{a})), \end{aligned}$$

so that

$$r_{ai}^2 = (\mathbf{r}'_i - \mathbf{R}\mathbf{a})^T (\mathbf{r}'_i - \mathbf{R}\mathbf{a}), \quad (2.90)$$

and this in general is obviously not  $r_{ai}^2$ . However, if the transformation  $\mathbf{R}$  is such that

$$\mathbf{b} = \mathbf{R}\mathbf{a} \quad \text{and} \quad \mathbf{a} = \mathbf{R}^T \mathbf{b}, \quad (2.91)$$

where  $\mathbf{b}$  is the position of another nucleus in the problem with the same charge as the nucleus whose position is  $\mathbf{a}$ , then it is clear that even though individual terms in the electron-nucleus attraction operator are *not* invariant, nevertheless the operator as a whole *is* invariant.

The generalization of this result is obvious. If the nuclear positions are divided into sets corresponding to nuclei of the same charge, the clamped nuclei Hamiltonian is invariant under all operators represented by orthogonal matrices  $\mathbf{R}$  such that if

$$\mathbf{b} = \mathbf{R}\mathbf{a}, \quad (2.92)$$

$\mathbf{b}$  is to be found in the same set as  $\mathbf{a}$  was found.<sup>8</sup>

To look at it another way, were the coordinates of a set of equivalent nuclei to be written as a row matrix of the coordinates  $\mathbf{a}_1 \mathbf{a}_2 \dots \mathbf{a}_p$  (so that the “row” is actually a  $3 \times p$  matrix), the effect of an invariance preserving operator (a *symmetry* operator) could be symbolized in the partitioned matrix form

$$(\mathbf{b}_1 \mathbf{b}_2 \dots \mathbf{b}_p) = (\mathbf{a}_1 \mathbf{a}_2 \dots \mathbf{a}_p) \mathbf{P}, \quad (2.93)$$

where  $\mathbf{P}$  is a  $p \times p$  *permutation matrix*, that is, one of the form

$$\mathbf{P} = \begin{pmatrix} 0 & 1 & 0 & 0 & \dots & \dots & 0 \\ 1 & 0 & 0 & 0 & \dots & \dots & 0 \\ \dots & \dots & \dots & \dots & \dots & \dots & \dots \\ \dots & \dots & \dots & \dots & \dots & \dots & \dots \\ 0 & 0 & 1 & 0 & \dots & \dots & 0 \end{pmatrix}, \quad (2.94)$$

where the permutation corresponds to the effective rearrangement of the nuclei in the electron-nucleus attraction operator. Permutation matrices have just one nonzero entry in any row or column and that entry is always 1 so that such matrices are always orthogonal matrices. Their determinant can, however, be  $\pm 1$  depending on the *parity* of the permutation.

Thus, to all intents and purposes, when considering the symmetry of a molecule to be represented by a clamped nuclei Hamiltonian, all we need to look at is those orthogonal operators that let equivalent nuclear positions carry a permutation representation of the operator in question. Any such operator is a symmetry operator of the problem. We thus never need to think about the electrons and it is usual in elementary books to start from the point reached here, as if the operations were carried out on the nuclear positions. From here one can go on to show, in the usual way, that the collection of symmetry operators form a group and that the group is a *point group* essentially corresponding to the geometrical figure formed by the equivalent nuclei in the nuclear framework.

Functions can always be visualized in terms of a fixed Cartesian basis and under the change (assumed orthogonal)  $\mathbf{r}' = \mathbf{R}\mathbf{r}$  or  $\mathbf{r} = \mathbf{R}^T \mathbf{r}'$  the change *induced* in a function  $f(\mathbf{r})$  is

$$\mathcal{O}_R f(\mathbf{r}) = \tilde{f}(\mathbf{r}) \equiv f(\mathbf{R}^T \mathbf{r}), \quad (2.95)$$

<sup>8</sup>Notice that in this approximation the *mass* of the nucleus is of no consequence, only the charge matters.

meaning that  $\tilde{f}(\mathbf{r})$  is constructed from  $f(\mathbf{r})$  by substituting  $(\mathbf{R}^T \mathbf{r})_\alpha$  for  $r_\alpha$  wherever it occurs in the prescription for  $f(\mathbf{r})$ .  $O_R$  symbolizes the operation in function space.

Considering the transformation of operators again, assuming that one specifies the operator form in a fixed basis, consider an operator  $A$  (assumed linear and Hermitian) such that

$$Af(\mathbf{r}) = g(\mathbf{r}), \quad (2.96)$$

and by formal operator algebra we can rewrite this to exhibit the effect of the operator  $O_R$  as

$$\begin{aligned} O_R Af(\mathbf{r}) &= O_R g(\mathbf{r}), \\ O_R Af(\mathbf{r}) &= O_R A O_R^{-1} O_R f(\mathbf{r}) = O_R g(\mathbf{r}), \\ O_R Af(\mathbf{r}) &= O_R A O_R^{-1} \tilde{f}(\mathbf{r}) = \tilde{g}(\mathbf{r}), \end{aligned} \quad (2.97)$$

so that we can say that if  $R$  induces  $O_R$  then it induces a change in the operators acting on the original function space such that

$$\tilde{A} = O_R A O_R^{-1}, \quad (2.98)$$

where the functions on which the operators act are implicit in the formalism.

Furthermore if the induced change is such that  $A = \tilde{A}$ , that is,  $A$  is an invariant operator, then

$$A = O_R A O_R^{-1}, \quad (2.99)$$

or

$$O_R A = A O_R,$$

or

$$O_R A - A O_R \equiv [O_R, A] = 0,$$

and we say that the  $O_R$  *commute* with  $A$ . We can thus characterize the symmetry operators in the function space that constitutes the domain of  $A$  as those operators which commute with  $A$ . In particular we are interested in the case when  $A$  is the Hamiltonian for the problem.

Now, in practice, (2.98) is not of much use for actually checking on the transformation properties of operators since it does not actually provide a specific rule for the construction of  $\tilde{A}$ . However as seen before, the actual variable names in an operator relation do not matter, so that if we regard  $\mathbf{R}^T \mathbf{r}$  as just a new variable name, say  $\mathbf{y}$ , then it follows immediately from (2.96) and (2.97) that  $\tilde{A}$  is just the operator  $A$  made up in the same basis as  $A$  but with  $(\mathbf{R}^T \mathbf{r})_\alpha$  for every occurrence of  $r_\alpha$  in the operator. This prescription is usable in an obvious way for multiplicative terms in the operator and, for derivative terms, a little thought shows that the replacement

$$\frac{\partial}{\partial r_\alpha} \rightarrow \sum_y (\mathbf{R}^T)_{\alpha y} \frac{\partial}{\partial r_y} = \sum_y R_{y\alpha} \frac{\partial}{\partial r_y} \quad (2.100)$$

is the appropriate one for the new operator set up on the original basis. (Compare with (2.81) and (2.82).)

Thus we see that the momentum operator, for example, is not generally an invariant operator since from (2.100)

$$\begin{aligned} \tilde{p}_\alpha &= \frac{\hbar}{i} \sum_y R_{y\alpha} \frac{\partial}{\partial r_y} = \sum_y R_{y\alpha} p_y, \\ \tilde{\mathbf{p}}_\alpha &= (\mathbf{R}^T \mathbf{p})_\alpha, \end{aligned} \quad (2.101)$$

and (Eq. 2.101) is the equation that relates the elements of the transformed operator to those of the untransformed operator on a fixed basis. In fact it is easy to see from (Eq. 2.101) that in this case the operators actually provide a basis for the representation of  $R$  by  $\mathbf{R}$  as

$$\bar{\mathbf{p}} = \mathbf{p}\mathbf{R}, \quad (2.102)$$

where the operators are written as a row matrix. The transformation of operators is a matter to which we shall return later, but for the moment let it simply be noted that the arguments presented earlier in this section show that the clamped nuclei Hamiltonian is an invariant operator if  $R$  is a point group operation and we shall now look at the behavior of its eigenfunctions under  $\mathbf{O}_R$ .

Any set of degenerate eigenfunctions of  $H$  carry a matrix representation of  $\mathbf{O}_R$ . Thus if we denote the set of degenerate eigenfunctions as  $f_1, f_2, \dots, f_n$  and treat these as a row matrix  $f$ , then we can write

$$\mathbf{O}_R \mathbf{f} = \mathbf{f}\mathbf{O}_R, \quad (2.103)$$

and we say that  $\mathbf{O}_R$  provides a matrix representation of  $\mathbf{O}_R$  in the basis  $f_i$  so that a set of such functions in a function space play exactly the same role as do the unit vectors in a coordinate space and are, therefore, sometimes called *basis functions* of the representation.

The representations provided in the basis of degenerate eigenfunctions are usually irreducible and can be chosen to be unitary matrices (in fact usually orthogonal matrices if the functions are real functions). In practice, what one is usually faced with is a collection of functions which have arbitrary (but known) transformation properties and what one actually wants to do is to adapt these functions so that they actually transform like the true eigenfunctions of the problem. This can be done by means of the group theoretical projection operator.

If the unitary matrix irreducible representation of the point group is known and denoted by  $\mathbf{D}^{(\mu)}(R)$ , where  $\mu$  labels the irreducible representation, then the projection operator is

$$\mathbf{P}_{ij}^{(\mu)} = \frac{n_\mu}{g} \sum_R (\mathbf{D}^{(\mu)}(R))_{ij}^* \mathbf{O}_R, \quad (2.104)$$

where  $g$  is the order of the group and  $n_\mu$  the dimension of  $\mathbf{D}^{(\mu)}(R)$ .<sup>9</sup> This projection operator is such that

$$\mathbf{P}_{ij}^{(\mu)} f = f_i^{(\mu)} \quad \text{or a null result}, \quad (2.105)$$

where  $f$  is an arbitrary function and  $f_i^{(\mu)}$  is the  $i$ th function in the row matrix  $\mathbf{f}^{(\mu)}$  such that

$$\mathbf{O}_R \mathbf{f}^{(\mu)} = \mathbf{f}^{(\mu)} \mathbf{D}^{(\mu)}(R). \quad (2.106)$$

The null result occurs in (Eq. 2.105) if the arbitrary function has no component that lies in the subspace defined by the  $f^{(\mu)}$ .

In practice one often makes do with the character projection operator based on the characters  $\chi^{(\mu)}$  of the irreducible representation,

$$\chi^{(\mu)}(R) = \sum_i (\mathbf{D}^{(\mu)}(R))_{ii}^*, \quad (2.107)$$

so that the character projection operator  $\mathbf{P}^{(\mu)}$  is

$$\mathbf{P}^{(\mu)} = \frac{n_\mu}{g} \sum_R (\chi^{(\mu)}(R))^* \mathbf{O}_R, \quad (2.108)$$

<sup>9</sup>The operator in this form is clearly only possible for finite groups but similar operators are constructible for most infinite groups of interest.

and produces from an arbitrary function (if not a null result) then a function which is said to *belong* to the  $\mu$ th irreducible representation but which in general transforms like a linear combination of the basis functions for  $\mathbf{D}^{(\mu)}$ .

In practice, therefore, everything depends on knowing the representations of the group in question (and the irreducible representations are usually tabulated) and on knowing how the chosen functions actually transform under the operations of the group.

It is helpful to think of constructing MOs as a linear combination of atomic orbitals (LCAOs) and as a preliminary to this the idea of an MO and of an AO need to be developed a bit further.

It might be thought that orbitals could be best determined by solving the relevant one-electron problem specified by  $h$ , (Eq. 2.49), for each molecule. This is not so easily done and if a wavefunction is constructed as a determinant of spin-orbitals so constructed it yields a very poor approximation to the electronic energy. This is because the electron interaction term is large and has not been considered in constructing the orbital. Thus to get useful orbitals the fact that the electrons interact strongly must somehow be incorporated into the single particle potential through some sort of effective field process. This was first attempted for atoms in the 1920s by W. Hartree and D. R. Hartree (1927, 1936) but without considering antisymmetry. Their method was developed by Fock (1930) and by Slater (1930) in a properly antisymmetric form. Molecules resisted this approach because it was extremely difficult to solve the one-electron problem with a potential that was not centrosymmetric. However since it was possible to get atomic orbitals, two approaches using them developed, one at the hands of Pauling (1939) using atomic orbitals directly and the other at the hands of Mulliken (1931) by writing molecular orbitals as a linear combination of atomic orbitals. The Pauling approach was called the Valence Bond (VB) method and the Mulliken one the Linear Combination of Atomic Orbitals Molecular Orbital (LCAO MO) method. Although it was the VB method that was used in the first successful molecular electronic structure calculation, on  $H_2$  by Heitler and London (1927), it was the LCAO MO method that became standard in quantum chemical calculations following the work of Roothaan (1951) in the 1950s. Although these methods will be considered in great detail elsewhere in this volume, their basis can best be considered here.

The most familiar atomic orbitals are those for the hydrogen atom which are usually designated according to their angular parts as  $s$  for  $l = 0$ ,  $p$  for  $l = 1$ ,  $d$  for  $l = 2$ , and so on where there are  $2l + 1$  orbitals of each type. For calculational purposes Slater proposed that the radial part of the orbital, while still centered upon the nucleus, should be of the form

$$Nr^{n-1} \exp -\xi r, \quad n = 1, 2, \dots, \quad (2.109)$$

where  $N$  is a normalizing factor, and  $\xi$  may be chosen at will or used as a variational parameter.

It is customary to use a real form for the angular parts of the orbital so that, for example, the three  $p$  orbitals are specified as

$$x \exp -\xi r, \quad y \exp -\xi r, \quad z \exp -\xi r. \quad (2.110)$$

The most widespread atomic orbital form in use at present is the Gaussian which has the radial part

$$Nr^{n-1} \exp -\xi r^2, \quad n = 1, 2, \dots \quad (2.111)$$

When it is not necessary to specify atomic orbitals in detail they will be denoted  $\eta_i(\mathbf{r})$ .

In elementary books it is often assumed that you can “eye-ball” the transformation properties from the “pictures” of the orbitals stuck on the nuclei. (Such pictures usually look a bit

like twisted sausages and doughnuts.) Such an approach is a bit risky and knowing how to do this sort of thing algebraically avoids getting into the nasty mess that often happens if one relies on the pictures. Indeed, it is clear that it is quite impossible to draw a picture of an orbital. The sausages and doughnuts, therefore, must be at most projection representations in three (or two) dimensions and it is not clear that the transformation of the picture in three (or two) dimensions really corresponds correctly to the induced transformation of the orbital in the function space.

If the atomic orbital  $\eta(\mathbf{r})$  is situated at the origin of coordinates and the origin is the invariant point of the point group operators, then any orbital constructed about this origin simply transforms under  $O_R$  to a new functional form in the space

$$O_R \eta(\mathbf{r}) = \tilde{\eta}(\mathbf{r}) = \eta(\mathbf{R}^T \mathbf{r}). \quad (2.112)$$

If, however, the orbital is developed about another origin, say  $\mathbf{a}$ , so that the functional form is

$$\eta((\mathbf{r} - \mathbf{a})), \quad (2.113)$$

then the situation is a little more involved. The coordinate point  $\mathbf{a}$  is not a variable of the problem, but a parameter in the function construction. It does not change under the transformation so that

$$\begin{aligned} O_R \eta((\mathbf{r} - \mathbf{a})) &= \eta((\mathbf{R}^T \mathbf{r} - \mathbf{a})) \\ &= \eta(\mathbf{R}^T (\mathbf{r} - \mathbf{Ra})), \end{aligned} \quad (2.114)$$

but clearly  $\mathbf{Ra}$  is some other fixed parameter point in the problem  $\mathbf{b}$ , say, so that

$$\begin{aligned} \eta(\mathbf{R}^T (\mathbf{r} - \mathbf{Ra})) &= \eta(\mathbf{R}^T (\mathbf{r} - \mathbf{b})) \\ &= \eta(\mathbf{R}^T \mathbf{r}_b). \end{aligned} \quad (2.115)$$

Effectively the origin of the function is changed, but about that new origin, the transformed function is constructed by the usual rules in terms of the variable  $\mathbf{r}_b = (\mathbf{r} - \mathbf{b})$ . Clearly if  $\eta(\mathbf{R}^T \mathbf{r})$  is  $\tilde{\eta}(\mathbf{r})$  then  $\eta(\mathbf{R}^T \mathbf{r}_b)$  will be  $\tilde{\eta}(\mathbf{r}_b)$  so that if one has worked out the transformation properties of an orbital at the origin ( $\mathbf{a} = 0$ ) then the functional form of the transformed orbital carries over immediately to an orbital at arbitrary origin  $\mathbf{a}$  given that  $\mathbf{b} = \mathbf{Ra}$  is known.

Thus if one chooses a set of AOs which are identical but on different centers then they carry a permutation representation of the operation, much like (♣ Eq. 2.94) but with appropriate transformation matrices in place of the 0s and 1s there. So if, for example, one had a set of identical s-orbitals with one on each center, the transformation matrices under any point group operation would just be 1, so that the matrix would remain just as in (♣ Eq. 2.94). But if one had a set of three equivalent p-functions on each center the 0s would become  $3 \times 3$  null matrices and the 1s would become those three-dimensional transformation matrices which represent the operation on a set of three equivalent p-functions at the origin and so on.

Once these transformation properties have been determined it is an easy matter to apply the projection operator either to construct functions that transform like irreducible representations or like a "special" representation.

Thus in practice we can always get one-particle symmetry functions relatively easily, but the symmetry problem is clearly more involved when it comes to considering many-particle functions.

The paradigm for an approximate many-particle function is a product of one-particle functions (*orbitals*)

$$\Phi(\mathbf{r}_1, \mathbf{r}_2, \mathbf{r}_3, \dots, \mathbf{r}_N) = \phi_1(\mathbf{r}_1)\phi_2(\mathbf{r}_2) \dots \phi_N(\mathbf{r}_N). \quad (2.116)$$

In thinking of approximate solutions to the clamped nuclei problem it is natural to think of the  $\phi_r$  as molecular-orbitals and the  $\mathbf{r}_i$  as the electron variables, but the discussion that follows is quite general and it need not even be the case that the variables are those of identical particles. Now from what has been said before it can always be supposed that the orbitals are adapted to particular irreducible representations of the invariance group of the Hamiltonian and that one desires an approximate solution which is also adapted to a particular irreducible representation. The variable-space for the product function on the right-hand side of  $\blacklozenge$  Eq. 2.116 is the *direct sum* of each of the variable-spaces for the particles, that is  $\mathbf{r}_1 \oplus \mathbf{r}_2 \oplus \mathbf{r}_3 \oplus \dots \oplus \mathbf{r}_N$ . The functions  $\phi_r$  built on each of these variable-spaces individually constitute a separate function space for each variable and the total function space is, therefore, the *direct product* of all these function spaces. If, for the moment, we restrict each of these function spaces to sufficient functions to carry irreducible representations of the invariance group, then the direct product function space is just

$$\phi^{(1)} \otimes \phi^{(2)} \otimes \dots \otimes \phi^{(N)}, \quad (2.117)$$

where the row matrix  $\phi^{(1)}$  contains  $\phi_1$  and is a basis for the representation  $\mathbf{D}^{(1)}$ , of dimension  $n_1$ , and so on, so that the total dimension of the space is  $n_1 \times n_2 \times \dots \times n_N = P$ .

The symmetry operation  $R$  has an orthogonal representative  $\mathbf{R}$  in each of the variable-spaces and it has a representative in the total variable-space which is the direct sum of  $N$  repeats of  $\mathbf{R}$ .

Thus the effect of  $O_R$  on the product function ( $\blacklozenge$  Eq. 2.117) is to produce

$$\phi^{(1)}\mathbf{D}^{(1)}(R) \otimes \phi^{(2)}\mathbf{D}^{(2)}(R) \dots \phi^{(N)}\mathbf{D}^{(N)}(R), \quad (2.118)$$

which, by the ordinary rules of manipulation for direct products, is

$$\phi^{(1)} \otimes \phi^{(2)} \otimes \dots \otimes \phi^{(N)}\mathbf{D}^{(1)}(R) \otimes \mathbf{D}^{(2)}(R) \dots \otimes \mathbf{D}^{(N)}(R). \quad (2.119)$$

The elements of the row matrix arising from the direct product of the orbitals can obviously be written (with suitable reordering if necessary) as a row matrix of functions like  $\blacklozenge$  Eq. 2.116 but involving such other partner orbitals as are necessary.

Now if it happens that *all* the original orbitals belong to *one*-dimensional irreducible representations of the invariance group, then the matrix of direct products of representations in  $\blacklozenge$  Eq. 2.119 is just a scalar, generally speaking  $\pm 1$ , so that, in this case,  $\Phi$  obviously belongs to an irreducible representation of the invariance group of the problem. Otherwise the matrix of direct products of representations generally constitutes a *reducible* representation of the invariance group and in this case the product function ( $\blacklozenge$  Eq. 2.116) and its partners do not, generally, carry an irreducible representation of the point group and must be suitably adapted to do so.

There are clearly two possible ways in which this might be done. One could start off from  $\Phi$  and project out the required components, or one could recognize that there is a matrix relationship between the unadapted set and the adapted set and try to determine the matrix elements from group theoretical arguments. Both approaches have their uses but since the second approach has not yet been considered, it is appropriate to speak of it now.

If, for the moment, we consider the direct product of just two irreducible representations, then it follows at once, from the character orthogonality theorem, that we can write down the number of times that any irreducible representation occurs in the reduction of the direct product representation. If we are thinking of representations  $\mu$  and  $\nu$  in the direct product and  $\sigma$  as

the resulting representation, let us call this number  $(\mu\nu\sigma)$ . It is zero or an integer and of course it is known once the character table for all the irreducible representations of a group are known. This means that we can find a transformation  $\mathbf{U}$  such that

$$\mathbf{U}^\dagger \mathbf{D}^{(\mu)} \otimes \mathbf{D}^{(\nu)} \mathbf{U} = \sum_{\sigma} (\mu\nu\sigma) \mathbf{D}^{(\sigma)}, \quad (2.120)$$

where a direct sum is implied on the right-hand side, which runs over all the representations in the group. In [Eq. 2.120](#) it is assumed that the representations  $\mathbf{D}^{(\mu)}$ , etc., are unitary so that from the definition of the direct product,  $\mathbf{D}^{(\mu)} \otimes \mathbf{D}^{(\nu)}$  is unitary and can, therefore, be reduced to irreducible form by means of a unitary transformation.

Now if we denote by  $\phi^{(\sigma)}$  the row of  $n_{\mu}$  basis functions for  $\mathbf{D}^{(\mu)}$ , then the set of  $n_{\sigma} = n_{\mu}n_{\nu}$  product functions  $\phi^{(\mu)} \otimes \phi^{(\nu)}$  are a basis for the direct product representations and clearly the set of product functions  $\phi_s^{(\sigma)}$ ,  $s = 1, 2, \dots, n$  defined by

$$\phi^{(\sigma)} = \phi^{(\mu)} \otimes \phi^{(\nu)} \mathbf{U} \quad (2.121)$$

are a basis for the reduced representation on the right-hand side of [Eq. 2.120](#). It is usual to rewrite ([Eq. 2.121](#)) in the form

$$\phi_s^{(\sigma)} = \sum_{i,j} \phi_i^{(\mu)} \phi_j^{(\nu)} (\mu i, \nu j | \sigma s), \quad (2.122)$$

and refer to the elements of the unitary matrix in [Eq. 2.122](#) as *vector-coupling* or *Clebsch-Gordan* coefficients.

Care is needed here, because if  $(\mu\nu\sigma)$  is zero then clearly ([Eq. 2.122](#)) makes no sense, but this can be taken care of at the formal level by defining the vector-coupling coefficient as zero if  $(\mu\nu\sigma)$  is zero. There is also obviously some ambiguity if  $(\mu\nu\sigma)$  is greater than one and it will then be necessary to define some standard ordering. But nevertheless, the ideas are clear enough. The point is that if the irreducible representations of the groups are known then it is always possible to discover the vector coupling coefficients and hence to synthesize product functions that carry irreducible representations. This process is often called vector-coupling and obviously having coupled a pair of functions one can then couple another one to that pair and so on. This technique finds its principal use in dealing with the construction of eigenfunctions of the rotation group, but it is a quite general procedure.

There are many different notations for the vector-coupling coefficients and great care must be exercised in determining just which convention a particular book is using, but it is perhaps appropriate to note that there is a common, pretty standard, notation in terms of the *Wigner 3-j* symbol defined, in our particular notation, so that (with the Wigner symbol as the object in brackets on the right-hand side)

$$(\mu i, \nu j | \sigma s)^* = [\sigma]^{1/2} \begin{pmatrix} \mu & \nu & \sigma \\ i & j & s \end{pmatrix}, \quad (2.123)$$

where  $[\sigma]$  is the dimensionality of the  $\sigma$ th irreducible representation. There are, obviously, different sets of 3-j symbols for every group, but the ones most commonly tabulated are those for the three-dimensional rotation group; they are also available for the crystallographic point groups. Whether one chooses synthetic or projective methods to construct many-particle symmetry functions is a matter of choice in any given problem.

Having considered the transformation properties of functions, consider how these properties may be used in the construction of matrix elements of operators and, from this, consider again how operators themselves transform.



Consider the matrix elements of an arbitrary operator  $A$  between two functions. We symbolize the matrix element  $A_{12}$  by

$$A_{12} = \int \phi_1^*(\mathbf{x}) A \phi_2(\mathbf{x}) d\mathbf{x}, \quad (2.124)$$

where the integral is a definite one over all space and over all coordinates and where  $d\mathbf{x}$  symbolizes the appropriate volume element. Since the variables of integration are dummy we may also write

$$A_{12} = \int \phi_1^*(\mathbf{y}) A' \phi_2(\mathbf{y}) d\mathbf{y}, \quad (2.125)$$

where  $A'$  symbolizes  $A$  made up with  $y$  just as  $A$  was made up with  $\mathbf{x}$ . But now let it be supposed that  $\mathbf{y}$  corresponds to a variable change induced by a transformation so that  $\mathbf{y} = \mathbf{R}^T \mathbf{x}$ . Then

$$A_{12} = \int \bar{\phi}_1^*(\mathbf{x}) \bar{A} \bar{\phi}_2(\mathbf{x}) |\mathbf{R}| d\mathbf{x}, \quad (2.126)$$

where  $\bar{A}$  is the transformed operator as in  $\blacktriangleright$  Eq. 2.98 and  $\bar{\phi}_i$  the transformed function as in  $\blacktriangleright$  Eq. 2.95.  $|\mathbf{R}|$  is the Jacobian of the transformation and since the matrix  $\mathbf{R}$  is orthogonal,  $|\mathbf{R}|$  is  $\pm 1$ . If it is  $-1$  then it can be shown that the signs of the limits change also so that the integral is unchanged and thus  $|\mathbf{R}|$  can always be treated as  $+1$ . Thus  $\blacktriangleright$  Eq. 2.126 may be rewritten as

$$A_{12} = \int \bar{\phi}_1^*(\mathbf{x}) \bar{A} \bar{\phi}_2(\mathbf{x}) d\mathbf{x}. \quad (2.127)$$

Now assume for a moment that  $A$  is  $H$  then of course  $\bar{A}$  is also  $H$  if  $\mathbf{R}$  is a symmetry operator of the problem; thus it is the case that

$$\int \phi_1^* H \phi_2 d\mathbf{x} = \int \bar{\phi}_1^* H \bar{\phi}_2 d\mathbf{x}. \quad (2.128)$$

But suppose it turned out that

$$\bar{\phi}_1 \equiv \mathbf{O}_R \phi_1 = -\phi_1, \quad (2.129)$$

and

$$\bar{\phi}_2 \equiv \mathbf{O}_R \phi_2 = \phi_2,$$

then one would have proved that

$$\int \phi_1^* H \phi_2 d\mathbf{x} = - \int \phi_1^* H \phi_2 d\mathbf{x}, \quad (2.130)$$

and clearly the only way for this to happen is for the integral to vanish. This is a familiar result as is its generalization, namely, that if  $\phi_1$  is a basis function for a particular irreducible representation and  $\phi_2$  is one for another irreducible representation, then the matrix element vanishes unless the direct product of these two representations is reducible to a direct sum of representations which includes the totally symmetric (unit) representation. It should be remembered that although the integral certainly vanishes if the totally symmetric representation is absent, even if this representation is present, the integral could also vanish, for reasons other than the symmetry considered. Thus in the context of the selection rules based on the matrix elements one can say that a particular transition is *forbidden* by symmetry, one cannot say that it is *allowed* by symmetry.

## Spin and Point Group Symmetry

So far spin has not been considered explicitly. It is usual to ignore it in discussions of point group symmetry because the total spin operator is invariant under all point group transformations and the axis orientation is defined by the fixed frame choice so there is a fixed internal choice for the  $z$ -axis. Thus it is regarded as sufficient to require that the spatial part of any trial function has the correct point group symmetry and then to form properly antisymmetric functions from the spatial parts and the spin eigenfunctions in the manner outlined earlier. If orbitals are used to construct the spatial part, then it is usual simply to extend the symmetry orbitals to become symmetry spin-orbitals. Returning to the functional form used in [Eq. 2.116](#) this would become

$$\Phi(\mathbf{x}_1, \mathbf{x}_2, \mathbf{x}_3, \dots, \mathbf{x}_N) = A\phi_1(\mathbf{x}_1)\phi_2(\mathbf{x}_2) \dots \phi_N(\mathbf{x}_N), \quad (2.131)$$

where  $A$  is the projection operator for the antisymmetric representation of the symmetric group of the electrons. It is usually just called the *antisymmetrizer*:

$$A = \frac{1}{N!} \sum_P \epsilon_P O_P,$$

where  $O_P$  is the permutation operator and  $\epsilon_P$  is the parity of the permutation.  $O_P$  operates on the electronic variables and should thus be associated with the inverse of a particular permutation. However since the symmetric group is ambivalent and the representation of interest is one-dimensional this is a distinction without a difference. In the case above where the initial function is an orbital product, the operator can equally well be treated as if it operated on the orbital index.

The space parts of the spin-orbitals  $\phi_i$  and  $\phi_j$  can be the same if the spin parts are different. If any two spin-orbitals are the same the projected function simply vanishes. This vanishing is the basis of what is usually called the ‘‘Pauli exclusion principle.’’ The function ([Eq. 2.131](#)) is clearly a determinant of spin-orbitals with the spin-orbital index designating a row (column) and the electron numbering designating a column (row). This was first recognized by Slater and so such determinants are called *Slater determinants* and often denoted by the shorthand

$$M|\phi_1(\mathbf{x}_1)\phi_2(\mathbf{x}_2) \dots \phi_N(\mathbf{x}_N)|,$$

where  $M$  is a normalizing factor.

Such Slater determinants are not themselves always spin eigenfunctions but they are eigenfunctions of  $S_z$ . They can be either coupled or projected to yield spin eigenfunctions for a particular  $M_s$  value and the resulting functions can then be further projected by the step-up operator

$$S_+ = S_x + iS_y$$

to produce functions with  $M_s + 1$  or the step-down operator

$$S_- = S_x - iS_y$$

to produce functions with  $M_s - 1$ .

The presence of spin in the trial function does not modify the previous point group symmetry discussion. However the requirements of spin and permutational symmetry may mean that a trial function is constrained so that it might not be possible to have a trial function with a particular point group symmetry and a specified spin symmetry. As an example consider a determinant of doubly occupied orbitals for four electrons symbolized as

$$M|\phi_1(\mathbf{r}_1)\alpha(s_1)\phi_1(\mathbf{r}_2)\beta(s_2)\phi_2(\mathbf{r}_3)\alpha(s_3)\phi_2(\mathbf{r}_4)\beta(s_4)|.$$

This determinant is a spin eigenfunction with  $S = 0$ . If the orbitals are point group symmetry orbitals, the only possible symmetry of the many particle function is that generated by the direct product of each orbital symmetry with itself followed by the direct product of the resulting symmetries. If the orbitals belong to one-dimensional irreps then the many particle function must belong to the totally symmetric representation of the point group. It is not possible to represent other symmetries with a function of this form.

## The Construction of Approximate Eigenfunctions of the Clamped Nuclei Hamiltonian

The basic mathematical tool used in the construction of approximate eigenfunctions is the variation theorem. This theorem asserts that for any square integrable function  $\Phi$  which is of a definite and allowed symmetry for the Hamiltonian, the quotient

$$\frac{\int \Phi^* H \Phi d\mathbf{x}}{\int \Phi^* \Phi d\mathbf{x}} = E \geq E_f, \quad (2.132)$$

where  $E_f$  is the lowest energy of the particular symmetry. The function  $\Phi$  is chosen to contain parameters which can be varied to minimize  $E$  to make it as close as possible to  $E_f$ . The function is usually scaled so that the denominator in the quotient is unity and the function with this scaling is said to be *normalized to unity* or just to be *normalized*. If  $\Phi$  is chosen as a linear combination of functions with the coefficients as the parameters then minimizing  $E$  leads to a secular problem the roots of which are upper bounds not only to the lowest states of the particular symmetry, but to excited states of increasing energy. At this stage the secular problem can be approximated and approximations to the eigenfunctions can be developed by perturbation theory.

It is usual to construct approximate solutions to the electronic Schrödinger equation in terms of functions composed of spin-orbitals  $\phi_r(\mathbf{x})$ . In general it is supposed that we have available a set of  $m (\geq N)$  orbitals  $\phi(\mathbf{r})$  and to each of these we attach an  $\alpha(s)$  or  $\beta(s)$  spin factor function to form the spin-orbitals. When we write  $\mathbf{x}$  as a variable designation we shall in future mean space *and* spin variables collectively. We can write formally

$$(\phi_1 \dots \phi_{2m}) = (\alpha \beta) \times (\phi_1 \dots \phi_m) \equiv \phi = \sigma \times \phi, \quad (2.133)$$

where  $\times$  denotes the standard direct (or Kronecker) product of matrices.

The  $N$ -electron functions  $\Phi_k$  are composed of Slater determinants of  $N$  spin-orbitals or perhaps as a fixed linear combination of a number of such determinants. The matrix elements of  $H$  between such functions can be written in terms of one- and two-electron integrals over the spin-orbitals thus

$$H_{kl} \equiv \langle \Phi_k | H | \Phi_l \rangle = \sum_{rs}^{kl} Q_{rs}^1 \langle \phi_r | h | \phi_s \rangle + \frac{1}{2} \sum_{rstu}^{kl} Q_{rs,tu}^2 \langle \phi_r \phi_s | g | \phi_t \phi_u \rangle, \quad (2.134)$$

where the sums go over all spin-orbitals and where  ${}^{kl}Q_{rs}^1$  and the  ${}^{kl}Q_{rs,tu}^2$  are simple coefficients sometimes called *projective reduction coefficients* or *coupling coefficients* or alternatively one- and two-particle *density matrix elements*. These coefficients will of course be zero if any of the spin-orbitals shown in their indices do not occur in the pair of functions considered.

The notation for the one and two-electron integrals is conventional,

$$\langle \phi_r | h | \phi_s \rangle = \int \phi_r^*(\mathbf{r}) h \phi_s(\mathbf{r}) d\mathbf{r}, \quad (2.135)$$

and

$$\langle \phi_r \phi_s | g | \phi_t \phi_u \rangle = \int \phi_r^*(\mathbf{r}_1) \phi_s^*(\mathbf{r}_2) g(\mathbf{r}_1, \mathbf{r}_2) \phi_t(\mathbf{r}_1) \phi_u(\mathbf{r}_2) d\mathbf{r}_1 d\mathbf{r}_2. \quad (2.136)$$

Similarly the overlap matrix elements can be written as

$$M_{kl} \equiv \langle \Phi_k | \Phi_l \rangle = N^{-1} \sum_{rs}^{kl} Q_{rs}^1 \langle \phi_r | \phi_s \rangle. \quad (2.137)$$

Now let it be supposed that from a given set of spin-orbitals all possible functions  $\Phi_k$  are constructed and that the resulting set has  $M$  members. The best wavefunctions that could be obtained from such a set would be a linear combination of these  $M$  terms with coefficients determined using the variation theorem. Use of the variation theorem on such a set leads to the familiar secular problem

$$[\mathbf{H} - E \mathbf{M}] = 0, \quad (2.138)$$

whose solutions give  $M$  eigenvalues  $E_1 \leq E_2 \leq E_3 \dots \leq E_M$  each of which is an upper bound to the first, second, third, and so on exact solution of the electronic Schrödinger problem.

In the special case where the spin-orbitals are orthonormal and the trial functions are Slater determinants the expressions for the projective reduction coefficients are both simple and limited, given by Slater's rules to be discussed in detail in later chapters in this work. With such a choice there are Hamiltonian matrix elements between functions that differ from each other only in two or fewer orbitals and  $M_{kl} = \delta_{kl}$ . The expressions for these coefficients when the orbitals are not orthogonal involve the overlap integrals  $S_{ij}$  between all the orbitals in the functions and there is no limitation on orbital differences between the functions and  $M_{kl}$  is not the unit matrix. Every electronic permutation must be considered in their evaluation. For non-orthogonal orbitals it is thus much more difficult to consider systems with more than a few electrons and, because atomic orbitals on different centers are not orthogonal, this difficulty has hindered the development of VB theory in a quantitative manner until very recently. An account of modern VB developments forms a later part of this handbook. Usually LCAO MOs are developed so as to be orthogonal so that given

$$\phi_i = \sum_{p=1}^m \eta_p C_{pi} \quad i = 1, 2, 3 \dots, m, \quad (2.139)$$

to evaluate the two-electron integral  $\langle \phi_i \phi_j | g | \phi_k \phi_l \rangle$  involves evaluating all the two-electron integrals  $\langle \eta_r \eta_s | g | \eta_t \eta_u \rangle$  and summing. To transform all the two-electron integrals would seem at first sight to involve  $m^8$  multiplications and additions and thus put it beyond computational possibility for anything other than a small number of orbitals. However it actually needs operations only of the order of  $m^4$ , which is bad enough, but can be dealt with.

Although it proved possible to develop the LCAO method with Slater orbitals for diatomic molecules, the evaluation of two-electron integrals when the atomic orbitals were centered on three or four distinct nuclei proved very difficult and is not, even now, commonly undertaken. However it proved possible by the use of Gaussian functions, as pioneered by McWeeny (1950) and developed by Boys (1950) in the 1950s to evaluate the two-electron integrals swiftly and to high precision. Tests on atoms and diatoms showed that although many more Gaussian functions were required to obtain results comparable with a given set of Slater orbitals, the

computational time involved was not much longer. Results using Gaussian functions are now regarded as standard for polyatomic systems.

For ease of exposition we shall for the moment assume that the orbitals  $\phi_r$  are orthonormal so that the spin-orbitals are also orthonormal. If the  $\Phi_k$  are then chosen as normalized Slater determinants or proper linear combinations of them, they too may be chosen to be an orthonormal set so that  $M_{kl} = \delta_{kl}$ . The secular problem then simplifies to

$$|\mathbf{H} - E \mathbf{1}_M| = 0, \quad (2.140)$$

and this is the form that is typically taken in a CI calculation with orthonormal MOs  $\phi_r$  and orthonormal configuration functions  $\Phi_k$ , while  $\blacktriangleright$  Eq. 2.138 is the form typically taken in a VB calculation where, in general, neither the orbitals nor the structure functions are orthonormal.

Let us consider what happens if we subject the spin functions to the transformations

$$\sigma \rightarrow \sigma \mathbf{U}(2), \quad (2.141)$$

and the orbitals to the transformations

$$\phi \rightarrow \phi \mathbf{U}(m), \quad (2.142)$$

where  $\mathbf{U}(n)$  is an  $n \times n$  unitary matrix. In this case the spin-orbitals change

$$\begin{aligned} \phi \rightarrow \phi' &= \sigma \mathbf{U}(2) \times \phi \mathbf{U}(m) \\ &= (\sigma \times \phi)(\mathbf{U}(2) \times \mathbf{U}(m)), \end{aligned} \quad (2.143)$$

and it is easy to show that the  $\phi'$  form an orthonormal set still.

If we now make up the  $M$  functions  $\Phi_k$  but using the spin-orbitals  $\phi'_k$  rather than the  $\phi_k$ , it is easy to show that the  $\Phi'_k$  continue to form an orthonormal set because the  $\phi_r$  are orthonormal. Since the set  $\Phi_k$  is complete, this means that the  $\Phi'_k$  are at most a unitary transformation of the  $\Phi_k$ , that is:

$$\Phi'_k = \sum_{n=1}^M \Phi_n U_{nk}(M), \quad (2.144)$$

where  $\mathbf{U}(M)$  is an  $M \times M$  unitary matrix. This in turn implies that the matrix  $\mathbf{H}$  is transformed as

$$\mathbf{H} \rightarrow \mathbf{H}' = \mathbf{U}^\dagger(M) \mathbf{H} \mathbf{U}(M). \quad (2.145)$$

The new secular problem is, therefore,

$$|\mathbf{H}' - E \mathbf{1}_M| = 0, \quad (2.146)$$

which can be rewritten as

$$|\mathbf{U}^\dagger(M)(\mathbf{H} - E \mathbf{1}_M)\mathbf{U}(M)| = 0, \quad (2.147)$$

and using the property

$$|\mathbf{A}\mathbf{B}| = |\mathbf{A}||\mathbf{B}|$$

of determinants of square matrix products it follows at once that the secular problem ( $\blacktriangleright$  Eq. 2.147) is identical with the secular problem ( $\blacktriangleright$  Eq. 2.140). Thus the energies are completely unchanged by this unitary transformation.

All possible unitary matrices of a given dimension, say  $n$ , form a group under matrix multiplication, a group that is usually written as  $U(n)$  and thus we can say that the secular problem is invariant under the operations that constitute the group  $U(2) \times U(m)$ .

It is wrong to think of this group as a transformation group in the same way as a point group. There is no coordinate transformation that corresponds to the unitary transformation on the orbital space. In this case the transformation on the function space is all that there is, the unitary matrices do not “correspond” to anything though of course, one can assert that each matrix formally represents a particular unitary operator if one wishes. If one does think in this way then we can regard the result that has just been shown as a very weak form of a fundamental result due to Wigner who showed that unitary invariance is a very deep invariance in any quantum mechanics based on square integrable eigenfunctions.

At one level the result just shown is quite useless because for  $m$  reasonably large  $M$  is astronomical. One can refine the result a little to make  $M$  less big, for one can show that if one starts off with a set of determinants each containing  $N_\alpha$   $\alpha$ -spin-orbitals and  $N_\beta$   $\beta$ -spin-orbitals ( $N_\alpha + N_\beta = N$ ) so that  $M_s = (N_\alpha - N_\beta)/2$  for every determinant, then it is sufficient to include only transformed functions with the same  $M_s$  value. Further one can show that if one starts off with functions which are fixed linear combinations of determinants which are spin eigenfunctions (i.e., have a particular expectation value  $S$  say, of  $S^2$ ), then again one only need consider the transformed functions that preserve  $S$ . But to give some idea of how big the  $M$  can be, the following figures are relevant. For a system where the number of electrons,  $N$ , is equal to 10 (as in  $\text{H}_2\text{O}$ ) and the number of orbitals,  $m$ , is equal to 30, the total number of determinants  $M$  is  $7.54 \times 10^{10}$ . If the process is restricted to those functions for which  $M_s = 0$ ,  $M$  drops to  $2.03 \times 10^{10}$  and if the process is further restricted to those functions for which  $S = 0$  then  $M$  becomes  $4.04 \times 10^9$ .

Clearly it is not possible to compute all the matrix elements and then to solve the secular problem. However it is possible to utilize the group theoretical results in the design of computational methods that yield tractable problems. The key to the connection between matrix element evaluation and the unitary group  $U(m)$  is because the Hamiltonian can be expressed in terms of the generators of this group. The spatial parts of the trial functions can be chosen to provide a basis for irreducible representations of  $U(m)$  corresponding to a particular choice of  $S$  and of  $M_s$  for spin symmetry by the use of *Weyl tableaux*. The required Young diagram for the particular choice of  $S$  and of  $M_s$  is constructed and then the conjugate diagram written down. Into this diagram the orbital indices are put in such a way that across any row the indices are nondecreasing and down any column they are strictly increasing. The resulting tableaux are the Weyl tableaux and each tableau labels a basis function for an irreducible representation of the group  $U(m)$  of dimension equal to the total number of tableaux. Thus for a three electron problem using four orbitals, choosing the Young diagram [2 1] would yield 20 distinct Weyl tableaux. Rather convenient rules may then be specified for matrix elements between such functions. This approach will be considered more fully later in this work.

There is, however, one particularly simple and commonly useful case that is appropriate to consider here. That is the case where the trial wavefunction is simply a single Slater determinant of doubly occupied orbitals and it is a commonly useful form because many molecules have an even number of electrons and their electronic ground states are, in many cases, totally symmetric singlet states. The expected value of the Hamiltonian for such a trial function is

$$E = 2 \sum_r \langle \phi_r | h | \phi_r \rangle + \sum_{rs} (2 \langle \phi_r \phi_s | g | \phi_r \phi_s \rangle - \langle \phi_r \phi_s | g | \phi_s \phi_r \rangle), \quad (2.148)$$

where the sum is over orbitals, the spin having been integrated out leaving only the spatial integrations to be performed. Using the form (► Eq. 2.139) for the orbitals  $E$  may be written as

$$E = 2tr\mathbf{hR} + tr\mathbf{GR},$$

where

$$h_{ij} = \langle \eta_i | \mathbf{h} | \eta_j \rangle,$$

$$R_{ij} = \sum_r C_{ir} C_{jr},$$

$$G_{ij} = 2J_{ij} - K_{ij}, \quad J_{ij} = \sum_{kl} R_{kl} \langle \eta_i \eta_k | \mathbf{g} | \eta_j \phi_l \rangle, \quad K_{ij} = \sum_{kl} R_{kl} \langle \eta_i \eta_k | \mathbf{g} | \eta_l \phi_j \rangle.$$

It can then be shown that the elements of  $\mathbf{C}$  that minimize the energy can be obtained by solving the generalized eigenvalue problem

$$\mathbf{h}^F \mathbf{C} = \mathbf{s} \mathbf{C} \boldsymbol{\epsilon},$$

where

$$\mathbf{h}^F = \mathbf{h} + \mathbf{G}, \quad S_{ij} = \langle \eta_i | \eta_j \rangle,$$

and  $\boldsymbol{\epsilon}$  is a diagonal matrix with the orbital energies  $\epsilon_r$  along the diagonal.

Because the construction of  $\mathbf{h}^F$  involves a knowledge of  $\mathbf{C}$  the construction of eigenvalues must start with a first guess at  $\mathbf{C}$  too, obtain an improved guess, and be continued until no further improvement occurs. There are a number of ways in which this may be done but a popular way is simply to solve the generalized eigenvalue problem iteratively. This scheme has given the name self-consistent field (SCF) to the method generally. The contributions of Hartree and of Fock to its development are sometimes acknowledged by denoting it the HF SCF method.

The SCF method is, at present, the most widely used method in computational chemistry and forms a central feature of all the commonly available computer packages for computational chemistry. Provided that the basis of AOs is full enough, the resulting functions yield energies that are often sufficiently good to enable meaningful distinctions to be made between molecules with different nuclear geometries and so to aid the interpretation of spectroscopic results and reaction mechanisms. However the basis of AOs cannot be made too large because of the number of electron repulsion integrals that must be computed and the difficulties of storing and manipulating these.

It is seen, however, that the distinctive feature in the calculation of the electronic energy is the potential term  $V(i)$ , all the other terms being of precisely the same form whatever the geometry of a given molecule and between molecules. The potential depends only upon the coordinates of a single particle and thus can be realized in terms of one-particle integrals. This is usually expressed by saying that the potential depends only upon the one-particle density functional. It was shown by Hohenberg and Kohn (1964) that the electronic energy depended on the density functional in a unique way and that, if the density functional was known, then so was the energy. This result has led to the development of variants on the SCF method which involve approximations to the density functional form and require many fewer integral evaluations than does the direct use of an LCAO MO SCF method. Thus much larger molecules can be tackled in this approach than would otherwise be possible.

## Conclusions

It seems fair to say that if one treats the nuclei as distinguishable particles and takes the sum of the electronic energy obtained as an eigenvalue of the clamped nuclei Hamiltonian and the classical nuclear repulsion energy as a potential, the geometrical structure of the minimum in

such a potential can be identified as the equilibrium molecular geometry. This can be done without appeal to the chemical bond, and without recognition of functional groups. Certain aspects of the transition state theory of chemical reactions can be rationalized in terms of structures anticipated using the potential at geometries away from the equilibrium one. If the occurrence of polar molecules is considered to be an aspect of molecular structure, polar molecules can be recognized from fixed nuclei electronic structure calculations by means of a dipole moment calculated as the sum of the electronic dipole and the classical nuclear dipole. And there are many other ways in which quantum mechanics formulated with the requirement that the nuclei may be treated as distinguishable clamped particles has been effectively used to illuminate chemical behavior.

However, even if this approach is regarded as giving a satisfactory account of chemical structure, it still remains to justify by full quantum mechanical means the treatment of the nuclei that it involves. But at present such a justification still eludes us. It may be in the future that the multiple well approach to nuclear permutational symmetry will be shown to be properly founded and thus the eigenvalues of the molecular Hamiltonian<sup>10</sup> to be just those anticipated from the previous approach; even so one will still be left with eigenfunctions which exhibit full permutation and rotation-inversion symmetry and it seems impossible to anticipate anything at all like classical chemical structure from these using the standard quantum mechanical machinery.

An obvious objection to this discussion is that the full symmetries of the Coulomb Hamiltonian we have been discussing are manifested necessarily by its stationary states, whereas chemists are concerned with time-dependent states that may exhibit less symmetry. The time-dependent Schrödinger equation simply describes unitary time evolution of a prior state and will not change symmetries; any given initial state is the result of some previous time evolution so what is required is a quantum mechanical theory of initial states that are consistent with chemistry; about that nothing is known. The most that it seems possible to say is that chemical structure can be teased out in terms of a chosen ansatz (the imposition of fixed, distinguishable nuclei) if one has a good idea of what one is looking for. It seems unlikely that one would ever guess that it was there in the full Coulomb Hamiltonian for a molecular formula unless one had decided on its presence in advance.

## References

- Born, M., & Huang, K. (1955). *Dynamical theory of crystal lattices*. Oxford: Oxford University Press.
- Born, M., & Oppenheimer, J. R. (1927). Zur Quantentheorie der molekeln. *Annalen der Physik*, 84, 457.
- Boys, S. F. (1950). Electronic wave functions. I. A general method of calculation for the stationary states of any molecular system. *Proceedings of the Royal Society of London. Series A, Mathematical and Physical Sciences*, 200, 542.
- Cassam-Chenai, P. (2006). On non-adiabatic potential energy surfaces. *Chemical Physics Letters*, 420, 354.
- Collins, M. A., & Parsons, D. F. (1993). Implications of rotation-inversion-permutation invariance for analytic molecular potential energy surfaces. *The Journal of Chemical Physics*, 99, 6756.
- Combes, J. M., & Seiler, R. (1980). Spectral properties of atomic and molecular systems. In R. G. Woolley (Ed.), *Quantum dynamics of molecules*. NATO ASI B57 (p. 435). New York: Plenum.
- Czub, J., & Wolniewicz, L. (1978). On the non-adiabatic potentials in diatomic molecules. *Molecular Physics*, 36, 1301.
- Deshpande, V., & Mahanty, J. (1969). Born-Oppenheimer treatment of the hydrogen atom. *American Journal of Physics*, 37, 823.

<sup>10</sup>The Coulomb Hamiltonian for the electrons and nuclei specified by the molecular formula.



- Fock, V. (1930). Näherungsmethode zur Lösung des quantenmechanischen Mehrkörperproblems. *Zeitschrift für Physik*, 61, 126.
- Frolov, A. M. (1999). Bound-state calculations of Coulomb three-body systems. *Physical Review A*, 59, 4270.
- Hagedorn, G., & Joye, A. (2007). Mathematical analysis of Born–Oppenheimer approximations. In F. Gesztesy, P. Deift, C. Galvez, P. Perry, & W. Schlag. (Eds.), *Spectral theory and mathematical physics: A festschrift in honor of Barry Simon's 60th birthday* (p. 203). London: Oxford University Press.
- Handy, N. C., & Lee, A. M. (1996). The adiabatic approximation. *Chemical Physics Letters*, 252, 425.
- Hartree, D. R. (1927). The wave mechanics of an atom with a non-Coulomb central field. Part I. Theory and methods. *Mathematical Proceedings of the Cambridge Philosophical Society*, 24, 89.
- Hartree, D. R., & Hartree, W. (1936). Self-consistent field, with exchange, for beryllium. II. The  $(2s)(2p)^3P$  and  $^1P$  excited states. *Proceedings of the Royal Society of London. Series A, Mathematical and Physical Sciences*, 154, 588.
- Heitler, W., & London, F. (1927). Wechselwirkung neutraler Atome und homöopolare Bindung nach der Quantenmechanik. *Zeitschrift für Physik*, 44, 455.
- Herrin, J., & Howland, J. S. (1997). The Born–Oppenheimer approximation: Straight-up and with a twist. *Reviews in Mathematical Physics*, 9, 467.
- Hinze, J., Aljiah, A., & Wolniewicz, L. (1998). Understanding the adiabatic approximation; The accurate data of  $H_2$  transferred to  $H_3^+$ . *Polish Journal of Chemistry*, 72, 1293.
- Hohenberg, P., & Kohn, W. (1964). Inhomogeneous electron gas. *Physical Review*, 136, 864.
- Hunter, G. (1975). Conditional probability amplitudes in wave mechanics. *International Journal of Quantum Chemistry*, 9, 237.
- Hunter, G. (1981). Nodeless wave functions and spiky potentials. *International Journal of Quantum Chemistry*, 19, 755.
- Kato, T. (1951). On the existence of solutions of the helium wave equation. *Transactions of the American Mathematical Society*, 70, 212.
- Klein, M., Martinez, A., Seiler, R., & Wang, X. P. (1992). On the Born–Oppenheimer expansion for polyatomic molecules. *Communications in Mathematical Physics*, 143, 607.
- Kołos, W., & Wolniewicz, L. (1963). Nonadiabatic theory for diatomic molecules and its application to the hydrogen molecule. *Reviews of Modern Physics*, 35, 473.
- Kutzelnigg, W. (2007). Which masses are vibrating or rotating in a molecule? *Molecular Physics*, 105, 2627.
- Longuet-Higgins, H. C. (1963). The symmetry groups of non-rigid molecules. *Molecular Physics*, 6, 445.
- McWeeny, R. (1950). Gaussian approximations to wave functions. *Nature*, 166, 21.
- Mohallem, J. R., & Tostes, J. G. (2002). The adiabatic approximation to exotic leptonic molecules: Further analysis and a nonlinear equation for conditional amplitudes. *Journal of Molecular Structure: Theochem*, 580, 27.
- Mulliken, R. S. (1931). Bonding power of electrons and theory of valence. *Chemical Reviews*, 9, 347.
- Nakai, H., Hoshino, M., Miyamoto, K., & Hyodo, S. (2005). Elimination of translational and rotational motions in nuclear orbital plus molecular orbital theory. *The Journal of Chemical Physics*, 122, 164101.
- Pauling, L. (1939). *The nature of the chemical bond*. Ithaca: Cornell University Press.
- Roothaan, C. C. J. (1951). New developments in molecular orbital theory. *Reviews of Modern Physics*, 23, 69.
- Slater, J. C. (1930). Note on Hartree's method. *Physical Review*, 35, 210.
- Sutcliffe, B. T. (2000). The decoupling of electronic and nuclear motions in the isolated molecule Schrödinger Hamiltonian. *Advances in Chemical Physics*, 114, 97.
- Sutcliffe, B. T. (2005). Comment on "Elimination of translational and rotational motions in nuclear orbital plus molecular orbital theory". *The Journal of Chemical Physics*, 123, 237101.
- Sutcliffe, B. T. (2007). The separation of electronic and nuclear motion in the diatomic molecule. *Theoretical Chemistry Accounts*, 118, 563.
- Thirring, W. (1981). *Quantum mechanics of atoms and molecules. A course in mathematical physics* (Vol. 3, E. M. Harrell, Trans.). Berlin: Springer.
- Wilson, E. B. (1979). On the definition of molecular structure in quantum mechanics. *International Journal of Quantum Chemistry*, 13, 5.
- Woolley, R. G., & Sutcliffe, B. T. (1977). Molecular structure and the Born–Oppenheimer approximation. *Chemical Physics Letters*, 45, 393.

# 3 Remarks on Wave Function Theory and Methods

Dariusz Kędziera<sup>1</sup> · Anna Kaczmarek-Kędziera<sup>2</sup>

<sup>1</sup>Department of Chemistry and Photochemistry of Polymers, Nicolaus Copernicus University, Toruń, Poland

<sup>2</sup>Department of Chemistry, Nicolaus Copernicus University, Toruń, Poland

<i>Introduction – What and Why?</i> .....	56
<i>Quantum Mechanics for Dummies</i> .....	57
<i>On the Way to Quantum Chemistry</i> .....	63
<i>Variational Principle – An Indicator</i> .....	66
<i>Perturbation Calculus – The Art of Estimation</i> .....	66
<i>One-Electron Approximation – Describe One and Say Something About All</i> .....	70
<i>Hartree–Fock Method – It Is Not that Sophisticated</i> .....	74
<i>Møller–Plesset Perturbation Theory – HF Is Just the Beginning</i> .....	78
<i>Beyond the HF Wave Function</i> .....	84
<i>Coupled Cluster Approximation – The Operator Strikes Back</i> .....	88
<i>Conclusions</i> .....	92
<i>Acknowledgments</i> .....	93
<i>References</i> .....	93

**Abstract:** Methods of computational chemistry seem to often be simply a melange of undecipherable acronyms. Frequently, the ability to characterize methods with respect to their quality and applied approximations or to ascribe the proper methodology to the physicochemical property of interest is sufficient to perform research. However, it is worth knowing the fundamental ideas underlying the computational techniques so that one may exploit the approximations intentionally and efficiently. This chapter is an introduction to quantum chemistry methods based on the wave function search in one-electron approximation.

## Introduction – What and Why?

---

Quantum chemistry is a branch of science originating from quantum mechanics that focuses on investigations of chemical systems. The mathematical roots of quantum chemistry allow it to be treated as a methodology for solving an eigenvalue equation for operators or – even simpler – finding solutions for some differential equations. We cannot totally escape this way of thinking, since this is how things really are. However, a chemist will comprehend quantum chemistry more as a helping tool in experimental work, supporting description of chemical reactions. A tool that plays a role similar to a spectrophotometer or a chromatographic column. A tool that can provide information about the system under consideration. A powerful tool, the popularization of which was achieved thanks to the fast progress of computer power and the hard work of people who made the transformation from pure theory to computer programs possible. Their efforts were appreciated – in 1998, the Nobel Prize was awarded to Walter Kohn “for his development of the density functional theory” and John Pople “for his development of computational methods.”

From the point of view of the experimentalist, the apparatus of quantum chemistry can be perceived similarly as the NMR spectrometer. One knows that the quality of the obtained NMR spectrum depends not only on the magnetic field of the magnet but also on the signal-processing capabilities. To successfully use NMR spectroscopy in experimental work, detailed knowledge about the technology of production and preparation of the magnets and electronic equipment is not a requisite. It is enough to keep in mind that with the given frequency one gets corresponding accuracy and information. All the rest is simply skill in sample preparation and expertise in spectrum interpretation. For effective usage of computational techniques of quantum chemistry, one must be aware of applied approximation to tune the accuracy of calculations and possess knowledge of the physicochemical phenomenon one wants to describe.

The aim of the present chapter is to provide a gentle introduction to basic quantum chemistry methods – the methods of solving the electronic Schrödinger equation. The chapter is intended for people starting their adventure with computational chemistry and wanting it to become the tool, not the aim itself.

When discussing quantum chemistry, we cannot totally avoid quantum mechanics. However, let us use another comparison: Traveling abroad it is good to know some basic expressions in the local language of the country you go to. It makes life easier and gives pleasure in interpersonal contacts. Still, no one expects a tourist to speak a language as fluently as a native speaker. Therefore, to efficiently apply computational techniques in experimental research one has to learn some basic quantum mechanical terms that will help during the journey through the remainder of this chapter.

## Quantum Mechanics for Dummies

We will begin with the basic terms of quantum mechanics. In this section, they will be introduced in an intuitive manner, to enable understanding of the next sections' content, even by beginners.

We consider a system of  $N$  electrons in the field produced by the potentials arising from nuclei (the nuclei are not treated as particles consisting of nucleons but just as a point source of the electrostatic potential). We are interested only in one particular case:

- The probability of finding the electrons of the considered system on the infinite distance from the nuclei is equal to zero. In other words, we want our system to constitute the whole entirety, not breaking into separate and independent parts (this would be the case of the interaction of two electrons with no attraction – two negative charges would repel each other to infinity).
- The energies of this system constitute the discrete spectrum.
- We want to know only the lowest value of energy (the wider approach can be found in the next volume of the present book).

With such limitations, we do not need to consider all of the different general cases and can simply concentrate on the bound state chemistry.

A central notion in quantum chemistry is a wave function. This is a function characterizing a state of the system. Therefore, it depends on the variables that are adequate for the given system. This means that the wave function has to depend, at least, on spatial coordinates describing motions of the particles in the investigated system. Moreover, the wave function depends on so-called spin variables (spin is an additional degree of freedom included a posteriori in nonrelativistic quantum mechanics). This spin dependency can be built into the wave function by introducing a spin function. For instance, for the electron with a label 1 its wave function depends on the spatial coordinates  $x_1$ ,  $y_1$ , and  $z_1$  and is multiplied by the spin function  $\alpha(\sigma_1)$  or  $\beta(\sigma_1)$ , where  $\sigma_1$  is a spin variable. The spin functions must fulfill the following requirements:

$$\int \alpha^*(\sigma_1)\alpha(\sigma_1)d\sigma_1 = \int \beta^*(\sigma_1)\beta(\sigma_1)d\sigma_1 = 1, \quad (3.1)$$

$$\int \alpha^*(\sigma_1)\beta(\sigma_1)d\sigma_1 = \int \beta^*(\sigma_1)\alpha(\sigma_1)d\sigma_1 = 0, \quad (3.2)$$

where the integration is carried out over the spin variable, which can be treated as the integration variable only. Such a construction may seem to be somehow unnatural; however, it is a convenient way of ascribing spins to the electrons without dealing with its origins.

In general, the wave function must depend on time to reproduce information about the time evolution of the system. However, since we are interested only in the ground state of the system, we can neglect the time dependency. Considering the bound state is equivalent to imposing the condition of the square integrability of the wave function. The integral over all variables in the full range must exist,

$$\int \int \dots \int f^* f d\tau = q, \quad (3.3)$$

where  $q$  is a finite real number. An asterisk under the integral denotes the complex conjugate; it comes from the fact that the wave function can be complex in general. The square-integrability

condition ensures that the wave function vanishes for the infinite values of all spatial variables, and, therefore, that our molecule is kept together. In the above expression, the integration intervals and the integration variables are not stated explicitly. For the investigated  $N$ -electron system, the wave function depends on the  $3N$  spatial variables (for each particle  $i$  we have  $x_i$ ,  $y_i$ , and  $z_i$  coordinates) and additionally  $N$  spin variables ( $\sigma_i$  for the particle  $i$ ):

$$f = f(x_1, y_1, z_1, \sigma_1, x_2, y_2, z_2, \sigma_2, \dots, x_N, y_N, z_N, \sigma_N). \quad (3.4)$$

The volume element in this  $4N$ -dimensional space is

$$d\tau = dV \cdot d\sigma, \quad (3.5)$$

where the spatial part can be written as

$$dV = dx_1 dy_1 dz_1 dx_2 dy_2 dz_2 \dots dx_N dy_N dz_N, \quad (3.6)$$

and the spin part is

$$d\sigma = d\sigma_1 d\sigma_2 \dots d\sigma_N. \quad (3.7)$$

The spatial variables change from  $-\infty$  to  $\infty$  and spin variables can take allowed values. One can see that writing all of the integrals, variables, and volume elements explicitly takes time and a lot of paper, even for relatively small systems. Therefore, one usually keeps them in mind, not writing them down.

The wave function contains all of the information about the state of the system. In order to extract it, operators are applied. An operator can be understood by an analogy to a function. The function ascribes a number to a number and the operator ascribes a function to another function. In other words, the operator is a recipe for how to obtain one function from another:

$$\hat{A}f = g. \quad (3.8)$$

We will denote operators by hats above the symbol to distinguish them from functions and numbers. One of the particularly interesting cases is when the function  $g$  is proportional to the function  $f$ ,

$$g = af, \quad (3.9)$$

where  $a$  is a number. Then [Eq. 3.8](#) takes the form

$$\hat{A}f = af. \quad (3.10)$$

[Equation 3.10](#) is called an eigenvalue equation of the operator  $\hat{A}$ . The function  $f$  fulfilling this equation is called an eigenfunction and  $a$  is an eigenvalue of the operator  $\hat{A}$ . The Schrödinger equation,

$$\hat{H}\Psi = E\Psi, \quad (3.11)$$

is a typical eigenvalue equation in which the Hamilton operator  $\hat{H}$  extracts the information about the energy  $E$  of the system from the wave function  $\Psi$ .

Like in the case of the wave function, we will not consider operators in general. Let us concentrate on the Hamilton operator and its properties to simplify our discussion. We need our operators ascribed to observables (Hamiltonian among others) to satisfy the following requirements:

- Linearity – the operators must fulfill the condition

$$\hat{A}(\alpha f + \beta g) = \alpha \hat{A}f + \beta \hat{A}g, \quad (3.12)$$

where now  $\alpha$  and  $\beta$  are numbers. This seems simple and obvious, however, it is not the property of all operators. For instance, the square root is not a linear operator, since the square root of the sum is not equal to the sum of the square roots.

- Real eigenvalues – only real values can be measured in a laboratory.

For these reasons, we will be interested in so-called Hermitian operators that can be defined by the relation

$$\int \int \dots \int f_1^* (\hat{A}f_2) d\tau = \int \int \dots \int f_2 (\hat{A}f_1)^* d\tau. \quad (3.13)$$

All the functions, variables, and integration intervals remain the same as in [Eq. 3.3](#). Writing of all these things in the expressions was already troublesome enough, and things become even more complicated when operators appear. In order to make life easier, Dirac notation can be applied. In this notation [Eq. 3.13](#) has the form

$$\langle f_1 | \hat{A} f_2 \rangle = \langle \hat{A} f_1 | f_2 \rangle, \quad (3.14)$$

where the left-hand side can be equivalently written as  $\langle f_1 | \hat{A} | f_2 \rangle$ , and the integral of [Eq. 3.3](#) becomes simply

$$\langle f | f \rangle = q. \quad (3.15)$$

In this very convenient notation it is also assumed that the integration intervals and variables flow from the context.

Let us look at Hermitian operators more carefully, considering them in the example of Hamiltonian. It has already been mentioned that such operators have real eigenvalues. Furthermore, the eigenfunctions of the Hermitian operator that correspond to different eigenvalues are orthogonal. In other words, for

$$\hat{H}f_1 = E_1 f_1 \quad \text{and} \quad \hat{H}f_2 = E_2 f_2, \quad (3.16)$$

where  $E_1 \neq E_2$  one has

$$\langle f_1 | f_2 \rangle = \langle f_2 | f_1 \rangle = 0. \quad (3.17)$$

This will be a very useful property, since it will cause various terms in complicated expressions to vanish. In the case of degeneration, or, in other words, when one of the eigenvalues corresponds to two or more eigenfunctions, the eigenfunctions  $f_1$  and  $f_2$  can be orthogonalized.

It is worth considering the integral

$$\langle f_1 | \hat{H} | f_1 \rangle. \quad (3.18)$$

Since  $f_1$  is the eigenfunction of  $\hat{H}$  with the eigenvalue  $E_1$ , it is obvious that

$$\langle f_1 | \hat{H} | f_1 \rangle = \langle f_1 | E_1 f_1 \rangle = E_1 \langle f_1 | f_1 \rangle. \quad (3.19)$$

It would be certainly more convenient if the result was a single number – the eigenvalue  $E_1$ . This would be the case if  $\langle f_1 | f_1 \rangle = 1$ , or if we say the function  $f_1$  was normalized to unity. It would be consistent with the interpretation of the integral  $\langle f_1 | f_1 \rangle$  as the probability of finding the system in the whole space – it should be surely equal 1. This is a very handy requirement. Any function that does not possess this property can be normalized by multiplying by the normalization factor  $\mathcal{N} = 1/\sqrt{\langle f_1 | f_1 \rangle}$ . Then, the new function  $\tilde{f}_1$  will be given as

$$\tilde{f}_1 = \mathcal{N} f_1. \quad (3.20)$$

This new function  $\tilde{f}_1$  is also an eigenfunction of the Hamiltonian, since  $f_1$  was only divided by the number  $\sqrt{\langle f_1 | f_1 \rangle}$  and Hamiltonian is linear:

$$\widehat{H}\tilde{f}_1 = \widehat{H}\mathcal{N}f_1 = \mathcal{N}\widehat{H}f_1 = \mathcal{N}E f_1 = E\mathcal{N}f_1 = E\tilde{f}_1. \quad (3.21)$$

In the case of unnormalized functions, the expression for the eigenvalue  $E_1$  can be obtained from  $\blacktriangleright$  Eq. 3.19:

$$E_1 = \frac{\langle f_1 | \widehat{H} | f_1 \rangle}{\langle f_1 | f_1 \rangle}. \quad (3.22)$$

However, many of the applied functions are not the eigenfunctions of the Hamiltonian. Therefore, let us investigate another interesting integral,

$$\langle g | \widehat{H} | g \rangle, \quad (3.23)$$

where  $g$  is not an eigenfunction of  $\widehat{H}$ . In order to calculate this integral, an alternate important property of the Hermitian operators needs to be exploited: the fact that their eigenfunctions constitute a complete basis set. Each function depending on the same variables as the eigenfunctions can be expressed as the linear combination of the basis functions. Now, this concept seems to be hard-core mathematics, however, anybody using computational techniques knows well that the two things one must input to the ab initio program are the method and the basis set. Hence, let us make a break from the general considerations of operators and abstract space functions and concentrate for a while on the basis set concept in the example of simple trigonometric functions.

In a calculus course, one learns how to express a function using a set of other functions. For example, consider  $\sin x$  function and expand it in the Taylor series around 0:

$$\sin x = \sum_{i=1}^{\infty} \frac{(-1)^{i-1}}{(2i-1)!} x^{2i-1} = x - \frac{x^3}{3!} + \frac{x^5}{5!} - \dots \quad (3.24)$$

In  $\blacktriangleright$  Eq. 3.24,  $\sin x$  function is expressed in the basis set of monomials:

$$\sin x = \sum_{k=1}^{\infty} c_k x^k, \quad (3.25)$$

where  $c_k$  are the expansion coefficients that need to be determined. In our case it is simple, since  $c_k$  result directly from the Taylor expansion and are equal:

$$c_k = \begin{cases} \frac{(-1)^{(k-1)/2}}{k!} & \text{for odd } k, \\ 0 & \text{for even } k. \end{cases} \quad (3.26)$$

The summation in  $\blacktriangleright$  Eqs. 3.24 and  $\blacktriangleright$  3.25 goes from 1 to  $\infty$ . In practice, finite and possibly short expansions are applied:

$$F_n(x) = \sum_{i=1}^n c_i x^i. \quad (3.27)$$

This truncation of the series introduces an approximation to our function.

Let us analyze the  $\sin x$  function in the range  $x \in \langle -\frac{\pi}{2}; \frac{\pi}{2} \rangle$ . The standard deviation works well as the accuracy measure:

$$\sigma_n = \sqrt{\int_{-\frac{\pi}{2}}^{\frac{\pi}{2}} (\sin x - F_n(x))^2 dx}. \quad (3.28)$$

■ Table 3-1

Taylor expansion of  $\sin x$  function and standard deviation for various expansion lengths

$n$	$F_n$	$\sigma_n$
1	$x$	$3.93 \cdot 10^{-1}$
3	$x - \frac{1}{6}x^3$	$4.05 \cdot 10^{-2}$
5	$x - \frac{1}{6}x^3 + \frac{1}{120}x^5$	$2.08 \cdot 10^{-3}$
7	$x - \frac{1}{6}x^3 + \frac{1}{120}x^5 - \frac{1}{5,040}x^7$	$6.39 \cdot 10^{-5}$

► Table 3-1 summarizes data for small  $n$  values. Increasing the number of expansion terms causes a decrease of the standard deviation values and more accurate representation of the original  $\sin x$  function. Given the required accuracy of the calculation, the necessary value length of the expansion,  $n$ , can be found.

The following question arises: why use Taylor expansion instead of  $\sin x$  function itself, if one needs to worry about the expansion accuracy? The answer is straightforward: simplifications and savings. It is much easier to operate on the polynomials than on the trigonometric functions (for instance, the integral  $\int (x^i)^2 dx$  is much easier to handle than  $\int \sin^2 x dx$ ). Moreover, the required accuracy can often be obtained with a relatively short expansion.

Let us now make the considerations more general. As was stated before, the set of eigenfunctions of the Hermitian operator  $\hat{H}$  is complete and orthonormal – functions are orthogonal and normalized:

$$\forall_{i,j} \langle f_i | f_j \rangle = \delta_{ij}, \quad (3.29)$$

where  $\delta_{ij}$  is a Kronecker symbol that takes value 1 for  $i = j$  and 0 otherwise. The basis set completeness means that each function depending on the same set of variables can be expressed by the basis functions:

$$g = \sum_{i=1}^{\infty} c_i f_i, \quad (3.30)$$

where coefficients  $c_i$  need to be found. Knowing the normalized  $g$  function makes this task simple, because of the orthonormality of the  $\{f_i\}$  set, the coefficients will be equal:

$$c_i = \langle f_i | g \rangle, \quad (3.31)$$

since

$$\langle f_i | g \rangle = \sum_{j=1}^{\infty} c_j \langle f_i | f_j \rangle = \sum_{j=1}^{\infty} c_j \delta_{ij} = c_i. \quad (3.32)$$

(Only one term for  $i = j$ ,  $c_i$ , remains, all other vanish for the Kronecker delta equals zero if  $i \neq j$ .) Similarly,

$$\langle g | g \rangle = \sum_{j=1}^{\infty} c_j^* c_j. \quad (3.33)$$

However, things are not that easy, since we usually apply the expansion (► Eq. 3.30) when we do not know the  $g$  function. Thus, the integrals (► Eqs. 3.31 and ► 3.33) should be perceived rather as the interpretation of the  $c_i$  coefficients than the direct recipe for the calculations. From



► Eq. 3.30, the  $g$  function can be treated as the linear combination of the  $f_i$  functions. Moreover (see ► Eq. 3.33), the probability that a system described by the function  $g$  is in the state  $f_j$  is given by  $c_j^* c_j$ .

Now let us consider the expression

$$\langle g | \widehat{H} | g \rangle \equiv \langle \widehat{H} \rangle_g, \quad (3.34)$$

when  $g$  is not the Hamiltonian eigenfunction. Using the expansion ► Eq. 3.30 and the fact that  $f_i$  are the Hamiltonian eigenfunctions (► Eq. 3.16), one obtains

$$\langle g | \widehat{H} | g \rangle = \sum_{j=1}^{\infty} c_j^* c_j E_j. \quad (3.35)$$

The above integral is called an average (expectation) value, and ► Eq. 3.35 for Hamiltonian carries the information about the average energy of the system in the state described by the  $g$  function. Looking closer at ► Eq. 3.35 shows that this average energy is simply a weighted average of all possible  $E_j$  energies of the system. The weights are determined by the  $c_j^* c_j$  products – the probability of finding the system in the  $f_j$  state. It should be noticed that we used the linearity of the Hamiltonian operator to achieve this result.

Conclusion? Very optimistic: we can say something about the sought energy value not knowing the eigenfunctions of the operator of interest, since for calculations of ► Eq. 3.35 we do not need  $f_j$  functions. Strange? Not at all, if we recall some linear algebra: using three basis vectors we can describe each and every point in the 3D space. Likewise, the wave function can be perceived as a vector, the Hermitian operator as the symmetric transformation matrix, an integral  $\langle f | g \rangle$  as the dot product, orthogonality of functions as orthogonality of vectors, and normalization as dividing the vector components by its length.

Now, when the “linear algebra” term has already appeared, let us see how it is applied for solving the eigenequation. Almost all calculations are performed by applying the basis functions. This means that the unknown function  $\Psi$  describing the investigated system is expressed in the basis of known functions  $\chi_i$  (see ► Eq. 3.30):

$$\Psi \approx \sum_{i=1}^n c_i \chi_i = \Phi, \quad (3.36)$$

where  $\Psi$  is the eigenfunction of the Hamiltonian corresponding to a given eigenvalue  $E$  (► Eq. 3.11). The task is to find such  $c_i$  coefficients that the function  $\Phi$  would be the best approximation to  $\Psi$ . Since  $\Phi$  is an approximation to the wave function, the corresponding energy will also be only approximated. Let us call the approximation  $E_\Phi$ . Basis functions  $\chi_i$  are not the Hamiltonian eigenfunctions, therefore, to estimate the energy, an average value must be calculated. Therefore, substituting ► Eq. 3.36 for ► Eq. 3.11 and multiplying by  $\Psi^* = \langle \sum_i c_i \chi_i |$

on both sides gives<sup>1</sup>

$$\text{LHS} = \left\langle \sum_i c_i \chi_i \left| \widehat{H} \right| \sum_j c_j \chi_j \right\rangle = \sum_i \sum_j c_i^* c_j \langle \chi_i \left| \widehat{H} \right| \chi_j \rangle, \quad (3.37)$$

$$\text{RHS} = E_\Phi \sum_i \sum_j c_i^* c_j \langle \chi_i \left| \chi_j \rangle. \quad (3.38)$$

In order to further simplify the notation, let us denote  $\langle \chi_i \left| \widehat{H} \right| \chi_j \rangle$  by  $H_{ij}$  and  $\langle \chi_i \left| \chi_j \rangle$  by  $S_{ij}$ . Then,

$$\sum_i \sum_j c_i^* c_j H_{ij} = E_\Phi \sum_i \sum_j c_i^* c_j S_{ij}. \quad (3.39)$$

Equivalently, in the matrix form

$$\mathbf{H}\mathbf{c} = \mathbf{S}\mathbf{c}E_\Phi, \quad (3.40)$$

where  $\mathbf{H}$  is the Hamiltonian matrix with the elements  $H_{ij}$ ,  $\mathbf{S}$  is called the overlap matrix and is built of the overlap integrals  $S_{ij}$ , and  $\mathbf{c}$  denotes the vector of the  $c_i$  coefficients. The basis sets applied in practice are usually non-orthogonal, which causes the off-diagonal terms in the  $\mathbf{S}$  matrix to not vanish.

Such a method of finding approximate eigenvalues and eigenvectors of the Hamiltonian is known as the Ritz method and is frequently applied in quantum chemistry.

This simple introduction of basic terms of quantum mechanics is obviously far from complete. One can notice the lack of further discussion of the degeneration, the continuum spectrum, and many other topics. For these we encourage the reader to dive into the following excellent books on quantum mechanics and chemistry: (Atkins and Friedman 2005; Griffiths 2004; Levine 2008; Lowe and Peterson 2005; McQuarrie and Simon 1997; Pielka 2007; Ratner and Schatz 2000; Szabo and Ostlund 1996).

## On the Way to Quantum Chemistry

For the sake of simplification, we assume that the energy of the ground state of our system differs from other energy values. This allows one to avoid embroilment in technical details that are unnecessary at this point. Our system is described by the wave function  $\Psi$  fulfilling the Schrödinger  $\blacktriangleright$  Eq. 3.11. It is important to notice that this eigenvalue equation can be solved exactly only for hydrogen atoms. Any more complicated system requires approximate techniques. In order to explain this complication, let us look into the Hamilton operator. For the system of  $N$  electrons and  $M$  nuclei the full Hamiltonian is a sum of the following terms:

<sup>1</sup> Here, different subscripts appear on the both sides of the integral. The sum does not depend on the name of the summation index, thus any subscript can be applied. However, one should not apply the same index on both sides of the integral, since it can cause the erroneous omission of the off-diagonal terms. Compare the overlap integral

$$\begin{aligned} \langle \Psi \left| \Psi \rangle &= \left\langle \sum_i c_i \chi_i \left| \sum_j c_j \chi_j \right\rangle = \langle c_1 \chi_1 + c_2 \chi_2 + c_3 \chi_3 + \dots \left| c_1 \chi_1 + c_2 \chi_2 + c_3 \chi_3 + \dots \right\rangle \\ &= c_1^* c_1 \langle \chi_1 \left| \chi_1 \rangle + c_1^* c_2 \langle \chi_1 \left| \chi_2 \rangle + c_1^* c_3 \langle \chi_1 \left| \chi_3 \rangle + \dots \end{aligned}$$

The explicit writing of all terms shows that not only the integrals  $\langle \chi_i \left| \chi_i \rangle$  with the same function on both sides are present, but also the contributions  $\langle \chi_i \left| \chi_j \rangle$  with  $i \neq j$ . Therefore, the diversification of the subscripts prevents mistakes.

- Kinetic energy of electrons,  $\widehat{T}_e$
- Kinetic energy of nuclei,  $\widehat{T}_n$
- Energy of interactions between electrons,  $\widehat{V}_{ee}$
- Energy of interactions between nuclei,  $\widehat{V}_{nn}$
- Energy of interactions between a nucleus and an electron,  $\widehat{V}_{ne}$

In the atomic units, these terms have the following form:

$$\widehat{T}_e = -\frac{1}{2} \sum_{i=1}^N \nabla_{\mathbf{r}_i}^2, \quad (3.41)$$

$$\widehat{T}_n = -\sum_{i=1}^M \frac{1}{2m_i} \nabla_{\mathbf{R}_i}^2, \quad (3.42)$$

$$\widehat{V}_{ee} = \sum_{i=1}^N \sum_{j>i}^N \frac{1}{r_{ij}}, \quad (3.43)$$

$$\widehat{V}_{nn} = \sum_{i=1}^M \sum_{j>i}^M \frac{Z_i Z_j}{R_{ij}}, \quad (3.44)$$

$$\widehat{V}_{ne} = -\sum_{i=1}^N \sum_{j=1}^M \frac{Z_j}{|\mathbf{r}_i - \mathbf{R}_j|}, \quad (3.45)$$

where  $m_i$  is the mass of the nucleus  $i$ ,  $Z_i$  stands for the nuclear charge, and  $r_{ij}$  denotes the distance between the electrons  $i$  and  $j$ ,  $r_{ij} = |\mathbf{r}_i - \mathbf{r}_j|$ . Likewise,  $R_{ij}$  refers to the internuclear distance,  $R_{ij} = |\mathbf{R}_i - \mathbf{R}_j|$ . The presence of the mutual distances between the particles causes a serious problem when solving the Schrodinger equation, it does not allow one to decouple the equations.

Fortunately, from the chemist's point of view, such a Hamiltonian is not very useful. The chemist is not interested in each and every bit of information one can get about any  $N$ -electron  $M$ -nuclei system, however, she or he is focused on the given molecule, its conformations, interactions with the environment, and properties (spectroscopic, magnetic, electric, and so on). What makes quantum mechanics a valuable tool for chemists is the Born–Oppenheimer approximation, discussed in detail in the previous chapter of this volume. Let us briefly summarize it to maintain consistent notation throughout the chapter.

The chemist is concerned with the relative positions of the nuclei in the molecule and with the internal energy, but not with the motions of the molecule as a whole. This motion can be excluded from our consideration, for example, by elimination of the center-of-mass translation. Moreover, the intermolecular (electrostatic) forces acting on electrons and nuclei would be similar. This would cause much slower internal motion of the heavy nuclei in comparison to light electrons. For this reason, the approximate description of electron motion with parametric dependence on the static positions of nuclei is justified. Such reasoning leads to adiabatic approximation and finally to Born–Oppenheimer approximation.

According to this approximation, the Hamiltonian can be written as

$$\widehat{H} = \widehat{T}_n + \widehat{H}_e + \widehat{V}_{nn}, \quad (3.46)$$

where  $\widehat{T}_n$  now has a meaning of nuclear kinetic energy of the molecule for which the center-of-mass is stopped (however, there are still oscillations and rotations), and

$$\widehat{H}_e = \widehat{T}_e + \widehat{V}_{ee} + \widehat{V}_{en}. \quad (3.47)$$

is called an electronic Hamiltonian, and it represents the energy of the system after omitting the nuclear kinetic energy term and nuclear repulsion. One can now focus on the solution of the equation of the form

$$[\widehat{T}_n(\mathbf{R}) + \widehat{H}_e(\mathbf{r}; \mathbf{R}) + \widehat{V}_{nn}(\mathbf{R})]\Psi(\mathbf{r}, \mathbf{R}) = E\Psi(\mathbf{r}, \mathbf{R}). \quad (3.48)$$

Here, the dependence on the electronic spatial variables  $\mathbf{r} = (x_1, y_1, z_1, \dots, x_N, y_N, z_N)$  and the nuclear spatial variables  $\mathbf{R} = (X_1, Y_1, Z_1, \dots, X_M, Y_M, Z_M)$  is written explicitly. The semicolon sign in the  $\widehat{H}_e$  term denotes the parametric dependence – for various  $\mathbf{R}$  the various electronic equations are obtained.

With such a Hamiltonian, it seems reliable to distinguish also the nuclear  $f(\mathbf{R})$  and electronic  $\Psi_e(\mathbf{r}; \mathbf{R})$  part in the wave function

$$\Psi(\mathbf{r}, \mathbf{R}) \approx \Psi_e(\mathbf{r}; \mathbf{R})f(\mathbf{R}), \quad (3.49)$$

which leads to a significant reduction of the problem.

Now  $\blacklozenge$  Eq. 3.48 can be separated into three equations:

$$\widehat{H}_e(\mathbf{r}; \mathbf{R})\Psi_e(\mathbf{r}; \mathbf{R}) = E_e(\mathbf{R})\Psi_e(\mathbf{r}; \mathbf{R}), \quad (3.50)$$

$$(\widehat{H}_e(\mathbf{r}; \mathbf{R}) + \widehat{V}_{nn}(\mathbf{R}))\Psi_e(\mathbf{r}; \mathbf{R}) = U(\mathbf{R})\Psi_e(\mathbf{r}; \mathbf{R}), \quad (3.51)$$

$$(\widehat{T}_n(\mathbf{R}) + \widehat{U}(\mathbf{R}))f(\mathbf{R}) = Ef(\mathbf{R}). \quad (3.52)$$

The first two describe electronic motion for a given position of nuclei. The difference between  $E_e(\mathbf{R})$  and  $U(\mathbf{R})$  is that in  $U(\mathbf{R})$  nuclear repulsion energy is taken into account. These equations are milestones in our considerations for two reasons. First, since we are now talking about “fixed positions of the nuclei,” finally we have got molecules instead of an unspecified system containing some electrons and some nuclei. The second is hidden in  $\blacklozenge$  Eq. 3.52: electronic energy and nuclear repulsion energy constitute the potential, in which nuclei are moving. That is why the proper description of electronic movement in a molecule is so important: The electrons glue the whole molecule together.

Our attention in the rest of the chapter will be focused only on  $\blacklozenge$  Eq. 3.50; hence, to simplify notation, all the subscripts denoting the electronic case will be omitted:

$$\widehat{H}_e \rightarrow \widehat{H}, \quad (3.53)$$

$$\Psi_e \rightarrow \Psi, \quad (3.54)$$

$$\widehat{H}_e\Psi_e(r; R) = E_e\Psi_e(r; R) \rightarrow \widehat{H}\Psi = E\Psi. \quad (3.55)$$

The electronic wave function  $\Psi$  satisfies all the requirements discussed in the previous sections, depends on the coordinates of  $N$  electrons, and additionally must be antisymmetric with respect to the exchange of coordinates of two electrons.<sup>2</sup>

It should be noted that the analytic solution of  $\blacklozenge$  Eq. 3.50 is not known even for the smallest molecule, i.e.,  $H_2$ . Therefore, the approximate techniques must be applied to extract the necessary information about molecules of interest. Quantum mechanics provides two tools:

- Variational principle
- Perturbation theory

<sup>2</sup>In order to explain the antisymmetry requirement, we have to refer again to theory that is beyond the scope of the present chapter. Let us simply state here that wave functions must be antisymmetric without belaboring the point. This will mean that the exchange of the coordinates of the two electrons causes the wave function to change the sign:  $\Psi(\tau_1, \tau_2) = -\Psi(\tau_2, \tau_1)$ .

## Variational Principle – An Indicator

The variational principle allows one to judge the quality of the obtained solutions. It can be formulated as follows: For the arbitrary trial function  $\chi$  that is square-integrable, differentiable, antisymmetric, and depends on the same set of variables as a sought ground state  $\Psi_0$  function, we have

$$E_0 \leq \frac{\langle \chi | \widehat{H} | \chi \rangle}{\langle \chi | \chi \rangle}, \quad (3.56)$$

where  $E_0$  is the ground state energy corresponding to  $\Psi_0$  (► Eq. 3.50). The important consequence of the variational principle is that, to estimate the energy of the system one does not need to solve the eigenequation (this we already know, see ► Eq. 3.35), and moreover – what is crucial – the estimated energy value will always not be lower than the exact eigenvalue  $E_0$ .

The proof of the inequality (► Eq. 3.56) is straightforward and can be derived from ► Eqs. 3.30 and ► 3.35. The function  $\chi$  that satisfies the above requirements can be expanded on the basis of the Hamiltonian eigenfunctions:

$$\chi = \sum_{i=0}^{\infty} c_i f_i, \quad (3.57)$$

where  $f_i$  fulfill the eigenproblem  $\widehat{H} f_i = E_i f_i$ . Thus,

$$\frac{\langle \chi | \widehat{H} | \chi \rangle}{\langle \chi | \chi \rangle} = \frac{\sum_{i=0}^{\infty} c_i^* c_i E_i}{\sum_{i=0}^{\infty} c_i^* c_i} \geq \frac{\sum_{i=0}^{\infty} c_i^* c_i E_0}{\sum_{i=0}^{\infty} c_i^* c_i} = E_0, \quad (3.58)$$

with the assumption that  $E_0$  is the lowest of all Hamiltonian eigenvalues (Atkins and Friedman 2005; Levine 2008; Lowe and Peterson 2005; McQuarrie and Simon 1997; Piela 2007; Szabo and Ostlund 1996).

## Perturbation Calculus – The Art of Estimation

Due to the variational principle that is satisfied for the electronic Hamiltonian, the group of methods of searching for parameters optimizing the energy value can be constructed. The way of verification of the given wave function is the corresponding energy value: the lower, the better. Besides this “quality control,” the variational principle does not give the prescription for the choice of the trial wave functions. Here comes the perturbation calculus – the method frequently applied in physics for the estimation of the functions or values on the basis of partial knowledge about the solutions of the investigated problem. We will consider here the Rayleigh–Schrödinger variant of the perturbation calculus (Atkins and Friedman 2005; Levine 2008; Lowe and Peterson 2005; McQuarrie and Simon 1997; Piela 2007; Ratner and Schatz 2000).

Let us assume that the total electronic Hamiltonian of the investigated system can be divided into

$$\widehat{H} = \widehat{H}^0 + \widehat{H}^1, \quad (3.59)$$

in such a fashion that we know the exact solutions of

$$\widehat{H}^0 \Psi_k^{(0)} = E_k^{(0)} \Psi_k^{(0)}, \quad (3.60)$$

where the subscript  $k$  enumerates the eigenvalues of the  $\widehat{H}^0$  operator in such a way that  $E_0^{(0)}$  is the lowest energy. Now, one can say that the operator  $\widehat{H}$  describes the system for which  $\widehat{H}^0$  is an unperturbed operator and  $\widehat{H}^1$  denotes a perturbation. We can assume that if the change in the system represented by  $\widehat{H}^1$  is minor, then the functions  $\Psi_k^{(0)}$  would be a good approximation to  $\Psi_k$ . Considering  $\widehat{H}^0$ , one postulates its Hermiticity and that its eigenvalues are not degenerate (in our case, for the ground state at least  $E_0^{(0)}$  must not be equal to any other eigenvalue). This condition will become clear in a moment.

Knowing only the unperturbed solutions (► Eq. 3.60), we would like to say something more about the ground state energy of the investigated system. Nothing is easier – we can calculate the average value of the full electronic Hamiltonian with the  $\Psi_0^{(0)}$  function. The variational principle states that the resulting energy will be not lower than the exact energy:

$$E_0 \leq \langle \Psi_0^{(0)} | \widehat{H}^0 + \widehat{H}^1 | \Psi_0^{(0)} \rangle = E_0^{(0)} + E_0^{(1)}. \quad (3.61)$$

The term modifying  $E_0^{(0)}$  is simply

$$E_0^{(1)} = \langle \Psi_0^{(0)} | \widehat{H}^1 | \Psi_0^{(0)} \rangle. \quad (3.62)$$

So far, the only new thing is the manner of partitioning the total energy into the energy of the unperturbed system and the corrections (where  $E_0^{(1)}$  is not the only term):

$$E_0 = E_0^{(0)} + E_0^{(1)} + E_0^{(2)} + \dots \quad (3.63)$$

Likewise, the wave function can be written as

$$\Psi_0 = \Psi_0^{(0)} + \Psi_0^{(1)} + \Psi_0^{(2)} + \dots, \quad (3.64)$$

where  $\Psi_0^{(1)}$ ,  $\Psi_0^{(2)}$  and so forth are the corrections to the wave function of the unperturbed system,  $\Psi_0^{(0)}$ . Now, the electronic Schrödinger ► Eq. 3.50 becomes

$$\begin{aligned} & (\widehat{H}^0 + \widehat{H}^1) (\Psi_0^{(0)} + \Psi_0^{(1)} + \Psi_0^{(2)} + \dots) \\ &= (E_0^{(0)} + E_0^{(1)} + E_0^{(2)} + \dots) (\Psi_0^{(0)} + \Psi_0^{(1)} + \Psi_0^{(2)} + \dots). \end{aligned} \quad (3.65)$$

Introducing the expansions (► Eqs. 3.63 and ► 3.64) does not increase our knowledge about the energy or the wave function; it is only a different way of expressing the unknowns by other unknowns. However, now we have a starting point for further investigations.

The comparison of the terms on the left- and right-hand side of the above expression is instructive. Let us regard as similar the terms with the same sum of the superscripts (so-called perturbation order, by analogy to the multiplication and ordering of polynomials). Simple multiplication in ► Eq. 3.65 and directing the terms of the same order to separate equations gives

$$\widehat{H}^0 \Psi_0^{(0)} = E_0^{(0)} \Psi_0^{(0)}, \quad (3.66)$$

$$\widehat{H}^0 \Psi_0^{(1)} + \widehat{H}^1 \Psi_0^{(0)} = E_0^{(0)} \Psi_0^{(1)} + E_0^{(1)} \Psi_0^{(0)}, \quad (3.67)$$

$$\widehat{H}^0 \Psi_0^{(2)} + \widehat{H}^1 \Psi_0^{(1)} = E_0^{(0)} \Psi_0^{(2)} + E_0^{(1)} \Psi_0^{(1)} + E_0^{(2)} \Psi_0^{(0)}, \quad (3.68)$$

⋮

These equations link the corrections to the wave function and to the energy. Before detailed investigation of the subsequent corrections, one more thing should be underlined. Up to now, the function  $\Psi_0$  is not normalized; only  $\Psi_k^{(0)}$  are normalized. Until the corrections to  $\Psi_0$  were found, we would not be able to normalize it. We can only write the normalization constant as  $\mathcal{N} = \frac{1}{\sqrt{\langle \Psi_0 | \Psi_0 \rangle}}$ . However, it is not necessary at this moment. Now the intermediate normalization condition is more useful:

$$\langle \Psi_0^{(0)} | \Psi_0 \rangle = 1. \quad (3.69)$$

Such a concept is based on the information that the eigenfunctions of  $\widehat{H}^0$  form an orthonormal complete set of functions (that is one of the reasons why the Hermiticity of  $\widehat{H}^0$  was required) and they can be applied to express any other function, for instance,  $\Psi_0$  as

$$\Psi_0 = \sum_{k=0}^{\infty} c_k \Psi_k^{(0)} = \Psi_0^{(0)} + \sum_{k \neq 0} c_k \Psi_k^{(0)}. \quad (3.70)$$

In this linear combination, the function  $\Psi_0^{(0)}$  has a distinguished meaning ( $c_0 = 1$ ); this is the approximation of the wave function of the considered system. Therefore, one can require that  $\Psi_0^{(0)}$  does not have a contribution to the higher corrections:  $\Psi_0^{(1)}$ ,  $\Psi_0^{(2)}$ , and so on:

$$\sum_{k \neq 0} c_k \Psi_k^{(0)} = \Psi_0^{(1)} + \Psi_0^{(2)} + \dots \quad (3.71)$$

Here, the benefits from the intermediate normalization are obvious: the function  $\Psi_0^{(0)}$  is orthogonal to each of the corrections (or, in other words, the corrections are defined in such a way that they are orthogonal to  $\Psi_0^{(0)}$ ).

Therefore, there is an additional set of equations to be satisfied:

$$\langle \Psi_0^{(0)} | \Psi_0^{(n)} \rangle = \delta_{0n}, \quad (3.72)$$

where the superscript  $n$  denotes the  $n$ -th order correction to the ground state wave function  $\Psi_0$ . Now we can go back to the [Eqs. 3.66–3.68](#) and extract the corrections to energy. For this purpose, each of the equations must be multiplied from the left-hand side by  $\Psi_0^{(0)}$  and integrated:

$$E_0^{(0)} = \langle \Psi_0^{(0)} | \widehat{H}^0 | \Psi_0^{(0)} \rangle, \quad (3.73)$$

$$E_0^{(1)} = \langle \Psi_0^{(0)} | \widehat{H}^1 | \Psi_0^{(0)} \rangle, \quad (3.74)$$

$$E_0^{(2)} = \langle \Psi_0^{(0)} | \widehat{H}^1 | \Psi_0^{(1)} \rangle, \quad (3.75)$$

⋮

The integrals  $\langle \Psi_0^{(0)} | \widehat{H}^0 | \Psi_0^{(n)} \rangle$  vanish, since

$$\langle \Psi_0^{(0)} | \widehat{H}^0 | \Psi_0^{(n)} \rangle = \langle \widehat{H}^0 \Psi_0^{(0)} | \Psi_0^{(n)} \rangle = E_0^{(0)} \langle \Psi_0^{(0)} | \Psi_0^{(n)} \rangle = 0. \quad (3.76)$$

Thus, obtaining the energy corrections of any order is straightforward. The general expression for the  $n$ -th order correction can be written as

$$E_0^{(n)} = \langle \Psi_0^{(0)} | \widehat{H}^1 | \Psi_0^{(n-1)} \rangle \quad \text{for } n > 1. \quad (3.77)$$

The problem is that to obtain the corrections to the energy in the second or higher orders, the corrections to the wave function are necessary. Then, let us try to find  $\Psi_0^{(1)}$ . This function can

be expressed as the linear combination of the functions from the orthonormal set  $\{\Psi_k^{(0)}\}$  for  $k \neq 0$ :

$$\Psi_0^{(1)} = \sum_{k \neq 0}^{\infty} c_k^{(1)} \Psi_k^{(0)}, \quad (3.78)$$

where  $c_k^{(1)}$  are the expansion coefficients in the first-order correction. Again, the whole thing reduces to finding the coefficients  $c_k$ . Substituting  $\blacktriangleright$  Eq. 3.78 to  $\blacktriangleright$  Eq. 3.67 gives

$$\left(\widehat{H}^0 - E_0^{(0)}\right) \sum_{k \neq 0}^{\infty} c_k^{(1)} \Psi_k^{(0)} = \left(E_0^{(1)} - \widehat{H}^1\right) \Psi_0^{(0)}. \quad (3.79)$$

Integrating this equation with the  $\Psi_l^{(0)}$  function leads to

$$\begin{aligned} \text{LHS} &= \langle \Psi_l^{(0)} | \widehat{H}^0 - E_0^{(0)} | \sum_{k \neq 0}^{\infty} c_k \Psi_k^{(0)} \rangle = \sum_{k \neq 0}^{\infty} c_k \langle \Psi_l^{(0)} | \widehat{H}^0 - E_0^{(0)} | \Psi_k^{(0)} \rangle \\ &= \sum_{k \neq 0}^{\infty} c_k (E_l^{(0)} - E_0^{(0)}) \langle \Psi_l^{(0)} | \Psi_k^{(0)} \rangle = \sum_{k \neq 0}^{\infty} c_k (E_l^{(0)} - E_0^{(0)}) \delta_{lk} \\ &= c_l (E_l^{(0)} - E_0^{(0)}) \end{aligned} \quad (3.80)$$

and

$$\begin{aligned} \text{RHS} &= \langle \Psi_l^{(0)} | E_0^{(1)} - \widehat{H}^1 | \Psi_0^{(0)} \rangle = E_0^{(1)} \langle \Psi_l^{(0)} | \Psi_0^{(0)} \rangle - \langle \Psi_l^{(0)} | \widehat{H}^1 | \Psi_0^{(0)} \rangle \\ &= -\langle \Psi_l^{(0)} | \widehat{H}^1 | \Psi_0^{(0)} \rangle. \end{aligned} \quad (3.81)$$

Altogether, these allow one to write the coefficients of the expansion ( $\blacktriangleright$  Eq. 3.78) as

$$c_l = \frac{\langle \Psi_l^{(0)} | \widehat{H}^1 | \Psi_0^{(0)} \rangle}{E_0^{(0)} - E_l^{(0)}}. \quad (3.82)$$

Hence, the first correction to the wave function is already known:

$$\Psi_0^{(1)} = \sum_{k \neq 0}^{\infty} \frac{\langle \Psi_k^{(0)} | \widehat{H}^1 | \Psi_0^{(0)} \rangle}{E_0^{(0)} - E_k^{(0)}} \Psi_k^{(0)}, \quad (3.83)$$

and, thereby, the second-order correction to the energy can be calculated as

$$E_0^{(2)} = \sum_{k \neq 0}^{\infty} \frac{\langle \Psi_k^{(0)} | \widehat{H}^1 | \Psi_0^{(0)} \rangle}{E_0^{(0)} - E_k^{(0)}} \langle \Psi_0^{(0)} | \widehat{H}^1 | \Psi_k^{(0)} \rangle. \quad (3.84)$$

This is also equivalently written as

$$E_0^{(2)} = \sum_{k \neq 0}^{\infty} \frac{|\langle \Psi_k^{(0)} | \widehat{H}^1 | \Psi_0^{(0)} \rangle|^2}{E_0^{(0)} - E_k^{(0)}}. \quad (3.85)$$

The energy difference in the denominator of the above expression cannot be equal to zero, and for this reason the non-degenerated ground state was assumed. The higher-order corrections are sought in a similar manner, which just requires more operations.

One of the interesting issues is the problem of variationality of the perturbation calculus built upon the variational Hamiltonian. This is, however, a sophisticated problem for advanced readers and will not be discussed here. It should be added, in summary, that the manner of



partitioning of the Hamilton operator was arbitrary. The only prerequisites were the Hermitian character of the operators (for the eigenfunctions to form the orthonormal set) and the non-degenerated ground state eigenenergy. Nothing more. One should also remember that, in practice, even solving the unperturbed problem cannot be performed exactly and the approximations must be applied. The consequence could be the loss of accuracy for higher-order corrections. Moreover, good convergence of the perturbation expansion can be expected when the consecutive corrections are small in comparison to the total estimated value. However, in such a case, the low orders of the series would reproduce the sought value with relatively good accuracy. Thus, application of the low orders of perturbation calculus is highly recommended.

## One-Electron Approximation – Describe One and Say Something About All

Equipped with general knowledge about the tools for the Schrödinger equation solution, one can move to many-electron systems.

The electronic Hamiltonian for any many-electron system in atomic units has the following form (compare  $\blacklozenge$  Eqs. 3.41–3.45):

$$\hat{H} = -\frac{1}{2} \sum_{i=1}^N \Delta_{\mathbf{r}_i} + \sum_{i=1}^N \sum_{j=1}^M \frac{Z_j}{|\mathbf{r}_i - \mathbf{R}_j|} + \sum_{i=1}^N \sum_{j=i+1}^N \frac{1}{|\mathbf{r}_i - \mathbf{r}_j|}. \quad (3.86)$$

Let us look more closely. In the first term, we sum up over the number of electrons  $N$ ; in the second term, the summations run over the number of electrons  $N$  and number of nuclei  $M$ ; and the third term contains the double sum over the number of electrons  $N$ . Thus, one can simplify the notation of the first two terms:

$$-\frac{1}{2} \sum_{i=1}^N \Delta_{\mathbf{r}_i} + \sum_{i=1}^N \sum_{j=1}^M \frac{Z_j}{|\mathbf{r}_i - \mathbf{R}_j|} = \sum_{i=1}^N \left( -\frac{1}{2} \Delta_{\mathbf{r}_i} + \sum_{j=1}^M \frac{Z_j}{|\mathbf{r}_i - \mathbf{R}_j|} \right). \quad (3.87)$$

Now, denoting the term in parenthesis by  $\hat{h}(i)$ ,

$$\hat{h}(i) = -\frac{1}{2} \Delta_{\mathbf{r}_i} + \sum_{j=1}^M \frac{Z_j}{|\mathbf{r}_i - \mathbf{R}_j|}, \quad (3.88)$$

we get the part of the Hamiltonian depending only on the coordinates of one electron,  $i$  (and nuclear coordinates, but it does not bother us). Hence, the total electronic Hamiltonian ( $\blacklozenge$  Eq. 3.86) can be rewritten as the sum of one-electron and two-electron contributions:

$$\hat{H} = \sum_{i=1}^N \hat{h}(i) + \sum_{i=1}^N \sum_{j=i+1}^N \hat{g}(i, j), \quad (3.89)$$

where we introduced a symbol:

$$\hat{g}(i, j) = \frac{1}{|\mathbf{r}_i - \mathbf{r}_j|}. \quad (3.90)$$

It should be noticed that each of the one-electron Hamiltonians  $\hat{h}(i)$  describes a single electron in the field of some potentials. Therefore, the exact solutions of the eigenvalue problem for these

one-electron operators are available. The problem lies in the  $\hat{g}(i, j)$  operator that couples two electrons together: It is not possible to separate their coordinates exactly.

All electronic Hamiltonians have the same general form; they differ only in the number of electrons  $N$  and the nuclear potential hidden in  $\hat{h}(i)$ . One can choose any possible chemical compounds and try to write the corresponding equations; however, one would soon note the similarity of all of them. Therefore, we will not invest time in describing the procedure for a polypeptide or a nanotube, but for simplicity we will start from the two-electron helium atom (the simplest many-electron system) and later try to generalize the considerations. For the helium atom:

- $N = 2$  – two electrons
- $M = 1$  – one nucleus

The generalization of the helium discussion into the larger ( $N$ -electron) systems should be straightforward:

$$\hat{h}(1) + \hat{h}(2) = \sum_{i=1}^2 \hat{h}(i) \longrightarrow \sum_{i=1}^N \hat{h}(i), \quad (3.91)$$

$$\hat{g}(1, 2) = \sum_{i=1}^2 \sum_{j=i+1}^2 \hat{g}(i, j) \longrightarrow \sum_{i=1}^N \sum_{j=i+1}^N \hat{g}(i, j), \quad (3.92)$$

and finally:

$$\hat{h}(i) = -\frac{1}{2} \Delta_{\mathbf{r}_i} + \frac{Z_1}{|\mathbf{r}_i - \mathbf{R}_1|} \longrightarrow -\frac{1}{2} \Delta_{\mathbf{r}_i} + \sum_{j=1}^M \frac{Z_j}{|\mathbf{r}_i - \mathbf{R}_j|}. \quad (3.93)$$

Recall that the exact solutions of the one-electron problem are known, and the task is to solve the full problem. The ideas of the perturbation theory were explained in the previous section. Now it is the time to apply the knowledge. The one-electron part can be treated as the unperturbed Hamiltonian and the rest as the perturbation:

$$\widehat{H}^0 = \hat{h}(1) + \hat{h}(2), \quad \widehat{H}^1 = \hat{g}(1, 2), \quad (3.94)$$

where the normalized solutions for the one-electron part are known:

$$\hat{h}(1)\phi_i(1) = \epsilon_i\phi_i(1), \quad (3.95)$$

$$\hat{h}(2)\phi_j(2) = \epsilon_j\phi_j(2). \quad (3.96)$$

These functions require more attention. Although the electronic Hamiltonian – and thereby the one-electron operators – do not act on the spin variables, the wave functions  $\phi_k$  must carry on the spin dependence. Therefore, the function  $\phi_k(l)$  is a product of the spatial part depending on the three spatial coordinates of the electron  $l$  and on the spin part, and is called a spin-orbital. For simplicity, the set of coordinates  $\tau_l$  is written as a label of the electron, i.e.,  $l$ . Such convention will be applied from now on, with an exception where the  $\tau_l$  labeling is really needed.

If an operator can be written as a sum of contributions acting on different variables, its eigenfunction takes a form of the product of the eigenfunctions of the subsequent operators in the summation. In the case of the helium atom, where  $\widehat{H}^0$  is a sum of  $\hat{h}(1)$  and  $\hat{h}(2)$ , the wave function  $\Psi(1, 2)$  can be denoted as the product of one-electron functions:

$$\Psi(1, 2) = \phi_i(1)\phi_j(2). \quad (3.97)$$

The eigenproblem for such a function gives the eigenvalue that is simply the sum of the one-electron eigenvalues:

$$\begin{aligned}
 [\hat{h}(1) + \hat{h}(2)] \phi_i(1)\phi_j(2) &= \hat{h}(1)\phi_i(1)\phi_j(2) + \hat{h}(2)\phi_i(1)\phi_j(2) \\
 &= [\hat{h}(1)\phi_i(1)] \phi_j(2) + [\hat{h}(2)\phi_j(2)] \phi_i(1) \\
 &= [\epsilon_i\phi_i(1)] \phi_j(2) + [\epsilon_j\phi_j(2)] \phi_i(1) \\
 &= [\epsilon_i + \epsilon_j] \phi_i(1)\phi_j(2).
 \end{aligned} \tag{3.98}$$

However, here the antisymmetry requirement should also be taken into account. The many-electron function must change the sign with respect to the exchange of labels of any two electrons:

$$\Psi(1, 2) = -\Psi(2, 1). \tag{3.99}$$

The product (● Eq. 3.97) is not antisymmetric; the interchange of the electron labels leads to

$$\Psi(2, 1) = \phi_i(2)\phi_j(1) \neq -\Psi(1, 2), \tag{3.100}$$

and the result is a function different from the original  $\Psi(1, 2)$ . But another function,

$$\Psi(1, 2) \sim [\phi_i(1)\phi_j(2) - \phi_i(2)\phi_j(1)], \tag{3.101}$$

satisfies the antisymmetry condition.

Moreover, the wave function  $\Psi(1, 2)$  has to be normalized. This can be achieved by calculating the following (overlap) integral:

$$\begin{aligned}
 \langle \Psi(1, 2) | \Psi(1, 2) \rangle &= \mathcal{N}(\phi_i(1)\phi_j(2) - \phi_j(1)\phi_i(2)) | \mathcal{N}(\phi_i(1)\phi_j(2) - \phi_j(1)\phi_i(2)) \rangle \\
 &= \mathcal{N}^2 \left( \langle \phi_i(1)\phi_j(2) | \phi_i(1)\phi_j(2) \rangle - \langle \phi_i(1)\phi_j(2) | \phi_j(1)\phi_i(2) \rangle \right. \\
 &\quad \left. - \langle \phi_j(1)\phi_i(2) | \phi_i(1)\phi_j(2) \rangle + \langle \phi_j(1)\phi_i(2) | \phi_j(1)\phi_i(2) \rangle \right).
 \end{aligned} \tag{3.102}$$

The spin-orbitals of electrons 1 and 2 are mutually independent, thus,

$$\langle \phi_i(1)\phi_j(2) | \phi_k(1)\phi_l(2) \rangle = \langle \phi_i(1) | \phi_k(1) \rangle \langle \phi_j(2) | \phi_l(2) \rangle = \delta_{ik}\delta_{jl}, \tag{3.103}$$

where  $\langle \phi_i(1) | \phi_k(1) \rangle = \delta_{ik}$  arises from the fact that the eigenfunctions of the Hermitian operator  $\hat{h}(1)$  form the orthonormal set. Hence, in ● Eq. 3.102 only the first and last integral will be non-vanishing, and, finally,

$$\langle \Psi(1, 2) | \Psi(1, 2) \rangle = 2\mathcal{N}^2 = 1, \tag{3.104}$$

and, therefore, the normalization constant  $\mathcal{N}$  must equal  $1/\sqrt{2}$ . In order to fulfill the normalization and the antisymmetry request, the trial wave function can be written as

$$\Psi(1, 2) = \frac{1}{\sqrt{2}} (\phi_i(1)\phi_j(2) - \phi_j(1)\phi_i(2)) = \frac{1}{\sqrt{2}} \begin{vmatrix} \phi_i(1) & \phi_i(2) \\ \phi_j(1) & \phi_j(2) \end{vmatrix}. \tag{3.105}$$

Thereafter, the expectation value of the Hamiltonian can be calculated using the same tricks as in  $\blacklozenge$  Eq. 3.102<sup>3</sup>:

$$\begin{aligned} \langle \widehat{H}(1,2) \rangle_{\Psi(1,2)} &= \langle \Psi(1,2) | \widehat{H}(1,2) | \Psi(1,2) \rangle \\ &= \langle \phi_i(1) | \hat{h}(1) | \phi_i(1) \rangle + \langle \phi_j(2) | \hat{h}(2) | \phi_j(2) \rangle \\ &\quad + \langle \phi_i(1) \phi_j(2) | \frac{1}{r_{12}} | \phi_i(1) \phi_j(2) \rangle \\ &\quad - \langle \phi_i(1) \phi_j(2) | \frac{1}{r_{12}} | \phi_j(1) \phi_i(2) \rangle. \end{aligned} \quad (3.106)$$

The only difference with respect to the overlap integral is that the integrals containing  $1/r_{12}$  cannot be separated.

In the spirit of perturbation calculus, the expectation value ( $\blacklozenge$  Eq. 3.106) can be treated as the energy corrected up to the first order of perturbation expansion. According to the variational principle, this integral is an upper bound of the exact energy of the two-electron system under consideration. The recipe for correcting the trial function is given by the perturbation theory: Apply functions corresponding to the remaining states of the unperturbed system in the expansion. In other words, in order to improve the wave function, the expansion built from products of the remaining states of the systems should be used.

Let us summarize. The many-electron function of the system can be approximately written as the antisymmetrized product of the one-electron functions being the solutions for the one-electron eigenvalue problem. This is the idea of the popular one-electron approximation (Atkins and Friedman 2005; Lowe and Peterson 2005; McQuarrie and Simon 1997; Ratner and Schatz 2000). In the  $N$ -electron case, one obtains the trial function as the antisymmetrized product of  $N$  one-electron functions that can be written in the form of the Slater determinant:

$$\Psi(1,2,\dots,N) = \frac{1}{\sqrt{N!}} \begin{vmatrix} \phi_1(1) & \phi_1(2) & \dots & \phi_1(N) \\ \phi_2(1) & \phi_2(2) & \dots & \phi_2(N) \\ \vdots & \vdots & \ddots & \vdots \\ \phi_N(1) & \phi_N(2) & \dots & \phi_N(N) \end{vmatrix}. \quad (3.107)$$

$1/\sqrt{N!}$  factor ensures the normalization of the wave function. Often, instead of writing the whole determinant, only the diagonal is written down:

$$\begin{vmatrix} \phi_1(1) & \phi_1(2) & \dots & \phi_1(N) \\ \phi_2(1) & \phi_2(2) & \dots & \phi_2(N) \\ \vdots & \vdots & \ddots & \vdots \\ \phi_N(1) & \phi_N(2) & \dots & \phi_N(N) \end{vmatrix} = |\phi_1(1)\phi_2(2)\dots\phi_N(N)|. \quad (3.108)$$

It is important to realize that the many-electron function in the form of the Slater determinant is only an approximation. Intuition tells us that describing the many-electron system using only one-electron functions cannot be exact. One needs to be aware of the fact that such an approach

<sup>3</sup> Since the value of the integral does not depend on the name of the variable, the obvious equality,  $\int_a^b f(x)dx = \int_a^b f(y)dy$ , in the above case takes the form

$$\langle \phi_i(1)\phi_j(2) | \frac{1}{r_{12}} | \phi_j(1)\phi_i(2) \rangle = \langle \phi_i(2)\phi_j(1) | \frac{1}{r_{12}} | \phi_j(2)\phi_i(1) \rangle.$$

causes the loss of some information included in the sought wave function. In particular, the one-electron function cannot “see” another electron, therefore, the terms coupling the mutual electron positions are missing in the one-electron approximation.

For example, consider the two-electron function (Piela 2007)

$$F(1,2) \sim (e^{-ar_1-br_2-cr_{12}} - e^{-ar_2-br_1-cr_{12}}), \quad (3.109)$$

where  $r_1, r_2$  are the electron-nucleus distances,  $r_{12}$  denotes the distance between two electrons, and  $a, b,$  and  $c$  stand for the coefficients.  $F(1,2)$  contains the factor  $c$  correlating the electron motions. In the one-electron approach, such a function would be approximated by the antisymmetrized function

$$f(1,2) \sim (e^{-ar_1-br_2} - e^{-ar_2-br_1}), \quad (3.110)$$

with total neglect of this correlation. From the practical point of view, this means that the trial function written as the single determinant does not allow reproduction of the exact electronic energy, even when using the best possible one-electron functions for its construction.

The question arises: why use such an approach, knowing from the very beginning that it is bad? The answer is simple. First, including the electron correlation in the wave function is very expensive. For two electrons, one additional term appears; for three, three terms; for four, six. In general, for  $N$  electrons there are  $N(N-1)/2$  terms (the triangle of the  $N \times N$  matrix without the diagonal elements). Therefore, the number of coefficients describing the electron correlation is much bigger than the number of one-electron terms. Calculating even the one-electron coefficients is very time-consuming, and, moreover, calculating the overlap integrals and Hamiltonian matrix elements becomes prohibitively complicated with the correlated functions. Second, perturbation theory provides ways of improving the results. Expansion built on a higher number of determinants will lead to better energy. Third, a chemist does not usually need exact data, but only an appropriate accuracy (furnishing a house does not require calliper measurements, just a quick glance to estimate the size of the door and the furniture).

Therefore, let us stick to the one-electron approximation. The next section will explain how to find the best possible spin-orbitals.

## Hartree–Fock Method – It Is Not that Sophisticated

---

Now we are prepared to concentrate on the methods for solving the electron equation. As you will see, they are only an extension of the already-discussed techniques. We start with the fundamental Hartree–Fock method.

The main goal of this approximation is to find the spin-orbitals applied for construction of the Slater determinant that will best reproduce the exact wave function. We again begin our considerations with the two-electron system. The problem is that the operator  $\hat{h}(i)$  does not contain the part arising from the potential of the second electron, and an operator responsible

for this missing part must be found. What we do know is that such an interaction is included in the two-electron part of  $\blacktriangleright$  Eq. 3.106:

$$\left\langle \frac{1}{r_{12}} \right\rangle_{\Psi(1,2)} = \langle \phi_i(1)\phi_j(2) | \frac{1}{r_{12}} | \phi_i(1)\phi_j(2) \rangle - \langle \phi_i(1)\phi_j(2) | \frac{1}{r_{12}} | \phi_j(1)\phi_i(2) \rangle. \quad (3.111)$$

Unfortunately,  $\blacktriangleright$  Eq. 3.111 contains the integrals that cannot be exactly separated into a product of the simpler integrals depending only on the coordinates of one electron. What we can propose is rewriting this equation in the following form:

$$\left\langle \frac{1}{r_{12}} \right\rangle_{\Psi(1,2)} = \langle \phi_i(1) | \hat{v}(1) | \phi_i(1) \rangle + \langle \phi_j(2) | \hat{v}(2) | \phi_j(2) \rangle + \text{the rest}, \quad (3.112)$$

where  $\hat{v}(1)$  and  $\hat{v}(2)$  are introduced to extract only the terms depending on the coordinates of a single electron from  $\blacktriangleright$  Eq. 3.111 and “the rest” is what remains from  $\left\langle \frac{1}{r_{12}} \right\rangle_{\Psi(1,2)}$  after this extraction.

If such extraction were possible, the operators  $\hat{v}(1)$  and  $\hat{v}(2)$  could be applied to improve our one-electron operators, which leads to the following equations:

$$[\hat{h}(1) + \hat{v}(1)] \phi_i(1) = \epsilon_i \phi_i(1), \quad (3.113)$$

$$[\hat{h}(2) + \hat{v}(2)] \phi_j(2) = \epsilon_j \phi_j(2). \quad (3.114)$$

The solutions of such equations (spin-orbitals  $\phi_i, \phi_j$ ) can be used to build up the Slater determinant. They ensure better approximation than  $\blacktriangleright$  Eqs. 3.95 and  $\blacktriangleright$  3.96, since they somehow provide for the influence of the second electron.

Therefore, our goal now is to utilize  $\blacktriangleright$  Eq. 3.106 (treating  $\phi_i$  and  $\phi_j$  as known functions) to find the best form of the operators  $\hat{v}(1)$  and  $\hat{v}(2)$ . Adding zero, written as

$$0 = \left\langle \frac{1}{r_{12}} \right\rangle_{\Psi(1,2)} - \left\langle \frac{1}{r_{12}} \right\rangle_{\Psi(1,2)}, \quad (3.115)$$

to  $\blacktriangleright$  Eq. 3.111 allows one to ascribe, for instance,

$$\begin{aligned} \langle \phi_i(1) | \hat{v}(1) | \phi_i(1) \rangle &= \langle \phi_i(1)\phi_j(2) | \frac{1}{r_{12}} | \phi_i(1)\phi_j(2) - \phi_j(1)\phi_i(2) \rangle, \\ \langle \phi_j(2) | \hat{v}(2) | \phi_j(2) \rangle &= \langle \phi_i(1)\phi_j(2) | \frac{1}{r_{12}} | \phi_i(1)\phi_j(2) - \phi_j(1)\phi_i(2) \rangle, \\ \text{the rest} &= -\langle \phi_i(1)\phi_j(2) | \frac{1}{r_{12}} | \phi_i(1)\phi_j(2) - \phi_j(1)\phi_i(2) \rangle. \end{aligned}$$

Consider in more detail the integral containing  $\hat{v}(1)$ . We want it to be expressed in such a way that only the coordinates of the electron labeled by 1 are explicitly written under the integral:

$$\begin{aligned} \langle \phi_i(1) | \hat{v}(1) | \phi_i(1) \rangle &= \langle \phi_i(1)\phi_j(2) | \frac{1}{r_{12}} | \phi_i(1)\phi_j(2) - \phi_j(1)\phi_i(2) \rangle \\ &= \int \int \phi_i^*(\tau_1)\phi_j^*(\tau_2) \frac{1}{r_{12}} \phi_i(\tau_1)\phi_j(\tau_2) d\tau_1 d\tau_2 \\ &\quad - \int \int \phi_i^*(\tau_1)\phi_j^*(\tau_2) \frac{1}{r_{12}} \phi_j(\tau_1)\phi_i(\tau_2) d\tau_1 d\tau_2 \end{aligned}$$

$$\begin{aligned}
&= \int \phi_i^*(\tau_1) \left( \int \phi_j^*(\tau_2) \frac{1}{r_{12}} \phi_j(\tau_2) d\tau_2 \right) \phi_i(\tau_1) d\tau_1 \\
&\quad - \int \phi_i^*(\tau_1) \left( \int \phi_j^*(\tau_2) \frac{1}{r_{12}} \phi_i(\tau_2) d\tau_2 \right) \phi_j(\tau_1) d\tau_1 \\
&= \int \phi_i^*(\tau_1) (\widehat{J}_j(1) \phi_i(\tau_1)) d\tau_1 \\
&\quad - \int \phi_i^*(\tau_1) (\widehat{K}_j(1) \phi_i(\tau_1)) d\tau_1 \\
&= \langle \phi_i(1) | \widehat{J}_j(1) | \phi_i(1) \rangle - \langle \phi_i(1) | \widehat{K}_j(1) | \phi_i(1) \rangle \\
&= \langle \phi_i(1) | \widehat{J}_j(1) - \widehat{K}_j(1) | \phi_i(1) \rangle, \tag{3.116}
\end{aligned}$$

where two operators were defined:

$$\widehat{J}_j(1) \phi_i(1) = \left( \int \phi_j^*(\tau_2) \frac{1}{r_{12}} \phi_j(\tau_2) d\tau_2 \right) \phi_i(1), \tag{3.117}$$

$$\widehat{K}_j(1) \phi_i(1) = \left( \int \phi_j^*(\tau_2) \frac{1}{r_{12}} \phi_i(\tau_2) d\tau_2 \right) \phi_j(1). \tag{3.118}$$

Despite a slightly different way of defining, they are still ordinary operators. An operator is a function of a function. The operators  $\widehat{J}_j(1)$  and  $\widehat{K}_j(1)$  act on the function  $\phi_i(1)$ , producing another function, as was written in [Eq. 3.8](#). The operator  $\widehat{J}_j(1)$  acting on  $\phi_i(1)$  transforms it into the same function:

$$\phi_i(1) \xrightarrow{\widehat{J}_j(1)} \left( \int \phi_j^*(\tau_2) \frac{1}{r_{12}} \phi_j(\tau_2) d\tau_2 \right) \phi_i(1), \tag{3.119}$$

and the operator  $\widehat{K}_j(1)$  produces  $\phi_j(1)$ :

$$\phi_i(1) \xrightarrow{\widehat{K}_j(1)} \left( \int \phi_j^*(\tau_2) \frac{1}{r_{12}} \phi_i(\tau_2) d\tau_2 \right) \phi_j(1). \tag{3.120}$$

The expressions on the right-hand side of the arrows are some functions of a dependent variable  $\tau_1$  (the integration eliminates the dependence on  $\tau_2$ , however, its result is not a number, but a function depending on  $\tau_1$ ). The interpretation of the  $\widehat{J}_j(1)$  and  $\widehat{K}_j(1)$  operators by ascribing them to observables is not straightforward. These operators appear in the equations when we try to write the interaction between two electrons as the average value of the one-electron operator calculated with the one-electron function. However, in fact, they do appear as the difference:

$$\hat{v}_i^{\text{HF}}(1) = \widehat{J}_j(1) - \widehat{K}_j(1). \tag{3.121}$$

And the physical sense should be sought in this difference. Here,  $\hat{v}_i^{\text{HF}}(1)$  is an operator of the average interaction of the electron labeled as 1, described by a spin-orbital  $\phi_i$  with the second electron characterized by  $\phi_j(2)$ . It should be noticed that the potential  $\hat{v}_i^{\text{HF}}(1)$  depends on  $\phi_j(2)$ , since this spin-orbital is necessary to define  $\widehat{J}_j(1)$  and  $\widehat{K}_j(1)$  operators.

Similarly,

$$\hat{v}_j^{\text{HF}}(2) = \widehat{J}_i(2) - \widehat{K}_i(2), \tag{3.122}$$

where the action of operators  $\widehat{J}_j(1)$  and  $\widehat{K}_j(1)$  on the function  $\phi_j(2)$  is defined by

$$\widehat{J}_i(2) \phi_j(2) = \left( \int \phi_i^*(\tau_1) \frac{1}{r_{12}} \phi_i(\tau_1) d\tau_1 \right) \phi_j(2) \tag{3.123}$$

$$\widehat{K}_i(2) \phi_j(2) = \left( \int \phi_i^*(\tau_1) \frac{1}{r_{12}} \phi_j(\tau_1) d\tau_1 \right) \phi_i(2). \tag{3.124}$$

Here, one more important circumstance should be mentioned. The electronic Hamiltonian does not depend on spin. However, the electronic wave function is spin dependent. During the construction of the HF equations, this dependence is introduced to the operators  $\widehat{K}$  since they depend on two different spin-orbitals.

Let us briefly review. We want to have a one-electron operator that includes the interaction between the electrons in some averaged way. Such an operator must depend on the function describing the motion of the second, adjacent, electron. Therefore, for the two-electron case, two coupled equations must be solved (► Eqs. 3.113 and ► 3.114). The word “coupled” that distinguishes this set of equations from ► Eqs. 3.95 and ► 3.96 is crucial. Denoting

$$\hat{f}_i(1) = \hat{h}(1) + v_i^{\text{HF}}(1), \quad (3.125)$$

one can rewrite the above equations as

$$\hat{f}_k(1)\phi_k(1) = \epsilon_k\phi_k(1), \quad \text{for } k = i, j. \quad (3.126)$$

$\hat{f}_i(1)$  is called the Fock operator and ► Eq. 3.114 gives the Hartree–Fock equations.

It should be noted that the label of electrons determines only the name of the integration variables, and the result of the integration does not depend on the name of the variable. Therefore, what is really important is the label of the spin-orbital. It will be even more pronounced in the  $N$ -electron case, when the electron labels are applied only to show that the operator acts on one or two electron coordinates. The form of the  $N$ -electron wave function depends only on the spin-orbitals and not on the electron labels; they are just the integration variables.

The most popular way of solving ► Eq. 3.126 is the iterative procedure. It starts from the guessed or chosen spin-orbitals  $\phi_i(1)$  and  $\phi_j(2)$  applied to construct the potentials  $\hat{v}_i^{\text{HF}}(1)$  and  $\hat{v}_j^{\text{HF}}(2)$ . Next, the obtained potentials are substituted to ► Eq. 3.125 and solutions of ► Eq. 3.126 give the improved form of the  $\phi_i(1)$  and  $\phi_j(2)$  spin-orbitals. These, on the other hand, are treated as the starting point again, and the whole procedure is repeated until the starting and final orbitals of the given iteration do not differ much. This technique is called self-consistent field (SCF). Often the abbreviations HF for Hartree–Fock method and SCF are used interchangeably. They can also be joined together as SCF–HF, denoting the self-consistent way of solving Hartree–Fock equations.

Let us assume that the spin-orbitals are already known. Concentrate on the calculations of the average value of the Hamiltonian with the determinant build of these spin-orbitals using the operators defined previously. Writing down the two-electron part:

$$\begin{aligned} \left\langle \frac{1}{r_{12}} \right\rangle_{\Psi(1,2)} &= \langle \phi_i(1) | \widehat{J}_j(1) - \widehat{K}_j(1) | \phi_i(1) \rangle \\ &= \langle \phi_j(2) | \widehat{J}_i(2) - \widehat{K}_i(2) | \phi_j(2) \rangle, \end{aligned}$$

one obtains the integrals that can be denoted by

$$\begin{aligned} J_{ij} &= \langle \phi_i(1) | \widehat{J}_j(1) | \phi_i(1) \rangle, \\ K_{ij} &= \langle \phi_i(1) | \widehat{K}_j(1) | \phi_i(1) \rangle. \end{aligned}$$

With this notation, the expression (► Eq. 3.106) takes the following form:

$$\langle \widehat{H}(1,2) \rangle_{\Psi(1,2)} = \langle \phi_i(1) | \hat{f}_i(1) | \phi_i(1) \rangle + \langle \phi_j(2) | \hat{f}_j(2) | \phi_j(2) \rangle - (J_{ij} - K_{ij}), \quad (3.127)$$



or, if one wants to apply the spin-orbital energies  $\epsilon$  calculated earlier:

$$\langle \widehat{H}(1, 2) \rangle_{\Psi(1,2)} = \epsilon_i + \epsilon_j - (J_{ij} - K_{ij}). \quad (3.128)$$

Now it is time to generalize these considerations into the  $N$ -electron case. The recipe for this transformation was given previously (🔗 Eqs. 3.91–3.93). For the system of  $N$  electrons, the set of  $N$ -coupled equations of the form

$$\hat{f}_i(1)\phi_i(1) = \epsilon_i\phi_i(1), \quad \text{for } i = 1, \dots, N \quad (3.129)$$

must be solved. Here,

$$f_i(1) = h(1) + \sum_{j \neq i}^N (\widehat{T}_j(1) - \widehat{K}_j(1)). \quad (3.130)$$

The summation in the expression for the one-electron Fock operator arises from the fact that now the given electron described by the spin-orbital  $i$  interacts with  $(N - 1)$  electrons in the states determined by the remaining spin-orbitals.

In searching for the ground state energy, one is interested in the lowest possible energy. Therefore, the functions of choice are the spin-orbitals corresponding to the lowest values of  $\epsilon$ . Such a set of spin-orbitals, called occupied, is opposite to any other solutions of the Fock equations corresponding to higher energies. These are known as virtual (unoccupied) orbitals.

Finally, the average value of the Hamiltonian can be written as

$$\langle \widehat{H}(1, 2, \dots, N) \rangle_{\Psi^{(0)}(N)} = \sum_{i=1}^N \epsilon_i - \sum_{i=1}^N \sum_{j>i}^N (J_{ij} - K_{ij}) = E_0^{\text{HF}}.$$

It should be emphasized that the energy estimated in this manner is not the simple sum of the orbital energies. If the terms  $\sum_{i=1}^N \sum_{j>i}^N (J_{ij} - K_{ij})$  are neglected, the double summation of the electron-electron interaction would take place (Atkins and Friedman 2005; Cramer 2004; Jensen 2006; Levine 2008; Lowe and Peterson 2005; McQuarrie and Simon 1997; Piela 2007; Ratner and Schatz 2000; Roos and Widmark 2002; Szabo and Ostlund 1996).

## Møller–Plesset Perturbation Theory – HF Is Just the Beginning

From here forward, we will treat the Hartree–Fock function as the basis for the further investigations and denote it as  $\Psi_0^{(0)}$ , where the subscript 0 indicates the ground state and the superscript (0) is the reference function. We will also omit the explicit writing of the dependence of the Hamiltonian and the wave function on the coordinates of  $N$  electrons. As a consequence,

$$\langle \Psi_0^{(0)} | \widehat{H} | \Psi_0^{(0)} \rangle = E_0^{\text{HF}}. \quad (3.131)$$

One of the possible ways of improving the HF results is the application of the perturbation theory (Atkins and Friedman 2005; Cramer 2004; Jensen 2006; Levine 2008; McQuarrie and Simon 1997; Piela 2007; Ratner and Schatz 2000; Szabo and Ostlund 1996). The Hamiltonian (🔗 Eq. 3.89) can be partitioned into the unperturbed part and the perturbation in the following manner:

$$\widehat{H}^0 = \sum_{i=1}^N \hat{f}(i), \quad \widehat{H}^1 = \sum_{i=1}^N \left( \sum_{j>i}^N \frac{1}{r_{ij}} - \hat{v}^{\text{HF}}(i) \right), \quad (3.132)$$

(compare  $\blacktriangleright$  Eq. 3.125). Up to the first order in the perturbation theory, the energy is

$$E_0^{\text{HF}} = E_0^{(0)} + E_0^{(1)} = \langle \Psi_0^{(0)} | \widehat{H}^0 + \widehat{H}^1 | \Psi_0^{(0)} \rangle = \langle \widehat{H} \rangle_{\Psi_0^{(0)}}. \quad (3.133)$$

The correction to the HF energy appears in the second order:

$$E_0^{(2)} = \sum_{k \neq 0}^{\infty} \frac{|\langle \Psi_0^{(0)} | \widehat{H}^1 | \Psi_k^{(0)} \rangle|^2}{E_0^{(0)} - E_k^{(0)}}. \quad (3.134)$$

During calculations, the expansion of the spin-orbitals in the finite basis set is applied. This allows identification of only the finite number of spin-orbitals. But the number of all possible  $\Psi_k^{(0)}$  functions can still be horrifyingly large. In practice, this is equivalent to the finite but long expansion in the above summation. In quantum chemistry we are interested in the best quality results with moderate expenses and are continuously searching for more economical methods.

Careful examination of the second-order energy correction  $E_0^{(2)}$  shows that a significant number of its terms do not contribute to the final result. Some work invested in the manipulation of expressions allows one not only to learn the basic computational apparatus but also to save a lot of effort.

In order to proceed comfortably, the notation should again be simplified. Let us drop the superscript (0) denoting the zeroth-order functions (other functions will not appear in our considerations). Additionally, we omit the subscript  $k$  from the determinants containing the virtual spin-orbitals. In return, we explicitly specify the pattern of spin-orbital exchange. Using  $\blacktriangleright$  Eq. 3.108, the Slater determinant can be written as

$$|\Psi_0\rangle = |\phi_1(1)\phi_2(2)\phi_3(3)\phi_4(4)\dots\phi_N(N)\rangle. \quad (3.135)$$

The numbers of the occupied spin-orbitals vary from 1 to  $N$ . Thus, the virtual spin-orbitals will be labeled starting from  $N+1$  onward. Now consider the example of the determinant in which the occupied spin-orbital  $\phi_3$  is exchanged for the virtual one,  $\phi_{N+8}$ . The new determinant can be written as

$$|\Psi_3^{N+8}\rangle = |\phi_1(1)\phi_2(2)\phi_{N+8}(3)\phi_4(4)\dots\phi_N(N)\rangle, \quad (3.136)$$

where the subscript in  $\Psi_3^{N+8}$  denotes the occupied orbital that is exchanged and the superscript denotes the virtual one that takes its place. To generalize, one could denote the occupied orbitals building the  $\Psi_0$  function by first alphabet letters  $a, b, c, d, \dots$  and the virtuals by  $p, q, r, s, \dots$ . Therefore,  $\Psi_3^{N+8}$  can be written as  $\Psi_a^p$ , where  $a = 3$  and  $p = N + 8$ . Likewise, any determinant can be represented.

Thereafter, the influence of the function choice on the values of the integrals appearing in the electronic energy calculations can be investigated. Similarly, as in the case of Hamiltonian, the integrals can also be divided into two groups with one-electron operator

$$\hat{o}_1 = \sum_{i=1}^N \hat{o}(i), \quad (3.137)$$

where in place of  $\hat{o}(i)$  operators  $\hat{h}, (i)$  or  $\hat{f}(i)$  will be used, and with two-electron operator,

$$\widehat{O}_2 = \sum_i \sum_{j>i} \left( \frac{1}{r_{ij}} \right). \quad (3.138)$$

To get a full picture we should analyze the following types of integrals:

$$\langle \Psi_0 | \hat{\sigma}_1 | \Psi_a^p \rangle \quad \text{and} \quad \langle \Psi_0 | \widehat{\mathcal{O}}_2 | \Psi_a^p \rangle, \quad (3.139)$$

$$\langle \Psi_0 | \hat{\sigma}_1 | \Psi_{ab}^{pq} \rangle \quad \text{and} \quad \langle \Psi_0 | \widehat{\mathcal{O}}_2 | \Psi_{ab}^{pq} \rangle, \quad (3.140)$$

$$\langle \Psi_0 | \hat{\sigma}_1 | \Psi_{abc}^{pqr} \rangle \quad \text{and} \quad \langle \Psi_0 | \widehat{\mathcal{O}}_2 | \Psi_{abc}^{pqr} \rangle. \quad (3.141)$$

Any other will be equal to zero (Levine 2008; Szabo and Ostlund 1996).

Recall that the determinant of the  $N \times N$  matrix can be represented as the sum of the  $N!$  products of the matrix elements. According to Laplace's formula, a determinant can be expanded along a row or a column. Thus, calculation of the  $\langle \Psi_0 | \hat{\sigma}_1 | \Psi_a^p \rangle$  integrals, when the occupied orbital  $a$  in  $\Psi_0$  has been exchanged with the virtual orbital  $p$  in  $\Psi_a^p$ , can be performed by expanding the determinant  $\Psi_0$  along the  $a$ -th row and the determinant  $\Psi_a^p$  along the  $p$ -th row:

$$\Psi_0 = \frac{1}{\sqrt{N!}} \sum_{i=1}^N \phi_a(i) C_{ai}, \quad (3.142)$$

$$\Psi_a^p = \frac{1}{\sqrt{N!}} \sum_{i=1}^N \phi_p(i) C_{pi}. \quad (3.143)$$

The cofactors  $C$  can be perceived as the  $(N-1)$ -electron determinants that have been obtained from  $\Psi_0$  and  $\Psi_a^p$  via the elimination of the  $a$ -th and  $p$ -th spin-orbitals, respectively. Thus, after elimination of what is different in the two determinants, we get both cofactors equal to each other. Hence,

$$\begin{aligned} \langle \Psi_0 | \hat{\sigma}_1 | \Psi_a^p \rangle &= \frac{1}{N!} \langle \sum_{i=1}^N \phi_a(i) C_{ai} | \sum_{j=1}^N \hat{\sigma}(j) | \sum_{k=1}^N \phi_p(k) C_{pi} \rangle \\ &= \frac{1}{N!} \sum_{i=1}^N \langle \phi_a(i) | \hat{\sigma}(i) | \phi_p(i) \rangle \langle C_{ai} | C_{pi} \rangle \\ &= \frac{1}{N} \sum_{i=1}^N \langle \phi_p(i) | \hat{\sigma}(i) | \phi_p(i) \rangle \\ &= \langle \phi_a(1) | \hat{\sigma}(1) | \phi_p(1) \rangle, \end{aligned} \quad (3.144)$$

where

$$\langle C_{ai} | C_{pi} \rangle = (N-1)!, \quad (3.145)$$

$$\sum_{i=1}^N \langle \phi_a(i) | \hat{\sigma}(i) | \phi_a(i) \rangle = N \langle \phi_a(1) | \hat{\sigma}(1) | \phi_a(1) \rangle \quad (3.146)$$

was applied. If the cofactors are not the same – this would be the case when the determinants differ from two or more spin-orbitals – the corresponding overlap matrix is equal to zero according to the orthogonality condition. Thus,

$$\begin{aligned} \langle \Psi_0 | \hat{\sigma}_1 | \Psi_a^p \rangle &= \langle \phi_a(1) | \hat{\sigma}(1) | \phi_p(1) \rangle, \\ \langle \Psi_0 | \hat{\sigma}_1 | \Psi_{ab}^{pq} \rangle &= 0, \\ \langle \Psi_0 | \hat{\sigma}_1 | \Psi_{abc}^{pqr} \rangle &= 0. \end{aligned} \quad (3.147)$$

Similar (but a little more time-consuming) considerations for the two-electron operators lead to the following expressions:

$$\begin{aligned}
 \langle \Psi_0 | \widehat{O}_2 | \Psi_a^p \rangle &= \sum_{i=1}^N \left( \langle \phi_a(1) \phi_i(2) | \frac{1}{r_{12}} | \phi_p(1) \phi_i(2) \rangle \right. \\
 &\quad \left. - \langle \phi_a(1) \phi_i(2) | \frac{1}{r_{12}} | \phi_i(1) \phi_p(2) \rangle \right) \\
 \langle \Psi_0 | \widehat{O}_2 | \Psi_{ab}^{pq} \rangle &= \langle \phi_a(1) \phi_b(2) | \frac{1}{r_{12}} | \phi_p(1) \phi_q(2) \rangle \\
 &\quad - \langle \phi_a(1) \phi_b(2) | \frac{1}{r_{12}} | \phi_q(1) \phi_p(2) \rangle \\
 \langle \Psi_0 | \widehat{O}_2 | \Psi_{abc}^{pqr} \rangle &= 0.
 \end{aligned} \tag{3.148}$$

In the first contact with these equations one can have the feeling that something is lost here. We start from the integrals with the  $N$ -electron functions and we finish with the integral of only the electrons labeled by 1 and 2. What happened to the rest? Again, it should be emphasized here that the electron labels symbolize only the integration variables. What matters is the functions of these variables, namely spin-orbitals. Thus, in the integral with the one-electron operator the electron label 1 means that the integration is performed only over the variables of one electron. Likewise, the two-electron operator integral depends on the variables of two electrons, which is symbolized by two labels: 1 and 2.

In the integration of one-electron expressions, the electron label can be omitted without any harm:  $\langle \phi_a(1) | \hat{o}_1 | \phi_a(1) \rangle$ . Likewise, in the two-electron case, we can declare that the spin-orbitals are written in the given order. So,

$$\langle \phi_x(1) \phi_y(2) | \frac{1}{r_{12}} | \phi_v(1) \phi_z(2) \rangle = \langle \phi_x \phi_y | \frac{1}{r_{12}} | \phi_v \phi_z \rangle. \tag{3.149}$$

Moreover, now there is no reason to explicitly write the  $\phi$  symbol. Thereby, the next simplification of the notation is obvious:

$$\begin{aligned}
 \langle \phi_a | \hat{o}_1 | \phi_a \rangle &= \langle a | \hat{o}_1 | a \rangle, \\
 \langle \phi_x \phi_y | \frac{1}{r_{12}} | \phi_v \phi_z \rangle &= \langle xy | \frac{1}{r_{12}} | vz \rangle,
 \end{aligned} \tag{3.150}$$

and, finally, since the combination of the integrals  $\langle xy | 1/r_{12} | vz \rangle - \langle xy | 1/r_{12} | zv \rangle$  appears frequently, the following symbol is introduced:

$$\langle xy || zv \rangle = \langle xy | \frac{1}{r_{12}} | vz \rangle - \langle xy | \frac{1}{r_{12}} | zv \rangle. \tag{3.151}$$

Now  $\blacktriangleright$  Eqs. 3.147 and  $\blacktriangleright$  3.148 can be rewritten as

$$\begin{aligned}
 \langle \Psi_0 | \hat{o}_1 | \Psi_a^p \rangle &= \langle a | \hat{o} | p \rangle, \\
 \langle \Psi_0 | \hat{o}_1 | \Psi_{ab}^{pq} \rangle &= 0, \\
 \langle \Psi_0 | \hat{o}_1 | \Psi_{abc}^{pqr} \rangle &= 0, \\
 \langle \Psi_0 | \widehat{O}_2 | \Psi_a^p \rangle &= \sum_{i=1}^N \langle ai || pi \rangle, \\
 \langle \Psi_0 | \widehat{O}_2 | \Psi_{ab}^{pq} \rangle &= \langle ab || pq \rangle, \\
 \langle \Psi_0 | \widehat{O}_2 | \Psi_{abc}^{pqr} \rangle &= 0.
 \end{aligned} \tag{3.152}$$

These simple equations, known as the Slater rules, allow for the following general remark: If the one-electron operator is integrated with functions that differ by more than one spin-orbital, the corresponding integral vanishes. Similarly, the result is zero for the integration of two-electron operators with functions differing by more than two spin-orbitals. Hitherto, only the integrals with  $\Psi_0$  were considered. However, it is easy to notice that functions  $\Psi_{ab}^{pq}$  and  $\Psi_{abc}^{pqr}$  differ by only one exchange (spin-orbital  $\phi_c \rightarrow \phi_r$ ), etc. Therefore, the above considerations can be also applied in any other cases.

In this abundance of equations our main goal cannot be lost: All these derivations were necessary to limit the types of the  $\Psi_k$  functions present in the MP2 energy expression. Now, with a recognition of the above Slater rules, one can safely neglect the integrals with the pairs of the  $\Psi_k$  functions differing with more than two spin-orbital exchanges. But this is not everything.

Let us consider the integral

$$\langle \Psi_0 | \widehat{H} | \Psi_a^p \rangle = \langle a | \widehat{h} | p \rangle + \sum_j (\langle a j | \frac{1}{r_{ij}} | p j \rangle - \langle a j | \frac{1}{r_{ij}} | j p \rangle). \quad (3.153)$$

Since

$$\langle a j | \frac{1}{r_{ij}} | p j \rangle = \langle a | \widehat{J}_j | p \rangle, \quad (3.154)$$

and

$$\langle a j | \frac{1}{r_{ij}} | j p \rangle = \langle a | \widehat{K}_j | p \rangle, \quad (3.155)$$

one gets

$$\langle \Psi_0 | \widehat{H} | \Psi_a^p \rangle = \langle a | \widehat{H}^0 | p \rangle, \quad (3.156)$$

which has to vanish, because

$$\langle a | \widehat{H}^0 | p \rangle = \langle a | \sum_{i=1}^N f(i) | p \rangle = \langle a | f | p \rangle = \epsilon_p \delta_{ap} = 0, \quad (3.157)$$

for it was assumed that  $a \neq p$ .

The obtained result,

$$\langle \Psi_0 | \widehat{H} | \Psi_a^p \rangle = 0, \quad (3.158)$$

is known as the Brillouin theorem. Applying it allows one also to show that

$$\langle \Psi_0 | \widehat{H}^1 | \Psi_a^p \rangle = 0. \quad (3.159)$$

Indeed, using

$$\widehat{H}^1 = \widehat{H} - \widehat{H}^0, \quad (3.160)$$

one obtains

$$\begin{aligned} \langle \Psi_0 | \widehat{H}^1 | \Psi_a^p \rangle &= \langle \Psi_0 | \widehat{H} | \Psi_a^p \rangle - \langle \Psi_0 | \widehat{H}^0 | \Psi_a^p \rangle \\ &= 0 - \left( \sum_{i=1}^N \epsilon_i \right) \langle \Psi_0 | \Psi_a^p \rangle \\ &= 0. \end{aligned} \quad (3.161)$$

Now is the time for an important conclusion: In order to calculate the correction to the energy in MP2, the functions arising from  $\Psi_0$  only by the exchange of precisely two spin-orbitals need to be applied. Not more, not less. Life becomes easier when not calculating zero contributions in a complicated way.

Let us exploit the above knowledge to transform  $\blacktriangleright$  Eq. 3.134. The integral on the right-hand side will be calculated with the functions  $\Psi_{ab}^{pq}$ . Assuming  $b > a$  and  $q > p$  allows avoidance of the integration with the same functions. The upper limit for the summations over  $a$  and  $b$  will be equal to  $N$ . For the remaining spin-orbitals it should be  $\infty$ ; however, in practice, the finite basis is applied and the upper limit will be determined by the basis set size. Let us look into the numerator of  $\blacktriangleright$  Eq. 3.134 carefully. Denoting the total Fock operator as  $\widehat{F} = \sum_i \hat{f}(i)$ , one gets

$$\begin{aligned} \langle \Psi_0 | \widehat{H}^1 | \Psi_{ab}^{pq} \rangle &= \langle \Psi_0 | \widehat{H} | \Psi_{ab}^{pq} \rangle - \langle \Psi_0 | \widehat{F} | \Psi_{ab}^{pq} \rangle \\ &= \langle ab | \frac{1}{r_{ij}} | pq \rangle - \langle ab | \frac{1}{r_{ij}} | qp \rangle, \end{aligned} \quad (3.162)$$

since

$$\langle \Psi_0 | \widehat{F} | \Psi_{ab}^{pq} \rangle = 0 \quad (3.163)$$

(integration of the one-electron operator with the functions differing by two spin-orbitals, see  $\blacktriangleright$  Eq. 3.152).

Now consider the denominator of  $\blacktriangleright$  Eq. 3.134. The energy of the ground state is simply a sum of  $N$  lowest spin-orbital energies:

$$E_0^{(0)} = \sum_{i=1}^N \epsilon_i. \quad (3.164)$$

The energy of the zeroth order for the function  $\Psi_{ab}^{pq}$  is a similar sum with  $\epsilon_a$  and  $\epsilon_b$  replaced by  $\epsilon_p$  and  $\epsilon_q$ :

$$E_{(ab)}^{(0)} = E_0^{(0)} - \epsilon_a - \epsilon_b + \epsilon_p + \epsilon_q. \quad (3.165)$$

Thus, the final form of  $\blacktriangleright$  Eq. 3.134 is

$$E_0^{(2)} = \sum_{b>a} \sum_{q>p} \frac{|\langle ab || pq \rangle|^2}{\epsilon_p + \epsilon_q - \epsilon_a - \epsilon_b}. \quad (3.166)$$

Why was it worth our hard work? Not only for satisfaction. These derivations are necessary to understand the mechanisms employed in computational methods of quantum chemistry. With the Slater rules it is straightforward to recognize the vanishing integrals. The double exchanges appear to be most important, since these are the only exchanges that give rise to the energy corrections in the MP2 method.

According to the perturbation calculus, the wave function corrected in the first order can be written as

$$\Psi \approx \Psi_0 + \sum_{k \neq 0} c_k \Psi_k, \quad (3.167)$$

where  $c_k$  is given by

$$c_k = \frac{\langle \Psi_0 | \widehat{H}^1 | \Psi_k \rangle}{E_0 - E_k}. \quad (3.168)$$

From the Slater rules it is easy to estimate that the only non-vanishing terms will arise from the double spin-orbital exchange in the wave function. The intuitive statement that the low-order corrections should have the larger impact and the above considerations lead to the most important accomplishment of this section: the largest contribution to the corrections of the Hartree–Fock function arises from the functions with the doubly exchanged spin-orbitals.

## Beyond the HF Wave Function

Having done all this hard work, one can now sit comfortably in an armchair and think. The main goal of the quantum chemistry is to find the best possible description of the state of the system (the best possible wave function). The exact solutions of the Hamiltonian eigenproblem are unavailable and all we have are approximations. We have become used to approximations in everyday life. The important thing is to realize that the Hartree–Fock solutions can be improved. At the beginning of this chapter, various properties of operators were discussed. Among others, it was stated that the eigenfunctions of the Hermitian operators constitute the complete sets and any other function of the same variables can be represented by applying them. The one-electron spin-orbitals that are the eigenfunctions of the Fock operator are accessible. They form the complete set, but only for the one-electron functions. However, they can be applied to build up the  $N$ -electron determinants. The set of all possible determinants is also complete and, therefore, can be applied to express any  $N$ -electron function (Cramer 2004; Jensen 2006; Levine 2008; Lowe and Peterson 2005; Piela 2007; Ratner and Schatz 2000; Roos and Widmark 2002; Szabo and Ostlund 1996):

$$\Psi = c_0 \Psi_0 + \sum_{a,p} c_a^p \Psi_a^p + \sum_{a,b,p,q} c_{ab}^{pq} \Psi_{ab}^{pq} + \sum_{a,b,c,p,q,r} c_{abc}^{pqr} \Psi_{abc}^{pqr} + \dots \quad (3.169)$$

For this purpose, only the coefficients  $c_0, c_a^p, c_{ab}^{pq}, c_{abc}^{pqr}, \dots$  need to be found. In the ideal case all the summations would be infinite and the problem must be reduced. Still, instead of using the infinite expansions, the finite and relatively small number of terms can be sufficient. Moreover, solving the Hartree–Fock equations in the finite basis, one possesses only the finite number of orbitals that can be exchanged.

Anyway, it is instructive to see how large the number of terms in  $\blacktriangleright$  Eq. 3.169 can be. Consider the methane molecule  $\text{CH}_4$ . Calculations with the minimal basis set (each orbital described by a single one-electron function; for carbon single functions for each of the orbitals,  $1s, 2s, 2p_x, 2p_y, 2p_z$ , and for hydrogen a single function for  $1s$  orbital) require 9 orbitals/18 spin-orbitals for the 10-electron system. From the probability theory the number of combinations ( $K$ ) of  $k$  elements from the  $n$ -element set can be calculated as

$$K = \binom{n}{k} = \frac{n!}{(n-k)!k!}. \quad (3.170)$$

In the case of methane, 10 electrons can be placed in 18 spin-orbitals on  $\binom{18}{10} = 43,758$  ways. This is equivalent to the 43,758 terms in the expansion ( $\blacktriangleright$  Eq. 3.169). Impressive. And one needs to remember that the minimal basis set gives relatively bad Hartree–Fock solutions and is not recommended in *ab initio* calculations. However, increasing the basis set size causes the number of expansion terms to grow dramatically. For instance, in the case of the so-called double- $\zeta$  basis set (two functions per each orbital) for methane, one has 36 spin-orbitals, which makes 254,186,856 combinations! And double- $\zeta$  is still not much....

Therefore, it is necessary to find some way to reduce the size of the problem. The symmetry of the molecules can be applied here, and the fact that the chosen determinants (or their linear combinations) must be the given functions of the spin operators can be beneficial. Moreover, one would like to eliminate from the expansion the determinants that are not crucial for the quality of the wave function, and their neglect does not cause the deterioration of the description of the system (or causes only slight deterioration). In other words, only the determinants

that have the significant contribution to the total energy must be chosen for the wave function construction. Let us begin with the classification of the determinants, taking into account the number of the spin-orbitals exchanged with respect to  $\Psi_0$ . For this purpose the averaged value of Hamiltonian calculated with  $\Psi$  will be useful. We can write the wave function expansion as

$$\Psi = c_0 \Psi_0 + \mathbf{S}c_S + \mathbf{D}c_D + \mathbf{T}c_T + \mathbf{Q}c_Q + \dots \quad (3.171)$$

The symbols' meaning can be clearly deciphered by comparison with [Eq. 3.169](#):  $\mathbf{S}$  denotes a vector build of the determinants constructed from  $\Psi_0$  by single exchanges and  $c_S$  is a vector of coefficients corresponding to the functions in  $\mathbf{S}$ :

$$\mathbf{S}c_S = \sum_a \sum_q c_a^q \Psi_a^q. \quad (3.172)$$

In other words,  $\mathbf{S}$  contains all the functions with the single exchanged spin-orbital. Similarly,  $\mathbf{D}$  would be the combination of the functions with double exchanges,  $\mathbf{T}$  with triple exchanges, and so forth. With such a notation, the function  $\Psi$  can be treated as the scalar product of the basis vectors  $\Psi_0, \mathbf{S}, \mathbf{D}, \dots$  and the coefficient vector

$$|\Psi\rangle = [|\Psi_0\rangle, |\mathbf{S}\rangle, |\mathbf{D}\rangle, |\mathbf{T}\rangle, |\mathbf{Q}\rangle, \dots] \cdot \begin{bmatrix} c_0 \\ c_S \\ c_D \\ c_T \\ c_Q \\ \vdots \end{bmatrix}. \quad (3.173)$$

Using this notation, the Hamiltonian  $\widehat{H}$  of the system can be linked in an elegant way to a matrix  $\mathbf{H}$ . Let us apply this form of the wave function for the calculation of the Hamiltonian average value. To simplify the expressions, let us limit ourselves to the truncated expansion:

$$\Psi_{SD} = [\Psi_0 \mathbf{S} \mathbf{D}] \begin{bmatrix} c_0 \\ c_S \\ c_D \end{bmatrix} = c_0 \Psi_0 + \mathbf{S}c_S + \mathbf{D}c_D. \quad (3.174)$$

The average value of the Hamiltonian can now be written as

$$\langle H \rangle_{\Psi_{SD}} = \langle \Psi_{SD} | \widehat{H} | \Psi_{SD} \rangle = [c_0 c_S c_D]^\dagger \begin{bmatrix} \langle \Psi_0 | \\ \langle \mathbf{S} | \\ \langle \mathbf{D} | \end{bmatrix} \widehat{H} [|\Psi_0\rangle, |\mathbf{S}\rangle, |\mathbf{D}\rangle] \begin{bmatrix} c_0 \\ c_S \\ c_D \end{bmatrix}. \quad (3.175)$$

The vector multiplication leads to the following expression:

$$\begin{aligned} \langle H \rangle_{\Psi_{SD}} &= c_0^* \langle \Psi_0 | \widehat{H} | \Psi_0 \rangle c_0 + c_0^* \langle \Psi_0 | \widehat{H} | \mathbf{S} \rangle c_S + c_0^* \langle \Psi_0 | \widehat{H} | \mathbf{D} \rangle c_D + c_S^\dagger \langle \mathbf{S} | \widehat{H} | \Psi_0 \rangle c_0 \\ &+ c_S^\dagger \langle \mathbf{S} | \widehat{H} | \mathbf{S} \rangle c_S + c_S^\dagger \langle \mathbf{S} | \widehat{H} | \mathbf{D} \rangle c_D + c_D^\dagger \langle \mathbf{D} | \widehat{H} | \Psi_0 \rangle c_0 \\ &+ c_D^\dagger \langle \mathbf{D} | \widehat{H} | \mathbf{S} \rangle c_S + c_D^\dagger \langle \mathbf{D} | \widehat{H} | \mathbf{D} \rangle c_D. \end{aligned} \quad (3.176)$$

Such an equation is not very useful, since we still do not know the  $c_0, c_S$  and  $c_D$  coefficients determining the  $\Psi_{SD}$  function. The only thing that can be said about them so far comes from the normalization requirement for  $\Psi_{SD}$ :

$$1 = c_0^* c_0 + c_S^\dagger c_S + c_D^\dagger c_D. \quad (3.177)$$



This is not enough to uniquely determine the wave function. However, going back to [Eq. 3.175](#) and multiplying only the inside vectors one obtains

$$\mathbf{H}_{\text{SD}} = \begin{bmatrix} \langle \Psi_0 | \\ \langle \mathbf{S} | \\ \langle \mathbf{D} | \end{bmatrix} \widehat{H} [ | \Psi_0 \rangle, | \mathbf{S} \rangle, | \mathbf{D} \rangle ] = \begin{bmatrix} \langle \Psi_0 | \widehat{H} | \Psi_0 \rangle & \langle \Psi_0 | \widehat{H} | \mathbf{S} \rangle & \langle \Psi_0 | \widehat{H} | \mathbf{D} \rangle \\ \langle \mathbf{S} | \widehat{H} | \Psi_0 \rangle & \langle \mathbf{S} | \widehat{H} | \mathbf{S} \rangle & \langle \mathbf{S} | \widehat{H} | \mathbf{D} \rangle \\ \langle \mathbf{D} | \widehat{H} | \Psi_0 \rangle & \langle \mathbf{D} | \widehat{H} | \mathbf{S} \rangle & \langle \mathbf{D} | \widehat{H} | \mathbf{D} \rangle \end{bmatrix}. \quad (3.178)$$

We can then associate finding the approximate Hamiltonian eigenvalues with its matrix in the  $\Psi_{\text{SD}}$  basis:

$$\langle H \rangle_{\Psi_{\text{SD}}} = [c_0^* \mathbf{c}_{\mathbf{S}}^\dagger \mathbf{c}_{\mathbf{D}}^\dagger] \begin{bmatrix} \langle \Psi_0 | \widehat{H} | \Psi_0 \rangle & \langle \Psi_0 | \widehat{H} | \mathbf{S} \rangle & \langle \Psi_0 | \widehat{H} | \mathbf{D} \rangle \\ \langle \mathbf{S} | \widehat{H} | \Psi_0 \rangle & \langle \mathbf{S} | \widehat{H} | \mathbf{S} \rangle & \langle \mathbf{S} | \widehat{H} | \mathbf{D} \rangle \\ \langle \mathbf{D} | \widehat{H} | \Psi_0 \rangle & \langle \mathbf{D} | \widehat{H} | \mathbf{S} \rangle & \langle \mathbf{D} | \widehat{H} | \mathbf{D} \rangle \end{bmatrix} \begin{bmatrix} c_0 \\ \mathbf{c}_{\mathbf{S}} \\ \mathbf{c}_{\mathbf{D}} \end{bmatrix}. \quad (3.179)$$

Because of the Hermitian character of the Hamilton operator, the  $\mathbf{H}_{\text{SD}}$  matrix is symmetric and real. Its diagonalization provides the set of the eigenvalues corresponding to its eigenvectors. We are interested in the ground state energy and, thus, we need only the lowest eigenvalue of the  $\mathbf{H}_{\text{SD}}$  matrix and the respective normalized eigenvector  $\Psi_{\text{SD}}$ .

Knowing the procedure for the finite basis (only Single- and double-orbital exchanges), we can see how it looks for the full [Eq. 3.171](#) expansion. The matrix notation leads to the average value of the Hamiltonian, written as

$$\langle H \rangle_{\Psi} = [c_0, \mathbf{c}_{\mathbf{S}}, \mathbf{c}_{\mathbf{D}}, \mathbf{c}_{\mathbf{T}}, \mathbf{c}_{\mathbf{Q}}, \dots] \begin{bmatrix} \langle \Psi_0 | \\ \langle \mathbf{S} | \\ \langle \mathbf{D} | \\ \langle \mathbf{T} | \\ \langle \mathbf{Q} | \\ \vdots \end{bmatrix} \widehat{H} [ | \Psi_0 \rangle, | \mathbf{S} \rangle, | \mathbf{D} \rangle, | \mathbf{T} \rangle, | \mathbf{Q} \rangle, \dots ] \begin{bmatrix} c_0 \\ \mathbf{c}_{\mathbf{S}} \\ \mathbf{c}_{\mathbf{D}} \\ \mathbf{c}_{\mathbf{T}} \\ \mathbf{c}_{\mathbf{Q}} \\ \vdots \end{bmatrix}. \quad (3.180)$$

The vector multiplication permits one to perceive the average value as the eigenproblem of the Hamiltonian matrix:

$$\mathbf{H} = \begin{bmatrix} \langle \Psi_0 | \widehat{H} | \Psi_0 \rangle & 0 & \langle \Psi_0 | \widehat{H} | \mathbf{D} \rangle & 0 & 0 & \dots \\ 0 & \langle \mathbf{S} | \widehat{H} | \mathbf{S} \rangle & \langle \mathbf{S} | \widehat{H} | \mathbf{D} \rangle & \langle \mathbf{S} | \widehat{H} | \mathbf{T} \rangle & 0 & \dots \\ \langle \mathbf{D} | \widehat{H} | \Psi_0 \rangle & \langle \mathbf{D} | \widehat{H} | \mathbf{S} \rangle & \langle \mathbf{D} | \widehat{H} | \mathbf{D} \rangle & \langle \mathbf{D} | \widehat{H} | \mathbf{T} \rangle & \langle \mathbf{D} | \widehat{H} | \mathbf{Q} \rangle & \dots \\ 0 & \langle \mathbf{T} | \widehat{H} | \mathbf{S} \rangle & \langle \mathbf{T} | \widehat{H} | \mathbf{D} \rangle & \langle \mathbf{T} | \widehat{H} | \mathbf{T} \rangle & \langle \mathbf{T} | \widehat{H} | \mathbf{Q} \rangle & \dots \\ 0 & 0 & \langle \mathbf{Q} | \widehat{H} | \mathbf{D} \rangle & \langle \mathbf{Q} | \widehat{H} | \mathbf{T} \rangle & \langle \mathbf{Q} | \widehat{H} | \mathbf{Q} \rangle & \dots \\ \vdots & \vdots & \vdots & \vdots & \vdots & \ddots \end{bmatrix}. \quad (3.181)$$

It can be clearly seen that some blocks in this matrix are equal to zero. This happens in two cases:

- The integrals between  $\Psi_0$  and functions of the  $\mathbf{S}$  type (single exchange of spin-orbitals) vanish due to the Brillouin theorem, as was shown in the previous section
- The integrals between the functions that differ by more than two exchanges, for instance,  $\mathbf{S}$  and  $\mathbf{Q}$  type, vanish due to the Slater rules

Even not knowing combinatorics one can expect that the number of functions in a block will grow drastically with and increase in the number of exchanges (block  $\mathbf{S}$  will contain less functions than  $\mathbf{D}$  etc.). A bit of thinking in the beginning would help to save a lot of time by not calculating zero integrals. Let's see: only in the case of  $\langle \Psi_0 | \widehat{H} | \mathbf{D} \rangle$  and  $\langle \mathbf{S} | \widehat{H} | \mathbf{S} \rangle$  blocks should all the elements be calculated. The remaining matrices are sparse. For example, the  $\langle \mathbf{D} | \widehat{H} | \mathbf{D} \rangle$

block contains the integrals of the following types:  $\langle \Psi_{ab}^{pq} | \widehat{H} | \Psi_{ab}^{pq} \rangle$  (the same function on both sides),  $\langle \Psi_{ab}^{pq} | \widehat{H} | \Psi_{ab}^{pr} \rangle$  (differing by one exchange),  $\langle \Psi_{ab}^{pq} | \widehat{H} | \Psi_{ab}^{rs} \rangle$  (differing by two exchanges),  $\langle \Psi_{ab}^{pq} | \widehat{H} | \Psi_{ac}^{pq} \rangle$  (differing by three exchanges), and  $\langle \Psi_{ab}^{pq} | \widehat{H} | \Psi_{dc}^{pq} \rangle$  (differing by four exchanges). Obviously, the two latter cases produce zeros.

With the large number of exchanges, the size of the blocks grows abruptly, but most of the elements would be equal to zero. The simplification in this case would be the limitation of the  $\mathbf{H}$  matrix size by the elimination of the functions including more than a given number of exchanges from the expansion. Let us leave only the single exchange block. Thus, the Hamiltonian matrix has the form

$$\mathbf{H}_S = \begin{bmatrix} \langle \Psi_0 | \widehat{H} | \Psi_0 \rangle & 0 \\ 0 & \langle \mathbf{S} | \widehat{H} | \mathbf{S} \rangle \end{bmatrix}. \quad (3.182)$$

This is the block diagonal matrix. One of the properties of such matrices is that their eigenvalue set is a sum of the eigenvalues of the diagonal blocks. This means that the lowest possible eigenvalue is  $E_0 = \langle \Psi_0 | \widehat{H} | \Psi_0 \rangle$  and, in consequence, there is no improvement in the ground state energy with respect to the Hartree–Fock theory when taking only the single orbital exchanges.

Hence, let us also include the functions of the  $\mathbf{D}$  type. Now the Hamilton matrix can be written as

$$\mathbf{H}_{SD} = \begin{bmatrix} \langle \Psi_0 | \widehat{H} | \Psi_0 \rangle & 0 & \langle \Psi_0 | \widehat{H} | \mathbf{D} \rangle \\ 0 & \langle \mathbf{S} | \widehat{H} | \mathbf{S} \rangle & \langle \mathbf{S} | \widehat{H} | \mathbf{D} \rangle \\ \langle \mathbf{D} | \widehat{H} | \Psi_0 \rangle & \langle \mathbf{D} | \widehat{H} | \mathbf{S} \rangle & \langle \mathbf{D} | \widehat{H} | \mathbf{D} \rangle \end{bmatrix}. \quad (3.183)$$

It is no longer a block diagonal matrix – all blocks contribute to its eigenvalues and one can count on some improvement. An interesting observation, however, is that here the functions with the single spin-orbital exchange also have influence on the energy via the  $\langle \mathbf{S} | \widehat{H} | \mathbf{D} \rangle$  and  $\langle \mathbf{D} | \widehat{H} | \mathbf{S} \rangle$  blocks.

Next, subsequent groups of functions can be applied containing more than two spin-orbital exchanges. However, the calculations become prohibitively expensive, even for moderate size of the systems, and the consecutive corrections are smaller and smaller. The distinguished character of the double spin-orbital exchange was already discussed within the MP2 method. Now one can also expect that including double exchanges produces reasonable results with the moderate computational cost. Then, why not save more and diagonalize only

$$\mathbf{H}_D = \begin{bmatrix} \langle \Psi_0 | \widehat{H} | \Psi_0 \rangle & \langle \Psi_0 | \widehat{H} | \mathbf{D} \rangle \\ \langle \mathbf{D} | \widehat{H} | \Psi_0 \rangle & \langle \mathbf{D} | \widehat{H} | \mathbf{D} \rangle \end{bmatrix} \quad (3.184)$$

instead of  $\mathbf{H}_{SD}$ ? This can be done; however, savings are not that great, since the number of  $\mathbf{S}$  functions is significantly smaller than the number of  $\mathbf{D}$  functions. Thus, if one can afford  $\mathbf{H}_D$  diagonalization,  $\mathbf{H}_{SD}$  diagonalization is probably also within easy reach.

The above reasoning has led to the sequence of quantum chemistry methods. The best results can be obtained within Full CI (FCI) by applying the full expansion (Eq. 3.171) within the given basis set. This is certainly the most expensive variant. Cheaper – but also worse – are, respectively, CISD based on the  $\mathbf{H}_{SD}$  matrix and CID neglecting single exchanges (Cramer 2004; Jensen 2006; Levine 2008; Lowe and Peterson 2005; Piela 2007; Ratner and Schatz 2000; Szabo and Ostlund 1996).

So far, the reference function has been a single determinant. Such an approach is very limited. For instance, it does not allow one to describe a dissociation process. Correct description of dissociation requires at least one determinant for each subsystem. And, even in the cases

when multi-determinant reference state description is not obligatory, such an elastic wave function will provide an improved description of the system of interest (Cramer 2004; Jensen 2006; Levine 2008; Piela 2007; Roos and Widmark 2002).

The multi-determinant wave function  $\Psi$  depends both on the expansion coefficients and on the spin-orbitals building up the determinants. Both these sets of variables can be optimized simultaneously. The particular case of this procedure, when taking only the first expansion term, is the Hartree–Fock approximation (SCF–HF). Therefore, the optimization of the multi-determinant wave function is called the multiconfiguration (MC) SCF method. Even without a detailed study of the MC–SCF equations, an improvement in the results with respect to the HF energy can be expected. However, this approach is much more expensive, since the spin-orbitals are optimized several times. Again, a time savings is desired. Therefore, let us search for the spin-orbitals with the highest influence on the total energy value. It has been observed that not all doubly exchanged functions provide the same contribution to the energy. Some improve the result more and others less. This is due to the spin-orbital energy differences. The exchange of the spin-orbitals of significantly different energies does not contribute much to the total energy improvement. Therefore, it can be requested that the exchange is included in calculations only if the energy difference between the involved spin-orbitals is smaller than some given value. Hence, only some groups of spin-orbitals can be exchanged.

Up to now, the spin-orbital notion was used. However, let us switch to the orbital language that is frequently used for MC–SCF considerations.

For the  $N$ -electron system, the orbitals can be divided into three groups:

- Core orbitals, which are not varied, since they have too low orbital energies, but are applied in the wave function expansion (doubly occupied orbitals)
- Active orbitals, which are exchanged in the expansion (partially occupied orbitals)
- Virtual orbitals, which are not varied and not applied in the expansion (unoccupied orbitals)

Instead of optimization of all the orbitals, only the active orbitals will be varied within the Complete Active Space Self-Consistent Field approximation (CASSCF). In the acronym of this method, the number of active orbitals and active electrons are also provided for the given system. For instance, CASSCF(6,4) denotes the calculations with the expansion including all the possible exchanges of the four electrons within the six active orbitals. The CASSCF approach leads to all possible exchanges in the given active space, and for a moderately sized system, the size of the active spaces can quickly exceed the computational resources. In such a case, the solution can be the Restricted Active Space Self-Consistent Field method (RASSCF), which supplies a way of limiting the size of the active space.

Additionally, one needs to remember that for a powerful tool such as perturbation theory, there is no obstacle to applying the multi-determinant reference function as the unperturbed function in perturbation calculus. Thus, similar to the SCF–HF and MP2 approaches, CASPT2 would be the second-order perturbation theory complete active space method – the perturbationally corrected CASSCF.

## Coupled Cluster Approximation – The Operator Strikes Back

---

It would seem that all the straightforward ways to improve wave function in the one electron approximation have been exploited. However, we now next discuss one of the most accurate (and simultaneously most expensive) methods applied in quantum chemistry.

The idea is simple. Consider again the expansion (► Eq. 3.171). Introducing an operator

$$\widehat{C} = \widehat{C}_0 + \widehat{C}_1 + \widehat{C}_2 + \widehat{C}_3 + \widehat{C}_4 + \dots, \quad (3.185)$$

defined as

$$\widehat{C}_0|\Psi_0\rangle = c_0|\Psi_0\rangle, \quad (3.186)$$

$$\widehat{C}_1|\Psi_0\rangle = \mathbf{S}\mathbf{c}_S, \quad (3.187)$$

$$\widehat{C}_2|\Psi_0\rangle = \mathbf{D}\mathbf{c}_D, \quad (3.188)$$

$$\widehat{C}_3|\Psi_0\rangle = \mathbf{T}\mathbf{c}_T, \quad (3.189)$$

$$\widehat{C}_4|\Psi_0\rangle = \mathbf{Q}\mathbf{c}_Q, \quad (3.190)$$

⋮

allows one to write ► Eq. 3.171 in a very compact form:

$$\Psi = \widehat{C}\Psi_0. \quad (3.191)$$

Now the problem of finding the appropriate expansion can be replaced by the problem of finding the adequate operator. This is the essence of the Coupled Cluster (CC) method. Here the assumption is made that the wave function can be expressed by

$$\Psi = e^{\widehat{T}}\Psi_0, \quad (3.192)$$

where  $\Psi_0$  is a reference function (depending on the approach, this can be the one-determinant HF function or the multi-determinant function arising from MC-SCF) and  $\widehat{T}$  is a sought operator. Applying the expansion of the exponential function, it can be written that

$$e^{\widehat{T}} = \hat{1} + \widehat{T} + \frac{1}{2!}\widehat{T}^2 + \frac{1}{3!}\widehat{T}^3 + \dots \quad (3.193)$$

Such an expanded form makes the interpretation of the  $\widehat{T}$  operators easier. Putting

$$\widehat{T} = \widehat{T}_1 + \widehat{T}_2 + \widehat{T}_3 + \widehat{T}_4 + \dots, \quad (3.194)$$

one can identify the subsequent  $\widehat{T}_i$  operators as corresponding to  $i$ -tuple exchanges of the spin-orbitals in the reference function:

$$\widehat{T}_1\Psi_0 = \sum_{a,p} t_a^p \Psi_a^p, \quad (3.195)$$

$$\widehat{T}_2\Psi_0 = \sum_{a,b,p,q} t_{ab}^{pq} \Psi_{ab}^{pq}, \quad (3.196)$$

and so forth. The coefficients  $t$  (called “amplitudes”) are in general not equivalent to the  $c$  coefficients in the CI expansion (see ► Eq. 3.171). In order to find their mutual relation, let us consider the approximate operator:

$$\widehat{T} \approx \widehat{T}_1 + \widehat{T}_2 + \widehat{T}_3 + \widehat{T}_4. \quad (3.197)$$

The operator (► Eq. 3.193) takes the form

$$\begin{aligned}
 e^{\widehat{T}_1 + \widehat{T}_2 + \widehat{T}_3 + \widehat{T}_4} &= \hat{1} \\
 &+ \widehat{T}_1 + \widehat{T}_2 + \widehat{T}_3 + \widehat{T}_4 \\
 &+ \frac{1}{2!} (\widehat{T}_1 + \widehat{T}_2 + \widehat{T}_3 + \widehat{T}_4)^2 \\
 &+ \frac{1}{3!} (\widehat{T}_1 + \widehat{T}_2 + \widehat{T}_3 + \widehat{T}_4)^3 \\
 &+ \frac{1}{4!} (\widehat{T}_1 + \widehat{T}_2 + \widehat{T}_3 + \widehat{T}_4)^4.
 \end{aligned} \tag{3.198}$$

Limiting ourselves to the terms corresponding to not more than four spin-orbital exchanges and writing it in the ordered way according to the number of exchanges, one gets

$$\begin{aligned}
 e^{\widehat{T}_1 + \widehat{T}_2 + \widehat{T}_3 + \widehat{T}_4} &\approx \hat{1} \\
 &+ \widehat{T}_1 \\
 &+ \widehat{T}_2 + \frac{1}{2} \widehat{T}_1^2 \\
 &+ \widehat{T}_3 + \widehat{T}_1 \widehat{T}_2 + \frac{1}{3} \widehat{T}_1^3 \\
 &+ \widehat{T}_4 + \widehat{T}_1 \widehat{T}_3 + \frac{1}{2} \widehat{T}_2^2 + \frac{1}{2} \widehat{T}_1^2 \widehat{T}_2 + \widehat{T}_1^4.
 \end{aligned} \tag{3.199}$$

Now the direct comparison can be made:

$$\widehat{C}_1 = \widehat{T}_1, \tag{3.200}$$

$$\widehat{C}_2 = \widehat{T}_2 + \frac{1}{2} \widehat{T}_1^2, \tag{3.201}$$

$$\widehat{C}_3 = \widehat{T}_3 + \widehat{T}_1 \widehat{T}_2 + \frac{1}{3} \widehat{T}_1^3, \tag{3.202}$$

$$\widehat{C}_4 = \widehat{T}_4 + \widehat{T}_1 \widehat{T}_3 + \frac{1}{2} \widehat{T}_2^2 + \frac{1}{2} \widehat{T}_1^2 \widehat{T}_2 + \widehat{T}_1^4. \tag{3.203}$$

We have the relation between the  $\widehat{C}_i$  and  $\widehat{T}_i$  operators, but still neither  $\widehat{C}_i$  nor  $\widehat{T}_i$  are known. Recall from the earlier sections that the double exchanges have a significant influence on the energy improvement with respect to the Hartree–Fock results. Taking double exchanges into account within the coupled cluster formalism means that the operators  $\widehat{T}_1$  and  $\widehat{T}_2$  need to be determined. However, as a side effect they also allow inclusion of some not negligible contributions arising from the triple and higher exchanges. In the above comparison, the  $\widehat{T}_1$  and  $\widehat{T}_2$  operators recover two out of three terms in  $\widehat{C}_3$  and three out of five terms in  $\widehat{C}_4$ . This is the power of the CC method.

Unfortunately, the strength of this method does not go together with ease of calculations. Obtaining the expressions for the operators  $\widehat{T}$  is ransomed with compromises. Not only is the operator expansion (► Eq. 3.194) truncated, but the basis set is finite. Moreover, the variational character of the method is sacrificed.

In order to realize the complications, let us consider step-by-step the energy calculation within the CC formalism. We begin, as usual, with the electron Schrödinger ► Eq. 3.50. Substituting ► Eq. 3.192 gives

$$\widehat{H} e^{\widehat{T}} \Psi_0 = E e^{\widehat{T}} \Psi_0. \tag{3.204}$$

Taking into account that, due to (► Eq. 3.193),

$$\langle \Psi_0 | \Psi \rangle = \langle \Psi_0 | e^{\widehat{T}} | \Psi_0 \rangle = \langle \Psi_0 | \Psi_0 \rangle = 1, \quad (3.205)$$

the energy can be calculated as

$$E = \langle \Psi_0 | \widehat{H} e^{\widehat{T}} | \Psi_0 \rangle = \langle \Psi_0 | \widehat{H} | \Psi \rangle. \quad (3.206)$$

This is not the Hamiltonian average value expression. Additionally, the operator inside the bracket is not hermitian. But, until we assume that (► Eq. 3.192) is true, such an approach works. We can also construct an integral:

$$\langle \Psi_{ab}^{Pq} | \widehat{H} e^{\widehat{T}} | \Psi_0 \rangle = E \langle \Psi_{ab}^{Pq} | e^{\widehat{T}} | \Psi_0 \rangle, \quad (3.207)$$

which is the consequence of ► Eq. 3.204 and will be applied in near future.

We should now concentrate on the way of determining the form of amplitudes. To simplify the considerations we can assume

$$\widehat{T} \approx \widehat{T}_2, \quad (3.208)$$

which is equivalent to the CCD variant. We are interested in finding the amplitudes  $t_{ab}^{Pq}$ . The final result of the calculations will be the approximate energy:

$$E_{\text{CCD}} = \langle \Psi_0 | \widehat{H} e^{\widehat{T}_2} | \Psi_0 \rangle. \quad (3.209)$$

The information about the amplitude  $t_{ab}^{Pq}$  can be extracted from the integral

$$t_{ab}^{Pq} = \langle \Psi_{ab}^{Pq} | \widehat{T}_2 | \Psi_0 \rangle \quad (3.210)$$

(see ► Eq. 3.196). However, the amplitudes are still not known, since we do not know the  $\widehat{T}_2$  operator. Therefore, one more equation is necessary to elicit the sought information. Let us begin with the approximated expression ► Eq. 3.207:

$$\begin{aligned} \langle \Psi_{ab}^{Pq} | \widehat{H} e^{\widehat{T}_2} | \Psi_0 \rangle &= E_{\text{CCD}} \langle \Psi_{ab}^{Pq} | e^{\widehat{T}_2} | \Psi_0 \rangle \\ &= \langle \Psi_0 | \widehat{H} e^{\widehat{T}_2} | \Psi_0 \rangle \langle \Psi_{ab}^{Pq} | e^{\widehat{T}_2} | \Psi_0 \rangle. \end{aligned} \quad (3.211)$$

The expansion (► Eq. 3.193) tailored to the present case,

$$e^{\widehat{T}_2} = \hat{1} + \widehat{T}_2 + \frac{1}{2} \widehat{T}_2^2 + \dots, \quad (3.212)$$

and substituted to the left-hand side of ► Eq. 3.211 gives

$$\langle \Psi_{ab}^{Pq} | \widehat{H} e^{\widehat{T}} | \Psi_0 \rangle = \langle \Psi_{ab}^{Pq} | \widehat{H} (\hat{1} + \widehat{T}_2 + \frac{1}{2} \widehat{T}_2^2) | \Psi_0 \rangle. \quad (3.213)$$

Further terms are not necessary; in such a case the functions on both sides of the integral would differ with four and more spin-orbital exchanges (and Hamiltonian is still a sum of one- and two-electron operators). Similarly, the expansion in the integral  $\langle \Psi_0 | \widehat{H} e^{\widehat{T}_2} | \Psi_0 \rangle$  will also be truncated on the second term:

$$\langle \Psi_0 | \widehat{H} e^{\widehat{T}_2} | \Psi_0 \rangle = \langle \Psi_0 | \widehat{H} (\hat{1} + \widehat{T}_2) | \Psi_0 \rangle. \quad (3.214)$$

Remembering that

$$E_0^{(0)} = \langle \Psi_0 | \widehat{H} | \Psi_0 \rangle, \quad (3.215)$$

one gets

$$\langle \Psi_0 | \widehat{H} e^{\widehat{T}_2} | \Psi_0 \rangle = E_0^{(0)} + \langle \Psi_0 | \widehat{H} \widehat{T}_2 | \Psi_0 \rangle. \quad (3.216)$$

The last integral on the right-hand side of  $\blacklozenge$  Eq. 3.211,  $\langle \Psi_{ab}^{pq} | e^{\widehat{T}} | \Psi_0 \rangle$ , can be non-vanishing only if the functions on the right and left side are the same. This is possible for

$$\langle \Psi_{ab}^{pq} | e^{\widehat{T}_2} | \Psi_0 \rangle = \langle \Psi_{ab}^{pq} | \widehat{T}_2 | \Psi_0 \rangle. \quad (3.217)$$

This is the integral that can provide information about the desired amplitudes of  $\blacklozenge$  Eq. 3.210. Putting all these together one gets

$$\langle \Psi_{ab}^{pq} | \widehat{H} (\widehat{1} + \widehat{T}_2 + \frac{1}{2} \widehat{T}_2^2) | \Psi_0 \rangle = (E_0 + \langle \Psi_0 | \widehat{H} \widehat{T}_2 | \Psi_0 \rangle) \langle \Psi_{ab}^{pq} | \widehat{T}_2 | \Psi_0 \rangle. \quad (3.218)$$

Therefore, the amplitude  $t_{ab}^{pq} = \langle \Psi_{ab}^{pq} | \widehat{T}_2 | \Psi_0 \rangle$  can be expressed as

$$t_{ab}^{pq} = \frac{\langle \Psi_{ab}^{pq} | \widehat{H} (\widehat{1} + \widehat{T}_2 + \frac{1}{2} \widehat{T}_2^2) | \Psi_0 \rangle}{E_0 + \langle \Psi_0 | \widehat{H} \widehat{T}_2 | \Psi_0 \rangle}. \quad (3.219)$$

Unluckily, this does not mean that the amplitudes are known. Still, the above expression also contains the  $t_{ab}^{pq}$  amplitudes on the right-hand side in the  $\widehat{T}_2$  operators. Moreover, all other amplitudes are also present on the right-hand side. The consequence of this aggravation is that the CC equations cannot be solved separately, one by one. All together, the complicated set of non-linear equations must be handled. The number of equations is equal to the number of sought amplitudes. This is the main reason for the huge computational cost of the CC calculations, even though the variationality of the method was abandoned (Atkins and Friedman 2005; Cramer 2004; Jensen 2006; Levine 2008; Piela 2007; Roos and Widmark 2002).

It can be seen that solving the CC equations is quite complicated, even in the simplified case of the CCD approach. If one wanted to use the variational Hamiltonian and apply its average value, the following integrals would appear:

$$\langle \Psi | \widehat{H} | \Psi \rangle = \langle \Psi_0 | e^{\widehat{T}^\dagger} \widehat{H} e^{\widehat{T}} | \Psi_0 \rangle = \langle e^{\widehat{T}} \Psi_0 | \widehat{H} | e^{\widehat{T}} \Psi_0 \rangle. \quad (3.220)$$

In order to calculate them, one needs to know the form of all the  $\widehat{T}_i$  operators, since not only the function on the right-hand side of the above integral will contain the exchanged spin-orbitals but also the function on the left-hand side. Therefore, one needs to calculate terms like  $\langle \widehat{T}_3 \Psi_0 | \widehat{H} | \widehat{T}_2 \Psi_0 \rangle$  and many others. This causes the significant increase of the computational costs of the CC method.

Like in the MPn case, the CC method is worth using for the short expansion of the  $\widehat{T}$  operator. Thus, relatively good accuracy is obtained with a moderate price.

## Conclusions

We have finally reached the end of the zeroth iteration in the process of learning quantum chemistry methods. The beginner may feel saturated or even overwhelmed, however, we hope that this chapter arouses interest. Our aim was to show that simple ideas underlie quantum chemistry methods. The purpose is to put complicated things in a simpler and more convenient form. One of the most popular rules in computational chemistry is as follows: “If you cannot calculate

something, divide it into parts in such a way that you can calculate some contribution while the other is too difficult.” For instance, nonrelativistic energy can be divided into HF energy and correlation energy. Correlation energy accounts for the contribution that we can not calculate in practice, but methods such as MP $n$ , CC, and CI allow one to find some part of it. It may happen (and it often does!) that what we can calculate will be enough.

This chapter should be treated as the introduction to more advanced handbooks or as a guide through the symbols and concepts applied in the later parts of this book. Thus, some of the concepts are just touched upon, and many are omitted. If the reader noticed this and wants to know more, it means that this chapter has met its goal.

## Acknowledgments

---

Authors are grateful to Dr Krzysztof Strasburger, Dr Andrej Antušek, Agnieszka Zawada, and Lukasz Mentel for helpful comments.

## References

---

- Atkins, P., & Friedman, R. (2005). *Molecular quantum mechanics*. Oxford, NY: Oxford University Press.
- Cramer, C. J. (2004). *Essentials of computational chemistry: Theories and models*. Chichester: Wiley.
- Griffiths, D. J. (2004). *Introduction to quantum mechanics* (2nd ed.). San Francisco: Benjamin Cummings.
- Jensen, F. (2006). *Introduction to computational chemistry*. Chichester: Wiley.
- Levine, I. N. (2008). *Quantum Chemistry* (6th ed.). Englewood Cliffs: Prentice Hall.
- Lowe, J. P., & Peterson, K. (2005). *Quantum chemistry* (3rd ed.). Boston: Academic.
- McQuarrie, D. A., & Simon, J. D. (1997). *Physical chemistry: A molecular approach*. Sausalito, CA: University Science Books.
- Piela, L. (2007). *Ideas of quantum chemistry*. Amsterdam: Elsevier.
- Ratner, M. A., & Schatz, G. C. (2000). *Introduction to quantum mechanics in chemistry*. Upper Saddle River: Prentice Hall.
- Roos, B. O., & Widmark, P.-O. (Eds.). (2002). *European summerschool in quantum chemistry*. Lund: Lund University.
- Szabo, A., & Ostlund, N. S. (1996). *Modern quantum chemistry: Introduction to advanced electronic structure theory*. Mineola: Dover Publications.





# 4 Directions for Use of Density Functional Theory: A Short Instruction Manual for Chemists

Heiko Jacobsen<sup>1</sup> · Luigi Cavallo<sup>2</sup>

<sup>1</sup>KemKom, New Orleans, LA, USA

<sup>2</sup>Department of Chemistry, University of Salerno Via Ponte don Melillo, Fisciano, Italy

<i>Introduction</i> .....	97
<i>DFT: A Paradigm Shift in Theoretical Chemistry</i> .....	98
Holes and Electron Pairs .....	102
Climbing Jacob's Ladder .....	104
First Rung: The Local Density Approximation .....	104
Second Rung: The Generalized Gradient Approximation .....	105
Third Rung: Meta-Functionals .....	106
Fourth Rung: Hyper-Functionals .....	106
Fifth Rung .....	107
Practical DFT and the Density Functional Zoo .....	107
<i>DFT: Computational Chemistry in Action</i> .....	109
Computational Performance .....	110
Properties of Molecular and Electronic Structure .....	111
Bond Lengths .....	112
Bond Angles .....	114
Vibrational Frequencies .....	115
Electron Affinities and Ionization Potentials .....	117
Atomization Energies .....	118
Heats of Formation .....	118
Energy Barriers .....	119
Bond Energies .....	120
Hydrogen Bonding .....	121
Weak Interactions .....	122
Spin States .....	123
Excited States .....	124
Orbitals in DFT .....	125

<b><i>DFTips</i></b> .....	<b>127</b>
B3LYP Is No Synonym for DFT .....	127
Choose Your DFT Method Carefully .....	128
Read the Fine Print .....	128
DFT Does Not Hold the Universal Answer to All Chemical Problems .....	128
Make DFT an Integral Part of Your Work .....	129
Follow Your Interests .....	129
 <b><i>A Concise Guide to the Literature</i></b> .....	 <b>129</b>
 <b><i>References</i></b> .....	 <b>130</b>
Books on DFT .....	130
Conceptual Developments and Applications of DFT .....	130
Practical Developments and Applications of DFT .....	131
Reviews and Overviews of DFT .....	132
Web Links .....	133

**Abstract:** Two aspects are quintessential if one seeks to successfully perform DFT calculations: A basic understanding of how the concepts and models underlying the various manifestations of DFT are built, and an essential knowledge of what can be expected from DFT calculations and how to achieve the most appropriate results. This chapter expands on the development and philosophy of DFT, and aims to illustrate the essentials of DFT in a manner that is intuitively accessible. An analysis of the performance and applicability of DFT focuses on a representative selection of chemical properties, including bond lengths, bond angles, vibrational frequencies, electron affinities and ionization potentials, atomization energies, heats of formation, energy barriers, bond energies hydrogen bonding, weak interactions, spin states, and excited states.

## Introduction

---

Density functional theory (DFT) is an enticing subject. It appeals to chemists and physicists alike, and it is entrancing for those who like to work on mathematical physical aspects of problems, for those who relish computing observable properties from theory, and for those who most enjoy developing correct qualitative descriptions of phenomena. It is this combination of a qualitative model that at the same time furnishes quantitative reliable estimates that makes DFT particularly attractive for chemists.

DFT is an alternative, and complementary, to wave function theory (WFT). Both approaches are variations of the basic theme of electronic structure theory, and both methods originated during the late years of the 1920s. Whereas WFT evolved rapidly and gained general popularity, DFT found itself in a state of shadowy existence. It was the appearance of the key papers by Hohenberg and Kohn (1964) and by Kohn and Sham (1965), generally perceived as the beginning of modern DFT, which changed the perception and level of acceptance of DFT. With the evolution of reliable computational technologies for DFT chemistry, and with the advent of the generalized gradient approximation (GGA) during the 1980s, DFT emerged as powerful tool in computational chemistry, and without exaggeration the 1990s can be called the decade of DFT in electronic structure theory. During this time period, despite the lack of a complete development, DFT was already competitive with the best WFT methods. Furthermore, the advancement of computational hardware as well as software has progressed to a state where DFT calculations of “real molecules” can be performed with high efficiency and without major technical hurdles.

Now, at the end of the first decade of the new millennium, it appears that DFT might have become a victim of its own success. DFT has transformed into an off-the-shelf technology and ready-to-crunch component, and often is used as such. However, it has become clear that the happy days of black-box DFT are over, and that not all the promises of DFT came to fruition. DFT has its own limitations and shortcomings, and the numbers obtained from DFT calculations begin to lose some of their awe-inspiring admiration they enjoyed about 10 years ago. At the same time, DFT is maturing into a standard research tool, used routinely by many experimental chemists to support their work.

We have composed our short instruction manual for chemists in view of the ontogeny of DFT. A chemist using DFT calculations should be aware of the fact that all approximations and simplifications of any general theory may lead to failures in computed data. Every principally correct theory, if not executed with specific care, may produce essentially wrong results, and therefore erroneous predictions. Two aspects are quintessential if one seeks to successfully

perform DFT calculations: A basic understanding of how the concepts and models underlying the various manifestations of DFT are built, and an essential knowledge of what can be expected from DFT calculations and how to achieve the most appropriate results. Thus, we have divided the main body of our directions into two parts.

In [▶ section “DFT: A Paradigm Shift in Theoretical Chemistry,”](#) we expand on the development and philosophy of DFT. We do not present a course or textbook work on DFT; the interested reader will find a selection of references to the literature for more elaborate and detailed descriptions. Rather, we aim to illustrate the essentials of DFT in a manner that is intuitively accessible. For this reason, we will avoid mathematical equations as much as possible, incorporate formulas into the flow of the text, and only on occasion add the odd numbered equation to the elaboration. As a consequence, we have to abandon the rigor that unambiguous and well-defined derivations require, and introduce a certain degree of sloppiness. We hope that such a treatment will facilitate the flow of our arguments and emphasize what we think are indispensable aspects of DFT.

In [▶ section “DFT: Computational Chemistry in Action,”](#) we present an analysis of the performance and applicability of DFT. We focus on a representative selection of chemical properties and system types, and base our review on the most recent benchmarking studies, which encompass several well-established density functionals together with the most recent efforts in the field. Due to the multitude of papers that report DFT applications, our analysis is far from complete, but we aim to present a representative snapshot of the current situation of DFT at the end of the first decade of the new millennium.

We will close our work with two additional short [▶ sections “DFTips”](#) and [▶ “A Concise Guide to the Literature,”](#) where we present the reader with a few tips about how to use DFT, and with a collection of selected references as a concise guide to the by now vast literature of DFT.

## DFT: A Paradigm Shift in Theoretical Chemistry

---

Density functional theory is primarily a theory of electronic ground state structure, which is based on the electron density distribution  $\rho(r)$ . In contrast to DFT, wave function theory is an approach to electronic structure, which is based on the many-electron wave function  $\Psi(r_n)$ . In order to put the innovation of DFT into proper perspective, we begin with a brief overview of WFT, before we illustrate the essentials and growth of DFT.

The objective of WFT is the exact solution of the time-independent Schrödinger equation (TISE),  $H\Psi = E\Psi$ , for a system of interest. (We recall that in quantum mechanics, associated with each measurable parameter in a physical system is an operator, and the operator associated with the energy of a system is called the Hamiltonian  $H$ . The Hamiltonian contains the operations associated with the kinetic and potential energies of all particles that comprise a system. We further note that the terms function, operator, and functional are to be understood such that a function is a prescription which maps one or more numbers to another number, an operator is a prescription which maps one function to another function, and a functional takes a function and provides a number.) The solution to the TISE yields the wave function  $\Psi$  as well as the energy  $E$  for the system of interest. In a systematic, variational search one looks for the wave function that produces the lowest energy, and arrives at a description for the system in its ground state.

If we consider a system of nuclei and  $N$  electrons, solving the TISE – within the Born–Oppenheimer separation of slow nuclear motion from fast electronic motion – yields the electronic molecular wave function,  $\Psi_{\text{el}}(r)$ . This wave function depends explicitly on the  $3N$  coordinates of all  $N$  electrons, all of which might undergo positional permutation due to repulsive Coulomb interaction. A first approximation to the challenging task of solving the TISE is to neglect interaction between electrons, and to reduce the function  $\Psi_{\text{el}}(r)$  of  $3N$  variables to a product of  $N$  functions  $\phi$  each depending only on three variables,  $\Psi_{\text{el}}(r) = \prod_{i=1,N} \phi_i(r_i)$ . Atomic orbitals are conveniently chosen to represent the functions  $\phi$ . However, such a Hartree product of atomic orbitals violates the Pauli exclusion principle due to the Fermion nature of electrons, and hence the appropriate form for a system of non-interacting electrons is a single determinant  $|\phi_1(r_1) \dots \phi_n(r_n)|$ , known as Slater-determinant. Such a wave function, from the mathematical properties of determinants, is antisymmetric with respect to exchange of two sets of electronic variables as it should be. One row of a Slater-determinant carries contributions from all atomic orbitals  $\phi$ , and is commonly referred to as molecular orbital (MO)  $\psi^{\text{MO}}$ . This approximate method for the determination of the ground state wave function and ground state energy is the well-known Hartree–Fock (HF) method.

Although in the HF method the electrons obey exchange as required by the Pauli exclusion principle, the electrons are non-interacting, and the movement of one electron within the system is independent from the movement of all other electrons. However, as the presence of Coulomb repulsion between electrons would suggest, the electrons move in a correlated fashion. In order to allow for electron correlation, configuration interaction (CI) is introduced in that the wave function is constructed as a linear combination of several Slater-determinants, obtained from a permutation of electron occupancies among all MOs available. Increasing the number of Slater-determinants increases the accuracy of the calculations, although the added accuracy comes with the price of added computational cost that often becomes the limiting factor for WFT calculations.

This brief exposition brings about two main differences between DFT and WFT. A WFT calculation in general, and increasing the accuracy of WFT calculations in particular, is computationally demanding. DFT seems to be more cost-efficient; after all, the simplest HF wave function  $\Psi_{\text{el}}(r)$  depends on  $3N$  spatial coordinates, whereas the probability distribution of electrons in space  $\rho(r)$  depends only on three coordinates. But there exist strategies for how the result of WFT can be systematically improved, whereas there is no methodical, standardized scheme to improve DFT calculations. In the following, we will explore reasons for the WFT–DFT differences.

In WFT, atoms and molecules constitute the basic systems of interest. Since the distribution and redistribution of electrons within atoms and molecules are central to chemical properties and reactivity, we now limit ourselves to systems comprised of  $N$  electrons in motion, with some two-particle interaction. The Hamiltonian of such a system reads  $H = T + U + V$ , where  $T$  and  $U$  denote the operators for kinetic energy and for electron–electron interaction energy, respectively. Whereas  $U$  results in the internal potential energy of our system, the moving electrons might in addition interact with an external potential, and the operation  $V$  recovers the potential energy due to this extra interaction. For systems of electrons that move in a field of fixed nuclei, the external potential  $V$  is always just the nuclear field. Systems of electrons in combination with fields of fixed nuclei represent the essential building blocks of matter such as molecules or solids. For a chemist, it might appear counterintuitive that nuclei, being an essential part of a molecule, represent an external potential, but the nuclear potential – although internal to a molecule – is external to the density of the moving electrons.

If we consider the external potential to be a uniformly distributed background positive charge, we arrive at the uniform or homogeneous electron gas (UEG or HEG), also known as jellium. At zero temperature, the properties of jellium depend solely upon the constant electron density distribution,  $\rho(r)=\text{const}$ . Such a treatment of electronic density, the Thomas–Fermi (TF) model, constitutes the origins of DFT (Parr and Yang 1989). The TF model is able to describe the kinetic energy of the UEG as functional of the electronic density, and later on Dirac added a density functional for the exchange energy as a conclusion of the Pauli principle. The UEG-formalism itself provides the basis for the local density approximation (LDA).

Before we proceed, we take a small step back to WFT. At the beginning of the 1950s, Slater (1951) described the then current situation in WFT as follows: “The Hartree–Fock equations furnish the best set of one-electron wave functions for use in a self-consistent approximation to the problem of the motion of electrons in the field of atomic nuclei. However, they are so complicated to use that they have not been employed except in relatively simple cases.” Facing the decision “Do you want to calculate it, or do you want it to be accurate?” Slater decided to replace the peculiar exchange term in the HF equations by something equivalent, yet easier to calculate. Slater used the free-electron approximation for the exchange potential, which, as Dirac has shown, could be expressed as a density functional. His new method, termed HFS, “was easy enough to apply so that we can look forward to using it even for heavy atoms” (Slater 1951), and in order to check its applicability, he performed calculations for the transition metal ion  $\text{Cu}^+$ . The exchange potential functional derived from the exchange energy functional contains one additional, scalable parameter  $\alpha$ , which led to the development of the  $X\alpha$ -method. This model enjoyed a significant amount of popularity among physicists, and is still a topic of ongoing research activities (Zope and Dunlap 2006). The HFS- or the  $X\alpha$ -method became the first practically used DFT-method in chemistry.

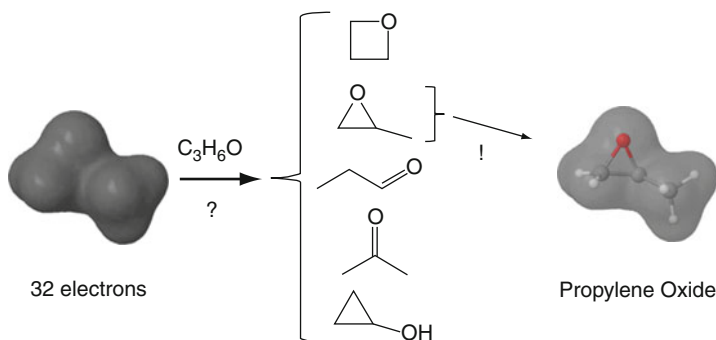
Two points that were fundamental for the progress of DFT were already anticipated within the advancements of the HFS- or  $X\alpha$ -method:

1. Every density functional method to some degree contains one or more empirical parameters. Therefore, DFT has often been regarded as “Yet another Semi-Empirical Method” (YaSEM). The Hartree–Fock–Slater model, which can be regarded as ancestor of modern DFT, is such an example. But whereas the HFS-method is intrinsically approximate, modern DFT is in principle exact (Kohn et al. 1996).
2. Transition metal chemistry has played and continues to play a major role in the progression of DFT. Work of Baerends and Ros (1978) is representative of the transition-metal-HFS era, and Ziegler’s contributions, summarized in his early review article (Ziegler 1991) have provided the impetus that changed the perception of calculations based on densities from YaSEM to DFT, “Das Future Tool.” A recent review article by Cramer and Truhlar (2009) is dedicated solely to developments and progress of DFT for transition metal chemistry.

At the heart of modern DFT is the rigorous, simple lemma of Hohenberg and Kohn (1964), which states that the specification of the ground state density,  $\rho(r)$ , determines the external potential  $V(r)$  uniquely,  $\blacktriangleright$  Eq. 4.1:

$$\rho(r) \rightarrow V(r)(\text{unique}). \quad (4.1)$$

This first theorem by Hohenberg and Kohn (HK-I) is not difficult to prove (Parr and Yang 1989), but for a chemist, the essentials of HK-I that given a density, only one external potential corresponds to that density, are intuitively clear. A pictorial representation of HK-I is shown



■ Fig. 4-1

Visualization of the first Hohenberg–Kohn theorem (density map drawn for a contour envelope of 0.01 a.u.)

in [Fig. 4-1](#); we consider the density created by 32 electrons that move around the external potential created by one oxygen, three carbon, and six hydrogen nuclei. By inspection of a density map of a certain density value, it becomes obvious that of all the atomic constellations considered, only one seems to be consistent with the shape of the density map. Such a consideration reflects ideas developed in the context of “conceptual DFT” (Geerlings et al. 2003). HK-I also expresses the fact that there is a one-to-one mapping between the potential  $V(r)$ , the particle density  $\rho(r)$ , and the ground state wave function  $\Psi_0$ , [Eq. 4.2](#):

$$\rho(r) \longleftrightarrow V(r) \longleftrightarrow \Psi_0. \quad (4.2)$$

This implies that all properties of a system are functionals of the ground state density, since any property may be determined as the expectation value of the corresponding operator. With the help of this lemma, a minimal principle for the energy as functional of  $\rho(r)$  can be derived. The second Hohenberg–Kohn theorem (HK-II) provides the necessary guidelines to obtain the ground state energy. Following HK-II, a variational principle is established, according to which the ground state density of a system of interest can be determined.

In order to put the promise of the HK theorems that all properties of a system can be obtained from its ground state density, into reality, one would need a construction that is computationally accessible while maintaining the formal exactness of HK-I and HK-II. To this end, Kohn and Sham (1965) introduced a fictitious system of  $N$  non-interacting electrons that have for their overall ground state density the same density as some real system of interest where the electrons do interact. Using some aspects of HF-theory, the ground state wave function  $\Psi_0$  of such a non-interacting system is described by a single Slater determinant. The orbitals, which form this Slater determinant, known as Kohn–Sham (KS) orbitals  $\phi_{KS}$ , are solutions of  $N$  single particle equations. Following the variational principle, the ground state energy and the ground state density are determined from variations in  $\phi_{KS}$ .

The essential contribution to the KS-energy comes from the so-called exchange correlation energy  $E_{XC}$ . It incorporates corrections to the kinetic energy due to the interacting nature of the electrons of the real system, all non-classical corrections to the electron–electron repulsion, as well as electron self-interaction corrections. If  $E_{XC}$  is ignored, the physical content of the theory becomes identical to that of the Hartree approximation. Thus, within the KS-formalism,



the electronic energy of the ground state of a system of  $N$  electrons moving within an external potential of nuclei is expressed – without approximations – as a functional of the ground state density,  $\blacktriangleright$  Eq. 4.3:

$$E[\rho] = T_s[\rho] + U[\rho(1), \rho(2)] + V_{\text{ne}}[\rho] + E_{\text{XC}}[\rho]. \quad (4.3)$$

In  $\blacktriangleright$  Eq. 4.3, the first term represents the kinetic energy of the system of  $N$  non-interacting electrons, the second term corresponds to the Coulombic repulsions between the total charge distributions at two different positions within the system, and the third term accounts for nuclear–electron interactions, due to the presence of an external potential. It is the fourth term, the functional for the exchange–correlation energy  $E_{\text{XC}}$ , which is responsible for the power and magic of DFT. What makes current DFT applications approximate is the unknown analytic expression of  $E_{\text{XC}}$ , for which an approximation is needed.

The KS formalism is closely related to the HF formalism. What differentiates the KS-operator from the HF-operator is the exchange–correlation potential  $V_{\text{XC}}$ .  $V_{\text{XC}}$  in turn is a functional derivative of the exchange–correlation energy  $E_{\text{XC}}$ . Furthermore, the Hamiltonian  $H$  operating on the wave function that is associated with the density of a fictitious system of  $N$  non-interacting electrons can be expressed as sum of one-electron operators.

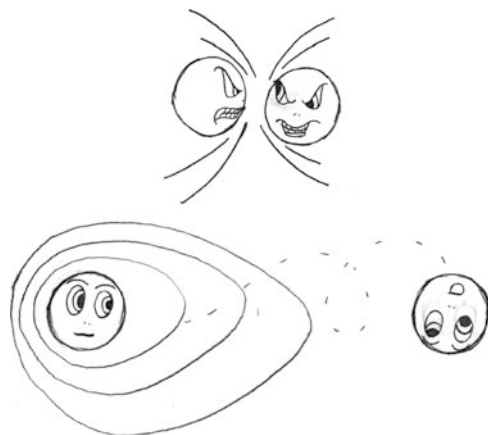
Whereas increasing the accuracy of HF calculations is accompanied with a steep increase in computational cost, increasing the accuracy of DFT calculations apparently requires modifications in  $V_{\text{XC}}$ , which – if at all – only lead to a moderate increase in computational cost. However, whereas it is well known how to systematically improve the accuracy and quality of HF calculations, no comparable strategy exists for DFT calculations within the confines of a KS-approach. It appears that a detailed knowledge of the exchange–correlation energy  $E_{\text{XC}}$  is essential for designing more accurate density functionals.

## Holes and Electron Pairs

The exchange–correlation energy  $E_{\text{XC}}$  is a relatively small part of the total energy of a typical system, although it is by far the largest part of “nature’s glue” that binds atoms together (Kurth and Perdew 2000). It arises because the electrons do not move randomly through the density but avoid one another. Ziegler (1995) illustrates the situation as follows: An electron will try to maximize the attraction from the nuclei and minimize the repulsion from the other electrons, as it moves around in the molecular framework. To do so, it creates an exclusion area or “no-fly zone” around itself into which no other electron can penetrate, as pictorially exemplified in  $\blacktriangleright$  Fig. 4-2. The exclusion zone is referred to as the exchange and correlation (XC) hole, and it is the way in which the XC-hole is modeled that distinguishes one electronic theory from another. Each density functional has its own characteristic XC-fingerprint.

The XC-hole also determines to a large part  $E_{\text{XC}}$ , which however contains three different contributions. The first is the potential energy of exchange, which also should include corrections for self-exchange or self-interaction. The second is the potential energy of correlation due to the effect of Coulomb repulsion. Both potential energies are negative, and determined by the nature of the XC-hole. The third contribution to  $E_{\text{XC}}$  is a smaller positive kinetic energy of correlation due to the extra swerving motion of the electrons as they avoid one another (Perdew et al. 2009).

The XC-hole arises from an extension of the concept of the unconditional one-electron probability density  $\rho(1)$  by considering pairs of electrons and a resulting conditional probability.



■ Fig. 4-2

**Electrons in distress:** While trying to maximize the attraction from the nuclei, an electron experiences enhanced repulsion from the other electron as it moves around in the molecular framework (*top*). To minimize the repulsion, each electron creates an exclusion area around itself, into which no other electron can penetrate (*bottom*) (Cartoon by Lauren Bertolino)

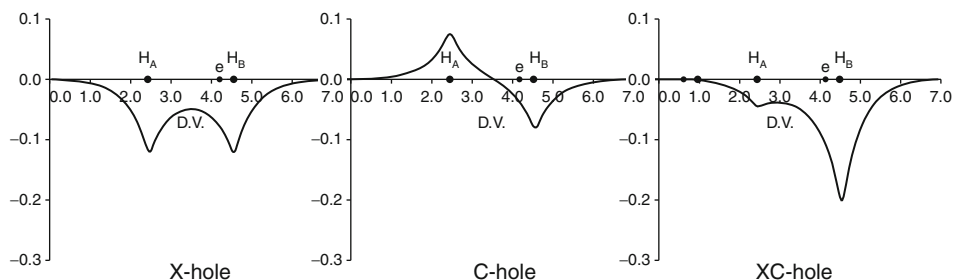
When a reference electron is known to be at position 1, the conditional probability  $\rho^{\text{cond}}(2, 1)$  of the other electron to be at position 2 can be written as the sum of the unconditional probability  $\rho(2)$  of the other electron and the XC-hole density  $\rho^{\text{XC-hole}}(2, 1)$ . Thus, the hole  $\rho^{\text{XC-hole}}(2, 1)$  describes how the conditional density of the other electron deviates from its unconditional density  $\rho(2)$ .

It is instructive to have a closer look at hole-profiles, and as simple example, we will consider the hydrogen molecule  $\text{H}_2$  with only two electrons or one electron pair. In ► Fig. 4-3, hole densities for  $\text{H}_2$  are shown; the two nuclei  $\text{H}_A$  and  $\text{H}_B$  are separated by 72 pm, and the reference electron is placed 15 pm to the left of nucleus  $\text{H}_B$ .

The XC-hole can be split into contributions from the exchange- or X-hole, which arises from the Fermion nature of an electron obeying the Pauli principle, and the correlation- or C-hole due to Coulomb repulsion within the pair of electrons. (The X-hole and C-hole are often referred to as Fermi hole and Coulomb hole, respectively).

The X-hole puts an emphasis on the reference electron. It creates a taboo zone for the other electron with a negative  $\rho^{\text{X-hole}}(2, 1)$  probability density not only around the region in space where the reference electron currently is, but also where it might be. Regions in the vicinity of both nuclei  $\text{H}_A$  and  $\text{H}_B$  are declared as “no-fly zone.” The C-hole on the other hand puts an emphasis on the other electron. It excludes regions where the other electron might experience Coulomb repulsion with the reference electron, but it also maps out regions where the other electron can benefit from attractive Coulomb interactions with nuclei. We see a negative  $\rho^{\text{C-hole}}(2, 1)$  probability density around  $\text{H}_B$  but a positive  $\rho^{\text{C-hole}}(2, 1)$  probability, a build-up of density, around  $\text{H}_A$  far away from the reference electron. Whereas the X- and C-hole illustrate exchange and correlation, only the combined XC-hole has physical meaning.

Before we continue, a short remark on the use of some language is in order. Since the terms local and nonlocal are often recurred to in the context of DFT, and often with different meanings, we briefly define how the terms local and nonlocal are used in this work. An approximation



■ Fig. 4-3

**Hole densities in the hydrogen molecule: Only the full XC-hole  $\rho^{\text{XC-hole}}(2,1)$  has physical meaning (Adapted from Baerends and Gritsenko (1997) with permission by the American Chemical Society)**

is said to be local if its energy density and related properties at any position of interest depend only on the electron density neighborhood of the given position. Otherwise, an approximation is said to be fully nonlocal. (We note that some physicists separate local approximations into “strictly local” and “semilocal.”)

From an inspection of Fig. 4-3 it appears that both the C-hole and the X-hole are inherently nonlocal (the same as the HF exchange energy). The XC-hole, too, must therefore be nonlocal, but its dominant contributions arise from the region around its reference electron – the XC-hole appears to be more local and less nonlocal than the X- or C-hole. This observation already anticipates that local density functionals might be able to produce approximate models for the nonlocal XC-hole.

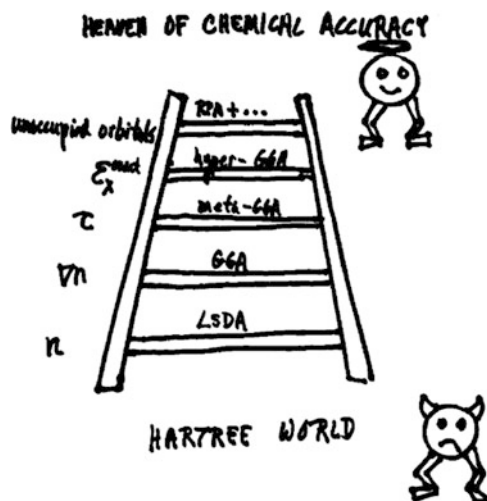
Although it seems that there exists no systematic approach like in WFT to improve the accuracy of DFT, the advancement of density functionals depends on more precise descriptions not only of the XC-hole but also of the exchange-correlation energy  $E_{\text{XC}}$ . This task can be approached in methodical manner.

## Climbing Jacob’s Ladder

Perdew and Schmidt (2001) compare the development of enhanced density functionals to a climb of Jacob’s ladder, leading the way from the Hartree world to the heaven of chemical accuracy, illustrated in Fig. 4-4. Each rung of the ladder adds a refinement to the approximation of the exchange-correlation energy.

### First Rung: The Local Density Approximation

The first rung employs only the local densities in the description of the exchange-correlation energy. This method is known as the local density approximation (LDA). (Although vital to the Fermion nature of electrons, so far we have treated spin rather nonvercal. But the issue of spin can be treated as well in density functional theory, and the local spin density approximation (LSD or LSDA) replaces the spin-averaged energy density with the energy density for a polarized homogeneous electron gas. LDA and LSDA are now often used synonymously.)



■ Fig. 4-4

The Jacob's ladder of density functional approximations to the exchange-correlation energy (Reprinted from Perdew et al. (2009), with permission by the American Chemical Society)

LDA takes its densities from the uniform electron gas (UEG), and an analytical form of a density functional for the exchange energy of the UEG can be derived (the same exchange energy as used in the HFS-method). No such expression exists for the correlation energy, but the UEG correlation energy can be calculated numerically and fit in various ways. One successful and popular parameterization comes from the work of Vosko, Wilk, and Nussair, referred to as VWN (Vosko et al. 1980).

LDA performs surprisingly well in predicting molecular properties that are based on relative energy differences within a given density. Molecular geometries for representative main group compounds could be reproduced in close agreement to the experiment (Versluis and Ziegler 1988). For transition metal complexes, metal-ligand separations are slightly underestimated, but still within acceptable conformity with X-ray data (Ziegler 1995). However, properties that are based on absolute energies differences between densities, such as bond energies, are not well described by LDA, where a clear overbinding tendency emerged. LDA is therefore a remarkably useful structural, though not thermochemical, tool. The disappointing performance of LDA in estimating thermochemical properties spawned the development of gradient-based methods, the second rung on Jacob's ladder.


## Second Rung: The Generalized Gradient Approximation

The second rung or generalized gradient approximation (GGA) adds the gradients of the local densities to the exchange-correlation picture. It became clear that the homogeneous electron gas is only of limited use as a model of the inhomogeneous electron density within molecules, and approximations for exchange and correlation energy were augmented by density gradients. (In the older literature, GGAs are sometimes called nonlocal (LDA/NL), since the gradient implies a directional change within the density.) Two early models for correlation (Perdew 1986) and exchange (Becke 1988b) in combination resulted in the BP86 functional, the GGA that was

most influential in the early developments of transition metal DFT (Ziegler 1991). Gradient corrections are essential for a quantitative estimate of bond energies as well as metal–ligand bond distances (Ziegler 1995).

### Third Rung: Meta-Functionals

The third rung adds the kinetic energy density to the description of density functionals (Tao et al. 2003), and addresses the smaller third contribution to  $E_{XC}$ . Such functionals are referred to as meta-functionals, and when built on second rung functionals, as meta-GGA (MGGA).

The first three rungs of Jacob's ladder all represent local functionals. They often work because of proper accuracy for a slowly varying density or because of error cancellation between exchange and correlation. Error cancellation can occur because the exact XC-hole is usually more localized around its reference electron than the exact X-hole (compare  Fig. 4-3). Regions in which no error cancellation is expected are regions where exchange dominates correlation (Perdew et al. 2009).

Climbing up the ladder, the approximations become more complicated, more sophisticated, and typically more accurate. Computation times increase modestly from the first to the third rungs and much more steeply after that. The added ingredients on each higher rung of the ladder can be used to satisfy more exact constraints or to achieve better agreement with experimental data (or both). These two strategies define the nonempirical and semiempirical approaches commonly used to improve density functionals. Beginning with the fourth rung, the nature of the density functionals changes from local to nonlocal.

### Fourth Rung: Hyper-Functionals

The fourth rung, which also represents the first fully nonlocal rung, adds the exact exchange energy density. Such a functional is termed hyper-GGA (hyper-HGGA). After reaching the second rung, DFT progressed rapidly and took one giant step from the second to the fourth rung, omitting meta-GGAs. Following the idea of adiabatic connection, Becke derived a functional for exchange, which contained contributions from the exact HF-exchange (Becke 1993a). He then designed an advanced functional for the exchange-correlation contribution containing three parameters for its various parts, including gradient corrections for correlation, gradient corrections for exchange, as well as an exact exchange contribution (Becke 1993b). These semi-empirical coefficients have been determined by a linear least-square fit to 56 atomization energies, 42 ionization potentials, eight proton affinities, and ten first-row total atomic energies. Becke's functional, combining HF-theory and DFT with the use of three empirical coefficients, was the first example and initiated the evolution of so-called hybrid-functionals. The hybrid functional B3LYP, based on Becke's parameterization, was to a large part responsible for the meteoric ascent of DFT during the 1990s.

While the first three rungs of Jacob's ladder require no fitting of experimental data, empiricism seems unavoidable on the fourth rung. This has caused some skepticism, and it appeared that the success of "empirical DFT" would eventually be responsible for the death of "true DFT." Gill humorously described the situation at the beginning of the new millennium in his obituary

to DFT (Gill 2001). The Jacob's ladder metaphor puts the addition of exact exchange to density functionals into proper perspective.

The step from the third rung to the fourth rung results in a new class of functionals, so-called HMGGAs. HMGGA functionals are currently a field of active development, and appear to produce promising results. M06, for example, is a HMGGA with good accuracy for a variety of different chemical applications ranging from transition metals over main group thermochemistry to barrier heights of chemical reactions. Thus, HMGGAs might be considered as a class of density functionals with broad applicability in chemistry (Zhao and Truhlar 2008). Whether HMGGA is read as hybrid-meta-GGA or hyper-meta-GGA is a matter of taste; fortunately, both specifications result in the same acronym.

## Fifth Rung

The fifth rung of Jacob's ladder adds exact correlation as new ingredient. One might think of this as an expansion of the density space of a system by adding virtual densities into the picture. One approach to this problem is the use of the random phase approximation (RPA). RPA in DFT in turn is closely related to time-dependent DFT (TD-DFT). The essence of RPA might be described as constructing the excited states of a system as a superposition of particle-hole excitations.

When building a fifth-rung density functional for the exchange-correlation energy, the RPA utilizes full exact exchange and constructs the correlation with the help of the unoccupied Kohn–Sham orbitals. Like the first three rungs of Jacob's ladder, the fifth rung requires no fitting. At the time of writing, fifth-rung methods have not yet been established as essential tools in computational chemistry.

In the early days of modern density functional theory, hazy clouds of ambiguity that enfolded the XC-hole obscured the view of Jacob's ladder. The existence of the third rung of Jacob's ladder was recognized before the fourth rung entered the Jacob's ladder picture (Becke and Roussel 1989), but at first it did not appear as a safe and secure stage for the ascent toward the heaven of chemical accuracy. Thus, although MGGAs predate HGGAs, the computational development of HGGAs predates that of MGGAs. Only after the clouds of ambiguity lifted, MGGAs became a recognized DFT-approach in computational chemistry, and HMGGAs began to appear.

The Jacob's ladder scheme is not the only way to arrive at exact functionals. When leaving the confines of ordinary KS-DFT methods, and using ideas from WFT, one arrives at ab initio density functional theory, the seamless connection of DFT and WFT (Bartlett et al. 2005). However, these methods have not yet established themselves as standard approaches in computational chemistry.

## Practical DFT and the Density Functional Zoo


---

A practical DFT-based calculation is in many ways similar to a traditional HF treatment in that the final outcome is a set of orbitals, the Kohn–Sham orbitals  $\phi^{\text{KS}}$ . The KS-orbitals are often expanded in terms of a basis set as in the traditional linear combination of atomic

orbital (LCAO) approach of traditional HF-methods. Most often, Gaussian-type basis functions are used to construct atomic orbitals (GTO). A major exception is the Amsterdam Density Functional suite of programs (ADF), where Slater-type basis functions (STO) are used (ADF 2010). ADF constitutes one of the first programs developed essentially for applications of DFT.

The evaluation of matrix elements of the Kohn–Sham exchange–correlation potential always requires at some step a 3D numerical integration. Solutions to the problem of carrying out 3D numerical integration for polyatomic systems to arbitrary precision (Becke 1988a) provided a major thrust for computational DFT, and proficient improvements were made in connection with developments of the ADF computer code (Boerrigter et al. 1988). The availability of economical numerical integration schemes made the choice of STOs over GTOs computationally compatible.

The local nature of the effective potential in the one-electron Kohn–Sham equations affords efficient computational schemes. During the development of ADF, the remaining Coulomb problem, the two-electron-integral “bottleneck,” has been addressed by the introduction of auxiliary basis sets, so-called “density fitting” (Baerends et al. 1973).

Many of the pioneering improvements made during the development of the ADF suite of programs have become standard tools in density functional calculations, and as a result, DFT calculations perform compatible to, if not better than HF-methods. We note that a density fit is not possible, when the chosen functional utilizes exact exchange. By now, a plethora of density functionals is available for electronic structure calculations. Towards the end of the first decade of the new millennium, Sousa and coworkers have presented an authoritative review, in which they evaluate the performance of over 50 different density functionals (Sousa et al. 2007). The authors also report the percentage of occurrences of the names of different functionals in journal titles and abstracts; we interpret these numbers as measure for usage and popularity of the corresponding functional. Although new functionals appear every year, the popularity ranking seems to possess some stability within a time interval of several years. Thus, in  Fig. 4-5,

FUNCTIONAL (YEAR)	TYPE	USAGE
B3LYP (1994)	HGGA	80%
BLYP (1988)	GGA	5%
B3PW91 (1993)	HGGA	4%
BP86 (1988)	GGA	3%
PBE (1996)	GGA	2%
BPW91 (1991)	GGA	1%
TPSS (2003)	MGGA	1%

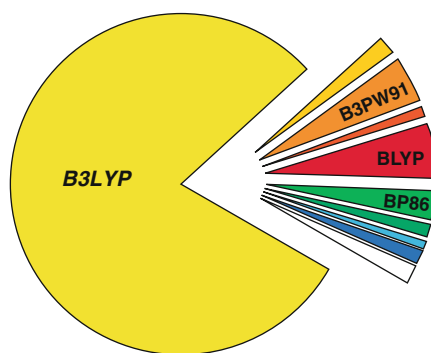





 Fig. 4-5

Most popular density functionals at the end of the first decade of the new millennium (Data based on results of extensive literature searches (Sousa et al. 2007))

we have compiled data for the seven most popular functionals, taken from the work of Sousa and coworkers, and include a popularity pie chart as well.

The key information conveyed in  Fig. 4-5 is the fact that B3LYP is by far the most popular density functional in chemistry, representing 80% of the total of occurrences of density functionals in the literature, in the period 1990–2006 (Sousa et al. 2007). Other popular density functionals such as BLYP, B3PW91, and BP86 acquire usage shares of 5% and less, and can only be considered as also-rans in the functional race.

It seems advisable to briefly talk about how to decipher the density functional code. With the advent of GGAs at the end of the 1980s, the abbreviation for each GGA-functional usually consisted of two parts: the first for exchange and the second for correlation. As an example, BP86 takes its exchange contribution from the work of Becke (1988b), and correlation from the work of Perdew (1986). Similarly, BLYP breaks down into B-exchange and LYP-correlation. Later, when gradient corrections for exchange and correlation were often taken from the same work, the functional is usually referred to by one combined code only. The GGA functional PBE takes its gradients for exchange as well as for correlation from the work of Perdew, Burke, and Ernzerhof. The same holds true for the MGGGA TPSS. Strictly spoken, the PBE functional should be referred to as PBEPBE. It is also possible that the individual parts are combined with other functionals, for example, PBELYP or BPBE. HGGAs usually contain one number that indicates the degree of parameterization when building the hybrid: B3LYP refers to a three-parameter mixing of B-exchange, LYP-correlation, and exact exchange, whereas B1LYP refers to a one-parameter hybrid density functional. As density functionals get more elaborate and more complex, the XC-coding is not always strictly followed. The HMGGA M06 and its variations (M06-L, M06-2X, M06-HF), for example, refer to a set of functionals developed at the University of Minnesota in 2006.

The pie chart presented in  Fig. 4-5 bears a striking resemblance to Pac-Man. Like the arcade game Pac-Man, often credited with being a landmark in video game history and virtually synonymous with video games, B3LYP has to be considered a landmark in electronic structure theory, and is often used as a synonym for DFT. However, the same as there is more to video games than just Pac-Man, there is more to density functional theory than just B3LYP. In  section “DFT: Computational Chemistry in Action,” we will explore the characteristics and capabilities of density functional in more detail.

The reader, who would like to know more about the details and derivations of DFT, will find valuable information about the basics in the “Chemist’s Guide to Density Functional Theory” (Koch and Holthausen 2002) and will learn more about advanced aspects in the “Primer in Density Functional Theory” (Fiolhais et al. 2003).

## DFT: Computational Chemistry in Action

---

The breakthrough of DFT coincided with a rise of computational power at the end of the last millennium. CPU architectures advanced from CISC- to RISC-designs, and supercomputers transformed from single vector-processors to computing clusters. However, as the computational power increased, the problems too became more and more demanding, and the molecules that found their way into input files for density functional programs grew bigger and bigger. Computing time remains to be a crucial factor when assessing the performance of



computational methods, and linear-scaling approaches are one of the great strengths of DFT (Yang 1991). However, these techniques fall out of the scope of our review and assessment, and we begin with a comparison of computational demands of representative density functionals, following standard approaches.

## Computational Performance

---

We start this section remarking that there is not something like “the best functional and basis set for all properties.” Rather, the specific methodological approach to be used depends from the specific problem at hand. Nevertheless, many functionals are robust enough to give rather reasonable results in a large series of chemical properties, and the scope of this section is to provide an overview of the performances of typical functionals and basis sets, trying to highlight which ones perform remarkably better or remarkably worse than the average, if this is known. Further, as a practical vademecum, the scope of this section is to give an overview of performances under “standard working conditions.” Thus, the focus will be on performances that can be expected when working with real-size systems (50–100 atoms including a transition metal), which requires a compromise between the computer resources available and the combination of functional and basis set used, rather than peak performances that can be reached with a sophisticated last generation functional in combination with a very extended basis. On the other hand, there are several excellent reviews that provide an accurate and critical assessment of the various methods, with a particular focus on the best performances that can be achieved, independently from the computational cost (Cramer and Truhlar 2009; Sousa et al. 2007). Methods that currently are computationally too expensive might become the standard computational tools in the future.

Finally, the number of possible functionals is very large, so that it is more confusing than enlightening to review all of them. In addition, it might well be that the best functional for a specific problem has not been tested in the several benchmarking studies published in the literature. As a general rule, before wasting huge amounts, computer power with the wrong functional and/or basis set, it is wiser to invest some time to read literature to find which computational method works better (or acceptably well) for a given problem, and possibly have a feeling of the accuracy through test calculations on small selected systems.

To give an idea of the relative cost of the various functionals, the relative computational time required by some functionals in two standard applications such as the calculations of the energy and of the first derivatives of the energy with respect to the atomic coordinates (which must be calculated at each geometry optimization step), and the calculation of the second derivatives of the energy with respect to the atomic coordinates (which must be calculated for vibrational analysis) is reported in ► [Table 4-1](#). The system considered in these calculations is a 70 atom Ru-complex whose brute formula is  $\text{RuC}_{31}\text{H}_{33}\text{Cl}_2\text{N}_3$ .

The data reported in ► [Table 4-1](#) clearly indicate that GGA calculations are computationally very effective. In addition, for DFT methods that do not rely on exact exchange, the performance can be further improved by using an auxiliary basis set to fit the electron density (usually called density fit or resolution of identity). Indeed, without this technical setup, the same GGA or MGGA functional – compare the BP86 (density-fit) and the simple BP86 values in ► [Table 4-1](#) – is roughly 50% slower. The same consideration applies when MGGA functionals are considered; compare the TPSS (density-fit) and the simple TPSS values in ► [Table 4-1](#). We note that this technical acceleration is not possible when the Hartree–Fock exchange must be evaluated,

■ Table 4-1

Relative performance of various functionals, as implemented in the Gaussian09 package, in the calculation of energy and gradients, or second derivatives, for an organometallic complex of formula  $\text{RuC}_{31}\text{H}_{33}\text{Cl}_2\text{N}_3$

Method		E + gradients	Second derivatives	E + gradients
		SVP		TZVP
BP86 (density fit)	GGA	1.0	1.0	1.6
BP86	GGA	1.5	1.9	4.1
PBE	GGA	1.5	1.8	4.2
B3LYP	HGGA	2.6	2.9	8.9
PBE1PBE	HGGA	3.0	3.2	9.2
TPSS (density fit)	MGGA	1.6	1.9	2.6
TPSS	MGGA	2.1	2.3	5.1
TPSSh	HMGGA	3.5	3.5	9.4
M06	HMGGA	3.6	4.0	10.6

and thus HGGA and HMGGA calculations cannot benefit from it. Generally speaking, there are marginal differences within a family of functionals, and HGGA functionals are roughly two to three times slower than GGA functionals. MGGA functionals, particularly when the resolution of identity technique is invoked, are roughly 50% slower than GGA functionals, and thus are quite faster than HGGA functionals. HMGGA functionals are roughly three to four times slower than GGA functionals. This relative speed between the different families of functionals is maintained when second derivatives are evaluated. Moving to the effect of the size of the basis set, calculations performed with a triple- $\zeta$  plus one polarization function of main group atoms results in an increase of the required computational time by a factor of 2–3 roughly. Thus, on going from an accelerated GGA functional in combination with a split-valence plus one polarization function basis set, to a HMGGA functional in combination with a triple- $\zeta$  plus one polarization function basis set results in an increase of the computational time by a factor of 10 roughly. In other words, a GGA/SVP calculation that would take 1 day would require more than 1 week, roughly, if performed at the HMGGA/TZVP level. This indicates that the selection of the most appropriate computational method (both functional and basis set) must be a trade between the accuracy needed and the computational time (or power) available. Of course, degradation of accuracy below the level required by the specific problem at hand is not possible.

## Properties of Molecular and Electronic Structure

To explore the capabilities of various density functionals, we have selected 12 representative properties of atoms and molecules. We begin with molecular structure (bond lengths, bond angles vibrational frequencies) and basics of electronic structure (electron affinities and ionization potentials). We then proceed to the energetics of transformations of molecules (atomization energies, heats of formation, energy barriers), which will carry us to chemical bonding. The nature of the chemical bond remains a central theme in theoretical chemistry, and we discuss regular bonds as well as weak bonds, all being at the focus of ongoing research activities (bond energies, hydrogen bonding, weak interactions). The issue of spin in DFT deserves

particular attention (spin states). Although DFT essentially is a ground state theory, excited states too can be treated with density functional theory, and with our last property we briefly touch this topic (excited states). Time-dependent density functional theory (TDDFT) is a topic in its own right, and an appropriate coverage of TDDFT falls out of the scope of the present work. The reader will find an entry into this excited field when studying the articles compiled by Marques and co-workers (2006).

The 12 topics we selected in no way exhaust the capabilities of DFT, and any property that can be treated with WFT, is in principle accessible with DFT as well. As an example, we refer the reader to a recent review by Neese (2009) that illustrates the capabilities of DFT in the field of molecular spectroscopy.

When evaluating the performance of computational methods, benchmarking is an essential procedure in which calculated properties are evaluated against accurate experimental data. By now, a large number of problem-specific databases have been established, which cover a wide variety of different physicochemical properties, such as proton affinities, atomization energies, barrier heights, reaction energies, and spectroscopic properties. However, these databases are not free from chemical biases, and often narrowed by the structural space of chemical intuition. There is always the risk that when following established procedures, benchmark studies might lose some of their general appeal. As to avoid the dangers of casual benchmarking, Korth and Grimme have developed a “mindless” DFT benchmarking protocol. Here, the databases consist of randomly generated molecules that rely on systematic constraints (Korth and Grimme 2009) rather than on what is supposed to be chemical insight.

In the following, we will make extensive reference to published benchmark studies. However, it might well be that a particular molecule of interest to the reader is not covered within one of the existing benchmark databases, and benchmark studies in general provide good starting points for calculations, but no guarantee for correctness.

## Bond Lengths

It is well established that almost any DFT approach, beyond LDA, is able to reproduce correctly the geometry of molecular systems composed of main group atoms. With the increase of computer resources it is becoming customary to test the performances of various methods through calculations on a rather large set of molecules, and to report statistical values. In one of such comparative studies, 17 closed-shell molecules composed by first-row atoms, for which accurate experimental geometries determined in the gas-phase was available, confirmed that the performance of commonly used GGA (BLYP, BPW91 and BP86) and HGGA (B3LYP, B3PW91 and B3P86) is quite accurate, although the mean unsigned error (MUE) on the bond length obtained with the GGA functionals, between 0.015 and 0.020 Å roughly, is slightly larger than that calculated with the HGGA functionals, usually below 0.010 Å (Wang and Wilson 2004). The convergence of the geometry was tested with respect to increasing basis set size from cc-pVDZ to aug-cc-pV5Z, and was shown to occur quickly. Convergence is typically reached at the triple- $\zeta$  level, and beyond this level minor fluctuations, in the order of 0.002 Å, were observed. Thus, excellent performances require that at least a triple- $\zeta$  basis set is used. Similar conclusions were reached in a different benchmark study on a dataset of 44 small molecules (Riley et al. 2007). Again, GGA functionals in combination with Pople basis sets of the 6-31G family result in MUE between 0.015 and 0.020 Å, while HGGA functional result in MUE below 0.010 Å. The MGGA functionals tested resulted in a minor improvement relative

to GGA functionals, while the tested HMGGA functionals substantially reproduce the performance of HGGA functionals. This indicates that the advantage of meta-functionals certainly is not in bond distances.

To give an idea of the performance of some popular functionals, and also to show the effect of the basis set, the dependence of the O–H bond length in water is reported in ► [Table 4-2](#) as an exemplary case. The data indicate that reasonable accurate bond lengths (within 0.02 Å from the experimental value) can be achieved with computationally cheap GGA functionals, and that HGGA performs slightly better with modest basis sets. As a general trend, the HGGA bond lengths are slightly shorter than the corresponding GGA value and, independent of the computational approach; slightly shorter bond lengths are predicted with basis sets of increasing quality.

As final result, we remark that with the extended aug-cc-pV5Z basis set the GGA values slightly overestimate the experimental value, whereas the HGGA values slightly underestimate it. Importantly, rather good results can be achieved also with relatively small basis sets, which allow calculating geometries for fairly large systems with a reasonable accuracy.

The very good performance of almost any functional to calculate accurately bond lengths of molecular systems composed by main group atoms is not replicated when bonds to transition metals are considered. Focusing on an extensive benchmark of 42 functionals on a database of 13 metal–ligand bond lengths, the MBL13/05 database, all functionals provide rather good results, with MUE normally between 0.01 and 0.02 Å when a basis set of triple- $\zeta$  quality is used (Schultz et al. 2005a). Extending the benchmark to a database containing the bond length of eight metal–metal dimers, the TMBL8/05 databases, the situation deteriorates. GGA functionals, including the popular BP86, BLYP, and PBE functionals, still provide rather good results, with MUE between 0.02 and 0.03 Å when a basis set of triple- $\zeta$  quality is used, while reducing the quality of the basis set to double- $\zeta$  deteriorates performances remarkably, with MUE between 0.06 and 0.09 Å (Schultz et al. 2005b). In the GGA family, the HTCH and OLYP functionals, with MUE greater than 0.03 Å, should be avoided. The rather good performance of GGA functionals is not replicated by HGGA functionals, including the popular B3LYP and PBE1PBE

■ **Table 4-2**

**Performance of selected functionals and basis sets in predicting the experimental value of the O–H bond length of water, 0.956 Å**

	BP86	revPBE	B3LYP	TPSS	TPSSh	M06
6-31G	0.985	0.984	0.976	0.983	0.978	0.970
SVP	0.976	0.974	0.967	0.974	0.969	0.963
6-31G(d,p)	0.974	0.973	0.965	0.972	0.967	0.960
TZVP	0.972	0.971	0.962	0.969	0.965	0.958
cc-pVDZ	0.978	0.977	0.969	0.977	0.972	0.964
cc-pVTZ	0.971	0.970	0.961	0.968	0.964	0.958
cc-pVQZ	0.970	0.968	0.960	0.968	0.963	0.956
cc-pV5Z	0.970	0.968	0.960	0.967	0.963	0.956
aug-cc-pVDZ	0.974	0.974	0.965	0.973	0.970	0.961
aug-cc-pVTZ	0.971	0.970	0.962	0.969	0.964	0.958
aug-cc-pVQZ	0.970	0.968	0.961	0.967	0.963	0.956
aug-cc-pV5Z	0.970	0.968	0.960	0.967	0.963	0.956

functionals, with MUE between 0.08 and 0.09 Å. In the HGGA family, the BH&HLYP and MPW1K functionals, with MUE greater than 0.12 Å, should be avoided. Interestingly, MGGA functionals do not perform as or better than GGA functionals in predicting bond lengths, but rather worse. Indeed, including also the popular BB95 and TPSS functionals, they result in MUE greater than 0.06 Å. Introduction of HF exchange partially improves the performance of MGGA functionals, and the tested HMGGA functionals, including the B1B95 and the TPSSh functionals, result in MUE between 0.03 and 0.07 Å (Schultz et al. 2005a). Finally, the M06 functional performs particularly poor, with a MUE of 0.131 Å (Zhao and Truhlar 2008).

To give an idea of the performance of some popular functionals in the calculation of the M-ligand distances and of the effect of the metal on the bond distance of the ubiquitous CO ligand, analysis of these distances in three typical binary carbonyl complexes involving first-row transition metals is reported in [Table 4-3](#).

Basically, all the functionals reproduce the experimental M-CO distances well within 0.02 Å, but many of the functionals tested underestimate the difference in the axial and equatorial Fe-CO distances. In this respect, HGGA and HMGGA functionals seem to perform slightly better, although there is quite a debate on the exact assignment of the Fe-CO distances in Fe(CO)<sub>5</sub>. Similar good behavior is shown by all the functionals in the prediction of the CO distance when bonded to a transition metal, although the GGA and MGGA functionals tested yield systematically longer CO distances. In this respect, HGGA and HMGGA functionals do perform slightly better.

## Bond Angles

The good performance of almost every functional to predict correctly bond lengths of molecular systems composed by main group atoms is confirmed in the case of bond angles. Again, a

Table 4-3

Performance of selected functionals, in combination with the TZVP basis set on all the atoms, in predicting the experimental value of the M-C and C-O bond length (in Å) in three first-row M(CO)<sub>n</sub> complexes

		Ni(CO) <sub>4</sub>		Fe(CO) <sub>5</sub>				Cr(CO) <sub>6</sub>	
		M-C	C-O	M-C <sub>eq</sub>	M-C <sub>ax</sub>	C-O <sub>eq</sub>	C-O <sub>ax</sub>	M-C	C-O
Exp.		1.838	1.141	1.803	1.811	1.133	1.117	1.918	1.141
BP86	GGA	1.828	1.151	1.809	1.810	1.157	1.153	1.910	1.155
PW91	GGA	1.824	1.149	1.805	1.806	1.154	1.151	1.906	1.153
revPBE	GGA	1.829	1.150	1.809	1.810	1.155	1.153	1.911	1.154
B3LYP	HGGA	1.845	1.137	1.820	1.828	1.142	1.138	1.926	1.141
PBE1PBE	HGGA	1.822	1.134	1.796	1.805	1.140	1.136	1.900	1.138
B98	HGGA	1.839	1.137	1.813	1.820	1.142	1.138	1.915	1.141
TPSS	MGGA	1.830	1.149	1.813	1.816	1.154	1.151	1.918	1.152
mPWKCIS	MGGA	1.832	1.150	1.810	1.811	1.156	1.153	1.911	1.154
BB95	MGGA	1.833	1.150	1.811	1.811	1.156	1.153	1.912	1.154
TPSSh	HMGGA	1.828	1.142	1.809	1.815	1.147	1.144	1.915	1.146
M06	HMGGA	1.848	1.133	1.820	1.821	1.139	1.135	1.920	1.138

benchmark study on 17 closed-shell molecules composed by first row atoms, for which accurate experimental geometries determined in the gas-phase was available, confirmed that the performance of commonly used GGA (BLYP, BPW91 and BP86) and HGGA (B3LYP, B3PW91 and B3P86) functionals is quite accurate, with a MUE between  $1.0^\circ$  and  $1.5^\circ$  (Wang and Wilson 2004). Differently from bond lengths, GGA and HGGA methods perform rather similarly on bond angles. Also for bond angles the convergence was tested with respect to increasing basis set size from cc-pVDZ to aug-cc-pV5Z, and was shown to occur quickly, and again convergence is typically reached at the triple- $\zeta$  level. Similar conclusions were reached in a different benchmark study on a dataset of 44 small molecules (Riley et al. 2007). All the functionals considered resulted in MUE between  $1.0^\circ$  and  $1.5^\circ$ , independent of the functional used.

To give an idea of the performance of some popular GGA and HGGA functionals, and also to show the effect of the basis set, the dependence of the H–O–H angle in water is reported in [Table 4-4](#) as an exemplary case. Accurate bond angles (within  $1.0^\circ$  from the experimental value) can be achieved with all functionals and moderate basis sets.

## Vibrational Frequencies

Benchmarking various DFT methods to reproduce accurately vibrational frequencies of 35 molecular systems composed by main group atoms revealed that GGA methods, with a MUE of roughly  $40\text{ cm}^{-1}$ , are among the most accurate functionals (Riley et al. 2007). Indeed, the performance of several HGGA methods was at least  $20\text{ cm}^{-1}$  worse, with MUE between 60 and  $80\text{ cm}^{-1}$ , and meta-functionals are not an improvement. As for other geometrical properties, accurate performance requires that a triple- $\zeta$  basis set be used. The GGA functionals also performed better than HGGA functionals in the prediction of the vibrational frequency in nine homonuclear 3d metal dimers, with a MUE around  $100\text{ cm}^{-1}$  for BLYP and BP86, and around  $120\text{ cm}^{-1}$  for B3LYP and B3P86. Nevertheless, both families of functionals resulted in a rather large deviation from accurate data (Barden et al. 2000).

■ Table 4-4

Performance of selected functionals and basis sets in predicting the experimental value of the H–O–H angle of water,  $105.2^\circ$

	BP86	revPBE	B3LYP	TPSS	TPSSh	M06
6-31G	107.2	107.1	108.3	107.1	107.7	109.4
SVP	102.2	102.1	103.1	102.3	102.7	103.3
6-31G(d,p)	103.1	103.0	104.0	103.3	103.7	104.5
TZVP	104.1	104.1	105.1	104.3	104.6	104.9
cc-pVDZ	101.7	101.7	102.7	104.9	102.3	102.8
cc-pVTZ	103.6	103.5	104.5	103.7	104.0	104.4
cc-pVQZ	103.9	104.0	104.9	104.0	104.3	104.8
cc-pV5Z	104.2	104.3	105.1	104.3	104.5	105.0
aug-cc-pVDZ	103.8	103.8	104.8	103.8	104.1	104.7
aug-cc-pVTZ	104.2	104.2	105.0	104.3	104.6	104.9
aug-cc-pVQZ	104.2	104.3	105.1	104.3	104.6	104.9
aug-cc-pV5Z	104.2	104.3	105.1	104.3	104.6	105.1

■ Table 4-5

Performance of selected functionals, in combination with the TZVP basis set on all the atoms, in predicting the symmetric frequency of the CO stretching mode in selected first-row transition metal binary carbonyl complexes

Method		Ni(CO) <sub>4</sub>		Fe(CO) <sub>5</sub>		Cr(CO) <sub>6</sub>		$\nu_{\text{Ni}} - \nu_{\text{Cr}}$
Exp.		2,061.3	%err	2,038.1	%err	2,003.0	%err	58.1
BP86	GGA	2,104.0	2.1	2,103.0	3.2	2,102.0	4.9	2.0
PW91	GGA	2,116.0	2.7	2,115.0	3.8	2,115.0	5.6	1.0
revPBE	GGA	2,110.0	2.4	2,109.0	3.5	2,109.0	5.3	1.0
B3LYP	HGGA	2,194.0	6.5	2,184.0	7.2	2,185.0	9.1	9.0
PBE1PBE	HGGA	2,232.0	8.3	2,223.0	9.1	2,223.0	11.0	9.0
B98	HGGA	2,212.0	7.3	2,202.0	8.0	2,197.0	9.7	15.0
TPSS	MGGA	2,121.0	2.9	2,116.0	3.8	2,117.0	5.7	4.0
mPWKICIS	MGGA	2,102.0	2.0	2,102.0	3.1	2,102.0	4.9	0.0
BB95	MGGA	2,100.0	1.9	2,100.0	3.0	2,100.0	4.8	0.0
TPSSh	HMGGA	2,169.0	5.2	2,162.0	6.1	2,162.0	7.9	7.0
M06	HMGGA	2,234.0	8.4	2,224.0	9.1	2,226.0	11.1	8.0

Next to each calculated frequency is reported the %error calculated as  $\%err = 100 * (\nu_{\text{exp}} / \nu_{\text{DFT}})$ . The final column reports the difference between the Ni(CO)<sub>4</sub> and the Cr(CO)<sub>6</sub> frequencies

The performance of various functionals in the prediction of the CO stretching frequency in typical binary carbonyl complexes with first-row transition metals is exemplified in [Table 4-5](#). Simple GGA and also MGGA functionals perform better, and are able to capture the experimental value with an accuracy of roughly 50–100 cm<sup>-1</sup>, while Hartree–Fock exchange seems to deteriorate results, since the HGGA and HMGGA functionals reproduce the experimental value with an accuracy of roughly 150–200 cm<sup>-1</sup>. In terms of percent, the GGA and MGGA functionals overestimate the experimental values by 3–4%, while the HGGA and HMGGA functional by 6–10%. While these results may seem quite accurate, almost all the functionals considered are unable to differentiate too little between metals. In fact, the experimental value decreases by 58.1 cm<sup>-1</sup> on going from Ni(CO)<sub>4</sub> to Cr(CO)<sub>6</sub>, but the functionals examined are unable to capture this difference. The best performing are the B98 functional, with a difference of merely 15.0 cm<sup>-1</sup>, and the HGGA and HMGGA with differences slightly smaller than 10 cm<sup>-1</sup>.

On the other hand, the simple BP86 GGA functional has also been tested in the prediction of the CO stretching frequency in rather large organometallic complexes. For these large and computationally demanding systems, which are displayed in [Fig. 4-6](#), computationally effective methods are needed.

The data reported in [Table 4-6](#) clearly show the very good performance of the BP86 functional, which is able to reproduce the higher frequency symmetric CO stretching with an error of roughly 20 cm<sup>-1</sup> only, and the lower frequency asymmetric CO stretching with an error of roughly 30 cm<sup>-1</sup>. Further, despite the poor performances discussed above in the ability of GGA functionals to differentiate between different binary M(CO)<sub>n</sub> complexes, comparison of the saturated N-heterocyclic carbene complexes (SIPr and SIMes) with their unsaturated counterparts (IPr and IMes) indicates that the DFT values reproduce the experimental finding that both CO stretches are about 1 or 2 cm<sup>-1</sup> smaller in the complexes with the unsaturated N-heterocyclic carbene ligand (Kelly et al. 2008).

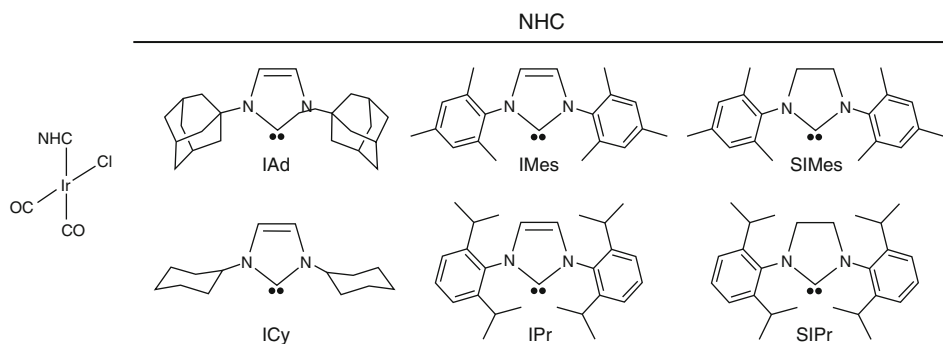


Fig. 4-6  
Iridium complexes that bear N-heterocyclic carbene ligands

Table 4-6  
Experimental and DFT calculated CO stretching frequencies, in  $\text{cm}^{-1}$ , in several N-heterocyclic carbene complexes

Method	Experimental		BP86	
(IAd)Ir(CO) <sub>2</sub> Cl	2,063.4	1,979.8	2,082	2,010
(ICy)Ir(CO) <sub>2</sub> Cl	2,064.8	1,981.2	2,083	2,015
(IPr)Ir(CO) <sub>2</sub> Cl	2,066.8	1,981.0	2,083	2,005
(SIPr)Ir(CO) <sub>2</sub> Cl	2,068.0	1,981.8	2,084	2,007
(IMes)Ir(CO) <sub>2</sub> Cl	2,066.4	1,979.8	2,084	2,007
(SIMes)Ir(CO) <sub>2</sub> Cl	2,068.0	1,981.8	2,085	2,008

## Electron Affinities and Ionization Potentials

A benchmark study of 24 molecules from the G2/97 dataset, with the addition of  $\text{PO}_2$ , indicated that, with some exceptions, DFT methods reproduce the electron affinity of molecular systems composed by main group atoms with a MUE close to  $4 \text{ kcal mol}^{-1}$ . Some hybrid functionals, such as the B98 functional, performs slightly better ( $\text{MUE} = 3.15 \text{ kcal mol}^{-1}$ ), while GGA functionals with the P86 correlation term usually perform rather poorly, with MUE around  $6 \text{ kcal mol}^{-1}$  (Riley et al. 2007). Finally, meta-functionals are not an improvement. As for any molecular system with a negative charge, the calculation of electron affinity requires that basis set containing diffuse functions are used. Moving to ionization potentials, the performance of the various methods on 36 molecules from the G2/97 dataset, with the addition of  $\text{PO}_2$ , substantially replicates that found for electron affinities, although the MUE, between 5 and  $6 \text{ kcal mol}^{-1}$ , is slightly larger (Wang and Wilson 2004). The B1B95 MHGGA functional provided the best performance, with a MUE of  $4.25 \text{ kcal mol}^{-1}$ .

Moving to selected cases, see Table 4-7, the BP86 GGA functional seems quite more accurate than the HGGGA B3LYP functional in predicting the electron affinity of highly unsaturated late transition metal  $\text{M}(\text{CO})_n$  complexes, but the HGGGA functional seems to be more accurate when the unsaturation at the metal is reduced (Zhou et al. 2001). These results exemplify the difficulty to extract trends from benchmarks, if the specific case at hand has not been included in the testing dataset.



■ Table 4-7

Calculated and experimental electron affinities, in kcal mol<sup>-1</sup>, for neutral late transition-metal M(CO)<sub>n</sub> complexes

System	Experimental	BP86/6-311G(d)	B3LYP/6-311G(d)
Mn(CO)	25.7	25.0	24.0
Fe(CO)	26.7	25.7	21.8
Ni(CO)	18.5	19.1	13.8
Fe(CO) <sub>2</sub>	28.1	32.6	–
Ni(CO) <sub>2</sub>	14.8	19.9	16.0
Ni(CO) <sub>3</sub>	24.8	35.3	27.9

## Atomization Energies

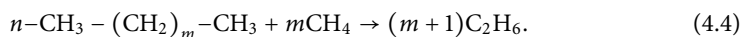
A benchmark study on 17 first-row closed-shell molecules indicated that in the calculation of the atomization energy with the Dunning correlation-consistent basis sets, the HGGA functionals, with a MUE of roughly 2.2 kcal mol<sup>-1</sup>, outperform GGA functionals, such as BLYP (MUE = 7.2 kcal mol<sup>-1</sup>), with BP86 performing particularly bad (MUE = 16.2 kcal mol<sup>-1</sup>) (Wang and Wilson 2004). In another benchmark study on the atomization energy of a dataset composed by 109 main groups organic and inorganic molecules, calculated with the MG3S basis set, HGGA functionals were again confirmed to perform well, with MUE smaller than 1.0 kcal mol<sup>-1</sup>, while GGA functionals, such as the PBE, with a MUE of 3.0 kcal mol<sup>-1</sup>, again performed poorly. The peak performance of 0.40 kcal mol<sup>-1</sup> was produced with the B1B95 functional, while the classic B3LYP resulted in a MUE of 0.91 kcal mol<sup>-1</sup>. Finally, HMGGGA functionals were shown to perform similarly to HGGA functionals (Zhao and Truhlar 2005b). On the other hand, GGA functionals perform well when the atomization energy of nine metal dimers in the TMAE9/05 database is calculated, with MUE in the range of 5–8 kcal mol<sup>-1</sup>. HGGA functionals, instead, resulted in MUE around 15–30 kcal mol<sup>-1</sup>, with only the B97-1, B97-2, and B98 functionals with MUE below 10 kcal mol<sup>-1</sup>. MGGA and HMGGGA functionals substantially replicate the results obtained with non-meta-functionals, although the M05 and M06 functionals result in the very low MUE of 6.9 and 4.7 kcal mol<sup>-1</sup>, respectively (Zhao and Truhlar 2008). These results are another indication that hybrid functionals usually perform better for molecules composed by main group atoms, whereas GGA and MGGA functionals perform better for transition metal chemistry.

## Heats of Formation

The accurate calculation of this property, even for rather simple molecular systems composed by main group atoms, still represents a challenge for several functionals. Indeed, the MUE on the heat of formation in a benchmark study on 24 molecules from the G2/97 dataset, with the addition of PO<sub>2</sub>, span the rather broad range of 10–30 kcal mol<sup>-1</sup>, even if basis set of rather good quality, such as the 6-31++G\* basis set, are used. Functionals to be avoided are those containing the P98 correlation term among the GGA, the BILYP and the B98 among the MGGA, the PBEKCIS among the MGGA, and the BBIK among the HMGGGA. On the other

side, good performances were obtained with the PBELYP, PW91LYP, MPWPW91 and MPW-PBE GGA functionals, the PBE1PBE and B3PW91 HGGA functionals, and finally the TPSS and the TPSSKCIS MGGA functionals. With these functionals the MUE on the heats of formation usually is below 10 kcal mol<sup>-1</sup> (Riley et al. 2007). Augmented correlation-consistent Dunning-type basis sets usually lead to slightly better performances. Nevertheless, recent results have cast a shadow on the common procedure to test heats of formation on small molecules. Indeed, it has been shown that almost all the functionals, including the popular B3LYP functional, are unable to predict correctly the heats of formation of *n*-alkanes (Curtiss et al. 1997, 2000). Due to the inability to describe properly long-range attractive dispersion interaction, practically all functionals introduce a systematic error in the calculation of the isodesmic stabilization energy,

► Eq. 4.4:



This systematic error ranges between 0.90 kcal mol<sup>-1</sup> for the HMGGGA MPWB1K functional and 1.82 kcal mol<sup>-1</sup> for the OLYP functional. The BP86 and PBE GGA functionals result in an error of 1.25 and 1.08 kcal mol<sup>-1</sup>, respectively, while the HGGA functional B3LYP results in an error of 1.33 kcal mol<sup>-1</sup>. While these errors may seem to be not dramatic, they are per CH<sub>2</sub> unit, so that the errors are between 10 and 20 kcal mol<sup>-1</sup> for a simple molecule such as *n*-decane (Wodrich et al. 2006).

## Energy Barriers

The performance of a series of functionals was tested to reproduce the barrier height for a series of reactions. Starting from hydrogen transfer reactions, the forward and backward barrier for the following three reactions OH<sup>•</sup> + CH<sub>4</sub> → CH<sub>3</sub><sup>•</sup> + H<sub>2</sub>O, OH<sup>•</sup> + H<sup>•</sup> → O(<sup>3</sup>P) + H<sub>2</sub>, and H<sup>•</sup> + H<sub>2</sub>S → HS<sup>•</sup> + H<sub>2</sub>, which constitute the BH6 database (Lynch and Truhlar 2003), GGA functionals systematically underestimate the barriers, with a MUE between 7.8 and 9.4 kcal mol<sup>-1</sup>. Better results were obtained with HGGA functionals, with MUE around 4.5–5.0 kcal mol<sup>-1</sup>. The mPWPW91 MGGA functional is not a clear improvement, with a MUE of 8.5 kcal mol<sup>-1</sup>, while HMGGGA functionals such as the mPW1PW91 and the MPW1K perform better, with MUE of 3.9 and 1.4 kcal mol<sup>-1</sup>, respectively (Zhao et al. 2004). Testing the functional on the larger BH42/04 database, consisting of 42 transition state barrier heights of hydrogen transfer reactions in mostly open-shell systems gave substantially similar results (Zhao and Truhlar 2004). The HGGA functionals underestimate barriers by a MUE of roughly 4 kcal mol<sup>-1</sup>, while HMGGGA functionals give better results, with peak performances from the BBIK, XBIK, and MPWB1K resulting in MUE around 1.2–1.3 kcal mol<sup>-1</sup>.

Moving to 38 transition state barrier heights for non-hydrogen transfer reactions constituting the NHTBH38/04 database, and comprising 12 barrier heights for heavy-atom transfer reactions, 16 barrier heights for nucleophilic substitution reactions, and 10 barrier heights for non-nucleophilic substitution unimolecular and association reactions, GGA functionals, such as the PBE, still approximate barriers severely, with a MUE of 8.64 kcal mol<sup>-1</sup>. HGGA functionals, such as the B3LYP and the PBE1PBE functionals perform better, although the MUE, around 4 kcal mol<sup>-1</sup>, still is quite large (Zhao et al. 2005). MGGA functionals perform similarly to the GGA functionals, while the performance of HMGGGA is rather scattered. For example, the TPSSh and the MPW1KCIS functionals do not perform impressively, with MUE of 6.6 and

4.6 kcal mol<sup>-1</sup>, respectively, while the MPW1K and the BBlK are very accurate, with MUE of 1.3 and 1.2 kcal mol<sup>-1</sup>, respectively (Zhao and Truhlar 2005b). The breakdown of these cumulative MUEs for selected functionals is reported in ► Table 4-8. Clearly, the most problematic cases are the transfer reaction of both hydrogen and heavy atoms. With the exception of the BBlK, all the other functionals fail to a large and embarrassing extent. For the HTBH38 dataset the M06 and M06-2X HMGGGA functionals, with MUE of 2.00 and 1.1 kcal mol<sup>-1</sup>, also perform well (Zhao and Truhlar 2005b). Barrier height of nucleophilic substitutions are predicted better, although GGA functionals still result in a too large MUE. Finally, the barrier heights of unimolecular and association reactions are predicted with reasonably accuracy by all functionals. Again, the performance of the BBlK functional is extremely good for the four classes of reactions considered. Similarly good and well balanced performances are also obtained with other HMGGGA functionals such as the PW6BK and the MPWBBlK functionals.

Similar extensive tests on another dataset, comprising the barrier height for 23 reactions of small systems with a radical transition state, also highlighted the good performances of the HMGGGA BBlK functional, with a MUE of 1.05 kcal mol<sup>-1</sup>, in predicting energy barriers. However, when the same functionals were tested on a dataset of 6 barrier heights of larger systems with a singlet transition state, the best performance was obtained with the simple HGGA BLYP functional, with a MUE of 2.58 kcal mol<sup>-1</sup>, the performance of the B3LYP functional, with a MUE of 3.10 kcal mol<sup>-1</sup>, was slightly worse, while all the HMGGGA functionals tested, including the BBlK functional, resulted in MUE greater than 4 kcal mol<sup>-1</sup> (Riley et al. 2007).

## Bond Energies

The performance of several functionals to predict bond energies on a database of 21 metal-ligand bond energies, the MBL21/05 database (Schultz et al. 2005a) indicated that GGA functionals predict metal-ligand bond energies with a MUE between 6 and 12 kcal mol<sup>-1</sup>, with the BLYP, PBE, and BP86 among the worst, and that performances can be quite better at the HGGA level, with MUE normally in the 5–7 kcal mol<sup>-1</sup> range. MGGA and HMGGGA functionals do not offer an improvement, as exemplified by the MUE of the TPSS and TPSSh functionals, 7.9 and 5.5 kcal mol<sup>-1</sup>, respectively, and by the recently developed M06 functional, with a MUE of 5.4 kcal mol<sup>-1</sup> (Zhao and Truhlar 2008).

► Table 4-8

Selected mean errors for HTBH38 and NHTBH38 databases

Method		Hydrogen transfer	Heavy atom transfer	Nucleophilic substitution	Unimolecular and association
PBE	GGA	9.32	14.93	6.97	3.35
BLYP	GGA	7.52	14.66	8.40	3.51
B3LYP	HGGA	4.23	8.49	3.25	2.02
PBEIPBE	HGGA	4.22	6.62	2.05	2.16
TPSS	MGGA	7.71	14.65	7.75	4.04
TPSSKClS	MGGA	4.69	9.26	4.88	2.12
TPSSh	HMGGGA	5.97	11.51	5.78	3.23
BBlK	HMGGGA	1.16	1.58	1.30	1.44

Taking again some selected binary carbonyl complexes of first-row transition metals as examples, the performance of various functionals in the prediction of the first bond dissociation energy is reported in [Table 4-9](#). The first clean result is that the binding energy is strongly affected by the basis set quality, and a triple- $\zeta$  basis set yields binding energies that are roughly 3–4 kcal mol<sup>-1</sup> lower. Focusing on the TZVP results, the GGA functionals examined consistently overestimate the CO binding energy in the three complexes by roughly 3–6 kcal mol<sup>-1</sup>. The PBE1PBE HGGA functional performs like the GGA functionals examined, whereas the B3LYP, and particularly the B98 functional, are among the best performing functionals. Meta-functionals only offer a marginal improvement.

## Hydrogen Bonding

Benchmarking various DFT methods to reproduce the H-bond interaction energy of ten systems composed by main group atoms revealed that HGGA functionals generally perform better than GGA functionals, with MUE around 0.5 kcal mol<sup>-1</sup>, and the B3LYP functional among the best. GGA functionals, instead, result in MUE between 0.5 and 2.0 kcal mol<sup>-1</sup>, with the BLYP, MPWPW91, and MPWPBE among the best performing (Riley et al. 2007). MGGA and HMGGA functionals perform close to the B3LYP functional. In all cases, the quality of the basis sets had a strong impact on the quality of the results, and at least a 6-31G(d,p) basis set should be used. Further tests were performed on a database consisting of the binding energies of six hydrogen bonding dimers, the HB6/04 database (Zhao and Truhlar 2005a). Also these tests indicated that the performance of GGA functionals is generally not very impressive, with MUE normally between 0.5 and 4 kcal mol<sup>-1</sup>, with the exception of the very well performing PBE functional,

■ Table 4-9

First metal-carbonyl dissociation energy, in kcal mol<sup>-1</sup>, for selected first-row transition metal systems

Exp.		Ni(CO) <sub>4</sub> 24.9 ± 2 <sup>a</sup>		Fe(CO) <sub>5</sub> 41.5 ± 2 <sup>b</sup>		Cr(CO) <sub>6</sub> 36.8 ± 2 <sup>b</sup>	
Method		SVP	TZVP	SVP	TZVP	SVP	TZVP
BP86	GGA	32.3	29.4	50.1	46.8	46.0	42.8
PW91	GGA	34.3	31.4	52.8	49.4	48.6	45.5
revPBE	GGA	33.9	30.9	52.1	48.6	48.2	44.9
B3LYP	HGGA	24.2	21.3	42.1	38.8	39.8	36.5
PBE1PBE	HGGA	29.2	26.4	50.1	47.1	46.1	43.4
B98	HGGA	25.6	22.8	44.7	41.8	41.5	38.6
TPSS	MGGA	32.9	30.5	50.8	48.1	46.2	43.8
mPWKCIS	MGGA	30.3	27.3	48.4	44.8	44.7	41.3
BB95	MGGA	30.4	27.4	48.8	45.2	45.4	42.4
TPSSh	HMGGA	31.2	28.6	50.0	47.4	45.5	43.0
M06	HMGGA	25.6	22.5	44.2	40.3	45.0	41.7

DFT values, calculated with the TZVP basis set on the metal, and the SVP or TZVP basis sets on CO

<sup>a</sup>Stevens et al. (1982)

<sup>b</sup>Lewis et al. (1984)

with a MUE of  $0.25 \text{ kcal mol}^{-1}$  only. On the average HGGA perform better, with MUE between  $0.3$  and  $1.0 \text{ kcal mol}^{-1}$ , with the PBE1PBE functional, with a MUE of  $0.27 \text{ kcal mol}^{-1}$ , among the best, while the B3LYP functional, with a MUE of  $0.87 \text{ kcal mol}^{-1}$ , does not perform impressively. Meta GGA and HGGA functionals are not a great improvement. These results have been achieved with the rather large aug-cc-pVTZ basis set, using the 6-31+G(d,p) basis set leads to slightly lower performances.

Extensive tests of the performance of the B3LYP and PW91 functionals in the case of H-bonded nucleic acid–base pairs indicated that the PW91 GGA functional replicates with better accuracy the MP2/aug-cc-pVQZ values than the B3LYP HGGA functional (Sponer et al. 2004). The B3LYP calculations underestimate the interaction energies by few  $\text{kcal mol}^{-1}$  with relative error of  $2.2 \text{ kcal mol}^{-1}$ . Representative values for Watson–Crick (G–C, A–T) purine–pyrimidine (G–U) and pyrimidine–pyrimidine (U–U) pairs are presented in [Table 4-10](#).

## Weak Interactions

For a long time one of the well known failures of DFT was in the description of long-range dispersion forces, which are the glue that keeps together van der Waals complexes and are at the basis of the well known  $\pi$ – $\pi$  stacking interactions. Members of the former family are the rare-gas dimers, that almost invariably are predicted to be unbound (or bound by effect of the basis set superposition error) by many GGA and HGGA functionals. Indeed, an extensive benchmark on the WI4/04 datasets, composed by four rare-gas dimers (HeNe, NeNe, HeAr, and NeAr) indicated that the B3LYP functional simply does not predict a energy well for three out of the four dimers if the basis set superposition error is corrected by the counterpoise procedure, and that even including the basis set superposition error the interaction energy are underestimated by  $0.23 \text{ kcal mol}^{-1}$ , and equilibrium distances are overestimated by more than  $1 \text{ \AA}$ . On the other hand, HMGGA functionals were shown to reproduce with good accuracy both the interaction energy and the equilibrium distance of these dimers, with MUE on the counterpoise corrected binding energies below  $0.05 \text{ kcal mol}^{-1}$  by several functionals, such as the X1B95 and the MPWB1K, and with MUE on the equilibrium distances as low as  $0.10 \text{ \AA}$ , which is a remarkable result for weakly interacting systems (Zhao and Truhlar 2004).

Enlarging the dataset to include also organic molecules, such as the  $\text{C}_6\text{H}_6$ –Ne, and the  $(\text{C}_2\text{H}_4)_2$  and  $(\text{CH}_4)_2$  dimers, indicated that standard GGA functionals systematically underestimate the interaction energy by a MUE of roughly  $0.4$ – $1.0 \text{ kcal mol}^{-1}$ , with the exception of the PBE functional, with a MUE of  $0.30 \text{ kcal mol}^{-1}$ . MGGA functionals do not perform much better, while a small improvement is shown by HGGA functionals, with the best results from

■ Table 4-10

H-bond interaction energy, in  $\text{kcal mol}^{-1}$ , of selected nucleic acid base pairs

Base pair	MP2/aug-cc-pVQZ	B3LYP/6-31G(d,p)	PW91/6-31G(d,p)
G:C Watson Crick	–27.7	–25.5	–27.7
A:T Watson Crick	–15.1	–12.3	–14.5
G:U Wobble	–15.7	–13.4	–14.8
U:U Calcutta	–9.6	–7.5	–8.7

B97-1 with a MUE of  $0.20 \text{ kcal mol}^{-1}$ . HMGGGA functionals do not offer better performances, although the largest MUE is reduced to  $0.64 \text{ kcal mol}^{-1}$  (Zhao and Truhlar 2005a). Finally, better performances were shown by the M05-2X and M06-2X functionals, with a MUE of only  $0.03$  and  $0.09 \text{ kcal mol}^{-1}$ , respectively, when applied to a dataset formed by the four rare-gas dimers above,  $\text{C}_6\text{H}_6\text{-Ne}$ ,  $\text{CH}_4\text{-Ne}$ , and the  $(\text{CH}_4)_2$  dimer. Surprisingly, on this reduced dataset the well performing B97-1 functional was not tested (Zhao and Truhlar 2005a).

Moving to  $\pi\text{-}\pi$  stacking interactions, the performance of a series of functionals was tested on the PPS5/05 database, which consists of binding energies of 5  $\pi\text{-}\pi$  stacking complexes, namely,  $(\text{C}_2\text{H}_2)_2$ ,  $(\text{C}_2\text{H}_4)_2$ , and sandwich, T-shaped and parallel-displaced  $(\text{C}_6\text{H}_6)_2$  (Zhao and Truhlar 2005b). Basically, all the functionals tested underestimated the binding energies in the PPS5/05 database, with MUE in the range of  $1.0\text{-}3.8 \text{ kcal mol}^{-1}$ . This is not a minor failure, since the average binding energy in the PPS5/05 dataset amounts to  $2.02 \text{ kcal mol}^{-1}$  only. The PBE GGA functional, with a MUE of  $2.1 \text{ kcal mol}^{-1}$ , performs better than the B3LYP HGGA functional, which results in a MUE of  $3.2 \text{ kcal mol}^{-1}$ . The best performances, slightly above  $1 \text{ kcal mol}^{-1}$ , are obtained with the PWB6K, PW6B95, and MPWB1K. A clear improvement is obtained with the M06-2X functional, with a MUE of  $0.30 \text{ kcal mol}^{-1}$  only. Reducing the amount of Hartree-Fock exchange deteriorates somewhat performances, as evidenced by the MUE of  $0.60 \text{ kcal mol}^{-1}$  yielded by the M06 functional (Zhao and Truhlar 2008).

Focusing on  $\pi\text{-}\pi$  stacking interactions between nucleic acid bases, which are fundamental to describe properly the base-base stacking in nucleic acids, the popular B3LYP is simply unable to find a minimum corresponding to the  $\text{A}\cdots\text{T}$  as well as the  $\text{G}\cdots\text{C}$  base pairs in a stacked geometry. Of the six functionals tested, only the MPWB1K and the PWB6K functionals resulted in stable stacked base pairs, with an underestimation of the stacking energy of roughly  $2\text{-}3 \text{ kcal mol}^{-1}$  (Zhao and Truhlar 2005c).

As a final remark, we note that a very simple cure to the failure of standard density functionals to predict dispersion interactions is to include an empirical C6-R-6 dispersion term. One of these functionals – B97-D – performs remarkably well for non-covalently bound systems including many pure van der Waals complexes (Grimme 2006).

## Spin States

The problem of a reliable prediction of the relative ordering of different spin states in transition metal complexes remains a tough challenge for DFT – not only for a quantitative judgment (energy separation between the different spin states) but also for a qualitative assessment (correct prediction of the spin ground state). There is general consensus that GGA functionals overestimate the stability of low-spin states, whereas the inclusion of Hartree-Fock exchange in the HGGA functionals results in an overestimation of the stability of high-spin states (Ghosh 2006; Swart 2008). This led to the development of the B3LYP\* functional, in which the amount of the Hartree-Fock exchange is reduced from 20% of the original B3LYP functional, to 15% (Reiher et al. 2001). Furthermore, it has been suggested that results obtained with Slater-type basis sets converge rapidly with the basis set size, while this convergence in case of Gaussian-type basis sets is much slower, and demanding basis sets like Dunning's correlation consistent basis are needed to achieve good results (Güell et al. 2008).

■ Table 4-11

Singlet-quintet splitting,  $E_{\text{singlet}} - E_{\text{quintet}}$  in kcal mol<sup>-1</sup>, for selected Fe complexes (Swart 2008)

	Fe(H <sub>2</sub> O) <sub>6</sub> <sup>2+</sup>	Fe(NH <sub>3</sub> ) <sub>6</sub> <sup>2+</sup>	Fe(bpy) <sub>3</sub> <sup>2+</sup>	MAD
CASPT2	46.6	20.3	-13.2	
BP86	28.4	5.1	-23.2	14.5
RPBE	34.3	6.3	-29.9	14.3
B3LYP	33.1	14.1	0.6	11.2
PBE1PBE	46.0	24.7	9.0	9.1
OPBE	49.3	19.0	-14.9	1.9

MAD mean absolute deviation

Besides the above general comment, benchmark tests of the different functionals in this case is often hampered by the problem of accurate reference data, and by the problem that functionals that seem to behave properly for a metal or system simply fail if the system changes (Ghosh 2006). Focusing on Fe complexes, a benchmark study versus CASPT2 values, see ● Table 4-11, indicated that the OPBE functional performs definitely better than commonly used GGA and HGGA functionals. In a similar study, the performance of some DFT functionals to describe CASPT2 results for a series of five Fe complexes indicated that the OLYP functional performed remarkably well in these cases, whereas the success of the HGGA PBE1PBE, B3LYP, and B3LYP\* functionals varied from case to case (Pierloot and Vancoillie 2008). Finally, another benchmark study, in which various properties of Fe<sub>2</sub>, Fe<sub>2</sub><sup>-</sup>, and FeO<sup>+</sup>, as obtained from a series of GGA, HGGA, MGGA, and HMGGA functionals, were calculated, indicated that no single functional was found to yield a satisfactory description of all characteristics for all states of these species (Sorkin et al. 2008). These results clearly indicate that the spin-state problem still is an open challenge for DFT.

## Excited States

Testing the performance of several functionals in the TD-DFT prediction of 21 valence and 20 Ry excitation energies in N<sub>2</sub>, O<sub>2</sub>, HCOOH, and tetracene indicated that valence excitations are easier to predict than Rydberg excitation. Indeed, valence excitations were predicted by 15 functionals with a MUE of 0.36 eV, while Rydberg excitations were predicted with a MUE of 1.13 eV. Focusing on valence excitations HMGGA functionals such as TPSSh, B98, and B97-3 are the best performers, with MUE as small as 0.25 eV. Nevertheless, GGA and HGGA functionals, with a MUE of 0.32 and 0.28 eV for the PBE and B3LYP functionals, respectively, also perform reasonably well. Differently, for the accurate prediction of Rydberg excitations a high amount of Hartree-Fock exchange, as in the M06-2X and M06-HF functionals, with MUE lower than 0.4 eV, is beneficial. With the exception of the also well-performing BMK functional, almost all the other functionals tested results in MUE greater than 0.78 eV, with the PBE and B3LYP functionals resulting in a MUE of 1.95 and 1.07 eV, respectively. When Rydberg and valence excitations are combined into a single database, the best average performance is of the M06-2X and BMK functionals, with a MUE around 0.35 eV (Zhao and Truhlar 2008).

With regards to charge-transfer excitations, the performance of 16 functionals was tested in the prediction of three charge-transfer excitation energies in tetracene and in the NH<sub>3</sub>·F<sub>2</sub> and



$C_2H_4 \cdots C_2F_4$  complexes. The average MUE over the 16 functionals examined, 3.86 eV, is depressive. The only working functional is M06-HF, with a MUE of 0.09 eV. However, the inclusion of Hartree–Fock exchange is not the only reason for this surprisingly good performance, since simple HF and the HFLYP functional result in MUE around 1 eV. With the exception of the M05-2X and M06-2X, with a MUE around 2.5 eV, all the other functionals tested resulted in a MUE greater than 3 eV (Zhao and Truhlar 2008). As a final note, it would be interesting to test the performance of the M06-HF on a larger database.

Moving to more complex organic molecules, the  $\pi \rightarrow \pi^*$  transitions of more than 100 dyes from the major classes of chromophores have been investigated using a TD-DFT with the PBE, PBE1PBE and long-range corrected hybrid functionals. The PBE1PBE and CAMB3LYP were shown to outperform all other approaches, with the latter functional especially adequate to treat molecules with delocalized excited states. The PBE1PBE functional resulted in a MUE of 22 nm (0.14 eV) with no deviation exceeding 100 nm (0.50 eV), thus delivering reasonable estimates of the color of most organic dyes of practical or industrial interest. Long-range functionals allowed a better description of the low-lying excited-state energies than HGGA functionals, and linearly corrected long-range approaches yield an average error of 10 nm (Jacquemin et al. 2008).

An extended test of the performance of 41 functionals in the calculation of the electronic absorption spectra of Cu and Zn complexes by TD-DFT methods indicated that HGGA functionals outperform GGA functionals. In case of the spin-unrestricted calculations on the  $Cu^{II}$ (thiosemicarbazonato) complex the functional best performing in the reproduction of the experimental spectra and geometry was the B1LYP, while the B3LYP functional was ranked 8. This order was not replicated in case of the spin-restricted  $Zn^{II}$ (thiosemicarbazonato) complex, where the best functional was PBE1PBE, with the B3LYP ranked 10. In both cases HGGA functionals did not offer an improvement. In almost all the cases the calculations underestimated the experimental excitation energies (Holland and Green 2010). Nevertheless, it maybe worth noting that the OPBE and the OBLYP functionals, which were shown to perform well in other cases, were not considered.

## Orbitals in DFT

---

Since chemists long have used and continue to use orbitals as natural language to explain and rationalize the complex reality of molecules that define the realms of inorganic and organic chemistry, we conclude with a few remarks on orbitals obtained from density functional calculations.

Originally, chemists have built their understanding of orbitals on constructs that resulted from WFT-analyzes, and such an orbital is usually referred to as molecular orbital (MO). One important aspect of an MO-analysis is the investigation of orbital-overlap. A simplified wave function theory that emphasizes this particular feature of orbital-interaction, the Extended Hückel-Theory (EHT), has revolutionized the general perception of molecular structure and reaction mechanisms.

Since the Kohn–Sham orbitals, introduced and used in DFT, serve a different purpose than creating a reasonable single determinantal wave function  $\Psi$ , chemists were seeking answers to the question “what do the Kohn–Sham orbitals and eigenvalues mean?” as DFT moved into the spotlight of electronic structure theory. A simple answer was based on a comparison of orbitals of small molecules ( $H_2O$ ,  $N_2$ ,  $PdCl_4^{2-}$ ) obtained from WFT (Hartree–Fock, EHT)





and DFT calculations: The shape and symmetry properties of the KS orbitals are very similar to those calculated by HF and EHT methods. The energy order of the occupied orbitals is in most cases in agreement between WFT and DFT methods. Overall, the KS orbitals are a good basis for qualitative interpretation of molecular orbitals (Stowasser and Hoffmann 1999). This simple conception of the meaning and use of KS orbitals by now has gained general acceptance, and chemists often use KS orbitals in ways that are familiar to them from MO-analysis.

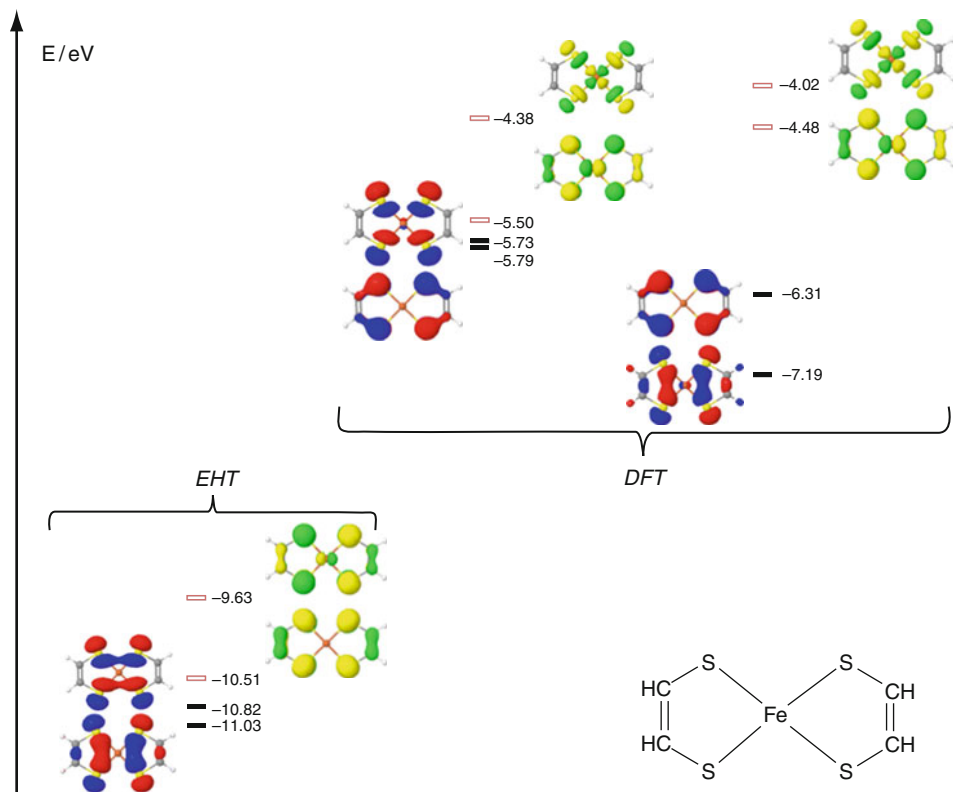
Bareends and Gritsenko (1997) have provided an answer to the same question based on fundamental concepts of density functional theory. Among other aspects, the authors identify the following two important characteristics of KS orbitals:

1. The highest occupied Kohn–Sham orbital energy is equal to the exact first ionization energy. This is a property that is very desirable in qualitative MO theory in general and is often simply assumed in such theories.
2. The lowest unoccupied Kohn–Sham orbital energy and all other virtual orbital energies are solutions in exactly the same potential as the occupied orbitals. They are therefore not shifted toward higher energies in the same way as Hartree–Fock virtual orbitals are – HF orbital energy differences are not estimates of excitation energies. Further, it has been observed empirically for a long time that KS-orbital energy differences are good approximations to excitation energies, and the KS-orbital energy differences play a role as a first approximation to the excitation energy in the treatment of excitation energies using time-dependent DFT.

The authors, therefore, recommend KS orbitals and one-electron energies as tools in the traditional qualitative MO-considerations on which much of the rationalizations of contemporary chemistry are based. The Kohn–Sham one-electron model and KS orbitals provide an ideal MO theoretical context to apply concepts such as “charge control” and “orbital control.” KS-orbitals usually follow the expected behavior, in terms of bonding and antibonding character in terms of geometrical distortions, and in terms of interaction with other atoms or molecules.

About 10 years later, Cramer and Truhlar (2009) presented a more conservative view of the use of KS-orbitals. One should be careful not to stretch the interpretation of KS-orbitals beyond its limits, since KS-orbitals correspond to a fictitious non-interacting system with the same electron density as the correct many-body function. Since the density computed from KS-orbitals is an approximation to the exact density, properties that depend on individual orbitals, with the exception of the energy of the highest occupied orbitals, should be interpreted with care. Nonetheless, many studies published in the literature do employ DFT molecular orbitals to interpret the electronic origins of chemical bonding and reactivity.

The quality of the KS orbitals depends to a large part on the ability of a chosen density functional to correctly represent the ground state density of a given molecule. In most cases, different density functionals produce qualitatively identical orbitals, which also agree with WFT orbitals. For molecules that might possess a spin-polarized ground state density, different methods of electronic structure calculation not only produce quantitatively different results, but also lead to qualitatively contrastive conclusions. One such case is illustrated in  Fig. 4-7. We leave it to the reader to decide whether or not chemically meaningful information can be extracted from the orbital picture as displayed in  Fig. 4-7.



■ Fig. 4-7

Energies and shapes of the two highest occupied (red-blue) and the two lowest unoccupied (yellow-green) KS-orbitals (contour envelope: 0.05 a.u.) of  $\text{Fe}(\text{S}_2\text{C}_2\text{H}_2)_2$  extracted from an unpolarized ground state density according to GGA and HGGA DFT calculations. The molecule was constructed according to  $D_{2h}$  symmetry with a Fe-S bond length of 220 pm. Also shown for the sake of comparison are orbitals obtained from an extended Hückel calculation

## DFTips

The advertent reader has noticed the many technical recommendations that we have given within the discussion of the 12 selected scenarios for properties of atoms and molecules. Here, we will close our instruction manual with a few pieces of general advice.

## B3LYP Is No Synonym for DFT

Some researchers hold the opinion that given the fact that the B3LYP functional has been identified as the most successful DFT method in an overwhelming number of systematic

investigations in very many areas of chemical research, there is no persuasive motivation to recommend its replacement by one of the other functionals. We do not agree with such a judgment. Although the B3LYP functional is largely responsible for DFT becoming one of the most popular tools in computational chemistry, it does have unsatisfactory performance issues, notably the unreliable results obtained for transition metal chemistry (Zhao and Truhlar 2008). One should become aware of the capabilities and shortcomings of particular density functionals. It might well be that B3LYP is the proper approach to many chemical problems, but choosing a functional for its previous success while ignoring its potential failures cannot be the right strategy to approach DFT calculations.

## Choose Your DFT Method Carefully

---

We agree with Burke's interpretation of "The Good, The Bad & The Ugly" (Burke 2010): It is good to choose one functional of each kind and stick with it. It is bad to run several functionals, and pick the "best" answer. And it is ugly to design your own functional with 2,300 parameters.

In view of the many functionals available, it is likely that one will find a functional that fits one's own particular problems. In view of possibilities offered by computational programs that make it fairly easy to create new sets of parameterized hybrid functionals, it is almost certain that for each chemical problem, the right functional can be designed.

Following such an approach, density functional calculations lose their generality and meaning. One should aim for consistency within one's calculations, rather than for the best agreement with experiment. If one chooses a particular functional for its characteristics and capabilities, the results of DFT calculations gain a predictive quality.

## Read the Fine Print

---

During the early days of HGGGA development, it became clear that B3LYP is not B3LYP (Hertwig and Koch 1997). Different programs based their implementation of the B3LYP functional on different models of the underlying LDA, and produced slightly different results for the same chemical problem. The same considerations apply to the gradient corrections for correlation; P86 requires a different choice of LDA than LYP. Some computer programs automatically make the right choice, while other programs rely on correct input instructions given by the user.

Familiarize yourself with the default values and basic implementations of your favorite DFT-code. Default values are chosen with much consideration, and most of the time are just adequate. However, for subtle problems you might find it necessary, for example, to change the accuracy of the numerical integration routines.

## DFT Does Not Hold the Universal Answer to All Chemical Problems

---

You can expect that not all of your DFT calculations will produce satisfying results. An increasing number of problem molecules are currently identified for which standard density

functionals fail to produce satisfactory results. Seemingly simple stereoelectronic effects in alkane isomers provided a serious challenge for many standard functionals, such as B3LYP, BLYP, or PBE (Grimme 2006). However, such failures are not bad news for DFT, but rather good news. The origin of the dissatisfying DFT performance has been carefully analyzed, and led to the design of improved functionals (Zhao et al. 2006). Be honest with your DFT-results and accept apparent failures – it might be just another small step climbing Jacob's ladder.

---

## Make DFT an Integral Part of Your Work

---

Although in some areas of chemical research DFT is at the verge of becoming a standard research tool, necessary for the complete characterization of new molecules, not every chemical problem warrants a full-fledged DFT investigation. However, if you structure your computational approach beginning with an elaboration of qualitative aspects before addressing a problem in a quantitative way, a few quick DFT calculations might provide you with valuable insights how to further pursue your line of work.

---

## Follow Your Interests

---

As final advice we will leave you with the words of Nobel Prize laureate Harold Kroto: Do something which interests you or which you enjoy, and do it to the absolute best of your ability. If it interests you, however mundane it might seem on the surface, still explore it because something unexpected often turns up just when you least expect it Kroto (2010).

We hope that our work could satisfy some old interests as well as perk some new interests. We wish that our short instruction manual serves as a valuable guide for the perplexed and provides some food for thought for the enlightened, be it in agreement or in disagreement. If you follow your interests, keep an open mind, and maintain a broad perspective, good things will happen.

---

## A Concise Guide to the Literature

---

The literature on DFT is large, and rich in excellent reviews and overviews. At the same time, while thousands of papers on DFT have been published, most of them will become out of date in the future, as the picture and perception of DFT, chemistry and science in general is in a state of constant flux. It was necessary to make a conscious selection that of course is not unbiased – some references represent the most recent developments in DFT, while others have been part of our DFT folder for a long time.

The reader will find references to books, review articles, and articles that illustrate developments and applications of DFT. In addition, we included a few references to the worldwide web.

## References

### Books on DFT

- Fiolhais, C., Nogueira, F., & Marques, M. (2003). *A primer in density functional theory, Lecture notes in physics*. Berlin: Springer.
- Koch, W., & Holthausen, M. C. (2002). *A chemist's guide to density functional theory* (2nd ed.). Weinheim: Wiley-VCH.
- Marques, M. A. L., Ullrich, C. A., Nogueira, F., Rubio, A., Burke, K., & Gross, E. K. U. (2006). *Time-dependent density functional theory, Lecture notes in physics*. Berlin, Heidelberg: Springer.
- Parr, R. G., & Yang, W. (1989). *Density functional theory of atoms and molecules*. New York: Oxford University Press.

### Conceptual Developments and Applications of DFT

- Baerends, E. J., & Ros, P. (1978). Evaluation of the LCAO Hartree-Fock-Slater method – Applications to transition-metal complexes. *International Journal of Quantum Chemistry*, 12, 169–190.
- Baerends, E. J., Ellis, D. E., & Ros, P. (1973). Self-consistent molecular Hartree-Fock-Slater calculations – I. The computational procedure. *Chemical Physics*, 2, 41–47.
- Bartlett, R. J., Lotrich, V. F., & Schweigert, I. V. (2005). *Ab initio* density functional theory: The best of both worlds? *Journal of Chemical Physics*, 123, 062205.
- Becke, A. D. (1988a). A multicenter numerical-integration scheme for polyatomic molecules. *Journal of Chemical Physics*, 88, 2547–2553.
- Becke, A. D. (1988b). Density-functional exchange-energy approximation with correct asymptotic behavior. *Physical Review A*, 38, 3098–3100.
- Becke, A. D. (1993a). A new mixing of Hartree-Fock and local density-functional theories. *The Journal of Physical Chemistry*, 98, 1372–1377.
- Becke, A. D. (1993b). Density-functional thermochemistry: 3. The role of exact exchange. *The Journal of Physical Chemistry*, 98, 5648–5652.
- Becke, A. D., & Roussel, M. R. (1989). Exchange holes in inhomogeneous systems – a coordinate-space model. *Physical Review A*, 98, 1372–1377.
- Boerrigter, P. M., te Velde, G., & Baerends, E. J. (1988). 3-dimensional numerical-integration for electronic-structure calculations. *International Journal of Quantum Chemistry*, 33, 87–113.
- Gill, P. M. W. (2001). Obituary: Density functional theory (1927–1993). *Australian Journal of Chemistry*, 54, 661–662.
- Grimme, S. (2006). Seemingly simple stereoelectronic effects in alkane isomers and the implications for Kohn-Sham density functional theory. *Angewandte Chemie International Edition*, 45, 4460–4464.
- Hertwig, R. H., & Koch, W. (1997). On the parameterization of the local correlation functional. What is Becke-3-LYP? *Chemical Physics Letters*, 268, 345–351.
- Hohenberg, P., & Kohn, W. (1964). Inhomogeneous electron gas. *Physical Review*, 136, B646–B871.
- Kohn, W., & Sham, L. J. (1965). Self-consistent equations including exchange and correlation effects. *Physical Review*, 140, A1133–A1138.
- Kurth, S., & Perdew, J. P. (2000). Role of the exchange-correlation energy: Nature's glue. *International Journal of Quantum Chemistry*, 77, 814–818.
- Perdew, J. P. (1986). Density-functional approximation for the correlation-energy of the inhomogeneous electron gas. *Physical Review B*, 33, 8822–8824.
- Perdew, J. P., & Schmidt, K. (2001). Jacob's ladder of density functional approximations for the exchange-correlation energy. In V. V. Doren, P. Geerlings, & C. V. Alsenoy (Eds.), *Density functional theory and its applications to materials* (pp. 1–20). Melville: AIP.
- Slater, J. C. (1951). A simplification of the Hartree-Fock method. *Physical Review*, 81, 385–390.
- Tao, J. M., Perdew, J. P., Staroverov, V. N., & Scuseria, G. E. (2003). Climbing the density functional ladder: Nonempirical meta-generalized gradient approximation designed for molecules and solids. *Physical Review Letters*, 91, 146401.
- Versluis, L., & Ziegler, T. (1988). The determination of molecular structures by density functional theory: The evaluation of analytical energy gradients by numerical integration. *Journal of Chemical Physics*, 88, 322–328.

- Vosko, S. H., Wilk, L., & Nusair, M. (1980). Accurate spin-dependent electron liquid correlation energies for local spin density calculations: A critical analysis. *Canadian Journal of Physics*, *58*, 1200–1211.
- Zope, R. R., & Dunlap, B. I. (2006). The limitations of Slater's element-dependent exchange functional from analytic density-functional theory. *Journal of Chemical Physics*, *124*, 044107.

## Practical Developments and Applications of DFT

- Barden, C. J., Rienstra-Kiracofe, J. C., & Schaefer, H. F. (2000). Homonuclear 3d transition-metal diatomics: A systematic density functional theory study. *Journal of Chemical Physics*, *113*, 690–700.
- Curtiss, L. A., Raghavachari, K., Redfern, P. C., & Pople, J. A. (1997). Assessment of Gaussian-2 and density functional theories for the computation of enthalpies of formation. *Journal of Chemical Physics*, *106*, 1063–1079.
- Curtiss, L. A., Raghavachari, K., Redfern, P. C., & Pople, J. A. (2000). Assessment of Gaussian-3 and density functional theories for a larger experimental test set. *Journal of Chemical Physics*, *112*, 7374–7383.
- Ghosh, A. (2006). Transition metal spin state energetics and noninnocent systems: Challenges for DFT in the bioinorganic arena. *Journal of Biological Inorganic Chemistry*, *11*, 712–714.
- Grimme, S. (2006). Semiempirical GGA-type density functional constructed with a long-range dispersion correction. *Journal of Computational Chemistry*, *27*, 1787–1799.
- Güell, M., Luis, J. M., Solá, M., & Swart, M. (2008). Importance of the basis set for the spin-state energetics of iron complexes. *The Journal of Physical Chemistry A*, *112*, 6384–6391.
- Holland, J. P., & Green, J. C. (2010). Evaluation of exchange-correlation functionals for time-dependent density functional theory calculations on metal complexes. *Journal of Computational Chemistry*, *31*, 1008–1014.
- Jacquemin, D., Perpète, E. A., Scuseria, G. E., Ciofini, I., & Adamo, C. (2008). TD-DFT performance for the visible absorption spectra of organic dyes: Conventional versus long-range hybrids. *Journal of Chemical Theory and Computation*, *4*, 123–135.
- Kelly, R. A., Clavier, H., Giudice, S., Scott, N. M., Stevens, E. D., Bordner, J., Samardjiev, I., Hoff, C. D., Cavallo, L., & Nolan, S. P. (2008). Determination of N-heterocyclic carbene (NHC) steric and electronic parameters using the [(NHC)Ir(CO)(2)Cl] system. *Organometallics*, *27*, 202–210.
- Korth, M., & Grimme, S. (2009). "Mindless" DFT Benchmarking. *Journal of Chemical Theory and Computation*, *5*, 993–1003.
- Lynch, B. J., & Truhlar, D. G. (2003). Small representative benchmarks for thermochemical calculations. *The Journal of Physical Chemistry A*, *107*, 8996–8999.
- Pierloot, K., & Vancoillie, S. J. (2008). Relative energy of the high-(T-5(2g)) and low-((1)A(1g)) spin states of the ferrous complexes [Fe(L)(NHS4)]: CASPT2 versus density functional theory. *Journal of Chemical Physics*, *128*, 034104.
- Reiher, M., Salomon, O., & Hess, B. A. (2001). Reparameterization of hybrid functionals based on energy differences of states of different multiplicity. *Theoretical Chemistry Accounts*, *107*, 48–55.
- Riley, K. E., Op't Holt, B. T., & Merz, K. M., Jr. (2007). Critical assessment of the performance of density functional methods for several atomic and molecular properties. *Journal of Chemical Theory and Computation*, *3*, 407–433.
- Schultz, N. E., Zhao, Y., & Truhlar, D. G. (2005a). Density functionals for inorganometallic and organometallic chemistry. *The Journal of Physical Chemistry A*, *109*, 11127–11143.
- Schultz, N. E., Zhao, Y., & Truhlar, D. G. (2005b). Databases for transition element bonding: Metal-metal bond energies and bond lengths and their use to test hybrid, hybrid meta, and meta density functionals and generalized gradient approximations. *The Journal of Physical Chemistry A*, *109*, 4388–4403.
- Sorkin, A., Iron, M. A., & Truhlar, D. G. (2008). Density functional theory in transition-metal chemistry: Relative energies of low-lying states of iron compounds and the effect of spatial symmetry breaking. *Journal of Chemical Theory and Computation*, *4*, 307–315.
- Sponer, J., Jurecka, P., & Hobza, P. (2004). Accurate interaction energies of hydrogen-bonded nucleic acid base pairs. *Journal of the American Chemical Society*, *126*, 10142–10151.

- Stevens, A. E., Feigerle, C. S., & Lineberger, W. C. (1982). *Journal of the American Chemical Society*, 104, 5026.
- Stowasser, R., & Hoffmann, R. (1999). What do the Kohn-Sham orbitals and eigenvalues mean? *Journal of the American Chemical Society*, 121, 3414–3420.
- Swart, M. (2008). Accurate spin-state energies for iron complexes. *Journal of Chemical Theory and Computation*, 4, 2057–2066.
- Wang, N. X., & Wilson, A. K. (2004). The behavior of density functionals with respect to basis set. I. The correlation consistent basis sets. *Journal of Chemical Physics*, 121, 7632–7646.
- Wodrich, M. D., Corminboeuf, C., & Schleyer, P. v. R. (2006). Systematic errors in computed alkane energies using B3LYP and other popular DFT functionals. *Organic Letters*, 8, 3631–3634.
- Yang, W. T. (1991). Direct calculation of electron density in density functional theory. *Physical Review Letters*, 66, 1438–1441.
- Zhao, Y., & Truhlar, D. G. (2004). Hybrid meta density functional theory methods for thermochemistry, thermochemical kinetics, and noncovalent interactions: The MPW1B95 and MPWB1K models and comparative assessments for hydrogen bonding and van der Waals interactions. *The Journal of Physical Chemistry A*, 108, 6908–6918.
- Zhao, Y., & Truhlar, D. G. (2005a). Benchmark databases for nonbonded interactions and their use to test density functional theory. *Journal of Chemical Theory and Computation*, 1, 415–432.
- Zhao, Y., & Truhlar, D. G. (2005b). Design of density functionals that are broadly accurate for thermochemistry, thermochemical kinetics, and nonbonded interactions. *The Journal of Physical Chemistry A*, 109, 5656–5667.
- Zhao, Y., & Truhlar, D. G. (2005c). How well can new-generation density functional methods describe stacking interactions in biological systems? *Physical Chemistry Chemical Physics*, 7, 2701–2705.
- Zhao, Y., & Truhlar, D. G. (2008). The M06 suite of density functionals for main group thermochemistry, thermochemical kinetics, noncovalent interactions, excited states, and transition elements: Two new functionals and systematic testing of four M06-class functionals and 12 other functionals. *Theoretical Chemistry Accounts*, 120, 215–241.
- Zhao, Y., Pu, J., Lynch, B. J., & Truhlar, D. G. (2004). Tests of second-generation and third-generation density functionals for thermochemical kinetics. *Physical Chemistry Chemical Physics*, 6, 673–676.
- Zhao, Y., Gonzalez-Garcia, N., & Truhlar, D. G. (2005). Benchmark database of barrier heights for heavy atom transfer, nucleophilic substitution, association, and unimolecular reactions and its use to test theoretical methods. *The Journal of Physical Chemistry A*, 109, 2012–2018.
- Zhao, Y., Schultz, N. E., & Truhlar, D. G. (2006). Design of density functionals by combining the method of constraint satisfaction with parametrization for thermochemistry, thermochemical kinetics, and noncovalent interactions. *Journal of Chemical Theory and Computation*, 2, 364–382.
- Zhou, M., Andrews, L., & Bauschlicher, C. (2001). Spectroscopic and theoretical investigations of vibrational frequencies in binary unsaturated transition-metal carbonyl cations, neutrals, and anions. *Chemical Reviews*, 101, 1931–1961.

## Reviews and Overviews of DFT

- Baerends, E. J., & Gritsenko, O. V. (1997). A quantum chemical view of density functional theory. *The Journal of Physical Chemistry A*, 101, 5383–5403.
- Cramer, C. J., & Truhlar, D. G. (2009). Density functional theory for transition metals and transition metal chemistry. *Physical Chemistry Chemical Physics*, 11, 10757–10816.
- Geerlings, P., De Proft, F., & Langenaeker, L. (2003). Conceptual density functional theory. *Chemical Review*, 103, 1793–1873.
- Kohn, W., Becke, A. D., and Parr, R. G. (1996). Density functional theory of electronic structure. *The Journal of Physical Chemistry*, 100, 12974–12980.
- Lewis, K. E., Golden, D. M., & Smith, G. P. (1984). *Journal of the American Chemical Society*, 106, 3905.
- Neese, F. (2009). Prediction of molecular properties and molecular spectroscopy with density functional theory: From fundamental theory to exchange-coupling. *Coordination Chemistry Reviews*, 253, 526–563.
- Perdew, J. P., Ruzsinszky, A., Constantin, L. A., Sun, J. W., & Csonka, G. I. (2009). Some fundamental issues in ground-state density functional theory: A guide for the perplexed. *Journal of Chemical Theory and Computation*, 5, 902–908.

- Sousa, S. F., Fernandes, P. A., & Ramos, M. J. (2007). General performance of density functionals. *The Journal of Physical Chemistry A*, *111*, 10439–10452.
- Zhao, Y., & Truhlar, D. G. (2008). Density functionals with broad applicability in chemistry. *Accounts of Chemical Research*, *41*, 157–167.
- Ziegler, T. (1991). Approximate density functional theory as practical tool in molecular energetics and dynamics. *Chemical Review*, *91*, 651–667.
- Ziegler, T. (1995). Density functional theory as practical tool in studies of organometallic energetics and kinetics. Beating the heavy metal blues with DFT. *Canadian Journal of Chemistry*, *73*, 743–761.

## Web Links

---

- ADE. (2010). Amsterdam density functional software. <http://www.scm.com/>. Accessed 12 Mar 2010.
- Burke, K. (2010). More basics of DFT. <http://dft.uci.edu/materials/tutorialsAPS08/tutorialKB.pdf>. Accessed 10 Mar 2010.
- Kroto, H. (2010). Autobiography. [http://nobelprize.org/nobel\\_prizes/chemistry/laureates/1996/kroto-autobio.html](http://nobelprize.org/nobel_prizes/chemistry/laureates/1996/kroto-autobio.html). Accessed 01 Mar 2010.





# 5 Introduction to Response Theory

*Thomas Bondo Pedersen*

Centre for Theoretical and Computational Chemistry, Department of Chemistry, University of Oslo, Oslo, Norway

<i>Introduction</i> .....	136
<i>Response Theory</i> .....	138
<i>The Linear Response Function</i> .....	140
<i>Quadratic and Higher-Order Response Functions</i> .....	145
<i>Static Response Functions</i> .....	147
<i>Gauge and Origin Invariance</i> .....	148
<i>Effects of Nuclear Motion</i> .....	151
<i>Further Reading</i> .....	155
<i>Acknowledgments</i> .....	155
<i>References</i> .....	156

**Abstract:** This chapter provides a concise introduction to quantum chemical response theory as implemented in a number of widely used electronic structure software packages. While avoiding technical derivations of response functions, the fundamental idea of response theory, namely, the calculation of field-induced molecular properties through changes in expectation values, is explained in a manner equally valid for approximate wave function and density functional theories. Contrasting response theory to textbook treatments of perturbation theory, key computational concepts such as iterative solution of response equations, and the identification and calculation of electronic excitation energies are elucidated. The wealth of information that can be extracted from approximate linear, quadratic, and higher-order response functions is discussed on the basis of the corresponding exact response functions. Static response functions and their identification and numerical calculation as energy derivatives are discussed separately. Practical issues related to the lack of gauge and origin invariance in approximate calculations are discussed without going into too much theoretical detail regarding the sources of these problems. Finally, the effects of nuclear motion (molecular vibrations, in particular) and how to include them in computational studies are treated in some detail.

## Introduction

---

The ultimate vision of computational chemistry is to provide a virtual laboratory for chemical explorations. The goal is not to replace but rather complement the real lab. In the virtual lab, it is easy to change “experimental” conditions and to experiment with hypothetical what-if scenarios. Virtual synthesis of chemical compounds can be done with a few mouse-clicks, whereas the virtual measurement of physical and chemical properties is the often burdensome task of a computational engine based on the laws of classical and/or quantum physics. Most research efforts, therefore, are aimed at improving the algorithms and approximations implemented in the computational engines. The main role of quantum chemical response theory, which is the subject of this chapter, is the virtual measurement of optical properties of molecules.

The scope of this chapter is to provide a rudimentary understanding of response theory as implemented in a number of molecular electronic structure packages based on wave function models or density functional theory. Only the general structure of response theory and its computer implementation are discussed, leaving out the often complicated details of advanced wave function and density functional models. For these details the reader is referred to the literature mentioned in the last section and references therein. Although the discussion of this chapter is restricted to nonrelativistic theory, it is the same line of reasoning that is applied in relativistic response theory. In conjunction with the chapter on applications of response theory, the reader should become sufficiently familiar with the concepts and practices of response theory to allow educated use of quantum chemistry software packages.

As the name indicates, response theory describes the response of a molecular system to external potentials such as electromagnetic fields. The meaning of external depends on the definition of the molecular system. For example, the magnetic field due to nuclear spins would typically be considered an external potential. The fundamental assumption is that the external potentials are weak compared to the internal potentials of the molecule. That is, the external potentials can be regarded as perturbations of the isolated molecule. This assumption can be justified by noting that the electric field strength in the hydrogen atom is on the order of  $10^{11} \text{ Vm}^{-1}$ , which is well above the external field strengths applied in almost all experimental

setups. Experimental observations are then rationalized by means of response functions, which may be expressed entirely in terms of states and energies of the unperturbed (isolated) molecule. Response functions are thus characteristic properties of a molecule. The objective of quantum chemical response theory is the computation of response functions from first principles.

Response functions quantify the field-induced change in a given observable such as the electric dipole moment. It is therefore necessary to know the state of the molecule before the field is applied. This unperturbed state is normally taken to be the molecular ground state, which is usually assumed to be non-degenerate. Calculation of the molecular ground state is, however, a daunting task and approximations are invoked in practice. We will use the clamped-nucleus Born–Oppenheimer approximation to separate the electronic degrees of freedom from the nuclear ones. Focusing on the response of the electronic ground state, the coupling between the nuclei and the external field is neglected. This is justified for field frequencies much larger than vibrational and rotational frequencies.

The electronic ground state  $|0\rangle$  is computed as an approximate solution to the time-independent Schrödinger equation, that is,

$$H_0|0\rangle \approx E_0|0\rangle \quad (5.1)$$

where  $H_0$  is the electronic Hamiltonian (see below) and  $E_0$  is the ground state energy in the absence of external fields. The approximate solution (energy and wave function or density) can be obtained using standard methods such as density functional theory (DFT), Hartree–Fock (HF) theory, multiconfigurational self-consistent field (MCSCF) theory, configuration interaction (CI), or coupled cluster (CC) theory. For fixed nuclear positions (clamped-nucleus approximation), the electronic Hamiltonian is given by

$$H_0 = \frac{1}{2m_e} \sum_{s=1}^{N_e} (\mathbf{p}^s)^2 - \sum_{s=1}^{N_e} \sum_{K=1}^{N_n} \frac{e^2 Z_K}{4\pi\epsilon_0 |\mathbf{r}^s - \mathbf{R}^K|} + \sum_{K=2}^{N_n} \sum_{L=1}^{K-1} \frac{e^2 Z_K Z_L}{4\pi\epsilon_0 |\mathbf{R}^K - \mathbf{R}^L|} + \sum_{s=2}^{N_e} \sum_{t=1}^{s-1} \frac{e^2}{4\pi\epsilon_0 |\mathbf{r}^s - \mathbf{r}^t|} \quad (5.2)$$

Here,  $N_e$  is the number of electrons,  $N_n$  is the number of nuclei,  $m_e$  is the mass of the electron,  $e$  is the elementary charge,  $\epsilon_0$  is the vacuum permittivity,  $\mathbf{r}^s$  and  $\mathbf{p}^s$  are the position and momentum operators of electron  $s$ , and  $\mathbf{R}^K$  and  $Z_K$  are the position and atomic number of nucleus  $K$ . Starting from the Schrödinger equation (Eq. 5.1), relativistic effects as described by the Breit–Pauli Hamiltonian can be treated as perturbations on an equal footing with external fields. Effects of nuclear motion (vibrations and rotations) can be estimated once the electronic response functions have been calculated.

Response functions are functions of the frequencies of the external fields, and although response theory is based on time-dependent perturbation theory, it is more appropriate to describe response theory as frequency-dependent rather than time-dependent. Nevertheless, response theory for approximate quantum chemical models is sometimes referred to as time-dependent, for example, time-dependent DFT (TDDFT) and time-dependent HF (TDHF) theory. Related by Fourier transformation, the time and frequency domains are two sides of the same coin. In practice, however, response functions are computed for a limited number of perturbation frequencies without any explicit reference to the time evolution of the quantum state.

## Response Theory

Approximate wave function and density functional theories provide information about the electronic structure of molecules in their electronic ground state. The information includes the electronic charge density, total energy, electric multipole moments (dipole, quadrupole, octupole, etc.), forces on the nuclei, and vibrational frequencies, which is sufficient to model a wide range of chemical phenomena. For example, equilibrium structures and transition states can be calculated from the forces, and vibrational frequencies are not only useful for the interpretation of vibrational spectra but also enable the calculation of thermochemical data from first principles. These theories are sufficient to model experimental conditions where only the electronic ground state is significantly populated.

When a molecule is subjected to external fields, however, quantum mechanics tells us that the electronic ground state responds by becoming a superposition of many electronic states. Response theory takes this wave function change into account and thus facilitates calculations of molecular properties beyond the reach of the ground state theory. Computation of the ground state response allows extraction of information about transitions from the ground state to excited states induced by one or more photons and even allows us to calculate properties of the excited states without explicitly computing the excited state wave functions.

Response theory describes the change in observable quantities such as electric and magnetic multipole moments due to external fields. The starting point of response theory therefore is the time evolution of the expectation value  $\langle A \rangle$  of an Hermitian operator  $A$  representing the observable quantity (e.g., the electric or magnetic dipole moment). In order to monitor the change in an observable quantity, we need to know the state of the molecule before the external field is switched on. As mentioned above, the electronic ground state  $|0\rangle$  is the proper choice under most experimental conditions. With this initial condition, the time evolution can be written as the perturbation expansion

$$\begin{aligned} \langle A \rangle &= \langle 0|A|0\rangle \\ &+ \int_{-\infty}^{\infty} \langle \langle A; V(\omega) \rangle \rangle_{\omega} \exp(-i\omega t) d\omega \\ &+ \frac{1}{2} \int_{-\infty}^{\infty} \int_{-\infty}^{\infty} \langle \langle A; V(\omega), V(\omega') \rangle \rangle_{\omega, \omega'} \exp(-i(\omega + \omega')t) d\omega d\omega' \\ &+ \dots \end{aligned} \tag{5.3}$$

where the operator  $V(\omega)$  describes the interaction between the electrons and the external field of frequency  $\omega$ . It should be noted that the perturbation expansion cannot generally be guaranteed to converge. Moreover, the perturbation expansion does not make sense when the external potential is comparable to or larger than the internal potential of the molecule. In most cases of practical interest, including the interaction of molecular electrons with laser fields, the perturbation expansion may be used.

Frequency-dependent response functions can only be computed within approximate electronic structure models that allow definition of the time-dependent expectation value. Hence, frequency-dependent response functions are not defined for approximate methods that provide an energy but no wave function. Such methods include Møller–Plesset (MP) perturbation theory, multiconfigurational second-order perturbation theory (CASPT2), and coupled cluster singles and doubles with non-iterative perturbative triples [CCSD(T)]. As we shall see later, it is possible to derive static response functions for such methods.

Common methods that do allow calculation of frequency-dependent response functions include DFT, HF, MCSCF, and members of the CC hierarchy of wave functions (CCSD(T) is not a member of this hierarchy, as it does not provide a wave function). In these models, the wave function (or density in the case of DFT) is written in terms of time-dependent parameters which are determined from the time-dependent Schrödinger equation with the initial condition that the approximate ground state wave function (or density) is recovered in the limit  $t \rightarrow -\infty$ , that is, before the external fields are switched on. The zeroth-order parameters are thus determined in the same way as in the ground state model, and response theory calculations are naturally performed on top of a standard ground state calculation. First-, second-, and higher-order parameters are determined from response equations that take into account the coupling with the external field in a manner consistent with the time-dependent Schrödinger equation. The response equations have the general matrix form (the detailed form of these matrices and vectors depend on the approximate theory used)

$$[\mathcal{H} - \omega\mathcal{S}] \lambda^{(n)}(\omega) = -\mathcal{V}^{(n)}(\omega) \quad (5.4)$$

where  $\lambda^{(n)}(\omega)$ , the unknown quantity in this equation, is a vector containing the  $n$ th-order ( $n > 0$ ) wave function parameters in a suitable order. While the matrices  $\mathcal{H}$  and  $\mathcal{S}$  only depend on the unperturbed ground state wave function, the vector on the right-hand side additionally depends on the lower-order wave function parameters  $\lambda^{(1)}, \lambda^{(2)}, \lambda^{(3)}, \dots, \lambda^{(n-1)}$  as well as on one or more perturbation operators  $V(\omega)$ . This implies that the solution of the first-order equations must be known before the second-order equations can be solved, and so on. The frequency  $\omega$  represents the sum of the frequencies corresponding to the perturbations included in the vector on the right-hand side of  $\blacklozenge$  Eq. 5.4.

Solving the response equations ( $\blacklozenge$  Eq. 5.4) is formally simple, namely,

$$\lambda^{(n)}(\omega) = -[\mathcal{H} - \omega\mathcal{S}]^{-1} \mathcal{V}^{(n)}(\omega) \quad (5.5)$$

where we assume that the matrix  $[\mathcal{H} - \omega\mathcal{S}]$  is non-singular. Those frequencies  $\omega$  for which the matrix is singular have a special significance, as will be discussed below. Since the matrices  $\mathcal{H}$  and  $\mathcal{S}$  only depend on the ground state wave function or density, they may in principle be computed once and for all. For each frequency and right-hand side vector we may then calculate the inverse  $[\mathcal{H} - \omega\mathcal{S}]^{-1}$  followed by a simple matrix-vector multiplication to obtain the response parameters according to  $\blacklozenge$  Eq. 5.5. Unfortunately, this simple solution strategy is too computationally demanding to be useful in practice. The large number of matrix elements in  $\mathcal{H}$  and  $\mathcal{S}$  makes it expensive to compute the matrices and to compute the inverse which, in addition, needs to be done for each frequency  $\omega$ . The number of matrix elements is given by the square of the number of ground state wave function parameters. For DFT or HF, for example, the number of ground state parameters is given by  $OV$  where  $O$  and  $V$  are the number of occupied and virtual (Kohn–Sham or HF) orbitals, respectively. For the more complicated coupled cluster singles and doubles (CCSD) wave function, the number of ground state wave function parameters is roughly  $O^2V^2/2$ . To get an impression of the orders of magnitude, consider a simple benzene molecule with the aug-cc-pVDZ basis set. In this case, there are approximately 3,600 DFT or HF ground state parameters and over six million CCSD parameters. The number of elements in the  $\mathcal{H}$  and  $\mathcal{S}$  matrices would therefore be approximately 13 million for DFT and HF, and  $36 \times 10^{12}$  for CCSD. For two benzene molecules, these numbers would increase to approximately 207 million matrix elements for DFT and HF, and  $10^{16}$  for CCSD. Just storing the matrices in computer memory would quickly pose an insurmountable problem, and a different solution strategy is needed.

Rather than straightforward application of [Eq. 5.5](#), the response equations ([Eq. 5.4](#)) are solved in an iterative procedure in which the matrices and vectors are projected onto a small subspace. In this procedure, an initial guess (a trial vector) is generated according to [Eq. 5.5](#) by neglecting all off-diagonal elements of  $\mathcal{H}$  and  $\mathcal{S}$  such that the inverse matrix  $[\mathcal{H} - \omega\mathcal{S}]^{-1}$  is readily computed. The iterations proceed by refining the trial vector until the norm of the residual vector

$$\mathbf{R} = (\mathcal{H} - \omega\mathcal{S})\lambda^{(n)} + \mathcal{V}^{(n)} \quad (5.6)$$

falls below a specified tolerance. Although quantum chemistry software packages provide reasonable default values for the tolerance, it may occasionally be necessary to lower the value to obtain sufficient accuracy in the computed response functions.

From the perturbative corrections to the wave function parameters we obtain perturbative corrections to the expectation value of the operator  $A$ , that is,

$$\langle A \rangle = \langle A \rangle^{(0)} + \langle A \rangle^{(1)} + \langle A \rangle^{(2)} + \dots \quad (5.7)$$

We may then identify response functions for each of the approximate electronic structure models by comparing with [Eq. 5.3](#):

$$\langle A \rangle^{(0)} = \langle 0|A|0 \rangle \quad (5.8)$$

$$\langle A \rangle^{(1)} = \int_{-\infty}^{\infty} \langle \langle A; V(\omega) \rangle \rangle_{\omega} \exp(-i\omega t) d\omega \quad (5.9)$$

$$\langle A \rangle^{(2)} = \frac{1}{2} \int_{-\infty}^{\infty} \int_{-\infty}^{\infty} \langle \langle A; V(\omega), V(\omega') \rangle \rangle_{\omega, \omega'} \exp(-i(\omega + \omega')t) d\omega d\omega' \quad (5.10)$$

⋮

Response theory deviates in one crucial aspect from the formulation of time-dependent perturbation theory in most textbooks on quantum mechanics: the response parameters  $\lambda^{(n)}$  are not explicitly expressed in terms of the excited states. As a consequence, knowledge of the excited state wave functions is not needed in response theory. Instead, we must solve the response equations ([Eq. 5.4](#)) for each set of perturbation operators  $V(\omega)$ . This is a tremendous computational advantage as there are significantly fewer perturbation operators, and hence response equations to solve, than excited states in virtually all cases of practical interest.

In order to illuminate the wealth of information that can be extracted from response functions for approximate wave functions, it is instructive to study the details of the exact response functions expressed in terms of electronic excited states.

## The Linear Response Function

The linear response function describing the first-order induced electric dipole moment due to an oscillating and spatially uniform electric field is related to the frequency-dependent electric dipole polarizability as

$$\alpha_{ij}(-\omega; \omega) = -\langle \langle \mu_i; \mu_j \rangle \rangle_{\omega} \quad (5.11)$$

The  $i$ th Cartesian component of the electronic electric dipole operator is given by

$$\mu_i = -e \sum_s r_i^s \quad (5.12)$$

where the sum is over all electrons in the molecule. This identification is obtained by substituting  $A \rightarrow \mu_i$  and  $V(\omega) \rightarrow -\boldsymbol{\mu} \cdot \mathbf{F}(\omega)$  in  $\blacktriangleright$  Eq. 5.3. The uniform electric field amplitude vector at frequency  $\omega$  is here represented by  $\mathbf{F}(\omega)$ . In an approximate calculation, the electric dipole polarizability is thus obtained by computing (minus) the linear response function from first-order wave function parameters determined by  $\blacktriangleright$  Eq. 5.4 with the three Cartesian components of the electric dipole operator as perturbation operators. Note that the response equations must be solved for each frequency.

More information can be extracted from the linear response function, however. This is most easily seen by studying the exact linear response function. Unlike the approximate theories, the exact linear response function is expressed in terms of the ground and excited states satisfying the time-independent Schrödinger equation

$$H_0|k\rangle = E_k|k\rangle \quad (5.13)$$

where  $k \geq 0$  and  $H_0$  is the molecular electronic Hamiltonian in the clamped-nucleus Born–Oppenheimer approximation,  $\blacktriangleright$  Eq. 5.2. The exact linear response function is given by

$$\langle\langle A; B \rangle\rangle_\omega = \frac{1}{\hbar} \sum_{k \neq 0} \left( \frac{\langle 0|A|k\rangle\langle k|B|0\rangle}{\omega - \omega_{k0}} - \frac{\langle 0|B|k\rangle\langle k|A|0\rangle}{\omega + \omega_{k0}} \right) \quad (5.14)$$

where  $\hbar\omega_{k0} = E_k - E_0$  is the excitation energy for the transition from the ground state to the  $k$ th excited state. This formulation of the linear response function is often referred to as the sum-over-states expression or spectral resolution.

The exact linear response function is singular at the molecular excitation energies, that is, it has poles at  $\omega = \pm\omega_{k0}$ . This is exploited in approximate theories to identify excitation energies as those frequencies for which the approximate linear response function is singular. In principle, the search for excitation energies could be done by scanning over frequencies in a manner analogous to measurements of absorption spectra. In practice, however, it is straightforward to identify the poles of the approximate linear response function as the frequencies for which the response equations ( $\blacktriangleright$  Eq. 5.4) are singular. As discussed above, this occurs at frequencies where the matrix  $\mathcal{H} - \omega\mathcal{S}$  cannot be inverted. This, in turn, occurs when  $\omega$  equals one of the eigenvalues  $w_n$  of the generalized eigenvalue problem

$$(\mathcal{H} - w_n\mathcal{S})\mathbf{V}_n = 0 \quad (5.15)$$

where  $\mathbf{V}_n$  is the eigenvector corresponding to the eigenvalue  $w_n$ . The generalized eigenvalue problem does not depend on the perturbation, and it can therefore be solved to directly obtain the excitation energies, identifying  $\omega_{k0} = w_k$ ,  $k = 1, 2, 3, \dots$ , without explicit calculation of neither the excited state wave functions nor their energies. The eigenvectors  $\mathbf{V}_n$  are the closest we get to an explicit wave function representation of the excited states in response theory. In practice, therefore, analysis of these eigenvectors is used to extract the (approximate) orbital nature of an excitation, for example, as a  $\pi - \pi^*$  orbital transition. Since we know the ground state energy  $E_0$  from the prerequisite unperturbed calculation, the excited state energy may be deduced from the excitation energy as

$$E_k = E_0 + \hbar\omega_{k0} \quad (5.16)$$

Solving the eigenvalue problem,  $\blacktriangleright$  Eq. 5.15, does not necessarily yield all excited states. With a spin-adapted wave function, only excited states with the proper spin symmetry would be produced. For example, only spin-singlet excited states can be found with a spin-singlet



wave function parameterization. Triplet states require a suitable spin-triplet adaptation of the wave function response. In unrestricted theories, the ground and excited states need not be spin eigenfunctions and the labeling of states as spin-singlet, spin-triplet, etc., is not well defined.

It is important to realize, however, that the number of eigenvalues  $w_n$  equals the number of excited states within a given approximate theory. Calculation of all eigenvalues is very computationally demanding. The number of excited states in an approximate theory equals the number of ground state wave function parameters, which grows quickly with the size of the molecule, as discussed above. One would most often be interested in just a few, typically on the order of 10, of the lowest excitation energies. Iterative techniques have been devised that allow the solution of  $\blacktriangleright$  Eq. 5.15 for a given number of eigenvalues and eigenvectors in ascending order. In order to calculate the excitation energy  $\omega_{k0}$ , it is therefore necessary to compute all excitation energies below this one as well, that is,  $\omega_{10}, \omega_{20}, \omega_{30}, \dots, \omega_{k-1,0}$ .<sup>1</sup> The iterative solution of the generalized eigenvalue problem ( $\blacktriangleright$  Eq. 5.15) is carried out by refining trial vectors and eigenvalues until the norm of the residuals

$$\mathbf{R}_n = (\mathcal{H} - w_n \mathcal{S}) \mathbf{V}_n \quad (5.17)$$

falls below a given tolerance.

Another important piece of information can be extracted from the pole structure of the linear response function. The residue of the linear response function at an excitation energy provides the one-photon transition strength:

$$\langle 0|A|k\rangle\langle k|B|0\rangle = \lim_{\omega \rightarrow \omega_{k0}} \hbar(\omega - \omega_{k0}) \langle\langle A; B \rangle\rangle_{\omega} \quad (5.18)$$

This observation allows us to identify transition moments between the ground state and the  $k$ th excited state,  $\langle 0|A|k\rangle$ , in approximate theories by computing the residue of the linear response function at the  $k$ th excitation energy. Again, this is achieved without explicitly computing the excited state wave function. In practice, the transition moment is expressed in terms of the  $k$ th eigenvector of  $\blacktriangleright$  Eq. 5.15 and the matrix representation of the operator  $A$  in the molecular orbital (or spin orbital) basis. It is therefore possible, in principle, to compute the linear response function for an approximate wave function using the sum-over-states expression with excitation energies calculated according to  $\blacktriangleright$  Eq. 5.15 and transition moments from  $\blacktriangleright$  Eq. 5.18. If all excitation energies and residues are included, the result is identical to the response function computed from the response equations ( $\blacktriangleright$  Eq. 5.4). From a computational point of view, of course, this approach is not advisable unless the combined number of perturbation operators and frequencies is larger than the number of excited states. This is practically never the case.

Within approximate wave function or density functional theories, it thus becomes possible to calculate one-photon absorption intensities such as the electric dipole oscillator strength of a transition from the ground state to the  $k$ th excited state from the following residue of the frequency-dependent electric dipole polarizability:

$$\begin{aligned} f_{k0} &= \frac{2m_e}{3e^2\hbar} \omega_{k0} \langle 0|\mu|k\rangle \cdot \langle k|\mu|0\rangle \\ &= -\frac{2m_e}{3e^2\hbar} \omega_{k0} \sum_i \lim_{\omega \rightarrow \omega_{k0}} \hbar(\omega - \omega_{k0}) \alpha_{ii}(-\omega; \omega) \end{aligned} \quad (5.19)$$

where  $m_e$  is the mass of the electron.

<sup>1</sup> Although techniques exist which solve an eigenvalue equation around a specific energy, these techniques are not used for quantum chemical calculations of excitation energies, as the energy range is rarely known in advance.

In approximate theories, the iterative solution of the response equations (► Eq. 5.4) becomes difficult and may even fail to converge when the frequency is too close to one of the excitation energies. As a consequence, linear response functions should only be calculated in transparent spectral regions. In absorptive spectral regions (“close” to an excitation energy), so-called anomalous dispersion is observed experimentally. Anomalous dispersion can be understood theoretically by taking into account the finite lifetime of the excited electronic states, leading to damped response theory. The exact damped linear response function is given by:

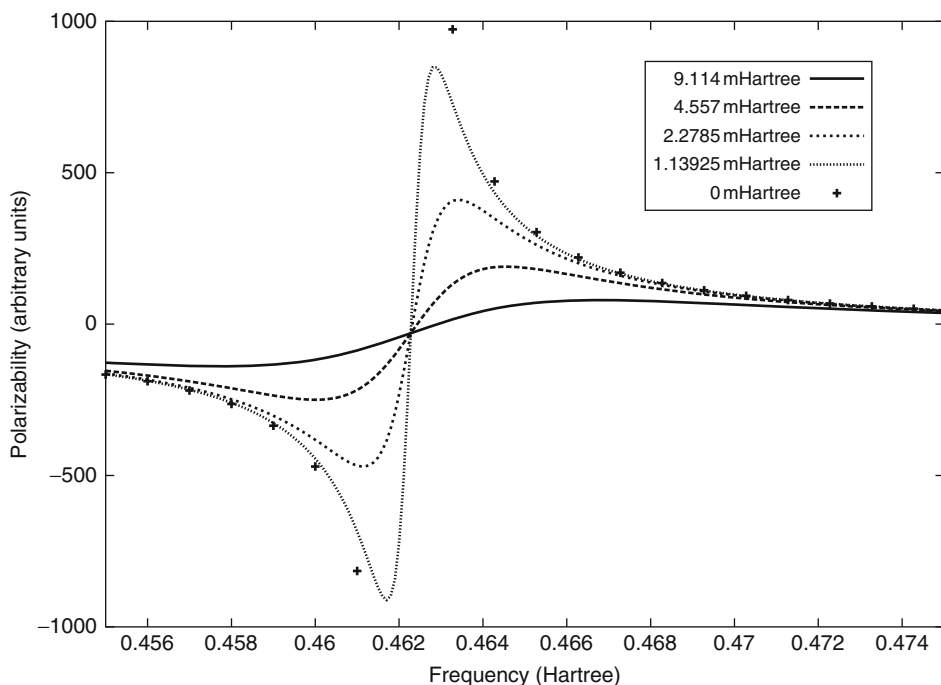
$$\langle\langle A; B \rangle\rangle_{\omega} = \frac{1}{\hbar} \sum_{k \neq 0} \left( \frac{\langle 0|A|k\rangle\langle k|B|0\rangle}{\omega - \omega_{k0} + i\Gamma_k/2} - \frac{\langle 0|B|k\rangle\langle k|A|0\rangle}{\omega + \omega_{k0} - i\Gamma_k/2} \right) \quad (5.20)$$

The broadening  $\Gamma_k$  is proportional to the probability of the excited state  $|k\rangle$  decaying into any of the other states, and it is related to the lifetime of the excited state as  $\tau_k = 1/\Gamma_k$ . For  $\Gamma_k = 0$ , the lifetime is infinite and ► Eq. 5.14 is recovered from ► Eq. 5.20. Unfortunately, it is not possible to account for the finite lifetime of each individual excited state in approximate theories based on the response equations (► Eq. 5.4). We would be forced to use a sum-over-states expression, which is computationally intractable. Moreover, the lifetimes cannot be adequately determined within a semiclassical radiation theory as employed here and a fully quantized description of the electromagnetic field is required. In addition, all decay mechanisms would have to be taken into account, for example, radiative decay, thermal excitations, and collision-induced transitions. Damped response theory for approximate electronic wave functions is therefore based on two simplifying assumptions: (1) all broadening parameters are assumed to be identical,  $\Gamma_1 = \Gamma_2 = \dots = \Gamma$ , and (2) the value of  $\Gamma$  is treated as an empirical parameter. With a single empirical broadening parameter, the response equations take the same form as in ► Eq. 5.4 with the substitution  $\omega \rightarrow \omega + i\Gamma/2$ , and the damped linear response function can be calculated from first-order wave function parameters, which are now inherently complex. For absorption spectra, this leads to a Lorentzian line-shape function which is identical for all transitions.

► Figure 5-1 shows the damped linear response function calculated from the real part of ► Eq. 5.20 with different values of the broadening. Only a section of the frequency spectrum around the lowest excitation energy is shown. With infinite lifetime ( $\Gamma = 0$ ), the linear response function goes to  $\pm\infty$  as the frequency approaches the excitation. This is avoided when the finite lifetime ( $\Gamma > 0$ ) is taken into account. In the absorptive region, the behavior of the damped linear response function depends strongly on the value of the broadening. Since the broadening parameter can be chosen freely, the results obtained in this region must be treated with great care: changing the value of the broadening could give a very different result. Sufficiently far from the excitation energy, on the other hand, the effect of the broadening is small and can be neglected. In the transparent region, we may therefore safely use the undamped linear response function.

A long list of molecular electromagnetic properties can be obtained by inserting suitable operators in the linear response function. The electric dipole polarizability is an important example. To further illustrate the procedure of obtaining molecular properties from linear response functions, we now consider the induced electric dipole moment due to higher-order multipole components of the electromagnetic field. The induced electric dipole moment due to a time-dependent uniform magnetic field is, to first order in the field, given by the electric dipole – magnetic dipole polarizability

$$G'_{ij}(-\omega; \omega) = -\text{Im}\langle\langle \mu_i; m_j \rangle\rangle_{\omega} \quad (5.21)$$



■ Fig. 5-1

The damped linear response function computed from the real part of  $\blacktriangleright$  Eq. 5.20 with the indicated values of the broadening  $\Gamma$  (corresponding to 0, 250, 500, 1,000, and 2,000  $\text{cm}^{-1}$ ). Electric dipole transition moments and excitation energies were obtained using CCSD for the hydrogen molecule with the aug-cc-pVDZ basis set

where the  $j$ th Cartesian component of the magnetic dipole operator is defined as

$$m_j = -\frac{e}{2m_e} \sum_s L_j^s \quad (5.22)$$

with the angular momentum operator of electron  $s$  given by  $\mathbf{L}^s = \mathbf{r}^s \times \mathbf{p}^s$ . This identification is obtained from  $\blacktriangleright$  Eq. 5.3 by substituting  $A \rightarrow \mu_i$  and  $V(\omega) \rightarrow -\mathbf{m} \cdot \mathbf{B}(\omega)$ , where  $\mathbf{B}(\omega)$  is the magnetic field amplitude at frequency  $\omega$ . Using multipole expansions of the electric and magnetic fields, the Maxwell equations show that a time-dependent uniform magnetic field is always accompanied by a quadrupolar electric field, and the contribution to the induced dipole moment from the electric dipole – electric quadrupole polarizability

$$a_{i,jk}(-\omega; \omega) = -\langle\langle \mu_i; q_{jk} \rangle\rangle_\omega \quad (5.23)$$

is of the same order of magnitude as  $\mathbf{G}'$ . Here,  $q_{jk} = -e \sum_s r_j^s r_k^s$  is the  $j, k$  component of the Cartesian electric quadrupole moment operator. The electric dipole – magnetic dipole and electric dipole – electric quadrupole polarizabilities govern the optical rotation of chiral molecules. For samples of randomly oriented molecules, the contribution from the electric dipole – electric quadrupole polarizability averages to zero, and only the trace (the sum of the diagonal elements) of the electric dipole – magnetic dipole polarizability contributes to the optical rotation. The

frequency-dependence of the linear response functions give rise to optical rotation dispersion. The residues of the electric dipole – magnetic dipole polarizability are related to the rotatory strength

$$R_{k0} = \text{Im} [\langle 0|\mu|k\rangle \cdot \langle k|\mathbf{m}|0\rangle] = - \sum_i \lim_{\omega \rightarrow \omega_{k0}} \hbar(\omega - \omega_{k0}) G'_{ii}(-\omega; \omega) \quad (5.24)$$

which determines the differential intensity of electronic circular dichroism spectra. If the molecules are oriented, the rotatory strength is a tensor (since the intensity will depend on the orientation of the molecule relative to the propagation direction of the photon) that also includes contributions from the residues of the electric dipole – electric quadrupole polarizability.

Finally, we note that the linear response function satisfies the permutation and conjugation relations

$$\langle\langle A; B \rangle\rangle_{\omega} = \langle\langle B; A \rangle\rangle_{-\omega} \quad (5.25)$$

$$\langle\langle A; B \rangle\rangle_{\omega}^* = \langle\langle A^{\dagger}; B^{\dagger} \rangle\rangle_{-\omega} \quad (5.26)$$

where the asterisk denotes complex conjugation and  $A^{\dagger}$  is the adjoint of the operator  $A$  ( $A^{\dagger} = A$  for Hermitian operators, by definition). It follows from these relations that the electric dipole polarizability is an even function of frequency,  $\alpha_{ij}(-\omega; \omega) = \alpha_{ij}(\omega; -\omega)$ , and a symmetric tensor,  $\alpha_{ij}(-\omega; \omega) = \alpha_{ji}(-\omega; \omega)$ , which implies that only six of the nine Cartesian components of the polarizability need to be computed. The permutation and conjugation relations are satisfied by approximate linear response functions as well.

## Quadratic and Higher-Order Response Functions

The quadratic response function describing the second-order induced electric dipole moment due to a uniform time-dependent electric field is related to the frequency-dependent electric dipole hyperpolarizability as

$$\beta_{ijk}(-\bar{\omega}; \omega, \omega') = -\langle\langle \mu_i; \mu_j, \mu_k \rangle\rangle_{\omega, \omega'} \quad (5.27)$$

where  $\bar{\omega} = \omega + \omega'$ . With a procedure completely analogous to that of the linear response functions, this identification is obtained by substituting  $A \rightarrow \mu_i$  and  $V(\omega) \rightarrow -\mu \cdot \mathbf{F}(\omega)$  in  $\blacklozenge$  Eq. 5.3. A variety of optical processes are governed by the electric hyperpolarizability depending on the values of the frequencies, including Second Harmonic Generation through  $\beta_{ijk}(-2\omega; \omega, \omega)$  and Optical Rectification through  $\beta_{ijk}(0; \omega, -\omega)$ . In an approximate calculation, the electric dipole hyperpolarizability can be obtained by computing (minus) the quadratic response function from first-order wave function parameters determined by  $\blacklozenge$  Eq. 5.4 with the three Cartesian components of the electric dipole operator as perturbation operators at each set of frequencies  $\omega$ ,  $\omega'$ , and  $\bar{\omega}$ . In accordance with Wigner's  $2n + 1$  rule, which states that the  $n$ th-order wave function parameters determine the response functions up to order  $2n + 1$ , second-order wave function parameters are not needed. In this context, the order of the response function corresponds to the number of operators it contains such that the ground state expectation value is of order 1, the linear response function is of order 2, the quadratic response function is of order 3, and so on. The  $2n + 1$  rule is essential for efficient computer implementations of response theory.

To learn more about the information that can be extracted from the quadratic response function in approximate calculations, we now study the exact one. Like the exact linear response

function, the exact quadratic response function can be calculated from excitation energies and transition matrix elements of the unperturbed molecule:

$$\begin{aligned} \langle\langle A; B, C \rangle\rangle_{\omega, \omega'} = \frac{1}{\hbar^2} P_{BC} \sum_{k, l \neq 0} & \left\{ \frac{\langle 0|A|k\rangle \langle k|\bar{B}|l\rangle \langle l|C|0\rangle}{(\omega + \omega' - \omega_{k0})(\omega' - \omega_{l0})} \right. \\ & + \frac{\langle 0|C|k\rangle \langle k|\bar{B}|l\rangle \langle l|A|0\rangle}{(\omega + \omega' + \omega_{l0})(\omega' + \omega_{k0})} \\ & \left. - \frac{\langle 0|B|k\rangle \langle k|\bar{A}|l\rangle \langle l|C|0\rangle}{(\omega + \omega_{k0})(\omega' - \omega_{l0})} \right\} \end{aligned} \quad (5.28)$$

The bar signals that the operator has been shifted to a zero-point defined by its ground state expectation value. For example,

$$\bar{B} = B - \langle 0|B|0\rangle I \quad (5.29)$$

where  $I$  is the identity operator. The operator  $P_{BC}$  permutes the pairs  $(B, \omega)$  and  $(C, \omega')$ :

$$P_{BC} f(B, \omega, C, \omega') = f(B, \omega, C, \omega') + f(C, \omega', B, \omega) \quad (5.30)$$

giving a total of six distinct terms in the quadratic response function. The quadratic response function is singular at the molecular excitation energies, that is, when  $\omega + \omega' = \pm\omega_{k0}$  or when  $\omega = \pm\omega_{k0}$  or when  $\omega' = \pm\omega_{k0}$  for some  $k > 0$ . These singularities can be avoided by taking into account the finite lifetime of the excited molecular states, as discussed for the linear response function in the previous section.

The quadratic response function, for exact as well as approximate states, satisfies the permutation and conjugation relations

$$\begin{aligned} \langle\langle A; B, C \rangle\rangle_{\omega, \omega'} &= \langle\langle A; C, B \rangle\rangle_{\omega', \omega} \\ &= \langle\langle B; A, C \rangle\rangle_{-\omega - \omega', \omega'} = \langle\langle B; C, A \rangle\rangle_{\omega', -\omega - \omega'} \\ &= \langle\langle C; A, B \rangle\rangle_{-\omega - \omega', \omega} = \langle\langle C; B, A \rangle\rangle_{\omega, -\omega - \omega'} \end{aligned} \quad (5.31)$$

$$\langle\langle A; B, C \rangle\rangle_{\omega}^* = \langle\langle A^\dagger; B^\dagger, C^\dagger \rangle\rangle_{-\omega, -\omega'} \quad (5.32)$$

The assumption, known as Kleinman symmetry, that the quadratic (and higher-order) response function is symmetric under interchange of any pair of operators is only true at zero frequency, as is easily verified from [Eq. 5.31](#). Note that the quadratic response function is symmetric when permuting the operators  $B$  and  $C$  at  $\omega = \omega'$ , which is the case for, for example, Second Harmonic Generation:  $\beta_{ijk}(-2\omega; \omega, \omega) = \beta_{ikj}(-2\omega; \omega, \omega)$ . Kleinman symmetry is often assumed in calculations of the electric dipole hyperpolarizability at low frequencies where it is approximately valid. This reduces the number of independent tensor elements and thus the computational effort.

Owing to the more complicated dependence on field frequencies, the residues of the quadratic response function provide more information than those of the linear response function. One of the most important residues of the quadratic response function is

$$\begin{aligned} & \lim_{\omega' \rightarrow \omega_{m0}} \hbar(\omega' - \omega_{m0}) \langle\langle A; B, C \rangle\rangle_{-\omega, \omega'} \\ &= - \left[ \frac{1}{\hbar} \sum_k \left( \frac{\langle 0|A|k\rangle \langle k|B|m\rangle}{\omega_{k0} - (\omega_{m0} - \omega)} + \frac{\langle 0|B|k\rangle \langle k|A|m\rangle}{\omega_{k0} - \omega} \right) \right] \langle m|C|0\rangle \end{aligned} \quad (5.33)$$

where the summation over  $k$  includes the ground state  $|0\rangle$ . The quantity in square brackets is an element of the transition matrix for two-photon excitation from the ground state to the excited state  $m$ . Another useful (double) residue is

$$\begin{aligned} \lim_{\omega \rightarrow -\omega_{n0}} \hbar(\omega' + \omega_{m0}) \left[ \lim_{\omega' \rightarrow \omega_{m0}} \hbar(\omega' - \omega_{m0}) \langle \langle A; B, C \rangle \rangle_{-\omega, \omega'} \right] \\ = \delta_{mn} \langle 0|A|0\rangle \langle 0|B|n\rangle \langle n|C|0\rangle - \langle 0|B|n\rangle \langle n|A|m\rangle \langle m|C|0\rangle \end{aligned} \quad (5.34)$$

From this expression it is possible to extract transition moments between excited states  $[\langle n|A|m\rangle]$ . With the specific choice  $n = m$  it thus becomes possible to compute excited state properties such as dipole moments from the quadratic response of the ground state.

Higher-order response functions (cubic, quartic, quintic, etc.) can also be written in terms of molecular excitation energies, and eigenstates. These functions possess singularities at the excitation energies, and the associated residues (single, double, etc. residues) can be used to identify a wide range of molecular properties. For example, residues of the cubic response function provide two-photon transition strengths (the product of two-photon transition matrix elements) and three-photon transition matrix elements, while the three-photon transition strength is obtained from the quintic response function. Linear response functions for the excited states can be extracted from the cubic response function. By calculating ground state response functions we may thus extract all molecular properties.

## Static Response Functions

The interaction between a molecule and time-independent external fields is described by frequency-independent perturbation operators. Time-independent fields are nonoscillating, and interactions with molecular electrons are therefore characterized by perturbation operators at zero frequency. The limit  $\omega \rightarrow 0$  is often referred to as the static limit and response functions at zero frequency are called static response functions. Although static response functions can be calculated in the same way as dynamic (frequency-dependent) ones, they are special in the sense that they are related to changes in ground state energy. For example, the electronic ground state energy of a molecule in the presence of a static uniform electric field,  $\mathbf{F}$ , can be expanded as

$$E = E_0 - \langle 0|\mu|0\rangle \cdot \mathbf{F} - \mathbf{F} \cdot \alpha(0; 0) \cdot \mathbf{F} + \dots \quad (5.35)$$

where  $E_0$  is the energy in the absence of the field. The expectation value of the dipole moment operator thus determines the first-order energy due to the field, whereas the static polarizability determines the second-order energy. Higher-order energy corrections are determined by the static hyperpolarizability, second hyperpolarizability, etc. This explains why ground state expectation values are often classified as first-order properties, linear response functions as second-order properties, and so on.

The relation between static response functions and energy corrections implies that molecular properties can be identified as derivatives of the total energy at zero field strength. For example,

$$\langle 0|\mu_i|0\rangle = -\frac{\partial E}{\partial F_i} \quad (5.36)$$

$$\alpha_{ij}(0; 0) = -\frac{\partial^2 E}{\partial F_i \partial F_j} \quad (5.37)$$

where it is implicitly understood that the derivatives must be evaluated at zero field strength ( $\mathbf{F} = \mathbf{0}$ ). Hence, the calculation of static response functions does not require a wave function and may therefore be computed with electronic structure theories that only provide the energy (e.g., MP2, CASPT2, and CCSD(T)).

Even if a quantum chemical software package does not feature an implementation of a given static response property, it is often possible to evaluate the property as an energy derivative by finite difference. Most packages allow the addition of external static fields to the Hamiltonian, making it possible to compute the energy at a specified field strength,  $E(\mathbf{F})$ . From the definition of the partial derivative, we may thus compute the dipole moment and polarizability from finite difference formulas such as

$$\frac{\partial E}{\partial F_i} \approx \frac{E(\delta_i) - E(-\delta_i)}{2\delta_i} \quad (5.38)$$

$$\frac{\partial^2 E}{\partial F_i^2} \approx \frac{E(\delta_i) - 2E(0) + E(-\delta_i)}{\delta_i^2} \quad (5.39)$$

$$\frac{\partial^2 E}{\partial F_i \partial F_j} \approx \frac{E(\delta_i, \delta_j) + E(-\delta_i, -\delta_j) - E(-\delta_i, \delta_j) - E(\delta_i, -\delta_j)}{4\delta_i \delta_j} \quad (5.40)$$

where  $\delta_i$  ( $\delta_j$ ) is a small field strength along the  $i$ th ( $j$ th) Cartesian direction. The error in these numerical derivative formulas is quadratic in the field strength which should therefore be chosen as small as possible. Choosing too small field strengths, however, may lead to numerical instabilities when computing the difference between two large and almost identical numbers. It is therefore advisable to conduct a convergence study with respect to the field strength when computing numerical derivatives.

A number of static perturbations arise from internal interactions or fields, which are neglected in the nonrelativistic Born–Oppenheimer electronic Hamiltonian. The relativistic correction terms of the Breit–Pauli Hamiltonian are considered as perturbations in nonrelativistic quantum chemistry, including Darwin corrections, the mass-velocity correction, and spin–orbit and spin–spin interactions. Some properties, such as nuclear magnetic resonance shielding tensors and shielding polarizabilities, are computed from perturbation operators that involve both internal and external fields.

## Gauge and Origin Invariance

As described above, molecular properties are identified as response functions by selecting the observable quantity whose change is to be monitored and the external field(s) inducing the change. The operator describing the coupling between the external field and the electrons is not unique, however. The electric field  $\mathbf{F}(\mathbf{r}, t)$  can be written in terms of the vector potential  $\mathbf{A}(\mathbf{r}, t)$  and the scalar potential  $\phi(\mathbf{r}, t)$  as

$$\mathbf{F}(\mathbf{r}, t) = -\frac{\partial \mathbf{A}(\mathbf{r}, t)}{\partial t} - \nabla \phi(\mathbf{r}, t) \quad (5.41)$$

while the magnetic field  $\mathbf{B}(\mathbf{r}, t)$  is given by

$$\mathbf{B}(\mathbf{r}, t) = \nabla \times \mathbf{A}(\mathbf{r}, t) \quad (5.42)$$

Since the electric and magnetic fields are obtained by differentiation, adding a constant to the vector and scalar potentials does not alter the physical electric and magnetic fields. More

generally, adding the gradient of a continuous function  $\xi(\mathbf{r}, t)$  to the vector potential, that is,  $\mathbf{A} \rightarrow \mathbf{A} + \nabla \xi$ , while subtracting the time-derivative of the same function from the scalar potential, that is,  $\phi(\mathbf{r}, t) \rightarrow \phi(\mathbf{r}, t) - \partial \xi / \partial t$  will not change the electric and magnetic fields. This feature is known as gauge invariance and implies that there is a manifold of scalar and vector potentials related by gauge transformations that describe the same physical field. This leads to a manifold of different quantum mechanical operators describing the interaction between the electrons and the field. The time-dependent Schrödinger equation is invariant under such gauge transformations and the computed properties therefore also should be invariant. This is indeed the case for exact response functions.

As an example, consider again the interaction between electrons and a uniform electric field. In [section “The Linear Response Function,”](#) the electric dipole polarizability was identified using the length gauge perturbation operator

$$V(\omega) = -\boldsymbol{\mu} \cdot \mathbf{F}(\omega) \quad (5.43)$$

An equally valid choice would have been the velocity gauge perturbation operator

$$V(\omega) = -\frac{ie}{\omega m_e} \mathbf{p} \cdot \mathbf{A}(\omega) \quad (5.44)$$

where  $\mathbf{A}(\omega)$  is the amplitude vector of the electromagnetic vector potential in the electric dipole approximation, and  $\mathbf{p} = \sum_s \mathbf{p}^s$  is the total electronic momentum operator. This operator leads to the following expression for the electric dipole polarizability

$$\alpha_{ij}(-\omega; \omega) = -\frac{ie}{\omega m_e} \langle\langle \mu_i; p_j \rangle\rangle_\omega \quad (5.45)$$

While [Eq. 5.11](#) is called the length gauge or dipole-length gauge expression, [Eq. 5.45](#) is often called the mixed gauge form since it involves both the electric dipole operator and the momentum operator. The length and mixed gauge polarizabilities are equivalent due to the equation of motion

$$\hbar\omega \langle\langle A; B \rangle\rangle_\omega = \langle\langle [A, H_0]; B \rangle\rangle_\omega + \langle 0|[A, B]|0 \rangle \quad (5.46)$$

which is satisfied by the exact linear response function, and due to the commutator relations

$$[\mu_j, H_0] = -\frac{ie\hbar}{m_e} p_j \quad (5.47)$$

$$[\mu_i, \mu_j] = 0 \quad (5.48)$$

Such relations (equation of motion and commutators) guarantee that exact linear response functions are gauge invariant. In addition, transition moments deduced from residues of the exact linear response function are also gauge invariant.

For approximate theories, however, different results are always obtained with different perturbation operators related by gauge transformations. The use of a finite basis set implies that operators are represented as finite matrices and, consequently, the commutator relations no longer hold. As the basis set quality is increased, the commutators converge to the exact values. Gauge invariance thus is recovered in the limit of a complete basis set, provided that the equation of motion [Eq. 5.46](#), is fulfilled. While this is the case in theories with fully variational orbitals such as DFT, HF, and MCSCF, it is not the case in approximate theories with fixed (nonvariational) orbitals such as CI and CC.



The exact quadratic and higher-order response functions satisfy similar equations of motion, for example,

$$\begin{aligned} \hbar(\omega + \omega') \langle \langle A; B, C \rangle \rangle_{\omega, \omega'} &= \langle \langle [A, H_0]; B, C \rangle \rangle_{\omega, \omega'} \\ &+ \langle \langle [A, B]; C \rangle \rangle_{\omega'} + \langle \langle [A, C]; B \rangle \rangle_{\omega} \end{aligned} \quad (5.49)$$

ensuring gauge invariance of higher-order molecular properties. In analogy to the case of the linear response function, the higher-order equations of motion are satisfied in approximate theories with variational determination of the orbitals such as DFT, HF, MCSCF, but not in theories such as CI and CC.

It is therefore necessary to specify which gauge (typically, length or velocity) is used when reporting computed response properties such as electric dipole (hyper-)polarizabilities and transition moments. With reasonably flexible basis sets, each of the DFT, HF, and MCSCF methods typically provide length and velocity gauge results that are quite close to each other, whereas CC results occasionally show significant differences between length and velocity gauge. For example, the specific optical rotation of (1S,4S)-norbornenone calculated at the CC singles and doubles (CCSD) level is  $-558 \text{ deg dm}^{-1} (\text{g/ml})^{-1}$  with the length gauge and  $-740 \text{ deg dm}^{-1} (\text{g/ml})^{-1}$  with the velocity gauge (corrected for an unphysical static limit, see below). The fundamental problem is that there is no general physical reason to trust one gauge formulation more than another.

In some cases, however, there may be good reasons for favoring one gauge formulation over others in approximate calculations. One such example is optical rotation which is governed by the trace of the electric dipole – magnetic dipole polarizability, whose length gauge formulation is given by [Eq. 5.21](#). Within the clamped-nucleus Born–Oppenheimer approximation, every electronic structure calculation is performed with fixed nuclear positions. The coordinate system used to specify the nuclear positions can be chosen arbitrarily. In particular, the results of the calculation should be independent of the choice of origin of the coordinate system.

Suppose that we translate the origin of the coordinate system along a vector  $\mathbf{O}$ . As a consequence, the positions of nuclei and electrons are shifted by the same vector, for example,  $\mathbf{r}^s \rightarrow \mathbf{r}^s - \mathbf{O}$ , and the electric dipole – magnetic dipole polarizability changes according to

$$\mathbf{G}'(-\omega; \omega) \rightarrow \mathbf{G}'(-\omega; \omega) + \frac{e}{2m_e} \text{Im} [\langle \langle \mu; \mathbf{p} \rangle \rangle_{\omega} \times \mathbf{O}] \quad (5.50)$$

which shows that the tensor is origin-dependent. The culprit is the origin-dependence of the magnetic dipole operator:

$$\mathbf{m} \rightarrow \mathbf{m} - \frac{e}{2m_e} \mathbf{p} \times \mathbf{O} \quad (5.51)$$

This translation of the operator can also be achieved by a particular type of gauge transformation of the magnetic vector potential, explaining why the term gauge-origin is often used for  $\mathbf{O}$  in the context of magnetic properties.

It can be shown that the trace of the tensor  $\mathbf{G}'$ , and hence the computed optical rotation of a sample of randomly oriented chiral molecules, is independent of the origin provided that the linear response function satisfies [Eq. 5.46](#) and that the commutator of [Eq. 5.47](#) is fulfilled. Consequently, approximate linear response calculations of the length gauge optical rotation depend on the chosen coordinate origin. On the other hand, the trace of the velocity gauge formulation of the electric dipole – magnetic dipole polarizability

$$\mathbf{G}'(-\omega; \omega) = \frac{e}{\omega m_e} \langle \langle \mathbf{p}; \mathbf{m} \rangle \rangle_{\omega} \quad (5.52)$$

is unconditionally independent of the chosen origin, also in approximate theories. (Note that  $\blacktriangleright$  Eq. 5.52 is only valid for real wave functions.) It may thus be argued that the velocity gauge formulation of optical rotation should be preferred over the length gauge expression. It must be added, however, that the velocity gauge optical rotation calculated with an approximate theory suffers from a serious artifact: it predicts a nonvanishing optical rotation at zero frequency (at zero frequency, there is no light and the optical rotation must be zero). This can be traced back to the lack of gauge invariance and is rectified by the modified velocity gauge where the static limit simply is subtracted from the linear response function, that is,  $\langle\langle p_i; m_i \rangle\rangle_\omega$  is replaced by  $\langle\langle p_i; m_i \rangle\rangle_\omega - \langle\langle p_i; m_i \rangle\rangle_0$ .

The most widely used technique for ensuring origin invariance of magnetic properties, however, is based on so-called Gauge Including Atomic Orbitals (GIAOs, also known as London Atomic Orbitals [LAOs]). Belonging to the class of perturbation-dependent basis sets, GIAOs are obtained from any conventional atomic orbital basis set by multiplying each basis function with a complex phase factor that depends explicitly on an external uniform static magnetic field. In a finite GIAO basis set, the magnetic dipole moment operator depends on the chosen coordinate origin according to

$$\mathbf{m} \rightarrow \mathbf{m} - \frac{i}{2\hbar} [\boldsymbol{\mu}, H_0] \times \mathbf{O} \quad (5.53)$$

which is identical to  $\blacktriangleright$  Eq. 5.51 in the limit of a complete basis set where the commutator of  $\blacktriangleright$  Eq. 5.47 is fulfilled. For fully variational approximate theories (DFT, HF, MCSCF), GIAOs thus remove the condition that the commutator must be fulfilled and the length gauge optical rotation becomes manifestly independent of origin. For approximate theories lacking variational orbital optimization (CI, CC), GIAOs are unable to remove the origin dependence of the length gauge optical rotation, since the equation of motion  $\blacktriangleright$  Eq. 5.46, is not satisfied. The velocity gauge formulation with GIAOs is origin-dependent in all approximate theories and, therefore, is never used.

The greatest strength of GIAOs lies in origin invariant calculation of molecular properties involving static uniform magnetic fields, including static magnetic properties such as magnetizabilities and rotational  $g$  tensors, and nuclear magnetic shieldings as well as optical properties aided by a static magnetic field such as magneto-optical activity. The use of GIAOs makes it possible to calculate the total energy in the presence of a static uniform magnetic field in an origin-independent manner for variational as well as nonvariational approximate theories, implying that the molecular properties identified as energy derivatives are independent of origin as well. In addition, owing to their being atomic eigenfunctions of the angular momentum operator correct to first order in the applied magnetic field, GIAOs provide vastly improved basis set convergence of static magnetic properties.

## Effects of Nuclear Motion

Within the clamped-nucleus Born–Oppenheimer approximation, electronic response functions are computed for fixed nuclear geometries. Just like the electronic ground state energy, the excitation energies and response functions thus become parametric functions of nuclear positions. For example, by solving the eigenvalue problem,  $\blacktriangleright$  Eq. 5.15, at a range of geometries, it becomes possible to compute excited state potential energy surfaces using  $\blacktriangleright$  Eq. 5.16 at each point. This, in turn, allows us to optimize excited state geometries using either a simple scan of

the excited state potential energy surface or analytic gradients derived from [Eq. 5.16](#). Since the ground state energy is required to compute the excited state energy in the response approach, calculations of excited state potential energy surfaces should only be carried out for geometries where the approximate wave function is valid. For single-reference methods such as HF and CC, one should only compute excitation energies (and thus excited state energies) for geometries not too far from the ground state equilibrium structure. As a consequence, these single-reference methods cannot be used to compute dissociative excited state surfaces, except at points close to the ground state equilibrium geometry. Multiconfigurational methods are required to describe such unbound excited states. For bound excited states, [Eq. 5.16](#) also provides a viable path to excited state vibrational frequencies and wave functions. Along with those of the ground state, it then becomes possible to calculate 0–0 transition energies rather than the vertical excitation energies provided by the poles of the response functions. In addition, the vibrational structure of electronic bands becomes amenable to theoretical computations.

Electronic ground state response functions are most often calculated at the (ground state) equilibrium geometry. The geometry optimization and response function evaluation may be performed at different levels of theory and using different basis sets. For example, it may be sufficient to optimize the geometry of a covalently bonded molecule at the DFT level of theory with a relatively small polarized basis set, while the response functions are evaluated at the CC level of theory (at the DFT equilibrium geometry) with a large polarized basis set augmented with diffuse functions to ensure the correct pole structure of the response functions. In other cases, it may be advantageous to use different DFT functionals and basis sets for the geometry optimization and property calculation.

If high accuracy is required, vibrational effects must be taken into account. In a proper adiabatic Born–Oppenheimer treatment, the ground state wave function would be written as a product of an electronic and a vibrational wave function. The response of this wave function should then be computed and subsequently used to construct vibronic response functions. The sum-over-states expressions would include contributions from vibrational states in the electronic ground and excited states. Since each set of vibrational wave functions is tied to a specific electronic state within the adiabatic Born–Oppenheimer approximation, this approach is not feasible in practice. Hence, the electronic properties are considered as electronic ground state properties and therefore, averaged in a vibrational state of the electronic ground state.

Computing the expectation value of the electronic property  $P(\mathbf{q})$ , which may be a response function or a sum of response functions depending parametrically on the dimensionless normal coordinates  $\mathbf{q}$ , in the vibrational state  $|v_0\rangle$  of the electronic ground state, the vibrational correction becomes

$$\Delta P = \langle v_0 | P(\mathbf{q}) | v_0 \rangle - P_0 \quad (5.54)$$

where  $P_0$  is the value of the electronic property at the equilibrium geometry. The analytic form of the dependence of  $P$  on normal coordinates normally is not known. Even if it were known, it would be too computationally demanding to evaluate the property on a grid of normal coordinates to fit the values to the analytic form. Instead, the property is expanded in a Taylor series. This implies that derivatives of the property with respect to the normal coordinates must be evaluated at the expansion point of the Taylor series. The property derivatives can themselves be expressed in terms of response functions (by considering the nuclear displacement terms of the Hamiltonian as perturbations), or they may be computed by numerical techniques analogous to the static properties of [section “Static Response Functions.”](#) The vibrational wave

functions may be computed in the same manner as in the ground state theory. That is, they are computed on the basis of the harmonic approximation and often include anharmonic effects to first order in perturbation theory. In another approach, the vibrational problem is viewed as so-called mode dynamics and solved in manner resembling electronic structure theory. This approach also makes it possible to compute the vibrational expectation value directly and only requires that an electronic structure program is available for computing energies and properties at specified nuclear geometries.

The relatively small difference between vibrational energy levels implies that a range of vibrational states are occupied at finite temperature. Including anharmonic effects to first order, the temperature-dependent vibrational correction can be expressed as:

$$\begin{aligned} \Delta P = & -\frac{1}{4\hbar} \sum_n \frac{1}{\omega_n} \frac{\partial P}{\partial q_n} \sum_m k_{nmm} \coth\left(\frac{\hbar\omega_m}{2k_B T}\right) \\ & + \frac{1}{4} \sum_n \frac{\partial^2 P}{\partial q_n^2} \coth\left(\frac{\hbar\omega_n}{2k_B T}\right) \end{aligned} \quad (5.55)$$

where the property derivatives are to be evaluated at the equilibrium geometry,  $\omega_n$  is the harmonic vibrational frequency of normal mode  $n$ ,  $k_B$  is the Boltzmann constant,  $T$  is the temperature, and the cubic (anharmonic) force constants are given by

$$k_{nmm} = \frac{\partial^3 E_0}{\partial q_n \partial q_m^2} \quad (5.56)$$

which is also evaluated at the equilibrium geometry ( $E_0$  is the electronic ground state energy surface,  $E_0 = E_0(\mathbf{q})$ ). The first term in [Eq. 5.55](#) accounts for the anharmonicity of the potential energy surface, whereas the second term is purely harmonic and arises from the curvature of the property surface. If anharmonic effects are neglected, only the second term is included. Anharmonic effects can be as large as the harmonic contribution and should generally be included, in particular when the molecule contains low-frequency vibrational modes (such as torsional motions). Most quantum chemistry programs are able to compute the harmonic vibrational frequencies and normal coordinates, and some also provide cubic force constants (if not, these can be computed numerically). The property derivatives are most often computed by numerical differentiation. At zero temperature, only the vibrational ground state is populated and the zero-point vibrational correction (ZPVC) is obtained from [Eq. 5.55](#) by taking the limit  $T \rightarrow 0$  where the hyperbolic cotangent factors approach 1. Once the property and energy derivatives have been calculated, the temperature-dependence of the vibrationally averaged property can be easily computed, including the ZPVC.

Conformationally flexible molecules are characterized by multiple low-lying minima on the potential energy surface, each minimum defining a conformer of the molecule. All conformers contribute to the experimentally observed property and must be taken into account in theoretical calculations. In the simplest approach, provided that the barriers separating the minima are sufficiently large, the vibrationally corrected property can be computed along the lines discussed above for each conformer (letting the conformer structure play the role of equilibrium geometry in each case). The total (observed) property is then obtained as a Boltzmann average of the results for each conformer:

$$\bar{P} = \sum_i^{\text{conformers}} \langle P \rangle_i X_i \quad (5.57)$$

Here,  $\langle P \rangle_i$  and  $X_i$  are the vibrationally corrected property and mole fraction of conformer  $i$ , respectively. Note that the same formula can be applied to compute the average of the purely electronic contribution to the property (i.e., not vibrationally corrected). The mole fraction is computed according to

$$X_i = \frac{\exp(-G_i/k_B T)}{\sum_j^{\text{conformers}} \exp(-G_j/k_B T)} \quad (5.58)$$

where  $G_i$  is Gibbs free energy of conformer  $i$ , which, assuming the ideal gas approximation, is given by

$$G_i = E_{0,i} + \epsilon_{0,i} + RT - TS_i \quad (5.59)$$

where  $R$  is the universal gas constant. The electronic ground state energy of conformer  $i$  is denoted  $E_{0,i}$  and  $\epsilon_{0,i}$  is the zero-point vibrational energy of conformer  $i$  in the harmonic oscillator approximation. The entropy is computed from the electronic, vibrational, and rotational partition functions,

$$S_i = -k_B T \ln(Z_{\text{el},i} Z_{\text{vib},i} Z_{\text{rot},i}) \quad (5.60)$$

$$Z_{\text{el},i} = 1 \quad (5.61)$$

$$Z_{\text{vib},i} = \sum_n g_{n,i}^{\text{vib}} \exp(-\epsilon_{n,i}/k_B T) \quad (5.62)$$

$$Z_{\text{rot},i} = \sum_m g_{m,i}^{\text{rot}} \exp(-\epsilon_{m,i}/k_B T) \quad (5.63)$$

The electronic partition function is unity, as only the electronic ground state is assumed populated. The vibrational energies of conformer  $i$ ,  $\epsilon_{n,i}$ , are computed in the harmonic oscillator approximation, which facilitates analytic summation over all vibrational levels. The rotational energy of conformer  $i$ ,  $\epsilon_{m,i}$ , is calculated within the rigid rotor approximation. The factors  $g_{n,i}^{\text{vib}}$  and  $g_{m,i}^{\text{rot}}$  are the degeneracies of the vibrational and rotational energy levels, respectively. Hence, the data needed to evaluate the Boltzmann average can be obtained from ground state calculations (electronic ground state energy at the equilibrium structure, harmonic vibrational energies, and rotational constants).

The simple Boltzmann averaging relies on a range of approximations that tend to benefit from fortuitous cancellation of errors. In particular, the assumption that the conformers can be treated as independent with no couplings between their vibrational states is fragile, as barriers are often insufficient to warrant the assumption. A more correct description would be obtained by solving the vibrational problem for the entire ground state potential energy surface instead of using a first-order anharmonic approximation in the vicinity of the minima. Calculation of the entire potential energy surface is, however, out of the question for all but the smallest systems. One way out might be to compute the nuclear motion using molecular dynamics and parametrized force fields, sampling the electronic property along the trajectory. Also this approach, however, may easily turn out to be too demanding in terms of the number of electronic structure calculations required.

## Further Reading

---

This section contains a short description of suggested references for further study of the concepts and techniques described above. The list of references is highly incomplete and should be considered as a mere starting point.

The time-independent perturbation operators describing internal molecular interactions are taken from the Breit–Pauli Hamiltonian, which includes relativistic corrections to the molecular electronic Hamiltonian of [Eq. 5.2](#). The Breit–Pauli Hamiltonian is discussed in more detail in the text books by Bethe and Salpeter (1957) and by Moss (1973). Appropriate operators for the interaction between charged particles and external electromagnetic fields are discussed in the paper by Fiutak (1963). The text book by Craig and Thirunamachandran (1984) contains derivations of a long range of optical properties in terms of exact molecular states, while Barron’s book (Barron 1982) is highly recommended for its thorough discussion of optical activity phenomena. The expressions derived in these books may be translated into response functions amenable to calculation by means of approximate wave functions.

Olsen and Jørgensen (1985, 1995) have derived and discussed response functions for exact, HF, and MCSCF wave functions in great detail, while Koch and Jørgensen (1990) presented a derivation for CC wave functions. The latter was modified by Pedersen and Koch (1997) to ensure proper symmetry of the response functions. Christiansen et al. (1998) have presented a derivation of dynamic response functions for variational as well as non-variational wave functions that resembles the way in which static response functions are deduced from energy derivatives. Linear and higher order response functions based on DFT have been presented by Sałek et al. (2002). Damped response theory has been discussed by Norman et al. (2001) in the context of HF and MCSCF response theory. Nonperturbative calculations of static magnetic properties at the HF level have been presented by Tellgren et al. (2008, 2009).

Gauge invariance of HF and MCSCF response theory has been shown in terms of the equations of motion for the response functions by Olsen and Jørgensen (1985, 1995), whereas the lack of gauge invariance in CC response theory was demonstrated by Pedersen et al. (Pedersen and Koch 1997; Pedersen et al. 2001). The use of GIAOs to ensure origin invariance of static magnetic properties has been discussed by Helgaker et al. (Helgaker and Jørgensen 1991; Olsen et al. 1995) and for optical rotations by Bak et al. (1995).

Different approaches to the calculation of vibrational corrections to response properties can be found in the work of Sauer and Pack (2000), Ruud et al. (2000), and Kongsted and Christiansen (2006). The Boltzmann averaging procedure for conformationally flexible molecule has been critically reviewed by Crawford and Allen (2009). Mort and Autschbach (2008) have proposed an approach based on a decoupling of hindered rotations from the remaining (high-frequency) vibrational modes, which allows for a separate calculation of the hindered rotations without invoking the harmonic approximation.

## Acknowledgments

---

The author wishes to thank Profs. Michał Jaszuński, Antonio Rizzo, T. Daniel Crawford, and Trygve Helgaker for commenting on the manuscript.

## References

- Bak, K. L., Hansen, A. E., Ruud, K., Helgaker, T., & Olsen, J. (1995). *Ab initio* calculation of electronic circular dichroism for *trans* - cyclooctene using London atomic orbitals. *Theoretica Chimica Acta*, 90, 441–458.
- Barron, L. D. (1982). *Molecular light scattering and optical activity*. Cambridge, MA: Cambridge University Press.
- Bethe, H. A., & Salpeter, E. E. (1957). *Quantum mechanics of one- and two-electron atoms*. New York: Academic Press.
- Christiansen, O., Jørgensen, P., & Hättig, C. (1998). Response functions from Fourier component variational perturbation theory applied to a time-averaged quasienergy. *International Journal of Quantum Chemistry*, 68, 1–52.
- Craig, D. P., & Thirunamachandran, T. (1984). *Molecular quantum electrodynamics*. London: Academic Press.
- Crawford, T. D., & Allen, W. D. (2009). Optical activity in conformationally flexible molecules: a theoretical study of large-amplitude vibrational averaging in (R)-3-chloro-1-butene. *Molecular Physics*, 107, 1041–1057.
- Fiutak, J. (1963). The multipole expansion in quantum theory. *Canadian Journal of Physics*, 41, 12–20.
- Helgaker, T., & Jørgensen, P. (1991). An electronic Hamiltonian for origin independent calculations of magnetic properties. *Journal of Chemical Physics*, 95, 2595–2601.
- Koch, H., & Jørgensen, P. (1990). Coupled cluster response functions. *Journal of Chemical Physics*, 93, 3333–3344.
- Kongsted, J., & Christiansen, O. (2006). Automatic generation of force fields and property surfaces for use in variational vibrational calculations of anharmonic vibrational energies and zero-point vibrational averaged properties. *Journal of Chemical Physics*, 125, 124108.
- Mort, B. C., & Autschbach, J. (2008). A pragmatic approach for the treatment of hindered rotations in the vibrational averaging of molecular properties. *European Journal of Chemical Physics and Physical Chemistry*, 9, 159–170.
- Moss, R. E. (1973). *Advanced molecular quantum mechanics*. London: Chapman and Hall.
- Norman, P., Bishop, D. M., Jensen, H. J. A., & Oddershede, J. (2001). Near-resonant absorption in the time-dependent self-consistent field and multi-configurational self-consistent field approximations. *Journal of Chemical Physics*, 115, 10323–10334.
- Olsen, J., Bak, K. L., Ruud, K., Helgaker, T., & Jørgensen, P. (1995). Orbital connections for perturbation-dependent basis sets. *Theoretica Chimica Acta*, 90, 421–439.
- Olsen, J., & Jørgensen, P. (1985). Linear and nonlinear response functions for an exact state and for an MCSCF state. *Journal of Chemical Physics*, 82, 3235–3264.
- Olsen, J., & Jørgensen, P. (1995). Time-dependent response theory with applications to self-consistent field and multiconfigurational self-consistent field wave functions. In D. R. Yarkony (Ed.), *Modern electronic structure theory* (Vol. 2, pp. 857–990). Singapore/River Edge: World Scientific.
- Pedersen, T. B., & Koch, H. (1997). Coupled cluster response functions revisited. *Journal of Chemical Physics*, 106, 8059–8072.
- Pedersen, T. B., Fernández, B., & Koch, H. (2001). Gauge invariant coupled cluster response theory using optimized nonorthogonal orbitals. *Journal of Chemical Physics*, 114, 6983–6993.
- Ruud, K., Astrand, P.-O., & Taylor, P. R. (2000). An efficient approach for calculating vibrational wave functions and zero-point vibrational corrections to molecular properties of polyatomic molecules. *Journal of Chemical Physics*, 112, 2668–2683.
- Salek, P., Vahtras, O., Helgaker, T., & Agren, H. (2002). Density-functional theory of linear and nonlinear time-dependent molecular properties. *Journal of Chemical Physics*, 117, 9630–9645.
- Sauer, S. P. A., & Packer, M. J. (2000). The *Ab initio* calculation of molecular properties other than the potential energy surface. In P. R. Bunker & P. Jensen (Eds.), *Computational molecular spectroscopy* (pp. 221–252). London: Wiley.
- Tellgren, E. I., Soncini, A., & Helgaker, T. (2008). Nonperturbative *ab initio* calculations in strong magnetic fields using London orbitals. *Journal of Chemical Physics*, 129, 154114.
- Tellgren, E. I., Helgaker, T., & Soncini, A. (2009). Non-perturbative magnetic phenomena in closed-shell paramagnetic molecules. *Physical Chemistry Chemical Physics*, 11, 5489–5498.

# 6 Intermolecular Interactions

*Alston J. Misquitta*

TCM Group, Cambridge, UK

School of Physics, Queen Mary, University of London, UK

<b>Introduction</b> .....	<b>159</b>
Definition of the Interaction Energy .....	160
The Two-Body Interaction Energy .....	160
Examples .....	162
<b>Practical Methods for the Two-Body Interaction Energy</b> .....	<b>164</b>
Supermolecular Methods .....	164
Density Functional Theory .....	165
Perturbation Theory .....	165
Symmetry-Adapted Perturbation Theory .....	165
Symmetry-Adapted Perturbation Theory Based on DFT .....	166
Density-Fitting .....	168
Higher-Order Contributions .....	169
Basis Sets: Charge-Transfer .....	170
Auxiliary Basis Sets .....	171
<b>Multipole Expansion for the Interaction Energy</b> .....	<b>171</b>
Damping Functions .....	174
<b>Many-Body Contributions to the Interaction Energy</b> .....	<b>174</b>
<b>Molecular Properties</b> .....	<b>176</b>
Distributed Multipoles .....	176
Distributed Polarizabilities .....	177
Williams–Stone–Misquitta (WSM) Distribution .....	177
Analyzing the Models .....	179
Distributed Dispersion Coefficients .....	180
<b>Case Studies</b> .....	<b>181</b>
Applications .....	181
Polarization in Organic Crystals .....	183
Crystal Structure Prediction .....	184
Outlook .....	184



<i>Programs</i> .....	186
<i>Annotated Bibliography</i> .....	186
<i>Acknowledgments</i> .....	187
<i>References</i> .....	187

**Abstract:** Van der Waals interactions determine a number of phenomena in the fields of physics, chemistry and biology. As we seek to increase our understanding of physical systems and develop detailed and more predictive theoretical models, it becomes even more important to provide an accurate description of the underlying molecular interactions. The goal of this chapter is to describe recent developments in the theory of intermolecular interactions that have revolutionised the field due to their comparatively low computational costs and high accuracies. These are the symmetry-adapted perturbation theory based on density functional theory (SAPT(DFT)) for interaction energies and the Williams–Stone–Misquitta (WSM) method for molecular properties in distributed form. These theories are applicable to systems of small organic molecules containing as many as 30 atoms each and have demonstrated accuracies comparable to the best electronic structure methods. We also discuss the numerical aspects of these theories and recent applications which demonstrate the range of problems that can now be approached with these accurate *ab initio* methods.

## Introduction

---

Intermolecular, or van der Waals, interactions are responsible for a wide variety of phenomena in the fields of physics, chemistry, and biology. The thermodynamic properties of gases, liquids, and solids depend on these interactions. In fact, many liquids and many solids would not exist without van der Waals forces. Amongst other properties that depend strongly on the van der Waals interactions are microwave and infrared spectra of molecular complexes and bulk phases. Due to their long-range nature, van der Waals forces determine the entrance channels for chemical reactions. Some of the more exotic systems in which van der Waals interactions play an important role are Bose–Einstein condensates (BECs) and helium nanodroplets (Chang et al. 2003; Xu et al. 2003). In biological systems, van der Waals interactions are particularly important, subtle, and often hard to model. The stability of DNA and RNA arise, in part, from the stacking energy (Hobza and Sponer 2002), which is determined by this interaction. One of the important problems in which van der Waals interactions play an important role is the problem of protein folding (Lehninger 1970).

This chapter is an introduction to the field of intermolecular interaction and to the modern *ab initio* electronic structure methods – primarily those based on perturbation theory – that have been developed to study them. We will be mainly concerned with applications to small organic molecules for which accuracies of the order of a  $\text{kJ mol}^{-1}$  or less are sufficient. High-accuracy calculations on small dimers can be orders of magnitude more accurate, but these are the subject of a specialist review (see Szalewicz et al. 2005 for a review and references). Nor are we concerned with empirical methods. Our focus will be on first principles methods for the interactions of closed-shell systems in the non-relativistic limit. In the last decade, *ab initio* methods have been used to successfully model the structure of liquid water. (Bukowski et al. 2007) studied the interactions between DNA base tetramers (Fiethen et al. 2008) and predicted the crystal structure of an organic molecule (Misquitta et al. 2008b). The goal of this chapter is to describe the main theoretical developments that have been responsible for these applications.

## Definition of the Interaction Energy

The interaction energy of a cluster of  $N$  interacting *rigid* molecules is defined to be

$$E_{\text{int}} = E_{ABC\dots} - E_A - E_B - E_C - \dots \quad (6.1)$$

Here  $E_{ABC\dots}$  is the energy of the cluster and  $E_X$ ,  $X = A, B, C$ , etc., is the energy of molecule  $X$ . Non-rigid molecules undergo a deformation in the cluster, with an associated *deformation energy cost*:  $\delta E_X = E_X(x_X^*) - E_X(x_X^0)$ , where  $x_X^0$  is the geometry of monomer  $X$  in isolation and  $x_X^*$  is the geometry in the cluster. This deformation energy cost should be included as part of the interaction energy defined above, but since this chapter is mainly concerned with the interactions of rigid molecules, we will assume that the deformation energies  $\delta E_X$  are obtained in a suitable manner, and concern ourselves only with the interaction energy defined by  $\blacktriangleright$  Eq. 6.1.

$E_{\text{int}}$  can be evaluated directly, but for computational efficiency as well as physical interpretation it is worthwhile to partition the  $N$ -body interaction energy into contributions from dimers, trimers, and so on. This leads to an exact reformulation of  $E_{\text{int}}$  that is known as the many-body expansion:

$$E_{\text{int}}(ABC\dots) = \sum_{X<Y} E_{\text{int}}(XY) + \sum_{X<Y<Z} \Delta E_{\text{int}}(XYZ) + \dots, \quad (6.2)$$

where  $\Delta E_{\text{int}}(XYZ)$  is the three-body correction, defined as

$$\Delta E_{\text{int}}(XYZ) = E_{\text{int}}(XYZ) - E_{\text{int}}(XY) - E_{\text{int}}(XZ) - E_{\text{int}}(YZ). \quad (6.3)$$

In the same way, we can define four-body corrections, five-body corrections, and so on. For a cluster of  $N$  molecules, this expansion terminates at the  $N$ -body correction.

The many-body expansion would not be of much use if we had to evaluate all terms in  $\blacktriangleright$  Eq. 6.2. But experience has shown that the expansion converges quickly and terms beyond those involving three bodies are not so important. This is fortunate as the two-body interactions are well understood and can be evaluated for moderate-sized molecules using a variety of methods, while good approximations are available for the terms involving three and more bodies, which usually arise from the effects of polarization in the cluster.

## The Two-Body Interaction Energy

The interaction energy of a pair of interacting molecules is defined as

$$E_{\text{int}} = E_{AB} - E_A - E_B. \quad (6.4)$$

If we calculate all three energies using a suitable electronic structure method – some of which will be described later – this definition provides a simple method for calculating the interaction energy of a pair of interacting molecules. This approach, known as the *supermolecular* method, provides us with a single number: the interaction energy  $E_{\text{int}}$ . We gain considerable physical insight into  $E_{\text{int}}$  by evaluating it not as the difference in energies suggested by the above definition, but through *perturbation theory*, which enables us to partition  $E_{\text{int}}$  into physical components: the electrostatic, induction (or polarization), dispersion, and exchange-repulsion energies. This breakup proves invaluable not only as an aid to interpretation, but also forms the basis for all analytic atom–atom potentials (Stone and Misquitta 2007).

Consider the dimer Hamiltonian partitioned as

$$H(\lambda) = H_0 + \lambda V, \quad (6.5)$$

where  $H_0 = H_A + H_B$  is the sum of the Hamiltonians of the unperturbed monomers  $A$  and  $B$ , and  $V$  is the intermonomer interaction operator that consists of electron–electron, electron–nuclear, and nuclear–nuclear interactions between the monomers. We may now carry out a Rayleigh–Schrödinger perturbation theory – also known as the *polarization expansion* (Jeziorski et al. 1994) – using as our zeroth-order wave function the unsymmetrized product  $\Phi_0 = \Phi_0^A \Phi_0^B$ . The zeroth-order energy is then  $E_0 = E_0^A + E_0^B$ . The interaction energy appears at first and higher orders in perturbation theory (setting  $\lambda = 1$ ):

$$E_{\text{int}} = E_{\text{pol}}^{(1)} + E_{\text{pol}}^{(2)} + \dots, \quad (6.6)$$

where we have used the subscript “pol” to indicate these are energies from the polarization expansion and do not include any of the effects of electron exchange between monomer. The individual terms in this series can be evaluated using the usual methods of perturbation theory (Stone 1996). At firstorder we have

$$E_{\text{pol}}^{(1)} = \langle \Phi_0^A \Phi_0^B | V \Phi_0^A \Phi_0^B \rangle, \quad (6.7)$$

which is identified as the electrostatic energy of the interacting dimer and can be written in terms of the unperturbed total charge densities of the monomers:

$$E_{\text{pol}}^{(1)} = E_{\text{elst}}^{(1)} = \iint \rho_A^{\text{tot}}(\mathbf{r}_1) \frac{1}{|\mathbf{r}_1 - \mathbf{r}_2|} \rho_B^{\text{tot}}(\mathbf{r}_2) d\mathbf{r}_1 d\mathbf{r}_2. \quad (6.8)$$

Here, the total charge density of monomer  $X$  is defined as

$$\rho_X^{\text{tot}} = \sum_{\alpha \in X} Z_\alpha \delta(\mathbf{r} - \mathbf{R}_\alpha) - \rho_X \quad (6.9)$$

where  $\rho_X$  is the unperturbed electronic charge density of the monomer and the term containing the Dirac delta functions represents the nuclear charge density.

At second order we get

$$E_{\text{pol}}^{(2)} = \sum_{rs} \frac{|\langle \Phi_0^A \Phi_0^B | V \Phi_r^A \Phi_s^B \rangle|^2}{E_0^A + E_0^B - E_r^A - E_s^B}, \quad (6.10)$$

where  $r$  and  $s$  label the excited states of monomers  $A$  and  $B$  respectively. The prime indicates that at least one of  $r$  or  $s$  refer to an excited state. The above expression can be split into two physically motivated terms: the second-order induction and second-order dispersion energies. The second-order induction energy is obtained when the summation in  $\blacktriangleright$  Eq. 6.10 is restricted to those dimer states including only one excited monomer. This has two natural contributions: the ground state of monomer  $A$  interacting with excitations on monomer  $B$ , and vice versa. Thus,

$$E_{\text{ind,pol}}^{(2)} = E_{\text{ind,pol}}^{(2)}(A) + E_{\text{ind,pol}}^{(2)}(B), \quad (6.11)$$

where,

$$E_{\text{ind,pol}}^{(2)}(A) = \sum_r \frac{|\langle \Phi_0^A \Phi_0^B | V \Phi_r^A \Phi_0^B \rangle|^2}{E_0^A - E_r^A}. \quad (6.12)$$

Similarly, we can define  $E_{\text{ind,pol}}^{(2)}(B)$ .

From  $\blacktriangleright$  Eq. 6.12, we see that  $E_{\text{ind,pol}}^{(2)}(A)$  may be interpreted as the second-order energy correction arising when the monomer A is perturbed by the external field  $\Omega_B$  of monomer B. Thus the second-order induction energy can be interpreted as a *response* to a static field, and is therefore also called the polarization energy.

The remaining part of the second-order term  $E_{\text{pol}}^{(2)}$  is the dispersion energy which is defined as

$$E_{\text{disp,pol}}^{(2)} = \sum_{r \neq 0} \sum_{s \neq 0} \frac{|\langle \Phi_0^A \Phi_0^B | V \Phi_r^A \Phi_s^B \rangle|^2}{E_0^A + E_0^B - E_r^A - E_s^B}. \quad (6.13)$$

The dispersion is purely quantum mechanical in origin and is the only term at second order in  $\lambda$  that describes intermonomer electron correlation. The second-order dispersion energy is long ranged, always negative, and exists between all types of molecules.

The starting wave function  $\Phi_0 = \Phi_0^A \Phi_0^B$  used in the polarization expansion is not antisymmetric with respect to electron interchanges between the monomers and thus cannot be expected to be reliable when overlap effects between the monomers become important. In this region, only a fully antisymmetric theory is valid. Various procedures exist to achieve the complete antisymmetrization and these are discussed by Jeziorski and Szalewicz (2002) and Szalewicz et al. (2005). The result is that corresponding to each of the three interaction energy components discussed above we get an exchange counterpart. At first order we get the first-order exchange-repulsion energy  $E_{\text{exch}}^{(1)}$ , and at second order we get the second-order exchange-induction and exchange-dispersion energies,  $E_{\text{ind,exch}}^{(2)}$  and  $E_{\text{disp,exch}}^{(2)}$ .

We now define the *total* induction and *total* dispersion energies as the sum of their polarization and exchange terms:

$$E_{\text{ind,tot}}^{(2)} = E_{\text{ind,pol}}^{(2)} + E_{\text{ind,exch}}^{(2)} \quad (6.14)$$

$$E_{\text{disp,tot}}^{(2)} = E_{\text{disp,pol}}^{(2)} + E_{\text{disp,exch}}^{(2)}. \quad (6.15)$$

These sums are the physically relevant energies; the individual components are useful from the theoretical standpoint, but are somewhat arbitrary and depend on the particular perturbation theory used.

Therefore, the total interaction energy can be defined as

$$E_{\text{int}} = E_{\text{elst}}^{(1)} + E_{\text{exch}}^{(1)} + E_{\text{ind,tot}}^{(2)} + E_{\text{disp,tot}}^{(2)} + \Delta E_{\text{int}}^{(3-\infty)}, \quad (6.16)$$

where the last term collects all contributions of third order and higher in the interaction operator  $V$ . We will describe the theoretical methods for calculating the interaction energy components in  $\blacktriangleright$  section “Perturbation Theory.” Now let us see the kind of interpretational power perturbation theory gives us by taking a look at a few examples.

## Examples

Based on the relative contributions of the interaction energy components, we can classify intermolecular bonds. For example, hydrogen-bonded complexes tend to be bound primarily by the electrostatic and induction (polarization) components of the interaction energy, while van der Waals complexes are bound primarily by the dispersion energy. Of course, most complexes will fall in between, so it is probably better not to regard such classifications as being rigorous, but they are useful as they provide us with a physical picture of the mechanisms of the intermolecular bond.

Interaction energies and components for three representative complexes are presented in **Table 6-1**. We have used both approaches: perturbation theory and the supermolecular method.

- *Hydrogen bonding*: At its minimum energy geometry, the water dimer shows a bonding pattern that is typical of hydrogen-bonded complexes (Buckingham et al. 2008). Binding is primarily due to the electrostatic and induction energies. In fact, this is the only one of the three complexes which is bound at first order, that is, the sum of the first-order energies is negative. Even so, the dispersion energy is certainly non-negligible and contributes almost 40% of the binding of this complex. The terms of third and higher orders contribute significantly to the binding of these complexes.
- *van der Waals bonding*: The benzene dimer in the sandwich geometry is a typical example of a van der Waals bound complex. The dimer is unbound at first order and the electrostatic and induction energies make minor contributions to the interaction energy. Almost all the binding arises at second order from the dispersion energy. Third- and higher-order terms are generally small for van der Waals complexes, and in this particular case, they are positive.
- *Intermediate case*: As an example of an intermediate case consider the so-called halogen-bonded complex  $\text{Cl}_2 \cdots \text{OH}_2$ . The exchange-repulsion energy of this complex is similar to that of the water dimer, but the electrostatic and induction energies are not as strong. The dispersion contributes a substantial fraction of the interaction energy, but less than for the benzene dimer. Third- and higher-order terms are quite large for this particular system.

**Table 6-1**

Interaction energy components for the water dimer, benzene dimer, and the  $\text{Cl}_2 \cdots \text{OH}_2$  complex. The water dimer is in its equilibrium geometry, the benzene dimer is in the parallel stacked geometry with center-of-mass separation 3.7 Å, and the  $\text{Cl}_2 \cdots \text{OH}_2$  complex is in a symmetrical complex with all atoms in a plane and  $\text{Cl}-\text{Cl} \cdots \text{O}$  collinear with  $r(\text{Cl} \cdots \text{O}) = 2.755$  Å. All energies are reported in  $\text{kJ mol}^{-1}$

Energy	$(\text{H}_2\text{O})_2$	$\text{Cl}_2 \cdots \text{OH}_2$	$(\text{C}_6\text{H}_6)_2$
Perturbation theory [SAPT(DFT)]:			
$E_{\text{elst}}^{(1)}$	-28.90	-19.24	-1.63
$E_{\text{exch}}^{(1)}$	23.97	24.96	20.99
$E_{\text{ind,pol}}^{(2)}$	-10.96	-16.09	-7.65
$E_{\text{ind,exch}}^{(2)}$	5.79	12.21	6.70
$E_{\text{ind,tot}}^{(2)}$	-5.16	-3.88	-0.95
$E_{\text{disp,pol}}^{(2)}$	-10.02	-12.49	-29.03
$E_{\text{disp,exch}}^{(2)}$	1.68	1.76	2.89
$E_{\text{disp,tot}}^{(2)}$	-8.34	-10.73	-26.14
$\Delta E_{\text{int}}^{(3-\infty)}$	-2.82	-3.24	+0.34
$E_{\text{int}}$	-21.26	-12.13	-7.39
Supermolecular:			
$E_{\text{int}}$ [MP(2)]	-20.34	-12.43	-15.23 <sup>a</sup>
$E_{\text{int}}$ [CCSD(T)]	-20.45	-11.21	-7.57 <sup>a</sup>

<sup>a</sup>From Sinnokrot et al. 2002. These energies are close to the basis set limit

By comparison, the supermolecular methods provide just the interaction energy: a single number. But perturbation theory does not provide only physical interpretation; the breakup of the interaction energy proves invaluable when constructing model interaction potentials (Stone and Misquitta 2007) and semi-empirical methods, some of which we shall see later.

## Practical Methods for the Two-Body Interaction Energy

### Supermolecular Methods

The two-body interaction energy can be calculated directly through  $\blacktriangleright$  Eq. 6.4 as the difference in energies of the dimer and the monomers. This approach, known as the *supermolecular method*, has the advantage of allowing  $E_{\text{int}}$  to be calculated using a variety of electronic structure methods. We will only briefly describe some aspects of this method below; for a more complete description see Chalasinski and Szczesniak (2000).

Two of the most commonly used electronic structure methods to evaluate  $E_{\text{int}}$  are MP2 (second-order Moller–Plesset perturbation theory) and CCSD(T) (coupled-cluster with singles and doubles and non-iterated triples). Interaction energies calculated using these methods are shown in  $\blacktriangleright$  Table 6-1. Interaction energies calculated using MP2 are usually close to those calculated using the more sophisticated and computationally expensive CCSD(T), but the exception is the benzene dimer system for which MP2 overestimates the binding by almost a factor of 2. This deserves some explanation.

Moller–Plesset perturbation theory starts from a Hartree–Fock description of the system and builds in electron correlation perturbatively. In MP2, electron correlation is described using second-order perturbation theory. For a pair of interacting molecules the two orders of perturbation theory are used to describe the dispersion interaction, and therefore cannot be used to simultaneously describe electron correlation *within* each of the interacting molecules. This seems to cause severe problems for systems with  $\pi$ -bonding for which MP2 is completely inappropriate. Recently, this problem has been corrected using a hybrid scheme in which the dispersion component of the MP2 interaction energy is replaced with the dispersion energy calculated using SAPT(DFT) (see below) (Pitonak and Hesselmann 2010).

The CCSD(T) method takes a very different approach to electron correlation and is today regarded as the reference method for many kinds of problems. However, the computational cost of CCSD(T) scales as the seventh power of the system size, and therefore this method cannot be applied to large systems.

One of the sources of error in a supermolecular calculation of the interaction energy is the basis set superposition error (BSSE). This is the artificially enhanced binding that occurs because of the use of finite basis sets. This problem has been discussed at length in the literature, so we will not get into details here. A simple way of correcting for this error was suggested by Boys and Bernardi (1970) who suggested that the BSSE could be reduced by using the dimer basis to calculate the monomer energies. This leads to the *counterpoise* (CP) corrected interaction energy defined as

$$E_{\text{int}}^{\text{CP}} = E_{AB}(AB) - E_A(AB) - E_B(AB). \quad (6.17)$$

Here  $E_A(AB)$  is the energy of A calculated in the dimer basis AB, and likewise for  $E_B(AB)$ . The CP form of the interaction energy should always be used, except possibly when the basis set is too poor. However, in this case, neither the CP corrected nor the uncorrected energies may be meaningful.

There is another aspect of the BSSE worth keeping in mind: An energy minimum on the CP corrected surface will generally occur at a different geometry from the corresponding minimum on the uncorrected surface. Since geometry optimizations are typically performed on the latter surface, the resulting structure will need to be re-optimized on a CP corrected surface, but this is often rather difficult and computationally expensive.

## Density Functional Theory

Density functional theory (DFT) is not presently suitable for intermolecular interactions (Tszuki and Lüthi 2001; van Mourik and Gdanitz 2002). The main reason for this failure of DFT is the highly non-local nature of the dispersion interaction which is present even when charge densities do not overlap. Since most density functionals are local or semi-local in the density, that is, they depend on the electron density and gradients of the density, they are unable to account for non-local correlations, and therefore cannot describe the dispersion energy.

Recently, there have been many attempts made to include the dispersion in DFT, either *explicitly* through a dispersion correction (Grimme 2004; Neumann and Perrin 2005) or *implicitly* through a non-local functional (Dion et al. 2004). The former method is necessarily empirical and makes *a priori* assumptions about the nature of the dispersion interaction. Though the latter methods are promising, it is still unclear if they are accurate enough in practice. Also recently, Becke and Johnson (2005) have proposed that the dispersion energy could be included in DFT through correlations in the exchange-hole dipole moments evaluated using the occupied orbitals. This method is promising and has been given a theoretical justification by Angyan (2007) and Hesselmann (2009).

In a recent development, Pernal et al. (2009) have used SAPT(DFT) (see below) interaction energies for a number of dimers to develop an exchange–correlation functional that does not include the dispersion energy. They have subsequently added the dispersion energy calculated from SAPT(DFT). This is a significant development as it is far better founded on theoretical grounds than other dispersion-corrected DFT methods. In practice a more efficient, but less accurate method could be to use dispersion models such as the WSM models described below.

## Perturbation Theory

---

### Symmetry-Adapted Perturbation Theory

Until recently, and possibly still so for certain applications, one of the most successful perturbation theories for intermolecular interactions was the symmetry-adapted perturbation theory (SAPT) (Jeziorski and Szalewicz 2002; Jeziorski et al. 1994). SAPT is a triple perturbation theory based on a Hartree–Fock description of the interacting monomers. Intramolecular correlation is built up using two of the perturbations, and intermolecular correlation by the third. SAPT has been applied to a large number of systems with very good success. See for example, applications



to the water dimer (Mas et al. 1997), the carbon dioxide dimer (Bukowski et al. 1999), the He–HCCCN dimer (Akin-Ojo et al. 2003), Ar–CO<sub>2</sub> dimer (Misquitta et al. 2000), and the Ne–HCN dimer (Murdachaw et al. 2001). However, SAPT, like the CCSD(T) method, is computationally expensive with scaling of  $\mathcal{O}(N^7)$ , where  $N$  is the size of the system (which can be taken to be the number of electrons), and quickly become impossible to apply as this size increases, and cannot be applied to systems of more than about ten atoms without a significant reduction to the level of correlation.

## Symmetry-Adapted Perturbation Theory Based on DFT

Fairly recently, Szalewicz, Misquitta, and Jeziorski (Misquitta and Szalewicz 2002, 2005; Misquitta et al. 2003, 2005b), and independently, Jansen and Hesselmann (Hesselmann and Jansen 2002a, b, 2003a, b) developed a variant of SAPT based on DFT that has largely superseded SAPT both in terms of accuracy as well as computational efficiency. In this method, termed SAPT(DFT) or DFT-SAPT, the interaction energy components are formulated to make their dependence on molecular properties like the charge density and density response functions explicit. These molecular properties are then calculated using DFT and linear-response time-dependent DFT. In some sense, DFT is used to describe intramolecular correlation effects, thereby significantly simplifying the perturbation theory as the intramolecular perturbation operators are no longer required.

The first-order electrostatic energy  $E_{\text{elst}}^{(1)}$  has already been shown to arise from the Coulomb interaction of the unperturbed total charge densities of the interacting monomers (Eq. 6.8). In SAPT(DFT), these densities are obtained from DFT. To see how the second-order induction and dispersion energies can be expressed in terms of molecular properties we need to define the frequency-dependent density susceptibility (FDDS):

$$\alpha_X(\mathbf{r}, \mathbf{r}' | \omega) = 2 \sum_{r \neq 0} \frac{E_r^X - E_0^X}{(E_r^X - E_0^X)^2 - \omega^2} \langle \Phi_0^X | \hat{\rho}_X(\mathbf{r}) | \Phi_r^X \rangle \langle \Phi_r^X | \hat{\rho}_X(\mathbf{r}') | \Phi_0^X \rangle, \quad (6.18)$$

where  $\omega$  is a frequency and  $\hat{\rho}_X(\mathbf{r}) = -\sum_{i \in X} \delta(\mathbf{r} - \mathbf{r}_i)$  is the electron density operator. The FDDS describes the linear response of the electron density to a frequency-dependent perturbation.

$E_{\text{ind,pol}}^{(2)}(A)$  can be written in terms of the FDDS evaluated at zero frequency (Magnasco and McWeeny 1991):

$$E_{\text{ind,pol}}^{(2)}(A) = -\frac{1}{2} \iint V_B(\mathbf{r}) \alpha_A(\mathbf{r}, \mathbf{r}' | 0) V_B(\mathbf{r}') d\mathbf{r} d\mathbf{r}' \quad (6.19)$$

where  $V_B(\mathbf{r}) = \int \rho_B^{\text{tot}}(\mathbf{r}') / |\mathbf{r} - \mathbf{r}'| d\mathbf{r}'$  is the electrostatic potential of monomer B, and similarly for  $E_{\text{ind,pol}}^{(2)}(B)$ . We therefore see that the induction energy is a *response* energy of the molecule to the potential arising from the interacting partner.

The dispersion energy involves the FDDSs of the two molecules evaluated at imaginary frequency (Longuet-Higgins 1965; Zaremba and Kohn 1976):

$$E_{\text{disp,tot}}^{(2)} = -\frac{1}{2\pi} \int_0^\infty d\omega \int d\mathbf{r}_1 d\mathbf{r}'_1 d\mathbf{r}_2 d\mathbf{r}'_2 \frac{\alpha_A(\mathbf{r}_1, \mathbf{r}'_1; i\omega) \alpha_B(\mathbf{r}_2, \mathbf{r}'_2; i\omega)}{|\mathbf{r}_1 - \mathbf{r}_2| |\mathbf{r}'_1 - \mathbf{r}'_2|}. \quad (6.20)$$

There is no easy way to interpret this expression which is a coupling of the response functions of the two molecules, but at imaginary frequency. However, see the discussion in Angyan (2007)

and Hesselmann (2009) where an approximate form of this expression is related to correlations in fluctuating exchange-holes of the monomers.

Linear-response time-dependent DFT, also known as coupled Kohn–Sham (CKS), provides us with a convenient framework for evaluating the FDDS. CKS theory has been used for some time now to obtain excitation energies of small systems (Grabo et al. 2000; Onida et al. 2002) and molecular properties like polarizabilities and hyperpolarizabilities (Adamo et al. 1999; Tozer and Handy 1998) (see Koch 2000 for a comprehensive summary), so it is not surprising that it can also be used to evaluate the second-order dispersion and induction energies through the FDDS (Hesselmann and Jansen 2003b; Misquitta et al. 2003). Within CKS theory (and also coupled Hartree–Fock (CHF) theory), the FDDS takes the form (Casida 1995; Colwell et al. 1995; Petersilka et al. 1996):

$$\alpha(\mathbf{r}, \mathbf{r}' | \omega) = \sum_{iv, i'v'} C_{iv, i'v'}(\omega) \phi_i(\mathbf{r}) \phi_v(\mathbf{r}) \phi_{i'}(\mathbf{r}') \phi_{v'}(\mathbf{r}'), \quad (6.21)$$

where the subscripts  $i$  and  $i'$  ( $v$  and  $v'$ ) denote occupied (virtual) molecular orbitals and  $\phi_i$  is a molecular orbital obtained from Kohn–Sham DFT. The coupling between the molecular orbitals is contained in the coefficients  $C_{iv, i'v'}(\omega)$  which are defined in Colwell et al. (1995), Ioannou et al. (1997), Misquitta et al. (2005b), and Podeszwa et al. (2006b). These coefficients involve Coulomb integrals of the molecular orbitals as well as integrals containing the functional derivative of the exchange–correlation potential. The method used to evaluate the coefficients  $C_{iv, i'v'}(\omega)$  is quite important as the dispersion energy calculated through  $\blacktriangleright$  Eq. 6.20 varies appreciably depending on the type of FDDS (Misquitta et al. 2005b).

The exchange energies depend explicitly on molecular wavefunctions through the interaction density matrix (Jeziorski et al. 1994; Moszyński et al. 1994). In SAPT(DFT), these energies are evaluated using Kohn–Sham molecular orbitals and, for the second-order exchange energies, the effect of orbital relaxation is estimated by scaling:

$$E_{\text{ind,exch}}^{(2)} = E_{\text{ind,exch}}^{(2)}(\text{KS}) \times \frac{E_{\text{ind,pol}}^{(2)}}{E_{\text{ind,pol}}^{(2)}(\text{KS})} \quad (6.22)$$

$$E_{\text{disp,exch}}^{(2)} = E_{\text{disp,exch}}^{(2)}(\text{KS}) \times \frac{E_{\text{disp,pol}}^{(2)}}{E_{\text{disp,pol}}^{(2)}(\text{KS})} \quad (6.23)$$

where the energies calculated without orbital relaxation are indicated by “KS,” that is, they use un-relaxed Kohn–Sham orbitals. The validity of using Kohn–Sham orbitals for the first-order exchange–repulsion energy has been justified by an asymptotic analysis of the exact and Kohn–Sham interaction density matrices (Misquitta and Szalewicz 2002) as well as extensive numerical tests (Misquitta and Szalewicz 2005). In the DFT–SAPT formulation, the second-order exchange energies are defined via coupled-response theory (Hesselmann et al. 2005).

*Exchange–correlation functional:* Which exchange–correlation functional should be used in SAPT(DFT) calculations? The short answer is that while SAPT(DFT) interaction energies are not very sensitive to the exchange–correlation functional used, it has been concluded from extensive numerical experiments that the asymptotically corrected (Tozer 2000; Tozer and Handy 1998) PBE0 (Adamo and Barone 1999) exchange–correlation functional results in the most accurate interaction energies for a variety of systems. For details see Hesselmann and Jansen (2002a), Misquitta and Szalewicz (2005), and Misquitta et al. (2005b). The PBE0 functional (also called PBE1PBE) is a hybrid functional with 75% of its exchange energy determined

from PBE and 25% from the so-called exact, or Hartree–Fock exchange. This means that the FDDS must also be constructed as the hybrid of the FDDSs from CKS and CHF theories. This is quite important as significant errors in the dispersion energy are introduced if the FDDS is constructed using CKS theory alone (Misquitta et al. 2005b). For large molecules, however, the terms in the coefficients  $C_{iv,i'v'}(\omega)$  that depend on the functional derivative of the exchange–correlation potential are computationally demanding to evaluate using the PBE functional. Instead, a more practical approach is to calculate these coefficients using the exchange-only LDA functional. Therefore, while the Kohn–Sham molecular orbitals and eigenvalues are obtained using the PBE0 functional, the FDDS is best constructed using the less accurate LDA+CHF kernel. This approximation results in a small (less than 1%) loss in accuracy which is more than compensated by an order of magnitude reduction in computational expense (Misquitta et al. 2005b).

*Asymptotic correction:* The asymptotic correction is needed to correct the tails of the exchange–correlation potential, and consequently, the density tails that are crucial for intermolecular interactions. In order to implement the asymptotic correction, accurate vertical ionization potentials (IPs) are needed for the monomers. When they are not available experimentally, good estimates may be obtained from the difference between the energies of the  $N$  and  $N - 1$  electron systems. The PBE0 functional is best suited for this calculation too as tests on atoms, diatoms, and small organic molecules have shown that it gives IPs with mean errors centered about 0.0 a.u. with a standard deviation of only 0.007 a.u. (Ernzerhof and Scuseria 1999). This correction is definitely needed if the individual interaction energy components are required to be accurate. However, it is cumbersome to apply for large systems, when a single IP may be questionable and local IPs are hard to define. In such cases, the asymptotic correction is best neglected, particularly if total interactions are all that is desired.

## Density-Fitting

The SAPT(DFT) interaction energy components are not evaluated directly through the expressions provided in the previous section, but are formulated to make use of a procedure known as density-fitting (DF) or the resolution of the identity (RI) (Dunlap 2000; Dunlap et al. 1979). The idea here is to expand pairs of molecular orbitals that appear in the energy expressions in an auxiliary basis. For example, we may perform the DF expansion of one such pair that appears in the FDDS defined through  $\blacktriangleright$  Eq. 6.21 as follows:

$$\rho_{iv}(\mathbf{r}) = \phi_i(\mathbf{r})\phi_v(\mathbf{r}) \approx \tilde{\rho}_{iv}(\mathbf{r}) = \sum_k D_{iv,k} \chi_k(\mathbf{r}), \quad (6.24)$$

where  $\chi_k$  are the auxiliary basis functions and  $D_{iv,k}$  are the expansion coefficients. In the standard density-fitting procedure (Dunlap et al. 1979), the fitted density  $\tilde{\rho}$  is found by minimizing the integrals

$$\Delta_{iv} = \iint (\tilde{\rho}_{iv}(\mathbf{r}) - \rho_{iv}(\mathbf{r})) \frac{1}{|\mathbf{r} - \mathbf{r}'|} (\tilde{\rho}_{iv}(\mathbf{r}') - \rho_{iv}(\mathbf{r}')) d\mathbf{r} d\mathbf{r}'. \quad (6.25)$$

With these expansions, the FDDS can be rewritten as (Misquitta et al. 2003)

$$\alpha(\mathbf{r}, \mathbf{r}' | \omega) = \sum_{k,l} \tilde{C}_{kl}(\omega) \chi_p(\mathbf{r}) \chi_q(\mathbf{r}'), \quad (6.26)$$

where  $\tilde{C}_{kl}(\omega)$  are the transformed coefficients given by  $\tilde{C}_{kl}(\omega) = \sum_{iv,i'v'} D_{iv,k} C_{iv,i'v'}(\omega) D_{i'v',l}$ . Now the FDDS defined through  $\blacktriangleright$  Eq. 6.21 involves a quadruple sum over molecular orbitals, but in  $\blacktriangleright$  Eq. 6.26 the sum is over only two indices. This represents a huge reduction in computational expense provided that the size of the density-fitting basis – commonly called the *auxiliary basis* – is of the same order as the size of the main basis (the basis used to obtain the molecular orbitals), which is indeed the case with optimized auxiliary basis sets.

With the density-fitted formulation of SAPT(DFT), commonly called DF-SAPT(DFT) or DF-DFT-SAPT, the computational cost of the second-order interaction energy scales as only  $\mathcal{O}(N^5)$  if hybrid functionals are used (Bukowski et al. 2005; Podeszwa et al. 2006b). In the DFT-SAPT implementation the FDDS is calculated without a contribution from CHF theory. This reduces the computational scaling for evaluating the FDDS to  $\mathcal{O}(N^4)$ , but the overall scaling is still  $\mathcal{O}(N^5)$  because of the 4-index two-electron integrals (Hesselmann et al. 2005). This is the same computational scaling as MP2, though DF-SAPT(DFT) calculations take a few times longer due to the additional complexity of the method. Compare this to the  $\mathcal{O}(N^7)$  scaling of SAPT and CCSD(T).

## Higher-Order Contributions

Contributions of third and higher order to the two-body interaction energy are often large and cannot be neglected. In particular, for systems of polarizable molecules with large permanent multipole moments terms of third and higher order can contribute as much as 30% of the binding energy at equilibrium geometries. Such systems tend to have a large  $E_{\text{ind,pol}}^{(2)}$ . Examples are the water dimer and the  $\text{Cl}_2 \cdots \text{OH}_2$  systems in  $\blacktriangleright$  Table 6-1. For dispersion-bound systems the higher-order contributions are smaller and constitute only as much as 5% of the total interaction energy (see the benzene dimer in  $\blacktriangleright$  Table 6-1) and can therefore be neglected if high accuracies are not required.

The most common method for approximating the terms of third and higher-order,  $E_{\text{int}}^{(3-\infty)}$ , is the  $\delta_{\text{int,resp}}^{\text{HF}}$  correction (Jeziorska et al. 1987; Moszynski et al. 1996):

$$E_{\text{int}}^{(3-\infty)} \approx \delta_{\text{int,resp}}^{\text{HF}} = E_{\text{int}}^{\text{HF}} - \left( E_{\text{elst}}^{(1)}(\text{HF}) + E_{\text{exch}}^{(1)}(\text{HF}) + E_{\text{ind,tot}}^{(2)}(\text{CHF}) \right), \quad (6.27)$$

where the  $E_{\text{int}}^{\text{HF}}$  is the counterpoise-corrected supermolecular interaction energy calculated using Hartree–Fock theory, and the interaction energies are calculated using Hartree–Fock orbitals (denoted by “HF”) or, for the second-order induction energy, using CHF theory. This approximation was used to evaluate  $E_{\text{int}}^{(3-\infty)}$  for the water dimer and  $\text{Cl}_2 \cdots \text{OH}_2$  systems ( $\blacktriangleright$  Table 6-1) for which this term contributes 13% and 27% of the total interaction energy.

There is evidence (Patkowski et al. 2006) that the  $\delta_{\text{int,resp}}^{\text{HF}}$  estimate is not appropriate for dispersion-bound systems, for which a better estimate of  $E_{\text{int}}^{(3-\infty)}$  is (Misquitta and Stone 2008a)

$$E_{\text{int}}^{(3-\infty)} \approx E_{\text{ind,tot}}^{(3)}(\text{KS}) \quad (6.28)$$

where  $E_{\text{ind,tot}}^{(3)}(\text{KS})$  is the total third-order induction energy evaluated without relaxation, that is, using uncoupled Kohn–Sham theory. This estimate has been used for the benzene dimer in  $\blacktriangleright$  Table 6-1.

For large systems it is quite conceivable that no clear distinction may be possible that would justify the use of either one of these approximations. In such cases, it would probably be better to use the  $\delta_{\text{int,resp}}^{\text{HF}}$  approximation rather than ignore the higher-order energies altogether.

## Basis Sets: Charge-Transfer

In general, the basis sets used to calculate intermolecular interaction energies need to be large and augmented with diffuse functions. In part, this is because of the second-order energies which are response energies. Consequently, the basis set has to be good enough to describe not only the charge density accurately (particularly in the region of the density tail), but also the *response* of the density to perturbations. These requirements are adequately met only by basis sets of the augmented triple- $\zeta$  kind (and larger), such as aug-cc-pVTZ (Kendall et al. 1992; Woon and Dunning 1994) and Sadlej-pVTZ (Sadlej 1992; Sadlej and Urban 1991).

However, when the overlap of the charge densities of the interacting monomers becomes significant (typically at around the equilibrium separation) the basis set must be flexible enough to describe the intermolecular electron–electron cusp as well as the intermolecular charge-transfer (CT). The former effect is manifested as part of  $E_{\text{disp,tot}}^{(2)}$  and the latter as part of  $E_{\text{ind,tot}}^{(2)}$ .

It is often quite difficult to converge  $E_{\text{disp,tot}}^{(2)}$  with basis set. This is because it is hard to describe the intermolecular electron–electron cusp in the bonding region using basis functions located on atomic sites only (Burcl et al. 1995). In this case, fairly high-angular-momenta functions are needed in order to do so. However, this leads to very large basis sets and a consequent increase in computational requirements. An alternative is to use basis sets augmented with the so-called *mid-bond* functions: a small set of basis functions located in the bonding region (see Burcl et al. 1995; Williams et al. 1995 and references therein). The dispersion energy is not so sensitive to the exact composition of the mid-bond basis, which is usually chosen to consist of a set of 3 *s*, 2 *p*, and 1 *d* diffuse functions (Mas et al. 1997). A convenient choice for the location of the mid-bond set has been given in Akin-Ojo et al. (2003).

An alternative to mid-bond functions is to use the basis set extrapolation scheme of Helgaker et al. (1997). For intermolecular interactions, this involves calculating  $E_{\text{disp,tot}}^{(2)}$  using two correlation-consistent basis sets, say the aug-cc-pVnZ and the aug-cc-pV(n + 1)Z Dunning bases. This energy can be fitted to the form  $a + b/X^3$  where  $X = n$  and  $n + 1$  and the constants determined. The complete basis set (CBS) estimate of  $E_{\text{disp,tot}}^{(2)}$  is obtained by extrapolating  $X \rightarrow \infty$ , that is, it is the constant *a*. This scheme has the advantage that it applies equally well to small as well as large molecules, for which the mid-bond scheme is potentially ambiguous. However, two electronic structure calculations need to be performed, so there is an increase in computational cost.

Charge transfer poses a very different problem. This subject is discussed more completely in Stone and Misquitta (2009) and Stone (1996). The CT energy is the part of the short-range induction energy that involves excitations from the occupied orbitals on one molecule into the virtual orbitals of another. Consequently, in Stone (1993) it was suggested that the CT energy could be calculated as the difference of  $E_{\text{ind,tot}}^{(2)}$  calculated in the dimer and monomer basis. The understanding here is that the monomer basis is localized, so excitations into the virtual space of the interacting partner should be suppressed. In any case, if CT excitations are to be correctly included, the induction energy should be calculated using the dimer basis. In practice, this is rather excessive, and it has been shown (Williams et al. 1995) that only a subset of the basis of the interacting partner need be included. This is typically taken to be just the functions of *s* and *p* symmetry. Thus, when calculating the induction energy of A in the presence of B, that is,  $E_{\text{ind,tot}}^{(2)}(A)$ , we use in addition to the basis set of A, the *s* and *p* symmetry functions of B located where the atomic sites of B would be. These ghost functions are known as the *far-bond* functions.

The combined basis consisting of functions on the molecule and the mid-bond and far-bond functions is referred to as the *monomer-centered plus* or “MC+” basis type. The “+” indicating the presence of the additional basis functions. A typical SAPT(DFT) calculation of the interaction energy would involve two such bases; one for each of the two interacting molecules.

The additional functions are required for the second-order energies. If all that is needed are the first-order energies, the MC basis can be used, that is, basis functions need be included only on the monomer. First-order electrostatic and exchange-repulsion energies calculated in such a basis are generally very close to those calculated in the larger MC+ type of basis if a triple- $\zeta$ -quality basis is used.

Finally, if each molecule is described using the dimer basis we obtain the DC or DC+ basis types; the latter additionally including the mid-bond set. These basis types must be used for supermolecular calculations of the interaction energy.

## Auxiliary Basis Sets

One downside of density-fitting is that the auxiliary basis used needs to be paired with the main basis. Nevertheless, optimized auxiliary basis sets are available (Weigend et al. 1998, 2002) for most of the commonly used main basis sets. These tend to be between two and three times larger than the main basis.

A few points should be noted when using density-fitting for intermolecular forces:

- The auxiliary basis used needs to be of the DC or DC+ type even if the main basis is of the MC or MC+ type. It is not clear why this is the case, but a failure to do so sometimes results in unacceptable errors in  $E_{\text{elst}}^{(1)}$  and  $E_{\text{ind,tot}}^{(2)}$ .
- The Sadlej-pVTZ basis does not have an optimized auxiliary basis associated with it, but experience suggests that the aug-cc-pVTZ auxiliary basis may be used.
- When using the Dunning aug-cc-pVnZ basis sets, higher accuracies may be obtained by using auxiliary basis sets optimized for the aug-cc-pV(n + 1)Z bases.

## Multipole Expansion for the Interaction Energy

One of the major strengths of perturbation theory is that each of the interaction energy components possesses a multipole expansion that allows us to evaluate the interaction energy analytically in terms of molecular properties alone, at least when the molecular charge densities do not overlap appreciably.

The intermolecular interaction operator  $V$  defined through  $\blacklozenge$  Eq. 6.5 can be written as

$$V = \sum_{\alpha \in A} \sum_{\beta \in B} \frac{q_{\alpha} q_{\beta}}{r_{\alpha\beta}}, \quad (6.29)$$

where  $\alpha$  ( $\beta$ ) label all the particles (electrons and nuclei) of monomers A (B),  $q_{\alpha}$  is the charge (in atomic units) of particle  $\alpha$ , and  $r_{\alpha\beta}$  is the inter-particle distance. If A and B are well separated so that their charges are distinct and do not overlap (strictly this is never exactly possible), we can expand the interaction operator in the multipole expansion to give (in the compact notation of Stone 1996):

$$V = \sum_{t,u} \hat{Q}_t^A T_{tu}^{AB} \hat{Q}_u^B. \quad (6.30)$$

There is a lot compressed in this expression so it is well that we spend some time unravelling it. First of all, the subscripts  $t$  and  $u$  label the angular momenta of the real spherical harmonics and take the  $lm$  values 00, 10, 11c, 11s, 20, 21c, 21s, 22c, 22s, ... (the labels “c” and “s” stand for cosine and sine respectively).  $\hat{Q}_t^A$  is the real form of the multipole moment operator of rank  $t$  centered on A and expressed in the local-axis system of A, while  $T_{tu}^{AB}$  is the so-called  $T$ -tensor that carries the distance and angular dependence. The  $T$ -function of ranks  $l_1$  and  $l_2$  has a distance dependence  $R^{-l_1-l_2-1}$  where  $R$  is the separation between the centers of A and B.

Using this form of the interaction energy operator, the first-order electrostatic energy can be written as

$$E_{\text{elst}}^{(1)}(\text{MP}) = \sum_{t,u} Q_t^A T_{tu}^{AB} Q_u^B, \quad (6.31)$$

where  $Q_t^A$  is now the rank  $t$  multipole moment of the total charge density of A. This expression, which follows directly from [Eqs. 6.8](#) and [Eq. 6.30](#), is convenient as multipole moments are relatively easy to calculate. Therefore, [Eq. 6.31](#) provides us an easy method for calculating the first-order electrostatic energy. But consider the following points:

- Contributions to the electrostatic energy that decay exponentially with separation  $R$  do not contribute to the multipole expansion. Such terms arise when the charge densities overlap and are therefore referred to as the *penetration* contributions to the interaction energy.
- The non-expanded electrostatic energy ([Eq. 6.8](#)) exhibits a  $R^{-1}$  divergence when the nuclei of the interacting molecules approach each other, but the multipole expansion introduces a higher-order divergence because it includes terms of the form  $R^{-n}$  with  $n > 1$ . These terms need to be *damped* out at short range. This is usually done using a *damping function*  $f_n(R)$  that has the property that  $f_n(R) \rightarrow R^n$  for small  $R$  and  $f_n(R) \rightarrow 1$  at large  $R$ . We will discuss specific forms of these functions later.

Therefore, we can write the electrostatic energy as

$$E_{\text{elst}}^{(1)} = Ae^{-\alpha R} + \sum_{t,u} Q_t^A f_{(tu)}(R) T_{tu}^{AB} Q_u^B, \quad (6.32)$$

where the first term is the exponential penetration contribution (that is usually negative) and the second is the damped multipole expansion of the electrostatic energy. In general, the coefficients  $A$  and  $\alpha$  in the penetration term will depend on orientation and possibly on distance. The exact form is not critical, what is important is that this term exists at short separations and that it can be large in magnitude.

This analysis also applies to the multipole expansions for the second-order induction and dispersion energies. But before getting to these, let us ask an important question: When is the single-center multipole expansion valid? To answer this question fully would take us beyond the scope of this chapter. Instead we will introduce the main ideas here without proof, and refer the reader to the detailed discussion in [Chap. 7](#) of Stone (1996).

A key concept is the idea of the sphere of divergence. This is defined as the sphere centered on the expansion center (typically the center-of-mass) and just enclosing all charges. For a molecule this poses a problem as the electronic density formally extends to infinity. But it has been shown (Stone and Alderton 1985) that for charge densities expressed as the sum of Gaussian functions, it is sufficient that the sphere enclose all nuclear sites. The multipole expansion is valid only if the spheres of divergence of all interacting molecules *do not overlap*.

This poses a problem for all but the smallest of molecules. For example, consider the benzene dimer in the sandwich configuration used in [Table 6-1](#). The equilibrium separation is about



3.7 Å, but the radius of a benzene molecule is about 2.4 Å, so the molecules would have to be at least 4.8 Å apart before the single-center multipole expansion could be used. And even then, the expansion would be only slowly convergent.

A solution to this problem is to use a multi-centered multipole expansion, more commonly called a *distributed multipole expansion*. In principle the centers could be arbitrarily chosen, but it is convenient to use the atomic nuclei as centers. The distributed multipole expansion of the intermolecular interaction operator  $V$  is

$$V = \sum_{a \in A} \sum_{b \in B} \sum_{tu} \hat{Q}_t^a T_{tu}^{ab} \hat{Q}_u^b, \quad (6.33)$$

which is similar to  $\blacktriangleright$  Eq. 6.30 except that now  $\hat{Q}_t^a$  is the rank  $t$  multipole moment operator for site  $a$ . We will define the precise form of these multipole moment operators later.

We are now in a position to define the distributed multipole expansions for  $E_{\text{elst}}^{(1)}$ ,  $E_{\text{ind,tot}}^{(2)}$ , and  $E_{\text{disp,tot}}^{(2)}$ . Recall that the exchange energies decay exponentially with molecular separation and have no expansion in  $1/R$ . Consequently, the multipole expansion for  $E_{\text{ind,tot}}^{(2)}$  is the same as that for  $E_{\text{ind,pol}}^{(2)}$  and will be denoted simply by  $E_{\text{ind}}^{(2)}(\text{MP})$ . Likewise for  $E_{\text{disp}}^{(2)}(\text{MP})$ . The damping functions have been omitted from the expansions given below. To insert them is straightforward: for every  $T_{tu}^{ab}$  include a damping function of the form  $f_{(tu)}(r_{ab})$ .

- Electrostatic energy: The generalization of the single-center expansion is straightforward and we get

$$E_{\text{elst}}^{(1)}(\text{MP}) = \sum_{a \in A} \sum_{b \in B} \sum_{tu} Q_t^a T_{tu}^{ab} Q_u^b. \quad (6.34)$$

- Second-order induction: The second-order induction energy for molecule A is given by

$$E_{\text{ind}}^{(2)}(\text{MP})(A) = -\frac{1}{2} \sum_{a,a' \in A} \sum_{b,b' \in B} \sum_{tu t' u'} Q_u^b T_{tu}^{ab} \alpha_{tt'}^{aa'} T_{t'u'}^{a'b'} Q_{u'}^{b'}, \quad (6.35)$$

where  $\alpha_{tt'}^{aa'}$  is the static polarizability of rank  $t$  by  $t'$  for sites  $a$  and  $a'$  and is defined by

$$\alpha_{tt'}^{aa'} = \iint \hat{Q}_t^a(\mathbf{r}) \alpha(\mathbf{r}, \mathbf{r}' | 0) \hat{Q}_{t'}^{a'}(\mathbf{r}') d\mathbf{r} d\mathbf{r}'. \quad (6.36)$$

Likewise, we define  $E_{\text{ind}}^{(2)}(\text{MP})(B)$ .

From  $\blacktriangleright$  Eq. 6.35 we see that the second-order induction energy of A is a *linear response* to permanent multipoles of B.

- Second-order dispersion: The second-order dispersion energy has the distributed multipole expansion

$$E_{\text{disp}}^{(2)}(\text{MP}) = -\frac{1}{2\pi} \sum_{a,a' \in A} \sum_{b,b' \in B} \sum_{tu t' u'} T_{tu}^{ab} T_{t'u'}^{a'b'} \int_0^\infty \alpha_{tt'}^{aa'}(i\omega) \alpha_{u'u'}^{bb'}(i\omega) d\omega, \quad (6.37)$$

where  $\alpha_{tt'}^{aa'}(i\omega)$  is the frequency-dependent distributed polarizability defined analogously to  $\blacktriangleright$  Eq. 6.36 and evaluated at imaginary frequency. This form of the asymptotic dispersion energy involves a quadrupole sum over sites and is too cumbersome for most applications. Instead, very often a simplification is made by *localizing* the distributed polarizabilities to obtain a polarizability description that contains terms that contain one site index only. With this simplification, the dispersion expansion involves a double sum over sites and can be cast



into the more familiar site–site form (Stone and Tough 1984):

$$\begin{aligned}
 E_{\text{disp}}^{(2)}(\text{MP}) &= -\frac{1}{2\pi} \sum_{a \in A} \sum_{b \in B} \sum_{tu t' u'} T_{tu}^{ab} T_{t' u'}^{ab} \int_0^\infty \alpha_{t t'}^a(i\omega) \alpha_{u u'}^b(i\omega) d\omega \\
 &= -\sum_{a \in A} \sum_{b \in B} \left( \frac{C_6^{ab}}{R_{ab}^6} + \frac{C_7^{ab}}{R_{ab}^7} + \frac{C_8^{ab}}{R_{ab}^8} + \dots \right). \quad (6.38)
 \end{aligned}$$

In general, the dispersion coefficients are angle dependent (Stone and Tough 1984), but for the special case of spherical sites (an idealization), they are independent of angle and only terms of even order survive.

## Damping Functions

As explained above, the divergence of the multipole expansions of the interaction energies must be damped out using *damping functions*. The exact form of the damping functions are not known, particularly for the induction energy, but experience from high-accuracy calculations on small dimers suggests that the damping functions from Tang and Toennies (1992), which are incomplete gamma functions, are probably the most suitable. The order- $n$  Tang–Toennies damping function takes the form

$$f_n(\beta R_{ab}) = 1 - \exp(-\beta R_{ab}) \sum_{k=0}^n \frac{(\beta R_{ab})^k}{k!} \quad (6.39)$$

where  $\beta$  is the damping constant which may be angle dependent, but is often assumed to be a simple constant dependent on the pair of sites ( $a, b$ ). Often, even the site dependence is dropped and  $\beta$  is assumed to depend on the molecular types alone.

In general, the damping constant  $\beta$  will need to be determined by comparison with the non-expanded energies [from SAPT(DFT)]. For the induction energy, since the multipole expansion does not include the charge transfer energies, the comparison should be made with  $E_{\text{ind,tot}}^{(2)}$  calculated in the MC basis. This differs from the recommendation in Misquitta and Stone (2008a) where it was suggested that the damping constant be derived from the ionization energies of the interacting molecules as

$$\beta = \sqrt{2I_A} + \sqrt{2I_B}, \quad (6.40)$$

where  $I_A$  and  $I_B$  are the molecular vertical ionization energies in atomic units. There is now evidence (Sebetci and Beran 2010) to suggest that this results in too small a damping when used to evaluate the many-body induction energy through the polarization expansion, potentially resulting in a divergence of the expansion. However, there is extensive evidence that this value of the damping constant is appropriate for the dispersion energy (Misquitta and Stone 2008b) and results in accurate dispersion energies even at molecular charge-density overlap.

## Many-Body Contributions to the Interaction Energy

In the condensed phase and in clusters, the two-body energy is often a poor approximation to the total interaction energy which can contain a substantial contribution from the many-body energies (► Eqs. 6.2 and ► 6.3). These terms contribute most strongly in systems of

polarizable molecules with strong permanent multipole moments such as those that exhibit strong hydrogen-bonding. For example, Milet et al. (1999) have shown that in clusters of water molecules, the three-body contribution to the interaction energy can be as much as 28% at the equilibrium geometries and even more – as much as 50% – at the barriers. Likewise, the many-body non-additive energies have been shown to be responsible for the structural properties of liquid water (Bukowski et al. 2006). Many-body effects are also present in dispersion-bound systems like the argon liquid (Bukowski and Szalewicz 2001) small trimers containing inert gases (Ernesti and Hutson 1997) and the benzene crystal (Podeszwa et al. 2008). In all cases the non-additive dispersion makes a small but non-negligible contribution to the total interaction energy.

The three-body correction (► Eq. 6.3) is the dominant source of non-additivity (Bukowski et al. 2006; Mas et al. 2003a, b). This correction may be calculated using the supermolecular approach, but the calculation is tedious and the BSSE needs to be corrected for. Nevertheless, this approach is possible for small clusters (Hodges et al. 1997). The most appropriate method for calculating the three-body correction is through a three-body version of SAPT(DFT) (Podeszwa and Szalewicz 2007). Using representative trimers of benzene, Podeszwa et al. (2008) have estimated the three-body SAPT(DFT) contribution to the lattice energy of the benzene crystal and have found the result to be in good agreement with experiment. However this cannot be done in general as the number of trimers in the condensed phase scales as the cube of the number of molecules. One solution is to construct an analytic representation of the three-body correction. Though this has been successfully done for water (Mas et al. 2003a, b), it is a formidable task, and is likely unreasonable to perform for most systems.

There are, however, alternative, computationally feasible procedures that are based on the (distributed) multipole forms of the induction and dispersion that are the dominant source of non-additivity in clusters (Bukowski and Szalewicz 2001; Mas et al. 2003b). The exchange non-additivity is significant in small clusters (Hodges et al. 1997; Milet et al. 1999), but it is relatively less important in large clusters and the condensed phase (Mas et al. 2003b).

From a detailed examination of the three-body SAPT energies for the argon liquid, Bukowski et al. (Bukowski and Szalewicz 2001) have concluded that the bulk of the three-body dispersion energy can be estimated using the Axilrod–Teller–Muto triple dipole term. For isotropic local distributed polarizabilities this takes the form (Stone 1996)

$$\Delta E_{\text{disp}}^{3\mu}(ABC) = \sum_{a \in A} \sum_{b \in B} \sum_{c \in C} C_9 \frac{(1 + 3 \cos \widehat{a} \cos \widehat{b} \cos \widehat{c})}{R_{ab}^3 R_{bc}^3 R_{ac}^3}, \quad (6.41)$$

where  $R_{ab}$ , etc., are the lengths of the sides and  $\widehat{a}$ ,  $\widehat{b}$ , and  $\widehat{c}$  are the angles of the triangle formed by the three atoms, and

$$C_9 = \frac{3}{\pi} \int_0^\infty \alpha^a(i\omega) \alpha^b(i\omega) \alpha^c(i\omega) d\omega. \quad (6.42)$$

One of the most efficient and convenient ways of approximating the many-body induction energy is through a *polarizability model* based on distributed polarizabilities. The many-body induction energy of a cluster of molecules can be calculated using a generalization of ► Eq. 6.35 (Stone 1996):

$$E_{\text{ind}}(\text{Many-body}) = \frac{1}{2} \sum_A \sum_{a \in A} \sum_{B \neq A} \sum_{b \in B} \sum_{tu} \Delta Q_t^a T_{tu}^{ab} Q_u^b. \quad (6.43)$$

Here  $\Delta Q_t^a$  is the *change* in multipole moment  $t$  at  $a$  due to the self-consistent polarization of site  $a$  in the field of all sites on other molecules and is given by

$$\Delta Q_t^a = - \sum_{a' \in A} \sum_{B \neq A} \sum_{b \in B} \sum_{t'v} \alpha_{tt'}^{aa'} T_{t'v}^{a'b} (Q_v^b + \Delta Q_v^b), \quad (6.44)$$

Notice that  $\bullet$  Eq. 6.44 must be solved iteratively for all molecules in the system, as the  $\Delta Q$  occur on both sides of the equation. The cumulative effect of the iterations is small for a dimer, but can be substantial for a cluster. As before, each of the  $T$ -functions should be associated with a suitable damping function. Mas et al. (2003b) have validated this model for the many-body energies in liquid water.

## Molecular Properties

In order to evaluate the distributed multipole forms of the interaction energy components we need to calculate distributed multipoles and distributed frequency-dependent polarizabilities of the interacting molecules.

There is no unique method for distributed molecular properties. Rather than get into a philosophical discussion of the concept of an *atom-in-a-molecule* (Matta and Bader 2006; Parr et al. 2005) (see also the discussion in Lillestolen and Wheatley 2008) we will adopt the more pragmatic approach and require that whatever the method used, the distributed properties be the most accurate possible within the constraints imposed by the model. Additionally, we also need the methods used to be numerically robust, applicable to small organic molecules, relatively easy to use, and theoretically consistent with the electronic structure method used to calculate the non-expanded energies, which, in our case, will be SAPT(DFT).

## Distributed Multipoles

The distribution of the multipole moments has been the subject of many decades of research (see Stone 1996 and Stone and Misquitta 2007 for reviews). The Distributed Multipole Analysis (DMA) of Stone and Alderton (1985) is widely used, and a recent modification (Stone 2005) overcomes a shortcoming of the earlier method that arose when diffuse functions were present in the basis.

A special case of distributed multipoles are the point charge models. Such models may be obtained in a variety of ways. In one of the most commonly used methods the charge model is required to reproduce (in a least-squares sense) the molecular electrostatic potential at a set of points around the molecule (Singh and Kollman 1984). These points are generally chosen to lie sufficiently far as to exclude or minimize the effects of penetration. Another possibility is to require that the charges best reproduce some of the molecular multipole moments.

The simplicity of the point charge models comes at a price. While such models may be adequate for systems with an insignificant contribution from the electrostatic energy, they are clearly inadequate for others, in particular, when hydrogen bonding is present. This is because hydrogen bonds are strongly directional (Buckingham and Fowler 1983; Buckingham et al. 2008), whereas the electrostatic interaction between two point charges is completely isotropic. Besides the energetic importance of the hydrogen bond, the strong directionality significantly

reduces the available configuration space. This can have important consequences in simulations and crystal energy landscape searches (Day et al. 2005).

*Basis set:* The higher-ranking multipoles require large and more diffuse basis sets to be well described. Experience has shown that an augmented triple- $\zeta$  basis is often adequate.

## Distributed Polarizabilities

The distributed polarizability is defined through  $\blacktriangleright$  Eq. 6.36. This definition suggests at least two methods for performing the distribution: one possibility is to require that the site multipole moment operator  $\hat{Q}_t^a$  is non-zero only around site  $a$ , and likewise for  $\hat{Q}_{t'}^{a'}$ . This *real-space* partitioning scheme has been implemented using integration grids (Le Sueur and Stone 1994) and Bader's theory of atoms in a molecule (Angyan et al. 1994). However, the shapes of the atomic domains in these schemes tend to be irregular, which could lead to artifacts in the higher-rank polarizabilities. Additionally, these methods tend to result in unphysically large charge-flow terms that are hard to localize. These terms are rank zero contributions to the polarizability (where one or both of the subscripts  $t$  and  $t'$  are 00 in  $\blacktriangleright$  Eq. 6.36) that describe the flow of charge along the molecule (Stone 1996). The effects of the charge-flow terms can often be described using higher-ranking polarizabilities, but in order to do so, the charge-flow terms must be small.

Yet another possibility is to partition the FDDS that appears in  $\blacktriangleright$  Eq. 6.36 into contributions from pairs of atoms. These are known as the *basis-space* partitioning methods. Early attempts to do so failed as the resulting polarizabilities were completely unphysical for large basis sets (Le Sueur and Stone 1993).

More recent methods (Gagliardi et al. 2004; Lillestolen and Wheatley 2007; Wheatley and Lillestolen 2008) have been more successful, but are either applicable only to the static polarizability or are too cumbersome to use routinely. Also very recently, distribution schemes were proposed by Williams and Stone (2003) and Misquitta and Stone (2006). These two methods have been combined into the Williams–Stone–Misquitta (WSM) method which has proved to be one of the most successful methods for obtaining distributed polarizabilities. This is what we will describe next.

## Williams–Stone–Misquitta (WSM) Distribution

The WSM method involves three stages. In the first, the constrained density-fitting scheme (Misquitta and Stone 2006) is used to calculate distributed, non-local polarizabilities. These are then *localized* in stage two. And subsequently, in the final stage, *refined* using a method based on Ref. Williams and Stone (2003).

*Stage 1:* From  $\blacktriangleright$  Eq. 6.26 we see that the density-fitted FDDS can be partitioned into atom–atom contributions by partitioning the auxiliary basis set into contributions from individual sites, that is,  $\{\chi\} = \{\chi^{(1)}, \chi^{(2)}, \dots\}$ , and then the FDDS can be written as

$$\alpha(\mathbf{r}, \mathbf{r}' | \omega) \approx \sum_{aa'} \alpha^{a,a'}(\mathbf{r}, \mathbf{r}' | \omega), \quad (6.45)$$

where the contribution from sites  $a$  and  $a'$  is given by

$$\alpha^{a,a'}(\mathbf{r}, \mathbf{r}'|\omega) = \sum_{p \in a, p' \in a'} \tilde{C}_{pp'}(\omega) \chi_p(\mathbf{r}) \chi_{p'}(\mathbf{r}'). \quad (6.46)$$

We can now insert  $\alpha^{a,a'}(\mathbf{r}, \mathbf{r}'|\omega)$  in  $\bullet$  Eq. 6.36 to define the distributed polarizability for sites  $(a, a')$ :

$$\alpha_{tt'}^{aa'}(\omega) = \sum_{p \in a, p' \in a'} \tilde{C}_{pp'}(\omega) \mathcal{N}_t^p \mathcal{N}_{t'}^{p'}, \quad (6.47)$$

where  $\mathcal{N}_t^p = \int \hat{Q}_t(\mathbf{r} - \mathbf{a}) \chi_p(\mathbf{r}) d^3\mathbf{r}$ , where  $\mathbf{a}$  is a suitable reference origin for site  $a$  that will typically be taken to be the nucleus. Here  $\hat{Q}_t(\mathbf{r} - \mathbf{a}) \equiv \hat{Q}_t^a$  is the multipole moment operator of rank  $t$ , centered on site  $a$ .

This simple idea fails when the standard density-fitting procedure is used. The resulting distributed polarizabilities are very sensitive to the auxiliary basis used (Misquitta and Stone 2006) and become unphysical as the basis grows larger and more complete. This is because in a large diffuse basis, diffuse functions on a site can be used to describe properties on another, adjacent site. This means that the basis functions located on a site are not representative of the site properties.

This problem can be overcome by modifying the density-fitting algorithm ( $\bullet$  section “Density-Fitting”) to include two additional constraints: one to impose orthogonality and the other to remove the non-physical terms (Misquitta and Stone 2006). With this modification, the density-fitted form of the FDDS leads to much more sensible values (Misquitta and Stone 2006) and are only weakly dependent on the basis set used.

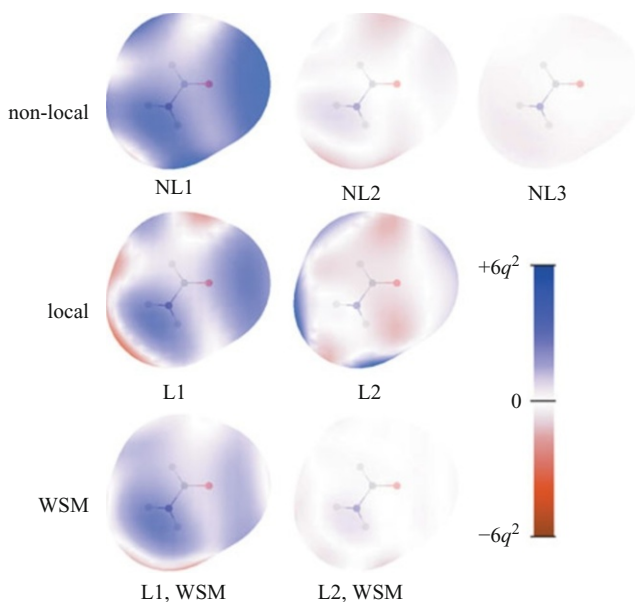
*Step 2:* The distributed polarizabilities obtained using this constrained density-fitting procedure contain non-local terms, that is, terms involving pairs of distinct sites. In contrast to other distribution methods, the non-local terms describing flow of charge from site to site are very small (around  $10^{-2}$  and  $10^{-3}$  a.u. in magnitude) for all systems, irrespective of the type of bonding involved. Nevertheless, non-local terms are best avoided as they complicate the description unnecessarily. The localization methods of Le Sueur and Stone (1994) and Lillestolen and Wheatley (2007) can be used to transform the non-local terms into local polarizabilities and remove the charge-flow terms altogether. The localization by this procedure causes a deterioration of the convergence properties of the model, because multipole expansions are used to move the polarizabilities around. In principle, the Le Sueur and Stone procedure can increase the radius of divergence of the description to be equal to the size of the molecule, thereby causing significant losses in accuracy for large molecules for which the Lillestolen and Wheatley localization method may be more appropriate. Thus, while good results have been obtained for molecules like formamide and urea, there is already an appreciable loss in accuracy for N-methyl propanamide (Misquitta and Stone 2006).

*Step 3:* The quality of the local polarizability model from the previous step can be dramatically improved using the method of Williams and Stone (2003). In this step, the local polarizabilities are *refined* by requiring them to reproduce a set of point-to-point polarizabilities which describe the response of the electrostatic potential at a point to the frequency-dependent potential produced by a unit oscillating point charge at another. Details of the refinement process are given in Misquitta and Stone (2008a) and Misquitta et al. (2008a).

## Analyzing the Models

The WSM method can be used to construct a variety of polarization models. These can include terms to rank 3 and can even be made isotropic. The refinement step ensures that whatever the choice of model, it will be the most accurate possible. A convenient way of assessing the accuracy of the models is by mapping induction energies onto a suitable surface around the molecule in question (Misquitta et al. 2008a). Such a mapping can be performed using a spherical energy probe which, for the induction energy, is best taken to be a point charge with charge  $qe$ . The induction energy of a molecule in the field of a point charge depends quadratically on the magnitude of the charge, and an appropriate value of  $q$  needs to be used in interpreting the energy scales in these maps. Setting  $q = 1$  gives the response to a unit charge, but this is larger than typical local charges in a molecule, which are not expected to exceed  $0.5e$ . The surface around the molecule is constructed using the algorithm described in Misquitta et al. (2008a).

In **Fig. 6-1** we show difference maps of the induction energy of the formamide molecule in the field of a unit point charge, computed using the non-local models, local models, and WSM local models, respectively. The large errors in the non-local rank 1 model, particularly near the oxygen and the polar hydrogen atoms, are quite clearly displayed. These errors are reduced in the rank 1 local model and are still smaller in the WSM rank 1 local model. The



**Fig. 6-1**

Difference maps of the induction energy ( $\text{kJ mol}^{-1}$ ) arising from a charge  $q$  atomic units on the  $\text{vdW}\times 2$  surface of formamide using distributed non-local description of ranks 1, 2, and 3, distributed local description of ranks 1 and 2 obtained from the non-local models using the Le Sueur and Stone localization technique (Le Sueur and Stone 1994), and WSM distributed local descriptions of ranks 1 and 2. The differences are taken against SAPT(DFT) second-order induction energies obtained using a molecular description with the Sadlej/MC basis set

largest residual errors always seem to occur in the same regions, perhaps indicating the need for higher-ranking polarizabilities on some sites than on others. At rank 2, the non-local model is in almost perfect agreement with SAPT(DFT), but the local model obtained using the Le Sueur and Stone localization method exhibits rather large deficiencies near the polar hydrogens. These are removed in the WSM rank 2 local model which is comparable in accuracy to the rank 2 non-local model.

## Distributed Dispersion Coefficients

Having obtained the localized frequency-dependent polarizabilities, we can now evaluate the dispersion coefficients that appear in [Eq. 6.38](#). The dispersion coefficients depend on integrals of the form

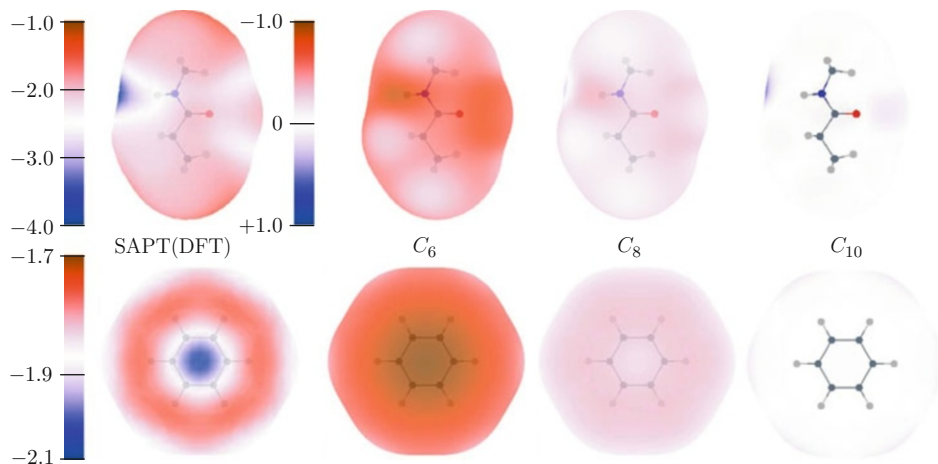
$$\int_0^\infty \alpha_{tt'}^a(iv) \alpha_{uu'}^b(iv) dv, \quad (6.48)$$

where rank- $l_1$  – rank- $l_1'$  and rank- $l_2$  – rank- $l_2'$  polarizability tensors contribute to a  $C_n$  coefficient with  $n = l_1 + l_1' + l_2 + l_2' + 2$ . At present, the WSM polarizabilities can be calculated to rank 3, so while we can calculate  $C_{10}$  and  $C_{12}$  terms, they will lack the contributions from the hexadecapole and higher-rank polarizabilities. However, this has been shown not to be a serious limitation (Misquitta and Stone 2008b).

*Basis sets:* For a good dispersion model the basis set needs to be large and diffuse. To be consistent with SAPT(DFT) interaction energies calculated using the MC+ (or DC+) basis types, the dispersion coefficients should be calculated using a more diffuse basis than was used for the monomer part of the SAPT(DFT) basis. This is to compensate for the effects of the mid-bond functions that cannot be used when calculating dispersion coefficients. For example, if an aug-cc-pVTZ MC+ basis is used to calculate SAPT(DFT) interaction energies, the dispersion model should be constructed from WSM polarizabilities calculated using a d-aug-cc-pVTZ basis (Misquitta and Stone 2008b).

*Models:* Dispersion models need to be rather elaborate before they are accurate enough to describe the dispersion energy at small separations. [Figure 6-2](#) shows dispersion energy maps for benzene and N-methyl propanamide using neon as a probe atom as described in Misquitta and Stone (2008b). From the error maps we see that the  $C_6$  dispersion models significantly underestimate the dispersion interaction, and it is only with the  $C_{10}$  model that we get a good representation of the dispersion. More examples are provided in Misquitta and Stone (2008b).

However, the  $C_{10}$  model is rather elaborate and unwieldy. For many applications simpler models may suffice. Fortunately, the WSM method allows the construction of far simpler *isotropic* dispersion models. Even more simplifications can be made by scaling the isotropic  $C_6$  WSM model to best reproduce the SAPT(DFT) dispersion energies (Misquitta and Stone 2008b), and the results are quite acceptable. From [Fig. 6-3](#) we see that the scaled isotropic  $C_6$  dispersion model (damped) is quite acceptable for the benzene dimer and is a significant improvement over the empirical dispersion model from a popular and well parameterized empirical potential. The significant failure occurs at the stacked configurations where anisotropy is essential to describe the dispersion interaction correctly.



■ Fig. 6-2

Dispersion energy maps of benzene and N-methyl propanamide with neon as a probe. The SAPT(DFT) dispersion energy  $E_{\text{disp,pol}}^{(2)}$  is displayed using an absolute scale in  $\text{kJ mol}^{-1}$ . The model dispersion energies are displayed as *differences* taken against  $E_{\text{disp,tot}}^{(2)}$  from SAPT(DFT). The models are not damped. The d-aug-cc-pVTZ basis has been used for N-methyl propanamide and the aug-cc-pVTZ basis for benzene

## Case Studies

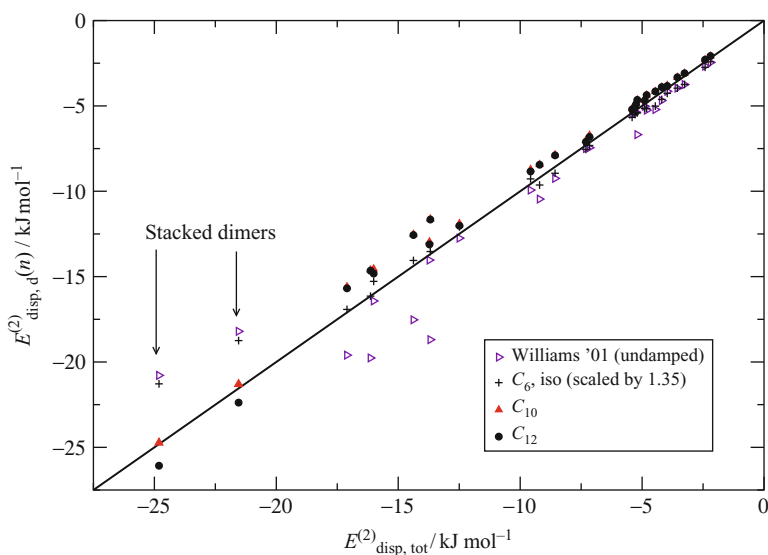
### Applications

Over the last few years, SAPT(DFT) has been used to study the interactions between a number of small and medium-sized molecules. Initial applications tended to focus on small systems such as dimers of rare gas atoms (Misquitta et al. 2005a; Podeszwa and Szalewicz 2005) where detailed comparisons were possible with the more established CCSD(T) method, from which the accuracy of SAPT(DFT) was validated. The agreement was generally excellent. Consider for example the  $\text{He}\cdots\text{CO}$  complex (● Fig. 6-4). The agreement of SAPT(DFT) energies with the CCSDT energies extrapolated to the complete basis set limit (Peterson and McBane 2005) is remarkable. By contrast, SAPT yields a potential energy curve that is somewhat too negative.

Subsequently, applications were made to larger systems such as the ethyne and benzene dimers (Hesselmann et al. 2005; Podeszwa and Szalewicz 2005) where, once again, the accuracy of the method was demonstrated. More recently, the DFT-SAPT implementation has been used to study the interaction of water on graphene (Jenness and Jordan 2009), DNA base pairs (Hesselmann et al. 2006), and DNA base pair tetramers (Fiethen et al. 2008). Calculations of such accuracy are simply not possible using conventional electronic structure methods in the supermolecular approach, particularly as the only correlated ab initio method with a reasonable computational scaling is MP2, and MP2 is not suitable for the interactions of systems with  $\pi$ -bonding (Sinnokrot et al. 2002).

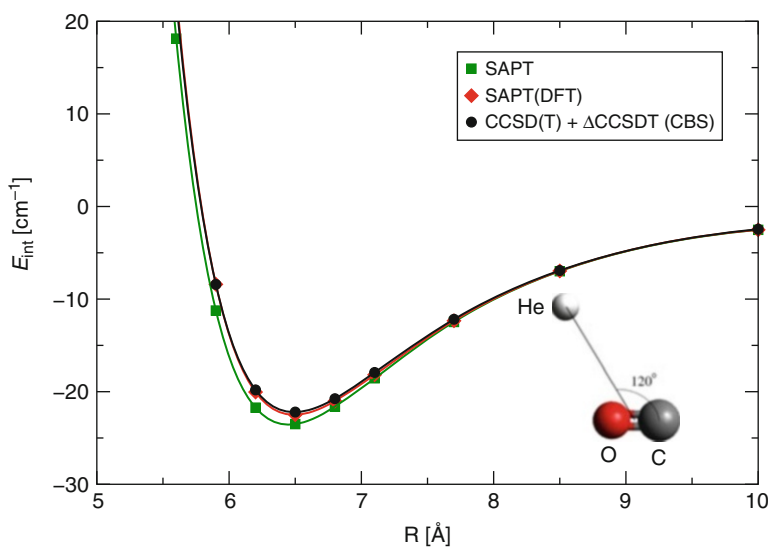
In a truly remarkable application on water, Bukowski et al. (2006) derived a SAPT(DFT) two-body potential, together with a three-body potential from SAPT (Mas et al. 2003a, b)





■ Fig. 6-3

Dispersion energies for the benzene dimer. Scatter plot of dispersion energies calculated using the damped anisotropic  $C_{10}$  and  $C_{12}$  models and the isotropic scaled  $C_6$  model plotted against  $E_{\text{disp,tot}}^{(2)}$  calculated using SAPT(DFT). Also shown are undamped dispersion energies calculated using the  $C_6$  parameters from the Williams' 01 potential (Williams 2001a, b)



■ Fig. 6-4

Interaction energy scan for the He...CO system. Comparison of SAPT, SAPT(DFT), and CCSDT (From Peterson and McBane 2005)

and a polarization model for the many-body effects, and were able to describe not only the vibrational-rotational tunneling spectrum of the water dimer and trimer, but also the structure of liquid water.

Complete potential energy surfaces of a few complexes have been calculated using SAPT(DFT). These include the CO dimer, for which ro-vibrational transitions were calculated and found to be in good agreement with experiment (Visser et al. 2005), and the benzene dimer (Podeszwa et al. 2006a). Recently, an anisotropic, transferable atom-atom potential for polycyclic aromatic hydrocarbons has been parametrized from SAPT(DFT) calculations on the benzene, naphthalene, anthracene, and pyrene dimers (Podeszwa and Szalewicz 2008; Totton et al. 2010). Such potentials could bring a new level of accuracy to the simulations of condensed matter.

## Polarization in Organic Crystals

One of the successes of the WSM polarizability models has been in describing the role of polarization in organic crystals (Welch et al. 2008). Amongst the many crystals of organic molecules studied by Welch et al. let us consider one here: oxalyl dihydrazide (Fig. 6-5). This molecule has been found to crystallize in five polymorphic forms. In the  $\alpha$  form, the molecular conformation is quite different from the other four, with two fewer internal hydrogen bonds. While the experimental lattice energies of these five forms are not known, it is generally expected that they should lie close together in energy. However, lattice energies calculated using methods that only

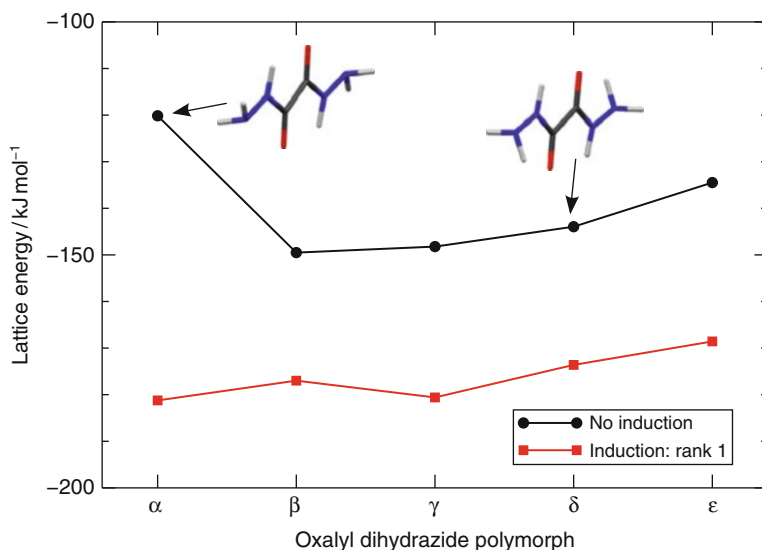


Fig. 6-5

Lattice energy of the five polymorphs of oxalyl dihydrazide calculated with and without an explicit polarization contribution. Without polarization, the  $\alpha$  form is too high in energy compared with the others, but on calculating the polarization contribution to the lattice energy self-consistently, the five forms are seen to be similar in energy, which is what would be expected for polymorphs (Welch et al. 2008)

modeled the exchange-repulsion, dispersion, electrostatic, and conformational energies predict the lattice energy of the  $\alpha$  form to be between 20 and 28 kJ mol<sup>-1</sup> higher than the others. Such a high energy is generally considered to be out of the range of possible polymorphism.

Using a WSM polarizability model, Welch et al. showed that this difference could be explained as arising from polarization (induction) effects that were missing in the empirical force fields (see [▶ Fig. 6-5](#)). When polarization is taken into account explicitly and added to the lattice energy (without subsequent lattice relaxation) all five polymorphs of oxalyl dihydrazide are seen to have a similar lattice energy. It is not hard to see why an explicit model was found to be important here. Empirical force fields (Williams 2001a, b) will always contain some of the effects of polarization in an average manner. This is why they work in many cases. But when there is a difference in the hydrogen-bonding network, such as happens in polymorphs of oxalyl dihydrazide where we see a difference in the number of intra and intermolecular hydrogen bonds, these potentials are no longer able to describe the relative energies of the systems, and we need an explicit treatment of the polarization. See Karamertzanis et al. (2008) for a detailed investigation of this instance of conformational polymorphism.

These effects will undoubtedly be important in other systems which involve different hydrogen-bonding environments such as biological molecules. It is very likely that even a simple treatment of polarization may significantly improve the predictions of the properties of such systems.

## Crystal Structure Prediction

---

One of the significant successes of the electronic structure methods described in this chapter is the high level of predictive power they have brought to the field of organic crystals. Consider that just about 20 years ago the inability of computational scientists to predict crystal structures of organic molecules was considered a “scandal” (Maddox 1988). While we still cannot claim to have solved the problem, we do now have a number of noteworthy successes in this field.

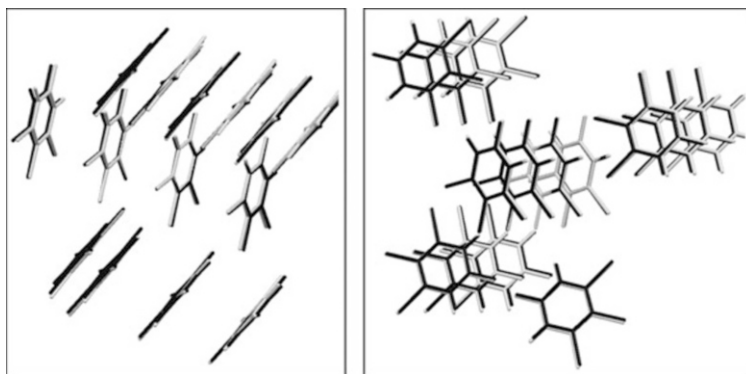
One of the target molecules in the 2007 blind test of organic crystal structure prediction organized by the Cambridge Crystallographic Data Center (CCDC) was 1,3-dibromo-2-chloro-5-fluorobenzene (C<sub>6</sub>Br<sub>2</sub>ClFH<sub>2</sub>). This molecule contains halogen atoms which are not well represented by most empirical potentials, primarily because they are strongly anisotropic (Day and Price 2003; Stone 1996) and empirical atom–atom potentials assume spherical atomic shapes. Using an anisotropic atom–atom potential calculated using first-order SAPT(DFT) energies and a dispersion model from WSM polarizabilities, Misquitta et al. (2008b) were able to predict a crystal structure for this system that was later found to correspond exactly with the experimental one ([● Fig. 6-6](#)) (Day et al. 2009). This was the first completely *ab initio* prediction of a crystal structure of an organic molecule.

Also recently, Podeszwa et al. (2008) have used potentials derived from SAPT(DFT) to model the crystal structures of cyclotrimethylene trinitramine (RDX) and benzene, the latter being arguably the more difficult of the two systems. This once again demonstrates the accuracy of force fields derived from SAPT(DFT) energies.

## Outlook

---

Applications such as these would have been almost unthinkable as little as a decade ago. It is developments in the theory of intermolecular forces together with improvements in our



■ Fig. 6-6

Two views of the overlay of the experimental (*black*) and predicted (*gray*) crystal structures of  $C_6Br_2ClFH_2$ . The two structures are hard to separate as the overlay is nearly perfect

computational resources that have made these calculations possible. We can only speculate where future developments will take us in the next few years. For many applications computational requirement will limit us to use atom–atom intermolecular potentials. We have already seen examples of the success of such potentials when derived using accurate *ab initio* methods, but this is only the beginning of what is possible. Accurate *ab initio* methods like SAPT(DFT) and the WSM method can be the basis of a new generation of atom–atom potentials that will surpass any empirical potential in accuracy.

While we have good reason for optimism, it is worthwhile bearing in mind that at least some of the successes described here are fortuitous. The crystal structure predictions listed above were successful because the observed crystal form corresponded to the global minimum in the free energy. However, this is not always true, particularly for industrially important polymorphic molecules for which kinetic effects can be important. If we are to fully understand the interplay between kinetic and thermodynamic effects, we first need to remove any uncertainty in our ability to model molecular interactions – probably of both the intra and intermolecular types.

This raises the question of intramolecular flexibility which has not yet been adequately addressed. The potential energy surface involving intermolecular and intramolecular degrees of freedom is a formidable object and so far has been constructed for only a small number of small dimers. Methods for the inclusion of internal degrees of freedom have been suggested (Jankowski 2004, 2008; Jankowski and Ziolkowski 2006; Murdachaew et al. 2002), but so far have been applied to dimers of small systems only. This remains one of the outstanding problems with this approach.

Yet another outstanding problem is the correct treatment of the interactions of small gap materials such as fullerenes. It is quite likely that second-order perturbation will not be adequate for such systems. Furthermore, the strong electron delocalization in these semi-conductor-like materials means that the standard atom–atom models of interaction fail due to their inherent assumption of locality (Misquitta et al. 2010). This is possibly the next hurdle to be faced by the theory of intermolecular interactions.

## Programs

---

There are a large number of programs that can be used to study intermolecular interactions. If the supermolecular method is used, practically any electronic structure program capable of using correlated methods like MP2 and CCSD(T) can be used. However, the following programs are likely more suited than most for this field.

- **SAPT2008:** (free, source available, parallel) The SAPT2008 program (Bukowski et al. 2002) contains implementations of both SAPT and DF-SAPT(DFT) and allows the calculation of three-body energies through the three-body SAPT and SAPT(DFT) theories. Besides the usual interaction energy corrections, this program also contains a variety of state-of-the-art energy components. The SAPT2008 program uses molecular orbitals and eigenvalues from a variety of SCF programs, but the DF-SAPT(DFT) module works only with the DALTON 2.0 program.
- **CAMCASP:** (free, source available, serial) The CAMCASP (Misquitta and Stone 2007) contains implementations of DF-SAPT(DFT), the WSM method for molecular properties, and a variety of modules and programs to analyze and interpret mechanisms of intermolecular interactions in small organic molecules (through interfaces with the ORIENT program) and construct analytic, polarizable atom–atom potentials for small organic molecules. Additionally, distributed multipoles can be calculated using CAMCASP through the included GDMA 2.2 module. This program has been used for almost all the results presented in this chapter. CAMCASP uses molecular orbitals and eigenvalues calculated using the DALTON 2.0 program (Helgaker et al. 2005).
- **ORIENT:** (free, source available, serial) ORIENT (Stone et al. 2006) is not an electronic structure program, but is a very versatile platform for calculating interaction energies of clusters, performing geometry optimizations, simulations and displaying energies using the Open-GL module. This program is used quite closely by CAMCASP through a variety of interfaces.
- **MOLPRO 2008:** (commercial, source available, parallel) The MOLPRO 2008 program (Werner et al. 2008) contains a number of state-of-the-art electronic structure methods including DF-DFT-SAPT. This program is probably the most computationally efficient implementation of SAPT(DFT), though the FDDS cannot include any fraction of CHF (see [▶ section “Symmetry-Adapted Perturbation Theory”](#)).
- **DALTON 2.0:** (free, source available, parallel) The DALTON 2.0 program (Helgaker et al. 2005) is used by both SAPT2008 and CAMCASP as the front-end to calculate the Kohn–Sham molecular orbitals and eigenvalues and some of the integrals needed to evaluate the FDDS.

## Annotated Bibliography

---

The papers highlighted in this section are meant to be the most recent or comprehensive in the subject. This list is by no means complete. They should be a good starting point for researchers entering the field.

- **Intermolecular forces:** The book by Stone (1996) is probably the most comprehensive introduction to the theory from the atomistic point of view. Israelachvili (2007) takes a very

different approach and is more concerned with the manifestations of these forces on surfaces, bulk media, and complex systems. Yet another approach is taken by Parsegian (2005) who tackles the Casimir forces between extended media in various geometries. The two volumes – (Wales 2005a, b) – offer articles on the current status of the field.

- Types of intermolecular bonds: An excellent overview of hydrogen bonds can be found in the article by Buckingham, Del Bene, and McDowell (Buckingham et al. 2008). In the last few years interest has developed in halogen bonded systems. See Bernal-Uruchurtu et al. (2009) for an introduction and an analysis based on a SAPT decomposition of the interaction energy.
- SAPT: The review articles by Jeziorski, Szalewicz, and others (Jeziorski and Szalewicz 1998, 2002; Jeziorski et al. 1994; Szalewicz 2002; Szalewicz et al. 2005) are probably the most comprehensive articles on symmetry-adapted perturbation theory. See also the discussion of these theories in Stone (1996). For a detailed examination of symmetry-forcing techniques and the convergence of intermolecular perturbation theories see Szalewicz et al. (2005).
- SAPT(DFT): The theory of the SAPT(DFT) method is described in Misquitta et al. (2005b) and DF-SAPT(DFT) in Podeszwa et al. (2006b). The DF-DFT-SAPT method is described in Hesselmann et al. (2005).
- Potentials: Obtaining an analytic expression for the intermolecular interaction energy in atom–atom form is often difficult. See Misquitta et al. (2008b) and Stone and Misquitta (2007) for a discussion of how this could be done.
- Crystal structure prediction: The field of organic crystal structure prediction remains one of the best testing grounds for intermolecular potentials. Accuracies need not be as high as that needed for spectroscopic calculations, but the effects of molecular flexibility and many-body non-additivity need to be accounted for. See Price (2008, 2009) for recent reviews of this subject. For a description of dispersion-corrected DFT methods specially parametrized for organic crystals see Neumann and Perrin (2005). For a comprehensive examination of the role of detailed distributed multipole models in this field see Day et al. (2005).

## Acknowledgments

---

The theoretical methods described in this chapter have been strongly influenced by Anthony Stone and Krzysztof Szalewicz. I owe particular thanks to Anthony who has had a strong influence on this chapter through the many discussions we have had and papers we have written together.

## References

---

- Adamo, C., & Barone, V. (1999). Toward reliable density functional methods without adjustable parameters: The pbe0 model. *Journal of Chemical Physics*, 110, 6158–6170.
- Adamo, C., Cossi, M., Scalmani, G., & Barone, V. (1999). Accurate static polarizabilities by density functional theory: Assessment of the PBE0 model. *Chemical Physics Letters*, 307, 265–271.
- Akin-Ojo, O., Bukowski, R., & Szalewicz, K. (2003). Ab initio studies of He-HCCCN interaction. *Journal of Chemical Physics*, 119, 8379–8396.
- Angyan, J. G. (2007). On the exchange-hole model of london dispersion forces. *Journal of Chemical Physics*, 127, 024108–8.
- Angyan, J. G., Jansen, G., Loos, M., Hattig, C., & Hess, B. A. (1994). Distributed polarizabilities using

- the topological theory of atoms in molecules. *Chemical Physics Letters*, 219, 267–273.
- Becke, A. D., & Johnson, E. R. (2005). Exchange-hole dipole moment and the dispersion interaction. *Journal of Chemical Physics*, 122, 154104.
- Bernal-Uruchurtu, M. I., Hernandez-Lamoneda, R., & Janda, K. C. (2009). On the unusual properties of halogen bonds: A detailed ab initio study of  $x_2\text{-(h}_2\text{o)}_1\text{-5}$  clusters ( $x=\text{cl}$  and  $\text{br}$ ). *Journal of Physical Chemistry A*, 113, 5496–5505.
- Boys, S. F., & Bernardi, F. (1970). The calculation of small molecular interactions by the differences of separate total energies. some procedures with reduced errors. *Molecular Physics*, 19, 553.
- Buckingham, A. D., & Fowler, P. W. (1983). Do electrostatic interactions predict structures of van der waals molecules? *Journal of Chemical Physics*, 79, 6426–6428.
- Buckingham, A. D., Bene, J. E. D., & McDowell, S. A. C. (2008). The hydrogen bond. *Chemical Physics Letters*, 463, 1–10.
- Bukowski, R., & Szalewicz, K. (2001). Complete ab initio three-body nonadditive potential in monte carlo simulations of vapor-liquid equilibria and pure phases of argon. *Journal of Chemical Physics*, 114, 9518.
- Bukowski, R., Sadlej, J., Jeziorski, B., Jankowski, P., Szalewicz, K., Kucharski, S. A., Williams, H. L., & Rice, B. M. (1999). Intermolecular potential of carbon dioxide dimer from symmetry-adapted perturbation theory. *Journal of Chemical Physics*, 110, 3785–3803.
- Bukowski, R., Cencek, W., Jankowski, P., Jeziorski, B., Jeziorska, M., Lotrich, V., Kucharski, S., Misquitta, A. J., Moszynski, R., Patkowski, K., Podeszwa, R., Rybak, S., Szalewicz, K., Williams, H., Wheatley, R. J., Wormer, P. E. S., & Zuchowski, P. S. (2002). SAPT2008: An ab initio program for many-body symmetry-adapted perturbation theory calculations of intermolecular interaction energies. University of Delaware and University of Warsaw. <http://www.physics.udel.edu/~szalewic/>. Accessed 18 July 2011
- Bukowski, R., Podeszwa, R., & Szalewicz, K. (2005). Efficient generation of the coupled Kohn–Sham dynamic susceptibility functions and dispersion energy with density fitting. *Chemical Physics Letters*, 414, 111–116.
- Bukowski, R., Szalewicz, K., Groenenboom, G., & van der Avoird, A. (2006). Interaction potential for water dimer from symmetry-adapted perturbation theory based on density functional description of monomers. *Journal of Chemical Physics*, 125, 044301.
- Bukowski, R., Szalewicz, K., Groenenboom, G. C., & van der Avoird, A. (2007). Predictions of the properties of water from first principles. *Science*, 315, 1249–1252.
- Burcl, R., Chalasinski, G., Bukowski, R., & Szczesniak, M. M. (1995). On the role of bond functions in interaction energy calculations:  $\text{Ar}\cdots\text{HCl}$ ,  $\text{Ar}\cdots\text{H}_2\text{O}$ ,  $(\text{HF})_2$ . *Journal of Chemical Physics*, 103, 1498–1507.
- Casida, M. E. (1995). Time-dependent density-functional response theory for molecules. In D. P. Chong (Ed.), *Recent advances in density-functional theory* (p. 155). Singapore: World Scientific.
- Chalasinski, G., & Szczesniak, M. M. (2000). State of the art and challenges of the ab initio theory of intermolecular interactions. *Chemical Reviews*, 100, 4227–4252.
- Chang, B., Akin-Ojo, O., Bukowski, R., & Szalewicz, K. (2003). Potential energy surface and rovibrational spectrum of  $\text{He-N}_2\text{O}$  dimer. *Journal of Chemical Physics*, 119, 11654.
- Colwell, S. M., Handy, N. C., & Lee, A. M. (1995). Determination of frequency-dependent polarizabilities using current density-functional theory. *Physical Review A*, 53, 1316–1322.
- Day, G. M., & Price, S. L. (2003). A nonempirical anisotropic atom-atom model potential for chlorobenzene crystals. *Journal of the American Chemical Society*, 125, 16434–16443.
- Day, G. M., Motherwell, W. D. S., & Jones, W. (2005). Beyond the isotropic atom model in crystal structure prediction of rigid molecules: Atomic multipoles versus point charges. *Crystal Growth and Design*, 5, 1023–1033.
- Day, G. M., Cooper, T. G., Cabeza, A. J. C., Hejczyk, K., Ammon, H. L., Boerrigter, S. X. M., Tan, J., Valle, R. G. D., Venuti, E., Jose, J., Gadre, S. R., Desiraju, G. R., Thakur, T. S., van Eijck, B. P., Facelli, J. C., Bazterra, V. E., Ferraro, M. B., Gavezzotti, A., Hofmann, D. W. M., Neumann, M., Leusen, F. J. J., Price, J. K. S. L., Misquitta, A. J., Karamertzanis, P. G., Welch, G., Scheraga, H. A., Arnaudova, Y. A., Schmidt, M. U., van de Streek, J., Wolf, A., & Schweizer, B. (2009). Significant progress in predicting the crystal structures of small organic molecules - a report on the fourth blind test. *Acta Crystallographica Section B*, 65, 107–125.
- Dion, M., Rydberg, H., Schroder, E., Langreth, D. C., & Lundqvist, B. I. (2004). Van der waals density functional for general geometries. *Physical Review Letters*, 92, 246401–246404.
- Dunlap, B. I. (2000). Robust and variational fitting. *Physical Chemistry Chemical Physics*, 2, 2113–2116.

- Dunlap, B. I., Connolly, J. W. D., & Sabin, J. R. (1979). On first-row diatomic molecules and local density models. *Journal of Chemical Physics*, *71*, 4993–4999.
- Ernesti, A., & Hutson, J. M. (1997). Non-additive intermolecular forces from the spectroscopy of van der waals trimers: A comparison of ar2-hf and ar2-hcl, including h/d isotope effects. *Journal of Chemical Physics*, *106*, 6288.
- Ernzerhof, M., & Scuseria, G. E. (1999). Assessment of the perdew–burke–ernzerhof exchange–correlation functional. *Journal of Chemical Physics*, *110*, 5029–5036.
- Fiethen, A., Jansen, G., Hesselmann, A., & Schutz, M. (2008). Stacking energies for average b-dna structures from the combined density functional theory and symmetry-adapted perturbation theory approach. *Journal of the American Chemical Society*, *130*, 1802–1803.
- Gagliardi, L., Lindh, R., & Karlstrom, G. (2004). Local properties of quantum systems: The lopro approach. *Journal of Chemical Physics*, *121*, 4494.
- Grabo, T., Petersilka, M., & Gross, E. K. U. (2000). Molecular excitation energies from time-dependent density functional theory. *Journal of Molecular Structure (Theochem)*, *501*, 353.
- Grimme, S. (2004). Accurate description of van der waals complexes by density functional theory including empirical corrections. *Journal of Computational Chemistry*, *25*, 1463–1473.
- Helgaker, T., Klopper, W., Koch, H., & Noga, J. (1997). Basis set convergence of correlated calculations on water. *Journal of Chemical Physics*, *106*, 9639–9646.
- Helgaker, T., Jensen, H. J. A., Joergensen, P., Olsen, J., Ruud, K., Aagren, H., Auer, A., Bak, K., Bakken, V., Christiansen, O., Coriani, S., Dahle, P., Dalskov, E. K., Enevoldsen, T., Fernandez, B., Haettig, C., Hald, K., Halkier, A., Heiberg, H., Hettema, H., Jonsson, D., Kirpekar, S., Kobayashi, R., Koch, H., Mikkelsen, K. V., Norman, P., Packer, M. J., Pedersen, T. B., Ruden, T. A., Sanchez, A., Saue, T., Sauer, S. P. A., Schimmelpfennig, B., Sylvester-Hvid, K. O., Taylor, P. R., & Vahtras, O. (2005). Dalton, a molecular electronic structure program, release 2.0. See <http://www.kjemi.uio.no/software/dalton/dalton.html>. Accessed 18 July 2011
- Hesselmann, A. (2009). Derivation of the dispersion energy as an explicit density- and exchange-hole functional. *Journal of Chemical Physics*, *130*, 084104–5.
- Hesselmann, A., & Jansen, G. (2002a). First-order intermolecular interaction energies from Kohn–Sham orbitals. *Chemical Physics Letters*, *357*, 464–470.
- Hesselmann, A., & Jansen, G. (2002b). Intermolecular induction and exchange-induction energies from coupled-perturbed Kohn–Sham density functional theory. *Chemical Physics Letters*, *362*, 319–325.
- Hesselmann, A., & Jansen, G. (2003a). The helium dimer potential from a combined density functional theory and symmetry-adapted perturbation theory approach using an exact exchange–correlation potential. *Physical Chemistry Chemical Physics*, *5*, 5010.
- Hesselmann, A., & Jansen, G. (2003b). Intermolecular dispersion energies from time-dependent density functional theory. *Chemical Physics Letters*, *367*, 778–784.
- Hesselmann, A., Jansen, G., & Schutz, M. (2005). Density-functional theory–symmetry-adapted intermolecular perturbation theory with density fitting: A new efficient method to study intermolecular interaction energies. *Journal of Chemical Physics*, *122*, 014103.
- Hesselmann, A., Jansen, G., & Schutz, M. (2006). Interaction energy contributions of h-bonded and stacked structures of the at and gc dna base pairs from the combined density functional theory and intermolecular perturbation theory approach. *Journal of the American Chemical Society*, *128*, 11730–11731.
- Hobza, P., & Spöner, J. (2002). Toward true dna base-stacking energies: Mp2, ccSD(t), and complete basis set calculations. *Journal of the American Chemical Society*, *124*, 11802.
- Hodges, M. P., Stone, A. J., & Xantheas, S. S. (1997). Contribution of many-body terms to the energy for small water clusters: A comparison of ab initio calculations and accurate model potentials. *Journal of Physical Chemistry A*, *101*, 9163–9168.
- Ioannou, A. G., Colwell, S. M., & Amos, R. D. (1997). The calculation of frequency-dependent polarizabilities using current density functional theory. *Chemical Physics Letters*, *278*, 278–284.
- Israelachvili, J. N. (2007). *Intermolecular and surface forces* (2nd edn.). Amsterdam: Academic.
- Jankowski, P. (2004). Approximate generation of full-dimensional ab initio van der waals surfaces for high-resolution spectroscopy. *Journal of Chemical Physics*, *121*, 1655–1662.
- Jankowski, P. (2008). Exploring the new three-dimensional ab initio interaction energy surface of the Ar–HF complex: Rovibrational calculations for Ar–HF and Ar–DF with vibrationally excited diatoms. *Journal of Chemical Physics*, *128*, 154311–11.
- Jankowski, P., & Ziolkowski, M. (2006). Fitting the derivative surfaces for full-dimensional



- interaction potentials. *Molecular Physics*, 104, 2293–2302.
- Jenness, G. R., & Jordan, K. D. (2009). Df-dft-sapt investigation of the interaction of a water molecule to coronene and dodecabenzocoronene: Implications for the water-graphite interaction. *Journal of Physical Chemistry C*, 113, 10242–10248.
- Jeziorski, B., & Szalewicz, K. (1998). *Encyclopedia of computational chemistry* (Vol. 2, p. 1376). Chichester: Wiley.
- Jeziorski, B., & Szalewicz, K. (2002). Symmetry-adapted perturbation theory. In S. Wilson (Ed.), *Handbook of molecular physics and quantum chemistry* (Vol. 8, Chap. 8, pp. 37–83). Chichester: Wiley.
- Jeziorska, M., Jeziorski, B., & Cizek, J. (1987). Direct calculation of the hartree-fock interaction energy via exchange-perturbation expansion. The He...He interaction. *International Journal of Quantum Chemistry*, 32, 149–164.
- Jeziorski, B., Moszynski, R., & Szalewicz, K. (1994). Perturbation theory approach to intermolecular potential energy surfaces of Van der Waals complexes. *Chemical Reviews*, 94, 1887–1930.
- Karamertzanis, P. G., Day, G. M., Welch, G. W. A., Kendrick, J., Leusen, F. J. J., Neumann, M. A., & Price, S. L. (2008). Modeling the interplay of inter- and intramolecular hydrogen bonding in conformational polymorphs. *Journal of Chemical Physics*, 128, 244708–17.
- Kendall, R. A., Dunning, T. H., & Harrison, R. J. (1992). Electron affinities of the first-row atoms revisited. systematic basis sets and wave functions. *Journal of Chemical Physics*, 96, 6796–6806.
- Koch, W. (2000). *A chemist's guide to density functional theory*. Weinheim, Chichester: Wiley.
- Le Sueur, C. R., & Stone, A. J. (1993). Practical schemes for distributed polarizabilities. *Molecular Physics*, 78, 1267–1291.
- Le Sueur, C. R., & Stone, A. J. (1994). Localization methods for distributed polarizabilities. *Molecular Physics*, 83, 293–308.
- Lehninger, A. L. (1970). *Biochemistry*. New York: Worth Publishers, Inc.
- Lillestolen, T. C., & Wheatley, R. J. (2007). First-principles calculation of local atomic polarizabilities. *Journal of Physical Chemistry A*, 111, 11141–11146.
- Lillestolen, T. C., & Wheatley, R. J. (2008). Redefining the atom: Atomic charge densities produced by an iterative stockholder approach. *Chemical Communications*, 5909–5911.
- Longuet-Higgins, H. C. (1965). Intermolecular forces. *Discussions of the Faraday Society*, 40, 7.
- Maddox, J. (1988). Crystals from first principles. *Nature*, 335, 201.
- Magnasco, V., & McWeeny, R. (1991). Weak interaction between molecules and their physical interpretations. In Z. B. Maksić (Ed.), *Theoretical models of chemical bonding* (Vol. 4, pp. 133–169). New York: Springer.
- Mas, E. M., Szalewicz, K., Bukowski, R., & Jeziorski, B. (1997). Pair potential for water from symmetry-adapted perturbation theory. *Journal of Chemical Physics*, 107, 4207–4218.
- Mas, E. M., Bukowski, R., & Szalewicz, K. (2003a). Ab initio three-body interactions for water. I. Potential and structure of water trimer. *Journal of Chemical Physics*, 118, 4386–4403.
- Mas, E. M., Bukowski, R., & Szalewicz, K. (2003b). Ab initio three-body interactions for water. II. Effects on structure and energetics of liquid. *Journal of Chemical Physics*, 118, 4404–4413.
- Matta, C. F., & Bader, R. F. W. (2006). An experimentalist's reply to 'what is an atom in a molecule?' *Journal of Physical Chemistry A*, 110, 6365–6371.
- Milet, A., Moszynski, R., Wormer, P. E. S., & van der Avoird, A. (1999). Hydrogen bonding in water clusters: Pair and many-body interactions from symmetry-adapted perturbation theory. *Journal of Physical Chemistry A*, 103, 6811–6819.
- Misquitta, A. J., & Stone, A. J. (2006). Distributed polarizabilities obtained using a constrained density-fitting algorithm. *Journal of Chemical Physics*, 124, 024111.
- Misquitta, A. J., & Stone, A. J. (2007). CAMCASP: A program for studying intermolecular interactions and for the calculation of molecular properties in distributed form. University of Cambridge. <http://www-stone.ch.cam.ac.uk/programs.html#CamCASP>. Accessed 18 July 2011
- Misquitta, A. J., & Stone, A. J. (2008a). Accurate induction energies for small organic molecules: I. Theory. *Journal of Chemical Theory and Computation*, 4, 7–18.
- Misquitta, A. J., & Stone, A. J. (2008b). Dispersion energies for small organic molecules: First row atoms. *Molecular Physics*, 106, 1631–1643.
- Misquitta, A. J., & Szalewicz, K. (2002). Intermolecular forces from asymptotically corrected density functional description of monomers. *Chemical Physics Letters*, 357, 301–306.
- Misquitta, A. J., & Szalewicz, K. (2005). Symmetry-adapted perturbation-theory calculations of intermolecular forces employing density-functional description of monomers. *Journal of Chemical Physics*, 122, 214109.

- Misquitta, A. J., Bukowski, R., & Szalewicz, K. (2000). Spectra of Ar-CO<sub>2</sub> from ab initio potential energy surfaces. *Journal of Chemical Physics*, *112*, 5308–5319.
- Misquitta, A. J., Jeziorski, B., & Szalewicz, K. (2003). Dispersion energy from density-functional theory description of monomers. *Physical Review Letters*, *91*, 33201.
- Misquitta, A., Podeszwa, R., Jeziorski, B., & Szalewicz, K. (2005a). Intermolecular potentials based on symmetry-adapted perturbation theory with dispersion energies from time-dependent density-functional calculations. *Journal of Chemical Physics*, *123*, 214103.
- Misquitta, A. J., Podeszwa, R., Jeziorski, B., & Szalewicz, K. (2005b). Intermolecular potentials based on symmetry-adapted perturbation theory with dispersion energies from time-dependent density-functional theory. *Journal of Chemical Physics*, *123*, 214103.
- Misquitta, A. J., Stone, A. J., & Price, S. L. (2008a). Accurate induction energies for small organic molecules: II. Models and numerical details. *Journal of Chemical Theory and Computation*, *4*, 19–32.
- Misquitta, A. J., Welch, G. W. A., Stone, A. J., & Price, S. L. (2008b). A first principles prediction of the crystal structure of C<sub>6</sub>Br<sub>2</sub>ClFH<sub>2</sub>. *Chemical Physics Letters*, *456*, 105–109.
- Misquitta, A. J., Spencer, J., Stone, A. J., & Alavi, A. (2010). Dispersion interactions between semiconducting wires. *Physical Review B*, *82*, 075312–075317.
- Moszyński, R., Jeziorski, B., Rybak, S., Szalewicz, K., & Williams, H. L. (1994). Many-body theory of exchange effects in intermolecular interactions. density matrix approach and applications to He-F<sup>-</sup>, He-HF, H<sub>2</sub>-HF, and Ar-H<sub>2</sub> dimers. *Journal of Chemical Physics*, *100*, 5080–5092.
- Moszyński, R., Heijmen, T. G. A., & Jeziorski, B. (1996). Symmetry-adapted perturbation theory for the calculation of hartree-fock interaction energies. *Molecular Physics*, *88*, 741–758.
- Murdachaw, G., Misquitta, A. J., Bukowski, R., & Szalewicz, K. (2001). Intermolecular potential energy surfaces and spectra of Ne-HCN complex from ab initio calculations. *Journal of Chemical Physics*, *114*, 764.
- Murdachaw, G., Szalewicz, K., & Bukowski, R. (2002). Efficient generation of flexible-monomer intermolecular potential energy surfaces. *Physical Review Letters*, *88*, 12320.
- Neumann, M. A., & Perrin, M.-A. (2005). Energy ranking of molecular crystals using density functional theory calculations and an empirical van der waals correction. *Journal of Physical Chemistry B*, *109*, 15531–15541.
- Onida, G., Reinig, L., & Rubio, A. (2002). Electronic excitations: Density-functional versus many-body greens-function approaches. *Reviews of Modern Physics*, *74*, 601.
- Parr, R. G., Ayers, P. W., & Nalewajski, R. F. (2005). What is an atom in a molecule? *Journal of Physical Chemistry A*, *109*, 3957–3959.
- Parsegian, V. A. (2005). *Van der Waals forces: A handbook for biologists, chemists, engineers, and physicists*. Cambridge, NY: Cambridge University Press.
- Patkowski, K., Szalewicz, K., & Jeziorski, B. (2006). Third-order interactions in symmetry-adapted perturbation theory. *Journal of Chemical Physics*, *125*, 154107.
- Pernal, K., Podeszwa, R., Patkowski, K., & Szalewicz, K. (2009). Dispersionless density functional theory. *Physical Review Letters*, *103*, 263201(4).
- Petersilka, M., Gossmann, U. J., & Gross, E. K. U. (1996). Excitation energies from time-dependent density-functional theory. *Physical Review Letters*, *76*, 1212–1215.
- Peterson, K. A., & McBane, G. C. (2005). A hierarchical family of three-dimensional potential energy surfaces for He-CO. *Journal of Chemical Physics*, *123*, 084314–15.
- Pitonak, M., & Hesselmann, A. (2010). Accurate intermolecular interaction energies from a combination of mp2 and tddft response theory. *Journal of Chemical Theory and Computation*, *6*, 168–178.
- Podeszwa, R., & Szalewicz, K. (2005). Accurate interaction energies for argon, krypton, and benzene dimers from perturbation theory based on the Kohn–Sham model. *Chemical Physics Letters*, *412*, 488.
- Podeszwa, R., & Szalewicz, K. (2007). Three-body symmetry-adapted perturbation theory based on Kohn–Sham description of the monomers. *Journal of Chemical Physics*, *126*, 194101.
- Podeszwa, R., & Szalewicz, K. (2008). Physical origins of interactions in dimers of polycyclic aromatic hydrocarbons. *Physical Chemistry Chemical Physics*, *10*, 2735–2746.
- Podeszwa, P., Bukowski, R., & Szalewicz, K. (2006a). Potential energy surface for the benzene dimer and perturbational analysis of  $\pi - \pi$  interactions. *Journal of Physical Chemistry A*, *110*, 10345–10354.
- Podeszwa, R., Bukowski, R., & Szalewicz, K. (2006b). Density-fitting method in symmetry-adapted perturbation theory based on Kohn–Sham description of monomers. *Journal of Chemical Theory and Computation*, *2*, 400–412.

- Podeszwa, R., Rice, B. M., & Szalewicz, K. (2008). Predicting structure of molecular crystals from first principles. *Physical Review Letters*, *101*, 115503.
- Price, S. L. (2008). Computational prediction of organic crystal structures and polymorphism. *International Reviews in Physical Chemistry*, *27*, 541–568.
- Price, S. L. (2009). Computed crystal energy landscapes for understanding and predicting organic crystal structures and polymorphism. *Accounts of Chemical Research*, *42*, 117–126.
- Sadlej, A. J. (1992). Medium-sized polarized basis sets for high-level correlated calculations of molecular electric properties. V. Fourth-row atoms Sn–I. *Theoretical Chemistry Accounts*, *81*, 339–354.
- Sadlej, A. J., & Urban, M. (1991). Medium-sized polarized basis sets for high-level correlated calculations of molecular electric properties. III. Alkali atoms (Li, Na, K, Rb) and alkaline-earth atoms (Be, Mg, Ca, Sr). *Theochem – Journal of Molecular Structure*, *80*, 147–171.
- Sebetci, A., & Beran, G. J. O. (2010). Spatially homogeneous qm/mm for systems of interacting molecules with on-the-fly ab initio force-field parametrization. *Journal of Chemical Theory and Computation*, *6*, 155–167.
- Singh, U. C., & Kollman, P. A. (1984). An approach to computing electrostatic charges for molecules. *Journal of Computational Chemistry*, *5*, 129–145.
- Sinnokrot, M. O., Valeev, E. F., & Sherrill, C. D. (2002). Estimates of the ab initio limit for pi-pi interactions: The benzene dimer. *Journal of the American Chemical Society*, *124*, 10887–10893.
- Stone, A. J. (1993). Computation of charge-transfer energies by perturbation theory. *Chemical Physics Letters*, *211*, 101–109.
- Stone, A. J. (1996). *The theory of intermolecular forces*. Oxford: Clarendon Press.
- Stone, A. J. (2005). Distributed multipole analysis: Stability for large basis sets. *Journal of Chemical Theory and Computation*, *1*, 1128–1132.
- Stone, A. J., & Alderton, M. (1985). Distributed multipole analysis—methods and applications. *Molecular Physics*, *56*, 1047–1064.
- Stone, A. J., & Misquitta, A. J. (2007). Atom–atom potentials from ab initio calculations. *International Reviews in Physical Chemistry*, *26*, 193–222.
- Stone, A. J., & Misquitta, A. J. (2009). Charge-transfer in symmetry-adapted perturbation theory. *Chemical Physics Letters*, *473*, 201–205.
- Stone, A. J., & Tough, R. J. A. (1984). Spherical tensor theory of long-range intermolecular forces. *Chemical Physics Letters*, *110*, 123–129.
- Stone, A. J., Dullweber, A., Engkvist, O., Fraschini, E., Hodges, M. P., Meredith, A. W., Nutt, D. R., Popelier, P. L. A., & Wales, D. J. (2006). Orient: A program for studying interactions between molecules, version 4.6. University of Cambridge. <http://www-stone.ch.cam.ac.uk/programs.html#Orient>. Accessed 18 July 2011
- Szalewicz, K. (2002). Hydrogen bond. In R. A. M. et al. (Ed.), *Encyclopedia of physical science and technology* (Vol. 7, 3rd edn., pp. 505–538). San Diego: Academic.
- Szalewicz, K., Patkowski, K., & Jeziorski, B. (2005). Intermolecular interactions via perturbation theory: From diatoms to biomolecules. In D. J. Wales (Ed.), *Intermolecular forces and clusters II* (Structure and bonding, Vol. 116, pp. 43–117). Berlin: Springer.
- Tang, K. T., & Toennies, J. P. (1992). The damping function of the van der Waals attraction in the potential between rare gas atoms and metal surfaces. *Surface Science Letters*, *279*, 203–206.
- Totton, T., Misquitta, A. J., & Kraft, M. (2010). A first principles development of a general anisotropic potential for polycyclic aromatic hydrocarbons. *Journal of Chemical Theory and Computation*, *6*, 683–695.
- Tozer, D. J. (2000). The asymptotic exchange potential in Kohn–Sham theory. *Journal of Chemical Physics*, *112*, 3507–3515.
- Tozer, D. J., & Handy, N. C. (1998). Improving virtual Kohn–Sham orbitals and eigenvalues: Application to excitation energies and static polarizabilities. *Journal of Chemical Physics*, *109*, 10180–10189.
- Tsuzuki, S., & Lüthi, H. P. (2001). Interaction energies of van der Waals and hydrogen bonded systems calculated using density functional theory: Assessing the pw91 model. *Journal of Chemical Physics*, *114*, 3949–3957.
- van Mourik, T., & Gdanitz, R. J. (2002). A critical note on density functional theory studies on rare-gas dimers. *Journal of Chemical Physics*, *116*, 9620–9623.
- Vissers, G. W. M., Hesselmann, A., Jansen, G., Wormer, P. E. S., & van der Avoird, A. (2005). New CO–CO interaction potential tested by rovibrational calculations. *Journal of Chemical Physics*, *122*(5), 054306. doi:10.1063/1.1835262.
- Wales, D. J. (Ed.). (2005a). *Intermolecular forces and clusters I* (Structure and bonding). Berlin: Springer.
- Wales, D. J. (Ed.). (2005b). *Intermolecular forces and clusters II* (Structure and Bonding). Berlin: Springer.
- Weigend, F., Haser, M., Patzelt, H., & Ahlrichs, R. (1998). RI-MP2: Optimized auxiliary basis

- sets and demonstration of efficiency. *Chemical Physics Letters*, 294, 143–152.
- Weigend, F., Kohn, A., & Hattig, C. (2002). Efficient use of the correlation consistent basis sets in resolution of the identity MP2 calculations. *Journal of Chemical Physics*, 116, 3175–3183.
- Welch, G. W. A., Karamertzanis, P. G., Misquitta, A. J., Stone, A. J., & Price, S. L. (2008). Is the induction energy important for modeling organic crystals? *Journal of Chemical Theory and Computation*, 4, 522–532.
- Werner, H.-J., Knowles, P. J., Lindh, R., Manby, F. R., Schütz, M., Celani, P., Korona, T., Mitrushenkov, A., Rauhut, G., Adler, T. B., Amos, R. D., Bernhardsson, A., Berning, A., Cooper, D. L., Deegan, M. J. O., Dobbyn, A. J., Eckert, F., Goll, E., Hampel, C., Hetzer, G., Hrenar, T., Knizia, G., Köppl, C., Liu, Y., Lloyd, A. W., Mata, R. A., May, A. J., McNicholas, S. J., Meyer, W., Mura, M. E., Nicklass, A., Palmieri, P., Pflüger, K., Pitzer, R., Reiher, M., Schumann, U., Stoll, H., Stone, A. J., Tarroni, R., Thorsteinsson, T., Wang, M., & Wolf, A. (2008). Molpro, version 2008.3, a package of ab initio programs. See <http://www.molpro.net>. Accessed 18 July 2011
- Wheatley, R. J., & Lillestolen, T. C. (2008). Local polarizabilities and dispersion energy coefficients. *Molecular Physics*, 106, 1545–1556.
- Williams, D. E. (2001a). Improved intermolecular force field for crystalline oxohydrocarbons including O-H...O hydrogen bonds. *Journal of Computational Chemistry*, 22, 1–20.
- Williams, D. E. (2001b). Improved intermolecular force field for molecules containing H, C, N, and O atoms, with applications to nucleoside and peptide crystals. *Journal of Computational Chemistry*, 22, 1154–1166.
- Williams, G. J., & Stone, A. J. (2003). Distributed dispersion: A new approach. *Journal of Chemical Physics*, 119, 4620–4628.
- Williams, H. L., Mas, E. M., Szalewicz, K., & Jeziorski, B. (1995). On the effectiveness of monomer-, dimer-, and bond-centered basis functions in calculations of intermolecular interaction energies. *Journal of Chemical Physics*, 103, 7374–7391.
- Woon, D. E., & T. H. Dunning, J. (1994). Gaussian basis sets for use in correlated molecular calculations. IV. Calculation of static. Electrical response properties. *Journal of Chemical Physics*, 100, 2975–2889.
- Xu, Y., Jager, W., Tang, J., & McKellar, A. R. W. (2003). *Physical Review Letters*, 91, 163401(4).
- Zaremba, E., & Kohn, W. (1976). Van der waals interaction between an atom and a solid surface. *Physical Review B*, 13, 2270–2285.



# 7 Molecular Dynamics Simulation: From “Ab Initio” to “Coarse Grained”

Chris Lorenz<sup>1</sup> · Nikos L. Doltsinis<sup>1,2</sup>

<sup>1</sup>Department of Physics, King’s College London, London, UK

<sup>2</sup>Institute for Solid State Theory, Department of Physics,  
University of Münster, Münster, Germany

<b>Introduction</b> .....	<b>197</b>
<b>Choosing the Right Method</b> .....	<b>197</b>
Theoretical Background .....	199
Born–Oppenheimer Approximation .....	199
Ab Initio Molecular Dynamics .....	200
Born–Oppenheimer Molecular Dynamics .....	201
Car–Parrinello Molecular Dynamics .....	201
Classical Molecular Dynamics .....	201
Verlet Algorithm .....	202
“Leap-Frog” Algorithm .....	203
Velocity Verlet Algorithm .....	203
Hybrid Quantum/Classical (QM/MM) Molecular Dynamics .....	204
Partitioning Schemes .....	204
Bonds Across the QM/MM Boundary .....	205
Coarse Grain Molecular Dynamics .....	207
<b>Interaction Potentials/Force Fields</b> .....	<b>208</b>
Classical Force Fields .....	208
Nonbonded Interactions .....	209
Bonded Interactions .....	212
Angle Bending Interactions .....	212
Torsional Interactions .....	213
First Principles Electronic Structure Methods .....	213
<b>Building the System/Collecting the Ingredients</b> .....	<b>215</b>
Setting Up an AIMD Simulation .....	215
Building a Molecule .....	215
Plane Waves and Pseudopotentials .....	215
Setting Up a Classical MD Simulation .....	217
Gathering Preliminary Information .....	218
Building the System .....	218

<b><i>Preparing an Input File</i></b> .....	<b>219</b>
Optimization Algorithms .....	219
Steepest Descent .....	219
Conjugate Gradient Methods .....	220
Direct Inversion of the Iterative Subspace .....	220
Controlling Temperature: Thermostats .....	221
Rescale Thermostat .....	222
Berendsen Thermostat .....	222
Nosé–Hoover Thermostat .....	223
Controlling Pressure: Barostats .....	223
Berendsen Barostat .....	224
Nosé–Hoover Barostat .....	224
Setting the Time Step .....	225
Born–Oppenheimer MD .....	225
Car–Parrinello MD .....	226
<b><i>Postprocessing</i></b> .....	<b>227</b>
Data Analysis .....	227
Spatial Distribution Functions .....	227
Time Correlation Functions .....	229
Visualization .....	230
<b><i>References</i></b> .....	<b>231</b>

**Abstract:** This chapter provides an overview of different hierarchical levels of molecular dynamics (MD) simulations spanning a wide range of time and length scales – from first principles approaches via classical atomistic methods to coarse graining techniques. The theoretical background of the most widely used methods and algorithms is briefly reviewed and practical instructions are given on the choice of input parameters for an actual computer simulation. In addition, important postprocessing procedures such as data analysis and visualization are discussed.

## Introduction

---

Molecular dynamics (MD) simulations in their different flavors are widely used in a large variety of research areas of Computational Physics and Chemistry. They represent a powerful tool to study the motion of atoms in molecules, liquids, and solids. The term MD typically refers to the propagation of point particles – atomic nuclei or effective particles combining several nuclei – according to the laws of classical mechanics. In particular, the forces acting on the particles are calculated “on the fly” only at discrete points along the trajectory. Following this definition, we discuss in this chapter Ab Initio MD (AIMD), i.e., the atomic forces are calculated from first principles, classical atomistic MD using analytical empirical interaction potentials (force-fields), which sometimes is referred to as force-field molecular dynamics, and coarse grain MD using analytical empirical potentials between effective particles representing groups of atoms. We exclude methods which go beyond classical nuclei, such as path integral MD (Tuckerman 2002; Tuckerman and Hughes 1998; Tuckerman et al. 1993) and wavepacket dynamics (Balint-Kurti 2008; Worth et al. 2008), or beyond the Born–Oppenheimer approximation (Doltsinis and Marx 2002a, b). This overview, furthermore, leaves out the vast area of semi-empirical methods (see for instance Bredow and Jug [2005] for a recent review) including self-consistent charge density functional tight-binding (SCC-DFTB) (Elstner et al. 1998) and empirical valence-bond (EVB) theory (Aqvist and Warshel 1993; Shurki and Warshel 2003; Warshel 1991, 2003).

The aim of this chapter is to offer practical guidance on how to choose the appropriate technique for a particular physical problem, how to set up a simulation, and how to analyze and visualize the output. In addition it should provide the theoretical background required to become a competent user of the available simulation software packages.

## Choosing the Right Method

---

When choosing which type of molecular dynamics simulations to perform, it is important to understand the capabilities of each technique. The differences in the various methods are basically dependent on the detail with which each one models a physical system.

The most detailed molecular dynamics simulation technique is the ab-initio (quantum) molecular dynamics simulation approach that explicitly models the electrons of the particles within the system. Whereas, force-field molecular dynamics simulations model the nuclear interactions of the particles within the system, and therefore do not explicitly model each electron. Then the method that incorporates the least amount of detail is that of coarse grain molecular dynamics models where multiple particles are grouped together before being represented by a single interaction “bead.”



Therefore, quantum molecular dynamics simulations will generate the most detailed modeling of interatomic interactions as electrons are the basis of all such interactions. Quantum simulations allow for certain phenomena like electron transport within a system to be modeled, which cannot be modeled in force-field or coarse grain molecular dynamics simulations because they do not explicitly model electrons. Also, in order to model chemical reactions, quantum simulations are the most accurate approach (Note: there have been force-field and coarse-grain molecular dynamics simulations that have modeled the formation and breaking of bonds, but some a priori knowledge must then be included in the model to allow for the reaction to take place). The major limitations of quantum simulations is that the simulations are very computationally intensive, which results in the capability to model only small system sizes ( $\sim 10^2$  particles) and time ( $\sim 10^{-12}$  s). Thus the systems that can be modeled are limited to small molecules or portions of larger molecules (i.e., specific amino acids within a protein).

Force-field molecular dynamics simulations offer the ability to model molecules at the particle level. Often, information from quantum simulations is used to develop the empirical equations (force-field) that are used to govern the interactions between particles. Because force-field molecular dynamics simulations use less detail than the quantum simulations, they are able to model systems that are significantly larger in size ( $\sim 10^6$  particles) for a longer period of time ( $< 10^{-6}$  s). Therefore, measuring the structural, mechanical, and/or transport properties of medium to large sized systems (i.e., proteins, functionalized nanoparticles, . . .) is possible.

Finally, coarse grain molecular dynamics simulations reduce the number of degrees of freedom within the simulated system even further by grouping several atoms into one interaction bead. Therefore, even larger system sizes and times (on the order of seconds) are accessible via these simulations. Several of the same properties measured via force-field molecular dynamics simulations can be measured with coarse grain molecular dynamics simulations (i.e., structural, mechanical, and transport properties). However, due to the reduced detail in the models of the molecules, it is not possible to investigate specific chemical interactions within a system, such as hydrogen bonding.

Once you have chosen the appropriate method for the particular system and property to be investigated, the next choice is what simulation package to use. For classical MD simulations, there are several free molecular dynamics packages that can be found on the web including DL\_POLY (Smith et al. 2002; Todorov and Smith 2009), GROMACS (van der Spoel et al. 2005a, b), HOOMD (Anderson et al. 2008; HOOMD 2009), LAMMPS (LAMMPS 2010; Plimpton 1995), MOLLY (Refson 2000, 2001), and NAMD (Bhandarkar et al. 2009; Phillips et al. 2005b), and there are also commercial packages including AMBER (Case et al. 2005, 2008), CHARMM (Brooks et al. 2009; CHARMM 2009), and GROMOS (GROMOS 2007; Scott et al. 1999). Generally, these codes can be divided into those that are mostly used for simulations of biological systems (AMBER, CHARMM, GROMACS, GROMOS, NAMD) and those that are more general simulation packages (HOOMD, LAMMPS, MOLLY). When choosing between these options, an important criterion is to choose a code that you feel comfortable using. Outside of comfort, another aspect to take into consideration is that packages will differ in the features they offer and the additional tools to perform analysis (usually lists of analysis tools can be found in the packages' documentation).

For AIMD simulations, the user may choose from a large number of codes, for instance, ABINIT (2010; Aulbur et al. 2000), CASTEP (2009; Clark et al. 2005; Segall et al. 2002), CONQUEST (2009; Bowler et al. 2006), CP2K (Hutter et al. 2009; VandeVondele et al. 2005, 2006), CPMD (Marx and Hutter 2000, 2009; Parrinello et al. 2008), CP-PAW (2006; Blochl 1994; Blochl et al. 2003), DACAPO (2006), FHI98md (2002; Bockstedte et al. 1997), NWChem

(2008; Kendall et al. 2000), ONETEP (2005; Skylaris et al. 2005), PINY (2005), PWscf (2009; Giannozzi et al. 2009), QuantumEspresso (2009; Giannozzi et al. 2009), SIESTA (2010; Artacho et al. 2008; Soler et al. 2002), S/PHI/nX (2009; Boeck 2009), or VASP (2009; Kresse and Furthmüller 1996).

## Theoretical Background

### Born–Oppenheimer Approximation

Let us begin by introducing our nomenclature and by reviewing some well-known basic relations within the Schrödinger formulation of quantum mechanics. A complete, nonrelativistic, description of a dynamic system of  $N$  atoms having the positions  $\mathbf{R} = \{\mathbf{R}_1, \mathbf{R}_2, \dots, \mathbf{R}_I, \dots, \mathbf{R}_N\}$  with  $n$  electrons located at  $\mathbf{r} = \{\mathbf{r}_1, \mathbf{r}_2, \dots, \mathbf{r}_i, \dots, \mathbf{r}_n\}$  would involve solving the time-dependent Schrödinger equation

$$\mathcal{H}\Phi(\mathbf{r}, \mathbf{R}; t) = i\hbar \frac{\partial}{\partial t} \Phi(\mathbf{r}, \mathbf{R}; t), \quad (7.1)$$

with the total Hamiltonian

$$\mathcal{H}(\mathbf{r}, \mathbf{R}) = \mathcal{T}(\mathbf{R}) + \mathcal{T}(\mathbf{r}) + \mathcal{V}_{\text{nn}}(\mathbf{R}) + \mathcal{V}_{\text{ne}}(\mathbf{r}, \mathbf{R}) + \mathcal{V}_{\text{ee}}(\mathbf{r}), \quad (7.2)$$

being the sum of kinetic energy of the atomic nuclei,

$$\mathcal{T}(\mathbf{R}) = -\frac{\hbar^2}{2} \sum_{I=1}^N \frac{\nabla_I^2}{M_I}, \quad (7.3)$$

kinetic energy of the electrons,

$$\mathcal{T}(\mathbf{r}) = -\frac{\hbar^2}{2m_e} \sum_{i=1}^n \nabla_i^2, \quad (7.4)$$

internuclear repulsion,

$$\mathcal{V}_{\text{nn}}(\mathbf{R}) = \frac{e^2}{4\pi\epsilon_0} \sum_{I=1}^{N-1} \sum_{J>I}^N \frac{Z_I Z_J}{|\mathbf{R}_I - \mathbf{R}_J|}, \quad (7.5)$$

electronic–nuclear attraction,

$$\mathcal{V}_{\text{ne}}(\mathbf{r}, \mathbf{R}) = -\frac{e^2}{4\pi\epsilon_0} \sum_{I=1}^N \sum_{i=1}^n \frac{Z_I}{|\mathbf{r}_i - \mathbf{R}_I|}, \quad (7.6)$$

and interelectronic repulsion,

$$\mathcal{V}_{\text{ee}}(\mathbf{r}) = \frac{e^2}{4\pi\epsilon_0} \sum_{i=1}^{n-1} \sum_{j>i}^n \frac{1}{|\mathbf{r}_i - \mathbf{r}_j|}. \quad (7.7)$$

Here,  $M_I$  and  $Z_I$  denote the mass and atomic number of nucleus  $I$ ;  $m_e$  and  $e$  are the electronic mass and elementary charge, and  $\epsilon_0$  is the permittivity of vacuum. The nabla operators  $\nabla_I$  and  $\nabla_i$  act on the coordinates of nucleus  $I$  and electron  $i$ , respectively. The total wavefunction  $\Phi(\mathbf{r}, \mathbf{R}; t)$  simultaneously describes the motion of both electrons and nuclei.

The Born–Oppenheimer approximation (Doltsinis and Marx 2002b; Kofos 1970; Kutzelnigg 1997) separates nuclear and electronic motion based on the assumption that the much faster electrons adjust their positions instantaneously to the comparatively slow changes in

nuclear positions. The electronic problem is then reduced to the time-independent (electronic) Schrödinger equation for clamped nuclei,

$$\mathcal{H}_{\text{el}}(\mathbf{r}; \mathbf{R})\Psi_k(\mathbf{r}; \mathbf{R}) = E_k(\mathbf{R})\Psi_k(\mathbf{r}; \mathbf{R}), \quad (7.8)$$

where  $\mathcal{H}_{\text{el}}(\mathbf{r}; \mathbf{R})$  is the electronic hamiltonian,

$$\mathcal{H}_{\text{el}}(\mathbf{r}, \mathbf{R}) = \mathcal{T}(\mathbf{r}) + \mathcal{V}_{\text{nn}}(\mathbf{R}) + \mathcal{V}_{\text{ne}}(\mathbf{r}, \mathbf{R}) + \mathcal{V}_{\text{ee}}(\mathbf{r}), \quad (7.9)$$

and  $\Psi_k(\mathbf{r}; \mathbf{R})$  is the electronic wavefunction of state  $k$ . Meanwhile, nuclear motion is described by

$$[\mathcal{T}(\mathbf{R}) + E_k(\mathbf{R})]\chi_k = i\hbar \frac{\partial}{\partial t}\chi_k \quad (7.10)$$

with the nuclear wavefunction  $\chi_k(\mathbf{R}, t)$  evolving on the potential energy surface  $E_k(\mathbf{R})$  of the electronic state  $k$ . The total wavefunction is then the direct product of the electronic and the nuclear wavefunction,

$$\Phi(\mathbf{r}, \mathbf{R}; t) = \Psi_k(\mathbf{r}, \mathbf{R})\chi_k(\mathbf{R}, t) \quad (7.11)$$

In the classical limit (Doltsinis and Marx 2002b), the nuclear wave equation (7.10) is replaced by Newton’s equation of motion

$$M_I \ddot{\mathbf{R}}_I = -\nabla_I E_k \quad (7.12)$$

For a great number of physical situations, the Born–Oppenheimer approximation can be safely applied. On the other hand, there are many important chemical phenomena such as charge transfer and photoisomerization reactions, whose very existence is due to the inseparability of electronic and nuclear motion. Inclusion of nonadiabatic effects is beyond the scope of this chapter and the reader is referred to the literature (e.g., Doltsinis 2006; Doltsinis and Marx 2002b) for more details.

The above approximations form the basis of conventional molecular dynamics, (7.7) Eqs. 7.12 together with (7.8) being the working equations. Thus, in principle, a classical trajectory calculation merely amounts to integrating Newton’s equations of motion (7.12). In practice, however, this deceptively simple task is complicated by the fact that the stationary Schrödinger equation (7.8) cannot be solved exactly for any many-electron system. The potential energy surface therefore has to be approximated using ab initio electronic structure methods or empirical interaction potentials (so-called force-field molecular dynamics Sutmann [2002] and Allen and Tildesley [1987]). The former approach, usually referred to as ab initio molecular dynamics (AIMD), will be the subject of section “Ab Initio Molecular Dynamics,” while the latter – force-field molecular dynamics – will be discussed in section “Classical Molecular Dynamics.”

## Ab Initio Molecular Dynamics

In the following, we shall focus on first principles molecular dynamics methods. Due to the high computational cost associated with ab initio electronic structure calculations of large molecules, computation of the entire potential energy surface prior to the molecular dynamics simulation is best avoided. A more efficient alternative is the evaluation of electronic energy and nuclear forces “on the fly” at each step along the trajectory.

## Born–Oppenheimer Molecular Dynamics

In the so-called Born–Oppenheimer implementation of such a scheme (Marx and Hutter 2000), the nuclei are propagated by integration of Eq. 7.12, where the exact energy  $E_k$  is replaced with the eigenvalue,  $\tilde{E}_k$ , of some approximate electronic Hamiltonian,  $\tilde{\mathcal{H}}_{\text{el}}$ , which is calculated at each time step. For the electronic ground state, i.e.,  $k = 0$ , the use of Kohn–Sham (KS) density functional theory (Dreizler and Gross 1990; Parr and Yang 1989) has become increasingly popular.

## Car–Parrinello Molecular Dynamics

In order to further increase computational efficiency, Car and Parrinello have introduced a technique to bypass the need for wavefunction optimization at each molecular dynamics step (Car and Parrinello 1985; Marx and Hutter 2000). Instead, the molecular wavefunction is dynamically propagated along with the atomic nuclei according to the equations of motion

$$M_I \ddot{\mathbf{R}}_I = -\nabla_I \langle \Psi_k | \tilde{\mathcal{H}}_{\text{el}} | \Psi_k \rangle \quad (7.13)$$

$$\mu_i \ddot{\psi}_i = -\frac{\delta}{\delta \psi_i^*} \langle \Psi_k | \tilde{\mathcal{H}}_{\text{el}} | \Psi_k \rangle + \sum_j \lambda_{ij} \psi_j, \quad (7.14)$$

where the KS one-electron orbitals  $\psi_i$  are kept orthonormal by the Lagrange multipliers  $\lambda_{ij}$ . These are the Euler–Lagrange equations

$$\frac{d}{dt} \frac{\partial \mathcal{L}}{\partial \dot{q}} = \frac{\partial \mathcal{L}}{\partial q}, \quad (q = \mathbf{R}_I, \psi_i^*) \quad (7.15)$$

for the Car–Parrinello Lagrangian (Car and Parrinello 1985)

$$\mathcal{L} = \sum_I \frac{1}{2} M_I \dot{\mathbf{R}}_I^2 + \sum_i \frac{1}{2} \mu_i \langle \dot{\psi}_i | \dot{\psi}_i \rangle - \langle \Psi_k | \tilde{\mathcal{H}}_{\text{el}} | \Psi_k \rangle + \sum_{ij} \lambda_{ij} (\langle \psi_i | \psi_j \rangle - \delta_{ij}) \quad (7.16)$$

that is formulated here for an arbitrary electronic state  $\Psi_k$ , an arbitrary electronic Hamiltonian  $\tilde{\mathcal{H}}_{\text{el}}$ , and an arbitrary basis (i.e., without invoking the Hellmann–Feynman theorem).

## Classical Molecular Dynamics

While first-principles molecular dynamics simulations deal with the electrons in a system, this results in a large number of particles that must be considered and therefore the calculations become significantly time-consuming. Classical molecular dynamics ignore electronic motions and calculate the energy of a system as a function of the nuclear positions only, and therefore are used to simulate larger, less detailed systems for larger timescales. The successive configurations of the system are generated by solving the differential equations that constitute Newton’s second law (Eq. 7.12):

$$\frac{d^2 X_I}{dt^2} = \frac{F_{X_I}}{M_I} \quad (7.17)$$

This equation describes the motion of a particle of mass  $M_I$  along one dimension ( $X_I$ ), where  $F_{X_I}$  is the force on the particle in that dimension. The solution of these differential equations

results in a trajectory that specifies how the positions and velocities of the particles in the system vary with time.

In realistic models of intermolecular interactions, the force on particle  $I$  changes whenever particle  $I$  changes its position or whenever another atom with which particle  $I$  interacts changes its position. Therefore the motions of all the particles are coupled together, which results in a many-body problem that cannot be solved analytically. Therefore finite difference methods are used to integrate the equations of motion.

Generally, the integration of  $\bullet$  Eq. 7.17 is broken into consecutive steps that are conducted at different times  $t$  that are separated by increments of  $\delta t$ , which is generally referred to as the time step. First, the total force on each particle in the system at time  $t$  is calculated as the vector sum of its interactions with other particles.

Then, assuming the force is constant over the course of the time step, the accelerations of the particles are calculated, which are then combined with positions and velocities of the particles at time  $t$  to determine the positions and velocities at time  $t + \delta t$ . Finally, the forces on the particles in their new positions are determined, and then new accelerations, positions, and velocities are determined at  $t + 2\delta t$  and so on.

A common approach in the various finite difference methods used to integrate the equations of motions for classical molecular dynamics simulations is that it is assumed that the positions, velocities, and accelerations (as well as all other dynamic properties) can be approximated using Taylor series expansions:

$$\mathbf{R}(t + \delta t) = \mathbf{R}(t) + \delta t \mathbf{V}(t) + \frac{1}{2} \delta t^2 \mathbf{A}(t) + \frac{1}{6} \delta t^3 \mathbf{B}(t) + \frac{1}{24} \delta t^4 \mathbf{C}(t) + \dots \quad (7.18)$$

$$\mathbf{V}(t + \delta t) = \mathbf{V}(t) + \delta t \mathbf{A}(t) + \frac{1}{2} \delta t^2 \mathbf{B}(t) + \frac{1}{6} \delta t^3 \mathbf{C}(t) + \dots \quad (7.19)$$

$$\mathbf{A}(t + \delta t) = \mathbf{A}(t) + \delta t \mathbf{B}(t) + \frac{1}{2} \delta t^2 \mathbf{C}(t) + \dots \quad (7.20)$$

where  $\mathbf{R}$  is the position,  $\mathbf{V}$  is the velocity,  $\mathbf{A}$  is the acceleration, and  $\mathbf{B}$  and  $\mathbf{C}$  are the third and fourth derivatives of the positions with respect to time, respectively.

## Verlet Algorithm

One of the most widely used finite difference methods in classical molecular dynamics simulations is the Verlet algorithm (Verlet 1967). In the Verlet algorithm, the positions and accelerations at time  $t$  and the positions from the previous time step  $\mathbf{R}(t - \delta t)$  are used to calculate the updated positions  $\mathbf{R}(t + \delta t)$  using the equation:

$$\mathbf{R}(t + \delta t) = 2\mathbf{R}(t) - \mathbf{R}(t - \delta t) + \delta t^2 \mathbf{A}(t). \quad (7.21)$$

While the velocities do not explicitly appear in  $\bullet$  Eq. 7.21, they can be calculated from the difference in position over the entire time step:

$$\mathbf{V}(t) = \frac{|\mathbf{R}(t + \delta t) - \mathbf{R}(t - \delta t)|}{2\delta t} \quad (7.22)$$

or the difference in position over a half time step ( $t + \frac{1}{2} \delta t$ ):

$$\mathbf{V}(t + \frac{1}{2} \delta t) = \frac{|\mathbf{R}(t + \delta t) - \mathbf{R}(t)|}{\delta t} \quad (7.23)$$

The fact that the velocities are not explicitly represented in the Verlet algorithm is one of the drawbacks to this method in that no velocities are available until the positions have been determined at the next time step. Also, in order to calculate the position of particles at  $t = \delta t$ , it is necessary to determine the positions at  $t = -\delta t$  since the algorithm requires the position at time  $t - \delta t$  to calculate the position at time  $t + \delta t$ . Often, this drawback is overcome by using the Taylor series to calculate  $\mathbf{R}(-\delta t) = \mathbf{R}(0) - \delta t \mathbf{V}(0) + \frac{1}{2} \delta t^2 \mathbf{A}(t) + \dots$ . A final drawback of the Verlet algorithm is that there may be a loss of precision in the resulting trajectories that result from the fact that the positions are calculated by adding a small term ( $\delta t^2 \mathbf{A}(t)$ ), to the difference of two larger terms ( $2\mathbf{R}(t)$  and  $\mathbf{R}(t - \delta t)$ ) in  $\blacklozenge$  Eq. 7.21.

## “Leap-Frog” Algorithm

In an attempt to improve upon the original Verlet algorithm, several variations have been developed. The leap-frog algorithm (Hockney 1970) is one of the variations that uses the following equations to update the positions:

$$\mathbf{R}(t + \delta t) = \mathbf{R}(t) + \delta t \mathbf{V}(t + \frac{1}{2} \delta t), \quad (7.24)$$

and the velocities:

$$\mathbf{V}(t + \frac{1}{2} \delta t) = \mathbf{V}(t - \frac{1}{2} \delta t) + \delta t \mathbf{A}(t). \quad (7.25)$$

In the leap-frog algorithm, the velocities  $\mathbf{V}(t + \frac{1}{2} \delta t)$  are first calculated from the velocities at time  $t - \frac{1}{2} \delta t$  and the accelerations at time  $t$  using  $\blacklozenge$  Eq. 7.24. Then the positions  $\mathbf{R}(t + \delta t)$  are calculated from the velocities  $\mathbf{V}(t + \frac{1}{2} \delta t)$  and the positions  $\mathbf{R}(t)$  using  $\blacklozenge$  Eq. 7.25. The algorithm gets its name from the fact that the velocities are calculated in manner such that they “leap-frog” over the positions to give their values  $t - \frac{1}{2} \delta t$ . Then the positions are calculated such that they “leap-frog” over the velocities, and then the algorithm continues.

The “leap-frog” algorithm improves upon the standard Verlet algorithm in that the velocity is explicitly included in the calculations and also the “leap-frog” algorithm does not require the calculation of the differences of large numbers so the precision of the calculation should be improved. However, the fact that the calculated velocities and positions are not synchronized in time results in the fact that the kinetic energy contribution to the total energy cannot be calculated for the time at which the positions are defined. In response to this shortcoming in the “leap-frog” algorithm, a formalism to calculate the velocities at time  $t$  has been developed that follows

$$\mathbf{V}(t) = \frac{[\mathbf{V}(t + \frac{\delta t}{2}) + \mathbf{V}(t - \frac{\delta t}{2})]}{2} \quad (7.26)$$

## Velocity Verlet Algorithm

The velocity Verlet method (Swope et al. 1982), which is a variation of the standard Verlet method, calculates the positions, velocities, and accelerations at the same time by using the following equations:

$$\mathbf{R}(t + \delta t) = \mathbf{R}(t) + \delta t \mathbf{V}(t) + \frac{1}{2} \delta t^2 \mathbf{A}(t) \quad (7.27)$$

$$\mathbf{V}(t + \delta t) = \mathbf{V}(t) + \frac{1}{2} \delta t [\mathbf{A}(t) + \mathbf{A}(t + \delta t)]. \quad (7.28)$$

The velocity Verlet method is a three-stage algorithm because the calculation of the new velocities (► Eq. 7.28) requires both the acceleration at time  $t$  and at time  $t + \delta t$ . Therefore, first, the positions at  $t + \delta t$  are calculated using ► Eq. 7.27 and the velocities and accelerations at time  $t$ . The velocities at time  $t + \frac{1}{2} \delta t$  are then calculated using

$$\mathbf{V}(t + \frac{1}{2} \delta t) = \mathbf{V}(t) + \frac{1}{2} \delta t \mathbf{A}(t). \quad (7.29)$$

Then the forces are computed from the current positions, which results in being able to calculate  $\mathbf{A}(t + \delta t)$ . Then the final step consists of calculating the velocities at time  $t + \delta t$  using

$$\mathbf{V}(t + \delta t) = \mathbf{V}(t + \frac{1}{2} \delta t) + \frac{1}{2} \delta t \mathbf{A}(t + \delta t). \quad (7.30)$$

Therefore, the velocity Verlet allows for the velocities and positions to be calculated in a time-synchronized manner, and thus allows for the kinetic energy contribution of the total energy. Also, the precision of the results will be improved upon those from the standard Verlet algorithm as there are no differences of large numbers within the formalism of the method.

The selection of the best time integration method for a given problem and the size of the time step to use will be discussed in section “Setting the Time Step.”

## Hybrid Quantum/Classical (QM/MM) Molecular Dynamics

The ab initio and classical simulation techniques discussed in the previous sections can be viewed as complementary. While AIMD is capable of dealing with electronic processes such as chemical reactions, charge transfer, and electronic excitations, its applicability is limited to systems of modest size, precluding its use in complex, large-scale biochemical simulations. Classical MD, on the other hand, can describe much larger systems on longer timescales, but misses any of the above-mentioned electronic effects, e.g., bond breaking and formation. The basic idea of the QM/MM approach is to combine the strengths of the two methods treating a chemically active region at the quantum level and the environment using molecular mechanics (i.e., a force-field). There are several excellent review articles on the QM/MM method in the literature (Senn and Thiel 2009; Thiel 2009).

### Partitioning Schemes

The entire system, **S**, is partitioned into a chemically active inner region, **I**, and a chemically inert outer region, **O**. If the border between these regions cuts through chemical bonds, so-called link atoms, **L**, are usually introduced to cap the inner region (see section “Bonds Across the QM/MM Boundary”).

#### Subtractive Scheme

In a subtractive scheme, the total energy,  $E_{\text{QM/MM}}^{\text{S}}$ , of the entire system,

$$E_{\text{QM/MM}}^{\text{S}} = E_{\text{MM}}^{\text{S}} + E_{\text{QM}}^{\text{I,L}} - E_{\text{MM}}^{\text{I,L}} \quad (7.31)$$

is calculated from three separate energy contributions: (1) the MM energy of the entire system,  $E_{MM}^S$ , (2) the QM energy of the active region (including any link atoms),  $E_{QM}^{I,L}$ , (3) the MM energy of the active region  $E_{MM}^{I,L}$ .

The role of the third term in  $\blacktriangleright$  Eq. 7.31 is to avoid double counting and to correct for any artifacts caused by the link atoms. For the latter to be effective, the force-field has to reproduce the quantum mechanical forces reasonably well in the link region.

### Additive Scheme

In an additive scheme, the total energy of the system is given by

$$E_{QM/MM}^S = E_{MM}^O + E_{QM}^{I,L} + E_{QM-MM}^{I,O} \quad (7.32)$$

The difference to the subtractive scheme is that here a pure MM calculation is performed for only the outer region and the interaction between QM and MM regions is achieved by an explicit coupling term,

$$E_{QM-MM}^{I,O} = E_{QM-MM}^{\text{bond}} + E_{QM-MM}^{\text{vdW}} + E_{QM-MM}^{\text{el}} \quad (7.33)$$

where  $E_{QM-MM}^{\text{bond}}$ ,  $E_{QM-MM}^{\text{vdW}}$ ,  $E_{QM-MM}^{\text{el}}$ , are bonded, van der Waals, and electrostatic interaction energies, respectively.

The simplest way to treat electrostatic interactions between the **I** and **O** subsystems is to assign fixed electric charges to all **I** atoms (*mechanical embedding*). In this case the QM problem is solved for the isolated subsystem **I** without taking into account the effects of the surrounding atomic charges in **O**. The majority of implementations use an *electrostatic embedding* scheme in which the MM point charges of region **O** are incorporated in the QM Hamiltonian through a QM-MM coupling term,

$$\hat{H}_{QM-MM}^{\text{el}} = - \sum_i^n \sum_{\alpha \in O} \frac{q_\alpha}{|\mathbf{r}_i - \mathbf{R}_\alpha|} + \sum_{I \in I+L} \sum_{\alpha \in O} \frac{q_\alpha Z_I}{|\mathbf{R}_I - \mathbf{R}_\alpha|} \quad (7.34)$$

where  $q_\alpha$  are the MM point charges at positions  $\mathbf{R}_\alpha$  (all other symbols as defined in section “Born–Oppenheimer Approximation”). In this way, the electronic structure of the QM region adjusts to the moving MM charge distribution. A problem that arises when an MM point charge is in close proximity to the QM electron cloud is overpolarization of the latter, sometimes referred to as “spill-out” effect. This can be avoided by modifying the Coulomb potential in the first term of  $\blacktriangleright$  Eq. 7.34 at short range (see for instance Laio et al. 2002).

At present, in all commonly used partitioning schemes, the partitions remain *fixed* over time, i.e., an MM atom cannot turn into a QM atom and *vice versa*. This can present a serious limitation, for instance, in the case of solvent diffusion through the chemically active region. A number of *adaptive* partitioning methods have been proposed to remedy this problem (Bulo et al. 2009; Heyden et al. 2007; Hofer et al. 2005; Kerdcharoen et al. 1996; Kerdcharoen and Morokuma 2002); however the computational overhead is enormous.

## Bonds Across the QM/MM Boundary

Partitioning the total system into QM and MM regions in such a way that cuts chemical bonds is best avoided. However, in many cases this is inevitable. Then one has to make sure that



any atoms participating in chemical reactions are at least three bonds away from boundary. Furthermore it is preferable to cut a bond that is unpolar and not part of a conjugated chain.

### Link Atoms

Cutting a single covalent bond will create a dangling bond which must be capped by a so-called link atom; in most applications a hydrogen atom is chosen. In the QM calculation, the atoms of region **I** together with the link atoms **L** are treated as an isolated molecule in the presence of the point charges of the environment **O**. The original QM–MM bond, cut by the partitioning, is only treated at the MM level.

### Boundary Atoms


Boundary atom schemes have been developed to avoid the artifacts introduced by a link atom. The boundary atom appears as a normal MM atom in the MM calculation, while carrying QM features to saturate the QM–MM bond and to mimic the electronic properties of the MM side. The QM interactions are achieved by placing a pseudopotential at the position of the boundary atom, parameterized to reproduce electronic properties of certain chemical end group, e.g., a methyl group in the case of a cut C–C bond. Among the various flavors that have been proposed, the pseudobond method for first principles QM calculations (Zhang 2005, 2006; Zhang et al. 1999) and the pseudopotential approach for plane-wave DFT (Laio et al. 2002) are the most relevant in the present context.

### Frozen Localized Orbitals

The basic idea behind the various frozen orbital methods (Amara et al. 2000; Assfeld and Rivail 1996; Assfeld et al. 1998; Day et al. 1996; Ferré et al. 2002; Fornili et al. 2003, 2006a, b; Gao et al. 1998; Garcia-Viloca and Gao 2004; Gordon et al. 2001; Grigorenko et al. 2002; Jensen et al. 1994; Jung et al. 2007; Kairys and Jensen 2000; Loos and Assfeld 2007; Monard et al. 1996; Murphy et al. 2000; Nemukhin et al. 2002, 2003; Philipp and Friesner 1999; Pu et al. 2004a, b, 2005; Sironi et al. 2007; Théry et al. 1994; Warshel and Levitt 1976) is to saturate the cut QM–MM bond by placing on either the MM or the QM atom at the boundary localized orbitals that have been determined in a prior quantum-mechanical SCF calculation on a model molecule containing the bond under consideration. To preserve the properties of the bond, the localized orbitals are then kept fixed in the subsequent QM/MM calculation. Different flavors are the Local SCF (LSCF) method (Assfeld and Rivail 1996; Assfeld et al. 1998; Ferré et al. 2002; Monard et al. 1996; Théry et al. 1994), extremely localized molecular orbitals (ELMOs) (Fornili et al. 2003, 2006b; Sironi et al. 2007), frozen core orbitals (Fornili et al. 2006a), optimized LSCF (Loos and Assfeld 2007), frozen orbitals (Murphy et al. 2000; Philipp and Friesner 1999), generalized hybrid orbitals (Amara et al. 2000; Gao et al. 1998; Garcia-Viloca and Gao 2004; Jung et al. 2007; Pu et al. 2004a, b, 2005), and effective fragment potentials (EFP) (Day et al. 1996; Gordon et al. 2001; Grigorenko et al. 2002; Jensen et al. 1994; Kairys and Jensen 2000; Nemukhin et al. 2002, 2003).

Of the three types of boundary treatment, the link atom method is the simplest both conceptually and in practice, and is hence the most widely used. The boundary atom and in particular the frozen orbital methods can potentially achieve higher accuracy but require careful a priori parametrization and bear limitations on transferability (Senn and Thiel 2009).

## Coarse Grain Molecular Dynamics

A large number of important problems in fields that are often studied using molecular dynamics simulations (i.e. soft condensed matter physics, structural biology, chemistry and materials science) take place over a time span of microseconds to seconds and distances of few hundred nanometers to a few microns. However, these time and length scales are still unattainable via quantum or force-field molecular dynamics methods despite significant computational hardware advances (Mervis 2001; Reed 2003; Shirts and Pande 2000) and the development of increasingly powerful software (Lindahl et al. 2001; MacKerell et al. 1998; Phillips et al. 2005a; Wang et al. 2004). Therefore one approach that has been utilized in order to be able to study these complex problems is to reduce the computational demand of the simulation by reducing the number of atoms represented and therefore the degrees of freedom of the simulated system. This procedure of reducing the number of atoms represented in a system is done by grouping atoms together and representing them as a single interaction site and is generally referred to as “coarse graining” of the system.  Figure 7-1 shows a comparison of the atomistic, united-atom and coarse grain representation.

The “bead-spring” coarse grain model of polymer chains that was created by Kremer and Grest in 1990 has served as the foundation for many of the coarse grain models that have been developed for a wide range of phenomena (at the current date this paper has been cited over 860 times) including various studies of polymers and biomolecules including DNA solutions. Many of the more recent coarse grain models have been developed for biological macromolecules since there are many examples of interesting biophysical phenomena that occur at large length and timescales. The most widely used coarse grain models for biological systems include the generic model of Lipowsky et al. (Goetz et al. 1999; Shillcock and Lipowsky 2002), the solvent-free model of Deserno et al. (Cooke et al. 2005), and the specific models of the Klein group (Shelley et al. 2001), the Voth group (which is called the Multi-Scale Coarse Grain model) (Izvekov and Voth 2005, 2006), and the Marrink group (called the MARTINI force-field) (Marrink et al. 2007). The above coarse grain models have generally been developed for lipid membranes, however there are also coarse grain force-fields for proteins (as reviewed in Tozzini [2005] and some more recent examples Betancourt and Omovie [2009] and Bereau and Deserno [2009]) and DNA (Khalid et al. 2008; Tepper and Voth 2005).

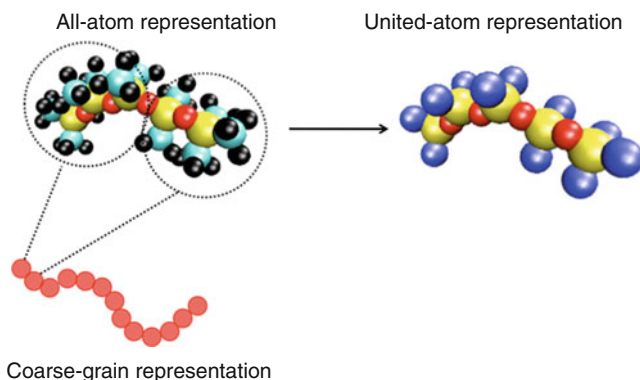


 Fig. 7-1

Atomistic, united-atom, and coarse grain representations of organic molecules

When developing a coarse grain model for a system, there are two important decisions to be made: (1) how many atoms to combine (coarse grain) into a single interaction site and (2) how to parameterize the coarse grain force-field. In deciding the number of atoms to combine into a single interaction site, one must consider the obvious trade-off of how much detail are you able to sacrifice in order to simulate larger length and/or timescale phenomena and still be able to actually accurately model the phenomena of interest. The least amount of coarse graining that has been used is represented by what is called a “united-atom” representation of a molecule where all “heavy” atoms (generally all non-hydrogen elements in a molecule) are represented and the “light” (i.e., hydrogen) atoms are grouped with the heavy atom to which they are bonded into one interaction site. United atom versions of many of the popular all-atom force-fields listed in section “Classical Force Fields” exist and have been successfully used in several studies. In addition to united-atom models, there are several existing coarse graining methods that will combine different number of atoms together into one interaction site.

In general, coarse grain systems are governed by similar potential terms as are found in atomistic models such as nonbond terms (both pair-wise interactions and electrostatic interactions), bond stretching terms, and then in more sophisticated models even angle and dihedral terms will be included as well. Generally, all specific models are parameterized based on comparison to atomistic simulations and/or detailed experimental data. Effective coarse grain potentials have been extracted from atomistic simulations using inverse Monte Carlo schemes (Elezgaray and Laguerre 2006; Lyubartsev 2005) or force matching approaches (Izvekov and Voth 2005, 2006). Another approach is to develop standard potential functions that are calibrated using thermodynamic data (Marrink et al. 2004). The advantage of the using either the inverse Monte Carlo or force matching schemes is that the resulting force-field will produce a higher level of accuracy and closer resemblance to atomistic simulations. However, these schemes produce force-fields that are useful for a given statepoint and therefore are not transferable. Whereas the advantages of the thermodynamic approach include that it produces a potential that has a broader range of applicability and also the thermodynamic approach does not require atomistic simulations to be done in the first place.

## Interaction Potentials/Force Fields

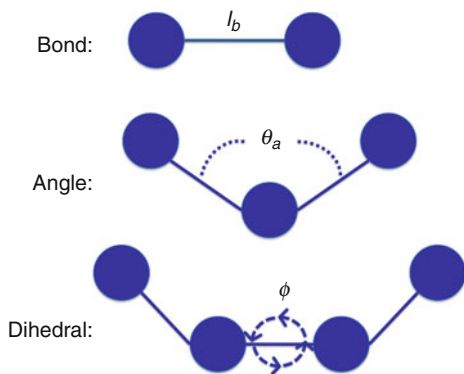
---

### Classical Force Fields

---

Classical, or empirical, force-fields are generally used to calculate the energy of a system as a function of the nuclear positions of the particles within the system, while ignoring the behavior of the individual electrons. As stated in the section “Born–Oppenheimer Approximation,” the Born–Oppenheimer approximation makes it possible to write the energy as a function of the nuclear coordinates. Another approximation that is key to the implementation of classical force-fields is that it is possible to model the relatively complex motion of particles within the system with fairly simple analytical models of inter and intra-molecular interactions. Generally, an empirical force-field consists of terms that model the nonbonded interactions ( $E_{\text{nonbond}}$ ), which include both the van der Waals and Coulombic interactions, the bonded interactions ( $E_{\text{bond}}$ ), the angle bending interactions ( $E_{\text{angle}}$ ), and the dihedral (bond rotations) interactions ( $E_{\text{dihedral}}$ ):

$$E(\mathbf{R}) = E_{\text{nonbond}} + E_{\text{bond}} + E_{\text{angle}} + E_{\text{dihedral}}. \quad (7.35)$$



■ Fig. 7-2

**Intramolecular terms of classical force-fields: bond, angle, and dihedral interactions**

► *Figure 7-2* presents representative cartoons of the bond, angle, and dihedral interactions from a molecular perspective. The form that each of these individual terms takes is dependent on the force-field that you are using. There are several different force-field options available for various systems. The best way to find the most suitable force-field for your specific problem is to conduct a literature and/or internet search in order to find which force-field has the capability to model the molecules you are interested in studying. However, if you are interested in modeling organic/biological molecules, there are several large force-fields that may be a good place to start, including Charmm (MacKerell et al. 1998), OPLS (Jørgensen et al. 1984), Amber (Cornell et al. 1995), and COMPASS (Sun et al. 1998). Likewise, there are several well-known large force-fields that can be used for solids like the BKS potential (van Beest et al. 1990) for oxides and the Embedded Atom Method (EAM) (Daw and Baskes 1983, 1984; Finnis and Sinclair 1984) and Modified Embedded Atom Method (MEAM) (Baskes 1992) force-fields, which are primarily used to model metals. In addition to defining the functional forms used for the various terms in the general potential formulation, a force-field will also define the variables used in the potential which are derived from a combination of quantum simulation results and experimental observations.

In the following sections, each of the terms in ► *Eq. 7.35* will be discussed further and typical functional forms that are used in the previously mentioned force-fields and others to represent each term will be shown.

We limit the discussion to simple non-polarizable force fields in which the individual atoms carry fixed charges. They capture many-body-effects such as electronic polarization only in an effective way. More sophisticated polarizable force fields have been developed over the past two decades (see for instance Ponder et al. [2010] and references therein) however they are computationally substantially more demanding.

## Nonbonded Interactions

There are two general forms of nonbonded interactions that need to be accounted for by a classical force-field: (1) the van der Waals (vdw) interactions and (2) the electrostatic interactions.

### van der Waals Interactions

In order to model the van der Waals interactions, we need a simple empirical expression that is not computationally intensive and that models both the dispersion and repulsive interactions that are known to act upon atoms and molecules. The most commonly used functional form of van der Waals energy ( $E_{\text{vdW}}$ ) in classical force-fields is the Lennard-Jones 12-6 function that has the form:

$$E_{\text{vdW}}(\mathbf{R}) = \sum_{I>J} 4\epsilon_{IJ} \left[ \left( \frac{\sigma_{IJ}}{R_{IJ}} \right)^{12} - \left( \frac{\sigma_{IJ}}{R_{IJ}} \right)^6 \right], \quad (7.36)$$

where  $\sigma_{IJ}$  is the collision diameter and  $\epsilon_{IJ}$  is the well depth of the interaction between atoms  $I$  and  $J$ . Both  $\sigma_{IJ}$  and  $\epsilon_{IJ}$  are adjustable parameters that will have different values to describe the interactions between different pairs of particles (i.e., the values of  $\sigma$  and  $\epsilon$  used to describe the interaction between two carbon atoms are different than the values of  $\sigma$  and  $\epsilon$  used to describe the interaction between a carbon and an oxygen).

➤ Equation 7.36 models both the attractive part (the  $R^{-6}$  term) and the repulsive part (the  $R^{-12}$  term) of the nonbonded interaction. Other formulations of the Lennard-Jones nonbond potential commonly have the same power law description of the attractive part of the potential, but will have different power law dependence for the repulsive part of the interaction, such as the Lennard-Jones 9-6 function:

$$E_{\text{vdW}}(\mathbf{R}) = \sum_{I>J} 4\epsilon_{IJ} \left[ \left( \frac{\sigma_{IJ}}{R_{IJ}} \right)^9 - \left( \frac{\sigma_{IJ}}{R_{IJ}} \right)^6 \right]. \quad (7.37)$$

When the nonbond interactions of a system that contains multiple particle types and multiple molecules are modeled using a Lennard-Jones type nonbond potential, it is necessary to be able to define the values of  $\sigma$  and  $\epsilon$  that apply to the interaction between particles of type  $I$  and  $J$ . The parameters for these cross interactions are generally found using one of the two following mixing rules. One common mixing rule is the Lorentz-Berthelot rule where the value of  $\sigma_{IJ}$  is found from the arithmetic mean of the two pure values and the value of  $\epsilon_{IJ}$  is the geometric mean of the two pure values:

$$\sigma_{IJ} = \frac{(\sigma_I + \sigma_J)}{2} \quad (7.38)$$

$$\epsilon_{IJ} = \sqrt{\epsilon_I \epsilon_J} \quad (7.39)$$

The other commonly used mixing rule is the one that defines both  $\sigma_{IJ}$  and  $\epsilon_{IJ}$  as the geometric mean of the values for the pure species:

$$\sigma_{IJ} = \sqrt{\sigma_I \sigma_J} \quad (7.40)$$

$$\epsilon_{IJ} = \sqrt{\epsilon_I \epsilon_J} \quad (7.41)$$

Most force-fields use the Lorentz-Berthelot mixing rule, however the OPLS force-field is one force-field that utilizes the geometric mixing rule.

In other nonbond pairwise potentials, the repulsive portion of the interaction is modeled with an exponential term, which is in better agreement with the functional form of the repulsive term determined from quantum mechanics. One example of such a potential is the Buckingham potential (Buckingham 1938):

$$E_{\text{vdW}}(\mathbf{R}) = \sum_{I<J} A_{IJ} \exp(-B_{IJ}R_{IJ}) - \left( \frac{C_{IJ}}{R_{IJ}^6} \right), \quad (7.42)$$

where  $A_{IJ}$ ,  $B_{IJ}$ , and  $C_{IJ}$  are adjustable parameters that will have unique values for different types of particles. Another form of the nonbond interaction is the Born–Mayer–Huggins potential (Fumi and Tosi 1964; Tosi and Fumi 1964):

$$E_{\text{vdW}}(\mathbf{R}) = \sum_{I < J} A_{IJ} \exp(B_{IJ}(\sigma_{IJ} - R_{IJ})) - \frac{C_{IJ}}{R_{IJ}^6} + \frac{D_{IJ}}{R_{IJ}^8}, \quad (7.43)$$

where  $A_{IJ}$ ,  $B_{IJ}$ ,  $C_{IJ}$ ,  $D_{IJ}$  and  $\sigma_{IJ}$  are adjustable parameters that will have unique values for different types of particles. The Born–Mayer–Huggins potential (► Eq. 7.43) is identical to the Buckingham potential (► Eq. 7.42) when  $\sigma = D = 0$ .

All of the nonbond potential functional forms that have been presented to this point take into account the effect that one particle has on another particle based solely on the distance between the two particles. However, in some systems like metals and alloys as well as some covalently bonded materials like silicon and carbon, the nonbonded potential is a function of more than just the distance between two particles. In order to model these systems, the embedded-atom method (EAM) (Daw and Baskes 1983, 1984; Finnis and Sinclair 1984) and modified embedded-atom method (MEAM) (Baskes 1992) utilize an embedding energy,  $F_I$ , which is a function of the atomic electronic density  $\rho_I$  of the embedded atom  $I$  and a pair potential interaction  $\phi_{IJ}$  such that

$$E_I(\mathbf{R}) = F_I \left( \sum_{J \neq I} \rho_I(R_{IJ}) \right) + \frac{1}{2} \sum_{J \neq I} \phi_{IJ}(R_{IJ}). \quad (7.44)$$

The multi-body nature of the EAM potential is a result of the embedding energy term.

So while the EAM and MEAM potentials have a term to account for multi-body interactions they are still only pair-wise potential, as are all the other nonbond potentials presented to this point. However, there are multi-body potentials that will explicitly account for how the presence of a third, fourth, ... atom affects the nonbond energy felt by any given atom. One example of a three-body potential is the Stillinger-Weber potential (Stillinger and Weber 1985):

$$E(\mathbf{R}) = \sum_I \sum_{J > I} \phi_2(R_{IJ}) + \sum_I \sum_{J \neq I} \sum_{K > J} \phi_3(R_{IJ}, R_{IK}, \theta_{IJK}), \quad (7.45)$$

where there is a two-body term  $\phi_2$ :

$$\phi_2(R_{IJ}) = A_{IJ} \epsilon_{IJ} \left[ B_{IJ} \left( \frac{\sigma_{IJ}}{R_{IJ}} \right)^{p_{IJ}} - \left( \frac{\sigma_{IJ}}{R_{IJ}} \right)^{q_{IJ}} \right] \exp \left( \frac{\sigma_{IJ}}{R_{IJ} - a_{IJ} \sigma_{IJ}} \right) \quad (7.46)$$

and a three-body term  $\phi_3$ :

$$\begin{aligned} \phi_3(R_{IJ}, R_{IK}, \theta_{IJK}) &= \lambda_{IJK} \epsilon_{IJK} \left[ \cos \theta_{IJK} - \cos \theta_{0,IJK} \right]^2 \\ &\times \exp \left( \frac{\gamma_{IJ} \sigma_{IJ}}{R_{IJ} - a_{IJ} \sigma_{IJ}} \right) \\ &\times \exp \left( \frac{\gamma_{IK} \sigma_{IK}}{R_{IK} - a_{IK} \sigma_{IK}} \right). \end{aligned} \quad (7.47)$$

The Stillinger-Weber potential has generally been used for modeling crystalline silicon; however, more recently it has also been used for organic molecules as well. Another example of a three-body interatomic potential is the Tersoff potential (Tersoff 1988, 1989), which also was created initially in an attempt to accurately model silicon solids.

### Electrostatic Interactions

Due to the fact that not all particles in a molecule have the same electronegativity, different particles will have stronger attractions to electrons than others. However, since classical force-fields do not model the flow of electrons, the different particles within a molecule are assigned a partial charge that remains constant during the course of a simulation. Generally these partial charges  $q_i$  are assigned to the nuclear centers of the particles. The electrostatic interaction between particles in different molecules or particles that are separated by at least two other atoms in a given molecule is calculated as the sum of the contributions between pairs of these partial charges using Coulomb's law:

$$E_{\text{coul}} = \sum_I \sum_J \frac{q_I q_J}{4\pi\epsilon_0 R_{IJ}} \quad (7.48)$$

where the charges of each particle are  $q_I$  and  $q_J$  and  $\epsilon_0$  is the dielectric constant.

In practice, an Ewald sum (Ewald 1921) is generally used to evaluate the electrostatic interactions within a classical MD simulation. However, this is a very computationally expensive algorithm to implement and it results in a computational cost of  $N^{3/2}$ , where  $N$  is the number of particles in the system. In order to obtain better computational scaling, fast Fourier transforms (FFTs) have been used to calculate the reciprocal space summation required within the Ewald sum. By using the FFT algorithm, one can reduce the cost of the electrostatic algorithm to  $N \log N$ . The most popular FFT algorithm that has been adopted for use in classical MD simulations is the particle-particle particle-mesh (pppm) approach (Hockney and Eastwood 1981; Luty et al. 1994, 1995).

### Bonded Interactions

The bonded interactions are needed to model the energetic penalty that will result from two covalently bonded atoms moving too close or too far away from one another. The most common functional form that is used to model the bond bending interactions is that of a harmonic term:

$$E_{\text{bond}} = \sum_{\text{bonds}} k_b (\ell_b - \ell_b^{(0)})^2 \quad (7.49)$$

where  $k_b$  is commonly referred to as the bond constant and is a measure of the bond stiffness and  $\ell_b^{(0)}$  is the reference length or often referred to the equilibrium bond length. Each of these parameters will vary depending on the types of particles that the bond is joining.

### Angle Bending Interactions

The angle bending interactions are also modeled in order to determine the energetic penalties of angles containing three different particles compressing or overextending such that they distort the geometry of a portion of a molecule away from its desired structure.

Again, the most common functional form to model the angle interactions is a harmonic expression:

$$E_{\text{angle}} = \sum_{\text{angles}} k_a (\theta_a - \theta_a^{(0)})^2 \quad (7.50)$$

where  $k_a$  is the angle constant and is a measure of the rigidity of the angle, and  $\theta_a^{(0)}$  is the equilibrium or reference angle.

## Torsional Interactions

The torsional interactions are generally modeled using some form of a cosine series. The OPLS force-field uses the following expression for its torsional term:

$$E_{\text{dihed}} = \sum_{\text{dihedrals}} \frac{1}{2} K_d^{(1)} [1 + \cos(\phi)] + \frac{1}{2} K_d^{(2)} [1 - \cos(2\phi)] + \frac{1}{2} K_d^{(3)} [1 + \cos(3\phi)] + \frac{1}{2} K_d^{(4)} [1 - \cos(4\phi)] \quad (7.51)$$

where  $K_d^{(i)}$  are the force constants for each cosine term and  $\phi$  is the measured dihedral angle. The Charmm force-field uses the following expression:

$$E_{\text{dihed}} = \sum_{\text{dihedrals}} K_d [1 + \cos(n\phi - d_d)], \quad (7.52)$$

where  $K_d$  is the force constant,  $n$  is the multiplicity of the dihedral angle  $\phi$ , and  $d_d$  is the shift of the cosine that allows one to more easily move the minimum of the dihedral energy.

## First Principles Electronic Structure Methods

For the electronic ground state, i.e.,  $k = 0$ , Kohn–Sham (KS) density functional theory is commonly used. In this case, the energy is given by

$$E_0 \approx E^{\text{KS}}[\rho] = T_s[\rho] + \int d\mathbf{r} v_{\text{ext}}(\mathbf{r})\rho(\mathbf{r}) + \frac{1}{2} \int d\mathbf{r} v_{\text{H}}(\mathbf{r})\rho(\mathbf{r}) + E_{\text{xc}} \quad (7.53)$$

with the kinetic energy of *noninteracting electrons*, i.e., using a Slater determinant as a wavefunction ansatz,

$$\Psi^{\text{KS}} = \frac{1}{\sqrt{n!}} \begin{vmatrix} \psi_1(\mathbf{x}_1) & \psi_2(\mathbf{x}_1) & \cdots & \psi_n(\mathbf{x}_1) \\ \psi_1(\mathbf{x}_2) & \psi_2(\mathbf{x}_2) & \cdots & \psi_n(\mathbf{x}_2) \\ \vdots & \vdots & \ddots & \vdots \\ \psi_1(\mathbf{x}_n) & \psi_2(\mathbf{x}_n) & \cdots & \psi_n(\mathbf{x}_n) \end{vmatrix} \quad (7.54)$$

$$T_s[\rho] = -\frac{1}{2} \sum_i^n f_i \int d\mathbf{r} \psi_i(\mathbf{r}) \nabla^2 \psi_i(\mathbf{r}) \quad (7.55)$$

where  $f_i$  is the number of electrons occupying orbital  $\psi_i$ , the external potential including nucleus–nucleus repulsion and electron–nucleus attraction,

$$v_{\text{ext}}(\mathbf{r}) = \sum_{I=1}^{N-1} \sum_{J>I}^N \frac{Z_I Z_J}{|\mathbf{R}_I - \mathbf{R}_J|} - \sum_{I=1}^N \frac{Z_I}{|\mathbf{r} - \mathbf{R}_I|} \quad (7.56)$$

the Hartree potential (electron–electron interaction)

$$v_{\text{H}}(\mathbf{r}) = \int d\mathbf{r}' \frac{\rho(\mathbf{r}')}{|\mathbf{r} - \mathbf{r}'|} \quad (7.57)$$

the exchange–correlation energy,  $E_{\text{xc}}$ , and the electron density

$$\rho(\mathbf{r}) = \sum_i^n f_i |\psi_i(\mathbf{r})|^2 \quad (7.58)$$



The orbitals which minimize the total, many-electron energy (► Eq. 7.53) are obtained by solving self-consistently the one-electron Kohn–Sham equations,

$$\left[ -\frac{1}{2}\nabla^2 + v_{\text{ext}}(\mathbf{r}) + v_{\text{H}}(\mathbf{r}) + \frac{\delta E_{\text{xc}}[\rho]}{\delta \rho(\mathbf{r})} \right] \psi_i(\mathbf{r}) = \epsilon_i \psi_i(\mathbf{r}) \quad (7.59)$$

DFT is exact in principle, provided that  $E_{\text{xc}}[\rho]$  is known, in which case  $E^{\text{KS}}$  (see ► Eq. 7.53) is an exact representation of the ground state energy  $E_0$  (see ► Eq. 7.8). In practice, however,  $E_{\text{xc}}[\rho]$  is not – and presumably never will be – known exactly; therefore (semiempirical) approximations are used.

The starting point for most density functionals is the *local density approximation* (LDA), which is based on the assumption that one deals with a homogeneous electron gas.  $E_{\text{xc}}$  is split into an exchange term  $E_x$  and a correlation term  $E_c$ . Within the LDA, the exchange functional is given exactly by Dirac (1930):

$$E_x^{\text{LDA}}[\rho] = \int \rho(\mathbf{r}) \epsilon_x^{\text{LDA}}(\rho(\mathbf{r})) d\mathbf{r} \quad (7.60)$$

where

$$\epsilon_x^{\text{LDA}}(\rho) = -\frac{3}{4} \left( \frac{3}{\pi} \right)^{\frac{1}{3}} \rho(\mathbf{r})^{\frac{1}{3}} \quad (7.61)$$

The LDA correlation functional, on the other hand, can only be approximated. We give here the most commonly used expression by Vosko et al. [1980], derived from Quantum Monte Carlo calculations:

$$E_c^{\text{LDA}}[\rho] = \int \rho(\mathbf{r}) \epsilon_c^{\text{LDA}}(\rho(\mathbf{r})) d\mathbf{r} \quad (7.62)$$

where

$$\epsilon_c^{\text{LDA}}(\rho) = A \left\{ \ln \left( \frac{x^2}{X} \right) + \frac{2b}{Q} \tan^{-1} \left( \frac{Q}{2x+b} \right) - \frac{bx_0}{X(x_0)} \left[ \ln \left( \frac{(x-x_0)^2}{X} \right) + \frac{2(b2x_0)}{Q} \tan^{-1} \left( \frac{Q}{2x+b} \right) \right] \right\} \quad (7.63)$$

with  $X = x^2 + bx + c$ ,  $x = \sqrt{r_s}$ ,  $r_s = \sqrt[3]{\frac{3}{4\pi\rho(\mathbf{r})}}$ ,  $Q = \sqrt{4c - b^2}$ ,  $x_0 = -0.104098$ ,  $A = 0.0310907$ ,  $b = 3.72744$ ,  $c = 12.9352$ .

This simplest approximation, LDA, is often too inaccurate for chemically relevant problems. A notable improvement is usually offered by so-called *semilocal* or *gradient corrected* functionals (*generalized gradient approximation* (GGA)), in which  $E_x$  and  $E_c$  are expressed as functionals of  $\rho$  and the first variation of the density,  $\nabla\rho$ :

$$E_x^{\text{GGA}}[\rho, \nabla\rho] = \int \rho(\mathbf{r}) \epsilon_x^{\text{GGA}}(\rho(\mathbf{r}), \nabla\rho) d\mathbf{r} \quad (7.64)$$

$$E_c^{\text{GGA}}[\rho, \nabla\rho] = \int \rho(\mathbf{r}) \epsilon_c^{\text{GGA}}(\rho(\mathbf{r}), \nabla\rho) d\mathbf{r} \quad (7.65)$$

Popular examples are the BLYP (Becke 1988; Lee et al. 1988), BP (Becke 1988; Polák 1986), and BPW91 (Becke 1988; Perdew et al. 1992) functionals. The expressions for  $\epsilon_{x,c}^{\text{GGA}}(\rho(\mathbf{r}), \nabla\rho)$  are complex and shall not be discussed here.

In many cases, accuracy can be further increased by using so-called *hybrid functionals*, which contain an admixture of Hartree–Fock exchange to KS exchange. Probably the most widely used hybrid functional is the three-parameter B3LYP functional (Becke 1993),

$$E_{xc}^{\text{B3LYP}} = aE_x^{\text{LDA}} + (1 - a)E_x^{\text{HF}} + b\Delta E_x^{\text{B}} + (1 - c)E_c^{\text{LDA}} + cE_c^{\text{LYP}} \quad (7.66)$$

where  $a = 0.80$ ,  $b = 0.72$ ,  $c = 0.81$ , and  $E_x^{\text{HF}}$  is the Hartree–Fock exchange energy evaluated using KS orbitals.

New functionals are constantly proposed in search of better approximations to the exact  $E_{xc}$ . Often functionals are designed to remedy a particular shortcoming of previous functionals, for instance, for dispersion interactions.

## Building the System/Collecting the Ingredients

### Setting Up an AIMD Simulation

#### Building a Molecule

In many cases, the coordinates of a molecular structure are available for download on the web, from crystallographic databases (CCDC 2010; ICSD 2009; PDB 2010; Reciprocal Net 2004; Toth 2009) or journal supplements. For relatively small molecules, an initial guess structure can be built using molecular graphics software packages such as `molDen` (2010).

#### Plane Waves and Pseudopotentials

The most common form of AIMD simulation employs DFT (see section “First Principles Electronic Structure Methods”) to calculate atomic forces, in conjunction with periodic boundary conditions and a plane wave basis set. Using a plane wave basis has two major advantages over atom-centered basis functions: (1) there is no *basis set superposition error* (Boys and Bernardi 1970; Marx and Hutter 2000) and (2) the Pulay correction (Pulay 1969, 1987) to the Hellmann–Feynman force, due to basis set incompleteness, vanishes (Marx and Hutter 2000, 2009).

##### Plane Wave Basis Set

As a consequence of Bloch’s theorem, in a periodic lattice, the Kohn–Sham orbitals (see [Eq. 7.59](#)) can be expanded in a set of plane waves (Ashcroft and Mermin 1976; Meyer 2006),

$$\psi_{\mathbf{k},j}(\mathbf{r}) = \sum_{\mathbf{G}} c_{\mathbf{G}}^{\mathbf{k},j} e^{i(\mathbf{k}+\mathbf{G})\mathbf{r}} \quad (7.67)$$

where  $\mathbf{k}$  is a wavevector within the Brillouin zone, satisfying Bloch’s theorem,

$$\psi(\mathbf{r} + \mathbf{T}) = e^{i\mathbf{k}\mathbf{T}} \psi(\mathbf{r}) \quad (7.68)$$

for any lattice vector  $\mathbf{T}$ ,

$$\mathbf{T} = N_1\mathbf{a}_1 + N_2\mathbf{a}_2 + N_3\mathbf{a}_3 \quad (7.69)$$

$N_1, N_2, N_3$  being integer numbers, and  $\mathbf{a}_1, \mathbf{a}_2, \mathbf{a}_3$  the vectors defining the periodically repeated simulation box.

In  $\blacklozenge$  Eq. 7.67, the summation is over all reciprocal lattice vectors  $\mathbf{G}$  which fulfill the condition  $\mathbf{G} \cdot \mathbf{T} = 2\pi M$ ,  $M$  being an integer number. In practice, this plane-wave expansion of the Kohn-Sham orbitals is truncated such that the individual terms all yield kinetic energies lower than a specified cutoff value,  $E_{\text{cut}}$ ,

$$\frac{\hbar^2}{2m} |\mathbf{k} + \mathbf{G}|^2 \leq E_{\text{cut}} \quad (7.70)$$

The plane-wave basis set thus has the advantage over other basis sets that convergence can be controlled by a single parameter, namely  $E_{\text{cut}}$ .

In this periodic setup, the electron density (see  $\blacklozenge$  Eq. 7.58) can be approximated by a sum over a mesh of  $N_{\text{kpt}}$   $\mathbf{k}$ -points in the Brillouin zone (Chadi and Cohen 1973; Monkhorst and Pack 1976; Moreno and Soler 1992),

$$\rho(\mathbf{r}) \approx \frac{1}{N_{\text{kpt}}} \sum_{\mathbf{k}} f_{\mathbf{k},j} |\psi_{\mathbf{k},j}(\mathbf{r})|^2 \quad (7.71)$$

Since the volume of the Brillouin zone,  $V_{\text{BZ}} = (2\pi)^3 / V_{\text{box}}$ , decreases with increasing volume of the simulation supercell,  $V_{\text{box}}$ , only a small number of  $\mathbf{k}$ -points need to be sampled for large supercells. For insulating materials (i.e., large bandgap), a single  $\mathbf{k}$ -point is often sufficient, typically taken to be  $\mathbf{k} = 0$  ( $\Gamma$ -point approximation).

### Pseudopotentials

While plane waves are a good representation of delocalized Kohn–Sham orbitals in metals, a huge number of them would be required in the expansion ( $\blacklozenge$  Eq. 7.67) to obtain a good approximation of atomic orbitals, in particular near the nucleus where they oscillate rapidly. Therefore, in order to reduce the size of the basis set, only the valence electrons are treated explicitly, while the core electrons (i.e., the inner shells) are taken into account implicitly through pseudopotentials combining their effect on the valence electrons with the nuclear Coulomb potential. This *frozen core approximation* is justified as typically only the valence electrons participate in chemical interactions. To minimize the number of basis functions the pseudopotentials are constructed in such a way as to produce nodeless atomic valence wavefunctions. Beyond a specified cutoff distance from the nucleus,  $R_{\text{cut}}$  the nodeless pseudo-wavefunctions are required to be identical to the reference all-electron wavefunctions.

### Normconserving Pseudopotentials

Normconserving pseudopotentials are generated subject to the condition that the pseudo-wavefunction has the same norm as the all-electron wavefunction and thus gives rise to the same electron density. Although normconserving pseudopotentials have to fulfill a (small) number of mathematical conditions, there remains considerable freedom in how to create them. Hence several different recipes exist (Bachelet et al. 1982; Goedecker et al. 1996; Hamann et al. 1979; Hartwigsen et al. 1998; Kerker 1980; Troullier and Martins 1990, 1991; Vanderbilt 1985).

Since pseudopotentials are generated using *atomic* orbitals as a reference, it is not guaranteed that they are *transferable* to any chemical environment. Generally, transferability is the better the smaller the cutoff radius  $R_{\text{cut}}$  is chosen. However, the reduction in the number of plane waves required to represent a particular pseudo-wavefunction – i.e., the *softness* of the corresponding pseudopotential – increases as  $R_{\text{cut}}$  gets larger. So  $R_{\text{cut}}$  has to be chosen carefully and there is always a trade-off between transferability and softness. An upper limit for

$R_{\text{cut}}$  is given by the shortest interatomic distances in the molecule or crystal the pseudopotential will be used for: one needs to make sure that the sum of the two cutoff radii of any two neighboring atoms is smaller than their actual spatial separation.

For each angular momentum  $l$ , a separate pseudopotential  $V_l^{\text{PS}}(r)$  is constructed. The total pseudopotential operator is written as

$$\hat{V}^{\text{PS}} = V_{\text{loc}}^{\text{PS}}(r) + \sum_l V_{\text{nl},l}^{\text{PS}}(r) \hat{P}_l \quad (7.72)$$

where the nonlocal part is defined as

$$V_{\text{nl},l}^{\text{PS}}(r) = V_l^{\text{PS}}(r) - V_{\text{loc}}^{\text{PS}}(r) \quad (7.73)$$

and the local part  $V_{\text{loc}}^{\text{PS}}(r)$  is taken to be the pseudopotential  $V_l^{\text{PS}}(r)$  for one specific value of  $l$ , typically the highest one for which a pseudopotential was created. The pseudopotential (Eq. 7.72) is called semi-local, since the projector  $\hat{P}_l$  only acts on the  $l$ -th angular momentum component of the wavefunction, but not on the radius  $r$ . (Note: a pseudopotential is called nonlocal if it is  $l$ -dependent.)

To achieve higher numerical efficiency, it is common practice to transform the semi-local pseudopotential (Eq. 7.72) to a fully nonlocal form,

$$\hat{V}^{\text{PS}} = V_{\text{loc}}^{\text{PS}}(r) + \sum_{ij} |\beta_i \rangle B_{ij} \langle \beta_j| \quad (7.74)$$

using the Kleinman-Bylander prescription (Kleinman and Bylander 1982).

### Vanderbilt Ultrasoft Pseudopotentials

An ultrasoft type of pseudopotential was introduced by Vanderbilt (1990) and Laasonen et al. [1993] to deal with nodeless valence states which are strongly localized in the core region. In this scheme the normconserving condition is lifted and only a small portion of the electron density inside the cutoff radius is recovered by the pseudo-wavefunction, the remainder is added in the form of so-called augmentation charges. Complications arising from this scheme are the nonorthogonality of Kohn–Sham orbitals, the density dependence of the nonlocal pseudopotential, and need to evaluate additional terms in atomic force calculations.

### How to Obtain Pseudopotentials?

There are extensive pseudopotential libraries available for download with the simulation packages CPMD (Parrinello et al. 2008), CP2K (Hutter et al. 2009) or online (Vanderbilt Ultra-Soft Pseudopotential Site 2006). However, before applying any pseudopotentials, they should always be tested against all-electron calculations. Pseudopotentials used in conjunction with a particular density functional should have been generated using the same functional.

In many cases, the required pseudopotential will not be available in any accessible library; in this case it may be generated using freely downloadable programs (Vanderbilt Ultra-Soft Pseudopotential Site 2006).

## Setting Up a Classical MD Simulation

There are two general stages that make up the preparation to conduct force-field molecular dynamics simulations: (1) gathering preliminary information and (2) building the actual system.

## Gathering Preliminary Information

Gathering the preliminary information before conducting the simulation is mostly focussed on making sure that the simulation is possible. First, it is important to identify the type and number of molecules that you wish to model. Then, it is necessary to find the force-field that will allow you to most accurately model the molecules and physical system that you want to simulate. A brief synopsis of some of the larger classical force-field parameter sets is given in section "Classical Force Fields". These force-fields and references may be good starting points in searching for the correct classical force-field to use for a given system, but the best way to find a specific force-field is to just conduct a search for research articles that may have been conducted on the same system. If no force-field parameters exist for the system of interest, then you can use configurations and energies from quantum simulations to parameterize a given force-field for your system. A methodology for how a force-field was parameterized originally is presented in the relevant paper; however, this is a complicated exercise and is probably best left to the experts.

## Building the System

After identifying that a force-field exists for the system you wish to model, the next step is to build the initial configuration of the molecules within the system. The initial configuration will consist of initial spatial coordinates of each atom in each given molecule. When building a large system consisting of several molecules of various types, it is easiest to write a computer code that contain the molecular structure and coordinates of each molecule present in the system, and then have the code replicate each molecule how ever many times is necessary in order to build the entire system. Alternatively, most of the molecular dynamics simulation packages previously mentioned have capabilities to build systems from a pdb file; however, these tools are often useful for only certain systems and force-fields. There is unfortunately no one tool which can be used to build any system with any force-field.

These initial configurations can represent a minimum energy structure either from another simulation (i.e., a final structure from a energy minimization in a quantum or classical Monte Carlo simulation can be used as the starting state for classical simulations), from experimental observation (i.e., the pdb database for crystallographic structures of proteins) or building the initial coordinates based upon the equilibrium bond distances and bond angles from the force-field.

The placement of the molecules within the simulation box can be done in a number of different ways as well. The molecules can be placed on the vertices of a regular lattice, or in any other regularly defined geometry that may be useful for conducting your simulation (i.e., in simulating the structural properties of micelles often times the surfactant molecules will initially be placed on the vertices of a buckey ball such that they are in a spherical configuration). Also, molecules can be placed at random positions within the simulation box. The one advantage of placing molecules at regularly spaced positions is that it is easier to insure that there is no overlapping of molecules, whereas with the randomly placed molecules it can be quite difficult to ensure that a placed molecule does not overlap with another molecule in the box (particularly for large or highly branched molecules).

In addition to containing the initial spatial coordinates of all of the molecules in the system, the initial configuration must also contain some additional information about the atoms and

molecules in the systems. Each atom in the configuration must contain a label of what atomic species (i.e., carbon, nitrogen, ...) it represents. This label will be different for each simulation code used but all of them will have some type of label as it will inform the simulation code what force-field values to use to represent the interactions of that atom. A list of all of the covalent bonds, the bond angles, and the dihedrals in the system will also need to be included in the initial configuration. The lists of the bonds, angles, and dihedrals contain an identifier for each atom that make up the bond, angle, or dihedral and then an identifier for the type that informs the simulation package which parameters to use in calculating the energy of the bond, angle, or dihedral. The final component of the initial configuration of a classical simulation is a list of all of the various types of atoms, bonds, angles, and dihedrals in the system along with their corresponding force-field parameters (i.e.,  $\epsilon$  and  $\sigma$  for atom types to describe their nonbond interactions, force constants, and equilibrium values for bond, angle, and dihedral types).

Finally, after building the initial configuration, the simulation is about ready to be performed. The last step is to choose the simulation variables and set up the input to the simulation package in order to convey these selections.

These options and the decision process behind choosing from the various options will be presented in the following sections.

## Preparing an Input File

### Optimization Algorithms

Optimization algorithms are often used to find stationary points on a potential energy surface, i.e., local and global minima and saddle points. The only place where they directly enter MD is in the case of Born–Oppenheimer AIMD, in order to converge the SCF wavefunction for each MD step. It is immediately obvious that the choice of optimization algorithm crucially affects the speed of the simulation.

### Steepest Descent

The Steepest Descent method is the simplest optimization algorithm. The initial energy  $E[\Psi_0] = E(\mathbf{c}_0)$ , which depends on the plane wave expansion coefficients  $\mathbf{c}$  (see [Eq. 7.67](#)), is lowered by altering  $\mathbf{c}$  in the direction of the negative gradient,

$$\mathbf{d}_n = -\frac{\partial E(\mathbf{c}_n)}{\partial \mathbf{c}} \equiv -\mathbf{g}_n \quad (7.75)$$

$$\mathbf{c}_{n+1} = \mathbf{c}_n + \Delta_n \mathbf{d}_n \quad (7.76)$$

where  $\Delta_n > 0$  is a variable step size chosen such that the energy always decreases, and  $n$  is the optimization step index. The steepest descent method is very robust; it is guaranteed to approach the minimum. However, the rate of convergence ever decreases as the energy gets closer to the minimum, making this algorithm rather slow.

## Conjugate Gradient Methods

The Conjugate Gradient method generally converges faster than the steepest descent method due to the fact that it avoids moving in a previous search direction. This is achieved by linearly combining the gradient vector and the last search vector,

$$\mathbf{c}_{n+1} = \mathbf{c}_n + \Delta_n \mathbf{d}_n \quad (7.77)$$

where

$$\mathbf{d}_n = -\mathbf{g}_n + \beta_n \mathbf{d}_{n-1} \quad (7.78)$$

Different recipes exist to determine the coefficient  $\beta_n$  (Jensen 2007) among which the Polak–Ribière formula usually performs best for non-quadratic functions,

$$\beta_n = \frac{\mathbf{g}_n^T (\mathbf{g}_n - \mathbf{g}_{n-1})}{\mathbf{g}_{n-1}^T \mathbf{g}_{n-1}} \quad (7.79)$$

In the case of a general non-quadratic function, such as the DFT energy, conjugacy is not strictly fulfilled and the optimizer may search in completely inefficient directions after a few steps. It is then recommended to restart the optimizer (setting  $\beta = 0$ ). Convergence can be improved by multiplying  $\mathbf{g}_n$  with a preconditioner matrix, e.g., an approximate inverse of the second derivatives matrix (Hessian in the case of geometry optimization)  $\tilde{\mathbf{H}}$ . The method is then called Preconditioned Conjugate Gradient (PCG). In the CPMD code, the matrix  $\tilde{\mathbf{H}}$  is approximated by

$$\tilde{\mathbf{H}} = \begin{cases} H_{GG'}^{\text{KS}} & \text{for } G \geq G_{\text{cut}} \\ H_{G_{\text{cut}}G_{\text{cut}}}^{\text{KS}} & \text{for } G < G_{\text{cut}} \end{cases} \quad (7.80)$$

where  $H_{GG'}^{\text{KS}}$  is the Kohn–Sham matrix in the plane-wave basis and  $G_{\text{cut}}$  is a cutoff value for the reciprocal lattice vector  $\mathbf{G}$  (set to a default value of 0.5 a.u.).

## Direct Inversion of the Iterative Subspace

Having generated a sequence of optimization steps  $\mathbf{c}_i$ , the Direct Inversion of the Iterative Subspace (DIIS) method (Császár and Pulay 1984; Hutter et al. 1994; Pulay 1980, 1982) is designed to accelerate convergence by finding the best linear combination of stored  $\mathbf{c}_i$  vectors,

$$\mathbf{c}_{n+1} = \sum_{i=1}^n a_i \mathbf{c}_i \quad (7.81)$$

Ideally, of course,  $\mathbf{c}_{n+1}$  is equal to the optimum vector  $\mathbf{c}_{\text{opt}}$ . Defining the error vector  $\mathbf{e}_i$  for each iteration as

$$\mathbf{e}_i = \mathbf{c}_i - \mathbf{c}_{\text{opt}} \quad (7.82)$$

► Eq. 7.81 becomes

$$\sum_{i=1}^n a_i \mathbf{c}_{\text{opt}} + \sum_{i=1}^n a_i \mathbf{e}_i = \mathbf{c}_{\text{opt}} \quad (7.83)$$

► Equation 7.83 is satisfied if

$$\sum_{i=1}^n a_i = 1 \quad (7.84)$$

and

$$\sum_{i=1}^n a_i \mathbf{e}_i = 0 \quad (7.85)$$

Instead of the ideal case  $\blacktriangleright$  Eq. 7.85, in practice one minimizes the quantity

$$\left\langle \sum_{i=1}^n a_i \mathbf{e}_i \middle| \sum_{j=1}^n a_j \mathbf{e}_j \right\rangle \quad (7.86)$$

subject to the constraint ( $\blacktriangleright$  Eq. 7.84), which is equivalent to solving the system of linear equations

$$\begin{pmatrix} b_{11} & b_{12} & \cdots & b_{1n} & -1 \\ b_{21} & b_{22} & \cdots & b_{2n} & -1 \\ \vdots & \vdots & \vdots & \vdots & \vdots \\ b_{n1} & b_{n2} & \cdots & b_{nn} & -1 \\ -1 & -1 & \cdots & -1 & 0 \end{pmatrix} \begin{pmatrix} a_1 \\ a_2 \\ \vdots \\ a_n \\ \lambda \end{pmatrix} = \begin{pmatrix} 0 \\ 0 \\ \vdots \\ 0 \\ -1 \end{pmatrix} \quad (7.87)$$

where

$$b_{ij} = \langle \mathbf{e}_i | \mathbf{e}_j \rangle \quad (7.88)$$

and the error vectors are approximated by

$$\mathbf{e}_i = -\tilde{\mathbf{H}}^{-1}(\mathbf{c}_{\text{opt}}) \mathbf{g}_i \quad (7.89)$$

using an approximate Hessian matrix  $\tilde{\mathbf{H}}$ , e.g.,  $\blacktriangleright$  Eq. 7.80.

## Controlling Temperature: Thermostats

If understanding the behavior of the system as a function of temperature is the aim of your study, then it is important to be able to control the temperature of your system. The temperature of the system is related to the time average of the kinetic energy, which generally can be calculated by

$$\langle \mathcal{H} \rangle_{NVT} = \frac{3}{2} N k_B T. \quad (7.90)$$

Below we introduce specific thermostating techniques for MD simulations at thermodynamic equilibrium, e.g., for calculating equilibrium spatial distribution and time-correlation functions. However, when MD simulations are performed on a system undergoing some *non-equilibrium* process involving exchange of energy between different parts of the system, e.g., when an energetic particle, such as an atom or a molecule, hits a crystal surface, or there is a temperature gradient across the system, one has to resort to specially developed techniques, see for example Kantorovich [2008], Kantorovich and Rompotis [2008] and Toton et al. [2010]. In these methods, based on the so-called Generalized Langevin Equation, the actual system on which MD simulations are performed is considered in contact with one (or more) heat bath(s) kept at constant temperature(s), and the dynamics of the system of interest reflects the fact that there is an interaction and energy transfer between the system and the surrounding heat bath(s).



## Rescale Thermostat

One obvious way to control the temperature of a system is to rescale the velocities of the atoms within the system (Woodcock 1971). The rescaling factor  $\lambda$  is determined from  $\lambda\sqrt{T_{\text{target}}/T_0}$ , where  $T_{\text{target}}$  and  $T_0$  are the target and initial temperatures, respectively. Then, the velocity of each atom is rescaled such that  $V_f = \lambda V_i$ . In practice, the inputs generally required to use a rescale thermostat include:

- $T_0$  – Initial temperature
- $T_{\text{target}}$  – Target temperature
- $\tau$  – Damping constant (i.e., frequency with which to apply the thermostat)
- $\delta T$  – Maximum allowable temperature difference from  $T_{\text{target}}$  before thermostat is applied
- $f_{\text{rescale}}$  – Fraction of temperature difference between current temperature and  $T_{\text{target}}$  is corrected during each application of thermostat

If it is desired to have a strict thermostat (i.e., when first starting a simulation that might have particles very near one another), then  $\delta T$  and  $\tau$  should have values of  $\sim 0.01T_{\text{target}}$  and 1 time step, respectively, and  $f_{\text{rescale}}$  should be near 1.0. However, if you wish to allow a more lenient thermostat, then the value of  $\delta T$  should be of the same order of magnitude as  $T_{\text{target}}$ ,  $\tau$  should be  $\sim 10^2$ – $10^3$  time steps, and  $f_{\text{rescale}} \sim 0.01$ – $0.1$ .

## Berendsen Thermostat

Another way to control the temperature is to couple the system to an external heat bath, which is fixed at a desired temperature. This is referred to as a Berendsen thermostat (Berendsen et al. 1984). In this thermostat, the heat bath acts as a reservoir of thermal energy that supplies or removes temperature as necessary. The velocities are rescaled each time step, where the rate of change in temperature is proportional to the difference in the temperature in the system  $T(t)$  and the temperature of the external bath  $T_{\text{bath}}$ :

$$\frac{dT(t)}{dt} = \frac{1}{\tau}(T_{\text{bath}} - T(t)) \quad (7.91)$$

which when integrated results in the change in temperature each time step:

$$\Delta T = \frac{\delta t}{\tau}(T_{\text{bath}} - T(t)). \quad (7.92)$$

In [Eqs. 7.91](#) and [7.92](#),  $\tau$  is the damping constant for the thermostat. In practice, the necessary inputs when using the Berendsen thermostat include:

- $T_{\text{bath}}$  – temperature of the external heat bath
- $\tau$  – damping constant for the thermostat

Obviously the amount of control that the thermostat imposes on the simulation is controlled by the value of  $\tau$ . If  $\tau$  is large, then the coupling will be weak and the temperature will fluctuate significantly during the course of the simulation. While if  $\tau$  is small, then the coupling will be strong and the thermal fluctuations will be small. If  $\tau = \delta t$ , then the result will be the same as the rescale thermostat, in general.

## Nosé–Hoover Thermostat

While the Berendsen thermostat is efficient for achieving a target temperature within your system, the use of a thermostat that represents a canonical ensemble once the system has reached a thermal equilibrium. The extended system method, which was originally introduced by Nosé [1984a, b] and then further developed by Hoover (1985), introduces additional degrees of freedom into the Hamiltonian that describes the system, from which equations of motion can be determined.

The extended system method considers the external heat bath as an integral part of the system by including an additional degree of freedom in the Hamiltonian of the system that is represented by the variable  $s$ . As a result, the potential energy of the reservoir is

$$E_{\text{pot}} = (f + 1)k_B T \ln s, \quad (7.93)$$

where  $f$  is the number of degrees of freedom in the physical system and  $T$  is the target temperature. The kinetic energy of the reservoir is calculated by

$$E_{\text{kin}} = \frac{Q}{2} \left( \frac{ds}{dt} \right)^2, \quad (7.94)$$

where  $Q$  is a parameter with dimensions of energy  $\times$  (time)<sup>2</sup> and is generally referred to as the “virtual” mass of the extra degree of freedom  $s$ . The magnitude of  $Q$  determines the coupling between the heat bath and the real system, thus influencing the temperature fluctuations.

Utilizing  $\blacktriangleright$  Eqs. 7.93 and  $\blacktriangleright$  7.94, and substituting the real variables for the corresponding Nosé variables, the equations of motion are found to be as follows:

$$\ddot{\mathbf{R}}_I = \frac{\mathbf{F}_I}{M_I} - \gamma \mathbf{R}_I, \quad (7.95)$$

$$\dot{\gamma} = -\frac{1}{\tau_{\text{NH}}} \left( \frac{f+1}{f} \frac{T_{\text{target}}}{T} - 1 \right), \quad (7.96)$$

where  $\gamma = \frac{\dot{s}}{s}$  and  $\tau_{\text{NH}} = \frac{Q}{fk_B T_{\text{target}}}$ . The variable  $\tau_{\text{NH}}$  is an effective relaxation time, or damping constant.

In practice, the inputs that are necessary when utilizing the Nosé–Hoover thermostat during a molecular dynamics simulation include

- $T_{\text{target}}$  – Target temperature
- $\tau_{\text{NH}}$  – Damping constant
- $Q$  – Fictitious mass of the additional degree of freedom  $s$

The most significant variable in the above list is  $Q$ . Large values of  $Q$  may cause poor temperature control, with the infinite limit resulting in no energy exchange between the temperature bath and the real system, which is the case of conventional molecular dynamics simulations resulting in the microcanonical ensemble. However, if  $Q$  is too small then the energy oscillates and the system will take longer in order to reach a thermal equilibrium.

## Controlling Pressure: Barostats

It may be desired to study the behavior of the simulated system while the pressure is held constant (i.e., pressure-induced phase transitions). Many experimental measurements are made

in conditions where the pressure and temperature are held constant and so it is of utmost importance to be able to accurately replicate these conditions in simulations.

One thing of note is that the pressure often fluctuates more than other quantities such as the temperature in an  $NVT$  molecular dynamics simulation or the energy in a  $NVE$  molecular dynamics simulation. This is due to the fact that the pressure is related to the virial term, which is the product of the positions of the particles in the system and the derivative of the potential energy function. These fluctuations will be observed in the instantaneous values of the system pressure during the course of the simulation, but the average pressure should approach the desired pressure. Since generally the temperature and number of atoms will also be held constant during constant pressure simulations, and the volume of the system will be allowed to change in order to arrive at the desired pressure, therefore, less compressible systems will show larger fluctuations in the pressure than the systems that are more easily compressed.

## Berendsen Barostat

Many of the approaches used for controlling the pressure are similar to those that are used for controlling the temperature. One approach is to maintain constant pressure by coupling the system to a constant pressure reservoir as is done in the Berendsen barostat (Berendsen et al. 1984), which is analogous to the way temperature is controlled in the Berendsen thermostat. The pressure change in the system is determined by

$$\frac{dP(t)}{dt} = \frac{1}{\tau_P} (P_0 - P(t)), \quad (7.97)$$

where  $\tau_P$  is time constant of the barostat,  $P_0$  is the desired pressure and  $P(t)$  is the system pressure at any time  $t$ . In order to accommodate this change in pressure, the volume of the box is scaled by a factor of  $\mu^3$  each time step, therefore the coordinates of each particle in the system are scaled by a factor of  $\mu$  (i.e.,  $\mathbf{R}_I(t + \delta t) = \mu^{1/3} \mathbf{R}_I(t)$ ), where

$$\mu = \left[ 1 - \frac{\delta t}{\tau_P} (P - P_0) \right]^{\frac{1}{3}}. \quad (7.98)$$

In practice, the inputs for the Berendsen barostat will include:

- $P_0$  – Desired pressure
- $\tau_P$  – Time constant of the barostat

One other input that may be included in the use of the Berendsen barostat is to define which dimensions are coupled during the pressure relaxation. For example, you could define that the pressure is relaxed in a way that the changes in all three dimensions are coupled and therefore all of the dimensions change at the same rate. On the other hand, the pressure relaxation can be handled in an anisotropic manner, such that none of the dimensions are coupled and each dimension will have its own scaling factor that results from the individual pressure components.

## Nosé–Hoover Barostat

Similar to the Nosé–Hoover thermostat, the extended system method has been applied to create a barostat (Hoover 1986) that is coupled with a Nosé–Hoover thermostat. In this case, the extra

degree freedom  $\eta$  corresponds to a “piston,” and it is added to the Hamiltonian of the system, which results in the following equations of motion:

$$\frac{d\mathbf{R}(t)}{dt} = \mathbf{V}(t) + \eta(t)(\mathbf{R}(t) - \mathbf{R}_{\text{COM}}), \quad (7.99)$$

$$\frac{d\mathbf{V}(t)}{dt} = \frac{\mathbf{F}(t)}{M} - [\chi(t) + \eta(t)]\mathbf{V}(t), \quad (7.100)$$

$$\frac{d\chi(t)}{dt} = \frac{1}{\tau_T^2} \left( \frac{T}{T_0} - 1 \right), \quad (7.101)$$

$$\frac{d\eta(t)}{dt} = \frac{1}{Nk_B T_0 \tau_P^2} V(t)(P - P_0), \quad (7.102)$$

$$\frac{dV(t)}{dt} = 3\eta(t)V(t) \quad (7.103)$$

where  $\mathbf{R}_{\text{COM}}$  are the coordinates of the center of mass of the system,  $\eta$  is the thermostat extra degree of freedom and can be thought of as a friction coefficient,  $\tau_T$  is the thermostat time constant,  $\chi$  is barostat extra degree of freedom and is considered a volume scaling factor and  $\tau_P$  is the barostat time constant. **•** Equations 7.102 and **•** 7.103 explicitly contain the volume of the simulation box,  $V(t)$ . Generally, this barostat is implemented using the approach described in Melchionna et al. [1993].

In addition to the variables that are a part of the equations of motion, there is a variable  $Q$  that represents the “mass” of the “piston.” This is analogous to the “mass” variable in the Nosé–Hoover thermostat. In practice, the required input for the Nosé–Hoover barostat will include:

- $P_0$  – Desired pressure
- $T_0$  – Desired temperature
- $\tau_P$  – Time constant of the barostat
- $\tau_T$  – Time constant of the thermostat
- $Q$  – The “mass” of the piston

Like in the case of the Nosé–Hoover thermostat, care must be taken when selecting the value of the variable  $Q$ . A small value of  $Q$  is representative of a piston with small mass, and thus will have rapid oscillations of the box size and pressure, whereas a large value of  $Q$  will have the opposite effect. The infinite limit of  $Q$  results in normal molecular dynamics behavior.

## Setting the Time Step

### Born–Oppenheimer MD

Since BO-MD is classical MD in the sense that the nuclei are classical particles, the same rules concerning the choice of time step apply to both BO-MD and atomistic force-field MD. The largest possible time step,  $\delta t$ , is determined by the fastest oscillation in the system – in many molecules this would be a bond stretching vibration involving hydrogen, e.g., CH, NH, or OH. It is immediately plausible that  $\delta t$  must be smaller than the shortest vibrational period in order to

resolve that motion and for the numerical integrator (see section “Classical Molecular Dynamics”) to be stable. Let us assume a particular molecule has an OH vibration at  $3,500\text{ cm}^{-1}$ , corresponding to a period of about 10 fs. Then the time step has to be chosen smaller than 10 fs. Using a harmonic approximation it can be shown that the Verlet algorithm is stable for  $\omega^2 \delta t^2 < 2$  (Sutmann 2006). In the present example this would dictate a maximum time step of 2 fs. However, although such a choice guarantees numerical stability, it results in deviations from the exact answer. Therefore, in practice smaller time steps – typically around 1 fs – are often used.

## Car-Parrinello MD

Although in CP-MD the nuclei are still treated as classical particles, the choice of time step can no longer be based solely on the highest nuclear frequency  $\omega_n^{\max}$ . We also need to consider the fictitious dynamics of the electronic degrees of freedom. In fact, the optimum simulation time step is closely linked to the value of the fictitious electron mass  $\mu$  as we will see in the following.

The fictitious mass  $\mu$  has to be chosen small enough to guarantee adiabatic separation of electronic and nuclear motion. This means that the frequency spectrum of the electronic degrees of freedom (Marx and Hutter 2009; Pastore et al. 1991)

$$\omega_{ph} = \sqrt{\frac{2(\epsilon_p - \epsilon_h)}{\mu}} \quad (7.104)$$

must not overlap with the vibrational spectrum of the nuclear system. The lowest electronic frequency according to  $\blacktriangleright$  Eq. 7.104 is

$$\omega^{\min} = \sqrt{\frac{2(\epsilon_{\text{LUMO}} - \epsilon_{\text{HOMO}})}{\mu}} \quad (7.105)$$

The highest electronic frequency is determined by the plane-wave cutoff energy  $E_{\text{cut}}$ ,

$$\omega^{\max} \approx \sqrt{\frac{2E_{\text{cut}}}{\mu}} \quad (7.106)$$

Thus the maximum simulation time step, which is inversely proportional to  $\omega^{\max}$ , thus obeys the relation

$$\Delta t^{\max} \propto \sqrt{\frac{\mu}{E_{\text{cut}}}} \quad (7.107)$$

According to  $\blacktriangleright$  Eq. 7.107 the maximum time step can be increased by simply increasing  $\mu$ . However, this would also result in a lowering of  $\omega_e^{\min}$  (see  $\blacktriangleright$  Eq. 7.105) and therefore in a smaller separation  $\omega_e^{\min} - \omega_n^{\max}$  between the nuclear and electronic spectra.

Let us discuss the above using some realistic numbers. In the case of the  $\text{H}_2\text{O}$  molecule, for example, the HOMO-LUMO gap with the BLYP functional is about 5.7 eV. Assuming a typical value of 400 a.u. for  $\mu$ , the minimum electronic frequency ( $\blacktriangleright$  Eq. 7.105) is ca.  $6,900\text{ cm}^{-1}$ . The highest energy molecular vibrational mode in a CP-MD simulation using these parameter values is the asymmetric stretch at about  $3,500\text{ cm}^{-1}$ . This means that electronic and nuclear spectra are well separated. A basis set cutoff of  $E_{\text{cut}} = 70\text{ Ry}$  ( $= 35\text{ a.u.}$ ) leads to a maximum electronic frequency ( $\blacktriangleright$  Eq. 7.106) of  $\approx 92,000\text{ cm}^{-1}$  corresponding to a vibrational period of 15 a.u.. Hence the CP-MD time step has to be smaller than this number. For water, a time

step/fictitious mass combination of 4 a.u./400 a.u. has been shown to be a good compromise between efficiency and accuracy (Kuo et al. 2004).

If we were to increase  $\mu$  to 1,000 a.u., we could afford a larger time step of about 6 a.u. (according to  $\blacktriangleright$  Eq. 7.107). However,  $\omega_e^{\min}$  ( $\blacktriangleright$  Eq. 7.105) would become ca.  $4,500 \text{ cm}^{-1}$ , dangerously close to  $\omega_n^{\max}$ . A simple trick that is often used to be able to afford larger time steps is to replace all hydrogen atoms by deuterium atoms thus downshifting  $\omega_n^{\max}$ . For systems with a small or even vanishing (e.g., metals) bandgap it is increasingly difficult or impossible to achieve adiabatic separation of electronic and nuclear degrees of freedom following the above considerations. A solution to this problem is the use of separate thermostats for the two subsystems (Marx and Hutter 2009; Sprik 1991)

## Postprocessing

### Data Analysis

#### Spatial Distribution Functions

For a system of  $N$  particles in a volume  $V$  at temperature  $T$ , the probability of molecule 1 being in the volume element  $d\mathbf{R}_1$  around the position  $\mathbf{R}_1$ , molecule 2 being in  $d\mathbf{R}_2$ , ..., molecule  $N$  being in  $d\mathbf{R}_N$  is given by McQuarrie [1992]

$$P^{(N)}(\mathbf{R})d\mathbf{R} = P^{(N)}(\mathbf{R}_1, \dots, \mathbf{R}_N)d\mathbf{R}_1, \dots, d\mathbf{R}_N = \frac{e^{-E(\mathbf{R})/kT}}{Z_N} \quad (7.108)$$

with the configuration integral

$$Z_N = \int_V e^{-E(\mathbf{R})/kT} d\mathbf{R} \quad (7.109)$$

where  $E(\mathbf{R})$  is the potential energy of the system at configuration  $\mathbf{R}$  (cf.  $\blacktriangleright$  Eqs. 7.8 and  $\blacktriangleright$  7.10).

For a subset of  $n$  molecules, the probability of molecule 1 being in  $d\mathbf{R}_1$ , ..., molecule  $n$  being in  $d\mathbf{R}_n$  is

$$P^{(n)}(\mathbf{R}_1, \dots, \mathbf{R}_n) = \frac{\int \dots \int e^{-E(\mathbf{R})/kT} d\mathbf{R}_{n+1} \dots d\mathbf{R}_N}{Z_N} \quad (7.110)$$

The probability of *any* molecule being in  $d\mathbf{R}_1$ , ..., *any* molecule  $n$  being in  $d\mathbf{R}_n$  is

$$\rho^{(n)}(\mathbf{R}_1, \dots, \mathbf{R}_n) = \frac{N!}{(N-n)!} P^{(n)}(\mathbf{R}_1, \dots, \mathbf{R}_n) \quad (7.111)$$

In a liquid the probability of finding any one molecule in  $d\mathbf{R}_1$ ,  $\rho^{(1)}(\mathbf{R}_1)d\mathbf{R}_1$ , is independent of  $\mathbf{R}_1$ . Therefore

$$\frac{1}{V} \int \rho^{(1)}(\mathbf{R}_1)d\mathbf{R}_1 = \rho^{(1)} = \frac{N}{V} = \rho \quad (7.112)$$

The dependence of the molecules of a liquid on all the other molecules, in other words, their correlation, is captured by the *correlation function*  $g^{(n)}(\mathbf{R}_1, \dots, \mathbf{R}_n)$ , which is defined by


$$\rho^{(n)}(\mathbf{R}_1, \dots, \mathbf{R}_n) = \rho^n g^{(n)}(\mathbf{R}_1, \dots, \mathbf{R}_n) \quad (7.113)$$

Using  $\blacktriangleright$  Eq. 7.111 we can thus write

$$g^{(n)}(\mathbf{R}_1, \dots, \mathbf{R}_n) = \frac{V^n N!}{N^n (N-n)!} \frac{\int \dots \int e^{-E(\mathbf{R})/kT} d\mathbf{R}_{n+1} \dots d\mathbf{R}_N}{Z_N} \quad (7.114)$$

The two-body correlation function  $g^{(2)}(\mathbf{R}_1, \mathbf{R}_2)$  is of particular interest as it can be determined in X-ray diffraction experiments. In the following we shall only consider the dependence of  $g^{(2)}$  on the interparticle distance  $R = R_{12} = |\mathbf{R}_1 - \mathbf{R}_2|$ , i.e., we have averaged over any angular dependence, and call  $g^{(2)}(R_{12}) = g(R)$  the *radial distribution function*. The quantity  $\rho g(R) d\mathbf{R}_I$  is proportional to the probability of finding another particle,  $I$ , in  $d\mathbf{R}_I$  if the reference particle is at the origin. Spherical integration yields

$$\int \rho g(R) 4\pi R^2 dR = N - 1 \approx N \quad (7.115)$$

showing that  $\rho g(R) 4\pi R^2 dR$  is the number of particles in the spherical volume element between  $R$  and  $R + dR$  about the central particle. The radial distribution function  $g(R)$  is proportional to the local density  $\rho(R) = \rho g(R)$  about a certain molecule. In a fluid,  $g(R) \rightarrow 1$  as  $R \rightarrow \infty$ , i.e., there is no long-range order and we "see" only the average particle density. At very short range, i.e.,  $R \rightarrow 0$ ,  $g(R) \rightarrow 0$ , due to the repulsiveness of the molecules. Examples from a CP-MD simulation of liquid water are shown in  Fig. 7-3.

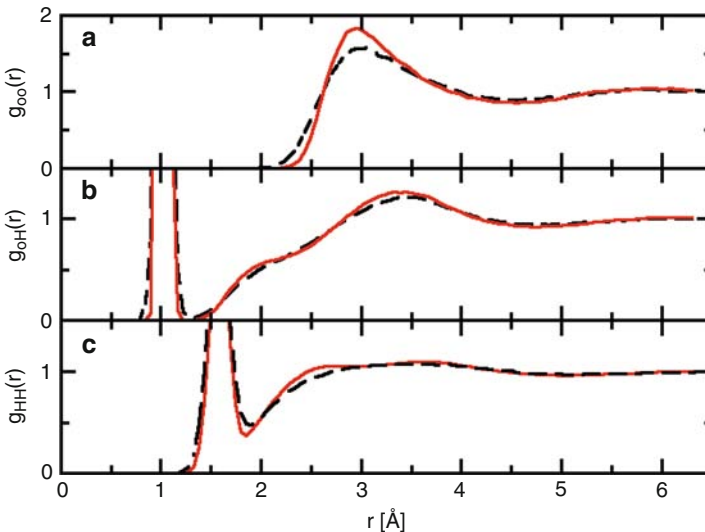
The radial distribution function  $g(R)$  provides a useful measure of the quality of a simulation as it can be compared to experimental – X-ray or neutron diffraction – data obtained by Fourier transform of the structure factor


$$h(k) = \rho \int [g(R) - 1] e^{i\mathbf{k}\mathbf{R}} d\mathbf{R} \quad (7.116)$$

where  $\mathbf{k}$  is the wave vector.

In addition to characterizing the structure of a liquid, the radial distribution function may also be used to calculate thermodynamic properties such as the total energy,

$$E = \frac{3}{2} NkT + 2\pi N\rho \int_0^\infty u(R)g(R)R^2 dR \quad (7.117)$$



 Fig. 7-3

Radial distribution function of liquid water from CP-MD simulations at 900 and 1,200 K, respectively

the pressure,

$$p = \rho kT - \frac{2}{3}\pi\rho^2 \int_0^\infty \frac{du(R)}{dR} g(R)R^3 dR \quad (7.118)$$

and the chemical potential,

$$\mu = kT \ln(\rho\Lambda^3) + 4\pi\rho \int_0^1 d\xi \int_0^\infty u(R)g(R, \xi)R^2 dR \quad (7.119)$$

where

$$\Lambda = \sqrt{\frac{h^2}{2\pi m kT}} \quad (7.120)$$

is the thermal de Broglie wavelength. By varying the coupling parameter  $\xi$  between 0 and 1, one can effectively take a molecule in and out of the system. It should be stressed that  $\blacktriangleright$  Eqs. 7.117–7.119 have been derived assuming a pairwise additive intermolecular potential  $u(R)$ .

We now define the *potential of mean force*, i.e., the interaction between  $n$  fixed molecules averaged over the configurations of the remaining molecules  $n + 1, \dots, N$ , as

$$w^{(n)}(\mathbf{R}_1, \dots, \mathbf{R}_n) = -kT \ln g^{(n)}(\mathbf{R}_1, \dots, \mathbf{R}_n) \quad (7.121)$$

The mean force acting on molecule  $J$  is then obtained from

$$\mathbf{f}_J^{(n)} = -\nabla_J w^{(n)} \quad (7.122)$$

## Time Correlation Functions

The classical *time autocorrelation function* of some vectorial function

$$\mathbf{A}(t) = \mathbf{A}(P(t), Q(t)) = \mathbf{A}(P, Q; t) \quad (7.123)$$

where  $Q(t)$  and  $P(t)$  are the generalized coordinate and momentum, respectively, is defined as

$$C(t) = \langle \mathbf{A}(0)\mathbf{A}(t) \rangle = \int \dots \int dP dQ \mathbf{A}(P, Q; 0)\mathbf{A}(P, Q; t) f(P, Q) \quad (7.124)$$

where  $f(P, Q)$  is the equilibrium phase space distribution function.

From the velocity autocorrelation function, for example, one can calculate the diffusion coefficient as

$$D = \frac{1}{3} \int_0^\infty \langle \mathbf{V}_I(0)\mathbf{V}_I(t) \rangle dt \quad (7.125)$$

where  $\mathbf{V}_I$  is the velocity of particle  $I$ . Alternatively, one can obtain the diffusion coefficient for long times from the associated *Einstein relation*,

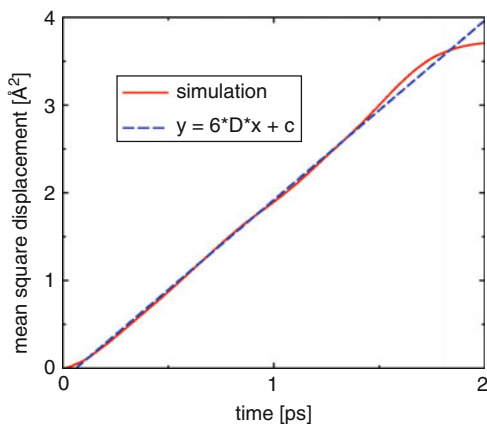
$$6tD = \langle |\mathbf{R}_I(t) - \mathbf{R}_I(0)|^2 \rangle \quad (7.126)$$

In practice,  $D$  is then determined from a linear fit to the *mean square displacement* (rhs of  $\blacktriangleright$  Eq. 7.126) as one sixth of the slope. An example is shown in  $\blacktriangleright$  Fig. 7-4.

Another common application of correlation functions is the calculation of IR absorption spectra. The lineshape function,  $I(\omega)$ , is given by the Fourier transform of the autocorrelation function of the electric dipole moment  $\mathbf{M}$ ,

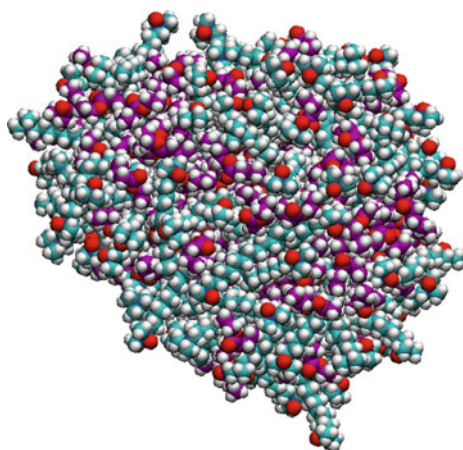
$$I(\omega) = \frac{1}{2\pi} \int_{-\infty}^\infty \langle \mathbf{M}(0)\mathbf{M}(t) \rangle e^{-i\omega t} dt \quad (7.127)$$





■ Fig. 7-4

Mean square displacement of liquid water from CP-MD simulations at 900 K and linear fit to determine the diffusion constant  $D$  using [Eq. 7.126](#)



■ Fig. 7-5

A snapshot of a micelle formed from DDAO molecules and oil molecules formed using the VMD software package ([VMD 2009](#))

## Visualization

Due to the nature of MD simulations, one of the most productive forms of analysis of a simulation is to be able to visualize the trajectory of the molecules of interest. This is particularly useful since experimental techniques are not able to produce visual pictures of atomistic interactions and therefore it is something that only simulations (at this point) are able to provide. In order to visualize a simulation trajectory there are several different very powerful computer packages that are commonly used. These software packages include VMD ([2009](#)), PyMol ([2010](#)), RasMol ([2008](#)), and several others ([Free Molecular Visualization Software 2008](#)). [Figure 7-5](#) shows an example of the type of pictures that can be made using the visualization software.

Each of these codes will generally accept the trajectory in any number of standard inputs (i.e., pdb, xyz,...) and then will generate snapshots which can be rendered individually or as a movie. In addition to providing the visualization, these codes have become progressively powerful analysis codes in their own right. They now have the ability to measure bond lengths, angles, and dihedrals as a function of time, determine the solvent accessible surface area, hydrogen bond network, and many other useful structural related properties of the system.

## References

- ABINIT. (2010). <http://www.abinit.org>. Accessed 02 July 2011.
- Allen, M. P., & Tildesley, D. J. (1987). *Computer simulation of liquids*. Oxford: Clarendon Press.
- Amara, P., Field, M. J., Alhambra, C., & Gao, J. (2000). The generalized hybrid orbital method for combined quantum mechanical/molecular mechanical calculations: Formulation and tests of the analytical derivatives. *Theoretical Chemistry Accounts*, 104, 336.
- Anderson, J. A., Lorenz, C. D., & Travestet, A. (2008). General purpose molecular dynamics simulations fully implemented on graphics processing units. *Journal of Computational Physics*, 227, 5342.
- Aqvist, J., & Warshel, A. (1993). Simulation of enzyme reactions using valence bond force fields and other hybrid quantum/classical approaches. *Chemical Reviews*, 93, 2523.
- Artacho, E., Anglada, E., Dieguez, O., Gale, J. D., Garcia, A., Junquera, J., Martin, R. M., Ordejón, P., Pruneda, J. M., Sánchez-Portal, D., & Soler, J. M. (2008). The SIESTA method; developments and applicability. *Journal of Physics: Condensed Matter*, 20, 064208.
- Ashcroft, N. W., & Mermin, N. D. (1976). *Solid state physics*. Philadelphia: Saunders College Publishing.
- Assfeld, X., & Rivail, J. L. (1996). Quantum chemical computations on parts of large molecules: The ab initio local self consistent field method. *Chemical Physics Letters*, 263, 100.
- Assfeld, X., Ferré, N., & Rivail, J. L. (1998). In J. Gao & M. A. Thompson (Eds.), *Combined quantum mechanical and molecular mechanical methods*, ACS Symp. Ser. (Vol. 712, p. 234). Washington: American Chemical Society.
- Aulbur, W. G., Jonsson, L., & Wilkins, J. W. (2000). Quasiparticle calculations in solids. *Solid State Physics*, 54, 1.
- Bachelet, G. B., Hamann, D. R., Schlüter, M. (1982). Pseudopotentials that work: From H to Pu. *Physical Review B*, 26, 4199.
- Balint-Kurti, G. G. (2008). Time-dependent and time-independent wavepacket approaches to reactive scattering and photodissociation dynamics. *International Reviews in Physical Chemistry*, 27, 507.
- Baskes, M. I. (1992). Modified embedded-atom potentials for cubic materials and impurities. *Physical Review B*, 46, 2727.
- Becke, A. D. (1988). Density-functional exchange-energy approximation with correct asymptotic behavior. *Physical Review A*, 38, 3098.
- Becke, A. D. (1993). Density-functional thermochemistry. III. The role of exact exchange. *Journal of Chemical Physics*, 98, 5648.
- Bereau, T., & Deserno, M. (2009). Generic coarse-grained model for protein folding and aggregation. *Journal of Chemical Physics*, 130, 235106.
- Berendsen, H. J. C., Postma, J. P. M., van Gunsteren, W. F., Nola, A. D., & Haak, J. R. (1984). Molecular dynamics with coupling to an external bath. *Journal of Chemical Physics*, 81, 3684.
- Betancourt, M. R., & Omovie, S. J. (2009). Pairwise energies for polypeptide coarse-grained models derived from atomic force fields. *Journal of Chemical Physics*, 130, 195103.
- Bhandarkar, M., Bhatele, A., Bohm, E., Brunner, R., Buelens, F., Chipot, C., Dalke, A., Dixit, S., Fiorin, G., Freddolino, P., Grayson, P., Gullingsrud, J., Gursoy, A., Hardy, D., Harrison, C., Héning, J., Humphrey, W., Hurwitz, D., Krawetz, N., Kumar, S., Kunzman, D., Lee, C., Mei, C., Nelson, M., Phillips, J., Sarood, O., Shinozaki, A., Zheng, G., & Zhu, F. (2009). NAMD User's Guide. Theoretical Biophysics Group, University of Illinois and Beckman Institute. <http://www.ks.uiuc.edu/Research/namd/>. Accessed 02 July 2011.
- Bloch, P. E. (1994). Projector augmented-wave method. *Physical Review B*, 50, 17953.
- Bloch, P. E., Forst, C. J., & Schimpl, J. (2003). Projector augmented wave method: Ab initio molecular dynamics with full wave functions. *Bulletin of Material Science*, 26, 33.

- Bockstedte, M., Kley, A., Neugebauer, J., & Scheffler, M. (1997). Density-functional theory calculations for poly-atomic systems: Electronic structure, static and elastic properties and ab initio molecular dynamics. *Computer Physics Communications*, 107, 187.
- Boeck, S. (2009). *Development and application of the S/PHI/nX library*. Saarbrücken: Südwestdeutscher Verlag für Hochschulschriften.
- Bowler, D. R., Choudhury, R., Gillan, M. J., & Miyazaki, T. (2006). Recent progress with large-scale ab initio calculations: The CONQUEST code. *Physica Status Solidi B*, 243, 989.
- Boys, S. F., & Bernardi, F. (1970). The calculation of small molecular interactions by the differences of separate total energies. Some procedures with reduced errors. *Molecular Physics*, 19, 553.
- Bredow, T., & Jug, K. (2005). Theory and range of modern semiempirical molecular orbital methods. *Theoretical Chemistry Accounts*, 113, 1.
- Brooks, B. R., Brooks, C. L., III, Mackerell, A. D., Nilsson, L., Petrella, R. J., Roux, B., Won, Y., Archontis, G., Bartels, C., Boresch, S., Caflisch, A., Caves, L., Cui, Q., Dinner, A. R., Feig, M., Fischer, S., Gao, J., Hodoscek, M., Im, W., Kuczera, K., Lazaridis, T., Ma, J., Ovchinnikov, V., Paci, E., Pastor, R. W., Post, C. B., Pu, J. Z., Schaefer, M., Tidor, B., Venable, R. M., Woodcock, H. L., Wu, X., Yang, W., York, D. M., & Karplus, M. (2009). CHARMM: The biomolecular simulation program. *Journal of Computational Chemistry*, 30, 1545.
- Buckingham, R. A. (1938). The classical equation of state of gaseous helium, neon and argon. *Proceedings of the Royal Society of London A*, 168, 264.
- Bulo, R. E., Ensing, B., Sikkema, J., & Visscher, L. (2009). Toward a practical method for adaptive QM/MM simulations. *Journal of Chemical Theory and Computation*, 5, 2212.
- Car, R., & Parrinello, M. (1985). Unified approach for molecular dynamics and density-functional theory. *Physical Review Letters*, 55, 2471.
- Case, D. A., Cheatham, T. E., III, Darden, T., Gohlke, H., Luo, R., Jr., K. M. M., Onufriev, A., Simmerling, C., Wang, B., & Woods, R. (2005). The Amber biomolecular simulation programs. *Journal of Computational Chemistry*, 26, 1668.
- Case, D. A., Darden, T. A., Cheatham, T. E., III, Simmerling, C. L., Wang, J., Duke, R. E., Luo, R., Crowley, M., Walker, R. C., Zhang, W., Merz, K. M., Wang, B., Hayik, S., Roitberg, A., Seabra, G., Kolossváry, I., Wong, F. K., Paesani, F., Vanicek, J., Wu, X., Brozell, S. R., Steinbrecher, T., Gohlke, H., Yang, L., Tan, C., Mongan, J., Hornak, V., Cui, G., Mathews, D. H., Seetin, M. G., Sagui, C., Babin, V., & Kollman, P. (2008). AMBER 10. San Francisco: University of California. <http://ambermd.org/>. Accessed 02 July 2011.
- CASTEP. (2009). <http://www.tcm.phy.cam.ac.uk/castep/>. Accessed 02 July 2011.
- CCDC. (2010). Cambridge crystallographic data centre. <http://www.ccdc.cam.ac.uk>. Accessed 02 July 2011.
- Chadi, D. J., & Cohen, M. L. (1973). Special points in the brillouin zone. *Physical Review B*, 8, 5747.
- CHARMM. (2009). <http://www.charmm.org/>. Accessed 02 July 2011.
- Clark, S. J., Segall, M. D., Pickard, C. J., Hasnip, P. J., Probert, M. J., Refson, K., & Payne, M. C. (2005). First principles methods using CASTEP. *Zeitschrift für Kristallographie*, 220, 567.
- CONQUEST. (2009). <http://hamlin.phys.ucl.ac.uk/NewCQWeb/bin/view>. Accessed 02 July 2011.
- Cooke, I. R., Kremer, K., & Deserno, M. (2005). Tunable generic model for fluid bilayer membranes. *Physical Review E*, 72, 011506.
- Cornell, W. D., Cieplak, P., Bayly, C. I., Gould, I. R., Merz, K. M., Jr., Ferguson, D. M., Spellmeyer, D. C., Fox, T., Caldwell, J. W., & Kollman, P. A. (1995). A second generation force field for the simulation of proteins, nucleic acids, and organic molecules. *Journal of American Chemical Society*, 117, 5179.
- CP-PAW. (2006). <http://orion.pt.tu-clausthal.de/paw/>. Accessed 02 July 2011.
- Császár, P., & Pulay, P. (1984). Geometry optimization by direct inversion in the iterative subspace. *Journal of Molecular Structure*, 114, 31.
- DACAPO. (2006). <https://wiki.fysik.dtu.dk/dacapo>. Accessed 02 July 2011.
- Daw, M. S., & Baskes, M. I. (1983). Semiempirical, quantum mechanical calculation of hydrogen embrittlement in metals. *Physical Review Letters*, 50, 1285.
- Daw, M. S., & Baskes, M. I. (1984). Embedded-atom method: Derivation and application to impurities, surfaces, and other defects in metals. *Physical Review B*, 29, 6443.
- Day, P. N., Jensen, J. H., Gordon, M. S., Webb, S. P., Stevens, W. J., Krauss, M., Garmer, D., Basch, H., & Cohen, D. (1996). An effective fragment method for modeling solvent effects in quantum mechanical calculations. *Journal of Chemical Physics*, 105, 1968.
- Dirac, P. A. M. (1930). Note on exchange phenomena in the Thomas atom. *Proceedings of the Cambridge Philosophical Society*, 26, 376.
- Doltsinis, N. L. (2006). In J. Grotendorst, F. Blügel, & D. Marx (Eds.), *Computational nanoscience: Do it yourself!* Jülich: NIC. <http://www2.fz-juelich.de/nic-series/volume31/doltsinis3.pdf>. Accessed 02 July 2011.

- Doltsinis, N. L., & Marx, D. (2002a). Nonadiabatic car-parrinello molecular dynamics. *Physical Review Letters*, 88, 166402.
- Doltsinis, N. L., & Marx, D. (2002b). First-principles molecular dynamics involving excited states and nonadiabatic transitions. *Journal of Theoretical and Computational Chemistry*, 1, 319–349.
- Dreizler, R. M., & Gross, E. K. U. (1990). *Density-functional theory*. Berlin: Springer.
- Elezgaray, J., & Laguerre, M. (2006). A systematic method to derive force fields for coarse-grained simulations of phospholipids. *Computer Physics Communications*, 175, 264.
- Elstner, M., Porezag, D., Jungnickel, G., Elsner, J., Haugk, M., Frauenheim, T., Suhai, S., & Seifert, G. (1998). Self-consistent-charge density-functional tight-binding method for simulations of complex materials properties. *Physical Review B*, 58, 7260.
- Ewald, P. P. (1921). Die Berechnung optischer und elektrostatischer Gitterpotentiale. *Annals of Physics*, 369, 253.
- Ferré, N., Assfeld, X., & Rivail, J. L. (2002). Specific force field parameters determination for the hybrid ab initio QM/MM LSCF method. *Journal of Computational Chemistry*, 23, 610.
- FHI98md. (2002). <http://www.fhi-berlin.mpg.de/th/fhimd/>. Accessed 02 July 2011.
- Finnis, M. W., & Sinclair, J. E. (1984). A simple empirical n-body potential for transition metals. *Philosophical Magazine A*, 29, 6443.
- Fornili, A., Sironi, M., & Raimondi, M. (2003). Determination of extremely localized molecular orbitals and their application to quantum mechanics/molecular mechanics methods and to the study of intramolecular hydrogen bonding. *Journal of Molecular Structure (THEOCHEM)*, 632, 157.
- Fornili, A., Loos, P.-F., Sironi, M., & Assfeld, X. (2006a). Frozen core orbitals as an alternative to specific frontier bond potential in hybrid Quantum Mechanics/Molecular Mechanics methods. *Chemical Physics Letters*, 427, 236.
- Fornili, A., Moreau, Y., Sironi, M., & Assfeld, X. (2006b). On the suitability of strictly localized orbitals for hybrid QM/MM calculations. *Journal of Computational Chemistry*, 27, 515.
- Free Molecular Visualization Software. (2008). <http://www.umass.edu/microbio/rasmol/othersof.htm>. Accessed 02 July 2011.
- Fumi, F. G., & Tosi, M. P. (1964). Ionic sizes and born repulsive parameters in the NaCl-type alkali halides I : The Huggins-Mayer and Pauling forms. *Journal of Physics and Chemistry of Solids*, 25, 31.
- Gao, J., Amara, P., Alhambra, C., & Field, M. J. (1998). A Generalized Hybrid Orbital (GHO) method for the treatment of boundary atoms in combined QM/MM calculations. *Journal of Physics Chemistry A*, 102, 4714.
- Garcia-Viloca, M., & Gao, J. (2004). Generalized hybrid orbital for the treatment of boundary atoms in combined quantum mechanical and molecular mechanical calculations using the semiempirical parameterized model 3 method. *Theoretical Chemistry Accounts*, 111, 280.
- Giannozzi, P., Baroni, S., Bonini, N., Calandra, M., Car, R., Cavazzoni, C., Ceresoli, D., Chiarotti, G. L., Cococcioni, M., Dabo, I., Corso, A. D., Fabris, S., Fratesi, G., de Gironcoli, S., Gebauer, R., Gerstmann, U., Gougoussis, C., Kokalj, A., Lazzeri, M., Martin-Samos, L., Marzari, N., Mauri, F., Mazzarello, R., Paolini, S., Pasquarello, A., Paulatto, L., Sbraccia, C., Scandolo, S., Sclauzero, G., Seitsonen, A. P., Smogunov, A., Umari, P., & Wentzcovitch, R. M. (2009). QUANTUM ESPRESSO: A modular and open-source software project for quantum simulations of materials. *Journal of Physics: Condensed Matter*, 21, 395502.
- Goedecker, S., Teter, M., & Hutter, J. (1996). Separable dual-space Gaussian pseudopotentials. *Physical Review B*, 54, 1703.
- Goetz, R., Compber, G., & Lipowsky, R. (1999). Mobility and elasticity of self-assembled membranes. *Physical Review Letters*, 82, 221.
- Gordon, M. S., Freitag, M. A., Bandyopadhyay, P., Jensen, J. H., Kairys, V., & Stevens, W. J. (2001). The effective fragment potential method: A QM-based MM approach to modeling environmental effects in chemistry. *The Journal of Physical Chemistry A*, 105, 105.
- Grigorenko, B. L., Nemukhin, A. V., Topol, I. A., & Burt, S. K. (2002). Modeling of biomolecular systems with the quantum mechanical and molecular mechanical method based on the effective fragment potential technique: Proposal of flexible fragments. *The Journal of Physical Chemistry A*, 106, 10663.
- GROMOS. (2007). BIOMOS b.v. laboratory of physical chemistry ETH Hnggerberg, HCI. <http://www.gromos.net/>. Accessed 02 July 2011.
- Hamann, D. R., Schlüter, M., Chiang, C. (1979). Norm-conserving pseudopotentials. *Physical Review Letters*, 43, 1494.
- Hartwigsen, C., Goedecker, S., & Hutter, J. (1998). Relativistic separable dual-space Gaussian pseudopotentials from H to Rn. *Physical Review B*, 58, 3641.
- Heyden, A., Lin, H., & Truhlar, D. G. (2007). Adaptive partitioning in combined quantum mechanical

- and molecular mechanical calculations of potential energy functions for multiscale simulations. *The Journal of Physical Chemistry B*, *111*, 2231.
- Hockney, R. W. (1970). The potential calculation and some applications. *Methods in Computational Physics*, *9*, 135.
- Hockney, R., & Eastwood, J. (1981). *Computer simulation using particles*. New York: McGraw-Hill.
- Hofer, T. S., Pribil, A. B., Randolf, B. R., & Rode, B. M. (2005). Structure and dynamics of solvated Sn(II) in aqueous solution: An ab initio QM/MM MD approach. *Journal of American Chemical Society*, *127*, 14231.
- HOOMD. (2009). <http://codeblue.umich.edu/hoomd-blue>. Accessed 02 July 2011.
- Hoover, W. G. (1985). Canonical dynamics: Equilibrium phase-space distributions. *Physical Review A*, *31*, 1695.
- Hoover, W. G. (1986). Constant-pressure equations of motion. *Physical Review A*, *34*, 2499.
- Hutter, J., Lüthi, H. P., & Parrinello, M. (1994). Electronic structure optimization in plane-wave-based density functional calculations by direct inversion in the iterative subspace. *Computational Materials Science*, *2*, 244.
- Hutter, J., Kohlmeyer, A., Mundy, C. J., Mohamed, F., Schiffmann, F., Tabacchi, G., Forbert, H., Bethune, I., Kuo, W., Krack, M., Iannuzzi, M., Guidon, M., McGrath, M., Kuehne, T. D., Laino, T., Borstnik, U., VandeVondele, J., & Weber, V. (2009). CP2K – a general program to perform molecular dynamics simulations. <http://cp2k.berlios.de>. Accessed 02 July 2011.
- ICSD. (2009). Inorganic crystal structure database. <http://www.fiz-karlsruhe.de/icsd.html>. Accessed 02 July 2011.
- Izvekov, S., & Voth, G. A. (2005). A multiscale coarse-graining method for biomolecular systems. *The Journal of Physical Chemistry B*, *109*, 2469.
- Izvekov, S., & Voth, G. A. (2006). Multiscale coarse-graining of mixed phospholipid/cholesterol bilayers. *Journal of Chemical Theory and Computation*, *2*, 637.
- Jensen, F. (2007). *Introduction to computational chemistry*. Chichester: Wiley.
- Jensen, J. H., Day, P. N., Gordon, M. S., Basch, H., Cohen, D., Garmer, D. R., Krauss, M., & Stevens, W. J. (1994). In D. A. Smith (Ed.), *Modeling the hydrogen bond*, ACS Symp. Ser. (Vol. 569, p. 139). Washington, DC: American Chemical Society.
- Jørgensen, W. L., Madura, J. D., & Swenson, C. J. (1984). Optimized intermolecular potential functions for liquid hydrocarbons. *Journal of American Chemical Society*, *106*, 6638.
- Jung, J., Choi, C. H., Sugita, Y., & Ten-no, S. (2007). New implementation of a combined quantum mechanical and molecular mechanical method using modified generalized hybrid orbitals. *Journal of Chemical Physics*, *127*, 204102.
- Kairys, V., & Jensen, J. H. (2000). QM/MM boundaries across covalent bonds: A frozen localized molecular orbital-based approach for the effective fragment potential method. *The Journal of Physical Chemistry A*, *104*, 6656.
- Kantorovich, L. (2008). Generalized Langevin equation for solids. I. Rigorous derivation and main properties. *Physical Review B*, *78*, 094304.
- Kantorovich, L., & Rompotis, N. (2008). Generalized Langevin equation for solids. II. Stochastic boundary conditions for nonequilibrium molecular dynamics simulations. *Physical Review B*, *78*, 094305.
- Kendall, R. A., Apra, E., Bernholdt, D. E., Bylaska, E. J., Dupuis, M., Fann, G. I., Harrison, R. J., Ju, J., Nichols, J. A., Nieplocha, J., Straatsma, T. P., Windus, T. L., & Wong, A. T. (2000). High performance computational chemistry: An overview of NWChem a distributed parallel application. *Computer Physics Communications*, *128*, 260.
- Kerdcharoen, T., Liedl, K. R., & Rode, B. M. (1996). A QM/MM simulation method applied to the solution of Li<sup>+</sup> in liquid ammonia. *Chemical Physics*, *211*, 313.
- Kerdcharoen, T., & Morokuma, K. (2002). ONIOM-XS: An extension of the ONIOM method for molecular simulation in condensed phase. *Chemical Physics Letters*, *355*, 257.
- Kerker, G. (1980). Non-singular atomic pseudopotentials for solid state applications. *The Journal of Physical Chemistry C*, *13*, L189.
- Khalid, S., Bond, P. J., Holyoake, J., Hawtin, R. W., & Sansom, M. S. P. (2008). DNA and lipid bilayers: Self-assembly and insertion. *Journal of the Royal Society Interface*, *5*, S241.
- Kleinman, L., & Bylander, D. M. (1982). *Physical Review Letters*, *48*, 1425.
- Kołos, W. (1970). Adiabatic approximation and its accuracy. *Advances in Quantum Chemistry*, *5*, 99.
- Kremer, K., & Grest, G. (1990). Dynamics of entangled linear polymer melts: A molecular-dynamics simulation. *Journal of Chemical Physics*, *92*, 5057.
- Kresse, G., & Furthmüller, J. (1996). Efficient iterative schemes for ab initio total-energy calculations using a plane-wave basis set. *Physical Review B*, *54*, 11169.
- Kuo, I.-F. W., Mundy, C. J., McGrath, M. J., Siepmann, J. I., VandeVondele, J., Sprik, M., Hutter, J., Chen, B., Klein, M. L., Mohamed, F., Krack, M., & Parrinello, M. (2004). Liquid water from first principles: Investigation of different sampling approaches. *The Journal of Physical Chemistry B*, *108*, 12990.

- Kutzelnigg, W. (1997). The adiabatic approximation I. The physical background of the Born-Handy ansatz. *Molecular Physics*, 90, 909.
- Laasonen, K., Pasquarello, A., Car, R., Lee, C., & Vanderbilt, D. (1993). Car-Parrinello molecular dynamics with Vanderbilt ultrasoft pseudopotentials. *Physical Review B*, 47, 10142.
- Laio, A., VandeVondele, J., & Rothlisberger, U. (2002). A Hamiltonian electrostatic coupling scheme for hybrid Car-Parrinello molecular dynamics simulations. *Journal of Chemical Physics*, 116, 6941.
- LAMMPS. (2010). <http://lammps.sandia.gov>. Accessed 02 July 2011.
- Lee, C., Yang, W., & Parr, R. C. (1988). Development of the Colle-Salvetti correlation-energy formula into a functional of the electron density. *Physical Review B*, 37, 785.
- Lindahl, E., Hess, B., & van der Spoel, D. (2001). GROMACS 3.0: A package for molecular simulation and trajectory analysis. *Journal of Molecular Modeling*, 7, 306.
- Loos, P.-F., & Assfeld, X. (2007). Self-consistent strictly localized orbitals. *Journal of Chemical Theory and Computation*, 3, 1047.
- Luty, B. A., Davis, M. E., Tironi, I. G., & van Gunsteren, W. F. (1994). A comparison of particle-particle, particle-mesh and Ewald methods for calculating electrostatic interactions in periodic molecular systems. *Molecular Simulation*, 14, 11.
- Luty, B. A., Tironi, I. G., & van Gunsteren, W. F. (1995). Lattice-sum methods for calculating electrostatic interactions in molecular simulations. *Journal of Chemical Physics*, 103, 3014.
- Lyubartsev, A. P. (2005). Multiscale modeling of lipids and lipid bilayers. *European Biophysics Journal*, 35, 53.
- MacKerell, A. D., Bashford, D., Bellott, M., Dunbrack, R. L., Evanseck, J. D., Field, M. J., Fischer, S., Gao, J., Guo, H., Ha, S., Joseph-McCarthy, D., Kuchnir, L., Kuczera, K., Lau, F. T. K., Mattos, C., Michnick, S., Ngo, T., Nguyen, D. T., Prodhom, B., Reiher, W. E., III, Raux, B., Schlenkrich, M., Smith, J. C., Store, R., Straub, J., Watanabe, M., Wiorkiewicz-Kuczera, J., Yin, D., & Karplus, M. (1998). All-atom empirical potential for molecular modeling and dynamics studies of proteins. *The Journal of Physical Chemistry B*, 102, 3586.
- Marrink, S. J., de Vries, A. H., & Mark, A. E. (2004). Coarse grained model for semiquantitative lipid simulations. *The Journal of Physical Chemistry B*, 108, 750.
- Marrink, S. J., Risselada, H. J., Yefimov, S., Tieleman, D. P., & de Vries, A. H. (2007). The MARTINI force field: Coarse grained model for biomolecular simulations. *The Journal of Physical Chemistry B*, 111, 7812.
- Marx, D., & Hutter, J. (2000). Ab initio molecular dynamics: Theory and implementation. In J. Grotendorst (Ed.), *Modern methods and algorithms of quantum chemistry*. Jülich: NIC. <http://www.theochem.ruhr-uni-bochum.de/research/marx/marx.pdf>. Accessed 02 July 2011.
- Marx, D., & Hutter, J. (2009). *Ab initio molecular dynamics: Basic theory and advanced methods*. Cambridge: Cambridge University Press.
- McQuarrie, D. A. (1992). *Statistical mechanics*. London: Academic.
- Melchionna, S., Cicciotti, G., & Holian, B. L. (1993). Hoover NPT dynamics for systems varying in shape and size. *Molecular Physics*, 78, 533.
- Mervis, J. (2001). NSF launches TeraGrid for academic research. *Science*, 293, 1235.
- Meyer, B. (2006). The pseudopotential plane wave approach. In J. Grotendorst, S. Blügel, & D. Marx (Eds.), *Computational nanoscience: Do it yourself!* Jülich: NIC. <http://www2.fz-juelich.de/nic-series/volume31/meyer1.pdf>. Accessed 02 July 2011.
- Molden. (2010). *A pre- and post processing program of molecular and electronic structure*. <http://www.cmbi.ru.nl/molden/>. Accessed 02 July 2011.
- Monard, G., Loos, M., Théry, V., Baka, K., & Rivail, J. L. (1996). Hybrid classical quantum force field for modeling very large molecules. *International Journal of Quantum Chemistry*, 58, 153.
- Monkhorst, H. J., & Pack, J. D. (1976). Special points for Brillouin-zone integrations. *Physical Review B*, 13, 5188.
- Moreno, J., & Soler, J. M. (1992). Optimal meshes for integrals in real- and reciprocal-space unit cells. *Physical Review B*, 45, 13891.
- Murphy, R. B., Philipp, D. M., & Friesner, R. A. (2000). Frozen orbital QM/MM methods for density functional theory. *Chemical Physics Letters*, 321, 113.
- Nemukhin, A. V., Grigorenko, B. L., Bochenkova, A. V., Topol, I. A., & Burt, S. K. (2002). A QM/MM approach with effective fragment potentials applied to the dipeptide-water structures. *Journal of Molecular Structure (THEOCHEM)*, 581, 167.
- Nemukhin, A. V., Grigorenko, B. L., Topol, I. A., & Burt, S. K. (2003). *Journal of Computational Chemistry*, 24, 1410.
- Nosé, S. (1984a). A unified formulation of the constant temperature molecular dynamics methods. *Journal of Chemical Physics*, 81, 511.
- Nosé, S. (1984b). A molecular dynamics method for simulations in the canonical ensemble. *Molecular Physics*, 52, 255.
- NWChem. (2008). [http://www.nwchem-sw.org/index.php/Main\\_Page](http://www.nwchem-sw.org/index.php/Main_Page). Accessed 02 July 2011.



- ONETEP. (2005). <http://www2.tcm.phy.cam.ac.uk/onetep/>. Accessed 02 July 2011.
- Parr, R. G., & Yang, W. (1989). *Density functional theory of atoms and molecules*. Oxford: Oxford University Press.
- Parrinello, M., Hutter, J., Marx, D., Focher, P., Tuckerman, M., Andreoni, W., Curioni, A., Fois, E., Roetlisberger, U., Giannozzi, P., Deutsch, T., Alavi, A., Sebastiani, D., Laio, A., Vande-Vondele, J., Seitsonen, A., & Billeter, S. (2008). Car–Parrinello molecular dynamics: An ab initio electronic structure and molecular dynamics program. <http://www.cpmo.org>. Accessed 02 July 2011.
- Pastore, G., Smargiassi, E., & Buda, F. (1991). Theory of ab initio molecular-dynamics calculations. *Physical Review A* 44, 6334.
- PDB. (2010). RCSB protein data bank. <http://www.rcsb.org/pdb>. Accessed 02 July 2011.
- Perdew, J. P., Chevary, J. A., Vosko, S. H., Jackson, K. A., Pederson, M. R., Singh, D. J., & Fiolhais, C. (1992). Atoms, molecules, solids, and surfaces: Applications of the generalized gradient approximation for exchange and correlation. *Physical Review B*, 46, 6671.
- Philipp, D. M., & Friesner, R. A. (1999). Mixed ab initio QM/MM modeling using frozen orbitals and tests with alanine dipeptide and tetrapeptide. *Journal of Computational Chemistry*, 20, 1468.
- Phillips, J. C., Braun, R., Wang, W., Gumbart, J., Tajkhorshid, E., Villa, E., Chipot, C., Skeel, R. D., Kale, L., & Schulten, K. (2005a). Scalable molecular dynamics with NAMD. *Journal of Computational Chemistry*, 26, 1781.
- Phillips, J. C., Braun, R., Wang, W., Gumbart, J., Tajkhorshid, E., Villa, E., Chipot, C., Skeel, R. D., Kale, L., & Schulten, K. (2005b). *Journal of Computational Chemistry*, 26, 1781.
- PINY. (2005). [http://homepages.nyu.edu/~mt33/PINY\\_MD/PINY.html](http://homepages.nyu.edu/~mt33/PINY_MD/PINY.html). Accessed 02 July 2011.
- Plimpton, S. J. (1995). Fast parallel algorithms for short-range molecular dynamics. *Journal of Computational Physics*, 117, 1.
- Polák, R. (1986). An investigation of the importance of many-centre effects in the diatomics-in-molecules approach. *Chemical Physics*, 103, 277.
- Ponder, J. W., Wu, C., Ren, P., Pande, V. S., Chodera, J. D., Schnieders, M. J., Haque, I., Mobley, D. L., Lambrecht, D. S., DiStasio, R. A., Jr., Head-Gordon, M., Clark, G. N. I., Johnson, M. E., & Head-Gordon, T. (2010). Current status of the AMOEBA polarizable force field. *The Journal of Physical Chemistry B*, 114, 2549.
- Pu, J., Gao, J., & Truhlar, D. G. (2004a). Combining Self-Consistent-Charge Density-Functional Tight-Binding (SCC-DFTB) with molecular mechanics by the Generalized Hybrid Orbital (GHO) method. *The Journal of Physical Chemistry A*, 108, 5454.
- Pu, J., Gao, J., & Truhlar, D. G. (2004b). Generalized Hybrid Orbital (GHO) method for combining ab initio Hartree-Fock wave functions with molecular mechanics. *The Journal of Physical Chemistry A*, 108, 632.
- Pu, J., Gao, J., & Truhlar, D. G. (2005). Generalized Hybrid-Orbital method for combining density functional theory with molecular mechanics. *ChemPhysChem*, 6, 1853.
- Pulay, P. (1969). Ab initio calculation of force constants and equilibrium geometries in polyatomic molecules I. Theory. *Molecular Physics*, 17, 197.
- Pulay, P. (1980). Convergence acceleration of iterative sequences. The case of SCF iteration. *Chemical Physics Letters*, 73, 393.
- Pulay, P. (1982). Improved SCF convergence acceleration. *Journal of Computational Chemistry*, 3, 556.
- Pulay, P. (1987). Analytical derivative methods in quantum chemistry. *Advances in Chemical Physics*, 69, 241.
- PWscf. (2009). <http://www.pwscf.org/home.htm>. Accessed 02 July 2011.
- PyMOL. (2010). <http://www.pymol.org>. Accessed 02 July 2011.
- QuantumEspresso. (2009). <http://www.quantum-espresso.org>. Accessed 02 July 2011.
- RasMol. (2008). <http://rasmol.org/>. Accessed 02 July 2011.
- Reciprocal Net. (2004). A distributed crystallography network for researchers, students and the general public. <http://www.reciprocalnet.org>. Accessed 02 July 2011.
- Reed, D. A. (2003). Grids, the TeraGrid, and beyond. *Computer*, 36, 62.
- Refson, K. (2000). Moldy: A portable molecular dynamics simulation program for serial and parallel computers. *Computer Physics Communications*, 126, 310.
- Refson, K. (2001). Moldy user's manual. <http://www.ccp5.ac.uk/moldy/moldy.html/>. Accessed 02 July 2011.
- Scott, W. R. P., Hünenberger, P. H., Tironi, I. G., Mark, A. E., Billeter, S. R., Fennen, J., Torda, A. E., Huber, T., Krüger, P., & van Gunsteren, W. F. (1999). The GROMOS biomolecular simulation program package. *The Journal of Physical Chemistry A*, 103, 3596.
- Segall, M. D., Lindan, P. L. D., Probert, M. J., Pickard, C. J., Hasnip, P. J., Clark, S. J., & Payne, M. C. (2002). First-principles simulation: Ideas, illustrations and the CASTEP code. *Journal of Physics: Condensed Matter*, 14, 2717.

- Senn, H. M., & Thiel, W. (2009). QM/MM methods for biomolecular systems. *Angewandte Chemie International Edition*, 48, 1198.
- Shelley, J. C., Shelley, M. Y., Reeder, R. C., Bandyopadhyay, S., Moore, P. B., & Klein, M. L. (2001). Simulations of phospholipids using a coarse grain model. *The Journal of Physical Chemistry B*, 105, 9785.
- Shillcock, J. C., & Lipowsky, R. (2002). Equilibrium structure and lateral stress distribution of amphiphilic bilayers from dissipative particle dynamics simulations. *Journal of Chemical Physics*, 117, 5048.
- Shirts, M., & Pande, V. S. (2000). Screen savers of the world unite! *Science*, 290, 1903.
- Shurki, A., & Warshel, A. (2003). Structure/function correlations of enzymes using MM, QM/MM and related approaches; methods, concepts, Pitfalls and current progress. In V. Daggett (Ed.), *Protein simulations*, Adv. Protein Chem. (Vol. 66, p. 249). San Diego: Academic.
- SIESTA. (2010). <http://www.icmab.es/siesta/>. Accessed 02 July 2011.
- Sironi, M., Genoni, A., Civera, M., Pieraccini, S., & Ghitti, M. (2007). Extremely localized molecular orbitals: Theory and applications. *Theoretical Chemistry Accounts*, 117, 685.
- Skylaris, C.-K., Haynes, P. D., Mostofi, A. A., & Payne, M. C. (2005). Introducing ONETEP: Linear-scaling density functional simulations on parallel computers. *Journal of Chemical Physics*, 122, 084119.
- Smith, W., Yong, C. W., & Rodger, P. M. (2002). DL\_POLY: Application to molecular simulation. *Molecular Simulation*, 28, 385.
- Soler, J. M., Artacho, E., Gale, J. D., Garcia, A., Junquera, J., Ordejón, P., & Sánchez-Portal, D. (2002). The SIESTA method for ab initio order-*N* materials simulation. *Journal of Physics: Condensed Matter*, 14, 2745.
- S/PHI/nX. (2009). <http://www.mpie.de/index.php?id=sxlib>. Accessed 02 July 2011.
- Språk, M. (1991). Computer simulation of the dynamics of induced polarization fluctuations in water. *The Journal of Physical Chemistry*, 95, 2283.
- Stillinger, F., & Weber, T. A. (1985). Computer simulation of local order in condensed phases of silicon. *Physical Review B*, 31, 5262.
- Sun, H., Ren, P., & Fried, J. R. (1998). The COMPASS force field: Parameterization and validation for phosphazenes. *Computational and Theoretical Polymer Science*, 8, 229.
- Sutmann, G. (2002). Classical molecular dynamics. In J. Grotendorst, D. Marx, & A. Muramatsu (Eds.), *Quantum simulations of complex many-body systems: From theory to algorithms*. Jülich: NIC. <http://www2.fz-juelich.de/nic-series/volume10/sutmann.pdf>. Accessed 02 July 2011.
- Sutmann, G. (2006). Molecular dynamics – vision and reality. In J. Grotendorst, S., Blügel, & D. Marx (Eds.), *Computational nanoscience: Do it yourself!* Jülich: NIC. <http://www2.fz-juelich.de/nic-series/volume31/sutmann.pdf>. Accessed 02 July 2011.
- Swope, W. C., Anderson, H. C., Berens, P. H., & Wilson, K. R. (1982). *Journal of Chemical Physics*, 76, 637.
- Tepper, H. L., & Voth, G. A. (2005). A coarse-grained model for double-helix molecules in solution: Spontaneous helix formation and equilibrium properties. *Journal of Chemical Physics*, 122, 124906.
- Tersoff, J. (1988). New empirical approach for the structure and energy of covalent systems. *Physical Review B*, 37, 6991.
- Tersoff, J. (1989). Modeling solid-state chemistry: Interatomic potentials for multicomponent systems. *Physical Review B*, 39, 5566.
- Théry, V., Rinaldi, D., Rivail, J. L., Maigret, B., & Ferenczy, G. G. (1994). Quantum mechanical computations on very large molecular systems: The local self-consistent field method. *Journal of Computational Chemistry*, 15, 269.
- Thiel, W. (2009). QM/MM methodology: Fundamentals, scope, and limitations. In J. Grotendorst, N. Attig, S. Blügel, & D. Marx (Eds.), *Multiscale simulation methods in molecular sciences*. Jülich: NIC. <http://www2.fz-juelich.de/nic-series/volume42/thiel.pdf>. Accessed 02 July 2011.
- Todorov, I. T., & Smith, W. (2009). *The DL\_POLY\_3 user manual*. [http://www.cse.scitech.ac.uk/ccg/software/DL\\_POLY/](http://www.cse.scitech.ac.uk/ccg/software/DL_POLY/). Accessed 02 July 2011.
- Tosi, M. P., & Fumi, F. G. (1964). Ionic sizes and born repulsive parameters in the NaCl-type alkali halides II : The generalized Huggins-Mayer form. *Journal of Physics and Chemistry of Solids*, 25, 45.
- Toth (2009). Information systems. <http://www.tothcanada.com>. Accessed 02 July 2011.
- Toton, D., Lorenz, C. D., Rompotis, N., Martsinovich, N., & Kantorovich, L. (2010). Temperature control in molecular dynamic simulations of non-equilibrium processes. *Journal of Physics Condensed Matter*, 22, 074205.
- Tozzini, V. (2005). Coarse-grained models for proteins. *Current Opinion in Structural Biology*, 15, 144.
- Troullier, N., & Martins, J. L. (1990). A straightforward method for generating soft transferable



- pseudopotentials. *Solid State Communications*, 74, 613.
- Troullier, N., & Martins, J. L. (1991). Efficient pseudopotentials for plane-wave calculations. *Physical Review B*, 43, 1993.
- Tuckerman, M. E. (2002). Path integration via molecular dynamics. In J. Grotendorst, D. Marx, & A. Muramatsu (Eds.), *Quantum simulations of complex many-body systems: From theory to algorithms*, Jülich: NIC. <http://www.fz-juelich.de/nic-series/volume10/tuckerman1.pdf>. Accessed 02 July 2011.
- Tuckerman, M. E., & Hughes, A. (1998). Path integral molecular dynamics. In B. J. Berne, G. Ciccotti, & D. F. Coker (Eds.), *Classical and quantum dynamics in condensed phase simulations* (p. 311). Singapore: World Scientific.
- Tuckerman, M. E., Berne, B. J., Martyna, G. J., & Klein, M. L. (1993). Efficient molecular dynamics and hybrid Monte Carlo algorithms for path integrals. *Journal of Chemical Physics*, 99, 2796.
- van Beest, B. W. H., Kramer, G. J., & van Santen, R. A. (1990). Force fields for silicas and aluminophosphates based on ab initio calculations. *Physical Review Letters*, 64, 1955.
- van der Spoel, D., Lindahl, E., Hess, B., Groenhof, G., Mark, A. E., & Berendsen, H. J. C. (2005a). GROMACS: Fast, flexible, and free. *Journal of Computational Chemistry*, 26, 1701.
- van der Spoel, D., Lindahl, E., Hess, B., van Buuren, A. R., Apol, E., Meulenhoff, P. J., Tieleman, D. P., Sijbers, A. L. T. M., Feenstra, K. A., van Drunen, R., & Berendsen, H. J. C. (2005b). Gromacs user manual version 4.0. <http://www.gromacs.org/>. Accessed 02 July 2011.
- Vanderbilt, D. (1985). Optimally smooth norm-conserving pseudopotentials. *Physical Review B*, 32, 8412.
- Vanderbilt, D. (1990). Soft self-consistent pseudopotentials in a generalized eigenvalue formalism. *Physical Review B*, 41, 7892.
- Vanderbilt Ultra-Soft Pseudopotential Site. (2006). <http://www.physics.rutgers.edu/~dhv/uspp/>. Accessed 02 July 2011.
- VandeVondele, J., Krack, M., Mohamed, F., Parrinello, M., Chassaing, T., & Hutter, J. (2005). Quickstep: Fast and accurate density functional calculations using a mixed Gaussian and plane waves approach. *Computer Physics Communications*, 167, 103.
- VandeVondele, J., Iannuzzi, M., & Hutter, J. (2006). Large scale condensed matter calculations using the Gaussian and augmented plane waves method. In *Computer simulations in condensed matter systems: From materials to chemical biology, Volume 1. Lecture notes in physics* (Vol. 703, p. 287). Berlin/Heidelberg: Springer.
- VASP. (2009). <http://cms.mpi.univie.ac.at/vasp/>. Accessed 02 July 2011.
- Verlet, L. (1967). Computer "Experiments" on classical fluids. I. Thermodynamical properties of Lennard-Jones molecules. *Physical Review*, 159, 98.
- VMD. (2009). <http://www.ks.uiuc.edu/Research/vmd/>. Accessed 02 July 2011.
- Vosko, S. H., Wilk, L., & Nusair, M. (1980). Accurate spin-dependent electron liquid correlation energies for local spin-density calculations – A critical analysis. *Canadian Journal of Physics*, 58, 1200.
- Wang, J. M., Wolf, R. M., Caldwell, J. W., Kollman, P. A., & Case, D. A. (2004). Toward direct determination of conformations of protein building units from multidimensional NMR experiments. V. NMR chemical shielding analysis of N-formyl-serinamide, a model for polar side-chain containing peptides. *Journal of Computational Chemistry*, 24, 1157.
- Warshel, A. (1991). *Computer modeling of chemical reactions in enzymes and solutions*. New York: Wiley.
- Warshel, A. (2003). Computer simulations of enzyme catalysis: Methods, progress, and insights. *Annual Review of Biophysics and Biomolecular Structure*, 32, 425.
- Warshel, A., & Levitt, M. (1976). Theoretical studies of enzymic reactions: Dielectric, electrostatic and steric stabilization of the carbonium ion in the reaction of lysozyme. *Journal of Molecular Biology*, 103, 227.
- Woodcock, L. V. (1971). Isothermal molecular dynamics calculations for liquid salts. *Chemical Physics Letters*, 10, 257.
- Worth, G. A., Meyer, H. D., Koepfel, H., Cederbaum, L. S., & Burghardt, I. (2008). Using the MCTDH wavepacket propagation method to describe multimode non-adiabatic dynamics. *International Reviews in Physical Chemistry*, 27, 569.
- Zhang, Y. (2005). A pseudobond approach to combining quantum mechanical and molecular mechanical methods. *Journal of Chemical Physics*, 122, 024114.
- Zhang, Y. (2006). Pseudobond ab initio QM/MM approach and its applications to enzyme reactions. *Theoretical Chemistry Accounts*, 116, 43.
- Zhang, Y., Lee, T.-S., & Yang, W. (1999). A pseudobond approach to combining quantum mechanical and molecular mechanical methods. *Journal of Chemical Physics*, 110, 46.

# 8 Statistical Mechanics of Force-Induced Transitions of Biopolymers

*Sanjay Kumar*

Department of Physics, Banaras Hindu University, Varanasi, India

<i>Introduction</i> .....	240
<i>Models</i> .....	241
Continuum Models .....	241
Lattice Models .....	244
Polymer and Critical Phenomena .....	245
<i>Methods and Techniques</i> .....	246
Generating Function Technique .....	246
Exact Enumeration Technique .....	248
Monte Carlo Simulation .....	249
Molecular Dynamics .....	250
<i>Applications</i> .....	254
<i>Conclusions</i> .....	256
<i>Acknowledgments</i> .....	257
<i>References</i> .....	257

**Abstract:** Single molecule force spectroscopy constitutes a robust method for probing the unfolding of biomolecules. Knowledge gained from statistical mechanics is helping to build our understanding about more complex structure and function of biopolymers. Here, we have reviewed some of the models and techniques that have been employed to study force-induced transitions in biopolymers. We briefly describe the merit and limitation of these models and techniques. In this context, we discuss statistical models of polymer along with numerical techniques, which may provide enhanced insight in understanding the unfolding of biomolecules.

## Introduction

---


Recent technological developments of experimental techniques, for example, optical tweezers, atomic force microscope, etc., made it possible to apply a force of the order of pN to manipulate the single biomolecules (Kumar and Li 2010; Rief et al. 1999, 1997; Tskhovrebova et al. 1997). Many interesting results, for example, structural, functional, and elastic properties of biomolecules, information about the kinetics of biomolecular reactions, and detection of molecular intermediates have been obtained (Bustamante et al. 2000; Cecconi et al. 2005; Smith et al. 1992, 1996). Moreover, these experiments also provided a platform to verify theoretical predictions based on the models developed in the framework of statistical mechanics (Bhattacharjee 2000; Giri and Kumar 2006; Kumar 2009; Kumar and Giri 2007; Kumar et al. 2005; Lubensky and Nelson 2000; Marenduzzo et al. 2001a; Zhou et al. 2006).

Many biological reactions involve large conformational changes which provide well-defined mechanical reaction coordinates, for example, the end-to-end distance of a polymer, that can be used to follow the progress of the reaction (Bustamante et al. 2004; Kumar et al. 2007). Such processes have been modeled by a simple two-state model (Bustamante et al. 2004). The applied force “tilts” the free energy surface along the reaction coordinate by an amount linearly dependent on the end-to-end distance. The kind of transitions induced by the applied force are the folding–unfolding transition of proteins, the stretching and unzipping transition of double-stranded DNA, or the ball–string transition of a polymer (Kumar and Li 2010). From thermodynamics point of view, the change in energy of system can be categorized into components related to the heat exchanged and the work done on or performed by the system. If the change in energy of the system is quite low then the system remains in quasi-static equilibrium. The aim of this chapter is to provide the concepts from statistical mechanics to describe the force-induced transitions of biopolymers. In [▶ section “Models”](#), we discuss some of the models of polymers, which have been used to study biopolymers in the presence of a force  $f$ . [▶ Section “Methods and Techniques”](#) dwells with few techniques used in statistical mechanics for polymers. Among these techniques, we choose an exact enumeration technique to study force-induced desorption of polymer adsorbed on the surface in [▶ section “Applications”](#). The method developed for homo-polymers can also be extended to study the protein unfolding and DNA unzipping in quasi static equilibrium. The chapter ends with some results based on model studies which are interesting for future experiments in [▶ section “Conclusions”](#).

## Models

Macromolecules from living organisms are called biopolymers which vary in their size, shape, and function. Polymers including biopolymers are made up of long chains of “monomer” units (de Gennes 1979; des Cloizeaux and Jannink 1990; Grosberg and Khokhlov 1994; Vanderzande 1998). The monomers can be of different natures. In DNA and RNA they are called nucleotides, and amino acids in proteins. Building blocks of simple artificial polymers can be group of just a few atoms, for example,  $\text{CH}_2$  in polyethylene or a complex structure in amino acids. The difference between polymers and biopolymers is in their structure. Biopolymers have generally well-defined structures. The most intensive theoretical study related to biomolecules can be performed with the help of all-atom simulations. All-atom models, which provide the most detailed description on the atomistic level, include the local interaction and interaction involved in non-bonded monomers. The later include the (6–12) Lennard-Jones potential, the electrostatic interaction, and the interaction with environment (Kumar and Li 2010). However, such study for a long chain is computationally demanding and is difficult to handle analytically. In order to get the key features, physicists attempt to simplify complex structures of biopolymers as much as possible. Such process is termed as coarse graining. They model polymer chains as threads or necklaces made of beads on a string which describes some essential properties of biopolymers (de Gennes 1979; des Cloizeaux and Jannink 1990; Grosberg and Khokhlov 1994; Vanderzande 1998) but not always. In the literature, coarse-grained models are divided into two broad categories: (1) Continuum models and (2) Lattice models, which are briefly discussed below.

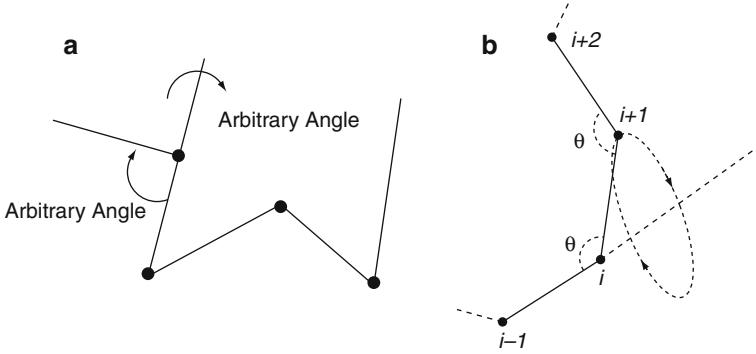
### Continuum Models

We briefly describe three models, namely, the Gaussian Chain model, Freely Jointed Chain (FJC) model, and Worm Like Chain (WLC) model, which have been extensively used to describe the force-extension curves of biopolymers. The advantages of these models come from their simplicity and allowing one to derive analytical expressions in a simple form. In these models a polymer chain consists of  $N$  beads (monomers) of contour length  $L$ . A point in  $d$ -dimensional space represents each monomer and the distance between two consecutive monomers is  $R_{i-1} - R_i$  (see  Fig. 8-1). The energy with force  $f$  (along  $x$ -direction) in Gaussian model is expressed as (Doi and Edwards 1986)

$$F = \frac{3k_B T}{2b} \int_0^{L=Nb} ds \left( \frac{\partial \mathbf{r}(s)}{\partial s} \right)^2 - f \hat{x}_0 \cdot \int_0^{Nb} ds \frac{\partial \mathbf{r}(s)}{\partial s}, \quad (8.1)$$

where  $b$  is the effective bond length known as the Kuhn length and  $\mathbf{r}(s)$  describes the local state at arc-length point  $s$ . For example, in the case of a flexible Gaussian chain,  $\mathbf{r}$  is a three-dimensional position vector, whereas for WLC case it represents the unit tangent vector.  $k_B$  is the Boltzmann constant and  $T$  the temperature of the system. Using the path integral technique (Doi and Edwards 1986; Kleinert 1990), the end-to-end distance distribution function of a chain under the force can be written as

$$P_N(\mathbf{R}, f) = \left( \frac{3}{2\pi N b^2} \right)^{(3/2)} \exp \left\{ -\frac{3}{2N b^2} \left( \mathbf{R} - \frac{N b^2 f \hat{x}_0}{3k_B T} \right)^2 \right\}. \quad (8.2)$$



■ Fig. 8-1

(a) Schematic of a freely jointed chain. (b) Freely rotating chain with fixed bond angle. These models do not incorporate excluded volume effects in their description

The  $x$ -component of  $\mathbf{R}$  can be expressed as

$$P_N(R_x, f) = \int dR_y dR_z P_N(R, f) \\ = \left( \frac{1}{2\pi N b^2} \right)^{(3/2)} \exp \left\{ -\frac{3}{2N b^2} \left( R_x - \frac{N b^2 f}{3k_B T} \right)^2 \right\}, \quad (8.3)$$

which gives the expression for the extension  $x$  in the presence of applied force  $f$  (Dai et al. 2003)

$$x(f) = \frac{N b}{3} \frac{f b}{k_B T}. \quad (8.4)$$

This is a linear force relation. The model describes the response of a single polymer chain under low force. The major limitation of the model is the property that the distance between two monomers can be extended without any limit. This shortcoming of Gaussian chain is removed in the FJC model, where the distance between two consecutive monomers (bond length) is kept fixed while the rotational angle occurs with equal probability (● Fig. 8-1b). The free energy of the system can be written as

$$F = -f \hat{x}_0 \cdot \sum_{n=1}^N \mathbf{r}_n, \quad (8.5)$$

where  $\mathbf{r}_n$  are bond vectors with constant length  $|\mathbf{r}_n| = b$ .

The distribution function of end-to-end vector  $\mathbf{R}$  in the presence of force  $f$  is defined as

$$P_N(\mathbf{R}, f) = \frac{\exp[\beta f \hat{x}_0 \cdot \mathbf{R}] P_N(\mathbf{R}, 0)}{\int d\mathbf{R} \exp[\beta f \hat{x}_0 \cdot \mathbf{R}] P_N(\mathbf{R}, 0)}, \quad (8.6)$$

where  $\beta = 1/k_B T$  and  $P_N(\mathbf{R}, 0)$  is the end-to-end distance distribution function in the absence of force  $f$ , which is given as

$$P_N(\mathbf{R}, 0) = \frac{1}{2^{N+1} (N-2)! \pi b^2 R} \sum_{n=0}^{[(N-R/b)/2]} (-1)^n \binom{N}{n} \\ \times (N-2n-R/b)^{N-2}. \quad (8.7)$$

The component of end-to-end distance along the  $x$ -direction may be obtained by integrating **►** Eq. 8.6 with respect to  $R_y$  and  $R_z$  as (Dai et al. 2003)

$$P_N(R_x, f) = \frac{\exp(\beta f R_x)}{[4\pi \sinh(\beta f b)/\beta f b]^N} P_N(R_x, 0), \quad (8.8)$$

where the value of  $P_N(R_x, 0)$  can be obtained from **►** Eq. 8.7.

The average extension along the force direction is

$$x(f) = bN \left[ -\frac{1}{\beta f b} + \coth(\beta f b) \right]. \quad (8.9)$$

One of the important characteristics of biopolymers not described by the FJC model is the stiffness of the chain. A more realistic model for many systems is that of the Freely Rotating Chain, or Worm Like Chain (WLC), which includes stiffness in its description. This model builds an extension of the FJC model with the assumptions that the bond angles are fixed at certain angle, but are free to rotate. This gives rise to a uniform distribution of dihedral angles. The end-to-end distance within the WLC model can be calculated by transfer matrix methods, numerical simulations, etc. One can find variational expressions for  $x$  as a function of  $f$  (Chatney et al. 2004; Marko and Siggia 1995; Rosa et al. 2003a). The one used extensively in the literature is (Marko and Siggia 1995)

$$f = \frac{k_B T}{2b} \left[ \frac{1}{(1-x/L)^2} - 1 + \frac{4x}{L} \right]. \quad (8.10)$$

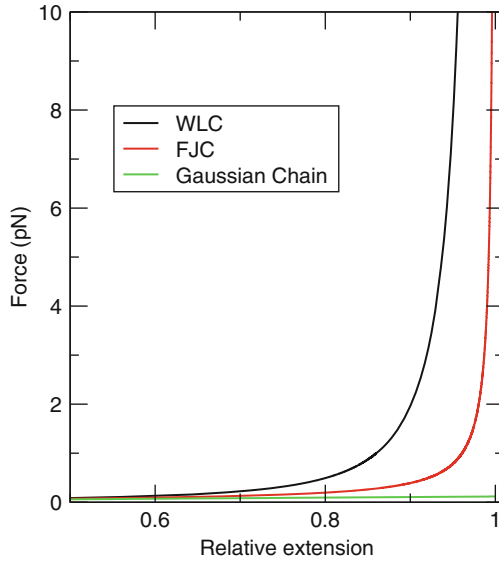
This equation also reduces to the Gaussian chain result in the small force regime i.e.,  $f < k_B T/b$  and for large force  $f > k_B T/b$ , it acquires the form

$$x = L \left( 1 - \sqrt{\frac{k_B T}{2fb}} \right). \quad (8.11)$$

One can see from this equation that the difference between the contour length  $L$  and the extension  $x$  varies as  $f^{-0.5}$ . The force-extension curves for the Gaussian chain, FJC and WLC are shown in **►** Fig. 8-2. The behavior of a biopolymer subjected to a large force as described by the WLC model is contrary to the behavior as described by the FJC model, whereas at low force all models show identical behavior. The Kuhn length of the WLC model corresponds to twice the persistence length. One of the important shortcomings is that all these models have only one free parameter, known as the persistence length or Kuhn length, and hence are not suitable when it comes to describing the entire force-extension curve involving many intermediates.

It is important to recall that all these models ignore crucial excluded volume effect, i.e., the space occupied by a monomer is not available to other monomers (de Gennes 1979). Apart from these, in a polymer solution three types of interactions may be present (de Gennes 1979): (1) monomer–monomer interactions, (2) monomer–solvent interaction, (3) solvent–solvent interaction.

If monomer–monomer (or solvent–solvent) interaction is more than the monomer–solvent interaction in the solution, such solvent is known as a poor solvent. However, if monomer–solvent interaction favors in the solution, the solvent is referred as a good solvent. It is possible by lowering the temperature, one can go from the expanded coil state to a compact globule state and such transition is known as a coil–globule transition and transition point is called  $\theta$ -point. Generally, force-induced transitions have been studied by these models where excluded volume



■ Fig. 8-2

Force-extension curves for the Gaussian chain, FJC, and WLC models

effects and attractive interactions between chain segments have been ignored and is thus well suited only for modeling the stretching of polymers in a good solvent (Kumar and Li 2010).

## Lattice Models

Any model designed to represent a polymer chain over a full range of physical conditions must include important effects such as excluded volume and attractive interactions as a starting point. In a simplified assumption, a linear biopolymer chain in a solvent can be described by a walk on a lattice in which a step or vertex of the walk represents a monomer. If the walk is allowed to cross itself without restriction such walk is referred as Random Walk, which is same as that of the Gaussian chain (de Gennes 1979; Vanderzande 1998). The excluded volume effect has been incorporated in the Random Walk model of polymer with a constraint that a lattice site cannot be visited more than once. This kind of walk is known as Self-Avoiding Walks (SAWs), which simulates a linear polymer chain in a good solvent (► Fig. 8-3a). A polymer chain in a poor solvent is modeled by Self-Attracting Self-Avoiding Walks (SASAWs) by including self-attraction among non-bonded monomers. This model exhibits collapse transition including the existence of  $\theta$ -point (de Gennes 1979; Vanderzande 1998). Various kinds of underlying lattices have been proposed in the literature to study the conformational properties of linear polymer chains. The choice of the lattice depends on the mathematical convenience, nature of the system, and the interactions present in the system. As far as universality is concerned, the nature of underlying lattice and the detail of interactions do not matter much and many important properties associated with polymers can be derived, which are in qualitative agreement with the experiments. Sometimes quantitative agreement has also been achieved particularly in determining

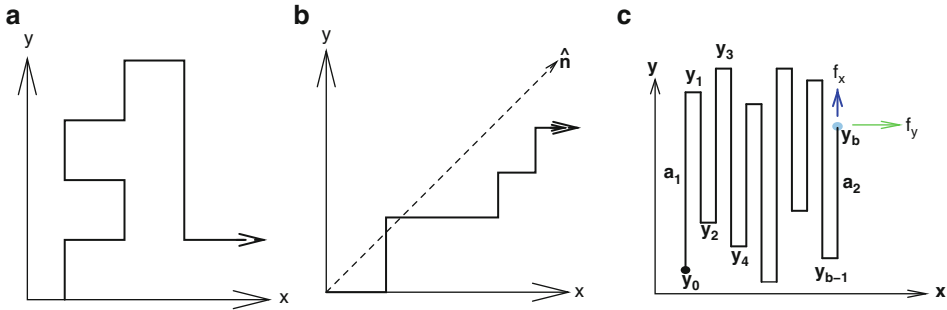


Fig. 8-3

Schematic diagrams of SASAW, DW, and PDSAW model. A force has been applied at one end (along  $x$ -axis) keeping other end fixed. In order to study the role of anisotropy, one may apply force along  $y$ -direction (Fig. 8-3c)

the critical exponents (de Gennes 1979; Vanderzande 1998). Therefore, SAWs with suitable interactions on lattice has been studied extensively in describing the various properties of polymers and biopolymers.

In addition to self-avoidance, one can also introduce additional constraint on the walks, for example, certain direction(s) is (are) not accessible to the walker, such walks are called Directed Walks (DWs) (Privman and Svrakic 1989; Vanderzande 1998). To define a directed walk, a preferred direction  $\hat{n}$  on the lattice is assigned. Walkers are allowed to take only those steps in the non-negative direction of  $\hat{n}$ . The directed walk can be seen as a model of polymer that is subject to some external force in the direction of  $\hat{n}$ , for example, flow in which the polymer is immersed or an electric field acting on electrically charged polymers. If the direction  $\hat{n}$  is assigned as shown in Fig. 8-3b and walks in the non-negative projection of  $\hat{n}$  are not allowed then such walks are called Fully Directed Walks (FDWs). If the direction  $\hat{n}$  is assigned, say, along the  $x$ -axis (Fig. 8-3c), then the walks are said to be the Partial Directed Walks (PDSAWs). For example in two dimensions, the walker can take step in  $\pm y$  directions but only in  $+x$  direction. The major advantage of the directed walk model of polymer is that it can be solved analytically and many important results may be derived exactly. The drawback is that it is too far from the real chain.

## Polymer and Critical Phenomena

It is known that the certain quantities associated with polymers modeled by SAWs for, example, number of distinct conformation ( $C_N$ ), number of closed polygons ( $P_N$ ), and end-to-end distance of chain ( $R_e$ ) of  $N$  monomers scale as (de Gennes 1979)

$$\begin{aligned} C_N &\sim \mu^N N^{\nu-1}, \\ P_N &\sim \mu^N N^{\alpha-3}, \\ R_e &\sim N^\nu, \end{aligned} \quad (8.12)$$

where  $\mu$  is the connectivity constant giving the number of choices per step for an infinitely long walk. From the phase transition and critical phenomena, we also know that certain physical



quantities like susceptibility ( $\chi$ ), specific heat ( $C$ ), and correlation length ( $\xi$ ) near the transition point  $T_C$  scale as

$$\begin{aligned}\chi &\sim \chi_0 \left| \frac{T - T_c}{T_c} \right|^{-\gamma}, \\ C &\sim C_0 \left| \frac{T - T_c}{T_c} \right|^{-\alpha}, \\ \xi &\sim \xi_0 \left| \frac{T - T_c}{T_c} \right|^{-\nu}.\end{aligned}\tag{8.13}$$

A relation between polymer statistics and phase transition was established by de Gennes (1979) and des Cloiseaux (1974) showing a correspondence between the polymer chain modeled by SAWs and the  $n$ -vector spin model of magnetization in the limit  $n \rightarrow 0$ . Similarities between correlation length ( $\xi$ ) and the end-to-end distance ( $R_e$ ) can be noticed by comparing  $\blacktriangleright$  Eqs. 8.12 and  $\blacktriangleright$  8.13. Correspondence between  $1/N$  and  $\frac{T-T_c}{T_c}$  is viewed as  $\frac{T-T_c}{T_c} \rightarrow 0$  and  $N \rightarrow \infty$ . This equivalence allowed polymer science to benefit from the vast knowledge accumulated in the study of critical phenomena. For example, the following relations, which are quite non-trivial to derive directly, are also valid here (de Gennes 1979):

$$\begin{aligned}\alpha + 2\beta + \gamma &= 2, \\ 2 - \alpha &= d\nu, \\ \gamma &= \nu(2 - \eta).\end{aligned}\tag{8.14}$$

Here,  $\alpha$ ,  $\beta$ ,  $\gamma$ , and  $\eta$  are the critical exponents and  $d$  represents the dimensionality of the system. The above equivalence may serve an important role in describing the long range behavior of the polymers.

## Methods and Techniques

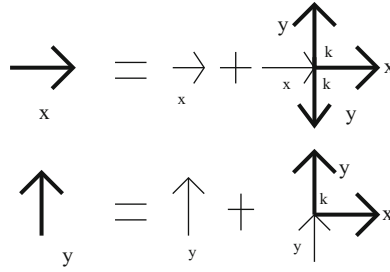
---

Methods and techniques used in critical phenomena can also be applied to polymers and biopolymers to gain further insight of the system. In the following, we discuss some of the techniques of statistical mechanics which have been used in analyzing the results of single molecule force spectroscopy.

### Generating Function Technique

---

The generating function technique is a very powerful technique, which may be adapted to study the conformational properties of biopolymers (Forgacs et al. 1995; Privman and Svrakic 1989). Here, we use a simple example to illustrate how the generating function approach can be applied and exact results can be derived. Let us consider a directed walk model of a polymer chain (Privman and Svrakic 1989; Vanderzande 1998). For simplicity, we consider partial directed walks (PDWs) in which the walker is allowed to move along  $x$ - and  $\pm y$ -axes only ( $\blacktriangleright$  Fig. 8-3c). As discussed above biopolymers are in general semi-flexible. Stiffness is introduced into the polymer chain by putting an energy cost  $\epsilon_b$  on every bend of the walk thus giving rise to an associated Boltzmann weight,  $k = e^{-\frac{\epsilon_b}{k_B T}}$ . For  $k = 1$  ( $\epsilon_b = 0$ ) the chain is said to be flexible,



■ Fig. 8-4

The diagrammatic representations of the recursion relations  $\blacktriangleright$  Eqs. 8.16 and  $\blacktriangleright$  8.17 for PDWs. The *thick arrows*  $X$  and  $Y$  denote all possible walks with the initial step (fugacity) along  $+x$  and  $\pm y$  directions

while for  $0 < k < 1$ , ( $0 < \epsilon_b < \infty$ ) the chain is said to be semi-flexible. The grand canonical partition function of such a chain can be written as (Mishra et al. 2003; Privman and Svrakic 1989)

$$\mathcal{Z}(z, k) = \sum_{N=0}^{\infty} \sum_{\text{all walks}} z^N k^{N_b}. \quad (8.15)$$

Here,  $z$  is the fugacity of the walk and  $N_b$  is the number of bends in a given configuration. In two dimensions, the grand canonical partition function defined by  $\blacktriangleright$  Eq. 8.15 may be expressed as a sum of two components of PDWs. The recursion relations for the case of a semi-flexible polymer chain are

$$X = z + z(X + 2kY), \quad (8.16)$$

and

$$Y = z + z(kX + Y). \quad (8.17)$$

Schematic representations of the above equations (for 2D) have been shown in  $\blacktriangleright$  Fig. 8-4. It may be noted that the first term of  $\blacktriangleright$  Eqs. 8.16 and  $\blacktriangleright$  8.17 is the fugacity of the walk and remain constant as  $z$ . Solving  $\blacktriangleright$  Eqs. 8.16 and  $\blacktriangleright$  8.17 we get

$$X = \frac{z + (2k - 1)z^2}{1 - 2z + z^2 - 2z^2k^2}, \quad (8.18)$$

$$Y = \frac{z + (k - 1)z^2}{1 - 2z + z^2 - 2z^2k^2}. \quad (8.19)$$

The partition function of the system can, therefore, be written as

$$\mathcal{Z}(z, k) = X + 2Y = \frac{(4k - 3)z^2 + 3z}{1 - 2z + z^2 - 2z^2k^2}. \quad (8.20)$$

The critical point for polymerization of an infinite chain is found from the relation

$$1 - 2z + z^2 - 2z^2k^2 = 0. \quad (8.21)$$

This leads to an expression for the critical value of the step fugacity as a function of  $k$ ,  $z_c = \frac{1}{(1+\sqrt{2k})}$ . In the limit  $k \rightarrow 1$ , it reduces to the well-known value for the flexible polymer chain in 2D (Privman and Svrakic 1989). The approach has been successfully applied to study the DNA unzipping and unfolding of collapse polymer (Marenduzzo et al. 2001a, b; Rosa et al. 2003a, b).

## Exact Enumeration Technique

The conformational properties of a polymer chain and phase transition phenomena can be understood if one has the complete information about the partition function of the chain. In the lattice model, the canonical partition function of a polymer chain is calculated (Domb and Lebowitz 1989) by enumerating all possible walks of a given length. For example, we show total number of conformations ( $C_N$ ) for  $N$  step walk in **Table 8-1**. The grand canonical partition function defined in **Eq. 8.15** can be written as

$$\mathcal{Z}(z) = \sum_N C_N z^N, \quad (8.22)$$

where  $z$  is the fugacity associated with each step of the walk. As the singularity of the partition function is associated with critical phenomena, the partition function defined in **Eq. 8.22** will follow  $\mathcal{Z}(z) \sim (1 - \mu z)^{-\gamma}$  in the thermodynamic limit. In most of the cases, where model is not analytically solvable, one uses numerical techniques (Domb and Lebowitz 1989) to calculate the partition function. Once the partition function is known, other thermodynamic variables can be calculated.

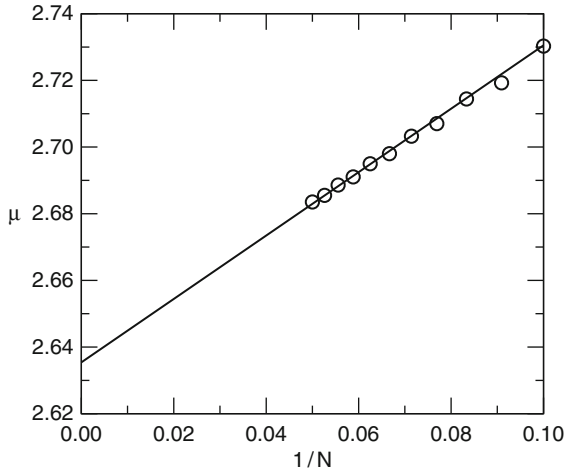
Since in a system of finite size the true phase transition cannot take place, therefore, one has to use suitable extrapolation scheme to calculate  $C_N$  in the limit  $N \rightarrow \infty$ . For this purpose suitable techniques, for example, ratio method, Pade approximants, differential approximation, etc. (Domb and Lebowitz 1989) can be used. In ratio method, the approximate value of  $\mu$  for  $N \rightarrow \infty$  can be calculated by taking the ratios of consecutive terms of the series. These quantities should, for large  $N$ , be a linear function of  $1/N$

$$\log \frac{C_{N+1}}{C_N} \simeq \log \mu + (\gamma - 1)\mathcal{O}(1/N), \quad (8.23)$$

**Table 8-1**

Values of  $C_N$  for different  $N$  for the square lattice. The value of  $C_N$  can be obtained numerically or one may see the following webpage: <http://www.ms.unimelb.edu.au/iwan/saw/series/sqsaw.ser>

$N$	$C_N$	$N$	$C_N$
1	4	16	17245332
2	12	17	46466676
3	36	18	124658732
4	100	19	335116620
5	284	20	897697164
6	780	...	...
7	2172	...	...
8	5916	...	...
9	16268	...	...
10	44100	...	...
11	120292	...	...
12	324932	...	...
13	881500	53	99121668912462180162908
14	2374444	54	263090298246050489804708
15	6416596	55	698501700277581954674604



■ Fig. 8-5

Variation of connectivity constant ( $\mu$ ) with  $1/N$  for SAW on square lattice. The linear extrapolation gives  $\mu = 2.636$  which is quite close to the best estimated value

where  $\mathcal{O}(1/N)$  lower order correction. A simple fit then gives estimates for  $\mu$  and  $\gamma$  (Domb and Lebowitz 1989). However, there is an odd-even effect in  $\frac{C_{N+1}}{C_N}$ . One can avoid this by using the square root of the successive ratios of  $C_N$  as  $\mu = \sqrt{\frac{C_{N+2}}{C_N}}$  and extrapolate it to  $N \rightarrow \infty$ . Linear extrapolation of  $\mu$  with  $\frac{1}{N}$  is shown in [Fig. 8-5](#).

## Monte Carlo Simulation

The Monte Carlo (MC) technique is extremely simple in principle and has been greatly expanded and applied to a wide variety of problems (Binder 1995; Grassberger et al. 1999; Landau and Binder 2005). The typical goal of Monte Carlo simulations is first to find out the ground state of a given system (optimization problem) and then calculate ensemble averages through random sampling (equilibrium problem). The core of this approach is a set of predefined moves, which are traditionally on the lattice but may be defined in free space. At each time step a move is selected and may be accepted or rejected based on some criterion, for example, Metropolis method (Binder 1995), which has been used extensively, is defined as follows:

1. Start with some initial configuration  $I$  at a given temperature  $T$
2. Define some rule to go from the present configuration to a new one
3. Compute the energy difference  $\Delta E = E_{\text{new}} - E_{\text{old}}$ , where  $E_{\text{new}}$  and  $E_{\text{old}}$  are energies of the system after and before the move
4. If  $\Delta E < 0$ , accept the move with new configuration. Otherwise, generate a random number  $r$  between 0 and 1 and accept the trial configuration if  $\exp(-\beta\Delta E) > r$ . Such choice of acceptance of move is known as Metropolis method
5. Repeat Steps 2–4 till enough configurations have been sampled
6. Repeat Steps 1–5 for different temperatures

The way in which temperature is decreased is known as the cooling process. Ideally one should try to devise an optimal way to find the annealing schedule, as the decrease rate and the number of MC steps per  $T$  can be varied during the numerical simulation. An important parameter to monitor during the annealing is the number of accepted moves that do not violate physical constraints. At high  $T$ , this number is very high but at low temperatures almost all moves may be rejected, and therefore, caution should be taken in sampling. One of the biggest advantages of the MC is that it can be very fast especially if the moves are selected carefully. The disadvantage is that it is not generally suitable for studying the dynamics since it is dependent on the move set, and method fails at low temperature. There are a number of good reviews and books available, and serious readers are advised to go through them (Binder 1997; Leckband and Israelachvili 2001; Muller et al. 2006; Muller-Plathe 1997).

## Molecular Dynamics

One of the important tools that has been employed in statistical mechanics is the molecular dynamics (MD) simulations (Allen and Tildesley 1987; Frenkel and Smit 2002). Quite frequently, this technique has been used to study the biomolecules (Kumar and Li 2010). Before studying the structural and dynamical properties of biomolecules, it is important to note that these molecules exhibit a wide range of time scales over which specific processes take place. For example, local motion, which involves atomic fluctuation, side chain motion, and loop motion occurs in the length scale of  $0.01\text{--}5 \text{ \AA}$  and the time involved in such process is of the order of  $10^{-15}$  to  $10^{-9}$  s. The motion of a helix, protein domain, or subunit falls under the rigid body motion whose typical length scales are in between  $1 \text{ \AA}$  and  $10 \text{ \AA}$  and time involved in such motion is in between  $10^{-9}$  and 1 s. Large-scale motion consists of helix-coil transition or folding-unfolding transition, which is more than  $5 \text{ \AA}$  in length and, time involved is about  $10^{-7}$  to  $10^{-4}$  s. Hence the basic goal of molecular dynamics is to understand the role of different length and time scales involved in describing the physical phenomena. Since MD simulation provides information at microscopic level, it is desirable to use the basic concepts of statistical mechanics to derive the macroscopic observable like pressure, energy, heat capacity, etc.

In MD one generates a sequence of points in phase space  $\Omega(p_i, q_i)$  where  $p_i$  is the momentum of the  $i$ th particle and  $q_i$  is the position as a function of time. These points belong to the same ensemble and correspond to different conformations (Allen and Tildesley 1987; Frenkel and Smit 2002). The ergodic hypothesis states that the ensemble average is equivalent to time average. Hence if one allows system to evolve in time indefinitely then system will pass through all possible states and thus corresponds to the time average. Therefore, the goal is to generate enough representative point such that equality is satisfied.

The method is based on Newton's second law of motion, that is, Frenkel and Smit (2002), Allen and Tildesley (1987)

$$\mathcal{F}_i = m_i \frac{d^2 \mathbf{r}}{dt^2} = - \frac{dE_p}{d\mathbf{r}_i}, \quad (8.24)$$

where  $\mathcal{F}_i$  is the applied force on the  $i$ -th particle of mass  $m_i$  and  $E_p$  is the potential energy of the system. The potential energy, in general, is a complicated function and there is no analytic solution to the equation of motion and therefore, one has to solve these equations numerically.

There are various algorithms/numeric schemes for integrating Newton's equations of motion (Allen and Tildesley 1987; Frenkel and Smit 2002). They are generally derived from

the Taylor expansion. The expansion for the positions ( $\mathbf{r}$ ), velocity ( $\mathbf{v}$ ), and acceleration ( $\mathbf{a}$ ) of the particles around some moment of time  $t$  are

$$r(t + \Delta t) = r(t) + v(t)\Delta t + \frac{1}{2}a(t)\Delta t^2 + \dots, \quad (8.25)$$

$$v(t + \Delta t) = v(t) + a(t)\Delta t + \frac{1}{2}b(t)\Delta t^2 + \dots, \quad (8.26)$$

$$a(t + \Delta t) = a(t) + b(t)\Delta t + \dots, \quad (8.27)$$

where  $\Delta t$  is the time step used in the simulation. In the following, we will discuss some of the common schemes of integration algorithm, which have been extensively used in literature.

- **Verlet algorithm:**

The Verlet algorithm uses positions and accelerations at time  $t$  and the positions from time  $t - \Delta t$  to calculate new positions at time  $t + \Delta t$ . In order to derive the Verlet algorithm one can write

$$r(t + \Delta t) = r(t) + v(t)\Delta t + \frac{1}{2}a(t)\Delta t^2, \quad (8.28)$$

$$r(t - \Delta t) = r(t) - v(t)\Delta t + \frac{1}{2}a(t)\Delta t^2. \quad (8.29)$$

The sum of these equations gives

$$r(t + \Delta t) = 2r(t) - r(t - \Delta t) + a(t)\Delta t^2. \quad (8.30)$$

The algorithm does not use the explicit form of velocities. The usefulness of the algorithm are it is simple to implement, and does not require large memory. The algorithm is of moderate precision.

- **Leap Frog algorithm:**

In this algorithm, the velocities are first computed at time  $t + \frac{\Delta t}{2}$  and then used to calculate the positions,  $r$ , at time  $t + \Delta t$ . The velocities leap over the positions and subsequently the positions leap over the velocities.

$$r(t + \Delta t) = r(t) + v(t + \frac{\Delta t}{2})\Delta t, \quad (8.31)$$

$$v(t + \Delta t) = v(t - \frac{\Delta t}{2}) + a(t)\Delta t. \quad (8.32)$$

The approximate form of velocities at time  $t$  is given by

$$v(t) = \frac{1}{2}[v(t + \frac{\Delta t}{2}) + v(t - \frac{\Delta t}{2})]. \quad (8.33)$$

The major gain in this process is that the velocities are explicitly calculated, however, the shortcoming of the algorithm is that velocities are not calculated at the same time as the positions.

- **The Velocity Verlet algorithm:**

It may be noted that in the Leap Frog algorithm, velocities are not defined at the same time as the positions. As a consequence kinetic and potential energies are also not defined at the same time, and hence one cannot directly compute the total energy in the Leap Frog algorithm. It is, however, possible to implement in the Verlet algorithm a form that uses

positions and velocities computed at same instant of times.

$$r(t + \Delta t) = r(t) + v(t)\Delta t + \frac{1}{2}a(t)\Delta t^2, \quad (8.34)$$

$$v(t + \Delta t) = v(t) + \frac{1}{2}[a(t) + a(t + \Delta t)]\Delta t. \quad (8.35)$$

It has to be emphasized here that the Velocity Verlet algorithm is not memory consuming, because it is not required to keep track of the velocity at every time step during the simulation. Moreover, the long-term results of Velocity Verlet are equivalent to the Semi-implicit Euler method, and there is no compromise on precision.

- **Beeman's algorithm:**

This algorithm is related to the Verlet algorithm and yields the same trajectories. However, it provides better estimate of the velocities and looks different than the Verlet algorithm.

$$r(t + \Delta t) = r(t) + v(t)\Delta t + \frac{2}{3}a(t)\Delta t^2 - \frac{1}{6}a(t - \Delta t)\Delta t^2, \quad (8.36)$$

$$v(t + \Delta t) = v(t) + v(t)\Delta t + \frac{1}{3}a(t)\Delta t + \frac{5}{6}a(t)\Delta t - \frac{1}{6}a(t - \Delta t)\Delta t. \quad (8.37)$$

The advantage of this algorithm is that it gives accurate expression for the velocities and better energy conservation. The disadvantage is that because of the complex expressions computation is much more time-consuming.

The procedure for a molecular dynamics simulation is subject to many user-defined variables. However, one should consider certain criteria in choosing these algorithms. It should conserve energy, momentum and computationally efficient so that long time step integration can be performed. Because the evaluation of the atomic positions is not performed on a continuous basis, but at intervals of a femtosecond (fs). Since this is the time-scale of stretches of the bonds with hydrogen atoms, these stretches should be constrained in order to permit time steps of 2 fs. The algorithm that permits this increase in simulation speed is called SHAKE (Frenkel and Smit 2002). Application of constraints on all bond lengths and bond angles would increase the permitted time step even more, without too much loss of information. Since most of the computational time is spent on evaluating the non-bonded interactions between atoms, the evaluation time step for non-bonded atom pairs can be increased to a small extent. Using a cut-off distance beyond which atoms are no longer considered to interact can significantly reduce the amount of non-bonded atom pairs.

It may be noted that MD is a scheme for studying the time evolution of a classical system of  $N$  particles in volume  $V$ , where total energy is a constant of motion. As pointed out earlier, time averages are equivalent to ensemble averages, the observables, say  $A$  evolves according to constant energy simulation and hence,

$$\langle A \rangle_{N,V,E} = \lim_{\tau \rightarrow \infty} \int_0^\tau A(t) dt. \quad (8.38)$$

It is possible to run many NVE simulations with different energies and result could be used in a Boltzmann-weighted average as

$$\langle A \rangle_{NVT} = \sum_E \langle A \rangle_{NVE} e^{-\beta E}. \quad (8.39)$$

However, such process is not very practical, because simulations are quite expensive in terms of time. Moreover, we require a lot of  $E$  values to have enough statistics, and to conserve energy

during simulation is a tough task. Thus, it is more appropriate to run simulation in constant temperature ensemble, that is, NVT. In the following, we will discuss some popular temperature control schemes (Allen and Tildesley 1987; Frenkel and Smit 2002).

### 1. Scaling velocities (Berendsen thermostat):

Since in the beginning, the system is not equilibrated and hence remains in the incorrect state. The potential energy is converted to thermal energy or thermal energy is being consumed during equilibration. In order to stop the temperature from drifting, one of the possible ways is to constrain instantaneous velocities scaled by a factor at each step

$$\mathbf{v}'_i = \sqrt{\frac{T_d}{T_i}} \mathbf{v}_i, \quad (8.40)$$

where  $T_d$  is desired temperature and  $T_i$  is instantaneous temperature given by  $T_i = \frac{2}{3Nk_B} \sum_i^N \frac{p_i^2}{2m_i}$  after  $i$ -th step. This influences the dynamics severely and does not give correct canonical ensemble because it does not generate fluctuations in temperature which are also present in the canonical ensemble. The method is good for initialization of phase.

A weaker formulation of this approach is the Berendsen thermostat where to keep temperature constant, system is coupled to an external heat bath of temperature  $T_0$ . The velocities are scaled in such a way that the rate of change of temperature is proportional to the difference in temperature between system and bath, that is,

$$\frac{dT}{dt} = \frac{T_0 - T(t)}{c}, \quad (8.41)$$

where  $c$  is coupling parameter of the system with a bath. The scaling factor for velocities is given by

$$\lambda = \sqrt{1 + \frac{\Delta t}{c} \left( \frac{T_0}{T(t - \Delta t/2)} - 1 \right)}. \quad (8.42)$$

### 2. Adding stochastic forces and/or velocities (Langevin thermostat):

This thermostat models the influence of a heat bath by adding to the velocity of each particle a small random (white) noise and a frictional force directly proportional to the velocity of that particle. These two factors are balanced to give a constant temperature. Since each particle is coupled to a local heat bath, the heat trapped in localized modes can be removed by using this model.

$$ma = -\xi v + f(r) + f'. \quad (8.43)$$

Here  $f(r)$  and  $f'$  are conservative force and random force respectively.  $\xi$  is the friction coefficient. The drawback of this thermostat is that momentum transfer is destroyed. So, it is not advisable to use Langevin thermostat in the simulations where one wishes to study the diffusion processes.

### 3. Nosé–Hoover thermostat:

The Berendsen thermostat is quite efficient for relaxing a system to the target temperature. However, once your system has reached equilibrium, it is important to probe a correct canonical ensemble. The Nosé–Hoover thermostat is an extended-system method for controlling the temperature of simulated system (Huenenberger 2005; Thijssen 1999). It allows temperatures to fluctuate about an average value, and uses a friction factor to control particle velocities. This particular thermostat can oscillate when a system is not in equilibrium.



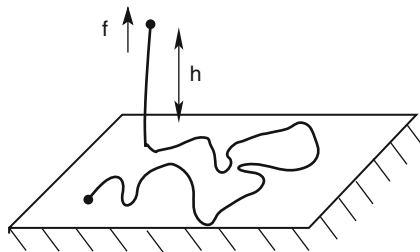
Therefore, it is recommended to use a weak-coupling method for initial system preparation (e.g., Berendsen thermostat), followed by data collection under the Nosé–Hoover thermostat. This thermostat produces a correct kinetic ensemble.

In this context, molecular dynamics simulation of nucleic acids have been considered as a bigger challenge because of the negative backbone charge and the poly-electrolyte behavior. In oligonucleotide dynamics simulations, particular attention should be paid to the atomic charges. The negatively charged phosphate groups may very well influence the trajectory. In contrast with molecular mechanics where a structural minimum is the end result, molecular dynamics offers so much information that is hard to quantify. Excellent reviews on molecular dynamics and its use in biochemistry and biophysics are numerous (see, e.g., Adcock and McCammon 2006 and references therein).

## Applications

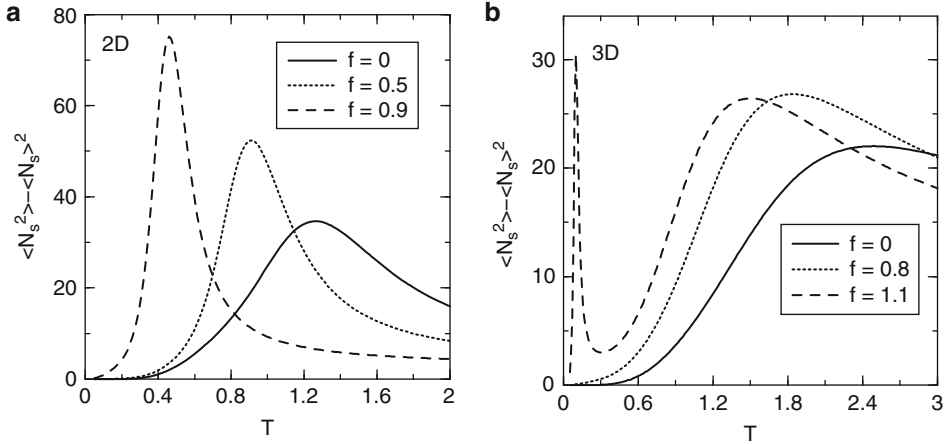
FJC and WLC models have been used in analyzing the force-extension curve obtained from SMFS experiments. In this context, molecular dynamics and Monte Carlo simulations have been found to be quite useful in understanding the phenomena. Since there is a lot of good literature available in this subject, we are not going to discuss them here again. In this section, we shall illustrate that lattice model along with exact enumeration technique which may provide enhanced insight in the mechanism involved in the force-induced transitions because exact density of states are available and the entire phase diagram can be probed exactly for small chains.

We consider SAWs that start from a point on an impenetrable surface and experience a force  $f$  in a direction perpendicular to the surface at the other end as shown in **Fig. 8-6**. The applied force, because of its direction, favors desorption and one expects a critical force ( $f_c$ ) for the desorption. At a given temperature ( $T$ ) when the applied force  $f$  is less than  $f_c(T)$  the polymer will be adsorbed, while for  $f > f_c(T)$  the polymer will be desorbed. The curve  $f_c(T)$ , therefore, gives the boundary that separates the desorbed phase from the adsorbed phase in the force–temperature ( $f, T$ ) plane (Mishra et al. 2005). Here,  $C_N(N_s, h)$  corresponds to the number of SAWs of  $N$  steps having  $N_s$  number of monomers on the surface and  $h$ , the



**Fig. 8-6**

Schematic diagram of the polymer chain adsorbed on the surface under the application of external force



■ Fig. 8-7

The dependence of critical force  $f_c(T)$  on  $T$  in (a) 2D and (b) 3D. The star corresponds to results obtained from the extrapolated values of the reduced free energy, and cross corresponds to the value obtained from finite size data of a step  $N = 20$  (3D) and  $N = 31$  (2D) respectively

height of the end-monomer away from the surface. In this case, the partition function may be defined as

$$Z_N(\omega, u) = \sum_{N_s, h} C_N(N_s, h) \omega^{N_s} u^h, \quad (8.44)$$

where  $\omega = e^{-\epsilon_s/k_B T}$  and  $u = e^{f/k_B T}$  are the Boltzmann weights for the surface interaction ( $\epsilon_s < 0$ ) and the applied force respectively. In the following, we set the Boltzmann constant  $k_B = 1$  and  $\epsilon_s = -1$ . For a fixed force  $f$ , we locate the adsorption–desorption transition temperature from the maximum of fluctuation in number of adsorbed monomers (i.e.,  $\langle N_s^2 \rangle - \langle N_s \rangle^2$ ) (see ► Fig. 8-7), where  $\langle N_s \rangle$  and  $\langle N_s^2 \rangle$  are defined as:

$$\langle N_s \rangle = \frac{1}{Z_N(\omega, u)} \sum_{N_s, h} N_s C_N(N_s, h) \omega^{N_s} u^h, \quad (8.45)$$

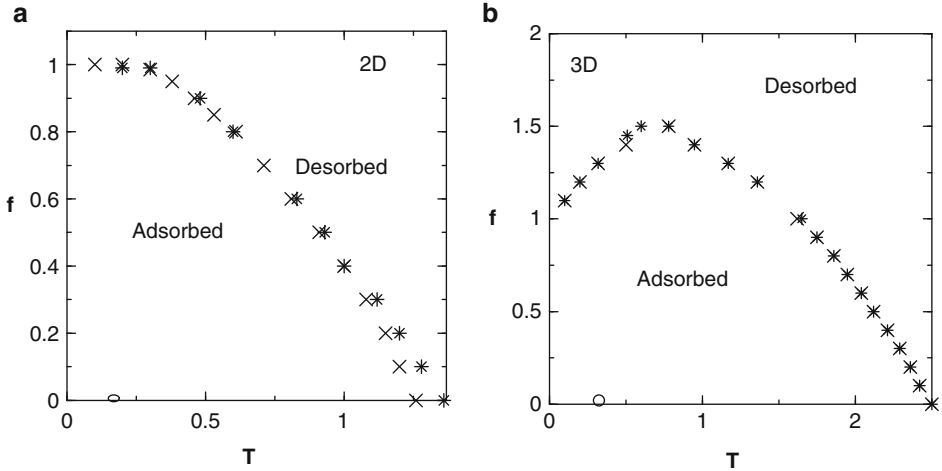
and

$$\langle N_s^2 \rangle = \frac{1}{Z_N(\omega, u)} \sum_{N_s, h} N_s^2 C_N(N_s, h) \omega^{N_s} u^h. \quad (8.46)$$

The force–temperature phase diagram is shown in ► Fig. 8-8. The occurrence of two maxima in fluctuation curve gives the signature of re-entrance in 3D, but absent in 2D (Mishra et al. 2005). Using the phenomenological argument and the probability distribution analysis, it was shown that the ground state entropy is responsible for the re-entrance which is absent in 2D (Mishra et al. 2005).

It is possible to obtain better estimates of phase boundaries by extrapolating  $\mu$  for the large  $N$ . The reduced free energy per monomer in this case is defined as

$$G(\omega, u) = \lim_{N \rightarrow \infty} \frac{1}{N} \log Z_N(\omega, u) = \log \mu_N(\omega, u). \quad (8.47)$$



■ Fig. 8-8

The dependence of critical force  $f_c(T)$  on  $T$  in (a) 2D and (b) 3D. The star corresponds to results obtained from the extrapolated values of the reduced free energy, and cross corresponds to the value obtained from finite size data of a step  $N = 20$  (3D) and  $N = 31$  (2D) respectively

$\mu_N(\omega, u)$  can be estimated from the partition functions found from the data of exact enumerations for finite  $N$  by extrapolating to large  $N$ . The fluctuation in terms of reduced free energy is given as  $\frac{\partial^2 G}{\partial(\log \omega)^2}$ .

The method described above has been applied to protein unfolding (Kumar and Giri 2005, 2007; Kumar et al. 2007), stretching of DNA (Kumar and Mishra 2008; Mishra et al. 2009), and unzipping of DNA (Giri and Kumar 2006; Kumar et al. 2005) and, many useful information about biomolecules have been derived which are in qualitative agreement with experiments.

## Conclusions

We have discussed some basic models of biopolymers and few techniques which have been used extensively in the past to understand the mechanism involved in force-induced transitions. In particular, we showed that lattice model along with exact enumeration technique may be used to interpret the results of SMFS. It is important to point out here that all the single molecule experiments have been performed to understand the structure and function of biopolymers in vivo by analyzing it in vitro. As a result, the effect of cellular environment has been ignored in all these studies. It is known that the interior of the cell contains different kinds of biomolecules like sugar, nucleic acids, lipids, etc. These macromolecules occupy about 40% of the total volume with steric repulsion among themselves. This confined environment induces phenomena like “molecular confinement” and “molecular crowding” and has major thermodynamic and kinetic consequences on the cellular processes. Recently Singh et al. (2009a, b) have used exact enumeration technique and showed that the molecular crowding has significant impact on the force-induced transitions. In order to have better understanding of force-induced transitions, it is advisable to perform SMFS experiments in the environment similar to a cell.

## Acknowledgments

We would like to thank D. Giri, A. R. Singh, and G. Mishra for many helpful discussions. Financial assistance from the Department of Science and Technology, New Delhi is gratefully acknowledged.

## References

- Adcock, S. A., & McCammon, J. A. (2006). Molecular Dynamics: Survey of methods for simulating the activity of proteins. *Chemical Reviews*, 106, 1589–1615.
- Allen, M. P., & Tildesley, D. J. (1987). *Computer simulations of liquids*. Oxford: Oxford Science.
- Bhattacharjee, S. M. (2000). Unzipping DNAs: Towards the first step of replication. *Journal of Physics A*, 33, L423–L428.
- Binder, K. (1995). *Monte Carlo and molecular dynamics simulations in polymer science*. New York: Oxford University Press.
- Binder, K. (1997). Applications of Monte Carlo methods to statistical physics. *Reports on Progress in Physics*, 60, 487–559.
- Bustamante, C., Smith, S. B., Liphardt, J., & Smith, D. (2000). Single-molecule studies of DNA mechanics. *Current Opinion in Structural Biology*, 10, 279–285.
- Bustamante, C., Chemla, Y. R., Forde, N. R., & Izhaky, D. (2004). Mechanical processes in biochemistry. *The Annual Review of Biochemistry*, 73, 705–748.
- Cecconi, C., Shank, E. A., Bustamante, C., & Marqusee, S. (2005). Direct observation of the three-state folding of a single protein molecule. *Science*, 309, 2057–2060.
- Chatney, D., Cocco, S., Monasson, R., & Thieffry, D. (2004). *Multiple aspects of DNA and RNA: From biophysics to bioinformatics: Lecture notes of the Les Houches Summer School*. The Netherlands: Elsevier.
- Cloizeaux, J. D. (1974). Langrangian theory for a self-avoiding random chain. *Physical Review A*, 10, 1665–1669.
- Dai, L., Liu, F., & Ou-Yang, Z.-C. (2003). Maximum-entropy calculation of the end-to-end distance distribution of force-stretched chains. *Journal of Chemical Physics*, 119, 8124.
- de Gennes, P. G. (1979). *Scaling concepts in polymer physics*. Ithaca/London: Cornell University Press.
- des Cloizeaux, J., & Jannink, G. (1990). *Polymers in solution*. Oxford: Clarendon.
- Doi, M., & Edwards, S. F. (1986). *The theory of polymer dynamics*. Oxford: Clarendon.
- Domb, C., & Lebowitz, J. L. (1989). *Phase transition and critical phenomena* (Vol. 13). New York: Academic.
- Forgacs, G., Lipowsky, R., & Nieuwenhuizen, T. M. (1995). *The behaviour of interfaces in ordered and disordered systems* (Vol. 14). Oxford: Clarendon.
- Frenkel, D., & Smit, B. (2002). *Understanding molecular simulation*. London: Academic.
- Giri, D., & Kumar, S. (2006). Effects of the eye phase in DNA unzipping. *Physical Review E*, 73, 050903(R).
- Grassberger, P., Nadler, W., & Barkema, G. T. (1999). *The Monte Carlo approach to biopolymers and protein folding*. Singapore: World Scientific.
- Grosberg, A. Y., & Khokhlov, A. R. (1994). *Statistical physics of macromolecules*. New York: American Institute of Physics.
- Huenenberger, P. (2005). Thermostat algorithms for molecular dynamics simulations. *Advances in Polymer Science*, 173, 105–149.
- Kleinert, H. (1990). *Path integrals in quantum mechanics, statistics, and polymer physics*. Singapore: World Scientific.
- Kumar, S. (2009). Can reentrance be observed in force induced transitions? *Europhysics Letters*, 85, 38003.
- Kumar, S., & Giri, D. (2005). Force-induced conformational transition in a system of interacting stiff polymers: Application to unfolding. *Physical Review E*, 72, 052901.
- Kumar, S., & Giri, D. (2007). Does changing the pulling direction give better insight into biomolecules? *Physical Review Letters*, 98, 048101.
- Kumar, S., Giri, D., & Bhattacharjee, S. M. (2005). Force induced tripple point for interacting polymers. *Physical Review E*, 71, 051804.
- Kumar, S., Jensen, I., Jacobsen, J. L., & Guttman, A. J. (2007). Role of conformational entropy in force induced biopolymer unfolding. *Physical Review Letters*, 98, 128101–128104.

- Kumar, S., & Li, M. (2010). Biomolecules under mechanical force. *Physics Reports*, 486, 1–74.
- Kumar, S., & Mishra, G. (2008). Force-induced stretched state: Effects of temperature. *Physical Review E*, 78, 011907.
- Landau, D. P., & Binder, K. (2005). *A guide to Monte Carlo simulations in statistical physics*. New York: Cambridge University Press.
- Leckband, D., & Israelachvili, J. (2001). Intermolecular forces in biology. *Quarterly Review of Biophysics*, 34, 105–267.
- Lubensky, D. K., & Nelson, D. R. (2000). Pulling pinned polymers and unzipping DNA. *Physical Review Letters*, 85, 1572–1575.
- Marenduzzo, D., Bhattacharjee, S. M., Maritan, A., Orlandini, E., & Seno, F. (2001a). Dynamical scaling of the DNA unzipping transition. *Physical Review Letters*, 88, 028102.
- Marenduzzo, D., Trovato, A., & Maritan, A. (2001b). Phase diagram of force-induced DNA unzipping in exactly solvable models. *Physical Review E*, 64, 031901.
- Marko, J., & Siggia, E. (1995). Stretching DNA. *Macromolecules*, 28, 8759–8770.
- Mishra, G., Giri, D., & Kumar, S. (2009). Stretching of a single stranded DNA: Evidence for structural transition. *Physical Review E*, 79, 031930.
- Mishra, P. K., Kumar, S., & Singh, Y. (2003). A simple and exactly solvable model for a semi flexible polymer chain interacting with a surface. *Physica A*, 323, 453–465.
- Mishra, P. K., Kumar, S., & Singh, Y. (2005). Force-induced desorption of a linear polymer chain adsorbed on an attractive surface. *Europhysics Letters*, 69, 102–108.
- Muller, M., Katsov, K., & Schick, M. (2006). Biological and synthetic membranes: What can be learned from a coarse-grained description? *Physics Reports*, 434, 113–176.
- Muller-Plathe, F. (1997). Coarse-graining in polymer simulation: From the atomistic to the mesoscopic scale and back. *ChemPhysChem*, 3, 754–769.
- Privman, V., & Svrakic, N. M. (1989). *Directed models of polymers, interfaces, and clusters*. Berlin: Springer.
- Rief, M., Clausen-Schaumann, H., & Gaub, H. E. (1999). Sequence-dependent mechanics of single DNA molecules. *Nature Structural Biology*, 6, 346–349.
- Rief, M., Gautel, M., Oesterhelt, F., Fernandez, J. M., & Gaub, H. E. (1997). Reversible unfolding of individual titin immunoglobulin domains by AFM. *Science*, 276, 1109–1112.
- Rosa, A., Hoang, T. X., Marenduzzo, D., & Maritan, A. (2003a). Elasticity of semiflexible polymers with and without self-interactions. *Macromolecules*, 36, 10095–10102.
- Rosa, A., Marenduzzo, D., Maritan, A., & Seno, F. (2003b). Mechanical unfolding of directed polymers in a poor solvent: Critical exponents. *Physical Review E*, 67, 041802.
- Singh, A. R., Giri, D., & Kumar, S. (2009a). Force induced unfolding of bio-polymers in a cellular environment: A model study. *Journal of Chemical Physics*, 131, 065103.
- Singh, A. R., Giri, D., & Kumar, S. (2009b). Effects of molecular crowding on stretching of polymers in poor solvent. *Physical Review E*, 79, 051801.
- Smith, S. B., Finzi, L., & Bustamante, C. (1992). Direct mechanical measurements of the elasticity of single DNA molecules by using magnetic beads. *Science*, 258, 1122–1126.
- Smith, S. B., Cui, Y., & Bustamante, C. (1996). Overstretching B-DNA: The elastic response of individual double-stranded and single-stranded DNA molecules. *Science*, 271, 795–799.
- Thijssen, J. M. (1999). *Computational physics*. Cambridge: Cambridge University.
- Tskhovrebova, L., Trinick, K., Sleep, J. A., & Simons, R. M. (1997). Elasticity and unfolding of single molecules of the giant muscle protein titin. *Nature*, 387, 308–312.
- Vanderzande, C. (1998). *Lattice models of polymers*. Cambridge: Cambridge University Press.
- Zhou, H. J., Zhou, J., Ou-Yang, Z. C., & Kumar, S. (2006). Collapse transition of two-dimensional flexible and semiflexible polymers. *Physical Review Letters*, 97, 158302.

# 10 Molecular Structure and Vibrational Spectra

*Jon Baker*

Parallel Quantum Solutions, Fayetteville, Arkansas, USA

<b>Introduction</b> .....	<b>294</b>
<b>Molecular Structure</b> .....	<b>295</b>
He <sub>2</sub> <sup>2+</sup> : An Illustrative Example .....	295
The Newton–Raphson Step .....	297
The Hessian Matrix and Hessian Updates .....	299
Transition State Searches .....	300
Choice of Coordinates .....	302
The Modified Newton–Raphson Step .....	303
GDHS .....	306
Geometry Optimization and Symmetry .....	307
Performance for Minimization .....	307
Minimization: An Example .....	310
Transition State Searches: An Example .....	318
Using Optimized Potential Scans in Transition State Searches .....	324
Comparison of Experimental and Theoretical Geometries .....	327
Geometry Optimization of Molecular Clusters .....	329
Geometry Optimization in the Presence of External Forces .....	330
<b>Molecular Vibrations</b> .....	<b>331</b>
1,2-Dichloroethane: An Illustrative Example .....	336
Scaled Quantum Mechanical Force Fields .....	342
1,2-Dichloroethane: A Further Analysis .....	343
Density Functional Theory and Weight Derivatives .....	352
<b>Conclusions</b> .....	<b>355</b>
<b>References</b> .....	<b>356</b>

**Abstract:** This chapter deals with two very important aspects of modern *ab initio* computational chemistry: the determination of molecular structure and the calculation, and visualization, of vibrational spectra. It deals primarily with the practical aspects of determining molecular structure and vibrational spectra computationally. Both minima (i.e., stable molecules) and transition states are discussed, as well as infrared (IR), Raman, and vibrational circular dichroism (VCD) spectra, all of which can now be computed theoretically.

## Introduction

---

This chapter deals with two very important aspects of modern *ab initio* computational chemistry: the determination of molecular structure and the calculation, and visualization, of vibrational spectra. The two things are intimately related as, once a molecular geometry has been found (as a stationary point on a potential energy surface at whatever level of theory is being used) it has to be characterized, which usually means that it has to be confirmed that the structure is a genuine minimum. This of course is done by vibrational analysis, i.e., by computing the vibrational frequencies and checking that they are all real.

A large percentage of the total expenditure in CPU cycles devoted to computational chemistry (variously estimated at between 60% and 85%) is spent optimizing geometries. In order to calculate various molecular properties, one first needs a reliable molecular structure so this is perhaps not surprising. Algorithms for geometry optimization are now highly advanced and usually very efficient and most of the quantum chemistry programs available for general use have solid and reliable geometry optimization modules. They also nearly all have analytical second derivatives, at least for the most common theoretical methods, which makes it relatively straightforward to compute vibrational frequencies once a structure has been found.

In this chapter I deal primarily with the practical aspects of determining molecular structure and vibrational spectra computationally. I consider both minima (i.e., stable molecules) and transition states, as well as infrared (IR), Raman, and vibrational circular dichroism (VCD) spectra, all of which can now be computed theoretically. The program used to carry out the calculations presented here is the PQS package developed by Parallel Quantum Solutions (PQS 2010), although any modern general purpose package (e.g. Gaussian, Turbomole, GAMESS) would do just as well. As the name implies, all the major *ab initio* functionality of this package is fully parallel, including energies, gradients, and second derivatives. PQS was chosen because (a) it is the package I actually use in all my application work; and (b) I am one of its principal authors. A review of the capabilities and parallel efficiency of the PQS package was published recently (Baker et al. 2009).

I have elected to use a standard level of *ab initio* theory for all of the examples presented in this chapter, namely, density functional theory (Hohenberg and Kohn 1964; Kohn and Sham 1965) (DFT) using the B3LYP (Becke 1993) (see also Hertwig and Koch (1997)) functional and the 6-31G\* (Ditchfield et al. 1971) basis set (B3LYP/6-31G\*). DFT is now the method of choice for routine chemical applications, and B3LYP – despite the large number of functionals developed since – is still one of the most popular. Many of the techniques and pitfalls in locating stable geometries are essentially independent of method, although DFT has its own issues as a result of the numerical quadrature required to handle many of the integrals; this will be discussed in some detail later. DFT is so popular that Hartree–Fock theory, which used to be the standard approach throughout the 1980s, has now almost disappeared other than as a precursor

for higher level post-SCF calculations. At the time of writing, the latter are beginning to make a bit of a comeback as the limitations of DFT are being reached, in particular its inability to systematically improve the wavefunction (and hence the results). A good introduction to DFT for those, like me, whose background is in traditional quantum chemistry is the now classic 1993 paper from (Johnson et al. 1993).

The Born–Oppenheimer approximation (Born and Oppenheimer 1927) (see also Wikipedia (2010)) is used throughout. This extremely important approximation, namely that electrons, being so much less massive, respond instantaneously to the motion of the nuclei, underpins the whole concept of the potential energy surface (PES). Stable arrangements of nuclei (stable or meta-stable molecules) correspond to local minima on the PES, first-order saddle points connecting two different minima correspond to transition states, and the “valleys” joining transition states to minima correspond to “reaction paths.” Electronic excitation is represented by a “jump” from one potential energy surface to another. We will be spending all of our time on the lowest energy (ground-state) PES.

## Molecular Structure

---

From a theoretical point of view the determination of a “molecular structure” means determining the geometry (i.e., the positions of atoms relative to one another) at a minimum (the bottom of a well) on the ground-state potential energy surface. Although a prerequisite, locating a minimum does not automatically mean that you have found the structure of a stable molecule; this depends on the barrier height, i.e., the energy required to get out of the well. The barrier height can be determined by locating the transition state, which for our purposes is defined as the highest energy point on the lowest energy path between reactants and products. (In a barrierless reaction, this will effectively be the energy of the products, assuming the reactant is taken to have the lower energy.) As a rough rule of thumb, if the barrier height is less than about 12–15 kcal mol<sup>-1</sup>, the system is kinetically unstable at room temperature.

Determining the geometry of a stable molecule therefore requires knowledge of both the minimum itself and the barrier height (i.e., effectively locating the transition state) for all possible decomposition reactions. Of course, the structures of many stable molecules can be derived from “chemical intuition” based on preexisting knowledge, but for new structures in particular the transition state is equally important and the practicing theoretician must be able to find both. In this section we discuss the methods available to do so.

## He<sub>2</sub><sup>2+</sup>: An Illustrative Example

---

The simplest possible molecular orbital approach to the bonding in the hydrogen molecule (H<sub>2</sub>) would consider the overlap between two 1s atomic orbitals on each hydrogen producing two molecular orbitals (MOs), one of which is bonding (the in-phase combination) and the other antibonding (the out-of-phase combination). H<sub>2</sub> is stable because its two electrons occupy the bonding orbital, giving an overall energy lowering compared to two separate H atoms.

Similar considerations applied to helium would suggest, quite rightly, that He<sub>2</sub> would not be stable, since both the bonding and antibonding MOs would be occupied, giving no net bonding. (In fact, as is well known, the antibonding MO is more antibonding than the bonding MO is

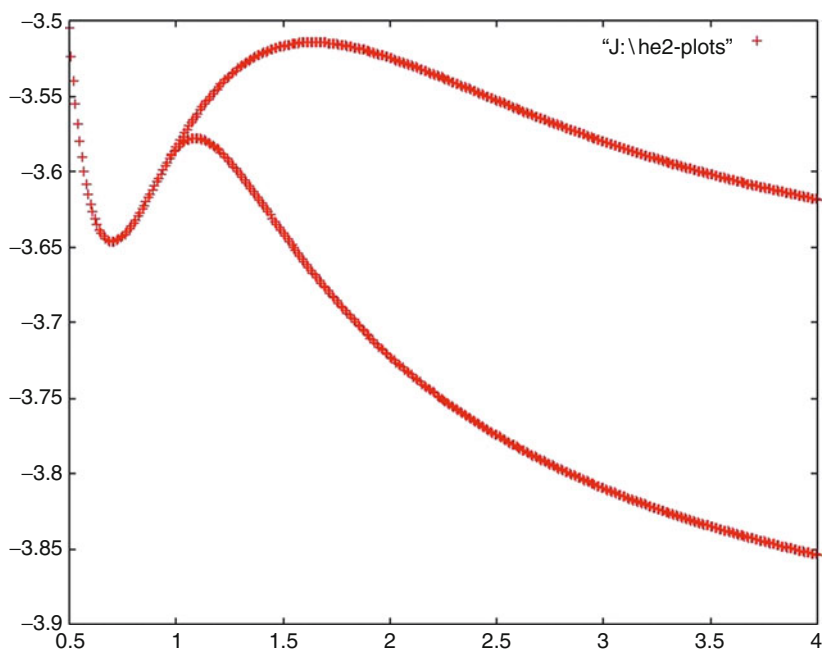


bonding.) What happens if the electrons in the antibonding MO are removed? On the one hand, there should be a strong bonding interaction, while on the other the resultant positive charge should cause the two nuclei to repel one another.

► *Figure 10-1* shows the ground-state PES of  $\text{He}_2^{2+}$ . This was obtained via a potential scan, varying the He–He distance from 0.6 to 4.0 Å in steps of 0.01 Å and computing the energy at each scanned distance. (An optimized potential scan – scanning one particular variable or combination of variables while optimizing all remaining degrees of freedom – is a useful tool for locating transition states, as will be seen later.) The upper curve shows the energy at the restricted RB3LYP/6-31G\* level, while the lower curve is the unrestricted equivalent (UB3LYP/6-31G\*). The two curves coalesce at He–He distances less than about 0.96 Å; at distances greater than this the restricted wavefunction is energetically unstable, i.e., a lower energy can be obtained by switching to the unrestricted formalism.

During the restricted (upper) scan full symmetry ( $D_{\infty h}$ ) was maintained and the system is a pure singlet. For the unrestricted scan, symmetry was turned off and the highest occupied (HOMO) and lowest unoccupied (LUMO) MOs, both alpha and beta spin, were allowed to mix; this results – as can be seen – in an ultimately much lower energy, but the spin symmetry is lost and the system wavefunction is no longer a pure singlet. (Spin contamination gradually rises with increasing He–He distance until at 4.0 Å  $\langle S^2 \rangle$  is 1.000 and the multiplicity is 2.236, i.e., the system is somewhat “greater” than a doublet.)

At B3LYP/6-31G\* the energy of two separate  $\text{He}^+$  ions is  $-3.9863 E_h$  and so, despite the spin contamination, the unrestricted curve gives a far better description of the dissociation of  $\text{He}_2^{2+}$



■ Fig. 10-1

Energy versus He–He distance (Å) for  $\text{He}_2^{2+}$  (RB3LYP/6-31G\* – upper curve; UB3LYP/6-31G\* – lower curve)


than the restricted one. This is a general feature of the dissociation of essentially all diatomic molecules and is well known.

The interesting feature from our point of view is that this simple, one-dimensional PES contains both a (local) minimum *and* a transition state, and both types of stationary point can be examined and discussed in relation to the *same* potential energy curve. This is the only one-dimensional potential energy curve that I am aware of that has this feature.

The gradient is zero at both turning points – minimum and transition state – on the potential energy curve. The key difference between them is of course the sign of the energy second derivative (the rate of change of the gradient) which is positive for a minimum and negative for a transition state.

In this example, we have the complete energy curve between He–He distances of 0.5–4.0 Å available to us, but in general of course (in particular for anything more complicated than a diatomic molecule) this would not be the case, and if we wanted to search for, say, a local minimum we would have to provide an initial approximation for the geometry, i.e., a guess for the minimum structure. We would then calculate the energy, the gradient and either calculate, or provide a reliable estimate for, the second derivative and use this information to predict: (a) how far away we are on the PES from the nearest local minimum, and (b) the step to take (length and direction) in order to get there. Note that only in the one-dimensional case are the first and second derivatives single numbers; typically they would be vectors (with elements  $dE/dv_i$ , where  $v_i$  is the  $i$ -th variable) and matrices (with elements  $d^2E/dv_i dv_j$ ), respectively.

Predicting the next step, i.e., how to change the current geometry to get to a new geometry that is closer to the desired stationary point than the old geometry was, is the job of the geometry optimization algorithm. For *ab initio* methods these algorithms can be very sophisticated as both the energy and the gradient are relatively expensive to compute (the second derivative is usually even more expensive), and so additional manipulations in the optimization algorithm in order to reduce the number of optimization cycles (i.e., the number of costly energy and gradient calculations) is more than justified. Not so in molecular mechanics where the energy and gradient cost very little and a highly efficient – in terms of CPU time – optimization algorithm is required.

It is obvious that one of the factors that determines how quickly a given geometry optimization will converge is the starting geometry. In our  $\text{He}_2^+$  example, in order to locate the metastable minimum, which occurs at a He–He distance of around 0.7 Å (shorter than in  $\text{H}_2$ , making this the shortest bond distance known), any initial starting bond length greater than ca. 1.2 Å – the distance in the transition state on the lower, unrestricted, curve – will almost inevitably lead to dissociation (see  Fig. 10-1). If you want to find the transition state then the closer you start to a He–He distance of around 1.2 Å the better off you will be.

## The Newton–Raphson Step

Consider a starting He–He distance of about 1.0 Å, i.e., midway between the bound minimum and the transition state. This could probably go either way, toward the minimum or the transition state. Which way it does go is guided by the curvature of the surface around the local region, i.e., by the nature of the second derivative. If we do a standard Taylor series expansion about the current point, then we have

$$E(x+h) = E(x) + h \frac{dE}{dx} + \frac{h^2}{2} \frac{d^2E}{dx^2} + \frac{h^3}{6} \frac{d^3E}{dx^3} + \dots \quad (10.1)$$

In the region about a local minimum (or maximum) the potential energy curve is more-or-less parabolic, so assuming we are in or close to this region we can ignore all terms in the Taylor series expansion (► Eq. 10.1) beyond the quadratic. Taking the derivative with respect to the displacement  $h$  gives

$$\frac{dE(x+h)}{dh} = \frac{dE}{dx} + h \frac{d^2E}{dx^2}. \quad (10.2)$$

At a stationary point  $\frac{dE(x+h)}{dh} = 0$  and so the displacement  $h$  that achieves this is

$$h = -\frac{\frac{dE}{dx}}{\frac{d^2E}{dx^2}} \quad \text{or} \quad h = -\frac{g}{H}, \quad (10.3)$$

where  $g$  is of course the gradient and  $H$  is the energy second derivative.

► Equation 10.3 is the well-known Newton–Raphson step in one dimension. The multidimensional equivalent of this is

$$\mathbf{h} = -\mathbf{H}^{-1}\mathbf{g}, \quad (10.4)$$

where  $\mathbf{h}$  is now a vector (a set of displacements for all variables),  $\mathbf{g}$  is the gradient vector, and  $\mathbf{H}$  is the second derivative matrix, commonly known as the Hessian matrix.

Going back to our  $\text{He}_2^+$  example we see that the Newton–Raphson step is normally in the direction of minus the gradient (just like a steepest descent step) with a step length determined by the magnitude of the second derivative. If the second derivative is positive, the step will be downhill (opposite to the gradient) whereas if the second derivative is negative, the step will be uphill (in the same direction as the gradient). Thus at a He–He distance of 1.0 Å (see ► Fig. 10-1) the step taken will be uphill toward the transition state if the surface curvature is negative and downhill toward the minimum if it is positive.

In the multidimensional case, we can always find a unitary transformation that diagonalizes the Hessian matrix (which is symmetric about its diagonal), i.e.,

$$\mathbf{D} = \mathbf{U}\mathbf{H}\mathbf{U}^T, \quad (10.5)$$

where  $\mathbf{D}$  is a diagonal matrix and the superscript  $\mathbf{T}$  represents a matrix transpose. The vectors in  $\mathbf{U}$  are known as eigenvectors and the diagonal elements of  $\mathbf{D}$  are the corresponding eigenvalues. Both the displacement vector  $\mathbf{h}$  and the gradient  $\mathbf{g}$  can be transformed into this new (diagonal) representation as

$$\mathbf{g}' = \mathbf{U}^T\mathbf{g}; \quad \mathbf{h}' = \mathbf{U}^T\mathbf{h}. \quad (10.6)$$

Substituting ► Eq. 10.5 into ► Eq. 10.4 gives

$$\mathbf{h} = -(\mathbf{U}\mathbf{D}^{-1}\mathbf{U}^T)\mathbf{g}. \quad (10.7)$$

Multiplying both sides by  $\mathbf{U}^T$  and rearranging gives

$$\mathbf{U}^T\mathbf{h} = (\mathbf{U}^T\mathbf{U})\mathbf{D}^{-1}(\mathbf{U}^T\mathbf{g}), \quad (10.8)$$

$$\mathbf{h}' = \mathbf{D}^{-1}\mathbf{g}'. \quad (10.9)$$

Diagonalizing the Hessian matrix results in a set of mutually orthogonal directions on the PES (the vectors in  $\mathbf{U}$ ) with the gradient along each direction given by the corresponding element in the vector  $\mathbf{g}'$  and the second derivative given by the corresponding diagonal matrix element in  $\mathbf{D}$ . Thus we see that the  $N$ -dimensional Newton–Raphson step is equivalent to  $N$  separate one-dimensional Newton–Raphson steps along the orthogonal directions given by the vectors in  $\mathbf{U}$ . If all the eigenvalues of the Hessian matrix (all the diagonal entries in  $\mathbf{D}$ )

are positive, then the step taken will attempt to minimize along all directions on the PES (all degrees of freedom) and will head downhill to the nearest minimum. If one (and only one) of the Hessian eigenvalues is negative, then the Newton–Raphson step will attempt to maximize (head uphill in energy) along that direction, while simultaneously minimizing along all the other directions, i.e., it will move toward a transition state. If the Hessian has two or more negative eigenvalues, then, left to its own devices, the optimization will head toward a second (or higher) order stationary point. As these are usually of much less interest than minima or transition states, the problem in these cases is normally how to take a decent optimization step when the Hessian signature (number of negative eigenvalues) is inappropriate for the stationary point being sought.

I have spent a lot of time on the Newton–Raphson step as it, or a modification thereof, forms the heart of virtually all advanced geometry optimization algorithms. It is usually a good step to take, particularly in the immediate region around the stationary point, and from a practical point of view it utilizes all the information that is likely to be available at the current point on the PES, i.e., first and second derivatives; there are very few codes that routinely compute derivatives higher than the second, and they would be prohibitively expensive in any case.

## The Hessian Matrix and Hessian Updates

---

As I hope the above discussion has shown, the Hessian matrix plays a very important role in determining the step direction, which depends on the surface curvature in the local region of the PES. However, care must be taken with the step length. Hessian information is only local and only applies in the region immediately surrounding the current point. If the predicted step length is small, then you are probably near to a stationary point, in which case the step is best taken “as is”; however too large steps are usually not wise and you can easily get lost. Consequently it is a good idea to impose a limit on the step size – either an overall limit on the total step length or limits on the size of individual step components (or indeed both). Some algorithms attempt to define a “trust radius” which limits the step size dynamically depending on the local nature of the PES (usually determined by comparing the actual energy change from that predicted from the Hessian assuming quadratic behavior). In PQS a simple user-defined maximum step length is imposed (default 0.3 au).

Calculation of the exact Hessian for *ab initio* wavefunctions is expensive and in many cases it can be replaced by an approximation with little effect on the optimization itself, i.e., on the number of optimization cycles required to reach convergence. In some cases having the exact Hessian is a definite disadvantage. If you are fairly close on the PES to the stationary point being sought then, although an exact Hessian will likely get you there faster, the reduction in the number of optimization cycles will probably not be enough to offset the extra computational time required to compute the Hessian in the first place. (The exception is if the surface is fairly flat – long, weak bonds, or, especially, floppy systems with flat torsional potentials – in which case an exact Hessian will be a tremendous help.) A good quality Hessian will usually help the most when you are not really close to a stationary point, but within the region where the surface curvature is still appropriate, i.e., the Hessian matrix still has the correct signature (all positive eigenvalues for a minimum and one, and only one, negative eigenvalue for a transition state). Computing an exact Hessian will almost certainly be a waste of time if you are a long way from where you finally end up; under these circumstances an exact Hessian will almost inevitably have more negative eigenvalues than required and the Newton–Raphson step alone will clearly be inappropriate. If you are searching for a minimum you will be far better off

using an alternative for the Hessian matrix which has all positive eigenvalues (such a matrix is known as positive-definite) which should keep the energy going down until you get closer to the stationary point. If the gradient is large, then a few steepest descent steps, possibly with a line search, might be in order, simply to lower the energy and get to a more appropriate region of the PES.

In fact, other than in exceptional circumstances, when searching for a minimum you do not normally need to compute a full Hessian matrix at all. In most cases reasonably good starting geometries can be derived simply from “chemical intuition,” for example, C–H bond lengths (except in the rare cases of bridging hydrogens) are likely to be of the order of 1 Å, so there is no point in using a starting geometry with C–H distances differing much from this value. Very reasonable estimates of stretching, bending and also torsional force constants (diagonal Hessian elements) are readily available – for example, stretching force constants via Badgers rule (Badger 1934, 1935) (see also Schlegel 1984) – which are perfectly adequate in the vast majority of cases. Consequently you can normally come up with an approximate estimate for at least the diagonal elements of the Hessian matrix at the starting geometry using some simple empirical rules.

Once you have taken a step from one point on the PES to another (hopefully closer to the final stationary point), then you can compute an energy and a gradient at the new geometry. This information can be utilized, together with the energy, gradient, and anything else that might be to hand from the old point (or points), not only to work out a new step (the job of the geometry optimization algorithm) but also to improve (update) the original approximation for the Hessian matrix. You can think of this as similar to determining the surface curvature by finite difference on the gradient; you know the gradient where you started, you take a small step, calculate a new gradient, and determine the curvature by forward differences. Of course, updating a Hessian matrix on a multidimensional energy surface is a lot more approximate than this as typically the step taken is fairly large and you are attempting to get an update for the whole Hessian from a step in just one direction.

There are a number of different Hessian updating formulae, e.g., Murtagh and Sargeant (1970) and Powell (1971), Broyden-Fletcher-Goldfarb-Shanno (BFGS) (Broyden 1970; Fletcher 1970, 1980; Goldfarb 1970; Shanno 1970), which can be used where appropriate depending on the nature of the stationary point being sought. (The exact details are not important.) For minimization the BFGS update is a popular one as, if you start out with a positive-definite Hessian matrix (with all positive eigenvalues), as needed for a minimum search, you are more likely to retain this desirable feature with BFGS than with the other updates. (You may see statements to the effect that the BFGS update *guarantees* retention of a positive-definite Hessian. This is not true. However, on those occasions – not too common, but they do occur – when the update fails in this regard, you can tell in advance that it is going to fail and either skip the update on that step or take a different one.)

## Transition State Searches

---

For a minimum search then, computing an exact Hessian matrix is rarely required. Things are unfortunately not so straightforward for transition state searches. First of all transition state geometries are not as obvious as are the geometries of stable minima and so it is often quite difficult to come up with good starting structures. This can be a major problem in itself. Secondly, the correct Hessian eigenvalue structure is much more important for a transition state than it is for a minimum. For a transition state search, the Hessian must have one, and only one,

negative eigenvalue, and furthermore the direction of negative curvature must correspond to that for the structure being sought; to the reaction coordinate if you will. Difficult transition state searches can be plagued with additional small negative Hessian eigenvalues continually reappearing which correspond to rotation of, e.g., methyl groups, way off the reaction path, i.e., on some side chain or other nowhere near the reaction center. These additional negative eigenvalues often interfere with the search algorithm making the final structure difficult to locate. And thirdly, there are no simple empirical rules generally available for estimating a reliable starting Hessian for transition state searches as there are for minima. All these factors make transition state searches more difficult than minimizations and in all but the simplest cases a good estimate of the Hessian for at least the region round the active center is essentially mandatory.

As is the case with minimization, once you are “on the right track,” it is not necessary to calculate fresh second derivative data at every optimization cycle, the Hessian matrix can be updated. Currently the best update for a transition state search is probably that proposed by Boffill (1994) which is a linear combination of the Powell (1971) and Murtagh and Sargeant (1970) updates. This is a more flexible update than BFGS and allows the eigenvalue structure of the Hessian to change, which is obviously important if you get too close to a minimum. Unfortunately, unlike the case with minimization, there is no update that preserves the negative eigenvalue once you have it, and it is all too easy to find that the updated Hessian has either too few (zero) or too many (two or more) negative eigenvalues.

There are transition state search algorithms that do not require an initial starting structure; instead they take as input the two minima that you wish to connect and attempt to derive some kind of “reaction path” connecting the two. Depending on the nature of the algorithm, the maximum energy structure on this path is either the transition state itself, or a pretty good estimate for it which is subsequently refined. The original algorithm of this type was the Linear Synchronous Transit (LST) approach of Halgren and Lipscomb (1977) which mapped each atom in the reactant to a corresponding atom in the product and derived the best linear path between them in a least-squares sense. The maximum energy structure along this path provided an estimate (unfortunately often not a particularly good one) of the transition state geometry which was subsequently used as input into a standard search algorithm.

An improvement over this was Quadratic Synchronous Transit (QST) (Bell and Crighton 1984; Bell et al. 1981), which attempted to maximize along the line joining reactant and product while minimizing in all directions “orthogonal” (or conjugate) to this. One can easily see the rationale behind this approach: if the direction to be maximized could be reliably isolated from all other directions (imagine a Hessian matrix with what will become the direction of negative curvature having all zero off-diagonal matrix elements, i.e.,  $H_{ii}$ ; all  $H_{ij} = 0$ ) then it would be straightforward to maximize along the one direction while minimizing in the subspace of all the other variables. Unfortunately maintaining the orthogonality between the isolated direction and the rest of the space (i.e., keeping  $H_{ij} = 0$ ,  $j \neq i$ ) is rather difficult, and so the algorithm can often get lost. Nonetheless, there are several more modern algorithms based on these approaches, for example from Peng and Schlegel (1993) and Ionova and Carter (1993).

If the “reaction coordinate” can be reliably confined to just a couple of (ideally one) variables, then a very good starting geometry for a transition state search can be obtained from an optimized potential scan. Here the variable in question is scanned over a range of values (hopefully including the value the variable has in the transition state) and at each scanned value all other degrees of freedom are minimized. In effect this involves a series of constrained optimizations over the scanned variable. Once again, the transition state is taken to be the geometry at the highest energy found during the scan. (If the highest energy occurs at either of the scan

endpoints then either the scan range needs to be extended or there is no transition state in the region of the PES that is being explored.) An optimized potential scan is easy to set up with PQS and is normally a very reliable method, albeit potentially time consuming, of obtaining an excellent transition state starting geometry provided that the principal reaction coordinate can be successfully identified.

## Choice of Coordinates

---

In the discussion so far the choice of coordinates in which to carry out minimizations or transition state searches has not been specifically mentioned, although in certain cases – for example, when considering a potential scan – it is implicitly assumed that variables familiar to chemists, such as bond lengths and angles, have been employed. Virtually all quantities of interest that are actually computed in *ab initio* quantum chemistry, such as first (gradient) and second (Hessian) derivatives are calculated in terms of Cartesian coordinates and the molecular geometry, regardless of how it may be input, is stored and manipulated internally as a set of Cartesians. However, Cartesian coordinates are usually not the best choice when it comes to actually carrying out a geometry optimization, because they are generally too coupled. The only case where they are regularly used in the actual geometry optimization itself is in molecular mechanics.

In the late 1960s and early 1970s the so-called *Z*-matrix was widely used in quantum chemistry, initially simply as a means of inputting the molecular geometry, but later as a means of defining a set of internal coordinates in which to carry out the optimization. With a *Z*-matrix, the geometry can be defined in terms familiar to a chemist using individual (primitive) bond lengths, bond angles, and torsions. The first atom defined in the *Z*-matrix is placed at the origin of a standard Cartesian axis system (i.e., at 0.0, 0.0, 0.0), the second is placed along the *Z* axis at a distance *R*<sub>1</sub>, say, and the third in the *XZ* plane at a distance, *R*<sub>2</sub>, from the second atom and making an angle, *A*<sub>1</sub>, with the first atom (or vice versa). Thereafter the position of all subsequent atoms is given in terms of a bond distance, a bond angle and, say, a torsion, relative to three previously defined atoms. In the days before graphical user interfaces (GUI) and model builders, the *Z*-matrix became a regular way of defining and reading a molecular geometry into the program doing the actual calculation. Dummy atoms could be included in the *Z*-matrix (and were needed to help define linear arrangements of three or more atoms for which the torsion was undefined) and, once geometry optimizations were regularly performed in *Z*-matrix coordinates, the writing of a successful *Z*-matrix became almost an art form, with the aim of defining the *Z*-matrix variables so that the value of any one of them could be changed without changing the values of any of the others, the idea being to reduce the coupling between the variables to a minimum.

A well-defined set of internal coordinates usually performs better in a geometry optimization, i.e., converges in less optimization cycles, than the same optimization carried out in Cartesian coordinates. The playing field can be leveled, particularly for standard organic molecules, if the geometry is preoptimized in advance using a molecular mechanics forcefield (ensuring a reliable starting geometry) and if second derivative information – computed very cheaply during the mechanics minimization – is transferred to the *ab initio* optimization (Baker and Hehre 1991). However, as the system to be optimized gets larger and/or more complicated, Cartesian coordinates become less and less competitive with respect to a good set of internal coordinates.

The *Z*-matrix is rarely used today. With the increasing popularity of GUIs and model builders it is no longer needed as a means of geometry input, and *Z*-matrix coordinates have



been superseded as a coordinate set for optimization, first by natural internal coordinates (Fogarasi et al. 1992; Pulay et al. 1979) and then by delocalized internal coordinates (Baker et al. 1996). The latter, which are linear combinations of stretches, bends, and torsions (as opposed to the individual primitive internals in a  $Z$ -matrix), are readily generated from an underlying set of Cartesian coordinates and decouple the coordinate set (in a linearized sense) to the maximum extent possible (Baker et al. 1996). In large systems, reductions in the number of optimization cycles to reach convergence by an order of magnitude or more compared to Cartesians can be readily achieved. There is an additional computational cost in using delocalized internal coordinates however, as the transformations required to convert the Cartesian gradient into the gradient over delocalized internals, and – in particular – to convert the new geometry in internals back into Cartesians for the next optimization step (the back-transformation), are expensive and increasingly so with increasing system size. They scale formally as  $O(N^3)$ , where  $N$  is a rough measure of the system size, although this can readily be reduced to  $O(N^2)$  (Baker et al. 1999). There have been attempts to reduce the scaling to  $O(N)$  (Farkas and Schlegel 1998; Paizs et al. 2000), but I think it is fair to say that these have not been entirely successful. It is principally because of the unfavorable scaling in the coordinate transformations that internal coordinates have not been adopted in molecular mechanics.

The cost of the coordinate transformations and the overall complexity of the algorithm is not really a factor in *ab initio* methods and the majority of geometry optimizations in modern quantum chemistry packages are carried out in delocalized internals (Baker et al. 1996) or in some other set of redundant internal coordinates (Peng et al. 1996; Pulay and Fogarasi 1992).

## The Modified Newton–Raphson Step

We have already seen that the Newton–Raphson step is a pretty good one provided that the eigenvalue structure of the Hessian matrix is appropriate to the stationary point being sought. What should you do if it is not? An early effort to take remedial action under these circumstances was due to Poppinger (1975) who proposed that, when searching for a transition state, if the negative eigenvalue was lost then take a step uphill in the direction of the lowest positive eigenvector, while if an additional (unwanted) negative eigenvalue appeared, then take a step downhill in the direction of the least negative eigenvector. While this approach should lead you back into the right region of the PES, it has at least two drawbacks. Firstly, unlike the Newton–Raphson step which, when appropriate, minimizes/maximizes along all directions on the PES (all Hessian modes) simultaneously, here you are minimizing/maximizing essentially along one direction only. Secondly, successive such steps following a particular Hessian mode tend to become linearly dependent, which degrades many of the standard Hessian updating procedures.

A much better step was subsequently proposed by Cerjan and Miller (1981) which involved modifying the standard Newton–Raphson step with a so-called shift parameter,  $\lambda$ . In terms of a diagonal Hessian representation, the Newton–Raphson step given by  $\blacklozenge$  Eq. 10.4 can be written as

$$\mathbf{h} = \sum_i - \frac{F_i \mathbf{U}_i}{d_i}, \quad (10.10)$$

where  $\mathbf{U}_i$  is the  $i$ -th eigenvector,  $d_i$  is the corresponding eigenvalue, and  $F_i = \mathbf{U}_i^T \mathbf{g}$  is the component of the gradient along the local eigenmode  $\mathbf{U}_i$ .



The modified Newton–Raphson step is given by

$$\mathbf{h} = \Sigma_i - \frac{F_i \mathbf{U}_i}{d_i - \lambda}, \quad (10.11)$$

where  $\lambda$  can be regarded as a shift parameter on the Hessian eigenvalues. A suitable choice of  $\lambda$  can guide the step in a particular direction; for example if  $\lambda$  is close to a particular eigenvalue  $d_i$ , then the step taken will be predominantly in the direction of the corresponding eigenvector. In the early to mid-1980s, several groups were working on this topic, and several alternative transition state search algorithms were proposed differing only in the recipe used to determine the value of  $\lambda$  (Banerjee et al. 1985; Cerjan and Miller 1981; Simons et al. 1983).

The principal optimization algorithm in PQS, both for minima and transition states, is the eigenvector following (EF) algorithm developed in 1986 (Baker 1986). It is based on the Rational Functional Optimization (RFO) approach of Simons and coworkers (Banerjee et al. 1985) which was found at the time to provide the best recipe for determining the shift parameter,  $\lambda$ . In this approach, the energy on the PES following a step  $\mathbf{h}$  is written as (see  $\blacktriangleright$  Eq. 10.1):

$$E(x + h) = E(x) + \frac{\mathbf{g}^T \mathbf{h} + \frac{1}{2} \mathbf{h}^T \mathbf{H} \mathbf{h}}{1 + \mathbf{h}^T \mathbf{S} \mathbf{h}}. \quad (10.12)$$

In the original formalism, the matrix  $\mathbf{S}$  was a diagonal scaling matrix but in most practical implementations (certainly in the EF algorithm) it is taken as a unit matrix.

Applying the stationary condition  $dE/dh = 0$  to  $\blacktriangleright$  Eq. 10.12 gives the RFO eigenvalue equation (Banerjee et al. 1985):

$$\begin{pmatrix} \mathbf{H} & \mathbf{g} \\ \mathbf{g}^T & 0 \end{pmatrix} \begin{pmatrix} \mathbf{h} \\ 1 \end{pmatrix} = \lambda \begin{pmatrix} \mathbf{S} & 0 \\ 0 & 1 \end{pmatrix} \begin{pmatrix} \mathbf{h} \\ 1 \end{pmatrix}. \quad (10.13)$$

The dimensionality of  $\blacktriangleright$  Eq. 10.13 is one more than the number of variables ( $n$ ). As it is an eigenvalue equation, there are  $(n + 1)$  eigenvalues,  $\lambda$ ; normally the lowest one,  $\lambda_1$ , is the one you need. Expanding out  $\blacktriangleright$  Eq. 10.13 gives

$$(\mathbf{H} - \lambda \mathbf{S})\mathbf{h} + \mathbf{g} = 0, \quad (10.14)$$

$$\mathbf{g}^T \mathbf{h} = \lambda. \quad (10.15)$$

In terms of a diagonal Hessian representation, and with  $\mathbf{S}$  a unit matrix,  $\blacktriangleright$  Eq. 10.14 rearranges to  $\blacktriangleright$  Eq. 10.11, and substitution of  $\blacktriangleright$  Eq. 10.4 into the diagonal form of  $\blacktriangleright$  Eq. 10.15 gives

$$\Sigma_i - \frac{F_i^2}{\lambda - b_i} = \lambda, \quad (10.16)$$

which can be used to iteratively evaluate  $\lambda$ .

The eigenvalues,  $\lambda$ , of  $\blacktriangleright$  Eq. 10.13 have the following properties (Banerjee et al. 1985):

1. The  $(n + 1)$  eigenvalues of  $\blacktriangleright$  Eq. 10.13 bracket the  $n$  eigenvalues of the Hessian:  $\lambda_i \leq d_i \leq \lambda_{i+1}$ .
2. At convergence to a minimum both  $\mathbf{g}$  and  $\mathbf{h}$  are  $\mathbf{0}$ . The lowest eigenvalue,  $\lambda_1$ , of  $\blacktriangleright$  Eq. 10.13 is also zero and the other  $n$  eigenvalues are those of the Hessian at the minimum point, i.e.,  $\lambda_{i+1} = d_i$  for all  $i$ . Thus, near a local minimum,  $\lambda_1$  is negative and approaches zero at convergence.
3. For a saddle-point of order  $\mu$  (i.e., a stationary point with  $\mu$  negative eigenvalues) the zero eigenvalue of  $\blacktriangleright$  Eq. 10.13 at convergence separates the  $\mu$  negative and  $(n - \mu)$  positive Hessian eigenvalues.

The separability of the positive and negative Hessian eigenvalues led Simons and coworkers to suggest that the problem be reformulated into  $\mu$  principal modes to be maximized and  $(n - \mu)$  modes to be minimized. There would be two shift parameters,  $\lambda_p$  and  $\lambda_n$ , one for modes along which the energy is to be maximized and the other for which it is minimized. The RFO eigenvalue equation (Eq. 10.11) could thus be partitioned into two smaller P-RFO equations, and each one solved separately.

For a transition state, in terms of a diagonal Hessian representation, this gives rise to the two matrix equations:

$$\begin{pmatrix} d_1 & F_1 \\ F_1 & 0 \end{pmatrix} \begin{pmatrix} h_1 \\ 1 \end{pmatrix} = \lambda_p \begin{pmatrix} h_1 \\ 1 \end{pmatrix}, \quad (10.17)$$

$$\begin{pmatrix} d_2 & \mathbf{0} & & F_1 \\ \mathbf{0} & \ddots & & \vdots \\ & & d_n & F_n \\ F_2 & \cdots & F_n & 0 \end{pmatrix} \begin{pmatrix} h_2 \\ \vdots \\ h_n \\ 1 \end{pmatrix} = \lambda_n \begin{pmatrix} h_2 \\ \vdots \\ h_n \\ 1 \end{pmatrix}. \quad (10.18)$$

$\lambda_p$  is the highest eigenvalue of Eq. 10.17; it is always positive and approaches zero at convergence.  $\lambda_n$  is the lowest eigenvalue of Eq. 10.18; it is always negative and again approaches zero at convergence.

The above discussion assumes that, for a transition state search, the energy is to be maximized along the lowest Hessian mode,  $d_1$ , and minimized along all the higher modes. However, as first pointed out by Cerjan and Miller (1981), it is possible to maximize along modes other than the lowest and in this way obtain transition states for alternative reactions and rearrangements from the same starting point. The ability of the algorithm to “walk” on the PES, maximizing along different Hessian eigenmodes, is why the algorithm is known as Eigenvector Following. For maximization along the  $k$ -th mode, instead of the lowest, Eq. 10.17 would be replaced by

$$\begin{pmatrix} d_k & F_k \\ F_k & 0 \end{pmatrix} \begin{pmatrix} h_k \\ 1 \end{pmatrix} = \lambda_p \begin{pmatrix} h_k \\ 1 \end{pmatrix}, \quad (10.19)$$

and Eq. 10.18 would now exclude the  $k$ -th mode but include the lowest. Since what was originally the  $k$ -th mode is the mode along which the negative eigenvalue is required, if the search is to be successful this mode must eventually become the lowest mode. The mode that is actually followed during each optimization cycle is the mode which has the largest overlap with the mode followed on the previous cycle. In this way the same mode should hopefully be followed from cycle to cycle as it makes its way through the ranks from  $k$ -th position to first (lowest). Once the mode being followed has become the lowest, mode-following is switched off and it is always the lowest mode that is followed.

Although it was developed primarily for transition states, the EF algorithm is also a very powerful minimizer. For minimization the standard RFO-step is taken (requiring a single shift parameter) using Eq. 10.13. Mode following for transition state searches is useful if you want to explore the PES in detail, but it is likely to be expensive and requires reliable Hessian information to be effective. There will almost certainly be more variables, and hence more Hessian modes, for a given system than there are different transition structures associated with that system; furthermore it is not always obvious which mode to follow at any given point in order to locate a transition state of a desired type. Beware of low energy modes which if followed will lead to rotational barriers for torsions in side chains rather than to the transition state for the main reaction being sought.

## GDIIS

As well as the EF algorithm, the PQS package has another algorithm for structure minimization: GDIIS (Csaszar and Pulay 1984). This is an extension of Pulay's ubiquitous DIIS (Direct Inversion in the Iterative Subspace) procedure for accelerating SCF convergence (Pulay 1980, 1982), only applied instead to geometry optimization.

The essence of the DIIS approach is that parameter vectors (in this case the geometry) generated in previous iterations  $\mathbf{x}_1, \mathbf{x}_2, \dots, \mathbf{x}_m$  are linearly combined to find the best geometry in the current iteration. We can express each parameter vector in terms of its deviation from the final solution,  $\mathbf{x}_f$ :  $\mathbf{x}_i = \mathbf{x}_f + \mathbf{e}_i$ . If the conditions  $\sum_i c_i \mathbf{e}_i = \mathbf{0}$  and  $\sum_i c_i = 1$  are satisfied, then it is also the case that  $\sum_i c_i \mathbf{x}_i = \mathbf{x}_f$ . The true error vectors,  $\mathbf{e}_i$ , are of course unknown. However, they can be approximated by  $\mathbf{e}_i = -\mathbf{H}^{-1} \mathbf{g}_i$  (i.e., by the Newton–Raphson step). Minimization of the norm of the residuum vector  $\sum_i c_i \mathbf{e}_i$  taking into account the constraint equation  $\sum_i c_i = 1$  leads to a system of  $m$  equations (Csaszar and Pulay 1984):

$$\begin{pmatrix} B_{11} & B_{12} & \dots & B_{1m} & 1 \\ B_{21} & B_{22} & \dots & B_{2m} & 1 \\ \vdots & \vdots & & \vdots & \vdots \\ B_{m1} & B_{m2} & \dots & B_{mm} & 1 \\ 1 & 1 & \dots & 1 & 0 \end{pmatrix} \begin{pmatrix} c_1 \\ c_2 \\ \vdots \\ c_m \\ -\lambda \end{pmatrix} = \begin{pmatrix} 0 \\ 0 \\ \vdots \\ 0 \\ 1 \end{pmatrix}, \quad (10.20)$$

where  $B_{ij} = \langle \mathbf{e}_i | \mathbf{e}_j \rangle$ , the scalar product of the error vectors  $\mathbf{e}_i$  and  $\mathbf{e}_j$ , and  $\lambda$  is a Lagrange multiplier.

The coefficients,  $c_i$ , obtained from  $\blacktriangleright$  Eq. 10.20 are used to calculate an intermediate interpolated geometry:

$$\mathbf{x}'_{m+1} = \sum_i c_i \mathbf{x}_i, \quad (10.21)$$

and a corresponding interpolated gradient vector

$$\mathbf{g}'_{m+1} = \sum_i c_i \mathbf{g}_i. \quad (10.22)$$

A new, independent geometry is generated from the interpolated geometry by acting on the interpolated gradient with the (approximate) Hessian,

$$\mathbf{x}_{m+1} = \mathbf{x}'_{m+1} - \mathbf{H}^{-1} \mathbf{g}'_{m+1}. \quad (10.23)$$

$\blacktriangleright$  Equation 10.20–10.23 constitute a complete cycle of the GDIIS method. Convergence can be tested for in the usual way (based on the gradient and the displacement from the previous step) or on the norm of the GDIIS residuum vector.

The size of the GDIIS subspace,  $m$ , increases by one after each optimization cycle. Experience with the method suggests that  $m$  should not be allowed to grow too large; once a predefined maximum size has been reached (say 20, the current default in PQS), the earliest vectors are dropped out as new vectors are added. Intermediate quantities (geometries and error vectors) within the GDIIS subspace need to be stored, so limiting the subspace size also limits the storage requirements of the method. (This is not really an issue with GDIIS, but is more important with DIIS, where potentially large-dimension Fock and possibly density matrices are stored.)

GDIIS was originally used in what is termed “static” mode, in which the original estimate for the Hessian matrix was used throughout the optimization procedure. In fact GDIIS performs very well with a simple unit matrix approximation for the Hessian. However, it certainly

performs better if the Hessian matrix is updated. It is particularly important that the Hessian approximation remain positive definite, and so the BFGS update is strongly recommended with the update skipped if it is determined that this property is in danger of being lost.

## Geometry Optimization and Symmetry

---

Many molecules have symmetry and it is definitely advantageous to utilize as much symmetry as possible during the calculation of the energy, the gradient and, if it is being computed, the Hessian. Various quantities, particularly the geometry and the gradient, can be symmetrized during the optimization step itself, thus removing numerical round-off error and resulting in a cleaner, and occasionally faster, optimization. Most programs can utilize at least Abelian point-group symmetry, resulting in savings in computational time by up to a factor of 8, depending on the molecular symmetry.

If symmetry is utilized during a geometry optimization it obviously restricts the search on the PES to structures that retain the molecular symmetry, i.e., it excludes symmetry-breaking geometries. This can be particularly useful during a transition state search as, if it is known that the motion in the transition state breaks symmetry, then the transition state search can be replaced by a minimization within a symmetry-restricted subspace, usually a much simpler prospect. For example, consider ethane. The minimum, lowest energy structure has staggered C–H bonds and  $D_{3d}$  symmetry. The transition state for rotation about the C–C bond has eclipsed C–H bonds and  $D_{3h}$  symmetry. The latter can in fact be found by a simple minimization utilizing  $D_{3h}$  point-group symmetry as the path to the  $D_{3d}$  minimum is unavailable under the symmetry constraint. The minimum under  $D_{3h}$  symmetry is actually a transition state once the symmetry constraint is removed.

This illustrates another pitfall that occasionally catches out the novice: A structure that has been minimized under a symmetry constraint is not necessarily a true minimum and its identity should be confirmed by a full vibrational analysis. As a corollary to this, a transition state located under a symmetry constraint may not be a true transition state either; it could have one (or more) symmetry breaking modes with negative curvature.

## Performance for Minimization

---

We have had a lot of theory. How well, for example, does the standard eigenvector following (EF) algorithm perform in practice? This is illustrated in [Table 10-1](#) for a selection of ten organic molecules, selected at random from the fragments library in the graphical user interface *PQSMol* available for use with PQS (2010). These systems were all optimized using a molecular mechanics force field (it is not important which one) and symmetrized prior to being stored.

There have of course been a number of previous comparisons of the performance of various optimization algorithms. I mention two in particular, as I was involved in them myself. In 1991 Baker and Hehre compared the performance of the EF and GDIIS minimization algorithms, as implemented in the version of *Spartan* available at that time, on a test set of 20 organic molecules with a variety of structural motifs (Baker and Hehre 1991). The two algorithms performed similarly, but the main focus of this paper was to demonstrate that, provided reliable second derivative information was available, i.e., a good starting Hessian, then Cartesian

■ Table 10-1

Number of optimization cycles required to reach convergence for ten average-sized organic molecules under a range of starting conditions<sup>a</sup>

Molecule	Formula	Atoms	Symm.	Cartesians		Delocalized internals		
				Unit <sup>b</sup>	PM3 <sup>c</sup>	Unit <sup>b</sup>	Default <sup>d</sup>	PM3 <sup>c</sup>
Alanine	C <sub>3</sub> H <sub>7</sub> NO <sub>2</sub>	13	C <sub>1</sub>	28	11	20	10	8
Indole	C <sub>8</sub> H <sub>7</sub> N	16	C <sub>s</sub>	22	5	11	5	5
Cycloheptane	C <sub>7</sub> H <sub>14</sub>	21	C <sub>2</sub>	27	6	23	5	6
Bicyclo-2,2,2-octane	C <sub>8</sub> H <sub>14</sub>	22	D <sub>3</sub>	12 <sup>e</sup>	10	29	8	8
Adamantane	C <sub>10</sub> H <sub>16</sub>	26	T <sub>d</sub>	12	3	11	4	4
cis-decalin	C <sub>10</sub> H <sub>18</sub>	28	C <sub>2</sub>	27	4	26	4	4
amp-5	C <sub>10</sub> H <sub>14</sub> N <sub>5</sub> O <sub>7</sub> P	37	C <sub>1</sub>	193 <sup>e</sup>	68	85	29	35
Porphine	C <sub>20</sub> H <sub>14</sub> N <sub>4</sub>	38	D <sub>2h</sub>	21	7	11	6	7
Sucrose	C <sub>12</sub> H <sub>22</sub> O <sub>11</sub>	45	C <sub>1</sub>	163	31	67	17	21
Cyclohexadecane	C <sub>16</sub> H <sub>32</sub>	48	S <sub>4</sub>	32	10	27	6	9

<sup>a</sup>Standard EF algorithm used with a maximum allowed stepsize in the optimization space of 0.3 au and a BFGS Hessian update; convergence criteria were the standard PQS defaults – maximum component of the gradient vector less than 0.0003 au and either a maximum predicted displacement of 0.0003 au or an energy change from the previous cycle of less than 10<sup>-6</sup> Eh

<sup>b</sup>Starting Hessian was a unit matrix

<sup>c</sup>Starting Hessian was computed using PM3 by central-differences on the Cartesian gradient

<sup>d</sup>Diagonal elements of the starting Hessian were estimated using simple empirical rules

<sup>e</sup>Converged to higher energy local minimum

coordinates were just as efficient as *Z*-matrix coordinates for routine geometry optimization. A later paper Baker (1993) did the same thing for Cartesians versus natural internal coordinates on a larger test set of 30 mainly organic molecules. This latter test set became a kind of “standard” for checking improved optimization algorithms and several papers showing minor enhancements in performance (as would be expected with the passage of time) for these 30 molecules were published subsequently (Bakken and Helgaker 2002; Eckert et al. 1997; Lindh et al. 1995; Swart and Bickelhaupt 2006). A similar test set is also available for transition structures (Baker and Chan 1996).

The conclusion in Baker (1993) was that with a reasonable starting geometry and a good initial Hessian, optimizations in Cartesian coordinates were as efficient as those employing natural internal coordinates. However, there were certainly signs that, as the system size increased, the use of natural internals became more and more advantageous even if a reliable starting Hessian was available, and it was further concluded that with no initial Hessian information, natural internals (for which read also delocalized internals which have more-or-less replaced them) were in general superior to both Cartesian and *Z*-matrix coordinates, and for unconstrained optimization were therefore the coordinates of first choice.

One of the issues with the published studies (Baker 1993; Baker and Hehre 1991) is that the size of the systems in both test suites (all molecules had less than 30 atoms, and most much less), although typical for the time (the early 1990s), is pretty small by today's standards. The molecules in ● Table 10-1 are about 50% larger on the average, four of them have more than

30 atoms, with the largest having 48. The level of theory used, B3LYP/6-31G\*, is also more typical of today. They are still only average-sized molecules, but nonetheless are representative as far as performance is concerned.

All the conclusions reached in the previous studies are fully supported by the results shown in [Table 10-1](#). The use of a decent Hessian, even just an approximate one at the starting geometry (in this case computed by central differences using the semiempirical PM3 method (Stewart 1989)), improves the performance of minimizations in Cartesian coordinates substantially, by up to a factor of almost 7 (cis-decalin) and by an average over all 10 molecules of around 3.5. Despite this, Cartesian coordinates are not really competitive with delocalized internals under the same conditions, taking about 45% more cycles on the average to reach convergence. The performance of Cartesians is notably worse for large, floppy molecules with no symmetry (amp-5 and sucrose). Perhaps surprisingly, the performance of delocalized internals using the standard default Hessian (estimating diagonal matrix elements only using simple empirical rules) is even better, with the number of optimization cycles being the same or less than with the PM3 starting Hessian for all systems except one (alanine).

Of some surprise, at least to me, is the relatively poor performance of internal coordinates when no Hessian information (a unit matrix) is used. They are certainly better than Cartesian coordinates under the same conditions, which require about 75% more cycles on the average to converge, but perform over three times worse than when the default diagonal Hessian is used, showing the advantages of even rudimentary information about the surface curvature.

One of the molecules in [Table 10-1](#), bicyclo-2,2,2-octane, took significantly less optimization cycles to converge in Cartesian coordinates with a unit Hessian (12) than with the same optimization in delocalized internal coordinates (29); the reverse is the case for all of the other systems. This apparent anomaly is due to the fact that the Cartesian unit Hessian optimization converged to a higher energy local minimum than the other optimizations. This was not the only occasion when this occurred: higher energy local minima were also found for amp-5 and to a lesser extent for sucrose and alanine (although in the latter case the difference was only 40  $\mu$ H and may well be simply due to premature convergence, a fairly common occurrence for unit Hessian Cartesian optimizations (Baker et al. 1996)).

These results support another assertion made in Baker (1993), namely, that Cartesian optimizations tend to converge to the nearest local minimum whereas optimizations in natural (or delocalized) internals tend to converge more globally. This global tendency, and that is really all it is, with the internal coordinate optimizations is principally due to the fact that relatively small displacements in internal coordinates can lead to large changes when the geometry is converted back to Cartesian coordinates. For example a small change in a central bond angle can lead to a large Cartesian displacement at the end of a lengthy attached side chain; such large displacements enable internal coordinate optimizations to “jump over” local minima. (This phenomenon was first observed in the days of the *Z*-matrix.)

This is an appropriate point to emphasize that all the optimization algorithms discussed so far in this chapter are local methods, aimed at locating a single stationary point. Whether this is the lowest energy structure on the entire PES, i.e., the global minimum, is quite another matter. The number of (mainly conformational) minima a molecule has increases dramatically with system size and the problem of locating the one with the lowest energy quite quickly becomes almost insurmountable. Additionally, of course, unless the global minimum is noticeably lower in energy than other low-lying local minima, there will be a Boltzmann distribution

at room temperature with several different minima having appreciable population; under these circumstances to talk about a well-defined structure does not make a lot of sense.

Problems in locating global minima have only recently become an issue in *ab initio* calculations as the size of the systems that can be handled using these techniques has increased significantly in recent years. A number of global search algorithms are available, although none of them are bulletproof (i.e., absolutely guaranteed to locate the global minimum in a finite time). The problem of global minimization is outside the scope of this chapter and the interested reader is referred to the existing literature for more detail (Pardalos et al. 1995).

## Minimization: An Example

► **Figure 10-2** shows the optimization output at each cycle in the standard default EF minimization of indole. There is more printout than normal for the first and last cycles as I have used a higher print flag in order to show more detail. The output is of course specific to PQS but would be similar – at least in terms of the quantities printed – in other programs.

At the beginning of each optimization cycle the current geometry is printed in Cartesian coordinates together with the point group ( $C_s$ ) and the number of degrees of freedom (29). Indole is planar and is oriented in the  $XY$  plane; consequently all  $Z$ -coordinates are zero. Next comes the SCF energy at that geometry and the Cartesian forces (the gradient – not normally printed). The latter should fully reflect the symmetry of the system, which it does in this case, and so all  $Z$ -gradient components are zero.

This is followed by a symmetry analysis of the set of delocalized internal coordinates generated for indole which results in the elimination of all primitive torsions, all of which are fixed by symmetry. This analysis is typically done once only as thereafter the delocalized internal coordinates formed and used on the first cycle are retained unaltered throughout the optimization. One does not have to do this; several algorithms (e.g., Schlegel and coworkers (Peng et al. 1996)) effectively regenerate a set of active delocalized internals on each optimization cycle although in most cases this is not necessary and does not improve the overall performance.

There is then a statement as to how many Hessian modes (eigenvectors) are used during the construction of the optimization step – this does not have to be all of them, but is usually most, and cannot be more than the total number of degrees of freedom – followed by a listing of the corresponding Hessian eigenvalues (the curvature along each of the eigenvector directions). In this particular optimization, a diagonal Hessian in the underlying space of primitive internals (individual stretches, bends and torsions) is estimated using empirical rules, and is then transformed into the space of selected delocalized internal coordinates,  $\mathbf{U}$ , via  $\mathbf{H} = \mathbf{U}^T \mathbf{H}_{\text{prim}} \mathbf{U}$  (Baker et al. 1996). The simple RFO step is then computed and taken, appropriate for minimization, resulting in a single shift parameter,  $\lambda$  (see ► Eq. 10.16), with a value of  $-0.01172058$ . The resulting step length of 0.174879 is below the default maximum of 0.3 and so no scaling of the step is required.

The parameter values, and their gradients and displacements are then printed out. As with the Cartesian forces, these are not normally printed, and are not particularly informative given that each coordinate is potentially a linear combination of all underlying primitive internals (minus the torsions in the case of indole). A persistently large gradient for a particular coordinate would suggest some problems with the overall coordinate set, suggesting that either the delocalized internals, the underlying primitives or likely both, should be regenerated.

\*\* GEOMETRY OPTIMIZATION IN DELOCALIZED INTERNAL COORDINATES \*\*  
Searching for a Minimum

Optimization Cycle: 1

Coordinates (Angstroms)			
ATOM	X	Y	Z
1 c	-1.128517	1.256320	0.000000
2 c	-2.175159	0.350932	0.000000
3 c	-1.944638	-1.056645	0.000000
4 c	-0.661806	-1.575795	0.000000
5 c	0.418576	-0.654407	0.000000
6 c	0.193566	0.736550	0.000000
7 n	1.801059	-0.848856	0.000000
8 c	1.464739	1.385216	0.000000
9 c	2.431380	0.400066	0.000000
10 h	-1.307547	2.344176	0.000000
11 h	-3.212371	0.726200	0.000000
12 h	-2.806900	-1.744633	0.000000
13 h	-0.476805	-2.662311	0.000000
14 h	2.242590	-1.695842	0.000000
15 h	1.641099	2.472979	0.000000
16 h	3.520733	0.566050	0.000000

Point Group: Cs      Number of degrees of freedom: 29

Energy is -363.810295355

Cartesian Forces (au)			
ATOM	X	Y	Z
1 c	0.0055736	-0.0029170	0.0000000
2 c	-0.0116662	-0.0021539	0.0000000
3 c	-0.0102295	0.0028293	0.0000000
4 c	0.0158848	-0.0032863	0.0000000
5 c	-0.0012122	-0.0121078	0.0000000
6 c	-0.0098733	0.0169732	0.0000000
7 n	-0.0277428	0.0598278	0.0000000
8 c	0.0127970	0.0051731	0.0000000
9 c	-0.0032541	0.0095309	0.0000000
10 h	0.0020479	-0.0106104	0.0000000
11 h	0.0092568	-0.0048346	0.0000000
12 h	0.0083209	0.0070569	0.0000000
13 h	-0.0025071	0.0095819	0.0000000
14 h	0.0262691	-0.0500248	0.0000000
15 h	-0.0010053	-0.0136614	0.0000000
16 h	-0.0126474	-0.0113918	0.0000000

■ Fig. 10-2  
(Continued)



Iterative generation of Internal Gradient  
 Eliminated 13 Coordinates due to Symmetry  
 Setting Up Default Hessian

Eliminating Redundant Primitive Internals from Space  
 Removed 40 Torsions  
 There are now 44 Primitive Internals

29 Hessian modes will be used to form the next step

Hessian Eigenvalues:

0.160000	0.160000	0.160000	0.160000	0.160000	0.160000
0.160000	0.220000	0.221923	0.226566	0.240305	0.246612
0.333419	0.333513	0.334083	0.334451	0.334655	0.334700
0.371362	0.386468	0.401879	0.411214	0.422264	0.441836
0.450459	0.468353	0.478270	0.480256	0.565271	

Minimum Search -- Taking Simple RFO Step

Searching for Lambda that Minimizes Along All modes

Value Taken Lambda = -0.01172058

Step Taken. Step size is 0.174879

Parameter Values and Displacements in Internal Coordinates

Coordinate	Current Value	Gradient	Displacement	New Value
1	0.101253	-0.014349	0.053801	0.155053
2	5.456291	0.008615	-0.016785	5.439506
3	0.217497	-0.007632	0.010903	0.228400
4	-3.211789	-0.009303	0.024794	-3.186995
5	-0.012152	-0.000858	0.006348	-0.005803
6	1.909226	0.003986	-0.024340	1.884886
7	-3.105834	-0.009981	0.008840	-3.096993
8	2.478733	0.002437	0.009541	2.488274
9	-6.023465	-0.014279	0.061052	-5.962413
10	1.567775	-0.024103	0.052225	1.620000
11	0.120409	0.004716	-0.000988	0.119421
12	0.470803	-0.006865	0.010435	0.481238
13	0.108849	0.029674	-0.072756	0.036093
14	-0.084456	-0.000889	-0.005425	-0.089881
15	-0.019703	-0.018787	0.045992	0.026288
16	-0.655038	-0.006993	0.018148	-0.636890
17	0.053151	0.028830	-0.077571	-0.024421
18	-0.542248	-0.008997	0.031837	-0.510411
19	0.418788	-0.009691	0.003553	0.422341
20	0.027192	-0.012413	0.020235	0.047427
21	-0.521699	-0.020982	0.035801	-0.485898
22	0.026544	0.014739	-0.036257	-0.009713

■ Fig. 10-2  
 (Continued)

23	0.025617	0.012415	-0.020628	0.004989
24	0.106965	-0.014751	0.019131	0.126096
25	0.010931	0.000862	0.003784	0.014715
26	0.078250	0.014521	-0.003008	0.075242
27	-0.017986	0.002536	0.000400	-0.017586
28	-0.036740	0.005844	-0.010000	-0.046740
29	0.059767	-0.010038	0.023970	0.083736

	Maximum	Tolerance	Cnvgd?
Gradient	0.029674	0.000300	NO
Displacement	0.077571	0.000300	NO
Energy change	*****	0.000001	NO

New Cartesian Coordinates Obtained by Inverse Iteration

Cycle: 1 Maximum deviation: 0.07757147 RMS deviation: 0.03247425  
 Cycle: 2 Maximum deviation: 0.00251062 RMS deviation: 0.00103769  
 Cycle: 3 Maximum deviation: 0.00000221 RMS deviation: 0.00000090  
 Cycle: 4 Maximum deviation: 0.00000000 RMS deviation: 0.00000000

Full backtransformation converged in 4 cycles

\*\* GEOMETRY OPTIMIZATION IN DELOCALIZED INTERNAL COORDINATES \*\*

Searching for a Minimum

Optimization Cycle: 2

Energy is -363.816456941

Hessian Updated using BFGS Update

24 Hessian modes will be used to form the next step

Hessian Eigenvalues:

0.151802	0.160279	0.220081	0.222573	0.225149	0.238697
0.243289	0.333210	0.333512	0.334201	0.334467	0.334607
0.343195	0.364439	0.384434	0.402067	0.410203	0.415618
0.442013	0.451793	0.468281	0.475225	0.483089	0.592272

Minimum Search -- Taking Simple RFO Step

Searching for Lambda that Minimizes Along All modes

Value Taken Lambda = -0.00036212

Step Taken. Stepsize is 0.041360

	Maximum	Tolerance	Cnvgd?
Gradient	0.004782	0.000300	NO
Displacement	0.016892	0.000300	NO
Energy change	-0.006162	0.000001	NO

■ Fig. 10-2  
(Continued)

\*\* GEOMETRY OPTIMIZATION IN DELOCALIZED INTERNAL COORDINATES \*\*  
 Searching for a Minimum

Optimization Cycle: 3

Energy is -363.816671150

Hessian Updated using BFGS Update

25 Hessian modes will be used to form the next step

Hessian Eigenvalues:

0.130519	0.160040	0.163016	0.220115	0.222415	0.225439
0.237352	0.243655	0.333380	0.333585	0.334086	0.334518
0.334959	0.343578	0.347729	0.392411	0.400153	0.404240
0.415041	0.441905	0.448922	0.467657	0.472002	0.481316
0.592359					

Minimum Search -- Taking Simple RFO Step

Searching for Lambda that Minimizes Along All modes

Value Taken Lambda = -0.00002978

Step Taken. Step size is 0.012738

	Maximum	Tolerance	Cnvgd?
Gradient	0.001411	0.000300	NO
Displacement	0.005681	0.000300	NO
Energy change	-0.000214	0.000001	NO

\*\* GEOMETRY OPTIMIZATION IN DELOCALIZED INTERNAL COORDINATES \*\*  
 Searching for a Minimum

Optimization Cycle: 4

Energy is -363.816687350

Hessian Updated using BFGS Update

26 Hessian modes will be used to form the next step

Hessian Eigenvalues:

0.125429	0.160015	0.160339	0.163176	0.219075	0.222406
0.225145	0.240033	0.248037	0.333477	0.333628	0.334164
0.334523	0.335030	0.340061	0.343940	0.388531	0.394562
0.402733	0.413258	0.443109	0.446921	0.466923	0.472407
0.484096	0.575065				

Minimum Search -- Taking Simple RFO Step  
 Searching for Lambda that Minimizes Along All modes  
 Value Taken Lambda = -0.00000167  
 Step Taken. Stepsize is 0.002748

	Maximum	Tolerance	Cnvgd?
Gradient	0.000329	0.000300	NO
Displacement	0.001530	0.000300	NO
Energy change	-0.000016	0.000001	NO

\*\* GEOMETRY OPTIMIZATION IN DELOCALIZED INTERNAL COORDINATES \*\*  
 Searching for a Minimum

Optimization Cycle: 5

		Coordinates (Angstroms)		
ATOM		X	Y	Z
1	c	-1.139936	1.251805	0.000000
2	c	-2.184123	0.336460	0.000000
3	c	-1.936378	-1.052260	0.000000
4	c	-0.639460	-1.552003	0.000000
5	c	0.409411	-0.626076	0.000000
6	c	0.184879	0.779966	0.000000
7	n	1.776536	-0.819763	0.000000
8	c	1.477261	1.408786	0.000000
9	c	2.412786	0.408513	0.000000
10	h	-1.341534	2.320123	0.000000
11	h	-3.211059	0.691818	0.000000
12	h	-2.774412	-1.743982	0.000000
13	h	-0.449126	-2.622400	0.000000
14	h	2.239283	-1.715056	0.000000
15	h	1.683185	2.470391	0.000000
16	h	3.492686	0.463678	0.000000

Point Group: Cs Number of degrees of freedom: 29

Energy is -363.816688224

		Cartesian Forces (au)		
ATOM		X	Y	Z
1	c	0.0000584	0.0000769	0.0000000
2	c	-0.0000324	-0.0000754	0.0000000
3	c	-0.0000236	0.0000544	0.0000000
4	c	0.0000253	0.0000010	0.0000000
5	c	0.0000447	0.0000047	0.0000000
6	c	-0.0000126	-0.0000224	0.0000000

■ Fig. 10-2  
 (Continued)

7	n	0.0000101	-0.0000947	0.0000000
8	c	-0.0000175	0.0000305	0.0000000
9	c	-0.0000117	-0.0000575	0.0000000
10	h	-0.0000167	-0.0000124	0.0000000
11	h	0.0000098	0.0000222	0.0000000
12	h	0.0000205	-0.0000148	0.0000000
13	h	-0.0000036	-0.0000004	0.0000000
14	h	-0.0000063	0.0000234	0.0000000
15	h	-0.0000125	0.0000115	0.0000000
16	h	-0.0000212	0.0000385	0.0000000

## Iterative generation of Internal Gradient

Cycle: 1 Maximum deviation: 0.00000045 RMS deviation: 0.00000017  
 Cycle: 2 Maximum deviation: 0.00000002 RMS deviation: 0.00000000  
 Cycle: 3 Maximum deviation: 0.00000000 RMS deviation: 0.00000000

Gradient converged in 3 cycles

Hessian Updated using BFGS Update

27 Hessian modes will be used to form the next step

Hessian Eigenvalues:

0.123423	0.145668	0.160015	0.160222	0.160354	0.219732
0.223230	0.234867	0.238794	0.266437	0.329579	0.333566
0.333688	0.334223	0.334658	0.336381	0.344207	0.373478
0.394783	0.402322	0.411472	0.445584	0.447885	0.466973
0.472563	0.490846	0.574440			

Minimum Search -- Taking Simple RFO Step

Searching for Lambda that Minimizes Along All modes

Value Taken Lambda = -0.00000011

Step Taken. Stepsize is 0.000794

## Parameter Values and Displacements in Internal Coordinates

Coordinate	Current Value	Gradient	Displacement	New Value
1	0.174852	0.000041	-0.000220	0.174632
2	5.446165	0.000048	-0.000143	5.446022
3	0.220440	-0.000048	0.000192	0.220632
4	-3.186512	-0.000013	0.000045	-3.186467
5	0.005499	0.000019	-0.000053	0.005447
6	1.881035	-0.000030	0.000240	1.881275
7	-3.115511	-0.000001	-0.000056	-3.115567
8	2.497738	0.000031	-0.000321	2.497417
9	-5.949299	0.000024	-0.000100	-5.949400
10	1.621591	-0.000050	0.000147	1.621738
11	0.121225	0.000010	-0.000072	0.121153
12	0.483100	0.000032	-0.000143	0.482958
13	0.028700	-0.000023	0.000133	0.028833

14	-0.091955	-0.000001	0.000091	-0.091864
15	0.036701	0.000029	-0.000142	0.036559
16	-0.640073	0.000000	0.000031	-0.640042
17	-0.040582	-0.000043	0.000238	-0.040343
18	-0.513581	0.000025	-0.000128	-0.513709
19	0.416043	0.000048	-0.000159	0.415884
20	0.049659	0.000005	0.000034	0.049693
21	-0.490411	0.000020	-0.000080	-0.490491
22	-0.031165	0.000042	-0.000214	-0.031380
23	0.006415	-0.000016	0.000033	0.006449
24	0.139909	-0.000005	0.000087	0.139996
25	0.020428	0.000004	-0.000045	0.020383
26	0.091251	0.000013	-0.000090	0.091161
27	-0.014788	0.000006	-0.000093	-0.014881
28	-0.049225	-0.000002	-0.000010	-0.049236
29	0.094109	0.000053	-0.000269	0.093840

	Maximum	Tolerance	Cnvgd?
Gradient	0.000053	0.000300	YES
Displacement	0.000321	0.000300	NO
Energy change	-0.000001	0.000001	YES

■ Fig. 10-2

#### PQS output for the minimization of indole

The convergence criteria – current value, tolerance, and whether or not convergence is satisfied – are then printed, together with details of the back-transformation (conversion of the current geometry in internal coordinates back into Cartesians, again not normally printed). This constitutes a complete optimization cycle.

On subsequent optimization cycles, assuming that the system is converging, the energy, the gradient components (both Cartesian and internal) and the step size should all decrease, with the latter two tending to zero. This is exactly what occurs for indole (see [Fig. 10-2](#)) which converges smoothly to the minimum energy structure. Another quantity that should tend to zero is the shift parameter,  $\lambda$ , which again clearly does so; its magnitude on the last cycle is 0.00000011. Note that, as previously stated (see the comments under [Eq. 10.16](#))  $\lambda$  is always negative and so approaches zero from below. The closer  $\lambda$  is to zero, the closer is the step taken to the simple Newton–Raphson step.

After the initial estimate, the Hessian matrix is updated at the beginning of each new optimization step. This is done using the BFGS update, as appropriate for a minimization. Indole is a planar, rigid molecule and so, not surprisingly, convergence is achieved quickly taking just five optimization cycles. At final convergence the displacement criteria is not fully satisfied; this is not an error as the default convergence criteria in PQS allow for just one of the displacement and energy change criteria to be satisfied (see the footnotes under [Table 10-1](#)); this is to prevent wasteful cycles near the end of the optimization for excessively floppy molecules for which relatively large displacements result in only small changes in energy. If it is desired that the displacement criterion be rigorously satisfied, then the energy criterion should be reduced so that it is almost impossible to satisfy (for example to  $10^{-8}$  Eh); Convergence can then only be achieved by satisfying the displacement criterion.

## Transition State Searches: An Example

► *Figure 10-3* shows the optimization output at each cycle (truncated for the intermediate cycles) in the standard default EF transition state search for the reaction  $\text{HCN} \leftrightarrow \text{HNC}$ . This is a very simple reaction but is still instructive. Both reactant and product are linear. Reaction can be considered to occur essentially by motion of the hydrogen atom in a semicircle centered about the midpoint of the C–N bond, with the  $\angle\text{HCN}$  angle going from  $180^\circ$  in HCN to  $0^\circ$  in HNC (CNH).

Consider the starting geometry. A first approximation to the transition state (TS) geometry might be to position the hydrogen atom directly vertically above the midpoint of the C–N bond. (The H–C distance of course has to be decided.) This corresponds to  $\angle\text{HCN}$  a bit less than  $90^\circ$ . However, knowing the relative energetics (HNC is less stable than HCN, the reaction as written is endothermic), the Hammond postulate (Hammond 1955) suggests that the TS is likely to resemble HNC more than HCN, in which case  $\angle\text{HCN}$  will very likely be noticeably less than  $90^\circ$ , i.e., relative to HCN we have a late transition state. Now this is only a simple consideration, but the use of “chemical intuition” in this way can potentially save several optimization cycles. In this particular example, it does not save much because the system as a whole only has three atoms and the transition state is fairly easy to locate, but starting with  $\angle\text{HCN} = 85^\circ$  instead of  $70^\circ$  costs an extra optimization cycle, and starting with  $\angle\text{HCN} = 130^\circ$  takes three more cycles. (The other starting parameters were  $r_{\text{C-N}} = 1.21 \text{ \AA}$  and  $r_{\text{H-C}} = 1.5 \text{ \AA}$ .) As has already been mentioned, a good initial Hessian is almost mandatory for a TS search and a full Hessian at the starting geometry was computed at the semiempirical PM3 level (Stewart 1989) for the  $\text{HCN} \leftrightarrow \text{HNC}$  reaction.

\*\* GEOMETRY OPTIMIZATION IN DELOCALIZED INTERNAL COORDINATES \*\*

Searching for a Transition State

Optimization Cycle: 1

		Coordinates (Angstroms)		
ATOM		X	Y	Z
1	c	-0.469846	0.571010	0.000000
2	n	-0.469846	-0.628990	0.000000
3	h	0.939693	0.057980	0.000000

Point Group: Cs      Number of degrees of freedom: 3

Energy is -93.319741527

		Cartesian Forces (au)		
ATOM		X	Y	Z
1	c	0.0404791	-0.0073674	0.0000000
2	n	0.0272344	0.0058884	0.0000000
3	h	-0.0677118	0.0014596	0.0000000

Iterative generation of Internal Gradient

Transforming Cartesian Hessian to Internal Coordinates

■ Fig. 10-3  
(Continued)

Hessian Transformation does not Include Derivative of B-matrix

3 Hessian modes will be used to form the next step

Hessian Eigenvalues:

-0.187665      0.238971      1.173533

Transition State Search -- Taking P-RFO Step

Searching for Lambda that Maximizes Along the Lowest mode

Value Taken      Lambda =    0.00189009

Searching for Lambda that Minimizes Along All other modes

Value Taken      Lambda =  -0.02788347

Calculated Step too Large. Step scaled by  0.888690

Step Taken. Stepsize is  0.300000

Parameter Values and Displacements in Internal Coordinates

Coordinate	Current Value	Gradient	Displacement	New Value
1	2.134802	0.074274	-0.131560	2.003242
2	-0.247567	-0.037317	0.203494	-0.044073
3	-3.170360	-0.032424	0.176868	-2.993492

	Maximum	Tolerance	Cnvgd?
Gradient	0.074274	0.000300	NO
Displacement	0.203494	0.000300	NO
Energy change	*****	0.000001	NO

New Cartesian Coordinates Obtained by Inverse Iteration

Cycle:  1 Maximum deviation:  0.20349400 RMS deviation:  0.17320508

Cycle:  2 Maximum deviation:  0.00532215 RMS deviation:  0.00463403

Cycle:  3 Maximum deviation:  0.00001577 RMS deviation:  0.00001192

Cycle:  4 Maximum deviation:  0.00000000 RMS deviation:  0.00000000

Full backtransformation converged in  4 cycles

\*\* GEOMETRY OPTIMIZATION IN DELOCALIZED INTERNAL COORDINATES \*\*

Searching for a Transition State

Optimization Cycle:  2

Energy is        -93.339112477

Hessian Updated using Powell/Murtagh-Sargent Update

Mixing factors:    0.645582 Powell

                    0.354418 Murtagh-Sargent

■ Fig. 10-3  
(Continued)



3 Hessian modes will be used to form the next step

Hessian Eigenvalues:

-0.196173      0.099238      1.154056

Transition State Search -- Taking P-RFO Step

Searching for Lambda that Maximizes Along the Lowest mode

Value Taken      Lambda =      0.00827163

Searching for Lambda that Minimizes Along All other modes

Value Taken      Lambda =      -0.02009120

Calculated Step too Large. Step scaled by 0.661233

Step Taken. Stepsize is 0.300000

	Maximum	Tolerance	Cnvgd?
Gradient	0.062199	0.000300	NO
Displacement	0.233225	0.000300	NO
Energy change	-0.019371	0.000001	NO

\*\* GEOMETRY OPTIMIZATION IN DELOCALIZED INTERNAL COORDINATES \*\*

Searching for a Transition State

Optimization Cycle: 3

Energy is -93.342916439

Hessian Updated using Powell/Murtagh-Sargent Update

Mixing factors: 0.556632 Powell

0.443368 Murtagh-Sargent

3 Hessian modes will be used to form the next step

Hessian Eigenvalues:

-0.214546      0.216669      1.155709

Transition State Search -- Taking P-RFO Step

Searching for Lambda that Maximizes Along the Lowest mode

Value Taken      Lambda =      0.00009941

Searching for Lambda that Minimizes Along All other modes

Value Taken      Lambda =      -0.00011765

Step Taken. Stepsize is 0.030919

	Maximum	Tolerance	Cnvgd?
Gradient	0.006976	0.000300	NO
Displacement	0.028637	0.000300	NO
Energy change	-0.003804	0.000001	NO

■ Fig. 10-3

(Continued)

\*\* GEOMETRY OPTIMIZATION IN DELOCALIZED INTERNAL COORDINATES \*\*

Searching for a Transition State

Optimization Cycle: 4

Energy is -93.342897201

Hessian Updated using Powell/Murtagh-Sargent Update

Mixing factors: 0.111685 Powell  
0.888315 Murtagh-Sargent

3 Hessian modes will be used to form the next step

Hessian Eigenvalues:

-0.203277 0.258806 1.161986

Transition State Search -- Taking P-RFO Step

Searching for Lambda that Maximizes Along the Lowest mode

Value Taken Lambda = 0.00000265

Searching for Lambda that Minimizes Along All other modes

Value Taken Lambda = -0.00000882

Step Taken. Stepsize is 0.006795

	Maximum	Tolerance	Cnvgd?
Gradient	0.001321	0.000300	NO
Displacement	0.004864	0.000300	NO
Energy change	0.000019	0.000001	NO

\*\* GEOMETRY OPTIMIZATION IN DELOCALIZED INTERNAL COORDINATES \*\*

Searching for a Transition State

Optimization Cycle: 5

Energy is -93.342899327

Hessian Updated using Powell/Murtagh-Sargent Update

Mixing factors: 0.377168 Powell  
0.622832 Murtagh-Sargent

3 Hessian modes will be used to form the next step

Hessian Eigenvalues:

-0.177469 0.279946 1.171011

Transition State Search -- Taking P-RFO Step

Searching for Lambda that Maximizes Along the Lowest mode

■ Fig. 10-3  
(Continued)

Value Taken      Lambda =    0.00000027  
 Searching for Lambda that Minimizes Along All other modes  
 Value Taken      Lambda =  -0.00000018  
 Step Taken.      Stepsize is  0.001445

	Maximum	Tolerance	Cnvgd?
Gradient	0.000343	0.000300	NO
Displacement	0.001440	0.000300	NO
Energy change	-0.000002	0.000001	NO

\*\* GEOMETRY OPTIMIZATION IN DELOCALIZED INTERNAL COORDINATES \*\*

Searching for a Transition State

Optimization Cycle:    6

Coordinates (Angstroms)			
ATOM	X	Y	Z
1 c	-0.341598	0.551098	0.000000
2 n	-0.417301	-0.638152	0.000000
3 h	0.758898	0.087054	0.000000

Point Group: Cs      Number of degrees of freedom:    3

Energy is            -93.342899294

Cartesian Forces (au)			
ATOM	X	Y	Z
1 c	0.0000015	0.0000201	0.0000000
2 n	-0.0000112	-0.0000468	0.0000000
3 h	0.0000097	0.0000043	0.0000000

Iterative generation of Internal Gradient

Cycle:    1    Maximum deviation:    0.00000053    RMS deviation:    0.00000036  
 Cycle:    2    Maximum deviation:    0.00000000    RMS deviation:    0.00000000

Gradient converged in    2 cycles

Hessian Updated using Powell/Murtagh-Sargent Update

Mixing factors:        0.600156 Powell  
                           0.399844 Murtagh-Sargent

3 Hessian modes will be used to form the next step

Hessian Eigenvalues:

-0.188567      0.275416      1.153882

■ Fig. 10-3  
 (Continued)

```

Transition State Search -- Taking P-RFO Step
Searching for Lambda that Maximizes Along the Lowest mode
Value Taken   Lambda =   0.00000000
Searching for Lambda that Minimizes Along All other modes
Value Taken   Lambda =   0.00000000
Step Taken.   Stepsize is  0.000133

```

```

Parameter Values and Displacements in Internal Coordinates
Coordinate   Current Value   Gradient   Displacement   New Value
    1             2.021093     -0.000032   -0.000069     2.021024
    2             0.137423     -0.000025   -0.000037     0.137386
    3            -2.754498      0.000023   -0.000108    -2.754606

                                Maximum   Tolerance   Cnvgd?
Gradient                0.000032    0.000300    YES
Displacement            0.000108    0.000300    YES
Energy change           0.000000    0.000001    YES

```

■ Fig. 10-3

PQS output for the HCN ↔ HNC Transition State Search

The output for a transition state search is of course similar to that for a minimization. Quantities such as the Cartesian geometry, the SCF energy, the forces, parameter values, and displacements are common to both TS searches and minimizations and are printed out in the same way. The first difference occurs in the treatment of the starting Hessian: for the indole minimization (● Fig. 10-2) a default Hessian, diagonal in the underlying space of primitive internals, is used whereas the TS search started with a full, albeit approximate, Cartesian Hessian which needs to be transformed into internal coordinates. This transformation is done once only, on the first optimization cycle, as thereafter the Hessian will be updated.

Note the comment printed on cycle 1 that the Hessian transformation does not include the derivative of the **B**-matrix. The **B**-matrix (Wilson et al. 1955) formally relates a displacement in internal coordinates (*q*) to one in Cartesian coordinates (*X*),  $\Delta q = B\Delta X$ , and it turns out that a full transformation of the Hessian to internal coordinates requires the derivative of the **B**-matrix; the precise equation is Pulay (1977):

$$\mathbf{H}^{\text{int}} = \mathbf{B}^{\text{inv}} \left( \mathbf{H}^{\text{cart}} - \mathbf{g}^{\text{int}} \frac{d\mathbf{B}}{d\mathbf{X}} \right) (\mathbf{B}^{\text{inv}})^{\text{T}}, \quad (10.24)$$

where

$$\mathbf{B}^{\text{inv}} = (\mathbf{B}\mathbf{B}^{\text{T}})^{-1}\mathbf{B}, \quad (10.25)$$

and a superscript <sup>T</sup> represents a matrix transpose.

If you require an *exact* transformation of all quantities from Cartesian to internal coordinates, then the  $d\mathbf{B}/d\mathbf{X}$  term must be included; however it is usually advantageous to leave it

out as its inclusion often changes the Hessian eigenvalue structure. In general, Cartesian Hessian matrices with a known eigenvalue structure will retain that structure if the  $d\mathbf{B}/d\mathbf{X}$  term is omitted; this is far from guaranteed when it is included. When starting off a geometry optimization (either a minimization or a TS search) using an optimized geometry and starting Hessian obtained from a previous calculation at a lower level of theory – a common occurrence – then the  $d\mathbf{B}/d\mathbf{X}$  term should almost certainly be omitted. Note that for a Hessian transformation at a stationary point, the gradient is zero in any case and so the  $d\mathbf{B}/d\mathbf{X}$  term will also be zero. For the HCN  $\leftrightarrow$  HNC TS search the starting Hessian has the correct eigenvalue structure, i.e., one negative eigenvalue, so our initial geometry was at least reasonable.

The other major difference from the indole minimization is with the shift parameter(s). A TS search uses the P-RFO step, as opposed to the simple RFO step used for minimization (see [Eqs. 10.17–10.19](#)), and so there are *two* shift parameters instead of just one. As explained previously, one shift parameter maximizes along the TS mode (the eigenvector with the negative eigenvalue), while the other minimizes along all the other Hessian modes. The first shift parameter is positive while the other is negative. On the first cycle the computed step length is initially greater than the default maximum of 0.3 and so the step is scaled down (by 0.888690).

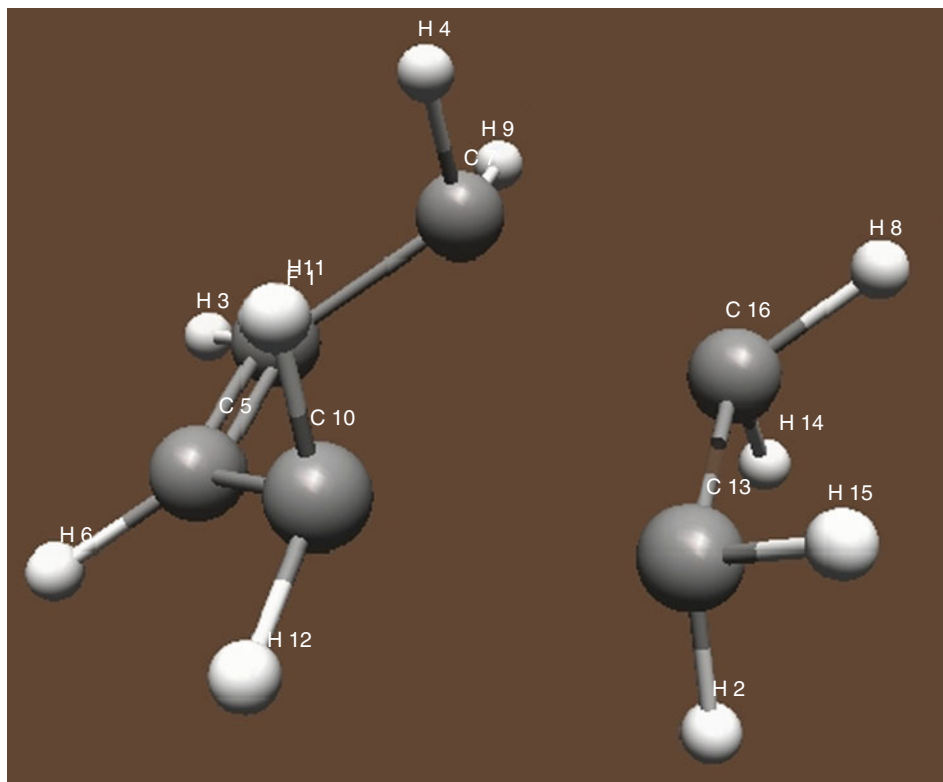
As with a minimization, on subsequent optimization cycles the gradient components and the step size should both decrease, tending to zero if the structure is converging. The two shift parameters,  $\lambda$ , also both tend to zero, one from above and the other from below. On the last cycle they are both zero to all eight decimal places printed out. The energy may increase or decrease, depending on whether the increase in energy from maximization along the TS mode is greater or smaller than the decrease in energy from minimization along all the other modes; the change in energy however should of course again tend to zero. (Overall a decrease in energy is the more likely, especially as the system gets larger, as the number of modes which are minimized becomes far greater than the single mode along which the energy is maximized.)

The Hessian update, at the beginning of each new optimization step, is done using the Bofill formula (Bofill 1994), which is the default for a TS search. This is a linear combination of the Powell (1971) and Murtagh and Sargent (1970) updates, and the two mixing coefficients are printed out. They vary from cycle to cycle, as can be seen ([Fig. 10-3](#)). The final TS geometry is well converged (in six cycles), with the three convergence criteria all well below their respective tolerances.

## Using Optimized Potential Scans in Transition State Searches

We turn now to a somewhat more complicated example, namely, a search for the transition state for the parent Diels–Alder reaction between *cis*-1,3-dibutadiene and ethylene to give cyclohexene. Here we use an optimized potential scan to obtain an initial approximation to the TS geometry. The starting geometry for the potential scan is shown in [Fig. 10-4](#). This was obtained by building cyclohexene using *PQSMol*, the graphical user interface for PQS (2010), and then stretching the appropriate C–C bonds (C<sub>10</sub>–C<sub>13</sub> and C<sub>7</sub>–C<sub>16</sub> as shown in [Fig. 10-4](#)) to separate off an ethylene fragment. The overall system symmetry ( $C_s$ ) was maintained using the symmetrization tools available in *PQSMol*. The  $\angle\text{HCH}$  angles in the ethylene fragment are likely to be too acute, but this will be rectified during the potential scan.

The C<sub>10</sub>–C<sub>13</sub> and C<sub>7</sub>–C<sub>16</sub> distances in the starting geometry (see [Fig. 10-4](#); the two distances are equivalent by symmetry) are 1.720 Å. What we are going to do is scan this distance



■ Fig. 10-4  
Starting structure for potential scan for Diels–Alder TS search

over a range of (increasing) values, at each scanned value optimizing all the remaining degrees of freedom. If the scanned variable(s) is a good approximation to the reaction coordinate, and if the value of the variable at the transition state geometry lies within the scanned range, then what we should see is a maximum in the energy somewhere along the scan. The (optimized) geometry at this energy maximum should be a very good approximation to the transition state.

An optimized potential scan is effectively a series of constrained geometry optimizations, with the constraint being the scanned variable. *PQS* has powerful algorithms for constrained optimization using the method of Lagrange multipliers (Baker 1992, 1997; Baker and Bergeron 1993). Because of the symmetry of the system, the scanned variable is not a single distance but rather a linear combination (with equal weights) of the  $C_{10}-C_{13}$  and  $C_7-C_{16}$  distances. The requested linear combination is normalized by the program and so the actual parameter scanned is  $\frac{1}{\sqrt{2}}[(r_{C_{10}-C_{13}}) + (r_{C_7-C_{16}})]$ . The potential energy scan module in *PQS* is capable of scanning any linear combination of primitive internal coordinates selected by the user.

The optimized energies at  $C_{10}-C_{13}$  and  $C_7-C_{16}$  distances from 1.720 Å to about 2.65 Å are shown in [Table 10-2](#). Note that, although the final level of theory used in this chapter for

■ Table 10-2

Optimized B3LYP/3-21G energies ( $E_n$ ) for the Diels–Alder Potential Scan at combined scan distances (in bohr) from 6.50 to 10.00 in steps of 0.25

Current value:	6.5000	Energy is	-233.352945649
Current value:	6.7500	Energy is	-233.341556134
Current value:	7.0000	Energy is	-233.328803153
Current value:	7.2500	Energy is	-233.315693812
Current value:	7.5000	Energy is	-233.303165136
Current value:	7.7500	Energy is	-233.292127679
Current value:	8.0000	Energy is	-233.283459373
Current value:	8.2500	Energy is	-233.277798713
Current value:	8.5000	Energy is	-233.275148592
Current value:	8.7500	Energy is	-233.274846534
Current value:	9.0000	Energy is	-233.276044729
Current value:	9.2500	Energy is	-233.278051315
Current value:	9.5000	Energy is	-233.280392073
Current value:	9.7500	Energy is	-233.282767273
Current value:	10.0000	Energy is	-233.285004883

all examples given is B3LYP/6-31G\*, the scan was actually carried out using the smaller 3-21G (Binkley et al. 1980) basis set. This is simply to save computer time. I expect the B3LYP/3-21G energy surface to be very similar to the B3LYP/6-31G\* one in this system, and since we are using the optimized scan to obtain a good, but still approximate, starting geometry for the proper TS search, there is no point using the larger basis set for the scan.

As can be seen in [Table 10-2](#), there is a clear energy maximum at a parameter value somewhere around 8.75. The parameter printed out is the sum of the two scanned C–C distances (unnormalized) given in atomic units (bohr); the maximum is equivalent to a C–C distance of 2.315 Å. During the scan, the first energy (from the starting geometry) took the most optimization cycles (12) to converge; thereafter each subsequent point typically converged in five to seven steps. Note that if the scanned range is insufficient to locate the maximum, it can simply be extended. For example, if the initial scan only went as far as 8.00 bohr (for the combined C–C distances), then it can be repeated for distances greater than this starting from the last optimized geometry found. That the scan needs to go to greater C–C distances is clear from the energy, which is increasing over the initial scan range; if it had been decreasing then one would need to go to shorter C–C distances.

The full B3LYP/6-31G\* TS search commenced using the optimized geometry at the scan maximum with a full Hessian matrix computed at this geometry using the 3-21G basis (the same basis as used in the scan). Not surprisingly this starting Hessian had the desired one negative eigenvalue, and the search converged in just four optimization cycles, indicating just how good the geometry resulting from the scan was. A full vibrational analysis at the B3LYP/6-31G\* level on the converged transition state structure indicated that it was indeed a genuine TS. The C<sub>10</sub>–C<sub>13</sub> and C<sub>7</sub>–C<sub>16</sub> distances in the final TS were 2.272 Å, very close to those in the structure at the scan maximum.

## Comparison of Experimental and Theoretical Geometries

Before turning to the second part of this chapter, the computational simulation of vibrational spectra, I want to make a few comments on the accuracy of theoretically computed geometries. Direct comparison with reliable experimental data shows that theoretical geometries are now really very accurate indeed, particularly for “normal” organic molecules. The level of theory used here, B3LYP/6-31G\*, is typically accurate for, say, bond angles to within a few degrees and bond lengths to within 0.02 Å at worst, and if any experimental bond distance differs by much more than this from the theoretical value, it is more likely in my opinion for experiment to be in error rather than theory. One needs to bear in mind that none of the experimental methods commonly used in molecular structure determination, X-ray crystallography, microwave spectroscopy, nuclear magnetic resonance (NMR) etc., measure a bond distance directly; rather some kind of spectrum (or pattern) is obtained which has to be interpreted, and bond distances are extracted indirectly from this. It was fairly typical in the early 1970s (and even into the 1980s) for X-ray diffraction structures to be published, as a set of Cartesian coordinates, which resulted in quite ridiculous bond distances involving hydrogen. This was due principally of course to the difficulty in locating hydrogen atoms because of the much lower electron density surrounding hydrogen nuclei compared to heavier elements, and the fact that this density could easily be displaced in bonds involving more electronegative atoms. From the mid-1970s onward it became increasingly more common for theoretically computed bond distances involving hydrogen to be used in the fitting of X-ray data; this also resulted in much better agreement with heavy atom bond distances as well (Schäfer 1983).

Another factor to be considered is that theory and experiment do not quite measure the same thing. Within the Born–Oppenheimer approximation (Born and Oppenheimer 1927; Wikipedia 2010), theory ideally determines the geometry at the bottom of the well, at the energy minimum, whereas this geometry is inaccessible to experiment due to the existence of zero-point vibrational energy. Such differences, however, are usually minor.

► **Table 10-3** provides a comparison between optimized B3LYP/6-31G\* and experimental geometrical parameters for a number of small, organic molecules. These results were taken from two papers published in the mid-1990s; a DFT study of some organic reactions (Baker et al. 1985) and a systematic DFT study of fluorination in methane, ethane, and ethylene (Muir and Baker 1996). The focus was mainly on the energetics, but many computed and experimental geometrical parameters were provided. The theoretical approaches did not include B3LYP, using instead a related functional (Becke’s original ACM (Becke 1993; see also Hertwig and Koch 1997), better known today as B3PW91), but I have reoptimized all the geometries at the B3LYP/6-31G\* level for compatibility with this chapter.

As can be seen from ► **Table 10-3**, the agreement between the computed and experimental geometrical parameters is excellent. The mean average deviation between the B3LYP/6-31G\* and experimental bond lengths is just 0.006 Å, with a maximum error (for the C–N triple bond in HCN) of 0.022 Å. The mean average deviation for bond angles is only 0.8°. Such results are typical.

Included in ► **Table 10-3** is the series of fluorine-substituted methanes: mono-, di-, tri-, and tetra-fluoromethane. These compounds exhibit a well-known substituent effect (the geminal effect) of decreasing C–F bond length (and increasing bond strength) with increasing fluorine substitution on the same carbon atom. This effect of fluorine (not seen with any of the other halogens) has been known for a long time (although there are still arguments about the explanation for it) and is very accurately reproduced by the theoretical calculations.



■ Table 10-3

Optimized B3LYP/6-31G\* and experimental geometrical parameters for a number of small organic molecules

Parameter	B3LYP	Experiment	Parameter	B3LYP	Experiment
Vinyl alcohol (CH <sub>2</sub> =CHOH)			trans-1,1,2,2-tetrafluoroethane (CHF <sub>2</sub> CHF <sub>2</sub> )		
rC–O	1.363	1.369	rC–C	1.524	1.518
rC=C	1.334	1.335	rC–F	1.360	1.350
rO–H	0.972	0.962	rC–H	1.095	1.098
rC–H	1.086	1.080	∠CCF	108.8	108.2
∠CCO	127.2	126.0	∠CCH	111.8	110.3
∠COH	108.7	108.5	∠FCF	108.8	107.3
Acetaldehyde (CH <sub>2</sub> CHO)			Carbonyl fluoride (CF <sub>2</sub> O)		
rC=O	1.211	1.210	rC=O	1.180	1.17
rC–C	1.508	1.515	rC–F	1.322	1.32
rC–H	1.114	1.128	∠FCF	107.8	112.5
∠CCO	124.7	124.1	Hydrogen fluoride (HF)		
trans-butadiene (CH <sub>2</sub> =CHCH=CH <sub>2</sub> )			rH–F	0.934	0.917
rC=C	1.341	1.349	Hydrogen (H <sub>2</sub> )		
rC–C	1.458	1.467	rH–H	0.743	0.741
∠C=CH	119.4	120.9	Water (H <sub>2</sub> O)		
∠CCC	124.3	124.4	rO–H	0.969	0.958
Ethylene (CH <sub>2</sub> =CH <sub>2</sub> )			∠HOH	103.6	104.5
rC=C	1.331	1.339	Formaldehyde (CH <sub>2</sub> O)		
rC–H	1.087	1.087	rC=O	1.206	1.208
∠CCH	121.9	121.3	rC–H	1.110	1.116
Cyclohexene (C <sub>6</sub> H <sub>10</sub> )			∠HCH	115.2	116.5
rC=C	1.337	1.334	Acetylene (C <sub>2</sub> H <sub>2</sub> )		
rC–C	1.510	1.50	rC–C	1.205	1.203
rC–C	1.537	1.52	rC–H	1.067	1.060
rC–C	1.535	1.54	Ethane (CH <sub>3</sub> CH <sub>3</sub> )		
∠CC=C	123.5	123.4	rC–C	1.531	1.535
∠CCC	112.0	112.0	rC–H	1.096	1.094
∠CCC	110.9	110.9	∠CCH	111.4	111.2
Tetrazine (C <sub>2</sub> N <sub>4</sub> H <sub>2</sub> )			Fluoromethane (CH <sub>3</sub> F)		
rN–N	1.326	1.321	rC–F	1.383	1.382
rC–N	1.339	1.334	rC–H	1.096	1.095
∠NCH	126.6	127.4	∠HCH	109.3	110.4
Hydrogen cyanide (HCN)			Difluoromethane (CH <sub>2</sub> F <sub>2</sub> )		
rC–N	1.157	1.135	rC–F	1.361	1.357
rC–H	1.070	1.066	rC–H	1.096	1.093
Nitrogen (N <sub>2</sub> )			∠HCH	112.2	113.7
rN–N	1.105	1.098	∠FCF	109.2	108.3

(Continued)

■ Table 10-3  
(Continued)

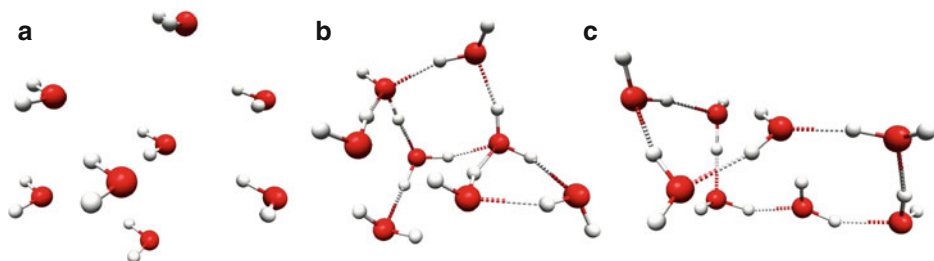
Parameter	B3LYP	Experiment	Parameter	B3LYP	Experiment
Cyclobutene (C <sub>4</sub> H <sub>6</sub> )			Trifluoromethane (CHF <sub>3</sub> )		
rC=C	1.340	1.342	rC-F	1.342	1.333
rC-C	1.519	1.517	rC-H	1.093	1.098
rC-C	1.573	1.566	∠FCF	108.6	108.8
∠CCC	86.5	85.5	Tetrafluoromethane (CF <sub>4</sub> )		
∠C=CC	94.4	94.2	rC-F	1.329	1.323

## Geometry Optimization of Molecular Clusters

The situation at the time of writing is that molecular structures for stable or metastable minima are readily located theoretically using powerful optimization algorithms usually carried out in natural, delocalized or redundant internal coordinates. The resulting structural parameters (computed using B3LYP or better with a decent basis set) are typically in excellent agreement with experimental results where these are available. The location of transition states can be more difficult, but perseverance usually brings its reward. Theoretical calculations are essentially the only means for providing structural data on transition states as they are extremely difficult to study experimentally.

One area where standard natural or delocalized internal coordinates are not the best choice is for optimizing the geometry of molecular clusters. For larger clusters the problem of global versus local minimization becomes an issue, but even for relatively small clusters (containing half-a-dozen or so molecules) deriving a set of coordinates suitable for an efficient optimization from stretches, bends, and torsions alone usually results in poor optimization performance. One reason for this is that there are really two different types of forces involved in determining the structure of a molecular cluster: the normal, fairly strong intramolecular forces that determine the geometry of each individual molecule, and the weak intermolecular forces that determine the arrangement of each molecule relative to the others. The latter are best described in terms of scaled inverse distance coordinates (*not* standard distances) and an efficient algorithm which uses normal primitive internal coordinates to describe the geometry of each molecule in the cluster, and scaled inverse distances (with a cutoff) to describe the relative position of the cluster molecules with respect to each other (Baker and Pulay 2000) is available in PQS. The resulting set of coordinates, which are linear combinations of standard primitive internals and scaled inverse distances, are known as cluster coordinates.

Examples of geometry optimization of some small molecular clusters are shown in ▶ [Table 10-4](#). Optimization performance using cluster coordinates (1/R with a 5 Å cutoff) is compared with Cartesian coordinates. A modest level of theory was used (Hartree-Fock with the 3-21G basis set) and all optimizations were started with a unit Hessian matrix. In most cases the starting geometry was poor, and very far from the final converged structure. No comparisons with natural or delocalized internal coordinates are included in ▶ [Table 10-4](#); with such poor starting geometries this is usually a waste of time as the large changes that occur in the relative positions of molecules in the cluster often result in individual bond angles, as defined, exceeding 180° causing problems with the various transformations, particularly the Cartesian



■ Fig. 10-5

Starting and final structures for optimization of the  $(\text{H}_2\text{O})_8$  cluster from [Table 10-4](#): (a) starting geometry, (b) final geometry cluster coords, (c) final geometry Cartesians

backtransformation. This is yet another reason why standard internal coordinates are inappropriate for optimizing the geometry of molecular clusters. This is not a problem with inverse distance (or simple distance) coordinates as these are defined essentially from zero to infinity.

As shown in [Table 10-4](#), cluster coordinates typically converge much faster than Cartesians (on average for the seven clusters shown by a factor of almost 5) and usually – but not always – to lower energy structures. (Five out of the seven converged to lower energies than the corresponding Cartesian optimizations, two to higher.) The starting and final geometries are shown for the eight water molecule cluster in [Fig. 10-5](#).

## Geometry Optimization in the Presence of External Forces

I want to end this section by briefly mentioning a simple but relatively new technique which has proven to be very useful in deriving potentially new molecular structures. It was originally developed to study the geometrical changes inferred in atomic force microscopy and similar experiments (known collectively as mechano-chemistry) (Beyer and Clausen-Schaumann 2005), but can be applied as a general optimization tool which also has potential for the location

■ Table 10-4

Comparison of the performance of cluster coordinates and Cartesian coordinates for the optimization of some small molecular clusters

Clusters	Cluster coordinates		Cartesian coordinates	
	Cycles	Energy	Cycles	Energy
4 × benzene	52	−917.687877	273	−917.680357
6 × DMSO	124	−3,292.233057	660	−3,292.192089
formamide + 6 × water	75	−621.674713	222	−621.687307
6 × methanol	39	−686.489506	301	−686.492821
5 × pyridine	108	−1,226.595255	479	−1,226.587376
3 × THF	65	−689.117483	348	−689.113449
8 × water	69	−604.913202	331	−604.911548
Average cycles	76		373	

of transition states. This is geometry optimization in the presence of external forces (Wolinski and Baker 2009) known as enforced geometry optimization (EGO). The force is applied along a straight line joining any two atoms in the molecule under study, either to push the two atoms together or to pull them apart. Whatever force is applied to one atom of the pair, an equal and opposite force is applied to the other. This ensures that there is no tendency for the molecule to translate or rotate; in essence it remains in place under simulated pressure. Forces can be applied between as many pairs of atoms as desired, although calculations to date have typically involved only a single pair of atoms.

If you are applying an external force to, say, push two atoms together in a stable molecule there will be a tendency for a bond to form between the two atoms. If the applied force is insufficient to form a bond (or if a bond won't form anyway), there will be some minor geometrical changes as the system endeavors to compensate for the excess force. If the applied force is sufficient, then what you should see is the energy rise as the two atoms are pushed together, then fall as the bond forms and additional molecular rearrangement occurs. The final "optimized" geometry will still involve a structural arrangement under considerable strain, but if this structure is allowed to relax (by reoptimizing with the additional force removed) it could well converge to a new, stable geometry, different from the initial structure. If it does so, then the maximum energy structure found as the two atoms were pushed together is often a reasonable estimate for the transition state joining the original and the new structure.

The method as described above has been used to find seven previously unknown geometrical isomers of  $C_{10}N_2H_8$ , starting from the ground-state geometry of *cis*-azobenzene, at the B3LYP/6-31G\* level by pushing together various pairs of atoms, one from each of the two benzene rings (Wolinski and Baker 2009). All of the new structures were classified by vibrational analysis, and all were found to be minima. Transition states between each of the new structures and *cis*-azobenzene were also located and characterized. Additional calculations were carried out at MP2/6-311G\*\* to ensure that the energetics remained stable. The technique overall shows considerable promise for the discovery of new chemistry and new chemical structures.

## Molecular Vibrations

---

A molecular system containing  $N$  atoms nominally has  $3N$  degrees of freedom. In Cartesian coordinates, one can consider each degree of freedom as separate  $X$ ,  $Y$ , or  $Z$  displacements of each atom about its equilibrium position. This atomic motion can be induced for example by heat or by interaction with light or other electromagnetic radiation. Because the atoms in a molecule are connected by chemical bonds, the various atomic motions are coupled. In a classical treatment, it turns out that three of these motions involve overall translation of the system as a whole (along the  $X$ ,  $Y$ , and  $Z$  directions of a standard Cartesian axis system), and three of them involve overall rotation of the system as a whole (about the same axes). These are known as rigid-body motions. The Cartesian axes pass through (they have their origin at) the center of mass of the system and the  $X$ ,  $Y$ , and  $Z$  axes coincide with the principal axes of inertia of the undistorted molecule. Under these rigid-body motions the positions of the atoms in the molecule relative to each other remain unchanged, and so the potential energy of the system in a vacuum is also unchanged. The remaining  $3N - 6$  coupled motions, which do affect the relative atomic positions and hence the potential energy, are classified as molecular vibrations.

(Note that a linear molecule has  $3N - 5$  vibrations, not  $3N - 6$ , as one of the rotations – that about its own axis – cannot be observed, and is effectively ignored.)

To a reasonable approximation, at least for small displacements, the vibrations in a polyatomic molecule can be described as a kind of simple harmonic motion. This is essentially equivalent to considering a chemical bond between two atoms as a weightless spring that obeys Hooke's law (i.e., the force is proportional to the displacement). The simplest vibration is that in a diatomic molecule, and we can refer back to the potential energy curve for  $\text{He}_2^{2+}$  (► Fig. 10-1) as an example. At the minimum, near the bottom of the well, the potential energy curve is indeed parabolic to a very good approximation.

The force/displacement equation for a diatomic molecule obeying Hooke's law is

$$F = -kq, \quad (10.26)$$

where  $F$  is the applied force,  $k$  is the so-called force constant, and  $q$  is the displacement from equilibrium. The negative sign indicates that the force exerted by the spring is in a direction opposite to that of the displacement. The potential energy stored in the spring (the integral of force over distance) is

$$E = \frac{1}{2}kq^2. \quad (10.27)$$

By Newton's second law of motion, the force can also be given by mass times acceleration

$$F = m \frac{d^2q}{dt^2}. \quad (10.28)$$

The two forces in ► Eqs. 10.26 and ► 10.28 are one and the same, and so the differential equation relating displacement,  $q$ , with time,  $t$ , for the harmonic oscillator is

$$m \frac{d^2q}{dt^2} + kq = 0. \quad (10.29)$$

The solution to ► Eq. 10.29 is

$$q(t) = A \cos(2\pi\nu t); \quad \nu = \frac{1}{2\pi} \sqrt{\frac{k}{m}}, \quad (10.30)$$

where  $A$  is the amplitude of the vibrational coordinate  $q$  and  $\nu$  is the fundamental frequency of the vibration. The "mass,"  $m$ , is actually the so-called reduced mass,  $\mu$ , which for a diatomic molecule A–B, with atomic masses  $m_A$  and  $m_B$ , respectively, is given by

$$\frac{1}{\mu} = \frac{1}{m_A} + \frac{1}{m_B}. \quad (10.31)$$

Using the reduced mass ensures that the center of mass of A–B remains unchanged during the vibrational motion.

From ► Eq. 10.27 the force constant,  $k$ , is given by

$$k = \frac{d^2E}{dq^2}. \quad (10.32)$$

The force constant in a one-dimensional system (a system with a single degree of vibrational freedom) is thus directly related to the curvature of the potential energy surface, i.e., the shape of the well. From the force constant, one can directly determine the fundamental frequency (via ► Eq. 10.30). In a polyatomic molecule the single  $d^2E/dq^2$  term is replaced by the Hessian

matrix,  $\mathbf{H}$  (often called the force constant matrix). In Cartesian coordinates this is the same Hessian matrix introduced in [Eq. 10.4](#) when discussing the Newton–Raphson step during a geometry optimization, and a classical treatment of molecular vibrations and the Newton–Raphson step both assume the same thing about the potential energy surface, namely that it is quadratic. The only major difference is that a vibrational analysis involves the atomic masses, whereas the potential energy surface is independent of mass. The fundamental vibrational frequencies for a polyatomic molecule can be extracted from the mass-weighted Hessian matrix, and the normal modes (the coupled motion of the atoms during the vibration) can be obtained by a suitable treatment of the Hessian eigenvectors. The precise steps involved are as follows:

1. Mass-weight the Cartesian Hessian matrix.

$$\mathbf{H}_{ij}^{\text{MW}} = \frac{\mathbf{H}_{ij}}{\sqrt{m_i m_j}}. \quad (10.33)$$

2. Project out the translations and rotations from the mass-weighted Hessian.

As discussed briefly above, the translational and rotational degrees of freedom can be separated out from the vibrations for a rigid body. This requires shifting the origin of the coordinate system to the center of mass, determining the principal moments and the rotation generators, setting up orthogonal coordinate vectors for translation and rotation about the principal axes of inertia, setting up a projection matrix  $\mathbf{P}$  from these vectors and using it to “remove” the translations and rotations from the Hessian matrix, leaving only the vibrational modes.

If the orthogonal set of vectors representing translation and rotation (there are six of them, each of length  $3N$ , where  $N$  is the number of atoms) are given by  $\mathbf{R}$ , then the projection matrix  $\mathbf{P}$  is formed by

$$\mathbf{P}_{ij} (i \neq j) = - \sum_k \mathbf{R}_{ik} \mathbf{R}_{jk}; \quad \mathbf{P}_{ii} = 1 - \sum_k \mathbf{R}_{ik} \mathbf{R}_{ik}, \quad (10.34)$$

and the projected Hessian is given by

$$\mathbf{H}^{\text{P}} = \mathbf{P} \mathbf{H}^{\text{MW}} \mathbf{P}^{\text{T}}. \quad (10.35)$$

3. Diagonalize the projected, mass-weighted Hessian matrix.

The effect of the projection leaves the eigenvectors of the Hessian corresponding to translations and rotations with exactly zero eigenvalues (or at least zero within numerical round-off error), allowing the  $3N - 6$  nonzero vibrations to be separated out. These are converted to  $\text{cm}^{-1}$  prior to print out, and the corresponding eigenvectors are mass-weighted and normalized to become the normal modes. The mass-weighting uses isotopically averaged atomic masses based on the average isotopic abundance for each atom.

At first sight it might be surprising that the Hessian matrix, which after all in *ab initio* molecular orbital theory is inherently quantum mechanical, is amenable to a purely classical treatment. This is because the Born–Oppenheimer approximation (Born and Oppenheimer [1927](#); Wikipedia [2010](#)) allows for a pretty good separation of the electronic and nuclear motion, allowing the latter to be treated classically. A quantum mechanical description of the simple harmonic oscillator leads to quantized energy levels given by

$$E_n = h\nu \left( n + \frac{1}{2} \right); \quad \nu = \frac{1}{2\pi} \sqrt{\frac{k}{m}}, \quad (10.36)$$

where the fundamental vibrational frequency,  $\nu$ , is exactly the same as in a classical description (Eq. 10.30). The quantum number,  $n$ , takes integer values 0, 1, 2, ... and so even in the vibrational ground-state ( $n = 0$ ) there is a residual energy,  $\frac{1}{2}h\nu$ , known as the zero-point energy. This is a fundamental quantum mechanical property of all oscillators at the absolute zero of temperature (Einstein and Stern 1913).

A molecular vibration is excited when the system absorbs a quantum of energy,  $h\nu$ , corresponding to the vibrational frequency,  $\nu$ , of one of its normal modes. This is commonly accomplished under standard conditions by interaction with infrared (IR) radiation. An IR spectrum can be recorded by passing a beam of infrared light covering a range of frequencies through the sample. This can be done by using a monochromatic beam which changes in wavelength over time, or by using a Fourier Transform instrument which effectively measures all wavelengths at once. From this a transmission (or absorbance) spectrum can be produced showing at which frequencies/wavelengths the sample absorbs.

Not all normal modes are IR active, i.e., result in the absorption of energy at the normal mode frequency. In order for a normal mode to be IR active, its motion must result in a change in the dipole moment of the vibrating molecule. For example, the totally symmetric C–H stretch in methane (in which all four C–H bonds are vibrating in the same way simultaneously) does not change the molecular dipole moment (which is zero in any case), and so this mode is IR inactive. Change one of the hydrogen atoms for a fluorine, however, and it is a different picture. In general, molecules with a permanent dipole moment in their ground-state geometries give rise to more intense signals in the IR spectrum (i.e., greater absorbance) than molecules in which a dipole moment is induced by the vibration itself.

Vibrational excitation can occur, and usually does, in conjunction with rotational excitations, resulting in vibration-rotation spectra. For straightforward IR vibrational spectra, the simultaneous rotational excitations result in broadening of the vibrational bands. Bands are additionally broadened if two (or more) normal modes have frequencies close to one another, as well as by instrument resolution and other experimental artifacts. Additional bands, other than those caused by vibrational fundamentals, can arise in the spectrum by the absorption of two or more quanta of energy simultaneously, giving rise to combination and overtone bands, and by further excitations from already vibrationally excited states which give rise to what are called hot bands.

It is worth noting at this point that although our analysis of vibrational motion derives from consideration of the simple harmonic oscillator, many common features observed in vibrational spectra are present precisely because the potential energy surface is not harmonic. For example, transitions between vibrational energy levels in the quantum harmonic oscillator formally allow the quantum number,  $n$ , to change only by 1 ( $\Delta n = \pm 1$ ). As the vibrational energy levels are equally spaced (see Eq. 10.36), this means that light of only one frequency can be absorbed, that of the vibrational fundamental for each normal mode, and there are no overtone bands. The  $\Delta n = \pm 1$  selection rule does not apply to an anharmonic oscillator and the observation of overtones is only possible because vibrations are anharmonic. A further consequence of anharmonicity is that the spacing between the vibrational energy levels decreases with increasing quantum number (eventually reaching a continuum allowing for vibrational dissociation) which results in the frequency of the first overtone being slightly less than twice the frequency of the vibrational fundamental.

IR spectroscopy is a very important method in molecular structure determination. Even though the normal modes depend on the whole molecule, certain structural motifs have very similar motions regardless of how many atoms the molecule contains. For example, virtually

all molecules containing a carbonyl group give rise to an intense (because of the bond polarity) signal in the IR spectrum around  $1,800\text{ cm}^{-1}$  due to excitation of the C=O stretch, thus allowing for the identification of this group. Theory can not only determine the fundamental frequencies and normal modes of a molecule, but by computing the dipole moment derivatives, it can reliably estimate the resulting band intensities as well, enabling the IR spectrum for the vibrational fundamentals to be predicted a priori.

Another technique used in vibrational spectroscopy is Raman scattering (Raman and Krishnan 1928). This normally uses visible light, which is typically scattered by the molecule. Most of the light is scattered elastically at the same frequency as the initial radiation (Rayleigh scattering), but a small amount interacts with the system, excites a vibrational mode, and is scattered inelastically at a lower frequency. If the system is already in a vibrationally excited state, then the scattered radiation can have a higher frequency than the initial radiation. These are known as Stokes and anti-Stokes Raman scattering, respectively. Raman scattering constitutes only a very small component of the total scattered radiation (only about one part in  $10^7$ ) and a major difficulty in Raman spectroscopy is to separate out the weak, inelastic scattering from the intense Rayleigh scattered light. The frequency difference corresponds to, e.g., the frequency of one of the molecules normal modes.

As with IR spectroscopy, not all of a molecules vibrations are active in the Raman spectrum. In order for a vibrational mode to be Raman active, the motion must result in a change in the polarizability of the electron charge cloud surrounding the molecule. The degree of change determines the intensity of the band. Whether or not a band is Raman, or indeed IR, active can be determined in advance by a symmetry analysis of the normal modes. In molecules with no symmetry, all bands are potentially both IR and Raman active, but if the molecule has symmetry then vibrations of certain symmetry types may be inactive in either the Raman or the IR spectrum, or both. For example, in a molecule with a center of symmetry (such as trans-1,2-dichloroethylene; point group  $C_{2h}$ ), the symmetric modes ( $a_g$  and  $b_g$  for  $C_{2h}$ ) are Raman active but IR inactive, and vice versa for the unsymmetric modes. The intensity of a Raman band can be determined theoretically by calculating the molecule's polarizability derivatives.

The polarization of Raman scattered light also contains useful structural information. This property can be measured by using plane polarized light and a polarization analyzer. Spectra recorded with the analyzer set both parallel and perpendicular to the excitation plane can be used to calculate the depolarization ratio of each vibrational mode. This provides insight into molecular orientation and the symmetry of the vibrational modes, as well as information about molecular shape. It is often used to determine macromolecular orientation in crystal lattices, liquid crystals, or polymer samples.

Yet another spectroscopic method that can be used to help determine molecular structure is vibrational circular dichroism (VCD). This technique detects differences in attenuation of left and right circularly polarized light passing through the sample. VCD is sensitive to the mutual orientation of groups of atoms in a molecule and provides three-dimensional structural information. It is especially important in the study of chirality and molecular conformation. Only chiral molecules have a VCD spectrum. In particular, molecules that have either a plane of symmetry or a center of symmetry are VCD inactive.

The differential absorption of polarized light in vibrational circular dichroism is proportional to the rotational strength, a quantity that depends on both the electric and magnetic dipole transition moments. For a vibrational transition from the ground ( $g$ ) to an excited vibrational state ( $e$ ), this is given by

$$R(g \rightarrow e) = \text{Im}(\langle g | \mu_{\text{el}} | e \rangle \langle e | \mu_{\text{mag}} | g \rangle), \quad (10.37)$$



where  $\mu_{el}$  and  $\mu_{mag}$  are the electric and magnetic dipole operators, respectively. These quantities can be calculated theoretically, enabling VCD intensities to be computed. For details see the review by Stephens and Lowe (1985). Modern computational approaches use so-called gauge-invariant atomic orbitals (GIAOs) for the magnetic component (Bak et al. 1995) (as does PQS) which are particularly efficient, and the computation of VCD rotational strengths as part of a vibrational analysis is now almost routine.

IR, Raman, and VCD spectroscopy all excite the same vibrational fundamentals. The respective vibrational spectra are different because the mechanism by which light is absorbed is different in each case, the amount of absorption depending on changes in the dipole moment, the polarizability and the rotational strength, respectively. All these quantities are amenable to computation, and modern *ab initio* theory can reliably predict the frequencies of a molecule's vibrational fundamentals as well as the intensity of the signal in IR, Raman, and VCD spectra. The latter in particular are greatly assisted by electronic structure calculations; comparison of experimental and theoretical VCD spectra enable absolute molecular conformations to be determined.

## 1,2-Dichloroethane: An Illustrative Example

► *Figure 10-6* shows the PQS output for a full vibrational and thermodynamic analysis of *trans (anti)* 1,2-dichloroethane following a geometry optimization under  $C_{2h}$  symmetry at the B3LYP/6-31G\* level of theory. It includes IR and Raman intensities obtained from the dipole moment and polarizability derivatives, respectively. (Because of its symmetry the system is not VCD active.) In PQS, dipole moment derivatives are computed analytically along with the Hessian matrix and atomic axial tensors (for VCD rotational strengths) (Bak et al. 1995) are computed in the same module that calculates NMR chemical shifts. Polarizability derivatives are obtained numerically by finite difference on the force (gradient) in the presence of a series of external electric fields. The number of applied fields varies with the molecular symmetry but requires a maximum of 12 separate single-point energy plus gradient calculations in the worst case (when the system is  $C_1$ ).

```
=====
Vibrational Frequency & Thermodynamics Module

Hessian read from file C2H4Cl2.hess

Translations and Rotations Projected Out of Hessian

Vibrational Frequencies in atomic units
0.000000   0.000000   0.000000   0.000000   0.000000   0.000000
0.023226   0.041718   0.057471   0.137739   0.146736   0.153218
0.199410   0.207432   0.225626   0.248960   0.255115   0.264838
0.295409   0.295559   0.606973   0.608510   0.617940   0.622129

There are 4 real representations:   ag   bg   au   bu
```

■ **Fig. 10-6**  
(Continued)

## \*\* VIBRATIONAL FREQUENCIES (CM\*\*-1) AND NORMAL MODES \*\*

Label:	1			2			3		
Symmetry:	au			bu			ag		
Frequency:	119.40			214.45			295.43		
IR Active:	YES			YES			NO		
IR Inten:	7.534			10.811			0.000		
dmux/dQ:	0.00000			-0.10225			0.00000		
dmuy/dQ:	0.00000			0.02513			0.00000		
dmuz/dQ:	0.08790			0.00000			0.00000		
Raman Active:	NO			NO			YES		
Raman Inten:	0.000			0.000			5.558		
Depolar:	0.000			0.000			0.384		
Rot.Strength:	0.654			0.635			0.000		
	X	Y	Z	X	Y	Z	X	Y	Z
c	0.000	0.000	0.301	-0.357	-0.019	0.000	0.023	0.223	0.000
cl	0.000	0.000	-0.125	0.144	0.001	0.000	-0.194	0.426	0.000
h	0.043	0.191	0.399	-0.409	0.090	0.011	0.050	-0.336	0.004
h	0.043	0.191	0.399	-0.409	0.090	0.011	-0.050	0.336	-0.004
h	-0.043	-0.191	0.399	-0.409	0.090	-0.011	-0.050	0.336	0.004
c	0.000	0.000	0.301	-0.357	-0.019	0.000	-0.023	-0.223	0.000
h	-0.043	-0.191	0.399	-0.409	0.090	-0.011	0.050	-0.336	-0.004
cl	0.000	0.000	-0.125	0.144	0.001	0.000	0.194	-0.426	0.000
Label:	4			5			6		
Symmetry:	bu			ag			au		
Frequency:	708.05			754.30			787.62		
IR Active:	YES			NO			YES		
IR Inten:	108.720			0.000			3.168		
dmux/dQ:	-0.06593			0.00000			0.00000		
dmuy/dQ:	0.32733			0.00000			0.00000		
dmuz/dQ:	0.00000			0.00000			0.05700		
Raman Active:	NO			YES			NO		
Raman Inten:	0.000			51.557			0.000		
Depolar:	0.000			0.305			0.000		
Rot.Strength:	-4.191			0.005			-0.313		
	X	Y	Z	X	Y	Z	X	Y	Z
c	-0.017	0.495	0.000	0.086	0.390	0.000	0.000	0.000	-0.065
cl	0.004	-0.187	0.000	-0.027	-0.101	0.000	0.000	0.000	0.009
h	0.031	0.329	-0.031	0.016	-0.403	0.050	0.422	0.123	0.234
h	0.031	0.328	-0.031	-0.017	0.403	-0.050	0.422	0.123	0.234
h	0.031	0.328	0.031	-0.016	0.403	0.050	-0.422	-0.123	0.234
c	-0.017	0.496	0.000	-0.086	-0.390	0.000	0.000	0.000	-0.065
h	0.031	0.328	0.031	0.017	-0.402	-0.050	-0.422	-0.123	0.234
cl	0.004	-0.187	0.000	0.027	0.101	0.000	0.000	0.000	0.009
Label:	7			8			9		

■ Fig. 10-6  
(Continued)

Symmetry:	bg			ag			au		
Frequency:	1025.07			1066.31			1159.83		
IR Active:	NO			NO			YES		
IR Inten:	0.000			0.000			1.739		
dmux/dQ:	0.00000			0.00000			0.00000		
dmuy/dQ:	0.00000			0.00000			0.00000		
dmuz/dQ:	0.00000			0.00000			-0.04223		
Raman Active:	YES			YES			NO		
Raman Inten:	10.492			6.766			0.000		
Depolar:	0.750			0.746			0.000		
Rot.Strength:	0.002			-0.001			2.024		
	X	Y	Z	X	Y	Z	X	Y	Z
c	0.000	0.000	-0.124	-0.371	0.060	0.000	0.000	0.000	0.035
cl	0.000	0.000	0.016	0.006	-0.008	0.000	0.000	0.000	-0.011
h	-0.170	-0.442	-0.135	0.415	-0.087	0.002	0.181	-0.465	-0.017
h	0.170	0.442	0.135	-0.415	0.087	-0.002	0.181	-0.465	-0.017
h	-0.170	-0.442	0.135	-0.414	0.087	0.002	-0.181	0.465	-0.017
c	0.000	0.000	0.124	0.371	-0.060	0.000	0.000	0.000	0.035
h	0.170	0.442	-0.135	0.414	-0.087	-0.002	-0.181	0.465	-0.017
cl	0.000	0.000	-0.016	-0.006	0.008	0.000	0.000	0.000	-0.011
Label:	10			11			12		
Symmetry:	bu			bg			ag		
Frequency:	1279.78			1311.42			1361.40		
IR Active:	YES			NO			NO		
IR Inten:	43.117			0.000			0.000		
dmux/dQ:	-0.01423			0.00000			0.00000		
dmuy/dQ:	-0.20980			0.00000			0.00000		
dmuz/dQ:	0.00000			0.00000			0.00000		
Raman Active:	NO			YES			YES		
Raman Inten:	0.000			11.740			11.310		
Depolar:	0.000			0.750			0.678		
Rot.Strength:	-13.415			-0.004			-0.002		
	X	Y	Z	X	Y	Z	X	Y	Z
c	0.056	-0.053	0.000	0.000	0.000	-0.082	-0.040	0.094	0.000
cl	-0.006	-0.007	0.000	0.000	0.000	-0.004	0.004	0.007	0.000
h	-0.222	0.444	0.008	-0.393	0.300	-0.045	-0.198	0.451	0.046
h	-0.222	0.444	0.008	0.393	-0.300	0.045	0.198	-0.451	-0.046
h	-0.222	0.444	-0.008	-0.393	0.300	0.045	0.198	-0.451	0.046
c	0.056	-0.053	0.000	0.000	0.000	0.082	0.040	-0.094	0.000
h	-0.222	0.444	-0.008	0.393	-0.300	-0.045	-0.198	0.451	-0.046
cl	-0.006	-0.007	0.000	0.000	0.000	0.004	-0.004	-0.007	0.000
Label:	13			14			15		
Symmetry:	ag			bu			ag		

■ Fig. 10-6  
(Continued)

Frequency:	1518.55			1519.32			3120.15		
IR Active:	NO			YES			NO		
IR Inten:	0.000			6.293			0.000		
dmux/dQ:	0.00000			-0.07728			0.00000		
dmuy/dQ:	0.00000			0.02192			0.00000		
dmuz/dQ:	0.00000			0.00000			0.00000		
Raman Active:	YES			NO			YES		
Raman Inten:	20.486			0.000			160.189		
Depolar:	0.743			0.000			0.085		
Rot.Strength:	-0.006			3.532			0.000		
	X	Y	Z	X	Y	Z	X	Y	Z
c	0.064	0.006	0.000	0.056	0.026	0.000	0.042	0.022	0.000
cl	0.000	0.002	0.000	0.001	0.002	0.000	0.000	0.000	0.000
h	0.365	0.155	0.300	-0.346	-0.191	-0.305	0.236	0.140	-0.416
h	-0.366	-0.156	-0.301	-0.345	-0.190	-0.303	-0.236	-0.140	0.416
h	-0.366	-0.156	0.301	-0.345	-0.190	0.303	-0.236	-0.140	-0.416
c	-0.063	-0.006	0.000	0.056	0.026	0.000	-0.042	-0.022	0.000
h	0.365	0.155	-0.300	-0.346	-0.191	0.305	0.236	0.140	0.416
cl	0.000	-0.002	0.000	0.001	0.002	0.000	0.000	0.000	0.000
Label:	16			17			18		
Symmetry:	bu			bg			au		
Frequency:	3128.05			3176.52			3198.06		
IR Active:	YES			NO			YES		
IR Inten:	16.489			0.000			5.976		
dmux/dQ:	0.08192			0.00000			0.00000		
dmuy/dQ:	0.10099			0.00000			0.00000		
dmuz/dQ:	0.00000			0.00000			-0.07828		
Raman Active:	NO			YES			NO		
Raman Inten:	0.000			106.923			0.000		
Depolar:	0.000			0.750			0.000		
Rot.Strength:	0.708			0.000			0.266		
	X	Y	Z	X	Y	Z	X	Y	Z
c	0.040	0.024	0.000	0.000	0.000	0.069	0.000	0.000	-0.069
cl	0.000	0.000	0.000	0.000	0.000	0.000	0.000	0.000	0.000
h	-0.238	-0.140	0.415	-0.245	-0.146	0.408	-0.248	-0.143	0.407
h	-0.238	-0.140	0.415	0.245	0.146	-0.408	-0.248	-0.143	0.407
h	-0.238	-0.140	-0.415	-0.245	-0.146	-0.408	0.248	0.143	0.407
c	0.040	0.024	0.000	0.000	0.000	-0.069	0.000	0.000	-0.069
h	-0.238	-0.140	-0.415	0.245	0.146	0.408	0.248	0.143	0.407
cl	0.000	0.000	0.000	0.000	0.000	0.000	0.000	0.000	0.000

STANDARD THERMODYNAMIC QUANTITIES AT 298.180 K AND 1.000 ATM

This Molecule has 0 Imaginary Frequencies

Zero point vibrational energy: 36.802 kcal/mol

■ Fig. 10-6  
(Continued)

```

Atom   1  Element  c  Has Mass  12.01115
Atom   2  Element  cl Has Mass  35.45270
Atom   3  Element  h  Has Mass   1.00794
Atom   4  Element  h  Has Mass   1.00794
Atom   5  Element  h  Has Mass   1.00794
Atom   6  Element  c  Has Mass  12.01115
Atom   7  Element  h  Has Mass   1.00794
Atom   8  Element  cl Has Mass  35.45270
Molecular Mass:   98.959460 amu
Principal axes and moments of inertia in atomic units:

          1          2          3
Eigenvalues --   62.16074  1242.14322  1281.43626
          X         0.36607   -0.93059   0.00000
          Y        -0.93059   -0.36607   0.00000
          Z         0.00000   0.00000   1.00000

Rotational Symmetry Number is  2
The Molecule is an Asymmetric Top
Translational Enthalpy:         0.889 kcal/mol
Rotational Enthalpy:           0.889 kcal/mol
Vibrational Enthalpy:          38.101 kcal/mol
gas constant (RT):             0.593 kcal/mol
Translational Entropy:         39.687 cal/mol.K
Rotational Entropy:            24.718 cal/mol.K
Vibrational Entropy:           7.625 cal/mol.K

Total Enthalpy:                 40.471 kcal/mol
Total Entropy:                  72.030 cal/mol.K

```

■ Fig. 10-6

**PQS vibrational frequency output for trans-1,2-dichloroethane**


The first thing printed out is the name of the file containing the Hessian matrix. In PQS a vibrational and thermodynamic analysis is done independently of the Hessian computation enabling a full vibrational analysis of isotopomers to be carried out from the same Hessian matrix simply by changing the atomic masses. Analysis is done on any matrix read from the Hessian file, including partial and/or approximate Hessians (e.g., an updated Hessian left over from a geometry optimization), so care must be taken that the source of the Hessian matrix is known. A vibrational analysis of an approximate Hessian will of course, at best, be only approximate; in particular an analysis based on a geometry optimized at one level of theory and a Hessian matrix computed at another (lower) level of theory is, strictly speaking, invalid.

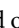
Then comes a list of the vibrational frequencies in atomic units after the translations and rotations have been projected out. This is simply a printout of the eigenvalues of the projected mass-weighted Hessian (see ► [Eq. 10.35](#)); as can be seen, the six eigenvalues corresponding to

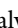

the translations and rotations are all zero. The remaining eigenvalues are all positive, showing that the optimized structure of trans-1,2-dichloroethane is a genuine minimum. As any decent chemist should know, 1,2-dichloroethane has two stable conformations, trans and gauche; the former is the more stable by around  $1.5 \text{ kcal mol}^{-1}$  (El Youssoufi et al. 1998a, b). This energy difference is sufficiently small that both conformers will be present, certainly at room temperature, and experimental vibrational spectra of 1,2-dichloroethane, unless recorded at very low temperature, will contain bands from the gauche as well as the more abundant trans conformer. This will be discussed in more detail later in this chapter.

This is followed by a list of all symmetry types possible for the vibrational modes. This is simply a list of the irreducible representations present in the character table for the molecule's symmetry point group; for trans-1,2-dichloroethane, having  $C_{2h}$  symmetry, this is  $a_g$ ,  $b_g$  (symmetric motions) and  $a_u$ ,  $b_u$  (antisymmetric).

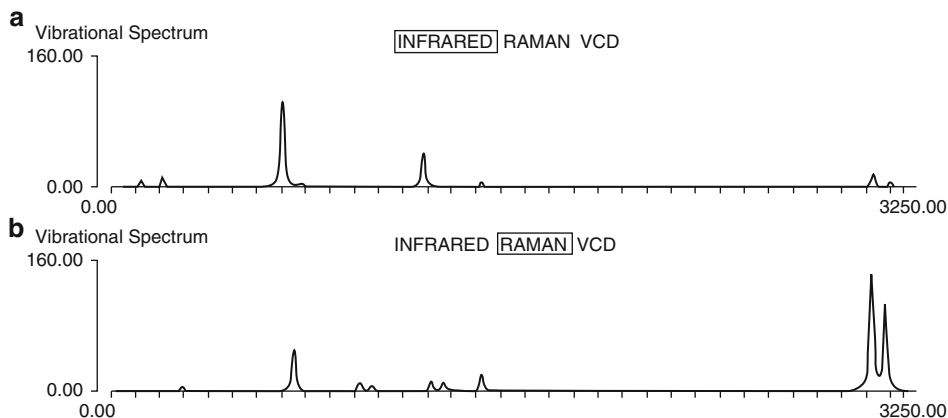
All  $3N - 6$  normal modes (Cartesian displacements for each atom) are then listed, together with as much information for each mode as is available, depending on which, if any, of the dipole derivatives, the polarizability derivatives or the rotational strengths have been computed for the molecule in question. For trans-1,2-dichloroethane all these quantities are available except the latter, so listed for each mode is its symmetry type, its frequency in wavenumbers ( $\text{cm}^{-1}$ ), whether or not the mode is IR active, the corresponding IR intensity, the  $X$ ,  $Y$  and  $Z$  dipole derivatives with respect to the motion in each normal mode, whether the mode is Raman active, its corresponding Raman intensity and its Raman depolarization ratio. If the molecule were VCD active, its rotational strength (relative intensity in a VCD spectrum) would also be printed.

As already noted, whether a mode is IR or Raman active can be determined in advance (although its intensity cannot) by group theoretical considerations and depends on its symmetry type. For trans-1,2-dichloroethane (because of its point group symmetry) each mode is *either* IR active *or* Raman active, but not both, and so IR and Raman spectroscopy excite completely different vibrational fundamentals. In the Raman spectrum, only bands of  $a_g$  and  $b_g$  symmetry will appear. These can be distinguished experimentally by measuring the depolarization ratio; according to theory (Wilson et al. 1955), the depolarization ratio of totally symmetric modes ( $a_g$  under  $C_{2h}$ ) is less than 0.75 (these are called polarized bands) whereas that of all other modes is 0.75 (depolarized bands). (See the depolarization ratios calculated for trans-1,2-dichloroethane in  Fig. 10-5.)

The vibrational analysis is followed by a standard, classical statistical thermodynamic analysis at 298.18 K (25°C) and 1 atm pressure. (For details, see McQuarrie (2000)). Computed quantities include the principal axes and moments of inertia, the rotational symmetry number and symmetry classification, and the translational, rotational, vibrational, and total enthalpy and entropy, respectively. Both the temperature and pressure can be altered from standard conditions and/or scanned across a requested range of values. The total zero-point energy at 0 K is given by  $\sum_v \frac{1}{2} h\nu$ , summed over all real frequencies (converted to  $\text{kcal mol}^{-1}$ ; see  Eq. 10.36).

The predicted IR and Raman spectra, based on the data printed out from the vibrational analysis in  Fig. 10-6 are shown in  Fig. 10-7. These are direct “screen captures” from PQSView, which is the job output and visualization component of the PQSMol GUI (PQS 2010). For each spectrum, the frequency range (horizontal axis), the intensity range (vertical axis), and the band half-width (fitted using a Lorentzian band profile) can be varied; it is also possible to “zoom in” on selected regions of the spectrum.

So how good are the results? First of all it should be noted that we would not expect theory to be able to exactly reproduce experimental vibrational spectra as factors such as intensity



■ Fig. 10-7

Simulated IR and Raman spectra using data derived from [Fig. 10-6](#): (a) IR Spectrum, (b) Raman Spectrum

and bandwidth depend strongly on experimental conditions (as to some extent do the frequencies themselves). Also, most importantly, the theoretical analysis assumes harmonic behavior, whereas the real spectrum is of course anharmonic. So we would expect the calculated vibrational fundamentals to deviate from experiment simply because they are harmonic, without even considering other sources of error (such as incomplete basis set and approximate treatment of electron correlation). For the level of theory used here, B3LYP/6-31G\*, the average (mean) error between computed (harmonic) vibrational fundamentals and experimentally observed (anharmonic) values is around  $50\text{ cm}^{-1}$ . For example, in a study of 900 individual vibrational fundamentals from 111 different small molecules using B3LYP and a polarized-valence triple-zeta basis, Schlegel and coworkers (Halls et al. 2001) found an average absolute deviation between theory and experiment of  $44.69\text{ cm}^{-1}$ .

Agreement with experiment can be much improved by scaling. This has been done since the early days of Hartree–Fock theory, when all computed HF/6-31G\* frequencies were regularly scaled by a factor of around 0.89. Optimized Hartree–Fock bond lengths are typically too short compared with experiment; hence computed frequencies are almost uniformly too high. Single scale factors, applied directly to computed vibrational fundamentals, have since been derived for a range of other wavefunctions, including post-HF and DFT. A recent paper from Radom and coworkers derived least-squares fitted scale factors for more than 100 different levels of theory (varying both the methodology and the basis set) (Merrick et al. 2007). Scale factors for DFT-based methods are much closer to unity than scale factors derived using Hartree–Fock (which completely neglects electron correlation) showing that the raw (unscaled) results are simply better. The scale factor for B3LYP/6-31G\* is 0.9614 (Merrick et al. 2007).

## Scaled Quantum Mechanical Force Fields

Although scaling of the computed vibrational frequencies using a single, global, scale factor is common, the first scaling methods applied to *ab initio* force constants used several different scale factors to correct for systematic errors in different types of molecular deformations, e.g.,

stretches, bends, or torsions. This procedure requires the transformation of the molecular force field (the Hessian matrix) into chemically meaningful internal coordinates and scales the resulting Hessian elements themselves. It cannot be applied directly to the calculated frequencies. It is thus less convenient than global scaling using a single scaling factor. Largely because of its simplicity, global scaling became popular, but using multiple scale factors yields much better results as was convincingly demonstrated by Blom and Altona in a series of papers starting in the mid-1970s (Blom and Altona 1976, 1977a, b; Blom et al. 1976). Their method forms the basis of the scaled quantum mechanical (SQM) procedure which has been in widespread use for over 25 years (Pulay et al. 1983).

In the original SQM procedure, the molecular geometry was expressed in terms of a full set of nonredundant natural internal coordinates (Fogarasi et al. 1992; Pulay et al. 1979). On the basis of chemical intuition, the natural internal coordinates of all molecules under consideration (there can be more than one) are sorted into groups sharing a common scale factor, and factors for each group are determined by a least-squares fit to experimental vibrational frequencies. Force constants, originally calculated in Cartesian coordinates, are transformed into the internal coordinate representation, and scaling is applied to the elements of the internal force constant matrix (not to the individual vibrational frequencies) according to

$$\mathbf{F}_{ij}(\text{scaled}) = \sqrt{s_i s_j} \mathbf{F}_{ij}, \quad (10.38)$$

where  $s_i$  and  $s_j$  are scaling factors for internal coordinates  $i$  and  $j$ , respectively.

The accuracy obtained by selective scaling in this way is naturally greater than if just a single global scaling factor were used. Additionally, scaling the force constant matrix also affects the resultant normal modes, and hence the calculated intensities (which are unaffected if only the frequencies are scaled), leading to better agreement with experimental intensities. Furthermore the vibrational frequencies derive directly from the (scaled) Hessian matrix, and are thus fully consistent with it; not the case at all if the frequencies are scaled directly.


The SQM procedure has been widely used in the interpretation of vibrational spectra. A further important role is the development of transferable scale factors which can be used to modify calculated force constants and so predict the vibrational spectrum *a priori*.

The SQM module in PQS uses a modified scaling procedure involving the scaling of individual valence coordinates (Baker et al. 1998) (not the linear combinations present in natural internal coordinates). This has immediate advantages in terms of ease of use, as no natural internals need to be generated (a procedure which may fail for complicated molecular topologies), and it simplifies the classification and presorting of the coordinates. In addition, the extra flexibility involved in the scaling of individual primitive internals generally leads to an increase in accuracy and to more transferable scale factors. On typical organic molecules one can expect average differences between predicted SQM and experimental fundamentals of around  $10 \text{ cm}^{-1}$  with maximum errors of about  $30 \text{ cm}^{-1}$  or so (Baker and Pulay 1998). In my experience, if differences greatly exceed this maximum, it is more likely that the observed experimental peaks have been misassigned than the predicted SQM frequency is wrong.

## 1,2-Dichloroethane: A Further Analysis

We are going to apply the SQM method to the existing Hessian matrix for trans-1,2-dichloroethane in order to improve the agreement with experiment; furthermore, we will also need to consider the gauche conformer which will almost certainly contribute to the experimental vibrational spectra at room temperature.



The results of a vibrational analysis of gauche-1,2-dichloroethane, optimized at the B3LYP/6-31G\* level, are shown in  Fig. 10-8. This is direct printout from the corresponding PQS log file (not the output file). In addition to the full output, PQS produces a summary output – the log file – which contains only data that is of direct interest to the user and omits all intermediate printout (such as integral and timing data, intermediate steps in an optimization etc.). As can be seen, the log file reproduces the thermodynamic analysis that is printed in the full output file, but provides only a summary of the vibrational analysis and completely omits the normal modes.

#### Vibrational frequencies and intensities

No.	Symm.	Freq.	IR	Raman	IR int.	Raman int.	Depol.	Rot.Str.
18	b	3172.85	YES	YES	6.495	21.936	0.7500	1.306
17	a	3159.99	YES	YES	0.688	107.324	0.7427	-1.162
16	a	3103.37	YES	YES	22.911	190.623	0.0225	-3.727
15	b	3094.75	YES	YES	3.074	48.934	0.7500	-2.061
14	a	1500.18	YES	YES	0.172	6.079	0.6749	-0.632
13	b	1495.96	YES	YES	10.565	19.427	0.7500	0.851
12	a	1364.60	YES	YES	25.618	6.217	0.7390	-18.289
11	b	1342.07	YES	YES	49.651	0.508	0.7500	-4.220
10	a	1246.88	YES	YES	1.274	19.900	0.7301	5.497
9	b	1178.97	YES	YES	1.164	7.360	0.7500	-4.560
8	a	1054.50	YES	YES	0.629	3.929	0.7451	2.522
7	a	960.62	YES	YES	13.324	6.693	0.4295	-5.248
6	b	904.47	YES	YES	19.675	1.655	0.7500	16.416
5	b	679.03	YES	YES	30.638	10.525	0.7500	-29.476
4	a	654.31	YES	YES	21.755	13.678	0.1022	19.772
3	b	409.09	YES	YES	9.479	2.353	0.7500	7.781
2	a	261.37	YES	YES	1.042	1.127	0.3706	-4.698
1	a	112.97	YES	YES	1.019	1.793	0.7446	-0.892

STANDARD THERMODYNAMIC QUANTITIES AT 298.180 K AND 1.000 ATM

This Molecule has 0 Imaginary Frequencies

Zero point vibrational energy: 36.734 kcal/mol

Atom	1	Element c	Has Mass	12.01115
Atom	2	Element cl	Has Mass	35.45270
Atom	3	Element h	Has Mass	1.00794
Atom	4	Element h	Has Mass	1.00794
Atom	5	Element h	Has Mass	1.00794
Atom	6	Element c	Has Mass	12.01115
Atom	7	Element h	Has Mass	1.00794
Atom	8	Element cl	Has Mass	35.45270

Molecular Mass: 98.959460 amu

Principal axes and moments of inertia in atomic units:

	1	2	3
Eigenvalues --	181.49676	849.35170	971.53423
X	-0.75466	0.00000	0.65612
Y	0.65612	0.00000	0.75466
Z	0.00000	1.00000	0.00000

 Fig. 10-8  
(Continued)

```

Rotational Symmetry Number is 2
The Molecule is an Asymmetric Top
Translational Enthalpy: 0.889 kcal/mol
Rotational Enthalpy: 0.889 kcal/mol
Vibrational Enthalpy: 37.940 kcal/mol
gas constant (RT): 0.593 kcal/mol
Translational Entropy: 39.687 cal/mol.K
Rotational Entropy: 25.130 cal/mol.K
Vibrational Entropy: 6.966 cal/mol.K

Total Enthalpy: 40.310 kcal/mol
Total Entropy: 71.783 cal/mol.K

```

■ Fig. 10-8

PQS vibrational frequency summary from the log file for *gauche*-1,2-dichloroethane

■ Table 10-5

Standard B3LYP/6-31G\* SQM scale factors relevant to 1,2-dichloroethane

Type		Scale factor
Stretch	rC–C	0.9207
Stretch	rC–H	0.9164
Stretch	rC–Cl	1.0438
Bend	∠CCCl	1.0144
Bend	∠CCH; ∠ClCH	0.9431
Bend	∠HCH	0.9016
Torsion	all	0.9523

*Gauche*-1,2-dichloroethane has  $C_2$  symmetry and formally all of its vibrational fundamentals are both IR and Raman active. (Additionally, unlike the *trans* conformer, it is also potentially VCD active.) However, several modes have only relatively low intensity and may therefore be difficult to see in the experimental spectrum, especially given that the *gauche* is the higher energy conformer and is only expected to comprise about 13–25% of the total at room temperature (El Youssoufi et al. 1998a, b). The computed B3LYP/6-31G\* energy difference between the *gauche* and *trans* conformers is 1.5 kcal mol<sup>-1</sup>, including (minor) zero-point energy effects.

In the paper that introduced the scaling of individual primitive internals into the SQM method (Baker et al. 1998), a set of 11 scale factors were derived from a test set of 30 molecules containing C, H, O, N and Cl at the B3LYP/6-31G\* level. These scale factors will be used “as is” to scale the raw Hessian data for both *trans* and *gauche*-1,2-dichloroethane. The seven scale factors appropriate for use with 1,2-dichloroethane as shown in ▶ Table 10-5.

There have been several experimental studies of the vibrational spectra of 1,2-dichloroethane. Of note are the 1975 IR and Raman measurements on the solid, liquid, and gaseous *trans* and *gauche* conformers from Mizushima and coworkers (1975), and the combined theoretical and FT-IR study of El Youssoufi et al. already referred to (El Youssoufi et al. 1998a, b). These results are summarized, together with the unscaled, scaled using a single scale factor (Merrick et al. 2007), and the SQM predicted fundamentals in ▶ Table 10-6.

The first thing to note from ▶ Table 10-6 is that the order and the symmetry assignments of the fundamentals is predicted to be exactly the same theoretically as found experimentally. The

■ Table 10-6

Comparison of experimental and theoretical (B3LYP/6-31G\*) vibrational fundamentals for gas-phase 1,2-dichloroethane and their assignments

Experiment		Scaled (SQM)	Scaled (0.9614)	Unscaled	Assignment
A <sup>a</sup>	B <sup>b</sup>				
<b>trans conformer</b>					
122 ( <i>a<sub>u</sub></i> )	123	117 ( <i>a<sub>u</sub></i> )	114 ( <i>a<sub>u</sub></i> )	119 ( <i>a<sub>u</sub></i> )	Torsion
221 ( <i>b<sub>u</sub></i> )	220	214 ( <i>b<sub>u</sub></i> )	206 ( <i>b<sub>u</sub></i> )	214 ( <i>b<sub>u</sub></i> )	CCCl def.
305 ( <i>a<sub>g</sub></i> )		296 ( <i>a<sub>g</sub></i> )	284 ( <i>a<sub>g</sub></i> )	295 ( <i>a<sub>g</sub></i> )	CCCl def.
727 ( <i>b<sub>u</sub></i> )	728	724 ( <i>b<sub>u</sub></i> )	681 ( <i>b<sub>u</sub></i> )	708 ( <i>b<sub>u</sub></i> )	C–Cl str.
772 ( <i>a<sub>g</sub></i> )		766 ( <i>a<sub>g</sub></i> )	725 ( <i>a<sub>g</sub></i> )	754 ( <i>a<sub>g</sub></i> )	C–Cl str.
772 ( <i>a<sub>u</sub></i> )	773	767 ( <i>a<sub>u</sub></i> )	758 ( <i>a<sub>u</sub></i> )	788 ( <i>a<sub>u</sub></i> )	CH <sub>2</sub> rock
996 ( <i>b<sub>g</sub></i> )		999 ( <i>b<sub>g</sub></i> )	985 ( <i>b<sub>g</sub></i> )	1,025 ( <i>b<sub>g</sub></i> )	CH <sub>2</sub> rock
1,057 ( <i>a<sub>g</sub></i> )		1,027 ( <i>a<sub>g</sub></i> )	1,025 ( <i>a<sub>g</sub></i> )	1,066 ( <i>a<sub>g</sub></i> )	C–C str.
1,124 ( <i>a<sub>u</sub></i> )	1,122	1,128 ( <i>a<sub>u</sub></i> )	1,115 ( <i>a<sub>u</sub></i> )	1,160 ( <i>a<sub>u</sub></i> )	CH <sub>2</sub> twist
1,233 ( <i>b<sub>u</sub></i> )	1,232	1,244 ( <i>b<sub>u</sub></i> )	1,231 ( <i>b<sub>u</sub></i> )	1,280 ( <i>b<sub>u</sub></i> )	CH <sub>2</sub> wag.
1,267 ( <i>b<sub>g</sub></i> )		1,273 ( <i>b<sub>g</sub></i> )	1,260 ( <i>b<sub>g</sub></i> )	1,311 ( <i>b<sub>g</sub></i> )	CH <sub>2</sub> twist
1,310 ( <i>a<sub>g</sub></i> )		1,322 ( <i>a<sub>g</sub></i> )	1,308 ( <i>a<sub>g</sub></i> )	1,361 ( <i>a<sub>g</sub></i> )	CH <sub>2</sub> wag.
1,431 ( <i>a<sub>g</sub></i> )		1,459 ( <i>a<sub>g</sub></i> )	1,460 ( <i>a<sub>g</sub></i> )	1,519 ( <i>a<sub>g</sub></i> )	CH <sub>2</sub> scissor
1,461 ( <i>b<sub>u</sub></i> )	1,460	1,460 ( <i>b<sub>u</sub></i> )	1,460 ( <i>b<sub>u</sub></i> )	1,519 ( <i>b<sub>u</sub></i> )	CH <sub>2</sub> scissor
2,979 ( <i>a<sub>g</sub></i> )		2,987 ( <i>a<sub>g</sub></i> )	3,000 ( <i>a<sub>g</sub></i> )	3,120 ( <i>a<sub>g</sub></i> )	CH <sub>2</sub> sym. str.
2,983 ( <i>b<sub>u</sub></i> )	2,983	2,994 ( <i>b<sub>u</sub></i> )	3,007 ( <i>b<sub>u</sub></i> )	3,128 ( <i>b<sub>u</sub></i> )	CH <sub>2</sub> sym. str.
3,001 ( <i>b<sub>g</sub></i> )		3,041 ( <i>b<sub>g</sub></i> )	3,054 ( <i>b<sub>g</sub></i> )	3,177 ( <i>b<sub>g</sub></i> )	CH <sub>2</sub> antisym. str.
3,009 ( <i>a<sub>u</sub></i> ) <sup>c</sup>	3,011	3,062 ( <i>a<sub>u</sub></i> )	3,075 ( <i>a<sub>u</sub></i> )	3,198 ( <i>a<sub>u</sub></i> )	CH <sub>2</sub> antisym. str.
<b>Mean error<sup>d</sup> (cm<sup>-1</sup>)</b>		<b>9.3 (30)</b>	<b>17.9 (47)</b>	<b>38.8 (145)</b>	
<b>gauche conformer</b>					
125 ( <i>a</i> )		111 ( <i>a</i> )	109 ( <i>a</i> )	113 ( <i>a</i> )	torsion
263 ( <i>a</i> )		260 ( <i>a</i> )	251 ( <i>a</i> )	261 ( <i>a</i> )	CCCl def.
411 ( <i>b</i> )		408 ( <i>b</i> )	393 ( <i>b</i> )	409 ( <i>b</i> )	CCCl def.
669 ( <i>a</i> )	668	663 ( <i>a</i> )	629 ( <i>a</i> )	654 ( <i>a</i> )	C–Cl str.
694 ( <i>b</i> )	694	689 ( <i>b</i> )	653 ( <i>b</i> )	679 ( <i>b</i> )	C–Cl str.
891 ( <i>b</i> )	891	889 ( <i>b</i> )	869 ( <i>b</i> )	904 ( <i>b</i> )	CH <sub>2</sub> rock
947 ( <i>a</i> )	948	938 ( <i>a</i> )	924 ( <i>a</i> )	961 ( <i>a</i> )	CH <sub>2</sub> rock
1,028 ( <i>a</i> )	1,027	1,021 ( <i>a</i> )	1,014 ( <i>a</i> )	1,055 ( <i>a</i> )	C–C str.
1,146 ( <i>b</i> )	1,146	1,146 ( <i>b</i> )	1,133 ( <i>b</i> )	1,179 ( <i>b</i> )	CH <sub>2</sub> twist
1,214 ( <i>a</i> )	1,214	1,211 ( <i>a</i> )	1,199 ( <i>a</i> )	1,247 ( <i>a</i> )	CH <sub>2</sub> twist
1,292 ( <i>b</i> )	1,292	1,303 ( <i>b</i> )	1,290 ( <i>b</i> )	1,342 ( <i>b</i> )	CH <sub>2</sub> wag.
1,315 ( <i>a</i> )	1,313	1,325 ( <i>a</i> )	1,312 ( <i>a</i> )	1,365 ( <i>a</i> )	CH <sub>2</sub> wag.
1,436 ( <i>b</i> )	1,437	1,438 ( <i>b</i> )	1,438 ( <i>b</i> )	1,496 ( <i>b</i> )	CH <sub>2</sub> scissor
1,446 ( <i>a</i> )		1,443 ( <i>a</i> )	1,442 ( <i>a</i> )	1,500 ( <i>a</i> )	CH <sub>2</sub> scissor
2,957 ( <i>b</i> )	2,957	2,971 ( <i>b</i> )	2,976 ( <i>b</i> )	3,095 ( <i>b</i> )	CH <sub>2</sub> sym. str.

(Continued)

■ Table 10-6  
(Continued)

Experiment		Scaled (SQM)	Scaled (0.9614)	Unscaled	Assignment
A <sup>a</sup>	B <sup>b</sup>				
2,966 (a)	2,963	2,971 (a)	2,983 (a)	3,103 (a)	CH <sub>2</sub> sym. str.
3,005 (a)		3,025 (a)	3,038 (a)	3,160 (a)	CH <sub>2</sub> antisym. str.
3,005 (b)	3,040	3,037 (b)	3,051 (b)	3,173 (b)	CH <sub>2</sub> antisym. str.
<b>Mean error<sup>d</sup> (cm<sup>-1</sup>)</b>		<b>5.4 (14)</b>	<b>16.1 (41)</b>	<b>40.9 (138)</b>	

<sup>a</sup>Ref. Mizushima et al. (1975)

<sup>b</sup>Ref. El Youssefi et al. (1998a, b)

<sup>c</sup>Reported as 3,040 cm<sup>-1</sup> in the solid

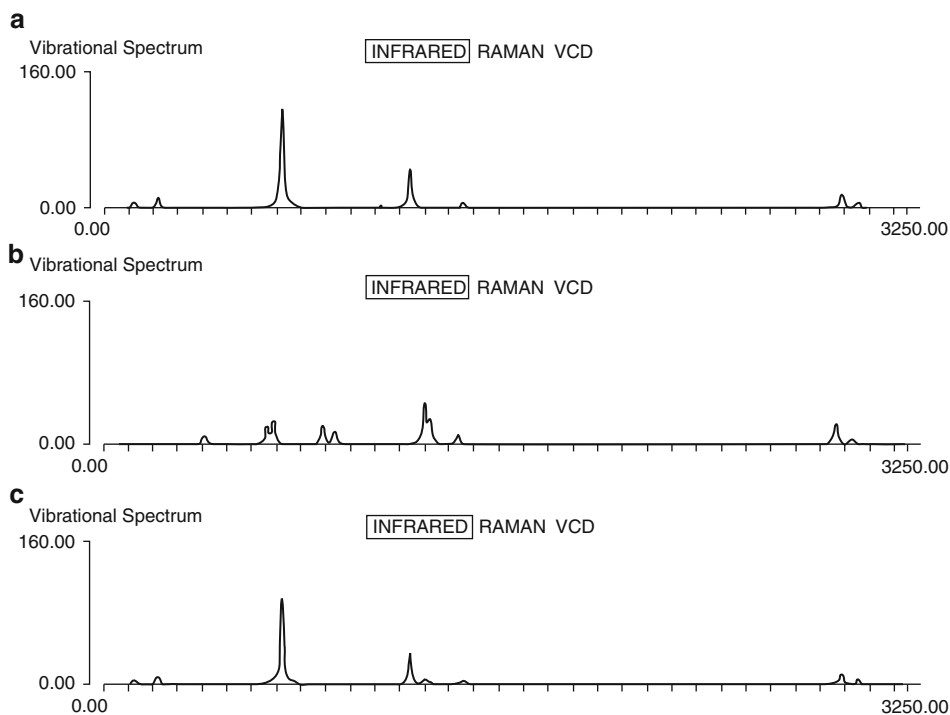
<sup>d</sup>Omitting the two highest fundamentals, maximum deviation in parentheses (see text)

actual assignments as to the type of motion for each vibrational mode can be readily checked by animating the mode and observing it visually. In this regard, theory is far easier to interpret than experiment. When you determine a vibrational fundamental computationally you automatically get its normal mode, its symmetry type, its IR and Raman intensities, its depolarization ratio, indeed the whole vibrational analysis, so there is absolutely no dispute as to the bands assignment. Additionally, it is possible to do an energy distribution analysis (Pulay and Torok 1966) of the normal modes which determines which primitive internals have more than a given weight (typically 3%) to each mode, often enabling the principal motion in the mode (assuming there is one) to be found without having to animate it.

The two sets of experimental fundamentals are for the most part in excellent agreement with each other and typically differ by 1–2 cm<sup>-1</sup> only. However, there are more serious discrepancies for the two highest frequencies. These are C–H stretches which, primarily due to tunneling, often show large differences from harmonic behavior, and both the position and the intensity of these bands in the experimental spectrum can deviate significantly from theoretical predictions. They are also often difficult to determine experimentally. In this case the highest frequency for the *gauche* conformer differs by 35 cm<sup>-1</sup> between the two sets of experimental values: 3,005 and 3,040 cm<sup>-1</sup>. Additionally, although the agreement in this region for the *trans* conformer looks fine, Mizushima and coworkers (1975) report a value for the *a<sub>u</sub>* C–H antisymmetric stretch in the solid of 3,040 cm<sup>-1</sup>, compared to 3,009 cm<sup>-1</sup> in the gas phase, a substantial difference. Because of these experimental differences, we have omitted the two highest frequency C–H stretches from our error analysis, and the mean average (unsigned) and maximum errors between theory and experiment is reported over 16 vibrational fundamentals (not 18).

The largest errors are of course found for the raw, unscaled frequencies, which show average differences from experiment for the two conformers of around 40 cm<sup>-1</sup> (and maximum errors of about 140 cm<sup>-1</sup>). These are in line with the average errors reported by Schlegel (Halls et al. 2001) previously mentioned. Despite the large average differences, even the unscaled B3LYP/6-31G\* frequencies are helpful in assigning the experimental spectrum as the order is the same as that found experimentally, even if the positions are off.

Scaling even using just a single scaling factor significantly improves the comparison with experiment, reducing the average error by well over 50%. However, the SQM results are by far the best and are genuinely predictive. Results for the *trans* conformer are typical for this approach (average error 9.3 cm<sup>-1</sup>, maximum error 30 cm<sup>-1</sup>) and those for the *gauche* are even



■ Fig. 10-9

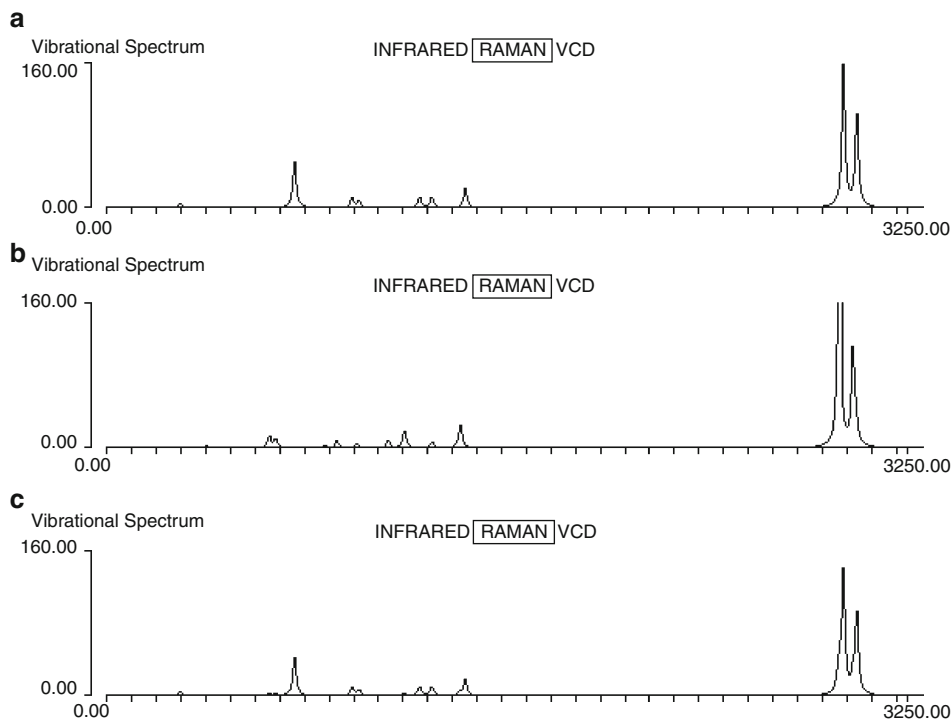
Predicted SQM IR spectra for 1,2-difluoroethane: (a) IR spectrum for *trans*-1,2-dichloroethane, (b) IR spectrum for *gauche*-1,2-dichloroethane, (c) IR spectrum for 1,2-dichloroethane at room temperature

better (average error  $5.4\text{ cm}^{-1}$ , maximum error  $14\text{ cm}^{-1}$ ). In the latter case, they are three times better than using a single scaling factor, both on the average and for the maximum deviation.

A recently published SQM reappraisal of the vibrational spectrum of toluene (Baker 2008) showed a similar average deviation from the 2005 experimental study of Keefe and coworkers (Bertie et al. 2005) of  $5.3\text{ cm}^{-1}$  (maximum error  $17\text{ cm}^{-1}$ ) and convincingly proposed that three observed bands either unassigned or assigned as combination bands were in fact fundamentals. In their 1998 SQM study of the vibrational spectra of several small fluorocarbons, Baker and Pulay (1998) proposed several reassignments to previously published experimental spectra and predicted the fundamental frequencies and IR intensities of nine other fluorocarbons for which there was, at that time, no experimental data. A subsequent jet-cooled FT-IR investigation by McNaughton and coworkers (Jiang et al. 2002) essentially confirmed all of the theoretical predictions.

The final SQM-predicted IR and Raman Spectra for 1,2-dichloroethane are shown in [▶ Fig. 10-9](#) and [▶ Fig. 10-10](#), respectively. In each case individual spectra for the *trans* and *gauche* conformers are given followed by a combined spectrum assuming a room-temperature distribution of 85% *trans* and 15% *gauche*.

Not surprisingly, because of its dominance at room temperature, the observed IR spectrum of 1,2-dichloroethane is predicted to look very much like that for the *trans*-conformer



■ Fig. 10-10

Predicted SQM Raman spectra for 1,2-dichloroethane: (a) Raman spectrum for *trans*-1,2-dichloroethane, (b) Raman spectrum for *gauche*-1,2-dichloroethane, (c) Raman spectrum for 1,2-dichloroethane at room temperature

alone. However there are some peaks due to the *gauche* form that should be visible in room-temperature spectra and their intensity should increase at higher temperature. In particular, the CH<sub>2</sub> wag. at  $\sim 1,300\text{ cm}^{-1}$  should have sufficient intensity to be seen in the IR spectrum and the CH<sub>2</sub> twist at  $1,211\text{ cm}^{-1}$  should be visible in the Raman spectrum.

In addition to their results for normal 1,2-dichloroethane, Mizushima et al. also reported the experimental vibrational fundamentals for the fully deuterated isotopomer (CD<sub>2</sub>ClCD<sub>2</sub>Cl) (Mizushima et al. 1975). These are compared with the SQM scaled frequencies (using the same scaling factors as for CH<sub>2</sub>ClCH<sub>2</sub>Cl) in Table 10-7. (As the Hessian matrix is independent of mass, the vibrational fundamentals for all possible isotopomers can be derived from a single Hessian matrix simply by changing the mass weighting.) The agreement is again excellent, with average errors (mean average deviation) of just over  $7\text{ cm}^{-1}$  and maximum errors around  $20\text{ cm}^{-1}$  for both deuterated conformers. There is one frequency for the *gauche* conformer where there is significant disagreement between theory and experiment (see Table 10-7); this is a *b* mode observed experimentally at  $707\text{ cm}^{-1}$  but predicted theoretically at  $752\text{ cm}^{-1}$ . In Table 3 in Mizushima et al. (1975) this frequency is in parentheses (the only one to be thus treated) which suggests that its value is uncertain. The *trans* conformer shows an intense band at precisely this frequency ( $707\text{ cm}^{-1}$ ) which is predicted to be the most intense band in the entire IR spectrum

■ Table 10-7

Comparison of experimental and theoretical (B3LYP/6-31G\*) vibrational fundamentals for fully deuterated 1,2-dichloroethane and their assignments

Experiment <sup>a</sup>	SQM	Assignment	Experiment <sup>a</sup>	SQM	Assignment
<b><i>trans</i> conformer</b>			<b><i>gauche</i> conformer</b>		
128 ( <i>a<sub>u</sub></i> )	107 ( <i>a<sub>u</sub></i> )	torsion	120 ( <i>a</i> )	106 ( <i>a</i> )	torsion
217 ( <i>b<sub>u</sub></i> )	201 ( <i>b<sub>u</sub></i> )	CCCl def.	229 ( <i>a</i> )	224 ( <i>a</i> )	CCCl def.
299 ( <i>a<sub>g</sub></i> )	292 ( <i>a<sub>g</sub></i> )	CCCl def.	365 ( <i>b</i> )	359 ( <i>b</i> )	CCCl def.
568 ( <i>a<sub>u</sub></i> )	566 ( <i>a<sub>u</sub></i> )	CD <sub>2</sub> rock	624 ( <i>a</i> )	616 ( <i>a</i> )	C–Cl str.
707 ( <i>b<sub>u</sub></i> )	701 ( <i>b<sub>u</sub></i> )	C–Cl str.	643 ( <i>b</i> )	620 ( <i>b</i> )	C–Cl str.
708 ( <i>a<sub>g</sub></i> )	709 ( <i>a<sub>g</sub></i> )	C–Cl str.	(707)( <i>b</i> )	752 ( <i>b</i> )	CD <sub>2</sub> rock
768 ( <i>b<sub>g</sub></i> )	770 ( <i>b<sub>g</sub></i> )	CD <sub>2</sub> rock	759 ( <i>a</i> )	766 ( <i>a</i> )	CD <sub>2</sub> rock
817 ( <i>a<sub>u</sub></i> )	815 ( <i>a<sub>u</sub></i> )	CD <sub>2</sub> twist	828 ( <i>a</i> )	822 ( <i>a</i> )	CD <sub>2</sub> twist
909 ( <i>a<sub>g</sub></i> )	895 ( <i>a<sub>g</sub></i> )	C–C str.	828 ( <i>b</i> )	826 ( <i>b</i> )	C–C str.
944 ( <i>b<sub>u</sub></i> )	946 ( <i>b<sub>u</sub></i> )	CD <sub>2</sub> wag.	941 ( <i>a</i> )	935 ( <i>a</i> )	CD <sub>2</sub> twist
975 ( <i>b<sub>g</sub></i> )	977 ( <i>b<sub>g</sub></i> )	CD <sub>2</sub> twist	1,022 ( <i>b</i> )	1,022 ( <i>b</i> )	CD <sub>2</sub> wag.
1,036 ( <i>a<sub>g</sub></i> )	1,046 ( <i>a<sub>g</sub></i> )	CD <sub>2</sub> wag.	1,052 ( <i>a</i> )	1,053 ( <i>a</i> )	CD <sub>2</sub> wag.
1,085 ( <i>b<sub>u</sub></i> )	1,078 ( <i>b<sub>u</sub></i> )	CD <sub>2</sub> sissor	1,067 ( <i>b</i> )	1,060 ( <i>b</i> )	CD <sub>2</sub> sissor
1,160 ( <i>a<sub>g</sub></i> )	1,146 ( <i>a<sub>g</sub></i> )	CD <sub>2</sub> sissor	1,153 ( <i>a</i> )	1,135 ( <i>a</i> )	CD <sub>2</sub> sissor
2,179 ( <i>a<sub>g</sub></i> )	2,180 ( <i>a<sub>g</sub></i> )	CD <sub>2</sub> sym. str.	2,171 ( <i>b</i> )	2,159 ( <i>b</i> )	CD <sub>2</sub> sym. str.
2,185 ( <i>b<sub>u</sub></i> )	2,180 ( <i>b<sub>u</sub></i> )	CD <sub>2</sub> sym. str.	2,171 ( <i>a</i> )	2,168 ( <i>a</i> )	CD <sub>2</sub> sym. str.
2,264 ( <i>b<sub>g</sub></i> )	2,271 ( <i>b<sub>g</sub></i> )	CD <sub>2</sub> antisym. str.	2,265 ( <i>a</i> )	2,256 ( <i>a</i> )	CD <sub>2</sub> antisym. str.
2,271 ( <i>a<sub>u</sub></i> )	2,282 ( <i>a<sub>u</sub></i> )	CD <sub>2</sub> antisym. str.	2,265 ( <i>b</i> )	2,261 ( <i>b</i> )	CD <sub>2</sub> antisym. str.
<b>MAD (cm<sup>-1</sup>)</b>	<b>7.3 (21)</b>		<b>7.7 (23)<sup>b</sup></b>		

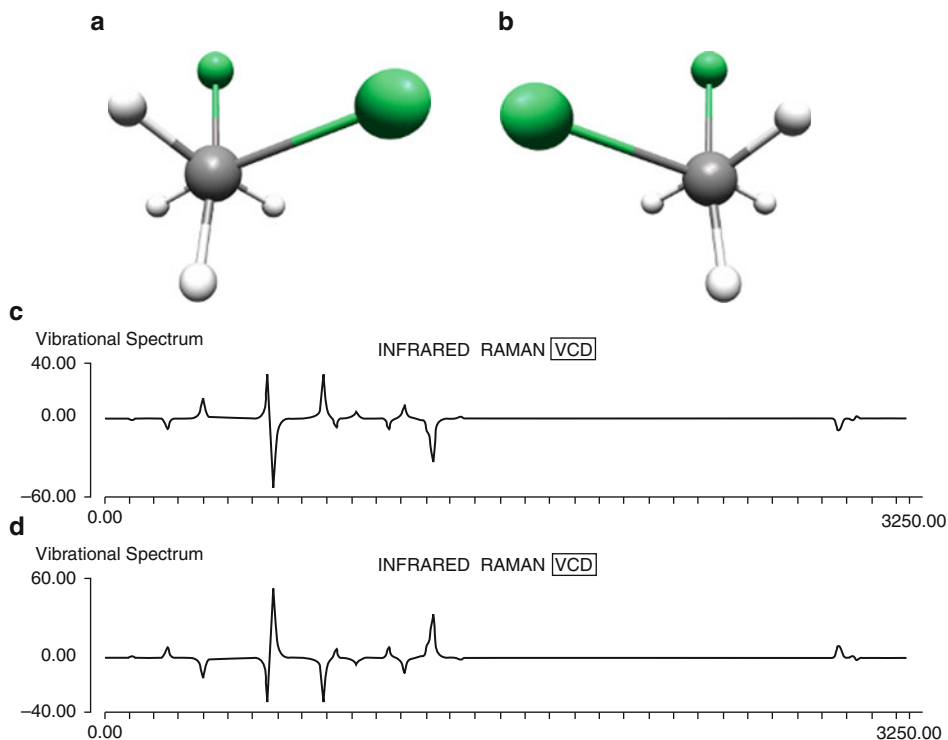
<sup>a</sup>From Ref. Mizushima et al. (1975); gas-phase where given, otherwise liquid

<sup>b</sup>Omitting mode in parentheses (707)

of deuterated 1,2-dichloroethane, and it may well be that a *gauche* mode was assumed to lie hidden under this intense band. The prediction here is that this is not the case, and there is an unassigned feature in the IR spectrum around 752 cm<sup>-1</sup> which should be assigned as a *gauche* fundamental. Because of the possible experimental misinterpretation, this mode was omitted from the error analysis.

As noted, *gauche*-1,2-dichloroethane is potentially VCD active. The two chiral forms of this molecule are shown in ● Fig. 10-11 together with their simulated VCD spectra. (They are denoted by *gauche*1 and *gauche*2, respectively; the rotational strengths given in ● Fig. 10-8 correspond to *gauche*1.) The VCD spectra for the two chiral conformers are precisely the opposite of each other; where one form has a positive rotational strength, the other has exactly the same magnitude but with a negative sign. In any real mixture of *gauche*-1,2-dichloroethane, however, both forms will be present in equal amounts, i.e., it will be a racemic mixture, and so overall there will be no observable VCD spectrum as everything will cancel. However, this clearly shows the potential of VCD spectroscopy to determine the absolute molecular configuration of a pure, chiral conformer.

Finally ● Table 10-8 compares optimized geometrical parameters for *trans*-1,2-dichloroethane with experimental electron diffraction data from Kvesethi as reported in El Youssoufi et al. (1998a, b).



■ Fig. 10-11

Predicted VCD spectra for the two chiral forms of *gauche*-1,2-dichloroethane: (a) *gauche*1, (b) *gauche*2, (c) simulated VCD spectrum of *gauche*1, (d) simulated VCD spectrum of *gauche*2

■ Table 10-8

Comparison of experimental and theoretical (B3LYP/6-31G\*) geometrical parameters for *trans*-1,2-dichloroethane

Parameter <sup>a</sup>	B3LYP/6-31G*	Experiment <sup>b</sup>
rC–C	1.518	1.528(6)
rC–Cl	1.815	1.796(3)
rC–H	1.090	1.120(10)
∠CCCl	109.2	108.9(0.3)
∠CCH	111.6	113.0(1.3)
τClCCCl	180.0	180.0

<sup>a</sup>Distances in Å and angles in degrees

<sup>b</sup>From Ref. Kveseth (1974), standard deviation in parentheses

I hope that the above has demonstrated just how useful modern theory can be for the prediction and interpretation of molecular vibrational spectra and the identification and assignment of vibrational fundamentals. I have attempted to show this with a fairly extensive theoretical study (carried out especially for this chapter) on one particular molecule, 1,2-dichloroethane, rather than merely summarizing the results of previous studies.



## Density Functional Theory and Weight Derivatives

Before concluding, I would like to comment on the use of weight derivatives in DFT calculations. As will be discussed, this has important ramifications for the reliable computation of DFT vibrational frequencies. Following Pople and coworkers (Johnson et al. 1993), we can write the DFT exchange-correlation energy as

$$E_{XC} = \int f(\rho) dr, \quad (10.39)$$

where  $\rho$  represents all the density dependence, of whatever form, in the density functional  $f(\rho)$ . This integral is too complicated to be evaluated analytically and numerical integration has to be used. Virtually all DFT programs employ an atomic partitioning scheme pioneered by Becke (1988) to evaluate this integral, which separates the molecular integral into atomic contributions which may then be individually treated using single-center techniques.

If this is done, we can replace  $\blacktriangleright$  Eq. 10.39 by

$$E_{XC} = \sum_A \sum_i \omega_{Ai} f(\rho; \mathbf{r}_{Ai}), \quad (10.40)$$

where the first summation is over all atoms,  $A$ , and the second is over the numerical quadrature grid points,  $i$ , for the current atom. The  $\omega_{Ai}$  are quadrature weights and the grid points,  $\mathbf{r}_{Ai}$  are given by  $\mathbf{r}_{Ai} = \mathbf{R}_A + \mathbf{r}_i$ , where  $\mathbf{R}_A$  is the position of nucleus  $A$  and  $\mathbf{r}_i$  represents a suitable quadrature grid centered on  $A$ .

Because the grid points are atom-centered they are not fixed in space, but “move with” the atom. This means that the derivative of  $\blacktriangleright$  Eq. 10.40 (needed for the DFT contribution to the gradient) formally has two parts:

$$\nabla_A E_{XC} = \sum_B \sum_i [\omega_{Bi} \nabla_A f(\rho; \mathbf{r}_{Bi}) + (\nabla_A \omega_{Bi}) f(\rho; \mathbf{r}_{Bi})]. \quad (10.41)$$

The first term in  $\blacktriangleright$  Eq. 10.41 looks like the numerical integral of the exchange-correlation contribution to the total energy gradient, and is the only term in a fixed grid, but the second term is formally needed and the implementation in Johnson et al. (1993) was the first time that this term – the weight derivative – was properly included.

The error in neglecting the weight-derivative term can be reduced to virtually zero by taking a large enough number of grid points, but for smaller grids its omission is not justified (Johnson et al. 1993). I suspect that the hope was that if the second term in  $\blacktriangleright$  Eq. 10.41 were properly included, then small grids would no longer give unreliable results, but if this was indeed the hope, it was quickly dashed when it was shown that small grids which included weight derivatives often gave worse results than calculations in which they were omitted (Baker et al. 1994). Basically you have to have a decent quadrature grid to get reliable gradients; if the grid is not good enough using weight derivatives will not save you, if it is good enough then you probably do not need weight derivatives. At least this is typically the case for the gradient.

One clear advantage of including weight derivatives is that the gradient zero coincides essentially exactly (for minimization) with the energy minimum. If the weight derivative term is omitted and grid quality is poor then there is a strong tendency for the energy to

■ Table 10-9

Optimized BLYP/6-31G\* geometrical parameters for hydrogen peroxide using numerical quadrature grids of decreasing quality with and without weight derivatives<sup>a</sup>

Grid quality <sup>b</sup>	Weight derivs	Geometrical parameters <sup>c</sup>			
		rO–O	rO–H	∠HOO	τHOOH
Conv.	yes	1.494	0.985	98.4	121.9
1	yes	1.494	0.985	98.4	122.0
1	no	1.494	0.985	98.4	121.9
2	yes	1.494	0.985	98.4	122.0
2	no	1.494	0.985	98.4	121.9
3	yes	1.495	0.985	98.4	122.8
3	no	1.493	0.986	98.6	118.3
4	yes	1.496	0.985	98.3	126.2
4	no	1.492	0.986	98.7	113.9
5	yes	1.502	0.983	97.7	142.8
5	no	1.493	0.986	98.4	114.3

<sup>a</sup>From Ref. Baker et al. (1994)

<sup>b</sup>1 = best grid, 5 = worst; Conv. represents converged results

<sup>c</sup>in Å and degrees

rise near the end of a geometry optimization as the gradient supposedly decreases. This was a common occurrence with many early DFT codes almost entirely due to sloppy numerical integration.

The kind of errors in geometries seen when the DFT integration grid gets increasingly worse is shown in ● Table 10-9 which gives geometrical parameters for BLYP/6-31G\* optimizations of hydrogen peroxide with a range of decreasing quality grids. The table is taken from Baker et al. (1994) for which see for more details. Results are shown with and without inclusion of the weight derivative term. As can be seen from ● Table 10-9, the HOOH torsion changes substantially with grid quality, as do some of the other parameters with the poorest quality grid. If anything, results with weight derivatives are worse than those without as grid quality worsens. The actual optimization for the poorest quality grid (grid 5) converged smoothly when weight derivatives were included, with the energy decreasing on every optimization cycle; it was only when examining the final geometry that one realizes that something is badly wrong.

The situation as far as the first energy derivative (the gradient) is concerned is that for reliable results you need a good quality grid, but if you have that then you don't really need to include weight derivatives (although there is no harm in doing so of course). For the second energy derivative (the Hessian matrix and hence vibrational frequencies) things are somewhat different. As convincingly demonstrated by Malagoli and Baker (2003), weight derivatives are essentially *de rigueur* for the reliable computation of vibrational frequencies, particularly if heavier elements (beyond the first row) are involved. However, the reason for this is not what you might think.

It turns out that there is a potential, major difficulty in integrating derivatives of basis functions that represent core electrons on their own atomic grid. Such basis functions have large

exponents and their contribution to the electron density consequently dies off very rapidly with increasing distance from the nucleus. Exponents of the order of a million or more are not at all uncommon, especially if the core – as is often the case – is represented by a contracted function, and such exponents only increase in magnitude with increasing atomic number. In order to accurately integrate a Gaussian function that dies off so rapidly a high density of points are needed near the nucleus. The numerical inaccuracy does not matter very much at all for the exchange-correlation energy, but for the gradient and especially for the second derivative, then a basis function  $\exp(-\omega r^2)$  which has a small value at some grid point near the nucleus, has a magnitude  $2\omega \exp(-\omega r^2)$  for its gradient and  $4\omega^2 \exp(-\omega r^2)$  for its second derivative. With  $\omega$  of the order of  $10^6$ , then the contribution of this function to the second derivative has a magnitude four trillion  $r^2$  times its contribution to the energy at that particular grid point, i.e., it has changed from something fairly small to something potentially large, as well as having a greater radial extent. Consequently it requires a far more accurate numerical integration than it previously had.

It is possible to ameliorate this inaccuracy by increasing the grid quality, but eventually with a large enough exponent, you will simply be swamped and it will not be possible to accurately integrate the function on any viable radial grid. The tremendous advantage of including the weight derivative term (as opposed to ignoring it and in effect assuming a fixed grid) is that, when considering any derivative term, because a grid “moves with” its atom there is no need to take the derivative of any basis function centered on that atom. Thus the highly inaccurate integration of basis functions with large exponents on their own atomic center no longer needs to be carried out. In other words, the inclusion of weight derivatives is so important for reliable frequencies with DFT, not because of anything inherent in the weight derivative term itself, but because, by including them, one can completely avoid a highly inaccurate numerical integration.

If you are using DFT code which does *not* have weight derivatives, then consider carrying out any vibrational analysis with a Hessian matrix computed numerically. As noted above, the gradient is normally reliable even without weight derivatives provided the quadrature grid is of sufficient quality. The calculation will almost certainly take longer compared to computing a fully analytical Hessian, but at least it should give reasonable results.

► **Table 10-10** shows the effects of not including weight derivatives in analytical Hessian matrices on the computed B3LYP/m6-31G\* harmonic vibrational frequencies for Fe(CO)<sub>5</sub>. (The m6-31G\* basis (Mitin et al. 2003) is a modified version of the 6-31G\* basis for first-row transition metals (Rassalov et al. 1998) that corrects deficiencies in the latter due to the lack of a sufficiently diffuse *d*-function in the 3*d*-shell.) This Table, taken from Malagoli and Baker (2003), shows analytical frequencies computed both with and without weight derivatives using the standard grid in PQS (which is perfectly adequate for DFT energies and gradients) as well as a much better quality grid; additionally it gives numerical frequencies derived from a Hessian obtained via central differences on the (analytical) gradient using the standard grid.

As can be seen, all computed frequencies are in excellent agreement with one another (all agreeing within  $1 \text{ cm}^{-1}$ ) except for those computed with the standard grid without weight derivatives. These results are terrible. Apart from the high frequency C–O stretches (above  $2,000 \text{ cm}^{-1}$ ), all the  $e'$  modes show significant errors, as do the  $a_2''$ . The low frequencies are completely wrong, the order of the fundamentals is incorrect, and there are two imaginary frequencies even though the geometry was minimized. All this is solely due to integration error.

■ Table 10-10

Computed B3LYP/m6-31G\* harmonic vibrational frequencies ( $\text{cm}^{-1}$ ) for  $\text{Fe}(\text{CO})_5^a$ 

Vib. mode	Standard grid		Better grid		Numerical Hessian
	No weight	Weight	No weight	Weight	
$e'$	150.09i	47.44	46.55	47.38	46.66
$e''$	100.44	98.96	98.46	98.81	98.99
$e'$	52.52	102.00	101.72	101.79	101.73
$a_2''$	122.60i	109.13	108.75	108.93	109.13
$a_2'$	349.78	350.44	349.78	350.33	350.20
$e''$	360.98	361.49	360.89	361.25	361.05
$a_1'$	419.73	419.44	419.74	419.41	419.35
$e'$	417.52	428.61	428.40	428.50	428.87
$a_1'$	441.88	441.57	441.85	441.57	441.46
$a_2''$	440.85	471.81	471.77	471.81	471.58
$e'$	463.61	484.05	484.22	484.01	484.18
$e''$	561.95	562.26	561.97	662.14	562.06
$a_2''$	579.54	620.21	620.05	620.22	620.49
$e'$	627.12	658.12	658.07	658.07	658.18
$e'$	2,089.44	2,089.55	2,089.59	2,089.40	2,090.10
$a_1'$	2,115.53	2,115.43	2,115.69	2,115.43	2,115.98
$a_2''$	2,116.03	2,116.09	2,116.20	2,116.20	2,116.65
$a_1'$	2,187.58	2,187.40	2,187.59	2,187.31	2,187.96

<sup>a</sup>From Malagoli and Baker (2003)

## Conclusions

Modern *ab initio* theory can compute a large number of molecular properties, particularly those for individual molecules – such as geometries and spectroscopic data – that are of direct relevance for experimental studies. This chapter has concentrated on molecular structure and vibrational spectroscopy where theory can be tremendously helpful to experimentalists. Theoretical data – for example, bond lengths involving hydrogen – are now regularly used as an aid when fitting X-ray and microwave data in order to extract geometrical parameters. IR, Raman and VCD spectra can readily be simulated theoretically, with reliable estimates of both band positions and intensities, especially if the raw data is scaled via an SQM treatment. I have tried to illustrate the latter in particular by concentrating for the most part on an extensive study of a single system using a standard level of theory (B3LYP/6-31G\*) rather than attempting to summarize results on a large number of molecules using a variety of theoretical methods.

Thirty years ago I was attending scientific meetings and conferences in which the theoretical chemists in the audience were often attempting to justify their existence to their experimental colleagues. At that time calculations were not especially helpful to the experimentalist. The standard level of theory for most applications was Hartree–Fock, with perhaps some higher level post-HF single-point energies to hopefully improve the energetics. Computed geometries were not particularly good, computed frequencies were typically much too high (indeed, the

paper introducing one of the first useable analytical Hartree–Fock second derivative codes (Pople et al. 1979) had only just been published), reaction energetics were fairly poor and barrier heights were simply not reliable. All that has changed. Today the experimentalist who refuses to consider any input from theory is just making things harder for him/herself. This is especially the case in the field covered by this chapter.

## References

- Badger, R. M. (1934). A relation between internuclear distances and bond force constants. *Journal of Chemical Physics*, 2, 128.
- Badger, R. M. (1935). The relation between the internuclear distances and force constants of molecules and its application to polyatomic molecules. *Journal of Chemical Physics*, 3, 710.
- Bak, K. L., Devlin, F. J., Ashvar, C. S., Taylor, P. R., Frisch, M. J., & Stephens, P. J. (1995). *Ab initio* calculation of vibrational circular dichroism spectra using gauge-invariant atomic orbitals. *Journal of Physical Chemistry*, 99, 14918.
- Baker, J. (1986). An algorithm for the location of transition states. *Journal of Computational Chemistry*, 7, 385.
- Baker, J. (1992). Geometry optimization in Cartesian coordinates: Constrained optimization. *Journal of Computational Chemistry*, 13, 240.
- Baker, J. (1993). Techniques for Geometry Optimization: A Comparison of Cartesian and Natural Internal Coordinates. *Journal of Computational Chemistry*, 14, 1085.
- Baker, J. (1997). Constrained optimization in delocalized internal coordinates. *Journal of Computational Chemistry*, 18, 1079.
- Baker, J. (2008). A scaled quantum mechanical reinvestigation of the vibrational spectrum of toluene. *Journal of Molecular Structure THEOCHEM*, 865, 49.
- Baker, J., & Bergeron, D. (1993). Constrained optimization in cartesian coordinates. *Journal of Computational Chemistry*, 14, 1339.
- Baker, J., & Chan, F. (1996). The location of transition states: A comparison of Cartesian, Z-matrix, and natural internal coordinates. *Journal of Computational Chemistry*, 17, 888.
- Baker, J., & Hehre, W. J. (1991). Geometry optimization in cartesian coordinates: The end of the Z-matrix? *Journal of Computational Chemistry*, 12, 606.
- Baker, J., & Pulay, P. (1998). Predicting the vibrational spectra of some simple fluorocarbons by direct scaling of primitive valence force constants. *Journal of Computational Chemistry*, 19, 1187.
- Baker, J., & Pulay, P. (2000). Efficient geometry optimization of molecular clusters. *Journal of Computational Chemistry*, 21, 69.
- Baker, J., Muir, M., & Andzelm, J. (1985). A study of some organic reactions using density functional theory. *Journal of Chemical Physics*, 102, 2063.
- Baker, J., Andzelm, J., Scheiner, A., & Delley, B. (1994). The effect of grid quality and weight derivatives in density functional calculations. *Journal of Chemical Physics*, 101, 8894.
- Baker, J., Kessi, A., & Delley, B. (1996). The generation and use of delocalized internal coordinates in geometry optimization. *Journal of Chemical Physics*, 105, 192.
- Baker, J., Jarzecki, A. A., & Pulay, P. (1998). Direct scaling of primitive valence force constants: An alternative approach to scaled quantum mechanical force fields. *Journal of Physical Chemistry A*, 102, 1412.
- Baker, J., Kinghorn, D., & Pulay, P. (1999). Geometry optimization in delocalized internal coordinates: An efficient quadratically scaling algorithm for large molecules. *Journal of Chemical Physics*, 110, 4986.
- Baker, J., Wolinski, K., Malagoli, M., Kinghorn, D., Wolinski, P., Magyarfalvi, G., Saebo, S., Janowski, T., & Pulay, P. (2009). Quantum chemistry in parallel with PQS. *Journal of Computational Chemistry*, 30, 317.
- Bakken, V., & Helgaker, T. (2002). The efficient optimization of molecular geometries using redundant internal coordinates. *Journal of Chemical Physics*, 117, 9160.
- Banerjee, A., Adams, N., Simons, J., & Shepard, R. (1985). Search for stationary points on surfaces. *Journal of Physical Chemistry*, 89, 52.
- Becke, A. D. (1988). A multicenter numerical integration scheme for polyatomic molecules. *Journal of Chemical Physics*, 88, 2547.
- Becke, A. D. (1993). Density-functional thermochemistry. III. The role of exact exchange. *Journal of Chemical Physics*, 98, 5648.
- Bell, S., & Crighton, J. S. (1984). Locating transition states. *Journal of Chemical Physics*, 80, 2464.

- Bell, S., Crighton, J. S., & Fletcher, R. (1981). A new efficient method for locating saddle points. *Chemical Physics Letters*, 82, 122.
- Bertie, J. E., Apelblat, V., & Keefe, C. D. (2005). Infrared intensities of liquids XXV: Dielectric constants, molar polarizabilities and integrated intensities of liquid toluene at 25°C between 4800 and 400 cm<sup>-1</sup>. *Journal of Molecular Structure*, 750, 78.
- Beyer, M., & Clausen-Schaumann, H. (2005). Mechanochemistry: The mechanical activation of covalent bonds. *Chemical Review*, 105, 2921.
- Binkley, J. S., Pople, J. A., & Hehre, W. J. (1980). Self-consistent molecular orbital methods. 21. Small split-valence basis sets for first-row elements. *Journal of the American Chemical Society*, 102, 939.
- Blom, C. E., & Altona, C. (1976). Application of self-consistent-field *ab initio* calculations to organic molecules II. Scale factor method for the calculation of vibrational frequencies from *ab initio* force constants: Ethane, propane and cyclopropane. *Molecular Physics*, 31, 1377.
- Blom, C. E., & Altona, C. (1977a). Application of self-consistent-field *ab initio* calculations to organic molecules IV. Force constants of propene scaled on experimental frequencies. *Molecular Physics*, 33, 875.
- Blom, C. E., & Altona, C. (1977b). Application of self-consistent-field *ab initio* calculations to organic molecules V. Ethene: General valence force field scaled on harmonic and anharmonic data, infrared and Raman intensities. *Molecular Physics*, 34, 177.
- Blom, C. E., Otto, L. P., & Altona, C. (1976). Application of self-consistent-field *ab initio* calculations to organic molecules III. Equilibrium structure of water, methanol and dimethyl ether, general valence force field of water and methanol scaled on experimental frequencies. *Molecular Physics*, 32, 1137.
- Boffill, J. M. (1994). Updated Hessian matrix and the restricted step method for locating transition structures. *Journal of Computational Chemistry*, 15, 1.
- Born, M., & Oppenheimer, R. (1927). Zur Quantentheorie der Molekeln. *Annalen der Physik*, 389, 457.
- Broyden, C. G. (1970). The convergence of a class of double-rank minimization algorithms. I: General considerations. *Journal of the Institute of Mathematics and Its Applications*, 6, 76.
- Cerjan, C. J., & Miller, W. H. (1981). On finding transition states. *Journal of Chemical Physics*, 75, 2800.
- Csaszar, P., & Pulay, P. (1984). Geometry optimization by direct inversion in the iterative subspace. *Journal of Molecular Structure THEOCHEM*, 114, 31.
- Ditchfield, R., Hehre, W. J., & Pople, J. A. (1971). Self-consistent molecular-orbital methods. IX. An extended Gaussian-type basis for molecular-orbital studies of organic molecules. *Journal of Chemical Physics*, 54, 724.
- Eckert, F., Pulay, P., & Werner, H.-J. (1997). *Ab initio* geometry optimization for large molecules. *Journal of Computational Chemistry*, 18, 1473.
- Einstein, A., & Stern, O. (1913). Einige Argumente für die Annahme einer molekularen Agitation beim absoluten Nullpunkt. *Annals of Physics*, 40, 551.
- El Youssoufi, Y., Herman, M., & Liévin, J. (1998a). The ground electronic state of 1,2-dichloroethane I. *Ab initio* investigation of the geometrical, vibrational and torsional structure. *Molecular Physics*, 94, 461.
- El Youssoufi, Y., Liévin, J., van der Auwera, J., Herman, M., Federov, A., & Snavely, D. L. (1998b). The ground electronic state of 1,2-dichloroethane II. Experimental investigation of the fundamental and overtone vibrations. *Molecular Physics*, 94, 473.
- Farkas, O., & Schlegel, H. B. (1998). Methods for geometry optimization of large molecules. I. An O(N<sup>2</sup>) algorithm for solving systems of linear equations for the transformation of coordinates and forces. *Journal of Chemical Physics*, 109, 7100.
- Fletcher, R. (1970). A new approach to variable metric algorithms. *The Computer Journal*, 13, 317.
- Fletcher, R. (1980). *Practical methods of optimization* (Vol. 1). New York: Wiley.
- Fogarasi, G., Zhou, X., Taylor, P. W., & Pulay, P. (1992). The calculation of *ab initio* molecular geometries: Efficient optimization by natural internal coordinates and empirical correction by offset forces. *Journal of the American Chemical Society*, 114, 8191.
- Goldfarb, D. (1970). A family of variable-metric methods derived by variational means. *Mathematics of Computation*, 24, 23.
- Halgren, T. A., & Lipscomb, W. N. (1977). The synchronous-transit method for determining reaction pathways and locating molecular transition states. *Chemical Physics Letters*, 49, 225.
- Halls, M. D., Velkovski, J., & Schlegel, H. B. (2001). Harmonic frequency scaling factors for Hartree-Fock, S-VWN, B-LYP, B3-LYP, B3-PW91 and MP2 with the Sadlej pVTZ electric property basis set. *Theoretical Chemistry Accounts*, 105, 413.
- Hammond, G. S. (1955). A correlation of reaction rates. *Journal of the American Chemical Society*, 77, 334.

- Hertwig, R. H., & Koch, W. (1997). On the parameterization of the local correlation functional. What is Becke-3-LYP? *Chemical Physics Letters*, 268, 345.
- Hohenberg, P., & Kohn, W. (1964). Inhomogeneous electron gas. *Physical Review B*, 136, 864.
- Ionova, I. V., & Carter, E. A. (1993). Ridge method for finding saddle points on potential energy surfaces. *Journal of Chemical Physics*, 98, 6377.
- Jiang, H., Appadoo, D., Robertson, E., & McNaughton, D. (2002). A comparison of predicted and experimental vibrational spectra in some small fluorocarbons. *Journal of Computational Chemistry*, 23, 1220.
- Johnson, B. G., Gill, P. M. W., & Pople, J. A. (1993). The performance of a family of density functional methods. *Journal of Chemical Physics*, 98, 5612.
- Kohn, W., & Sham, L. J. (1965). Self-consistent equations including exchange and correlation effects. *Physical Review A*, 140, 1133.
- Kveseth, K. (1974). Conformational analysis. 1. The temperature effect on the structure and composition of the rotational conformers of 1,2-Dichloroethane as studied by gas electron diffraction. *Acta Chemica Scandinavica A*, 28, 482.
- Lindh, R., Bernhardsson, A., Karlström, G., & Malmquist, P.-A. (1995). On the use of a Hessian model function in molecular geometry optimizations. *Chemical Physics Letters*, 241, 423.
- Malagoli, M., & Baker, J. (2003). The effect of grid quality and weight derivatives in density functional calculations of harmonic vibrational frequencies. *Journal of Chemical Physics*, 119, 12763.
- McQuarrie, D. A. (2000). *Statistical mechanics*. California: University Science Books.
- Merrick, J. P., Moran, D., & Radom, L. (2007). An evaluation of harmonic vibrational frequency scale factors. *Journal of Physical Chemistry A*, 111, 11683.
- Mitin, A. V., Baker, J., & Pulay, P. (2003). An improved 6-31G\* basis set for first-row transition metals. *Journal of Chemical Physics*, 118, 7775.
- Mizushima, S., Shimanouchi, T., Harada, I., Abe, Y., & Takeuchi, H. (1975). Infrared and Raman Spectra of 1,2-Dichloroethane and its deuterium compound in the gaseous, liquid, and solid states. *Canadian Journal of Physics*, 53, 2085.
- Muir, M. & Baker, J. (1996). A systematic density functional study of fluorination in methane, ethane and ethylene. *Molecular Physics*, 89, 211.
- Murtagh, B. A., & Sargent, R. W. H. (1970). Computational experience with quadratically convergent minimisation methods. *Computer Journal*, 13, 185.
- Paizs, B., Baker, J., Suhai, S., & Pulay, P. (2000). Geometry optimization of large biomolecules in redundant internal coordinates. *Journal of Chemical Physics*, 113, 6566.
- Pardalos, P. M., Shalloway, D., & Xue, G. (Eds.). (1995). *Global minimization of nonconvex functions: Molecular conformation and protein folding*. Providence: American Mathematical Society.
- Peng, C., & Schlegel, H. B. (1993). Combining synchronous transit and quasi-newton methods to find transition states. *Israel Journal of Chemistry*, 33, 449.
- Peng, C., Ayala, P. Y., Schlegel, H. B., & Frisch, M. J. (1996). Using redundant internal coordinates to optimize equilibrium geometries and transition states. *Journal of Computational Chemistry*, 17, 49.
- Pople, J. A., Krishnan, R., Schlegel, H. B., & Binkley, J. S. (1979). Derivative studies in Hartree-Fock and Møller-Plesset theories. *International Journal of Quantum Chemistry: Symposium*, 13, 225.
- Poppinger, D. (1975). On the calculation of transition states. *Chemical Physics Letters*, 35, 550.
- Powell, M. J. D. (1971). Recent advances in unconstrained optimization. *Mathematical Programming*, 1, 26.
- PQS (2010). *PQS version 4.0*. Parallel Quantum Solutions 2013 Green Acres Road, Suite A, Fayetteville, AR 72703. Email: sales@pqs-chem.com; URL: <http://www.pqs-chem.com>.
- Pulay, P. (1977). *Direct use of the gradient for investigating molecular energy surfaces*. New York: Plenum.
- Pulay, P. (1980). Convergence acceleration of iterative sequences. The case of SCF iteration. *Chemical Physics Letters*, 73, 393.
- Pulay, P. (1982). Improved SCF convergence acceleration. *Journal of Computational Chemistry*, 3, 556.
- Pulay, P., & Fogarasi, G. (1992). Geometry optimization in redundant internal coordinates. *Journal of Chemical Physics*, 96, 2856.
- Pulay, P., & Torok, F. (1966). On the parameter form of the force constant matrix II. Investigation of the assignment with the aid of the parameter form. *Acta Chimica Academiae Scientiarum Hungaricae*, 47, 273.
- Pulay, P., Fogarasi, G., Pang, F., & Boggs, J. E. (1979). Systematic *ab initio* gradient calculation of molecular geometries, force constants, and dipole moment derivatives. *Journal of the American Chemical Society*, 101, 2550.

- Pulay, P., Fogarasi, G., Pongor, G., Boggs, J. E., & Vargha, A. (1983). Combination of theoretical *ab initio* and experimental information to obtain reliable harmonic force constants. Scaled quantum mechanical (QM) force fields for glyoxal, acrolein, butadiene, formaldehyde, and ethylene. *Journal of the American Chemical Society*, *105*, 7037.
- Raman, C. V., & Krishnan, K. S. (1928). A new type of secondary radiation. *Nature*, *121*, 501.
- Rassalov, V. A., Pople, J. A., Ratner, M. A., & Windus, T. L. (1998). 6-31G\* basis set for atoms K through Zn. *Journal of Chemical Physics*, *109*, 1223.
- Schäfer, L. (1983). The *ab initio* gradient revolution in structural chemistry: The importance of local molecular geometries and the efficacy of joint quantum mechanical and experimental procedures. *Journal of Molecular Structure*, *100*, 51.
- Schlegel, H. B. (1984). Estimating the hessian for gradient-type geometry optimizations. *Theoretica Chimica Acta*, *66*, 333.
- Shanno, D. F. (1970). Conditioning of quasi-Newton methods for function minimization. *Mathematics of Computation*, *24*, 647.
- Simons, J., Jorgensen, P., Taylor, H., & Ozment, J. (1983). Walking on potential energy surfaces. *Journal of Physical Chemistry*, *87*, 2745.
- Stephens, P. J., & Lowe, M. A. (1985). Vibrational circular dichroism. *Annual Review of Physical Chemistry*, *36*, 213.
- Stewart, J. J. P. (1989). Optimization of parameters for semiempirical methods I. Method. *Journal of Computational Chemistry*, *10*, 209.
- Swart, M., & Bickelhaupt, F. M. (2006). Optimization of strong and weak coordinates. *International Journal of Quantum Chemistry*, *106*, 2536.
- Wikipedia (2010). The article "Born–Oppenheimer approximation."
- Wilson, E. B., Decius, J. C., & Cross, P. C. (1955). *Molecular vibrations*. New York: McGraw-Hill.
- Wolinski, K., & Baker, J. (2009). Theoretical predictions of enforced structural changes in molecules. *Molecular Physics*, *107*, 2403.





# 9 Molecular Mechanics: Method and Applications

Valeri Poltev

Autonomous University of Puebla, Mexico

<b>Introduction</b> .....	<b>260</b>
<b>Foundations and General Scheme of Molecular Mechanics. Atoms as Elementary</b>	
<b>Units of the Matter</b> .....	<b>261</b>
General Expression and Terms of Molecular System Energy .....	261
Intramolecular Contributions to Molecular System Energy .....	262
Intermolecular and Non-bonded Intramolecular Interactions .....	263
General Remarks on Molecular Mechanics, its Accuracy, and Applicability .....	264
<b>A Bit of History. The “Precomputer” and Early Computer-Aided MM Calculations</b> ....	
First MM Applications to Three-Dimensional Structure and Thermodynamics of Organic Molecules .....	265
The Role of Molecular Crystal Study on the First Steps of Molecular Mechanics .....	266
Molecular Mechanics on the First Steps of Molecular Biology. Molecular Mechanics and Protein Physics .....	267
Molecular Mechanics on the First Steps of the Biophysics of Nucleic Acids .....	269
<b>The Problems and Doubts of Further Development of the MM Approach</b> .....	
Two Hypothetical Approaches to Choice of MM Formulae and Parameters .....	275
Various Schemes of Water Molecules in MM Calculations .....	276
<b>Modern Molecular Mechanics Force Fields and Their Applications</b> .....	
Allinger’s Force Fields and Programs .....	278
Merck Molecular Force Field (MMFF94) .....	278
The Force Fields and Programs Designed by Scheraga and Coauthors .....	279
Force Fields and Programs Developed by Kollman and Coauthors .....	280
Other Popular Force Fields and MM Software. CHARMM, OPLS, and GROMOS ...	281
<b>Conclusions</b> .....	
.....	286
<b>References</b> .....	
.....	287

The ultimate justification for the many severe approximations and assumptions made in the present work comes from the fact that the agreement between the simple calculations and the available experimental data is as good as it is.

N. L. Allinger, *J. Am. Chem. Soc.*, **81**, 5727, 1959

**Abstract:** A short survey of the general principles and various applications of molecular mechanics (MM) is presented. The origin of molecular mechanics and its evolution is followed starting from “pre-computer” and the first computer-aided estimations of the structure and potential energy of simple molecular systems to the modern force fields and the large system computations. The problem of “classic mechanics” description of essentially quantum properties and processes is considered. Various approaches to a selection of force field mathematical expressions and parameters are reviewed. The relation between MM simplicity and “physical nature” of the properties and events is examined. The possibility of a priori predictions of the properties of large systems is discussed in view of modern improvements of MM scheme. Quantum chemistry contributions to MM description of complex molecular and biomolecular systems are considered.

## Introduction

---

Molecular mechanics (MM) deals with a classical (“mechanistic,” i.e., Newtonian mechanics) description of molecular and supramolecular systems. The simplified assumptions and approximations enable one to use MM for wide applications to various systems, starting from simple low molecular weight molecules (such as numerous hydrocarbons) to large biomolecular complexes (such as those of proteins, nucleic acids, and membrane fragments) or material assemblies of many thousands of atoms. During a period of a bit longer than a half of a century the number of publications using this approach grew by many orders of magnitude. It was rather easy to follow nearly all the works related to MM calculations in the 1960s and in the early 1970s (and the author of this chapter tried to do so); today it is very difficult to follow all the papers related to the MM approach, even in a rather restricted area of application (e.g., to biopolymer structure and function). Thus it is impossible to consider all the applications of MM in a short survey, and the choice of the material for this chapter is “a matter of taste” of the author, who refers readers to other monographs and chapters for more general descriptions of the modern state and some of extended applications of MM; for recent references see, e.g., (Allinger 2010; Cramer 2004; Leach 2001; Ramachandran et al. 2008).

The MM method is used now not only in theoretical and computational works but also as a part of experimental studies (e.g., many X-ray and NMR-derived structures of proteins, nucleic acids, and their complexes with other molecules deposited in Protein Data Bank (Berman et al. 2003) and Nucleic Acid Data Bank (Berman et al. 1992) are the results of MM refinements). The MM semiempirical terms are used in some quantum mechanics computations, e.g., in the DFT-D method (Antony and Grimme 2006; Jurecka et al. 2007). We will follow the evolution of MM from the first “precomputer” and early computer-aided (i.e., before the era of personal computers) works to modern complex simulations impossible without supercomputers.

The rapid extension of MM simulations is a result of development of new branches of natural science related to molecular biology with its numerous applications, to directed synthesis of new substances with desirable properties (including new drugs and new materials for the industry), and many other areas of so-called nanoscience. The MM simulations enable one to perform a

preliminary selection of the compounds with desirable properties before experimental testing, and even before chemical synthesis itself. Sometimes it is impossible to rationalize completely experimental results without the construction of atom-level mechanistic model. In many cases the model cannot be derived from experimental data only, e.g., the accuracy of X-ray diffraction patterns for biopolymer fragments is not sufficient for the extraction of precise atom coordinates due to a complexity of the system and inherent irregularities of atom positions (e.g., delocalization of water molecules). In other cases the complex molecular system cannot be characterized by a single three-dimensional structure but by a set of conformations. MM simulations enable one to construct habitual atom-level molecular models of sufficiently complex systems favorable from an energy viewpoint. These models can be visualized by computer graphics programs and are ready to use for further investigations and refinements.

## Foundations and General Scheme of Molecular Mechanics. Atoms as Elementary Units of the Matter

---

The modern MM can be considered as an extension of the simple atom-and-bond representation of molecules and their complexes in chemistry. Scaled paper images, hand-made primitive models of atoms and bonds from wood and wire enabled subtle scientists to construct in 1950s the first successful models of proteins and DNA. The pioneering papers of Nobel Prize-winning authors can be mentioned in this relation (Pauling et al. 1951; Watson and Crick 1953). Ball-and-stick and space-filling plastic models as well as their computer images are widely used until for both teaching and investigation.

## General Expression and Terms of Molecular System Energy

---

The MM approach is a generalization and quantitative representation of these models via mathematic expressions (a set of such expressions together with numerical coefficients usually referred to as the force field). The modern mathematical expressions common in the MM method and for most force fields are the result of nearly a half of century of efforts of many researchers, trials and errors of both well-known and widely cited authors, as well as of those who contributed to specific parts of the computations of nonbonded energy for selected classes of molecules. In this section we will describe the general scheme and the main common assumptions of the MM method, leaving any references to specific papers for later sections. In the framework of the simple scheme (the so-called “Class I” model, the main subject of this survey), the systems (molecules or their complexes) are considered to consist of atoms, each atom being simulated as a single point particle. Molecular mechanics describes molecules in terms of “bonded atoms” (atoms in molecule), their positions are distorted from some idealized (equilibrium) geometry due to nonbonded interactions with the atoms of the same molecule or other molecules. Some papers consider not only atoms but lone pairs of electrons, chemical bonds, and other points as centers of interactions.

The first principal approximation of MM method is the additivity for several levels of calculations, namely, the additivity of energy terms responsible for the contributions of different physical nature, and the additivity of contributions of the atoms. The simple (“minimalist”) representation of the potential energy of a molecule or molecular complex as a function of atom

coordinates,  $\mathbf{R}$ , can be represented by a sum of four main terms each term being a sum of many contributions (● Eq. 9.1).

$$\Delta E(\mathbf{R}) = \sum E_b + \sum E_a + \sum E_t + \sum E_{nb} \quad (9.1)$$

The summing up in the terms is over all the chemical bonds (the first term), valence angles (the second term), torsion angles (the third term), and all the pairs of atoms non-bonded to each other or to a common third atom (the last term). The energy terms depend on mutual positions of atoms and on the adjustable constants (parameters); the parameters are suggested to be transferable between atoms and molecules of the same type. The transferability of the force field parameters is the second important assumption of MM, and the number of atom types depends on particular force field.

### Intramolecular Contributions to Molecular System Energy

The first and the second terms (sums of ● Eq. 9.1) refer to the energy changes due to variations of bond lengths, stretching (● Eq. 9.2), and bond angles, bending (● Eq. 9.3). These terms are usually modeled as harmonic potentials centered on equilibrium values of bond lengths and bond angles, respectively, i.e., “simple Hook’s law” dependences are used.

$$E_b = k b_i (l_i - l_i^0)^2 \quad (9.2)$$

$$E_a = k a_i (\alpha_i - \alpha_i^0)^2 \quad (9.3)$$

In these equations,  $l_i$  and  $\alpha_i$ , the current values of bond lengths and angles; parameters  $l_i^0$  and  $\alpha_i^0$ , equilibrium values for bond lengths and angles of this type;  $k b_i$  and  $k a_i$ , stretch and bend force constants, respectively. These adjustable parameters depend on types of atoms forming the bond or the valence angle. Some force fields may also contain cubic and higher-order contributions to these terms, or sometimes more flexible Morse potential can be used instead; additionally, “cross terms” can be included to account for correlations between stretch and bend components. In the latter case the terms depending on both bond length and angle variations are added. The third sum of the expression ● Eq. 9.1 refers to the changes of torsion energy; it is responsible for interactions of electron shells of two atoms, A and D (and of two bonds A–B and C–D), which are connected through an intermediate chemical bond B–C.

$$E_t = k t_i (1 + \cos(n_i \varphi_i - \delta_i)) \quad (9.4)$$

This periodic function (integer  $n_i$  being the periodicity) contains the current value  $\varphi_i$  of the angle  $i$  of the rotation around B–C chemical bond (the angle between the two planes defined by atoms A, B, and C and by B, C, and D), and three parameters ( $k t_i$ ,  $n_i$ , and  $\delta_i$ ;  $n_i$  is multiplicity and  $\delta_i$  is the phase angle) for each type of torsion (for each combination of four neighbor atoms of the molecule). These parameters can be estimated from experimental data on the structure and properties of the molecule considered and of related molecules, then they (as well as  $l_i^0$ ,  $\alpha_i^0$ ,  $k b_i$ , and  $k a_i$  of ● Eqs. 9.2 and ● 9.3) should be adjusted by trial computations. Many force fields include terms responsible for “improper” torsions or out-of-plane bending, i.e., terms related to four atoms not forming consecutive chemical bonds, which function as correction factors for out-of-plane deviations (for example, they can be used to keep aromatic rings planar). These terms can be expressed via harmonic potentials like those for bond stretching and valence angle bending. Cross terms depending on both torsion angle and bond length or valence angle are added in some force fields.

## Intermolecular and Non-bonded Intramolecular Interactions

The last sum of the  $\blacktriangleright$  Eq. 9.5 refers to so-called non-bonded interactions,  $E_{nb}$ , of all the atom pairs not bonding to each other or to the same third atom,  $\blacktriangleright$  Eq. 9.5. Each atom–atom term is usually represented by a sum of electrostatic, Coulomb (the first term of  $\blacktriangleright$  Eq. 9.5) and van der Waals (the second and the third terms of  $\blacktriangleright$  Eq. 9.5) interactions.

$$E_{ij}(r_{ij}) = Kq_i q_j / r_{ij} - A_{ij} / r_{ij}^6 + B_{ij} / r_{ij}^{12} \quad (9.5)$$

This equation contains  $r_{ij}$ , the current distance between  $i$  and  $j$  atoms;  $q_i$  and  $q_j$ , effective atom charges;  $A_{ij}$  and  $B_{ij}$ , adjustable parameters responsible for dispersion (London) attraction and short-range repulsion interactions, respectively. The atomic charges are usually derived using calculations via various quantum chemistry methods; effective dielectric constant implicitly accounting for surrounding can be used (this value may be distant dependent). The  $A_{ij}$  and  $B_{ij}$  coefficient can be preliminarily estimated via equilibrium inter-atomic distance and energy values at equilibrium for neutral pairs of atoms ( $\rho_{ij}$  and  $\epsilon_{ij}$ , respectively), and followed by the adjustment to reference experimental data. Most of the early force fields used for description of van der Waals interactions Buckingham (6-exp) potential instead of Lennard–Jones (6-12) as in  $\blacktriangleright$  Eq. 9.5. The total expression for nonbonded interaction term are usually referred as (1-6-12) or (1-6-exp) potential relating to the dependency of the terms on the inter-atom distance. The Buckingham potential is more flexible (it has three adjustable parameters instead of two for 6-12 potentials for each atom pair type) and has more physics basis for really existent distances (due to exponential dependence of electron wave functions on the distance from nuclei), but it is less convenient for computations. It has a maximum at short distance, and then trends to negative infinite value. A majority of the modern force fields utilize 6-12 expressions for description of van der Waals interactions, the total atom-atom potential being referred as 1-6-12 one. Some force fields substitute 6-12 potential with 10-12 for the interactions of hydrogen atoms of hydrogen bonds in order to describe more sharp distance dependence in the most important area of energy minimum corresponding to H-bond formation (referred as 1-10-12 potential). More complex expressions (including those dependent on the angles between two straight lines connected three atoms of H-bond) were used for H-bond description in some early potential sets. The nonbonded terms of the intramolecular energy related to 1-4 interactions (i.e., the interactions between atoms in a molecule separated by three chemical bonds) are frequently accounted for with a coefficient less than 1 (1-4 scaling) as these interactions are already included into torsion term ( $\blacktriangleright$  Eq. 9.4). To reduce the number of adjustable  $A_{ij}$  and  $B_{ij}$  parameters of Lennard–Jones potential (and corresponding parameters of other potentials), the combination rules for  $\rho$  and  $\epsilon$  values for pairs of different atoms are usually applied.

$$\rho_{ij} = \rho_i + \rho_j; \epsilon_{ij} = (\epsilon_i \epsilon_j)^{1/2} \quad (9.6)$$

Some force fields apply the combination rules directly to the coefficients of van der Waals terms.

The calculations of potential energy via  $\blacktriangleright$  Eq. 9.1 are used to search for local energy minima (mutual atom positions corresponding to possible stable configurations), to construct and analyze multidimensional energy surfaces, to follow trajectory of movement (in MD, molecular dynamics simulations), or to study averaged thermodynamic and geometry characteristics (via MC, Monte Carlo sampling) of the systems.

## General Remarks on Molecular Mechanics, its Accuracy, and Applicability

---

The first computer (and all “precomputer”) applications of mechanistic approach to molecule conformations and interactions ignored certain energy terms (e.g., stretching, bending, torsion, or electrostatic ones). Some modern works ignore certain terms in order to reduce the number of variables of energy function, e.g., considering the bond lengths as the constants (their changes in many cases are very small and have no influence on energy and geometry of minimal energy structures). The simplest of such approaches considers bond lengths and valence angles as constants, ignores torsion energy (the contributions of the first three terms of [Eq. 9.1](#) being zeros), and utilizes “hard sphere approach” to nonbonded interactions. This approach is a mathematical representation of plastic (or wood, iron, etc.) space-filling mechanical models or their computer images. The configurations are forbidden when any two non-bonded atoms are closer to each other than a sum of van der Waals radii (these configurations have infinite positive energy), all other being allowed (with zero energy). Already this oversimplified approach enables one to obtain some important results, e.g., to reject certain configurations and even possibly to synthesize the molecule with inevitably too close positions of non-bonded atoms. The first “Ramachandran maps” for proteins (which will be discussed in the next section) have demonstrated allowed and forbidden regions on two-dimensional plots of the fragment of polypeptide chain. These maps were subsequently improved using more realistic MM functions or quantum mechanics calculations.

Most modern MM computations include additional terms besides those already mentioned. These terms refer to direct imposition of experimental data (e.g., NMR-derived restraints on inter-atom distances or global characteristics of the macromolecule) and describe specific quantum effects not accounted for by standard MM force field formulae.

The complexity of mathematic expressions and the number of parameters depend on the systems considered. The problem of “which atoms pertain to the same type and which ones are of different types” is considered by the authors of specific force fields and software depending on the tasks and computer resources. The atom type may depend not only on the chemical element and electron shell configuration, but on neighbor atoms and on the structure of the whole molecular fragment (e.g., the carbons of six-member and five-member aromatic rings having the same three bonded atoms may be considered as pertaining to different atom types). The more broad the applications that are planned for the force field, the greater the number of atom types that should be involved, and the more complex force field formulae that should be constructed. The first works that deal with the tasks related to specific systems (e.g., the conformations of saturated hydrocarbons or peptide fragments) usually contained a few parameters; the modern force fields may contain thousands of parameters (in spite of use of combination rules mentioned above).

Various physical considerations can be used for preliminary estimation of mathematic expressions and parameter values (rather simplified considerations were used in [Eqs. 9.2–9.5](#)). It is important to emphasize that neither dependences nor values of parameters can be “derived” (directly calculated) from universal principles or measured by any experimental method. The stretch and bend constants (of [Eqs. 9.2](#) and [9.3](#)) can be evaluated using infra-red spectra; equilibrium bond lengths and valence angles can be estimated from X-ray data for simple molecules. The  $A_{ij}$  coefficients of the attraction part of van der Waals interactions can be evaluated (and really were calculated and used without refinement in the first MM works) via approximate formulae for dispersion interactions; however, their exact values for the certain class of the systems should be adjusted by comparison with experimental data

or with the most exact quantum chemistry results after trial computations for reference set of related systems. The same is valid for other terms and their parameters. Some parameters have rather simple physical meaning and restricted areas of possible values (e.g., equilibrium distances between bonded atoms or barriers to rotation about the bonds), other parameters have only approximate relation to physical values (atom charges,  $B_{ij}$  coefficients of Lennard–Jones potential). As all the parameters are adjustable ones, only the values of total energy and the equilibrium geometry of the molecular system can be compared with experimental data, and consequently have the strict physical meaning, not the individual contributions or the values of the individual parameters. As various force fields utilize different reference sets of data, the individual parameters are not transferable between different force fields even in cases where they use the same mathematical expressions. Different force fields may result in the nearly equal energy and geometry of local minima configurations but rather different values of the individual term contributions. Thus individual terms of the energy may have very approximate physical interpretation, although in some cases it is interesting to evaluate the certain energy contributions and to follow their changes for different molecular complexes and different configurations (and many researchers include these evaluations in their publications).

It is worth mentioning that preliminary consideration of MM scheme has resulted already in some doubts and objections. Generally speaking, the classical description of the essentially quantum molecular systems cannot be exact and full. Most of the terms in [Eqs. 9.2–9.5](#) refer to the first approximation or to the first term of expansion of the corresponding interaction energy. The atoms are not points, they have dipole and quadrupole moments (not only charges), charge distribution in a molecule is continuous, the polarization or electron delocalization interactions are not considered in the classical “minimalist” MM approach, the contributions of three-body and four-body interactions can be essential ones. Many attempts have been undertaken to overcome these inherent difficulties of the MM method as well as to justify the assumptions and simplifications; we will consider some of these attempts below. Few remarks for justification of the main principles of MM method are described here.

The possibility of consideration of atoms as elementary subunits of the molecular systems is a consequence of Born–Oppenheimer or adiabatic approximation (“separation” of electron and nuclear movements); all quantum chemistry approaches start from this assumption. Additivity (or linear combination) is a common approach to construction of complex functions for physical description of the systems of various levels of complexity (cf. orbital approximation, MO LCAO approximation, basis sets of wave functions, and some other approximations in quantum mechanics). The final justification of the method is good correlation of the results of its applications with the available experimental data and the potential to predict the characteristics of molecular systems before experimental data become available. It can be achieved after careful parameter adjustment and proper use of the force field in the area of its validity. The contributions not considered explicitly in the force field formulae are included implicitly into parameter values of the energy terms considered.

## A Bit of History. The “Precomputer” and Early Computer-Aided MM Calculations

---

The quantitative estimations of molecular properties via simple atom-level mechanics representations originate from the communications of Hill (1946, 1948), Westheimer and Mayer (1946), and Barton (1948, 1950). All these papers refer to conformations of organic molecules. It is



interesting to mention that mathematic expression of potential energy suggested in the pioneering work of Hill (1946) contains common for all the modern force fields stretch and bend components (• Eqs. 9.2 and • 9.3 of previous section) as well as the Lennard–Jones terms of non-bonded interaction energy. Westheimer and Mayer (1946) suggested use of exponential terms for description of steric repulsion. The first calculations for selected conformations of rather simple (“medium size”) molecules (such as diphenil derivatives) (Westheimer and Mayer 1946), cis-decalin, and steroids in the papers of Barton (1948, 1950) were performed manually or using desk calculators. Some researchers constructed “hand-made” models of steel or wood (e.g., of cyclic saturated hydrocarbons in the papers of Allinger (1959)) for careful measurements of geometry parameters. The importance of quantitative estimations of nonbonded interactions for considerations of three-dimensional structure of organic molecules was emphasized starting from the first mechanical considerations, as was clearly shown by Bartell (1960). He illustrated the preference of the “soft sphere” over “hard sphere” approach to the analysis of hydrocarbon structures, and suggested one of the first (6-12) parameters for hydrocarbons (Bartell 1960). Already mentioned above, rather approximate calculations clearly demonstrated the utility of MM approach to the problems of organic chemistry as well as the need for further extensive computations and searching for more reliable parameters. We will refer to all these quantitative theoretical considerations of molecular properties as MM, not depending on use of this term by the authors, and on methods of estimation of different types of interactions.

Rapid expansion of MM method starting from the 1960s was provoked by an introduction of computers into all the branches of natural science. In this section we will briefly consider some examples of the first computer-aided applications of the MM method to three research areas, namely, physical organic chemistry (these works can be considered as a continuation of the “precomputer” papers mentioned above), the structure and properties of molecular crystals, and the interactions and conformations of biopolymers.

## First MM Applications to Three-Dimensional Structure and Thermodynamics of Organic Molecules

---

The first paper on a computer study of organic molecule conformations was related to saturated hydrocarbons (Hendrickson 1961). The angle bending, torsion, and (6-exp) van der Waals contributions to the conformation energy were taken into account, while constant values were assigned to bond lengths. The computer calculations of cyclo-alkanes containing 5, 6, and 7 carbon atoms enabled the author to consider various conformers and to reproduce and rationalize the experimental data. During 1960s and the beginning of 1970s, such computations were performed by several groups of investigators. Hendrickson (1962, 1973, and references therein) and Allinger and Sprague (1973 and references therein) extended the MM approach to more complex hydrocarbons, including those with delocalized electronic systems. Allinger's computations took into account bond stretching in addition to terms used by Hendrickson. The electrostatic term has not been included in these papers as hydrocarbons are non-polar molecules; it was introduced later when more broad sets of molecules became to be considered.

The most important results of early MM computations of organic compounds can be illustrated by the Engler et al. paper (1973) titled “Critical Evaluation of Molecular Mechanics.” The calculations for various hydrocarbons have been performed using two rather different force fields, their own and that of Allinger et al. The two force fields have substantially different parameters as different sets of experimental characteristics were used for parameter adjustment. It results in significant difference of separate terms of the energy, which may vary by several times

or even be positive for one force field and negative for another one. Nevertheless, total energies and relative values for various conformations calculated by two force fields are close to each other for most of compounds considered. Some disagreements between the results obtained via two parameter sets are discussed, and a need for their further refinement was mentioned; two phrases of the paper abstract can be considered as characteristics of whole situation with MM approach for that time: “*Most of the available data are reproduced with an accuracy rivaling that achieved by the experimental methods*” and “*The molecular mechanics method, in principle, must be considered to be competitive with experimental determination of the structures and enthalpies of molecules.*”

Since the publication of above mentioned papers, the theoretical conformational analysis using MM force fields has become an inherent part of physical studies of organic molecules. It became clear that, in spite of difficulties with the parameter choice, the MM calculations are not only a useful tool in rationalizing experimental observations, and in reproducing and predicting the structure and energy characteristics of “medium size” organic molecules with experimental accuracy, they can also help in the elaboration of pathways of chemical synthesis. Separate mathematical expressions and parameters are transformed into *force fields*, i.e., to complete and verified sets of the formulae and constants, and ready-to-use computer programs. One of the first such force fields and programs was the MM1 program based on the paper by Allinger and Sprague (1973), which then was followed by MM2, MM3, and MM4 force fields and software for broad class of organic molecules. The inclusion of new atom types and new terms of energy, as well as parameter refinement continued for years, and we will discuss these program sets in the following sections, together with other force fields and software.

## The Role of Molecular Crystal Study on the First Steps of Molecular Mechanics

---

The first publications on the MM approach to molecule conformations mentioned above deal with *intramolecular* interactions. The first works on such an approach to *intermolecular* interactions belong to one of the pioneers and founders of MM, A. I. Kitaigorodsky (other spellings, Kitaigorodskii, Kitajgorodskij, Kitaygorodsky), though he did not use the term “Molecular Mechanics.” Nearly at the same period (the 1950s) as Hill and Westheimer, usually mentioned as initiators of MM approach, he suggested to considering mechanic models of molecular systems quantitatively via mathematical expressions. In the 1950s he foresaw the applications of the method to various problems of physics and physical chemistry of organic and biological molecules, including the problems of crystal structure, adsorption, and conformational transitions. We refer to the most frequently cited works of Kitaigorodsky (1961, 1973), although his first publications and congress presentations on the subject date from the 1950s (many of them were not published in English). Kitaigorodsky used structure and thermodynamic data on the crystals of organic molecules for adjustment of parameters of atom–atom potential functions for calculations of nonbonded interaction energy. This term of the total energy is dominant for molecular crystals. The method of atom–atom potentials was suggested as a generalization of the “principle of close packing” of molecules in molecular crystals he discovered earlier; his book (Kitaigorodski 1959) describing this principle is still widely cited. Later he demonstrated that this principle is a consequence of a more general atom–atom approach to potential energy of molecular crystals. Kitaigorodsky was the first researcher to suggest considering the interactions of non-bonded atoms in a molecule and of such atoms of different molecules via the same mathematic expressions and parameters (applications of

MM approach to biopolymers would be impossible without this suggestion). The studies of molecular crystals via the MM approach were important not only for the intrinsic problems of crystallography, but they enabled one to derive potential functions for nonbonded interactions and to test the fidelity and accuracy of the approach itself using extensive sets of available quantitative data on structure and energy of molecular crystals. Such justification was important for the first steps of the MM approach and for its extension to various branches of natural science.

Some energy terms were ignored in the first MM works on conformations of organic molecules, but it is impossible to predict a priori what types of contributions to intramolecular interactions energy (sums in [Eq. 9.1](#)) can be reasonably neglected for specific types of molecules. Considering crystal structure of nearly rigid molecules (e.g., aromatic rings) it is possible to ignore (at least in the first approximation) all the terms but the last one in [Eq. 9.1](#). This assumption is just a consequence of examination of the geometry of series of related molecules in crystals (e.g., aromatic hydrocarbons consisting of six-atom rings); all of them have nearly equal values of bond lengths and angles not depending on molecular complexity and the type of crystal packing. For hydrocarbons it is possible (again at least for the initial studies) to ignore electrostatic contributions as well (the molecules have no dipole moment, and all the estimations of atom charges result in small values, less than 0.1 of electron charge). Kitaigorodsky suggested step-by-step selection of potential functions starting from molecules of nearly neutral atoms of two types (hydrocarbons) and introducing next atom types one-by-one for selecting next parameters. His pioneering works on molecular crystals were followed by more extensive computations by other authors. Some of these works were inspired by his ideas and followed his methodology (e.g., first papers of Williams (1966, 1967)) other researchers performed computations using different expressions for nonbonded potentials and additional terms of the energy (e.g., Lifson and Warshel 1968; Warshel and Lifson 1970). The common set of (6-exp) parameters for C...C, C...H, and H...H intermolecular interactions was obtained by Williams (1967) from energy and structure calculations for crystals of both aromatic and aliphatic hydrocarbons. Warshel and Lifson (1970) derived “consistent force field” parameters for description of both intermolecular and intramolecular interactions in crystals. This set contains both parameters for van der Waals interactions and other terms of energy mentioned in the previous section. Mason and coauthors (e.g., Craig et al. 1965; Rae and Mason 1968; Mason 1969) used a combined approach to calculations of intermolecular interactions in crystals, namely, repulsive terms were calculated at an atom–atom level while attractive ones were considered on a bond–bond level. Such an approach and other changes of simple atom–atom scheme are not convenient for computations, and we would like to cite a phrase from Mason’s paper comparing his and Kitaigorodsky’s methods: “Although the representation of the attractive potential by spherically symmetric atom–atom interactions cannot be justified theoretically, it has been outstandingly successful in predicting the properties of crystals” (Mason 1969). We will not cite later publications on the crystal studies via MM approach, but we would like to mention that early papers (of the 1960s and 1970s) enabled the researchers to suggest potential functions for calculations of nonbonded interactions and to demonstrate a possibility to predict energy and structure characteristics of the crystals via this computational approach. The calculations for molecular crystals became a part of the selection and test of the parameters during elaboration of nearly all modern force field. Later MM calculations for molecular crystals enabled researchers to examine the approximations accepted in force field elaboration and to derive force field versions with additional terms of energy (including polarization and additional to atom centers, e.g., Williams and Weller (1983)).

## Molecular Mechanics on the First Steps of Molecular Biology. Molecular Mechanics and Protein Physics

Development of molecular biology and biophysics in the 1960s required a quantitative consideration of the conformations and interactions of proteins, nucleic acids, and biomolecules in general. The problems of biological importance were to rationalize the structure and conformational properties of the proteins and nucleic acids, namely to understand the contributions of the subunits and to construct the models of the most favorable conformations of the fragments. We already mentioned in a previous section that the first successful models of regular structures of proteins and DNA duplex were constructed using “hand-made” fragments of paper, wood, wire in 1950s. For understanding, explanation, and prediction of molecular level mechanisms of biopolymer functions, it was necessary to work out the method of quantitative simulation of the three-dimensional structure and properties of biomolecules. The first molecular mechanics considerations of biopolymer fragments were performed in 1960s. We will follow briefly such studies for proteins and DNA in a few paragraphs below.

The general problems on proteins that can be in principle solved via MM simulations are (1) the construction of three-dimensional structure of the macromolecule and prediction of the pathways of “protein folding” using restricted experimental data (ideally, the primary structure only); (2) the refinement of experimental structure (X-ray diffraction patterns usually do not supply us with information sufficient for precise atom coordinate assignment). The whole problem of the proteins functioning as enzymes cannot be solved via MM only, as chemical reactions are beyond the MM approach, quantum mechanics considerations are indispensable. Nevertheless, the MM approach is useful for the problems of enzyme-substrate complex formation and of molecular recognition, which are crucial for protein functions.

First of all, two important results on protein structure obtained before classical MM computations should be mentioned. The atom-level structures of  $\alpha$ -helical and  $\beta$ -sheet fragments of polypeptide chains were designed by Linus Pauling and Robert Corey in (1951) using hand-made models of wood (Pauling and Corey 1951; Pauling et al. 1951). Such regular structures are the intrinsic parts of the majority of the proteins. The success in the construction of these first models of the regular protein fragments (as well as of the DNA duplex) primarily depended on correct subunits geometry and a potential to predict the correct scheme of hydrogen-bond formation, all other contributions to intramolecular interactions being of secondary importance. The regular structures imply H-bond formation between N–H donors and C=O acceptors of the peptide groups of the same chain for  $\alpha$ -helix, and of other chain or of distant parts of the same chain for  $\beta$ -sheet. As was pointed out more than half of century ago (Eisenberg 2003), “In major respects, the Pauling–Corey–Branson models were astoundingly correct, including bond lengths that were not surpassed in accuracy for >40 years”.

The second important “precomputer” result refers to construction via hard-sphere models of a two-dimensional map for possible (and impossible) conformations of the dipeptide unit, the so-called Ramachandran plot (Ramachandran et al. 1963). The polypeptide backbone consists of repeating peptide groups connected via  $C_\alpha$  atoms, the latter being connected to hydrogen atoms and amino-acid residue (the first atom of the residue is designated as the  $C_\beta$  atom). The peptide group is practically planar, and the only single bonds in the peptide chain are those between the  $C_\alpha$  atom and two neighbor peptide groups ( $C_\alpha$ –N–H of one group, the torsion angle for rotation about this bond is designated as  $\Phi$ , and  $C_\alpha$ –C=O of the next group, the torsion angle for rotation about this bond is designated as  $\Psi$ ). Using mathematical expressions for atom coordinates suggesting fixed bond lengths and bond angles, Ramachandran et al. (1963)

constructed the two-dimensional  $\Phi - \Psi$  maps with two sets of van der Waals atom radii, “normally allowed” and “outer limit,” i.e., normal and shortened radii. The main part of the maps for all the amino-acid residues except glycyl corresponds to the conformations forbidden due to shortened atom-atom contacts, while  $\alpha$ -helix and  $\beta$ -sheet fall into the allowed regions. For glycyl residue the allowed regions were considerably more extended. It took about half a year to construct these maps using a desk calculator (Ramachandran 1990); later such maps were computationally constructed using various force fields and quantum mechanics methods; superposition of  $\Phi - \Psi$  combinations corresponding to experimentally or computationally constructed three-dimensional structure of proteins and peptides on a Ramachandran plot helps to check and rationalize the protein models nearly a half of century. The consideration of dependence of a Ramachandran plot on amino acid residue via a hard sphere approach enabled (Leach et al. 1966a) to evaluate semi-quantitatively the parts of a two-dimensional map corresponding to allowed conformations for different amino-acid residues (from about 50% of all conceivable conformations for glycyl to only 5% for valyl). The evaluation of steric restrictions emphasizes their important role as a determinant in protein conformation; the consideration of  $\alpha$ -helices demonstrated that the preference of the right-handed ones in comparison to left-handed helices is due essentially to interactions of the  $C_{\beta}$  atom of the side chains with atoms in adjacent peptide units of the backbone (Leach et al. 1966b). The “hard sphere” approach was applied to search for allowed conformations of cyclic oligopeptides, e.g., Némethy and Scheraga (1965).

The main conclusion of the “hard sphere” works was that steric effects are one of the most important factors in determining polypeptide conformations. “Many conformations of a polypeptide can be classed as energetically unfavorable without consideration of other kinds of interactions; however, the method breaks down to the extent that it cannot discriminate between those conformations that are sterically allowed. The contribution that this method made is that more than half of all the conceivable polypeptide conformations are now known to be ruled out by steric criteria alone (Scott and Scheraga 1966a). Nearly at the same time (the middle of 1960s) as the above mentioned hard sphere considerations of peptides, the first applications of MM formulae to protein structure were started using “soft atoms”; and the first parameters of potential functions suitable for peptide subunits calculations were suggested. The first such works were published by three groups of researchers, namely those of De Santis and Liquori (De Santis et al. 1965), Flory (Brant and Flory 1965), and Scheraga (Scott and Scheraga 1966a). All these works were preceded by the publications of the authors related to synthetic polymers, and various contributions to the potential functions were primarily studied by them when considering synthetic polymers and their fragments. The bond lengths, valence angles, and planar peptide group in the all the early studies of polypeptides were fixed.

De Santis et al. (1963) have carried out the calculations of the van der Waals term of the energy using different potentials for regular conformations of linear polymers as functions of torsion angles of monomer units. The deepest minima of the conformational diagrams were found very near to the experimental structures, as obtained by X-ray fiber diffraction methods, for a series of polymers investigated including polyethylene, poly(tetrafluoroethylene), poly(oxy-methylene), and polyisobutylene. When the calculations were extended to the polypeptides (polyglycine, poly-L-alanine, and poly-L-proline), good agreement with the experiments was obtained as well (De Santis et al. 1965). After nearly 30 years De Santis wrote, “While other contributions to the conformational energy are included in the calculations, the dominant role of the van der Waals interactions remains well established as the main determinant of the conformational stability of macromolecules” (De Santis 1992).

Brant and Flory (1965) have carried out the calculations on peptide unit energy in which they included torsion potentials, van der Waals (6-exp) interactions, and dipole-dipole interactions between the permanent dipole moments of near-neighbor peptide groups. The conformational energies were used by Brant and Flory in statistical mechanical calculations of the mean-square unperturbed end-to-end distance of various polypeptide chains. They concluded that it was necessary to include the dipole-dipole electrostatic interactions in the energy calculations to obtain agreement between the calculated and experimentally determined chain dimensions, and thus that these interactions are important in determining polypeptide conformations.

The first publication of Scheraga's group related to "soft atoms," MM simulations related to proteins (on helical structures of polyglycine and poly-L-alanine (Scott and Scheraga 1966a) included, besides contributions considered in the paper of Brant and Flory (1965), explicit accounting of hydrogen bonds and interactions of atom charges of peptide group. Rather complex expression for dipole-dipole energy of interactions between peptide groups used by Brant and Flory (1965) was substituted by Coulomb atom-atom terms, and (6-exp) expressions for van der Waals interactions were substituted in this paper and subsequent publications by (6-12) potentials, but an additional complicated expression for description of hydrogen bond energy was added. The method and parameters for calculation of torsion and van der Waals energies were earlier developed by Scott and Scheraga (1966b) for normal hydrocarbons and polyethylene; for these systems other contributions to the energy dependence on conformation can be neglected. These parameters were used then for proteins calculations. It is interesting to note that both groups of authors (those of Flory and of Scheraga) applied without further refinement the approximate Slater-Kirkwood equation for calculation of coefficient for attractive term of van der Waals energy (the coefficients were expressed via polarizabilities and effective numbers of electrons of the interacting atoms) and van der Waals radii for calculation of repulsion term parameters. The approximate character of such parameters is evident, but good agreement with experimental results was obtained in the both publications (Brant and Flory 1965; Scott and Scheraga 1966a). The existence of polyglycine and poly-L-alanine regular  $\alpha$ -helices was rationalized as a consequence of favorable both H-bond and van der Waals interactions, while helices of other possible types ( $\omega$  and  $3_{10}$ ) lie in relatively high-energy regions, and for isolated helices these structures have been excluded (Scott and Scheraga 1966a).

The above mentioned calculations of Scheraga et al. on protein simulations were followed by a series of publications related to both improvements of the method (both parameter adjustments and new term additions) and of simplifications of computations. Such changes in the methods enable them to obtain preliminary results on peptides of up to 20 amino-acid residues already in 1967 (Gibson and Scheraga 1967a,b). The improvements to the method relate to enlarging the equilibrium radii of atoms, assigning partial charges to each atom (but neglecting the electrostatic contribution when the atoms are not close together), and introduction of orientation-dependent term for H-bond description instead of complicated formulae of the previous paper (Scott and Scheraga 1966a). Additional terms were introduced to account for the presence of disulfide bridges (Gibson and Scheraga 1967b). The simplified account for solvent contribution to the energy has been included, considering the effect of removing the nearest-neighbor to peptide water molecules (Gibson and Scheraga 1967a). The simplification of the model refers to introducing "extended atom," i.e., CH, CH<sub>2</sub>, and CH<sub>3</sub> groups were considered as the single atom to reduce the number of interactions that had to be computed (this approach was used later in many force fields and such potential functions are commonly referred as "united atom" potentials). Scheraga's group continued the improvement of the parameters and



the method continuously until recent years. It resulted in the release of ECEPP (Empirical Conformational Energy Program for Peptides) (Momany et al. 1975), ECEPP/2 (Sippl et al. 1984), ECEPP/3 (Némethy et al. 1992), and the next versions of the force fields and software. We will discuss these studies below, however, first we will mention some improvements performed in the first half of 1970s. The most important improvements relate to description of H-bond potential by (10-12) expression (McGuire et al. 1972) (some other force fields adopted such dependence for description of interaction between hydrogen atom capable to participate in H-bond and atom-acceptor of H-bond), to calculation of partial charges via semi-empirical CNDO/2 method (Yan et al. 1970), and to adjustment of repulsion part of van der Waals interactions to crystal data for extensive set of molecules including amino acid crystals (Momany et al. 1974, 1975). The results of the crystal calculations led to an internally self-consistent set of interatomic potential energies for interactions between all types of atoms found in polypeptides (ECEPP force field (Momany et al. 1975)). The bond lengths and bond angles were obtained from a survey of the crystal structures and were considered as fixed for each of amino acid residue (Scheraga's force fields differ in this feature from the most of other widely used force fields). The authors mentioned that the potential functions can be improved further, but the long time is required to develop new ones, and the present ones will be very useful for calculations on polypeptides and proteins in the foreseeable future (Momany et al. 1975). They used the preliminary set of potential functions to refine X-ray structures of some proteins, lysozyme,  $\alpha$ -lactalbumin, and rubredoxin (Rasse et al. 1974; Warme et al. 1974).

We will not consider details of these papers; instead we will mention the first publication on MM refinement of X-ray protein structure of Levitt and Lifson (1969). The refinements of protein structures (myoglobin and lysozyme) have been performed via two steps by minimization of the energy function containing all the MM terms and an additional term describing deviation of the atom coordinates from their values obtained from X-ray diffraction studies (penalty functions). The initial co-ordinates of a protein molecule have been obtained from measurements on a rigid wire model, built according to electron density maps derived from X-ray diffraction measurements. Three energy terms (corresponding bond stretching, bond angle bending, and torsion potentials) supplemented by penalty functions were used at the first step. In the second step, non-bonded and hydrogen-bonded interactions were included, and penalty functions were omitted. The authors mentioned that energy function parameters are preliminary, intended for protein simulation in aqueous solution, differing significantly from those of Scheraga, and subject to further improvement. The nonbonded potentials were strongly attractive between non-polar, hydrophobic groups and those polar groups that can form hydrogen bonds. Other interactions between polar groups unable to form hydrogen bonds, and those between polar and non-polar groups, are made entirely repulsive (Levitt and Lifson 1969). The refined structures are close to X-ray diffraction ones and do not contain short atom-atom contacts or unusual bond lengths and valence angles. Starting from rough model coordinates, the method minimizes the assumed total potential energy of the protein molecule to give a refined conformation (Levitt and Lifson 1969).

## Molecular Mechanics on the First Steps of the Biophysics of Nucleic Acids

---

The problems related to the MM approach to nucleic acid structure and functions differ in some aspects from those for proteins. The main computational tasks in the 1960s in the area of the nucleic acids were to rationalize the structure of native and modified DNA duplexes, t-RNAs,

synthetic polynucleotides, i.e., to understand the contribution of the subunits (the bases, sugars, ionized phosphate groups, counter-ions, and surrounding water) to three-dimensional structure, and to evaluate the contributions of interactions of different physical nature to structure and functions of nucleic acids. The extensive applications of the MM approach to nucleic acids commenced a few years after those for proteins. The same is true for the adjustment of MM parameters for calculations of nucleic acids. Such a situation can be explained by “special role” of DNA in cells as a heredity material as well as by expectations of “specific” forces between the bases as conjugated molecules with delocalized electron system. Many researchers considered the electron exchange via H-bonds in base pairs and exchange interactions between stacked bases as the crucial contributions to nucleic acid functioning. It took some years before pioneers of a quantum mechanics approach to biochemical problems would write: “The possible contributions of resonance energy stabilization through electronic delocalization across the hydrogen bond for horizontal interactions and of overlapping of their  $\pi$ -electronic cloud or of charge-transfer complexation for the vertical interactions appear to be of much smaller order the magnitude than the stabilization increments due to van der Waals-London forces” (Pullman and Pullman 1968).

The author of this survey was the first researcher since the application of MM formulae in 1966 to consider the interactions of nucleic acids subunits. We will now briefly follow the route of investigations of nucleic acid interactions to the “classic” MM approach. The first quantitative estimation of interactions of bases in DNA duplex via formulae of intermolecular interactions was performed by De Voe and Tinoco (1962). They used so-called molecule dipole approximation, i.e., permanent and induced electric point dipoles were placed into the center of each base. The energy of interaction between two paired or stacked bases was suggested to be a sum of the interactions of permanent dipoles, permanent dipole-induced dipole, and of induced dipoles (London dispersion interaction). Such an approximation does not enable them to obtain qualitatively correct results (e.g., the energy of interaction between the bases in Watson-Crick A:T pair was positive), but the computational problem of evaluation of interaction energy changes on the formation of the specific nucleic acid conformation was defined in this paper. That is why it is cited in hundreds of publications over nearly a half of century; many of them, including those of the author of this survey, were inspired by the paper of De Voe and Tinoco (1962). Shortly it became clear that such an approximation is invalid for this system, not depending on dipole location, as well as after replacement of point dipoles by “real” ones, i.e., by dipoles of definite size. Bradley et al. (1964) suggested that the main contribution into base-base interaction energy is of a Coulomb electrostatic nature, which can be calculated in “monopole approximation.” The point charges were calculated via semi-empirical methods of quantum chemistry and placed on each atom of the bases. This paper was followed by the papers of Nash and Bradley related to calculations of base-base interactions. One of their papers should be mentioned in relation to the general progress and development of MM approach. Starting from various mutual in-plane positions for all the combinations of RNA bases, the calculations and search for minima of electrostatic energy was performed (Nash and Bradley 1966). Van der Waals energy was taken into account in “hard sphere” approximation, i.e., any non-hydrogen atom pair should not be closer than sum of van der Waals radii. As a result of the calculations, 27 energy minima were obtained that have two or more short N-H...O or N-H...N contacts (with N...N or N...O distances about 3 Å) corresponding to nearly linear or bifurcated hydrogen bonds. The results enabled Nash and Bradley to rationalize the available experimental data on base crystals data, as well as base-base complex formation in solutions and polynucleotides. It appeared that the observed base pairings with two H-bonds in crystals always correspond to one of the computed geometries of lowest energy (Nash and Bradley 1966). Some additional regularities



of base pairing obtained later using more rigorous approaches could be derived from the results of this paper. We will not discuss this and other interesting works of Bradley and coauthors in more detail, but it is important to emphasize that Bradley and co-workers' (1964) "monopole" approach to calculations of the base interaction was the first attempt to consider the electrostatic energy in the framework of the modern MM scheme. The above mentioned calculations of Scheraga's group with inclusion of point charges of peptide group were started 2 years after the Bradley's publication.

The subsequent studies on the quantitative evaluation of the interactions and three-dimensional structure of nucleic acid fragments were continued via two routes. One of the approaches suggested construction of a MM force field parameterized to nucleic acids interactions; another way implied calculations using more rigorous physics concepts and molecular characteristics in a hope to understand physical nature of interactions. The first such works were performed by Pullman's group and referred to interactions of the bases in fixed positions (e.g., Pullman et al. 1966). Considering the energy of interactions as a sum of electrostatic, polarization, and dispersion terms, two approximations were applied, "dipole" and "monopole," mentioning that "it may be preferable to treat the problem in the 'monopole' approximation because of the shortage of the intermolecular distances, with respect to the molecular dimensions" (Pullman et al. 1966). The so-called monopole approximation assumed representation of charge distribution of the molecule by point atom charges and it was applied to electrostatic energy only (following Bradley et al. 1964), while two other terms were actually calculated in dipole approximation, considering the total dipole of one molecule placed into its center induced by the charge distribution of the second one (Pullman et al. 1966). This approach was later augmented by inclusion of the short-range repulsion term and representation of the molecule as a set of "many-centered multipole distributions obtained from ab initio SCF calculations (charges, dipoles, and quadrupoles located on the atoms and the middles of segments joining pairs of atoms)" (Langlet et al. 1981). We will not consider subsequent progress in this way of nucleic acid computations because new schemes (e.g., Gresh et al. 1986 and references herein) do not correspond to the MM approach. Nevertheless, it is worth mentioning that the sophisticated schemes of base-base computations had no advantage for rationalization and prediction of experimental results in comparison to the "standard" MM scheme reviewed in the next paragraph.

In the middle of 1960s the author of this survey proposed the first atom-atom scheme and numerical parameters (Poltev and Sukhorukov 1967) for the calculation of interactions of nucleic acid bases (the terms "force field" and "molecular mechanics" were not widely used those years). This scheme had three source points, namely, idea of De Voe and Tinoco (1962) on quantitative estimations of interactions of nucleic acid subunits, "monopole" approximation of Bradley et al. (1964) for electrostatic interactions of the bases, and Kitaygorodsky (1961) atom-atom approach to calculations of van der Waals interactions in molecular crystals. That time there was no calculation scheme suitable for quantitative considerations of nucleic acid interactions and structure, and some "molecular-mechanics type" computations for other molecular systems can be used for approximate comparison only. We refer here only to later papers summarizing some preliminary adjustments and applications of the approach (Poltev and Shulyupina 1986; Poltev and Sukhorukov 1970). When calculating the interactions of nucleic acid bases or other conjugated heterocyclic molecules, only the term  $\sum E_{nb}$  of  $\blacktriangleright$  Eq. 9.1 was considered, corresponding to all the pair-wise interactions of atoms not pertaining to the same molecule. The bond lengths and valence angles were fixed and corresponded to averaged experimental geometry for each of the bases (like those for amino-acid residues and peptide backbone

in Sheraga's force field (Momany et al. 1975)). The atom-atom terms contained electrostatic, London attraction, and short-range repulsion contributions. This scheme was the first one assigning different parameters of van der Waals terms to the atoms of the same chemical element but different electron shell configuration (e.g., aromatic and aliphatic carbons, pyridine and pyrrole nitrogens, keto and enol oxygens). These parameters were preliminarily evaluated with approximate London formulae (for  $A_{ij}$  of Eq. 9.5) and enlarged van der Waals radii of atoms (for  $B_{ij}$  of Eq. 9.5 or corresponded values for the firstly used 6-exp potentials). The final values of the parameters were selected after step-by-step calculations and comparison with experimental data for crystals containing the atoms of some types only (starting from graphite, then aromatic hydrocarbons, pyrazine, and benzoquinone, and finally the bases). The effective charges of atoms were calculated via a simple semi-empirical quantum chemistry method (of Huckel and Del Re for  $\pi$ -electrons and  $\sigma$ -electrons, respectively) with the parameters adjusted to reproduce experimental values of dipole moments for related molecules. The primary scheme (Poltev and Sukhorukov 1967, 1970) contained a polarization term as well, but it was shortly eliminated due to its small value for many cases and to avoid difficulties related to non-additivity of atom-atom and molecule-molecule interactions. The parameter set was then amplified by consistent parameters for the sugar-phosphate backbone (Zhurkin et al. 1980) and for water-DNA interactions (Poltev et al. 1984). This simple MM scheme, specially adjusted to nucleic acid interactions, enables us to rationalize an extended set of experimental data and to forecast some nucleic acid properties before experimental evidence. Variability of DNA helix parameters (Khutorsky and Poltev 1976), dependence of mutual base positions on nucleotide sequence (Polozov et al. 1973), pathways for all the base-substitution errors (Poltev and Bruskov 1978), and DNA duplexes with mispairs (Chuprina and Poltev 1983) were predicted by such calculations before experimental data became available. The parameters of this simple scheme were later refined several times (like any other force field scheme discussed above and below) via adjustment to new experimental data and quantum mechanical considerations. We will mention here only one more series of early MM calculations related to nucleic acids performed by Indian scientists Renugopalakrishnan, Lakshminarayanan, and Sasisekharan (coauthor of Ramachandran (1963) paper on  $\Phi - \Psi$  plot for proteins). They suggested the first complete set of parameters for calculations of the conformations of nucleic acid fragments (Renugopalakrishnan et al. 1971, and references herein). The atom charges crucial for the base interactions was calculated via the same procedure as in our earlier papers (e.g., Poltev and Sukhorukov 1970).

## The Problems and Doubts of Further Development of the MM Approach

---

As follows from the previous section, the usefulness of the MM approach had already been demonstrated in the first decade of its extensive applications and modifications. At the same time, the problems of justification and of pathways for future development of the approach had arisen. From the very beginning it was clear that the method could not provide the exact description of the structures and processes due to its semi-empirical nature. The interesting problem of the method is the relative extent of empiricism and physical meaning of the scheme and its parameters.

## Two Hypothetical Approaches to Choice of MM Formulae and Parameters

Two opposite approaches can be considered. In the framework of the first one it is necessary to describe the physical nature of the system in the most exact way, e.g., to employ more exact equations for description of the interaction energy or/and more detailed representation of the system considering not only point atoms but other centers of interactions, not restricting the scheme with scalar values but introducing vectors (e.g., dipole moments) or tensors (e.g., anisotropic polarizability). In the framework of the second approach it would be possible to consider energy expressions as entirely empirical ones and to adjust the parameters to experimental data (or, later, to reliable quantum mechanical results) until the closest coincidence (e.g., via the least squares method). Unsuccessful attempts at consistent and strict use of both approaches were undertaken during the first two decades of the MM computer simulations.

The second approach mentioned above is practically impossible to realize; usually there is neither sufficient quantitative experimental data to derive the form of dependences of the energy on inter-atomic distances nor to obtain the coefficients of already accepted potential form (e.g., of Lennard-Jones). Even in a case where we have a sufficient number of experimental values, the equations for parameter calculations have no single definite solution. This was demonstrated in the paper of Momany et al. (1968). These authors tried to adjust the coefficient of (6-12) potentials for C-C, C-H, and H-H interactions for benzene molecule to the energy and structure data on benzene crystal. Using three sets of experimental data for different temperatures, they obtained entirely repulsive contribution from C-C interactions. This means that qualitative estimations (relative values of attraction terms for various atoms, of equilibrium radii, of atom charges in the same or similar molecules, etc.) should be taken into account in adjustment the parameters of the force field. Most modern force fields originate from previous sets of expressions and parameters derived from simple qualitative considerations (e.g., simplified formulae of dispersion term, van der Waals radii of atoms), and take into account these considerations automatically (e.g., using previous approximate parameters values as starting points).

As for the first approach, the more complex expressions of the energy have been suggested since the end of 1960s; such expressions are used in some modern force fields, i.e., the next terms in the expansions of the energy are incorporated into stretching, bending, and van der Waals contributions. The inclusion of additional terms requires new parameters. Usually the number of reliable quantitative values is not sufficient, and such an approach becomes useful in cases where the area of applications of the force field is restricted to a certain type of similar molecules (e.g., hydrocarbons). In any case, the expressions for each term remain the approximate ones, and more coefficients should be adjusted according to experimental data. The more complex representation of the molecular system as compared to a set of point atoms was proposed by several researchers (including the author of this survey). Such a representation seems the most natural for atoms with lone pairs of electrons (inclusion of additional points for electrostatic interactions of pyridine nitrogen or keto oxygen located at the centers of lone-pair orbitals) or for atoms with  $\pi$ -orbitals (additional points for aromatic heterocycles located above and below the ring planes). Additional lone pair centers for electrostatic interactions are included in some modern force fields for better reproduction of electric field around the molecules and the directionality of hydrogen bonds.

Although the introduction of such centers seems physically based, an inconsistency in such an approach can be detected rather easily. When assigning the negative charged interaction centers to some electron orbitals (and hence positively charged centers to nuclei locations),

it seems natural to assign additional centers to chemical bonds (sites of the highest electron density between the nuclei). As a result, we have several times more centers (more computer resources are needed), and several times more adjustable parameters. Such an approach was consistently implemented into force field suggested by Scheraga and coauthors. The first version was titled EPEN (empirical potential using electrons and nuclei, Shipman et al. 1975), and an improved version, EPEN/2, was released 3 years later (Snir et al. 1978). In this model, the molecular interactions are modeled through distributed interaction sites, which account for the nuclei and electronic clouds. The positive charges are located at the atomic nuclei, and the negative charge centers are located off the nuclei. The bonding electrons are located along the bonds, while the lone-pair and  $\pi$ -electrons are located off the bonds. The energy of interaction is approximated by the sum of the coulomb interactions between all point charge centers, an exponential repulsion to represent electron–electron overlap repulsion, and an  $R^{-6}$  ( $R$  = distance) attraction to simulate attractive energies between the nuclei. The distances between the charge locations are the method parameters; they are fixed in the molecule fragments. The parameterization was optimized by least square fits to spectroscopic, crystallographic, and thermodynamic data. This approach (as well as other approaches considering many additional to atom centers of interactions) is not widely used in MM calculations. The situation can be accounted for by restrictions imposed by fixed geometry of the molecule fragments, as well as by need for the parameter adjustment for molecules other than considered by the approach authors.

## Various Schemes of Water Molecules in MM Calculations

---

The only molecule frequently represented by more interaction centers than the number of atoms is the water molecule. In view of importance of water for life and for description of the biomolecular interactions, as well as of “anomalous” physical properties of water in liquid and solid states, hundreds of models and their modifications of water molecule have been proposed. We will mention here only few of most frequently used and cited rigid models with 3, 4, 5, and 6 sites of interactions. The first water molecule model (frequently referred as the BF model) was proposed by Bernal and Fowler (1933). This model may be considered the earliest molecular model suitable for MM calculations, and it was used for Monte Carlo calculations of liquid water performed over nearly a half of century for comparison with some later models (Jorgensen et al. 1983). The model contains four interaction sites, three charged sites (two positive centers located at the hydrogen atoms and one negative center displaced by 0.15 Å from oxygen atom in the direction of H–O–H bisector), and one center for van der Waals interactions located on oxygen atom. It is interesting to note that Bernal and Fowler (1933) performed approximate evaluations of intermolecular interaction energy by the (1-6-12) potential functions. Jorgensen et al. (1983) used nearly the same position of centers and slightly modified charges in TIP4P four-site water model (one of their popular Transferable Intermolecular Potentials). Matsuoka et al. (1976) derived more complex four-site model from potential surface of water dimer constructed via *ab initio* quantum mechanics calculations with configuration interactions. The analytical expression for interaction potential function between two water molecules consists of pair-wise Coulomb interactions of three charges located similar to BF or TIP4P models and exponential interactions of all the three atoms of one molecule with the atoms of the other one. This model (the so-called MCY model) was widely used during the first decade of liquid water simulations.

We will not consider many models, including the earliest ones, that consist of three, five, or more centers, but only briefly mention some of rigid models cited up to the present time and widely used in modern force fields. Stillinger and Rahman (1974) suggested the five-site

model with two positive centers (hydrogen atoms), two negative centers (located at oxygen lone pairs), and one center (oxygen atom) for Lennard–Jones interactions. The model has been used successfully to study a wide variety of properties of liquid water. Mahoney and Jorgensen (2001), after extensive Monte Carlo simulations and parameter adjustments, suggested a five-site model TIP5P, which enabled them to describe the density anomaly of liquid water better than previously existing models. Nada and Van der Eerden (2003) designed a six-site model of a water molecule. Three of these sites are the three atoms of the molecule (they interact through a Lennard–Jones potential), and the three other sites are negative point charges (O atom is electrically neutral; the two H atoms carry positive charges). The model can be considered a combination of TIP4P and TIP5P models of Jorgensen. The Monte Carlo simulations of ice and water show that the six-site model reproduces well the real structural and thermodynamic properties of ice and water near the melting point.

Further progress in the study of water properties and its interactions with other molecules is related to new models introducing flexibility to the molecule (incorporating bond stretching and angle bending terms into interaction energy) and with the inclusion of electronic polarization. These effects are important for the quantitative description of water properties in liquid and solid states as well as of phase transitions. We will not consider these attempts here, as most modern force fields continue using three-site rigid water models for computations of the systems containing organic and bioorganic molecules. Two such models, namely TIP3P of Jorgensen et al. (1983) and SPC of Berendsen et al. (1981) should be mentioned. They have three interaction sites centered on the nuclei. Each site has a partial charge for computing the Coulomb energy, and the only one site (oxygen atom) for Lennard–Jones interactions. The TIP3P model demonstrates better reproduction of experimental water properties (Jorgensen et al. 1983); and this model or its modifications is frequently used in biomolecular computations. Most modern force fields enable users to employ both simple rigid water models (TIP3P, SPC, TIP4P) and flexible and polarizable ones.

## Modern Molecular Mechanics Force Fields and Their Applications

---

The MM computations during the first two decades were mainly performed by researchers using their own force fields and homemade computer programs. Most modern publications refer to standard, ready-to-use software with implemented (or sometimes slightly modified) force field parameters. The number of program and parameter packages is great and new or newly modernized software and force fields appear every year. We will present below a short overview of the selected program sets and the force fields most frequently used for study of biomolecular systems. Some of them have already been mentioned in previous sections.

### Allinger's Force Fields and Programs

---

The MM family of force fields designed by Allinger and coauthors is widely used for calculations on small and medium-size organic molecules. The first parameter set (MM1) was described in 1973 (Allinger and Sprague 1973); and the MM1 program was released through the *Quantum Chemistry Program Exchange* in 1976. The force field and the program were followed by a series of improved and extended for various classes of organic molecules versions MM2, MM3, MM4 (see Lii et al. 2005 for references to previous papers). These force fields have been parameterized

based on the most comprehensive and highest quality experimental data, including the electron diffraction, vibrational spectra, heats of formation, and crystal structures. The results of calculations were verified via comparison with high level ab initio quantum chemistry computations, and the parameters were additionally adjusted. The last program version MM4 includes complex force field equations (including additional terms to harmonic potentials for stretching and bending, and cross-terms) and various calculation options (e.g., prediction of frequencies and intensities of vibrational spectra; and calculating the entropy and heat of formation for a molecule at various temperatures). MM4's molecular dynamics option creates a description of the vibrational and conformational motion of molecules as a function of time. The program examines the atoms of a molecule and their environment, and decides which atom type is appropriate. The program includes more energy terms and more complicated expressions for some terms than most of the other popular MM force fields. The force field contains a greater number of the constants that are adjusted to an extended set of experimental data. The stretching and bending energy terms include higher order contributions, several cross-terms are inserted, the electrostatic contribution includes interactions of bond dipoles. It is interesting to note that the MM3 version, after adjustment to amides and peptides, provided the authors (Lii and Allinger 1991) with the structural results for cyclic peptides and the protein Crambin comparable with the better specialized protein force fields including ECEPP and AMBER.

## Merck Molecular Force Field (MMFF94)

This force field was developed for a broad range of molecules, primarily of importance for drug design. It differs from Allinger's and many other popular force fields in several aspects. The core portion of MMFF94 was primarily derived from high-quality computational quantum chemistry data (up to MP4SDQ/TZP level of theory) for a wide variety of chemical systems of interest to organic and medical chemists (Halgren 1996, 1999b). Nearly all MMFF94 parameters were determined in a mutually consistent fashion from the full set of available computational data. The force field reproduces well both computational and experimental data, including experimental bond lengths (0.014 Å rms), bond angles (1.2° rms), vibrational frequencies, conformational energies, and rotational barriers. The mathematics expressions of the force field differ from many other force fields. The expressions for stretching and bending energies (like Allinger's force fields) contain additional to harmonic terms, stretch-bend cross terms, and out-of-plane terms. The van der Waals energy is expressed by buffered (7-14) potentials (Eq. 9.9, the designations are the same as in Eqs. 9.2–9.7)

$$E_{vdW} = \varepsilon_{ij} (1.07\rho_{ij}/r_{ij} + 0.07\rho_{ij})^7 ((r_{ij}^7/\rho_{ij}^7 + 0.07\rho_{ij}^7) - 2) \quad (9.7)$$

The electrostatic term contains buffering constant as well. The MMFF94 version was developed for molecular dynamics simulations; the MMFF94s version (Halgren 1999a) was modified for energy minimization studies (s in the title means static). Both versions provide users with nearly the same results for majority of molecules and complexes. Additional parameters of the force field and careful adjustment to high-level reference data appeared after force field's publication, resulting in good reproduction of an extended set of experimental data on conformational energies of the molecules (Halgren 1999b). Nevertheless Bordner et al. (2003) revealed that MMFF94 values of sublimation energy for a set of compounds are systematically 30–40% lower than experimental data. It can be explained by “computational nature” of MMFF parameters when non-additive contributions do not accounted for implicitly.

## The Force Fields and Programs Designed by Scheraga and Coauthors

As already mentioned, the first MM parameter set for the simulation of proteins was described in 1975 by Scheraga and coauthors (Momany et al. 1975); their ECEPP program (Empirical Conformational Energy Program for Peptides) was released through the *Quantum Chemistry Program Exchange* in the same year. This force field family has been refined continuously up until the last few years. We will briefly describe two versions of Scheraga's force field used for studies of protein three-dimensional structure and protein folding up to recent time, ECEPP/3 (Némethy et al. 1992) and ECEPP-05 (Arnautova et al. 2006). The ECEPP/3 force field in turn is a modified version of ECEPP/2; it contains updated parameters for proline and oxyproline residues. The ECEPP force fields utilize fixed bond lengths and bond angles obtained from a survey of the crystal structures for each of amino acid residue. The peptide energy is calculated and minimized as a function of torsion angles only, and it is a significant advantage for minimization approaches as it drastically reduces the variable space that must be considered. The energy function of the ECEPP/3 force field consists of torsion and non-bonded (Coulomb and van der Waals) terms (► Eq. 9.4 and ► 9.5). The partial charges of atoms are calculated by the molecular orbital CNDO/2 method, the parameters of (6-12) term are adjusted by comparison with crystal data. The (6-12) terms are substituted by (10-12) terms for the interactions of the hydrogen atoms capable of participating in H bonds with H-bond acceptor atoms. In spite of the appearance of new improved and augmented versions of ECEPP force field, the ECEPP/3 is used until recently for protein simulations (e.g., McAllister and Floudas 2010).

The ECEPP-05 force field (Arnautova et al. 2006 and references therein) is adjusted to both new experimental data and quantum mechanical results. Like previous ECEPP force fields ECEPP-05 utilizes the fixed bond lengths and bond angles but has some distinctive features as compared to both ECEPP/3 version and many other popular force fields. The van der Waals term of the energy is modeled by using the “6-exp” potential function

$$E_{ij} = -A_{ij}r_{ij}^{-6} + B_{ij}\exp(-C_{ij}r_{ij}) \quad (9.8)$$

where  $r_{ij}$  is the distance between atoms  $i$  and  $j$  of different molecules (or monomers);  $A_{ij}$ ,  $B_{ij}$ , and  $C_{ij}$  are parameters of the potential. The combination rules for these parameters are used for describing heteroatomic interactions.

$$A_{ij} = (A_{ii}A_{jj})^{1/2}; B_{ij} = (B_{ii}B_{jj})^{1/2}; C_{ij} = (C_{ii} + C_{jj})/2 \quad (9.9)$$

The parameters of (6-exp) potentials were derived using the so-called global-optimization-based method consisting of two steps. An initial set of parameters is derived from quantum mechanical interaction energies (at MP2/6-31G\* level of ab initio theory) of dimers of selected molecules; in the second step the initial set is refined to satisfy the following criteria: the parameters should reproduce the observed crystal structures and sublimation enthalpies of related compounds, and the experimental crystal structure should correspond to the global minimum of the potential energy.

The atomic charges were fitted to reproduce the molecular ab initio electrostatic potential, calculated at HF/6-31G\* level; the fitting was carried out using the restrained electrostatic potential (RESP) method taken from the AMBER program. The method was applied to obtain a single set of charges using several conformations of a given molecule (the multiple-conformation-derived charges). An additional point charge (with zero nonbonded parameters)



is used to model the lone-pair electrons of  $sp^2$  nitrogen. The torsional parameters of the side chains of the 20 naturally occurring amino acids were computed by fitting to rotational energy profiles obtained from *ab initio* MP2/6-31G\*\* calculations. The peptide backbone torsional parameters were obtained by fitting the energies to the  $\Phi - \Psi$  energy maps of terminally blocked glycine and alanine amino acids constructed at MP2/6-31G\*\*//HF/6-31G\*\* level of theory. The performance of the force field was evaluated by simulating crystal structures of small peptides.

As the important problems of protein structure and function as well as of natural science as a whole refer to prediction of three-dimensional structure and pathways of folding of proteins, Scheraga and coauthors have modified and augmented the force fields mentioned above with some theoretical approaches and concepts. We will note a few of them related directly to MM calculations. The all-atom ECEPP05 force field was coupled with an implicit solvent-accessible surface area model (ECEPP05/SA, Arnautova and Scheraga 2008). Recognizing the impossibility of searching enormous conformational space of a real protein with an all-atom potential function, a hierarchical procedure was developed whose two main features are the initial use of a united-residue, UNRES, potential function and an efficient procedure, and conformational space annealing, CSA (Scheraga et al. 2002, and references therein). The protein is first optimized with the low-resolution UNRES model (Liwo et al. 1999). In the UNRES force field, the backbone is represented as a virtual-bond chain of  $C_\alpha$  atoms, and the side chains are depicted as ellipsoids. The interaction sites are the united-atom side chains, and the centers of the peptide groups between  $C_\alpha$  atoms. The lowest-energy UNRES conformation, as well as a set of distinct low-energy conformations, are then converted to all-atom models. Finally, the all-atom models are refined with the EDMC method, with inclusion of continuum hydration model.

The search for low-energy “native-like” structures includes several minimization and Monte Carlo procedures. The simplest of the MC methods is Monte Carlo with minimization, MCM, i.e., a Metropolis Monte Carlo algorithm in which every trial state is first energy-minimized before the Boltzmann acceptance criterion is applied. The EDMC (Electrostatically Driven Monte Carlo) method employs a move set in which individual peptide groups are selected at random and rotated “in place” (i.e., the conformational change is localized to the peptide group as much as possible) so as to optimize the alignment of its dipole moment with the local electric field. The methodology assumes that a protein molecule is driven toward the native structure by the combined action of electrostatic interactions and stochastic conformational changes associated with thermal movements (Ripoll and Scheraga 1988). The use of force fields and methods enabled Scheraga and coauthors not only to rationalize but to predict some interesting features of protein three-dimensional structure and pathways of folding. “With increasing refinement of the computational procedures, the computed results are coming closer to experimental observations, providing an understanding as to how physics directs the folding process” (Scheraga 2008).

## Force Fields and Programs Developed by Kollman and Coauthors

---

The computer software and force fields referred to as “AMBER” (Assisted Model Building with Energy Refinement) are the most popular of those designed for a wide class of biomolecules, including proteins and nucleic acids. The first description of the computer program AMBER appeared in 1981 (Weiner and Kollman 1981), and the first detailed specification of the force field was published 3 years later (Weiner et al. 1984). The force field contained the usual “minimalist”



set of energy terms (🔗 Eqs. 9.1–9.6 of this survey), the parameters being adjusted to both experimental and quantum mechanics data. Although preliminary parameters and calculations for the fragments of nucleic acids and proteins have been published by the authors since 1981, the set of parameters of 1984 was carefully reviewed and presented as a consistent force field for both proteins and nucleic acids. The parameters of their previous publications and those of other authors were used as starting points for the adjustment. Preliminary estimations of equilibrium bond lengths and angles were adopted from microwave and neutron diffraction studies, and atomic charges are obtained by fitting a partial charge model to electrostatic potentials calculated by *ab initio* quantum mechanical calculations (with minimal STO 3G basis set). The (10-12) potential was included for description of H-bonding (this term was deleted in new versions of AMBER force fields and software). The force field accounted for implicit solvent by using distance dependent dielectric constant ( $\epsilon = R_{ij}$ ); a united atom approach enabled one to perform calculations of sufficiently extended systems (such as fragments of DNA double helix of a few nucleotide pairs or peptides of dozens of amino acid residues). In spite of several deficiencies of the first AMBER force field (e.g., too short distances in stacking complexes due to short equilibrium radii for van der Waals interactions, defects in atomic charges due to very approximate quantum mechanics data), hundreds of papers were published with this force field and the program. In 2005, even after release of several new and improved AMBER force field versions, the paper (Weiner et al. 1984) was the tenth most-cited one in the history of the *Journal of the American Chemical Society* (Case et al. 2005).

Since publication of these papers, new versions of both force fields and program sets have been released. Cornell et al. (1995) published the “second generation” AMBER force field for simulating the structures, conformational energies, and interaction energies of proteins, nucleic acids, and many related organic molecules in condensed phases. The charges were determined using the calculations with 6-31G\* basis set and restrained electrostatic potential (RESP) fitting, and were shown to reproduce interaction energies, free energies of solvation, and conformational energies of small molecules to a good degree of accuracy. The new van der Waals parameters were derived to account for liquid properties. Retaining most of the torsion parameters of “the previous generation” of force field, the improvement of potentials for peptide backbone were performed for  $\Phi$  and  $\Psi$  dihedrals, as well as for the nucleoside  $\chi$  dihedrals by adding extra Fourier terms. This “second generation” force field is usually referred as *ff94* (parameter set *parm94*).

There are a number of AMBER parameter sets, with names beginning with “ff” and followed by a two-digit year number, such as “ff99” We will briefly mention some new features of these force fields. Some of versions differ from *ff94* by minor (but important for some problems) modifications. The *ff96* force field differs from *ff94* one only in the peptide  $\Phi$ – $\Psi$  torsional potential, and *parm96* was developed because it was clear that *parm94* overstabilized  $\alpha$  helices relative to  $\beta$  sheets. Thus, *parm94* seems adequate for comparing structures with similar secondary structures, but *parm96* seems to more accurately represent the relative stability of  $\alpha$  and  $\beta$  secondary structures. The improved version *ff99* (Wang et al. 2000) was developed using the restrained electrostatic potential (RESP) approach to derive the partial charges. The adjustment of point charges and torsion constants for the set of 34 molecules to the highest level *ab initio* model (GVB/LMP2) and experimental data enabled the authors to reproduce data for a 55-molecule set with better accuracy than MM3, MMFF, and CHARMM force fields. It was demonstrated that “a well-parameterized harmonic force field with a reliable charge method can describe the structure and intramolecular energies for organic systems very well” (Wang et al. 2000). The authors tried to use the adjusted parameters (*parm99*) in nonadditive models (which

include polarization), and obtained “reasonable results using the same parameters derived for the additive model, although additional torsional parameterization is required to achieve the same high level of accuracy as that found using the additive model” (Wang et al. 2000). This force field has been widely used for more than 10 years. The other AMBER force field, “a third-generation point-charge all-atom force field for proteins” (referred as ff03) was developed by Duan et al. (2003). The main difference from previous force fields is that all quantum mechanical calculations were done in the condensed phase with continuum solvent models and an effective dielectric constant of  $\epsilon = 4$ . Initial tests on peptides demonstrated a high-degree of similarity between the calculated and the statistically measured Ramachandran maps for glycine and alanine peptide fragments. One more AMBER force field, referred as GAFF (General Amber Force Field), should be mentioned (Wang et al. 2004). GAFF was designed as an extension of the AMBER force fields to be compatible with existing versions for proteins and nucleic acids, and has parameters for most organic molecules of pharmaceutical importance that are composed of H, C, N, O, S, P, and halogens. The parameterization is based on more than 3,000 MP2/6-31G\* optimizations and 1,260 MP4/6-31G(d,p) single-point calculations. Unlike most conventional force fields, parameters for all combinations of atom types are not contained in an exhaustive table, but are determined algorithmically for each input molecule, based on the bonding topology (which determines the atom types) and the geometry. A completely automated, table-driven procedure (called *antechamber*, a part of the late versions of AMBER program set) was developed to assign atom types, charges, and force field parameters to almost any organic molecule (Wang et al. 2006). New versions of AMBER software work with several force fields. The newest AMBER 11 version (Case et al. 2010) supports CHARMM fixed-charge force fields as well.

The initial AMBER force fields and program packages (due to the state of the theory and computer facilities) were generally aimed at the search for energy minima of separate molecular systems in vacuum. The current Amber versions are strongly aimed at simulations (molecular dynamics, evaluations of free energy changes) of biomolecules in water solutions. Both explicit solvent models (using TIP3P, TIP4P, TIP5P, and SPC water models as well as models of some organic solvents) and implicit ones are supported. By default, explicit solvation models involve electrostatic interactions handled by a particle-mesh Ewald (PME) procedure, and long-range Lennard–Jones attractions are treated by a continuum model. The PME is a modified form of Ewald summation, a method to efficiently calculate the infinite range Coulomb interaction under periodic boundary conditions, and PME is a modification to accelerate the Ewald reciprocal sum to near linear scaling, using the three-dimensional fast Fourier transform (3DFFT).

An accurate description of the aqueous environment is essential for atom-level biomolecular simulations, but may become very expensive computationally. An implicit model replaces the discrete water molecules by an infinite continuum medium with some of the dielectric and “hydrophobic” properties of water. The continuum implicit solvent models have several advantages over the explicit water representation, especially in molecular dynamics simulations (e.g., they are often less expensive, and generally scale better on parallel machines; they correspond to instantaneous solvent dielectric response; the continuum model corresponds to solvation in an infinite volume of solvent, there are no artifacts of periodic boundary conditions; estimating free energies of solvated structures is much more straightforward than with explicit water models). Despite the fact that the methodology represents an approximation at a fundamental level, it has in many cases been successful in calculating various macromolecular properties (Case et al. 2005).

The total energy of a solvated molecule can be written as a sum of molecule's energy in vacuum (gas phase), and the free energy of transferring the molecule from vacuum into solvent, that is, it is typically assumed that solvation free energy can be decomposed into electrostatic and nonelectrostatic parts. The above decomposition is the basis of the widely used PB/SA (Poisson-Boltzman solvent accessible surface area) scheme. Amber follows this way to compute the nonelectrostatic part of the energy. The most time-consuming part of solvation energy estimations is the computation of the electrostatic contribution. Amber employs one of the most popular for biomolecular applications the finite-difference method (FDPB) and analytic generalized Born (GB) method. In the GB model, a molecule in solution is represented as a set of spherical cavities of dielectric constant of 1 with charges at their centers embedded in a polarizable dielectric continuum solvent of a higher dielectric constant.

New versions of AMBER software support the option of allowing part of the system to be described quantum mechanically in an approach known as a hybrid (or coupled potential) QM/MM simulation. Both semi-empirical and the Density Functional Theory-based Tight Binding (DFTB) Hamiltonian can be used. The system may contain both two non-bonded parts and covalently bonded QM and MM sub-systems (Case et al. 2010).

The AMBER software and AMBER force fields are widely used for the simulation of various systems of biological and material science importance. Some researchers develop proper additions and corrections to "standard" parameters for better description of specific systems. We refer to only two of many such examples. Perez et al. (2007) reparameterized the parm99 force field for nucleic acid simulations, improving the representation of the  $\alpha/\gamma$  conformational space, which seems to be poorly represented in very long DNA MD simulations with available AMBER force fields. Song et al. (2008) adjusted the AMBER force field to reproduce conformational properties of an oxidative DNA lesion, 2,6-diamino-4-hydroxy-5-formamidopyrimidine.

## Other Popular Force Fields and MM Software. CHARMM, OPLS, and GROMOS

---

The force fields and program packages listed below are used for nearly the same type of simulations as those considered above. The main differences relate to the organization of the programs and to the role of experimental data and quantum mechanics results in force field parameter adjustment. The first versions of force fields and programs as well as the whole research programs were initiated by such pioneers of MM applications as Karplus (CHARMM, Chemistry at HARvard Molecular Mechanics), Jorgensen (OPLS, Optimized Potentials for Liquid Simulations), Gunsteren and Berendsen (GROMOS (GRONingen MOlecular Simulation package), and GROMACS (GRONingen MACHine for Chemical Simulation). The progress and improvement of the force fields and programs are connected to comparison with the approaches and results of other programs. The parameterization of a second-generation AMBER force field (Cornell et al. 1995) was influenced by Jorgensen OPLS potentials for proteins (Jorgensen and Tirado-Rives 1988), whereas these OPLS united atom potentials adopted bond stretch, angle bend, and torsional terms from the AMBER united-atom force field (Weiner et al. 1984). The OPLS parameters for the 20 neutral peptide residues were obtained primarily via Monte Carlo simulations for the 36 organic liquids, and the parameterization for the charged protein residues was performed via comparisons with ab initio results for ion-molecule complexes

(6-31G(d) basis set) and on Monte Carlo simulations for hydrated ions (Jorgensen and Tirado-Rives 1988). The OPLS-AA (all atom) force field (Jorgensen et al. 1996) retain most of bond stretch and angle bending parameters from AMBER all atom force fields, but torsion and non-bonding constants are reparameterized utilizing both experimental and ab initio (RHF/6-31G\* level) data. This force field was improved for peptides by means of refitting the key Fourier torsional coefficients using accurate ab initio data (LMP2/cc-pVTZ(-f)//HF/6-31G\*\* level) as the target (Kaminski et al. 2001).

Most popular program sets utilize various force fields, not only those developed in the research groups of the authors of the program with the same title. The software suite GROMACS (Groningen MACHine for Chemical Simulation) was developed by the Berendsen group at the University of Groningen, The Netherlands, starting in the early 1990s. This fast program for molecular dynamics simulation does not have a force field of its own, but is compatible with the GROMOS, OPLS, and AMBER force fields. The GROMACS (Van der Spoel et al. 2005) was developed and optimized especially for use on PC-clusters. It originated from the Fortran package GROMOS developed by van Gunsteren and Berendsen (Van Gunsteren et al. 1987). The GROMOS force fields are united atom force fields, i.e., without explicit aliphatic (non-polar) hydrogens. The latest version, GROMOS05 (Christen et al. 2005), utilizes new versions of GROMOS force field sets (53A5 and 53A6) based on extensive reparameterization of the previous GROMOS force field (Oostenbrink et al. 2004). In contrast to the parameterization of most of other biomolecular force fields, this parameterization of the GROMOS force field is based primarily on reproducing the free enthalpies of hydration and apolar solvation for a range of organic compounds.

Very popular for the computations of wide range of macromolecular systems are the CHARMM (Chemistry at HARvard Macromolecular Mechanics) program and force field sets. The computations include energy minimization, molecular dynamics, and Monte Carlo simulations. CHARMM originated with Martin Karplus's group at Harvard University; the first publication of the CHARMM program and force field was in 1983 (Brooks et al. 1983). Several versions of both software and force field have since been released. Improvement to the programs and force fields have progressed to date. The mathematical expressions for calculation of CHARMM energy are nearly the same as "minimalist" ones for other force fields (MacKerell 2004). The minor differences with, e.g., AMBER or OPLS force fields relate to inclusion of harmonic improper and Urey-Bradley terms. The parameters of various versions of force field are consistently adjusted with emphasis to specific molecules to be applied. The first versions of CHARMM force fields were aimed primary towards protein molecular dynamics simulations. Then, the special adjustments were performed for the simulations of the nucleic acids (Foloppe and MacKerell 2000), and for lipids (Klauda et al. 2008). The improvement of parameters for specific molecules has continued, while other parameters can be used from the previous versions. Raman et al. (2010) recently extended the CHARMM additive carbohydrate all-atom force field to enable modeling glycosidic linkages in carbohydrates involving furanoses. As in most of popular modern force fields, both the ab initio quantum mechanics computations and experimental data for solid and liquid states are used in adjustment of the parameters of CHARMM force fields. The distinct feature of this adjustment relates to charge adscription. Like OPLS force fields (Jorgensen et al. 1996), CHARMM utilizes the so-called supramolecular approach. The partial atomic charges are adjusted to reproduce ab initio (HF/6-31G\* level) minimum interaction energies and geometries of model compounds with water or for model compound dimers (with energy and distance

corrections for reproducing the correct experimental densities). On the other hand, the use of ab initio data on small clusters to optimize the van der Waals parameters leads to poorly condensed phase properties. This requires that the optimization of these parameters be performed by empirical fitting to reproduce thermodynamics properties from condensed phase simulations, taking into account the relative values of the parameters obtained from high-level ab initio data on interactions of the model compounds with rare gases (Klauda et al. 2008).

It is interesting to mention that multiple adjustments of different force fields mentioned above resulted in an increase of similarity in both corresponding parameters values and the results of applications to complex molecular systems (such as protein and nucleic acid fragments), but many differences remain.

## Conclusions

---

The MM computation approach to the study of the molecular systems arose about a half of century ago and today has become a useful and powerful research tool for many branches of natural science. During this period of development, the number of publications utilizing this approach increased by a few orders of magnitude. This increase continues up to present, followed by the appearance of new journals and a flow of MM publications into the journals of a wide area of coverage. The MM considers the molecular systems via a classic Newtonian mechanics approach, i.e., using classical approximation to essentially quantum systems. The MM suggests representation of the system energy as a sum of terms responsible for interactions of various physical nature.

The minimalist MM approach involves the simple expressions for chemical bond stretching, bond angle bending, rotation about the bond, and nonbonded van der Waals and Coulomb contributions calculated via additive atom-atom scheme. The force fields (sets of mathematical formulae and numerical parameters) are derived from simple physical considerations followed by adjustment to the experimental data and precise quantum mechanics results. The additivity of the terms responsible for separate atom contributions and for interactions of different physical nature, and transferability of the parameters between atoms and molecules of similar structure are the main assumptions of the MM approach. Development of the approach results in elaboration of a variety of computer software and force fields for simulating different molecular systems of biological, medical, and industrial importance. Various force fields differ in the complexity of mathematical expressions and in the relative role of experimental and quantum mechanics results used for the parameter adjustment. The development of algorithms for MM applications (including those for molecular dynamics and Monte Carlo techniques) and the increase of computer power has enabled researchers to approach such complex problems as predicting the pathways of the formation of the biopolymer's three-dimensional structure, molecular recognition in various biological processes, and assistance in creation of compounds with desirable properties (including drugs and industrial materials). Several force fields have been elaborated recently, going beyond the atom-atom approach and the additivity principle. There are programs utilizing the united atom approach to energy calculations and a hierarchical procedure for consideration of the complex systems. It may be predicted that the role of MM computations in the pure and applied science will arise synchronously with arising the role of computers in the human life.

## References

- Allinger, N. L. (1959). Conformational analysis. III. Applications to some medium ring compounds. *Journal of the American Chemical Society*, *81*, 5727.
- Allinger, N. L. (2010). *Molecular structure: Understanding steric and electronic effects from molecular mechanics*. New Jersey: Wiley.
- Allinger, N. L., & Sprague, J. T. (1973). Calculation of the structures of hydrocarbons containing delocalized electronic systems by the molecular mechanics method. *Journal of the American Chemical Society*, *95*, 3893.
- Antony, J., & Grimme, S. (2006). Density functional theory including dispersion corrections for intermolecular interactions in a large benchmark set of biologically relevant molecules. *Physical Chemistry Chemical Physics*, *8*, 5287.
- Arnautova, Y. A., & Scheraga, H. A. (2008). Use of decoys to optimize an all-atom force field including hydration. *Biophysical Journal*, *95*, 2434.
- Arnautova, Y. A., Jagielska, A., & Scheraga, H. A. (2006). A new force field (ECEPP-05) for peptides, proteins and organic molecules. *Journal of Chemical Physics*, *110*, 5025.
- Bartell, L. S. (1960). On the effects of intramolecular van der Waals forces. *Journal of Chemical Physics*, *32*, 827.
- Barton, D. H. R. (1948). Interaction between non-bonded atoms, and the structure of cis-Decalin. *Journal of Chemical Society*, 340.
- Barton, D. H. R. (1950). The conformation of the steroid nucleus. *Experientia*, *6*, 316.
- Berendsen, H. J. C., Postma, J. P. M., von Gunstaren, W. F., & Hermans, J. (1981). Interaction models for water in relation to protein hydration. In B. Pullman (Ed.), *Intermolecular forces* (pp. 331–342). Dordrecht: Reidel.
- Berman, H. M., Olson, W. K., Beveridge, D. I., Westbrook, J., Gelbin A., Demeny T., Hsieh S.-H., Srinivasan, A. R., & Schneider, B. (1992). The nucleic acid database. A comprehensive relational database of three-dimensional structures of nucleic acids. *Biophysical Journal*, *63*, 751.
- Berman, H. M., Henrick, K., & Nakamura, H. (2003). Announcing the worldwide protein data bank. *Nature Structural & Molecular Biology*, *10*, 980.
- Bernal, J. D., & Fowler, R. H. (1933). A theory of water and ionic solution, with particular reference to hydrogen and hydroxyl ions. *Journal of Chemical Physics*, *1*, 515.
- Bordner, A. J., Cavasotto, C. N., & Abagyan, R. A. (2003). Direct derivation of van der Waals force field parameters from quantum mechanical interaction energies. *The Journal of Physical Chemistry B*, *107*, 9601.
- Bradley, D. F., Lifson, S., & Honig, B. (1964). Theory of optical and other properties of biopolymers: Applicability and elimination of the first-neighbor and dipole-dipole approximations. In B. Pullman (Ed.), *Electronic aspects of biochemistry*. New York: Academic.
- Brant, D. A., & Flory, P. J. (1965). The configuration of random polypeptide chains. II. Theory. *Journal of the American Chemical Society*, *87*, 2791.
- Brooks, B. R., Bruccoleri, R. E., Olafson, B. D., States, D. J., Swaminathan, S., & Karplus, M. (1983). CHARMM: A program for macromolecular energy, minimization, and dynamics calculations. *Journal of Computational Chemistry*, *4*, 187.
- Case, D. A., Cheatham T. E., III, Darden, T., Gohlke, H., Luo, R., Merz, K. M., Jr., Onufriev, A., Simmerling, C., Wang, B., & Woods, R. J. (2005). The amber biomolecular simulation programs. *Journal of Computational Chemistry*, *26*, 1668.
- Case, D. A., Darden, T. A., Cheatham T. E., III, Simmerling, C. L., Wang, J., Duke, R. E., Luo, R., Walker, R. C., Zhang, W., Merz, K. M., Roberts, B., Wang, B., Hayik, S., Roitberg, A., Seabra, G., Kolossváry, I., Wong, K. F., Paesani, F., Vanicek, J., Liu, J., Wu, X., Brozell, S. R., Steinbrecher, T., Gohlke, H., Cai, Q., Ye, X., Wang, J., Hsieh, M.-J., Cui, G., Roe, D. R., Mathews, D. H., Seetin, M. G., Sagui, C., Babin, V., Luchko, T., Gusarov, S., Kovalenko, A., & Kollman, P. A. (2010). *AMBER 11*. San Francisco: University of California.
- Chuprina, V. P., & Poltev, V. I. (1983). Possible conformations of double-helical polynucleotides containing incorrect base pairs. *Nucleic Acids Research*, *11*, 5205.
- Cornell, W. D., Cieplak, P., Bayly, C. I., Gould, I., Merz, K., Jr., Ferguson, D., Spellmeyer, D., Fox, T., Caldwell, J., & Kollman, P. (1995). A second generation force field for the simulation of proteins, nucleic acids, and organic molecules. *Journal of the American Chemical Society*, *117*, 5179.
- Craig, D. P., Mason, R., Pauling, P., & Santry, D. P. (1965). Molecular packing in crystals of the aromatic hydrocarbons. *Proceedings of the Royal Society A*, *286*, 98.
- Cramer, C. J. (2004). *Essentials of computational chemistry: Theories and models*. Chichester: Wiley.
- Christen, M., Hunenberger, P. H., Bakowies, D., Baron, R., Burgi, R., Geerke, D. P., Heinz, T. N., Kastenholz, M. A., Krautler, V., Oostenbrink, C.,



- Peter, C., Trzesniak, D., & Van Gunsteren, W. F. (2005). The GROMOS software for biomolecular simulation: GROMOS05. *Journal of Computational Chemistry*, 26, 1719.
- De Santis, P. (1992). Conformational energy calculations of macromolecules. *Current Contents*, 34, 8.
- De Santis, P., Giglio, E., Liquori, A. M., & Ripamonti, A. (1963). Stability of helical conformations of simple linear polymers. *Journal of Polymer Science Part A*, 1, 1383.
- De Santis, P., Giglio, E., Liquori, A. M., & Ripamonti, A. (1965). Van der Waals interaction and stability of helical polypeptide chains. *Nature*, 206, 456.
- De Voe, H., & Tinoco, I., Jr. (1962). The stability of helical polynucleotides: Base contributions. *Journal of Molecular Biology*, 4, 500.
- Duan, Y., Wu, C., Chowdhury, S., Lee, M. C., Xiong, G., Zhang, W., Yang, R., Cieplak, P., Luo, R., Lee, T., Caldwell, J., Wang, J., & Kollman, P. (2003). A point-charge force field for molecular mechanics simulations of proteins based on condensed-phase quantum mechanical calculations. *Journal of Computational Chemistry*, 24, 1999.
- Eisenberg, D. (2003). The discovery of the  $\alpha$ -helix and  $\beta$ -sheet, the principal structural features of proteins. *Proceedings of the National Academy of Sciences of the United States of America*, 100, 11207.
- Engler, E. M., Andose, J. D., & Schleyer, P. R. (1973). Critical evaluation of molecular mechanics. *Journal of the American Chemical Society*, 95, 8005.
- Foloppe, N., & MacKerell, A. D., Jr. (2000). All-atom empirical force field for nucleic acids: I. Parameter optimization based on small molecule and condensed phase macromolecular target data. *Journal of Computational Chemistry*, 21, 86.
- Gibson, K. D., & Scheraga, H. A. (1967a). Minimization of polypeptide energy. I. Preliminary structures of bovine pancreatic ribonuclease S-peptide. *Proceedings of the National Academy of Sciences of the United States of America*, 58, 420.
- Gibson, K. D., Scheraga, H. A. (1967b). Minimization of polypeptide energy. II. Preliminary structures of oxytocin, vasopressin, and an octapeptide from ribonuclease. *Proceedings of the National Academy of Sciences of the United States of America*, 58, 1317.
- Gresh, N., Claverie, P., & Pullman, A. (1986). Intermolecular interactions: Elaboration on an additive procedure including an explicit charge-transfer contribution. *International Journal of Quantum Chemistry*, 29, 101.
- Halgren, T. A. (1996). Merck molecular force field. I. Basis, form, scope, parameterization, and performance of MMFF94. *Journal of Computational Chemistry*, 17, 490.
- Halgren, T. A. (1999a). MMFF VI. MMFF94s option for energy minimization studies. *Journal of Computational Chemistry*, 20, 720.
- Halgren, T. A. (1999b). MMFF VII. Characterization of MMFF94, MMFF94s, and other widely available force fields for conformational energies and for intermolecular-interaction energies and geometries. *Journal of Computational Chemistry*, 20, 730.
- Hendrickson, J. B. (1961). Molecular geometry. I. Machine computation of the common rings. *Journal of the American Chemical Society*, 83, 4537.
- Hendrickson, J. B. (1962). Molecular geometry. II. methyl-cyclohexanes and cycloheptanes. *Journal of the American Chemical Society*, 84, 3355.
- Hendrickson, J. B. (1973). Molecular geometry. VIII. Proton magnetic resonance studies of cycloheptane conformations. *Journal of the American Chemical Society*, 95, 494.
- Hill, T. L. (1946). On steric effects. *Journal of Chemical Physics*, 14, 465.
- Hill, T. L. (1948). Steric effects. I. Van der Waals potential energy curves. *Journal of Chemical Physics*, 16, 399.
- Jorgensen, W. L., Chandrasekhar, J., Madura, J. D., Impey, R. W., & Klein, M. L. (1983). Comparison of simple potential functions for simulating liquid water. *Journal of Chemical Physics*, 79, 926.
- Jorgensen, W. L., & Tirado-Rives, J. (1988). The OPLS potential functions for proteins. Energy minimizations for crystals of cyclic peptides and crambin. *Journal of the American Chemical Society*, 110, 1657.
- Jorgensen, W. L., Maxwell, D. S., & Tirado-Rives, J. (1996). Development and testing of the OPLS all-atom force field on conformational energetics and properties of organic liquids. *Journal of the American Chemical Society*, 118, 11226.
- Jurecka, P., Cerny, J., Hobza, P., & Salahub, D. R. (2007). Density functional theory augmented with an empirical dispersion term. Interaction energies and geometries of 80 non-covalent complexes compared with ab initio quantum mechanics calculations. *Journal of Computational Chemistry*, 28, 555.
- Kaminski, G. A., Friesner, R. A., Tirado-Rives, J., & Jorgensen, W. L. (2001). Evaluation and reparameterization of the OPLS-AA force field for proteins via comparison with accurate quantum chemical calculations on peptides. *The Journal of Physical Chemistry B*, 105, 6474.

- Khutorsky, V. E., & Poltev, V. I. (1976). Conformations of double-helical nucleic acids. *Nature*, 264, 483.
- Kitaigorodski, A. I. (1959). *Organic chemical crystallography*. New York: Consultants Bureau.
- Kitaigorodsky, A. I. (1961). The interaction curve of non-bonded carbon and hydrogen atoms and its application. *Tetrahedron*, 14, 230.
- Kitaigorodsky, A. I. (1973). *Molecular crystals and molecules*. New York: Academic.
- Klauda, J. B., Venable, R. M., MacKerell, A. D., Jr., & Pastor, R. W. (2008). Considerations for lipid force field development. *Current Topics in Membranes*, 60, 1.
- Langlet, J., Claverie, P., Caron, F., & Boeue, J. C. (1981). Interactions between nucleic acid bases in hydrogen bonded and stacked configurations: The role of the molecular charge distribution. *International Journal of Quantum Chemistry*, 20, 299.
- Leach, A. R. (2001). *Molecular modelling: Principles and applications*. Harlow: Prentice Hall (Pearson Education).
- Leach, S. J., Némethy, G., & Scheraga, H. A. (1966a). Computation of the sterically allowed conformations of peptides. *Biopolymers*, 4, 369.
- Leach, S. J., Némethy, G., Scheraga, H. A. (1966b). Intramolecular steric effects and hydrogen bonding in regular conformations of polyamino acids. *Biopolymers*, 4, 887.
- Levitt, M., & Lifson, S. (1969). Refinement of protein conformations using a macromolecular energy minimization procedure. *Journal of Molecular Biology*, 46, 269.
- Lifson, S., & Warshel, A. (1968). Consistent force field for calculations of conformations, vibrational spectra, and enthalpies of cycloalkane and *n*-alkane molecules. *Journal of Chemical Physics*, 49, 5116.
- Lii, L.-H., & Allinger, N. L. (1991). The MM3 force field for amides, polypeptides and proteins. *Journal of Chemical Physics*, 12, 186.
- Lii, L.-H., Chen, K.-H., Johnson, G. P., French, A. D., & Allinger, N. L. (2005). The external-anomeric torsional effect. *Carbohydrate Research*, 340, 853.
- Liwo, A., Lee, J., Ripoll, D. R., Pillardy, J., & Scheraga, H. A. (1999). Protein structure prediction by global optimization of a potential energy function. *Proceedings of the National Academy of Sciences of the United States of America*, 96, 5482.
- MacKerell, A. D., Jr. (2004). Empirical force fields for biological macromolecules: Overview and issues. *Journal of Computational Chemistry*, 25, 1584.
- Mahoney, M. W., & Jorgensen, W. L. (2001). Quantum, intramolecular flexibility, and polarizability effects on the reproduction of the density anomaly of liquid water by simple potential functions. *Journal of Computational Chemistry*, 115, 10758.
- Mason, R. (1969). The intermolecular potential and structure of crystals of aromatic molecules. *Molecular Crystals and Liquid Crystals*, 9, 3.
- Matsuoka, O., Clementi, E., & Yoshimine, M. (1976) CI Study of the water dimer potential surface. *Journal of Chemical Physics*, 64, 1351.
- McAllister, S. R., & Floudas, C. A. (2010). An improved hybrid global optimization method for protein tertiary structure prediction. *Computational Optimization and Applications*, 45, 377.
- McGuire, R. F., Momany, F. A., & Scheraga, H. A. (1972). Energy parameters in polypeptides. V. An empirical hydrogen bond potential function based on molecular orbital calculations. *Journal of Physical Chemistry*, 76, 375.
- Momany, F. A., Vanderkooi, G., & Scheraga, H. A. (1968). Determination of intermolecular potentials from crystal data. I. General theory and application to crystalline benzene at several temperatures. *Proceedings of the National Academy of Sciences*, 61, 429.
- Momany, F. A., Carruthers, L. M., & Scheraga, H. A. (1974). Intermolecular potentials from crystal data. IV. Application of empirical potentials to the packing configurations and lattice energies in crystals of amino acids. *Journal of Physical Chemistry*, 78, 1621.
- Momany, F. A., McGuire, R., Burgess, A., & Scheraga, H. (1975). Energy parameters in polypeptides. VII. Geometric parameters, partial atomic charges, nonbonded interactions, hydrogen bond interactions, and intrinsic torsional potentials for the naturally occurring amino acids. *Journal of Physical Chemistry*, 79, 2361.
- Nada, H., & van der Eerden, J. P. J. M. (2003). An intermolecular potential model for the simulation of ice and water near the melting point: A six-site model of H<sub>2</sub>O. *Journal of Chemical Physics*, 118, 7401.
- Nash, H. A., & Bradley, D. F. (1966). Calculation of the lowest energy configurations of nucleotide base pairs on the basis of an electrostatic model. *Journal of Chemical Physics*, 45, 1380.
- Némethy, G., & Scheraga, H. A. (1965). Theoretical determination of sterically allowed conformations of a polypeptide chain by a computer method. *Biopolymers*, 3, 155.
- Némethy, G., Gibson, K. D., Palmer, K. A., Yoon, C. N., Paterlini, G., Zagari, A., Rumsey, S., &



- Scheraga, H. A. (1992) Energy parameters in polypeptides. 10. Improved geometrical parameters and nonbonded interactions for use in the ECEPP/3 algorithm, with application to proline-containing peptides. *Journal of Physical Chemistry*, 96, 6472.
- Oostenbrink, C., Villa, A., Mark, A. E., & van Gunsteren, W. F. (2004). A biomolecular force field based on the free enthalpy of hydration and solvation: The GROMOS force-field parameter sets 53A5 and 53A6. *Journal of Computational Chemistry*, 25, 1656.
- Pauling, L., & Corey, R. B. (1951). The pleated sheet, a new layer configuration of polypeptide chains. *Proceedings of the National Academy of Sciences of the United States of America*, 37, 251.
- Pauling, L., Corey, R. B., & Branson, H. R. (1951). The structure of proteins: Two hydrogen-bonded helical configurations of the polypeptide chain. *Proceedings of the National Academy of Sciences of the United States of America*, 37, 205.
- Perez, A., Marchan, I., Svozil, D., Sponer, J., Cheatham, T. E., Laughton, C. A., & Orozco, M. (2007). Refinement of the AMBER force field for nucleic acids: Improving the description of  $\alpha/\beta$  conformers. *Biophysical Journal*, 92, 3817.
- Polozov, R. V., Poltev, V. I., & Sukhorukov, B. I. (1973). Relation of the interactions of nucleic acid bases to the helical conformations of polynucleotides. *Studia Biophysica*, 40, 13.
- Poltev, V. I., & Bruskov, V. I. (1978) On molecular mechanisms of nucleic acid synthesis fidelity aspects I. Contribution of base interactions. *Journal of Theoretical Biology*, 70, 69.
- Poltev, V. I., & Shulyupina, N. V. (1986). Simulation of interactions between nucleic-acid bases by refined atom-atom potential functions. *Journal of Biomolecular Structure & Dynamics*, 3, 739.
- Poltev, V. I., & Sukhorukov, B. I. (1967). Theoretical examination of the physical nature of the intermolecular interactions determining the conformational state of polynucleotides. *Biophysics (Moscow)*, 12, 879.
- Poltev, V. I., & Sukhorukov, B. I. (1970). Semiempirical calculations of interaction energy of DNA nitrous bases. *Studia Biophysica*, 24/25, 179.
- Poltev, V. I., Grokhilina, T. I., & Malenkov, G. G. (1984). Hydration of nucleic-acid bases studied using novel atom-atom potential functions. *Journal of Biomolecular Structure & Dynamics*, 2, 413.
- Pullman, A., & Pullman, B. (1968). Aspects of the electronic structure of the purine and pyrimidine bases of the nucleic acids and of their interactions. *Advances in Quantum Chemistry*, 4, 267.
- Pullman, B., Claverie, P., & Caillet, J. (1966). Van der Waals-London interactions and the configuration of hydrogen-bonded purine and pyrimidine Pairs. *Proceedings of the National Academy of Sciences of the United States of America*, 55, 904.
- Rae, A. I. M., & Mason, R. (1968). The intermolecular potential and the lattice energy of benzene. *Proceedings of the Royal Society*, 304, 487.
- Ramachandran, G. N. (1990). This week's citation classic. *Current Contents*, 10, 119.
- Ramachandran, G. N., Ramakrishnan, C., & Sasisekharan, V. (1963). Stereochemistry of polypeptide chain configurations. *Journal of Molecular Biology*, 7, 95.
- Ramachandran, K. I., Deepa, G., & Namboori, K. (2008). *Computational chemistry and molecular modeling: Principles and applications*. Berlin: Springer.
- Raman, E. P., Guvench, O., & MacKerell, A. D., Jr. (2010). CHARMM additive all-atom force field for glycosidic linkages in carbohydrates involving furanoses. *Journal of Physical Chemistry B*, 114, 12981.
- Rasse, D., Warme, P. K., & Scheraga, H. A. (1974). Refinement of the X-ray structure of rubredoxin by conformational energy calculations. *Proceedings of the National Academy of Sciences of the United States of America*, 71, 3736.
- Renugopalakrishnan, V., Lakshminarayanan, A. V., & Sasisekharan, V. (1971) Stereochemistry of nucleic acids and polynucleotides III. Electronic charge distribution. *Biopolymers*, 10, 1159.
- Ripoll, D. R., Scheraga, H. A. (1988) On the multiple-minima problem in the conformational analysis of polypeptides. II. An electrostatically driven Monte Carlo method. Tests on poly(L-alanine). *Biopolymers*, 27, 1283.
- Scheraga, H. A. (2008). From helix-coil transitions to protein folding. *Biopolymers*, 89, 479.
- Scheraga, H. A., Pillardy, J., Liwo, A., Lee, J., Czaplowski, C., Ripoll, D. R., Wedemeyer, W. J., & Arnautova, Y. A. (2002). Evolution of physics-based methodology for exploring the conformational energy landscape of proteins. *Journal of Computational Chemistry*, 23, 28.
- Scott, R. A., & Scheraga, H. A. (1966a). Conformational analysis of macromolecules. III. Helical structures of poly-glycine and poly-L-alanine. *Journal of Chemical Physics*, 45, 2091.
- Scott, R. A., & Scheraga, H. A. (1966b). Conformational analysis of macromolecules. II. The rotational isomeric states of the normal hydrocarbons. *Journal of Chemical Physics*, 44, 3054.

- Shipman, L. L., Burgess, A. W., & Scheraga, H. A. (1975). A new approach to empirical intermolecular and conformational potential energy functions. I. Description of model and derivation of parameters. *Proceedings of the National Academy of Sciences of the United States of America*, 72, 543.
- Sippl, M. J., Némethy, G., & Scheraga, H. A. (1984). Intermolecular potentials from crystal data. 6. Determination of empirical potentials for O-H...O=C hydrogen bonds from packing configurations. *Journal of Physical Chemistry*, 88, 6231.
- Snir, J., Nemenoff, R. A., & Scheraga, H. A. (1978). A revised empirical potential for conformational, intermolecular, and solvation studies. 5. Development and testing of parameters for amides, amino acids and peptides. *Journal of Physical Chemistry*, 82, 2527.
- Song, K., Hornak, V., de los Santos, C., Grollman, A. P., & Simmerling, C. (2008). Molecular mechanics parameters for the FapydG DNA lesion. *Journal of Computational Chemistry*, 29, 17.
- Stillinger, F. H., & Rahman, A. (1974). Improved simulation of liquid water by molecular dynamics. *Journal of Chemical Physics*, 60, 1545.
- Van der Spoel, D., Lindahl, E., Hess, B., Groenhof, G., Mark, A. E., & Berendsen, H. J. C. (2005). GRO-MACS: Fast, flexible, and free. *Journal of Computational Chemistry*, 26, 1701.
- Van Gunsteren, W., Fand, H. J., & Berendsen, C. (1987). *Groningen molecular simulation (GROMOS) library manual*. Groningen: BIOMOS.
- Wang, J., Cieplak, P., & Kollman, P. A. (2000). How well does a restrained electrostatic potential (RESP) model perform in calculating conformational energies of organic and biological molecules? *Journal of Computational Chemistry*, 21, 1049.
- Wang, J., Wolf, R. M., Caldwell, J. W., Kollman, P. A., & Case, D. A. (2004). Development and testing of a general amber force field. *Journal of Computational Chemistry*, 25, 1157.
- Wang, J., Wang, W., Kollman, P. A., & Case, D. A. (2006). Automatic atom type and bond type perception in molecular mechanical calculations. *Journal of Molecular Graphics & Modelling*, 25, 247.
- Warme, P. K., Momany, F. A., Rumball, S. V., & Scheraga, H. A. (1974). Computation of structures of homologous proteins;  $\alpha$ -lactalbumin from lysozyme. *Biochemistry*, 13, 768.
- Warshel A., & Lifson, S. (1970). Consistent force field calculations. II. Crystal structures, sublimation energies, molecular and lattice vibrations, molecular conformations, and enthalpies of alkanes. *Journal of Chemical Physics*, 53, 582.
- Watson, J. D., & Crick, F. H. C. (1953). A structure for deoxyribose nucleic acid. *Nature*, 171, 737.
- Weiner, P., & Kollman, P. (1981). AMBER: Assisted model building with energy refinement. A general program for modeling molecules and their interactions. *Journal of Computational Chemistry*, 2, 287.
- Weiner, S. J., Kollman, P. A., Case, D. A., Singh, U. C., Ghio, C., Alagona, G., Profeta, S., Jr., & Weiner, P. (1984). A new force field for molecular mechanical simulation of nucleic acids and proteins. *Journal of the American Chemical Society*, 106, 765.
- Westheimer, F. H., & Mayer, J. E. (1946). The theory of the racemization of optically active derivatives of diphenyl. *Journal of Chemical Physics*, 14, 733.
- Williams, D. E. (1966). Nonbonded potential parameters derived from crystalline aromatic hydrocarbons. *Journal of Chemical Physics*, 45, 3770.
- Williams, D. E. (1967). Nonbonded potential parameters derived from crystalline hydrocarbons. *Journal of Chemical Physics*, 47, 4680.
- Williams, D. E., & Weller, R. R. (1983). Lone-pair electronic effects on the calculated ab initio SCF-MO electric potential and the crystal structures of azabenzene. *Journal of the American Chemical Society*, 105, 4143.
- Yan, J. F., Momany, F. A., Hoffmann, R., & Scheraga, H. A. (1970). Energy parameters in polypeptides. II. Semiempirical molecular orbital calculations for model peptides. *Journal of Physical Chemistry*, 74, 420.
- Zhurkin, V. B., Poltev, V. I., & Florentiev, V. L. (1980). Atom-atom potential functions for conformational calculations of nucleic-acids. *Molecular Biology (Moscow), English Translation*, 14, 882.



# 11 Molecular Electric, Magnetic, and Optical Properties

*Michał Jaszuński<sup>1</sup> · Antonio Rizzo<sup>2</sup> · Kenneth Ruud<sup>3</sup>*

<sup>1</sup>Institute of Organic Chemistry, Polish Academy of Sciences, Warszawa, Poland

<sup>2</sup>Istituto per i Processi Chimico Fisici del Consiglio Nazionale delle Ricerche, Pisa, Italy

<sup>3</sup>Centre for Theoretical and Computational Chemistry, Department of Chemistry, University of Tromsø, Tromsø, Norway

<b>Introduction</b> .....	<b>363</b>
<b>The Molecular Hamiltonian</b> .....	<b>364</b>
The Molecular Breit–Pauli Hamiltonian .....	365
Small Terms Due to the Scalar Potential in the Hamiltonian .....	367
The Magnetic Vector Potential .....	368
Small Terms Due to the Vector Potential in the Hamiltonian .....	369
<b>Response Theory</b> .....	<b>372</b>
Molecular Response: Definitions, Symbols .....	372
Expansions of Energy and Multipole Moments .....	375
<b>Electric Properties</b> .....	<b>376</b>
Electric Multipole Moments .....	377
Dipole and Quadrupole Moments .....	378
The Origin of the Frequency-Dependent Electric Dipole Polarizability and Hyperpolarizabilities .....	379
Dipole Polarizability .....	381
First Dipole Hyperpolarizability .....	383
Second Dipole Hyperpolarizability .....	385
Cauchy Moments .....	386
Long-Range Dispersion Interaction Coefficients .....	387
Electric Field Gradient at the Nucleus, Nuclear Quadrupole Coupling Constant .....	388
One-Photon Absorption, Excitation Energies, and Transition Moments .....	389
Two-Photon Absorption .....	392
<b>Magnetic Properties</b> .....	<b>393</b>
Magnetizability .....	393
Rotational <i>g</i> Tensor .....	396

<b><i>Birefringences and Dichroisms</i></b> .....	<b>398</b>
Optical Rotation .....	401
Circular Dichroism .....	404
Natural (Electronic) Circular Dichroism .....	404
Two-Photon Circular Dichroism .....	405
Faraday Effect .....	406
Hypermagnetizabilities, Cotton–Mouton Effect .....	407
Electric-Field-Gradient-Induced Birefringence .....	409
Magnetic Circular Dichroism .....	410
<b><i>Nuclear Spin-Related Properties</i></b> .....	<b>411</b>
NMR Effective Spin Hamiltonian .....	411
Nuclear Magnetic Shielding .....	414
Shielding Derivatives .....	418
Spin-Orbit Corrections to Nuclear Magnetic Shielding .....	419
Nuclear Spin Rotation Constants .....	420
NMR Indirect Spin–Spin Coupling .....	421
<b><i>Electron Spin-Related Properties</i></b> .....	<b>424</b>
Spin-Orbit Coupling Constants .....	425
Phosphorescence .....	426
ESR Effective Spin Hamiltonian .....	426
ESR Electronic $g$ -Tensor .....	428
Zero-Field Splitting .....	429
ESR Hyperfine Coupling Tensors .....	430
<b><i>Conclusions</i></b> .....	<b>432</b>
<b><i>Acknowledgment</i></b> .....	<b>433</b>
<b><i>References</i></b> .....	<b>433</b>

**Abstract:** The theory and applications of *ab initio* methods for the calculation of molecular properties are reviewed. A wide range of properties characterizing the interactions of molecules with external or internal sources of static or dynamic electromagnetic fields (including nonlinear properties and those related to nuclear and electron spins) is considered. Emphasis is put on the properties closely connected to the parameters used to describe experimentally observed spectra. We discuss the definitions of these properties, their relation to experiment, and give some remarks regarding various computational aspects. Theory provides a unified approach to the analysis of molecular properties in terms of average values, transition moments, and linear and nonlinear responses to the perturbing fields. Several literature examples are given, demonstrating that theoretical calculations are becoming easier, and showing that computed *ab initio* molecular properties are in many cases more accurate than those extracted from experimentally observed data.

## Introduction

---

The term “molecular properties” is generally used to denote properties characterizing the interactions of molecules with internal or external sources of static or dynamic electromagnetic fields. In the description of a complex quantum-mechanical system consisting of a molecule and a field it is convenient, both in theory and in experiment, to introduce an approximation that separates the molecule, the field, and the molecule–field interaction. One can then introduce an additional approximation and analyze the effects of the interaction only for the molecule, assuming a passive role of the interaction-induced changes in the field. In this way we can describe the interaction between the field and the molecule in terms of what we can consider intrinsic properties of the molecule.

Most spectroscopic methods assume that the experiment can be described in terms of these molecule–field interactions. There is, therefore, often a very close connection between the parameters used to describe the experimental spectra and the molecular properties that describe the molecule–field interactions probed by the experiment. The set of properties describing the influence of external electric and magnetic fields – static and time-dependent, spatially uniform or nonuniform – can be used to determine parameters that enter into the analysis of different experimental spectra. In particular, optical properties describe the interactions of a molecule with an external electromagnetic radiation field, and characterize both linear and nonlinear responses to the fields. Other sets of molecular properties describe the interactions of external magnetic fields and the magnetic fields due to the spins of all particles – that is, nuclear spins (specific for each nuclear isotope) and electron spin. These properties determine the parameters entering the analysis of Nuclear Magnetic Resonance (NMR) and Electron Spin Resonance (ESR) experiments. Additional fields can be created by the presence of neighboring molecules, and various effects due to weak long-range intermolecular interactions can also be described in terms of molecular properties. The treatment of molecular vibrational properties is in many cases based on the same principles as the formalism explored here; however, the calculation of such properties differs quite substantially from that of electronic properties due to the different quantum-mechanical treatments of the electronic and nuclear motions, and for this reason we will not consider vibrational properties in this chapter.

## The Molecular Hamiltonian

Our starting point for electronic structure calculations of molecules is the time-independent, field-free nonrelativistic Schrödinger equation for the electronic degrees of freedom of a molecule

$$\hat{H}^{(0)}\Psi = E\Psi, \quad (11.1)$$

where  $\Psi$  is the wave function describing the electronic state of the molecule,  $E$  the energy of this state, and  $\hat{H}^{(0)}$  the Hamilton operator for the system, given by

$$\hat{H}^{(0)} = \frac{1}{2m_e} \sum_i \hat{p}_i^2 - \frac{e^2}{4\pi\epsilon_0} \sum_{iK} \frac{Z_K}{r_{iK}} + \frac{e^2}{8\pi\epsilon_0} \sum_{i \neq j} \frac{1}{r_{ij}} + \frac{e^2}{8\pi\epsilon_0} \sum_{K \neq L} \frac{Z_K Z_L}{R_{KL}}, \quad (11.2)$$

where the first term corresponds to the kinetic energy of the electrons,  $\mathbf{p}_i = -i\hbar\nabla_i$  is the linear momentum operator of particle  $i$ , the second term is the attractive potential between the electrons and the nuclei, the third term the electron–electron repulsion potential, and the last term the repulsive potential for the interaction between the nuclear point charges. In  $\blacklozenge$  Eq. 11.2,  $e$  is the elementary charge,  $Z_K e$  is the charge of nucleus  $K$ ,  $\epsilon_0$  is the electric constant (electric permittivity of vacuum), and  $m_e$  the mass of the electron. We use  $\mathbf{r}_i$  and  $\mathbf{R}_K$  to denote the vectors giving the position of electron  $i$  and nucleus  $K$  with respect to a chosen origin of the molecular frame. If needed, for a specific frame of interest, we use the notation

$$\mathbf{r}_{iO} = \mathbf{r}_i - \mathbf{O} \quad (11.3)$$

to emphasize that the positions are given relative to an origin  $\mathbf{O}$ . We define vectors between two different points in space with the directional convention

$$\mathbf{R}_{KL} = \mathbf{R}_K - \mathbf{R}_L, \quad (11.4)$$

corresponding to a vector pointing from nucleus  $L$  to nucleus  $K$ . In the summations over electrons or nuclei, we always assume – unless explicitly stated otherwise – that the summation runs over all the particles of a given type in the molecule. Whenever needed, we shall use for vector and tensor coordinates the following subscripts:

- Greek symbols for unspecified molecular frame coordinates; for these coordinates the Einstein summation convention is applied
- $x, y, z$  for specific molecular frame coordinates (for instance, determined by molecular symmetry)
- $X, Y, Z$  for laboratory frame coordinates
- $1, 2, 3$  when the tensor is specified using its own principal axes and values
- $a, b, c$  for coordinates defined by the moment of inertia  $\mathbf{I}$

where  $\mathbf{I} = \sum_K M_K \mathbf{R}_K \mathbf{R}_K^T$  and  $M_K$  is the mass of nucleus  $K$ .

The Hamiltonian in  $\blacklozenge$  Eq. 11.2 does not take into account the interactions with external electric or magnetic fields. Moreover, so far we have neglected numerous other interactions, related to the existence of the electron and nuclear spins (and the corresponding magnetic moments), their interactions with external fields, and relativistic effects. Thus, for the study of molecular properties which depend on these interactions we need to consider a more general approach, based for instance on the Breit–Pauli Hamiltonian (Dyall and Faegri Jr. 2007; Moss 1973). In many cases the contributions to molecular properties due to the additional terms appearing in the Breit–Pauli Hamiltonian can be estimated using the available solutions of the (nonrelativistic) Schrödinger equation and perturbation theory.

## The Molecular Breit–Pauli Hamiltonian

There are several ways to introduce and justify the use of the Breit–Pauli Hamiltonian. One can start from the Dirac equation which involves the relativistic Hamiltonian for the free electron, and extend it by applying various approximations to many electrons in the field generated by the nuclei. We will not discuss here the steps taken in the reduction of the Dirac Hamiltonian to the Breit–Pauli Hamiltonian (Dyall and Faegri Jr. 2007; Moss 1973). Instead, we only list the various contributions appearing in the Breit–Pauli Hamiltonian. The approximate form of the Breit–Pauli Hamiltonian we will discuss is accurate to order  $\alpha_{fs}^2$ , where  $\alpha_{fs}$  is the fine structure constant, and higher-order corrections are not considered at this stage (we will include later selected terms of the order  $\alpha_{fs}^4$  needed for the calculation of response properties in the presence of magnetic fields). Finally, even though some of the operators appearing in the electronic Breit–Pauli Hamiltonian are of little interest from the point of view of molecular properties, they are included here for completeness.

The purely electronic contributions to the Breit–Pauli Hamiltonian can be written as (Bethe and Salpeter 1957, p. 170; Moss 1973):

$$\hat{H}_{el}^{BP} = \sum_i \left( \frac{\pi_i^2}{2m_e} - e\phi \right) \quad (11.5)$$

$$- \mathbf{m}_i \cdot \mathbf{B} \quad (11.6)$$

$$+ \frac{\alpha_{fs}^2}{4m_e} \mathbf{m}_i \cdot (\boldsymbol{\pi}_i \times \mathbf{F} - \mathbf{F} \times \boldsymbol{\pi}_i) \quad (11.7)$$

$$+ \frac{e\hbar^2 \alpha_{fs}^2}{8m_e^2} (\nabla \cdot \mathbf{F}) \quad (11.8)$$

$$- \frac{\alpha_{fs}^2}{8m_e^3} \pi_i^4 \quad (11.9)$$

$$+ \frac{\alpha_{fs}^2}{2m_e^2} (\mathbf{m}_i \cdot \mathbf{B}) \pi_i^2 \quad (11.10)$$

$$+ \frac{1}{4\pi\epsilon_0} \sum_{j \neq i} \left\{ \frac{e^2}{2} \frac{1}{r_{ij}} \right. \quad (11.11)$$

$$\left. - \frac{e^2 \alpha_{fs}^2}{4m_e^2} \left[ \frac{\boldsymbol{\pi}_i \cdot \boldsymbol{\pi}_j}{r_{ij}} + \frac{(\boldsymbol{\pi}_i \cdot \mathbf{r}_{ij})(\mathbf{r}_{ij} \cdot \boldsymbol{\pi}_j)}{r_{ij}^3} \right] \right\} \quad (11.12)$$

$$+ \frac{e\alpha_{fs}^2}{2m_e} \frac{\mathbf{m}_i \cdot (\mathbf{r}_{ij} \times \boldsymbol{\pi}_i)}{r_{ij}^3} \quad (11.13)$$

$$- \frac{e\alpha_{fs}^2}{m_e} \frac{\mathbf{m}_i \cdot (\mathbf{r}_{ij} \times \boldsymbol{\pi}_j)}{r_{ij}^3} \quad (11.14)$$

$$+ \frac{\alpha_{fs}^2}{2} \left[ \frac{\mathbf{m}_i \cdot \mathbf{m}_j}{r_{ij}^3} - \frac{3(\mathbf{m}_i \cdot \mathbf{r}_{ij})(\mathbf{r}_{ij} \cdot \mathbf{m}_j)}{r_{ij}^5} - \frac{8\pi}{3} \delta(\mathbf{r}_{ij}) \mathbf{m}_i \cdot \mathbf{m}_j \right] \quad (11.15)$$

$$\left. - \frac{\pi e^2 \hbar^2 \alpha_{fs}^2}{2m_e^2} \delta(\mathbf{r}_{ij}) \right\} \quad (11.16)$$



where  $\delta(\mathbf{r}_{ij})$  is the Dirac delta function

$$\delta(\mathbf{r}_{ij}) = 0 \quad \text{for} \quad \mathbf{r}_{ij} \neq 0; \quad \int_V \delta(\mathbf{r}_{ij}) d^3\mathbf{r} = 1. \quad (11.17)$$

In addition to these purely electronic contributions, we must also consider the interactions that involve simultaneously one of the electrons and one of the nuclei:

$$\hat{H}_{eN}^{\text{BP}} = \frac{1}{4\pi\epsilon_0} \sum_{iK} Z_K \left[ -\frac{e^2}{r_{iK}} \right. \quad (11.18)$$

$$\left. + \frac{e\alpha_{fs}^2}{2m_e} \frac{\mathbf{m}_i \cdot (\mathbf{r}_{iK} \times \boldsymbol{\pi}_i)}{r_{iK}^3} \right. \quad (11.19)$$

$$\left. + \frac{\pi e^2 \hbar^2 \alpha_{fs}^2}{2m_e^2} \delta(\mathbf{r}_{iK}) \right]. \quad (11.20)$$

Finally, we have the contributions arising from the nuclei only

$$\hat{H}_{\text{nucl}}^{\text{BP}} = \sum_K \left[ Z_K e \phi_K - \mathbf{m}_K \cdot \mathbf{B} \right. \quad (11.21)$$

$$\left. + \sum_{L \neq K} \frac{e^2}{8\pi\epsilon_0} \frac{Z_K Z_L}{R_{KL}} \right]. \quad (11.22)$$

We have omitted in these equations all the terms dependent on the (inverse) masses of the nuclei. In the purely electronic and purely nuclear parts we have not included the rest mass of the particles. In the above equations we have introduced the mechanical momentum

$$\boldsymbol{\pi}_i = \mathbf{p}_i - q_i \mathbf{A}(\mathbf{r}_i), \quad (11.23)$$

where  $\mathbf{A}(\mathbf{r}_i)$  is the magnetic vector potential experienced by electron  $i$ , and  $q_i$  is the charge of the particle, which for an electron is  $-e$ . The corresponding magnetic field induction is  $\mathbf{B}$  (see below).  $\phi$  represents the external scalar electrostatic potential, and the electric field due to this external potential is  $\mathbf{F} = -\nabla\phi$ . We have also introduced the magnetic moment of the electron  $\mathbf{m}_i$ , which is related to the electron spin through

$$\mathbf{m}_i = -g_e \frac{e\hbar}{2m_e} \mathbf{s}_i = -g_e \mu_B \mathbf{s}_i, \quad (11.24)$$

where  $g_e$  is the electron  $g$  factor and the Bohr magneton  $\mu_B$  is the unit for magnetic moments. In a similar manner,  $\mathbf{m}_K$  is the nuclear magnetic moment, related to the nuclear spin  $\mathbf{I}_K$  as

$$\mathbf{m}_K = \hbar \gamma_K \mathbf{I}_K = \mu_N g_K \mathbf{I}_K, \quad (11.25)$$

where  $\gamma_K$  is the nuclear magnetogyric ratio,  $\mu_N = e\hbar/2m_p$  is the nuclear magneton,  $m_p$  the proton mass, and  $g_K$  is the  $g$  factor of nucleus  $K$ , unique for each isotope. For a detailed description of the different terms appearing in the Breit–Pauli Hamiltonian we refer to Moss (1973). The Breit–Pauli Hamiltonian,  $\blacklozenge$  Eqs. 11.5–11.22, does not contain explicitly any coupling between the nuclear magnetic moments  $\mathbf{m}_K$  and the magnetic moments of the electrons  $\mathbf{m}_i$ . In  $\blacklozenge$  sections “The Magnetic Vector Potential” and  $\blacklozenge$  “Small Terms Due to the Scalar Potential in the Hamiltonian,” we introduce these interactions by establishing a magnetic vector potential for the nuclear magnetic moments in a similar manner to the magnetic vector potential for the external magnetic field induction. These interactions, important for determining the observable NMR and ESR spectra, will thus appear through the couplings arising when we expand

$\pi_i^2$  (and the spin–Zeeman term leading to  $\blacktriangleright$  Eq. 11.6) using the full mechanical momentum operator given in  $\blacktriangleright$  Eq. 11.23.

The Breit–Pauli Hamiltonian describes a number of contributions that can be considered small compared to the nonrelativistic Hamiltonian given in  $\blacktriangleright$  Eq. 11.2. These contributions are thus ideally suited to be treated by perturbation theory, at least as long as we do not consider the heaviest atoms of the periodic table, where the relativistic effects become substantial and the lack of a variational bound for the Breit–Pauli Hamiltonian makes any perturbation approach fail. For the energy of molecules consisting of light atoms, the relativistic effects can to a first approximation often be treated considering only the mass-velocity ( $\blacktriangleright$  Eq. 11.9) and one-electron Darwin ( $\blacktriangleright$  Eq. 11.20) terms.

Some of the terms included in the Breit–Pauli Hamiltonian also describe small interactions that can be probed experimentally by inducing suitable excitations in the electron or nuclear spin space, giving rise to important contributions to observable NMR and ESR parameters. In particular, for molecular properties for which there are interaction mechanisms involving the electron spin, also the spin-orbit interaction ( $\blacktriangleright$  Eqs. 11.13 and  $\blacktriangleright$  11.14) becomes important. The Breit–Pauli Hamiltonian in  $\blacktriangleright$  Eqs. 11.5–11.22, however, only includes molecule–external field interactions through the presence of a scalar electrostatic potential  $\phi$  (and the associated electric field  $\mathbf{F}$ ) and the appearance of the magnetic vector potential in the mechanical momentum operator ( $\blacktriangleright$  Eq. 11.23). In order to extract in more detail the interaction between the electronic structure of a molecule and an external electromagnetic field, we need to consider in more detail the form of the scalar and vector potentials.

## Small Terms Due to the Scalar Potential in the Hamiltonian

Let us begin with the simplest example, the interaction of a molecule with a static electric field. This interaction can be described by the Hamiltonian

$$\hat{H} = \hat{H}^{(0)} - e \sum_i \phi(\mathbf{r}_i) + e \sum_K Z_K \phi(\mathbf{R}_K), \quad (11.26)$$

where we have neglected the spin-orbit and relativistic terms given in  $\blacktriangleright$  Eqs. 11.7 and  $\blacktriangleright$  11.8. We can expand the potential around a common origin

$$\phi(\mathbf{r}_i) = \phi(0) + \frac{\partial \phi}{\partial r_{i\alpha}} r_{i\alpha} + \frac{1}{2} \frac{\partial^2 \phi}{\partial r_{i\alpha} \partial r_{i\beta}} r_{i\alpha} r_{i\beta} + \dots \quad (11.27)$$

with a similar expansion for the potential at the position of the nuclei,  $\phi(\mathbf{R}_K)$ . Recalling that the electric field due to the external potential is  $\mathbf{F} = -\nabla \phi$ , we can rewrite  $\blacktriangleright$  Eq. 11.26 in terms of electric multipole operators

$$\hat{H} = \hat{H}^{(0)} + Q\phi(0) + \hat{H}^F \cdot \mathbf{F} + \hat{H}^{\nabla F} \cdot \nabla \mathbf{F} + \dots, \quad (11.28)$$

where  $Q$  is the total charge of the molecule. We note that the multipole operators are defined with respect to the chosen common origin. For a neutral system, the first two contributions describing the field effects are given by the:

- External electric field perturbation:

$$\hat{H}^F = -\boldsymbol{\mu}, \quad (11.29)$$

where the electric dipole operator is

$$\hat{\mu}_\alpha = -e \sum_i \hat{r}_{i\alpha} + e \sum_K Z_K R_{K\alpha}. \quad (11.30)$$

- External electric field gradient perturbation:

$$\hat{H}^{\nabla F} = -\frac{1}{3} \hat{\Theta}, \quad (11.31)$$

where the electric quadrupole operator in its traceless form is

$$\hat{\Theta}_{\alpha\beta} = -\frac{e}{2} \sum_i (3\hat{r}_{i\alpha}\hat{r}_{i\beta} - \hat{r}_i^2 \delta_{\alpha\beta}) + \frac{e}{2} \sum_K Z_K (3R_{K\alpha}R_{K\beta} - R_K^2 \delta_{\alpha\beta}). \quad (11.32)$$

The interaction due to the external field gradient can also be expressed in terms of the second moments (traced form)

$$\hat{q}_{\alpha\beta} = -e \sum_i \hat{r}_{i\alpha}\hat{r}_{i\beta} + e \sum_K Z_K R_{K\alpha}R_{K\beta}. \quad (11.33)$$

Later we shall discuss also the effects due to the:

- Electric field gradient at the nucleus K:

$$\begin{aligned} \hat{V}_{\alpha\beta}^K &= \frac{1}{4\pi\epsilon_0} e \sum_i \frac{3\hat{r}_{iK,\alpha}\hat{r}_{iK,\beta} - \hat{r}_{iK}^2 \delta_{\alpha\beta}}{r_{iK}^5} \\ &\quad - \frac{1}{4\pi\epsilon_0} e \sum_{L \neq K} Z_L \frac{3R_{LK,\alpha}R_{LK,\beta} - R_{LK}^2 \delta_{\alpha\beta}}{R_{LK}^5}, \end{aligned} \quad (11.34)$$

since we will need it to describe the interaction with the nuclear quadrupole moments,  $\mathbf{Q}_K$ , described by the interaction Hamiltonian

$$\hat{H}^{V^K} = -\frac{1}{2} \sum_K \mathbf{V}^K \mathbf{Q}_K. \quad (11.35)$$

## The Magnetic Vector Potential

We consider a molecule in which the magnetic field arises from two primary sources, an external magnetic field induction and the permanent magnetic moments of nuclei possessing a spin. In the minimal coupling approximation, the mechanical momentum operator (► Eq. 11.23) is given as

$$\boldsymbol{\pi}_i = \mathbf{p}_i + e\mathbf{A}^{\mathbf{B}}(\mathbf{r}_i) + e \sum_K \mathbf{A}^{\mathbf{m}^K}(\mathbf{r}_i), \quad (11.36)$$

where the superscripts indicate the different sources of the magnetic vector potential. In ► Eq. 11.36 we have explicitly indicated that we are interested in the magnetic vector potential at the positions of the electrons.

The magnetic vector potential is not uniquely defined, and we have to choose the gauge (Jackson 1998). In the Coulomb gauge, that is, where the magnetic vector potential is divergence free at all points in space,

$$\nabla \cdot \mathbf{A}(\mathbf{r}) = 0, \quad (11.37)$$

we may choose the vector potential describing the interaction with the external magnetic field induction and with the magnetic moments of the nuclei in the form

$$\mathbf{A}(\mathbf{r}_i) = \frac{1}{2} \mathbf{B} \times \mathbf{r}_{iO} + \alpha_{fs}^2 \sum_K \frac{\mathbf{m}_K \times \mathbf{r}_{iK}}{r_{iK}^3}. \quad (11.38)$$

It can easily be verified that the magnetic vector potential (Eq. 11.38) is divergence free. Since the magnetic field induced by the magnetic vector potential is given by

$$\mathbf{B} = \nabla \times \mathbf{A}^B(\mathbf{r}_i), \quad (11.39)$$

we can add any scalar differentiable potential  $\nabla\Lambda$  to the magnetic vector potential in Eq. 11.38 without changing the description of the magnetic field induction experienced by the molecule (since  $\nabla \times (\nabla\Lambda) = 0$ ). There are, therefore, multiple definitions of the magnetic vector potential that describe the same magnetic field induction, and thus the same physical situation. This invariance with respect to the choice of magnetic vector potential may be lost in approximate calculations. This in turn leads to what is known as the gauge dependence of computed magnetic properties, an undesirable feature of approximate calculations – the results depend on an arbitrary factor in the calculation. In practice, when interactions with external magnetic fields are considered, special computational methods are introduced to bypass this problem and to obtain reliable and unambiguous gauge-origin independent results. We will return to this point when we consider magnetic properties in section “Magnetic Properties.”

## Small Terms Due to the Vector Potential in the Hamiltonian

Having now established the form of the vector potential, we return to the molecular Hamiltonian. In the presence of magnetic fields, the kinetic energy is defined by the mechanical momentum operator, Eq. 11.23 (instead of the linear momentum operator), and in addition we need to consider the Zeeman term, Eq. 11.6. We can expand all the terms appearing in the kinetic energy, using the vector potential in the mechanical momentum, and introduce the magnetic field induction in the Zeeman term. This yields the following form of the Hamiltonian:

$$\hat{H} = \hat{H}^0 - i \frac{e\hbar}{m_e} \sum_i \mathbf{A}(\mathbf{r}_i) \cdot \nabla_i + \frac{e^2}{2m_e} \sum_i \mathbf{A}^2(\mathbf{r}_i) + \sum_i \mathbf{m}_i \cdot (\nabla_i \times \mathbf{A}(\mathbf{r}_i)), \quad (11.40)$$

where  $\hat{H}^0$  indicates the Hamiltonian in Eq. 11.2. In this equation we have taken advantage of the commutator relation  $[\mathbf{A}(\mathbf{r}_i), \nabla_i] = 0$  (this relation holds true for our choice of the Coulomb gauge, see Eq. 11.37). Inserting the magnetic vector potential, Eq. 11.38, into Eq. 11.40 we get

$$\hat{H} = \hat{H}^0 + \hat{H}^B \mathbf{B} + \sum_K \hat{H}^{K(\text{PSO})} \mathbf{m}_K \quad (11.41)$$

$$+ \mathbf{B}^T \hat{H}^{B,B} \mathbf{B} + \sum_K \mathbf{B}^T \hat{H}^{B,K} \mathbf{m}_K + \frac{1}{2} \sum_{K \neq L} \mathbf{m}_K^T \hat{H}^{K,L(\text{DSO})} \mathbf{m}_L \quad (11.42)$$

$$+ \sum_i \mathbf{m}_i \hat{H}^{s,B} \mathbf{B} + \sum_{iK} \mathbf{m}_i \hat{H}^{K(\text{FC})} \mathbf{m}_K + \sum_{iK} \mathbf{m}_i \hat{H}^{K(\text{SD})} \mathbf{m}_K. \quad (11.43)$$

The summation over the nuclear magnetic moments in the last term of Eq. 11.42 should include contributions quadratic in  $\mathbf{m}_K$ , but since these contributions do not correspond to any

measurable quantity, we have restricted the summation to different nuclei. We note also that these neglected terms are divergent, which shows the limitations of the applied theory.

Let us analyze the explicit expressions for the different operators in [Eqs. 11.41–11.43](#), which are obtained by inserting the magnetic vector potential [Eq. 11.38](#) into [Eq. 11.40](#). The contributions in [Eq. 11.41](#) arise from the unperturbed Hamiltonian and from the term linear in  $\mathbf{A}(\mathbf{r}_i)$ . The operators involved are:

- Magnetic dipole operator

$$\hat{H}^B = \frac{e}{2m_e} \sum_i \mathbf{l}_{iO} = \frac{\mu_B}{\hbar} \sum_i \mathbf{l}_{iO} = -i\mu_B \sum_i (\mathbf{r}_{iO} \times \nabla_i) = -\mathbf{m}. \quad (11.44)$$

The magnetic dipole moment is proportional to the angular momentum, the coefficient of proportionality being the magnetogyric ratio  $\gamma_e = e/2m_e$ . The orbital angular momentum of electron  $i$  is defined as

$$\mathbf{l}_{iO} = \mathbf{r}_{iO} \times \mathbf{p}_i = -i\hbar \mathbf{r}_{iO} \times \nabla_i. \quad (11.45)$$

The magnetic dipole operator describes the magnetic moment induced by the angular momentum of the electrons arising from the orbital motion, in contrast to the magnetic moment arising from the electron spin which we discuss when we consider the spin–Zeeman interaction.

- Paramagnetic spin-orbit operator

$$\hat{H}^{K(\text{PSO})} = \alpha_{\text{fs}}^2 \frac{2\mu_B}{\hbar} \sum_i \frac{\mathbf{l}_{iK}}{r_{iK}^3}. \quad (11.46)$$

The paramagnetic spin-orbit interaction, often called the orbital hyperfine interaction, describes the interaction of the magnetic moment induced by the orbital motion of the electrons with the nuclear magnetic moments.

The contributions in [Eq. 11.42](#) arise from the term quadratic in  $\mathbf{A}(\mathbf{r}_i)$  in [Eq. 11.40](#). They involve the following operators:

- Diamagnetic magnetizability operator

$$\hat{H}^{\text{B,B}} = \frac{e^2}{8m_e} \sum_i \left( r_{iO}^2 \mathbf{1} - \mathbf{r}_{iO} \mathbf{r}_{iO}^T \right), \quad (11.47)$$

where  $\mathbf{1}$  is a  $3 \times 3$  unit matrix. This operator is closely related to the second moment of the electronic charge, and thus reflects the size of the electron density distribution. The diamagnetic magnetizability tensor is a symmetric  $3 \times 3$  tensor operator, and has, therefore, in general six independent tensor operator elements.

- Diamagnetic shielding operator

$$\hat{H}^{\text{B,K}} = \alpha_{\text{fs}}^2 \frac{e^2}{2m_e} \sum_i \frac{(\mathbf{r}_{iO} \cdot \mathbf{r}_{iK}) \mathbf{1} - \mathbf{r}_{iO} \mathbf{r}_{iK}^T}{r_{iK}^3}. \quad (11.48)$$

The diamagnetic shielding tensor describes the interaction of the magnetic field induction with the nuclear magnetic moment, mediated by the orbital motion of the electrons. We note that the diamagnetic shielding tensor is a  $3 \times 3$  nonsymmetric tensor operator, and thus in general has nine independent elements.

- Diamagnetic spin-orbit operator

$$\hat{H}^{\text{K,L(DSO)}} = \alpha_{\text{fs}}^4 \frac{e^2}{2m_e} \sum_i \frac{(\mathbf{r}_{iK} \cdot \mathbf{r}_{iL}) \mathbf{1} - \mathbf{r}_{iK} \mathbf{r}_{iL}^T}{r_{iK}^3 r_{iL}^3}. \quad (11.49)$$

The diamagnetic spin-orbit operator describes the direct interaction between the two orbital magnetic moments induced in the electron density by the presence of the magnetic moments of nuclei  $K$  and  $L$ . As for the diamagnetic shielding operator, this is a  $3 \times 3$  nonsymmetric tensor operator, with in general nine independent elements.

Finally, the terms in  $\blacktriangleright$  Eq. 11.43 arise from the spin–Zeeman term, the last term in  $\blacktriangleright$  Eq. 11.40.

- Spin–Zeeman operator

$$\hat{H}^{s,B} = -\mathbf{1}. \quad (11.50)$$

The spin–Zeeman operator describes the direct interaction of an electron spin with the external magnetic field induction, and does not act on the spatial coordinates of the electrons, acting only in spin space (this contribution thus vanishes for closed-shell systems). We note that it is customary to describe this term in the Hamiltonian using the electron spin explicitly rather than the electron magnetic moment.

- Fermi contact (FC) operator

$$\hat{H}^{K(\text{FC})} = -\alpha_{\text{fs}}^2 \frac{8\pi}{3} \sum_i \delta(\mathbf{r}_{iK}) \mathbf{1}. \quad (11.51)$$

The Fermi contact operator acts both in the spin and in the spatial space of the electronic coordinates, often leading to a very different behavior of the response properties than for instance the  $\hat{H}^{K(\text{PSO})}$  operator. The Fermi contact operator represents the direct interaction of the electron spin-magnetic moment with the nuclear magnetic moment at the position of the nucleus, and can also be considered to be a measure of the spin-polarization at the nucleus.

- Spin–dipole (SD) operator

$$\hat{H}^{K(\text{SD})} = -\alpha_{\text{fs}}^2 \sum_i \frac{3 \mathbf{r}_{iK} \mathbf{r}_{iK}^T - r_{iK}^2 \mathbf{1}}{r_{iK}^5}. \quad (11.52)$$

The spin–dipole operator is in the form of a classical dipole–dipole interaction between the magnetic dipole of the nucleus and the magnetic dipole of the electron.

For the contributions involving the electronic spin operators through the electron spin-magnetic moment  $\mathbf{m}_i$  – that is,  $\hat{H}^{K(\text{FC})}$  and  $\hat{H}^{K(\text{SD})}$  – we need to keep track of the electron spin index and of the nuclear spin index. Due to the nature of the Dirac delta function appearing in the operator for  $\hat{H}^{K(\text{FC})}$ , this operator is diagonal in the two tensor indices, that is

$$\hat{H}_{\alpha\beta}^{K(\text{FC})} = \hat{H}_{\text{iso}}^{K(\text{FC})} \delta_{\alpha\beta}. \quad (11.53)$$

Both the Fermi contact and the spin–dipole operators can be derived considering the magnetic field induction created by the vector potential describing the nuclear magnetic moment

$$\begin{aligned} \nabla \times \mathbf{A}^{\mathbf{m}_K}(\mathbf{r}_i) &= \alpha_{\text{fs}}^2 \nabla \times \frac{\mathbf{m}_K \times \mathbf{r}_{iK}}{r_{iK}^3} \\ &= \alpha_{\text{fs}}^2 \left( \sum_i \frac{3 \mathbf{r}_{iK} \mathbf{r}_{iK}^T - r_{iK}^2 \mathbf{1}}{r_{iK}^5} + \frac{8\pi}{3} \sum_i \delta(\mathbf{r}_{iK}) \mathbf{1} \right) \mathbf{m}_K, \end{aligned} \quad (11.54)$$

which can be derived using standard vector product formulas.

We shall in later sections also discuss the effects of the spin-orbit interaction. The total spin-orbit (SO) interaction operator (McWeeny 1992) can be defined combining the terms included in [Eqs. 11.13](#), [11.14](#), and [11.19](#) as

$$\begin{aligned}\hat{H}^{\text{SO}} &= -\frac{e}{8\pi\epsilon_0 m_e} \alpha_{\text{fs}}^2 \left[ \sum_{iK} Z_K \frac{\mathbf{m}_i \cdot \mathbf{l}_{iK}}{r_{iK}^3} - \sum_{i \neq j} \frac{(\mathbf{m}_i + 2\mathbf{m}_j) \cdot \mathbf{l}_{ij}}{r_{ij}^3} \right] \\ &\equiv \hat{H}^{\text{SO}(1)} + \hat{H}^{\text{SO}(2)}.\end{aligned}\quad (11.55)$$

The corrections to the  $\hat{H}^{\text{SO}}$  operator, [Eq. 11.55](#), which account for the presence of magnetic fields, arise through the angular momentum operators (Fukui et al. 1996):

$$\mathbf{l}_{iK} = \mathbf{r}_{iK} \times [-i\hbar \nabla_i + e\mathbf{A}(\mathbf{r}_i)] \quad (11.56)$$

$$\mathbf{l}_{ij} = \mathbf{r}_{ij} \times [-i\hbar \nabla_i + e\mathbf{A}(\mathbf{r}_i)]. \quad (11.57)$$

The first part of the vector potential, related to the external magnetic field, causes the  $\hat{H}^{\text{SO}}$  operator to contain two contributions

$$\hat{H}^{\text{SO,B}} = \hat{H}^{\text{SO,B}(1)} + \hat{H}^{\text{SO,B}(2)}, \quad (11.58)$$

$$\hat{H}^{\text{SO,B}(1)} = -\frac{e^2}{16\pi\epsilon_0 m_e} \alpha_{\text{fs}}^2 \left[ \sum_{iK} Z_K \mathbf{m}_i \cdot \frac{(\mathbf{r}_{iO} \cdot \mathbf{r}_{iK}) \mathbf{1} - \mathbf{r}_{iO} \mathbf{r}_{iK}^T}{r_{iK}^3} \cdot \mathbf{B} \right], \quad (11.59)$$

$$\hat{H}^{\text{SO,B}(2)} = \frac{e^2}{16\pi\epsilon_0 m_e} \alpha_{\text{fs}}^2 \left[ \sum_{i \neq j} (\mathbf{m}_i + 2\mathbf{m}_j) \cdot \frac{(\mathbf{r}_{iO} \cdot \mathbf{r}_{ij}) \mathbf{1} - \mathbf{r}_{iO} \mathbf{r}_{ij}^T}{r_{ij}^3} \cdot \mathbf{B} \right]. \quad (11.60)$$

Similarly, the second part of the vector potential related to the magnetic moment of nucleus  $K$  leads to

$$\hat{H}^{\text{SO,K}} = \hat{H}^{\text{SO,K}(1)} + \hat{H}^{\text{SO,K}(2)}, \quad (11.61)$$

$$\hat{H}^{\text{SO,K}(1)} = -\frac{e^2}{8\pi\epsilon_0 m_e} \alpha_{\text{fs}}^4 \left[ \sum_M Z_M \sum_i \mathbf{m}_i \cdot \frac{(\mathbf{r}_{iK} \cdot \mathbf{r}_{iM}) \mathbf{1} - \mathbf{r}_{iK} \mathbf{r}_{iM}^T}{r_{iK}^3 r_{iM}^3} \cdot \mathbf{m}_K \right], \quad (11.62)$$

$$\hat{H}^{\text{SO,K}(2)} = \frac{e^2}{8\pi\epsilon_0 m_e} \alpha_{\text{fs}}^4 \left[ \sum_{i \neq j} (\mathbf{m}_i + 2\mathbf{m}_j) \cdot \frac{(\mathbf{r}_{iK} \cdot \mathbf{r}_{ij}) \mathbf{1} - \mathbf{r}_{iK} \mathbf{r}_{ij}^T}{r_{iK}^3 r_{ij}^3} \cdot \mathbf{m}_K \right]. \quad (11.63)$$

## Response Theory

### Molecular Response: Definitions, Symbols

The formalism we use to compare theory with experiment is based on the analysis of the expectation value of some operator of interest. We denote the time-dependent reference state as  $|\hat{0}(t)\rangle$

and consider hermitian (in general time-dependent) perturbing operators. The response functions correspond to the Fourier coefficients in the expansion of the time-dependent expectation value of an operator  $A$  (Olsen and Jørgensen 1995):

$$\begin{aligned} \langle \tilde{0}(t) | A | \tilde{0}(t) \rangle &= \langle 0 | A | 0 \rangle + \int_{-\infty}^{\infty} \langle \langle A; V^{\omega_1} \rangle \rangle e^{-i\omega_1 t} d\omega_1 \\ &+ \frac{1}{2} \int_{-\infty}^{\infty} \int_{-\infty}^{\infty} \langle \langle A; V^{\omega_1}, V^{\omega_2} \rangle \rangle e^{-i(\omega_1 + \omega_2)t} d\omega_1 d\omega_2 \\ &+ \frac{1}{6} \int_{-\infty}^{\infty} \int_{-\infty}^{\infty} \int_{-\infty}^{\infty} \langle \langle A; V^{\omega_1}, V^{\omega_2}, V^{\omega_3} \rangle \rangle e^{-i(\omega_1 + \omega_2 + \omega_3)t} d\omega_1 d\omega_2 d\omega_3 + \dots, \end{aligned} \quad (11.64)$$

where each  $V^{\omega_i}$  represents a time-dependent perturbation operator. We have omitted the infinitesimal factors, which ensure that the perturbations are switched on adiabatically and vanish for  $t = -\infty$ .

In the analysis of the different terms in  $\blacklozenge$  Eq. 11.64 for the case of exact electronic states, the zeroth-order response function is the expectation value of the operator  $A$  in the reference state  $|0\rangle$ ,  $\langle 0 | A | 0 \rangle$ . The first-order, or linear, response function and its residue are given in the sum-over-states form by (Olsen and Jørgensen (1995), Sasagane et al. (1993)):

$$\begin{aligned} \langle \langle A; B \rangle \rangle_{\omega_1} &= -\frac{1}{\hbar} \sum_P \sum_n \frac{\langle 0 | A | n \rangle \langle n | B | 0 \rangle}{\omega_n - \omega_1} \\ &= -\frac{1}{\hbar} \sum_n \left[ \frac{\langle 0 | A | n \rangle \langle n | B | 0 \rangle}{\omega_n - \omega_1} + \frac{\langle 0 | B | n \rangle \langle n | A | 0 \rangle}{\omega_n + \omega_1} \right]. \end{aligned} \quad (11.65)$$

The poles correspond to the excitation energies of the system. In addition, from the residues:

$$\lim_{\omega_1 \rightarrow \omega_e} \hbar(\omega_1 - \omega_e) \langle \langle A; B \rangle \rangle_{\omega_1} = \langle 0 | A | e \rangle \langle e | B | 0 \rangle, \quad (11.66)$$

$$\lim_{\omega_1 \rightarrow -\omega_e} \hbar(\omega_1 + \omega_e) \langle \langle A; B \rangle \rangle_{\omega_1} = -\langle 0 | B | e \rangle \langle e | A | 0 \rangle, \quad (11.67)$$

we can extract information about the transition matrix elements. The second-order, or quadratic, response function is defined as

$$\langle \langle A; B, C \rangle \rangle_{\omega_1, \omega_2} = -\frac{1}{\hbar^2} \sum_P \sum_{m, n} \frac{\langle 0 | A | m \rangle \langle m | B | n \rangle \langle n | C | 0 \rangle}{(\omega_m - \omega_\sigma)(\omega_n - \omega_2)}. \quad (11.68)$$

In  $\blacklozenge$  Eq. 11.68 and in the expressions given below,  $\omega_\sigma$  equals the sum of the other frequencies ( $\omega_\sigma = \sum_i \omega_i$ ) and  $P$  permutes the operators and the associated frequencies. For example, in  $\blacklozenge$  Eq. 11.68,  $P$  permutes  $A(-\omega_\sigma)$ ,  $B(\omega_1)$ ,  $C(\omega_2)$ . We note that different expressions for nonlinear response functions, involving operators of the form  $\bar{B} = B - \langle 0 | B | 0 \rangle$ , are obtained when the state  $|0\rangle$  is omitted from the summations (see, e.g., Sasagane et al. 1993).

For the quadratic and cubic response functions there is a variety of residues, and we present only expressions for the residues that are of practical interest. A single residue of a quadratic response function is

$$\lim_{\omega_2 \rightarrow \omega_f} \hbar(\omega_2 - \omega_f) \langle \langle A; B, C \rangle \rangle_{\omega_1, \omega_2} = -\frac{1}{\hbar} \left[ \sum_P \sum_m \frac{\langle 0 | A | m \rangle \langle m | B | f \rangle}{(\omega_m - \omega_\sigma)} \right] \langle f | C | 0 \rangle. \quad (11.69)$$



This type of residue is used for instance to evaluate two-photon transition amplitudes, the  $B$  term in magnetic circular dichroism or the transition moments in phosphorescence. A double residue of the quadratic response function, given by

$$\begin{aligned} & \lim_{\omega_1 \rightarrow -\omega_f} \hbar(\omega_1 + \omega_f) \lim_{\omega_2 \rightarrow \omega_e} \hbar(\omega_2 - \omega_e) \langle\langle A; B, C \rangle\rangle_{\omega_1, \omega_2} \\ & = -\langle 0|B|f\rangle \langle f|(A - \langle 0|A|0\rangle)|e\rangle \langle e|C|0\rangle, \end{aligned} \quad (11.70)$$

allows us to determine (from a knowledge of the reference state  $|0\rangle$  only) the transition moment between two other states,  $|e\rangle$  and  $|f\rangle$ .

For the particular choice of  $|e\rangle = |f\rangle$ , we obtain

$$\begin{aligned} & \lim_{\omega_1 \rightarrow -\omega_e} \hbar(\omega_1 + \omega_e) \lim_{\omega_2 \rightarrow \omega_e} \hbar(\omega_2 - \omega_e) \langle\langle A; B, C \rangle\rangle_{\omega_1, \omega_2} \\ & = -\langle 0|B|e\rangle (\langle e|A|e\rangle - \langle 0|A|0\rangle) \langle e|C|0\rangle, \end{aligned} \quad (11.71)$$

which allows us to extract the expectation value  $\langle e|A|e\rangle$ . In this way, using a double residue of the quadratic response function from the reference state function we can compute first-order properties of another state.

Finally, the third-order, or cubic, response function can be expressed as

$$\langle\langle A; B, C, D \rangle\rangle_{\omega_1, \omega_2, \omega_3} = -\frac{1}{\hbar^3} \sum_P \sum_{m, n, q} \frac{\langle 0|A|m\rangle \langle m|B|n\rangle \langle n|C|q\rangle \langle q|D|0\rangle}{(\omega_m - \omega_\sigma)(\omega_n - \omega_2 - \omega_3)(\omega_q - \omega_3)}. \quad (11.72)$$

From the discussed residues, we can determine properties explicitly dependent on different electronic states, for instance all the transition moments coupling the reference state  $|0\rangle$  and other states  $|e\rangle$  (from linear response residues) and all the one-photon transition moments coupling other pairs of states (from quadratic response double residues). In addition, from single residues of the second- and third-order response functions we can identify two- and three-photon transition matrix elements.

The frequency(time)-independent properties are a special case of the response functions ( $\omega_1 = \omega_2 = \dots = 0$ ) and correspond to energy derivatives. We shall use a simplified notation omitting the subscripts indicating the (zero) frequencies for these properties. The response function, is therefore, in this case written as  $\langle\langle A; B, C, D, \dots \rangle\rangle$ .

For time-dependent oscillatory perturbations, the response functions can be related to the derivatives of the time-averaged quasienergy (Christiansen et al. 1998; Saue 2002). The derivation, based on a time-dependent variational principle and the time-dependent Hellman-Feynman theorem, shows explicitly the symmetry of the response functions with respect to the permutation of all the operators.

We do not describe in this chapter the standard basis sets and wave function models in use in quantum chemistry, referring instead the interested reader to other chapters in this handbook and to a recent textbook (Helgaker et al. 2000). We only note that response theory has been formulated and corresponding programs have been implemented for most of the standard approximations, such as:

- RHF, the restricted Hartree-Fock model
- MCSCF, the multiconfigurational self-consistent field model
- DFT, density-functional theory

- MP2, the Møller–Plesset second-order perturbation theory, which in the case of frequency-dependent perturbations has to be replaced by an iterative optimization of the perturbation amplitudes, as described by the CC2 model (Christiansen et al. 1995)
- CCSD, the coupled-cluster singles-and-doubles model
- CCSD(T), CCSD with a noniterative perturbative treatment of the triples correction, which in the case of frequency-dependent response functions has to be replaced by an iterative triples correction, as described by the CC3 model (Koch et al. 1997)
- FCI, full configuration-interaction theory

There are also a couple of models designed primarily for the purpose of calculating response functions – that is, they cannot be derived in terms of energy or quasienergy derivatives of the energy expression for an electronic structure method. We note here the second-order polarization propagator approximation [SOPPA (Enevoldsen et al. 1998; Nielsen et al. 1980)], SOPPA using CCSD correlation amplitudes [SOPPA(CCSD) (Sauer 1997)], as well as the equation-of-motion CCSD model [EOM-CCSD (Perera et al. 1994a; Stanton and Bartlett 1993)].

In general, the accuracy of the computed molecular properties reflects the accuracy of the approach used for the unperturbed reference state. There is, however, one significant difference between variational and perturbative, nonvariational approximations which should be kept in mind in the calculation of properties. The response equations which hold for the exact wave function are in general not fulfilled for nonvariational wave function models, even in the limit of a complete basis set. For instance, in the MP2 and coupled-cluster approximations, the static first-order properties, which should be computed as the first energy derivatives, do not correspond to simple expectation values – corrections arising from orbital relaxation must in general be taken into account. Similarly, in the calculation of higher-order molecular properties when the basis set depends explicitly on the applied perturbations (such as geometrical distortions, or magnetic field perturbations described using London atomic orbitals), orbital relaxation corrections should be included (Gauss and Stanton 1995). We note, however, that as the excitation level is increased (triple excitations, etc.), the importance of orbital relaxation is reduced, since in the limit of the full CI wave function, which is exact, no orbital relaxation is necessary.

## Expansions of Energy and Multipole Moments

The static properties can be defined by an expansion of the total energy

$$\begin{aligned}
 E = E^{(0)} &- \mu_{\alpha} F_{\alpha} - \frac{1}{2} \alpha_{\alpha\beta} F_{\alpha} F_{\beta} - \frac{1}{6} \beta_{\alpha\beta\gamma} F_{\alpha} F_{\beta} F_{\gamma} - \frac{1}{24} \gamma_{\alpha\beta\gamma\delta} F_{\alpha} F_{\beta} F_{\gamma} F_{\delta} + \dots \\
 &- \frac{1}{3} \Theta_{\alpha\beta} F_{\alpha} F_{\beta} - \frac{1}{3} A_{\alpha,\beta\gamma} F_{\alpha} F_{\beta\gamma} - \frac{1}{6} C_{\alpha\beta,\gamma\delta} F_{\alpha\beta} F_{\gamma\delta} + \dots \\
 &- \frac{1}{2} \xi_{\alpha\beta} B_{\alpha} B_{\beta} - \frac{1}{2} \zeta_{\gamma,\alpha\beta} B_{\alpha} B_{\beta} F_{\gamma} - \frac{1}{4} \eta_{\gamma\delta,\alpha\beta} B_{\alpha} B_{\beta} F_{\gamma} F_{\delta} + \dots \\
 &+ \sigma_{K,\alpha\beta} B_{\alpha} m_{K,\beta} + \dots
 \end{aligned} \tag{11.73}$$

For a molecule in a radiation field, the definitions of the frequency-dependent properties are related to the induced (in general also frequency-dependent) multipole moments. Let us consider a small harmonic perturbation of angular frequency  $\omega$  from a plane-wave radiation field. We then have (Barron 2004):

- The induced electric dipole moment  $\mu$

$$\mu_\alpha = \alpha_{\alpha\beta} F_\beta + \frac{1}{\omega} G'_{\alpha\beta} \dot{B}_\beta + \frac{1}{3} A_{\alpha,\beta\gamma} F_{\beta\gamma} + \dots \quad (11.74)$$

$$+ \frac{1}{\omega} \alpha'_{\alpha\beta} \dot{F}_\beta + G_{\alpha\beta} B_\beta + \frac{1}{3\omega} A'_{\alpha,\beta\gamma} \dot{F}_{\beta\gamma} + \dots, \quad (11.75)$$

- The induced electric quadrupole moment  $\Theta$

$$\Theta_{\alpha\beta} = A_{\gamma,\alpha\beta} F_\gamma - \frac{1}{\omega} D'_{\gamma,\alpha\beta} \dot{B}_\gamma + C_{\alpha\beta,\gamma\delta} F_{\gamma\delta} + \dots \quad (11.76)$$

$$- \frac{1}{\omega} A'_{\gamma,\alpha\beta} \dot{F}_\gamma + D_{\gamma,\alpha\beta} B_\gamma + \frac{1}{\omega} C'_{\alpha\beta,\gamma\delta} \dot{F}_{\gamma\delta} + \dots, \quad (11.77)$$

- The induced magnetic dipole moment  $m'$

$$m'_\alpha = \xi_{\alpha\beta} B_\beta + \frac{1}{3\omega} D'_{\alpha,\beta\gamma} \dot{F}_{\beta\gamma} - \frac{1}{\omega} G'_{\beta\alpha} \dot{F}_\beta + \dots \quad (11.78)$$

$$+ \frac{1}{\omega} \xi'_{\alpha\beta} \dot{B}_\beta + \frac{1}{3} D_{\alpha,\beta\gamma} F_{\beta\gamma} + G_{\beta\alpha} F_\beta + \dots, \quad (11.79)$$

where  $\dot{F}$  and  $\dot{B}$  denote the time derivatives of the fields and we have considered only linear response properties.

The properties we have included are the electric multipole polarizabilities –  $\alpha_{\alpha\beta}$ , dipole–dipole,  $A_{\alpha,\beta\gamma}$ , dipole–quadrupole; and  $C_{\alpha\beta,\gamma\delta}$ , quadrupole–quadrupole – as well as the mixed polarizabilities –  $G_{\alpha\beta}$ , electric dipole–magnetic dipole,  $D_{\gamma,\alpha\beta}$ , magnetic dipole–electric quadrupole and the magnetizability (magnetic dipole–magnetic dipole polarizability)  $\xi_{\alpha\beta}$ . The frequency-dependent response properties labeled with a prime vanish for  $\omega = 0$ , and the properties specified in the second rows of the equations (🔗 Eqs. 11.75, 🔗 11.77, 🔗 11.79) are zero for reference states described by real wave functions (in practice, closed-shell nondegenerate systems).

We note that in the expansion of the induced dipole moment, higher-order corrections may also be important, in particular in connection with electric-field perturbations. For instance, considering only electric dipole contributions, it is customary to also include contributions to  $\mu_\alpha$  arising from frequency-dependent hyperpolarizabilities (see 🔗 Eq. 11.84 below).

## Electric Properties

In this section we consider molecular properties which characterize the interactions with static and/or frequency-dependent electric fields. The electric properties of a molecule determine the electric properties of the bulk sample, such as the relative permittivity (dielectric constant) and the refractive index. In addition, the electric properties can be used to describe intermolecular forces.

Only static and dynamic molecular properties involving electric dipole and quadrupole operators will be discussed below. However, electric properties related to higher-order electric multipole operators can also be determined in a similar manner to the properties described here, in terms of expectation values, linear and nonlinear response functions. Nevertheless, it should be kept in mind that although the same formalism is applied in the calculation of response functions involving octupole, hexadecapole, and higher moments, in practice it may

■ Table 11-1

Unit conversion factors for selected electric properties

	1 a.u.	SI		esu	
$F$	$E_h e^{-1} a_0^{-1}$	$5.142\,206 \times 10^{11}$	$V\,m^{-1}$	$1.715\,3 \times 10^7$	statvolt $cm^{-1}$
$\mu$	$ea_0$	$8.478\,353 \times 10^{-30}$	$C\,m$	$2.541\,7 \times 10^{-18}$	statvolt $cm^2$ <sup>a</sup>
$\Theta$	$ea_0^2$	$4.486\,551 \times 10^{-40}$	$C\,m^2$	$1.345\,0 \times 10^{-26}$	statvolt $cm^3$
$\alpha$	$e^2 a_0^2 E_h^{-1}$	$1.648\,777 \times 10^{-41}$	$C^2\,m^2\,J^{-1}$	$1.481\,8 \times 10^{-25}$	$cm^3$
$\beta$	$e^3 a_0^3 E_h^{-2}$	$3.206\,362 \times 10^{-53}$	$C^3\,m^3\,J^{-2}$	$8.639\,2 \times 10^{-33}$	statvolt <sup>-1</sup> $cm^4$
$\gamma$	$e^4 a_0^4 E_h^{-3}$	$6.235\,381 \times 10^{-65}$	$C^4\,m^4\,J^{-3}$	$5.036\,7 \times 10^{-40}$	statvolt <sup>-2</sup> $cm^5$
$V^K$	$E_h e^{-1} a_0^{-2}$	$9.717\,365 \times 10^{21}$	$V\,m^{-2}$	$3.241\,4 \times 10^{15}$	statvolt $cm^{-2}$ <sup>b</sup>

<sup>a</sup> 1 Debye =  $10^{-18}$  statvolt  $cm^2$

<sup>b</sup> The nuclear quadrupole moments, needed to compare the calculated NQCC with experiment (▶ section “Electric Field Gradient at the Nucleus, Nuclear Quadrupole Coupling Constant”), are usually given in barn; 1 barn =  $10^{-28}$   $m^2$

be difficult to obtain accurate results for these moments and related molecular properties. For instance, significantly larger basis sets with more polarization and diffuse functions may be required than for the properties involving lower-order electric moments.

Most theoretical results are obtained in atomic units (a.u.), whereas experimental data often are given in SI or esu units. In ▶ Table 11-1 some useful conversion factors are given.

## Electric Multipole Moments

The permanent multipole moments characterize the charge distribution in a molecule. The zeroth-order (monopole) moment corresponds to the total charge, the first moment to the dipole, the second to the quadrupole, and so on. The multipole moments can be computed as expectation values of the multipole moment operators discussed in ▶ section “Small Terms Due to the Scalar Potential in the Hamiltonian.” As for the operators, we can use the primitive or traceless forms for the quadrupole and higher-order moments. The traceless multipole moments describe the deviation from an isotropic charge distribution. For instance, the traceless quadrupole moment vanishes for a spherical charge distribution when the center of the sphere coincides with the origin, since the transformation from the primitive (traced) quadrupole moment  $q_{\alpha\beta}$  to the traceless quadrupole moment  $\Theta_{\alpha\beta}$  eliminates the isotropic contribution. The traceless multipole moment of order  $n$  is defined by  $2n + 1$  components, whereas the traced tensor involves  $(n + 2)(n + 1)/2$  independent quantities. A tabulation of nonzero symmetry-independent elements of multipole moments ( $\mu$  = dipole,  $\Theta$  = quadrupole,  $\Omega$  = octupole, and  $\Phi$  = hexadecapole) for different point groups is given by Kielich (1972).

In general, when the multipole expansion of the potential is used to describe the influence of a static electric field, only the first nonzero moment is unambiguously defined. The next, higher-order multipole moments depend on the choice of origin, and when computed with respect to the origin of the coordinate system, they depend on the position of the molecule in space. This can be seen from ▶ Eq. 11.30, where a shift of the chosen common origin for the expansion of the potential by a vector  $\mathbf{D}$  for a molecule with the total charge  $Q$  leads to a change of  $Q\mathbf{D}$  in the dipole moment; similarly, for a neutral molecule with a nonzero dipole moment, the quadrupole moment will change.

## Dipole and Quadrupole Moments

From the multipole expansion of the energy in the presence of a static electric field, [Eq. 11.73](#), we find that the  $\alpha$ -component of the static permanent dipole moment is defined as the electric field derivative of  $E(\mathbf{F})$

$$\mu_\alpha = - \left. \frac{\partial E(\mathbf{F})}{\partial F_\alpha} \right|_{\mathbf{F}=0}. \quad (11.80)$$

For wave functions that fulfill the Hellman–Feynman theorem we can compute the dipole moment as the expectation value

$$\mu_\alpha = \langle 0 | \hat{\mu}_\alpha | 0 \rangle, \quad (11.81)$$

where  $\hat{\mu}_\alpha$  is the  $\alpha$ -component of the dipole moment operator defined in [Eq. 11.30](#). Obviously, the expectation value expression is correct for the exact wave function. Furthermore, for most approximate wave functions it is much easier to compute the expectation value than to calculate the energy derivative. However, the results differ when the method used does not fulfill the Hellman–Feynman theorem. In this case, one can either derive the analytic expressions which reproduce the correct definition of the electric field derivative of  $E(\mathbf{F})$  (see for instance the discussion of the coupled cluster approach in Helgaker et al. 2000) or use the finite field method and numerical differentiation.

The finite-field method appears to be very simple and has been often applied, but it has some drawbacks. First, the values of  $E(\mathbf{F})$  depend not only on the dipole moment, but also on the polarizability and hyperpolarizabilities, and high accuracy of the computed values of  $E(\mathbf{F})$  is required to perform the numerical differentiation accurately. Moreover, the presence of the finite electric field may lower the symmetry of the system, making the calculations much more time-consuming.

[Figure 11-1](#), taken from Bak et al. (2000), illustrates the accuracy of equilibrium geometry dipole moments calculated for a series of small molecules. In Bak et al. (2000), the dipole moments of 11 molecules were studied at various levels of approximation using a sequence of basis sets, with the CCSD(T)/aug-cc-pVQZ results providing the benchmark values. The normal distribution of errors with respect to the reference values, shown in [Fig. 11-1](#), demonstrates the systematic improvements of the computed results with increasing basis set and improved treatment of electron correlation effects.

The expectation value of  $\hat{\Theta}$ , that is, the traceless electric quadrupole operator as defined in [Eq. 11.32](#) following Buckingham (1967),

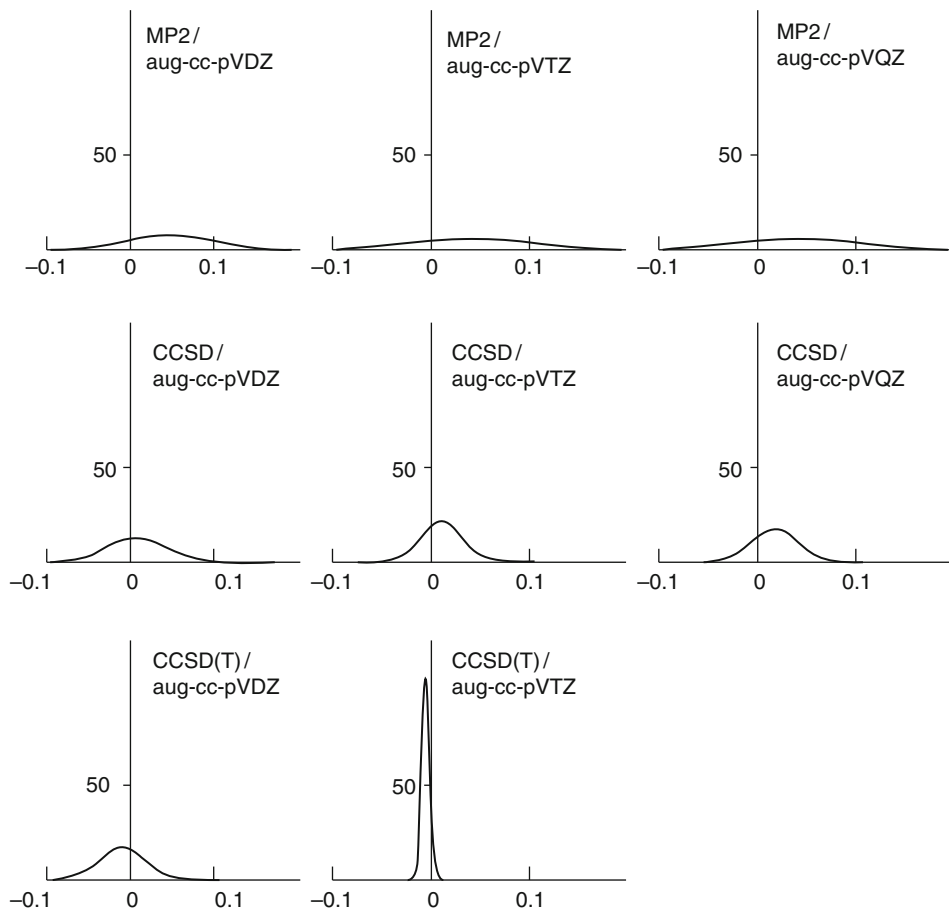
$$\Theta_{\alpha\beta} = \langle 0 | \hat{\Theta}_{\alpha\beta} | 0 \rangle = -3 \frac{\partial E(\nabla\mathbf{F})}{\partial F_{\alpha\beta}}, \quad (11.82)$$

can be related to the expectation values of second moments,  $q_{\alpha\beta} = \langle 0 | \hat{q}_{\alpha\beta} | 0 \rangle$ , by a simple linear transformation, the same as that connecting the corresponding operators, [Eqs. 11.32](#) and [11.33](#). Both  $\Theta$  and  $\mathbf{q}$  are rank two, symmetric tensors.

For molecules with an  $n$ -fold rotation axis with  $n \geq 3$ :

$$\Theta \equiv \Theta_{zz} = -2\Theta_{yy} = -2\Theta_{xx}, \quad (11.83)$$

where  $z$  coincides with the rotation axis. In experiment, two diagonal components of  $\Theta$  are measured.



■ Fig. 11-1

Correlation and basis set dependence of the dipole moment – normal distribution of errors (in Debye) (Reproduced by permission from Bak et al. (2000))

## The Origin of the Frequency-Dependent Electric Dipole Polarizability and Hyperpolarizabilities

The electric dipole moment  $\tilde{\mu}$  in the presence of an applied spatially homogeneous non-monochromatic electric field  $\sum_i \mathbf{F}^{\omega_i}$  (where  $\omega_i$  indicates the circular frequency) can be written as

$$\begin{aligned}
 \tilde{\mu}_\alpha^{\omega_\sigma} &= \mu_\alpha \delta(\omega_\sigma = 0) + \alpha_{\alpha\beta}(-\omega_\sigma; \omega_1) F_\beta(\omega_1) \\
 &+ \frac{1}{2} \sum_{\omega_1, \omega_2} \beta_{\alpha\beta\gamma}(-\omega_\sigma; \omega_1, \omega_2) F_\beta(\omega_1) F_\gamma(\omega_2) \\
 &+ \frac{1}{6} \sum_{\omega_1, \omega_2, \omega_3} \gamma_{\alpha\beta\gamma\delta}(-\omega_\sigma; \omega_1, \omega_2, \omega_3) F_\beta(\omega_1) F_\gamma(\omega_2) F_\delta(\omega_3) + \dots,
 \end{aligned} \tag{11.84}$$

where  $\mu_\alpha$  is the unperturbed electric dipole moment. In this phenomenological expansion (which we use to describe elastic light scattering processes) the summations over optical frequencies will be restricted in order to preserve a constant  $\omega_\sigma$  equal to the sum of optical frequencies

$$\omega_\sigma = \sum_i \omega_i. \quad (11.85)$$

► Equation 11.84 defines the components of the dynamic electric dipole polarizability tensor,  $\alpha_{\mu\nu}(-\omega_\sigma; \omega_1)$ , those of the first electric dipole hyperpolarizability,  $\beta_{\mu\nu\eta}(-\omega_\sigma; \omega_1, \omega_2)$ , and those of the second electric dipole hyperpolarizability  $\gamma_{\mu\nu\eta\xi}(-\omega_\sigma; \omega_1, \omega_2, \omega_3)$ . The combination of frequencies and the presence or absence of static fields characterize various nonlinear processes. The calculations can be done for any combination of frequencies satisfying ► Eq. 11.85, but only selected examples of the most commonly studied optical phenomena will be discussed below (see, e.g., Willets et al. 1992 and Bogaard and Orr 1975 for more details).

► Figure 11-2 shows how some of these processes can be interpreted in terms of electronic transitions between ground and excited states. The excited states can be treated as virtual states, but if one of the excitation energies is close to the frequency of the light, the contribution of that state is often dominant. Simplified models that include in the analysis only a few excited states can be used when these computed states describe well the real, physical states of the molecule which are relevant for the property studied. However, it is important to emphasize that even though these few-states models in many cases may give qualitative insight into the electronic processes, the convergence of the sum-over-states expansion for the (hyper)polarizabilities (see ► Eqs. 11.65, ► 11.68, and ► 11.72) with respect to the number of excited states included in the summation is in general very slow (Wiberg et al. 2006). We should also keep in mind that if an excitation energy equals a frequency, we have a very different situation in which we have to consider the finite lifetime of the excited state and also deal with the absorption process.

In experiment, the molecule is often perturbed by a combination of a static and a dynamic electric field. We then have, assuming a monochromatic dynamic field,

$$F_\alpha(t) = F_\alpha^0 + F_\alpha^\omega \cos(\omega t), \quad (11.86)$$

and therefore the time dependence of the polarization can be described as

$$\mu_\alpha(t) = \mu_\alpha^0 + \mu_\alpha^\omega \cos(\omega t) + \mu_\alpha^{2\omega} \cos(2\omega t) + \mu_\alpha^{3\omega} \cos(3\omega t) + \dots, \quad (11.87)$$

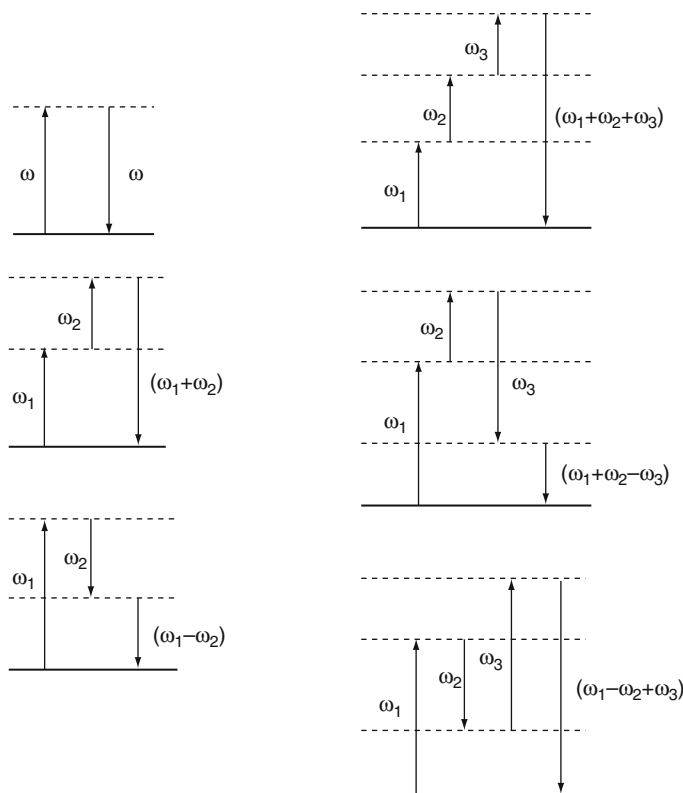
where  $\mu_\alpha^{n\omega}$  are the Fourier amplitudes to be determined. In order to compare the measured polarization at a certain frequency to the theoretical expressions, we insert ► Eq. 11.86 into ► Eq. 11.84 and use the relations between  $\cos^n(\omega t)$  and  $\cos(n\omega t)$ . We obtain

$$\begin{aligned} \mu_\alpha^0 &= \mu_\alpha + \alpha_{\alpha\beta}(0; 0)F_\beta^0 + \frac{1}{2}\beta_{\alpha\beta\gamma}(0; 0, 0)F_\beta^0 F_\gamma^0 + \frac{1}{6}\gamma_{\alpha\beta\gamma\delta}(0; 0, 0, 0)F_\beta^0 F_\gamma^0 F_\delta^0 \\ &\quad + \frac{1}{4}\beta_{\alpha\beta\gamma}(0; -\omega, \omega)F_\beta^\omega F_\gamma^\omega + \frac{1}{4}\gamma_{\alpha\beta\gamma\delta}(0; 0, -\omega, \omega)F_\beta^0 F_\gamma^\omega F_\delta^\omega, \end{aligned} \quad (11.88)$$

$$\begin{aligned} \mu_\alpha^\omega &= \alpha_{\alpha\beta}(-\omega; \omega)F_\beta^\omega + \beta_{\alpha\beta\gamma}(-\omega; \omega, 0)F_\beta^\omega F_\gamma^\omega \\ &\quad + \frac{1}{2}\gamma_{\alpha\beta\gamma\delta}(-\omega; \omega, 0, 0)F_\beta^\omega F_\gamma^0 F_\delta^0 + \frac{1}{8}\gamma_{\alpha\beta\gamma\delta}(-\omega; \omega, -\omega, \omega)F_\beta^\omega F_\gamma^\omega F_\delta^\omega, \end{aligned} \quad (11.89)$$

$$\mu_\alpha^{2\omega} = \frac{1}{4}\beta_{\alpha\beta\gamma}(-2\omega; \omega, \omega)F_\beta^\omega F_\gamma^\omega + \frac{1}{4}\gamma_{\alpha\beta\gamma\delta}(-2\omega; \omega, \omega, 0)F_\beta^\omega F_\gamma^\omega F_\delta^0, \quad (11.90)$$

$$\mu_\alpha^{3\omega} = \frac{1}{24}\gamma_{\alpha\beta\gamma\delta}(-3\omega; \omega, \omega, \omega)F_\beta^\omega F_\gamma^\omega F_\delta^\omega, \quad (11.91)$$



■ Fig. 11-2

**Linear and nonlinear optical properties – a schematic illustration of the involved transitions for (left, top to bottom):  $\alpha(-\omega; \omega)$ ;  $\beta(-(\omega_1 + \omega_2); \omega_1, \omega_2)$ ; and  $\beta(-(\omega_1 - \omega_2); \omega_1, -\omega_2)$ ; (right, top to bottom)  $\gamma(-(\omega_1 + \omega_2 + \omega_3); \omega_1, \omega_2, \omega_3)$ ;  $\gamma(-(\omega_1 + \omega_2 - \omega_3); \omega_1, \omega_2, -\omega_3)$ , and  $\gamma(-(\omega_1 - \omega_2 + \omega_3); \omega_1, -\omega_2, \omega_3)$**

where we have truncated the expansions at  $\cos(3\omega t)$ . Using the expansions given above and the expansion in [Eq. 11.84](#) we can compare the experimentally measured polarization and the theoretical estimates.

## Dipole Polarizability

The frequency-dependent electric dipole polarizability is, next to the dipole moment, the most important effect characterizing the response of a molecule to electromagnetic radiation. It is a second-order symmetric tensor determined by the linear response function

$$\alpha_{\alpha\beta}(-\omega; \omega) = -\langle \hat{\mu}_\alpha; \hat{\mu}_\beta \rangle_\omega. \quad (11.92)$$

The frequency dependence of the polarizability may be described using the Cauchy moments ([section “Cauchy Moments”](#)).



For the static dipole polarizability  $\alpha(0;0)$  we have

$$\alpha_{\alpha\beta}(0;0) = - \left. \frac{\partial^2 E(\mathbf{F})}{\partial F_\alpha \partial F_\beta} \right|_{\mathbf{F}=0}, \quad (11.93)$$

and the energy derivative can be evaluated using the finite-field approach (i.e., computing numerically the differences between  $E(\mathbf{F})$  and  $E(0)$ ).

Numerous molecular properties which describe nonlinear effects, such as the Kerr effect (► section “Second Dipole Hyperpolarizability”) or magnetic circular dichroism (► section “Magnetic Circular Dichroism”), arising in the presence of radiation and additional electric or magnetic fields, are interpreted as derivatives of the dipole polarizability (Michl and Thulstrup 1995). They can be calculated as higher-order response functions. Similarly, relativistic corrections to the polarizabilities for heavy atoms can be estimated from higher-order response functions including the mass-velocity and Darwin operators, ► Eqs. 11.9 and ► 11.20, as additional perturbations (Kirpekar et al. 1995).

In isotropic fluids, the experimentally measured quantity is usually the scalar component of the  $\alpha$  tensor given by the isotropic average, defined as

$$\alpha_{\text{iso}} = \frac{1}{3} \alpha_{\eta\eta}. \quad (11.94)$$

The polarizability anisotropy may be defined as

$$(\alpha_{\text{anis}})^2 = \frac{(3\alpha_{\mu\nu}\alpha_{\mu\nu} - \alpha_{\mu\mu}\alpha_{\nu\nu})}{2}, \quad (11.95)$$

which, using the components of the diagonalized tensor, leads to

$$\alpha_{\text{anis}} = 2^{-1/2} [(\alpha_{xx} - \alpha_{yy})^2 + (\alpha_{yy} - \alpha_{zz})^2 + (\alpha_{zz} - \alpha_{xx})^2]^{1/2}. \quad (11.96)$$

For linear molecules,  $\alpha_{\text{anis}}$  reduces to the difference between the parallel and perpendicular components,

$$\alpha_{\text{anis}} = \alpha_{\parallel} - \alpha_{\perp}. \quad (11.97)$$

The macroscopic property related to the molecular polarizability  $\alpha$  is the dielectric constant  $\epsilon$ , defined by the ratio of the permittivity of the medium to the electric constant,  $\epsilon_0$ . It is also related to the refractive index  $n$  ( $n = \sqrt{\epsilon}$ , assuming the vacuum magnetic permeability to be equal to 1). The quantity measured in a dielectric constant experiment is

$$\tilde{\alpha} = \left( \frac{\tilde{\mu}_Z^F}{F} \right)_{F \rightarrow 0} = \langle \alpha_{II} \rangle_{\Omega} + \frac{\mu_Z^2}{3kT}, \quad (11.98)$$

where we use the notation  $\langle \dots \rangle_{\Omega}$  for the average over all the orientations,  $k$  is the Boltzmann constant, and  $T$  is the temperature. The temperature-dependent term is proportional to the square of the dipole moment, the temperature-independent term is the isotropic average of the polarizability (using ► Eq. 11.94 we can obtain a corresponding expression in terms of properties calculated in the molecular frame of reference).

The anisotropy of the electric dipole polarizability can be determined in Rayleigh scattering experiments, where the observed depolarization of the incident light is a function of  $(\alpha_{\text{anis}})^2$  (Bonin and Kresin 1997).

The static electric dipole polarizability of the He atom has been studied in more detail than any other response property of any other atomic or molecular system. Not only is the non-relativistic value known accurately, and the relativistic corrections computed, but – in a recent

benchmark calculation – the quantum-electrodynamic corrections have also been analyzed and numerous effects related to the nuclear mass have been taken into account (Łach et al. 2004).

Standard energy-optimized basis sets are not suitable for accurate calculations of electric polarizabilities. The simplest solution – adding the necessary polarization and diffuse functions – makes the basis sets too large to enable efficient calculations for large molecules. Significantly smaller basis sets, designed considering the electric-field dependence of the orbitals (Benkova et al. 2005; Sadlej 1988), provide results of similar or better quality at lower computational cost.

A practical problem that may be encountered in calculations using very extended basis sets is the appearance of linear dependencies in the basis set. This may make the response equations (as well as the equations determining the molecular energy/density) ill-conditioned and the calculations slowly convergent; in exceptional cases it may even be impossible to converge the equations. The problem is normally resolved by removing the linear dependencies in the basis set, or by removing manually the most diffuse basis functions from the basis set.

Electron correlation effects on the isotropic polarizability are in general moderate, being at the most 5–10% of the uncorrelated value and for nondipolar systems always leading to an increased polarizability. Correlation effects are usually larger on the individual tensor components than on the isotropic polarizability, and can, therefore, be expected to be more important for the polarizability anisotropies. In general, Hartree–Fock polarizability anisotropies cannot be considered accurate enough to allow for a quantitative comparison with experimental observations, or for the interpretation of the ellipticity arising in some birefringences, where the polarizability anisotropies often constitute an important (and dominant) orientational contribution.

DFT in general reproduces quite well correlation effects in the polarizability of small molecular systems. In particular, polarizability anisotropies calculated using DFT will usually be in better agreement with experiment. However, due to the local nature of the exchange–correlation functionals and the lack of general implementations of current density functionals, DFT does not perform so well for extended conjugated systems (Champagne et al. 2000). We will return briefly to this point when discussing calculations of hyperpolarizabilities.

## First Dipole Hyperpolarizability

The first electric dipole hyperpolarizability, given by the quadratic response function

$$\beta_{\alpha\beta\gamma}(-\omega_{\sigma}; \omega_1, \omega_2) = -\langle\langle \hat{\mu}_{\alpha}; \hat{\mu}_{\beta}, \hat{\mu}_{\gamma} \rangle\rangle_{\omega_1, \omega_2}, \quad (11.99)$$

has physical meaning only when  $\omega_{\sigma} = \omega_1 + \omega_2$ .

The static dipole hyperpolarizability  $\beta(0;0,0)$  can be obtained evaluating the third derivative of the energy. When we consider dynamic fields, the processes of particular interest are:

---

Second Harmonic Generation (SHG)	$\beta_{\mu\nu\eta}^{\text{SHG}}(-2\omega; \omega, \omega) = -\langle\langle \hat{\mu}_{\mu}; \hat{\mu}_{\nu}, \hat{\mu}_{\eta} \rangle\rangle_{\omega, \omega}$
dc-Pockels Effect (dc-P) or Electro-Optic Pockels Effect (EOPE)	$\beta_{\mu\nu\eta}^{\text{EOPE}}(-\omega; \omega, 0) = -\langle\langle \hat{\mu}_{\mu}; \hat{\mu}_{\nu}, \hat{\mu}_{\eta} \rangle\rangle_{\omega, 0}$
Optical Rectification (OR)	$\beta_{\mu\nu\eta}^{\text{OR}}(0; \omega, -\omega) = -\langle\langle \hat{\mu}_{\mu}; \hat{\mu}_{\nu}, \hat{\mu}_{\eta} \rangle\rangle_{\omega, -\omega}$

---

According to  $\blacktriangleright$  Eqs. 11.88–11.91, in these processes we deal with a perturbation of frequency  $\omega$  (and a static field in the Pockels effect) and we consider the resulting dipole moment oscillating with frequency  $2\omega$ , frequency  $\omega$  or static, respectively.

The general definition of the quadratic response function,  $\blacktriangleright$  Eq. 11.68, indicates its symmetry with respect to permutation of operators. Thus, for all the dipole hyperpolarizabilities we have

$$\beta_{\mu\nu\eta}(-\omega_\sigma; \omega_1, \omega_2) = \beta_{\mu\eta\nu}(-\omega_\sigma; \omega_2, \omega_1). \quad (11.100)$$

Also the relation

$$\beta_{\mu\nu\eta}(-\omega_\sigma; \omega_1, \omega_2) = \beta_{\nu\mu\eta}(\omega_1; -\omega_\sigma, \omega_2) \quad (11.101)$$

holds, and we have, for instance,  $\beta_{\mu\nu\eta}^{\text{OR}}(0; \omega, -\omega) = \beta_{\eta\nu\mu}^{\text{EOPE}}(-\omega; \omega, 0)$ . We note that this relation does not hold for macroscopic samples due to the differences in the local fields experienced by the molecule in these two different experimental setups.

In the case of the first hyperpolarizability, the measured quantity is the vector component of  $\beta$  in the direction of the permanent dipole moment  $\mu$ , defining the molecular  $z$  axis. The relevant averages are given by:

$$\beta_{\parallel} = \frac{1}{5}(\beta_{z\eta\eta} + \beta_{\eta z\eta} + \beta_{\eta\eta z}), \quad (11.102)$$

$$\beta_{\perp} = \frac{1}{5}(2\beta_{z\eta\eta} - 3\beta_{\eta z\eta} + 2\beta_{\eta\eta z}), \quad (11.103)$$

where the same sequence of optical frequencies (not given explicitly) is used for the laboratory axes and the molecular axes.

The number of independent nonzero tensor elements depends on the nonlinear optical process and on the symmetry of the molecule, see for instance Bogaard and Orr (1975). For example,  $\beta^{\text{SHG}}$  is symmetric with respect to the permutation of the second and third indices (see  $\blacktriangleright$  Eq. 11.100) and this can be used to simplify the equations for the parallel and perpendicular components. For nonzero frequencies, the number of independent tensor components to be computed decreases when Kleinman's symmetry (Kleinman 1972) is assumed – that is, we assume that we can permute the indices of the incoming light without changing the corresponding frequencies,

$$\beta_{\mu\nu\eta}(-\omega_\sigma; \omega_1, \omega_2) \approx \beta_{\mu\eta\nu}(-\omega_\sigma; \omega_1, \omega_2). \quad (11.104)$$

Although for  $\omega_1 \neq \omega_2$  this is only an approximation and these two tensor components are not equal, Kleinman's symmetry is often applied for low frequencies, where it is usually found to be a reasonable approximation.

The basis set requirements for the calculation of first hyperpolarizabilities are much the same as for the linear polarizability. However, as the first hyperpolarizability probes even higher-order electric-field-perturbed densities of the molecule, care should be exercised to ensure that the basis set is sufficiently saturated with respect to diffuse polarizing functions. Special basis sets have been developed for the calculation of hyperpolarizabilities by Pluta and Sadlej (1998), though the same basis sets that can be used for polarizabilities in most cases give reliable estimates also for first hyperpolarizabilities.

Due to the fact that the first hyperpolarizability involves multiple virtual excited states ( $\blacktriangleright$  Eq. 11.68), the property has proven to be more sensitive to electron correlation effects than the polarizability (Christiansen et al. 2006). Molecules with push–pull conjugated structures are often characterized by large first hyperpolarizabilities. Due to the problems facing many

commonly used local exchange-correlation functionals, DFT has been shown to have difficulties describing correctly nonlinear optical properties such as the first hyperpolarizability for extended systems (Champagne et al. 2000). The recently introduced Coulomb-attenuated B3LYP functional (CAM-B3LYP), see Yanai et al. (2004) has, in contrast, shown quite good performance also for rather extended systems (Paterson et al. 2006).

## Second Dipole Hyperpolarizability

The second dipole hyperpolarizability is described by the cubic response function

$$\gamma_{\alpha\beta\gamma\delta}(-\omega_\sigma; \omega_1, \omega_2, \omega_3) = -\langle\langle \hat{\mu}_\alpha; \hat{\mu}_\beta, \hat{\mu}_\gamma, \hat{\mu}_\delta \rangle\rangle_{\omega_1, \omega_2, \omega_3}, \quad (11.105)$$

where  $\omega_\sigma = \omega_1 + \omega_2 + \omega_3$ .

Similarly to the lower-order static polarizabilities, the hyperpolarizability  $\gamma(0;0,0,0)$  corresponds to an energy derivative and can be computed using the finite-field approach. Among the possible frequency-dependent third-order processes, the most relevant are:

---

Electric Field – Induced Second Harmonic Generation (dc-SHG, ESHG, EFISH)

$$\gamma_{\mu\nu\eta\xi}^{\text{ESHG}}(-2\omega; \omega, \omega, 0) = -\langle\langle \hat{\mu}_\mu; \hat{\mu}_\nu, \hat{\mu}_\eta, \hat{\mu}_\xi \rangle\rangle_{\omega, \omega, 0},$$

Third Harmonic Generation (THG)

$$\gamma_{\mu\nu\eta\xi}^{\text{THG}}(-3\omega; \omega, \omega, \omega) = -\langle\langle \hat{\mu}_\mu; \hat{\mu}_\nu, \hat{\mu}_\eta, \hat{\mu}_\xi \rangle\rangle_{\omega, \omega, \omega},$$

Electro-optical or dc-Kerr effect (EOKE, dc-Kerr)

$$\gamma_{\mu\nu\eta\xi}^{\text{dc-Kerr}}(-\omega; \omega, 0, 0) = -\langle\langle \hat{\mu}_\mu; \hat{\mu}_\nu, \hat{\mu}_\eta, \hat{\mu}_\xi \rangle\rangle_{\omega, 0, 0},$$

Optical or ac-Kerr effect (OKE, ac-Kerr)

$$\gamma_{\mu\nu\eta\xi}^{\text{ac-Kerr}}(-\omega_1; \omega_1, \omega_2, -\omega_2) = -\langle\langle \hat{\mu}_\mu; \hat{\mu}_\nu, \hat{\mu}_\eta, \hat{\mu}_\xi \rangle\rangle_{\omega_1, \omega_2, -\omega_2},$$

Intensity-Dependent Refractive Index or Degenerate Four Wave Mixing (IDRI or DFWM)

$$\gamma_{\mu\nu\eta\xi}^{\text{IDRI}}(-\omega; \omega, \omega, -\omega) = -\langle\langle \hat{\mu}_\mu; \hat{\mu}_\nu, \hat{\mu}_\eta, \hat{\mu}_\xi \rangle\rangle_{\omega, \omega, -\omega},$$

dc Optical Rectification (dc-OR, EFior)

$$\gamma_{\mu\nu\eta\xi}^{\text{dc-OR}}(0; \omega, -\omega, 0) = -\langle\langle \hat{\mu}_\mu; \hat{\mu}_\nu, \hat{\mu}_\eta, \hat{\mu}_\xi \rangle\rangle_{\omega, -\omega, 0}.$$


---

The experimentally measured quantities in isotropic fluids are usually the scalar components of the tensor  $\gamma$  given by the isotropic average:

$$\gamma_{\parallel} = \frac{1}{15}(\gamma_{\xi\eta\eta\xi} + \gamma_{\xi\eta\xi\eta} + \gamma_{\xi\xi\eta\eta}), \quad (11.106)$$

$$\gamma_{\perp} = \frac{1}{15}(2\gamma_{\xi\eta\eta\xi} - \gamma_{\xi\xi\eta\eta}), \quad (11.107)$$

where the same sequence of optical frequencies, not given explicitly above, is used for the laboratory axes and the molecular axes.

As for the first hyperpolarizability, the number of independent nonzero tensor elements depends on the optical process and on the symmetry of the molecule. For example,  $\gamma^{\text{THG}}$  is symmetric with respect to the second, third, and fourth indices, and this can be used to simplify  $\blacktriangleright$  Eqs. 11.106–11.107. For instance, the average value that should be compared with the experimental THG parallel component becomes

$$\gamma_{\parallel}^{\text{THG}} = \frac{1}{5} \gamma_{\xi\xi\eta\eta}^{\text{THG}}. \quad (11.108)$$

Experimentally, if all fields have parallel polarization, one can measure the parallel components of the first and second hyperpolarizabilities which take into account the classical orientational averaging. In the case of ESHG, with the optical field polarized perpendicular to the static field, one measures the perpendicular components, and in the case of a dc-Kerr experiment, the differences between the parallel and perpendicular components.

In the ESHG experiment a laser beam passes through the sample in a static electric field and a weak, collinear, frequency-doubled beam is detected. Absolute values for the hyperpolarizabilities cannot be extracted; the signal from the sample is compared to that of a known buffer gas (ultimately helium, for which there are accurate theoretical values (Bishop and Pipin 1989)) or a solid. In analogy with the derivation for  $\tilde{\alpha}$ , the classical thermal averaging yields

$$\tilde{\gamma}^{\text{ESHG}} = \left( \tilde{\beta}_{ZZZ}^F / F \right)_{F \rightarrow 0} = \langle \gamma_{ZZZZ} \rangle_{\Omega} + \frac{\mu_z \langle \beta_{ZZZ} \rangle_{\Omega}}{3kT}. \quad (11.109)$$

The molecular hyperpolarizabilities  $\gamma^{\text{ESHG}}$  and  $\beta^{\text{SHG}}$  can be obtained in this experiment. For non-centrosymmetric molecules a series of measurements over a range of temperatures has to be performed, whereas for centrosymmetric molecules  $\beta = 0$  and thus a single measurement at one temperature is sufficient.

The majority of existing experimental data on hyperpolarizabilities are derived from ESHG and dc-Kerr measurements (Shelton and Rice 1994). The dc-Kerr effect differs from the other nonlinear optical processes as it allows for absolute measurements without the need for a reference measurement. The measured molar Kerr constant is (Shelton and Rice 1994):

$$A^{\text{dc-Kerr}} = \frac{N_A}{81\epsilon_0} \left[ \frac{3}{2} (\langle \gamma_{ZZZZ} \rangle_{\Omega} - \langle \gamma_{XXZZ} \rangle_{\Omega}) + \mu_z (\langle \beta_{ZZZ} \rangle_{\Omega} - \langle \beta_{XXZ} \rangle_{\Omega}) / kT \right. \\ \left. + \frac{3}{10kT} \left( \alpha_{\alpha\beta} \alpha_{\alpha\beta}^0 - \langle \alpha_{ZZ} \rangle_{\Omega} \langle \alpha_{ZZ}^0 \rangle_{\Omega} + \frac{1}{kT} \mu_z^2 (\alpha_{zz} - \langle \alpha_{ZZ} \rangle_{\Omega}) \right) \right], \quad (11.110)$$

where  $N_A$  is Avogadro's number, and it involves both dynamic hyperpolarizabilities ( $\gamma^{\text{dc-Kerr}}$  and  $\beta^{\text{EOPE}}$ ) as well as static (superscript 0) and dynamic polarizabilities.

The computational requirements for the second hyperpolarizability are more or less the same as for the first hyperpolarizability. Although the number of studies that analyze the importance of electron correlation effects (not including here DFT) is rather limited, the available results confirm in general the findings made for the first hyperpolarizabilities (Christiansen et al. 2006).

## Cauchy Moments

Response functions for a system in its electronic ground state are analytic functions of the frequency arguments, except at the poles that occur when a frequency or a sum of frequencies is

equal to an excitation energy. Thus, for frequencies below the first pole, the linear, quadratic, or cubic response functions can be expanded in power series (Hättig and Jørgensen 1998). Let us consider in more detail the simplest case when only electric dipole operators are involved and the frequency dependence of the (hyper)polarizabilities is of interest. The Cauchy series – that is, the power series expansion of the frequency-dependent polarizability – is usually written as:

$$\alpha(-\omega; \omega) = \sum_{k=0}^{\infty} \omega^{2k} S(-2k-2) = S(-2) + \omega^2 S(-4) + \omega^4 S(-6) + \dots, \quad (11.111)$$

where  $S(-2) = \alpha(0; 0)$ . This expansion is valid also for purely imaginary frequency arguments.

Similar expansions may be applied to describe the dispersion effects for hyperpolarizabilities. Often, the power series expansion in the frequency arguments may be truncated at second order leading to:

$$\alpha_{\text{iso}}(-\omega_{\sigma}; \omega_1) = \alpha_{\text{iso}}(0; 0) \left[ 1 + \mathcal{A}^{\alpha} (\omega_{\sigma}^2 + \omega_1^2) + \mathcal{O}(\omega_i^4) \right], \quad (11.112)$$

$$\beta_{\parallel}(-\omega_{\sigma}; \omega_1, \omega_2) = \beta_{\parallel}(0; 0, 0) \left[ 1 + \mathcal{A}^{\beta} (\omega_{\sigma}^2 + \omega_1^2 + \omega_2^2) + \mathcal{O}(\omega_i^4) \right], \quad (11.113)$$

$$\gamma_{\parallel}(-\omega_{\sigma}; \omega_1, \omega_2, \omega_3) = \gamma_{\parallel}(0; 0, 0, 0) \left[ 1 + \mathcal{A}^{\gamma} (\omega_{\sigma}^2 + \omega_1^2 + \omega_2^2 + \omega_3^2) + \mathcal{O}(\omega_i^4) \right]. \quad (11.114)$$

Each expansion contains only a single second-order dispersion coefficient  $\mathcal{A}$ . Since these coefficients for different optical processes of a given order are equivalent (Bishop 1995), they express the dispersion of frequency-dependent properties in a way that is transferable between different optical processes, for instance  $\mathcal{A}^{\beta}$  describes both the second-harmonic generation and the (dc-)electro-optic Pockels effect.

## Long-Range Dispersion Interaction Coefficients

For neutral, closed-shell weakly interacting systems, one of the dominant contributions to the interaction energy at large intermolecular distances is the dispersion energy. It can be analyzed using perturbation theory, and for two atoms or molecules  $A$  and  $B$ , we find (McWeeny 1992):

$$E_{\text{disp}}^{AB} = -\frac{1}{\hbar} \sum_{n \neq 0}^A \sum_{m \neq 0}^B \frac{|\langle 0^A 0^B | \hat{V}^{AB} | n^A m^B \rangle|^2}{\omega_{n0}^A + \omega_{m0}^B}, \quad (11.115)$$

where  $\hat{V}^{AB}$  denotes the intersystem interaction,  $|0^A\rangle$  and  $|n^A\rangle$  represent the ground and excited states of system  $A$ ,  $\omega_{n0}^A$  is the excitation energy, and similarly for system  $B$ .

We would like to express the dispersion energy in terms of response properties of molecules  $A$  and  $B$  since this allows for a physical interpretation of the dispersion interaction. Such an expression is obtained applying an integral transform to avoid the summation of the  $A$  and  $B$  excitation energies in the denominator of  $\blacktriangleright$  Eq. 11.115 and using the multipole expansion of the perturbing operator  $\hat{V}^{AB}$ .

For the second-order dispersion interaction between closed-shell atoms  $A$  and  $B$  we have:

$$E_{\text{disp}}^{AB}(R) = -\frac{C_6^{AB}}{R^6} - \frac{C_8^{AB}}{R^8} - \frac{C_{10}^{AB}}{R^{10}} - \dots, \quad (11.116)$$

where the coefficient for the dipole–dipole term can be written as (Langhoff et al. 1971):

$$C_6^{AB} = \frac{\hbar}{(4\pi\epsilon_0)^2} \frac{3}{\pi} \int_0^\infty \alpha^A(-i\omega; i\omega) \alpha^B(-i\omega; i\omega) d\omega. \quad (11.117)$$

This equation is known as the Casimir–Polder formula. The polarizability at imaginary frequencies,  $\alpha(-i\omega; i\omega)$ , can be obtained for instance using  $\blacktriangleright$  Eq. 11.111 with an imaginary value of  $\omega$ . The  $C_n^{AB}$ ,  $n > 6$  coefficients depend on similar higher-order multipole polarizabilities of one or both atoms. The same approach can be applied for atom–molecule and molecule–molecule interactions considering individual tensor components of the required polarizabilities. It can also be used for three-body interactions, and to describe the dispersion contributions to the pair polarizability function (Fowler et al. 1994).

To determine the long-range dispersion coefficients we need the values of  $\alpha(-i\omega; i\omega)$  for the whole range of imaginary frequencies, whereas the radius of convergence of the power series expansion of the polarizability ( $\blacktriangleright$  11.111) is determined by the lowest excitation energy. However, using analytic continuation of the Cauchy expansion (Langhoff and Karplus 1970) we can obtain all the required values of  $\alpha(-i\omega; i\omega)$  and thus we can determine accurate values of the dispersion interaction coefficient  $C_6^{AB}$ . The polarizabilities at imaginary frequencies can also be obtained directly, solving the complex linear response equations (Norman et al. 2003).

Qualitatively correct estimates of the dispersion energy are obtained in the perturbational approach even using the dispersion coefficients  $C_n$  calculated at the DFT level. It has been shown that a successful description of intermolecular forces for large molecules may be obtained in this manner (Misquitta et al. 2005; Podeszwa and Szalewicz 2008).

## Electric Field Gradient at the Nucleus, Nuclear Quadrupole Coupling Constant

The *electric field gradient* (EFG) tensor at the nucleus  $K$  –  $V_{\alpha\beta}^K$  – corresponds to the expectation value (Baker et al. 1989; Fowler et al. 1989) of the EFG operator  $\hat{V}^K$  given by  $\blacktriangleright$  Eq. 11.34:

$$V_{\alpha\beta}^K = \langle 0 | \hat{V}_{\alpha\beta}^K | 0 \rangle, \quad (11.118)$$

where the traceless form of the operator  $\hat{V}^K$  is used. The components of the diagonalized EFG tensor, given in its own (EFG) principal axis system, fulfill therefore the equation

$$V_{zz}^K + V_{yy}^K + V_{xx}^K = 0. \quad (11.119)$$

They are by definition arranged so that

$$|V_{zz}^K| \geq |V_{yy}^K| \geq |V_{xx}^K|. \quad (11.120)$$

For the asymmetry parameter  $\eta_K$  defined as

$$\eta_K = \frac{V_{xx}^K - V_{yy}^K}{V_{zz}^K}, \quad (11.121)$$

we thus have  $0 \leq \eta_K \leq 1$ .

On the other hand, for comparison with experimental data derived from the hyperfine structure of rotational spectra, tensor components defined in the principal axes of inertia system must be used.

For quadrupolar nuclei – that is, nuclei for which the nuclear spin quantum number  $I_K \geq 1$ , the *nuclear quadrupole coupling* tensor is defined as  $-eQ_K \mathbf{V}^K / \hbar$ , where  $eQ_K$  is the electric quadrupole moment of the nucleus. There is an interaction of the nuclear quadrupole moment tensor with the EFG at the nucleus, mediated by the nuclear spin  $\mathbf{I}_K$  and described by the operator:

$$\mathcal{H}^{\text{Nq}} = \frac{1}{2} \sum_K \frac{-eQ_K}{I_K(2I_K - 1)} \mathbf{I}_K^T \mathbf{V}^K \mathbf{I}_K. \quad (11.122)$$

The *nuclear quadrupole coupling constant* (NQCC) is defined as  $-eQ_K V_{zz}^K / \hbar$ . The EFG at the nucleus affects the NMR relaxation processes, thus it is relevant in the analysis of the linewidths of NMR signals. The linewidth is proportional to the inverse relaxation time (Abragam 1961), that is:

$$\Delta\nu_{1/2} \propto \frac{1}{T_q} = \frac{3}{40} \frac{2I_K + 3}{I_K^2(2I_K - 1)} \left(1 + \frac{\eta_K^2}{3}\right) \left(\frac{eQ_K}{\hbar} V_{zz}^K\right)^2 \tau_c, \quad (11.123)$$

where  $\Delta\nu_{1/2}$  is the width of the peak at half of the maximum intensity and  $\tau_c$  is the correlation time for the quadrupole coupling relaxation.

From the formal  $1/r_K^3$  dependence of the operator in  $\blacklozenge$  Eq. 11.34, we realize that the basis used to calculate this property must be flexible in the core region and the outer-core/inner-valence region. This is an important requirement, as many modern basis sets are quite heavily contracted in these regions (since the orbitals do not change much in this region when going from the atomic to the molecular system). In general, much of the same basis set requirements as those arising in the calculation of nuclear shielding constants (and to some extent also the spin-spin coupling constants) apply, and we refer to  $\blacklozenge$  section “Nuclear Spin-Related Properties” for further discussion.

An important application of theoretically calculated electric field gradients at the nucleus is in the determination of nuclear quadrupole moments. The interaction between the nuclear quadrupole moments and the electric field gradient at the nucleus can be measured with unprecedented accuracy (compared to other experimental approaches for determining nuclear quadrupole moments) in microwave spectroscopy. These interactions give rise to the fine structure in the rotational spectrum of the molecule. Highly accurate estimates for the electric field gradient at the nucleus can often be calculated theoretically (since this is a first-order molecular property). By combining these theoretical results with experimental observations, accurate values of the nuclear quadrupole moments can be obtained, and this approach has been used to revise previously estimated nuclear quadrupole moments (see, e.g., Kellö and Sadlej 1998).

## One-Photon Absorption, Excitation Energies, and Transition Moments

Calculations of one-photon absorption enable the determination of the extinction coefficient  $\varepsilon$ , describing the attenuation of the intensity of an incoming light beam when passing through a sample of absorbing species. In the lowest-order perturbative expansion of the interaction between light and matter,  $\varepsilon$  is related to the excitation energy and  $\langle 0 | \boldsymbol{\mu} | n \rangle$ , the transition moment between the ground  $|0\rangle$  and excited  $|n\rangle$  electronic states. The derived quantities are the dipole strength

$${}^n D_{\alpha\beta} = \langle 0 | \hat{\mu}_\alpha | n \rangle \langle n | \hat{\mu}_\beta | 0 \rangle, \quad (11.124)$$



and the oscillator strength. In the length gauge, the latter can be written as

$$f_{0n}^r = \frac{2m_e\omega_{0n}}{3\hbar e^2} \langle 0 | \hat{\mu}_\alpha | n \rangle \langle n | \hat{\mu}_\alpha | 0 \rangle = \frac{2m_e}{3e^2} \lim_{\omega \rightarrow \omega_{0n}} (\omega - \omega_{0n}) \omega \langle \langle \hat{\mu}_\alpha; \hat{\mu}_\alpha \rangle \rangle_\omega. \quad (11.125)$$

Using the hypervirial relationship

$$\langle 0 | \hat{p}_\alpha | n \rangle = im_e \omega_{0n} \langle 0 | \hat{r}_\alpha | n \rangle, \quad (11.126)$$

we obtain in the velocity gauge

$$f_{0n}^v = \frac{2}{3\hbar m_e \omega_{0n}} \langle 0 | \hat{p}_\alpha | n \rangle \langle n | \hat{p}_\alpha | 0 \rangle = \frac{2}{3m_e} \lim_{\omega \rightarrow \omega_{0n}} (\omega - \omega_{0n}) \omega^{-1} \langle \langle \hat{p}_\alpha; \hat{p}_\alpha \rangle \rangle_\omega, \quad (11.127)$$

and in the mixed length-velocity gauge

$$f_{0n}^{rv} = -\frac{2i}{3\hbar e} \langle 0 | \hat{\mu}_\alpha | n \rangle \langle n | \hat{p}_\alpha | 0 \rangle = -\frac{2i}{3e} \lim_{\omega \rightarrow \omega_{0n}} (\omega - \omega_{0n}) \langle \langle \hat{\mu}_\alpha; \hat{p}_\alpha \rangle \rangle_\omega, \quad (11.128)$$

respectively (Hansen and Bouman 1980).

To illustrate the differences between oscillator strengths computed in different approaches, we present in [Table 11-2](#) the results for the  $1^1\Sigma_g^+ \rightarrow 1^1\Pi_u$  singlet transition in the  $N_2$  molecule. The HF results and the results for the hierarchy of coupled-cluster approximations (CCS, CC2, CCSD and CC3) show the role of the wave function model. In addition, the role of the basis set is shown in the sequence of the results for the d-aug-cc-pVXZ correlation-consistent basis sets (Kendall et al. 1992), with  $X = D, T, Q,$  and  $5$ , abbreviated in the table as daDZ, daTZ, daQZ, and da5Z, respectively. At the HF level the hypervirial relationship ([Eq. 11.126](#)) is fulfilled in complete basis sets and the differences between computed oscillator strengths are only due to the incompleteness of the basis set. We observe that all the HF results converge with  $X$ , and the da5Z values are almost identical. In the CC methods, in addition to the differences arising due to basis set incompleteness,  $f_{0n}^r$ ,  $f_{0n}^v$ , and  $f_{0n}^{rv}$  may differ even for a complete basis set since [Eq. 11.126](#) is not satisfied. This difference should be diminishing as we approach the full CI limit, and in fact for a given one-electron basis the differences between  $f_{0n}^r$ ,  $f_{0n}^v$ , and  $f_{0n}^{rv}$  follow the sequence  $CCS > CC2 \approx CCSD > CC3$ . Finally, we note that for evaluating the accuracy of the results the gauge invariance of a calculated oscillator strength is a necessary, but not sufficient requirement. Gauge invariance has been obtained for large basis sets both at the HF and at the CC3 level, whereas the correlated values differ significantly from the HF results, and only the CC3 results can be expected to be of high accuracy.

The Thomas–Reiche–Kuhn (TRK) sum rule, which can be written in terms of the dipole oscillator strengths as

$$\sum_n f_{0n} = N_{el}, \quad (11.129)$$

where  $N_{el}$  is the total number of electrons, can be used as another test of the accuracy of the calculations.

Of particular concern are Rydberg states, characterized by a very diffuse orbital occupied by the excited electron. DFT in general fails to properly describe Rydberg-excited states, as many of the common exchange-correlation functionals do not display the correct asymptotic behavior for the  $-1/r$  operator. This deficiency of modern exchange-correlation functionals can be partially rectified by introducing the correct asymptotic behavior for the exchange-correlation functional (Tozer and Handy 1998). It is worth noting that the time-dependent Hartree–Fock (TDHF) theory does not display the same problems in describing Rydberg states, due to use

■ Table 11-2

Oscillator strength and excitation energy ( $\omega_{0n}$ , in eV) for the singlet transition  $1^1\Sigma_g^+ \rightarrow 1^1\Pi_u$  of  $N_2$ ; results taken from Pawłowski et al. (2004)

Model	Basis set	$f_{0n}^r$	$f_{0n}^v$	$f_{0n}^{rv}$	$f_{0n}^r - f_{0n}^v$	$\omega_{0n}$
HF	daDZ	0.1669	0.1725	0.1697	-0.0055	13.26
	daTZ	0.1702	0.1724	0.1713	-0.0022	13.22
	daQZ	0.1709	0.1717	0.1713	-0.0008	13.22
	da5Z	0.1714	0.1715	0.1715	-0.0001	13.22
CCS	daDZ	0.1629	0.1485	0.1556	0.0144	13.27
	daTZ	0.1662	0.1504	0.1582	0.0158	13.24
	daQZ	0.1670	0.1511	0.1589	0.0158	13.23
	da5Z	0.1675	0.1512	0.1592	0.0163	13.23
CC2	daDZ	0.1202	0.1144	0.1172	0.0058	12.42
	daTZ	0.1239	0.1211	0.1225	0.0028	12.58
	daQZ	0.1248	0.1230	0.1239	0.0018	12.65
	da5Z	0.1263	0.1238	0.1251	0.0025	12.69
CCSD	daDZ	0.1671	0.1617	0.1644	0.0055	12.80
	daTZ	0.1757	0.1729	0.1743	0.0029	13.00
	daQZ	0.1794	0.1769	0.1782	0.0025	13.08
	da5Z	0.1822	0.1788	0.1805	0.0034	13.11
CC3	daDZ	0.1844	0.1806	0.1825	0.0037	12.71
	daTZ	0.2046	0.2045	0.2046	0.0002	12.87
	daQZ	0.2141	0.2147	0.2144	-0.0006	12.92
	da5Z	0.2196	0.2194	0.2195	0.0002	12.94

of the exact exchange operator. However, the lack of electron correlation effects in TDHF may limit the applicability of this approach for excited states in general.

To account for the broadening of the experimental spectrum (related not only to the finite lifetime of the electronic state, but also to the rovibrational structure, collisions, and other aspects of the interaction between light and matter), and in particular to investigate whether certain bands may be hidden in the experimental spectrum due to overlapping bands, simple Lorentzian line broadening is often added in the form

$$L(\nu) \approx \frac{\tilde{\Gamma}}{\pi} \left[ \frac{1}{(\nu_0 - \nu)^2 + \tilde{\Gamma}^2} \right], \quad (11.130)$$

where  $\tilde{\Gamma}$  is related to the lifetime of the excited state, and  $\nu_0$  is the frequency of the electronic excitation. Assuming an isolated absorption band,  $\tilde{\Gamma}$  is equal to half the width of the absorption band at half height (the value of  $\tilde{\Gamma}$  is often adjusted in the calculations to fit the experimental data). It is common also to employ a Gaussian function to reproduce the line broadening

$$L(\nu) = \frac{2}{\Gamma\sqrt{2\pi}} e^{-2(\nu-\nu_0)^2/\Gamma^2}, \quad (11.131)$$

and we have  $\tilde{\Gamma} = \Gamma\sqrt{(\ln 2)/2}$ .

Finally, we recall that the transition moment between two excited states  $\langle m | A | n \rangle$  can be obtained using only the reference state wave function from a double residue of the quadratic

response function  $\blacklozenge$  Eq. 11.70 (and if  $|m\rangle = |n\rangle$ ) we may in this way determine the expectation value of  $A$  in the excited state).

## Two-Photon Absorption

In experimental studies of two- and multi-photon absorption processes, the multiphoton transition strength, a function of all the frequencies of all photons absorbed, is analyzed. For two laser sources of circular frequency  $\omega_1$  and  $\omega_2$  with associated wavelengths  $\lambda_1$  and  $\lambda_2$ , the two-photon transition strength  $\delta(\omega_1, \omega_2)$  for the transition between states  $|0\rangle$  and  $|n\rangle$  in isotropic samples is given by, see e.g., Craig and Thirunamachandran (1984):

$$\begin{aligned} \delta_{0n}^{\text{TPA}}(\omega_1, \omega_2) = & F S_{\alpha\alpha}^{0n}(\omega_1, \omega_2) S_{\beta\beta}^{0n,*}(\omega_1, \omega_2) + G S_{\alpha\beta}^{0n}(\omega_1, \omega_2) S_{\alpha\beta}^{0n,*}(\omega_1, \omega_2) + \\ & + H S_{\alpha\beta}^{0n}(\omega_1, \omega_2) S_{\beta\alpha}^{0n,*}(\omega_1, \omega_2), \end{aligned} \quad (11.132)$$

where F, G, and H are numbers depending on the polarization state of the two photons and on the geometrical setup (mutual direction of the laser beams) (Craig and Thirunamachandran 1984; McClain 1974) and, in the dipole approximation,

$$S_{\alpha\beta}^{0n}(\omega_1, \omega_2) = \frac{1}{\hbar} \sum_m \left\{ \frac{(\hat{\mu}_\alpha)_{0m} (\hat{\mu}_\beta)_{mn}}{\omega_{m0} - \omega_1} + \frac{(\hat{\mu}_\beta)_{0m} (\hat{\mu}_\alpha)_{mn}}{\omega_{m0} - \omega_2} \right\} \quad (11.133)$$

is the second-rank, two-photon tensor. In  $\blacklozenge$  Eq. 11.133 the summation runs over the whole set of excited states, the energy conservation relation  $\omega_1 + \omega_2 = \omega_{n0}$  applies, and off-resonance conditions are implied – that is, the frequencies  $\omega_1$  and  $\omega_2$  are sufficiently far off the values at which the denominators vanish. The tensor is nonsymmetric in the exchange of the two frequencies except for  $\omega_1 = \omega_2$ . For the special case of a one-color beam – that is, a monochromatic light source – the transition matrix is symmetric and (using  $\omega = \omega_1 = \omega_2$ )

$$\delta_{0n}^{\text{TPA}}(\omega) = S_{\lambda\lambda}^{0n}(\omega) S_{\mu\mu}^{0n,*}(\omega) + 2 S_{\lambda\mu}^{0n}(\omega) S_{\lambda\mu}^{0n,*}(\omega) \quad (11.134)$$

for linear polarization of the incident light and

$$\delta_{0n}^{\text{TPA}}(\omega) = -S_{\lambda\lambda}^{0n}(\omega) S_{\mu\mu}^{0n,*}(\omega) + 3 S_{\lambda\mu}^{0n}(\omega) S_{\lambda\mu}^{0n,*}(\omega) \quad (11.135)$$

for circular polarization, respectively.

It can be shown that the two-photon absorption transition rate (cross section) can be obtained from the single residue of the cubic response function (Hättig et al. 1998a). Two-photon absorption transition amplitudes  $S_{\alpha\beta}^{0n}(\omega_1, \omega_2)$ ,  $\blacklozenge$  Eq. 11.133, can also be extracted from the single residue of a quadratic response function, see  $\blacklozenge$  Eq. 11.69 above.

The following relations hold for the matrix elements of the two-photon transition tensor

$$S_{\alpha\beta}^{0n}(\omega) = S_{\beta\alpha}^{0n}(\omega_{n0} - \omega), \quad (11.136)$$

$$S_{\alpha\beta}^{0n}(\omega) = S_{\alpha\beta}^{n0}(-\omega)^*. \quad (11.137)$$

For methods which do not fulfill  $\blacklozenge$  Eq. 11.137 (such as the coupled cluster approach), one can instead use the two-photon transition strength (Hättig et al. 1998b):

$$F_{\alpha\beta,\gamma\delta}^{0n}(\omega) = \frac{1}{2} \{ S_{\alpha\beta}^{0n}(-\omega) S_{\gamma\delta}^{n0}(\omega) + S_{\gamma\delta}^{0n,*}(-\omega) S_{\alpha\beta}^{0n,*}(\omega) \}, \quad (11.138)$$

where  $S_{\alpha\beta}^{0n}(\omega)$  and  $S_{\alpha\beta}^{n0}(\omega)$  are the left and right transition moments.

Three-photon absorption has been described through the single residue of the cubic response function (Cronstrand et al. 2003). Similarly to two-photon absorption, one can discuss the third-order (left and right) transition moments and strengths (Hättig et al. 1998a) and define the three-photon transition strengths in this manner for nonvariational wave functions. There has been a rather limited number of theoretical studies of three-photon absorption processes and these will therefore not be discussed any further here.

In general, the computational requirements for the calculation of molecular properties from the residues of the response functions inherit the requirements from the response functions themselves; that is, the selection of the basis sets has to be done considering the operators appearing in the expression for the transition moments and excited-state properties. However, as the residues are connected to specific excited states, the nature of the probed excited state also needs to be considered.

## Magnetic Properties

Let us now consider perturbations involving external static magnetic fields only. In this case, the number of observable molecular properties that arise is rather limited. This is due in part to the fact that the strength of the magnetic field perturbation of the molecular energy is much smaller than the electric field perturbational strength, but also because only even-order interactions will survive for closed-shell molecules. This is normally referred to as quenching of the induced magnetic moment, and can also be seen as an explanation why there are no permanent magnetic dipoles in such systems. The quenching of the magnetic moment in closed-shell molecules can easily be understood by considering that for any orbitally nondegenerate state, one can always choose the wave function to be real. For such a state, the expectation value of the magnetic moment is given as

$$\langle 0 | \hat{H}_\alpha^B | 0 \rangle = \langle 0 | \hat{H}_\alpha^{B*} | 0 \rangle^* = -\langle 0 | \hat{H}_\alpha^B | 0 \rangle^* = 0, \quad (11.139)$$

since the magnetic dipole operator is Hermitian and purely imaginary (see [Eq. 11.44](#)).

## Magnetizability

The magnetizability yields the first nonvanishing (second order in the external magnetic field) contribution to the energy of interaction between an external magnetic field and a closed-shell molecule

$$\Delta E(\mathbf{B}) = -\frac{1}{2} B_\alpha \xi_{\alpha\beta} B_\beta, \quad (11.140)$$

where  $\xi$  is a symmetric tensor of rank two with a total of six independent elements. For isotropic samples, the magnetizability is expressed in the principal axis system in which the tensor is diagonal, and in addition to the isotropic magnetizability defined in a standard manner as

$$\xi_{\text{iso}} = \frac{1}{3} \xi_{\alpha\alpha}, \quad (11.141)$$

two anisotropies:

$$\xi_{\text{anis1}} = \xi_{33} - (\xi_{11} + \xi_{22})/2, \quad (11.142)$$

$$\xi_{\text{anis2}} = \xi_{11} - (\xi_{22} + \xi_{33})/2, \quad (11.143)$$

Table 11-3

Unit conversion factors for magnetizability

	1 a.u.	SI	CGS
$\xi$	$(e\hbar/m_e)^2 E_h^{-1}$	$7.89104 \times 10^{-29} \text{ JT}^{-2}$	$4.7521 \text{ ppm cgs/ppm cm}^3 \text{ mol}^{-1}$

are usually defined, with  $|\xi_{33}| \leq |\xi_{22}| \leq |\xi_{11}|$ . However, results reported in the literature often do not follow these definitions, and care should be exercised when comparing with experiment to ensure that the same conventions are used for defining the anisotropies. For unit conversion factors, see Table 11-3.

Two contributions to the magnetizability appear in the nonrelativistic electronic Hamiltonian in the presence of a magnetic vector potential Eq. 11.40. One arises as an expectation value of the diamagnetic magnetizability operator, see Eq. 11.47. The second involves a linear response contribution arising from the interaction of the magnetic dipole operator Eq. 11.44 with itself. We can, therefore, calculate the magnetizability from the expression:

$$\xi_{\alpha\beta} = -2\langle 0 | \hat{H}_{\alpha\beta}^{\text{B},\text{B}} | 0 \rangle - \langle \langle \hat{H}_{\alpha}^{\text{B}}; \hat{H}_{\beta}^{\text{B}} \rangle \rangle = - \left. \frac{\partial^2 E(\mathbf{B})}{\partial B_{\alpha} \partial B_{\beta}} \right|_{\mathbf{B}=0}, \quad (11.144)$$

where the last equality shows that the magnetizability can be obtained as an energy derivative and it holds because the magnetic fields discussed here are static.

A negative magnetizability corresponds to an induced magnetic moment of the molecule opposing the applied magnetic field, and is experimentally manifested by the molecule trying to get away from the poles of a magnet and thus align itself across the applied magnetic field, an effect that is referred to as *diamagnetism*. The opposite effect, where the induced magnetic moment enforces the magnetic field, is referred to as *paramagnetism*, and in this case the molecule will seek to orient itself in the direction of the poles of the magnet and therefore along the magnetic field.

The diagonal elements of the first contribution to the magnetizability in Eq. 11.144 are negative since

$$\xi_{\alpha\beta}^{\text{dia}} = -2\langle 0 | \hat{H}_{\alpha\beta}^{\text{B},\text{B}} | 0 \rangle = -\frac{e^2}{4m_e} \langle 0 | \hat{r}_O^2 \delta_{\alpha\beta} - \hat{r}_{O,\alpha} \hat{r}_{O,\beta} | 0 \rangle, \quad (11.145)$$

and this part is for this reason referred to as the diamagnetic contribution. The linear response function contribution to the magnetizability (including the negative sign, see Eq. 11.144) is always positive and is therefore referred to as the paramagnetic contribution. For closed-shell molecules, the expectation value almost always dominates, and these molecules are therefore diamagnetic. Exceptions occur for molecules for which there are near degeneracies in the electronic ground state. Then the denominator of the linear response function (Eq. 11.65) may become small, leading to such an increase of the magnitude of the paramagnetic term that the overall magnetizability becomes positive. A well known and often studied example is the BH molecule (Ruud et al. 1995; Sauer et al. 1993).

Although the expression for the magnetizability in Eq. 11.144 is conceptually simple and can in principle be used straightforwardly, the gauge origin problem turns out to be difficult. In order to ensure gauge-origin independent magnetizabilities, as well as significantly improve the basis set convergence, London atomic orbitals should be used when calculating magnetizabilities.

A London orbital is obtained from a conventional basis function by multiplying it by an imaginary phase factor

$$\omega_{\mu}(\mathbf{B}, \mathbf{R}_M) = \exp\left(-\frac{i}{\hbar} e \mathbf{A}_M \cdot \mathbf{r}\right) \chi_{\mu}(\mathbf{R}_M). \quad (11.146)$$

$\chi_{\mu}$  is here an ordinary basis function, such as a Gaussian or a Slater-type basis function. The magnetic vector potential appearing in the imaginary phase factor is defined as

$$\mathbf{A}_M = \frac{1}{2} \mathbf{B} \times \mathbf{R}_{OM} = \frac{1}{2} \mathbf{B} \times (\mathbf{R}_M - \mathbf{O}). \quad (11.147)$$

The effect of this complex phase factor is to move the global gauge origin  $\mathbf{O}$  to the “best” gauge origin for the basis function located at center  $\mathbf{R}_M$ , namely, the nucleus  $M$  to which the basis function is attached.

When London atomic orbitals (LAOs, known also as gauge-including atomic orbitals – GIAOs) are used, the definition of dia- and paramagnetic contributions to the magnetizability in  $\blacktriangleright$  Eq. 11.144 can no longer be used. We can instead define (Ruud and Helgaker 1997):

$$\xi_{\alpha\beta}^{\text{dia}}(\mathbf{O}) = -2\langle 0 | \hat{H}_{\alpha\beta}^{\text{B,B}} | 0 \rangle, \quad (11.148)$$

$$\xi_{\alpha\beta}^{\text{para,Lon}}(\mathbf{O}) = \xi_{\alpha\beta}^{\text{Lon}} - \xi_{\alpha\beta}^{\text{dia}}(\mathbf{O}). \quad (11.149)$$

This partitioning leads to dia- and paramagnetic contributions that display the correct gauge origin dependence also for finite basis sets, since the diamagnetic contribution,  $\xi_{\alpha\beta}^{\text{dia}}$  in  $\blacktriangleright$  Eq. 11.148, is an expectation value, and therefore it has the correct origin dependence. Furthermore, expectation values in general show fast basis set convergence. Therefore the significant improvement in convergence of both the total magnetizability and the diamagnetic magnetizability ensures fast basis set convergence also for the paramagnetic contribution,  $\blacktriangleright$  Eq. 11.149.

To illustrate the importance of using London orbitals when calculating magnetizabilities, we consider in  $\blacktriangleright$  Table 11-4 the magnetizability (and rotational  $g$  tensor, *vide infra*) of the  $\text{PF}_3$  molecule. We note that the isotropic magnetizability calculated using the aug-cc-pVDZ basis set and without London atomic orbitals is wrong by a factor of almost three compared to the estimated Hartree–Fock limit. As shown in  $\blacktriangleright$  Table 11-4, even when the aug-cc-pV5Z basis containing more than 500 basis functions is used, the results obtained using  $\blacktriangleright$  Eq. 11.144 are still more than 10% off the results obtained with London atomic orbitals, which can be expected to be very close to the Hartree–Fock limit considering the excellent basis set convergence of the London atomic orbital magnetizabilities. In contrast, all the calculations using London orbitals

$\blacksquare$  Table 11-4

**Basis set convergence of the SCF magnetizability (in a.u.) and rotational  $g$  tensor of  $\text{PF}_3$  calculated without and with London atomic orbitals, Ruud and Helgaker (1997)**

	aug-cc-pVDZ		aug-cc-pVTZ		aug-cc-pVQZ		aug-cc-pV5Z	
	No-Lon	Lon	No-Lon	Lon	No-Lon	Lon	No-Lon	Lon
$\xi^{\text{iso}}$	-16.55	-6.80	-11.50	-6.67	-9.06	-6.61	-7.66	-6.57
$\Delta\xi$	-3.66	-0.25	-0.77	-0.32	0.48	-0.33	-0.28	-0.34
$g_{\parallel}$	0.0845	-0.0618	0.0159	-0.0636	-0.0181	-0.0643	-0.0461	-0.0649
$g_{\perp}$	0.0890	-0.0378	0.0162	-0.0380	-0.0181	-0.0383	-0.0274	-0.0385

are within 3% of the LAO aug-cc-pV5Z results. More importantly, the anisotropy is off by an order of magnitude at the aug-cc-pVDZ level, and even has the wrong sign at the aug-cc-pVQZ basis (containing 345 basis functions) if London orbitals are not used.

Computational studies have shown that unless the ground electronic state is nearly degenerate with the lowest excited states, electron correlation effects on the isotropic magnetizability are in general negligible. All published results of correlated calculations of the magnetizability of closed-shell molecules without close-lying excited states have found electron correlation effects to be less than 3% in most cases, much smaller than any uncertainty in experimentally determined magnetizabilities for such molecular systems. Results within 1–2% of the Hartree–Fock limit can be obtained using the very modest-sized aug-cc-pVDZ basis set of Woon and Dunning (1994). The important point in the construction of a suitable basis set is the inclusion of diffuse polarizing functions in order to ensure highly accurate magnetizabilities.


Commonly adopted exchange-correlation functionals (e.g., B3LYP, BLYP) are in general less efficient in recovering correlation effects on molecular magnetic properties than they are in recovering correlation effects on vibrational spectra or electric properties. Indeed, in many cases DFT may perform worse than Hartree–Fock in the calculation of isotropic magnetizabilities. A set of new functionals designed specifically for the calculation of magnetic properties has been developed by Keal and Tozer (2003). However, recent CCSD benchmark calculations indicate that the results obtained with one of these functionals deteriorate when vibrational corrections and solvent effects are taken into account (Lutnæs et al. 2009).

The isotropic magnetizabilities are in general very little affected by nonelectronic contributions such as zero-point vibrational corrections, dielectric medium effects, or weak intermolecular forces. The situation is very different for the magnetizability anisotropy, which may display both fairly large electron correlation effects as well as sizeable contributions from nonelectronic contributions.

Although highly accurate theoretical calculations using coupled-cluster wave functions have demonstrated that correlation effects are in general small (Gauss et al. 2007), and that nonelectronic contributions are small as noted above, agreement with experimentally determined magnetizabilities is in general poor. Part of the reason for this is the general lack of experimental gas-phase magnetizabilities. However, more important for the apparent disagreement between theory and experiment may be the fact that isotropic magnetizabilities are almost exclusively determined *relative* to the magnetizability of reference compounds. It has been suggested that the reference values used to determine experimental magnetizabilities are inaccurate (Ruud et al. 2000).

## Rotational $g$ Tensor

---

The magnetizability describes the magnetic moment induced in a molecule by an external magnetic field induction, and how this induced magnetic moment in turn can interact with the external magnetic field and lead to an energy correction. A molecule also has its own source of a magnetic moment, arising from the rotational motion. Since the molecule consists of charged particles, the nuclei, and the electrons, the overall rotation of these particles will generate a small magnetic moment. In the case of the external-field-induced magnetic moment, the vector potential and the electron magnetogyric ratio determine the form of the magnetic dipole operator in  Eq. 11.44. For the magnetic moment induced by the molecular rotation, the magnitude

of the rotational angular momentum  $\mathbf{J}$  is determined by the rotational quantum numbers of the molecule, giving rise to a rotationally induced magnetic moment

$$m_a^J = \frac{\mu_N}{\hbar} \sum_{a,b} g_{ab}^J J_b, \quad (11.150)$$

where  $\mu_N$  is the nuclear magneton and the rotational  $g$  tensor (also called the molecular  $g$  factor) is defined as

$$g^J = g^{J,\text{nucl}} + g^{J,\text{el}} = m_p \mathbf{I}^{-1} \sum_K Z_K \left( R_{K,\text{CM}}^2 \mathbf{1} - \mathbf{R}_{K,\text{CM}} \mathbf{R}_{K,\text{CM}}^T \right) - \frac{4m_p m_e}{e^2} \mathbf{I}^{-1} \xi^{\text{para}}(\mathbf{R}_{\text{CM}}). \quad (11.151)$$

In  $\blacklozenge$  Eq. 11.151 we have introduced the moment of inertia tensor  $\mathbf{I}$  and we have used the definition of  $\xi^{\text{para}}$  as given in  $\blacklozenge$  Eq. 11.149, which is applicable both when using London orbitals and when using conventional basis sets. Both the nuclear positions and magnetic dipole operators are defined with respect to the center of mass of the molecule, as this is the point about which the molecule rotates.

There are two contributions to the rotationally induced magnetic moment, one arising from the rotation of the nuclear framework, and one arising because of the rotation of the electron density, and these contributions are opposite in sign because the linear response function  $\xi^{\text{para}}$  in  $\blacklozenge$  Eq. 11.151 is positive. This rotationally induced magnetic moment is an example of a nonadiabatic effect. If the electrons were able to adjust their positions and momenta instantaneously to any change in the nuclear configuration, the magnetic moment created by the electrons and the nuclei would have the same magnitude but opposite sign, due to the different charges of the particles. However, this description, corresponding to the Born–Oppenheimer approximation, is not exact, and in fact a small permanent magnetic moment will arise from the decoupling of the electronic and nuclear rotation.

The rotational magnetic moment can interact with either internal or external sources of magnetic moments or magnetic fields. If the rotational magnetic moment interacts with the nuclear magnetic moment it gives rise to a contribution to the energy, discussed in more detail in  $\blacklozenge$  section “Nuclear Spin Rotation Constants,” which involves the nuclear spin–rotation constant. If we apply an external magnetic field and consider the interaction of this field with the magnetic moment created by the molecular rotation, the interaction energy is (Flygare 1974; Gauss et al. 1996):

$$\Delta E = -\frac{\mu_N}{\hbar} \sum_{a,b} B_a g_{ab}^J J_b, \quad (11.152)$$

where  $J_a$  is the rotational quantum number along the principal rotational axis  $a$ .

The rotational  $g$  tensor is a tensor of rank two with in principle nine independent elements. The rotational magnetic moment is only well defined in the principal rotational axis system, where the moment of inertia tensor is diagonal, and only the diagonal elements of  $g^J$  in this principal axes system contribute to the rotational Zeeman effect (Flygare 1974; Gauss et al. 1996).

We also note that if we can determine both the magnetizability and the rotational  $g$  factor, we can indirectly determine the molecular quadrupole moment from the equation:

$$q_{cc} = \frac{2m_e}{e} (\xi_{aa} + \xi_{bb} - 2\xi_{cc}) + \frac{e}{2m_p} (g_{aa}^J I_{aa} + g_{bb}^J I_{bb} - 2g_{cc}^J I_{cc}). \quad (11.153)$$

This relation shows that microwave Zeeman spectroscopy can be an important source of molecular quadrupole moments. From a theoretical point of view, this equation does not provide any



additional information compared to calculating the molecular quadrupole moment directly as an expectation value, since the relationship (Eq. 11.153) is fulfilled exactly for any wave function.

The electronic contribution to the rotational  $g$  factor is important in high-resolution microwave spectroscopy even in the absence of an external magnetic field. In Eq. 11.150 we introduced the magnetic moment induced by the rotation of the molecular framework. Instead of letting this induced magnetic moment interact with an external magnetic field induction, we can let it interact with the rotational moment of the molecule. This gives a correction to the molecular energy which is quadratic in the rotational quantum number  $J$ . In ordinary microwave spectroscopy, the leading energy contribution is related to the moment of inertia tensor and is also quadratic in  $J$ . Therefore, the energy correction related to  $g^J$  can be treated as a correction to the moment of inertia tensor, and it is customary to introduce an effective inverse moment of inertia tensor defined as (Flygare 1974):

$$\mathbf{I}_{\text{eff}}^{-1} = \mathbf{I}^{-1} \left( \mathbf{1} - \frac{m_e}{m_p} g^{J,\text{el}} \right). \quad (11.154)$$

When comparing highly accurate theoretical estimates of moments of inertia directly with the results observed in high-resolution microwave spectroscopy, it is essential to take into account these nonadiabatic corrections. It is particularly noteworthy that the experimental determination of the equilibrium geometry involves the estimation of the effects of the rotational  $g$  tensor on the moment of inertia tensor, and that it is currently possible to calculate these effects with an accuracy much higher than obtainable from experimental data alone. Therefore, the use of highly accurate experimental data, for instance from rotational spectra, combined with highly accurate calculations of small corrections to these quantities, is currently the most accurate way to obtain experimental equilibrium geometries (Stanton et al. 2001) (for a related analysis of diatomic systems, see Sauer et al. 2005).

As the rotational  $g$  tensor includes a linear response function involving two magnetic dipole operators, similar computational requirements apply for this property as for the magnetizability. We can therefore expect that the direct calculation of the rotational  $g$  tensor using Eq. 11.151 will display very slow basis set convergence. However, London orbitals are very efficient in getting fast basis set convergence, as illustrated for  $\text{PF}_3$  in Table 11-4.

In microwave or molecular beam experiments, all of the three diagonal elements of the rotational  $g$  tensor are determined. As for the magnetizability, the individual tensor components show some dependence on electron correlation effects, and in order to allow for the calculated results to be within the very tight experimental errors bars for the rotational  $g$  tensor elements, electron correlation and the effects of zero-point vibrational corrections need to be included. This is illustrated for the water molecule in Table 11-5.

## Birefringences and Dichroisms

The consequences of the fact that an electromagnetic wave has both a frequency-dependent electric field component and a frequency-dependent magnetic field component have so far not been discussed. The two components are perpendicular to each other, as well as perpendicular to the direction of the propagation of the light beam. Moreover, we have not discussed the implications of the possible polarization of the light beam. Light experienced in everyday life

■ Table 11-5

Electron correlation effects and zero-point vibrational corrections to the rotational  $g$  tensor components of  $\text{H}_2\text{O}$ . The molecule is located in the  $xz$ -plane with the dipole moment along the  $z$ -axis ( $g^j$  is dimensionless)

Computational method	$g_{xx}^j$	$g_{yy}^j$	$g_{zz}^j$
Hartree–Fock (Ruud et al. 1998)	0.6635	0.6814	0.7342
RASSCF (Ruud et al. 1998)	0.651(1)	0.667(3)	0.728(3)
CCSD (Gauss et al. 2007)	0.6545	0.6707	0.7304
CCSD(T) (Gauss et al. 2007)	0.6543	0.6690	0.7308
RASSCF+ZPV (Ruud et al. 1998)	0.637(1)	0.640(3)	0.709(3)
Exp. (Molecular beam) (Verhoeven and Dymanus 1970)	0.645(6)	0.657(1)	0.718(7)
Exp. (Microwave Zeeman) (Kukolich 1969)	0.6465(20)	0.6650(20)	0.7145(20)

is mostly nonpolarized – that is, the tip of the electric or magnetic field vectors moves randomly in the plane perpendicular to the propagation direction. With the use of appropriate tools, unpolarized light can be turned into a wide variety of polarization states, becoming linearly, elliptically, or circularly polarized. In these cases, the tip of the field vector(s) oscillates in the plane containing the direction of propagation (linear polarization) or rotates along a circle (circular polarization) or an ellipse (elliptical polarization) in the plane perpendicular to it. The polarization of light plays an important role in the interactions of light with a molecule.

Birefringences and dichroisms are two aspects of this interaction which are closely related to the polarization status of light. They arise through a variety of different mechanisms and interactions between the electromagnetic field and the molecule, but they are all characterized by the simultaneous measurements of the refractive (birefringences) or absorptive (dichroisms) index of light along two directions, different with respect to some predefined laboratory or molecular frame. The difference in the dispersion or absorption in these two directions is described by a quantity of a specific sign and magnitude. All these properties give detailed information about the molecular structure, and in particular some of them can distinguish between a sample and its mirror image. Distinguishable mirror images can occur naturally, in chiral molecules where the mirror image of the molecule cannot be superimposed on the original molecule itself – that is, for so-called enantiomers – or they can occur by introducing an asymmetry in the experimental setup that makes the mirror image of the experimental design impossible to superimpose on the original setup. In the latter case, since the experimental design is itself chiral, the observed effect does not vanish even if the molecule is not chiral. We note that only molecules possessing no improper or rotation-reflection axes may be chiral.

It is instructive to start by giving some examples of birefringences, before discussing the details of the most important birefringences and dichroisms. Let us consider first an isotropic liquid sample subject to a strong external static electric field. The refractive index  $n_{\parallel}$  experienced by the component of the polarization vector aligned parallel to the direction of the external field  $\mathbf{F}$  in this case differs from the index of refraction  $n_{\perp}$  for the component aligned perpendicular to the direction of the vector  $\mathbf{F}$  (Kerr 1875a, b). As a consequence, the initially linearly polarized light beam will exit the region of the sample with an ellipticity. This is an example of a *linear birefringence*

$$\Delta n^{\text{lin}} = n_{\parallel} - n_{\perp}, \quad (11.155)$$

and the effect is known as electric-field-induced optical birefringence or more often as the Kerr (electro-optical) effect. It exhibits a quadratic dependence on the strength of the applied electric field. Its existence is due mainly to the fact that the external electric field, in a system possessing an anisotropic electric dipole polarizability tensor, tends to align the molecules preferentially in its direction.

Other mechanisms in general also contribute to the emergence of an anisotropy, the most important being the effect of electronic rearrangements. They play a role through the higher-order polarizabilities of the system, in particular through the second electric-dipole hyperpolarizability  $\gamma$  and, in the presence of permanent electric dipoles, through the first electric-dipole hyperpolarizability  $\beta$  (Kerr 1875a, b). Other examples of linear birefringences are the Cotton–Mouton and Buckingham effects, briefly discussed below, and the Jones and magneto-electric birefringences, which occur when linearly polarized light goes through an isotropic fluid perpendicularly to both static electric and magnetic fields.

*Circular birefringence* is observed when the two circular components of a linearly polarized beam propagate with different circular velocities, and therefore an anisotropy arises between the two refractive indices  $n_+$  and  $n_-$ :

$$\Delta n^{\text{circ}} = n_+ - n_- \quad (11.156)$$

The net result is a rotation of the plane of polarization. An example of a circular birefringence is *optical activity*, which is observed when a medium composed of chiral molecules (with an excess of one enantiomer) is subject to linearly polarized electromagnetic radiation. The dependence of the corresponding anisotropy on the wavelength is described by the optical rotatory dispersion (ORD). The Faraday effect, discussed below, is another well-known example of a circular birefringence.

An *axial birefringence* occurs with unpolarized light, and an example is the so-called magnetochiral birefringence (Barron and Vrbancich 1984; Kalugin et al. 1999). It can be seen in isotropic samples composed of chiral molecules, and it is observed when a static magnetic induction field is switched on parallel to the direction of propagation of the unpolarized probe beam. The refractive index experienced by the beam propagating parallel to the external magnetic field,  $n_{\uparrow\uparrow}$ , becomes different from that experienced by a beam propagating antiparallel to the field,  $n_{\uparrow\downarrow}$

$$\Delta n^{\text{ax}} = n_{\uparrow\uparrow} - n_{\uparrow\downarrow} \quad (11.157)$$

The corresponding anisotropy has a different sign for the different enantiomers.

An external field will have an orientational effect on the molecules of the sample, and this is a mechanism responsible for the emergence of birefringences. In the presence of external fields the sample becomes anisotropic, and the extent to which this happens depends on the temperature. Indeed, the general form of the optical anisotropy (for measurements taken at a fixed pressure) is usually of the form

$$\Delta n \propto A_0 + \frac{A_1}{T} + \frac{A_2}{T^2} + \dots, \quad (11.158)$$

where the term  $A_0$  includes all contributions arising from the reorganization of the electrons due to the action of the external field(s), whereas the terms  $A_1, A_2, \dots$  are connected to different mechanisms of reorientation of the molecules, involving the interaction of the field(s) with permanent electric or magnetic multipole moments. The temperature-dependent terms vanish for systems of spherical symmetry; the contributions exhibiting a nonlinear dependence are usually

connected to the presence of permanent electric or magnetic dipole moments, or higher-order processes involving more complicated interactions between fields and multipoles.

When the inducing field is time dependent, the birefringence is said to be “optically induced.” In general, the information provided by birefringences induced by static fields can differ from that obtained observing the corresponding optically induced phenomena. For example, in the static Kerr effect of dipolar molecules, an important role is played by the permanent dipoles, which tend to be aligned by the static field. This contribution vanishes for dynamic inducing fields, where the birefringence arises only from the rearrangement of the anisotropy of the electric dipole polarizability. The contribution resulting from the interaction with permanent multipoles averages over time to zero.

## Optical Rotation

The first contribution to the induced electric dipole moment in  $\blacktriangleright$  Eq. 11.74 from the time dependence of the magnetic field,  $\omega^{-1}G'$ , gives rise to two different observable properties. In the dispersive region, this property determines the optical rotatory power, or just optical rotation (OR) for short, and in the absorptive region it determines the rotational strength observed in electronic circular dichroism (ECD).

There are no terms bilinear in the electric and magnetic fields in the Hamiltonian, therefore  $G'$ , the mixed electric dipole–magnetic dipole polarizability (see also  $\blacktriangleright$  Eq. 11.74), can be expressed as a linear response function:

$$G'_{\alpha\beta}(-\omega; \omega) = -\frac{2\omega}{\hbar} \sum_{n \neq 0} \mathcal{I}m \frac{\langle 0 | \hat{\mu}_\alpha | n \rangle \langle n | \hat{m}_\beta | 0 \rangle}{\omega_n^2 - \omega^2} = -\mathcal{I}m \langle \langle \hat{\mu}_\alpha; \hat{m}_\beta \rangle \rangle_\omega. \quad (11.159)$$

We note that  $G'$  vanishes if the electromagnetic field is static ( $\omega = 0$ ), see the discussion in  $\blacktriangleright$  section “Expansions of Energy and Multipole Moments.” For unit conversion factors, see  $\blacktriangleright$  Table 11-6.

Measurements of optical rotation are almost exclusively carried out on liquid samples (though gas-phase measurements recently became possible (Müller et al. 2000)) and we will, therefore, be concerned primarily with the rotational average of the  $G'$  tensor, which is described by the quantity  $^{\text{ORD}}\beta$  defined as

$$^{\text{ORD}}\beta = -\frac{1}{3\omega} G'_{\alpha\alpha}. \quad (11.160)$$

The most common experimental setup involves the determination of the rotation of plane-polarized light as it passes through a sample in which there is an excess of one enantiomer. The standard optical rotation  $[\alpha]_D^{25}$ , proportional to  $^{\text{ORD}}\beta$ , is reported for light with a frequency corresponding to the sodium D-line (589.3 nm) at a temperature of 25°C.

**Table 11-6**

**Unit conversion factors for electric dipole–magnetic dipole polarizability**

	1 a.u.	SI	CGS
$G'$	$e^2 a_0^3 \hbar^{-1}$	$3.60702 \times 10^{-35} \text{ C}^2 \text{ m}^3 \text{ J}^{-1} \text{ s}^{-1}$	$1.08136 \times 10^{-27} \text{ Fr cm G}^{-1}$

Because the mixed electric dipole–magnetic dipole polarizability involves the magnetic dipole operator, in approximate calculations  $G'$  carries an origin dependence. Indeed, the individual tensor elements of  $G'$  are origin dependent. The trace of  $G'$  must be origin independent, since the optical rotation is an experimental observable. In non-isotropic media, contributions to the optical rotation tensor arise from the mixed electric dipole–electric quadrupole polarizability  $A$ ,

$$A_{\alpha,\beta\gamma}(-\omega; \omega) = -\langle\langle \hat{\mu}_\alpha; \hat{\Theta}_{\beta\gamma} \rangle\rangle_\omega, \quad (11.161)$$

(see the last term in  $\blacktriangleright$  Eq. 11.74), and it is the combination of the  $G'$  and  $A$  contributions that is gauge-origin independent for exact wave functions. The contribution from  $A$  vanishes in isotropic samples, since this mixed electric dipole–electric quadrupole polarizability is traceless.

For approximate variational wave functions, the origin independence of the trace of  $G'$  is only achieved in the limit of a complete basis set. One way to overcome this problem is to introduce local gauge origins by using London atomic orbitals (Helgaker et al. 1994).

The dispersion of the optical rotation was for a long time also the focus of much experimental attention through optical rotatory dispersion measurements. Even after it became customary to restrict the optical rotation measurements to a single frequency, ORD served as an important tool for determining excitation energies in chiral molecules, although it has now been surpassed by electronic circular dichroism for these purposes (see  $\blacktriangleright$  section “Circular Dichroism”).

At the sodium frequency, the optical rotation is rather small for most molecules. However, the individual diagonal elements of the mixed electric dipole–magnetic dipole polarizability may be fairly large in absolute value, often canceling each other in the trace. This is illustrated for a few selected molecules in  $\blacktriangleright$  Table 11-7. Consequently, the optical rotation is highly sensitive to numerical errors in the tensor components, because small residual errors in the individual tensor components, arising from the solution of the linear response equations, may lead to substantial errors in  ${}^{\text{ORD}}\beta$ . Another consequence of this cancellation is that  ${}^{\text{ORD}}\beta$  is very sensitive to the choice of molecular geometry, as well as zero-point vibrational effects (Ruud et al. 2001), since the small changes introduced by these effects in the molecular charge distribution, and thus on the different diagonal elements of  $G'$ , can give rather large effects on  ${}^{\text{ORD}}\beta$ .

The sensitivity of the optical rotation is perhaps most clearly illustrated in the case of conformationally flexible molecules – that is, molecules that have a significant population of multiple stable minima. As exemplified for paraconic acid (a substituted  $\gamma$ -butyrolactone) in  $\blacktriangleright$  Table 11-8, different molecular conformations can have optical rotations that differ by orders of magnitude and even in sign. A thorough conformational search is therefore mandatory before the absolute sign of the optical rotation (or any birefringence or dichroism for that matter) is determined from theoretical calculations for conformationally flexible molecules. The

■ Table 11-7

The diagonal elements of the mixed electric dipole–magnetic dipole polarizability and the trace of the tensor for a few selected molecules (in a.u.,  $[\alpha]_D^{25}$  in  $\text{deg cm}^3 \text{ dm}^{-1} \text{ g}^{-1}$ )

Molecule	$\omega^{-1}G'_{xx}$	$\omega^{-1}G'_{yy}$	$\omega^{-1}G'_{zz}$	${}^{\text{ORD}}\beta$	$[\alpha]_D^{25}$
H <sub>2</sub> O <sub>2</sub> ( $\phi = 120^\circ$ )	-1.201	0.387	0.960	-0.049	-55.3
(+)-methyloxirane	-0.820	-0.812	1.587	0.015	10.2
(+)-camphor	0.240	4.891	-5.847	0.239	60.5

DFT/B3LYP results obtained with the Sadlej polarized basis sets, taken from Giorgio et al. (2004)

■ Table 11-8

The specific optical rotation ( $[\alpha]_D^{25}$  in  $\text{deg cm}^3 \text{dm}^{-1} \text{g}^{-1}$ ) for different conformers of (S)-(-)-paraconic acid calculated using different basis sets and at DFT/B3LYP and MP2 optimized geometries<sup>a</sup>

Conformer	DFT geometries			MP2 geometry
	6-311++G**	aug-cc-pVDZ	aug-cc-pVDZ	aug-cc-pVDZ
<b>A</b>	-31.27	-42.35 <sup>b</sup>	-47.91	-10.58
<b>B</b>	152.79	144.53 <sup>b</sup>	145.76	<sup>c</sup>
<b>C</b>	112.01	95.73 <sup>b</sup>	91.47	109.74
<b>D</b>	-250.61	-245.03 <sup>b</sup>	-253.88	-251.71
<b>E</b>	-19.21	-10.78 <sup>b</sup>	0.36	-13.49
<b>F</b>	-188.13	-182.86 <sup>b</sup>	-182.67	-217.33
$[\alpha]_D^{25}$	+14.78	+6.72	+4.40	-85.23

<sup>a</sup>The bottom line of the table gives the total specific optical rotation  $[\alpha]_D^{25}$  (all conformations weighted by the Boltzmann distribution). All the results taken from Marchesan et al. (2005)

<sup>b</sup>The optical rotations were calculated for the B3LYP/6-311++G\*\* geometries

<sup>c</sup>An energy minimum corresponding to a **B**-like conformer could not be found

optical rotation of the flexible molecule can then be determined by Boltzmann averaging over the dominant molecular conformations.

In order to ensure reasonably well-converged results for the optical rotation, basis sets of polarized valence double-zeta quality are required, and sets such as the aug-cc-pVDZ of Woon and Dunning (1994), or the polarized triple-zeta basis of Sadlej (1988) have been shown to perform well for calculations of optical rotation. Most importantly, diffuse *p* functions in the outer regions of the electron density, which in most cases is described by the electron density of hydrogen atoms, are required to ensure qualitatively correct results (Zuber and Hug 2004).

Since the optical rotation is very sensitive even to small changes in the electron density, electron correlation effects should also be taken into account in order to get accurate results. Due to the fact that chiral molecules in general have very low symmetry, if any symmetry at all, the only viable approach for calculating electron correlation effects in chiral molecules is currently density functional theory (Ruud et al. 2003; Stephens et al. 2001). Methods such as MP2 and CCSD could also be used to describe electron correlation, but due to their nonvariational nature it is not ensured that gauge-origin independent results can be obtained in the conventional length-gauge formulation even in the limit of a complete basis set. In principle, the use of the dipole velocity gauge will ensure that the calculated results are independent of the gauge origin. For all but the smallest basis sets, the differences between the velocity and the length gauges are not very large, with the length gauge in general performing better. However, in the case of the optical rotation an additional complication arises: whereas  $G'$  given by Eq. 11.159 will vanish in the limit of a static field, this is not the case for the dipole-velocity analogue of the optical rotation. It has been suggested that the much slower basis set convergence of the optical rotation compared to other properties calculated using the velocity-gauge formulation can be improved by subtracting the static-limit value of the corresponding response function (Pedersen et al. 2004), such that

$$G' \propto \langle \langle \hat{p}_\alpha; \hat{l}_\beta \rangle \rangle_\omega - \langle \langle \hat{p}_\alpha; \hat{l}_\beta \rangle \rangle_0. \quad (11.162)$$

Since there are no empirical rules relating the stereochemistry of a molecule to the observed sign of the optical rotation, an important area of application for optical rotation calculations would be the combined theoretical and experimental determination of absolute configurations. However, this is a difficult task due in part to the large variations with geometry in the optical rotation of conformationally flexible molecules, and in part because of the small magnitude of  $^{\text{ORD}}\beta$ . These factors make the sign of the optical rotation hard to determine with confidence. One way to increase the predictive power of the calculations is to change the frequency of the incident light to shorter wavelengths. The magnitude of the optical rotation increases dramatically as the frequency approaches that of a resonance. Thus, if both theory and experiment could determine the optical rotation at frequencies closer to electronic excitation energies, theoretical calculations could provide a much more reliable proof of the absolute configuration of the molecule (Giorgio et al. 2004).

## Circular Dichroism

### Natural (Electronic) Circular Dichroism

Let us now turn to the lowest-order absorption process involving mixed electric and magnetic perturbations. This property, which is the absorptive analogue of the optical rotation, is known as *electronic circular dichroism* (ECD) or just CD for short.

The differential absorption of circularly polarized light, corresponding to the difference between the absorptive index of the two circular components of linearly polarized light, is proportional to the rotational strength, which is normally calculated as the residue of the linear response mixed electric dipole–magnetic dipole polarizability:

$$\lim_{\omega \rightarrow \omega_{n0}} \frac{\hbar}{\omega - \omega_{n0}} \langle \langle \hat{\mu}_\alpha; \hat{m}_\beta \rangle \rangle_\omega = \langle 0 | \hat{\mu}_\alpha | n \rangle \langle n | \hat{m}_\beta | 0 \rangle. \quad (11.163)$$

Since this expression corresponds to the infinite lifetime approximation for the excited state, only a single number will be obtained at the frequency of the electronic excitation.

In general  ${}^nR$ , the rotatory strength for the transition  $|0\rangle \rightarrow |n\rangle$ , includes an electric dipole–magnetic dipole contribution

$${}^nR_{\alpha\beta}^m = -\frac{3ie^2}{4m_e} (\delta_{\alpha\beta} \langle 0 | \mathbf{r} | n \rangle \langle n | \mathbf{I}^T | 0 \rangle - \langle 0 | \hat{r}_\beta | n \rangle \langle n | \hat{l}_\alpha | 0 \rangle), \quad (11.164)$$

and an electric dipole–electric quadrupole contribution

$${}^nR_{\alpha\beta}^Q = -\frac{3\omega_{n0}e^2}{4} \varepsilon_{\alpha\gamma\delta} \langle 0 | \hat{r}_\gamma | n \rangle \langle n | \hat{q}_{\delta\beta} | 0 \rangle. \quad (11.165)$$

For randomly oriented molecules, the averaging leaves only the electric dipole–magnetic dipole contribution and the scalar rotatory strength is given by

$${}^nR = -\frac{ie^2}{2m_e} \langle 0 | \mathbf{r}^T | n \rangle \langle n | \mathbf{I} | 0 \rangle, \quad (11.166)$$

corresponding to  $\blacktriangleright$  Eq. 11.163. These expressions are given in the length gauge. In the velocity gauge

$${}^nR_{\alpha\beta}^m = \frac{3e^2}{4m_e^2\omega_{n0}} (\delta_{\alpha\beta} \langle 0 | \mathbf{p} | n \rangle \langle n | \mathbf{I}^T | 0 \rangle - \langle 0 | \hat{p}_\beta | n \rangle \langle n | \hat{l}_\alpha | 0 \rangle), \quad (11.167)$$

and

$${}^n R_{\alpha\beta}^Q = \frac{3e^2}{4m_e^2\omega_{n0}} \varepsilon_{\alpha\gamma\delta} \langle 0 | \hat{p}_\gamma | n \rangle \langle n | \hat{T}_{\delta\beta}^+ | 0 \rangle, \quad (11.168)$$

where  $\mathbf{T}^+$  indicates the “velocity” form of the electric quadrupole operator

$$\mathbf{T}^+ = -(\mathbf{r}\mathbf{p} + \mathbf{p}\mathbf{r}). \quad (11.169)$$

This form has an advantage in comparison to the length form. Although with a translation of the reference frame the magnetic dipole and electric quadrupole components change, the total tensor in the velocity gauge is invariant to such a change of origin. For the length gauge, this invariance depends in addition on the fulfillment of the hypervirial relation,  $\blacktriangleright$  Eq. 11.126.

## Two-Photon Circular Dichroism

Two-photon circular dichroism (Tinoco 1975) arises in chiral systems due to the differential absorption of two photons, of which at least one is circularly polarized (De Boni et al. 2008). In this sense it can be seen as the nonlinear extension of ECD. The observable, the anisotropy of the two-photon transition strength, is proportional to the two-photon rotatory strength (Jansík et al. 2005; Rizzo et al. 2006; Tinoco 1975):

$${}^n R^{\text{TPCD}}(\omega) = -b_1[\mathcal{B}_1(\omega)]_{0n} - b_2[\mathcal{B}_2(\omega)]_{0n} - b_3[\mathcal{B}_3(\omega)]_{0n}, \quad (11.170)$$

where  $b_1$ ,  $b_2$ , and  $b_3$  are numbers, simple combinations of the analogous polarization and setup-related coefficients F, G, and H given for two-photon absorption in  $\blacktriangleright$  Eqs. 11.132. The molecule-related parameters  $\mathcal{B}_1$ ,  $\mathcal{B}_2$ , and  $\mathcal{B}_3$  take the form:

$$[\mathcal{B}_1(\omega)]_{0n} = \frac{1}{\omega^3} \mathcal{M}_{\rho\sigma}^{\text{p},0n}(\omega) \mathcal{P}_{\rho\sigma}^{\text{p}^*,0n}(\omega), \quad (11.171)$$

$$[\mathcal{B}_2(\omega)]_{0n} = \frac{1}{2\omega^3} \mathcal{T}_{\rho\sigma}^{+,0n}(\omega) \mathcal{P}_{\rho\sigma}^{\text{p},0n}(\omega), \quad (11.172)$$

$$[\mathcal{B}_3(\omega)]_{0n} = \frac{1}{\omega^3} \mathcal{M}_{\rho\rho}^{\text{p},0n}(\omega) \mathcal{P}_{\sigma\sigma}^{\text{p}^*,0n}(\omega), \quad (11.173)$$

and they are, therefore, appropriate contractions of generalized two-photon second-rank tensors, like the one given in  $\blacktriangleright$  Eq. 11.133. Indeed, these tensors are defined (for the general case of two photons of different frequency) as follows:

$$\mathcal{P}_{\alpha\beta}^{\text{p},0n}(\omega_1, \omega_2) = \frac{1}{\hbar} \sum_m \left\{ \frac{(\hat{\mu}_\alpha^{\text{p}})_{0m} (\hat{\mu}_\beta^{\text{p}})_{mn}}{\omega_{m0} - \omega_1} + \frac{(\hat{\mu}_\beta^{\text{p}})_{0m} (\hat{\mu}_\alpha^{\text{p}})_{mn}}{\omega_{m0} - \omega_2} \right\}, \quad (11.174)$$

$$\mathcal{M}_{\alpha\beta}^{\text{p},0n}(\omega_1, \omega_2) = \frac{1}{\hbar} \sum_m \left\{ \frac{(\hat{\mu}_\alpha^{\text{p}})_{0m} (\hat{m}_\beta)_{mn}}{\omega_{m0} - \omega_1} + \frac{(\hat{m}_\beta)_{0m} (\hat{\mu}_\alpha^{\text{p}})_{mn}}{\omega_{m0} - \omega_2} \right\}, \quad (11.175)$$

$$\mathcal{T}_{\alpha\beta}^{+,0n}(\omega_1, \omega_2) = \frac{1}{\hbar} \varepsilon_{\beta\rho\sigma} \sum_m \left\{ \frac{(\hat{T}_{\alpha\rho}^+)_{0m} (\hat{\mu}_\sigma^{\text{p}})_{mn}}{\omega_{m0} - \omega_1} + \frac{(\hat{\mu}_\sigma^{\text{p}})_{0m} (\hat{T}_{\alpha\rho}^+)_{mn}}{\omega_{m0} - \omega_2} \right\}, \quad (11.176)$$

where we have introduced the velocity form of the dipole operator,

$$\hat{\mu}_\alpha^{\text{p}} = -\frac{e}{m_e} \sum_i \hat{p}_{i\alpha}. \quad (11.177)$$



Within the formalism of response theory, the second-rank tensors of interest are obtained from the single residues of appropriate quadratic response functions, see [Eq. 11.69](#). The quadratic response functions of relevance for two-photon circular dichroism are:

$$\langle\langle \hat{\mu}_\alpha^p; \hat{\mu}_\beta^p, V^{\omega_n} \rangle\rangle_{\omega_1, \omega_2} \Rightarrow \mathcal{P}_{\alpha\beta}^{p,0n}(\omega_1, \omega_2), \quad (11.178)$$

$$\langle\langle \hat{\mu}_\alpha^p; \hat{m}_\beta, V^{\omega_n} \rangle\rangle_{\omega_1, \omega_2} \Rightarrow \mathcal{M}_{\alpha\beta}^{p,0n}(\omega_1, \omega_2), \quad (11.179)$$

$$\varepsilon_{\beta\rho\sigma} \langle\langle \hat{T}_{\alpha\rho}^+; \hat{\mu}_\sigma^p, V^{\omega_n} \rangle\rangle_{\omega_1, \omega_2} \Rightarrow \mathcal{T}_{\alpha\beta}^{+,0n}(\omega_1, \omega_2), \quad (11.180)$$

where  $V^{\omega_n}$  is an arbitrary operator (corresponding to the excitation vector to the state  $n$ ). Single residues of quadratic response functions are efficiently and accurately computed nowadays with a number of wave function models. Nevertheless, DFT has been used almost exclusively in the few theoretical studies of two-photon circular dichroism that have been published (Jansik et al. 2007, 2008).

## Faraday Effect

In 1846, Faraday observed that when a static magnetic field was applied with its direction parallel to the direction of propagation of linearly polarized light traversing a transparent sample (glass, liquid, gas), the plane of polarization of the beam was rotated (Faraday 1846a, b). It was the first ever experimental evidence of a birefringence phenomenon, and in particular of a circular birefringence, and the effect is often referred to as the *Faraday effect* or magnetic field-induced optical rotation. The rotation is proportional to the optical anisotropy, see [Eq. 11.156](#), and this depends linearly on the strength of the applied magnetic induction field. The mechanisms governing this effect involve the interaction of the static external magnetic induction field with the oscillating electric field of the light wave and with the electric multipoles of the sample. The term “magnetic optical rotatory dispersion” (MORD) is often used to denote the frequency dispersion of the Faraday effect, and thus of the corresponding circular birefringence.

For a fluid sample, the rotation with respect to the molecular frame becomes (Barron 2004; Buckingham and Stephens 1966):

$$\phi = V(\omega) B_z l \propto \omega \varepsilon_{\alpha\beta\gamma} (\alpha'_{\alpha\beta,\gamma} + \frac{1}{kT} \langle 0 | \hat{m}_\gamma | 0 \rangle \alpha'_{\alpha\beta}) B_z l, \quad (11.181)$$

where  $l$  is the path length, we have introduced the Verdet constant  $V(\omega)$ , and  $\alpha'^B$  denotes the magnetic field derivative of  $\alpha'$ , the antisymmetric electric dipole polarizability. The second term in the parentheses vanishes for closed-shell systems, as the magnetic dipole is quenched,  $\langle 0 | \hat{m}_\gamma | 0 \rangle = 0$ .

The Verdet constant of a closed-shell system, free of orbital degeneracies both in the ground and in the excited state, is therefore obtained from the response function (Jaszuński et al. 1994; Parkinson and Oddershede 1997):

$$V(\omega) \propto i \omega \varepsilon_{\alpha\beta\gamma} \langle\langle \hat{\mu}_\alpha; \hat{\mu}_\beta, \hat{m}_\gamma \rangle\rangle_{\omega,0}. \quad (11.182)$$

This contribution is sometimes referred to as the  $B$  term contribution to the Verdet constant. For molecules containing orbital degeneracies additional contributions arise (the  $A$  and  $C$  terms), in analogy with the closely related phenomenon – magnetic circular dichroism, discussed in [section “Magnetic Circular Dichroism.”](#) For unit conversion factors, see [Table 11-9](#).

Table 11-9

Unit conversion factors for the Verdet constant

	1 a.u.	SI	CGS
$V(\omega)$	$\text{rad } e a_0 \hbar^{-1}$	$8.03961 \times 10^4 \text{ rad T}^{-1} \text{ m}^{-1}$	$2.76382 \times 10^2 \text{ min G}^{-1} \text{ cm}^{-1}$

## Hypermagnetizabilities, Cotton–Mouton Effect

The *Cotton–Mouton effect* (CME) is a magnetic induction field-induced linear birefringence, observed in the presence of a strong magnetic induction field  $\mathbf{B}$  with a component perpendicular to the direction of propagation of the beam. It is mainly due to the tendency of both the electric field associated with the light beam and the magnetic induction field to align the molecules exhibiting both an anisotropic electric dipole polarizability and an anisotropic magnetizability tensor (according to the Langevin–Born theory (Born 1918; Langevin 1910)). The rearrangement of the electron density again plays a part through the mixed electric and magnetic hyperpolarizabilities, or hypermagnetizabilities.

The experimental quantity connected to the hypermagnetizability is the molar Cotton–Mouton constant  ${}_m C$ . Semiclassically, for fluids composed of closed-shell systems (Buckingham and Pople 1956; Fowler and Buckingham 1989; Jamieson 1991):

$${}_m C = \frac{2\pi N_A}{27} [\Delta\eta + Q(T)], \quad (11.183)$$

where  $\Delta\eta$  is the hypermagnetizability anisotropy

$$\Delta\eta = \frac{1}{15} (3\eta_{\alpha\beta,\alpha\beta} - \eta_{\alpha\alpha,\beta\beta}), \quad (11.184)$$

and

$$Q(T) = \frac{1}{15kT} (3\alpha_{\alpha\beta}\xi_{\alpha\beta} - \alpha_{\alpha\alpha}\xi_{\beta\beta}). \quad (11.185)$$

In  $\blacktriangleright$  Eq. 11.185,  $\alpha$  is the (frequency-dependent) electric polarizability tensor, and  $\xi$  the magnetizability tensor. The two contributions to the molar Cotton–Mouton constant in  $\blacktriangleright$  Eq. 11.183 are, therefore, a temperature-independent term related to the hypermagnetizability  $\eta_{\alpha\beta,\gamma\delta}$  and a temperature-dependent molecular orientational part – the “Langevin term.”

When the magnetizability is expressed as a power series in the perturbing electric field:

$$\xi_{\alpha\beta}(\mathbf{F}) = \xi_{\alpha\beta} + \zeta_{\gamma,\alpha\beta}F_\gamma + \frac{1}{2}\eta_{\gamma\delta,\alpha\beta}F_\gamma F_\delta + \dots, \quad (11.186)$$

the expansion coefficients  $\zeta_{\gamma,\alpha\beta}$  and  $\eta_{\gamma\delta,\alpha\beta}$  define the molecular first and second hypermagnetizability. The first indices of  $\zeta$  and  $\eta$  refer to the electric field and the last two to the magnetic field. In fluids, the experimentally measured property is related to the anisotropy of  $\eta$ . From the expansion above it can be seen that the static hypermagnetizability  $\eta$  corresponds to the fourth derivative of the molecular energy:

$$\eta_{\alpha\beta,\gamma\delta} = - \left. \frac{\partial^4 E(\mathbf{F}, \mathbf{B})}{\partial F_\alpha \partial F_\beta \partial B_\gamma \partial B_\delta} \right|_{\mathbf{F}, \mathbf{B}=0}. \quad (11.187)$$

It can also be expressed in terms of  $\xi(\mathbf{F})$  – the magnetizability dependent on  $\mathbf{F}$ :

$$\eta_{\alpha\beta,\gamma\delta} = \left. \frac{\partial^2 \xi_{\gamma\delta}}{\partial F_\alpha \partial F_\beta} \right|_{\mathbf{F}=0}, \quad (11.188)$$

or  $\alpha(\mathbf{B})$  – the polarizability dependent on  $\mathbf{B}$ :

$$\eta_{\alpha\beta,\gamma\delta}(\omega) = \left. \frac{\partial^2 \alpha(-\omega; \omega)_{\alpha\beta}}{\partial B_\gamma \partial B_\delta} \right|_{\mathbf{B}=0}, \quad (11.189)$$

and we have indicated in the latter equation that it holds also for the frequency-dependent polarizability.

The hypermagnetizability is given as a sum of paramagnetic and diamagnetic contributions:

$$\eta_{\alpha\beta,\gamma\delta}(\omega) = \eta_{\alpha\beta,\gamma\delta}^{\text{para}}(-\omega; \omega, 0, 0) + \eta_{\alpha\beta,\gamma\delta}^{\text{dia}}(-\omega; \omega, 0), \quad (11.190)$$

corresponding to a sum of a cubic response and a quadratic response function (Rizzo et al. 1997):

$$\eta_{\alpha\beta,\gamma\delta}^{\text{para}}(-\omega; \omega, 0, 0) = -\langle \langle \hat{\mu}_\alpha; \hat{\mu}_\beta, \hat{m}_\gamma, \hat{m}_\delta \rangle \rangle_{\omega,0,0}, \quad (11.191)$$

$$\eta_{\alpha\beta,\gamma\delta}^{\text{dia}}(-\omega; \omega, 0) = \langle \langle \hat{\mu}_\alpha; \hat{\mu}_\beta, \hat{\xi}_{\gamma\delta}^{\text{B,B}} \rangle \rangle_{\omega,0}, \quad (11.192)$$

where (see for comparison  $\blacktriangleright$  Eq. 11.145) the “diamagnetic magnetizability operator” in the second term is

$$\hat{\xi}_{\alpha\beta}^{\text{B,B}} = -2\hat{H}_{\alpha\beta}^{\text{B,B}}. \quad (11.193)$$

We recall here that the magnetic dipole moment and diamagnetic magnetizability operators, and thus the partitioning of the hypermagnetizability into para- and diamagnetic components, may depend on the chosen gauge origin.

Finite field approaches corresponding to  $\blacktriangleright$  Eqs. 11.188 and  $\blacktriangleright$  11.189 have been used (Rizzo et al. 1997). In these calculations  $\eta_{\alpha\beta,\gamma\delta}$  is obtained combining the available analytic linear response methods with the numerical finite difference approach. The frequency-dependent electric dipole polarizability can be computed in the presence of a magnetic induction field, and the hypermagnetizability is obtained by numerical differentiation. This approach (Cybulski and Bishop 1994; Tellgren et al. 2008) in general requires complex algebra as the perturbation is purely imaginary, whereas most electronic structure codes use real wave functions. In the more often used finite field approach based on  $\blacktriangleright$  Eq. 11.188, one computes the magnetizability  $\xi$  with and without an external electric field perturbation. However, in this approach only the static value of the required hypermagnetizability is obtained. Analytic calculations of the quadratic and cubic responses  $\blacktriangleright$  Eqs. 11.192 and  $\blacktriangleright$  11.191 also including London orbitals to ensure gauge origin independence can nowadays be carried out (Thorvaldsen et al. 2008). The effect of the London orbitals on improving the basis set convergence appears to be small.

For atoms, choosing the origin of the gauge at the nucleus automatically makes the dependence on the gauge vanish, and there is no advantage in using LAOs. Moreover, the evaluation of  $\Delta\eta$  may be reduced to the calculation of the Cauchy moments  $S(-2n)$  and of the dipole–dipole–quadrupole hyperpolarizability frequency dispersion coefficients (Coriani et al. 1999a; Rizzo et al. 1997). For unit conversion factors, see  $\blacktriangleright$  Table 11-10.

**Table 11-10**

**Unit conversion factors for hypermagnetizability**

	1 a.u.	SI	CGS
$\eta$	$(ea_0^2)^2 (e\hbar/m_e)^2 E_h^{-3}$	$2.98425 \times 10^{-52} \text{ C}^2 \text{ m}^2 \text{ J}^{-1} \text{ T}^{-2}$	$2.68211 \times 10^{-44} \text{ cm}^3 \text{ G}^{-2}$

## Electric-Field-Gradient-Induced Birefringence

As a magnetic induction field can give rise to an optical anisotropy through its interaction with the anisotropic magnetizability of a molecule, so can an electric field gradient, through its coupling with a permanent molecular quadrupole moment. The corresponding birefringence (Buckingham 1959; Buckingham and Disch 1963) is commonly called *electric-field-gradient-induced birefringence*, more recently *Buckingham birefringence*, and it exhibits a linear dependence on the strength of the electric field gradient. Besides the orientational Langevin–Born-type effect, acting on quadrupolar molecules and due to both the electric field associated with the light wave and to the static external field gradient, it also involves the rearrangement of the electron density as a consequence of the electron interaction with the electric and magnetic wave vectors associated with the beam and with the externally applied electric field gradient. In this case, mixed electric-dipole, electric-quadrupole, and magnetic-dipole hyperpolarizabilities play their role in determining the strength of the effect. Buckingham birefringence has been often employed for the determination of molecular quadrupole moments (Buckingham 1959; Buckingham and Disch 1963).

For an ideal gas at constant pressure, for light propagating along the Z axis

$$\Delta n = n_X - n_Y = \frac{N_A \nabla F}{15 V_m \epsilon_0} s = \frac{3 \nabla F}{2 V_m} {}_m Q(\omega, T), \quad (11.194)$$

$${}_m Q(\omega, T) = \frac{2 N_A}{45 \epsilon_0} s, \quad (11.195)$$

where  $V_m$  is the molar volume,  $\nabla F$  is the external electric field gradient arranged so that  $\nabla F = \nabla F_{XX} = -\nabla F_{YY}$  and  $\nabla F_{ZZ} = 0$ .  $\blacktriangleright$  Equation 11.195 introduces the Buckingham constant  ${}_m Q$ , which depends through the quantity  $s$  on the circular frequency of the light and on the temperature. For non-dipolar systems, where the quadrupole moment does not depend on the choice of origin,

$$s = b(\omega) + \frac{1}{kT} \Theta_{\alpha\beta} \alpha_{\alpha\beta}(-\omega; \omega), \quad (11.196)$$

involving the molecular quadrupole moment  $\Theta_{\alpha\beta}$  and the frequency-dependent electric dipole polarizability  $\alpha_{\alpha\beta}(-\omega; \omega)$ . The temperature-independent contribution is

$$b(\omega) = B_{\alpha\beta, \alpha\beta}(-\omega; \omega, 0) - \mathcal{B}_{\alpha, \alpha\beta, \beta}(-\omega; \omega, 0) - \frac{5}{\omega} \varepsilon_{\alpha\beta\gamma} J'_{\alpha, \beta, \gamma}(-\omega; \omega, 0), \quad (11.197)$$

and is a combination of three mixed hyperpolarizabilities:

$$B_{\alpha\beta, \gamma\delta}(-\omega; \omega, 0) = \langle\langle \hat{\mu}_\alpha; \hat{\mu}_\beta, \hat{\Theta}_{\gamma\delta} \rangle\rangle_{\omega, 0}, \quad (11.198)$$

$$\mathcal{B}_{\alpha, \beta\gamma, \delta}(-\omega; \omega, 0) = \langle\langle \hat{\mu}_\alpha; \hat{\Theta}_{\beta\gamma}, \hat{\mu}_\delta \rangle\rangle_{\omega, 0}, \quad (11.199)$$

$$J'_{\alpha, \beta, \gamma}(-\omega; \omega, 0) = i \langle\langle \hat{\mu}_\alpha; \hat{m}_\beta, \hat{\mu}_\gamma \rangle\rangle_{\omega, 0}. \quad (11.200)$$

The expressions are somewhat more complex for dipolar fluids (Buckingham and Longuet-Higgins 1968), where the quadrupole moment becomes origin dependent. The formal expression for  $s$ ,  $\blacktriangleright$  Eq. 11.196, does not change provided that we refer to a frequency-dependent origin for the quadrupole operator, commonly labeled as the “effective quadrupole center” (Rizzo and Coriani 2005; Rizzo et al. 2007). For any other choice of the origin we have

$$s = b(\omega) + \frac{1}{kT} \left\{ \Theta_{\alpha\beta} \alpha_{\alpha\beta}(-\omega; \omega) - \mu_\alpha \left[ A_{\beta, \alpha\beta}(-\omega; \omega) + \frac{5}{\omega} \varepsilon_{\alpha\beta\gamma} G'_{\beta\gamma}(-\omega; \omega) \right] \right\}. \quad (11.201)$$

The effective quadrupole center is defined as the point in space where the last term in  $\blacktriangleright$  Eq. 11.201, involving the molecular dipole moment  $\mu_\alpha$  and the mixed polarizabilities  $A_{\alpha,\beta\gamma}(-\omega; \omega)$  and  $G'_{\alpha\beta}(-\omega; \omega)$ , vanishes.

## Magnetic Circular Dichroism

For a medium that is isotropic in the absence of magnetic fields, the Faraday  $A$ ,  $B$ , and  $C$  terms determining the MCD of a transition from the electronic state  $|0\rangle$  to the electronic state  $|n\rangle$  are defined as (Buckingham and Stephens 1966; Schatz and McCaffery 1969; Stephens 1976):

$$A(0 \rightarrow n) = \frac{1}{2} [\langle n | \mathbf{m} | n \rangle - \langle 0 | \mathbf{m} | 0 \rangle] \cdot \mathcal{I}m \left( \langle 0 | \boldsymbol{\mu} | n \rangle \times \langle n | \boldsymbol{\mu} | 0 \rangle \right), \quad (11.202)$$

$$B(0 \rightarrow n) = \mathcal{I}m \left\{ \sum_{k \neq 0} \frac{\langle k | \mathbf{m} | 0 \rangle}{\omega_{k0}} \cdot \langle 0 | \boldsymbol{\mu} | n \rangle \times \langle n | \boldsymbol{\mu} | k \rangle + \sum_{k \neq n} \frac{\langle n | \mathbf{m} | k \rangle}{\omega_{kn}} \cdot \langle 0 | \boldsymbol{\mu} | n \rangle \times \langle k | \boldsymbol{\mu} | 0 \rangle \right\}, \quad (11.203)$$

$$C(0 \rightarrow n) = \frac{1}{2} \langle 0 | \mathbf{m} | 0 \rangle \cdot \mathcal{I}m \left( \langle 0 | \boldsymbol{\mu} | n \rangle \times \langle n | \boldsymbol{\mu} | 0 \rangle \right), \quad (11.204)$$

where an average over the molecular orientations has been made. These tensors correspond to the single residues of the tensors that determine the Verdet constant of the Faraday effect ( $\blacktriangleright$  section “Faraday Effect”). With the convention used here, the Faraday terms given in  $\blacktriangleright$  Eqs. 11.202–11.204 are three times those of Buckingham and Stephens (1966). The  $A$  term exists only if either  $|0\rangle$  or  $|n\rangle$  is degenerate, whereas the  $C$  term is nonvanishing only if  $|0\rangle$  is degenerate.

The  $B$  terms exist in all cases, independently of the appearance of any ground- and excited-state degeneracies. We can rearrange  $\blacktriangleright$  Eq. 11.203 recalling that  $(\hat{\mu}_\alpha)_{lm}^* = (\hat{\mu}_\alpha)_{lm}$ ,  $(\hat{m}_\alpha)_{lm}^* = -(\hat{m}_\alpha)_{lm}$ , and  $\mathcal{I}m(z) = -i(z - z^*)/2$ , and we find that the  $B(0 \rightarrow n)$  term can be written in terms of a single residue of a quadratic response function (Coriani et al. 1999b; Olsen and Jørgensen 1985) as:

$$B(0 \rightarrow n) = i\varepsilon_{\alpha\beta\gamma} \left( \lim_{\omega \rightarrow \omega_{n0}} \hbar(\omega - \omega_{n0}) \langle \langle \hat{\mu}_\gamma; \hat{m}_\beta, \hat{\mu}_\alpha \rangle \rangle_{0,\omega} \right). \quad (11.205)$$

By analogy to the spectral representation expression for the single residue we may also write (Olsen and Jørgensen 1985):

$$\lim_{\omega \rightarrow \omega_{n0}} \hbar(\omega - \omega_{n0}) \langle \langle \hat{\mu}_\gamma; \hat{m}_\beta, \hat{\mu}_\alpha \rangle \rangle_{0,\omega} = M_{\mu_\alpha}^{0 \leftarrow n} M_{m_\beta \mu_\gamma}^{n \leftarrow 0}(0), \quad (11.206)$$

where  $M_{\mu_\alpha}^{0 \leftarrow n}$  and  $M_{m_\beta \mu_\gamma}^{n \leftarrow 0}(0)$  indicate specific one- and (formally) two-photon transition matrix elements between state  $|0\rangle$  and state  $|n\rangle$ , respectively.

In a recent experimental study of the ethylene MCD spectrum (Snyder et al. 2004), the assignment of the transitions was revised. The proposed new assignment is in agreement with earlier ab initio calculations of the  $B$  term in ethylene (Coriani et al. 1999b). Recently, also calculations of the  $A$  term of magnetic circular dichroism appeared (Seth et al. 2004). We also note that both the  $A$  and  $B$  terms come out directly from calculations using the complex polarization propagator approach (Solheim et al. 2008).

## Nuclear Spin-Related Properties

---

In the electronic Schrödinger equation defined by the Hamiltonian of [Eq. 11.2](#), there are no terms dependent on the isotopic species of the nuclei. The electron–nucleus and nucleus–nucleus interactions are described only as interactions of point charges. In particular, no hyperfine interactions dependent on the nuclear magnetic moments are included. To determine molecular properties dependent on the nuclear magnetic dipole moments we thus considered an extension of this Hamiltonian, [Eqs. 11.41–11.43](#), assuming that the magnetically active nuclei are represented by point magnetic dipoles. The related properties of the nucleus – its spin and magnetogyric constant – enter the definitions of the molecular properties as known, constant factors.

All the effects which determine the existence of nuclear magnetic resonance (NMR) spectra are due to the magnetic moments of the nuclei. Each magnetically active nucleus contributes to the magnetic field through the magnetic vector potential [Eq. 11.38](#). In the NMR spectrum we observe the effects due to the interaction of this locally induced magnetic field with the applied external magnetic field and with other magnetically active nuclei in the molecule. The richness of the NMR spectrum arises from the dependence of both these interactions on the electronic structure. Within a molecule, each nucleus is shielded by the electrons, and due to this shielding the effective, local magnetic field differs for different nuclei. Similarly, the interaction of two magnetic dipole moments – determining the spin–spin coupling in NMR spectra – depends not only on the distance between two nuclei, but also on the electronic structure of the molecule. Moreover, in contrast to the direct dipole–dipole interaction, this electron-mediated contribution – the indirect spin–spin coupling tensor – does not vanish in isotropic media. We focus in this section on the calculation of the linear response properties that determine these effects.

Due to the importance of NMR spectroscopy in modern chemical research, the shielding and spin–spin coupling constants are undoubtedly the most important properties which depend on the nuclear spin. Nevertheless, we analyze here also other phenomena proportional to the magnetic moment of a nucleus. The existence of an external magnetic field affects the rotational spectrum; similarly, splittings in the rotational spectrum will also appear due to the field associated with the nuclear magnetic dipole moment and these splittings are described by the nuclear spin–rotation constant (NSRC). Indeed, in high-resolution molecular beam and microwave spectroscopies, the effective Hamiltonians describing the rotational spectrum include the contributions to the rotational energy levels due to the presence of the spin–rotation interactions, as well as the interactions between two nuclear spin–magnetic moments, and the electric field gradients at the nuclei (see Vaara et al. (2002) and references therein for more details).

### NMR Effective Spin Hamiltonian

---

Let us first consider the standard interpretation of the NMR spectrum. The parameters used to define it – the shielding constants and spin–spin coupling constants – are obtained from an effective NMR Hamiltonian  $\mathcal{H}^{\text{NMR}}$ . This operator acts in the space defined by all possible arrangements of the nuclear spins. The eigenvalues of  $\mathcal{H}^{\text{NMR}}$  determine the transition energies as the differences between different nuclear spin states in the molecule, and the eigenvectors

determine the arrangement of the nuclear spins with respect to the external field. The effective NMR Hamiltonian is written as (Abragam 1961):

$$\mathcal{H}^{\text{NMR}} = - \sum_K \mathbf{B}^T (1 - \sigma_K) \mathbf{m}_K + \frac{1}{2} \sum_{K \neq L} \mathbf{m}_K^T (\mathbf{D}_{KL} + \mathbf{K}_{KL}) \mathbf{m}_L, \quad (11.207)$$

where  $\sigma_K$  is the shielding tensor (see [section “Nuclear Magnetic Shielding”](#)) and  $\mathbf{K}_{KL}$  is the reduced indirect spin–spin coupling tensor (see [section “NMR Indirect Spin–Spin Coupling”](#)). We recall that the nuclear magnetic dipole moment is related to the nuclear spin,  $\mathbf{m}_K = \mu_N g_K \mathbf{I}_K$ , see [Eq. 11.25](#). Finally,  $\mathbf{D}_{KL}$  is the direct interaction of the magnetic dipoles. The effective Hamiltonian does not include the  $\mathcal{H}^{\text{Nq}}$  operator, [Eq. 11.122](#), which describes the interactions due to the quadrupole moment of the nucleus and the electric field gradient at the nucleus (as discussed in [section “Electric Field Gradient at the Nucleus, Nuclear Quadrupole Coupling Constant,”](#)  $\mathcal{H}^{\text{Nq}}$  can be related to the contributions quadratic in  $\mathbf{I}_K$ ). The reason for this is that in isotropic media the nuclear quadrupole interaction does not contribute to the nuclear spin energy levels, but only to the relaxation processes in the nuclear spin system – thus, it only affects the shapes of the spectral lines, and not their positions.

The effective NMR Hamiltonian  $\mathcal{H}^{\text{NMR}}$  has no explicit dependence on the electronic structure. It includes two electron-independent contributions, the nuclear Zeeman term  $-\mathbf{B}^T \cdot \mathbf{m}_K$  and the classical direct dipolar coupling of the nuclear magnetic moments  $\mathbf{m}_K^T \mathbf{D}_{KL} \mathbf{m}_L$ . All the effects of the electronic structure are incorporated in the nuclear magnetic shielding tensors  $\sigma_K$ , and the reduced indirect nuclear spin–spin coupling tensors  $\mathbf{K}_{KL}$ .

In order to calculate the shielding and indirect spin–spin coupling tensors, we employ the perturbation expansion of the molecular Hamiltonian, discussed in [section “The Molecular Hamiltonian.”](#) As indicated by [Eq. 11.207](#), in the perturbation expansion of the Schrödinger equation we have to consider all contributions that are either linear or bilinear in  $\mathbf{B}$  and  $\mathbf{m}_K$  for the shielding constants, and those linear or bilinear in  $\mathbf{m}_K$  and  $\mathbf{m}_L$  for the indirect spin–spin coupling constants. Since the perturbing operators are time independent, both the shielding and spin–spin coupling tensors can be expressed as energy derivatives.

For a rotating molecule in an isotropic medium, the NMR spin Hamiltonian may be written as (assuming the external magnetic field is directed along the  $Z$  axis):

$$\mathcal{H}_{\text{iso}}^{\text{NMR}} = - \sum_K B (1 - \sigma_K) m_{K,Z} + \frac{1}{2} \sum_{K \neq L} K_{KL} \mathbf{m}_K^T \cdot \mathbf{m}_L. \quad (11.208)$$

The direct spin–spin couplings  $\mathbf{D}_{KL}$  are purely anisotropic and vanish in the rotational averaging, while for the shielding and indirect spin–spin coupling tensors the averaging leads to what is commonly referred to as the nuclear shielding constants  $\sigma_K$  and the reduced indirect nuclear spin–spin coupling constants  $K_{KL}$ :

$$\sigma_K = \frac{1}{3} \text{Tr } \sigma_K, \quad (11.209)$$

$$K_{KL} = \frac{1}{3} \text{Tr } \mathbf{K}_{KL}. \quad (11.210)$$

The name “scalar coupling” is sometimes used for the indirect spin–spin interaction; this is rather unfortunate, and one should keep in mind that we discuss a tensor even when the individual components are not observed.

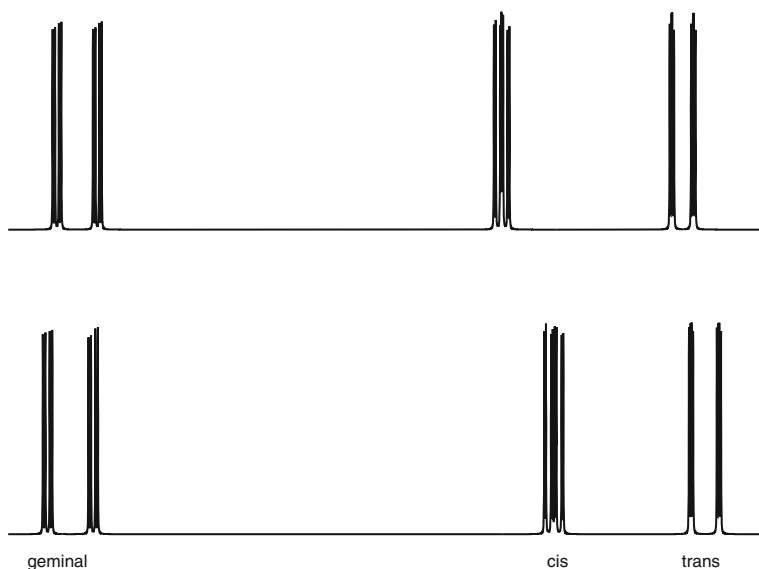
The numerical values of the shielding and indirect spin–spin coupling constants are determined in experiment by fitting the solutions of the nuclear spin equation with the effective

Hamiltonian  $\blacktriangleright$  Eq. 11.208 to the observed spectrum. The NMR spin Hamiltonian is usually not expressed in terms of the reduced indirect spin–spin coupling tensors  $\mathbf{K}_{KL}$ , but rather in terms of the indirect spin–spin coupling tensors  $\mathbf{J}_{KL}$ , which are related to the reduced tensors as:

$$\mathbf{J}_{KL} = \frac{1}{h} \mu_N g_K \mu_N g_L \mathbf{K}_{KL}. \quad (11.211)$$

The reduced coupling tensors  $\mathbf{K}_{KL}$  are independent of the nuclear  $g$  factors, and therefore, in contrast to  $\mathbf{J}_{KL}$ , can be used to compare the strengths of the couplings between nuclei with different  $g_K$  values.

An example of an NMR spectrum is shown in  $\blacktriangleright$  Fig. 11-3. The positions of the three groups of peaks are determined by the shielding constants and the fine structure within each group of peaks is determined by the spin–spin coupling constants. Both proton spectra have been simulated assuming no coupling to C atoms (i.e., for  $^{12}\text{C}$ ). We note here that the changes in the energy levels due to the screening of the nuclear magnetic moments, reflected in the magnetic shielding constants, depend on the external magnetic field induction, whereas the changes induced by the spin–spin coupling constants (the splitting within each group of lines) are independent of the external magnetic field induction.



$\blacksquare$  Fig. 11-3

Simulated 500 MHz proton NMR spectra of  $\text{C}_2\text{H}_3\text{F}$ . *Top* – ab initio, *bottom* – experimental values of shielding and spin–spin coupling constants. The labels define the position of the relevant proton with respect to the fluorine. The shielding constants and the Fermi contact contributions to the coupling constants were computed at the CCSD level, the other theoretical values are taken from Helgaker et al. (1997), where the experimental data were also discussed



## Nuclear Magnetic Shielding

The nuclear magnetic shielding tensor  $\sigma_K$  can be determined from the equation:

$$\left. \frac{\partial^2 E(\mathbf{B}, \mathbf{m}_K)}{\partial \mathbf{B} \partial \mathbf{m}_K} \right|_{\mathbf{B}=0, \mathbf{m}_K=0} = \sigma_K - \mathbf{1}, \quad (11.212)$$

where the second term represents the direct Zeeman interaction between the nucleus and the field. From the form of the energy derivative, as well as the bilinear nature of the interaction described by the shielding tensor appearing in the effective NMR Hamiltonian, it is clear that in the molecular Hamiltonian the terms that are linear and bilinear in the external magnetic field induction and the nuclear magnetic moments should be considered. Collecting them and writing the contributions in terms of expectation values and response functions, we find for closed-shell systems:

$$\sigma_{K,\alpha\beta} = \langle 0 | \hat{H}_{\alpha\beta}^{B,K} | 0 \rangle + \langle \langle \hat{H}_{\alpha}^B; \hat{H}_{\beta}^{K(\text{PSO})} \rangle \rangle = \sigma_{K,\alpha\beta}^{\text{dia}} + \sigma_{K,\alpha\beta}^{\text{para}}. \quad (11.213)$$

As for the magnetizability, there are two contributions to the shielding: the so-called diamagnetic contribution  $\sigma_K^{\text{dia}}$ , which is obtained as the expectation value  $\langle 0 | \hat{H}_{\alpha\beta}^{B,K} | 0 \rangle$  and the paramagnetic contribution  $\sigma_K^{\text{para}}$ , calculated as a linear response function  $\langle \langle \hat{H}_{\alpha}^B; \hat{H}_{\beta}^{K(\text{PSO})} \rangle \rangle$ .

The shielding tensor is a nonsymmetric tensor of rank two. The principal axis system (PAS) is determined by the diagonalization of the symmetric part of the tensor. The shielding constant, already introduced in [Eq. 11.209](#), is defined as the isotropic part; we can also define the anisotropy (Smith et al. 1992)

$$\sigma_{\text{anis}} = \sigma_{33}^{\text{PAS}} - \frac{1}{2}(\sigma_{11}^{\text{PAS}} + \sigma_{22}^{\text{PAS}}), \quad (11.214)$$

as well as the asymmetry:

$$\eta_{\text{asym}} = \frac{(\sigma_{22}^{\text{PAS}} - \sigma_{11}^{\text{PAS}})}{(\sigma_{33}^{\text{PAS}} - \sigma_{\text{iso}}^{\text{PAS}})}, \quad (11.215)$$

where it is assumed for the principal axis components of the shielding tensor that  $\sigma_{33}^{\text{PAS}} \geq \sigma_{22}^{\text{PAS}} \geq \sigma_{11}^{\text{PAS}}$ . Unfortunately, there are different conventions for the ordering of the principal shielding axes which can lead to much confusion when comparing literature values of anisotropies and asymmetries. To circumvent these problems it has been proposed that shielding tensor results should be reported in terms of the span and the skew, defined as (Mason 1993):

$$\Omega_{\text{span}} = \sigma_{33}^{\text{PAS}} - \sigma_{11}^{\text{PAS}}, \quad (11.216)$$

$$\kappa_{\text{skew}} = \frac{3(\sigma_{\text{iso}} - \sigma_{22}^{\text{PAS}})}{\Omega_{\text{span}}}. \quad (11.217)$$

The antisymmetric part does not affect the standard NMR spectrum (that is why the rank-1 tensor has been disregarded above); however, it affects the relaxation rates (Anet et al. 1990).

Since the magnetic dipole operator appears in the expression for the paramagnetic contribution to the shielding tensor, the calculated quantity will depend on the choice of a global gauge origin. Similarly, for the diamagnetic contribution an origin dependence can easily be seen from the definition of the operator  $\hat{H}^{B,K}$  in [Eq. 11.48](#). Hence, the partitioning of the nuclear shielding into dia- and paramagnetic contributions depends on the choice of global

gauge origin. Any interpretation attributed to the individual contributions is, therefore, limited to the applied computational approximation – in particular, care should be exercised when results for different nuclei in different molecules are compared. When the gauge origin is chosen to be the nucleus of study, the paramagnetic contribution to the shielding tensor is related to the electronic contribution to the nuclear spin-rotation constant; see [▶ Eq. 11.231](#) below. We note, however, that this relation is true only in a nonrelativistic approach.

The dependence of the dia- and paramagnetic contributions to the shielding on a global gauge origin means that in approximate calculations the nuclear magnetic shielding tensors will display a dependence on a gauge origin. This can be avoided through the introduction of local gauge origins, as described in [▶ section “Magnetic Properties.”](#) In addition to the London orbital approach other methods have also been applied to enable the calculation of origin-independent nuclear magnetic shielding constants, such as the individual gauge for localized orbitals (IGLO) method developed by Kutzelnigg (Kutzelnigg 1980; Schindler and Kutzelnigg 1982) and various continuous transformation of the origin of the current density (CTOCD) methods developed by Lazzeretti, Malagoli, and Zanasi (Lazzeretti and Zanasi 1996; Lazzeretti et al. 1994; Zanasi et al. 1995).

The shielding constant is dimensionless, and is expressed in ppm (parts per million). This unit reflects the role of the shielding in comparison to the electron-independent direct Zeeman interaction of the nuclear magnetic moment with the external field ([▶ Eq. 11.208](#)). We can get a physical understanding of the nuclear shielding by considering that the electrons in the molecule create an additional magnetic field, acting as a correction proportional to the external field and leading to the local magnetic field

$$\mathbf{B}_K^{\text{loc}} = (\mathbf{1} - \sigma_K) \mathbf{B}. \quad (11.218)$$

When  $\sigma_K$  is positive, it means that the presence of electrons leads to a decreased local magnetic field experienced by the nuclear magnetic moments – that is, the electron density shields the nuclear magnetic moments from the external magnetic field, a concept that explains the origins of the term shielding constant (we note that shielding constants can also be negative). The values of the shielding constants for various elements differ widely, as do their variations with molecular structure. In general the variation of the shielding constants increases with increasing atomic number – ranging from 10–10<sup>2</sup> ppm for light atoms to  $\approx 10^4$  ppm for Pb (see also [▶ Table 11-11](#)). The range of shielding constants for a particular nucleus is relevant when we compare the computed and experimental spectra, for instance to assign the peaks in the NMR spectrum to specific nuclei. The required accuracy for the shielding of hydrogen may be  $\approx 0.1$  ppm, whereas for carbon or nitrogen nuclei it may be sufficient to obtain results accurate to  $\approx 5$  ppm.

Let us also briefly consider the shielding constants in paramagnetic molecules. In this case we have a total electron spin  $S$  which implies a set of  $2S + 1$  degenerate spin states. These different states will be split when an external magnetic field is applied to the sample. The ensemble average of the projection of the spin operator along the  $Z$  axis can be obtained in much the same way as the magnetization induced in a molecular sample containing unpaired electrons as:

$$\langle S_Z \rangle = -\frac{g_e}{2} \frac{S(S+1)}{3kT} B_Z. \quad (11.219)$$

The total magnetic moment of the electrons becomes directly proportional to the external magnetic field induction, and thus additional contributions to the nuclear shielding constant arise,

Table 11-11

Absolute shielding (in ppm) of selected nuclei in commonly used standard reference molecules<sup>a, b</sup>

NMR standard		Primary source	Absolute shielding		Shift $\delta$	
Nucleus, standard	Absolute shielding					
<sup>1</sup> H in TMS(l)	32.873	H <sub>2</sub>	26.2886	Sundholm and Gauss (1997)	6.584	Jackowski et al. (2010)
<sup>13</sup> C in TMS(l)	186.37	CO	0.6	Raynes et al. 1989	185.77	Jackowski et al. (2000)
<sup>15</sup> N in CH <sub>3</sub> NO <sub>2</sub> (l)	-135.8	NH <sub>3</sub>	264.54	Jameson et al. 1981	-400.34	Jameson et al. 1981
<sup>17</sup> O in H <sub>2</sub> O(l)	287.5	CO	-62.74	Wasylishen and Bryce (2002)	350.2	Wasylishen and Bryce (2002)

<sup>a</sup>See the references for experimental details and error bars

<sup>b</sup>Gas phase NMR or isolated molecule ab initio values for primary source, (l) = liquid

since we need to consider new terms linear and bilinear in the nuclear and electronic magnetic moments. From the terms in the molecular Hamiltonian introduced in section “Small Terms Due to the Vector Potential in the Hamiltonian” we see that these are the hyperfine interactions involving the Fermi contact and spin–dipole operators,  $\hat{H}^{K(\text{FC})}$  and  $\hat{H}^{K(\text{SD})}$  given in Eqs. 11.51 and 11.52, respectively. Using the ensemble average for the spin-projection given in Eq. 11.219, we find that the contributions to the nuclear shielding constants due to these hyperfine interactions are (Rinkevicius et al. 2003):

$$\sigma_{K,\alpha\beta}^{\text{con,FC}} = \frac{4\mu_B^2}{3kT} S(S+1) \langle 0 | \hat{H}_{\alpha\beta}^{K(\text{FC})} | 0 \rangle, \quad (11.220)$$

$$\sigma_{K,\alpha\beta}^{\text{con,SD}} = \frac{4\mu_B^2}{3kT} S(S+1) \langle 0 | \hat{H}_{\alpha\beta}^{K(\text{SD})} | 0 \rangle. \quad (11.221)$$

These contributions are closely related to the hyperfine interactions observed in ESR spectroscopy (see section “ESR Hyperfine Coupling Tensors”). The above expressions have been derived assuming  $kT$  to be much larger than the separation of the different electronic spin states. We have also for simplicity ignored higher-order corrections arising from the spin-orbit interaction, which for many open-shell species can be quite significant.

It is worth noticing that the so-called contact contributions to the nuclear shielding tensor, Eqs. 11.220 and 11.221, are temperature dependent, and thus behave differently than the orbital contributions. Experimentally, the contact contributions are often quite large and assumed to vary much more with molecular structure than the dia- and paramagnetic contributions, and thus these latter two terms are often assumed constant in different chemical species or taken to be identical to closely related closed-shell molecules. However, theoretical studies have shown that this is a rather crude approximation, and it may fail to correctly describe the total shifts due to the contact and orbital terms (Rinkevicius et al. 2003).

A direct comparison of calculated shielding constants with experiment is hampered by the difficulty in experimentally determining the absolute shielding constants calculated by theory. The lack of experimental data for absolute shielding constants has many origins: first, the shielding constant is defined as a correction to the direct interaction between the external magnetic

field induction and the bare nuclear magnetic moment. However, it is impossible to experimentally determine this direct interaction. Moreover, determining the magnetic field induction of an NMR spectrometer with sufficient accuracy is difficult.

The shielding constant can be considered as a measure of the local field experienced by a nuclear magnetic moment due to the shielding of the external magnetic field by the electron density. The *relative* difference in the local magnetic fields around different nuclei provides similar information and for this reason experimental NMR studies report the *chemical shift*  $\delta_K$  defined as:

$$\begin{aligned}\delta_K &= \frac{\sigma_K(\text{reference}) - \sigma_K(\text{sample})}{1 - \sigma_K(\text{reference})} \\ &\cong \sigma_K(\text{reference}) - \sigma_K(\text{sample}).\end{aligned}\quad (11.222)$$

The trends for the absolute shielding are thus reversed to those for the chemical shift – that is,  $\delta_K < \delta_L$  means that the nucleus  $K$  is more shielded than nucleus  $L$ . The chemical shifts are taken relative to the shielding in a selected molecule (see [Table 11-11](#)); for instance, liquid tetramethylsilane (TMS) is used as a standard reference for  $^{13}\text{C}$ . Unfortunately, large molecules in solution or in condensed phase are chosen for many nuclei to define experimental chemical shifts. It is not yet possible to perform benchmark calculations for these standard systems; moreover, it is often not even possible to compute the shielding in these reference compounds at the same level of accuracy as for smaller molecules that are of interest.

There is a semi-experimental approach for determining absolute shielding scales, based on the relationship between the paramagnetic shielding constant and the nuclear spin-rotation constants, as indicated in [Eq. 11.231](#) below. The absolute shielding constants have been used to obtain the magnetic dipole moments of bare nuclei from NMR spectra – in this case, it is not sufficient to measure the chemical shifts. Similarly to the electric quadrupole moments, improved values of the nuclear magnetic dipole moments can now be determined applying increasingly accurate absolute shielding constants obtained in *ab initio* calculations for small molecules (Jaszuński and Jackowski 2008).

The use of perturbation-dependent basis sets is mandatory in theoretical studies of nuclear shielding constants. This is particularly important in order to ensure that the calculated shielding constants are independent of the choice of gauge origin. At the same time, for smaller basis sets, the use of perturbation-dependent basis sets improves basis set convergence compared to calculations only employing conventional basis sets. Moreover, the convergence may be significantly improved by applying property-optimized basis sets, such as the pcS-n basis sets optimized by Jensen for DFT calculations of the shielding constants (Jensen 2008).

For atomic systems, theory can determine rather accurately the absolute shielding constants. First, fairly large nonelectronic contributions such as the zero-point vibrational corrections are absent. Secondly, because of symmetry only the diamagnetic term – an expectation value, which is much easier to compute than an accurate value of the response function – contributes. For instance, for the hydrogen atom the nonrelativistic shielding constant can be calculated as:

$$\sigma^{\text{dia}} = \alpha_{\text{fs}}^2 \frac{e^2}{3m_e} \left\langle 0 \left| \frac{1}{r_{iK}} \right| 0 \right\rangle = 17.750454 \text{ ppm}.\quad (11.223)$$

In a similar manner, explicitly correlated calculation of the  $1/r_{iK}$  expectation value leads to an absolute shielding constant for the helium atom of 59.9367794 ppm (Drake 2006) (the most accurate value obtained in a recent study including relativistic, quantum-electrodynamic, and nuclear mass effects is  $\sigma_{\text{He}} = 59.96743$  ppm (Rudziński et al. 2009)). For all the rare-gas atoms the

shielding constants have been computed using a four-component relativistic approach (Vaara and Pyykkö 2003). The calculations were performed within the Dirac–Hartree–Fock approximation and, if we assume that the electron correlation effects are small, they provide the shielding scale for the rare gas atoms.

The development of efficient methods – using perturbation-dependent basis sets and highly correlated wave functions for the calculation of nuclear magnetic shieldings – has allowed in practice to reach high accuracy also for shielding constants in molecules (see the reviews by Gauss and Stanton 2002 and Helgaker et al. 1999). For instance, the use of carefully chosen basis sets with the CCSD(T) method has enabled calculations of the equilibrium shielding constants with an accuracy of about 1–3 ppm for  $^{13}\text{C}$  shieldings in a range of molecules (Auer et al. 2003). Most importantly, it has been demonstrated that systematic convergence of the results with improvement in the level of the calculation can be achieved. In order to obtain highly accurate shielding constants comparable with experiment, in addition to the effects of electron correlation, vibrational effects also have to be considered. The latter are obviously mandatory to estimate the isotopic substitution effects, since for a fixed molecular geometry the shielding constants are independent of the nuclear masses. The most accurate and reliable results are presently obtained in this manner – within the CCSD(T) approach, applying GIAOs and taking into account the vibrational effects [see for instance a recent  $^{19}\text{F}$  shielding study (Harding et al. 2008a)]. CCSD(T) shielding constants may be computed for increasingly large molecules, as shown by benzene calculations with basis sets including up to 474 functions (Harding et al. 2008b). Higher-order coupled-cluster methods have also been developed, but so far their application has been limited to small molecules (Kállay and Gauss 2004). At the HF or DFT level, shielding constants may nowadays be computed for molecules with more than 1,000 atoms, with basis sets including over 10,000 functions (Kussmann and Ochsenfeld 2007; Ochsenfeld et al. 2004).

In practice, care should be exercised when using the data of [Table 11-11](#) to analyze experimental chemical shifts and computed absolute shielding values. The differences between various levels of approximation in the theory are often difficult to foresee, and variations of the experimental conditions may also lead to unpredictable changes in the shielding. When a particular approximation is used in a sequence of calculations, a comparison of the calculated chemical shifts with the corresponding experimental data might be more appropriate. Moreover, whereas there is no guarantee that zero-point vibrational effects or changes due to intermolecular interactions will be identical for nuclei of interest in two molecules (or even within a single molecule), one may expect that these effects partly cancel out for two nuclei (Ruud et al. 2001), and thus that higher accuracy may be achieved for chemical shifts than for absolute shielding constants.

To obtain the shielding constants in ppm, the computed values in a.u. are multiplied by  $10^6 \times \alpha_{\text{fs}}^2 \cong 53.25136$ .

## Shielding Derivatives

The nuclear shielding depends, as does the molecular energy itself, on additional sources of perturbations, such as electric and magnetic fields. Assuming these perturbations to be static, we may perform a Taylor expansion of the nuclear shielding tensor in the presence of the additional perturbations. As the simplest example, let us mention the perturbation–induced changes

in the shielding in the presence of a static electric field. They can be described in terms of so-called shielding polarizabilities (a review was given by Raynes 1996), where for instance the first shielding polarizability is given by:

$$\left. \frac{\partial \sigma_K(\mathbf{F})}{\partial \mathbf{F}} \right|_{\mathbf{F}=0} = \left. \frac{\partial^3 E(\mathbf{B}, \mathbf{m}_K, \mathbf{F})}{\partial \mathbf{B} \partial \mathbf{m}_K \partial \mathbf{F}} \right|_{\mathbf{B}, \mathbf{m}_K, \mathbf{F}=0} = \langle \langle \hat{H}^{B,K}; \boldsymbol{\mu} \rangle \rangle + \langle \langle \hat{H}^B; \hat{H}^{K(\text{PSO})}, \boldsymbol{\mu} \rangle \rangle. \quad (11.224)$$

We note that there is a route to origin-independent shielding polarizabilities, as the combination of origin-independent linear response calculations of the shielding constant in the presence of a finite electric field can be used in a finite-field procedure. This allows for the calculation of origin-independent shielding polarizabilities using for instance London atomic orbitals (Rizzo and Gauss 2002).

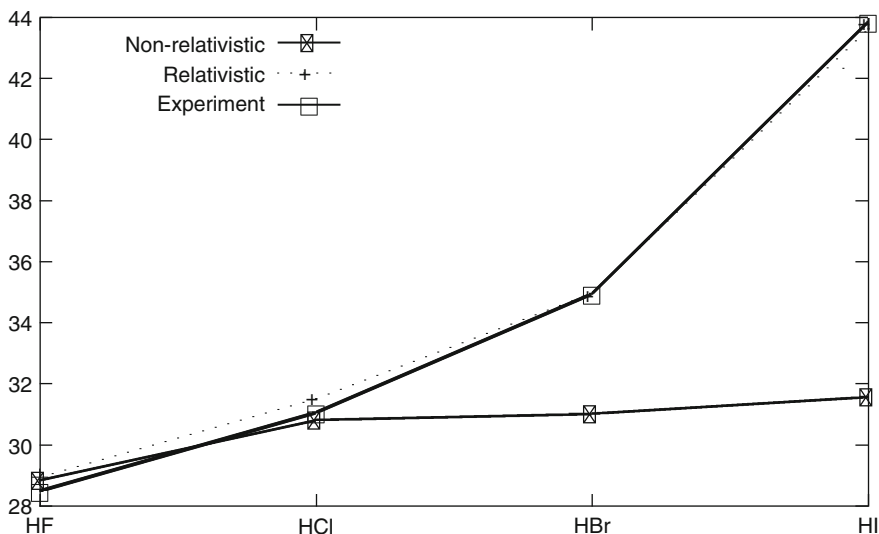
### Spin-Orbit Corrections to Nuclear Magnetic Shielding

The formalism presented above for calculating the nuclear shielding constants works well for molecules containing elements from the first two or three rows of the periodic table. However, when the molecule contains heavier nuclei, this formalism may fail to reproduce correctly even the qualitative features of all the shielding constants, also for light elements such as hydrogen or carbon in a molecule. A classic example of this failure of  $\blacklozenge$  Eq. 11.213 is shown in  $\blacklozenge$  Fig. 11-4, which illustrates the hydrogen shielding in the hydrogen halides. Whereas the hydrogen shielding observed experimentally increases strongly with increasing atomic number, only a small increase is observed when  $\blacklozenge$  Eq. 11.213 is used to calculate the shielding constants. The reason for this failure can be traced to relativistic effects, and in the case of the hydrogen shielding in  $\blacklozenge$  Fig. 11-4 to the effects of the spin-orbit interactions.

Some of the most important relativistic effects – such as the discussed spin-orbit contributions to the shielding of light elements bonded to heavy atoms – can be calculated using perturbation theory, beginning with the nonrelativistic treatment and considering the spin-orbit operator as an additional perturbation representing one of the relativistic corrections. The spin-orbit operator provides a coupling between the orbital magnetic moment of the electron, in the case of NMR induced by an external magnetic field induction, and either its own or another electron's spin-magnetic moment. This induced spin-magnetic moment may in turn interact with the nuclear magnetic moments through the Fermi contact ( $\blacklozenge$  Eq. 11.51) or spin-dipolar ( $\blacklozenge$  Eq. 11.52) mechanism. These contributions involve three perturbing operators, and they are thus proportional to quadratic response functions such as  $\langle \langle \hat{H}^{K(\text{FC})} + \hat{H}^{K(\text{SD})}; \hat{H}^{\text{SO}}, \hat{H}^{\text{B}} \rangle \rangle$ .

In addition, in the presence of an external magnetic field there is a term in the spin-orbit operator which is proportional to the external magnetic field induction (we recall here the discussion of the general form of the spin-orbit operators in  $\blacklozenge$  section “Small Terms Due to the Vector Potential in the Hamiltonian,”  $\blacklozenge$  Eqs. 11.58–11.60). The operator  $\hat{H}^{\text{SO}, \text{B}^{(n)}}$  can in turn interact with the Fermi contact and spin-dipole operators, leading to second-order contributions to the shielding tensor which are proportional to triplet linear response functions (Vaara et al. 1999) of the form  $\langle \langle \hat{H}^{K(\text{FC})} + \hat{H}^{K(\text{SD})}; \hat{H}^{\text{SO}, \text{B}^{(n)}} \rangle \rangle$ .

For the shielding constants of the heavy elements themselves, relativistic effects arising from the other terms in the Breit–Pauli Hamiltonian (see  $\blacklozenge$  section “The Molecular Breit–Pauli Hamiltonian”) are in general found to be more important than the spin-orbit corrections (Manninen et al. 2003). In general, relativistic effects on the heavy-atom shielding are due to a large number of contributions (Fukui et al. 1996; Ruiz de Azúa et al. 2003) in contrast to



■ Fig. 11-4

The proton shielding constants (in ppm) in the HX series (X = F, Cl, Br, I) calculated with and without spin-orbit coupling contributions. Also included are the available experimental data. The theoretical data are CASSCF results from Vaara et al. (1998)

the hydrogen shieldings in molecules containing heavy elements, which are dominated by the spin-orbit corrections. Although there have been several studies of scalar relativistic effects on shielding, yielding results in good agreement with four-component Dirac–Hartree–Fock methods, the Breit–Pauli Hamiltonian is not variationally bound and thus the perturbation theory approach may fail for heavy elements.

## Nuclear Spin Rotation Constants

The interaction between the nuclear magnetic dipole and the effective magnetic field of a rotating molecule at that nucleus leads to a splitting in the rotational spectrum (Flygare 1974; Gauss et al. 1996). This splitting is usually expressed in terms of the nuclear spin  $\mathbf{I}_K$  and the total rotational angular momentum  $\mathbf{J}$  as

$$\Delta E_K = -\mathbf{I}_K^T \mathcal{M}_K \mathbf{J}, \quad (11.225)$$

where  $\mathcal{M}_K = \mathcal{M}_K^{\text{el}} + \mathcal{M}_K^{\text{nucl}}$  is the nuclear spin–rotation tensor in the Born–Oppenheimer approximation. More precisely, the energy shift depends on the nuclear magnetic moment interacting with the magnetic field induced by the molecular rotation, so we shall proceed from the equivalent equation,

$$\Delta E_K = -\frac{2\pi}{\mu_{\text{NGK}}} \mathbf{m}_K^T \mathcal{M}_K \mathbf{J}. \quad (11.226)$$

The electronic contribution  $\mathcal{M}_K^{\text{el}}$  is a second-order property

$$\mathcal{M}_K^{\text{el}} = -\frac{\mu_N g_K}{2\pi} \left. \frac{\partial^2 E^{\text{el}}}{\partial \mathbf{m}_K \partial \mathbf{J}} \right|_{\mathbf{m}_K, \mathbf{J}=0}, \quad (11.227)$$

and thus it can be obtained from the linear response function  $\mathbf{I}^{-1} \langle \langle \hat{H}^{K(\text{PSO})}; \hat{l}_K \rangle \rangle$ , where  $\mathbf{I}$  is the moment-of-inertia tensor and the angular momentum is evaluated with respect to nucleus  $K$ . The nuclear contribution is

$$\mathcal{M}_K^{\text{nucl}} = \alpha_{\text{fs}}^2 \mu_N g_K \sum_{L \neq K} Z_L \frac{R_{LK}^2 \mathbf{1} - \mathbf{R}_{LK} \mathbf{R}_{LK}^T}{R_{LK}^3} \mathbf{I}^{-1}. \quad (11.228)$$

The principal axes of the nuclear spin–rotation tensor are determined by the molecular moment of inertia. Indeed, the magnetic moment induced by the rotational motion is well defined only in the rotation frame. Spin–rotation constants are related to the difference between the total shielding (for instance obtained using LAOs) and the diamagnetic part of the shielding derived from a conventional calculation with  $\mathbf{R}_K$  as the global gauge origin,  $\sigma_K^{\text{dia}}(\mathbf{R}_K)$ ,

$$\mathcal{M}_K^{\text{el}} = \mathcal{M}_K - \mathcal{M}_K^{\text{nucl}} = \frac{\hbar}{\mu_B} \frac{\mu_N g_K}{2\pi} \left[ \sigma_K - \sigma_K^{\text{dia}}(\mathbf{R}_K) \right] \mathbf{I}^{-1} \quad (11.229)$$

in analogy with our definition of the paramagnetic magnetizability,  $\blacktriangleright$  Eq. 11.149. Hence,  $\mathcal{M}_K^{\text{el}}$  is related to the correspondingly defined paramagnetic shielding:

$$\sigma_K^{\text{para}}(\mathbf{R}_K) = \langle \langle -\mathbf{m}(\mathbf{R}_K); \hat{H}^{K(\text{PSO})} \rangle \rangle, \quad (11.230)$$

as (Flygare 1974):

$$\sigma_K^{\text{para}}(\mathbf{R}_K) = \frac{\mu_B}{\hbar} \frac{2\pi}{\mu_N g_K} \mathcal{M}_K^{\text{el}} \mathbf{I}. \quad (11.231)$$

The additional contributions to the spin–rotation constants arising in paramagnetic molecules have been discussed by Minaev et al. (2003).

As the spin–rotation interaction splits lines in the rotational spectrum, the unit of the spin–rotation constant is kHz.

## NMR Indirect Spin–Spin Coupling

The interaction of the magnetic dipoles of two nuclei, including also the classic dipolar interaction between the bare nuclei, can be determined (compare  $\blacktriangleright$  section “NMR Effective Spin Hamiltonian”) from perturbation theory as the second derivative of the energy

$$\left. \frac{\partial^2 E(\mathbf{m}_K, \mathbf{m}_L)}{\partial \mathbf{m}_K \partial \mathbf{m}_L} \right|_{\mathbf{m}_K=0, \mathbf{m}_L=0} = \mathbf{K}_{KL} + \mathbf{D}_{KL}, \quad (11.232)$$

where  $\mathbf{K}_{KL}$  is the reduced indirect spin–spin coupling tensor given as the derivative of  $E^{\text{el}}(\mathbf{m}_K, \mathbf{m}_L)$ , and  $\mathbf{D}_{KL}$  describes the direct interaction of two nuclear dipoles. The reduced spin–spin coupling constants, independent of the nuclear magnetogyric ratios, should be used (for instance) to compare the strength of the coupling between pairs of different nuclei, and to analyze relative accuracies of calculated constants.



In standard gas- or liquid-phase NMR spectra the interaction of magnetic dipoles leads to a splitting of the lines of the spectrum, described by the NMR indirect spin–spin coupling constant  $J_{KL}$ . This constant is the trace of the tensor (● 11.211):

$$J_{KL} = \frac{1}{h} \mu_N g_K \mu_N g_L \mathbf{K}_{KL}.$$

The total spin–spin coupling tensor includes (see, e.g., Vahtras et al. 1992b) the so-called diamagnetic spin-orbit contribution  $-\langle 0 | \hat{H}^{K,L(\text{DSO})} | 0 \rangle$  – obtained as the expectation value of the corresponding operator (● 11.49), and a sum of linear response terms  $\langle\langle \hat{H}^{K(\text{PSO})}; \hat{H}^{L(\text{PSO})} \rangle\rangle$  and  $\langle\langle \hat{H}^{K(\text{FC})} + \hat{H}^{K(\text{SD})}; \hat{H}^{L(\text{FC})} + \hat{H}^{L(\text{SD})} \rangle\rangle$ .

The paramagnetic spin-orbit operator  $\hat{H}^{K(\text{PSO})}$  (● 11.46) does not depend on electron spin, whereas the Fermi contact  $\hat{H}^{K(\text{FC})}$  and spin–dipole  $\hat{H}^{K(\text{SD})}$  operators (● Eqs. 11.51, ● 11.52) are electron-spin dependent. Therefore, as shown for instance by the sum-over-states description, in the calculation of the PSO term only singlet excited states have to be considered. In contrast, the FC–FC, SD–SD, and mixed FC–SD contributions depend on the triplet excited states. This leads to computational difficulties when the reference state function is not stable with respect to triplet perturbations. For instance, when the HF approximation is used to describe the reference state, completely meaningless results may be obtained.

$J_{KL}$  is an asymmetric tensor, and the different terms (DSO, PSO, SD, FC, and mixed SD–FC) yield contributions of different symmetry. For example, the term  $\langle\langle \hat{H}^{K(\text{FC})}; \hat{H}^{L(\text{FC})} \rangle\rangle$  is fully isotropic, whereas the terms  $\langle\langle \hat{H}^{K(\text{FC})}; \hat{H}^{L(\text{SD})} \rangle\rangle$  are fully anisotropic. Therefore, if we are only interested in the isotropic value of the spin–spin coupling constant, we can express it as the sum of four contributions:

$$J_{KL} = J_{KL}^{\text{DSO}} + J_{KL}^{\text{PSO}} + J_{KL}^{\text{SD}} + J_{KL}^{\text{FC}}, \quad (11.233)$$

and we do not need to compute the SD–FC terms. They have to be included when all the tensor components are required (see Buckingham and Love (1970), Buckingham et al. (1982), Jameson (1987) for details).

In addition to NMR spectra, microwave spectra also may provide information on the spin–spin coupling (Vaara et al. 2002). In particular, for diatomic molecules accurate data can be obtained from molecular beam electric and magnetic resonance when the splitting of a single rotational–vibrational state can be observed. One of the parameters of this splitting (usually called  $c_4$ ) is equal to the isotropic value of the indirect spin–spin coupling tensor, another one ( $c_3$ ) depends both on the direct coupling ( $\propto R_{KL}^{-3}$ ) and on the anisotropy of the tensor.

In contrast to the shielding constants, London orbitals are neither needed nor used in any calculation of spin–spin coupling constants. There is no dependence of the perturbing operators on the external magnetic field and thus no gauge origin problem.

The basis-set dependence of the Fermi contact term has been often a source of problems in the calculation of spin–spin coupling constants. To describe properly the response to the  $\delta(\mathbf{r}_{iK})$  perturbation we need a basis set which is sufficiently flexible in the region of the nucleus. An illustration of the slow convergence of computed  $J^{\text{FC}}$  values for the simplest example – the HD molecule – is given in ● Table 11-12. We can see that practically only the last added function does not affect the result, whereas there are very few other properties where an *s*-type function with so high exponents as 150,000 would be needed for the H atom.

In general, two modifications of the standard energy-optimized basis sets are needed: the standard functions should be uncontracted and tight *s*, *p*, and *d* functions should be added. The *s*-type functions are of particular importance for the Fermi contact contribution, whereas

■ Table 11-12

The Fermi contact contribution to the spin–spin coupling constant of HD (in Hz), calculated using the CCSD Polarization Propagator Approximation (Oddershede et al. 1988)

Basis set <sup>a</sup>	Added <i>s</i> -function exponent	$J^{FC}$
10s6p2d		38.98
11s6p2d	5,000	39.24
12s6p2d	15,000	39.69
13s6p2d	50,000	39.77
14s6p2d	150,000	39.93
15s6p2d	500,000	39.94

<sup>a</sup>Gaussian-type functions. The effects of additional functions of *p*- and *d*-type symmetry are negligible

■ Table 11-13

$C_2H_2$ , all the contributions to the spin-spin coupling constants (in Hz)<sup>a</sup>

	$^1J(CC)$	$^1J(CH)$	$^2J(CH)$	$^3J(HH)$
DSO	0.01	0.31	−1.35	−3.59
PSO	6.67	−0.84	5.58	4.80
SD	9.04	0.43	1.02	0.57
FC	172.34	247.40	47.77	9.43
Total	188.07	247.29	53.02	11.22

<sup>a</sup>Jaszuński and Ruud (2001), RASSCF-1/cc-pCVQZsu2 results

other functions may be more relevant for the other contributions. Various basis sets constructed in this way have been successfully used in ab initio and DFT calculations; further improvement of convergence with the basis set extension is achieved reoptimizing the exponents and contraction coefficients (Benedikt et al. 2008; Jensen 2006).

In ► *Table 11-13* we present, as an example, the different contributions to all the coupling constants in acetylene. The dominant role of the FC term is typical for many molecules, in particular for large coupling constants in organic compounds. The SD contribution is often small, and therefore (being most expensive to calculate) it is sometimes neglected or analyzed at a lower level of accuracy than the other terms. In some cases such an approach is, however, not possible. For instance, the FC, PSO, and SD terms, respectively, dominate for different coupling constants in  $ClF_3$  (Jaszuński 2004).

To illustrate the accuracy of the results that may be achieved for small molecules, we present in ► *Table 11-14* the values for all the coupling constants in acetylene. The comparison with experimental data clearly demonstrates that it is necessary to consider the effects of vibration and rotation (zero-point vibrations and temperature).

Finally, we note that  $J_{KL}$  is very sensitive to variations in the molecular geometry. It has been repeatedly observed that the best results are obtained when the same approximation (for instance DFT functional and basis set) is used for geometry optimization and for the following calculation of spin–spin coupling constants. We refer to the recent reviews discussing the calculation of spin–spin coupling constants (Aucar 2008; Helgaker et al. 2008; Krivdin and Contreras 2007) for a discussion of many practical issues and numerous examples of successful applications.

The unit of  $J$  is Hz;  $K$  is given in  $kg\ m^{-2}\ s^{-2}\ A^{-2} = N\ A^{-2}\ m^{-3} = T^2J^{-1}$  (Raynes 1992).

■ Table 11-14

**C<sub>2</sub>H<sub>2</sub>, indirect spin–spin coupling constants (in Hz)**

	<sup>1</sup> J(CC)	<sup>1</sup> J(CH)	<sup>2</sup> J(CH)	<sup>3</sup> J(HH)
Experiment, measured <sup>a</sup>	174.78 ± 0.02	247.56 ± 0.05	50.14 ± 0.05	9.62 ± 0.05
Nuclear motion contributions <sup>b</sup>	–10.255	4.866	–3.703	–1.272
Equilibrium geometry, from experiment <sup>c</sup>	185.04	242.70	53.84	10.89
Equilibrium geometry, ab initio, MCSCF <sup>d</sup>	184.68	244.27	53.08	10.80

<sup>a</sup>Gas phase, Jackowski et al. (2000)

<sup>b</sup>Wigglesworth et al. (2000)

<sup>c</sup>Calculated using the nuclear motion contributions given above

<sup>d</sup>Jaszuński and Ruud (2001). FC term – RASSCF-4; other contributions – RASSCF-1

## Electron Spin–Related Properties

Electron spin resonance (ESR) and NMR are in principle very similar from a theoretical point of view, involving excitations and de-excitations in the electron and nuclear spin space, respectively. Thus, the effective Hamiltonians have much the same appearance in ESR and NMR theory, and the structure of the interactions is also very similar from a purely theoretical point of view.

However, from a computational viewpoint, there is a large difference between electron and nuclear spin interactions. In the case of the nuclear spin interactions, the Born–Oppenheimer approximation allowed us to decouple the nuclear spin wave function from the electronic wave function. This is not possible for the electron spin; indeed, the change in the electron spin state directly affects also the spatial part of the total electronic wave function. This is in principle not a problem. In *spin-unrestricted* approaches, the  $\alpha$  and  $\beta$  electrons are treated separately, and changes of electron spin through perturbation theory expressions can quite straightforwardly be included. However, since the spatial part of the orbitals of the  $\alpha$  and  $\beta$  spins may differ, the total electron spin is no longer necessarily a good quantum number (as required for the exact wave function), giving rise to what is often referred to as *spin contamination*. Spin contamination can be avoided forcing the spin to be a good quantum number, for instance by demanding that the spatial orbitals for the  $\alpha$  and  $\beta$  electrons are the same and writing the wave function as a fixed linear combination of Slater determinants referred to as configuration-state functions (CSFs). We also note that many open-shell wave functions of low and intermediate spin have strong multireference character, putting severe constraints on the wave function models that can be used. An alternative approach to address low and intermediate spin states is through the use of broken symmetry states (Noodleman 1981).

We recall that the Hamiltonian,  $\blacklozenge$  Eq. 11.2, does not involve the electron spin. Spin-restricted implementations of electronic structure methods, therefore, only optimize the wave function parameters of the same spin symmetry as the reference wave function. Since operators that change the spin symmetry are known not to contribute to the ground-state energy (at least in the nonrelativistic picture in which spin-orbit effects are ignored), such spin-breaking wave function parameters are left undefined. This has the consequence that average values of

triplet-perturbing operators cannot be accurately calculated in spin-restricted approaches, and an alternative approach to circumvent this problem has been proposed (Fernandez et al. 1992). Furthermore, in the calculation of second-order properties, such as for instance spin–spin coupling constants discussed in [▶ section “NMR Indirect Spin–Spin Coupling,”](#) triplet instabilities in the wave function may occur. We have discussed this problem in [▶ section “NMR Indirect Spin–Spin Coupling”](#) and we will not dwell further on this here. We only note that these considerations apply to all properties discussed in the following sections.

## Spin-Orbit Coupling Constants

The spin–orbit coupling constant is obtained from the single residue of a triplet linear response function:

$$\lim_{\omega \rightarrow \omega_f} \hbar(\omega - \omega_f) \langle \langle \hat{H}^{\text{SO}}; V^{\omega_f} \rangle \rangle_{\omega}, \quad (11.234)$$

where  $V^{\omega_f}$  is an arbitrary operator (corresponding to the excitation vector). There are two terms in the spin-orbit interaction operator  $\hat{H}^{\text{SO}}$  ([▶ Eq. 11.55](#)); the contribution to the spin-orbit coupling from the two-electron part is usually smaller than the one-electron contribution, though it is as large as 30% for the spin–orbit coupling constant in triplet  $\text{O}_2$  (Vahtas et al. 1992c).

The two-electron spin-orbit integrals calculated using the operators in [▶ Eqs. 11.13](#) and [▶ 11.14](#) of the Breit–Pauli Hamiltonian have three spatial components and lower symmetry than conventional two-electron repulsion integrals, and the cost of calculating these integrals is therefore very high. In order to reduce the costs of computations of spin-orbit effects, building on the observation that the one-electron contribution dominates, either scaled one-electron spin-orbit approximations are used (in which an effective nuclear charge is introduced) (Kosegi et al. 1995) or atomic mean-field approaches are utilized (Hess et al. 1996). In the latter approach, the two-electron interactions are included in a mean-field sense, in principle similar to the way the two-electron repulsion is included in a mean-field sense in Hartree–Fock calculations.

The spin-orbit coupling is the major intramolecular interaction mechanism responsible for intersystem crossings, such as singlet–triplet transitions. It should be kept in mind that, in contrast to, for example, external fields,  $\hat{H}^{\text{SO}}$  does not describe a perturbation which has a well-defined physical meaning and arbitrarily modified strength. It is our description of the system which provides first a set of singlet and triplet states and only next includes  $\hat{H}^{\text{SO}}$  and yields the values of the spin-orbit coupling constants. Indeed, within a relativistic framework, the spin-orbit interaction appears naturally and is included variationally in the optimization of the wave function. The spin-orbit effects often differ quite substantially in their behavior from the scalar relativistic effects (as for instance illustrated in the case of the hydrogen shielding constants in molecules containing heavy elements). It is therefore important, in order to get physical insight into the role of various relativistic effects, that spin-orbit effects can be addressed separately from other effects in a four-component framework, and an approach for achieving such a decomposition of the relativistic effects at the four-component level has been proposed (Visscher and Sauer 2000).

The spin-orbit coupling constant is normally reported in  $\text{cm}^{-1}$ .

## Phosphorescence

When the spin-orbit operator  $\hat{H}^{\text{SO}}$  is taken into account, the ground and excited state, which we assume here to be of singlet and triplet spin multiplicity, respectively, are no longer pure spin states –  $|^1_0^{(0)}\rangle$  and  $|^3_f^{(0)}\rangle$  – but are contaminated by, to first order in perturbation theory:

$$|^3_0^{(1)}\rangle = - \sum_{^3_n} \frac{|^3_n^{(0)}\rangle \langle ^3_n^{(0)} | \hat{H}^{\text{SO}} | ^1_0^{(0)} \rangle}{\omega_n}, \quad (11.235)$$

$$|^1_f^{(1)}\rangle = \sum_{^1_n} \frac{|^1_n^{(0)}\rangle \langle ^1_n^{(0)} | \hat{H}^{\text{SO}} | ^3_f^{(0)} \rangle}{\omega_f - \omega_n}. \quad (11.236)$$

Including these first-order corrections to the ground- and excited-state wave functions in the expression for the dipole transition moment, we find that the first-order nonvanishing contribution to the dipole transition moment between a singlet and a triplet state may be written in terms of a residue of a quadratic response function (Olsen and Jørgensen 1995; Vahtras et al. 1992a):

$$\langle ^1_0 | \boldsymbol{\mu} | ^3_f \rangle^{(1)} = \lim_{\omega \rightarrow \omega_f} \hbar(\omega - \omega_f) \langle \langle \boldsymbol{\mu}; \hat{H}^{\text{SO}}, V^\omega \rangle \rangle_{0,\omega} / \langle ^3_f | V^\omega | ^1_0 \rangle, \quad (11.237)$$

where  $V^\omega$  is an arbitrary triplet operator (determining the excitation vector) and  $\omega$  matches the singlet-triplet excitation energy.

The phosphorescent radiative lifetime  $\tau_k$  of the  $k$ th triplet spin component of state  $|^3_f\rangle$  is obtained from the relation:

$$\frac{1}{\tau_k} = \frac{4\omega_f^3 \alpha_{\text{fs}}^3}{3\hbar} \sum_{\nu} |\langle ^1_0 | \hat{\mu}_{\nu} | ^3_{fk} \rangle|^2, \quad (11.238)$$

and thus depends not only on the transition moment from the ground to the excited state, but also on the excitation energy. The transition moments may vary for different polarizations of the light, and the average phosphorescent lifetime is dominated by the shortest lifetime, corresponding to the polarization with the largest partial transition rate. The total transition rate is given in  $\text{s}^{-1}$ , the total lifetime being its inverse.

## ESR Effective Spin Hamiltonian

The effective ESR Hamiltonian, including also contributions from the nuclear spins and nuclear quadrupole moments (the latter primarily observable in electron-nuclear double resonance – ENDOR – spectroscopy), may be written as (Harriman 1978):

$$\mathcal{H}^{\text{ESR}} = \mathcal{H}^{\text{ex}} + \mathcal{H}^{\text{sZ}} + \mathcal{H}^{\text{ZFS}} + \mathcal{H}^{\text{hf}} + \mathcal{H}^{\text{nZ}} + \mathcal{H}^{\text{Nq}}. \quad (11.239)$$

Like the NMR effective Hamiltonian, the ESR effective Hamiltonian contains no reference to the electronic structure of the molecule, and the different contributions to the ESR Hamiltonian thus describe phenomenologically the interactions present in the molecule.

The first term in  $\blacktriangleright$  Eq. 11.239,  $\mathcal{H}^{\text{ex}}$ , contributes to the overall energy of interaction between electronic spin states, but the energy differences are in general too large to be observed by ESR

spectroscopy. This exchange contribution accounts for the difference in energy between states of different multiplicity, and the Hamiltonian

$$\mathcal{H}^{\text{ex}} = -2\mathcal{J}\mathbf{s}_1 \cdot \mathbf{s}_2, \quad (11.240)$$

is often referred to as the Heisenberg Hamiltonian. It is important in the analysis of the spin states in open-shell species. However, since to a large extent it defines an intrinsic relation between different electronic states of a molecule, we do not consider it to describe a molecular property in the sense we have defined, and we will, therefore, not discuss this contribution any further.

The second term in  $\blacklozenge$  Eq. 11.239,  $\mathcal{H}^{\text{SZ}}$ , is the electron spin–Zeeman interaction describing the interaction between the spin-magnetic moment of the electron and the external magnetic field induction

$$\mathcal{H}^{\text{SZ}} = \mu_B \mathbf{S}^T \mathbf{g} \mathbf{B}, \quad (11.241)$$

where  $\mathbf{g}$  is the electron  $g$  tensor. We use here  $\mathbf{S}$  to indicate the total effective spin of the system. For a free electron, the strength of this interaction would be determined by  $\blacklozenge$  Eq. 11.6 and thus be given by the free electron  $g$  factor ( $g_e \approx 2.0023193$ , in which the quantum-electrodynamic corrections to the electron  $g$  factor are included). However, unpaired electrons in a molecule experience a local magnetic field, arising from a partial shielding (or deshielding) due to the other electrons in the molecule, which leads to a shift relative to  $g_e$ , and therefore:

$$\mathbf{g} = g_e \mathbf{1} + \Delta \mathbf{g}. \quad (11.242)$$

$\mathcal{H}^{\text{ZFS}}$  is the spin–spin interaction:

$$\mathcal{H}^{\text{ZFS}} = \mathbf{S}^T \mathbf{D} \mathbf{S}, \quad (11.243)$$

which gives rise to the zero-field splitting of the ESR spectrum, since it can be observed even without an external magnetic field. It is described by the dipole interaction between the spin-magnetic dipoles of two unpaired electrons, and is thus only present in states with more than one unpaired electron, such as for instance triplet states. This term will in general lead to a splitting of the different spin sublevels in the triplet state.

The electronic  $g$  tensor and the electron spin–spin interactions (if present) are in most cases the dominating contributions to the ESR spectrum. The interactions of the spin-magnetic moments of the electrons with the nuclear magnetic moments give rise to hyperfine interaction in the ESR spectrum described by  $\mathcal{H}^{\text{hf}}$ :

$$\mathcal{H}^{\text{hf}} = \sum_K \left( A_K^{\text{fc}} \mathbf{S}^T \cdot \mathbf{I}_K + \mathbf{S}^T \mathbf{A}_K^{\text{sd}} \mathbf{I}_K \right). \quad (11.244)$$

There are thus hyperfine interactions arising from all nonzero nuclear magnetic moments. We note from  $\blacklozenge$  Eq. 11.244 that the hyperfine interactions in general can be divided into two contributions. The first term is purely isotropic and has the form of a contact interaction, whereas the second term  $A_K^{\text{sd}}$  corresponds to the dipolar interaction of the electron spin-magnetic moment and the nuclear magnetic moment, and is purely anisotropic. The isotropic hyperfine interaction measures the spin density at a given nucleus.

The last terms in  $\blacklozenge$  Eq. 11.239 are in general not observable in ESR spectroscopy, because of the increased linewidths due to the presence of the unpaired electrons. The nuclear Zeeman interaction is given by:

$$\mathcal{H}^{\text{NZ}} = -\mu_N \sum_K g_K \mathbf{B}^T \cdot \mathbf{I}_K, \quad (11.245)$$

and is analogous to the interaction included in the NMR effective Hamiltonian  $\blacklozenge$  Eq. 11.207, where the shift with respect to the nuclear  $g$  factor was described in terms of the shielding constant. The final term, the nuclear quadrupole interaction  $\mathcal{H}^{\text{Nq}}$ , also only involves the two nuclear spins and has already been discussed in  $\blacklozenge$  section “Electric Field Gradient at the Nucleus, Nuclear Quadrupole Coupling Constant.”

## ESR Electronic $g$ -Tensor

In this section we concentrate on the part of the ESR effective Hamiltonian describing the interaction between the electron spin and the external magnetic field,  $\blacklozenge$  Eq. 11.241. In the case of molecules with a single open-shell electronic doublet state, as well as high-spin radicals in the strong field limit, the energy difference between the eigenvalues of the effective ESR Hamiltonian can be written as

$$\Delta E = \mu_B \sqrt{\mathbf{B}^T \mathbf{G} \mathbf{B}}, \quad (11.246)$$

where we have introduced the so-called symmetric  $\mathbf{G}$  tensor, measured in experiment, and defined as  $\mathbf{G} = \mathbf{g} \cdot \mathbf{g}^T$ . The shift in the  $g$  factor may be anisotropic, and thus the  $\mathbf{g}$  tensor is a  $3 \times 3$  nonsymmetric tensor. Both  $\mathbf{G}$  and  $\mathbf{g}$  tensors provide the same information and are thus suitable for analyzing EPR data. We emphasize that the effective Hamiltonian employed here requires the use of degenerate perturbation theory for a proper analysis, since we consider states that are degenerate in the absence of the perturbation. We do not discuss these aspects in detail here, referring instead to Löwdin and Goscinski (1999) for a general introduction to this topic, and to Rinkevicius et al. (2008) for the  $g$  tensor in particular.

Within degenerate perturbation theory at the nonrelativistic level, there are in principle two contributing terms arising from expectation values of the spin–Zeeman ( $\blacklozenge$  Eq. 11.50) and the magnetic dipole operator ( $\blacklozenge$  Eq. 11.44), respectively. The latter can be shown to be zero, and the effect of the spin–Zeeman operator is to recover the free-electron  $g$  factor,  $g_e$ . Thus, within a purely nonrelativistic picture, there would be no effect of the electronic structure of the molecule on the interaction between an external magnetic field and the magnetic moment of the unpaired electron.

Including relativistic effects to order  $\alpha_{\text{fs}}^2$  leads to three corrections to the electronic  $g$  tensor (we consider here only the shift  $\Delta \mathbf{g}$  relative to the free-electron value):

$$\Delta \mathbf{g} = \Delta \mathbf{g}^{\text{SO}} + \Delta \mathbf{g}^{\text{RMC}} + \Delta \mathbf{g}^{\text{GC}} + \mathcal{O}(\alpha_{\text{fs}}^4). \quad (11.247)$$

Of these three contributions, the linear response contribution arising from the spin-orbit operator interacting with the orbital magnetic dipole operator is in most cases dominating, giving corrections to the  $g$  tensor of the form:

$$\Delta g_{\alpha\beta}^{\text{SO}} = \frac{2}{\langle S_Z \rangle} \langle \langle \hat{H}_{\alpha}^{\text{B}}, \hat{H}_{\beta}^{\text{SO}} \rangle \rangle, \quad (11.248)$$

where  $\langle S_Z \rangle$  is the expectation value of the  $z$  component of the total electron spin. The relativistic mass correction  $\Delta \mathbf{g}^{\text{RMC}}$  and gauge correction  $\Delta \mathbf{g}^{\text{GC}}$  contributions are obtained as expectation values:

$$\Delta g_{\alpha\beta}^{\text{RMC}} = \frac{2}{\langle S_Z \rangle} \langle 0 | \hat{H}_{\alpha\beta}^{\text{SZ/KE}} | 0 \rangle, \quad (11.249)$$

$$\Delta g_{\alpha\beta}^{\text{GC}} = \frac{2}{\langle S_Z \rangle} \langle 0 | \hat{H}_{\alpha\beta}^{\text{GC}} | 0 \rangle. \quad (11.250)$$

Here,  $\hat{H}^{SZ/KE}$  is the kinetic energy correction to the spin–Zeeman term given in the Breit–Pauli Hamiltonian (► Eq. 11.10), whereas  $\hat{H}^{GC} = \hat{H}^{SO,B(1)} + \hat{H}^{SO,B(2)}$  is the sum of the one- and two-electron magnetic-field corrections to the spin-orbit operator, (► Eqs. 11.59 and ► 11.60. Higher-order relativistic corrections have also been derived (Rinkevicius et al. 2008). We note, however, that the electron  $g$  tensor is a property for which a two- or four-component relativistic framework provides the most elegant expression, with the  $g$  tensor being reduced to a simple expectation value of the orbital magnetic dipole operator (see for instance van Lenthe et al. (1997)).

As for other open-shell properties, most calculations employ unrestricted approaches, in which conventional response-theory methodology can be used to calculate the relevant quantities if performed starting from a nonrelativistic wave function and using perturbation theory to include the relativistic corrections, as applied in Geurts et al. (1980), Noodleman and Baerends (1984). Spin-restricted approaches have also been applied, though it is important in this case to ensure that the triplet-perturbing operators acting on an open-shell reference state properly take all possible excitations into account (Rinkevicius et al. 2008). We also note that multireference CI and MCSCF wave functions have been used to calculate the  $g$  tensor of small molecules (see, e.g., Engström et al. (1998), Lushington and Grein (1996)).

The computed electronic  $g$  tensor will in general also be origin dependent in approximate calculations, since it depends on the external magnetic field. The origin dependence of the orbital magnetic dipole operator is canceled by the origin dependence of the gauge-correction term for exact states and wave functions. This means that in approximate calculations, care should be exercised to ensure gauge origin independence, for instance using London atomic orbitals (Ciofini et al. 2004). In general, however, electronic  $g$  tensors appear to be less sensitive than other properties to the choice of gauge origin (see for instance Kacprzak and Kaupp 2004), although exceptions have been observed.

## Zero-Field Splitting

In degenerate perturbation theory, the ZFS of a spin-degenerate state  $^{2S+1}\Psi_0$  is evaluated from the eigenvalues of the matrix

$$|\mathcal{H}_{ij}^{\text{ZFS}} - W\delta_{ij}| = 0, \quad (11.251)$$

where

$$\mathcal{H}_{ij}^{\text{ZFS}} = \langle ^{2S+1}\Psi_0^i | \hat{H}^{S,S} | ^{2S+1}\Psi_0^j \rangle - \sum_{n,\lambda} \sum_k \frac{\langle ^{2S+1}\Psi_0^i | \hat{H}^{\text{SO}} | ^{\lambda}\Psi_n^k \rangle \langle ^{\lambda}\Psi_n^k | \hat{H}^{\text{SO}} | ^{2S+1}\Psi_0^j \rangle}{\lambda E_n - E_0}. \quad (11.252)$$

In these expressions,  $^{\lambda}\Psi_n^k$  is the zeroth-order wave function,  $\lambda$  is the multiplicity of the state,  $S$  is the total spin quantum number, and the indices  $i, j, k = M_S$  determine the projection of the total spin (Minaev et al. 2003; Vahtras et al. 2002). As the operator couples two electron spins, ZFS will only occur in molecules with at least two unpaired electrons.

As for many other properties, the zero-field splitting has two distinct contributions. The first contribution in (► Eq. 11.252) is an expectation value of the two-electron spin–spin dipole–dipole



coupling operator,

$$\hat{H}^{S,S} = \frac{\alpha_{fs}^2}{2} \sum_{j \neq i} \left[ \frac{\mathbf{m}_i \cdot \mathbf{m}_j}{r_{ij}^3} - \frac{3(\mathbf{m}_i \cdot \mathbf{r}_{ij})(\mathbf{r}_{ij} \cdot \mathbf{m}_j)}{r_{ij}^5} \right], \quad (11.253)$$

whereas the other term is the indirect interaction between the spin-magnetic moments of two electrons, mediated through the interaction between the orbital magnetic moments in the spin-orbit operator. For transition-metal complexes, the spin-orbit effects, often dominated by a few close-lying electronic states, can be included in a limited sum-over-states expansion (Bolvin 2006) or using ligand-field theory (Neese and Solomon 2003). The electron spin-spin interaction can, however, be dominant in molecules with weak spin-orbit interactions, such as triplet states of organic molecules (Vahtras et al. 2002).

We can represent the zero-field splitting as

$$\mathcal{H}^{ZFS} = \mathbf{S}^T \mathbf{D} \mathbf{S}, \quad (11.254)$$

and in a basis that diagonalizes  $\mathbf{D}$ , it is customary to write

$$\mathcal{H}^{ZFS} = D \left[ S_z^2 - \frac{1}{3} S(S+1) \right] + E \left[ S_x^2 - S_y^2 \right], \quad (11.255)$$

in which  $D = D_{zz} - \frac{1}{2}(D_{xx} + D_{yy})$  and  $E = \frac{1}{2}(D_{xx} - D_{yy})$ , and there are thus only two independent parameters for the spin-spin coupling constants. There is in principle a contribution involving the total spin multiplied by the isotropic value of  $D$ , but since it does not contribute to the splitting of the electron spin levels, it does not affect the ESR spectrum.

There have not been too many studies, in particular using highly correlated wave functions, of the basis set and correlation requirements for the direct spin-spin interaction to the zero-field splitting. For the spin-orbit contribution, the basis set requirements follow to a large extent those applicable for the spin-orbit correction to the  $g$  tensor. Otherwise, an accurate description of the relevant electronic excited states contributing to the spin-orbit contribution is required, which by itself may be a challenge in the case of transition-metal complexes (Bolvin 2006).

## ESR Hyperfine Coupling Tensors

The ESR hyperfine splitting constants  $A_K$  appear in the ESR spin Hamiltonian  $\blacktriangleright$  Eq. 11.239 in the term  $\mathcal{H}^{hf}$  dependent on  $\mathbf{S}^T \mathbf{A}_K \mathbf{I}_K$ . This contribution couples the electron and nuclear magnetic moments, and thus provides very detailed information about the structure of radicals, in much the same manner as shielding constants do in NMR spectroscopy. To compute this correction, we thus need to select in the perturbation expansion all the terms bilinear in  $\mathbf{S}$  and  $\mathbf{m}_K$ .

Considering the expansion of the spin-Zeeman term in  $\blacktriangleright$  Eq. 11.40, when we insert the magnetic vector potential arising due to the nuclear magnetic moments, we find two contributions that are bilinear in the electron spin and nuclear magnetic moments, namely:

$$\mathbf{A}_K = \mathbf{A}_K^{fc} + \mathbf{A}_K^{sd}. \quad (11.256)$$

The purely isotropic contribution to the hyperfine interaction  $\mathbf{A}_K^{fc} = A_K^{fc} \mathbf{1}$  and the purely anisotropic contribution  $\mathbf{A}_K^{sd}$  (Fernandez et al. 1997) in  $\blacktriangleright$  Eq. 11.256 are due to the Fermi contact ( $\blacktriangleright$  Eq. 11.51) and the spin-dipole ( $\blacktriangleright$  Eq. 11.52) operators, respectively. Both contributions can in

principle be calculated as expectation values of the respective operators, using the spin-density matrix  $\mathbf{D}^{\alpha-\beta}$  (i.e., the difference between the density matrices for  $\alpha$  and  $\beta$  spin):

$$\mathbf{A}_K^{\text{fc}} = -\frac{1}{2}g_K g_e \mu_B \mu_N \langle S_Z \rangle^{-1} \sum_{\mu\nu} \left\langle \phi_\mu \left| \hat{H}^{K(\text{FC})} \right| \phi_\nu \right\rangle D_{\mu\nu}^{\alpha-\beta}, \quad (11.257)$$

$$\mathbf{A}_K^{\text{sd}} = -\frac{1}{2}g_K g_e \mu_B \mu_N \langle S_Z \rangle^{-1} \sum_{\mu\nu} \left\langle \phi_\mu \left| \hat{H}^{K(\text{SD})} \right| \phi_\nu \right\rangle D_{\mu\nu}^{\alpha-\beta}. \quad (11.258)$$

There are also contributions of the order  $\alpha_{\text{fs}}^4$  – a linear response contribution  $\langle\langle \hat{H}^{\text{SO}}; \hat{H}^{K(\text{PSO})} \rangle\rangle$  due to relativistic effects caused by the spin-orbit operator and expectation values  $\langle 0 | \hat{H}^{\text{SO}, K(1)} | 0 \rangle$  and  $\langle 0 | \hat{H}^{\text{SO}, K(2)} | 0 \rangle$ , ► Eqs. 11.62–11.63 (see Neese (2003), Arbužnikov et al. (2004)).

The ESR hyperfine coupling is determined by triplet perturbations. Thus, in principle one should use an unrestricted wave function to describe the reference state. However, it is also possible to use a spin-restricted wave function (Fernandez et al. 1992) and take into account the triplet nature of the perturbation in the definition of the response. Within such a (e.g., SCF or MCSCF) restricted-unrestricted approach, first-order properties are given as the sum of the usual expectation value term and a response correction that takes into account the change of the wave function induced by the perturbation (of the type  $\langle 0^{(1)} | H^0 | 0 \rangle$ ). This restricted-unrestricted approach has also been extended to restricted Kohn–Sham density functional theory (Rinkevicius et al. 2004).

In general, the most severe basis set requirements come from the isotropic hyperfine interactions, the anisotropic contribution in general being well converged with basis sets that perform well for the isotropic contribution. We mention in particular that there are basis sets specifically designed for calculations of hyperfine coupling constants (EPR-III) using density functional

■ Table 11-15

Calculated isotropic hyperfine coupling constants (in MHz) of transition metal compounds and their dependence on the exchange-correlation functionals; results taken from Rinkevicius et al. (2004)

Molecule	Isotope	BP86	BLYP	B3LYP	UBP86	UBLYP	UB3LYP	Expt.
TiO	<sup>47</sup> Ti	−245.0	−252.7	−248.6	−251.0	−257.5	−252.8	−241.0(60)
	<sup>17</sup> O	−11.5	−11.3	−7.9	−8.2	−8.2	−4.9	n.a. <sup>a</sup>
VN	<sup>51</sup> V	1321.8	1367.5	1317.4	1393.5	1432.6	1388.9	1311.8
	<sup>14</sup> N	8.7	8.2	4.7	6.2	6.0	3.2	n.a.
VO	<sup>51</sup> V	780.2	808.4	791.2	821.0	847.8	829.5	778.0(2)
	<sup>17</sup> O	−6.9	−6.0	−2.5	−3.1	−2.7	1.1	0(4)
MnO	<sup>55</sup> Mn	507.8	527.9	508.6	526.8	543.1	521.8	479.9 (100)
	<sup>17</sup> O	−5.6	−7.0	−9.4	−5.4	−6.6	−8.0	n.a.
MnH	<sup>55</sup> Mn	355.8	360.7	209.7	380.	380.0	331.8	279.4(12)
	<sup>1</sup> H	24.7	34.3	28.1	25.8	35.6	28.0	20.7 (39)
TiF <sub>3</sub>	<sup>47</sup> Ti	−127.5	−131.4	−158.2	−216.6	−218.0	−192.2	−184.4(4), −177.1(4)
	<sup>19</sup> F	17.1	18.8	1.6	5.0	8.7	−5.6	8.3(4), 8.0(4)
MnO <sub>3</sub>	<sup>55</sup> Mn	1262.2	1267.6	1476.2	2009.3	2042.4	1735.5	1613(6)
	<sup>17</sup> O	−3.9	−6.2	−6.4	−4.1	−5.1	2.6	n.a.

<sup>a</sup>Not available

theory (Barone 1995). In general, for main-group elements, DFT does not display a particularly strong sensitivity on the choice of exchange–correlation functional, and provides results in quite good agreement with CCSD(T) (Perera et al. 1994b).

Even though the majority of calculations of hyperfine coupling constants are performed using unrestricted approaches, the importance of spin contamination and its effect on the hyperfine coupling constants remains somewhat unclear, in particular in DFT calculations. Whereas restricted and unrestricted approaches give more or less identical results for simple radicals, the situation is less clear in the case of transition metal compounds, and a few examples of the differences between restricted and unrestricted approaches are collected in [Table 11-15](#), based on the results reported by Rinkevicius et al. (2004). We note that the differences between restricted and unrestricted approaches in general are small for the same functional, but that these differences become significant when spin contamination can be a problem, for instance for  $\text{TiF}_3$  and  $\text{MnO}_3$ .

The hyperfine coupling constants are usually reported in MHz; the contributions evaluated in a.u. need to be multiplied by  $g_K g_e \mu_B \mu_N$ .

## Conclusions

---

We end this discussion of molecular properties with some additional comments related both to theory and to experiment. First of all, we have mainly discussed nonrelativistic methods, since these are still dominant in practical applications. The approach starting with a nonrelativistic description of the molecular system and introducing relativistic effects as a correction/perturbation has obviously some limitations and cannot be applied in highly accurate studies of molecules containing heavy elements. There are different approaches that start from a relativistic description of the unperturbed molecule (using one-, two-, or four-component wave functions), and we refer for a discussion of relativistic methods applied in the theory of molecular properties to Reiher and Wolf (2009) and Saue (2002). There is an increasing number of successful applications of these methods, for example, in the study of NMR shielding constants (Autschbach 2007; Kaupp 2004; Maldonado and Aucar 2009) and spin–spin coupling constants (Autschbach 2008).

Secondly, we have not discussed in any detail the effects of nuclear motion. Methods used to calculate these vibrational corrections, for both zero-point vibrational effects and temperature effects, have been described elsewhere in this book. There are, however, other effects that should also be considered. We have not discussed the role of the purely vibrational contributions to molecular (electric) properties (Bishop 1990), which in certain cases can be as large as the electronic contributions (Kirtman et al. 2000). Moreover, in conformationally flexible molecules one has to consider the effects of large nuclear motions. For instance, for a proper comparison with experiment, it may not be sufficient to perform an *ab initio* calculation for a single molecular structure. In experiment one will always observe the average value of the different thermally accessible isomers (rotamers, conformers), and in order to allow for a direct comparison with these experimental observations, a Boltzmann average of the properties of these isomers must be computed. This is particularly important when the properties of the isomers are very different, possibly even differing in sign (Pecul et al. 2004).

Finally, most experimental data are not obtained in the gas phase. Therefore, in order to have a faithful comparison with experiment, the effects of the solvent must be considered. There is

an increasing number of studies of molecular properties in the presence of a solvent; we refer to a recent review for more details (Mennucci and Cammi 2007). Molecular dynamics or Monte Carlo procedures can be used when it is necessary to describe the nuclear dynamics in more detail, for example, for a better description of solvent effects or when considering sophisticated isomerization processes (Böhm et al. 2007; Møgelhøj et al. 2008, 2009).

The theory of molecular properties has for a long time provided a precise description of the interactions of a molecule with external and internal fields. In the last years, progress in the development and implementation of computational methods has enabled increasingly accurate calculations of such properties, often yielding results more accurate than experimental data. We note here that a molecular property is always defined as a quantity characterizing an isolated molecule, in a particular state, subject to particular perturbation(s) – conditions not easily achieved in experiment.

Theoretical calculations may thus provide insight into the electronic origins of the behavior of a molecule in the presence of electromagnetic fields, and help disentangle the contributions of solvents, vibrational effects, molecular rotation, and other small perturbations to the experimental observation. By combining the information obtainable in experiment with the tools of analysis offered by quantum-chemical calculations, a better understanding of the interactions between molecules and electromagnetic fields can be achieved, which in turn may facilitate for instance the design of molecules and functional materials with specific responses to external perturbations.

## Acknowledgment

---

We are grateful to Dr. Stephan Sauer and to Dr. Olav Vahtras for many helpful comments. We are indebted to Dr. Anna Kaczmarek-Kędziera for help in the editing of the manuscript.

## References

---

- Abragam, A. (1961). *The principles of nuclear magnetic resonance*. Oxford: Oxford University Press.
- Anet, F. A. L., O'Leary, D. J., Wade, C. G., & Johnson, R. D. (1990). NMR relaxation by the antisymmetric component of the shielding tensor: A longer transverse than longitudinal relaxation time. *Chemical Physics Letters*, 171, 401.
- Arbuznikov, A. V., Vaara, J., & Kaupp, M. (2004). Relativistic spin-orbit effects on hyperfine coupling tensors by density-functional theory. *Journal of Chemical Physics*, 120, 2127.
- Aucar, G. A. (2008). Understanding NMR J-couplings by the theory of polarization propagators. *Concepts in Magnetic Resonance Part A*, 32, 88.
- Auer, A. A., Gauss, J., & Stanton, J. F. (2003). Quantitative prediction of gas-phase  $^{13}\text{C}$  nuclear magnetic shielding constants. *Journal of Chemical Physics*, 118, 10407.
- Autschbach, J. (2007). Density functional theory applied to calculating optical and spectroscopic properties of metal complexes: NMR and optical activity. *Coordination Chemistry Reviews*, 251, 1796.
- Autschbach, J. (2008). Two-component relativistic hybrid density functional computations of nuclear spin-spin coupling tensors using Slater-type basis sets and density-fitting techniques. *Journal of Chemical Physics*, 129, 094105. Erratum: 130, 209901 (2009).
- Bak, K. L., Gauss, J., Helgaker, T., Jørgensen, P., & Olsen, J. (2000). The accuracy of molecular dipole moments in standard electronic structure calculations. *Chemical Physics Letters*, 319, 563.
- Baker, J., Buckingham, A. D., Fowler, P. W., Steiner, E., Lazzarotti, P., & Zanasi, R. (1989). The electrostatic model of field gradients at nuclei – an application to hydrogen-bonded complexes of

- HCl. *Journal of the Chemical Society, Faraday Transactions 2*, 85, 901.
- Barone, V. (1995). Structure, magnetic properties and reactivities of open-shell species from density functional and self-consistent hybrid methods. In D. P. Chong (Ed.), *Recent advances in density functional methods* (Vol. 1, p. 287). Singapore: World Scientific.
- Barron, L. D. (2004). *Molecular light scattering and optical activity*. Cambridge: Cambridge University Press.
- Barron, L. D., & Vrbancich, J. (1984). Magneto-chiral birefringence and dichroism. *Molecular Physics*, 51, 715.
- Benedikt, U., Auer, A. A., & Jensen, F. (2008). Optimization of augmentation functions for correlated calculations of spin-spin coupling constants and related properties. *Journal of Chemical Physics*, 129, 064111.
- Benkova, Z., Sadlej, A. J., Oakes, R. E., & Bell, S. E. J. (2005). Reduced-size polarized basis sets for calculations of molecular electric properties. I. The basis set generation. *Journal of Computational Chemistry*, 26, 145.
- Bethe, H., & Salpeter, E. (1957). *Quantum mechanics of one- and two-electron atoms*. New York: Academic.
- Bishop, D. M. (1990). Molecular vibrational and rotational motion in static and dynamic electric fields. *Reviews of Modern Physics*, 62, 343.
- Bishop, D. M. (1995). Dispersion formula for the average first hyperpolarizability  $\beta$ . *Journal of Chemical Physics*, 95, 5489.
- Bishop, D. M., & Pipin, J. (1989). Improved dynamic hyperpolarizabilities and field-gradient polarizabilities for helium. *Journal of Chemical Physics*, 91, 3549.
- Bogaard, M. P., & Orr, B. J. (1975). Electric Dipole Polarizabilities of Atoms and Molecules. In A. D. Buckingham (Ed.), *International review of science, physical chemistry, molecular structure, and properties, series 2* (Vol. 2, p. 149). London: Butterworths.
- Böhm, M. C., Ramirez, R., & Schulte, J. (2007). On the influence of vibrational modes and intramolecular isomerization processes on the NMR parameters of bullvalene: A Feynman path integral – ab initio investigation. *Chemical Physics*, 342, 1.
- Bolvin, H. (2006). An alternative approach to the g-matrix: Theory and applications. *ChemPhysChem*, 7, 1575.
- Bonin, K. D., & Kresin, V. V. (1997). *Electric-dipole polarizabilities of atoms, molecules and clusters*. Singapore: World Scientific.
- Born, M. (1918). Elektronentheorie des natürlichen optischen Drehungsvermögens isotroper und anisotroper Flüssigkeiten. *Annalen der Physik*, 55, 177.
- Buckingham, A. D. (1959). Direct method of measuring molecular quadrupole moments. *Journal of Chemical Physics*, 30, 1580.
- Buckingham, A. D. (1967). Permanent and induced molecular moments and long-range intermolecular forces. *Advances in Chemical Physics*, 12, 107.
- Buckingham, A. D., & Disch, R. L. (1963). The quadrupole moment of the carbon dioxide molecule. *Proceedings of the Royal Society A*, 273, 275.
- Buckingham, A. D., & Longuet-Higgins, H. C. (1968). The quadrupole moments of dipolar molecules. *Molecular Physics*, 14, 63.
- Buckingham, A. D., & Love, I. (1970). Theory of the anisotropy of nuclear spin coupling. *Journal of Magnetic Resonance*, 2, 338.
- Buckingham, A. D., & Pople, J. A. (1956). A theory of magnetic double refraction. *Proceedings of the Physical Society, Section B*, 69, 1133.
- Buckingham, A. D., & Stephens, P. J. (1966). Magnetic optical activity. *Annual Review of Physical Chemistry*, 17, 399.
- Buckingham, A. D., Pyykkö, P., Robert, J. B., & Wiesenfeld, L. (1982). Symmetry rules for the indirect nuclear spin-spin coupling tensor revisited. *Molecular Physics*, 46, 177.
- Champagne, B., Perpète, E. A., Jacquemin, D., van Gisbergen S. J. A., Baerends, E. J., Soubra-Ghaoui, C., Robins, K. A., & Kirtman, B. (2000). Assessment of conventional density functional schemes for computing the dipole moment and (hyper)polarizabilities of push-pull  $\pi$ -conjugated systems. *Journal of Physical Chemistry A*, 104, 4755.
- Christiansen, O., Koch, H., & Jørgensen, P. (1995). The second-order approximate coupled cluster singles and doubles model CC2. *Chemical Physics Letters*, 243, 409.
- Christiansen, O., Jørgensen, P., & Hättig, C. (1998). Response functions from Fourier component variational perturbation theory applied to a time-averaged quasienergy. *International Journal of Quantum Chemistry*, 68, 1.
- Christiansen, O., Coriani, S., Gauss, J., Hättig, C., Jørgensen, P., Pawłowski, F., & Rizzo, A. (2006). Accurate nonlinear optical properties for small molecules. In M. G. Papadopoulos, A. J. Sadlej, & J. Leszczynski (Eds.), *Non-linear optical properties of matter: From molecules to condensed phases* (p. 51). Dordrecht: Springer.
- Ciofini, I., Adamo, C., & Barone, V. (2004). Complete structural and magnetic characterization of biological radicals in solution by an integrated

- quantum mechanical approach: Glycyl radical as a case study. *Journal of Chemical Physics*, 121, 6710.
- Coriani, S., Hättig, C., & Rizzo, A. (1999a). The electric-field-gradient-induced birefringence of helium, neon, argon, and SF<sub>6</sub>. *Journal of Chemical Physics*, 111, 7828.
- Coriani, S., Jørgensen, P., Rizzo, A., Ruud, K., & Olsen, J. (1999b). Ab initio determinations of magnetic circular dichroism. *Chemical Physics Letters*, 300, 61.
- Craig, D. P., & Thirunamachandran, T. (1984). *Molecular quantum electrodynamics. An introduction to radiation molecule interaction*. Mineola: Dover Publications, Inc.
- Cronstrand, P., Luo, Y., Norman, P., & Ågren, H. (2003). Ab initio calculations of three-photon absorption. *Chemical Physics Letters*, 375, 233.
- Cybulski, S. M., & Bishop, D. M. (1994). Calculations of magnetic properties. V. Electron-correlated hypermagnetizabilities (Cotton-Mouton effect) for H<sub>2</sub>, N<sub>2</sub>, HF, and CO. *Journal of Chemical Physics*, 101, 424.
- De Boni, L., Toro, C., & Hernández, F. E. (2008). Synchronized double L-scan technique for the simultaneous measurement of polarization-dependent two-photon absorption in chiral molecules. *Optics Letters*, 33, 2958.
- Drake, G. W. F. (2006). High precision calculations for helium. In G. W. F. Drake (Ed.), *Springer handbook of atomic, molecular and optical physics* (p. 199). New York: Springer.
- Dyall, K. G., & Faegri, K., Jr. (2007). *Introduction to relativistic quantum chemistry*. USA: Oxford University Press.
- Enevoldsen, T., Oddershede, J., & Sauer, S. P. A. (1998). Correlated calculations of indirect nuclear spin-spin coupling constants using second-order polarization propagator approximations: SOPPA and SOPPA(CCSD). *Theoretical Chemistry Accounts*, 100, 275.
- Engström, M., Minaev, B., Vahtras, O., & Ågren, H. (1998). Linear response calculations of electronic g-factors and spin-rotational coupling constants for diatomic molecules with a triplet ground state. *Chemical Physics*, 237, 149.
- Faraday, M. (1846a). XLIX. Experimental researches in electricity. Nineteenth series. *Philosophical Magazine*, 28, 294.
- Faraday, M. (1846b). Experimental researches in electricity. Nineteenth series. *Philosophical Transactions of the Royal Society of London*, 136, 1.
- Fernandez, B., Jørgensen, P., Byberg, J., Olsen, J., Helgaker, T., & Jensen, H. J. Aa. (1992). Spin polarization in restricted electronic structure theory: Multiconfiguration self-consistent-field calculations of hyperfine coupling constants. *Journal of Chemical Physics*, 97, 3412.
- Fernandez, B., Christiansen, O., Jørgensen, P., Byberg, J., Gauss, J., & Ruud, K. (1997). Hyperfine and nuclear quadrupole coupling in chlorine and fluorine dioxides. *Journal of Chemical Physics*, 106, 1847.
- Flygare, W. H. (1974). Magnetic interactions in molecules and an analysis of molecular electronic charge distribution from magnetic parameters. *Chemical Reviews*, 74, 653.
- Fowler, P. W., & Buckingham, A. D. (1989). The magnetic hyperpolarizability anisotropy of some two-electron systems. *Molecular Physics*, 67, 681.
- Fowler, P. W., Lazzarotti, P., Steiner, E., & Zanasi, R. (1989). The theory of Sternheimer shielding in molecules in external fields. *Chemical Physics*, 133, 221.
- Fowler, P. W., Hunt, K. L. C., Kelly, H. M., & Sadlej, A. J. (1994). Multipole polarizabilities of the helium atom and collision-induced polarizabilities of pairs containing He or H atoms. *Journal of Chemical Physics*, 100, 2932.
- Fukui, H., Baba, T., & Inomata, H. (1996). Calculation of nuclear magnetic shieldings. X. Relativistic effects. *Journal of Chemical Physics*, 105, 3175. Erratum: 106, 2987 (1997).
- Gauss, J., & Stanton, J. F. (1995). Coupled-cluster calculations of nuclear magnetic resonance chemical shifts. *Journal of Chemical Physics*, 103, 3561.
- Gauss, J., & Stanton, J. F. (2002). Electron-correlated approaches for the calculation of NMR chemical shifts. *Advances in Chemical Physics*, 123, 355.
- Gauss, J., Ruud, K., & Helgaker, T. (1996). Perturbation-dependent atomic orbitals for the calculation of spin-rotation constants and rotational g tensors. *Journal of Chemical Physics*, 105, 2804.
- Gauss, J., Ruud, K., & Kállay, M. (2007). Gauge-origin independent calculation of magnetizabilities and rotational g tensors at the coupled-cluster level. *Journal of Chemical Physics*, 127, 074101.
- Geurts, P. J. M., Bouten, P. C. P., & van der Avoird, A. (1980). Hartree-Fock-Slater-LCAO calculations on the Cu(II) bis(dithiocarbamate) complex; Magnetic coupling parameters and optical spectrum. *Journal of Chemical Physics*, 73, 1306.
- Giorgio, E., Viglione, R., Zanasi, R., & Rosini, C. (2004). Ab initio calculation of optical rotatory dispersion (ORD) curves: A simple and reliable approach to the assignment of the molecular absolute configuration. *Journal of the American Chemical Society*, 126, 12968.

- Hansen, A. E., & Bouman, T. D. (1980). Natural chiroptical spectroscopy: Theory and computations. *Advances in Chemical Physics*, 44, 545.
- Harding, M. E., Lenhart, M., Auer, A. A., & Gauss, J. (2008a). Quantitative prediction of gas-phase  $^{19}\text{F}$  nuclear magnetic shielding constants. *Journal of Chemical Physics*, 128, 244111.
- Harding, M. E., Metzroth, T., Gauss, J., & Auer, A. A. (2008b). Parallel calculation of CCSD and CCSD(T) analytic first and second derivatives. *Journal of Chemical Theory and Computation*, 4, 64.
- Harriman, J. E. (1978). *Theoretical foundations of electron spin resonance*. New York: Academic.
- Hättig, C., Christiansen, O., & Jørgensen, P. (1998a). Multiphoton transition moments and absorption cross sections in coupled cluster response theory employing variational transition moment functionals. *Journal of Chemical Physics*, 108, 8331.
- Hättig, C., Christiansen, O., & Jørgensen, P. (1998b). Coupled cluster response calculations of two-photon transition probability rate constants for helium, neon and argon. *Journal of Chemical Physics*, 108, 8355.
- Hättig, C., & Jørgensen, P. (1998). Dispersion coefficients for first hyperpolarizabilities using coupled cluster quadratic response theory. *Theoretical Chemistry Accounts*, 100, 230.
- Helgaker, T., Ruud, K., Bak, K. L., Jørgensen, P., & Olsen, J. (1994). Vibrational Raman optical-activity calculations using London atomic orbitals. *Faraday Discussions*, 99, 165.
- Helgaker, T., Jaszunski, M., & Ruud, K. (1997). Ab initio calculation of the NMR shielding and indirect spin-spin coupling constants of fluoroethylene. *Molecular Physics*, 91, 881.
- Helgaker, T., Jaszunski, M., & Ruud, K. (1999). Ab initio methods for the calculation of NMR shielding and indirect spin-spin coupling constants. *Chemical Reviews*, 99, 293.
- Helgaker, T., Jørgensen, P., & Olsen, J. (2000). *Molecular electronic-structure theory*. Chichester: Wiley.
- Helgaker, T., Jaszunski, M., & Pecul, M. (2008). The quantum-chemical calculation of NMR indirect spin-spin coupling constants. *Progress in Nuclear Magnetic Resonance Spectroscopy*, 53, 249.
- Hess, B. A., Marian, C. M., Wahlgren, U., & Gropen, O. (1996). A mean-field spin-orbit method applicable to correlated wavefunctions. *Chemical Physics Letters*, 251, 365.
- Jackowski, K., Wilczek, M., Pecul, M., & Sadlej, J. (2000). Nuclear magnetic shielding and spin-spin coupling of 1,2- $^{13}\text{C}$ -enriched acetylene in gaseous mixtures with xenon and carbon dioxide. *Journal of Physical Chemistry A*, 104, 5955. Erratum: 104, 9806 (2000).
- Jackowski, K., Makulski, W., & Wasylishen, R. E. (2011). To be published.
- Jackson, D. A. (1998). *Classical electrodynamics* (3rd ed.). New York: Wiley.
- Jameson, C. J. (1987). Spin-spin coupling. In J. Mason (Ed.), *Multinuclear NMR* (p. 89). New York: Plenum Press.
- Jameson, C. J., Jameson, A. K., Oppusunggu, D., Wille, S., Burrell, P. M., & Mason, J. (1981).  $^{15}\text{N}$  nuclear magnetic shielding scale from gas phase studies. *Journal of Chemical Physics*, 74, 81.
- Jamieson, M. J. (1991). A time-dependent Hartree-Fock study of dispersion in the Cotton-Mouton effect for the helium isoelectronic sequence. *Chemical Physics Letters*, 183, 9.
- Jansik, B., Rizzo, A., & Ågren, H. (2005). Response theory calculations of two-photon circular dichroism. *Chemical Physics Letters*, 414, 461.
- Jansik, B., Rizzo, A., & Ågren, H. (2007). Ab initio study of the two-photon circular dichroism in chiral natural amino acids. *The Journal of Physical Chemistry B*, 111, 446. Erratum: 111, 2409 (2007).
- Jansik, B., Rizzo, A., Ågren, H., & Champagne, B. (2008). Strong two-photon circular dichroism in helicenes: A Theoretical investigation. *Journal of Chemical Theory and Computation*, 4, 457.
- Jaszunski, M. (2004). Ab initio study of the shielding and spin-spin coupling constants in  $\text{ClF}_3$ ,  $\text{PF}_3$  and  $\text{PF}_5$ . *Chemical Physics Letters*, 385, 122.
- Jaszunski, M., & Jackowski, K. (2008). Nuclear magnetic dipole moments from NMR spectra - quantum chemistry and experiment. In S. G. Karshenboim (Ed.), *Precision physics of simple atoms and molecules. Lecture notes in physics* (Vol. 745, p. 233). Springer, Berlin, Heidelberg.
- Jaszunski, M., & Ruud, K. (2001). Spin-spin coupling constants in  $\text{C}_2\text{H}_2$ . *Chemical Physics Letters*, 336, 473.
- Jaszunski, M., Jørgensen, P., Rizzo, A., Ruud, K., & Helgaker, T. (1994). MCSCF calculations of Verdet constants. *Chemical Physics Letters*, 222, 263.
- Jensen, F. (2006). The basis set convergence of spin-spin coupling constants calculated by density functional methods. *Journal of Chemical Theory and Computation*, 2, 1360.
- Jensen, F. (2008). Basis set convergence of nuclear magnetic shielding constants calculated by density functional methods. *Journal of Chemical Theory and Computation*, 4, 719.
- Kacprzak, S., & Kaupp, M. (2004). Electronic g-tensors of semiquinones in photosynthetic reaction centers. A density functional study. *The Journal of Physical Chemistry B*, 108, 2464.



- Kállay, M., & Gauss, J. (2004). Analytic second derivatives for general coupled-cluster and configuration-interaction models. *Journal of Chemical Physics*, 120, 6841.
- Kalugin, N. K., Kleindienst, P., & Wagnière, G. H. (1999). The magnetochiral birefringence in diamagnetic solutions and in uniaxial crystals. *Chemical Physics*, 248, 105.
- Kaupp, M. (2004). Relativistic effects on NMR chemical shifts. In P. Schwerdtfeger (Ed.), *Relativistic electronic structure theory. Part 2. Applications* (p. 552). Amsterdam: Elsevier.
- Keal, T. W., & Tozer, D. J. (2003). The exchange-correlation potential in Kohn–Sham nuclear magnetic resonance shielding calculations. *Journal of Chemical Physics*, 119, 3015.
- Kellö, V., & Sadlej, A. J. (1998). The quadrupole moment of the  $^{39}\text{K}$  and  $^{41}\text{K}$  nuclei from microwave data for KF and KCl. *Chemical Physics Letters*, 292, 403.
- Kendall, R. A., Dunning, T. H., Jr., & Harrison, R. J. (1992). Electron affinities of the first-row atoms revisited. Systematic basis sets and wave functions. *Journal of Chemical Physics*, 96, 6796.
- Kerr, J. (1875a). XL. A new relation between electricity and light: Dielectric media birefringent. *Philosophical Magazine*, 50, 337.
- Kerr, J. (1875b). LIV. A new relation between electricity and light: Dielectric media birefringent (second paper). *Philosophical Magazine*, 50, 446.
- Kielich, S. (1972). General molecular theory and electric field effects in isotropic dielectrics. In M. Davies (Ed.), *Specialist periodical report, dielectric and related molecular processes* (Vol. 1, p. 192). London: Chemical Society.
- Kirpekar, S., Oddershede, J., & Jensen, H. J. Aa. (1995). Relativistic corrections to molecular dynamic dipole polarizabilities. *Journal of Chemical Physics*, 103, 2983.
- Kirtman, B., Champagne, B., & Luis, J. M. (2000). Efficient treatment of the effect of vibrations on electrical, magnetic, and spectroscopic properties. *Journal of Computational Chemistry*, 21, 1572.
- Kleinman, D. A. (1972). Nonlinear dielectric polarization in optical media. *Physical Review*, 126, 1977.
- Koch, H., Christiansen, O., Jørgensen, P., Sánchez de Merás, A. M. J., & Helgaker, T. (1997). The CC3 model: An iterative coupled cluster approach including connected triples. *Journal of Chemical Physics*, 106, 1808.
- Kosegi, S., Gordon, M. S., Schmidt, M. W., & Matsunaga, N. (1995). Main group effective nuclear charges for spin-orbit calculations. *Journal of Physical Chemistry*, 99, 12764.
- Krivdin, L. B., & Contreras, R. H. (2007). Recent advances in theoretical calculations of indirect spin-spin coupling constants. In *Annual Reports on NMR Spectroscopy* (Vol. 61, p. 133).
- Kukolich, S. G. (1969). Measurement of the molecular  $g$  values in  $\text{H}_2\text{O}$  and  $\text{D}_2\text{O}$  and hyperfine structure in  $\text{H}_2\text{O}$ . *Journal of Chemical Physics*, 50, 3751.
- Kussmann, J., & Ochsenfeld, C. (2007). Linear-scaling method for calculating nuclear magnetic resonance chemical shifts using gauge-including atomic orbitals within Hartree–Fock and density-functional theory. *Journal of Chemical Physics*, 127, 054103.
- Kutzelnigg, W. (1980). Theory of magnetic-susceptibilities and NMR chemical shifts in terms of localized quantities. *Israel Journal of Chemistry*, 19, 193.
- Lach, G., Jeziorski, B., & Szalewicz, K. (2004). Radiative corrections to the polarizability of helium. *Physical Review Letters*, 92, 233001.
- Langevin, P. (1910). Sur les biréfringences électrique et magnétique. *Radium, Paris*, 7, 249.
- Langhoff, P. W., & Karplus, M. (1970). Application of Padé approximants to dispersion force and optical polarizability computations. In G. A. Baker Jr, J. L. Gammel (Eds.), *The Padé approximant in theoretical physics* (pp. 41–97). New York: Academic.
- Langhoff, P. W., Gordon, R. G., & Karplus, M. (1971). Comparisons of dispersion force bounding methods with applications to anisotropic interactions. *Journal of Chemical Physics*, 55, 2126.
- Lazzeretti, P., & Zanasi, R. (1996). Molecular magnetic properties via formal annihilation of paramagnetic contribution to electronic current density. *International Journal of Quantum Chemistry*, 60, 249.
- Lazzeretti, P., Malagoli, M., & Zanasi, R. (1994). Computational approach to molecular magnetic properties by continuous transformation of the origin of the current density. *Chemical Physics Letters*, 220, 299.
- Löwdin, P.-O., & Goscinski, O. (1999). Studies in perturbation theory. XIV. Treatment of constants of motion, degeneracies and symmetry properties by means of multidimensional partitioning. *International Journal of Quantum Chemistry*, 5, 685.
- Lushington, G. H., & Grein, F. (1996). The electronic  $g$ -tensor of MgF: A comparison of ROHF and MRD–CI level results. *International Journal of Quantum Chemistry*, 60, 1679.
- Lutnæs, O. B., Teale, A. M., Helgaker, T., Tozer, D. J., Ruud, K., & Gauss, J. (2009). Benchmarking



- density-functional-theory calculations of rotational  $g$  tensors and magnetizabilities using accurate coupled-cluster calculations. *Journal of Chemical Physics*, *131*, 144104.
- Maldonado, A. F., & Aucar, G. A. (2009). The UKB prescription and the heavy atom effects on the nuclear magnetic shielding of vicinal heavy atoms. *Physical Chemistry Chemical Physics*, *11*, 5615.
- Manninen, P., Lantto, P., Vaara, J., & Ruud, K. (2003). Perturbational ab initio calculations of relativistic contributions to nuclear magnetic resonance shielding tensors. *Journal of Chemical Physics*, *119*, 2623.
- Marchesan, D., Coriani, S., Forzato, C., Nitti, P., Pitacco, G., & Ruud, K. (2005). Optical rotation calculation of a highly flexible molecule: The case of paraconic acid. *Journal of Physical Chemistry A*, *109*, 1449.
- Mason, J. (1993). Conventions for the reporting of nuclear magnetic shielding (or shift) tensors suggested by participants in the NATO ARW on NMR shielding constants at the University of Maryland, College Park, July 1992. *Solid State Nuclear Magnetic Resonance*, *2*, 285.
- McClain, W. M. (1974). Two-photon molecular spectroscopy. *Accounts of Chemical Research*, *7*, 129.
- McWeeny, R. (1992). *Methods of molecular quantum mechanics* (2nd ed.). London: Academic.
- Mennucci, B., & Cammi, R. (2007). *Continuum solvation models in chemical physics: From theory to applications*. Chichester: Wiley.
- Michl, J., & Thulstrup, E. W. (1995). *Spectroscopy with polarized light*. Weinheim: VCH.
- Minaev, B., Loboda, O., Rinkevicius, Z., Vahtras, O., & Ågren, H. (2003). Fine and hyperfine structure in three low-lying  $^3\Sigma^+$  states of molecular hydrogen. *Molecular Physics*, *101*, 2335.
- Misquitta, A. J., Podaszwa, R., Jeziorski, B., & Szalewicz, K. (2005). Intermolecular potentials based on symmetry-adapted perturbation theory with dispersion energies from time-dependent density-functional calculations. *Journal of Chemical Physics*, *123*, 214103.
- Mogelhøj, A., Aidas, K., Mikkelsen, K. V., & Kongsted, J. (2008). Solvent effects on the nitrogen NMR shielding and nuclear quadrupole coupling constants in 1-methyltriazoles. *Chemical Physics Letters*, *460*, 129.
- Mogelhøj, A., Aidas, K., Mikkelsen, K. V., Sauer, S. P. A., & Kongsted, J. (2009). Prediction of spin-spin coupling constants in solution based on combined density functional theory/molecular mechanics. *Journal of Chemical Physics*, *130*, 134508.
- Moss, R. E. (1973). *Advanced molecular quantum mechanics*. London: Chapman and Hall.
- Müller, T., Wiberg, K. B., & Vaccaro, P. H. (2000). Cavity ring-down polarimetry (CRDP): A new scheme for probing circular birefringence and circular dichroism in the gas phase. *Journal of Physical Chemistry A*, *104*, 5959.
- Neese, F. (2003). Metal and ligand hyperfine couplings in transition metal complexes: The effect of spin-orbit coupling as studied by coupled perturbed Kohn-Sham theory. *Journal of Chemical Physics*, *118*, 3939.
- Neese, F., & Solomon, E. I. (2003). Interpretation and calculation of spin-Hamiltonian parameters in transition metal complexes. In J. S. Miller, & M. Drillon (Eds.), *Magnetism: Molecules to materials IV* (p. 345). Weinheim: Wiley.
- Nielsen, E. S., Jørgensen, P., & Oddershede, J. (1980). Transition moments and dynamic polarizabilities in a second order polarization propagator approach. *Journal of Chemical Physics*, *73*, 6238.
- Noodleman, L. (1981). Valence bond description of antiferromagnetic coupling in transition metal dimers. *Journal of Chemical Physics*, *74*, 5737.
- Noodleman, L., & Baerends, E. J. (1984). Electronic structure, magnetic properties, ESR, and optical spectra for 2-iron ferredoxin models by LCAO-X $\alpha$  valence bond theory. *Journal of the American Chemical Society*, *106*, 2316.
- Norman, P., Jiemchoorj, A., & Sernelius, B. E. (2003). Polarization propagator calculations of the polarizability tensor at imaginary frequencies and long-range interactions for the noble gases and n-alkanes. *Journal of Chemical Physics*, *118*, 9167.
- Ochsenfeld, C., Kussmann, J., & Koziol, F. (2004). Ab initio NMR spectra for molecular systems with a thousand and more atoms: A linear-scaling method. *Angewandte Chemie International Edition*, *43*, 4485.
- Oddershede, J., Geertsens, J., & Scuseria, G. E. (1988). Nuclear spin-spin coupling constant of hydrogen molecule with deuterium (HD). *Journal of Physical Chemistry*, *92*, 3056.
- Olsen, J., & Jørgensen, P. (1985). Linear and nonlinear response functions for an exact state and for an MCSCF state. *Journal of Chemical Physics*, *82*, 3235.
- Olsen, J., & Jørgensen, P. (1995). Time-dependent response theory with applications to self-consistent field and multiconfigurational self-consistent field wave functions. In D. R. Yarkony (Ed.), *Modern electronic structure theory* (p. 857). Singapore: World Scientific.

- Parkinson, W. A., & Oddershede, J. (1997). Response function analysis of magnetic optical rotation. *International Journal of Quantum Chemistry*, *64*, 599.
- Paterson, M. J., Christiansen, O., Pawłowski, F., Jørgensen, P., Hättig, C., Helgaker, T., & Salek, P. (2006). Benchmarking two-photon absorption with CC3 quadratic response theory, and comparison with density-functional response theory. *Journal of Chemical Physics*, *124*, 054322.
- Pawłowski, F., Jørgensen, P., & Hättig, C. (2004). Gauge invariance of oscillator strengths in the approximate coupled cluster triples model CC3. *Chemical Physics Letters*, *389*, 413.
- Pecul, M., Ruud, K., Rizzo, A., & Helgaker, T. (2004). Conformational effects on the optical rotation of alanine and proline. *Journal of Physical Chemistry A*, *108*, 4269.
- Pedersen, T. B., Koch, H., Boman, L., & Sánchez de Merás, A. M. J. (2004). Origin invariant calculation of optical rotation without recourse to London orbitals. *Chemical Physics Letters*, *393*, 319.
- Perera, S. A., Sekino, H., & Bartlett, R. J. (1994a). Coupled-cluster calculations of indirect nuclear coupling constants: The importance of non-Fermi contact contributions. *Journal of Chemical Physics*, *101*, 2186.
- Perera, S. A., Watts, J. D., & Bartlett, R. J. (1994b). A theoretical study of hyperfine coupling constants. *Journal of Chemical Physics*, *100*, 1425.
- Pluta, T., & Sadlej, A. J. (1998). HyPol basis sets for high-level-correlated calculations of electric dipole hyperpolarizabilities. *Chemical Physics Letters*, *297*, 391.
- Podeszwa, R., & Szalewicz, K. (2008). Physical origins of interactions in dimers of polycyclic aromatic hydrocarbons. *Physical Chemistry Chemical Physics*, *10*, 2735.
- Raynes, W. T. (1992). Letter to editor. *Magnetic Resonance in Chemistry*, *30*, 686.
- Raynes, W. T. (1996). Electric field effects on shielding constants. In D. M. Grant & R. K. Harris (Eds.), *Encyclopaedia of NMR* (p. 1846). New York: Wiley.
- Raynes, W. T., McVay, R., & Wright, S. J. (1989). An improved  $^{13}\text{C}$  nuclear shielding scale. *Journal of the Chemical Society, Faraday Transactions 2*, *85*, 759.
- Reiher, M., & Wolf, A. (2009). *Relativistic quantum chemistry*. Weinheim: Wiley.
- Rinkevicius, Z., Vaara, J., Telyatnyk, L., & Vahtras, O. (2003). Calculations of nuclear magnetic shielding in paramagnetic molecules. *Journal of Chemical Physics*, *118*, 2550.
- Rinkevicius, Z., Telyatnyk, L., Vahtras, O., & Ågren, H. (2004). Density functional theory for hyperfine coupling constants with the restricted-unrestricted approach. *Journal of Chemical Physics*, *121*, 7614.
- Rinkevicius, Z., de Almeida, K. J., Oprea, C. I., Vahtras, O., Ågren, H., & Ruud, K. (2008). Degenerate perturbation theory for electronic  $g$  tensors: Leading-order relativistic effects. *Journal of Chemical Theory and Computation*, *4*, 1810.
- Rizzo, A., & Coriani, S. (2005). Birefringences: A Challenge for both theory and experiment. *Advances in Quantum Chemistry*, *50*, 143.
- Rizzo, A., & Gauss, J. (2002). Shielding polarizabilities calculated at the coupled-cluster singles and doubles level augmented by a perturbative treatment of triple excitations. *Journal of Chemical Physics*, *116*, 869.
- Rizzo, C., Rizzo, A., & Bishop, D. M. (1997). The Cotton-Mouton effect in gases: Experiment and theory. *International Reviews in Physical Chemistry*, *16*, 81.
- Rizzo, A., Jansík, B., Pedersen, T. B., & Ågren, H. (2006). Origin invariant approaches to the calculation of two-photon circular dichroism. *Journal of Chemical Physics*, *125*, 064113.
- Rizzo, A., Frediani, L., & Ruud, K. (2007). An ab initio investigation of the Buckingham birefringence of furan, thiophene, and selenophene in cyclohexane solution. *Journal of Chemical Physics*, *127*, 164321.
- Rudziński, A., Puchalski, M., & Pachucki, K. (2009). Relativistic, QED, and nuclear mass effects in the magnetic shielding of  $^3\text{He}$ . *Journal of Chemical Physics*, *130*, 244102.
- Ruiz de Azúa, M. C., Melo, J. I., & Giribet, C. G. (2003). Orbital contributions to relativistic corrections of the NMR nuclear magnetic shielding tensor originated in scalar field-dependent operators. *Molecular Physics*, *101*, 3103.
- Ruud, K., & Helgaker, T. (1997). The magnetizability, rotational  $g$  tensor, and quadrupole moment of  $\text{PF}_3$  revisited. *Chemical Physics Letters*, *264*, 17.
- Ruud, K., Helgaker, T., Bak, K. L., Jørgensen, P., & Olsen, J. (1995). Accurate magnetizabilities of the isoelectronic series  $\text{BeH}^-$ ,  $\text{BH}$ , and  $\text{CH}^+$ . The MCSCF-GIAO approach. *Chemical Physics*, *195*, 157.
- Ruud, K., Vaara, J., Lounila, J., & Helgaker, T. (1998). Vibrationally averaged magnetizabilities and rotational  $g$  tensors of the water molecule. *Chemical Physics Letters*, *297*, 467.
- Ruud, K., Taylor, P. R., & Jaszunski, M. (2000). Comment on "On the magnetic susceptibility of fluorine." *Journal of Physical Chemistry A*, *104*, 168.

- Ruud, K., Åstrand, P.-O., & Taylor, P. R. (2001). Zero-point vibrational effects on proton shieldings: Functional-group contributions from ab initio calculations. *Journal of the American Chemical Society*, 123, 4826.
- Ruud, K., Taylor, P. R., & Åstrand, P.-O. (2001). Zero-point vibrational effects on optical rotation. *Chemical Physics Letters*, 337, 217.
- Ruud, K., Stephens, P. J., Devlin, F. J., Taylor, P. R., Cheeseman, J. R., & Frisch, M. J. (2003). Coupled-cluster calculations of optical rotation. *Chemical Physics Letters*, 373, 606.
- Sadlej, A. J. (1988). Medium-size polarized basis sets for high-level correlated calculations of molecular electric properties. *Collection of Czechoslovak Chemical Communications*, 53, 1995.
- Sasagane, K., Aiga, F., & Itoh, R. (1993). Higher-order response theory based on the quasienergy derivatives: The derivation of the frequency-dependent polarizabilities and hyperpolarizabilities. *Journal of Chemical Physics*, 99, 3738.
- Saue, T. (2002). Post Dirac-Fock-methods - Properties. In P. Schwerdtfeger (Ed.), *Relativistic electronic structure theory. Part I. Fundamentals* (p. 332). Amsterdam: Elsevier.
- Sauer, S. P. A. (1997). Second-order polarization propagator approximation with coupled-cluster singles and doubles amplitudes - SOPPA(CCSD): The polarizability and hyperpolarizability of  $\text{Li}^-$ . *Journal of Physics B: Atomic, Molecular and Optical Physics*, 30, 3773.
- Sauer, S. P. A., Enevoldsen, T., & Oddershede, J. (1993). Paramagnetism of closed shell diatomic hydrides with six valence electrons. *Journal of Chemical Physics*, 98, 9748.
- Sauer, S. P. A., Jensen, H. J. Aa., & Ogilvie, J. F. (2005). Quantum-chemical calculations of radial functions for rotational and vibrational  $g$  factors, electric dipolar moment and adiabatic corrections to the potential energy for analysis of spectra of  $\text{HeH}^+$ . *Advances in Quantum Chemistry*, 48, 319.
- Schatz, P. N., & McCaffery, A. J. (1969). Faraday effect. *Quarterly Review of the Chemical Society*, 23, 552.
- Schindler, M., & Kutzelnigg, W. (1982). Theory of magnetic susceptibilities and NMR chemical shifts in terms of localized quantities. II. Application to some simple molecules. *Journal of Chemical Physics*, 76, 1919.
- Seth, M., Ziegler, T., Banerjee, A., Autschbach, J., van Gisbergen, S. J. A., & Baerends, E. J. (2004). Calculation of the A term of magnetic circular dichroism based on time dependent-density functional theory I. Formulation and implementation. *Journal of Chemical Physics*, 120, 10942.
- Shelton, D. P., & Rice, J. E. (1994). Measurements and calculations of the hyperpolarizabilities of atoms and small molecules in the gas phase. *Chemical Reviews*, 94, 3.
- Smith, S. A., Palke, W. E., & Gerig, J. T. (1992). The Hamiltonians of NMR. Part I. *Concepts in Magnetic Resonance*, 4, 107.
- Snyder, P. A., Atanasova, S., & Hansen, R. W. C. (2004). Ethylene. Experimental evidence for new assignments of electronic transitions in the  $\pi \rightarrow \pi^*$  energy region. Absorption and magnetic circular dichroism measurements with synchrotron radiation. *Journal of Physical Chemistry A*, 108, 4194.
- Solheim, H., Ruud, K., Coriani, S., & Norman, P. (2008). Complex polarization propagator calculations of magnetic circular dichroism spectra. *Journal of Chemical Physics*, 128, 094103.
- Stanton, J. F., & Bartlett, R. J. (1993). The equation of motion coupled-cluster method. A systematic biorthogonal approach to molecular excitation energies, transition probabilities, and excited state properties. *Journal of Chemical Physics*, 98, 7029.
- Stanton, J. F., Gauss, J., & Christiansen, O. (2001). Equilibrium geometries of cyclic  $\text{SiC}_3$  isomers. *Journal of Chemical Physics*, 114, 2993.
- Stephens, P. J. (1976). Magnetic circular dichroism. *Advances in Chemical Physics*, 35, 197.
- Stephens, P. J., Devlin, F. J., Cheeseman, J. R., & Frisch, M. J. (2001). Calculation of optical rotation using density functional theory. *Journal of Physical Chemistry A*, 105, 5356.
- Sundholm, D., & Gauss, J. (1997). Isotope and temperature effects on nuclear magnetic shieldings and spin-rotation constants calculated at the coupled-cluster level. *Molecular Physics*, 92, 1007.
- Tellgren, E. I., Soncini, A., & Helgaker, T. (2008). Nonperturbative ab initio calculations in strong magnetic fields using London orbitals. *Journal of Chemical Physics*, 129, 154114.
- Thorvaldsen, A. J., Ruud, K., Rizzo, A., & Coriani, S. (2008). Analytical calculations of frequency-dependent hypermagnetizabilities and Cotton-Mouton constants using London atomic orbitals. *Journal of Chemical Physics*, 129, 164110.
- Tinoco, I. (1975). Two-photon circular dichroism. *Journal of Chemical Physics*, 62, 1006.
- Tozer, D. J., & Handy, N. C. (1998). Improving virtual Kohn-Sham orbitals and eigenvalues: Application to excitation energies and static polarizabilities. *Journal of Chemical Physics*, 109, 10180.
- Vaara, J., Jokisaari, J., Wasylishen, R. E., & Bryce, D. L. (2002). Spin-spin coupling tensors as determined by experiment and computational

- chemistry. *Progress in Nuclear Magnetic Resonance Spectroscopy*, 41, 233.
- Vaara, J., & Pyykkö, P. (2003). Relativistic, nearly basis-set-limit nuclear magnetic shielding constants of the rare gases He–Rn: A way to absolute nuclear magnetic resonance shielding scales. *Journal of Chemical Physics*, 118, 2973.
- Vaara, J., Ruud, K., Vahtras, O., Ågren, H., & Jokisaari, J. (1998). Quadratic response calculations of the electronic spin-orbit contribution to nuclear shielding tensors. *Journal of Chemical Physics*, 109, 1212.
- Vaara, J., Ruud, K., & Vahtras, O. (1999). Second- and third-order spin-orbit contributions to nuclear shielding tensors. *Journal of Chemical Physics*, 111, 2900.
- Vahtras, O., Ågren, H., Jørgensen, P., Jensen, H. J. Aa., Helgaker, T. and Olsen, J. (1992a). Multiconfigurational quadratic response functions for singlet and triplet perturbations: The phosphorescence lifetime of formaldehyde. *Journal of Chemical Physics*, 97, 9178.
- Vahtras, O., Ågren, H., Jørgensen, P., Jensen, H. J. Aa., Padkjær, S. B., & Helgaker, T. (1992b). Indirect nuclear spin-spin coupling constants from multiconfiguration linear response theory. *Journal of Chemical Physics*, 96, 6120.
- Vahtras, O., Ågren, H., P., J., Jensen, H. J. Aa., Helgaker, T., & Olsen, J. (1992c). Spin-orbit coupling constants in a multiconfiguration linear response approach. *Journal of Chemical Physics*, 96, 2118.
- Vahtras, O., Loboda, O., Minaev, B., Ågren, H., & Ruud, K. (2002). Ab initio calculations of zero-field splitting parameters. *Chemical Physics*, 279, 133.
- van Lenthe, E., Wormer, P. E. S., & van der Avoird, A. (1997). Density functional calculations of molecular g-tensors in the zero-order regular approximation for relativistic effects. *Journal of Chemical Physics*, 107, 2488.
- Verhoeven, J., & Dymanus, A. (1970). Magnetic properties and molecular quadrupole tensor of the water molecule by beam-maser Zeeman spectroscopy. *Journal of Chemical Physics*, 52, 3222.
- Visscher, L., & Saue, T. (2000). Approximate relativistic electronic structure methods based on the quaternion modified Dirac equation. *Journal of Chemical Physics*, 113, 3996.
- Wasylishen, R. E., & Bryce, D. L. (2002). A revised experimental absolute magnetic shielding scale for oxygen. *Journal of Chemical Physics*, 117, 10061.
- Wiberg, K. B., Wang, Y. G., Wilson, S. M., Vaccaro, P. H., & Cheeseman, J. R. (2006). Sum-over-states calculation of the specific rotations of some substituted oxiranes, chloropropionitrile, ethane, and norbornene. *Journal of Physical Chemistry A*, 110, 13995.
- Wigglesworth, R. D., Raynes, W. T., Kirpekar, S., Oddershede, J., & Sauer, S. P. A. (2000). Nuclear spin-spin coupling in the acetylene isotopomers calculated from ab initio correlated surfaces for  $^1\text{J}(\text{C,H})$ ,  $^1\text{J}(\text{C,C})$ ,  $^2\text{J}(\text{C,H})$ , and  $^3\text{J}(\text{H,H})$ . *Journal of Chemical Physics*, 112, 3735. Erratum: 114, 9192 (2001).
- Willets, A., Rice, J., Burland, D. M., & Shelton, D. P. (1992). Problems in the comparison of theoretical and experimental hyperpolarizabilities. *Journal of Chemical Physics*, 97, 7590.
- Woon, D. E., & Dunning, T. H., Jr. (1994). Gaussian basis sets for use in correlated molecular calculations. IV. Calculation of static electrical response properties. *Journal of Chemical Physics*, 100, 2975.
- Yanai, T., Tew, D. P., & Handy, N. C. (2004). A new hybrid exchange-correlation functional using the Coulomb-attenuating method (CAM-B3LYP). *Chemical Physics Letters*, 393, 51.
- Zanasi, R., Lazzarotti, P., Malagoli, M., & Piccinini, F. (1995). Molecular magnetic properties within continuous transformations of origin of the current density. *Journal of Chemical Physics*, 102, 7150.
- Zuber, G., & Hug, W. (2004). Rarefied basis sets for the calculation of optical tensors. I. The importance of gradients on hydrogen atoms for the Raman scattering tensor. *Journal of Physical Chemistry A*, 108, 2108.



# 12 Weak Intermolecular Interactions: A Supermolecular Approach

Mark Waller · Stefan Grimme

Organisch-Chemisches Institut, Westfälische Wilhelms-Universität  
Münster, Münster, Germany

<b>Introduction</b> .....	<b>444</b>
Hydrogen-Bonded Complexes .....	445
Aromatic $\pi \dots \pi$ Stacking .....	446
Other Interaction Types .....	447
Interaction Energy .....	448
<b>Methods</b> .....	<b>448</b>
Coupled Cluster .....	449
Quantum Monte Carlo .....	449
Møller–Plesset Perturbation theory .....	449
Spin Component Scaled MP2 .....	450
Hartree–Fock .....	451
Density Functional Theory .....	451
DFT-D .....	452
Range Separated and Dispersion Functionals .....	453
Dispersion Calibrated Effective Potentials .....	454
SemiEmpirical Methods .....	454
Molecular Mechanics .....	455
<b>Basis Sets</b> .....	<b>455</b>
<b>Counterpoise Correction</b> .....	<b>457</b>
<b>Benchmark Sets</b> .....	<b>457</b>
<b>Performance Considerations</b> .....	<b>459</b>
<b>Concluding Remarks and Recommendations</b> .....	<b>461</b>
<b>References</b> .....	<b>462</b>

**Abstract:** Weak intermolecular interactions, which are ubiquitous in biological and materials chemistry, are fast becoming more routinely and accurately investigated owing to the increased performance of computational methods being actively developed. A vast array of pragmatic methods have been proposed using empirical, semi-empirical, density functional theory, and ab initio approaches, which all serve to widen the scope of feasible problems. Especially for the calculation of the important London dispersion interactions, significant progress has been achieved. Herein, we present a general overview on a number of illustrative strategies used to routinely investigate structures and energies of such systems. The composition and advantages/disadvantages of different benchmark sets, which have been found to be of crucial importance in assessing such a wide range of methods is discussed. Finally, a number of experience-based perspectives are provided in relation to the scaling and accuracy of the “more popular” methods used when investigating non-covalent interactions.

A present trend in quantum chemistry is on cheap and reliable methods that effectively solve present-day problems in biological and materials chemistry. Quantum chemistry now confidently looks beyond small polyatomic molecules and toward large supramolecular complexes; this represents an area on the cutting edge of simulation sciences.

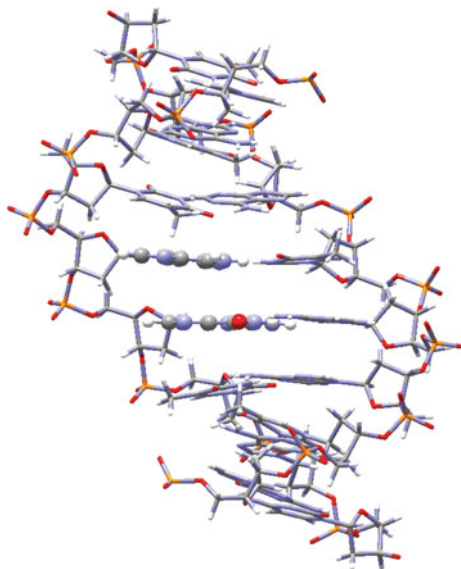
This chapter deals with weak intermolecular (non-covalent) interactions between molecules in the gas phase. These interactions are essential for the quantitative description and understanding of complex molecular aggregates in physics (e.g., surface science), chemistry, and molecular biology. The same interactions also occur in an intramolecular fashion between atoms or groups in one molecule. One of the big advantages of the supermolecular approach described herein is that it can handle both situations on an equal footing. Just for convenience and due to space limitations, we will consider here only intermolecular cases (complexes of at least two molecules). The reader should, however, keep in mind that much of what we are saying about quantum chemical methods similarly holds for the quantum chemical simulation of protein folding.

The following chapter is a pragmatic overview on “current” methods that are useful in obtaining reliable data from quantum chemical calculations, with a strong focus on methods used (and developed) primarily to study such non-covalent interactions. Weak intermolecular interactions in the solid or solution phase are almost completely neglected here, this is by no means a reflection on their importance, rather a way of restricting the scope of this chapter to a particular stream of research. A thorough description of the underlying theory of molecular interactions is presented in Volume I written by Alston Misquita. Only a succinct overview of weak intermolecular interactions is given below to “*set the scene.*”

## Introduction

---

The individual stabilization of weak interactions is to a good approximation additive and is, therefore, extremely important. Weak molecular interactions are characterized by stabilization energies of typically less than  $\Delta E < -30$  kJ/mol (Suresh and Naik 2000) per pair of interacting atoms (fragments). Therefore, in normal physiochemical environments, there is a continuous formation and breaking of such molecular interactions. The resultant combined interaction energies can be responsible for some substantial effects on, e.g., molecular conformation and reactivity. However, one should keep in mind that due to additive property, complexes made out of about 100 atoms can have non-covalent (gas phase) interaction energies more resembling that of covalent bonds (i.e., 300–500 kJ/mol).



■ Fig. 12-1

Deoxyribonucleic acid (DNA) highlighting the intrastrand interaction (*blue bracket*) between the two ball-and-stick base pairs, and the interstrand interaction (*red bracket*) which is between the lower ball-and-stick base and the adjacent base rendered as tubes

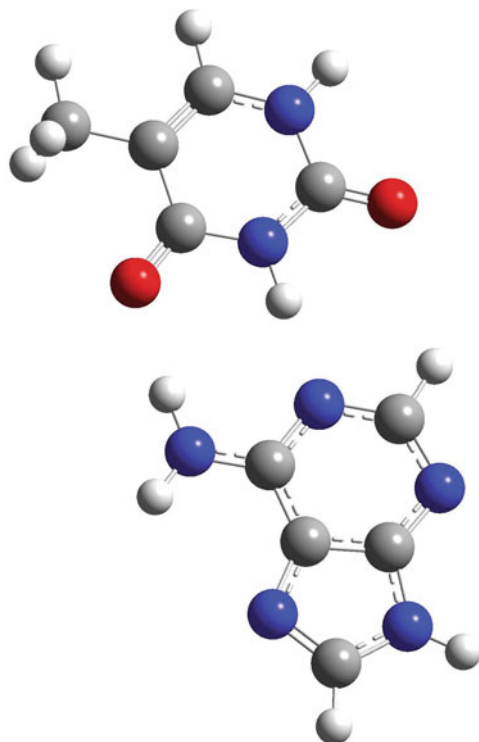
In chemistry and biochemistry, weak interactions are a hot topic of interest, especially within the emerging areas of molecular recognition (Desiraju and Steiner 1999), self-assembly (Hyla-Kryspin et al. 2004), supramolecular chemistry, and general host-guest interactions (Arunan and Gutowsky 1993; Desiraju and Steiner 1999; Hyla-Kryspin et al. 2004; Kim et al. 2000; Sharma et al. 2009; Sinnokrot et al. 2002; Steed et al. 1979; Tsuzuki and Luthi 2004; Tsuzuki et al. 1994). Weak interactions are fundamental in many aspects of biology with the quintessential example being the elegant double helix of DNA, resulting from a subtle interplay of weak interactions (Antony and Grimme 2008), see ► Fig. 12-1.

Furthermore, the secondary and tertiary structure of proteins, membrane structures, and complex intracellular particles such as ribosomes are all maintained by a variety of weak interactions (Wong 2009). Structure-based drug design is therefore dependent upon an understanding of the geometric and energetic aspects of these abundant interactions. Since pharmaceutical agents often bind to biological targets under the control of weak interactions, deconvolution of such host-receptor interactions into separate quantifiable interactions enables drug designers to make subtle modifications and then predict the consequences using modeling techniques.

## Hydrogen-Bonded Complexes

The electron distribution in covalent bonds is frequently polarized due to electronegativity differences of the atoms involved. The lone pair(s) on electron-rich atoms such as oxygen or nitrogen are attractive targets for terminal electron-poor atoms such as hydrogen on adjacent molecules. A hydrogen bond develops wherever a LP-bearing electronegative atom (acceptor)





■ Fig. 12-2

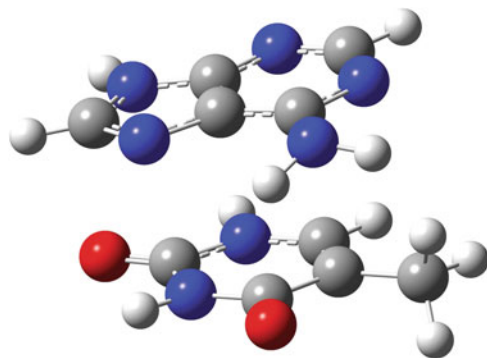
The Watson and Crick (interstrand) adenine-thymine hydrogen-bonded base pair

and a hydrogen atom that is bound covalently to another electronegative atom (donor) are sufficiently near, see ► Fig. 12-2.

Hydrogen bonds are typically strong if the atoms (donor, hydrogen, and acceptor) are collinear. The strength of their interactions reduces drastically for H-bonds which depart significantly from collinearity. The length of hydrogen bonds depends on the type of the constituent groups, but is typically 2.5–3.5 Å (between donor and acceptor nuclei) (Desiraju and Steiner 1999). Molecules may develop both inter- and intramolecular hydrogen bonds. So-called weak H-bonding, e.g., between C–H and fluorine atoms (with interactions in the range 3–10 kJ/mol) are a current topic of research (Hyla-Kryspin et al. 2004).

## Aromatic $\pi \dots \pi$ Stacking

When aromatic rings are oriented favorably, they may develop a stabilizing interaction known as “ $\pi \dots \pi$  stacking” (i.e., involving the  $\pi$  electrons). The  $\pi \dots \pi$  interaction is known to influence reactions, stabilize complexes, and influence structure. It follows that the estimation of the energetic and structural features of these interactions would be extremely useful in understanding many important chemical phenomena (► Fig. 12-3).



■ Fig. 12-3  
The (intrastrand) adenine–thymine stacked base pair

A myriad of experimental and theoretical methods have been employed to investigate  $\pi \dots \pi$ -stacking interactions. State-of-the-art electronic structure methods such as Møller–Plesset perturbation and coupled-cluster methods (see below) show that dispersive forces play the primary stabilizing role in  $\pi$ -stacked complexes (Arunan and Gutowsky 1993; Kim et al. 2000; Sinnokrot et al. 2002; Steed et al. 1979; Tsuzuki and Luthi 2004; Tsuzuki et al. 1994), while the electrostatic forces are responsible for details of the geometrical arrangements. Dispersion is a result of electron correlation, therefore methods that ignore electron correlation cannot be used at all and those that make drastic approximations to it must be carefully validated. The challenge of adequately describing the dispersion interaction is a major focus of the following chapter.

The non-covalent interactions in biological systems are of significant interest, e.g., in purine riboswitches binding sites (Sharma et al. 2009). The interactions of benzene and polycyclic aromatic hydrocarbons (PAHs) can be extended to real-world applications such as investigating the interaction of stacked graphene–nucleobase complexes (Antony and Grimme 2008). Concave buckyball catchers (Wong 2009) were investigated using sophisticated computational methods (e.g., DFT-D and SCS-MP2) explained later within this chapter. Fullerenes and carbon nanotubes (CNT) (Dappe et al. 2009), self-assembled of molecular tweezers formed by discrete biomolecular  $\pi$ -stacks (Lohr et al. 2009), and  $C_{60}$ -derived nanobaskets (dos Santos et al. 2009) were all investigated in 2009 using methods directly developed to model dispersion in an efficient manner. An interesting question was raised by Grimme, asking whether “special  $\pi \dots \pi$ -stacking interactions really exist?” (Grimme 2008).

## Other Interaction Types

The “weak” interaction energy discussed in detail below can be decomposed into various physically meaningful components, i.e., attractive electrostatic, polarization, and dispersion interactions and the repulsive Pauli exchange term. The sum of dispersion and Pauli repulsion is often called van der Waals interaction. In the various types of non-covalent interactions, these contributions are contained to a different degree. For example, there is a continuous transition from a purely dispersion bound van der Waals complex like the methane dimer to the ammonia

dimer which already has partial H-bonding character to the water dimer as the H-bonding prototype complex. The typical H-bond has strong electrostatic and polarization contributions but only small (but non-negligible) dispersion forces. Pauli-repulsion is always present and mainly determined by the distance (wave function overlap) between the fragments. The benzene dimer on the other hand would be unbound when one could switch off the dispersion term. From the above, it is clear that only an accurate account of all these physically important contributions will lead to a consistent description of non-covalent interactions in general.

## Interaction Energy

---

The interaction energy can be calculated with any of the methods outlined within this chapter, to a varying degree of accuracy. Adopting a “*Supramolecular approach*,” the interaction energy is defined as

$$\Delta E^{\text{int}} = E(AB) - E(A) - E(B), \quad (12.1)$$

where  $E(A)$ ,  $E(B)$ , and  $E(AB)$  are the electronic energies of the monomers  $A$ ,  $B$ , and of the complex  $AB$ , respectively. This concept of interaction energy can be extended to a general multi-body regime:

$$\Delta E^{\text{int}} = E(A_1, A_2, A_3, \dots, A_N) - \sum_{i=1}^N E(A_i). \quad (12.2)$$

When investigating multi-body effects, the question of cooperative and anti-cooperative interactions can become an additional consideration of the utmost importance.

When one adopts a supramolecular approach using *ab initio* methods, one has to be mindful of the strengths, and limitations, of a given method:

- Is a particular method size-consistent?
- Does a particular method provide an adequate description of electron correlation?
- Is the use of a particular finite basis set sufficient?
- Does the method inherently have problems in the description of the electronic structure of  $A$  or  $B$ ?

Within this chapter, we shall seek to answer such questions in a general overarching fashion.

An alternative to the supramolecular approach is symmetry adapted perturbation theory (SAPT) that computes the interaction energy directly (Chipman and Hirschfelder 1980; Jeziorski et al. 1978, 1980). The SAPT method has been shown to be suitable for studying weak intermolecular interactions and, in general, provides results similar to the current “gold standard” CCSD(T) (see below). Although this method has been instrumental to the understanding of weak intermolecular interactions, we have omitted details to rein in the scope of the chapter.

## Methods

---

A general overview of the methods, in particular those developed to particularly address weak intermolecular interactions, will be given. The in-depth theoretical details of the underlying methods are given in other parts of this handbook and shall not be restated here in any depth.

This should ensure that readers of different levels (and background) could gain some insight into how such calculations may be performed.

Ab initio methods are naturally more computational expensive than empirical or semiempirical methods. However, they have the obvious advantage that no parameters need to be derived beforehand, which is often laborious and time consuming. The advantage of semiempirical methods are obviously speed, compared to their fully ab initio brethren. A discussion on describing weak intermolecular interactions would be obviously incomplete without an overview of the classical methods.

A strong disclaimer is that we cannot possibly cover all methods derived to compute weak intermolecular interactions, and the methods that we choose to cover shall inevitably date rather quickly. Neither of these considerations is avoidable within such a large and dynamic field of research, and this should hardly be taken as a negative.

## Coupled Cluster

---

Coupled cluster with singles and doubles excitations (CCSD) is a size-consistent post-HF electron correlation method. The wavefunction,  $\Psi$ , in coupled cluster theory is formulated in terms of a cluster (exponential) expansion including the single and double excitation operators  $\hat{T}_1$  and  $\hat{T}_2$ . The effect of triple excitations (T) is calculated with perturbation theory.

CCSD(T) has become, and remains, the “gold-standard” for studying weak intermolecular interactions in the gas phase. The accuracy of this method in general surpasses that of experimental determination and marks the limit of what is feasible using current computing resources.

## Quantum Monte Carlo

---

Quantum Monte Carlo (QMC) effectively solves the many-body problem by a random walk through the electronic configuration space; it has been shown to be a promising method in quantum chemistry. One of the major advantages of QMC is the ability to perform massively parallel calculations, which can effectively increase the scope of what is computationally tractable by distributing the work over hundreds or even thousands of processors. QMC is a general method and, therefore, also has been applied recently to the computation of non-covalent interactions (e.g., the S22 data set) (Korth et al. 2008).

## Møller–Plesset Perturbation theory

---

Møller–Plesset second-order perturbation theory (MP2) is a common method used in computational chemistry to include electron correlation as an extension to Hartree–Fock (HF) theory which neglects Coulomb correlation and thus also misses all dispersion effects. The perturbation is the difference between the Fock-operator and the exact electronic Hamiltonian.

In general, MP2 is a substantial improvement upon Hartree–Fock for all types of non-covalent interactions. The largest advantage of using second-order perturbation is, however, the inclusion of dispersion interactions. The method in general overestimates such an interaction; however, a number of strategies have been developed to address this problem. For example,

Hobza et al. was the first to show that MP2/6-31G(0.25)\* (i.e., with spatially expanded polarization functions) works well in a number of cases due to error compensation (Hobza and Šponer 1996).

Local (truncated) correlation methods, for example, LMP2, have the advantage of superior scaling behavior of the computation time with system size. In addition, they remove to large extent the basis set superposition error (explained below in ► section “Counterpoise Correction”). Such local methods have been applied to weak intermolecular interactions in combination with density fitting approximations (Goll et al. 2008; Hill and Platts 2008).

A further way to correct for the overestimation of MP2 for dispersion bound complexes is MP2.5 (Pitonák et al. 2009). This is a sum of MP2/CBS (complete basis set limit) interaction energies and a scaled third-order energy contribution obtained in small or medium size basis sets. MP2.5 results agree very closely with the estimated CCSD(T)/CBS interaction energies for weak intermolecular interactions. In particular, a very balanced treatment of hydrogen-bonded compared to stacked complexes is achieved with MP2.5. The main advantage of the approach is that it employs only a single empirical parameter and is thus based on two rigorously defined, asymptotically correct ab initio methods, MP2 and MP3. The method is an accurate and computationally feasible alternative to CCSD(T) for the computation of the properties of various kinds of non-covalently bound systems.

## Spin Component Scaled MP2

The total MP2 correlation energy is partitioned into parallel- and antiparallel-spin components that may be separately scaled. The two parameters  $p_s$  and  $p_t$  (scaling factors), whose values can be justified by basic theoretical arguments, were optimized on a thermochemical benchmark set (Grimme 2003).

$$E^{\text{corr}}(\text{SCS-MP2}) = p_s E_{\uparrow\downarrow} + p_t E_{\uparrow\uparrow\downarrow\downarrow}. \quad (12.3)$$

It was shown, that the new method performs significantly better than standard MP2. Significant improvements are especially observed for cases which are usually known as MP2 pitfalls, while cases already described well with MP2 remain almost unchanged. Also, for difficult systems including strong (nondynamical) correlation effects, the improved MP2 method clearly outperforms DFT(B3LYP) and yields results of QCISD or sometimes QCISD(T) quality (QCISD is a variant of CCSD). The uniformity with which the new method improves upon MP2, thereby rectifying many of its problems and suggests it as a valuable quantum chemical method for the investigation of weak intermolecular interactions.

In an effort to simplify and reduce the scaling of the SCS-MP2 method, Head-Gordon has proposed a scaled opposite-spin (SOS) method. The SOS-MP2 method completely neglects the antiparallel-spin contribution to the MP2 energy and scales the parallel contribution by a factor of 1.3 (Jung et al. 2004). The Head-Gordon group has also developed a method, termed modified opposite-spin (MOS), in an attempt to provide a better description of long-range interactions (Lochan et al. 2005). The SCS(MI)-MP2 (MI: molecular interaction) was specifically designed to treat intermolecular interactions (Distasio and Head-Gordon 2007).

SCSN-MP2 is another parameterization of the spin scaling parameters which completely neglects the contribution from antiparallel-spin electron pairs to the MP2 energy while scaling the parallel contribution by 1.76 (Hill and Platts 2007). These spin-component scaled for nucleobases (SCSN) parameters were obtained by minimizing, with respect to SCS parameters,

the RMS interaction energy error relative to the best available literature values, over a set of ten stacked nucleic acid base pairs. The applicability of this scaling to a wide variety of non-covalent interactions is verified through evaluation of a larger set of model complexes, including those dominated by dispersion and electrostatics.

One disadvantage of all SCS variants (except when the scaling factors add to a value of two) is that asymptotically (for large interfragment distances) the correct dispersion energy is not obtained. Although this is of less importance in many complexes, one should keep this in mind when very extended systems are considered.

## Hartree–Fock

---

Hartree–Fock theory is a well-established method in computational chemistry. Therefore, no details on the method or implementation are given here. It suffices to say that Hartree–Fock theory is adequately accurate for hydrogen-bonding interactions (with, however, significant underbinding) in organic first-row compounds. Hartree–Fock, however, fails spectacularly for dispersion bound complexes. A dispersion corrected Hartree–Fock method (HFD) was proposed (Hepburn et al. 1975) and has seen some applications. Its main further disadvantage is the systematic overestimation of dipole moments and underestimation of the fragment polarizability. These two issues are much better described by DFT (at the same cost) so that Hartree–Fock can be considered as being more or less completely outdated.

## Density Functional Theory

---

Density functional theory (DFT) has gained huge popularity due to its ability to provide good accuracy, and due to its favorable scaling, in a timely fashion. Although it has been shown, and is commonly known, that an exact exchange correlation functional is possible, it remains ever elusive. To make matters worse, “traditional” (Kohn–Sham) DFT in present approximations does not provide a correct description of the dispersion interactions.


Density functional theory still remains “plagued” by an abundance of functionals developed with a plethora of design goals. Some grouping of functionals was proposed by Perdew and Schmidt (2001) using the “Jacob’s ladder” metaphor. In this metaphor, functionals may be grouped according to their formulation:

- First-rung functionals are only dependent upon the density and are known as local density approximation (LDA). Although LDA does overestimate the interaction energies in some dispersion bound systems (but for the wrong reasons), its accuracy can only be described as sporadic, and therefore its application in intermolecular interactions is NOT recommended.
- Second-rung functionals utilize in addition the gradient of the density, known as generalized gradient approximation (GGA). They typically show repulsive behavior for dispersion bound complexes similar to Hartree–Fock.
- Third-rung functionals further include the kinetic energy density or Laplacian (second derivative) of the density. These functionals show only marginal improvements over their second-rung counterparts.
- Fourth-rung functionals include Hartree–Fock exchange and are known as hybrid-GGAs. A number of hybrid functionals have been intentionally parameterized using datasets that

include dispersion bound complexes, e.g., M05 (Zhao et al. 2005, 2006) and M06 (Zhao and Truhlar 2006a, b, 2008) (and variants thereof) from Truhlar and coworkers. The BHandH (Becke 1993) has been shown to give reasonable answers for particular problems of interest, but should be used with extreme caution (Swart et al. 2007; Waller et al. 2006).

- Fifth-rung functionals include the occupied and virtual orbitals simultaneously and are known as double hybrid functionals. They offer a superior description of long range-dispersion, while maintaining some quantum mechanical rigor. By their very nature, the current implementations are fundamentally semiempirical. A general *ansatz* for a combination of Kohn-sham DFT and perturbation theory is based on the following expression for the exchange-correlation energy  $E_{xc}$ :

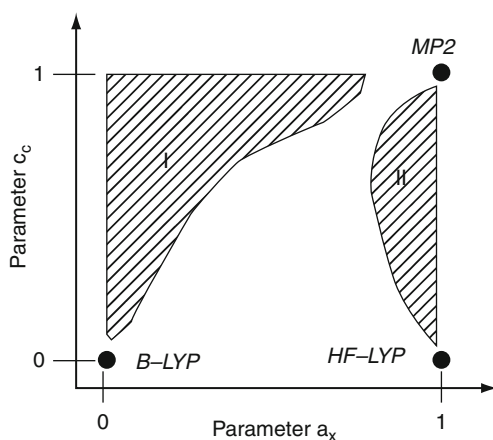
$$E_{xc} = (1 - a_x)E_x^{\text{GGA}} + a_x E_x^{\text{HF}} + (1 - c_c)E_c^{\text{GGA}} + c_c E_c^{\text{PT2}}. \quad (12.4)$$


If  $c_c = 0$  and  $a_x \neq 0$ , then a fourth-rung functional; If  $c_c = 0$  and  $a_x = 0$ , then a second-rung functional is recovered, see  Fig. 12-4.

The details of many “garden variety” density functionals are not discussed in this chapter, rather only recently developed schemes that specifically address shortcomings of density functionals in accurately describing weak intermolecular interactions.

## DFT-D

An empirical method to account for dispersive interactions in practical calculations with the density functional theory (termed DFT-D) (Grimme 2006) has been tested for a wide variety of molecular complexes. As in previous schemes, the dispersive energy is described by a damped interatomic potential of the form  $C_6 R^{-6}$ . The use of pure (non-hybrid), gradient-corrected density functionals (e.g., BLYP or PBE), together with the resolution-of-the-identity



 Fig. 12-4

Schematic description of possible methods arising from different combinations of HF exchange and PT2 mixing parameters. The *dashed areas* I and II can be excluded by physical reasoning. B-LYP is a second-rung GGA and in HF-LYP the correlation energy is mixed with Hartree–Fock

(RI) approximation for the Coulomb integrals, allows for an efficient computation of large systems (as is often required for supramolecular chemistry).

By using a global scaling factor for the atomic  $C_6$  coefficients, the functional dependence of the results could be strongly reduced. The double counting of correlation effects for strongly bound complexes is found to be insignificant if steep damping functions are employed. For stacked aromatic systems and the important base pairs, the DFT-D(BLYP) model seems to be even superior to standard MP2 treatments (which are known to systematically overbind). The good results obtained, in a variety of diverse examples, suggest that the DFT-D approach is a practical tool for describing weak intermolecular interactions. Furthermore, the DFT-D data may be used to calibrate much simpler (e.g., force-field) potentials. Alternatively, the optimized structures may be used as input for more accurate ab initio calculations of the interaction energies (Grimme 2006b).

The dispersive correction term in DFT-D is given by

$$E_{\text{disp}} = -s_6 \sum_{i=1}^{N_{\text{at}}-1} \sum_{j=i+1}^{N_{\text{at}}} \frac{C_6^{ij}}{R_{ij}^6} f_{\text{dmp}}(R_{ij}), \quad (12.5)$$

where  $N$  is the number of atoms in the system,  $C_6^{ij}$  denotes the dispersion coefficient for atom pair  $ij$ ,  $s_6$  is a global scaling factor (see below), and  $R_{ij}^{ij}$  is the interatomic distance. The damping function is

$$f_{\text{dmp}}(R) = \frac{1}{1 + e^{-\alpha(R/R_0-1)}}, \quad (12.6)$$

where  $R_0$  is the sum of atomic respective van der Waals (cut-off) radii, see [Fig. 12-5](#).

This simple approach has recently been improved regarding accuracy, less empiricism (the most important parameters  $R_0$  and  $C_6$  are computed ab initio), and general applicability to most elements of the periodic table (Grimme et al. 2010). An important change in this so-called DFT-D3 method is that the  $C_6$  dispersion coefficients are dependent on the molecular structure which accounts for subtle effects, e.g., the hybridization state of an atom changes.

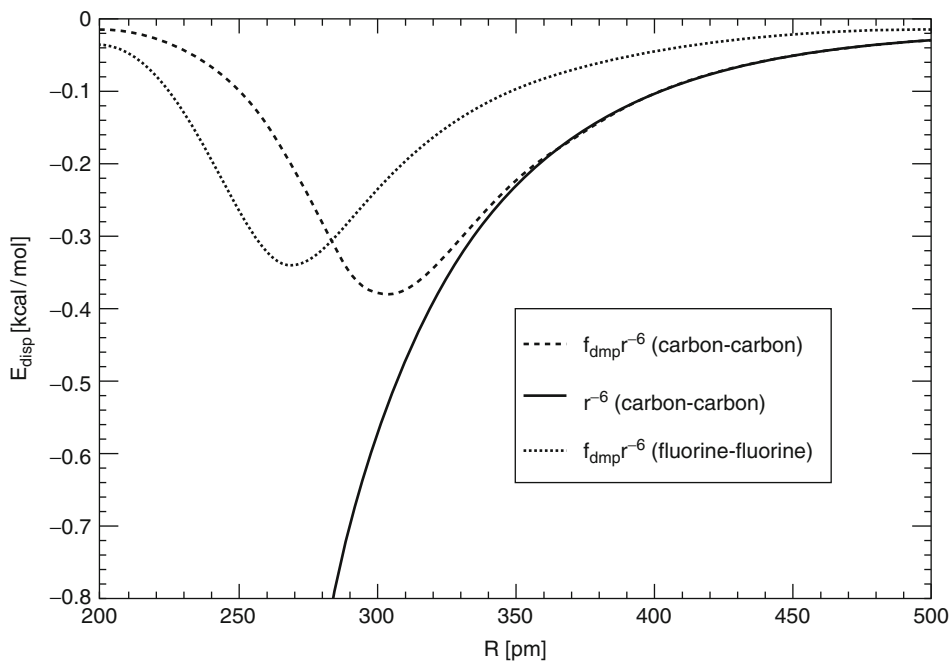
The DFT-D method does not only work for molecular complexes and intramolecular dispersion effects but is rather general, and Sauer and coworkers extended this correction to periodic systems (Kerber et al. 2008).

## Range Separated and Dispersion Functionals

An alternative method is the nonlocal van der Waals density functional (vdW-DF) of Langreth and Lundqvist and coworkers (Andersson et al. 1996; Lundqvist et al. 1995). In vdW-DF, the nonlocal correlation is calculated explicitly in a non-empirical manner. It is typically used with standard GGAs like PBE or revPBE which introduces some inconsistency, as this results in an unbalanced treatment of computed interaction energies and equilibrium distances. The overall quality of vdW-DF results for typical non-covalent complexes is not better than with DFT-D but requires substantially more computation time.

The range-separated hybrid (RSH+MP2) (Ángyán et al. 2005; Gerber and Ángyán 2007) employs MP2 to account for the dispersion interaction, HF for long-range exchange, and, finally, LDA for short-range exchange and correlation. The method provides promising results for rare gas complexes but has not thoroughly been tested on standard benchmark sets (see [section "Benchmark Sets"](#)). The basic idea is similar to that of double-hybrid functionals.





■ Fig. 12-5

Dispersion correction (Eq. 12.5) for two carbon and two fluorine atoms ( $s_6 = 1.0$ ) separated by a distance  $R$ . The solid line shows the undamped potential for comparison

## Dispersion Calibrated Effective Potentials

A Dispersion-Corrected Atom-Centered Potential (DCACP) is a novel approach whereby the “missing” dispersion effect in traditional DFT is introduced using a suitably engineered effective core potential (ECP) (von Lilienfeld et al. 2004). The fitted atom–electron potentials in the DCACP method have been shown to perform well for weak intermolecular interactions (Arey et al. 2009; Tapavicza et al. 2007). Importantly, for practical purposes, the parameterized DCACPs are somewhat transferable to atoms in a wide range of different chemical environments (Lin and Rothlisberger 2008; Lin et al. 2007a, b; von Lilienfeld et al. 2005). This approach, however, has the same disadvantage as standard DFT-D in that the atomic parameters do not change with the electronic environment.

## SemiEmpirical Methods

Traditionally, it has been generally believed that semiempirical methods are not particularly well suited to hydrogen bonding problems. In order to overcome these limitations, the PM6 method has been re-parameterized and additional empirical terms were added to increase the accuracy of this semiempirical hamiltonian for describing weak intermolecular interactions (PM6-DH) (Řezáč et al. 2009) and the second generation corrections scheme PM6-DH2 (Korth et al. 2010).

Such empirical corrections for the semiempirical methods brings about a new frontier in large simulations.

Another approach was proposed by Tuttle and Thiel (2008), starting with the OM $x$  family of methods and adopting the dispersion correction of Grimme (2004). This particular combination was referred to as OM $x$ -D. The authors found it necessary to rescale the empirical  $s_6$  parameter (see above). Similarly, Hillier et al. (McNamara and Hillier 2007) proposed the AMI-D and PM3-D to alleviate some of the shortcomings of some more traditional semiempirical Hamiltonians.

The RMI $_{BH}$  method (Feng et al. 2009) was constructed by adding Gaussian functions to the core–core repulsion items in the original AM1 formula. It was demonstrated that RMI $_{BH}$  provides good agreement with the values of both high-level calculations and experiments for the binding energies of biological hydrogen-bonded systems.

Somewhat removed is the density functional based tight-binding method (DFTB), which is based on a second-order expansion of the Kohn-Sham total energy, employing a self-consistent redistribution of Mulliken charges (SCC-DFTB) (Elstner et al. 1998). It also employs dispersion corrections similar to the DFT-D method and has successfully been applied, e.g., to nuclear-base stacking problems (Elstner et al. 2001).

## Molecular Mechanics

---

The empirically fitted force-fields such as CHARMM (Brooks et al. 1983), AMBER (Case et al. 2008), and GROMOS (Scott et al. 1999) perhaps perform better than one might originally imagine. Most importantly for the focus of this chapter are the noncovalent interactions, as naturally the interaction energy of a supramolecular complex should be dominated by the non-covalent terms. Therefore, a good description of such noncovalent interactions requires a balanced description of the electrostatic and van der Waals energies. Typically standard force-fields utilize the Coulomb's law for the electrostatic part and do not consider polarization. By judicious adjustment of the partial charges, one may strive to effectively model hydrogen-bonded interactions. Furthermore, one recognizes that the expression for the van der Waals interaction is normally represented as a Lennard-Jones potential. The  $r^{-12}$  term describing the Pauli repulsion and the  $r^{-6}$  term describing the long-range attractive dispersion forces. The vdW parameters may also be fitted to reproduce experimentally derived structures.

## Basis Sets

---

Most *ab initio* and DFT schemes employ the LCAO method. The molecular orbitals are expanded using an orbital basis set – a collection of mathematical functions used to model the spatial variation of the orbitals. Historically, Slater-type orbitals were used due to their geometric similarity to the hydrogenic orbitals. They also remain a common choice in semiempirical MO theory. However, they do have a significant drawback in that there are no general and numerically stable solutions for the many-center integrals involving Slater-type orbitals. Consequently, most practitioners of quantum chemistry turned to Gaussian type orbitals.

Larger basis sets give rise to more accurate representations of the MOs. Practical considerations have dictated the need for optimization of basis sets to best describe molecular properties

within a sensible computational time. This has led to the development of various basis sets each with differing characteristics reflecting their intended applications. The use of such optimized finite basis sets does produce reasonably accurate geometries (as the particular choice of a basis set does not strongly influence computed structures). However, energies are much more basis set dependent.

One may use two contracted GTOs per atomic orbital, as in the so-called double-zeta basis sets (Lochan et al. 2005), as this provides much greater flexibility. Split-valence basis sets partition the atomic orbitals into core and valence regions. The core AO's are assigned a minimal basis, while the valence orbitals are described at the double-zeta level.

The Pople style basis sets (Binkley et al. 1980; Dobbs and Hehre 1986, 1987a, b; Gordon et al. 1982; Hehre et al. 1969; Pietro et al. 1982) have received widespread use in the computational community. They may be described as:  $X - YZg$  where  $X$  is the number of primitive Gaussians used to describe the core atomic orbitals. The valence orbitals are composed of a linear combination of  $Y$  and  $Z$  primitive Gaussian functions, respectively. Split-valence triple- and quadruple-zeta basis sets are also used, denoted as  $X - YZWg$ ,  $X - YZ WVg$ , etc.

The correlation consistent (cc) basis sets devised by Dunning (1989) were designed to converge systematically to the complete-basis-set (CBS) limit when used in conjunction with extrapolation techniques, see below. They may be described as: cc-pVNZ where  $N = D, T, Q, 5, 6, \dots$  (D=double zeta, T=triple zeta, etc.).

Alternatively, the Ahlrichs style split-valence basis sets (Schaefer et al. 1992) are also ubiquitous in computational chemistry. Practically, extended AO basis sets of polarized TZV or QZV quality should be employed. Because the Ahlrichs basis sets have been carefully optimized variationally, the basis set superposition error (described below) is much smaller than with Pople or Dunning sets of about the same size. These expansions are consistently available for all elements of the periodic table.

Diffuse functions, denoted in Pople-type sets by a plus sign, +, and in Dunning-type sets by "aug" (abbreviation of "augmented"), are shallow Gaussian basis functions with large exponents. The diffuse functions are essential for the "tail" portion of the atomic orbitals, which are distant from the atomic nuclei. The diffuse basis functions are important when considering intermolecular complexes (a) to effectively span the intermolecular region and (b) to accurately describe the fragment polarizabilities. So-called polarization functions are also necessary for weak interactions to improve the flexibility of the wave function. These are functions with higher angular momentum than in the occupied ground state atomic orbitals.

The RI approximation is a method to approximate four-index two electron integrals without having any significant effect on the accuracy of results (Eichkorn et al. 1995). It requires specific auxiliary basis functions, which are available for many standard basis sets. The method is most efficient in GGA and MP2 calculations where it saves a factor of 10–20 in computation time for larger systems. It is also available in hybrid-GGA and Hartree–Fock treatments, but the savings are less (about a factor of 2–3). RI (also called density fitting) is strongly recommended in all treatments of larger complexes and is available in many major quantum chemistry codes.

Extrapolation schemes are employed to relieve the errors associated by using a truncated basis set. It is most often used to improve the computed correlation energy but also Hartree–Fock or DFT energies can be extrapolated. A number of schemes have been proposed and routinely used within the literature, a brief survey of some of the more popular schemes in chronological order: Martin (1996) and later Martin and Taylor (1997), Helgaker et al. (1998), Truhlar (1998), and Lee (2005) correction scheme. In the mostly employed standard scheme, two computations with basis sets of systematically improved quality (e.g., Dunning sets with

$X = 2, Y = 3$  or  $X = 3, Y = 4$ ) are required. The correlation energy is obtained by

$$E_{XY}^{\infty} = \frac{E_X^{\text{corr}} X^3 - E_Y^{\text{corr}} Y^3}{X^3 - Y^3}. \quad (12.7)$$

Basis set extrapolation also reduces considerably the basis set superposition error (see below).

## Counterpoise Correction

---

The basis set superposition error (BSSE) arises as a direct result of basis set truncation. This truncation for a dimer or complex is less severe as it is for the monomer as the dimer basis set is the union of the two-monomer basis sets. This leads to an artificial energy lowering of the dimer compared to the monomers and leads to a too low (negative) interaction energy. The so-called *counterpoise correction* (CP) is the standard procedure for calculating an interaction energy using a supermolecular approach. The counterpoise corrected interaction energy is

$$\Delta E^{\text{CP}} = E_{AB}(AB) - E_{AB}(A) - E_{AB}(B), \quad (12.8)$$

where  $E_{AB}(A)$  and  $E_{AB}(B)$  denote the total energies of monomers  $A$  and  $B$ , respectively, computed with the dimer basis set of  $AB$ , i.e., in the calculation of monomer  $A$  including the basis set of the  $B$  monomer (but neglecting the nuclear charges and electrons of  $B$ ). In this way, the basis set for each monomer becomes of about the same size as for the dimer thereby creating a more balanced description.

The counterpoise correction typically overestimates the BSSE since the monomer basis set is enhanced not only by empty orbitals of the other fragment, but also by orbitals occupied by electrons of the other monomer molecule which are excluded by the Pauli principle. Thus, if CP-corrected and uncorrected interaction energies are plotted as function of basis set size, they approach from above and below, respectively, the true interaction energy at the complete basis set (CBS) limit. CP corrections are mandatory for all double-zeta calculations and with MP2 or CCSD(T) also for triple-zeta basis treatments. In triple-zeta basis set (e.g., cc-pVTZ or TZVPP) DFT calculations, the BSSE is typically less than 5–10% of the interaction energy which makes the laborious CP correction unnecessary. If sets of valence quadruple-zeta are used, it seems as if the error of the CP procedure is often similar to the (uncorrected) BSSE, but this is system-dependent and more definite conclusions about this issue requires further work.

## Benchmark Sets

---

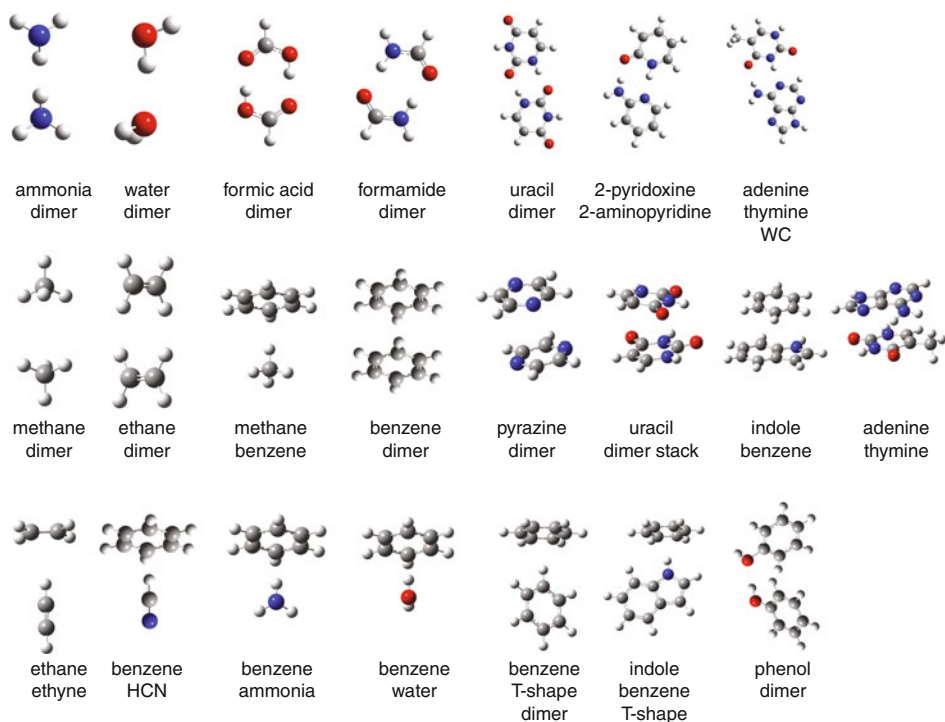
The importance of validating and assessing the relative strengths, and pitfalls, of a given theoretical method is often achieved using validation against standardized data sets. This circumvents the need to meta-analyze inhomogeneous studies (different basis sets, density functionals, etc.) of diverse molecular systems. Computational chemistry should ideally be predictive, and by having a clear and widely accepted set of references, one can preempt the magnitude of expected errors.

The development of force fields, semiempirical parameters, or even indeed density functionals, are reliant upon such carefully constructed datasets. What is needed is a good balance of diversity and relevance, when creating such a benchmark set. A benchmark set should ideally be able to expose systematic errors for different methods.

The BEDGB dataset (Řezáč et al. 2008) contains a number of subsets; S22 (Jurečka et al. 2006) has been used extensively in benchmarking weak intermolecular interactions, see Fig. 12-6; S26 (Riley and Hobza 2007) augments four extra molecules into the S22 dataset; Small Halogen Bonding Complexes (Riley and Hobza 2008) contains six complexes calculated at the CCSD(T)/aug-cc-pVTZ CP level of theory; JSCH-2005 (Jurečka et al. 2006) is a larger benchmark of non-covalent complexes; Set of five small peptides (Valdes et al. 2008) contains aromatic side chains and includes the P26 set; SCAI (Berka et al. 2009) – representative interactions of amino acid side chains.

The Minnesota non-covalent interaction databases were compiled by Truhlar et al. Benchmark Database of Noncovalent Interactions (2006): HB6/04 (Zhao et al. 2006; Zhao and Truhlar 2005a, b) is a hydrogen bond database that consists of the equilibrium binding energies of six hydrogen bonding dimers; DI6/04 (Zhao et al. 2006; Zhao and Truhlar 2005b, 2005) database contains the binding energies of six dipole interaction complexes; WI7/05 (Zhao et al. 2006, 2005; Zhao and Truhlar 2005a) database consists of the binding energies of seven weak interaction complexes; PPS5/05 (Zhao et al. 2005; Zhao and Truhlar 2005a) database consists of binding energies of five  $\pi \dots \pi$ -stacking complexes; CT7/04 (Zhao et al. 2005, 2006; Zhao and Truhlar 2005b) database consists of binding energies of seven charge transfer complexes.

When a collection of the different constituents of the Minnesota non-covalent interaction databases is made (HB6/04, DI6/04, WI7/05, PPS5/05, and CT7/04) the superset contains 31



■ Fig. 12-6  
The S22 dataset

complexes with many dimers in common with the S22 dataset. As these two databases are rather similar, for the remaining chapter, we will focus on the S22 dataset, see [Fig. 12-5](#), to assess performance.

## Performance Considerations

The methods were, more or less, presented above in order of decreasing accuracy. The higher-level *ab initio* methods are more accurate than the lower methods, as expected. The density functionals tend to roughly follow the Jacob's ladder analogy in terms of accuracy for the S22 dataset. Less accurate, for the S22, are the semiempirical methods with the empirical ones performing even worse. In order to provide a visual indication of the relevant methods [Fig. 12-7](#) displays plots of the normal error distributions. One can immediately note that most methods are shifted to the right of the  $y$ -axis with CCSD(T) being the reference values. The higher-level methods again tend to be more narrow in their error distribution.

The dramatic gains in accuracy when one investigates weak intermolecular interactions at the DFT and MP2 levels of theory (with and without corrections) are displayed in [Fig. 12-8](#).

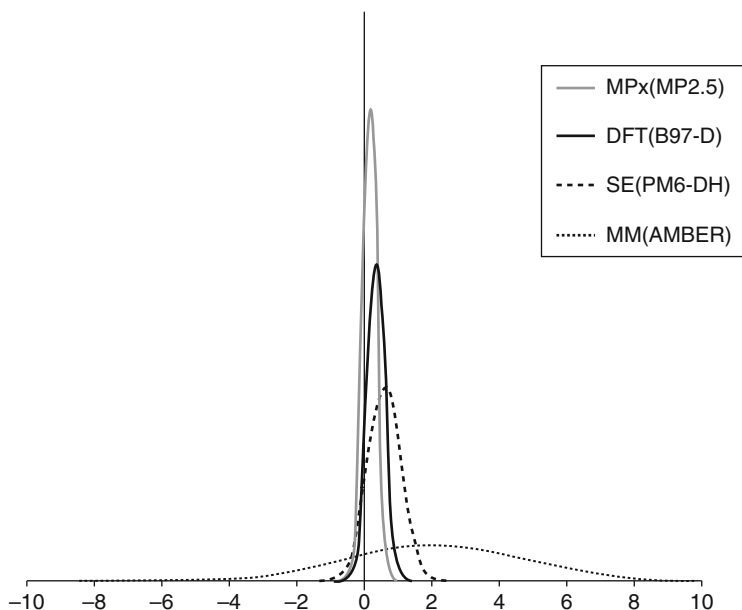
Timing considerations (typically scaling) are important when one considers computational efficiency. Diminishing returns does occur with *ab initio* methods, and one must remain mindful of the desired accuracy and computational resources on hand. Such a delicate balancing act is crucial for practitioners of computational chemistry.

The computation time  $t(cpu)$  required to execute a given quantum chemical method to obtain the energy follows a power law with respect to the number of electrons in the system, i.e.,

$$t(cpu) = a(N_{el})^b, \quad (12.9)$$

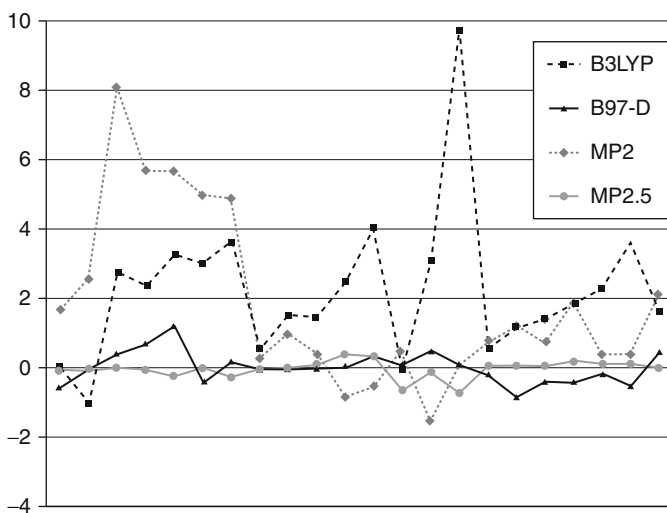
where  $a$  and  $b$  are constants which are characteristic for each method and its implementation. While  $b$  determines how fast the computation time increases with increasing system size (often abbreviated by the term “order  $n$ ”, i.e., an “order  $n$ ” method means  $b = n$ ), the prefactor  $a$  measures how efficiently the given combination of hard- and software performs the task. Although in general methods with small  $b$  are preferred, it is important to mention that to some extent a large value of  $b$  can be compensated by a small  $a$  so that formally “expensive” methods can sometimes be a better choice. Because the prefactor is very strongly influenced by many technical parameters, we present in [Table 12-1](#) the computation times (single-point energy only) for two examples ordered according to formal scaling behavior.

It is seen ([Table 12-1](#)) that a realistic evaluation of the performance requires consideration of not too small systems and basis sets. The aug-cc-pVDZ results for the water dimer and the cc-pVDZ values for the benzene dimer, however, nicely illustrate the steep increase of the computation time with the level of sophistication. While RI-MP2 is not much more costly than HF (and even DFT), higher-level correlation methods (in particular CCSD(T)) already for medium-sized systems lead to a substantial increase in computation time. The timings for the two systems also allow to check if the formal scaling laws hold. For example, for the water and benzene dimers, the system size increases by a about a factor of four which translates for  $b = 4$  to a computation time ratio of  $4^4 = 256$  which is worse than the actually observed factor of about 50. The timings also show that already for a medium-sized system like the benzene dimer, CCSD(T) calculations with reasonable basis sets (at least aug-cc-pVDZ) are prohibitive in routine applications.



■ Fig. 12-7

The normal error distribution (in kcal/mol) for Møller-Plesset (MP), density functional theory (DFT), semiempirical (SE), molecular mechanics (MM)



■ Fig. 12-8

The individual errors (in kcal/mol) for (a) DFT (b) DFT-D (c) MP2 (d) MP2.5 across the entries of the S22 dataset

■ Table 12-1

Computation times (in seconds on one Intel CoreDuo T9300 2.50 GHz CPU) for two non-covalently bound complexes with different quantum chemical methods

Method	Formal scaling exponent $b$	Water dimer ( $N_{el}=20$ )	Benzene dimer ( $N_{el}=84$ )
AM1	3	0.5	0.6
DFT(semi-local)	3	12.7	78.3
Hartree–Fock	4	5.6 (10.8)	278
RI-MP2	5	7.2 (12.5)	301
CCSD	6	11.7 (47.7)	17,284
CCSD(T)	7	14.1 (72.9)	25,810

Except for AM1, all calculations have been performed with a small cc-pVDZ (or aug-cc-pVDZ in parentheses) AO basis set and using the ORCA program package

## Concluding Remarks and Recommendations

The aim of a developing a diverse set of well-balanced methods that can treat weak and strong inter- and intramolecular interactions continues to be a dominate area of computational chemistry. The ubiquitous nature of the weak intermolecular interactions in “state-of-the-art” materials and biomedical sciences ensures that work in this direction shall continue unabated.

The nature of fundamental intermolecular interactions were briefly introduced; a general impression of the relative strengths and weaknesses of different methods; basis sets; basis set extrapolation schemes; counterpoise correction schemes; and benchmark sets was presented. The chapter has concluded with overarching summary for the expected accuracy of the particular methods.

We finally want to make some general recommendations how “weak interactions” should be treated by quantum chemical methods:

1. Whenever possible, simple, approximate methods that are unavoidable in many practical applications should be checked or benchmarked against large (or complete) basis set CCSD(T) results. Often one can identify the main interactions and construct suitable model systems for this task. If the one-particle basis set issues and the basis set superposition error are carefully considered, CCSD(T) errors are <5% of the true interaction energies.
2. The simpler CCSD and MP3 ab initio methods are much less reliable (but still computationally expensive) and should not be used. In the “wave function world,” MP2 can (with some faults) also be recommend because the cost/performance ratio is rather good. MP2 should not be used for unsaturated or more strongly correlated (metallic) cases for which SCS-MP2 is a reliable alternative. If the systems are not too large (<50 atoms), MP2.5 can be used as well.
3. An interesting ab initio alternative when the system can be separated into chemically meaningful fragments is symmetry adapted perturbation theory (SAPT) that is complementary to the here-described supermolecular approach. Its main advantage is that it is free of BSSE and that it provides a natural partitioning of the interaction energy into physically meaningful components.
4. When the issue of London dispersion interactions is carefully considered with DFT, this yields a similar or often even better performance than MP2. Of the several approaches in this area, the DFT-D method has proven as an accurate and robust computational tool.



The main advantage of DFT-based approaches is that they can be applied also in electronically complicated situations (e.g., metal-containing systems) when MP $n$ -based methods fail.

5. The biggest problem in DFT is the choice of the functional approximation. In many cases, computationally cheap (meta-)GGAs (e.g., BLYP, PBE, or TPSS) can be recommended. Such functionals should not be used when the self-interaction error (e.g., in charged open shell systems) plays a role. Then, hybrid functionals are required which also have less tendency for over-polarization. The currently highest level of approximation in DFT is represented by double-hybrid functionals (e.g., B2PLYP) that also perform very well for non-covalent interactions.
6. An important performance issue, that is unfortunately occasionally overlooked, is the tremendous computational savings gained by applying the resolution of the identity (RI) approximation when evaluating the two-electron integrals. This approximation, in combination with the development of well-performing “auxiliary” basis sets, has dramatically opened up new frontiers in large-scale calculations. We do not wish to comment on the accuracy of the various RI approximations, but we have experienced particularly good performance with the implementations in TURBOMOLE, ORCA, MOLPRO and Q-CHEM.
7. Semiempirical methods (and this also holds for many forcefields) mainly suffer from a poor description of the electrostatic interactions which, e.g., is demonstrated by their notoriously bad performance for hydrogen-bonded systems (for which even the simplest GGAs work very well). Because also their description of polarization (induction) contributions to binding is deficient, these methods can only be recommended for nonpolar systems or as parts in ONIOM-type approaches to describe the outer regions of a quantum chemical system.

## References

- Andersson, Y., Langreth, D. C., & Lundqvist, B. I. (1996). van der Waals interactions in density-functional theory. *Physical Review Letters*, *76*, 102.
- Ángyán, J. G., Gerber, I. C., Savin, A., & Toulouse, J. (2005). van der Waals forces in density functional theory: Perturbational long-range electron-interaction corrections. *Physical Review A*, *72*, 012510.
- Antony, J., & Grimme, S. (2008). Structures and interaction energies of stacked graphene–nucleobase complexes. *Physical Chemistry Chemical Physics*, *10*, 2722–2729.
- Arey, J. S., Aeberhard, P. C., Lin, I.-C., & Rothlisberger, U. (2009). Hydrogen bonding described using dispersion-corrected density functional theory. *The Journal of Physical Chemistry B*, *113*, 4726–4732.
- Arunan, E., & Gutowsky, H. S. (1993). The rotational spectrum, structure and dynamics of a benzene dimer. *Journal of Chemical Physics*, *98*, 4294.
- Becke, D. (1993). A new mixing of Hartree–Fock and local density-functional theories. *Journal of Chemical Physics*, *98*, 1372–1377.
- Benchmark Database of Noncovalent Interactions. (2006). [http://comp.chem.umn.edu/database\\_noncov/noncovalent.htm](http://comp.chem.umn.edu/database_noncov/noncovalent.htm). Accessed 13 February 2010.
- Berka, K., Laskowski, R., Riley, K. E., Hobza, P., & Vondrasek, J. (2009). Representative amino acid side chain interactions in proteins. A comparison of highly accurate correlated *ab initio* quantum chemical and empirical potential procedures. *Journal of Chemical Theory and Computation*, *5*, 982–992.
- Binkley, J. S., Pople, J. A., & Hehre, W. J. (1980). Self-consistent molecular orbital methods. 21. Small split-valence basis sets for first-row elements. *Journal of the American Chemical Society*, *102*, 939–947.
- Brooks, B. R., Bruccoleri, R. E., Olafson, B. D., States, D. J., Swaminathan, S., & Karplus, M. (1983). CHARMM: A program for macromolecular energy, minimization, and dynamics calculations. *Journal of Computational Chemistry*, *3*, 187–217.
- Case, D. A., Darden, T. A., Cheatham, T. E. I., Simmerling, C. L., Wang, J., Duke, R. E., Luo,

- R., Crowley, M., Walker, R. C., Zhang, W., Merz, K. M., Jr., Wang, B., Hayik, S., Roitberg, A., Seabra, G., Kolossváry, I., F.Wong, K., Paesani, F., Vanicek, J., Wu, X., Brozell, S. R., Steinbrecher, T., Gohlke, H., Yang, L., Tan, C., Mongan, J., Hornak, V., Cui, G., Mathews, D. H., Seetin, M. G., Sagui, C., Babin, V., & Kollman, P. A. (2008). *AMBER 10*. San Francisco: University of California.
- Chipman, D. M., & Hirschfelder, J. O. (1980). On symmetry in the polarization expansion for intermolecular forces. *Journal of Chemical Physics*, *73*, 5164.
- Dappe, Y. J., Ortega, J., & Flores, F. (2009). Intermolecular interaction in density functional theory: Application to carbon nanotubes and fullerenes. *Physical Review B*, *79*, 165409.
- Desiraju, G. R., & Steiner, T. (1999). The weak hydrogen bond: In structural chemistry and biology. In *IUCr monographs on crystallography* (Vol. 9). Oxford: Oxford University Press/International Union of Crystallography Oxford.
- Distasio, R. A., Jr., & Head-Gordon, M. (2007). Optimized spin-component scaled second-order Møller-Plesset perturbation theory for intermolecular interaction energies. *Molecular Physics*, *105*, 1073–1083.
- Dobbs, K. D., & Hehre, W. J. (1986). Molecular orbital theory of the properties of inorganic and organometallic compounds 4. Extended basis sets for third- and fourth-row, main-group elements. *Journal of Computational Chemistry*, *7*, 359–378.
- Dobbs, K. D., & Hehre, W. J. (1987a). Molecular orbital theory of the properties of inorganic and organometallic compounds 5. Extended basis sets for first-row transition metals. *Journal of Computational Chemistry*, *8*, 861.
- Dobbs, K. D., & Hehre, W. J. (1987b). Molecular orbital theory of the properties of inorganic and organometallic compounds. 6. Extended basis sets for second-row transition metals. *Journal of Computational Chemistry*, *8*, 880–893.
- dos Santos, S. G., Pires, M. S., Lemos, V., Freire, V. N., Caetano, E. W. S., Galvão, D. S., Sato, F., & Albuquerque, E. L. (2009). C<sub>60</sub>-derived nanobaskets: Stability, vibrational signatures, and molecular trapping. *Nanotechnology*, *20*, 395701.
- Dunning, T. H., Jr. (1989). Gaussian basis sets for use in correlated molecular calculations. I. The atoms boron through neon and hydrogen. *Journal of Chemical Physics*, *90*, 1007–1023.
- Eichkorn, K., Treutler, O., Öhm, H., Häser, M., & Ahlrichs, R. (1995). Auxiliary basis sets to approximate Coulomb potentials. *Chemical Physics Letters*, *240*, 283–290.
- Elstner, M., Porezag, D., Jungnickel, G., Elsner, J., Haugk, M., Frauenheim, T., Suhai, S., & Seifert, G. (1998). Self-consistent-charge density-functional tight-binding method for simulations of complex materials properties. *Physical Review B*, *58*, 7260.
- Elstner, M., Hobza, P., Frauenheim, T., Suhai, S., & Kaxiras, E. (2001). Hydrogen bonding and stacking interactions of nucleic acid base pairs: A density-functional-theory based treatment. *Journal of Chemical Physics*, *114*, 5149.
- Feng, F., Wang, H., Fang, W., & Yu, J. (2009). Can semiempirical quantum models calculate the binding energy of hydrogen bonding for biological systems? *Journal of Theoretical and Computational Chemistry*, *4*, 691–711.
- Gerber, I. C., & Ángyán, J. G. (2007). London dispersion forces by range-separated hybrid density functional with second order perturbational corrections: The case of rare gas complexes. *Journal of Chemical Physics*, *126*, 044103.
- Goll, E., Leininger, T., Manby, F., Mitrushchenkov, A., Werner, H.-J., & Stoll, H. (2008). Local and density fitting approximations within the short-range/long-range hybrid scheme: Application to large non-bonded complexes. *Physical Chemistry Chemical Physics*, *10*, 3353.
- Gordon, M. S., Binkley, J. S., Pople, J. A., Pietro, W. J., & Hehre, W. J. (1982). Self-consistent molecular-orbital methods. 22. Small split-valence basis sets for second-row elements. *Journal of the American Chemical Society*, *104*, 2797–2803.
- Grimme, S. (2003). Improved second-order Møller-Plesset perturbation theory by separate scaling of parallel- and antiparallel-spin pair correlation energies. *Journal of Chemical Physics*, *118*, 9095.
- Grimme, S. (2004). Accurate description of van der Waals complexes by density functional theory including empirical corrections. *Journal of Computational Chemistry*, *25*, 1463–1473.
- Grimme, S. (2006a). Semiempirical GGA-type density functional constructed with a long-range dispersion correction. *Journal of Computational Chemistry*, *27*, 1787–1799.
- Grimme, S. (2006b). Semiempirical hybrid density functional with perturbative second-order correlation. *Journal of Chemical Physics*, *124*, 034108–16.
- Grimme, S. (2008). Do special noncovalent  $\pi$ - $\pi$  stacking interactions really exist? *Angewandte Chemie International Edition*, *47*, 3430–3434.
- Grimme, S., Antony, J., Ehrlich, S., & Krieg, H. (2010). A consistent and accurate *ab initio* parametrization of density functional dispersion correction (DFT-D) for the 94 elements H–Pu. *Journal of Chemical Physics*, *132*, 154104.

- Halkier, A., Helgaker, T., Jørgensen, P., Klopper, W., Koch, H., Olsen, J., & Wilson, A. K. (1998). Basis-set convergence in correlated calculations on Ne. *Chemical Physics Letters*, 286, 243–252.
- Hehre, W. J., Stewart, R. F., & Pople, J. A. (1969). Self-consistent molecular-orbital methods. I. use of Gaussian expansions of Slater-type atomic orbitals. *Journal of Chemical Physics*, 51, 2657.
- Hepburn, J., Scoles, G., & Penco, R. (1975). A simple but reliable method for the prediction of intermolecular potentials. *Chemical Physics Letters*, 36, 451.
- Hill, J. G., & Platts, J. A. (2007). Spin-component scaling methods for weak and stacking interactions. *Journal of Chemical Theory and Computation*, 3, 80–85.
- Hill, J. G., & Platts, J. A. (2008). Calculating stacking interactions in nucleic acid base-pair steps using spin-component scaling and local second order Møller-Plesset perturbation theory. *Physical Chemistry Chemical Physics*, 10, 2785–2791.
- Hobza, P., & Šponer, J. (1996). MP2 and CCSD(T) calculations on H-bonded and stacked formamide...formamide and formamidine...formamidine dimers. *Journal of Molecular Structure (THEOCHEM)*, 388, 115–120.
- Hyla-Kryspin, I., Haufe, G., & Grimme, S. (2004). Weak hydrogen bridges: A systematic theoretical study on the nature and strength of C–H...F–C interactions. *Chemistry – A European Journal*, 10, 3411–3422.
- Jeziorski, B., Chalasinski, G., & Szalewicz, K. (1978). Symmetry forcing and convergence properties of perturbation expansions for molecular interaction energies. *International Journal of Quantum Chemistry*, 14, 271.
- Jeziorski, B., Schwalm, W. A., & Szalewicz, K. (1980). Analytic continuation in exchange perturbation theory. *Journal of Chemical Physics*, 73, 6215.
- Jung, Y., Lochan, R. C., Dutoi, A. D., & Head-Gordon, M. (2004). Scaled opposite-spin second order Møller-Plesset correlation energy: An economical electronic structure method. *Journal of Chemical Physics*, 121, 9793–9802.
- Jurečka, P., Šponer, J., Černý, J., & Hobza, P. (2006). Benchmark database of accurate (MP2 and CCSD(T) complete basis set limit) interaction energies of small model complexes, DNA base pairs, and amino acid pairs. *Physical Chemistry Chemical Physics*, 8, 1985–1993.
- Kerber, T., Sierka, M., & Sauer, J. (2008). Application of semiempirical long-range dispersion corrections to periodic systems in density functional theory. *Journal of Computational Chemistry*, 29, 2088–2097.
- Kim, K. S., Tarakeshwar, P., & Lee, J. Y. (2000). Molecular clusters of  $\pi$ -systems: Theoretical studies of structures, spectra, and origin of interaction energies. *Chemical Reviews*, 100, 4145.
- Korth, M., Lüchow, A., & Grimme, S. (2008). Toward the exact solution of the electronic Schrödinger equation for noncovalent molecular interactions: Worldwide distributed quantum Monte Carlo calculations. *The Journal of Physical Chemistry A*, 112, 2104–2109.
- Korth, M., Pitoňák, M., Řezáč, J., & Hobza, P. (2010). A transferable H-bonding correction for semiempirical quantum-chemical methods. *Journal of Chemical Theory and Computation*, 6, 344–352.
- Lee, J. S. (2005). Accurate *ab initio* determination of binding energies for rare-gas dimers by basis set extrapolation. *Theoretical Chemistry Accounts*, 113, 87–94.
- Lin, I.-C., & Rothlisberger, U. (2008). Describing weak interactions of biomolecules with dispersion-corrected density functional theory. *Physical Chemistry Chemical Physics*, 10, 2730.
- Lin, I.-C., Coutinho-Neto, M. D., Felsenheimer, C., von Lilienfeld, O. A., Tavernelli, I., & Rothlisberger, U. (2007a). Library of dispersion-corrected atom-centered potentials for generalized gradient approximation functionals: Elements H, C, N, O, He, Ne, Ar, and Kr. *Physical Review B*, 75, 205131.
- Lin, I.-C., von Lilienfeld, O. A., Coutinho-Neto, M. D., Tavernelli, I., & Rothlisberger, U. (2007b). Predicting noncovalent interactions between aromatic biomolecules with London-Dispersion-Corrected DFT. *The Journal of Physical Chemistry B*, 111, 14346.
- Lochan, R. C., Jung, Y., & Head-Gordon, M. (2005). Scaled opposite spin second order Møller-Plesset theory with improved physical description of long-range dispersion interactions. *The Journal of Physical Chemistry A*, 109, 7598–7605.
- Lohr, A., Grüne, M., & Würthner, F. (2009). Self-assembly of Bis(merocyanine) Tweezers into discrete bimolecular  $\pi$ -stacks. *Chemistry – A European Journal*, 15, 3691–3705.
- Lundqvist, B. I., Andersson, Y., Shao, H., Chan, S., & Langreth, D. C. (1995). Density functional theory including van der Waals forces. *International Journal of Quantum Chemistry*, 56, 247–255.
- Martin, J. M. L. (1996). *Ab initio* total atomization energies of small molecules – towards the basis set limit. *Chemical Physics Letters*, 259, 669.
- Martin, J. M. L., & Taylor, P. R. (1997). Benchmark quality total atomization energies of small polyatomic molecules. *Journal of Chemical Physics*, 106, 8620.

- McNamara, J. P., & Hillier, I. H. (2007). Semiempirical molecular orbital methods including dispersion corrections for the accurate prediction of the full range of intermolecular interactions in biomolecules. *Physical Chemistry Chemical Physics*, 9, 2362.
- Perdew, J. P., & Schmidt, K. (2001). Jacob's Ladder of density functional approximations for the exchange-correlation energy. In V. Van-Doren, C. V. Alsenoy, & P. Geerlings (Eds.), *Density functional theory and its applications to materials* (p. 1). New York: American Institute of Physics Press.
- Pietro, W. J., Francl, M. M., Hehre, W. J., Defrees, D. J., Pople, J. A., & Binkley, J. S. (1982). Self-consistent molecular orbital methods. 24. Supplemented small split-valence basis sets for second-row elements. *Journal of the American Chemical Society*, 104, 5039–5048.
- Pitoňák, M., Neogrády, P., Cerný, J., Grimme, S., & Hobza, P. (2009). Scaled MP3 non-covalent interaction energies agree closely with accurate CCSD(T) benchmark data. *ChemPhysChem*, 10, 282–289.
- Řezáč, J., Jurečka, P., Riley, K. E., Černý, J., Valdes, H., Pluháčková, K., Berka, K., Řezáč, T., Pitoňák, M., Vondrášek, J., & Hobza, P. (2008). Quantum chemical benchmark energy and geometry database for molecular clusters and complex molecular systems ([www.begdb.com](http://www.begdb.com)): A users manual and examples. *Collection of Czechoslovak Chemical Communications*, 73, 1261–1270. <http://www.begdb.com/>.
- Řezáč, J., Fanfrlik, J., Salahub, D., & Hobza, P. (2009). Semiempirical quantum chemical PM6 method augmented by dispersion and H-bonding correction terms reliably describes various types of noncovalent complexes. *Journal of Chemical Theory and Computation*, 5, 1749–1760.
- Riley, K. E., & Hobza, P. (2007). Assessment of the MP2 method, along with several basis sets, for the computation of interaction energies of biologically relevant hydrogen bonded and dispersion bound complexes. *The Journal of Physical Chemistry A*, 111, 8257–8263.
- Riley, K., & Hobza, P. (2008). Investigations into the nature of halogen bonding including symmetry adapted perturbation theory analyses. *Journal of Chemical Theory and Computation*, 4, 232–242.
- Schaefer, A., Horn, H., & Ahlrichs, R. (1992). Fully optimized contracted Gaussian basis sets for atoms Li to Kr. *Journal of Chemical Physics* 97, 2571–2577.
- Scott, W. R. P., Hünenberger, P. H., Tironi, I. G., Mark, A. E., Billeter, S. R., Fennen, J., Torda, A. E., Huber, T., Krüger, P., & van Gunsteren, W. F. (1999). The GROMOS biomolecular simulation program package. *The Journal of Physical Chemistry A*, 103, 3596–3607.
- Sharma, P., Sharma, S., Chawla, M., & Mitra, A. (2009). Modeling the noncovalent interactions at the metabolite binding site in purine riboswitches. *Journal of Molecular Modeling*, 15, 633–649.
- Sinnokrot, M. O., Valeev, E. F., & Sherrill, C. D. (2002). Estimates of the *Ab Initio* limit for  $\pi$ - $\pi$  interactions: The benzene dimer. *Journal of the American Chemical Society*, 124, 10887.
- Steed, J. M., Dixon, T. A., & Klemperer, W. (1979). Molecular beam studies of benzene dimer, hexafluorobenzene dimer, and benzene-hexafluorobenzene. *Journal of Chemical Physics*, 70, 4940.
- Suresh, S. J., & Naik, V. M. (2000). Hydrogen bond thermodynamic properties of water from dielectric constant data. *Journal of Chemical Physics*, 113, 9272.
- Swart, M., van der Wijst, T., Guerra, C. F., & Bickelhaupt, F. M. (2007).  $\pi$ - $\pi$  stacking tackled with density functional theory. *Journal of Molecular Modeling*, 13, 1245–1257.
- Tapavicza, E., Lin, I-C von Lilienfeld, O. A., Tavernelli, I., Coutinho-Neto, M. D., & Rothlisberger, U. (2007). Weakly bonded complexes of aliphatic and aromatic carbon compounds described with dispersion corrected density functional theory. *Journal of Chemical Theory and Computation*, 3, 1673–1679.
- Truhlar, D. G. (1998). Basis-set extrapolation. *Chemical Physics Letters*, 294, 45–48.
- Tsuzuki, S., & Luthi, H. P. (2004). Interaction energies of van der Waals and hydrogen bonded systems calculated using density functional theory: Assessing the PW91 model. *Journal of Chemical Physics*, 114, 3949.
- Tsuzuki, S., Uchimaru, T., & Tanabe, K. (1994). Basis set effects on the intermolecular interaction of hydrocarbon molecules obtained by an *ab initio* molecular orbital method: Evaluation of dispersion energy. *Journal of Molecular Structure (THEOCHEM)*, 307, 107.
- Tuttle, T., & Thiel, W. (2008). OMx-D: Semiempirical methods with orthogonalization and dispersion corrections. Implementation and biochemical application. *Physical Chemistry Chemical Physics*, 10, 2159.
- Valdes, H., Pluháčková, K., Pitoňák, M., Řezáč, J., & Hobza (2008). Benchmark database on isolated small peptides containing an aromatic side chain: Comparison between wave function and density functional theory methods and empirical

- force field. *Physical Chemistry Chemical Physics*, *10*, 2747–2757.
- von Lilienfeld, O. A., Tavernelli, I., Röhrlisberger, U., & Sebastiani, D. (2004). Optimization of effective atom centered potentials for London dispersion forces in density functional theory. *Physical Review Letters*, *93*, 153004.
- von Lilienfeld, O. A., Tavernelli, I., Rothlisberger, U., & Sebastiani, D. (2005). Performance of optimized atom-centered potentials for weakly bonded systems using density functional theory. *Physical Review B*, *71*, 195119.
- Waller, M. P., Robertazzi, A., Platts, J. A., Hibbs, D. E., & Williams, P. A. (2006). Hybrid density functional theory for  $\pi$ -stacking interactions: Application to benzenes, pyridines, and DNA bases. *Journal of Computational Chemistry*, *27*, 491–504.
- Wong, B. (2009). Noncovalent interactions in supramolecular complexes: A study on corannulene and the double concave buckycatcher. *Journal of Computational Chemistry*, *30*, 51–56.
- Zhao, Y., Schultz, N. E., & Truhlar, D. G. (2005). Exchange-correlation functional with broad accuracy for metallic and nonmetallic compounds, kinetics, and noncovalent interactions. *Journal of Chemical Physics*, *123*, 161103.
- Zhao, Y., Schultz, N. E., & Truhlar, D. G. (2006). Design of density functionals by combining the method of constraint satisfaction with parametrization for thermochemistry, thermochemical kinetics, and noncovalent interactions. *Journal of Chemical Theory and Computation*, *2*, 364.
- Zhao, Y., & Truhlar, D. G. (2005a). Design of density functionals that are broadly accurate for thermochemistry, thermochemical kinetics, and nonbonded interactions. *The Journal of Physical Chemistry A*, *109*, 5656.
- Zhao, Y., & Truhlar, D. G. (2005b). Benchmark databases for nonbonded interactions and their use to test density functional theory. *Journal of Chemical Theory and Computation*, *1*, 415.
- Zhao, Y., & Truhlar, D. G. (2006a). A new local density functional for main-group thermochemistry, transition metal bonding, thermochemical kinetics, and noncovalent interactions. *Journal of Chemical Physics*, *125*, 194101.
- Zhao, Y., & Truhlar, D. G. (2006b). Density functional for spectroscopy: No long-range self-interaction error, good performance for Rydberg and charge-transfer states, and better performance on average than B3LYP for ground states. *The Journal of Physical Chemistry A*, *110*, 13126.
- Zhao, Y., & Truhlar, D. G. (2008). The M06 suite of density functionals for main group thermochemistry, thermochemical kinetics, noncovalent interactions, excited states, and transition elements: Two new functionals and systematic testing of four M06-class functionals and 12 other functionals. *Theoretical Chemistry Accounts*, *120*, 215–241.

# 13 Chemical Reactions: Thermochemical Calculations

*John D. Watts*

Department of Chemistry and Biochemistry, Jackson State University,  
Jackson, MS, USA

<b>Introduction</b> .....	<b>468</b>
<b>General Aspects of Thermochemical Calculations</b> .....	<b>469</b>
Calculating the $\Delta H$ , $\Delta S$ , and $\Delta G$ for a Chemical Reaction .....	469
Preliminary Comments on Accuracy .....	470
<b>Examples</b> .....	<b>471</b>
Case Study: $3\text{H}_2(\text{g}) + \text{N}_2(\text{g}) \rightarrow 2\text{NH}_3(\text{g})$ .....	471
Small Basis Set Study .....	472
Study with Extended “Pople-Type” Basis Sets .....	473
Effect of Geometry .....	474
Results from Correlation-Consistent Basis sets .....	475
Thermochemistry of Species with F–O Bonds .....	477
Calculating the Heat of Formation of $\text{H}_2\text{SO}_2$ .....	479
<b>Acknowledgments</b> .....	<b>481</b>
<b>References</b> .....	<b>481</b>

**Abstract:** This chapter provides an introduction to the calculation of thermochemical data for chemical reactions using quantum chemical methods. The basic procedure is first described, namely, obtaining molecular structures and electronic energies of reactants and products, followed by vibrational frequency calculations and evaluation of thermal corrections. Since it is harder to obtain a given accuracy for some types of reactions than others, some discussion is provided on classes of reactions (e.g., isodesmic reactions) for which a given accuracy is easier to achieve than for a general reaction. Three examples illustrate different aspects of thermochemical calculations. The first example, the formation of ammonia from its elements, illustrates a variety of basis set and correlation effects on calculated data. The second example is concerned with calculations on small fluorine-oxygen species and a systematic side-by-side comparison of coupled-cluster and density-functional methods, including the use of isodesmic reactions. The third example describes the use of high-level coupled-cluster calculations to predict the standard enthalpy of formation of  $S(OH)_2$ .

## Introduction

---

The term “chemical reactions” obviously covers a wide range of phenomena. The purpose of this chapter is to address some of the basic issues that one faces when using quantum chemical methods to calculate thermodynamic properties of chemical reactions. The focus here is more on the electronic problem than the nuclear problem, i.e., more on the potential energy surface than on motion thereon. The emphasis also is on gas-phase processes.

Fundamentally, the quantities to be calculated in thermochemical studies are the changes in enthalpy, entropy, and Gibbs free energy for a chemical reaction. From the standard Gibbs free energy change, the equilibrium constant may be obtained. At the most basic level, thermochemical data must be calculated for the reactants and products. This necessitates the calculation of minimum energy structures for all reactant and product species, followed by the calculation of harmonic vibrational frequencies, and thermal corrections. Very often one will seek to improve the results by high-level single-point energy calculations at the geometries obtained at lower-level methods, and using thermal corrections from a lower-level method. Another point is that the ultimate goal in a thermochemical study is often not the  $\Delta H$ ,  $\Delta S$ , or  $\Delta G$  of the reaction(s) directly studied. Rather, these quantities for one reaction are to be combined with data for another reaction, leading ultimately, for example, to an estimate of the standard heat of formation for a particular species. Sometimes experimental data may be incorporated in some way, and one often has some freedom in choosing which reactions to employ. The choices one makes can have a significant effect on the accuracy of the final answer, and hence the overall success of the project.

It is appropriate to mention a few monographs at this point. These provide a wide range of information on studying the thermochemistry of reactions by quantum chemical methods. The first of these is by Hehre et al. (1986). It summarizes a lot of studies using the theoretical-model chemistry approach pioneered by John A. Pople, as well as providing information on background theory and what have come to be called the Pople-type basis sets. Although this book is almost 25 years old, it is still a useful source. Hehre's book (Hehre 2003), which is provided as part of the Spartan software, is in some respects an update of (Hehre et al. 1986), providing new data, including data from various density-functional theory (DFT) methods. A different type of book is that by Helgaker et al. (2000). Most of it is devoted to a thorough and advanced presentation of the theory behind quantum chemical methods, but it also presents



some numerical results on enthalpy changes using very large basis sets. A volume edited by Irikura and Frirup (1998) covers a range of issues in computational thermochemistry. Finally, a textbook by Lewars (2003) is very readable and has useful material on thermochemistry.

The plan of this chapter is as follows. The next section first addresses some general aspects of performing calculations and some points to be considered when planning a project that will yield thermochemical data. Afterwards, it looks at some points concerning the accuracy of results obtained. The third and final section is split into a discussion of three types of studies that involve thermochemical calculations. The first examines in some detail the formation of (gaseous) ammonia from its elements. Various effects of basis set and method are illustrated. The second is concerned with obtaining accurate heats of formation on fluorine-oxygen species, especially using DFT methodology. The third is concerned with obtaining an accurate heat of formation of  $\text{H}_2\text{SO}_2$ , for which experimental thermochemical data are lacking.

## General Aspects of Thermochemical Calculations

### Calculating the $\Delta H$ , $\Delta S$ , and $\Delta G$ for a Chemical Reaction

We consider a general gas-phase chemical reaction  $aA(g) + bB(g) \rightarrow cC(g) + dD(g)$ . In quantum chemical calculations, the enthalpy change for this reaction is calculated from the enthalpies of the species involved:

$$\Delta H^0 = cH_C + dH_D - [aH_A + bH_B].$$

This equation differs from the calculation of  $\Delta H^0$  from standard enthalpies of formation ( $\Delta H_f^0$ ), although it is equivalent to it. We return to the issue of obtaining  $\Delta H_f^0$  in theoretical methods later. At first sight, the notion of the enthalpy of a substance ( $H_A$ ,  $H_B$ ,  $H_C$ , and  $H_D$ ) might be confusing: there is after all no such thing as an “absolute enthalpy.” The quantities  $H_A$ ,  $H_B$ ,  $H_C$ , and  $H_D$  are relative enthalpies, but they are enthalpies of substances *relative to the so-called quantum chemical standard state*. The quantum chemical standard state consists of infinitely separated electrons and nuclei of a substance. For example, the quantum chemical enthalpy of the water molecule is the enthalpy relative to an O nucleus, two protons, and ten electrons, all infinitely separated. The quantum chemical standard state is the zero of the potential energy in the usual quantum chemical Hamiltonian. To make a parallel with experimental thermochemistry, the  $\Delta H_f^0$  of a substance is its molar enthalpy relative to the enthalpy of its elements in their standard states.

Next we consider how the enthalpies are calculated. The quantum chemical enthalpy of a substance has electronic, nuclear, and  $PV$  contributions. The nuclear contribution consists of translational, rotational, and vibrational contributions. Hence:

$$H_A = E(A)_{\text{elec}} + E(A)_{\text{trans}} + E(A)_{\text{rot}} + E(A)_{\text{vib}} + PV.$$

The electronic contribution is the quantum chemical energy, that is, the energy of the stationary, nonrotating, non-vibrating system relative to the quantum chemical standard state; it is sometimes referred to as the bottom-of-the-well energy. The translational energy is the classical kinetic energy of a gas, and just depends on temperature. The rotational energy depends on the molecular structure, and the vibrational energy depends on the vibrational levels of the molecule. The rotational and vibrational contributions depend on the temperature. In practice, the rotational and vibrational contributions are usually evaluated using the rigid-rotor and harmonic oscillator models. Equations for the various contributions are given in many places, for



example, the textbook by McQuarrie and Simon (1999). A technical note on the Gaussian Web site by Ochterski (2000) is also recommended. Along with the equations, a sample output from the Gaussian software is explained. Calculating the enthalpy of a species thus requires a geometry optimization to obtain the molecular structure and a vibrational frequency calculation. The electronic energy is the energy at the optimized geometry.

The first step is to select a particular method and basis set that will be used to optimize the geometry and obtain vibrational frequencies. Several factors will be considered in this choice:

1. The method and basis set selected should give a satisfactory geometry and vibrational frequencies that are not *qualitatively* different from the true results.
2. The required computational resources should be available for the geometry optimization and frequency calculation. This is not a trivial matter: a geometry optimization involves several force calculations, and each force calculation typically requires 2–3 times the time required for an energy calculation. In addition to more processor time, further resources may be needed, for example, additional disk space. Even more resources are needed for frequency calculations. If vibrational frequencies are calculated by finite differences of gradients, calculations at lower symmetries than the molecule's symmetry are needed, and these require substantially more resources.
3. Ideally the method and basis set will be capable of providing reasonably accurate electronic energy differences, that is,  $\Delta E_{\text{elec}} = cE(C)_{\text{elec}} + dE(D)_{\text{elec}} - [aE(A)_{\text{elec}} + bE(B)_{\text{elec}}]$ . In practice, however, it is very common to use a higher-level method and/or basis set to provide an improved estimate for  $\Delta E_{\text{elec}}$  by performing “single-point” energy calculations at the geometries obtained with a smaller basis set.  $\Delta E_{\text{elec}}$  is the major contribution to  $\Delta H$ , and it is more sensitive to quantum chemical method and basis set than are the other components of  $H$ . In conclusion, then, the method chosen for the geometry and frequency calculations is frequently not the method used for refined  $\Delta E_{\text{elec}}$  calculations, especially in high-accuracy work. In fact, in high-accuracy work, it is also common to employ extrapolation techniques to estimate higher-level corrections.

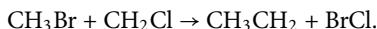
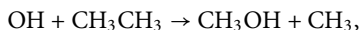
## Preliminary Comments on Accuracy

---

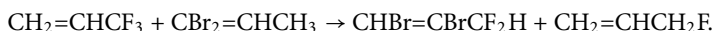
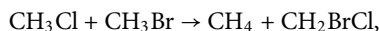
Naturally, one of the key questions concerns the level of theory needed to obtain a particular accuracy. There is no simple answer, but a few general comments are appropriate at this point (Hehre 2003; Hehre et al. 1986). The more similar are the reactants and products, the easier it should be to obtain accurate results. Similar in this sense means having similar chemical environments and bonding patterns in reactants and products. If the reactants and products are “similar” it might be anticipated that the errors in the calculations on reactants and products are similar and to a significant degree cancel out. On the other hand, when there is less similarity, such cancelation is not expected, and higher-level calculations are likely to be needed for the same accuracy. For example, in the reaction  $\text{N}_2 + 3\text{H}_2 \rightarrow 2\text{NH}_3$ , the reactants and products are rather dissimilar: the reactants have an N–N triple bond and an H–H single bond, while the products have N–H single bonds. Another view is that the hybridization states of the N in reactants and products are different. Accurately calculating the  $\Delta H^0$  for the above “simple” reaction in fact is not at all an easy task. Both large basis sets and a high-level treatment of electron correlation are needed. Some numerical data to illustrate these points will be presented. It has long been known (Hehre et al. 1986) that it is especially difficult to obtain accurate results

for reactions that have different numbers of unpaired electrons in reactants and products, for example, homolytic dissociation reactions.

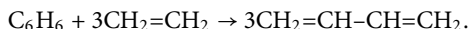
Several classes of reactions have been defined that display some degree of similarity in reactants and products. These include isogyric, isodesmic, and homodesmotic reactions. In isogyric reactions (Pople et al. 1983), the numbers of pairs of electrons in reactants and products is the same (and hence so is the number of unpaired electrons). For example, the following are isogyric processes:



Isogyric reactions constitute a very large group of reactions and it should not be assumed that it is easy to calculate the  $\Delta H^0$  of a general isogyric reaction. However, overall it tends to be easier to obtain an accurate  $\Delta H^0$  for an isogyric reaction than for a non-isogyric reaction. Any reaction that involves closed-shell reactants and products, such as the formation of ammonia from elements, is isogyric. Isodesmic and homodesmotic reactions are more restricted. In isodesmic reactions (Hehre et al. 1970), the number of bonds of each type and the number of lone pairs of each type are the same in reactants and products. For example:



Homodesmotic reactions (George et al. 1975) are a subset of isodesmic reactions. For organic compounds, the reactants and products have equal numbers of carbon atoms with the same hybridization. In addition, there are equal numbers of carbon atoms with each number of C–H bonds in reactants and products. Two examples, taken from a IUPAC document (Minkin 1999), are as follows:



It is expected and has been amply verified (Hehre 2003; Hehre et al. 1986) that calculating  $\Delta H$  for isodesmic and homodesmotic reactions is less demanding than for reactions in which reactants and products are less similar. Of course, this is of no apparent help if the target reaction is not one of these types. However, in a significant number of cases, it is possible to take advantage of (say) an isodesmic reaction in calculating a particular quantity of interest, such as a heat of formation.

A term commonly used in theoretical thermochemistry is “chemical accuracy.” This normally means an accuracy of  $1 \text{ kcal mol}^{-1}$  or about  $4 \text{ kJ mol}^{-1}$ . Achieving this accuracy is certainly not easy, and a lot of effort has been expended in trying to do so for reactions of relatively small molecules.

## Examples

---

### Case Study: $3\text{H}_2(\text{g}) + \text{N}_2(\text{g}) \rightarrow 2\text{NH}_3(\text{g})$

---

In this section we discuss the calculation of the  $\Delta H^0$  of this reaction by different methods and basis sets. Although many other choices could have been made, this example illustrates many important points that are likely to apply to other cases. We begin by considering the calculation

of the change in electronic energies,  $\Delta E_{\text{elec}}$ . In fact, an experimental value of  $\Delta E$  (the elec subscript is omitted hereafter in this section) can be derived by starting from the observed  $\Delta H^0$  and using known molecular structures and vibrational frequencies to obtain an “experimental”  $\Delta E$ . Thus, we shall be assessing the ability of theoretical methods to calculate the experimental  $\Delta E$ . Hehre et al. estimated this value to be  $-37 \text{ kcal mol}^{-1}$  (Hehre et al. 1986, p. 283), but the later estimate of  $-39.5 \text{ kcal mol}^{-1}$  (Helgaker et al. 2000, p. 866) by Helgaker et al. is probably more reliable. The  $\Delta H^0$  is  $-22.1 \text{ kcal mol}^{-1}$ .

## Small Basis Set Study

We begin with results of calculations at geometries obtained with the Hartree–Fock (HF) method and the 6-31G\* basis set. In [Table 13-1](#) we report  $\Delta E$  values from the HF method and several correlated methods. The correlated methods used are second- and third-order perturbation theory (MP2 and MP3), fourth-order perturbation theory including single, double, and quadruple excitations (MP4SDQ), fourth-order perturbation theory including single, double, triple, and quadruple excitations (MP4), coupled-cluster singles-and-doubles (CCSD), and CCSD with noniterative treatment of triple excitations (CCSD(T)). Two well-known DFT treatments, namely, the BLYP and B3LYP functionals, are also used. Five basis sets are used. These are the 6-31G\* basis set and four extensions thereof, namely, 6-31G\*\*, 6-31+G\*, 6-31+G\*\*, and 6-31++G\*\*. The 6-31G\* basis set is a double-zeta valence basis set augmented with a set of d polarization functions on Li and heavier atoms. The 6-31+G\* set adds a set of diffuse s and p functions to Li and heavier atoms to the 6-31G\* basis set. The 6-31G\*\* set includes a set of p polarization functions on H atoms. The 6-31+G\*\* extends 6-31G\*\* by adding a set of diffuse s and p functions to Li and heavier atoms. Finally, the 6-31++G\*\* set has a diffuse s set on H atoms. References for these basis sets are given in (Hehre et al. 1986). The basis sets considered here are not expected to give very high accuracy. However, they are a convenient starting point and the results illustrate several important points. The results with the 6-31G\* and 6-31+G\* basis sets can be discounted since these basis sets are not adequate for use with correlated methods for this example: in the calculations on  $\text{H}_2$  these basis sets do not include any polarization functions. For the MP and CC methods, one can see a large change in  $\Delta E$  on going from 6-31G\* to

■ Table 13-1

Calculated  $\Delta E$  values for  $3\text{H}_2(\text{g}) + \text{N}_2(\text{g}) \rightarrow 2\text{NH}_3(\text{g})$  (units are  $\text{kcal mol}^{-1}$ )

	6-31G*	6-31G**	6-31+G*	6-31+G**	6-31++G**
HF	-27.8	-33.3	-32.2	-37.9	-38.1
MP2	-16.9	-28.1	-23.8	-34.9	-35.3
MP3	-23.7	-35.6	-30.3	-42.0	-42.4
MP4SDQ	-19.4	-30.6	-25.9	-36.9	-37.3
MP4	-13.8	-26.3	-20.7	-32.9	-33.4
CCSD	-19.5	-30.8	-26.0	-37.0	-37.4
CCSD(T)	-15.3	-27.9	-22.1	-34.4	-34.9
BLYP	-20.5	-27.8	-29.9	-37.4	-36.3
B3LYP	-29.2	-35.9	-37.0	-43.9	-43.3

6-31G<sup>\*\*</sup>. Likewise, there is a significant effect on going from 6-31+G<sup>\*</sup> to 6-31+G<sup>\*\*</sup>. Both show the importance of polarization functions on H.

Several features are shown by the data in [Table 13-1](#). Looking at basis set effects first, we see that for all methods there is an appreciable effect on going from the 6-31G<sup>\*\*</sup> to the 6-31+G<sup>\*\*</sup> basis set. This is the effect of adding diffuse functions to the N atom: it is 4.6 kcal mol<sup>-1</sup> for the HF method and slightly more for the correlated methods. Adding the H diffuse s functions, that is, going from 6-31+G<sup>\*\*</sup> to 6-31++G<sup>\*\*</sup>, has a smaller effect. It decreases  $\Delta E$  for the HF, MP, and CC methods, but increases it for BLYP and B3LYP. It should be borne in mind that effects of diffuse functions depend on the size of the rest of the basis set, but here they are definitely important. These results illustrate that diffuse functions can be important even when all species are neutral.

Several trends among the different correlated methods are noteworthy. The MP2 results are much closer to the MP4 or MP4SDQ results than to the MP3 results. In fact, the MP3 results seem to be somewhat exceptional. This underscores the widely held view that MP3 calculations rarely offer any benefits: they demand considerably more resources than MP2 calculations but do not usually improve MP2 results. This is certainly the case here. For all basis sets, the MP2 results are between the MP4SDQ and MP4 results. This is not to be expected in general, but is nonetheless noteworthy. There are close parallels between CCSD and MP4SDQ and between CCSD(T) and MP4. CC methods can be viewed as summing certain classes of terms in the perturbation series to infinite order. CCSD includes all of the contributions in MP4SDQ to infinite order, along with certain other terms. There is a similar relationship between CCSD(T) and MP4. The closeness the CC and MP methods suggests relatively minor importance of infinite-order effects. Again, this is certainly not true in all cases, especially difficult cases, for which the CC methods are expected to perform better than the MP methods. The effect of connected triple excitations, that is, the difference between MP4SDQ and MP4 or between CCSD and CCSD(T), is about 3 kcal mol<sup>-1</sup>, and so triple excitations are necessary for “chemical accuracy.”

It is premature to make judgments about accuracy based on the data in [Table 13-1](#) since the basis sets are relatively small. A few noteworthy trends are apparent, however. The MP2, MP4, and CCSD(T) results seem to be getting closer to the experimental value as the basis set size increases. The HF result with the largest basis set is actually quite close to experiment, but this cannot generally be counted on. The two DFT sets of results show contrasting behavior. BLYP performs better for the larger basis sets, but this is not true for B3LYP for this example. It should be remembered that the effects of basis set and correlated methods are not additive. Differences between a pair of methods can depend on the basis set being used.

## Study with Extended “Pople-Type” Basis Sets

We now examine the results when a set of larger Pople-type basis sets is used. These are based on a triple-zeta valence description. The effects of adding diffuse functions and using multiple sets of polarization effects are considered. The 6-311G<sup>\*\*</sup> basis set is a triple-zeta valence basis set, augmented with a set of polarization functions for all atoms. 6-311++G<sup>\*\*</sup> includes in addition a set of diffuse functions on all atoms. In the 6-311++G(2df,2pd) and 6-311++G(3df,3pd), multiple sets of polarizations are used on all atoms.

Comparing the 6-311G<sup>\*\*</sup> results with the 6-31G<sup>\*\*</sup> data in [Table 13-1](#), one sees a change of about 1 kcal mol<sup>-1</sup>, but not in the same direction for all methods. At the HF, MP2, CCSD, and CCSD(T) levels, the magnitude of  $\Delta E$  decreases, while it increases for BLYP and B3LYP

on going from 6-31G\*\* to 6-311G\*\*. Adding diffuse functions to 6-311G\*\* again has a significant effect, 4 kcal mol<sup>-1</sup> for HF, about 5 kcal mol<sup>-1</sup> for MP2, CCSD, and CCSD(T), and about 6 kcal mol<sup>-1</sup> for BLYP and B3LYP. As in [Table 13-1](#), diffuse functions make  $\Delta E$  more negative. The effect of expanding the polarization space illustrates a significant difference between methods. For the HF method, the effect is comparatively small, and it decreases the magnitude of  $\Delta E$ . For the conventional correlated methods, that is, MP2, CCSD, and CCSD(T), expanding the polarization space increases the magnitude of  $E$  by about 7 kcal mol<sup>-1</sup>, making it more negative. There is a comparatively small difference between the two largest polarization spaces. For BLYP and B3LYP there is little effect on  $\Delta E$  on going beyond the 6-311++G\*\* basis set. The comparative insensitivity of the DFT methods to polarization is rightly cited as an advantage of these methods over conventional wave function-based correlation methods. It is well known that the results of the latter converge more slowly with respect to basis set expansion.

One difference between [Tables 13-1](#) and [13-2](#) is that the effect of triple excitations is slightly smaller with the larger basis sets used in [Table 13-2](#). As observed in [Table 13-1](#), the MP2 method seems to perform very well since its results are between those of CCSD and CCSD(T). Concerning agreement with experiment (-39.5 kcal mol<sup>-1</sup> (Helgaker et al. 2000)), results with the largest basis set show best agreement for CCSD(T). Of course, the effects of several additional factors need to be assessed. These include further basis set extensions and the effect of using the actual minimum energy geometries for the respective methods.

## Effect of Geometry

Geometries of all species were calculated using the 6-311++G(3df,3pd) basis set for six methods (HF, MP2, CCSD, CCSD(T), BLYP, and B3LYP), and the  $\Delta E$  values were calculated. The results are shown in [Table 13-3](#) below, along with the  $\Delta E$  values obtained with the same basis set and the HF/6-31G\* geometries.

The data in [Table 13-3](#) show that the effect of geometry in this case is comparatively small, just under 1 kcal mol<sup>-1</sup> for CCSD(T), for example. This is not to say that using a low-level geometry such as HF/6-31G\* is generally recommended. Rather, the choice of geometry should be carefully considered, with factors such as desired accuracy and available resources being considered. Certainly, with extended basis sets, obtaining a CCSD(T) geometry can be very time consuming, and this has to be weighed against benefits. In practice, it is advisable to study the effect of geometry on the final results using both some low-level and intermediate-level geometries before obtaining a very high-level geometry.

■ Table 13-2

Calculated  $\Delta E$  values for  $3\text{H}_2(\text{g}) + \text{N}_2(\text{g}) \rightarrow 2\text{NH}_3(\text{g})$  using extended Pople-type basis sets (units are kcal mol<sup>-1</sup>)

	6-311G**	6-311++G**	6-311++G(2df,2pd)	6-311++G(3df,3pd)
HF	-32.4	-36.4	-35.1	-34.5
MP2	-27.3	-32.9	-40.7	-40.3
CCSD	-29.4	-34.4	-41.6	-41.2
CCSD(T)	-27.0	-32.2	-40.2	-39.9
BLYP	-28.6	-35.5	-36.5	-36.3
B3LYP	-36.3	-42.3	-42.9	-42.6

■ **Table 13-3**  
Effect of geometries on  $\Delta E$ .

HF	MP2	CCSD	CCSD(T)	BLYP	B3LYP
-34.5	-40.3	-41.2	-39.9	-36.3	-42.6
-34.2	-38.6	-40.7	-39.1	-35.9	-42.4

The basis set is 6-311++G(3df,3pd). The first row data are for the HF/6-31G<sup>+</sup> geometry. The second row data are for the optimized geometries of the different methods with the 6-311++G(3df,3pd) basis set. Units are kcal mol<sup>-1</sup>

■ **Table 13-4**  
Calculated  $\Delta E$  values for  $3\text{H}_2(\text{g}) + \text{N}_2(\text{g}) \rightarrow 2\text{NH}_3(\text{g})$  using the cc-pVXZ (X = D, T, Q) basis sets (units are kcal mol<sup>-1</sup>)

	cc-pVDZ	cc-pVTZ	cc-pVQZ
HF	-32.4	-34.0	-34.9
MP2	-23.6	-34.2	-37.3
CCSD	-26.7	-36.9	-39.7
CCSD(T)	-24.0	-34.8	-37.9
BLYP	-26.1	-30.9	-33.3
B3LYP	-34.1	-38.5	-40.6

## Results from Correlation-Consistent Basis sets

Within the family of so-called Pople-type basis sets, 6-311++G(3df,3pd) is the largest standard set. Even though this basis set is quite large, it is not a complete basis set for correlated methods. Better basis sets for the systematic description of electron correlation, the so-called correlation-consistent (cc) basis sets, were developed some years later, the first being published in 1989 (Dunning Jr. 1989). The largest of such sets are recognized as providing a pathway to basis set completeness. At the same time, these basis sets are quite large, and basis set completeness for wave function-based correlated methods generally requires the use of an extrapolation. The cc basis sets were developed in such a way as to permit reasonably reliable extrapolation to the complete basis set result. Of course, the larger the basis sets used in the extrapolation, the more reliable the extrapolation is likely to be. Helgaker et al. (2000) discuss the convergence and performance of the cc sets quite extensively.

We have calculated the  $\Delta E$  using two series of the cc basis sets. The first series used the cc-pVDZ, cc-pVTZ, and cc-pVQZ basis sets. The cc-pVDZ set is a valence double-zeta set with one set of polarization functions (p for H, d for Li-Ar). In terms of contracted functions, it is equivalent to 6-31G<sup>\*\*</sup>. The cc-pVTZ and cc-pVQZ sets are valence triple- and quadruple-zeta sets. They have multiple sets of polarization functions (2p1d and 2d1f for cc-pVTZ; 3p2d1f and 3d2f1g for cc-pVQZ). In the second series, we have used the augmented sets, namely, aug-cc-pVDZ, aug-cc-pVTZ, and aug-cc-pVQZ. These contain a set of diffuse functions for each angular momentum, for example, there are diffuse s, p, and d sets in cc-pVDZ. In terms of contracted functions, the cc-pVTZ set is the same size as 6-311G(2df,2pd). The aug-cc-pVTZ set would be expected to be similar in accuracy to 6-311++G(2df,2pd). The next table shows the results from the cc-pVDZ, cc-pVTZ, and cc-pVQZ basis sets (► [Table 13-4](#)).

At the HF level, there is a small change as the basis set is extended, as observed with the other basis sets considered in this section. For MP2, CCSD, and CCSD(T), there is a considerable

■ Table 13-5

Calculated  $\Delta E$  values for  $3\text{H}_2(\text{g}) + \text{N}_2(\text{g}) \rightarrow 2\text{NH}_3(\text{g})$  using the aug-cc-pVXZ (X = T, Q) basis sets (units are kcal mol<sup>-1</sup>)

	cc-pVTZ	cc-pVQZ
HF	-36.2	-35.7
MP2	-38.6	-38.7
CCSD	-40.8	-41.0
CCSD(T)	-39.1	-39.3
BLYP	-35.4	-35.2
B3LYP	-42.3	-42.1

change from cc-pVDZ to cc-pVTZ (over 10 kcal mol<sup>-1</sup>), followed by a much smaller change on going to cc-pVQZ. The changes for BLYP and B3LYP are smaller. It is natural to wonder how well converged are the cc-pVQZ results. Larger basis sets in the cc series have been defined, and one could employ these in calculation on these systems (Helgaker et al. 2000). An alternative, mentioned above, is to use an extrapolation formula to estimate the complete basis set result. For example, to use the L<sup>-3</sup> extrapolation the formula (Halkier et al. 1998; Helgaker et al. 2000):

$$W(\infty) = \frac{M^3 W(M) - N^3 W(N)}{M^3 - N^3}$$

could be applied to a pair of  $\Delta E$  values for a method. In this formula,  $M$  and  $N$  are the highest angular momentum quantum numbers of two basis sets, while  $W(M)$  and  $W(N)$  are the values of the quantity being extrapolated with the two corresponding basis sets. For example, suppose we extrapolate the CCSD(T) results with the cc-pVTZ and cc-pVQZ basis sets:  $M = 3$  (for the f functions in cc-pVTZ),  $W(3) = -34.8$ ,  $N = 4$  (for the g functions in cc-pVQZ), and  $W(4) = -37.9$ . Applying the extrapolation formula, the result is  $-40.2$  kcal mol<sup>-1</sup>. Applying the extrapolation formula to the cc-pVDZ and cc-pVTZ data for CCSD(T) yields  $-39.3$  kcal mol<sup>-1</sup>. In this case, both extrapolations give quite similar results. This will not always be the case. The larger the basis sets used in the extrapolation, the more reliable the result should be. The next set of results to consider are those with the augmented cc basis sets. These are shown in the **Table 13-5**.

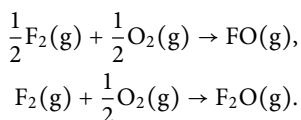
Going from cc-pVTZ to aug-cc-pVTZ the  $\Delta E$  decreases by about 4 kcal mol<sup>-1</sup> for the correlated methods and just over 2 kcal mol<sup>-1</sup> for HF. The effect of adding diffuse functions to cc-pVQZ is smaller, namely, about 1.5 kcal mol<sup>-1</sup> for the correlated methods. The diffuse functions in aug-cc-pVTZ effectively make up for some the valence basis set incompleteness in cc-pVTZ, while cc-pVQZ is more complete, so the effect of the diffuse functions is smaller. The difference between the aug-cc-pVTZ and aug-cc-pVQZ results is very small in this case.

Finally, based on the data in **Table 13-5** and an experimentally derived value of  $\Delta E$  of  $-39.5$  kcal mol<sup>-1</sup> (Helgaker et al. 2000), one can see the CCSD(T) results approaching chemical accuracy for this problem. MP2 also performs very well in this case, but this is not always the case. Helgaker et al. (2000) report an extrapolated CCSD(T) result from cc-pcV5Z and cc-pcV6Z values of  $-39.6$  kcal mol<sup>-1</sup>. The cc-pcVXZ basis sets include additional functions to account for core correlation effects that are not included in the cc-pVXZ sets.

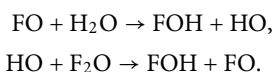
## Thermochemistry of Species with F–O Bonds

Species containing F–O bonds have provided a significant challenge for theoretical methods over the years. The most celebrated case is fluorine peroxide, the theoretical structure of which is arguably an unsolved problem, as is its heat of formation. As far as thermochemistry is concerned, getting reliable, chemically accurate heats of formation for several fundamental species (e.g., FO, F<sub>2</sub>O, HOF, FOO, and F<sub>2</sub>O<sub>2</sub>) is very difficult. For some of these species (FOO and F<sub>2</sub>O<sub>2</sub>) additional difficulties are possible uncertainties in experimental data, which make it more difficult to assess the quality of theoretical data. One theoretical strategy is to use the most advanced theoretical methods (e.g., CCSD(T)) and large basis sets, perhaps including attempted extrapolation to the (estimated) basis set limit. Such calculations place severe demands on resources and are applicable only to relatively small species, but they should be capable of chemical accuracy when carried far enough. Another strategy is to use DFT methods. These are much less demanding computationally and thus can be applied to much larger species. The key issue is their accuracy: can they provide sufficient accuracy on small species to be applied with confidence on larger species? A study by Ventura et al. (1999) involves a comparative study of two functionals and the CCSD(T) method for species with F–O bonds, which we now discuss.

Ventura et al. undertook this study since there were conflicting reports on the suitability of DFT methods for systems containing F–O bonds. Their first goal was to provide a systematic, side-by-side comparison of two functionals, namely, B3LYP and B3PW91, and the CCSD(T) method using the same large atomic natural orbital basis set. The basis set chosen was an uncontracted 14s9p4d3f set (for N, O, and F) combined with an uncontracted 8s4p3d set for H. Two strategies were used to calculate heats of formation: (a) calculating the enthalpy changes for the defining equations of  $\Delta H_f^0$  (referred to hereafter as the direct method) and (b) calculating the enthalpy changes for appropriate isodesmic equations and then using experimental data on all but one species to calculate the enthalpy of formation of the unused species. For example, approach (a) would use the following equations for FO and F<sub>2</sub>O:



The isodesmic approaches for FO and F<sub>2</sub>O used the equations



To calculate the heat of formation of FO, for example, one would calculate the  $\Delta H^0$  of the first equation and then combine this result with experimental standard enthalpies of formation of H<sub>2</sub>O, HOF, and OH:

$$\Delta H_f^0(\text{FO}) = \Delta H_f^0(\text{HO}) + \Delta H_f^0(\text{HOF}) - \Delta H_f^0(\text{H}_2\text{O}) - \Delta H^0.$$

DFT and CCSD(T) approaches were used to obtain a series of standard enthalpies of formation using both the direct (referred to by the authors as the diatomic approach) and isodesmic approaches. The species with F–O bonds studied were FO, HOF, and F<sub>2</sub>O. In addition, the authors calculated heats of formation of the H, N, O, and F atoms, the OH and NO radicals, and H<sub>2</sub>O.

The general findings of Ventura et al. can be summarized as follows. The DFT methods performed better using the isodesmic method than they did for the direct method. For the



■ Table 13-6

Calculated and experimental  $\Delta H_f^0$  of FO, HOF, and F<sub>2</sub>O (units are kcal mol<sup>-1</sup>; the data are from Ventura et al. 1999)

	Experiment	B3PW91		B3LYP		CCSD(T)	
		Iso	Direct	Iso	Direct	Iso	Direct
FO	26.06	25.75 26.42	24.93	26.50 26.29	24.31	28.01 27.20	26.42
HOF	-20.60	-20.30 -20.41	-18.84	-21.05 -20.36	-19.20	-22.56 -19.45	-20.83
F <sub>2</sub> O	5.86	5.67	5.78	5.62	5.48	4.71	6.52

■ Table 13-7

Calculated and experimental  $\Delta H_f^0$  of FO and HOF using the 6-31G\* basis set (units are kcal mol<sup>-1</sup>; the data are from Ventura et al. 1999)

	Experiment	B3PW91		B3LYP		CCSD(T)	
		Iso	Direct	Iso	Direct	Iso	Direct
FO	26.06	26.44	23.08	27.04	24.53	30.28	26.24
HOF	-20.60	-20.99	-13.60	-21.56	-13.47	-24.83	-13.16

CCSD(T) method, however, the reverse was true. For the isodesmic method, the DFT methods perform better than the CCSD(T) method, but CCSD(T) performs better than the DFT methods for the direct method. Overall the performance of all methods is generally very good. Representative data are shown in the table below (● Table 13-6).

Two values are given for the isodesmic method for FO and HOF, one for each of the two equations given above. Whether the isodesmic or direct method is used for the DFT approaches, the results are impressive, especially considering that the time required for these calculations is a fraction of that needed for CCSD(T). The CCSD(T) results would likely be improved slightly with larger basis sets, while the effect is likely to be much smaller for the DFT methods.

Another instructive aspect of the work of Ventura et al. (1999) comes from the use of the 6-31G\* basis set. Such a basis set is obviously not expected to be accurate enough for a direct calculation of the heat of formation of a molecule. However, as the following data show, when the isodesmic approach is used, very promising results are obtained (● Table 13-7).

For HOF in particular, one can see that the isodesmic approach is a major improvement over the direct method for all methods. This illustrates the potential value of isodesmic approaches. The good result obtained for CCSD(T) for FO with the 6-31G\* is no doubt fortuitous. Ventura et al. (1999) do not report results for F<sub>2</sub>O using the 6-31G\* basis set.

One cautionary comment worth making here concerns the use of experimental data in schemes with isodesmic reactions. The success of such schemes obviously depends on the reliability of the experimental data, certainly requiring chemical accuracy in the experimental data. For FO, HOF, and F<sub>2</sub>O, this appears to be the case. As mentioned above, this is probably not true for all F–O containing species. Some theoretical studies (Feller and Dixon 2003; Karton et al. 2009) have found a disagreement between high-quality calculated data and experimental data for FOO and F<sub>2</sub>O<sub>2</sub> and recommend revision and/or a new determination of experimental data for these species.

## Calculating the Heat of Formation of H<sub>2</sub>SO<sub>2</sub>

In a recent study (Napolion et al. 2008), isomers of H<sub>2</sub>SO<sub>2</sub> were investigated theoretically using the CCSD(T) and other methods. Part of that study was calculating the standard heat of formation of the lowest energy isomer, namely, the C<sub>2</sub> conformer of sulfoxylic acid, S(OH)<sub>2</sub>. This species has been detected experimentally, but no structural, spectroscopic (e.g., infrared), or thermochemical data have been measured. There had been some prior theoretical estimates, but the variations were significant. In 1978, using bond energy estimates, Benson (Benson 1978) estimated  $\Delta H_f^0$  to be  $-69.3 \pm 4.1 \text{ kcal mol}^{-1}$ . Wang and Zhang (2002) calculated  $\Delta H_f^0$  in two ways using the G3B3 and G3//MP2 procedures. First, they calculated the enthalpy change for dissociation to atoms. Then they used the experimental  $\Delta H_f^0$  values of atoms to obtain a  $\Delta H_f^0$  for S(OH)<sub>2</sub>. With this approach they obtained values of  $-65.2$  (G3B3) and  $-65.9 \text{ kcal mol}^{-1}$  (G3//MP2), which are at the lower end of Benson's estimate. However, Wang and Zhang were concerned about possible inaccuracies in the atomization procedure, so they also used a procedure that involved isodesmic reactions. This gave estimates of  $-69.5 \text{ kcal mol}^{-1}$  (G3B3) and  $-68.3$  to  $-70.0 \text{ kcal mol}^{-1}$  (G3//MP2). Wang and Zhang's preferred value was  $-69.3 \text{ kcal mol}^{-1}$ . Our strategy was to use the CCSD(T) method with extended basis sets, including correlation-consistent basis sets and L<sup>-3</sup> extrapolation.

A direct approach to calculating the  $\Delta H_f^0$  was not possible since the standard state of sulfur is solid sulfur. Instead, two schemes were devised, each of which involved calculating the  $\Delta H^0$  of a reaction that could be combined with experimental data to yield an estimate of the required  $\Delta H_f^0$ . In the limit of an exact calculation, both schemes will give the same final result. Hence, the closeness of the two estimates is to some extent a measure of the accuracy. The two schemes are as follows.

*Scheme 1:* The standard enthalpy change for the reaction  $\text{S(OH)}_2(\text{g}) \rightarrow \text{SO}_2(\text{g}) + \text{H}_2(\text{g})$  was calculated. The  $\Delta H_f^0$  was then calculated from

$$\Delta H_f^0 = \Delta H_f^0(\text{SO}_2) + \Delta H_f^0(\text{H}_2) - \Delta H_{rxn}^0 = -70.9 \text{ kcal mol}^{-1} - \Delta H_{rxn}^0,$$

using the calculated  $\Delta H_{rxn}^0$  and experimental data for SO<sub>2</sub> and H<sub>2</sub>.

*Scheme 2:* The standard enthalpy change for the reaction  $\text{S(OH)}_2(\text{g}) \rightarrow \text{H}_2\text{S}(\text{g}) + \text{O}_2(\text{g})$  was calculated. The  $\Delta H_f^0$  was then calculated from

$$\Delta H_f^0 = \Delta H_f^0(\text{H}_2\text{S}) + \Delta H_f^0(\text{O}_2) - \Delta H_{rxn}^0 = -4.8 \text{ kcal mol}^{-1} - \Delta H_{rxn}^0,$$

using the calculated  $\Delta H_{rxn}^0$  and experimental data for SO<sub>2</sub> and H<sub>2</sub>.

The difference

$$\Delta H_f^0(\text{Scheme 1}) - \Delta H_f^0(\text{Scheme 2})$$

is equal to  $\Delta H^0(\text{Expt.}) - \Delta H^0(\text{Calc.})$  for the reaction  $\text{H}_2\text{S}(\text{g}) + \text{O}_2(\text{g}) \rightarrow \text{SO}_2(\text{g}) + \text{H}_2(\text{g})$ . For our most complete calculations (see below), the difference is only  $-0.6 \text{ kcal mol}^{-1}$ , which is within chemical accuracy. This is a significant achievement since it is well known to be very difficult to obtain accurate thermochemical data on SO<sub>2</sub>. This suggests that our strategy is suitable for calculating the  $\Delta H_f^0$  of S(OH)<sub>2</sub>.

■ Table 13-8

CCSD(T) values of  $\Delta E$ ,  $\Delta H^0$ , and  $\Delta H_f^0$  from Scheme 1 (see above) in kcal mol<sup>-1</sup>

	$\Delta E$	$\Delta H^0$	$\Delta H_f^0$
6-311++G(2d,2p)	8.2	1.8	-72.7
6-311++G(3df,3pd)	5.1	-1.3	-69.6
ANO-TZP	8.1	1.7	-72.6
cc-pV(D+d)Z	8.6	2.2	-73.1
cc-pV(T+d)Z	3.9	-2.4	-68.5
cc-pV(Q+d)Z	4.0	-2.4	-68.6
aug-cc-pV(D+d)Z	13.3	6.9	-77.8
aug-cc-pV(T+d)Z	5.5	-0.9	-70.1
aug-cc-pV(Q+d)Z	4.5	-1.9	-69.0
Extrapolation <sup>a</sup>	4.1	-2.3	-68.6
Extrapolation <sup>b</sup>	3.8	-2.6	-68.3

<sup>a</sup>Extrapolation based on the cc-pVTZ and cc-pVQZ results

<sup>b</sup>Extrapolation based on the aug-cc-pVTZ and aug-cc-pVQZ results

The results of our calculations are shown in ► [Tables 13-8](#) and ► [13-9](#) (see below). Each table shows three quantities.  $\Delta E$  is the energy change of the reaction for stationary nuclei at 0 K.  $\Delta H^0$  is the calculated standard enthalpy change of the reaction at 298.15 K, obtained from  $\Delta E$  and the unscaled CCSD(T)/6-311++G(2d,2p) thermal correction (-6.4 and -5.4 kcal mol<sup>-1</sup> for Schemes 1 and 2, respectively).  $\Delta H_f^0$  is the calculated standard enthalpy of formation of S(OH)<sub>2</sub> at 298.15 K, obtained as indicated above.

Before discussing the data, a note on the cc basis sets used is needed. When the cc basis sets for third-row elements such as sulfur were first developed, the numbers of polarization functions used were the same as in the basis sets for the second-row elements (e.g., 1d for cc-pVDZ, 2d1f for cc-pVTZ, and so on). It was subsequently found that the d set for third-row elements was inadequate and needed to be expanded by adding a set of “tight” d functions. The resulting basis sets are referred to as cc-pV(X+d)Z and aug-cc-pV(X+d)Z. For H and second-row elements, these sets are the same as the original cc-pVXZ and aug-cc-pVXZ sets, but for third-row elements they have an extra set of d functions.

Looking at ► [Table 13-8](#), one sees that there are quite small differences between the triple- and quadruple-zeta results, the largest being 1.1 kcal mol<sup>-1</sup> between the aug-cc-pV(T+d)Z and aug-cc-pV(Q+d)Z results. Consequently, the extrapolated results differ little from the cc-pV(Q+d)Z and aug-cc-pV(Q+d)Z values. Also, the two extrapolated results differ by only 0.3 kcal mol<sup>-1</sup>. The 6-311++G(3df,3pd) basis set performs fairly well overall. The cc-pV(D+d)Z and aug-cc-pV(D+d)Z results are not as good, especially the latter.

The data in ► [Table 13-9](#) show greater sensitivity to basis set than do those in ► [Table 13-8](#), no doubt a reflection of the demands on the basis set in calculations on SO<sub>2</sub>. In ► [Table 13-9](#), one can see much larger differences between the triple- and quadruple-zeta results. Not surprisingly, the extrapolation has a larger effect than in ► [Table 13-8](#). However, the two extrapolations give  $\Delta H_f^0$  values that differ by only 0.1 kcal mol<sup>-1</sup>. The 6-311++G(3df,3pd) basis set is seen not to perform as well in ► [Table 13-9](#) as in ► [Table 13-8](#). The deficiencies of the smaller basis sets are more apparent in ► [Table 13-9](#) than in ► [Table 13-8](#).

■ Table 13-9

CCSD(T) values of  $\Delta E$ ,  $\Delta H^0$ , and  $\Delta H_f^0$  from Scheme 2 (see above) in kcal mol<sup>-1</sup>

	$\Delta E$	$\Delta H^0$	$\Delta H_f^0$
6-311++G(2d,2p)	56.5	51.2	-56.0
6-311++G(3df,3pd)	62.6	57.2	-62.1
ANO-TZP	63.9	58.6	-63.4
cc-pV(D+d)Z	43.4	38.0	-42.8
cc-pV(T+d)Z	61.4	56.1	-60.9
cc-pV(Q+d)Z	65.3	60.0	-64.8
aug-cc-pV(D+d)Z	57.5	52.1	-56.9
aug-cc-pV(T+d)Z	64.6	59.2	-64.1
aug-cc-pV(Q+d)Z	66.6	61.3	-66.1
Extrapolation <sup>a</sup>	68.2	62.9	-67.7
Extrapolation <sup>b</sup>	68.1	62.7	-67.6

<sup>a</sup>Extrapolation based on the cc-pVTZ and cc-pVQZ results<sup>b</sup>Extrapolation based on the aug-cc-pVTZ and aug-cc-pVQZ results

A measure of the quality of the results can be obtained by comparing the  $\Delta H_f^0$  values in **▶ Tables 13-8** and **▶ 13-9**. Even for the aug-cc-pV(Q+d)Z basis set, there is a 2.9 kcal mol<sup>-1</sup> difference, which is not within chemical accuracy, of course. However, the corresponding extrapolated values in the two tables differ by less than 1 kcal mol<sup>-1</sup>, which is within chemical accuracy. Our best results for  $\Delta H_f^0$ , then, are 1–2 kcal mol<sup>-1</sup> above Benson's mean value and in the range of values obtained by Wang and Zhang byisodesmic reactions, rather than their estimates based on dissociation reactions. Our reaction enthalpies predict that decomposition of S(OH)<sub>2</sub> to SO<sub>2</sub> + H<sub>2</sub> is slightly exothermic, while decomposition to H<sub>2</sub>S + O<sub>2</sub> is strongly endothermic.

## Acknowledgments

This work was supported in part by the National Science Foundation. Calculations performed in this work on the formation of NH<sub>3</sub> were run on a QS4-2800C computer from Parallel Quantum Solutions, LLC using the Gaussian 2003 software.

## References

- Benson, S. W. (1978). Thermochemistry and kinetics of sulfur-containing molecules and radicals. *Chemical Reviews*, 78, 23–35.
- Dunning Jr., T. H. (1989). Gaussian basis sets for use in correlated molecular calculations. I. The atoms boron through neon and hydrogen. *Journal of Chemical Physics*, 90, 1007–1023.
- Feller, D., & Dixon, D. A. (2003). Coupled cluster theory and multireference configuration interaction study of FO, F<sub>2</sub>O, FO<sub>2</sub>, and FOOF. *Journal of Physical Chemistry A*, 107, 9641–9651.
- George, P., Trachtman, M., Bock, C. W., & Brett, A. M. (1975). An alternative approach to the problem of assessing stabilization energies in cyclic

- conjugated hydrocarbons. *Theoretica Chimica Acta*, 38, 121–129.
- Halkier, A., Helgaker, T., Jørgensen, P., Klopper, W., Koch, H., Olsen, J., & Wilson, A. K. (1998). Basis-set convergence in correlated calculations on Ne, N<sub>2</sub>, and H<sub>2</sub>O. *Chemical Physics Letters*, 286, 243–252.
- Hehre, W. J. (2003). *A guide to molecular mechanics and quantum chemical calculations*. Irvine: Wavefunction, Inc.
- Hehre, W. J., Ditchfield, R., Radom, L., & Pople, J. A. (1970). Molecular orbital theory of the electronic structure of organic compounds. V. Molecular theory of bond separation. *Journal of the American Chemical Society*, 92, 4796–4801.
- Hehre, W. J., Radom, L., v. R. Schleyer, P., & Pople, J. A. (1986). *Ab initio molecular orbital theory*. New York: Wiley.
- Helgaker, T., Jørgensen, P., & Olsen, J. (2000). *Molecular electronic-structure theory*. Chichester: Wiley.
- Irikura, K. K., & Frirup, D. J., (Eds.). (1998). *Computational thermochemistry*. Washington: American Chemical Society.
- Karton, A., Parthiban, S., & Martin, J. M. (2009). Post-CCSD(T) ab initio thermochemistry of halogen oxides and related hydrides XOX, XOOX, HOX, XO<sub>n</sub>, and HXO<sub>n</sub> (X = F, Cl), and evaluation of DFT methods for these systems. *Journal of Physical Chemistry A*, 113, 4802–4816.
- Lewars, E. (2003). *Computational chemistry*. Boston: Kluwer
- McQuarrie, D. A., & Simon, J. D. (1999). *Molecular thermodynamics*. Sausalito: Science Books.
- Minkin, V. I. (1999). Glossary of terms used in theoretical organic chemistry. *Pure and Applied Chemistry*, 71, 1919–1981.
- Napoliion, B., Huang, M.-J., & Watts, J. D. (2008). Coupled-cluster study of isomers of H<sub>2</sub>SO<sub>2</sub>. *Journal of Physical Chemistry A*, 112, 4158–4164.
- Ochterski, J. W. (2000). Thermochemistry in Gaussian. [http://Gaussian.com/g\\_whitepap/thermo.htm](http://Gaussian.com/g_whitepap/thermo.htm).
- Pople, J. A., Frisch, M. J., Luke, B. T., & Binkley, J. S. (1983). A Møller-Plesset study of the energies of AH<sub>n</sub> molecules (A = Li to F). *International Journal of Quantum Chemistry Symposium*, 17, 307–320.
- Ventura, O. N., Kieninger, M., & Cachau, R. E. (1999). Density functional theory is more accurate than coupled-cluster theory in the study of the thermochemistry of species containing the F–O bond. *Journal of Physical Chemistry A*, 103, 147–151.
- Wang, L., & Zhang, J. (2002). Ab initio calculation on thermochemistry of CH<sub>3</sub>SO<sub>x</sub>H (x = 1 – 3) and H<sub>2</sub>SO<sub>y</sub> (y = 2,3). *Journal of Molecular Structure: THEOCHEM*, 581, 129–138.

# 14 Calculation of Excited States: Molecular Photophysics and Photochemistry on Display

Luis Serrano-Andrés<sup>1</sup> · Juan José Serrano-Pérez<sup>1,2</sup>

<sup>1</sup>Instituto de Ciencia Molecular, Universitat de València, Valencia, Spain

<sup>2</sup>Department of Chemistry, Imperial College London Computational & Structural Research Group, London, UK

<i>Introduction</i> .....	485
<i>Spectroscopy Overview</i> .....	486
<i>Electronic Structure Calculations</i> .....	493
General Overview .....	493
Methods, Advantages, and Drawbacks .....	496
Basis Sets .....	502
Methods for Excited States .....	504
<i>How to Compute Excited States</i> .....	510
How to Start: Selection of Goals, Methods, Geometries .....	510
Molecular Photophysics: Computing Absorption and Emission Spectra .....	512
An Application Example: Psoralen .....	512
Practical Aspects .....	516
Computing Rydberg States .....	520
An Application Example: Water .....	520
Practical Aspects .....	523
Electronic States of Anionic Systems .....	524
An Application Example: p-benzosemiquinone Radical Anion .....	524
Practical Aspects .....	527
Photochemistry: On the Trail of the Energy .....	531
An Application Example: Thymine .....	531
Practical Aspects .....	535
Photoinduced Reactions in Bimolecular Systems .....	544
An Application Example of Reactivity: Cytosine Dimer .....	544
An Application Example of Energy Transfer: Psoralen + O <sub>2</sub> .....	548
Practical Aspects .....	553

<i>Conclusions</i> .....	556
<i>Acknowledgments</i> .....	557
<i>References</i> .....	557

**Abstract:** <sup>1</sup> Excited states participate in photoinduced events as well as in thermally activated reactions, even in many cases in which only the ground state is believed to be involved. Life on Earth also depends, both directly and indirectly, on the influence that light has on chemistry. The energy of the Sun's visible and ultraviolet radiation promotes processes that not only permit the continued existence of life on the planet, but which are keys for evolution by means of mutations. To study a system in an excited state, far away from its optimum situation, is a challenge for chemists, both experimentalists and theoreticians. This chapter is focused on the practical aspects related to the calculation of excited states in molecular systems by using quantum-chemical methods, a type of study that escapes in many cases from the well-established computational strategies used for the molecular ground states, both because of the complexity of the problem itself and for the methodological requirements. A short review of the spectroscopic and photochemical panorama will be provided first in order to explain which are the main parameters and processes to be determined, followed by a compact description of the most relevant and employed quantum-chemical methods and computational strategies for excited states. A number of applied examples of actual calculations on paradigmatic excited state problems will be provided in the different subchapters, followed in each case by comments on practical issues occurring in the calculations. With these cases we will try to demonstrate that in the last years the quantum-chemical studies on excited states have reached the required maturity to interpret and predict, at a molecular level, different types of chemical situations.

## Introduction

---

Computing electronic excited states with quantum chemical methods is much more complex than doing it for ground states, because it implies not only coping with higher solutions of the electronic Hamiltonian with diverse character and therefore requiring more complex methods, but also to solve a plethora of new situations, such as hypersurface crossings and coupling between the states, that usually requires to abandon convenient approximations like Born–Oppenheimer (see Szabo and Ostlund 1996), for instance.

Molecules, consisting of electrically charged nuclei and electrons, may interact with the oscillating electric and magnetic fields of light. Spectroscopic experiments demonstrate that energy can be absorbed or emitted by molecules (and atoms) in discrete amounts, corresponding to precise changes in energy of the molecule (or atom) concerned. As matter, light is a form of energy that exhibits both wave- and particle-like properties. Absorption of the relevant frequencies from incident radiation raises molecules from lower to higher levels. Electrons in molecules occupy molecular orbitals (MOs) with precise energy levels. Transitions from lower, filled orbitals, to upper (higher energy), empty orbitals usually involve absorption of radiation in the UV and visible parts of the spectrum. Much smaller quantities of energy are linked to changes in the vibrational and rotational energy of the molecule. The understanding of the spectroscopic phenomena in the light of molecular orbital theory has opened new avenues in the comprehension of the photoinduced events.

The molecule in excited state is often prone to react in an easier way than in the ground state. The excess energy of an excited species can alter its reactivity and is particularly significant in the case of electronic excitation because of the energies involved are of similar order of magnitude

---

<sup>1</sup>Dedicated to the memory of Luis Serrano–Andrés, great scientist, teacher and friend, who passed away recently



as bond energies. Electronic excitations can then have a considerable effect on the structure of a species. Accordingly, the energies correspond roughly with typical activation energies for many reactions, which are too high to be reached from the ground but not from the excited state. The new electronic rearrangement may be also the key of the reactivity since the molecule in an excited state may exhibit nucleophilic or electrophilic properties different than those of its ground state.

Three modern developments have been produced in the last years that are the key for the comprehension of the photophysics and photochemistry of many chemical and biochemical phenomena: (1) rapid advances in quantum-chemical methods allow to study the excited states with high accuracy; (2) improved molecular beams techniques permit studies of isolated molecules, despite their sometimes low vapor pressure and propensity for thermal decomposition, and (3) the revolutionary impact that femtosecond laser and multiphoton techniques have had on the study of the electronic energy relaxation processes. Indeed, now it is possible to get information about reaction intermediates at very short times from femtochemical techniques, and, more than ever, the participation of quantum chemistry to interpret such findings has become crucial. A constructive interplay between theory and experiment can provide an insight into the chemistry of the electronic state that cannot be easily derived from the observed spectra alone.

From the theoretical viewpoint, the calculation of excited states is still a very complex task. Considering the many different electronic structure situations occurring in the potential energy hypersurfaces (PEHs) of the excited molecular systems, the only methods generally applicable to all of them are the multiconfigurational approaches. The application of these procedures requires a lot of skill and experience, and the limitations on the size of the problem are noticeable. Single-reference (black-box) methods only work in certain regions of the PEHs. In general, the excited state problem can be considered heavily multiconfigurational. New tools and strategies are required for excited states at the highest levels of calculation: optimization of minima, transition states, hypersurface crossings (conical intersections), and reaction paths, whereas states couplings (nonadiabatic, electronic, spin-orbit) need to be computed. This solves only the first part of the problem, that is, the solution of the time-independent Schrödinger equation. Once the potential represented by the PEHs is obtained, time-dependent equations have to be solved to finally determine reaction rates, states lifetimes, or populations. Coupling at the proper level those two types of calculations, static and dynamic approaches representing the electronic structure and reaction dynamics problems, respectively, is still a task under development.

## Spectroscopy Overview

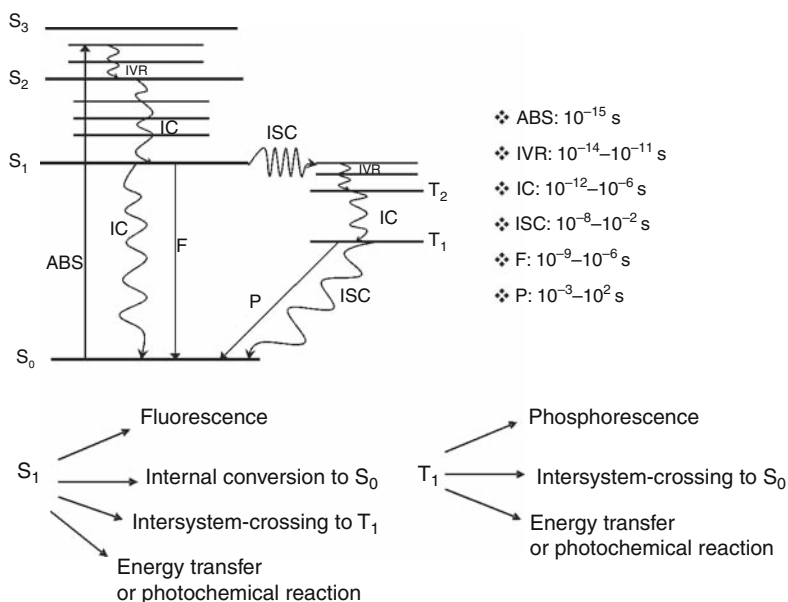
---

The concept of PEHs comes from the Born–Oppenheimer approximation, based on the separation of electronic and nuclear motion due to the large difference in mass between these particles, and assumes that the electrons follow the nuclei instantaneously during the motion of the latter. Therefore, an electronic and a nuclear Hamiltonian can be defined. Solving the electronic Schrödinger equation provides us a description of the movement of electrons, whereas we consider the rotation, vibration, and translation of the molecule solving the nuclear counterpart. The solution of the electronic Schrödinger equation is the energy of a particular nuclear configuration. The total energy for fixed nuclei must also include the constant (within this approximation) nuclear repulsion potential. The value of this total potential energy for every

possible nuclear configuration is specifically the potential energy hypersurface. Photophysical and photochemical processes take place through interactions between PEHs. For the specific case of close degeneracies between the surfaces, where ultrafast energy transfers occur, the Born–Oppenheimer approximation breaks down and special methods in order to localize, optimize, and study the crossing structures are required.

The absorption of photons for a molecule is hardly a static problem. After the absorption (ABS) of one photon, a state of the same multiplicity as the ground state is mainly populated. Direct absorption to states of different multiplicity are only possible if the states heavily interact, for instance, by spin-coupling effects. Actually, in the general case, the energy goes to a vibrational excited state of an electronic excited state of the molecule. Straight afterward, a non-radiative decay occurs, with emission of heat (IVR, intramolecular vibrational relaxation), toward more stable structures of the state PEH, in many cases the state minimum. It might frequently happen that along the decay other states cross and, if appropriately coupling, the system can evolve toward other electronic states of the same multiplicity via a non-radiative internal conversion (IC). Finally, the molecule arrives to the lowest-lying singlet excited state,  $S_1$ , from which the molecule may emit (F, fluorescence) and return to the ground state. Alternatively, a non-radiative transition between two states of different multiplicity is also possible (ISC, intersystem-crossing). By successive internal conversions the system reaches the lowest-lying triplet excited state,  $T_1$ , from which the molecule may emit (P, phosphorescence).

► **Figure 14-1** contains a simplified Jablonski diagram summarizing the main photophysical and photochemical effects undergone by a molecular system. It is common to reserve the word photophysics to processes not involving the generation of new photospecies, that is, just



■ Fig. 14-1

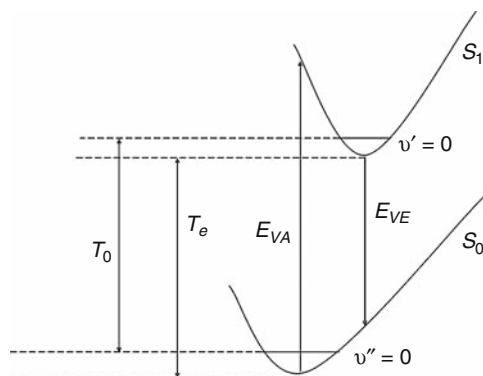
Jablonski's diagram, lifetimes of the basic photophysical processes and deexcitation pathways from the lowest-lying excited states of a molecule

to decays leading to emission or returns to the ground state. However, nonradiative internal conversions or intersystem crossing are also considered photochemical processes, therefore the use of both terms is somewhat loose. A proper nomenclature for excited states is not easy to establish. The less ambiguous (and less informative too) form is purely enumerative:  $S_0$ ,  $S_1$ ,  $T_1$ ,  $T_2$ , where S represents a singlet state and T stands for the triplet states, and the states are ordered by energy. In symmetric systems, it is convenient to use the labels derived from group theory. A state is then described in terms of the behavior of the electronic wave function under the symmetry operations of the point group which the molecule belongs to ( $1^1A_g$ ,  $2^3B_{3u}$ , ...), including the energy ordering, multiplicity, and symmetry label. Classical nomenclatures, such as those developed by Mulliken (N, V, T), Kasha ( $1^1\pi\pi^*$ ,  $3^3\sigma\pi^*$ ), and Platt ( $1^1L_a$ ,  $3^3B_b$ ), highlighting the type of orbitals implied in the excitation, can be useful in different cases.

The basic information required to rationalize a photoinduced phenomenon is the energy levels of the excited solutions and the probability of energy (population) transfer from one state to the other. In the semiclassical treatment of the interaction radiation-matter, whereas we treat the molecule quantum-mechanically, the radiation field is seen as a classical wave obeying Maxwell's equations.

The electric and magnetic fields of the radiation will interact with the atomic or molecular electrons giving a time-dependent perturbation. Solving the time-dependent Schrödinger equation provides us the comprehension of absorption and stimulated emission, whereas to explain spontaneous emission we need the machinery of quantum electrodynamics. The resonance condition provided by the energy differences between the different PEHs of the corresponding states relates to the absorbed or emitted energy quanta. Regarding the transfer probability, it is related with the strength of the interaction between the time-dependent field and the multipolar (the dipole,  $d$ , approach is usually enough) charge distribution of the molecular system. Such strength is proportional to the transition dipole moment (TDM) (► Fig. 14-2).

As an initial feature, the electronic states produce a superposition of bands which characterize the absorption spectrum. The range of absorbed energies fluctuates between the vertical absorption energy,  $E_{VA}$  (difference between the minimum of the ground state and the excited state at the same geometry, that is, the Franck-Condon transition), and the adiabatic transition



■ Fig. 14-2

Vertical energies and band origins. Vibrational states are labeled with the greek character  $\nu$

or band origin,  $T_e$  (difference between the excited state and the ground state at their respective optimized equilibrium geometries): it is the minimal energy difference allowed in absorption if the assumption that all excitations begin from the relaxed ground state is considered, as well as the largest energy emitted from the relaxed excited state. In many cases, the determination of  $T_e$  provides enough information to assign band origins; however, the zero-point vibrational energy (ZVE) has to be included in both initial and final states to get the vibrational band origin,  $T_0$ , which can be directly compared to the experimental value, at least that obtained in the gas phase or in molecular beams. In addition, there is another magnitude named vertical emission energy,  $E_{VE}$ , which is the difference between the excited state and the ground state at the relaxed geometry of the former. The Franck–Condon principle stipulates that the vertical absorption can be related with the experimental band maximum. In fact, this is hardly the case, except when the ground and excited states have very similar geometries, and in this case the  $T_0$  transition ( $S_0 v'' = 0 \rightarrow S_1 v' = 0$ ) yields the most intense peak. The vertical excitation has, however, no experimental counterpart, whereas to get a true band maximum, the band vibrational profile must be computed. The only direct comparison relates the theoretical and experimental band origins,  $T_0$  actually. Trying to assess the quality of a theoretical approach by comparing theoretical vertical excitations and experimental band maxima is one of the most frequent mistakes seen in the literature.

Regarding the transfer probability, far from the conical intersection regions the Fermi's Golden Rule is employed, in which the one-photon (optical) transition probability between two states  $|n\rangle \rightarrow |m\rangle$  is proportional to the square of the TDM between such states:  $\text{TDM} = \langle m|d|n\rangle$ . Two- and higher-order multiphoton probabilities can be also obtained. Based on symmetry considerations, selection rules for electronic transitions have been developed because only the totally symmetric matrix elements yield allowed nonzero probabilities (at first order). Using the so-computed electronic TDM, it is useful to estimate the electronic oscillator strength as  $f = (2/3)E_{VA}\text{TDM}^2$ , with  $E_{VA}$  being the vertical energy difference. The oscillator strength is a classically derived magnitude that represents the relative area of the electronic transition band and that it can be compared with the experimental estimation based in shapes and bandwidths. On the other hand, the vibrational contributions to the band intensity (or, in general, the strength of the transfer) can be obtained by computing the TDM between vibrational states. If belonging to the same electronic states, infrared or Raman intensities can be produced, otherwise electronic band vibrational profiles can be obtained. The vibrational TDM is proportional to the vibrational overlap term between the electronic states,  $\langle v_m|v_n\rangle$ , which are called the Franck–Condon factors (the probability of transition is proportional to its square). The vibrational profiles are basically related to the differences in geometry existing from the initial to the final electronic state and, therefore, the most intense progressions proceed through the normal modes which trigger the aforesaid changes. Within the harmonic approach, the complete TDM with respect the nuclear coordinates  $Q_i$  is defined as the Herzberg–Teller expansion:

$$\begin{aligned} \text{TDM} = & \text{TDM}(Q_0)\langle v_m(Q)|v_n(Q)\rangle \\ & + \sum_K \left( \frac{\partial \text{TDM}(Q)}{\partial Q_K} \right)_{Q_0} \langle v_m(Q)|Q_K|v_n(Q)\rangle + \dots \end{aligned}$$

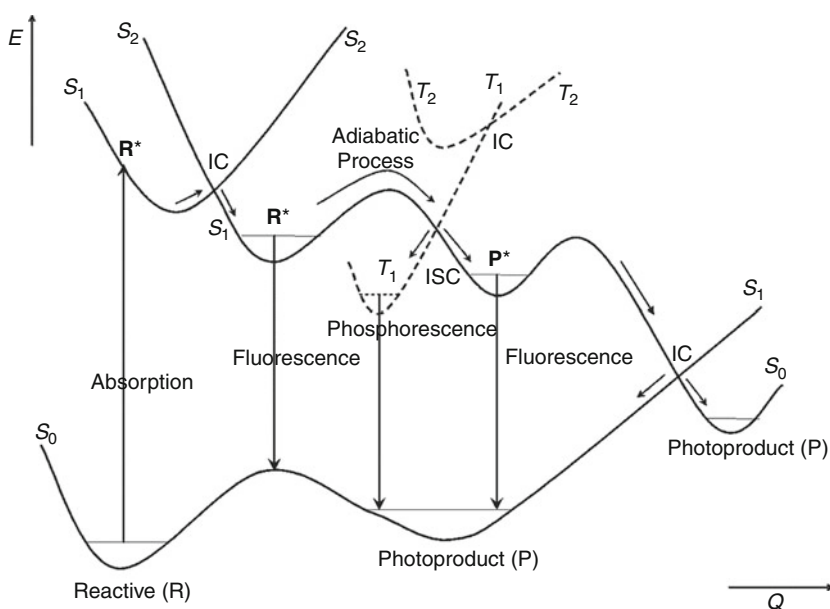
Each one of the terms has an electronic and a vibrational component. The neglect of all terms except the first one is known as the Condon approximation, a usual way to proceed but only applicable for the one-photon dipole-allowed transitions. Otherwise,  $\text{TDM}(Q_0)$  is zero by symmetry and the first term vanishes. Nonetheless, this approximation is valid only when the

Born–Oppenheimer approximation is also valid. Otherwise, the phenomenon of vibronic coupling arises, which gives rise to other approximations (the term vibronic should be reserved to solutions obtained in non-Born–Oppenheimer cases, although is frequently used improperly). From the calculation of transition dipole moments, radiative lifetimes can also be obtained, both in fluorescence and phosphorescence by using the Einstein coefficients ( $A_{21}$ ) and the Strickler–Berg relationships (Strickler and Berg 1962):

$$A_{21} = \frac{1}{\tau_{\text{rad}}} = 2.142005 \cdot 10^{10} E_{\text{VE}}^3 \text{TDM}_{1 \rightarrow 2}^2, \quad (14.1)$$

where  $\tau_{\text{rad}}$  is the radiative lifetime measured in  $\text{s}^{-1}$ . The use of  $T_e$  instead of  $E_{\text{VE}}$  is more representative of the energy of the emission.

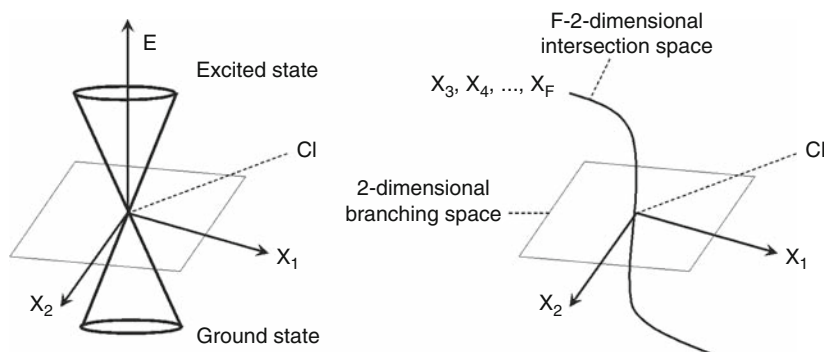
To study photophysical and photochemical processes on theoretical grounds, we need to determine the topography of the potential surfaces of the implied states (see [Fig. 14-3](#)). According to the different reaction paths through what a system might evolve, one can normally make the following classification that defines the photochemical panorama: adiabatic and non-adiabatic photochemistry. In an adiabatic reaction path, once vertical absorption takes place, the system proceeds along the hypersurface of the excited state to reach a local (or absolute) minimum leading in some cases to an emitting feature. On the contrary, in a non-adiabatic photochemical reaction, one part of the reaction takes place on the higher-state hypersurface and after a nonradiative jump at the surface crossing (or funnel) continues on the lower-state hypersurface. In a typical closed-shell ground-state molecule, the reaction usually begins on the potential energy surface of the excited state ( $S_1$  or higher) at the Franck–Condon geometry



■ Fig. 14-3

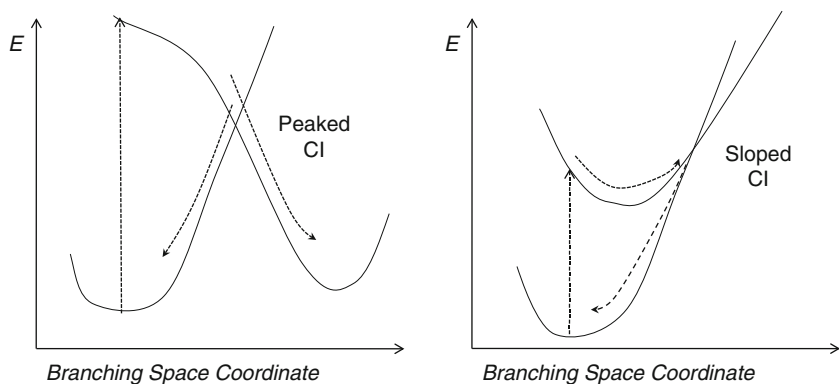
Scheme of the main photophysical and photochemical molecular events. Notice that the order of the states changes along the nuclear coordinate,  $Q$

(i.e., at the ground-state equilibrium geometry) and evolves either to the  $S_1$  state minimum, from which it might emit, or to a crossing region with the ground state. Depending on the properties of such crossing, the process will end up on the reactant minimum or a new photoproduct minimum on the ground-state surface ( $S_0$ ). The crossings between the excited state relevant from the photochemical view and the ground state are frequent, and they represent the basis of the spectroscopic phenomena. Therefore, a molecule evolving through the PEH of an excited state may well enter in a crossing region between two hypersurfaces during the lifetime of such an excited state. Hence, the lifetime of excited states is determined by the barriers that separate the excited states at the Franck–Condon geometry from the low-lying crossings. There are two types of crossings: conical intersections (CI), when the two interacting hypersurfaces have the same multiplicity, and (within the nonrelativistic approximation) singlet–triplet crossings (STC) or any other crossing between states that have different multiplicity (Bearpark and Robb 2007; Domcke et al. 2004; Herzberg and Longuet-Higgins 1963; Robb et al. 1996; Teller 1937). Therefore, internal conversions take place through CIs, and intersystem crossings through STCs. The name of conical intersection (see [Fig. 14-4](#)) reflects the fact that a cone-shaped crossing is obtained when the energy of the states is plotted against the two privileged coordinates, the gradient differential vector,  $x_1$ , and the nonadiabatic coupling vector,  $x_2$ . Thus the total coordinate space  $F$ -dimensional is divided in two: the intersecting space (of dimension  $F - 2$ ), in which both states are degenerated, and the branching space (of 2 dimensions). The most pronounced difference between the slopes of both hypersurfaces occurs along  $x_1$ , whereas along  $x_2$  the optimum nuclear displacement which mixes the two adiabatic wave functions in the CI point takes place. Actually, the intersection space is an hyperline that consists of an infinite number of CI points, i.e., a  $(F - 8)$ -dimensional intersection space. To locate a CI point is equivalent to minimize the energy in the intersection space. In the case of STCs (if the nonrelativistic Hamiltonian is considered), we have only one privileged coordinates since the nonadiabatic coupling vector vanishes. Therefore we should refer this feature as an hyperplane, since we are moving along a  $(F - 1)$ -dimension space.



■ Fig. 14-4

**Description of a conical intersection.** The vectors  $x_1$  and  $x_2$  span the branching space. They are called the gradient difference (GD) vector and the derivative coupling (DC) vector. The DC vector measures the distortion of the system providing the maximum coupling between the electronic states involved in the crossing. The GD vector measures the distortion of the system leading to the largest variation of the energy difference between the two electronic states involved in the crossing



■ Fig. 14-5

Scheme of the limit characters displayed by the conical intersections. For a peaked CI, the two minima lie on the two different sides of the CI point and the gradients of the two intersecting PEHs are directed toward different directions. Conversely, for a sloped CI, the excited-state and ground-state minima lie on the same side (the gradients of the two PEHs point in the same direction), then the probability of re-crossing is higher and the efficiency of funneling is lower

As the Born–Oppenheimer approximation is not valid in regions where the electronic states become too close, it is logical that the nonadiabatic transfer is faster than the radiative relaxation. In essence, the former is based on the structure of the vibronic states. Certainly, the smaller is the gap between the states, the larger is the transfer probability.

Conical intersections may be peaked or sloped (see Atchity et al. 1991; Ben-Nun and Martínez 2000, and ● Fig. 14-5).

If the connection between the two surfaces is sloped, the funnel may well be more efficient. In addition, the degeneracy at a crossing point can also be lifted at second order. As a consequence, we can choose a coordinate system in which to mix the branching and intersection space coordinates to remove this splitting and preserve the degeneracy to second order. These new coordinates give the curvature of the conical intersection hyperline and determine whether one has a minimum or a saddle point on it. These studies may also provide the vibrational modes that must be stimulated in order to enhance nonradiative decay because they decrease the energy gap and can lead to a CI (see Paterson et al. 2004; Sicilia et al. 2007).

A computational strategy can be designed, namely the Photochemical Reaction Path approach, in which the mechanism of the photoinduced process is accounted for by determining the fate of the energy on the populated state by computing the reaction profile. The whole process can be described by computing Minimum Energy Paths (MEPs), describing the lowest-energy, and therefore most favorable, although not unique, path for energy decay. The MEP is often built as steepest descent paths, guaranteeing the absence of barriers along the path. Each step requires the minimization of the PEH on a hyperspherical cross-section of the hypersurface centered on the initial geometry and characterized by a predefined radius. The optimized structure is taken as the center of a new hypersphere of the same radius, and the procedure is iterated until the bottom of the energy surface is reached. Mass-weighted coordinates are used, therefore the MEP coordinate corresponds to the so-called Intrinsic Reaction Coordinate (IRC), measured in a.u., that is,  $\text{bohr} \cdot (\text{amu})^{1/2}$ . The end of the path and the states crossed along

the computed profile will inform about the fate of the energy, and, in particular, of the location of possible radiative minima and surface crossings, CIs and STCs. More crucial than the presence of a crossing is its accessibility. The path of available energy should reach the crossing region to take place. Otherwise, if a too high energy barrier hinders the access to the crossing, the feature could be totally ineffective.

## Electronic Structure Calculations

---

The development of Quantum Mechanics was spread over by Erwin Schrödinger, Werner Heisenberg, and Paul Dirac in the 1920s. The wave and particle aspects of matter are reconciled by the Schrödinger equation for stationary states,  $\mathbf{H}\Psi = E\Psi$ . The Hamiltonian operator,  $\mathbf{H}$ , is associated to the total energy of a physical system and is the sum of the kinetic energy and the potential energy operators associated with electrons and nuclei ( $\mathbf{H} = \mathbf{T}_e + \mathbf{T}_N + \mathbf{V}_{NN} + \mathbf{V}_{Ne} + \mathbf{V}_{ee}$ ). This is an eigenvalue problem, in which wave functions  $\Psi$  are the eigenfunctions of  $\mathbf{H}$  and  $E$  stands for the corresponding eigenvalues (energies). The main challenge in Quantum Chemistry is that we cannot solve exactly the Schrödinger equation, except for one-electron systems, due to the electron repulsion term present in the Hamiltonian. Quantum-chemical methods look for approximate solutions of the equation, employing computational numerical methods typically based on the variational principle and perturbation theory. A point worth bearing in mind is that none of these models is applicable under all circumstances. Actually, we should get the best method in order to find what it has been wisely defined as “the right answer for the right reason.”

The physics of electron correlation is hidden in the Hamiltonian itself. The Coulomb repulsion given by the term  $r^{-1}$  present in the  $\mathbf{V}_{ee}$  energy, the inverse distance between two electrons, increases enormously in the regions close to  $r_{ij} = 0$ , preventing that two electrons may occupy the same space. Therefore, the motion of any two electrons is not independent but it is correlated. The phenomenon is known as electron correlation. Moreover, the statement that two electrons are correlated is equivalent to express that the probability of finding two electrons at the same point in space is zero. The instantaneous position of electron  $i$  forms the center of a region that electron  $j$  will avoid. For this reason, it is stated that each electron, as described by the exact wave function  $\Phi$ , is surrounded by a Coulomb hole. However, electron correlation is not taken into account properly by many approximate methods. The effect of neglecting electron correlation partly in approximate quantum-chemical approaches has great impact in the computed molecular spectroscopic properties of interest.

## General Overview

---

We can group computational-chemical methods in three basic categories (see for instance Atkins and Friedman 1997; Helgaker et al. 2004):

- Ab initio methods, in which the complete Hamiltonian is used, all the integrals are solved numerically, and no essential parametrization is employed
- Semiempirical methods, in which a simpler Hamiltonian is used or integrals are adjusted to experimental values or ab initio results

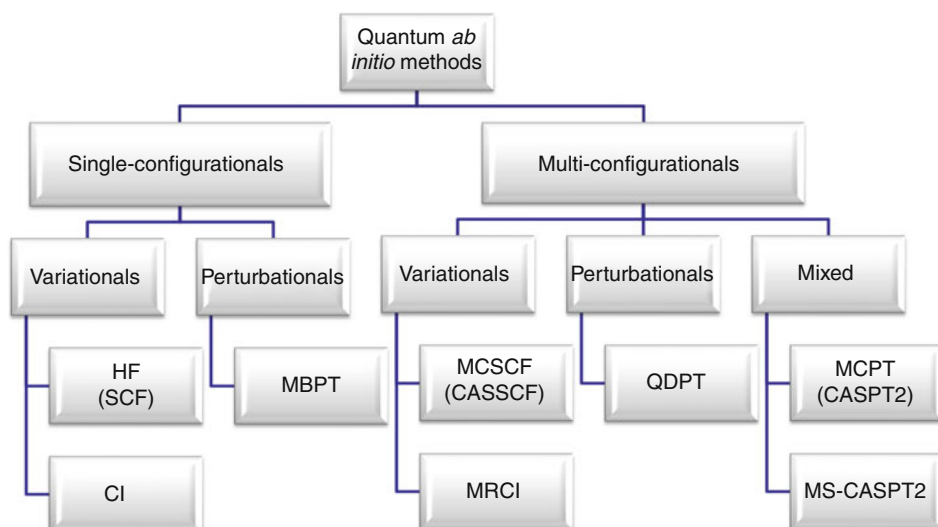


- Molecular mechanics, in which we solve Newton's equation of motion, only valid for situations where no bonds are broken or formed, i.e., conformational changes

Obviously, the larger is the system under study, the less accurate is the available method. Despite their inherent drawbacks, classical semiempirical methods are still employed in large systems, whereas modern semiempirical methods, based on the Density Functional Theory, have a widespread use. A combined approach, QM/MM (Quantum Mechanics/Molecular Mechanics) treats an internal part of the problem with QM methods, whereas the surroundings or a large part of a macromolecule (for instance, a protein) is introduced using classical mechanics.

According to the number of configurations used to build the reference wave function, the *ab initio* methods can be classified in the following two categories (see [Fig. 14-6](#)):

- *Single-configuration methods.* They are typically based in the single Hartree–Fock (HF) reference, which determines the optimal ground-state energy and MOs (molecular orbitals). Post-HF methods introduce the electron correlation usually at the Configuration Interaction (CI), Coupled-Cluster (CC) or perturbative (PT) Møller–Plesset (MP, or PT in general) levels. The coupled-cluster methods with singly and doubly excited configurations, including the effect of triple excitations by perturbation theory CCSD(T), as well as related approaches, yield accurate results in well-defined ground-state situations and are considered as benchmark results for small to medium molecules. In general, the applicability of the methods in this group is restricted to situations where a single reference wave function is adequate for the description of a chemical process, something not generally true for bond-breaking cases, degeneracies, and excited states
- *Multiconfigurational methods.* Part of the electronic correlation is already included in the reference wave function, normally by using a Multiconfigurational Self-Consistent-Field



■ Fig. 14-6

**Ab initio methods**

(MCSCF) wave function, which determines a set of MOs. The remaining electron correlation effects are accounted for by MRCI, MRCC, or MRPT techniques, where MR stands for multireference. They have a more ample range of applicability (ground state, excited states, transition states) than single-reference methods

The variation principle states that given a normalized wave function that satisfies the appropriate boundary conditions, then the expectation value of the Hamiltonian is an upper bound to the exact ground-state energy. In the linear variational problem, the trial function is a linear combination of basis functions, in general using the Linear Combination of Atomic Orbitals (LCAO) approach. On the other hand, in perturbation theory, the total Hamiltonian of the system is divided into two pieces: a zeroth-order part, which has known eigenfunctions and eigenvalues, and a perturbation part. The exact energy and wave function are then expressed as an infinite sum of contributions of increasing complexity. If we have chosen the zeroth-order Hamiltonian wisely, then the perturbation is small and the expansion (i.e., the sum of the 1st-, 2nd-, ...,  $n$ th-order energies) converges quickly.

The simplest wave function to describe a many-electron system is a Slater determinant built by orthogonal one-electron wave functions. Electrons are fermions and accordingly they have to be described by an antisymmetric wave function. For an  $N$ -electron system, the Slater determinant has the form:

$$\Psi(x_1, x_2, \dots, x_N) = (N!)^{-1/2} \begin{vmatrix} \chi_i(x_1) & \chi_j(x_1) & \dots & \chi_k(x_1) \\ \chi_i(x_2) & \chi_j(x_2) & \dots & \chi_k(x_2) \\ \vdots & \vdots & \ddots & \vdots \\ \chi_i(x_N) & \chi_j(x_N) & \dots & \chi_k(x_N) \end{vmatrix} = |\chi_i \chi_j \dots \chi_k| \quad (14.2)$$

without specifying which electron is in which orbital. To simplify the notation, a normalized Slater determinant is represented by only showing the diagonal elements of the determinant. The constant  $(N!)^{-1/2}$  is a normalization factor. The wave function for an electron that describes both the spatial distribution and its spin is called spin orbital,  $\chi_i(x_i)$ . Since the Hamiltonian employed does not depend on the electronic spin, each spin orbital can be expressed by multiplying the spatial orbital,  $\psi_j(r_i)$ , by the spin function,  $\omega$  ( $\alpha$  – spin up and  $\beta$  – spin down):  $\chi_i(x_i) = \psi_j(r_i) \cdot \omega$ . A complete set for describing the spin of an electron consists of two orthogonal functions  $\alpha(\omega_i)$  and  $\beta(\omega_i)$ .

A single-determinant wave function has several interesting properties. Firstly, it is worth noting that spin orbitals must be linearly independent, otherwise the value of the determinant is zero. It is obvious that interchanging two rows of the Slater determinant, which is equivalent to interchanging the coordinates of two electrons, changes the sign of the determinant. The requirement of the antisymmetry principle is automatically fulfilled. Having two columns of the determinant identical, that is, two electrons occupying the same spin orbital, makes the determinant zero. Thus, no more than one electron can occupy a spin orbital (Pauli exclusion principle). When a linear transformation of the set  $\{\chi_i\}$  is carried out,  $\chi'_i = \sum_j \chi_j \cdot A_{ji}$ , where  $A_{ji}$  is an element of the matrix  $\mathbf{A}$  of dimension  $N \times N$ , with a value for its determinant,  $\det(\mathbf{A})$ , different from zero, then  $\Psi' = \det(\mathbf{A})\Psi$ . The wave functions  $\Psi'$  and  $\Psi$  differ just in a constant and, therefore, represent the same physical situation. Since the set of spin orbitals is linearly independent, we can always choose a transformation matrix  $\mathbf{A}$  so that the resulting spin orbitals  $\chi'_i$  become orthonormal. Therefore, no restriction at all is imposed when we choose from the beginning an orthonormal set of spin orbitals. It just makes the computation of the Hamiltonian matrix elements involving Slater determinants easier. A Slater determinant is completely

specified by the spin orbitals used to build it, and any unitary transformation of them is equally valid. Two sets of spin orbitals related by a unitary transformation ( $\mathbf{A}^\dagger = \mathbf{A}^{-1}$ ), which keeps the orthonormality of the spin orbitals, yield the same Slater determinant. Slater determinants formed from orthonormal spin orbitals are normalized and N-electron Slater determinants that have different spin orbitals are orthogonal. In other words, a Slater determinant is completely specified by the spin orbitals used to build it and any unitary transformation of them is equally valid (each result of such a linear transformation represents the same physical situation).

There are two types of spin orbitals: restricted spin orbitals, which are constrained to have the same spatial function for  $\alpha$  and  $\beta$  spin functions; and unrestricted spin orbitals, which have different spatial functions for  $\alpha$  and  $\beta$  spins. A restricted set of spin orbitals has the form:  $\chi_i(x) = \psi_j(r) \cdot \alpha(\omega) / \psi_j(r) \cdot \beta(\omega)$ , whereas an unrestricted set has the form:  $\chi_i(x) = \psi_j^\alpha(r) \cdot \alpha(\omega) / \psi_j^\beta(r) \cdot \beta(\omega)$ .

Essentially, all practical calculations for generating solutions to the electronic Schrödinger equation are performed with molecular orbital methods: the zeroth-order wave function is constructed as one or two Slater determinants and the MOs are expanded in a set of atomic orbitals, the basis set. In a subsequent step, the wave function may be improved by adding electron correlation by either CI, MP, or CC methods. Nevertheless, there is another equivalent theory to get approximate solutions of this eigenvalue equation: the valence bond (VB) theory. The main drawback is that this theory leads to awkward calculations. On the positive side, conceptually it is much closer to the experimentalist's language since it may be regarded as a quantitative version of the resonance structure of electronic structure, with ionic structures and covalent structures of molecules. The VB method assumes that the wavefunction of a molecule may be written as a linear superposition of mathematical functions which represent canonical electronic structures: structures in which electrons are assigned to specific atoms and then paired (spinwise) leading to covalent and ionic structures, the combination of which represents the wave function. The VB description of a bond as the result of two overlapping and localized orbitals is in contrast to the MO approach where a bond between two atoms arises as a sum over (small) contributions from many delocalized orbitals.

Classical valence bond theory is very successful in providing a qualitative explanation for many aspects. One of the great merits of VB theory is its pictorially intuitive wave function that is expressed as a linear combination of chemically meaningful structures. It is this feature that has made VB theory so popular in the 1930–1950s. However, VB theory was “defeated” by MO theory for two main reasons: (1) mathematical simplicity and (2) several “failures” of the VB theory (actually due to misuse of very simplified versions of the theory). Currently, VB theory is coming of age in all the branches of theoretical chemistry (excited states, dynamics, environmental effects, and so on), with the development of faster, and more accurate *ab initio* VB methods, and with generation of new post-Pauling concepts. The Renaissance of VB theory is marked by surge in the following two-pronged activity: (1) creation of general qualitative models based on VB theory and (2) development of new methods and softwares that enable applications to moderate sized molecules.

## Methods, Advantages, and Drawbacks

The Hartree–Fock method is the simplest *ab initio* approach. We can equate closed-shell HF theory to single determinant theory, and we are thus interested in finding a set of spin orbitals

$\{\chi_a\}$  such that the single determinant formed from them,  $|\Psi_0\rangle = |\chi_1\chi_2\chi_3 \dots \chi_a\chi_b \dots \chi_N\rangle$  is the best possible approximation to the ground state of the  $N$ -electron system described by an electronic Hamiltonian  $\mathbf{H}$ . The expectation value of the energy,  $E_0 = \langle\Psi_0|H|\Psi_0\rangle$ , is a linear combination of one-electron integrals,  $\langle i|h|j\rangle$  and two-electron integrals,  $\langle ij|kl\rangle$ . According to the properties of a Slater determinant, electrons are not uncorrelated in a HF wave function. At least the probability of finding two electrons with parallel spins at the same point in the space is zero, the so-called exchange correlation, which is incorporated by the antisymmetric condition of the wave function for fermions. The phenomenon is known as the Fermi hole. We are, therefore, facing a model of independent particles where the behavior of certain electrons is not fully independent because the Fermi hole simulates somehow the Coulomb hole. Consequently, only Fermi correlation is accounted for by the HF wave function.

By minimizing  $E_0$  with respect to the choice of spin orbitals  $\{\chi_a\}$ , varying them with the only restriction that they remain orthonormal,  $\langle\chi_a|\chi_b\rangle = \delta_{ab}$ , one can arrive to the Hartree–Fock conditions. In doing so, one obtains an equation that defines the best spin orbitals, the ones that minimize  $E_0$ . This equation for the best (Hartree–Fock) spin orbitals is the Hartree–Fock integro-differential equation  $f|\chi_a\rangle = \varepsilon_a|\chi_a\rangle$ , for the  $N$ -occupied spin orbitals  $\{\chi_a\}$ . Each of the solutions  $\{\chi_j\}$  has a spin orbital energy  $\varepsilon_j$ . The  $N$  spin orbitals with the lowest orbital energies are just the spin orbitals occupied in  $|\Psi_0\rangle$  for which we use the indices  $a, b$ , etc. The remaining infinite number of spin orbitals with higher energies are the virtual spin orbitals, which we label with the indices  $r, s$ , etc.

The Fock operator  $f$  is the sum of a core-Hamiltonian operator  $h(1)$ , which is the kinetic energy and potential energy for attraction to the nuclei of a single  $a$  electron, and an effective one-electron potential called the Hartree–Fock potential  $v^{\text{HF}}(1)$ , which contains the Coulomb term (the total averaged potential acting on the electron in  $\chi_a$ , arising from the  $N - 1$  electrons in the other spin orbitals) and the exchange term (which arises because of the antisymmetric nature of the determinantal wave function). This is the essence of the HF approximation: to replace the complicated many-electron problem by a one-electron problem in which electron–electron repulsion is treated in an average way. What is more, since the Fock operator has a functional dependence, through the coulomb and exchange operators, on the solutions  $\{\chi_a\}$  of the pseudo-eigenvalue equation, Hartree–Fock equations are actually nonlinear equations and will need to be solved by iterative procedures. The matrix representation of the Fock operator in the basis of spin orbitals eigenfunctions is diagonal with diagonal elements equal to the orbital energies.

The exact solution to this integro-differential equation corresponds to the “exact” HF spin orbitals. In practice, it is only possible to solve this equation exactly (i.e., as an integro-differential equation) for atoms. In practice, for molecules, the spin orbitals are expanded as a combination of one-electron atomic base functions and the set of matrix equations are solved. Only as the basis set approaches completeness, i.e., as one approaches the HF limit, will the spin orbitals be the exact HF orbitals.

It can be shown that any single determinant wave function  $|\Psi_0\rangle$  formed from a set of spin orbitals  $\{\chi_a\}$  retains a certain degree of flexibility in the spin orbitals; the spin orbitals can be mixed among themselves without changing the expectation value  $E_0 = \langle\Psi_0|H|\Psi_0\rangle$ . Furthermore, for a single determinant wave function, any expectation value is invariant to an arbitrary unitary transformation of the spin orbitals, since a transformed single determinant  $|\Psi'_0\rangle$  can at most differ from the original determinant  $|\Psi_0\rangle$  by a phase factor and, obviously, any observable property depends on  $|\Psi|^2$ , as we stated before. Thus the spin orbitals that make the total energy stationary are not unique, and no particular physical significance can be given to a particular set

of spin orbitals. Localized spin orbitals, for instance, are not more “physical” than delocalized spin orbitals. Indeed, there exist a set of spin orbitals for which the eigenvalue matrix is diagonal, and we obtain just the equation  $f|\chi_a\rangle = \varepsilon_a|\chi_a\rangle$ , and this set is called “canonical spin orbitals.” The canonical spin orbitals, which are a solution to this equation, will generally be delocalized and form a basis for an irreducible representation of the point group of the molecule.

It was in 1951 that Roothaan published his equations (see Roothaan 1951), considering molecular orbitals that were restricted to be linear combinations of a set of three-dimensional one-electron functions,  $\phi_\mu$ . Thus,  $\psi_i$  is a linear combination of these functions  $\phi_\mu$  (basis set):  $\psi_i = \sum C_{\mu i} \cdot \phi_\mu$ . If the set  $\{\phi_\mu\}$  was complete, this would be an exact expansion, and any complete set  $\{\phi_\mu\}$  could be used. Unfortunately, this one is always restricted, for practical computational reasons, to a finite set of  $N$  basis functions. As the basis set becomes more and more complete, this expansion leads to more and more accurate representations of the “exact” molecular orbitals, which are eigenfunctions of the Fock operator. For any finite basis set, we will obtain molecular orbitals which are exact only in the space spanned by the aforesaid finite basis. In addition, since the electronic energy (the output of the quantum mechanical calculation) is variational, the better the basis set, the lower the total energy. As the basis set becomes more and more complete, the total energy approaches the Hartree–Fock limit. Of course, by the variational principle, the Hartree–Fock-limit energy is still above the “exact” energy, which here can be taken as the energy obtained from an exact solution to the nonrelativistic Schrödinger equation in the Born–Oppenheimer approximation.

Variation of the total energy was then carried out respect to the coefficients  $C_{\mu i}$  of such a linear combination. This leads to a set of algebraic equations which can be written in matrix form,  $\mathbf{FC} = \mathbf{SCE}$ , where  $\mathbf{F}$  is the matrix representation of the Fock operator (which can be divided into the core-Hamiltonian matrix, that is, integrals involving the one-electron operator  $h(i)$  describing the kinetic energy and nuclear attraction of the electron  $i$ , plus the two-electron terms),  $\mathbf{C}$  is the matrix of coefficients,  $\mathbf{S}$  is the overlap matrix, and  $\mathbf{E}$  is the diagonal energy matrix. The columns of  $\mathbf{C}$  describe the molecular orbitals, i.e., the coefficients describing  $\psi_1$  are in the first column, with the corresponding energy  $\varepsilon_1$ , those describing  $\psi_2$  are in the second column, and so on. If  $\mathbf{S}$  is the unit matrix (i.e., if we have an orthonormal basis set), then we would have  $\mathbf{FC} = \mathbf{CE}$ , and Roothaan’s equations would just have the form of the usual matrix eigenvalue problem. Increasing the flexibility of the one-electron basis set  $\{\phi_\mu\}$ , the HF energy  $E_0$  will progressively reach the Hartree–Fock limit.

The approximation has its limitations, in particular the lack of electronic correlation energy. For instance, Restricted Hartree–Fock (RHF) solution predicts incorrectly the dissociation of molecules into open-shell fragments (like  $\text{H}_2 \rightarrow 2\text{H}$ ) given that both electrons are forced to occupy the same spatial molecular orbital (MO), when they should belong to infinitely separated atoms in the dissociated solution. This means that some electron–electron repulsion remains even at infinity, which is the source of a spurious term in the total energy (different from twice the energy of two hydrogen atoms). Alternatively, the products of dissociation are not just  $2\text{H}$ , but also include, incorrectly,  $\text{H}^-$  and  $\text{H}^+$ . However, the poor behavior of closed-shell RHF calculations upon dissociation to open-shell products does not detract from their utility as reference function in the region of equilibrium: the potential surface obtained from a closed-shell RHF calculation will not be parallel in regions of the surface characterizing dissociation limit, but it will be reasonably parallel near the region of the equilibrium geometry. It is worth mentioning that the VB wave function for  $\text{H}_2$ ,  $\Psi = C_{\text{cov}}\Psi_{\text{cov}} + C_{\text{ion}}\Psi_{\text{ion}}$ , with the covalent and ionic counterparts, contains “left–right” correlation which is necessary for a correct description of dissociation of the  $\text{H}_2$  molecule.

Within the HF approach, a slight improvement can be achieved in dealing with open-shell systems with the restricted open-shell (ROHF) and the unrestricted Hartree–Fock (UHF) procedures. In the former, all electrons, except those that are explicitly required to occupy open-shell orbitals, occupy closed-shell MOs. In the latter, electrons of different spin, in general, are described by different sets of spatial orbitals, although the obtained wave function is typically contaminated with higher spin state solutions. The approximation leads to two integro-differential eigenvalue equations which are coupled and cannot be solved independently. The introduction of a basis leads to the Pople–Nesbet equations,  $\mathbf{F}^\alpha \mathbf{C}^\alpha = \mathbf{S}^\alpha \mathbf{C}^\alpha \mathbf{E}^\alpha$  and  $\mathbf{F}^\beta \mathbf{C}^\beta = \mathbf{S}^\beta \mathbf{C}^\beta \mathbf{E}^\beta$ . When  $N^\alpha = N^\beta$ , a restricted solution to the Roothaan equations is a solution to the unrestricted Pople–Nesbet equations. In general those approaches, which can serve as reference for post-HF methods in ground-state cases, are not accurate enough to compute excited states.

The lack of correlation is the actual source of all errors. In particular, a Slater determinant incorporates exchange correlation, i.e., the motion of two electrons with parallel spins is correlated (the so-called Fermi correlation). Unfortunately, the motion of electrons with opposite spins remains uncorrelated. It is common to define correlation energy,  $E_{\text{corr}}$ , as the difference between the exact nonrelativistic energy of the system,  $\varepsilon_0$ , and the Hartree–Fock energy,  $E_0$ , obtained in the limit that the basis set approaches completeness:  $E_{\text{corr}} = \varepsilon_0 - E_0$ . The simplest manner to understand the inclusion of the correlation effects is through the method of configuration interaction (CI). The basic idea is to diagonalize the N-electron Hamiltonian in a basis of N-electron functions: we represent the exact wave function as a linear combination of N-electron trial functions and use the linear variational method.

$$|\Phi\rangle = C_0|\Psi_0\rangle + \sum_{ra} C_a^r |\Psi_a^r\rangle + \sum_{a<b;r<s} C_{ab}^{rs} |\Psi_{ab}^{rs}\rangle + \dots \quad (14.3)$$

If the basis were complete, we would obtain the exact energies of all the electronic states of the system. In spite of providing the exact solution of a many-electron problem, we can handle only a finite set of N-electron trial functions. As a result, the CI method provides only upper bounds to the exact energies. Specifically, the lowest eigenvalue,  $\varepsilon_0$ , will be an upper bound to the ground-state energy of the system. When all the N-electron wave functions are taken into account, the calculation is named full configuration interaction (FCI) and the corresponding eigenvalues and eigenvectors computed are exact within the space spanned by the finite basis set. Despite the great advances in FCI technology in the last few years, the size of the eigenvalue problem becomes rapidly too large to be handled by modern computers. As a result, FCI solutions are only available for very small molecular systems. In contrast to HF, the FCI energy of  $\text{H}_2$  properly describes the dissociation. However, within a minimal basis set approach, the FCI potential curve does not agree very well with the exact one provided by Kolos and Wolniewicz due to the lack of flexibility of such a basis set. The truncation of both N-electron basis and one-electron basis is the main source of inaccuracies in quantum-chemical calculations (► Fig. 14-7).

As mentioned earlier, for computational reasons, we have to truncate the full CI matrix or equivalently the CI expansion for the wave function, considering only those configurations which differ from the HF ground-state wave function by no more than a predetermined number of spin orbitals. The simplest version of this scheme is to deal with single and double excitation out of  $|\Psi_0\rangle$ : a SDCI calculation. SDCI and, in fact, all forms of truncated CI deteriorate as the number of electrons increases. The truncation of the CI expansion leads to problems of size-extensivity. For instance, in a DCI calculation, by definition the wave function of each monomer

$$\begin{aligned} & \text{N-electron basis set} \\ \langle \Phi \rangle &= C_0 |\Psi_0\rangle + \sum_{ra} C_a^{rs} |\Psi_a^r\rangle + \sum_{a<b; r<s} C_{ab}^{rs} |\Psi_{ab}^{rs}\rangle + \dots \\ & \text{1-electron basis set} \\ \langle \Phi_i \rangle &= |\chi_i \chi_j \dots \chi_N\rangle \quad \chi_i = \phi_i \vec{\omega} / \vec{\omega} = \alpha, \beta \\ \phi_i(\vec{r}) &= \sum_{\mu=1}^K C_{\mu i} \phi_{\mu}(\vec{r}) \quad \phi_{\mu}(\vec{r}) = \sum_K d_{K\mu} g_K \end{aligned}$$

■ Fig. 14-7

**Many-electron expansion (CI) and one-electron expansion (basis set).** The total wave function,  $\Phi$ , is a linear combination of N-electron wave functions  $\Psi_0, \Psi_a^r$ , etc. Each one of these functions is an antisymmetrized and normalized product of spin orbitals,  $\chi_i$ . Each of them is constituted by a one-electron wave function,  $\psi_i$ , and a spin function,  $\omega$ . Each one-electron wave function is defined as a linear combination of a set of basis functions,  $\phi_{\mu}$ , which are used to be contracted gaussian functions, CGTFs (linear combinations of a set of primitive functions,  $g_K$ )

contains double excitations within the monomer. If we restrict the supermolecule trial function to double excitations, we exclude the possibility that both monomers are simultaneously doubly excited, since this represents a quadruple excitation in the supermolecule. It is now common to differentiate size-extensivity and size-consistency. The latter was originally employed by Pople as a criterion for a well-constructed quantum-chemical method, indicating that the energy computed for two noninteracting molecules should be exactly twice that calculated for only one isolated molecule, that is, a property that described the additive separability of the wave function. Recently, the concept has been extended to include not only the fragmentation limit but the entire process, that is, qualitatively all regions of the potential energy hypersurface must be qualitatively correct. For instance, both RHF and UHF wave functions are size consistent in the first sense, considering that they properly describe a separated  $H_2$  dimer system, but for a closed-shell molecule dissociating into open-shell fragments the RHF descriptions fails, and therefore does not conform to the broader size-consistency concept. On the other hand, size extensivity, analogously to the extensivity concept in thermodynamics, refers to the correct, linear, scaling of a method with the number of electrons, and its fulfillment leads to methods in which calculations with differing number of electrons can be compared, like those related to ionization processes. Otherwise, the error of the method increases with the size of the system. At the noninteracting limit size extensivity implies size consistency, but this latter property has the requirement of correct fragmentation, which does not depend on the mathematical scaling. Therefore, RHF and UHF approaches are always size extensive, but RHF does not provide proper dissociation in open-shell cases, and it is therefore non-size-consistent, as any other method such as single-reference coupled-cluster (CC) or perturbation approaches (PT) which use RHF as reference wave function. On the other hand any truncated configuration interaction approximation is not size extensive, whereas CC and PT are. In the case of the multiconfigurational methods, the size-consistency depends on the selected reference – generally they are size consistent – and the size extensivity varies with the approach. MRCI is formally a truncated CI approach and therefore is not size extensive, as CASPT2 – multiconfigurational complete active space perturbation theory up to second order – and similar methods, which are formally not size extensive either, but in practice the effects are irrelevant, in particular for the most common implementation (see Taylor 2007).



It is worth mentioning that using a better-variational method only ensures to get a better variational energy, but a priori we cannot say nothing regarding properties other than the energy. For instance, the dipole moment of CO is ca. zero, and to obtain the correct sign of the vector (actually, greater than zero: +0.044 a.u. experimentally) is a tricky problem. A DCI calculation with the 200 most important double excitations has a lower energy than a SDCI procedure with 138 doubles + 62 singles. Still, the DCI calculation predicts the wrong sign of the dipole moment (-0.072 a.u.), just the contrary that the SDCI calculation (+0.030 a.u.). To improve the result it is necessary to employ CCSD(T) (+0.047 a.u.) (Paschoal et al. 2009).

There is another clever way to introduce in the wave function enough correlation effects to get a good account of the nature of the chemical problem, for instance, in a dissociation path of a diatomic molecule. Such procedure implies to improve the reference wave function by including more than one determinant or electronic configuration in its description. Adding more than one configuration means to get their weights in a linear combination. Therefore, the central idea of a multiconfigurational self-consistent field (MCSCF) calculation is to build the wave function as a truncated CI expansion

$$|\Psi_{\text{MCSCF}}\rangle = \sum_I c_I |\Psi_I\rangle, \quad (14.4)$$

in which both the expansion coefficients and the orthonormal orbitals contained in  $|\Psi_I\rangle$  are optimized simultaneously. For a closed-shell system, if only one determinant is included in such an expansion, the MCSCF and HF methods become identical. In the minimal basis set description of  $\text{H}_2$ ,  $\Psi_{\text{MCSCF}}$  is identical to the FCI wave function. However, if an extended basis set is used, the MCSFC energy will be above and nearly parallel to the FCI energy but below the energy obtained from any two-configuration CI expansion based on canonical HF MOs.

The correlation energy introduced in a MCSCF wave function is usually named nondynamic, static, or large-range correlation energy, and the corresponding wave function must be built in such way that includes most of near-degenerate electronic configurations, that is, all those which basically contribute to define the reference function along the chemical process under study. An example is a bond breaking. A proper MCSCF description should include both the bonding and antibonding distribution of the electrons, and the corresponding MOs. The optimization procedure at each region of the PEH will determine the relative weight of each configuration at that point and the proper MOs. Improving the reference in such manner helps to the post-HF approaches to account for the remaining correlation effects, named dynamic or short-range. It is like starting the race from a more advantageous position.

One of the most successful and systematic procedures to account for the correlation energy, which is not variational but is size extensive at each order, is the perturbation theory. Using different zeroth-order Hamiltonians, Møller–Plesset perturbation theory (MPPT), also named many-body perturbation theory (MBPT), yields the energy and the wave function corrected up to  $n$  order following a Taylor series expansion. Although, in general, higher perturbation orders improve the result, it has been proved that it leads to divergences at infinite order. Second- and fourth-order perturbation (MP2, MP4) results are much better than the SCF and SDCI ones. The most recent family of methods based on a single reference is that based on the coupled-cluster (CC) approach, in which the correlation energy is introduced size-extensively by increasing the excitation level. CC methods for the ground state, especially when including up to triple excitations, have become, in practice, the most accurate quantum-chemical approaches for many systems.



No matter how good is the quality of the post-HF method for the inclusion of the correlation energy, when based on a single HF reference, the accuracy of the results largely decreases in many situations, like those related with dissociations, degeneracies, and excited states. For instance, regarding the dissociation problem, the potential curve calculated at any level based on a RHF reference is not satisfactory at long range. The problem is the starting point: the exact wave function at large  $R$  cannot be described by a single determinant. The results largely improve its accuracy when a multiconfigurational or multireference (MR) wave function is used as a reference, for instance, in the MRCI, MRCC, or MRMP approaches. Recovering correlation energy does not require so large effort in this case, for instance, lower perturbation (MP) or excitation (CC) levels. As a drawback, the complexity of the methods increases.

On the other hand, the semiempirical DFT approach has become the most widespread quantum-chemical method in the last years. It allows us to treat large systems in a relatively short time taking into account electron correlation. The basic idea is that the energy of an electronic system can be written in terms of the electron density,  $\rho$ . For a system of  $N$  electrons,  $\rho(\mathbf{r})$  denotes the total electron density at a particular point in space  $\mathbf{r}$ . The electronic energy  $E$  is said to be a functional of the electron density, denoted  $E[\rho]$ , in the sense that for a given function  $\rho(\mathbf{r})$ , there is a single corresponding energy. It is not necessary to compute a wave function, but, unfortunately, the Hohenberg–Kohn theorem does not inform about the form of the functional dependence of energy on the density: it confirms only that such a functional exists. So the procedures should resort to approximate derivations with adjustable parameters. This is the reason why functionals proliferate to hundreds in the literature. Some of them, like the Becke3-Lee-Yang-Parr (B3LYP) functional, is the most popular in the literature, not because its overall accuracy but of its balance and its controlled flaws. There is no systematic way to improve a functional, just to derive another one with different parameters. It is typical to use one functional per each situation, something that makes the predictability of the results somewhat questionable. On the contrary, *ab initio* calculations, if allowed by the size of the problem, can be hierarchically improved in a known direction enlarging the  $N$ -electron and/or the one-electron basis.

## Basis Sets

---

The choice of the one-particle space is a most important decision when setting up any calculation, and there is no point in trying to improve the result if the selection of the one-electron basis set is not adequate. This is especially true for the calculation of excited states, in which states of very different nature (for instance, compact and diffuse) have particular requirements that must be fulfilled simultaneously when selecting the basis set. In a strict mathematical sense, many different types of basis set functions  $\{\phi_\mu\}$  can be used. Gaussian-type functions (GTFs,  $g \propto e^{-\alpha r^2}$ ) are the more widespread in spite of being ill-behaved in both close and far away of the nuclei. Nevertheless, four-center integrals (that is, two-electron repulsion integrals) are very easy to evaluate with GTFs, and, in addition, the basis set can be improved by employing contracted Gaussian functions, CGTFs, which are linear combinations of primitive GTFs. To build a CGTFs, the primitive functions have to be optimized, both exponents and contraction coefficients. According to the number of basis functions, it is common to distinguish among minimal basis set (a single basis function per occupied atomic orbital), double- $\zeta$  (two basis functions per atomic orbital), triple- $\zeta$ , split-valence (duplication only affects to valence layer whereas minimal basis set is used for core orbitals), etc.

Ground-state calculations have made extensive use of the so-called Pople basis sets: STO-G, 3-21G, 6-31G. These basis sets are built using segmented contraction, which means that each primitive functions contributes to one or a limited number of contracted function only. Exponents and coefficients were optimized using the HF approach. Valence basis sets are too limited to get accurate results, and therefore additional functions have to be added, named polarization functions (6-31G\* or 6-31G(d), which means that polarization functions are added to second-period atoms; and 6-31G\*\* or 6-31G(d,p), which means that, additionally, polarization functions are added to hydrogen atoms). These are functions of higher angular momentum than those of valence type and are necessary in order to describe the changes of the electronic density of an atom in the molecule. Diffuse functions (6-31+G, 6-31++G) can be also added which are more extended in the space, that is, with smaller exponents, to describe better situations such as anions or Rydberg states. A 6-31G basis set for the C atom ( $1s^2 2s^2 2p^2$ ) is described as  $(10s4p)/[3s2p]$ , i.e., 10 primitives s and 4 primitives p (22 primitives:  $1s \times 6 + 2s \times 3 + 2s \times 1 + 2p \times 3 + 2p \times 1$ ) are contracted to three combined functions s and two combined functions p (nine contracted functions:  $1s, 2s, 2s', 2p, 2p'$ ). The basic flaw of Pople's basis sets is that they have been built with a method lacking correlation energy. The consequence is that they are very poor in recovering correlation effects in post-HF methods. In order to get better values, more polarization of diffuse functions have to be added to compensate the lack of flexibility of these basis set.

If the ultimate goal is to perform correlated calculations, it would seem preferable to include correlation in the construction of the basis set. For correlated calculations, the basis set requirements are different and more demanding since we must also provide a virtual orbital space capable of recovering a large part of the correlation energy. It is often sufficient to correlate only the valence electrons. This is the case for correlation consistent (cc) or Atomic Natural Orbitals (ANO) basis sets. Correlation consistent basis sets are designed so that functions which contribute in similar amounts of correlation energy are included at the same stage, independently of the function type. We can add polarization functions (cc-pVDZ. . .) or diffuse functions (augmented, aug). They need fewer primitives than ANOs, and each contracted basis comes from a different primitive set and the exponents of polarization functions are optimized by correlated calculations within a segmented contraction scheme.

On the other hand, ANO-type basis sets arise as eigenfunctions of the first-order reduced density matrix of the atom. They give the most rapidly convergent CI expansion, and to obtain a given accuracy one requires fewer configurations formed from NOs than configurations formed from any other orthonormal basis. The occupation number is a reference of its significance in the wave function and the truncation of the orbital space by elimination of the ANOs whose occupation numbers are small produces the least possible error on the wave function. The coefficients of ANOs obtained in a correlated calculation of the ground state of the atom represent the coefficients of the basis functions within a general contraction scheme (all primitives on a given atom and of a given angular momentum enter all the contracted functions having that angular momentum, but with different contraction coefficients, which improves the flexibility). This yields basis of any size with a unique calculation with the primitive set, and since the same primitive set for all contractions is used, a smaller basis is always a subset of a larger basis. In other words, we can enlarge our basis set without changing of vector space (Almlöf and Taylor 1986; Almlöf and Taylor 1991). An improvement of the original scheme takes into account an average density matrix to build the basis set (including ground state, excited state, cation, anion, atom into an electric field, see Widmark et al. (1990)). In general, ANO basis set will require less contracted functions than the other basis to get the same results. Recently, all electron ANO

basis sets, including correlation effects for all periodic system elements, have been generated (Roos et al. 2005). It has also been observed that for extremely accurate calculations, only ANO basis sets can provide the best answer (see, e.g., Martin et al. 1997).

A final type of approach regarding the one-electron basis sets is the combination of inner-shell pseudopotentials (including typically relativistic effects) with valence basis sets and the use of embedded potentials to represent atomic environments.

## Methods for Excited States

---

Based on the methods described in the previous section, specific algorithms to deal with electronic excited states have been developed. In this section, the most commonly employed approaches will be briefly summarized (see also Merchán and Serrano-Andrés 2005; Serrano-Andrés and Merchán 2005).

Starting by the single-configurational methods that use the HF solution as reference wave function, an approach which has lost popularity because of its poor performance is the method named Configuration Interaction-Singles (CIS). The essence of the method is to consider that an excited state can be described by a singly excited determinant formed by replacing, with respect to the reference wave function, an occupied spin orbital with a virtual spin orbital. The drawbacks of such a description may be partially compensated if a linear combination of all possible single excited determinants is used to build the excited state wave function. In general, the CIS excitation energies are largely overestimated due to the absence of correlation energy effects. It is more common to find in the literature cases in which CIS yields the wrong order and state nature than the proper ones, simply because the differential correlation energy affects the excited states unevenly and because the intrinsic character of the states is multiconfigurational (Foresman et al. 1992).

In the light of the previous discussion, the logical method to deal with excited states should be multireference CI (MRCI) (Buenker et al. 2000). Consider a wave function of CI type expanded in a many-electron basis set of determinants. As in the  $H_2$  molecule, it is possible to select a number of determinants to describe the correct dissociation limit. When the energy is minimized with respect to the coefficients of the expansion, the configuration interaction (CI) method is employed. It should be kept in mind that actual calculations are performed using either spin-adapted Configuration State Functions (CSFs: appropriate linear combination of Slater determinants) or determinants as a  $N$ -electronic basis set (Slater determinants lead to more efficient CI algorithms), whereas CSFs lead to shorter CI expansions and, obviously, spin eigenfunctions, i.e., singlet, doublet, triplet states...). In case that the expansion contains more than one configuration, the process is denoted as MRCI. The wave function  $|\Psi\rangle$  is a multireference function and, at least, the singly and doubly excited determinants generated from each reference determinant  $|m\rangle$  are taken into account. Unfortunately, MRCI-based approaches are restricted to molecular systems of small molecular size (containing up to 6–7 atoms), where dynamic correlation can be fully retrieved. Otherwise, truncation of the many-electron functions involved in the MRCI expansion might easily lead to large errors in the computed excitation energies.

Another type of methods applied to the calculation of excited states are the propagator approaches (Oddershede 1987). The underlying technique, also called Green's function approach, equation-of-motion or linear response theory in its different forms, can be applied to

various types of methodologies: single- or multi-reference configuration interaction, coupled-cluster, or density functional. The essentials of the technique consider that once a molecule is subjected to a linear time-dependent electric field fluctuating with frequency  $\omega$ , a second-order property as the frequency-dependent ground-state polarizability of the system is well approximated by

$$\alpha_{\omega} = \sum_{i \neq 0}^{\text{states}} \frac{|\langle \Psi_0 | r | \Psi_i \rangle|^2}{\omega - \Delta E_i}, \quad (14.5)$$

where the denominator of the expression involves the frequency of the field and the excitation energies ( $\Delta E_i$ ) characterizing the excited states (1), while the numerator of each term is the square of the transition dipole moment between the ground and the corresponding excited state. Using complex function analysis, it is possible to obtain the poles of the expression, that is, the values for which the frequency corresponds to the excitation energies and the denominator goes to zero, while the residues provide the numerators, in this case, the one-photon absorption matrix elements. The peculiarity of the propagator approaches is that the wave functions of the individual states are not necessarily computed to obtain excitation energies and transition probabilities, while its quality relies on the type of reference wave function. Except for very elaborated implementations, usual propagator approaches have also the same problems as all single-reference procedures.

The family of methods CCS, CC2, and CC3 is based on response theory (Koch and Jørgensen 1990). The CCS approach is equivalent to the single excited configuration interaction or Tamm–Dancoff approach. The iterative hybrid CC2 and CC3 procedures introduce approximations to account for the level of excitation. They have been defined for systems with closed-shell ground-states, although some Equation of Motion EOM-CC procedures also deal with open-shell ground state cases. In order to get accurate excitation energies and properties, the single-configuration coupled-cluster methods should include high excitation levels to compensate both the poor reference wave function and the multiconfigurational character of the excited states. CC-based methods are, up-to-date and in practice, the most accurate methods to compute excited states in small to medium size molecules with closed-shell ground states, but only for those states which are well described by singly excited configurations, in systems where the ground state has a clear single-configuration character, and close to the equilibrium geometry. Triple excitations have to be anyway included in the cluster expansion if accuracy is intended. The precision of the single-reference CC methods decreases in systems with open-shell ground states and vanishes (up to several eVs of error) for multiconfigurational cases, like the  $2^1A_1$  state of ozone. The inclusion of quadruple excitations, unpractical so far, would improve some of those results, although the only solution in prospect to beat in accuracy the lower level and less expensive multireference perturbation approaches such as CASPT2, is to use multireference coupled-cluster (MRCC) methods, in which the required excitation level will be expected lower. However, the development of such methods is still in their infancy, and the initial results are not very promising.

Before continuing with the ab initio procedures, in particular the MRMP theory most employed in this chapter, the use of DFT approaches for excited states will be discussed. The implementation, known with the unfortunate name of Time-Dependent DFT (TD-DFT) approach (no time-dependency is accounted for) should be expected to be able to deal with large systems were ab initio methods become too expensive. Unfortunately, these methods fail dramatically in too many situations: charge transfer states, multiconfigurational states, doubly or highly-excited states, and even introduce large and systematic errors in valence states of large

$\pi$  extended systems. In some cases, the deviations can be as large as 5–6 eV, especially in cases in which the ground state is poorly defined by the HF configuration. Even when many different parameterizations have been tried and different functionals developed in order to correct the flaws of the method, so far no single functional is able to solve most of them simultaneously. Much worse than that (and this is common for all single-configurational approaches), they cannot describe at all degenerate situations like conical intersections, which are the core of the quantum-chemical description of the excited states.

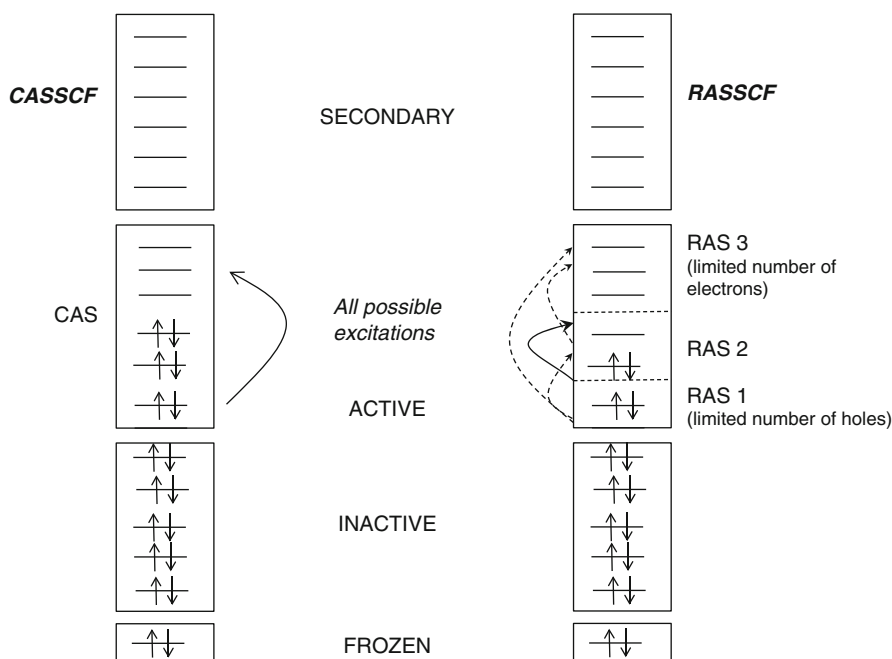
An hybrid derivation, known as DFT/MRCI is unarguably the best DFT-based procedure for excited states. It consists of an MRCI expansion with multiconfigurational wave functions replacing the HF orbitals with Kohn–Sham orbitals in the building of CSFs. The Hamiltonian, however, is heavily modified with empirical parameters, and only a few situations can be handled. The objective is to recover dynamic correlation by means of DFT and static correlation by means of MRCI. In this way, severe size-extensivity problems can be avoided even for systems with many valence electrons. Currently, optimized parameter sets for the effective DFT/MRCI Hamiltonian are available in combination with the B3LYP functional. The accuracy in energy is about 0.2–0.3 eV, and other properties are well balanced as well. Additionally, it is very appropriate to compute SOC, including a spin-dependent Hamiltonian (Grimme and Waletzke 1999; Kleinschmidt et al. 2001).

As already mentioned, a multiconfigurational description of the reference wave function helps enormously to recover the overall correlation effects. Starting from a good reference, the method used for such a recovery does not need to be extremely elaborated. That is why multiconfigurational second-order Møller–Plesset theory, the CASPT2 method, based on a Complete Active Space SCF (CASSCF) zeroth-order wave function, has become the most successful method for excited states. As this is the procedure in which most of the examples of the chapter will be based on, a more detailed description of the procedure will be given. Nowadays, the CASPT2//CASSCF methodology has proved the best ratio quality of the results/computational cost. At the CASSCF level (a particular case of MCSCF), both the many-electron-function coefficients of the MCSCF expansion and the coefficients included in the expansion of each molecular orbital are optimized simultaneously (see [Eq. 14.3](#)). Their variations are considered as rotations in an orthonormalized vector space. In the CASSCF method, the orbitals are classified in three categories, depending on the role they play in building the  $N$ -electron wave function: inactive, active, and secondary orbitals. Inactive and active orbitals are occupied in the wave functions, whereas the remaining of the orbital space, given by the size of the one-electron basis set employed, is constituted by secondary orbitals, also called external or virtual. Inactive orbitals are doubly occupied in all the CASSCF configurations. The rest of the electrons (called active electrons) occupy active orbitals. The CASSCF wave function is formed by a linear combination of all the possible configurations that can be built by distributing the active electrons among the active orbitals and are consistent with a given spatial and spin symmetry. That is, in the configuration space spanned by the active orbitals, the CASSCF function is complete (CASCI space, equivalent to FCI). Inactive orbitals are also optimized in the variational process, but they are treated as in the restricted HF function. The CASSCF energy is invariant to rotations among the active orbitals (Roos et al. 1979).

Essentially, we construct for a given state a multiconfigurational wave function which includes all configurations generated by a set of active orbitals and active electrons that fulfils spin and spatial symmetry requirements. This provides the nondynamic correlation effects due to configurations which are very close in energy. Several states that belong to a same symmetry are usually computed by means of a State-Average (SA) CASSCF calculation, where a functional

of energy is defined as average of a number of states, that, if required, although it is not recommended, can be weighted. From a SA-CASSCF calculation, a single set of average orbitals and a number of orthogonal wave functions equal to the number of roots used in the average process are obtained. In this manner, it is sometimes possible to overcome the problem of “root flipping,” that is, the interchange of roots along the CASSCF optimization procedure. For a given spatial and spin symmetry, the treatment of excited states is preferably performed by using SA-CASSCF calculations. In principle, it is also possible to make a single CASSCF calculation for higher roots, optimizing just one state. Nevertheless, experience shows that in most cases it can only be achieved for the second root of a given irreducible representation. Wave functions obtained in a SA-CASSCF calculation are orthogonal among them, whereas those obtained from different CASSCF calculations are not. In the latter cases, the wave function is rather poor and cannot be used for a further correlated calculations, although sometimes it may be useful to perform CASSCF optimizations.

On the other hand, the Restricted Active Space Self-Consistent Field (RASSCF) method is a more general extension of the CASSCF method. Now, there are three subspaces within the active orbitals: RAS1 (orbitals that are doubly occupied except for a maximum number of holes allowed in this orbital subspace), RAS2 (in these orbitals, all possible occupations are allowed), and RAS3 (orbitals that are unoccupied except for a maximum number of electrons allowed in this subspace). CASSCF calculations can be performed by allowing orbitals only in the RAS2 space. A single reference SDCl wave function is obtained by allowing a maximum of two holes



■ Fig. 14-8  
CASSCF and RASSCF methods

in RAS1 and a maximum of two electrons in RAS3, while RAS2 is empty (Malmqvist et al. 1990; Olsen et al. 1988) (● Fig. 14-8).

Either by using CASSCF or RASSCF, the active space provided by the user of a CASSCF calculation represents a key point to obtain accurate theoretical predictions once dynamic correlation has subsequently been taken into account, for instance, at the CASPT2 or RASPT2 levels. The properties of a CASSCF wave function depend on the active space. Thus, a valence CASSCF is size-extensive (the computed energy within a given methods scales linearly with the number of particles) and the corresponding CASPT2 results become also nearly size-extensive (formally the CASPT2 method is not size-extensive, but it is in practice, in particular the MOLCAS implementation). As in any quantum-chemical approach, one has to make sure that the method has enough flexibility, i.e., the active space is the appropriate one, to describe the chemical process under consideration. It is important to mention here the power of the CAS State Interaction (CASSI) approach, which provides orthogonal wave functions and transition densities from CASSCF or RASSCF wave functions optimized independently for a number of excited states of whatever symmetry (Malmqvist and Roos 1989).

Valence-bond methods have increased its applicability recently. One example is the CASVB (complete active space valence bond) method. A CASVB wave function can be obtained simply by transforming a canonical CASSCF function and readily interpreted in terms of the well-known classical VB resonance structures. The total CASVB wave function is identical to the canonical CASSCF wave function. In other words, the MO description and the VB description are equivalent, at least at the level of CASSCF. The CASVB method provides an alternative tool for describing the correlated wave functions.

The CASPT2 (complete active space perturbation theory to second order) method (Andersson et al. 1992) includes the remaining dynamic correlation due to short-range electronic interactions. This method can be seen as a conventional non-degenerate perturbation theory, that is, a single state is independently considered, with the particularity that this zeroth-order wavefunction is multiconfigurational (CASSCF). The wave function is corrected up to first order and, consequently, the energy is corrected up to second order. The set of functions required to compute the first-order correction of the wave function is formed by those that interact with the zeroth-order wave function through the Hamiltonian in the Rayleigh–Schrödinger perturbation theory, and it is known as the first-order interacting space. Taking into account the one and two particle nature of the Hamiltonian, the first-order interaction space, called hereafter  $V_{SD}$ , comprises the functions generated by singly and doubly excited configurations from the zeroth-order (CASSCF) wave function. As a matter of fact, the configurational space is divided in four subspaces:  $V_0$  (one-dimension space expanded by the reference function  $|0\rangle$  of the studied states),  $V_K$  (orthogonal to  $|0\rangle$  in the restricted FCI subspace used to generate the CAS function), the aforesaid  $V_{SD}$  (space expanded by the singles and doubles replacements from  $|0\rangle$ ), and  $V_{TQ\dots}$  (space that contains the excitations of higher order). Regarding orbitals, they are classified into frozen (doubly occupied, not correlated), inactives (doubly occupied in the reference function), actives (with any occupation, between 0 and 2, in the reference function) and secondary (empty in the reference function). Recently, a new shifted zeroth-order Hamiltonian named IPEA has been designed and set up with a value 0.25 a.u. into the default for the MOLCAS implementation (Ghigo et al. 2004). The new formulation solves previous effects for open-shell cases in which the correlation effects were overshoot. The net effect of this correction is to slightly increase the excitation energies. In any case care has to be taken when comparing present with previous CASPT2 results.



The normalized wave function is corrected up to first order. The weight of the reference function,  $C_0^2$ , can be used as a simple and rapid criterion of quality for the perturbation treatment carried out. Ideally, in order to get a fast convergence in the perturbation series, the weight should be close to unity. Nevertheless, its value depends on the number of correlated electrons. Thus, upon enlarging the molecular system the reference weight decreases. The electronic excited states considered should have a similar magnitude for the weight as compared to the ground state, employing the same active space. Sometimes intruder states appear in the second-order calculation, which are normally related to the occurrence of large coefficients in the first-order expansion, leading to a low value for the reference weight. Analysis of the states with large coefficients (intruder states) may give a hint about the type of reformulation in the perturbation partition necessary to overcome the problem. Thus, a new CASSCF calculation might be designed comprising in the active space the MOs implied in the description of the previous intruder states. It is the proper action to be taken when intruder states are strongly interacting with the CASSCF reference wave function, because it points out to obvious deficiencies in the choice of the active space. Intruder states are often present in the treatment of excited states of small organic compounds when the active space does not include the full  $\pi$  valence system. Thus, the low weight for the zeroth-order wave function in such a case just tells us that the active space has to be enlarged in a way that previous intruder states would be treated variationally, that is, they should be moved to the active space. It is also frequent to find calculations where the reference weight of the excited state is “somewhat low” compared to that of the ground state, but a particular state cannot be identified as intruder in the first-order wave function, which is instead characterized by a large number of low-energy minor contributions. It occurs often in the simultaneous computation of valence and Rydberg states, where the one-electron valence basis set has been augmented with Rydberg-type functions. This is a typical case when using large and diffuse basis sets like ANOs. We have to face then accidental near-degeneracy effects, implying weakly interacting intruder states, and the level-shift (LS) technique is especially useful in order to check the validity of the perturbation treatment performed. The level-shift CASPT2 (LS-CASPT2) method removes efficiently weak intruder states by the addition of a shift parameter  $\epsilon$ , to the zeroth-order Hamiltonian and a subsequent back correction of its effect to the second-order energy.

Many times, one has to apply both strategies: enlargement of the active space to overcome the problem of severe intruder states, and, with the enlarged active space, the LS technique is applied in order to minimize the effect of weakly interacting intruder states. Since a constant added to a linear and Hermitian operator (like  $\mathbf{H}$ ) does not affect its eigenfunctions but it is added to its eigenvalues (let  $k$  be a constant; as long as  $\mathbf{H}\Psi = E\Psi$ , then  $(\mathbf{H} + k)\Psi = \mathbf{H}\Psi + k\Psi = E\Psi + k\Psi = (E + k)\Psi$ ), the energies of the states may be altered, but this is a price that must be paid. However, it is desirable that the shift parameter is as small as possible. For instance, results at  $\epsilon = 0.0$  (standard CASPT2), 0.1, 0.2, 0.3, and 0.4 a.u. are sufficient to establish the proper behavior of the LS-CASPT2 results. It is extremely dangerous to rely on just one result because the appearance of an accidental near degeneracy might lead to large errors in the excitation energies. In order to demonstrate the proper performance of the LS-CASPT2 technique, calibration calculations of that type always have to be carried out. The best choice for  $\epsilon$  is the lowest possible value capable of removing intruder states. In order to avoid singularities, currently the technique so-called imaginary level-shift should be employed. The dependence of the energy on the imaginary level-shift parameter is of minor relevance (see Forsberg and Malmqvist 1997; Roos et al. 1996).



Finally, the multistate CASPT2 (MS-CASPT2) procedure has to be mentioned. It represents an extension of the CASPT2 method for the perturbation treatment of chemical situations that require two or more reference states. The procedure implies the use of an effective Hamiltonian in which the diagonal terms are the single-root, and non-orthogonal, CASPT2 solutions, whereas the interacting terms form the off-diagonal components. The diagonalization of the Hamiltonian, after symmetrization, provides a set of MS-CASPT2 energies and orthogonal states ready to describe situations such as avoided crossings and near-degeneracy of valence and Rydberg states, which cannot be fully accounted for by just using a single-reference perturbation treatment. A new wave function, named Perturbatively Modified CAS-CI (PMCAS-CI), is obtained built as a combination of the previous SA-CASSCF states, which has been in many cases improved from the previous set. This approach is not free of problems, as it will be discussed along this chapter (Finley et al. 1999; Serrano-Andrés et al. 2005).

The CASPT2 approach, especially when combined with ANO-type basis set functions, has proved to give a balanced and accurate description of all types of excited states and electronic structure cases, independently of their nature. The energy and the wave function are treated in general in an unbiased way. As all other quantum-chemical methods, the results heavily rely on the proper determination of the structural parameters, that is, the geometry optimizations. Because of their computational cost, geometries are obtained at lower levels of calculations than energies. In many cases, analytical gradients, more convenient for optimization processes, are not available at the highest level of calculation (they are, for instance, at the MRCI level, see Shepard et al. (1992) or for CASPT2 applicable to small molecules, see Celani and Werner (2003)). This is why most of the calculations use the mixed strategy, for instance, CASPT2 energies and CASSCF geometries (CASPT2//CASSCF), but also MRCI//CASSCF or CC3//CC2. Some problems related with this inconsistency will be discussed during the chapter.

It can be finally commented that, recently, the RASPT2 approach, in which a RASSCF wave function is used as reference for multiconfigurational perturbation theory has been made available, using all tools related with CASPT2, for instance allowing MS-RASPT2 calculations (Malmqvist et al. 2008). Benchmark studies are currently under way in order to determine the best partition schemes for the RASSCF active spaces. Prospectively, the approach will largely extend the applicability of the MRMP calculations.

## How to Compute Excited States

---

### How to Start: Selection of Goals, Methods, Geometries

---

Quantum-chemical methods provide information for excited states directly applicable to explain and predict the spectroscopy, photophysics, and photochemistry of molecular systems. A balanced description of the different electronic states is required in order to obtain the initial, basic data, that is, energy differences and transition probabilities, in an accurate way. This goal is a much more difficult task for excited states as compared to the ground state. First, one has to deal with many classes of excited states, each one showing different sensitivity to the amount of electronic correlation energy and, also, flexible one-electron basis functions able to describe all effects simultaneously are required, in general larger than that used in ground-state quantum chemistry. Then, it is necessary to compute extremely complicated potential energy hypersurfaces where the number of minima, transition states, and surface crossings like conical

intersections, is multiplied. Because of the inherent complexity of the problems, the methods and algorithms to compute excited states are not as widespread as for ground states or are still under development.

In this section, we are going to illustrate different examples for the calculation of excited states using presently available quantum-chemical techniques. In each subsection, we will proceed in the same manner, first, by describing an actual example taken from the literature, and, after, practical aspects which explain the choices made. The results obtained will be then discussed, including new cases if necessary.

Before introducing the first example, let's make some comments on the initial way to tackle the problem. Our goal, in principle for a typical ground-state closed-shell case, will be focused in the lowest-lying singlet and triplet excited states of the molecule. Most of the interesting spectroscopy and photochemistry will take place in the low-lying states, although higher states are relevant in other contexts. Properties of interest provided by static electronic structure quantum-chemical calculations that help to rationalize the photophysical and photochemical processes in a molecule are: molecular structures, charge and spin distributions, electronic and vibrational energies, oscillator strengths, dipole and transition moments and their directions, radiative lifetimes, nonadiabatic, vibronic, spin-orbit, and electronic couplings. In a second step, in reaction dynamics calculations, reaction rates, lifetimes, and population distributions can be provided.

Which method is the most appropriate for the purpose of that research? The initial questions to answer is what is the goal of the study, how far can it go, how many questions can be solved, and, especially, which is the accuracy required in the study. All this depends in most cases on the complexity and the size of the system. Of course, the best ratio quality/CPU time should be looked for, but it is useless to carry out calculations, no matter how cheap they are, with methods that cannot provide accuracy to make conclusive predictions. Apart from checking carefully the literature, calibrations will be typically necessary. Both methods and basis sets should be tested, and several steps to approach to the problem are maybe necessary. We can start by using less expensive semiempirical classical or TD-DFT methods in order to understand the problem and its requirements, and then move to more sophisticated coupled-cluster or multiconfigurational approaches, depending on the goals of the research. The same with basis sets. 6-31G-type basis sets are practical because of their reduced time requirements, but they are less accurate and in many cases using them may degrade too much our results. Calibrating the obtained values with fully correlated methods or higher-quality basis sets like Dunning's correlation consistent or ANO-type basis sets is always a requirement. Obviously the program package we should use has to balance all aspects we have mentioned. Normally a combination of them will be necessary: versatile programs, such as GAUSSIAN, GAMESS, or QCHEM; packages specialized in DFT implementations, like ADF, TURBOMOLE, or NWCHEM; suites focused on CC algorithms such as DALTON or ACES II; or programs especially designed for multiconfigurational methods like MOLCAS or MOLPRO, these more generally applicable to the calculation of excited states.

A point to bear in mind is that there are different types of excited states, and each of them has different theoretical requirements. A valence state can be viewed as a promotion from one occupied molecular orbital to a virtual one. On the other hand, a Rydberg state, in a simple MO theory, is the result of exciting one electron from one occupied molecular orbital to an atomic-like orbital of higher quantum number. Valence excited states are more compact than the diffuse Rydberg states. A valence state can be denoted as covalent or zwitterionic according to the type of valence bond (VB) structures. Covalent and zwitterionic states are described by

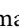
hole-hole and hole-pair VB structures, respectively. What is more, the label ionic is reserved to states with an actual charge separation. On the other hand, if a pair of nearly degenerated nonbonding orbitals is occupied with a total of two electrons in the ground state, the molecule is called biradical. In addition, there are charge transfer states, in which an electron is transferred from one occupied orbital of a molecule to a virtual orbital of another molecule (or the same molecule, if it is intramolecular).

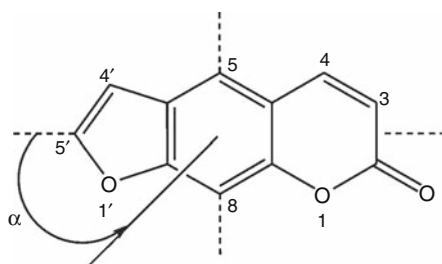
Excited states can be also classified according to the main types of configurations involved in their description, in relation to the ground state: singly excited states, doubly excited states, and so on. Rydberg states are usually well described by only one singly excited configuration. Multiconfigurational singlet excited states with a large contribution of doubly excited configurations are normally covalent. Singlet excited states of zwitterionic character are described by one or several singly excited configurations. In anionic systems, new types of excited states are present, such as the resonance states or the multipole-bound (dipole, basically) states, where the bonding energy is the result of the interaction between the additional electron and the multipole moments of the molecule.


## Molecular Photophysics: Computing Absorption and Emission Spectra

### An Application Example: Psoralen

The simplest approach to the electronic state problem is the determination of the photophysics of an isolated molecule, that is, to reproduce its absorption and emission spectra. As mentioned, let's first describe in its full extent a case, the psoralen molecule, and later the choices made can be analyzed (see Serrano-Pérez et al. 2006, 2008a, b, c, d).

Furocoumarins (also named psoralens, see  Fig. 14-9) are a class of heterocyclic compounds with a known phototherapeutic activity. These systems have been found to possess mutagenic properties when applied in conjunction with near UV-A light (320–400 nm) exposure. The technique so-called PUVA therapy (psoralen + UV-A) has been specifically designed to treat different skin disorders such as psoriasis and vitiligo. It is generally assumed that there is an oxygen-independent mechanism, which implies a [2+2]-photocycloaddition of psoralen and a pyrimidine DNA base monomer, and there is also an oxygen-dependent mechanism, in which energy transfer between the furocoumarin and molecular oxygen present in the cellular



 Fig. 14-9

Psoralen labeling. The *arrow* defines the positive angles of both the dipole moment and electronic transition moment directions with respect to the pseudosymmetry long axis

environment is produced generating cytotoxic singlet molecular dioxygen. It is believed that the state protagonist of the photosensitizing action, in both cases, is the lowest-lying triplet excited state of psoralen. Initially, our main goal is to describe the absorption spectrum of the molecule, and we do it by computing the lowest-lying singlet and triplet states at the optimized structure of the ground state (i.e., those distances, angles, and dihedral angles which make the energy minimum), what is typically known as the Franck–Condon geometry. Later, the mechanisms for triplet state population can be determined.

Using CASSCF multiconfigurational wave functions as reference, the second-order perturbation theory through the CASPT2 method was employed to include dynamic correlation energy in the calculation of the electronic excited states. The imaginary level-shift technique was employed in order to prevent the effect of intruder states. A shift parameter of 0.3 a.u. was selected by checking the stability in the excitation energies. The molecular symmetry was constrained to the  $C_S$  point group. An atomic natural orbital (ANO-L)-type basis set, contracted to C,O [4s3p1d]/H [2s1p] was used throughout. The carbon and oxygen 1s core electrons were kept frozen in the second-order perturbation step. Geometries were obtained by computing analytical gradients at the RASSCF level of calculation for the ground and the lowest singlet and triplet excited states. In the optimization of the  $A'$  states, an active space of 14  $a''$  active orbitals and 16 electrons, i.e., the full  $\pi$  system of the molecule, has been employed, and up to quadruple excitations were considered (eight orbitals in RAS1 space and six orbitals in RAS3 space). Within the irreducible representations ( $a'$ ,  $a''$ ) of the  $C_S$  group, this active space can be labeled as (0, 14). An additional oxygen lone-pair orbital was included in the active space (1, 14) in order to optimize the lowest  $A''$  excited state. In all the remaining calculations, CASSCF wave functions were generated as state-average (SA) CASSCF roots of a given symmetry. Based on preliminary RASSCF calculations and using the criterion of the largest natural orbitals occupations for the states of interest, the CASSCF active space was reduced to include 12 active electrons and 12 active orbitals (0, 12) for  $A'$  roots and 14 active electrons and 13 active orbitals (1, 12) for  $A''$  roots. The CAS state interaction method (CASSI) was used to compute transition properties, including the spin-orbit coupling (SOC) elements between selected states.

At the Franck–Condon (FC) geometry, the lowest singlet excited states  $2^1A'$  ( $\pi\pi^*$ ),  $1^1A''$  ( $n\pi^*$ ), and  $3^1A'$  ( $\pi\pi^*$ ) lie at 3.98, 5.01, and 5.03 eV, respectively (see [Table 14-1](#)). Whereas the transition to the  $n\pi^*$  state is predicted with negligible intensity, the  $\pi\pi^*$  states have related oscillator strengths of 0.027 and 0.107. Unlike other states, the  $3^1A'$  state has a high dipole moment, 8.70 D, differing by more than 2.5 D from that of the ground state, and therefore the associated transition is expected to undergo a red shift (bathochromic effect) in polar environments. The recorded absorption spectra in different solvents, from cyclohexane to water, display a weak and structured band ranging from 360 to 270 nm (3.44–4.77 eV). Depending on the band resolution and the environment, one or two maxima near 330 and 280 nm (3.76 and 4.43 eV, respectively) have been described. The present computed results suggest that this set of features can be better assigned just to the  $2^1A'$  ( $\pi\pi^*$ ) transition, with the weak  $n\pi^*$  band lying beneath. In that case, the observed band profile should be attributed to vibrational structure. This explanation is not unlikely, considering that a noticeable rearrangement of the molecular bond distances occurs at the  $2^1A'$  minimum.

Although less relevant regarding the phototherapeutic properties, we will describe the higher-energy region of the absorption spectrum. Transitions to the  $4^1A'$  (5.22 eV) and  $5^1A'$  (5.30 eV) ( $\pi\pi^*$ ) excited states have oscillator strengths of 0.064 and 0.331, respectively. The recorded spectra show a single and sharp band peaking near 248 nm (5.00 eV) in cyclohexane and 240 nm (5.16 eV) in ethanol and water. In principle, the observed feature can be assigned to transition to the  $3^1A'$  state at 5.03 eV. Moreover, taking into account our computed results, an

■ Table 14-1

Computed excitation energies  $\Delta E$  (eV) at CASPT2 level, oscillator strengths  $f$ , dipole moments  $\mu$  (D), dipole moment directions  $\mu_{\text{dir}}$  (deg), and transition dipole moment directions  $\text{TDM}_{\text{dir}}$  (deg) for the low-lying electronic transitions of psoralen

State	$\Delta E$	$f$	$\mu$	$\mu_{\text{dir}}$	$\text{TDM}_{\text{dir}}$
$1^1A'$	–	–	6.25	128	–
$2^1A'(\pi\pi^*)$	3.98	0.027	6.50	132	4
$1^1A''(nO\pi^*)$	5.01	0.000	2.07	130	–
$3^1A'(\pi\pi^*)$	5.03	0.107	8.72	132	5
$4^1A'(\pi\pi^*)$	5.22	0.064	7.07	–23	–10
$5^1A'(\pi\pi^*)$	5.30	0.331	7.07	–37	102
$6^1A'(\pi\pi^*)$	5.70	0.091	7.37	–37	30
$1^3A'(\pi\pi^*)$	3.27	–	5.40	124	–
$2^3A'(\pi\pi^*)$	3.55	–	5.35	125	–
$3^3A'(\pi\pi^*)$	4.08	–	5.48	127	–
$1^3A''(n\pi^*)$	4.85	–	2.15	111	–

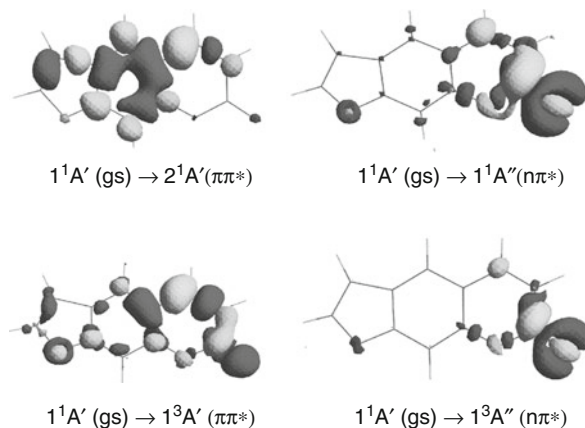
additional and more intense band can be expected at higher energies (5.30 eV). The measured band is probably a combination of both transitions.

Three other  $^3A'\pi\pi^*$  states are next in energy at 3.55, 4.08, and 4.66 eV. The nature of the low-lying transitions of each symmetry, which are those basically responsible for the photophysical properties of psoralen, can be graphically described by computing the differential electron density plots as displayed in [Fig. 14-10](#). Transition to the  $S_1\pi\pi^*$  state is mainly benzene-like, with the charge migration concentrated in the central benzenoid ring. On the contrary, that related to the  $T_1\pi\pi^*$  state has its major contributions in the pyrone ring, with high participation of the carbonyl oxygen and a shift in the density away from the pyrone ring  $C_3-C_4$  bond, which will be later discussed as an essential feature of the photophysics of the system. Also in [Fig. 14-10](#), we find the expected differential density plots of the  $n\pi^*$  states centered on the carbonyl group. Transition dipole moment directions ( $\text{TDM}_{\text{dir}}$ ) indicate that the three lowest  $\pi\pi^*$  features have nearly parallel polarizations, that is, they are aligned with the long axis of the molecule, while transition to the  $5^1A'$  state has essentially perpendicular polarization. Regarding the vertical excitations to the triplet states, the  $1^3A'\pi\pi^*$  ( $T_1$ ) state lies at 3.27 eV, near 0.7 eV below the  $2^1A'$  ( $S_1$ ) state.

Fluorescence has been reported for psoralen in polar solvents starting ( $T_0$ ) at 350 nm (3.54 eV) with a maximum at 409 nm (3.03 eV). Phosphorescence has also been recorded in solution with band origin at 456 nm (2.72 eV) and a maximum between 460 and 490 nm (2.7–2.5 eV).

The fluorescence and phosphorescence quantum yields were measured in ethanol as  $\Phi_F = 0.019 - 0.02$  and  $\Phi_P = 0.13$ , respectively. The obtained ratio  $\Phi_F/\Phi_P$  is approximately 7.1. The total phosphorescence decay time ( $\tau_P$ ) has been reported 1.1 s in glycerol-water and 0.66 s in ethanol. With those data, the phosphorescence radiative lifetime  $\tau_{\text{rad}} (= \tau_P \cdot \Phi_P)$  can be therefore expected between 8 and 5 s.

The low-lying singlet excited state  $2^1A'(\pi\pi^*)$  is responsible for the lowest-energy absorption and emission fluorescence bands (see [Table 14-2](#)). Vertically, at the ground-state geometry, the transition energy is computed to be 3.98 eV and, upon relaxation of the geometry,



■ Fig. 14-10

Differential electron density for the main valence transitions in psoralen computed at the ground-state optimized geometry. The electron density is shifted upon light-induced excitation from darker to lighter regions

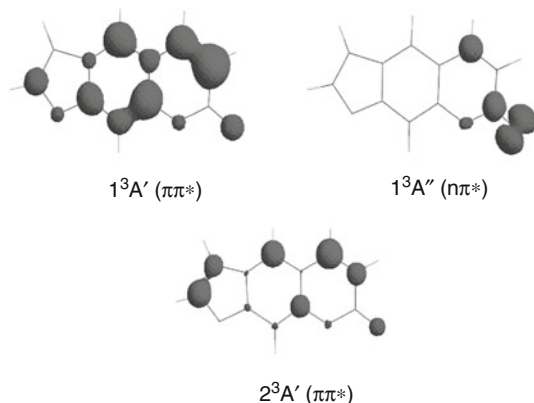
■ Table 14-2

Computed and experimental excitation energies (eV) and emission radiative lifetimes ( $\tau_{\text{rad}}$ ) relevant for the photophysics of psoralen

Theoretical (CASPT2)					
State	$E_{\text{VA}}$	$T_e$	$E_{\text{VE}}$	$\tau_{\text{rad}}$	
$2^1A'(\pi\pi^*)$	3.98	3.59	3.45	74 ns	
$1^1A''(n_O\pi^*)$	5.01	3.91	2.78	3 $\mu\text{s}$	
$1^3A'(\pi\pi^*)$	3.27	2.76	2.29	28 s	
$1^3A''(n_O\pi^*)$	4.85	3.84	2.79	9 ms	
Experimental (data in ethanol)					
State	$\text{Abs}_{\text{max}}$	$T_0$	$E_{\text{max}}$	$\tau_{\text{rad}}$	
$2^1A'(\pi\pi^*)$	3.7–4.3	3.54	3.03	–	
$1^1A''(n_O\pi^*)$	–	–	–	–	
$1^3A'(\pi\pi^*)$	–	2.7	2.7	5–8 s	
$1^3A''(n_O\pi^*)$	–	–	–	–	

$E_{\text{VA}}$  vertical absorption,  $T_e$  adiabatic electronic band origin,  $E_{\text{VE}}$  vertical emission,  $\text{Abs}_{\text{max}}$  experimental absorption maximum,  $T_0$  experimental band origin, and  $E_{\text{max}}$  emission maximum

the band origin ( $T_e$ ) decreases to 3.59 eV. This means that the range of absorption goes from 3.59 to 3.98 eV, well within the PUVA action. A similar relaxation is observed experimentally between the lowest-energy absorption band maximum and the band origin. The structural changes of the computed equilibrium geometries for the ground ( $S_0$ ) and the  $2^1A'(\pi\pi^*)$  ( $S_1$ ) states affect the bond alternation of the system, mainly in the central ring (cf. [Figs. 14-10](#) and [14-11](#)), as expected from the differential charge density plots. By using the Strickler–Berg relationship, a fluorescence radiative lifetime of 74 ns is calculated for the  $S_1$  state. The low-lying  $1^1A''(n\pi^*)$  state (vertically  $S_2$ ) becomes relaxed by more than 1 eV upon geometry optimization.



■ Fig. 14-11

**Spin density for the low-lying triplet states in psoralen computed at the ground-state optimized geometry**

Although the  $1^1A''$  ( $n\pi^*$ ) minimum belongs to the  $S_1$  hypersurface, the final  $T_e$  value is about 0.3 eV higher in energy than the computed and measured band origin for  $2^1A'$  ( $\pi\pi^*$ ). Therefore the  $n\pi^*$  state is not a plausible candidate for the fluorescence, which is better attributed to the  $\pi\pi^*$  state.

The  $1^3A'$  ( $\pi\pi^*$ ) state is the clear protagonist of the phosphorescence. The computed band origin at 2.76 eV perfectly relates to the observed value in solution at 2.72 eV. The relaxation energy is about 0.5 eV. The largest structural change is produced in the  $C_3-C_4$  bond of the pyrone ring, which enlarges by near 0.13 Å from the ground-state value. The computed spin population, displayed in ► Fig. 14-II, is mainly placed on each of the carbon atoms forming the bond. In that way, psoralen becomes highly reactive in its lowest triplet state through its pyrone  $C_3-C_4$  bond. This finding is the cornerstone of the photophysics of psoralen, which has been repeatedly proposed to take place through a reactive triplet state. The computed phosphorescence radiative lifetime is 28 s, somewhat higher than those estimated experimentally from the quantum yield and the total relaxation time, 5 and 8 s. For the  $2^3A'$  ( $\pi\pi^*$ ) state, the spin population is placed mainly on the carbon atoms forming both  $C=C$  bonds, that is,  $C_3-C_4$  (pyrone) and  $C_{4'}-C_{5'}$  (furan).

## Practical Aspects

### Selection of Geometries

Any quantum-chemical calculation starts with the definition of the molecular geometry. As mentioned in ► section “Methods, Advantages, and Drawbacks,” we can safely assume that the absorption spectrum is initiated at the ground state equilibrated geometry. An optimization is therefore required, in principle at the highest reasonable level of theory. DFT (with a proper functional) works well for most closed-shell cases, and it is a fully correlated method. Other ab initio methods that also include all correlation energy will be more accurate, but also more computationally expensive: MP2, CCSD, CASPT2 (with numerical gradients for small molecules). Although the best choice is not to use any symmetry restriction and let the system to find the



lowest-energy solution, it is possible to make approximations and, for instance, let the system to be planar ( $C_s$  point group), like in the case of psoralen and save computational time, especially if experiment give some indication along these lines. In order to confirm that the obtained point is a true minimum, it would be desirable to perform a frequency analysis, although computing Hessians (second derivatives) is an expensive task. If too demanding, maybe is feasible to compute the Hessian at lower levels of theory and check the outcome. Of course, if possible, one should compare the result with experimental (X-ray or electron diffraction, for instance) data. To compute emission, we have to optimize excited states too, a more difficult task than for ground states only at reach of few methods: CASSCF, RASSCF, CASPT2, and CCSD, to mention the most reliable ones (the two latter only for small systems). If the ground state is optimized with a better method than the ground state, some unbalance in the results may occur. It can be a good idea to get the different states optimized at the same level, like CASSCF or RASSCF. The choice of RASSCF in the psoralen example is motivated by the impossibility of including all  $\pi$  space into a CASSCF calculation. Although safe in many cases, the exclusion of some MOs, like, for instance, the lowest-energy nodeless  $\pi$  orbital, may lead to problems if the excluded orbital, instead of becoming delocalized and having then no biased effect, tends to localize unbalancing the calculations. It is worth noticing that CASSCF (RASSCF) gives very good geometries in  $\pi$ -conjugated systems, probably because of some compensation between the obtained single and double bonds lengths.

#### Accuracy of the Excitation Energies and how to compare with experiment

It is time to decide if the method and strategy employed is accurate enough to solve the problem. In principle, the accuracy should be established by previous experience if the electronic structure problem is under control. We cannot expect a TD-DFT calculation to be more accurate than 0.5–0.4 eV, much less if the problem has no closed-shell ground state or a charge transfer character (except for specific functionals like CAMB3LYP, see Peach et al. (2008)). Choosing one functional for each molecule makes theoretical chemistry useless as a predictive tool. It is much better to stick into one procedure and know their limitations. Coupled-cluster results, EOM-CC(T) or CC3, are much more accurate, sometimes near 0.2–0.1 eV if pushed to the limit, but this also relies on being far from degenerate situations or multiconfigurational ground states (see Grein (2009),  $1^1B_2$  state of ozone: CCSD(T) 1.81 eV vs. best estimation 4.11 eV, or Kowalski (2005),  $2^1A_1$  state of ozone: EOMCCSD 9.82 eV vs. best estimation 4.33 eV). Multiconfigurational calculations, CASPT2 in particular, can reach also 0.2–0.1 eV in most cases, although the result may degrade if the reference is not well described. More important that all we have said: accuracy with respect to what? Many studies discussing the precision of a method for excited states compare their vertical excitation energies with what experiment initially offers, absorption maxima. This is wrong and misleading. A vertical excitation energy computed at the electronic ground-state equilibrium geometry is a purely theoretical concept without experimental counterpart. The Franck–Condon principle relates such value with the absorption (not emission) maximum, but this approximation will be true only in the case that the ground and excited minima take place at the same geometry. Apart from that, an experimentally determined absorption maximum depends on the concentration of the sample, the apparatus, the environment, the temperature, the pressure, etc. In the most favorable case, vertical absorption and emission maximum will differ by near 0.1 eV from an experimental gas-phase or molecular beam maximum. Typically, those cases display as maximum feature the band origin or  $T_0$  transition. Indeed, the true experimental data to compare with this band origin, that theory computes as the energy difference between the states minima, also named the adiabatic energy



difference,  $T_e$  if it is just electronic energies or  $T_0$  – the true comparable value – if the zero-point energy correction has been included. The situation is even worse for the emission, where the FC principle is hardly fulfilled. In the psoralen example, a good agreement has been obtained for the band origins: computed  $T_e$  3.57 and 2.76 eV and measured  $T_0$  3.54 and 2.7 eV for fluorescence and phosphorescence, respectively. In most cases,  $T_e$  and  $T_0$  differ by close to 0.1 eV. On the other hand, the vertical emission is typically much lower than the emission maxima.

### How to Deal with Symmetry

Unfortunately, the topic is too extensive to be treated here. For practical cases, the reader is referred to the advances examples in the MOLCAS program manual (see <http://www.teokem.lu.se/molcas>). Group theory may be very useful in a calculation on excited states, especially because it allows dividing the states in each one of the irreducible representations (since a symmetry operation leaves a molecule unchanged) and consequently reduce the computational effort. Unfortunately, the molecular symmetry is typically only found for ground states, and most of the photochemistry takes place at distorted asymmetric structures, especially for organic systems. Linear molecules or many inorganic complexes can however be studied making an extensive use of the symmetry, as well as other systems if absorption, and sometimes emission, spectra are studied. Symmetry is particularly useful in multiconfigurational calculations to reduce the active space requirements. Also, symmetry permits prediction of intensities when following selection rules or analysis of the polarization or dipole moment directions. Normally, one should have at hand the character tables and also the Wigner–Witmer rules, as those found in Herzberg books. Finally, it is necessary to warn about symmetry breaking problems, in which a bad selection of the method or the active space may lead to find spurious lower-energy solutions.

### How to Obtain Intensities and Band Shapes: Vibrational Contributions

Apart from the energies, computing electronic oscillator strengths,  $f$ , provides information about the relative intensity of the different transitions, initially for those states allowed in one-photon (optical) spectroscopy. Group theory indicates that one-photon allowed transitions of the molecule are those in which the direct product of the symmetries of the initial state, the corresponding dipole moment component ( $x$ ,  $y$  or  $z$ ), and the final state belong to the totally symmetric irreducible representation of the point group of the molecule:

$$\int \psi_m^* \hat{d}_{el} \psi_n d\tau_{el} \Rightarrow \Gamma(\psi_m) \otimes \Gamma(\hat{d}_{el}) \otimes \Gamma(\psi_n). \quad (14.6)$$

For instance, in the case of a  $C_s$  molecule like psoralen (in the  $XY$  plane), the allowed transitions are those in which the aforesaid direct product is  $A'$ . Otherwise, the transition is forbidden. In other words, from the ground state  $A'$ , the accessible states are  $A'$  if the light is  $x$ -polarized or  $y$ -polarized, and  $A''$  if the light is  $z$ -polarized. If the light is  $x$ -polarized, for instance, the transition  $A' \rightarrow A'$  is allowed, whereas the transition  $A' \rightarrow A''$  is forbidden. The magnitude of the adimensional  $f$  has to be compared to the area beneath the band representing the transition, not to the height. Frequently, especially in gas-phase spectra, weak bands such as the Rydberg transitions are the highest because they sit on top of the more intense, although broader, valence bands. Notice that the range of energies of a band depends on the length of the vibrational progressions, which, in turn, relies on the difference in geometries with the ground state. The larger is the difference, the broader and extended will be the band. Flexible systems like  $NH_2$  or C=O-based spectra like that of formaldehyde extends their valence bands and spread their

intensity by several eVs. In many occasions it may be required to compute the vibrational profile of different electronic bands and plot them together. This is an expensive task because, requires the calculation of Hessians, FC factors, and sometimes the derivatives of such factors and of TDMs in order to obtain vibrational TDMs. This is, however, the only procedure to elucidate complex cases, for instance, that of the lowest single valence 5.5–6.5 eV band of pyrrole, which contains two valence and four Rydberg bands which have all to be resolved (see Roos et al. 2002). Ideally, and in order to get all actual excitation bands, calculations on vibrational TDMs should be complemented with the inclusion of vibronic couplings, in which more than one electronic state is considered at the same time (breaking the Born–Oppenheimer approach), an example of what can be found in the pioneering studies of Domcke and coworkers on the pyrazine molecule (Domcke et al. 1993).

### How to Add Environmental Effects

Adding the effects of the environment for excited states accurately is, if possible, even more complex than for the ground state. Usual procedures use cavity models such as Onsager's or the Polarized Continuum Model (PCM), with the additional consideration of the non-equilibration of the electronic response for the excited states that leads to divide the reaction field in slow, inertial, and fast, optical, parts. Results obtained with cavity models cannot be expected to be as accurate as those for the isolated system when compared with gas-phase results, among other things, because using large basis sets as those required for excited states will force the charge to leave the cavity and provide non-physical results. In many cases, the information yielded by the dipole moment of the states will be informative enough for qualitative purposes. In the psoralen example, it was discussed how states with dipole moments larger than that of the ground state were expected to stabilize in polar solvents (and undergo a spectral red-shift) than those with smaller dipole moments (blue-shift), typical case of the  $n\pi^*$  states, which, additionally, tend to directly interact with protic solvents forming hydrogen bonds and pushing the excitation energy up in energy, sometimes even 0.5 eV. These interactions cannot be included by the cavity models and specific molecules have to be applied, even several solvation shells. Careful microhydration experiments allow nowadays comparison with such type of calculations.

Solvation is a very dynamical phenomenon which requires also the inclusion of statistical effects. More sophisticated studies require the employment of dynamical approaches making use of statistical mechanics, such as Monte Carlo type of calculations. Solvent molecules can be then simulated by point charges (like in QM/MM approaches as it will be discussed later) and dynamical time shots with their positions taken for a subsequent quantum chemical calculation. The required property will be obtained as an average of the different conformations, as some studies on 2-aminopurine reported recently have shown.

### Active Spaces for Multiconfigurational Methods

As a large part of studies on excited states, and especially in photochemistry, employ multiconfigurational approaches, it is necessary to understand the process of selection of an appropriate active space (AS) for such computations. An active space should contain all orbitals and electrons relevant for the chemical process under study. The size and nature of the AS define the type of states and processes the multiconfigurational method will compute. Obviously, there is no single choice, and the size is limited to 14–15 or 30–30 orbitals/electrons in CASSCF and RASSCF calculations, respectively, depending on the type of partitions made. It is important to emphasize that the selection depends on the problem. If one is only interested in low-lying excited states, maybe a small AS is enough for that purpose. On the other hand, more states

imply larger ASs. In photochemistry the situation is worse, because the AS must be flexible enough to include all MOs participating in the process in all different regions of the PEHs which are chemically relevant. For instance, each bond that breaks means that the AS should contain both the corresponding bonding and antibonding MOs. In the psoralen example above the highest-lying  $\pi\pi^*$ , MOs plus one lone-pair MO from the carbonyl oxygen were selected because the purpose was to compute the low-lying spectra. The selection was a combination of experience and use of tools like performing a RASSCF calculation on several roots with enlarged active spaces to analyze the MOs participation in the different states and eliminate those orbitals with occupation numbers  $<0.05$  and  $>1.95$  in all roots of interest. If Rydberg states were to be computed, they should be added into the active space too. Making a TD-DFT calculation also helps to select the AS. As a general rule, it is wise to have in the AS one “virtual correlating” MO for each heavily occupied MO, for instance, each  $\pi$  MO with its corresponding “correlating”  $\pi^*$  MO. This is not necessary for lone-pair orbitals. Other well-known requirements relates to the need to include a second “correlating” d shell (4d) when computing the excited states of first-row transition metals, or more specific rules for very heavy elements. One big advantage of using symmetry in the calculations is the possibility of splitting the AS following the symmetry requirements, always when the energy differences are computed between states computed with the same AS size. The reader is referred to the specialized literature and the MOLCAS manual.

The recently developed RASPT2 method has opened the field to the use of larger RASSCF ASs. Special care has to be taken in the proper distribution of the MOs into the three RAS sub-spaces, and in the inclusion of an excitation level high enough (triples typically) from and to RAS1/RAS3 to get accurate results. The method is still under calibration, but it is a big step forward for the application of the methodology to larger and more complex systems. Typical improvements include the placement of Rydberg MOs or the second d-shell into the RAS3 space.

## Computing Rydberg States

---

### An Application Example: Water

How do we understand a Rydberg state? If we extract one electron from each of the MOs of a neutral molecule, the system becomes positively charged. An electrostatic interaction is therefore established between the molecular cation and the negative electron up to the moment that this ends up as a free electron, that is, at the energy named ionization potential (IP). While the electron leaves the molecule many metastable situations, the Rydberg states, take place, one series from each of the MOs converging to the respective IPs. Obviously, the electrons will be located relatively far from the molecule, therefore the Rydberg states will differ in extension from the compact valence ones and will require basis sets that generate large and diffuse orbitals able to represent them. Typically, the Rydberg states are labeled, and even represented, in the united-atom approach, that is, by using atomic-type orbitals, because they “see” the molecule as a single atom. The Rydberg states are of interest in gas-phase photochemistry; because of their diffuseness, they are strongly affected by external fields and solvation. Solution chemistry does not contain Rydberg transitions.

Treating simultaneously valence and Rydberg states is not that simple. It requires methods able to deal with the mixing of configurations and orbitals in the wave function. In the past, the literature has been plagued with discussions about how physical is the effect of the valence-Rydberg mixing. In most cases, such mixing was just a consequence of the lack of electron

correlation in the calculation of the wave function. Then, both valence and Rydberg orbitals and configurations mix, and valence states, become more diffuse and Rydberg states more compact, with specially dangerous consequences for the valence states, which are extremely sensitive to the mixing. Therefore, if a calculation does not provide clear and compact valence states the result is always suspicious.

Not always the mixing is spurious. One intriguing case is the water molecule. A comprehensive ab initio study performed in 1974 by Goddard and Hunt characterized all the computed states below 11.7 eV as having Rydberg nature, a result supported at the configuration interaction (CI) level. The electronic spectrum of water in the gas phase is currently interpreted as composed either of different Rydberg series or implying excited states with a significant Rydberg character at the ground-state equilibrium geometry. The lowest-energy band of the gas-phase electronic spectrum of water is broad (6.8–8.2 eV), with poorly defined vibrational progressions, and has its maximum absorption around 7.4 eV. There is a unanimous agreement in assigning the lowest-energy band to the  $1^1B_1$  state, but the valence, Rydberg or mixed valence-Rydberg, nature of the state is still under debate.

In  $C_{2v}$  symmetry, the ground state of the water molecule is mainly described by the electronic configuration  $(1a_1)^2(2a_1)^2(1b_2)^2(3a_1)^2(1b_1)^2$ . The latter orbital is nonbonding. The valence orbitals comprise the four highest occupied MOs listed above and two unoccupied orbitals of  $a_1$  and  $b_2$  symmetries ( $4a_1$  and  $2b_2$  orbitals). The valence excited states can interact with the corresponding Rydberg states of the same symmetry and close in energy. For instance, the valence singly excited  $1b_1 \rightarrow 4a_1$  configuration could be mixed with the  $1b_1 \rightarrow 3s$ ,  $1b_1 \rightarrow 3p_z$ ,  $1b_1 \rightarrow 3d_{x^2-y^2}$ , and  $1b_1 \rightarrow 3d_{z^2}$  Rydberg states.

The properties of the lowest-lying electronic states were studied in the light of CASPT2//CASSCF procedure (see Rubio et al. 2008). The coupling of the CASSCF wave functions via dynamic correlation was dealt by using the MS-CASPT2 method. In this way, all the states of a given symmetry are allowed to interact under the influence of dynamic correlation, and the possible erratic valence-Rydberg mixing can be removed. Properties of the states were determined from the PMCAS-CI wave functions.

The next table lists some properties of the low-lying electronic states of the water molecule, employing (after calibration) a one-electron basis set  $O[5s4p2d1f]/H[3s2p1d]+(2s2p2d)$ , being the diffuse  $2s2p2d$  set, located at the oxygen atom only, necessary to properly describe Rydberg states. Indeed, if no Rydberg orbital is included into the active space, the CASSCF calculation will only yield roots corresponding to valence states. Rydberg and valence orbitals must be treated simultaneously, and this is not possible if there is no Rydberg orbital in the active space. The full valence active space comprises six orbitals with eight electrons and corresponds to (3120), labels that represents each one of the irreducible representations of the point group  $(a_1b_1b_2a_2)$ .

Regarding the first excited state,  $1^1B_1$ , it has a diffuse nature according to the value of  $\langle r^2 \rangle$ , more than twice that of the ground state, but appreciably lower than that obtained for a pure Rydberg state as the  $2^1B_1$  ( $1b_1 \rightarrow 3p_z$ ) state ( $\langle r^2 \rangle = 64$  a.u.). As the state is mainly described by the singly excited  $1b_1 \rightarrow 3s/4a_1$  configuration (75% in the PMCAS-CI wave function), the valence-Rydberg character of the state arises mainly from the nature of the excited orbital, labeled here as  $3s/4a_1$  to highlight its intermediate character valence ( $4a_1$ )-Rydberg ( $3s$ ), and not from configurational mixing (🔗 [Table 14-3](#)).

We can get further insight into the nature of such a state analyzing its evolution with respect to the O–H internuclear distance. For the sake of simplicity, we have considered the symmetrical stretching of both O–H bonds, preserving thus the  $C_{2v}$  symmetry of the system. MS-CASPT2 calculations were performed for the three lowest roots of  $1^1B_1$  symmetry using the

Table 14-3

Computed MS-CASPT2 vertical transition energies ( $\Delta E$ , eV), oscillator strengths ( $f$ ), and orbital extensions ( $\langle r^2 \rangle$ , a.u.) from the PMCAS-CI wave functions for the lowest-lying singlet states of the water molecule at the ground-state equilibrium geometry

State	$\Delta E$	$f$	$\langle r^2 \rangle$
$1^1A_1$			13
$1^1B_1(1b_1 \rightarrow 3s/4a_1)$	7.50	0.033	30
$1^1A_2(1b_1 \rightarrow 3p_y/2b_2)$	9.27	Forbidden	43
$2^1A_1(3a_1 \rightarrow 3s/4a_1)$	9.86	0.032	45

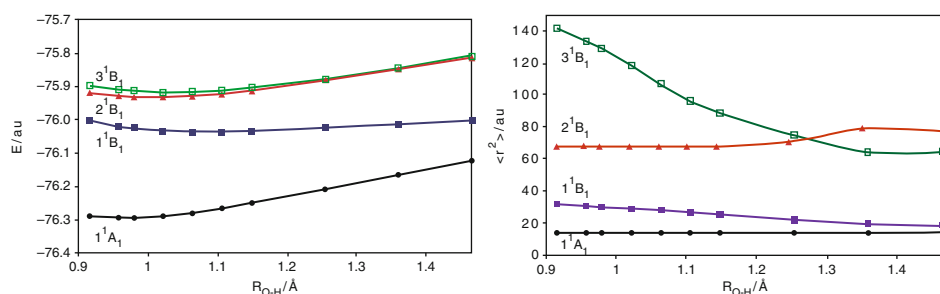


Fig. 14-12

Symmetrical stretching of the O–H bonds in the ground and low-lying  $1^1B_1$  states of the water molecule. Potential energy curves referred to the corresponding ground-state minimum (left) and computed  $\langle r^2 \rangle$  values

O[5s4p1d]/H[2s1p]+(2s2p2d) basis set (since now we will use the same basis sets for each state, one for vertical transitions, another for potential curves analysis) and the (5120) active space (full valence active space plus two extra Rydberg orbitals of  $a_1$  symmetry). The bond angle was kept fixed at  $104.5^\circ$ .

The second and third  $1^1B_1$  states have Rydberg character at all distances examined since they show high values of  $\langle r^2 \rangle$  in comparison with the ground state. However, the situation is clearly different for the  $1^1B_1$  state. The evolution of the computed  $\langle r^2 \rangle$  with the O–H distance shows that the state is getting more and more valence character when stretching the O–H bond as a result mainly of the changes undergone by the virtual orbital: the energy of the antibonding  $4a_1$  orbital decrease when lengthening the O–H distance separating this orbital from the related  $3s$ -Rydberg orbital. In other words, the nature of the  $1^1B_1$  state evolves from a valence-Rydberg mixing type ( $1b_1 \rightarrow 3s/4a_1$ ) at the ground-state equilibrium geometry to a valence character ( $1b_1 \rightarrow 4a_1$ ) at O–H bond lengths around  $1.25 \text{ \AA}$  and longer, which corresponds only to a symmetrical bond stretching of  $0.3 \text{ \AA}$  from the ground-state equilibrium value. Accordingly, the second  $1^1B_1$  root becomes the Rydberg state ( $1b_1 \rightarrow 3s$ ) at O–H distances longer than  $1.32 \text{ \AA}$ . This state constitutes an example of MO Rydbergization postulated by Mulliken. The reason for such behavior is probably that both valence and  $2s$  Rydberg MOs share the same energy and position in space, yielding therefore a common mixed state (Fig. 14-12).

A similar analysis of the  $1^1A_2$  state shows another example of Rydbergization, as its nature evolves from ( $1b_1 \rightarrow 3p_y/2b_2$ ), with a 73% weight at PMCAS-CI wave function at geometries close to the ground-state equilibrium geometry to ( $1b_1 \rightarrow 2b_2$ ) at O–H distances longer than

$\sim 1.217 \text{ \AA}$ , where the second  $^1A_2$  state becomes the  $1b_1 \rightarrow 3p_y$  Rydberg state. Indeed, the diffuse nature of the  $^1A_2$  state decreases when increasing the O–H distance. Calculations of the stretching potential energy curves were performed using the active space (3141) with eight active electrons.

On the other hand, the  $2^1A_1$  state is characterized mainly by means of the  $3a_1 \rightarrow 3s/4a_1$  configuration, with a weight of 70% at the PMACAS-CI wave function, and by  $1b_1 \rightarrow 3p_x$ , with a weight of 28%. This state is closely related to the  $3^1A_1$  state, which is characterized by the same configuration but in different proportion (69% and 28%, respectively). Since the  $1b_1 \rightarrow 3p_x$  one-electron promotion is a pure Rydberg excitation, its contribution increases the configurational mixing of the state. Calculations carried out using the active space (4220) show that the valence character of the state increases with the stretching the O–H bonds due to the increment of the weight of the singly excited  $3a_1 \rightarrow 3s/4a_1$  configuration in the PMACAS-CI wave function of the state together with the transformation of the excited orbital toward a valence  $4a_1$  orbital. To sum up, the  $2^1A_1$  state is a valence-Rydberg state at the ground-state equilibrium geometry and the mixing is not only due to the nature of the excited orbital ( $3s/4a_1$ ), but also to configurational mixing involving the Rydberg  $1b_1 \rightarrow 3p_y$  excitation.

In the light of these results, it is concluded that the electronic spectrum of gas-phase water has a predominant Rydberg character at the Franck–Condon geometry, in line with the general view, although a certain degree of valence character has been shown to exist in the three lowest singlet states, a property that increases far from the FC region.

## Practical Aspects

### How to Solve Valence-Rydberg Mixing

Many methods are unable to solve properly the valence-Rydberg mixing because they do not include enough correlation effects in the calculation of the wave function, for instance, TD-DFT, CASSCF, RASSCF, or even CC2. In many cases, the problem is aggravated by the use of excessively diffuse basis set functions. For instance, aug-cc- or 6-31++G-type basis sets are already too diffuse, becoming even more when atom-centered and combined in the LCAO approach. The excess of uncontracted diffuse functions has been found necessary to compensate the poor recovery of the correlation energy of the underlying valence basis sets. A procedure to reduce the mixing problems and even to make the obtained Rydberg solutions identifiable is to employ molecule-centered uncontracted functions, as explained in the previous example. Typically, orbitals, excitations, and even population analysis are more clearly represented in such cases.

If the mixing persists, and it can be observed by comparing the orbital extension (second Cartesian moment  $\langle r^2 \rangle$ ) of the valence state with that of the ground state, which should be similar and different from that of the Rydberg state, the only solution is to increase the level of correlation used to compute the wave function. In the CC treatments, it might mean to include the triple excitations. For multiconfigurational studies, it means to make the CASPT2 states to interact and display orthogonal solutions via the MS-CASPT2 method. Ethene is the most paradigmatic case. A CASPT2(2e,9MOs)/ANO-L C[5s4p2d] / H[3s2p] + 1s1p1d calculation yielded an expected  $^1B_{1u}$  valence and Rydberg states at 8.45 and 8.93 eV with orbital extensions  $\langle x^2 \rangle$  52 and 50 a.u., and with related oscillator strengths 0.261 and 0.166, respectively (see Finley et al. 1998; Müller et al. 1999). Several errors plague these results. First, the ground state extension was 12 a.u., therefore none of the two states seemed to have proper valence character. Also, Rydberg states cannot have oscillator strength values close to those of valence states.

Second, the correct energetic values are known to be  $\sim 8.0$  and  $9.33$  eV, respectively, leading then to deviations of  $\pm 0.4$  eV. A clear mixing of states was obtained at the CASSCF level (in which our wave function was obtained) that CASPT2 could not solve properly for the energies. Using the multistate MS-CASPT2 method makes both states to interact. By diagonalization of the effective interaction Hamiltonian, a new set of states is obtained. The new wave functions, PM-CASCI, are linear combination of the previous SA-CASSCF references built with the eigenvectors of the MS treatment. The new results provide two new solutions for the  $^1B_{1u}$  valence and Rydberg states at  $7.98$  and  $9.33$  eV with orbital extensions  $\langle x^2 \rangle$  of  $20$  and  $82$  a.u., and with related oscillator strengths  $0.360$  and  $0.051$ , respectively, leading to a proper interpretation of the spectrum.

A proof that the valence-Rydberg mixing problem is just a problem of lack of correlation in the wave function is obtained when performing RASSCF/RASPT2 calculations on the ethene molecule. When a calculation including all valence  $\sigma$ ,  $\pi$ ,  $\pi^*$ ,  $\sigma^*$  and Rydberg orbitals in the RAS active spaces is carried out, the mixing vanishes even at the RASSCF level and compact valence and diffuse Rydberg states are obtained separated. The RASPT2 step, without the need of a multistate treatment, produces already the correct results.

### Focusing on the Valence States

Is it possible to ignore the Rydberg states and focus on the valence spectrum? Logically, this depends on the system and also on our goals. A system with a solvated or proteinic environment perturbs so much the diffuse transitions that it is safe to ignore the Rydberg solutions. For isolated systems, the simultaneous treatment of valence and Rydberg states seems unavoidable, for instance, in pyrrole, where the lowest-energy excited single state is of Rydberg character. Using poor basis sets like 6-31G\* type or excluding in general the diffuse functions from the basis set or the Rydberg orbitals from an active space may seem a solution (the Rydberg states cannot be represented in such case), but the obtained “valence” solutions will most probably be of mixed type.

For larger systems the, exclusion of the Rydberg orbitals from the basis or the active space may be less dangerous. Valence states decrease much more in energy with the enlargement of the molecule or the complexity of the chromophore than Rydberg states. It is unusual to find Rydberg series below  $4.5$ – $5.0$  eV. Therefore, if one is interested in computing low-lying valence states in a large molecule, it might be safe to first estimate where the lowest-energy Rydberg state is placed and consider that valence states below such energy are treated accurately with compact basis sets. From one to other molecule, this estimation can be done using the respective IPs, which are a good measure of where the Rydberg series are being located energetically. On the other hand, the geometry of the Rydberg states tends to be similar to that of the molecular cation, typically different from that of the valence states. A way to simplify the calculations in many systems may be to use a compact valence basis set to get the geometry of valence states that, far from the FC region, might not suffer of mixing with the Rydberg states. A recent example can be found in the literature for  $1,1'$ -bicyclohexyliden (see Pérez-Hernández et al. 2008).

## Electronic States of Anionic Systems

---

### An Application Example: p-benzoemiquinone Radical Anion

When computing excited states in anionic systems, several cautions should be taken into account. In some molecules, certain states in the anion may lie below the ground state of the



neutral system, for instance, those in which the actual electron affinity is positive. Most of the electronic states in anions, including in many cases the ground state, are, however, higher in energy than the ground state of the neutral system and represent temporary anion states, which means that they are unstable with respect to electron detachment. They are typically named Temporary Negative Ion (TNI) states, resonances, or anionic valence-bound states. Conventional quantum-chemical techniques cannot be applied in general to the study of these temporary states since they lie in the continuum of the neutral species plus the free electron. It has been shown that it is, however, possible to obtain well-localized solutions with *ab initio* methods such as CASSCF and others. Those eigenvalues can be regarded as discrete representations of the TNI or anion resonance states. The metastable states of anions can be classified as either shape or core-excited resonances. From the electronic structure standpoint, shape resonances originate in the attachment of the electron to a virtual orbital of the neutral ground state. Alternatively, they can be viewed as the result of the promotion of the unpaired electron of the LUMO to higher-lying virtual orbitals. Core-excited resonances can be seen, on the other hand, as arising from the attachment of an extra electron to an excited state of the neutral molecule. They can be divided into Feshbach and core-excited shape resonances, depending on their energetic position with respect to the excited state of the neutral molecule involved. The former lie below the parent state of the neutral, whereas the latter are located above.

The theoretical treatment of temporary negative ions can proceed via the use of scattering theory or the employment of modified bound-state quantum chemical techniques. The latter requires the use of stabilization methods for the obtained solutions, for instance, by decreasing the exponents of the diffuse functions. It is of general knowledge that any quantum chemical calculation in anions requires a basis set including extra diffuse functions. Besides the discrete valence TNI states, also named valence-bound (VB) anion states, diffuse states described by a singly excited configuration involving a diffuse orbital can be also obtained, and they have been sometimes erroneously interpreted as Rydberg states. Singly excited Rydberg states are not present on monoanions because there is no specific direct electrostatic interaction between the neutral molecule and the electron; doubly excited Rydberg states would be instead present at high energies. Then, if not Rydberg states, what is the nature of the diffuse states that a quantum-chemical calculation finds interleaved between the valence excited states of the anion? In the cases where the neutral system has a dipole moment larger than a critical value established between 1.26 and 2.50 D, metastable solutions known as dipole-bound (DB) anion states should be found consequence of the interaction between the additional electron and the dipole moment of the neutral system. These states will have small binding energies (i.e., they will be more stable than the neutral ground state), but in some cases, they may appear higher than the neutral state because of deficiencies of the quantum-chemical treatment. Upon improvement of the level of the calculation, they should end up with a positive binding energy. In systems with smaller dipole moments, however, spurious diffuse solutions are also present together with the VB and DB states, but they are an artificial consequence of the calculation, in particular of the structure of the one-electron basis set, which forces a confinement effect (known as the basis set cage effects) leading to erroneous results. In the low dipole moment molecules, these diffuse solutions for the excited states of the anion try to simulate the neutral molecule plus a free electron by placing the extra electron into the most diffuse orbital available. The computed energy for these states strongly depends on the diffuseness of the basis set employed. In practice, the only way to check if the obtained result is correct is to analyze the stability of the energy, for instance, with the increase of the diffuseness of the basis set, as it will be discussed below.



We have a hint of how to analyze ionic systems in the monodeterminant HF approach. The Koopman's theorem stated that given an  $N$ -electron HF single determinant  $|\Psi_0\rangle = |\chi_1 \chi_2 \dots \chi_c \dots \chi_N\rangle$ , the ionization potential (IP) to produce and  $(N - 1)$ -electron single determinant by removing an electron from spin orbital  $\chi_c$ , and the electron affinity (EA) to produce and  $(N + 1)$ -electron single determinant by adding an electron to spin orbital  $\chi_r$ , are just  $\text{IP} = {}^{N-1} E_c - {}^N E_0 = -\varepsilon_c$  and  $\text{EA} = {}^N E_0 - {}^{N+1} E_r = -\varepsilon_r$ , respectively; that is, the corresponding orbital energies of the protagonist spin orbitals. This "frozen orbital" approximation assumes that the spin orbitals in the  $(N \pm 1)$ -electron states are identical with those of the  $N$ -electron state, neglecting the relaxation of the spin orbitals in the ionized states. As a result, Koopman's theorem calculations tend to produce too positive IPs and too negative EAs. In addition, we should take into account the correlation effects, which one obtains in going beyond the HF approximation, which will produce further corrections. In general, Koopman's ionization potentials are reasonable first approximations to the experimental ones. On the contrary, Koopman's electron affinities are often inaccurate. Obviously, correlated methods are needed to determine quantitatively such properties.

The ground state of the anion can be then lower (positive EA) or higher (negative EA) in energy than the ground state of the neutral system. How about the excited states of the anion? They will lie in general higher than the neutral ground state, in the continuum region. As mentioned, it is possible to obtain discrete solutions of the Hamiltonian corresponding to the valence-bound states of the anion, but, because of the confinement effect of the basis set functions, other solutions in which the electrons are placed in the diffuse orbitals will be also present. In a series of calculations on the *p*-benzosemiquinone radical anion ( $p\text{BQ}^-$ , nonpolar in the neutral form), a number of experiments were performed (see Pou-Amérgigo et al. 2000). Apart from the clearly localized valence-bound anionic states, a number of supposedly diffuse states were obtained interleaved with the valence states. What are those solutions? They are spurious solutions caused by the cage effect of the basis set. By decreasing the orbital exponents in the C and O basis sets, it was observed that, while the valence states remained in energy, the "diffuse" solutions started to decrease their absolute energy. The instability remained until their energy converged to the energy of the neutral system, while the electron becomes free and detached from the molecule, an effect that is observed because it always ends up on the most diffuse orbital available. Once identified, the stable solutions above the neutral ground state energy can be TNI states or anion resonances, whereas the instable solutions can be neglected as spurious. The apolar character of  $p\text{BQ}^-$  prevents the molecule to have dipole bound anion states (although it has quadrupole-bound states).

The CASPT2 study on  $p\text{BQ}^-$  used a basis set of ANO-L type C[4s3p1d]/H[2s1p] plus a set of 1s1p1d diffuse functions centered in the molecule and an active space of 9 MOs of valence  $\pi\pi^*$  type, (03010301), distributed into the  $D_{2h}$  irreducible representations ( $a_g b_{3u} b_{2u} b_{1g} b_{1u} b_{2g} b_{3g} a_u$ ). The adiabatic electroaffinity (AEA), obtained as the difference between the ground states of the neutral and anion  $p\text{BQ}$  at their respective geometries was computed as  $-0.33$  eV (CASSCF) and  $2.01$  eV (CASPT2), as compared to the  $1.9$  eV measured in experiment. The result clearly highlights the fundamental role of the correlation effects. Two series of calculations on the excited states were performed to analyze the spectrum of the system at the geometries of neutral and anion  $p\text{BQ}$ . The former results can be compared with those obtained from photodetachment measurements, whereas the latter are better related to the electron attachment or electron transmission spectroscopy (ETS). ● Table 14-4 summarizes the results.

■ Table 14-4

Computed and experimental excitation energies (eV) and oscillator strengths of the *p*-benzosemiquinone radical anion

State	Anion absorption				State	Attachment energies <sup>a</sup>			
	Theoretical <sup>b</sup>		Experimental <sup>c</sup>			Theoretical		Experimental <sup>d</sup>	
	$E_{VA}$	$f$	$A_{max}$	$f$		AE <sup>e</sup>	SF <sub>6</sub>	ETS	EI
$1^2B_{2g}$	–	–	–	–	$1^2B_{2g}$	–1.64			
$1^2B_{3g}$	2.25	Forbidden	2.41	Forbidden	$1^2A_u$	0.91	0.70	0.72	0.77
$1^2B_{3u}$	2.80	0.05	2.7/3.1	0.15/0.06	$1^2B_{2u}$	0.96			
$1^2A_u$	2.82	0.17	2.7/3.1	0.15/0.06	$1^2B_{3u}$	1.31	1.35	1.46	1.6
$1^2B_{1g}$	3.25	Forbidden	–	Forbidden	$2^2B_{3u}$	1.87	1.90	2.15	2.0
$2^2B_{3u}$	3.56	0.32	3.8/3.9	0.50/0.35	$1^2B_{1g}$	1.99			

<sup>a</sup>Electron attachment energies at neutral ground state geometry

<sup>b</sup> $E_{VA}$ : vertical excitation energy at the anion ground state geometry

<sup>c</sup>Absorption maxima in acetonitrile/water

<sup>d</sup>SF<sub>6</sub> scavenger spectra (SF<sub>6</sub>), electron transmission spectroscopy (ETS), and vibrational excitation by electron impact (EI)

<sup>e</sup>Adiabatic energy difference: energy difference between the anion state and the neutral ground state geometry at such geometry

Whereas most of the assignments, made to  $\pi\pi^*$  valence-bound states, seem to be explained, the observed band near 2.7–2.9 eV in the *p*BQ<sup>–</sup> absorption spectrum could not be initially resolved because the degeneracy of the  $1^2B_{3u}$  and  $1^2A_u$  states, both leading to one-photon allowed transitions. This broad band had two main peaks at 2.7 and 3.1 eV, which could be attributed to one or other states. In principle, the transition to the  $1^2A_u$  was computed with larger oscillator strength, but that does not guarantee that the highest peaks correspond to such a state. The vibrational profile of the transitions to both states was therefore computed at the CASPT2//CASSCF level of calculation by obtaining vibrational energies and TDMs, which required geometries optimizations and Hessians for both states and resolution of the vibrational Hamiltonian. As a result, it was confirmed that the two highest bands at 2.7 and 3.1 eV corresponded to the initial quanta in the vibrational progression of the breathing mode in the  $1^2B_{3u}$  state, whereas the  $1^2A_u$  transition, even when broader, extended to higher energies displaying a larger band area but not so high peaks. Such result proves the danger implicit in the use of vertical excitation energies matching band maxima to assign molecular spectra.

## Practical Aspects

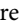
### Basis Sets and Spurious Solutions in Anions

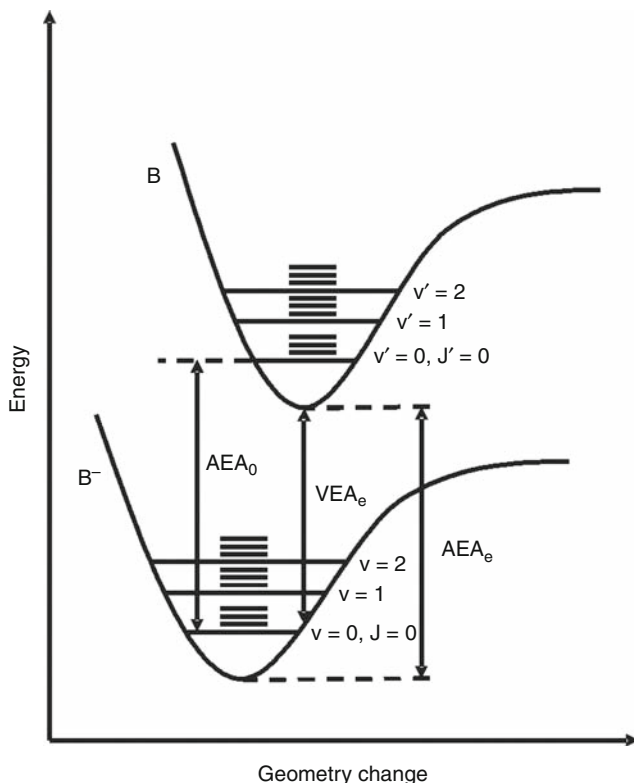
Closely controlling the quality of our basis set and its effects on our states will confirm the validity of our results. Let us illustrate this aspect with another example. Neutral nitromethane (CH<sub>3</sub>NO<sub>2</sub>) has a dipole moment of 3.46 D. A standard ANO-L C,N [4s3p2d]/H[3s1p1d] basis set is used supplemented with a set of 1s diffuse functions (eight primitives) with exponents for the diffuse functions explicitly optimized to deal with Rydberg states. At the CASSCF optimized

geometry for the neutral molecule, the lowest state of the anion is 0.530 eV above the neutral ground state at the MS-CASPT2 level. Just by scaling the exponents of the diffuse functions by a factor 0.5 in both the neutral ground state and the lowest anion state, the energy difference decreases to 0.250 eV. Scaling instead the exponents by 0.1 leads to an energy difference of  $-0.022$  eV, that is, the lowest state of the anion has converged below the energy of the neutral system. Increasing further the diffuseness of the basis set does not vary the result, which corresponds to a dipole-bound state of the anion with a small binding energy of 0.022 eV (experimental value 0.012 eV). The lowest valence-bound anion state is computed, adiabatically, 0.23 eV below the neutral ground state of the molecule at the CCSD(T) level. This state remains basically stable with the increase of the diffuseness of the basis set and it is, in general, better represented by using diffuse functions localized in the positive sites of the molecule. To test the stability of the solutions obtained, other techniques have been developed, such as increasing the effective positive nuclear charge, adding specific counter ions to fix the negative charge, or using penalty functions or electric fields, such the dielectric continuum cavities, which will highly perturb the diffuse solutions.

### Negative Electron Affinities

Ionization potentials and electron affinities are intrinsic properties of the DNA and RNA nucleic acid bases (NABs) whose determination enables a deep understanding of all phenomena related to the electron donor and acceptor abilities of the NABs, such as those involving charge transfer and transport along the DNA strand. Determination of the EAs of NABs is difficult both experimentally and theoretically, and the uncertainties range up to several eV, including also changes in the sign of the energies, because both VB and DB anions may be located within a small range of energies, and therefore determination of accurate EAs is uncertain, especially because the type of anion formed may vary with the different experimental conditions. Apart from that, new difficulties interfere the experimental determination of EAs of nucleobases as the presence of different tautomers of the nucleobases which are close in energy in the gas phase. In particular, the canonical (keto) form of guanine, which is the biologically relevant tautomer, has a very low concentration in the vapor, and there is no direct experimental value reported for the corresponding EA.

The electron affinity of a neutral molecule is the energy required for detaching an electron from a singly charged negative ion, or equivalently, the energy released when an electron is attached to the neutral system. Thus, the electron affinity of a neutral molecule can be defined as the energy difference between the ground state of the neutral system and that of the anion. A positive EA implies that the anion is more stable than the neutral species. As in the case of the ionization potential, three theoretical magnitudes (see  Fig. 14-13) are used for describing this transition: the vertical electronic energy difference ( $VEA_e$  or VEA) between the ground states of the neutral system and the anion at the equilibrium geometry of the neutral molecule, the adiabatic energy gap ( $AEA_e$ ) between the minima of the neutral and anion molecule ground states, and the corrected adiabatic property ( $AEA_0$  or AEA) with the addition of the zero-point vibrational energy correction (ZPE). Thus, positive VEAs indicate that the molecule acts as a trap for an excess electron, with an attachment energetically favored and, therefore, the anion can be created spontaneously. In this case, positive AEAs follows, and the system becomes stable, that is, it does not undergo autodetachment and can take part in chemical reactions. On the other hand, negative values for VEAs and AEAs represent the TNI states, existing in short periods of time and becoming prone to photodetachment.



■ Fig. 14-13

EA diagram ( $B + 1e^- \rightarrow B^-$ ). Definitions of the theoretical magnitudes related to EA are graphically shown through the electronic, vibrational, and rotational potential energy levels. Those magnitudes are  $VEA_e$  (vertical electronic electron affinity, from the neutral ground-state minimum),  $AEA_e$  (adiabatic electronic electron affinity, from minimum to minimum), and  $AEA_0$  (adiabatic electron affinity including the zero-point vibrational corrections of the minima)

Analysis of the experimental literature on nucleobase EAs shows an extremely confuse situation, ranging from clearly negative values ( $-0.56$  eV) up to largely positive energies ( $1.51$  eV), and including EAs close to  $0$  eV. In general, determination of EAs represents a technical challenge, especially when they have negative values, and in many cases it is based on indirect measurements. Negative electron affinities can be experimentally measured by electron transmission spectroscopy. The technique is able to detect negative ion resonance states, which are energetically unstable with respect to electron autodetachment. It is unclear when the experiment is measuring vertical (VEA) or adiabatic (EAs) attachments, or if the indirectly obtained data truly represent the molecular EAs. In general, however, ETS is the only direct experimental technique which is expected to provide actual VB anions in the region of the resonance states. In particular for gas-phase NABs (except G, which cannot be isolated), ETS measurements report EAs values clearly in the negative region (from  $-0.22$  to  $-0.54$  eV).

In order to compute accurate theoretical results for the VEA and AEA of NABs different levels of theory were taken into account, employing the MP2, CCSD, and

CCSD(T), and the CASSCF and CASPT2 methods, in conjunction with the 6-31G\*, cc-pVDZ, aug-cc-pVDZ, ANO-L C,N,O[4s3p1d]/H[2s1p] (hereafter ANO-L 431/21), and ANO-L C,N,O[4s3p2d1f]/H[3s2p1d] (hereafter ANO-L 4321/321) basis sets. Methods and basis sets were selected to obtain the most accurate values from preliminary calculations on atomic systems, in which the required levels of highly flexible enough basis sets and strongly correlated methods to obtain predictive EAs were determined. Geometry optimizations of both neutral and anionic NABs were carried out at the MP2/6-31G(d), MP2/aug-cc-pVDZ, CASSCF/cc-pVDZ, CASSCF/ANO-L 431/21, and CCSD/aug-cc-pVDZ levels of theory. No symmetry restrictions ( $C_1$  symmetry) were imposed, whereas all minima were characterized by computing second derivatives at the same level, except in the case of CCSD/aug-cc-pVDZ where the geometries were tested comparing with the optimized parameters at the other levels of theory. At the respective equilibrium structures, additional CASPT2 and CCSD(T) calculations were performed to account for the most accurate energy values. ZPE corrections were included at different levels using the harmonic approach. The active space for the CASSCF calculations in geometry optimizations comprises the full  $\pi$ -valence system, except the molecular orbital localized mainly on the nitrogen atom of the  $\text{NH}_2$  group in the case of cytosine, adenine, and guanine, whose occupation number is very close to two. This MO is further included in conjunction with the lone pair electrons and orbitals of the heteroatoms in the final CASSCF and CASPT2 calculations of VEAs and AEAs, except when the large ANO-L 4321/321 basis set was employed (see Roca-Sanjuán et al. 2006, 2008a).

The analysis of the results shows that neither DFT procedures nor the MP2 method have the required accuracy, either by the known problems of DFT to deal with negative centers or by the spin contamination problem that affects MP2. CCSD(T)//CCSD/aug-cc-pVDZ and CASPT2(IPEA)/ANO-L 4321/321 //CASSCF/ANO-L 431/21 will be established as the most accurate procedures, both for vertical and adiabatic EAs. It must be emphasized here that the main factor to achieve accurate results for the VEA of NABs by using ab initio methods is the employment of atomic one-electron basis sets flexible enough to describe both the spatial distributions of electrons and their correlation effects and including functions decaying slowly with the radial distance. The CASPT2//CASSCF strategy has the advantage to compute several states of the system, and it is possible to easily distinguish between the different solutions. Single-reference methods are not free of problems, because they can only obtain the lowest solution. For instance, at the corresponding geometry of the neutral species, adenine and guanine, in which the VB anion state lies much higher than other diffuse states, the CCSD and CCSD(T) computations lead initially to a diffuse and low-energy spurious solution in which a delocalized electron is located far from the molecule in a diffuse orbital. Finally, the sequence of stable solutions obtained for the VEAs of NABs using the reference CCSD(T) and CASPT2(IPEA) levels of theory is established as  $U \approx T > C > A > G$ , ranging from  $-0.61$  eV (U) to  $-1.14$  eV (G). Therefore, for guanine is less favorable to accept an electron at the neutral molecule geometry.

Regarding gas-phase adiabatic EAs, those for uracil and thymine were determined very close to zero, whereas cytosine has a small negative AEA. The sequence of AEAs for isolated NABs can be established as  $0 \text{ eV} \sim U \sim T > C > G > A$ . Purines are much less favorable than pyrimidines to retain the electron attached to the neutral nucleobase, and after geometry relaxation adenine becomes the poorest electron acceptor of all NABs, in contrast to what occurred for the vertical EAs, in which guanine had the more negative value. To understand the differences among these compounds, it can be also analyzed how the inductive effect (and the number of stable resonance structures) makes more or less stable the new center of negative charge created by the addition of the new electron. It should not be forgotten that the

accepting properties of the systems will largely change in solvated or biological environments. For instance, a recent calculation performed for the EAs of the cytosine molecule within a chain of oligomers,  $dC_{18} \times dG_{18}$ , employing a CASPT2/MM approach led the AEA of cytosine to change from  $-0.26$  eV in vacuo to  $0.69$  eV in the biological surrounding, becoming therefore the molecule a strong electron acceptor.

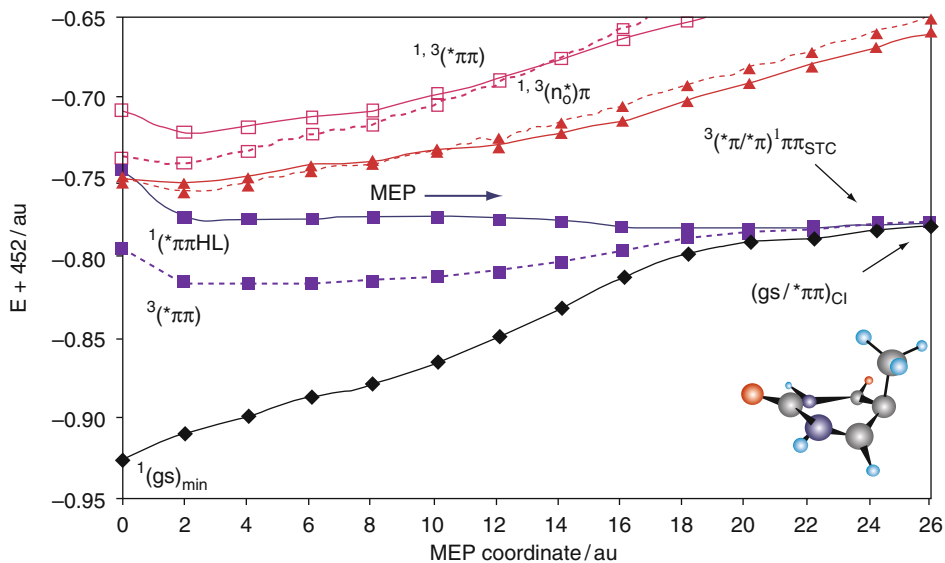
## Photochemistry: On the Trail of the Energy

---

### An Application Example: Thymine

The energy absorbed by a molecule can be released radiatively, that is, slowly emitted via fluorescence or phosphorescence, or nonradiatively. In that case, it can give rise to productive photochemistry, yielding photoproducts different from the initial species, or it can become unproductive, meaning that it is dissipated to the environment through the vibrational degrees of freedom, ending in some cases in the initial ground state of the system. Photophysics and photochemistry is typically a combination of all such processes. From the theoretical viewpoint, the best initial strategy to understand the photochemical processes is trying to follow closely the path of the energy from the initially populated states at the FC region toward favorable regions of the PEHs. That means to trace the lowest-energy possible pathway until reaching an energy barrier, that is, a minimum, or a transition state, or a hypersurface crossing, in particular conical intersections (CIs), the protagonists of the ultrafast radiationless nonadiabatic energy transfers between PEHs. The only strategy that guarantees finding PEH points along the lowest-energy path is the computation of a minimum energy path (MEP), that is, a steepest-descendent pathway. The procedure is performed generally in mass-weighted coordinates, and it is equivalent to the Intrinsic Reaction Path approach. Once localized, the crossings and CIs, the estimation of their accessibility, and the calculation of the interstate couplings (like the SOC between singlet and triplet states) and transfer probabilities will help understand and predict favorable IC and ISC processes. The described strategy is named as the Photochemical Reaction Path approach, and it can be applied to solve a large number of photochemical problems.

An interesting example of nonproductive photochemistry can be found in important compounds such as the DNA/RNA natural nucleobases, which were determined a long time ago as basically nonfluorescent. Modern femtochemical techniques have determined fluorescence decay times in the DNA/RNA nucleobase monomers, nucleosides, and nucleotides in different media to be ultrafast. In particular, molecular beam measurements reported two main decay lifetimes near 100 fs and few ps in all five natural NABS: thymine, uracil, cytosine, adenine, and guanine (Crespo-Hernández et al. 2004). Finding ultrafast decays in a molecule suggests the presence of extremely efficient internal conversion channels, and therefore the presence of accessible conical intersections, in particular one connecting the initially populated bright spectroscopic  $\pi\pi^*$  singlet and the ground state, yielding therefore nonfluorescent species. The ultrashort lifetime of nucleobases is an intrinsic molecular property as it has been proved in recent years both from theory and experiment. Indeed, such photoprotective properties may well be very important at the beginning of life in our planet given that there are evidences that point out that life began on Earth millions of years before the development of the ozone layer. The ultrafast decay channels of the nucleobases may have favored photostable natural nucleobases against less stable derivatives (Serrano-Andrés and Merchán 2009). This type of photochemical mechanisms may have been operative as natural selection processes reaching



■ Fig. 14-14

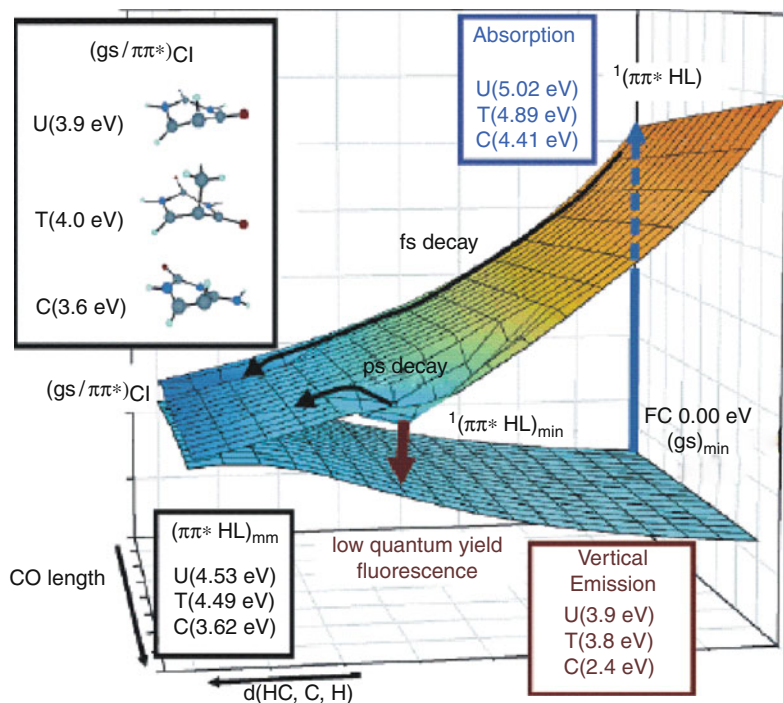
Evolution of the ground and lowest singlet excited states for thymine from the FC geometry along the  $^1(\pi\pi^* \text{ HL})$

in that way the genomic stability until the development of the ozone layer and complexes mechanisms of repair of DNA.

Thymine photophysics is here selected as an illustration of the computational strategies mentioned above (see Merchán et al. 2006; Serrano-Pérez et al. 2007b). **Figure 14-14** displays the CASPT2 energies of the lowest-lying singlet and triplet states of thymine along the MEP calculated for thymine on the bright  $^1(\pi\pi^* \text{ HL}, \text{HOMO} \rightarrow \text{LUMO})$  state from the FC geometry. The level of the calculation was CASPT2//CASSCF(14e<sup>-</sup>, 10MOs)/ANO-S C,N,O[3s2p1d]/H[2s1p]. Apart from the radius of the hypersphere controlling the distance from the initial geometry, not any other restriction was imposed to the calculations.

From thymine ground state and upon near-UV absorption at the FC region, most of the population reaches initially singlet excited states, and in particular, it is the transition to the  $^1(\pi\pi^* \text{ HL})$  excited state at 4.89 eV which has the largest oscillator strength up to 6 eV, that is, 0.167. The ultrafast nonradiative decay undergone by thymine in the femtosecond range can be rationalized by the barrierless character of the path leading from the FC region toward a CI seam with the ground state,  $(\text{gs}/^1\pi\pi^*)_{\text{CI}}$ . Unlike simple geometry optimizations, the use of the MEP technique guarantees the absence of energy barriers along the lowest-energy path. The structure of the CI at the end of the MEP can be characterized as ethene-like, a diradical species (as many CI are) involving combined stretching and twisting of the ethylenic bond and leading to a screw-boat (S) conformation  $^5\text{S}_6$  for the six-membered ring. The presence of an accessible CI explains also the low fluorescence quantum yield ( $\sim\phi_F = 10^{-4}$ ) detected for thymine with band origin at 4.5 eV in water. This weak emission can be related to the presence of a high-lying planar  $^1(\pi\pi^* \text{ HL})$  minimum computed adiabatically from the ground state at 4.49 eV, whereas a nonfluorescent  $^1(n_O\pi^*)$  minimum is found at 4.05 eV with a minor contribution to





■ Fig. 14-15

Global scheme of the photochemistry of uracil (U), thymine (T) and cytosine (C) as suggested by the CASPT2 calculations

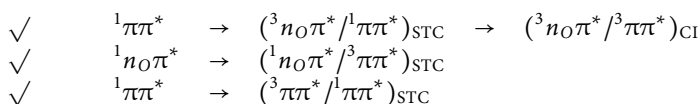
the emissive properties. As recently estimated by means of reaction dynamics, the near 100 fs decay detected in natural nucleobases can be related to the barrierless path from the FC to the CI region. Although other slower singlet decay pathways could be estimated proceeding through the low-lying  $n\sigma\pi^*$  state, that crosses the MEP at high energies and has its own CI with the ground state, still the main relaxation path for the energy runs along the computed  $^1(\pi\pi^* \text{HL})$  barrierless MEP, which will transfer most of the energy toward the ground state and back to the original species. Such behavior means that the systems are largely photostable, as it has been proved for natural and methylated nucleobases, and that the mechanism can be considered an intrinsic property of the systems. ● Figure 14-15 illustrates such mechanism for the pyrimidine nucleobases, thymine, uracil, and cytosine, although the basics also hold true for the purine systems, adenine and guanine (Merchán et al. 2006; Serrano-Andrés et al. 2006, 2008; ?). Further insight can be only obtained when reaction dynamic calculations are performed on larger regions of the PEHs (see, for instance, Szymczak et al. (2009)).

The decay along the singlet manifold is not the only procedure for energy relaxation. Efficient population of the triplet manifold can also take place, essentially through intersystem crossing (ISC) processes taking place along the main decay process on  $^1(\pi\pi^* \text{HL})$  or via photosensitization from endogenous or exogenous species. Triplet states are frequent intermediates in different types of photoinduced reactions. Both their usual diradical character and long lifetimes make them reactive species prone to interact with other systems. Among the most

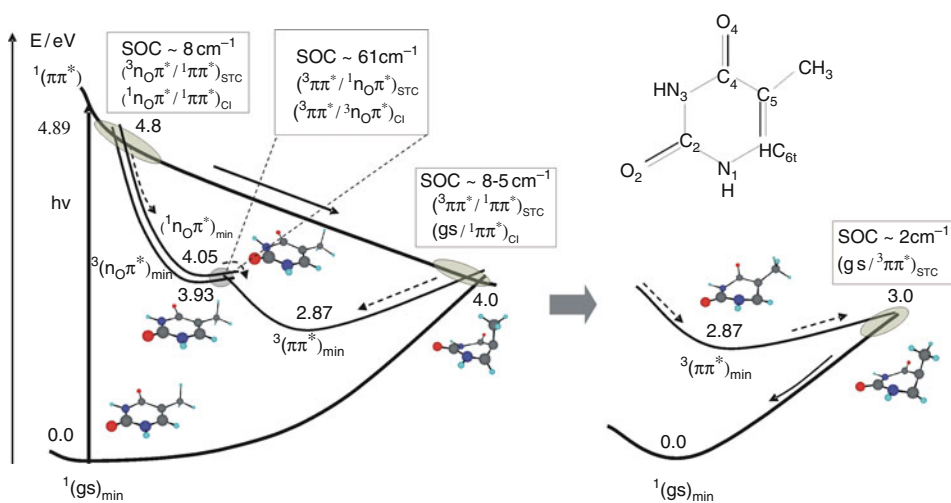


important reactions involving triplet states, those related to DNA/RNA purine and pyrimidine nucleobases have undoubtedly attracted more attention, in particular the photodimerization of pyrimidine nucleobases, considered to be the most frequent DNA lesion taking place after UV light irradiation. Through their triplet states, DNA/RNA nucleobases may not be as photostable as expected. As seen in ► Fig. 14-14, along the  $^1(\pi\pi^*)$  HL state, MEP is clear that two singlet-triplet crossings (STC) are accessible, and therefore two ISC processes may take place: at 4.8 eV with the  $^3(n_O\pi^*)$  triplet state,  $(^3n_O\pi^*/^1\pi\pi^*)_{STC}$ , and at 4.0 eV, further along the relaxation path and near the ethene-like CI with the ground state, directly with the lowest  $^3(\pi\pi^*)$  T<sub>1</sub> triplet state,  $(^3\pi\pi^*/^1\pi\pi^*)_{STC}$ , a structure displaying the same type of screw-boat puckered geometry with a stretched and twisted double bond C<sub>5</sub>=C<sub>6</sub> as at the  $(gs/^1\pi\pi^*)_{CI}$  CI. Efficient ISC requires both small singlet-triplet energy gaps and large spin-orbit coupling elements at the regions of degeneracy. As compared to IC, taken place essentially in small zones where the seam of CIs becomes accessible, the regions of the potential energy hypersurfaces for effective ISC are more extensive.


► Figure 14-16 includes a scheme describing the population of T<sub>1</sub> based on our CASPT2 calculations, and three are the suggested competitive mechanisms from the initially populated singlet state by means of STC processes:



Regarding the higher-energy ISC process, the  $^3(n_O\pi^*)$  triplet state can be populated from  $^1(\pi\pi^*)$  in the STC crossing region, in which a high SOC of  $8\text{ cm}^{-1}$  has been computed favoring the process. From such region, a MEP on the  $^3(n_O\pi^*)$  state leads directly to its energy minimum,  $^3(n_O\pi^*)_{min}$ , placed at 3.93 eV adiabatically from the ground state. Basically degenerated,



■ Fig. 14-16 Scheme, based on CASPT2 results, of the photochemistry of thymine focused on the population of the lowest-energy triplet state

we have located a conical intersection connecting the triplet states  $^3(n_O\pi^*)$  and  $^3(\pi\pi^*)$ , facilitating the population switch toward the lowest  $^3(\pi\pi^*)$  state. Another computed MEP on the  $T_1$  hypersurface leads from  $(^3n_O\pi^*/^3\pi\pi^*)_{CI}$  to the  $^3(\pi\pi^*)$  state minimum. A second ISC channel also relates with an  $n\pi^*$  state. In our results, as well as in previous theoretical studies, the presence of the low-lying  $^1(n_O\pi^*)$  state is confirmed, lying almost isoenergetic with the lowest ethene-like  $(gs/^1\pi\pi^*)_{CI}$  CI near 4.0 eV. The  $^1(n_O\pi^*)$  state may then be related to the observed dark state in pyrimidine nucleobases in solution. Additionally, we have found that, as both singlet and triplet  $^{1,3}(n_O\pi^*)$  states have almost parallel hypersurfaces because of the typical small singlet-triplet splitting of  $n\pi^*$ -type states, near degeneracy structures with the lowest  $^3(\pi\pi^*)$  state are equal to both states. Therefore, close to the  $(^3\pi\pi^*/^3n_O\pi^*)_{CI}$  CI, we have found a singlet-triplet crossing  $(^3\pi\pi^*/^1(n_O\pi^*))_{STC}$ . The extremely large computed SOC terms,  $\sim -61\text{ cm}^{-1}$ , guarantee also an efficient ISC process in the region, confirming this mechanism as relevant for the overall process. In principle, in different environments such as in polar solvents, it is expected that the  $n\pi^*$ -type excited state will destabilize with respect to  $\pi\pi^*$ -type excited states. Despite those effects, both singlet and triplet  $n_O\pi^*$ -type states are estimated to lie in the solvent below the  $^1(\pi\pi^* \text{ HL})$  state at the FC geometry, confirming the existence of the STC crossing upon decay along the  $^1(\pi\pi^* \text{ HL})$  state. Finally, a third ISC channel directly connecting the lowest  $\pi\pi^*$  states is found at low energies with SOC values ranging  $5\text{--}8\text{ cm}^{-1}$ . The profile of the computed MEP in  Fig. 14-16 suggests that the lowest-energy ISC mechanism may enhance its efficiency with respect to the other nucleobases resulting in larger quantum yields because the region for the energy transfer near to the end of the MEP seems to be much more extended. The presence of three basic ISC funnels in thymine (occurring also in uracil and adenine but not in guanine and cytosine where the higher-energy  $n\pi^*$ -mediated channels are absent) successfully explains for the first time the wavelength dependence on the measured ISC quantum yield ( $\phi_{ISC}$ ) reported in thymine (uracil and adenine too) on the basis of the location and accessibility of the two STC crossing regions upon the initial excitation conditions. In the case of thymine, the  $\phi_{ISC}$  value increases from  $3.9 \times 10^{-3}$  at 280 nm (4.43 eV) to  $5.2 \times 10^{-2}$  at 240 nm (5.17 eV). At low excitation energies, only the lowest-lying ISC computed to take place close to 4.0 eV will be activated. At higher-energies, however, the channels near 4.8 eV will be additionally activated, increasing the overall triplet formation yield.

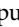
From any of the STC or CI regions, the lowest triplet state is populated by any of the previous ISC processes and reaches its minimum, as proved by the computed MEPs. The high reactivity attributed to this triplet state originates from its partial diradical character on  $C_5$  and  $C_6$ . The minimum is placed at 2.87 eV, adiabatically from the ground state optimized minimum. As a final aspect of the evolution along the triplet manifold in thymine, we have located the singlet-triplet crossing connecting the  $^3(\pi\pi^*)$  and the ground state, and mapped the MEP leading from such STC toward  $^3(\pi\pi^*)_{min}$ . The crossing is placed at near 3.0 eV from the ground state minimum, what means that there is a relatively small barrier of 0.13 eV ( $3.0\text{ kcal mol}^{-1}$ ) to reach  $(gs/^3\pi\pi^*)_{STC}$  from  $^3(\pi\pi^*)_{min}$ . The computed electronic SOC is, however, somewhat low,  $\sim 2\text{ cm}^{-1}$ , predicting for the triplet state a long lifetime and a slow relaxation, becoming therefore prone to undergone reactivity (Merchán et al. 2005; Serrano-Pérez et al. 2007b).

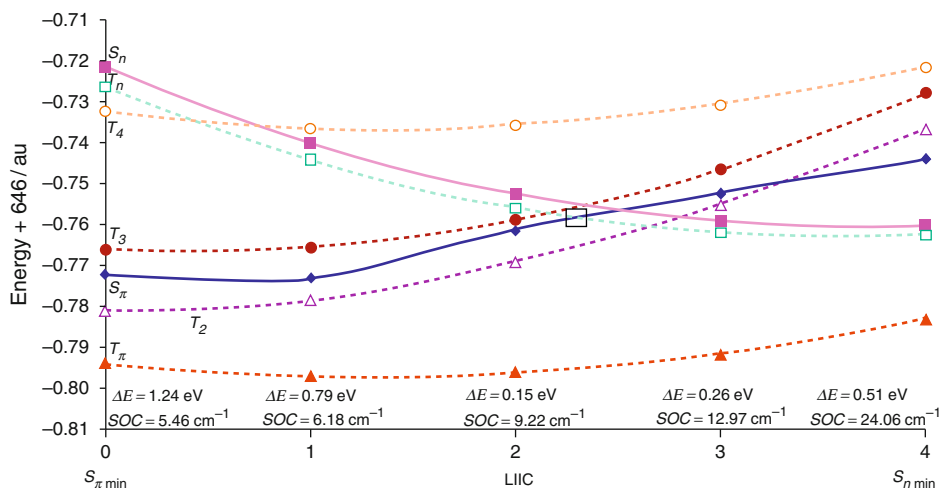
## Practical Aspects

### Reaction Paths: MEP Verses Other Approaches

Computing minimum energy paths (MEP) is an expensive procedure in which each point of the MEP is obtained from individual optimizations. Special care is required in the selection

of active spaces, which should be flexible enough and appropriate along the whole path, and the radius of the hypersphere, which should be not too small or too large. When the steepest-descendent MEP ends finding an energy barrier, for instance, as frequently in the minimum of the state, other procedures should be employed. It must occur also that the calculation of the MEP is too expensive. It is possible to continue using the MEP algorithm upward, that is, by increasing the hypersphere radius increasing energy paths can be computed. Other procedure is to search for a transition state (TS) along the path that represents the energy barrier. More general strategies are normally required to map the full profile of the reaction linking two pre-defined regions of the PEHs. One possibility is performing a relaxed scan, that is, varying by specific amounts one internal coordinate which is expected to be the leading structural modification along the path and, at each selected value, to perform a restricted geometry optimization in which only such coordinate is frozen. Relaxed scans are extremely dangerous and should be used with caution, because they often produce unconnected and useless paths. There is no guarantee that the lowest-energy value for each of the selected frozen-coordinate structures belongs to a connected path. In many cases, the results will jump from one region of the PEH to another along a profile that should represent a reaction path but does not at all. In general, the only relatively safe case in which a relaxed path can be used is that leading to a dissociation of an atom, because in this case the path has a descendent character while the bond length is increased.

Instead of a relaxed scan is preferable to make a linear interpolation in internal coordinates (LIIC). This is a predefined path in which each structure is generated from the previous one by adding linearly to each internal coordinate the geometrical change of the initial and final structures divided by the number of steps. The advantage of this profile is that the points belong to a connected path. The disadvantage is that it will most probably give rise to too high energy barriers, although they will always be upper bounds of the actual barrier. For instance, in a study of the photophysics of psoralen, it was determined that the MEP from the FC region led the system to the minimum of the initially populated  $S_1^1(\pi\pi^*)$  state. Psoralen is a strongly emitting system, especially by phosphorescence (in a ratio 7/1 with respect to fluorescence). Emission from the  $S_1^1(\pi\pi^*)$  minimum explains the fluorescence of the system, but, what about phosphorescence? The population of the triplet manifold seems not to take place close to the FC region, and no relevant STC crossing takes place soon along the MEP. Therefore, an effective triplet formation has to take place by depopulating the singlet state minimum by an accessible STC. The  $T_1$  ( $T_\pi$ ) state lies much lower in energy than the  $S_1$  ( $S_\pi$  state, both vertically ( $\sim 0.6$  eV) and adiabatically ( $\sim 1.2$  eV). Direct interaction between the singlet and triplet vertical excited states is unlikely, and therefore another mechanism has to be found, involving most probably population of higher-energy triplet states and subsequently internal conversion toward  $T_1$ . The qualitative El-Sayed rules indicate that the spin-orbit coupling is large between states of  $\pi\pi^*$  and  $n\pi^*$  types and small between states of the same character. In addition, it is known that the ISC process is enhanced in molecules with heavy atoms (the heavy-atom effect) because the SOC terms increase. There are two necessary conditions to be fulfilled for an effective ISC to take place: low energy gap and high spin-orbit coupling between a singlet and a triplet state. Thus, the nonradiative decay to a triplet state should occur along the relaxation pathway of  $S_\pi$ , starting from the Franck–Condon region, and in close vicinities of a singlet-triplet crossing. A LIIC profile was computed (see  Fig. 14-17) from  $(S_\pi)_{\text{MIN}}$  to the minimum of the  $1^1A''$ ,  $(S_n)_{\text{MIN}}$ , a path considered to be appropriate to find the singlet-triplet crossing, since both  $S_n$  and  $T_n$  states share the same basic structure and energetics (see Serrano-Pérez et al. 2007a). At half of the path the  $S_\pi$  and  $T_n^3(n\pi^*)$  states cross, and the SOC value is high enough ( $9 \text{ cm}^{-1}$ ) to guarantee an efficient ISC. A barrier of 0.4 eV, surely an upper bound, has to be overcome to reach the  $T_n$  state.



■ Fig. 14-17

LIIC path for psoralen. The crossing region between  $S_1$  and  $T_n$  is highlighted with a square

The geometry closer to the crossing point was used as initial geometry to initiate a search at the CASSCF level for a singlet-triplet crossing (STC) between  $S\pi$  and  $T_n$ , that is,  $(S\pi/T_n)_X$ . As expected, the main change in geometry from the minimum of  $S\pi$  to the optimized structures of  $S_n$  or  $T_n$  is related to the length of the C=O bond, much larger ( $\sim 0.15$  Å) than the ground state value for the  $n\pi^*$  states. It is not surprising that the STC structure displays an intermediate value of 1.220 Å. The SOC term in STC is computed as 6.4  $\text{cm}^{-1}$ . As displayed in Fig. 14-18, the barrier from  $(S\pi)_{\text{MIN}}$  to  $(S\pi/T_n)_X$  was computed 0.36 eV at the CASPT2 level. This is still a large energy barrier; however, the crossing is now below the energy of the  $S\pi$  state at the FC geometry, and therefore the system has enough excess energy to access the STC region and make the ISC process to take place.

Once the  $T_n$  state is efficiently populated through a favorable ISC mechanism, it will quickly evolve toward the nearby energy minimum,  $(T_n)_{\text{MIN}}$ , placed 0.11 eV below  $(S\pi/T_n)_X$ . At those geometries,  $T_n$  is the second-energy excited triplet state and can be expected that the energy follows a pathway for favorable internal conversion (IC) toward the low-lying  $T_\pi$  state. Actually, a conical intersection has been found,  $(T_n/T_\pi)_{\text{CI}}$ , placed isoenergetic with  $(T_n)_{\text{MIN}}$ . An efficient IC will therefore take place transferring the population to  $T_\pi$ , which will subsequently evolve to its own minimum,  $(T_\pi)_{\text{MIN}}$ , from where phosphorescence (P) will take place. Additionally, the molecule may react with thymine or transfer its energy to the molecular oxygen exerting the photosensitizing action. The family of furocoumarins (8-MOP, 5-MOP, khellin, TMP, and 3-CPS) was studied at the same grounds showing that all the compounds share the same mechanism of population of  $T_\pi$ . The differences in the values of the barriers (to reach the crossing regions on the hypersurfaces), besides the values of SOC, are actually the key points in considering the photosensitizing ability of each compound.

A final remark should be introduced. Considering that  $n\pi^*$  states tend to destabilize in polar solvents, the  $(T_n)$ -mediated mechanism here proposed will surely decrease its importance in polar media, remaining a plausible candidate for the efficient population of the low-lying  $T_\pi$  triplet state in the gas phase. Indeed, the relevance of out-of-plane displacements for the relaxation of the  $S\pi$  state has been emphasized recently at DFT/MRCI level of theory, together with

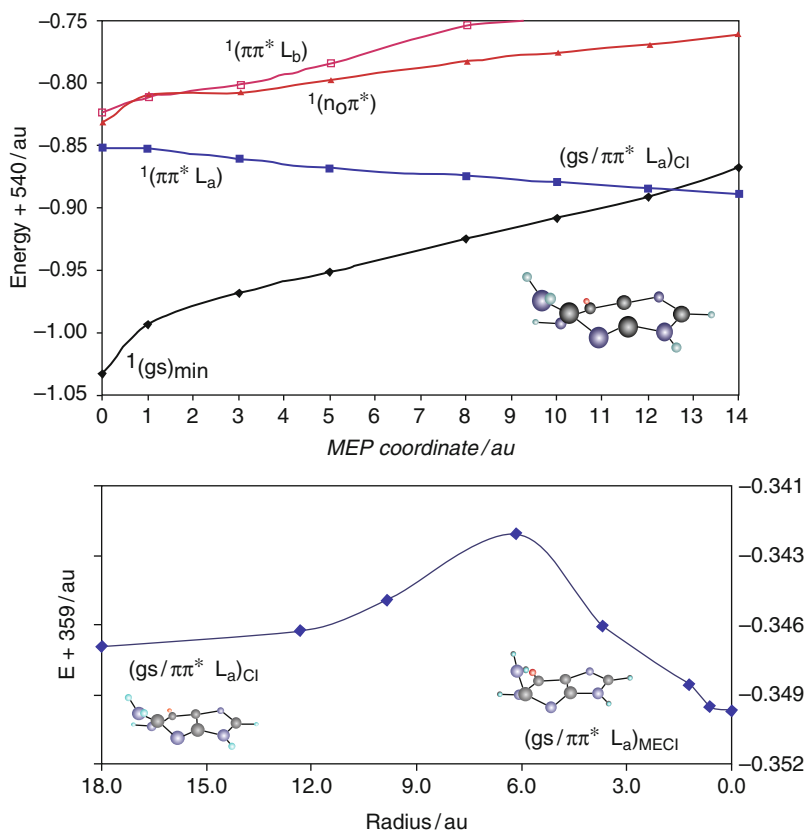


available at a high level of theory, like that at the MRCI level in the COLUMBUS code (see Lischka et al. 2004).

In many cases, however, it is safe enough just to compute the minimum energy crossing point (MECP), discarding the calculation of nonadiabatic coupling, because the obtained solution already defines the crossing region accurately enough. Even when the MECI (or MECP) is found, nothing guarantees that this is going to be the relevant structure from the photochemical viewpoint. It might happen that the MECI is placed in a region that it cannot be easily accessed from the main energy decay paths of the molecule. Therefore, the accessibility of the region is the key point making a CI (or a seam of CIs) relevant for the photochemistry. The next example can properly illustrate this idea. In the same manner as described for thymine, the MEP from the FC region on the bright  $^1(\pi\pi^*)$  HL state was computed for guanine at the CASPT2//CASSCF (14e<sup>-</sup>,12MOs)/ANO-S C,N,O[3s2p1d]/H[2s1p] level of calculation (see [Fig. 14-1](#), top), leading, through a barrierless path, to a crossing with the ground state at the end of the MEP. Independently, a MECI search was carried out to find the lowest-energy CI ([Fig. 14-19](#), bottom, right), which provided a geometry somewhat different from that obtained at the end of the MEP. To solve the problem, a CASSCF path was computed along the seam of CIs ([Fig. 14-19](#), bottom). The points of this profile have been computed to belong to the seam, that is, both the ground and the  $^1(\pi\pi^*)$  states are degenerated, and by successive optimizations in which the radius of the hypersphere has been increased from the initial MECI structure. It is clear that the MECI energy is lower than any other point of the seam, but also that a barrier separates that structure from a CI which is higher in energy but accessible from the end of the MEP (the actual source of the energy) and whose structure is quite similar to that of the end of the MEP ([Fig. 14-19](#), bottom, left). That CI is the relevant funnel for the photochemistry of guanine.

Other serious problems can be found when computing PEHs crossings, although it is as general issue in quantum chemistry. Determination of molecular structures is one of the most time-consuming steps in computational chemistry. It is therefore a typical strategy to use lower-level methodologies to locate singular-point geometries (minima, transition states, conical intersections...) and correct then the energetics by employing higher-level methods. Implicit in this procedure is the problem of the differential correlation effects. We shall check this issue in the case of the location of conical intersections (or any other hypersurface crossing). A usual protocol employed for that purpose is named CASPT2//CASSCF, meaning that geometries have been determined at the CASSCF level and, at those structures, the energies have been computed at the CASPT2 level. CASSCF includes the static or long-range correlation effects and provides wave functions which describe qualitatively the electronic states and form the reference for subsequent calculations. The remaining short-range correlation effects, dynamical electron correlation, are included by means of a second-order perturbative treatment, CASPT2. Depending on the nature of the state, the effects of the static and dynamical correlation energies differ, affecting directly to the description of the hypersurface. [Figure 14-20](#) summarizes what we have called the differential correlation effects on the location of surface crossing within the CASPT2//CASSCF protocol. It is important to recall that this problem is general in quantum chemistry if two levels of theory are being used to compute geometries and energies, e.g., CCSD(T)//CCSD or MRCI//CASSCF.

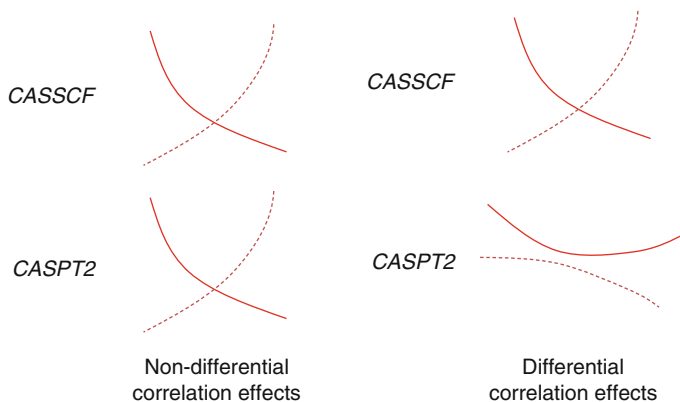
Turning to our example, two main situations do actually occur. In cases where the PEHs computed at the CASSCF and CASPT2//CASSCF levels behave approximately parallel (Case A), the CASSCF optimized geometries will be in general correct, despite they have been computed at a lower level of theory. It means that the dynamical correlation contributions are quite regular and similar for the two states in ample regions of the PEH. In these situations, two-step



■ Fig. 14-19

CASPT2 low-lying singlet states along the MEP from the FC region on the  $1(\pi\pi^* HL)$  state in guanine (top) and seam of CIs (bottom) computed from the MECI structure (bottom, right) to the CI close to the end of the MEP (bottom, left)

computational strategies like CASPT2//CASSCF can be confidently applied. When dynamical correlation is markedly different for the states considered and varies significantly along the PEH of interest, geometry optimization has to be carried out at the highest correlated level (Case B). Otherwise, the uneven contributions of dynamical correlation may lead to unphysical crossings and interactions between the two electronic states. The crossing can be then placed at a different geometry or it may never occur! Normally, states of ionic (in the valence-bound sense) nature have larger amounts of dynamical correlation in contrast to covalent states, in which the static correlation is able to recover large fractions of the total correlation energy. When both types of states are involved in a crossing, it is clear that a CASSCF description will give an unbalanced picture of the hypersurfaces and, obviously, of the crossing, which can be recovered only by inclusion of the dynamical correlation, with CASPT2 for instance, even in the searching of states crossing. In difficult cases, it can be convenient to map a grid of CASPT2 points in the region of the CASSCF CI to find the degeneracy at the highest level, or, if possible, to compute the CI with CASPT2, more specifically, with MS-CASPT2, considering that CASPT2 provides



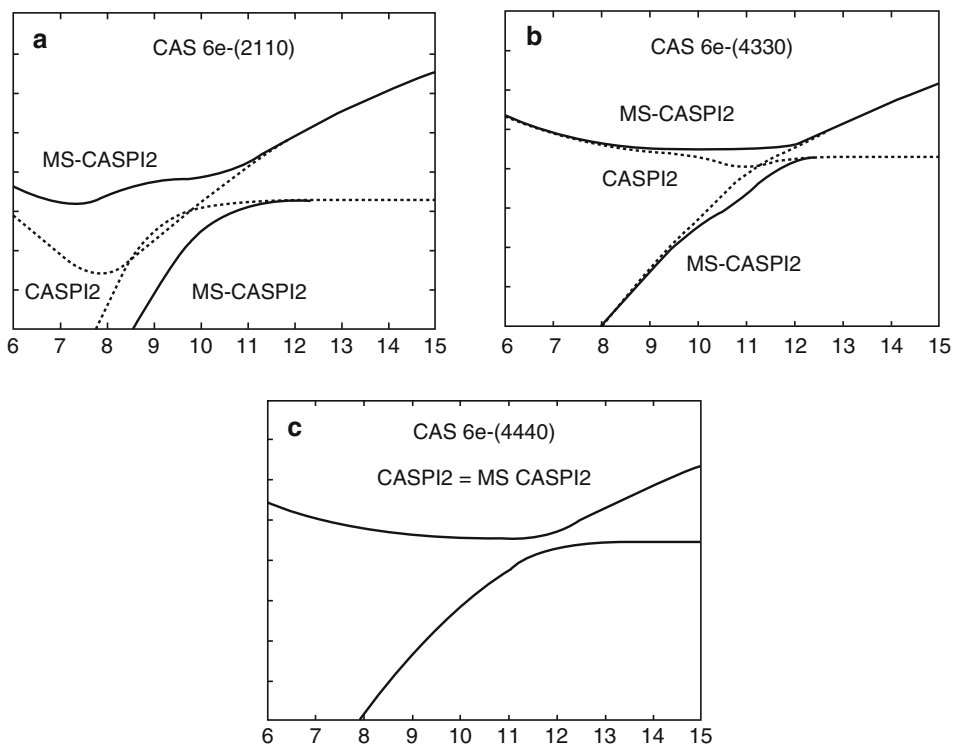
■ Fig. 14-20  
Different effects of correlation within the CASPT2//CASSCF protocol

non-orthogonal and therefore mixed solutions. This is a tricky issue that was studied recently and requires careful consideration.

► *Figure 14-21* displays the result of CASPT2/MS-CASPT2/ANO-L Li [4s2p]/F [4s3p1d] calculations on the lowest-lying  $^1\Sigma^+$  states of the LiF molecule along its dissociation path (see Serrano-Andrés and Merchán 2005). The lowest state has ionic and covalent character at short and long distances, respectively, because the lowest dissociation channel leads to the ground states of the neutral atoms, whereas the opposite occurs for the second state. At intermediate distances, the lowest ionic and next covalent states interact and change their character smoothly thanks to the multiconfigurational treatment. According to the non-crossing rule for states of the same spin and spatial symmetry that holds true for diatomic molecules, the two curves cannot become degenerate and instead an avoided crossing should take place. In the sample calculations, the results of three different active spaces and two levels of calculation, CASPT2 and MS-CASPT2, have been displayed. In cases A and B, the CASPT2 curves (dotted lines) incorrectly cross or touch. The reason is that in a single-state perturbation theory each root is not orthogonal to the others.

Neglecting the state interaction leads to unphysical crossing situations. On the contrary, the multistate treatment of MS-CASPT2 (solid lines) makes the two states to interact. The corresponding orthogonal solutions display therefore a “correct” avoided crossing. In case A the employed AS is the minimal one (one 2s orbital from Li and three 2p orbitals from F). Although the MS-CASPT2 solution yields a formally correct avoided crossing, the state interaction is overestimated, giving rise to a large energy splitting at too short distances (as compared to higher-level MS-CASPT2 or MRCI calculations) because of the too large value of the off-diagonal elements in the multistate effective Hamiltonian. A better treatment is obtained for enlarged active spaces in B and, especially, C, in which the increased space allows for angular correlation in the AS and the CASPT2 and MS-CASPT2 solutions match, undoubtedly because the initial CASPT2 states were including most of the interaction effects. Unfortunately in most cases the enlargement of the active space will not be possible. A good strategy is testing different spaces to check the stability of the results. The right solution seems to be between the CASPT2 and the MS-CASPT2 ones. In the worst case, the CASPT2 result is generally not so bad after all.





■ Fig. 14-21

CASPT2 (dotted lines) and MS-CASPT2 (solid lines) calculations on the lowest-lying  $1\Sigma^+$  states of the LiF molecule

► **Table 14-5** compiles the results of CASPT2 and MS-CASPT2 calculations on the two lowest singlet states of the  $C_{2h}$  ethylene dimer using a cc-pVDZ basis set computed at the MECP point upon the increase of the AS (see Serrano-Andrés and Merchán 2005). In order to provide a proper multistate treatment, the off-diagonal elements of the effective Hamiltonian have to be small and similar, otherwise the matrix symmetrization will be erroneous, whereas the energy split undergone by the original states once diagonalized the matrix will be excessive. Indeed, although the CASPT2 energy differences between the states remained always small ( $<3.35$  kcal mol $^{-1}$ ), the splitting largely increases at the MS-CASPT2 level, especially when the off-diagonal elements  $H_{12}$  and  $H_{21}$  most differ. It is only with the largest active space (angular  $\sigma - \pi$  correlation has been included in the active space in this case, 4,242) that the elements become smaller and the MS-CASPT2 reduces. Values close to 2 kcal mol $^{-1}$  can be considered small enough to identify such feature as a CI point within the accuracy of the method. What happens when a CI search is performed blindly using MS-CASPT2 solutions? Typically, it occurs that the obtained solutions are too separated and, apparently, the closest-energy solutions correspond to an avoided crossing. This is probably a wrong answer derived from that fact that the active space is too small and the MS-CASPT2 method is overshooting the interaction of the CASPT2 solutions. If it is not possible to increase the AS (maybe MS-RASPT2 is a solution), it is better trusting in the CASPT2 energies.

■ Table 14-5

Computed MS-CASPT2 energies and off-diagonal Hamiltonian matrix elements for the MECP point of the  $1^1A_g/2^1A_g$  states in the  $C_{2h}$  ethylene dimer<sup>a</sup>

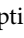
Active spaces	$\Delta E_{\text{CASPT2}}$ (kcal mol <sup>-1</sup> )	$-H_{12}$ (kcal mol <sup>-1</sup> )	$-H_{21}$ (kcal mol <sup>-1</sup> )	$-(H_{12} + H_{21})$ (kcal mol <sup>-1</sup> )	$\Delta E_{\text{MS-CASPT2}}$ (kcal mol <sup>-1</sup> )
2,020, 4e <sup>-</sup>	0.41	1.96	2.44	2.20	4.42
3,030, 4e <sup>-</sup>	2.08	2.09	2.89	2.49	5.40
4,040, 4e <sup>-</sup>	3.35	2.60	5.12	3.86	8.41
4,040, 8e <sup>-</sup>	2.76	2.51	5.48	4.00	8.46
4,242, 12e <sup>-</sup>	2.13	1.27	0.03	0.65	2.49

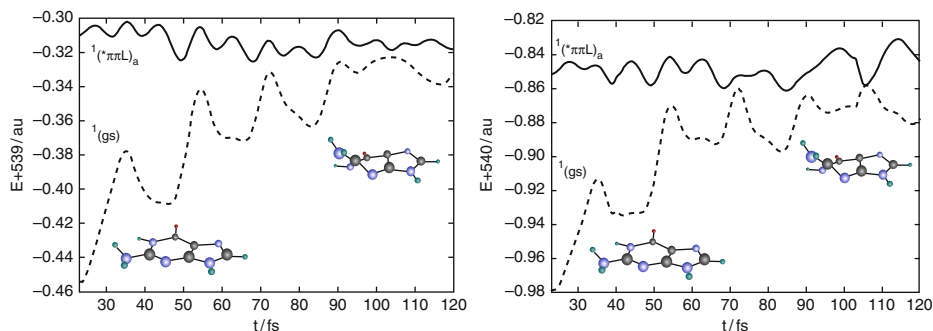
<sup>a</sup>The MS-CASPT2 calculations comprise two roots at the CASPT2(2,020, 4e<sup>-</sup>) optimized  $1^1A_g/2^1A_g$  MECP geometry

### Setting the Path for Dynamics

Mapping the PEHs of the molecular systems is not but the initial stage of the calculations. Once the topography of the hypersurfaces is obtained by solving the time-independent Schrödinger equation, the evolution of the nuclei on that potential must be described. Studying the reaction dynamics (RD) of the system implies considering time dependence and the statistical distribution on a sample of molecules. Several procedures can be followed, from the most expensive approach, solving the time-dependent Schrödinger equation, typically along specific reaction coordinates, to the semiclassical approaches, in which quantum-chemical information is used to solve the classical Newton equations. When properly averaged, the obtained data yield, in principle, predictive data for reaction rates, state lifetimes, and population distribution. We will not discuss dynamical calculations here, but will simply try to emphasize that the quality of a RD calculation, no matter how sophisticated, strongly relies on the quality of the underlying quantum-chemical description of the PEHs.

In other words, the dynamics is always as good as the quantum chemistry employed to describe the PEH. Expensive RD calculations tend to use analytical potentials fitted with quantum-chemical parameters, a technique filled with problems. The other approach is known as direct or “on the fly” reaction dynamics, meaning that the quantum-chemical information is obtained at each of the points of a trajectory and passed to the RD step. The basic difficulty stays: how good is the description of the PEHs and how this affects to the RD results?

In the study of thymine described above, it was found that when using lower levels of calculation, for instance, a 6-31G\* basis set or a small active space, the CASSCF MEPs run in wrong regions of the PEHs, something that only occurred in thymine and uracil, not in purine bases. The MEP FC  $^1(\pi\pi^*)$  leads in this case to the high-energy planar minimum and not to the low-lying CI with the ground state, an outcome obtained only when increasing the quality of the calculation by using ANO-type basis sets, larger active spaces or CASPT2 gradients. It is obvious that the RD description will be strongly affected by the quality of the underlying quantum-chemical description. As an illustration,  Fig. 14-22 includes two sample trajectories computed in the guanine molecule on the lowest-energy  $^1(\pi\pi^*)$  state starting near the FC region. The calculations used a Verlet-type algorithm for the classical part (which gives the solution of the equations of motion, i.e., how position, velocity, and acceleration change over time) and CASSCF(12,10) or CASPT2(12,10)/6-31G(d,p) quantum-chemical energies and gradients computed “on the fly” at intervals of 5 fs. In this preliminary study, most of the computed trajectories starting close to the FC region were shown to follow a similar path than the MEP,



■ Fig. 14-22

Sample CASSCF (*left*) and CASPT2 (*right*) semiclassical trajectories run on the lowest-energy  $^1(\pi\pi L^*)$  state of guanine from the FC region

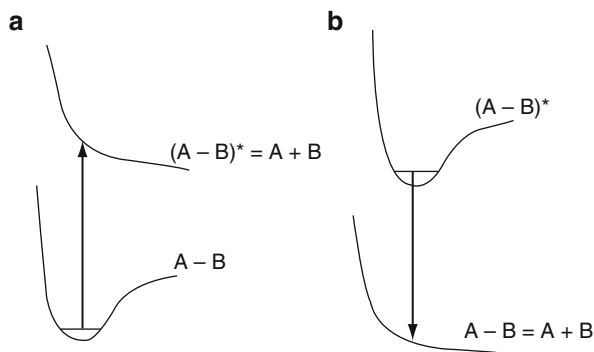
that is, leading to the region of CI with the ground state, and this is done in times close to 100 fs, explaining the ultrafast lifetime measured for the molecule in molecular beams (see Serrano-Andrés et al. 2008). From that point, the complications continue with the selection of the surface hopping algorithm for the population transfer, the diabatic description of the crossing regions, the re-evaluation of the reaction step, etc. (see, just as one of the many examples the use of the NEWTON-X reaction dynamics approach (Barbatti et al. 2007)).

## Photoinduced Reactions in Bimolecular Systems

The theoretical description of photoinduced bimolecular reactions requires specific strategies and procedures that will be illustrated here with two examples. First, the cytosine dimer, which forms an excimer in the ground state and it is also able to react yielding a photoadduct in the ground state. Second, the energy transfer reaction between psoralen and molecular oxygen, in which the lowest-energy triplet states are the protagonists.

### An Application Example of Reactivity: Cytosine Dimer

One intriguing aspect of UV-irradiated DNA is the appearance of red-shifted long-lived emissive states not found in base monomers, whereas the DNA absorption spectra closely resemble that of the monomers. This phenomenon is called excimer fluorescence, reflecting the relevant role assumed to be played by the corresponding excited dimer (excimer) of the biopolymer, given the similarity between the emission from dinucleotides and polynucleotides (Eisinger and Shulman 1968). Recent experimental results in the light of time- and wavelength-resolved fluorescent techniques using 80 picoseconds (ps) excitation pulses make readily apparent the longer-decay components and red-shifted emission that it was assumed to arise from excimer formation. Because of the slow rate of energy relaxation, these long-lived states associated to excimer-like states have been suggested as the precursors of the DNA photolesions, including photodimers (Schreier et al. 2007).



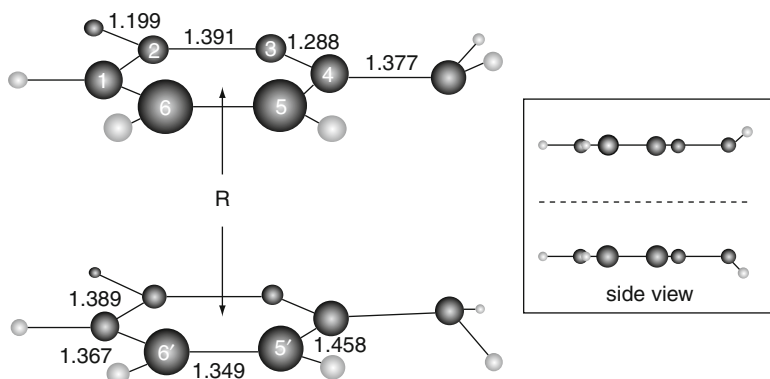
■ Fig. 14-23

(a) The nonexcited molecule (or a set of molecules; notice that A and B can be both atoms or molecules) is in a bound state; once excited, the molecules evolve to a dissociative state. (b) An excimer is a combination of atoms (or molecules) such that it is bound only in the excited state, and then it dissociates as soon as the system relaxes

Classically, an excimer (homodimer) or exciplex (heterodimer) is defined as a dimer system which is bound in the excited state and dissociative in the ground state (see [Fig. 14-23](#)). The existence of excimers between DNA nucleobases was proven theoretically by means of CASPT2(12,12)/ANO-S C,N,O [3s2p1d]/H [2s1p] calculations (see Olaso-González et al. 2006). Potential energy curves (PECs) with respect to the intermolecular separation ( $R$ ) of two cytosine molecule kept at the ground-state geometries were built (see [Fig. 14-24](#)). The structure allows for an effective and natural interaction of two cytosine molecules in the biologically relevant *cis-syn* stereoisomer. The ground-state PEC is repulsive at the CASSCF level, whereas the lowest singlet excited state is weakly bound. In contrast, at the CASPT2 level (see [Fig. 14-25](#)), when dynamic correlation is taken into account, the ground-state  $S_0$  and the three lowest singlet excited states ( $S_1$ ,  $S_2$ , and  $S_3$ ) have well defined minima with binding energies of a few tenths of an eV.

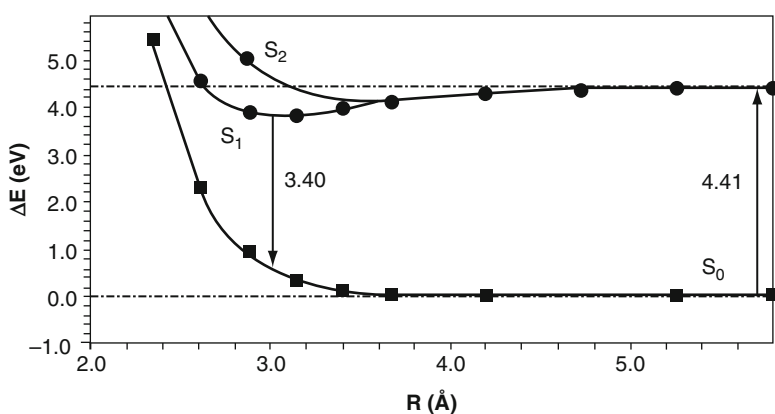
The Basis Set Superposition Error (BSSE) is corrected by means of the counterpoise procedure, an important aspect that will be discussed later. In the figure energies are referred to two ground-state cytosine molecules separated about 20 a.u. In the asymptotic limit,  $S_1$  and  $S_2$  become degenerate, which is consistent with the fact that they are related to the equivalent situations  $C+C^*$  and  $C^*+C$ , where C and  $C^*$  stand for the ground-state cytosine and its lowest singlet excited state, respectively. The absorption  $S_0 \rightarrow S_1$  calculated at 20 a.u. (4.41 eV) corresponds to the monomer absorption. On the other hand, the vertical emission from the minimum of  $S_1$  is calculated at 3.40 eV, and it can be considered the source of emission observed in DNA or oligomer samples. In particular, the fluorescence maximum was reported in aqueous solution for the dimer  $d(C)_2$  and the 15-mer  $d(C)_{15}$  at 3.22 eV, considerably red-shifted as compared to that of the monomer (3.96 eV).

Since that theoretical determination, the existence of excimers in DNA and their role as precursors for phenomena like the red-shifted DNA emission, charge transports in the DNA strand, the formation of nucleobase photoadducts, and, in general, the control of the decay dynamics of excited DNA has been determined both theoretically and experimentally. Crespo-Hernández et al. (2004), for instance, have shown by using femtosecond transient absorption



■ Fig. 14-24

Labeling for the cytosine dimer. Bond distances (in Å) correspond to the ground-state equilibrium geometry of the monomer. The homodimer system displays  $C_5$  symmetry, being the mirror symmetry plane represented by a *dashed line* in the side-view inset

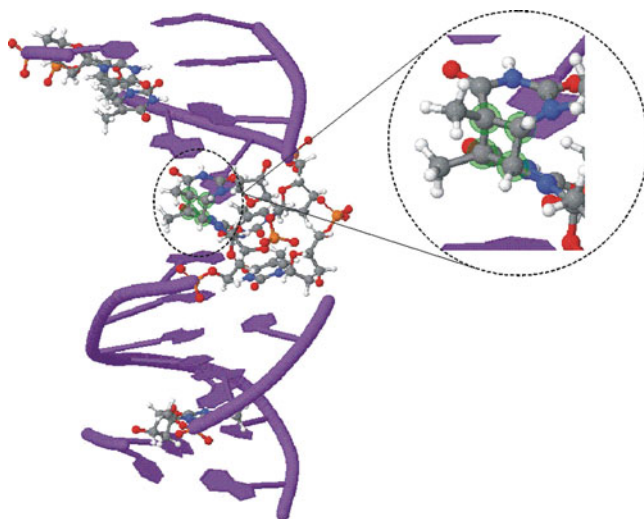


■ Fig. 14-25

BSSE-corrected CASPT2 (12,12) potential energy curves built with respect to the distance cytosine-cytosine arranged in a face-to-face disposition

spectroscopy that excimers are formed in high yields in a variety of synthetic DNA oligonucleotides and conclude that excited-state dynamics of A·T DNA is controlled by base stacking. CASPT2 calculations explained also the dynamics of the adenine dimer by the presence of the excimers.

As an illustration of bimolecular reactions, the formation of pyrimidine nucleobase adducts in the excited state will be presented here (see Roca-Sanjuán et al. 2008b; Serrano-Pérez et al. 2008d). Among the possible photoreactions that pyrimidine (Pyr) bases of nucleic acids may undergo upon ultraviolet (UV) irradiation, cyclobutane thymine dimers (T<>T or CBT) formed by intrastrand adjacent thymine bases (see ► Fig. 14-26) constitute one of the major photoinduced lesions, particularly in cellular DNA, in spite of the direct repairment by a light-activated mechanism (DNA photolyase) in which abnormal bonds are cleaved. Unrepaired or



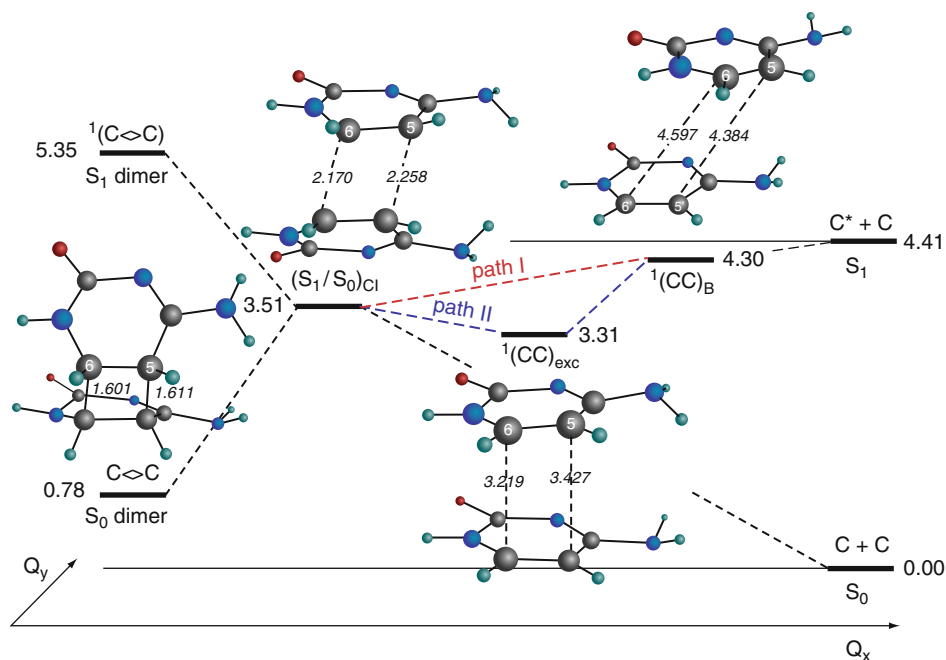
■ Fig. 14-26

Photocycloaddition between two adjacent molecules of thymine is a particular class of pericyclic [2+2] reaction allowed photochemically and not thermally. It is one of the most usual lesion on DNA. In this picture, taken from a structure obtained in the Protein Data Bank and visualized by Jmol program, the cyclobutane ring is highlighted

misrepaired thymine or cytosine dimers and the resultant mutations may well lead to the development of skin cancer. The major of Pyr<>Pyr photoproducts. The relatively smaller degree of flexibility of A-DNA compared to B-DNA to achieve the right orientations that become prone to react has been related to the greater resistance of A-DNA to Pyr<>Pyr formation.

Dimerization seems to occur only for thymine residues that are already in a reactive arrangement at the instant of excitation because the rate of formation by favorably oriented thymine pairs is much faster than the rate of orientation change. The dimerization reaction occurs both in the singlet and triplet manifolds (see Bosca et al. 2006; Cadet et al. 1992). Focusing on the singlet states, a CI must drive the ultrafast formation of the cycloadduct. Figure 14-27 displays an scheme of the energy levels of the cytosine dimer in its lowest-lying singlet states based on CASPT2(12,12)/ANO-S C,N,O[3s2p1d]/H[2s1p] results (BSSE corrected). The lines connecting the different solutions represent the different evolution paths followed by the system.

Initially, upon absorption of UV-light radiation in the 4.4 eV region, the system can undergo two types of processes. Nearly unstacked pairs will localize its excitation in one of the monomers and evolve in a ultrafast way toward the ground state via the CI of the monomer, located at 3.6 eV. Other pairs will form an excimer through the stacking interaction of the  $\pi$  clouds of the nucleobases, displaying much larger lifetimes, as it has been already determined experimentally. The binding interaction in the excimer will depend on the conformational arrangement of the nucleobase pair. Whereas the most common DNA confirmation, B-DNA, displays a very small interaction, strongly overlap situations like the face-to-face parallel arrangement yields the largest binding energy. The cytosine dimer has an excimer structure even lower than the CI leading the system to the formation of the ground state photoadduct CBT. This peculiarity and the presence of both  $S_0/S_1$  CIs, that of the monomer and the one related to CBT, almost



■ Fig. 14-27

Scheme based on CASPT2 calculations of the dimerization photochemistry of the cytosine dimer after UV-light absorption


isoenergetic and therefore competitive, makes the yield of formation of CBT adducts much smaller than in the case of the thymine dimer, where the CI of the adduct is the lowest and easily accessible feature.

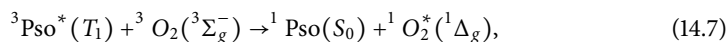
### An Application Example of Energy Transfer: Psoralen + O<sub>2</sub>

Photomedicine applies the principles of photobiology, photochemistry, and photophysics to the diagnosis and therapy of diseases. One of the most active research areas in this field is photodynamic therapy (PDT), in which the affected living tissue is treated with a combination of a photosensitizer, activated by UV light, and molecular oxygen in its ground triplet state,  $^3\Sigma_g^-$ . Oxygen is present in the cellular environment ready to transform into singlet oxygen  $^1O_2$  ( $^1\Delta_g$ ), which is a strong electrophilic species that reacts with different compounds including some components of the cellular membrane causing cell death by apoptosis. An energy transfer (ET) process triggered by electronic coupling between a molecule in an excited state, the donor (D\*), and a molecule, the acceptor (A) or quencher within a collision complex, is the mechanism through what the reaction takes place, a process that strongly depends on the inter-fragment distance. In general, ET processes, at large separation between the moieties (20–30 Å or even larger), the electronic coupling arises from the Coulomb interaction between electronic transitions that, under the dipole approximation, reduces to the known Förster's

dipole–dipole coupling. The process is actually a nonradiative transfer of energy occurring whenever the emission spectrum of D overlaps with the absorption spectrum of A (although no intermediate photon takes part on it). It is the electric field around  $D^*$ , behaving like a field generated by a classical oscillating dipole, the cause of the excitation of A. At larger separations than Förster's, fluorescence resonance ET (with photon emission by  $D^*$  and subsequent absorption by A) becomes more efficient than excitation ET. At shorter interfragment distances, however, the so-called Dexter exchange coupling predominates, arising from the exchange integrals that account for the indistinguishability of the electrons in many-electron wave functions. This factor decreases steeply with separation. If the interaction is assumed weak and overlap between  $D^*$  and A wave functions is produced, Fermi's Golden Rule for coupled transitions can be applied. Such processes have been studied theoretically in depth in recent years, in particular for singlet–singlet ET processes implying an exchange of electrons of the same spin but different energies, that is, the spin state of each fragment is conserved. In PDT, the actual mechanism is, on the other hand, an intermolecular triplet–triplet energy transfer (TET), that is, a process of exchanging both spin and energy between a pair or molecules or molecular fragments. These reactions are commonly used to efficiently populate the triplet states of many organic molecules.

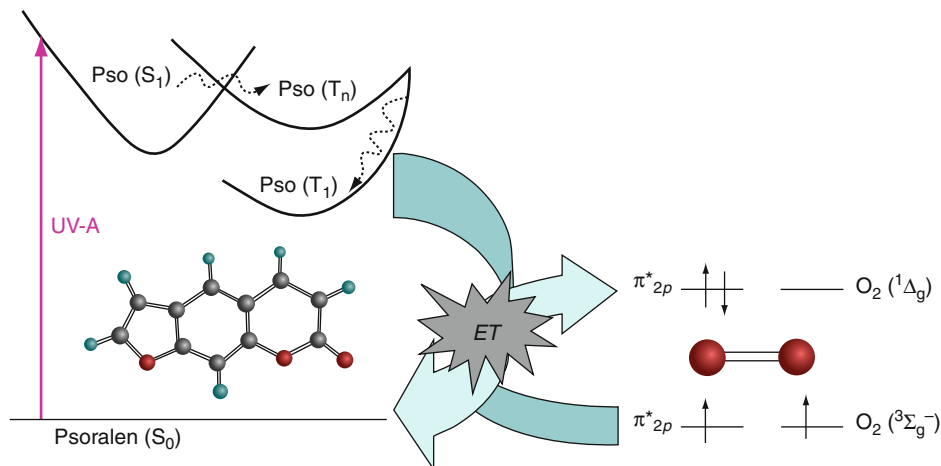
TET processes can be therefore understood as two simultaneous ETs with spin exchange between the interacting fragments and it is similar to the Dexter coupling for singlet–singlet ET, in particular because, as it depends on an electron exchange mechanism, it only takes place at short donor–acceptor distances ( $<10 \text{ \AA}$ ). In TET the Förster's mechanism will not contribute, because at short distances the dipole approximation breaks down and because the transitions are dipole forbidden. The electronic coupling is not the only key factor that determines the efficiency of the ET process, but also the resonance condition, that is, the energy available in the donor must be at least equal or higher than that required to populate the excited state of the acceptor. If this is the case, the process is usually controlled by diffusion and described as exothermic. In the opposite situation, that is, if the energy of the acceptor is lower than that of the donor, the process becomes thermally activated and lies in the endothermic region. That means that there is an energy barrier whose height will depend on the nature of the acceptor, either classical (for rigid systems) or nonclassical (flexible systems which might find conformations for efficient, non-vertical TET), with a corresponding larger or smaller, respectively, decay in the process rate.

Besides the reaction with DNA nucleobases, psoralen can also interact with molecular oxygen to exert its photosensitizing action. Singlet oxygen and other reactive species of oxygen induce photooxidation of lipids and are considered responsible for cell membrane damaging effects, causing also the appearance of erythema and pigmentation activity in the human skin. In particular, the TET process taking place between psoralen and molecular oxygen is (see also  Fig. 14-28):

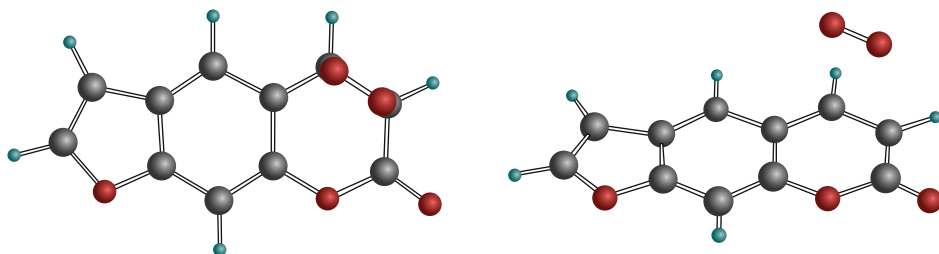


where activated psoralen behaves as a donor in its lowest triplet state, and triplet ground-state oxygen is the acceptor. The lowest excited singlet state of molecular oxygen ( ${}^1\Delta_g$ ) is located at 0.97 eV. Furocoumarins (psoralen, 8-MOP, 5-MOP, khellin, TMP, and 3-CPS) have their lowest-lying triplet  $T_1$  state energy at least 1.4 eV higher than the oxygen singlet state, what makes the TET exothermic and diffusion-controlled, with molecular oxygen behaving as a rigid, classical acceptor.





■ Fig. 14-28  
Scheme of the oxygen-dependent PUVA mechanism



■ Fig. 14-29  
Psoralen- $\text{O}_2$  supermolecule. The molecular oxygen was placed parallel to the reactive pyrone double bond of psoralen

A recent study (see Serrano-Pérez et al. 2009) performed employing the CASPT2/ANO-LC,O[4s3p1d]/H[2s1p] methodology estimated the electronic coupling at some specific disposition of the moieties (psoralen and  $\text{O}_2$ ). Looking for an appropriate arrangement yielding the most effective TET process is nontrivial and, in general, not even relevant, in particular in diffusion-controlled systems which may form a collision complex at short distances. It is important, however, to estimate reaction rates and lifetimes at different intermolecular distances. Furthermore,  $\text{M-O}_2$  interaction potentials are very weak, and the potential surfaces are generally characterized by multiple shallow minima. Hence, it is necessary to consider different orientations when approaching  $\text{M}$  and  $\text{O}_2$  through a basic interfragment coordinate, here the distance  $R$ . Previous studies on systems composed by two ethylene molecules ( $\text{Et-Et}$ ), by the methaniminium cation and ethylene ( $\text{MetN}^+-\text{Et}$ ), and by ethylene and molecular oxygen ( $\text{Et-O}_2$ ), show that the face-to-face (FF) arrangement is the most appropriate orientation (see ► Fig. 14-29).

The geometries of both psoralen and molecular oxygen were kept fixed at the CASSCF optimized triplet excited ( $\text{T}_1$ ) state structure and the triplet ground ( $^3\Sigma_g^-$ ) state experimental

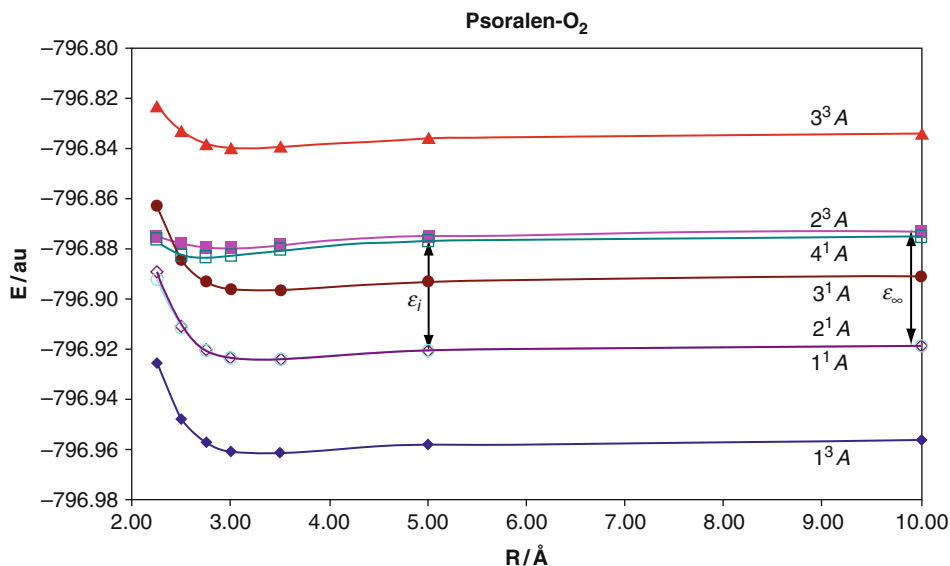


Fig. 14-30

Potential energy curves of the low-lying excited states of the supermolecule psoralen-molecular oxygen along the interfragment distance ( $R$ ). The energy coupling  $H'$  is obtained as half of the energy difference  $|\varepsilon_\infty - \varepsilon_i|$  between the initial  $4^1A$  ( $T_1$  of psoralen and  ${}^3\Sigma_g^-$  of  $O_2$ ) and final  $1^1A$  ( $S_0$  of psoralen and  ${}^1\Delta_g$  of  $O_2$ ) states of the supermolecule at infinite distance ( $\varepsilon_\infty$ , zero coupling situation) and at each of the distances ( $\varepsilon_i$ )

geometry, respectively. The active space employed was 14 electrons/11 orbitals (8/7 located in the furocoumarin and 6/4 located in  $O_2$ ). The active space was validated after comparing the results with previous findings in the isolated psoralen and control calculations on the oxygen molecule with larger active spaces and basis sets. The four lowest singlet states and the three lowest triplet states of the supermolecule were computed. The molecule behaves as a donor in its triplet state, and it is capable to transfer its energy to molecular oxygen in its triplet ground state to generate the singlet ground state furocoumarin and excited singlet oxygen ( ${}^1\Delta_g$ ). The energy of the triplet state of the furocoumarin is much higher than the energy of the oxygen  ${}^1\Delta_g$  state (computed 1.09 eV, experimental 0.97 eV), and the process falls clearly into the exothermic regime, expected to be controlled by diffusion. **Figure 14-30** displays the potential energy curves of the lowest-lying singlet and triplet states of the supermolecule psoralen- $O_2$  in a FF arrangement with respect to the  $C_3=C_4$  bond of the pyrone ring (the reactive bond in the triplet state, where the spin density is basically located at different intermolecular distances). The states of the supermolecule protagonist of the TET are  $4^1A$  ( $T_1$  of psoralen +  ${}^3\Sigma_g^-$  of  $O_2$ ), as initial energy level, and  $1^1A$  ( $S_0$  of psoralen +  ${}^1\Delta_g$  of  $O_2$ ), as the final outcome of the process in which both moieties have changed spin and energy. Within the present approach, the electronic coupling ( $H'$ ) is obtained as half the difference  $|\varepsilon_\infty - \varepsilon_i|$ , where  $\varepsilon_\infty$  and  $\varepsilon_i$  are the energy gaps between the states  $4^1A$  and  $1^1A$  at infinite distance (at 10 Å in the current computation) and at the different interfragment distances, respectively. In this way, the coupling represents the perturbation introduced in each state due to the interaction within the dimer. It is important

to notice how advantageous that definition is, because the results are in practice independent of the number of states considered. Notice that the BSSE problem does not affect the results of the coupling, which uses energy differences between states computed at the same geometry. As a result, the BSSE correction vanishes when the energy gap is computed. In other cases, known as non-vertical TET systems, the geometry of the acceptor can be distorted to better accept the photosensitization from the donor. In such situations, the search for regions of state degeneracy with enhanced effectiveness for the ET transfer may be convenient. This is not the case for the present example, in which the acceptor is a rigid oxygen molecule and the process is basically diffusion controlled.

► **Table 14-6** compiles the values of the electronic coupling computed at the different inter-nuclear distances, related with the ET rates and lifetimes. In the weak coupling regime in which the electronic interaction is smaller than the vibrational reorganization energy, the rate for triplet–triplet energy transfer ( $k_{\text{TET}}$ ), and the corresponding lifetime ( $\tau_{\text{TET}}$ ), between the donor and the acceptor can be estimated using Fermi's Golden Rule:

$$k_{\text{TET}} = \frac{1}{\tau_{\text{TET}}} = \frac{4\pi^2}{h} |\langle \psi_i | \hat{H} | \psi_j \rangle|^2 \rho_E = \frac{4\pi^2}{h} (H')^2 \rho_E, \quad (14.8)$$

where the matrix element of the Hamiltonian,  $H'$ , is the electronic part of the energy transfer (i.e., the electronic coupling) and  $\rho_E$  is the density of vibrational states in the initial and final states and their spectral overlap. The inverse of the rate is the lifetime of energy transfer. To obtain the TET rates, we have taken values of  $\rho_E = 200 \text{ eV}^{-1}$  and  $(4\pi^2/h) = 9.554 \times 10^{15} \text{ eV}^{-1} \text{ s}^{-1}$ . This order of magnitude for the value of the density of states was used previously as a good estimation in systems of this size.

The whole process of generation of singlet oxygen from psoralen does not only depend on the efficiency of the TET from the triplet state of the photosensitizer, but also on the rate of formation of the triplet state itself. As shown previously, in psoralen the crucial step to populate the triplet manifold in the gas phase is the intersystem crossing (ISC) process between the initially populated singlet  $S_\pi$  ( $\pi\pi^*$ ) state and the lowest-lying triplet  $T_n$  ( $n\pi^*$ ) state. The latter state evolves subsequently toward the lowest triplet  $T_1$  ( $\pi\pi^*$ ) state via a corresponding (and essentially barrierless and ultrafast) internal conversion (IC).

In a similar manner as for ► **Eq. 14.8**, the estimation of the rate constant, here for nonradiative ISC ( $k_{\text{ISC}}$ ), can be obtained as:

$$k_{\text{ISC}} = \frac{4\pi^2}{h} |H_{\text{SO}}|^2 \rho_E, \quad (14.9)$$

■ **Table 14-6**

ET analysis of Psoralen-O<sub>2</sub> system along the distance between the two moieties

R/Å	H' /eV	$k_{\text{TET}}/\text{s}^{-1}$	$\tau_{\text{TET}}/\text{s}$
10.00	0.0000	–	–
5.00	0.0012	$1.43 \times 10^9$	$6.98 \times 10^{-10}$
3.50	0.0038	$1.41 \times 10^{10}$	$7.10 \times 10^{-11}$
3.00	0.0357	$1.21 \times 10^{12}$	$8.23 \times 10^{-13}$
2.75	0.0870	$7.23 \times 10^{12}$	$1.38 \times 10^{-13}$
2.50	0.1966	$3.69 \times 10^{13}$	$2.71 \times 10^{-14}$
2.25	0.3833	$1.40 \times 10^{14}$	$7.13 \times 10^{-15}$

where  $H_{SO}$  stands for the spin-orbit coupling terms for the nonradiative transition  $S_\pi (\pi\pi^*) \rightarrow T_n (n\pi^*)$ . An estimated value of  $200 \text{ eV}^{-1}$  will be employed for  $\rho_E$  as used for psoralen in studies explicitly computing vibronic factors.

The ISC nonradiative process corresponds to the transfer  $S_\pi (\pi\pi^*) \rightarrow T_n (n\pi^*)$  in each furocoumarin donor, a process which will take place more efficiently in the region of the  $(S_\pi/T_n)_{STC}$  singlet-triplet crossing, and that subsequently will give rise to an ultrafast population of the lowest  $T_\pi (\pi\pi^*)$  by internal conversion in the triplet manifold. The spin-orbit coupling factors near the crossing point between  $S_\pi$  and  $T_n$ , along the LIIC performed in a previous study, is  $9.2 \text{ cm}^{-1}$  (see [Fig. 14-17](#)). As a result, the  $k_{ISC}$  rate computed was  $3.58 \times 10^9 \text{ s}^{-1}$ . Additionally, to the  $H_{SO}$  strength, the presence of energy barriers in the potential energy hypersurfaces may strongly affect the value of the rate constants, which can be corrected using the Arrhenius exponential term in the framework of the transition state theory. As a qualitative estimation of these effects, a corrected ISC rate ( $k'_{ISC}$ ) can be obtained from:

$$k'_{ISC} = k_{ISC} e^{-\Delta E/RT}, \quad (14.10)$$

where  $k_{ISC}$  is that computed from [Eq. 14.9](#),  $\Delta E$  is the energy of the barrier from the initial electronic singlet to the triplet state,  $R$  is the ideal gas constant, and  $T$  the temperature (298 K). In this particular context,  $\Delta E$  will be estimated as the energy difference between the singlet  $S_\pi (\pi\pi^*)$  state, populated at the Franck–Condon geometry, and the triplet  $T_n (n\pi^*)$  state in the computed crossing point with the singlet state  $(S_\pi/T_n)_X$ , considering that the energy obtained initially to populate  $S_\pi$  will be available, at least, to surmount the barrier and populate  $T_n$ .

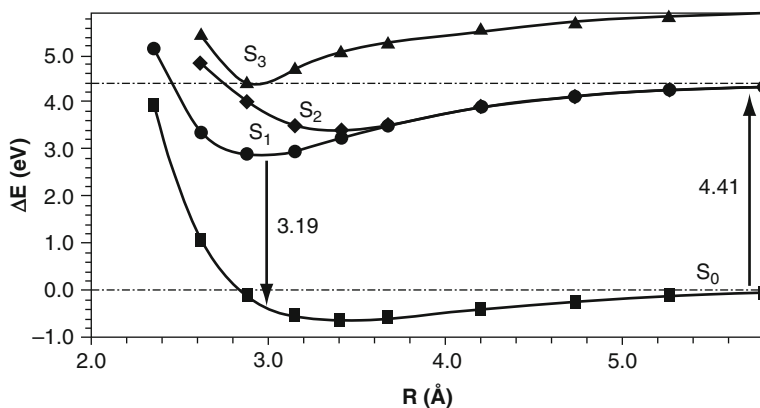
In a previous section, we considered as a barrier the energy difference between the minimum of the  $S_\pi$  state and the crossing point  $(S_\pi/T_n)_X$ , which is 0.36 eV, but the present approach accounts for the excess vibrational energy available in the system from the initially populated  $S_\pi$  state (at the Franck–Condon geometry) to the crossing point (0.03 eV), which seems to be more relevant in this context, where the interest focuses on rate constants. The results were  $1.11 \times 10^9 \text{ s}^{-1}$  and 0.90 ns for  $k'_{ISC}$  and  $\tau'_{ISC}$ , respectively.

Within this methodology, we can compute the photosensitizing effectiveness, regarding the generation of singlet oxygen, of other furocoumarins and other photosensitizers in general, analyzing the effectiveness of populating  $T_\pi$  as well. Since molecules (donors) that share the same basic structure are known to possess almost the same electronic coupling (against a common acceptor), the first part of this study may well be more interesting if different families of compounds are compared. On the contrary, we should rely on the different way to populate the lowest-lying triplet excited state. In studies performed on the family of furocoumarins (psoralen, 8-MOP, 5-MOP, khellin, TMP, and 3-CPS), the latter, 3-carbethoxypsoralen, was found with the largest ISC rate.

## Practical Aspects

### The Basis Set Superposition Error (BSSE) for Excited States

The use of finite basis sets derives in a specific defect of the quantum-chemical calculation known as the Basis Set Superposition Error (BSSE). The majority of the contribution to the energy of a system comes from the internal electrons. If the basis set of an atom is deficient in the core region, a molecular method recovers a large amount of energy correcting this deficient area with the basis set of the other atoms. The BSSE is therefore related with the improper inclusion of the correlation energy in a quantum-chemical calculation. Although present in all



■ Fig. 14-31

CASPT2 (12,12) potential energy curves built with respect the distance cytosine–cytosine arranged in a face-to-face way without the inclusion of the CP correction for BSSE

practical cases, as BSSE strongly depends on the separation between the different centers, its effects only become crucial in dimers and aggregates, that is, when energies at large internuclear distances are compared to those at short distances. In general, the result of ignoring BSSE is both a shortening of bond lengths and an increasing of bond energies because the net effect is an increase of the energy in absolute value. This error is a purely mathematical artifact owing to the fact that the supermolecule possesses a larger basis set than the isolated monomers and as a result the potential energy surface is altered. There are some methods to correct this error like the counterpoise (CP) or the Chemical Hamiltonian Approach (CHA) procedures.

In the previous study on the formation of the excimer of the cytosine dimer, the correction of the BSSE effect was necessary. Figure 14-31 displays the same PECs as in Fig. 14-25, but excluding the BSSE correction. All states seem now to be bound, including the ground state, and compared to the BSSE-corrected results, the vertical emission takes place at 3.19 eV instead of 3.40 eV. Table 14-6 collects the numerical results on the system.

The CASPT2 ground-state binding energy in the uncorrected result is substantial, 0.62 eV, but the system becomes unbound by  $-0.15$  eV when the BSSE is included, that is, the ground state dimer at  $3.416$  Å is 0.15 eV above the sum of two ground-state monomers. The CP-BSSE corrections seem to be large. With inclusion of the BSSE, both  $S_1$  and  $S_2$  are bound ( $CP - E_b$  is positive). Because of the cancelation of BSSE corrections, the vertical emission remains like the direct CASPT2 result once that the BSSE has been taken into account.

The corrected minimum for  $S_1$  is obtained at  $R = 3.076$  Å, with a vertical emission of 3.40 eV and a binding energy  $CP - E_b$  of 0.58 eV. Thus, our best estimate has a difference of 0.18 eV with respect to the emission maximum datum obtained experimentally. It is worth recalling that the computed vertical transition does not have experimental counterpart, and for a truly correct comparison with experiment, vibrational resolution of the band should be computed in order to determine the band maximum (Table 14-7).

The CP procedure has been followed here to take into account the BSSE, a strategy that is known to slightly overestimate the effect. The method corrects the energy at each geometry by subtracting from the full energy of the supermolecule twice the difference between the energy

■ Table 14-7

**Binding energies ( $E_b$ ), basis set superposition error (BSSE) obtained through the counterpoise method (CP-BSSE), and the corrected binding energy (CP- $E_b$ ), computed at the CASPT2 level**

State	Geometry	R	$E_b$	CP-BSSE	CP- $E_b$
$S_0$	$S_0$	3.416	0.62	0.77	-0.15
$S_1^a$	$S_1$	2.954	1.51	0.97	0.54
$S_0$	$S_1$	2.954	0.29	0.97	-0.68
$S_2$	$S_2$	3.376	0.99	0.74	0.25

<sup>a</sup>The CASPT2 vertical emission (fluorescence), including the CP-BSSE correction leads to 3.19 eV, as the result of (4.41 eV - 0.54 eV - 0.68 eV)

of the fragment using its own basis set and the energy of the fragment using the full basis, but placing the basis functions of the opposite fragment in ghost centers, that is, at the same position as the atoms but with no atoms on them. This subtracted energy is what is known as the BSSE in the CP correction procedure. Obviously the error will decrease when the distance between the fragments decreases, therefore at large internuclear distances the BSSE vanishes. The uncorrected binding energies will then be larger than they should be because they are computed as differences between the energy of the minimum of the supermolecule (with large and stabilizing BSSE effects) and the summed energy of the independent fragments (with no BSSE). The CP method was developed for ground states, and it can be directly extended to excited states only in those cases in which the excitation is clearly localized in one of the fragments. For delocalized situations, it is not possible to define a consistent procedure. As observed in [Table 14-6](#), however, BSSE values are the same for ground and excited states at a common geometry, for instance here, 0.97 eV both for the  $S_0$  and  $S_1$  states at the  $S_1$  geometry. This is a systematic behavior, in particular for methods like CASPT2, in which a previous common set of State-Average MOs has been used for both states. Therefore, it can be concluded that it is safe to assign the same BSSE correction for ground and excited states at the same geometry, considering also that the inter-fragment distance is the most important parameter to modulate the extent of the BSSE. Let's finally add that ANO basis sets, large and flexible, produce larger BSSE effects than lower quality basis sets.

### Computation of Electronic Couplings

The calculation of the electronic coupling matrix element  $H'$  is the crucial part in the determination of ET rates and lifetimes. The extent of the coupling controls the energy transfer process, specifically the passage from one state to another, and it can be taken as a measure of the efficiency of the ET process. Different procedures to estimate the ET coupling have been developed based on diabatic localized dimer calculations, monomer transition densities or transition dipole moments, and a supermolecule ansatz of the dimer, whereas generalization of such approaches to determine TET couplings are also available. From all procedures, an energy gap based method such as the supermolecule dimer approach, in which the value of the coupling is obtained as half of the splitting or perturbation between the interacting states, has been shown to be convenient and accurate, and it will be valid in the weak regime where the interaction is not strong. It is clear that its accuracy strongly relies on the quality of the quantum-chemical method used to perform the electronic structure calculations, something guaranteed by the

highly reliable and accurate CASPT2 method. It has also the additional advantage that their results are not affected by the BSSE because they are obtained as energy differences at the different internuclear distances.

## Conclusions

---

Quantum Mechanics helps in explaining natural phenomena from theoretical physics (particles, strings) and theoretical chemistry (chemical reactions, intermolecular forces) to the most complex theoretical biology. The complexity level increases as the simplicity of models decrease due to the growing number of variables to be dealt with and the difficulty in simulating the environment. The challenge lies in the ascertainment that life takes place into hierarchically structured matter (macromolecules, cells, tissues, organs, and entities), and it requires the action of several physical properties of its constituent elements on the whole: the interactions among them and with the environment.

Interaction of light with tissues or, in general, living or nonliving entities is a complex phenomenon which lies on the borders among physics, chemistry, and biology. Specifically, the quantum chemistry of the excited state has experienced an outstanding development in the last decades. Improved algorithms and computational strategies, and obviously faster computers, have contributed to increasing the accuracy of the theoretical description of the photochemical phenomena. Although quantitative determinations in realistic biological systems are still far into the future, medium-size systems and their processes are already at reach of quantum-chemical models. Even more, state-of-the-art experimental techniques, such those related to femtosecond lasers, cannot be properly interpreted without the support of accurate calculations, in a way that a constructive interplay between theory and experiment shows particularly rewarding.

We are witnesses of how the walls which blocked our understanding of photochemical and photophysical processes are being slowly demolished. Step by step larger systems and more complex processes can be studied with accuracy. In fact, it has been theory which has provided modern photochemistry with the proper framework formed by the potential energy hypersurfaces, their interaction through conical intersections and states coupling, and the molecular evolution along such potentials. Unfortunately there are not many methods able to compute properly excited states, and the available ones are complex and sometimes of limited applicability. Multiconfigurational approaches (MRCI, MRPT, and MRCC) give the most general and unbiased description of all types of excitations and situations, either valence, Rydberg or anionic states, bound and dissociated situations, involving open and closed-shell ground states. Among the available approaches, the CASPT2 method has proved to better balance applicability and accuracy at a relatively low computational cost, although new developments and refinements are soon to come, like RASPT2. Single configurational methods (CC, TDDFT, CIS...) must be used with caution because they do not give a balanced treatment of all situations in excited-state chemistry, for instance, for degenerate cases like conical intersections. Apart from having proper methods, they must be provided with the required tools, like geometry optimizers, algorithms to search for conical intersections, to compute state couplings or trajectories for the nuclei. One-electron basis sets must be also selected with caution. The simultaneous calculation of valence and Rydberg states is necessary in those regions where both types of states are present, and properly solving valence-Rydberg mixing requires specific strategies. The calculation of anionic excited states requires their own cautions, such as checking the convergence of

the resonance solutions by means of different stabilization methods. On the other hand, when dealing with finite one-electron functions and comparing fragment energies with bonded situations, the problem of BSSE arises. In such a situation, the BSSE corrections may well be very important and the phenomenon should be taken into account.

In summary, the excited state quantum chemistry cannot be undertaken routinely because of its complexity. Some of the tools available for the ground state are not even developed yet for the excited state. In order to get accurate and predictive results, one has to calibrate carefully the computational procedure and determine the requirements in each situation. In this manner, an accuracy of 0.2–0.1 eV is currently expected for the excitation energies, almost an order of magnitude larger than previously. Undoubtedly, the development and refinement of quantum-chemical methods (the software) and computers (the hardware) are making easier the study of the interaction radiation-matter, a still unfinished task with fascinating challenges in the foreseeable future.

## Acknowledgments

The authors thank to all the members of the Quantum Chemistry for the Excited State (QCEX-Val) group from the University of Valencia for their valuable contributions and to all their coworkers along the years. Financial support is acknowledged from projects CTQ2007-61260, CTQ2010-14892, and CSD2007-0010 Consolider-Ingenio in Molecular Nanoscience of the Spanish MICINN/FEDER.

## References

- Almlöf, J., & Taylor, P. R. (1986). General contraction of Gaussian basis sets. I. Atomic natural orbitals for first- and second-row atoms. *The Journal of Chemical Physics*, *86*, 4070–4077.
- Almlöf, J., & Taylor, P. R. (1991). Atomic Natural Orbital (ANO) basis sets for quantum chemical calculations. *Advances in Quantum Chemistry*, *22*, 301–373.
- Andersson, K., Malmqvist, P.-Å., & Roos, B. O. (1992). Second-order perturbation theory with a complete active space self-consistent field reference function. *The Journal of Chemical Physics*, *96*, 1218–1226.
- Atchity, G. J., Xantheas, S. S., & Ruedenberg, K. (1991). Potential-energy surfaces near intersections. *The Journal of Chemical Physics*, *95*, 1862–1876.
- Atkins, P. W., & Friedman, R. S. (1997). *Molecular quantum mechanics* (3rd ed.). Oxford: Oxford University Press.
- Barbatti, M., Granucci, G., Persico, M., Ruckebauer, M., Vazdar, M., Eckert-Maksić, M., & Lischka, H. (2007). The on-the-fly surface-hopping program system Newton-X: Application to *ab initio* simulation of the nonadiabatic photodynamics of benchmark systems. *Journal of Photochemistry & Photobiology A*, *190*, 228–240.
- Bearpark, M. J., & Robb, M. A. (2007). *Conical intersection species as reactive intermediates*. Hoboken: Wiley.
- Ben-Nun, M., & Martínez, T. J. (2000). Photodynamics of ethylene: *Ab initio* studies of conical intersections. *Chemical Physics*, *259*, 237–248.
- Bosca, F., Lhiaubet-Vallet, V., Cuquerella, M. C., Castell, J. V., & Miranda, M. A. (2006). The triplet energy of thymine in DNA. *Journal of the American Chemical Society*, *128*, 6318–6319.
- Buenker, R. J., Hirsch, G., Li, Y., Gu, J., Alekseyev, A. B., Liebermann, H., & Kimura, M. (2000). *Ab initio calculations of excited state potential functions* (pp. 135–168). Chichester: Wiley.
- Cadet, J., Anselmino, C., Douki, T., & Voituriez, L. (1992). New trends in photobiology: Photochemistry of nucleic acids in cells. *Journal of Photochemistry and Photobiology B: Biology*, *15*, 277–298.
- Celani, P., & Werner, H.-J. (2003). Analytical energy gradients for internally contracted second-order



- multireference perturbation theory. *The Journal of Chemical Physics*, 119, 5044–5057.
- Crespo-Hernández, C., Cohen, B., Hare, P., & Kohler, B. (2004). Ultrafast excited-state dynamics in nucleic acids. *Chemical Reviews*, 104, 1977–2019.
- Domcke, W., Sobolewski, A. L., & Woywood, C. (1993). Internal conversion funnel in benzene and pyrazine: Adiabatic and diabatic representation. *Chemical Physics Letters*, 203, 220–226.
- Domcke, W., Yarkony, D. R., & Köppel, H. (Eds.). (2004). *Conical intersections. Electronic structure, dynamics & spectroscopy*. River Edge: World Scientific.
- Eisinger, J., & Shulman, R. G. (1968). Excited electronic states of DNA. *Science*, 161, 1311–1319.
- Finley, J., Malmqvist, P.-Å., Roos, B. O., & Serrano-Andrés, L. (1998). The multi-state CASPT2 method. *Chemical Physics Letters*, 288, 299–306.
- Finley, J., Malmqvist, P.-Å., Roos, B. O., & Serrano-Andrés, L. (1999). The multi-state CASPT2 method. *Chemical Physics Letters*, 288, 299–306.
- Foresman, J. B., Head-Gordon, M., Pople, J. A., & Frisch, M. J. (1992). Toward a systematic molecular orbital theory for excited states. *The Journal of Physical Chemistry*, 96, 135–149.
- Forsberg, N., & Malmqvist, P.-Å. (1997). Multiconfiguration perturbation theory with imaginary level shift. *Chemical Physics Letters*, 274, 196–204.
- Ghigo, G., Roos, B. O., & Malmqvist, P.-Å. (2004). A modified definition of the zeroth-order Hamiltonian in multiconfigurational perturbation theory (CASPT2). *Chemical Physics Letters*, 396, 142–149.
- Goddard, W. A., & Hunt, W. J. (1974). The Rydberg nature and assignments of excited states of the water molecule. *Chemical Physics Letters*, 24, 464–471.
- Grein, F. (2009). Coupled cluster and density functional studies on geometries and energies of excited  $C_{2v}$  states of ozone. *The Journal of Chemical Physics*, 130, 124118.
- Grimme, S., & Waletzke, M. (1999). A combination of Kohn–Sham density functional theory and multi-reference configuration interaction methods. *The Journal of Chemical Physics*, 111, 5645.
- Helgaker, T., Jørgensen, J., & Olsen, J. (2004). *Molecular electronic-structure theory*. Chichester: Wiley.
- Herzberg, G., & Longuet-Higgins, L. C. (1963). Intersection of potential energy surfaces in polyatomic molecules. *Discussions of the Faraday Society*, 35, 77–82.
- Kleinschmidt, M., Tatchen, J., & Marian, C. M. (2001). Spin-orbit coupling of DFT/MRCI wavefunctions: Method, test calculations, and application to thiophene. *Journal of Computational Chemistry*, 23, 824–833.
- Koch, H., & Jørgensen, P. (1990). Coupled cluster response functions. *The Journal of Chemical Physics*, 93, 3333–3344.
- Kowalski, K. (2005). Completely renormalized EOM-CCSD(T) method employing independent optimization of the cluster product terms. *Chemical Physics Letters*, 411, 306–310.
- Lischka, H., Dallos, M., Szalay, P. G., Yarkoni, D. R., & Shepard, R. (2004). Analytic evaluation of nonadiabatic coupling terms at the MR-CI level. I. Formalism. *The Journal of Chemical Physics*, 120, 7322–7329.
- Malmqvist, P.-Å., & Roos, B. O. (1989). The CASSCF state interaction method. *Chemical Physics Letters*, 155, 189–194.
- Malmqvist, P.-Å., Rendell, A., & Roos, B. O. (1990). The restricted active space self-consistent-field method, implemented with a split graph unitary group approach. *The Journal of Physical Chemistry*, 94, 5477–5482.
- Malmqvist, P.-Å., Pierloot, K., Shahi, A. R. M., Cramer, C. J., & Agliardi, L. (2008). The restricted active space followed by second-order perturbation theory method: Theory and application to the study of  $CuO_2$  and  $Cu_2O_2$  systems. *The Journal of Chemical Physics*, 128, 204109.
- Martin, J. M. L., Taylor, P. R., & Lee, T. J. (1997). The harmonic frequencies of benzene. A case for atomic natural orbital basis sets. *Chemical Physics Letters*, 275, 414–422.
- Merchán, M., & Serrano-Andrés, L. (2005). *Ab initio methods for excited states*. Amsterdam: Elsevier.
- Merchán, M., Serrano-Andrés, L., Robb, M., & Blancafort, L. (2005). Triplet-state formation along the ultrafast decay of excited singlet cytosine. *Journal of the American Chemical Society*, 127, 1820–1825.
- Merchán, M., González-Luque, R., Climent, T., Serrano-Andrés, L., Rodríguez, E., Reguero, M., & Peláez, D. (2006). Unified model for the ultrafast decay of pyrimidine nucleobases. *The Journal of Physical Chemistry B*, 110, 26471–26476.
- Müller, T. H., Dallos, M., & Lischka, M. (1999). The ethylene  $1^1B_{1u}V$  state revisited. *The Journal of Chemical Physics*, 110, 7176–7184.
- Oddershede, J. (1987). Propagator methods. *Accounts of Chemical Physics*, 69, 201–239.
- Olaso-González, G., Roca-Sanjuán, D., Serrano-Andrés, L., & Merchán, M. (2006). Toward the understanding of DNA fluorescence: The singlet excimer of cytosine. *The Journal of Chemical Physics*, 125, 231102.

- Olsen, J., Roos, B. O., Jørgensen, P., & Jensen, H. J. A. (1988). Determinant based configuration interaction algorithms for complete and restricted configuration interaction spaces. *The Journal of Chemical Physics*, 89, 2185–2192.
- Paschoal, D., Costa, M. F., Junqueira, G. M. A., & Santos, H. F. D. (2009). *Ab initio* calculation of electric properties for the BH, CO, CS and N<sub>2</sub> molecules. *Journal of Molecular Structure: THEOCHEM*, 913, 200–206.
- Paterson, M. J., Bearpark, M. J., Robb, M. A., & Blancafort, L. (2004). The curvature of the conical intersection seam: An approximate second-order analysis. *The Journal of Chemical Physics*, 121, 11562–11571.
- Peach, M. J. G., Benfield, P., Helgaker, T., & Tozer, D. J. (2008). Excitation energies in density functional theory: An evaluation and a diagnostic test. *The Journal of Chemical Physics*, 128, 044118.
- Pou-Amérgigo, R., Serrano-Andrés, L., Merchán, M., Ortí, E., & Forsberg, N. (2000). A theoretical determination of the low-lying electronic states of the *p*-benzosemiquinone radical anion. *Journal of the American Chemical Society*, 122, 6067–6077.
- Pérez-Hernández, G., González, L., & Serrano-Andrés, L. (2008). Rydberg or valence? The long-standing question in the UV absorption spectrum of 1,1'-bicyclohexylidene. *ChemPhysChem*, 9, 2544–2549.
- Robb, M. A., Bernardi, F., & Olivucci, M. (1996). Conical intersections as a mechanistic feature of organic-photochemistry. *Pure and Applied Chemistry*, 67, 783–789.
- Roca-Sanjuán, D., Rubio, M., Merchán, M., & Serrano-Andrés, L. (2006). *Ab initio* determination of the ionization potentials of DNA and RNA nucleobases. *The Journal of Chemical Physics*, 125, 084302.
- Roca-Sanjuán, D., Merchán, M., Serrano-Andrés, L., & Rubio, M. (2008a). *Ab initio* determination of the electron affinities of DNA and RNA nucleobases. *The Journal of Chemical Physics*, 129, 095104.
- Roca-Sanjuán, D., Olaso-González, G., González-Ramírez, I., Serrano-Andrés, L., & Merchán, M. (2008b). Molecular basis of DNA photodimerization: Intrinsic production of cyclobutane cytosine dimers. *Journal of the American Chemical Society*, 130, 10768–10779.
- Roos, B. O., Taylor, P. R., & Siegbahn, P. E. M. (1979). A complete active space SCF method (CASSCF) using a density matrix formulated super-CI approach. *Chemical Physics*, 48, 157–173.
- Roos, B. O., Andersson, K., Fülcher, M. P., Serrano-Andrés, L., Pierloot, K., Merchán, M., & Molina, V. (1996). Applications of level shift corrected perturbation theory in electronic spectroscopy. *Journal of Molecular Structure: THEOCHEM*, 388, 257–276.
- Roos, B. O., Malmqvist, P.-Å., Molina, V., Serrano-Andrés, L., & Merchán, M. (2002). Theoretical characterization of the lowest-energy absorption band of pyrrole. *The Journal of Chemical Physics*, 116, 7526–7537.
- Roos, B. O., Lindh, R., Malmqvist, P.-Å., & Widmark, P.-O. (2005). New relativistic ANO basis sets for actinide atoms. *Chemical Physics Letters*, 409, 295–299.
- Roothaan, C. C. J. (1951). New developments in molecular orbital theory. *Reviews of Modern Physics*, 23, 69–89.
- Rubio, M., Serrano-Andrés, L., & Merchán, M. (2008). Excited states of the water molecule: Analysis of the valence and Rydberg character. *The Journal of Chemical Physics*, 128, 104305.
- Schreier, W. J., Schrader, T. E., Soller, F. O., Gilch, P., Crespo-Hernández, C. E., Swaminathan, V. N., Carell, T., Zinth, W., & Kohler, B. (2007). Thymine dimerization in DNA is an ultrafast photoreaction. *Science*, 315, 625–629.
- Serrano-Andrés, L., & Merchán, M. (2005). Quantum chemistry of the excited state: 2005 overview. *Journal of Molecular Structure: THEOCHEM*, 729, 99–108.
- Serrano-Andrés, L., & Merchán, M. (2009). Are the five natural DNA/RNA base monomers a good choice for natural selection? A photochemical perspective. *Journal of Photochemistry and Photobiology C: Photochemistry Reviews*, 10, 21–32.
- Serrano-Andrés, L., Merchán, M., & Lindh, R. (2005). Computation of conical intersections by using perturbation techniques. *The Journal of Chemical Physics*, 122, 104107.
- Serrano-Andrés, L., Merchán, M., & Borin, A. C. (2006). Adenine and 2-aminopurine: Paradigms of modern theoretical photochemistry. *Proceedings of the National Academy of Sciences of the United States of America*, 103, 8691–8696.
- Serrano-Andrés, L., Merchán, M., & Borin, A. C. (2008). A three-state model for the photophysics of guanine. *Journal of the American Chemical Society*, 130, 2473–2484.
- Serrano-Pérez, J., Serrano-Andrés, L., & Merchán, M. (2006). A theoretical insight into the photophysics of psoralen. *The Journal of Chemical Physics*, 124, 124502.
- Serrano-Pérez, J., Serrano-Andrés, L., & Merchán, M. (2007a). Quantum chemical study on the

- population of the lowest triplet state of psoralen. *Chemical Physics Letters*, 434, 107–110.
- Serrano-Pérez, J., González-Luque, R., Serrano-Andrés, L., & Merchán, M. (2007b). On the intrinsic population of the lowest triplet state of thymine. *The Journal of Physical Chemistry*, 111, 11880–11883.
- Serrano-Pérez, J., Merchán, M., & Serrano-Andrés, L. (2008a). Photosensitization and phototherapy with furocoumarins: A quantum-chemical study. *Chemical Physics*, 347, 422–435.
- Serrano-Pérez, J., González-Luque, R., Merchán, M., & Serrano-Andrés, L. (2008b). The family of furocoumarins: Looking for the best photosensitizer for phototherapy. *Journal of Photochemistry and Photobiology A: Chemistry*, 199, 34–41.
- Serrano-Pérez, J., Merchán, M., & Serrano-Andrés, L. (2008c). Photoreactivity of furocoumarins and DNA in PUVA therapy: Formation of psoralen-thymine adducts. *The Journal of Physical Chemistry B*, 112, 14002–14010.
- Serrano-Pérez, J., González-Ramírez, I., Coto, P., Serrano-Andrés, L., & Merchán, M. (2008d). Theoretical insight into the intrinsic ultrafast formation of cyclobutane pyrimidine dimers in UV-irradiated DNA: Thymine versus cytosine. *The Journal of Physical Chemistry B*, 112, 14096–14098.
- Serrano-Pérez, J., Olaso-González, G., Merchán, M., & Serrano-Andrés, L. (2009). Singlet oxygen generation in PUVA therapy studied using electronic structure calculations. *Chemical Physics*, 360, 85–96.
- Shepard, R., Lischka, H., Szalay, P. G., Kovar, T., & Ernzerhof, M. (1992). A general multireference configuration interaction gradient program. *The Journal of Chemical Physics*, 96, 2085–2098.
- Sicilia, F., Bearpark, M. J., Blancafort, L., & Robb, M. A. (2007). An analytical second-order description of the S0/S1 intersection seam: Fulvene revisited. *Theoretical Chemistry Accounts*, 118, 241–251.
- Strickler, S. J., & Berg, R. A. (1962). Relationship between absorption intensity and fluorescence lifetime of molecules. *The Journal of Chemical Physics*, 37, 814–822.
- Szabo, A., & Ostlund, N. S. (1996). *Modern quantum chemistry: Introduction to advanced electronic structure theory*. Mineola: Dover Publications, Inc.
- Szymczak, J. J., Barbatti, M., Soo Hoo, J. T., Adkins, J. A., Windus, T.-L., Nachtigallová, D., & Lischka, H. (2009). Photodynamics simulations of thymine: Relaxation into the first excited singlet state. *The Journal of Physical Chemistry A*, 113, 12686–12693.
- Taylor, P. R. (2007). *Lecture notes in quantum chemistry: European summerschool*. Berlin: Springer.
- Teller, E. (1937). The crossing of potential surfaces. *The Journal of Physical Chemistry*, 41, 109–116.
- Widmark, P.-O., Malmqvist, P.-Å., & Roos, B. O. (1990). Density matrix averaged atomic natural orbital (ANO) basis sets for correlated molecular wave functions. *Theoretica Chimica Acta*, 77, 291–306.

# 15 Solvent Effects in Quantum Chemistry

*Gerald Monard · Jean-Louis Rivail*

Theoretical Chemistry and Biochemistry Group SRSMC,  
Nancy-University CNRS Boulevard des Aiguillettes,  
Vandoeuvre-les-Nancy, France

<i>Introduction: Importance of Solvent Effects in Chemistry</i> .....	562
<i>The Supermolecule Model</i> .....	562
<i>Continuum Models</i> .....	563
<i>The Full Quantum Approaches of Liquids</i> .....	565
<i>The Quantum Mechanical/Molecular Mechanical (QM/MM) Models</i> .....	566
<i>Other Statistical Approaches of the Solvent</i> .....	567
Reference Interaction Site Model (RISM) .....	567
Langevin Dipole Model (LD) .....	568
<i>The Future of Studies in the Liquid State</i> .....	568
<i>References</i> .....	568

**Abstract:** The properties of a molecule may change quite substantially when passing from the isolated state to a solution, and computational chemistry requires the possibility of taking into account the effects of a solvent on molecular properties. These changes are mainly due to long range interactions, and electrostatics involving a large number of solvent molecules play the major role in the phenomenon and free energy changes have to be evaluated. Statistical calculations by means of usual Monte Carlo or molecular dynamics coupled with a full quantum chemical description of a sample representative of the solution is still out of reach for standard molecular modeling computations nowadays. Nevertheless, several simplified approaches are available to evaluate the free energy changes which appear when an isolated molecule, as described by standard quantum computations, undergoes the influence of a solvent and to predict the changes in the molecular properties which are the consequences of solvation. In this chapter, we develop the principles of the most usual methods that a computational chemist can find in standard codes or can implement more or less easily to approach the solvent effects in quantum chemistry investigations.

## Introduction: Importance of Solvent Effects in Chemistry

---

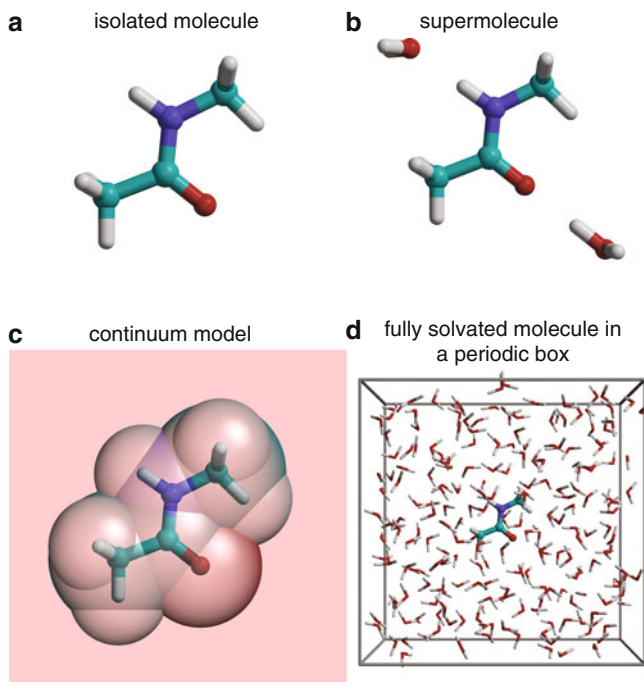
Most of the chemical reactions as well as experimental structure determinations are performed in solutions. On the contrary, usual quantum chemical computations usually deal with isolated chemical species. This may lead to erroneous conclusions. For instance, the addition of bromine to an ethylenic hydrocarbon is known for having a different mechanism in the gas phase and in solution. In this example, the velocity constant vary by a factor of  $10^{10}$  when going from carbon tetrachloride to water as a solvent (Reichardt 1979), although the mechanism is the same. These features are confirmed by appropriate quantum chemical computations which show that the transition state of ethylene-bromine would be dissymmetric and 55 kcal/mol above the van der Waals complex in the case of the isolated species (Yamabe et al. 1988), while with a simple simulation of the solvent effect one finds a symmetric transition state lying 30.79 kcal/mol above the van der Waals complex in a non dipolar solvent and 0.02 kcal/mol in water (Assfeld 1994).

A full quantum mechanical treatment of a sample containing the solute and a number of solvent molecules large enough to simulate the solution is still out of reach of usual quantum chemical computations not only because the system of interest should be pretty large but also because the free energy computations would require a statistical treatment on millions of configurations of this system. One is therefore led, in general, to use model systems, simplified expressions of interatomic interactions allowing either statistical simulations or the derivation of molecular distribution functions or some semi-empirical approaches. In this vade mecum, we summarized different ways of modeling solvent effects in quantum chemistry. This includes the supermolecule model, the continuum and semi-macroscopic models, the full quantum description of liquids, the QM/MM methods (see [Fig. 15-1](#)), and the use of analytical molecular distribution functions (Hirata 2003). All these approaches have their limits, and one is led to choose one or the other according to the kind of problem being addressed.

## The Supermolecule Model

---

In some cases, in particular that of aqueous solutions, the specific interactions may be modeled by means of a supermolecule made of an aggregate of the solute and a limited number of solvent molecules treated as an isolated single molecular system at the desired quantum chemical level.



■ Fig. 15-1

The different approaches for modeling a solute molecule in a solvent. From *top left to bottom right*: (a) the isolated molecule (gas phase); (b) the supermolecule (solute with a few solvent molecules); (c) the continuum approach (the molecule is inserted in a cavity surrounded by a dielectric continuum); (d) the fully solvated system (the solute is inserted in a periodic box filled with solvent molecules)

This approach may give useful information on strong intermolecular interactions (Catak et al. 2009; Harb et al. 2004) but cannot model correctly the effect of the solvent because the long-range electrostatic interactions, which play an important role in a liquid (Buckingham 1967, 1978), are not taken into account. An efficient way to model these long-range electrostatic interactions is to use a continuum model.

## Continuum Models

These models are by far the most widely used in current computational chemistry nowadays, and several review articles give an overview of them (Rivail and Rinaldi 1996; Tomasi 2004; Tomasi et al. 2005). They are based upon the consideration of the solvent as a continuous medium characterized by its macroscopic properties: bulk dielectric permittivity, possibly surface tension. The solute is assumed to occupy a cavity surrounded by this continuum. The free energy of interaction between this molecule and its surrounding may be analyzed as the sum of three contributions:

- The free energy variation of the system when the cavity is created in the bulk of the liquid. This can be considered as an increase of its free area and is a positive free energy variation.

- The dispersion-repulsion energy arising between a polarizable solute and the solvent molecules of finite size, which is always a negative contribution.
- The electrostatic free energy arising from the polarization of the solvent by the charge distribution of the solute. The result of this polarization is a non zero electrostatic potential within the cavity which perturbs the charge distribution of the solute, leading to changes in the solute's structure, compared with the isolated molecule (Luque et al. 2003).

The earlier attempt to approach the electrostatic contribution to the free energy of solvation is due to Kirkwood (1934). This model is based on a multipole expansion of the charge distribution of the solute at the center of a spherical cavity surrounded by a continuum represented by the dielectric permittivity of the solvent. When this expansion is limited to rank 1 which corresponds to a pure dipole  $\mu$ , one finds the Onsager model (Onsager 1936) in which the electrostatic contribution to the free energy of solvation by a solvent of dielectric constant  $\epsilon$  of a molecule having a dipole moment  $\mu$  in a cavity of radius  $a$  takes the expression:

$$\Delta G = -\frac{1}{2a^3} \frac{2(\epsilon - 1)}{2\epsilon + 1} \mu^2. \quad (15.1)$$

Onsager has shown, in the case of a pure liquid made of dipolar, polarizable molecules, that the dielectric constant of the liquid is fairly well predicted when the volume of the cavity is equal to the apparent molecular volume in the liquid. This finding gives a hint to the estimate of the volume of the cavity which is a parameter in the Kirkwood model. In the case of a non neutral solute, the charge  $q$  corresponds to the multipole of rank 0 and the corresponding term in the multipole expansion is the well-known Born formula (Born 1920) giving the free energy of solvation of charged solutes:

$$\Delta G = -\frac{1}{a} \frac{\epsilon - 1}{\epsilon} q^2. \quad (15.2)$$

This approach which has the advantage of giving an analytical formula of the free energy of solvation has been extended to ellipsoidal (Rinaldi and Rivail 1973) and spheroidal cavities (Rivail and Terryn 1982) and has been applied long ago to quantum chemical computations, at various levels of approximation (Rinaldi et al. 1983). As the perturbation to the wavefunction depends on the charge distribution of the solute which is defined by the wavefunction to be computed, the computational scheme requires self consistency combined with the usual self consistent computational algorithms for quantum chemistry. This is frequently referred as the Self Consistent Reaction Field (SCRF) where the solute is polarized by the solvent which is, in return, polarized by the solute. Nowadays, this model has been extended to cavities of any shape using a multicentric multipole expansion on all the atoms of the solute (Rinaldi et al. 2004). In all these approaches, the first and second derivatives of energy are computed allowing a full geometry optimization and the determination of the stationary points in the potential energy surface and the computation of the harmonic vibrational frequencies (Rinaldi et al. 2006).

A closely related approach, using the same kind of molecular cavity has been developed by Tomasi et al. (1981). In this model, the multipole expansion is replaced by a numerical computation of the electrostatic potential inside the cavity, due to the polarization of the boundary by the solute. This model also has been improved along the years. It has various versions all known under the acronym of PCM (Cancès et al. 1997) which are implemented in the Gaussian suites of programs, and a closely related model is available in the Jaguar package (Marten et al. 1996; Tannor et al. 1994).

Rather, different approaches are based on the so-called generalized Born model in which the charge distribution of the solute is represented by point charges on all atoms and the solute–solvent interaction is defined by a sum of the Born contributions of each atom in which the reciprocal of the sphere radius in [Eq. 15.2](#) is replaced by a parameterized empirical formula. The most elaborated applications of this model is found in the series of SM $x$  models of Cramer and Truhlar ( $x = 1$  to 8 nowadays, corresponding to successive improvements) (Cramer and Truhlar 1991, 2008).

Finally, to simplify the electrostatic algorithm some methods start with a dielectric permittivity  $\epsilon = \infty$  corresponding to a conductor like solvent and then correct the result either by the ratio  $2(\epsilon - 1)/(2\epsilon + 1)$  of the Onsager factor of the actual dielectric permittivity of the solvent to the limiting value when  $\epsilon = \infty$ , or by the ratio of the Born factors:  $(\epsilon - 1)/\epsilon$ . It is noteworthy that the difference may not be negligible for low dielectric constants. This approximation has first been introduced in the COSMO model (Klamt and Schüürmann 1993). A version of the PCM model, known as C-PCM (Barone and Cossi 1998) uses the same approximation to evaluate the electrostatic solvation term.

The importance of any kind of solvents, including the non polar ones has to be emphasized because some people claim that the properties in a non polar solvent should be close to the gas state. The experimental results mentioned in (Reichardt 1979) show that it is not true, and this can also be seen in the case of the Born or Onsager models. If one considers a solvent such as cyclohexane with a dielectric permittivity close to 2, one sees that the electrostatic free energy of solvation is for the former and the latter model respectively 50% and 40% of the limiting value at infinite permittivity. Similarly, one also notices that for high dielectric permittivities, these terms do not vary noticeably when this constant varies, justifying the COSMO-type models in particular in the case of water and highly polar solvents.

The quantitative use of continuum models requires care. The absolute values of free energies of solvation depend on many parameters. The electrostatic contribution mainly depends on the shape and volume of the cavity. The most widely used shapes are defined by the “molecular surface” (Pascual-Ahuir and Silla 1990; Silla et al. 1991) defined after the atomic radii (Bondi 1964) multiplied by a factor of the order of 1.3. A test for the choice of this parameter can be the comparison of the volume of the cavity with the apparent molecular volume of the solute (when known) in the liquid state or in the solution like in the Onsager’s theory of the dielectric permittivity of pure polar liquids.

The non electrostatic contributions are far more difficult to model. Usually, they are evaluated by empirical formulae which, in the most favorable cases, introduce some error bars. The models parameterized on a large number of experimental data, such as SM8 (Cramer and Truhlar 1991, 2008), are probably rather reliable although one may deal with a case which is an exception. Conversely, variations of solvation energy for systems in which the non electrostatic terms are assumed not to vary significantly, such as conformational equilibria, may be approached rather safely by means of these computational efficient models.

## The Full Quantum Approaches of Liquids

---

A reliable computation of free energies in a molecular system requires the use of statistical mechanics on a sample which can be considered as macroscopically representative. In the case of solutions, this requires more than one hundred solvent molecules and the computation of



an enormous number of different configurations. Full quantum chemical studies are now possible thanks to some specific algorithms but they are still lengthy. An efficient approach uses a standard semi-empirical code, reparameterized to account properly for intermolecular energies (Bernal-Uruchurtu and Ruiz-López 2000; Bernal-Uruchurtu et al. 2000), coupled with a linear scaling divide and conquer algorithm (Dixon and Merz 1996, 1997), which allows the simulation of a set of 216 water molecules in a quite affordable computer time (Monard et al. 2005). The use of fast DFT methods can now replace the semi-empirical ones (Hu et al. 2007) and one may anticipate that in the near future, the theoretical and algorithmic improvements will make possible the use of non empirical treatments. The use of plane wave basis sets (Todorova et al. 2006; VandeVondele et al. 2005) is another attempt to improve the efficiency of the codes.

In contrast with the previous approaches in which the energy and the forces calculated at each configuration of the system are computed within the usual Born-Oppenheimer approximation (BOMD), the Car-Parrinello unified approach for molecular dynamics and DFT (Car and Parrinello 1985) is an efficient alternative to the simulation of macroscopic samples although it requires rather large computational facilities and time. The CPMD package is available for such computations which require some expertise to be ran safely (Marx and Hutter 2000). A comparison of CPMD and BOMD simulations may be useful to determine the best computational procedures (Kuo et al. 2006). Car-Parrinello computations are widely applied to the simulation of liquids, mainly water (Izvekov and Voth 2002) but other liquids are also considered (Bakó et al. 2006). All these full QM approaches are, for the time being, mainly limited to the understanding of the structural properties of pure liquids.

## The Quantum Mechanical/Molecular Mechanical (QM/MM) Models

---

Chemical studies usually deal with a solute which can be a single molecule or a molecular complex or transition state in a chemical reaction. In such systems, the role of the solvent is mainly a physical perturbation which can be simulated at a lower theoretical level than that required for the study of the subsystem of chemical interest. The success of continuum models confirms this statement. In order to describe the solution at the molecular level and to perform full statistical mechanics computations on a model of macroscopic sample, one may set up some computationally efficient approaches by limiting the quantum chemical study to the solute and using one of the usual classical force-fields to represent the solvent molecules. The computation of the statistical averages can be done by means of either Monte Carlo or molecular dynamics algorithms. The so-called QM/MM models are now widely used in such chemical studies.

The Hamiltonian is a sum of three terms:  $H_{QM}$ , the usual quantum Hamiltonian of the solute,  $H_{MM}$ , the classical Hamiltonian corresponding to the configuration of the solvent  $H_{QM/MM}$ , which corresponds to the interaction energy between the classical solvent molecules and the quantum solute (Monard et al. 2003). The first two Hamiltonians are well defined by the choice of the quantum methodology and the classical force field chosen to model the liquid. The definition of the interaction Hamiltonian is far more difficult. It is usually made of a sum of van der Waals interaction energies between the classical atoms of the solvent and the quantum atoms of the solute, the long-range electrostatic interactions between the classical solvent molecules and the electron distribution and the nuclei of the solute and the possible specific interactions (hydrogen bonds). This is the most delicate part of the methodology, which requires specific parameterizations for each kind of quantum chemical method used as well as each classical

force field. A large number of papers have been published on this problem (Freindorf and Gao 1996; Freindorf et al. 2005; Giese and York 2007; Luque et al. 2000; Riccardi et al. 2004). For specific problems, useful methodologies have been set up to determine the most appropriate parameters (Martín et al. 2002).

Once the methodology has been defined, running a computation requires the usual molecular dynamics or Monte Carlo codes, but the necessity of taking into account a large number of configurations makes any improvements which accelerate the process very valuable. One of the time consuming step is the computation of the long-range electrostatic interactions for which some algorithms, such as the use of Ewald sum (Nam et al. 2005) or periodic boundary conditions (Laino et al. 2006), may become very efficient to compute accurate free energies (Gao et al. 2005).

Various methods and levels of approximation can be used for the QM part of the studies, from semi-empirical (Cummins and Gready 1997; Geerke et al. 2008), empirical Valence Bond (Sumner and Iyengar 2008) to correlated levels (Kongsted et al. 2003; Woods et al. 2008). QM/MM simulations also work with the Car-Parrinello methodology (Laio et al. 2002).

QM/MM methods have now reached a good level of achievement and have opened the way to refined studies of molecular structure and reactivity in the liquid state (Hu and Yang 2009). However, may be one of the last remaining challenges for QM/MM methods is to correctly and efficiently handle reactivity problems where one or more solvent molecules are directly implied in the chemical mechanism. The usual solution found in literature is to choose among all solvent molecules the unique molecule which will react with the solute. Some solutions which take into account the dynamical nature of the first solvation shell have been suggested so far (Kerdcharoen and Morokuma 2002, 2003; Tongraar et al. 1998; Tongraar and Rode 2004), but they have not been applied to reactivity problems yet.

## Other Statistical Approaches of the Solvent

### Reference Interaction Site Model (RISM)

Integral equations of the liquid state provide us, in principle, with a rigorous statistical description of the liquid, although, to solve them, one is forced to use several approximations, in particular various closure conditions to get pair correlation functions (Hansen and McDonald 1976). These approaches have been successfully used to describe simple liquids. In the case of polyatomic molecules, the difficulty increases rapidly with the number of sites and the nature of the interatomic potential. Nonetheless, a Reference Interaction Site Model (RISM) has been proposed to extend the treatment to polyatomic liquids (Chandler and Andersen 1972) and has been successfully applied to several problems dealing with molecular solutions (Hirata and Rossky 1982). Some routines are now available to solve the RISM equations. These equations have also been coupled with a quantum computation of the solute (Ten-no et al. 1993). The interatomic potentials have the standard Lennard-Jones expression in which the electrostatic interactions are developed on a basis of point charges. Therefore, the electronic distribution of the solute is limited to effective partial charges  $q_\lambda$  located on the atoms (denoted by a greek index here  $\lambda$ ). The Hartree-Fock equations are modified by introducing a perturbative potential on each atom  $\lambda$  of the solute:

$$V_\lambda = \rho \sum_{j \in S} q_j \int_0^\infty r^{-1} g_{\lambda j}(r, q_\lambda) 4\pi r^2 dr, \quad (15.3)$$

where  $\rho$  is the solvent density and  $g_{\lambda j}(r, q_{\lambda})$  is the radial distribution function of the  $j$ th site of solvent molecules S relative to the  $\lambda$ th site of the solute molecule. This function is given by the RISM equations. The RISM-SCF cycle simultaneously optimizes the pair correlation functions and the electronic wavefunctions. This approach has been successfully applied to the study of solvent effects on the electronic spectra of carbonyl compounds (Ten-no et al. 1994).

## Langevin Dipole Model (LD)

---

Between a macroscopic description of the solvent represented by the continuum models and a microscopic approach where all solvent atoms are explicitly represented, there exists an alternative semi-macroscopic approach: the Langevin Dipole model. This model treats the solvent (usually water) explicitly but in a simplified way. It represents the time average polarization of the solvent molecules by a cubic grid of polarizable dipoles (Warshel 1991; Warshel and Russel 1984). According to the Langevin equation (Langevin 1905), the electrostatic field of the solute reorients and polarizes the grid point dipoles. While this method has been successfully applied to the computation of the free energy of solvation of small neutral and ionic molecular solutes at a quantum level (Florián and Warshel 1997, 1999; Kongsted et al. 2009), the Langevin Dipole model has been mostly used to represent the electrostatic interactions between water as a solvent and proteins through the Protein Dipoles/Langevin Dipoles (PDL) method (Roca et al. 2007; Warshel et al. 2006).

## The Future of Studies in the Liquid State

---

The number of selected papers dealing with various approaches of the liquid state and solutions clearly indicate that taking into account the influence of the solvent in quantum chemical studies will soon become quite usual. The large variety of methods allows us to adapt the level of modeling to the accuracy required to get useful chemical information. The methodology is still expected to improve in the near future. In particular, the full quantum treatment of a solution which takes advantage of the advances in quantum modeling of pure liquids seems to be at hand, especially when one can use different quantum levels for the solute and for the solvent. Like in the case of QM/MM the key feature is the proper treatment of the interaction between both subsystems but one can be confident to the quantum chemists to find the proper solutions to this problem.

## References

---

- Assfeld, X. (1994). PhD Dissertation, Université Henri Poincaré, Nancy.
- Bakó, I., Hutter, J., & Pálinkás, G. (2006). Car-Parrinello molecular dynamics simulation of liquid formic acid. *Journal of Physical Chemistry A*, 110, 2188.
- Barone, V., & Cossi, M. (1998). Quantum calculation of molecular energies and energy gradients in solution by a conductor solvent model. *Journal of Physical Chemistry A*, 102, 1995.
- Bernal-Uruchurtu, M. I., & Ruiz-López, M. F. (2000). Basic ideas for the correction of semiempirical methods describing H-bonded systems. *Chemical Physics Letters*, 330, 118.
- Bernal-Uruchurtu, M. I., Martins-Costa, M. T. C., Millot, C., & Ruiz-López, M. F. (2000).

- Improving description of hydrogen bonds at the semiempirical level: Water-water interactions as test case. *Journal of Computational Chemistry*, *21*, 572.
- Bondi, A. (1964). van der Waals volumes and radii. *Journal of Physical Chemistry*, *68*, 441.
- Born, M. (1920). Volumen und hydrationswärme der Ionen. *Zeitschrift für Physik*, *1*, 45.
- Buckingham, A. (1967). Permanent and induced molecular moments and long-range intermolecular forces. *Advances in Chemical Physics*, *12*, 107.
- Buckingham, A. (1978). Basic theory of intermolecular forces: Applications to small molecules. In B. Pullman (Ed.), *Intemolecular interactions, from Diatomics to Biopolymers* (Vol. 1, p. 1). New York: Wiley.
- Cancès, E., Menucci, B., & Tomasi, J. (1997). A new integral equation formalism for the polarizable continuum model: Theoretical background and applications to isotropic and anisotropic dielectrics. *Journal of Chemical Physics*, *107*, 3032.
- Catak, S., Monard, G., Aviyente, V., & Ruiz-López, M. F. (2009). Deamidation of asparagine residues: Direct hydrolysis versus succinimide-mediated deamidation mechanisms. *Journal of Physical Chemistry A*, *113*, 1111.
- Car, R., & Parrinello, M. (1985). Unified approach for molecular dynamics and density-functional theory. *Physical Review Letters*, *55*, 2471.
- Chandler, D., & Andersen, H. C. (1972). Optimized cluster expansions for classical fluids. II. Theory of molecular liquids. *Journal of Chemical Physics*, *57*, 1930.
- Cramer, C. J., & Truhlar, D. G. (1991). Molecular orbital theory calculations of aqueous solvation effects on chemical equilibria. *Journal of the American Chemical Society*, *113*, 8552.
- Cramer, C. J., & Truhlar, D. G. (2008). A universal approach to solvation modeling. *Accounts of Chemical Research*, *41*, 760.
- Cummins, P. L., & Gready, J. E. (1997). Coupled semiempirical molecular orbital and molecular mechanics model (QM/MM) for organic molecules in aqueous solution. *Journal of Computational Chemistry*, *18*, 1496.
- Dixon, S. L., & Merz, K. M., Jr. (1996). Semiempirical molecular orbital calculations with linear system size scaling. *Journal of Chemical Physics*, *104*, 6643.
- Dixon, S. L., & Merz, K. M., Jr. (1997). Fast, accurate semiempirical molecular orbital calculations for macromolecules. *Journal of Chemical Physics*, *107*, 879.
- Florián, J., & Warshel, A. (1997). Langevin dipoles model for *ab initio* calculations of chemical processes in solution: Parametrization and application to hydration free energies of neutral and ionic solutes and conformational analysis in aqueous solution. *Journal of Physical Chemistry B*, *101*, 5583.
- Florián, J., & Warshel, A. (1999). Calculations of hydration entropies of hydrophobic, polar, and ionic solutes in the framework of the langevin dipoles solvation model. *Journal of Physical Chemistry B*, *103*, 10282.
- Freindorf, M., & Gao, J. (1996). Optimization of the Lennard-Jones parameters for a combined *ab initio* quantum mechanical and molecular mechanical potential using the 3-21G basis set. *Journal of Computational Chemistry*, *17*, 386.
- Freindorf, M., Shao, Y., Furlani, T. R., & Kong, J. (2005). Lennard-Jones parameters for the combined QM/MM method using the B3LYP/6-31G\*/AMBER potential. *Journal of Computational Chemistry*, *26*, 1270.
- Gao, D., Svoronos, P., Wong, P. K., Maddalena, D., Hwang, J., & Walker, H. (2005). pK<sub>a</sub> of acetate in water: A computational study. *Journal of Physical Chemistry A*, *109*, 10776.
- Geerke, D. P., Thiel, S., Thiel, W., & van Gunsteren, W. F. (2008). QM-MM interactions in simulations of liquid water using combined semi-empirical/classical Hamiltonians. *Physical Chemistry Chemical Physics*, *10*, 297.
- Giese, T. J., & York, D. M. (2007). Charge-dependent model for many-body polarization, exchange, and dispersion interactions in hybrid quantum mechanical/molecular mechanical calculations. *Journal of Chemical Physics*, *127*, 194101.
- Hansen, J. P., & McDonald, I. R. (1976). *Theory of simple liquids*. London: Academic Press.
- Harb, W., Bernal-Uruchurtu, M., & Ruiz-López, M. (2004). An improved semiempirical method for hydrated systems. *Theoretical Chemistry Accounts*, *112*, 204.
- Hirata, F. (2003). *Molecular theory of solvation*. Dordrecht: Kluwer.
- Hirata, F., & Rossky, P. J. (1982). Application of an extended RISM equation to dipolar and quadrupolar fluids. *Journal of Chemical Physics*, *77*, 509.
- Hu, H., & Yang, W. (2009). Development and application of *ab initio* QM/MM methods for mechanistic simulation of reactions in solution and in enzymes. *Journal of Molecular Structure THEOCHEM*, *898*, 17.
- Hu, H., Lu, Z., Elsner, M., Hermans, J., & Yang, W. (2007). Simulating water with the self-consistent-charge density functional tight

- binding method: From molecular clusters to the liquid state. *Journal of Physical Chemistry A*, *111*, 5685.
- Izvekov, S., & Voth, G. A. (2002). Car-Parrinello molecular dynamics simulation of liquid water: New results. *Journal of Chemical Physics*, *116*, 10372.
- Kerdcharoen, T., & Morokuma, K. (2002). ONIOM-XS: An extension of the ONIOM method for molecular simulation in condensed phase. *Chemical Physics Letters*, *355*, 257.
- Kerdcharoen, T., & Morokuma, K. (2003). Combined quantum mechanics and molecular mechanics simulation of  $\text{Ca}^{2+}$ /ammonia solution based on the ONIOM-XS method: Octahedral coordination and implication to biology. *Journal of Chemical Physics*, *118*, 8856.
- Kirkwood, J. (1934). Theory of solutions of molecules containing widely separated charges with special application to zwitterions. *Journal of Chemical Physics*, *2*, 351.
- Klamt, A., & Schüürmann, G. (1993). COSMO – a new approach to dielectric screening in solvents with explicit expressions for the screening energy and its gradient. *Journal of the Chemical Society Perkin Transactions*, *2*, 799.
- Kongsted, J., Osted, A., & Mikkelsen, K. V. (2003). Coupled cluster/molecular mechanics method: Implementation and application to liquid water. *Journal of Physical Chemistry A*, *107*, 2578.
- Kongsted, J., Söderhjelm, P., & Ryde, U. (2009). How accurate are continuum solvation models for drug-like molecules? *The Journal of Computer-Aided Molecular Design*, *23*, 395.
- Kuo, I.-F. W., Mundy, C. J., McGrath, M. J., & Stepmann, J. I. (2006). Time-dependent properties of liquid water: A comparison of Car-Parrinello and Born-Oppenheimer molecular dynamics simulations. *Journal of Chemical Theory and Computation*, *2*, 1274.
- Laino, T., Mohamed, F., Laio, A., & Parrinello, M. (2006). An efficient linear-scaling electrostatic coupling for treating periodic boundary conditions in QM/MM simulations. *Journal of Chemical Theory and Computation*, *2*, 1370.
- Laio, A., VandeVondele, J., & Rothlisberger, U. (2002). A Hamiltonian electrostatic coupling scheme for hybrid Car-Parrinello molecular dynamics simulations. *Journal of Chemical Physics*, *116*, 6941.
- Langevin, P. (1905). Magnétisme et Théorie des électrons. *Annales de Chimie-Physique*, *8*, 70.
- Luque, F. J., Reuter, N., Cartier, A., & Ruiz-López, M. F. (2000). Calibration of the Quantum/Classical Hamiltonian in Semiempirical QM/MM AM1 and PM3 Methods. *Journal of Physical Chemistry A*, *104*, 10923.
- Luque, F., Curutchet, C., Muñoz-Muriedas, J., Bidon-Chanal, A., Sorietas, I., Morreale, A., Gelpi, J. L., & Orozco, M. (2003). Continuum solvation models: Dissecting the free energy of solvation. *Physical Chemistry Chemical Physics*, *5*, 3827.
- Marten, B., Kim, K., Cortis, C., Friesner, R. A., Murphy, R. B., Rignalda, M. N., Sitkoff, D., & Honig, B. (1996). New model for calculation of solvation free energies: Correction of self-consistent reaction field continuum dielectric theory for short-range hydrogen-bonding effects. *Journal of Physical Chemistry*, *100*, 11775.
- Martín, M. E., Aguilar, M. A., Chalmet, S., & Ruiz-López, M. F. (2002). An iterative procedure to determine Lennard-Jones parameters for their use in quantum mechanics/molecular mechanics liquid state simulations. *Chemical Physics*, *284*, 607.
- Marx, D., & Hutter, J. (2000). *Ab initio* molecular dynamics: Theory and Implementation. In J. Grotendorst (Ed.), *Modern methods and algorithms of quantum chemistry*, (p. 301). Jülich: John von Neumann Institute for Computing, NIC series.
- Miertus, S., Scrocco, E., & Tomasi, J. (1981). Electrostatic interaction of a solute with a continuum. A direct utilization of *ab initio* molecular potentials for the prevision of solvent effects. *Chemical Physics*, *55*, 117.
- Monard, G., Bernal-Uruchurtu, M. I., van der Vaart, A., Merz, K. M., Jr., & Ruiz-López, M. F. (2005). Simulation of liquid water using semiempirical hamiltonians and the divide and conquer approach. *Journal of Physical Chemistry A*, *109*, 3425.
- Monard, G., Prat-Resina, X., González-Lafont, A., & Lluch, J. M. (2003). Determination of enzymatic reaction pathways using QM/MM methods. *International Journal of Quantum Chemistry*, *93*, 229.
- Nam, K., Gao, J., & York, D. M. (2005). An efficient linear-scaling ewald method for long-range electrostatic interactions in combined QM/MM calculations. *Journal of Chemical Theory and Computation*, *1*, 2.
- Onsager, L. (1936). Electric moments of molecules in liquids. *Journal of the American Chemical Society*, *58*, 1486.
- Pascual-Ahuir, J. L., & Silla, E. J. (1990). GEPOL: An improved description of molecular surfaces. I. Building the spherical surface set. *Journal of Computational Chemistry*, *11*, 1047.
- Reichardt, C. (1979). *Solvent effects in organic chemistry*. Weinheim, New York: Verlag Chemie.

- Riccardi, D., Li, G., & Cui, Q. (2004). Importance of van der Waals Interactions in QM/MM Simulations. *Journal of Physical Chemistry B*, 108, 6467.
- Rinaldi, D., & Rivail, J. L. (1973). Polarizabilités moléculaires et effet diélectrique de milieu à l'état liquide. Étude théorique de la molécule d'eau et de ses dimères. *Theoretica Chimica Acta*, 32, 57.
- Rinaldi, D., Ruiz-López, M. F., & Rivail, J. L. (1983). *Ab initio* SCF calculations on electrostatically solvated molecules using a deformable three axes ellipsoidal cavity. *Journal of Chemical Physics*, 78, 834.
- Rinaldi, D., Bouchy, A., Rivail, J. L., & Dillet, V. (2004). A self-consistent reaction field model of solvation using distributed multipoles. I. Energy and energy derivatives. *Journal of Chemical Physics*, 120, 2343.
- Rinaldi, D., Bouchy, A., & Rivail, J. L. (2006). A self-consistent reaction field model of solvation using distributed multipoles. II: Second energy derivatives and application to vibrational spectra. *Theoretical Chemistry Accounts*, 116, 664.
- Rivail, J., & Rinaldi, D. (1996). Liquid-state quantum chemistry: Computational applications of the polarizable continuum models. In J. Leszczynski (Ed.), *Computational chemistry, review of current trends* (p. 139). Singapore: World Scientific Publishing.
- Rivail, J. L., & Terryn, B. (1982). Free-energy of an electric charge distribution separated from an infinite dielectric medium by a 3 axes ellipsoidal cavity – application to the study of molecular solvation. *Journal of Chemical Physics*, 79, 1.
- Roca, M., Messer, B., & Warshel, A. (2007). Electrostatic contributions to protein stability and folding energy. *FEBS Letters*, 581, 2065.
- Silla, E. J., Tuñón, I., & Pascual-Ahuir, J. L. (1991). GEPOL: An improved description of molecular surfaces II. Computing the molecular area and volume. *Journal of Computational Chemistry*, 12, 1077.
- Sumner, I., & Iyengar, S. S. (2008). Combining quantum wavepacket *ab initio* molecular dynamics with QM/MM and QM/QM techniques: Implementation blending ONIOM and empirical valence bond theory. *Journal of Chemical Physics*, 129, 054109.
- Tannor, D. J., Marten, B., Friesner, R. M. R. A., Sitkoff, D., Nicholls, A., Rignalda, M., Goddard, W., & Honig, B. (1994). Accurate first principles calculation of molecular charge distributions and solvation energies from *Ab Initio* quantum mechanics and continuum dielectric theory. *Journal of American Chemical Society*, 116, 11875.
- Ten-no, S., Hirata, F., & Kato, S. (1993). A hybrid approach for the solvent effect on the electronic structure of a solute based on the RISM and Hartree-Fock equations. *Chemical Physics Letters*, 214, 391.
- Ten-no, S., Hirata, F., & Kato, S. (1994). Reference interaction site model self-consistent field study for solvation effect on carbonyl compounds in aqueous solution. *Journal of Chemical Physics*, 100, 7443.
- Todorova, T., Seitsonen, A. P., Hutter, J., Kuo, I.-F. W., & Mundy, C. J. (2006). Molecular dynamics simulation of liquid water: Hybrid density functionals. *Journal of Physical Chemistry B*, 110, 3685.
- Tomasi, J. (2004). Thirty years of continuum solvation chemistry: A review, and prospects for the near future. *Theoretical Chemistry Accounts*, 112, 184.
- Tomasi, J., Mennucci, B., & Cammi, R. (2005). Quantum Mechanical Continuum Solvation Models. *Chemical Reviews*, 105, 2999.
- Tongraar, A., Liedl, K. R., & Rode, B. M. (1998). Born-Oppenheimer *ab initio* QM/MM dynamics simulations of Na<sup>+</sup> and K<sup>+</sup> in water: From structure making to structure breaking effects. *Journal of Physical Chemistry A*, 102, 10340.
- Tongraar, A., & Rode, B. M. (2004). Dynamical properties of water molecules in the hydration shells of Na<sup>+</sup> and K<sup>+</sup>: *Ab initio* QM/MM molecular dynamics simulations. *Chemical Physics Letters*, 385, 378.
- VandeVondele, J., Krack, M., Mohamed, F., Parrinello, M., Chassaing, T., & Hutter, J. (2005). Quickstep: Fast and accurate density functional calculations using a mixed Gaussian and plane waves approach. *Computer Physics Communications*, 167, 103.
- Warshel, A. (1991). *Computer modeling of chemical reactions in enzymes and solutions*. New York: Wiley.
- Warshel, A., & Russel, S. T. (1984). Calculations of electrostatic interactions in biological systems and in solutions. *Quarterly Review of Biophysics*, 17, 283.
- Warshel, A., Sharma, P. K., Kato, M., & Parson, W. W. (2006). Modeling electrostatic effects in proteins. *Biochimica et Biophysica Acta*, 1764, 1647.
- Woods, C. J., Manby, F. R., & Mulholland, A. J. (2008). An efficient method for the calculation of quantum mechanics/molecular mechanics free energies. *Journal of Chemical Physics*, 128, 014109.
- Yamabe, S., Minato, T., & Inagaki, S. (1988). *Ab initio* structures of transition-states in electrophilic addition-reactions of molecular halogens with ethene. *Journal of the Chemical Society Chemical Communications*, 532, 35.



# 16 Auxiliary Density Functional Theory: From Molecules to Nanostructures

*Patrizia Calaminici*<sup>1</sup> · *Victor-Daniel Domínguez-Soria*<sup>1</sup> · *Roberto Flores-Moreno*<sup>2</sup> · *Gabriel Ulises Gamboa-Martínez*<sup>1</sup> · *Gerald Geudtner*<sup>1</sup> · *Annick Goursot*<sup>3</sup> · *Dennis R. Salahub*<sup>4</sup> · *Andreas M. Köster*<sup>1</sup>  
<sup>1</sup>Departamento de Química, CINVESTAV, Avenida Instituto Politécnico Nacional 2508, México, Distrito Federal, Mexico

<sup>2</sup>Departamento de Química, CUCEI, Universidad de Guadalajara, Guadalajara, Jalisco, Mexico

<sup>3</sup>Institut Charles Gerhardt, UMR 5253 CNRS, Ecole de Chimie de Montpellier, Montpellier, Cédex 5, France

<sup>4</sup>Department of Chemistry, IBI – Institute for Biocomplexity and Informatics, ISEEE – Institute for Sustainable Energy, Environment, Economy, University of Calgary, Calgary, Alberta, Canada

<b>Introduction</b> .....	<b>575</b>
<b>Theory</b> .....	<b>576</b>
Kohn–Sham Density Functional Theory .....	576
The LCGTO Kohn–Sham Method .....	578
Auxiliary Density Functional theory .....	582
Auxiliary Density Perturbation theory .....	584
<b>Applications</b> .....	<b>586</b>
Dynamics of Sodium Clusters .....	586
Summary .....	589
Structure of Zeolites .....	590
Models and Methodology .....	592
Calculated Geometries and Properties .....	594
Summary .....	598
Stability of Giant Fullerenes .....	598
Computational Details .....	599
Results and Discussion .....	600
Summary .....	602



<i>Conclusion</i> .....	603
<i>Acknowledgments</i> .....	603
<i>References</i> .....	603

**Abstract:** The working equations of auxiliary density functional theory (ADFT) and auxiliary density perturbation theory (ADPT) are derived in the framework of the linear combination of Gaussian type orbital expansion. The ADFT and ADPT implementations in the density functional theory program deMon2k are discussed. The use of ADFT and ADPT in first-principle Born–Oppenheimer molecular dynamics at the pico- to nanosecond time scale is reviewed. In particular, the long-standing mystery of the discrepancy between experiment and computations for the polarizability of small sodium clusters is resolved. Applications of the parallel deMon2k ADFT implementation to systems on the nanometer scale are reviewed. This includes Al-zeolites and giant fullerenes. It is shown that structures as large as  $C_{540}$  can be fully optimized without any symmetry constraints in the ADFT framework employing all-electron basis sets within a few days.

## Introduction

---

Within the broad spectrum of computational methods included in this “Vademecum,” this chapter will focus on Density Functional Theory (DFT) as implemented in the software package deMon, the most recent version of which is known as deMon2k (Köster et al. 2006).

DFT has shown solid progress since its formal beginnings in the theorems of Hohenberg and Kohn (1964) and Kohn and Sham (1965) and its even older roots dating back to the early work of Thomas and Fermi (Fermi 1927, 1928a, b; Thomas 1927), Slater (1951) and others (Gaspar 1954; Schwarz 1972). Our deMon program, too, has a significant track record of steady improvement over the years.

Looking back to the 1960s and early 1970s, the most popular DFT method was the  $X\alpha$ -Scattered Wave (SW) method of Slater and Johnson (Johnson 1966; Johnson and Smith 1970). This method, with its unsightly Muffin-Tin potential, was the trailblazer for DFT in molecular applications. It had good success for the spectroscopy of inorganic complexes, including those containing transition metals (Johnson and Messmer 1974; Johnson and Smith 1971, 1972; Messmer et al. 1975, 1978; Salahub 1978; Weber et al. 1977). But the lack of a full potential prevented the SW technique from performing even such simple tasks as geometry optimizations which, at the time, were coming under control by the usual wave function–based methods of quantum chemistry, at least for simple molecules. Hence  $X\alpha$ -SW remained a rather specialized fringe methodology, which was either ignored or scorned by main-stream quantum chemists.

The 1970s and early 1980s saw work that changed all of that. A few “ab initio quantum chemists” got interested in DFT and slowly but surely brought over some of the methodology and techniques that would allow a broader and broader base of functionality for DFT codes. This was the case for the earliest versions of deMon (Casida et al. 1996; St-Amant and Salahub 1990) as well as for several other codes, such as LCGTO- $X\alpha$  (Dunlap and Rösch 1990), DGAUSS (Andzelm and Wimmer 1992), ADF (Velde et al. 2001), and DMOL (Delley 1990). The deMon program, for example, was based on Gaussian functions and much of the machinery comes over to the DFT world straightforwardly, although some aspects like numerical integration (Becke 1987) remain special. Now geometry optimizations held no mystery for the DFT codes and one could start to think about real chemical applications. Then, in the late 1980s, the holy grail of chemical accuracy was reached, at least for organic thermochemistry, with the development of hybrid functionals (Becke 1993a, b). This really got the chemists interested in DFT and that interest has persisted until today.

In parallel, a broad range of physical and chemical properties and processes came into range. The 1990s saw the development of powerful methodology that included NMR chemical shifts and coupling constants (Malkin et al. 1993a, b, 1994; Valerio et al. 1998), core-electron spectroscopies (Triguero and Pettersson 1998; Triguero et al. 1998), optical properties through the Time-Dependent-DFT (TD-DFT) (Casida 1995; Jamorski et al. 1996) approach, photoelectron spectroscopy including the ZEKE (Zero Electron Kinetic Energy) technique (Calaminici et al. 2001, 2003; Yang et al. 1996), molecular polarizabilities and hyperpolarizabilities (Calaminici et al. 1998, 1999, 2000; Guan et al. 1995; Sim et al. 1992), and many others. DFT and programs like deMon were now established as components of the quantum chemical tool kit. The first decade of the twenty-first century, like its predecessors, continued to show steady progress. Born–Oppenheimer Molecular Dynamics (Calaminici et al. 2007b; Gamboa Martinez et al. 2008; Krishnamurty et al. 2003, 2008a, b; Vázquez-Pérez et al. 2009; Wei and Salahub 1994, 1997; Wei et al. 2000) have now become “routine” (though sometimes costly) for systems with a hundred or so atoms for simulation times of tens or even hundreds of picoseconds. Geometry optimizations and transition state searches (del Campo and Köster 2008) can now be performed for systems containing several hundred atoms (Calaminici et al. 2009; Dominguez-Soria et al. 2007, 2008), the thousand-atom barrier has been broken (Dominguez-Soria et al. 2009; Salahub et al. 2005), thanks mainly to the development of ADFT (Auxiliary Density Functional Theory) (Köster et al. 2004b). Hybrid, QM/MM, and QM/QM’ methodologies (Bertran et al. 2010; Lev et al. 2010) are now being applied with considerable confidence to systems with a level of complexity that would not have been contemplated just a few years ago.

So, at the present time deMon2k is one of the most powerful “pure DFT” codes available. In the next section, we will present the underlying theory, including a description of ADFT and Auxiliary Density Perturbation Theory, a rather new non-iterative alternative to the Coupled Perturbed Kohn–Sham (CPKS) methodology. Then, in the Applications section, we will describe three recent studies that represent the state of the art in “pure DFT” on large and/or difficult molecular and cluster problems, the largest of which are well into the nano-regime. We solve a long-standing mystery of the discrepancy between experiment and computations for the polarizabilities of sodium clusters (up to the nonamer) – finite-temperature effects are the key. In the second application, large models for Na<sup>+</sup> and protonated Al zeolites are constructed and the acidic sites are analyzed, including important vibrational effects. Finally the structures of giant fullerenes, up to C<sub>540</sub> have been optimized using full all-electron basis sets. The results confirm that for all of the large fullerenes a faceted shape is preferred over a spherical shape. The calculated binding energies are in the diamond range, but considerably below the value for graphene.

## Theory

---

### Kohn–Sham Density Functional Theory

---

Density functional theory (DFT) is based on the Hohenberg–Kohn theorem (Hohenberg and Kohn 1964). According to this theorem the ground state energy,  $E$ , of a many electron system with the external potential  $v(\mathbf{r})$  can be expressed by the following density functional (Dreizler and Gross 1990; Parr and Yang 1989):

$$E[\rho] = T[\rho] + \int \rho(\mathbf{r}) v(\mathbf{r}) d\mathbf{r} + V_{ee}[\rho]. \quad (16.1)$$

Here  $\rho(\mathbf{r})$  is the electron density,  $T[\rho]$  is the kinetic energy, and  $V_{ee}[\rho]$  collects all electron–electron interaction energies. A major technical problem is the accurate description of the kinetic energy functional  $T[\rho]$ . In the Kohn–Sham approximation this problem is avoided by introducing orbitals of a non-interacting reference system. Levy and Perdew (Levy 1979; Levy and Perdew 1985) have shown that these orbitals are delivered by the following minimization procedure:

$$T_{\text{KS}}[\rho] = \min_{\Psi \rightarrow \rho} \langle \Psi | \hat{T} | \Psi \rangle. \quad (16.2)$$

Here  $\Psi$  is a Slater determinant composed of the Kohn–Sham orbitals  $\psi_i(\mathbf{r})$ , and  $T_{\text{KS}}[\rho]$  is the corresponding Kohn–Sham kinetic energy. This energy can be calculated from the occupied orbitals of the non-interacting system,

$$T_{\text{KS}}[\rho] = -\frac{1}{2} \sum_i^{\text{occ}} \langle \psi_i[\rho] | \nabla^2 | \psi_i[\rho] \rangle. \quad (16.3)$$

These Kohn–Sham orbitals are functionals of the density and can be derived from it as shown by Parr and coworkers (Zhao and Parr 1992, 1993; Zhao et al. 1994). Imposing the constraint that occupied orbitals of the non-interacting system reproduce the true ground state density,

$$\rho(\mathbf{r}) = \sum_i^{\text{occ}} |\psi_i(\mathbf{r})|^2, \quad (16.4)$$

to the variation  $\blacktriangleright$  Eq. 16.2 and using a local Lagrange multiplier  $v_{\text{KS}}(\mathbf{r})$ , the following set of equations is obtained:

$$\left( -\frac{1}{2} \nabla^2 + v_{\text{KS}}(\mathbf{r}) \right) \psi_i(\mathbf{r}) = \epsilon_i \psi_i(\mathbf{r}). \quad (16.5)$$

These are the Kohn–Sham equations and  $v_{\text{KS}}(\mathbf{r})$  determines (within a trivial constant) the external potential of the Kohn–Sham reference system.

In order to find a more explicit representation of  $v_{\text{KS}}(\mathbf{r})$  we now rewrite the energy functional  $\blacktriangleright$  Eq. 16.1 using the Kohn–Sham kinetic energy term  $\blacktriangleright$  Eq. 16.3 and the explicit expression for the classic electronic interaction (Coulomb) energy,

$$J[\rho] = \frac{1}{2} \iint \frac{\rho(\mathbf{r})\rho(\mathbf{r}')}{|\mathbf{r} - \mathbf{r}'|} d\mathbf{r} d\mathbf{r}', \quad (16.6)$$

It then follows:

$$E[\rho] = T_{\text{KS}}[\rho] + \int \rho(\mathbf{r}) v(\mathbf{r}) d\mathbf{r} + J[\rho] + E_{\text{xc}}[\rho]. \quad (16.7)$$

Here the newly introduced exchange–correlation energy functional is defined as:

$$E_{\text{xc}}[\rho] \equiv T[\rho] - T_{\text{KS}}[\rho] + V_{ee}[\rho] - J[\rho]. \quad (16.8)$$

This quantity collects all non-classical interactions between the electrons and the difference of the kinetic energies of the interacting and non-interacting system. The accuracy of the Kohn–Sham method is mainly determined by the quality of the approximation used for the calculation of  $E_{\text{xc}}[\rho]$ . The kinetic energy difference appearing in  $E_{\text{xc}}[\rho]$  is on the order of magnitude of the correlation energy (Almbladh and Pedroza 1984).

Based on the Hohenberg–Kohn theorem, the ground state density minimizes the energy functional  $\blacktriangleright$  Eq. 16.7 and hence satisfies the Euler equation:

$$\mu = \frac{\delta E[\rho]}{\delta \rho(\mathbf{r})}, \quad (16.9)$$

where  $\mu$  is the Lagrange multiplier associated with the normalization of the electronic density to the number of electrons  $n$  in the system:

$$\int \rho(\mathbf{r}) d\mathbf{r} = n. \quad (16.10)$$

The functional derivative of the energy functional  $\blacktriangleright$  Eq. 16.7 yields:

$$\begin{aligned} \frac{\delta E[\rho]}{\delta \rho(\mathbf{r})} &= \frac{\delta T_{\text{KS}}[\rho]}{\delta \rho(\mathbf{r})} + v(\mathbf{r}) + \int \frac{\rho(\mathbf{r}')}{|\mathbf{r} - \mathbf{r}'|} d\mathbf{r}' + \frac{\delta E_{\text{xc}}[\rho]}{\delta \rho(\mathbf{r})} \\ &= \frac{\delta T_{\text{KS}}[\rho]}{\delta \rho(\mathbf{r})} + v_{\text{KS}}(\mathbf{r}). \end{aligned} \quad (16.11)$$

Thus, the Kohn–Sham potential has the following explicit form:

$$v_{\text{KS}}(\mathbf{r}) = v(\mathbf{r}) + \int \frac{\rho(\mathbf{r}')}{|\mathbf{r} - \mathbf{r}'|} d\mathbf{r}' + v_{\text{xc}}[\rho; \mathbf{r}], \quad (16.12)$$

where the exchange-correlation potential is defined as:

$$v_{\text{xc}}[\rho; \mathbf{r}] \equiv \frac{\delta E_{\text{xc}}[\rho]}{\delta \rho(\mathbf{r})}. \quad (16.13)$$

Substituting  $\blacktriangleright$  Eq. 16.12 in  $\blacktriangleright$  Eq. 16.5 yields the canonical Kohn–Sham orbital equations:

$$\left( -\frac{1}{2}\nabla^2 + v(\mathbf{r}) + \int \frac{\rho(\mathbf{r}')}{|\mathbf{r} - \mathbf{r}'|} d\mathbf{r}' + v_{\text{xc}}[\rho; \mathbf{r}] \right) \psi_i(\mathbf{r}) = \epsilon_i \psi_i(\mathbf{r}). \quad (16.14)$$

These equations have to be solved iteratively to reach self-consistency. They can be cast in matrix form yielding Roothaan–Hall-like equations (Hall 1951; Roothaan 1951).

## The LCGTO Kohn–Sham Method

In the linear combination of Gaussian-type orbitals (LCGTO) ansatz the Kohn–Sham orbitals are expanded in atomic orbitals:

$$\psi_i(\mathbf{r}) = \sum_{\mu} c_{\mu i} \mu(\mathbf{r}). \quad (16.15)$$

In our notation  $\mu(\mathbf{r})$  represents an atomic orbital and  $c_{\mu i}$  the corresponding molecular orbital coefficient. To avoid unnecessary complications in the presentation we restrict ourselves to the closed-shell case. The extension to the open-shell formalism (Binkley et al. 1974; Pople and Nesbet 1954; Roothaan 1960) is straightforward. With the LCGTO expansion we find for the electron density  $\blacktriangleright$  Eq. 16.4:

$$\rho(\mathbf{r}) = \sum_{\mu, \nu} P_{\mu\nu} \mu(\mathbf{r}) \nu(\mathbf{r}). \quad (16.16)$$

$P_{\mu\nu}$  represents an element of the closed-shell density matrix defined as:

$$P_{\mu\nu} \equiv 2 \sum_i^{\text{occ}} c_{\mu i} c_{\nu i}. \quad (16.17)$$

Using the above expansions for the Kohn–Sham orbitals  $\blacktriangleright$  Eq. 16.15 and the density  $\blacktriangleright$  Eq. 16.16, the Kohn–Sham energy expression  $\blacktriangleright$  Eq. 16.7 can be rewritten in terms of atomic orbitals,

$$E = \sum_{\mu,\nu} P_{\mu\nu} H_{\mu\nu} + \frac{1}{2} \sum_{\mu,\nu} \sum_{\sigma,\tau} P_{\mu\nu} P_{\sigma\tau} \langle \mu\nu \| \sigma\tau \rangle + E_{xc}[\rho], \quad (16.18)$$

with

$$H_{\mu\nu} = \langle \mu | -\frac{1}{2} \nabla^2 | \nu \rangle - \sum_C^{\text{Atoms}} \langle \mu | \frac{Z_C}{|\mathbf{r}-\mathbf{C}|} | \nu \rangle \quad (16.19)$$

and

$$\langle \mu\nu \| \sigma\tau \rangle \equiv \iint \frac{\mu(\mathbf{r})\nu(\mathbf{r})\sigma(\mathbf{r}')\tau(\mathbf{r}')}{|\mathbf{r}-\mathbf{r}'|} d\mathbf{r} d\mathbf{r}'. \quad (16.20)$$

where the symbol  $\|$  represents the  $1/|\mathbf{r}-\mathbf{r}'|$  operator.

The SCF convergence is based on this energy expression. The  $H_{\mu\nu}$  in  $\blacktriangleright$  Eq. 16.18 denotes elements of the one electron Hamiltonian matrix. They are built from the kinetic and nuclear attraction energy of the electrons and describe the motion of an electron in the nuclear framework. The computation of this matrix has a formal quadratic scaling with the number of basis functions  $N$  of the system. The second term in  $\blacktriangleright$  Eq. 16.18 represents the Coulomb repulsion energy of the electrons. In contrast to Hartree-Fock theory the calculation of the Coulomb and exchange energies are separated in DFT. The Coulomb term introduces a formal  $N^4$  scaling. The exchange-correlation energy can be obtained by means of an integral of the following type:

$$E_{xc}[\rho] = \int \rho(\mathbf{r}) \epsilon_{xc}[\rho] d\mathbf{r}. \quad (16.21)$$

In general, the explicit form of the exchange-correlation energy density,  $\epsilon_{xc}[\rho]$ , will not permit an analytic solution of this integral. Therefore, a three-dimensional numerical integration has to be performed. It scales formally as  $N^2 \times G$ , where  $G$  denotes the number of grid points in the numerical integration.

From the above discussion it follows that the calculation of the Coulomb repulsion energy represents the most demanding computational task in  $\blacktriangleright$  Eq. 16.18. The introduction of the variational approximation of the Coulomb potential (Dunlap et al. 1979; Mintmire and Dunlap 1982; Mintmire et al. 1982) reduces the formal scaling of this term to  $N^2 \times M$ , where  $M$  is the number of auxiliary functions which is usually three to five times  $N$ . This technique is nowadays used in most LCGTO-DFT programs. It is identical to the so-called resolution of the identity (RI) (Flores-Moreno and Ortiz 2009; Hamel et al. 2001; Vahtras et al. 1993) that cropped up in wave function methods, too. The variational approximation of the Coulomb potential, as implemented in deMon2k, is based on the minimization of the following self-interaction term:

$$\mathcal{E}_2 = \frac{1}{2} \iint \frac{[\rho(\mathbf{r}) - \tilde{\rho}(\mathbf{r})][\rho(\mathbf{r}') - \tilde{\rho}(\mathbf{r}')] }{|\mathbf{r}-\mathbf{r}'|} d\mathbf{r} d\mathbf{r}'. \quad (16.22)$$

The approximate density  $\tilde{\rho}(\mathbf{r})$  is expanded in primitive Hermite Gaussians (Köster 2003) which are centered at the atoms:

$$\tilde{\rho}(\mathbf{r}) = \sum_{\bar{k}} x_{\bar{k}} \bar{k}(\mathbf{r}). \quad (16.23)$$

The primitive Hermite Gaussian auxiliary functions are indicated by a bar. An (unnormalized) auxiliary function  $\bar{k}(\mathbf{r})$  centered at atom  $\mathbf{C}$  with exponent  $\zeta_{\bar{k}}$  has the form:

$$\bar{k}(\mathbf{r}) = \left( \frac{\partial}{\partial C_x} \right)^{\bar{k}_x} \left( \frac{\partial}{\partial C_y} \right)^{\bar{k}_y} \left( \frac{\partial}{\partial C_z} \right)^{\bar{k}_z} e^{-\zeta_{\bar{k}}(\mathbf{r}-\mathbf{C})^2}. \quad (16.24)$$

In deMon2k, these auxiliary functions are normalized with respect to the Coulomb norm and grouped into *s*, *spd*, and *spdfg* sets. The exponents are shared within each of these sets (Andzelm et al. 1985, 1987). Based on the exponent range of the primary atomic basis set an automatic generation of auxiliary function sets, indicated by the abbreviation GEN, is available in deMon2k. A detailed description is given in Calaminici et al. (2007a) for all-electron calculations and in Calaminici et al. (2005) for effective and model core potential calculations.

With the LCGTO expansion for  $\rho(\mathbf{r})$  and  $\tilde{\rho}(\mathbf{r})$  we obtain the following representation for  $\mathcal{E}_2$ :

$$\begin{aligned} \mathcal{E}_2 &= \frac{1}{2} \sum_{\mu,\nu} \sum_{\sigma,\tau} P_{\mu\nu} P_{\sigma\tau} \langle \mu\nu \| \sigma\tau \rangle \\ &\quad - \sum_{\mu,\nu} \sum_{\bar{k}} P_{\mu\nu} \langle \mu\nu \| \bar{k} \rangle x_{\bar{k}} + \frac{1}{2} \sum_{\bar{k},\bar{l}} x_{\bar{k}} x_{\bar{l}} \langle \bar{k} \| \bar{l} \rangle. \end{aligned} \quad (16.25)$$

The two- and three-center electron repulsion integrals are defined as:

$$\langle \bar{k} \| \bar{l} \rangle \equiv \iint \frac{\bar{k}(\mathbf{r})\bar{l}(\mathbf{r}')}{|\mathbf{r} - \mathbf{r}'|} d\mathbf{r} d\mathbf{r}', \quad (16.26)$$

$$\langle \mu\nu \| \bar{k} \rangle \equiv \iint \frac{\mu(\mathbf{r})\nu(\mathbf{r})\bar{k}(\mathbf{r}')}{|\mathbf{r} - \mathbf{r}'|} d\mathbf{r} d\mathbf{r}'. \quad (16.27)$$

The expansion coefficients  $x_{\bar{k}}$  of the approximate density are determined by the minimization of  $\mathcal{E}_2$ :

$$\frac{\partial \mathcal{E}_2}{\partial x_{\bar{m}}} = - \sum_{\mu,\nu} P_{\mu\nu} \langle \mu\nu \| \bar{m} \rangle + \sum_{\bar{k}} x_{\bar{k}} \langle \bar{k} \| \bar{m} \rangle = 0 \quad \forall \bar{m}. \quad (16.28)$$

At this point it is useful to introduce the Coulomb matrix,

$$\mathbf{G} = \begin{pmatrix} \langle \bar{1} \| \bar{1} \rangle & \langle \bar{1} \| \bar{2} \rangle & \dots & \langle \bar{1} \| \bar{m} \rangle \\ \langle \bar{2} \| \bar{1} \rangle & \langle \bar{2} \| \bar{2} \rangle & \dots & \langle \bar{2} \| \bar{m} \rangle \\ \vdots & \vdots & \ddots & \vdots \\ \langle \bar{m} \| \bar{1} \rangle & \langle \bar{m} \| \bar{2} \rangle & \dots & \langle \bar{m} \| \bar{m} \rangle \end{pmatrix}, \quad (16.29)$$

and the Coulomb vector

$$\mathbf{J} = \begin{pmatrix} \sum_{\mu,\nu} P_{\mu\nu} \langle \mu\nu \| \bar{1} \rangle \\ \sum_{\mu,\nu} P_{\mu\nu} \langle \mu\nu \| \bar{2} \rangle \\ \vdots \\ \sum_{\mu,\nu} P_{\mu\nu} \langle \mu\nu \| \bar{m} \rangle \end{pmatrix}. \quad (16.30)$$

With  $\mathbf{G}$  and  $\mathbf{J}$  the following system of inhomogeneous equations for the determination of the fitting coefficients, collected in  $\mathbf{x}$ , can be formulated:

$$\mathbf{G} \mathbf{x} = \mathbf{J}. \quad (16.31)$$

A straightforward solution is obtained by the inversion of the Coulomb matrix  $\mathbf{G}$ :

$$\mathbf{x} = \mathbf{G}^{-1} \mathbf{J}. \quad (16.32)$$

Because  $\mathbf{G}$  is symmetric and positive definite its inversion can be very efficiently performed via Cholesky decomposition (Press et al. 1992). However, if very large auxiliary function sets

are used the Coulomb matrix tends to become ill-conditioned. As a consequence the Cholesky decomposition might fail. For this reason in deMon2k we perform by default a singular value decomposition (SVD) of  $\mathbf{G}$  at the initial SCF and use in the following energy calculations (e.g., in a geometry optimization or molecular dynamics run) a numerical solver (Dominguez-Soria et al. 2009) that acts only on the non-redundant space of the SVD. This has proven to be a good compromise between accuracy and efficiency. The approach is suitable for systems with thousands of atoms and tight SCF convergence criteria ( $10^{-9}$  a.u.). The SVD threshold can be altered by the keyword MATINV (Köster et al. 2010). Its default value is  $10^{-6}$ .

After the description of the calculation of the fitting coefficients we now turn to the energy and SCF calculation. Because  $\mathcal{E}_2$  is positive definite the following inequality holds:

$$\frac{1}{2} \sum_{\mu,\nu} \sum_{\sigma,\tau} P_{\mu\nu} P_{\sigma\tau} \langle \mu\nu \| \sigma\tau \rangle \geq \sum_{\bar{k}} \sum_{\mu,\nu} P_{\mu\nu} \langle \mu\nu \| \bar{k} \rangle x_{\bar{k}} - \frac{1}{2} \sum_{\bar{k},\bar{l}} x_{\bar{k}} x_{\bar{l}} \langle \bar{k} \| \bar{l} \rangle.$$

With this inequality an approximate SCF energy, which is based on  $\blacklozenge$  Eq. 16.18, can be derived:

$$E = \sum_{\mu,\nu} P_{\mu\nu} H_{\mu\nu} + \sum_{\bar{k}} \sum_{\mu,\nu} P_{\mu\nu} \langle \mu\nu \| \bar{k} \rangle x_{\bar{k}} - \frac{1}{2} \sum_{\bar{k},\bar{l}} x_{\bar{k}} x_{\bar{l}} \langle \bar{k} \| \bar{l} \rangle + E_{\text{xc}}[\rho]. \quad (16.33)$$

The variation of this energy expression with respect to the molecular orbital coefficients, constraining the Kohn–Sham orbitals to be orthonormal,

$$\sum_{\mu,\nu} c_{\mu i} S_{\mu\nu} c_{\nu j} = \delta_{ij} \quad \forall \quad i, j, \quad (16.34)$$

yields:

$$\frac{\partial E}{\partial c_{\mu i}} = 2 \sum_{\nu} \left( H_{\mu\nu} + \sum_{\bar{k}} \langle \mu\nu \| \bar{k} \rangle x_{\bar{k}} + \langle \mu | v_{\text{xc}}[\rho] | \nu \rangle \right) c_{\nu i} - 2 \sum_{\nu} \sum_j S_{\mu\nu} c_{\nu j} \epsilon_{ji} \quad \forall \quad \mu, i. \quad (16.35)$$

Here, the derivative of the exchange–correlation energy, restricting ourselves to local functionals for clarity, was developed according to Gel'fand and Fomin (1963):

$$\frac{\partial E_{\text{xc}}[\rho]}{\partial c_{\mu i}} = \int \frac{\delta E_{\text{xc}}[\rho]}{\delta \rho(\mathbf{r})} \frac{\partial \rho(\mathbf{r})}{\partial c_{\mu i}} d\mathbf{r} = 2 \sum_{\nu} \langle \mu | v_{\text{xc}}[\rho] | \nu \rangle c_{\nu i}. \quad (16.36)$$

The  $\epsilon_{ji}$  in  $\blacklozenge$  Eq. 16.35 are the undetermined Lagrange multipliers. Because the electronic density is invariant to unitary transformations of the occupied molecular orbitals (MOs) it is possible (and convenient) to choose a set of MOs for which the off-diagonal multipliers are zero. These MOs are called canonical and are the solutions of the canonical Kohn–Sham equations,

$$\mathbf{Kc} = \mathbf{Sc}\boldsymbol{\epsilon}, \quad (16.37)$$

with the elements of the Kohn–Sham matrix  $\mathbf{K}$  defined as:

$$K_{\mu\nu} \equiv H_{\mu\nu} + \sum_{\bar{k}} \langle \mu\nu \| \bar{k} \rangle x_{\bar{k}} + \langle \mu | v_{\text{xc}}[\rho] | \nu \rangle. \quad (16.38)$$

In  $\blacklozenge$  Eq. 16.37,  $\mathbf{S}$  represents the overlap matrix,  $\mathbf{c}$  the molecular orbital coefficient matrix, and  $\boldsymbol{\epsilon}$  the diagonal matrix of the Lagrange multipliers, that is, the Kohn–Sham orbital energies.



As can be seen from [Eq. 16.38](#) the Kohn–Sham matrix elements depend on the fitting coefficients  $x_{\bar{k}}$  and the molecular orbital coefficients  $c_{\mu i}$  via the dependence of the exchange–correlation potential on the orbital density  $\rho(\mathbf{r})$ . In deMon2k this theoretical model is selected by the keyword specification VXCTYPE BASIS (Köster et al. 2010) and is often referred to as the BASIS approach. It should be noted that the SCF convergence can be guided either by the molecular orbital coefficients or by the fitting coefficients that arise from the variational fitting of the Coulomb potential. In any case the variational fitting of the Coulomb potential turns the original energy minimization into a MinMax variation (Köster et al. 2002). In deMon2k the SCF convergence is guided by the fitting coefficients because they form a vector rather than a matrix. As a result memory efficient SCF convergence acceleration methods suitable for very large systems are available (Köster et al. 2009).

Due to the use of efficient three-center electron repulsion integral algorithms (Köster 1996, 2003) the numerical integration of the exchange–correlation energy and potential is the computationally most demanding task in this approach. Therefore, a more efficient approach for the calculation of the exchange–correlation energy and potential is desirable. In fact, the use of auxiliary functions for the calculation of the exchange–correlation energy and potential has a long history in DFT methods (Baerends et al. 1973; Sambe and Felton 1975). In programs like deMon-KS (Casida et al. 1996), DGAUSS (Andzelm and Wimmer 1992), or GTOFF (Trickey et al. 2004) the exchange–correlation potential is expanded in auxiliary functions as proposed by Sambe and Felton (1975). The expansion coefficients are obtained by a least squares fit on a grid. Because this fit and the corresponding energy expression are not variational only approximate gradients and higher energy derivatives are available.

## Auxiliary Density Functional theory

As an alternative to the fitting of the exchange–correlation potential by auxiliary functions the direct use of the auxiliary function density from the variational fitting of the Coulomb potential for the calculation of the exchange–correlation potential has been investigated over the last years (Belpassi et al. 2006; Birkenheuer et al. 2005; Janetzko et al. 2008; Köster 1998; Köster et al. 2004b; Laikov 1997). The resulting energy expression, from now on named the auxiliary density functional theory (ADFT) energy, is variational and has the form (Köster et al. 2004b):

$$E = \sum_{\mu, \nu} P_{\mu\nu} H_{\mu\nu} + \sum_{\bar{k}} \sum_{\mu, \nu} P_{\mu\nu} \langle \mu\nu \| \bar{k} \rangle x_{\bar{k}} - \frac{1}{2} \sum_{\bar{k}, \bar{l}} x_{\bar{k}} x_{\bar{l}} \langle \bar{k} \| \bar{l} \rangle + E_{xc}[\tilde{\rho}]. \quad (16.39)$$

In deMon2k, this theoretical model is selected by the keyword specification VXCTYPE AUXIS (Köster et al. 2010), that is the default setting, and often referred to as the AUXIS approach. Because the approximate density is a linear combination of auxiliary functions the density calculation at each grid point scales linearly. In contrast, with the orbital density, products of basis functions have to be evaluated. Obviously, this represents a considerable simplification of the grid work. In particular, using auxiliary function sets that share the same exponents reduces considerably the number of expensive exponential function evaluations at each grid point. Moreover, by using Hermite Gaussian auxiliary functions the Hermite polynomial recurrence relations (Saunders 1983) can be used for the function calculations on the grid. For the numerical integration of the exchange–correlation energy and potential adaptive and fixed grids

(Köster et al. 2004a; Krack and Köster 1998) of various qualities are available in deMon2k. The default setting guarantees energy accuracies in the range of  $10^{-5}$  a.u. for most systems. Higher accuracies can be selected with the GRID keyword (Köster et al. 2010).

The variation of the ADFT energy expression  $\blacktriangleright$  Eq. 16.39 with respect to the molecular orbital coefficients, again constraining the Kohn–Sham orbitals to orthonormality  $\blacktriangleright$  Eq. 16.34, yields:

$$\frac{\partial E}{\partial c_{\mu i}} = 2 \sum_{\nu} \left( H_{\mu\nu} + \sum_{\bar{k}} \langle \mu\nu \| \bar{k} \rangle (x_{\bar{k}} + z_{\bar{k}}) \right) c_{\nu i} - 2 \sum_{\nu} \sum_j S_{\mu\nu} c_{\nu j} \epsilon_{ji} \quad \forall \mu, i. \quad (16.40)$$

The derivative of the exchange–correlation energy, again restricting ourselves to local functionals, now contains the fitted density:

$$\frac{\partial E_{xc}[\tilde{\rho}]}{\partial c_{\mu i}} = \int \frac{\delta E_{xc}[\tilde{\rho}]}{\delta \tilde{\rho}(\mathbf{r})} \frac{\partial \tilde{\rho}(\mathbf{r})}{\partial c_{\mu i}} d\mathbf{r}. \quad (16.41)$$

The resulting functional derivative defines the exchange–correlation potential calculated with the fitted density:

$$v_{xc}[\tilde{\rho}; \mathbf{r}] \equiv \frac{\delta E_{xc}[\tilde{\rho}]}{\delta \tilde{\rho}(\mathbf{r})}. \quad (16.42)$$

The derivative of the fitted density with respect to molecular orbital coefficients is given by:

$$\frac{\partial \tilde{\rho}(\mathbf{r})}{\partial c_{\mu i}} = \sum_{\bar{l}} \frac{\partial x_{\bar{l}}}{\partial c_{\mu i}} \bar{l}(\mathbf{r}). \quad (16.43)$$

After differentiation of  $\blacktriangleright$  Eq. 16.32 it follows for the derivative of the fitted density:

$$\frac{\partial \tilde{\rho}(\mathbf{r})}{\partial c_{\mu i}} = 2 \sum_{\bar{k}, \bar{l}} \sum_{\nu} c_{\nu i} \langle \mu\nu \| \bar{k} \rangle G_{\bar{k}\bar{l}}^{-1} \bar{l}(\mathbf{r}). \quad (16.44)$$

Substituting this expression and the definition of the approximate exchange–correlation potential  $\blacktriangleright$  Eq. 16.42 into  $\blacktriangleright$  Eq. 16.41 yields:

$$\frac{\partial E_{xc}[\tilde{\rho}]}{\partial c_{\mu i}} = 2 \sum_{\bar{k}} \sum_{\nu} c_{\nu i} \langle \mu\nu \| \bar{k} \rangle z_{\bar{k}}, \quad (16.45)$$

with

$$z_{\bar{k}} = \sum_{\bar{l}} G_{\bar{k}\bar{l}}^{-1} \langle \bar{l} | v_{xc}[\tilde{\rho}] \rangle. \quad (16.46)$$

In order to distinguish the  $x_{\bar{k}}$  and  $z_{\bar{k}}$  coefficients we name them Coulomb and exchange–correlation coefficients, respectively. The corresponding Kohn–Sham matrix elements are defined as:

$$K_{\mu\nu} = H_{\mu\nu} + \sum_{\bar{k}} \langle \mu\nu \| \bar{k} \rangle (x_{\bar{k}} + z_{\bar{k}}). \quad (16.47)$$

These matrix elements depend only on the fitting coefficients. In contrast to the traditional fitting of the exchange–correlation potential ADFT employs the fitted density for the exchange–correlation potential calculation and hence the numerical integration of  $v_{xc}$  is not avoided. However, the work on the grid is considerably reduced because only one-center terms are

involved in the integrals in  $\blacktriangleright$  Eq. 16.46. Despite the fact that these terms are evaluated numerically, the calculation of the Kohn–Sham elements  $\blacktriangleright$  Eq. 16.47 scales linearly (Köster et al. 2003). Because the ADFT energy is variational, analytic gradients (Köster et al. 2004b) and higher energy derivatives can be formulated.

## Auxiliary Density Perturbation theory

For second energy derivatives that appear in the calculation of polarizabilities, chemical hardness, van der Waals coefficients, vibrational frequencies and other second order properties, the perturbed density matrix is required. McWeeny’s self-consistent perturbation (SCP) theory (Diercksen and McWeeny 1966; Dodds et al. 1977; McWeeny 1962, 2001; McWeeny and Diercksen 1968; McWeeny et al. 1977) represents a direct approach for the calculation of this matrix. For the clarity of the presentation we assume perturbation-independent basis and auxiliary functions and restrict ourselves to closed-shell systems. Under these conditions the elements of the perturbed density matrix are given by the SCP formalism of McWeeny et al. (1977):

$$P_{\mu\nu}^{(\lambda)} \equiv \frac{\partial P_{\mu\nu}}{\partial \lambda} = 2 \sum_i^{\text{occ}} \sum_a^{\text{uno}} \frac{\mathcal{K}_{ia}^{(\lambda)}}{\varepsilon_i - \varepsilon_a} (c_{\mu i} c_{\nu a} + c_{\mu a} c_{\nu i}). \quad (16.48)$$

Extension to the case of perturbation dependent basis and auxiliary functions is straightforward. However, a number of extra terms appear which only distract from the discussion. In  $\blacktriangleright$  Eq. 16.48  $\lambda$  denotes the perturbation parameter, for example, an electric field component in the calculation of polarizabilities,  $\varepsilon_i$  and  $\varepsilon_a$  orbital energies of the  $i$ th occupied and  $a$ th unoccupied orbital, and  $\mathcal{K}_{ia}^{(\lambda)}$  the perturbed Kohn–Sham matrix in the molecular orbital representation:

$$\mathcal{K}_{ia}^{(\lambda)} = \sum_{\mu,\nu} c_{\mu i} c_{\nu a} K_{\mu\nu}^{(\lambda)}, \quad (16.49)$$

with

$$K_{\mu\nu}^{(\lambda)} = H_{\mu\nu}^{(\lambda)} + \sum_{\bar{k}} \langle \mu\nu | \bar{k} \rangle (x_{\bar{k}}^{(\lambda)} + z_{\bar{k}}^{(\lambda)}). \quad (16.50)$$

The perturbation of the exchange–correlation coefficients is given by:

$$z_{\bar{k}}^{(\lambda)} = \sum_I G_{\bar{k}I}^{-1} \langle \bar{I} | v_{\text{xc}}^{(\lambda)}[\tilde{\rho}] \rangle. \quad (16.51)$$

Since  $v_{\text{xc}}[\tilde{\rho}; \mathbf{r}]$  itself is a (local) functional of the density it follows:

$$\begin{aligned} \langle \bar{I} | v_{\text{xc}}^{(\lambda)}[\tilde{\rho}] \rangle &= \iint \bar{l}(\mathbf{r}) \frac{\delta v_{\text{xc}}[\tilde{\rho}; \mathbf{r}]}{\delta \tilde{\rho}(\mathbf{r}')} \frac{\partial \tilde{\rho}(\mathbf{r}')}{\partial \lambda} d\mathbf{r} d\mathbf{r}' \\ &= \sum_{\bar{m}} \langle \bar{I} | f_{\text{xc}}[\tilde{\rho}] | \bar{m} \rangle x_{\bar{m}}^{(\lambda)}, \end{aligned} \quad (16.52)$$

with the exchange–correlation kernel defined as:

$$f_{\text{xc}}(\mathbf{r}, \mathbf{r}') = \frac{\delta^2 E_{\text{xc}}[\tilde{\rho}]}{\delta \tilde{\rho}(\mathbf{r}') \delta \tilde{\rho}(\mathbf{r})} = \frac{\delta v_{\text{xc}}[\tilde{\rho}; \mathbf{r}]}{\delta \tilde{\rho}(\mathbf{r}')}. \quad (16.53)$$

Compared to the standard LCGTO kernel  $\langle \mu\nu | f_{xc} | \sigma\tau \rangle$  the scaling of the kernel calculation is reduced by almost two orders of magnitude in the ADPT approach. With this result we now rewrite the perturbed Kohn–Sham matrix elements in molecular orbital representation as:

$$\mathcal{K}_{ia}^{(\lambda)} = \mathcal{H}_{ia}^{(\lambda)} + \sum_{\bar{k}, \bar{l}} \langle ia \| \bar{k} \rangle M_{\bar{k}\bar{l}} x_{\bar{l}}^{(\lambda)}, \quad (16.54)$$

with

$$M_{\bar{k}\bar{l}} = \delta_{\bar{k}\bar{l}} + \sum_{\bar{m}} G_{\bar{k}\bar{m}}^{-1} \langle \bar{m} | f_{xc}[\bar{\rho}] | \bar{l} \rangle. \quad (16.55)$$

On the other hand we find as the derivative of the fitting equation system  $\blacklozenge$  Eq. 16.31:

$$\sum_{\bar{k}} G_{\bar{m}\bar{k}} x_{\bar{k}}^{(\lambda)} = \sum_{\mu, \nu} P_{\mu\nu}^{(\lambda)} \langle \mu\nu \| \bar{m} \rangle. \quad (16.56)$$

Substituting  $\blacklozenge$  Eqs. 16.54 and  $\blacklozenge$  16.56 into  $\blacklozenge$  Eq. 16.48 yields:

$$\begin{aligned} \sum_{\mu, \nu} P_{\mu\nu}^{(\lambda)} \langle \mu\nu \| \bar{m} \rangle &= 4 \sum_i^{\text{occ}} \sum_a^{\text{uno}} \frac{\langle \bar{m} \| ia \rangle \mathcal{H}_{ia}^{(\lambda)}}{\varepsilon_i - \varepsilon_a} \\ &\quad + 4 \sum_i^{\text{occ}} \sum_a^{\text{uno}} \sum_{\bar{k}, \bar{l}} \frac{\langle \bar{m} \| ia \rangle \langle ia \| \bar{k} \rangle}{\varepsilon_i - \varepsilon_a} M_{\bar{k}\bar{l}} x_{\bar{l}}^{(\lambda)} \\ &= \sum_{\bar{k}} G_{\bar{m}\bar{k}} x_{\bar{k}}^{(\lambda)}. \end{aligned} \quad (16.57)$$

We now define the elements of the Coulomb coupling matrix as:

$$A_{\bar{k}\bar{l}} = \sum_i^{\text{occ}} \sum_a^{\text{uno}} \frac{\langle \bar{k} \| ia \rangle \langle ia \| \bar{l} \rangle}{\varepsilon_i - \varepsilon_a}. \quad (16.58)$$

Similarly, the elements of the perturbation vector are given by:

$$b_{\bar{k}}^{(\lambda)} = \sum_i^{\text{occ}} \sum_a^{\text{uno}} \frac{\langle \bar{m} \| ia \rangle \mathcal{H}_{ia}^{(\lambda)}}{\varepsilon_i - \varepsilon_a}. \quad (16.59)$$

With these matrices and vectors,  $\blacklozenge$  Eq. 16.57 can now be recasted into:

$$(\mathbf{G} - 4\mathbf{A}\mathbf{M}) \mathbf{x}^{(\lambda)} = 4\mathbf{b}^{(\lambda)} \iff \mathbf{x}^{(\lambda)} = \left( \frac{1}{4} \mathbf{G} - \mathbf{A}\mathbf{M} \right)^{-1} \mathbf{b}^{(\lambda)}. \quad (16.60)$$

In the case of perturbation-dependent basis and auxiliary functions only  $\mathbf{b}^{(\lambda)}$  has to be modified. The matrix that needs to be inverted is exactly the same as in  $\blacklozenge$  Eq. 16.60. Thus, the calculation of the perturbed fitting coefficients is reduced to the solution of the above inhomogeneous equation system. In contrast to the traditional coupled-perturbed Kohn–Sham equation system (Fournier 1990; Komornicki and Fitzgerald 1993) the dimension of  $\blacklozenge$  Eq. 16.60 is  $M^2$  and, therefore, the memory requirement for the solution of this equation system is similar to that of the fitting equation system  $\blacklozenge$  Eq. 16.31 in the corresponding SCF calculation. With the perturbed fitting coefficients, the perturbed Kohn–Sham matrix can be constructed via  $\blacklozenge$  Eq. 16.54 and the perturbed density matrix can then be calculated by  $\blacklozenge$  Eq. 16.48.


So far  $\blacklozenge$  Eq. 16.60 has been applied successfully for the calculation of static and dynamic molecular polarizabilities (Carmona-Espíndola et al. 2010; Flores-Moreno and Köster 2008; Shedge et al. 2010) using local and gradient-corrected functionals as well as for the calculation of Fukui functions (Flores-Moreno 2010; Flores-Moreno et al. 2008). Calculation of second derivatives with respect to nuclear displacements is currently under development.

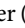

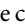
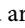
## Applications

### Dynamics of Sodium Clusters

In this section, we review the results obtained from a recent systematic study of the temperature dependency of the polarizabilities of small sodium clusters at a reliable first-principles all-electron level of theory (Calaminici et al. 2007b; Gamboa Martinez et al. 2008).

Static polarizability measurements have been used for a long time to gain insight into the electronic structure of small clusters (Bonin and Kresin 1997; Knickelbein 2001, 2003, 2004). Because the polarizability is very sensitive to the distribution of the valence electron density it can also be used as an indicator for chemical reactivity (Pearson 1973; Politzer 1987). Therefore, the study of the size dependency of the polarizability of simple clusters yields results of fundamental importance to chemistry and physics. A particular example resides in the polarizability studies on sodium clusters which were of paramount importance for the derivation of the jellium model (Knight et al. 1984). Today, this model is used with great success in cluster science (Bergeron et al. 2004, 2005). Several series of experimental data on sodium cluster polarizabilities are available in the literature (Knight et al. 1985; Molof et al. 1974a, b; Rayane et al. 1999; Tikhonov et al. 2001). In the pioneering work of Knight et al. (1984) the static polarizabilities of sodium clusters in a size range from 2 to 40 sodium atoms were studied. Later on Rayane et al. (1999) repeated these measurements for a smaller size range from 2 to 22 sodium atoms. Most recently, Tikhonov et al. (2001) measured the polarizability of selected sodium clusters up to 93 atoms. The overall agreement between these different experiments is quite satisfying. Nevertheless, discrepancies exist.

In  [Fig. 16-1](#), the experimental data series of sodium cluster polarizabilities are plotted together with our theoretical values.

In particular, the pronounced oscillating behavior observed by Knight et al. up to the hexamer ( [Fig. 16-1a](#), dots) was not confirmed by the more recent study of Rayane and co-workers ( [Fig. 16-1a](#), squares). To emphasize the spread between these two experimental data sets we have connected the data points in  [Fig. 16-1](#) by vertical lines. This figure also shows that for the larger sodium clusters with 7, 8 and 9 atoms excellent agreement between the reported data sets exist. The heptamer and octamer polarizabilities were also measured by Tikhonov et al. (2001) and are in good agreement with the depicted experimental data in  [Fig. 16-1](#), too.

In order to resolve the discrepancy in the measured polarizabilities of the smaller sodium clusters many theoretical studies have been performed over the last two decades (see, for example, Politzer (1987), Chandrakumar et al. (2004), Kümmel et al. (2000), Blundell et al. (2000), Kronik et al. (2000) and references therein). Most calculations employed density functional theory (Hohenberg and Kohn 1964; Kohn and Sham 1965) but wave function-based studies are also available (Chandrakumar et al. 2004). A comparison of these theoretical studies reveals that the static polarizabilities of sodium clusters are severely underestimated at all reliable levels of theory. Over the last two decades different corrections have been proposed to resolve this long-standing discrepancy between theory and experiment. More recently, it has been speculated that the mismatch between calculated and measured sodium cluster polarizabilities is due to finite temperature effects (Blundell et al. 2000; Kronik et al. 2000; Kümmel et al. 2000). In fact, this idea was already mentioned in the original experimental work (Knight et al. 1985). However, a systematic study of the temperature dependence of sodium cluster polarizabilities at a reliable first-principles all-electron level of theory was still absent until very recently we have finally closed this gap by performing a temperature dependent

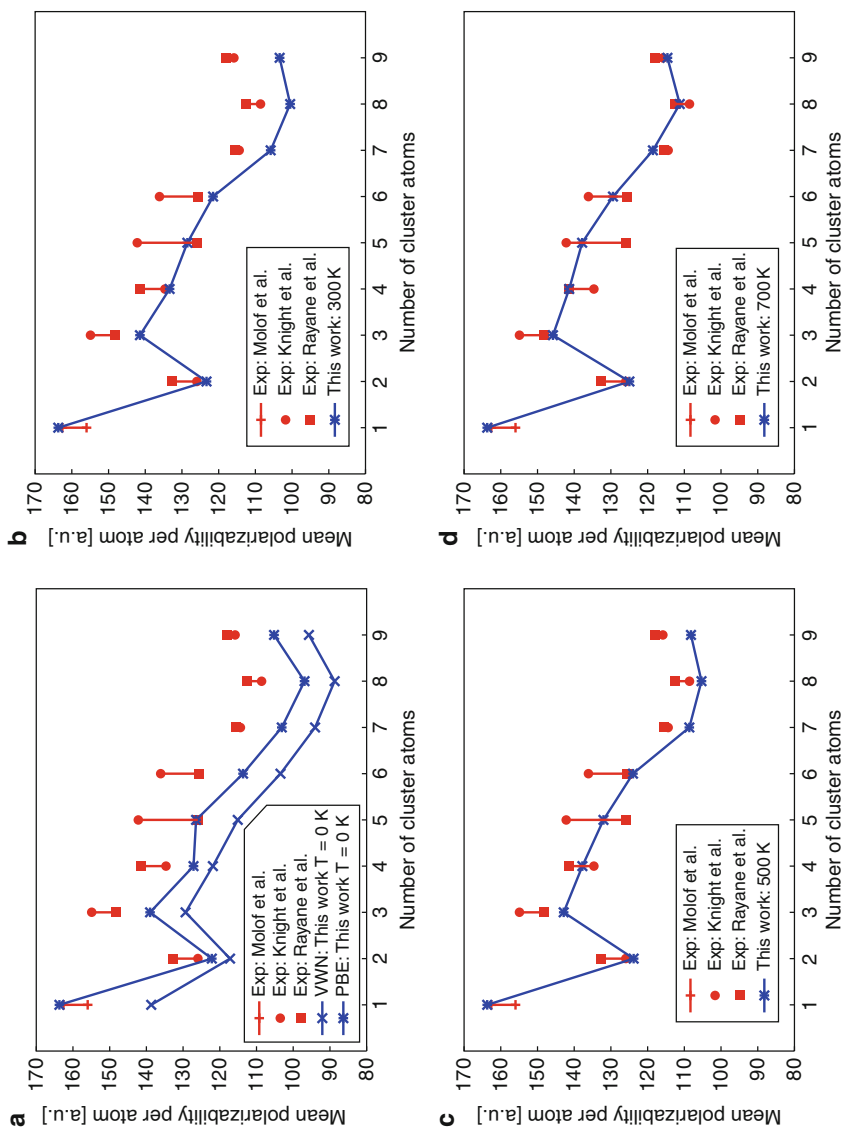
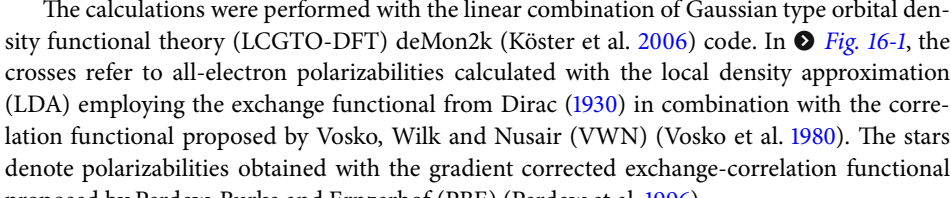


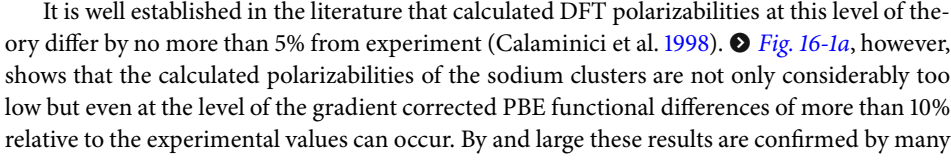
Fig. 16-1

Experimental and theoretical mean polarizabilities per atom [a.u.] of  $\text{Na}_n$  ( $n = 2-9$ ) clusters. The theoretical values are calculated at the VWN/TZVP-FIP/GEN-A2\* (crosses) and PBE/TZVP-FIP/GEN-A2\* (stars) level of theory. These values are connected in order to guide the eye. The individual graphs display calculated polarizabilities at 0 (a), 300 (b), 500 (c), and 700 K (d)

polarizability study of small sodium clusters by employing Born–Oppenheimer molecular dynamics (BOMD) simulations (Calaminici et al. 2007b; Gamboa Martinez et al. 2008).

The calculations were performed with the linear combination of Gaussian type orbital density functional theory (LCGTO-DFT) deMon2k (Köster et al. 2006) code. In  Fig. 16-1, the crosses refer to all-electron polarizabilities calculated with the local density approximation (LDA) employing the exchange functional from Dirac (1930) in combination with the correlation functional proposed by Vosko, Wilk and Nusair (VWN) (Vosko et al. 1980). The stars denote polarizabilities obtained with the gradient corrected exchange–correlation functional proposed by Perdew, Burke and Ernzerhof (PBE) (Perdew et al. 1996).

The cluster structures were optimized at the corresponding level of theory employing a double zeta valence polarization (DZVP) basis set (Godbout et al. 1992). For the polarizability calculations a triple zeta valence polarization (TZVP) basis set augmented with field induced polarization (FIP) function was used (Calaminici et al. 1999). All calculations were performed in the framework of auxiliary density functional theory (ADFT) (Köster et al. 2004b) with A2 or GEN-A2\* auxiliary function sets (Calaminici et al. 2007a). The latter was used in the analytical calculation of the cluster polarizabilities (Flores-Moreno and Köster 2008).

It is well established in the literature that calculated DFT polarizabilities at this level of theory differ by no more than 5% from experiment (Calaminici et al. 1998).  Fig. 16-1a, however, shows that the calculated polarizabilities of the sodium clusters are not only considerably too low but even at the level of the gradient corrected PBE functional differences of more than 10% relative to the experimental values can occur. By and large these results are confirmed by many other theoretical calculations.

In order to study the dynamics of small sodium clusters at finite temperatures Born–Oppenheimer molecular dynamics (BOMD) calculations were performed at the above described PBE/DZVP/A2 level of theory. For each cluster, from the dimer to the nonamer, 18 trajectories were recorded in a temperature range from 50 to 900 K with intervals of 50 K. Each trajectory has a length of 220 ps and was recorded with a time step of 2 ps. Similar statistics have already been successfully applied to determine the melting temperatures of sodium clusters with LDA pseudo-potential DFT molecular dynamics (Chacko et al. 2005).

The temperature in the canonical BOMD simulation was controlled by a Nosé–Hoover chain thermostat (Hoover 1985; Martyna et al. 1992; Nosé 1984). In order to study the temperature dependency of the sodium cluster polarizabilities the polarizability tensor  $\alpha$  was calculated along the recorded trajectories. For this purpose the first 20 ps of each trajectory were discarded and  $\alpha$  was then calculated in 100 fs time steps along the remaining 200 ps. Due to the computational demand of the analytical polarizability calculation along the BOMD trajectories we employed the LDA kernel. Thus, the computational level for the calculation of the temperature dependent part of the cluster polarizabilities was VWN/TZVP-FIP/GEN-A2\*. The temperature dependent mean sodium cluster polarizability was then calculated as:

$$\bar{\alpha}(T) = \bar{\alpha}^{\text{PBE}}(0) + \delta\bar{\alpha}^{\text{VWN}}(T), \quad (16.61)$$

with

$$\bar{\alpha}(T) = \frac{1}{3} [\bar{\alpha}_{xx}(T) + \bar{\alpha}_{yy}(T) + \bar{\alpha}_{zz}(T)]. \quad (16.62)$$

This approximation assumes that the temperature dependency of  $\bar{\alpha}(T)$ , namely,  $\delta\bar{\alpha}(T)$  is the same at PBE and VWN levels of theory. It should be remembered that the geometries are of course always determined from PBE BOMD calculations.

In  $\blacktriangleright$  Fig. 16-1, the calculated cluster polarizabilities at 0 (a), 300 (b), 500 (c), and 700 K (d) are depicted. As this figure shows the individual cluster polarizabilities increase with temperature. Somewhere between 500 and 700 K the calculated  $\bar{\alpha}(T)$  per atom match into the experimental data sets. In particular, the comparison of the calculated and experimental  $\bar{\alpha}(T)$  per atom at 700 K for  $\text{Na}_7$ ,  $\text{Na}_8$ , and  $\text{Na}_9$ , for which excellent agreement between the different experimental data sets exist, is very satisfying. Moreover, it is interesting to note that the oscillating behavior of the  $\bar{\alpha}$  per atom for the smaller clusters, which was observed in the original measurement (Knight et al. 1985) and also appears, less pronounced, in the  $T = 0$  K PBE calculations ( $\blacktriangleright$  Fig. 16-1a, stars), disappears at higher temperatures. Instead, the  $\bar{\alpha}$  per atom decreases monotonically from  $\text{Na}_3$  to  $\text{Na}_8$ . Therefore, we can conclude that the finite temperature polarizabilities of small sodium clusters do not reflect individual molecular structures. Instead, they only reflect the shell closing at the dimer and octamer consistent with the jellium model.

Our BOMD calculations also show that cluster fragmentations are not important for the cluster polarizabilities. Such fragmentations occur in our simulations above 800 K.

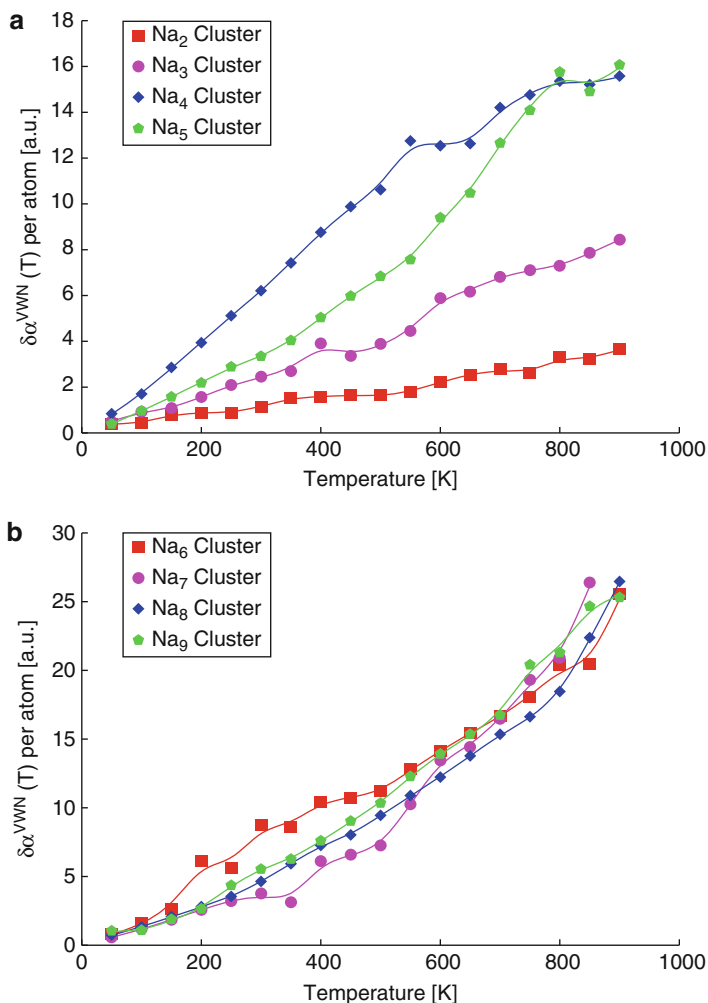
The change in the trend of the  $\bar{\alpha}$  per atom for the small sodium clusters with increasing temperature is due to the different temperature dependencies of the individual cluster polarizabilities. In  $\blacktriangleright$  Fig. 16-2 the temperature dependencies of the individual cluster polarizabilities are presented. As this figure shows, for the smaller clusters up to the pentamer ( $\blacktriangleright$  Fig. 16-2a) the behavior of  $\text{Na}_4$  is particular. Over a large temperature range up to 600 K the  $\delta\bar{\alpha}(T)$  value for this cluster changes almost ideally linearly with the temperature. A closer analysis reveals that in this temperature range the  $D_{2h}$  rhombic structure of  $\text{Na}_4$  rearranges only in the molecular plane. At 600 K and above, three-dimensional rearrangements occur. In this case the temperature dependency of the polarizability reflects directly the dynamics of the cluster rearrangement.  $\blacktriangleright$  Figure 16-2a also shows that  $\delta\bar{\alpha}(T)$  increases considerably faster with temperature for  $\text{Na}_4$  than for  $\text{Na}_5$ . As a result, the bump in the static  $T = 0$  K PBE polarizabilities at the pentamer ( $\blacktriangleright$  Fig. 16-1a) disappears in the finite temperature polarizabilities. For the larger clusters we found very similar temperature dependencies of  $\delta\bar{\alpha}(T)$  for  $\text{Na}_8$  and  $\text{Na}_9$  ( $\blacktriangleright$  Fig. 16-2b). The shape of our  $\text{Na}_8$  temperature dependent polarizability resembles previous studies with the extended Thomas–Fermi approximation (Blundell et al. 2000). The enlarged sodium hexamer polarizabilities in the temperature range between 200 and 600 K are due to the coexistence of two isomers, planar and pentagonal-pyramidal, as was already previously speculated in Calaminici et al. (1999).

## Summary

In this section, the results obtained by the first systematic study of the temperature dependency of the sodium cluster polarizabilities at a reliable first-principle all-electron level of theory were reviewed. The main results of this study are summarized as follows:

1. The calculated  $\bar{\alpha}(T)$  per atom match well the available experimental data sets at around 700 K.
2. The long-standing discrepancy between theory and experiment is resolved by inclusion of finite temperature effects in the electronic structure calculation.
3. The calculated finite temperature sodium cluster polarizabilities show characteristic minima at the dimer and octamer as expected from the jellium model.
4. Individual molecular structures besides these two are not resolved in the calculated finite temperature sodium cluster polarizabilities.





■ Fig. 16-2

Change of the mean polarizability per atom with temperature for  $\text{Na}_n$  clusters with  $n = 2-5$  (a) and  $n = 6-9$  (b). The calculations were performed at the VWN/TZVP-FIP/GEN-A2\* level of theory

## Structure of Zeolites

In this section, the calculated structural parameters and energetic properties of Na- and H-mordenites (MOR), using cluster models with more than 400 atoms will be reviewed. These calculations (Dominguez-Soria et al. 2007, 2008) were performed in the framework of ADFT, using both the local (LDA) and the generalized gradient approximation (GGA), employing all-electron basis sets. For this study, the most populated T3, T4, and T1 Al sites have been investigated, using two different MOR models, each containing two isolated Al sites. A detailed analysis of the structures, 3D contours of the molecular electrostatic potential (MEP), binding energies of Na cations and protons and Brønsted O–H harmonic frequencies are discussed. If

possible, comparison with available experimental results is made. The structural changes among Si/Al substitution as well as Na/H exchange are discussed, as well.

Diffusion, adsorption, and reactivity of molecules within micro- or mesoporous materials are specifically related with the physico-chemical properties of the material structures. It was originally underlined by D erouane et al. (1988) that the interactions of the host molecules with the material surfaces depend on the volume, shape, and topology of the cavities, which generate particular organizations of these molecules. The inter-relationship between the porous materials and the host molecules has been referred to as “confinement” and attributed a large role in the selectivity and catalytic activity of zeolite materials, in particular, in acid-catalyzed reactions (Anquetil et al. 1999; Smirnov and Thibault-Starzyk 1999; Thibault-Starzyk et al. 1998).

Computer modeling based on *ab initio* techniques have been used in recent years to provide a better understanding of the physico-chemical processes involved in the protonation of reactants. They lead to somewhat different conclusions, according to the methods applied and the reactions studied:


1. A confinement effect should originate from van der Waals interactions between the reactants and the zeolite framework (Rungsirisakun et al. 2005).
2. Protonated products are stabilized by the long range electrostatic effects of the framework (Demuth et al. 2001; Rozanska et al. 2003, 2005; Vos et al. 2001).
3. Confinement acts through the stabilizing interaction of the framework oxygens on protonated transition states, which are also favored when matched with the zeolite cavities, van der Waals interactions being dominant when neutral species are considered (Demuth et al. 2001; Rozanska et al. 2003, 2005; Vos et al. 2001).


These results obtained with modern computational methods demonstrate that the concept of confinement is now widely invoked but not yet clearly quantified, differing with the level of accuracy and approximation. The relative influence of the local structure on the Br onsted acid strengths (large vs. small cavities), of the solid-reactant dispersion interactions, and of electrostatic polarization effects on the reactants has not really been quantified yet. We believe that such a study necessitates first to set up an accurate and also efficient methodology in order to answer the following fundamental questions:

1. Is the Br onsted acid strength different in small and large cavities and what is the role of the local site geometry on this property?
2. How dependent on the cavity size is the stabilization of the guest molecule through long range dispersion and electrostatic polarization due to the solid framework?

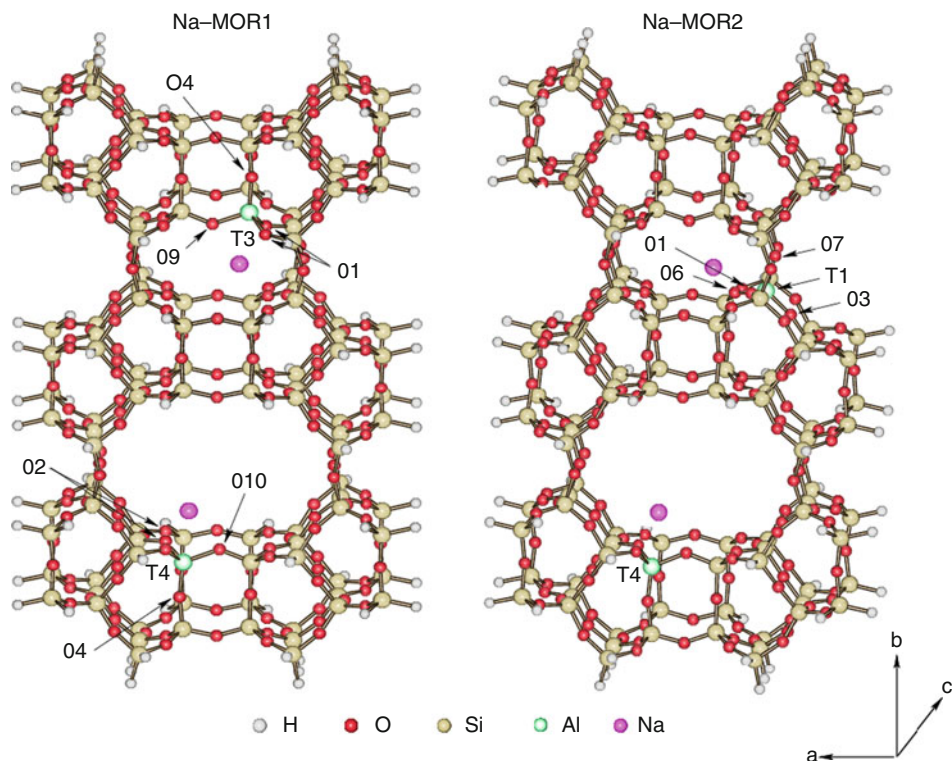
We have recently focused our attention on the first question (Dominguez-Soria et al. 2007, 2008), studying the structure and the intrinsic properties of mordenite (MOR) cationic sites, in particular sodium binding energies and acid strengths. For these studies we proposed a new methodological approach based on very large model clusters, which can eventually be embedded in a classical environment, which we believe is a promising alternative to the idealized periodic representation of a zeolitic solid. This is particularly important for zeolites where the experimental Si/Al ratio is not very large, that is, when the solid contains an Al distribution which can hardly be represented as periodic. In the next sections, we will compare our results with those reported experimentally for natural and synthetic zeolites. In [▶ section “Models and Methodology,”](#) we discuss the zeolite models that we have chosen and the applied methodology. In [▶ section “Calculated Geometries and Properties,”](#) we report the calculated geometries and properties and discuss them with respect to experiment and other theoretical results. The results obtained so far are summarized in [▶ section “Summary”](#).

## Models and Methodology

Mordenites are natural and synthetic zeolites with Si/Al ratios of 4.3 to 6.0 in the former case and 5.0 to 12.0 in the latter (Jacobs and Martens 1987; Passaglia 1975). Synthetic mordenites are used for acidic catalysis. MOR catalysts are synthesized in the Na-form followed by a mild treatment with  $\text{NH}_4\text{Cl}$  which leads to H-exchanged forms. The MOR structure can be described as composed of edge-sharing five-membered (5-m) rings of tetrahedra forming chains along the *c* crystallographic axis (Meier 1961). Their architectures comprise large mono-directional accessible 12-m ring channels of  $\text{TO}_4$  tetrahedra where T stands for either Si or Al and small 8-m ring channels, which are interconnected through 8-m ring tubes. The topological symmetry of MORs is orthorhombic with space group *Cmcm* having in the unit cell four symmetrically independent tetrahedral sites, usually called T1, T2, T3, and T4. T1 and T2 sites connect four different rings, while the T3 and T4 sites constitute the 4-m rings of the zeolite framework (Meier 1961). Since the first structural study of natural mordenite by Meier (1961), much work has been performed to solve several problems about the real symmetry of the solid due to the presence of Al tetrahedra and extra-framework cations, framework defects, and other structural distortions (Alberti 1997; Alberti et al. 1986). Having different Si/Al ratios, natural and synthetic zeolites also have different Al distribution patterns and slightly different T–O bond lengths (Schlenker et al. 1979). Our strategy in this study for the determination of the structure and intrinsic properties of the catalyst has been to use clusters containing 120 tetrahedra, sufficiently large to enclose the main 12m-rings and the side pocket 8m-rings. These models include two unit cells along *a* and *b* whereas the  $2 \times c$  dimension has been cut at the middle of the second 12m-ring channel (see  Fig. 16-3).

The substitution of Si by Al has previously been studied extensively for natural and synthetic mordenites (Alberti 1997; Alberti et al. 1986; Ito and Saioto 1985; Schlenker et al. 1979; Simonic and Armbruster 2004). Following these results based on crystal structure refinement (Alberti 1997; Alberti et al. 1986) and IR intensities of the OH stretching bands (Yang et al. 2001), it has been proposed that the Brønsted sites of MOR are related to an Al occupancy with the probability  $\text{T3} > \text{T4} > \text{T1} > \text{T2}$ , associated with a relative population of the OH sites which is probably larger in the 12-ring channel for natural zeolites (Alberti et al. 1986). The T4 site has also been proposed as the most probable candidate for Al substitution by Demuth et al. based on the relative stability of Al embedded clusters with Al substituted in turn at the four possible sites (Demuth et al. 2001). Due to the low probability of Al in T2, and the high probability of more Al sites in the main channel (Alberti 1997), we have selected two models with the distributions T4, T3 and T4, T1, associated with both Na cations (Na-MOR1, Na-MOR2) and protons (H-MOR1 and H-MOR2). The original models have been cut from a solid with the appropriate Al distribution, generated using the Cerius2 program (Cerius2 2005) and terminated with hydrogens. In order to constrain the structure of the cluster to that of the solid, the coordinates of the terminal hydrogen atoms, positioned along the Si–O bonds, have been fixed during the subsequent optimizations, all other atomic coordinates being relaxed.  Figure 16-3 illustrates the two models Na-MOR1 and Na-MOR2. In order to test the influence of the Al content on the mordenite geometrical parameters, we have also studied the same model without Al atoms, as will be discussed later.

For these studies we have used an ADFT-based approach, using a linear combination of atomic orbitals, as implemented in the deMon2k program (Köster et al. 2006). Geometry optimizations and molecular electrostatic potential (MEP) calculations were performed at the local level using the correlation functional proposed by Vosko et al. (1980), whereas energetic properties (binding energies and proton affinities) have also been evaluated using



■ Fig. 16-3

Structures, T and O atoms legend of the studied mordenite models. The orientation of the three crystallographic axis *a*, *b*, and *c* is also given

the exchange-correlation functional of Perdew et al. (1996). DFT-optimized double zeta plus valence polarization (DZVP) basis sets were employed for all atoms (Godbout et al. 1992). For the fitting of the density, the A2 auxiliary function set was used (Godbout et al. 1992). The exchange-correlation potential was numerically integrated on an adaptive grid (Köster et al. 2004a). The grid accuracy was set to  $10^{-5}$  a.u. in all calculations. The Coulomb energy was calculated by the variational fitting procedure proposed by Dunlap et al. (1979) and Mintmire and Dunlap (1982). A quasi-Newton method in internal redundant coordinates with analytical energy gradients was used for the structure optimization (Reveles and Köster 2004). The convergence was based on the Cartesian gradient and displacement vectors with a threshold of  $10^{-4}$  and  $10^{-3}$  a.u., respectively. For the geometry optimization of the mordenite structures the parallel version of deMon2k (Calaminici et al. 2006; Geudtner et al. 2006) was used. Each mordenite model possesses more than 400 atoms with around 6,000 orbital basis functions and 11,000 auxiliary functions. The calculations were performed on six or eight 2.4 GHz Intel Xeon CPUs. These nodes were connected with a Myrinet switch. The geometry optimization of such models takes about 13 days on 8 CPUs. In this time roughly 25 optimization steps are performed. The cation binding energies (BE) to the framework have been calculated using the formula:  $BE = E(\text{neutral model}) - E(\text{cation}) - E(\text{anionic model})$ . The O–H stretching frequencies of the H-MOR1 model have been calculated within the harmonic approximation. This normal

mode being uncoupled with all the other vibrational modes of the model, its frequency has been calculated using a partial Hessian analysis, as proposed by Li et al. (Li and Jensen 2002).

## Calculated Geometries and Properties

### General Structural Parameters of the Mordenite Models

Our purpose here was to simulate averaged bond length and bond angle data that can be compared with those provided by X-ray experiments performed on natural and synthetic mordenites with various Si/Al ratios. Comparison with available theoretical data was also presented (Dominguez-Soria et al. 2007). The main geometrical parameters (T–O bonds and T–O–T bond angles) of the fully siliceous and sodium mordenite models have been compared in Table 1 of Ref. Dominguez-Soria et al. (2007) with experimental data. The calculated values have been averaged over Na-MOR1 and Na-MOR2, namely, considering different Al distributions. This procedure mimics the experimental averaging over the non-distinguishable Si and Al positions. Among several experimental structures of natural mordenites (Alberti 1997; Alberti et al. 1986; Ito and Saioto 1985; Schlenker et al. 1979; Simoncic and Armbruster 2004), the structure obtained by Alberti et al. (1986) has been chosen for comparison together with the experimental structure of a natural and a synthetic Na-mordenite (Simoncic and Armbruster 2004).

As we have shown in Table 1 of Ref. Dominguez-Soria et al. (2007), the calculated bond lengths are very comparable with the experimental results, within 0.02 Å. We have noticed that this uncertainty is of the same order of magnitude as that obtained in previous theoretical work using the LDA level of theory and periodic boundary conditions (Demuth et al. 2001). The systematic lengthening of the T–O bonds in our calculations with respect to standard experimental bond distances could be interpreted in terms of a correction for thermal motions as given in Ref. Simoncic and Armbruster (2004). The average values of the T–O–T bond angles, presented in Table 2 of Ref. Dominguez-Soria et al. (2007), are in good agreement with experiment, within 4°, which is also the average difference of our calculated bond angles with respect to those reported previously by Demuth et al. (2001). It is worth noting that the isotropic temperature factors provided by X-ray refinements for the zeolite oxygens are all very large (2.4–4.6 Å<sup>2</sup>) (Alberti et al. 1986; Simoncic and Armbruster 2004), leading to a substantial uncertainty on the oxygen positions. It was also shown that the averaged bond length and bond angle are rather insensitive to the Al content of the model. This allowed us to compare our models containing two Al sites with experimental mordenites which contain about 4–6 Al per unit cell.

### Al Sites of Na-MOR

#### Previous Data for Extra-Framework Cations

Experimentally, the positions of the extra-framework cations are not easily determined. Moreover, there is a clear difference between natural and synthetic mordenites, due to the different natures of their extra-framework cations, as it was demonstrated in the literature (Simoncic and Armbruster 2004). Whereas Ca and K cations predominate in natural mordenites, synthetic zeolites are grown using Na cations, leading, presumably, to different locations of the (Al, cation) pairs; although T3 remains slightly more populated than the other sites, the distribution of Al among the possible T sites is much more balanced according to the pattern reported by Simoncic et al. (Simoncic and Armbruster 2004) (for an Al content of 6, one can expect 1.3 Al at T1 and T4, 0.8 at T2, and 2 at T3). Consequently, the Na cations compensating the Al charges are

found distributed within two regions, that is, the side pocket and the main channel. Due to the presence of water, about 60% of the cations cannot be precisely determined, presumably being located mainly in the main channel (Simoncic and Armbruster 2004). The remaining cations are found either bonded to three oxygens around T3 in the side pocket or pushed downward into the 8m-ring tube.

Since our study concerns Na-MOR models, we focus on comparing our results with the experimental data provided for synthetic Na-mordenites. Previous theoretical work on Na-mordenite used periodic models involving eight (Al, Na) pairs per unit cell, and results were compared with the natural zeolite data available (Demuth et al. 2001). The choice of occupying only T3 and T4 sites with equal populations was made, leading then to a strong concentration of cations in each cavity, related to the high symmetry of the solid. Therefore, it is hardly possible to make a direct comparison with this study, concerning the Na positions with respect to the framework oxygens.

### Analysis of the Properties of the Cationic Sites in Na-MOR1 and Na-MOR2

The substitution of one Si by Al in the framework generates one negative charge, which has to be compensated by the presence of a counterion. The framework negative charge is distributed among the framework oxygens, more particularly to the four oxygens adjacent to Al. The location of the cation thus depends on the local geometry around the T site for large Si/Al ratios, that is, when the Al sites can be considered isolated. In these conditions, it is well established that smaller Al–O–Si angles are generally associated with larger electrostatic potentials, that is, larger attractive interactions with an incoming positive charge (Goursot et al. 1998). In order to locate the most probable positions of the counterions, we have used the well-known strategy of approximating the cation position by searching the largest electrostatic interaction of the system density with a positive point charge. To do so the molecular electrostatic potential (MEP) was calculated around the three  $\text{AlO}_4$  T4, T3 and T1 tetrahedra. The contour plots of these MEPs are illustrated in Fig. 2a, b and c of Ref. Dominguez-Soria et al. (2007), respectively. These MEP values have been calculated for the optimized structures of the corresponding T anions, at the T4 and T3 sites in Na-MOR1 and at the T4 and T1 sites in Na-MOR2, respectively. As expected, the MEP wells in Na-MOR1 surround the two O2 and O10 in the main channel at T4 and the two O1 and O9 at T3 in the side pocket. The lowest MEP minimum at T4 is located between the two O2 and O10 (−4.13 eV). The lowest minimum at T3 is located close to O9 (−4.22 eV). In Na-MOR2, the MEPs at T4 are identical to the ones calculated for T4 in Na-MOR1, showing that the two Al sites are independent. Interestingly, the T1 site of Na-MOR2 belongs to both the main channel and the side pocket. The O1 and O6 adjacent oxygens are in the side pocket, whereas O3 and O7 are located in the main channel (► Fig. 16-3). The MEP well at T1 is essentially located within the side pocket, with the lowest minimum close to O6 (−3.94 eV). It is worthwhile to underline that the MEP values at O7 and O3, that is, in the main channel, are equal to −3.60 and −3.10 eV, respectively, showing that a compensating  $\text{Na}^+$  or  $\text{H}^+$  at those oxygens is unfavored with respect to O6. This result indicates that the counterion at T1 will be more stable within the side pocket than in the main channel, at least after dehydration. This conclusion is also valid for protons (Dominguez-Soria et al. 2007).

Si substitution by Al leads, as expected, to lengthening the T–O bonds and decreasing the T–O–Si angles. The average elongation of the T–O bonds reaches 0.115 for T1, 0.124 for T3, and 0.123 Å for T4. The corresponding T–O–Si averaged decrease is found to be 3.3°, 7.2°, and 8.3° for T1, T3, and T4, respectively. These changes are in a reasonable range, with a lower variation for the T1 site, due to its more rigid environment. The optimized structures of the  $\text{Na}^+$



sites were reported in Table 3 of Ref. Dominguez-Soria et al. (2007), as well as the Na binding energies to the framework. From the reported Na–O distances, the cation can be considered as bi-coordinated at T4 and T1 and mono-coordinated at T3. This result correlates with the calculated positions of the MEP minima, as shown in Fig. 2 of Ref. Dominguez-Soria et al. (2007). Interestingly we noticed that the shortest Na–O distances correspond to the smallest Al–O–Si angles (smaller Al–O–Si angles correlate with more electron density available for cations in the O lone pair due to better hybridization conditions) (Goursot et al. 1998). This result can be considered as the physical reason why the cation at T1 is located inside the side pocket. Moreover, this finding allows us to anticipate the preferred oxygen for protonation, that is, O10 at T4, O9 at T3, and O6 at T1.

The calculated Na binding energies follow the ordering  $T3 > T4 \approx T1$ , which is very comparable with that indicated by the MEPs. This result indicates that electrostatics governs the cation – framework binding. Moreover, we noticed that the use of the PBE GGA exchange–correlation functionals does not modify the trend established on the basis of LDA calculations. For sites T1, T3, and T4, it can be pointed out that the ordering of the Na binding energies reproduces the (Na, Al) population pattern, reported for synthetic Na-MOR. This result supports the suggestion of Simoncic et al. that there is a synergistic effect (Al, Si) order during the growth of the solid (Simoncic and Armbruster 2004). Finally, we remark that the binding properties found at T1 and T3 are different, although both sites belong to the side pocket. This is related to a sum of different effects, the prominent one being most probably the global electrostatic potential felt by the cation. For the same reason, T1 and T4 present comparable binding properties, despite their different locations in the zeolite framework. It is important here to stress that these conclusions are made on the basis of the existence of two independent Al sites. If several (Al, Na) pairs are present within the side pockets, the distribution of the cations would most probably be governed by their mutual repulsion (Campana et al. 1997).

For isolated sites, we have found that both T1 and T3 compensating cations are located in the side pocket area. In synthetic mordenites, at least two sites in side pockets are substituted by Al ( $\approx 2.5$ ). Since the binding of  $\text{Na}^+$  at T3 is favored with respect to that at T1, the three short Na–O bonds indicated by experiment (to O1, O1' and O9) can then be related to our calculated values at T3. In the presence of a second  $\text{Na}^+$  to compensate Al in T1, one can expect that the mutual repulsion of the two cations will modify their position. Taking into account their relative stability, the experimental evidence that the other cation is pushed downward to the main cavity (Simoncic and Armbruster 2004) is supported by our results. Moreover we could argue further about Na-MOR with 6 Al per unit cell: this Al content would imply the presence of three (Na, Al) pairs in the side pockets (presumably two at T3 and one at T1). In this situation, one may expect that only two cations will remain inside the pocket, whereas the third one will be pushed outside due to cation–cation repulsion (this argument is verified by classical molecular mechanics simulations using Cerius2 associated with the cvff-aug-ionic force field (Demuth et al. 2001).

### Al Sites of H-MOR

As for the Na-MOR models, the protonated structures have been optimized, the original proton positions being those of the respective lowest MEP minima. At T4, the MEP well is situated at equivalent distances from the two O2 and O10. Whereas the  $\text{Na}^+$  cation at T4 was found at equal distances from O10 and O2, the optimized position of the proton corresponds to a bonding to O2. In a previous theoretical study of the relative energies of various H-MOR models, the O2 protonation was also found to be more favorable than the O10 protonation (Li and Jensen 2002).

Consistency with the mentioned relationship between Al–O–Si bond angle values and cation binding energies would lead one to expect comparable proton affinities at O2 and O10. At T1 and T3, the proton attaches to O6 and O9, respectively. Moreover, the O2–H and O6–H bonds are pointing toward the center of the 8m-ring which contains the T4 and T1 site, respectively, these bonds lying in the 8m-ring planes. The proton at T4 can thus be reached by a molecule being in the main channel as well as coming from the side pocket. In contrast, the O9–H bond at T3 is pointing toward the center of the side pocket.

We could see that the Al–O bonds which do not connect to a proton are only a little changed with respect to those of the Na-MOR models, with a maximum elongation of about 0.05 Å. As expected, the Al–O(H) bonds are elongated by about 0.12–0.16 Å with respect to the same bonds in the Na-MOR models. This effect is due to the covalent character of the OH bond, which induces the weakening of the Al–O bonds, whereas the Na<sup>+</sup>-oxygens interactions are weaker and essentially electrostatic. The presence of the sodium cation, bonded to two O (T4, T1) or one O (T3) had thus much less impact on the Si–O–Al framework than that of the proton.

In contrast with the Na binding energies, we found that the proton affinity values are more sensitive to the inclusion of the GGA correction, leading to increased values with respect to LDA and to non-significant differences among the three acid sites (less than 0.08 eV) if one takes into account all methodological errors. From these values, we conclude that the sites belonging to the main channel and to the side pocket display similar proton affinities, showing thus that the strength of the O–H bond is not dependent on the local structure of the studied sites. It is worth noting that proton affinities are not related to relative energies of models with different H-sites, which are reported in previous theoretical work (Demuth et al. 2001), relative total energies being essentially related with relative Al site stabilities.

In order to complete the description of the OH bond strength, the vibrational harmonic frequencies of O2–H and O9–H in the H-MOR1 model have been calculated. The values are 3,667 cm<sup>-1</sup> for O9–H at T3 and 3,659 cm<sup>-1</sup> for O2–H at T4, with IR intensities of 174 and 182 km mol<sup>-1</sup>, respectively. These frequencies, not corrected by any scaling factor, can be considered similar within the theoretical error bar. This result is consistent with the corresponding proton affinity found for the proton at O9 (T3) with respect to O2 (T4). They are shifted toward higher energies by about 50 cm<sup>-1</sup> with respect to the reported Infra-Red (IR) experimental asymmetric band at about 3,610 cm<sup>-1</sup>. The comparison of our results with X-ray and IR experimental data allows us to suggest that the O9H stretching vibration (T3 site) is not responsible for the observed low-energy component at 3,585 cm<sup>-1</sup>.

Due to the similarity of the model and method used for both vibrations, it is most probable that the lower energy vibration is related to another Brønsted hydroxyl originated from the following:

1. Proton migration, after dehydration, to another oxygen, especially if both T1 and T3 sites are aluminated, leading to different local interactions.
2. The presence of two T3 and one T1 aluminated sites in the side pocket (Simonic and Armbruster 2004) will induce different MEP surfaces and different electrostatics.
3. The presence of a (100) defect layer (Simonic and Armbruster 2004) that induces geometry changes in the side pockets which are not reproduced in our models.

We can thus argue that our models with isolated Al sites (Si/Al = 23) show that main channel and side pocket hydroxyls are energetically not different because of their framework environment. Their different energetical behaviors are most probably generated by the different content of framework Al at the 12-membered ring-channels and in the side pockets obtained after crystallization.



## Summary

In this work, Na and protonated models of a mordenite zeolite, including Al in T1, T3 and T4 crystallographic sites, were studied using all-electron DFT calculations. From the analysis of the obtained results, the following conclusions can be drawn:

1. A good agreement with experimental bond length and bond angle data reported for synthetic Na-mordenites has been obtained.
2. The binding energies of the Na cation follows the same ordering as the populations of Al T sites, as derived from X-ray measurements on synthetic Na-mordenites; this result shows the existence of a synergic effect between cations and (Al, Si) order during the growth of the solid, as suggested experimentally.
3. The compensating cation at the T1 site is found to be more stable in the side pocket than in the main channel, which questions the assignments of the T1-associated proton to a main channel location.
4. The calculated proton affinities at T1, T3, and T4 sites are equivalent, indicating that these Brønsted sites have similar acid strengths. One can thus infer that the different acidic behaviors at the different sites (Marie et al. 2000, 2004) do not originate from different acid strengths of these OH sites. This leads to the suggestion that the MOR acidic properties are more related to the electronic structure of the base than to effects of the solid framework.

Thus, for the evaluation of differences in local acidity, the presence of the associated base (CO, CH<sub>3</sub>CN, NH<sub>3</sub>, etc...) has to be taken into account. Further work in this direction is currently in progress in our laboratories.

## Stability of Giant Fullerenes

Fullerenes are carbon nanostructures formed by the closing of a graphitic sheet with the needed curvature supplied by intersecting, among a given number of graphitic hexagons, of 12 pentagons (Andreoni 2007; Kadish and Ruoff 2007). These carbon aggregates have been experimentally known for more than 20 years (Kroto et al. 1985) and, consequently, a large number of works, experimental as well as theoretical, focused on this subject (see, for example, Refs. Seifert et al. (1996), Cioslowski (1995), Boltalina et al. (2000), Bühl and Hirsch (2001), and references therein).

One main reason for the great interest in the study of fullerenes is certainly to be found in their particularly appealing geometrical form. The best known fullerene is the so-called buckminsterfullerene that contains 60 carbon atoms (C<sub>60</sub>) and is composed of 12 pentagonal carbon rings located around the vertices of an icosahedron and 20 hexagonal carbon rings at the centers of icosahedral faces (Kroto et al. 1985).

Larger fullerenes that have an icosahedral symmetry can be constructed (Itoh et al. 1996; Kroto and McKay 1988) as well. These clusters, known as *giant fullerenes*, can be thought of as cut-out pieces of graphene that are folded into their final shapes (icosahedrons). This kind of procedure generates 12 pentagonal carbon rings situated around vertices of an icosahedron, while all other carbon rings are hexagonal. Giant or large fullerenes have been the subject of different theoretical studies in the last years. We address the interested reader to Refs. Dunlap et al. (1991), York et al. (1994), Bakowies et al. (1995), Scuseria (1995), Scuseria (1996), Xu and Scuseria (1996), Haddon et al. (1997), Bates and Scuseria (1998), Heggie et al. (1998), Geudtner

et al. (2006), Dunlap and Zope (2006), Shao et al. (2006), Shao et al. (2007), Zope et al. (2008), and references therein.

Most of these studies were focused either on understanding if the shape of these clusters is spherical or faceted (Bakowies et al. 1995; Bates and Scuseria 1998; Geudtner et al. 2006; Scuseria 1995, 1996; Xu and Scuseria 1996; York et al. 1994), on calculating their response properties (Zope et al. 2008) or testing new algorithms developed for the investigation of large systems (Dunlap and Zope 2006; Geudtner et al. 2006). Most previous first-principles theoretical studies of large fullerenes have been performed either at the Hartree-Fock level of theory using symmetry restrictions and relatively small basis sets or employing analytic density-functional theory (Bakowies et al. 1995; Bates and Scuseria 1998; Dunlap and Zope 2006; Haddon et al. 1997; Heggie et al. 1998; Scuseria 1995, 1996; Shao et al. 2006, 2007; Xu and Scuseria 1996; York et al. 1994; Zope et al. 2008).

In a recent study we have performed state-of-the-art calculations on the large  $C_{180}$ ,  $C_{240}$ ,  $C_{320}$ , and  $C_{540}$  fullerenes by employing the linear combination of Gaussian-type orbitals density functional theory (LCGTO-DFT) approach (Calaminici et al. 2009). The structures of these clusters were fully optimized without any symmetry constraints. This work represents the first systematic study on large fullerenes based on non-symmetry, adapted first-principles calculations, and it demonstrates the capability of ADFT for energy calculations and structure optimizations of large scale structures without any symmetry constraint.

In the next two sections, the computational details will be presented and the most important results we have obtained in terms of structural changes, of the evolution of the bond lengths and of the calculated binding energies, will be reviewed.

## Computational Details

All calculations were performed using the DFT program deMon2k (Köster et al. 2006). The exchange-correlation potential was numerically integrated on an adaptive grid (Köster et al. 2004a). The grid accuracy was set to  $10^{-5}$  in all calculations. The Coulomb energy was calculated by the variational fitting procedure proposed by Dunlap et al. (1979) and Mintmire and Dunlap (1982). The calculation of the exchange-correlation energy was performed with the auxiliary function density (Köster et al. 2004b), that is, auxiliary density functional theory was used. The structure optimizations were performed with the local density approximation (LDA) employing the Dirac exchange functional (Dirac 1930) in combination with the correlation functional from Vosko, Wilk, and Nusair (VWN) (Vosko et al. 1980). DFT optimized double zeta plus valence polarization (DZVP) all-electron basis sets optimized for local functionals (Godbout et al. 1992) were employed. For the structure optimization a quasi-Newton method in internal redundant coordinates with analytic energy gradients was used (Reveles and Köster 2004). The geometry optimizations were performed using the parallel version of the deMon2k code (Calaminici et al. 2006; Geudtner et al. 2006). The convergence was based on the Cartesian gradient and displacement vectors with a threshold of  $10^{-4}$  and  $10^{-3}$  a.u., respectively.

The diamond and graphene calculations were performed in the same theoretical framework using the cyclic cluster model (CCM) (Janetzko et al. 2008). The obtained energies using the CCM are in the range of other calculated cohesive energies for graphene (Dunlap and Boettger 1996; Trickey et al. 1992). Because the fullerenes and graphene calculations are performed within the same theoretical framework, the relative energy differences found here are reliable.

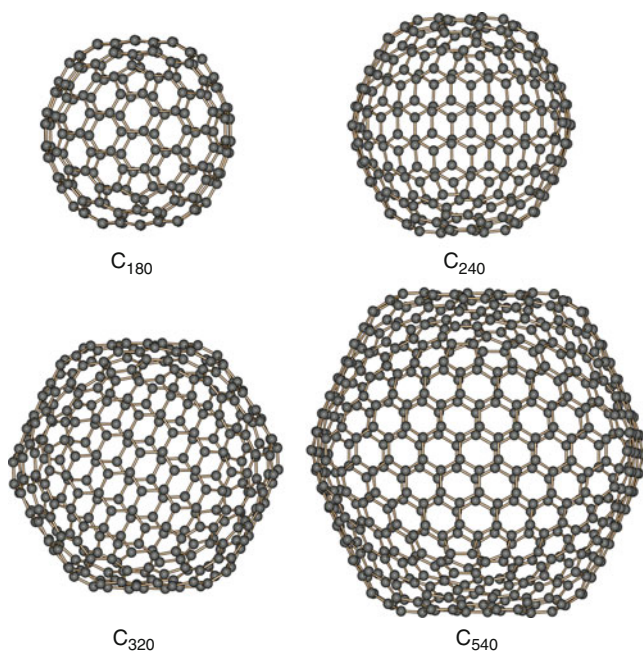
## Results and Discussion

The DFT optimized singlet structures of  $C_{180}$ ,  $C_{240}$ ,  $C_{320}$ , and  $C_{540}$  are depicted in [Fig. 16-4](#). These structures have been fully optimized at the all-electron level using DZVP basis sets in combination with the VWN functional.

A long standing discussion in the literature addresses the question of whether giant fullerenes prefer a faceted or a spherical shape. This question was raised considering pictures obtained by transmission electron microscopy (TEM) that have shown evidence of possible spheroidal structures in concentric carbon particles (Iijima 1980; Ugarte 1992, 1995).

Using a divide-and-conquer method for density functional calculations the structure and stability of  $C_{240}$  were studied and the most stable structure was claimed to be highly spherical (York et al. 1994). However, this result was not confirmed by any successive theoretical work that have clearly shown evidence of a faceted shape for this fullerene (Bakowies et al. 1995; Bates and Scuseria 1998; Dunlap et al. 1991; Haddon et al. 1997; Scuseria 1995, 1996; Xu and Scuseria 1996). Depending on the viewing axis, simulated TEM of icosahedral fullerenes can provide either images with spherical or with faceted shapes (Scuseria 1995). In addition, an explanation of why experimental results showed rounder shapes for large fullerenes was also given (Scuseria 1995).

As [Fig. 16-4](#) shows our first-principles based structure optimizations predict that larger fullerenes,  $C_{240}$ ,  $C_{320}$ , and  $C_{540}$ , prefer a faceted shape. Moreover, even for the smallest fullerene here studied,  $C_{180}$ , there is clear evidence that the faceted shape is preferred over a spherical shape if first-principles all-electron optimizations without any symmetry restriction are performed (see [Fig. 16-4](#)). Details about the timing of these calculations are reported in Ref.



■ Fig. 16-4

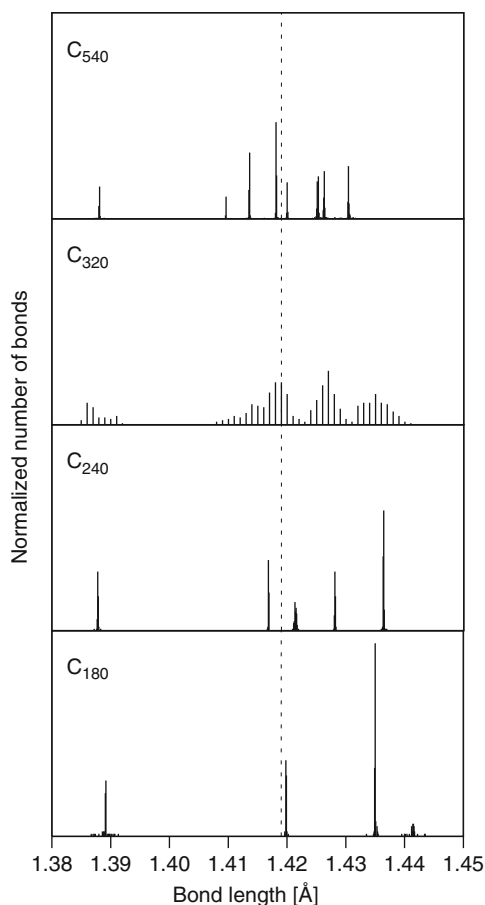
Optimized structure of  $C_{180}$ ,  $C_{240}$ ,  $C_{320}$  and  $C_{540}$  fullerenes. The calculations have been performed with the VWN functional in combination with DZVP basis sets

Geudtner et al. (2006) where it is shown that the optimization of such large fullerenes is feasible within a few days on a parallel architecture with 32–64 cores.

We noticed that the obtained results are in agreement with most of the previous reported theoretical studies (Bakowies et al. 1995; Bates and Scuseria 1998; Dunlap et al. 1991; Haddon et al. 1997; Scuseria 1995, 1996; Xu and Scuseria 1996).


In order to gain more insight into the structural changes of these systems as the number of carbon atoms increases, a detailed analysis of the bond length evolution was performed. In **Fig. 16-5**, the normalized number of bonds for  $C_{180}$ ,  $C_{240}$ ,  $C_{320}$ , and  $C_{540}$  are plotted versus the bond length. The dashed line at 1.419 Å represents the graphene bond length obtained from the periodic (CCM) deMon2k calculation.


Most obvious from this figure is the difference of  $C_{320}$  to all other fullerenes. In fact, whereas usually a discrete distribution of bond lengths is found, in  $C_{320}$ , a wide, in some ranges almost continuous bond length distribution is observed. This clearly indicates a break in the expected high symmetry of the system. Our studies show that the  $C_{320}$  fullerene possesses a ground state potential energy surface (PES) of higher multiplicity, most likely either triplet or quintet. Further test calculations indicated that for this fullerene also in the cases of triplet and quintet



**Fig. 16-5**

Normalized number of bonds for  $C_{180}$ ,  $C_{240}$ ,  $C_{320}$ , and  $C_{540}$  versus the bond lengths (in Å)

PESs the continuous bond length distribution observed for the singlet PES persists. Of course, only non-symmetry-adapted optimizations can lead to such a result. To the best of our knowledge this symmetry breaking in larger fullerenes due to their electronic structure has never been observed in previous calculations. As  Fig. 16-4 shows the observed symmetry breaking does not alter the global shape of the giant fullerene.

For the other systems,  $C_{180}$ ,  $C_{240}$ , and  $C_{540}$ , the expected discrete bond length distribution is obtained, indicating that the symmetry of the electronic structures matches with the expected geometrical symmetry. In these systems, the number of different bond lengths increases with system size and an accumulation of bond lengths around the graphene bond length is observed ( Fig. 16-5).

More surprising is the trend that the longest bond length in the cluster shortens with increasing cluster size. This indicates that delocalization increases with cluster size despite the global building pattern, that is, the appearance of 12 pentagons.

With the aim of guiding future desirable experiments on large fullerenes and to gain more information about their stability we have also explored the behavior of the binding energy of the studied fullerenes with increasing fullerene size. The results of the uncorrected binding energy (in eV) per carbon atom obtained with the VWN functional have been illustrated in Fig. 3 of Ref. Calaminici et al. (2009) showing that the binding energy increases monotonically with the increase in the number of carbon atoms. This indicates that the large fullerenes become more and more stable with increasing size. However, the increase turned out to be very moderate. We have also included the basis set superposition error (BSSE) in the calculation of the binding energies. The inclusion of the BSSE decreases the calculated binding energies of each studied fullerene by 0.02 eV but without altering the trend (Calaminici et al. 2009).

From the comparison of the CCM calculations we found that the calculated binding energy of  $C_{540}$  of 8.75 eV is very close to the cohesive energy of diamond (8.78 eV). This result indicates that  $C_{540}$  has a similar binding energy to diamond which fuels the hope that such giant fullerenes could indeed be prepared. However, the binding energy of even the largest studied fullerene,  $C_{540}$ , is still far away from the corresponding value in graphene which was calculated to be 8.91 eV (Janetzko et al. 2008).

## Summary

In this section, the results obtained from state-of-the-art density functional theory calculations performed on large fullerenes, such as  $C_{180}$ ,  $C_{240}$ ,  $C_{320}$ , and  $C_{540}$ , have been reviewed. The study was carried out with all electron basis sets, and all structures were fully optimized without any symmetry restriction. The results obtained can be summarized as follows:

1. This work confirms that for all large fullerenes studied here a faceted shape is preferred over the spherical shape.
2. The analysis of the bond length evolution reveals for  $C_{320}$  a qualitatively different pattern than for the other fullerenes. The most likely explanation for this difference is a symmetry breaking in the electronic structure of this large fullerene.
3. The shortening of the longest bond length with increasing cluster size indicates that delocalization increases with cluster size.
4. The calculated binding energies are in the range of diamond but considerably below the graphene value. Thus, even giant fullerenes as those reviewed in this section are only meta-stable.

## Conclusion

---

This chapter highlights recent developments in auxiliary density functional theory (ADFT) and their implementation in deMon2k. The simplifications associated with ADFT permit an efficient parallel code structure that is suitable for research applications in the nano-regime with chemical accuracy. The presented Born–Oppenheimer molecular dynamics simulation shows that simulation times on the nanosecond time scale can be reached with ADFT. As the here presented applications show this opens new and exciting perspectives for computational chemistry and material simulations with first-principle methods.

The development of ADFT in deMon2k is also a very educative example for the interplay of Theoretical Chemistry and Computer Science. The simplifications of the Kohn–Sham method by employing an atom-centered auxiliary density for the calculation of the Kohn–Sham potential yields simple and very efficient parallel algorithms. A typical example is the SCF acceleration by the MinMax procedure. Because only fitting vectors are involved it can be applied to systems with hundreds of atoms like the here discussed zeolites and fullerenes. Another example is the formulation of the non-iterative auxiliary density perturbation theory (ADPT) that substitutes the computationally cumbersome CPKS method in ADFT.

The increased use of ADFT in the deMon Developers community over the last years has considerably enhanced our understanding of this fitting approach. While the present authors are responsible for errors or omissions in this small chapter, the credit for the advances in ADFT and ADPT is shared with a much wider group cited in the references here and elsewhere.

## Acknowledgments

---

Financial support from CONACYT (U48775, 60117-F and 130726), ICYTDF (PIFUTP08-87 and PICCO-10-47), and CIAM (107310) is gratefully acknowledged. Parts of this chapter have been realized with the help of the bilateral CONACYT-CNRS project 16871.

## References

---

- Alberti, A. (1997). Location of Brønsted sites in mordenite. *Zeolites*, 19, 411.
- Alberti, A., Davoli, P., & Vezzalini, G. (1986). The crystal-structure refinement of a natural mordenite. *Zeitschrift für Kristallographie*, 175, 249.
- Almbladh, C. O., & Pedroza, A. C. (1984). Density-functional exchange-correlation potentials and orbital eigenvalues for light atoms. *Physical Review A*, 29, 2322.
- Andreoni, W. (2007). *The physics of fullerene-based and fullerene-related materials*. Dordrecht: Kluwer Academic Publishers.
- Andzelm, J., & Wimmer, E. (1992). Density functional Gaussian-type-orbital approach to molecular geometries, vibrations, and reaction energies. *Journal of Chemical Physics*, 96, 1280.
- Andzelm, J., Radzio, E., & Salahub, D. R. (1985). Compact basis sets for LCAO-LSD calculations. Part I: Method and bases for Sc to Zn. *Journal of Computational Chemistry*, 6, 520.
- Andzelm, J., Russo, N., & Salahub, D. R. (1987). Ground and excited states of group IVA diatomics from local-spin-density calculations: Model potentials for Si, Ge, and Sn. *Journal of Chemical Physics*, 87, 6562.
- Anquetil, R., Saussey, J. C., & Lavalley, J. C. (1999). Confinement effect on the interaction of hydroxy groups contained in the side pockets of H-mordenite with nitriles; a FT-IR study. *Physical Chemistry Chemical Physics*, 1, 555.
- Baerends, E. J., Ellis, D. E., & Ros, P. (1973). Self-consistent molecular Hartree-Fock-Slater

- calculations I. The computational procedure. *Chemical Physical*, 2, 41.
- Bakowies, D., Bühl, M., & Thiel, W. (1995). Can large fullerenes be spherical? *Journal of the American Chemical Society*, 117, 10113.
- Bates, K. R., & Scuseria, G. E. (1998). Why are buckyonions round? *Theoretica Chimica Acta*, 99, 29.
- Becke, A. D. (1987). A multicenter numerical integration scheme for polyatomic molecules. *Journal of Chemical Physics*, 88, 2547.
- Becke, A. D. (1993a). A new mixing of Hartree–Fock and local density-functional theories. *Journal of Chemical Physics*, 98, 1372.
- Becke, A. D. (1993b). Density-functional thermochemistry. III. The role of exact exchange. *Journal of Chemical Physics*, 98, 5648.
- Belpassi, L., Tarantelli, F., Sgamellotti, A., & Quiney, H. M. (2006). Electron density fitting for the Coulomb problem in relativistic density-functional theory. *Journal of Chemical Physics*, 124, 124104.
- Bergeron, D. E., Castleman, A. W., Jr., Morisato, T., & Khanna, S. N. (2004). Formation of  $Al_{13}I^-$ : Evidence for the superhalogen character of  $Al_{13}$ . *Science*, 304, 84.
- Bergeron, D. E., Roach, P. J., Castleman, A. W., Jr., Jones, N. O., & Khanna, S. N. (2005). Al cluster superatoms as halogens in polyhalides and as alkaline earths in iodide salts. *Science*, 307, 231.
- Bertran, O., Trickey, S. B., & Torras, J. (2010). Incorporation of deMon2k as a new parallel quantum mechanical code for the PUPIL system. *Journal of Computational Chemistry*, 31, 2669.
- Binkley, J. S., Pople, J. A., & Dobosh, P. A. (1974). The calculation of spin-restricted single-determinant wavefunctions. *Molecular Physics*, 28, 1423.
- Birkenheuer, U., Gordienko, A. B., Nasluzov, V. A., Fuchs-Rohr, M. K., & Rösch, N. (2005). Model density approach to the Kohn–Sham problem: Efficient extension of the density fitting technique. *International Journal of Quantum Chemistry*, 102, 743.
- Blundell, S. A., Guet, C., & Zope, R. R. (2000). Temperature dependence of the polarizability of sodium clusters. *Physical Review Letters*, 84, 4826.
- Boltalina, O. V., Ioffe, I. N., Sidorov, L. N., Seifert, G., & Vietze, K. (2000). Ionization energy of fullerenes. *Journal of the American Chemical Society*, 122, 9745.
- Bonin, K. D., & Kresin, V. V. (1997). *Electric-dipole polarizabilities of atoms, molecules and clusters*. Singapore: World Scientific.
- Bühl, M., & Hirsch, A. (2001). Spherical aromaticity of fullerenes. *Chemical Review*, 101, 1153.
- Calaminici, P., Jug, K., & Köster, A. M. (1998). Density functional calculations of molecular polarizabilities and hyperpolarizabilities. *Journal of Chemical Physics*, 109, 7756.
- Calaminici, P., Jug, K., & Köster, A. M. (1999). Static polarizabilities of  $Na_n$  ( $n < 9$ ) clusters: An all-electron density functional study. *Journal of Chemical Physics*, 111, 4613.
- Calaminici, P., Köster, A. M., Vela, A., & Jug, K. (2000). Comparison of static polarizabilities of  $Cu_n$ ,  $Na_n$ , and  $Li_n$  ( $n < 9$ ) clusters. *Journal of Chemical Physics*, 113, 2199.
- Calaminici, P., Köster, A. M., Carrington, T., Roy, P. N., Russo, N., & Salahub, D. R. (2001).  $V_3$ : Structure and vibrations from density functional theory, Franck–Condon factors, and the pulsed-field ionization zero-electron-kinetic energy spectrum. *Journal of Chemical Physics*, 114, 4036.
- Calaminici, P., Köster, A. M., & Salahub, D. R. (2003). Negative ion photoelectron spectra simulation of  $V_3O$  from a density functional study. *Journal of Chemical Physics*, 118, 4913.
- Calaminici, P., Flores-Moreno, R., & Köster, A. M. (2005). A density functional study of structures and vibrations of  $Ta_3O$  and  $Ta_3O^-$ . *Computing Letters*, 1, 164.
- Calaminici, P., Dominguez-Soria, V. D., Geudtner, G., Hernandez-Marin, E., & Köster, A. M. (2006). Parallelization of three-center electron repulsion integrals. *Theoretica Chimica Acta*, 115, 221.
- Calaminici, P., Janetzko, F., Köster, A. M., Mejia-Olvera, R., & Zuniga-Gutierrez, B. (2007a). Density functional theory optimized basis sets for gradient corrected functionals: 3d transition metal systems. *Journal of Chemical Physics*, 126, 044108.
- Calaminici, P., Köster, A. M., & Gamboa Martinez, G. U. (2007b). Temperature dependence of the polarizability of sodium clusters: An all-electron density functional study. In G. Maroulis & T. Simos (Eds.), *Computational methods in science and engineering, theory and computation: Old problems and new challenges* (Vol. 1, pp. 207–211). New York: AIP Conference Proceedings Melville.
- Calaminici, P., Geudtner, G., & Köster, A. M. (2009). First-principle calculations of large fullerenes. *Journal of Chemical Theory and Computation*, 5, 29.
- Campana, L., Selloni, A., Weber, J., & Goursot, A. (1997). Cation siting and dynamical properties of zeolite offretite from first-principles molecular dynamics. *Journal of Physical Chemistry*, 101, 9932.



- Carmona-Espíndola, J., Flores-Moreno, R., & Köster, A. M. (2010). Time-dependent auxiliary density perturbation theory. *Journal of Chemical Physics*, 133, 084102.
- Casida, M. E. (1995). Time-dependent density functional response theory for molecules. In P. D. Chong (Ed.), *Recent advances in density functional methods*. Singapore: World Scientific Publishing Co.
- Casida, M. E., Daul, C., Goursot, A., Köster, A. M., Pettersson, L. G. M., Proynov, E., St.-Amant, A., Salahub, D. R., Duarte, H., Godbout, N., Guan, J., Jamorski, C., Leboeuf, M., Malkin, V., Malkina, O., Sim, F., & Vela, A. (1996). *deMon-KS Version 3.4, deMon Software*. Montréal: Université de Montréal.
- Cerius2 (2005). *Version 4.10*. San Diego: Accelrys Inc.
- Chacko, S., Kanhere, D. G., & Blundell, S. A. (2005). First principles calculations of melting temperatures for free Na clusters. *Physical Review B*, 71, 155407.
- Chandrakumar, K. R. S., Ghanty, T. K., & Ghosh, S. K. (2004). Static dipole polarizability and binding energy of sodium clusters  $\text{Na}_n$  ( $n = 1 - 10$ ): A critical assessment of all-electron based post-Hartree-Fock and density functional methods. *Journal of Chemical Physics*, 120, 6487.
- Cioslowski, J. (1995). *Electronic structure calculations on fullerenes and their derivatives*. New York: Oxford University Press.
- del Campo, J. M., & Köster, A. M. (2008). A hierarchical transition state search algorithm. *Journal of Chemical Physics*, 129, 024107.
- Delley, B. (1990). An all-electron numerical method for solving the local density functional for polyatomic molecules. *Journal of Chemical Physics*, 92, 508.
- Demuth, T., Benco, L., Hafner, J., Toulhouat, H., & Hutschka, F. (2001). *Ab initio* investigation of the adsorption of benzene in mordenite. *Journal of Chemical Physics*, 114, 3703.
- Dérouane, E. G., André, J. M., & Lucas, A. A. (1988). Surface curvature effects in physisorption and catalysis by microporous solids and molecular sieves. *Journal of Catalysis*, 110, 58.
- Diercksen, G. H. F., & McWeeny, R. (1966). Self-consistent perturbation theory. I. General formulation and some applications. *Journal of Chemical Physics*, 44, 3554.
- Dirac, P. A. M. (1930). Note on exchange phenomena in the Thomas atom. *Proceedings of the Cambridge Philosophical Society*, 26, 376.
- Dodds, J. L., McWeeny, R., Raynes, W. T., & Riley, J. P. (1977). SCF theory for multiple perturbations. *Molecular Physics*, 33, 611.
- Dominguez-Soria, V. D., Calaminici, P., & Goursot, A. (2007). Theoretical study of the structure and properties of Na-MOR and H-MOR zeolite models. *Journal of Chemical Physics*, 127, 154710.
- Dominguez-Soria, V. D., Calaminici, P., & Goursot, A. (2008). Theoretical study of the structure and properties of Na-MOR and H-MOR zeolite models. In A. Gedeon, P. Massiani, & F. Babonneau (Eds.), *Studies in surface science and catalysis, zeolites and related materials: Trends, targets and challenges, Proceedings of 4th International FEZA Conference* (Vol. 174, p. 717). Amsterdam: Elsevier.
- Dominguez-Soria, V. D., Geudtner, G., Morales, J. L., Calaminici, P., & Köster, A. M. (2009). Robust and efficient density fitting. *Journal of Chemical Physics*, 131, 124102.
- Dreizler, R. M., & Gross, E. K. U. (1990). *Density functional theory*. Berlin: Springer.
- Dunlap, B., & Boettger, J. C. (1996). Local-density-functional study of the fullerenes, graphene and graphite. *Journal of Physics B*, 29, 4907.
- Dunlap, B. I., & Rösch, N. (1990). The Gaussian-type orbitals density-functional approach to finite systems. *Advances in Quantum Chemistry*, 21, 317.
- Dunlap, B. I., & Zope, R. R. (2006). Efficient quantum-chemical geometry optimization and the structure of large icosahedral fullerenes. *Chemical Physics Letters*, 422, 451.
- Dunlap, B. I., Connolly, J. W. D., & Sabin, J. R. (1979). On first-row diatomic molecules and local density models. *Journal of Chemical Physics*, 71, 4993.
- Dunlap, B. I., Brenner, D. W., Mintmire, J. W., Mowrey, R. C., & White, C. T. (1991). Local density functional electronic structures of three stable icosahedral fullerenes. *Journal of Physical Chemistry*, 95, 8737.
- Fermi, E. (1927). A statistical method for the determination of some atomic properties. *Rendiconti Accademia Lincei*, 6, 602.
- Fermi, E. (1928a). A statistical method for the determination of some properties of the atom and its application to the theory of the periodic system of the elements. *Zeitschrift für Physik*, 48, 73.
- Fermi, E. (1928b). On the statistical deduction of some atomic properties. Application to the theory of the periodic system of the elements. *Rendiconti Accademia nazionale dei Lincei*, 7, 342.
- Flores-Moreno, R. (2010). Symmetry conservation in Fukui functions. *Journal of Chemical Theory and Computation*, 6, 48.
- Flores-Moreno, R., & Köster, A. M. (2008). Auxiliary density perturbation theory. *Journal of Chemical Physics*, 128, 134105.



- Flores-Moreno, R., & Ortiz, J. V. (2009). Integral approximations in *ab initio* electron propagator calculations. *Journal of Chemical Physics*, *131*, 124110.
- Flores-Moreno, R., Melin, J., Ortiz, J. V., & Merino, G. (2008). Efficient evaluation of analytic Fukui functions. *Journal of Chemical Physics*, *129*, 224105.
- Fournier, R. (1990). Second and third derivatives of the linear combination of Gaussian type orbitals–local spin density energy. *Journal of Chemical Physics*, *92*, 5422.
- Gamboa Martinez, G., Calaminici, P., & Köster, A. M. (2008). How important are temperature effects for cluster polarizabilities? *Journal of Physical Chemistry A*, *112*, 11969.
- Gaspar, R. (1954). Über eine Approximation des Hartreefockschen Potentials durch eine Universelle Potentialfunktion. *Acta Physica Academiae Scientiarum Hungaricae*, *3*, 263.
- Gel'fand, I. M., & Fomin, S. V. (1963). *Calculus of variations*. Englewood Cliffs: Prentice Hall.
- Geudtner, G., Janetzko, F., Köster, A. M., Vela, A., & Calaminici, P. (2006). Parallelization of the deMon2k code. *Journal of Computational Chemistry*, *27*, 483.
- Godbout, N., Salahub, D. R., Andzelm, J., & Wimmer, E. (1992). Optimization of gaussian-type basis-sets for local spin-density functional calculations. 1. Boron through neon, optimization technique and validation. *Canadian Journal of Physics*, *70*, 560.
- Goursot, A., Fajula, F., Daul, C., & Weber, J. (1998). Study of the molecular electrostatic potentials of zeolites: the acidity in offretite. *Journal of Physical Chemistry*, *92*, 4456.
- Guan, J. G., Casida, M. E., Köster, A. M., & Salahub, D. R. (1995). All-electron local and gradient-corrected density-functional calculations of  $\text{Na}_n$  dipole polarizabilities for  $n=1-6$ . *Physical Review B*, *52*, 2184.
- Haddon, R. C., Scuseria, G. E., & Smalley, R. E. (1997).  $\text{C}_{240}$  – The most chemically inert fullerene? *Chemical Physics Letters*, *272*, 38.
- Hall, G. G. (1951). The molecular orbital theory of chemical valency. 8. A method of calculating ionization potentials. *Proceedings of the Royal Society of London Series B*, *205*, 541.
- Hamel, S., Casida, M. E., & Salahub, D. R. (2001). Assessment of the quality of orbital energies in resolution-of-the-identity Hartree–Fock calculations using deMon auxiliary basis sets. *Journal of Chemical Physics*, *114*, 7342.
- Heggie, M. I., Terrones, M., Eggen, B. R., Jungnickel, G., Jones, R., Latham, C. D., & Briddon, P. R. (1998). Quantitative density-functional study of nested fullerenes. *Physical Review B*, *57*, 13339.
- Hohenberg, P., & Kohn, W. (1964). Inhomogeneous electron gas. *Physical Review*, *136*, B864.
- Hoover, W. G. (1985). Canonical dynamics: Equilibrium phase-space distributions. *Physical Review A*, *31*, 1695.
- Iijima, S. (1980). Direct observation of the tetrahedral bonding in graphitized carbon-black by high-resolution electron-microscopy. *Journal of Crystal Growth*, *50*, 675–683.
- Ito, M., & Saioto, Y. (1985). The crystal-structure of ion-exchanged mordenite. *Bulletin of the Chemical Society of Japan*, *58*, 3035.
- Itoh, S., Ordejon, P., Drabold, D. A., & Martin, R. M. (1996). Structure and energetics of giant fullerenes: An order- $N$  molecular-dynamics study. *Physical Review B*, *53*, 2132.
- Jacobs, P. A., & Martens, G. A. (1987). *Synthesis in highsilica aluminosilicate zeolites*. Amsterdam: Elsevier.
- Jamorski, C., Casida, M. E., & Salahub, D. R. (1996). Dynamic polarizabilities and excitation spectra from a molecular implementation of time-dependent density-functional response theory:  $\text{N}_2$  as a case study. *Journal of Chemical Physics*, *104*, 5134.
- Janetzko, F., Köster, A. M., & Salahub, D. R. (2008). Development of the cyclic cluster model formalism for Kohn-Sham auxiliary density functional theory methods. *Journal of Chemical Physics*, *128*, 024102.
- Johnson, K. H. (1966). “Multiple-Scattering” model for polyatomic molecules. *Journal of Chemical Physics*, *45*, 3085.
- Johnson, K. H., & Messmer, R. P. (1974). Clusters, chemisorption and catalysis. *Journal of Vacuum Science & Technology*, *11*, 236.
- Johnson, K. H., & Smith, F. C. (1970). Cluster-wave approach to the electronic structures of complex molecules and solids. *Physical Review Letters*, *24*, 139.
- Johnson, K. H., & Smith, F. C. (1971). Scattered-wave model for the electronic structure and optical properties of the permanganate ion. *Chemical Physics Letters*, *10*, 219.
- Johnson, K. H., & Smith, F. C. (1972). Chemical bonding of a molecular transition-metal ion in a crystalline environment. *Physical Review B*, *5*, 831.
- Kadish, K. M., & Ruoff, R. S. (2007). *Fullerenes: Chemistry, physics, and technology*. New York: Wiley.

- Knickelbein, M. B. (2001). Electric dipole polarizabilities of Ni<sub>12–58</sub>. *Journal of Chemical Physics*, *115*, 5957.
- Knickelbein, M. B. (2003). Electric dipole polarizabilities of Nb<sub>2–27</sub>. *Journal of Chemical Physics*, *118*, 6230.
- Knickelbein, M. B. (2004). Electric dipole polarizabilities of copper clusters. *Journal of Chemical Physics*, *120*, 10450.
- Knight, W. D., Clemenger, K., de Heer, W. A., Saunders, W. A., Chou, M. Y., & Cohen, M. L. (1984). Electronic shell structure and abundances of sodium clusters. *Physical Review Letters*, *52*, 2141.
- Knight, W. D., Clemenger, K., de Heer, A. W., & Saunders, W. A. (1985). Polarizability of alkali clusters. *Physical Review B*, *31*, 2539.
- Kohn, W., & Sham, L. J. (1965). Self-consistent equations including exchange and correlation effects. *Physical Review*, *140*, A1133.
- Komornicki, A., & Fitzgerald, G. (1993). Molecular gradients and Hessians implemented in density functional theory. *Journal of Chemical Physics*, *98*, 1398.
- Köster, A. M. (1996). Efficient recursive computation of molecular integrals for density functional methods. *Journal of Chemical Physics*, *104*, 4114.
- Köster, A. M. (1998). *Habilitation thesis*. Universität Hannover.
- Köster, A. M. (2003). Hermite Gaussian auxiliary functions for the variational fitting of the Coulomb potential in density functional methods. *Journal of Chemical Physics*, *118*, 9943.
- Köster, A. M., Calaminici, P., Gómez, Z., & Reveles, J. U. (2002). Density functional theory calculations of transition metal clusters. In K. Sen (Ed.), *Reviews of modern quantum chemistry, a celebration of the contribution of Robert G. Parr*. River Edge: World Scientific.
- Köster, A. M., Goursot, A., & Salahub, D. R. (2003). DeMon. In J. McCleverty, T. J. Meyer, & B. Lever (Eds.), *Comprehensive coordination chemistry-II, from biology to nanotechnology* (Vol. 1). Amsterdam: Elsevier.
- Köster, A. M., Flores-Moreno, R., & Reveles, J. U. (2004a). Efficient and reliable numerical integration of exchange-correlation energies and potentials. *Journal of Chemical Physics*, *121*, 681.
- Köster, A. M., Reveles, J. U., & del Campo, J. M. (2004b). Calculation of exchange-correlation potentials with auxiliary function densities. *Journal of Chemical Physics*, *121*, 3417.
- Köster, A. M., Calaminici, P., Casida, M. E., Flores-Moreno, R., Geudtner, G., Goursot, A., Heine, T., Ipatov, A., Janetzko, F., del Campo, J. M., Patchkovskii, S., Reveles, J. U., Salahub, D. R., & Vela, A. (2006). *The deMon developers*. Mexico-City: Cinvestav. <http://www.demon-software.com>.
- Köster, A. M., del Campo, J. M., Janetzko, F., & Zuniga-Gutierrez, B. (2009). A MinMax self-consistent-field approach for auxiliary density functional theory. *Journal of Chemical Physics*, *130*, 114106.
- Köster, A. M., Geudtner, G., Calaminici, P., Casida, M. E., Flores-Moreno, R., Goursot, A., Janetzko, F., Reveles, J. U., Vela, A., & Salahub, D. R. (2010). *The deMon2k user's guide*. <http://www.demon-software.com>.
- Krack, M., & Köster, A. M. (1998). An adaptive numerical integrator for molecular integrals. *Journal of Chemical Physics*, *108*, 3226.
- Krishnamurty, S., Heine, T., & Goursot, A. (2003). Influence of dynamics on the structure and NMR chemical shift of a zeolite precursor. *Journal of Physical Chemistry B*, *104*, 5728.
- Krishnamurty, S., Stefano, M., Mineva, T., Bégu, S., Devoisselle, J. M., Goursot, A., Zhu, R., & Salahub, D. R. (2008a). Lipid thermodynamics: Melting is molecular. *ChemPhysChem*, *9*, 2321.
- Krishnamurty, S., Stefano, M., Mineva, T., Bégu, S., Devoisselle, J. M., Goursot, A., Zhu, R., & Salahub, D. R. (2008b). Density functional theory-based conformational analysis of a phospholipid molecule (Dimyristoyl Phosphatidylcholine). *Journal of Physical Chemistry B*, *112*, 13433.
- Kronik, L., Vasiliev, I., & Chelikowsky, J. R. (2000). *Ab initio* calculations for structure and temperature effects on the polarizabilities of Na<sub>n</sub> (n < ~20) clusters. *Physical Review B*, *62*, 9992.
- Kroto, H. W., & McKay, K. (1988). The formation of quasi-icosahedral spiral shell carbon particles. *Nature*, *331*, 328.
- Kroto, H. W., Heath, J. R., O'Brien, S. C., Curl, R. F., & Smalley, R. E. (1985). C<sub>60</sub>: Buckminsterfullerene. *Nature (London)*, *318*, 162.
- Kümmel, S., Akola, J., & Manninen, M. (2000). Temperature dependence of the polarizability of sodium clusters. *Physical Review Letters*, *84*, 4826.
- Laikov, D. N. (1997). Fast evaluation of density functional exchange-correlation terms using the expansion of the electron density in auxiliary basis sets. *Chemical Physics Letters*, *281*, 151.
- Lev, B., Zhang, R., de la Lande, A., Salahub, D. R., & Noskov, S. Y. (2010). The QM-MM interface for CHARMM-deMon. *Journal of Computational Chemistry*, *31*, 1015.
- Levy, M. (1979). Universal variational functionals of electron densities, first-order density matrices, and natural spin-orbitals and solution of the

- v-representability problem. *Proceedings of the National Academy of Sciences*, 76, 6062.
- Levy, M., & Perdew, J. P. (1985). In R. M. Dreizler & J. da Providencia (Eds.), *Density functional methods in physics*. New York: Plenum.
- Li, H., & Jensen, G. H. (2002). Partial Hessian vibrational analysis: The localization of the molecular vibrational energy and entropy. *Theoretica Chimica Acta*, 107, 211.
- Malkin, V. G., Malkina, O. L., & Salahub, D. R. (1993a). Calculations of NMR shielding constants by uncoupled density functional theory. *Chemical Physics Letters*, 204, 80.
- Malkin, V. G., Malkina, O. L., & Salahub, D. R. (1993b). Calculations of NMR shielding constants beyond uncoupled density functional theory. IGLO approach. *Chemical Physics Letters*, 204, 87.
- Malkin, V. G., Malkina, O. L., Casida, M. E., & Salahub, D. R. (1994). Nuclear magnetic resonance shielding tensors calculated with a sum-over-states density functional perturbation theory. *Journal of the American Chemical Society*, 116, 5898.
- Marie, O., Thibault-Starzyk, F., & Lavalley, J. C. (2000). Confirmation of the strongest nitriles-hydroxy groups interaction in the side pockets of mordenite zeolites. *Physical Chemistry Chemical Physics*, 2, 5341.
- Marie, O., Massiani, P., & Thibault-Starzyk, F. (2004). Infrared evidence of a third Brønsted site in mordenites. *Journal of Physical Chemistry B*, 108, 5073.
- Martyna, G. J., Klein, M. L., & Tuckerman, M. (1992). Nosé-Hoover chains: The canonical ensemble via continuous dynamics. *Journal of Chemical Physics*, 97, 2635.
- McWeeny, R. (1962). Perturbation theory for the Fock-Dirac density matrix. *Physical Review*, 126, 1028.
- McWeeny, R. (2001). *Methods of molecular quantum mechanics* (2nd reprinting). London: Academic.
- McWeeny, R., & Dierksen, G. H. F. (1968). Self-consistent perturbation theory. II. Extension to open shells. *Journal of Chemical Physics*, 49, 4852.
- McWeeny, R., Dodds, J. L., & Sadlej, A. J. (1977). Generalization for perturbation-dependent non-orthogonal basis set. *Molecular Physics*, 34, 1779.
- Meier, W. M. (1961). The crystal structure of mordenite (ptilolite). *Zeitschrift für Kristallographie*, 115, 439.
- Messmer, R. P., Tucker, C. W., & Johnson, K. H. (1975). A comparison of SCF- $X\alpha$  and extended Hückel methods for metal clusters. *Chemical Physics Letters*, 36, 423.
- Messmer, R. P., Salahub, D. R., & Davenport, J. W. (1978). Calculation of angular dependence of photoemission for the Al(100) + O system using a simple molecular orbital cluster model. *Chemical Physics Letters*, 57, 29.
- Mintmire, J. W., & Dunlap, B. I. (1982). Fitting the Coulomb potential variationally in linear-combination-of-atomic-orbitals density-functional calculations. *Physical Review A*, 25, 88.
- Mintmire, J. W., Sabin, J. R., & Trickey, S. B. (1982). Local-density-functional methods in two-dimensionally periodic systems. Hydrogen and beryllium monolayers. *Physical Review B*, 26, 1743.
- Molof, R. W., Miller, T. M., Schwartz, H. L., Benderson, B., & Park, J. T. (1974a). Measurements of the average electric dipole polarizabilities of the alkali dimers. *Journal of Chemical Physics*, 61, 1816.
- Molof, R. W., Schwartz, H. L., Miller, T. H., & Beder-son, B. (1974b). Measurements of electric dipole polarizabilities of the alkali-metal atoms and the metastable noble-gas atoms. *Physical Review A*, 10, 1131.
- Nosé, S. (1984). A unified formulation of the constant temperature molecular dynamics methods. *Journal of Chemical Physics*, 81, 511.
- Parr, R. G., & Yang, W. (1989). *Density-functional theory of atoms and molecules*. New York: Oxford University Press.
- Passaglia, E. (1975). Crystal-chemistry of mordenites. *Contributions to Mineralogy and Petrology*, 50, 65.
- Pearson, R. G. (1973). Hard and soft acids and bases. *Journal of the American Chemical Society*, 85, 3533.
- Perdew, J. P., Burke, K., & Ernzerhof, M. (1996). Generalized gradient approximation made simple. *Physical Review Letters*, 77, 3865.
- Politzer, P. (1987). A relationship between the charge capacity and the hardness of neutral atoms and groups. *Journal of Chemical Physics*, 86, 1072.
- Pople, J. A., & Nesbet, R. K. (1954). Self-consistent orbitals for radicals. *Journal of Chemical Physics*, 22, 571.
- Press, W. H., Teukolsky, S. A., Vetterling, W. T., & Flannery, B. P. (1992). *Numerical recipes in FORTRAN* (2nd ed.). Cambridge: Cambridge University Press.
- Rayane, D., Allouche, A. R., Benichou, E., Antoine, R., Aubert-Frecon, M., Dugourd, P., Broyer, M., Ristori, C., Chandezon, F., Hubert, B. A., & Guet, C. (1999). Static electric dipole polarizabilities of alkali clusters. *The European Physical Journal D*, 9, 243.

- Reveles, J. U., & Köster, A. M. (2004). Geometry optimization in density functional methods. *Journal of Computational Chemistry*, 25, 1109.
- Roothaan, C. C. J. (1951). New developments in molecular orbital theory. *Reviews of Modern Physics*, 23, 69.
- Roothaan, C. C. J. (1960). Self-consistent field theory for open shells of electronic systems. *Reviews of Modern Physics*, 32, 179.
- Rozanska, X., van Santen, R. A., Demuth, T., Hutschka, F., & Hafner, J. (2003). A periodic DFT study of isobutene chemisorption in proton-exchanged zeolites: Dependence of reactivity on the zeolite framework structure. *Journal of Physical Chemistry B*, 107, 1309.
- Rozanska, X., Barbosa, L. A. M. M., & van Santen, R. A. (2005). A periodic density functional theory study of cumene formation catalyzed by H-Mordenite. *Journal of Physical Chemistry B*, 109, 2203.
- Rungsirisakun, R., Jansang, B., Pantu, P., & Limtrakul, J. (2005). The adsorption of benzene on industrially important nanostructured catalysts (H-BEA, H-ZSM-5, and H-FAU): Confinement effects. *Journal of Molecular Structure*, 239, 733.
- Salahub, D. R. (1978). Electronic-structure of  $B_4H_8Fe(CO)_3$  - comparison of SCF-X $\alpha$ -SW molecular orbital theory with ultraviolet photoelectron-spectrum. *Journal of the Chemical Society, Chemical Communications*, 9, 385.
- Salahub, D. R., Weber, J., Goursot, A., Köster, A. M., & Vela, A. (2005). Applied density functional theory and the deMon codes 1964 to 2004. In C. E. Dykstra, G. Frenking, K. S. Kim, & G. Scuseria (Eds.), *Theory and applications of the computational chemistry: The first 40 years*. Amsterdam: Elsevier.
- Sambe, H., & Felton, R. H. (1975). A new computational approach to Slater's SCF-X $\alpha$  equation. *Journal of Chemical Physics*, 62, 1122.
- Saunders, V. R. (1983). *Methods in computational physics* (p. 1). Dordrecht: Reidel.
- Schlenker, J. L., Pluth, J. J., & Smith, J. V. (1979). Positions of cations and molecules in zeolites with the mordenite framework. 9. Dehydrated H-mordenite via acid exchange. *Materials Research Bulletin*, 14, 849.
- Schwarz, K. (1972). Optimization of the statistical exchange parameter  $\alpha$  for the free atoms H through Nb. *Physical Review B*, 5, 2466.
- Scuseria, G. E. (1995). The equilibrium structures of giant fullerenes: Faceted or spherical shape? An *ab initio* Hartree-Fock study of icosahedral  $C_{240}$  and  $C_{540}$ . *Chemical Physics Letters*, 243, 193.
- Scuseria, G. E. (1996). *Ab Initio* calculations of fullerenes. *Science*, 271, 942.
- Seifert, G., Vietze, K., & Schmidt, R. (1996). Ionization energies of fullerenes - size and charge dependence. *Journal of Physics B*, 29, 5183.
- Shao, N., Gao, Y., Yoo, S., An, W., & Zeng, X. C. (2006). Search for lowest-energy fullerenes:  $C_{98}$  to  $C_{110}$ . *Journal of Physical Chemistry A*, 110, 7672.
- Shao, N., Gao, Y., & Zeng, X. C. (2007). Search for lowest-energy fullerenes 2:  $C_{38}$  to  $C_{80}$  and  $C_{112}$  to  $C_{120}$ . *Journal of Physical Chemistry C*, 111, 17671.
- Shedge, S. V., Carmona-Espindola, J., Pal, S., & Köster, A. M. (2010). Comparison of the auxiliary density perturbation theory and the noniterative approximation to the coupled perturbed Kohn-Sham method: Case study of the polarizabilities of disubstituted azoarene molecules. *Journal of Physical Chemistry A*, 114, 2357.
- Sim, F., Salahub, D. R., & Chin, S. (1992). The accurate calculation of dipole moments and dipole polarizabilities using Gaussian-based density functional methods. *International Journal of Quantum Chemistry*, 43, 463.
- Simoncic, P., & Armbruster, T. (2004). Peculiarity and defect structure of the natural and synthetic zeolite mordenite: A single-crystal X-ray study. *American Mineralogist*, 89, 421.
- Slater, J. C. (1951). A simplification of the Hartree-Fock method. *Physical Review*, 81, 385.
- Smirnov, K., & Thibault-Starzyk, F. (1999). Confinement of acetonitrile molecules in mordenite. A computer modeling study. *Journal of Physical Chemistry B*, 103, 8595.
- St-Amant, A., & Salahub, D. R. (1990). New algorithm for the optimization of geometries in local density functional theory. *Chemical Physics Letters*, 169, 387.
- Thibault-Starzyk, F., Travert, A., Saussey, J. C., & Lavalley, J. C. (1998). Correlation between activity and acidity on zeolites: A high temperature infrared study of adsorbed acetonitrile. *Topics in Catalysis*, 6, 111.
- Thomas, L. H. (1927). The calculation of atomic fields. *Mathematical Proceedings of the Cambridge Philosophical Society*, 23, 542.
- Tikhonov, G., Kasperovich, V., Wong, K., & Kresin, V. V. (2001). A measurement of the polarizability of sodium clusters. *Physical Review A*, 64, 063202.
- Trickey, S. B., Müller-Plate, F., Dierksen, G. H. F., & Boettger, J. C. (1992). Interplanar binding and lattice relaxation in a graphite dilayer. *Physical Review B*, 45, 4460.
- Trickey, S. B., Alford, J. A., & Boettger, J. C. (2004). Methods and implementation of Robust, high-precision Gaussian basis DFT calculations

- for periodic systems: The GTOFF code. In J. Leszczynski (Ed.), *Computational materials science, theoretical and computational chemistry* (Vol. 15, p. 171). Amsterdam: Elsevier.
- Triguero, L., & Pettersson, L. G. M. (1998). MO and DFT approaches to the calculation of X-ray absorption/emission spectra of nitrogen atom adsorbed on Cu(100). *Surface Science*, 398, 70.
- Triguero, L., Pettersson, L. G. M., & Ågren, H. (1998). Calculations of X-ray emission spectra of molecules and surface adsorbates by means of density functional theory. *Journal of Physical Chemistry A*, 102, 10599.
- Ugarte, D. (1992). Curling and closure of graphitic networks under electron-beam irradiation. *Nature*, 359, 7071-7091.
- Ugarte, D. (1995). Onion-like graphitic particles. *Carbon*, 33, 989-993.
- Vahtras, O., Almlöf, J., & Feyereisen, M. W. (1993). Integral approximations for LCAO-SCF calculations. *Chemical Physics Letters*, 213, 514.
- Valerio, G., Goursot, A., Vetrivel, R., Malkina, O., & Malkin, V. (1998). Calculation of  $^{29}\text{Si}$  and  $^{27}\text{Al}$  MAS NMR chemical shifts in zeolite- $\beta$  using density functional theory: Correlation with lattice structure. *Journal of the American Chemical Society*, 120, 11426.
- Vásquez-Pérez, J. M., Gamboa Martínez, G. U., Köster, A. M., & Calaminici, P. (2009). The discovery of unexpected isomers in sodium heptamers by Born-Oppenheimer molecular dynamics. *Journal of Chemical Physics*, 131, 124126.
- Velde, G. T., Bickelhaupt, F. M., Baerends, E. J., Guerra, C. F., Van Gisbergen, S. J. A., Snijders, J. G., & Ziegler, T. (2001). Chemistry with ADF. *Journal of Computational Chemistry*, 22, 931.
- Vos, A. M., Rozanska, X., Schoonheydt, R. A., van Santen, R. A., Hutschka, F., & Hafner, J. (2001). A theoretical study of the alkylation reaction of toluene with methanol catalyzed by acidic mor-denite. *Journal of the American Chemical Society*, 123, 2799.
- Vosko, S. H., Wilk, L., & Nusair, M. (1980). Accurate spin-dependent electron liquid correlation energies for local spin-density calculations - a critical analysis. *Canadian Journal of Physics*, 58, 1200.
- Weber, J., Berthou, H., & Jorgensen, C. K. (1977). Application of the MS X $\alpha$  method to the understanding of satellite excitations in inner shell photoelectron spectra of lanthanide trifluorides. *Chemical Physics Letters*, 45, 1.
- Wei, D. Q., & Salahub, D. R. (1994). Hydrated proton clusters and solvent effects on the proton transfer barrier: A density functional study. *Journal of Chemical Physics*, 101, 7633.
- Wei, D. Q., & Salahub, D. R. (1997). Hydrated proton clusters: *Ab initio* molecular dynamics simulation and simulated annealing. *Journal of Chemical Physics*, 106, 6086.
- Wei, D. Q., Proynov, E. I., Milet, A., & Salahub, D. R. (2000). Solvation of the hydroxide anion: A combined DFT and molecular dynamics study. *Journal of Physical Chemistry A*, 104, 2384.
- Xu, C. H., & Scuseria, G. E. (1996). An O(N) tight-binding study of carbon clusters up to C $_{8640}$ : The geometrical shape of the giant icosahedral fullerenes. *Chemical Physics Letters*, 262, 219.
- Yang, D. S., Zgierski, M. Z., Berces, A., Hackett, P. A., Roy, P. N., Martinez, A., Carrington, T., Salahub, D. R., Fournier, R., Pang, T., & Chen, C. F. (1996). Vibrational and geometric structures of Nb $_3$ C $_2$  and Nb $_3$ C $_2^+$  from pulsed field ionization-zero electron kinetic energy photoelectron spectra and density functional calculations. *Journal of Chemical Physics*, 105, 10663.
- Yang, Y., Trafford, K., Kresnawahjuesa, O., Sepa, J., Gorte, R. J., & White, D. (2001). An examination of confinement effects in high-silica zeolites. *Journal of Physical Chemistry B*, 105, 1935.
- York, D., Lu, J. P., & Yang, W. (1994). Density-functional calculations of the structure and stability of C $_{240}$ . *Physical Review B*, 49, 8526.
- Zhao, Q., & Parr, R. G. (1992). Quantities T $_s$ [n] and T $_c$ [n] in density-functional theory. *Physical Review A*, 46, 2337.
- Zhao, Q., & Parr, R. G. (1993). Constrained-search method to determine electronic wave functions from electronic densities. *Journal of Chemical Physics*, 98, 543.
- Zhao, Q., Morrison, R. C., & Parr, R. G. (1994). From electron densities to Kohn-Sham kinetic energies, orbital energies, exchange-correlation potentials, and exchange-correlation energies. *Physical Review A*, 50, 2138.
- Zope, R. R., Baruah, T., Pederson, M. R., & Dunlap, B. I. (2008). Static dielectric response of icosahedral fullerenes from C $_{60}$  to C $_{2160}$  characterized by an all-electron density functional theory. *Physical Review B*, 77, 115452.

# 17 Guide to Programs for Non-relativistic Quantum Chemistry Calculations

*Tao Zeng · Mariusz Klobukowski*

Department of Chemistry, University of Alberta, Edmonton, Alberta,  
Canada

<b>Introduction</b> .....	<b>612</b>
<b>Free Software</b> .....	<b>614</b>
GAMESS-US .....	614
Firefly .....	616
GAMESS-UK .....	616
Dalton .....	617
NWChem .....	619
ORCA .....	620
PSI3 .....	621
ACES II .....	622
ACES III .....	623
CFOUR .....	623
COLUMBUS .....	623
MPQC .....	624
<b>Commercial Software</b> .....	<b>624</b>
Gaussian .....	624
Molcas .....	625
Q-Chem .....	625
Turbomole .....	625
Molpro .....	625
Jaguar .....	625
PQS .....	625
Spartan .....	625
HyperChem .....	625
Ampac 9 .....	625
<b>References</b> .....	<b>626</b>



**Abstract:** This chapter reviews most of the widely used non-relativistic quantum chemistry program packages. Considering that information about availability and capabilities of the free quantum chemistry programs is more limited than that of the commercial ones, the authors concentrated on the free programs. More specifically, the reviewed programs are free for the academic community. Features of these programs are described in detail. The capabilities of each free program can generally be categorized into five fields: independent electron model; electron correlation treatment; excited state calculation; nuclear dynamics including gradient and hessian; and parallel computation. Examples of input files for the Møller–Plesset calculation of formaldehyde are presented for most of the free programs to illustrate how to create the input files. The main contributors of each free program and their institutions are also introduced, with a brief history of program development if available. All the key references of the cited algorithms and the hyperlinks of the home page of each program (both free and commercial) are given in this review for the interested readers. As the most important information of every cited free program's documentation has been extracted here, it is appropriate to consider this chapter to be the manual of manuals.

## Introduction

---

Computational quantum chemistry has been experiencing recently a period of tremendous growth. As the capabilities of computer hardware increased, so did the appetites of researchers for modeling tools. Many computer packages became available, both commercially and as free programs, the latter usually requiring a simple registration procedure to obtain and use the code. The free access is usually restricted to researchers from academic institutions and the programs are sometimes unsupported; however, an associated users' discussion forum often accompanies the program. In this chapter, we will review the software that is currently available, focusing on packages that are familiar to the reviewers. In addition to outlining the unique capabilities of each program, we added the URL links to the home pages to allow the readers to follow the latest developments of each code.

The programs that use only the density functional theory and the programs for relativistic calculations at the level of Dirac theory and beyond are reviewed in other chapters.

All the reviewed programs carry out fundamental tasks of a computational chemist or a computational molecular physicist: calculation of energy for various hamiltonians; evaluation of gradients of energy (needed to locate stationary points on the potential energy surface); evaluation of the energy hessian (required to analyze the character of the located stationary point, identify local minima and saddle points, and perform vibrational frequency calculation); and evaluation of basic properties (population analysis, dipole moments). The components of the programs include basis set libraries and pseudopotentials.

At the Hartree-Fock level (Hartree 1928; Fock 1930), the energies for closed-shell systems are evaluated using the restricted Hartree-Fock (RHF) method (Hall and Lennard-Jones 1951; Roothaan 1951). For the open-shell molecules, there are several methods that are available in most programs: the unrestricted Hartree-Fock (UHF) method (Pople and Nesbet 1954), several variants of the restricted open-shell Hartree-Fock (ROHF) method (Hsu et al. 1976; McWeeny and Diercksen 1968), and the generalized valence bond (GVB) method (Bobrowicz and Schaefer 1977).

The wavefunction based on a single-configuration Hartree-Fock method is often inadequate to describe bonding in a molecule, and in such a case several multi-configuration methods are used; the approach is usually called multi-configuration self-consistent field (MCSCF) (Olsen et al. 1983; Roos 1983, 1994; Schmidt and Gordon 1998; Shepard 1987; Werner 1987), and its practical implementations are the full orbital reaction space (FORS) (Ruedenberg et al. 1982a, b, c) and complete active space (CAS) (Roos 1987).

Beyond Hartree-Fock, the energies (and wavefunctions) may be improved at several levels: various orders of the perturbation method at the Møller–Plesset level (1934) (MP2, MP3, MP4); for open-shell systems we could use either unrestricted MP2 (Pople et al. 1976) or one of several variants of the perturbation method based on the ROHF wavefunction: the Z-averaged perturbation theory (ZAPT) (Lee and Jayatilaka 1993; Lee et al. 1994) and RMP (Knowles et al. 1980; Lauderdale et al. 1991); configuration interaction (CI) method (Brooks and Schaefer 1979; Ivanic and Ruedenberg 2001).

Very accurate energies may be obtained using the coupled-cluster theory (CC) (Paldus 2005; Shavitt and Bartlett 2009).

Excited states may be studied using the general post-Hartree-Fock methods listed above, or some specialized techniques, such as configuration interaction with single substitutions (CIS) (Foresman et al. 1992), time-dependent density functional theory (TDDFT) (Dreuw and Head-Gordon 2005; Elliott et al. 2009), equations-of-motion coupled cluster (EOM-CC) (Kowalski and Piecuch 2004; Włoch et al. 2005).

Solvent effects may be treated using several models: self-consistent reaction field (SCRf) (Karelson et al. 1986, 1993; Kirkwood 1934; Tapia and Goscinski 1975), polarizable continuum model (PCM) (Cammi and Tomasi 1995; Miertuš et al. 1981; Tomasi and Persico 1994; Tomasi et al. 2005), surface and simulation of volume polarization for electrostatics (SS(V)PE) (Chipman 1997, 2000, 2002), and conductor-like screening model (COSMO) (Baldrige and Klamt 1997; Klamt 1995; Klamt and Schüürmann 1993).

Even though the programs described in this chapter are referred to as “non-relativistic” (i.e., using single-component wavefunction), for molecules containing heavy atoms it is necessary to include at least scalar relativistic effects. A popular method of adding relativistic corrections is based on the formalism developed by Douglas and Kroll (1974) and by Hess (1986, 1989), and is usually referred to as DKH $n$  (where  $n$  denotes the order of the method).

Some scalar relativistic effects are included implicitly in calculations if pseudopotentials for heavy atoms are used to mimic the presence of core electrons; there are several families of pseudopotentials available: the effective core potentials (ECP) (Cundari and Stevens 1993; Hay and Wadt 1985; Kahn et al. 1976; Stevens et al. 1984), energy-adjusted pseudopotentials (Cao and Dolg 2006; Dolg 2000; Peterson 2003; Peterson et al. 2003), averaged relativistic effective potentials (AREP) (Hurley et al. 1986; LaJohn et al. 1987; Ross et al. 1990), model core potentials (MCP) (Klobukowski et al. 1999), and ab initio model potentials (AIMP) (Huzinaga et al. 1987).

For very large molecular systems several programs offer semiempirical hamiltonians (Stewart 1990), including Modified Neglect of Differential Overlap (MNDO) (Dewar and Thiel 1977), Semi-Ab initio Model 1 (SAM1) (Dewar et al. 1993), Austin Model 1 (AM1) (Dewar et al. 1985), Parametric Method 3 (PM3) (Stewart 1989), and Parametric Method 6 (PM6) (Stewart 2007) (the PM3 parameterization is available in the MOPAC2009 program which is freely available to academics, see <http://openmopac.net/downloads.html>). Zerner’s modification of the Intermediate Neglect of Differential Overlap approach (ZINDO) (Ridley and Zerner 1973) (see also Zerner 1991) is available in the ArgusLab program <http://www.arguslab.com/index.htm>.



The present Guide will focus on those programs that are freely available to academic community. In describing the capabilities of the programs we heavily borrowed from the available documentation. Commercial programs for ab initio computational chemistry (including several that employ semiempirical methods) will be mentioned only very briefly, guiding the reader to relevant home pages on the Internet.

Several collections of references to quantum chemistry software may be found on the Internet [http://en.wikipedia.org/wiki/Quantum\\_chemistry\\_computer\\_programs](http://en.wikipedia.org/wiki/Quantum_chemistry_computer_programs).

## Free Software

---

Free access to computer programs discussed in the present section is sometimes restricted to academic researchers. Please consult the Internet links for each program for specific restrictions.

## GAMESS-US

---

GAMESS-US (GAMESS = General Atomic and Molecular Electronic Structure System) is one of the early programs for the large-scale ab initio calculations in the public domain (Gordon and Schmidt 2005; Schmidt et al. 1993). The origins of GAMESS-US go back to the National Resources for Computations in Chemistry (NRCC), where the original GAMESS was assembled before 1981 (Dupuis et al. 1980). Since 1982 the development of GAMESS-US was carried out in the research group of Mark Gordon, first at North Dakota State and then at Iowa State University, with several research groups across the world making their contributions. The code is a good illustration of the care and effort that go into the development of any modern ab initio code: the October 2010 (Release 2) version has 769,161 lines of code and 221,147 lines of comments.

The capabilities of GAMESS-US are listed below:

- Analytic gradients and Hessians for RHF, ROHF, UHF, GVB, and MCSCF wavefunctions that are used to locate stationary points on the potential energy surface and identify their character (local minimum or transition state).
- MP2 energy and gradients for RHF, ROHF, and UHF wavefunctions.
- CI energy for very general CI excitation schemes (Ivanic 2003a, b; Ivanic and Ruedenberg 2001).
- Several methods of evaluating the CC energy, such as CC with single and double excitations (CCSD), with perturbative triples excitations (CCSD(T)), and including the latest completely renormalized (CR) CR-CC(2,3) method (Piecuch and Włoch 2005; Piecuch et al. 2002); numerical gradients for the CC methods are available.
- Excited states may be treated using the CIS, TDDFT, multi-configurational quasi-degenerate perturbation theory (MCQDPT) (Nakano 1993a, b), and equation-of-motion coupled-cluster (EOM-CC) methodologies.
- There are many ubiquitous density functionals available.
- Extensive basis set libraries.
- Pseudopotentials: both effective core potentials and model core potentials are available.
- The intrinsic reaction coordinate method allows for checking whether the path from a transition state connects the two minima that correspond to the required reactant and product.
- Anharmonic vibrational analysis via the vibrational self-consistent field (VSCF) method (Chaban et al. 1999).

- Many molecular properties may be calculated (static polarizability and hyperpolarizability; frequency-dependent polarizability; electric moments; electric field and electric field gradient).
- Solvent effects may be studied via continuum solvation methods using effective fragment potentials (EFP) (Adamovic et al. 2003; Day et al. 1996; Gordon et al. 2007; Jensen et al. 1984), polarizable continuum model (PCM), surface and simulation of volume polarization for electrostatics (SS(V)PE), conductor-like screening model (COSMO), and self-consistent reaction field (SCRF).
- A unique feature of the program is its ability to carry out all-electron calculations based on the Fragment Molecular Orbital (FMO) method (Fedorov and Kitaura 2007, 2009).
- Several possibilities for carrying out multi-reference perturbation calculations; spin-orbit coupling may be treated as a perturbation.
- For spin-orbit coupling CI wave functions, two-component natural orbitals (natural spinors) may be formed and analyzed (Zeng et al. 2011a, b)
- Scalar relativistic effects may be included at the levels of DKH2, DKH3, normalized elimination of small components (NESC) (Dyall 2002), and relativistic elimination of small components (RESC) (Nakajima and Hirao 1999) methods.
- Semiempirical Hamiltonians (AM1, PM3, and MNDO) are available.

The input style is illustrated below for the MP2 energy calculation for formaldehyde  $\text{H}_2\text{CO}$  at the experimental geometry  $r(\text{CH}) = 1.116 \text{ \AA}$ ,  $r(\text{CO}) = 1.208 \text{ \AA}$ ,  $\angle(\text{HCH}) = 116.5^\circ$ . The basis set is the correlation consistent cc-pVDZ basis (Dunning 1989), used in the form of spherical Gaussian functions.  $C_{2v}$  point group symmetry is used. In this example, the geometric structure of formaldehyde is defined in terms of internal coordinates (bond lengths, bond angles, and dihedral angles) in the representation known as Z-matrix. For  $\text{H}_2\text{CO}$ , the first line in the Z-matrix definition specifies the starting atom, in this case oxygen O. The second line, C 1 1 . 208, defines the second atom, carbon, which is connected to the first atom and the CO bond length equals 1.208  $\text{ \AA}$ . The first hydrogen atom is defined on the third line, H 2 1 . 116 1 121 . 75; this H atom is connected to the second atom (carbon), the CH bond length equals 1.116  $\text{ \AA}$ , and the bond angle H-C(2)-O(1) equals 121.75°. Finally, the fourth line, H 2 1 . 116 1 121 . 75 3 180 . 0, defines the second hydrogen atom, which is connected to the second atom (C) with the CH bond length of 1.116  $\text{ \AA}$ , the bond angle H-C(2)-O(1) of 121.75°, and the dihedral angle H(4)-C(2)-O(1)-H(3) of 180.0°.

```
$contrl mplevl=2 runtyp=energy coord=zmt ispher=1 $end
$basis gbasis=ccd $end
$data
H2CO at experimental geometry (CRC, p. 9-36)
cnv 2

O
C 1 1.208
H 2 1.116 1 121.75
H 2 1.116 1 121.75 3 180.0
$end
```

The home page of the program is <http://www.msg.ameslab.gov/GAMESS/>.

## Firefly

Formerly known as PC-GAMESS, the Firefly was developed on the basis of GAMESS-US, ending with the 1999 version. The program has been extensively modified, with large sections written to increase the efficiency of the program. The program is available as binaries for Windows-based computers as well as the Macintosh computers. The development of the code took place at the lab of A. A. Granovsky (Moscow State University). Some interesting features of the program are:

- The Møller–Plesset energy corrections may be calculated up to the fourth order (MP2, MP3, and MP4).
- Compression of files allows for very large calculations to be carried out; the compression is accomplished via packing of integrals, matrix elements, and their indices reduces file size and input/output (I/O) time.
- Faster MCQDPT algorithm and availability of XMCQDPT implementation.
- Integral code allows for fast evaluation of generally-contracted basis sets (Raffenetti 1973), such as atomic natural orbitals (ANO) (Almlöf 1987).

Sample input file is illustrated below for the same MP2 energy calculation. At present, the program's internal library does not have the cc-pVDZ basis set; in order to avoid the explicit (and thus rather lengthy) definition of this basis, the double-zeta basis set of Dunning and Hay (Dunning and Hay 1977) is used instead. This input file also illustrates an alternative definition of the geometric structure of a molecule: in terms of Cartesian coordinates (according to Firefly's defaults, in Ångströms), with only the symmetry-nonequivalent atoms defined. Each line defining atomic Cartesian coordinates specifies also the atom name and its nuclear charge.

```
$contrl mplevl=2 runtyp=energy d5=1 $end
$basis  gbasis=DH $end
$data
H2CO at experimental geometry (CRC, p. 9-36)
cnv 2

O      8.0      0.0000000000      0.0000000000      -0.6036077039
C      6.0      0.0000000000      0.0000000000      0.6043922961
H      1.0      0.9489930831      0.0000000000      1.1916470349
$end
```

Home page <http://classic.chem.msu.su/gran/gamesh/index.html>.

## GAMESS-UK

This code also originated from the NRCC code (Dupuis et al. 1980) and has been extensively modified by the Daresbury Laboratory (UK) group that included M. F. Guest, J. H. van Lenthe, J. Kendrick, K. Schöffel, P. Sherwood, and R. J. Harrison. A good summary of the code's features has been published (Guest et al. 2005). A summary of the program's capabilities is given below:

- Gradients and Hessians for many energies (RHF, ROHF, UHF, MCSCF, CASSCF).
- Energies of the excited states and corresponding transition moments may be calculated using the multi-reference CI method (MR-DCI). For the studies of electronically excited

states, direct random-phase approximation (RPA) and multiconfigurational linear response (MCLR) (Fuchs et al. 1993) excitation energies and oscillator strengths are also available.

- Ionization potentials may be calculated using the Green's function methodology (Cederbaum and Domcke 1977) and the two-particle-hole Tamm-Dancoff method (Schirmer and Cederbaum 1978).
- MP2 (energies and gradients) and MP3 (energies).
- Multi-reference second order perturbation method (CASPT2 method); multi-reference MP3 method (MR-MP3) is also available.
- CCSD and CCSD(T) energies.
- Many density functionals for the density functional theory calculations.
- Many properties may be evaluated, among them atomic charges (derived from Mulliken and Löwdin population analysis, natural population analysis (Read and Weinhold 1983; Read et al. 1985), and electrostatic potentials), polarizabilities, hyperpolarizabilities, and magnetizabilities.
- Semiempirical Hamiltonians (MNDO, MINDO/3, AM1, PM3, PM5, and MNDO-d) are available.
- Pseudopotentials (Hay and Wadt 1985; Roy et al. 2008) may be employed, with many pseudopotentials included in the library.
- The effects of the solvent may be modeled using the direct reaction field (DRF) method (de Vries et al. 1995; Duijnen and de Vries 1996).
- Relativistic effects may be treated using the zeroth-order regular approximation (ZORA) (Faas et al. 1995).

Sample input file for the H<sub>2</sub>CO calculation at the MP2/cc-pVDZ level of theory is shown below; notice that the symmetry of the molecule is determined by the program.

```
title
  H2CO at experimental geometry (CRC, p. 9-36)
zmatrix angstrom
  O
  C 1 1.208
  H 2 1.116  1 121.75
  H 2 1.116  1 121.75  3 180.0
end
harmonic
basis cc-pVDZ
scftype mp2
enter
```

Home page is <http://www.cfs.dl.ac.uk/gamess-uk/index.shtml>.

## Dalton

---

To quote from the authors of the program, “the Dalton program system is designed to allow convenient, automated determination of a large number of molecular properties based on an HF, density functional theory (DFT), MP2, coupled cluster, or MCSCF reference wave function.” Given the great flexibility of Dalton’s computational capabilities, the authors describe it as

directed at experts in ab initio calculations. The program has been developed at the University of Oslo.

A very short list of Dalton's capabilities is shown below; for those interested in the evaluation of molecular properties we suggest that Dalton's manual be consulted (<http://www.kjemi.uio.no/software/dalton/dalton.html>).

- Complete Active Space (CAS) or Restricted Active Space (RAS) wave functions.
- Calculation of excited states and core hole states.
- Several coupled-cluster (CC) wave functions.
- MP2 and explicitly correlated RI2-MP2 triples models.
- Dalton can calculate a large variety of molecular properties at many levels of theory: linear, quadratic, and cubic frequency-dependent response properties.
- Linear second-order polarization propagator approach (SOPPA) (Nielsen et al. 1980).
- NMR properties (magnetizabilities, nuclear shieldings, and all contributions to nuclear spin-spin coupling constants).
- EPR properties (electronic  $g$ -tensor, hyperfine coupling tensor, and zero-field splitting tensor).
- Circular dichroism properties (electronic circular dichroism, vibrational circular dichroism, and Raman optical activity).
- Gauge-origin independent magnetic properties.
- Solvent effects may be modeled via the self-consistent reaction field (SCRf) to arbitrary order in the multipole expansion.
- First-order properties for ground states: dipole and quadrupole moments, second moments of the electronic charge distribution and electric field gradients at the nuclei, as well as scalar-relativistic one-electron corrections (Darwin and mass velocity).
- Relativistic two-electron Darwin correction to the ground state.
- Excitation energies may be calculated for several levels of the coupled-cluster wavefunctions.
- Density functional theory.
- Effective core potentials.

Input file for the calculation of the MP2/cc-pVDZ energy of H<sub>2</sub>CO is shown below; the symmetry of the molecule is determined by the program.

```

BASIS
cc-pVDZ
Z-matrix input

  4  0
ZMAT
O   1  8.0
C   2  1  1.208  6.0
H   3  2  1.116  1  121.75  1.0
H   4  2  1.116  1  121.75  3  180.0  0  1.0

**DALTON INPUT
.RUN WAVE FUNCTION
**WAVE FUNCTIONS

```

```
.HF
.MP2
*MP2 INPUT
.MP2 FROZEN
  2 0 0 0
**END OF INPUT
```

Home page <http://www.kjemi.uio.no/software/dalton/dalton.html>.

## NWChem

---

The program has been developed in the Molecular Sciences Software Group at the Pacific Northwest National Laboratory (Richland, WA, USA). The authors of the program state that “NWChem is a computational chemistry package designed to run on high-performance parallel supercomputers. Code capabilities include the calculation of molecular electronic energies and analytic gradients using Hartree-Fock self-consistent field (SCF) theory, Gaussian density function theory (DFT), and second-order perturbation theory. For all methods, geometry optimization is available to determine energy minima and transition states.” Furthermore, they add that “Classical molecular dynamics capabilities provide for the simulation of macromolecules and solutions, including the computation of free energies using a variety of force fields.” Details of the NWChem program system were described (Kendall et al. 2000).

Features of the program include:

- Spin-orbit density functional theory.
- Electron correlation energies may be calculated using many methods, including linearized coupled-cluster doubles (LCCD), coupled-cluster doubles (CCD), linearized coupled-cluster singles and doubles (LCCSD), coupled-cluster singles and doubles (CCSD), coupled-cluster singles, doubles, and triples (CCSDT), coupled-cluster singles, doubles, and active triples (CCSDTA), coupled-cluster singles, doubles, triples, and quadruples (CCSDTQ), CCSD and perturbative connected triples (CCSD(T)), CCSD and perturbative connected triples (CCSD[T]), completely renormalized CCSD[T] method (CR-CCSD[T]), completely renormalized CCSD(T) method (CR-CCSD(T)), CCSD and perturbative locally renormalized CCSD(T) correction (LR-CCSD(T)), quadratic configuration interaction singles and doubles (QCISD), configuration interaction singles and doubles (CISD), configuration interaction singles, doubles, and triples (CISDT), configuration interaction singles, doubles, triples, and quadruples (CISDTQ), second-, third-, and fourth-order Møller-Plesset perturbation theory (MP2, MP3, and MP4).
- Multi-configuration SCF wavefunctions.
- Selected configuration interaction with perturbation correction.
- Effective core potentials that allow to include both the scalar relativistic effects and spin-orbit effects (Pacios and Christiansen 1985).
- Relativistic corrections may be added at the levels of DKH2 and ZORA.
- Solvent effects may be described using COSMO (Baldrige and Klamt 1997; Klamt 1995; Klamt and Schüürmann 1993).
- For the studies of excited states, the CIS, time-dependent Hartree-Fock (TDHF), and TDDFT methods are available.

- Anharmonic vibrational analysis may be carried out using the VSCF method (Chaban et al. 1999).

Sample input file for the H<sub>2</sub>CO calculation at the MP2/cc-pVDZ level of theory is shown below; the symmetry of the molecule is determined by the program. The Cartesian coordinates of all atoms must be defined, and the atomic symbol must be used as atom name, eliminating the need to define nuclear charges.

```
echo
start h2co
geometry units angstrom
  O      0.00000      0.00000      -0.60361
  C      0.00000      0.00000      0.60439
  H      0.94899      0.00000      1.19165
  H     -0.94899      0.00000      1.19165
end
basis
  O library cc-pvdz
  C library cc-pvdz
  H library cc-pvdz
end
task mp2 energy
mp2
  freeze core 2
end
```

Home page <http://www.emsl.pnl.gov/capabilities/computing/nwchem/>.

## ORCA

The principal developer of the code has been Frank Neese, first at the Max Planck Institute for Bioinorganic Chemistry in Mülheim and then at the University of Bonn. In the words of the program's author, "ORCA is a flexible, efficient and easy-to-use general purpose tool for quantum chemistry with specific emphasis on spectroscopic properties of open-shell molecules. It features a wide variety of standard quantum chemical methods ranging from semiempirical methods to DFT to single- and multireference correlated ab initio methods. It can also treat environmental and relativistic effects." An abbreviated list of program's features includes:

- Calculation of MP2 and RI-MP2 energies and gradients.
- Coupled cluster methods.
- CASSCF wavefunction.
- Scalar relativistic corrections at the levels of Douglas-Kroll, ZORA, and the infinite-order relativistic approximation (IORA) (Dyall and van Lenthe 1999).
- Excited states energies may be calculated using the CIS, CIS(D), and TDDFT methods.
- Multi-reference CI and perturbation theory.
- Many properties may be calculated, including spin-orbit coupling, hyperfine and quadrupole couplings, the EPR *g*-tensor, and zero-field splitting.

Sample input file for calculation of the MP2/cc-pVDZ energy of H<sub>2</sub>CO is shown below (the symmetry of the molecule is determined by the program).

```
! MP2 RHF cc-pVDZ
* int 0 1
C(1)  0 0 0 0.00  0.0  0.00
O(2)  1 0 0 1.208  0.0  0.00
H(3)  1 2 0 1.116 121.75  0.00
H(3)  1 2 3 1.116 121.75  180.00
*
```

Home page <http://www.thch.uni-bonn.de/tc/orca/>.

## PSI3

In the description of the designers of the code, C.D. Sherrill, T.D. Crawford, and E.F. Valeev (from Georgia Institute of Technology and Virginia Tech), "the PSI3 suite of quantum chemical programs is designed for efficient, high-accuracy calculations of properties of small to medium-sized molecules. The package's current capabilities include a variety of Hartree-Fock, coupled cluster, complete-active-space self-consistent-field, and multi-reference configuration interaction models." PSI3, written in the programming languages C and C++ (rather than in the Fortran language, which has been traditionally used in computational quantum chemistry), was recently reviewed (Crawford et al. 2007).

Some interesting features of the program are:

- Arbitrarily high angular momentum levels in integrals and derivative integrals (up to *m*-type functions have been tested).
- Coupled cluster methods including CC2, CCSD, CCSD(T), and CC3 with RHF, ROHF, UHF, and Brueckner orbitals.
- Determinant-based CI including CASSCF, RAS-CI, and full CI.
- MP2 and MP2-R12 methods.
- Methods for excited state: CIS, CIS(D), random phase approximation (RPA), EOM-CCSD, and CC3.
- Analytic energy gradients for CCSD based on RHF, ROHF, and UHF orbitals.
- Coupled cluster linear response methods for static and dynamic polarizabilities and optical rotation.
- Diagonal Born–Oppenheimer correction (DBOC) for RHF, ROHF, UHF, and CI wave functions.

Sample input file for the H<sub>2</sub>CO calculation at the MP2/cc-pVDZ level of theory is shown below (symmetry of the molecule is determined by the program).

```
psi: (
label = "H2CO at experimental geometry (CRC, p. 9-36)"
wfn = mp2
reference = rhf
basis = "cc-pVDZ"
zmat = (
O
C 1 1.208
```



```

H 2 1.116 1 121.75
H 2 1.116 1 121.75 3 180.0
)
)

```

Home page <http://www.psicode.org/>.

## ACES II

The program ACES II (Advanced Concepts in Electronic Structure) was developed in the research group of R.J Bartlett at the Quantum Theory Project (QTP) of the University of Florida in Gainesville. The program's backbone was written in the early 1990s and has undergone extensive developments since that time. ACES II focused on the coupled-cluster theory (Paldus 2005 and its applications (Bartlett 2005; Bartlett and Musiał 2007).

Single point energy calculations may be carried out for the following cases:

- Independent particle models RHF, UHF, and ROHF.
- Correlation methods utilizing RHF and UHF reference determinants, including MBPT(2), MBPT(3), SDQ-MBPT(4), MBPT(4), CCD, CCSD, CCSD(T), CCSD+TQ\*(CCSD), CCSD(TQ), CCSDT-1, CCSDT-2, CCSDT-3, QCISD, QCISD(T), QCISD(TQ), UCCS(4), UCCSD(4), CID, and CISD.
- Correlation methods that can use ROHF reference determinants include MBPT(2), CCSD, CCSDT, CCSD(T), CCSDT-1, CCSDT-2, and CCSDT-3.
- Correlation methods that can use quasi-restricted Hartree-Fock (QRHF) or Brueckner orbital reference determinants include CCSD, CCSDT, CCSD(T), CCSDT-1, CCSDT-2, and CCSDT-3.
- Two-determinant CCSD calculations for open-shell singlet state.
- Equation-of-motion CCSD calculation of dynamic polarizabilities and of NMR spin-spin coupling constants.
- Equation-of-motion CCSD calculations of excitation energies.
- Kohn-Sham DFT density functional methods combined with a wide selection of density functionals.

Analytical gradients may be calculated for:

- Independent particle models RHF, UHF, and ROHF.
- Correlation methods utilizing RHF and UHF reference determinants, including MBPT(2), MBPT(3), SDQ-MBPT(4), MBPT(4), CCD, CCSD, CCSD+T(CCSD), CCSD(T), CCSDT-1, CCSDT-2, CCSDT-3, QCISD, QCISD(T), UCC(4), UCCSD(4), CID, and CISD.
- Correlation methods that can utilize ROHF reference determinants, including MBPT(2), CCSD, and CCSD(T).
- Correlation methods that can utilize QRHF reference determinants, including CCSD.
- Two-determinant CCSD calculations for open-shell singlet state based on QRHF orbitals.
- EOM-CCSD for excited states.
- TD-CCSD analytical derivatives.

Analytical Hessians may be carried out for the independent particle models RHF, UHF, and ROHF.

Home page <http://www.qtp.ufl.edu/ACES/>.

## ACES III

---

The program represents a significant advance in parallel processing and resulted from completely rewriting ACES II for efficiency in parallel calculations. The parallel technology, based on the super instruction assembly language (SIAL) that marked the progress from ACES II to ACES III was discussed by Bartlett and co-workers (Lotrich et al. 2008).

Home page <http://www.qtp.ufl.edu/ACES/>.

## CFOUR

---

The four C's in the name of the program stand for Coupled-Cluster techniques for Computational Chemistry. The predecessor of this program was known as the Mainz-Austin-Budapest version of ACES II which was replaced by CFOUR in April 2009 (see <http://www.aces2.de/>). At present, the development of the program is continued at the University of Mainz (J. Gauss), at the University of Texas at Austin (J.F. Stanton and M.E. Harding), and at Eötvös Loránd University (P.G. Szalay).

Some of the features of the program are:

- NMR chemical shifts.
- Many properties, including nuclear spin-rotation constants, magnetizabilities, rotational  $g$ -tensors, indirect spin-spin coupling constants.
- Electronically excited states may be calculated via CIC, CIS(D), and several EOM-CC methods; the ionized and electron-attached states may be described via EOM-CC methods.
- Anharmonic force-field calculations may be carried out.
- Vibrationally averaged properties.
- Relativistic corrections.
- Diagonal Born–Oppenheimer corrections.
- Automated additivity and basis-set extrapolation schemes.
- Basis sets up to  $i$ -type Gaussian functions.
- Effective core potentials.

Home page <http://www.cfour.de/>.

## COLUMBUS

---

COLUMBUS originated in 1980 at the Ohio State University and was developed by I. Shavitt, H. Lischka (University of Vienna), and R. Shepard (Battelle Columbus Laboratories). The program was designed to carry out a variety of multireference calculations on ground and excited states of molecules (Lischka et al. 2006). Specific features include:

- Geometry optimization to find minima and saddle points.
- Searches for minima on the crossing seam (conical intersections).
- General MCSCF with quadratic convergence including state averaging.
- Direct MR-CISD (single and double excitations), using an arbitrary set of reference configurations.
- Multireference averaged coupled-pair-functional (MR-ACPF) and multi-reference average quadratic coupled-cluster (MR-AQCC) with size-extensivity corrections.

- Spin-orbit CI (based on graphical unitary group approach) (Yabushita et al. 1999).
- Search for conical intersections may be done at the MRCI level.
- For excited states, MCSCF, MR-CISD, and MR-AQCC-LRT transition moments may be calculated.
- Finite field method for second-order properties (polarizabilities).

Home page <http://www.univie.ac.at/columbus/>.

## MPQC

---

The Massively Parallel Quantum Chemistry (MPQC) program is an object-oriented code that was written in C++. The work on the code has been initiated by C.L. Janssen at the Sandia National Laboratories (USA).

The capabilities of MPQC include:

- Energies and gradients are available for closed shell, unrestricted and general restricted open shell Hartree-Fock and density functional methods.
- Energies may be calculated for the second-order open-shell perturbation theory.
- Energies and gradients may be evaluated for the second-order closed-shell Møller–Plesset perturbation theory (MP2).
- MP2 energies of closed-shell systems, including an R12 correlation factor and using an auxiliary basis set, are supported.

Home page <http://www.mpqc.org/index.php>.

## Commercial Software

---

For the details of commercial software the reader is referred to the links listed below for the most up-to-date information about each program. For completeness, both ab initio and semiempirical programs are included.

## Gaussian

---

One of the first programs for large-scale calculations in the commercial domain, dating its origins to 1970, is currently in its 2009 edition.<sup>1</sup>

Please see home page <http://www.gaussian.com/>.

---

<sup>1</sup> The original 13,370 lines of Gaussian 70 code were released to general public via the now defunct Quantum Chemistry Program Exchange (QCPE). Historic information about QCPE may be found on [http://www.ccl.net/ccl/qcpe/QCPE\\_removed/](http://www.ccl.net/ccl/qcpe/QCPE_removed/). QCPE offered as the first ab initio program Polyatom (Version 1 with 3,275 lines of code) was made available by Csizmadia et al. in 1964. It is worth mentioning in passing that the fees that QCPE charged for the programs were very modest by today's standards: \$175 for codes greater than 10,000 lines plus \$35 for media and handling. The programs grew as new capabilities were added: in 1974 Polyatom (Version II for IBM 360) grew to 20,000 lines, while the 1980 release of Gaussian (IBM Version II) contained about 60,000 lines of code. The current status of QCPE was explained in a brief note saved in Computational Chemistry List <http://ccl.net/chemistry/resources/messages/2009/06/04.001-dir/index.html>

## Molcas

---

Please see home page <http://www.teokem.lu.se/molcas/introduction.html>

## Q-Chem

---

Please see home page <http://www.q-chem.com/>

## Turbomole

---

Please see home page <http://www.turbomole.com/>

## Molpro

---

Please see home page <http://www.molpro.net/>

## Jaguar

---

Please see home page <https://www.schrodinger.com/products/14/7/>.

## PQS

---

Parallel Quantum Solutions. Please see home page <http://www.pqs-chem.com/software.shtml>

## Spartan

---

Please see home page <http://www.wavefun.com/>

## HyperChem

---

Please see home page <http://www.hyper.com/>

## Ampac 9

---

Please see home page <http://www.semichem.com/>

## Acknowledgments

The work was partly supported by the Research Grant No. G12121041441 to MK from the Natural Sciences and Engineering Research Council of Canada.

## References

- Adamovic, I., Freitag, M. A., & Gordon, M. S. (2003). Density functional theory based effective fragment potential method. *The Journal of Chemical Physics*, *118*, 6725–6732.
- Almlöf, J. (1987). General contraction of Gaussian basis sets. I. Atomic natural orbitals for first- and second-row atoms. *The Journal of Chemical Physics*, *86*, 4070–4077.
- Baldridge, K., & Klamt, A. (1997). First principles implementation of solvent effects without outlying charge error. *The Journal of Chemical Physics*, *106*, 6622–6633.
- Bartlett, R. J. (2005). How and why coupled-cluster theory became the pre-eminent method in an ab initio quantum chemistry. In C. E. Dykstra, G. Frenking, K. S. Kim, & G. E. Scuseria (Eds.), *Theory and applications of computational chemistry: The first forty years* (pp. 1191–1221). Amsterdam/Boston: Elsevier.
- Bartlett, R. J., & Musiał, M. (2007). Coupled-cluster theory in quantum chemistry. *Reviews of Modern Physics*, *79*, 291.
- Bobrowicz, F. W., & Schaefer H. F., III. (1977). The self-consistent field equations for generalized valence bond and open-shell Hartree-Fock wave functions. In H. F. Schaefer III (Ed.), *Methods of electronic structure theory (modern theoretical chemistry)* (Vol. 3, pp. 79–127). New York/London: Plenum.
- Brooks, B. R., & Schaefer, H. F., III. (1979). The graphical unitary group approach to the electron correlation problem. Methods and preliminary applications. *The Journal of Chemical Physics*, *70*, 5092–5106.
- Cammi, R., & Tomasi, J. (1995). Remarks on the use of the apparent surface charges (ASC) methods in solvation problems: Iterative versus matrix-inversion procedures and the renormalization of the apparent charges. *Journal of Computational Chemistry*, *16*, 1449–1458.
- Cao, X., & Dolg, M. (2006). Relativistic energy-consistent ab initio pseudopotentials as tools for quantum chemical investigations of actinide systems. *Coordination Chemistry Reviews*, *250*, 900–910.
- Cederbaum, L. S., & Domcke, W. (1977). Theoretical aspects of ionization potentials and photoelectron spectroscopy: A Green's function approach. *Advances in Chemical Physics*, *36*, 205–344.
- Chaban, G. M., Jung, J. O., & Gerber, R. B. (1999). Ab initio calculation of anharmonic vibrational states of polyatomic systems: Electronic structure combined with vibrational self-consistent field. *The Journal of Chemical Physics*, *111*, 1823–1829.
- Chipman, D. M. (1997). Charge penetration in dielectric models of solvation. *The Journal of Chemical Physics*, *106*, 10194–10206.
- Chipman, D. M. (2000). Reaction field treatment of charge penetration. *The Journal of Chemical Physics*, *112*, 5558–5565.
- Chipman, D. M. (2002). Comparison of solvent reaction field representations. *Theoretical Chemistry Accounts*, *107*, 80–89.
- Crawford, T. D., Sherrill, C. D., Valeev, E. F., Fermann, J. T., King, R. A., Leininger, M. L., Brown, S. T., Janssen, C. L., Seidl, E. T., Kenny, J. P., & Allen, W. D. (2007). PSI3: An open-source ab initio electronic structure package. *Journal of Computational Chemistry*, *28*, 1610–1616.
- Csizmadia, I. G., Harrison, M. C., Moskowitz, J. W., Seung, S., Sutcliffe, B. T., & Barrett, M. P. (1964). *Quantum Chemistry Program Exchange*, *11*, 47.
- Cundari, T. R., & Stevens, W. J. (1993). Effective core potential methods for the lanthanides. *The Journal of Chemical Physics*, *98*, 5555–5565.
- Day, P. N., Jensen, J. H., Gordon, M. S., Webb, S. P., Stevens, W. J., Krauss, M., Garmer, D., Basch, H., & Cohen, D. (1996). An effective fragment method for modeling solvent effects in quantum mechanical calculations. *The Journal of Chemical Physics*, *105*, 1968–1986.
- de Vries, A. H., van Duijnen, P. T., Juffer, A. H., Rullmann, J. A. C., Dijkman, J. P., Merenga, H., & Thole, B. T. (1995). Implementation of reaction field methods in quantum chemistry computer codes. *Journal of Computational Chemistry*, *16*, 37–55.
- Dewar, M. J. S., & Thiel, W. (1977). Ground states of molecules. 38. The MNDO method. Approximations and parameters. *Journal of the American Chemical Society*, *99*, 4899–4906.

- Dewar, M. J. S., Zoebisch, E. G., Healy, E. F., & Stewart, J. J. P. (1985). AM1: A new general purpose quantum mechanical molecular model. *Journal of the American Chemical Society*, *107*, 3902–3909.
- Dewar, M. J. S., Jie, C., & Yu, J. (1993). SAM1: the first of a new series of general purpose quantum mechanical molecular models. *Tetrahedron*, *49*, 5003–5038.
- Dolg, M. (2000). Effective core potentials. In J. Grotendorst (Ed.), *Modern methods and algorithms of quantum chemistry* (Vol. 1, pp. 479–508). Jülich: John von Neumann Institute for Computing.
- Douglas, M., & Kroll, N. M. (1974). Quantum electrodynamic corrections to the fine structure of helium. *Annals of Physics*, *82*, 89–155.
- Dreuw, A., & Head-Gordon, M. (2005). Single-reference ab initio methods for the calculation of excited states of large molecules. *Chemical Reviews*, *105*, 4009–4037.
- Duijnen, P. T. V., & de Vries, A. H. (1996). Direct reaction field force field: A consistent way to connect and combine quantum-chemical and classical descriptions of molecules. *International Journal of Quantum Chemistry*, *60*, 1111–1132.
- Dunning, T. H. (1989). Gaussian basis sets for use in correlated molecular calculations. I. The atoms boron through neon and hydrogen. *The Journal of Chemical Physics*, *90*, 1007–1023.
- Dunning, T. H., & Hay, P. J. (1977). Gaussian basis sets for molecular calculations. In H. F. Schaefer III (Ed.), *Methods of electronic structure theory (modern theoretical chemistry)* (Vol. 3, pp. 1–27). New York/London: Plenum.
- Dupuis, M., Spangler, D., & Wendoloski, J. (1980). *NRCC software catalog* (Vol. 1, Program No. QG01 GAMESS Tech. rep.) Berkeley: National Resource for Computations in Chemistry, University of California.
- Dyall, K. G. (2002). A systematic sequence of relativistic approximations. *Journal of Computational Chemistry*, *23*, 786–793.
- Dyall, K. G., & van Lenthe, E. (1999). Relativistic regular approximations revisited: An infinite-order relativistic approximation. *The Journal of Chemical Physics*, *111*, 1366–1372.
- Elliott, P., Furche, F., & Burke, K. (2009). Excited states from time-dependent density functional theory. *Reviews in Computational Chemistry*, *26*, 91–166.
- Faas, S., Snijders, J. G., van Lenthe, J. H., van Lenthe, E., & Baerends, E. J. (1995). The ZORA formalism applied to the Dirac-Fock equation. *Chemical Physics Letters*, *246*, 632–640.
- Fedorov, D. G., & Kitaura, K. (2007). Extending the power of quantum chemistry to large systems with the fragment molecular orbital method. *The Journal of Physical Chemistry A*, *111*, 6904–6914.
- Fedorov, D. G., & Kitaura, K. (2009). *The fragment molecular orbital method: Practical applications to large molecular systems*. Boca Raton: CRC Press.
- Fock, V. A. (1930). Näherungsmethode zur Lösung des quantenmechanischen Mehrkörperproblems. *Zeitschrift für Physik*, *61*, 126–148.
- Foresman, J. B., Head-Gordon, M., Pople, J. A., & Frisch, M. J. (1992). Toward a systematic molecular orbital theory for excited states. *The Journal of Physical Chemistry*, *96*, 135–149.
- Fuchs, C., Bonačić-Koutecký, V., & Koutecký, J. (1993). Compact formulation of multiconfigurational response theory. Applications to small alkali metal clusters. *The Journal of Chemical Physics*, *98*, 3121–3140.
- Gordon, M. S., & Schmidt, M. W. (2005). Advances in electronic structure theory: GAMESS a decade later. In C. E. Dykstra, G. Frénking, K. S. Kim, & Scuseria, G. E. (Eds.), *Theory and applications of computational chemistry: The first forty years* (pp. 1167–1189). Amsterdam: Elsevier.
- Gordon, M. S., Slipchenko, L. V., Li, H., & Jensen, J. H. (2007). The effective fragment potential: A general method for predicting intermolecular interactions. In D. Spellmeyer & R. Wheeler (Eds.), *Annual reports in computational chemistry* (Vol. 3, pp. 177–193). Amsterdam: Elsevier.
- Guest, M. F., Bush, I. J., van Dam, H. J. J., Sherwood, P., Thomas, J. M. H., van Lenthe, J. H., Havenith, R. W. A., & Kendrick, J. (2005). The GAMESS-UK electronic structure package: algorithms, developments and applications. *Molecular Physics*, *103*, 719–747.
- Hall, G. G., & Lennard-Jones, J. (1951). The molecular orbital theory of chemical valency. III. Properties of molecular orbitals. *Proceedings of the Royal Society of London. Series A, Mathematical and Physical Sciences*, *202*, 155–165.
- Hartree, D. R. (1928). The wave mechanics of an atom with a non-coulomb central field. Part I. Theory and methods. *Mathematical Proceedings of the Cambridge Philosophical Society*, *24*, 89–110.
- Hay, P. J., & Wadt, W. R. (1985). Ab initio effective core potentials for molecular calculations. Potentials for K to Au including the outermost core orbitals. *The Journal of Chemical Physics*, *82*, 299–310.

- Hess, B. A. (1986). Relativistic electronic-structure calculations employing a two-component no-pair formalism with external-field projection operators. *Physical Review A*, 33, 3742–3748.
- Hess, B. A. (1989). Revision of the Douglas-Kroll transformation. *Physical Review A*, 39, 6016–6017.
- Hsu, H., Davidson, E. R., & Pitzer, R. M. (1976). An SCF method for hole states. *The Journal of Chemical Physics*, 65, 609–613.
- Hurley, M. M., Pacios, L. F., Christiansen, P. A., Ross, R. B., & Ermler, W. C. (1986). Ab initio relativistic effective core potentials with spin-orbit operators. II. K through Kr. *The Journal of Chemical Physics*, 84, 6840–6853.
- Huzinaga, S., Seijo, L., Barandiarán, Z., & Klobukowski, M. (1987). The ab initio model potential method. Main group elements. *The Journal of Chemical Physics*, 86, 2132–2145.
- Ivanic, J. (2003a). Direct configuration interaction and multiconfigurational self-consistent-field method for multiple active spaces with variable occupations. I. Method. *The Journal of Chemical Physics*, 119, 9364–9376.
- Ivanic, J. (2003b). Direct configuration interaction and multiconfigurational self-consistent-field method for multiple active spaces with variable occupations. II. Application to oxoMn(salen) and N<sub>2</sub>O<sub>4</sub>. *The Journal of Chemical Physics*, 119, 9377–9385.
- Ivanic, J., & Ruedenberg, K. (2001). Identification of deadwood in configuration spaces through general direct configuration interaction. *Theoretical Chemistry Accounts*, 106, 339–351.
- Jensen, J. H., Day, P. N., Gordon, M. S., Basch, H., Cohen, D., Garmer, D. R., Krauss, M., & Stevens, W. J. (1984). An effective fragment method for modeling intermolecular hydrogen bonding-effects on quantum mechanical calculations. In D. A. Smith (Ed.), *Modeling the hydrogen bond*, ACS symposium (Vol. 569, pp. 139–151). New York: ACS.
- Kahn, L. R., Baybutt, P., & Truhlar, D. G. (1976). Ab initio effective core potentials: Reduction of all-electron molecular structure calculations to calculations involving only valence electrons. *The Journal of Chemical Physics*, 65, 3826–3853.
- Karelson, M. M., Katritzky, A. R., & Zerner, M. C. (1986). Reaction field effects on the electron distribution and chemical reactivity of molecules. *International Journal of Quantum Chemistry*, 30, 521–527.
- Karelson, M., Tamm, T., & Zerner, M. C. (1993). Multicavity reaction field method for the solvent effect description in flexible molecular systems. *The Journal of Physical Chemistry*, 97, 11901–11907.
- Kendall, R. A., Aprà, E., Bernholdt, D. E., Bylaska, E. J., Dupuis, M., Fann, G. I., Harrison, R. J., Ju, J., Nichols, J. A., Nieplocha, J., Straatsma, T. P., Windus, T. L., & Wong, A. T. (2000). High performance computational chemistry: An overview of NWChem a distributed parallel application. *Computer Physics Communications*, 128, 260–283.
- Kirkwood, J. G. (1934). Theory of solutions of molecules containing widely separated charges with special application to zwitterions. *The Journal of Chemical Physics*, 2, 351–361.
- Klamt, A. (1995). Conductor-like screening model for real solvents: A new approach to the quantitative calculation of solvation phenomena. *The Journal of Physical Chemistry*, 99, 2224–2235.
- Klamt, A., & Schüürmann, G. (1993). COSMO: A new approach to dielectric screening in solvents with explicit expressions for the screening energy and its gradient. *Journal of the Chemical Society, Perkin Transactions*, 2, 799–805.
- Klobukowski, M., Huzinaga, S., & Sakai, Y. (1999). Model core potentials: Theory and applications. In J. Leszczynski (Ed.), *Computational chemistry: Reviews of current trends* (Vol. 3, pp. 49–74). Singapore: World Scientific.
- Knowles, P. J., Andrews, J. S., Amos, R. D., Handy, N. C., & Pople, J. A. (1980). Restricted Møller-Plesset theory for open-shell molecules. *Chemical Physics Letters*, 186, 130–136.
- Kowalski, K., & Piecuch, P. (2004). New coupled-cluster methods with singles, doubles, and non-iterative triples for high accuracy calculations of excited electronic states. *The Journal of Chemical Physics*, 120, 1715–1738.
- LaJohn, L. A., Christiansen, P. A., Ross, R. B., Atashroo, T., & Ermler, W. C. (1987). Ab initio relativistic effective core potentials with spin-orbit operators. III. Rb through Xe. *The Journal of Chemical Physics*, 87, 2812–2824.
- Lauderdale, W. J., Stanton, J. F., Gauss, J., D., W. J., & Bartlett, R. J. (1991). Many-body perturbation theory with a restricted open-shell Hartree-Fock reference. *Chemical Physics Letters*, 187, 21–28.
- Lee, T. J., & Jayatilaka, D. (1993). An open-shell restricted Hartree-Fock perturbation theory based on symmetric spin orbitals. *Chemical Physics Letters*, 201, 1–10.
- Lee, T. J., Rendell, A. P., Dyall, K. G., & Jayatilaka, D. (1994). Open-shell restricted Hartree-Fock perturbation theory: Some considerations and comparisons. *The Journal of Chemical Physics*, 100, 7400–7409.

- Lischka, H., Shepard, R., Shavitt, I., Pitzer, R. M., Dallos, M., Müller, Th., Szalay, P. G., Brown, F. B., Ahlrichs, R., Böhm, H. J., Chang, A., Comeau, D. C., Gdanitz, R., Dachsel, H., Ehrhardt, C., Ernzerhof, M., Höchtel, P., Irlé, S., Kedziora, G., Kovar, T., Parasuk, V., Pepper, M. J. M., Scharf, P., Schiffer, H., Schindler, M., Schüler, M., Seth, M., Stahlberg, E. A., Zhao, J.-G., Yabushita, S., Zhang, Z., Barbatti, M., Matsika, S., Schuurmann, M., Yarkony, D. R., Brozell, S. R., Beck, E. V., & Blauddau, J.-P. (2006). *COLUMBUS, an ab initio electronic structure program, release 5.9.1*.
- Lotrich, V., Flocke, N., Ponton, M., Yau, A. D., Perera, A., Deumens, E., & Bartlett, R. J. (2008). Parallel implementation of electronic structure energy, gradient, and hessian calculations. *The Journal of Chemical Physics*, *128*, 194104/1–15.
- McWeeny, R., & Diercksen, G. H. F. (1968). Self-consistent perturbation theory. II. Extension to open shells. *The Journal of Chemical Physics*, *49*, 4852–4856.
- Miertuš, S., Scrocco, E., & Tomasi, J. (1981). Electrostatic interaction of a solute with a continuum. A direct utilization of ab initio molecular potentials for the prevision of solvent effects. *Chemical Physics*, *55*, 117–129.
- Møller, Ch., & Plesset, M. S. (1934). Note on an approximation treatment for many-electron systems. *Physical Review*, *46*, 618–622.
- Nakajima, T., & Hirao, K. (1999). A new relativistic theory: a relativistic scheme by eliminating small components (RESC). *Chemical Physics Letters*, *302*, 383–391.
- Nakano, H. (1993a). MCSCF reference quasidegenerate perturbation theory with Epstein-Nesbet partitioning. *The Journal of Chemical Physics*, *99*, 7983–7992.
- Nakano, H. (1993b). Quasidegenerate perturbation theory with multiconfigurational self-consistent-field reference functions. *Chemical Physics Letters*, *207*, 372–378.
- Nielsen, E. S., Jørgensen, P., & Oddershede, J. (1980). Transition moments and dynamic polarizabilities in a second order polarization propagator approach. *The Journal of Chemical Physics*, *73*, 6238–6246.
- Olsen, J., Yeager, D. L., & Jørgensen, P. (1983). Optimization and characterization of a multiconfigurational self-consistent field (MCSCF) state. *Advances in Chemical Physics*, *54*, 1–176.
- Pacios, L. F., & Christiansen, P. A. (1985). Ab initio relativistic effective potentials with spin-orbit operators. I. Li through Ar. *The Journal of Chemical Physics*, *82*, 2664–2671.
- Paldus, J. (2005). The beginnings of coupled-cluster theory: an eyewitness account. In C. E. Dykstra, G. Frenking, K. S. Kim, & G. E. Scuseria (Eds.), *Theory and applications of computational chemistry: The first forty years* (pp. 115–147). Amsterdam: Elsevier.
- Peterson, K. A. (2003). Systematically convergent basis sets with relativistic pseudopotentials. I. Correlation consistent basis sets for the post-d Group 13 – 15 elements. *The Journal of Chemical Physics*, *119*, 11099–11112.
- Peterson, K. A., Figgen, D., Goll, E., Stoll, H., & Dolg, M. (2003). Systematically convergent basis sets with relativistic pseudopotentials. II. Small-core pseudopotentials and correlation consistent basis sets for the post-d Group 16 – 18 elements. *The Journal of Chemical Physics*, *119*, 11113–11123.
- Piecuch, P., & Włoch, M. (2005). Renormalized coupled-cluster methods exploiting left eigenstates of the similarity-transformed Hamiltonian. *The Journal of Chemical Physics*, *123*, 224105/1–10.
- Piecuch, P., Kucharski, S. A., Kowalski, K., & Musiał, M. (2002). Efficient computer implementation of the renormalized coupled-cluster methods: The R-CCSD[T], R-CCSD(T), CR-CCSD[T], and CR-CCSD(T) approaches. *Computer Physics Communications*, *149*, 7196.
- Pople, J. A., & Nesbet, R. K. (1954). Self-consistent orbitals for radicals. *The Journal of Chemical Physics*, *22*, 571–572.
- Pople, J. A., Binkley, J. S., & Seeger, R. (1976). Theoretical models incorporating electron correlation. *International Journal of Quantum Chemistry*, *S10*, 1–19.
- Raffenetti, R. C. (1973). General contraction of Gaussian atomic orbitals: Core, valence, polarization, and diffuse basis sets; Molecular integral evaluation. *The Journal of Chemical Physics*, *58*, 4452–4458.
- Read, A. E., & Weinhold, F. (1983). Natural bond orbital analysis of near-Hartree-Fock water dimer. *The Journal of Chemical Physics*, *78*, 4066–4073.
- Read, A. E., Weinstock, R. B., & Weinhold, F. (1985). Natural population analysis. *The Journal of Chemical Physics*, *83*, 735–746.
- Ridley, J. E., & Zerner, M. C. (1973). Intermediate neglect of differential overlap techniques for spectroscopy: pyrrole and the azines. *Theoretical Chemistry Accounts: Theory, Computation, and Modeling*, *32*, 111–134.
- Roos, B. O. (1983). The multiconfiguration SCF method. In G. H. F. Diercksen & S. Wilson (Eds.), *Methods in computational molecular physics* (pp. 161–187). Dordrecht: D. Reidel.



- Roos, B. O. (1987). The CASSCF method and its application in electronic structure calculations. *Advances in Chemical Physics*, 69, 339–445.
- Roos, B. O. (1994). The multiconfiguration SCF theory. In B. O. Roos (Ed.), *Lecture notes in quantum chemistry* (Vol. 58, pp. 177–254). Berlin: Springer.
- Roothaan, C. C. J. (1951). New developments in molecular orbital theory. *Reviews of Modern Physics*, 23, 69–89.
- Ross, R. B., Powers, J. M., Atashroo, T., Ermler, W. C., LaJohn, L. A., & Christiansen, P. A. (1990). Ab initio relativistic effective core potentials with spin-orbit operators. IV. Cs through Rn. *The Journal of Chemical Physics*, 93, 6654–6670.
- Roy, L. E., Hay, P. J., & Martin, R. L. (2008). Revised basis sets for the LANL effective core potentials. *Journal of Chemical Theory and Computation*, 4, 1029–1031.
- Ruedenberg, K., Schmidt, M. W., Gilbert, M. M., & Elbert, S. T. (1982a). Are atoms intrinsic to molecular electronic wavefunctions? I. The FORS model. *Chemical Physics*, 71, 41–49.
- Ruedenberg, K., Schmidt, M. W., Gilbert, M. M., & Elbert, S. T. (1982b). Are atoms intrinsic to molecular electronic wavefunctions? II. Analysis of FORS orbitals. *Chemical Physics*, 71, 51–64.
- Ruedenberg, K., Schmidt, M. W., Gilbert, M. M., & Elbert, S. T. (1982c). Are atoms intrinsic to molecular electronic wavefunctions? III. Analysis of FORS configurations. *Chemical Physics*, 71, 65–78.
- Schirmer, J., & Cederbaum, L. S. (1978). The two-particle-hole Tamm-Dancoff approximation (2ph-TDA) equations for closed-shell atoms and molecules. *Journal of Physics B: Atomic and Molecular Physics*, 11, 1889–1900.
- Schmidt, M. W., & Gordon, M. S. (1998). The construction and interpretation of MCSCF wavefunctions. *Annual Review of Physical Chemistry*, 49, 233–266.
- Schmidt, M. W., Baldridge, K. K., Boatz, J. A., Elbert, S. T., Gordon, M. S., Jensen, J. H., Koseki, S., Matsunaga, N., Nguyen, K. A., Su, S., Windus, T. L., Dupuis, M., & Montgomery, J. J. A. (1993). General atomic and molecular electronic structure system. *Journal of Computational Chemistry*, 14, 1347–1363.
- Shavitt, I., & Bartlett, R. J. (2009). *Many-body methods in chemistry and physics: MBPT and coupled-cluster theory*. Cambridge, UK: Cambridge University Press.
- Shepard, R. (1987). The MCSCF method. *Advances in Chemical Physics*, 69, 63–200.
- Stevens, W. J., Basch, H., & Krauss, M. (1984). Compact effective potentials and efficient shared-exponent basis sets for the first- and second-row atoms. *The Journal of Chemical Physics*, 81, 6026–6033.
- Stewart, J. J. P. (1989). Optimization of parameters for semiempirical methods. I. Method. *Journal of Computational Chemistry*, 10, 209–220.
- Stewart, J. J. P. (1990). MOPAC: A semiempirical molecular orbital program. *Journal of Computer-Aided Molecular Design*, 4, 1–103.
- Stewart, J. J. P. (2007). Optimization of parameters for semiempirical methods V: Modification of NDDO approximations and application to 70 elements. *Journal of Molecular Modeling*, 13, 1173–1213.
- Tapia, O., & Goscinski, O. (1975). Self-consistent reaction field-theory of solvent effects. *Molecular Physics*, 29, 1653.
- Tomasi, J., & Persico, M. (1994). Molecular interactions in solution: An overview of methods based on continuous distributions of the solvent. *Chemical Reviews*, 94, 2027–2094.
- Tomasi, J., Mennucci, B., & Cammi, R. (2005). Quantum mechanical continuum solvation models. *Chemical Reviews*, 105, 2999–3093.
- Werner, H. (1987). Matrix formulated direct MCSCF and multiconfiguration reference CI methods. *Advances in Chemical Physics*, 69, 1–62.
- Włoch, M., Gour, J. R., Kowalski, K., & Piecuch, P. (2005). Extension of renormalized coupled-cluster methods including triple excitations to excited electronic states of open-shell molecules. *The Journal of Chemical Physics*, 122, 214107/1–15.
- Yabushita, S., Zhang, Z., & Pitzer, R. M. (1999). Spin-orbit configuration interaction using the graphical unitary group approach and relativistic core potential and spin-orbit operators. *The Journal of Physical Chemistry*, 103, 5791–5800.
- Zeng, T., Fedorov, D. G., Schmidt, M. W., & Klobukowski, M. (2011a). *The Journal of Chemical Physics*, 134, 214107/1–214107/9.
- Zeng, T., Fedorov, D. G., Schmidt, M. W., & Klobukowski, M. (2011b). *The Journal of Chemical Theory and Computation*, 7, 2864–2875.
- Zerner, M. C. (1991). Semiempirical molecular orbitals methods. In K. B. Lipkowitz & D. B. Boyd (Eds.), *Reviews in computational chemistry* (Vol. 2, pp. 313–365). New York: VCH Publishers.

# 18 Functional Nanostructures and Nanocomposites – Numerical Modeling Approach and Experiment

Malgorzata Makowska-Janusik<sup>1</sup> · Abdel-Hadi Kassiba<sup>2</sup>

<sup>1</sup>Institute of Physics, Jan Dlugosz University, Czestochowa, Poland

<sup>2</sup>Institut de Recherche en Ingénierie Moléculaire et Matériaux Fonctionnels FR CNRS 2575 – Laboratoire de Physique de l’Etat Condensé, UMR CNRS 6087, Université du Maine, Le Mans Cedex 9, France

<i>Introduction</i> .....	632
<i>Nanocomposite Materials</i> .....	634
General Features .....	634
SiC-Based Nanomaterials and Nanocomposites .....	635
<i>Theoretical Background</i> .....	637
DFT and Semiempirical Codes .....	638
Molecular Dynamics .....	640
<i>Numerical Simulations of IR and Raman Spectra</i> .....	641
<i>Vibrational Density of States (VDOS) and Luminescence Features</i> .....	644
Experimental Results .....	645
Theoretical Analysis and Computational Results .....	648
VDOS Fingerprints of Nanoparticles .....	648
Photoluminescence Responses of SiC Nanoparticles .....	648
<i>Nonlinear Optical Properties of Composite Materials</i> .....	654
Pockels Effects in Hybrid Nanocomposites .....	654
Photoinduced SHG in Host–Guest SiC-Based Nanocomposites .....	655
Molecular Dynamics Simulations .....	656
Quantum Chemical Computations .....	659
<i>Conclusions</i> .....	662
<i>References</i> .....	663

**Abstract:** This chapter reports numerical models devoted to predict the optical and vibrational properties of nanoparticles treated as isolated objects or confined in host matrixes. The theoretical data obtained by the numerical simulations were confronted with the experimental investigations carried out by several spectroscopic methods such as Raman, IR, and UV-Vis absorption as well as photoluminescence. As model cluster systems, the physical properties of nanosized silicon carbide (SiC) particles in vacuum were numerically modeled. The computer simulations were also performed for SiC confined in polymeric matrix, namely, poly(methyl methacrylate), poly-*N*-vinylcarbazole, and polycarbonate. The obtained host-guest nanocomposites exhibit original optical and electro-optical features.

The considered systems were built using molecular dynamic simulations method and the full atomistic modeling of the composite materials was performed using CVFF method. The equilibrated geometries of nanocomposites were used to evaluate their key physical features. Particularly, the electronic and vibrational properties of SiC were calculated in the cluster approach model. The suitable cluster size and the nature of terminating bonds used to saturate the outermost nanograin surface were judiciously evaluated with the criterion to achieve consistent agreement with experimental results such as IR absorption, Raman, vibrational density of states and photoluminescence responses. The role of SiC clusters and its interaction with the surrounding polymer were investigated for the hybrid host-guest nanocomposites and their electro-optical functionalities were evaluated. The polarizability and first-order hyperpolarizabilities responsible for second harmonic generation and Pockels effect were calculated using DFT method. Then, taking into account the environmental interaction between host and guest molecules the optical susceptibilities were predicted. The effect of the local electric fields involved at the organic-inorganic interfaces on the NLO parameters was taken into account for each system. Additionally it was found that polymer environment reconstructs the surface of the SiC nanograin, which contributes critically to the NLO properties of hybrid materials. Finally, the chapter shows in exhaustive way that the developed methodologies associating key experimental works and relevant numerical methods allows to tailor the suitable nanostructured materials with the optimal physical responses.

## Introduction

---

The realization of functional nanosized materials has been achieved thanks to the development of innovative methods for the synthesis and the characterization of physical properties required for potential technological applications. So far, several domains have benefited from properties offered by nanostructured systems. Examples are the superplasticity in mechanics, the efficiency of luminescence in optics, the gain in memory storage in magnetism, the tendency to develop molecular transistor in electronics and realization of therapeutic structures based on functional nanoparticles in medicine. All these facts underline the importance of nanomaterials and their usefulness for new technologies.

From fundamental aspects, nanosized structures exhibit quite different properties compared to their parent bulk-like materials (Norris and Bawendi 1995). Thus, the electronic density of states related to nanoparticles exhibits quantified features in similar way as the optical emission spectra might be related to those of artificial atoms (Kagan et al. 1996). The quantum confinement effect alters both electrons and phonons mean-free paths in the nanostructures. The consequence on the electronic features lies in the bandgap widening for semiconducting

nanoparticles, while the vibrational density of states exhibits broad shape due to reduction of the mean-free paths of phonons. Obviously, the size reduction of particles favours the role played by the surface atoms since their fraction dominates those involved in the nanoparticle core (Alivisatos et al. 1988). From engineering aspects, the suitable tools such as AFM (atomic force microscopy) or STM (scanning tunneling microscopy) were developed to tailor and functionalize nanostructures with a precision at the atomic scale. Alternatively, a great attention was paid to the lithography process using X-ray or electrons to design high density of nanoscale components required for miniaturized devices leading to nanoelectronic technologies.

Several approaches were developed to synthesize nanoparticles with wide range of chemical formula from inorganic up to organic components, and with well-controlled size distributions. However, except some fundamental analysis of luminescence phenomena in colloidal solutions or an improvement of mechanical properties of composites by suitable sintering, the potential technological applications of nanoparticles remain very limited. The key approach to take benefit from the physical properties of such nanoobjects requires their organization in host matrixes, which may be organic or inorganic composition. The functional nanomaterials processed by combining different components give rise to nanocomposites with properties different than those of individual constituents. As a main reason, the phenomena at the interface play a key role in the physical responses of composites in nanoscale. The numerical simulations devoted to predict optimal geometry of nanostructures and their physical properties contribute efficiently to the development of functional materials. The geometry of the model clusters, their structural order, and the surface states constitute crucial parameters which monitor the achievement of stable structures and determine physical responses combined with optimal time consumption. Wide possibilities are offered by theoretical investigations of clusters or large nanoparticles treated as isolated objects or associated to host matrixes. This last configuration, realized in host-guest nanocomposites, offers unique possibilities to take benefit from high specific surfaces of nanoparticles and the interface effects, which monitor their physical properties (Ricciardi et al. 2000).

The present chapter reports experimental works and numerical models applied to nanoparticles and nanocrystals treated as isolated objects or alternatively confined in host matrixes. Numerical modeling and predictive physical properties constitute innovative approach, which offers exhaustive support for experimental investigations on nanostructures. The considered architectures used for numerical simulations can be modulated in a large extent with respect to the size of nanoparticles and the chemical composition of their core and surface feature as well as the interactions involved at the interface. To evaluate the potentialities of nanoobjects, which are able to draw functional architectures applicable in electronics or in optics, the cluster model taking advantage of semiempirical methods and DFT codes was developed. The silicon carbide (SiC) components were chosen as the representative of wide bandgap semiconducting nanocrystals. In a first stage, the proposed numerical methodology proceeds by building suitable cluster geometries according to their related ordered bulk crystalline structures restricting any geometry optimization or structural relaxation. This is fundamental requirement to suppress any structural disorder, which occurs from amorphous arrangement, relaxation, or reconstruction. However, the effect of the surface ordering and the chemical composition of nanoobjects on their physical properties were considered with the criterion that the optimal structural features should reproduce similar physical responses of the investigated powder-like samples. Numerical simulations based on DFT and semiempirical methods were developed to predict accurately the electronic structure of the nanostructures. Optical absorption curves, infrared (IR) and Raman spectra as well as photoluminescence responses under several optical

excitations were theoretically calculated and their relevance was compared to experimental spectroscopic data obtained on synthesized nanoparticles. In addition to the intrinsic behavior of nanoparticles, the doping effect on their core and surface structure was modeled. Thus, the incorporation of oxygen atoms into the surface layer of nanocrystals point out the dramatic changes in a calculation of the electronic structure compared to nonoxidized nanoparticles. In a similar approach, doping of nanoparticle core by appropriate elements, such as nitrogen, is suitable to modify the semiconducting nanocrystal bandgap and the optical behavior of the investigated nanostructures.

Based on above-mentioned nanoobjects, the investigated nanocomposite material was built in several configurations. It was composed on the inorganic nanocrystals and host organic or inorganic matrixes. Its electronic and optical behaviors predicted theoretically show remarkable agreement with experimental results. Furthermore, the theoretical approach supported by experiment proves that host matrix may play key role to enhance some physical responses of the nanocomposites. Among the considered architectures, those related to organic–inorganic structures based on SiC nanocrystals embedded in polymer matrix were found of particular interest in electro-optical applications. An inorganic–inorganic medium was also investigated. In such case, the SiC nanocrystals arranged in selective inorganic dielectric matrixes were taken into consideration.

The applied numerical methods use molecular dynamics with suitable force field required for the geometry optimization of the realistic composites. Mastering of such tools allows drawing homogeneous distribution of nanocrystals in the host matrixes with valuable criterion of the stability and the structural equilibrium. The free volume around nanocrystal embedded into host media, the distribution of bond lengths terminating nanocrystal surfaces, and the mobility of the nanoobjects inside the matrix can be evaluated depending on interactions involved at the host–guest interface. With regard to the interface role, several organic media were considered by modeling their interactions with the inorganic nanocrystals through the polar character of polymer chains. Simulations using semiempirical and DFT methodology have demonstrated the relevance of the predicted electro-optical performances of the nanocomposites compared to those demonstrated experimentally.

All the developed works contribute to point out the relevance of the numerical methods and the cluster model, in isolated state or confined in host matrix, to account quantitatively for the key physical phenomena in nanostructured systems.

## Nanocomposite Materials

---

### General Features

---

Nanocomposites have attracted a great interest in wide range of areas including thermomechanical features, dielectrics, optics, or electronics. Depending on the searched application, several architectures can be tailored such as core-shell nanomaterials, host–guest media or porous matrixes with functional groups grafted on the offered specific large surfaces (Henglein 1993; Alivisatos 1996). The main characteristics of such materials lie in the possibility to combine not only the relevant features of individual components but also the effects generated at the interface. These last contributions can even dominate the physical behavior of the media and induce new properties. As examples, the enhancement of the photoluminescence in host–guest

nanocomposites or the high dielectric response originates from large interfacial polarization at the nanoparticle interface. These particular cases underline the importance of the nanocomposites for several functionalities. They are also good candidates for experimental and numerical investigations with regard to the wide range of physical phenomena. Furthermore, their syntheses can be achieved simply by homogeneous and regular distribution of nanoparticles in host matrixes or alternatively by their surfaces functionalization using active molecules. In the case of nanoparticles, it is well known that the size reduction causes decreasing of the mean-free path of electrons and phonons leading to the quantum confinement effect. Such effect is experimentally traduced when the electronic, magnetic, thermodynamic, or spectral properties are probed (Dabbousi et al. 1997). The reference size scale of semiconducting nanostructured materials related to the quantum confinement effect is defined by the exciton Bohr radius. Any material dimension below this characteristic length leads to important quantum effects (Timp 1999) which cause, for example, blueshift of characteristic absorption spectra (Sapra et al. 2003), vibrational density of states accompanying normal Raman modes of crystalline structure, as well as the appearance of peaks connected with transition between exciton states (Wang et al. 1987). On the other hand, the quantum confinement effect is desired in nonlinear optics and luminescence (Schmitt-Rink et al. 1987), because the significant molecular dipole moment is caused by the large changes of the charge and energy distribution at the outermost grain surfaces (Manna et al. 2000). This is a fundamental criterion, which leads to the applications of such nanomaterials in linear and nonlinear optics (NLO).

The Maxwell-Garnet nanocomposites are characterized by the nanoparticles being unbounded to the polymeric chain. Also no long-range order can be established in such media (Fischer et al. 1995). Additionally, these structures used in optics should be transparent in selective spectral windows depending on the searched applications. Other treatments, such as the optical or electrical poling, are also required to create structural gratings or non-centrosymmetric media notably for optoelectronic applications. However, the main drawback of nanocomposites based on host-guest structures lies in the easy agglomeration, which overcame their eventual technological applications. In general, particular treatments are required to disperse correctly nanoparticles in the host media in order to take the benefit from their large specific surfaces and then from the interfacial effects. It is worth noting that polyvinyl alcohol matrix incorporating CdS nanocrystals even with loading rate as high as 50 wt% of the guest elements prevent their agglomeration (Akimov et al. 1992). This explain the reason why the NLO properties are widely investigated in structures based on CdS, PbS, CdSe, PbSe, GaAs or CuCl nanocrystals (Beecroft and Ober 1997).

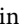

## SiC-Based Nanomaterials and Nanocomposites


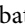
---

The present studies are mainly devoted to silicon carbide (SiC)-based materials in the form of isolated clusters, nanoparticles, or several architectures, which exhibit various original features. The interests in SiC is motivated by the large offered possibilities from structural aspects as well as physical responses such as electronic, optics, photovoltaic or dielectric properties. Additionally, beyond good thermal stability and mechanical hardness, the SiC is versatile from structural aspect (more than 170 polytypes), electronic behavior (a variable energy gap from 2.4 to 3.3 eV) as well as photorefractive properties (Vonsovici et al. 2000). As matter of fact, the nanocrystalline size modulates all the intrinsic parameters involved in the parent bulk materials. When nanoparticles are associated with suitable matrixes, promising new potentialities

such as charge transfer, NLO, and electro-optical effects are demonstrated (Kityk et al. 2000). However, in composites made from polymers and SiC nanoparticles, the interfaces govern the optical or electro-optical responses, and a great challenge lies in the control of the particle surface states. From the wide variety of SiC polymorphic structures, only the 3C-SiC and 6H-SiC crystalline orders were studied and the influence of the organic host matrixes on their optical properties was examined experimentally and supported by numerical simulations. Poly(methyl methacrylate) (PMMA), poly-*N*-vinylcarbazole (PVK), and polycarbonate (PC) were chosen as hosts due to their optical transparencies and improved thermomechanical properties. Some experiments are hereafter reported to point out the key features of the morphology, composition, vibrational and structural order in SiC nanoparticles. The selective experimental data are devoted to shed light on the theoretical model, which will be developed in forthcoming sections.

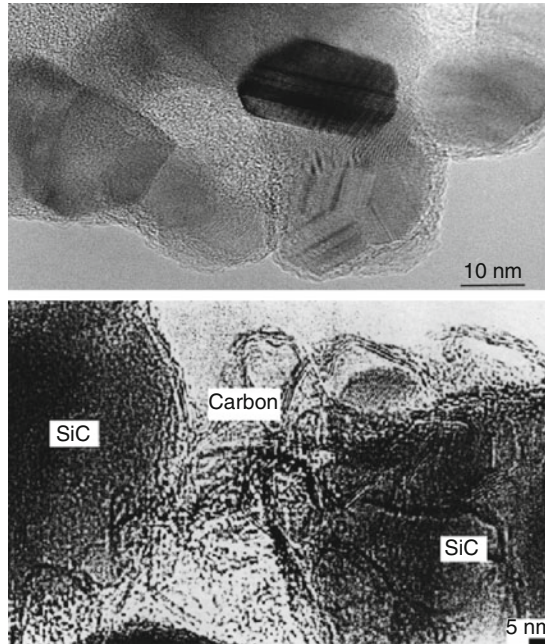
The built of realistic clusters or host-guest nanocomposites require effective experimental tools such as transmission electron microscopy (TEM) images, which illustrate the involved crystalline order both in the core and in the outermost particle surfaces. Second relevant information deals with the experimental vibrational spectra of SiC. The validity of theoretical construction of small-size clusters and evaluation of their physical properties should follow the experimental behavior. Also, IR and Raman experiments were performed on the SiC nanoparticles and will serve as reference for testing the relevance of the carried out numerical simulations performed. Representative experimental data, required for the initiation of theoretical model, are hereafter reported and consist in morphology and vibrational features of SiC nanoparticles.

For the morphology aspects, it is worth noting that nanoparticles of SiC can be synthesized by laser pyrolysis of gaseous mixture constituted by  $\text{SiH}_4$  and  $\text{C}_2\text{H}_2$  as source of Si and C, respectively. The synthesis method leads to nanoparticles with the shape and organization illustrated in  Fig. 18-1. The investigated SiC nanograins consist in the cubic and hexagonal structures with the C/Si ratio in the range 1.10–0.85 and particle size about 20–30 nm (Charpentier et al. 1999). Careful analyses of the TEM images show the occurrence of carbon layers arranged on the particle surfaces ( Fig. 18-1). These experimental facts point out a key property, which can be adopted in numerical simulations of SiC clusters. This will be taken into consideration by saturating the external surface of modeled cluster by carbon atoms in coherence with the real atomic organization of investigated batches.

A second aspect of the relevant experimental information required for a sound numerical approach can be found in the typical Raman spectra obtained on representative SiC batches ( Fig. 18-2). The spectra recorded using the 514.5 nm radiation of an Ar laser excitation correspond to SiC batches with C/Si ratio equal to 1.04, 1.02, and 0.85, respectively. The sample with higher carbon content than mentioned exhibits similar features as those for the nanopowder batch with C/Si ratio about 1.04. It can be seen from  Fig. 18-2 that the characteristic Raman lines of the different components (C, SiC, Si) are present at different wavenumber ranges with particular high scattering efficiency of surface located C–C or Si–Si bonds with respect to the nanoparticle core Si–C bonds. This is particularly shown through the intensity of the bands at  $1,603\text{ cm}^{-1}$  or  $1,350\text{ cm}^{-1}$  and  $520\text{ cm}^{-1}$  associated to C–C and Si–Si surface bonds, respectively compared to the core Si–C bands (Kassiba et al. 2002a) located in the range  $750\text{--}980\text{ cm}^{-1}$ .

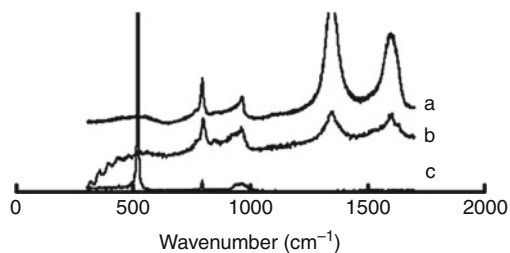
The numerical model, which will be developed, should conciliate optimal size of clusters, realistic organization of the clusters composition at their outermost surfaces and lead to sound theoretical vibrational and optical responses. These parameters will be exhaustively discussed in the applications part of numerical simulations.





■ Fig. 18-1

High-resolution TEM images of SiC nanoparticles: *top* – evidence of crystallization fringes; *bottom* – presence of carbon graphene sheets on the nanoparticle surfaces in nanopowders synthesized with an excess of carbon (Charpentier et al. 1999) (● *Figure 1a* has been reproduced with permission from Bouclé et al. (2006). ● *Figure 1b* has been reproduced with permission from Kassiba et al. (2002a))



■ Fig. 18-2

Raman spectra of the SiC nanoparticles for different C/Si ratios (a: 1.04, b: 1.02, c: 0.85) with high scattering efficiency of the surface bonds (C–C, Si–Si) compared to the core bonds (Si–C) (Reproduced with permission from Kassiba et al. (2002a))

## Theoretical Background

The quantum chemical models, developed for numerical modeling of materials, offer a relevant support for several experimental effects demonstrated on nanostructures. The developed



theories and numerical approaches allow exhaustive and more quantitative interpretations of experimental results. Additionally, numerical simulations can tailor predictive physical properties of nanomaterials with suitable chemical compositions, optimal sizes, and geometries. A wide range of computational simulation methods was extensively used in physics and chemistry including *ab initio* (Payne et al. 1992) or semiempirical codes (Di Bella et al. 1992). However, a relevant tool to simulate nanocrystals and related nanocomposites consists in the density functional theory (DFT) (Koch and Holthausen 2001). In spite of *ab initio* and DFT efficiencies, semiempirical methods are particularly relevant to model and analyze physical features of composite systems. Additionally, the molecular dynamic simulations are required to build the material configurations and to optimize the molecular geometries in polymeric environment.

## DFT and Semiempirical Codes

In quantum chemical approach, the electronic structure may be described by many electron wave functions such as  $\Psi(r_1, r'_2, \dots, r_N)$  or alternatively by using the electron density distribution  $n(r_i)$  required for the density functional theory (DFT). The starting point of DFT theory is based on the lemma of Hohenberg and Kohn, which specifies that the ground state density  $n(r)$  determines the external potential  $v_{ext}(r)$  (Hohenberg and Kohn 1964). For given  $v_{ext}(r)$  the energy functional of  $n(r)$  may be defined by

$$E_{v(r)}[n(r)] = \int v_{ext}(r)n(r)dr + F[n(r)], \quad (18.1)$$

where the functional  $F[n(r)]$  depend on the electron density distribution as follows:

$$F[n(r)] = T_s[n(r)] + \frac{1}{2} \int \frac{n(r)n(r')}{|r-r'|} drdr' + E_{XC}[n(r)]. \quad (18.2)$$

The  $T_s[n(r)]$  represents the kinetic energy expressed in term of the density  $n(r)$ . The second term of  $\blacklozenge$  Eq. 18.2 characterizes the interaction energy and the last one describe exchange-correlation (XC) energy  $E_{XC}$ . In consequence the Euler-Lagrange equation may be written as so-called Kohn-Sham (SK) equation:

$$\left( -\frac{1}{2}\nabla^2 + v_{ext}(r) + \int \frac{n(r')}{|r-r'|} dr' + v_{XC}(r) - \varepsilon_j \right) \varphi_j(r) = 0, \quad (18.3)$$

where  $n(r) = \sum_{j=1}^N |\varphi_j(r)|^2$  with  $\varphi_j(r)$  representing an individual system state and the XC potential defined by  $v_{XC}(r) = \delta E_{XC}[n(r)]/\delta n(r)$ . The local  $\blacklozenge$  Eq. 18.3 must be solved self-consistently by calculating the XC potential in each operation cycle. The main encountered problem is to find the appropriate expression of  $E_{XC}[n(r)]$ . Several approaches were developed to estimate the relevant  $E_{XC}[n(r)]$  function. In the local density approximation (LDA), the exchange-correlation energy may be calculated by using the expression (Kohn and Sham 1965):

$$E_{XC}^{LDA}[n(r)] \equiv \int \varepsilon_{XC}[n(r)]n(r)dr. \quad (18.4)$$

$\varepsilon_{XC}$  is the XC energy per particle of interacting electron gas with a density  $n$ . This method assumes that the electron density is uniform throughout the molecule. The KS orbitals in the LDA approximation are usually very close to Hartree-Fock orbitals and the method is appropriate to be used when the length over which  $n(r)$  varies is larger than the particle spacing.

More elaborated level of approximations is the so-called generalized gradient approximations (GGA) giving the  $E_{XC}$  as follows:

$$E_{XC}^{GGA} [n(r)] \equiv \int f [n(r), |\nabla n(r)|] dr, \quad (18.5)$$

where the function  $f [n(r), |\nabla n(r)|]$  should be chosen judiciously. Thus, with respect to LDA, GGA approximation includes terms, which depend on the density gradient.

The following section, even if general purposes are considered, will focus on optical parameters being exploited in the remaining part of the chapter. In this context, we consider the DFT, which is very attractive technique for the computation of many-atom systems. This method is less time consuming than other traditional computational methods and may be used for systems including even more than 200 atoms (Kohn et al. 1996). By the DFT technique, relevant physical properties may be calculated, but time-dependent (TD) phenomena are still not well explored. However, the calculations in the frame of TD-DFT technique using the LDA approximation yield satisfactory results notably for optical parameters such as polarizabilities, even if they are overestimated (van Gisbergen et al. 1995). The rigorous foundation for TD-DFT was given by Runge and Gross (1984). According to their model, the first-order change in density  $n(r)$  is related to the TD change in the external potential  $v_{ext}(r)$ :

$$\delta n(r, \omega) = \int dr' \chi(r, r', \omega) \delta v_{ext}(r', \omega). \quad (18.6)$$

The  $\chi(r, r', \omega)$  is the linear response function which is, in general, difficult to estimate. Alternatively the change in the density  $n(r)$  may be defined using response function  $\chi_s(r, r', \omega)$  of the noninteracting system, in combination with an effective potential  $v_{eff}(r)$ :

$$\delta n(r, \omega) = \int dr' \chi_s(r, r', \omega) \delta v_{eff}(r', \omega), \quad (18.7)$$

in which the response function may be calculated using rule:

$$\chi_s(r, r', \omega) = \sum_k^{occ.} \sum_l^{unocc.} \left\{ N_k \phi_k(r) \phi_l(r) \phi_l(r') \phi_k(r') \times \left( \frac{1}{(\epsilon_k - \epsilon_l) + \omega} + \frac{1}{(\epsilon_k - \epsilon_l) - \omega} \right) \right\}. \quad (18.8)$$

The  $\phi_k$  and  $\phi_l$  are associated to the occupied and unoccupied virtual Kohn–Sham orbitals with the energies  $\epsilon_k$  and  $\epsilon_j$ , respectively. All these parameters are calculated in the approximation of standard DFT procedure. The effective potential  $v_{eff}(r)$  from  $\blacklozenge$  Eq. 18.7 depends on the  $n(r)$  density variation:

$$\delta v_{eff}(r, \omega) = \delta v_{ext}(r, \omega) + \int dr' \frac{\delta n(r', \omega)}{|r - r'|} + \delta v_{XC}(r, \omega). \quad (18.9)$$

The change in the XC potential is given by XC kernel term  $f(r, r', \omega)$  as

$$\delta v_{XC}(r, \omega) = \int dr' f_{xc}(r, r'; \omega) \delta n(r', \omega). \quad (18.10)$$

In the variety of LDA approximation also called adiabatic LDA (ALDA), the kernel term is local in space as well as in time and may be written as

$$f_{XC}^{ALDA}(r, r'; \omega) = \delta(r - r') \frac{d^2}{dn^2} [n \epsilon_{XC}(n)] \Big|_{n=n_0(r)}, \quad (18.11)$$

where  $n_0(r)$  is converged SCF density. The parameterization for the XC energy density  $\epsilon_{xc}$  of a homogeneous electron gas is used according to Vosko-Wilk-Nusair rule (Vosko et al. 1980).

On the other hand, the Coulomb and XC term in  $\blacklozenge$  Eq. 18.9 may be combined into an induced potential  $v_{ind}$ . The potential is known in all points of the numerical integration grid and it allows the calculation of the first-order change in the density  $\delta n(r)$  (van Gisbergen et al. 1995). Also, this value is used to calculate the polarizability:

$$\alpha_{ij}(\omega) = -\frac{2}{E} \int dr \delta n_i(r, \omega) r_j, \quad (18.12)$$

where  $i$  and  $j$  denote the Cartesian coordinates  $x, y, z$ .  $E$  characterizes an intensity of external electric field. The hyperpolarizabilities are calculated by using a finite field method.

Among the available LDA approximations, the ALDA option is the most advanced one and may be used to calculate TD parameters of molecules with a large number of constituents. On the other hand, semiempirical method constitutes good alternative for molecules, which exceed the size of those practically accessible to ab initio methods. Semiempirical formalism ignores all core electrons and makes major simplification of the mathematics procedure. This relies on Hartree–Fock (HF) formalism, but replaces some of the mathematical terms by data (parameters) derived from experimental or computational results. The mentioned approach parameterizes the HF integrals. The various types of semiempirical methods use different numbers and types of parameters and new approaches rely on Neglect of Differential Diatomic Overlap (NDDO) formalism. One of them is Parameterization Method 3 (PM3) (Stewart 1991), which is widely used for rapid estimation of molecular properties and has been recently extended to include many elements such as some transition metals. The PM3 method is all valence model, which constrains two-center two-electron integrals. All integrals  $(\mu\nu|\lambda\sigma)$  are retained, provided that  $\mu$  and  $\nu$  are on the same atomic center and  $\lambda$  and  $\sigma$  are also on the same atomic center. It is not necessary for  $\mu$  and  $\nu$  go be at the same atomic center with  $\lambda$  and  $\sigma$ . The PM3 method may be used to calculate energy and geometry of inorganic compounds (Cramer 2002).

## Molecular Dynamics

One of the principal theoretical method, particularly devoted to calculate the time-dependent behavior of molecular systems, deals with molecular dynamics simulation (MD). This method is suitable to give precise insights on the structure and dynamics of composite materials. As examples, MD simulations generate for a given system, the atomic positions and velocities, which are afterward converted into macroscopic observables such as pressure, energy, and heat capacities. Basically, MD simulations proceed by the integration of the Newton equations of motions leading to the trajectories and determine the dynamics of particles (positions and velocities) correctly known during the time, past or future. Such trajectories allow obtaining the average values of physical properties.

In the following, let us outline briefly, the main idea behind MD simulation process. The force acting on an atom can be expressed as the gradient of the potential energy  $V$ :

$$F_i = -\nabla_i V = m_i \frac{d^2 r_i}{dt^2}. \quad (18.13)$$

$V$  is a function of the position of all the atoms in the system. Due to the complicated nature of this function, there is no analytical solution of the equations of motion. It can be solved numerically using different algorithms such as the Verlet, leap-frog, or Beeman's procedure (Cramer 2002).

The potential energy may be calculated using quantum chemical methods, which need to solve the Schrödinger equation. However, with regard to high number of atoms required for real composite systems, empirical energy functions are more suitable to solve the problem than other methods such as *ab initio*. Among the most commonly used semiempirical methods to estimate potential energy functions, we consider those referred as AMBER, CHARMM, GRO-MOS, or OPLS/AMBER force fields (Cramer 2002). When hybrid nanocomposites based on polymeric matrix and inorganic nanoclusters are concerned, the approximation of all-atom consistent valence force field (CVFF) (Kitson and Hagler 1988) is particularly recommended. Indeed, this can successfully reproduce biophysical (Lau et al. 1994), crystalline (Ma et al. 1997), or host-guest polymeric systems (Makowska-Janusik et al. 2004). The potential energy can be computed as a summation of the contributions due to bond stretching, bond bending, dihedral angle torsion, and nonbonded particles interactions:

$$V = \sum_{\text{all bonds}} V_{\text{bond}}(l_i) + \sum_{\text{all angles}} V_{\text{angle}}(\theta_i) + \sum_{\text{all dihedral angles}} V_{\text{torsional}}(\phi_i) + \sum_{\text{all pairs } i,j} V_{\text{nonbonded}}(r_{ij}) \quad (18.14)$$

where  $l_i$ ,  $\theta_i$ , and  $\phi_i$  refer to bond length, bond angle, and dihedral angle, respectively. The  $r_{ij}$  is a distance between atoms  $i$  and  $j$ . The interactions of nonbonded particles are modeled using the Lennard-Jones 12-6 potential and the Coulombic potential due to fixed partial charges. The interactions of bonded atoms are based on a fixed list of neighbours.

In general, the molecular dynamics simulations are performed under conditions of constant N, V, E (the microcanonical ensemble) or at constant N, T, and P. Beyond to obtain the average, simulated structures which can be compared to experimental ones, MD contributes to characterize and understand the dynamic changes at macroscopic scale.

## Numerical Simulations of IR and Raman Spectra

The vibrational signatures are drastically modified in the nanosized particles compared to the corresponding bulk structures. These modifications are revealed by a widening and position shifts of the vibrational bands. Furthermore, the structural reconstruction at the surface of nanograins and the electron-phonon interactions play a key role on the optical and vibrational properties. In this context, spectroscopic methods such as Raman and IR are suitable tools to probe the surface reconstruction and size effects through the features of the bands related to active vibration modes. The fundamental IR absorption or Raman spectra are based on rules related to dipole moments and polarizabilities of molecules. Thus, for IR technique, when clusters or molecular complexes are considered, the intensity of their characteristic bands may be calculated according to the following formulation:

$$I^{(IR)} \approx \frac{1}{\hbar} \sum \frac{\omega_{0n} |\mu_{0n}|^2}{\omega_{0n} - \omega_0}, \quad (18.15)$$

where  $\mu_{0n}$  is a transition dipole moment which couples the ground state  $|0\rangle$  and excited state  $|n\rangle$  of the system.  $\hbar\omega_{0n}$  represents the excitation energy between both mentioned states. The

situation is quite different for Raman spectra, which require the formation of induced dipole moment depending on the polarizability and on the probing radiation:

$$\mu_i^{(ex)} = \alpha_{ij} E_j, \quad (18.16)$$

where  $i, j = x, y, z$  represent the directions of the molecular referential frame and  $\alpha_{ij}$  is the component of the polarizability tensor, which may be computed by the following expression:

$$[\alpha_{ij}]_{mn} \approx \frac{\langle m | \mu_i | n \rangle \langle n | \mu_j | m \rangle}{\hbar \omega_n - \hbar \omega_m}, \quad (18.17)$$

$|m\rangle$  and  $|n\rangle$  represent the involved states of the molecular system. According to a simple approach, the Raman intensity may be calculated by using the following expression:

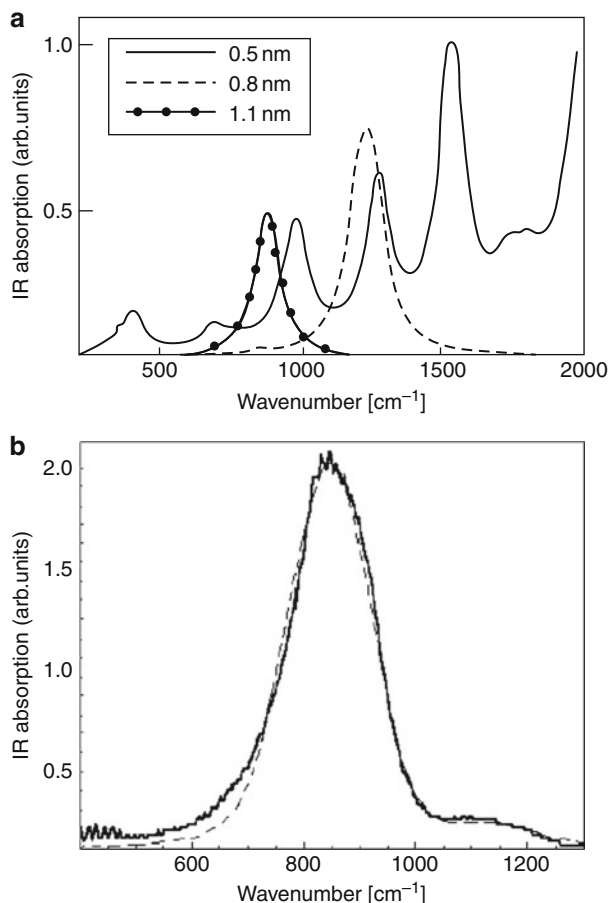
$$I_{nm}(\omega) = I_0 (\omega_0 - \omega_{mn})^4 [\alpha_{ij}]_{mn} [\alpha_{ij}]_{mn}^* f(\omega), \quad (18.18)$$

where  $f(\omega)$  represents the Lorentzian line shape taking into account the finite lifetime of the scattering and  $\omega_0$  represents the pulsation of the probing light.

All computational works described in the next subsection were done using HyperChem software. The IR and Raman spectra were calculated for fixed structures such as the polytypes 3C-SiC and 6H-SiC as well as for the amorphous SiC clusters with different sizes. The nanograins were covered by amorphous carbon shell. The chosen saturation of the model cluster is in accordance with the surface carbon sheet observed in TEM images (► Fig. 18-1). The structure of external carbon shell was optimized by the total energy minimization, which was performed using conjugated gradient method with criterion  $0.1 \text{ kcal mol}^{-1} \text{ \AA}^{-1}$ . The calculations were done applying semiempirical method with parameterization PM3 at the SCF RHF and UHF level (Weiner et al. 1986). As the criterion of the SCF convergence, the value equal to  $10^{-7} \text{ eV}$  was chosen.

The calculations of IR and Raman spectra were performed using semiempirical method with the same parameters as mentioned above. Several clusters with fixed cubic structure and different size were considered. The corresponding IR spectra are summarized in ► Fig. 18-3a. The theoretical data are compared to the experimental ones performed for the samples referred as SiC229 (► Fig. 18-3b). In as-formed state, the nanoparticles exhibit spherical shape with a diameter about 10 nm and an average composition close to the stoichiometric one. Each nanoparticle consists of several small nanocrystals (2–5 nm as diameter) separated by stacking faults at their boundaries. The average sample structure probed by  $^{29}\text{Si}$  NMR consists of 10% of 3C-SiC, 10% of 6H-SiC, and 80% of amorphous phase (Bouclé et al. 2002) (see ► Table 18-1). This is a consequence of the low nanocrystals dimension and the structural disorder at the their boundaries.

The experimental IR spectrum (► Fig. 18-3b) was satisfactorily fitted by combining two spectra calculated for clusters with sizes about 1.1 nm and different structures: cubic and amorphous ones. These theoretical contributions were superimposed with appropriate weighting factors in order to fit spectra nicely to the experimental result. The performed calculations account satisfactorily for the empirical data. The proposed cluster model is in agreement with structural investigations done by TEM and NMR technique. The experimental results give a precise insight on the structures involved into nanograins. It shows nanoparticles consisted of cubic, hexagonal, and amorphous arrangement. Additionally, it is worth noting that a minimal cluster size about 1.1 nm is required to reproduce the main features of experimental IR spectra of SiC nanograins.



■ Fig. 18-3

(a) IR absorption spectra simulated for the 3C-SiC clusters with sizes 0.5 nm, 0.8 nm, and 1.1 nm; (b) IR spectra for the SiC clusters obtained experimentally (solid line) and theoretically (dashed line) (Reproduced with permission from Makowska-Janusik et al. (2005))

The vibrational frequencies of smaller clusters exhibit large shifts to higher wave numbers. This is expected from behavior dominated by surface like atoms when the cluster size is drastically reduced.

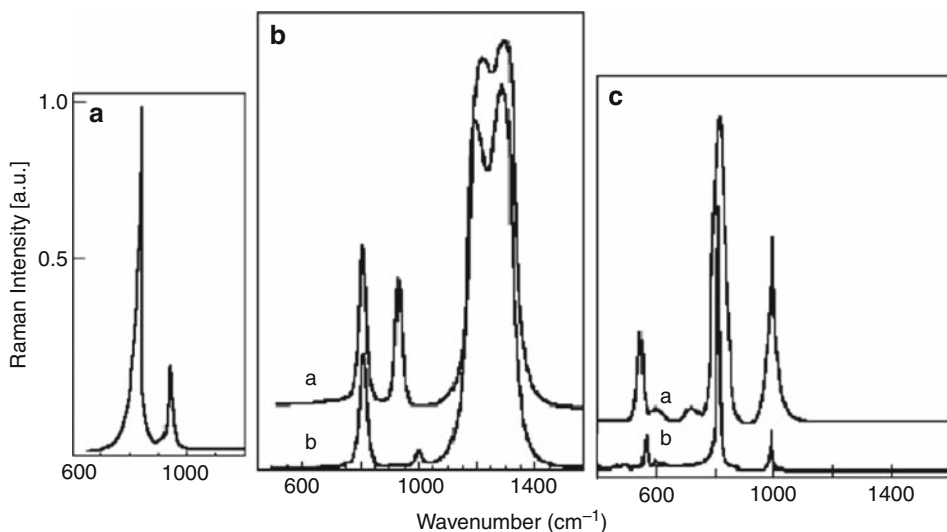
The same cluster geometries used for the simulations of IR spectra were also considered to model the Raman spectra as summarized in ▶ Fig. 18-4. The obtained results are in remarkable agreement with the experimental data (▶ Fig. 18-2) and point out the enhanced Raman signal from the elements in excess. Both atomic bonding around vacancies within the nanocrystallite and the excess of carbon at the outermost particle surfaces seem to be characterized by high Raman scattering efficiency compared to the intrinsic vibrational modes involved in perfect crystalline SiC structures. By limiting the computational procedure to only the harmonic interactions, we were able to show the stoichiometric effects of SiC nanocrystalline on the Raman signature. Thus, the performed calculations draw a realistic distribution of C and Si excess within the nanoparticles and support the experimental effective screening of SiC

■ Table 18-1

Structural properties of SiC nanosized powders inferred from  $^{29}\text{Si}$  MAS-NMR investigations.

Sample	6H-SiC (%)	3C-SiC (%)	Amorphous SiC*
SiC218	10	40	50
SiC229	9	7	84
SiC238	29	26	45
SiC241	38	26	36

\*The rate of amorphous fraction is overestimated due to the short spin-lattice relaxation time of amorphous structure compared to that in 3C-SiC and 6H-SiC lattices



■ Fig. 18-4

Calculated Raman spectra for (I) ideal SiC cubic-like fragment; (II) hexagonal-like (a) and cubic-like (b) SiC fragment with carbon excess (20%); and (III) with excess of silicon (2%) (Reproduced with permission from Kassiba et al. (2002a))

core particles from the laser excitation. The structure with an excess of Si was obtained by introducing defects exchanging carbon atom by silicon compared to those in an ideal crystal structure.

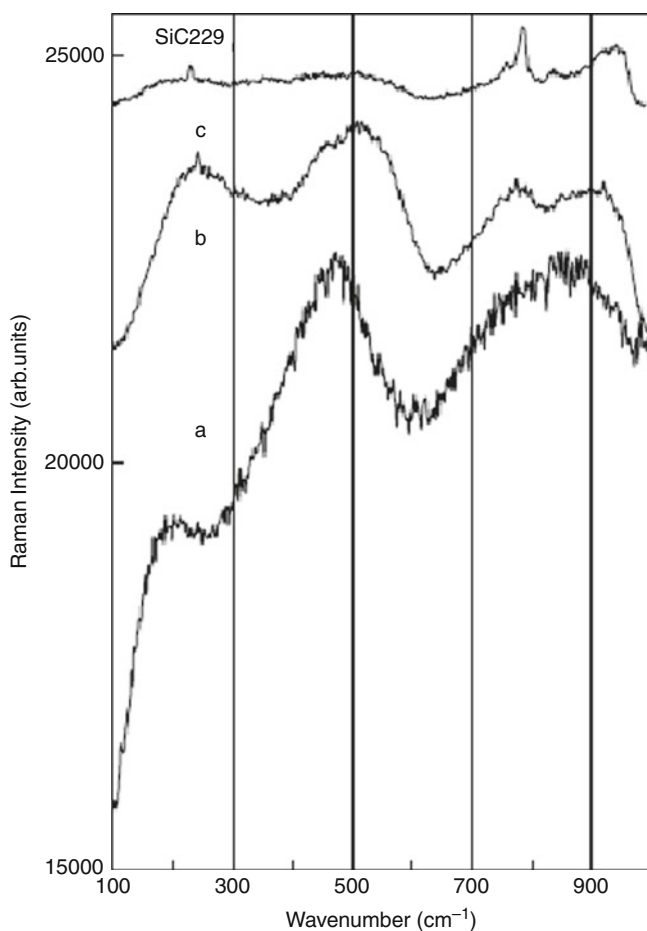
## Vibrational Density of States (VDOS) and Luminescence Features

The Raman signatures of SiC nanoparticles inform on the vibrational properties of the involved structures and on the degrees of organization and their stoichiometry. Any departure from perfect crystalline order, silicon or carbon excess leads to additional features, such as broad

vibrational bands, vibrational density of states (VDOS), or photoluminescence (PL) superimposed to normal modes. A combination of suitable Raman experiments and theoretical calculations, which allow exhaustive computation of Raman spectra taking into account VDOS and PL features, contribute to point out the nanoparticles structures and their surface states.

## Experimental Results

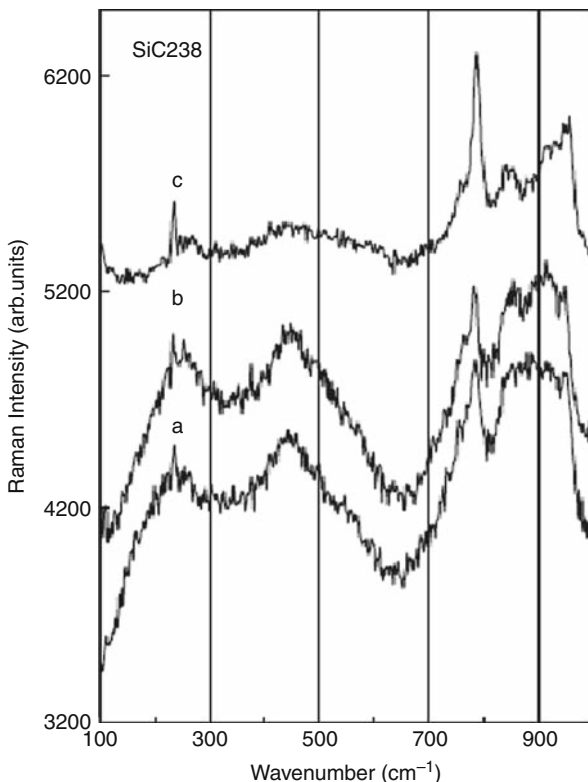
The Raman analysis of the involved structure within the nanopowders shows broad and structured features in the low wavenumber range. This is clearly exemplified for two representative batches such as SiC238 and SiC229 (● *Figs. 18-5* and ● *18-6*, ● *Table 18-1*). The Raman spectra



■ Fig. 18-5

Raman scattering signal in SiC229 sample for the as-formed nanopowders (a) and after annealing at 1,200°C (b) and 1,400°C (c). SiC Raman bands associated to TO and LO active modes are well resolved after annealing at 1,400°C (Reproduced with permission from Makowska-Janusik et al. (2005))



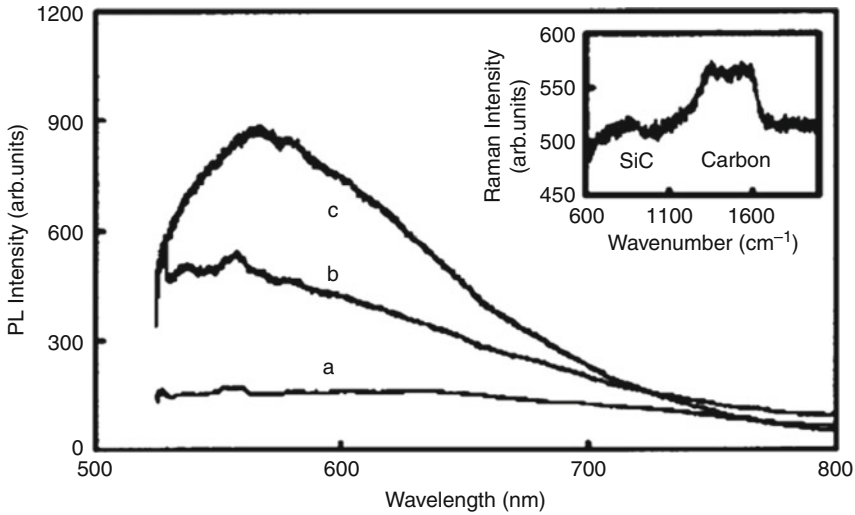


■ Fig. 18-6

Low-frequency Raman spectra of SiC<sub>238</sub> nanopowders versus annealing. (a) as-formed powder, (b) annealing at 1,200°C, and (c) annealing at 1,400°C. SiC Raman active modes at 795 and 967 cm<sup>-1</sup> are well resolved after annealing at 1,400°C (Reproduced with permission from Makowska-Janusik et al. (2005); Kassiba et al. (2007))

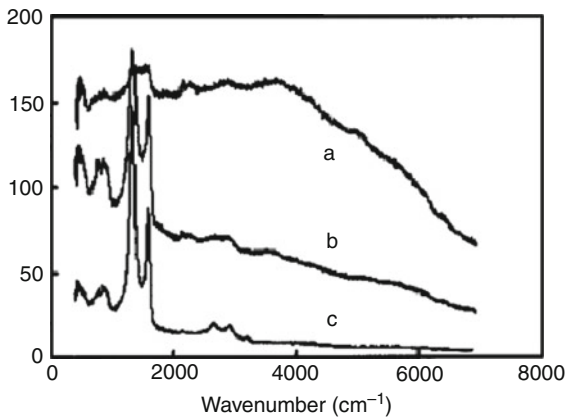
exhibit two main bands located in the ranges (100–600 cm<sup>-1</sup>) and (700–1,000 cm<sup>-1</sup>). A possible assignment of such details lies in VDOS signatures from the acoustic and optic modes of the SiC structures (Zhang and Xu 2002). The main difference between the SiC<sub>229</sub> (nanoparticles composed of several nanocrystals) and SiC<sub>238</sub> sample (nanoparticles as single nanocrystals, see ► Table 18-1) lies in their structure. The structure SiC<sub>229</sub> gives enhanced intensity of the VDOS signals compared to SiC<sub>238</sub> batch (► Figs. 18-5 and ► 18-6). Obviously, the annealing suppresses the broad details from the spectrum with regard to more improved surface states for both the crystalline order and the homogeneity as well. However, a precise insight and confirmation of the signal origin require exhaustive calculation of the vibrational responses from SiC clusters by using the same numerical tools developed for IR spectra analyses.

Let us first address the main experimental facts probed by micro-Raman analysis. Using the 514.5-nm laser radiation of Ar<sup>+</sup> on the SiC<sub>229</sub> samples in the as-formed batch and oxidized ones, broad PL features are demonstrated in the wavelength range 514–800 nm (► Fig. 18-7). The large PL intensity is obtained on the sample oxidized at the highest temperature. The same experiments were done on samples SiC<sub>238</sub> with a large nanocrystalline size (► Fig. 18-8).



■ Fig. 18-7

Broad photoluminescence bands on the Raman spectra of SiC<sub>229</sub> samples: (a) the as-formed sample and heated samples under oxygen, at temperatures 440°C (b) and 970°C (c) The intensities are normalized by weighting factors 1/3 (a), 1 (b), and 1/10 (c) (Reproduced with permission from Kassiba et al. (2002b))



■ Fig. 18-8

Experimental Raman spectra evidencing broad PL signal from the as-formed SiC samples: (a) SiC<sub>229</sub>, (b) SiC<sub>241</sub>, and (c) SiC<sub>238</sub>. The weighting factors are 1/10 (a), 1 (b), and 1 (c) (Reproduced with permission from Kassiba et al. (2002b))

Furthermore, for the SiC<sub>238</sub> and SiC<sub>229</sub> samples, annealing under argon at 1,400°C contributes to the emergence of well-defined SiC Raman bands and reduction of the broad PL features (Kassiba et al. 2002b). Improvement of the crystalline structures and modification of the particle surfaces by a release of carbon excess are the main effects of the annealing treatment (Charpentier et al. 1999).

## Theoretical Analysis and Computational Results

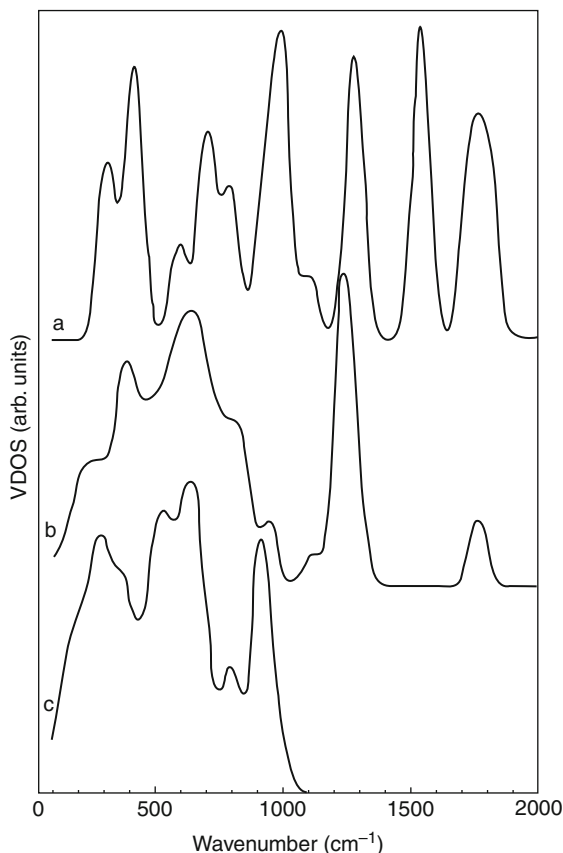
### VDOS Fingerprints of Nanoparticles

The size reduction of particles modifies the vibrational features mainly through the phonon confinement effect, which causes large changes on the dispersion relation compared to the bulk parent material. Additionally, the interface effects play a key role in the vibrational responses inferred from Raman or IR experiments. From the previously reported Raman and IR data obtained for SiC nanostructured materials, the size is drastically manifested on the shape of the spectra. Indeed, the experimental results show the manifestation of features, which can be identified to some contribution from vibrational density of states (VDOS). The assignment is made in detriment to broad luminescence features, which can be induced by some dangling bonds or any electronic active centers involved at the surface. Obviously, the expected concentration of such electronic centers is presumably high with respect to the high specific surfaces, which characterize the investigated nanoparticles ( $\sim 50 \text{ m}^2 \text{ g}^{-1}$ ). VDOS signatures are plausibly caused by the surface reconstruction and the amorphous structure, which occurs at the outermost nanoparticle surface and modify the phonon dispersion curves. As a relevant approach, the computer simulations are very helpful to discriminate between the luminescence and VDOS features. In this context, using the same methodology as developed for theoretical Raman spectra, the VDOS calculations were performed. The obtained results give additional evidences of the relevance of the used model. The developed approaches consider effects such as the broken translational symmetry at the nanocrystal boundaries or the size-induced changes on the electronic band structures and vibrational properties (Lin and Chang 1998). It was clearly demonstrated that the numerical methods contribute efficiently to identify the features of the low wavenumber Raman spectrum and particularly to discriminate between VDOS signatures and the luminescence features due to radiative recombination from defects of different kinds (dangling bonds, stoichiometry departure (Kassiba et al. 2002b), radicals).

Theoretical spectra were obtained by using SiC clusters with different diameters as shown in [Fig. 18-9](#). Additionally, the calculations for clusters with fixed diameter at 1.1 nm and different structures cubic, hexagonal, and amorphous were performed ([Fig. 18-10](#)). The computed VDOS spectra for amorphous clusters seem closer to the experimental curves obtained on the as-formed nanopowders ([Figs. 18-7](#) and [18-8](#)). This suggests that the main contribution to the experimental VDOS comes from the amorphous fractions of the nanoparticles in agreement with the structural NMR characterizations.

### Photoluminescence Responses of SiC Nanoparticles

In order to prove the relevance of the cluster model used to simulate properties of SiC, calculations of photoluminescence (PL) spectra were also performed using the same tools as for IR simulations. The computational results were obtained on clusters with a size about 1.1 nm as a critical size to reproduce the main features of IR and Raman spectra of the investigated nanoparticles. A carbon shell was used to saturate the built cluster. It is in agreement with real organization of nanoparticles when slight carbon excess is used during the synthesis process (carbon to silicon ratio about 1.04). Three types of model clusters, differ by the structural organization fixed as 3C-SiC, 6H-SiC and amorphous one obtained by full geometry optimization,



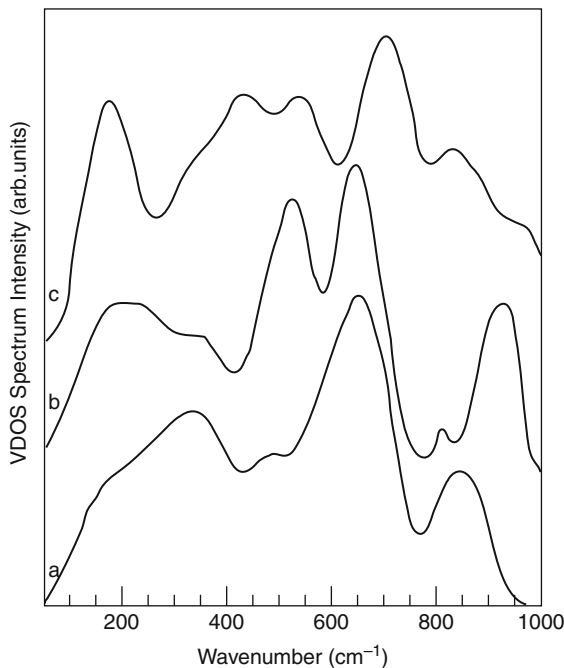
■ Fig. 18-9

Calculated vibrational density of states for SiC clusters with cubic structure and different cluster sizes: (a) 0.5 nm, (b) 0.8 nm, and (c) 1.1 nm (Reproduced with permission from Makowska-Janusik et al. (2005))

were built. In the performed constructions, the cluster cores may differ from the ideal cubic and hexagonal structure by an introduction of defects such as Si and C vacancies. The simulations were done using a semiempirical method with parameterization PM3 as mentioned above for IR simulations. The cluster was treated as a large molecule for which vibrational and electronic states are determined by quantum chemical codes.

As main idea, PL intensity model was developed for the theoretical approach concerning an emission process in nanoclusters. A transition between the electronic cluster states  $|j\rangle$  and  $|k\rangle$  manifested by a dipolar radiation are characterized by a single spectral line at the frequency  $\omega_{jk}$ . The intensity of spectral line, per unit source volume and per solid angle unit, reads as follows:

$$I_{jk}(\omega_{jk}) \approx \frac{4\omega_{jk}^4}{3\pi^3 c^3} |\mu_{jk}|^2, \quad (18.19)$$



■ Fig. 18-10

Calculated vibrational density of states in the low-wavenumber range for SiC nanoclusters (1.1 nm) with cubic SiC (a), hexagonal (b) and amorphous (c) arrangements obtained by a full geometry optimization of the Si–C bonds (Reproduced with permission from Makowska-Janusik et al. (2005))

where  $\mu_{jk}$  represents the transition dipole moment between two electronic cluster states  $|j\rangle$  and  $|k\rangle$ . For the theoretical photoluminescence spectrum description, the relevant relation was used as the following formulation:

$$I_{PL}(\omega) \approx \sum_{j=1}^n \frac{\sum_{i=x,y,z} |\mu_{0j}^{(i)}|^2}{(\omega - \omega_{0j})^2 + (\frac{\Gamma}{2})^2} + \sum_{j=1}^n \sum_{k=j+1}^n \frac{\sum_{i=x,y,z} |\mu_{jk}^{(i)}|^2}{(\omega - \omega_{jk})^2 + (\frac{\Gamma}{2})^2}. \quad (18.20)$$

In this expression, the finite lifetime ( $\approx 1/\Gamma$ ) characterize the emission processes traduced by Lorentzian shape for the spectral lines. The summation parameter  $n$  represents the number of excited states.  $\omega_{0j}$  and  $\omega_{jk}$  are the frequencies of transition between the ground  $|0\rangle$  and excited  $|j\rangle$  states and between two excited states  $|j\rangle$  and  $|k\rangle$ , respectively. According to the approach developed in molecular systems (Oudar and Chemla 1977), transition dipole moment describing the elements for two excited states was calculated as the difference between the dipole moments for the  $|j\rangle$  and  $|k\rangle$  states. Such an analytical expression allows a straightforward evaluation of the PL spectra in the cluster approach.

Due to the electron–phonon interactions, which contribute to the emission process by phonon-assisted transitions, the above expression may be modified to take into account the vibrational states. In that case, the dipole momentum matrix elements include both electronic

and vibrational terms. However, with respect to the Franck–Condon rule, only the dipole momentum elements for the final transition states are affected by the vibrational contribution. In this framework, the following expression written below:

$$I_{PL}(\omega) \approx \sum_{j=1}^n \sum_{l=1}^m \frac{\sum_{i=x,y,z} \left| \mu_j^{(i)} - \mu_0^{(i)} \cdot \mu_{\Omega l}^{(i)} \right|^2}{\left[ \omega - (\omega_{0j} \pm \omega_{\Omega l}) \right]^2 + \left( \frac{\Gamma}{2} \right)^2} + \sum_{j=1}^n \sum_{k=j+1}^n \sum_{l=1}^m \frac{\sum_{i=x,y,z} \left| \mu_j^{(i)} - \mu_k^{(i)} \cdot \mu_{\Omega l}^{(i)} \right|^2}{\left[ \omega - (\omega_{jk} \pm \omega_{\Omega l}) \right]^2 + \left( \frac{\Gamma}{2} \right)^2} \quad (18.21)$$

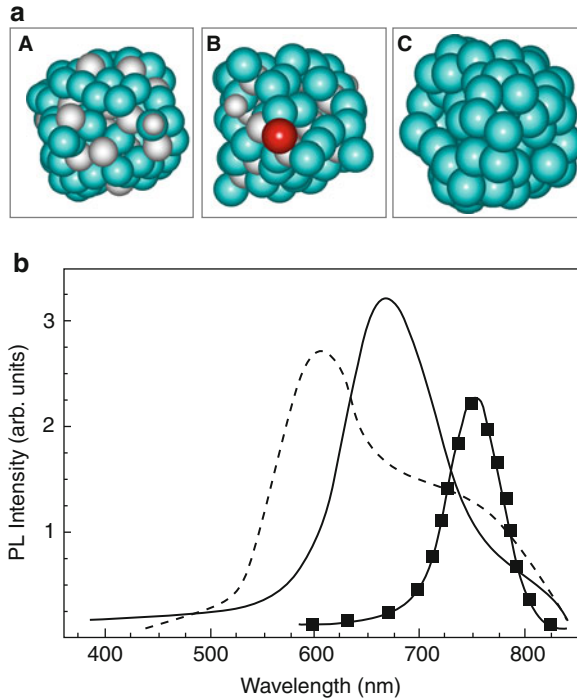
was used for an evaluation of the PL response from different cluster configurations with  $\mu_{\Omega l}$  being the dipole momentum element for the vibrational states  $|l\rangle$  with energies  $\hbar\omega_{\Omega l}$ .

The above cluster model with the derived formula for the emission process was used to model PL responses from 3C–SiC and 6H–SiC under and excitation line sets at 337 nm. The choice is dictated by the need to probe the interbands emission by using excitation line energy higher than the bandgap of SiC structure. In this case, the calculated emission bands were found centered around 410 and 380 nm and correspond to pseudo-optical gap at 3.02 and 3.26 eV for the two considered cluster structures, respectively. These values differ from the bulk-like optical gap, which are 2.4 eV for 3C–SiC and 3.0 eV for 6H–SiC. The large blueshift of the calculated PL lines in 3C–SiC compared to the bulk-like gap can be explained by the confinement effects due to the small cluster size. Indeed, the cluster size of 1.1 nm is situated largely well below the exciton Bohr radius (5.4 nm), which characterizes the semiconducting and undoped SiC structures.

However, it is well known that real nanoparticles exhibit a non-negligible amount of dangling bonds at the outermost surfaces or vacancies in the nanoparticle cores. Furthermore, a stoichiometry departure at the surface due to carbon excess or stacking faults in the particle cores are present in real nanoparticles. Also, as a large molecular complex, SiC cluster should exhibit intermediate energy levels and electronic states allowed inside the bandgap.

Probing the PL response from states due to imperfections of SiC clusters it requires the use of smaller excitation energies. For the numerical simulations, three cluster configurations depicted in **Fig. 18-11a** were built. There were the amorphous SiC structure, the carbon cluster, and the defected SiC created by including Si–O bonds to traduce the oxidation effect. For the emission process, the PL spectra were calculated by using excitation radiation lines located between 460 and 520 nm. The chosen cluster configurations give rise to visible photoluminescence bands centered in the red and near IR wavelengths. A superposition of the theoretical spectra with appropriate weighting factors and line widths is relevant approach, which allows straightforward interpretation of the set of PL responses from the SiC nanoparticles (**Fig. 18-11b**).

Comparing the experimental results in **Figs. 18-7** and **18-8** with the calculated PL spectra summarized in **Fig. 18-11b**, we may note the relevance of the carried out PL simulations. Particularly, the simulations on SiC cluster with oxygen substitution and experimental spectra in oxidized nanoparticles of SiC229 sample show good analogy of the relevant details. Obviously, the calculated PL signal is blueshifted with respect to the experimental PL spectrum of the oxidized sample at 970°C. The close features between theory and experiments point out the relevance of implemented theoretical model for PL simulations. The assignment of the features of the PL spectra is correctly done and discriminates between structural peculiarities and the role of the surface composition induced by stoichiometry departure or oxidation effect on nanoparticle surfaces.

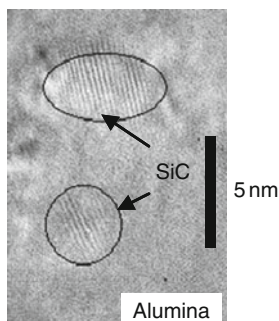


■ Fig. 18-11

(a) Examples of clusters used for the numerical simulations of PL spectra A: 3C-SiC cluster; B: defected SiC cluster using Si-O bonds; C: amorphous carbon cluster; (b) Theoretical PL spectra of SiC clusters with different structures and defects: amorphous structure (solid line); 3C-SiC with Si-O bonds (dashed line) and amorphous carbon cluster (line with squares). The excitation line has a wavelength in the range  $460 \text{ nm} < \lambda_{\text{exc}} < 520 \text{ nm}$  (Reproduced with permission from Kassiba et al. (2002b))

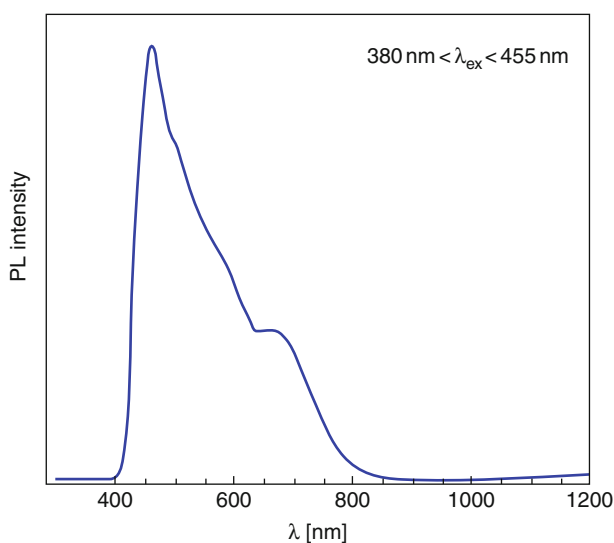
To interpret correctly the experimental PL signatures from isolated nanoparticles as discussed above, the theoretical models were tested to account for the PL responses when SiC nanocrystals are confined in alumina matrix. The experimental organization of the nanostructure is depicted in Fig. 18-12. Experimental PL spectra were investigated using Xe lamp and selecting the spectral line equal to 280 nm. However, the low intensity of the PL spectrum (Fig. 18-14) recorded at temperature 70 K is a consequence of small size and low quantity of SiC nanocrystals involved in the thin composite film (aluminum/nc-SiC). Nonetheless, the shape of PL signal is quite resolved and it may be compared to the performed calculations depicted in Fig. 18-13. The used cluster in this case is made from crystalline structure such as 6H-SiC with an introduction of carbon vacancies. The positions of the experimental and calculated bands are in good agreement but larger spectrum holds for theoretical data. The broadening is a consequence of the experiments being carried out at low temperature where phonons have a less contribution compared to experiments at room temperature.

To sum up the approaches applied to SiC nanoparticles, we underline that relevant numerical methods were developed and exhaustive analyses of experimental vibrational and



■ Fig. 18-12

Co-deposition by radio frequency sputtering of SiC cluster confined in alumina matrix. Fringes due to crystallization are clearly seen on the surrounded regions on the picture

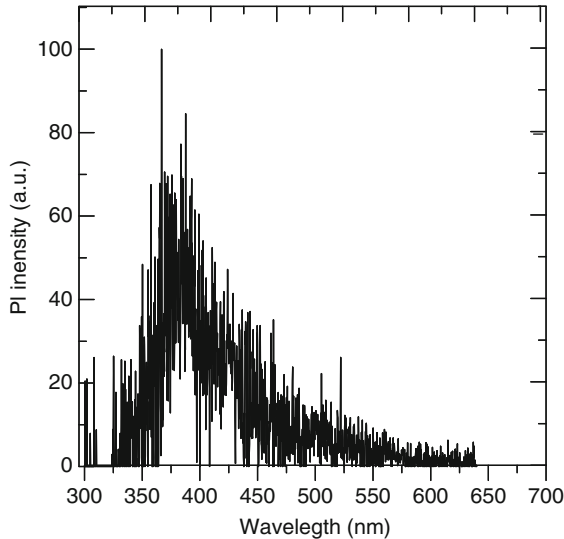


■ Fig. 18-13

Calculated photoluminescence spectra of 6H-SiC cluster with carbon vacancies (Reproduced with permission from Kassiba et al. (2007))

luminescence spectra were achieved. The theoretical model treats the cluster with an optimal size as a molecular complex for which the electronic and vibrational states are evaluated by quantum chemical codes. Experimental IR and Raman spectra obtained on SiC nanoparticles are quite well reproduced by numerical simulations based on the developed cluster approach. The experimental PL spectra were also satisfactorily accounted using appropriate clusters with several configurations (amorphous SiC, crystalline with vacancies and carbon cluster). These choices are dictated by the real organization of the SiC nanoparticles generally probed by high-resolution electron microscopy as clearly stated above. The good agreement between numerical simulations and the experimental IR and Raman spectra requires parameterizing





■ Fig. 18-14  
Photoluminescence of Aluminum/nc-SiC composite film recorded at 70 K. The used Xe excitation line has a wavelength at 280 nm

correctly the real organization of the nanograins. Within such requirement, the efficiency of the developed model is thus clearly demonstrated to analyze the linear optical behavior and vibrational features of SiC clusters. For a completeness of the methodology, the forthcoming paragraph is dedicated to model hybrid materials such as host-guest nanocomposites where the SiC nanocrystals play the key role of active vectors for nonlinear optical features.


## Nonlinear Optical Properties of Composite Materials

### Pockels Effects in Hybrid Nanocomposites

The linear electro-optical (EO) behavior, i.e., the Pockels effect, constitutes a manifestation of nonlinear optical features of anisotropic and non-centro-symmetric media. Functional architectures based on host polymer matrixes and guest SiC nanoparticles (nc-SiC) as active chromophores were realized. The intrinsic dipole moments of the chromophore combined with the eventual polarization at the interfaces with the host matrix constitute the physical origin of the electro-optical responses. The experiments were carried out in hybrid materials based on SiC nanocrystals and matrixes such as PVK, PMMA, or PC.

Beyond a good transparency and thermomechanical properties (Sanetra et al. 2001), the chosen polymers exemplify several features. Thus, PMMA or PC contains polar groups, which facilitate and keep macroscopic polarization, which may be induced by electrical poling. At the opposite, the PVK polymer exhibits photoconductivity. The consequence is to annihilate the macroscopic polarization and then to limit the Pockels effect in hybrid nanocomposite such as PVK/nc-SiC. Despite the role of the polymers, the characteristics of the SiC nanoparticles

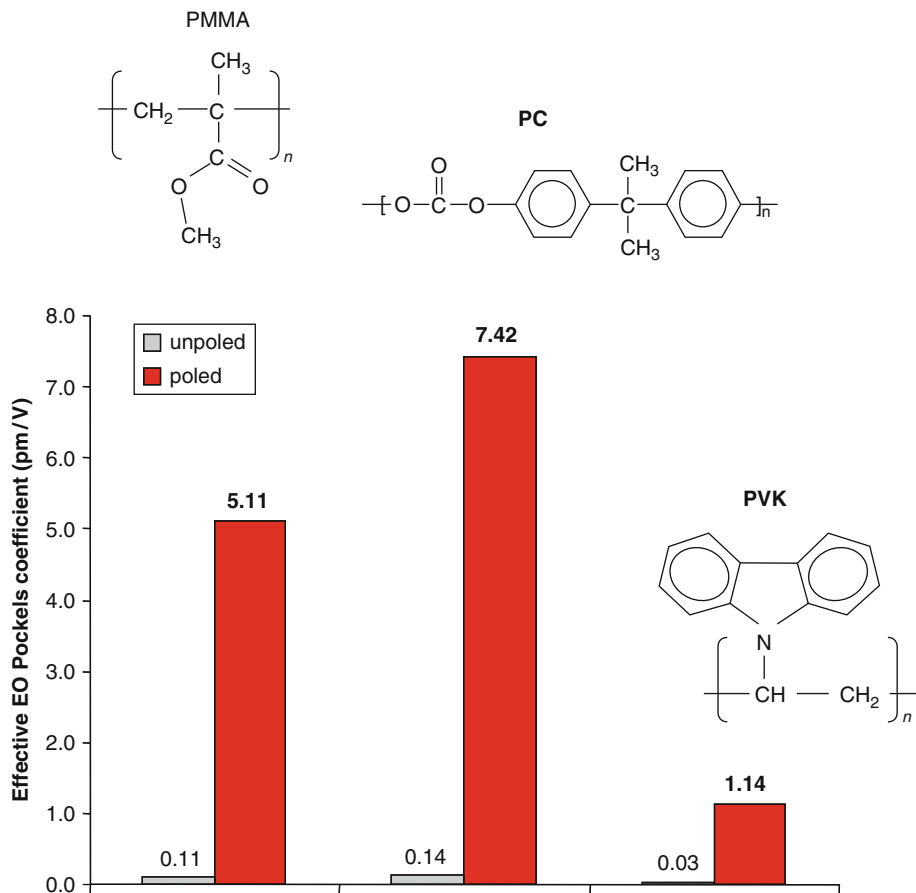
play also a key role on the electro-optical effect. Indeed, the crystalline order in the nanoparticle core has a crucial influence on the searched phenomena due to the main requirement of non-centrosymmetric media. With regard to the crystalline structures such as 6H-SiC and 3C-SiC involved in the nanoparticles, the Pockels effects is allowed and can be demonstrated on the investigated nanograins. Additionally, the nature of the nanoparticle surface (composition, crystalline order) monitors the polarization involved at the interfaces between polymer and nc-SiC. Indeed, a local charge neutrality departure holds at the interfaces and exhibits an easy polarization under an applied electric field, contributing then to enhance the EO responses.

In the performed EO experiments, three hybrid nanocomposites were synthesized using the above polymers and two SiC nanoparticle batches (SiC229, SiC218) with concentrations in the range 0.5–3 wt%. All samples were submitted to electrical poling required for the creation of structural anisotropy and non-centrosymmetric media (Bouclé et al. 2002). Linear EO measurements were performed using Senarmont setup with a dynamic regime, i.e., probing under AC voltage. The EO response depends drastically on the dispersion quality of the nanoparticles in the polymer matrix leading to homogenous films. The effective Pockels coefficients  $r_{eff}$  obtained for all investigated hybrid materials are reported in  Fig. 18-15. The results point out the role of electrical poling to enhance the EO parameters. Additionally, the nature of the polymer host matrix is crucial on the obtained EO responses. These results suggest that the interfaces between the SiC nanoparticles and the surrounding polymer media play a key role in the observed linear EO phenomenon. Particularly the interfacial polarizations involved between the SiC nanoparticles and the polar polymer contribute to EO coefficients, which are as important as those involved in the well-known traditional monocrystalline such as LiNbO<sub>3</sub>.

In the hybrid materials based on the SiC nanoparticles and host polymer matrixes, the origin of the EO behaviour is intimately connected to the hyperpolarizabilities intrinsically involved in the SiC and depends on the interactions at the host-guest interfaces. The intrinsic effect originates from the nanocrystallite bulk in agreement with the EO behavior of 3C-SiC thin films (Vonsovici et al. 2000). The effect of the surrounding polymer on the nanocrystal nonlinear optical behavior was evaluated by numerical methods. In this case the molecular dynamic technique was first used to build the relevant architectures, which combine SiC nanocrystals and the polymers. In a second step, the EO parameters were computed and exhaustive comparison with experimental results was achieved and underlines the strength of the developed theoretical and numerical approaches.

## Photoinduced SHG in Host-Guest SiC-Based Nanocomposites

A second aspect of the nonlinear optical behaviour of SiC based nanocomposites was demonstrated through the photoinduced second harmonic generation (PISHG) experiments (Kityk et al. 2000). The nanocomposites were made from SiC nanocrystals with several structural fractions such as hexagonal and cubic polytypes. The PISHG measurements were performed in nanocomposites based on SiC218 nanocrystals embedded into oligoetheracrylate photopolymer matrix. With increasing the power of the photoinducing nitrogen laser pulses the SHG maximum output signal increases and achieves its saturation at the pumping photon fluxes of about 1.6 GW/cm<sup>2</sup>. It is necessary to underline that the maximum of photoinduced SHG signal is achieved for the hexagonality (6H-SiC crystalline fraction in the nanocrystallite) of about 95% but at very low temperature (4.2–20 K). For the room temperature, it is more preferable is to take batches with higher amount of cubic phase. The measurements have been carried out



■ Fig. 18-15

Effective electro-optical Pockels coefficient as function of the polymer nature and the electrical poling. The used concentration of SiC218 nanoparticles is 1%

for different concentration of the nanocrystallite chromophores. The investigations have shown that the optimal concentration of the embedded SiC nanopowders lies within the  $0.8 \pm 1.6\%$ . The oligoetheracrylate photopolymers may also vanish the SHG output signal values (Czerwinski et al. 1997). Therefore the main contribution to the nonlinear optical susceptibility in this case belongs to host-guest interfaces.

## Molecular Dynamics Simulations

Three host-guest systems were built and their structural and physical features were simulated. The model hybrid materials consist of PMMA/nc-SiC, PC/nc-SiC, and PVK/nc-SiC composites. For each system, the starting structure was generated using Hyper-Chem program package. The unit cell of each structure consists of one SiC cluster surrounded by one polymer chain of

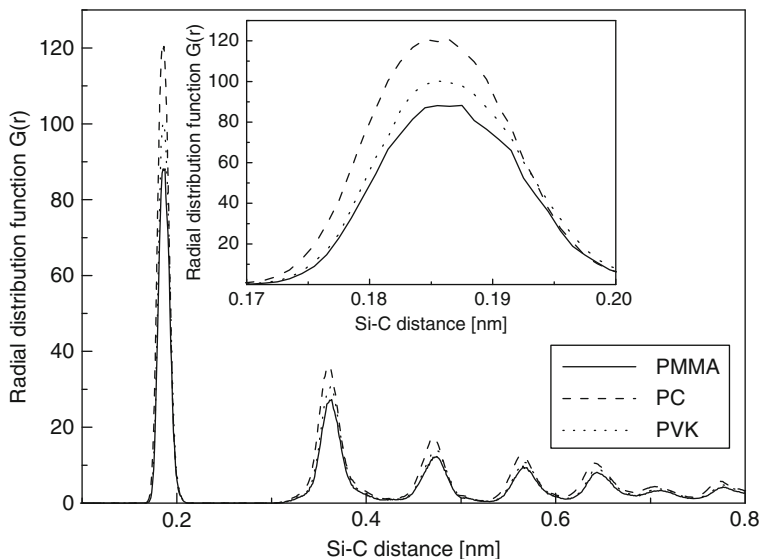
PMMA (90-mer) with molecular wt. 9,012.58 amu, one PC (50-mer) chain (wt. 12,716.21 amu), or one PVK (50-mer) chain (wt. 9,664.45 amu). The structures and specific features of the used polymers are reported in [Fig. 18-15](#). The density of each polymer was about 1.20 g/cm<sup>3</sup> and corresponds to the solid state of the considered matrices.

The SiC cluster was built with defined crystalline structure mainly from the cubic and hexagonal arrangements with a diameter about 1.1 nm as it was used for the above carried out simulations of IR, Raman, and PL signatures. Each cluster was composed by 216 atoms and possesses a mass about 4,330.48 amu. The simulated unit cell of the nanocomposite structure was cubic with an edge length of 27.10 Å, 29.99 Å, 28.34 Å for the PMMA/nc-SiC, PC/nc-SiC and PVK/nc-SiC system, respectively. The mass fraction of SiC embedded into the polymer host matrix was about 48.05 wt% for PMMA/nc-SiC, 34.05 wt% for PC/nc-SiC, and 44.81 wt% for PVK/nc-SiC system.

MD simulations were performed using the GROMACS software. A leap-frog algorithm was used to integrate Newton's equations of motion (Hockney et al. 1974). The potential energy was computed as a summation of the contributions of bonded terms and nonbonded interactions such as Lennard-Jones 12-6 potential and a Coulomb potential. Bonded interactions were based on fixed list of atoms and nonbonded ones on a dynamic list. The atomic charges of the system's constituents were obtained using DFT calculations described below. The pair list was updated at each step of the MD run. To make the neighbor list, a grid search algorithm was used with a cutoff parameter equal to 1.3 nm. Bond interactions are represented by harmonic potentials, while angle and dihedral distortions are modeled by a simple cosine function. The potential function of the modeled system is described via all-atom consistent valence force field (CVFF) (Kitson and Hagler 1988). The relevant parameters of SiC<sub>4</sub> and CSi<sub>4</sub> tetrahedral bonding potentials are presented elsewhere (Mirgorodsky et al. 1995). Note however that among the considered approach, the CVFF force field has been used successfully to model a wide variety of biophysical, crystal, and host-guest systems (Lau et al. 1994).

At the beginning of simulations, the geometry of each investigated system was optimized using an energy minimization tool based on the steepest descent method with a convergence criterion of 10 kcal mol<sup>-1</sup> Å<sup>-1</sup>. All MD simulations were conducted with a constant number of particles, volume, and temperature (NVT ensemble) by applying periodic boundary condition. The stabilization of the temperature to the required value about 300 K was carried out by increments of 2° using Nose-Hoover thermostat (Hoover 1985; Nose 1984). Each investigated system was first evaluated during 2 ns at temperature 300 K using a time step of 1 fs to allow a relaxation and an achieved equilibrium regime for the system. At this stage, the data were not used in the subsequent analysis. The stability of total energy was reached after about 1.5 ns of MD runs. However, a second execution of the simulation is generally performed at 300 K, with time step of 1 fs and the coordinates were stored every 1,000 steps. Furthermore, the Particle Mesh Ewald (PME) summation (Essman et al. 1995) was employed for the electrostatic long-range interactions. The cutoff distance for integrating the coordination numbers was larger than the nearest-neighbour distance of a perfect 3C-SiC crystal structure.

From the MD simulations, the resulting structure of SiC cluster can be characterized by its radial distribution function (RDF). The atomic RDFs of Si-C atoms distances recorded at the end of MD simulations are shown in [Fig. 18-16](#). The maximum of RDFs plot, for each investigated polymeric matrix is located at 0.189 nm. Such value is in agreement to the nearest-neighbor distance in 3C-SiC structure and the corresponding peak is related to a C-Si-C configuration. In such nanocrystalline structures, vibrations of atoms around their equilibrium positions are involved with relatively small amplitudes leading to slight variations of interatomic



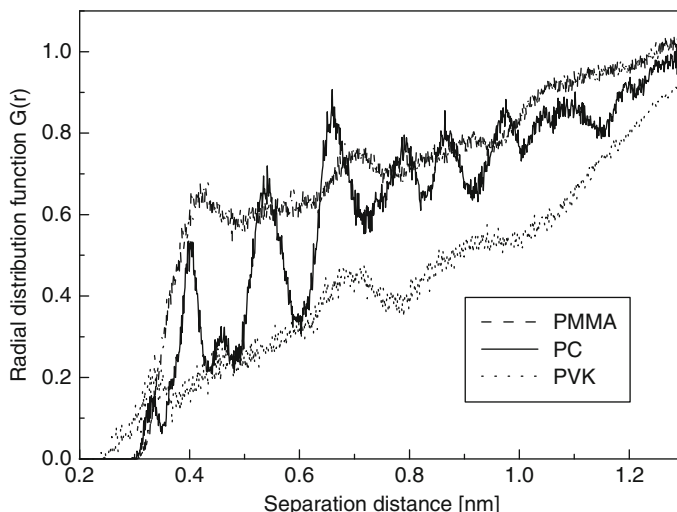
■ Fig. 18-16

**Atomic radial distribution function  $G(r)$  between the Si and C atoms of the 3C-SiC clusters embedded into PMMA, PVK, and PC polymeric matrix (Reproduced with permission from Makowska-Janusik et al. (2006))**

distances. The second peak on the RDF plot, centered at distance 0.378 nm, is related to Si-C farthest-neighbor distances. The computed RDFs of Si-C distances do not change with the nature of the polymer host matrix. One may conclude that the geometry of the 3C-SiC cluster is very stable. The averaged distances between Si and C atoms are no longer affected by the MD simulations performed at  $T = 300$  K which is very far from the melting point of the SiC. We may also note that the internal Si-C bond lengths inside the investigated clusters are not altered from the surrounding polymeric matrices.

The main goal of the performed simulation procedures is not to simulate the structure of SiC clusters but it is rather dedicated to determine the polymeric environment around them. The spatial distribution of the SiC clusters in polymeric matrix was investigated through the estimation of the intermolecular RDFs. This was calculated between the outermost Si-C cluster surface atoms and the center of mass (COM) of four polymeric groups. For the PMMA matrix the following groups were taken into account: methyl group bonded to the backbone carbon atom, methyl group bonded to COO, COO group and CH<sub>2</sub>. The RDFs between SiC cluster and the PC polymer were calculated for the two benzene rings, for C-(CH<sub>3</sub>)<sub>2</sub> group and the C=O one. For the PVK, four groups were chosen including the COM of the two benzene rings, that of CH<sub>2</sub> group and the N atom. In order to show the spatial distribution of the SiC cluster surrounded by the polymer environment, only the nearest distances between the cluster and polymeric groups are drawn (● Fig. 18-17).

The RDF related to the PMMA-SiC distances is evaluated for the methyl group bonded to COO. It is the nearest polymeric group to the SiC cluster with the distance equal to 0.40 nm. For the PC and PVK host polymers, the benzene rings and the carbazole groups were respectively considered. The SiC clusters embedded into the PC matrix show shorter distances (0.34 nm) to the polymer groups compared to our finding for PMMA matrix (0.40 nm). Similar remarks



■ Fig. 18-17 Intermolecular radial distribution functions for the distance between last Si–C surface atoms of SiC cluster and the polymer chains (Reproduced with permission from Makowska-Janusik et al. (2006))

on the involved short distance can be made in the case of the PVK matrix. This testifies that PVK groups can be closer to SiC cluster than the PMMA groups. As a consequence, the free space around the SiC cluster is larger in PMMA-based composites than in the case of PVK host media. As the matter of fact, the free space around SiC clusters incorporated into PMMA matrix is the highest from all investigated matrixes and has the same value as it was calculated for variety of organic chromophores (Makowska-Janusik et al. 2004). Finally, with regard to the nanocomposite order, it is worth noticing that all observed RDFs are typical for amorphous environments. No long-range order exists for considered systems except in the case of PC-based nanocomposite where the regular oscillations of RDF plot suggest some ordering degree.

## Quantum Chemical Computations

The optical properties of the SiC cluster were calculated in the rare gas cluster approach and local field modification using 216 atoms with the geometry of an isolated 3C–SiC structure. Described below quantum chemical computations were performed using Amsterdam Density Functional (ADF) package implementing Slater-type basis sets. All calculations were performed with the standard double- $\zeta$  basis sets available in ADF and described in the cited references. The polarizability  $\alpha$  and first hyperpolarizability  $\beta$  were calculated by using ADF-RESPONSE module within a frame of time-dependent DFT (TDDFT) theory. The local density approximation (LDA) for the potential and kernel was used. It composes the local Slater exchange functional and the uniform electron gas local correlation functional due to Vosko, Wilk, and Nusair (VWN) procedure (Vosko et al. 1980). All the clusters were rotated to maximally align the ground-state dipole moment along the Z-axis.

■ Table 18-2

Average local fields ( $F$ ) on COM of SiC in PMMA, PVK, and PC matrixes

System	$F_x$ [GV/m]	$F_y$ [GV/m]	$F_z$ [GV/m]	$F$ [GV/m]
PMMA/SiC	-0.34	-0.68	0.99	1.28
PVK/SiC	-0.18	-0.81	-0.93	1.25
PC/SiC	5.16	-4.44	11.98	13.78

In the frame of local field theory, linear and nonlinear macroscopic susceptibilities are related to molecular properties by local field factors. In discrete local field theory, the local fields are computed by considering the molecular environment rigorously. The intensity of the created electric field depends on the arrangement of the polarized molecules around the point of interest, in our case in the center of mass (COM) of the SiC cluster. Using the MD simulations results, the host–guest structures were considered to calculate the electrostatic interaction between the host polymer and the SiC cluster. The local electric field was calculated for each system in the COM of the SiC cluster. The calculations were carried out for each snapshot of the MD simulations via the boundary condition and then averaged. The influence of the next neighbor cells were taken into account with a cutoff defined by the difference between two calculated electric fields being less than  $\Delta F = 10^{-3}$  GV/m. The calculated electric fields related to the different nanocomposites are summarized in [Table 18-2](#). In order to evaluate the electrostatic intermolecular interactions, the data from the last range of 0.5 ns related to the MD run were considered. The obtained electric fields were used to predict the linear and nonlinear response of investigated composites as it was developed for the poled host–guest polymer systems (Reis et al. 2004).

In [Table 18-3](#) the electric properties calculated by DFT method on SiC cluster in several environments are reported. The energy-splitting  $\Delta E_{HOMO-LUMO}$  value for an isolated SiC cluster is in agreement with the work reported elsewhere (Reboredo et al. 2004) and shows a blueshift compared to the bulk 3C–SiC due to the used small cluster size. For the case of SiC cluster surrounded by polymeric matrixes, the  $\Delta E_{HOMO-LUMO}$  values are somehow reduced compared to an isolated SiC cluster. The environment contributes to narrowing the energy gap of the SiC clusters and increases the static dipole moment, which characterizes a given SiC grain. The most striking results concern the large effects from PC host matrixes. This is traced through the high local electric field induced in the COM of the investigated clusters (see [Table 18-2](#)) and also on the large dipole moment involved on the nanograins ([Table 18-3](#)). Generally, each considered polymer matrix delocalizes charge density of the semiconducting cluster. One can conclude that all investigated polymers should be appropriate to use them like matrixes keeping the SiC clusters.

On the other hand, the polarizability  $\alpha$  and hyperpolarizability  $\beta$  related to the electro-optical effect of the SiC clusters are calculated using Hartree–Fock and time-dependent DFT approaches at  $\lambda = 0.633 \mu\text{m}$ . The calculations are performed for an isolated cluster and then for the one embedded into polymer matrix. The effects of the surrounding media are taken into account via local field theory using the point-dipole approach. The obtained results are compared with the experimental data published recently (Bouclé et al. 2006). The obtained polarizabilities  $\alpha$  and hyperpolarizabilities  $\beta(\omega; 0, \omega)$  are summarized in [Table 18-3](#). Even with large differences observed on the local field calculations (see [Table 18-2](#)) in the different

■ Table 18-3

Molecular electric dipole moment  $\mu$ , HOMO-LUMO energy splitting  $\Delta E_{HOMO-LUMO}$ , polarizability  $\alpha(\omega)$  and hyperpolarizability  $\beta(\omega; 0, \omega)$  of the SiC cluster calculated in vacuum and polymeric environment ( $\lambda = 633 \text{ nm}$ ;  $1 \text{ au} = 0.16487 \times 10^{-40} \text{ C}^2 \text{ m}^2 \text{ J}^{-1}$  for  $\alpha$  and  $1 \text{ au} = 0.32066 \times 10^{-52} \text{ C}^3 \text{ m}^3 \text{ J}^{-2}$  for  $\beta$ )

Molecule	$\mu$ [D]	$\Delta E_{HOMO-LUMO}$ [eV]	$\alpha_{av}$ [au]	$\beta_{vec}(\omega; 0, \omega)$ [au]
SiC	5.86	3.40	2069.2	743.6
SiC in PMMA	17.54	3.30	2071.1	1951.5
SiC in PVK	9.19	3.26	2069.4	897.4
SiC in PC	69.82	1.31	2098.3	235400.0

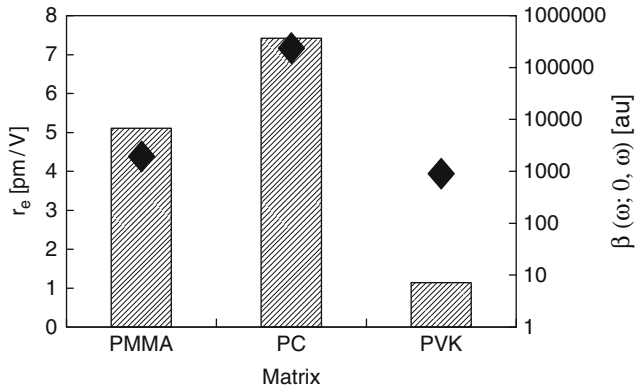
environments, the linear optical properties seem independent on the nature of polymers. The average value  $\alpha_{av}$  calculated in the local field approximation is about 1% lower in isolated cluster compared to the one located in a polymeric environment. Also, one may notice that the calculated local field has a tendency to be parallel to the direction of the molecular dipole moment. The absolute value of local field obtained for the PMMA and PVK matrixes are larger compared to the result obtained for the molecular crystals (Reis et al. 1998) but remains comparable with the previously investigated other guests in PMMA-based composites (Reis et al. 2004). It is worth noting the large electrical interactions involved between nc-SiC and the host polymer PC compared to those involved in the case of the PMMA- or PVK-based nanocomposites.

According to the carried out calculations, the environmental effect seems more important on the NLO properties than on the linear ones. All the considered host matrixes contribute to enhance drastically the hyperpolarizability  $\beta(\omega; 0, \omega)$  compared to the one involved in isolated 3C-SiC clusters. The largest effect is obtained on the PC-based nanocomposites due to the high local field involved at the COM of the SiC cluster. With regard to the available experimental works on electro-optical behavior of SiC nanocrystals in polymer matrixes, the hyperpolarizability coefficients are used to evaluate the linear electro-optical parameters. Figure 18-18 summarizes the experimental effective EO parameters  $r_e$  and the calculated hyperpolarizability parameters for the SiC nanocrystals embedded in the different polymeric matrixes (PMMA, PVK, and PC). The experimental results are compared to those defined from the  $\beta(\omega; 0, \omega)$  hyperpolarizability related to the EO effect and computed in local field approach. In practice, presented comparison is not straightforward. The  $r_e$  parameter depends not only on the effective hyperpolarizability  $\beta(\omega; 0, \omega)$  of considered molecule but also on the unit cell volume, density of active molecules, and the order parameters of the system. However, one main task of interest consists in analyzing the behavior of the electro-optical activity with respect to the used host matrix. One can conclude that the variation of the theoretical  $\beta(\omega; 0, \omega)$  values is in qualitative agreement with the experimental results.

The highest theoretical value of  $\beta(\omega; 0, \omega)$  is obtained for the PC/nc-SiC nanocomposites and seems to correlate with the experimental finding. It is worth noting that what we have addressed from the carried out analysis is to underline the general evolution of the effective EO coefficients and the hyperpolarizability parameters. More elaborated treatments should be performed on the nanocomposites and particularly the behavior under electrical poling.

Based on such approach, the EO properties discussed above can be improved by more elaborated approaches using MD simulations of the electrically treated media. In this context, the calculations of the macroscopic optical properties should be supplemented by the local field





■ Fig. 18-18

Linear effective EO parameter  $r_e$  experimentally obtained for the different kind of polymeric matrixes (bars) and hiperpolarizability  $\beta(\omega; 0, \omega)$  calculated via the local field theory (diamonds) (Reproduced with permission from Makowska-Janusik et al. (2006))

factor calculations. This approach can be combined with the permanent environmental effect on a perturbation of molecular surface. This is matter of current developments and actual scope.

## Conclusions

The development of innovative experimental approaches for the synthesis of functional nanostructured materials and the investigations of their key features was accompanied by theoretical and numerical approaches. This combination is dictated by the eventual lack of models and theories of bulk-like media to describe the real behavior from nanosized systems. Straightforward analyses and relevant interpretations of experimental responses require numerical simulations for the evaluation of the underlying physical properties of nanoparticles as isolated objects or associated with suitable host matrixes. Based on this methodology, the effects of broken translation symmetry at the nanocrystal boundaries or the size inducing electronic band structure and vibrational changes with respect to infinite media can be accounted quantitatively. This chapter summarizes the peculiarities of physical features of isolated nanoparticles and nanocomposites and describes the role of interface, which monitors electronic, optical, or vibrational phenomena. The conjugation of the different investigation approaches including experiments, theories, and simulations was applied to model nanosized materials based on SiC. This material has intrinsically versatile behaviors from structural (wide polytype family), electronic, and optical aspects as well. The interest from SiC-based nanostructures is also motivated by the technological applications of SiC in devices for high-power electronics, integrated optics, or photovoltaic applications. The development of the new methodology to improve the expected functionalities of SiC based nanosized architectures is a challenging investigation. This consists in the prediction of key properties from numerical simulations, the demonstration of their relevance using suitable experimental tools and finally, the establishment of the necessary feedback to enhance the physical responses for targeted applications.

The developed approach contributes to discriminate between experimental spectra of VDOS, the IR bands, and those due to photoluminescence (PL) phenomena. For the usefulness of nanosized crystalline materials, the cluster model was developed. It brings view on the physical properties of real nanostructured materials based on non-boundary condition calculations. Several geometries and structures of the clusters were tested and the suitable cluster size was determined for correct analysis of the experimental facts. A good agreement between experiments (IR, Raman) and the numerical simulation underline the strength of the developed methodology to describe correctly the physical properties of nanosized objects. Thus, theoretical VDOS spectra clarify their origin as mainly due to amorphous fraction of the SiC nanoparticles. In the PL investigations, the electron-phonon interactions play crucial role in the emission process through the phonon-assisted transitions stated on the theoretical model and the corresponding numerical simulations. The approach was developed on three representative cluster configurations to give precise insight on the experimental PL spectra even after oxidation treatments. However, it is worth noting that the construction of any cluster configuration and the evaluation of its physical peculiarities is generally dictated by the real organization of the SiC nanoparticles being precisely probed by high-resolution electron microscopy. This is the main requirement, which make us confident in the relevance of the carried out numerical analysis of vibrational and luminescence experiments.

In SiC-based nanocomposites, the simulations of the system proceed by numerical construction and geometry optimizations of the representative unit cell made from SiC cluster possessing appropriate size and the surrounding molecular arrangement of host matrix. The approaches were applied to the polymer host matrixes such as PMMA, PC, and PVK used for the evaluation of the electro-optical properties of hybrid nanocomposites. The geometry of structures was optimized using MD simulations with realistic parameters for the local order in SiC cluster and the boundary conditions defined by the interface features. The key parameter evaluated from MD simulations consists in the RDF between the cluster and the polymeric groups. Comparative analysis of the RDF features was then carried out depending on the polymer nature. In the final step of simulation work, the time-dependent DFT approach was used to evaluate the polarizability and hyperpolarizability parameters of SiC components. The dependence of these parameters on the host polymer matrixes was found similar to that of effective linear electro-optical parameters measured experimentally in the nanocomposites. The qualitative agreement between experimental responses and the numerical results in SiC based nanocomposites justify the validity and the generalization of the developed numerical methods to analyze the electro-optical behaviors of other nanostructured systems.

## References

---

- Akimov, I. A., Denisjuk, I. Yu., & Meshkov, A. M. (1992). Semiconductor nanocrystals in a polymeric matrix: new optical media. *Optics and Spectroscopy*, 72, 558–562.
- Alivisatos, A. P. (1996). Perspectives on the physical chemistry of semiconductor nanocrystals. *Journal of Physical Chemistry*, 100, 13226–13239.
- Alivisatos, A. P., Harris, A. L., Levinos, N. J., Steigerwald, M. L., & Brus, L. E. (1988). Electronic states of semiconductor clusters - homogeneous and inhomogeneous broadening of the optical spectrum. *Journal of Chemical Physics*, 89, 4001–4011.
- Beecroft, L. L., & Ober, C. K. (1997). Nanocomposite materials for optical applications. *Chemistry of Materials*, 9, 1302–1317 and revivied there.

- Bouclé, J., Kassiba, A., Emery, J., Kityk, I. V., Makowska-Janusik, M., Sanetra, J., Herlin-Boime, N., & Mayne, M. (2002). Local electrooptic effect of the SiC large-sized nanocrystallites incorporated in polymer matrixes. *Physics Letters A* 302, 196–202.
- Bouclé, J., Kassiba, A., Makowska-Janusik, M., Herlin-Boime, N., Reynaud, C., Desert, A., Emery, J., Bulou, A., Sanetra, J., Pud, A. A., & Kodjikian, S. (2006). Linear electro-optical behavior of hybrid nanocomposites based on silicon carbide nanocrystals and polymer matrixes. *Physical Review B*, 74, 205417–205411.
- Charpentier, S., Kassiba, A., Bulou, A., Monthieux, M., & Cauchetier, M. (1999). Effect of excess carbon and vibrational properties in ultrafine SiC powders. *The European Physical Journal Applied Physics*, 8, 111–121.
- Cramer, C. J. (2002). *Essentials of computational chemistry*. West Sussex: Wiley.
- Czerwinski, M., Bieleninik, J., Napieralski, J., Kityk, I. V., Kasperczyk, J., & Merwinski, R. I. (1997). Role of heteropolar bonds in ocm-2 oligocarbon-atomethacrylate. *European Polymer Journal*, 33, 1441–1447.
- Dabbousi, B. O., Rodriguez-Viejo, J., Mikulec, F. V., Heine, J. R., Mattoussi, H., Ober, R., Jensen, K. F., & Bawendi, M. G. (1997). (CdSe)ZnS core-shell quantum dots: synthesis and characterization of a size series of highly luminescent nanocrystallites. *Journal of Physical Chemistry B*, 101, 9463–9475.
- Di Bella, S., Ratner, M. A., & Marks, T. J. (1992). Design of chromophoric molecular assemblies with large second-order optical nonlinearities. A theoretical analysis of the role of intermolecular interactions. *Journal of American Chemical Society*, 114, 5842–5849.
- Essman, U., Perera, L., Berkowitz, M. L., Darden, T., Lee, H., & Pedersen, L. G. (1995). A Smooth particle Mesh Ewald method. *Journal of Chemical Physics*, 103, 8577–9593.
- Fischer, G. L., Boyd, R. W., Gehr, R. J., Jenekhe, S. A., Osaheni, J. A., Sipe, J. E., & Weller-Brophy, L. A. (1995). Enhanced nonlinear optical response of composite materials. *Physical Review Letters*, 74, 1871–1874.
- Henglein, A. (1993). Physicochemical properties of small metal particles in solution: “Micro-electrode” reactions, chemisorption, composite metal particles, and the atom-to-metal transition. *Journal of Physical Chemistry*, 97, 5457–5471.
- Hockney, R. W., Goel, S. P., & Eastwood, J. W. (1974). Quiet high-resolution computer models of a plasma. *Journal of Computational Physics*, 14, 148–158.
- Hohenberg, P., & Kohn, W. (1964). Inhomogeneous electron gas. *Physical Review B*, 136, 864–871.
- Hoover, W. G. (1985). Canonical dynamics: equilibrium phase-space distributions. *Physical Review A*, 31, 1695–1697.
- Kagan, C. R., Murray, C. B., & Bawendi, M. G. (1996). Long-range resonance transfer of electronic excitations in close-packed CdSe quantum-dot solids. *Physical Review B*, 54, 8633–8643.
- Kassiba, A., Makowska-Janusik, M., Boucle, J., Bardeau, J.-F., Bulou, A., Herlin, N., Mayne, M., & Armand, X. (2002a). Stoichiometry and interface effects on the electronic and optical properties of SiC nanoparticles. *Diamond and Related Materials*, 11, 1243–1247.
- Kassiba, A., Makowska-Janusik, M., Boucle, J., Bardeau, J.-F., Bulou, A., & Herlin-Boime, N. (2002b). Photoluminescence features on the Raman spectra of quasistoichiometric SiC nanoparticles: experimental and numerical simulations. *Physical Review B*, 66, 155317–1–155317–7.
- Kassiba, A., Bouclé, J., Makowska-Janusik, M., Errien, N. (2007). Some fundamental and applicative properties of [polymer/nano-SiC] hybrid nanocomposites. *Journal of Physics: Conference Series*, 79, 012002–1–012002–10.
- Kitson, D. H., & Hagler, A. T. (1988). Theoretical studies of the structure and molecular dynamics of a peptide crystal. *Biochemistry*, 27, 5246–5257.
- Kityk, I. V., Makowska-Janusik, M., Kassiba, A., & Plucinski, K. J. (2000). SiC nanocrystals embedded in oligoetheracrylate photopolymer matrixes; new promising nonlinear optical materials. *Optical Materials*, 13, 449–453.
- Kohn, W., & Sham, L. (1965). Self-consistent equations including exchange and correlation effects. *Physical Review A*, 140, 1133–1138.
- Kohn, W., Becke, A. D., & Parr, R. G. (1996). Density functional theory of electronic structure. *Journal of Physical Chemistry*, 100, 12974–12980.
- Koch, W., & Holthausen, M. C. (2001). *A chemist's guide to density functional theory* (2nd edn.). Wiley-VCH, Verlag GmbH. ISBN: 3-527-30372-3
- Lau, K. F., Alper, H. E., Thacher, T. S., & Stouch, T. R. (1994). Effects of switching functions on the behavior of liquid water in molecular dynamics simulations. *Journal of Physical Chemistry*, 98, 8785.
- Lin, S. Y., & Chang, S. T. (1998). Variations of vibrational local modes and electronic states of hydrogenated amorphous silicon carbide under thermal annealing. *Journal of Physics and Chemistry of Solids*, 59, 1399–1405.

- Ma, B., Lii, J. H., Chen, K., & Allinger, N. L. (1997). A molecular mechanics study of the cholesteryl acetate crystal: evaluation of interconversion among  $r_g$ ,  $r_z$ , and  $r_a$  bond lengths. *Journal of the American Chemical Society*, *119*, 2570–2573.
- Makowska-Janusik, M., Reis, H., Papadopoulos, M. G., Economou, I. G., & Zacharopoulos, N. (2004). Molecular dynamics simulations of electric field poled nonlinear optical chromophores incorporated in a polymer matrix. *The Journal of Physical Chemistry B*, *108*, 588–596.
- Makowska-Janusik, M., Kassiba, A., Bouclé, J., Bardeau, J.-F., Kodjikian, S., & Désert, A. (2005). Vibrational density of states in silicon carbide nanoparticles: experiments and numerical simulations. *Journal of Physics: Condensed Matter*, *17*, 5101–5110.
- Makowska-Janusik, M., Kassiba, A., Failleau, G., & Bouclé, J. (2006). Interface effects on the NLO properties of guest-host materials. *Materials Science*, *24*, 891–900.
- Manna, L., Scher, E. C., & Alivisatos, A. P. (2000). Synthesis of soluble and processable rod-, arrow-, teardrop-, and tetrapod-shaped CdSe nanocrystals. *Journal of the American Chemical Society*, *122*, 12700–12706.
- Mirgorodsky, A. P., Smirnov, M. B., Abdelmounim, E., Merle, T., & Quintard, P. E. (1995). Molecular approach to the modeling of elasticity and piezoelectricity of SiC polytypes. *Physical Review B*, *52*, 3993.
- Norris, D. J., & Bawendi, M. G. (1995). Structure in the lowest absorption feature of CdSe quantum dots. *Journal of Chemical Physics*, *103*, 5260–5268.
- Nose, S. (1984). A molecular dynamics method for simulations in the canonical ensemble. *Molecular Physics*, *52*, 255–268.
- Oudar, J. L., & Chemla, D. S. (1977). Hyperpolarizabilities of the nitroanilines and their relations to the excited state dipole moment. *Journal of Chemical Physics*, *66*, 2664–2668.
- Payne, M. C., Teter, M. P., Allan, D. C., Arias, T. A., & Joannopoulos, J. D. (1992). Iterative minimization techniques for *ab initio* total-energy calculations: molecular dynamics and conjugate gradients. *Reviews of Modern Physics*, *64*, 1045–1097.
- Reboredo, F. A., Pizzagalli, L., & Galli, G. (2004). Computational engineering of the stability and optical gaps of SiC quantum dots. *Nano Letters*, *4*, 801–804.
- Reis, H., Papadopoulos, M.G., & Munn, R. W. (1998). Calculation of macroscopic first-, second-, and third-order optical susceptibilities for the urea crystal. *Journal of Chemical Physics*, *109*, 6828–6838.
- Reis, H., Makowska-Janusik, M., & Papadopoulos, M. G. (2004). Nonlinear optical susceptibilities of poled guest-host systems: a computational approach. *Journal of Physical Chemistry B*, *108*, 8931–8940.
- Ricciardi, G., Rosa, A., van Gisbergen, S. J. A., & Baerends, E. J. (2000). A density functional study of the optical spectra and nonlinear optical properties of heteroleptic tetrapyrrole sandwich complexes: the porphyrinato-porphyrinato-zirconium(IV) complex as a case study. *Journal of Physical Chemistry A*, *104*, 635–643.
- Runge, E., & Gross, E. K. U. (1984). Density-functional theory for time-dependent systems. *Physical Review Letters*, *52*, 997–1000.
- Sanetra, J., Bogdal, D., Niziol, S., Armatys, P., & Pielichowski, J. (2001). Electroluminescence of poly(N-vinylcarbazole) (PVK) and its blends with 3-(2-methacrylate-ethoxy)carbonyl dimethylcoumarine. *Synthesis Materials*, *121*, 1731–1732.
- Sapra, S., Nanda, J., Anand, A., Bhat, S. V., & Sarma, D. D. (2003). Optical and magnetic properties of manganese doped zinc sulfide nanoclusters. *Journal for Nanoscience and Nanotechnology*, *3*, 392–400.
- Schmitt-Rink, S., Miller, D. A. B., & Chemla, D. S. (1987). Theory of the linear and nonlinear optical properties of semiconductor microcrystallites. *Physical Review B*, *35*, 8113–8125.
- Stewart, J. J. P. (1991). Optimization of parameters for semiempirical methods. III Extension of PM3 to Be, Mg, Zn, Ga, Ge, As, Se, Cd, In, Sn, Sb, Te, Hg, Tl, Pb, and Bi. *Journal of Computational Chemistry*, *12*, 320–341 and revised there.
- Timp, G. (1999). *Nanotechnology*. New York: Springer.
- van Gisbergen, S. J. A., Snijders, J. G., & Baerends, E. J. (1995). A density functional theory study of frequency-dependent polarizabilities and Van der Waals dispersion coefficients for polyatomic molecules. *Journal of Chemical Physics*, *103*, 9347–9354.
- Vonsovici, A., Reed, G. T., & Evans, A. G. R. (2000).  $\beta$ -SiC-on insulator waveguide structures for modulators and sensor systems. *Materials Science in Semiconductor Processing*, *3*, 367–374.
- Vosko, S. H., Wilk, L., & Nusair, M. (1980). Accurate spin-dependent electron liquid correlation energies for local spin density calculations: a critical analysis. *Canadian Journal of Physics*, *58*, 1200–1211.

- Wang, Y., Suna, A., Mahler, W., & Kasowski R. (1987). PbS in polymers. From molecules to bulk solids. *Journal of Chemical Physics*, 87, 7315–7322.
- Weiner, S. J., Kollman, P. A., Nguyen, D. T., & Case, D. A. (1986). An all atom force field for simulations of proteins and nucleic acids. *Journal of Computational Chemistry*, 7, 230–252.
- Zhang, H., & Xu, Z. (2002). Microstructure of nanocrystalline SiC films deposited by modified plasma-enhanced chemical vapor deposition. *Optical Materials*, 20, 177–181.

# 19 Structures and Stability of Fullerenes, Metallofullerenes, and Their Derivatives

Alexey A. Popov

Leibniz-Institute for Solid State and Materials Research (IFW Dresden),  
Dresden, Germany

Chemistry Department, Moscow State University, Moscow, Russia

<i>Introduction</i> .....	668
<i>Structures and Stability of Empty Fullerenes</i> .....	670
Definition of Fullerenes and Enumeration of Their Isomers .....	670
The Isolated Pentagon Rule and Steric Strain .....	671
The Isomers of IPR Fullerenes .....	677
<i>Bonding, Structures, and Stability of Endohedral Metallofullerenes</i> .....	684
Metal-Cage Bonding in Endohedral Metallofullerenes .....	684
Isomerism in Endohedral Metallofullerenes: Stability of the Charged Carbon Cages ...	687
Isomerism in Endohedral Metallofullerenes: The Cluster Size Factor .....	692
Violation of the Isolated Pentagon Rule in Endohedral Metallofullerenes .....	695
<i>Structures and Stability of Fullerene Derivatives</i> .....	696
Addition of $X_2$ to $C_{60}$ – Isomers of $C_{60}X_2$ and General Considerations .....	696
Addition of H and F to $C_{60}$ – Contiguous Addition, Benzene Rings, and Failures of AM1 .....	698
Addition of Bulky Groups to $C_{60}$ : Bromination and Perfluoroalkylation .....	701
Addition to $C_{70}$ and Higher Fullerenes .....	706
<i>Acknowledgments</i> .....	710
<i>References</i> .....	710

**Abstract:** This chapter describes general principles in the stability and bonding of empty fullerenes, endohedral fullerenes, and exohedral derivatives of empty fullerenes. First, an overview of the structural properties of empty fullerenes is given. The problem of isomers' enumeration is described and the origin of the intrinsic steric strain of the fullerenes is discussed in terms of POAV ( $\pi$ -orbital vector analysis) leading to the isolated pentagon rule (IPR). Finally, theoretical studies of the isomers of fullerenes are discussed. In the second part of the chapter, bonding phenomena and molecular structures of endohedral metallofullerenes (EMFs) are reviewed. First, the bonding situation in EMFs is discussed in terms of ionic/covalent dichotomy. Then, the factors determining isomers of EMFs, including those favoring formation of non-IPR cage isomers, are reviewed. In the third part, general principles governing addition of atomic addends and trifluoromethyl radicals to fullerenes are analyzed.

## Introduction

---

Carbon cluster research, originally the field of scientists interested in  $C_n$  species that might exist in deep space, "landed" on Earth with two discoveries that eventually changed the face of carbon science in particular and the nanoscience/nanotechnology in general. The first discovery was reported in 1985, when Kroto, Curl, Smalley, and coworkers made the Noble-prize-winning suggestion that the high-mass peaks in the mass spectra of laser-evaporated graphite belonged to closed-cage structures now known as fullerenes (Kroto et al. 1985). These molecules remained the playthings of mass spectrometrists, the only scientists who could "observe" fullerenes by producing them in situ in infinitesimal amounts, until 1990 when Krätschmer and coworkers discovered that this "new form of carbon" can be produced in bulk (i.e., macroscopic) amounts by the arc-burning of graphite (Krätschmer et al. 1990).  $C_{60}$  followed by  $C_{70}$  are the major fullerenes produced by arc-burning, however, starting from  $C_{72}$ , classical fullerene cages are possible for each even number, and many of such fullerenes (known as *higher fullerenes*) are produced as well. Studies of higher fullerenes are complicated by the increasing number of possible isomers, even if the strict isolated pentagon rule (IPR; see below for more details) is applied. The fullerenes with the number of atoms less than 60 are also available, but still remain exotic objects. Thus, the world of fullerenes themselves is very rich, but they also provide uncountable possibilities for further chemical modifications.

One of the attractive properties of fullerenes intrinsic to their closed-cage structure is the possibility of using them as robust containers for other species. The first evidence that metal atoms can be put inside fullerenes was reported in 1985 and was based on mass spectrometry (Heath et al. 1985), while the first bulk samples of fullerenes with metal atoms inside (endohedral metallofullerenes; hereinafter EMFs) were obtained in 1991 by laser evaporation (Chai et al. 1991) or arc-discharge (Alvarez et al. 1991) of the graphite rods mixed with lanthanum oxide. In the first decade after the discovery of macroscopic fullerene production the field of EMFs remained very "hot." Many metals were put inside fullerenes during this time, and many new molecules were reported (Shinohara 2000), but the yields of EMFs were very low (usually on the order of 1% of the empty fullerenes in the arc-discharge soot). Until 1999, EMFs were mostly molecules with one to three metal atoms encapsulated in the carbon cage. In 1999 it was found that the presence of nitrogen gas in the arc-burning reactor resulted in metal-nitride cluster fullerenes (NCFs) with the composition  $M_3N@C_{2n}$  ( $M=Sc, Y, Gd-Lu$ ;  $2n = 68-96$ ; the symbol "@" in the formula denotes how the EMF molecule is divided into the endohedral cluster,

the composition of which is given before this symbol, and the carbon cage with optional exohedrally attached groups, which follow after this symbol) to be produced (Dunsch and Yang 2007; Stevenson et al. 1999). In 2001 it was discovered that some “conventional” EMFs actually had  $C_2$  carbide units inside the cage. For example, “ $Sc_3@C_{82}$ ” and “ $Sc_2@C_{86}$ ” were shown to be  $Sc_3C_2@C_{80}$  and  $Sc_2C_2@C_{84}$ , respectively (Iiduka et al. 2005; Wang et al. 2001). Judicious choice of the nitrogen source led the group in Dresden to the invention of the reactive atmosphere method, in which the use of ammonia in the arc-burning reactor resulted in NCFs as major fullerene products (Dunsch et al. 2003, 2004). The same method with the use of  $CH_4$  resulted in  $Sc_3CH@C_{80}$  (Krause et al. 2007). Recently, oxides  $Sc_4O_{2,3}@C_{80}$  were synthesized using copper nitrate as the source of oxygen (Stevenson et al. 2008), while the use of guanidium thiocyanate afforded formation of sulfide clusterfullerenes  $M_2S@C_{82}$  ( $M=Sc, Y, Dy, Lu$ ) (Dunsch et al. 2010). The chemical route to open the empty fullerene cage, insert the small molecule inside (e.g.,  $H_2$ ), and then close the carbon cage was also recently reported (Komatsu et al. 2005). Finally, it is also possible to introduce one or two atoms of inert gases into the fullerene by high pressure–high temperature treatment (Saunders et al. 1993).

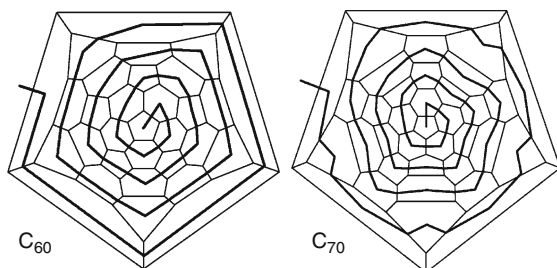
Another important property of fullerenes from the chemist’s point view is a very rich  $\pi$ -system based on the formal  $sp^2$  hybridization state of all carbon atoms. In chemical reactions fullerenes behave as polyalkenes (original expectations of the “superaromatic” properties were not confirmed) and thus exhibit very rich addition chemistry. That is, numerous cycloaddition reactions and addition of the groups forming one single bond to the fullerene core (such as atoms, e.g., halogens or hydrogen, or radicals, e.g., alkyl groups) are reported (Hirsch and Brettreich 2005).

Development of fullerene science was always accompanied – and sometimes preceded – by theoretical studies. The principles governing stability of fullerenes were revealed in late 1980s and early 1990s with the use of computational approaches, and such important data as relative energies of the fullerene isomers are still available only from the results of quantum-chemical calculations. Likewise, the most mysterious question about the fullerenes – why and how they are formed – is successfully addressed by theoreticians (Irle et al. 2003, 2006). The rise of the fullerene era to a large extent coincided with a dramatic increase in the capabilities of computational chemistry – either from advances in hardware, software, or theory itself. If studies of fullerenes in the mid-1980s, even by semiempirical approaches, were possible only in special laboratories, presently, at the end of the first decade of the twenty-first century, accurate DFT calculations can be done by virtually any scientist using a standard office computer. Yet, the large size of fullerenes and their derivatives still imposes serious limitations: even now it is barely possible to perform post Hartree-Fock *ab initio* calculations. Thus, DFT is the method of choice in fullerene chemistry, and will probably remain so in years to come. Although MP2 calculations are becoming more feasible (Darzynkiewicz and Scuseria 1997; Haser et al. 1991; Krapp and Frenking 2007), a significant increase of computational demands in many cases is not justified by the reliability of the results when compared to DFT (the modeling of noncovalent interaction, the weak point of DFT, is, however, an important exception). Routine use of methods with higher scaling than MP2 is still very difficult at present.

In this chapter we will show how quantum-chemical calculations can assist in studies of fullerenes. In particular, we will discuss prediction and elucidation of the molecular structures of the empty fullerenes, endohedral metallofullerenes, and selected fullerene derivatives. Taking into the account the huge amount of literature published on this subject, any review of the field is necessarily incomplete. We will not try to cover the whole field; instead, we will focus on several representative examples.







■ Fig. 19-1  
Unwinding  $C_{60}$  and  $C_{70}$  into spirals (thick black line)

There is a simple way to solve the problem of checking the uniqueness of the given fullerene. One can consider the spiral codes given in [Eq. 19.3](#) and [Eq. 19.4](#) as numbers, which can then simply be compared to each other. For the spirals of  $C_{60}$  under discussion, [Eq. 19.3](#) < [Eq. 19.4a](#) < [Eq. 19.4b](#). The spiral with the smallest number is called a *canonical* spiral; all non-canonical spirals should be sorted out. Thus, in addition to checking whether a given spiral can be wound up into a fullerene, one should also check if it is canonical. This problem can be also solved straightforwardly: if it is found that the spiral forms a fullerene, this fullerene should then be unwound into all possible spirals, the canonical one should be found among them and compared to the testing spiral.

The algorithm outlined above has been proved to be very successful, and its use in enumeration of the fullerene isomers is now standard. Importantly, the sequential number of the given fullerene isomer (i.e., the number of the isomer in the list of all isomers generated for the given fullerene by the spiral algorithm) is its sufficient and unique identifier. Usually, in designation of the fullerene isomer, one also adds its symmetry (to be precise, the highest symmetry possible for this topology of atoms; the ground state structure of the molecule can have lower symmetry), and we will use this notation in this chapter.

To conclude this section, we note that the spiral codes in [Eq. 19.3](#) and [Eq. 19.4](#) can be further simplified, taking into account that each fullerene has only 12 pentagons, and hence the spiral code can be uniquely defined by the numbers of the pentagon positions. In this notation, the spiral of  $C_{60}$  in [Eq. 19.3](#) is written as:

$$1\ 7\ 9\ 11\ 13\ 15\ 18\ 20\ 22\ 24\ 26\ 32 \quad (19.5)$$

This notation is usually used in the literature, including the famous “Atlas of Fullerenes” (Fowler and Manolopoulos 1995a).

## The Isolated Pentagon Rule and Steric Strain

The importance of exhaustive systematic enumeration of all isomers for a given fullerene becomes clear when the problem of structure elucidation of fullerenes is raised. Highly symmetric structures of  $C_{60}$  and  $C_{70}$  were proposed as a result of playing with the models. However, the success of this approach was to a large extent fortuitous, and this is hardly possible for other fullerenes. Of course, an unambiguous elucidation of the molecular structure might be possible through single-crystal X-ray diffraction studies. However, the quasi-spherical shape of

fullerene molecules results in strong disorder, which in most cases precludes reliable elucidations of the isomeric structures. This problem can be solved by chemical functionalization of fullerenes (e.g., via chlorination and perfluoroalkylation) and X-ray studies of their derivatives (Kareev et al. 2008a; Shustova et al. 2007; Simeonov et al. 2007; Troyanov and Tamm 2009b), but this promising approach is not always applicable. Thus, since early 1990s and up to now,  $^{13}\text{C}$  NMR spectroscopy has been the most important method in structural studies of newly isolated fullerenes. However, through the number of lines and their relative intensities,  $^{13}\text{C}$  NMR spectrum gives at best only the symmetry of the fullerene molecule, but not the exact isomeric pattern. Therefore, it is necessary that *all* isomers with NMR-determined symmetry are considered as possible structural guesses. Quantum-chemical calculations and studies by other spectroscopic techniques can be then used to determine the most appropriate structure.

► **Table 19-1** lists the total amount of possible isomers of fullerenes  $C_n$  for different  $n$ . These numbers clearly show that consideration of *all* isomers is hardly feasible for the low-symmetric structures. For instance, 99918 isomers are possible for  $C_{90}$ , and the information that an experimentally studied isomer has  $C_2$  symmetry allows one to reduce the structural guesses to 1266 isomers, which is still not very feasible. On the other hand, the number of isomers formed in arc-discharge synthesis is usually rather low. Therefore, it seems possible and highly desirable to develop some simple rules to reduce the number of isomers that should be considered.

The most successful rule of this sort is the isolated pentagon rule (IPR) proposed by H. Kroto back in 1987 on the basis of general considerations (Kroto 1987) and by Schmalz and coworkers in 1988 on the basis of more careful considerations of the sources of strain in carbon clusters and Hückel calculations (Schmalz et al. 1988). The IPR rule states that the fullerene isomers with adjacent pentagons are less stable than the isomers in which pentagons are surrounded only by hexagons (i.e., pentagons are *isolated*). In subsequent works numerous isomers of fullerenes were studied and the number of the pentagon-pentagon edges was found to be a parameter exhibiting very good correlation to the stability of the fullerenes. ► **Figure 19-2a** shows the correlation between the number of pentagon-pentagon edges and the relative energies of all 1812 isomers of  $C_{60}$  calculated at the QCFF/PI level of theory (Austin et al. 1995) (QCFF/PI is an inexpensive semiempirical computational approach combining classical mechanics for  $\sigma$ -bonds and the Pople-Pariser-Par method for  $\pi$ -system). The correlation is close to the linear

■ **Table 19-1**

**The total number of isomers of  $C_{60}$ – $C_{102}$  fullerenes and the number of fullerene  $C_{90}$  isomers of different symmetry types compared to the number of corresponding IPR isomers**

$C_n$	Total	IPR	$C_n$	Total	IPR	$C_{90}$ -symmetry group	Total	IPR
60	1,812	1	86	63,761	19	$C_{90} - C_1$	97936	16
70	8,149	1	88	81,738	35	$C_{90} - C_2$	1266	16
72	11,190	1	90	99,918	46	$C_{90} - C_5$	655	6
74	14,246	1	92	126,409	86	$C_{90} - C_3$	3	0
76	19,151	2	94	153,493	134	$C_{90} - C_{2v}$	50	7
78	24,109	5	96	191,839	187	$C_{90} - D_3$	4	0
80	31,924	7	98	231,017	259	$C_{90} - D_5$	1	0
82	39,718	9	100	285,914	450	$C_{90} - D_{3h}$	1	0
84	51,592	24	102	445,092	616	$C_{90} - D_{5h}$	2	1

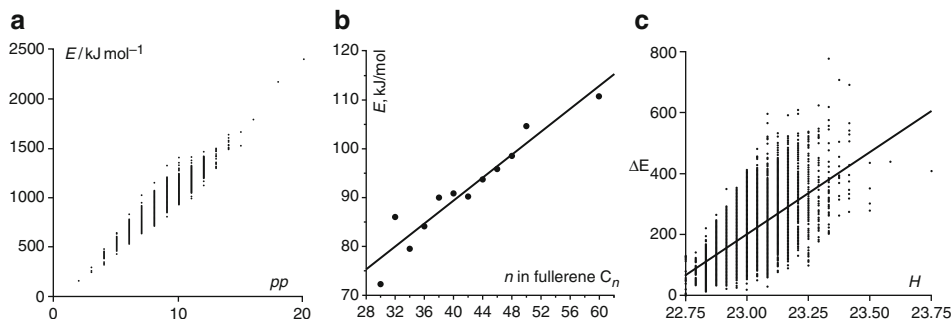


Fig. 19-2

(a) The relative energy of  $C_{60}$  isomers computed at the QCFF/PI level as a function of the number of pentagon/pentagon edges (Reproduced with permission from (Austin et al. 1995), © (1995) American Chemical Society); (b) energy penalty for the pentagon adjacency as a function of the fullerene size (Based on the data from Campbell et al. 1996); (c) relative energy of the IPR isomers of  $C_{116}$  computed at the QCFF/PI level as a function of the steric strain parameter  $H$  (Reproduced with permission from (Achiba et al. 1998a), © (1998) American Chemical Society)

form, and the energy penalty for one pentagon-pentagon edge, 111 kJ/mol for  $C_{60}$ , can be estimated from the slope of the fitted line. In a detailed study of the  $C_{30}$ – $C_{60}$  fullerene isomers at the QCFF/PI level (Campbell et al. 1996), it was found that the penalty is increasing with the cage size (► Fig. 19-2b), from 72 kJ/mol for  $C_{30}$  to 105 kJ/mol for  $C_{50}$ . The study of 55  $C_{76}$  isomers of  $D_2$  and higher symmetry at the QCFF/PI level (Austin et al. 1994) has shown that the penalty of the pentagon adjacency can be estimated as 150 kJ/mol (but this value is probably overestimated since the non-IPR isomers with lower symmetry can be more stable). The study of all 40 isomers of  $C_{40}$  at various levels of theory, including DFT (B3LYP, BLYP, and LDA), the Hartree-Fock method, semiempirical methods (AM1, PM3, MNDO, QCFF/PI), the density-functional based tight-binding method (DFTB), and molecular mechanics (MM), has shown that for all methods except for MM the penalty for  $C_{40}$  isomers falls in the narrow range of 82–100 kJ/mol (Albertazzi et al. 1999). In particular, B3LYP/STO-3G and QCFF/PI values are 92 and 91 kJ/mol, respectively, which confirms that the predictions on the broader range of isomers obtained at the QCFF/PI levels are also reliable. It should be noted, however, that the increase of the basis set to 6-31G\* resulted in a 13% increase in the penalty at the BLYP level, showing that the basis set effects can be rather important.

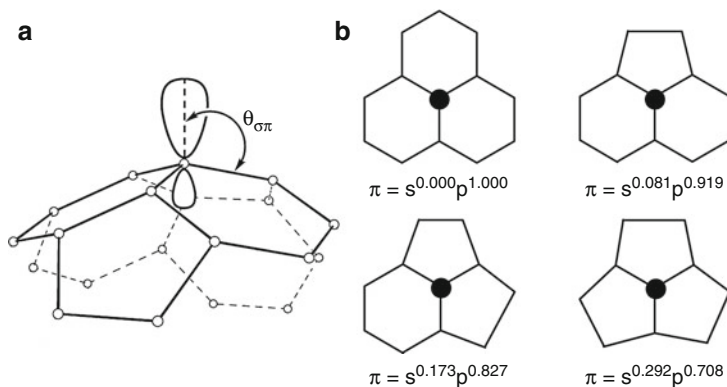
The energy penalty for the pentagon adjacency is sufficiently large to suggest that all non-IPR isomers can be sorted out for higher fullerenes (relative energies of the isolable fullerene isomers are usually less than 100 kJ/mol; see below). Increase of the energy penalty with the cage size is another factor favoring the application of the IPR. Indeed, the rule is strictly followed by all experimentally available empty fullerenes (the notable exclusion is  $C_{72}$ , which is discussed below). For the experimentally accessible fullerenes, the IPR reduces the number of possible isomers to be considered from many thousands to tens and hundreds (► Table 19-1). It is, however, possible to stabilize pentagon adjacencies by exohedral derivatization or by coordination to the metal atoms in EMFs (Tan et al. 2009), and hence larger sets of isomers have to be considered in these cases.

High energy penalty is the result of the combination of at least two factors. First, a pair of adjacent pentagons (pentalene) has an 8-electron  $\pi$ -system and is antiaromatic. Another factor, which is probably more important, is the steric strain induced by adjacent pentagons. The formal hybridization state of carbon in fullerenes is  $sp^2$ . Thus, carbon atoms should be planar (by this, we mean that it has three neighboring carbon atoms in the same plane). From the geometrical point of view, planarity is achieved when a carbon atom is located on the fusion of three hexagons. In this case,  $\pi$ -orbitals ( $p_z$ ) of the neighboring atoms are exactly parallel and the optimal overlap of these orbitals is achieved. However, one cannot build fullerene only from hexagons – pentagons are necessary to make closed-cage structures. The carbon atoms in pentagons are not planar any more (the small angle of  $108^\circ$  vs  $120^\circ$  in hexagons has to be compensated by the out-of-plane shift of the central atom), which results in *rehybridization*, the effect easily explainable in terms of  $\pi$ -orbital axis vector (POAV) analysis. POAV is defined as the vector that forms equal angles (POAV angles,  $\theta_{\sigma\pi}$ ) to all three  $\sigma$ -bonds (it is assumed that  $\sigma$ -orbitals are aligned toward the neighboring atoms). Admixing of  $s$ -orbitals into the hybrid  $\pi$ -orbital (the essence of rehybridization) can be quantified from geometrical point of view as:

$$m = \frac{2 \sin^2(\theta_{\sigma\pi} - \pi/2)}{1 - 3 \sin^2(\theta_{\sigma\pi} - \pi/2)} \quad (19.6)$$

where  $m$  determines admixture of  $s$ -orbital to the hybrid  $\pi$ -orbital ( $\pi = s^m p$ ; for perfect  $sp^2$  hybridization,  $\theta_{\sigma\pi} = 90^\circ$  and  $m = 0$ ). When  $m$  is not equal to zero,  $\pi$ -orbitals of the neighboring atoms are not parallel any more. Because of this misalignment, the  $\pi$ -orbital overlap is reduced, and therefore the  $\pi$ -bonding is weakened, the effect being the stronger the larger the value of  $m$ . ▶ *Figure 19-3b* shows possible junctions of pentagon and hexagons and hybrid  $\pi$ -orbital of the central atom computed for idealized polygonal bond angles. Misalignment of  $\pi$ -orbitals increases with the increase of the number of fused pentagons, and the IPR is a manifestation of this tendency.

It is obvious from ▶ *Fig. 19-3* that all fullerenes are inherently strained. For instance, it was estimated that the steric strain constitutes approximately 80% of the excess energy of  $C_{60}$  with



■ Fig. 19-3

(a) Definition of the  $\theta_{\sigma\pi}$  angle in the POAV approach; (b) the component of the hybrid  $\pi$ -orbital of the central atom in different junctions of pentagons and hexagons computed for idealized polygonal bond angles (Based on the data from Fowler and Manolopoulos 1995a)

respect to graphite (Haddon 1993). To quantify the steric strain, Raghavachari introduced the concept of hexagonal indices (Raghavachari 1992). The neighbor index  $k$  of a given hexagon is the number of its edges which are shared with other hexagons, and every fullerene isomer can be characterized by a set of indices  $h_k$  ( $k = 0 - 6$ ), where  $h_k$  is the number of hexagons with neighbor index  $k$ . In the aforementioned study of 1812 isomers of  $C_{60}$ , it was shown that the parameter

$$H = \sum_k k^2 h_k \quad (19.7)$$

also gives good linear correlation with the relative energies of the isomers.

The concept of hexagonal indices was in fact invented to explain relative stabilities of the IPR isomers. As each hexagon in the IPR isomer is adjacent to at least three other hexagons,  $h_0$ ,  $h_1$ , and  $h_2$  indices are equal to 0, and the combination of four indices ( $h_3, h_4, h_5, h_6$ ) is sufficient to characterize hexagon adjacencies in a given fullerene isomer (Fowler and Manolopoulos 1995a; Raghavachari 1992). Raghavachari suggested that to minimize the steric strain, the indices of all hexagons should be as close to each other as possible. In other words, the lowest strain energy can be achieved when the non-planarity is uniformly distributed over the whole carbon cage. Hence, the lowest strain is expected for those structures, in which all hexagons have the same neighborhood (all indices are equal), the condition fulfilled only for highly symmetric  $C_{60} - I_h(1)$ ,  $C_{80} - I_h(7)$ , and  $C_{80} - D_{5h}(6)$  in the whole range of IPR fullerenes  $C_{2n}$  with  $2n < 120$  (Fowler and Manolopoulos 1995a). More complex conditions were derived for other IPR fullerenes, namely:

$$(h_3, h_4, h_5, h_6) = \begin{cases} (80 - n, 3n/2 - 90, 0, 0); \rightarrow 60 \leq n \leq 80 \\ (0, 70 - n/2, n - 80, 0); \rightarrow 80 \leq n \leq 140 \\ (0, 0, 60, n/2 - 70); \rightarrow 140 \leq n \end{cases} \quad (19.8)$$

► **Table 19-2** lists optimal combinations of hexagonal indices as well as fullerene isomers in the range of  $C_{70} - C_{90}$  with such sets of indices. Importantly,  $C_{72}$  is the only fullerene that has no isomers satisfying these conditions.

#### ■ Table 19-2

**Optimal hexagon indices, the IPR isomers with optimal hexagon indices, and the lowest energy IPR  $C_{2n}$  and  $C_{2n}^{6-}$  isomers ( $2n = 76-90$ )**

$C_{2n}$	$(h_3, h_4, h_5, h_6)$	The least-strain IPR isomers <sup>a</sup>	The lowest energy $C_{2n}$ IPR isomers <sup>b</sup>	The lowest energy $C_{2n}^{6-}$ IPR isomers <sup>c</sup>
$C_{76}$	(4,24,0,0)	$T_d(2)$	$D_2(1)$	$T_d(2)$
$C_{78}$	(2,27,0,0)	$D_{3h}(5)$	$C_{2v}(3)$	$D_{3h}(5)$
$C_{80}$	(0,30,0,0)	$D_{5h}(6), I_h(7)$	$D_{5d}(1), D_2(2)$	$D_{5h}(6), I_h(7)$
$C_{82}$	(0,29,2,0)	$C_{2v}(9)$	$C_2(3)$	$C_{2v}(9)$
$C_{84}$	(0,28,4,0)	$D_2(21), D_2(22), D_{2d}(23)$	$D_2(22), D_{2d}(23)$	$D_2(21)$
$C_{86}$	(0,27,6,0)	$D_3(19)$	$C_2(17)$	$D_3(19)$
$C_{88}$	(0,26,8,0)	$D_2(35)$	$C_3(17)$	$D_2(35)$
$C_{90}$	(0,25,10,0)	$C_2(40), C_2(41), C_2(43), C_2(44), C_2(45)$	$C_2(45)$	$C_2(43)$

<sup>a</sup>based on the data from (Fowler and Manolopoulos 1995a)

<sup>b</sup>see ► **Table 19-3** for more details

<sup>c</sup>based on the data from (Popov and Dunsch 2007a)

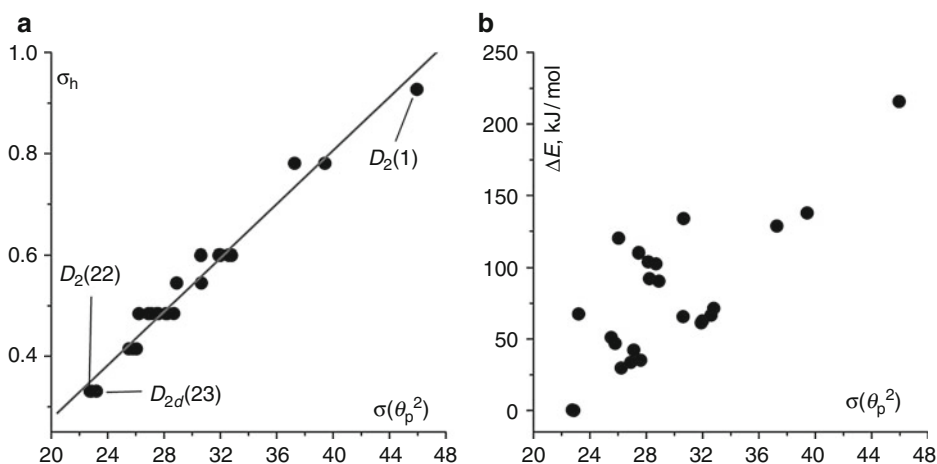
As a numerical parameter to quantify the steric strain in IPR fullerenes, one can use the standard deviation of the index distribution (Fowler and Manolopoulos 1995a):

$$\sigma_h = \sqrt{\langle k^2 \rangle - \langle k \rangle^2} \quad (19.9)$$

where

$$\langle k^i \rangle \Big|_{i=1,2} = \left( \sum_{k=3}^{k=6} k^i h_k \right) \cdot \left( \sum_{k=3}^{k=6} h_k \right)^{-1} \quad (19.10)$$

It was also shown that  $\sigma_h$  correlates well with the standard deviation of the square of POAV pyramidalization angle,  $\sigma(\theta_p^2)$  ( $\theta_p = \theta_{\sigma\pi} - 90$ ), as can be seen in **Fig. 19-4a** for a set of 24 IPR isomers of  $C_{84}$  (Boltalina et al. 2009). Therefore,  $\sigma_h$  and  $\sigma(\theta_p^2)$  can be used interchangeably to quantify the steric strain, the later parameter being more universal (for instance, it can be equally used for fullerene derivatives, in which some carbon atoms are in  $sp^3$  hybridization state). **Fig. 19-4b** also plots the relative energies ( $\Delta E$ ) of  $C_{84}$  computed at the B3LYP/6-31G\* level of theory versus  $\sigma(\theta_p^2)$ . The lack of correlations between  $\Delta E$  and  $\sigma(\theta_p^2)$  for the isomers with medium values of these parameters indicates that for IPR fullerenes, the other (e.g., electronic) factors are at least equally important as the steric strain. As a result, the lowest energy isomers for  $C_{76}$ – $C_{90}$  are usually not the isomers with the lowest steric strain (see **Table 19-2**), and steric strain analysis is not widely used now in the studies of higher fullerenes of medium size. If a larger set of isomers is considered (e.g., 6,063 IPR isomers  $C_{116}$ ), then the steric strain indicators (such as  $H$  in **Eq. 19.7**) indeed show correlation with the relative energies, at least at the QCFF/PI level (**Fig. 19-2c**) (Achiba et al. 1998a). However, the standard deviation of 75 kJ/mol is still too large, and such data can be of help only to sort out some high-energy isomer. Below we will show that more precise schemes have been developed based on the combination of topological motifs and their increments (Cioslowski et al. 2000).



**Fig. 19-4**

(a) Correlation between  $\sigma(\theta_p^2)$  and  $\sigma_h$  parameters for 24 IPR isomer of  $C_{84}$  (Based on the data from Boltalina et al. 2009); for a fitted line,  $R^2 = 0.97$ ; (b) correlation between  $\sigma(\theta_p^2)$  and B3LYP/6-31G\*-computed relative energies of 24 IPR isomer of  $C_{84}$  (Based on the data from Sun and Kertesz 2001b)

## The Isomers of IPR Fullerenes

With the advent of the IPR, the number of fullerene isomers to be considered was drastically reduced and detailed computations of reasonable (i.e., IPR) isomers and comparison to the experimental results became feasible. In this section we will review the results of the search of the most stable isomers of fullerenes beyond  $C_{70}$  (starting from  $C_{70}$ , at least one IPR isomer is possible for each even number of atoms). It is necessary to point out that the term *stability* comprises some ambivalence. It can be used in terms of *thermodynamic* stability, which in the studies of isomers means low relative energy, or in terms of *kinetic* stability, which implies reactivity of the compound in the given experimental conditions (in the studies of fullerenes it is usually determined by the HOMO–LUMO gap). When predicting the possible isomeric structure of fullerenes, it is necessary to consider a combination of both thermodynamic and kinetic stability factors, the former determining the possibility of the formation of the given fullerene, and the latter showing whether a given fullerene can be extracted from the soot and further processed by standard fullerene separation techniques. In fact, conclusions based on thermodynamic stability can be valid only when the reaction is close to the equilibrium (which is hard to prove for fullerenes). Moreover, for the equilibrium, Gibbs energies (rather than relative energies) should be taken into account, and it was shown by Slanina and coworkers that the equilibrium composition can be significantly altered at high temperatures (Slanina et al. 2004b). On the other hand, there are some examples (see below) showing that if thermodynamically stable fullerene has small HOMO–LUMO gap, it is possibly produced but remains in the insoluble part of the soot after extraction (presumably because of its polymerization). In this respect, a combination of the relative energy and the HOMO–LUMO gap still seem to be convenient parameters for the basic characterization of the fullerene isomers. **Table 19-3** lists the data on the relative energies of some higher fullerene isomers obtained using B3LYP and PBE0 (also known as PBE1PBE) hybrid DFT functionals. B3LYP results are compiled from several works by different groups and are obtained mainly with the use of 6-31G or 6-31G\* basis sets (Chen et al. 2001; Slanina et al. 2000; Sun and Kertesz 2000, 2001b, 2002; Sun 2003a, b; Zhao et al. 2003), while PBE0 values are results of single-point calculations with 6-311G\* basis set and DFTB-optimized atomic coordinates (Shao et al. 2006, 2007). **Table 19-3** also lists PBE0-obtained HOMO–LUMO gaps. **Figure 19-5** shows the structures of the major isomers of  $C_{60}$  and  $C_{72}$ – $C_{84}$ .

The first fullerene after  $C_{70}$ ,  $C_{72}$ , is a “missing” fullerene since it has never been obtained in considerable amounts. The sole IPR isomers of  $C_{72}$  with  $D_{6d}$  molecular symmetry is predicted to have large HOMO–LUMO gap (1.42 eV at the PBE/TZ2P level), however, DFT calculations (Kobayashi and Nagase 1997b, 2002b; Slanina et al. 2004a) supported also by the measurements of electron affinity of  $C_{72}$  (Boltalina et al. 2000a) show that trace amounts of  $C_{72}$  present in the fullerene extract are most probably based on the non-IPR  $C_{2v}$ (11188) isomer, which is 46–48 kJ/mol more stable than the IPR  $D_{6d}$ (1) isomer at the DFT level of theory (**Table 19-3**). Thus,  $C_{72}$  is the only empty fullerene  $C_n$  ( $n > 70$ ) which violates IPR.

$C_{74}$  represents to some extent the opposite situation to  $C_{72}$ : according to DFT calculations, the sole IPR isomer of  $C_{74}$ ,  $D_{3h}$ (1), has small HOMO–LUMO gap and probably has a triplet ground state (Kovalenko and Khamatgalimov 2003). This fullerene was also thought to be “missing” for a long time, until it was shown that it is insoluble in common fullerene solvents (Karataev 1998), most probably because of polymerization.  $C_{74}$  as well as some other “insoluble” fullerenes can be solubilized by either electrochemical (Diener and Alford 1998) or chemical modification (Goryunkov et al. 2004b; Shustova et al. 2006, 2007). For instance,



■ Table 19-3

Relative energies (kJ/mol) and HOMO–LUMO gap (eV) in selected isomers of C<sub>72</sub>–C<sub>94</sub> fullerenes as computed at the B3LYP and PBE0//DFTB levels of theory

C <sub>n</sub>	Sym.	B3LYP	PBE0	Gap	Ref. <sup>a</sup>	C <sub>n</sub>	Sym.	B3LYP	PBE0	Gap	Ref. <sup>a</sup>
C <sub>72</sub>	D <sub>6d</sub> (1)	0.0	0.0	2.64	[b,c]	C <sub>86</sub>	C <sub>2</sub> (17)	0.0	0.0	1.58	[b,d]
	C <sub>2v</sub>	-48.1	-46.1	1.63			C <sub>s</sub> (16)	25.9	23.6	1.97	
C <sub>74</sub>	D <sub>3h</sub> (1)	0.0	0.0	0.74	[b,c]		C <sub>1</sub> (12)	43.1	43.5	1.24	
C <sub>76</sub>	D <sub>2</sub> (1)	0.0	0.0	2.10	[b,c]		C <sub>1</sub> (11)	43.5	45.9	1.17	
	T <sub>d</sub> (2)		91.2	0.71			C <sub>3</sub> (18)	47.3	46.7	1.27	
C <sub>78</sub>	C <sub>2v</sub> (3)	0.0	0.0	1.71	[b,c]	C <sub>88</sub>	C <sub>s</sub> (17)	0.0	0.0	1.60	[f,d]
	D <sub>3h</sub> (5)	18.8	22.7	1.55			C <sub>2</sub> (33)	9.6	8.9	1.80	
	C <sub>2v</sub> (2)	27.6	26.3	2.15			C <sub>2</sub> (7)	10.9	5.1	1.63	
	D <sub>3</sub> (1)	41.4	41.3	1.71			C <sub>1</sub> (11)	43.5			
	D <sub>3h</sub> (4)	102.9					C <sub>2</sub> (20)	47.7	45.3	1.40	
C <sub>80</sub>	D <sub>2</sub> (2)	0.0	0.0	1.39	[b,c]	C <sub>90</sub>	C <sub>2</sub> (45)	0.0	0.0	1.74	[g,d]
	D <sub>5d</sub> (1)	9.2	1.1	1.15			C <sub>2v</sub> (46)	14.2	12.8	1.87	
	C <sub>2v</sub> (3)	11.7	17.1	0.95			C <sub>s</sub> (35)	15.1	12.0	1.91	
	C <sub>2v</sub> (5)	27.7					C <sub>1</sub> (30)	28.5	27.1	1.81	
	D <sub>3</sub> (4)	37.2					C <sub>2</sub> (28)	34.3	32.4	1.75	
C <sub>82</sub>	C <sub>2</sub> (3)	0.0	0.0	1.69	[b,d]	C <sub>92</sub>	C <sub>2</sub> (40)	36.8	39.6	1.45	
	C <sub>s</sub> (4)	16.2	17.8	1.63			C <sub>1</sub> (32)	38.5			
	C <sub>s</sub> (2)	27.4	27.3	1.69			C <sub>2</sub> (18)	46.9	43.6	1.52	
	C <sub>2</sub> (1)	32.1	33.2	1.28			D <sub>3</sub> (28)	51.4	0.0	2.20	[h,d]
	C <sub>2</sub> (5)	34.1	38.5	1.33			D <sub>2</sub> (84)	0.0	20.5	1.98	
	C <sub>s</sub> (6)	51.1	57.0	1.14			C <sub>2</sub> (26)	102.6	22.2	1.73	
C <sub>84</sub>	D <sub>2d</sub> (23)	0.0	0.0	2.15	[e,d]	C <sub>94</sub>	C <sub>1</sub> (38)	51.1	22.2	1.89	
	D <sub>2</sub> (22)	0.4	2.5	2.07			D <sub>2</sub> (82)	84.9	24.1	1.76	
	D <sub>6h</sub> (24)	29.7	30.3	2.46			D <sub>2</sub> (81)	134.7	40.5	1.61	
	C <sub>s</sub> (16)	33.7	34.5	1.96			C <sub>2</sub> (43)	15.5	0.0	1.91	[i,d]
	C <sub>2</sub> (11)	35.2	36.4	1.70			C <sub>s</sub> (42)	15.1	8.3	1.99	
	D <sub>3d</sub> (19)	42.3					C <sub>s</sub> (44)	35.1	25.2	1.74	
	C <sub>s</sub> (15)	47.0	50.6	1.60			C <sub>2</sub> (133)	0.0	29.4	1.66	
	C <sub>1</sub> (12)	51.1					C <sub>2</sub> (61)	24.7	33.4	1.63	
	D <sub>2d</sub> (4)	61.3					C <sub>1</sub> (37)	64.0	33.8	1.71	
	C <sub>s</sub> (14)	62.7					C <sub>1</sub> (34)	25.9	35.0	1.55	
	C <sub>2v</sub> (18)	65.4					C <sub>1</sub> (15)	33.9	43.6	1.44	
	D <sub>2</sub> (5)	66.4					C <sub>1</sub> (91)		44.7	1.50	

<sup>a</sup>In each pair of references, the first one is for B3LYP values, the second one is for PBE0/6-311G\*//DFTB values

<sup>b</sup>B3LYP/6-31G\* (Chen et al. 2001)

<sup>c</sup>Shao et al. 2007

<sup>d</sup>Shao et al. 2006

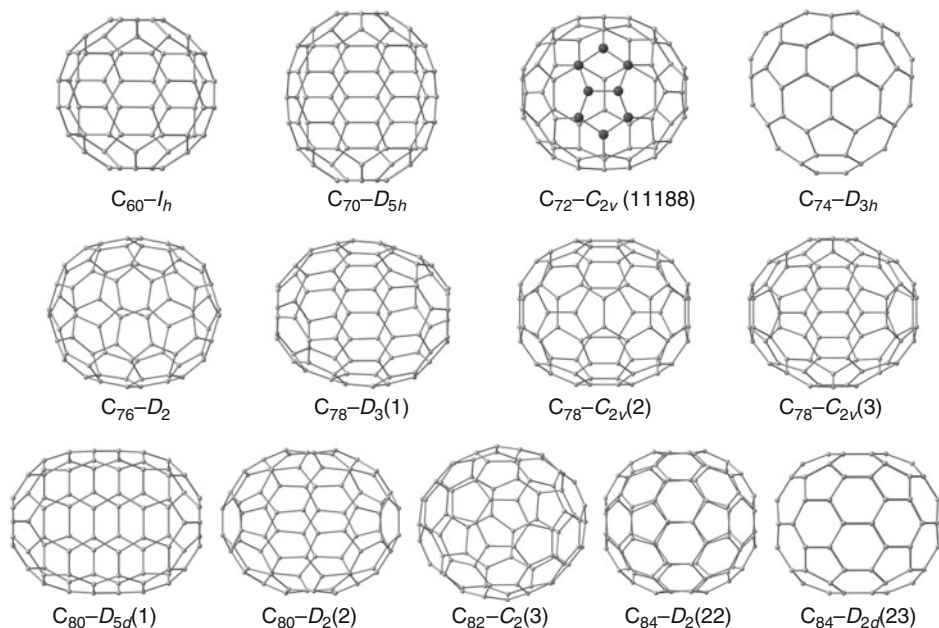
<sup>e</sup>B3LYP/6-31G\* (Sun and Kertesz 2001b)

<sup>f</sup>B3LYP/6-31G (Sun 2003a)

<sup>g</sup>B3LYP/6-31G (Sun 2003b)

<sup>h</sup>B3LYP/6-31G\*//SAM1 (Slanina et al. 2000)

<sup>i</sup>B3LYP/6-31G\*//SAM1 (Zhao et al. 2003)



■ Fig. 19-5

**Molecular structures of  $C_{60}$ ,  $C_{70}$ , and selected higher fullerenes. The atoms in adjacent pentagon pair in  $C_{72}$  are highlighted**

trifluoromethylation of “insoluble” fullerene mixture afforded  $C_{74}(CF_3)_{12}$  as a major product, and  $D_{3h}(1)$  carbon cage in this compound was unambiguously confirmed by single-crystal X-ray diffraction (Shustova et al. 2007).

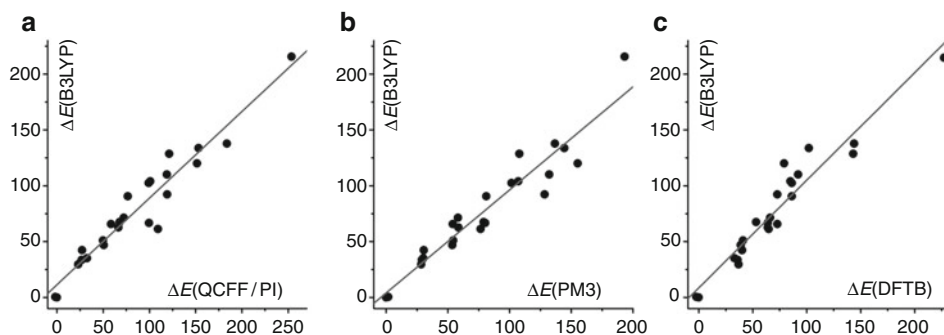
Identity of  $C_{76}$  as  $D_2(1)$  isomer was unambiguously confirmed by  $^{13}C$  NMR spectroscopy in the very early studies of the higher fullerenes (Ettl et al. 1991). According to DFT calculations,  $D_2(1)$  is considerably more stable than the second IPR isomer,  $T_d(2)$ . Moreover, the latter is subject to Jahn-Teller distortion (the actual symmetry is  $D_2$ ) and has a small HOMO–LUMO gap. Recently, it was shown that  $C_{76}-T_d(2)$  is probably also formed in the fullerene synthesis but remains insoluble; however, it can be solubilized and characterized in the form of trifluoromethyl derivative  $(C_{76}-T_d(2))(CF_3)_{12}$  (Shustova et al. 2006).

$C_{78}$  has five IPR isomers; four of them are quite stable (their  $\Delta E$  covers the range of 41 kJ/mol) and are proved to be formed in the arc-discharge synthesis. Three isomers,  $D_3(1)$ ,  $C_{2v}(2)$ , and  $C_{2v}(3)$ , are obtained in approximately comparable amounts (the actual ratio depends on the pressure used in the synthesis) and can be easily extracted from the soot as they have comparably high HOMO–LUMO gaps (Kikuchi et al. 1992; Wakabayashi et al. 1994). The isomer  $D_{3h}(5)$ , although it is the second in the stability order (► Table 19-3), can be found in the fullerene extract in much smaller amounts (Simeonov et al. 2008). A possible reason is the low HOMO–LUMO gap, which results in the poor solubility. Indeed, this isomer was found among the “insoluble” fullerenes, its structure being unambiguously confirmed by the single-crystal X-ray structure of the trifluoromethyl derivative,  $(C_{78}-D_{3h}(5))(CF_3)_{12}$  (Shustova et al. 2007).

From seven IPR isomers of  $C_{80}$ , only the two most stable structures (● [Table 19-3](#)),  $D_2(1)$  and  $D_{5d}(2)$ , are obtained in the form of empty fullerenes (Hennrich et al. 1996; Wang et al. 2000b). DFT predicts that they are almost isoenergetic (the  $D_2(1)$  isomer is somewhat more stable), but  $D_{5d}(2)$  isomer has considerably smaller HOMO–LUMO gap. Besides, the higher symmetry of  $D_{5d}(2)$  isomer also reduces its content if entropy factors at higher temperatures are taken into account. As a result, the yield of  $D_2(1)$  is about 30 times higher (Wang et al. 2000b). Isolation of  $(C_{80}-C_{2v}(5))(CF_3)_{12}$  after trifluoromethylation of the “insoluble” fullerene mixture has shown that  $C_{80}-C_{2v}(5)$  is also produced in the arc-discharge synthesis (Shustova et al. 2006).  $C_{2v}(5)$  isomer is rather stable but has small HOMO–LUMO gap ( $\Delta E = 25$  kJ/mol, gap = 0.71 eV at the B3LYP/6-31G\* level). Importantly, icosahedral  $C_{80}-I_h(7)$  isomer, which should have the least steric strain among all IPR isomer of  $C_{80}$ , is in fact the least stable isomer ( $\Delta E = 114$  kJ/mol at the B3LYP/6-31G\* level of theory (Slanina et al. 2008). The reason is its electronic instability – in the ideal icosahedral symmetry, its HOMO is fourfold degenerate and is occupied by two electrons. BP/TZVP studies have shown that it has  $D_{2h}$  symmetry in the ground state, and its singlet and triplet states are isoenergetic (Furche and Ahlrichs 2001). However, this isomer becomes the most stable  $C_{80}$  isomer in the hexaanionic state, when its HOMO is fully occupied, which makes it a key structure for the endohedral metallofullerenes (see section “Bonding, Structures, and Stability of Endohedral Metallofullerenes” of this chapter).

$C_{82}$  has seven IPR isomers, but only one of them,  $C_2(3)$ , was isolated in pure form (Kikuchi et al. 1992; Zalibera et al. 2007).  $C_2(3)$  is the most stable isomer of  $C_{82}$  and has large HOMO–LUMO gap (Sun and Kertesz 2001a), so its high abundance is not surprising. Meanwhile,  $C_s(4)$  isomer is also rather stable and has similar gap, but this isomer has never been observed. The studies of the “insoluble” fullerene fraction have shown that  $C_2(5)$  isomer is also formed in the arc-discharge synthesis, as verified by the isolation and characterization of its  $CF_3$  derivative,  $(C_{82}-C_2(5))(CF_3)_{12}$  (Shustova et al. 2006).

Starting from  $C_{84}$ , the increase in the number of possible structures becomes quite significant (see ● [Table 19-1](#)), which seriously complicates the studies, both experimentally and theoretically. This fact also increases the value of theoretical studies, since they can help in sorting out unrealistic isomers. The question of high importance in this situation is how to handle the rapidly increasing number of isomers. The obvious strategy of choice is to use several (usually two) computational approaches, first the “cheap” one (for instance, semiempirical method) for the whole set of isomers, and then the more expensive but more reliable approach (usually DFT) for a reduced set of structures. It is important that the “cheap” method should be also sufficiently reliable so that the possible errors in the relative energies should be not very high, and a reasonable cut-off in the relative energies might be applied for the subsequent higher level computations. Twenty-four IPR isomers of  $C_{84}$  form a convenient training set, since it is still feasible to perform a full DFT study for all of them. ● [Figure 19-6](#) compares relative energies of 24 isomers obtained at the B3LYP/6-31G\* level (Sun and Kertesz 2001b) to those obtained with three semiempirical approaches widely used in the fullerene chemistry, QCFF/PI, MNDO, and DFTB. One can see that in all cases the correlation is quite reasonable ( $R^2 \approx 0.92$ ), and the standard deviations ( $\sigma_E$ ) is less than  $\sim 20$  kJ/mol. Roughly estimating the energy cut-off for the isomers computed by means of “cheap” method as  $3\sigma_E$ , one can consider then only the isomers with  $\Delta E < 3\sigma_E$  for the subsequent DFT study (the cut-off should be appropriately increased, of course, if one is interested in the whole set of isomers within the given energy window). Assessment study of three semiempirical approaches, MNDO, AM1, and PM3, in predicting relative energies of fullerene isomers in comparison to B3LYP/6-31G\* was reported for a set of fullerenes including  $C_{30}-C_{50}$ , all IPR isomers of  $C_{72}-C_{86}$ , and selected isomers of  $C_{88}-C_{102}$



■ Fig. 19-6

Correlations between relative energies of 24 IPR isomer of  $C_{84}$  computed at the B3LYP/6-31G\* level and those computed using QCFF/PI (a), PM3 (b), and DFTB (c), all values are in kJ/mol.  $R^2$  values for the fitted lines are 0.925, 0.912, and 0.925, respectively

(Chen and Thiel 2003). Quite good correlations were found between the results of DFT and semiempirical calculations for higher fullerenes ( $R^2 = 0.92$ , 0.88, and 0.86, for MNDO, AM1, and PM3, respectively; standard deviations are 20–25 kJ/mol), while for small fullerenes with a large number of pentagon adjacencies performance of semiempirical methods was significantly worse. In another work, AM1 and PM3 methods were compared to DFTB and B3LYP/6-31G\* for all IPR isomers of  $C_{72}$ – $C_{86}$  fullerenes and selected isomers of  $C_{28}$ – $C_{36}$  (Zheng et al. 2005). At variance with the results in (Chen and Thiel 2003), the authors have found that AM1 and PM3 performed rather bad ( $R^2 = 0.77$  and 0.73, respectively, for  $C_{72}$ – $C_{86}$ ), while DFTB-predicted values were close to B3LYP/6-31G\* ( $R^2 = 0.88$  and 0.93 for NCC and SCC-variants of DFTB, respectively). The significant difference in performance of AM1 and PM3 methods reported by two groups is quite remarkable. Close comparison of the relative energies from the two works shows that the difference in relative energies predicted for the *same* isomers by the *same* method can be as high as 50 kJ/mol, and in one case ( $C_{3v}(8)$  isomer of  $C_{82}$ ) reaches 75 kJ/mol. At the same time, both works report the same values for the isomer of  $C_{84}$  and agree in that semiempirical methods give reliable predictions for this fullerene.

$C_{84}$  is also a special case among the higher fullerenes since, on the one hand, it is the most abundant empty fullerene after  $C_{60}$  and  $C_{70}$  (at least, if all  $C_{84}$  isomers are taken together); on the other hand, it provides the broadest range of the isomers characterized for one fullerene. The lowest energy is predicted by many approaches for  $D_2(22)$  and  $D_{2d}(23)$  isomers, separated from the other isomers by the gap of ca 30 kJ/mol (● Table 19-3). They are essentially isoenergetic ( $\Delta E$  varies within few kJ/mol in favor of one or another isomer depending on the method) and have large HOMO–LUMO gaps. Indeed, these are the isomers produced in the largest amounts (the  $D_2$  to  $D_{2d}$  ratio is ca 2:1 and varies depending on the conditions of synthesis) (Kikuchi et al. 1992).  $C_{84}$  also serves as a good example to emphasize that with the increase of the number of isomers the density of their distribution in the energy scale is also increasing. The energies of at least 12 isomers fall in the range of  $\Delta E = 30$ –71 kJ/mol at the B3LYP/6-31G\* level (Sun and Kertesz 2001b), and many of them can be isolated as “minor” isomers, including (in the order of their yield)  $C_2(11)$ ,  $C_s(16)$ ,  $C_s(14)$ ,  $D_{2d}(4)$ , and  $D_2(5)$  (Dennis et al. 1999). Isolation of  $D_{6h}(24)$  and  $D_{3d}(19)$  isomers from the arc-discharge soot of Gd-doped composite rods was also reported

(note that these isomers were not formed in noticeable amounts with pure graphite rods) (Tagmatarchis et al. 1999). Recent perfluoroalkylation of the higher fullerene mixture resulted in the isolation and single-crystal X-ray characterization of the derivatives of several  $C_{84}$  isomers, including  $(C_{84}-C_{2v}(18))(C_2F_5)_{12}$ , the carbon cage isomer of which has not been found in the previous studies (Tamm et al. 2009b).

For  $C_{86}$ , two isomers, with  $C_2$  and  $C_s$  symmetry, could be isolated from the arc-discharge soot and characterized by  $^{13}C$  NMR spectroscopy (Miyake et al. 2000). From 19 IPR isomer of  $C_{86}$ , 6 have  $C_2$  symmetry and 3 have  $C_s$  symmetry. DFT calculations show that isomers  $C_2(17)$  and  $C_s(16)$  have the lowest energies and large HOMO–LUMO gaps and hence can be assigned to the experimentally observed structures (Sun and Kertesz 2002). The assignment was also confirmed by comparison of B3LYP/6-31G computed and experimentally measured  $^{13}C$  NMR chemical shifts (Sun and Kertesz 2002). Recently, trifluoromethylation of the mixture of higher fullerenes afforded, among the other compounds,  $CF_3$  derivatives of  $C_{86}$ ,  $C_{86}(CF_3)_{16}$  and  $C_{86}(CF_3)_{18}$ , all assigned to the  $C_2(17)$  cage by means of single-crystal X-ray diffraction study (Trojanov and Tamm 2009b).

In the most recent experimental study of  $C_{88}$ , three isomers of this fullerene were isolated and assigned by  $^{13}C$  NMR spectroscopy to one  $C_s$  and two  $C_2$ -symmetric structures (Miyake et al. 2000). Among 35 IPR isomers of  $C_{88}$ , 11 and 7 structures have  $C_s$  and  $C_2$  symmetry, respectively. DFT calculations show that  $C_s(17)$  has the lowest energy, followed by  $C_2(7)$  and  $C_2(33)$  isomers, all within the range of 10 kJ/mol (Table 19-3). These three structures have large HOMO–LUMO gaps and are separated from the less stable isomers by a gap of at least 30 kJ/mol. Therefore, they can be readily assigned to the experimentally observed structures, which is also confirmed by the comparison of the B3LYP/6-31G computed  $^{13}C$  NMR spectra to the experimental data (Sun 2003b). Recently, the presence of  $C_2(33)$  isomer in the arc-discharge produced fullerene mixture was confirmed by the isolation and single-crystal X-ray diffraction characterization of  $(C_{88}-C_2(33))(CF_3)_{18}$  among the other trifluoromethylation products of higher fullerenes (Trojanov and Tamm 2009a).

Detailed experimental study of  $C_{90}$  has shown that at least five isomers are formed in the arc-discharge synthesis, and that the major fraction is a mixture of  $C_2$  and  $C_{2v}$ -symmetric isomers (Achiba et al. 1995). The B3LYP/STO-3G calculations of all 46 IPR isomers with subsequent B3LYP/6-31G calculations of the isomers with  $\Delta E < 100$  kJ/mol have shown that the lowest energy structures are  $C_2(45)$  and  $C_{2v}(46)$  (Sun 2003b). Analogous result was also obtained in the DFTB and PBE0/6-311G\*/DFTB study (Shao et al. 2006). Therefore,  $C_2(45)$  and  $C_{2v}(46)$  are the most probable candidates for the main major isomers of  $C_{90}$ . Chlorination of the mixture of higher fullerenes resulted in  $C_{90}Cl_{32}$  with  $C_{2v}(46)$  and  $C_s(34)$  cage isomers, thus confirming that at least the  $C_{2v}(46)$  isomer is indeed formed in the arc-discharge (Kemnitz and Trojanov 2009). At the same time, the trifluoromethylation product,  $C_{90}(CF_3)_{12}$ , was assigned to the  $C_1(32)$  isomer ( $\Delta E = 38.5$  kJ/mol, B3LYP/6-31G) (Kareev et al. 2008b). Very recently,  $D_{5h}(1)$  isomer ( $\Delta E = 76.2$  kJ/mol, B3LYP/6-31G) was isolated from the soot produced by vaporization of  $Sm_2O_3$ /graphite rods and characterized by single-crystal X-ray diffraction (Yang et al. 2010).

Isolation and  $^{13}C$  NMR characterization of five major isomers of  $C_{92}$ , of which two have  $C_2$  symmetry and three have  $D_2$  symmetry, has been reported (Achiba et al. 1998b), however, further spectroscopic details were not given. In another work, one  $C_2$ -symmetric isomer and inseparable mixture of at least three other isomers were obtained from dysprosium arc-burned soot (Tagmatarchis et al. 2002).  $C_{92}(CF_3)_{16}$  with either  $D_2(81)$  or  $D_2(82)$  carbon cage was identified among the other products of the trifluoromethylation of the higher fullerene mixture (Trojanov and Tamm 2009a). Results of DFT studies are more controversial for  $C_{92}$  than for

smaller fullerenes discussed above (► [Table 19-3](#)). Two detailed studies were reported, one based on the screening of the whole set of IPR isomers at the semiempirical SAM1 level with subsequent B3LYP/6-31G\*//SAM1 calculations (Slanina et al. 2000), while another study included screening at the DFTB level followed by PBE0/6-311G\*//DFTB calculations of the most stable isomers (Shao et al. 2006). As can be seen in ► [Table 19-3](#), the two approaches resulted in substantially different relative energies and stability order of the isomers. While B3LYP//SAM1 approach favors  $D_2(84)$  isomer as the most stable one, PBE0//DFTB predicts that  $D_3(28)$  is 20 kJ/mol lower in energy than  $D_2(84)$ . Full optimization of  $D_3(28)$  and  $D_2(84)$  isomers at the B3LYP/6-311G\* and PBE0/6-311G\* levels of theory in (Shao et al. 2006) showed that the former is indeed more stable by 18.2 and 20.8 kJ/mol, respectively, in very close agreement with the results of PBE0//DFTB calculations. It appears thus that PBE0//DFTB values are more reliable than the results of B3LYP//AM1 calculations.

Experimental structural information on the empty fullerenes beyond  $C_{92}$  is very scarce and usually limited to the mixtures of isomers. X-ray crystallographic study of  $C_{94}(CF_3)_{20}$  and  $C_{96}(C_2F_5)_{12}$  obtained by perfluoroalkylation of the higher fullerene mixture with subsequent HPLC separation proved formation of  $C_{94}-C_2(61)$  and  $C_{96}-C_1(145)$  isomers in the arc-discharge synthesis (Tamm et al. 2009a), but these data are inconclusive since the actual isomeric composition of the initial fullerene mixture remains unknown. Yet, a lot of calculations were performed for larger fullerenes, and systematic information on the lowest energy isomers is available up to  $C_{180}$ .

The aforementioned PBE0/6-311G\*//DFTB study was performed for all IPR fullerenes in the  $C_{82}-C_{120}$  range as well as for all IPR and non-IPR isomers of  $C_{38}-C_{80}$  fullerenes (Shao et al. 2006, 2007). For the most stable isomer,  $^{13}C$  NMR spectra were also predicted for comparison with experiment.

In another series of works, the most stable isomers of  $C_{122}$  to  $C_{180}$  were identified (Xu et al. 2006, 2008). To screen the huge number of the isomers, the authors used the empirical scheme of Cioslowski and coworkers (Cioslowski et al. 2000). According to the original scheme, formation enthalpies of fullerenes were factorized into contributions of 25 independent structural motifs, namely 6-member rings with their first and second neighbors, and the contributions of the motifs were fitted using the energies of 115 IPR fullerenes in the  $C_{60}-C_{180}$  size range computed at the B3LYP/6-31G\* level. In 2008, parameters were re-fitted using the energies of 536 fullerene molecules in the  $C_{60}-C_{160}$  range (Xu et al. 2008). The serious advantage of this empirical method is that it is very inexpensive, and the energies can be estimated with high accuracy without quantum-chemical calculations. B3LYP/6-31G\* calculations were then used by the authors to determine the lowest energy isomers (Xu et al. 2006, 2008). The same authors also performed benchmarking computations of  $C_{116}$ ,  $C_{118}$ , and  $C_{120}$  isomers to analyze performance of QCFF/PI, AM1, PM3, MNDO, and tight-binding (TB) methods in comparison to B3LYP/6-31G\*//B3LYP/3-21G (Xu et al. 2007). It was found that, in contrast to the relative energies of the medium-size higher fullerenes such as  $C_{84}$ , for large fullerenes semiempirical methods performed badly and did not show any reasonable correlations with DFT-predicted relative energies. However, it should be noted that DFT is not a panacea itself. DFT has difficulties with description of the extended  $\pi$ -systems (Reimers et al. 2003), and hence it is possible that DFT is also not reliable for large fullerenes. Unfortunately, results of computations for larger fullerenes cannot be verified by experimental information at this moment.

In conclusion, numerous studies have shown that the most stable isomers of the middle-size higher fullerenes predicted by DFT are usually the major isomers in the experimentally produced fullerene mixtures. At the same time, it is also clear that experimental results cannot



be fully described by considering only thermodynamic control (equilibrium), since some other *unknown* factors are also important in determining the isomeric composition. For instance, it is not clear yet why some stable isomers are not formed in the arc-discharge synthesis; besides, the influence of the metals on the distribution of the arc-discharge produced fullerene isomers is not understood.

## Bonding, Structures, and Stability of Endohedral Metallofullerenes

### Metal-Cage Bonding in Endohedral Metallofullerenes

Since La@C<sub>82</sub> was first isolated in 1991, the nature of the metal-fullerene bonding was of interest to researchers. Because of the radical nature of La@C<sub>82</sub> as well as other M<sup>III</sup>@C<sub>82</sub> (M=Y, Sc), the ESR spectroscopy appeared useful in revealing the main features of the electronic structure of EMFs. Small hyperfine splitting constant of the metal observed in the spectra indicated that the spin density in M@C<sub>82</sub> is presumably localized on the fullerene cage. This, along with the high electron affinity of fullerenes, resulted in the concept of the endohedral metallofullerenes as non-dissociative salts (e.g., La<sup>3+</sup>@C<sub>82</sub><sup>3-</sup>), with the metal cation encapsulated in the negatively charged carbon cage. Likewise, ionic model is often used to describe electronic structure of endohedral fullerenes with more complex encapsulated species, such as dimetallofullerenes (e.g., (La<sup>3+</sup>)<sub>2</sub>@C<sub>80</sub><sup>6-</sup>), nitride clusterfullerenes (e.g., (Sc<sub>3</sub>N)<sup>6+</sup>@C<sub>80</sub><sup>6-</sup>), or carbide clusterfullerenes (e.g., (Sc<sup>3+</sup>)<sub>2</sub>C<sub>2</sub><sup>2-</sup>@C<sub>82</sub><sup>4-</sup>).

The concept of the ionic metal-fullerene bonding was further developed by Kobayashi et al. (Kobayashi and Nagase 1998; Nagase et al. 1997). The authors analyzed the spatial distribution of electrostatic potential inside fullerene and showed that it has large negative values inside negatively charged carbon cages. This results in the strong stabilization of the metal cations if they are placed inside fullerene anions thus favoring formation of EMFs. Importantly, the minimum of the electrostatic potential in C<sub>82</sub><sup>3-</sup> was found in the position where metal resides in M@C<sub>82</sub> as predicted by calculations (Kobayashi and Nagase 1998; Lu et al. 2000) or shown by experimental X-ray diffraction studies (Takata et al. 2003). At the same time, it was also found that electrostatic potential inside C<sub>80</sub><sup>6-</sup> has no distinguishable minima, and hence there are no distinct bonding sites for metal atoms or clusters in C<sub>80</sub>-I<sub>h</sub>(7). This is indeed confirmed by several computational studies of La<sub>2</sub>@C<sub>80</sub>-I<sub>h</sub>(7) (Kobayashi et al. 1995; Shimotani et al. 2004; Zhang et al. 2007) and Sc<sub>3</sub>N@C<sub>80</sub>-I<sub>h</sub>(7) (Campanera et al. 2002; Gan and Yuan 2006; Kobayashi et al. 2001; Popov and Dunsch 2008; Yanov et al. 2006). For La<sub>2</sub>@C<sub>80</sub> it is shown that there are two almost isoenergetic minima for positions of La atoms, with D<sub>2h</sub> and D<sub>3d</sub> molecular symmetries, and each minimum is multiplied by the group symmetry operations of I<sub>h</sub> group. As a result, La<sub>2</sub> unit exhibits almost free rotation inside C<sub>80</sub> cage, and the charge density of La atoms forms a pentagonal-dodecahedron as revealed by synchrotron radiation powder diffraction study (Nishibori et al. 2001). Another important argument in favor of the ionic model is the carbon cage isomerism of EMFs, which shows a good correlation with the relative stability of the appropriately charged empty cages, as will be discussed in detail below.

Although the ionic model explains some spectroscopic and structural properties of EMFs, there are numerous studies which indicate that this model is oversimplified. While the analysis of MO energy levels in the EMFs and the corresponding empty cages can be indeed interpreted as an electron transfer to the cage from the metal, experimental (Alvarez et al. 2002; Kessler et al.

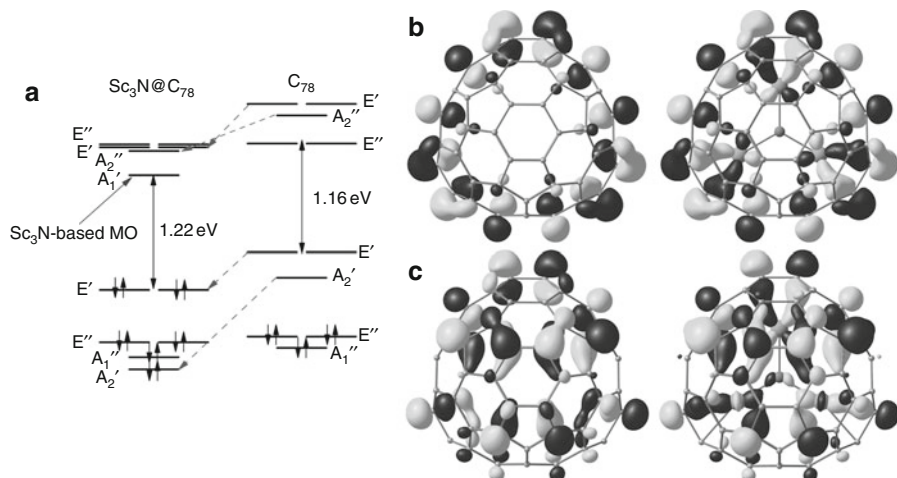


Fig. 19-7

(a) Frontier Kohn-Sham MO levels in  $\text{Sc}_3\text{N}@C_{78}-D_{3h}(5)$  and  $C_{78}-D_{3h}(5)$ , the *dash arrows* show correspondence between the orbitals of the empty cage and  $\text{Sc}_3\text{N}@C_{78}$ ; (b) LUMO ( $A_2'$ ) MO of  $C_{78}$  and corresponding occupied orbital in  $\text{Sc}_3\text{N}@C_{78}$ ; (c) LUMO+1 ( $E'$ , only one component is shown) in  $C_{78}$  and corresponding occupied orbital in  $\text{Sc}_3\text{N}@C_{78}$  (Based on the data from Krause et al. 2006 and Popov 2009)

1997) and theoretical (Campanera et al. 2002; Lu et al. 2000; Muthukumar and Larsson 2008; Nagase et al. 1997; Yang et al. 2008) studies clearly show a substantially non-zero population of  $nd$ -levels of the endohedral metal atoms. The mixing of the cluster and fullerene MOs as well as the corresponding change of the orbital energies in EMF when compared to the MOs of the empty cage are the most apparent for  $\text{Sc}_3\text{N}@C_{78}$  (Fig. 19-7) (Campanera et al. 2002; Krause et al. 2006). In many other EMFs the metal contribution to individual  $\pi$ -MO orbitals of the cage is very small; yet, the significant metal-cage interaction can be also revealed when the electron density distribution is analyzed (Liu et al. 2006; Popov and Dunsch 2008; Wu and Hagelberg 2008; Yang et al. 2008; Popov 2009). This can be best done with the use of promolecule deformation density approach, i.e., by visualizing the changes in the electron density distribution  $\Delta\rho = [\rho(\text{Mol}) - \rho(\text{Ref})]$ , where  $\rho(\text{Mol})$  is the electron density of the molecule under study, while  $\rho(\text{Ref})$  is the electron density of the reference system. A natural choice of the reference system in the studies of EMFs can be either non-interacting metal atoms or clusters (e.g.,  $\text{Sc}_3\text{N}$ ) and corresponding  $C_{2n}$  molecules or metal or cluster cations (e.g.,  $\text{Sc}_3\text{N}^{6+}$ ) and appropriately charged  $C_{2n}$  anions (e.g.,  $C_{2n}^{6-}$ ). In particular, when two sixfold charged ions were taken as a reference, a considerable concentration of the density at Sc atoms was found in all  $\text{Sc}_3\text{N}@C_{2n}$  ( $2n = 68, 78, 80$ ) EMFs (Popov and Dunsch 2008; Popov 2009), the effect referred to by some researchers as “back-donation” (Liu et al. 2006; Wu and Hagelberg 2008). The  $\Delta\rho$  plots have also revealed that metal-cage bonds are not localized (such as, e.g., carbon-carbon bonds) but can be better described by “coordination” bonds such as those found in transition metal complexes (Cortés-Guzmán and Bader 2005).

The cluster-cage bonding in  $\text{Sc}_3\text{N}@C_{78}$  and  $\text{Sc}_3\text{N}@C_{80}$  was also analyzed using the energy decomposition method (Campanera et al. 2002). The authors have shown that after the



$\text{Sc}_3\text{N}^{6+}$  cation is encapsulated inside  $\text{C}_{78,80}^{6-}$  cages, a strong orbital mixing and an electronic reorganization take place.

Computed atomic charges are also much smaller than the values expected for the purely ionic bonding. For instance, net Bader, Mulliken, and NBO charges of the  $\text{Sc}_3\text{N}$  cluster in  $\text{Sc}_3\text{N}@C_{80}$  are +3.50, +2.88, and +2.99, respectively, at the B3LYP/6-311G\* level of theory (Popov and Dunsch 2008); another group reported the net  $\text{Sc}_3\text{N}$  charges of +1.28 (Mulliken), +1.10 (Hirshfeld), +0.94 (Voronoi) (Valencia et al. 2008) at the BP/TZVP level of theory with ZORA relativistic corrections. Note that the charges strongly depend both on the method of theory used to compute wavefunction and on the electron density partitioning, but all reported values are significantly smaller than +6 expected for the ionic  $\text{Sc}_3\text{N}^{6+}@C_{60}^{6-}$ .

In summary, from the molecular orbital point of view, the mechanism of the metal(cluster)-cage interactions in EMFs can be described by the formal transfer of the appropriate number of electrons from the endohedral species to the carbon cage with subsequent coordination of the metal cations by the cage as a “ligand” and reoccupation of the metal *nd* orbitals (see also (Liu et al. 2006) for a more detailed discussion). Note that in most cases there are no special localized orbitals that could be responsible for the cage-to-cluster electron transfer. Instead, this kind of interaction occurs through the overlap of many cage  $\pi$ -orbitals with *nd* orbitals of the metal. One of the consequences of this type of bonding is a spin-charge separation found in the radical-anions of the EMFs with the metal-localized LUMO (such as  $\text{Sc}_3\text{N}@C_{80}$ ,  $\text{La}_2@C_{72,78,80}$ ,  $\text{Ti}_2\text{C}_2@C_{78}$ ). In these anions, the spin density is mostly localized on the metal atoms, however, the changes of the metal charges compared to the neutral state of the EMF molecule are rather small; instead, the surplus charge is mostly delocalized over the carbon cage (Popov and Dunsch 2008).

Since the effect of the metal-cage bonding in EMFs is best revealed in the analysis of the electron density as a whole, rather than by studying the individual MOs, it is natural to use the method based on the analysis of the electron density for the quantitative description of the metal-cage interactions in EMFs. The quantum theory of atoms in molecules (QTAIM) developed by Bader is probably the most refined and well-established method for the analysis of the topology of the electron density frequently used for the revealing and quantifying of the bonding situation between the atoms (Bader 1990; Matta and Boyd 2007). Kobayashi and Nagase analyzed a topology of the electron density distribution in  $\text{Sc}_2@C_{84}$ ,  $\text{Ca}@C_{72}$ , and  $\text{Sc}_2@C_{66}$  using QTAIM (Kobayashi and Nagase 1999, 2002a). Their studies have shown that although the bond critical points (BCPs: critical points of the electron density, in which the density has a minimum along one axis and has a maximum in the plane perpendicular to this direction) could be found between Sc or Ca and certain carbon atoms of the cage, the values of the electron density at BCPs ( $\rho_{bcp}$ ) were very small (0.05 a.u. for Sc-C and 0.01–0.02 a.u. for Ca-C), and the Laplacian of the density ( $\nabla^2\rho_{bcp}$ ) at metal-carbon BCPs was always positive. The authors concluded that such values for these descriptors are signatures of the highly ionic character of the metal-cage bonding. However, care should be taken when the bonding in transition metal compound is analyzed with QTAIM (Cortés-Guzmán and Bader 2005). It was revealed that for transition metals  $\nabla^2\rho_{bcp}$  values are usually positive, while  $\rho_{bcp}$  are small because of the diffuse character of electron distribution (Macchi and Sironi 2003) and hence these values alone cannot be proper descriptors of the bonding situation. Therefore, more specific descriptors should be applied in the analysis of the bonds involving transition metals, and the analysis of the *energy density* appears more useful than the analysis of the electron density alone. While kinetic energy density, *G*, is positive everywhere, potential energy density, *V*, is negative everywhere, and their sum, the total energy density *H*, defines which of the energy

components is dominating. Cremer and Kraka suggested that bonding between the atoms can be considered as covalent if the total energy density at BCP,  $H_{bcP}$ , is negative (Cremer and Kraka 1984).

The in-depth study of the metal-cage and intra-cluster bonding by DFT and QTAIM was recently reported for the four major classes of endohedral metallofullerenes, including monometallofullerenes, dimetallofullerenes, metal-nitride clusterfullerenes, metal-carbide clusterfullerenes, as well as  $Sc_3CH@C_{80}$  and  $Sc_4O_x@C_{80}$  ( $x = 2, 3$ ) (Popov and Dunsch 2009). The analysis of the bond critical point indicators showed that both the intra-cluster and the metal-cage interactions in EMFs were characterized by the negative total energy density, which means that bonding in EMFs exhibits a high degree of covalency. Furthermore, from the point of the electron density distribution, the interior of the EMF molecules was found to be a complex topological object, with many critical points, unpredictable number of the bond paths, and large bond ellipticities, similar to the bonding situation in the complexes of transition metals with  $\pi$ -carbocyclic ligands (Farrugia et al. 2009). In this respect, the analysis of the metal-cage bonding based only on the properties of the bond paths was found to be insufficient, and the metal-cage delocalization indices,  $\delta(M, C)$ , were also analyzed (by definition,  $\delta(M, C)$  is number of the electron pairs shared by the atoms M and C, which is very similar to the “bond order” in Lewis definition). It was found that in the majority of EMFs,  $\delta(M, C)$  values do not exceed 0.25; however, when summed over all metal-cage interactions, values of  $\delta(M, \text{cage})$  close to 2–3 were obtained. While QTAIM atomic charges of the metal atoms were found to be approximately two times smaller than their formal oxidation states, the total number of the electron pairs shared by the metal atoms with the EMF molecule,  $\Delta(M)$ , was found to be close to the typical valence of the given element (► Table 19-4).

To conclude the section on the metal-cage bonding in EMFs, it appears useful to distinguish two ways to determine the charge on the atom in endohedral fullerene: (1) a “formal” charge and (2) the “actual” charge. The formal charge is integer and implies that the metal (cluster)–cage bonding is purely ionic. As such, formal charges do not describe the actual electron distribution in the endohedral fullerenes, but still appear to be useful in understanding the spectroscopic and structural properties of endohedral fullerenes. For instance, compounds with the same formal cage and metal charges exhibit very similar absorption and vibrational spectra. In the next section we will show that the formal charge of the cage largely determines the isomeric structure of a given endohedral fullerene.

The “actual” charge should represent the electron density distribution in the endohedral fullerenes, but unfortunately there are no unique ways to partition the electron density between the atoms. Depending on the definition and the method of theory used to evaluate the charges, they can vary in a large range in the same molecule as already noted for  $Sc_3N@C_{80}$ . However, whatever method is used, computed charges are always considerably smaller than the formal charges, which is a clear manifestation of the covalent contribution to the metal-cage interactions. At the same time, the charges are still considerably large to indicate that ionic contribution to the cluster-cage bonding is also important.

## Isomerism in Endohedral Metallofullerenes: Stability of the Charged Carbon Cages

One of the specific features of the endohedral metallofullerenes is that their carbon cage isomers are usually different from those of the isolated empty fullerenes. This fact can be understood by

■ Table 19-4

QTAIM atomic charges ( $q$ ) of the metal atoms and the clusters, and the metal-cage and metal-cluster electron-pair sharing in EMFs<sup>a</sup>

EMF	$q(M)$ QTAIM	$q(\text{cluster})$ QTAIM	$q(\text{cluster})$ formal	$\delta(M, \text{cluster})$	$\delta(M, \text{cage})$	$\Delta(M)$
$C_2\text{-Ca}@C_{72}$	1.50		2		1.34	1.34
$C_3\text{-Ca}@C_{82}$	1.52		2		1.21	1.22
$C_5\text{-Sc}@C_{82}$	1.60		3		2.71	2.71
$D_3\text{-Sc}_3\text{N}@C_{68}$	1.74	3.45	6	0.81	1.89	2.70
$C_3\text{-Sc}_3\text{N}@C_{80}$	1.76	3.50	6	0.82	1.77	2.59
$D_2\text{-Sc}_2\text{C}_2@C_{84}$	1.72	2.01	4	0.63	2.00	2.63
$C_5\text{-Sc}_3\text{C}_2@C_{80}$	1.67, 1.67	3.30	6	0.86, 0.63	1.87, 2.13	2.73, 2.76
$C_3\text{-Sc}_3\text{CH}@C_{80}$	1.72	3.48	6	0.82	1.82	2.64
$C_1\text{-Sc}_4\text{O}_2@C_{80}$	1.41, 1.75	3.66	6	1.21, 1.32	1.74, 1.41	2.97, 2.65
$C_1\text{-Sc}_4\text{O}_3@C_{80}$	1.87, 1.82	3.47	6	1.43, 1.11	1.07, 1.48	2.52, 2.60
$C_2\text{-Ti}_2\text{C}_2@C_{78}$	1.67	2.17	6	0.82	3.29	4.11
$C_5\text{-Y}@C_{82}$	1.80		3		2.54	2.54
$C_5\text{-Y}_2@C_{82}$	1.35	2.69	4	0.63	2.25	2.88
$C_5\text{-Y}_2@C_{79}\text{N}$	1.52	3.04	5	0.37	2.37	2.74
$C_2\text{-Y}_3\text{N}@C_{78}$	1.90	3.90	6	0.83	1.76	2.61
$D_3\text{-Y}_3\text{N}@C_{80}$	1.90	3.87	6	0.85	1.77	2.62
$D_2\text{-Y}_3\text{N}@C_{88}$	1.93	3.95	6	0.79	1.65	2.44
$C_1\text{-Y}_2\text{C}_2@C_{82}$	1.89	2.40	4	0.66	1.90	2.56
$C_2\text{-La}@C_{72}$	1.91		3		2.72	2.72
$C_{2v}\text{-La}@C_{82}$	1.82		3		2.69	2.69
$D_{2h}\text{-La}_2@C_{80}$	1.65	3.29	6	0.08	2.95	3.04
$C_2\text{-La}_3\text{N}@C_{88}$	1.88	3.92	6	0.95	1.98	2.93
$C_2\text{-La}_3\text{N}@C_{96}$	1.89	3.99	6	0.90	1.89	2.80

<sup>a</sup>  $\delta(M, \text{cluster})$  is the number of the electron pairs shared by the metal with the cluster;  $\delta(M, \text{cage})$  is the number of the electron pairs shared by the metal with the carbon cage;  $\Delta(M)$  is the total number of the electron pairs shared by M with all other atoms of the molecule; when EMF has inequivalent metal atoms, corresponding values are averaged, unless they are significantly different; in the latter cases, different values are listed in the table separated by comma. Based on the QTAIM-B3LYP/6-311G\* calculations from (Popov and Dunsch 2009)

taking into account the electron transfer from the encapsulated species as discussed in the previous section. Using the semiempirical QCFF/PI method, Fowler and Zerbetto have shown that charging dramatically changes relative stabilities of the fullerene isomers (Fowler and Zerbetto 1995b). For instance,  $I_h(7)$  isomer of  $C_{80}$ , being the least stable structure for (+2) and (0) charge states, is the lowest energy structure for (-4) and (-6). In agreement with this finding, it was shown that the most stable isomer of  $\text{La}_2@C_{80}$  has  $I_h(7)$  cage, as opposed to the  $D_2$ -symmetric empty  $C_{80}$  (Kobayashi et al. 1995). Variation of the relative energies of  $C_{82}$  isomers in the negatively charged states was analyzed by Kobayashi and Nagase at the HF/3-21G//AM1 level to rationalize experimentally observed isomers of  $M@C_{82}$  (Kobayashi and Nagase 1997a, 1998). The authors have found that while  $C_2(3)$  is the lowest energy isomer of the neutral  $C_{82}$ , the  $C_{2v}(9)$  cage is the most stable for both  $C_{82}^{2-}$  and  $C_{82}^{3-}$  as well as for  $M@C_{82}$  ( $M=\text{Ca}, \text{Sc}, \text{Y}, \text{La}, \text{etc.}$ )

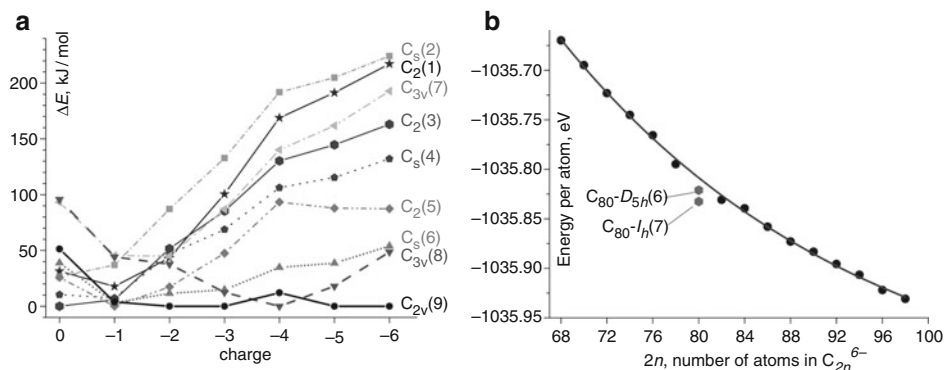


Fig. 19-8

(a) Relative energies IPR isomers of  $C_{82}$  computed at the PBE/TZ2P level in different charge states (Based on the data from Popov 2009); (b) PBE/TZ2P computed energies of the most stable  $C_{2n}^{6-}$  hexaanions on the per-atomic basis plotted as a function of the cage size (Based on the data from Popov and Dunsch 2007a)

(Kobayashi and Nagase 1997a, 1998). This finding is confirmed by experimental  $^{13}\text{C}$  NMR studies of  $\text{La}@C_{82}$  and  $\text{Ce}@C_{82}$  anions (Akasaka et al. 2000; Tsuchiya et al. 2005; Wakahara et al. 2004). Recently, DFT calculations of  $C_{82}^{4-}$  isomers were reported (Valencia et al. 2008) and the  $C_{3v}(8)$  isomer was shown to be the most stable tetraanion, in line with the finding of this cage in the most abundant isomers of  $\text{Sc}_2C_2@C_{82}$  (Iiduka et al. 2006; Nishibori et al. 2006a) and  $\text{Y}_2C_2@C_{82}$  (Inoue et al. 2004; Nishibori et al. 2006b). The data on the relative energies of all IPR  $C_{82}$  isomers in (0)-(−6) charge states obtained at the PBE/TZ2P level (Popov 2009) are summarized in Fig. 19-8a. DFT calculations show that  $C_{2v}(9)$  is the most stable isomer for all charge states starting from (−2), however, there is a change in favor of  $C_{3v}(8)$  for (−4) (Valencia et al. 2008). Note also that starting from (−3) charge state, the IPR isomers  $C_{2v}(9)$ ,  $C_{3v}(8)$ , and  $C_s(6)$  are considerably more stable than the other IPR isomers; as a result, only these isomers are found for  $M^{III}@C_{82}$  and  $M_2C_2@C_{82}$ .

The data on representative fullerenes discussed above show that (1) the relative energies of the fullerene isomers are dramatically affected by the charge and (2) the stability of the isomers of appropriately charged empty fullerenes provides a good estimation to the relative stability of the cage isomers of endohedral fullerenes. Thus, though ionic model is not realistic for the description of the electron density distribution in endohedral metallofullerenes, it can be useful for understanding the carbon cage isomerism of endohedral fullerenes.

In the last decade, the higher yields, increased stability, and broad variety of the formed structures attracted special attention to the family of nitride clusterfullerenes. Their electronic structure may be conceived as a result of a formal sixfold electron transfer from the  $M_3^{III}\text{N}$  cluster to the fullerene. Predicting of the lowest energy isomers of  $M_3\text{N}@C_{2n}$  endohedral fullerenes is a difficult task since, in addition to the carbon cage isomerism, different orientation of the  $M_3\text{N}$  cluster inside the cage can give structures with substantially different relative energies; besides, DFT calculations of the molecules with transition metals are more complex than those of the empty fullerenes. In this respect, attempts were made to predict the possible structures of  $M_3\text{N}@C_{2n}$  molecules based on the calculation for the empty fullerenes.

The simple use of this formal sixfold electron transfer in  $M_3N@C_{2n}$  to predict the most suitable cage isomers capable of encapsulating a nitride cluster was proposed by Poblet and coworkers. It was supposed that only the fullerenes with a considerable gap between LUMO+2 and LUMO+3 (which become HOMO and LUMO, respectively, in the  $C_{2n}^{6-}$  hexaanion and presumably in  $M_3N@C_{2n}$ ) should be considered as suitable hosts for nitride clusters (Campanera et al. 2005). With the application of this criterion, only  $C_{60}$ ,  $C_{78}-D_{3h}(5)$ ,  $C_{80}-I_h(7)$ , and  $C_{80}-D_{5h}(6)$  were found to be suitable cage isomers among all IPR fullerenes in the  $C_{60}-C_{84}$  range. Indeed, besides  $C_{60}$ , which is too small to host a  $Sc_3N$  cluster, only these and no other IPR cage isomers were found for  $Sc_3N@C_{2n}$  clusterfullerenes. Later this work was expanded by considering also all IPR isomer in the  $C_{86}-C_{100}$  range (Valencia et al. 2007), and the isomers with the largest orbital gaps found for  $C_{86}$  and  $C_{88}$  hexaanions ( $D_3(19)$  and  $D_2(35)$ , respectively) were those proved to exist in  $Tb_3N@C_{86}$  and  $Tb_3N@C_{88}$  by single-crystal X-ray diffraction studies (Zuo et al. 2007).

A different approach to the search of the suitable cage isomers for nitride clusterfullerenes is based on the stability of the hexaanions (Popov and Dunsch 2007a, d; Yang et al. 2007a, b). In the view of the correlation found between the relative energies of the empty fullerenes in appropriate charge state and the relative energies of endohedral fullerenes, it was suggested that the suitable cage isomers of  $M_3N@C_{2n}$  should be found among the most stable isomers of  $C_{2n}^{6-}$ . The growing number of endohedral fullerenes violating IPR shows that non-IPR isomers should also be included in the search. Importantly, good correlation was found between the relative energies of the  $C_{2n}^{6-}$  isomers computed at the AM1 and DFT levels of theory (Yang et al. 2007b). Since optimization of the structure of the fullerene at AM1 levels normally takes only about 1–2 min with the standard office computer, this fact dramatically facilitates the search of the stable isomers. That is, screening of *all* possible isomers can be done at AM1 level, and only few lowest energy  $C_{2n}^{6-}$  isomers (and corresponding  $M_3N@C_{2n}$  isomers) can then be studied at the higher – and more computationally demanding – level of theory. By screening through the large number of the  $C_{70}^{6-}$ ,  $C_{76}^{6-}$ , and  $C_{78}^{6-}$  isomers, the molecular structures of  $Sc_3N@C_{70}$  (Yang et al. 2007b),  $M_3N@C_{78}$  ( $M=Dy, Tm$ ) (Popov et al. 2007d), and  $DySc_2N@C_{76}$  (Yang et al. 2007a) were proposed, all violating the IPR. The structural guesses were then confirmed by comparison of the experimental and DFT-computed vibrational spectra.

The full search of the most favorable cage isomers of  $Sc_3N@C_{2n}$  and  $Y_3N@C_{2n}$  ( $2n = 68-98$ ) at the PBE/TZ2P level was reported in 2007 (Popov and Dunsch 2007a). For  $C_{68}-C_{88}$ , both IPR and non-IPR isomers were considered, which however resulted in the huge number of possible structures (for instance, there are totally 81,738 for  $C_{88}$ ). Taking into account that metal atoms in all known non-IPR fullerenes are coordinated to the adjacent pentagon pairs, the authors suggested that only the isomers with such pairs should be considered (while the structures with three or more adjacent pentagons could be omitted). This assumption considerably reduced the number of the isomers (e.g., 16,717 isomers were studied for  $C_{88}$ ), making the computations more feasible.

► **Table 19-5** lists the lowest energy isomers of  $C_{2n}^{6-}$  found in that work with their relative energies and HOMO–LUMO gaps computed at the PBE/TZ2P level; experimentally available structurally characterized EMFs are listed in the last column. Importantly, the isomers shown to exist by single-crystal X-ray studies can be found among the lowest energy isomers of  $C_{2n}^{6-}$ .  $C_{78}-C_2(22,010)$  and  $C_{82}-C_s(39,663)$  isomers were predicted as possible structures of  $M_3N@C_{78}$  and  $M_3N@C_{82}$  (Popov and Dunsch 2007a, d) before their structures were confirmed by single-crystal X-ray studies of  $Gd_3N@C_{78}$  and  $Gd_3N@C_{82}$  (Beavers et al. 2009; Mercado et al. 2008). Even better correlation with experimental data is found if the relative energies of

■ Table 19-5

The lowest energy  $C_{2n}^{6-}$  ( $2n = 68-88$ ) isomers with their relative energies (kJ/mol) and HOMO–LUMO gaps (eV) computed at the PBE/TZ2P level of theory, and the experimentally available EMFs with corresponding carbon cages (Based on the data from Popov and Dunsch 2007a)

$C_{2n}$	Isomer		$\Delta E$	Gap	Exp. EMFs
C <sub>68</sub>	D <sub>3</sub> (6,140)	non-IPR	0.0	1.20	Sc <sub>3</sub> N@C <sub>68</sub>
C <sub>70</sub>	C <sub>2v</sub> (7,854)	non-IPR	0.0	1.24	Sc <sub>3</sub> N@C <sub>70</sub>
C <sub>72</sub>	D <sub>2</sub> (10,611)	non-IPR	0.0	1.12	M <sub>2</sub> @C <sub>72</sub> (M=La, Ce)
C <sub>74</sub>	C <sub>2</sub> (13,295)	non-IPR	0.0	1.22	not known
C <sub>76</sub>	C <sub>5</sub> (17,490)	non-IPR	0.0	1.12	DySc <sub>2</sub> N@C <sub>76</sub>
C <sub>78</sub>	D <sub>3h</sub> (5)	IPR	0.0	1.21	M <sub>2</sub> @C <sub>78</sub> (M=La, Ce), Ti <sub>2</sub> C <sub>2</sub> @C <sub>78</sub> , Sc <sub>3</sub> N@C <sub>78</sub>
	C <sub>2</sub> (22,010)	non-IPR	59.1	1.60	M <sub>3</sub> N@C <sub>78</sub> (M=Dy, Tm, Gd)
C <sub>80</sub>	I <sub>h</sub> (7)	IPR	0.0	1.83	M <sub>2</sub> @C <sub>80</sub> (M=La, Ce), M <sub>3</sub> N@C <sub>80</sub> (M=Sc, Y, Gd–Lu), Sc <sub>3,4</sub> C <sub>2</sub> @C <sub>80</sub> , Sc <sub>4</sub> O <sub>2,3</sub> @C <sub>80</sub>
	D <sub>5h</sub> (6)	IPR	88.2	1.51	Ce <sub>2</sub> @C <sub>80</sub> , M <sub>3</sub> N@C <sub>80</sub> (M=Sc, Y, RE)
C <sub>82</sub>	C <sub>2v</sub> (9) <sup>b</sup>	IPR	0.0	0.79	not known
	C <sub>2v</sub> (39,705) <sup>b</sup>	non-IPR	30.1	1.32	not known
	C <sub>5</sub> (39,663) <sup>b</sup>	non-IPR	61.2	1.42	M <sub>3</sub> N@C <sub>82</sub> (M=Y, Gd, Tm, Dy, Tb)
C <sub>84</sub>	D <sub>2</sub> (21)	IPR	0.0	0.80	not known
	C <sub>5</sub> (51,365)	non-IPR	1.8	1.34	M <sub>3</sub> N@C <sub>84</sub> (M=Y, Gd, Tm, Dy, Tb)
C <sub>86</sub>	D <sub>3</sub> (19)	IPR	0.0	1.51	M <sub>3</sub> N@C <sub>86</sub> (M=Y, Gd, Tm, Dy, Tb)
C <sub>88</sub>	D <sub>2</sub> (35)	IPR	0.0	0.97	M <sub>3</sub> N@C <sub>88</sub> (M=Y, Gd, Tm, Dy, Tb)

<sup>b</sup>For Y<sub>3</sub>N@C<sub>82</sub>, the relative energies for isomers C<sub>2v</sub>(9), C<sub>2v</sub>(39,705), and C<sub>5</sub>(39,663) are 29.6, 0.0, and 32.6 kJ/mol, respectively, at the PBE/TZ2P level

Sc<sub>3</sub>N@C<sub>2n</sub> and Y<sub>3</sub>N@C<sub>2n</sub> isomers are considered (Popov and Dunsch 2007a). It is remarkable that C<sub>2n</sub><sup>6-</sup> isomers with high thermodynamic stability (i.e., low relative energy) quite often exhibit high kinetic stability (i.e., large HOMO–LUMO gap). As a result, the IPR isomers proposed by the group of Poblet (Campanera et al. 2005; Valencia et al. 2007) in most cases coincide with predictions based on the relative stability of the hexaanions (Popov and Dunsch 2007a).

The broad range of the fullerene sizes studied (Popov and Dunsch 2007a) enabled the authors to follow the general trends in their stabilities. To compare the energies of the fullerenes of different size, the absolute energies were normalized to the number of atoms in the given fullerene. Figure 19-8b plots the normalized energies of the most stable C<sub>2n</sub><sup>6-</sup> isomers versus the number of atoms. The smooth decrease of the energy with the increase of the fullerene size is the result of a combination of two factors: (1) the decrease of the curvature of the cage, which results in smaller curvature-induced strain, and (2) the decrease of the on-site Coulomb repulsions of six surplus electrons in C<sub>2n</sub><sup>6-</sup> with the increase of the cage size. There is, however, a significant deviation from the smooth curve found for C<sub>80</sub>–I<sub>h</sub>(7) and C<sub>80</sub>–D<sub>5h</sub>(6) isomers. These isomers are 185 and 98 kJ/mol more stable than they might be if they were like all other fullerenes (i.e., like those which obey the smooth decay in the normalized energy). The enhanced stability of the two C<sub>80</sub><sup>6-</sup> isomers explains the increased yield of M<sub>3</sub>N@C<sub>80</sub> compared to all other cage sizes. Besides, it explains why the C<sub>80</sub>–I<sub>h</sub>(7) isomer is always the most preferable structure

in other clusterfullerenes with formal sixfold electron transfer to the cage, such as  $\text{La}_2@C_{80}$ ,  $\text{Sc}_4\text{O}_{2,3}@C_{80}$  (Stevenson et al. 2008), and  $\text{Sc}_4\text{C}_2@C_{80}$  (Wang et al. 2009).

The exclusive stability of the  $I_h(7)$  and  $D_{5h}(6)$  isomers of  $C_{80}^{6-}$  can be rationalized using the concept of hexagon indices (Raghavachari 1992) discussed in section “Structures and Stability of Empty Fullerenes.” The lowest-strain condition (all indices are equal) is fulfilled only for  $C_{60}-I_h(1)$ ,  $C_{80}-I_h(7)$  and  $C_{80}-D_{5h}(6)$  in the whole range fullerenes  $C_{2n}$  with  $2n < 120$  (Fowler and Manolopoulos 1995a). Thus, the exceptional stability of two  $C_{80}^{6-}$  isomers can be explained by the favorable distribution of the pentagons, which leads to the least steric strain. Moreover, the list of the least-strained IPR isomers (► [Table 19-2](#)) perfectly corresponds to the lowest energy IPR isomers of  $C_{76}^{6-}-C_{90}^{6-}$  (Popov and Dunsch 2007a). For larger cages these conditions are less instructive, because many of the IPR isomers satisfy them. Interestingly, the relative energies of the IPR  $C_{2n}^{6-}$  isomers follow the rationalization of the stability based on the steric strain much better than the relative energies of the uncharged IPR fullerenes, which usually violate the requirement of the minimized strain (the only exclusions are  $C_{84}$  and  $C_{90}$ ; see ► [Table 19-2](#)). Very recently, this phenomenon was clarified by Poblet and co-workers (Rodríguez-Fortea et al. 2010). The authors have suggested that the relative stabilities of the isomers of multiply charged fullerene anions are largely determined by the on-site Coulomb repulsion. Since the negative charge in anions is mostly localized on the pentagons because of their non-planarity, the lowest-energy structures should be those in which the maximal separation (and hence the most uniform distribution) of the pentagons is achieved. The authors have constructed the inverse pentagon separation index to show that its correlation with the relative stabilities of the isomers is improving with the increase of the charge. Thus, minimization of the on-site Coulomb repulsion and minimization of the steric strain are achieved by fulfillment of the same condition, namely the most uniform distribution of the pentagons. If for the non-charged fullerenes the steric strain factor can be outweighed by other factors such as stability of the  $\pi$ -system (and hence the lowest strain condition is usually violated), with the increase of the negative charge on the cage the Coulomb repulsion sooner or later outweighs all other factors. Therefore, to predict the lowest energy isomers of the EMFs with high formal charge of the cage (such as  $M_3N@C_{2n}$ ) one can apply the same arguments as were developed in early 1990s to find the isomers of empty fullerenes with the lowest steric strain.

## Isomerism in Endohedral Metallofullerenes: The Cluster Size Factor

The carbon cage stability is very important in determining the molecular structure of endohedral fullerenes, however, the isolated structures are not always based on the lowest energy isomers of the hollow anions. In addition to the high stability, the cage should also provide a suitable shape for enclosed metal atoms or clusters; that is, there should be enough inner space in the cage for the endohedral species. If then a fullerene has adjacent pentagon pairs, they should be located in such a way that their coordination by the endohedral metal atoms is possible. This factor can be especially important for the nitride clusterfullerenes since the shape of the cluster itself imposes significant limitations on the possible location of the binding sites.

► [Figure 19-9a](#) plots the relative energies of the twenty lowest-energy isomers of  $C_{72}^{6-}$  and corresponding  $\text{Sc}_3\text{N}@C_{72}$  isomers calculated at the PBE/TZ2P level. The significant difference between the two sets of data is observed. While the most stable isomer of  $C_{72}^{6-}$  is  $D_2(10611)$  (Slanina et al. 2006a; Popov and Dunsch 2007a), this cage isomer is destabilized for



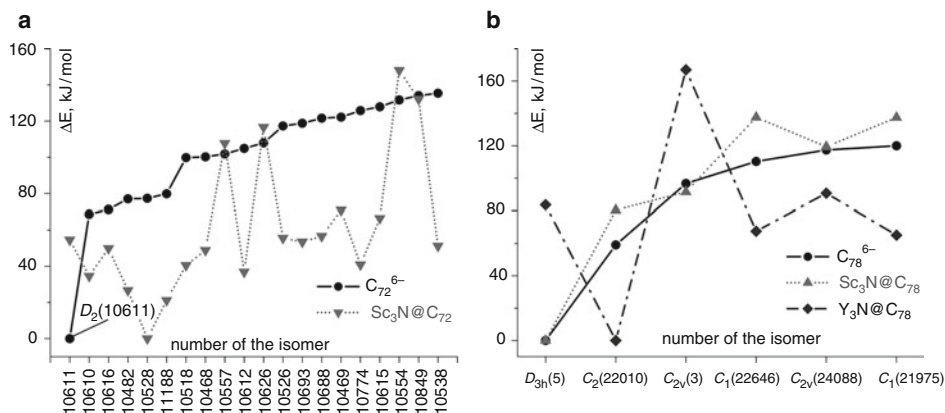


Fig. 19-9

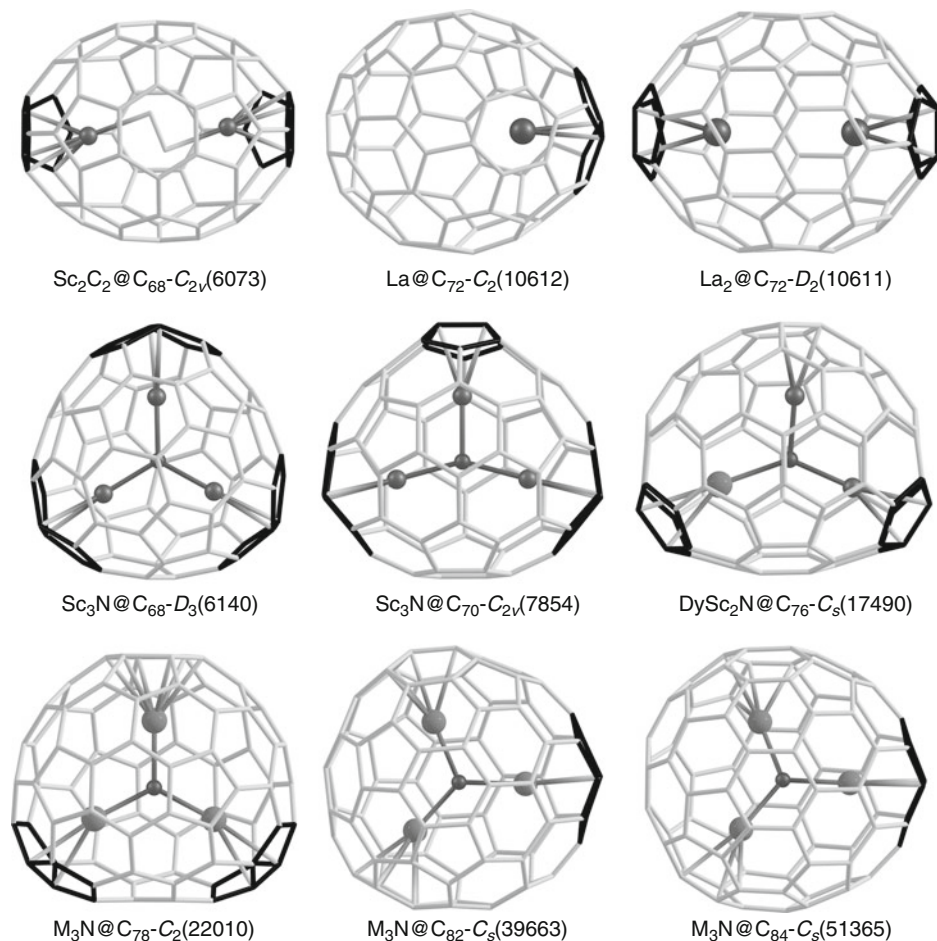
(a) Relative energies of  $C_{72}^{6-}$  and corresponding  $Sc_3N@C_{72}$  isomer computed at the PBE/TZ2P level (Based on the data from Popov and Dunsch 2007a); (b) Relative energies of  $C_{78}^{6-}$  and corresponding  $Sc_3N@C_{78}$  and  $Y_3N@C_{78}$  isomer computed at the PBE/TZ2P level (Based on the data from Popov et al. 2007d)

$Sc_3N@C_{72}$ , and the lowest energy is found for  $Sc_3N@C_{72}$  with  $C_s(10528)$  cage. The explanation of this phenomenon becomes clear when the structures of the cage isomers are analyzed.  $C_{72}-D_2(10,611)$  has elongated shape with two adjacent pentagon pairs on the opposite poles of the cage (Fig. 19-10). It is impossible to coordinate both pentagon pairs at once with the Sc atoms of the triangular  $Sc_3N$  cluster, and hence one pentagon pair in  $Sc_3N@C_{72}-D_2(10,611)$  is not stabilized by the metal, which explains the high relative energy found for this isomer by theory. The lowest energy  $C_{72}^{6-}$  isomer with favorable location of adjacent pentagon pairs is  $C_s(10528)$ , and it corresponds to the most stable isomer of  $Sc_3N@C_{72}$ . However, this isomer is based on the relatively unstable carbon cage and, besides, it has a small HOMO-LUMO gap (0.39 eV at the PBE/TZ2P level). As a result, the  $Sc_3N@C_{72}$  nitride clusterfullerene has never been observed experimentally. Similar situation was also found for  $C_{74}^{6-}$  and  $Sc_3N@C_{74}$ , which also has never been observed. Since the bimetallic cluster is more flexible, the steric factor is less important for dimetallofullerenes, and  $La_2@C_{72}$  is based on the lowest energy  $D_2(10,611)$  cage isomer (Kato et al. 2003; Lu et al. 2008).

A different situation was found for the clusterfullerenes based on  $C_{78}$  (Popov et al. 2007d).

Figure 19-9b compares relative energies of the lowest energy isomers of  $C_{78}^{6-}$  and  $M_3N@C_{78}$  ( $M=Sc, Y$ ). The most stable  $C_{78}^{6-}$  isomer is IPR  $D_{3h}(5)$ , which is followed by the non-IPR  $C_2(22,010)$  isomer with two adjacent pentagon pairs. The relative energies of  $Sc_3N@C_{78}$  isomers closely follow those of  $C_{78}^{6-}$ , which agrees with the formation of the  $Sc_3N@C_{78}-D_{3h}(5)$  isomer (Olmstead et al. 2001).  $C_{78}-D_{3h}(5)$  was also proved for  $M_2@C_{78}$  ( $M=La, Ce$ ) and  $Ti_2C_2@C_{78}$  (Cao et al. 2004, 2008; Tan and Lu 2005; Sato et al. 2006; Yumura et al. 2005; Yamada et al. 2008). However, with the increase of the cluster size from  $Sc_3N$  to  $Y_3N$  the relative energies of the  $M_3N@C_{78}$  isomers are changed dramatically. The isomer based on the  $D_{3h}(5)$  cage is significantly destabilized, and the lowest energy is now found for the  $Y_3N@C_{78}-C_2(22,010)$  (84 kJ/mol more stable than  $Y_3N@C_{78}-D_{3h}(5)$ ). The dramatic change in the stability of the isomers can be explained by insufficient size of the  $C_{78}-D_{3h}(5)$  cage for encapsulation of the clusters larger than  $Sc_3N$ . As a result,  $Y_3N$  cluster is forced to be pyramidal in  $Y_3N@C_{78}-D_{3h}(5)$  (nitrogen atoms





■ Fig. 19-10

Molecular structures of the non-IPR endohedral metallofullerenes. Carbon cages are shown in grey except for the adjacent pentagon pairs, which are shown in black. In  $\text{M}_3\text{N}@C_{78}$ ,  $\text{M}_3\text{N}@C_{82}$ , and  $\text{M}_3\text{N}@C_{84}$ , M can be Y, Gd, Dy, Tm, Tb, and possibly some other lanthanides

is displaced from the plane of the metal atoms by 0.554 Å), which is an indication of the strong strain exerted by the cage. On the contrary, the inner space in  $C_{78}\text{-}C_2(22,010)$  isomer is sufficient to retain the planar shape of the  $\text{Y}_3\text{N}$  cluster (● Fig. 19-10). Results of these calculations were supported by experimental spectroscopic studies of  $\text{Tm}_3\text{N}@C_{78}$  and the major isomer of  $\text{Dy}_3\text{N}@C_{78}$  (Popov et al. 2007d) and by single-crystal X-ray diffraction studies of  $\text{Gd}_3\text{N}@C_{78}$  (Beavers et al. 2009).

$\text{M}_3\text{N}@C_{80}\text{-}I_h(7)$  represent another important example of the cluster size influence on the stability of the clusterfullerenes (Popov and Dunsch 2007a). The lowest energy isomers for  $C_{80}^{6-}$  and  $\text{Sc}_3\text{N}@C_{80}$  are  $I_h(7)$  and  $D_{5h}(6)$ , and there is a gap of approximately 80 kJ/mol between these two isomers and the gap of approximately 120 kJ/mol between  $D_{5h}(6)$  and all other, less stable isomers. Stability order of  $C_{80}^{6-}$  and  $\text{Sc}_3\text{N}@C_{80}$  isomers is rather close, but relative energies

of unstable  $\text{Sc}_3\text{N}@C_{80}$  isomers are 20–40 kJ/mol smaller than those in  $C_{80}^{6-}$ . These data agree with formation of  $\text{Sc}_3\text{N}@C_{80}-I_h(7)$  as the most abundant product of the  $\text{Sc}_3\text{N}@C_{2n}$  clusterfullerene synthesis, followed by  $\text{Sc}_3\text{N}@C_{80}-D_{5h}(6)$  as the second most abundant structure. With the increase of the cluster size to the  $\text{Y}_3\text{N}$ , the  $I_h(7)$  isomer is still the most stable one, and the energy difference between  $I_h(7)$  and  $D_{5h}(6)$  isomers is almost the same as in the  $\text{Sc}_3\text{N}@C_{80}$  series, but all other isomers of  $\text{Y}_3\text{N}@C_{80}$  are significantly stabilized with respect to the  $I_h(7)$  isomer. For instance, relative energies of the  $D_{5h}(6)$  and non-IPR  $C_1(28325)$  isomers are quite close (70.2 and 90.0 kJ/mol, respectively). Similar to the case of  $\text{M}_3\text{N}@C_{78}$ , this can be explained by the relatively small size of almost spherical  $C_{80}-I_h(7)$  and  $C_{80}-D_{5h}(6)$  cages, which leads to the increase of the strain when large  $\text{M}_3\text{N}$  clusters are encapsulated. As a result,  $\text{M}_3\text{N}@C_{80}-I_h(7)$  is still the most abundant nitride clusterfullerene for the clusters up to the size of  $\text{Gd}_3\text{N}$ , but overall yields are suppressed compared to the clusterfullerenes with smaller clusters (Krause and Dunsch 2005). For the larger cluster size ( $\text{M}=\text{Nd}$ ,  $\text{Pr}$ ,  $\text{Ce}$ ,  $\text{La}$ ) Echegoyen and coworkers have shown that the larger cages (in particular,  $C_{88}$ ) are produced in higher yield than that of  $\text{M}_3\text{N}@C_{80}$  (Chaur et al. 2008).

## Violation of the Isolated Pentagon Rule in Endohedral Metallofullerenes

The specific feature of endohedral fullerenes is that the isolated pentagon rule, which imposes a strict limitation on the possible isomers of empty fullerenes, is often violated when a metal or a cluster are encapsulated inside the cage. Such possibility was first suggested by Kobayashi et al. in theoretical studies of  $\text{Ca}@C_{72}$  isomers (Kobayashi and Nagase 1997b), and the first experimental evidence was provided in 2000 when  $\text{Sc}_2@C_{66}-C_{2v}(4,348)$  (Wang et al. 2000a) and  $\text{Sc}_3\text{N}@C_{68}-D_3(6,140)$  (Stevenson et al. 2000) were isolated. Since that time, a lot of non-IPR endohedral fullerenes have been reported (► Fig. 19-10), including  $\text{Sc}_2\text{C}_2@C_{68}-C_{2v}(6,073)$  (Shi et al. 2006),  $\text{Sc}_3\text{N}@C_{70}-C_{2v}(7,854)$  (Yang et al. 2007b),  $\text{La}@C_{72}-C_2(10,612)$  (Wakahara et al. 2006),  $\text{La}_2@C_{72}-D_2(10,611)$  (Kato et al. 2003; Lu et al. 2008),  $\text{DySc}_2\text{N}@C_{76}-C_s(17,490)$  (Yang et al. 2007a),  $\text{M}_3\text{N}@C_{78}-C_2(22,010)$  ( $\text{M}=\text{Dy}$ ,  $\text{Tm}$ ,  $\text{Gd}$ ) (Beavers et al. 2009; Popov et al. 2007d),  $\text{Gd}_3\text{N}@C_{82}-C_s(39,663)$  (Mercado et al. 2008), and  $\text{M}_3\text{N}@C_{84}-C_s(51,365)$  ( $\text{M}=\text{Tb}$ ,  $\text{Gd}$ ,  $\text{Tm}$ ) (Beavers et al. 2006; Zuo et al. 2008). The non-IPR isomers were also proposed for  $\text{Sc}_2@C_{76}-C_s(17,490)$  (Popov and Dunsch 2007a),  $\text{Ca}@C_{72}-C_2(10,612)$  or  $C_{2v}(11,188)$  (Kobayashi and Nagase 1997b; Nagase et al. 1999) and the minor isomer of  $\text{Yb}@C_{74}$ ,  $C_1(13,393)$  or  $C_1(14,049)$  (Slanina et al. 2006b). The state of the art in the studies of non-IPR fullerenes has been recently reviewed (Tan et al. 2009).

The tendency to violate the IPR in endohedral fullerenes can be explained by the changes of the relative energies of the fullerene isomers with the increase of the cage charge. It was shown already in 1995 that for  $C_{60}$ , the non-IPR  $C_{2v}(1,809)$  isomer with two pairs of adjacent pentagons is substantially less stable than the IPR isomer in the neutrally charge state, but with the increase of the negative charge on the cage, the difference in the relative energies is diminishing, reaching almost zero for  $(-4)$  and inverting for  $(-6)$  states (Fowler and Zerbetto 1995b). Recently, semiempirical and DFT calculations for the whole set of 6,332 isomers of  $C_{68}$  in 0,  $(-2)$ ,  $(-4)$ , and  $(-6)$  charge states were reported (Chen et al. 2008). This study has shown that the lowest energy isomers of  $C_{68}^{4-}$  and  $C_{68}^{6-}$  are  $C_{2v}(6,073)$  and  $D_3(6140)$ , in agreement with isolation of these isomers for  $\text{Sc}_2\text{C}_2@C_{68}$  (Shi et al. 2006) and  $\text{Sc}_3\text{N}@C_{68}$  (Olmstead et al. 2003; Stevenson et al. 2000), respectively. By plotting the relative energies of the isomers of the same

charge versus the number of pentagon adjacencies, the authors have found that the penalty for a pentagon adjacency is decreasing from 92 kJ/mol in  $C_{68}$  to 70 kJ/mol in  $C_{68}^{6-}$  at the AM1 level, confirming that the increase of the charge stabilizes pentagon adjacencies.

An explanation of the stabilization of the pentagon adjacencies in metallofullerenes was proposed by Slanina et al. (2006a). The authors noted that the pentalene (a unit of two fused pentagons) is an  $8\pi$  anti-aromatic system in the neutrally charged state, but becomes  $10\pi$  aromatic in the dianionic state (Zywietz et al. 1998). In a similar fashion, when the metal in the non-IPR endohedral fullerene is coordinated to the pentagon pair, it donates two electrons to the pentalene unit to make it aromatic. This reasoning agrees with the fact that the maximum number of pentagon pairs found in endohedral fullerenes is equal to the half of the formal charge of the cage: three pairs for (6<sup>-</sup>) charge as in  $Sc_3N@C_{68}$  (Olmstead et al. 2003; Stevenson et al. 2000) or  $Sc_3N@C_{70}$  (Yang et al. 2007b), two pairs for (4<sup>-</sup>) state as in  $Sc_2C_2@C_{68}$  (Shi et al. 2006), and one pair for (3<sup>-</sup>) and (2<sup>-</sup>) states as in  $La@C_{72}$  (Wakahara et al. 2006) and  $Ca@C_{72}$  (Kobayashi and Nagase 1997b).

A correlation of the total number of adjacent pentagon pairs in the lowest-energy isomers of  $C_{2n}^{6-}$  ( $2n = 68-88$ ) with the cage size was revealed in (Popov and Dunsch 2007a). The authors found a pronounced tendency to decrease the number of pentagon pairs in the molecules with the increase of the cage size: while three pairs are common for  $C_{68}^{6-}$  and  $C_{70}^{6-}$  isomers, two and one pairs are preferable for  $C_{72}^{6-}-C_{78}^{6-}$  and  $C_{80}^{6-}-C_{86}^{6-}$ , respectively. At the same time, relative energies of the non-IPR isomers are increasing with respect to the IPR isomers, and starting from  $C_{86}$  formation of the non-IPR fullerenes is not expected (at least, for the cages with the formal charge of 6<sup>-</sup> and smaller). Indeed, the largest cage reported to date for any non-IPR fullerene is  $C_{84}-C_s$  (51365) (Beavers et al. 2006; Zuo et al. 2008). This tendency agrees with the increase of energy penalty for the adjacent pentagon pair in the empty fullerenes with increase of the cage size as discussed in the section "The Isolated Pentagon Rule and Steric Strain." With the increase of the cage size a more uniform distribution of the pentagon-induced strain over the fullerene is possible and hence, localization of such a strain in pentagon adjacencies should become more unfavorable than for the smaller cages. Besides, for the charged cages, the influence of the charging of the fullerene should be diminished with the growth of the cage size and hence its stabilizing role for the pentagon adjacencies is leveled down for larger fullerenes.

## Structures and Stability of Fullerene Derivatives

### Addition of $X_2$ to $C_{60}$ – Isomers of $C_{60}X_2$ and General Considerations

The  $C_{60}$  molecule has two types of C–C bonds, hexagon/hexagon (hex/hex) edges and pentagon/hexagon (pent/hex) edges. Determination of their bondlengths by different experimental and theoretical methods gives the values of ca 1.40 and 1.45 Å, respectively. As might be expected, these values fall in the range of the bondlengths typical for conjugated systems; yet, they also show that there are formal *double* and *single* bonds in  $C_{60}$ , and it is more appropriate to call it polyalkene rather than superaromatic molecule. The chemical properties of fullerenes are to a large extent determined by the presence of the conjugated double bonds, and vast majority of fullerene reactions are *addition* reactions. We will not cover here the cycloaddition, mainly because quantum chemical approaches are not so helpful in predicting and elucidation molecular structures of the reaction products. Thus, we will focus on the addition of atoms or groups

that form single bonds to the fullerene core (i.e., atoms or radicals, “X” hereafter). Such reactions, on the one hand, often occur at rather high temperatures allowing close-to-equilibrium distribution of the products and, on the other hand, addition of such groups allows multiple possibilities from the point of the distribution of the groups on the surface of the fullerene. For instance, there are 23 possible isomers of  $C_{60}X_2$ , 4,190 isomers of  $C_{60}X_4$ , 4,184,70 isomers of  $C_{60}X_6$ , and the number of possible isomers is growing rapidly with the further increase of the number of the added groups (Balasubramanian 1991). It is therefore desirable to find the principles which govern addition of the addends to the fullerenes, the task to be naturally addressed by theoreticians. It should be also noted that equilibrium or close-to-equilibrium distribution of the products in the addition reaction (i.e., thermodynamic control) is a necessary prerequisite for the conclusions based on the relative energies of isomers to be valid. Otherwise, kinetic factors can be equally or even more important than the relative stability of the isomers, and theoretical predictions of the products are severely complicated.

All possible isomers which can be obtained by the addition of two hydrogen atoms to  $C_{60}$  (addition of the odd number of groups leads to the highly reactive radicals and therefore is not considered here) were studied at the PM3 level of theory by Dixon and coworkers (Matsuzawa et al. 1992). An AM1 study of the relative stabilities of  $C_{60}X_2$  isomers for  $X=H, F, Cl, Br, CH_3$ , and  $t-C_4H_9$  was reported in 2003 (Clare and Kepert 2003a). Let us consider several possible isomers of  $C_{60}X_2$  (Fig. 19-11a). The simplest addition pathway is when two X groups are added to one double bond of  $C_{60}$ ; the rest of the  $\pi$ -system of the fullerene remains unchanged (in other words, this is 1,2-addition to a cyclohexatriene). If then two groups are attached to one hexagon in *para* position (1,4-addition to a cyclohexatriene), the  $\pi$ -system of the fullerene has to be adjusted by relocating one double bond to the pent/hex edge. All other variants of addition require more pronounced changes in the  $\pi$ -system of  $C_{60}$  and lead to the larger number of double bonds in pentagons (DBIPs). It was discovered that the number of DBIPs is an important parameter showing perfect correlation with the stability of the isomers of  $C_{60}X_2$  (Fig. 19-11b): the larger the number of DBIPs, the lower stability of the given isomer (Matsuzawa et al. 1992).

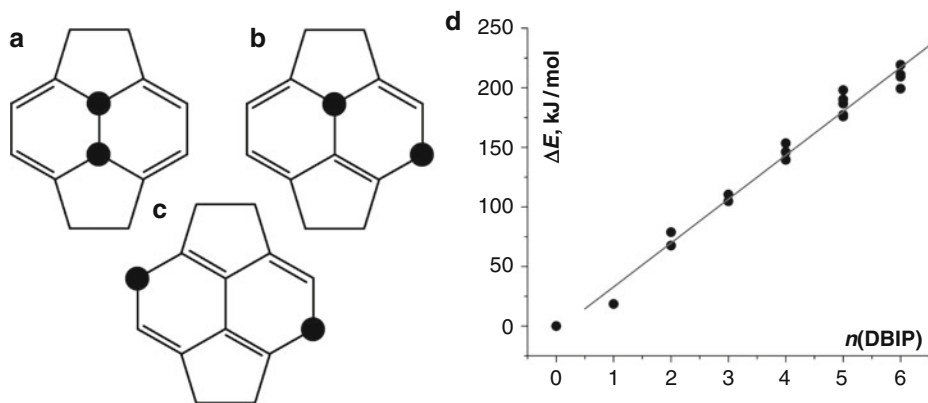


Fig. 19-11

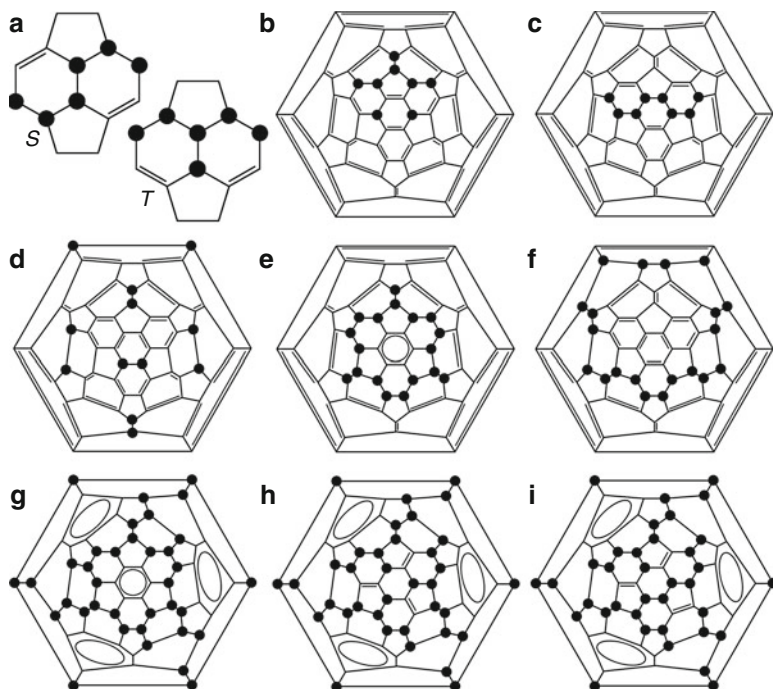
(a)–(c) Fragments of the lowest energy isomers of  $C_{60}H_2$ : (a) 1,2-addition; (b) 1,4-addition; (d) relative energies of  $C_{60}H_2$  isomers computed at the AM1 level as a function of the number of double bonds in pentagons (DBIPs) (Based on the data from Clare and Kepert 2003a)

From the slope of the fitted line, the penalty for each DBIP in  $C_{60}H_2$  can be estimated as 36 and 37 kJ/mol at the PM3 and AM1 levels, respectively. The penalty is virtually independent on the nature of X, being 39 kJ/mol for  $C_{60}F_2$  and 37 kJ/mol for  $C_{60}(t-C_4H_9)_2$  at the AM1 level (Clare et al. 2003a). Obviously, “1,2”-addition should be the most preferable from the energetic point of view, and 1,2- $C_{60}X_2$  is indeed the most stable isomer for X=H and F (Dixon et al. 1992; Clare et al. 2003a) in good agreement with the experimental structures of  $C_{60}H_2$  (Henderson and Cahill 1993) and  $C_{60}F_2$  (Boltalina et al. 2000b). However, in the 1,2- $C_{60}X_2$ , the X groups are experiencing eclipsing interactions. With the increase of the size of the groups, the influence of the steric factor is increasing and can balance the destabilizing effect of DBIP. Indeed, either semiempirical or DFT calculations show that for the bulky groups (such as Br or  $CF_3$ ), 1,4-addition is more preferable (Dixon et al. 1992; Clare and Kepert 2003a; Goryunkov et al. 2003). Furthermore, for even larger groups such as  $t-C_4H_9$ , the isomer with two DBIPs and  $t-C_4H_9$  groups on different hexagons (⦿ Fig. 19-11d) is the most stable at the B3LYP/6-31G\*//AM1 level (at the same time, AM1 method predicts that 1,4- $C_{60}(C_4H_9)_2$  is the lowest energy isomer) (Clare and Kepert 2003a).

The studies of  $C_{60}X_2$  isomers allow one to conclude that the structures of the products of the multiple addition of X groups should be a result of the interplay of at least two factors: (1) destabilizing double bonds in pentagons and (2) destabilizing eclipsing interactions of bulky groups. It can be expected that for the relatively small atoms such as H or F, multiple 1,2-addition is preferable, while for the bulky groups, multiple 1,4-addition is to be expected. Detailed studies of the multiple additions of various groups (in particular, H and Br) to fullerenes performed by Clare and Kepert in 1990s using AM1 method confirmed these suggestions (Clare and Kepert 1993, 1994a, b, c, 1995a, b, 1999a, b, 2002a; Kepert and Clare 1996). In brief, the methodology of the authors included a search of the most stable isomers of  $C_{60}X_n$ , sorting out majority of the unstable structures, and then a search of the most stable isomers of  $C_{60}X_{n+2}$  based on the several most stable isomers of  $C_{60}X_n$ . Gradual increase of  $n$  allowed Clare and Kepert to cover broad range of compositions, reveal some general principles of the multiple addition to  $C_{60}$  and other fullerenes, and predict several addition patterns which were indeed found later in the experimental studies. In the remaining parts of this chapter, we will discuss several examples of the addition patterns to  $C_{60}$  and  $C_{70}$ .

## Addition of H and F to $C_{60}$ – Contiguous Addition, Benzene Rings, and Failures of AM1

Early on semiempirical calculations of  $C_{60}H_2$  and  $C_{60}F_2$  have shown that 1,2-isomers are 18–19 kJ/mol lower in energy than 1,4-isomers, and then all other structures are substantially less stable (Dixon et al. 1992; Matsuzawa et al. 1992; Clare and Kepert 1993). Based on this fact, in their investigation of the multiple addition of hydrogen atoms to  $C_{60}$ , Clare and Kepert considered only 1,2-addition (addition to hex/hex edges). In the AM1 study (Clare and Kepert 1993), they have found that the most energetically favorable would be consequent addition of  $H_2$  molecules to hex/hex edges in a pathway, which eventually leads to  $T_h$ -symmetric  $C_{60}H_{12}$  with all CH–CH edges separated from each other (⦿ Fig. 19-12d). While this addition pattern has never been experimentally verified for  $C_{60}H_{12}$  or  $C_{60}F_{12}$ , it was indeed proved for many hexakis-cycloadducts such as  $C_{60}(C(COOEt)_2)_6$  (Lamparth et al. 1995; Hirsch and Vostrowsky 2001).



■ Fig. 19-12

**Addition patterns typical for small groups (H, F). (a) S and T addition motifs; (b) lowest energy C<sub>5</sub> isomer of C<sub>60</sub>F<sub>8</sub>; (c) C<sub>5</sub>-C<sub>60</sub>F<sub>8</sub> with S-motif; (d) T<sub>h</sub>-C<sub>60</sub>X<sub>12</sub> with isolated CX-CX edges; (e) crown C<sub>3v</sub>-C<sub>60</sub>X<sub>18</sub> with isolate benzene ring; (f) D<sub>5d</sub>-C<sub>60</sub>X<sub>20</sub> with S-type loop around equator; (g) T-C<sub>60</sub>X<sub>36</sub>; (h) C<sub>3</sub>-C<sub>60</sub>X<sub>36</sub>; (i) C<sub>1</sub>-C<sub>60</sub>X<sub>36</sub>**

Further addition to hex/hex edges in T<sub>h</sub>-C<sub>60</sub>H<sub>12</sub> inevitably requires formation of longer CH-(CH)<sub>x</sub>-CH strings. It was, however, found that formation of C<sub>6</sub>H<sub>6</sub> is energetically unfavorable, and -(CH)<sub>x</sub>- strings should be built up from the edge-sharing C<sub>6</sub>H<sub>4</sub> hexagons. Two motifs of the string growth, S and T (● Fig. 19-12a), have been indicated (Clare and Kepert 1994b).

Among many addition patterns studied by Clare and Kepert for C<sub>60</sub>H<sub>n</sub> (n ≤ 20), two are of particular interest. For C<sub>60</sub>H<sub>18</sub>, C<sub>3v</sub>-symmetric “crown” structure built from combination of S and T motifs (● Fig. 19-12e) was shown to be one of the most stable isomers (Clare and Kepert 1994b). In this molecule, -(CH)<sub>x</sub>- string forms a loop, which isolates one hexagon from the rest of the π-system. The isolated hexagon is highly aromatic, and the carbon cage is flattened in its neighborhood. Discovered first in 1994 in the theoretical study, in 1996 this addition pattern was proved by <sup>1</sup>H NMR spectroscopy for the experimentally available C<sub>60</sub>H<sub>18</sub> (Darwish et al. 1996), and later the same pattern was found in C<sub>60</sub>F<sub>18</sub> (Neretin et al. 2000). Consecutive extension of the S-motif leads to the closure of the -(CH)<sub>20</sub>- string in a loop around the fullerene equator with formation of the D<sub>5d</sub>-symmetric C<sub>60</sub>H<sub>20</sub> (● Fig. 19-12f) (Clare and Kepert 1994a). This addition pattern was found experimentally in C<sub>60</sub>F<sub>20</sub> (Boltalina et al. 2001), whose structure was recently confirmed by a single-crystal X-ray diffraction study (Shustova et al. 2010).



The crown motif with isolated benzene-like ring proposed for  $C_{60}H_{18}$  was then found common for highly hydrogenated  $C_{60}$  (Clare and Kepert 1994a, b, 1999a). In particular,  $C_{60}H_{36}$  was studied in detail because a compound with this composition was among the first  $C_{60}$  derivatives ever synthesized by different methods (Haufler et al. 1990; Attalla et al. 1993; Ruchardt et al. 1993), but its structure remained unclear for more than a decade. For  $C_{60}H_{36}$ , combination of several crown motifs can lead up to four isolated benzene ring as in the  $T$ -symmetric isomer (► Fig. 19-12g), but in the AM1 studies some isomers with two or three benzene rings were found to be equally stable (Clare and Kepert 1999a). Almost identical results were obtained at the AM1 level for isomers of  $C_{60}F_{36}$  (Clare and Kepert 1999a), whose structure also could not be unambiguously elucidated in the first synthetic studies. It was also found in the studies of  $C_{60}X_{36}$  and  $C_{60}X_{48}$  that double bonds in pentagons are not destabilizing any more at high degrees of functionalization (Clare and Kepert 1997, 1999a, 2002a). For instance, the most stable isomers of  $C_{60}F_{48}$  have all their six double bonds in pentagons (Clare and Kepert 1997).

In early 2000s, when routine DFT calculations have become feasible for the fullerene derivatives, Clare and Kepert reconsidered some of their earlier results by comparing AM1 to B3LYP/6-31G\*//AM1. One of the main conclusions of these studies was the understanding that one should treat results of AM1 calculations with caution.

First, it was found that AM1 underestimated the energy difference between 1,2 and 1,4-isomers of  $C_{60}X_2$  by ca 10 kJ/mol (at least, when compared to the results of DFT calculations), and the error accumulated at higher degrees of addition. As a result, while AM1 calculations predicted the  $C_{60}H_6$ ,  $C_{60}H_{12}$ , and  $C_{60}H_{18}$  structures with, respectively, one, two, and three *skew pentagonal pyramidal* (SPP) motifs (► Fig. 19-13d) to be the most stable isomers for their compositions (Clare and Kepert 1996), DFT calculations showed that these addition motifs are energetically unfavorable. For instance,  $C_{60}H_{18}$  with three SPP motifs is 73.8 kJ/mol more stable than the “crown”  $C_{3v}$ - $C_{60}H_{18}$  isomer at the AM1 level, but the latter is 256.8 kJ/mol more stable at the B3LYP/6-31G\*//AM1 level (Clare and Kepert 2003b). This agrees with the fact that hydro- or fluorofullerenes with SPP motifs have never been observed experimentally.

Second, DFT studies have shown that for the low degree of additions, the most stable are those isomers, which have  $-(CH)_x-$  strings, rather than isolated CH-CH fragments (Clare et al. 2003a). At the AM1 level, the most stable isomer of  $C_{60}H_4$  is 13.4 kJ/mol level lower in energy than the  $C_s$ -symmetric isomer with  $C_6H_4$  fragment, while at the B3LYP/6-31G\* level the latter is lower in energy by 15.3 kJ/mol. Likewise, the isomer of  $C_{60}H_6$  with the  $S$ -motif is 31.5 kJ/mol lower in energy at the B3LYP/6-31G\*//AM1 level than the isomer with three isolated CH-CH fragments, while at the AM1 level the latter is more stable by 24 kJ/mol. For the isomers of  $C_{60}H_8$ , analogous energy differences increase to 59.7 and 31.1 kJ/mol, respectively. The preference of the contiguous addition at the early stages of fluorination was proved experimentally by  $^{19}F$  NMR spectroscopy (Boltalina et al. 2002).

It is instructive to show that although contiguous addition appears to be the rule supported by both experimental and DFT studies, the other possibilities should not be completely abandoned. In the experimental studies of low  $C_{60}$  fluorides,  $C_s$ -symmetric isomer of  $C_{60}F_8$  was isolated (Boltalina et al. 2002).  $C_s$  symmetry is not compatible with the  $S$ -type string, and the authors proposed a contiguous addition pattern with  $T$ -motif and two additional fluorine atoms attached at the both ends of the string. However, later calculations have shown that such a structure would be unstable. Sandall and Fowler performed a broad search of all possible structures of  $C_s$  symmetry compatible with NMR data (Sandall and Fowler 2003). After calculations of more than 500 isomers using MNDO, AM1, and PM3 methods and – for selected structures – Hartree-Fock method with STO-3G and 6-31G\* basis sets, the authors have found that the most suitable

isomer indeed has *T*-motif, but two additional fluorine atoms are added in a non-contiguous way with formation of 1,4- $C_6F_2$  hexagon (► Fig. 19-12b). In a recent study it was shown that two isomers of  $C_{60}F_8$  are actually formed in the synthesis, aforementioned isomer with  $C_s$  symmetry and another one, also with  $C_s$  symmetry (Goryunkov et al. 2006b). Exhaustive DFT PBE/TZ2P calculations performed by the authors confirmed assignment of the  $C_s$  isomer to the structure proposed by Sandall and Fowler and showed that another  $C_s$ -isomer is based on the *S*-motif. At the PBE/TZ2P level, *S*- $C_s$  isomer of  $C_{60}F_8$  is 5.5 kJ/mol lower in energy.

The third failure of semiempirical methods revealed in the comparative AM1/DFT studies is that AM1 strongly underestimates stabilizing factor of the isolated benzene rings. Comparison of the relative energies of the isomers of  $C_{60}H_{36}$  with different number of benzene rings computed at the AM1 and B3LYP/6-31G\*//AM1 levels of theory shows that AM1-predicted relative energies should be adjusted by ca 60 kJ/mol per benzene ring to match the DFT-predicted values (Clare and Kepert 2002b). For instance, at the AM1 level the relative energies of  $S_6$  (2 rings),  $C_3$  (3 rings) and *T* (4 rings) isomers of  $C_{60}H_{36}$  are 0.0, 19.4, and 52.0 kJ/mol, while at the B3LYP/6-31G\*//AM1 level the values change to 0.0, -40.7, and -77.5 kJ/mol, respectively (Clare and Kepert 2002a). In a similar study of  $C_{60}H_{36}$  isomers at the PM3 and PBE/TZ2P levels of theory, it was found that PM3-computed relative energies should be corrected by approximately 67 kJ/mol per benzene ring to match the DFT results (Popov et al. 2004). For the isomers of  $C_{60}F_{36}$ , AM1-predicted relative energies should be corrected by approximately 30 kJ/mol per ring to match B3LP/6-31G\*//AM1 energies (Clare and Kepert 2002b). At the same time, relative energies of the isomers with the same number of benzene ring are reliably predicted by semiempirical approaches (Clare and Kepert 2002b; Popov et al. 2006). Thus, semiempirical methods were unable to predict the most stable isomers of  $C_{60}H_{36}$  and  $C_{60}F_{36}$ . At the same time, DFT calculations correctly predicts that *T*,  $C_3$ , and  $C_1$  isomers shown in ► Fig. 19-12g-i are the most stable isomers, in perfect agreement with the experimental results, which show that both  $C_{60}H_{36}$  and  $C_{60}F_{36}$  are obtained as mixtures of these three isomers (Boltalina et al. 1998; Gakh and Tuinman 2001, 2003; Avent et al. 2002; Hitchcock and Taylor 2002; Popov et al. 2006). It should be noted that formation of isolated benzene rings is very important stabilizing factor in the multiple addition to fullerenes and it has been observed for many addends and many fullerenes. The failure of semiempirical methods in adequate prediction of the relative energies of isomers with such fragments is therefore a very serious problem and makes these methods hardly applicable when the broad search of the possible isomers is necessary. Good results demonstrated by DFTB in the studies of the fullerenes of different size show that this method might be useful for fullerene derivatives as well, but to our knowledge, benchmark calculations for fullerene derivatives with DFTB are not available yet.

## Addition of Bulky Groups to $C_{60}$ : Bromination and Perfluoroalkylation

In contrast to H and F, bromine atom is sufficiently large to make eclipsing interactions strongly repulsive, so that 1,4 addition of two Br atoms is more energetically preferable than 1,2 addition either at the AM1 ( $\Delta E = 5.1$  kJ/mol) or DFT levels of theory (2.4 kJ/mol at B3LYP/6-31G\*//AM1, 2.1 kJ/mol at LDA/DNP//AM1, and 14.0 kJ/mol at the PBE/TZ2P levels) (Dixon et al. 1992; Clare and Kepert 1995a, 2001). At the same time, the difference in the energy of 1,2- and 1,4-isomers is not very large, and hence the possibility of 1,2-addition should be also considered. Indeed, in the AM1 study of  $C_{60}Br_4$  isomers, it was found that two lowest energy isomers are results of the

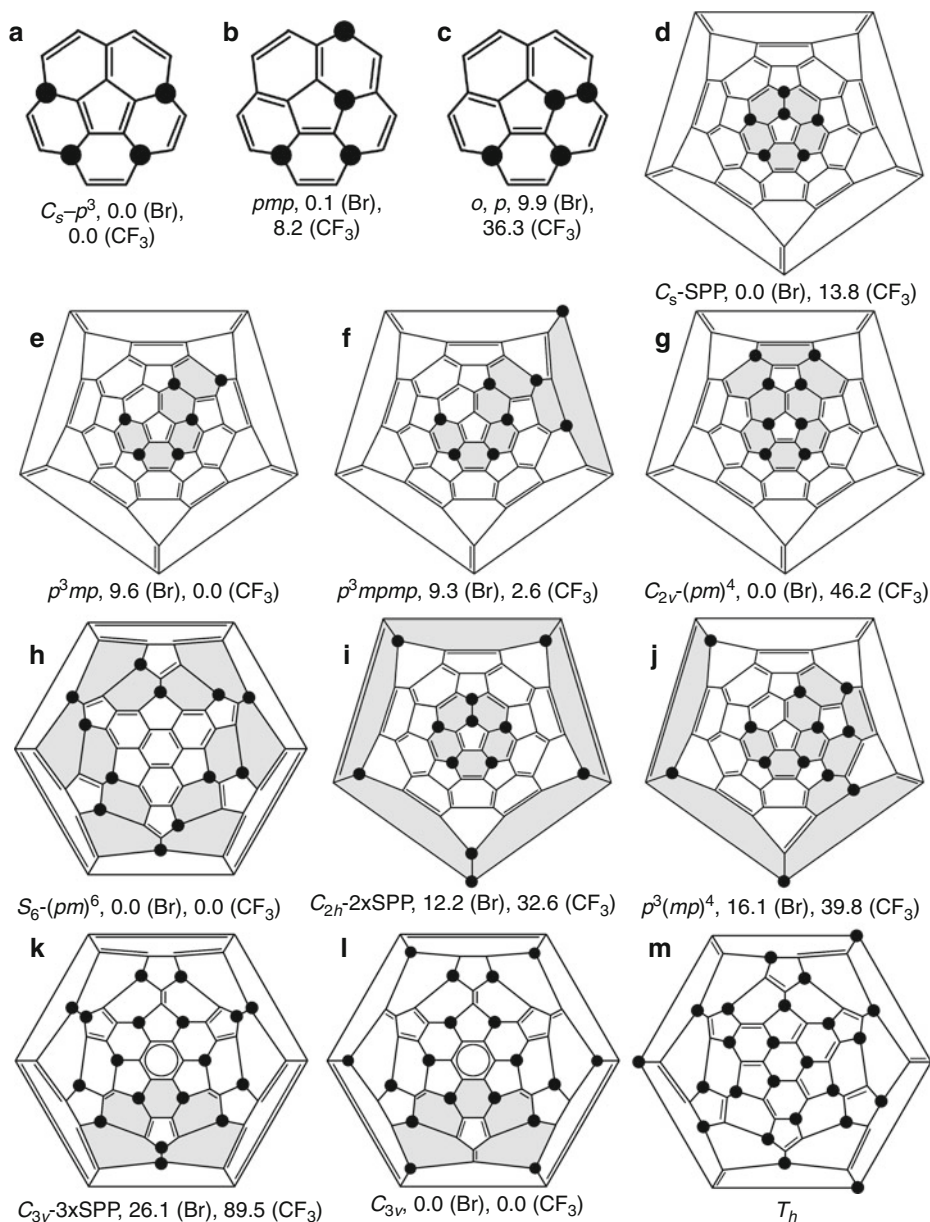


consecutive 1,4 additions, while the third most stable isomer was a result of a combined 1,2- and 1,4-additions (● Fig. 19-13a-c) (Clare and Kepert 1995a). Regression analysis of the relative energies of  $C_{60}Br_4$  isomers as a function of the number of different structural motifs (such as  $C_6Br$ ,  $C_6Br_2$ ,  $C_6Br_3$ , etc. hexagons) revealed that the most stable isomer of bromofullerenes might be obtained through formation of ribbons (also referred to as “strings”) of edge-sharing  $C_6Br_2$  hexagons, rather than by addition of pairs of bromine atoms to the distant parts of  $C_{60}$ . Thus, the most stable isomer has *para-para-para* string ( $p^3$  hereafter), while the second most stable isomer has *para-meta-para* string (*pmp* hereafter) (● Fig. 19-13a, b). The relative energy of *pmp* isomer at the PBE/TZ2P (AM1) level of theory with respect to the  $p^3$  isomer is 0.1 (6.7) kJ/mol, while the next in stability order with one *ortho*- and one *para*- $C_6Br_2$  hexagons is 9.9 (11.0) kJ/mol less stable (the DFT calculations reported hereafter for bromofullerenes at the PBE/TZ2P level with effective-core potential basis set for the Br atoms were performed specifically for this chapter).

Further addition of Br atoms to the three most stable isomer of  $C_{60}Br_4$  confirmed the preference of the string formation (Clare and Kepert 1995a). However, the most stable isomer at the AM1 level has a special  $C_s$ -symmetric addition pattern titled by some authors as “skew pentagonal pyramid” (SPP, ● Fig. 19-13d). This addition pattern includes one pair of Br atoms bonded to neighboring carbon atoms, and is 21.8 kJ/mol more stable than the second most stable isomer with a  $p^3mp$  ribbon (● Fig. 19-13e). At the PBE/TZ2P level, the energy difference between SPP and  $p^3mp$  isomers is reduced to 9.6 kJ/mol. Experimentally isolated  $C_{60}Br_6$  indeed has the SPP pattern (Birkett et al. 1992), and this addition motif was also found for some other addends, including Cl (Birkett et al. 1993) and  $CF_3$  (Kareev et al. 2006). It should be noted that formation of SPP- $C_{60}X_6$  derivatives for relatively large X is also favorable kinetically if the radical addition mechanism is adopted (Rogers and Fowler 1999).

Next two added Br atoms continue the tendency of the ribbon formation. At the AM1 level, the most stable isomer of  $C_{60}Br_8$  has  $p^3mpmp$  ribbon (● Fig. 19-13f), while DFT (PBE/TZ2P) shows that the isomer in which the ribbon is closed to a  $C_{2v}$ -symmetric loop ( $(pm)^4$ , ● Fig. 19-13g) is 9.3 kJ/mol more stable. The latter motif is indeed observed in the experimentally isolated  $C_{60}Br_8$  (Birkett et al. 1992). AM1 calculations have also shown that the isomers with the SPP motif and an additional *para*- $C_6Br_2$  hexagon on the opposite part of  $C_{60}$  are also equally stable (Clare and Kepert 1995a).

While there are no experimentally isolated  $C_{60}Br_x$  compounds between  $C_{60}Br_8$  and  $C_{60}Br_{24}$ , theoretical studies of the intermediate compositions were still very useful for predicting the general trends in the addition of bulky groups (Clare and Kepert 1995a, b). In particular, a remarkable prediction was done for  $C_{60}Br_{12}$ . The authors have shown that the most stable isomers in SPP and ribbon series are the  $C_{2h}$ -isomer with two SPP motifs on the opposite sides of  $C_{60}$  and the  $S_6$ -symmetric isomer in which the ribbon is closed to a loop around the equator of the carbon cage (● Fig. 19-13h, i). At the AM1 level,  $C_{2h}$  isomer is 6.8 kJ/mol more stable, while PBE/TZ2P favors the  $S_6$ -isomer by 12.2 kJ/mol. Though not available experimentally for  $C_{60}Br_{12}$ , both addition patterns have been found for  $C_{60}(CF_3)_{12}$  derivatives (Popov et al. 2007c; Troyanov et al. 2006). In further addition of Br atoms, the competition between SPP motifs and ribbons is continued up to  $C_{60}Br_{18}$ , for which the isomer with three SPP moieties was predicted to be the lowest energy structure (Clare and Kepert 1995b). For even larger number of Br atoms, SPP motif does not provide stable structures any more, and the most stable isomer of  $C_{60}Br_{24}$  is  $T_h$ -symmetric structure in which all Br atoms are bonded to the non-neighboring carbon atoms (24 is the largest number of addends for which such a restriction is possible) (Clare and Kepert 1995a; Fowler et al. 1999). This isomer corresponds to the experimentally available structure of  $C_{60}Br_{24}$  (Tebbe et al. 1992).



■ Fig. 19-13

$C_{60}X_n$  addition patterns typical for bulky groups (for  $C_{60}Br_n$  and  $C_{60}(CF_3)_n$ , PBE/TZ2P-computed relative energies (kJ/mol) are listed). (a)–(c) isomers of  $C_{60}X_4$ ; (d)–(e) isomers of  $C_{60}X_6$ ; (d)–(e) isomers of  $C_{60}X_8$ ; (h)–(j) isomers of  $C_{60}X_{12}$ ; (k)–(l) isomers of  $C_{60}X_{18}$ ; (m)  $T_h-C_{60}X_{24}$ . Symmetry group of the isomer is indicated only when it is different from  $C_1$ . Ribbons of edge-shared  $C_6X_2$ -hexagons are shaded (except for  $C_{60}X_{18}$ , here shaded are one SPP and one isolated fulvene moiety, respectively)

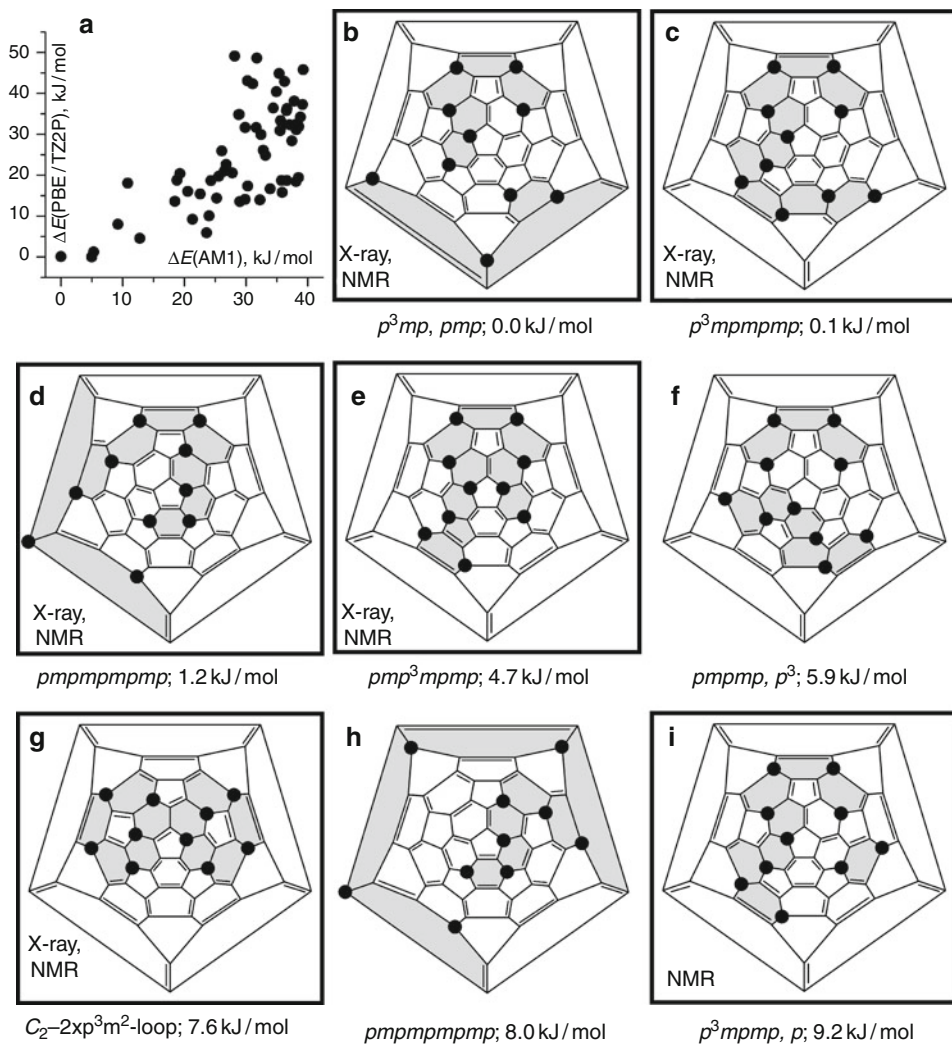
Significant progress achieved in the last years in the perfluoroalkylation of fullerenes initiated exhaustive theoretical studies of  $C_{2n}(CF_3)_x$  isomers with the aim to find the most stable structure(s) for each composition. Since the studies were performed almost a decade after the AMI-based analysis of  $C_{60}Br_x$  addition patterns by Clare and Kepert, they have strongly benefited from the serious progress in hardware. Instead of the maximum of about 100 structures reported in the early exploratory studies, up to thousands and tens of thousands isomers were routinely studied for  $CF_3$  derivatives, and results of the AMI studies were then verified by DFT calculations. Besides, the isolation of  $C_{60}(CF_3)_n$  derivatives with each even  $n$  from 2 to 18 (in many cases each composition is also presented by several isomers) enabled more detailed comparison between experimental and theoretical results.

Both AMI and DFT (PBE/TZ2P) unambiguously show that 1,4-isomer of  $C_{60}(CF_3)_2$  is much more stable than the 1,2-isomer, the DFT relative energy of the latter being 34.7 kJ/mol (Goryunkov et al. 2004a). The energy difference is more pronounced than for the  $C_{60}Br_2$ , which clearly shows that  $CF_3$  is bulkier than bromine. Therefore, in the compounds with larger number of  $CF_3$  groups, 1,2-addition is to be avoided. Indeed, the most stable isomers of  $C_{60}(CF_3)_4$  are  $p^3$  ( $\Delta E = 0.0$  kJ/mol at the PBE/TZ2P level) and  $pmp$  ( $\Delta E = 8.2$  kJ/mol) structures, just like for  $C_{60}Br_4$ , however the *o*, *p*- $C_{60}(CF_3)_4$  isomer, the third stable for  $C_{60}Br_4$ , is 36.3 kJ/mol less stable than  $p^3$ - $C_{60}(CF_3)_4$  (for  $C_{60}Br_4$  its relative energy is 9.9 kJ/mol) (Goryunkov et al. 2004a). The  $pmp$  is the major isolable isomer of  $C_{60}(CF_3)_4$ , while the more stable  $p^3$  isomer appears to be too reactive and is isolated only in the form of its epoxide  $C_{60}(CF_3)_4O$  (Goryunkov et al. 2003; Kareev et al. 2006).

The trend revealed for  $C_{60}(CF_3)_4$  in comparison to  $C_{60}Br_4$  is further emphasized for six added groups. For  $CF_3$ , the ribbon addition motifs are noticeably more preferable than the SPP motif. The most stable isomer of  $C_{60}(CF_3)_6$  has  $p^3mp$  addition pattern, while the SPP isomer is 13.8 kJ/mol less stable (for  $C_{60}Br_6$ , SPP is 9.6 kJ/mol lower in energy) (Dorozhkin et al. 2007). The SPP- $C_{60}(CF_3)_6$  still can be isolated, but its yield is ca 20 times lower than the yield of the major,  $p^3mp$  isomer (Kareev et al. 2006).

Another difference between  $CF_3$  and Br which becomes apparent for further additions is that  $CF_3$  groups are sufficiently bulky to experience repulsive interaction when two groups are in one pentagon, even though they are not bonded to the neighboring carbon atoms. Thus, the stable ribbon addition pattern of  $C_{60}Br_x$  with  $C_5Br_2$  pentagons are destabilized for  $CF_3$  groups (although some stable isomer still can have them). For instance, the most stable  $C_{2v}$ -symmetric addition pattern of  $C_{60}Br_8$  (9.3 kJ/mol more stable than  $p^3mpmp$ ) is 46.2 kJ/mol less stable than the  $p^3mpmp$  isomer of  $C_{60}(CF_3)_8$  at the PBE/TZ2P level (Goryunkov et al. 2007). The  $p^3mpmp$  isomer itself is the second most stable ( $\Delta E = 2.6$  kJ/mol, PBE/TZ2P), while the lowest energy was predicted for one of the isomers with  $p^3mp,p$  addition pattern (i.e., addition pattern of the lowest energy  $p^3mp$ - $C_{60}(CF_3)_6$  isomer with an additional isolated *para*- $C_6(CF_3)_2$  hexagon). Theoretical results agree well with experimental isolation of one  $p^3mpmp$ , three  $p^3mp,p$ , and one  $pmpmpmp$  isomers of  $C_{60}(CF_3)_8$  (Goryunkov et al. 2007; Popov et al. 2007c).

Fortuitously, performance of the AMI method for addition of bulky groups is much better than for the consecutive 1,2-additions of H and F, which encourages the use of AMI for the prescreening of thousands isomers of  $C_{60}(CF_3)_n$ . Although there is rather poor correlation between AMI and PBE/TZ2P values (❶ Fig. 19-14a), the trend in the energies of the most stable isomers is correctly predicted by AMI. For instance, when all isomers of  $C_{60}(CF_3)_{10}$  obtained by a combination 1,4-additions were studied at the AMI level and then a cutoff of 40 kJ/mol was applied to the AMI results for the consequent PBE/TZ2P calculations, the most stable isomers within the range of ca 15 kJ/mol could be identified (Popov et al. 2007c). ❷ Figure 19-14



■ Fig. 19-14

(a) Correlation between relative energies of  $\text{C}_{60}(\text{CF}_3)_{10}$  isomers computed at the AM1 and PBE/TZP levels of theory; (b)–(i) Schlegel diagrams of the eight lowest energy isomers of  $\text{C}_{60}(\text{CF}_3)_{10}$  (PBE/TZ2P-computed relative energies are also listed, based on the data from Popov et al. 2007a). Experimentally characterized compounds are framed in *black* (“X-ray” means single crystal X-ray diffraction; “NMR” means  $^{19}\text{F}$  NMR spectroscopy). Ribbons of edge-shared  $\text{C}_6(\text{CF}_3)_2$ -hexagons are *shaded*

shows addition patterns and relative energies of the eight most stable isomers of  $\text{C}_{60}(\text{CF}_3)_{10}$ . Except for one isomer, which has two symmetry-related  $p^3m^2$  loops, all other structures have ribbon addition patterns similar to those of  $\text{C}_{60}(\text{CF}_3)_8$ . Six isomers of  $\text{C}_{60}(\text{CF}_3)_{10}$  are characterized experimentally by single-crystal X-ray diffraction and/or  $^{19}\text{F}$  NMR spectroscopy, and all of them fall in the range of  $\Delta E < 10$  kJ/mol confirming reliability of the DFT predictions.

The splitting of the  $^{19}\text{F}$  NMR lines due to the through-space interaction of the fluorine atoms of  $\text{CF}_3$  groups in the same hexagon allows experimental identification of the lengths of the ribbon, and when combined with results of DFT calculations of the relative energies, these data allow unambiguous identification of the addition pattern. Molecular structures of several isomers of  $\text{C}_{60}(\text{CF}_3)_{10}$  were elucidated this way by a combination of NMR and DFT, and some of them were later confirmed by X-ray studies (Popov et al. 2007c).

Two key addition motifs predicted by Clare and Keprt for  $\text{C}_{60}\text{Br}_{12}$ , double-SPP pattern and  $S_6$ -symmetric loop (► Fig. 19-13h, i), have been identified experimentally for  $\text{C}_{60}(\text{CF}_3)_{12}$  (Popov et al. 2007c; Troyanov et al. 2006). Extensive AM1 and DFT calculations showed that the  $S_6$ -loop isomer is at least 19 kJ/mol more stable than all other isomer of  $\text{C}_{60}(\text{CF}_3)_{12}$ , while the  $C_{2h}$ -(2×SPP) isomer is 32.6 kJ/mol less stable (Kareev et al. 2007). The third isolated isomer of  $\text{C}_{60}(\text{CF}_3)_{12}$  with ribbon motif and two  $\text{C}_5(\text{CF}_3)_2$  pentagons (● Fig. 19-13j) has been found to be 39.8 kJ/mol less stable than the  $S_6$ -isomer, showing that kinetic factors can be also important in the isomeric distribution of  $\text{C}_{60}(\text{CF}_3)_x$  derivatives even at 500°C (Kareev et al. 2007).

When addition of more than 12  $\text{CF}_3$  groups is considered, one has to consider that fullerenes have only 12 pentagons, and hence it is impossible to avoid formation of destabilizing  $\text{C}_5(\text{CF}_3)_2$  pentagons. Therefore, when  $\text{CF}_3$  groups are too crowded on the fullerene surface, results of 1,2-addition can be not as destabilizing as at the lower addition stages. Exhaustive AM1 and DFT calculations have shown that for  $\text{C}_{60}(\text{CF}_3)_{14}$ , the lowest energy isomer with one SPP fragment is only 0.4 kJ/mol less stable than the most stable ribbon isomer with two  $\text{C}_5(\text{CF}_3)_2$  pentagons; however, experimentally characterized isomers of  $\text{C}_{60}(\text{CF}_3)_{14}$  do not have SPP fragments (Omelyanyuk et al. 2007). Likewise, for  $\text{C}_{60}(\text{CF}_3)_{16}$ , SPP and ribbon isomers are equally stable; moreover, it was found that stable addition patterns with  $\text{CF}_3$  groups on adjacent carbon atoms can be realized without formation of the SPP moiety, and one of the experimentally characterized  $\text{C}_{60}(\text{CF}_3)_{16}$  isomers has  $o\text{-C}_6(\text{CF}_3)_2$  hexagon (Troyanov et al. 2007). For  $\text{C}_{60}(\text{CF}_3)_{18}$ , theoretical studies have shown that the most stable isomer has  $C_{3v}$ -symmetry, two isolated benzene rings, three isolated fulvene fragments, nine  $\text{C}_5(\text{CF}_3)_2$  pentagons, and no  $\text{CF}_3$  groups on adjacent carbon atoms (► Fig. 19-13l) (Troyanov et al. 2007). DFT calculations show that this isomer is 89.5 kJ/mol more stable than the isomer with triple SPP motif, which also has one benzene ring (► Fig. 19-13k). Moreover, even for  $\text{C}_{60}\text{Br}_{18}$  this isomer is 26.1 kJ/mol more stable than the structure with three SPP moieties. Recently, the isomer of  $\text{C}_{60}(\text{CF}_3)_{18}$  with this addition pattern has indeed been isolated and characterized by single-crystal X-ray diffraction (Samokhvalova et al. 2009). Up to now, 18 is the largest number of  $\text{CF}_3$  groups in structurally characterized  $\text{C}_{60}(\text{CF}_3)_x$  derivatives; the  $T_h$ -symmetric  $\text{C}_{60}\text{X}_{24}$  motif known for  $\text{X}=\text{Br}$  and  $\text{Cl}$  could not be reached yet for  $\text{CF}_3$  derivatives.

## Addition to $\text{C}_{70}$ and Higher Fullerenes

$I_h\text{-C}_{60}$  has only two types of C–C bonds, which can be straightforwardly classified according to their bondlengths as “single” and “double” bonds. For  $\text{C}_{70}$  and higher fullerenes, the symmetry in most cases is much lower, and the lengths of C–C bonds are more uniformly distributed. It is therefore almost impossible to make an unambiguous classification of the bond types, and the relevant chemical properties (such as addition pathways) are much harder to predict.

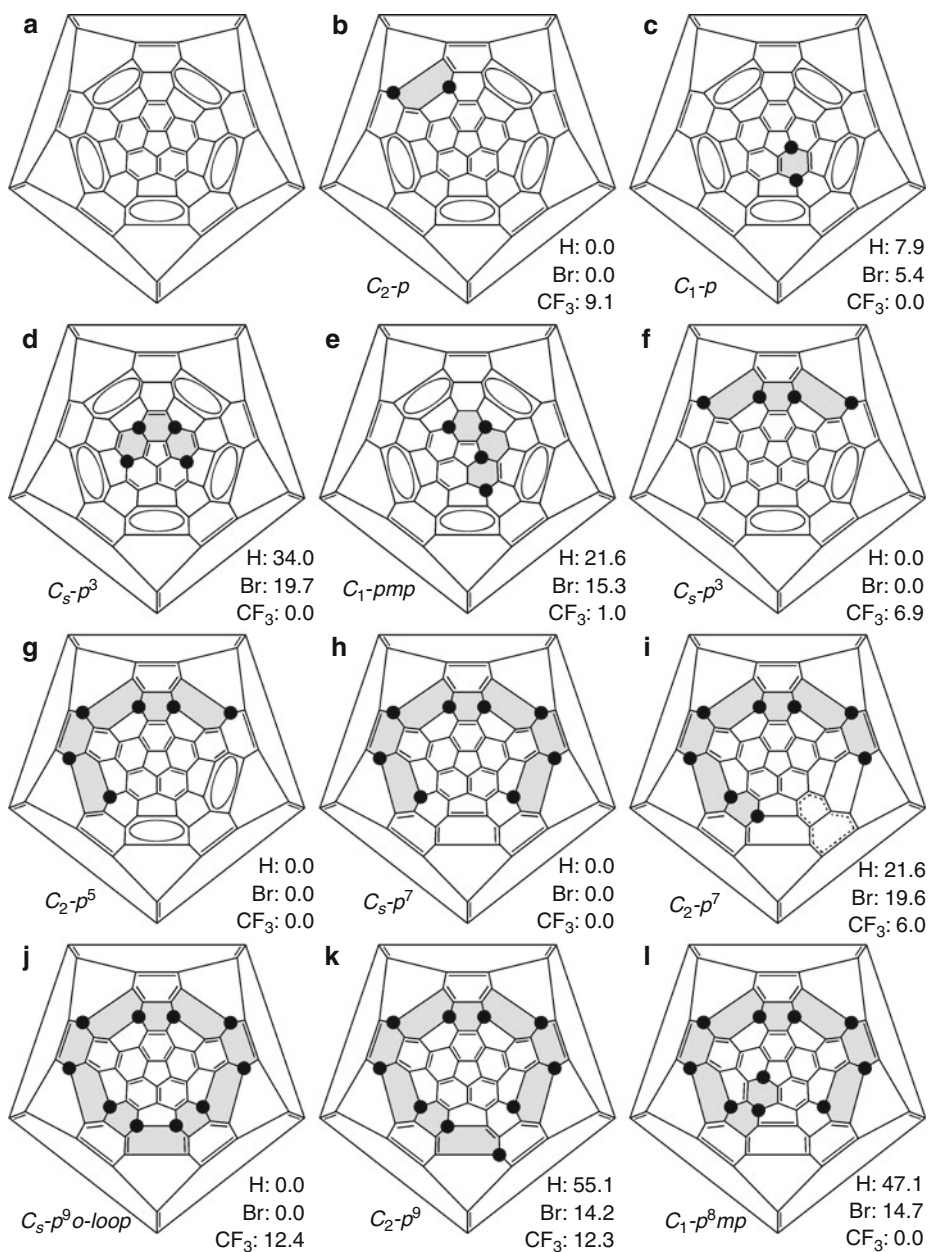
The structure of  $\text{C}_{70}$  can be described as a combination of two  $\text{C}_{60}$ -like hemispheres on the poles separated by the belt of 10 carbon atoms and five benzene-like rings around the equator (● Fig. 19-15a). The bonds between the belt carbon atoms are significantly elongated



compared to  $C_{60}$  values; besides, these atoms are located on triple hexagon junctions. Clare and Kepert reported AM1 study of the addition patterns of  $C_{70}X_n$  derivatives ( $n = 2-12$ ,  $X = H, F, Br, C_6H_5$ ) (Clare and Kepert 1999b). For  $C_{70}H_2$ , the authors have found that 1,2-addition is energetically preferable in the pole region, while the lowest energy 1,4-addition occurs at the equator. The AM1-computed energy difference between the most stable 1,2- and 1,4-isomers is only 4.4 kJ/mol, which can be compared to 18 kJ/mol for  $C_{60}H_2$ . Such a considerable difference between the relative energies of  $C_{70}H_2$  and  $C_{60}H_2$  isomer can be explained by the fact that the 1,4-addition at the equator of  $C_{70}$  does not generate destabilizing double bond in any pentagon. For  $C_{70}H_4$ , the isomer with  $p^3$ -string at the equator (● Fig. 19-15) is in fact 9.1 kJ/mol lower in energy than the isomer obtained by two 1,2-additions. The studies of  $C_{70}H_n$  with  $n = 6-10$  further emphasized the preference of consecutive 1,4-additions with formation of the  $p^{n-1}$ -ribbon along the equator of the carbon cage. The most stable  $C_{70}H_6$  and  $C_{70}H_8$  isomers in these series are, respectively, 28.0 and 54.3 kJ/mol lower in energy than the isomers obtained by 1,2-addition. Note that  $p^5$  and  $p^7$ -strings at the equator of  $C_{70}$  can be realized as either  $C_s$  or  $C_2$ -symmetric isomers. For  $C_{70}H_6$ ,  $C_2-p^5$  isomer is 76.6 kJ/mol more stable than the  $C_s-p^5$  pattern (56.6 kJ/mol at the PBE/TZ2P level (Dorozhkin et al. 2006a), while for  $C_{70}H_8$ , the  $C_s-p^7$  isomer is 34.7 kJ/mol (21.6 kJ/mol at the PBE/TZ2P level) more stable than  $C_2-p^7$ . The most stable isomer at the next addition step is obtained by the closure of the  $p^7$  ribbon via addition of two atoms to pent/hex junction with formation of the  $C_s-p^9 o$ -loop (● Fig. 19-15), which cuts the  $\pi$ -system of the fullerene into two non-communicating parts. This structure is 26.9 kJ/mol more stable than the  $C_2-p^9$  isomer, obtained by the growth of the equatorial ribbon via one more 1,4-addition step. Computations for the bulkier Br and  $C_6H_5$  groups have also shown that formation of the ribbon around the cage equator is the most referable addition motif in  $C_{70}$  (Clare and Kepert 1999b). Even for  $C_6H_5$ , the sterically strained  $C_s-p^9 o$ -loop addition pattern is more stable for  $C_{70}X_{10}$  than  $C_2-p^9$  isomer. Results of these calculations agree very well with experimental data. Except for  $C_{70}(CF_3)_{10}$  discussed below, the majority of experimentally available  $C_{70}X_{10}$  compounds ( $X = H, Cl, Br, Ph, CH_3$ ) have  $C_s-p^9 o$ -loop (Birkett et al. 1995; Avent et al. 1997; Spielmann et al. 2000; Al-Matar et al. 2002; Troyanov et al. 2003), and only bulky  $OO^tBu$  groups form the decakis-adduct with  $C_2-p^9$  addition pattern (Xiao et al. 2005). Some  $C_{70}X_n$  compounds with less than ten added groups have also been reported, and most of them also have equatorial string addition patterns. Thus, both computational and experimental data confirm that the most energetically stable addition motif for  $C_{70}$  is formation of the string from *para*- $C_6X_2$  hexagons around the cage equator, and even for hydrogen this motif might be more preferable than the consecutive 1,2-additions.

Trifluoromethylation of  $C_{70}$  deserves separate attention since, like for  $C_{60}$ , this reaction was studied recently in great details, and many compounds from  $C_{70}(CF_3)_2$  to  $C_{70}(CF_3)_{18}$  (each composition being presented by several isomers) have been isolated and structurally characterized (Goryunkov et al. 2005, 2006a; Kareev et al. 2005; Dorozhkin et al. 2006a,b; Ignat'eva et al. 2006; Popov et al. 2007b). The experimental studies were usually combined with and sometimes preceded by detailed theoretical analysis at the AM1 and PBE/TZ2P level.

It was found that the two lowest energy isomers of  $C_{70}(CF_3)_2$  have a *p*- $C_6(CF_3)_2$  hexagon on the pole of the molecule, and these structures are assigned to the experimentally available isomer (Dorozhkin et al. 2006a; Popov et al. 2007b). The most stable isomer with equatorial addition is 9.1 kJ/mol higher in energy at the PBE/TZ2P level of theory; meanwhile, the same method shows that the isomer of  $C_{70}H_2$  with equatorial addition is 7.9 kJ/mol more stable than the isomer with *p*- $C_6H_2$  hexagon on the pole. The reason for such a difference is most probably a much higher curvature of  $C_{70}$  cage at the poles as compared to the almost flat equator. Therefore,



■ Fig. 19-15

(a) Schlegel diagram of  $C_{70}$ ; (b)–(l) addition patterns of selected  $C_{70}X_n$  derivatives and the relative energies of their isomer (kJ/mol, PBE/TZ2P level of theory) for  $X=H, Br,$  and  $CF_3$ ; Ribbons of edge-shared  $C_6X_2$ -hexagos are shaded. Based on the data from (Dorozhkin et al. 2006a) and additional computations performed for this chapter

the distance between two  $\text{CF}_3$  groups is longer for  $p\text{-C}_6(\text{CF}_3)_2$  hexagon on the pole than for the hexagon on the equator, hence the repulsion between the groups is weaker on the pole. For  $\text{C}_{70}\text{H}_2$ , repulsion between the atoms is a less important factor, and the equatorial addition is more preferable.

Addition on the pole is more preferable for  $\text{C}_{70}(\text{CF}_3)_4$  as well. Similar to  $\text{C}_{60}(\text{CF}_3)_4$ , the most stable isomers have  $C_s\text{-}p^3$  and  $C_1\text{-}pmp$  ribbons with the energy difference of only 1.0 kJ/mol (PBE/TZ2P) (Dorozhkin et al. 2006a). Both can be isolated experimentally, however the  $p^3$  isomer is kinetically unstable, and the isolable form is its epoxide  $\text{C}_{70}(\text{CF}_3)_4\text{O}$  (Popov et al. 2007b). DFT calculations have also shown that there are at least 15 other isomers of  $\text{C}_{70}(\text{CF}_3)_4$  within the range of 20 kJ/mol, including the isomer with  $C_s\text{-}p^3$  string at the equator ( $\Delta E = 6.9$  kJ/mol, PBE/TZ2P), but no other structure has been characterized experimentally. Note that the model calculations of  $\text{C}_{70}\text{H}_4$  and  $\text{C}_{70}\text{Br}_4$  isomers at the PBE/TZ2P level have also shown that the equatorial addition is more energetically preferable for H and even Br (relative energy of the pole  $C_s\text{-}p^3$  isomer is 19.7 and 34.0 kJ/mol for Br and H, respectively, versus the equatorial  $C_s\text{-}p^3$  isomer).

Starting from  $\text{C}_{70}(\text{CF}_3)_6$ , addition switches to the equatorial motif. Like for many other groups (H, Cl, Br, Ph), the lowest energy isomer has a  $C_2\text{-}p^5$  ribbon at the equator, and this is indeed the most abundant experimentally characterized isomer (Dorozhkin et al. 2006a). For  $\text{C}_{70}(\text{CF}_3)_8$ , the two most stable isomers have  $C_s\text{-}p^7$  and  $C_2\text{-}p^7$  ( $\Delta E = 6.0$  kJ/mol, PBE/TZ2P) ribbons, and both isomers could be isolated and characterized by single-crystal X-ray diffraction (Goryunkov et al. 2005; Mutig et al. 2008).

For  $\text{C}_{70}(\text{CF}_3)_{10}$ , the large size of  $\text{CF}_3$  groups again makes the lowest energy addition pattern different from that for other addends. Repulsion of  $\text{CF}_3$  groups on adjacent carbon atoms destabilizes the  $C_s\text{-}p^9 o$ -loop isomer of  $\text{C}_{70}(\text{CF}_3)_{10}$ , and the most stable isomer is obtained if the  $C_s\text{-}p^7$  equatorial ribbon is continued by the  $mp$  fragment which is crawling to the pole again, as in the early stages of addition, and forming as a result  $C_1\text{-}p^7 mp$  ribbon (Kareev et al. 2005). The  $C_2\text{-}p^9$  string is 12.3 kJ/mol less stable followed by  $C_s\text{-}p^9 o$ -loop (12.4 kJ/mol). For comparison, the  $C_1\text{-}p^7 mp$  isomer of  $\text{C}_{70}\text{Br}_{10}$  is 14.7 kJ/mol less stable than the  $C_s\text{-}p^9 o$ -loop. In accordance with its DFT-predicted high thermodynamic stability, the  $C_1\text{-}p^7 mp$  is the most abundant  $\text{C}_{70}(\text{CF}_3)_{10}$  isomer, and it can be obtained with unprecedented high yield (Popov et al. 2007b).  $C_2\text{-}p^9$  as well as three other less stable minor isomers could be also structurally characterized, but their yield is much lower; the  $C_s\text{-}p^9 o$ -loop has never been found (Popov et al. 2007b).

The stable addition pattern of the major  $\text{C}_{70}(\text{CF}_3)_{10}$  isomer is found in all lowest energy and experimentally isolated addition patterns of  $\text{C}_{70}(\text{CF}_3)_{12-18}$ . For instance, four isolated isomers of  $\text{C}_{70}(\text{CF}_3)_{12}$  have  $p^7 mp_p$  patterns, while  $\text{C}_{70}(\text{CF}_3)_{16}$  and  $\text{C}_{70}(\text{CF}_3)_{18}$  have SPP fragment on the pole with  $p^7 mp$  and  $p^7 mpmp$  ribbons, respectively (Avdoshenko et al. 2006; Goryunkov et al. 2006a; Ignat'eva et al. 2006). Exhaustive theoretical studies have shown that these structures are the lowest energy isomers.

One of the important findings revealed in the studies of the multiple addition to  $\text{C}_{70}$  is the fact that the isomers in which addends are bonded to the carbon atoms on the triple hexagon junctions (THJs) are very unstable. This rule is fulfilled for all  $\text{C}_{70}$  derivatives with low and medium addition rate, and from all known derivatives of  $\text{C}_{70}$  the only violation of this rule is  $\text{C}_{70}\text{F}_{38}$  (Hitchcock et al. 2005). Moreover, it was found that this is also a strict rule for higher fullerenes (Trojanov and Kemnitz 2005; Shustova et al. 2006, 2007; Kareev et al. 2008b). Thus, when considering the possible isomers of  $\text{C}_{2n}\text{X}_m$ , one can exclude addition to triple hexagon junctions. This fact can dramatically reduce the number of possible isomers. For instance, in



the experimental study of the trifluoromethylation of the “insoluble” small HOMO–LUMO gap fullerenes, the conditions were optimized to produce  $C_{2n}(CF_3)_{12}$  as major products (Shustova et al. 2006).  $^{19}F$  NMR spectroscopy then enabled identification of the symmetry of the derivatives and the relative location of the groups (i.e., number and length of the ribbons). Note that the cage isomers of the studied fullerenes were unknown. As a result, millions of isomers were possible for these derivatives. However, when the rule about the triple hexagon junctions was taken into account and combined with the condition that  $CF_3$  groups cannot share the same pentagon (12 is the largest number of the groups added to any fullerene which can be distributed with one group per pentagon), the number of possible isomers was reduced to only a few structures for all possible cage isomers, and the DFT studies of all compatible structures could easily identify the experimental structures and determine their carbon cage isomers (Shustova et al. 2006). Interestingly, in contrast to the empty fullerenes, multiple addition of  $CF_3$  groups to THJ carbon atoms was found for  $Sc_3N@C_{80}$  (Shustova et al. 2009, 2011) showing that the endohedral cluster and electron transfer to the carbon cage dramatically change chemical properties of fullerenes.

## Acknowledgments

I would like to thank my colleagues in IFW Dresden, Moscow State University, and Colorado State University for a fruitful collaboration in the studies of fullerenes. A majority of the computations were performed using facilities of Scientific Research Center of the Moscow State University. Financial support from Alexander von Humboldt Foundation and DFG are deeply acknowledged.

## References

- Achiba, Y., Kikuchi, K., Aihara, Y., Wakabayashi, T., Miyake, Y., & Kainosho, M. (1995). *Higher fullerenes – structure and properties*. Science and technology of fullerene materials. Materials Research Society symposium proceedings, Pittsburgh.
- Achiba, Y., Fowler, P. W., Mitchell, D., & Zerbetto, F. (1998a). Structural predictions for the  $C_{116}$  molecule. *Journal of Physical Chemistry A*, 102(34), 6835–6841.
- Achiba, Y., Miyake, Y., Ishiwatari, H., Kainosho, M., & Kikuchi, K. (1998b). *NMR characterization of higher fullerenes up to  $C_{94}$* . Materials Research Society 1998 Fall Meeting. Boston.
- Akasaka, T., Wakahara, T., Nagase, S., Kobayashi, K., Waelchli, M., Yamamoto, K., Kondo, M., Shirakura, S., Okubo, S., Maeda, Y., Kato, T., Kako, M., Nakadaira, Y., Nagahata, R., Gao, X., Van Caemelbecke, E., & Kadish, K. M. (2000).  $La@C_{82}$  anion. An unusually stable metallofullerene. *Journal of the American Chemical Society*, 122(38), 9316–9317.
- Al-Matar, H., Sada, A. K. A., Avent, A. G., Taylor, R., & Wei, X. W. (2002). Methylation of [70]fullerene. *Journal of the Chemical Society-Perkin Transactions*, 2, 1251–1256.
- Albertazzi, E., Domene, C., Fowler, P. W., Heine, T., Seifert, G., Van Alsenoy, C., & Zerbetto, F. (1999). Pentagon adjacency as a determinant of fullerene stability. *Physical Chemistry Chemical Physics*, 1(12), 2913–2918.
- Alvarez, M. M., Gillan, E. G., Holczer, K., Kaner, R. B., Min, K. S., & Whetten, R. L. (1991).  $La_2C_{80}$  – a soluble dimetallofullerene. *Journal of Physical Chemistry*, 95(26), 10561–10563.
- Alvarez, L., Pichler, T., Georgi, P., Schwiager, T., Peisert, H., Dunsch, L., Hu, Z., Knupfer, M., Fink, J., Bressler, P., Mast, M., & Golden, M. S. (2002). Electronic structure of pristine and intercalated  $Sc_3N@C_{80}$  metallofullerene. *Physical Review B*, 66(3), 035107.

- Attala, M. I., Vassallo, A. M., Tattam, B. N., & Hanna, J. V. (1993). Preparation of hydrofullerenes by hydrogen radical-induced hydrogenation. *Journal of Physical Chemistry*, 97(24), 6329–6331.
- Austin, S. J., Fowler, P. W., Orlandi, G., Manolopoulos, D. E., & Zerbetto, F. (1994). Relative stabilities of  $C_{76}$  isomers – a numerical test of the fullerene isolated-pentagon rule. *Chemical Physics Letters*, 226(1–2), 219–225.
- Austin, S. J., Fowler, P. W., Manolopoulos, D. E., Orlandi, G., & Zerbetto, F. (1995). Structural motifs and the stability of fullerenes. *Journal of Physical Chemistry*, 99(20), 8076–8081.
- Avdoshenko, S. M., Goryunkov, A. A., Ioffe, I. N., Ignat'eva, D. V., Sidorov, L. N., Pattison, P., Kemnitz, E., & Troyanov, S. I. (2006). Preparation, crystallographic characterization and theoretical study of  $C_{70}(CF_3)_{16}$  and  $C_{70}(CF_3)_{18}$ . *Chemical Communications*, (23), 2463–2465.
- Avent, A. G., Benito, A. M., Birkett, P. R., Darwish, A. D., Hitchcock, P. B., Kroto, H. W., Locke, I. W., Meidine, M. F., O'Donovan, B. F., Prassides, K., Taylor, R., Walton, D. R. M., & van Wijnkoop, M. (1997). The structure of fullerene compounds. *Journal of Molecular Structure*, 437, 1–9.
- Avent, A. G., Clare, B. W., Hitchcock, P. B., Kepert, D. L., & Taylor, R. (2002).  $C_{60}F_{36}$ : There is a third isomer and it has  $C_1$  symmetry. *Chemical Communications*, 2006(20), 2370–2371.
- Bader, R. F. W. (1990). *Atoms in molecules – a quantum theory*. Oxford: Oxford University Press.
- Balasubramanian, K. (1991). Enumeration of isomers of polysubstituted  $C_{60}$  and application to NMR. *Chemical Physics Letters*, 182(3–4), 257–262.
- Beavers, C. M., Zuo, T. M., Duchamp, J. C., Harich, K., Dorn, H. C., Olmstead, M. M., & Balch, A. L. (2006).  $Tb_3N@C_{84}$ : An improbable, egg-shaped endohedral fullerene that violates the isolated pentagon rule. *Journal of the American Chemical Society*, 128(35), 11352–11353.
- Beavers, C. M., Chaur, M. N., Olmstead, M. M., Echegoyen, L., & Balch, A. L. (2009). Large metal ions in a relatively small fullerene cage: The structure of  $Gd_3N@C_2(22010)-C_{78}$  departs from the isolated pentagon rule. *Journal of the American Chemical Society*, 131(32), 11519–11524.
- Birkett, P. R., Hitchcock, P. B., Kroto, H. W., Taylor, R., & Walton, D. R. M. (1992). Preparation and characterization of  $C_{60}Br_6$  and  $C_{60}Br_8$ . *Nature*, 357(6378), 479–481.
- Birkett, P. R., Avent, A. G., Darwish, A. D., Kroto, H. W., Taylor, R., & Walton, D. R. M. (1993). Preparation and  $^{13}C$  NMR spectroscopic characterization of  $C_{60}Cl_6$ . *Journal of the Chemical Society-Chemical Communications*, 1993(15), 1230–1232.
- Birkett, P. R., Avent, A. G., Darwish, A. D., Kroto, H. W., Taylor, R., & Walton, D. R. M. (1995). Formation and characterization of  $C_{70}Cl_{10}$ . *Journal of the Chemical Society-Chemical Communications*, (6), 1995683–684.
- Boltalina, O. V., Street, J. M., & Taylor, R. (1998).  $C_{60}F_{36}$  consists of two isomers having  $T$  and  $C_3$  symmetry. *Journal of the Chemical Society-Perkin Transactions*, 2(3), 649–653.
- Boltalina, O. V., Ioffe, I. N., Sidorov, L. N., Seifert, G., & Vietze, K. (2000a). Ionization energy of fullerenes. *Journal of the American Chemical Society*, 122(40), 9745–9749.
- Boltalina, O. V., Lukonin, A. Y., Street, J. M., & Taylor, R. (2000b).  $C_{60}F_2$  exists! *Chemical Communications*, 2000(17), 1601–1602.
- Boltalina, O. V., Markov, V. Y., Troshin, P. A., Darwish, A. D., Street, J. M., & Taylor, R. (2001).  $C_{60}F_{20}$ : “Saturnene”, an extraordinary squashed fullerene. *Angewandte Chemie-International Edition*, 40(4), 787–789.
- Boltalina, O. V., Darwish, A. D., Street, J. M., Taylor, R., & Wei, X. W. (2002). Isolation and characterisation of  $C_{60}F_4$ ,  $C_{60}F_6$ ,  $C_{60}F_8$ ,  $C_{60}F_7CF_3$  and  $C_{60}F_2O$ , the smallest oxahomofullerene; the mechanism of fluorine addition to fullerenes. *Journal of the Chemical Society-Perkin Transactions*, 2(2), 251–256.
- Boltalina, O. V., Popov, A. A., & Strauss, S. H. (2009). Physicochemical properties and the unusual structure of fullerenes: Single-crystal X-ray structures of fullerenes and their derivatives. In H. Dodziuk (Ed.), *Strained hydrocarbons: Beyond the Van't Hoff and Le Bel hypothesis* (pp. 225–238). Weinheim: Wiley-VCH.
- Campanera, J. M., Bo, C., Olmstead, M. M., Balch, A. L., & Poblet, J. M. (2002). Bonding within the endohedral fullerenes  $Sc_3N@C_{78}$  and  $Sc_3N@C_{80}$  as determined by density functional calculations and reexamination of the crystal structure of  $Sc_3N@C_{78}-Co(OEP)-1.5(C_6H_6)-0.3(CHCl_3)$ . *Journal of Physical Chemistry A*, 106(51), 12356–12364.
- Campanera, J. M., Bo, C., & Poblet, J. M. (2005). General rule for the stabilization of fullerene cages encapsulating trimetallic nitride templates. *Angewandte Chemie-International Edition*, 44(44), 7230–7233.
- Campbell, E. E. B., Fowler, P. W., Mitchell, D., & Zerbetto, F. (1996). Increasing cost of pentagon adjacency for larger fullerenes. *Chemical Physics Letters*, 250(5–6), 544–548.
- Cao, B. P., Wakahara, T., Tsuchiya, T., Kondo, M., Maeda, Y., Rahman, G. M. A., Akasaka, T., Kobayashi, K., Nagase, S., & Yamamoto, K.

- (2004). Isolation, characterization, and theoretical study of  $\text{La}_2@C_{78}$ . *Journal of the American Chemical Society*, 126(30), 9164–9165.
- Cao, B., Nikawa, H., Nakahodo, T., Tsuchiya, T., Maeda, Y., Akasaka, T., Sawa, H., Slanina, Z., Mizorogi, N., & Nagase, S. (2008). Addition of adamantylidene to  $\text{La}_2@C_{78}$ : Isolation and single-crystal X-ray structural determination of the monoadducts. *Journal of the American Chemical Society*, 130, 983–989.
- Chai, Y., Guo, T., Jin, C. M., Haufler, R. E., Chibante, L. P. F., Fure, J., Wang, L. H., Alford, J. M., & Smalley, R. E. (1991). Fullerenes with metals inside. *Journal of Physical Chemistry*, 95(20), 7564–7568.
- Chaur, M. N., Melin, F., Elliott, B., Kumbhar, A., Athans, A. J., & Echegoyen, L. (2008). New  $\text{M}_3\text{N}@C_{2n}$  endohedral metallofullerene families ( $\text{M}=\text{Nd}$ , Pr, Ce;  $n=40\text{--}53$ ): Expanding the preferential templating of the  $C_{88}$  cage and approaching the  $C_{96}$  Cage. *Chemistry – A European Journal*, 14(15), 4594–4599.
- Chen, Z. F., Cioslowski, J., Rao, N., Moncrieff, D., Buhl, M., Hirsch, A., & Thiel, W. (2001). Endohedral chemical shifts in higher fullerenes with 72–86 carbon atoms. *Theoretical Chemistry Accounts*, 106(5), 364–368.
- Chen, Z. F., & Thiel, W. (2003). Performance of semiempirical methods in fullerene chemistry: Relative energies and nucleus-independent chemical shifts. *Chemical Physics Letters*, 367(1–2), 15–25.
- Chen, D. L., Q., T. W., Feng, J. K., & Sun, C. C. (2008).  $C_{68}$  fullerene isomers, anions, and their metallofullerenes: Charge-stabilizing different isomers. *ChemPhysChem*, 9, 454–461.
- Cioslowski, J., Rao, N., & Moncrieff, D. (2000). Standard enthalpies of formation of fullerenes and their dependence on structural motifs. *Journal of the American Chemical Society*, 122(34), 8265–8270.
- Clare, B. W., & Kepert, D. L. (1993). Structures and stabilities of hydrofullerenes  $C_{60}H_n$ . *Theochem-Journal of Molecular Structure*, 281, 45–52.
- Clare, B. W., & Kepert, D. L. (1994a). An analysis of the 63 Possible isomers of  $C_{60}H_{36}$  containing a threefold axis – a new structure for  $C_{60}H_{20}$ . *Theochem-Journal of Molecular Structure*, 315, 71–83.
- Clare, B. W., & Kepert, D. L. (1994b). Structures and stabilities of hydrofullerenes – completion of a tetrahedral fused quadruple crown structure and a double crown structure at  $C_{60}H_{36}$ . *Theochem-Journal of Molecular Structure*, 304, 181–189.
- Clare, B. W., & Kepert, D. L. (1994c). Structures and stabilities of hydrofullerenes. Completion of crown structures at  $C_{60}H_{18}$  and  $C_{60}H_{24}$ . *Theochem-Journal of Molecular Structure*, 303, 1–9.
- Clare, B. W., & Kepert, D. L. (1995a). Stereochemical patterns in bromofullerenes  $C_{60}Br_2$  to  $C_{60}Br_{12}$ . *Theochem-Journal of Molecular Structure*, 340, 125–142.
- Clare, B. W., & Kepert, D. L. (1995b). Stereochemical patterns in bromofullerenes,  $C_{60}Br_{12}$  to  $C_{60}Br_{24}$ . *Theochem-Journal of Molecular Structure*, 358, 79–94.
- Clare, B. W., & Kepert, D. L. (1996). Fullerene hydrides based on skew pentagonal pyramidal arrangements of hydrogen atoms. *Theochem-Journal of Molecular Structure*, 363, 179–190.
- Clare, B. W., & Kepert, D. L. (1997). An analysis of the 94 possible isomers of  $C_{60}F_{48}$  containing a three-fold axis. *Journal of Molecular Structure-Theochem*, 389, 97–103.
- Clare, B. W., & Kepert, D. L. (1999a). The structures of  $C_{60}F_{36}$  and new possible structures for  $C_{60}H_{36}$ . *Journal of Molecular Structure-Theochem*, 466, 177–186.
- Clare, B. W., & Kepert, D. L. (1999b). The structures of  $C_{70}X_n$ ,  $X=\text{H}$ , F, Br,  $C_6H_5$  and  $n=2\text{--}12$ . *Theochem-Journal of Molecular Structure*, 491, 249–264.
- Clare, B. W., & Kepert, D. L. (2001). Structures and stabilities of adducts of carbenes and fullerenes,  $C_{60}(\text{CR}_2)_n$ ,  $R=\text{H}$ ,  $\text{CH}_3$ ,  $C_4H_9$  and  $n=1\text{--}6$ . *Journal of Molecular Structure-Theochem*, 548, 61–91.
- Clare, B. W., & Kepert, D. L. (2002a). Structures of  $C_{60}H_n$  and  $C_{60}F_n$ ,  $n=36\text{--}60$ . *Journal of Molecular Structure-Theochem*, 589, 209–227.
- Clare, B. W., & Kepert, D. L. (2002b). Structures, stabilities and isomerism in  $C_{60}H_{36}$  and  $C_{60}F_{36}$ . A comparison of the AM1 Hamiltonian and density functional techniques. *Journal of Molecular Structure-Theochem*, 589, 195–207.
- Clare, B. W., & Kepert, D. L. (2003a). Early stages in the addition to  $C_{60}$  to form  $C_{60}X_n$ ,  $X=\text{H}$ , F, Cl, Br,  $\text{CH}_3$ ,  $C_4H_9$ . *Journal of Molecular Structure-Theochem*, 621(3), 211–231.
- Clare, B. W., & Kepert, D. L. (2003b). Structures, stabilities and isomerism in  $C_{60}H_n$ ,  $n=2\text{--}36$ . A comparison of the AM1 Hamiltonian and density functional techniques. *Journal of Molecular Structure-Theochem*, 622(3), 185–202.
- Cortés-Guzmán, F., & Bader, R. F. W. (2005). Complementarity of QTAIM and MO theory in the study of bonding in donor–acceptor complexes. *Coordination Chemistry Reviews*, 249(5–6), 633–662.

- Cremer, D., & Kraka, E. (1984). Chemical bonds without bonding electron density – Does the difference electron-density analysis suffice for a description of the chemical bond? *Angewandte Chemie-International Edition in English*, 23(8), 627–628.
- Darwish, A. D., Avent, A. G., Taylor, R., & Walton, D. R. M. (1996). Structural characterisation of  $C_{60}H_{18}$ ; a  $C_{3v}$  symmetry crown. *Journal of the Chemical Society-Perkin Transactions*, 2(10), 2051–2054.
- Darzynkiewicz, R. B., & Scuseria, G. E. (1997). Noble gas endohedral complexes of  $C_{60}$  buckminsterfullerene. *Journal of Physical Chemistry A*, 101(38), 7141–7144.
- Dennis, T. J. S., Kai, T., Asato, K., Tomiyama, T., & Shinohara, H. (1999). Isolation and characterization by  $^{13}C$  NMR spectroscopy of [84]fullerene minor isomers. *Journal of Physical Chemistry A*, 103(44), 8747–8752.
- Diener, M. D., & Alford, J. M. (1998). Isolation and properties of small-bandgap fullerenes. *Nature*, 393(6686), 668–671.
- Dixon, D. A., Matsuzawa, N., Fukunaga, T., & Tebbe, F. N. (1992). Patterns for addition to  $C_{60}$ . *Journal of Physical Chemistry*, 96(15), 6107–6110.
- Dorozhkin, E. I., Ignat'eva, D. V., Tamm, N. B., Goryunkov, A. A., Khavrel, P. A., Ioffe, I. N., Popov, A. A., Kuvychko, I. V., Streletskiy, A. V., Markov, V. Y., Spandl, J., Strauss, S. H., & Boltalina, O. V. (2006a). Synthesis, characterization, and theoretical study of stable isomers of  $C_{70}(CF_3)_n$  ( $n=2, 4, 6, 8, 10$ ). *Chemistry – A European Journal*, 12(14), 3876–3889.
- Dorozhkin, E. I., Ignat'eva, D. V., Tamm, N. B., Vasilyuk, N. V., Goryunkov, A. A., Avdoshenko, S. M., Ioffe, I. N., Sidorov, L. N., Pattison, P., Kemnitz, E., & Troyanov, S. I. (2006b). Structure of 1,4,10,19,25,41- $C_{70}(CF_3)_6$ , isomer with unique arrangement of addends. *Journal of Fluorine Chemistry*, 127(10), 1344–1348.
- Dorozhkin, E. I., Goryunkov, A. A., Ioffe, I. N., Avdoshenko, S. M., Markov, V. Y., Tamm, N. B., Ignat'eva, D. V., Sidorov, L. N., & Troyanov, S. I. (2007). Synthesis, structure, and theoretical study of lower trifluoromethyl derivatives of [60]fullerene. *European Journal of Organic Chemistry*, 2007(30), 5082–5094.
- Dunsch, L., & Yang, S. (2007). Metal nitride cluster fullerenes: Their current state and future prospects. *Small*, 3(8), 1298–1320.
- Dunsch, L., Georgi, P., Krause, M., & Wang, C. R. (2003). New clusters in endohedral fullerenes: The metalnitrides. *Synthetic Metals*, 135(1–3), 761–762.
- Dunsch, L., Krause, M., Noack, J., & Georgi, P. (2004). Endohedral nitride cluster fullerenes – formation and spectroscopic analysis of  $L_{3-x}M_xN@C_{2n}$  ( $0 \leq x \leq 3$ ;  $n = 39, 40$ ). *Journal of Physics and Chemistry of Solids*, 65(2–3), 309–315.
- Dunsch, L., Yang, S., Zhang, L., Svitova, A., Oswald, S., & Popov, A. A. (2010). Metal sulfide in a  $C_{82}$  fullerene cage: A new form of endohedral clusterfullerenes. *Journal of the American Chemical Society*, 132(15), 5413–5421. doi: 10.1021/ja909580j.
- Ettl, R., Chao, I., Diederich, F., & Whetten, R. L. (1991). Isolation of  $C_{76}$ , a chiral ( $D_2$ ) allotrope of carbon. *Nature*, 353(6340), 149–153.
- Farrugia, L. J., Evans, C., Lentz, D., & Roemer, M. (2009). The QTAIM approach to chemical bonding between transition metals and carbocyclic rings: A combined experimental and theoretical study of  $(\eta^5-C_5H_5)Mn(CO)_3$ ,  $(\eta^6-C_6H_6)Cr(Co)_3$ , and  $(E)-\{(\eta^5-C_5H_4)CF=CF(\eta^5-C_5H_4)\}(\eta^5-C_5H_5)_2Fe_2$ . *Journal of the American Chemical Society*, 131(3), 1251–1268.
- Fowler, P. W., & Manolopoulos, D. E. (1995a). *An atlas of fullerenes*. Oxford: Clarendon Press.
- Fowler, P. W., & Zerbetto, F. (1995b). Charging and equilibration of fullerene isomers. *Chemical Physics Letters*, 243(1–2), 36–41.
- Fowler, P. W., Rogers, K. M., Somers, K. R., & Troisi, A. (1999). Independent sets and the prediction of addition patterns for higher fullerenes. *Journal of the Chemical Society-Perkin Transactions*, 2(10), 2023–2027.
- Furche, F., & Ahlrichs, R. (2001). Fullerene  $C_{80}$ : Are there still more isomers? *Journal of Chemical Physics*, 114(23), 10362–10367.
- Gakh, A. A., & Tuinman, A. A. (2001). 'Fluorine dance' on the fullerene surface. *Tetrahedron Letters*, 42(41), 7137–7139.
- Gakh, A. A., Romanovich, A. Y., & Bax, A. (2003). Thermodynamic rearrangement synthesis and NMR structures of  $C_1$ ,  $C_3$ , and  $T$  isomers of  $C_{60}H_{36}$ . *Journal of the American Chemical Society*, 125(26), 7902–7906.
- Gan, L. H., & Yuan, R. (2006). Influence of cluster size on the structures and stability of trimetallic nitride fullerenes  $M_3N@C_{80}$ . *ChemPhysChem*, 7(6), 1306–1310.
- Goryunkov, A. A., Kuvychko, I. V., Ioffe, I. N., Dick, D. L., Sidorov, L. N., Strauss, S. H., & Boltalina, O. V. (2003). Isolation of  $C_{60}(CF_3)_n$  ( $n=2, 4, 6, 8, 10$ ) with high compositional purity. *Journal of Fluorine Chemistry*, 124(1), 61–64.
- Goryunkov, A. A., Ioffe, I. N., Kuvychko, I. V., Yankova, T. S., Markov, V. Y., Streletskiy, A. A., Dick, D. L., Sidorov, L. N., Boltalina, O. V.,

- & Strauss, S. H. (2004a). Trifluoromethylated [60]fullerenes: Synthesis and characterization. *Fullerenes Nanotubes and Carbon Nanostructures*, 12(1–2), 181–185.
- Goryunkov, A. A., Markov, V. Y., Ioffe, I. N., Bolskar, R. D., Diener, M. D., Kuvychko, I. V., Strauss, S. H., & Boltalina, O. V. (2004b).  $C_{74}F_{38}$ : An exohedral derivative of a small-bandgap fullerene with  $D_3$  symmetry. *Angewandte Chemie-International Edition*, 43(8), 997–1000.
- Goryunkov, A. A., Dorozhkin, E. I., Ignat'eva, D. V., Sidorov, L. N., Kemnitz, E., Sheldrick, G., & Troyanov, S. I. (2005). Crystal and molecular structures of  $C_{70}(CF_3)_8$ -PhMe. *Mendeleev Communications*, 15(6), 225–227.
- Goryunkov, A. A., Ignat'eva, D. V., Tamm, N. B., Moiseeva, N. N., Loffe, I. N., Avdoshenko, S. M., Markov, V. Y., Sidorov, L. N., Kemnitz, E., & Troyanov, S. I. (2006a). Preparation, crystallographic characterization, and theoretical study of  $C_{70}(CF_3)_{14}$ . *European Journal of Organic Chemistry*, 2006, 2508–2512.
- Goryunkov, A. A., Kareev, I. E., Ioffe, I. N., Popov, A. A., Kuvychko, I. V., Markov, V. Y., Goldt, I. V., Pimenova, A. S., Serov, M. G., Avdoshenko, S. M., Khavrel, P. A., Sidorov, L. N., Lebedkin, S. F., Mazej, Z., Zemva, B., Strauss, S. H., & Boltalina, O. V. (2006b). Reaction of  $C_{60}$  with  $KMnF_4$  – isolation and characterization of a new isomer of  $C_{60}F_8$  and re-evaluation of the structures of  $C_{60}F_7(CF_3)$  and the known isomer of  $C_{60}F_8$ . *Journal of Fluorine Chemistry*, 127(10), 1423–1435.
- Goryunkov, A. A., Dorozhkin, E. I., Tamm, N. B., Ignat'eva, D. V., Avdoshenko, S. M., Sidorov, L. N., & Troyanov, S. I. (2007). Synthesis and molecular structure of 1,6,11,16,18,24,27,36- $C_{60}(CF_3)_8$ . *Mendeleev Communications*, 17(2), 110–112.
- Haddon, R. C. (1993). Chemistry of the fullerenes – the manifestation of strain in a class of continuous aromatic-molecules. *Science*, 261(5128), 1545–1550.
- Haser, M., Almlof, J., & Scuseria, G. E. (1991). The equilibrium geometry of  $C_{60}$  as predicted by 2nd-Order (MP2) perturbation-theory. *Chemical Physics Letters*, 181(6), 497–500.
- Haufler, R. E., Conceicao, J., Chibante, L. P. F., Chai, Y., Byrne, N. E., Flanagan, S., Haley, M. M., O'Brien, S. C., Pan, C., Xiao, Z., Billups, W. E., Ciufolini, M. A., Hauge, R. H., Margrave, J. L., Wilson, L. J., Curl, R. F., & Smalley, R. E. (1990). Efficient production of  $C_{60}$  (Buckminsterfullerene),  $C_{60}H_{36}$ , and the solvated buckide ion. *Journal of Physical Chemistry*, 94(24), 8634–8636.
- Heath, J. R., O'Brien, S. C., Zhang, Q., Liu, Y., Curl, R. F., Tittel, F. K., & Smalley, R. E. (1985). Lanthanum complexes of spheroidal carbon shells. *Journal of the American Chemical Society*, 107(25), 7779–7780.
- Henderson, C. C., & Cahill, P. A. (1993).  $C_{60}H_2$  – synthesis of the simplest  $C_{60}$  hydrocarbon derivative. *Science*, 259(5103), 1885–1887.
- Henrich, F. H., Michel, R. H., Fischer, A., Richard-Schneider, S., Gilb, S., Kappes, M. M., Fuchs, D., Burk, M., Kobayashi, K., & Nagase, S. (1996). Isolation and characterization of  $C_{80}$ . *Angewandte Chemie-International Edition in English*, 35(15), 1732–1734.
- Hirsch, A., & Brettreich, M. (2005). *Fullerenes. Chemistry and reactions*. Weinheim: Wiley.
- Hirsch, A., & Vostrowsky, O. (2001).  $C_{60}$  hexakisadducts with an octahedral addition pattern – a new structure motif in organic chemistry. *European Journal of Organic Chemistry*, 2001, 829–848.
- Hitchcock, P. B., & Taylor, R. (2002). Single crystal X-ray structure of tetrahedral  $C_{60}F_{36}$ : The most aromatic and distorted fullerene. *Chemical Communications*, 2002(18), 2078–2079.
- Hitchcock, P. B., Avent, A. G., Martsinovich, N., Troshin, P. A., & Taylor, R. (2005).  $C_2 C_{70}F_{38}$  is aromatic, contains three planar hexagons, and has equatorial addends. *Chemical Communications*, 2005(1), 75–77.
- Ignat'eva, D. V., Goryunkov, A. A., Tamm, N. B., Ioffe, I. N., Avdoshenko, S. M., Sidorov, L. N., Dimitrov, A., Kemnitz, E., & Troyanov, S. I. (2006). Preparation, crystallographic characterization and theoretical study of two isomers of  $C_{70}(CF_3)_{12}$ . *Chemical Communications*, 2006(16), 1778–1780.
- Iiduka, Y., Wakahara, T., Nakahodo, T., Tsuchiya, T., Sakuraba, A., Maeda, Y., Akasaka, T., Yoza, K., Horn, E., Kato, T., Liu, M. T. H., Mizorogi, N., Kobayashi, K., & Nagase, S. (2005). Structural determination of metallofullerene  $Sc_3C_{82}$  revisited: A surprising finding. *Journal of the American Chemical Society*, 127(36), 12500–12501.
- Iiduka, Y., Wakahara, T., Nakajima, K., Tsuchiya, T., Nakahodo, T., Maeda, Y., Akasaka, T., Mizorogi, N., & Nagase, S. (2006).  $^{13}C$  NMR spectroscopic study of scandium dimetallofullerene,  $Sc_2@C_{84}$  vs.  $Sc_2C_2@C_{82}$ . *Chemical Communications*, 2006(19), 2057–2059.
- Inoue, T., Tomiyama, T., Sugai, T., Okazaki, T., Suetatsu, T., Fujii, N., Utsumi, H., Nojima, K., & Shinohara, H. (2004). Trapping a  $C_2$  radical in endohedral metallofullerenes: Synthesis and

- structures of  $(Y_2C_2)@C_{82}$  (Isomers I, II, and III). *Journal of Physical Chemistry B*, 108(23), 7573–7579.
- Irle, S., Zheng, G. S., Elstner, M., & Morokuma, K. (2003). From  $C_2$  molecules to self-assembled fullerenes in quantum chemical molecular dynamics. *Nano Letters*, 3(12), 1657–1664.
- Irle, S., Zheng, G. S., Wang, Z., & Morokuma, K. (2006). The  $C_{60}$  formation puzzle “solved”: QM/MD simulations reveal the shrinking hot giant road of the dynamic fullerene self-assembly mechanism. *Journal of Physical Chemistry B*, 110(30), 14531–14545.
- Karataev, V. I. (1998). Anomalous properties of  $C_{74}$  fullerene. *Molecular Crystals and Liquid Crystals Science and Technology Section C-Molecular Materials*, 11(1–2), 57–58.
- Kareev, I. E., Kuvychko, I. V., Popov, A. A., Lebedkin, S. F., Miller, S. M., Anderson, O. P., Strauss, S. H., & Boltalina, O. V. (2005). High-temperature synthesis of the surprisingly stable  $C_1-C_{70}(CF_3)_{10}$  isomer with a *para'-meta-para* ribbon of nine  $C_6(CF_3)_2$  edge-sharing hexagons. *Angewandte Chemie-International Edition*, 44(48), 7984–7987.
- Kareev, I. E., Shustova, N. B., Kuvychko, I. V., Lebedkin, S. F., Miller, S. M., Anderson, O. P., Popov, A. A., Strauss, S. H., & Boltalina, O. V. (2006). Thermally stable perfluoroalkylfullerenes with the skew-pentagonal-pyramid pattern:  $C_{60}(C_2F_5)_4O$ ,  $C_{60}(CF_3)_4O$ , and  $C_{60}(CF_3)_6$ . *Journal of the American Chemical Society*, 128(37), 12268–12280.
- Kareev, I. E., Shustova, N. B., Peryshkov, D. V., Lebedkin, S. F., Miller, S. M., Anderson, O. P., Popov, A. A., Boltalina, O. V., & Strauss, S. H. (2007). X-ray structure and DFT study of  $C_1-C_{60}(CF_3)_{12}$ . A high-energy, kinetically-stable isomer prepared at 500 degrees C. *Chemical Communications*, 2007(16), 1650–1652.
- Kareev, I. E., Kuvychko, I. V., Shustova, N. B., Lebedkin, S. F., Bubnov, V. P., Anderson, O. P., Popov, A. A., Boltalina, O. V., & Strauss, S. H. (2008a).  $C_1-(C_{84} - C_2(11))(CF_3)_{12}$ : Trifluoromethylation yields structural proof of a minor  $C_{84}$  cage and reveals a principle of higher fullerene reactivity. *Angewandte Chemie-International Edition in English*, 47, 6204–6207.
- Kareev, I. E., Popov, A. A., Kuvychko, I. V., Shustova, N. B., Lebedkin, S. F., Bubnov, V. P., Anderson, O. P., Seppelt, K., Strauss, S. H., & Boltalina, O. V. (2008b). Synthesis and X-ray or NMR/DFT structure elucidation of Twenty-One new trifluoromethyl derivatives of soluble cage isomers of  $C_{76}$ ,  $C_{78}$ ,  $C_{84}$ , and  $C_{90}$ . *Journal of the American Chemical Society*, 130, 13471–13489.
- Kato, H., Taninaka, A., Sugai, T., & Shinohara, H. (2003). Structure of a missing-caged metallofullerene:  $La_2@C_{72}$ . *Journal of the American Chemical Society*, 125(26), 7782–7783.
- Kemnitz, E., & Troyanov, S. I. (2009). Connectivity patterns of two  $C_{90}$  isomers provided by the structure elucidation of  $C_{90}Cl_{32}$ . *Angewandte Chemie International Edition*, 48(14), 2584–2587.
- Keper, D. L., & Clare, B. W. (1996). Stereochemical patterns formed by addition to fullerene  $C_{60}$ . *Coordination Chemistry Reviews*, 155, 1–33.
- Kessler, B., Bringer, A., Cramm, S., Schlebusch, C., Eberhardt, W., Suzuki, S., Achiba, Y., Esch, F., Barnaba, M., & Cocco, D. (1997). Evidence for incomplete charge transfer and la-derived states in the valence bands of endohedrally doped  $La@C_{82}$ . *Physical Review Letters*, 79(12), 2289–2292.
- Kikuchi, K., Nakahara, N., Wakabayashi, T., Suzuki, S., Shiromaru, H., Miyake, Y., Saito, K., Ike-moto, I., Kainosho, M., & Achiba, Y. (1992). NMR characterization of isomers of  $C_{78}$ ,  $C_{82}$  and  $C_{84}$  fullerenes. *Nature*, 357(6374), 142–145.
- Kobayashi, K., & Nagase, S. (1997a). Structures of the  $Ca@C_{82}$  isomers: A theoretical prediction. *Chemical Physics Letters*, 274(1–3), 226–230.
- Kobayashi, K., Nagase, S., Yoshida, M., & Osawa, E. (1997b). Endohedral metallofullerenes. Are the isolated pentagon rule and fullerene structures always satisfied? *Journal of the American Chemical Society*, 119(51), 12693–12694.
- Kobayashi, K., & Nagase, S. (1998). Structures and electronic states of  $M@C_{82}$  ( $M=Sc, Y, La$  and lanthanides). *Chemical Physics Letters*, 282(3–4), 325–329.
- Kobayashi, K., & Nagase, S. (1999). Bonding features in endohedral metallofullerenes. Topological analysis of the electron density distribution. *Chemical Physics Letters*, 302(3–4), 312–316.
- Kobayashi, K., & Nagase, S. (2002a). A stable unconventional structure of  $Sc_2@C_{66}$  found by density functional calculations. *Chemical Physics Letters*, 362(5–6), 373–379.
- Kobayashi, K., & Nagase, S. (2002b). Structures and electronic properties of endohedral metallofullerenes; theory and experiment. In T. Akasaka & S. Nagase (Eds.), *Endofullerenes: A new family of carbon custers* (pp. 99–119). Dordrecht: Kluwer.
- Kobayashi, K., Nagase, S., & Akasaka, T. (1995). A theoretical study of  $C_{80}$  and  $La_2@C_{80}$ . *Chemical Physics Letters*, 245(2–3), 230–236.
- Kobayashi, K., Sano, Y., & Nagase, S. (2001). Theoretical study of endohedral metallofullerenes:  $Sc_{3-n}La_nN@C_{80}$  ( $n=0-3$ ). *Journal of Computational Chemistry*, 22(13), 1353–1358.



- Komatsu, K., Murata, M., & Murata, Y. (2005). Encapsulation of molecular hydrogen in fullerene  $C_{60}$  by organic synthesis. *Science*, 307(5707), 238–240.
- Kovalenko, V. I., & Khamatgalimov, A. R. (2003). Open-shell fullerene  $C_{74}$ : Phenalenyl-radical substructures. *Chemical Physics Letters*, 377(3–4), 263–268.
- Krapp, A., & Frenking, G. (2007). Is this a chemical bond? A theoretical study of  $Ng_2@C_{60}$  ( $Ng = He, Ne, Ar, Kr, Xe$ ). *Chemistry – A European Journal*, 13(29), 8256–8270.
- Krättschmer, W., Lamb, L. D., Fostiropoulos, K., & Huffman, D. R. (1990). Solid  $C_{60}$  – a new form of carbon. *Nature*, 347(6291), 354–358.
- Krause, M., & Dunsch, L. (2005). Gadolinium nitride  $Gd_3N$  in carbon cages: The influence of cluster size and bond strength. *Angewandte Chemie-International Edition*, 44(10), 1557–1560.
- Krause, M., Popov, A., & Dunsch, L. (2006). Vibrational structure of endohedral fullerene  $Sc_3N@C_{78}(D_{3h})$ : Evidence for a strong coupling between the  $Sc_3N$  cluster and  $C_{78}$  cage. *ChemPhysChem*, 7(8), 1734–1740.
- Krause, M., Ziegls, F., Popov, A. A., & Dunsch, L. (2007). Entrapped bonded hydrogen in a fullerene: The five-atom cluster  $Sc_3CH$  in  $C_{80}$ . *Chemphyschem*, 8(4), 537–540.
- Kroto, H. W. (1987). The Stability of the fullerenes  $C_{24}$ ,  $C_{28}$ ,  $C_{32}$ ,  $C_{36}$ ,  $C_{50}$ ,  $C_{60}$  and  $C_{70}$ . *Nature*, 329(6139), 529–531.
- Kroto, H. W., Heath, J. R., O'Brien, S. C., Curl, R. F., & Smalley, R. E. (1985).  $C_{60}$  – Buckminsterfullerene. *Nature*, 318(6042), 162–163.
- Lamparth, I., Maichlemosmer, C., & Hirsch, A. (1995). Reversible template-directed activation of equatorial double-bonds of the fullerene framework – regioselective direct synthesis, crystal-structure, and aromatic properties of  $T_h-C_{66}(COOEt)_{12}$ . *Angewandte Chemie-International Edition in English*, 34(15), 1607–1609.
- Liu, D., Hagelberg, F., & Park, S. S. (2006). Charge transfer and electron backdonation in metallofullerenes encapsulating  $NSc_3$ . *Chemical Physics*, 330(3), 380–386.
- Lu, J., Zhang, X. W., Zhao, X. G., Nagase, S., & Kobayashi, K. (2000). Strong metal-cage hybridization in endohedral  $La@C_{82}$ ,  $Y@C_{82}$  and  $Sc@C_{82}$ . *Chemical Physics Letters*, 332(3–4), 219–224.
- Lu, X., Nikawa, H., Nakahodo, T., Tsuchiya, T., Ishitsuka, M. O., Maeda, Y., Akasaka, T., Toki, M., Sawa, H., Slanina, Z., Mizorogi, N., & Nagase, S. (2008). Chemical understanding of a Non-IPR metallofullerene: Stabilization of encaged metals on fused-pentagon bonds in  $La_2@C_{72}$ . *Journal of the American Chemical Society*, 130, 9129–9136.
- Macchi, P., & Sironi, A. (2003). Chemical bonding in transition metal carbonyl clusters: Complementary analysis of theoretical and experimental electron densities. *Coordination Chemistry Reviews*, 238–239, 383–412.
- Manolopoulos, D. E., May, J. C., & Down, S. E. (1991). Theoretical-studies of the fullerenes –  $C_{34}$  to  $C_{70}$ . *Chemical Physics Letters*, 181(2–3), 105–111.
- Matsuzawa, N., Dixon, D. A., & Fukunaga, T. (1992). Semiempirical calculations of dihydrogenated buckminsterfullerenes,  $C_{60}H_2$ . *Journal of Physical Chemistry*, 96(19), 7594–7604.
- Matta, C. F., & Boyd, R. J. (Eds.). (2007). *The quantum theory of atoms in molecules. From solid state to DNA and drug design*. Weinheim: Wiley.
- Mercado, B. Q., Beavers, C. M., Olmstead, M. M., Chaur, M. N., Walker, K., Holloway, B. C., Echegoyen, L., & Balch, A. L. (2008). Is the isolated pentagon rule merely a suggestion for endohedral fullerenes? The structure of a second egg-shaped endohedral fullerene— $Gd_3N@C_2(39663)-C_{82}$ . *Journal of the American Chemical Society*, 130(25), 7854–7855.
- Miyake, Y., Minami, T., Kikuchi, K., Kainosho, M., & Achiba, Y. (2000). Trends in structure and growth of higher fullerenes isomer structure of  $C_{86}$  and  $C_{88}$ . *Molecular Crystals and Liquid Crystals*, 340, 553–558.
- Muthukumar, K., & Larsson, J. A. (2008). A density functional study of  $Ce@C_{82}$ : Explanation of the Ce preferential bonding site. *Journal of Physical Chemistry A*, 112, 1071–1075.
- Mutig, T., Ioffe, I. N., Kemnitz, E., & Troyanov, S. I. (2008). Crystal and molecular structures of  $C_2-C_{70}(CF_3)_8-1.5PhMe$ . *Mendeleev Communications*, 18, 73–75.
- Nagase, S., Kobayashi, K., & Akasaka, T. (1997). Recent progress in endohedral dimetallofullerenes. *Theochem-Journal of Molecular Structure*, 398, 221–227.
- Nagase, S., Kobayashi, K., & Akasaka, T. (1999). Unconventional cage structures of endohedral metallofullerenes. *Journal of Molecular Structure-Theochem*, 462, 97–104.
- Neretin, I. S., Lyssenko, K. A., Antipin, M. Y., Slovokhotov, Y. L., Boltalina, O. V., Troshin, P. A., Lukonin, A. Y., Sidorov, L. N., & Taylor, R. (2000).  $C_{60}F_{18}$ , a flattened fullerene: Alias a hexa-substituted benzene. *Angewandte Chemie-International Edition*, 39(18), 3273–3276.
- Nishibori, E., Takata, M., Sakata, M., Taninaka, A., & Shinohara, H. (2001). Pentagonal-dodecahedral  $La_2$  charge density in  $[80-I_h]$  fullerene:  $La_2@C_{80}$ .

- Angewandte Chemie-International Edition*, 40(16), 2998–2999.
- Nishibori, E., Ishihara, M., Takata, M., Sakata, M., Ito, Y., Inoue, T., & Shinohara, H. (2006a). Bent (metal)<sub>2</sub>C<sub>2</sub> clusters encapsulated in (Sc<sub>2</sub>C<sub>2</sub>)@C<sub>82</sub>(III) and (Y<sub>2</sub>C<sub>2</sub>)@C<sub>82</sub>(III) metallofullerenes. *Chemical Physics Letters*, 433(1–3), 120–124.
- Nishibori, E., Narioka, S., Takata, M., Sakata, M., Inoue, T., & Shinohara, H. (2006b). A C<sub>2</sub> molecule entrapped in the pentagonal-dodecahedral Y<sub>2</sub> cage in Y<sub>2</sub>C<sub>2</sub>@C<sub>82</sub>(III). *ChemPhysChem*, 7(2), 345–348.
- Olmstead, M. H., de Bettencourt-Dias, A., Duchamp, J. C., Stevenson, S., Marciu, D., Dorn, H. C., & Balch, A. L. (2001). Isolation and structural characterization of the endohedral fullerene Sc<sub>3</sub>N@C<sub>78</sub>. *Angewandte Chemie-International Edition*, 40(7), 1223–1225.
- Olmstead, M. M., Lee, H. M., Duchamp, J. C., Stevenson, S., Marciu, D., Dorn, H. C., & Balch, A. L. (2003). Sc<sub>3</sub>N@C<sub>68</sub>: Folded pentalene coordination in an endohedral fullerene that does not obey the isolated pentagon rule. *Angewandte Chemie-International Edition*, 42(8), 900–903.
- Omelyanyuk, N. A., Goryunkov, A. A., Tamm, N. B., Avdoshenko, S. M., Ioffe, I. N., Sidorov, L. N., Kemnitz, E., & Troyanov, S. I. (2007). New trifluoromethylated derivatives of [60]fullerene, C<sub>60</sub>(CF<sub>3</sub>)<sub>n</sub> with n = 12 and 14. *Chemical Communications*, 2007(45), 4794–4796.
- Popov, A. A. (2009). Metal-cage bonding, molecular structures and vibrational spectra of endohedral fullerenes: Bridging experiment and theory. *Journal of Computational and Theoretical Nanoscience*, 6(2), 292–317.
- Popov, A. A., & Dunsch, L. (2008). Hindered cluster rotation and <sup>45</sup>Sc hyperfine splitting constant in distonoid anion radical Sc<sub>3</sub>N@C<sub>80</sub>, and spatial spin charge separation as a general principle for anions of endohedral fullerenes with metal-localized lowest unoccupied molecular orbitals. *Journal of the American Chemical Society*, 130(52), 17726–17742.
- Popov, A. A., & Dunsch, L. (2009). The bonding situation in endohedral metallofullerenes as studied by quantum theory of atoms in molecules (QTAIM). *Chemistry – A European Journal*, 15(38), 9707–9729.
- Popov, A. A., Senyavin, V. M., Granovsky, A. A., & Lobach, A. S. (2004). Vibrational spectra and molecular structure of the hydrofullerenes C<sub>60</sub>H<sub>18</sub>, C<sub>60</sub>D<sub>18</sub> and C<sub>60</sub>H<sub>36</sub> as studied by IR and Raman spectroscopy and first-principle calculations. In T. N. Veziroglu (Ed.), *Hydrogen materials science and chemistry of carbon nanomaterials* (Vol. 172, pp. 347–356). NATO Science Series II: Mathematics, Physics and Chemistry. Dordrecht: Kluwer Academic.
- Popov, A. A., Senyavin, V. M., Boltalina, O. V., Seppelt, K., Spandl, J., Feigerle, C. S., & Compton, R. N. (2006). Infrared, Raman, and DFT vibrational spectroscopic studies of C<sub>60</sub>F<sub>36</sub> and C<sub>60</sub>F<sub>48</sub>. *Journal of Physical Chemistry A*, 110(28), 8645–8652.
- Popov, A. A., & Dunsch, L. (2007a). Structure, stability, and cluster-cage interactions in nitride clusterfullerenes M<sub>3</sub>N@C<sub>2n</sub> (M=Sc, Y; 2n = 68–98): A density functional theory study. *Journal of the American Chemical Society*, 129(38), 11835–11849.
- Popov, A. A., Kareev, I. E., Shustova, N. B., Lebedkin, S. F., Strauss, S. H., Boltalina, O. V., & Dunsch, L. (2007b). Synthesis, spectroscopic and electrochemical characterization, and DFT study of seventeen C<sub>70</sub>(CF<sub>3</sub>)<sub>n</sub> derivatives (n = 2, 4, 6, 8, 10, 12). *Chemistry – A European Journal*, 14(1), 107–121.
- Popov, A. A., Kareev, I. E., Shustova, N. B., Stukalin, E. B., Lebedkin, S. F., Seppelt, K., Strauss, S. H., Boltalina, O. V., & Dunsch, L. (2007c). Electrochemical, spectroscopic, and DFT study of C<sub>60</sub>(CF<sub>3</sub>)<sub>n</sub> frontier orbitals (n = 2–18): The link between double bonds in pentagons and reduction potentials. *Journal of the American Chemical Society*, 129(37), 11551–11568.
- Popov, A. A., Krause, M., Yang, S. F., Wong, J., & Dunsch, L. (2007d). C<sub>78</sub> cage isomerism defined by trimetallic nitride cluster size: A computational and vibrational spectroscopic study. *Journal of Physical Chemistry B*, 111(13), 3363–3369.
- Raghavachari, K. (1992). Ground state of C<sub>84</sub>: Two almost isoenergetic isomers. *Chemical Physics Letters*, 190(5), 397–400.
- Reimers, J. R., Cai, Z.-L., Bilic, A., & Hush, N. S. (2003). The appropriateness of density-functional theory for the calculation of molecular electronics properties. *Annals of the New York Academy of Sciences*, 1006, 235–251.
- Rogers, K. M., & Fowler, P. W. (1999). A model for pathways of radical addition to fullerenes. *Chemical Communications*, 1999(23), 2357–2358.
- Rodriguez-Forteza, A., Alegret, N., Balch, A. L., & Poblet, J. M. (2010). The maximum pentagon separation rule provides guideline for the structures of endohedral metallofullerenes. *Nature Chemistry*, 2(11), 955–961.
- Ruchardt, C., Gerst, M., Ebenhoch, J., Beckhaus, H. D., Campbell, E. E. B., Tellmann, R., Schwarz, H., Weiske, T., & Pitter, S. (1993). Bimolecular radical formation through H-transfer 3. Transfer hydrogenation and deuteration of buckminsterfullerene



- C<sub>60</sub> by 9,10-dihydroanthracene and 9,9',10,10'[D<sub>4</sub>]dihydroanthracene. *Angewandte Chemie-International Edition in English*, 32(4), 584–586.
- Samokhvalova, N. A., Khavrel, P. A., Markov, V. Y., Samokhvalov, P. S., Goryunkov, A. A., Kemnitz, E., Sidorov, L. N., & Troyanov, S. I. (2009). Isolation and structural characterization of the most stable, highly symmetric isomer of C<sub>60</sub>(CF<sub>3</sub>)<sub>18</sub>. *European Journal of Organic Chemistry*, 2009(18), 2935–2938.
- Sandall, J. P. B., & Fowler, P. W. (2003). The energies of some isomers of C<sub>60</sub>F<sub>8</sub>: The use of experimental and theoretical considerations to limit candidate structures. *Organic & Biomolecular Chemistry*, 1(6), 1061–1066.
- Sato, Y., Yumura, T., Suenaga, K., Moribe, H., Nishide, D., Ishida, M., Shinohara, H., & Iijima, S. (2006). Direct imaging of intracage structure in titanium-carbide endohedral metallofullerene. *Physical Review B*, 73(19), 193401.
- Saunders, M., Jimenezvazquez, H. A., Cross, R. J., & Poreda, R. J. (1993). Stable compounds of Helium and Neon – He@C<sub>60</sub> and Ne@C<sub>60</sub>. *Science*, 259(5100), 1428–1430.
- Schmalz, T. G., Seitz, W. A., Klein, D. J., & Hite, G. E. (1988). Elemental carbon cages. *Journal of the American Chemical Society*, 110(4), 1113–1127.
- Shao, N., Gao, Y., Yoo, S., An, W., & Zeng, X. C. (2006). Search for lowest-energy fullerenes: C<sub>98</sub> to C<sub>110</sub>. *Journal of Physical Chemistry A*, 110(24), 7672–7676.
- Shao, N., Gao, Y., & Zeng, X. C. (2007). Search for lowest-energy fullerenes 2: C<sub>38</sub> to C<sub>80</sub> and C<sub>112</sub> to C<sub>120</sub>. *Journal of Physical Chemistry C*, 111(48), 17671–17677.
- Shi, Z. Q., Wu, X., Wang, C. R., Lu, X., & Shinohara, H. (2006). Isolation and characterization of Sc<sub>2</sub>C<sub>2</sub>@C<sub>68</sub>: A metal-carbide endofullerene with a non-IPR carbon cage. *Angewandte Chemie-International Edition*, 45(13), 2107–2111.
- Shimotani, H., Ito, T., Iwasa, Y., Taninaka, A., Shinohara, H., Nishibori, E., Takata, M., & Sakata, M. (2004). Quantum chemical study on the configurations of encapsulated metal ions and the molecular vibration modes in endohedral dimetallofullerene La<sub>2</sub>@C<sub>80</sub>. *Journal of the American Chemical Society*, 126(1), 364–369.
- Shinohara, H. (2000). Endohedral metallofullerenes. *Reports on Progress in Physics*, 63(6), 843–892.
- Shustova, N. B., Kuvychko, I. V., Bolskar, R. D., Seppelt, K., Strauss, S. H., Popov, A. A., & Boltalina, O. V. (2006). Trifluoromethyl derivatives of insoluble small-HOMO–LUMO-gap hollow higher fullerenes. NMR and DFT structure elucidation of C<sub>2</sub>-(C<sub>74</sub>-D<sub>3h</sub>)(CF<sub>3</sub>)<sub>12</sub>, C<sub>5</sub>-(C<sub>76</sub>-T<sub>d</sub>(2))(CF<sub>3</sub>)<sub>12</sub>, C<sub>2</sub>-(C<sub>78</sub>-D<sub>3h</sub>(5))(CF<sub>3</sub>)<sub>12</sub>, C<sub>5</sub>-(C<sub>80</sub>-C<sub>2v</sub>(5))(CF<sub>3</sub>)<sub>12</sub>, and C<sub>2</sub>-(C<sub>82</sub>-C<sub>2</sub>(5))(CF<sub>3</sub>)<sub>12</sub>. *Journal of the American Chemical Society*, 128(49), 15793–15798.
- Shustova, N. B., Newell, B. S., Miller, S. M., Anderson, O. P., Bolskar, R. D., Seppelt, K., Popov, A. A., Boltalina, O. V., & Strauss, S. H. (2007). Discovering and verifying elusive fullerene cage isomers: Structures of C<sub>2</sub>-p<sup>11</sup>-(C<sub>74</sub>-D<sub>3h</sub>)(CF<sub>3</sub>)<sub>12</sub> and C<sub>2</sub>-p<sup>11</sup>-(C<sub>78</sub>-D<sub>3h</sub>(5))(CF<sub>3</sub>)<sub>12</sub>. *Angewandte Chemie-International Edition*, 46(22), 4111–4114.
- Shustova, N. B., Chen, Y.-S., Mackey, M. A., Coumbe, C. E., Phillips, J. P., Stevenson, S., Popov, A. A., Strauss, S. H., & Boltalina, O. V. (2009). Sc<sub>3</sub>N@(C<sub>80</sub>-I<sub>h</sub>(7))(CF<sub>3</sub>)<sub>14</sub> and Sc<sub>3</sub>N@(C<sub>80</sub>-I<sub>h</sub>(7))(CF<sub>3</sub>)<sub>16</sub>. Endohedral metallofullerene derivatives with exohedral addends on four and eight triple-hexagon junctions. Does the Sc<sub>3</sub>N cluster control the addition pattern or vice versa? *Journal of the American Chemical Society*, 131(48), 17630–17637.
- Shustova, N. B., Mazej, Z., Chen, Y.-S., Popov, A. A., Strauss, S. H., & Boltalina, O. V. (2010). Saturnene revealed: X-ray crystal structure of D<sub>5d</sub>-C<sub>60</sub>F<sub>20</sub> formed in reactions of C<sub>60</sub> with A<sub>x</sub>MF<sub>y</sub> fluorinating agents (A = Alkali Metal; M = 3d Metal). *Angewandte Chemie International Edition*, 49, 812–815.
- Shustova, N. B., Peryshkov, D. V., Kuvychko, I. V., Chen, Y.-S., Mackey, M. A., Coumbe, C. E., Heaps, D. T., Confait, B. S., Heine, T., Phillips, J. P., Stevenson, S., Dunsch, L., Popov, A. A., Strauss, S. H., & Boltalina, O. V. (2011). Poly(perfluoroalkylation) of metallic nitride fullerenes reveals addition-pattern guidelines: Synthesis and characterization of a family of Sc<sub>3</sub>N@C<sub>80</sub>(CF<sub>3</sub>)<sub>n</sub> (n = 2–16) and their radical anions. *Journal of the American Chemical Society*, 133(8), 2672–2690.
- Simeonov, K. S., Amsharov, K. Y., & Jansen, M. (2007). Connectivity of the chiral D<sub>2</sub>-symmetric isomer of C<sub>76</sub> through a crystal-structure determination C<sub>76</sub>Cl<sub>18</sub>·TiCl<sub>4</sub>. *Angewandte Chemie-International Edition*, 46(44), 8419–8421.
- Simeonov, K. S., Amsharov, K. Y., Krokos, E., & Jansen, M. (2008). An Epilogue on the C<sub>78</sub>-fullerene family: The discovery and characterization of an elusive isomer. *Angewandte Chemie International Edition*, 47, 6283–6285.
- Slanina, Z., Zhao, X., Deota, P., & Osawa, E. (2000). Relative stabilities of C<sub>92</sub> IPR fullerenes. *Journal of Molecular Modeling*, 6(2), 312–317.
- Slanina, Z., Ishimura, K., Kobayashi, K., & Nagase, S. (2004a). C<sub>72</sub> isomers: The IPR-satisfying cage is disfavored by both energy and entropy. *Chemical Physics Letters*, 384(1–3), 114–118.

- Slanina, Z., Zhao, X., Uhlik, F., Lee, S. L., & Adamowicz, L. (2004b). Computing enthalpy-entropy interplay for isomeric fullerenes. *International Journal of Quantum Chemistry*, 99(5), 640–653.
- Slanina, Z., Chen, Z. F., Schleyer, P. V., Uhlik, F., Lu, X., & Nagase, S. (2006a). La<sub>2</sub>@C<sub>72</sub> and Sc<sub>2</sub>@C<sub>72</sub>: Computational characterizations. *Journal of Physical Chemistry A*, 110(6), 2231–2234.
- Slanina, Z., Uhlik, F., & Nagase, S. (2006b). Computed structures of two known Yb@C<sub>74</sub> isomers. *Journal of Physical Chemistry A*, 110(47), 12860–12863.
- Slanina, Z., Uhlik, F., Sheu, J. H., Lee, S. L., Adamowicz, L., & Nagase, S. (2008). Stabilities of fullerenes: Illustration on C<sub>80</sub>. *Match-Communications in Mathematical and in Computer Chemistry*, 59, 225–238.
- Spielmann, H. P., Weedon, B. R., & Meier, M. S. (2000). Preparation and NMR characterization of C<sub>70</sub>H<sub>10</sub>: Cutting a fullerene pi-system in half. *Journal of Organic Chemistry*, 65(9), 2755–2758.
- Stevenson, S., Rice, G., Glass, T., Harich, K., Cromer, F., Jordan, M. R., Craft, J., Hadju, E., Bible, R., Olmstead, M. M., Maitra, K., Fisher, A. J., Balch, A. L., & Dorn, H. C. (1999). Small-bandgap endohedral metallofullerenes in high yield and purity. *Nature*, 401(6748), 55–57.
- Stevenson, S., Fowler, P. W., Heine, T., Duchamp, J. C., Rice, G., Glass, T., Harich, K., Hajdu, E., Bible, R., & Dorn, H. C. (2000). Materials science – A stable non-classical metallofullerene family. *Nature*, 408(6811), 427–428.
- Stevenson, S., Mackey, M. A., Stuart, M. A., Phillips, J. P., Easterling, M. L., Chancellor, C. J., Olmstead, M. M., & Balch, A. L. (2008). A distorted tetrahedral metal oxide cluster inside an icosahedral carbon cage. Synthesis, isolation, and structural characterization of Sc<sub>4</sub>(μ<sup>3</sup>-O)<sub>2</sub>@I<sub>h</sub>-C<sub>80</sub>. *Journal of the American Chemical Society*, 130(36), 11844–11845.
- Sun, G. Y. (2003a). Assigning the major isomers of fullerene C<sub>88</sub> by theoretical <sup>13</sup>C NMR spectra. *Chemical Physics Letters*, 367(1–2), 26–33.
- Sun, G. Y. (2003b). Theoretical <sup>13</sup>C NMR chemical shifts of the stable isomers of fullerene C<sub>90</sub>. *Chemical Physics*, 289(2–3), 371–380.
- Sun, G. Y., & Kertesz, M. (2000). Theoretical <sup>13</sup>C NMR spectra of IPR isomers of fullerenes C<sub>60</sub>, C<sub>70</sub>, C<sub>72</sub>, C<sub>74</sub>, C<sub>76</sub>, and C<sub>78</sub> studied by density functional theory. *Journal of Physical Chemistry A*, 104(31), 7398–7403.
- Sun, G. Y., & Kertesz, M. (2001a). Identification for IPR isomers of fullerene C<sub>82</sub> by theoretical <sup>13</sup>C NMR spectra calculated by density functional theory. *Journal of Physical Chemistry A*, 105(22), 5468–5472.
- Sun, G. Y., & Kertesz, M. (2001b). Isomer identification for fullerene C<sub>84</sub> by <sup>13</sup>C NMR spectrum: A density-functional theory study. *Journal of Physical Chemistry A*, 105(21), 5212–5220.
- Sun, G. Y., & Kertesz, M. (2002). <sup>13</sup>C NMR spectra for IPR isomers of fullerene C<sub>86</sub>. *Chemical Physics*, 276(2), 107–114.
- Tagmatarchis, N., Avent, A. G., Prassides, K., Dennis, T. J. S., & Shinohara, H. (1999). Separation, isolation and characterisation of two minor isomers of the [84]fullerene C<sub>84</sub>. *Chemical Communications*, 1999(11), 1023–1024.
- Tagmatarchis, N., Arcon, D., Prato, M., & Shinohara, H. (2002). Production, isolation and structural characterization of [92]fullerene isomers. *Chemical Communications*, 2002(24), 2992–2993.
- Takata, M., Nishibori, E., Sakata, M., & Shinohara, H. (2003). Synchrotron radiation for structural chemistry – endohedral natures of metallofullerenes found by synchrotron radiation powder method. *Structural Chemistry*, 14(1), 23–38.
- Tamm, N. B., Sidorov, L. N., Kemnitz, E., & Troyanov, S. I. (2009a). Crystal structures of C<sub>94</sub>(CF<sub>3</sub>)<sub>20</sub> and C<sub>96</sub>(C<sub>2</sub>F<sub>5</sub>)<sub>12</sub> reveal the cage connectivities in C<sub>94</sub>(61) and C<sub>96</sub>(145) fullerenes. *Angewandte Chemie International Edition*, 48, 9102–9104.
- Tamm, N. B., Sidorov, L. N., Kemnitz, E., & Troyanov, S. I. (2009b). Isolation and structural X-ray investigation of perfluoroalkyl derivatives of six cage isomers of C<sub>84</sub>. *Chemistry – A European Journal*, 15(40), 10486–10492.
- Tan, K., & Lu, X. (2005). Ti<sub>2</sub>C<sub>80</sub> is more likely a titanium carbide endohedral metallofullerene (Ti<sub>2</sub>C<sub>2</sub>)@C<sub>78</sub>. *Chemical Communications*, 2005(35), 4444–4446.
- Tan, Y.-Z., Xie, S.-Y., Huanh, R.-B., & Zheng, I.-S. (2009). The stabilization of fused-pentagon fullerene molecules. *Nature Chemistry*, 1, 450–460.
- Tebbe, F. N., Harlow, R. L., Chase, D. B., Thorn, D. L., Campbell, G. C., Calabrese, J. C., Heron, N., Young, R. J., & Wasserman, E. (1992). Synthesis and single-crystal X-ray structure of a highly symmetrical C<sub>60</sub> derivative, C<sub>60</sub>Br<sub>24</sub>. *Science*, 256(5058), 822–825.
- Troyanov, S. I., & Kemnitz, E. (2005). Synthesis and structures of fullerene bromides and chlorides. *European Journal of Organic Chemistry*, 2005(23), 4951–4962.
- Troyanov, S. I., Popov, A. A., Denisenko, N. I., Boltalina, O. V., Sidorov, L. N., & Kemnitz, E. (2003). The first X-ray crystal structures of halogenated [70]fullerene: C<sub>70</sub>Br<sub>10</sub> and C<sub>70</sub>Br<sub>10</sub>·3Br<sub>2</sub>. *Angewandte Chemie-International Edition*, 42(21), 2395–2398.

- Troyanov, S. I., Dimitrov, A., & Kemnitz, E. (2006). Selective synthesis of a trifluoromethylated fullerene and the crystal structure of  $C_{60}(CF_3)_{12}$ . *Angewandte Chemie-International Edition*, 45(12), 1971–1974.
- Troyanov, S. I., Goryunkov, A. A., Dorozhkin, E. I., Ignat'eva, D. V., Tamm, N. B., Avdoshenko, S. M., Ioffe, I. N., Markov, V. Y., Sidorov, L. N., Scheurel, K., & Kemnitz, E. (2007). Higher trifluoromethylated derivatives of  $C_{60}$ ,  $C_{60}(CF_3)_{16}$  and  $C_{60}(CF_3)_{18}$  – Synthesis, structure, and theoretical study. *Journal of Fluorine Chemistry*, 128(5), 545–551.
- Troyanov, S. I., & Tamm, N. B. (2009a). Cage connectivities of  $C_{88}(33)$  and  $C_{92}(82)$  fullerenes captured as trifluoromethyl derivatives,  $C_{88}(CF_3)_{18}$  and  $C_{92}(CF_3)_{16}$ . *Chemical Communications*, 2009(40), 6035–6037.
- Troyanov, S. I., & Tamm, N. B. (2009b). Crystal and molecular structures of trifluoromethyl derivatives of fullerene  $C_{86}$ ,  $C_{86}(CF_3)_{16}$  and  $C_{86}(CF_3)_{18}$ . *Crystallography Reports*, 54(4), 598–602.
- Tsuchiya, T., Wakahara, T., Maeda, Y., Akasaka, T., Waelchli, M., Kato, T., Okubo, H., Mizorogi, N., Kobayashi, K., & Nagase, S. (2005). 2D NMR characterization of the  $La@C_{82}$  anion. *Angewandte Chemie-International Edition*, 44(21), 3282–3285.
- Valencia, R., Rodriguez-Forteza, A., & Poblet, J. M. (2007). Large fullerenes stabilized by encapsulation of metallic clusters. *Chemical Communications*, (40), 4161–4163.
- Valencia, R., Rodriguez-Forteza, A., & Poblet, J. M. (2008). Understanding the stabilization of metal carbide endohedral fullerenes  $M_2C_2@C_{82}$  and related systems. *Journal of Physical Chemistry A*, 112(20), 4550–4555.
- Wakabayashi, T., Kikuchi, K., Suzuki, S., Shiromaru, H., & Achiba, Y. (1994). Pressure-controlled selective isomer formation of fullerene- $C_{78}$ . *Journal of Physical Chemistry*, 98(12), 3090–3091.
- Wakahara, T., Kobayashi, J., Yamada, M., Maeda, Y., Tsuchiya, T., Okamura, M., Akasaka, T., Waelchli, M., Kobayashi, K., Nagase, S., Kato, T., Kako, M., Yamamoto, K., & Kadish, K. M. (2004). Characterization of  $Ce@C_{82}$  and its anion. *Journal of the American Chemical Society*, 126(15), 4883–4887.
- Wakahara, T., Nikawa, H., Kikuchi, T., Nakahodo, T., Rahman, G. M. A., Tsuchiya, T., Maeda, Y., Akasaka, T., Yoza, K., Horn, E., Yamamoto, K., Mizorogi, N., Slanina, Z., & Nagase, S. (2006).  $La@C_{72}$  having a non-IPR carbon cage. *Journal of the American Chemical Society*, 128(44), 14228–14229.
- Wang, C. R., Kai, T., Tomiyama, T., Yoshida, T., Kobayashi, Y., Nishibori, E., Takata, M., Sakata, M., & Shinohara, H. (2000a).  $C_{66}$  fullerene encaging a scandium dimer. *Nature*, 408, 426–427.
- Wang, C. R., Sugai, T., Kai, T., Tomiyama, T., & Shinohara, H. (2000b). Production and isolation of an ellipsoidal  $C_{80}$  fullerene. *Chemical Communications*, (7), 557–558.
- Wang, C. R., Kai, T., Tomiyama, T., Yoshida, T., Kobayashi, Y., Nishibori, E., Takata, M., Sakata, M., & Shinohara, H. (2001). A scandium carbide endohedral metallofullerene:  $(Sc_2C_2)@C_{84}$ . *Angewandte Chemie-International Edition*, 40(2), 397–399.
- Wang, T.-S., Chen, N., Xiang, J.-F., Li, B., Wu, J.-Y., Xu, W., Jiang, L., Tan, K., Shu, C.-Y., Lu, X., & Wang, C.-R. (2009). Russian-Doll-Type metal carbide endofullerene: Synthesis, isolation, and characterization of  $Sc_4C_2@C_{80}$ . *Journal of the American Chemical Society*, 131(46), 16646–16647.
- Wu, J., & Hageberg, F. (2008). Computational study on  $C_{80}$  enclosing mixed trimetallic nitride clusters of the form  $Gd_4M_{3-x}N$  ( $M=Sc, Sm, Lu$ ). *Journal of Physical Chemistry C*, 112(15), 5770–5777.
- Xiao, Z., Wang, F. D., Huang, S. H., Gan, L. B., Zhou, J., Yuan, G., Lu, M. J., & Pan, J. Q. (2005). Regiochemistry of [70]fullerene: Preparation of  $C_{70}((OOBu)^-tBu)_n$ , ( $n = 2, 4, 6, 8, 10$ ) through both equatorial and cyclopentadienyl addition modes. *Journal of Organic Chemistry*, 70(6), 2060–2066.
- Xu, L., Cai, W. S., & Shao, X. G. (2006). Prediction of low-energy isomers of large fullerenes from  $C_{132}$  to  $C_{160}$ . *Journal of Physical Chemistry A*, 110(29), 9247–9253.
- Xu, L., Cai, W. S., & Shao, X. G. (2007). Performance of the semiempirical AM1, PM3, MNDO, and tight-binding methods in comparison with DFT method for the large fullerenes  $C_{116}$ – $C_{120}$ . *Journal of Molecular Structure-Theochem*, 817(1–3), 35–41.
- Xu, L., Cai, W., & Shao, X. (2008). Systematic search for energetically favored isomers of large fullerenes  $C_{122}$ – $C_{130}$  and  $C_{162}$ – $C_{180}$ . *Computational Materials Science*, 41, 522–528.
- Yamada, M., Wakahara, T., Tsuchiya, T., Maeda, Y., Kako, M., Akasaka, T., Yoza, K., Horn, E., Mizorogi, N., & Nagase, S. (2008). Location of the metal atoms in  $Ce_2@C_{78}$  and its bis-silylated derivative. *Chemical Communications*, (5), 558–560.
- Yang, S., Popov, A. A., & Dunsch, L. (2007a). The role of an asymmetric nitride cluster on a fullerene

- cage: The non-IPR endohedral DySc<sub>2</sub>N@C<sub>76</sub>. *Journal of Physical Chemistry B*, 111(49), 13659–13663.
- Yang, S. F., Popov, A. A., & Dunsch, L. (2007b). Violating the isolated pentagon rule (IPR): The endohedral non-IPR cage of Sc<sub>3</sub>N@C<sub>70</sub>. *Angewandte Chemie-International Edition*, 46(8), 1256–1259.
- Yang, S., Yoon, M., Hicke, C., Zhang, Z., & Wang, E. (2008). Electron transfer and localization in endohedral metallofullerenes: Ab initio density functional theory calculations. *Physical Review B*, 78, 115435.
- Yang, H., Beavers, C. M., Wang, Z., Jiang, A., Liu, Z., Jin, H., Mercado, B. Q., Olmstead, M. M., & Balch, A. L. (2010). Isolation of a small carbon nanotube: The surprising appearance of D<sub>5h</sub>(1)-C<sub>90</sub>. *Angewandte Chemie International Edition*, 49(5), 886–890.
- Yanov, I., Kholod, Y., Simeon, T., Kaczmarek, A., & Leszczynski, J. (2006). Local minima conformations of the Sc<sub>3</sub>N@C<sub>80</sub> endohedral complex: Ab initio quantum chemical study and suggestions for experimental verification. *International Journal of Quantum Chemistry*, 106(14), 2975–2980.
- Yumura, T., Sato, Y., Suenaga, K., & Iijima, S. (2005). Which do endohedral Ti<sub>2</sub>C<sub>80</sub> metallofullerenes prefer energetically: Ti<sub>2</sub>@C<sub>80</sub> or Ti<sub>2</sub>C<sub>2</sub>@C<sub>78</sub>? A theoretical study. *Journal of Physical Chemistry B*, 109(43), 20251–20255.
- Zalibera, M., Rapta, P., & Dunsch, L. (2007). In situ ESR–UV/VIS/NIR spectroelectrochemistry of an empty fullerene anion and cation: The C<sub>82</sub>:3 isomer. *Electrochemistry Communications*, 9(12), 2843–2847.
- Zhang, J., Hao, C., Li, S. M., Mi, W. H., & Jin, P. (2007). Which configuration is more stable for La<sub>2</sub>@C<sub>80</sub>, D<sub>3d</sub> or D<sub>2h</sub>? Recomputation with ZORA methods within ADF. *Journal of Physical Chemistry C*, 111(22), 7862–7867.
- Zhao, X., Slanina, Z., Goto, H., & Osawa, E. (2003). Theoretical investigations on relative stabilities of fullerene C<sub>94</sub>. *Journal of Chemical Physics*, 118(23), 10534–10540.
- Zheng, G. S., Irle, S., & Morokuma, K. (2005). Performance of the DFTB method in comparison to DFT and semiempirical methods for geometries and energies of C<sub>20</sub>–C<sub>86</sub> fullerene isomers. *Chemical Physics Letters*, 412(1–3), 210–216.
- Zuo, T. M., Beavers, C. M., Duchamp, J. C., Campbell, A., Dorn, H. C., Olmstead, M. M., & Balch, A. L. (2007). Isolation and structural characterization of a family of endohedral fullerenes including the large, chiral cage fullerenes Tb<sub>3</sub>N@C<sub>88</sub> and Tb<sub>3</sub>N@C<sub>86</sub> as well as the I<sub>h</sub> and D<sub>5h</sub> isomers of Tb<sub>3</sub>N@C<sub>80</sub>. *Journal of the American Chemical Society*, 129(7), 2035–2043.
- Zuo, T., Walker, K., Olmstead, M. M., Melin, F., Holloway, B. C., Echegoyen, L., Dorn, H. C., Chaur, M. N., Chancellor, C. J., Beavers, C. M., Balch, A. L., & Athans, A. J. (2008). New egg-shaped fullerenes: Non-isolated pentagon structures of Tm<sub>3</sub>N@C<sub>s</sub>(51365)-C<sub>84</sub> and Gd<sub>3</sub>N@C<sub>s</sub>(51365)-C<sub>84</sub>. *Chemical Communications*, 2008(9), 1067–1069.
- Zywietz, T. K., Jiao, H., Schleyer, R., & de Meijere, A. (1998). Aromaticity and antiaromaticity in oligocyclic annelated five-membered ring systems. *Journal of Organic Chemistry*, 63(10), 3417–3422.



# 20 Structures and Electric Properties of Semiconductor clusters

*Panagiotis Karamanis*

Groupe de Chimie Théorique et Réactivité, ECP, IPREM UMR 5254,  
Université de Pau et de Pays de l'Adour, PAU Cedex, France

<i>Introduction</i> .....	724
<i>Structural Properties of Semiconductor Clusters</i> .....	725
The Ground-State Structure .....	725
Structural Determination .....	727
Silicon Clusters .....	729
Selected Structural Studies .....	729
The Si <sub>6</sub> and Si <sub>36</sub> Cases .....	731
III–V and II–VI Semiconductor Clusters .....	734
General Features .....	734
Gallium Arsenide Clusters .....	735
II–VI Semiconductor Clusters .....	737
<i>Electric Polarizabilities and Hyperpolarizabilities of Clusters</i> .....	740
Definitions and Theory .....	740
Cluster (Hyper)Polarizabilities: Computational Approach .....	741
Semiconductor Cluster (Hyper)polarizabilities: General Trends and Selected Studies .....	746
General Trends .....	746
Selected Studies .....	748
<i>Concluding Remarks</i> .....	751
<i>References</i> .....	751

**Abstract:** Materials that exhibit an electrical resistivity between that of conductor and insulator are called semiconductors. Devices based on semiconductor materials, such as transistors, solar cells, light-emitting diodes, digital integrated circuits, solar photovoltaics, and much more, are the base of modern electronics. Silicon is used in most of the semiconductor devices while other materials such as germanium, gallium arsenide, and silicon carbide are used for specialized applications. The obvious theoretical and technological importance of semiconductor materials has led to phenomenal success in making semiconductors with near-atomic precision such as quantum wells, wires, and dots. As a result, there is a lot of undergoing research in semiconductor clusters of small and medium sizes both experimentally and by means of computational chemistry since the miniaturization of devices still continues. In the next pages, we are going to learn which the most studied semiconductor clusters are, we will explore their basic structural features and visit some of the most representative *ab initio* studies that are considered as works of reference in this research realm. Also, we are going to be introduced to the theory of the electric properties applied in the case of clusters by visiting some of the most illustrative studies into this research area. It is one of the purposes of this presentation to underscore the strong connection between the electric properties of clusters and their structure.

## Introduction

---

About two decades ago Robert Pool stated: “Clusters are strange morsels of matter: when metals or semiconductors are shrunk down to clumps only 10 or 100 atoms in size, they become a “totally new class of materials” with potentially valuable applications” (Pool 1990). This distinctive behavior of clusters has triggered an explosion of scientific work in this area and it is in close relation with the dramatic development of a new field in science. This field is now widely known as “*nanoscience*.” The term nanoscience comes from the terms “nano” and “science.” The word “nano” is used to define a specific length of one billionth of a meter. This size scale resides between bulk materials and typical molecular dimensions. Thus, nanoscience is associated with the study of structures, materials, and devices, which are larger than the typical molecules but extremely small, usually in the range from 0.1 to 100 nm. The increasing importance of this area and its rapid expansion is owed mainly to the requirements of modern technologies for a vast diversity of new materials with more than one function. The field of nanoscience is highly multidisciplinary and joins different disciplines such as chemistry, applied physics, materials science, colloidal science, device physics, supramolecular chemistry, and even more, mechanical and electrical engineering. As a matter of fact, nanoscience can be viewed as extension of most of existing sciences into the nanoscale or the upgrade of the existing molecular sciences to the nanoscale dimensions.

Among nano-objects clusters occupy a large part of the big picture. The so-called nanoclusters apart from a bridge between molecules and solids are systems with properties of their own which are considerably different from those of the bulk materials and from those of their constituent parts (atoms and molecules). Under specific conditions those species can be considered as the building modules of nano-objects which are the foundations of nanoscience. Clusters are aggregates of atoms or molecules in the size of few nanometers and their constitution ranges between 10 and  $10^6$  atoms. They can be built from only one type of atoms such as the homogeneous silicon clusters, or from more than one element such as the heterogeneous gallium

arsenide binary clusters. Atomic clusters can be met in neutral or charged forms while their atoms bind together by almost all of the main bond types such as covalent, ionic, van der Waals, and metallic.

Amongst the different types of clusters that have been the subject of numerous studies in the past, clusters which originate from semiconductor materials have attracted considerable attention. In spite of their origin, these entities are not necessarily semiconductors. Their basic bonding features resemble those of the metals but they keep as well some of the covalent bonding characteristics which dominate in semiconductor nanocrystals.

The purpose of this presentation is to bring together the most representative *ab initio* studies of the non-bulk-like structural and electric properties of semiconductor clusters. Both of these two different property classes are closely related to each other and have occupied the interest of the researcher in numerous studies.

## Structural Properties of Semiconductor Clusters

---

Excluding clusters built from carbon (fullerenes) then the most studied semiconductor clusters are those made from silicon (Si) and gallium arsenide (GaAs). GaAs clusters belong to the so-called III–V group of semiconductors which are formed between the elements of groups 13 and 15. Also, there is a significant amount of work focusing on the II–VI semiconductor clusters which are formed between the elements of the 12 and 15 groups. Especially for the latter clusters there is significant amount of reported experimental and theoretical work due to their unique optical properties. The most studied II–VI semiconductor clusters are those built from cadmium sulfide which have served as prototypes for studies of the effect of quantum confinement on electronic and optical properties of semiconductor nano-objects. For instance, CdS quantum dots which are water soluble and biocompatible (Bruchez et al. 1998), are potentially useful as fluorescent biological labels since they are characterized by large optical gaps. Also, cadmium selenide and telluride clusters have attracted considerable attention due to their narrow bandgaps and large Bohr exciton radii. The last characteristic implies that nanostructures built from those systems are expected to exhibit strong quantum confinement and this feature makes both CdSe and CdTe nano-objects very interesting to explore their properties. Other kinds of semiconductor clusters that have been the subject of a notable number of computational studies are clusters built from GaN, GaP, InP, InAs, ZnO, ZnS, AlP, HgTe, Ge, SnTe, BeTe, BiTe, BN, BAs, and BP.

## The Ground-State Structure

---

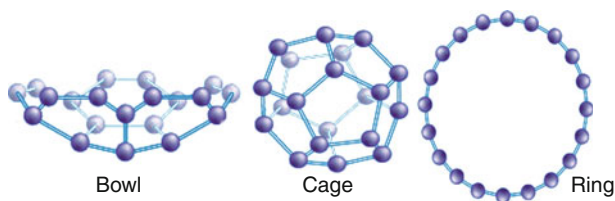
In principle, the most favorable atom arrangement of a cluster should be the one that is characterized by the smallest total energy. This structure is generally called the *ground-state structure* and at zero or low enough temperatures should be the mathematical global minimum of the potential energy of a cluster as a function of the coordinates of the atomic centers (the potential energy surface, PES). The arrangement of the atoms in the ground-state structure is the one that is considered in the majority of cluster property studies, assuming that most of those properties are defined by the properties of the lowest energy configuration. As a result, a respectable



number of various computational schemes have been developed and proposed in order to treat the *ground-state structure* problem in an accurate and efficient manner. However, the solution to this problem is neither obvious nor simple. In the contrary, it corresponds to a task of extremely high computational complexity. The problem becomes even harder given that the available experimental methods are not yet in the position to provide the necessary microscopic structural details for the complete understanding of clusters structures in order for the developed theoretical methods to be verified or improved. Also, the developed computational methods face certain difficulties that are mainly delivered from “practical” limitations of the algorithms used or restrictions of the quantum chemical methods in the precise calculation of the potential energy surface of a given cluster. Accordingly, in several cases the global minimum of the potential energy cluster surface exhibits a strong dependence on the quantum chemical method one uses in order to explore it (Karamanis et al. 2007b). A classical example of the above statement is the case of  $C_{20}$ . This cluster is the smallest possible fullerene, and experiments suggest that it should be a planar ring (Castro et al. 2002; Dugourd et al. 1998; Prinzbach et al. 2000). However, detailed theoretical studies (Grossman et al. 1995) by means of quantum Monte Carlo, all-electron fixed-node quantum Monte Carlo (Sokolova et al. 2000), single- and multireference MP2 methods (Grimme and Mück-Lichtenfeld 2002) and high-level ab initio methods (An et al. 2005) pointed out the bowl and the cage structures as more stable. The answer to this puzzle is that both experiments and theory are correct since if one introduces finite-temperature corrections to the calculations then ring structure becomes more stable (see [Fig. 20-1](#)).

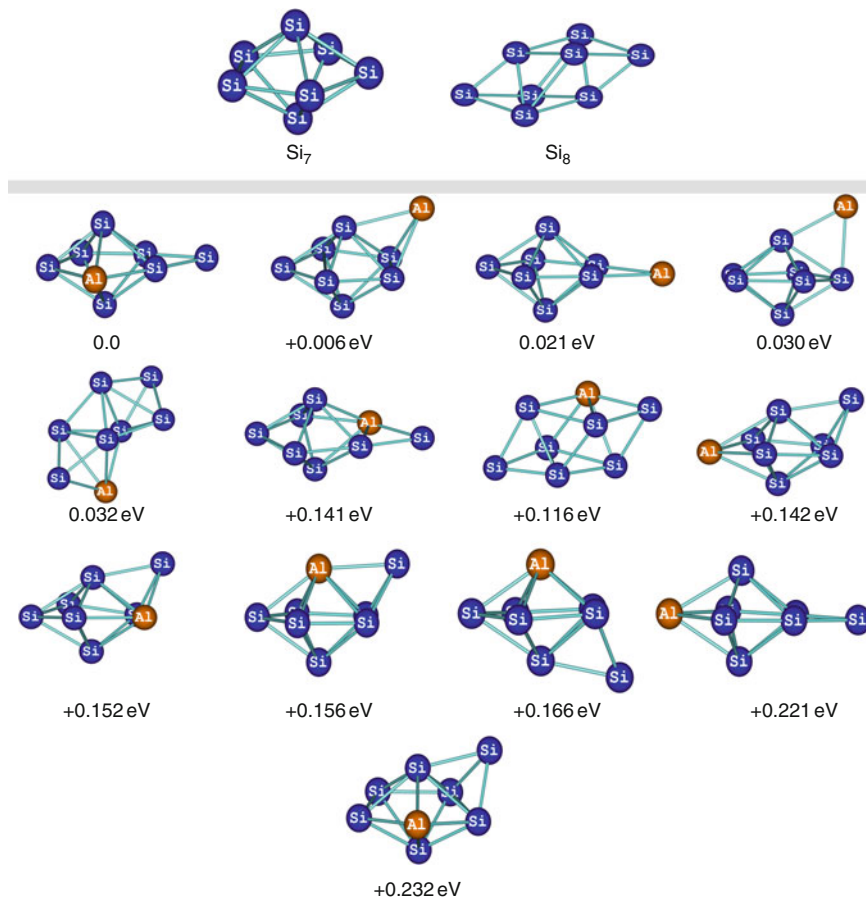
Furthermore, some specific clusters show a peculiar behavior well known as “fluxional behavior.” This behavior is connected with the fact that at a given temperature the clusters are expected to be in some sort of thermal equilibrium rapidly interconverting from one stable isomer to the other due to fast and sometimes drastic atomic rearrangements. During a structural rearrangement of this kind, the resulting “isomerization” leads to structures characterized by different bonding patterns. Thus, it would not be irrational for one to claim that *there is no guarantee that the theoretically predicted ground states are favored in all situations and condition*.

In order to overcome such problems many studies extend their property investigations to stationary points which correspond to cluster configurations energetically close to the ground state. These clusters are *meta-stable species* and their study is expected to complement the investigations which focus on the narrow area of the global minima. A demonstration of the numerous stable local minima that exist even for clusters of small size is given in [Fig. 20-2](#)



■ Fig. 20-1

The three different structures of  $C_{20}$  competing for the ground state



■ Fig. 20-2

Ground state structures and low lying isomers of  $\text{AlSi}_7$  in comparison with the lowest energy structures of  $\text{Si}_7$  and  $\text{Si}_8$

which depicts the ground-state structures of aluminum-doped clusters along with several low-lying isomers which are extremely close in energy (Karamanis et al. 2010).

## Structural Determination

There are two major classes of global computational methods: the *unbiased* and the *seeded* methods. The first class works independently of initial cluster configurations and is considered as the most significant and reliable but the more computationally demanding. The second class utilizes a set of initial structures as *seeds* and they are usually faster than the unbiased; however, there is always the possibility of disregarding configurations of low energy that are not expected. Another optional way of finding the most favorable structures of clusters is based on guiding principles and structural rules stability principles, such those that have

been originally developed and tested over the years for boranes and carboranes and bisboranes. Although this kind of approach is more of an art than of an automatic algorithmic computational approach it has been utilized with remarkable success in various systems such as pure or doped silicon cluster, or clusters made from gallium arsenide, cadmium sulfide, selenide, or telluride (see for instance, Al-Laham and Raghavachari 1991, 1993; Lipscomb 1966; Zdetsis 2008, 2009; Williams 1992; Gutsev et al. 2008a, b; Raghavachari and Logovinsky 1985, Raghavachari and Rohlfing 1988; Matxain et al. 2000, 2001, 2003, 2004). In any case though, whatever the method chosen, one has to deal with the existence of a vast number of local minima even in the case of clusters composed by few atoms.

Let us now see in brief some of the developed algorithms that have been used in cases that involve semiconductor clusters. The most commonly used computational schemes in finding the ground-state structures of semiconductor clusters are those based on genetic algorithms that simulate the evolution in nature through natural selection. This approach utilizes concepts such as chromosome mixing, mutations, and the selection of the fittest. Another family of algorithms is the so-called *basin hopping* which use canonical Monte Carlo simulations at a certain temperature. The basic idea of the basin hopping algorithms is to lower the energetic barriers that separate the various local minima of a cluster by leaving the number and the kinds of the local minima unchanged. This has been proven very efficient in scanning different areas of the potential energy surface and has been successfully applied in cases of clusters up to 100 atoms. A different approach which has been applied in a great variety of systems is the thermal simulated annealing. This method lets the system to evolve initially at a high temperature and then a cooling down procedure starts by reducing gradually the temperature of the system to zero temperature. At each step some neighbor structures are considered based on probability rules and then it is decided whether this new structures are accepted or not following certain energy criteria (e.g. by moving to states of lower energy). As a result, the search space which contains appropriate solutions to the problem considerably narrows down. However, if the free energy global minimum changes at low temperatures where dynamical relaxation is slow, the algorithms may become stuck in the structure corresponding to the high-temperature free energy global minimum. Thus, although this algorithm is easy to follow and understand because of its physical concepts, it is less efficient than methods based on genetic and basin hopping algorithms. Finally, another method that has been developed to treat the problem of rich potential energy surfaces close to the minimum is the so-called Global Search Algorithm of Minima (GSAM) (Marchal et al. 2009, 2010, 2011). In brief, the GSAM includes three major parts: the first part is devoted to the generation of an initial guess set of structures for a large number of cluster structures randomly generated by several techniques. The second part performs an automatic selection of the most appropriate structures through a special pattern recognition technique (Karamanis et al. 2009), which are expected to lead to different local minima. Finally, the third part comprises full geometry optimizations of the selected configurations. This last part yields the most stable cluster structures and the structure which corresponds to the ground state among them.

Further information into the subject of the methods that have been used to treat cluster structural problems in a global manner can be found in the Refs. Bazterra et al. (2004), Biswas and Hamann (1986), Blaisten-Barojas and Levesque (1986), Hamad et al. (2005), Ho et al. (1998), Hossain et al. (2007), Jelski et al. (1991), Menon and Subbaswamy (1995), Nair et al. (2004), Pedroza and Da Silva (2007), Sokolova et al. (2000), Tekin and Hartke (2004), Yoo et al. (2004, 2008), Yoo and Zeng (2005, 2004).

## Silicon Clusters

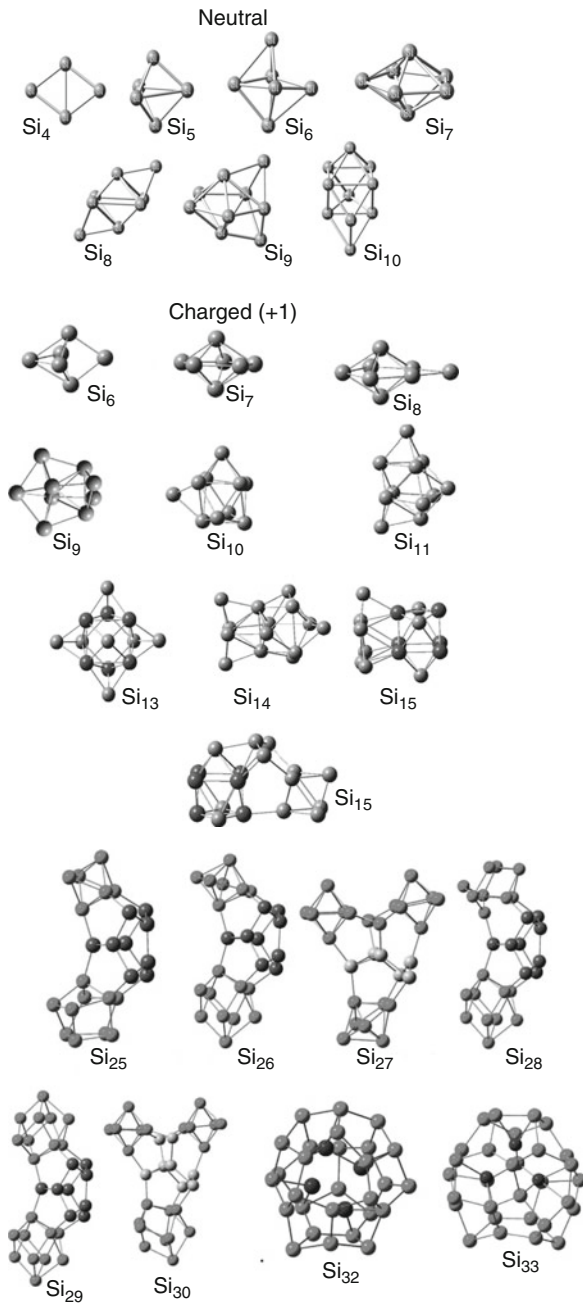
### Selected Structural Studies

As we have already mentioned, among the various semiconductor clusters studied during the past two decades, those made from silicon have attracted most of the attention. A significant number of algorithms and computational strategies have been employed to identify the ground states and the low-lying isomers of silicon clusters of small and medium size with remarkable success. As a result, it is now a common sense that the silicon atoms of a cluster are “different” from those of the bulk material.

It is evident that most of the studies on silicon clusters concern their neutral forms. However, it is impossible to neglect investigations on charged clusters since they have led to very significant results and conclusions (Lyon et al. 2009; Xiao et al. 2002; Nigam et al. 2004; Wei et al. 1997; Li et al. 2003, Li 2005; Zhou and Pan 2008). One of the most impressive investigations on this subject is the recent study reported by Lyon et al. who studied for the first time the experimental infrared spectra of positively charged silicon bare clusters up to 21 atoms in the gas phase. In this study the experimental spectra were compared to theoretical spectral predictions and the authors managed to make unambiguous structural assignments for these species (► Fig. 20-3). This work is one of the most recent proofs confirming that the silicon clusters which have been predicted one way or another by theory also exist in the gas phase.

In the case of the neutral clusters up to 13 atoms, the most stable structures are not planar except  $\text{Si}_3$  and  $\text{Si}_4$ . Mainly they prefer polyhedral structures of rather high symmetry. Raghavachari and Logovinsky (1985), Fournier et al. (1992), Li (2005), and Yu et al. (2002) have established the basic structural patterns of those small species which nowadays are considered as systems of reference. For those species, Zhu and Zeng (2003) provided accurate geometries computed at high levels of theory. A recent study performed by Zdzetsis (2007a, b) have showed that silicon clusters of 5 up to 13 atoms, and their dianions follow common structural motifs of the corresponding closo-boranes. Among the small clusters with 2 up to 13 atoms there are two species of remarkable interest. These species are the  $\text{Si}_6$  and  $\text{Si}_{10}$  which are considered as magic clusters because of their high stability. The six-atomic silicon cluster has attracted the attention of many researchers due the existence of three almost isoenergetic structures that compete for the ground state. Namely, the distorted (compressed) octahedron of  $D_{4h}$  symmetry and two trigonal bipyramidal shapes of lower  $C_{2v}$  symmetry, the edge-capped and face-capped trigonal bipyramids. On the other hand  $\text{Si}_{10}$  is also known as an extremely stable entity and it has been used as a building module of larger structures (Raghavachari and Rohlffing 1988; Mitas et al. 2000; Rohlffing and Raghavachari 1990; Grossman et al. 1995).

From  $n=14$  the shapes of the most stable structures become prolate (Zhu et al. 2004; Yoo and Zeng 2005). An interesting structural feature of the stacked prolate structures is that they are built from blocks that in fact are smaller stable clusters such as the  $\text{Si}_9$  tri-capped trigonal prism or the  $\text{Si}_6$  puckered-hexagonal-ring. For instance  $\text{Si}_{11}$  and  $\text{Si}_{15}$  are built upon the tricapped-trigonal-prism of  $\text{Si}_9$  while  $\text{Si}_6$  puckered-hexagonal-ring motifs can be identified for silicon clusters with 16–20 atoms. This is the most reliable explanation of their stability since it is related to the stability of their building blocks. This finding is of crucial importance since it may open new directions in the nanomaterial and single nanoparticle design.



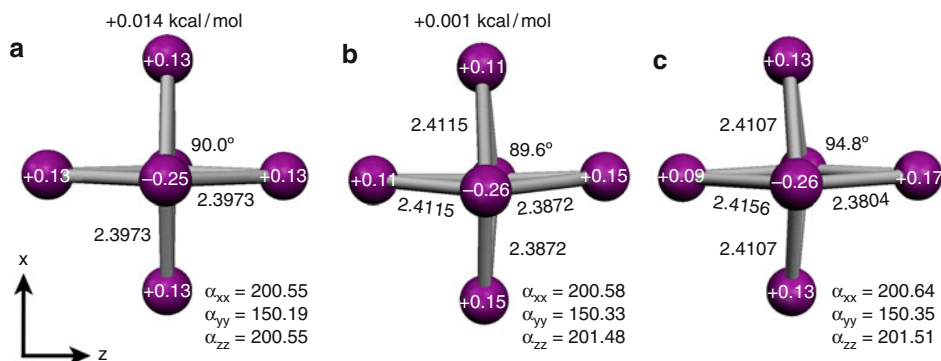
■ Fig. 20-3

Ground-state structures of neutral and charged silicon clusters. Stable structures of neutral silicon clusters

After  $n = 19$ , hollow near-spherical shapes start to show significant stability. From  $n = 24$ , the near-spherical structure with interior atoms becomes nearly degenerated with the prolate configurations (Jarrold and Bower 1992; Jarrold and Constant 1991; Kaxiras and Jackson 1993). However, up to  $n = 25$ , the stacked prolate structures are still the most stable. Finally, although clusters with more than 25 atoms are not very well studied and their ground-state structures are either unknown or under debate (Bai et al. 2006), there are recent studies that yielded very interesting results. For instance, Yoo and coworkers (Avramov et al. 2007; Yoo et al. 2008, 2004; Yoo and Zeng 2006, 2005) searched for generic structural features as well as patterns of structural evolution for the low-lying silicon clusters up to the size of 80 atoms by studying the structures and relative stability of different cluster shapes families. Their results indicate that for some cluster sizes such as  $\text{Si}_{39}$ ,  $\text{Si}_{40}$ , and  $\text{Si}_{50}$ , the fullerene cage motifs consistently are more stable than other kind of cage structures.


### The $\text{Si}_6$ and $\text{Si}_{36}$ Cases

To demonstrate the difficulty in studying the structures and properties of clusters even of small size even when are built from only one element, and the complexity in interpreting computational and experimental results of diverse sources we shall revisit two distinctive cases: One concerns the small  $\text{Si}_6$  cluster and the other the larger  $\text{Si}_{36}$ . As mentioned,  $\text{Si}_6$  is a particularly stable cluster and along with  $\text{Si}_{10}$  coincides with clusters found abundantly in the experiment. **Figure 20-4** shows three optimized structures of  $\text{Si}_6$  at the CCSD(T) level and the natural atomic charges computed with the CCD density. It is obvious that although the two  $C_{2v}$  isomers keep the characteristics of their symmetry group as they were defined in the starting point geometries, they are almost identical with the distorted octahedron and their energy separations are extremely smaller than expected. The  $C_{2v}$  face-capped isomer and the distorted octahedron are lying only 0.001 and 0.014 kcal/mol higher in energy than the edge-capped isomer, respectively. Additionally, MP2 polarizability tensor values (au) at the CCSD(T) optimized




**Fig. 20-4**

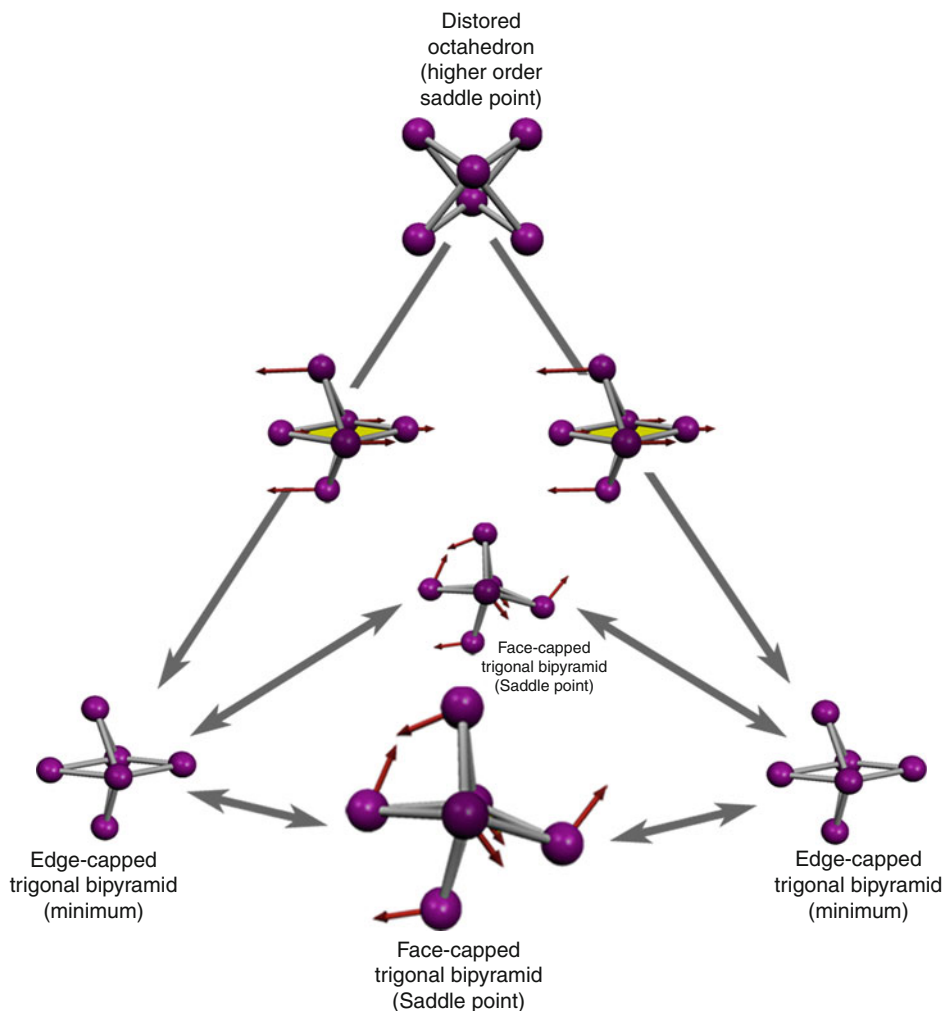
CCSD(T)/6-311G(2d) optimized structures of the three isomers of  $\text{Si}_6$ , atomic charges after a natural bond orbital analysis at the CCD level and MP2/6-311G(2d) polarizabilities (au). All drawn bond lengths are in Å and dihedral angles in degrees. Structure **a** is of  $D_{4h}$  symmetry, structures **b** (face-capped) and **c** (edge-capped) of  $C_{2v}$  symmetry.

geometries (also included in  Fig. 20-2) show that the two  $C_{2v}$  structures are almost as polarizable as the  $D_{4h}$  structure in all three directions. Consequently, the two trigonal bipyramid structures could be viewed as slightly distorted tetragonal bipyramidal shapes belonging to the  $C_{2v}$  point group.

A careful literature search shows that these three structures compete for the ground state. More specifically, all electron and core potential geometry optimizations at Hartree–Fock (HF) level by Raghavachari and Rohlfing prefer an edge-capped trigonal bipyramidal shape of  $C_{2v}$  symmetry while MP2 geometry optimizations favor a distorted octahedron of  $D_{4h}$  symmetry. On the other hand, higher order correlated method based on Møller–Plesset perturbation theory with the standard 6-31G(d) basis set by Zdetsis (2001) showed that the MP2 predicted structure of  $D_{4h}$  symmetry is unstable. Additionally, density functional theory (DFT) (Karamanis et al. 2007b) shows an fluctuating preference between the  $C_{2v}$  face-capped,  $C_{2v}$  edge-capped trigonal bipyramids. It is evident that there is an obvious disagreement between different theoretical approaches.

Let us now explore the most important experimental results concerning this problem. Raman experiments by Honea et al. (1993) of matrix isolated clusters, supported indirectly the MP2/6-31G(d) structure of  $D_{4h}$  symmetry. Their conclusions were based on two arguments: The first was the number of visible bands in both spectra which characterize species of  $D_{4h}$  symmetry, and second, the agreement between the experimental and scaled theoretical harmonic frequencies computed at the MP2/6-31G(d) level with the small 6-31G(d) standard basis set. The strongest arguments used to reject the other two candidates were two: first, geometry optimizations at MP2 level starting from either face-capped or edge-capped trigonal bipyramidal shapes collapsed to the distorted octahedron of  $D_{4h}$  symmetry; second, the other two structures were predicted to have a larger number of active vibrational bands than observed in both experimental Raman and IR spectra. Obviously such a puzzling problem rarely has solely one answer. Indeed, the resolution to this puzzle is twofold. On one hand the source of the disagreement among the various methods used hides in the particular capabilities of each method in the treatment of the pseudo Jahn–Teller effect (PJTE) (Karamanis et al. 2007b). According to general Jahn–Teller theory the only source of instability in any molecular systems is the proper Jahn–Teller effect, for degenerated states (Renner Teller effect in linear systems), and pseudo-Jahn–Teller for non-degenerated ones. PJTE is a part of modern JT interaction theory (Bersuker 2001) and its importance in the formation of the equilibrium structures of clusters has been demonstrated by Garcia-Fernandez et al. (2006) and by Pushpa et al. (2004). In the  $Si_6$  case, geometry optimizations with methods based on Møller–Plesset perturbation theory, which have been demonstrated not to treat the PJTE correctly, predict that the distorted octahedron of  $D_{4h}$  symmetry is the ground-state structure, while, methods which do provide PJTE treatment (DFT, HF) suggest that the distorted octahedron is unstable and undergoes PJTE distortions. On the other hand, the flat potential energy surface is connected with a fluxional behavior of  $Si_6$  (Zdetsis 2007b) caused by the couplings between the electronic motion and soft nuclear vibrations due to the second-order Jahn–Teller effect under the influence of “electron deficiency” and the resulting charge smoothing process. The soft nuclear motion that is implied by the calculation is shown in  Fig. 20-5. Of course, this kind of discrepancies in cluster structures can hardly be identified by experimental means since in such a flexible (or fluxional) system with low barriers, the consideration of separate “conformers” is probably not appropriate at all, and experimental spectroscopic properties are just an average of all structures. This has been highlighted in the recent work of Fielicke et al. (2009) who used tunable far-infrared-vacuum-ultraviolet two-color ionization to obtain vibrational spectra of neutral silicon clusters





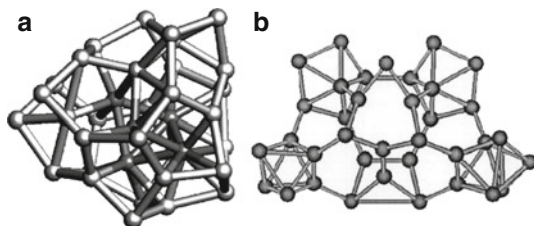
■ Fig. 20-5

Schematic representation of the three competing structures of  $\text{Si}_6$  based on the normal modes of the imaginary frequencies at CCSD(T) level of theory with the split valence Pople-like Basis set 6-311G(2d)

in the gas phase. Their results show clearly that it is almost impossible to distinguish the three different structures by means of vibrational spectroscopy.

Another example that demonstrates the complexity in determining the ground-state structures of larger clusters, and the importance of exploring the complete space when searching for atomic cluster is the case of  $\text{Si}_{36}$  (Bazterra et al. 2002; Sun et al. 2003). This cluster is one of the first large species that have been studied using first principles within the density functional framework (Sun et al. 2003). The structure that was initially proposed as the most stable was a stuffed fullerene-like configuration of near-spherical shape (► Fig. 20-6 structure a).





■ Fig. 20-6

### Two competing structures of $\text{Si}_{36}$

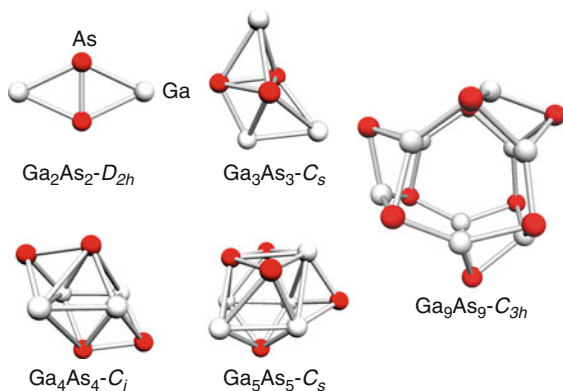
This structure seemed to confirm the up to that time experimental findings according to which a shape transition from prolate shapes to compact ones is occurring as the size of silicon clusters grows. Nonetheless, a subsequent study (Bazterra et al. 2002) based on a global approach using genetic algorithms, showed that a totally different structure lies lower in energy than the one previously adopted (● Fig. 20-6 structure b). Once more, the structure of  $\text{Si}_{36}$  proposed by Bazterra et al. can be envisioned as an assembly of smaller, stable clusters.

## III–V and II–VI Semiconductor Clusters

### General Features

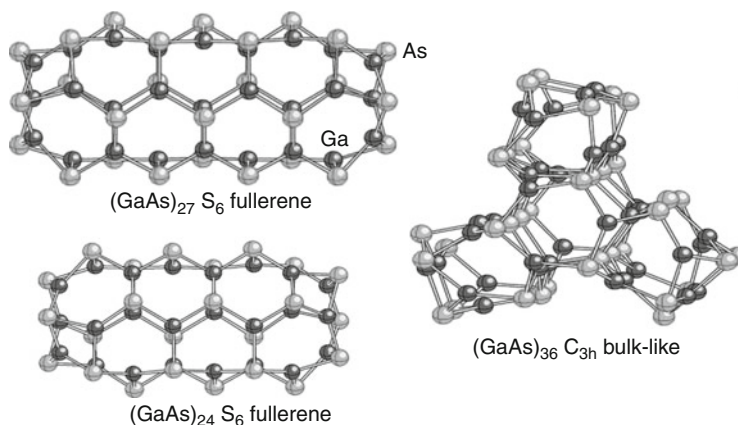
The III–V and II–VI semiconductor clusters are isoelectronic with the elements of the group 13 and 15. For instance, gallium arsenide clusters of the type  $\text{Ga}_n\text{As}_n$  have the same number of electrons with  $\text{Ge}_{2n}$  clusters while the analogue  $\text{Al}_n\text{P}_n$  clusters are isoelectronic with the corresponding  $\text{Si}_{2n}$  cluster species. For clusters of these two semiconductor families with even number of electrons, the preferred spin multiplicity is the singlet, where all electrons are in pairs. Triplets and larger spin multiplicities are always higher in energy (Gutsev et al. 2010). In the case of nonstoichiometric GaAs clusters which are species with even number of electrons, thus, open shell systems the preferred spin multiplicity is the doublet (Karamanis et al. 2009).

The basic bonding pattern in the compound III–V and II–VI semiconductor clusters is the alternating arrangement of their atoms (● Figs. 20-7 and ● 20-8). The alternating A-B type of bonding is a result of the polarity of these entities which is owed to the electronegativity difference between their atoms. As a result, the bonding in clusters formed by atoms with large electronegativity differences is expected to be more ionic than in clusters built from atoms characterized by smaller differences. For instance, the spectroscopic electronegativity differences  $\Delta\chi_{s\text{pec}}$  converted to Pauling scaling between the As and the atoms Ga and In are 0.455 and 0.555, respectively. Accordingly, the bonding in III–V compound clusters built from As and Ga is expected to be of less ionic (or of more covalent character) than clusters built from In and As. However, although the alternating A-B type of bonding is generally observed for this class of semiconductor clusters due to the polarity of their bonding, there are some cases in which homo-atomic bonds are detected between the electronegative atoms. For example the ground-state structures of  $\text{Ga}_4\text{As}_4$  (● Fig. 20-9) and  $\text{Al}_5\text{P}_5$  (● Fig. 20-8) are characterized by As–As and P–P bonds. On the other hand, this bonding feature is not favorable for II–VI semiconductors which also do not favor endohedral structures.



■ Fig. 20-7

Established ground-state structures of  $Ga_n As_n$  clusters with  $n = 2-5$  and 9. Such structure as for  $n = 9$  is the most stable also in the cases of  $Al_9P_9$  and  $Cd_9(S, Se, Te)_9$

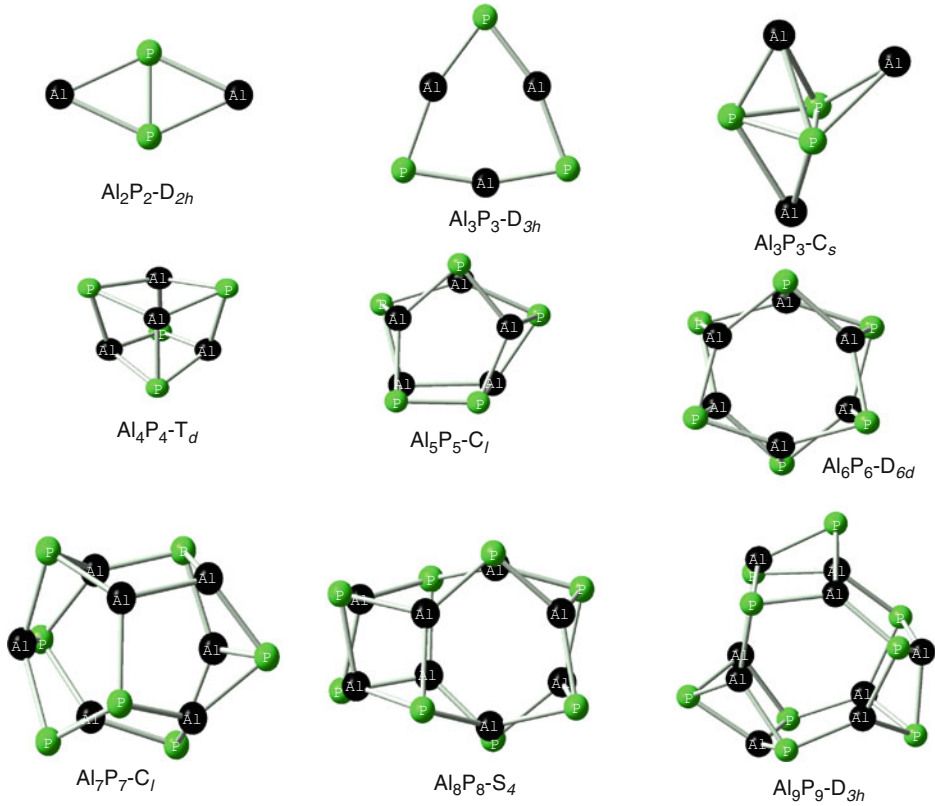


■ Fig. 20-8

Fullerene and bulk-like structures of large GaAs clusters (Gutsev et al. 2010)

## Gallium Arsenide Clusters

Combined experimental and computational studies have led to very interesting and important conclusions concerning microscopic feature of those systems such as their bonding and electronic structures. For instance, the revealed even/odd alternation in the photoionization cross section obtained with an ArF excimer laser (6.4 eV) indicated that clusters of any composition composed by even numbers of atoms (e.g.,  $Ga_1As_5$ ,  $Ga_2As_4$ ,  $Ga_3As_3$ ,  $Ga_4As_2$ ,  $Ga_5As_1$ ) have singlet ground states, whereas odd numbered clusters of any composition (e.g.,  $Ga_1As_4$ ,  $Ga_2As_3$ ,  $Ga_3As_2$ ,  $Ga_4As_1$ ) have doublet ground states with an unpaired electron in a weakly bound HOMO. This sort of electronic structure clearly indicates that the structural and bonding features of the produced small GaAs clusters should be dramatically different from the tetrahedral  $sp^3$  hybridization of the bulk. Both of those indirect experimental conclusions—assumptions



■ Fig. 20-9  
Structures of aluminum phosphide clusters

have been verified by all the later computational studies on those species which clearly showed that the singlet closed shell forms of the even-numbered GaAs clusters are the most stable than any other electronic configuration and their structures are completely different from the bulk (see: O'Brien et al. 1985; Lou et al. 1992; Karamanis et al. 2007a; Gutsev et al. 2008a, b).

Let us now make a brief review of the most representative studies of those important species starting from GaAs clusters which are the most studied species from those belonging to the III-V semiconductor family. Current and future applications of those species, in their nano or bulk, forms are very promising and interestingly diverse, extending from fuel cells Schaller and Klimov (2006) and optoelectronic sensors (Chen et al. 2004) to spintronics (spin-based electronics), medical diagnostics, and quantum computing (see Calarco et al. 2003; Michalet et al. 2005; Wolf et al. 2001).

Pioneering studies performed by O'Brien et al. on supersonic cluster beams of GaAs clusters generated by laser vaporization of discs made from pure GaAs brought theory closer to the experimental reality by providing cluster species of sizes suitable for very precise theoretical computations. As a result, the structural and bonding features of small GaAs clusters have occupied the interest of the researchers in the early cluster computational studies. For instance,

Graves and Scuseria (1991) studied the first members of these systems using the Hartree–Fock (HF) method. Liao and Balasubramanian (1992) by means of the multireference configuration interaction method with singles and doubles (MRCISD) made a reference estimation of the bond lengths and angles of  $(\text{GaAs})_2$ ; Lou et al. (1992) studied the structures and the bonding of small GaAs clusters up to 10 atoms while Andreoni within the Car–Parinello molecular dynamics approach studied the stoichiometric systems up to the ten-atomic  $\text{Ga}_5\text{As}_5$ . Later, Song et al. (1994) applied a fourth-order many body perturbation theory to study species from 2 to 4 atoms ( $\text{Ga}_n\text{As}_n$  with  $n = 2-4$ ). The interest in studying those systems remains intense even the recent years and a respectable variety of different methods have been applied. For instance, Costales et al. (2002) applied a DFT-GGA method for the systems up to the trimer, Zhao et al. (2006), Zhao and Cao (2001), Zhao et al. (2000) used another level of DFT-GGA approach for  $(\text{GaAs})_n$  ( $n = 6-9$ ) while Karamanis et al. (2007b) revisited the previous reported results using second-order many body perturbation theory (MP2) up to clusters with 18 atoms. More recently, Gutsev et al. (2008a, b) extended the earlier studies and reported structures up to 32 atoms with the DFT framework. In addition, there are some reported attempts in studying non-stoichiometric species and the influence of the composition on their properties. One of the most representative works in this field is the investigation of structural and electronic properties of  $\text{Ga}_m\text{As}_n$  clusters reported by Feng et al. (2007); Gutsev et al. (2010) studied the electronic and geometrical structures of neutral  $(\text{GaAs})_n$  clusters using density functional theory with generalized gradient approximation and relativistic effective core potentials for  $n = 17-40, 48$ , and  $54$ . Also, they examined the energetic preference of tubular and non-tubular cages with increasing  $n$  and found that tubular cages are generally lower in total energy than the other cage isomers. Along with the cage structures, they probed structures cut off from a zinc blende lattice, tailoring the surface atoms in such a way as to have no dangling bonds. They found that the lowest energy state of  $(\text{GaAs})_{36}$  has a bulk-like structure with 12 tetrahedrally coordinated inner atoms (► Fig. 20-7). Finally, Gutsev and coworkers (Karamanis et al. 2011) studied the structure and properties of prolate  $(\text{GaAs})_n$  clusters up to 120 atoms corresponding to the (2, 2) and (3, 3) armchair and (6, 0) zigzag capped single-wall tubes within the generalized gradient approximation (DFT-GGA). It was found that the bandgap in all three series does not converge to the GaAs bulk value when the cluster length increases.

## II–VI Semiconductor Clusters

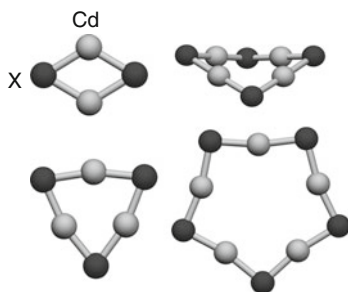
The synthesis of ZnO, ZnS, ZnSe, CdS, CdSe, and CdTe nanostructures which shape an important category of optically active materials with strong size dependence of their exciton energy (see: Alivisatos 1996; Swaminathan et al. 2006; Murray et al. 2000; Peng et al. 1998, 2000) have inspired most of the studies on II–VI semiconductor clusters. The respective nanomaterials can be synthesized in a great variety of sizes and shapes (spheres, rods, tetrapods or branched and core-shell structures) and they have been used for a wide assortment of applications, including quantum light emitting diodes pigments, biological tagging, and solar cells (Gur et al. 2005). Particularly, for CdSe clusters, correlations between their structure and properties have been highlighted by Jose et al. (2006).

One of the most fascinating features of this class of semiconductor clusters is the size dependence of the HOMO–LUMO bandgap which is distinguishable in their luminescence properties. For instance, it has been shown that by adjusting the particle size of colloidal

CdSe–CdS core–shell nanoparticles the fluorescence can be tuned between blue and red. Motivated by those findings, in nanoparticles, Sanville et al. (2006) used direct laser ablation to produce ZnS, CdS, and CdSe clusters and found that clusters composed of 6 and 13 monomer units were ultrastable in all cases. Kasuya et al. (2004) by means of mass spectral analysis of CdSe nanoparticles found that  $(\text{CdSe})_{33}$  and  $(\text{CdSe})_{34}$  are so stable that they grow in preference to any other chemical compositions to produce macroscopic quantities with a simple solution method. First-principles calculations predict that these clusters are puckered  $(\text{CdSe})_{28}$ -cages, with four- and six-membered rings based on the highly symmetric octahedral analogues of fullerenes, accommodating inside their framework either  $(\text{CdSe})_5$  or  $(\text{CdSe})_6$  to form a three-dimensional network with essentially heteropolar  $sp^3$ -bonding.

Let us now see in brief the most cited computational studies for this very interesting class of cluster species. Behrman et al. (1994) have shown that ZnO clusters can form stable, fullerene-like structures while Hamad et al. (2005) provided evidences that ZnS clusters can form onion-like or alternatively “double bubble” structures. Matxain et al. (2000) studied systematically the structures of small ZnO clusters with up to nine atoms and demonstrated that three-dimensional structures may be envisioned as being built from  $\text{Zn}_2\text{O}_2$  and  $\text{Zn}_3\text{O}_3$  rings. Also, the same group (Matxain et al. 2001, 2003) have found that clusters built from ZnS, ZnSe, and CdO clusters can form stable one-dimensional ring structures (● Fig. 20-10).

For species made from Cd and the chalcogenides S, Se Gurin (1998) studied small  $\text{Cd}_x\text{S}_y$  and  $\text{Zn}_x\text{S}_y$  ( $x, y \leq 6$ ) clusters, Troparevsky and Chelikowsky (2001), Troparevsky et al. (2002) reported structures of  $\text{Cd}_n(\text{S}, \text{Se})_n$  with up to 8 atoms, Deglmann et al. (2002) used density functional theory potential surface investigations to study small CdS, and CdSe clusters, up to the heptamer while CdSe large clusters have been investigated further using large crystal structure sections with up to 198 atoms. Also, Matxain et al. (2004) and Jha et al. (2008) reported ring and spherical structures with up to 16 atoms while Sanville et al. (2006) obtained geometries and energies of the neutral and positively charged  $\text{M}_n\text{X}_n$  clusters up to  $n = 16$  ( $\text{M} = \text{Zn}, \text{Cd}$  and  $\text{X} = \text{S}, \text{Se}$ ). Their results showed that one-dimensional structures are favored for some cluster sizes while three-dimensional structures may be envisioned as being built from  $\text{Cd}_2(\text{S}, \text{Se})_2$  and  $\text{Cd}_3(\text{S}, \text{Se})_3$  rings. At this point it is important to stress that contrary to what is reported in several studies about CdX clusters, the five-atom rings are not totally planar. Instead, they maintain distorted envelope structures of  $\text{C}_1$  symmetry due to the weakening of the steric repulsion between the metal atoms as the size of the ring increases. As, a result the planar structure is a transition point in each cluster’s potential energy surface characterized by soft imaginary

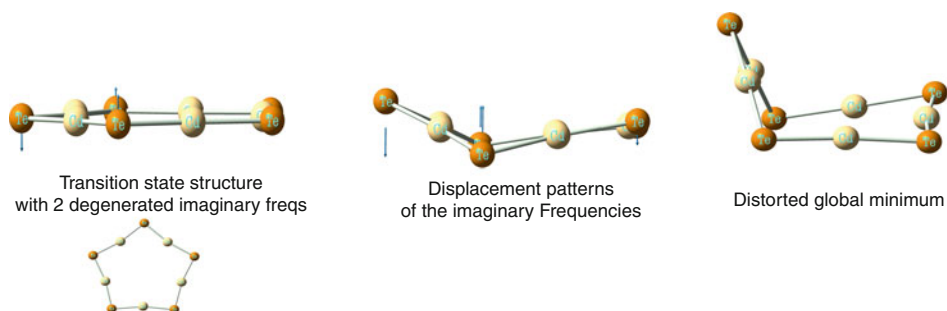


■ Fig. 20-10

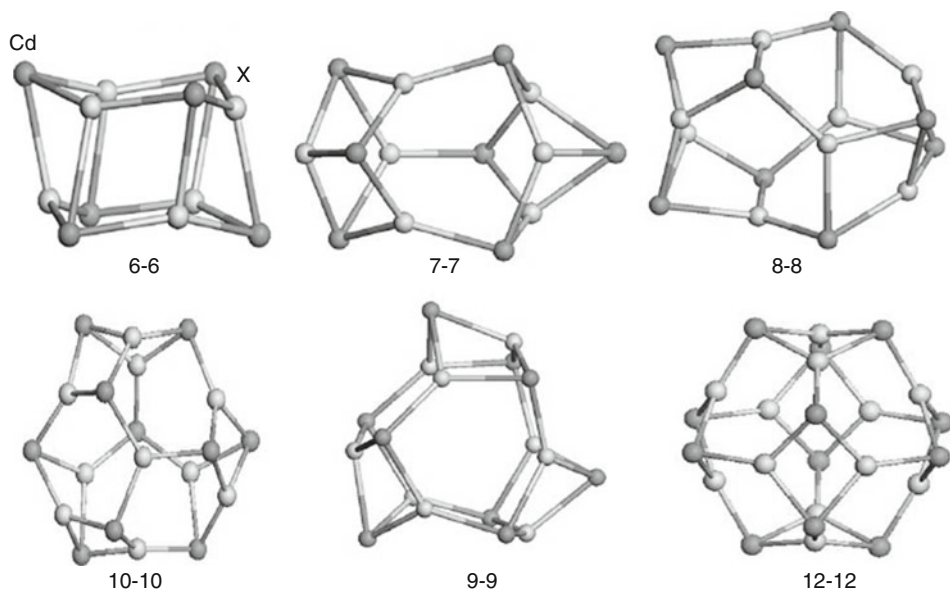
Ring structure-types of  $\text{MnX}_n$  ( $\text{M} = \text{Zn}, \text{Cd}$  and  $\text{X} = \text{S}, \text{Se}, \text{Te}$ ) small clusters

frequencies frequencies of a few  $\text{cm}^{-1}$  which indicate a very floppy system that is expected to exhibit fluxional behavior (► Fig. 20-11).

Lastly, small  $\text{Cd}_n\text{Te}_n$  and  $\text{Hg}_n\text{Te}_n$  clusters have attracted the attention of several groups (see for instance Wang et al. 2004, 2008, 2009). Especially HgTe clusters are very interesting since this material is considered as a semimetal with a small negative bandgap around  $=0.14\text{ eV}$  at 300 K and a semimetal-to-semiconductor can be produced by size quantization making HgTe nano-objects promising candidates as optical amplifiers (► Fig. 20-12).



■ Fig. 20-11  
Displacement patterns and ground-state structure of  $\text{Cd}_5\text{Te}_5$



■ Fig. 20-12  
Typical cage structures of  $\text{Cd}_n\text{X}_n$  ( $X = \text{S}, \text{Se}, \text{Te}$ ) clusters

## Electric Polarizabilities and Hyperpolarizabilities of Clusters

### Definitions and Theory

The electric dipole (hyper)polarizabilities describe the response of a molecular system to an external electric field. Briefly, the polarizabilities (or linear polarizabilities) are used to express the ability of the electronic density of a molecular or cluster entity to distort under the influence of weak external fields such as the field generated by a charge in close distance. The hyperpolarizabilities (or nonlinear polarizabilities) describe the same response to laser beams. Large polarizabilities imply easily polarized molecules, whereas, small polarizabilities correspond to molecules in which the electronic density is considerably insensitive to electric field perturbations. Large hyperpolarizabilities involve molecules which can interact with intense electric fields in a “nonlinear” manner and the corresponding materials are known as nonlinear optical materials. The polarizabilities are associated with fundamental chemical concepts such as global softness (Vela and Gázquez 1990), basicity–acidity (Headley 1987), electronegativity (Nagle 1990), and stability (Hohm 2000), (Parr and Chattaraj 1991). On the other hand, the hyperpolarizabilities are closely related to the nonlinear optical behavior of materials in such processes as the second harmonic generation (SHG) (or frequency doubling), the third harmonic generation (THG), the sum frequency generation (SFG), the optical Kerr effect, and others which are expected to find application in a wide range of future technologies (see Bloembergen 1996 and references therein).

For clusters, polarizability is one of the few microscopic quantities that are available from experiment (Backer 1997) and is linked both to macroscopic and microscopic features of the matter such as the bulk dielectric constants and chemical bonding, respectively. Hence, this property can provide valuable information about crucial microscopic cluster features and the behavior of low dimensional systems that may be used in nanotechnology applications where nano-objects are subjected in small electric perturbations. On the other hand, given that the macroscopic nonlinear optical properties of materials are governed by the microscopic molecular hyperpolarizabilities, the study of those properties on clusters (Leitsmann et al. 2005) may offer a new ground in the search of new nonlinear optical materials with potential applications in future nanostructure technologies. The nonlinear behavior could be employed for amplification, modulation, and changing the frequency of optical signals, similar to how nonlinearities of valves and transistors are used to govern the processes in traditional electric chips and circuits.

The microscopic (hyper)polarizabilities are studied by means of the so-called theory of the response functions which is of importance for all molecular and cluster entities (Roman et al. 2006). The most commonly used approach in studying the linear and nonlinear optical properties of clusters is the so-called semiclassical one. According to this approach a classical treatment is used to describe the response of the cluster to an external field (radiation) while the system itself is treated using the laws and techniques of quantum mechanics. This is done by using a Hamiltonian which combines both of the above treatments:

$$H = H^0 - \hat{\mu}_a F_a - \frac{1}{3} \hat{\Theta}_{\alpha\beta} F_{a\beta} - \frac{1}{15} \hat{\Omega}_{\alpha\beta\gamma} F_{\alpha\beta\gamma} - \frac{1}{105} \hat{\Phi}_{\alpha\beta\gamma\delta} F_{\alpha\beta\gamma\delta} + \dots \quad (20.1)$$

$H^0$  is the Hamiltonian which represents the free of the field system and the coefficients denoted with the Greek capital letters stand for the tensors of the dipole quadrupole, octupole, and hexadecapole moments which are used to implement the field perturbation ( $F$ ) into the new Hamiltonian. The expectation value after the implementation of this modified operator on the



wavefunction is the perturbed energy of the system due to the influence of the field which in the case of a static field  $F$  can be written using a Taylor series expansion as

$$E^P = E^0 - \mu_\alpha F_\alpha - \frac{1}{3} \Theta_{\alpha\beta} F_\alpha F_\beta - \frac{1}{15} \Omega_{\alpha\beta\gamma} F_\alpha F_\beta F_\gamma - \frac{1}{105} \Phi_{\alpha\beta\gamma\delta} F_\alpha F_\beta F_\gamma F_\delta + \dots - \frac{1}{2} a_{\alpha\beta} F_\alpha F_\beta - \frac{1}{3} A_{\alpha,\beta\gamma} F_{\alpha,\beta\gamma} - \frac{1}{6} C_{\alpha\beta,\gamma\delta} F_{\alpha\beta,\gamma\delta} - \frac{1}{15} E_{\alpha,\beta\gamma\delta} F_{\alpha,\beta\gamma\delta} + \dots - \frac{1}{6} \beta_{\alpha\beta\gamma} F_\alpha F_\beta F_\gamma - \frac{1}{6} B_{\alpha\beta,\gamma\delta} F_\alpha F_\beta F_\gamma F_\delta - \frac{1}{24} \gamma_{\alpha\beta\gamma\delta} F_\alpha F_\beta F_\gamma F_\delta + \dots \quad (20.2)$$

$E^P$  is the energy of the atomic or molecular system in the presence of the static electric field ( $F$ ),  $E^0$  is its energy in the absence of the field,  $\mu_\alpha$  corresponds to the permanent dipole moment of the system,  $\alpha_{\alpha\beta}$  to the static dipole polarizability tensor and  $\beta_{\alpha\beta\gamma}$ ,  $\gamma_{\alpha\beta\gamma\delta}$  to the first and second dipole hyperpolarizabilities, respectively. Greek subscripts denote tensor components and can be equal to x, y, and z and each repeated subscript implies summation over x, y, and z as follows:

$$\frac{1}{2} a_{\alpha\beta} F_\alpha F_\beta = \frac{1}{2} \sum_{\alpha,\beta=x,y,z} a_{\alpha,\beta} F_\alpha F_\beta \quad (20.3)$$

In the case of a weak uniform (homogenous) field, the above expression becomes more simplified:

$$E^P = E^0 - \mu_\alpha F_\alpha - \frac{1}{2} \alpha_{\alpha\beta} F_\alpha F_\beta - \frac{1}{6} \beta_{\alpha\beta\gamma} F_\alpha F_\beta F_\gamma - \frac{1}{24} \gamma_{\alpha\beta\gamma\delta} F_\alpha F_\beta F_\gamma F_\delta + \dots \quad (20.4)$$

The properties that are routinely computed and discussed are the mean (or average) static dipole polarizability ( $\bar{\alpha}$ ), the anisotropy ( $\Delta\alpha$ ) of the polarizability tensor, the vector component of the first hyperpolarizability tensor in the direction of the ground state permanent dipole moment ( $\beta_{\parallel}$ ), the total first-order hyperpolarizability  $\beta_{tot}$ , and the scalar component of the second hyperpolarizability tensor  $\bar{\gamma}$ . Those quantities are related to the experiment and in terms of the Cartesian components are defined as

$$\bar{\alpha} = \frac{1}{3} (\alpha_{xx} + \alpha_{yy} + \alpha_{zz}) \quad (20.5)$$

$$\Delta\alpha = \left(\frac{1}{2}\right)^{1/2} [(\alpha_{xx} - \alpha_{yy})^2 + (\alpha_{xx} - \alpha_{zz})^2 + (\alpha_{zz} - \alpha_{yy})^2 + 6(\alpha_{xy}^2 + \alpha_{xz}^2 + \alpha_{zy}^2)]^{1/2} \quad (20.6)$$

$$\beta_{\parallel} = \frac{3/5 (\beta_x \mu_x + \beta_y \mu_y + \beta_z \mu_z)}{|\mu|} \quad (20.7)$$

$$\begin{aligned} \text{where } \beta_x &= \beta_{xxx} + \beta_{xyy} + \beta_{xzz} \\ \beta_y &= \beta_{yxx} + \beta_{yyy} + \beta_{yzz} \\ \beta_z &= \beta_{zxx} + \beta_{zyy} + \beta_{zzz} \end{aligned}$$

$$\beta_{tot} = (\beta_x^2 + \beta_y^2 + \beta_z^2)^{1/2} \quad (20.8)$$

$$\bar{\gamma} = 1/5 (\gamma_{xxxx} + \gamma_{yyyy} + \gamma_{zzzz} + 2\gamma_{xxyy} + 2\gamma_{yyzz} + 2\gamma_{xxzz}) \quad (20.9)$$

## Cluster (Hyper)Polarizabilities: Computational Approach

The majority of the undergoing theoretical (hyper)polarizability studies on semiconductor clusters rely on conventional ab-initio and density functional methods (DFT) As it is broadly



accepted the ab initio approach leads to accurate (hyper)polarizability predictions and most of the reported attempts rely on a hierarchy of ab initio methods of increasing predictive capability such as the Hartree–Fock approximation (HF), the Møller–Plesset (MP) many body perturbation theory, and also on the coupled cluster theory such as singles and doubles coupled-cluster (CCSD), and singles and doubles coupled-cluster with an estimate of connected triple excitations via a perturbational treatment (CCSD(T)) (further reading for those quantum chemical methods can be found in Szabo and Ostlun (1989), and Helgaker et al. (2000). Although this computational strategy is not always straightforward and in most of the cases computationally demanding, leads to reliable predictions of cluster (hyper)polarizabilities giving also crucial and detailed information about the electron correlation effects on the properties of interest. On the other hand the density functional approach (Koch and Holthausen 2000) is by far less computationally costly and allows the treatment of large systems; however, the reliability of DFT results rely heavily on the ability of the functional applied each time to describe the response of the system to an external electric field (see Karamanis et al. 2011 and references therein)

Looking carefully at  $\blacklozenge$  Eq. 20.4 it becomes obvious that the computation of polarizabilities and hyperpolarizabilities in the case of static fields is in fact a mathematical derivation issue of the cluster energy with respect to the applied field. Consequently, the best accuracy can be achieved by finding and using the analytic expressions of the following relations:

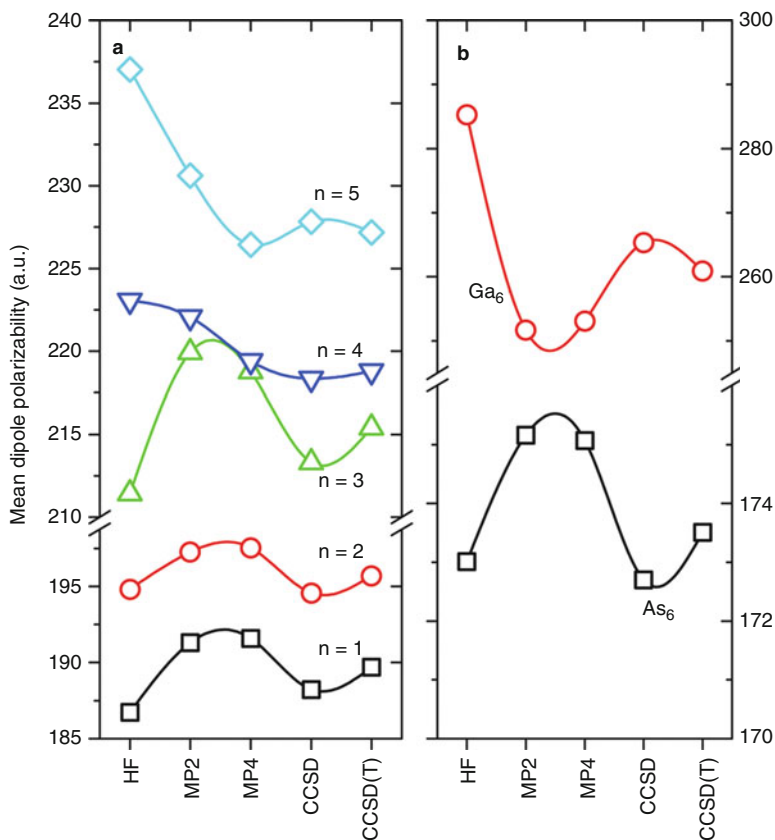
$$-\left(\frac{\partial^2 E}{\partial F^2}\right) = a_{static, F=0} \quad (20.10)$$

$$-\left(\frac{\partial^3 E}{\partial F^3}\right) = \beta_{static, F=0} \quad (20.11)$$

$$-\left(\frac{\partial^4 E}{\partial F^4}\right) = \gamma_{static, F=0} \quad (20.12)$$

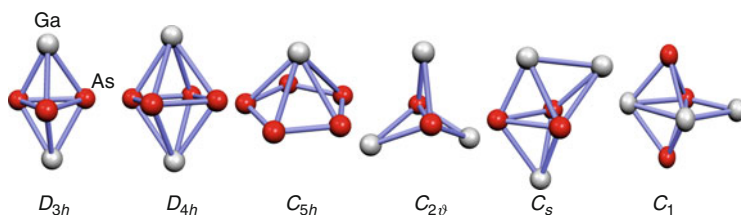
In the case of the linear polarizability, the majority of the available quantum chemical software is able to evaluate analytically the first field derivative of the energy yielding in a straightforward manner all components of the polarizability tensor. In most of the cases the type of the calculation has to be indicated in the command line of the input file and the polarizabilities of the system are returned after the calculation ends. Unfortunately no analytical evaluation of the high-order field derivatives of the energy is available in all commercial packages for all methods. What is more, for methods of high accuracy such as the CC methods, this option is not available even for the linear polarizabilities. To overcome this problem several numerical procedures have been developed. The most applied numerical solution to this mathematical problem is the one provided by the so called finite field approach. According to this approach, first a field perturbation of different magnitudes and along different directions is added to the Hamiltonian. Then the wavefunction is “solved” for each perturbation and the energy of the perturbed system is obtained. Lastly the differentiation of energy of the system with respect to the applied field is performed numerically and the coefficients of the  $\blacklozenge$  Eq. 20.4 are obtained ( $\blacklozenge$  Figs. 20-13 and  $\blacklozenge$  20-14).

Let us now demonstrate a simple example of the above process which will show us how the  $\blacklozenge$  Eq. 20.4 can be utilized in order to calculate all the components of the polarizability tensor for a cluster without symmetry ( $C_1$  point group). For this symmetry group there are three independent components of the dipole moment ( $\mu_x$ ,  $\mu_y$  and  $\mu_z$ ) and the six for the dipole polarizability: three principal (axial) components  $\alpha_{xx}$ ,  $\alpha_{yy}$ , and  $\alpha_{zz}$  and three transversal ones



■ Fig. 20-13

Method performance on the computation of the mean polarizabilities of  $\text{Ga}_n\text{As}_m$  clusters with  $m + n = 6$  in comparison with the performance on the computation of the mean polarizabilities of  $\text{Ga}_6$  and  $\text{As}_6$  clusters



■ Fig. 20-14

Gallium arsenic clusters of various symmetries

$\alpha_{xy} = \alpha_{yx}$ ,  $\alpha_{zy} = \alpha_{yz}$ , and  $\alpha_{xz} = \alpha_{zx}$ . The three principal ones can be computed by applying a weak electric field (of 0.0005–0.005 au strength) along each Cartesian direction, as follows:

$$\mu_a \approx \frac{E(-F_a) - E(F_a)}{2F_a} \quad (20.13)$$

$$\alpha_{aa} \approx \frac{2E(0) - E(-F_a) - E(F_a)}{F_a^2} \quad (20.14)$$

In the same manner, the transversal components can be obtained by applying fields in each  $\alpha\beta$  plane along each  $\pi/4$  diagonal between  $x$ ,  $y$ , and  $z$  axis (this is done by applying fields of equal strengths ( $F_\alpha = F_\beta$ ) at each  $xy$ ,  $yz$  and  $xz$  planes). In this case one obtains the following equation:

$$\alpha_{\alpha\beta} \approx \frac{E(F_\alpha) + E(F_\beta) - E(F_\alpha, F_\beta) - E(0)}{F_\alpha F_\beta} \quad (20.15)$$

In the case of centrosymmetric structures, the computation of the dipole polarizability becomes more straightforward since the permanent dipole moment and the transversal components of dipole polarizability of those systems are vanishing. In this case we have

$$\alpha_{aa} \approx \frac{E(0) - E(F_a)}{F_a^2} \quad (20.16)$$

Provided that a suitable field is chosen, the above computational approach leads to quite reliable polarizability values. The advantage of this approach is that it gives the flexibility to the user to compute the polarizabilities of a given system using a variety of post Hartree–Fock methods only by computing the energies of the free clusters with and without the field.

The described approach can be applied to other response properties apart from the perturbed energies provided that the method used for their computations satisfy the Hellmann–Feynman theorem (Feynman 1939; Hellmann 1937) according to which the derivative of the total energy with respect to the field is equivalent with the expectation value of the derivative of the Hamiltonian with respect to the field. In this case, one can safely use the following relationships:

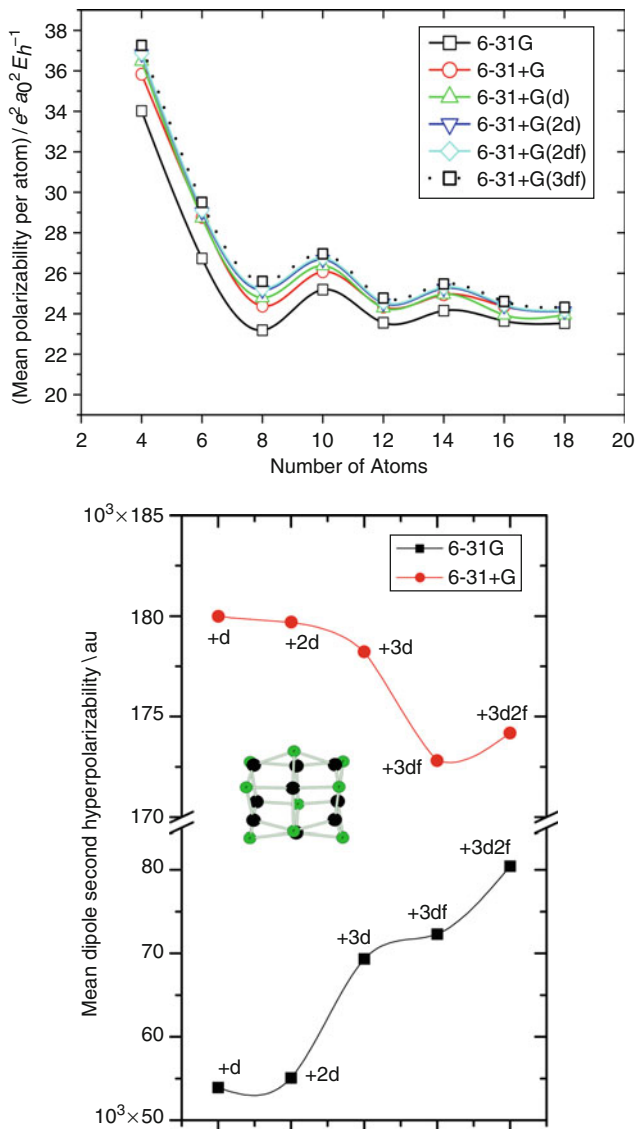
$$-\left(\frac{\partial^4 E}{\partial F^4}\right) = \left(\frac{\partial^3 \mu}{\partial F^3}\right) = \left(\frac{\partial^2 \alpha}{\partial F^2}\right) = \left(\frac{\partial \beta}{\partial F}\right) = \gamma_{static, F=0} \quad (20.17)$$

$$-\left(\frac{\partial^3 E}{\partial F^3}\right) = \left(\frac{\partial^2 \mu}{\partial F^2}\right) = \left(\frac{\partial \alpha}{\partial F}\right) = \beta_{static, F=0} \quad (20.18)$$

$$-\left(\frac{\partial^2 E}{\partial F^2}\right) = \left(\frac{\partial \mu}{\partial F}\right) = a_{static, F=0} \quad (20.19)$$

These relations can be used in all cases where the approximation to the true wavefunction is variationally optimized with respect to the Hamiltonian. This holds in the case of the SCF approach and all the DFT methods in which the energy of the systems is obtained through an iterative process. Contrary, in the case of the finite-order Møller–Pleset perturbation theory, (MP2, MP3, MP4), which is not variational, the relations  $\bullet$  Eqs. 20.17–20.19 do not hold and the calculations of the properties of interest should be extracted using only the energy derivatives.

Another key point in (hyper)polarizability calculations of clusters, as in all molecular systems, is the basis set choice. This has been clearly demonstrated in previous basis set studies on semiconductor clusters (see for instance Karamanis et al. 2006a, b, 2007a, 2008a; Maroulis et al. 2003, 2007; Papadopoulos et al. 2005, 2006). In general the polarizabilities are less sensitive to the basis set used than the first and second hyperpolarizabilities (see  $\bullet$  Fig. 20-15) Systematic basis set studies on cluster polarizabilities using basis sets of increasing size emphasize the importance of the diffuse  $s$   $p$  Gaussian type functions (GTFs) and the effect of GTFs of polarization functions and functions of higher angular momentum such as  $f$  functions Also it has been



■ Fig. 20-15

Basis set effect, at the Hartree–Fock level of theory, on the mean dipole polarizabilities per atom of the ground state structures of aluminum phosphide cluster of the type  $Al_nP_n$  with  $n=2-9$ , and basis set effect on the mean second hyperpolarizability of  $Al_9P_9$

illustrated that as the cluster size increases the overall basis set effect on the mean polarizability gradually decreases (Karamanis et al. 2011).

Besides the methods and techniques described above there are also some theoretical methods that have been developed to treat the polarizabilities of clusters in a different manner from that described above. One of those schemes has been used by Jackson et al. (2007) and relies on partitioning the volume of a system into atomic volumes and using the charge

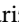
distributions within the atomic volumes to define quantities such as *atomic* dipole moments and polarizabilities. In a second step each of the latter quantities are further decomposed into two components: the dipole (or local) and the charge-transfer component. The summation of each component over all of the atoms gives the local and charge-transfer parts of the total system dipole moment and polarizability. This treatment allows one to perform a site-specific analysis of dielectric properties of finite systems and, also, to obtain an insight about the contribution of each atom or of any desired building block of the cluster. The specific method has been applied to silicon clusters with up to 28 atoms which were subjected to a small external electric field. The obtained results showed clearly a strong dependence of the individual atomic polarizabilities, as well as their dipole and charge-transfer components, on the site location of the atom within the cluster. For atoms at peripheral sites those properties are substantially larger than for atoms at the interior sites, and the more peripheral atoms are characterized by larger polarizabilities. The same conclusion was drawn later by Krishtal et al. (2010).

An alternative methodology which uses electrostatic interaction schemes to predict the evolution of cluster polarizabilities has been developed and tested on silicon clusters by Guillaume et al. (2009). This approach accepts the electrostatic nature of the dominant intra- and intermolecular interactions of a bulk material which is under the influence of external electric fields. This bottom-up approach allows the treatment very large clusters, enabling to reach the convergence of the response of the bulk material up to a point where adding new cluster units in the system would not change significantly the response of the material.

Further reading about the computational aspects of (hyper)polarizabilities on clusters and other molecules can be found in the following: Buckingham (1967), McLean and Yoshimine (1967), Marks and Ratner (1995), Kanis et al. (1994), Brédas et al. (1994), Bishop et al. (1997), Xenides (2006), Xenides and Maroulis (2000, 2006), Champagne et al. (2002), Maroulis (2008, 2004, 2003), Maroulis et al. (2007, 2003), Pouchan et al. (2004), Maroulis and Pouchan (2003), Papadopoulos and coworkers (Avramopoulos et al. 2004; Raptis et al. 1999; Reis et al. 2000); Karamanis and coworkers (Hohm et al. 2000; Kurtz et al. 1990; Luis et al. 2000).

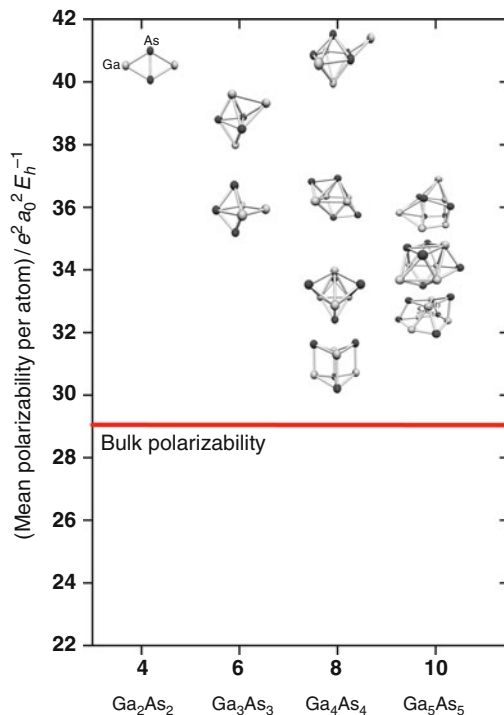
## Semiconductor Cluster (Hyper)polarizabilities: General Trends and Selected Studies

### General Trends

Semiconductor cluster polarizabilities have been the subject of some very important experimental studies via beam-deflection techniques (Backer 1997; Schlecht et al. 1995; Schnell et al. 2003; Schäfer et al. 1996; Kim et al. 2005) while they have been extensively studied using quantum chemical and density functional theory. In this research realm, one of the areas intensively discussed is the evolution of the cluster's polarizabilities per atom (PPA) with the cluster size. The PPA is obtained by dividing the mean polarizability of a given system by the number of its atoms. Such property offers a straightforward tool to compare the microscopic polarizability of a given cluster with the polarizability of the bulk (see  Fig. 20-16) as the latter is obtained by the "hard sphere" model with the bulk dielectric constant via the Clausius–Mossotti relation :

$$\bar{\alpha} = \frac{3}{4\pi} \left( \frac{\varepsilon - 1}{\varepsilon + 2} \right) v_{at} \quad (20.20)$$

where  $v_{at}$  is the volume per atom in the unit cell of the bulk and  $\varepsilon$  is the static dielectric constant of the bulk.



■ Fig. 20-16

Comparison between computed polarizabilities of small GaAs clusters and the polarizability of the bulk. The polarizabilities have been computed at the MP2 level of theory

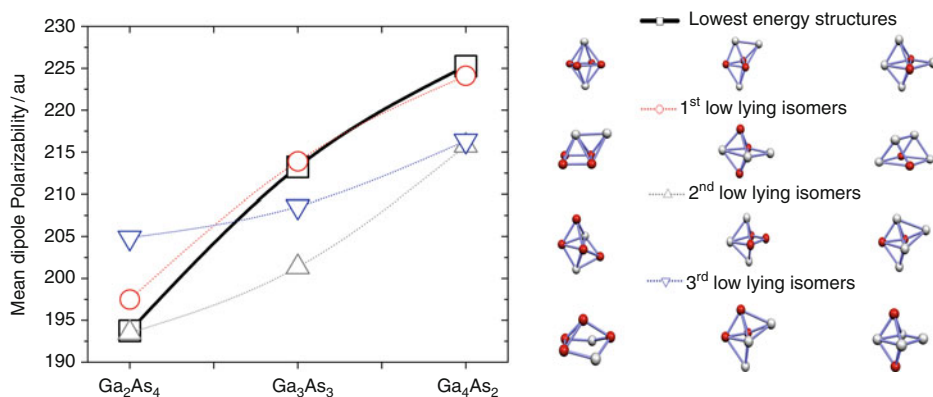
Most of the obtained knowledge on the polarizabilities of semiconductor clusters has emerged as the result of extensive studies of such species as silicon and gallium arsenide which have served well as models for the better understanding of the (hyper)polarizability evolution of semiconductor clusters. Also other kinds of clusters built from different elements such as aluminum phosphide, cadmium sulphide, selenide, and telluride have attracted the attention of several researchers and the corresponding studies have led to interesting conclusions. Those studies suggest that cluster polarizabilities are very different from the known polarizabilities of bulk materials. In general the PPAs of small semiconductor cluster are larger than the polarizability of the bulk (● Fig. 20-16). For instance, in all studied cases the theoretical predicted polarizabilities of small semiconductor clusters (e.g., Si, AlP, CdSe, CdS, GaAs) are found higher than the bulk polarizability and converge to the bulk limit from above. Also, the polarizability dependence of the cluster size is strong and as a rule cluster species exhibit strong and nonmonotonic size variations. In addition there is a strong dependence of the polarizability on the shape of the cluster. It has been shown that for species which maintain closed cage-like structures (i.e., close to the spherical shape), the polarizability per atom (PPA) decreases with clusters size (● Fig. 20-15) (see for instance (Jackson et al. 2004, 2005; Karamanis et al. 2008b, c; Zhang et al. 2004). On the other hand the per atom polarizabilities of clusters which maintain prolate structures (e.g., tubular clusters) increase as a function of the cluster size (Jackson et al. 2005; Karamanis et al. 2008b, 2011). Another important issue is the dependence

of the electric polarizabilities on the cluster bonding. It has been shown that semiconductor clusters which favor structures characterized by covalent bonds are expected to exhibit larger polarizabilities than clusters which tend to form ionic structures. This dependence is significantly more intense in the case of the second hyperpolarizability. The general rule that holds in this case is that semiconductor clusters which are characterized by significant electron transfer from the electropositive atoms (ionic bonding) to the electronegative ones are less hyperpolarizable than species in which the electron transfer is smaller (covalent bonding) (Karamanis et al. 2008d; Krishtal et al. 2010). This variation explains the nonmonotonic size variations of the mean PPAs of small binary semiconductor clusters. Also, both polarizabilities and hyperpolarizabilities of clusters have been proven very sensitive to the cluster elemental constitution. For instance, InAs clusters are more (hyper)polarizable than GaAs, AlP, AlAs, InP, and GaP clusters while CdTe clusters, are far more (hyper)polarizable than CdS and CdSe clusters (Karamanis and Pouchan 2009). What is more, the strong correlation between the polarizabilities of semiconductor clusters and their composition is also significant. In the case of GaAs clusters it has been demonstrated both experimentally and theoretically that Ga-rich gallium arsenide clusters are more polarizable than As-rich clusters due to the larger polarizability of Ga (Fig. 20-17) (Karamanis et al. 2009). Lastly, it was shown that the cluster shape dominates the magnitude of the second hyperpolarizabilities of large clusters (Karamanis and Pouchan 2011).

## Selected Studies

### Polarizabilities

Let us now briefly explore some of the most representative studies in the subject of the polarizabilities of Si and GaAs clusters that have attracted considerable attention. One of the first studies has been reported by Vasiliev et al. (1997). In that work the authors computed the polarizabilities of small  $\text{Si}_n$ ,  $\text{Ge}_n$  ( $n \leq 10$ ), and  $\text{Ga}_n\text{As}_m$  ( $n + m \leq 8$ ) clusters and they found that the polarizabilities of all systems are higher than the values estimated from the “hard sphere” model



■ Fig. 20-17

Composition-dependent polarizabilities of small  $\text{Ga}_n\text{As}_m$  with clusters  $n + m = 6$  computed at the B2PLYP/aug-cc-pVDZ-PP level

using  $\blacktriangleright$  Eq. 20.20. Also they evidenced that the computed per atom polarizabilities tend to decrease with increasing the cluster size and they related this trend to the one observed in the case of metallic clusters, for which the polarizability bulk limit is approached from above. This observation was considered as an evidence for the “metallic-like” nature of small semiconductor clusters. Two similar studies about silicon clusters up to 20 atoms by Jackson et al. (1999) and up to 28 atoms by Deng et al. (2000) confirmed the reported trends regarding to the PPA evolution with size and the metallic nature of silicon semiconductor clusters. The same conclusion has been reported also in later studies by Bazterra et al. (2002) and Maroulis et al. (2003). In the case of GaAs clusters the early results reported by Vasiliev et al. (1997) have been confirmed by Torrens (2002) with an interacting-induced-dipoles polarization model and have been extended up to 18 atoms by Karamanis et al. (2007a, 2008). Furthermore, the polarizability ordering in the case of the III–V dimers has been established:  $\text{In}_2\text{As}_2 > \text{In}_2\text{P}_2 > \text{Al}_2\text{As}_2 > \text{Ga}_2\text{As}_2 > \text{Al}_2\text{P}_2 > \text{Ga}_2\text{P}_2$  (Karamanis et al. 2008a).

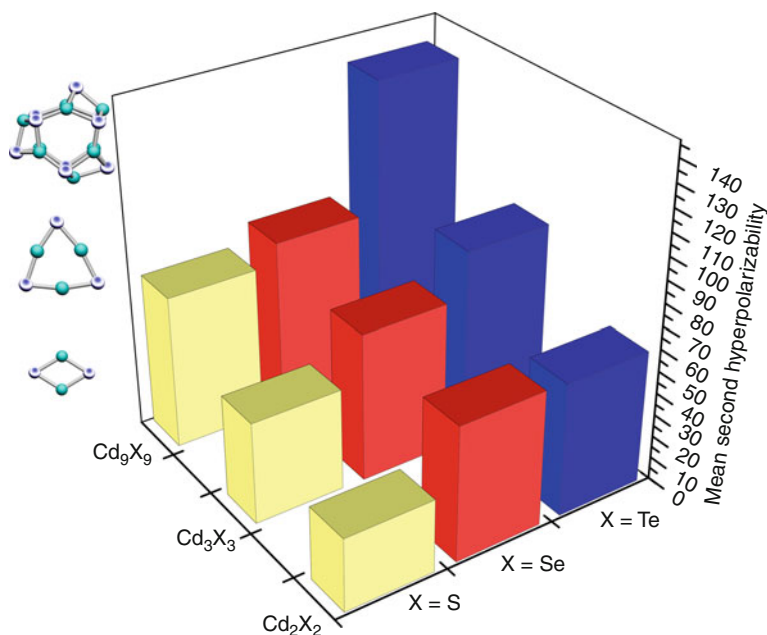
### Hyperpolarizabilities

In the domain of the nonlinear polarizabilities of semiconductor clusters (i.e., the second dipole hyperpolarizability and third polarizability) the reported studies are fewer than in the case of the linear polarizabilities. However, this field is very promising due to the properties that the compound semiconductors possess. With respect to their interaction with intense electric fields compound semiconductors are characterized by high sensitivity, high speed, and they may operate at a wide variety of wavelengths in the near-infrared range. In particular the compound III–V and II–VI semiconductors such as GaAs, InP, and CdS possess the two properties needed for the existence of the photorefractive effect, the photoconductivity, and the electro-optic effect. These properties are very crucial in electro-optical technology; and alloptical information technology, thus the study of clusters and nano-objects of those materials are essential, first for better understanding the properties of the bulk material and second for the research of new nano-materials with improved nonlinear optical properties (Bechstedt et al. 2007; Adolph and Bechstedt 1998; Hughes and Sipe 1996; Bergfeld and Daum 2003; Bloembergen 1996; Butcher and Cotter 1990; Powell et al. 2002; Vijayalakshmi et al. 2002).

At the microscopic level, one of the first studies into this matter was reported by Korambath and Karna (2000) who studied the first dipole hyperpolarizabilities of GaN, GaP, and GaAs clusters within the *ab initio* time-dependent Hartree–Fock method using an even-tempered Gaussian basis set and demonstrated that the magnitudes of the calculated (hyper)polarizabilities depend on the size of the cluster. Lan et al. (2003) studied the hyperpolarizabilities of  $\text{Ga}_3\text{As}_3$ ,  $\text{Ga}_3\text{Sb}_3$ ,  $\text{In}_3\text{P}_3$ ,  $\text{In}_3\text{As}_3$ , and  $\text{In}_3\text{Sb}_3$  clusters using a similar approach based on the time-dependent Hartree–Fock (TDHF) formalism combined with sum-over-states (SOS) method and found that the charge transferred from the  $\pi$ -bonding to  $\pi^*$ -antibonding orbitals between III and V group atoms under the influence of an electric field make a significant contribution to the second-order polarizability. The first *ab initio* attempt in treating the hyperpolarizabilities of semiconductor using methods of high sophistication such as CC and MP has been reported by Maroulis and Pouchan who explored the second hyperpolarizabilities of cadmium sulfide clusters. Their results showed that the mean second hyperpolarizability per atom of those species decreases rapidly with the cluster size. A second attempt on systems of increasing size has been reported by Lan et al. (2006). These authors studied several small GaAs clusters up to 10 atoms within the time-dependent density functional theory and reported that the dynamic behavior of  $\beta$  and  $\gamma$  show that the small  $\text{Ga}_n\text{As}_m$  clusters are expected as good candidates for nonlinear optical properties due to the avoidance of linear resonance photoabsorption. An application



of the time-dependent DFT (TD-DFT) theory on the hyperpolarizabilities of clusters can be found in the work of Sen and Chakrabarti (2006) who studied the second hyperpolarizabilities of CdSe clusters. In their conclusions, it is highlighted that these clusters have a high nonlinear optical activity. Karamanis et al. (2007a) reported ab initio values at the HF, MP2 level of theory for stoichiometric GaAs clusters up to 18 atoms and showed that as the size of the cluster increases the per atom mean second hyperpolarizability decreases fast and converges to a specific value. Finally, the significance of the bonding on the nonlinear polarizabilities of small clusters has been demonstrated by Karamanis and Leszczynski (2008) in a hyperpolarizability study of stoichiometric aluminum phosphide clusters up to 18 atoms. The conclusions of investigations on aluminum phosphide clusters have been extended later to several types of III-V semiconductor in a comparative hyperpolarizability study by Karamanis et al. (2008a). In that study the relative mean static dipole hyperpolarizabilities of the  $X_2Y_2$  type ( $X = \text{Al, Ga, In}$  and  $Y = \text{P, As}$ ) clusters have been established in several levels of theory,  $\bar{\gamma}$ :  $\text{In}_2\text{As}_2 > \text{In}_2\text{P}_2 \cong \text{Al}_2\text{As}_2 > \text{Al}_2\text{P}_2 \cong \text{Ga}_2\text{As}_2 > \text{Ga}_2\text{P}_2$ . This classification follows the size ordering of the electropositive atoms. Ga is slightly smaller than Al, while In is far more larger than both Ga and Al. The atomic radius of  $\text{Ga}(3d^{10}4s^24p^1)$  is slightly smaller than the  $\text{Al}(3s^23p^1)$  atomic radius, despite its larger number of electrons. This is caused by the insufficient shielding that the  $3d^{10}$  electrons provide to the  $4s^24p^1$  valence electrons of Ga. As a result, the valence electrons of Ga experience a larger attraction from the nuclear charge than the electrons of Al. Considering that the (hyper)polarizabilities are valence-related properties, the described peculiarity of the



■ Fig. 20-18

Comparisons between the second-order mean hyperpolarizabilities (divided by  $10^3$ ) of CdS, CdSe, and CdTe clusters computed at the HF/aug-cc-pVDZ-PP level of theory

Ga atoms can explain qualitatively the smaller hyperpolarizabilities of both  $\text{Ga}_2\text{P}_2$  and  $\text{Ga}_2\text{As}_2$  compared to  $\text{Al}_2\text{P}_2$  and  $\text{Al}_2\text{As}_2$  clusters.

The dynamic-second order hyperpolarizabilities of  $\text{Si}_3$  and  $\text{Si}_4$  have been explored by Lan et al. (2008) using the coupled cluster cubic response theory. These authors reported that  $\text{Si}_3$  and  $\text{Si}_4$  clusters exhibit wide non-resonant optical region. The same approach has been used by Lan and Feng (2009) in the study of the nonlinear response of another class of semiconductor clusters, namely, the  $\text{SiC}_n$  and  $\text{Si}_n\text{C}$ . In this work it was demonstrated that the size dependence of the first-order hyperpolarizabilities of the  $\text{SiC}_n$  clusters, which have approximate Si-terminated linear chain geometry, is similar to that observed in  $\pi$ -conjugated organic molecules. Lastly concerning the (hyper)polarizabilities of other II–VI clusters apart from CdS there two reported studies on their hyperpolarizabilities. The first (Li et al. 2008) deals with the ground states and low-lying isomers of stoichiometric  $(\text{ZnO})_n$  clusters with  $n = 2\text{--}12$  using finite field approach within density functional theory framework and the second (Karamanis et al. 2009) involves a comparative study of CdS, CdSe, CdTe with respect to their second hyperpolarizabilities (Fig. 20-18). Both of those studies demonstrate the structural and size dependence of those properties while the second one reveal that CdTe clusters are far more (hyper)polarizable than CdS and CdSe, verifying previous experimental work reported by Wu et al. (2003) which provided evidences that that CdTe nanoparticles exhibit stronger nonlinear optical properties than nanoparticles built from CdS and CdSe.

## Concluding Remarks

---

In this brief review, we made an attempt to present some of the most illustrative computational investigations of the structural properties of semiconductor clusters. We have chosen to present studies that had as subject cluster species which have attracted most of the attention of the researchers the last two decades and have served as models in the better understanding of cluster properties. Therefore it must be emphasized that although this chapter does not cover the vast number of studies that have been reported during the previous years, it can be utilized as starting material for those who are interested in contributing in this field, or simply, as a guide for those who wish to get some general information about the structural and bonding features of semiconductor clusters. Finally, in this chapter we have revisited most of the recent studies that focus on the electric properties of those species which also demonstrate in a comprehensive manner that clusters and electric properties such as the dipole polarizabilities and especially hyperpolarizabilities are strongly related.

## References

---

- Adolph, B., & Bechstedt, F. (1998). Ab initio second-harmonic susceptibilities of semiconductors: generalized tetrahedron method and quasiparticle effects. *Physical Review B - Condensed Matter and Materials Physics*, 57(11), 6519–6526.
- Alivisatos, A. P. (1996). Semiconductor clusters, nanocrystals, and quantum dots. *Science*, 271(5251), 933–937.
- Al-Laham, M. A., & Raghavachari, K. (1991). Theoretical study of small gallium arsenide clusters. *Chemical Physics Letters*, 187(1–2), 13–20.
- Al-Laham, M. A., & Raghavachari, K. (1993). Theoretical study of  $\text{Ga}_4\text{As}_4$ ,  $\text{Al}_4\text{P}_4$ , and  $\text{Mg}_4\text{S}_4$  clusters. *Journal of Chemical Physics*, 98(11), 8770–8776.

- An, W., Gao, Y., Bulusu, S., & Zeng, X. (2005). Ab initio calculation of bowl, cage, and ring isomers of  $C_{20}$  and  $C_{20}^-$ . *Journal of Chemical Physics*, 122, 204109/1–204109/8.
- Avramopoulos, A., Reis, H., Li, J., & Papadopoulos, M. G. (2004). The dipole moment, polarizabilities, and first hyperpolarizabilities of HArF. A computational and comparative study. *Journal of the American Chemical Society*, 126(19), 6179–6184.
- Avramov, P. V., Fedorov, D. G., Sorokin, P. B., Chernozatonskii, L. A., & Gordon, M. S. (2007). Atomic and electronic structure of new hollow-based symmetric families of silicon nanoclusters. *Journal of Physical Chemistry C*, 111(51), 18824–18830.
- Backer, J. A. (1997). Molecular beam studies on semiconductor clusters: polarizabilities and chemical bonding. *Angewandte Chemie (International Edition in English)*, 36(13–14), 1390–1404.
- Bai, J., Cui, L.-F., Wang, J., Yoo, S., Li, X., & Jellinek, J., et al. (2006). Structural evolution of anionic silicon clusters  $Si_N(20 \leq N \leq 45)$ . *Journal of Physical Chemistry A*, 110(3), 908–912.
- Bazterra, V. E., Caputo, M. C., Ferraro, M. B., & Fuentealba, P. (2002). On the theoretical determination of the static dipole polarizability of intermediate size silicon clusters. *Journal of Chemical Physics*, 117(24), 11158–11165.
- Bazterra, V. E., Oña, O., Caputo, M. C., Ferraro, M. B., Fuentealba, P., & Facelli, J. C. (2004). Modified genetic algorithms to model cluster structures in medium-size silicon clusters. *Physical Review A - Atomic, Molecular, and Optical Physics*, 69(5B), 053202/1–053202/7.
- Bechstedt, F., Adolph, B., & Schmidt, W. G. (1999). Ab initio calculation of linear and nonlinear optical properties of semiconductor structures. *Brazilian Journal of Physics*, 29(4), 643–651.
- Behrman, E. C., Foehrweiser, R. K., Myers, J. R., French, B. R., & Zandler, M. E. (1994). Possibility of stable spheroid molecules of ZnO. *Physical Review A*, 49(3), R1543–R1549.
- Bergfeld, S., & Daum, W. (2003). Second-harmonic generation in GaAs: experiment versus theoretical predictions of  $\chi_{xyz}^{(2)}$ . *Physical Review Letters*, 90(3), 036801/1–036801/4.
- Bersuker, I. B. (2001). Modern aspects of the Jahn-Teller effect theory and applications to molecular problems. *Chemical Reviews*, 101(4), 1067–1114.
- Biswas, R., & Hamann, D. R. (1986). Simulated annealing of silicon atom clusters in langevin molecular dynamics. *Physical Review B*, 34(2), 895–901.
- Bishop, D. M., Kirtman, B., & Champagne, B. (1997). Differences between the exact sum-over-states and the canonical approximation for the calculation of static and dynamic hyperpolarizabilities. *Journal of Chemical Physics*, 107(15), 5780–5787.
- Blaisten-Barojas, E., & Levesque, D. (1986). Molecular-dynamics simulation of silicon clusters. *Physical Review B*, 34(6), 3910–3916.
- Bloembergen, N. (1996). In *Nonlinear optics* (4th ed.). Singapore: World Scientific.
- Brédas, J. L., Adant, C., Tackx, P., Persoons, A., & Pierce, B. M. (1994). Third-order nonlinear optical response in organic materials: theoretical and experimental aspects. *Chemical Reviews*, 94(1), 243–278.
- Bruchez Jr., M., Moronne, M., Gin, P., Weiss, S., & Alivisatos, A. P. (1998). Semiconductor nanocrystals as fluorescent biological labels. *Science*, 281(5385), 2013–2016.
- Buckingham, A. D. (1967). Permanent and induced molecular moments and long-range intermolecular forces. *Advances in Chemical Physics*, 12, 107–142.
- Butcher P. N., & Cotter, D. (1990). *The elements of nonlinear optics*. Cambridge: Cambridge University Press.
- Calarco, T., Datta, A., Fedichey, P., Pazy, E., & Zoller, P. (2003). Spin-based all-optical quantum computation with quantum dots: understanding and suppressing decoherence. *Physical Review A - Atomic, Molecular, and Optical Physics*, 68(1), 012310/1–012310/21.
- Castro, A., Marques, M. A. L., Alonso, J. A., Bertsch, G. F., Yabana, K., & Rubio, A. (2002). Can optical spectroscopy directly elucidate the ground state of  $C_{20}$ ? *Journal of Chemical Physics*, 116(5), 1930–1933.
- Champagne, B., Spassova, M., Jadin, J.-B., & Kirtman, B. (2002). Ab initio investigation of doping-enhanced electronic and vibrational second hyperpolarizability of polyacetylene chains. *Journal of Chemical Physics*, 116(9), 3935–3946.
- Chen, W., Zhang, J. Z., & Joly, A. G. (2004). Optical properties and potential applications of doped semiconductor nanoparticles. *Journal of Nanoscience and Nanotechnology*, 4(8), 919–947.
- Costales, A., Kandalam, A. K., Franco, R., & Pandey, R. (2002). Theoretical study of structural and vibrational properties of  $(AlP)_n$ ,  $(AlAs)_n$ ,  $(GaP)_n$ ,  $(GaAs)_n$ ,  $(InP)_n$ , and  $(InAs)_n$  clusters with  $n=1, 2, 3$ . *Journal of Physical Chemistry B*, 106(8), 1940–1944.
- Deglmann, P., Ahlrichs, R., & Tsereteli, K. (2002). Theoretical studies of ligand-free cadmium

- selenide and related semiconductor clusters. *Journal of Chemical Physics*, 116(4), 1585–1597.
- Deng, K., Yang, J., & Chan, C. T. (2000). Calculated polarizabilities of small S clusters. *Physical Review A - Atomic, Molecular, and Optical Physics*, 61(2), 252011–252014.
- Dugourd, P., Hudgins, R. R., Tenenbaum, J. M., & Jarrold, M. F. (1998). Observation of new ring isomers for carbon cluster anions. *Physical Review Letters*, 80(19), 4197–4200.
- Feng, Y. P., Boo, T. B., Kwong, H. H., Ong, C. K., Kumar, V., & Kawazoe, Y. (2007). Composition dependence of structural and electronic properties of  $\text{Ga}_m\text{As}_n$  clusters from first principles. *Physical Review B - Condensed Matter and Materials Physics*, 76(4), 045336/1–045336/8.
- Fournier, R., Sinnott, S. B., & DePristo, A. E. (1992). Density functional study of the bonding in small silicon clusters. *Journal of Chemical Physics*, 97(6), 4149–4161.
- Feynman, R. P. (1939). Forces in Molecules. *Physical Reviews*, 56(4), 340.
- Fielicke, A., Lyon, J. T., Haertelt, M., Meijer, G., Claes, P., & De Haeck, J., et al. (2009). Vibrational spectroscopy of neutral silicon clusters via far-IR-VUV two color ionization. *Journal of Chemical Physics*, 131(17), 171105/1–171105/6.
- García-Fernández, P., Bersuker, I. B., & Boggs J. E. (2006). The origin of molecular distortions: a proposed experimental test. *Journal of Chemical Physics*, 124(6), 044321/1–044321/7.
- Graves, R. M., & Scuseria, G. E. (1991). Ab initio theoretical study of small GaAs clusters. *Journal of Chemical Physics*, 95(9), 6602–6606.
- Grimme, S., & Mück-Lichtenfeld, C. (2002). Structural isomers of  $\text{C}_{20}$  revisited: the cage and bowl are almost isoenergetic. *ChemPhysChem*, 3(2), 207–209.
- Grossman, J. C., Mitas, L., & Raghavachari, K. (1995). Structure and stability of molecular carbon: importance of electron correlation. *Physical Review Letters*, 75(21), 3870–3873.
- Guillaume, M., Champagne, B., Bógú, D., & Pouchan, C. (2009). Electrostatic interaction schemes for evaluating the polarizability of silicon clusters. *Journal of Chemical Physics*, 130(13)
- Gur, I., Fromer, N. A., Geier, M. L., & Alivisatos, A. P. (2005). Materials science: air-stable all-inorganic nanocrystal solar cells processed from solution. *Science*, 310(5747), 462–465.
- Gurin, V. S. (1998). Ab-initio calculations of small  $\text{Cd}_x\text{S}_y$  and  $\text{Zn}_x\text{S}_y$  ( $x, y \leq 6$ ) clusters. *Solid State Communications*, 108(6), 389–392.
- Gutsev, G. L., O'Neal Jr., R. H., Saha, B. C., Mochena, M. D., Johnson, E., & Bauschlicher Jr., C. W. (2008a). Optical properties of  $(\text{GaAs})_n$  clusters ( $n=2-16$ ). *Journal of Physical Chemistry A*, 112(43), 10728–10735.
- Gutsev, G. L., Johnson, E., Mochena, M. D., & Bauschlicher Jr., C. W. (2008b). The structure and energetics of  $(\text{GaAs})_n$ ,  $(\text{GaAs})_n^-$ , and  $(\text{GaAs})_n^+$  ( $n=2-15$ ). *Journal of Chemical Physics*, 128(14), 144707/1–144707/9.
- Gutsev, G. L., Mochena, M. D., Saha, B. C., & Derosa P. A. (2010). Structures and properties of  $(\text{GaAs})_n$  clusters. *Journal of Computational and Theoretical Nanoscience*, 7, 1–10.
- Hamad, S., Richard, C., Catlow, A., Spanó, E., Matxain, J. M., & Ugalde, J. M. (2005). Structure and properties of ZnS nanoclusters. *Journal of Physical Chemistry B*, 109(7), 2703–2709.
- Headley, A. D. (1987). Substituent effects on the basicity of dimethylamines. *Journal of the American Chemical Society*, 109(8), 2347–2348.
- Hellmann, H. (1937). *Einführung in die Quantenchemie* (p. 285). Leipzig: Franz Deuticke.
- Helgaker, T., Jørgensen, P., & Olsen, J. (2000). *Molecular Electronic-Structure Theory*. Chichester: Wiley.
- Ho, K.-M., Shvartsburg, A. A., Pan, B., Lu, Z.-Y., Wang, C.-Z., Wacker, J. G., Fye J. L., & Jarrold M. F. (1998). Structures of medium-sized silicon clusters. *Nature*, 392, 582–585.
- Hohm, U. (2000). Is there a minimum polarizability principle in chemical reactions? *Journal of Physical Chemistry A*, 104(36), 8418–8423.
- Hohm, U., Loose, A., Maroulis, G., & Xenides, D. (2000). Combined experimental and theoretical treatment of the dipole polarizability of  $\text{P}_4$  clusters. *Physical Review A - Atomic, Molecular, and Optical Physics*, 61(5), 532021–532026.
- Honea, E. C., Ogura, A., Murray, C. A., Raghavachari, K., Sprenger, W. O., Jarrold, M. F., & Brown, W. L. (1993). Raman spectra of size-selected silicon clusters and comparison with calculated structures. *Nature*, 366(6450), 42–44.
- Hossain, D., Hagedberg, F., Pittman Jr., C. U., & Saebo, S. (2007). Structures and stabilities of clusters of  $\text{Si}_{12}$ ,  $\text{Si}_{18}$ , and  $\text{Si}_{20}$  containing endohedral charged and neutral atomic species. *Journal of Physical Chemistry C*, 111(37), 13864–13871.
- Jackson, K. A., Yang, M., Chaudhuri, I., & Frauenheim, T. (2005). Shape, polarizability, and metallicity in silicon clusters. *Physical Review A - Atomic, Molecular, and Optical Physics*, 71(3), 1–6.
- Jackson, K., Yang, M., & Jellinek, J. (2007). Site-specific analysis of dielectric properties of finite systems. *Journal of Physical Chemistry C*, 111(48), 17952–17960.

- Jackson, K., Pederson, M., Wang, C.-Z., & Ho, K.-M. (1999). Calculated polarizabilities of intermediate-size Si clusters. *Physical Review A - Atomic, Molecular, and Optical Physics*, 59(5), 3685–3689.
- Jackson, K. A., Horoi, M., Chaudhuri, I., Frauenheim, T., & Shvartsburg, A. A. (2004). Unraveling the shape transformation in silicon clusters. *Physical Review Letters*, 93(1), 013401/1–013401/4.
- Jarrold, M. F., & Bower, J. E. (1992). Mobilities of silicon cluster ions: the reactivity of silicon sausages and spheres. *The Journal of Chemical Physics*, 96(12), 9180–9190.
- Jarrold, M. F., & Constant, V. A. (1991). Silicon cluster ions: evidence for a structural transition. *Physical Review Letters*, 67(21), 2994–2997.
- Jelski, D. A., Swift, B. L., Rantala, T. T., Xia, X., & George, T. F. (1991). Structure of the Si<sub>45</sub> cluster. *Journal of Chemical Physics*, 95(11), 8552–8560.
- Jha, P. C., Seal, P., Sen, S., Ågren, H., & Chakrabarti, S. (2008). Static and dynamic polarizabilities of (CdSe)<sub>n</sub> (n=1–16) clusters. *Computational Materials Science*, 44(2), 728–732.
- Jose, R., Zhanpeisov, N. U., Fukumura, H., Baba, Y., & Ishikawa, I. (2006). Structure-property correlation of CdSe clusters using experimental results and first-principles DFT calculations. *Journal of the American Chemical Society*, 128(2), 629–636.
- Kanis, D. R., Ratner, M. A., & Marks, T. J. (1994). Design and construction of molecular assemblies with large second-order optical nonlinearities. quantum chemical aspects. *Chemical Reviews*, 94(1), 195–242.
- Kasuya, A., Sivamohan, R., Barnakov, Y. A., Dmitruk, I. M., Nirasawa, T., & Romanyuk, V. R., et al. (2004). Ultra-stable nanoparticles of CdSe revealed from mass spectrometry. *Nature Materials*, 3(2), 99–102.
- Karamanis, P., Maroulis, G., & Pouchan, C. (2006a). Basis set and electron correlation effects in all-electron ab initio calculations of the static dipole polarizability of small cadmium selenide clusters, (CdSe)<sub>n</sub>, n=1,2,3,4. *Chemical Physics*, 331(1), 19–25.
- Karamanis, P., Maroulis, G., & Pouchan, C. (2006b). Molecular geometry and polarizability of small cadmium selenide clusters from all-electron Ab initio and density functional theory calculations. *Journal of Chemical Physics*, 124(7), 071101/1–071101/2.
- Karamanis, P., Begue, D., & Pouchan, C. (2007a). Ab initio finite field (hyper)polarizability computations on stoichiometric gallium arsenide clusters Ga<sub>n</sub>As<sub>n</sub> (n=2–9). *Journal of Chemical Physics*, 127(9), 094706/1–094706/10.
- Karamanis, P., Zhang-Negrerie, D., & Pouchan, C. (2007b). A critical analysis of the performance of conventional ab initio and DFT methods in the computation of Si<sub>6</sub> ground state. *Chemical Physics*, 331(2–3), 417–426.
- Karamanis, P., Pouchan, C., & Leszczynski, J. (2008a). Electric dipole (hyper)polarizabilities of selected X<sub>2</sub>Y<sub>2</sub> and X<sub>3</sub>Y<sub>3</sub> (X=Al, Ga, In and Y=P, As): III-V semiconductor clusters. An ab initio comparative study. *Journal of Physical Chemistry A*, 112(51), 13662–13671.
- Karamanis, P., Xenides, D., & Leszczynski, J. (2008b). Polarizability evolution on natural and artificial low dimensional binary semiconductor systems: a case study of stoichiometric aluminum phosphide semiconductor clusters. *Journal of Chemical Physics*, 129(9), 094708/1–094708/12.
- Karamanis, P., Xenides, D., & Leszczynski, J. (2008c). The polarizabilities of small stoichiometric aluminum phosphide clusters Al<sub>n</sub>P<sub>n</sub> (n=2–9). Ab initio and density functional investigation. *Chemical Physics Letters*, 457(1–3), 137–142.
- Karamanis, P., & Leszczynski, J. (2008d). Correlations between bonding, size, and second hyperpolarizability ( $\gamma$ ) of small semiconductor clusters: ab initio study on Al<sub>n</sub>P<sub>n</sub> clusters with n=2, 3, 4, 6, and 9. *Journal of Chemical Physics*, 128(15), 154323/1–154323/10.
- Karamanis, P., Pouchan, C., & Maroulis, G. (2008). Structure, stability, dipole polarizability and differential polarizability in small gallium arsenide clusters from all-electron ab initio and density-functional-theory calculations. *Physical Review A - Atomic, Molecular, and Optical Physics*, 77(1), 013201/1–013201/6.
- Karamanis, P., Carbonnière, P., & Pouchan, C. (2009). Structures and composition-dependent polarizabilities of open- and closed-shell gan asm semiconductor clusters. *Physical Review A - Atomic, Molecular, and Optical Physics*, 80(5), 053201/1–053201/11.
- Karamanis, P., & Pouchan, C. (2009). How large are the microscopic electronic dipole (hyper)polarizabilities of Cd<sub>n</sub>Te<sub>n</sub> bare clusters compared to those of Cd<sub>n</sub>S<sub>n</sub> and Cd<sub>n</sub>Se<sub>n</sub>? A systematic ab initio study. *Chemical Physics Letters*, 474(1–3), 162–167.
- Karamanis, P., Marchal, R., Carbonnière, P., & Pouchan, C. (2010). Doping effects on the electric response properties of Silicon clusters. A global structure-property investigation of AlSi<sub>n-1</sub> clusters (n=3–10). *Chemical Physics Letters*, 474(1–3), 59–64.
- Karamanis, P., Pouchan, C., Weatherford, C. A., & Gutsev, G. L. (2011). Evolution of properties

- in prolate (GaAs)<sub>n</sub> clusters. *Journal of Physical Chemistry C*, 115(1), 97–107.
- Karamanis, P., & Pouchan, C. (2011). On the shape dependence of cluster (hyper)polarizabilities. A combined ab initio and DFT study on large fullerene-like gallium arsenide semiconductor clusters. *International Journal of Quantum Chemistry*, 111(4), 788–796.
- Kaxiras, E., & Jackson, K. (1993). Shape of small silicon clusters. *Physical Review Letters*, 71(5), 727–730.
- Kim, H.-Y., Sofo, J. O., Velegol, D., Cole, M. W., & Mukhopadhyay, G. (2005). Static polarizabilities of dielectric nanoclusters. *Physical Review A - Atomic, Molecular, and Optical Physics*, 72(5), 1–8.
- Koch, W., & Holthausen, M. C. (2000). *A Chemist's guide to density functional theory*. Chichester: Wiley.
- Korambath, P. P., & Karna, S. P. (2000). (Hyper)polarizabilities of GaN, GaP, and GaAs clusters: an ab initio time-dependent Hartree-Fock study. *Journal of Physical Chemistry A*, 104(20), 4801–4804.
- Krishtal, A., Senet, P., Van Alsenoy, C. (2010) Origin of the size-dependence of the polarizability per atom in heterogeneous clusters: the case of AlP clusters. *Journal of Chemical Physics*, 133(15), 154310/1–154310/11.
- Kurtz, H. A., Stewart, J. J. P., & Dieter, K. M. (1990). Calculation of the nonlinear optical properties of molecules. *Journal of Computational Chemistry*, 11(1), 82–87.
- Lan, Y.-Z., Cheng, W.-D., Wu, D.-S., Shen, J., Huang, S.-P., Zhang, H., Gong, Y.-J., & Li, F.-F. (2006). A theoretical investigation of hyperpolarizability for small Ga<sub>n</sub>As<sub>m</sub> (n + m = 4–10) clusters. *Journal of Chemical Physics*, 124(9), 094302/1–094302/8.
- Lan, Y., Cheng, W., Wu, D., Li, X., Zhang, H., & Gong, Y. (2003). TDHF-SOS treatments on linear and nonlinear optical properties of III-V semiconductor clusters (Ga<sub>3</sub>As<sub>3</sub>, Ga<sub>3</sub>Sb<sub>3</sub>, In<sub>3</sub>P<sub>3</sub>, In<sub>3</sub>As<sub>3</sub>, In<sub>3</sub>Sb<sub>3</sub>). *Chemical Physics Letters*, 372 (5–6), 645–649.
- Lan, Y.-Z., Feng, Y.-L., Wen, Y.-H., & Teng, B.-T. (2008). Dynamic second-order hyperpolarizabilities of Si<sub>3</sub> and Si<sub>4</sub> clusters using coupled cluster cubic response theory. *Chemical Physics Letters*, 461(1–3), 118–121.
- Lan, Y.-Z., & Feng, Y.-L. (2009). Study of absorption spectra and (hyper)polarizabilities of SiC<sub>n</sub> and Si<sub>n</sub>C (n = 2–6) clusters using density functional response approach. *Journal of Chemical Physics*, 131(5), 054509/1–054509/11.
- Leitsmann, R., Schmidt, W. G., Hahn, P. H., & Bechstedt, F. (2005). Second-harmonic polarizability including electron-hole attraction from band-structure theory. *Physical Review B - Condensed Matter and Materials Physics*, 71(19), 195209/1–195209/10.
- Li, B.-X. (2005). Stability of medium-sized neutral and charged silicon clusters. *Physical Review B - Condensed Matter and Materials Physics*, 71(23), 1–7.
- Li, L., Zhou, Z., Wang, X., Huang, W., He, Y., & Yang, M. (2008). First-principles study of static polarizability, first and second hyperpolarizabilities of small-sized ZnO clusters. *Physical Chemistry Chemical Physics*, 10(45), 6829–6835.
- Li, B.-X., Cao, P.-L., & Zhou, X.-Y. (2003). Electronic and geometric structures of Si<sub>n</sub>- and Si<sub>n</sub><sup>+</sup> (n = 2–10) clusters and in comparison with Si<sub>n</sub>. *Physica Status Solidi (B) Basic Research*, 238(1), 11–19.
- Liao, D. W., & Balasubramanian, K. (1992). Electronic structure of the III-V tetramer clusters and their positive ions. *Journal of Chemical Physics*, 96(12), 8938–8947.
- Lipscomb, W. N. (1966). Framework rearrangement in boranes and carboranes. *Science*, 153(3734), 373–378.
- Lou, L., Nordlander, P., & Smalley, R. E. (1992). Electronic structure of small GaAs clusters. II. *Journal of Chemical Physics*, 97(3), 1858–1864.
- Luis, J. M., Duran, M., Champagne, B., & Kirtman, B. (2000). Determination of vibrational polarizabilities and hyperpolarizabilities using field-induced coordinates. *Journal of Chemical Physics*, 113 (13), 5203–5213.
- Lyon, J. T., Gruene, P., Fielicke, A., Meijer, G., Janssens, E., & Claes, P., et al. (2009). Structures of silicon cluster cations in the gas phase. *Journal of the American Chemical Society*, 131(3), 1115–1121.
- Marchal, R., Carbonnière, P., & Pouchan, C. (2009). A global search algorithm of minima exploration for the investigation of low lying isomers of clusters from density functional theory-based potential energy surfaces: the example of Si<sub>n</sub> (n = 3, 15) as a test case. *Journal of Chemical Physics*, 131(11), 114105/1–114105/9.
- Marchal, R., Carbonnière, P., & Pouchan, C. (2010). A global search algorithm of minima exploration for the investigation of low lying isomers of clusters from DFT-based potential energy surface. A theoretical study of Si<sub>n</sub> and Si<sub>n-1</sub>Al clusters. *International Journal of Quantum Chemistry*, 110(12), 2256–2259.



- Marchal, R., Carbonnière, P., & Pouchan, C. (2011). On the Structures of Non-Stoichiometric GaAsm Clusters ( $5 n < + m < 8$ ). *Journal of Computational and Theoretical Nanosciences*, 8(4), 568–578.
- Maroulis, G., Karamanis, P., & Pouchan, C. (2007). Hyperpolarizability of GaAs dimer is not negative. *Journal of Chemical Physics*, 126(15), 154316/1–154316/5.
- Maroulis, G. (2008). How large is the static electric (hyper)polarizability anisotropy in HXeI? *Journal of Chemical Physics*, 129(4), 044314/1–044314/6.
- Maroulis, G. (2004). Bonding and (hyper) polarizability in the sodium dimer. *Journal of Chemical Physics*, 121(21), 10519–10524.
- Maroulis, G., Bugué, D., & Pouchan, C. (2003). Accurate dipole polarizabilities of small silicon clusters from ab initio and density functional theory calculations. *Journal of Chemical Physics*, 119(2), 794–797.
- Maroulis, G. (2003). Accurate electric multipole moment, static polarizability and hyperpolarizability derivatives for N<sub>2</sub>. *Journal of Chemical Physics*, 118(6), 2673–2687.
- Maroulis, G., & Pouchan, C. (2003). Size and electric dipole (hyper)polarizability in small cadmium sulfide clusters: an ab initio study on (CdS)<sub>n</sub>, n = 1, 2, and 4. *Journal of Physical Chemistry B*, 107(39), 10683–10686.
- Marks, T. J., & Ratner, M. A. (1995). Design, synthesis, and properties of molecule-based assemblies with large second-order optical nonlinearities. *Angewandte Chemie (International Edition in English)*, 34(2), 155–173.
- Matxain, J. M., Fowler, J. E., & Ugalde, J. M. (2000). Small clusters of II-VI materials: Zn<sub>n</sub>O<sub>i</sub>, i = 1–9. *Physical Review A - Atomic, Molecular, and Optical Physics*, 62(5), 053201/1–053201/10.
- Matxain, J. M., Mercero, J. M., Fowler, J. E., & Ugalde, J. M. (2001). Small clusters of group-(II-VI) materials: Zn<sub>n</sub>X<sub>i</sub>, X = Se, Te, i = 1–9. *Physical Review A. Atomic, Molecular, and Optical Physics*, 64(5), 532011–532018.
- Matxain, J. M., Mercero, J. M., Fowler, J. E., & Ugalde, J. M. (2003). Clusters of group II-VI materials: Cd<sub>i</sub>O<sub>i</sub> (i ≤ 15). *Journal of Physical Chemistry A*, 107(46), 9918–9923.
- Matxain, J. M., Mercero, J. M., Fowler, J. E., & Ugalde, J. M. (2004). Clusters of II-VI materials: Cd<sub>i</sub>X<sub>i</sub>, X = S, Se, Te, i ≤ 16. *Journal of Physical Chemistry A*, 108(47), 10502–10508.
- McLean, A. D., & Yoshimine, M. (1967). Theory of molecular polarizabilities. *Journal of Chemical Physics*, 47(6), 1927–1935.
- Menon, M., & Subbaswamy, K. R. (1995). Structure and stability of Si<sub>45</sub> clusters: a generalized tight-binding molecular-dynamics approach. *Physical Review B*, 51(24), 17952–17956.
- Michalet, X., Pinaud, F. F., Bentolila, L. A., Tsay, J. M., Doose, S., & Li, J. J., et al. (2005). Quantum dots for live cells, in vivo imaging, and diagnostics. *Science*, 307(5709), 538–544.
- Mitas, L., Grossman, J. C., Stich, I., & Tobik, J. (2000). Silicon clusters of intermediate size: energetics, dynamics, and thermal effects. *Physical Review Letters*, 84(7), 1479–1482.
- Murray, C. B., Kagan, C. R., & Bawendi, M. G. (2000). Synthesis and characterization of monodisperse nanocrystals and close-packed nanocrystal assemblies. *Annual Review of Materials Science*, 30, 545–610.
- Nagle, J. K. (1990). Atomic polarizability and electronegativity. *Journal of the American Chemical Society*, 112(12), 4741–4747.
- Nair, N. N., Bredow, T., & Jug, K. (2004). Molecular dynamics implementation in MSINDO: study of silicon clusters. *Journal of Computational Chemistry*, 25(10), 1255–1263.
- Nigam, S., Majumder, C., & Kulshreshtha, S. K. (2004). Structural and electronic properties of Si<sub>n</sub>, Si<sub>n</sub><sup>+</sup>, and AlSi<sub>n</sub><sup>-1</sup> (n = 2–13) clusters: theoretical investigation based on ab initio molecular orbital theory. *Journal of Chemical Physics*, 121(16), 7756–7763.
- O'Brien, S. C., Liu, Y., Zhang, Q., Heath, J. R., Tittel, F. K., & Curl, R. F., et al. (1985). Supersonic cluster beams of III-V semiconductors: Ga<sub>x</sub>As<sub>y</sub>. *Journal of Chemical Physics*, 84(7), 4074–4079.
- Papadopoulos, M. G., Reis, H., Avramopoulos, A., Erkoç, S., & Amirouche, L. (2005). A comparative study of the dipole polarizability of some Zn clusters. *Journal of Physical Chemistry B*, 109(40), 18822–18830.
- Papadopoulos, M. G., Reis, H., Avramopoulos, A., Erkoç, S., & Amirouche, L. (2006). Polarizabilities and second hyperpolarizabilities of Zn<sub>m</sub>Cd<sub>n</sub> clusters. *Molecular Physics*, 104(13–14), 2027–2036.
- Parr, R. G., & Chattaraj, P. K. (1991). Principle of maximum hardness. *Journal of the American Chemical Society*, 113(5), 1854–1855.
- Pedroza, L. S., & Da Silva, A. J. R. (2007). Ab initio monte carlo simulations applied to Si<sub>3</sub> cluster. *Physical Review B - Condensed Matter and Materials Physics*, 75(24), 245331/1–245331/10.
- Peng, X., Wickham, J., & Alivisatos, A. P. (1998). Kinetics of II-VI and III-V colloidal semiconductor nanocrystal growth: 'Focusing' of size distributions. *Journal of the American Chemical Society*, 120(21), 5343–5344.

- Peng, X., Manna, L., Yang, W., Wickham, J., Scher, E., Kadavanich, A., et al. (2000). Shape control of CdSe nanocrystals. *Nature*, 404(6773), 59–61.
- Pool, R. (1990). Clusters: strange morsels of matter. *Science*, 248(4960), 1186–1188.
- Pouchan, C., Bégue, D., & Zhang, D. Y. (2004). Between geometry, stability, and polarizability: density functional theory studies of silicon clusters  $Si_n$  ( $n=3-10$ ). *Journal of Chemical Physics*, 121(10), 4628–4634.
- Powell, G. D., Wang, J.-F., & Aspnes, D. E. (2002). Simplified bond-hyperpolarizability model of second harmonic generation. *Physical Review B - Condensed Matter and Materials Physics*, 65(20), 205320/1–205320/8.
- Prinzbach, H., Weller, A., Landenberger, P., Wahl, F., Wörth, J., Scott, L. T., et al. (2000). Gas-phase production and photoelectron spectroscopy of the smallest fullerene,  $C_{20}$ . *Nature*, 407(6800), 60–63.
- Pushpa, R., Narasimhan, S., & Waghmare, U. (2004). Symmetries, vibrational instabilities, and routes to stable structures of clusters of Al, Sn, and As. *Journal of Chemical Physics*, 121(11), 5211–5220.
- Raghavachari, K., & Logovinsky, V. (1985). Structure and bonding in small silicon clusters. *Physical Review Letters*, 55(26), 2853–2856.
- Raghavachari, K., & Rohlfing, C. M. (1988). Bonding and stabilities of small silicon clusters: a theoretical study of  $Si_7$ – $Si_{10}$ . *Journal of Chemical Physics*, 89(4), 2219–2234.
- Raptis, S. G., Papadopoulos, M. G., & Sadlej, A. J. (1999). The correlation, relativistic, and vibrational contributions to the dipole moments, polarizabilities, and first and second hyperpolarizabilities of ZnS, CdS, and HgS. *Journal of Chemical Physics*, 111(17), 7904–7915.
- Reis, H., Papadopoulos, M. G., & Boustani, I. (2000). DFT calculations of static dipole polarizabilities and hyperpolarizabilities for the boron clusters  $B_n$  ( $n=3-8, 10$ ). *International Journal of Quantum Chemistry*, 78(2), 131–135.
- Rohlfing, C. M., & Raghavachari, K. A. (1990). Theoretical study of small silicon clusters using an effective core potential. *Chemical Physics Letters*, 167(6), 559–565.
- Roman, E., Yates, J. R., Veithen, M., Vanderbilt, D., & Souza, I. (2006). Ab initio study of the nonlinear optics of III-V semiconductors in the terahertz regime. *Physical Review B - Condensed Matter and Materials Physics*, 74(24), 245204/1–245204/9.
- Sanville, E., Burnin, A., & BelBruno, J. J. (2006). Experimental and computational study of small ( $n=1-16$ ) stoichiometric zinc and cadmium chalcogenide clusters. *Journal of Physical Chemistry A*, 110(7), 2378–2386.
- Schäfer, R., Schlecht, S., Woencckhaus, J., & Becker, J. A. (1996). Polarizabilities of isolated semiconductor clusters. *Physical Review Letters*, 76(3), 471–474.
- Schaller, R. D., & Klimov, V. I. (2006). Non-poissonian exciton populations in semiconductor nanocrystals via carrier multiplication. *Physical Review Letters*, 96(9), 1–4.
- Schlecht, S., Schäfer, R., Woencckhaus, J., & Becker, J. A. (1995). Electric dipole polarizabilities of isolated gallium arsenide clusters. *Chemical Physics Letters*, 246(3), 315–320.
- Schnell, M., Herwig, C., & Becker, J. A. (2003). Analysis of semiconductor cluster beam polarization taking small permanent dipole moments into account. *Zeitschrift Fur Physikalische Chemie*, 217(8), 1003–1030.
- Sen, S., & Chakrabarti, S. (2006). Frequency-dependent nonlinear optical properties of CdSe clusters. *Physical Review B - Condensed Matter and Materials Physics*, 74(20), 205435/1–205435/7.
- Sokolova, S., Lüchow, A., & Anderson, J. B. (2000). Energetics of carbon clusters  $C_{20}$  from all-electron quantum monte carlo calculations. *Chemical Physics Letters*, 323(3–4), 229–233.
- Song, K. M., Ray, A. K., & Khowash, P. K. (1994). On the electronic structures of GaAs clusters. *Journal of Physics B: Atomic, Molecular and Optical Physics*, 27(8), 1637–1648.
- Sun, Q., Wang, Q., Jena, P., Waterman, S., & Kawazoe, Y. (2003). First-principles studies of the geometry and energetics of the  $Si_{36}$  cluster. *Physical Review A - Atomic, Molecular, and Optical Physics*, 67(6), 632011–632016.
- Swaminathan, P., Antonov, V. N., Soares, J. A. N. T., Palmer, J. S., & Weaver, J. H. (2006). Cd-based II-VI semiconductor nanostructures produced by buffer-layer-assisted growth: structural evolution and photoluminescence. *Physical Review B - Condensed Matter and Materials Physics*, 73(12), 1–8.
- Szabo, A., & Ostlund, N. S. (1989). *Modern quantum chemistry*. New York: MacMillan.
- Tekin, A., & Hartke, B. (2004). Global geometry optimization of small silicon clusters with empirical potentials and at the DFT level. *Physical Chemistry Chemical Physics*, 6(3), 503–509.
- Torrens, F. (2002). Fractal dimension of different structural-type zeolites and of the active sites. *Physica E (Amsterdam)*, 13, 67.
- Troparevsky, M. C., & Chelikowsky, J. R. (2001). Structural and electronic properties of CdS



- and CdSe clusters. *Journal of Chemical Physics*, 114(2), 943–949.
- Troparevsky, M. C., Kronik, L., & Chelikowsky, J. R. (2002). Ab initio absorption spectra of CdSe clusters. *Physical Review B - Condensed Matter and Materials Physics*, 65(3), 33311–33314.
- Vasiliev, I., Ögüt, S., & Chelikowsky, J. R. (1997). Ab initio calculations for the polarizabilities of small semiconductor clusters. *Physical Review Letters*, 78(25), 4805–4808.
- Vela, A., & Gázquez, J. L. (1990). A relationship between the static dipole polarizability, the global softness, and the Fukui function. *Journal of the American Chemical Society*, 112(4), 1490–1492.
- Vijayalakshmi, S., Lan, A., Iqbal, Z., & Grebel, H. (2002). Nonlinear optical properties of laser ablated silicon nanostructures. *Journal of Applied Physics*, 92(5), 2490–2494.
- Wang, B.-C., Chou, Y.-M., Deng, J.-P., & Dung, Y.-T. (2008). Structural and optical properties of passivated silicon nanoclusters with different shapes: a theoretical investigation. *Journal of Physical Chemistry A*, 112(28), 6351–6357.
- Wang, J., Ma, L., Zhao, J., & Jackson, K. A. (2009). Structural growth behavior and polarizability of  $Cd_nTe_n$  ( $n=1-14$ ) clusters. *Journal of Chemical Physics*, 130(21), 214307/1–214307/8.
- Wang, X. Q., Clark, S. J., & Abram, R. A. (2004). Ab initio calculations of the structural and electronic properties of  $Hg_mTe_n$  cluster. *Physical Review B - Condensed Matter and Materials Physics*, 70(23), 1–6.
- Wei, S., Barnett, R. N., & Landman, U. (1997). Energetics and structures of neutral and charged sin ( $n \leq 10$ ) and sodium-doped  $Si_nNa$  clusters. *Physical Review B - Condensed Matter and Materials Physics*, 55(12), 7935–7944.
- Williams, R. E. (1992). The polyborane, carborane, carbocation continuum: architectural patterns. *Chemical Reviews*, 92(2), 177–207.
- Wolf, S. A., Awschalom, D. D., Buhrman, R. A., Daughton, J. M., Von Molnár, S., Roukes, M. L., et al. (2001). Spintronics: a spin-based electronics vision for the future. *Science*, 294(5546), 1488–1495.
- Wu, F., Lewis, J. W., Kliger, D. S., & Zhang, J. Z. (2003). Unusual excitation intensity dependence of fluorescence of CdTe nanoparticles. *Journal of Chemical Physics*, 118(1), 12–16.
- Xenides, D. (2006). (Hyper)polarizability dependence on the interatomic distance of  $N_4$  ( $T_d$ ): fourth order polynomials and third order derivatives. *Journal of Molecular Structure: Theochem*, 764(1–3), 41–46.
- Xenides, D., & Maroulis, G. (2000). Basis set and electron correlation effects on the first and second static hyperpolarizability of  $SO_2$ . *Chemical Physics Letters*, 319(5–6), 618–624.
- Xenides, D., & Maroulis, G. (2006). Electric polarizability and hyperpolarizability of  $BrCl(X 1\Sigma^+)$ . *Journal of Physics B: Atomic, Molecular and Optical Physics*, 39(17), 3629–3638.
- Xiao, C., Hagelberg, F., & Lester Jr., W. A. (2002). Geometric, energetic, and bonding properties of neutral and charged copper-doped silicon clusters. *Physical Review B - Condensed Matter and Materials Physics*, 66(7), 754251–7542523.
- Yoo, S., Shao, N., & Zeng, X. C. (2008). Structures and relative stability of medium- and large-sized silicon clusters. VI. Fullerene cage motifs for low-lying clusters  $Si_{39}$ ,  $Si_{40}$ ,  $Si_{50}$ ,  $Si_{60}$ ,  $Si_{70}$ , and  $Si_{80}$ . *Journal of Chemical Physics*, 128(10), 104316/1–104316/9.
- Yoo, S., & Zeng, X. C. (2006). Structures and relative stability of medium-sized silicon clusters. IV. motif-based low-lying clusters  $Si_{21}$ – $Si_{30}$ . *Journal of Chemical Physics*, 124(5), 1–6.
- Yoo, S., & Zeng, X. C. (2005). Structures and stability of medium-sized silicon clusters. III. Reexamination of motif transition in growth pattern from  $Si_{15}$  to  $Si_{20}$ . *Journal of Chemical Physics*, 123(16), 1–6.
- Yoo, S., Zhao, J., Wang, J., & Xiao, C. Z. (2004). Endohedral silicon fullerenes  $Si_n$  ( $27 \leq n \leq 39$ ). *Journal of the American Chemical Society*, 126(42), 13845–13849.
- Yu, D. K., Zhang, R. Q., & Lee, S. T. (2002). Structural transition in nanosized silicon clusters. *Physical Review B - Condensed Matter and Materials Physics*, 65(24), 2454171–2454176.
- Zdetsis, A. D. (2001). The real structure of the  $Si_6$  cluster. *Physical Review A. Atomic, Molecular, and Optical Physics*, 64(2), 023202/1–023202/4.
- Zdetsis, A. D. (2007a). Analogy of silicon clusters with deltahedral boranes: how far can it go? reexamining the structure of  $sin$  and  $sin 2^-$ ,  $n=5-13$  clusters. *Journal of Chemical Physics*, 127(24), 244308/1–244308/6.
- Zdetsis, A. D. (2007b). Fluxional and aromatic behavior in small magic silicon clusters: a full ab initio study of  $Si_n$ ,  $Si_n^{1-}$ ,  $Si_n^{2-}$ , and  $Si_n^{1+}$ ,  $n=6, 10$  clusters. *Journal of Chemical Physics*, 127(1), 014314/1–014314/10.
- Zdetsis, A. D. (2008). High-stability hydrogenated silicon-carbon clusters: a full study of  $Si_2C_2H_2$  in comparison to  $Si_2C_2$ ,  $C_2B_2H_4$ , and other similar species. *Journal of Physical Chemistry A*, 112(25), 5712–5719.
- Zdetsis, A. D. (2009). Silicon-bismuth and germanium-bismuth clusters of high stability.

- Journal of Physical Chemistry A*, 113(44), 12079–12087.
- Zhang, D. Y., Bégué, D., & Pouchan, C. (2004). Density functional theory studies of correlations between structure, binding energy, and dipole polarizability in  $\text{Si}_9$   $\text{Si}_{12}$ . *Chemical Physics Letters*, 398(4–6), 283–286.
- Zhao, J., Xie, R.-R., Zhou, X., Chen, X., & Lu, W. (2006). Formation of stable fullerene-like  $\text{Ga}_n$   $\text{As}_n$  clusters ( $6 \leq n \leq 9$ ): gradient-corrected density-functional theory and a genetic global optimization approach. *Physical Review B - Condensed Matter and Materials Physics*, 74(3), 035319/1–035319/2.
- Zhao, W., & Cao, P.-L. (2001). Study of the stable structures of  $\text{Ga}_6\text{As}_6$  cluster using FP-LMTO MD method. *Physics Letters, Section A: General, Atomic and Solid State Physics*, 288(1), 53–57.
- Zhao, W., Cao, P.-L., Li, B.-X., Song, B., & Nakamatsu, H. (2000). Study of the stable structures of  $\text{Ga}_4\text{As}_4$  cluster using FP-LMTO MD method. *Physical Review B - Condensed Matter and Materials Physics*, 62(24), 17138–17143.
- Zhou, R. L., & Pan, B. C. (2008). Low-lying isomers of  $\text{Si}_n^+$  and  $\text{Si}_n^-$  ( $n=31-50$ ) clusters. *Journal of Chemical Physics*, 128(23), 234302/1–234302/6.
- Zhu, X., & Zeng, X. C. (2003). Structures and stabilities of small silicon clusters: ab initio molecular-orbital calculations of  $\text{Si}_7$ – $\text{Si}_{11}$ . *Journal of Chemical Physics*, 118(8) 3558–3570.
- Zhu, X. L., Zeng, X. C., Lei, Y. A., & Pan, B. (2004). Structures and stability of medium silicon clusters. II. Ab initio molecular orbital calculations of  $\text{Si}_{12}$ – $\text{Si}_{20}$ . *Journal of Chemical Physics*, 120(19), 8985–8995.



# 21 Structures, Energetics, and Spectroscopic Fingerprints of Water Clusters $n = 2-24$

Soohaeng Yoo · Sotiris S. Xantheas

Chemical & Material Sciences Division, Pacific Northwest National Laboratory, Richland, WA, USA

<i>Introduction</i> .....	762
<i>Models of Intermolecular Interactions</i> .....	763
Quantum Models from Electronic Structure Calculations .....	764
Electron Correlation and Orbital Basis Set .....	765
The Basis Set Superposition Error Correction .....	765
Extrapolation to the Complete Basis Set Limit .....	767
<i>Global Minimum Structures of the <math>n = 2-10</math> Water Clusters</i> .....	767
<i>The Global Minima of Medium-Sized Water Clusters in the Range <math>11 \leq n \leq 16</math></i> .....	771
<i>The Transition from “All-Surface” to “Internally Solvated” Clusters at <math>n = 17</math></i> .....	775
Validation from Electronic Structure Calculations .....	776
Spectroscopic Signature .....	777
<i>The Family of Minima for <math>(\text{H}_2\text{O})_{20}</math></i> .....	778
The Four Major Families of Minima .....	780
Vibrational Spectra .....	780
<i>The First Few Water Cages</i> .....	782
Significance .....	782
The Pentagonal Dodecahedron (D-cage) $(\text{H}_2\text{O})_{20}$ Cluster .....	782
The Tetrakaidecahedron (T-Cage) $(\text{H}_2\text{O})_{24}$ Cluster .....	785
<i>Outlook</i> .....	786
<i>Acknowledgments</i> .....	787
<i>References</i> .....	788

**Abstract:** This chapter discusses the structures, energetics, and vibrational spectra of the first few ( $n \leq 24$ ) water clusters obtained from high-level electronic structure calculations. The results are discussed in the perspective of being used to parameterize/assess the accuracy of classical and quantum force fields for water. To this end, a general introduction with the classification of those force fields is presented. Several low-lying families of minima for the medium cluster sizes are considered. The transition from the “all surface” to the “fully coordinated” cluster structures occurring at  $n = 17$  and its spectroscopic signature is presented. The various families of minima for  $n = 20$  are discussed together with the low-energy networks of the pentagonal dodecahedron ( $\text{H}_2\text{O}$ )<sub>20</sub> water cage. Finally, the low-energy networks of the tetrakaidecahedron (T-cage) ( $\text{H}_2\text{O}$ )<sub>24</sub> cluster are shown and their significance in the construction of periodic lattices of structure I (sI) of the hydrate lattices is discussed.

## Introduction

---

Water's function as a universal solvent and its role in mediating several biological functions that are responsible for sustaining life has created tremendous interest in the understanding of its structure at the molecular level (Ball 2008). Due to the size of the simulation cells and the sampling time needed to compute many macroscopic properties, most of the initial simulations are performed using a classical force field, whereas several processes that involve chemistry are subsequently probed with electronic structure based methods. A significant effort has therefore been devoted toward the development of classical force fields for water (Robinson et al. 1996). Clusters of water molecules are useful in probing the intermolecular interactions at the microscopic level as well as providing information about the subtle energy differences that are associated with different bonding arrangements within a hydrogen-bonded network. They moreover render a quantitative picture of the nature and magnitude of the various components of the intermolecular interactions such as exchange, dispersion, induction, etc. They can finally serve as a vehicle for the study of the convergence of properties with increasing size.

Over the last decade, there have been tremendous advances in the experimental (Cruzan et al. 1996a, b, 1997; Liu et al. 1994, 1996a, b, 1997a, b; Pugliano and Saykally 1992; Suzuki and Blake 1994; Viant et al. 1997) and theoretical (Xantheas 1994, 1996a; Xantheas and Dunning 1993a, b) studies of the structural, spectral, and energetic properties of water clusters, as well as refinements of the macroscopic structural experimental data for liquid water (Hura et al. 2000; Soper 2000; Sorenson et al. 2000). These developments have created a unique opportunity for incorporating molecular level information into classical force fields for water as well as using the available database of cluster energetics for the assessment of their accuracy. The process of developing interaction potentials is by no means straightforward, and the different approaches that are used to model the various components of the underlying physical interactions have their own advantages and shortcomings. Some of the outstanding issues that are associated with the development of models based on molecular level information are the shortage or scarcity of experimental data for clusters. To this end, an alternative approach based on the use of *ab initio* results for water clusters can be put into practice.

Assuming that the route of parameterization of an interaction potential for water from the cluster results is adopted, the question naturally arises of the level of accuracy that needs to be attained so the models can produce meaningful and accurate results for the macroscopic properties of extended systems such as the bulk liquid and ice. In the subsequent sections, we

will present the results of ab-initio electronic structure calculations for cluster sizes up to 24 water molecules and we will address some important features of their structural and spectral properties. We will finally present results on the first few water cages that are the constituents of the three-dimensional hydrate networks.

## Models of Intermolecular Interactions

Force fields describing intermolecular interactions can be in general classified into two categories: (1) classical and (2) quantum models, the characteristics of which are outlined in [Fig. 21-1](#). Classical potentials consist of force fields that employ an analytic expression, in conjunction with several adjustable parameters, for the potential energy surface (PES) as a function of the coordinates of the atoms in the system. In contrast, for quantum models, the PES is computed by considering both the position of the nuclei and the distribution of the electrons of the system, and it is obtained by solving Schrödinger's equation.

The choice of the adjustable parameters used in conjunction with classical potentials can result to either *effective* potentials that implicitly include the nuclear quantization and can therefore be used in conjunction with classical simulations (albeit only for the conditions they were parameterized for) or *transferable* ones that attempt to best approximate the Born–Oppenheimer PES and should be used in nuclear quantum statistical simulations. Representative examples of effective force fields for water consist of TIP4P (Jorgensen et al. 1983), SPC/E (Berendsen et al. 1987) (pair-wise additive), and Dang-Chang (DC) (Dang and Chang 1997) (polarizable, many-body). The “polarizable” potentials contain – in addition to the pairwise additive term – a classical induction (polarization) term that explicitly (albeit approximately) accounts for many-body effects to infinite order. These effective potentials are fitted to reproduce bulk-phase experimental data (i.e., the enthalpy at  $T = 298$  K and the radial distribution functions at ambient conditions) in classical molecular dynamics simulations of liquid water. Despite their simplicity, these models describe some experimental properties of liquid

	Quantum		Classical			
Wave function	$\psi(\vec{r}; \vec{R})$		No electronic degrees of freedom			
Energy	$E = \langle \psi   \hat{H}   \psi \rangle$		$E = E(\vec{R}; a_i)$			
Potential energy surface	Born-Oppenheimer		“Effective”		Born-Oppenheimer	
Zero-point energy	Explicitly included		Implicitly included		Explicitly included	
Simulation methodology	Classical	Quantum	Classical	Quantum	Classical	Quantum
Transferability across different environments	NO	YES	NO <sup>§</sup>	NO <sup>¶</sup>	NO	YES

<sup>§</sup> appropriate only for the environment that the ZPE has been effectively included

<sup>¶</sup> double-counting

■ Fig. 21-1

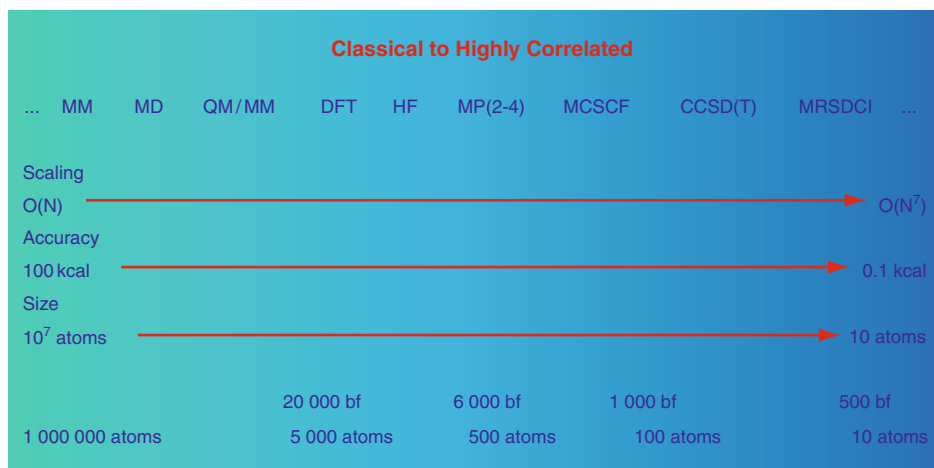
Characteristics of classical and quantum potential models

water at ambient conditions quite well but usually fail for conditions and environments that are not parameterized for, and so they have limited predictive power. On the other hand, force fields such as the Effective Fragment Potential (EFP) (Adamovic et al. 2003; Day et al. 1996; Gordon et al. 2001; Jensen and Gordon 1998; Netzloff and Gordon 2004), the SAPT-5 (Bukowski et al. 2007; Szalewicz et al. 2009), and the family of Thole-type models (TTM (Burnham et al. 1999), TTM-2F (Burnham and Xantheas 2002a), TTM2.1-F (Fanourgakis and Xantheas 2006), TTM3-F (Fanourgakis and Xantheas 2008), and TTM4-F (Burnham et al. 2008)) are examples of transferable potentials that are fitted to high-level first principles electronic structure results of the PESs of small water clusters, usually the water dimer and trimer, and should be used in conjunction with nuclear quantum statistical simulations.

The availability of energetic information for water clusters (such as binding energies) is of paramount importance in both fitting transferable potentials as well as assessing their performance. Currently, binding energies of small water clusters, even the water dimer, are not available experimentally but can only be obtained from high-level electronic structure calculations.

## Quantum Models from Electronic Structure Calculations

► *Figure 21-2* shows the spectrum of methods that are used to describe intermolecular interactions ranging from the classical descriptions, such as Molecular Mechanics (MM), up to the highly correlated ones, including Coupled Cluster with Single, Double, and perturbative estimates of Triple excitations [CCSD(T)] and Multi Reference Singles and Doubles Configuration Interaction (MRSDCI). Methods on the left part of the spectrum have the advantage of low formal scaling and as such allow for the treatment of large systems, but they are also associated with large inaccuracies. In contrast, methods to the right side of ► *Fig. 21-2* have the disadvantage



► Fig. 21-2

Models of intermolecular interactions: from classical to highly correlated

of high formal scaling (as much as  $\sim O(N^9)$ , where  $N$  is the system size) and are more appropriate for smaller systems for which high accuracy is achieved. Currently, the state of the art consists of the application of highly correlated methods such as CCSD(T) to a cluster of about 24 water molecules ( $\sim 1,100$  basis functions and 270 electrons), a calculation that can sustain a performance of 1.4 Petaflop/s (Apra et al. 2009).

## Electron Correlation and Orbital Basis Set

The cluster energies are obtained from the solution of the nonrelativistic Schrödinger equation for each system. The expansion of the trial many-electron wave function delineates the *level of theory* (description of electron correlation), whereas the description of the constituent orbitals is associated with the choice of the *orbital basis set*. A recent review (Dunning 2000) outlines a path, which is based on hierarchical approaches in this double expansion in order to ensure convergence of both the correlation and basis set problems. It also describes the application of these hierarchical approaches to various chemical systems that are associated with very diverse bonding characteristics, such as covalent bonds, hydrogen bonds and weakly bound clusters.

As regards the description of the electron correlation problem it has been recognized that the coupled cluster method (Bartlett and Purvis 1978; Cizek 1966, 1969; Coester 1958; Coester and Kümmel 1960; Kucharski and Bartlett 1992; Purvis and Bartlett 1982), which includes all possible single, double, triple, etc. excitations from a reference wave function, represents a viable route toward obtaining accurate energetics for hydrogen-bonded dimers (Halkier et al. 1999; Peterson and Dunning 1995). Among its variations, the CCSD(T) approximation (Raghavachari et al. 1989, 1990), which includes the effects of triple excitations perturbationally, represents an excellent compromise between accuracy and computational efficiency and has been recently coined as the “gold standard of quantum chemistry.” The CCSD(T) approximation scales as  $N^6$  for the iterative solution of the CCSD part, plus an additional single  $N^7$  step for the perturbative estimate of the triple excitations. This represents a substantial additional expense over the widely used second-order perturbation level (Møller and Plesset 1934) of theory (MP2) which formally scales as  $N^5$ .

For the basis set expansion, the *correlation-consistent* (cc-pVnZ) orbital basis sets of Dunning and coworkers (Dunning 1989; Dunning et al. 1998; Kendall et al. 1992), ranging from double to quintuple zeta quality ( $n = D, T, Q, 5$ ), offer a systematic path in approaching the complete basis set (CBS) limit. These sets were constructed by grouping together all basis functions that contribute roughly equal amounts to the correlation energy of the atomic ground states. In this approach, functions are added to the basis sets in shells. The sets approach the complete basis set (CBS) limit, for each succeeding set in the series provides an evermore accurate description of both the atomic radial and angular spaces. The extension of those sets to include additional diffuse functions for each angular momentum function present in the standard basis yields the *augmented correlation consistent* (aug-cc-pVnZ) sets. The exponents of those additional diffuse functions were optimized for the corresponding negative ions.

## The Basis Set Superposition Error Correction

The use of a finite basis set in electronic structure calculations has been known to overestimate the interaction energy (Clementi 1967) ( $\Delta E$ ) of a weakly bound dimer complex, a quantity



defined as

$$\Delta E = E_{AB}^{\alpha\cup\beta}(AB) - E_A^\alpha(A) - E_B^\beta(B), \quad (21.1)$$

where superscripts indicate the basis set; subscripts, the molecular system; and parentheses, the geometries for which the energies are obtained. In this notation, the term  $E_{AB}^{\alpha\cup\beta}(AB)$  is the energy of the dimer ( $AB$ ) at its equilibrium geometry  $AB$  with the basis set of the two fragments  $aUb$ . The overestimation comes from the fact that the basis functions that are centered on the one fragment help lower the energy of the other fragment and vice versa, a situation first termed “Basis Set Superposition Error” (BSSE) by Liu and McLean (1973). Boys and Bernardi (1970) originally proposed two approaches to circumvent this problem, introducing corrections via the “point counterpoise” (pCP) and the “function counterpoise” (fCP) methods, the latter being nowadays almost exclusively adopted in electronic structure calculations of intermolecular interaction energies (Chalasinski and Szczesniak 1994; van Duijneveldt et al. 1994).

For a dimer of two interacting moieties (extension to larger clusters is straightforward), the fCP correction is:

$$\Delta E(\text{fCP}) = E_{AB}^{\alpha\cup\beta}(AB) - E_{AB}^{\alpha\cup\beta}(A) - E_{AB}^{\alpha\cup\beta}(B). \quad (21.2)$$

► Equations 21.1 and ► 21.2 will not converge to the same result as the basis set increases toward the Complete Basis Set (CBS) limit since the reference energies of fragments  $A$  and  $B$  are computed at different geometries, viz. the dimer vs. the isolated fragments. Alternatively, if the BSSE correction is estimated via the equation (Xantheas 1996b)

$$\Delta E(\text{BSSE}) = E_{AB}^{\alpha\cup\beta}(AB) - E_{AB}^{\alpha\cup\beta}(A) - E_{AB}^{\alpha\cup\beta}(B) + E_{rel}^\alpha(A) + E_{rel}^\beta(B) \quad (21.3)$$

where

$$E_{rel}^\alpha(A) = E_{AB}^\alpha(A) - E_A^\alpha(A) \quad (22.3a)$$

$$E_{rel}^\beta(B) = E_{AB}^\beta(B) - E_B^\beta(B) \quad (22.3b)$$

represent the energy penalty for distorting the fragments from their isolated geometries to the ones that adopt due to their interaction in the complex, then it is readily seen that after substitution of ► Eqs. 22.3a and ► 22.3b into ► Eq. 21.3 and collecting terms, the BSSE correction (► Eq. 21.3) can be cast as:

$$\Delta E(\text{BSSE}) = \Delta E - \left\{ E_{AB}^{\alpha\cup\beta}(A) - E_A^\alpha(A) \right\} - \left\{ E_{AB}^{\alpha\cup\beta}(B) - E_B^\beta(B) \right\}. \quad (22.4)$$

► Equations 21.1 and ► 22.4 do converge to the same result at the CBS limit since the terms in the brackets in ► Eq. 22.4 will numerically approach zero as the basis sets  $\alpha$  and  $\beta$  tend toward CBS, viz.

$$\lim_{\alpha, \beta \rightarrow \text{CBS}} \Delta E(\text{BSSE}) = \lim_{\alpha, \beta \rightarrow \text{CBS}} \Delta E. \quad (22.5)$$

The importance of this correction, although previously recognized (Emsley et al. 1978; Smit et al. 1978; van Lenthe et al. 1987), has rarely been applied (Eggenberger et al. 1991; Kendall et al. 1989; Leclercq et al. 1983; Mayer and Surjan 1992; van Duijneveldt-van de Rijdt and van Duijneveldt 1992) until the problems arising from omitting it, especially for (1) strongly bound hydrogen-bonded complexes exhibiting large fragment relaxations and (2) calculations employing large basis sets, were noted. It should be emphasized that for some strongly hydrogen-bonded dimers such as  $F^-(H_2O)$  and  $OH^-(H_2O)$ , the energy penalty term is quite large ( $\geq 5$  kcal/mol) and its omission will lead to erroneous results as regards the magnitude

and convergence of the uncorrected and BSSE-corrected values of the interaction energy as the basis set increases. This large energy penalty is caused by the strong interaction between the ion and water, a fact that results in a large elongation of the hydrogen-bonded OH bond causing the water molecule to adopt a configuration that is far from its isolated equilibrium geometry. A further consequence of this effect is the large red shift in the corresponding OH stretching vibration, a fact that has been experimentally verified.

## Extrapolation to the Complete Basis Set Limit

Application of the family of these sets to a variety of chemical systems (see Reference Dunning (2000) and references therein) – ranging from the very weakly bound (by around 0.01 kcal/mol) rare gas diatomics, to intermediate strength hydrogen-bonded neutral (2–5 kcal/mol), singly charged ion-water (10–30 kcal/mol) clusters, and single-bond diatomics (50–100 kcal/mol), to very strong (>200 kcal/mol) multiply charged metal–water clusters and multiple bond diatomics – has permitted a *heuristic* extrapolation of the computed electronic energies and energy differences to the CBS limit. Among the various approaches that have been proposed (Bunge 1970; Fast et al. 1999; Feller 1992; Halkier et al. 1999; Klopper 1995; Martin 1996; Termath et al. 1991; Wilson and Dunning 1997; Xantheas and Dunning 1993c) in order to arrive at the CBS limit, we have relied on the following two:

1. A polynomial with inverse powers of 4 and 5 (4–5 polynomial):

$$\Delta E = \Delta E_{\text{CBS}} + \gamma / (\ell_{\text{max}} + 1)^4 + (\ell_{\text{max}} + 1)^5 \quad (22.6)$$

where  $\ell_{\text{max}}$  is the value of the highest angular momentum function in the basis set and

2. An exponential dependence on the cardinal number of the basis set  $n$  ( $n = 2, 3, 4, 5$  for the sets of double through quintuple zeta quality, respectively):

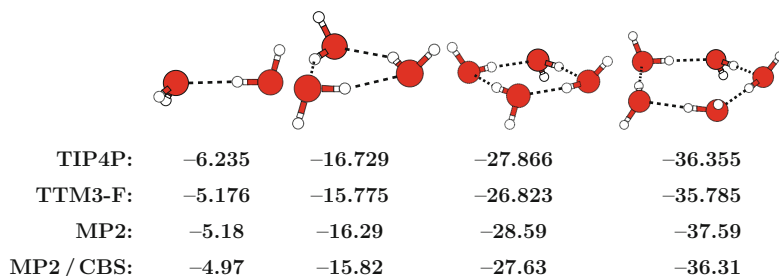
$$\Delta E = \Delta E_{\text{CBS}} + \alpha \bullet \exp(-\beta \bullet n). \quad (22.7)$$

It should be noted that in nearly every case, this “extrapolation” procedure only accounts for a very small change when compared to the “best” computed quantity with the largest basis set [usually the (aug)-cc-pV5Z or, computer resources permitting, the (aug)-cc-pV6Z]. This result suggests that effective convergence of the respective properties (such as structure and relative energies) has already been achieved with the largest basis sets of this family.

## Global Minimum Structures of the $n = 2-10$ Water Clusters

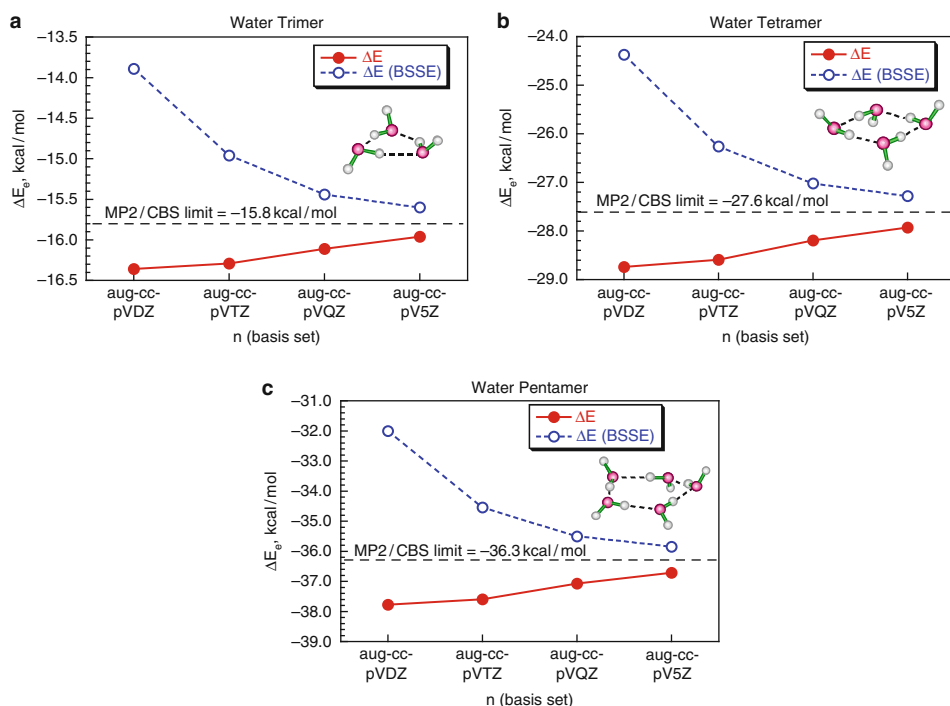
► *Figure 21-3* shows the global minimum structures of the water clusters  $n = 2-5$  and ► *Fig. 21-4* shows the variation of their uncorrected and BSSE-corrected binding energies from MP2 calculations with the correlation-consistent basis sets (Xantheas et al. 2002). The CBS limit of –15.8 kcal/mol for the cyclic trimer was estimated from MP2 binding energies with basis sets up to aug-cc-pV5Z.

It is worth noting that extrapolating the uncorrected and BSSE-corrected binding energies using ► *Eqs. 22.6* and ► *22.7* yields CBS limits that are within 0.01 kcal/mol from each other, while the extrapolation process itself results in minimal (<0.2 kcal/mol) changes with respect to the best computed numbers with the largest aug-cc-pV5Z set. For the cyclic water tetramer, the



■ Fig. 21-3

Global minimum energy structures for  $(\text{H}_2\text{O})_n$ ,  $n = 1-5$  are the same for the TIP4P and TTM3-F potentials and the MP2 level of theory. The binding energies ( $D_e$ ) at the MP2 level of theory (kcal/mol) were calculated with the aug-cc-pVTZ basis set

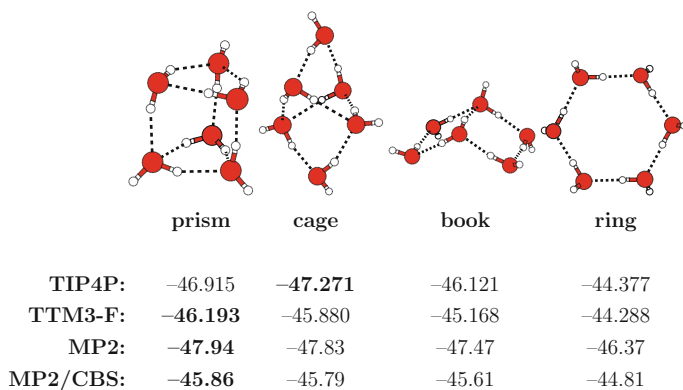


■ Fig. 21-4

The variation of the uncorrected (solid circles) and BSSE-corrected (open circles) binding energies from MP2 calculations with different basis sets for the global minimum structures of water clusters  $n = 3-5$ . The figure is reprinted with permission from reference Xantheas et al. (2002). © 2002 American Institute of Physics

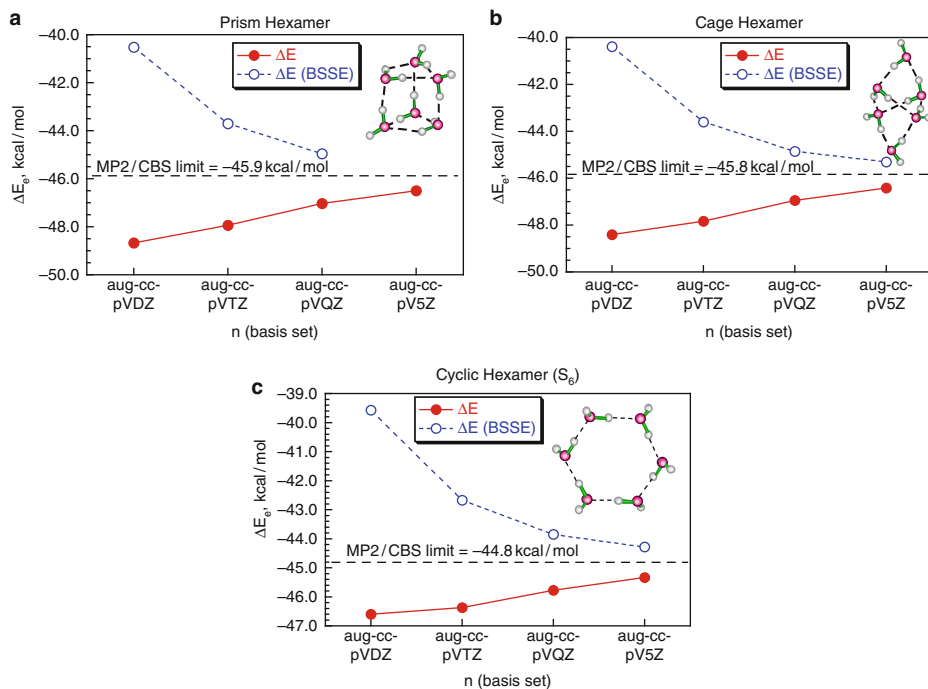
CBS limit estimated using the 4–5 polynomial (see [Eq. 22.6](#)) is  $-27.6$  kcal/mol. The extrapolation of the uncorrected and BSSE-corrected binding energies results in identical estimates for the CBS limit, which is just 0.3 kcal/mol away from the best computed value with the aug-cc-pV5Z set. The same trend is observed for the cyclic water pentamer with an estimated CBS limit of  $-36.3$  kcal/mol. Both the effective pair-wise TIP4P (Wales and Hodges 1998) potential and the transferable, polarizable, many-body TTM3-F do yield these structures as the global minima and in agreement with the results of the MP2 calculations. The unique common feature of the global minimum structures of water clusters in the  $n = 3-5$  size range is a cyclic (or ring) structure motif with the same direction of in-the-ring hydrogen bonding network in a *homodromic* direction (Xantheas 2000). These homodromic hydrogen bonding networks, i.e., those exhibiting donor-acceptor (da) arrangements between all water molecules, are associated with the largest non-additivities among other networks present in low-lying minima of small ( $n = 3-5$ ) water clusters. These cyclic (or ring) structures, especially for  $n = 4$  and 5 are of particular importance since they consist of the building blocks for the global minimum structures of water clusters in the size range  $n = 6-20$ .

The water hexamer has four distinct almost isoenergetic isomers that lie within 1 kcal/mol from each other (see [Figs. 21-5](#) and [21-6](#)) (Xantheas et al. 2002). Four distinct low-lying isomers are known as the prism, cage, book, and ring ( $S_6$ ) structures. The prism isomer (bilayer of a trimer ring) is the global minimum at the MP2 level of theory with all basis sets, while the cage isomer becomes the global minimum when zero-point energy corrections are included. The MP2/CBS limits are estimated at  $-45.86$  kcal/mol for the prism isomer and at  $-45.79$  kcal/mol for the cage isomer, respectively. We have also estimated MP2/CBS limits of  $-45.61$  kcal/mol for the book isomer and  $-44.81$  kcal/mol for the ring isomer of  $S_6$  symmetry. The calculations indicate that the “transition” from a quasi-planar, ring motif to a more compact, cage-like structure occurs for  $n = 6$ . A first difference among the results with classical water potentials was found for this cluster. The TIP4P potential predicts the cage isomer as the global minimum (Wales and Hodges 1998), while the TTM3-F potential favors the prism isomer in agreement with the result of the MP2 calculations.



**Fig. 21-5**

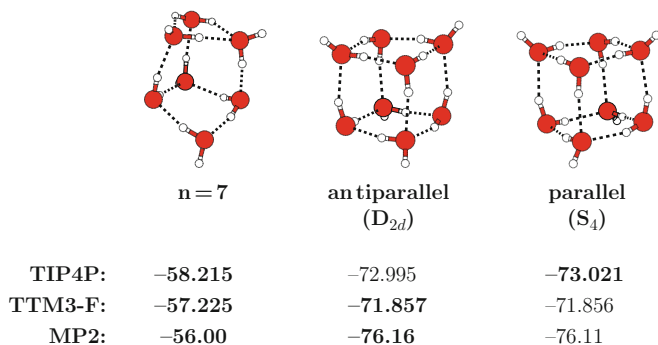
Global minimum energy structures and binding energies (kcal/mol) for  $(\text{H}_2\text{O})_6$ . The TIP4P potential prefers the cage-like hexamer, while the TTM3-F potential the prism-like one. The prism-like hexamer becomes the global minimum structure at the MP2/aug-cc-pVTZ level of theory



■ Fig. 21-6

The variation of the uncorrected (solid circles) and BSSE-corrected (open circles) binding energy from MP2 calculations with different basis sets for the water hexamer ( $n = 6$ ). The figure is reprinted with permission from reference Xantheas et al. (2002). © 2002 American Institute of Physics

The water heptamer ( $n = 7$ ) is an intermediate structure between the hexamer and the octamer. Note that water hexamer prefers to be a prism isomer (bilayer of cyclic ring trimer) and the water octamer a bilayer of the cyclic tetramer. The global minimum structure of the water heptamer consists of a cyclic trimer and cyclic tetramer on each layer as shown in ► Fig. 21-7. The water octamer ( $n = 8$ ) has two nearly isoenergetic forms having  $D_{2d}$  and  $S_4$  symmetry as the low-energy structures (see ► Figs. 21-7 and ► 21-8) (Xantheas and Aprà 2004). These are comprised of two stacked cyclic tetramers and the distinction between those two isoenergetic isomers lies in the direction of the two in-the-ring hydrogen bonding networks that can be either along the same (or **parallel**) for the  $S_4$  isomer or opposite (or **antiparallel**) for the  $D_{2d}$  isomer. The variation of the MP2 binding energies with basis set is graphically illustrated in ► Fig. 21-8 for the two isomers. The best estimated BSSE-corrected MP2/CBS limits obtained with the 4–5 polynomial (cf. ► Eq. 22.6) are  $-72.94$  kcal/mol and  $-72.78$  kcal/mol for the **antiparallel** ( $D_{2d}$ ) and the **parallel** ( $S_4$ ) isomers, respectively. The corresponding BSSE-corrected MP2/CBS limits estimated with the exponential extrapolation (via ► Eq. 22.7) are  $-72.42$  kcal/mol for the **antiparallel** and  $-72.35$  kcal/mol for the **parallel** isomers, respectively. Note that the MP2 energy difference between both isomers is quite small of  $\sim 0.2$  kcal/mol for both extrapolation methods. Given the *heuristic* nature of the two extrapolation methods to arrive at the CBS limit and these caveats,



■ Fig. 21-7

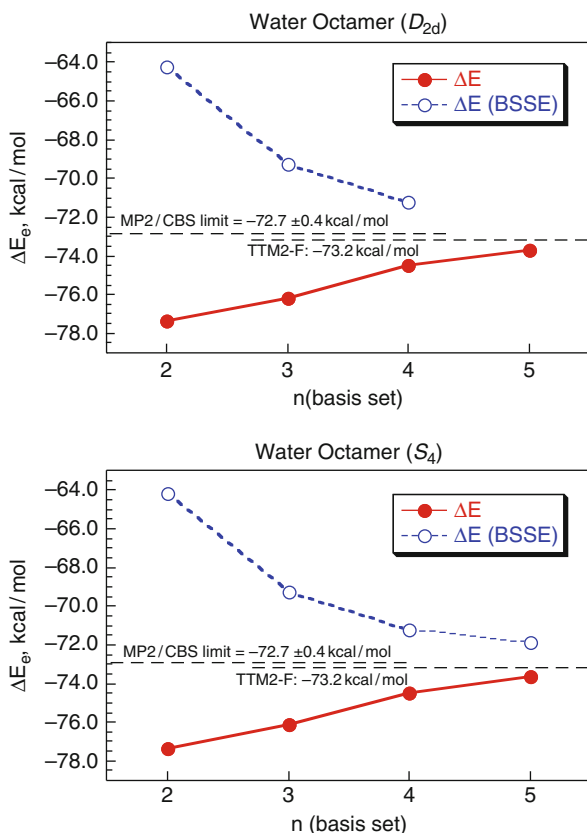
The global minimum energy structures and binding energies (kcal/mol) for  $(\text{H}_2\text{O})_7$  and  $(\text{H}_2\text{O})_8$ . For  $n = 7$ , the TIP4P and TTM3-F potentials have the same global minimum. For  $n = 8$ , the TIP4P potential favors the parallel circular arrangement of hydrogen bonds of two ring tetramers, while TTM3-F, the antiparallel arrangement. At the MP2/aug-cc-pVTZ level of theory, the antiparallel arrangement is preferred in agreement with the TTM3-F result

it is difficult and probably futile to assign a CBS limit for the binding energy with an “error bar” smaller than this quantity ( $\sim 0.4$  kcal/mol), which arises from the extrapolation procedure. As can be seen from [Fig. 21-8](#), we suggest a value of  $-72.7 \pm 0.4$  kcal/mol for the MP2/CBS limit of the binding energy for both isomers of the water octamer, keeping in mind that the **antiparallel** isomer is always lower in energy by  $\sim 0.05$  kcal/mol than the **parallel** one. As regards the results of classical potentials, TIP4P predicts the **parallel** isomer (Wales and Hodges 1998), while TTM3-F the **antiparallel** isomer as the global minimum structure in agreement with the results of the MP2 calculations.

► [Figure 21-9](#) shows the global minimum structures for  $n = 9$  and 10. The TIP4P and TTM3-F potentials predict the same global minimum structure of  $(\text{H}_2\text{O})_9$ , consisting of the cyclic tetramer and the cyclic pentamer on each layer. The water decamer ( $n = 10$ ) has two nearly isoenergetic isomers consisting of two stacked cyclic pentamers. These two isoenergetic isomers are distinguished by the direction of the in-the-ring hydrogen bonding networks as we have previously discussed for the two isomers of the water octamer. The **antiparallel** isomer of water decamer has the opposite direction of the in-the-ring hydrogen bonding networks on each layer, while the **parallel** isomer has the same direction. The TIP4P potential predicts the **parallel** isomer (Wales and Hodges 1998), whereas the TTM3-F potential predicts the **antiparallel** isomer as the global minimum structure that is consistent with the results of the MP2 calculations.

## The Global Minima of Medium-Sized Water Clusters in the Range $11 \leq n \leq 16$

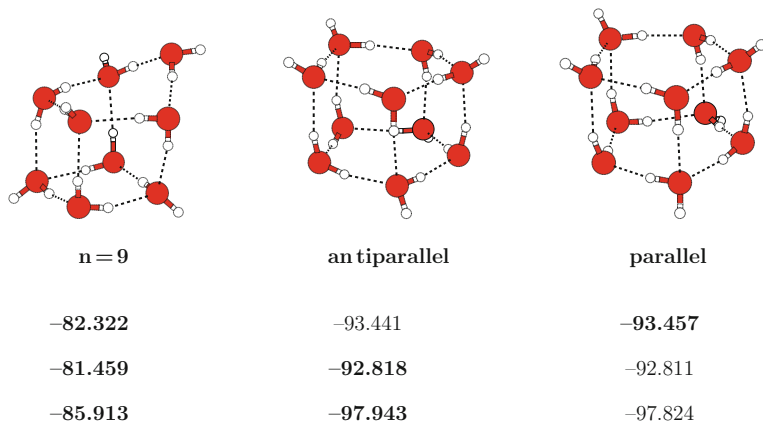
During the last 20 years, the search for the global minima of medium-sized water clusters has received much theoretical attention (Bulusu et al. 2006; Day et al. 2000; Fanourgakis et al. 2004, 2005; Hartke 2003; Kazimirski and Buch 2003; Koga et al. 2000; Lagutchenkov et al. 2005;



■ Fig. 21-8

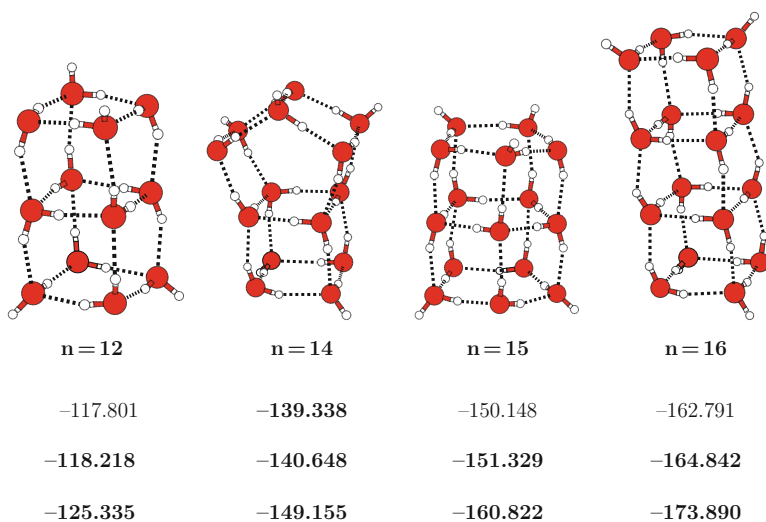
The variation of the uncorrected (solid circles) and BSSE-corrected (open circles) binding energy from MP2 calculations with different basis sets for the water octamer ( $n = 8$ ). The figure is reprinted with permission from reference Xantheas and Aprà (2004). © 2004 American Institute of Physics

Lee et al. 1995, 2001; Nigra and Kais 1999; Sadlej 2001; Tsai and Jordan 1993; Wales and Hodges 1998) and several previous ab initio calculations (Day et al. 2000; Fanourgakis et al. 2004, 2005; Koga et al. 2000; Lee et al. 1995, 2001; Sadlej 2001; Tsai and Jordan 1993) suggested that the global minima of medium-sized water clusters in the  $n = 11-16$  range mainly consist of the building blocks of the antiparallel octamer and the antiparallel decamer isomers. ▶ Figure 21-10 shows the global minimum structures for  $n = 12, 14, 15$ , and 16 at the MP2 level of theory. In detail, the global minima of  $(\text{H}_2\text{O})_{12}$  and  $(\text{H}_2\text{O})_{16}$  are stacked cube structures with the antiparallel arrangement of the in-the-ring hydrogen bonding networks that are built from the building blocks of the antiparallel octamer. For the global minimum of  $(\text{H}_2\text{O})_{15}$ , the antiparallel decamer was used as the building block to form a stacked pentagonal prism. In the case of the global minimum structure of  $(\text{H}_2\text{O})_{14}$ , two building blocks of the antiparallel octamer and decamer were used to obtain a fused square-pentagon prism structure. The TIP4P potential fails in predicting these arrangements as the global minima for  $n = 12, 15$  and 16. It rather uses the parallel octamer and the parallel decamer isomers as starting points to build the global minimum structures of



■ Fig. 21-9

The global minimum energy structures and binding energies (kcal/mol) of  $(\text{H}_2\text{O})_9$  and  $(\text{H}_2\text{O})_{10}$ . The TIP4P and TTM3-F potentials predict the same global minimum structure for  $(\text{H}_2\text{O})_9$ , which is based on the antiparallel arrangement of hydrogen bonding in  $(\text{H}_2\text{O})_8$ . For  $(\text{H}_2\text{O})_{10}$  (stacking of two pentagon rings), the TIP4P potential favors the parallel arrangement, while the TTM3-F potential the antiparallel arrangement. The binding energies at the MP2/aug-cc-pVTZ level of theory are listed

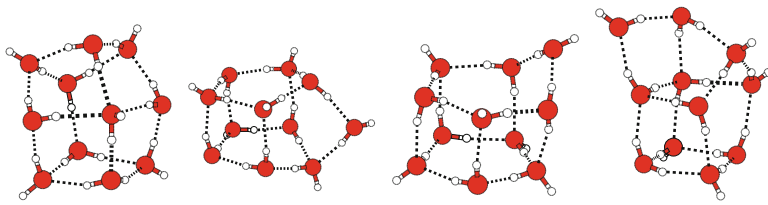


■ Fig. 21-10

The global minimum of  $(\text{H}_2\text{O})_n$  for  $n = 12, 14-16$ . The TIP4P potential predicts a different global minimum for  $n = 12, 15$  and  $n = 16$ . The MP2/aug-cc-pVDZ energies are listed

water clusters for  $n = 12, 15$ , and  $16$  since these were the most stable isomers for  $n = 8$  and  $n = 10$  (see ► Figs. 21-7 and ► 21-9) (Wales and Hodges 1998). In contrast, the TTM3-F potential again predicts the arrangements in agreement with the MP2 results.





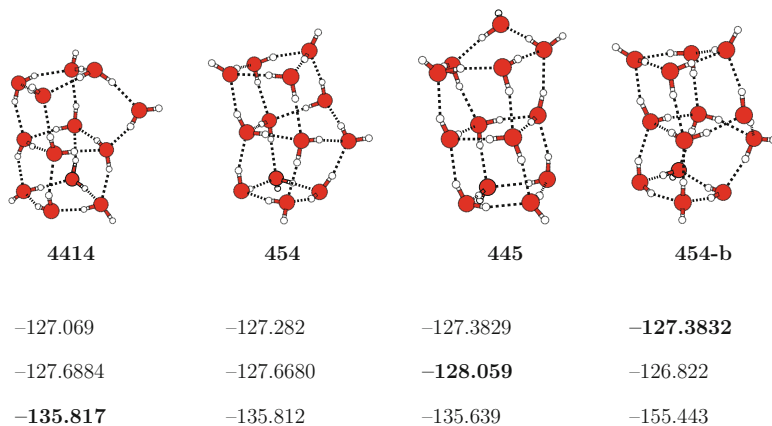
	434	515	551	443
TIP4P:	-82.322	-93.441	-93.457	-93.457
TTM3-F:	-101.771	-101.629	-101.653	-102.964
MP2:	-107.611	-107.485	-107.270	-107.134

■ Fig. 21-11

The isomers of  $(\text{H}_2\text{O})_{11}$ . The (443) isomer is the global minimum structure with the TIP4P and TTM3-F potentials. The (434) isomer has the lowest binding energy ( $D_e$ ) at the MP2/aug-cc-pVTZ level theory. Binding energies are shown in kcal/mol. The figure is reprinted with permission from reference Bulusu et al. (2006). © 2006 American Chemical Society

In the case of the odd-numbered water clusters ( $n = 11$  and 13), it is not as easy to build the global minimum structures starting from most stable networks of the octamer and decamer clusters. Figure 21-11 shows the four distinct structural families of the low-lying isomers of  $(\text{H}_2\text{O})_{11}$  (Bulusu et al. 2006). Two families labeled as (515) and (551) are built from the stacked pentagon  $(\text{H}_2\text{O})_{10}$  (antiparallel decamer, the global minimum of  $(\text{H}_2\text{O})_{10}$  as shown in Fig. 21-9). The (515) isomer can be viewed as constructed by adding one water molecule between the top and middle layers of the antiparallel decamer isomer, whereas the (551) isomer from inserting one water molecule into the top layer. The families labeled as (443) and (434) are built from the stacked cube  $(\text{H}_2\text{O})_{12}$  isomer, which consists of three layers of cyclic tetramers: the (443) isomer can be built by removing one water molecule from the top layer of the global minimum of  $(\text{H}_2\text{O})_{12}$  and the (434) isomer by removing one water molecule from the middle layer of the stacked cube structure of  $(\text{H}_2\text{O})_{12}$ . The MP2 results indicate that the low-lying isomers of the (434) and (515) families are the most probable candidates for the global minimum. Since the maximum MP2 energy difference for all four distinct almost isoenergetic isomers is very small ( $\sim 0.5$  kcal/mol), the inclusion of zero-point energy corrections is important to identify the global minimum. When zero-point energy corrections (albeit at the harmonic level) were included, the (515) isomer becomes the global minimum structure of  $(\text{H}_2\text{O})_{11}$ . Both the TIP4P and TTM3-F potentials predict the (443) isomer as the global minimum.

Figure 21-12 shows four distinct isomers for  $(\text{H}_2\text{O})_{13}$  as the low-lying isomers of  $(\text{H}_2\text{O})_{13}$  (Bulusu et al. 2006). Note that the three isomers (441a), (454a), and (445) can be built from the antiparallel global minimum of  $(\text{H}_2\text{O})_{12}$ , as shown in Fig. 21-10. However, the (454-b) isomer, which is the global minimum structure predicted by TIP4P, is built from the parallel  $(\text{H}_2\text{O})_{12}$  in accordance with the fact that this is the global minimum structure of  $(\text{H}_2\text{O})_{12}$  predicted by TIP4P. For completeness, the (441a) isomer can be built by adding one water molecule vertically between the top and middle layers of the antiparallel isomer of  $(\text{H}_2\text{O})_{12}$ . The (454a) and (454-b) isomers can be built by inserting one water molecule into the middle layer of the



■ Fig. 21-12

The isomers of  $(\text{H}_2\text{O})_{13}$ . The MP2 energies were calculated with the aug-cc-pVDZ basis set. The figure is reprinted with permission from reference Bulusu et al. (2006). © 2006 American Chemical Society

**antiparallel** and **parallel**  $(\text{H}_2\text{O})_{12}$  isomers, respectively. The (445) isomer can be constructed by inserting one water molecule into the top water layer. The MP2 calculations predict that the (4414) isomer is the most stable isomer of the  $(\text{H}_2\text{O})_{13}$  cluster and the (454) isomer is the next lowest isomer. Since the maximum MP2 energy difference for four distinct isoenergetic isomers of  $(\text{H}_2\text{O})_{13}$  is very small ( $\sim 0.4$  kcal/mol), we furthermore estimate the effect of the zero-point energy correction to the relative stability of the isomers. The (4414) isomer remains as the global minimum structure of  $(\text{H}_2\text{O})_{13}$  after including harmonic zero-point energy corrections. The TTM3-F potential predicts the (445) isomer as the global minimum structure of  $(\text{H}_2\text{O})_{13}$ .

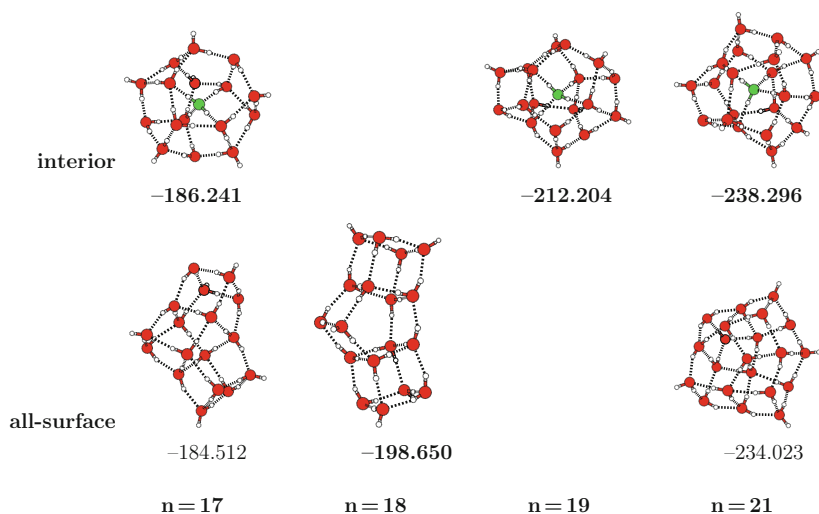
## The Transition from “All-Surface” to “Internally Solvated” Clusters at $n = 17$

So far we have discussed in ● section “Global Minimum Structures of the  $n = 2-10$  Water Clusters” that the structural “transition” from a quasi-planar ring motif to a more compact, cage-like structure, which occurs at  $n = 6$ . For the smaller clusters, the need to maximize hydrogen bonding results in all the atoms being on the surface of the cluster. However, as the cluster grows, there is a point where more compact, fully connected structures are formed, in which water molecules are fully coordinated (i.e., they have two donors and two acceptors of hydrogen bonds) like in an average arrangement in the liquid environment. Several experiments (Beuhler and Friedman 1982; Haberland 1984; Hermann et al. 1982; Lin 1973; Nagashima et al. 1986; Niedner-Schatteburg and Bondybey 2000; Schindler et al. 1996; Searcy and Fenn 1974; Stace and Moore 1983; Yang and Castleman 1989) such as expansion of ionized water vapor (Beuhler and Friedman 1982; Searcy and Fenn 1974), ion bombardment of ice surfaces (Haberland 1984), as well as black-body-radiation-induced dissociation studies (Niedner-Schatteburg and Bondybey 2000; Schindler et al. 1996) suggested a prevailed magic cluster of the  $\text{H}_3\text{O}^+(\text{H}_2\text{O})_{20}$  cluster consisting of a clathrate-like pentagonal dodecahedron structure.

This magic cluster of  $\text{H}_3\text{O}^+(\text{H}_2\text{O})_{20}$  indicates the transition from the “all-surface” to “internally solvated” clusters. Note that this kind of transition for the neutral water clusters has not yet been identified experimentally. For a cluster of that size, the number of isomers increases dramatically with size. A detailed discussion of this problem will be presented in the following section “The Family of Minima for  $(\text{H}_2\text{O})_{20}$ .” In brief, a global search algorithm (Hartke 2003; Li and Scheraga 1987; Wales and Scheraga 1999) has been previously used in order to identify low-energy structures of clusters of that size. That global search approach of an evolutionary algorithm combined with the TTM2-F potential predicted that for the neutral water clusters, the transition from “all-surface” to “internally solvated” occurs for  $(\text{H}_2\text{O})_{17}$  (Hartke 2003). Figure 21-13 shows the alternation between the all-surface and interior minima at the  $n = 17-21$  cluster regime predicted by the TTM2-F interaction potential. The solvated water molecule with a tetrahedral network is highlighted in green color. The TIP4P potential predicts that the transition from “all-surface” to “internally solvated” clusters occurs for  $(\text{H}_2\text{O})_{19}$ . Both the TIP4P and TTM3-F potentials predicted the same global minimum structures for  $n = 18$  and 20. The lowest energy structure predicted with TIP4P has a slightly different hydrogen bonding orientation for  $n = 19$  when compared to the global minimum structure predicted by TTM2-F.

## Validation from Electronic Structure Calculations

Since the TIP4P and TTM3-F classical water potentials predicted different global minimum structures for  $n = 17$  and 21, we concentrated our efforts in comparing the relative stabilities of



■ Fig. 21-13

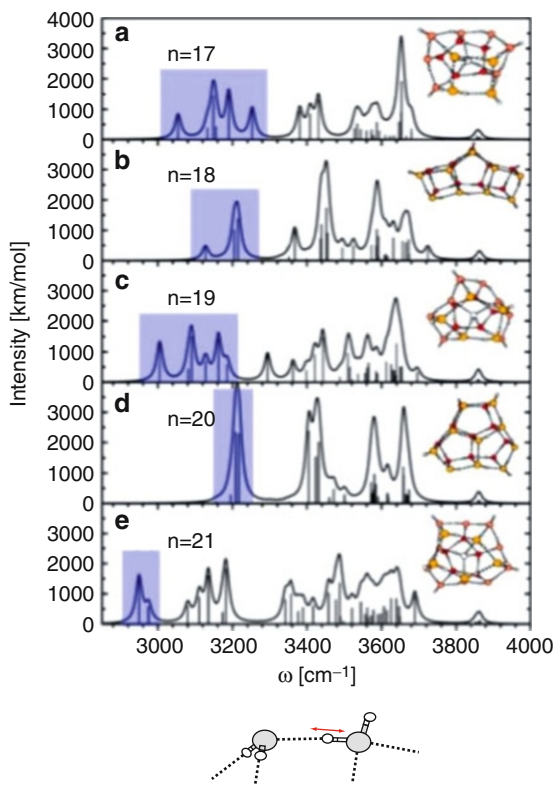
The transition from “all-surface” to “internally solvated” clusters in the range of  $n = 17-21$ . The binding energies were calculated at the MP2/aug-cc-pVDZ level of theory. The figure is reprinted with permission from reference Lagutchenkov et al. (2005). © 2005 American Institute of Physics

the two different arrangements predicted by the two models from electronic structure calculations. The results (Lagutchenkov et al. 2005) obtained at the MP2 level of theory with the aug-cc-pVDZ and aug-cc-pVTZ basis sets are shown in [▶ Fig. 21-13](#). For the  $n = 17$  cluster, MP2 calculations with both basis sets predicted the “interior” structure to be more stable, in agreement with the predictions of the TTM2-F potential. Inclusion of differential zero-point energy corrections (0.45 kcal/mol at B3LYP/TZVP level of theory) furthermore tends to increase the energy difference between the two isomers in favor of the “interior” configuration. Our best estimate for the energy difference between the “all-surface” and “interior” isomers of  $n = 17$  is 1.43 kcal/mol (1.88 kcal/mol including zero-point energy corrections) at the MP2/aug-cc-pVTZ level of theory. For the  $n = 21$  cluster, a similar behavior was found between the most stable “all-surface” and “interior” isomers. The basis set effect at the MP2 level of theory also results in decreasing the energy difference, where as the inclusion of zero-point energy corrections tends to stabilize the “interior” configuration with respect to the “all-surface” one. The TTM2-F potential predicts the correct ordering between the two different arrangements, yielding an energy difference that is almost half of the MP2/aug-cc-pVTZ value. At this level of theory, the “interior” configuration is stabilized by 3.71 kcal/mol (4.11 kcal/mol including zero-point energy corrections) with respect to the “all-surface” one for  $n = 21$ . Therefore, the MP2 calculations provided a reliable benchmark that validated the predictions of the TTM2-F potential as regards the onset of the “all-surface” to “interior” configurations occurring at  $n = 17$ .

## Spectroscopic Signature

As noted earlier, the ab initio investigation of the relative stability of the various hydrogen bonding networks in the  $n = 17-21$  cluster regime has identified the existence of a transitional size regime where preferential stabilization alternates between “all-surface” (all atoms on the surface of a cluster) and “internally solvated” (one water molecule at the center of the cluster, fully solvated) configurations with the addition or the removal of a single water molecule.

This behavior has been previously suggested based on the results of the TTM2-F interaction potential. It is qualitatively different from the picture that simple, pairwise-additive potentials like TIP4P suggest. The onset of the appearance of the first “interior” configuration in water clusters occurs for  $n = 17$ . The observed structural alternation between “interior” ( $n = 17, 19, 21$ ) and “all-surface” ( $n = 18, 20$ ) global minima in the  $n = 17-21$  cluster regime is accompanied by a corresponding spectroscopic signature, namely the undulation in the position of the most red-shifted OH stretching vibrations (indicated by the shaded area in [▶ Fig. 21-14](#)) according to the trend: “interior” configurations exhibit more red-shifted OH stretching vibrations than “all-surface” ones (see [▶ Fig. 21-14](#)). These most red-shifted OH stretching vibrations form distinct groups in the intramolecular region of the spectra and correspond to localized vibrations of donor OH stretches that have the following characteristics: (1) the hydrogen-bonded OH group belongs to a water molecule that has a “free” (non-hydrogen-bonded) OH stretch and (2) the bound OH group acts as a donor to a neighboring water molecule via a water dimer-like hydrogen bond (i.e., a hydrogen bond in which the dihedral angle between the free OH of the donor molecule and the bisector of the HOH angle of the acceptor molecule is  $180^\circ$ , as seen in the lower panel of [▶ Fig. 21-14](#)).



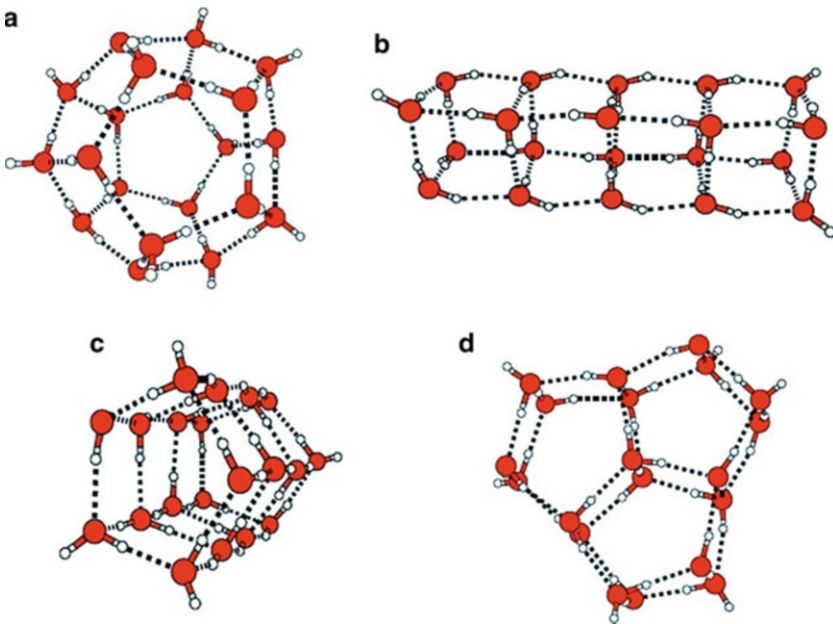
■ Fig. 21-14

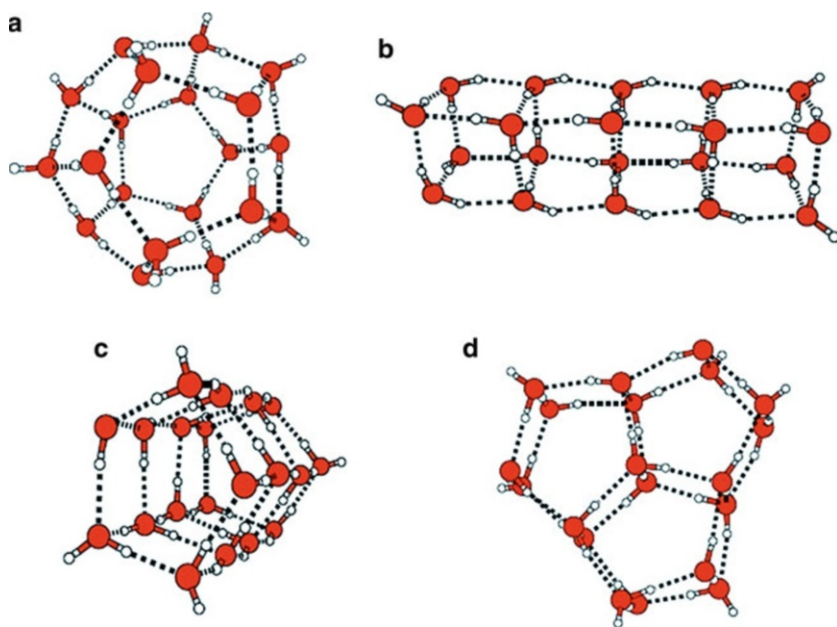
Intramolecular spectra in the 3,000–4,000  $\text{cm}^{-1}$  region associated with the hydrogen-bonded and free OH stretching vibrations for  $n = 17-21$  [(a)–(e)] at the B3LYP/TZVP level of theory. The stick diagram of the computed frequencies is also shown. Shaded area denotes the most red-shifted OH stretching vibrations. The figure is reprinted with permission from reference Lagutchenkov et al. (2005). © 2005 American Institute of Physics

## The Family of Minima for $(\text{H}_2\text{O})_{20}$

Interest in the family of water clusters for  $n = 20$  stems from the fact that one of the families of minima is the dodecahedron which has been proposed as a model for inclusion compounds and constitutes a building block of type I ice clathrate (we will discuss this in detail in ▶ section “The First Few Water Cages”) The structure of  $(\text{H}_2\text{O})_{20}$  has been the subject of debate due to the existence of various major families of minima which are energetically in close proximity and the disagreement as to which was the global minimum (Fanourgakis et al. 2004).

We have previously briefly discussed (see ▶ section “The Transition from “All-Surface” to “Internally Solvated” Clusters at  $n = 17$ ”) the issue regarding the number of isomers increasing dramatically with cluster size. The assignment of the structural motif of the neutral  $(\text{H}_2\text{O})_{20}$

cluster represents a much more difficult task especially in the absence of experimental information (such as rotational constants or infrared spectra) that can yield definitive structural information. For typical clusters of that size, even for a fixed position of the Oxygen atom network, there exists a multitude of arrangements of the hydrogen atoms in a manner consistent with the cluster analog of the Bernal-Fowler ice rules (Hobbs 1974; Petrenko and Whitworth 1999) For instance, just for the dodecahedral arrangement of the oxygen atom network in  $(\text{H}_2\text{O})_{20}$ , the application of graph theoretical techniques (Kuo et al. 2001; McDonald et al. 1998) yields an estimate of 30,026 symmetry-distinct hydrogen bond topologies which are likely candidates for local minimum structures. For this reason, extensive sampling of the  $n = 20$  cluster potential energy surface (PES) has been performed only with classical interaction potentials. Using the “basin-hopping” method combined with the TIP4P potential, Wales and Hodges (Wales and Hodges 1998) identified four major families of  $(\text{H}_2\text{O})_{20}$  which, based on the arrangement of the oxygen atom network, they classified as (a) dodecahedron, (b) fused cubes, (c) face-sharing pentagonal prisms, and (d) edge-sharing pentagonal prisms. Representative candidates of these families of minima are illustrated in  Fig. 21-15. The relative energetic order of the four families is predicted to be (d)-(b)-(c)-(a) with TIP4P. An evolutionary algorithm used by Hartke in conjunction with TTM2-F interaction potentials resulted in the edge-sharing pentagonal prism as the global minimum. The global minimum structure is in fact qualitatively



■ Fig. 21-15

The lowest energy isomers within the four-families of minima for  $(\text{H}_2\text{O})_{20}$ : (a) dodecahedron, (b) fused cubes, (c) face-sharing pentagonal prisms, and (d) edge-sharing pentagonal prisms. The figure is reprinted with permission from reference Fanourgakis et al. (2004). © 2004 American Institute of Physics

identical for TTM2-F and TIP4P, and it is an all-surface one. The edge-sharing pentagonal prism (d) is lower by 11.2 (TIP4P) and by 13.98 kcal/mol (TTM2-F) than the dodecahedral family (a).

## The Four Major Families of Minima

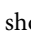
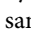
---

First principles electronic structure calculations at the MP2 level of theory with the family of augmented correlation-consistent basis sets up to quadruple zeta quality were used to estimate complete basis set (CBS) binding energies  $D_e$  for the lowest energy structures within each of the four low-lying families of minima as follows: (a) dodecahedron (−200.1 kcal/mol, 30 hydrogen bonds), (b) fused cubes (−212.6 kcal/mol, 36 hydrogen bonds), (c) face-sharing pentagonal prisms (−215.0 kcal/mol, 35 hydrogen bonds), and (d) edge-sharing pentagonal prisms (−217.9 kcal/mol, 34 hydrogen bonds) (Fanourgakis et al. 2004). Among the various interaction potentials, TTM2-F (Burnham and Xantheas 2002b) was found to predict the absolute cluster binding energies to within 1% from the corresponding MP2/CBS values. These calculations also yielded the first harmonic vibrational spectra of the lowest energy isomers within each family as a means of providing the necessary information for their future spectroscopic identification.

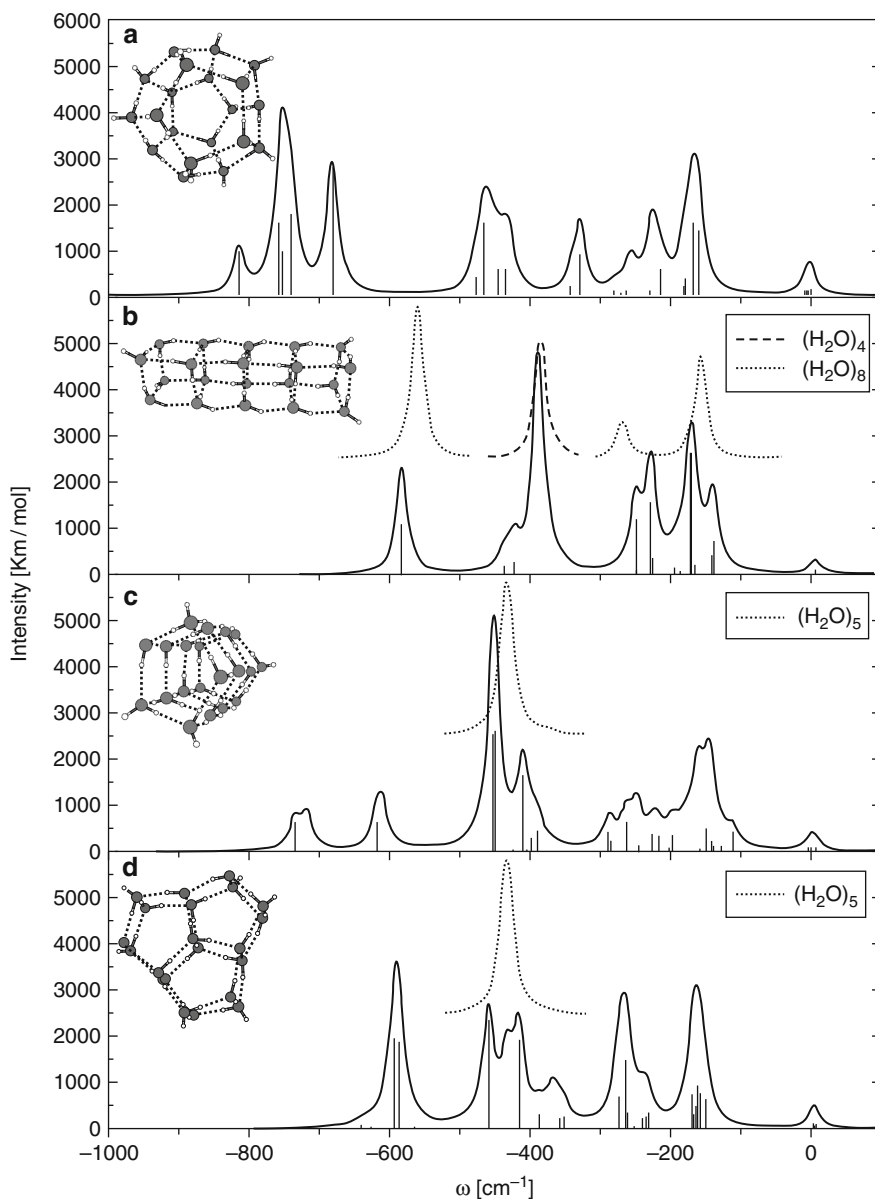
Zero-point energy corrections do not change the relative order of the four different networks, although they reduce the separation between the highest-lying dodecahedron structure and the lowest-lying edge-sharing pentagonal prism isomer from 17.8 kcal/mol to 15.0 kcal/mol.

## Vibrational Spectra

---

The IR spectra of the four low-lying families of minima of  $(\text{H}_2\text{O})_{20}$  exhibit different features in the OH stretching region that can be used for their spectroscopic assignment. These are shown in  Fig. 21-16. Some of these spectral features are reminiscent of their constituent water tetramer and pentamer fragments. The dodecahedral network is associated with the most red-shifted (by 700–800  $\text{cm}^{-1}$  with respect to the monomer) OH stretching vibrations among the four isomers and shows the richest structure in the 3,000–4,000  $\text{cm}^{-1}$  range. The lowest edge-sharing pentagonal prisms family of isomers displays IR intense bands that are red-shifted by  $\sim 600 \text{ cm}^{-1}$  with respect to the average of the symmetric and antisymmetric OH stretching vibrations in the water monomer. A common feature of the vibrational spectra that is shared by all four networks is that the *most* red-shifted, IR-active OH stretching vibrations exhibit the same characteristics previously found for the most stable isomers of  $n = 17-21$  ( Fig. 21-14), namely that they belong to fragments that have a “free” OH stretch and act as donors to a neighboring water molecule along a hydrogen bond which resembles a gas-phase dimer arrangement. It is conceivable that the second characteristic directly affects the energetic stability of the isomer within the corresponding family.

The computed spectra can be used as guides for the spectroscopic assignment of the lowest energy edge-sharing pentagonal prism isomer in molecular beams or the higher-lying networks in other environments such as helium droplets or cryogenic *para*-hydrogen solids that can facilitate the formation of higher energy cluster isomers.



■ Fig. 21-16

Intramolecular spectra in the  $3,000-4,000\text{ cm}^{-1}$  region associated with the OH stretching vibrations. The stick diagram of the frequencies is also shown. The IR spectra for the water ring tetramer, pentamer, and octamer cube are shown for comparison. The figure is reprinted with permission from reference Fanourgakis et al. (2004). © 2004 American Institute of Physics



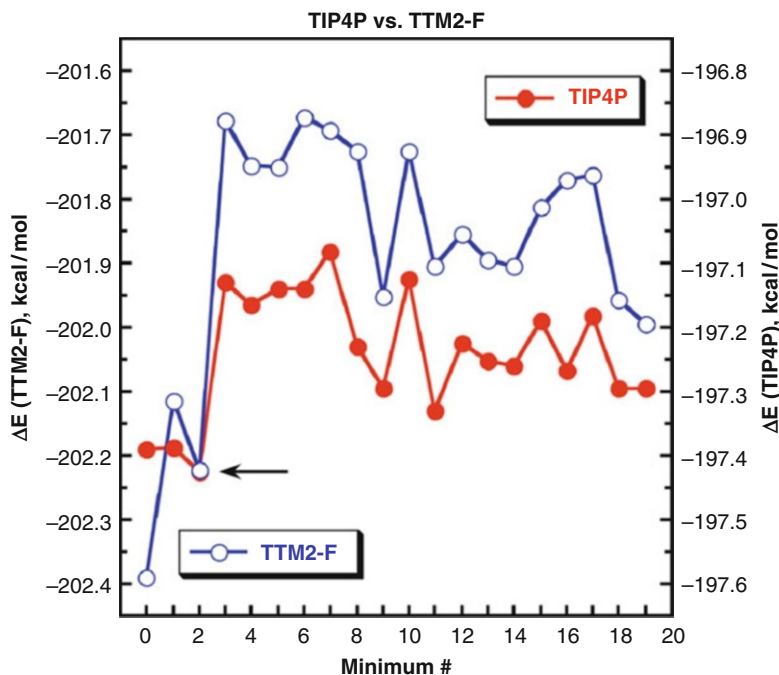
## The First Few Water Cages

### Significance

Gas hydrates are naturally occurring in situ in the deep oceans and permafrost regions of the earth (Mao et al. 2007; Sloan 1998). Their potential importance as inclusion compounds relevant to energy problems such as hydrogen storage has been recently highlighted. All of the clathrate hydrate forming natural gases adopt one of the following three crystal structures (Jeffrey et al. 1967; Ripmeester et al. 1987): (1) sI (cubic,  $Pm\bar{3}n$ ), (2) sII (cubic,  $Fd\bar{3}m$ ) and (3) sH (hexagonal,  $P6/mmm$ ). These three-dimensional lattices are constructed from the following water cages: (1) the pentagonal dodecahedron (D-cage), which consists of 20 water molecules that form 12 pentagonal faces ( $5^{12}$ ); (2) the tetrakaidecahedron (T-cage), which consists of 24 water molecules that form 12 pentagonal and 2 hexagonal faces ( $5^{12}6^2$ ); (3) the hexakaidecahedron (H-cage), which consists of 28 water molecules that form 12 pentagonal and 4 hexagonal faces ( $5^{12}6^4$ ); (4) the irregular dodecahedron, which consists of 20 water molecules that form 3 tetragonal, 6 pentagonal, and 3 hexagonal faces ( $4^35^66^3$ ); and (5) the icosahedron, that consists of 36 water molecules that form 12 pentagonal and 8 hexagonal faces ( $5^{12}6^8$ ). In the previous notation,  $p^nq^m$  identifies the underlying Oxygen atom network of the constituent cages, with  $p$ ,  $q$  being the size of the polygons and  $n$ ,  $m$  the number of faces; for instance,  $5^{12}6^2$  denotes 12 pentagonal and 2 hexagonal faces. The unit cell of the three-dimensional (sI) hydrate periodic structure is made of 2 units of the  $5^{12}$  cage and 6 units of the  $5^{12}6^2$  cage. In a similar manner, the unit cell of the (sII) hydrate lattice is constructed from 16 units of the  $5^{12}$  cage and 8 units of the  $5^{12}6^4$  cage. This hydrate lattice (sII) has been recently considered for practical applications in energy storage as it was shown to meet current US Department of Energy's target densities for an onboard hydrogen storage system (Mao et al. 2006; Schüth 2005). Finally, the unit cell of the (sH) hydrate is more complex since it is constructed from 3 units of the  $5^{12}$  cage, 2 units of the  $4^35^66^3$  cage, and 1 unit of the  $5^{12}6^8$  cage. The constituent cages of those three hydrate lattices are often used as models to probe the relevant guest/host interactions from electronic structure calculations to derive intermolecular potentials that can be then used for the full system of the periodic lattice and the molecular guests.

### The Pentagonal Dodecahedron (D-cage) ( $\text{H}_2\text{O}$ )<sub>20</sub> Cluster

The analysis of the relative energetics of the various dodecahedron isomers is performed using the previous results (Wales and Hodges 1998) of Wales and Hodges as the starting point. These authors have used the basin-hopping Monte Carlo method (Li and Scheraga 1987; Wales and Scheraga 1999) in conjunction with the classical TIP4P (Jorgensen et al. 1983) potential in order to obtain the global and low-lying local minima of the pentagonal dodecahedron family of isomers. The list of the first 19 minima obtained with the TIP4P potential by Wales and Hodges were used as starting geometries for optimization with the TTM2-F (Burnham and Xantheas 2002b, c; Burnham et al. 1999) interaction potential (see [Fig. 21-17](#)). In that figure, the global minimum obtained with TIP4P for the dodecahedron corresponds to minimum #2 in the list and is indicated by an arrow. In general, there is a good correspondence between the TIP4P and TTM2-F relative isomer energetics, except for the isomer indicated as minimum "0" in the list. That isomer labeled by "0" is the one suggested as the global minimum from the combinatorial optimization with the "strong" and "weak" hydrogen bonds (SWB) model (Kirov 1996)



■ Fig. 21-17

Binding energies of the first 19 isomers of the pentagonal dodecahedron ( $\text{H}_2\text{O}$ )<sub>20</sub> cluster with the TIP4P (filled circles) and TTM2-F (open circles) potentials. The TIP4P global minimum corresponds to minimum #2 and is indicated with an arrow. Minimum “0” is the isomer predicted from the SWB model. The figure is reprinted with permission from reference Kirov et al. (2008). © 2008 Elsevier

when the intermolecular interactions were computed with the ST2 (Stillinger and Rahman 1974) interaction potential.

In order to further assess the validity of the predictions of the empirical interaction potentials regarding the relative stability of isomers for the pentagonal dodecahedron, we have carried out electronic structure calculations for the 20 minima that are included in Fig. 21-17 (Kirov et al. 2008). The TTM2-F optimal structures (which are qualitatively similar to the ones obtained by TIP4P) for the 20 minima labeled 0–19 were used as starting points in the geometry optimization at both the density functional (DFT) (Hohenberg and Kohn 1964; Kohn and Sham 1965) and MP2 (Møller and Plesset 1934) levels. In the DFT calculations, Becke’s gradient-corrected exchange-correlation density functional (B3LYP) (Becke 1988, 1993) was used in conjunction with Ahlrichs’ polarized triple- $\zeta$  (TZVP) basis set (Schäfer et al. 1994). As for the previous cases, the MP2 optimizations were performed using Dunning’s (Dunning 1989; Kendall et al. 1992) augmented correlation-consistent basis sets of double- $\zeta$  (aug-cc-pVDZ) quality.

The binding energies of these 20 isomers of the dodecahedron ( $\text{H}_2\text{O}$ )<sub>20</sub> are shown in Fig. 21-18 at the B3LYP/TZVP (open circles) and MP2/aug-cc-pVDZ (filled squares) levels of theory (Kirov et al. 2008). The order of isomers has been maintained the same as in

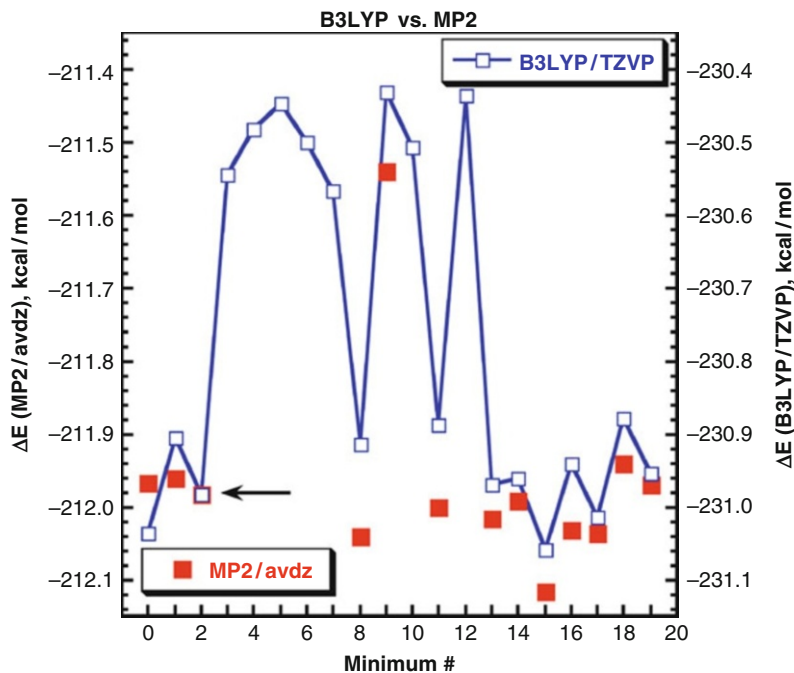
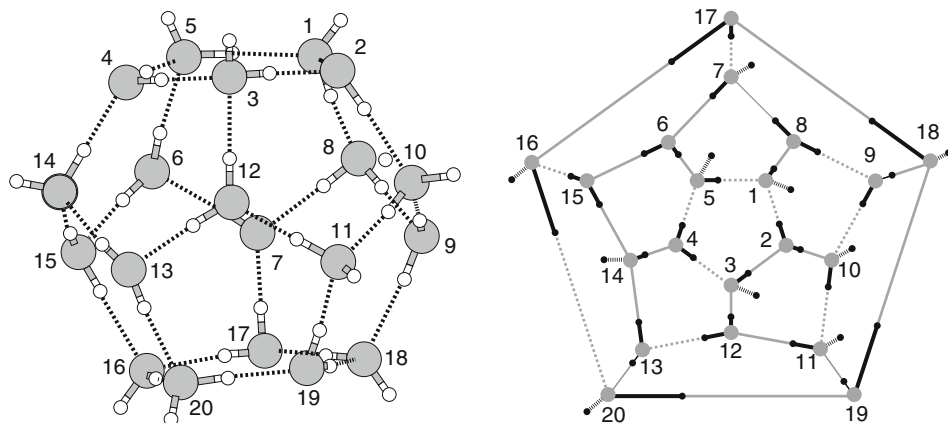


Fig. 21-18

Binding energies of the first 19 isomers of the pentagonal dodecahedron ( $\text{H}_2\text{O}$ )<sub>20</sub> cluster at the B3LYP/TZVP (open squares) and MP2/aug-cc-pVDZ (filled squares) levels of theory. The TIP4P global minimum corresponds to minimum #2 and is indicated with an arrow. Minimum “0” is the isomer predicted from the SWB model. The figure is reprinted with permission from reference Kirov et al. (2008). © 2008 Elsevier

Fig. 21-16 for a direct comparison. We first note that B3LYP/TZVP also predicts minimum “0” to be more stable than minimum #2 (the global dodecahedron minimum of TIP4P model) as was the case with TTM2-F potential. However, it yields an even lower energy structure (minimum #15). The energetic stabilization of minimum #15 is also confirmed during subsequent MP2/aug-cc-pVDZ optimizations. Based on the results of the DFT and MP2 calculations, we therefore suggest minimum #15 as the global minimum for the dodecahedron family of ( $\text{H}_2\text{O}$ )<sub>20</sub>. Its binding energy ( $D_e$ ) is  $-231.01$  kcal/mol (B3LYP/TZVP) and  $-212.10$  kcal/mol (MP2/aug-cc-pVDZ). The three-dimensional structure and its two-dimensional mapping onto the corresponding Schlegel diagram (Schlegel 1883) for the newly found global minimum are shown in Fig. 21-19. Schlegel diagrams assist in categorizing the various isomers by offering a helpful two-dimensional visual representation of the connectivity of the underlying hydrogen bonding network. Their construction is based on the principle that the nodes and lines of the graph correspond to the vertices and edges of the corresponding polyhedron. The hydrogen bonding network is naturally preserved upon this dimensional reduction from the 3D structure (left) to the 2D graph (right). In order to better indicate the correspondence between the two representations, we also indicate the numbering of the oxygen atoms in Fig. 21-19.



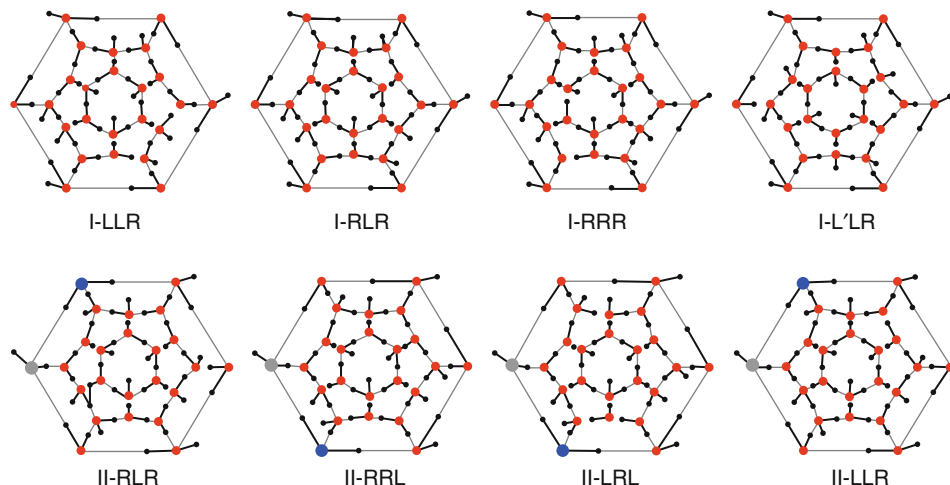
■ Fig. 21-19

The lowest energy isomer of the dodecahedron predicted at the MP2 level of theory. *Left panel:* 3D structure. *Right Panel:* Schlegel diagram indicating the “strong” (dimer-like, solid lines) and “weak” (dashed lines) nearest-neighbor ( $n-n$ ) molecular arrangements. The figure is reprinted with permission from reference Kirov et al. (2008). © 2008 Elsevier

## The Tetrakaidecahedron (T-Cage) ( $\text{H}_2\text{O}$ )<sub>24</sub> Cluster


For a fixed position of the Oxygen atoms in the  $5^{12}6^2$  ( $\text{H}_2\text{O}$ )<sub>24</sub> cage cluster, there are 3,043,836 symmetry distinct configurations arising from the different hydrogen positions that are consistent with the ice rules. The application of the SWEB discrete model with subsequent refinement at the DFT and MP2 levels of theory yields the first few ( $\sim 100$ ) low-lying networks. The Schlegel diagrams (Schlegel 1883) (2D projections of the 3D structures) of the ten lowest minima of the T-cage (fully optimized at the MP2/aug-cc-pVDZ level of theory) are shown in ▶ Fig. 21-20 (Yoo et al. 2009). The various networks are labeled using the R or L designation, depending on whether the direction of the donor H atoms in the three concentric rings starting from the inner one is either clockwise (R) or counterclockwise (L). For example, the RLR isomer corresponds to an arrangement in which the H atoms are arranged in a clockwise (for the inner and outer circles) and a counterclockwise direction (for the middle circle). Primes are used to indicate different arrangements of the vertical H atoms that connect the three rings. Therefore, the L'LR network has the same connectivity and direction as LLR for the three rings but differs in the direction of the vertical H atoms. The ten lowest-lying minima of the T-cage can be furthermore grouped into three families (indicated as I, II and III in ▶ Fig. 21-20) depending on the donor-acceptor connectivity of the top hexagonal face. For this six-member hydrogen-bonded ring, isomers in family (I) isomers have only donor-acceptor (da) water molecules, whereas isomers in families (II) and (III) have both double donor (dd) and double acceptor (aa) water molecules. The (dd)/(aa) molecules are indicated with blue and gray colors in ▶ Fig. 21-20. It should be noted that all ten minima shown in ▶ Fig. 21-20 have a zero total dipole moment. Their relative order at the MP2/aug-cc-pVDZ level of theory with respect to the most stable LLR network of family (I) (I-LLR) is identical with the larger aug-cc-pVTZ basis set at the MP2 level of theory.

Starting from any of those low-lying isomers of the T-cage the three-dimensional periodic lattice of the (sl) hydrate can now be constructed. In the 46-molecule unit cell of the (sl) lattice



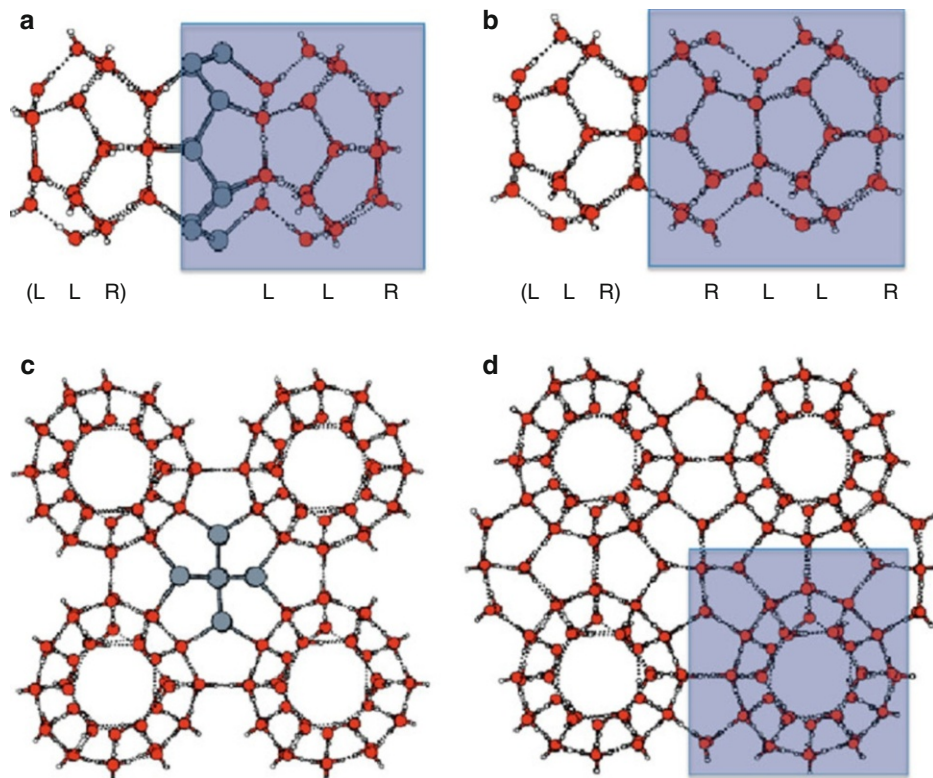
■ Fig. 21-20

Schlegel diagrams of the ten lowest minima of the T-cage  $(\text{H}_2\text{O})_{24}$  cluster obtained at the MP2/aug-cc-pVDZ level of theory. The figure is reprinted with permission from reference Yoo et al. (2009). © 2009 American Chemical Society

two adjacent T-cages are surrounded by six D-cages. When two T-cage isomers sharing a common hexagonal face are used as the building blocks, the positions of the hydrogen atoms of the rest of 36 molecules ( $2 \times 24 - 6 - 6$ ) can be determined. In this manner, the possible networks of the (sI) hydrate unit cell are dramatically reduced. The proposed “bottom-up” approach, which starts from the constituent cages and builds up the three-dimensional lattice, can be used to construct three-dimensional unit cells of the (sI) hydrate from the low-energy networks of their constituent cages. In  Fig. 21-21 the process of constructing a periodic unit cell of the (sI) hydrate lattice starting from the lowest-lying I-LLR isomer is illustrated.

## Outlook

The study of small- to medium-sized water clusters offers an important, molecular-level insight into the fundamental interactions between water molecules. It provides information about the nature and magnitude of the cooperative effects that govern the structural and dynamic properties of the more complex aqueous environments. The structures of the first few water clusters are controlled by the need to maximize the amount of hydrogen bonding and as such they are inhomogeneous and under-coordinated, resulting in structures in which all atoms are on the surface of the cluster. This hydrogen bonding environment is very different than the on-the-average homogeneous, fully coordinated one that is found in aqueous systems. As the cluster grows there is a point where fully coordinated molecules in the inside of the cluster are observed. The onset of this transition from the “all-surface” to “fully coordinated” molecules occurs at  $n = 17$ . Classical force fields for water are essential in probing the plethora of isomers especially for the larger ( $n > 21$ ) clusters. They can be used in conjunction with new approaches for the efficient



■ Fig. 21-21

Schematic approach for building the (sl) hydrate lattice from the low-lying networks of the T-cage. The connectivity of the O atoms between the two cages (without hydrogen atoms) is highlighted in gray. The blue box indicates the (sl) cubic unit cell (46 water molecules). The figure is reprinted with permission from reference Yoo et al. (2009). © 2009 American Chemical Society

sampling of the configuration space in order to obtain the low-lying isomers of clusters in this size regime. The structures of the small- and medium-sized water clusters are essential in order to assess the accuracy of those force fields in developing transferable models that can be used in different environments such as liquid water, ice, at aqueous interfaces, or around charged species or hydrophobic surfaces. Given the fact that accurate energetics for the interaction even between two water molecules is not currently available experimentally, the use of high-level first principles electronic structure calculations to obtain the cluster energetics represents an indispensable and currently irreplaceable path toward understanding aqueous environments.

## Acknowledgments

This work was supported by the Division of Chemical Sciences, Geosciences and Biosciences, Office of Basic Sciences, U.S. Department of Energy. Battelle operates the Pacific Northwest National Laboratory for the U.S. Department of Energy. This research was performed in part using the Molecular Science Computing Facility (MSCF) in the Environmental Molecular



Sciences Laboratory, a national scientific user facility sponsored by the Department of Energy's Office of Biological and Environmental Research. Additional computer resources were provided by the Office of Basic Energy Sciences, US Department of Energy at the National Energy Research Scientific Computing Center, a U.S. Department of Energy's Office of Science user facility at Lawrence Berkeley National Laboratory.

## References

- Adamovic, I., Freitag, M. A., & Gordon, M. S. (2003). Density functional theory based effective fragmentation potential method. *Journal of Chemical Physics*, *118*, 6725-6732.
- Apra, E., Rendell, A. P., Harrison, R. J., Tippraju, V., deJong, W. A., & Xantheas, S. S. (2009). Liquid water: Obtaining the right answer for the right reasons. In *Proceedings of the conference on high performance computing networking, storage and analysis*. Portland: ACM.
- Ball, P. (2008). Water: Water-an enduring mystery. *Nature*, *452*, 291-292.
- Bartlett, R. J., & Purvis, G. D. (1978). Many-body perturbation theory, coupled-pair many-electron theory, and the importance of quadruple excitation for the correlation problem. *International Journal of Quantum Chemistry*, *14*, 561-581.
- Becke, A. D. (1988). Density-functional exchange-energy approximation with correct asymptotic behavior. *Physical Review A*, *38*, 3098-3100.
- Becke, A. D. (1993). Density-functional thermochemistry. III. The role of exact exchange. *Journal of Chemical Physics*, *98*, 5648.
- Berendsen, H. J. C., Grigera, J. R., & Straatsma, T. P. (1987). The missing term in effective pair potentials. *Journal of Physical Chemistry*, *91*, 6269-6271.
- Beuhler, R. J., & Friedman, L. (1982). A study of the formation of high molecular-weight water cluster ions ( $m/e < 59000$ ) in expansion of ionized gas mixtures. *Journal of Chemical Physics*, *77*, 2549-2557.
- Boys, S. F., & Bernardi, F. (1970). Calculation of small molecular interactions by differences of separate total energies - some procedures with reduced errors. *Molecular Physics*, *19*, 553.
- Bukowski, R., Szalewicz, K., Groenenboom, G. C., & van der Avoird, A. (2007). Predictions of the properties of water from first principles. *Science*, *315*, 1249-1252.
- Bulusu, S., Yoo, S., Apra, E., Xantheas, S., & Zeng, X. C. (2006). Lowest-energy structures of water clusters  $(\text{H}_2\text{O})_{11}$  and  $(\text{H}_2\text{O})_{13}$ . *Journal of Physical Chemistry A*, *110*, 11781-11784.
- Bunge, C. F. (1970). Electronic wave functions for atom. II. Some aspects of convergence of configuration interaction expansion for ground states of He isoelectronic series. *Theoretica Chimica Acta*, *16*, 126.
- Burnham, C. J., & Xantheas, S. S. (2002a). Development of transferable interaction models for water. I. Prominent features of the water dimer potential energy surface. *Journal of Chemical Physics*, *116*, 1479-1492.
- Burnham, C. J., & Xantheas, S. S. (2002b). Development of transferable interaction models for water. IV. A flexible, all-atom polarizable potential (TTM2-F) based on geometry dependent charges derived from an ab initio monomer dipole moment surface. *Journal of Chemical Physics*, *116*, 1479-1492.
- Burnham, C. J., & Xantheas, S. S. (2002c). Development of transferable interaction models for water. III. Reparametrization of an all-atom polarizable rigid model (TTM2-R) from first principles. *Journal of Chemical Physics*, *116*, 1500-1510.
- Burnham, C. J., Li, J., Xantheas, S. S., & Leslie, M. (1999). The parametrization of a Thole-type all-atom polarizable water model from first principles and its application to the study of water clusters ( $n = 2-21$ ) and the phonon spectrum of ice Ih. *Journal of Chemical Physics*, *110*, 4566-4581.
- Burnham, C. J., Anick, D. J., Mankoo, P. K., & Reiter, G. F. (2008). The vibrational proton potential in bulk liquid water and ice. *Journal of Chemical Physics*, *128*, 154519.
- Chalasinski, G., & Szczesniak, M. M. (1994). Origins of structure and energetics of van-der-waals clusters from ab-initio calculations. *Chemical Reviews*, *94*, 1723-1765.
- Cizek, J. (1966). On correlation problem in atomic and molecular systems. Calculation of wavefunction components in urchell-type expansion using quantum-field theoretical methods. *Journal of Chemical Physics*, *45*, 4256.
- Cizek, J. (1969). *Advances in Chemical Physics*, *14*, 35.

- Clementi, E. (1967). Study of electronic structure of molecules. II. Wavefunctions for  $\text{NH}_3 + \text{HCl} \rightarrow \text{NH}_4\text{Cl}$  reaction. *Journal of Chemical Physics*, *46*, 3851-3880.
- Coester, F. (1958). Bound states of a many-particle system. *Nuclear Physics*, *7*, 421-424.
- Coester, F., & Kümmel, K. (1960). Short-range correlations in nuclear wave functions. *Nuclear Physics*, *17*, 477-485.
- Cruzan, J. D., Braly, L. B., Brown, M. G., Loeser, J. G., & Saykally, R. J. (1996a). Quantifying hydrogen bond cooperativity in water: VRT spectroscopy of the water tetramer. *Science*, *271*, 59-62.
- Cruzan, J. D., Brown, M. G., Liu, K., Braly, L. B., & Saykally, R. J. (1996b). The far-infrared vibration-rotation-tunneling spectrum of the water tetramer-d8. *Journal of Chemical Physics*, *105*, 6634-6644.
- Cruzan, J. D., Viant, M. R., Blake, G. A., & Saykally, R. J. (1997). Terahertz laser vibration-rotation tunneling spectroscopy of the water tetramer. *Journal of Physical Chemistry A*, *101*, 9022-9031.
- Dang, L. X., & Chang, T. M. (1997). Molecular dynamics study of water clusters, liquid, and liquid-vapor interface of water with many-body potentials. *Journal of Chemical Physics*, *106*, 8149-8159.
- Day, P. N., Jensen, J. H., Gordon, M. S., Webb, S. P., Stevens, W. J., Krauss, M., Garmer, D., Basch, H., & Cohen, D. (1996). An effective fragment method for modeling solvent effects in quantum mechanical calculations. *Journal of Chemical Physics*, *105*, 1968-1986.
- Day, P. N., Pachter, R., Gordon, M. S., & Merrill, G. N. (2000). A study of water clusters using the effective fragment potential and Monte Carlo simulated annealing. *Journal of Chemical Physics*, *112*, 2063-2073.
- Dunning, T. H., Jr. (1989). Gaussian basis sets for use in correlated molecular calculations. I. The atoms boron through neon and hydrogen. *Journal of Chemical Physics*, *90*, 1007-1023.
- Dunning, T. H., Jr. (2000). A road map for the calculation of molecular binding energies. *Journal of Physical Chemistry A*, *104*, 9062-9080.
- Dunning, T. H., Jr., Peterson, K. A., & Woon, D. E. (1998). *Encyclopedia of computational chemistry*. New York: Wiley.
- Eggenberger, R., Gerber, S., Huber, H., & Searles, D. (1991). Basis set superposition errors in intermolecular structures and force-constants. *Chemical Physics Letters*, *183*, 223-226.
- Emsley, J., Hoyte, O. P. A., & Overill, R. E. (1978). Ab initio calculations on very strong hydrogen-bond of biformate anion and comparative esterification studies. *Journal of the American Chemical Society*, *100*, 3303-3306.
- Fanourgakis, G. S., & Xantheas, S. S. (2006). The flexible, polarizable, thole-type interaction potential for water (TTM2-F) revisited. *Journal of Physical Chemistry A*, *110*, 4100-4106.
- Fanourgakis, G. S., & Xantheas, S. S. (2008). Development of transferable interaction potentials for water. V. Extension of the flexible, polarizable, Thole-type model potential (TTM3-F, v. 3.0) to describe the vibrational spectra of water clusters and liquid water. *Journal of Chemical Physics*, *128*, 074506.
- Fanourgakis, G. S., Aprà, E., & Xantheas, S. S. (2004). High-level ab initio calculations for the four low-lying families of minima of  $(\text{H}_2\text{O})_{20}$ . I. Estimates of MP2/CBS binding energies and comparison with empirical potentials. *Journal of Chemical Physics*, *121*, 2655-2663.
- Fanourgakis, G. S., Aprà, E., de Jong, W. A., & Xantheas, S. S. (2005). High-level ab initio calculations for the four low-lying families of minima of  $(\text{H}_2\text{O})_{20}$ . II. Spectroscopic signatures of the dodecahedron, fused cubes, face-sharing pentagonal prisms, and edge-sharing pentagonal prisms hydrogen bonding networks. *Journal of Chemical Physics*, *122*, 134304.
- Fast, P. L., Sanchez, M.L., & Truhlar, D. G. (1999). Infinite basis limits in electronic structure theory. *Journal of Chemical Physics*, *111*, 2921-2926.
- Feller, D. (1992). Application of systematic sequences of wave-functions to the water dimer. *Journal of Chemical Physics*, *96*, 6104-6114.
- Gordon, M. S., Freitag, M. A., Bandyopadhyay, P., Jensen, J. H., Kairys, V., & Stevens, W. J. (2001). The effective fragment potential method: A QM-based MM approach to modeling environmental effects in chemistry. *Journal of Physical Chemistry A*, *105*, 293-307.
- Haberland, H. (1984). *Electronic and atomic collisions*. New York: Elsevier.
- Halkier, A., Klopper, W., Helgaker, T., Jorgensen, P., & Taylor, P. R. (1999). Basis set convergence of the interaction energy of hydrogen-bonded complexes. *Journal of Chemical Physics*, *111*, 9157-9167.
- Hartke, B. (2003). Size-dependent transition from all-surface to interior-molecule structures in pure neutral water clusters. *Physical Chemistry Chemical Physics*, *5*, 275-284.
- Hermann, V., Kay, B. D., & Castleman, A. W., Jr. (1982). Evidence for the existence of structures in gas-phase homomolecular clusters of water. *Chemical Physics*, *72*, 185-200.
- Hobbs, P. V. (1974). *Ice physics*. Oxford: Clarendon.



- Hohenberg, P., & Kohn, W. (1964). Inhomogeneous electron gas. *Physical Review*, 136, B864.
- Hura, G., Sorenson, J. M., Glaeser, R. M., & Head-Gordon, T. (2000). A high-quality x-ray scattering experiment on liquid water at ambient conditions. *Journal of Chemical Physics*, 113, 9140-1948.
- Jeffrey, G. A., Jordan, T. H., & McMullan, R. K. (1967). Clathrate hydrates of some amines. *Science*, 155, 689.
- Jensen, J. H., & Gordon, M. S. (1998). An approximate formula for the intermolecular Pauli repulsion between closed shell molecules. II. Application to the effective fragment potential method. *Journal of Chemical Physics*, 108, 4772-4782.
- Jorgensen, W. L., Chandrasekhar, J., Madura, J. D., Impey, R. W., & Klein, M. L. (1983). Comparison of simple potential functions for simulating liquid water. *Journal of Chemical Physics*, 79, 926-935.
- Kazimirski, J. K., & Buch, V. (2003). Search for low energy structures of water clusters  $(\text{H}_2\text{O})_n$ ,  $n = 20-22$ , 48, 123, and 293. *Journal of Physical Chemistry*, 107, 9762-9775.
- Kendall, R. A., Dunning, T. H., Jr., & Harrison, R. J. (1992). Electron affinities of the first-row atoms revisited. Systematic basis sets and wave functions. *Journal of Chemical Physics*, 96, 6796-6806.
- Kendall, R. A., Simons, J., Gutowski, M., & Chalasinski, G. (1989). Ab initio energy and structure of  $\text{H}^-(\text{H}_2)_2$ . *Journal of Physical Chemistry*, 93, 621-625.
- Kirov, M. V. (1996). Conformational combinatorial analysis of polyhedral water clusters. *Journal of Structural Chemistry*, 37, 84-91.
- Kirov, M. V., Fanourgakis, G. S., & Xantheas, S. S. (2008). Identifying the most stable networks in polyhedral water clusters. *Chemical Physics Letters*, 461, 108-188.
- Klopper, W. (1995). Limiting values for Møller-Plesset second-order correlation energies of polyatomic systems: A benchmark study on Ne, HF,  $\text{H}_2\text{O}$ ,  $\text{N}_2$ , and He...He. *Journal of Chemical Physics*, 102, 6168-6179.
- Koga, K., Parra, R. D., Tanaka, H., & Zeng, X. C. (2000). Ice nanotube: What does the unit cell look like? *Journal of Chemical Physics*, 113, 5037-5040.
- Kohn, W., & Sham, L. J. (1965). Self-consistent equations including exchange and correlation effects. *Physical Review*, 140, A1133.
- Kucharski, S. A., & Bartlett, R. J. (1992). The coupled-cluster single, double, triple, and quadruple excitation method. *Journal of Chemical Physics*, 97, 4282-4288.
- Kuo, J.-L., Coe, J. V., & Singer, S. J. (2001). On the use of graph invariants for efficiently generating hydrogen bond topologies and predicting physical properties of water clusters and ice. *Journal of Chemical Physics*, 114, 2527-2540.
- Lagutchenkov, A., Fanourgakis, G. S., Niedner-Schatteburg, G., & Xantheas, S. S. (2005). The spectroscopic signature of the "all-surface" to "internally solvated" structural transition in water clusters in the  $n = 17 \sim 21$  size regime. *Journal of Chemical Physics*, 122, 194310.
- Leclercq, J. M., Allavena, M., & Bouteiller, Y. (1983). On the basis set superposition error in potential surface investigations. I. Hydrogen-bonded complexes with standard basis set-functions. *Journal of Chemical Physics*, 78, 4606-4611.
- Lee, C., Chen, H., & Fitzgerald, G. (1995). Chemical bonding in water clusters. *Journal of Chemical Physics*, 122, 1266-1269.
- Lee, H. M., Suh, S. B., & Kim, K. S. (2001). Structures, energies, and vibrational spectra of water undecamer and dodecamer: An ab initio study. *Journal of Chemical Physics*, 114, 10749-10756.
- Li, Z., & Scheraga, H. A. (1987). Monte-Carlo-minimization approach to the multiple-minima problem in protein folding. *Proceedings of the National Academy of Sciences of the United States of America*, 84, 6611-6615.
- Lin, S. S. (1973). Detection of large water clusters by a low re-quadrupole mass filter. *Review of Scientific Instruments*, 44, 516.
- Liu, B., & McLean, A. D. (1973). Accurate calculation of attractive interaction of two ground-state helium-atoms. *Journal of Chemical Physics*, 59, 4557-4558.
- Liu, K., Loeser, J. G., Elrod, M. J., Host, B. C., Rzepiela, J. A., Pugliano, N., & Saykally, R. J. (1994). Dynamics of structural rearrangements in the water trimer. *Journal of the American Chemical Society*, 116, 3507-3512.
- Liu, K., Brown, M. G., Cruzan, J. D., & Saykally, R. J. (1996a). Vibration-rotation tunneling spectra of the water pentamer: Structure and dynamics. *Science*, 271, 62-64.
- Liu, K., Brown, M. G., Carter, C., Saykally, R. J., Gregory, J. K., & Clary, D. C. (1996b). Characterization of a cage form of the water hexamer. *Nature*, 381, 501-503.
- Liu, K., Brown, M. G., & Saykally, R. J. (1997a). Terahertz laser vibration rotation tunneling spectroscopy and dipole moment of a cage form of the water hexamer. *Journal of Physical Chemistry A*, 101, 8995-9010.
- Liu, K., Brown, M. G., Cruzan, J. D., & Saykally, R. J. (1997b). Terahertz laser spectroscopy of the water pentamer: Structure and hydrogen

- bond rearrangement dynamics. *Journal of Physical Chemistry A*, 101, 9011–9021.
- Mao, W. L., Mao, H.-K., Meng, Y., Eng, P. J., Hu, M. Y., Chow, P., Cai, Y. Q., Shu, J., & Hemley, R. J. (2006). X-ray-induced dissociation of  $\text{H}_2\text{O}$  and formation of an  $\text{O}_2\text{-H}_2$  alloy at high pressure. *Science*, 314, 636–638.
- Mao, W. L., Koh, C. A., & Sloan, E. D. (2007). Clathrate hydrates under pressure. *Physics Today*, 60(10), 42.
- Martin, J. M. L. (1996). Ab initio total atomization energies of small molecules - Towards the basis set limit. *Chemical Physics Letters*, 259, 669–678.
- Mayer, I., & Surjan, P. R. (1992). Monomer geometry relaxation and the basis set superposition error. *Chemical Physics Letters*, 191, 497–499.
- McDonald, S., Ojamae, L., & Singer, S. J. (1998). Graph theoretical generation and analysis of hydrogen-bonded structures with applications to the neutral and protonated water cube and dodecahedral clusters. *Journal of Physical Chemistry A*, 102, 2824–2832.
- Møller, C., & Plesset, M. S. (1934). Note on an approximation treatment for many-electron systems. *Physical Review*, 46, 618–622.
- Nagashima, U., Shinohara, H., & Tanaka, H. (1986). Enhanced stability of ion clathrate structures for magic number water clusters. *Journal of Chemical Physics*, 84, 209–214.
- Netzloff, H. M., & Gordon, M. S. (2004). The effective fragment potential: Small clusters and radial distribution functions. *Journal of Chemical Physics*, 121, 2711–2714.
- Niedner-Schatteburg, G., & Bondybey, V. E. (2000). FT-ICR studies of solvation effects in ionic water cluster reactions. *Chemical Reviews*, 100, 4059–4086.
- Nigra, P., & Kais, S. (1999). Pivot method for global optimization: A study of water clusters  $(\text{H}_2\text{O})_N$  with  $2 \leq N \leq 33$ . *Chemical Physics Letters*, 305, 433–438.
- Peterson, K. A., Dunning, T. H., Jr. (1995). Benchmark calculations with correlated molecular wave-functions. 7. Binding-energy and structure of the HF dimer. *Journal of Chemical Physics*, 102, 2032–2041.
- Petrenko, V. F., & Whitworth, R. W. (1999). *Physics of ice*. New York: Oxford University Press.
- Pugliano, N., & Saykally, R. J. (1992). Measurement of quantum tunneling between chiral isomers of the cyclic water trimer. *Science*, 257, 1937–1940.
- Purvis, G. D., & Bartlett, R. J. (1982). A full coupled-cluster singles and doubles model - The inclusion of disconnected triples. *Journal of Chemical Physics*, 76, 1910–1917.
- Raghavachari, K., Trucks, G. W., Pople, J. A., & Head-Gordon, M. (1989). A 5th-order perturbation comparison of electron correlation theories. *Chemical Physics Letters*, 157, 479–483.
- Raghavachari, K., Pople, J. A., Replogle, E. S., & Head-Gordon, M. (1990). 5th-order Møller-plesset perturbation-theory - comparison of existing correlation methods and implementation of new methods correct to 5th-order. *Journal of Physical Chemistry*, 94, 5579.
- Ripmeester, J. A., Tse, J. S., Ratcliffe, C. I., & Powell, B. M. (1987). A new clathrate hydrate structure. *Nature*, 325, 135–136.
- Robinson, G. W., Zhu, S.-B., Singh, S., & Evans, M. W. (1996). *Water in biology, chemistry and physics. Experimental overviews and computational methodologies*. Singapore: World Scientific.
- Sadlej, J. (2001). Theoretical study of structure and spectra of cage clusters  $(\text{H}_2\text{O})_n$ ,  $n = 11, 12$ . *Chemical Physics Letters*, 333, 485–492.
- Schäfer, A., Huber, C., & Ahlrichs, R. (1994). Fully optimized contracted Gaussian basis sets of triple zeta valence quality for atoms Li to Kr. *Journal of Chemical Physics*, 100, 5829.
- Schindler, T., Berg, C., Niedner-Schatteburg, G., & Bondybey, V. E. (1996). Protonated water clusters and their black body radiation induced fragmentation. *Chemical Physics Letters*, 250, 301–308.
- Schlegel, V. (1883). *Verh. Kais. Leopold.-Carolin. Dtsch. Akad. Naturforsch.*, 44, 343.
- Schüth, F. (2005). Technology: Hydrogen and hydrates. *Nature*, 434, 712–713.
- Searcy, J. Q., & Fenn, J. B. (1974). Clustering of water on hydrated protons in supersonic free jet expansion. *Journal of Chemical Physics*, 61, 5282–5288.
- Sloan, E. D., Jr. (1998). *Clathrate hydrates of natural gases* (2nd ed.). New York: Marcel Dekker.
- Smit, P. H., Derissen, J. L., & van Duijneveldt, F. B. (1978). Role of distortion energy in ab initio calculated dimerization energy of formic acid. *Journal of Chemical Physics*, 69, 4241–4244.
- Soper, A. K. (2000). The radial distributions of water and ice from 220 to 673 K and at pressure up to 400 Mpa. *Chemical Physics*, 258, 121–137.
- Sorenson, J. M., Hura, G., Glaeser, R. M., & Head-Gordon, T. (2000). What can x-ray scattering tell us about the radial distribution functions of water? *Journal of Chemical Physics*, 113, 9149–1961.
- Stace, A. J., & Moore, C. (1983). A correlation between structure and reactivity in ion clusters. *Chemical Physics Letters*, 96, 80–84.

- Stillinger, F. H., & Rahman, A. (1974). Molecular-dynamics study of liquid water under high pressure. *Journal of Chemical Physics*, 60, 1545.
- Suzuki, S., & Blake, G. A. (1994). Pseudorotation in the  $D_2O$  trimer. *Chemical Physics Letters*, 229, 499.
- Szalewicz, K., Leforestier, C., & van der Avoird, A. (2009). Towards the complete understanding of water by a first-principles computational approach. *Chemical Physics Letters*, 482, 1-14.
- Termath, V., Klopper, W., & Kutzelnigg, W. (1991). Wave-functions with terms linear in the inter-electronic coordinates to take care of the correlation cusp. II. second-order Møller-Plesset (MP2-R12) calculations on closed-shell atoms. *Journal of Chemical Physics*, 94, 2002-2019.
- Tsai, C. J., & Jordan, K. D. (1993). Theoretical study of small water clusters: Low-energy fused cubic structures for  $(H_2O)_n$ ,  $n = 8, 12, 16$ , and 20. *Journal of Physical Chemistry*, 97, 5208-5210.
- van Duijneveldt, F. B., van Duijneveldt-van de Rijdt, J. G. C. M., & van Lenthe, J. H. (1994). State of the art in counterpoise theory. *Chemical Reviews*, 94, 1873.
- van Duijneveldt-van de Rijdt, J. G. C. M., & van Duijneveldt, F. B. (1992). Convergence to the basis-set limit in abinitio calculations at the correlated level on the water dimer. *Journal of Chemical Physics*, 97, 5019.
- van Lenthe, J. H., van Duijneveldt-van de Rijdt, J. G. C. M., & van Duijneveldt, F. B. (1987). *Advances in Chemical Physics*, 69, 521.
- Viant, M. R., Cruzan, J. D., Lucas, D. D., Brown, M. G., Liu, K., & Saykally, R. J. (1997). Pseudorotation in water trimer isotopomers using terahertz laser spectroscopy. *Journal of Physical Chemistry A*, 101, 9032-9041.
- Wales, D. J., & Hodges, M. P. (1998). Global minima of water clusters  $(H_2O)_n$ ,  $n \leq 21$ , described by an empirical potential. *Chemical Physics Letters*, 286, 65-72.
- Wales, D. J., & Scheraga, H. A. (1999). Global optimization of clusters, crystals, and biomolecules. *Science*, 285, 1368-1372.
- Wilson, A. K., & Dunning, T. H., Jr. (1997). Benchmark calculations with correlated molecular wave functions. X. Comparison with "exact" MP2 calculations on Ne, HF,  $H_2O$ , and  $N_2$ . *Journal of Chemical Physics*, 106, 8718-8726.
- Xantheas, S. S. (1994). Ab initio studies of cyclic water clusters  $(H_2O)_n$ ,  $n = 1-6$ . II. Analysis of many-body interactions. *Journal of Chemical Physics*, 100, 7523-7534.
- Xantheas, S. S. (1996a). Significance of higher-order many-body interaction energy terms in water clusters and bulk water. *Philosophical Magazine Part B*, 73, 107-115.
- Xantheas, S. S. (1996b). On the importance of the fragment relaxation energy terms in the estimation of the basis set superposition error correction to the intermolecular interaction energy. *Journal of Chemical Physics*, 104, 8821-8824.
- Xantheas, S. S. (2000). Cooperativity and hydrogen bonding network in water clusters. *Chemical Physics*, 258, 225-231.
- Xantheas, S. S., & Aprà, E. (2004). The binding energies of the  $D_{2d}$  and  $S_4$  water octamer isomers: High-level electronic structure and empirical potential results. *Journal of Chemical Physics*, 120, 823-828.
- Xantheas, S. S., & Dunning, T. H., Jr. (1993a). The structure of the water trimer from ab initio calculations. *Journal of Chemical Physics*, 98, 8037-8040.
- Xantheas, S. S., & Dunning, T. H., Jr. (1993b). Ab initio studies of cyclic water clusters  $(H_2O)_n$ ,  $n = 1-6$ . I. Optimal structures and vibrational spectra. *Journal of Chemical Physics*, 99, 8774-8792.
- Xantheas, S. S., & Dunning, T. H., Jr. (1993c). Theoretical estimate of the enthalpy of formation of sulfhydryl radical (HSO) and HSO-SOH isomerization energy. *Journal of Physical Chemistry*, 97, 18-19.
- Xantheas, S. S., Burnham, C. J., & Harrison, R. J. (2002). Development of transferable interaction models for water. II. Accurate energetics of the first few water clusters from first principles. *Journal of Chemical Physics*, 116, 1493-1499.
- Yang, X., & Castleman, A. W. (1989). Large protonated water clusters  $H^+(H_2O)_n$  ( $1 \leq n < 60$ ): The production and reactivity of clathrate-like structures under thermal conditions. *Journal of the American Chemical Society*, 111, 6845-6846.
- Yoo, S., Kirov, M. V., & Xantheas, S. S. (2009). Low-energy networks of the T-cage  $(H_2O)_{24}$  cluster and their use in constructing periodic unit cells of the structure I (sI) hydrate lattice. *Journal of the American Chemical Society*, 131, 7564-7566.

# 22 Fundamental Structural, Electronic, and Chemical Properties of Carbon Nanostructures: Graphene, Fullerenes, Carbon Nanotubes, and Their Derivatives

Tandabany C. Dinadayalane · Jerzy Leszczynski

Interdisciplinary Center for Nanotoxicity, Department of Chemistry and Biochemistry, Jackson State University, Jackson, Mississippi, USA


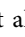
<i>Introduction to Carbon Nanostructures</i> .....	795
Graphene .....	797
Fullerenes .....	800
Natural Abundance of Fullerenes .....	804
Fullerene Nano-Capsules .....	805
Isolated Pentagon Rule (IPR) in Fullerenes .....	806
Common Defects in Fullerenes .....	810
Carbon Nanotubes (CNTs) .....	811
Discovery and Classification of CNTs .....	811
Various Defects in Carbon Nanotubes .....	815
 <i>Computational Approaches Used to Study Carbon Nanostructures: An Overview</i> .....	 817
 <i>Structural, Electronic and Chemical Properties of Graphene, Fullerenes and SWCNTs</i> .....	 820
Graphene .....	820
Hydrogenation of Graphene with and Without Defects .....	821
Fullerenes .....	824
Computational Studies of Fullerene Isomers .....	824
Giant Fullerenes .....	827
Local Strain in Curved Polycyclic Systems: POAV and Pyramidalization Angle .....	828
Stone–Wales Defect in C <sub>60</sub> .....	831
Computational Studies on Vacancy Defects in Fullerene C <sub>60</sub> .....	831

Computational Studies of Single-Walled Carbon Nanotubes .....	834
Covalent Functionalization of SWCNTs: H and F Atom Chemisorptions .....	838
Theoretical Studies on Common Defects in SWCNTs .....	844
Stone–Wales Defect .....	844
Topological Ring Defects .....	846
Topological Ring Defects: Single- and Di-Vacancy .....	847
<b><i>Outlook of Potential Applications of Carbon Nanostructures</i></b> .....	<b>851</b>
<b><i>Summary and Outlook</i></b> .....	<b>852</b>
<b><i>Acknowledgments</i></b> .....	<b>854</b>
<b><i>References</i></b> .....	<b>854</b>

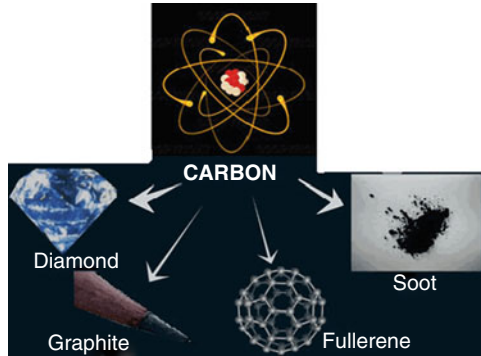
**Abstract:** This chapter provides information on various carbon allotropes, and in-depth details of structures, electronic and chemical properties of graphene, fullerenes, and single-walled carbon nanotubes (SWCNTs). We have given an overview of different computational methods that were employed to understand various properties of carbon nanostructures. Importance of application of computational methods in exploring different sizes of fullerenes and their isomers is given. The concept of isolated pentagon rule (IPR) in fullerene chemistry has been revealed. The computational and experimental studies involving Stone–Wales (SW) and vacancy defects in fullerene structures are discussed in this chapter. The relationship between the local curvature and the reactivity of the defect-free and defective fullerene and single-walled carbon nanotubes has been revealed. We reviewed the influence of different defects in graphene on hydrogen addition. The viability of hydrogen and fluorine atom additions on the external surface of the SWCNTs is revealed using computational techniques. We have briefly pointed out the current utilization of carbon nanostructures and their potential applications.

## Introduction to Carbon Nanostructures

---

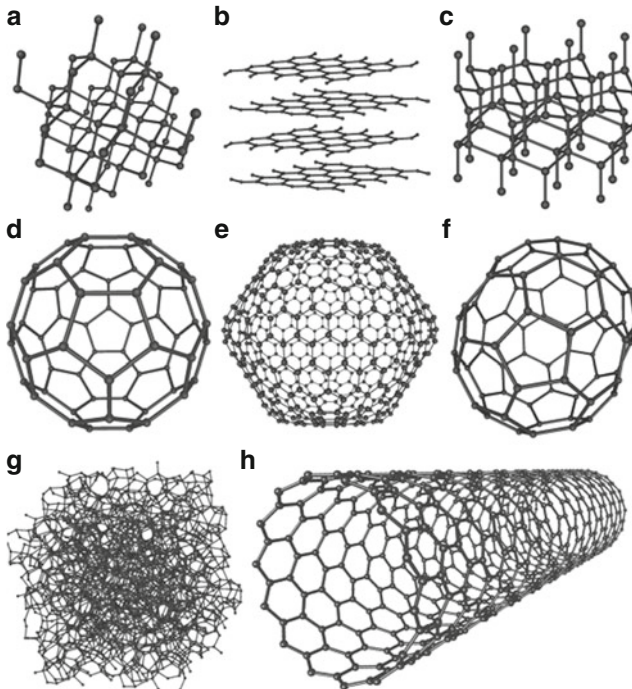
Carbon is one of the first few elements known in antiquity. The pure forms of this element include diamond and graphite, which have been known for few thousand years (<http://www.nndc.bnl.gov/content/elements.html>; Pierson 1993; Wikipedia - <http://en.wikipedia.org/wiki/Carbon>). Both of these materials are of immense importance in industry and in everyday life. Diamond and graphite are termed as giant structures since, by means of a powerful microscope, one could see millions and millions of atoms, all connected together in a regular array. Diamond would appear as a rigid and rather complex system like some enormous scaffolding construction. Carbon is also the major atomic building block for life. All life forms on Earth have carbon central to their composition. More than ten million carbon-containing compounds are known. Compounds containing only carbon atoms, particularly nano-sized materials are intriguing and attract attention of scientists working in various disciplines. Before 1985, scientists deemed that there were only three allotropes of carbon, namely, diamond, graphite, and amorphous carbon such as soot and charcoal. Soccer-ball-shaped molecule comprising of 60 carbon atoms, C<sub>60</sub> buckyball named fullerene was discovered in 1985 and it is another interesting carbon allotrope (Kroto et al. 1985). Carbon nanotubes (CNTs), a spin-off product of fullerene, were reported in 1991 by Iijima (1991). Important well-known carbon materials are depicted in  Fig. 22-1. The publication of transmission electron microscope (TEM) images of CNTs by Iijima was a critical factor in convincing a broad community that “there is plenty of room at the bottom” and many new structures can exist at the nanoscale.  Figure 22-2 shows eight allotropes of carbon. In addition to graphene, fullerenes, and carbon nanotubes, there are few other uncommon carbon nanostructures such as nanohorns (Iijima et al. 1999; Poonjarernsilp et al. 2009), nano-onions (Palkar et al. 2008; Zhou et al. 2009), nanobuds (He and Pan 2009; Nasibulin et al. 2007a, b; Wu and Zeng 2009), peapods (Launois et al. 2010; Li et al. 2009a; Smith et al. 1998), nanocups (Chun et al. 2009), and nanotori (Liu et al. 1997; Sano et al. 2001).

We performed a quick search in SciFinder on “fullerene” and “carbon nanotubes” to reveal their importance and growth in current science, engineering, and technology. Nearly 39,000 references were obtained for the word “fullerene,” while ~45,000 references were obtained for



■ Fig. 22-1

Well-known carbon materials



■ Fig. 22-2

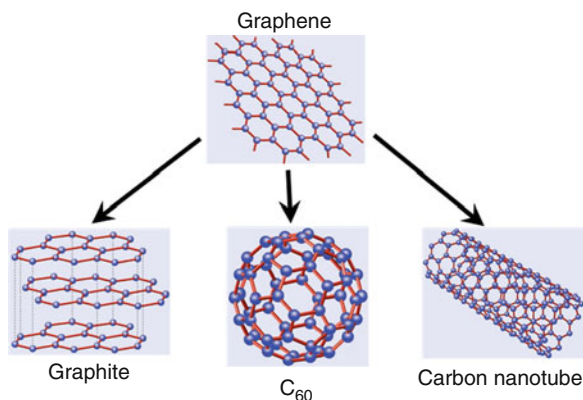
Eight allotropes of carbon: (a) Diamond, (b) Graphite, (c) Lonsdaleite, (d)  $C_{60}$  (Buckminsterfullerene or buckyball), (e)  $C_{540}$ , (f)  $C_{70}$ , (g) Amorphous carbon, and (h) single-walled carbon nanotube or buckytube (The picture adopted from Wikipedia – [http://en.wikipedia.org/wiki/Allotropes\\_of\\_carbon](http://en.wikipedia.org/wiki/Allotropes_of_carbon))



“carbon nanotubes” when we searched these topics in October 2009. This is indicative that carbon nanomaterials have gained a momentum with the development of nanotechnology as the driving force of the modern science and engineering. Among various carbon nanostructures, CNTs play a special role in the nanotechnology era. The design and discovery of new materials is always exciting for the potential of new applications and properties (Cohen 1993; Serra et al. 1999). In this chapter, we aim to present an overview of carbon nanostructures, with a particular interest on structural, electronic, and chemical properties of graphene, fullerenes, and carbon nanotubes. Important topological defects in the graphene, fullerenes, and carbon nanotubes will be delineated. Thus, this chapter is intended to be an informative guide of carbon nanostructures and to provide description of current computational chemistry applications involving these species to facilitate the pursuit of both newcomers to this field and experienced researchers in this rapidly emerging area.

## Graphene

Carbon displays a unique feature of making a chemically stable two-dimensional (2D), one-atom thick membrane called graphene in a three-dimensional (3D) world. Each carbon atom in graphene is covalently bonded to three other carbon atoms with  $sp^2$  hybridization. Graphene is the thinnest known material and in the same time it is the strongest material ever to be measured. It can sustain current densities six orders of magnitude higher than that of copper. It has extremely high strength, very high thermal conductivity and stiffness, and is impermeable to gases (Geim 2009). Well-known forms of carbon-containing molecules that derived from graphene are graphite, fullerene, and carbon nanotube, which are depicted in **Fig. 22-3**. Graphite consists of stacked layers of graphene sheets separated by 0.3 nm and is stabilized by weak van der Waals forces (He and Pan 2009). Buckminsterfullerene ( $C_{60}$ ) is formed from graphene balled into a sphere by including some pentagons and hexagons




**Fig. 22-3**


**Carbon-containing molecules (graphite, Buckminsterfullerene ( $C_{60}$ ), and carbon nanotube) derived from graphene**



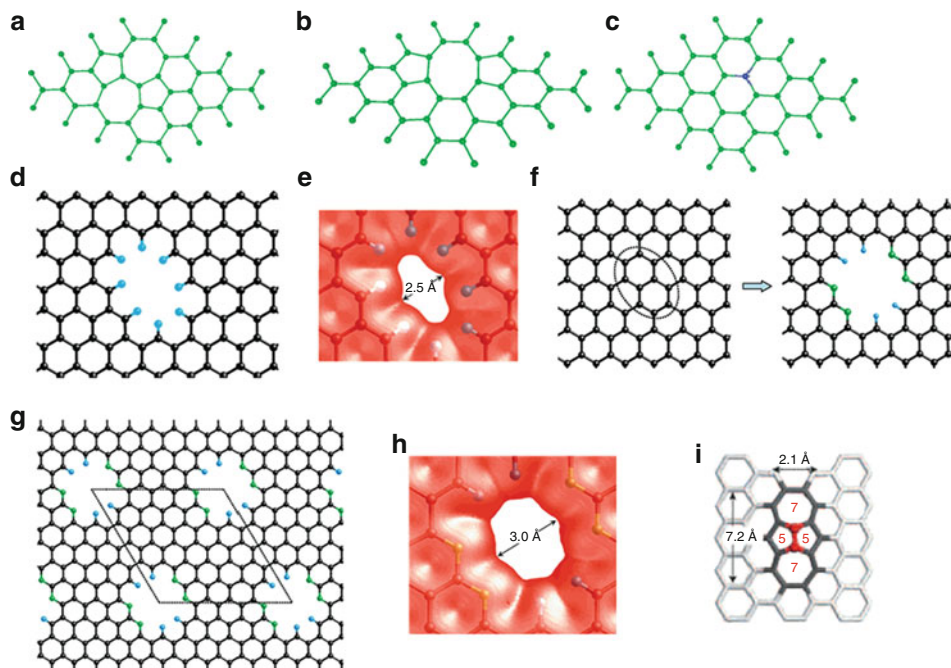
into the lattice (Kroto et al. 1985). Carbon nanotubes can be viewed as rolled-up cylinders of graphene. Therefore, graphene can be called “the mother” of all these three  $sp^2$  carbon structures.

It was presumed that planar graphene cannot exist in free state since they are unstable compared to curved structures such as soot, nanotubes, and fullerenes. This presumption has changed since Novoselov et al. prepared graphitic sheets including single graphene layer and studied their electronic properties (Novoselov et al. 2004, 2005a). The detailed information of growth and isolation of graphene has been provided in the recent review by Geim (2009). Graphene is a prospective material for nanoelectronics. The electron transport in graphene is described by Dirac-like equation (Geim and Novoselov 2007; Novoselov et al. 2005b; Ponomarenko et al. 2008). The experimental realization of graphene motivates several studies focusing on fundamental physics, materials science, and device applications (Abanin et al. 2006; Geim and Novoselov 2007; Novoselov et al. 2004, 2005a, b; Pereira et al. 2009; Ponomarenko et al. 2008). The studies pertinent to the chemistry of graphene sheets have also been reported (Abanin et al. 2006; Avouris et al. 2007; Geim and Novoselov 2007; Neto et al. 2009; Pereira et al. 2009). Graphene research is a hot topic in this decade, thanks to the recent advances in technology for growth, isolation, and characterization of graphene.

Graphene sheets need not always be as perfect as one thinks. Various defects such as Stone–Wales (SW) (Stone and Wales 1986), vacancies (Carlson and Scheffler 2006), pore-defects (Jiang et al. 2009), and substitution atoms (Miwa et al. 2008; Zhu et al. 2005) can occur in the thin graphene sheet. Like the creation of vacancies by knocking atoms out of the graphene sheet, surplus atoms can be found as ad-atoms on the graphene surface. Ad-dimer defect can be introduced to graphene and is characterized by two adjacent five-membered rings instead of two adjacent seven-membered rings in Stone–Wales defect. Therefore, ad-dimer defect is called as Inverse Stone–Wales (ISW) defect.  Figure 22-4 depicts some of the common defects in graphene sheet.

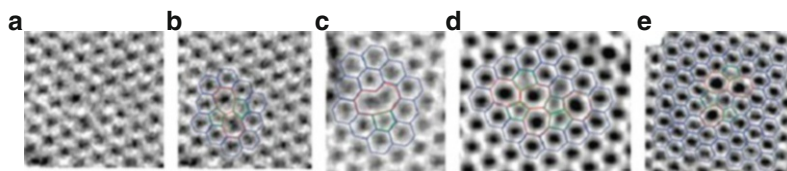
Experimental observations of defects in graphene have been reported recently (Meyer et al. 2008; Wang et al. 2008). Zettl and coworkers showed the direct image of Stone–Wales defects in graphene sheets using transmission electron microscopy (TEM) and explored their real-time dynamics. They found that the dynamics of defects in extended, two-dimensional graphene membranes are different than in closed-shell graphenes such as nanotubes or fullerenes (Meyer et al. 2008). High-resolution transmission electron microscopy (HRTEM) and atomic force microscopy (AFM) have been useful in identifying various defects in graphene. AFM and HRTEM images of graphene sheet with different defects are shown in  Fig. 22-5. The effect of various defects on the physical and chemical properties of graphene was studied theoretically (Boukhvalov and Katsnelson 2008; Carpio et al. 2008; Duplock et al. 2004; Lherbier et al. 2008; Li et al. 2005). The characteristics of typical defects and their concentrations in graphene sheets are unclear.

Computational and experimental studies concerning defects in graphene sheet are critically important for basic understanding of this novel system and such understanding will be helpful for scientists who actively work on applications of graphene-based materials. Although the surface physics of graphene sheets is currently at the center of attention, its chemistry has remained largely unexplored. Like any other molecule, graphene can involve in chemical reactions. The chemical functionalization is probably one of the best approaches to detect imperfections in a graphene sheet (Boukhvalov and Katsnelson 2008). The functionalized graphene can be suitable for specific applications. Research on bended, folded, and scrolled graphene is rapidly growing now.



■ Fig. 22-4

Defects in graphene sheet; the segment of graphene containing (a) the Stone–Wales (SW) defect; (b) a bivacancy; (c) a nitrogen substitution impurity; (d) an all-hydrogen saturated pore in graphene; (e) the pore electron density isosurface of all-hydrogen passivated porous graphene; (f) creation of a nitrogen-functionalized pore within a graphene sheet: the carbon atoms in the dotted circle are removed, and four dangling bonds are saturated by hydrogen, while the other four dangling bonds (DBs) together with their carbon atoms are replaced by nitrogen atoms; (g) the hexagonally ordered porous graphene. The *dotted lines* indicate the unit cell of the porous graphene; (h) the pore electron density isosurface of nitrogen-functionalized porous graphene; (i) An Inverse Stone–Wales (ISW) defect. Color code for (d), (f), and (g): C, black; N, green; H, cyan. Isosurface is at  $0.02 e/\text{Å}^3$  (The pictures were reprinted with permission from refs. Jiang et al. (2009) and Boukhvalov and Katsnelson (2008). Copyright 2008 and 2009 American Chemical Society)



■ Fig. 22-5

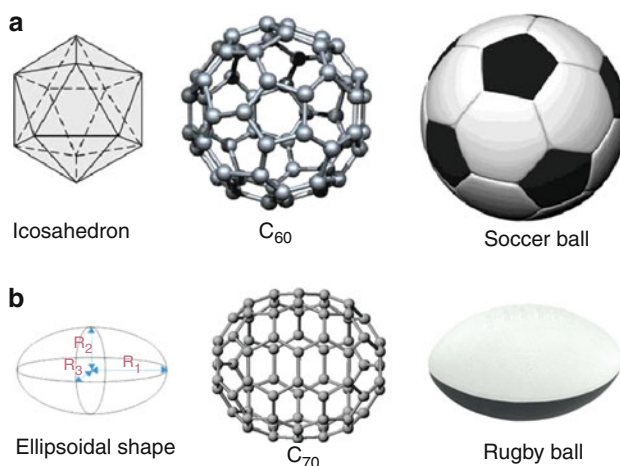
(a) HRTEM image of a single graphene layer (atoms appear white). (b) Image of graphene with Stone–Wales defect (atomic configuration superimposed for easy recognition). (c) Image of vacancy defect with atomic configuration. (d) Defect image with atomic configuration consisting of four pentagons (*green*) and four heptagons (*red*). (e) Defect image with atomic configuration consisting of three pentagons (*green*) and three heptagons (*red*) (Pictures were reprinted with permission from ref. Meyer et al. (2008). Copyright 2008 American Chemical Society)

## Fullerenes

Discovery of fullerene  $C_{60}$  and other fullerene molecules, isolated pentagon rule (IPR) in fullerenes:


The fullerene era started in 1985; Kroto and his colleagues obtained cold carbon clusters when they carried out an experiment to simulate the condition of red giant star formation. With the use of the mass spectrometer, they found a large peak commensurate with 60 carbon atoms (Kroto et al. 1985). The molecule  $C_{60}$  was proposed to have a football structure, known to mathematicians as the truncated icosahedron. The shape is composed of 12 pentagons located around the vertices of an icosahedron and 20 hexagon rings placed at the centers of icosahedral faces. The  $C_{60}$  molecule was named “Buckminsterfullerene” in honor of the renowned architect Buckminster Fuller, who designed geodesic domes based on similar pentagonal and hexagonal structures. The carbon atoms in  $C_{60}$  fullerene are arranged in exactly the same way, albeit much smaller, as the patches of leather found on the common football (► Fig. 22-6a).


Since the remarkable discovery of fullerenes in 1985 (Kroto et al. 1985), these new carbon allotropes have received significant attention from the scientific community and still exhibit vast interest (Lu and Chen 2005; Thilgen and Diederich 2006). The 1996 Nobel Prize in Chemistry was awarded to Sir Harold W. Kroto, Robert F. Curl, and the late Richard E. Smalley for their discovery of fullerenes. Essentially, the most prominent representative of the fullerene family is  $C_{60}$ . In early 1990, a method was discovered for producing macroscopic amounts of this fascinating molecule (Krätschmer et al. 1990). This breakthrough allowed scientists to explore the properties of  $C_{60}$  and understand its chemistry. Krätschmer et al. characterized the fullerene  $C_{60}$  using mass spectroscopy, infrared spectroscopy, electron diffraction, and X-ray diffraction (Krätschmer et al. 1990). Both Kroto et al. (1985) and Krätschmer et al. (1990), by means of mass spectroscopy, also characterized the fullerene  $C_{70}$ . Pure  $C_{60}$  and  $C_{70}$  fullerenes were isolated and separated by Kroto and coworkers (Taylor et al. 1990). The stable fullerenes of  $C_{60}$




■ Fig. 22-6

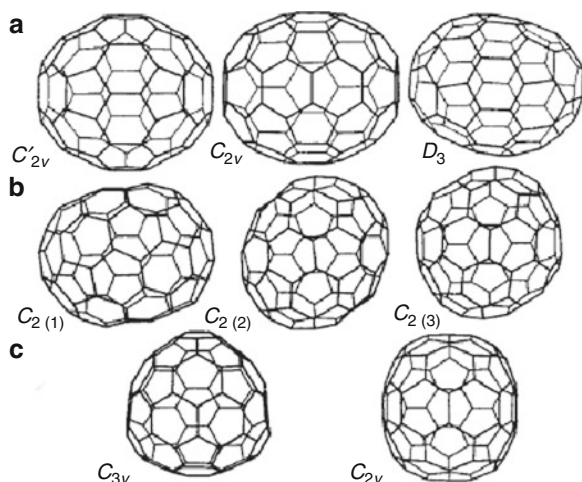
The structures of fullerenes  $C_{60}$  and  $C_{70}$  and their familiar shapes.  $C_{60}$  and  $C_{70}$  are in icosahedron ( $I_h$ ) and  $D_{5h}$  point groups

and  $C_{70}$  were reported in the ratio of approximately 5:1.  $^{13}\text{C}$  nuclear magnetic resonance (NMR) spectroscopy was used to characterize the fullerenes (Taylor et al. 1990). These two molecules are members of a homologous series of hollow closed-cage molecules. The fullerene  $C_{70}$  belongs to a class of nonspherical fullerenes. It adopts an ellipsoidal shape (point group  $D_{5h}$ ) and it looks like “Rugby Ball” as shown in  Fig. 22-6b. Existence of  $C_{60}$  was predicted by Eiji Osawa in 1970 (Kagaku 1970). However, his prediction did not reach Europe or America since it was published in a Japanese magazine.

In the eighteenth century, the Swiss mathematician Leonhard Euler demonstrated that a geodesic structure must contain 12 pentagons to close into a spheroid, although the number of hexagons may vary. Later research by Smalley and his colleagues showed that there should exist an entire family of these geodesic-dome-shaped carbon clusters (Kroto et al. 1985). Fullerenes form with an even number  $n \geq 20$  of three connected vertices,  $3n/2$  edges, 12 pentagonal faces, and  $(n-20)/2$  hexagonal faces (Fowler and Manolopoulos 1995; Kroto et al. 1985). Thus,  $C_{60}$  has 20 hexagons, whereas its “rugby-ball”-shaped cousin  $C_{70}$  has 25 hexagons. As hexagons are added or removed, the molecule begins to lose its roundness. Giant fullerenes take on a pentagonal shape. Smaller fullerenes look like asteroids. One should note that all of the fullerenes have the same Gaussian curvature sign; therefore, all of them have a convex surface. The Buckminsterfullerene  $C_{60}$ , shown in  Fig. 22-6, has a spherical-like shape and the full group of symmetry of the icosahedron ( $I_h$ ), which means that it could be rotated by the angle of  $2\pi/5$  around the center of each pentagon and reflected in the mirror located on each plane of its symmetry. Another class of spherical fullerenes like  $C_{140}$  and  $C_{260}$  lacks the mirror symmetry  $h$ , hence their maximum symmetry group is icosahedral ( $I$ ) (Terrones et al. 2002).

The fullerenes  $C_{60}$  and  $C_{70}$  were identified in carbon flames and their ratios depend on the temperature, pressure, carbon/oxygen ratio, and residence time in the flame (Howard et al. 1991). The molecular structure of  $C_{70}$  was deduced from electron diffraction using a simulated-annealing method (McKenzie et al. 1992). Scientists tried to understand the crystal structures of  $C_{60}$  and  $C_{70}$  using X-ray diffraction technique (David et al. 1991, 1992; Fischer et al. 1991; Valsakumar et al. 1993). At ambient temperature and pressure,  $C_{60}$  crystals have face centered cubic (fcc) structure with a lattice constant of 14.17 Å (David et al. 1991), while the  $C_{70}$  crystals adopt to a hexagonal close packed (hcp) structure with  $a = 10.1$  Å and  $c = 17.0$  Å (David et al. 1992). The average diameters of  $C_{60}$  and  $C_{70}$  fullerenes are about 7 and 9 Å, respectively. Since the discovery of  $C_{60}$  followed by  $C_{70}$  (Kroto et al. 1985; Taylor et al. 1990), different sizes of carbon cage fullerenes were revealed. In early 1990, Diederich et al. isolated the carbon cages of  $C_{76}$ ,  $C_{84}$ ,  $C_{90}$ , and  $C_{94}$ , and these fullerenes were characterized by mass spectrometry,  $^{13}\text{C}$  NMR, electronic absorption (ultraviolet/visible), and vibrational (infrared) spectroscopy techniques (Diederich et al. 1991a). As compared with  $C_{60}$  and  $C_{70}$ , the isolation of higher fullerenes is really challenging, and their characterization is complicated by the presence of a varying number of isomers.

Fullerenes are generally represented by a formula  $C_n$ , where  $n$  is an even number and denotes the number of carbon atoms present in the cage. Theoretical calculations predicted that fullerenes larger than  $C_{76}$  should have at least two isomeric forms (Manolopoulos and Fowler 1991). For fullerenes  $C_{84}$  and  $C_{96}$ , 24 and 187 distinct isomers were predicted, respectively (Manolopoulos and Fowler 1991, 1992). Three isomers for  $C_{78}$  and two isomers for  $C_{84}$  were isolated and characterized by  $^{13}\text{C}$  NMR spectroscopy (Kikuchi et al. 1992a). Some of the isomers of  $C_{78}$  and  $C_{82}$  proposed by experimental  $^{13}\text{C}$  NMR spectroscopy are depicted in  Fig. 22-7. Many of the unique properties of fullerenes originate from their unusual cage structures. Therefore, determining the ground state geometries of the fullerenes was considered to be an important step in understanding their unusual properties.




■ Fig. 22-7


The structures of fullerene isomers suggested by the  $^{13}\text{C}$  NMR measurements. (a) Three isomers of  $C_{78}$  fullerene with  $C'_{2v}$ ,  $C_{2v}$ , and  $D_3$  point group. (b) Three structural candidates for  $C_{82}$  fullerene with  $C_2$  symmetry. (c) Structures of  $C_{3v}$ - and  $C_{2v}$ - $C_{82}$  isomers (The picture was reprinted by permission from Macmillan Publishers Ltd.: Nature, ref. Kikuchi et al. (1992a), copyright 1992)

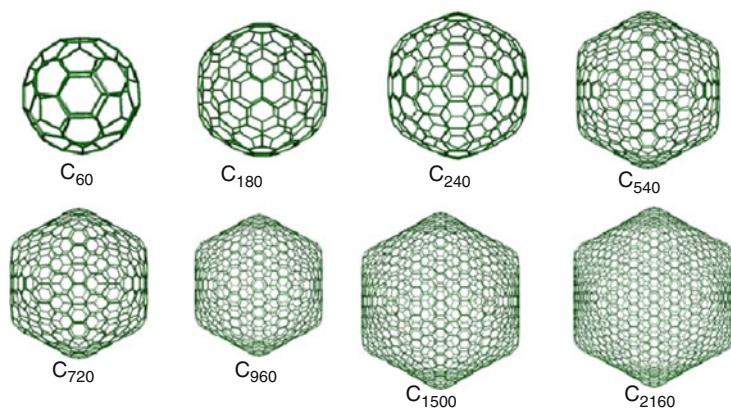
Experimental works are very limited for higher fullerenes beyond  $C_{84}$  because such species are difficult to isolate in pure form in quantities suitable for comprehensive study. Synthesis of  $C_{60}$ , in isolable quantities, was achieved using flash vacuum pyrolysis (FVP) technique by Scott and coworkers by 12 steps in 2002 and no other fullerenes were formed as by-products (Scott et al. 2002). Very recently, Amsharov and Jensen synthesized larger fullerene  $C_{78}$  using the same FVP technique used for  $C_{60}$  synthesis (Amsharov and Jensen 2008). This shows a promise for the synthesis of higher fullerenes. It is noteworthy to mention that there has been lot of experimental and theoretical studies involving fragments of fullerenes, called “buckybowls” (Barth and Lawton 1966; Dinadayalane and Sastry 2001, 2002a, b; Dinadayalane et al. 2001, 2002, 2003, 2004; Mehta and Rao 1998; Mehta et al. 1997; Priyakumar and Sastry 2001a, b, c; Sakurai et al. 2003; Sastry and Priyakumar 2001; Sastry et al. 1993, 2000; Seiders et al. 1999, 2001; Sygula and Rabideau 1999; Wu and Siegel 2006). The smallest buckybowl “corannulene” was synthesized nearly 20 years prior to the discovery of fullerene  $C_{60}$  (Barth and Lawton 1966). Another small fragment of  $C_{60}$  called “sumanene” was successfully synthesized in 2003 after so many futile attempts by different groups (Sakurai et al. 2003).


Fullerene can be classified into (a) classical fullerene and (b) nonclassical fullerene. The former is a closed carbon cage containing 12 pentagons and any number of hexagons, while the latter can have heptagons, octagons, and an additional number of pentagons or squares. Growing classical fullerenes from nonclassical fullerenes, for example from  $C_{50}$  to  $C_{60}$  by the dimer addition, was proposed (Hernández et al. 2001). However, there is no clear experimental evidence for fullerene formation through this route. Helden et al. showed the experimental evidence for the formation of fullerenes by collisional heating of carbon rings in the gas phase (Helden et al. 1993). Various mechanisms have been proposed so far for the formation of fullerenes. They can be divided into two major models: the pentagon road (PR) model (Klein and Schmalz 1990; Maruyama and Yamaguchi 1998; Smalley 1992), and the fullerene road (FR) model (Heath 1991).



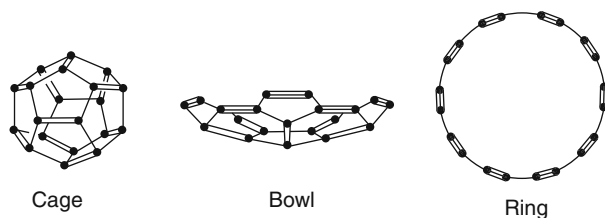
Since the discovery of  $C_{60}$ , scientists showed vast interest in larger fullerenes. Therefore, the family of fullerenes increased, and now it also includes  $C_{70}$ ,  $C_{76}$ ,  $C_{78}$ ,  $C_{82}$ ,  $C_{84}$ ,  $C_{86}$ ,  $C_{88}$ ,  $C_{90}$ ,  $C_{92}$ ,  $C_{94}$ , and  $C_{96}$  (Diederich et al. 1991a, b; Kikuchi et al. 1992b; Kimura et al. 1995; Miyake et al. 2000; Mizorogi and Aihara 2003; Taylor et al. 1992, 1993). The fundamental understanding of the size dependence of the closed carbon cage structures is important for tailoring these systems for possible nanotechnology applications. Larger fullerenes that have an icosahedral symmetry can also be constructed. This procedure generates 12 pentagons positioned around vertices of an icosahedron, while all other carbon rings are hexagonal. In general, there are two kinds of fullerenes with  $I_h$  symmetry, one being  $n = 60 k^2$  and the other  $n = 20 k^2$ ; where  $n$  is the number of carbon atoms and  $k$  is any positive integer (Miyake et al. 2000).  Figure 22-8 depicts some of the giant fullerene structures, where  $C_{180}$  and  $C_{720}$  belong to  $180 k^2$  family of icosahedral fullerenes, but all other structures belong to  $60 k^2$  family of icosahedral fullerenes. For more than a decade, these giant fullerenes have been fascinating molecules for theoreticians (Calaminici et al. 2009; Dulap and Zope 2006; Dunlap et al. 1991; Gueorguiev et al. 2004; Lopez-Urias et al. 2003; Tang and Huang 1995; Tang et al. 1993; Zope et al. 2008).

The closed carbon cages smaller than  $C_{60}$  consist of adjacent pentagons. Such smaller fullerenes are predicted to have unusual electronic, magnetic, and mechanical properties that arise mainly from the high curvature of their molecular surface (Kadish and Ruoff 2002). A dodecahedron consisting of 20 carbon atoms with only pentagon rings is topologically the smallest possible fullerene. The well-known isomers of  $C_{20}$  are cage, bowl, and ring as shown in  Fig. 22-9. The bowl shaped isomer is reminiscent of corannulene. The realization of the smallest carbon closed-cage  $C_{20}$ , which exclusively contains 12 pentagons, was doubtful until 2000. The  $C_{20}$  closed cage has extreme curvature and high reactivity, which led to doubts about its existence and stability (Wahl et al. 1993). Prinzbach et al. produced the smallest fullerene  $C_{20}$  from its perhydrogenated form in the gas phase and also obtained the bowl- and ring-shaped isomers for comparison purposes (Prinzbach et al. 2000). All these structures were characterized by photoelectron spectroscopy (PES) and their electron affinities vary significantly (Prinzbach et al. 2000). Theoretical calculations at different levels predicted dissimilar



 Fig. 22-8

The structures of giant fullerenes (Reprinted with permission from Zope et al. (2008). Copyright 2008 by the American Physical Society)



■ Fig. 22-9

Isomers of  $C_{20}$ : cage-, bowl-, and ring-shaped structures (Reprinted by permission from Macmillan Publishers Ltd.: Nature, ref. Prinzbach et al. (2000), copyright 2000)

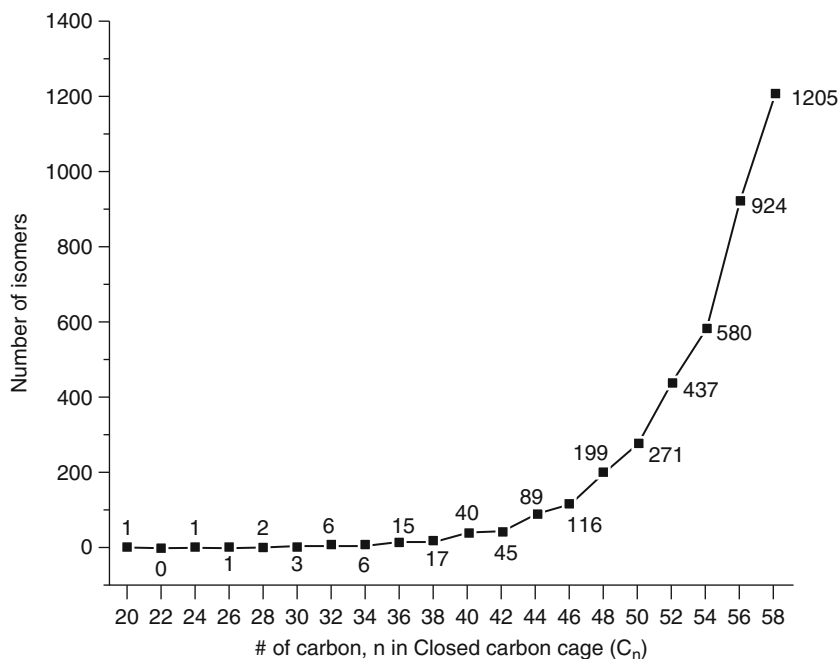
energetic ordering for these three isomers. However, all revealed very small relative energies of isomers. MP2 method predicted the fullerene to be the most stable followed by the bowl and then the ring, and this prediction is very similar to the calculations of density functional theory (DFT) using the local density approximation (LDA). Complete reversal of the stability ordering was obtained in the calculations with Becke–Lee–Yang–Parr (BLYP) functional. Some other DFT functionals predicted the bowl to be the most stable structure, closely followed by the fullerene isomer (Scuseria 1996). Hybrid density functional theory and time-dependent DFT formalism validated the synthesis of the smallest cage fullerene  $C_{20}$  by comparing the computed photoelectron spectra with the experimental results (Saito and Miyamoto 2001).

Closed-cage structure of  $C_{36}$  was detected by mass spectroscopy in very early days of fullerene science (Kroto 1987; Robinson et al. 1984). Zettl's group claimed the first preparation of  $C_{36}$  in the solid form (Piskoti et al. 1998). However, the existence of  $C_{36}$  has not been fully confirmed to date.  $C_{36}$  has 15 conventional fullerene isomers; out of which, the  $D_{6h}$  and  $D_{2d}$  have a minimal number of pentagons (Fowler and Manolopoulos 1995). Therefore, these two are potential candidates for the most stable structure. In general, the number of isomers increases as the carbon cage size increases for these small fullerenes as shown in ● Fig. 22-10.

Fullerenes from  $C_{20}$  to  $C_{58}$  have been extensively studied by theoreticians (Fowler and Manolopoulos 1995; Scuseria 1996; Shao et al. 2007). They have been predicted to have narrow HOMO–LUMO gaps and high reactivity. Lu and Chen reviewed the structures, aromaticity, reactivity, and other properties of the smaller fullerenes that is, less than 60 carbon atoms (Lu and Chen 2005). Readers may refer to the review by Lu and Chen and the references therein for detailed understanding and further knowledge if required (Lu and Chen 2005). Selected structures of smaller fullerenes and their isomers are depicted in ● Fig. 22-11. Schlegel diagram is commonly used by scientists to sketch the fullerenes in planar view, which is very helpful in identifying atoms and the C–C bonding networks (Fowler and Heine 2001; Thilgen and Diederich 2006; Troyanov and Tamm 2009). ● Figure 22-12 depicts the Schlegel diagram for fullerenes  $C_{20}$ ,  $C_{36}$ ,  $C_{60}$ , and  $C_{70}$ .

## Natural Abundance of Fullerenes

Scientists are actively involved in discovering the presence of natural fullerenes on Earth. Interestingly, occurrence of fullerenes such as  $C_{60}$  and  $C_{70}$  was reported in shungite, a meta-anthracite coal from a deposit near Shunga, Russia (Buseck et al. 1992). Heymann et al. reported



■ Fig. 22-10

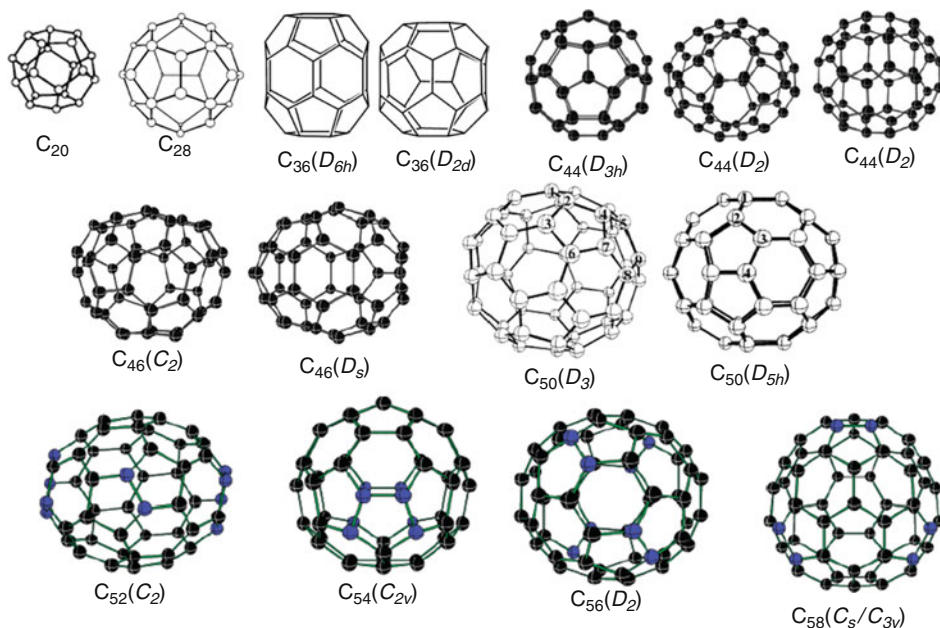
Number of isomers for the closed carbon cages from  $C_{20}$  to  $C_{58}$  (Data was taken from ref. Fowler and Manolopoulos (1995))

the presence of  $C_{60}$  at very low concentrations in Cretaceous–Tertiary boundary sites in New Zealand (Heymann et al. 1994). Fullerenes ( $C_{60}$  and  $C_{70}$ ) were found in a unit of shock-produced impact breccias (Onaping Formation) from the Sudbury impact structure in Ontario, Canada (Becker et al. 1994). The abundance of naturally occurring fullerenes was found in carbon materials, for example, coal, rocks, interstellar media, and even dinosaur eggs (Heymann et al. 2003).

### Fullerene Nano-Capsules

In the area of fullerene science, one should not forget to mention an interesting property of holding the atoms or ions or molecules inside the fullerene cage (Thilgen and Diederich 2006). Fullerenes are potential nano-capsules. Experimental detection of the nano-capsules of fullerenes such as  $La@C_{60}$ ,  $La@C_{70}$ ,  $La@C_{74}$ ,  $La@C_{76}$ ,  $La@C_{78}$ ,  $La@C_{82}$ , and  $Ce_2@C_{80}$  was reported (Kessler et al. 1997; Kubozono et al. 1996; Moro et al. 1993; Saunders et al. 1993; Thilgen and Diederich 2006; Yamada et al. 2005, 2010). Fullerenes are known in the field of radioactive chemistry/physics. Radioactive nuclear materials can be stored by encapsulating inside the fullerenes.  $U@C_{28}$ ,  $Gd@C_{60}$ , and  $Gd@C_{82}$  are few examples of encapsulated radioactive materials (Guo et al. 1992; Kubozono et al. 1996). The stability of these metallic fullerenes could bring the new effective solution of the radioactive waste elimination. For the substance enclosed in





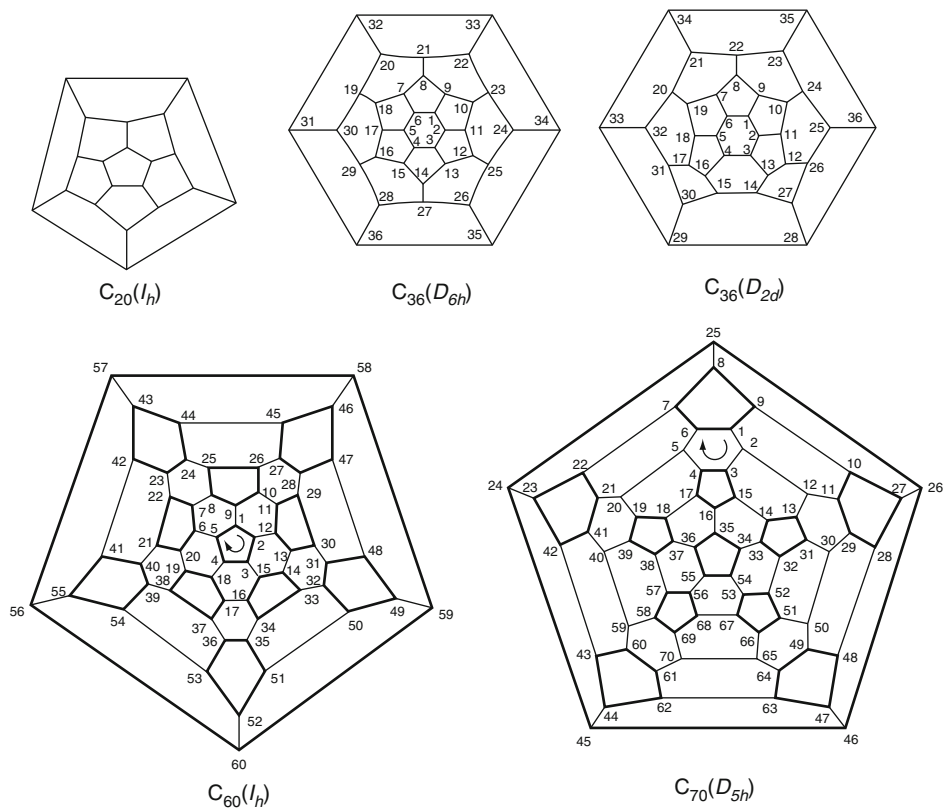
■ Fig. 22-11

Representative structures of smaller fullerenes and low-energy isomers are given for some of them. The pentagon–pentagon fusions are highlighted in blue color only for  $C_{52}$ ,  $C_{54}$ ,  $C_{56}$ , and  $C_{58}$ . The point groups are given in parentheses (Reprinted with permission from ref. Lu and Chen (2005). Copyright 2005 American Chemical Society)

the fullerene nano-capsule, carbon atoms act like a defense shield and the fullerene containers are good for protecting their contents from water and acid. The structures, stabilities, and reactivities of encapsulated fullerenes (nano-capsules) and doped fullerenes have been the subject of theoretical interest (Guo et al. 1992; Lu et al. 2000; Park et al. 2005; Simeon et al. 2005; Wang et al. 2003; Wu and Hagelberg 2008; Zhao and Pitzer 1996). The closed-cage “fullerenes” or “heterofullerenes” can be placed inside the single-walled carbon nanotubes, for example,  $C_{60}@SWCNT$  (Hirahara et al. 2000; Okada 2007; Smith et al. 1999). Leszczynski and coworkers have explored the mechanism of the catalytic activity of fullerene derivatives using reliable computational methods (Sulman et al. 1999; Yanov et al. 2004). Fullerenes are certainly worthy of scientific study because of their unique shape and intriguing properties.

### Isolated Pentagon Rule (IPR) in Fullerenes

A wide range of methods available for producing fullerenes concluded that  $C_{60}$  is the most abundant and is followed by  $C_{70}$  (Kadish and Ruoff 2002). The pristine  $C_{60}$  ( $I_h$ ) contains two different C–C bonds: the one at the junction of two six-membered rings and the other one at the junction of a five- and a six-membered ring. These two bonds are usually labeled as a [6,6] and [5,6] C–C bonds respectively. The pristine  $C_{70}$  ( $D_{5h}$ ) has eight distinguishable C–C bonds. It has been known to chemists that energetically it is not favorable to have two pentagons sharing

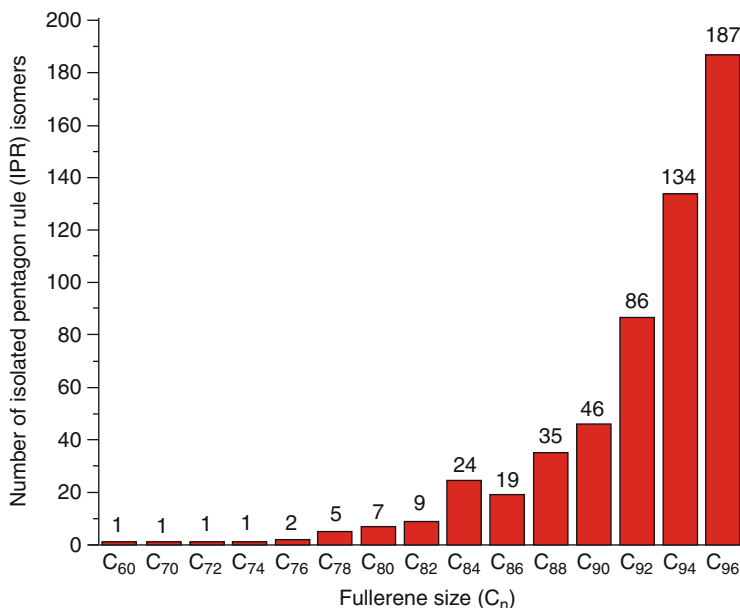


■ Fig. 22-12

Schlegel diagrams of  $C_{20}$ ,  $C_{36}$ ,  $C_{60}$ , and  $C_{70}$  fullerenes. The point groups are given in parentheses, systematic numbering recommended by IUPAC (Pictures were reprinted with permission from ref. Thilgen and Diederich (2006). Copyright 2006 American Chemical Society. Ref. Fowler and Heine (2001). Copyright 2001 Royal Society of Chemistry)

the same C–C bond. There are 1,812 mathematical ways of forming a closed cage with 60 carbon atoms (isomers), but the Buckminsterfullerene  $C_{60}$  ( $I_h$ ) is the most special and stable because all of its pentagons are isolated by hexagons. This condition is called the “isolated pentagon rule” (IPR), which tends to make fullerenes more stable (Fowler and Manolopoulos 1995).

In fact,  $C_{60}$  is the smallest fullerene cage that obeys the isolated pentagon rule. Fullerenes  $C_{62}$ ,  $C_{64}$ ,  $C_{66}$ , or  $C_{68}$  do not satisfy the IPR. The next fullerene, which follows the IPR, is  $C_{70}$  (it has 8,149 possible isomers). Also,  $C_{72}$  has an IPR structure. Most of the higher fullerenes have proven to follow IPR (Kroto 1987). Only one IPR-obeying isomer exists for  $C_{60}$  and for  $C_{70}$  (Fowler and Manolopoulos 1995), while the number of possible IPR isomers increases rapidly with increase in the size of the fullerenes as shown in ● Fig. 22-13. Fullerene  $C_{78}$  has five isomers that satisfy the IPR. Three isomers (two with  $C_{2v}$  and one with  $D_3$  symmetry) out of these five were identified and characterized using  $^{13}\text{C}$  NMR spectra (Kikuchi et al. 1992a). The fourth isomer ( $D_{3h}$ - $C_{78}$ ) has been recently separated and characterized in the form of

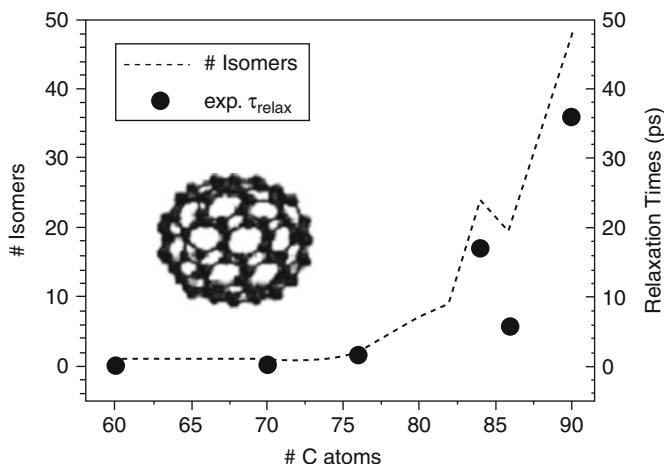


■ Fig. 22-13

Fullerene size versus number of isolated pentagon rule (IPR) isomers (The data was taken from ref. Manolopoulos and Fowler (1992))

$C_{78}(CF_3)_{12}$  (Shustova et al. 2006, 2007), and the last one has been synthesized using FVP technique (Amsharov and Jensen 2008). According to Manolopoulos and Fowler (Manolopoulos and Fowler 1991),  $C_{82}$  has nine IPR-satisfying isomers, out of which three isomers with  $C_2$  symmetry were experimentally characterized using  $^{13}C$  NMR spectroscopy, which gave 41 NMR lines with nearly equal intensity (Kikuchi et al. 1992a).

There are 24 geometric isomers satisfying IPR and 51,568 non-IPR isomers are possible for fullerene  $C_{84}$  (Fu et al. 2009). Earlier experimental  $^{13}C$  NMR spectroscopy studies characterized two IPR isomers with  $D_2$  and  $D_{2d}$  point groups (Kikuchi et al. 1992a; Taylor et al. 1993). Third isomer was also identified and reported (Achiba et al. 1995; Crassous et al. 1999). Pure  $D_2-C_{84}$  was synthesized by Dennis et al. in 1998 (Dennis and Shinohara 1998). A theoretical study revealed that  $C_{84}$  cage is special in the family of fullerenes from  $C_{60}$  to  $C_{90}$  since the number of preferable isomers for  $C_{84}$  is more than that of  $C_{86}$  fullerene. Okada and Saito provided the geometries of all of the 24 IPR isomers of fullerene  $C_{84}$  along with their point groups (Okada and Saito 1996). Miyake et al. separated two IPR isomers of  $C_{86}$  out of possible 19 isomers using multistage HPLC (high performance liquid chromatography) (Miyake et al. 2000) and these two isomers were characterized to have  $C_2$  and  $C_s$  point groups by  $^{13}C$  NMR spectroscopy (Taylor et al. 1993). Burda et al. showed the experimental evidence for the photoisomerization of higher fullerenes. They confirmed the theoretical prediction that  $C_{86}$  has less number of IPR-satisfying isomers (19 isomers) than  $C_{84}$  (24 isomers) (► Fig. 22-14) (Burda et al. 2002). Experimental studies based on  $^{13}C$  NMR spectroscopy revealed that fullerenes  $C_{88}$  and  $C_{92}$  possess 35 and 86 IPR isomers respectively, and HPLC was used to separate the isomers (Achiba et al. 1996; Miyake et al. 2000; Tagmatarchis et al. 2002). Computational methods were used to calculate



■ Fig. 22-14

Correlation between the number of isomers (dotted line as a visual guide) for each fullerene and the time constant for the formation of the lowest excited singlet state monitored at 550 nm (dots) (Reprinted with permission from ref. Burda et al. (2002). Copyright 2002 American Chemical Society)

relative energies of the IPR isomers and the  $^{13}\text{C}$  NMR spectra of fullerenes (Shao et al. 2006; Slanina et al. 2000a, b; Sun 2003). The computed  $^{13}\text{C}$  NMR spectra were interpreted with the available experimental data (Beavers et al. 2006; Chaur et al. 2009a, b; Melin et al. 2007; Rojas et al. 2007; Scheina and Friedrich 2008; Shao et al. 2006; Slanina et al. 2000a, b; Sun 2003; Xie et al. 2004). Theoretical calculations predicted that  $\text{C}_{88}$  (33) is one of the most stable IPR isomers (Shao et al. 2006). The number provided in the parenthesis is the isomer number. Very recently, consistent to the theoretical prediction, Troyanov and Tamm reported the isolation and X-ray crystal structures of trifluoromethyl derivatives of  $\text{C}_{88}$  (33) and  $\text{C}_{92}$  (82) fullerene isomers complying with the isolated pentagon rule (Troyanov and Tamm 2009).

Rojas et al. have shown the experimental evidence of the decreasing trend in the gas-phase enthalpy of formation and strain energy per carbon atom as the size of the cluster increases. Thus, the fullerenes become more stable as they become larger in size (Rojas et al. 2007). Interestingly, molecules encapsulated inside the carbon cages stabilize the fullerene isomers that violate IPR (Beavers et al. 2006; Fu et al. 2009; Thilgen and Diederich 2006). Several IPR and non-IPR endohedral fullerenes (single metal, di-metal, or tri-metal nitride encapsulated fullerenes) were isolated and characterized experimentally (Beavers et al. 2006; Chaur et al. 2009a, b; Fu et al. 2009; Melin et al. 2007; Thilgen and Diederich 2006), and their isolation motivated significant theoretical interest (Fu et al. 2009; Park et al. 2005; Wu and Hagelberg 2008). Dinadayalane and Sastry explored the structures and relative energies of the IPR isomers of buckybowls using computational methods (Dinadayalane and Sastry 2003). Scheina and Friedrich have recently proposed head-to-tail exclusion rule in explaining the stability of carbon cage structures that obey the IPR (Scheina and Friedrich 2008).

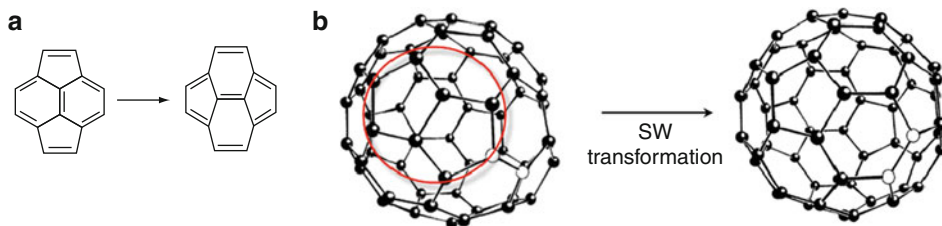
Fullerenes with less than 60 carbon atoms cannot have isolated pentagons and therefore they should be highly unstable and reactive. Xie et al. synthesized non-IPR  $D_{5h}$ - $\text{C}_{50}$  fullerene, which is a little sister of  $\text{C}_{60}$ , by introduction of chlorine atoms at the most reactive pentagon-pentagon

vertex fusions. They confirmed the  $D_{5h}$ - $C_{50}$  structure by mass spectrometry, infrared, Raman, ultraviolet-visible, and fluorescence spectroscopic techniques (Xie et al. 2004). The report of novel small cage “Saturn-shaped”  $C_{50}Cl_{10}$  structure encourages the possibility of obtaining other small non-IPR fullerenes and their derivatives. The investigations of the properties and applications of small fullerenes and their derivatives are now open.

## Common Defects in Fullerenes

Stone and Wales examined rotation of C–C bonds in various fullerene structures using approximate Huckel calculations. The  $90^\circ$  rotation of C–C bond in fullerene is called Stone–Wales (SW) or “pyracylene” rearrangement (► Fig. 22-15) (Stone and Wales 1986). Austin et al. reported that 94% of all fullerene  $C_{60}$  isomers can rearrange to Buckminsterfullerene by SW transformation (Austin et al. 1995). The  $C_{78}$  cage represents the smallest fullerene in which SW rearrangement can give stable IPR isomers:  $C_{78}:5 (D_{3h}) \leftrightarrow C_{78}:3 (C_{2v}) \leftrightarrow C_{78}:2 (C_{2v}) \leftrightarrow C_{78}:4 (D_{3h})$ ; where the numbers 5, 3, 2, and 4 indicate the isomer numbers (Austin et al. 1995). In case of higher fullerenes, the number of IPR isomers that can be transformed one into another by SW rearrangement considerably increases. For example, the SW transformation gives 9 and 24 stable IPR isomers for  $C_{82}$  and  $C_{84}$ , respectively (Fowler and Manolopoulos 1995). The SW transformation is usually thought to be the possible mechanism for achieving fullerene isomers (Austin et al. 1995; Fowler and Manolopoulos 1995; Stone and Wales 1986).

It was proposed that fullerenes can have seven-membered rings in addition to five- and six-membered rings (Taylor 1992). Troshin et al. isolated and characterized the  $C_{58}$  fullerene derivatives in which the cage structure contains the seven-membered ring. The structures were characterized using mass spectrometry, IR spectroscopy, and NMR spectroscopy (Troshin et al. 2005). Smalley and coworkers found that laser irradiation can fragment  $C_{60}$  into  $C_{58}$ ,  $C_{56}$ ,  $C_{54}$ , and other smaller cages with even number of carbon atoms via losing  $C_2$  fragments (O’Brien et al. 1988). The formation of seven-membered rings was considered to play an important role in the fragmentation process of fullerenes (Murry et al. 1993). The laser desorption ionization of products generated from the reactions of  $C_{60}$  with  $O_3$  gives the odd-numbered clusters such as  $C_{59}$ ,  $C_{57}$ ,  $C_{55}$ , and  $C_{53}$  (Christian et al. 1992; Deng et al. 1993). Vacancy defects destroy the original topology of five- and six-membered rings in fullerenes (Christian et al. 1992; Deng et al.



■ Fig. 22-15

(a) Stone–Wales or “pyracylene” transformation in fullerenes interchanges pentagons and hexagons; (b) Stone–Wales transformation of  $C_{2v}$  isomer of  $C_{60}$  with two adjacent pentagons gives the most stable  $I_h$  Buckminsterfullerene; the C–C bond involved in  $90^\circ$  rotation is highlighted and the two adjacent pentagons are marked in the fullerene structure in left hand-side

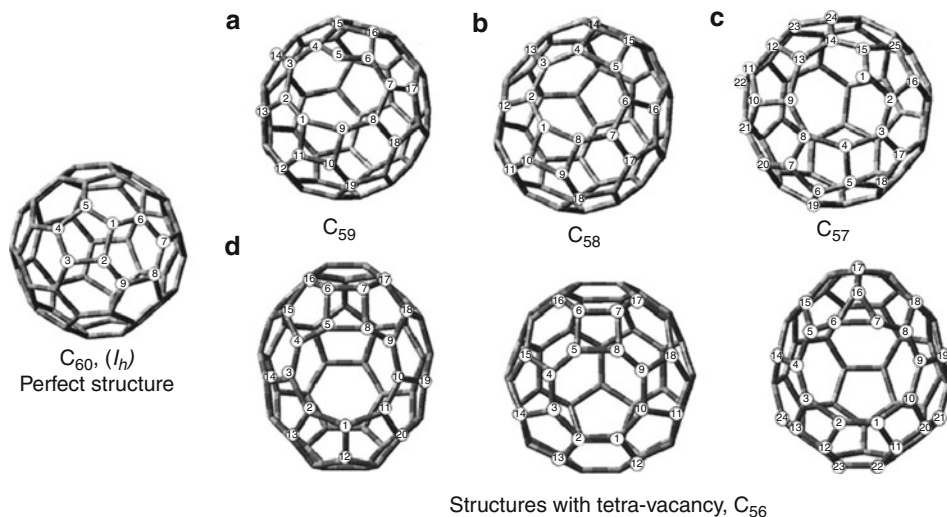


Fig. 22-16

Buckminsterfullerene (perfect structure); vacancy defect fullerenes generated from  $C_{60}$ : (a) mono-vacancy, (b) di-vacancy, (c) tri-vacancy, (d) three different structures of tetra-vacancy (Reprinted with permission from Hu and Ruckenstein (2004). Copyright 2004, American Institute of Physics)

1993; Hu and Ruckenstein 2003; Hu and Ruckenstein 2004; Lee and Han 2004; Murry et al. 1993; O'Brien et al. 1988). They generate various sizes of rings such as four-, seven-, eight-, and nine-membered rings and also produce the new five- and six-membered rings depending on the number of carbon atom vacancies (Fig. 22-16) (Christian et al. 1992; Deng et al. 1993; Hu and Ruckenstein 2003; Hu and Ruckenstein 2004; Lee and Han 2004; Murry et al. 1993; O'Brien et al. 1988).

## Carbon Nanotubes (CNTs)


### Discovery and Classification of CNTs

Modern “nanotechnology revolution” was flourished by the discovery of fullerenes and has been escalating since the isolation of multi- and single-walled carbon nanotubes. The detection of carbon nanotubes by Iijima in 1991 is one of the landmarks in nanotechnology (Iijima 1991). In the interview to Nature Nanotechnology, Iijima told that the discovery of carbon nanotubes was unexpected but not entirely accidental because he had accumulated a lot of experience in looking at short-range order in carbon species such as amorphous carbon and very thin graphite sheets (Iijima 2007). The discovery of Buckminsterfullerene by Kroto, Curl, Smalley, and coworkers motivated Iijima’s interest in finding out new carbon allotropes (Kroto et al. 1985).

There are two structural forms of carbon nanotubes: multi-walled carbon nanotubes (MWCNTs) and single-walled carbon nanotubes (SWCNTs). The former one was reported in



the journal *Nature* in 1991 by Iijima (1991). The SWCNTs were reported for the first time in back-to-back papers in *Nature* in 1993 independently by Iijima as well as Bethune groups (Berthe et al. 1993; Iijima and Ichihashi 1993). The existence of carbon nanotubes was reported as early as 1952 and also in 1976 (Oberlin et al. 1976; Radushkevich and Lukyanovich 1952). However, those reports did not reach the wide range of scientific community because they were published in unpopular journals and at that time, no fabrication process was known that would lead to the synthesis of macroscopic amounts of carbon nanotubes (Oberlin et al. 1976; Radushkevich and Lukyanovich 1952). Monthioux and Kuznetsov have recently documented the history of carbon nanotube discovery since 1952 (Monthioux and Kuznetsov 2006).

High-resolution electron microscopy (HREM) images of the CNTs showed the resemblance of a “Russian doll” structural model that is based on hollow concentric cylinders capped at both ends. The model structures of multi-walled and single-walled carbon nanotubes are shown in  Fig. 22-17. Wide range of methods such as arc-evaporation of graphite, laser ablation, chemical vapor deposition (CVD), vapor phase decomposition, or disproportionation of carbon-containing molecules, etc., have been reported for the synthesis of multi-walled and single-walled carbon nanotubes (Dresselhaus et al. 2001). It remains unclear whether SWCNTs and MWCNTs are formed via the same mechanism. It is also unclear whether various methods used to produce carbon nanotubes are mechanistically consistent (Dresselhaus et al. 2001). For the transformation pathway, fullerenes are known to be a suitable carbon source for MWCNT growth under certain conditions (Suchanek et al. 2001). An ideal MWCNT consists of cylindrical tubes in which the neighboring tubes are weakly bonded through van der Waals forces. The MWCNT is incommensurate when each of its walls has its own chirality independent of other walls.

SWCNT, which is a one-dimensional (1D) system, can be considered as the conceptual rolling of a section of two-dimensional (2D) graphene sheet into a seamless cylinder forming the nanotube. The structure of SWCNT is uniquely described by two integers ( $n, m$ ), which refer to the number of  $\vec{a}_1$  and  $\vec{a}_2$  unit vectors of the 2D graphene lattice that are contained in the chiral vector,  $C_h = n\vec{a}_1 + m\vec{a}_2$ . The chiral vector determines whether the nanotube is a semiconductor, metal, or semimetal. From the ( $n, m$ ) indices, one can calculate the nanotube diameter ( $d_t$ ), the chirality or chiral angle ( $\theta$ ), the electronic energy bands, and the density of electronic states. The nanotube diameter ( $d_t$ ) determines the number of carbon atoms in the

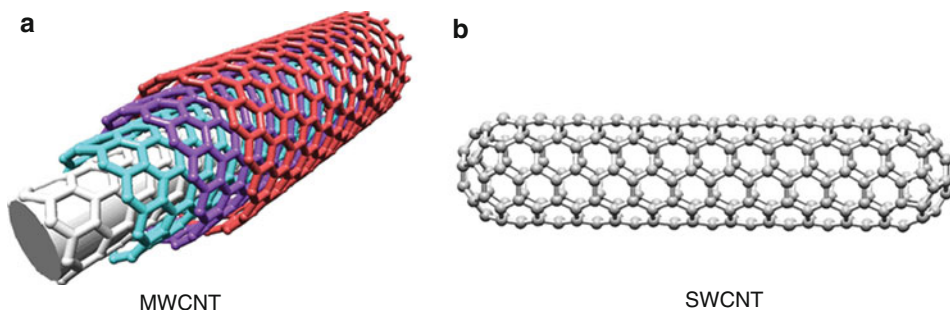



 Fig. 22-17 Representative structures of (a) multi-walled (b) single-walled carbon nanotubes

circular cross section of the nanotube shell, one atom in thickness (Saito et al. 1998). The tube diameter and chiral angle can be written in terms of  $(n, m)$  as


$$\begin{aligned} \text{Tube diameter, } d_t &= (\sqrt{3}/\pi) a_{cc} \left( \sqrt{m^2 + mn + n^2} \right) \\ \text{Chiral angle, } \theta &= \tan^{-1} \left\{ \sqrt{3} m / (2n + m) \right\}, \end{aligned}$$

where  $a_{cc}$  is the nearest-neighbor carbon atom distance of 1.421 Å.

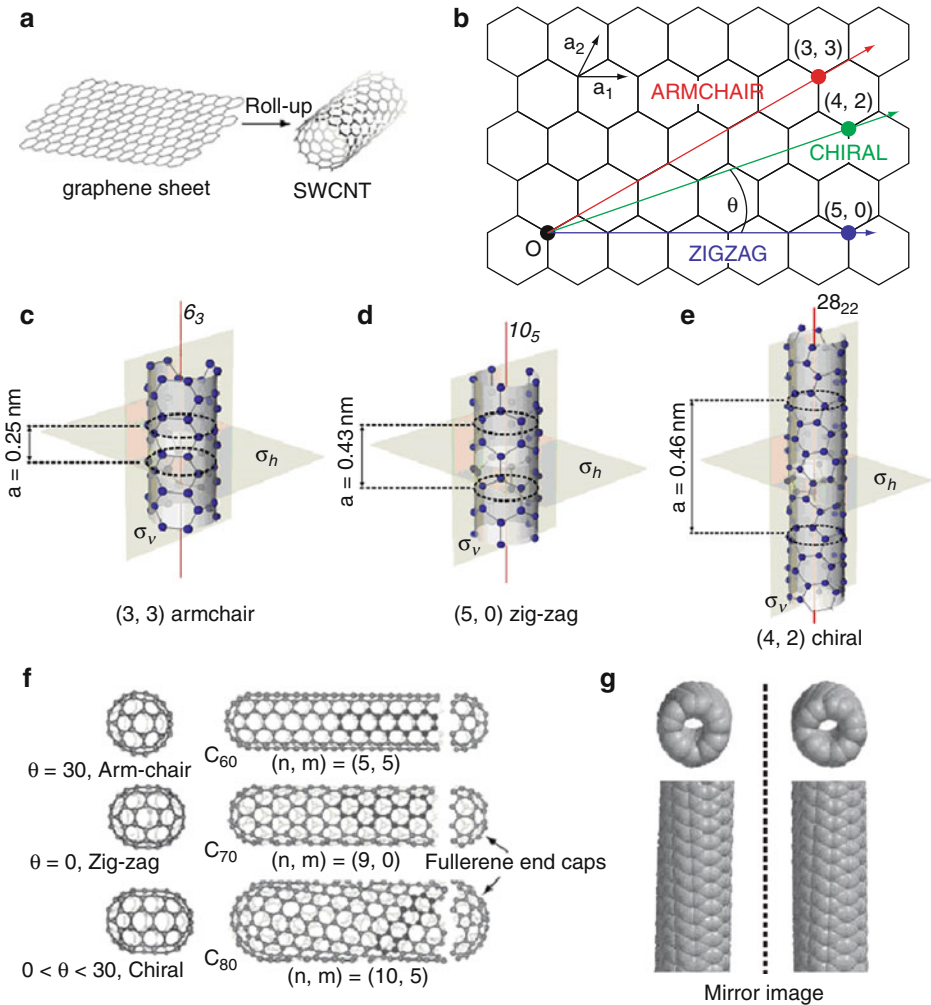
Among the large number of possible  $C_h$  vectors, there are two inequivalent high-symmetry directions. These are termed “zigzag” and “armchair” and are designated by  $(n,0)$  and  $(n,n)$ , respectively. Either achiral (armchair and zigzag) or chiral SWCNTs can be constructed depending on the orientation of the six-membered rings with respect to the nanotube axis. Schematic representation of the structures of armchair, zigzag, and chiral SWCNTs are shown in  Fig. 22-18. Theoretical studies in 1992 predicted that the electronic properties of “ideal” SWCNTs depend on the width and chirality of the tubes (Hamada et al. 1992; Mintmire et al. 1992; Saito et al. 1992). The electronic properties of a SWCNT vary in periodic way between being metallic and semiconductor. SWCNTs are metals if  $(n-m)/3$  represent an integer, otherwise they are called semiconductors (Dresselhaus et al. 2002).

Several metallic  $(n, m)$  nanotubes have almost the same diameter  $d_t$  (from 1.31 to 1.43 nm), but have different chiral angles:  $\theta = 0, 8.9, 14.7, 20.2, 24.8,$  and  $30.0^\circ$  for nanotubes (18, 0), (15, 3), (14, 5), (13, 7), (11, 8), and (10, 10), respectively (Dresselhaus et al. 2002). Few people realize that CNTs constitute a large family with a wide variety of sizes and properties, which are determined by their structure and composition, including chirality, number of walls, ordering of the wall, defects, surface functionalization, and other features.

Strano has recently sorted out chiral SWCNTs into left-handed and right-handed tubes, which is an important milestone for studying of SWCNTs (Strano 2007). Significant progress has been made in the area of carbon nanotubes. Scientists are able to disperse, identify, sort, and now also isolate various types of carbon nanotubes (Arnold et al. 2006; Peng et al. 2007; Strano 2003, 2007). Specific methods have been found to grow long SWCNTs and control the nanotube diameters (Lu et al. 2008; Zhang et al. 2008). Controlled synthesis of nanotubes opens up exciting opportunities in nanoscience and nanotechnology (Dai 2002). A range of methods have been found for effective separation of metallic and semiconducting SWCNTs. Although some synthetic procedures have been known, they are not easy methods for synthesizing bulk quantities of metallic and semiconducting SWCNTs (Zhang et al. 2008). Very recently, scientists have succeeded the preferential growth of SWCNTs with metallic conductivity (Rao et al. 2009a).

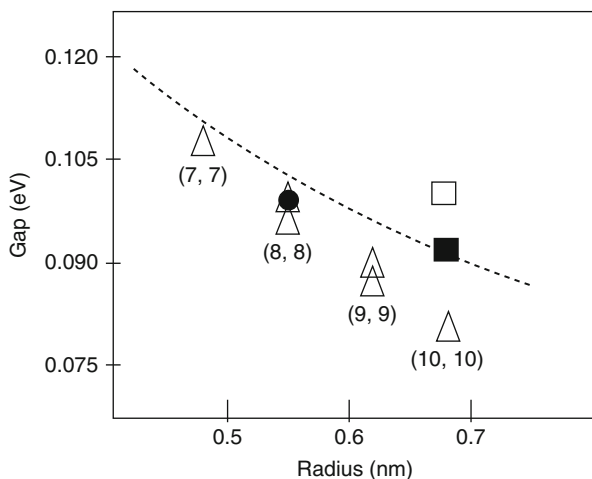
Raman and electronic spectroscopy techniques are useful in characterizing metallic and semiconducting SWCNTs. The radial breathing mode (RBM) in Raman spectra of SWCNTs is helpful in determining the diameter and chiral indices  $(n, m)$  of the nanotubes (Dresselhaus et al. 2002; Dresselhaus et al. 2005, 2007; Harutyunyan et al. 2009; Rao et al. 2009a). Experimental results pointed out decreasing band gap with increasing radius of the armchair SWCNTs ( Fig. 22-19) (Ouyang et al. 2002). Another breakthrough in carbon nanotube chemistry has been accounted by Zhang and Zuo, who have determined a quantitative atomic structure of MWCNT containing five walls with diameter ranging from  $\sim 17$  to 46 Å and the C–C bond lengths of individual SWCNTs using electron diffraction technique (Zhang and Zuo 2009). Their results indicate that there are three different bond lengths in chiral walls and two different bond lengths in achiral walls (Zhang and Zuo 2009). Electron diffraction technique has been used in determination of atomic structure of SWCNTs and the chiral indices  $(n,m)$  of





■ Fig. 22-18

(a) The roll-up of graphene sheet into SWCNT; (b) picture shows how to roll-up graphene sheet to generate three different types of SWCNTs; (c) (3,3) armchair SWCNT; (d) (5,0) zigzag SWCNT; (e) (4,2) chiral SWCNT; (f) three types of SWCNTs (armchair, zigzag, and chiral) with fullerene end caps. These can be viewed as the growth of SWCNTs by adding several layers of hexagonal rings at middle of different fullerenes; (g) Mirror image of the chiral SWCNT; The structures (c), (d), and (e) are given exactly same types of SWCNTs that are mentioned in (b). In (c)–(e),  $\sigma_v$  and  $\sigma_h$  indicate the vertical plane of symmetry and horizontal plane of symmetry, respectively. Further, in these three structures, the red line is the axis of rotation; the distance of one unit cell for these three types of SWCNTs is provided; the number of carbon atoms ( $x$ ) in each layer and the number of layers ( $y$ ) required for one unit cell is given as  $x_y$ , for example –  $6_3$  means six carbon atoms in each layer and three layers required for one unit cell of (3,3) armchair SWCNT (Pictures (b) and (g) were reprinted by permission from Macmillan Publishers Ltd.: Nature Nanotech., ref. Strano (2007), copyright 2007)



■ Fig. 22-19

**Tube radius versus observed band gap.** Each experimental data point ( $\Delta$ ) represents an average gap value measured on a distinct  $(n,n)$  tube. Theoretical results (solid square, open square, and solid circle) are also shown for comparison (Reprinted with permission from ref. Ouyang et al. (2002). Copyright 2002 American Chemical Society)

CNTs (Jiang et al. 2007; Qin 2007). Rao et al. have revealed the efficient growth of SWCNTs of diameter 1–3 nm from diamond nanoparticles and fullerenes (Rao et al. 2009b).

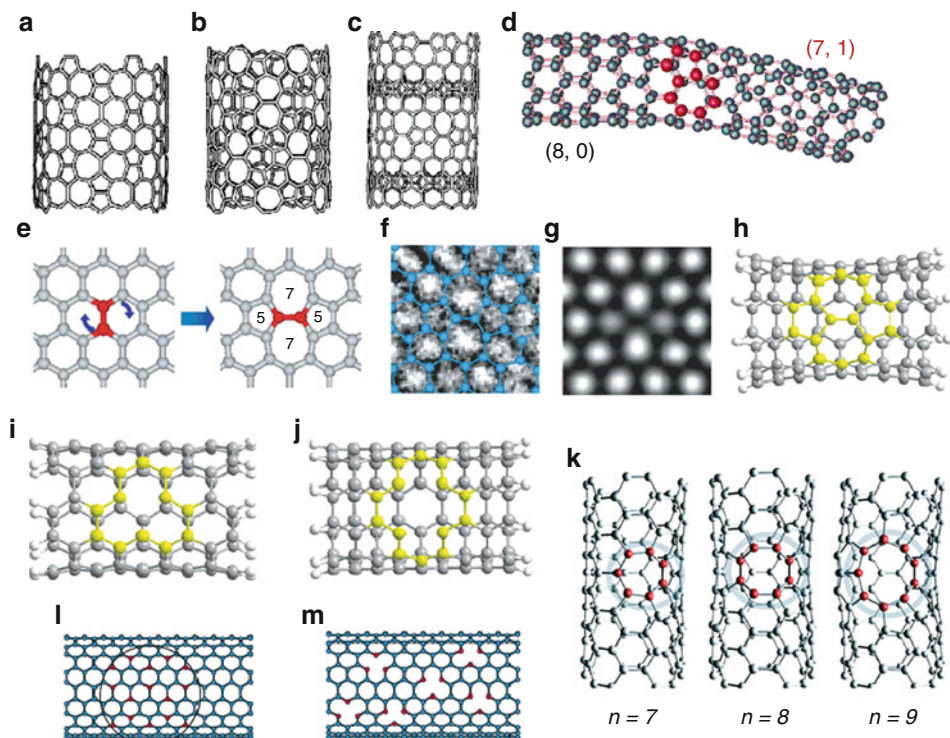
SWCNTs have stimulated vast interest due to their unique structural, mechanical, electronic, thermal, and chemical properties, and their potential applications in diversified areas. There has been enormous growth in patents related to carbon nanotubes, fuelled by predictions that the market for nanotubes will be \$9 billion by 2020. Between 1994 and 2006 it was estimated that 1,865 nanotube-related patents were issued in the USA. Still, there is a cumulative backlog of more than 4,500 patent applications relevant to CNT as reported in 2008 (MacKenzie et al. 2008).

Since there are reports of the natural abundance of fullerenes (Becker et al. 1994; Buseck et al. 1992; Heymann et al. 1994, 2003), the issue of the natural occurrence of carbon nanotubes has also attracted the attention of researchers. In 2004, Esquivel et al. published TEM images that appear to be MWCNTs isolated from a Greenland ice core (Esquivel and Murr 2004). Velasco-Santos reported the images of hollow carbon fibers from oil-well samples (Velasco-Santos et al. 2003). However, we do not have any evidence so far for naturally occurring SWCNTs.

## Various Defects in Carbon Nanotubes

Carbon nanotubes are not as perfect as they were thought to be earlier. Defects such as pentagons, heptagons, Stone–Wales defects, vacancies, ad-atoms, and dopants can occur in the nanotube during the growth or in processing and handling of the CNTs (Charlier 2002).

► *Figure 22-20* depicts different types of defects in SWCNTs. Heptagon defects are found to play a crucial role in the topology of nanotube-based molecular junctions, for making X and Y type



■ Fig. 22-20

(a) to (c) Nonchiral Haeckelite nanotubes of similar diameter; (a) Nanotube segment containing only heptagons and pentagons paired symmetrically. (b) Nanotube segment exhibiting repetitive units of three agglomerated heptagons, surrounded by alternating pentagons and hexagons. (c) Nanotube segment containing pentalene and heptalene units bound together and surrounded by six-membered rings. (d) Atomic structure of an (8,0)–(7,1) intermolecular junction; the large red balls denote the atoms forming the pentagon–heptagon pair. (e) The SW transformation leading to the 5-7-7-5 defect, generated by rotation of a C–C bond in a hexagonal network. (f) HRTEM image obtained for the atomic arrangement of the SW defect. (g) Simulated HRTEM image for the model shown in (f). (h) (5,5) armchair SWCNT with a Stone–Wales defect. (i) Ideal single vacancy (SV) defect in (5,5) armchair SWCNT. (j) Ideal double vacancy defect in (5,5) armchair SWCNT. (k) Defect (5,5) SWCNT with seven ( $n = 7$ ), eight ( $n = 8$ ), and nine ( $n = 9$ ) membered rings. (l) SWCNT doped with boron [B atoms are bonded to three C atoms; B in red spheres; C in blue spheres]. (m) SWCNT doped with nitrogen [N atoms are bonded to two C atoms; N in red spheres; C in blue spheres] (Pictures (a)–(d), (l) and (m) were reprinted with permission from ref. Charlier (2002). Copyright 2002 American Chemical Society. Pictures (e)–(g) were reprinted by permission from Macmillan Publishers Ltd.: Nature, ref. Suenaga et al. (2007), copyright 2007. Pictures (h)–(j) were reprinted with permission from ref. Yang et al. (2006a). Copyright 2006 American Chemical Society. Picture (k) was reprinted with permission from Nishidate and Hasegawa (2005). Copyright 2005 by the American Physical Society)

nanotube connections (Menon and Srivastava 1997). Long ago, theoretical studies proposed that pentagon–heptagon pair can be found in the intramolecular junctions of two SWCNT segments of different chirality (● Fig. 22-20d) (Charlier et al. 1996; Chico et al. 1996). Recent experimental study revealed that ion irradiation has induced defects in the SWCNTs and the dangling bonds produced by irradiation are rapidly saturated (Chakraborty et al. 2007).

Low-energy electron and photon also induce damage in SWCNTs (Suzuki and Kobayashi 2007). The defect formation in SWCNTs is strongly dependent on the nanotube diameter, suggesting that the curvature-induced strain energy plays crucial role in the damage (Suzuki and Kobayashi 2007). The defect formation and healing are reversible processes (Berthe et al. 2007; Suzuki and Kobayashi 2007). The defects in the SWCNTs affect their electronic, optical, and chemical properties. A competition between the defect formation and healing at room temperature or even below was reported. Raman spectroscopy, electrical measurements, and photoluminescence (PL) spectroscopy were used to examine the defect formation. However, the type of defects was not confirmed. Chemically stable topological defect, Stone–Wales defect, was ruled out because the activation energy for the defect healing was quite small ( $\sim 1$  eV). Low-energy electron and photon can break C–C bonds in SWCNTs, as it was concluded based on energetic criterion. Thus, the experimental study proposed that the defects may be a vacancy and an ad-atom (Suzuki and Kobayashi 2007).

The Stone–Wales defect is one of the important defects in carbon nanotubes. Stone and Wales showed that a dipole consisting of a pair of five- and seven-membered rings could be created by  $90^\circ$  rotation of a C–C bond in a hexagonal network (Stone and Wales 1986). Such a dipole was later called Stone–Wales defect. SW transformation is thought to play important role during the growth of carbon nanotubes. Miyamoto et al. reported an unambiguous identification of SW defect in carbon and boron nitride nanotubes using photoabsorption and vibrational spectroscopy (Miyamoto et al. 2004). Experimental vibrational frequency of  $1,962\text{ cm}^{-1}$  was reported to be a signature in identifying SW defect in carbon nanotube (Miyamoto et al. 2004). Identifying and characterizing topological defects in SWCNTs are highly challenging tasks. A powerful microscope with high resolution and high sensitivity is required for characterizing the topological defects in CNTs. Using HRTEM, the first direct image of the pentagon–heptagon pair defect (Stone–Wales defect) in the SWCNT has been reported recently (Suenaga et al. 2007). Computational studies examined the structures and defect formation energies of the SWCNTs with defects containing different sizes of rings (seven-, eight-, and nine-membered rings) (Nishidate and Hasegawa 2005), and different types of defects (Amorim et al. 2007; Dinadayalane and Leszczynski 2007a, b; Ding 2005; Wang et al. 2006; Yang et al. 2006a, b).

## Computational Approaches Used to Study Carbon Nanostructures: An Overview

---

Theory and computation play important role in understanding structures and reactivity of carbon nanosystems such as graphene, fullerenes, and carbon nanotubes. Computational nanoscience often complements the experiments and is very useful for the design of novel carbon nanomaterials as well as predicting their properties. Theory is helpful in obtaining knowledge on the mechanism of reactions and fragmentations of carbon clusters. Thus, we provide an overview of the computational approaches employed to study various carbon nanostructures in this chapter. Carbon nanostructures are very large systems. Hence, performing very high-level quantum chemical calculations is not possible even using modern supercomputers.

Many-body empirical potentials, empirical tight-binding molecular dynamics, and local density functional (LDF) methods were used to perform electronic structure calculations of carbon nanosystems including fullerenes and model CNTs in early of the last decade (Robertson et al. 1992; Zhang et al. 1993). In the mid-1990s, electronic structure calculations for large fullerenes with  $I_h$  point group were performed using Huckel approximation (Tang and Huang 1995). In the late 1990s, scientists performed geometry optimizations for large fullerenes using molecular mechanics (MM3), semiempirical methods (MNDO (Dewar and Thiel 1977), AM1 (Dewar et al. 1985), and PM3 (Stewart 1989)), and Semi-Ab Initio Model 1 (SAM1) (Dewar et al. 1993). The single-point energy calculations were affordable at that time using ab initio Hartree-Fock (HF) method in combination with small basis sets such as 3-21G and 4-31G (Slanina et al. 1997). The computing power has been tremendously increasing since 2000. Thus, currently theoreticians enjoy investigating medium size molecules using reliable quantum chemical methods and exploring carbon nanoclusters beyond molecular mechanics and semiempirical methods.

The popular B3LYP functional, which is a combination of Becke's three-parameter (B3) (Becke 1993) hybrid functional incorporating exact exchange with Lee, Yang, and Parr's (LYP) (Lee et al. 1988) correlation functional, has been employed with small and medium size basis sets like STO-3G, 3-21G, 4-31G, and 6-31G(d) for calculations on fullerenes and carbon nanotubes (Bettinger et al. 2003; Dinadayalane and Leszczynski 2007b; Feng et al. 2005; Matsuo et al. 2003; Yumura et al. 2005a, b; Zhou et al. 2004). Computational studies indicate that the B3LYP functional can yield reliable answers for the properties of carbon compounds and carbon nanostructures (Bettinger et al. 2003; Dinadayalane and Leszczynski 2007b; Feng et al. 2005; Matsuo et al. 2003; Yumura et al. 2005a, b; Zhou et al. 2004). PBE1PBE/6-311G(d) level has been used for calculating relative energies and  $^{13}\text{C}$  NMR spectra of fullerene isomers (Shao et al. 2006, 2007). The PBE1PBE functional was concluded to be very reliable DFT functional since it yields the same relative energy ordering as the high-level coupled cluster calculations for the top three isomers of  $\text{C}_{20}$  (cage, bowl, and ring isomers) (An et al. 2005).

In comparison with ab initio MP2 or CCSD methods, DFT is less time consuming and computationally feasible for large carbon nanosystems. For studying chemical reactivity in fullerenes and nanotubes, ONIOM approach is more cost-effective than treating the whole molecule with DFT. ONIOM is a hybrid methodology in which the molecule is partitioned into two or more fragments. The most important part (one fragment) of the molecule is treated with high-level method and the other parts are treated with low-level methods (Maseras and Morokuma 1995; Morokuma et al. 2006; Osuna et al. 2009). Osuna et al. have recently examined the performance of ONIOM approach by taking different density functional theory levels against the experimental results for the Diels-Alder reaction between cyclopentadiene and  $\text{C}_{60}$  (Osuna et al. 2009). Two-layer ONIOM approach ONIOM(B3LYP/6-31G(d) : AM1), where B3LYP/6-31G(d) and AM1 are used for high and low layers, has been utilized to study chemisorption of alkoxide ions with the perfect and Stone-Wales defective armchair (5,5) SWCNTs of cap-ended and H-terminated structures (Wanbayer and Ruangpornvisuti 2008).

Independent theoretical studies considered DFT methods in investigating the structures and properties of SWCNTs (Akdin et al. 2007; Amorim et al. 2007; Andzelm et al. 2006; Bettinger 2005; Dinadayalane and Leszczynski 2007a, b; Govind et al. 2008; Lu et al. 2005; Nishidate and Hasegawa 2005; Robertson et al. 1992; Wang et al. 2006; Yang et al. 2006a, b; Zhang et al. 1993). The B3LYP functional with double- $\zeta$  basis set was often employed to investigate the electronic structures of pristine and defect SWCNTs, and also the influence of defects

on functionalization of SWCNTs (Akdim et al. 2007; Andzelm et al. 2006; Dinadayalane and Leszczynski 2007b; Govind et al. 2008; Lu et al. 2005). Sometimes, more than one basis set was utilized for the exploration of defective SWCNTs and the viability of metal adsorption in the defect tubes (Yang et al. 2006b). DFT with periodic boundary condition (PBC) as implemented in Gaussian 03 program package (Frisch et al. 2003) was used to examine the reactivity of Stone–Wales defect in (5,5) and (10,0) SWCNTs (Bettinger 2005). The unit cell should be carefully chosen for the calculations involving PBC in order to simulate the tubes of infinite length. Popular DFT methods fail to provide reliable answers for  $\pi$ – $\pi$  interactions involving fullerenes and other carbon clusters (Cuesta et al. 2006; Kar et al. 2008; Shukla and Leszczynski 2009). Although calculations at the MP2 and CCSD(T) levels are required to obtain very reliable results for  $\pi$ -stacking interactions (Dinadayalane et al. 2007a; Lee et al. 2007; Sinnokrot and Sherrill 2004), they are not possible for such large systems with current computational facilities. Recently developed meta-hybrid density functional (M06-2X) has been reported to be a promising functional to calculate the binding energies for  $\pi$ – $\pi$  interactions involving large carbon nanostructures (Zhao and Truhlar 2007, 2008).

Using powerful supercomputers, performing static and dynamic calculations at high-level *ab initio* and DFT methodologies is affordable for graphene and carbon nanotubes. Very recently, density functional theory (PBE functional Perdew et al. 1996) calculations with plane-wave basis sets and periodic boundary conditions (PBCs) were employed to understand small molecule interactions with the defective graphene sheets (Jiang et al. 2009). Vienna *ab initio* simulation package (VASP) has been used in several studies to perform static and dynamic calculations (Kresse and Furthmüller 1996a, b). Theoretical calculations are helpful to understand the electronic structure of graphene sheets and SWCNTs, and their viability as ion separation systems and gas sensors (Jiang et al. 2009; Li et al. 2009b; Nishidate and Hasegawa 2005). The Stone–Wales defect formation energy for graphene and CNTs has been calculated using DFT, invoking the local density approximation to the exchange–correlation potential as implemented in VASP (Ertekin et al. 2009).

The mechanical properties of CNTs have been the interest of theoreticians for the last two decades (Avila and Lacerda 2008; Chandra et al. 2004; Dereli and Sungu 2007; Yakobson et al. 1996). An array of methods has been employed for computing the Young's modulus of MWCNTs and different types of SWCNTs (armchair, zig zag, chiral). A wide range of Young's modulus values has been reported in the literature (Avila and Lacerda 2008; Chandra et al. 2004; Dereli and Sungu 2007; Mielke et al. 2004; WenXing et al. 2004; Yakobson et al. 1996). Most of the molecular dynamics methods used so far are classical or tight binding (Avila and Lacerda 2008; Chandra et al. 2004; Dereli and Sungu 2007; WenXing et al. 2004; Yakobson et al. 1996). Quantum chemical calculations on mechanical properties of carbon nanotubes or graphene sheets are scarce since they are still highly time consuming (Mielke et al. 2004). It is not of our interest to discuss mechanical properties in this chapter since there are many papers and some of classic reviews on this subject available (Avila and Lacerda 2008; Chandra et al. 2004; Dereli and Sungu 2007; Mielke et al. 2004; WenXing et al. 2004; Yakobson et al. 1996). By using DFT and time-dependent DFT methods, one can obtain IR, Raman, NMR, and UV spectra. Recent advances in computer hardware and *ab initio* electronic structure methods have brought a substantial improvement in the capabilities of quantum chemists to predict and study the properties of carbon nanostructures. However, the application of state-of-the-art quantum chemical methods to study the structures and properties of large carbon nanoclusters (graphenes, fullerenes, and CNTs) is still a great challenge.

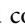


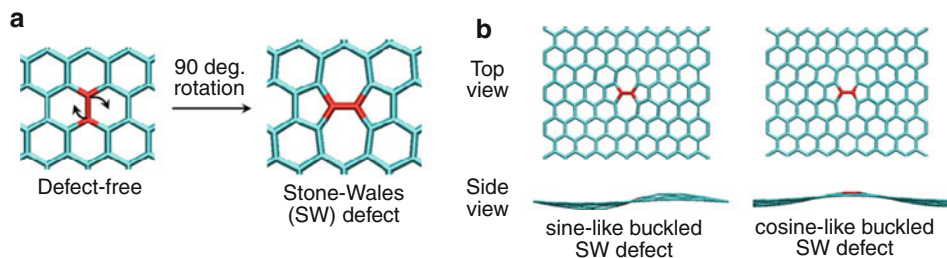
## Structural, Electronic and Chemical Properties of Graphene, Fullerenes and SWCNTs

### Graphene

The recent experimental investigation of mechanical properties of monolayer graphene reports a breaking strength of  $\sim 40$  N/m and the Young's modulus of  $\sim 1.0$  TPa (Lee et al. 2008). Graphene displays a thermal conductivity of  $\sim 5,000$  Wm $^{-1}$  K $^{-1}$  at room temperature (Balandin et al. 2008). Graphene chemistry is expected to play an important role in producing graphene-based materials. In this chapter, we outline the Stone–Wales defect in graphene, chemisorption process (covalent functionalization) on graphene, and the influence of defects on chemisorption; particular interest is given to hydrogen chemisorption. Chemical functionalization in graphene should produce new 2D systems with distinct electronic structures and different electrical, optical, and chemical properties. Chemical changes can probably be induced even locally. The first known example of hydrogenated graphene is graphane, which is a 2D hydrocarbon with one hydrogen atom attached to every site of the honeycomb lattice (Elias et al. 2009; Sofo et al. 2007).

Stone–Wales defect is expected to enhance the tendency of graphitic layers to roll up into other carbon nanostructures such as fullerenes and nanotubes. Therefore, in-depth understanding of Stone–Wales defect in graphene is required. It is known that pentagons and heptagons induce curvature in graphitic materials. In perfect graphene, the equilibrium C–C bond length is reported as 1.42 Å using PBE functional with the plane-wave code CPMD (Hutter et al.). Further details of the calculations can be obtained from the paper of Ma et al (Ma et al. 2009). The C–C bond shared by two heptagons of the SW defect in graphene is compressed to 1.32 Å using the same method. Density functional theory and quantum Monte Carlo simulations reveal that the structure of the SW defect in graphene is not simple. Ma et al. have systematically studied the polycyclic hydrocarbon size dependence on the structural distortion caused by the Stone–Wales defect formation. They considered different systems ranging from the smallest analog of SW defect, azupyrene (C<sub>16</sub>H<sub>10</sub>) to 1D tape-like structure of C<sub>50</sub>H<sub>28</sub>, and finally, to 2D planar cluster of C<sub>228</sub>H<sub>38</sub>. As known earlier, azupyrene is planar. The optimized bond length of the C–C bond at the center of azupyrene is 1.38 Å, which is longer than the corresponding C–C bond length of 1.32–1.33 Å observed for the SW defect in graphene (Ma et al. 2009).

Large carbon clusters exhibit a tendency to buckle upon the creation of SW defects. Vibrational frequency calculations of the flat graphene sheet with the Stone–Wales defect reveal that the structure is not a local minimum, but instead has two imaginary frequencies. The true minimum is a sine-like structure in which the C–C bond at the defect core is  $\sim 0.01$  Å longer than in the flat defect. Furthermore, many C–C bonds are slightly elongated in the buckled structure compared to the flat defect structure. The cosine-like SW defect structure was obtained as a transition state connecting to sine-like SW defect structure. The optimized structures of sine-like and cosine-like SW defect graphenes are depicted in  Fig. 22-21. Vibrational frequencies also revealed that the maximum phonon frequencies corresponding to the stretch of the rotated C–C bond for the flat and buckled SW structure are 1,880 and 1,774 cm $^{-1}$ , respectively. The corresponding frequency computed for perfect graphene is 1,612 cm $^{-1}$  (Ma et al. 2009). Theoretical study pointed out that for a graphene sheet of C<sub>228</sub>H<sub>38</sub> containing a SW defect, the sine-like buckled structure becomes more stable (by  $\sim 10$  meV) than the flat SW defect (Ma et al. 2009).



■ Fig. 22-21

(a) Stone–Wales transformation by 90° rotation of C–C bond in graphene sheet; (b) top and side views of sine-like and cosine-like buckled SW defect graphene sheets (The pictures were reprinted with permission from Ma et al. (2009). Copyright 2009 by the American Physical Society)

## Hydrogenation of Graphene with and Without Defects

Chemical modification of graphene has been less explored (Geim and Novoselov 2007). Attachment of atomic hydrogen to each site of the graphene lattice to create graphane is an elegant idea (Sofa et al. 2007). As a result, the hybridization of carbon atoms changes from  $sp^2$  to  $sp^3$ , thus removing the conducting p-bands and opening energy gap (Boukhvalov et al. 2008; Sofa et al. 2007). In experiment, the fully hydrogenated graphene called “graphane” was produced by exposing graphene to hydrogen plasma discharge. Raman spectroscopy and transmission electron microscopy confirmed the reversible hydrogenation of single-layer graphene (Elias et al. 2009).

Li et al. have investigated the structural and electronic properties of graphane using DFT PW91 functional with plane-wave basis set applying periodic boundary conditions as implemented in VASP (Li et al. 2009b). Computations revealed that hydrogenation of graphene nanoribbon is experimentally viable and the electronic properties of graphane are completely different from graphene nanoribbons. Figure 22-22 depicts the structures of graphane. Two types of graphane nanoribbons (zigzag and armchair edge) can be obtained by cutting the optimized graphane layer. The edge carbon atoms were all saturated with H atoms to avoid the effects of dangling bonds. The bond lengths of edge C–C and C–H bonds are almost as the inner C–C (1.52 Å) and C–H (1.11 Å) bonds. The calculated C–C bond length is similar to the bond length of 1.53 Å in diamond ( $sp^3$  carbon atoms) and is longer than 1.42 Å characteristic of  $sp^2$  carbon in graphene. Both spin-unpolarized and spin-polarized computations yielded same energy for ground state graphane nanoribbons (Li et al. 2009b).

Figure 22-23a shows that computed band gap decreases monotonically with increasing ribbon width for both zigzag and armchair nanoribbons. Graphane nanoribbons are semiconductors. The formation energy increases with increasing ribbon width (Figure 22-23b) irrespective of the type, indicating that narrow ribbons are more likely to form than the wider ribbons (Li et al. 2009b). Sofa et al. investigated the structures, formation energies, and vibrational frequencies of graphane using DFT with plane-wave basis set (Sofa et al. 2007). They found two favorable conformations of graphane: chair-like conformer with the hydrogen atoms alternating on both sides of the plane and the boat-like conformer with the hydrogen atoms alternating in pairs. Chair conformer has one type of C–C bond (1.52 Å), while boat conformer



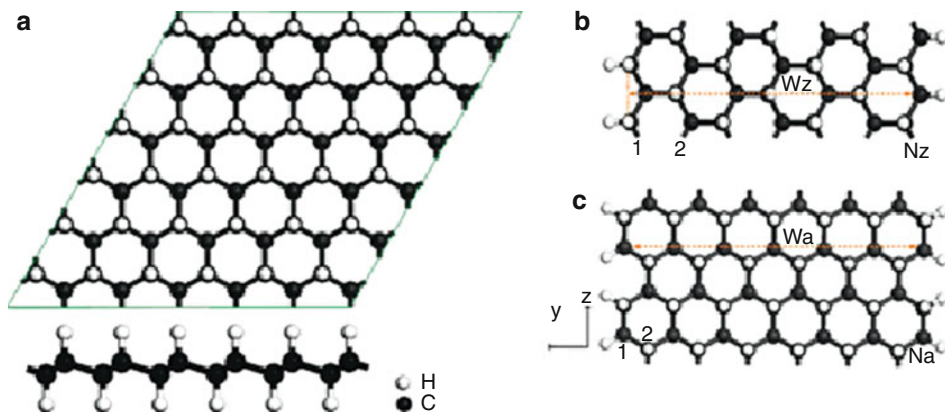


Fig. 22-22

(a) Top (*upper*) and side (*lower*) view of a 2D graphene layer. Geometric structures of the (b) 7-zigzag and (c) 13-armchair graphene nanoribbons. The ribbons are periodic along the  $z$ -direction. The ribbon widths are denoted by  $W_z$  and  $W_a$ , respectively (Reprinted with permission from ref. Li et al. (2009b). Copyright 2009 American Chemical Society)

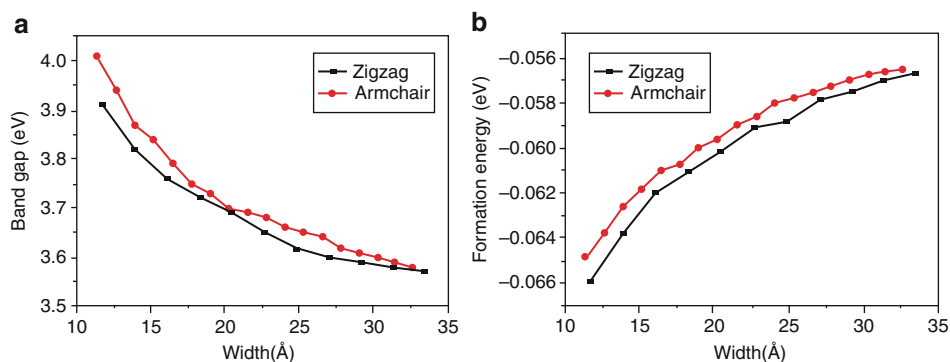
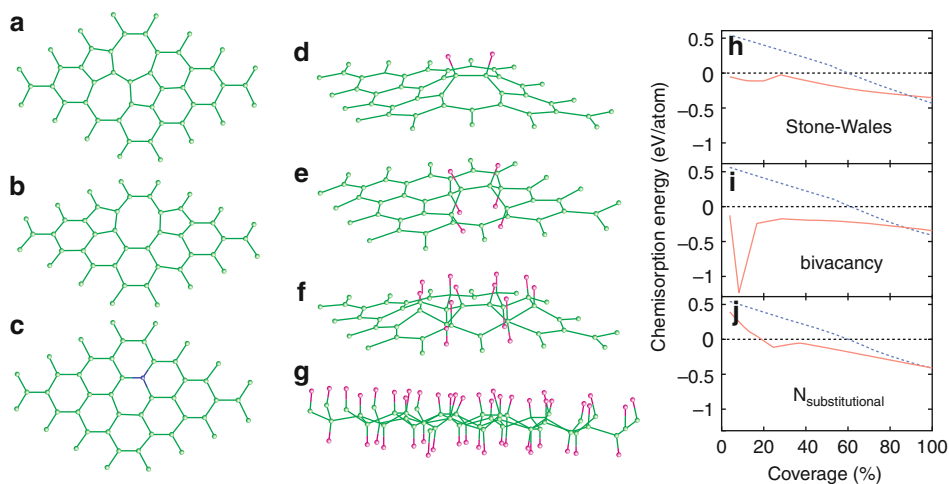


Fig. 22-23

Variation of the band gap (a) and the formation energy (b) of zigzag ( $6 \leq N_z \leq 16$ ) and armchair ( $10 \leq N_a \leq 27$ ) graphene nanoribbons as a function of ribbon width.  $N$  is the number of zigzag chains for a zigzag ribbon and the number of dimer lines along the ribbon direction for an armchair ribbon (Reprinted with permission from ref. Li et al. (2009b). Copyright 2009 American Chemical Society)

possesses two different types of C–C bonds (bond lengths of 1.52 Å and 1.56 Å). The boat conformer is less stable than the chair conformer due to the repulsion of the two hydrogen atoms bonded to first neighbor carbon atoms on the same side of the sheet. This repulsion results in slightly longer C–C bonds in boat conformer. Calculated C–H bond stretching frequencies are 3,026 and 2,919  $\text{cm}^{-1}$  for the boat and chair conformers respectively. These C–H stretching modes are IR active and they should be useful in characterizing these two types of conformers of graphane (Sofa et al. 2007).

Using density functional calculations, Boukhvalov and Katsnelson have studied hydrogenation of graphene sheets with defects such as Stone–Wales (SW), bivacancies, nitrogen substitution impurities, and zigzag edges (Boukhvalov and Katsnelson 2008). They performed calculations for chemisorptions of hydrogen atoms on the defects in the graphene from low to high coverage. The optimized geometries of the graphene supercells with various types of defects as well as their hydrogenated structures are depicted in ► Fig. 22-24, which also displays the computed chemisorption energy as the function of coverage for the graphene containing different defects. The chemisorption energy of a single hydrogen atom to the defect-free graphene was given as 1.5 eV, while those of 0.30 eV for SW defects, 0.93 eV for bivacancies, and 0.36 eV for substitution impurities of nitrogen in graphene were reported. This indicates the significant influence of defects on single hydrogen atom chemisorption energy in graphene. The calculated chemisorption energy for different nonequivalent carbon atoms of the graphene containing SW defect reveals that the chemisorption energy for the entire area surrounding the SW defect is lower compared to the perfect graphene. Further, the defects also decrease the chemisorption energy of two hydrogen atoms at adjacent positions compared to the defect-free graphene. It was reported that, for the complete coverage, the binding energy is smaller for the hydrogen chemisorption of graphene with defects than the perfect graphene. Thus, completely hydrogenated graphene is less stable with defects than without them (Boukhvalov and Katsnelson 2008).



► Fig. 22-24

Optimized geometric structures for graphene supercell containing (a) the Stone–Wales defect, (b) a bivacancy, and (c) a nitrogen substitution impurity. Optimized structures for the Stone–Wales (SW) defect functionalized by (d) 2, (e) 6, (f) 14 hydrogen atoms, and (g) completely covered by hydrogen. Green circles represent carbon atoms, violet circles represent hydrogen atoms, and blue circles represent nitrogen atoms. Hydrogen atom chemisorption energy per atom as a function of coverage for a graphene sheet containing (h) a Stone–Wales (SW) defect, (i) a bivacancy, and (j) a nitrogen substitution impurity. The blue dashed line represents the results for the ideal infinite graphene sheet (Reprinted with permission from ref. Boukhvalov and Katsnelson (2008). Copyright 2008 American Chemical Society)

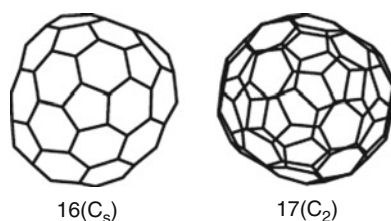
Graphenes with various kinds of defects may have different types of properties and applications. Therefore, obtaining knowledge on graphenes with defects is important. DFT calculations showed only physisorption of water molecule with perfect graphene, while the vacancy defect greatly assists the dissociative chemisorption of water molecules in the graphene (Cabrera-Sanfeliix and Darling 2007; Kostov et al. 2005). There can be many possible reaction pathways for the dissociation of water molecule over defective sites in the graphene (Kostov et al. 2005). Computational studies provide evidence that defects such as Stone–Wales and vacancy strongly influence the chemisorption of functional groups in the graphene (Boukhvalov and Katsnelson 2008; Boukhvalov et al. 2008; Cabrera-Sanfeliix and Darling 2007; Kostov et al. 2005).

## Fullerenes

### Computational Studies of Fullerene Isomers

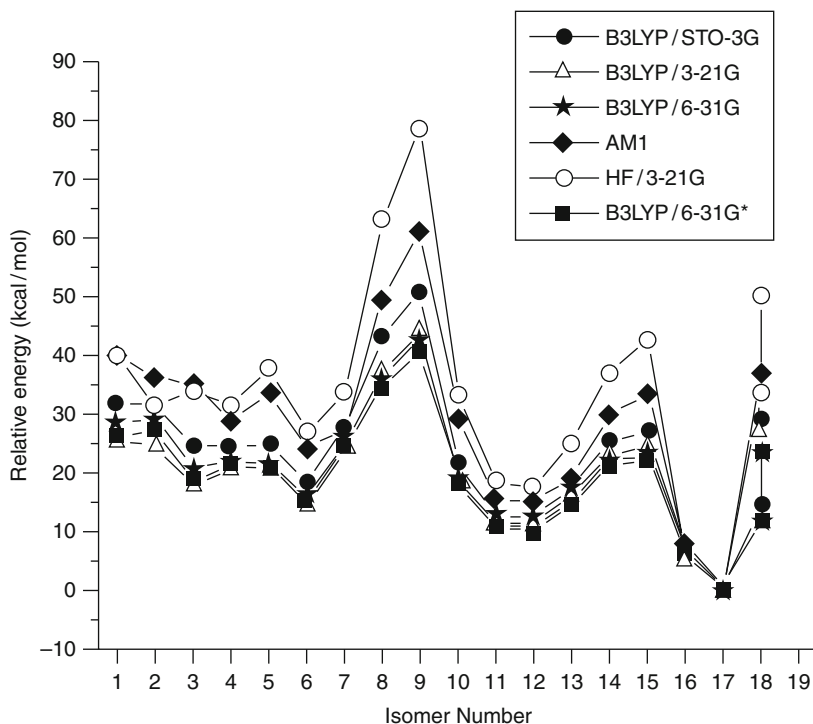
Computational methods were employed to systematically search and study the low-lying isomeric structures of fullerenes, and such thorough investigations have been useful to predict the best candidates for the lowest-energy structures of higher fullerenes because of the growing experimental interest (Shao et al. 2006, 2007; Slanina et al. 2000a, b; Sun 2003; Sun and Kertesz 2002; Zhao et al. 2004a, b). Fullerene  $C_{86}$  has 19 possible isomers obeying IPR and all of these isomers were studied by Sun and Kertesz using B3LYP functional with different basis sets (Sun and Kertesz 2002). Among 19 isomers, the isomer **17** with  $C_2$  symmetry is the most stable followed by isomer **16** with  $C_s$  symmetry and these two isomers are shown in [Fig. 22-25](#). It should be noted that these two isomers were experimentally observed. At the B3LYP/6-31G level, isomer **16** was predicted to be about 6 kcal/mol less stable than isomer **17**, albeit the former has slightly larger HOMO–LUMO gap than the latter. The variation of relative stability at different theoretical levels for all 19 IPR satisfying isomers of  $C_{86}$  is depicted in [Fig. 22-26](#). The relative stabilities were calculated with respect to the lowest-energy isomer (**17**). The HF/3-21G level and the semiempirical AM1 Hamiltonian overestimate the relative energies compared to the density functional theory levels (Sun and Kertesz 2002).

Experimental study identified two isomers of fullerene  $C_{86}$  and characterized them using  $^{13}C$  NMR spectroscopy (Miyake et al. 2000). Based on the experimental NMR spectra,  $C_2$  and  $C_s$  point groups were assigned for the two isomers, but there are more than one  $C_2$  and  $C_s$



■ Fig. 22-25

Two experimentally observed IPR isomers of fullerene  $C_{86}$ . Their point groups are given in parentheses (Reprinted with permission from ref. Sun and Kertesz (2002). Copyright 2002 Elsevier)

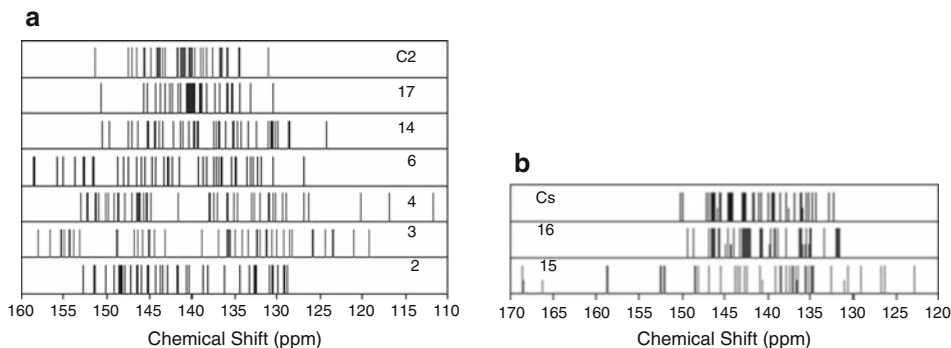


■ Fig. 22-26

The relative energy of IPR satisfying isomers of  $C_{86}$  at various levels of theory. Isomers 1, 5, 7, 11, 12, and 13 have  $C_1$  symmetry. Isomers 2, 3, 4, 6, 14, and 17 possess  $C_2$  point group. Isomers 9 and 10 have  $C_{2v}$  point group. Isomers 8, 15, and 16 have  $C_s$  point group. Isomers 18 and 19 possess  $C_3$  and  $D_3$  point groups respectively (The data was taken from ref. Sun and Kertesz (2002))

isomers. Theoretical calculations play crucial role in identifying the correct structure by comparing theoretical and experimental  $^{13}\text{C}$  NMR spectra. Sun and Kertesz calculated the  $^{13}\text{C}$  NMR chemical shifts for all of the 19 IPR isomers of  $C_{86}$ , except isomer 8. Theoretical  $^{13}\text{C}$  NMR spectra complement the experimental spectra as evidenced from Fig. 22-27. Computational study revealed that isomer 17 has high thermodynamic and kinetic stability among the six IPR isomers of  $C_{86}$  possessing  $C_2$  point group. The computed NMR spectrum of isomer 17 supports the results of experimental spectrum. Among the  $C_s$  isomers, the second most stable isomer 16 has large HOMO–LUMO gap (Sun and Kertesz 2002). Isomers 6, 10, 11, 12, 13, and 18 were predicted to have relative energies less than 20 kcal/mol and moderate HOMO–LUMO gap, thus indicating the possibility of experimental realization (Sun and Kertesz 2002).

Okada and Saito proposed the number of extractable fullerenes among the IPR-satisfying isomers of fullerenes from  $C_{60}$  to  $C_{90}$ . They found that  $C_{84}$  is unique since the number of preferable isomers is more than for other fullerenes and this was attributed to the abundant production of  $C_{84}$  after  $C_{60}$  and  $C_{70}$ . Okada and Saito computationally studied all 24 IPR-satisfying isomers of  $C_{84}$  (Okada and Saito 1996). A complete set of 187 isomers that obey IPR of fullerene  $C_{96}$  was systematically investigated using various theoretical methods including



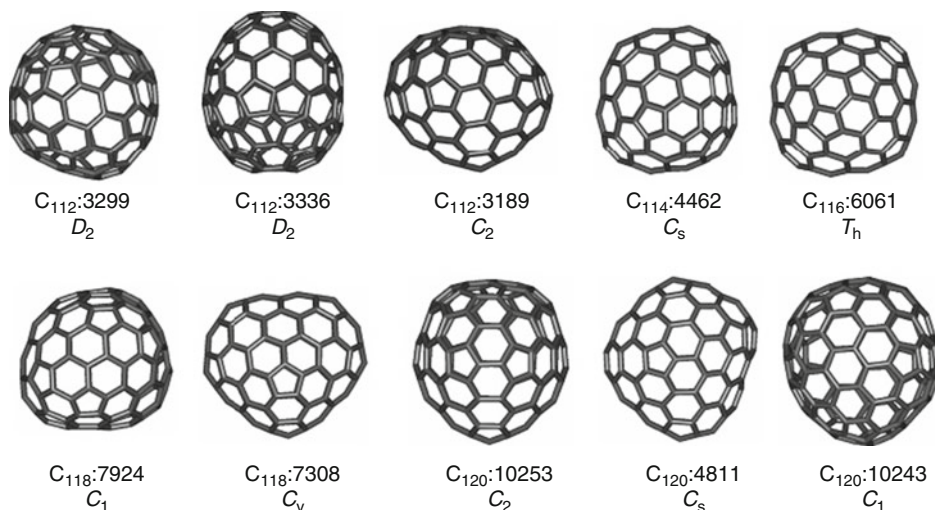
■ Fig. 22-27

Experimental and theoretical  $^{13}\text{C}$  NMR spectra of (a)  $\text{C}_2$  isomers of fullerene  $\text{C}_{86}$ . (b)  $\text{C}_s$  isomers of fullerene  $\text{C}_{86}$ . Theoretical spectra are labeled by isomer number and experimental spectrum labeled by symmetry (Reprinted with permission from ref. Sun and Kertesz (2002). Copyright 2002 Elsevier)

molecular mechanics (MM3), semiempirical (AM1, MNDO, and PM3) and quantum mechanical (HF/4-31G and B3LYP/6-31G) methods. All of the theoretical levels unequivocally predicted that isomer **183** with  $D_2$  point group is the lowest-energy one. The relative energies for some of the isomers were reported to be quite method-sensitive and varied dramatically with different methods. The computational study highlighted the importance of the entropy effect in examining the relative stability of IPR-obeying isomers of fullerene  $\text{C}_{96}$  (Zhao et al. 2004a). A large set of 450 IPR isomers of  $\text{C}_{100}$  has been explored using the above-mentioned semiempirical and molecular mechanics (MM3) methods. Systematic theoretical calculations predicted the isomer with  $D_2$  point group (isomer **449**) as the lowest energy by all of the methods employed (Zhao et al. 2004b).

Recently, Shao et al. have searched the lowest-energy isomer of the fullerenes  $\text{C}_{38}$  to  $\text{C}_{80}$  and  $\text{C}_{112}$  to  $\text{C}_{120}$ . For the first set ( $\text{C}_{38}$  to  $\text{C}_{80}$ ), all IPR and all non-IPR isomers were considered, and only IPR-satisfying isomers were considered for the second set of fullerenes ( $\text{C}_{112}$  to  $\text{C}_{120}$ ) (Shao et al. 2007). Thus, a large set of molecules was taken for optimizations at the semiempirical density functional-based tight-binding (DFTB) method and the single-point energy calculations at the DFT (Shao et al. 2007). It is known that the fullerene with large HOMO–LUMO gap and high-symmetry is not necessarily the lowest-energy structure. The decreasing trend of HOMO–LUMO gap was reported with increasing the fullerene size (Shao et al. 2006, 2007). An unexpected manner of pentagonal adjacency was observed in the low-lying isomers in the series of fullerenes  $\text{C}_{38}$  to  $\text{C}_{80}$  (Shao et al. 2007).

In a comprehensive computational study, Shao et al. identified 20 isomers as the best candidates for the lowest-energy structures. Among the 20 isomers, 10 isomers with relative energies less than 1 kcal/mol are depicted in ● Fig. 22-28 (Shao et al. 2007). Computational study proposed that these 10 isomers can be observed experimentally. The  $^{13}\text{C}$  NMR chemical shifts for these 10 isomers were calculated. Theoretical study predicted that  $\text{C}_{116}$ :**6061** can be more easily isolated and characterized in the laboratory than other higher fullerenes from  $\text{C}_{112}$  to  $\text{C}_{120}$  (Shao et al. 2007). In a different study, Shao et al. proposed the seven best candidates of the lowest-energy isomers for the fullerenes  $\text{C}_{98}$  to  $\text{C}_{110}$  based on the systematic study using DFTB



■ Fig. 22-28

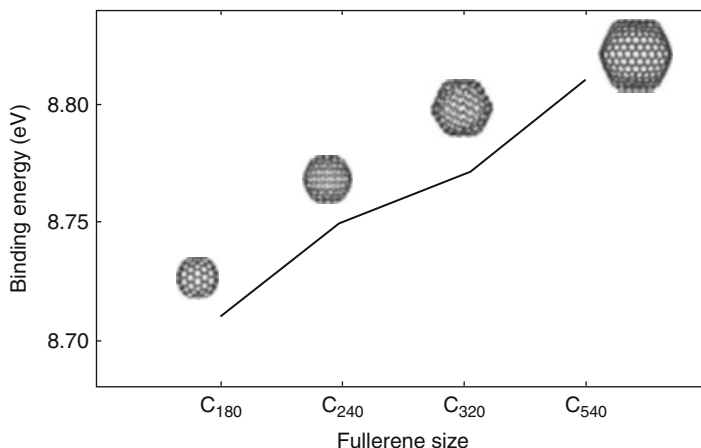
Best candidates for the lowest-energy structure of higher fullerenes ( $C_{112}$  to  $C_{120}$ ). The isomer number and point group are given (Reprinted with permission from ref. Shao et al. (2007). Copyright 2007 American Chemical Society)

and DFT methods. They pointed out that  $C_{102}$  ( $C_1$ : 603) and  $C_{108}$  ( $D_2$ : 1771) isomers can be easily synthesized (Shao et al. 2006).

Fullerene  $C_{50}$  and  $C_{50}Cl_{10}$  were computationally studied using B3LYP/6-31G(d) level due to the experimental report of the latter compound (Lu et al. 2004). The computational study thoroughly explored the structures, relative energies, HOMO, LUMO energies, and HOMO–LUMO gap for low-lying isomers of  $C_{50}$  and its anions. The computed IR, Raman,  $^{13}C$  NMR, and UV-Vis spectra of the  $C_{50}Cl_{10}$  with  $D_{5h}$  symmetry showed very good agreement with the reported experimental data. The pentagon–pentagon fusions were found to be the active sites of addition reactions in both  $D_3$  and  $D_{5h}$  symmetric isomers of fullerene  $C_{50}$ . It was observed that HOMO and LUMO coefficients of  $C_{50}$  ( $D_{5h}$ ) are distributed around the equatorial pentagon–pentagon fusion sites. This was given as a reason for the binding of Cl atoms around the equatorial pentagon–pentagon fusion sites of  $C_{50}$  yielded  $C_{50}Cl_{10}$  (Lu et al. 2004).

## Giant Fullerenes

Giant fullerenes have been the subject of theoretical interests (Calaminici et al. 2009; Dulap and Zope 2006; Dunlap et al. 1991; Gueorguiev et al. 2004; Lopez-Urias et al. 2003; Zope et al. 2008). Very recently, the structures and stabilities of the giant fullerenes  $C_{180}$ ,  $C_{240}$ ,  $C_{320}$ , and  $C_{540}$  have been investigated using high-level density functional theory calculations (Calaminici et al. 2009). The results of the uncorrected binding energy (in eV) per carbon atom for the giant fullerenes obtained using the VWN functional are depicted in ► Fig. 22-29. The inclusion of the basis set superposition error (BSSE) decreases the calculated binding energies but does not alter the trend. The increasing trend of binding energy indicates that the large fullerenes



■ Fig. 22-29

Binding energy (in eV) for C<sub>180</sub>, C<sub>240</sub>, C<sub>320</sub>, and C<sub>540</sub> fullerenes. The calculations have been performed with the VWN functional in combination with DZVP basis sets (Reprinted with permission from ref. Calaminici et al. (2009). Copyright 2009 American Chemical Society)

become more and more stable with increasing size. Fullerene C<sub>540</sub> has a similar binding energy to diamond, giving the hope that such giant fullerenes could be prepared. However, the binding energy per carbon atom of the fullerene, C<sub>540</sub>, is considerably lower than that of graphene (Calaminici et al. 2009). Gueorguiev et al. performed the calculations for giant fullerenes using semiclassical approximation LR-LCAO (Linear Response model in the framework of the Linear Combination of Atomic Orbitals). They reported the decreasing trend of HOMO–LUMO gaps (except C<sub>20</sub>) and the considerably large increase of the static polarizability as increasing the size of the fullerene cage (► Fig. 22-30) (Gueorguiev et al. 2004). The static dipole polarizability per atom in C<sub>2160</sub> is three times larger than that in C<sub>60</sub> (Dunlap et al. 1991).

### Local Strain in Curved Polycyclic Systems: POAV and Pyramidalization Angle

Fullerenes experience large strain energy because of their spherical shape. The curvature-induced pyramidalization of the carbon atoms of fullerenes weakens the  $\pi$ -conjugation. The curved  $\pi$ -conjugation in carbon networks of fullerenes has not only  $\pi$ -character but also substantial s-character. The  $\pi$ -orbital axis vector (POAV) analysis developed by Haddon is useful in measuring the local curvature of the nonplanar conjugated organic molecules, fullerenes, and SWCNTs (Haddon 1993; Haddon and Scott 1986). In general, the sp<sup>2</sup>-hybridized carbon atom prefers to be in the planar arrangement, but it is pyramidalized in fullerenes. The local strain of carbon framework in fullerenes and SWCNTs is reflected in the pyramidalization angle  $\theta_p$  at the carbon atoms (Niyogi et al. 2002). The pyramidalization angle ( $\theta_p$ ) equals to the difference between the  $\pi$ -orbital axis vector (POAV) and the normal right angle 90°: Thus,  $\theta_p = (\theta_{\sigma\pi} - 90^\circ)$ , where the  $\theta_{\sigma\pi}$  is the angle between the  $\pi$ -orbital of the conjugated atom and the  $\sigma$ -orbital of the surrounding atoms. As shown in ► Fig. 22-31, the pyramidalization angle



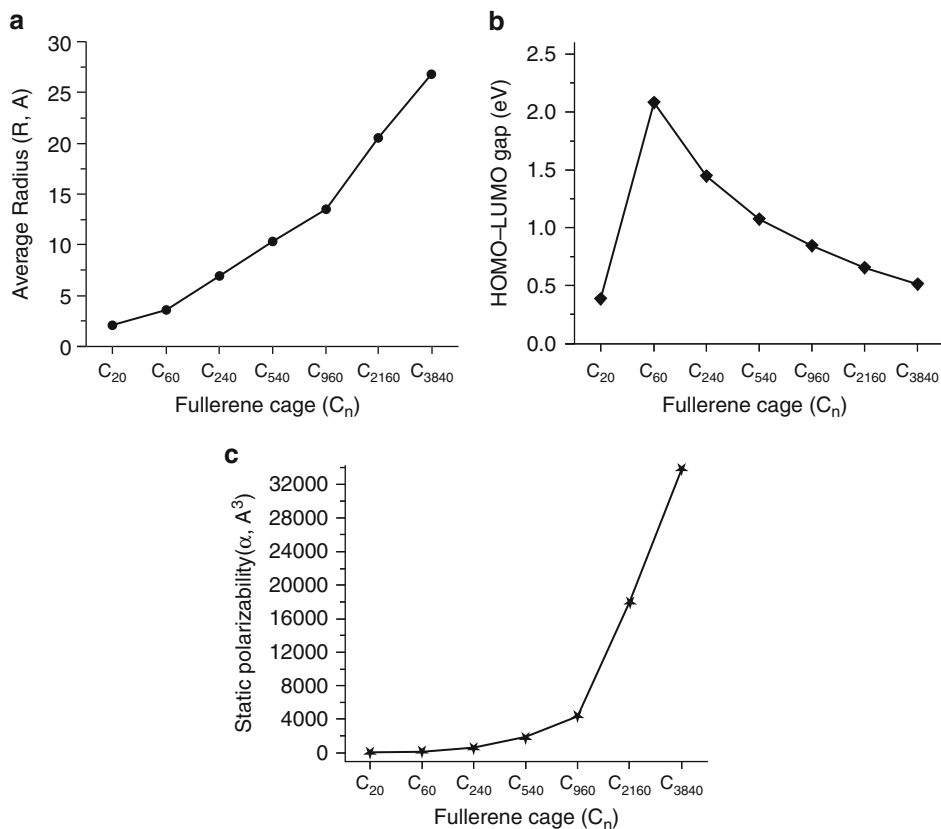


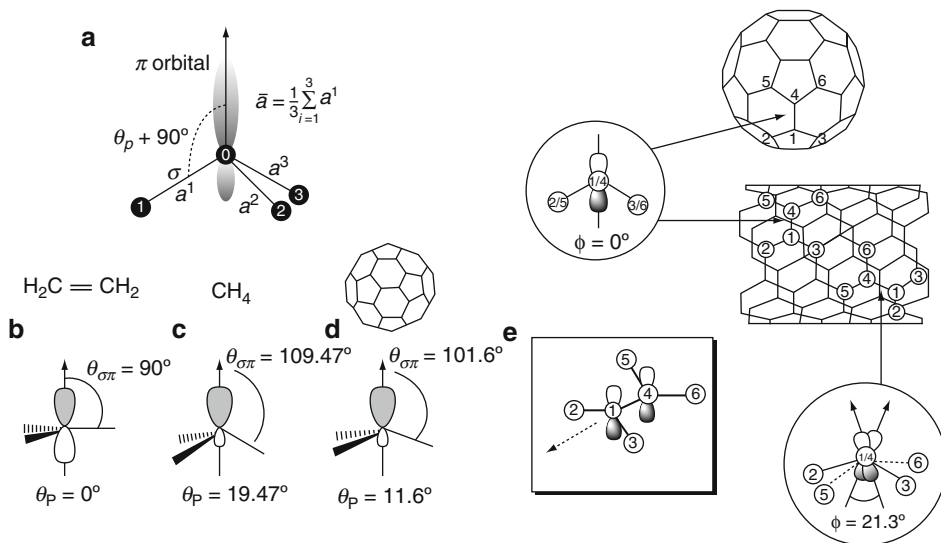
Fig. 22-30

The variation of (a) radius ( $R$ , Å), (b) HOMO–LUMO gap (eV), and (c) static polarizability as increasing the size of the fullerene cage ( $C_{20}$ ,  $C_{60}$ ,  $C_{240}$ ,  $C_{540}$ ,  $C_{960}$ ,  $C_{2160}$ , and  $C_{3840}$ ) (The data for the plots was taken from ref Guerguiev et al. (2004))

is 0 and  $19.47^\circ$  for a planar  $sp^2$ -hybridized carbon and a tetrahedral  $sp^3$ -hybridized carbon, respectively. All carbon atoms in the icosahedral  $C_{60}$  have the same  $\theta_{\sigma\pi}$  of  $\sim 11.6^\circ$ .

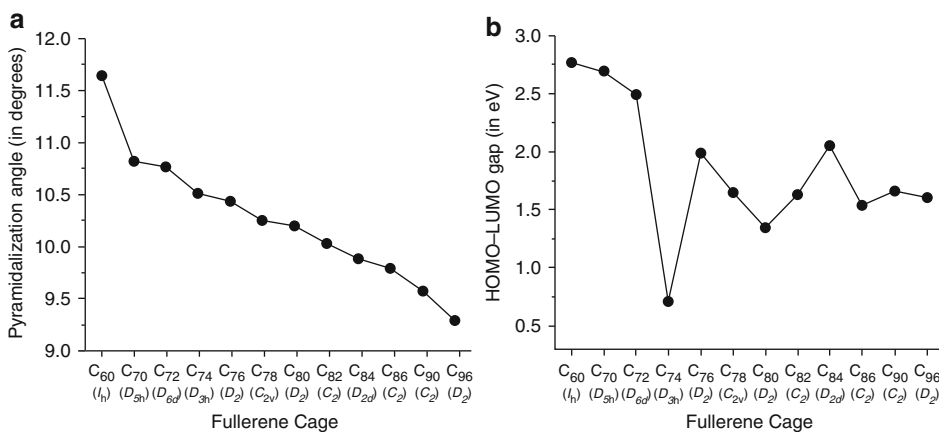
Pyramidalization angle of a carbon atom in fullerenes and SWCNTs is helpful in predicting the chemical reactivity (Akdim et al. 2007; Bettinger 2005; Dinadayalane and Leszczynski 2007a, b; Lu and Chen 2005; Lu et al. 2005). The larger pyramidalization angle of carbon atom indicates the higher reactivity toward addition reactions in the curved systems of fullerenes and SWCNTs. The curvature-induced pyramidalization and the  $\pi$ -orbital misalignment cause local strain in SWCNTs (Fig. 22-32). Hence, carbon atoms of SWCNTs are more reactive than that of a perfect graphene sheet (Niyogi et al. 2002; Park et al. 2003). Cyranski et al. studied the structures and energetics of the 12 lowest-energy isomers of neutral, closed-shell IPR fullerenes  $C_{60}$ – $C_{96}$  using B3LYP/6-31G(d) level. They obtained the decreasing values of pyramidalization angles, while no regular trend was obtained for HOMO–LUMO gaps with increasing size of fullerenes (Fig. 22-32) (Cyranski et al. 2004).





■ Fig. 22-31

(a) Pyramidalization angle ( $\theta_p$ ) is defined by the angle between the  $\pi$  orbital and  $\sigma$  bond  $-90^\circ$  so that  $\theta_p = 0^\circ$  for a graphene sheet and  $\theta_p = 19.47^\circ$  for  $\text{sp}^3$ -hybridized carbon. For practical reasons, we take the average of three  $\theta_p$  values. (b)  $\theta_p$  for a perfect planar  $\text{sp}^2$ -hybridized carbon atom (e.g., in  $\text{C}_2\text{H}_4$ ), (c)  $\theta_p$  for a perfect tetrahedral  $\text{sp}^3$ -hybridized carbon atom (e.g.,  $\text{CH}_4$ ), (d)  $\theta_p$  for a nonplanar  $\text{sp}^2$ -hybridized carbon atom (e.g., C atom in  $\text{C}_{60}$  or SWCNT). (e) The  $\pi$ -orbital misalignment angle ( $\phi$ ) along the C1–C4 bond in the (5,5) SWCNT and the fullerene  $\text{C}_{60}$  (Pictures were reprinted with permission from refs. Lu and Chen (2005), Niyogi et al. (2002), and Park et al. (2003). Copyright 2002, 2003, and 2005 American Chemical Society)




■ Fig. 22-32

(a) Variation of pyramidalization angle for the carbon atom of the most stable IPR fullerene as increasing the size of fullerene size. (b) Variation of HOMO–LUMO gap for the most stable IPR fullerene as increasing the size of fullerene size. The point groups are given in the parentheses. The values for these graphs were taken from ref. Cyranski et al. (2004)

Decachloro-derivative of  $C_{50}$  fullerene has been synthesized and experimental characterization confirmed the existence of  $C_{50}$  cage. Two  $C_{20}$  caps and five  $C_2$  units around the equator are present in the  $C_{50}$  core of  $C_{50}Cl_{10}$  (Xie et al. 2004). The calculated pyramidalization angle for the carbon atoms of the  $C_{20}$  caps of fullerene  $C_{50}$  ranges from 10.7 to 12.88°, which are comparable to that of  $C_{60}$  (11.68°). However, a large pyramidalization angle (15.58°) is obtained for the equatorial C atoms (pentagon–pentagon fusion). Such large value was attributed to high reactivity of those carbon atoms in addition reactions to form exohedral adducts (Chen 2004; Lu et al. 2004). Such structural features were reasoned for the instability of a bare  $C_{50}$  cage and the stability of  $C_{50}Cl_{10}$  (Chen 2004).

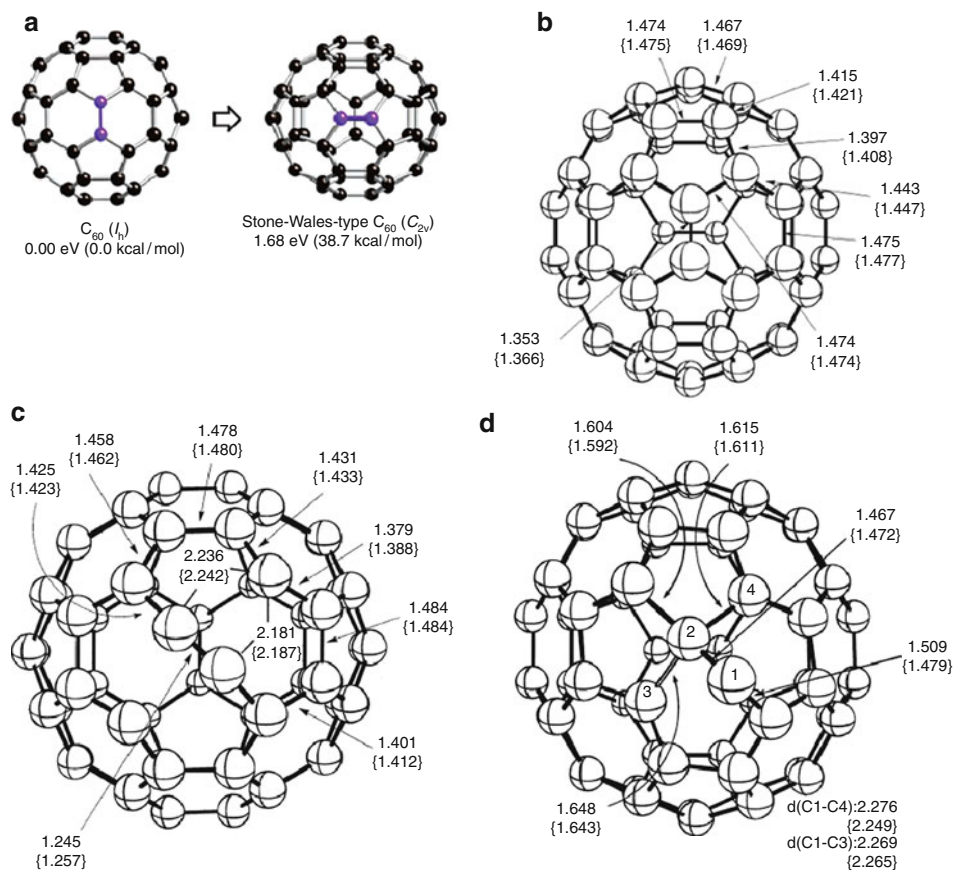
### Stone–Wales Defect in $C_{60}$

Fullerene isomers are likely to interconvert through Stone–Wales transformation (Stone and Wales 1986; Troyanov and Tamm 2009). Very recently, experimental study has reported that the chlorine functionalized  $D_2-C_{76}$  IPR isomer transformed to non-IPR isomer and this transformation was proposed to include seven single Stone–Wales rearrangements (Ioffe et al. 2009). Computational chemists strived to understand the energy barriers for the Stone–Wales transformation and the possible mechanisms involved in this rearrangement, particularly considering the  $C_{60}$  fullerene (Bettinger et al. 2003; Eggen et al. 1996; Yumura et al. 2007). Stone–Wales transformation is a thermally forbidden rearrangement by following the orbital symmetry considerations of Woodward and Hoffmann (Woodward and Hoffmann 1969). The icosahedral  $C_{60}$  fullerene (Buckminsterfullerene) gives an isomer of  $C_{60}$  with  $C_{2v}$  point group that violates the isolated pentagon rule. Two different pathways namely, concerted and stepwise pathways and two different (symmetric and asymmetric) transition states were identified theoretically for the Stone–Wales transformation in  $C_{60}$  fullerene. The  $C_{60} - C_{2v}$  isomer, which is a Stone–Wales type defect structure with two adjacent pentagons, was reported to be less stable by 33.9–38.7 kcal/mol (1.47–1.68 eV) than the Buckminsterfullerene using various density functional theory levels (Yumura et al. 2007).

Bettinger et al. listed the C–C bond lengths of  $C_{60}$  ( $I_h$ ) and the activation barrier for the Stone–Wales defect transformation through different transition states at various levels of theory (Bettinger et al. 2003). Computed geometries of Buckminsterfullerene at different levels showed shorter [6,6] C–C bond length than the [5,6] C–C bond length, in consistent with experimental results (Bettinger et al. 2003).  Figure 22-33 depicts the concerted  $C_2$  symmetric transition state and asymmetric transition state involved in SW transformation of  $C_{60} - I_h$  to  $C_{60} - C_{2v}$ . The intrinsic reaction coordinate calculations by Bettinger et al. support the concerted pathway rather than stepwise pathway for the SW transformation in the  $C_{60}$  fullerene. Based on the computed activation energies, both concerted and stepwise pathways are highly competitive (Bettinger et al. 2003). The rigorous computational study of SW transformation in Buckminsterfullerene revealed that the empirical schemes such as Tersoff–Brenner potentials and density functional–based tight-binding (DF-TB) underestimate the barrier heights, and semiempirical AM1 appears to be promising for such investigations (Bettinger et al. 2003).

### Computational Studies on Vacancy Defects in Fullerene $C_{60}$

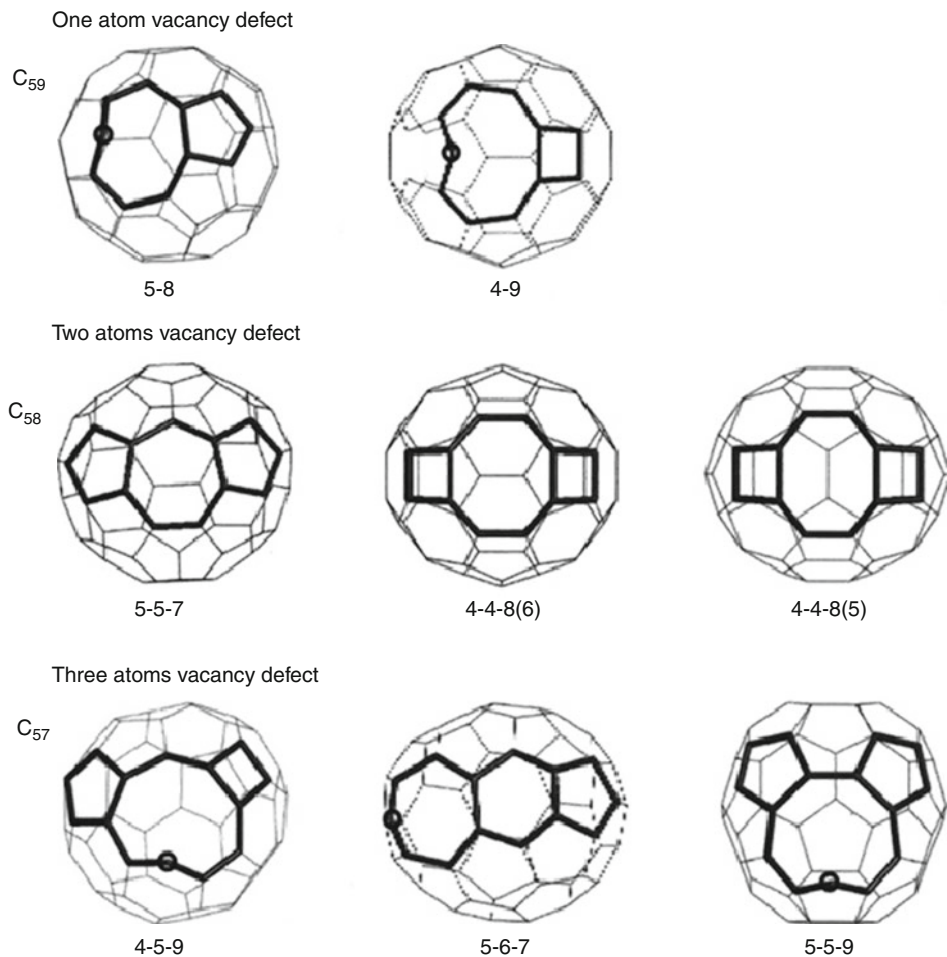
Vacancy defects in fullerene  $C_{60}$  were studied using quantum chemical methods (Hu and Ruckenstein 2003; Hu and Ruckenstein 2004; Lee and Han 2004). They were generated by



■ Fig. 22-33

(a) Buckminsterfullerene to  $C_{60} - C_{2v}$  with Stone–Wales defect generated by the  $90^\circ$  rotation of the C–C bond in blue color of  $C_{60} (I_h)$ . (b) Optimized structure of the  $C_{2v}$  symmetry isomer. (c) Structure of the  $C_2$  symmetry transition state for the concerted Stone–Wales transformation pathway. (d) Structure of the asymmetric transition state between carbene intermediate and  $C_{60} - C_{2v}$  isomer. Bond lengths were obtained at the B3LYP/6-31G\* and PBE/6-31G\* (in curly brackets) levels of theory and are given in Å (Pictures were reprinted with permission from ref. Bettinger et al. (2003) and Yumura et al. (2007). Copyright 2003 and 2007 American Chemical Society)

removal of 1–4 carbon atoms in  $C_{60}$  as shown in ► Figs. 22-34 and ► 22-35. Different modes are possible to remove carbon atoms from  $C_{60}$  to generate vacancy defects; hence, different sizes of rings (4, 7, 8, and nine-membered rings) were produced by removing carbon atoms in  $C_{60}$ . Removing one, two, three, and four adjacent carbon atoms from the  $C_{60}$  cluster generates two, three, three, and six different isomers for the  $C_{59}$ ,  $C_{58}$ ,  $C_{57}$ , and  $C_{56}$  clusters, respectively (Hu and Ruckenstein 2004; Lee and Han 2004). The odd-numbered clusters have unsaturated carbon, which favors being located in a six-membered ring rather than a five-membered ring. Two atom vacancies give structure with seven- and eight-membered rings, whereas one atom vacancy gives the structure with nine-membered ring. Four atom vacancies provide the most

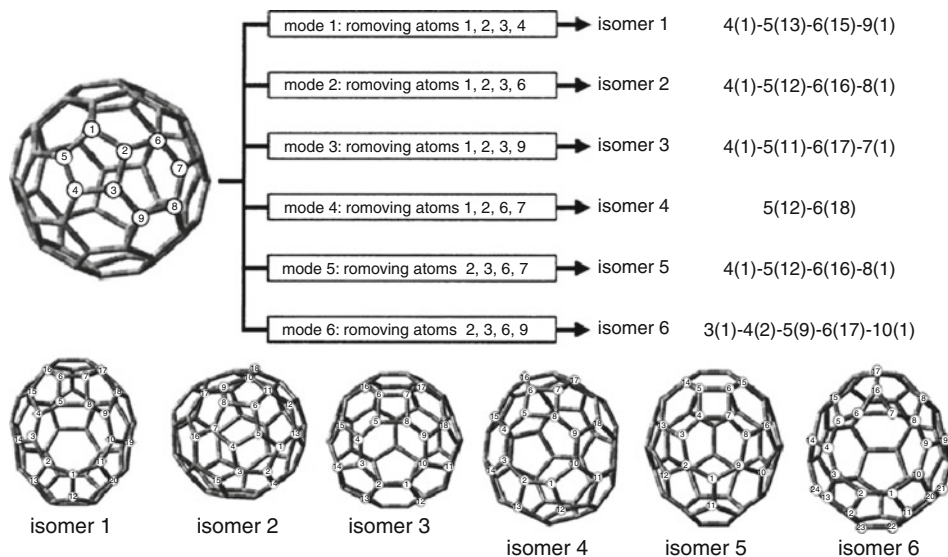


■ Fig. 22-34

B3LYP/6-31G(d) optimized structures of  $C_{59}$ ,  $C_{58}$ , and  $C_{57}$  clusters. Description indicates *highlighted rings*. "A-B" denotes A- and B-membered ring. Circle denotes an unsaturated atom (Reprinted with permission from Lee and Han (2004). Copyright 2004, American Institute of Physics)

stable structure with only five- and six-membered rings. Thus, increasing the number of vacancies need not increase the size of the hole (Hu and Ruckenstein 2003; Hu and Ruckenstein 2004).

The singlet structures are more stable than the triplet ones for  $C_{58}$  cluster, while the reverse is true in case of  $C_{57}$  clusters. The reported stabilization energy per atom at the B3LYP/6-311G(d)//B3LYP/6-31G(d) level is 2.18, 1.49, and 3.10 kcal/mol for the  $C_{59}$ ,  $C_{58}$ , and  $C_{57}$ , respectively. Quantum chemical calculations provide relationship between structure and stability of the defect fullerene clusters (Hu and Ruckenstein 2003; Hu and Ruckenstein 2004; Lee and Han 2004). In case of removal of four adjacent carbon atoms in  $C_{60}$ , additional five-membered rings are formed in geometry optimizations (e.g., isomer 1 in Fig. 22-35). The isomer 4 has only five- and six-membered rings (12 five-membered rings and 18 six-membered



■ Fig. 22-35

Different modes to generate isomers of  $C_{60}$  with four vacancies by removing four adjacent atoms from the perfect  $C_{60}$  structure. Structures of isomers 1–6 of defect  $C_{60}$  with four vacancies. The ring size and the number of rings (in parentheses) for each isomer is given (taken from ref. Hu and Ruckenstein 2004); for example, isomer 1 – 4(1)-5(13)-6(15)-9(1) means one 4-membered, thirteen 5-membered, fifteen 6-membered, one 9-membered rings (Reprinted with permission from Hu and Ruckenstein (2004). Copyright 2004, American Institute of Physics)

rings) and was predicted to be the most stable among the isomers depicted in [Fig. 22-35](#). The stability energy for the isomers generated by removing four carbon atoms has the following sequence: Isomer 4 > isomer 3 > isomer 2 > isomer 5 > isomer 6 > isomer 1. All defect clusters have lower stability energy per atom than  $C_{60}$ . The removal of carbon atoms from  $C_{60}$  increases the HOMO and decreases the LUMO energy. Consequently, the defect structures exhibit lower HOMO–LUMO gap compared to  $C_{60}$ . No relationship was obtained between the stability energy per carbon atom and the HOMO–LUMO gap for the defect carbon clusters of  $C_{60}$  (Hu and Ruckenstein 2003).

## Computational Studies of Single-Walled Carbon Nanotubes

Computational chemists have explored the structures, electronic properties, and reactivities of SWCNTs of varying length and diameter (Bettinger 2004; Dinadayalane and Leszczynski 2009; Dinadayalane et al. 2007b; Galano 2006; Kaczmarek et al. 2007; Matsuo et al. 2003; Niyogi et al. 2002; Yang et al. 2006c). They also tried to understand the influence of different defects on these properties at reliable theoretical methods within the limitations of hardware and software (Akdim et al. 2007; Andzelm et al. 2006; Bettinger 2005; Dinadayalane and Leszczynski 2007a, b; Govind et al. 2008; Lu et al. 2005; Nishidate and Hasegawa 2005; Wanbayer and Ruangpornvisuti 2008; Wang et al. 2006; Yang et al. 2006a, b). A series of finite-length hydrogen

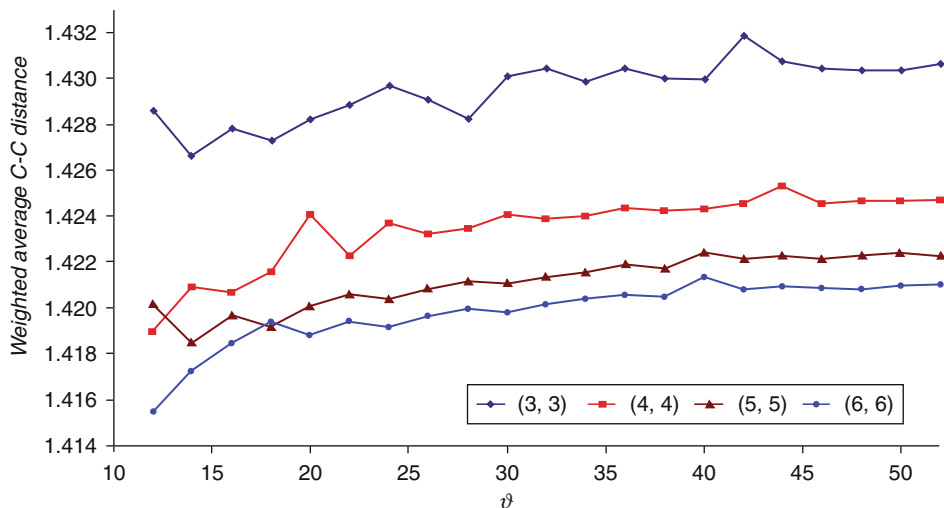


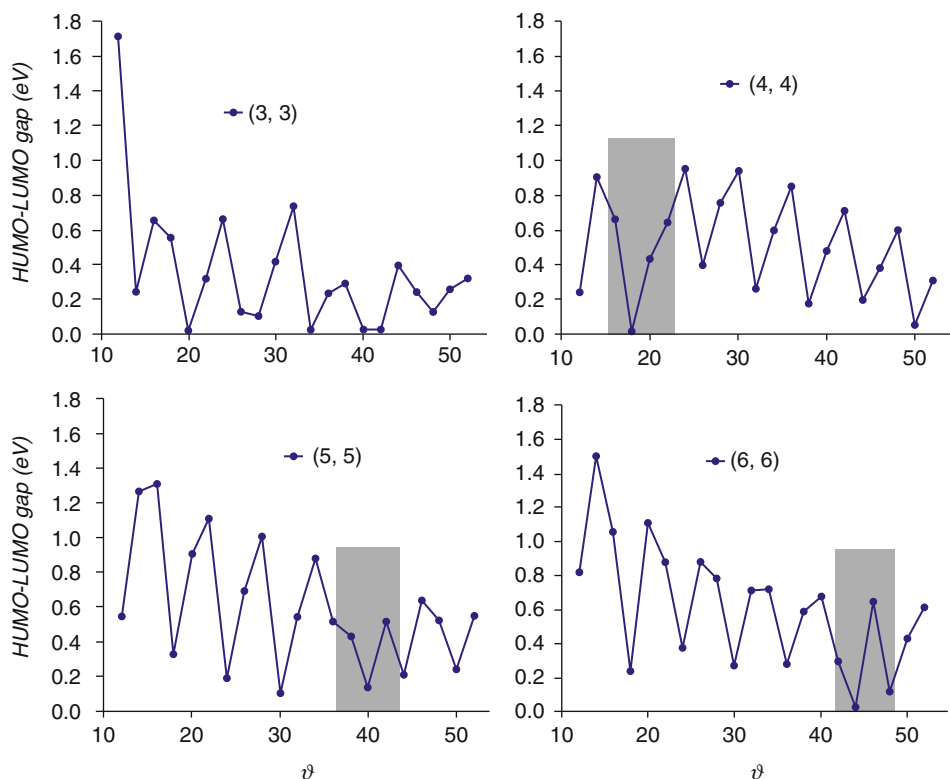
Fig. 22-36

Calculated weighted average values of the C–C distance as a function of the tube length for armchair  $(n,n)$  SWCNTs (Reprinted with permission from ref. Galano 2006. Copyright 2006 Elsevier)

terminated armchair SWCNTs have been computationally studied to obtain knowledge on the influence of diameter and length on the structural and electronic properties (Galano 2006). The optimized armchair  $(n,n)$  SWCNTs possess  $D_{nh}$  and  $D_{nd}$  point groups for  $\vartheta/2$  even and odd, respectively. The different lengths of the armchair SWCNTs have the general formula  $C_{(2n)k}H_{4n}$  with  $k = \vartheta/2$ . Galano considered (3,3), (4,4), (5,5), and (6,6) armchair SWCNTs with  $k$  of 6–26 (i.e., from 6 to 26 carbon atom layers) (Galano 2006). There are two types of bonds in the perfect  $(n,n)$  armchair SWCNTs: one is perpendicular to the tube axis ( $r_I$ ) and another one is nearly parallel to the tube axis ( $r_{II}$ ). The maximum difference between  $r_I$  and  $r_{II}$  was obtained in case of the narrow diameter (3,3) tube. Galano found that the influence of diameter on the weighted average values of the C–C distances is larger than the influence of the tube length (Fig. 22-36) (Galano 2006).

The frontier molecular orbitals (HOMO and LUMO) play important role in SWCNTs since they are helpful in predicting number of ground state properties of molecules. According to Huckel theory, the  $(n,n)$  armchair SWCNTs should be metallic (Saito et al. 1998), but the finite-length armchair SWCNTs are semiconducting with a finite size of the HOMO–LUMO gap (Cioslowski et al. 2002). The computed HOMO–LUMO gaps for (3,3) to (6,6) SWCNTs were reported to be lower than the corresponding value for fullerene  $C_{60}$ . The HOMO–LUMO gap oscillates as the tube length increases for all of these armchair tubes (Fig. 22-37). The behavior of narrow diameter (3,3) tube is different from other armchair SWCNTs (Galano 2006).

Matsuo et al. classified the structures of finite-length armchair (5,5) and (6,6) SWCNTs as Kekule, incomplete Clar, and complete Clar networks depending on the exact length of the tubes. The (5,5) and (6,6) SWCNTs were elongated layer by layer of 10 and 12 carbon atoms, respectively (Matsuo et al. 2003). The local aromaticity of different lengths of the tubes was evaluated using the NICS (Nucleus Independent Chemical Shift) calculations (GIAO-SCF/6-31G\*\*/HF/6-31G\* level). Matsuo et al. pointed out that the geometry of  $C_{50}H_{10}$  is similar to



■ Fig. 22-37

Variations of HOMO–LUMO gaps as increasing the tube length for the armchair SWCNTs. There is no periodicity in (3,3) tube and the shaded region indicated the broken periodicity in other tubes (Reprinted with permission from ref. Galano (2006). Copyright 2006 Elsevier)

the equatorial belt of the fullerene  $C_{70}$ . Bond lengths of optimized structures exhibit oscillation with increase in tube length for both (5,5) and (6,6) armchair SWCNTs. The schematic structures of Kekule, incomplete Clar and complete Clar networks for (5,5) and (6,6) SWCNTs are depicted in [Fig. 22-38](#) along with the NICS values of dissimilar benzenoid rings. The energy of frontier molecular orbitals and HOMO–LUMO gap also oscillate as the length of the nanotube increases ([Fig. 22-39](#)). The Kekule structure shows larger HOMO–LUMO gap than other two. It was reported that the band gap will eventually disappear at a certain tube length (Matsuo et al. 2003).

The pyramidalization angle ( $\theta_p$ ) and  $\pi$ -orbital misalignment angles are useful to gauge the reactivity of the carbon atom sites of SWCNTs. The end caps of SWCNTs resemble fullerene hemisphere, thus the end caps are expected to be more reactive than sidewalls irrespective of the diameter of the SWCNTs. Carbon atoms in fullerene are more distorted than those in the corresponding SWCNTs. For example, the carbon atom of (10,10) armchair SWCNT has the pyramidalization angle ( $\theta_p$ ) of about  $3.0^\circ$ , while the carbon atom of the fullerene with corresponding radius (fullerene  $C_{240}$ ) has the  $\theta_p$  of about  $9.7^\circ$  (the hemisphere of fullerene  $C_{240}$  can be capped to (10,10) SWCNT) (Niyogi et al. 2002). Chen et al. mentioned that the pyramidalization angle of the C atoms of the sidewalls of SWCNTs is smaller compared to that



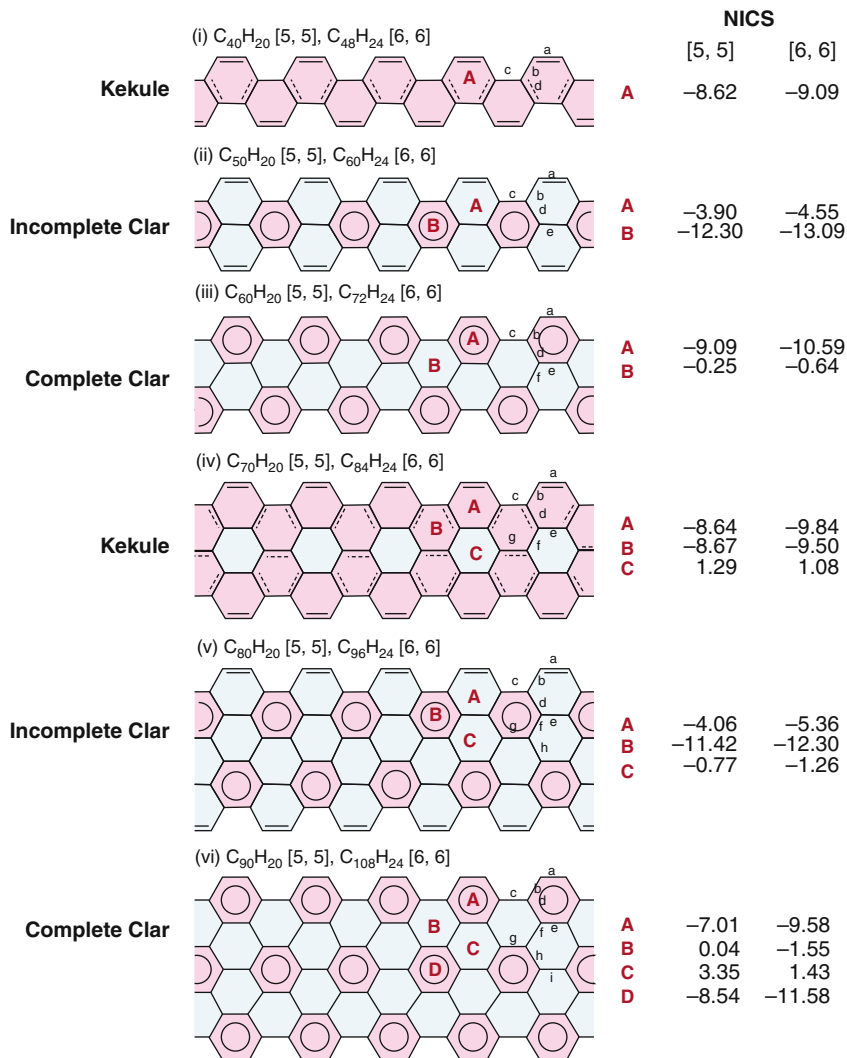
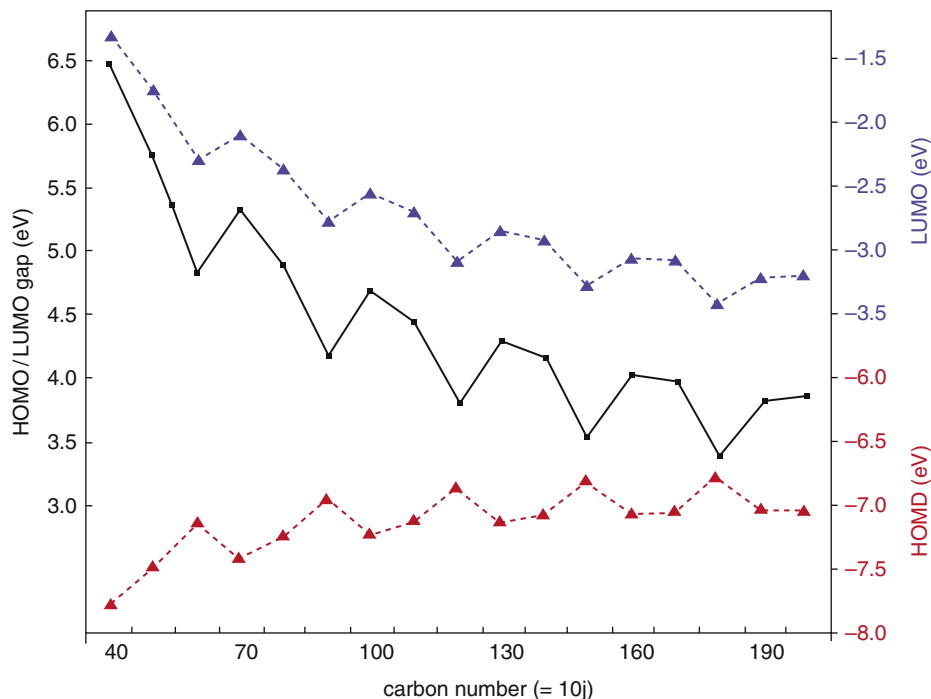


Fig. 22-38

Schematic structures and color-coded NICS maps of finite length (5,5) and (6,6) SWCNTs. Hydrogen atoms are omitted for clarity. Chemical bonds are schematically represented by using single bond (solid single line; bond length  $>1.43$  Å), double bond (solid double line; bond length  $<1.38$  Å), single bond halfway to double bond (solid-dashed line;  $1.43$  Å  $>$  bond length  $>1.38$  Å), and Clar structure (i.e., ideal benzene). NICS coding: red, aromatic  $< -4.5$ ; blue, nonaromatic  $> -4.5$  (Reprinted with permission from ref. Matsuo et al. (2003). Copyright 2003 American Chemical Society)

of the fullerenes of same radius. As a consequence, the covalent functionalization to SWCNTs is less favorable compared to fullerenes of same radius (Chen et al. 2003). The  $\pi$ -orbital misalignment is likely to be a main source of strain in the SWCNTs. For both armchair and zigzag SWCNTs, the pyramidalization angle and the  $\pi$ -orbital misalignment angle decrease with increase in diameter of the tube (► Fig. 22-40) (Niyogi et al. 2002).



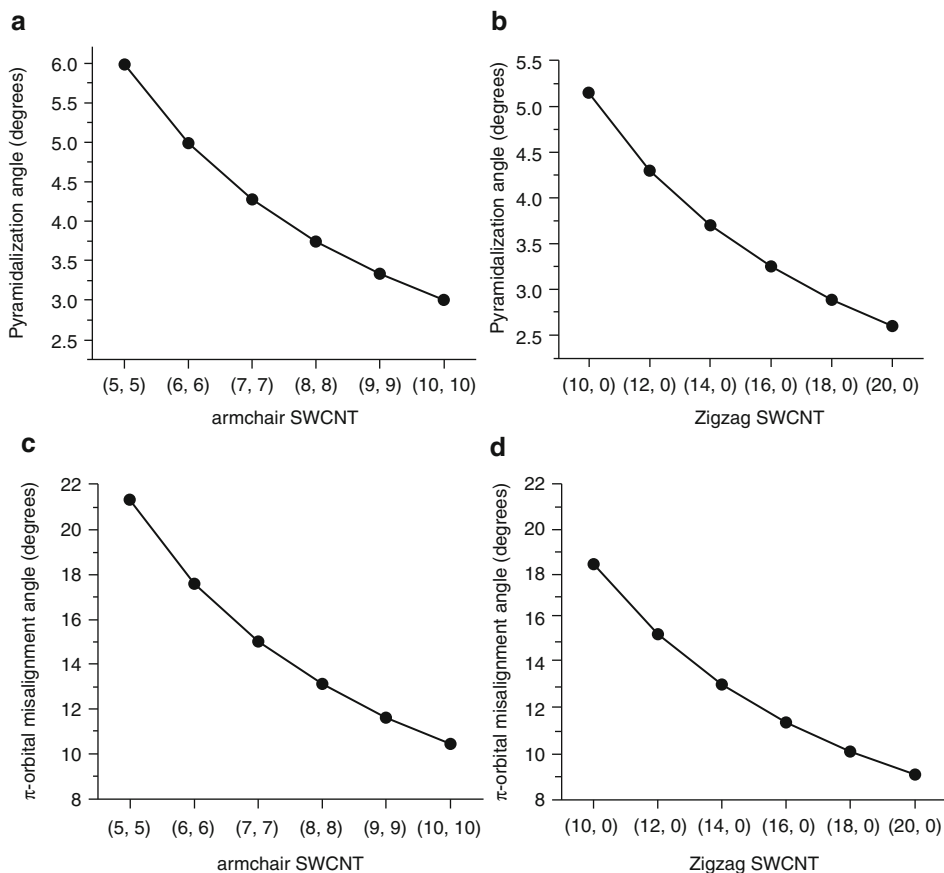


■ Fig. 22-39

Variation of HOMO, LUMO energies and HOMO–LUMO gap with increase in tube length of (5,5) armchair SWCNT ( $C_{10j}H_{20}$ ) (Reprinted with permission from ref. Matsuo et al. (2003). Copyright 2003 American Chemical Society)

## Covalent Functionalization of SWCNTs: H and F Atom Chemisorptions

The covalent functionalization of SWCNTs, which modifies the properties of the tubes, has become a challenging field of research for the past few years (Bettinger 2006; Hirsch 2002; Niyogi et al. 2002; Vostrowsky and Hirsch 2004). Functionalization of tubes is considered to be promising to produce carbon nanotube–based materials for selective applications (Bettinger 2006; Cho et al. 2008; Denis et al. 2009). The binding of hydrogen with SWCNTs has generated lot of experimental and theoretical interests due to their potential application in hydrogen storage (Dillon et al. 1997; Dinadayalane and Leszczynski 2009; Dinadayalane et al. 2007b; Kaczmarek et al. 2007; Nikitin et al. 2005; Ormsby and King 2007; Yang et al. 2006c; Zhang et al. 2006). Scientists have tried to obtain knowledge on the mechanism of hydrogen adsorption in SWCNTs. They attempt to design and achieve the viable nanotube-based hydrogen storage material to meet the Department of Energy (DOE) target of 6.5 wt% at ambient temperature (Dillon et al. 1997; Dinadayalane and Leszczynski 2009; Dinadayalane et al. 2007b; Kaczmarek et al. 2007; Nikitin et al. 2005; Ormsby and King 2007; Yang et al. 2006c; Zhang et al. 2006). The experimental investigations reported the chemisorption of H atoms on the surface of SWCNTs as promising approach to meet DOE's target of hydrogen storage (Nikitin et al. 2005; Zhang et al. 2006). Our group as well as others have investigated the chemisorption of low occupancy of

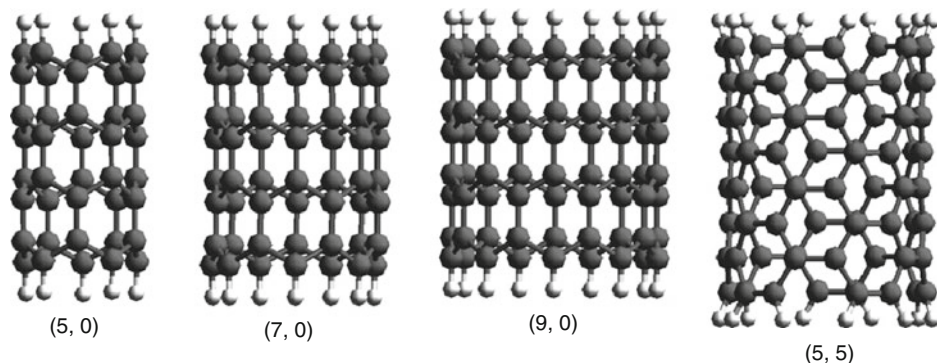


■ Fig. 22-40

The change of pyramidalization angle (a,b) at the carbon atom and the  $\pi$ -orbital misalignment angle (c,d) between two adjacent carbon atoms of armchair (a,c) and zigzag (b,d) SWNTs. The  $\pi$ -orbital misalignment angle is zero for the carbon atoms of the circumferential bond in armchair tube and axial bond in zigzag tube (The data was taken from ref. Niyogi et al. (2002))

hydrogen atoms on the surface of SWCNTs (Dinadayalane and Leszczynski 2009; Dinadayalane et al. 2007b; Kaczmarek et al. 2007; Ormsby and King 2007; Yang et al. 2006c). The covalent functionalization of SWCNTs by H atoms is a hot topic. Thus, we discuss the quantum chemical studies of the hydrogen chemisorption on different types of SWCNTs.

Yang et al. studied, using DFT and ONIOM calculations, the chemisorption of atomic hydrogen(s) on the open-ended finite-size (5,0), (7,0), and (9,0) zigzag and (5,5) armchair SWCNTs (● Fig. 22-41) (Yang et al. 2006c). They compared the binding energies obtained for nanotubes with results of the model graphene sheet in order to examine the effect of curvature. It was reported that the chemisorptions of H atoms to the exterior wall of the SWCNTs are more favorable than the interior walls. The H chemisorption has strong dependence of tube diameter and helicity or chirality in both interior (endohedral) and exterior (exohedral) addition. In case of single H atom addition, the binding energy (chemisorption energy), which is



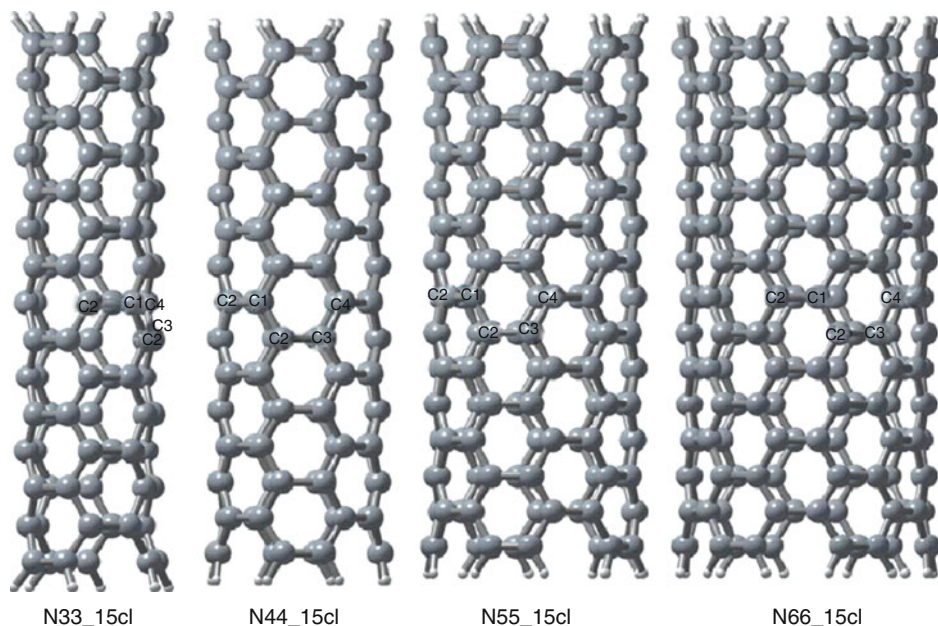
■ Fig. 22-41

Finite-size small carbon nanotube models of (5,0), (7,0), and (9,0) zigzag and (5,5) armchair SWCNTs considered for low occupancy of H chemisorptions (Reprinted with permission from ref. Yang et al. (2006c). Copyright 2006 American Chemical Society)

the reaction energy for H chemisorption with SWCNT, decreases with increase in tube diameter. In the chemisorption of two hydrogen atoms in the interior and exterior walls of (5,0) and (7,0) SWCNTs, two hydrogen atoms prefer to bind at alternate positions rather than adjacent positions. This was attributed to the crowding effect when two hydrogen atoms occupy in the adjacent positions. In case of (5,0) SWCNT, chemisorption of ten hydrogen atoms (33% coverage) decreases the magnitude of chemisorption energy, which is further decreased by an increase the coverage to 50%. Similar to the situation in zigzag SWCNTs, two hydrogen atoms prefer to attach at alternate carbon sites rather than adjacent sites in the graphene sheet. Significantly large deviation of chemisorption energy between the graphene sheet and zigzag SWCNTs (H atoms chemisorbed on the exterior wall) was reported. It was found that the chemisorptions of H atoms with small diameter SWCNTs are much more favorable than with the graphene sheet (Yang et al. 2006c).

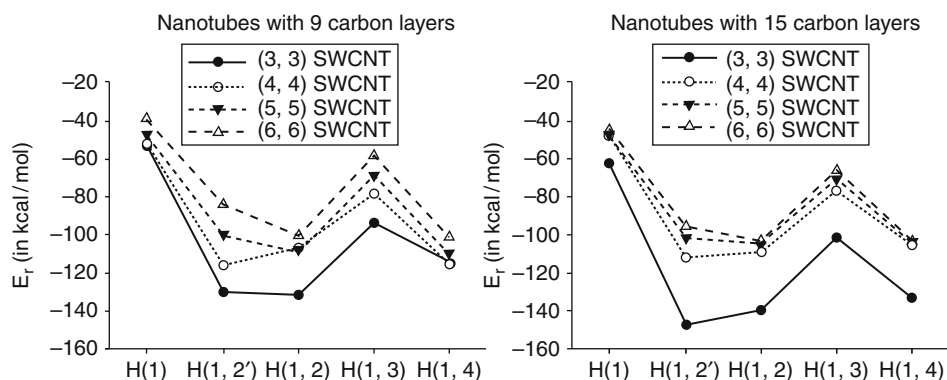
We have recently investigated a single hydrogen chemisorption, the preference of the positions (i.e., 1-2, 1-2', 1-3, or 1-4 positions) for the chemisorption of two hydrogen atoms considering (3,3), (4,4), (5,5), and (6,6) armchair SWCNTs of 9 and 15 carbon atom layers (Dinadayalane et al. 2007b). The SWCNTs of 15 carbon layers considered in our study are shown in ● Fig. 22-42. The addition of H atoms on the outer wall of SWCNT (exohedral addition) has only been considered in our study. We performed DFT calculations using B3LYP/6-31G(d) level for full geometry optimizations. The finite-length SWCNTs were capped with hydrogen atoms to avoid dangling bonds. The reaction energies for hydrogen chemisorption ( $E_r$ ) on the external surface of SWCNTs have been calculated using the formula  $E_r = E_{SWCNT+nH} - E_{SWCNT} - nE_H$ , where  $E_{SWCNT+nH}$  denotes the total energy of hydrogen chemisorbed nanotube; n represents the number of hydrogen atoms chemisorbed;  $E_{SWCNT}$  and  $E_H$  correspond to the energies of pristine nanotube and the hydrogen atom, respectively. The reaction energy  $E_r$  can also be considered as hydrogen chemisorption energy. The chemisorption of hydrogen is an exothermic process if the value of  $E_r$  is negative (Dinadayalane et al. 2007b).

We have observed the rupture of circumferential C1-C2' bond when two hydrogen atoms were chemisorbed in case of (3,3) SWCNT of 15 carbon layers. As shown in ● Fig. 22-43, the reactions of single as well as two hydrogen chemisorptions on the surface of armchair SWCNTs



■ Fig. 22-42

Structures of (3,3), (4,4), (5,5), and (6,6) armchair SWCNTs of 15 carbon layers (15cl) considered for the chemisorption of one and two H atoms. The carbon atom sites for attachment of H atoms are shown (Reprinted with permission from ref. Dinadayalane et al. (2007b). Copyright 2007 American Chemical Society)



■ Fig. 22-43

The variation of reaction energies at the B3LYP/6-31G(d) level for the chemisorption of one and two hydrogen atoms on the external surface of (3,3), (4,4), (5,5), and (6,6) armchair single-walled carbon nanotubes (SWCNTs) (Reprinted with permission from ref. Dinadayalane et al. (2007b). Copyright 2007 American Chemical Society)

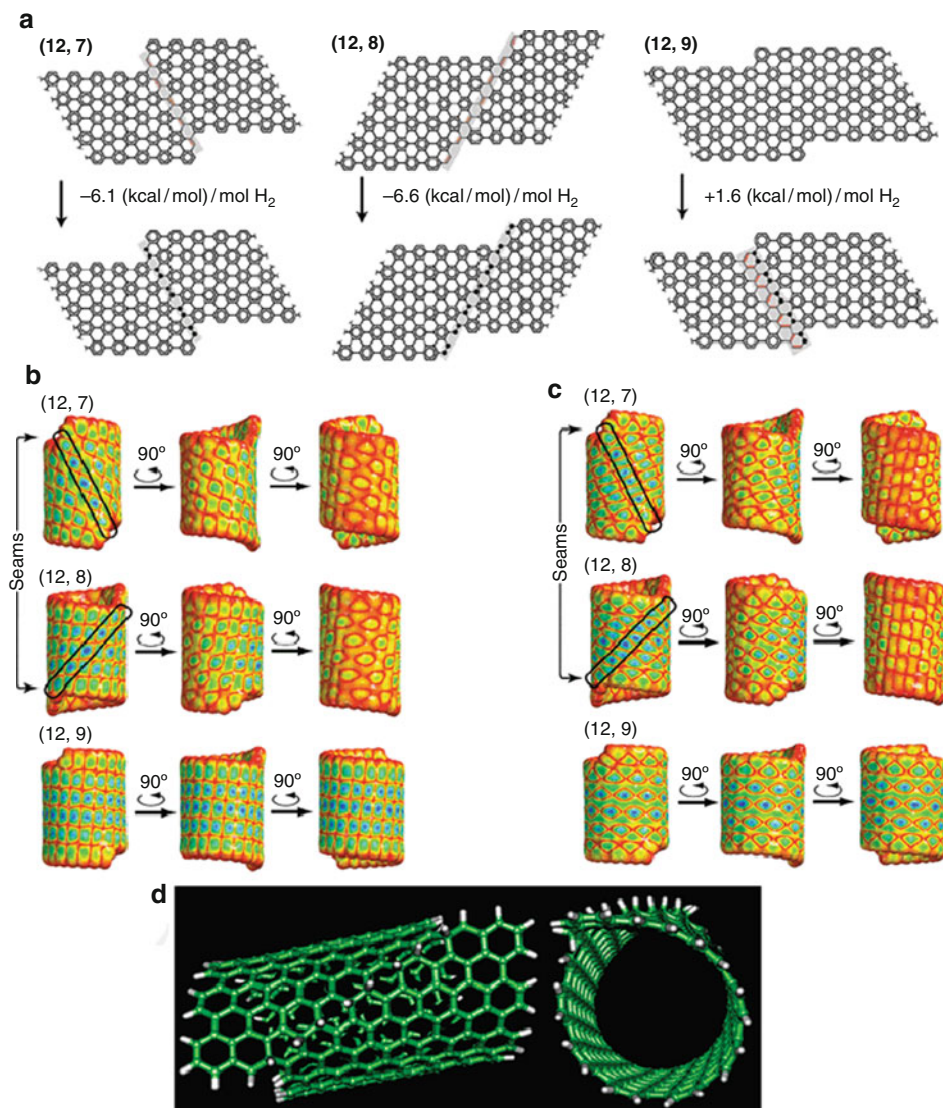
are highly exothermic. The reaction energy for the addition of two H atoms is more than two times that of one H chemisorption except for H(1,3) addition. Our computational study revealed a competition between H(1,2) and H(1,4) addition in case of (5,5) and (6,6) SWCNTs, but such competition was not seen in case of narrow diameter (3,3) and (4,4) SWCNTs. Increasing the length of the tube has pronounced effect on the reaction energy of hydrogen chemisorption. In case of armchair SWCNTs, the chemisorption of two hydrogen atoms at alternate positions is thermodynamically less favored compared to H(1,2) and H(1,2') additions regardless of the length and diameter of the tubes (Dinadayalane et al. 2007b). The least positional preference of H(1,3) for armchair SWCNTs is different compared to the results of zigzag type nanotubes by Yang et al. (2006c), Dinadayalane et al. (2007b). We found that the H chemisorption on nanotubes of different diameters and the positions of two hydrogen atoms chemisorbed on the surface of armchair SWCNTs can be characterized by C–H stretching frequencies of chemisorbed hydrogen atoms (Dinadayalane et al. 2007b). In the investigation of chemisorption of H atoms with (3,3) and (4,4) SWCNTs of different lengths, we found that changing the length of the nanotube has significant effect on the reaction energy of hydrogen chemisorption, HOMO–LUMO gap of pristine and hydrogen chemisorbed SWCNTs (Kaczmarek et al. 2007).

Ormsby and King predicted the reactivity pattern for the hydrogenation in chiral SWCNTs (Ormsby and King 2007). Investigations involving chiral SWCNTs are more challenging than for zigzag and armchair SWCNTs because single unit cell contains many atoms; consequently, more computational resources require. Computational study demonstrated that hydrogenation of the fully benzenoid (12,9) SWCNT was significantly less energetic (by  $\sim 8$  kcal/mol per mol  $H_2$ ) than the hydrogenation of (12,7) and (12,8) SWCNTs (Fig. 22-44a). Furthermore, the hydrogenation at an internal Clar double bond or bonds was reported to be more exothermic than at randomly selected internal bonds. Like other polycyclic aromatic hydrocarbons, hydrogenation of double bonds is energetically preferred over hydrogenation of aromatic sextets. The frontier molecular orbitals (HOMO and LUMO) of chiral SWCNTs have maximum amplitude at the double bonds suggesting that Clar's model also predicts the kinetic reactivity. Thus, the frontier molecular orbitals are useful in predicting the favorable sites for hydrogenation in chiral SWCNTs (Ormsby and King 2007).

In the early 2000s, experimentalists found that partial fluorination of the SWCNTs could be used as a technique for cutting the nanotubes of varying lengths. However, the mechanism of cutting is not yet clear (Gu et al. 2002). In a computational study, Bettinger observed a strong oscillation of reaction energy for the addition of F atom on the external surface of (5,5) SWCNT of varying lengths (Fig. 22-45). The computed reaction energy oscillation ranges from 43 to 68 kcal/mol at the UB3LYP/6-31G(d) level using UPBE/3-21G optimized geometries. The shortest tube exhibited the highest exothermicity. The energy oscillation was reported to be periodic with large exothermicity for the fully benzenoid frameworks, in agreement with their smaller band gaps compared to Kekule and incomplete Clar structures. Computational study demonstrated that the addition of F atom to the sidewall of SWCNT strongly depends on the length of the nanotube (Bettinger 2004). As observed in H atom addition (Dinadayalane et al. 2007b; Kaczmarek et al. 2007; Yang et al. 2006c), the F atom addition to the sidewalls of SWCNTs transforms the carbon atom hybridization from  $sp^2$  to  $sp^3$  (Bettinger 2004).

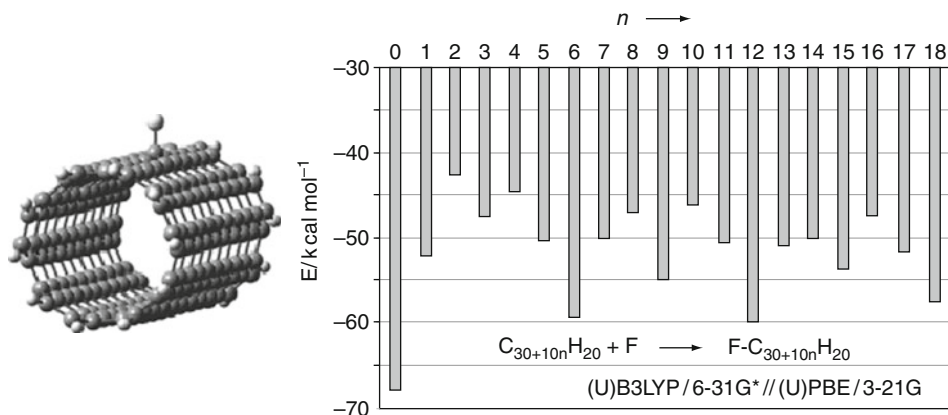
The chemical reactivity of carbon nanotubes is governed by the local atomic structure. As mentioned earlier, the pyramidalization angle is an important parameter in predicting the chemical reactivity of SWCNTs. Park et al. predicted the hydrogenation and fluorination energies of each carbon from its pyramidalization angle for zigzag SWCNTs (Fig. 22-46). They formulated the  $E_{\text{total}}$  for chemisorption of H and F atom on the external surface of zigzag tubes





■ Fig. 22-44

(a) Hydrogenation of equivalent vectors of (12,7), (12,8), and (12,9) chiral SWCNT segments (planar representation). (b) HOMO plotted on the isodensity surface for (12,7), (12,8), and (12,9) chiral SWCNTs. (c) LUMO plotted on the isodensity surface for (12,7), (12,8), and (12,9) chiral SWCNTs. (d) The hydrogenated model chiral SWCNT (*side* and *top* views). The locations of double bond seam are indicated in (b) and (c). HOMO and LUMO isodensity surface structures generated at AM1 method (Reprinted with permission from ref. Ormsby and King (2007). Copyright 2007 American Chemical Society)



■ Fig. 22-45

Variation of reaction energy for the addition of F atom to (5,5) armchair SWCNT of different lengths ( $n$  – increasing number of carbon layers) (Reprinted with permission from ref. Bettinger (2004). Copyright 2004 American Chemical Society)

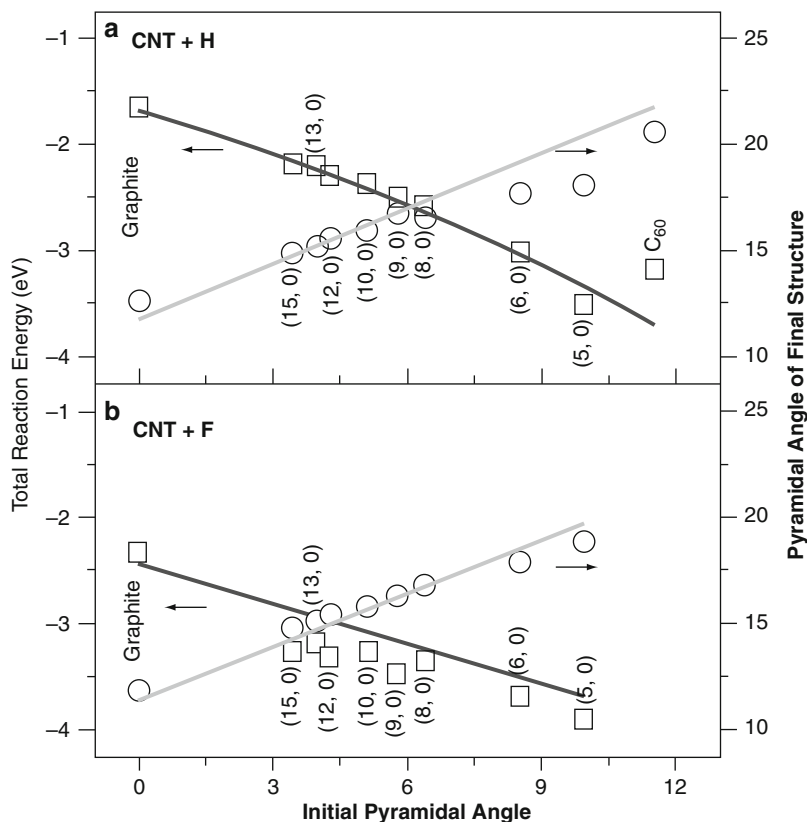
of different diameters as a function of pyramidalization angle of the binding site of tubes. They revealed that the metallic zigzag SWCNTs are slightly more reactive than the semiconducting SWCNTs. Furthermore, the fluorination is more viable than the hydrogenation (Park et al. 2003).

## Theoretical Studies on Common Defects in SWCNTs

Investigating the atomic defects is important in tailoring the electronic properties of SWCNTs. Recent experimental study reported a method to selectively modify the electronic properties of semiconductor SWCNTs by the creation and annihilation of point defects on their surface with the tip of a scanning tunneling microscope (STM) (Berthe et al. 2007). Such experimental study motivates theoreticians to explore the structures, energetics, reactivities, and electronic properties of SWCNTs containing different types of defects.

### Stone–Wales Defect

The Stone–Wales defect can be created by  $90^\circ$  rotation of one of the C–C bonds in the hexagonal network of SWCNTs. Two types of C–C bonds exist in each of armchair and zigzag SWCNTs. Therefore, one can generate Stone–Wales defect in two different orientations in both armchair and zigzag SWCNTs (► Fig. 22-47). DFT calculations revealed that the formation energies of (5,5) SWD\_II and (10,0) SWD\_II are lower than those of (5,5) SWD\_I, and (10,0) SWD\_I. The computed formation energies of (5,5) SWD\_I, (5,5) SWD\_II, (10,0) SWD\_I, and (10,0) SWD\_II are 66.4 (2.88 eV), 57.0 (2.47 eV), 68.9 (2.99 eV), and 63.0 (2.73 eV) kcal/mol, respectively. The formation energy was calculated as the relative energy of the Stone–Wales defective tube with



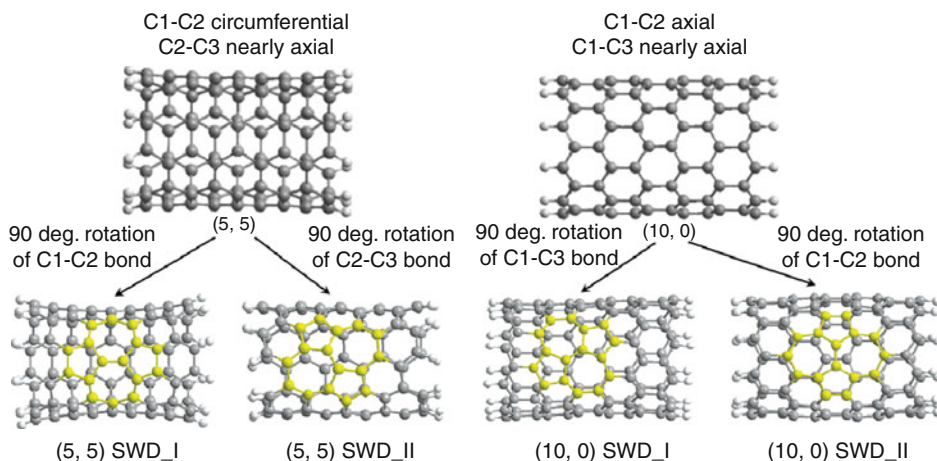
■ Fig. 22-46

DFT-computed  $E_{\text{total}}$  ( $\square$ ) and pyramidalization angle ( $\theta_P$ ) values ( $\circ$ ) for fully relaxed configurations and their estimated values (solid curves) for (a) hydrogenation, and (b) fluorination (Reprinted with permission from ref. Park et al. (2003). Copyright 2003 American Chemical Society)

respect to the corresponding defect-free SWCNT. It was reported that the formation of Stone–Wales defect causes no change in the HOMO–LUMO gaps (Yang et al. 2006a, b).

We have investigated the structures, formation energies, reactivities of Stone–Wales defect with two different orientations and different locations from the end of tube in armchair (5,5) SWCNTs of  $C_{80}H_{20}$  (I) and  $C_{100}H_{20}$  (II) (► Fig. 22-48a) (► Dinadayalane and Leszczynski 2007b). We employed HF/4-31G, HF/6-31G(d), B3LYP/3-21G, and B3LYP/6-31G(d) levels of theory. HF/4-31G level overestimates the Stone–Wales defect formation energy compared to B3LYP/6-31G(d) level. Our study revealed that B3LYP/3-21G level, which provides reasonable energy estimation, may be employed for large nanotube systems to compute the defect formation energies when the calculations at the B3LYP functionals with large basis sets are prohibitive. Our study showed that the Stone–Wales defective (5,5) armchair SWCNTs generated by rotation of nearly axial bond (ABR) are more stable than those created by circumferential bond rotation (CBR) as shown in ► Fig. 22-48b. The SW defect structures generated by ABR show lower HOMO–LUMO gap than those created by CBR and the defect-free SWCNTs (Dinadayalane and Leszczynski 2007b).





■ Fig. 22-47

**Generation of Stone–Wales defect with different orientations in (5,5) armchair and (10,0) zigzag SWCNTs. The atoms in the Stone–Wales defect region are highlighted in yellow color (Reprinted with permission from ref. Yang et al. (2006a). Copyright 2006 American Chemical Society. Reprinted with permission from Yang et al. (2006b). Copyright 2006, American Institute of Physics)**

Bettinger demonstrated in a comprehensive computational study that some of the bonds of SW defect show higher reactivity than pristine tube, others are less reactive (Bettinger 2005). Computational studies explained the reactivity of carbon atom sites based on the pyramidalization angles (Akdim et al. 2007; Bettinger 2005; Lu et al. 2005). Lu et al. investigated addition of O, CH<sub>2</sub>, and O<sub>3</sub> across C–C bonds of SW defective and defect-free armchair SWCNTs. They showed that the central C–C bond of the SW defect in armchair SWCNT (SW defect generated by CBR) is chemically less reactive than that in the perfect tube and it was attributed to small local curvature in the carbon atoms of central C–C bond of the SW defect (Lu et al. 2005). We found that the values of pyramidalization angles do not completely explain the reactivity of different bonds of SW defect region for cycloaddition reactions and the reactivity may arise from various other reasons, in addition to topology. We concluded that the cycloaddition reactions across the C–C bond shared by two heptagons (7–7 ring fusion) need not always be less reactive than the corresponding bond in the pristine structure and the reactivity of that bond depends on the orientation of the SWD in the SWCNTs (Dinadayalane and Leszczynski 2007b).

## Topological Ring Defects

Nishidate and Hasegawa calculated the formation energies of  $n$ -membered topological ring defects with  $n = 7$  (heptagon),  $n = 8$  (octagon),  $n = 9$  (enneagon) in (5,5) armchair and (8,0) zigzag SWCNTs (► Fig. 22-49a). They used both local density approximation (LDA) and the generalized gradient approximation (GGA: PW91). The spin-polarized projector augmented-wave (PAW) implemented in VASP code was employed for calculations and periodic boundary condition was used (Nishidate and Hasegawa 2005).

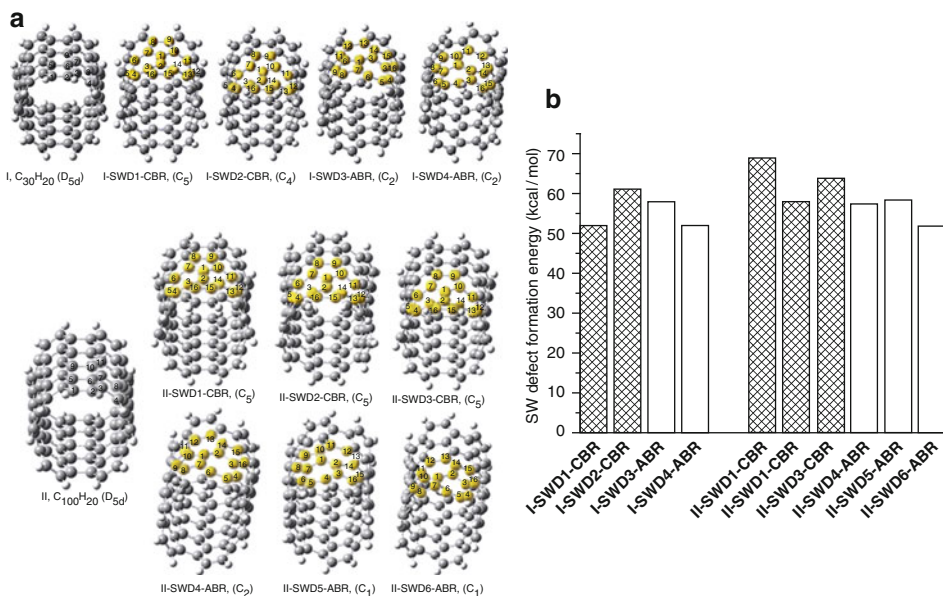


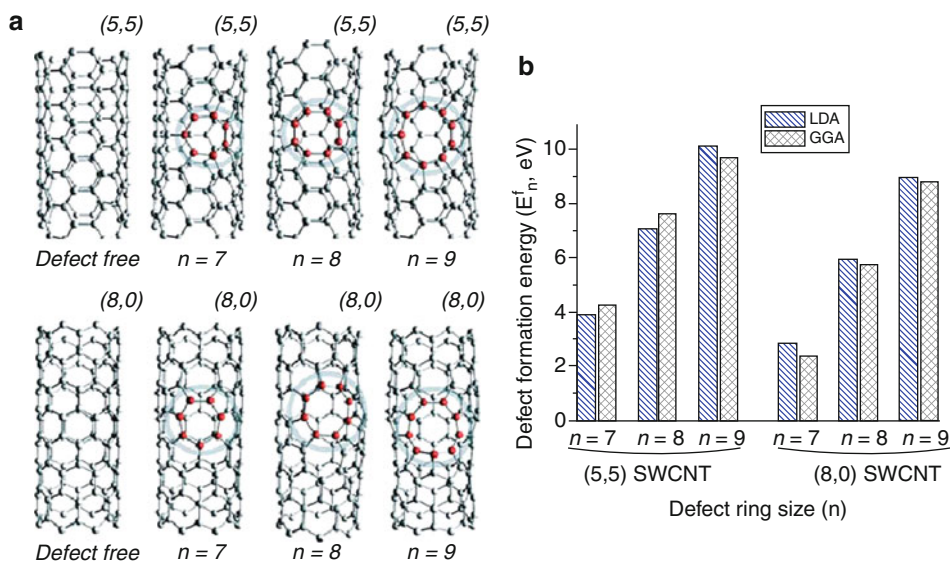
Fig. 22-48

(a) B3LYP/6-31G(d) level optimized structures of defect-free (5,5) armchair SWCNTs and the Stone–Wales defect tubes generated by the 90° rotation of circumferential and nearly axial C–C bonds. (b) The Stone–Wales defect formation energy obtained at the B3LYP/6-31G(d) level (Reprinted with permission from ref. Dinadayalane and Leszczynski (2007b). Copyright 2007 Elsevier)

The defect formation energy ( $E_f^n$ ) of  $n$ -membered rings was calculated as the energy difference between the total energy of defective SWCNT ( $E_{\text{tot}}^n$ ) and that of the pristine SWCNT ( $E_{\text{tot}}$ ); that is,  $E_f^n = E_{\text{tot}}^n - E_{\text{tot}}$ . The number of atoms of each defective SWCNT is the same as that of the corresponding SWCNT. Computational study showed that the defect formation energy increases with increase in defect ring size ( $n$ ) (Fig. 22-49b). In general, LDA method yielded higher defect formation energy than generalized gradient approximation. The SWCNTs were reported to be more fragile than the graphene sheet for defect formation. Distortion of the SWCNTs became larger as the defect ring size increases (Nishidate and Hasegawa 2005).

## Topological Ring Defects: Single- and Di-Vacancy

An ideal single vacancy (SV) with three dangling bonds (DBs) was generated by removing one carbon atom from the perfect (5,5) and (10,0) SWCNTs. Upon geometry optimization, an ideal SV with three dangling bonds rearranged into a pentagonal ring and one DB (Yang et al. 2006a). Hence, this defect is called a 5-1DB defect (Lu and Pan 2004; Yang et al. 2006a). In case of (5,5) SWCNT, the optimization of the ideal SV resulted in two different 5-1DB defects. The structures were named as (5,5) SV\_I and (5,5) SV\_II as shown in Fig. 22-50. The latter structure was reported to be energetically more favorable (by 1.20 eV) than the former. A similar behavior



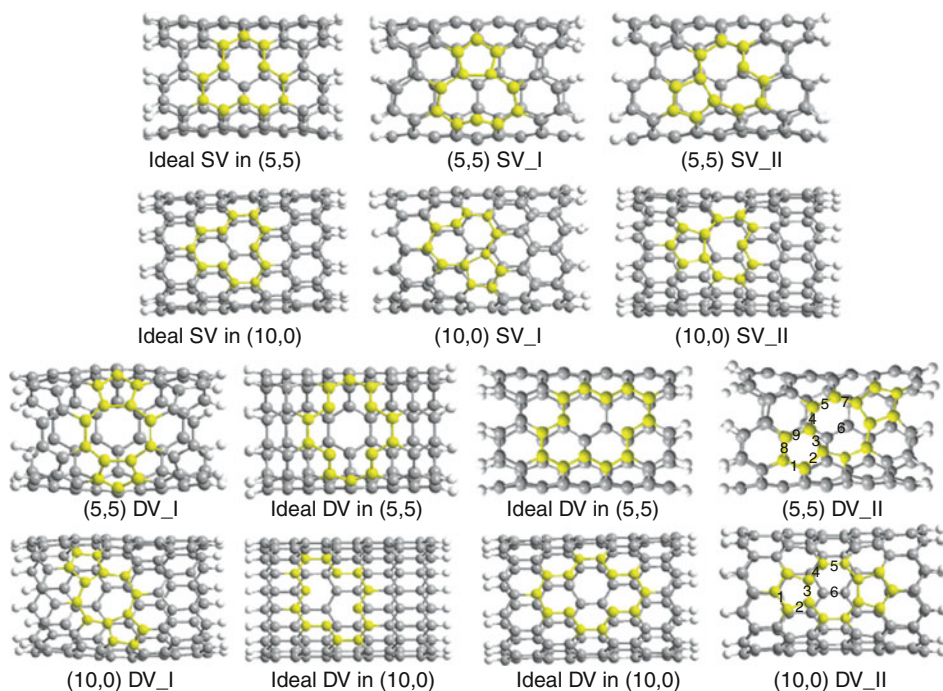
■ Fig. 22-49

(a) Fully relaxed structures of the defect-free and the defective (5,5) (*upper panel*) and (8,0) (*lower panel*) SWCNTs obtained by the GGA calculations. Gray balls and rods are the carbon atoms and bonds shorter than 1.5 Å, respectively. Carbon ring defects (given in red color) are indicated by the thick circles. (b) Defect formation energy ( $E_f^n$ ) of  $n$ -membered carbon rings for (5,5) and (8,0) calculated using LDA and GGA (The pictures in (a) and the data for (b) were taken with permission from Nishidate and Hasegawa (2005). Copyright 2005 by the American Physical Society)

was observed for (10,0) zigzag SWCNT. The bond length of the new C–C bond forming five-membered ring is 1.64 Å in (5,5) SV\_I, while that of 1.55 Å was obtained for (5,5) SV\_II (Yang et al. 2006a). Lu and Pan found using tight-binding calculations that the single vacancy defect formation energy for  $(n,n)$  armchair SWCNTs increases monotonically with increasing tube radii. The formation energy curve of single vacancy defects in the zigzag  $(n,0)$  SWCNTs is periodic, which is mainly characterized by metallic  $(n,0)$  tubes (such as (6,0), (9,0), (12,0), (15,0), etc.) (Lu and Pan 2004).

An ideal di-vacancy can be generated by removing two carbon atoms. Two different orientations are possible because of the presence of two different types of bonds in both (5,5) armchair and (10,0) zigzag SWCNTs. Upon geometry optimizations, SWCNTs with ideal di-vacancies yielded 5-8-5 (five-eight-five-membered rings) defects in two different orientations in both armchair and zigzag type tubes. Computational study revealed that (5,5) DV\_II and (10,0) DV\_II configurations are energetically more favorable than (5,5) DV\_I and (10,0) DV\_I by 0.97 and 0.63 eV, respectively (Yang et al. 2006a). Yang et al. mentioned that (5,5) DV\_II and (10,0) DV\_II can be obtained by removing the carbon atoms with the dangling bond from (5,5) SV\_II and (10,0) SV\_II, which are the most stable configurations among the possible types of SVs in each type of tubes (Yang et al. 2006a).

The di-vacancy in graphene as well as SWCNTs generates structures possessing two pentagons side by side with an octagon (585 structure) as a result of geometry optimization.

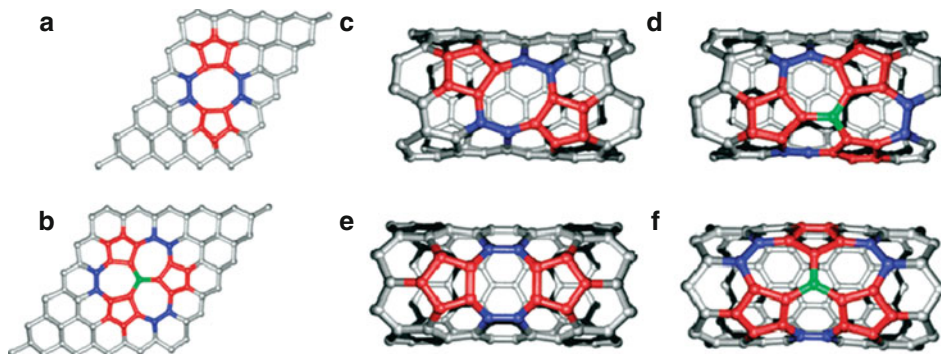


■ Fig. 22-50

Configurations of the single (SV) and double (DV) vacancies. Ideal SV and DV mean one and two carbon atoms removed from pristine and the structures were not relaxed. Single and double vacancies in two different orientations (I and II) given for (5,5) and (10,0) SWCNTs. Carbon atoms in defect region are given in *yellow color* (Reprinted with permission from ref. Yang et al. (2006a). Copyright 2006 American Chemical Society)

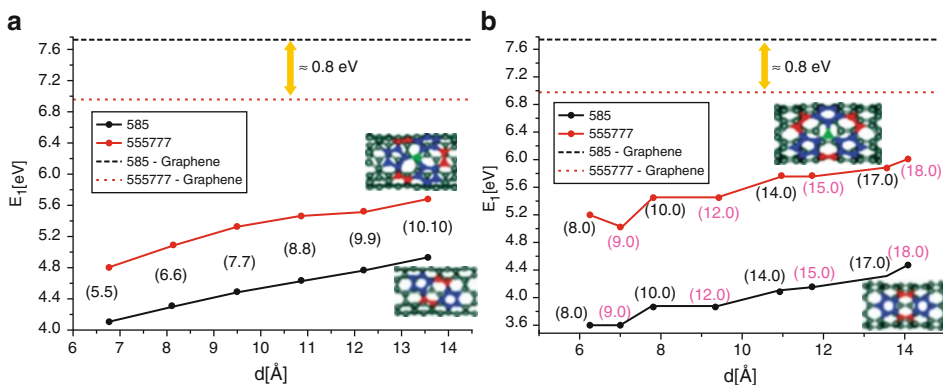
The 585 configuration can reconstruct further into a complex structure composed of three pentagons and three heptagons, called 555777 defect structure. In fact, 555777 configuration is more stable than 585 configuration in graphene. Amorim et al. investigated the stability of these types of configurations, derived by di-vacancies, in armchair and zigzag SWCNTs considering different tube diameters (Amorim et al. 2007). The 585 defect in SWCNTs has two possible orientations with respect to the tube axis: perpendicular and tilted in armchair, and parallel and tilted in zigzag SWCNTs. For the (5,5) SWCNT, the perpendicular orientation is less stable than the tilted one by  $\sim 3.5$  eV. In case of (8,0) SWCNT, the tilted orientation is less stable by  $\sim 2.7$  eV than the parallel one. In their study, Amorim et al. have considered only the tilted and the parallel orientations of defects for armchair and zigzag SWCNTs, respectively (🔗 Fig. 22-51) (Amorim et al. 2007).

In contrast to graphene, the 585 defect was predicted to be more stable than the 555777 defect in both armchair and zigzag SWCNTs. Both 585 and 555777 defects in nanotubes (both armchair and zigzag) are more stable than in graphene. The defect formation energy increases monotonically as the diameter of the armchair SWCNT increases (🔗 Fig. 22-52a). The energy difference between the 585 defect and the 555777 defect was computed to be  $\sim 1.6$  eV in case



■ Fig. 22-51

Ball and stick models for the final geometries of the defects: (a) 585 and (b) 555777 in graphene; (c) 585 tilted and (d) 555777 in the (5,5) armchair SWCNT; (e) 585 parallel and (f) 555777 in the (8,0) zigzag SWCNT. The carbon atoms in pentagons are marked in red, the ones that complete either the octagons or the heptagons are colored in blue, and the ones at the center of the  $C_3$  symmetry operation in the 555777 defects are colored green. All the others are colored gray (Reprinted with permission from ref. Amorim et al. (2007). Copyright 2007 American Chemical Society)



■ Fig. 22-52

Formation energy vs diameter for the 585 and 555777 defects in (a) armchair and (b) zigzag SWCNTs. The limits for graphene were given in both graphs (Reprinted with permission from ref. Amorim et al. (2007). Copyright 2007 American Chemical Society)

of zigzag tubes, while the difference was reported to be  $\sim 0.7$  eV for armchair SWCNTs. Zigzag SWCNTs exhibited oscillations in the formation energies and the oscillations were related to the alternation between semiconductor and metallic character of the  $(n,0)$  zigzag SWCNTs (► Fig. 22-52b) (Amorim et al. 2007).




## Outlook of Potential Applications of Carbon Nanostructures

Graphene is used as a base material for nanoelectromechanical systems (NEMS) due to its lightweight and stiffness properties (Bunch et al. 2007; Robinson et al. 2008). Graphene-based resonators have notable advantages in comparison with nanotubes. Reduced graphene oxide films are used to make drum resonators. The high Young's modulus, extremely low mass, and large surface area make the graphene-based resonators ideally suited for use as mass, force, and charge sensors (Ekinici et al. 2004; Knobel and Cleland 2003; Lavrik and Datskos 2003). Graphene can be used for metallic transistor applications and ballistic transport. One of the potential applications of graphene sheet is its use as membrane for separation (Jiang et al. 2009). Graphene may be useful for electro- and magneto-optics (Geim 2009). Graphene (fully hydrogenated graphene) nanoribbons have quite promising applications in optics and opto-electronics due to the wide band gap. Graphene may also be used for transistor applications (Novoselov et al. 2004). Research into applications for carbon graphene nanosheets has focused on their uses as platforms for next-wave microchips, active materials in field emitter arrays for flat panel screen displays, in biological sensors and medical imaging devices, in solar energy cells, and in high-surface area electrodes for use in bioscience. Graphene is a possible replacement material where carbon nanotubes are presently used (Xia et al. 2009). Recent study revealed that graphene-based liquid crystal devices (LCDs) show excellent performance with high contrast ratio. Thus, LCDs might be graphene's first realistic commercial application (Blake et al. 2008).

Fullerenes hold possibilities of application in many areas including antiviral activity, enzyme inhibition, DNA cleavage, photodynamic therapy, electron transfer, ball bearings, lightweight batteries, new lubricants, nanoscale electrical switches, new plastics, antitumor therapy for cancer patients, and combustion science and astrophysics (Dresselhaus et al. 1996). The fullerene derivatives obtained by attachment of electron donor moieties are used as photovoltaic devices. The supramolecular design of molecular assemblies involving fullerenes holds the possibility to reach new efficient photovoltaic devices (Hudhomme and Cousseau 2007). Fullerenes show promising biomedical applications (Bakry et al. 2007; Bosi et al. 2003; Mashino et al. 2003; Stoilova et al. 2007; Thrash et al. 1999). The fullerene derivatives showed antibacterial and antiproliferative activities; they inhibited bacteria and cancer cell growth effectively (Mashino et al. 2003). Cationic fullerenes have been identified to work as antimicrobial photosensitizers. Bis-functionalized C<sub>60</sub> derivatives have shown the activity against HIV-1 and HIV-2 strains (Bosi et al. 2003). The antiviral activity of fullerene derivatives is based on several biological properties including their unique molecular architecture and antioxidant activity (Bakry et al. 2007). Fullerenes derivatized by hydrophilic moieties are capable of carrying drugs and genes for the cellular delivery (Thrash et al. 1999). The localization of the metallofullerol in bone might be useful chemotherapeutic agent for treatment of leukemia and bone cancer (Thrash et al. 1999).

Several potential applications have been proposed for carbon nanotubes; for example, conductive and high-strength composites, energy storage and energy conversion devices, sensors, field emission display and radiation sources, and nanotube-based semiconductor devices (Baughman et al. 2002; Sinha and Yeow 2005). Supercapacitors with carbon nanotube electrodes can be used for devices that require higher power capabilities than batteries. Nanotubes have potential application as hydrogen storage (Dinadayalane and Leszczynski 2009). CNTs can be added to aircraft to offer EMI (Electromagnetic Interference) shielding and lightning strike protection. They will also make the aircraft stronger and lighter, allowing for larger payloads and

greater fuel efficiency. They may be used in commercial aircraft and in notebook computers to efficiently draw away generated heat without adding additional weight (Sinha and Yeow 2005). Nanotube films may be used by the automobile industry to make cars and trucks stronger yet lighter, and therefore, more fuel efficient.

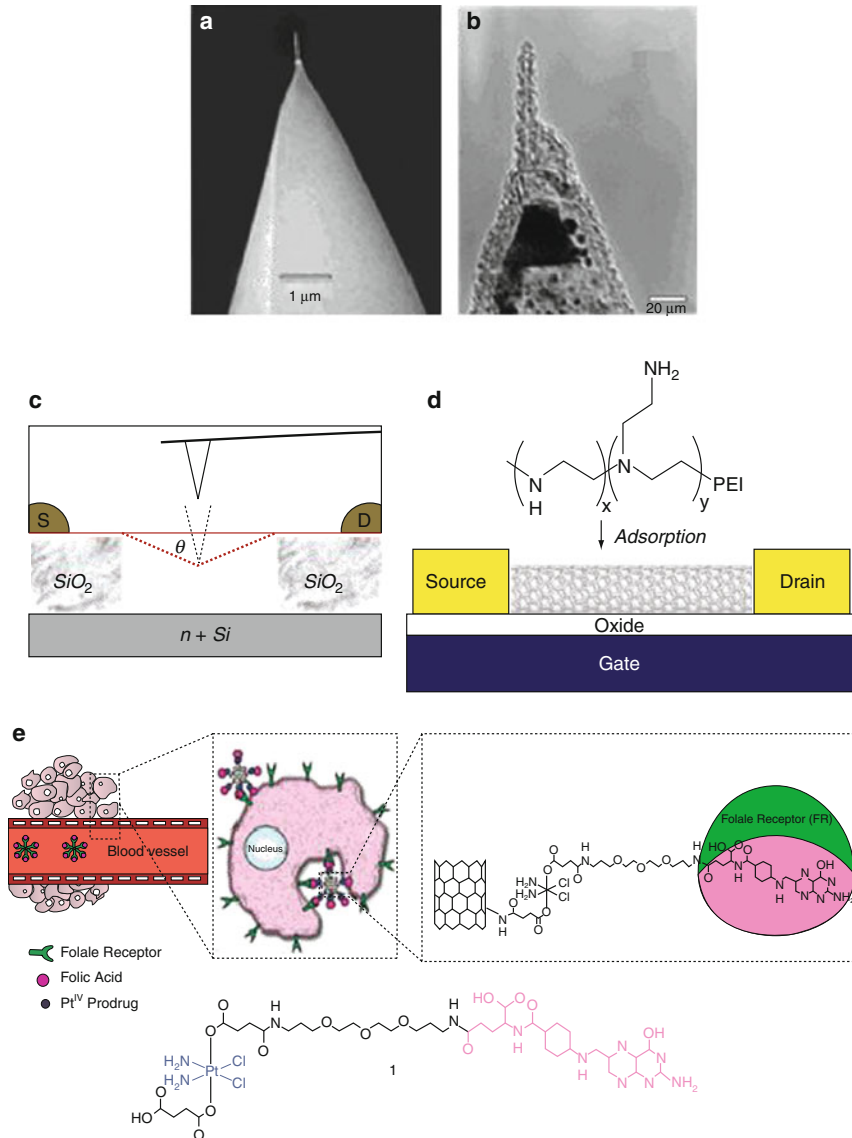
MWCNTs show great potential for use in nanofluidic devices because of their high mechanical strength and fluid transport ability at near-molecular length scales (Sinha and Yeow 2005). Due to the advantages of miniature size of the nanotube and the small amount of material required, the carbon nanotubes are being explored for chemical sensing applications. SWCNTs are promising materials for building high performance nano-sensors and devices (Close et al. 2008). Defects in SWCNTs play important role in chemical sensing applications (Robinson et al. 2006). CNTs can be used as implanted sensors to monitor pulse, temperature, blood glucose, heart's activity level, and can also be used for repairing damaged cells or killing them by targeting tumors by chemical reactions (Sinha and Yeow 2005). Some of the selected applications of carbon nanotubes are shown in  Fig. 22-53.

Potential biological and biomedical applications of CNTs are under investigation (Dhar et al. 2008; Karousis et al. 2009; Liu et al. 2007; Sinha and Yeow 2005). Carbon nanotubes have potential to make miniature biological electronic devices, including probes and sensors (Sotiropoulou and Chaniotakis 2003; Stevens et al. 2000, 2004). Water-soluble peptidomimetic-functionalized carbon nanotubes have been reported to have antitrypsin activity (Dhar et al. 2008). Functionalized and water-soluble SWCNTs have been explored to find biological applications in the area of drug delivery (Dhar et al. 2008; Karousis et al. 2009; Liu et al. 2007). CNTs could be used as potential delivery tools for peptide-based synthetic vaccines. CNTs are currently being considered as suitable substrate for neuronal growth, as ion channel blockers, as vectors for gene transfection (Sinha and Yeow 2005). Carbon nanotubes have provided possibilities for applications in nanotechnology. Continuous and optimistic research efforts in the area of carbon nanotubes are required to realize lot of breakthrough commercial applications.

## Summary and Outlook

---

In this chapter, we provided vital information and up-to-date research on carbon nanostructures, particularly graphene, fullerenes, and carbon nanotubes, which are critical in the nanotechnology revolution. This chapter also covered the modeling aspects, especially the current trends of computational chemistry applications in understanding the structures, reactivity, and other properties of above, mentioned carbon nanostructures, and their importance in supporting the experimental results. Many aspects of basic research and practical application requirements have been motivating both theoreticians and experimentalists to gain better understanding about the carbon nanostructures. Obtaining knowledge on a specific class of chemical reactions with graphene, fullerenes, and SWCNTs is required for making novel materials as well as to produce carbon-based nanomaterials for specific applications. Computational investigations provide opportunity to understand the structures, binding of atoms/molecules with the carbon nanotubes. Systematic and careful computational chemistry approaches could have important implications for the rational design of novel CNT composite materials, novel nanotube-based sensors, as well as for the development of new chemical strategies for SWCNT functionalization. Strong interactions between experimentalists and theoreticians working in



■ Fig. 22-53

(a) and (b) Electron micrographs of two different AFM cantilever tips, each with a nanotube attached; (a) An SEM (scanning electron microscope) micrograph of a nanotube. (b) A TEM (transmission electron microscope) micrograph of a nanotube (Reprinted with permission from ref. Stevens et al. (2000). Copyright 2000 Institute of Physics). (c) Nanoelectromechanics of suspended nanotubes – Experimental scheme for measuring the electromechanical property of the nanotube. (d) The SWCNT evolves into an n-type FET (field-effect transistors) after adsorption of PEI (polyethyleneimine) (Pictures (c) and (d) were reprinted with permission from ref. Dai (2002). Copyright 2002 American Chemical Society). (e) Folate receptor (FR)-mediated targeting and SWCNT-mediated delivery of Pt containing complex (Reprinted with permission from ref Dhar et al. (2008). Copyright 2008 American Chemical Society)



the area of carbon nanostructures will enhance the real-time applications rapidly. Future efforts should not only provide high-tech nano-devices but also address fundamental scientific questions. Further exciting developments in nanoscience and nanotechnology are expected.

## Acknowledgments

This work was supported by the High Performance Computational Design of Novel Materials (HPCDNM) Project funded by the Department of Defense (DoD) through the U.S. Army/Engineer Research and Development Center (Vicksburg, MS); Contract # W912HZ-06-C-0057 and by the Office of Naval Research (ONR) grant 08PRO2615-00/N00014-08-1-0324. We also acknowledge the support from National Science Foundation (NSF) for Interdisciplinary Center for Nanotoxicity (ICN) through CREST grant HRD-0833178.

## References

- Abanin, D. A., Lee, P. A., & Levitov, L. S. (2006). Spin-filtered edge states and quantum hall effect in graphene. *Physical Review Letters*, *96*, 176803-1-176803-4.
- Achiba, Y., Kikuchi, K., Aihara, Y., Wakabayashi, Y., Miyake, Y., & Kainosho, M. (1995). In P. Bernier, D. S. Bethune, L. Y. Chiang, T. W. Ebbesen, R. M. Metzger, & J. W. Mintmire (Eds.), *Higher fullerenes: Structure and properties* (Materials research society symposium proceedings, Vol. 359, p. 3). Pittsburgh, PA: Materials Research Society.
- Achiba, Y., Kikuchi, K., Aihara, Y., Wakabayashi, T., Miyake, Y., & Kainosho, M. (1996). In W. Andreoni (Ed.), *The chemical physics of fullerenes, 10 and 5 years later* (p. 139). Dordrecht: Kluwer.
- Akdim, B., Kar, T., Duan, X., & Pachter, R. (2007). Density functional theory calculations of ozone adsorption on sidewall single-wall carbon nanotubes with Stone-Wales defects. *Chemical Physics Letters*, *445*, 281-287.
- Amorim, R. G., Fazzio, A., Antonelli, A., Novaes, F. D., & da Silva, A. J. R. (2007). Divacancies in graphene and carbon nanotubes. *Nano Letters*, *7*, 2459-2462.
- Amsharov, K. Y., & Jensen, M. (2008). A C<sub>78</sub> Fullerene precursor: Toward the direct synthesis of higher fullerenes. *Journal of Organic Chemistry*, *73*, 2931-2934.
- An, W., Gao, Y., Bulusu, S., & Zeng, X. C. (2005). Ab initio calculation of bowl, cage, and ring isomers of C<sub>20</sub> and C<sub>20</sub><sup>-</sup>. *Journal of Chemical Physics*, *122*, 204109-1-204109-8.
- Andzelm, J., Govind, N., & Maiti, A. (2006). Nanotube-based gas sensors – Role of structural defects. *Chemical Physics Letters*, *421*, 58-62.
- Arnold, M. S., Green, A. A., Hulvat, J. F., Stupp, S. I., & Hersam, M. C. (2006). Sorting carbon nanotubes by electronic structure using density differentiation. *Nature Nanotechnology*, *1*, 60-65.
- Austin, S. J., Fowler, P. W., Manolopoulos, D. E., & Zerbetto, F. (1995). The Stone-Wales map for C<sub>60</sub>. *Chemical Physics Letters*, *235*, 146-151.
- Avila, A. F., & Lacerda, G. S. R. (2008). Molecular mechanics applied to single-walled carbon nanotubes. *Materials Research*, *11*, 325-333.
- Avouris, P., Chen, Z. H., & Perebeinos, V. (2007). Carbon-based electronics. *Nature Nanotechnology*, *2*, 605-615.
- Bakry, R., Vallant, R. M., Najam-ul-Haq, M., Rainer, M., Szabo, Z., Huck, C. W., & Bonn, G. K. (2007). Medicinal applications of fullerenes. *International Journal of Nanomedicine*, *2*, 639-649.
- Balandin, A. A., Ghosh, S., Bao, W., Calizo, I., Teweldebrhan, D., Miao, F., & Lau, C. N. (2008). Superior thermal conductivity of single-layer graphene. *Nano Letters*, *8*, 902-907.
- Barth, W. E., & Lawton, R. G. (1966). Dibenzo[ghi, mno]fluoranthene. *Journal of the American Chemical Society*, *88*, 380-381.
- Baughman, R. H., Zakhidov, A. A., & de Heer, W. A. (2002). Carbon nanotubes-the route toward applications. *Science*, *297*, 787-792.
- Beavers, C. M., Zuo, T., Duchamp, J. C., Harich, K., Dorn, H. C., Olmstead, M. M., & Balch, A. L. (2006). Tb<sub>3</sub>N@C<sub>84</sub>: An improbable, egg-shaped endohedral fullerene that violates the isolated

- pentagon rule. *Journal of the American Chemical Society*, 128, 11352–11353.
- Becke, A. D. (1993). Density-functional thermochemistry. III. The role of exact exchange. *Journal of Chemical Physics*, 98, 5648–5652.
- Becker, L., Bada, J. L., Winans, R. E., Hunt, J. E., Bunch, T. E., & French, B. M. (1994). Fullerenes in the 1.85-billion-year-old Sudbury impact structure. *Science*, 265, 642–645.
- Berthe, M., Yoshida, S., Ebine, Y., Kanazawa, K., Okada, A., Taninaka, A., Takeuchi, O., Fukui, N., Shinohara, H., Suzuki, S., Sumitomo, K., Kobayashi, Y., Grandidier, B., Stievenard, D., & Shigekawa, H. (2007). Reversible defect engineering of single-walled carbon nanotubes using scanning tunneling microscopy. *Nano Letters*, 7, 3623–3627.
- Bethune, D. S., Klang, C.-H., de Vries, M. S., Gorman, G., Savoy, R., Vazquez, J., & Beyers, R. (1993). Cobalt-catalysed growth of carbon nanotubes with single-atomic-layer walls. *Nature*, 363, 605–607.
- Bettinger, H. F. (2004). Effects of finite carbon nanotube length on sidewall addition of fluorine atom and methylene. *Organic Letters*, 6, 731–734.
- Bettinger, H. F. (2005). The reactivity of defects at the sidewalls of single-walled carbon nanotubes: The Stone-Wales defect. *The Journal of Physical Chemistry B*, 109, 6922–6924.
- Bettinger, H. F. (2006). Addition of carbenes to the sidewalls of single-walled carbon nanotubes. *Chemistry - A European Journal*, 12, 4372–4379.
- Bettinger, H. F., Yakobson, B. I., & Scuseria, G. E. (2003). Scratching the surface of Buckminsterfullerene: The barriers for Stone-Wales transformation through symmetric and asymmetric transition states. *Journal of the American Chemical Society*, 125, 5572–5580. and references therein.
- Blake, P., Brimicombe, P. D., Nair, R. R., Booth, T. J., Jiang, D., Schedin, F., Ponomarenko, L. A., Morozov, S. V., Gleeson, H. F., Hill, E. W., Geim, A. K., & Novoselov, K. S. (2008). Graphene-based liquid crystal device. *Nano Letters*, 8, 1704–1708.
- Bosi, S., Ros, T. D., Spalluto, G., Balzarini, J., & Prato, M. (2003). Synthesis and anti-HIV properties of new water-soluble bis-functionalized[60]fullerene derivatives. *Bioorganic and Medicinal Chemistry Letters*, 13, 4437–4440.
- Boukhvalov, D. W., & Katsnelson, M. I. (2008). Chemical functionalization of graphene with defects. *Nano Letters*, 8, 4373–4379.
- Boukhvalov, D. W., Katsnelson, M. I., & Lichtenstein, A. I. (2008). Hydrogen on graphene: Electronic structure, total energy, structural distortions and magnetism from first-principles calculations. *Physical Review B*, 77, 035427-1–035427-7.
- Bunch, J. S., van der Zande, A. M., Verbridge, S. S., Frank, I. W., Tanenbaum, D. M., Parpia, J. M., Craighead, H. G., & McEuen, P. L. (2007). Electromechanical resonators from graphene sheets. *Science*, 315, 490–493.
- Burda, C., Samia, A. C. S., Hathcock, D. J., Huang, H., & Yang, S. (2002). Experimental evidence for the photoisomerization of higher fullerenes. *Journal of the American Chemical Society*, 124, 12400–12401.
- Buseck, P. R., Tshipursky, S. J., & Hettich, R. (1992). Fullerenes from the geological environment. *Science*, 257, 215–217.
- Cabrera-Sanfelix, P., & Darling, G. R. (2007). Dissociative adsorption of water at vacancy defects in graphite. *The Journal of Physical Chemistry C*, 111, 18258–18263.
- Calaminici, P., Geudtner, G., & Koster, A. M. (2009). First-principle calculations of large fullerenes. *Journal of Chemical Theory and Computation*, 5, 29–32.
- Carlson, J. M., & Scheffler, M. (2006). Structural, electronic, and chemical properties of nanoporous carbon. *Physical Review Letters*, 96, 046806-1–046806-4.
- Carpio, A., Bonilla, L. L., de Juan, F., & Vozmediano, M. A. H. (2008). Dislocations in graphene. *New Journal of Physics*, 10, 053021-1–053021-13.
- Chakraborty, A. K., Woolley, R. A. J., Butenko, Y. V., Dhanak, V. R., Siller, L., & Hunt, M. R. C. (2007). A photoelectron spectroscopy study of ion-irradiation induced defects in single-wall carbon nanotubes. *Carbon*, 45, 2744–2750.
- Chandra, N., Namila, S., & Shet, C. (2004). Local elastic properties of carbon nanotubes in the presence of Stone-Wales defects. *Physical Review B*, 69, 094101-1–094101-12.
- Charlier, J.-C. (2002). Defects in carbon nanotubes. *Accounts of Chemical Research*, 35, 1063–1069.
- Charlier, J.-C., Ebbesen, T. W., & Lambin, Ph. (1996). Structural and electronic properties of pentagon-heptagon pair defects in carbon nanotubes. *Physical Review B*, 53, 11108–11113.
- Chaur, M. N., Valencia, R., Rodríguez-Fortea, A., Poblet, J. M., & Echegoyen, L. (2009a). Trimetallic nitride endohedral fullerenes: Experimental and theoretical evidence for the  $M_3N^{6+}@C_{2n}^{6-}$  model. *Angewandte Chemie, International Edition*, 48, 1425–1428.
- Chaur, M. N., Melin, F., Ortiz, A. L., & Echegoyen, L. (2009b). Chemical, electrochemical, and structural properties of endohedral metallofullerenes. *Angewandte Chemie, International Edition*, 48, 7514–7538.

- Chen, Z. (2004). The smaller fullerene  $C_{50}$ , isolated as  $C_{50}Cl_{10}$ . *Angewandte Chemie, International Edition*, 43, 4690–4691.
- Chen, Z., Thiel, W., & Hirsch, A. (2003). Reactivity of the convex and concave surfaces of single-walled carbon nanotubes (SWCNTs) towards addition reactions: Dependence on the carbon-atom pyramidalization. *Chemical Physics and Physical Chemistry*, 4, 93–97.
- Chico, L., Crespi, V. H., Benedict, L. X., Louie, S. G., & Cohen, M. L. (1996). Pure carbon nanoscale devices: Nanotube heterojunctions. *Physical Review Letters*, 76, 971–974.
- Cho, E., Shin, S., & Yoon, Y.-G. (2008). First-principles studies on carbon nanotubes functionalized with azomethine ylides. *The Journal of Physical Chemistry C*, 112, 11667–11672.
- Christian, J. F., Wan, Z., & Anderson, S. L. (1992).  $O^+ + C_{60} \cdot C_{60}O^+$  production and decomposition, charge transfer, and formation of  $C_{59}O^+$ . Dopeyball or  $[CO@C_{58}]^+$ . *Chemical Physics Letters*, 199, 373–378.
- Chun, H., Hahm, M. G., Homma, Y., Meritz, R., Kuramochi, K., Menon, L., Ci, L., Ajayan, P. M., & Jung, Y. J. (2009). Engineering low-aspect ratio carbon nanostructures: Nanocups, nanorings, and nanocontainers. *ACS Nano*, 3, 1274–1278.
- Cioslowski, J., Rao, N., & Moncrieff, D. (2002). Electronic structures and energetics of [5,5] and [9,0] single-walled carbon nanotubes. *Journal of the American Chemical Society*, 124, 8485–8489.
- Close, G. F., Yasuda, S., Paul, B., Fujita, S., & Wong, H. S. P. (2008). A 1 GHz integrated circuit with carbon nanotube interconnects and silicon transistors. *Nano Letters*, 8, 706–709.
- Cohen, M. L. (1993). Predicting useful materials. *Science*, 261, 307–308.
- Crassous, J., Rivera, J., Fender, N. S., Shu, L., Echevoyen, L., Thilgen, C., Herrmann, A., & Diederich, F. (1999). Chemistry of  $C_{84}$ : Separation of three constitutional isomers and optical resolution of  $D_2-C_{84}$  by using the Bingel-retro-Bingel strategy. *Angewandte Chemie, International Edition*, 38, 1613–1617.
- Cuesta, I. G., Pedersen, T. B., Koch, H., & de Meras, A. S. (2006). Carbon nanorings: A challenge to theoretical chemistry. *Chemical Physics and Physical Chemistry*, 7, 2503–2507.
- Cyranski, M. K., Howard, S. T., & Chodkiewicz, M. L. (2004). Bond energy, aromatic stabilization energy and strain in IPR fullerenes. *Chemical Communications*, 2458–2459.
- Dai, H. (2002). Carbon nanotubes: Synthesis, integration, and properties. *Accounts of Chemical Research*, 35, 1035–1044.
- David, W. I. F., Ibberson, R. M., Matthewman, J. C., Prassides, K., Dennis, T. J. S., Hare, J. P., Kroto, H. W., Taylor, R., & Walton, D. R. M. (1991). Crystal structure and bonding of ordered  $C_{60}$ . *Nature*, 353, 147–149.
- David, V. P., Lin, X., Zhang, H., Liu, S., & Kappes, M. M. (1992). Transmission electron microscopy of  $C_{70}$  single crystals at room temperature. *Journal of Materials Research*, 7, 2440–2446.
- Deng, J.-P., Ju, D.-D., Her, G.-R., Mou, C.-Y., Chen, C.-J., Lin, Y.-Y., & Han, C.-C. (1993). Odd-numbered fullerene fragment ions from  $C_{60}$  oxides. *Journal of Physical Chemistry*, 97, 11575–11577.
- Denis, P. A., Iribarne, F., & Faccio, R. (2009). Hydrogenated double wall carbon nanotubes. *Journal of Chemical Physics*, 130, 194704–1–194704–10.
- Dennis, T. J. S., & Shinohara, H. (1998). Isolation and characterisation of the two major isomers of [84]fullerene ( $C_{84}$ ). *Chemical Communications*, 619–620.
- Derehi, G., & Sungu, B. (2007). Temperature dependence of the tensile properties of single-walled carbon nanotubes: O(N) tight-binding molecular-dynamics simulations. *Physical Review B*, 75, 184104–1–184104–6.
- Dewar, M. J. S., & Thiel, W. (1977). Ground states of molecules. 38. The MNDO method. Approximations and parameters. *Journal of the American Chemical Society*, 99, 4899–4907.
- Dewar, M. J. S., Zoebisch, E. G., Healy, E. F., & Stewart, J. J. P. (1985). Development and use of quantum mechanical molecular models. 76. AM1: A new general purpose quantum mechanical molecular model. *Journal of the American Chemical Society*, 107, 3902–3909.
- Dewar, M. J. S., Jie, C., & Yu, J. (1993). SAM1: The first of a new series of general purpose quantum mechanical molecular models. *Tetrahedron*, 49, 5003–5038.
- Dhar, S., Liu, Z., Thomale, J., Dai, H., & Lippard, S. J. (2008). Targeted single-wall carbon nanotube-mediated Pt(IV) prodrug delivery using folate as a homing device. *Journal of the American Chemical Society*, 130, 11467–11476.
- Diederich, F., Ettl, R., Rubin, Y., Whetten, R. L., Beck, R., Alvarez, M., Anz, S., Sensharma, D., Wudl, F., Khemani, K. C., & Koch, A. (1991a). The higher fullerenes: Isolation and characterization of  $C_{76}$ ,  $C_{84}$ ,  $C_{90}$ ,  $C_{94}$ , and  $C_{70}O$ , an oxide of  $D_{5h}-C_{70}$ . *Science*, 252, 548–551.
- Diederich, F., Whetten, R. L., Thilgen, C., Ettl, R., Chao, I., & Alvarez, M. M. (1991b). Fullerene isomerism: Isolation of  $C_{2v}-C_{78}$  and  $D_3-C_{78}$ . *Science*, 254, 1768–1770.

- Dillon, A. C., Jones, K. M., Bekkedahl, T. A., Kiang, C. H., Bethune, D. S., & Heben, M. J. (1997). Storage of hydrogen in single-walled carbon nanotubes. *Nature*, *386*, 377–379.
- Dinadayalane, T. C., & Leszczynski, J. (2007a). Toward nanomaterials: Structural, energetic and reactivity aspects of single-walled carbon nanotubes. In P. B. Balbuena & J. M. Seminario (Eds.), *Nanomaterials: Design and simulation* (Theoretical and computational chemistry, Vol. 18, pp. 167–199). Amsterdam: Elsevier.
- Dinadayalane, T. C., & Leszczynski, J. (2007b). StoneWales defects with two different orientations in (5, 5) single-walled carbon nanotubes: A theoretical study. *Chemical Physics Letters*, *434*, 86–91.
- Dinadayalane, T. C., & Leszczynski, J. (2009). Toward understanding of hydrogen storage in single-walled carbon nanotubes by chemisorption mechanism. In J. Leszczynski & M. K. Shukla (Eds.), *Practical aspects of computational chemistry: Methods, concepts and applications* (pp. 297–313). Netherlands: Springer.
- Dinadayalane, T. C., & Sastry, G. N. (2001). Synthetic strategies toward buckybowls and C<sub>60</sub>: Benzannulation is remarkably facile compared to cyclopentannulation. *Tetrahedron Letters*, *42*, 6421–6423.
- Dinadayalane, T. C., & Sastry, G. N. (2002a). Structure-energy relationships in curved polycyclic aromatic hydrocarbons: Study of benzo-corannulenes. *Journal of Organic Chemistry*, *67*, 4605–4607.
- Dinadayalane, T. C., & Sastry, G. N. (2002b). An assessment of semiempirical (MNDO, AM1 and PM3) methods to model buckybowls. *Journal of Molecular Structure (Theochem)*, *579*, 63–72.
- Dinadayalane, T. C., & Sastry, G. N. (2003). Isolated pentagon rule in buckybowls: A computational study on thermodynamic stabilities and bowl-to-bowl inversion barriers. *Tetrahedron*, *59*, 8347–8351.
- Dinadayalane, T. C., Priyakumar, U. D., & Sastry, G. N. (2001). Theoretical studies on the effect of sequential benzannulation to corannulene. *Journal of Molecular Structure (Theochem)*, *543*, 1–10.
- Dinadayalane, T. C., Priyakumar, U. D., & Sastry, G. N. (2002). Ring closure synthetic strategies toward buckybowls: Benzannulation versus cyclopentannulation. *Journal of the Chemical Society, Perkin Transactions 2*, 94–101.
- Dinadayalane, T. C., Deepa, S., & Sastry, G. N. (2003). Is peri hydrogen repulsion responsible for flattening buckybowls? The effect of ring annelation to the rim of corannulene. *Tetrahedron Letters*, *44*, 4527–4529.
- Dinadayalane, T. C., Deepa, S., Reddy, A. S., & Sastry, G. N. (2004). Density functional theory study on the effect of substitution and ring annelation to the rim of corannulene. *Journal of Organic Chemistry*, *69*, 8111–8114.
- Dinadayalane, T. C., Gorb, L., Simeon, T., & Dodziuk, H. (2007a). Cumulative p-p interaction triggers unusually high stabilization of linear hydrocarbons inside the single-walled carbon nanotube. *International Journal of Quantum Chemistry*, *107*, 2204–2210.
- Dinadayalane, T. C., Kaczmarek, A., Lukaszewicz, J., & Leszczynski, J. (2007b). Chemisorption of hydrogen atoms on the sidewalls of armchair single-walled carbon nanotubes. *The Journal of Physical Chemistry C*, *111*, 7376–7383.
- Ding, F. (2005). Theoretical study of the stability of defects in single-walled carbon nanotubes as a function of their distance from the nanotube end. *Physical Review B*, *72*, 245409-1–245409-7.
- Dresselhaus, M. S., Dresselhaus, G., & Eklund, P. C. (1996). *Science of fullerenes and carbon nanotubes: Their properties and applications*. California: Academic.
- Dresselhaus, M. S., Dresselhaus, G., & Avouris, Ph. (Eds.). (2001). *Carbon nanotubes: Synthesis, structure, properties, and applications*. Berlin: Springer.
- Dresselhaus, M. S., Dresselhaus, G., Jorio, A., Filho, A. G. S., Pimenta, M. A., & Saito, R. (2002). Single nanotube Raman spectroscopy. *Accounts of Chemical Research*, *35*, 1070–1078.
- Dresselhaus, M. S., Dresselhaus, G., Saito, R., & Jorio, A. (2005). Raman spectroscopy of carbon nanotubes. *Physics Reports*, *409*, 47–99.
- Dresselhaus, M. S., Dresselhaus, G., & Jorio, A. (2007). Raman spectroscopy of carbon nanotubes in 1997 and 2007. *The Journal of Physical Chemistry C*, *111*, 17887–17893.
- Dulap, B. I., & Zope, R. R. (2006). Efficient quantum-chemical geometry optimization and the structure of large icosahedral fullerenes. *Chemical Physics Letters*, *422*, 451–454.
- Dunlap, B. I., Brenner, D. W., Mintmire, J. W., Mowrey, R. C., & White, C. T. (1991). Local density functional electronic structures of three stable icosahedral fullerenes. *Journal of Physical Chemistry*, *95*, 8737–8741.
- Duplock, E. J., Scheffler, M., & Lindan, P. J. D. (2004). Hallmark of perfect graphene. *Physical Review Letters*, *92*, 225502-1–225502-4.
- Eggen, B. R., Heggie, M. I., Jungnickel, G., Latham, C. D., Jones, R., & Briddon, P. R. (1996). Autocatalysis during fullerene growth. *Science*, *272*, 87–89.

- Ekinci, K. L., Huang, X. M. H., & Roukes, M. L. (2004). Ultrasensitive nanoelectromechanical mass detection. *Applied Physics Letters*, 84, 4469–4471.
- Elias, D. C., Nair, R. R., Mohiuddin, T. M. G., Morozov, S. V., Blake, P., Halsall, M. P., Ferrari, A. C., Boukhvalov, D. W., Katsnelson, M. I., Geim, A. K., & Novoselov, K. S. (2009). Control of graphenes properties by reversible hydrogenation: Evidence for graphane. *Science*, 323, 610–613.
- Ertekin, E., Chrzan, D. C., & Daw, M. S. (2009). Topological description of the Stone-Wales defect formation energy in carbon nanotubes and graphene. *Physical Review B*, 79, 155421–155421-17.
- Esquivel, E. V., & Murr, L. E. (2004). A TEM analysis of nanoparticles in a polar ice core. *Materials Characterization*, 52, 15–25.
- Feng, X., Irle, S., Witek, H., Morokuma, K., Vidic, R., & Borguet, E. (2005). Sensitivity of ammonia interaction with single-walled carbon nanotube bundles to the presence of defect sites and functionalities. *Journal of the American Chemical Society*, 127, 10533–10538.
- Fischer, J. E., Heiney, P. A., McGhie, A. R., Romanow, W. J., Denenstein, A. M., McCauley, J. P., Jr., & Smith, A. B., III. (1991). Compressibility of solid C<sub>60</sub>. *Science*, 252, 1288–1290.
- Fowler, P. W., & Heine, T. (2001). Stabilisation of pentagon adjacencies in the lower fullerenes by functionalisation. *Journal of the Chemical Society, Perkin Transactions 2*, 487–490.
- Fowler, P. W., & Manolopoulos, D. E. (1995). *An atlas of fullerenes*. New York: Oxford University Press.
- Frisch, M. J., et al. (2003). *Gaussian 03, revision E.1*. Pittsburg, PA: Gaussian, Inc.
- Fu, W., Xu, L., Azurmendi, H., Ge, J., Fuhrer, T., Zuo, T., Reid, J., Shu, C., Harich, K., & Dorn, H. C. (2009). <sup>89</sup>Y and <sup>13</sup>C NMR cluster and carbon cage studies of an yttrium metallofullerene family, Y<sub>3</sub>N@C<sub>2n</sub> (n = 40–43). *Journal of the American Chemical Society*, 131, 11762–11769 and references therein.
- Galano, A. (2006). On the influence of diameter and length on the properties of armchair single-walled carbon nanotubes: A theoretical chemistry approach. *Chemical Physics*, 327, 159–170.
- Geim, A. K. (2009). Graphene: Status and prospects. *Science*, 324, 1530–1534.
- Geim, A. K., & Novoselov, K. S. (2007). The rise of graphene. *Nature Materials*, 6, 183–191.
- Govind, N., Andzelm, J., & Maiti, A. (2008). Dissociation chemistry of gas molecules on carbon nanotubes Applications to chemical sensing. *IEEE Sensors Journal*, 8, 837–841.
- Gu, Z., Peng, H., Hauge, R. H., Smalley, R. E., & Margrave, J. L. (2002). Cutting single-wall carbon nanotubes through fluorination. *Nano Letters*, 2, 1009–1013.
- Gueorguiev, G. K., Pacheco, J. M., & Tomanek, D. (2004). Quantum size effects in the polarizability of carbon fullerenes. *Physical Review Letters*, 92, 215501-1–215501-4.
- Guo, T., Diener, M. D., Chai, Y., Alford, M. J., Hauffler, R. E., McClure, S. M., Ohno, T., Weaver, J. H., Scuseria, G. E., & Smalley, R. E. (1992). Uranium stabilization of C<sub>28</sub>: A tetravalent fullerene. *Science*, 257, 1661–1663.
- Haddon, R. C. (1993). Chemistry of the fullerenes: The manifestation of strain in a class of continuous aromatic molecules. *Science*, 261, 1545–1550.
- Haddon, R. C., & Scott, L. T. (1986).  $\pi$ -Orbital conjugation and rehybridization in bridged annulenes and deformed molecules in general:  $\pi$ -Orbital axis vector analysis. *Pure and Applied Chemistry*, 58, 137–142.
- Hamada, N., Sawada, S., & Oshiyama, A. (1992). New one-dimensional conductors: Graphitic microtubules. *Physical Review Letters*, 68, 1579–1581.
- Harutyunyan, A. R., Chen, G., Paronyan, T. M., Pigos, E. M., Kuznetsov, O. A., Hewaparakrama, K., Kim, S. M., Zakharov, D., Stach, E. A., & Sumanasekera, G. U. (2009). Preferential growth of single-walled carbon nanotubes with metallic conductivity. *Science*, 326, 116–120.
- He, H. Y., & Pan, B. C. (2009). Electronic structures and Raman features of a carbon nanobud. *The Journal of Physical Chemistry C*, 113, 20822–20826.
- Heath, J. R. (1991). *ACS Symposium Series*, 24, 1–23.
- Helden, G. v., Gotts, N. G., & Bowers, M. T. (1993). Experimental evidence for the formation of fullerenes by collisional heating of carbon rings in the gas phase. *Nature*, 363, 60–63.
- Hernández, E., Ordejón, P., & Terrones, H. (2001). Fullerene growth and the role of nonclassical isomers. *Physical Review B*, 63, 193403-1–193403-4.
- Heymann, D., Chibante, L. P. F., Brooks, R. R., Wolbach, W. S., & Smalley, R. E. (1994). Fullerenes in the cretaceous-tertiary boundary layer. *Science*, 265, 645–647.
- Heymann, D., Jenneskens, L. W., Jehlicka, J., Koper, C., & Vlietstra, E. (2003). Terrestrial and extraterrestrial fullerenes. *Fullerenes, Nanotubes, and Carbon Nanostructures*, 11, 333–370.
- Hirahara, K., Suenaga, K., Bandow, S., Kato, H., Okazaki, T., Shinohara, H., & Iijima, S. (2000). One-dimensional metallofullerene crystal generated inside single-walled carbon nanotubes. *Physical Review Letters*, 85, 5384–5387.

- Hirsch, A. (2002). Functionalization of single-walled carbon nanotubes. *Angewandte Chemie, International Edition*, 41, 1853–1859.
- Howard, J. B., Mckinnon, J. T., Makarovskiy, Y., Lafleur, A. L., & Johnson, M. E. (1991). Fullerenes  $C_{60}$  and  $C_{70}$  in flames. *Nature*, 352, 139–141. <http://www.nndc.bnl.gov/content/elements.html>.
- Hu, Y. H., & Ruckenstein, E. (2003). Ab initio quantum chemical calculations for fullerene cages with large holes. *Journal of Chemical Physics*, 119, 10073–10080.
- Hu, Y. H., & Ruckenstein, E. (2004). Quantum chemical density-functional theory calculations of the structures of defect  $C_{60}$  with four vacancies. *Journal of Chemical Physics*, 120, 7971–7975.
- Hudhomme, P., & Cousseau, J. (2007). Plastic solar cells using fullerene derivatives in the photoactive layer. In F. Langa & J.-F. Nierengarten (Eds.), *Fullerenes: Principles and applications*. London: Royal Society of Chemistry.
- Hutter, J. et al. Computer code CPMD, version 3.11 (copyright IBM Corp. 1990–2008; copyright für Festkörperforschung Stuttgart, Germany, 1997–2001), <http://www.cpmd.org/>.
- Iijima, S. (1991). Helical microtubules of graphitic carbon. *Nature*, 354, 56–58.
- Iijima, S. (2007). A career in carbon. *Nature Nanotechnology*, 2, 590–591.
- Iijima, S., & Ichihashi, T. (1993). Single-shell carbon nanotubes of 1-nm diameter. *Nature*, 363, 603–605.
- Iijima, S., Yudasaka, M., Yamada, R., Bandow, S., Suenaga, K., Kokai, F., & Takahashi, K. (1999). Nano-aggregates of single-walled graphitic carbon nano-horns. *Chemical Physics Letters*, 309, 165–170.
- Ioffe, I. N., Goryunkov, A. A., Tamm, N. B., Sidorov, L. N., Kemnitz, E., & Troyanov, S. I. (2009). Fusing pentagons in a fullerene cage by chlorination: IPR  $D_2-C_{76}$  rearranges into non-IPR  $C_{76}Cl_{24}$ . *Angewandte Chemie, International Edition*, 48, 5904–5907.
- Jiang, H., Nasibulin, A. G., Brown, D. P., & Kauppinen, E. I. (2007). Unambiguous atomic structural determination of single-walled carbon nanotubes by electron diffraction. *Carbon*, 45, 662–667.
- Jiang, D., Cooper, V. R., & Dai, S. (2009). Porous graphene as the ultimate membrane for gas separation. *Nano Letters*, 9, 4019–4024.
- Kaczmarek, A., Dinadayalane, T. C., Lukaszewicz, J., & Leszczynski, J. (2007). Effect of tube length on the chemisorptions of one and two hydrogen atoms on the sidewalls of (3,3) and (4,4) single-walled carbon nanotubes: A theoretical study. *International Journal of Quantum Chemistry*, 107, 2211–2219.
- Kadish, K. M., & Ruoff, R. S. (Eds.). (2002). *Fullerene: Chemistry, physics and technology*. New York: Wiley.
- Kagaku (1970). 25, pp. 854.
- Kar, T., Bettinger, H. F., Scheiner, S., & Roy, A. K. (2008). Noncovalent  $\pi$ - $\pi$  stacking and CH- $\pi$  interactions of aromatics on the surface of single-wall carbon nanotubes: An MP2 study. *The Journal of Physical Chemistry C*, 112, 20070–20075.
- Karousis, N., Papi, R. M., Siskos, A., Vakalopoulou, P., Glezakos, P., Sarigiannis, Y., Stavropoulos, G., Kyriakidis, D. A., & Tagmatarchis, N. (2009). Peptidomimetic functionalized carbon nanotubes with antitrypsin activity. *Carbon*, 47, 3550–3558.
- Kessler, B., Bringer, A., Cramm, S., Schlebusch, C., Eberhardt, W., Suzuki, S., Achiba, Y., Esch, F., Barnaba, M., & Cocco, D. (1997). Evidence for incomplete charge transfer and La-derived states in the valence bands of endohedrally doped  $La@C_{82}$ . *Physical Review Letters*, 79, 2289–2292.
- Kikuchi, K., Nakahara, N., Wakabayashi, T., Suzuki, S., Shiromaru, H., Miyake, Y., Saito, K., Ikemoto, I., Kainosho, M., & Achiba, Y. (1992a). NMR characterization of isomers of  $C_{78}$ ,  $C_{82}$  and  $C_{84}$  fullerenes. *Nature*, 357, 142–145.
- Kikuchi, K., Nakahara, N., Wakabayashi, T., Honda, M., Matsumiya, H., Moriwaki, T., Suzuki, S., Shiromaru, H., Saito, K., Yamauchi, K., Ikemoto, I., & Achiba, Y. (1992b). Isolation and identification of fullerene family:  $C_{76}$ ,  $C_{78}$ ,  $C_{82}$ ,  $C_{84}$ ,  $C_{90}$  and  $C_{96}$ . *Chemical Physics Letters*, 188, 177–180.
- Kimura, T., Sugai, T., Shinohara, H., Goto, T., Tohji, K., & Matsuoka, I. (1995). Preferential arc-discharge production of higher fullerenes. *Chemical Physics Letters*, 246, 571–576.
- Klein, D. J., & Schmalz, T. G. (1990). In I. Hargittai (Ed.), *Quasicrystals, networks, and molecules of fivefold symmetry* (p. 239). New York: VCH.
- Knobel, R. G., & Cleland, A. N. (2003). Nanometre-scale displacement sensing using a single electron transistor. *Nature*, 424, 291–293.
- Kostov, M. K., Santiso, E. E., George, A. M., Gubbins, K. E., & Nardelli, M. B. (2005). Dissociation of water on defective carbon substrates. *Physical Review Letters*, 95, 136105-1–136105-4.
- Krätschmer, W., Lamb, L. D., Fostiropoulos, K., & Huffman, D. R. (1990). Solid  $C_{60}$ : A new form of carbon. *Nature*, 347, 354–358.
- Kresse, G., & Furthmüller, J. (1996a). Efficient iterative schemes for ab initio total-energy calculations using a plane-wave basis set. *Physical Review B*, 54, 11169–11186.



- Kresse, G., & Furthmuller, J. (1996b). Efficiency of ab-initio total energy calculations for metals and semiconductors using a plane-wave basis set. *Computational Materials Science*, 6, 15–50.
- Kroto, H. W. (1987). The stability of the fullerenes  $C_n$ , with  $n = 24, 28, 32, 36, 50, 60$  and 70. *Nature*, 329, 529–531.
- Kroto, H. W., Heath, J. R., O'Brien, S. C., Curl, R. F., & Smalley, R. E. (1985).  $C_{60}$ : Buckminsterfullerene. *Nature*, 318, 162–163.
- Kubozono, Y., Maeda, H., Takabayashi, Y., Hiraoka, K., Nakai, T., Kashino, S., Emura, S., Ukita, S., & Sogabe, T. (1996). Extractions of  $Y@C_{60}$ ,  $Ba@C_{60}$ ,  $La@C_{60}$ ,  $Ce@C_{60}$ ,  $Pr@C_{60}$ ,  $Nd@C_{60}$ , and  $Gd@C_{60}$  with aniline. *Journal of the American Chemical Society*, 118, 6998–6999.
- Launois, P., Chorro, M., Verberck, B., Albouy, P.-A., Rouziere, S., Colson, D., Foget, A., Noe, L., Kataura, H., Monthieux, M., & Cambedouzou, J. (2010). Transformation of  $C_{70}$  peapods into double walled carbon nanotubes. *Carbon*, 48, 89–98.
- Lavrik, N. V., & Datskos, P. G. (2003). Femtogram mass detection using photothermally actuated nanomechanical resonators. *Applied Physics Letters*, 82, 2697–2699.
- Lee, S. U., & Han, Y.-K. (2004). Structure and stability of the defect fullerene clusters of  $C_{60}$ :  $C_{59}$ ,  $C_{58}$ , and  $C_{57}$ . *Journal of Chemical Physics*, 121, 3941–3942.
- Lee, C., Yang, W., & Parr, R. G. (1988). Development of the Colle-Salvetti correlation-energy formula into a functional of the electron density. *Physical Review B*, 37, 785–789.
- Lee, C., Kim, D., Jurecka, P., Tarakeshwar, P., Hobza, P., & Kim, K. S. (2007). Understanding of assembly phenomena by aromatic-aromatic interactions: Benzene dimer and the substituted systems. *The Journal of Physical Chemistry. A*, 111, 3446–3457.
- Lee, C., Wei, X., Kysar, J. W., & Hone, J. (2008). Measurement of the elastic properties and intrinsic strength of monolayer graphene. *Science*, 321, 385–388.
- Lherbier, A., Blase, X., Niquet, Y.-M., Triozon, N., & Roche, S. (2008). Charge transport in chemically doped 2D graphene. *Physical Review Letters*, 101, 036808-1–036808-4.
- Li, L., Reich, S., & Robertson, J. (2005). Defect energies of graphite: Density-functional calculations. *Physical Review B*, 72, 184109-1–184109-10.
- Li, J., Wu, C., & Guan, L. (2009a). Lithium insertion/extraction properties of nanocarbon materials. *The Journal of Physical Chemistry C*, 113, 18431–18435.
- Li, Y., Zhou, Z., Shen, P., & Chen, Z. (2009b). Structural and electronic properties of graphene nanoribbons. *The Journal of Physical Chemistry C*, 113, 15043–15045.
- Liu, J., Dai, H., Hafner, J. H., Colbert, D. T., Smalley, R. E., Tans, S. J., & Dekker, C. (1997). Fullerene 'crop circles.' *Nature*, 385, 780–781.
- Liu, Z., Sun, X., Nakayama-Ratchford, N., & Dai, H. (2007). Supramolecular chemistry on water-soluble carbon nanotubes for drug loading and delivery. *ACS Nano*, 1, 50–56.
- Lopez-Urias, F., Terrones, M., & Terrones, H. (2003). Electronic properties of giant fullerenes and complex graphitic nanostructures with novel morphologies. *Chemical Physics Letters*, 381, 683–690.
- Lu, X., & Chen, Z. (2005). Curved pi-conjugation, aromaticity, and the related chemistry of small fullerenes ( $< C_{60}$ ) and single-walled carbon nanotubes. *Chemical Reviews*, 105, 3643–3696.
- Lu, A. J., & Pan, B. C. (2004). Nature of single vacancy in achiral carbon nanotubes. *Physical Review Letters*, 92, 105504-1–105504-4.
- Lu, J., Zhang, X., & Zhao, X. (2000). Metal-cage hybridization in endohedral  $La@C_{60}$ ,  $Y@C_{60}$  and  $Sc@C_{60}$ . *Chemical Physics Letters*, 332, 51–57.
- Lu, X., Chen, Z., Thiel, W., Schleyer, P. v. R., Huang, R., & Zheng, L. (2004). Properties of fullerene[50] and  $D_{5h}$  decachlorofullerene[50]: A computational study. *Journal of the American Chemical Society*, 126, 14871–14878.
- Lu, X., Chen, Z., & Schleyer, P. V. R. (2005). Are Stone-Wales defect sites always more reactive than perfect sites in the sidewalls of single-wall carbon nanotubes? *Journal of the American Chemical Society*, 127, 20–21.
- Lu, J., Yuan, D., Liu, J., Leng, W., & Kopley, T. E. (2008). Three dimensional single-walled carbon nanotubes. *Nano Letters*, 8, 3325–3329 and references therein.
- Ma, J., Alfe, D., Michaelides, A., & Wang, E. (2009). Stone-Wales defects in graphene and other planar  $sp^2$ -bonded materials. *Physical Review B*, 80, 033407-1–033407-4.
- MacKenzie, K. J., See, C. H., Dunens, O. M., & Harris, A. T. (2008). Do single-walled carbon nanotubes occur naturally? *Nature Nanotechnology*, 3, 310.
- Manolopoulos, D. E., & Fowler, P. W. (1991). Structural proposals for endohedral metal-fullerene complexes. *Chemical Physics Letters*, 187, 1–7.
- Manolopoulos, D. E., & Fowler, P. W. (1992). Molecular graphs, point groups, and fullerenes. *Journal of Chemical Physics*, 96, 7603–7614.
- Maruyama, S., & Yamaguchi, Y. (1998). A molecular dynamics demonstration of annealing to a perfect  $C_{60}$  structure. *Chemical Physics Letters*, 286, 343–349.

- Maseras, F., & Morokuma, K. (1995). IMOMM: A new integrated ab initio + molecular mechanics geometry optimization scheme of equilibrium structures and transition states. *Journal of Computational Chemistry*, *16*, 1170–1179.
- Mashino, T., Nishikawa, D., Takahashi, K., Usui, N., Yamori, T., Seki, M., Endo, T., & Mochizuki, M. (2003). Antibacterial and antiproliferative activity of cationic fullerene derivatives. *Bioorganic and Medicinal Chemistry Letters*, *13*, 4395–4397.
- Matsuo, Y., Tahara, K., & Nakamura, E. (2003). Theoretical studies on structures and aromaticity of finite-length armchair carbon nanotubes. *Organic Letters*, *5*, 3181–3184.
- McKenzie, D. R., Davis, C. A., Cockayne, D. J. H., Muller, D. A., & Vassallo, A. M. (1992). The structure of the  $C_{70}$  molecule. *Nature*, *355*, 622–624.
- Mehta, G., & Rao, H. S. P. (1998). Synthetic studies directed towards bucky-balls and bucky-bowls. *Tetrahedron*, *54*, 13325–13370.
- Mehta, G., Panda, G., Yadav, R. D., & Kumar, K. R. (1997). A synthetic approach towards Pinakene, a  $C_{28}H_{14}$  fragment of [70]-fullerene. *Indian Journal of Chemistry (Section B)*, *36*, 301–302.
- Melin, F., Chaur, M. N., Engmann, S., Elliott, B., Kumbhar, A., Athans, A. J., & Echegoyen, L. (2007). The large  $Nd_3N@C_{2n}$  ( $40 \leq n \leq 49$ ) cluster fullerene family: Preferential templating of a  $C_{88}$  cage by a trimetallic nitride cluster. *Angewandte Chemie, International Edition*, *46*, 9032–9035.
- Menon, M., & Srivastava, D. (1997). Carbon nanotube T junctions: Nanoscale metal-semiconductor-metal contact devices. *Physical Review Letters*, *79*, 4453–4456.
- Meyer, J. C., Kisielowski, C., Erni, R., Rossell, M. D., Crommie, M. F., & Zettl, A. (2008). Direct imaging of lattice atoms and topological defects in graphene membranes. *Nano Letters*, *8*, 3582–3586.
- Mielke, S. L., Troya, D., Zhang, S., Li, J.-L., Xiao, S., Car, R., Ruoff, R. S., Schatz, G. C., & Belytschko, T. (2004). The role of vacancy defects and holes in the fracture of carbon nanotubes. *Chemical Physics Letters*, *390*, 413–420.
- Mintmire, J. W., Dunlap, B. I., & White, C. T. (1992). Are fullerene tubules metallic? *Physical Review Letters*, *68*, 631–634.
- Miwa, R. H., Martins, T. B., & Fazzio, A. (2008). Hydrogen adsorption on boron doped graphene: An ab initio study. *Nanotechnology*, *19*, 155708-1–155708-7.
- Miyake, Y., Minami, T., Kikuchi, K., Kainosho, M., & Achiba, Y. (2000). Trends in structure and growth of higher fullerenes isomer structure of  $C_{86}$  and  $C_{88}$ . *Molecular Crystals and Liquid Crystals*, *340*, 553–558.
- Miyamoto, Y., Rubio, A., Berber, S., Yoon, M., & Tomanek, D. (2004). Spectroscopic characterization of Stone-Wales defects in nanotubes. *Physical Review B*, *69*, 121413-1–121413-4.
- Mizorogi, N., & Aihara, J. (2003). PM3 localization energies for the isolated-pentagon isomers of the  $C_{84}$  fullerene. *Physical Chemistry Chemical Physics*, *5*, 3368–3371.
- Monthieux, M., & Kuznetsov, V. L. (2006). Who should be given the credit for the discovery of carbon nanotubes? *Carbon*, *44*, 1621–1623.
- Moro, L., Ruoff, R. S., Becker, C. H., Lorents, D. C., & Malhotra, R. (1993). Studies of metallofullerene primary soots by laser and thermal desorption mass spectrometry. *Journal of Physical Chemistry*, *97*, 6801–6805.
- Morokuma, K., Wang, Q., & Vreven, T. (2006). Performance evaluation of the three-layer ONIOM method: Case study for a zwitterionic peptide. *Journal of Chemical Theory and Computation*, *2*, 1317–1324.
- Murry, R. L., Strout, D. L., Odom, G. K., & Scuseria, G. E. (1993). Role of  $sp^3$  carbon and 7-membered rings in fullerene annealing and fragmentation. *Nature*, *366*, 665–667.
- Nasibulin, A. G., Pikhitsa, P. V., Jiang, H., Brown, D. P., Krashenninnikov, A. V., Anisimov, A. S., Queipo, P., Moiala, A., Gonzalez, D., Lientschnig, G., Hassanien, A., Shandakov, S. D., Lolli, G., Resasco, D. E., Choi, M., Tomanek, D., & Kauppinen, E. I. (2007a). A novel hybrid carbon material. *Nature Nanotechnology*, *2*, 156–161.
- Nasibulin, A. G., Anisimov, A. S., Pikhitsa, P. V., Jiang, H., Brown, D. P., Choi, M., & Kauppinen, E. I. (2007b). Investigations of nanobud formation. *Chemical Physics Letters*, *446*, 109–114.
- Neto, A. H. C., Guinea, F., Peres, N. M. R., Novoselov, K. S., & Geim, A. K. (2009). The electronic properties of graphene. *Reviews of Modern Physics*, *81*, 109–162.
- Nikitin, A., Ogasawara, H., Mann, D., Denecke, R., Zhang, Z., Dai, H., Cho, K., & Nilsson, A. (2005). Hydrogenation of single-walled carbon nanotubes. *Physical Review Letters*, *95*, 225507-1–225507-1.
- Nishidate, K., & Hasegawa, M. (2005). Energetics of lithium ion adsorption on defective carbon nanotubes. *Physical Review B*, *71*, 245418-1–245418-6.
- Niyogi, S., Hamon, M. A., Hu, H., Zhao, B., Bhowmik, P., Sen, R., Itkis, M. E., & Haddon, R. C. (2002). Chemistry of single-walled carbon nanotubes. *Accounts of Chemical Research*, *35*, 1105–1113.



- Novoselov, K. S., Geim, A. K., Morozov, S. V., Jiang, D., Zhang, Y., Dubonos, S. V., Grigorieva, I. V., & Firsov, A. A. (2004). Electric field effect in atomically thin carbon films. *Science*, 306, 666–669.
- Novoselov, K. S., Jiang, D., Schedin, F., Booth, T. J., Khotkevich, V. V., Morozov, S. V., & Geim, A. K. (2005a). Two-dimensional atomic crystals. *Proceedings of the National Academy of Sciences of the United States of America*, 102, 10451–10453.
- Novoselov, K. S., Geim, A. K., Morozov, S. V., Jiang, D., Katsnelson, M. I., Grigorieva, I. V., Dubonos, S. V., & Firsov, A. A. (2005b). Two-dimensional gas of massless Dirac fermions in graphene. *Nature*, 438, 197–200.
- Oberlin, A., Endo, M., & Koyama, T. (1976). Filamentous growth of carbon through benzene decomposition. *Journal of Crystal Growth*, 32, 335–349.
- O'Brien, S. C., Heath, J. R., Curl, R. F., & Smalley, R. E. (1988). Photophysics of buckminsterfullerene and other carbon cluster ions. *Journal of Chemical Physics*, 88, 220–230.
- Okada, S. (2007). Radial-breathing mode frequencies for nanotubes encapsulating fullerenes. *Chemical Physics Letters*, 438, 59–62.
- Okada, S., & Saito, S. (1996). Number of extractable fullerene isomers and speciality of C<sub>84</sub>. *Chemical Physics Letters*, 252, 94–100.
- Ormsby, J. L., & King, B. T. (2007). The regioselectivity of addition to carbon nanotube segments. *Journal of Organic Chemistry*, 72, 4035–4038.
- Osuna, S., Morera, J., Cases, M., Morokuma, K., & Sola, M. (2009). Diels-Alder reaction between cyclopentadiene and C<sub>60</sub>: An analysis of the performance of the ONIOM method for the study of chemical reactivity in fullerenes and nanotubes. *The Journal of Physical Chemistry. A*, 113, 9721–9726.
- Ouyang, M., Huang, J.-L., & Lieber, C. M. (2002). Fundamental electronic properties and applications of single-walled carbon nanotubes. *Accounts of Chemical Research*, 35, 1018–1025.
- Palkar, A., Kumbhar, A., Athans, A. J., & Echegoyen, L. (2008). Pyridyl-functionalized and water-soluble carbon nano onions: First supramolecular complexes of carbon nano onions. *Chemistry of Materials*, 20, 1685–1687.
- Park, S., Srivastava, D., & Cho, K. (2003). Generalized chemical reactivity of curved surfaces: Carbon nanotubes. *Nano Letters*, 3, 1273–1277.
- Park, S. S., Liu, D., & Hagelberg, F. (2005). Comparative investigation on non-IPR C<sub>68</sub> and IPR C<sub>78</sub> fullerenes encaging Sc<sub>3</sub>N molecules. *The Journal of Physical Chemistry. A*, 109, 8865–8873.
- Peng, X., Komatsu, N., Bhattacharya, S., Shimawaki, T., Aonuma, S., Kimura, T., & Osuka, A. (2007). Optically active single-walled carbon nanotubes. *Nature Nanotechnology*, 2, 361–365.
- Perdew, J. P., Burke, K., & Ernzerhof, M. (1996). Generalized gradient approximation made simple. *Physical Review Letters*, 77, 3865–3868.
- Pereira, V. M., Neto, A. H. C., & Peres, N. M. R. (2009). Tight-binding approach to uniaxial strain in graphene. *Physical Review B*, 80, 045401-1–045401-8.
- Pierson, H. O. (1993). *Handbook of carbon, graphite, diamonds and fullerenes: Processing, properties and applications*. New Jersey: Noyes Publications.
- Piskoti, C., Yarger, J., & Zettl, A. (1998). C<sub>36</sub>, a new carbon solid. *Nature*, 393, 771–774.
- Ponomarenko, L. A., Schedin, F., Katsnelson, M. I., Yang, R., Hill, E. W., Novoselov, K. S., & Geim, A. K. (2008). Chaotic Dirac billiard in graphene quantum dots. *Science*, 320, 356–358.
- Poonjarernsilp, C., Sano, N., Tamon, H., & Charinpanitkul, T. (2009). A model of reaction field in gas-injected arc-in-water method to synthesize single-walled carbon nanohorns: Influence of water temperature. *Journal of Applied Physics*, 106, 104315-1–104315-7.
- Prinzbach, H., Weiler, A., Landenberger, P., Wahl, F., Worth, J., Scott, L. T., Gelmont, M., Olevano, D., & Issendorff, B. v. (2000). Gas-phase production and photoelectron spectroscopy of the smallest fullerene, C<sub>20</sub>. *Nature*, 407, 60–63.
- Priyakumar, U. D., & Sastry, G. N. (2001a). Heterobuckybowls: A theoretical study on the structure, bowl-to-bowl inversion barrier, bond length alternation, structure-inversion barrier relationship, stability, and synthetic feasibility. *Journal of Organic Chemistry*, 66, 6523–6530.
- Priyakumar, U. D., & Sastry, G. N. (2001b). Tailoring the curvature, bowl rigidity and stability of heterobuckybowls: Theoretical design of synthetic strategies towards heterosumanenes. *Journal of Molecular Graphics and Modelling*, 19, 266–269.
- Priyakumar, U. D., & Sastry, G. N. (2001c). Theory provides a clue to accomplish the synthesis of sumanene, C<sub>21</sub>H<sub>12</sub>, the prototypical C<sub>3v</sub>-buckybowl. *Tetrahedron Letters*, 42, 1379–1381.
- Qin, L.-C. (2007). Determination of the chiral indices (n, m) of carbon nanotubes by electron diffraction. *Physical Chemistry Chemical Physics*, 9, 31–48.
- Radushkevich, L. V., & Lukyanovich, V. M. (1952). O strukture ugljeroda, obrazujucesjosja pri termiceskom razlozenii oksii ugljeroda na zeleznom kontakte. *Zurn. Fisic. Chim.*, 26, 88–95.
- Rao, C. N. R., Voggu, R., & Govindaraj, A. (2009a). Selective generation of single-walled

- carbon nanotubes with metallic, semiconducting and other unique electronic properties. *Nanoscale*, *1*, 96–105.
- Rao, F., Li, T., & Wang, Y. (2009b). Growth of all-carbon single-walled carbon nanotubes from diamonds and fullerenes. *Carbon*, *47*, 3580–3584.
- Robertson, D. H., Brenner, D. W., & Mintmire, J. W. (1992). Energetics of nanoscale graphitic tubules. *Physical Review B*, *45*, 12592–12595.
- Robinson, J. A., Snow, E. S., Badescu, S. C., Reinecke, T. L., & Perkins, F. K. (2006). Role of defects in single-walled carbon nanotube chemical sensors. *Nano Letters*, *6*, 1747–1751.
- Robinson, J. T., Perkins, F. K., Snow, E. S., Wei, Z., & Sheehan, P. E. (2008). Reduced graphene oxide molecular sensors. *Nano Letters*, *8*, 3137–3140.
- Rohlfing, E. A., Cox, D. M., & Kaldor, A. (1984). Production and characterization of supersonic carbon cluster beams. *Journal of Chemical Physics*, *81*, 3322–3330.
- Rojas, A., Martínez, M., Amador, P., & Torres, L. A. (2007). Increasing stability of the fullerenes with the number of carbon atoms: The experimental evidence. *The Journal of Physical Chemistry. B*, *111*, 9031–9035.
- Saito, M., & Miyamoto, Y. (2001). Theoretical identification of the smallest fullerene,  $C_{20}$ . *Physical Review Letters*, *87*, 035503-1–035503-4.
- Saito, R., Fujita, M., Dresselhaus, G., & Dresselhaus, M. S. (1992). Electronic structure of chiral graphene tubules. *Applied Physics Letters*, *60*, 2204–2206.
- Saito, R., Dresselhaus, G., & Dresselhaus, M. S. (1998). *Physical properties of carbon nanotubes*. London: Imperial College Press.
- Sakurai, H., Daiko, T., & Hirao, T. (2003). A synthesis of sumanene, a fullerene fragment. *Science*, *301*, 1878.
- Sano, M., Kamino, A., Okamura, J., & Shinkai, S. (2001). Ring closure of carbon nanotubes. *Science*, *293*, 1299–1301.
- Sastry, G. N., & Priyakumar, U. D. (2001). The role of heteroatom substitution in the rigidity and curvature of buckybowl. A theoretical study. *Journal of the Chemical Society, Perkin Transactions 2*, 30–40.
- Sastry, G. N., Jemmis, E. D., Mehta, G., & Shah, S. R. (1993). Synthetic strategies towards  $C_{60}$ . Molecular mechanics and MNDO study on sumanene and related structures. *Journal of the Chemical Society, Perkin Transactions 2*, 1867–1871.
- Sastry, G. N., Rao, H. S. P., Bednarek, P., & Priyakumar, U. D. (2000). Effect of substitution on the curvature and bowl-to-bowl inversion barrier of bucky-bowls. Study of mono-substituted corannulenes ( $C_{19}XH_{10}$ ,  $X = B^-, N^+, P^+$  and Si). *Chemical Communications*, 843–844.
- Saunders, M., Jiménez-Vázquez, H. A., Cross, R. J., & Poreda, R. J. (1993). Stable compounds of helium and neon:  $He@C_{60}$  and  $Ne@C_{60}$ . *Science*, *259*, 1428–1430.
- Scheina, S., & Friedrich, T. (2008). A geometric constraint, the head-to-tail exclusion rule, may be the basis for the isolated-pentagon rule in fullerenes with more than 60 vertices. *Proceedings of the National Academy of Sciences of the United States of America*, *105*, 19142–19147.
- Scott, L. T., Boorum, M. M., McMahon, B. J., Hagen, S., Mack, J., Blank, J., Wegner, H., & de Meijere, A. (2002). A rational chemical synthesis of  $C_{60}$ . *Science*, *295*, 1500–1503.
- Scuseria, G. E. (1996). Ab initio calculations of fullerenes. *Science*, *271*, 942–945.
- Seiders, T. J., Elliot, E. L., Grube, G. H., & Siegel, J. S. (1999). Synthesis of corannulene and alkyl derivatives of corannulene. *Journal of the American Chemical Society*, *121*, 7804–7813.
- Seiders, T. J., Baldrige, K. K., Grube, G. H., & Siegel, J. S. (2001). Structure/energy correlation of bowl depth and inversion barrier in corannulene derivatives: Combined experimental and quantum mechanical analysis. *Journal of the American Chemical Society*, *123*, 517–525.
- Serra, S., Cavazzoni, C., Chiarotti, G. L., Scandolo, S., & Tosatti, E. (1999). Pressure-induced solid carbonates from molecular  $CO_2$  by computer simulation. *Science*, *284*, 788–790.
- Shao, N., Gao, Y., Yoo, S., An, W., & Zeng, X. C. (2006). Search for lowest-energy fullerenes:  $C_{98}$  to  $C_{110}$ . *The Journal of Physical Chemistry. A*, *110*, 7672–7676.
- Shao, N., Gao, Y., & Zeng, X. C. (2007). Search for lowest-energy fullerenes 2:  $C_{38}$  to  $C_{80}$  and  $C_{112}$  to  $C_{120}$ . *The Journal of Physical Chemistry C*, *111*, 17671–17677.
- Shukla, M. K., & Leszczynski, J. (2009). Fullerene ( $C_{60}$ ) forms stable complex with nucleic acid base guanine. *Chemical Physics Letters*, *469*, 207–209.
- Shustova, N. B., Kuvychko, I. V., Bolskar, R. D., Seppelt, K., Strauss, S. H., Popov, A. A., & Boltalina, O. V. (2006). Trifluoromethyl derivatives of insoluble small-HOMO-LUMO-Gap hollow higher fullerenes. NMR and DFT structure elucidation of  $C_2-(C_{74}-D_{3h})(CF_3)_{12}$ ,  $C_5-(C_{76}-T_d(2))(CF_3)_{12}$ ,  $C_2-(C_{78}-D_{3h}(5))(CF_3)_{12}$ ,  $C_5-(C_{80}-C_{2v}(5))(CF_3)_{12}$ , and  $C_2-(C_{82}-C_2(5))(CF_3)_{12}$ . *Journal of the American Chemical Society*, *128*, 15793–15798.
- Shustova, N. B., Newell, B. S., Miller, S. M., Anderson, O. P., Bolskar, R. D., Seppelt, K., Popov,

- A. A., Boltalina, O. V., & Strauss, S. H. (2007). Discovering and verifying elusive fullerene cage isomers: Structures of  $C_{2-p}^{11}-(C_{74}-D_{3h})(CF_3)_{12}$  and  $C_{2-p}^{11}-(C_{78}-D_{3h}(5))(CF_3)_{12}$ . *Angewandte Chemie, International Edition*, 46, 4111–4114.
- Simeon, T. M., Yanov, I., & Leszczynski, J. (2005). Ab initio quantum chemical studies of fullerene molecules with substitutes  $C_{59}X$  [X = Si, Ge, Sn],  $C_{59}X^-$  [X = B, Al, Ga, In], and  $C_{59}X$  [X = N, P, As, Sb]. *International Journal of Quantum Chemistry*, 105, 429–436.
- Sinha, N., & Yeow, J. T.-W. (2005). Carbon nanotubes for biomedical applications. *IEEE Transactions on NanoBioscience*, 4, 180–195.
- Sinnokrot, M. O., & Sherrill, C. D. (2004). Highly accurate coupled cluster potential energy curves for the benzene dimer: Sandwich, T-shaped, and parallel-displaced configurations. *The Journal of Physical Chemistry A*, 108, 10200–10207.
- Slanina, Z., Zhao, X., Lee, S.-L., & Osawa, E. (1997).  $C_{90}$  temperature effects on relative stabilities of the IPR isomers. *Chemical Physics*, 219, 193–200.
- Slanina, Z., Uhlik, F., Yoshida, M., & Osawa, E. (2000a). A computational treatment of 35 IPR isomers of  $C_{88}$ . *Fullerene Science and Technology*, 8, 417–432.
- Slanina, Z., Zhao, X., Deota, P., & Osawa, E. (2000b). Relative stabilities of  $C_{92}$  IPR fullerenes. *Journal of Molecular Modeling*, 6, 312–317.
- Smalley, R. E. (1992). Self-assembly of the fullerenes. *Accounts of Chemical Research*, 25, 98–105.
- Smith, B. W., Monthieux, M., & Luzzi, D. E. (1998). Encapsulated  $C_{60}$  in carbon nanotubes. *Nature*, 396, 323–324.
- Smith, B. W., Monthieux, M., & Luzzi, D. E. (1999). Carbon nanotube encapsulated fullerenes: A unique class of hybrid materials. *Chemical Physics Letters*, 315, 31–36.
- Sofo, J. O., Chaudhari, A. S., & Barber, G. D. (2007). Graphane: A two-dimensional hydrocarbon. *Physical Review B*, 75, 153401-1–153401-4.
- Sotiropoulou, S., & Chaniotakis, N. A. (2003). Carbon nanotube array-based biosensor. *Analytical and Bioanalytical Chemistry*, 375, 103–105.
- Stevens, R. M. D., Frederick, N. A., Smith, B. L., Morse, D. E., Stucky, G. D., & Hansma, P. K. (2000). Carbon nanotubes as probes for atomic force microscopy. *Nanotechnology*, 11, 1–5.
- Stevens, R. M. D., Nguyen, C. V., & Meyyappan, M. (2004). Carbon nanotube scanning probe for imaging in aqueous environment. *IEEE Transactions on NanoBioscience*, 3, 56–60.
- Stewart, J. J. P. (1989). Optimization of parameters for semiempirical methods I. Method. *Journal of Computational Chemistry*, 10, 209–220.
- Stoilova, O., Jérôme, C., Detrembleur, C., Mouithys-Mickalad, A., Manolova, N., Rashkova, I., & Jérôme, R. (2007).  $C_{60}$ -containing nanostructured polymeric materials with potential biomedical applications. *Polymer*, 48, 1835–1843.
- Stone, A. J., & Wales, D. J. (1986). Theoretical studies of icosahedral  $C_{60}$  and some related species. *Chemical Physics Letters*, 128, 501–503.
- Strano, M. S. (2003). Probing chiral selective reactions using a revised Kataura plot for the interpretation of single-walled carbon nanotube spectroscopy. *Journal of the American Chemical Society*, 125, 16148–16153.
- Strano, M. S. (2007). Carbon nanotubes: Sorting out left from right. *Nature Nanotechnology*, 2, 340–341.
- Suchanek, W. L., Libera, J. A., Gogotsi, Y., & Yoshimura, M. (2001). Behavior of  $C_{60}$  under hydrothermal conditions: Transformation to amorphous carbon and formation of carbon nanotubes. *Journal of Solid State Chemistry*, 160, 184–188.
- Suenaga, K., Wakabayashi, H., Koshino, M., Sato, Y., Urita, K., & Iijima, S. (2007). Imaging active topological defects in carbon nanotubes. *Nature Nanotechnology*, 2, 358–360.
- Sulman, E., Yanov, I., & Leszczynski, J. (1999). An active site model and the catalytic activity mechanism of the new fullerene-based catalyst -  $(\eta^2-C_{60})Pd(PPh_3)_2$ . *Fullerenes, Nanotubes and Carbon Nanostructures*, 7, 467–484.
- Sun, G. (2003). Assigning the major isomers of fullerene  $C_{88}$  by theoretical  $^{13}C$  NMR spectra. *Chemical Physics Letters*, 367, 26–33.
- Sun, G., & Kertesz, M. (2002).  $^{13}C$  NMR spectra for IPR isomers of fullerene  $C_{86}$ . *Chemical Physics*, 276, 107–114.
- Suzuki, S., & Kobayashi, Y. (2007). Healing of low-energy irradiation-induced defects in single-walled carbon nanotubes at room temperature. *The Journal of Physical Chemistry C*, 111, 4524–4528.
- Sygula, A., & Rabideau, P. W. (1999). Non-pyrolytic syntheses of buckybowls: Corannulene, cyclopentacorannulene, and a semibuckminsterfullerene. *Journal of the American Chemical Society*, 121, 7800–7803.
- Tagmatarchis, N., Arcon, D., Prato, M., & Shinohara, H. (2002). Production, isolation and structural characterization of [92]fullerene isomers. *Chemical Communications*, 2992–2993.
- Tang, A. C., & Huang, F. Q. (1995). Electronic structures of giant fullerenes with  $I_h$  symmetry. *Physical Review B*, 51, 13830–13832.

- Tang, A. C., Li, Q. S., Liu, C. W., & Li, J. (1993). Symmetrical clusters of carbon and boron. *Chemical Physics Letters*, 201, 465–469.
- Taylor, R. (1992). The third form of carbon: A new era in chemistry. *Interdisciplinary Science Reviews*, 17, 161–170.
- Taylor, R., Hare, J. P., Abdul-Sada, A. K., & Kroto, H. W. (1990). Isolation, separation and characterisation of the fullerenes  $C_{60}$  and  $C_{70}$ : The third form of carbon. *Journal of the Chemical Society, Chemical Communications*, 1423–1425.
- Taylor, R., Langley, G. J., Dennis, T. J. S., Kroto, H. W., & Walton, D. R. M. (1992). A mass spectrometric NMR study of fullerene-78 isomers. *Journal of the Chemical Society, Chemical Communications*, 1043–1046.
- Taylor, R., Langley, G. J., Avent, A. G., Dennis, T. J. S., Kroto, H. W., & Walton, D. R. M. (1993).  $^{13}C$  NMR spectroscopy of  $C_{76}$ ,  $C_{78}$ ,  $C_{84}$  and mixtures of  $C_{86}$ – $C_{102}$ ; anomalous chromatographic behaviour of  $C_{82}$ , and evidence for  $C_{70}H_{12}$ . *Journal of the Chemical Society, Perkin Transactions 2*, 1029–1036.
- Terrones, M., Terrones, G., & Terrones, H. (2002). Structure, chirality, and formation of giant icosahedral fullerenes and spherical graphitic onions. *Structural Chemistry*, 13, 373–384.
- Thilgen, C., & Diederich, F. (2006). Structural aspects of fullerene chemistry - A journey through fullerene chirality. *Chemical Reviews*, 106, 5049–5135.
- Thrash, T. P., Cagle, D. W., Alford, J. M., Wright, K., Ehrhardt, G. J., Mirzadeh, S., & Wilson, L. J. (1999). Toward fullerene-based radiopharmaceuticals: High-yield neutron activation of endohedral  $^{165}Ho$  metallofullerenes. *Chemical Physics Letters*, 308, 329–336.
- Troshin, P. A., Avent, A. G., Darwish, A. D., Martsinovich, N., Abdul-Sada, A. K., Street, J. M., & Taylor, R. (2005). Isolation of two seven-membered ring  $C_{58}$  fullerene derivatives:  $C_{58}F_{17}CF_3$  and  $C_{58}F_{18}$ . *Science*, 309, 278–281.
- Troyanov, S. I., & Tamm, N. B. (2009). Cage connectivities of  $C_{88}$  (33) and  $C_{92}$  (82) fullerenes captured as trifluoromethyl derivatives,  $C_{88}(CF_3)_{18}$  and  $C_{92}(CF_3)_{16}$ . *Chemical Communications*, 6035–6037.
- Valsakumar, M. C., Subramanian, N., Yousuf, M., Sahu, P. Ch., Hariharan, Y., Bharathi, A., Sastry, V. S., Janaki, J., Rao, G. V. N., Radhakrishnan, T. S., & Sundar, C. S. (1993). Crystal structure and disorder in solid  $C_{70}$ . *Physical Review B*, 48, 9080–9085.
- Velasco-Santos, C., Martínez-Hernández, A. L., Consultchi, A., Rodríguez, R., & Castaño, V. M. (2003). Naturally produced carbon nanotubes. *Chemical Physics Letters*, 373, 272–276.
- Vostrowsky, O., & Hirsch, A. (2004). Molecular peapods as supramolecular carbon allotropes. *Angewandte Chemie, International Edition*, 43, 2326–2329.
- Wahl, F., Worth, J., & Prinzbach, H. (1993). The pagodane route to dodecahedranes: An improved approach to the  $C_{20}H_{20}$  parent framework; partial and total functionalizations - Does  $C_{20}$ -fullerene exist? *Angewandte Chemie (International Edition in English)*, 32, 1722–1726.
- Wanbayor, R., & Ruangpornvisuti, V. (2008). Theoretical study of adsorption of  $C_1$ – $C_3$  alkoxides on various cap-ended and open-ended armchair (5,5) single-walled carbon nanotubes. *Carbon*, 46, 12–18.
- Wang, G.-W., Zhang, X.-H., Zhan, H., Guo, Q.-X., & Wu, Y.-D. (2003). Accurate calculation, prediction, and assignment of  $^3He$  NMR chemical shifts of Helium-3-encapsulated fullerenes and fullerene derivatives. *Journal of Organic Chemistry*, 68, 6732–6738.
- Wang, C., Zhou, G., Liu, H., Wu, J., Qiu, Y., Gu, B.-L., & Duan, W. (2006). Chemical functionalization of carbon nanotubes by carboxyl groups on Stone-Wales defects: A density functional theory study. *The Journal of Physical Chemistry. B*, 110, 10266–10271.
- Wang, X., Tabakman, S. M., & Dai, H. (2008). Atomic layer deposition of metal oxides on pristine and functionalized graphene. *Journal of the American Chemical Society*, 130, 8152–8153.
- WenXing, B., ChangChun, Z., & WanZhao, C. (2004). Simulation of Young's modulus of single-walled carbon nanotubes by molecular dynamics. *Physica B*, 352, 156–163.
- Wikipedia - <http://en.wikipedia.org/wiki/Carbon>.
- Woodward, R. B., & Hoffmann, R. (1969). The conservation of orbital symmetry. *Angewandte Chemie (International Edition in English)*, 8, 781–853.
- Wu, J., & Hugelberg, F. (2008). Computational study on  $C_{80}$  enclosing mixed trimetallic nitride clusters of the form  $Gd_xM_{3-x}N$  ( $M = Sc, Sm, Lu$ ). *The Journal of Physical Chemistry C*, 112, 5770–5777.
- Wu, Y.-T., & Siegel, J. S. (2006). Aromatic molecular-bowl hydrocarbons: Synthetic derivatives, their structures, and physical properties. *Chemical Reviews*, 106, 4843–4867. and references therein.
- Wu, X., & Zeng, X. C. (2009). Periodic graphene nanobuds. *Nano Letters*, 9, 250–256.
- Xia, J., Chen, F., Li, J., & Tao, N. (2009). Measurement of the quantum capacitance of graphene. *Nature Nanotechnology*, 4, 505–509.

- Xie, S.-Y., Gao, F., Lu, X., Huang, R.-B., Wang, C.-R., Zhang, X., Liu, M.-L., Deng, S.-L., & Zheng, L.-S. (2004). Capturing the labile fullerene[50] as  $C_{50}Cl_{10}$ . *Science*, *304*, 699.
- Yakobson, B. I., Brabec, C. J., & Bernholc, J. (1996). Nanomechanics of carbon tubes: Instabilities beyond linear response. *Physical Review Letters*, *76*, 2511–2514.
- Yamada, M., Nakahodo, T., Wakahara, T., Tsuchiya, T., Maeda, Y., Akasaka, T., Kako, M., Yoza, K., Horn, E., Mizorogi, N., Kobayashi, K., & Nagase, S. (2005). Positional control of encapsulated atoms inside a fullerene cage by exohedral addition. *Journal of the American Chemical Society*, *127*, 14570–14571.
- Yamada, M., Akasaka, T., & Nagase, S. (2010). Endohedral metal atoms in pristine and functionalized fullerene cages. *Accounts of Chemical Research*, *43*, 92–102.
- Yang, S. H., Shin, W. H., Lee, J. W., Kim, S. Y., Woo, S. I., & Kang, J. K. (2006a). Interaction of a transition metal atom with intrinsic defects in single-walled carbon nanotubes. *The Journal of Physical Chemistry B*, *110*, 13941–13946.
- Yang, S. H., Shin, W. H., & Kang, J. K. (2006b). Ni adsorption on Stone-Wales defect sites in single-wall carbon nanotubes. *Journal of Chemical Physics*, *125*, 084705-1–084705-5.
- Yang, F. H., Lachawiec, A. J., Jr., & Yang, R. T. (2006c). Adsorption of spillover hydrogen atoms on single-wall carbon nanotubes. *The Journal of Physical Chemistry. B*, *110*, 6236–6244.
- Yanov, I., Leszczynski, J., Sulman, E., Matveeva, V., & Semagina, N. (2004). Modeling of the molecular structure and catalytic activity of the new fullerene-based catalyst ( $\eta^2-C_{60}$ )Pd(PPh<sub>3</sub>)<sub>2</sub>: An application in the reaction of selective hydrogenation of acetylenic alcohols. *International Journal of Quantum Chemistry*, *100*, 810–817.
- Yumura, T., Nozaki, D., Bandow, S., Yoshizawa, K., & Iijima, S. (2005a). End-cap effects on vibrational structures of finite-length carbon nanotubes. *Journal of the American Chemical Society*, *127*, 11769–11776.
- Yumura, T., Sato, Y., Suenaga, K., & Iijima, S. (2005b). Which do endohedral Ti<sub>2</sub>C<sub>80</sub> metallofullerenes prefer energetically: Ti<sub>2</sub>@C<sub>80</sub> or Ti<sub>2</sub>C<sub>2</sub>@C<sub>78</sub>? A theoretical study. *The Journal of Physical Chemistry. B*, *109*, 20251–20255.
- Yumura, T., Kertesz, M., & Iijima, S. (2007). Local modifications of single-wall carbon nanotubes induced by bond formation with encapsulated fullerenes. *The Journal of Physical Chemistry. B*, *111*, 1099–1109.
- Zhang, J., & Zuo, J. M. (2009). Structure and diameter-dependent bond lengths of a multi-walled carbon nanotube revealed by electron diffraction. *Carbon*, *47*, 3515–3528.
- Zhang, B. L., Wang, C. Z., Ho, K. M., Xu, C. H., & Chan, C. T. (1993). The geometry of large fullerene cages: C<sub>72</sub> to C<sub>102</sub>. *Journal of Chemical Physics*, *98*, 3095–3102.
- Zhang, G., Qi, P., Wang, X., Lu, Y., Mann, D., Li, X., & Dai, H. (2006). Hydrogenation and hydrocarbonation and etching of single-walled carbon nanotubes. *Journal of the American Chemical Society*, *128*, 6026–6027.
- Zhang, H., Cao, G., Wang, Z., Yang, Y., Shi, Z., & Gu, Z. (2008). Influence of ethylene and hydrogen flow rates on the wall number, Crystallinity, and length of millimeter-long carbon nanotube array. *The Journal of Physical Chemistry C*, *112*, 12706–12709 and references therein.
- Zhao, K., & Pitzer, R. M. (1996). Electronic structure of C<sub>28</sub>, Pa@C<sub>28</sub>, and U@C<sub>28</sub>. *Journal of Physical Chemistry*, *100*, 4798–4802.
- Zhao, Y., & Truhlar, D. G. (2007). Size-selective supramolecular chemistry in a hydrocarbon nanoring. *Journal of the American Chemical Society*, *129*, 8440–8442.
- Zhao, Y., & Truhlar, D. G. (2008). Computational characterization and modeling of buckyball tweezers: Density functional study of concave convex interactions. *Physical Chemistry Chemical Physics*, *10*, 2813–2818.
- Zhao, X., Slanina, Z., & Goto, H. (2004a). Theoretical studies on the relative stabilities of C<sub>96</sub> IPR fullerenes. *The Journal of Physical Chemistry A*, *108*, 4479–4484.
- Zhao, X., Goto, H., & Slanina, Z. (2004b). C<sub>100</sub> IPR fullerenes: Temperature-dependent relative stabilities based on the Gibbs function. *Chemical Physics*, *306*, 93–104.
- Zhou, Z., Steigerwald, M., Hybertsen, M., Brus, L., & Friesner, R. A. (2004). Electronic structure of tubular aromatic molecules derived from the metallic (5,5) armchair single wall carbon nanotube. *Journal of the American Chemical Society*, *126*, 3597–3607.
- Zhou, L., Gao, C., Zhu, D. D., Xu, W., Chen, F. F., Palkar, A., Echegoyen, L., & Kong, E. S.-W. (2009). Facile functionalization of multilayer fullerenes (carbon nanonions) by nitrene chemistry and grafting from strategy. *Chemistry - A European Journal*, *15*, 1389–1396.

- Zhu, Z. H., Hatori, H., Wang, S. B., & Lu, G. Q. (2005). Insights into hydrogen atom adsorption on and the electrochemical properties of nitrogen-substituted carbon materials. *The Journal of Physical Chemistry. B*, 109, 16744–16749.
- Zope, R. R., Baruah, T., Pederson, M. R., & Dunlap, B. I. (2008). Static dielectric response of icosahedral fullerenes from  $C_{60}$  to  $C_{2160}$  characterized by an all-electron density functional theory. *Physical Review B*, 77, 115452-1–115452-5.



# 23 Optical Properties of Quantum Dot Nano-composite Materials Studied by Solid-State Theory Calculations

*Ying Fu · Hans Ågren*

Division of Theoretical Chemistry and Biology, School of Biotechnology,  
Royal Institute of Technology, Stockholm, Sweden

<i>Introduction</i> .....	870
<i>Solid-State <math>k \cdot p</math> Theory</i> .....	871
<i>Excitons in Nanostructures</i> .....	875
<i>Polarization and Optical Properties of Exciton-Polaritons</i> .....	878
<i>Exciton-Polariton Photonic Crystals</i> .....	882
Photonic Dispersion of QD Dimer Systems .....	883
Lossless Dielectric Constant of QD Dimer Systems .....	887
<i>Multiple-Photon and Multiple-Carrier Processes</i> .....	889
Multiphoton Process .....	889
Impact Ionization and Auger Recombination .....	891
<i>Summary</i> .....	896
<i>References</i> .....	897



**Abstract:** This chapter reviews the fundamental concepts of excitons and excitonic polaritons and their extraordinary optical properties in quantum dot nano-composite materials. By starting with the optical excitation of an exciton in the nanostructure we show that the effective dielectric constant of the nanostructure becomes significantly modified due to the exciton generation and recombination, resulting in high positive and negative dielectric constants. We also discuss single exciton generation by multiple photons and multiple exciton generation by single photon. All these nonlinear optical properties of quantum dot nano-composite materials offer novel possibilities and are expected to have deep impact in nanophotonics.

## Introduction

---

Materials with nanoscale features have the potential to revolutionize optoelectronics, permitting new and interesting device and system capabilities. The key design element is the geometry, that is, size and shape, which defines the properties of the nanostructured material and has led to the expectation of new and/or significantly improved physical, electrical, and optical properties. To precisely engineer light–matter interaction at the nanoscale, electron-hole pairs, that is, excitons, and their coupling with photons, exciton-polaritons, are becoming increasingly important. Excitons are of great interest in nanoscience because it has been discovered that their properties can be dictated by the size and the shape of a nanostructure in which they are confined, in addition to the constitution of the nanostructure. The new aspect of excitons that is prevalent in or even defining nanoscience is that the physical size and shape of the nanostructure are parameters that significantly influence their properties.

Exciton polaritons were intensively studied in the 1960s and 1970s, and their manifestation in various optical phenomena, including light reflection and transmission, photoluminescence, and resonant light scattering are well established and documented by now, see, for example, the dedicated volume (Sturge and Rashba 1982) and references therein. We refer to Kavokin (2007) that presents detailed discussions of energy dispersion of exciton-polaritons in microcavities (largely about quantum wells, QWs), to Scholes and Rumbles (2006) for a very intuitive description of excitons in nanoscale systems and a detailed review about excitons in polymers and nanotubes, and to Weisbuch et al. (2000) for research and development of excitons and photons in confined structures from three-dimensionally (3D) extended states (bulk) to atom-like quantum dots (QDs) and their applications in light emitting devices.

In semiconductor technology, the geometric miniaturization of individual components and devices have been scaling according to Moore's Law (International Technology Roadmap for Semiconductors; Fu et al. 2006a). Photonics has also been catching up (Thylén et al. 2006) but at a slow pace due to the limitations imposed by the diffraction limit. Resonant excitonic states in nanostructures, after coupling with light to form excitonic polaritons, provide a source for both high and negative dielectric constant (Fu et al. 2006b, 2008; Zia et al. 2006), thus offering novel possibilities to drastically increase the integration density and new functionalities in photonics at the nanoscale. Rapid growth of nanotechnology also greatly expands the clinical opportunities. Colloidal QDs are highly fluorescent with excellent photochemical stability, extreme brightness, and broad excitation spectral range, which have been introduced successfully in many fluorescence-based optical imaging applications (Medintz et al. 2005). Surface-modified and water-soluble QDs open a new era in cell imaging and bio-targeting as transport vehicles

■ Table 23-1

Atomic structures of typical elements making up common semiconductors

Element	Core electrons	Valence electrons
IV-Si	$1s^2 2s^2 2p^6$	$3s^2 3p^2$
IV-Ge	$1s^2 2s^2 2p^6 3s^2 3p^6 3d^{10}$	$4s^2 4p^2$
III-Ga	$1s^2 2s^2 2p^6 3s^2 3p^6 3d^{10}$	$4s^2 4p^1$
V-As	$1s^2 2s^2 2p^6 3s^2 3p^6 3d^{10}$	$4s^2 4p^3$
II-Cd	$1s^2 2s^2 2p^6 3s^2 3p^6 3d^{10} 4s^2 4p^6 4d^{10}$	$5s^2$
VI-Se	$1s^2 2s^2 2p^6 3s^2 3p^6 3d^{10}$	$4s^2 4p^4$

for therapeutic drug delivery to different diseases such as cancer and atherosclerosis (Derfus et al. 2007; Molnár et al. 2010; Vashist et al. 2006).

In this chapter we concentrate on nano-semiconductor systems, where it has become possible during the last 15 years to handle and control single excitons. More specifically we focus on excitons and exciton-polaritons in semiconductor QDs. This chapter presents first a theoretical background of the solid-state theory, the exciton and the coupling between the exciton and the photon (excitonic polariton). Optical properties of exciton polaritons in nanostructures and their photonic engineering are then discussed.

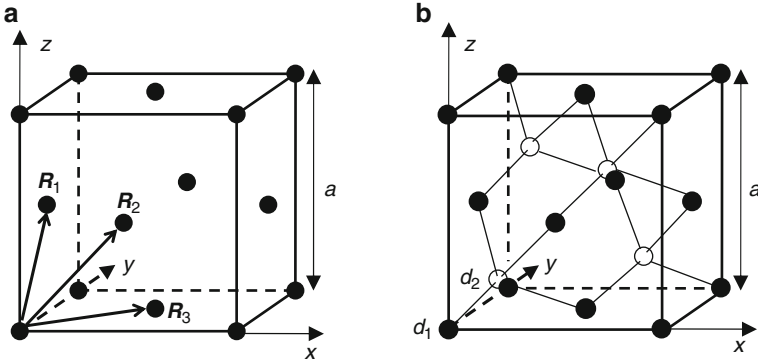
## Solid-State $k \cdot p$ Theory

The theoretical description of electronic and optical properties of nanostructures is currently advancing using modern quantum methodologies such as pseudo potential, tight-binding, and atomistic semi-empirical pseudo potential methods (Allan and Delerue 2008; Franceschetti et al. 2006; Jiang et al. 2009; Rabani and Baer 2008). However, these studies have been limited to light atoms and small nanostructure sizes. Our target nanostructure systems are about 10 nm in diameter and even more where macroscopic micrometer scale solid-state theory is well developed.

In isolated atoms the energy levels are sharply defined. When two atoms are brought close to each other their electron wave functions overlap. As a result of the interaction between the electrons, it turns out that each single state of the isolated atom splits into two states with different energies. The degree of splitting increases as the inter-atomic separation decreases. Similarly, if five atoms are placed in close proximity, then each original energy level splits into five new levels. The same process occurs in a solid, where there are roughly  $10^{28}$  atoms/m<sup>3</sup>. The energy levels associated with each state of the isolated atom spread into essentially continuous energy bands separated from each other by energy gaps.

Before further examining the various properties of semiconductors it is extremely useful to examine the atomic structure of some of the elements which make up commonly used semiconductors as listed in ● Table 23-1.

A very important conclusion can be drawn about the elements making up the semiconductors: The outmost valence electrons are made up of electrons in either the  $s$ - or  $p$ -type orbitals. While this conclusion is strictly true for elements in the atomic form, it turns out that even in crystalline semiconductors the electrons in the valence band (VB) and conduction band (CB) retain this  $s$ - or  $p$ -type character. The core electrons are usually not of interest, except



■ Fig. 23-1

(a) Face-centered cubic (fcc) lattice with primitive translation vectors  $R_1$ ,  $R_2$ , and  $R_3$ . (b) Zincblende crystal structure where  $d_1$  and  $d_2$  denote two different atoms (can be identical such as in Si crystal in which case the lattice structure is called diamond). In both (a) and (b),  $a$  denotes the lattice constant

of some special characterization-type experiments. Note that II–VI compounds such as CdSe are normally complicated and their lattice structures are hexagonal.

In general, it is found that when atoms exchange or share valence electrons so that the complement of quantum states is completed, they have a lower electrostatic energy for their combined electron patterns than when they are separate. For example, silicon has four valence electrons grouped in two closely spaced energy levels ( $3s$  and  $3p$ , see ▶ Table 23-1); it can combine with other silicon atoms by sharing four valence electrons with four surrounding silicon atoms in an endless array. The atoms around any one atom are centered at the corners of a regular tetrahedron: the tetrahedral bond. This creates the diamond crystal structure.

Essentially all semiconductors of interest for electronics and optoelectronics have the face-centered cubic (fcc) structure. However, they have two atoms per basis. The coordinates of the two basis atoms are  $(000)$  and  $(a/4)(111)$ , indicated in  $d_1$  and  $d_2$  in ▶ Fig. 23-1b. Here  $a$  is normally denoted as the crystal lattice constant. If the two atoms of the basis are identical, the structure is called the diamond structure. Semiconductors such as silicon, germanium, and carbon fall into this category. If the two atoms are different, for example, GaAs, AlAs, and CdS, the structure is called zincblende.

The intrinsic property of a crystal is that the environment around a given atom or group of atoms is exactly the same as the environment around another atom or similar group of atoms. Many of the properties of crystals and many of the theoretical techniques used to describe crystals derive from such a periodicity of crystalline structures. This suggests the use of Fourier analysis in the form of *real space–reciprocal space* or *wave vector space* duality for crystal problem discussions. Many concepts are best understood in terms of functions of the wave vector. We prefer to describe a wave with wavelength  $\lambda$  as a plane wave with wave vector  $\mathbf{k}$  of magnitude  $2\pi/\lambda$  and propagation direction perpendicular to the wave front. The space of the wave vectors is called the reciprocal space.

The  $\mathbf{k} \cdot \mathbf{p}$  method is much used in analyzing semiconductor nanostructures as it gives a good approximation of the states close to the  $\Gamma$  point ( $\mathbf{k} = 0$ ), which is the most relevant region for many device applications. The approximation is given with good accuracy, while in many

nanostructure calculations, this is the only feasible numerical model that can be implemented (even though it is still much restricted due to the computational capability).

The goal is essentially to solve the Schrödinger equation for a nanostructure to get the eigenenergies and their associated eigenvectors (wave functions). The wave functions usually have too high frequencies to be feasible to calculate explicitly using numerical methods on computers as an inordinately high number of grid points would be necessary to capture an acceptable numerical representation of the wave function. A solution is to separate the wave functions into an oscillatory part and a modulating part which is of the same scale as the heterostructure. This is the basic idea of the envelope function approximation – the modulating part is called the envelope function. We write the envelope function as a Bloch function:

$$\psi_{nk}(\mathbf{r}) = e^{i\mathbf{k}\cdot\mathbf{r}} u_{nk}(\mathbf{r}) \quad (23.1)$$

where  $n$  is the state index and  $\mathbf{k}$  is the wave vector. The Schrödinger equation for this wave function is simply

$$\left[ \frac{\mathbf{p}^2}{2m_0} + V(\mathbf{r}) \right] \psi_{nk}(\mathbf{r}) = E_n(\mathbf{k}) \psi_{nk}(\mathbf{r}) \quad (23.2)$$

Substituting the factorization into the equation requires some care in evaluating the product of the momentum operator  $\mathbf{p}$  and the two parts of the wave function. With  $\mathbf{p} = -i\hbar\nabla$  and knowing from vector calculus that  $\nabla e^{i\mathbf{k}\cdot\mathbf{r}} = i\mathbf{k}e^{i\mathbf{k}\cdot\mathbf{r}}$ , the product of the momentum operator and the wave function becomes

$$-i\hbar\nabla \left[ e^{i\mathbf{k}\cdot\mathbf{r}} u_{nk}(\mathbf{r}) \right] = -i\hbar e^{i\mathbf{k}\cdot\mathbf{r}} (\nabla + i\mathbf{k}) u_{nk}(\mathbf{r}) = e^{i\mathbf{k}\cdot\mathbf{r}} (\mathbf{p} + \hbar\mathbf{k}) u_{nk}(\mathbf{r}) \quad (23.3)$$


Applying the momentum operator a second time gives  $e^{i\mathbf{k}\cdot\mathbf{r}} (\mathbf{p} + \hbar\mathbf{k})^2 u_{nk}(\mathbf{r})$ , so the Schrödinger equation can be written in the following way that the oscillatory part will cancel out:

$$e^{i\mathbf{k}\cdot\mathbf{r}} \left[ \frac{(\mathbf{p} + \hbar\mathbf{k})^2}{2m_0} + V(\mathbf{r}) \right] u_{nk}(\mathbf{r}) = e^{i\mathbf{k}\cdot\mathbf{r}} E_n(\mathbf{k}) u_{nk}(\mathbf{r}) \quad (23.4)$$

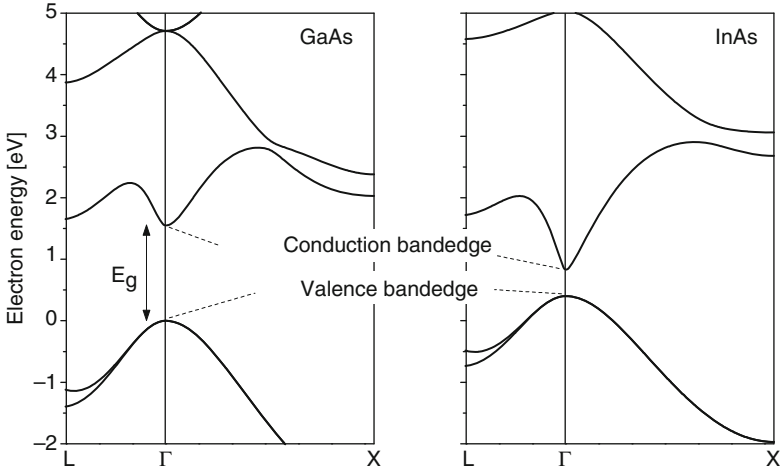
Expanding the  $(\mathbf{p} + \hbar\mathbf{k})^2$  term gives

$$\left[ \frac{\mathbf{p}^2}{2m_0} + V(\mathbf{r}) + \frac{\hbar\mathbf{k}\cdot\mathbf{p}}{m_0} + \frac{\hbar^2 k^2}{2m_0} \right] u_{nk}(\mathbf{r}) = E_n(\mathbf{k}) u_{nk}(\mathbf{r}) \quad (23.5)$$

The first two terms are identical to the original Hamiltonian, so if the two other terms are treated as a small perturbation the Hamiltonian can be expressed as  $(H_0 + H_1 + H_2) u_{nk}(\mathbf{r}) = E_n(\mathbf{k}) u_{nk}(\mathbf{r})$ , and treat  $H_1 = (\hbar/m_0)\mathbf{k}\cdot\mathbf{p}$  and  $H_2 = \hbar^2 k^2/2m_0$  as first-order and second-order perturbations, respectively.

If the equation is solved for  $\mathbf{k} = 0$  with only  $H_0$  remaining nonzero, the result is a set of eigenvectors  $u_{n0}(\mathbf{r})$ , typically at the optimal points such as the  $\Gamma$  point in  Fig. 23-2 which shows the energy band structure of most common GaAs and InAs bulk materials. For the following discussion we express the eigenfunction using Dirac notation as  $|n\rangle$ , and eigenvalues  $E_n$ . These form a complete basis set with orthogonal eigenfunctions which can be used in perturbation calculations of states with  $\mathbf{k} \neq 0$ .

As the atoms of the elements making up the semiconductors are brought together to form the crystal, the valence electronic states are perturbed by the presence of neighboring atoms.



■ Fig. 23-2  
Energy band structures of electrons in GaAs and InAs bulk materials

While the original atomic functions describing the valence electrons, of course, no longer are eigenstates of the problem, their characteristics can be used as a good approximate set of basis states to describe the “crystalline” electrons. For most semiconductor materials of interest, the atomic functions required to describe the outermost electrons are  $s$ ,  $p_x$ ,  $p_y$ , and  $p_z$  types, as shown by [Table 23-1](#). A common approach of choosing the above  $|n\rangle$  at the  $\Gamma$  point is to follow Kane (1957) and define a set of eight states, that is,  $u_{nk}(\mathbf{r})$  in [Eq. 23.1](#) at  $\mathbf{k} = 0$ ,  $|S \uparrow\rangle$ ,  $|X \uparrow\rangle$ ,  $|Y \uparrow\rangle$ ,  $|Z \uparrow\rangle$ ,  $|S \downarrow\rangle$ ,  $|X \downarrow\rangle$ ,  $|Y \downarrow\rangle$ ,  $|Z \downarrow\rangle$ , where the arrows indicate spin up and down.  $|X, Y, Z\rangle$  denotes degenerate VBs while  $|S\rangle$  denotes the CB. Other remote bands are not included unless specifically required.

The eigen function for a given  $\mathbf{k}$  is a linear combination of the basis functions:

$$u_{nk}(\mathbf{r}) = \sum_m c_{nm}(\mathbf{k})|m\rangle \quad (23.6)$$

so the objective is now to find the coefficients  $c_{nm}$  that form our envelope parts together with the basis functions at  $\Gamma$ .

If we substitute this linear combination into the Schrödinger equation, we get

$$H \sum_m c_{nm}(\mathbf{k})|m\rangle = \sum_m c_{nm}(\mathbf{k})H|m\rangle = E_n(\mathbf{k}) \sum_m c_{nm}(\mathbf{k})|m\rangle \quad (23.7)$$

Multiply this on the left with the conjugate of any, say  $|\ell\rangle$ , of the basis functions, and we obtain

$$\sum_m c_{nm}(\mathbf{k})\langle\ell|H|m\rangle = E_n(\mathbf{k}) \sum_m c_{nm}(\mathbf{k})\langle\ell|m\rangle = E_n(\mathbf{k})c_{n\ell}(\mathbf{k}) \quad (23.8)$$

The right-hand part is the result of wave function’s orthonormal property.

Inserting the expanded  $\mathbf{k} \cdot \mathbf{p}$  Hamiltonian [Eq. 23.5](#), multiplying with the conjugate, and integrating over an unit cell using the fact that the basis functions are orthonormal gives

$$\sum_m \left[ \left( E_m + \frac{\hbar^2 k^2}{2m_0} \right) \delta_{\ell m} + \frac{\hbar}{m_0} \langle\ell|\mathbf{k} \cdot \mathbf{p}|m\rangle \right] c_{nm}(\mathbf{k}) = E_n(\mathbf{k})c_{n\ell}(\mathbf{k}) \quad (23.9)$$

The first-order approximation is thus

$$E_n(\mathbf{k}) = E_n + \frac{\hbar^2 k^2}{2m_0}, \quad c_{nm}(\mathbf{k}) = \delta_{nm} \quad (23.10)$$

The second-order approximation is thus given by

$$E_n(\mathbf{k}) = E_n + \frac{\hbar^2 k^2}{2m_0} + \frac{\hbar}{m_0} \sum_{\ell \neq n} \frac{|\langle \ell | \mathbf{k} \cdot \mathbf{p} | n \rangle|^2}{E_n - E_\ell} \quad (23.11)$$

The result can be expressed in terms of an effective mass  $m^*$ :

$$E_n(\mathbf{k}) = E_n + \sum_{i,j} \frac{\hbar^2}{2m_{ij}^*} k_i k_j \quad (23.12)$$

where  $i, j = x, y, z$ , and

$$\frac{m_0}{m_{ij}^*} = \delta_{ij} + \frac{2}{m_0} \sum_{\ell \neq n} \frac{\langle n | p_i | \ell \rangle \langle \ell | p_j | n \rangle}{E_n - E_\ell} \quad (23.13)$$

Note here that the effective mass can be anisotropic which can be utilized for optical coupling in quantum well photodetection (Xu et al. 1994).

It can be easily seen that a narrow bandgap, which leads to two states being close to each other, gives a small effective mass which agrees very well with the experimental data which indicates that InSb has both the smallest bandgap and the lowest effective mass. By a series of experiments the parameters for the  $\mathbf{k} \cdot \mathbf{p}$  Hamiltonian can be determined, and the final result is a matrix with many material-dependent parameters and no arbitrary parameters to adjust. Details of the  $\mathbf{k} \cdot \mathbf{p}$  Hamiltonian for III–V and II–VI semiconductor materials are well documented in reviews (Madelung 1991, 1992; Vurgaftman et al. 2001).

## Excitons in Nanostructures

After reviewing some solid state theory, we are now capable of modeling excitons and exciton-polaritons in semiconductor nanostructures. We first study and model the exciton in general, then excitons in QD-based nanostructures, and finally applications of QD excitons and exciton-polaritons. Details of exciton theory can be found in Dimmock (1967) and Fu and Willander (1999).

As discussed in the previous section, the energy band structure of electrons in a semiconductor consists of energy bands separated by band gaps. At absolute zero temperature, a pure semiconductor is characterized by having only completely occupied and completely empty energy bands. The highest occupied bands are referred as VBs and the lowest unoccupied band is the CB. Let  $H_0$  be the Hamiltonian of the nanostructure under investigation, then

$$H_0 \psi_{v\mathbf{k}_h}(\mathbf{r}_h) = E_v(\mathbf{k}_h) \psi_{v\mathbf{k}_h}(\mathbf{r}_h)$$

denotes the VB state and

$$H_0 \psi_{c\mathbf{k}_e}(\mathbf{r}_e) = E_c(\mathbf{k}_e) \psi_{c\mathbf{k}_e}(\mathbf{r}_e)$$

the CB state. We consider an optical absorption process in which an allowed electric dipole (not ultra intense excitation) transition raises an electron from a filled VB state to an empty CB state. The properties of a system with an electron missing from a VB state  $\psi_{v\mathbf{k}_h}$  can be described

by considering a single particle of positive charge in the state, that is, the VB hole. The exact expression of the interaction potential between the CB electron and VB hole is rather complicated. For commonly used semiconductor systems, and when the electron and hole are widely separated and moving relatively slowly with respect to one another, the Coulomb interaction between them is screened and given by Dimmock (1967)

$$V(\mathbf{r}_e - \mathbf{r}_h) = -\frac{e^2}{4\pi\epsilon_\infty|\mathbf{r}_e - \mathbf{r}_h|} \quad (23.14)$$

where  $\epsilon_\infty$  is the high-frequency dielectric constant.

The exciton state is described by the two-particle wave function

$$\psi_{c\mathbf{k}_e}(\mathbf{r}_e)\psi_{v\mathbf{k}_h}(\mathbf{r}_h)$$

The total wave vector of the excited state is  $\mathbf{K} = \mathbf{k}_e + \mathbf{k}_h$ . Because of the Coulomb interaction,  $\psi_{c\mathbf{k}_e}(\mathbf{r}_e)\psi_{v\mathbf{k}_h}(\mathbf{r}_h)$  does not represent an eigen state of the system. We approximate the eigen state of the exciton by a linear combination of electron-hole states


$$\Psi_{n\mathbf{K}}(\mathbf{r}_e, \mathbf{r}_h) = \sum_{c\mathbf{k}_e, v\mathbf{k}_h} A_{n\mathbf{K}}(c\mathbf{k}_e, v\mathbf{k}_h)\psi_{c\mathbf{k}_e}(\mathbf{r}_e)\psi_{v\mathbf{k}_h}(\mathbf{r}_h) \quad (23.15)$$

where  $n$  is the quantum index of the exciton state. By introducing the Fourier transform of  $A_{n\mathbf{K}}(c\mathbf{k}_e, v\mathbf{k}_h)$ ,

$$\psi_{n\mathbf{K}}(\mathbf{r}_e, \mathbf{r}_h) = \frac{1}{\Omega} \sum_{\mathbf{k}_e, \mathbf{k}_h} e^{i\mathbf{k}_e \cdot \mathbf{r}_e} e^{i\mathbf{k}_h \cdot \mathbf{r}_h} A_{n\mathbf{K}}(c\mathbf{k}_e, v\mathbf{k}_h) \quad (23.16)$$

where  $\Omega$  is the normalization volume, it is easy to show that  $\psi_{n\mathbf{K}}(\mathbf{r}_e, \mathbf{r}_h)$  satisfies the differential equation

$$\left[ E_c(-i\nabla_e) - E_v(-i\nabla_h) + V(\mathbf{r}_e - \mathbf{r}_h) \right] \psi_{n\mathbf{K}}(\mathbf{r}_e, \mathbf{r}_h) = E \psi_{n\mathbf{K}}(\mathbf{r}_e, \mathbf{r}_h) \quad (23.17)$$

where  $E_c(-i\nabla_e)$  is the expression obtained by replacing  $\mathbf{k}_e$  in the power-series expansion of  $E_c(\mathbf{k}_e)$  by  $-i\nabla_e$ . The result is valid provided  $E_c(\mathbf{k}_e)$  and  $E_v(\mathbf{k}_h)$  are analytic and can be expanded in powers of  $\mathbf{k}_e$  and  $\mathbf{k}_h$ . In the effective mass approximation of  Eq. 23.12, the exciton Hamiltonian becomes

$$H_0 = -\frac{\hbar^2 \nabla_e^2}{2m_e^*} - \frac{\hbar^2 \nabla_h^2}{2m_h^*} - \frac{e^2}{4\pi\epsilon_\infty|\mathbf{r}_e - \mathbf{r}_h|} \quad (23.18)$$

where  $m_e^*$  and  $m_h^*$  are effective masses of electron and hole.

It is easier to introduce the relative and centre-of-mass coordinates  $\mathbf{r}_e - \mathbf{r}_h$  and  $\mathbf{R} = (m_e^* \mathbf{r}_e + m_h^* \mathbf{r}_h)/(m_e^* + m_h^*)$  to solve the above exciton Hamiltonian

$$H_0 = -\frac{\hbar^2 \nabla_{\mathbf{R}}^2}{2(m_e^* + m_h^*)} - \frac{\hbar^2 \nabla_{\mathbf{r}_e - \mathbf{r}_h}^2}{2m_r^*} - \frac{e^2}{4\pi\epsilon_\infty|\mathbf{r}_e - \mathbf{r}_h|} \quad (23.19)$$

where  $1/m_r^* = 1/m_e^* + 1/m_h^*$  is the reduced effective mass.

For three-dimensionally extended bulk material, the part of the wave function in  $\mathbf{R}$  contains a factor of  $e^{i\mathbf{K} \cdot \mathbf{R}}$ , the part in the relative coordinates contains a hydrogenic  $\psi_{n\mathbf{K}}(\mathbf{r}_e, \mathbf{r}_h) = \psi_{n\mathbf{K}}(\mathbf{r}_e - \mathbf{r}_h)$ , so that the exciton wave function and its energy are

$$e^{i\mathbf{K} \cdot \mathbf{R}} \psi_{n\mathbf{K}}(\mathbf{r}_e, \mathbf{r}_h), \quad E_{n\mathbf{K}} = \frac{\hbar^2 \mathbf{K}^2}{2(m_e^* + m_h^*)} - \frac{m_r^* e^4}{2\epsilon_\infty^2 n^2} \quad (23.20)$$

and the wave function of the ground exciton state ( $n = 1$ ) corresponding to the last two terms of the Hamiltonian  $\blacktriangleright$  Eq. 23.19 is

$$\psi_{1K}(\mathbf{r}_e, \mathbf{r}_h) = \frac{1}{\sqrt{\pi a_{\text{Br}}^3}} e^{-|\mathbf{r}_e - \mathbf{r}_h|/a_{\text{Br}}} \quad (23.21)$$

where  $a_{\text{Br}} = 4\pi\epsilon_\infty \hbar^2 / m_r^* e^2$  is the Bohr radius of the exciton in the semiconductor material. In three-dimensionally confined nanostructures, the center of mass of the exciton is not mobile so that we simply let  $\mathbf{K} = 0$  in  $\blacktriangleright$  Eqs. 23.20 and  $\blacktriangleright$  23.21.

We now study the effect of excitons on the optical transition. The probability that the system makes an electronic transition from the ground state  $\Psi_0$  to an excited (exciton) state  $\Psi_{nK}(\mathbf{r}_e, \mathbf{r}_h)$  is proportional to

$$|\langle \Psi_{nK} | e^{i\mathbf{q}\cdot\mathbf{r}} \mathbf{a} \cdot \mathbf{p} | \Psi_0 \rangle|^2 \quad (23.22)$$

where  $\mathbf{p}$  is the momentum operator,  $\mathbf{q}$  and  $\mathbf{a}$  are, respectively, the wave vector and polarization vector of the photon. By  $\blacktriangleright$  Eq. 23.15 we obtain

$$\langle \Psi_{nK} | \mathbf{p} | \Psi_0 \rangle = \sum_{c\mathbf{k}_e, v\mathbf{k}_h} A_{nK}(c\mathbf{k}_e, v\mathbf{k}_h) \langle \psi_{c\mathbf{k}_e} | \mathbf{p} | \theta \psi_{v\mathbf{k}_h} \rangle \quad (23.23)$$

where  $\theta$  is the time-reversal operator and  $\theta \psi_{v\mathbf{k}_h}$  is the unoccupied VB state out of which the electron was excited. Denoting  $\theta \psi_{v\mathbf{k}_h} = \psi_{v-\mathbf{k}_h}$  as the hole state and making use of the negligible  $\mathbf{q}$  (the photon wave vector is negligibly small so that  $\mathbf{K} = 0$ ) so that  $\mathbf{k}_e = -\mathbf{k}_h \equiv \mathbf{k}$ ,

$$\langle \Psi_{n0} | \mathbf{p} | \Psi_0 \rangle = \sum_{\mathbf{k}} A_{n0}(c\mathbf{k}, v - \mathbf{k}) \langle \psi_{c\mathbf{k}} | \mathbf{p} | \psi_{v\mathbf{k}} \rangle \quad (23.24)$$

where we have neglected the contribution from all other bands except the VB and CB in the vicinity of the Fermi level.

Under normal device operation conditions,  $\langle \psi_{c\mathbf{k}} | \mathbf{p} | \psi_{v\mathbf{k}} \rangle \approx \mathbf{p}_{cv}$  which is independent of  $\mathbf{k}$  over the range of  $\mathbf{k}$  involved,

$$\langle \Psi_{n0} | \mathbf{p} | \Psi_0 \rangle = \mathbf{p}_{cv} \sum_{\mathbf{k}} A_{n0}(c\mathbf{k}, v - \mathbf{k}) \quad (23.25)$$

By  $\blacktriangleright$  Eq. 23.16 the transition probability is therefore proportional to

$$|\langle \Psi_{n0} | \mathbf{p} | \Psi_0 \rangle|^2 = \mathbf{p}_{cv}^2 |\psi_{n0}(\mathbf{r}_e, \mathbf{r}_h)|_{\mathbf{r}_e=\mathbf{r}_h}^2 \quad (23.26)$$

Note that the optical transition is also constrained to  $\mathbf{K} = 0$  since the photon wave vector is negligibly small. For spherical state  $\psi_{n0}(0)$  is nonzero only for  $s$ -type states of  $\blacktriangleright$  Eq. 23.21 (the reader can refer to the hydrogen atom in many quantum mechanics textbooks) and  $|\psi_{n0}(0)|^2 \propto 1/n^3$  so that

$$|\langle \Psi_{n0} | \mathbf{p} | \Psi_0 \rangle|^2 \propto \frac{1}{n^3} \quad (23.27)$$

which shows that only the low-energy exciton states (small  $n$ ) can be probed optically for bulk materials.

The exciton binding energy  $E_{10}$  in  $\blacktriangleright$  Eq. 23.20 for the ground exciton state ( $n = 1$ ) in commonly used bulk semiconductors is less than 10 meV so that their room temperature luminescence is very weak (exciton thermally dissolved so that  $n$  is large). Moreover, exciton Bohr radii, that is, the effective spatial extensions of the excitons, in bulk materials are also quite extended, see  $\blacktriangleright$  Table 23-2.



■ Table 23-2

Excitons in common semiconductor (Fu et al. 2000; Madelung 1991, 1992) (low temperature for IV and III-V).  $E_g$  denotes the band gap between VB and CB

	Si	GaAs	AlAs	InAs	CdSe	ZnO
$m_h^*$ (heavy hole)	0.537	0.51	0.409	0.35	0.45/1.0	0.59
$m_e^*$ (electron)	1.026	0.067	0.71	0.0239	0.13	0.28
$E_g$ [eV]	1.170	1.519	2.229	0.418	1.842	3.435
$a_{Br}$ [nm]	15.2	11.6	8.6	38.1	5.4	1.8
$E_{10}$ [meV]	14.3	4.2	20.0		13.2	60.0

In high quality semiconductor nanostructures, quantum size effects prevail and subband formation strongly influences the exciton as the electron and hole are forced to stay in a very confined spatial area. Coulomb interaction between the electron and hole, that is, the exciton binding energy, becomes much increased. Even at room temperature the sharp exciton lines can be detected in the absorption spectra of AlGaAs/GaAs multiple QWs (Miller et al. 1982), which can hardly be observed in bulk GaAs samples.

One of the reasons for the fast development of ZnO and related materials is their large excitonic binding of about 60 meV which binds the electron and hole strongly in bulk ZnO even at room temperature (Sun et al. 2002). A photonic switch operating by controlling exciton excitation in ZnO QWs via an optical near field has been reported, where ZnO QWs were in the form disks with a disk diameter of 80 nm and the heights of 2 nm (in a structure composed of one single-QW and three double-QW) and 3.5 nm in the one double-QW case (Yatsui et al. 2007, 2008). Another development based on the large exciton binding energy of ZnO was the room-temperature polariton laser (Zamfirescu et al. 2002).

➤ Equation 23.27 tells us that the major reason for studying and developing semiconductor nanostructures for optical applications refers to the forced quantum confinement. The exciton will not dissolve even when the exciton binding is comparable or smaller than the thermal energy. Light-matter interaction in the forms of optical exciton generation and radiative recombination is much enhanced, resulting in many novel nanostructure-based optoelectronic applications.

## Polarization and Optical Properties of Exciton-Polaritons

In this section, we study the optical properties of excitons in nanostructures. We start with the detailed analysis of optical absorption in which an allowed electric dipole transition creates an exciton  $\Psi_{nK}$  from a filled VB and in this scheme the wave function of the initial state (the filled VB) is simply unity denoted by  $\Psi_0$  in the formalism of second quantization. Assume that our electron-hole system is initially in its ground state  $\Psi_0$  for time  $t < 0$ . We switch on an external radiation of  $\mathbf{E}(\mathbf{r}, t)$  for  $t \geq 0$ ; the first-order perturbation Hamiltonian is

$$V = \int \mathbf{d}(\mathbf{r}) \cdot \mathbf{E}(\mathbf{r}, t) d\mathbf{r} \quad (23.28)$$

where  $\mathbf{d}(\mathbf{r})$  is the dipole-moment operator given by,

$$\mathbf{d}(\mathbf{r}) = -e\mathbf{r}_e\delta(\mathbf{r} - \mathbf{r}_e) + e\mathbf{r}_h\delta(\mathbf{r} - \mathbf{r}_h) \quad (23.29)$$

where  $e$  is the charge unit. We denote the wave function of the electron-hole system as  $|\mathbf{r}_e, \mathbf{r}_h, t\rangle$ , its time-dependent Schrödinger equation is then

$$i\hbar \frac{\partial}{\partial t} |\mathbf{r}_e, \mathbf{r}_h, t\rangle = (H_0 + V) |\mathbf{r}_e, \mathbf{r}_h, t\rangle \quad (23.30)$$

where  $H_0$  is given by  $\blacktriangleright$  Eq. 23.18.

By the first-order perturbation approximation where we consider only the exciton ground state  $\Psi_0$  to one excited excitonic state  $\Psi_{nK}(\mathbf{r}_e, \mathbf{r}_h, t)$  the time-dependent wave function

$$|\mathbf{r}_e, \mathbf{r}_h, t\rangle = |\Psi_0(t)\rangle + c_{nK}(t) |\Psi_{nK}(\mathbf{r}_e, \mathbf{r}_h, t)\rangle \quad (23.31)$$

Here we simply assume that  $|c_{nK}(t)| \ll 1$ . We will discuss this more closely in the coming sections.

We now formally denote both  $\Psi_0(t)$  and  $\Psi_{nK}(\mathbf{r}_e, \mathbf{r}_h, t)$  as eigen functions of  $H_0$  such that

$$\begin{aligned} H_0 \Psi_0(t) &= E_0 \Psi_0(t) = \hbar\omega_0 \Psi_0(t) \\ H_0 \Psi_{nK}(\mathbf{r}_e, \mathbf{r}_h, t) &= E_{nK} \Psi_{nK}(\mathbf{r}_e, \mathbf{r}_h, t) = \hbar\omega_{nK} \Psi_{nK}(\mathbf{r}_e, \mathbf{r}_h, t) \\ \Psi_0(t) &= \Psi_0 e^{-i\omega_0 t} \\ \Psi_{nK}(\mathbf{r}_e, \mathbf{r}_h, t) &= \Psi_{nK}(\mathbf{r}_e, \mathbf{r}_h) e^{-i\omega_{nK} t} \end{aligned} \quad (23.32)$$

Substituting  $\blacktriangleright$  Eq. 23.31 into  $\blacktriangleright$  Eq. 23.30 leads to

$$\begin{aligned} i\hbar \frac{\partial \Psi_0(t)}{\partial t} + i\hbar \frac{\partial c_{nK}(t)}{\partial t} \Psi_{nK}(\mathbf{r}_e, \mathbf{r}_h, t) + i\hbar c_{nK}(t) \frac{\partial \Psi_{nK}(\mathbf{r}_e, \mathbf{r}_h, t)}{\partial t} \\ = H_0 \Psi_0(t) + c_{nK}(t) H_0 \Psi_{nK}(\mathbf{r}_e, \mathbf{r}_h, t) + V \Psi_0(t) + c_{nK}(t) V \Psi_{nK}(\mathbf{r}_e, \mathbf{r}_h, t) \end{aligned}$$

By  $\blacktriangleright$  Eqs. 23.32,

$$\begin{aligned} \hbar\omega_0 \Psi_0(t) + i\hbar \frac{\partial c_{nK}(t)}{\partial t} \Psi_{nK}(\mathbf{r}_e, \mathbf{r}_h, t) + \hbar\omega_{nK} c_{nK}(t) \Psi_{nK}(\mathbf{r}_e, \mathbf{r}_h, t) \\ = E_0 \Psi_0(t) + c_{nK}(t) E_{nK} \Psi_{nK}(\mathbf{r}_e, \mathbf{r}_h, t) + V \Psi_0(t) + c_{nK}(t) V \Psi_{nK}(\mathbf{r}_e, \mathbf{r}_h, t) \end{aligned}$$

which is

$$i\hbar \frac{\partial c_{nK}(t)}{\partial t} \Psi_{nK}(\mathbf{r}_e, \mathbf{r}_h, t) = V \Psi_0(t) + c_{nK}(t) V \Psi_{nK}(\mathbf{r}_e, \mathbf{r}_h, t) \quad (23.33)$$

Multiplying the above equation by  $\langle \Psi_{nK}(\mathbf{r}_e, \mathbf{r}_h, t) |$  we come to

$$\frac{\partial c_{nK}(t)}{\partial t} = \frac{1}{i\hbar} \langle \Psi_{nK}(\mathbf{r}_e, \mathbf{r}_h, t) | \int \mathbf{d}(\mathbf{r}) \cdot \mathbf{E}(\mathbf{r}, t) \mathbf{d}\mathbf{r} | \Psi_0(t) \rangle \quad (23.34)$$

It can be shown (Fu and Willander 1999)

$$\begin{aligned} \langle \Psi_{nK}(\mathbf{r}_e, \mathbf{r}_h) | \int \mathbf{d} \cdot \mathbf{E}(\mathbf{r}, t) \mathbf{d}\mathbf{r} | \Psi_0(\mathbf{r}_e, \mathbf{r}_h) \rangle \\ = \frac{e}{\omega_{nK} m_0} \int \psi_{nK}^*(\mathbf{r}, \mathbf{r}) \mathbf{p}_{cv} \cdot \mathbf{E}(\mathbf{r}, t) \mathbf{d}\mathbf{r} \end{aligned} \quad (23.35)$$

where  $\psi_{nK}(\mathbf{r}, \mathbf{r})$  is obtained from  $\Psi_{nK}(\mathbf{r}_e, \mathbf{r}_h)$  by setting  $\mathbf{r}_e = \mathbf{r}_h = \mathbf{r}$ . Thus,

$$\frac{\partial c_{nK}(t)}{\partial t} = \frac{1}{i\hbar} \frac{e}{\omega_{nK} m_0} \int \psi_{nK}^*(\mathbf{r}, \mathbf{r}) \mathbf{p}_{cv} \cdot \mathbf{E}(\mathbf{r}, t) \mathbf{d}\mathbf{r} e^{i(\omega_{nK} - \omega_0)t} \quad (23.36)$$

Note that optical couplings among excitonic states are zero because of the quantum selection rules. As well, only a limited number of excitonic states have nonzero optical couplings with the ground state.

In reality  $\omega_0 = 0$  since this is the reference state where the VB is completely filled and the CB is empty. Furthermore, we can very well describe the excitation radiation as  $\mathbf{E}(\mathbf{r}, t) = \mathbf{E}(\mathbf{r}, \omega) e^{-i\omega t}$ , so that integrating the above equation we obtain immediately

$$c_{n\mathbf{K}}(t) = \frac{e^{i(\omega_{n\mathbf{K}} - \omega)t}}{\hbar(\omega_{n\mathbf{K}} - \omega + iy)} \frac{e}{\omega_{n\mathbf{K}} m_0} \int \psi_{n\mathbf{K}}^*(\mathbf{r}, \mathbf{r}) \mathbf{p}_{cv} \cdot \mathbf{E}(\mathbf{r}, \omega) d\mathbf{r} \quad (23.37)$$

Before we move on, let us discuss the spatial distribution of the exciton wave function. Excitons are normally categorized into two types. The Frenkel exciton is an excited electronic state where the electron and the hole are situated in the same molecule or atom. Because of their small radius, the Frenkel excitons usually are considered to be local. The large-radius Wannier–Mott exciton in bulk semiconductors is relatively weakly bound due to a typically large exciton Bohr radius. A hybrid state of Wannier–Mott exciton and Frenkel exciton in different heterostructure configurations involving QDs was found to exist at the interfaces of the QDs and the surrounding organic medium with complimentary properties of both kinds of excitons (Birman and Huang 2007).

In heterostructures both the CB electrons and the VB holes will experience extra potential energies such as band offsets. For low-energy Frenkel excitons in a QD, the electrons and holes are confined within the same QD volume (type-I exciton) so that we will have a common potential energy  $V(|\mathbf{R} - \mathbf{a}|)$  that confines the exciton, where  $\mathbf{R}$  is the center of mass of the exciton (see  $\blacktriangleright$  Eq. 23.19),  $\mathbf{a}$  denotes the center of the QD. For common semiconductor QDs, the radius of the QD,  $R_{\text{QD}}$ , is in the order of the exciton Bohr radius  $a_{\text{Br}}$  so that one may neglect the free motion of the center of mass of the electron-hole pair in the QD, that is,  $\mathbf{K} = 0$  in  $\blacktriangleright$  Eq. 23.20. For the ground state of the exciton we can approximate  $V(|\mathbf{R} - \mathbf{a}|) = 0$  when  $|\mathbf{R} - \mathbf{a}| < R_{\text{QD}}$  and  $V(|\mathbf{R} - \mathbf{a}|) = \infty$  elsewhere so that the wave function corresponding to the motion of the center of mass becomes (Gasiorowicz 1996)

$$\frac{1}{\sqrt{2\pi R_{\text{QD}} |\mathbf{R} - \mathbf{a}|}} \sin\left(\frac{\pi |\mathbf{R} - \mathbf{a}|}{R_{\text{QD}}}\right) \quad (23.38)$$

for  $|\mathbf{r} - \mathbf{a}| \leq R_{\text{QD}}$ . The wave function is zero elsewhere. We thus finally obtain the total wave function of the exciton ground state inside the QD

$$\frac{1}{\sqrt{2\pi R_{\text{QD}} |\mathbf{R} - \mathbf{a}|}} \sin\left(\frac{\pi |\mathbf{R} - \mathbf{a}|}{R_{\text{QD}}}\right) \frac{1}{\sqrt{\pi a_{\text{Br}}^3}} e^{-|r_e - r_h|/a_{\text{Br}}} u_c(\mathbf{r}_e) u_v(\mathbf{r}_h) \quad (23.39)$$

Here Bloch functions  $u_c(\mathbf{r}_e)$  and  $u_v(\mathbf{r}_h)$  at CB and VB bandedges are included, see  $\blacktriangleright$  Eqs. 23.1 and  $\blacktriangleright$  23.6.

The polarization of the excited exciton in a QD centered at  $\mathbf{a}$  is

$$\mathbf{P}_a(\mathbf{r}, t) = \sum_{n\mathbf{K}} \langle \Psi_{n\mathbf{K}}(\mathbf{r}_e, \mathbf{r}_h, t) | \mathbf{d}(\mathbf{r}) | \Psi_0(\mathbf{r}_e, \mathbf{r}_h) \rangle c_{n\mathbf{K}}^*(t) c_0(t) + \text{c.c.} \quad (23.40)$$

where  $\mathbf{d}$  is the dipole of the exciton given by  $\blacktriangleright$  Eq. 23.29. Since the wave function  $\blacktriangleright$  Eq. 23.39 of the exciton is confined and real, the polarization of the exciton in the QD excited by an external electromagnetic field  $\mathbf{E}(\mathbf{r}, t)$  is (Fu et al. 1997, 2000)

$$\begin{aligned} \mathbf{P}_a(\mathbf{r}, t) = & \sum_{n\mathbf{K}} \frac{e^2 \mathbf{p}_{cv} e^{-i\omega t}}{\hbar(\omega_{n\mathbf{K}} - \omega + iy) \omega_{n\mathbf{K}}^2 m_0^2} \\ & \times \psi_{n\mathbf{K}}(\mathbf{r}, \mathbf{r}) \int \psi_{n\mathbf{K}}(\mathbf{r}', \mathbf{r}') \mathbf{p}_{cv} \cdot \mathbf{E}(\mathbf{r}', \omega) d\mathbf{r}' \end{aligned} \quad (23.41)$$

By assuming small spatial variation of the excitation field within the QD, an effective permittivity is defined for the QD exciton polariton by writing

$$\mathbf{D}(\mathbf{r}, \omega) = \epsilon_{\infty} \mathbf{E}(\mathbf{r}, \omega) + \mathbf{P}(\mathbf{r}, \omega) = \epsilon_{\text{QD}}(\mathbf{r}, \omega) \mathbf{E}(\mathbf{r}, \omega) \quad (23.42)$$

where  $\epsilon_{\infty}$  is the background dielectric constant of the QD material, and

$$\epsilon_{\text{QD}}(\mathbf{r}, \omega) = \epsilon_{\infty} \left( 1 + \sum_{n\mathbf{K}} \frac{2\omega_{\text{LT}}}{\omega_{n\mathbf{K}} - \omega + i\gamma} \frac{\sin \alpha_{n\mathbf{K}}}{\alpha_{n\mathbf{K}}} \right) \quad (23.43)$$

where  $\alpha_{n\mathbf{K}} = \pi|\mathbf{r} - \mathbf{a}|/R_{\text{QD}}$ .  $\epsilon_{\infty}\omega_{\text{LT}}a_{\text{Br}}^3 = e^2 p_{cv}^2 / \pi \hbar \omega_{n\mathbf{K}}^2 m_0^2$ .  $\omega_{\text{LT}}$  is normally referred to be the exciton longitudinal-transverse splitting. The above equation was obtained under the perturbation approximation and thus can also be accounted at a semiclassical level by adding a Lorentz-oscillator term to the dielectric function (Andreani et al. 2005).

Notice that  $\epsilon_{\text{QD}}(\mathbf{r}, \omega)$  in the above equation is position-dependent. Making an average over the QD volume results in an effective dielectric constant

$$\epsilon_{\text{QD}}(\omega) = \epsilon_{\infty} \left[ 1 + \sum_{n\mathbf{K}} \frac{6\omega_{\text{LT}}}{\pi^2 (\omega_{n\mathbf{K}} - \omega + i\gamma)} \right] \quad (23.44)$$

For a normal system without any extra external modifications except the incident electromagnetic field of  $\mathbf{E}(\mathbf{r}, t)$  under investigation, the occupation of excited exciton state,  $|c_{n\mathbf{K}}(t)|^2$ , is small (the first-order perturbation condition). Moreover, this occupation of the excited state is also much smaller than the ground state, see  $\bullet$  Eq. 23.31, so that an optical absorption dominates. This means that the optical field is absorbed during the exciton excitation following its propagation through the QD. The situation is normally referred to as optical loss, for example, in photodetectors.

Optical gain is achieved in light-emitting and laser devices by population inversion. To achieve optical gain in the QD, we increase the occupation of the exciton state. Here we consider such a pumping process that the exciton population of the excited exciton state  $c_{n\mathbf{K}}^{(0)}$  is finite at time  $t = 0$  so the time-dependent wavefunction becomes

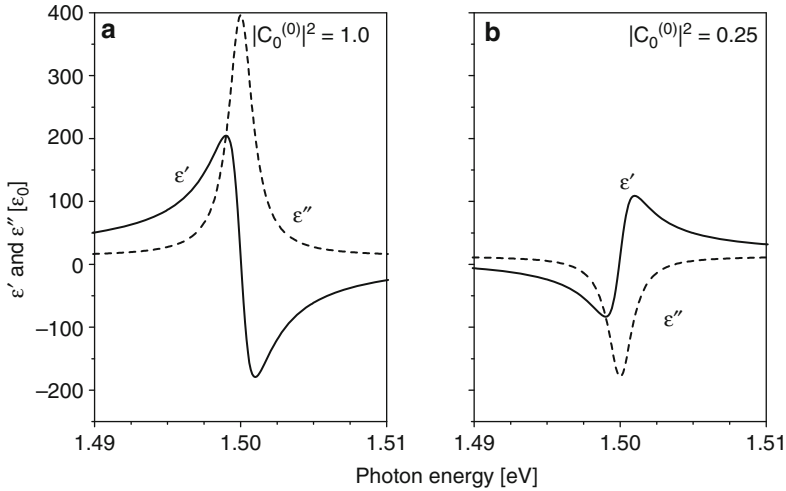
$$|\mathbf{r}_e, \mathbf{r}_h, t\rangle = \left[ c_0^{(0)} + c_0(t) \right] |\Psi_0(\mathbf{r}_e, \mathbf{r}_h)\rangle + \sum_{n\mathbf{K}} \left[ c_{n\mathbf{K}}^{(0)} + c_{n\mathbf{K}}(t) \right] |\Psi_{n\mathbf{K}}(\mathbf{r}_e, \mathbf{r}_h, t)\rangle \quad (23.45)$$

due to the external electromagnetic field  $\mathbf{E}(\mathbf{r}, t)$ . We can obtain (Fu et al. 2008)

$$\epsilon_{\text{QD}}(\omega) = \epsilon_{\infty} \left[ 1 + \sum_{n\mathbf{K}} \frac{6(2|c_0^{(0)}|^2 - 1)\omega_{\text{LT}}}{\pi^2 (\omega_{n\mathbf{K}} - \omega + i\gamma)} \right] \quad (23.46)$$

Let us write  $\epsilon = \epsilon' + i\epsilon''$ ,

$$\begin{aligned} \epsilon'_{\text{QD}}(\omega) &= \epsilon_{\infty} \left[ 1 + \sum_{n\mathbf{K}} \frac{6(2|c_0^{(0)}|^2 - 1)(\omega_{n\mathbf{K}} - \omega)\omega_{\text{LT}}}{\pi^2 [(\omega_{n\mathbf{K}} - \omega)^2 + \gamma^2]} \right] \\ \epsilon''_{\text{QD}}(\omega) &= \epsilon_{\infty} \left[ 1 + \sum_{n\mathbf{K}} \frac{6(2|c_0^{(0)}|^2 - 1)\gamma\omega_{\text{LT}}}{\pi^2 [(\omega_{n\mathbf{K}} - \omega)^2 + \gamma^2]} \right] \end{aligned} \quad (23.47)$$



■ Fig. 23-3

Dielectric coefficients of the QD before (a) and after (b) the excited exciton state in the QD becomes populated.  $\epsilon_\infty = 12.8$ ,  $\hbar\omega_{nK} = 1.5$  eV,  $\hbar\omega_{LT} = 5$  meV, and  $\hbar\gamma = 1$  meV for typical II–VI semiconductor QDs, for example, colloidal PbSe/ZnSe QD

Since  $\epsilon''$  represents the energy loss of the incident electromagnetic field, we observe that the QD is lossy when  $|c_0^{(0)}|^2 < 1/2$ , it becomes transparent when  $|c_0^{(0)}|^2 = 1/2$ , and optical gain will occur when  $|c_0^{(0)}|^2 > 1/2$ . At the same time, the polarization changes sign.

► Figure 23-3 shows the calculated dielectric constant for one QD before and after some fraction of the exciton states becomes populated. In this example, II–VI PbSe/ZnSe QD in a CdSe background is assumed and  $\hbar\gamma = 1.0$  meV. In ► Fig. 23-3 and throughout this chapter we write  $\epsilon = \epsilon' + i\epsilon''$ , where  $\epsilon'$  and  $\epsilon''$  are expressed in units of  $\epsilon_0$ . Here we observe the possibility of finding low-loss negative dielectric constant.

As shown in ► Fig. 23-3, a huge effective permittivity is expected in the vicinity of  $\omega_{nK}$ , with which the energy dispersions of photonic crystals based on QD arrays were derived (Fu et al. 2000) to understand photonic band gaps observed in CdS QDs embedded in fcc porous silica matrices (Vlasov et al. 1997). A close-packed 3D array of spherical CuCl QDs in air was shown by extended Maxwell-Garnett theory and rigorous layer-multiple-scattering method to have a negative refractive index within the region of the excitonic resonance (Yannopapas 2007). The structure was proposed for subwavelength imaging (the loss is however formidably high) (Yannopapas 2008).

## Exciton-Polariton Photonic Crystals

As shown by ► Eq. 23.43, the effective dielectric coefficient of the QD is strongly modified when the exciton state in the QD is resonantly excited by an incident electromagnetic field. The contrast between this exciton effective dielectric coefficient and the background material can thus be utilized to construct a photonic crystal when the QDs are positioned in space in

a periodic manner.  $\blacktriangleright$  Equation 23.43 was coupled to the electromagnetic field to study the optical dispersion of exciton-polariton crystals (Fu et al. 2000; Ivchenko et al. 2000) stimulated by the experimental works of fcc structured silica opals (Vlasov et al. 1997).

Maxwell equations describing the incident electromagnetic field in the QD photonic crystal, free of charges and free of drift-diffusion current, are written as

$$\begin{aligned}\nabla \times [\nabla \times \mathbf{E}(\mathbf{r})] &= \mu_0 \omega^2 \mathbf{D}(\mathbf{r}) \\ \nabla \cdot \mathbf{D}(\mathbf{r}) &= 0\end{aligned}\quad (23.48)$$

in the MKS unit system, where  $\mathbf{E}(\mathbf{r})$  is the electric field,  $\mathbf{D}(\mathbf{r})$  is the displacement vector, and  $\omega$  is the angular frequency of the incident electromagnetic field. Here we have assumed that the QD consists of uniform isotropic linear media, for which  $\mathbf{D} = \epsilon_\infty \mathbf{E}$  and  $\mathbf{B} = \mu_0 \mathbf{H}$ .  $\mathbf{H}$  is the magnetizing field and  $\mathbf{B}$  is the magnetic field.  $\mu_0$  is the magnetic constant (permeability of free space). The nonlocal material equation relating  $\mathbf{D}(\mathbf{r})$  and  $\mathbf{E}(\mathbf{r})$  is (Fu et al. 1997)

$$\mathbf{D}(\mathbf{r}) = \epsilon_\infty \mathbf{E}(\mathbf{r}) + \sum_{\mathbf{a}} \mathbf{P}_{\mathbf{a}}(\mathbf{r}) \quad (23.49)$$

where  $\mathbf{P}_{\mathbf{a}}(\mathbf{r})$  is the polarization contribution from the excited exciton in a QD centered at  $\mathbf{a}$ , that is,  $\blacktriangleright$  Eq. 23.41. We have neglected the overlap of exciton envelope functions centered at different QDs so that excitons excited in different QDs are assumed to be coupled only via the electromagnetic field.

By denoting  $\mathbf{P} = \sum_{\mathbf{a}} \mathbf{P}_{\mathbf{a}}(\mathbf{r})$ , it follows from the second  $\blacktriangleright$  Eq. 23.48 and  $\blacktriangleright$  Eq. 23.49 that

$$\nabla \cdot \mathbf{E}(\mathbf{r}) = -\frac{1}{\epsilon} \nabla \cdot \mathbf{P}(\mathbf{r}) \quad (23.50)$$

so that the first  $\blacktriangleright$  Eq. 23.48 can be rewritten as

$$\nabla^2 \mathbf{E}(\mathbf{r}) + k^2 \mathbf{E}(\mathbf{r}) = -\frac{k_0^2}{\epsilon_0} \left\{ \mathbf{P}(\mathbf{r}) + \frac{1}{k^2} \nabla [\nabla \cdot \mathbf{P}(\mathbf{r})] \right\} \quad (23.51)$$

where  $k_0 = \omega/c$ ,  $k = k_0 n = \omega n/c$ , and  $n = \sqrt{\epsilon_\infty/\epsilon_0}$ .

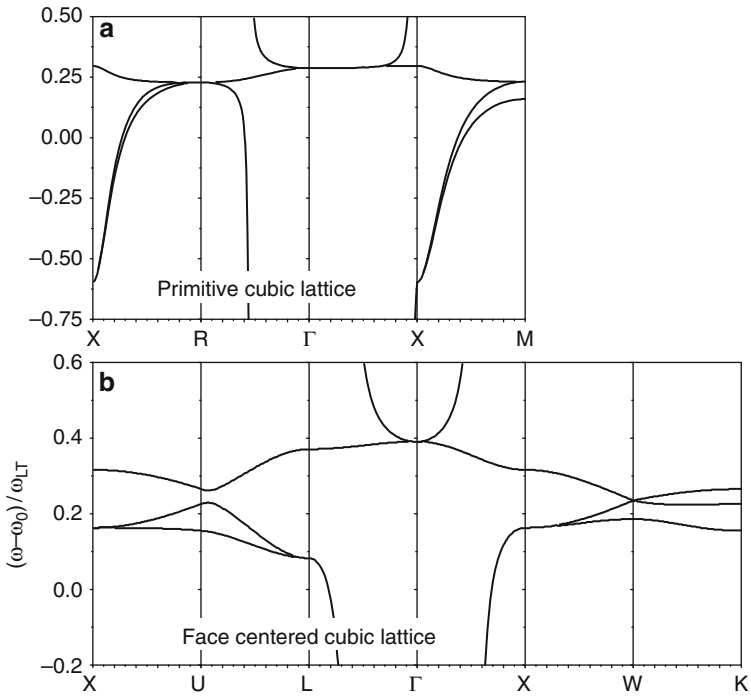
Bloch-like solutions of  $\blacktriangleright$  Eq. 23.51 satisfying

$$\mathbf{E}_{\mathbf{q}}(\mathbf{r} + \mathbf{a}) = e^{i\mathbf{q} \cdot \mathbf{a}} \mathbf{E}_{\mathbf{q}}(\mathbf{r}) \quad (23.52)$$

is the photonic band structure.  $\blacktriangleright$  Figure 23-4 shows the dispersion relationships of primitive-cubic and fcc QD photonic crystals (Fu et al. 2000). An overall bandgap, most prominent along the  $\Lambda$  ( $\Gamma$ -L) line (the [111] direction) is observed in the fcc lattice (Zeng et al. 2006a).

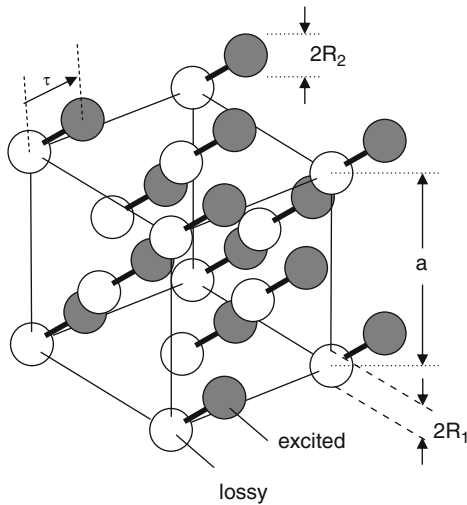
## Photonic Dispersion of QD Dimer Systems

As demonstrated by  $\blacktriangleright$  Eqs. 23.47 and  $\blacktriangleright$  Fig. 23-3,  $e'_{\text{QD}}$  can be adjusted to be positively large as well as negative by tuning the initial occupation condition of the exciton state in the QD. However, optical loss is not avoidable when a single type of QDs is used. To tackle the loss issue, we construct a QD dimer photonic crystal by positioning two types of spherical QDs, having radii  $R_1$  and  $R_2$ , respectively, in a fcc lattice having a lattice constant  $a$ , see  $\blacktriangleright$  Fig. 23-5. The lossy QDs, that is, type-I QDs (exciton energies are  $\hbar\omega_1$ ) occupy the normal fcc lattice sites, while the already excited QDs, type-II QDs ( $\hbar\omega_2$ ) are displaced from the type-I QDs by  $\boldsymbol{\tau}$ . Let  $c_{ai}$  be the occupation of the ground state of QD  $i$  positioned at lattice site  $\mathbf{a}$ , that is, the valence



■ Fig. 23-4

Photonic dispersion relation of QD photonic crystals. (a) Primitive cubic lattice. (b) Face-centered cubic lattice



■ Fig. 23-5

Schematic QD dimer system in a face-centered cubic (fcc) lattice structure.  $R_1$  and  $R_2$  denote the radii of the QDs and  $a$  the lattice constant of the fcc lattice

band is completely filled and the conduction band is completely empty, the contribution of an excited exciton state in a QD  $ai$  to the dielectric polarization is given by

$$\mathbf{P}_{ai}(\mathbf{r}) = \frac{e^2 \mathbf{p}_{cv}}{\hbar(\omega_{ai} - \omega + i\gamma)\omega_{ai}^2 m_0^2} \psi_{ai}(\mathbf{r}, \mathbf{r}) \int \psi_{ai}^*(\mathbf{r}', \mathbf{r}') \mathbf{p}_{cv} \cdot \mathbf{E}(\mathbf{r}') d\mathbf{r}' \quad (23.53)$$

by referring to  $\blacktriangleright$  Eqs. 23.41 and  $\blacktriangleright$  23.46.

We seek again for Bloch-like solutions of  $\blacktriangleright$  Eq. 23.51 satisfying  $\blacktriangleright$  Eq. 23.52. We expand the vector function  $\mathbf{E}_q(\mathbf{r})$  in the Fourier series

$$\mathbf{E}_q(\mathbf{r}) = \sum_{\mathbf{g}} e^{i(\mathbf{q}+\mathbf{g})\cdot\mathbf{r}} \mathbf{E}_{\mathbf{q}+\mathbf{g}} \quad (23.54)$$

Where  $\mathbf{g}$  are the reciprocal lattice vectors. Denote  $a_1 = \sqrt{2|c_1|^2 - 1}$ ,  $a_2 = \sqrt{2|c_2|^2 - 1}$ ,  $v_0 = a^3/4$  is the volume of the primitive unit cell of the fcc lattice,  $\phi_i = a_i \psi_i$  and  $t = \epsilon \omega_{LT} \pi a_{Br}^3$ , the excitonic polarization becomes

$$\mathbf{P}(\mathbf{r}) = \sum_{ai} \frac{t}{\omega_i - \omega + i\gamma} \phi_{ai}(\mathbf{r}, \mathbf{r}) \int \phi_{ai}^*(\mathbf{r}', \mathbf{r}') \mathbf{E}(\mathbf{r}') d\mathbf{r}' \quad (23.55)$$

Note that the excitonic wave function is real so that we have dropped off the complex conjugation of the wave function in the integrals in  $\blacktriangleright$  Eq. 23.53. The two integrals in the above equation can be transformed into

$$\begin{aligned} \int \phi_{1,a}(\mathbf{r}) \mathbf{E}(\mathbf{r}) d\mathbf{r} &= e^{i\mathbf{q}\cdot\mathbf{a}} \sum_{\mathbf{g}} I_{1,\mathbf{q}+\mathbf{g}} \mathbf{E}_{\mathbf{q}+\mathbf{g}} \equiv e^{i\mathbf{q}\cdot\mathbf{a}} \Lambda_1 \\ \int \phi_{2,a+\tau}(\mathbf{r}) \mathbf{E}(\mathbf{r}) d\mathbf{r} &= e^{i\mathbf{q}\cdot\mathbf{a}} \sum_{\mathbf{g}} I_{2,\mathbf{q}+\mathbf{g}} \mathbf{E}_{\mathbf{q}+\mathbf{g}} \equiv e^{i\mathbf{q}\cdot\mathbf{a}} \Lambda_2 \end{aligned} \quad (23.56)$$

where  $I_{1,\mathbf{q}+\mathbf{g}} = \int \phi_{1,0}(\mathbf{r}) e^{i(\mathbf{q}+\mathbf{g})\cdot\mathbf{r}} d\mathbf{r}$ ,  $I_{2,\mathbf{q}+\mathbf{g}} = \int \phi_{2,0}(\mathbf{r}) e^{i(\mathbf{q}+\mathbf{g})\cdot(\mathbf{r}+\tau)} d\mathbf{r}$ . The sums  $\sum_a \phi_{1,a}(\mathbf{r}) e^{i\mathbf{q}\cdot\mathbf{a}}$  and  $\sum_{a+\tau} \phi_{2,a+\tau}(\mathbf{r}) e^{i\mathbf{q}\cdot\mathbf{a}}$  satisfy the translational symmetry and can be presented as

$$\begin{aligned} \sum_a \phi_{1,a}(\mathbf{r}) e^{i\mathbf{q}\cdot\mathbf{a}} &= \sum_{\mathbf{g}} e^{i(\mathbf{q}+\mathbf{g})\cdot\mathbf{r}} \frac{I_{1,\mathbf{q}+\mathbf{g}}^*}{v_0} \\ \sum_{a+\tau} \phi_{2,a+\tau}(\mathbf{r}) e^{i\mathbf{q}\cdot\mathbf{a}} &= \sum_{\mathbf{g}} e^{i(\mathbf{q}+\mathbf{g})\cdot\mathbf{r}} \frac{I_{2,\mathbf{q}+\mathbf{g}}^*}{v_0} \end{aligned} \quad (23.57)$$

The linear equations for the space harmonics  $\mathbf{E}_{\mathbf{q}+\mathbf{g}}$  can thus be written

$$\begin{aligned} &(|\mathbf{q} + \mathbf{g}|^2 - k^2) \mathbf{E}_{\mathbf{q}+\mathbf{g}} \\ &= \frac{k_0^2 t}{v_0} \left[ 1 - \frac{1}{k^2} (\mathbf{q} + \mathbf{g})^2 \right] \left[ \frac{I_{1,\mathbf{q}+\mathbf{g}}^*}{\omega_1 - \omega + i\gamma} \Lambda_1 + \frac{I_{2,\mathbf{q}+\mathbf{g}}^*}{\omega_2 - \omega + i\gamma} \Lambda_2 \right] \end{aligned} \quad (23.58)$$

Let  $S(\mathbf{Q})_{\alpha\beta} = \delta_{\alpha\beta} - Q_\alpha Q_\beta / k^2$ ,  $\alpha, \beta = x, y, z$ ,  $\delta_{\alpha\beta}$  is the Kronecker symbol. Dividing  $\blacktriangleright$  Eq. 23.58 by  $(|\mathbf{q} + \mathbf{g}|^2 - k^2)$ , multiplying it by  $I_{1,\mathbf{q}+\mathbf{g}}$ , and summing over  $\mathbf{g}$ :

$$\begin{aligned} &\sum_{\mathbf{g}} I_{1,\mathbf{q}+\mathbf{g}} \mathbf{E}_{\mathbf{q}+\mathbf{g}} = \Lambda_1 \\ &= \frac{k_0^2 t}{v_0} \sum_{\mathbf{g}} \frac{\widehat{S}(\mathbf{q} + \mathbf{g})}{|\mathbf{q} + \mathbf{g}|^2 - k^2} \left[ \frac{|I_{1,\mathbf{q}+\mathbf{g}}|^2}{\omega_1 - \omega + i\gamma} \Lambda_1 + \frac{I_{1,\mathbf{q}+\mathbf{g}} I_{2,\mathbf{q}+\mathbf{g}}^*}{\omega_2 - \omega + i\gamma} \Lambda_2 \right] \\ &= \widehat{M}_1(\omega, \mathbf{q}) \Lambda_1 + \widehat{M}_2(\omega, \mathbf{q}) \Lambda_2 \end{aligned} \quad (23.59)$$



where

$$\begin{aligned}\widehat{M}_1(\omega, \mathbf{q}) &= \frac{k_0^2 t}{(\omega_1 - \omega + iy)v_0} \sum_{\mathbf{g}} \frac{\widehat{S}(\mathbf{q} + \mathbf{g})}{|\mathbf{q} + \mathbf{g}|^2 - k^2} |I_{1, \mathbf{q} + \mathbf{g}}|^2 \\ \widehat{M}_2(\omega, \mathbf{q}) &= \frac{k_0^2 t}{(\omega_2 - \omega + iy)v_0} \sum_{\mathbf{g}} \frac{\widehat{S}(\mathbf{q} + \mathbf{g})}{|\mathbf{q} + \mathbf{g}|^2 - k^2} I_{1, \mathbf{q} + \mathbf{g}} I_{2, \mathbf{q} + \mathbf{g}}^* \end{aligned} \quad (23.60)$$

Similarly, dividing  $\bullet$  Eq. 23.58 by  $(|\mathbf{q} + \mathbf{g}|^2 - k^2)$ , multiplying it by  $I_{2, \mathbf{q} + \mathbf{g}}$ , and summing over  $\mathbf{g}$ ,

$$\begin{aligned}\sum_{\mathbf{g}} I_{2, \mathbf{q} + \mathbf{g}} \mathbf{E}_{\mathbf{q} + \mathbf{g}} &= \Lambda_2 \\ &= \frac{k_0^2 t}{v_0} \sum_{\mathbf{g}} \frac{\widehat{S}(\mathbf{q} + \mathbf{g})}{|\mathbf{q} + \mathbf{g}|^2 - k^2} \left[ \frac{I_{2, \mathbf{q} + \mathbf{g}} I_{1, \mathbf{q} + \mathbf{g}}^*}{\omega_1 - \omega + iy} \Lambda_1 + \frac{|I_{2, \mathbf{q} + \mathbf{g}}|^2}{\omega_2 - \omega + iy} \Lambda_2 \right] \\ &= \widehat{M}_3(\omega, \mathbf{q}) \Lambda_1 + \widehat{M}_4(\omega, \mathbf{q}) \Lambda_2 \end{aligned} \quad (23.61)$$

where

$$\begin{aligned}\widehat{M}_3(\omega, \mathbf{q}) &= \frac{k_0^2 t}{(\omega_1 - \omega + iy)v_0} \sum_{\mathbf{g}} \frac{\widehat{S}(\mathbf{q} + \mathbf{g})}{|\mathbf{q} + \mathbf{g}|^2 - k^2} I_{2, \mathbf{q} + \mathbf{g}} I_{1, \mathbf{q} + \mathbf{g}}^* \\ \widehat{M}_4(\omega, \mathbf{q}) &= \frac{k_0^2 t}{(\omega_2 - \omega + iy)v_0} \sum_{\mathbf{g}} \frac{\widehat{S}(\mathbf{q} + \mathbf{g})}{|\mathbf{q} + \mathbf{g}|^2 - k^2} |I_{2, \mathbf{q} + \mathbf{g}}|^2 \end{aligned} \quad (23.62)$$

We arrive at the vector equations

$$\begin{aligned}[I - \widehat{M}_1(\omega, \mathbf{q})] \Lambda_1 &= \widehat{M}_2(\omega, \mathbf{q}) \Lambda_2 \\ [I - \widehat{M}_4(\omega, \mathbf{q})] \Lambda_2 &= \widehat{M}_3(\omega, \mathbf{q}) \Lambda_1 \end{aligned} \quad (23.63)$$

where  $I$  is a  $3 \times 3$  unit matrix. We can rewrite the above equations as

$$D = \begin{pmatrix} 1 - M_{1,11} & -M_{1,12} & -M_{1,13} & -M_{2,11} & -M_{2,12} & -M_{2,13} \\ -M_{1,21} & 1 - M_{1,22} & -M_{1,23} & -M_{2,21} & -M_{2,22} & -M_{2,23} \\ -M_{1,31} & -M_{1,32} & 1 - M_{1,33} & -M_{2,31} & -M_{2,32} & -M_{2,33} \\ M_{3,11} & M_{3,12} & M_{3,13} & M_{4,11} - 1 & M_{4,12} & M_{4,13} \\ M_{3,21} & M_{3,22} & M_{3,23} & M_{4,21} & M_{4,22} - 1 & M_{4,23} \\ M_{3,31} & M_{3,32} & M_{3,33} & M_{4,31} & M_{4,32} & M_{4,33} - 1 \end{pmatrix} \quad (23.64)$$

$$\begin{aligned}M_{1, \alpha\beta}(\Omega, \mathbf{q}) &= \frac{8}{\pi v_0} \frac{\omega_{\text{LT}} R_1^3 |a_1|^2}{(\omega_1 - \omega + iy)} \sigma_{11, \alpha\beta}(\Omega, \mathbf{q}) \\ M_{2, \alpha\beta}(\Omega, \mathbf{q}) &= \frac{8}{\pi v_0} \frac{\omega_{\text{LT}} (R_1 R_2)^{3/2} a_1 a_2^*}{(\omega_2 - \omega + iy)} \sigma_{12, \alpha\beta}(\Omega, \mathbf{q}) \\ M_{3, \alpha\beta}(\Omega, \mathbf{q}) &= \frac{8}{\pi v_0} \frac{\omega_{\text{LT}} (R_1 R_2)^{3/2} a_1^* a_2}{(\omega_1 - \omega + iy)} \sigma_{21, \alpha\beta}(\Omega, \mathbf{q}) \\ M_{4, \alpha\beta}(\Omega, \mathbf{q}) &= \frac{8}{\pi v_0} \frac{\omega_{\text{LT}} R_2^3 |a_2|^2}{(\omega_2 - \omega + iy)} \sigma_{22, \alpha\beta}(\Omega, \mathbf{q}) \\ \sigma_{st, \alpha\beta}(\Omega, \mathbf{q}) &= \sum_{\mathbf{g}} \frac{f(|\mathbf{g} + \mathbf{q}| R_s) f(|\mathbf{g} + \mathbf{q}| R_t) S_{\alpha\beta}(\mathbf{g} + \mathbf{q})}{\Omega^2(\mathbf{g} + \mathbf{q}) - \Omega^2} e^{i(s-t)(\mathbf{g} + \mathbf{q}) \cdot \boldsymbol{\tau}} \\ f(x) &= \frac{\pi^2 \sin x}{x(\pi^2 - x^2)} \end{aligned}$$

$$\begin{aligned}\Omega &= \frac{\omega}{\omega_1} \\ \Omega(\mathbf{Q}) &= \frac{c|\mathbf{Q}|}{\omega_1 n}\end{aligned}\quad (23.65)$$

where  $s, t = 1, 2$ . The exciton-polariton dispersion  $\omega(\mathbf{q})$  satisfies the equation

$$\text{Det}|D| = 0 \quad (23.66)$$

Note that by setting  $|c_1|^2 = 0$  and  $|c_2|^2 = 0.5$  (type-II QDs are totally transparent) we retrieve the case of a photonic crystal composed of only type-I QDs (Fu et al. 2000), see [Fig. 23-4](#). By setting  $|c_1|^2 = |c_2|^2 = 0$  and  $\omega_1 = \omega_2$  we retrieve the case of a compound QD photonic crystal (Zeng et al. 2006b).

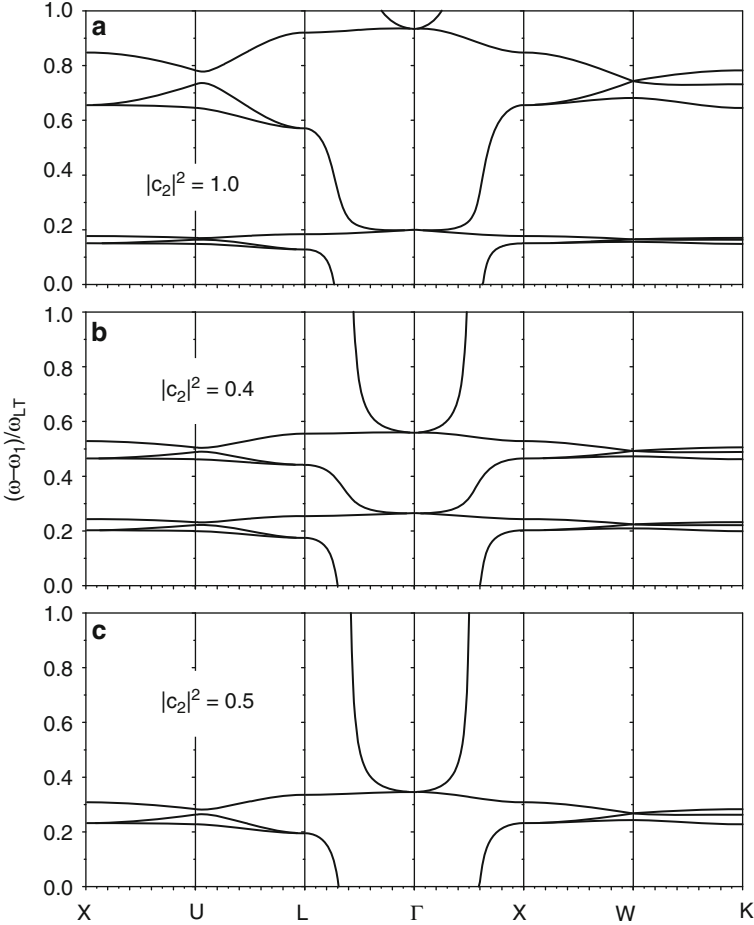
The dispersion relationship  $\omega(\mathbf{q})$  for a QD dimer fcc lattice is presented in [Fig. 23-6](#). The lattice is denoted by its lattice constant  $a$ , which is set to be  $0.95a_{\text{Bragg}}$  (which is 116 nm for GaAs), where  $a_{\text{Bragg}} = c\pi/\omega_{1n}$ . The lossy type-I QDs ( $\hbar\omega_1 = 1.5$  eV) occupy the normal fcc lattice sites, while the excited type-II QDs ( $\hbar\omega_2 = 1.503$  eV) are displaced by  $\boldsymbol{\tau} = (a/2, a/2, a/2)$ .  $\hbar\omega_{\text{LT}} = 5$  meV. Here we observe the modification of the photonic band structure of the QD dimer system by pumping one type of the QDs (type-II QDs), which evolves from the one of only type-I QDs ( $|c_1|^2 = 0$ , i.e., at their ground exciton state) when type-II QDs are transparent [ $|c_2|^2 = 0.5$ , [Fig. 23-6c](#)] to the compound system [ $|c_2|^2 = 1.0$ , [Fig. 23-6a](#)]. We can observe modified but still characteristic features of the photonic dispersions of individual type-I and type-II QDs in their separate photonic crystal formats in the compound system, see [Fig. 23-4](#). More specifically, the resonance features of type-I QDs around  $(\omega - \omega_1)/\omega_{\text{LT}} = 0.3$  in [Fig. 23-6d](#) become compressed by the radiative interaction between type-I QDs and type-II QDs, and they are also shifted down to around 0.18 in [Fig. 23-6a](#).

By varying  $|c_2|^2$  from 0.0 to 1.0 we find that the solutions of [Eq. 23.66](#) are symmetric with respect to  $|c_2|^2$  and  $1 - |c_2|^2$  when  $c_1 = 0$ . Thus, [Fig. 23-6a](#) represents also the photonic dispersion of the QD dimer system when both type-I and type-II QDs are all initially at their ground exciton states, that is,  $|c_1|^2 = |c_2|^2 = 0$ . Thus the modification of the exciton state (from ground state to excited state) in one type of QDs in the dimer system does not affect the feature of the dispersion structure.

## Lossless Dielectric Constant of QD Dimer Systems

As shown by [Fig. 23-4](#), the exciton polarization provides possibilities of generating positively high dielectric constant as well as negative dielectric constant at the cost of disturbing the external electromagnetic field (either loss or gain). At least in the photonic crystal composed of one type of QDs (either lossy or gain), the dielectric modulation is always accompanied by loss or gain. The idea of the QD dimer system discussed in the previous sub-section is to compensate the loss of type-I QDs by the gain of type-II QDs, while still maintaining dielectric modulation. More specifically, we require  $\epsilon'' = 0$  at some frequencies in order to achieve lossless dielectric modulation for various optoelectronics applications.

In the following, we consider a PbSe/ZnSe QD assembly such as [Fig. 23-5](#) immersed in a medium of dielectric constant  $\epsilon_i$ . The macroscopic dielectric constant  $\epsilon$  for the ensemble of the



■ Fig. 23-6

Energy dispersion relationships of QD dimer systems in the fcc lattice.  $R_1 = a/4$ ,  $R_2 = a/5$ ,  $\hbar\omega_1 = 1.5 \text{ eV}$ ,  $\hbar\omega_2 = 1.503 \text{ eV}$ ,  $\hbar\omega_{LT} = 5 \text{ meV}$ ,  $a = 0.95a_{\text{Bragg}}$ ,  $\tau = (a/2, a/2, a/2)$ .  $|c_1|^2 = 0$ . (a)  $|c_2|^2 = 1.0$  (complete excitation), (b)  $|c_2|^2 = 0.4$ , (c)  $|c_2|^2 = 0.5$  (type-II QDs are total transparent)

QDs can be described by the dielectric theory of Maxwell-Garnett (1906) and Gittleman and Abeles (1977), which for two QD species can be written as

$$\frac{\epsilon - \epsilon_i}{\epsilon + 2\epsilon_i} = x_1 \frac{\epsilon_{\text{QD1}} - \epsilon_i}{\epsilon_{\text{QD1}} + 2\epsilon_i} + x_2 \frac{\epsilon_{\text{QD2}} - \epsilon_i}{\epsilon_{\text{QD2}} + 2\epsilon_i} \quad (23.67)$$

where  $x_i$  is the volume fraction of the  $i$ -th QD species. While  $\blacktriangleright$  Eq. 23.67 works best for  $x_i$  less than 0.4, there is evidence that useful information can be available with higher concentrations (Cohen et al. 1973).  $\blacktriangleright$  Figure 23-7a shows the spectra of  $\epsilon'_{\text{QD}}$  and  $\epsilon''_{\text{QD}}$  of the two types of QDs. For the combination of two types of QDs, that is, the QD dimer system, one type is lossy and the other gain, immersed in a conducting polymer with an effective dielectric constant  $\epsilon_i = 1.8$ , the optical spectrum is presented in  $\blacktriangleright$  Fig. 23-7b.

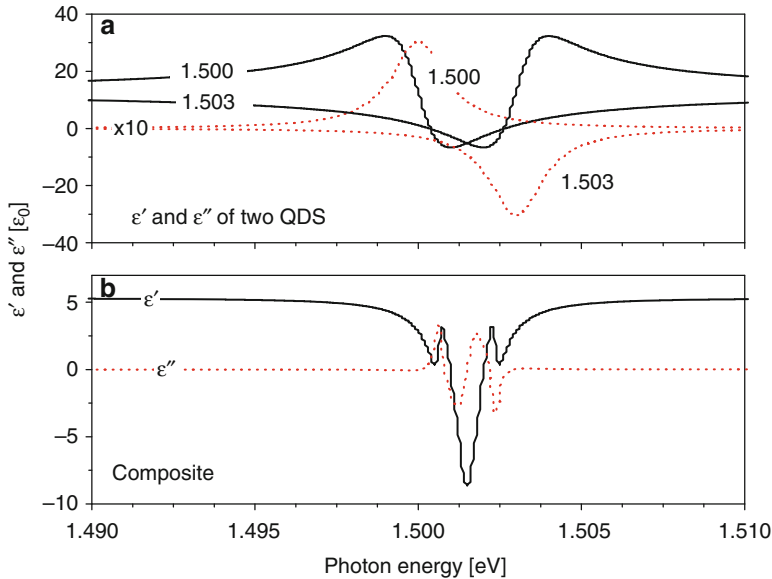


Fig. 23-7

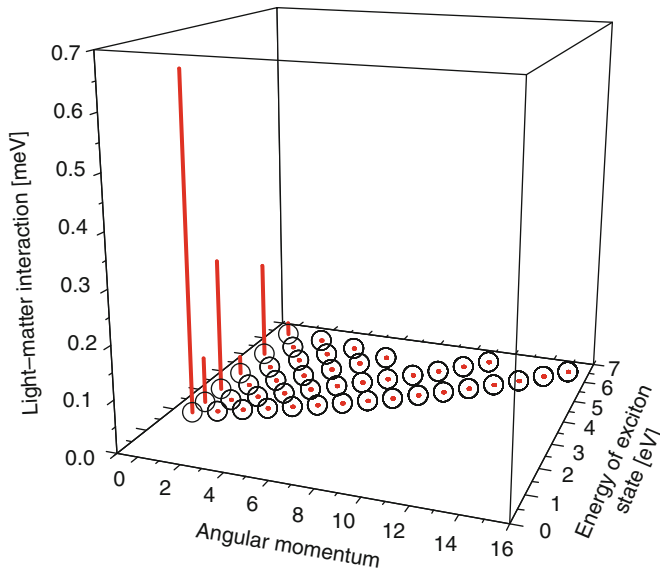
(a) Dielectric constants of type-I QDs at 1.500 eV and  $|c^{(0)}|^2 = 1.0$ , and type-II QDs at 1.503 eV and  $|c^{(0)}|^2 = 0.0$ . Solid lines:  $\epsilon'$ ; Dotted lines:  $\epsilon''$ . Note that  $\epsilon''$  is magnified by 10. (b) QD dimer system after immersing the two types of QDs in  $\epsilon_i = 1.8$ . The densities of two types of QDs are  $7 \times 10^{16} \text{ cm}^{-3}$ . Adapted from Fu et al. (2008)

Figure 23-7 shows that a mixture of two types of QDs such as Fig. 23-5 can produce an effective dielectric constant that is lossless and negative, thus permitting, in concept, arbitrarily small scaling of the optical mode volume in the field of nanophotonics (Fu et al. 2008). Another binary mixture of lossy QDs and plasmonic silver nanorods was also shown to have a negative  $\epsilon$  and compensated optical loss by using finite-difference time-domain calculations (Bratkovsky et al. 2008).

## Multiple-Photon and Multiple-Carrier Processes

### Multiphoton Process

Another important aspect about the optical properties of QDs is the multiphoton process which has been widely applied in recent years in biological and medical imaging after the pioneer work of Goepfert-Mayer (1931), Lami et al. (1996), Helmchen et al. (1996), Yokoyama et al. (2006). The multiphoton process has largely been treated theoretically by steady-state perturbation approaches, for example, the scaling rules of multiphoton absorption by Wherrett (1984) and the analysis of two-photon excitation spectroscopy of CdSe QDs by Schmidt et al. (1996). Non-perturbation time-dependent Schrödinger equation was solved to analyze the ultrafast (fs) and ultra-intense (in many experiments the optical power of laser pulse peak can reach



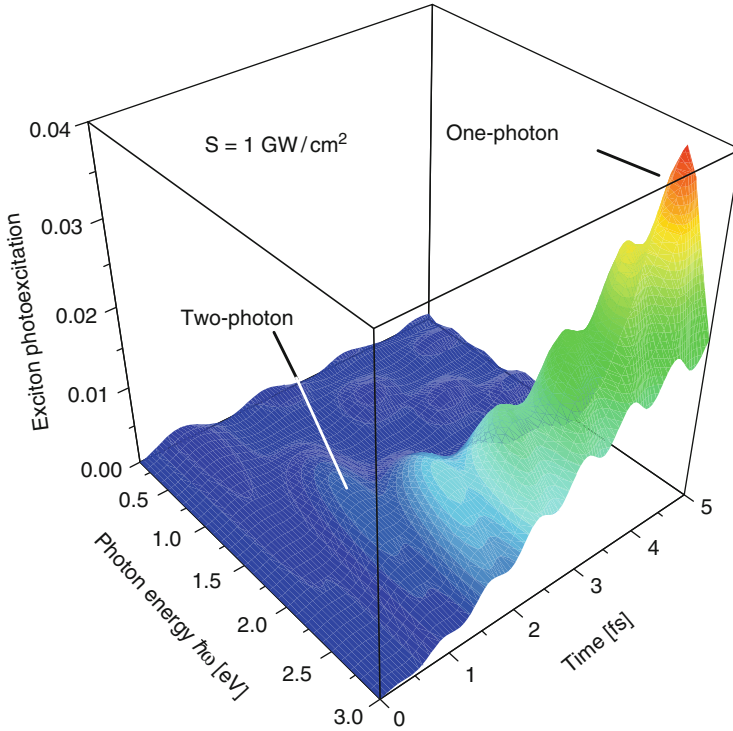
■ Fig. 23-8

Exciton states (open circles) confined in the QD and their corresponding light-matter interactions (vertical lines). Adapted from Fu et al. (2009)

GW/cm<sup>2</sup>) dynamics of multiphoton processes in QDs that are highly fluorescent with excellent photochemical stability, extreme brightness, and broad excitation spectral range (Fu et al. 2006c, 2007).

For spherical QDs the exciton wave function can be expressed by a radial function and spherical harmonics. The degeneracy of each exciton state is  $2(2\ell + 1)$ , where  $\ell$  is the quantum number of the angular momentum. Figure 23-8 shows the exciton states (open circles) confined in the QD as well as their corresponding light-matter interactions (vertical lines). For spherical QDs, only exciton states having zero angular momenta ( $\ell = 0$ ) have nonzero relaxation energies. Moreover, only confined exciton states (i.e., both the electron and hole states that compose the exciton state under discussion are confined) have significant light-matter interaction.

In the ultrashort regime, after a continuous-wave optical excitation is switched on at  $t = 0$ , Figure 23-9 shows that the time to reach peak two-photon excitation is much shorter than the one-photon excitation. Moreover, the multiphoton excitation spectral range is very broad. From about 1.0 to 2.5 eV (i.e., two-photon excitation range), the calculated excited exciton rate is much larger than the occupation of the first-excited exciton so that the emission spectrum is expected to be dominated by the recombination of the ground-state exciton. It was concluded by the theoretical simulation that experimentally observed strong multiphoton excitations can be reproduced when optical transitions among all confined states in the QD and an additional few hundred extended states in the barrier are taken into account (Fu et al. 2006c). This agrees with the experimental results of multi-particle (Huxter and Scholes 2006) and multi-exciton dynamics (Suffczyński et al. 2006).



■ Fig. 23-9

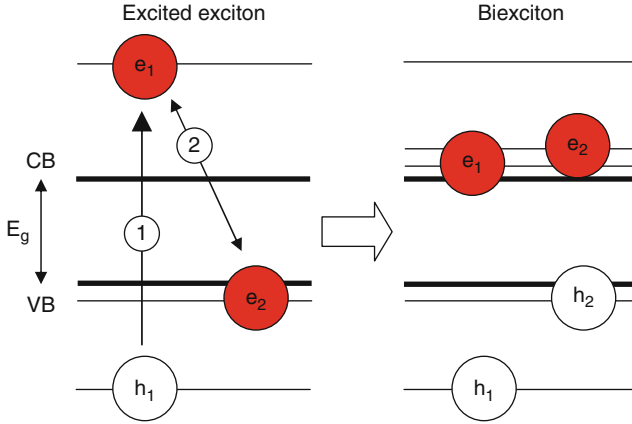
Multiphoton excitation of QD exciton in an ultrashort period excited by a continuous wave light source switched on at  $t = 0.5$  denotes the optical power of the excitation light source. Adapted from Fu et al. (2006c)

## Impact Ionization and Auger Recombination

Nozik proposed that impact ionization might be enhanced in semiconductor QDs to increase the efficiency of solar cells up to about 66% (Nozik 2002). This was later verified experimentally by Schaller and Klimov (2004). Impact ionization was reported to produce multiple exciton generation (MEG) per photon in a QD that results in a very high quantum yield (up to 300% when the photon energy reaches four times the QD bandgap) in QD solar cells (Hanna et al. 2004). Multiple carrier extraction ( $> 100\%$ ) was observed at photon energies greater than 2.8 times the PbSe QD bandgap with about 210% measured at 4.4 times the bandgap (Kim et al. 2008). In a recent communication in Nano Letters, Trinh et al. (2008) showed compelling support for carrier multiplication in PbSe QDs.

We concentrate here on reviewing impact ionization and Auger recombination in QDs using the solid-state theory. As shown in ► Fig. 23-10, a highly photoexcited electron and hole pairs can evolve into a multiple-exciton state through impact ionization. The carrier-carrier interaction is expressed by the Coulomb potential in the form of

$$V = \frac{e^2}{4\pi\epsilon|\mathbf{r}_1 - \mathbf{r}_2|} \quad (23.68)$$



■ Fig. 23-10

Schematic depiction of impact ionization of a high-energy electron-hole pair. (1) Electron-hole pair ( $e_1$  and  $h_1$ ) is generated, for example, by a photon. (2)  $e_2$  gets excited from a VB state to a CB state via Coulomb interaction with  $e_2$ , leaving hole  $h_2$  behind. The reverse process is referred to be Auger recombination

to account for the two-body interaction of two electrons from an initial state  $\phi_j(\mathbf{r}_1)\psi_i(\mathbf{r}_2)\exp[-i(E_j + E_i)t/\hbar]$ , that is, one electron occupying a VB state

$$\phi_j(\mathbf{r}_1)\exp(-iE_jt/\hbar)$$

and another electron occupying a CB state

$$\psi_i(\mathbf{r}_2)\exp(-iE_it/\hbar)$$

to a final state

$$\frac{1}{\sqrt{2}} \begin{vmatrix} \psi_n(\mathbf{r}_1)\psi_m(\mathbf{r}_1) \\ \psi_n(\mathbf{r}_2)\psi_m(\mathbf{r}_2) \end{vmatrix} \exp[-i(E_n + E_m)t/\hbar] \quad (23.69)$$

in the CB. Notice that the two electrons in the final state are not distinguishable so that we use a Slater determinant.

Other ionization pathways exist such as one electron occupying a low-energy VB state falls into  $h_1$  and the released energy excites another electron from the VB to the CB. Auger recombination can be expressed similarly.

Before discussing the QD case, let us consider the computation of an Auger-type process in solid states that an incident high-energy CB electron with a wave vector  $\mathbf{k}_1$  collides with a second electron that occupies a VB state  $\mathbf{k}_2$ , resulting in two CB electrons  $\mathbf{k}'_1$  and  $\mathbf{k}'_2$ . The general expression for the scattering matrix element of this process is

$$\int \int \Psi_{c\mathbf{k}'_1}^*(\mathbf{r}_1)\Phi_{v\mathbf{k}_2}^*(\mathbf{r}_2) \frac{1}{|\mathbf{r}_1 - \mathbf{r}_2|} \Psi_{c\mathbf{k}'_1}(\mathbf{r}_1)\Psi_{c\mathbf{k}'_2}(\mathbf{r}_2) d\mathbf{r}_1 d\mathbf{r}_2 \quad (23.70)$$

where  $\Psi_{c\mathbf{k}}(\mathbf{r})$  [ $\Phi_{v\mathbf{k}}(\mathbf{r})$ ] denotes the total wave function of the CB electron (VB hole) state  $\mathbf{k}$ . For semiconductor systems and within the effective mass approximation,

$\Psi_{ck}(\mathbf{r}) = \psi_{ck}(\mathbf{r})u_{ck}(\mathbf{r})$  and  $\Phi_{vk}(\mathbf{r}) = \phi_{vk}(\mathbf{r})u_{vk}(\mathbf{r})$ , where  $\psi$  and  $\phi$  are envelope functions of the CB electron and VB hole, respectively, and  $u$ 's are periodic Bloch functions, the above expression becomes

$$\int \int \psi_{ck_1}^*(\mathbf{r}_1)u_{ck_1}^*(\mathbf{r}_1)\phi_{vk_2}^*(\mathbf{r}_2)u_{vk_2}^*(\mathbf{r}_2) \frac{1}{|\mathbf{r}_1 - \mathbf{r}_2|} \quad (23.71)$$

$$\times \psi_{ck'_1}(\mathbf{r}_1)u_{ck'_1}(\mathbf{r}_1)\psi_{ck'_2}(\mathbf{r}_2)u_{ck'_2}(\mathbf{r}_2) d\mathbf{r}_1 d\mathbf{r}_2 \quad (23.72)$$

See, for example, Eq. 6.128 in Ridley (1988). Following overlap integrals are thus involved

$$I_1 = \int_{\text{cell}} u_{ck_1}^*(\mathbf{r}_1)u_{ck'_1}(\mathbf{r}_1) d\mathbf{r}_1$$

$$I_2 = \int_{\text{cell}} u_{vk_2}^*(\mathbf{r}_2)u_{ck'_2}(\mathbf{r}_2) d\mathbf{r}_2 \quad (23.73)$$

in the evaluation of the Auger-type scattering processes. The first overlap integral can be approximated to unity. Because of the orthogonality of  $u$  functions for different bands but the same  $\mathbf{k}$ , the second overlap integral  $I_2$  is, in crudest approximation, zero. This, however, is not correct since the periodic Bloch functions are functions of wave vectors. More specifically, we can write

$$u_{ck}(\mathbf{r}) = u_c(\mathbf{r}) + \mathbf{k}\nabla_k u_c(\mathbf{r}) + \dots$$

$$u_{vk}(\mathbf{r}) = u_v(\mathbf{r}) + \mathbf{k}\nabla_k u_v(\mathbf{r}) + \dots \quad (23.74)$$

for small  $\mathbf{k}$ , where  $u_c(\mathbf{r})$  and  $u_v(\mathbf{r})$  are periodic Bloch functions at the CB and VB bandedges, respectively.  $\int_{\text{cell}} u_v^*(\mathbf{r}_2)u_c(\mathbf{r}_2) d\mathbf{r}_2 = 0$ . Substituting these expressions into the overlap integrals we obtain the squared overlap integral in terms of the heavy-hole mass  $m_v$  (Landsberg and Adams 1973; Ridley 1988)

$$|I_2|^2 = \frac{\hbar^2}{2E_g} \left( \frac{1}{m_0} + \frac{1}{m_v} \right) |\mathbf{k}_2 - \mathbf{k}'_2|^2 \quad (23.75)$$

where  $E_g$  is the energy band gap of the bulk material. By using the inverse Bohr radius of shallow impurities as a measure about the  $\mathbf{k}$  values, Landsberg and Adams obtained  $|I_2| = 0.223$  for shallow-impurity-assisted Auger-type processes in bulk CdS and  $|I_2| = 0.265$  in GaAs (Landsberg and Adams 1973). Note that the inverse Bohr radius of shallow impurities in bulk semiconductors is small. For QDs under investigation, the effective Bohr radius of the electron and hole distribution is largely determined by the QD size, which is about 5 nm, that is, very small compared with the Bohr radius of shallow impurities in bulk semiconductors (about 100 nm in CdS and GaAs Landsberg and Adams 1973). This results in a large value of  $|I_2|$ . Under this specific circumstance we approximate  $|I_2| = 1$ . In other words, the electrons and holes in QDs, described by effective masses in the presence of the QD confinement potentials, interact with each other via the Coulomb force of  $\odot$  Eq. 23.68 (Abrahams 1954). The approach has been adopted for describing carrier interactions in many electronic devices such as tunnel junctions where the kinetic energies of relevant carriers are large, see for examples Takenaka et al. (1979) and Rodina et al. (2002).

By the scattering theory and the generalized Golden rule (Landau and Lifshitz 1965) and denoting  $\langle \phi_j \psi_i | \hat{T}(t) | \phi_j \psi_i \rangle \approx e^{-w_{ji}t/2}$  as the temporal development  $\hat{T}(t)$  of state  $ji$ , it is easy to obtain

$$w_{ji} = \frac{2\pi}{\hbar} \sum_{nm \neq ji} |\langle \phi_j \psi_i | V | \psi_n \psi_m \rangle|^2 \delta(E_j + E_i - E_n - E_m) \quad (23.76)$$

$\Gamma_{ji} = \hbar w_{ji}/2$  is the relaxation energy and  $1/w_{ji}$  the decaying time. In numerical calculations the  $\delta$  functions in the above equation are replaced by  $\Gamma_{ji}/[\Gamma_{ji}^2 + (E_j + E_i - E_n - E_m)^2]$  and  $\Gamma_{ji}$  is



to be calculated by the above equation in a self-consistent way that the left and right sides of **Eq. 23.76** equal after knowing the interaction values of  $\langle \phi_j \psi_i | V | \psi_n \psi_m \rangle^2$ .

Numerical calculations of the Coulomb interaction **Eq. 23.68** are not trivial. They were simplified in Allan and Delerue (2008) by using a screened Coulomb potential involving one-electron wave functions which were derived for bulk semiconductor materials (Landsberg 1991). To calculate the impact ionization interaction from an initial state of  $R_{\ell_1}(r_1)Y_{\ell_1 m_1}(\theta_1, \phi_1)R_{\ell_2}(r_2)Y_{\ell_2 m_2}(\theta_2, \phi_2)$  to a final state  $R_{\ell_3}(r_1)Y_{\ell_3 m_3}(\theta_1, \phi_1)R_{\ell_4}(r_2)Y_{\ell_4 m_4}(\theta_2, \phi_2)$  (the first term one in **Eq. 23.69**), we notice

$$\frac{1}{4\pi|\mathbf{r}_1 - \mathbf{r}_2|} = \sum_{\ell=0}^{\infty} \sum_{m=-\ell}^{\ell} \frac{1}{2\ell+1} \frac{r_{<}^{\ell}}{r_{>}^{\ell+1}} Y_{\ell m}^*(\theta_2, \phi_2) Y_{\ell m}(\theta_1, \phi_1) \quad (23.77)$$

where  $r_{<} = \min\{|\mathbf{r}_1|, |\mathbf{r}_2|\}$  and  $r_{>} = \max\{|\mathbf{r}_1|, |\mathbf{r}_2|\}$  so that the impact ionization energy consists of

$$\begin{aligned} & \frac{r_{<}^{\ell}}{r_{>}^{\ell+1}} R_{\ell_1}(r_1)R_{\ell_2}(r_2)R_{\ell_3}(r_1)R_{\ell_4}(r_2)Y_{\ell_1 m_1}^*(\theta_1, \phi_1)Y_{\ell_2 m_2}^*(\theta_2, \phi_2) \\ & \times Y_{\ell m}^*(\theta_2, \phi_2)Y_{\ell m}(\theta_1, \phi_1)Y_{\ell_3 m_3}(\theta_1, \phi_1)Y_{\ell_4 m_4}(\theta_2, \phi_2) \end{aligned} \quad (23.78)$$

for which we utilize the addition theorem for spherical harmonics (Cohen-Tannoudji et al. 1991)

$$\begin{aligned} Y_{\ell_1 m_1} Y_{\ell_2 m_2} &= \sum_{\ell=|\ell_1-\ell_2|}^{\ell_1+\ell_2} \sqrt{\frac{(2\ell_1+1)(2\ell_2+1)}{4\pi(2\ell+1)}} \\ & \times C(\ell 0 | \ell_1 0; \ell_2 0) C(\ell m_1 + m_2 | \ell_1 m_1; \ell_2 m_2) Y_{\ell m_1+m_2} \end{aligned} \quad (23.79)$$

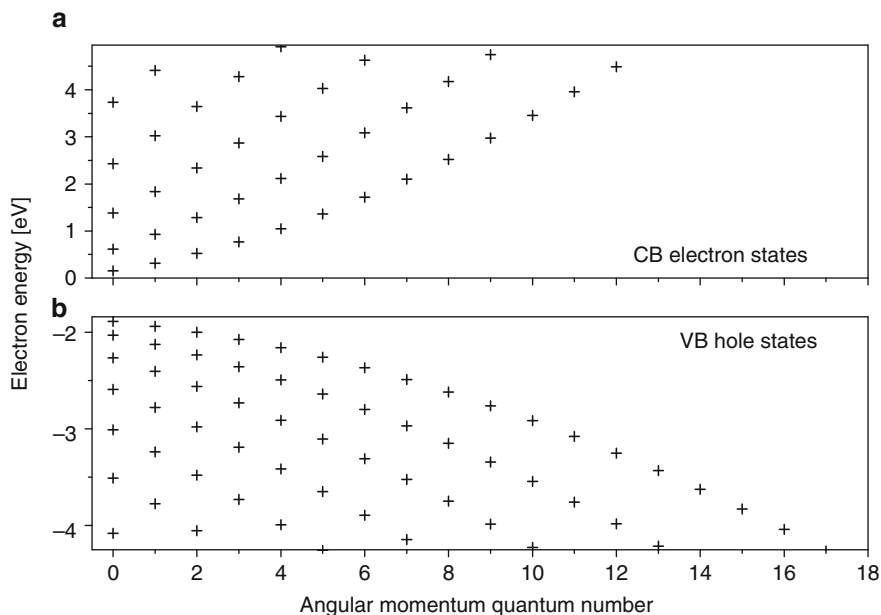
where  $C(\ell m_1 + m_2 | \ell_1 m_1; \ell_2 m_2)$  is the CG-coefficient.

A more detailed analysis shows a few selection rules for  $\ell$ 's and  $m$ 's such as  $m_4 - m_2 = m_1 - m_3$ . However, these selection rules can be easily fulfilled in nanoscale QDs because of the large number of available states confined in the QDs (see further discussion below). The most important qualitative selection rules refer to the radial functions that

$$\begin{aligned} & \int \int \frac{r_{<}^{\ell}}{r_{>}^{\ell+1}} R_{\ell_1}(r_1)R_{\ell_2}(r_2)R_{\ell_3}(r_1)R_{\ell_4}(r_2) \\ &= \int_0^a R_{\ell_1}(r_1)R_{\ell_3}(r_1) \left[ \int_0^{r_1} \frac{r_2^{\ell}}{r_1^{\ell+1}} R_{\ell_2}(r_2)R_{\ell_4}(r_2)r_2^2 dr_2 \right. \\ & \left. + \int_{r_1}^a \frac{r_1^{\ell}}{r_2^{\ell+1}} R_{\ell_2}(r_2)R_{\ell_4}(r_2)r_2^2 dr_2 \right] r_1^2 dr_1 \end{aligned} \quad (23.80)$$

which shows that a direct spatial overlap between  $R_{\ell_2}(r_2)$  (VB hole state) and  $R_{\ell_4}(r_4)$  (CB electron state) will result in a large impact ionization. Impact ionization in type-II QDs is thus negligible since the electron-hole wave function overlap is small. Furthermore, to ensure energy conservation,  $R_{\ell_1}(r)$  is normally a high-energy CB state, while both  $R_{\ell_3}(r)$  and  $R_{\ell_4}(r)$  are low-energy CB states. Impact ionization in many core-shell-structured QDs (e.g., Fu et al. 2007) could be small since the high-energy wave functions are much more extended (extended into shells) than the ground-state wave function (deeply confined in the core region).

We now consider a spherical CdSe QD in vacuum with a radius of  $a$ . The energy bandgap of bulk CdSe material is 1.74 eV (room temperature) and the exciton Bohr radius is 4.9 nm, the quantum confinement energies for CB electrons is 4.95 and 2.5 eV for the VB holes, and the electron and hole effective masses are  $m_c^* = 0.14m_0$  and  $m_v = 0.46m_0$ , respectively,  $m_0$



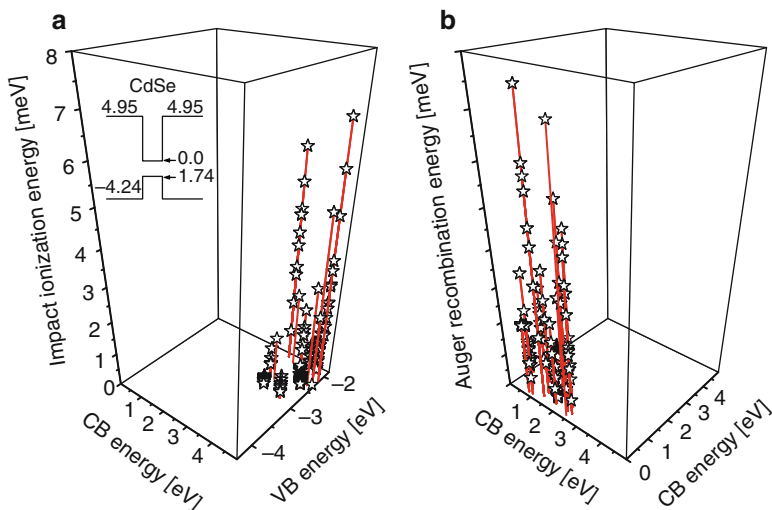
■ Fig. 23-11

(a) Conduction-band (CB) electron states and (b) valence-band (VB) hole states confined in a spherical CdSe QD with a radius of 4 nm as functions of angular momentum quantum number  $\ell$

is the electron rest mass (Madelung 1992). In numerical calculations we also include a shell of vacuum with a thickness of 20 nm to account for the penetration of wave functions of high-energy states from the QD volume to the vacuum (the results are compared with the ones when a shell of 10 nm thick vacuum shell is included and no significant differences are observed). We include all the confined energy states in the QD (i.e., energy levels below the vacuum state) of all possible combinations of CB electron states and VB hole states that form the initial state of the impact ionization, then all possible combinations of two final CB electron states. Each single-particle state is denoted by its energy,  $R(r)$ ,  $\ell$  and  $m$ . Spherical harmonics (i.e.,  $\ell$  and  $m$ ) is calculated using the addition theorem, while the radial integration is to be performed numerically.

► Figure 23-11 shows the CB electron states and VB hole states confined in a spherical CdSe QD with a radius of 4 nm as functions of angular momentum quantum number  $\ell$ . Note that states with  $\ell \neq 0$  are  $(2\ell + 1)$ -fold degenerate. We pick up one of the CB state from ► Fig. 23-11a and one VB state from ► Fig. 23-11b to calculate the total impact ionization energy to all possible combinations of two final CB states in ► Fig. 23-11a, which is shown in ► Fig. 23-12a.

► Figure 23-12a conforms with what can be expected intuitively that the initial CB state has to be high while the VB state low in order to fulfil the energy conservation requirement. Furthermore, high-energy states can be highly degenerate because of large  $\ell$  so  $\Gamma$  can be also high. For the case of ► Fig. 23-12 where  $a = 4$  nm, we observe a maximal  $\Gamma$  of about 7 meV. We further observe tens of  $\Gamma$  over 4 meV while majorities are about 1 meV. These are very high as compared with the light-matter interaction of only 0.065 meV in a similar CdSe QD (Fu et al. 2009), thus we can be very optimistic about MEG processes in colloidal QDs, as has been much



■ Fig. 23-12

(a) Impact ionization energy between initial CB state(s) and initial VB state(s). Inset shows the band structure of the CdSe QD in vacuum. (b) Auger recombination. The QD radius  $a = 4$  nm. Adapted from Fu et al. (2010)

reported and also anticipated for significant solar cell applications. For the CdSe QDs under investigation, the MEG effect can be expected when the excitation radiation energy exceeds a threshold of about  $2E_g$  (note that  $E_g$  is the energy of the ground exciton state, that is, nanocrystal energy gap in Schaller et al. (2005)) when the QD radius  $a = 4.8$  nm, while the threshold energy will be  $2.8E_g$  when  $a = 4.0$  nm, and  $3.5E_g$  for  $a = 3.0$  nm.

The Auger recombination process (reverse process of the impact ionization) shown in **Fig. 23-12b** can be similarly analyzed. Note that the energy range of the initial CB states in the Auger recombination processes is much wider than the impact ionization, especially for small QDs. This is due to the large density of states at high energy so that there are more available final CB states for two initial CB states to interact via the Auger recombination process.

## Summary

We have briefly reviewed fundamental theory of excitons and excitonic polaritons in nanostructures. Experimental characterization and application-specific developments using excitons and excitonic polaritons in nanostructures at the electronic and photonic engineering levels have also been briefly discussed. A realization of the potential applications is intimately tied to the control of the geometry and localization of the nanoscale features. Positioning of the nanostructures not only allows for reproducible communication with the environment, but is also necessary for defining the interaction between nanostructures. Solid-state-based nanostructures such as self-assembled QDs provide excellent communication to the environment. The geometry control of these QD size is though relatively poor by the current molecular beam epitaxy (MBE) and metal-organic vapour phase epitaxy (MOVPE) techniques. The size of colloidal II–VI QDs can be very well controlled during the chemical synthetic processes and

many colloidal II–VI QDs used in bioimaging applications are core-multishells formed so that possible effects of the surface and external environment on the exciton in the central core region are minimal. However, the interconnection to the environment becomes a major issue, for example, for photocarrier extraction in solar cell applications. We will, nevertheless, surely witness a further fast development in the research and we hope that this chapter provides some foundation for the understanding and simulation of excitons and exciton polaritons in nanostructures.

## References

- Abrahams, E. (1954). Electron-electron scattering in Alkali metals. *Physical Review*, 95, 839–910.
- Allan, G., & Delerue, C. (2008). Influence of electronic structure and multiexciton spectral density on multiple-exciton generation in semiconductor nanocrystals: Tight-binding calculations. *Physical Review B*, 77, 125340(10).
- Andreani, L. C., Gerace, D., & Agio, M. (2005). Exciton-polaritons and nanoscale cavities in photonic crystal slabs. *Physica Status Solidi (B)*, 242, 2197–2209.
- Birman, J. L., & Huong, N. Q. (2007). Wannier-Frenkel hybrid exciton in organic-semiconductor quantum dot heterostructures. *Journal of Luminescence*, 125, 196–200.
- Bratkovsky, A., Ponizovskaya, E., Wang, S.-Y., Holmström, P., Thylén, L., Fu, Y., & Ågren, H. (2008). A metal-wire/quantum-dot composite metamaterial with negative  $\epsilon$  and compensated optical loss. *Applied Physics Letters*, 93, 193106(3).
- Cohen, R. W., Cody, G. D., Coutts, M. D., & Abeles, B. (1973). Optical properties of granular silver and gold films. *Physical Review B*, 8, 3689–3701.
- Cohen-Tannoudji, C., Diu, B., & Laloe, F. (1991). *Quantum mechanics* (Vol. 2, p. 1046). New York: Wiley-Interscience.
- Derfus, A. M., Chen, A. A., Min, D.-H., Ruoslahti, E., & Bhatia, S. N. (2007). Targeted quantum dot conjugates for siRNA delivery. *Bioconjugate Chemistry*, 18, 1391–1396.
- Dimmock, J. O. (1967). Chapter 7 Introduction to the theory of exciton states in semiconductors. In R. K. Willardson & A. C. Beer (Eds.), *Semiconductors and Semimetals* (Vol. 3, pp. 259–319). New York: Academic.
- Franceschetti, A., An, J. M., & Zunger, A. (2006). Impact ionization can explain carrier multiplication in PbSe quantum dots. *Nano Letters*, 6, 2191–2195.
- Fu, Y., & Willander, M. (1999). Chapter 1 Elemental and compound semiconductors. In *Physical model of semiconductor quantum devices* (pp. 1–22). Boston: Kluwer.
- Fu, Y., Willander, M., Ivchenko, E. L., & Kiselev, A. A. (1997). Four-wave mixing in microcavities with embedded quantum wells. *Physical Review*, B55, 9872–9879.
- Fu, Y., Willander, M., & Ivchenko, E. L. (2000). Photonic dispersions of semiconductor-quantum-dot-array-based photonic crystals in primitive and face-centered cubic lattices. *Superlattices and Microstructures*, 27, 255–264.
- Fu, Y., Willander, M., & Xu, Q.-X. (2006a). Chapter 5 Quantum effects and nanofabrications in scaling metal-oxide-semiconductor devices. In A. A. Balandin & K. L. Wang (Eds.), *Handbook of semiconductor nanostructures and nanodevices* (Vol. 5, pp. 229–256). Los Angeles: American Scientific Publishers.
- Fu, Y., Berglind, E., Thylén, L., & Ågren, H. (2006b). Optical transmission and waveguiding by excitonic quantum dot lattices. *Journal of the Optical Society of America B*, 23, 2441–2447.
- Fu, Y., Han, T.-T., Luo, Y., & Ågren, H. (2006c). Multiphoton excitation of quantum dots by ultra-short and ultra-intense laser pulse. *Applied Physics Letters*, 88, 221114(3).
- Fu, Y., Han, T.-T., Ågren, H., Lin, L., Chen, P., Liu, Y., Tang, G.-Q., Wu, J., Yue, Y., & Dai, N. (2007). Design of semiconductor CdSe-core ZnS/CdS-multishell quantum dots for multiphoton applications. *Applied Physics Letters*, 90, 173102(3).
- Fu, Y., Thylén, L., & Ågren, H. (2008). A lossless negative dielectric constant from quantum dot exciton polaritons. *Nano Letters*, 8, 1551–1555.
- Fu, Y., Ågren, H., Kowalewski, J. M., Brismar, H., Wu, J., Yue, Y., Dai, N., & Thylén, L. (2009). Radiative and nonradiative recombination of photoexcited excitons in multi-shell-coated CdSe/CdS/ZnS quantum dots. *Europhysics Letters*, 86, 37003(6).
- Fu, Y., Zhou, Y.-H., Su, H., Boey, F. Y. C., & Ågren, H. (2010). Impact ionization and Auger recombination rates in semiconductor quantum dots. *Journal of Physical Chemistry C*, 114, 3743–3747.
- Gasiorowicz, S. (1996). *Quantum physics* (p. 178). New York: Wiley.

- Gittleman, J. I., & Abeles, B. (1977). Comparison of the effective medium and the Maxwell-Garnett predictions for the dielectric constants of granular metals. *Physical Review B*, 15, 3273–3275.
- Hanna, M. C., Ellingson, R. J., Beard, M., Yu, P., Micic, O.I., & Nozik, A.J. (2004, October 25–28). *Quantum dot solar cells: High efficiency through multiple exciton generation*. 2004 DOE Solar Energy Technologies Program Review Meeting, Denver, Colorado.
- Helmchen, F., Svododa, K., Denk, W., Kleinfeld, D., & Tank, D. W. (1996). In vivo dendritic calcium dynamics in deep-layer cortical pyramidal neurons. *Nature Neuroscience*, 2, 989–996.
- Huxter, V. M., & Scholes, G. D. (2006). Nonlinear optical approach to multiexciton relaxation dynamics in quantum dots. *Journal of Chemical Physics*, 125, 144716–144712.
- International Technology Roadmap for Semiconductors. [www.itrs.net](http://www.itrs.net).
- Ivchenko, E. L., Fu, Y., & Willander, M. (2000). Exciton polaritons in quantum-dot photonic crystals. *Physics of the Solid State*, 42, 1756–1765.
- Jiang, J., Gao, B., Han, T.-T., & Fu, Y. (2009). Ab initio study of energy band structures of GaAs nanoclusters. *Applied Physics Letters*, 94, 092110(3).
- Kane, E. O. (1957). Band structure of indium antimonide. *Journal of Physics and Chemistry of Solids*, 1, 249.
- Kavokin, A. (2007). Exciton-polaritons in microcavities: Present and future. *Applied Physics A*, 89, 241–246.
- Kim, S. J., Kim, W. J., Sahoo, Y., Cartwright, A. N., & Prasad, P. N. (2008). Multiple exciton generation and electrical extraction from a PbSe quantum dot photoconductor. *Applied Physics Letters*, 92, 31107(3).
- Lami, J.-F., Gilliot, P., & Hirliemann, C. (1996). Observation of interband two-photon absorption saturation in CdS. *Physical Review Letters*, 77, 1632–1635.
- Landau, L. D., & Lifshitz, E. M. (1965). *Quantum mechanics* (2nd ed., p. 129). Oxford: Pergamon Press.
- Landsberg, P. T. (1991). *Recombination in semiconductors*. London: Cambridge University Press.
- Landsberg, P. T., & Adams, M. J. (1973). Theory of donor-acceptor radiative and Auger recombination in simple semiconductors. *Proceedings of the Royal Society of London A*, 334, 523–539.
- Madelung, O. (Ed.). (1991). *Semiconductors group IV elements and III-V compounds*. Berlin: Springer.
- Madelung, O. (Ed.). (1992). *Data in science and technology: Semiconductors other than group IV elements and III-V compounds*. Boston: Springer.
- Maxwell-Garnett, J. C. (1906). Colours in metal glasses, in metallic films, and in metallic solutions. II. *Philosophical Transactions of the Royal Society of London*, 205, 237–288.
- Mayer, M. G. (1931). Elementary processes with two quantum jumps. *Annalen Der Physik (Leipzig)*, 9, 273–294.
- Medintz, I. L., Uyeda, H. T., Goldman, E. R., & Mattoussi, H. (2005). Quantum dot bioconjugates for imaging, labelling and sensing. *Nature Materials*, 4, 435–446.
- Miller, D. A. B., Chemla, D. S., Eilenberg, D. J., Smith, P. W., Gossard, A. C., & Tsang, W. T. (1982). Large room-temperature optical nonlinearity in GaAs/Ga<sub>1-x</sub>Al<sub>x</sub>As multiple quantum well structures. *Applied Physics Letters*, 41, 679–681.
- Molnár, M., Fu, Y., Friberg, P., & Chen, Y. (2010). Optical characterization of colloidal CdSe quantum dots in endothelial progenitor cells. *Journal of Nanobiotechnology*, 8, 2. doi:10.1186/1477-3155-8-2.
- Nozik, A. J. (2002). Quantum dot solar cells. *Physica E: Low-dimensional Systems and Nanostructures*, 14, 115–120.
- Rabani, E., & Baer, R., (2008). Distribution of multiexciton generation rates in CdSe and InAs nanocrystals. *Nano Letters*, 8, 4488–4492.
- Ridley, B. K. (1988). *Quantum processes in semiconductors* (pp. 269–278). Oxford: Clarendon Press.
- Rodina, P., Ebert, U., Hundsdoerfer, W., & Grekhov, I. (2002). Tunneling-assisted impact ionization fronts in semiconductors. *Journal of Applied Physics*, 92, 958–964.
- Schaller, R. D., & Klimov, V. I. (2004). High efficiency carrier multiplication in PbSe nanocrystals: Implications for solar energy conversion. *Physical Review Letters*, 92, 186601(4).
- Schaller, R. D., Agranovich, V. M., & Klimov, V. I. (2005). Mechanism for high-efficiency carrier multiplication in semiconductor nanocrystals: Direct photogeneration of multiexcitons via virtual single-exciton states. *Nature Physics*, 1, 189–194.
- Schmidt, M. E., Blanton, S. A., Hines, M. A., & Guyot-Sionnest, P. (1996). Size-dependent two-photon excitation spectroscopy of CdSe nanocrystals. *Physical Review B*, 53, 12629–12632.
- Scholes, G. D., & Rumbles, G. (2006). Excitons in nanoscale systems. *Nature Materials*, 5, 683–696.
- Sturge, M. D., & Rashba, E. I. (Eds.). (1982). *Excitons*. Amsterdam: North-Holland.
- Suffczynski, J., Kazmierczuk, T., Goryca, M., Piechal, B., Trajnerowicz, A., Kowalik, K., Koszacki, P., Golnik, A., Korona, K. P., Nawrocki, M., & Gaj, J. A. (2006). Excitation mechanisms of individual CdTe/ZnTe quantum dots studied

- by photon correlation spectroscopy. *Physical Review B*, 74, 085319(7).
- Sun, H. D., Makino, T., Segawa, Y., Kawasaki, M., Ohtomo, A., Tamura, K., & Koinuma, H. (2002). Enhancement of exciton binding energies in ZnO/ZnMgO multiquantum wells. *Journal of Applied Physics*, 91, 1993–1997.
- Takenaka, N., Inoue, M., & Inuishi, Y. (1979). Influence of inter-carrier scattering on hot electron distribution function in GaAs. *Journal of the Physical Society of Japan*, 47, 861–868.
- Thylén, L., He, S., Wosinski, L., & Dai, D. (2006). The Moore's Law for photonic integrated circuits. *Journal of Zhejiang University Science A*, 7, 1961–1967.
- Trinh, M. T., Houtepen, A. J., Schins, J. M., Hanrath, T., Piris, J., Knulst, W., Goossens, A. P. L. M., & Siebbeles, L. D. A. (2008). In spite of recent doubts carrier multiplication does occur in PbSe nanocrystals. *Nano Letters*, 8, 1713–1718.
- Vashist, S. K., Tewari, R., Bajpai, R. P., Bharadwaj, L. M., & Raiteri, R. (2006). Review of quantum dot technologies for cancer detection and treatment. *Azojono Journal of Nanotechnology Online*, 2, 1–14, 10.2240/azojono0113.
- Vlasov, Y. A., Astratov, V. N., Karimov, O. Z., Kaplyanskiy, A. A., Bogomolov, V. N & Prokofiev, A. V. (1997). Existence of a photonic pseudo-gap for visible light in synthetic opals. *Physical Review*, B55, R13357–13360.
- Vurgaftman, I., Meyer, J. R., & Ram-Mohan, L. R. (2001). Band parameters for III-V compound semiconductors and their alloys. *Journal Of Applied Physics*, 89, 5815–5875.
- Weisbuch, C., Benisty H., & Houdré, R. (2000). Overview of fundamentals and applications of electrons, excitons and photons in confined structures. *Journal of Luminescence*, 85, 271–293.
- Wherrett, B. S. (1984). Scaling rules for multiphoton interband absorption in semiconductors. *Journal of the Optical Society of America B-Optical Physics*, 1, 67–72.
- Xu, W.-L., Fu, Y., Willander, M., & Shen, S. C. (1994). Theory of normal incident absorption for the intersubband transition in *n*-type indirect-gap semiconductor quantum wells. *Physical Review B*, 49, 13760–13766.
- Yannopapas, V. (2007). Artificial magnetism and negative refractive index in three-dimensional metamaterials of spherical particles at near-infrared and visible frequencies. *Applied Physics A*, 87, 259–264.
- Yannopapas, V. (2008). Subwavelength imaging of light by arrays of metal-coated semiconductor nanoparticles: A theoretical study. *Journal of Physics: Condensed Matter*, 20, 255201–255208.
- Yatsui, T., Sangu, S., Kawazoe, T., Ohtsu, M., An, S. J., Yoo, J., & Yi, G.-C. (2007). Nanophotonic switch using ZnO nanorod double-quantum-well structures. *Applied Physics Letters*, 90, 223110(3).
- Yatsui, T., Yib, G.-C., & Ohtsu, M. (2008). Progress in developing nanophotonic integrated circuits. *Proceedings of SPIE*, 7007, 700703(8).
- Yokoyama, H., Guo, H., Yoda, T., Takashima, K., Sato, K.-I., Taniguchi, H., & Ito, H. (2006). Two-photon bioimaging with picosecond optical pulses from a semiconductor laser. *Optics Express*, 14, 3467–3471.
- Zamfirescu, M., Kavokin, A., Gil, B, Malpuech, G., & Kaliteevski, M. (2002). ZnO as a material mostly adapted for the realization of room-temperature polariton lasers. *Physical Review B*, 65, 161205(4).
- Zeng, Y., Fu, Y., Chen, X., Lu, W., & Ågren, H. (2006a). Complete band gaps in three-dimensional quantum-dot photonic crystals. *Physical Review B*, 74, 115325(5).
- Zeng, Y., Chen, X.-S., Lu, W., Fu, Y. (2006b). Exciton polaritons of nano-spherical-particle photonic crystals in compound lattices. *The European Physical Journal B*, 49, 313–318.
- Zia, R., Schuller, J. A., Chandran, A., & Brongersma, M. L. (2006). Plasmonics: The next chip-scale technology. *Materials Today*, 9, 20.



# 24 Modeling of Quasi-One-Dimensional Carbon Nanostructures with Density Functional Theory

Veronica Barone<sup>1</sup> · Oded Hod<sup>2</sup> · Juan E. Peralta<sup>1</sup>

<sup>1</sup>Department of Physics, Central Michigan University, Mount Pleasant, Michigan, USA

<sup>2</sup>Department of Chemical Physics, School of Chemistry, The Sackler Faculty of Exact Sciences, Tel Aviv University, Tel Aviv, Israel

<i>Density Functional Theory with Periodic Boundary Conditions</i> .....	903
<i>Structure–Property Relations in Single-Walled Carbon Nanotubes and Graphene</i>	
<i>Nanoribbons</i> .....	905
Single-Walled Carbon Nanotubes .....	905
Graphene Nanoribbons .....	906
<i>Modeling the Optical Spectrum of Single-Walled Carbon Nanotubes and Graphene</i>	
<i>Nanoribbons</i> .....	912
Single-Walled Carbon Nanotubes .....	912
Graphene Nanoribbons .....	915
<i>Chemistry at the Edges of Graphene</i> .....	916
<i>Finite Size Effects in Low-Dimensional Graphitic Materials</i> .....	918
Quantum Confinement in Graphitic Systems .....	918
Edge Effects in Graphitic Systems .....	921
<i>Electromechanical Properties of One-Dimensional Graphitic Structures</i> .....	926
Carbon Nanotubes in NEMS Applications .....	926
Graphene Nanoribbons in NEMS Applications .....	930



<i>Concluding Remarks</i> .....	932
<i>Acknowledgments</i> .....	932
<i>References</i> .....	932

**Abstract:** The purpose of this chapter is to describe and review examples of how theoretical investigations can be applied to elucidate the behavior of carbon nanostructures and to understand the physical mechanisms taking place at the molecular level. We will place a special emphasis in theoretical works utilizing density functional theory. We assume that the reader is familiar with the basics of density functional theory as well as the electronic properties of single-walled carbon nanotubes and graphene nanoribbons (GNRs). We do not intend to present an extensive review; instead, we focus on several examples to illustrate the powerful predictive capabilities of current computational approaches.

## Density Functional Theory with Periodic Boundary Conditions

---

The focus of this chapter is on carbon structures that are elongated, predominantly one-dimensional systems. For most modeling purposes, these structures can be considered as periodic in one dimension. There are many software packages either free or commercially available to perform density functional theory (DFT) calculations using periodic boundary conditions. In fact, these type of calculations are routine in condensed matter physics and became very popular recently in the quantum chemistry community. One of the most widely used approaches for DFT calculations with periodic boundary conditions is the combination of the local density approximation (LDA) or the generalized gradient approximation (GGA) and plane waves. This approach usually involves only valence electrons, while the effect of core electrons is represented with pseudopotentials. Many modern pseudopotential calculations use ultrasoft pseudopotentials, which were first developed by Vanderbilt in the early 1990s (Vanderbilt 1990). Full-potential all-electron calculations can also be performed using plane waves, although they are somewhat computationally expensive for routine calculations. On the other hand, another class of software packages employ localized basis functions such as Gaussians. These basis functions allow not only an all-electron treatment of the system but also present the flexibility of pseudopotential calculations when heavy atoms are involved. In most cases, dealing with systems involving first- and second-row elements in an all-electron fashion can be routinely done. Another advantage of localized basis functions is that periodic boundary conditions can be explicitly imposed in either one, two, or three dimensions, in contrast to plane waves, which are naturally periodic in three dimensions and therefore approaches such as the super-cell are commonly used to reduce the dimensionality from three to two or one at the price of increasing the computational cost. The main advantage of plane waves over Gaussian basis functions is that the basis set convergence is more controlled. The basis set convergence of Gaussian-type orbitals is well known for molecules and there are tens of available basis sets developed for different purposes (see for instance the EMSL library Feller 1996, 2007). However, the basis set convergence of Gaussian functions is less known for periodic systems, especially for properties like the bandgap. Another disadvantage of Gaussians is that available basis for molecular systems cannot always be straightforwardly employed in periodic boundary conditions calculations due to linear dependencies that occur in periodic structures, limiting in practice the use of large exponents (Gruneich and Hess 1998).

When using localized functions, in general, the basis set needs to be carefully chosen in order to obtain sensible results. It is important to point out that using either localized basis or plane waves, different properties can have different basis set convergence behavior, and the fact that one property such as the energy is converged (within a given criterion) does not imply that

all properties are converged. In single-walled carbon nanotubes (SWNTs), for instance, the choice of the Gaussian basis set does not seem to have a significant impact on the bandgap. In [Table 24-1](#), we show the bandgap (obtained as Kohn–Sham band energy differences) of the (10,0) SWNT calculated with different functionals and standard Gaussian basis sets. The initial SWNT geometry was obtained with the *Tubegen* program (Frey and Doren 2005) and then relaxed using the different functionals and basis sets indicated in each column. For each optimized structure, we calculate the bandgap of the system with the different functionals and basis sets. As shown in [Table 24-1](#), the bandgap does not depend significantly on the level of theory utilized for the geometry optimization, or the basis set. [Table 24-1](#) illustrates, however, the dependence of the bandgap upon the choice of the exchange–correlation (XC) functional. This shows that for SWNTs, the choice of the XC functional has a larger impact on the calculated bandgap and related properties.

There are several options available in DFT software packages for the choice of the approximate XC functional. The most widely used XC functionals depend either on the electronic density (local[-spin] density approximation or L[S]DA) or on the electronic density and its gradient (generalized gradient approximation or GGA). For example, in [Table 24-1](#) we employ the combination of Dirac exchange and the parameterization of Vosko et al. (1980) for correlation in the LSDA functional and the GGA functional of Perdew, Burke, and Ernzerhof (PBE) (1996). Comparing with available experimental data, these families of functionals usually perform well for structural properties but have some deficiencies for energetics and electronic properties. Other type of approximate XC functionals include an orbital dependency either through quantities such as the kinetic energy density or Hartree–Fock (HF) type of exchange (for a thorough review, see Kümmel and Kronik 2008). Examples of orbital-dependent functionals are the meta-GGA TPSS (Tao et al. 2003), or the hybrid functionals PBE0 (Adamo and Barone 1999; Ernzerhof and Scuseria 1999; Perdew et al. 1997) (also known as PBEh), and B3LYP (Becke 1993). These type of functionals generally show some improvement over the LSDA and GGA but are computationally more demanding. In particular, due to the nature of the HF approximation, hybrid functionals in extended systems can be extremely demanding for metallic and small bandgap systems (Paier et al. 2007). An alternative to standard hybrid functionals for extended systems are the short-range hybrid functionals such as HSE (Heyd et al. 2003, 2006). These functionals truncate the long-range tail of the electron–electron interaction in the exchange contribution to the electronic energy. In this way, the remaining (short-range) part of the HF exchange can be efficiently evaluated (Adamson et al. 1996, 1999). It has been shown that this truncation has little effect on the properties of finite systems and at the same

■ **Table 24-1**

**Bandgaps (in eV) for the (10,0) SWNT obtained with different functionals (LDA, PBE, and HSE, shown row-wise) and basis sets (3-21G, 3-21G\*, and 6-31G\*, shown column-wise).**

	LDA optimized			PBE optimized			HSE optimized		
	3-21G	3-21G*	6-31G*	3-21G	3-21G*	6-31G*	3-21G	3-21G*	6-31G*
LDA	0.79	0.79	0.78	0.77	0.77	0.76	0.79	0.79	0.77
PBE	0.80	0.80	0.79	0.78	0.78	0.76	0.79	0.79	0.78
HSE	1.00	1.00	0.98	0.97	0.97	0.96	0.99	0.99	0.98

The structure was optimized using the functional and basis set indicated in each column. Calculations were performed with the Gaussian development program (Frisch et al. 2006)

time provides an efficient route for hybrid DFT calculations in extended systems (Heyd and Scuseria 2004).

Most commonly available functionals, either derived from nonempirical grounds or using fitting procedures, are meant to approximate only the electronic ground state, and not excited states. Moreover, although in “static” DFT, Kohn–Sham eigenvalues are often used to evaluate the energy bandgap, there is no formal justification for this: The formal theoretical framework is provided by time-dependent DFT (Runge and Gross 1984). For a review, see Onida et al. (2002). Therefore, the evaluation of the energy bandgaps and related properties from DFT calculations needs to be carried out with care. From a pragmatic viewpoint, Kohn–Sham eigenvalues are often used to distinguish between metals and semiconductors and to estimate excitation energies. LSDA and GGA Kohn–Sham gaps usually underestimate experimental data and sometimes small-gap semiconductors are erroneously predicted to be metallic. Kohn–Sham gaps from hybrid functional calculations, on the other hand are, in general, in better agreement with experimental gaps (Barone et al. 2005a, b; Heyd et al. 2005; Kümmel and Kronik 2008; Peralta et al. 2006), although they tend to overestimate, in general, the available experimental data. Short-range hybrid functionals improve upon regular hybrids and provide good agreement with experiments and more sophisticated many-electron approaches (Barone et al. 2005b; Batista et al. 2006).

## Structure–Property Relations in Single-Walled Carbon Nanotubes and Graphene Nanoribbons

### Single-Walled Carbon Nanotubes

Carbon nanotubes are one of the most fascinating carbon nanostructures. Although soon after the discovery of fullerenes in 1985 (Kroto et al. 1985) there were many speculations about the possibility of synthesizing long and narrow graphitic cage-like structures, the synthesis of the first carbon nanotubes was reported by Iijima in 1991. After that seminal work, several new routes toward the synthesis of single- and multi-walled carbon nanotubes were developed.

The electronic properties of SWNT were first studied within the so-called zone-folding scheme (ZF) (Hamada et al. 1992; Saito et al. 1992, 1998). This scheme is based on the tight-binding (TB) approximation for the two-dimensional honeycomb lattice and the subsequent quantization of the wave vector associated with the radial direction of the nanotube. In this framework, the electronic structure of SWNTs is determined by the allowed values of the quantized wave vector. Within this approach, each nanotube, characterized by the indices  $(n, m)$ , can be either metallic if  $(2n + m)/3 = k$ , with  $k$  integer, or semiconducting for  $k$  non-integer (with a bandgap that depends on the inverse diameter,  $1/d$ ). This versatility in the electronic behavior, that depends *only* on the geometric structure of the tubes, ignited a large amount of experimental and theoretical efforts with the promise of novel technological applications based on these unique nanostructured materials.

In 1998, Tang et al. produced SWNTs grown in zeolite channels with diameters of about 4 Å (Tang et al. 1998). From the optical spectrum and the possible diameter distributions, these tubes were identified as the (3,3), (4,2), and (5,0) (Li et al. 2001). In 2004, the thinnest SWNTs, with diameters of about 3 Å were grown inside multi-walled nanotubes. Because of the small diameter, the possible  $(n, m)$  indices of these narrow SWNT were predicted to be (2,2), (4,0),

and (3,1) (Zhao et al. 2004). DFT calculations pointed out the importance of curvature effects, especially for narrower nanotubes which present a significant  $\sigma$ - $\pi$  hybridization not accounted for in the ZF scheme (Blase et al. 1994; Gülseren et al. 2002; Mintmire et al. 1992; Reich et al. 2002). Although the ZF scheme works reasonably well for the average diameter SWNT of about 10 Å, several studies confirmed the profound effect of the  $\sigma$ - $\pi$  hybridization in small diameter SWNT on their electronic properties.

DFT calculations have shown that the zigzag (5,0) SWNT, which should be a semiconductor according to the zone-folding scheme, is indeed metallic (Barone and Scuseria 2004; Cabria et al. 2003; Li et al. 2001; Liu and Chan 2002; Machón et al. 2002; Springborg and Satpathy 1994). The same holds true for the zigzag (4,0) SWNT (Barone and Scuseria 2004; Cabria et al. 2003). Although it is tempting to assume that narrower tubes tend to be metallic due to the  $\sigma$ - $\pi$  hybridization, it has been shown that the narrowest chiral tubes (4,3) and (3,1) present the largest bandgaps of all SWNTs (1.7 and 1.3 eV, respectively, obtained with the HSE functional) (Barone and Scuseria 2004). Due to curvature effects, most narrow semiconducting SWNTs become indirect gap semiconductors and largely deviate from the ZF  $1/d$  predictions.

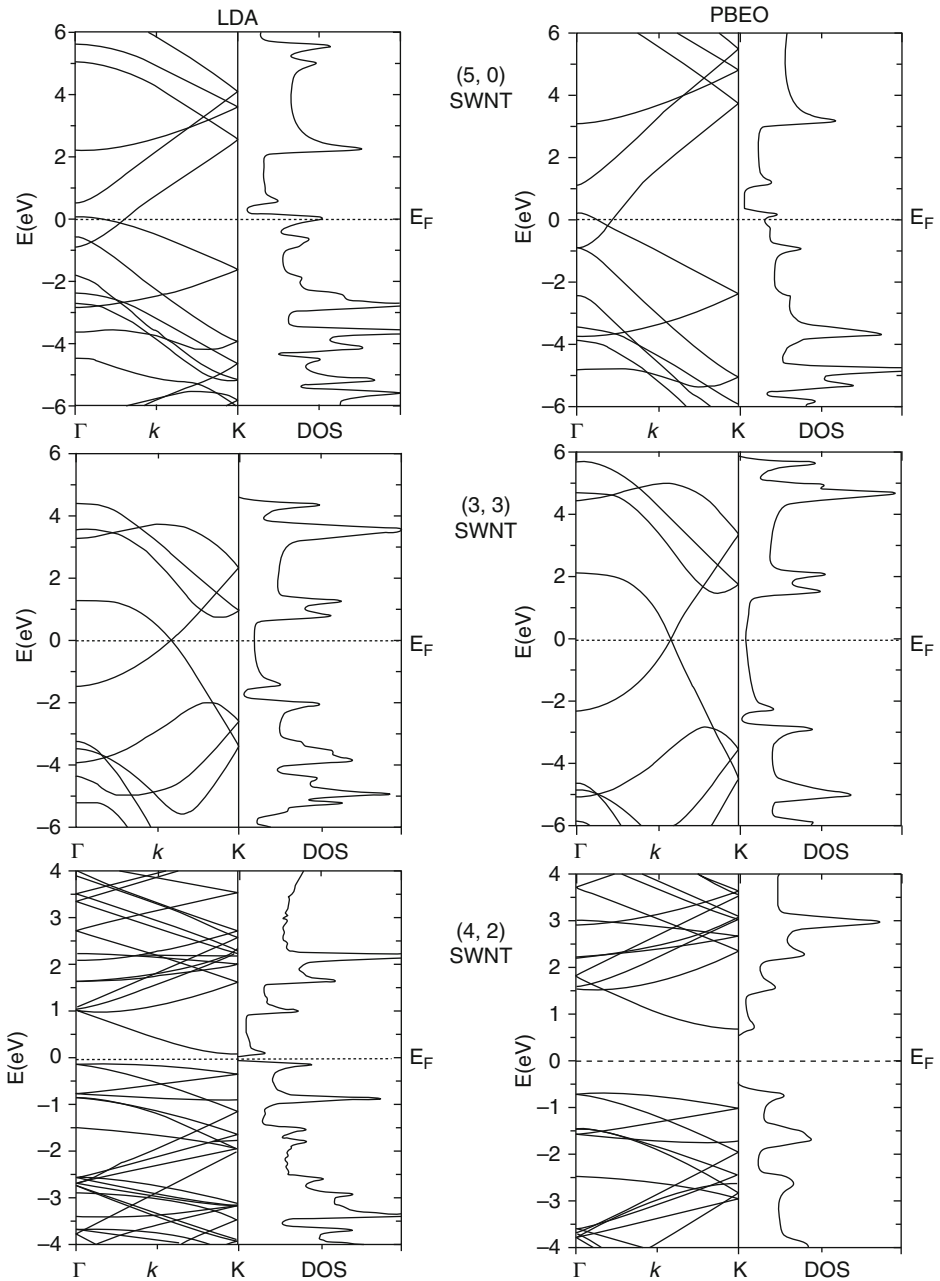
On the modeling side, we note that the calculated electronic properties of narrow nanotubes strongly depend on the exchange-correlation functional used. In [Fig. 24-1](#) we show the band structure and density of states (DOS) for the three narrow (5,0), (3,3), and (4,2) nanotubes obtained with LDA and the hybrid PBE0 functionals. The largest differences are found for the chiral semiconducting tube for which PBE0 predicts a bandgap as large as 1.36 eV. However, as we show in [section “Modeling the Optical Spectrum of Single-Walled Carbon Nanotubes and Graphene Nanoribbons,”](#) while the bandgap of SWNTs is largely underestimated by LSDA, it is also significantly overestimated by PBE0.

## Graphene Nanoribbons

Graphene, a single layer of graphite, has attracted a lot of attention since 2004 when it was isolated for the first time as a stand-alone two-dimensional all-carbon network (Novoselov et al. 2004). Since then, major accomplishments in their production have been achieved and now, lower dimensional graphene derivatives are routinely created in the lab (Berger et al. 2006; Cai et al. 2010; Han et al. 2007; Ritter and Lyding 2009; Wang et al. 2008; Yang et al. 2008). Recent studies point to graphene and its derivatives as one of the most promising materials for technological applications ranging from spintronic devices to energy storage media (Bhardwaj et al. 2010; Son et al. 2006b).

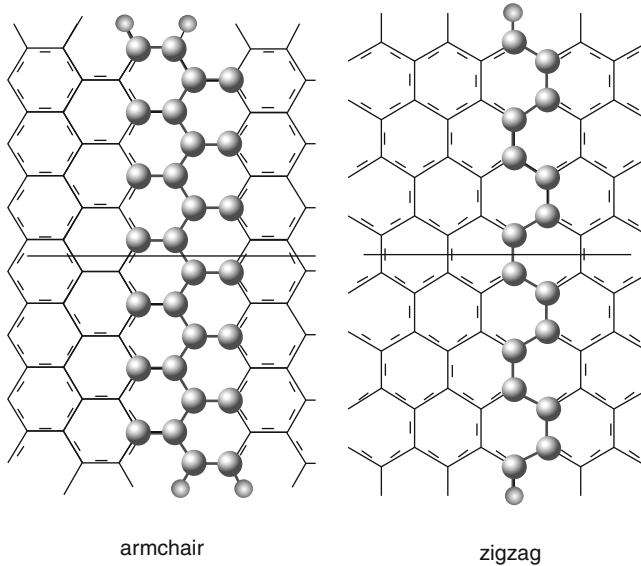
By cutting a quasi-one-dimensional structure out of a two-dimensional graphene sheet, it is possible to obtain a flat structure usually referred to as a graphene nanoribbon (GNR). These ribbons can also be thought of as unwrapped nanotubes of a given chirality. In [Fig. 24-2](#) we present a scheme of the two extreme crystallographic orientations of the GNRs axis: armchair (AGNR) and zigzag (ZGNR). Dangling bonds at the edges are usually passivated with hydrogen atoms for the purpose of performing computational studies as it is very difficult to experimentally determine the chemical nature of the edges.

One of the earliest theoretical investigations of the electronic properties of these materials was reported by Fujita et al. (1996). In that work, the authors report striking differences between armchair and zigzag GNRs. Most notably, the authors found that magnetism can



■ Fig. 24-1

Band structure and electronic density of states for the (5,0), (3,3), and (4,2) SWNT. (a) Obtained at the LDA/6-31G\* level. (b) Obtained at the PBE0/6-31G\* level

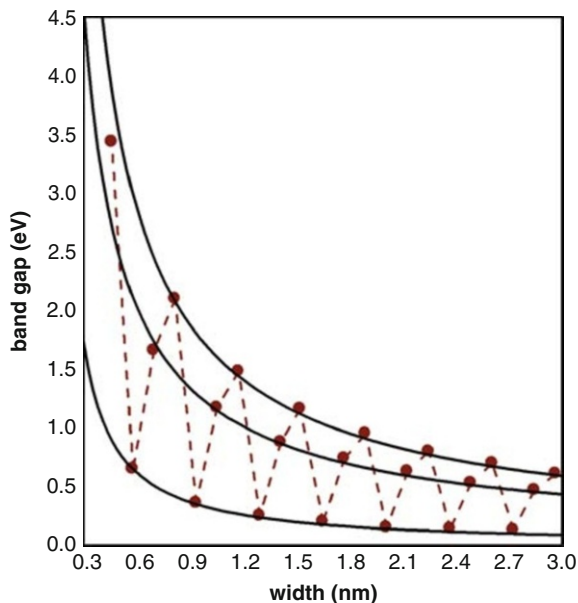


■ Fig. 24-2

**Schematic representation of the fundamental cell of an armchair and a zigzag graphene nanoribbon. The horizontal line represents the translational vector**

arise in nanometer-scale graphitic fragments in the zigzag configuration due to the appearance of localized edge states. According to TB calculations these edge states are manifested as flat bands near the Fermi energy in the band structure of the system. We will return to the case of ZGNRs later in this section. AGNRs do not present such edge states. Instead, the bandgap of these ribbons is predicted to vary with a three fold periodicity as a function of their width, changing from metallic to semiconducting as one consecutively increases their width (Ezawa 2006). When electronic correlation effects are taken into account via DFT, similar bandgap oscillations appear. Nevertheless, a major difference is identified. While in the TB calculations, at certain widths, AGNRs appear to become metallic, DFT calculations predict all AGNRs to be semiconducting (Barone et al. 2006; Son et al. 2006a). In Fig. 24-3, we present DFT results for the bandgap of armchair ribbons as a function of their width. As shown in this figure, ultra-narrow graphene nanoribbons with widths up to 1 nm present the largest bandgaps in the range of 1–3 eV. For the range of widths covered by the DFT calculations (up to 3 nm), no significant quenching of the energy gap oscillations is observed (Barone et al. 2006). However, GNRs are expected to reach the graphene limit of zero bandgap for sufficiently large widths.

We note that the armchair GNRs bandgaps presented in Fig. 24-3 can be separated into three groups, namely, the points forming the envelope of the maxima of the oscillations, those forming the envelope of the minima of the oscillations, and the remaining intermediate points. It is possible then to extrapolate the behavior of each of these subgroups independently to larger widths. Such an extrapolation can be performed using an inverse power law with two fitting parameters (Barone et al. 2006). This simple rule presents the correct asymptotic behavior and provides qualitative information on the electronic structure of ribbons beyond the range of



■ Fig. 24-3

Bandgap of H-terminated armchair GNRs as a function of the width obtained with the HSE functional (Reprinted (Adapted) with permission from Barone et al. (2006). © (2006) American Chemical Society)

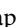
widths studied by first-principles calculations. From these calculations, it is shown that in order to obtain an AGNR with a bandgap comparable to that of Ge (0.67 eV) or InN (0.7 eV), it will be necessary to go to a range of widths between 2 and 3 nm. If a larger band gap material is needed (like Si, 1.14 eV, or GaAs, 1.43 eV), the width of the AGNR must be reduced to as low as 1–2 nm. The extrapolation to wider ribbons also shows that an AGNR of about 8 nm will present a bandgap smaller than 0.2 eV. It is interesting to note that when the first DFT calculations on these systems were carried out, it seemed impossible to produce nanoribbons as narrow as a few nanometers. Only 3 years later, the fabrication and electrical measurement of nanoribbons with widths down to a few nanometers are performed routinely in many laboratories around the world (Wang et al. 2008; Yang et al. 2008; Berger et al. 2006; Cai et al. 2010; Han et al. 2007; Ritter and Lyding 2009).

Experimentally, it has been demonstrated that the energy gap in graphene nanoribbons can be tuned during fabrication and that the energy gap scales inversely with the ribbon width (Chen et al. 2007; Han et al. 2007). Suspended GNRs with widths below 10 nm have been synthesized by a chemical route (Wang et al. 2008). However, the uncontrollable character of these methods restrict the quality of the GNR's edges and consequently limit their applications. Novel, organic synthetic protocols leading to graphene type molecules with different sizes have been presented recently (Yang et al. 2008; Cai et al. 2010). This route should provide perfect edged narrow graphene nanoribbons with widths up to 12 nm.



In zigzag graphene nanoribbons, quantum confinement is accompanied by the existence of pronounced edge states localized around the zigzag edges. As mentioned before, the existence of these edge states have been suggested theoretically more than a decade ago (Fujita et al. 1996; Klein 1994; Kobayashi 1993; Nakada et al. 1996; Tanaka et al. 1987). Recently, such states along the zigzag edges of graphite have been experimentally observed (Kobayashi et al. 2005, 2006; Niimi et al. 2005). One of the most interesting characteristics of these edge states in graphite is their predicted magnetic character (Fujita et al. 1996; Kusakabe and Maruyama 2003; Son et al. 2006a; Wakabayashi et al. 1999). Early theoretical predictions of graphene edge states were based on TB and Hubbard models (Fujita et al. 1996; Nakada et al. 1996; Tanaka et al. 1987), Huckel theory (Klein 1994), and the DV- $X\alpha$  method (Kobayashi 1993; Tsukada et al. 1983). A more chemically oriented interpretation of the structure and electronic character of the different edges has recently been given using Clar's sextet theory, a well-known tool for the study of aromaticity in organic materials (Balaban and Klein 2009; Baldoni et al. 2008; Wassmann et al. 2008).

The magnetic character carried by the zigzag edge states has a dominant effect on the electronic structure of the system. If one views a ZGNR as unrolling an armchair SWNT, one would naively expect both systems to have similar electronic character while replacing the symmetry of a "particle in a ring" type of boundary conditions with that of a "particle in a box." Therefore, since all armchair SWNTs are metallic in nature, it can be assumed that all ZGNRs would be metallic as well. When performing spin-restricted DFT calculations, this indeed turns out to be the case (Son et al. 2006b). Nevertheless, if the spin degree of freedom is taken into account via the unrestricted DFT scheme, the spin-polarized character of the electronic ground state of the ZGNR is revealed (Son et al. 2006b). Here, the electronic edge state on one zigzag edge has one spin flavor while the corresponding state on the other zigzag edge has the opposite spin flavor. This antiparallel edge spin alignment is a direct consequence of the antiferromagnetic coupling of spins on adjacent sites within the hexagonal carbon lattice. In contrast to the case of the metallic armchair SWNTs, the magnetic ground state exhibits a finite bandgap, and therefore, all ZGNRs become semiconducting (Son et al. 2006b). This is an excellent example showing how edge states may dominate the electronic character of the system.

The existence of such spin-polarized edge states opens a venue for controlling the electronic properties of GNRs. One possible scheme was recently suggested where an in-plane electric field, applied perpendicular to the axis of the ribbon, drives the system into a half-metallic state (Son et al. 2006b). Due to the field-induced charge separation, a local gating with opposite charge polarization occurs at the edges of the ribbons. This in turn, shifts the local DOS at both edges with respect to one another thus increasing the bandgap of electrons with one spin flavor and reducing the bandgap of the opposite spins (see  Fig. 24-4). By changing the intensity of the applied electric field, one can control the ratio of the bandgaps of the two spin components up to a point where the bandgap of one spin flavor completely vanishes while the other spin flavor presents a large bandgap. A system in such a half-metallic state may serve as a perfect spin filter in nanospintronic devices.

The half-metallic behavior exhibited by zigzag ribbons under an external electric field was first obtained using the LSDA functional. Shortly after, calculations in a large cluster model of a zigzag GNR performed using the hybrid B3LYP challenged those findings arguing that the inclusion of HF exchange prevents the half-metallic behavior (Rudberg et al. 2007). However, Kan et al. (2007) and Hod et al. (2007a) independently found half-metallicity in periodic zigzag nanoribbons using the B3LYP and HSE functionals, respectively.

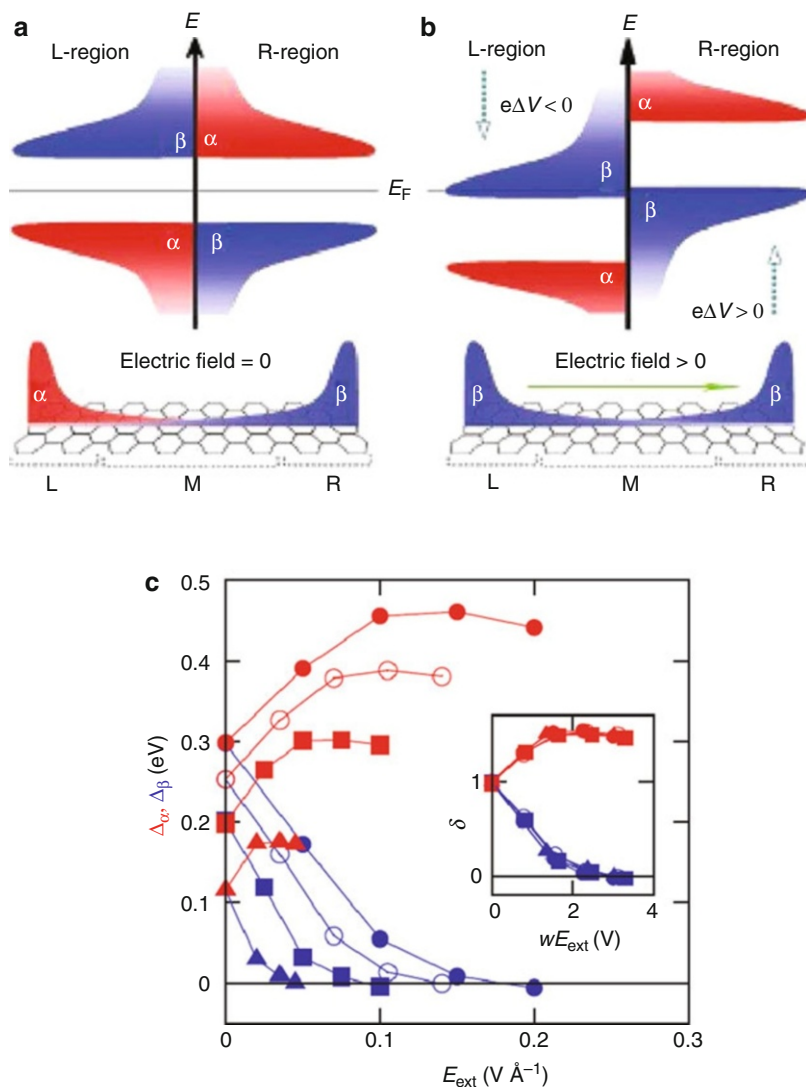


Fig. 24-4

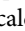
(a) Schematic density of states diagram of the electronic states of a zigzag GNR in the absence of an applied electric field. (b) Schematic density of states diagram in the presence of a transverse electric field. The electrostatic potential on the *left edge* is lowered, whereas the one on the *right edge* is raised. (c) Dependence of half-metallicity on system size. Red denotes the bandgap of  $\alpha$ -spin, and blue the gap of  $\beta$ -spin as function of  $E_{ext}$  for the 8-GNR (filled circles), 11-GNR (open circles), 16-GNR (squares), and 32-GNR (triangles). The rescaled gaps for the various widths collapse to a single function as shown in the inset (Reprinted with permission from Macmillan Publishers Ltd: Nature (Son et al. 2006b), © (2006))

## Modeling the Optical Spectrum of Single-Walled Carbon Nanotubes and Graphene Nanoribbons


### Single-Walled Carbon Nanotubes

Characterization methods for single-walled carbon nanotubes based on optical absorption have attracted much attention during the past few years. Experiments based on photoluminescence (Bachilo et al. 2002; Weisman and Bachilo 2003), resonant Raman spectroscopy (Fantini et al. 2004; Telg et al. 2004), and Rayleigh scattering (Sfeir et al. 2006) have been reported in which optical transitions are obtained as fingerprints of a certain  $(n,m)$  SWNT. Optical transitions were first studied theoretically within the tight-binding approach considering the excitations as inter-band transitions. Within this framework, the optical spectra is generally obtained by utilizing the random-phase approximation (RPA) for the imaginary part of the dielectric function  $\epsilon$  (for a review, see Onida et al. 2002)

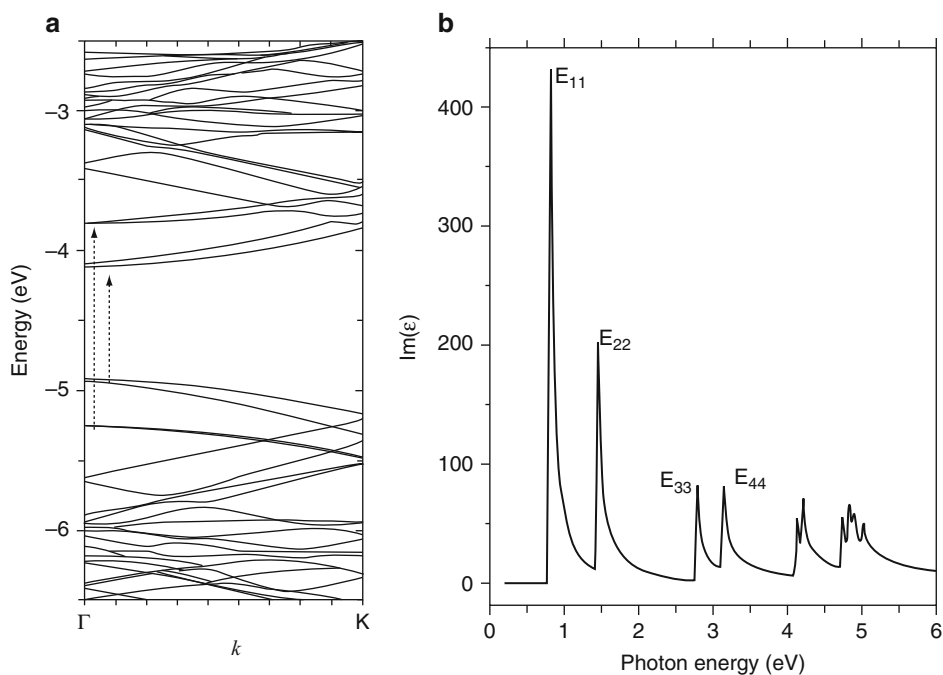
$$\text{Im}(\epsilon) = \frac{1}{\omega^2} \sum_{\mathbf{k}} \sum_{o,u} |\langle \psi_o^{\mathbf{k}} | \mathbf{p} | \psi_u^{\mathbf{k}} \rangle|^2 \delta(\epsilon_o^{\mathbf{k}} - \epsilon_u^{\mathbf{k}} - \omega), \quad (24.1)$$

where  $\mathbf{p}$  is the linear momentum operator and the indices  $o$  and  $u$  stand for occupied and unoccupied Bloch orbitals, respectively. An example of the band structure and optical spectrum for a semiconducting tube obtained from DFT calculations is shown in  Fig. 24-5. Allowed optical transitions, marked with arrows in the band structure of panel (a), produce a peak in the optical spectrum (panel (b)). Within the RPA the first-order optical transition corresponds to the fundamental gap of the semiconducting SWNT (generally dipole-allowed).

The relation between the optical transitions and the diameter of the nanotubes (Kataura plot) (Kataura et al. 1999) was used as a useful guide for experimentalists in characterizing nanotubes samples. However, Kataura plots based on conventional TB calculations present serious limitations (Bachilo et al. 2002). DFT calculations utilizing local and semi-local functionals are well known to underestimate the bandgap of semiconductors significantly. This holds also true for higher order optical transitions. Hybrid functionals have been shown to improve significantly the description of the bandgap in semiconducting materials (Heyd and Scuseria 2004; Heyd et al. 2005). In the specific case of semiconducting nanotubes, commonly employed hybrid functionals, like B3LYP or PBE0 significantly overestimate the bandgap (Barone et al. 2005b).

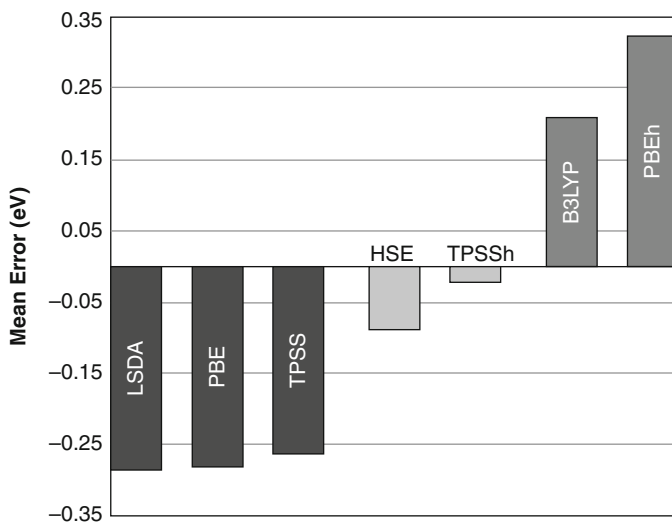
Despite the excitonic character of optical transitions in SWNTs (Spataru et al. 2004), the hybrid meta-GGA TPSS and the screened-exchange hybrid HSE provide excellent agreement with experiments for the optical gap (Barone et al. 2005b) as depicted in  Fig. 24-6 where the mean error for the first-order optical transition with respect to experimental values in a set of ten semiconducting nanotubes is shown. It is worth pointing out, however, that DFT-based approaches cannot predict the strength of exciton binding energies due to the mean-field nature of the approximation.

First-principles calculations including electron–electron interactions beyond the mean field theory have shown the excitonic character of optical transitions in SWNTs with large exciton binding energies (of up to 1 eV for the (8,0) SWNT) (Spataru et al. 2004). These predictions have been corroborated by experiments (Shaver et al. 2007; Wang et al. 2005). Unfortunately, these calculations are too demanding for routine calculations in large diameter tubes, and unlikely to be practical to study the effect of defects and functionalization.



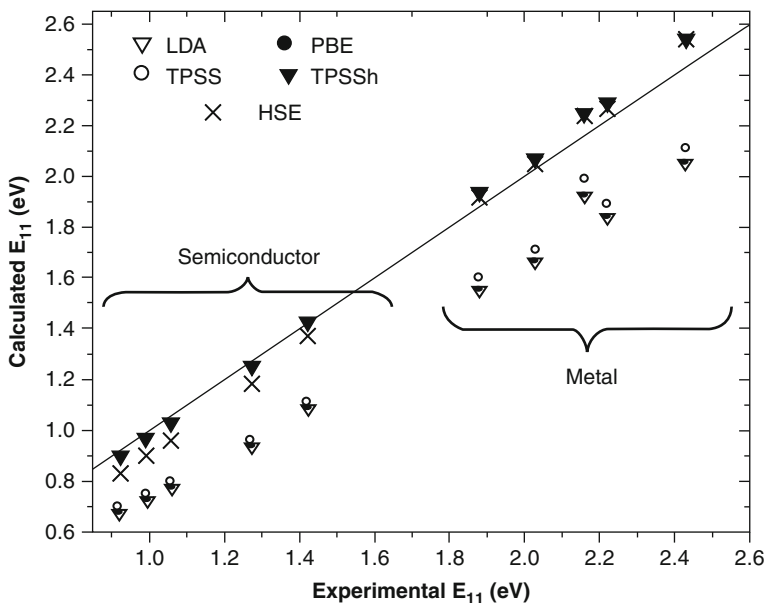
■ Fig. 24-5

Band structure (a) and optical spectrum (b) of the semiconducting (10,8) SWNT (Reprinted (Adapted) with permission from Barone et al. (2005b). © (2005) American Chemical Society)



■ Fig. 24-6

$E_{11}$  mean errors in a set of ten semiconducting SWNTs calculated with different functionals



■ Fig. 24-7

Calculated versus experimental first optical excitation energies for semiconducting and metallic SWNTs (Reprinted (Adapted) with permission from Barone et al. (2005a). © (2005) American Chemical Society)

The success of the hybrid functionals HSE and TPSSh in predicting the peak position of optical transitions has been attributed to unknown error cancellations (Kümmel and Kronik 2008; Spataru et al. 2008). However, excitonic effects in metallic nanotubes are up to two orders of magnitude smaller than in semiconducting tubes (Deslippe et al. 2007) and remarkably, the same hybrid functionals that are able to describe the optical peaks in semiconducting tubes also produce excellent results in metallic tubes (Barone et al. 2005a).

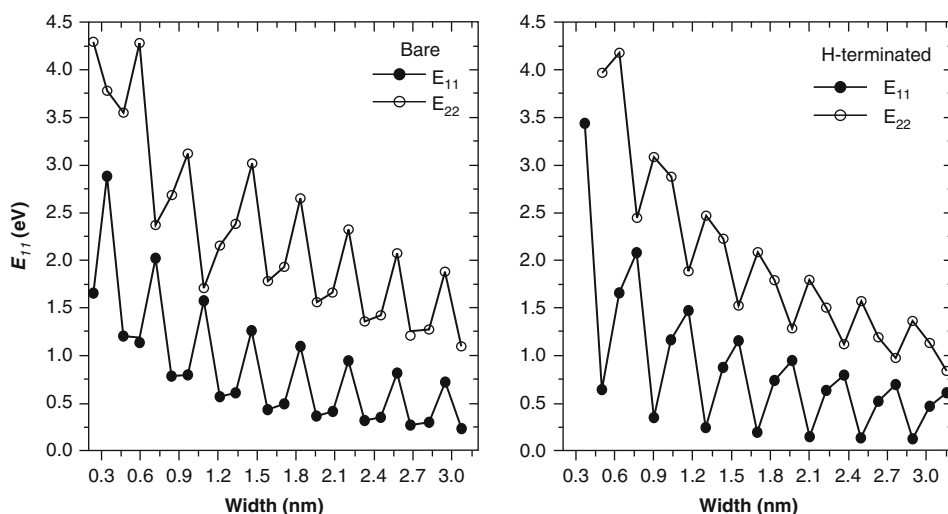
As a first example of the predictive capabilities of these functionals, we show in ● Fig. 24-7 calculated first-order optical transitions,  $E_{11}$  as a function of the corresponding experimental values in a set of five semiconducting and five metallic chiral nanotubes. All non-hybrid functionals employed here (LDA, PBE, and TPSS) underestimate  $E_{11}$  in metallic tubes by approximately 0.3 eV. This error is comparable to the error for  $E_{11}$  in semiconducting tubes. The best overall performance is achieved by the hybrids TPSSh and HSE, which yield comparable first-order transitions in the case of metallic SWNTs.

As a second example, we compare in ● Table 24-2 first-order transitions calculated using the hybrid TPSSh and HSE functionals (Barone et al. 2005a), and calculations considering GW plus electron-hole interactions (GW + e-h) (Spataru et al. 2008), with experimental values. Here, it is worth to point out the results obtained with hybrid functionals, that predict peak positions in agreement with more complex quasiparticle and excitonic effects approaches. An explanation for this behavior has been recently presented by Brothers et al. (2008).

■ Table 24-2

First-order optical transitions (eV) in metallic and semiconducting tubes calculated using the hybrid TPSSH and HSE functionals (Barone et al. 2005a, b), GW plus electron–hole interactions (GW + e–h) (Spataru et al. 2008), and experimental values

Tube	TPSSH	HSE	GW + e–h	Exp.	Reference (Exp.)
Semiconductor					
(10,0)	1.04	0.97	1.00	1.07	Bachilo et al. (2002)
(11,0)	1.19	1.12	1.21	1.20	Bachilo et al. (2002)
Metallic					
(12,0)	2.25	2.24	2.25	2.16	Fantini et al. (2004)
(10,10)	1.89	1.86	1.84	1.89	Fantini et al. (2004)



■ Fig. 24-8

Dependence of the first ( $E_{11}$ ) and second ( $E_{22}$ ) optical transition energies on the width of bare (*left panel*) and hydrogen-terminated (*right panel*) GNRs, at the HSE/6-31G\* level of theory (Reprinted (Adapted) with permission from Barone et al. (2006). © (2006) American Chemical Society)

## Graphene Nanoribbons

Theoretical and experimental studies reveal that the optical peaks of AGNRs might be utilized as tools to determine the nature of their edges (Barone et al. 2006; Pimenta et al. 2007). The first calculations of the optical spectrum of GNRs was presented by Barone et al. (2006) by means of DFT using the screened-exchange hybrid HSE functional. As expected from an inter-band transitions framework, first optical excitations present the corresponding oscillations as a function of the width. Second-order transitions also exhibit these oscillations, as shown in Fig. 24-8.

For armchair ribbons with hydrogen terminations there is a shift between the oscillation of the first and second optical transition energies such that the local maxima of  $E_{11}$  coincide with the local minima of  $E_{22}$ . This is expected to give rise to a doublet in the optical spectrum. A similar doublet is expected to appear for bare GNRs with widths smaller than 1.2 nm. Nevertheless,

for larger widths, the bandgap oscillations of the first and second optical transition energies of bare ribbons are in phase and the doublet is expected to disappear. This effect should provide a practical way of revealing information on the size and the nature of the edges of GNRs. Many-body approaches later pointed out that due to the one-dimensional nature of GNRs, and like in the case of SWNTs, their optical spectrum is dominated by excitonic effects with binding energies as high as 1.4 eV for a 1.2 nm wide ribbon (Prezzi et al. 2008; Yang et al. 2007).

## Chemistry at the Edges of Graphene

---

The question of what is at the edges of graphene has fascinated researchers in the area (Radovic and Bockrath 2005), especially, since the possibility of finding magnetic edge states was openly discussed in terms of the type of chemical bond that is expected to appear for bare and hydrogen-terminated edges (Radovic and Bockrath 2005). The question of how magnetic and electronic properties of nanoribbons depend upon chemical functionalization and doping has been partially addressed by several studies. One of the first studies along this line of research was presented by Hod et al. (2007a). In this study, the authors assumed that in most synthetic scenarios GNRs edges will most likely be oxidized with an unknown effect on their electronic properties. The oxidation schemes considered in these calculations included hydroxyl, lactone, ketone, and ether groups. The authors have shown that these oxidized ribbons are, in general, more stable than hydrogen-terminated GNRs (see [Fig. 24-9](#)). These configurations maintain a spin-polarized ground state with antiferromagnetic ordering localized at the edges, similar to the fully hydrogenated counterparts. Edge oxidation has been found to lower the onset electric field required to induce half-metallic behavior (see [section “Graphene Nanoribbons”](#)) and extend the overall field range at which the systems remain half-metallic. When the edges of the ribbon are fully or partially hydrogenated, the field intensity needed to switch the system to the half-metallic regime is about  $0.4 \text{ V/\AA}$  and the range at which the half-metallic behavior is maintained is of  $0.3 \text{ V/\AA}$ . Nevertheless, when the edges are fully oxidized, the system turns half-metallic at a lower field intensity ( $0.2 \text{ V/\AA}$ ) and the range of half-metallic behavior is doubled to  $0.6 \text{ V/\AA}$ . Unfortunately, it is found that oxygen-containing groups at the edges have a minor effect on the energy difference between the antiferromagnetic ground state and the above-lying ferromagnetic state. This indicates a weak site-to-site exchange coupling and therefore oxygen terminations do not increase the spin coherence length in these systems.

Gunlycke et al. (2007) also studied the effect of oxygen and imine groups and found that transport and magnetic properties are greatly affected by the nature of the chemical groups at the edges. The electronic properties of ribbons with edge carbons presenting two hydrogen or two fluorine atoms were also studied and it was found that in narrow GNRs the  $sp^3$  type of edge carbon results in a non-spin-polarized state (Kudin 2008). Kan et al. (2007) studied the effect of combining donor and acceptor groups at different edges of zigzag nanoribbons using DFT in the GGA. Within this approach, the authors found a half-metallic behavior without an external field for some particular chemical decorations. Cervantes-Sodi et al. (2008a, b) investigated the electronic properties of chemically modified ribbons and observed that chemical modifications of zigzag ribbons can lift the spin degeneracy which promotes a semiconducting-metal transition, or a half-semiconducting state, with the two spin channels having a different bandgap, or a spin-polarized half-semiconducting state, where the spins in the valence and conduction bands are oppositely polarized. The authors find that edge functionalization studied in

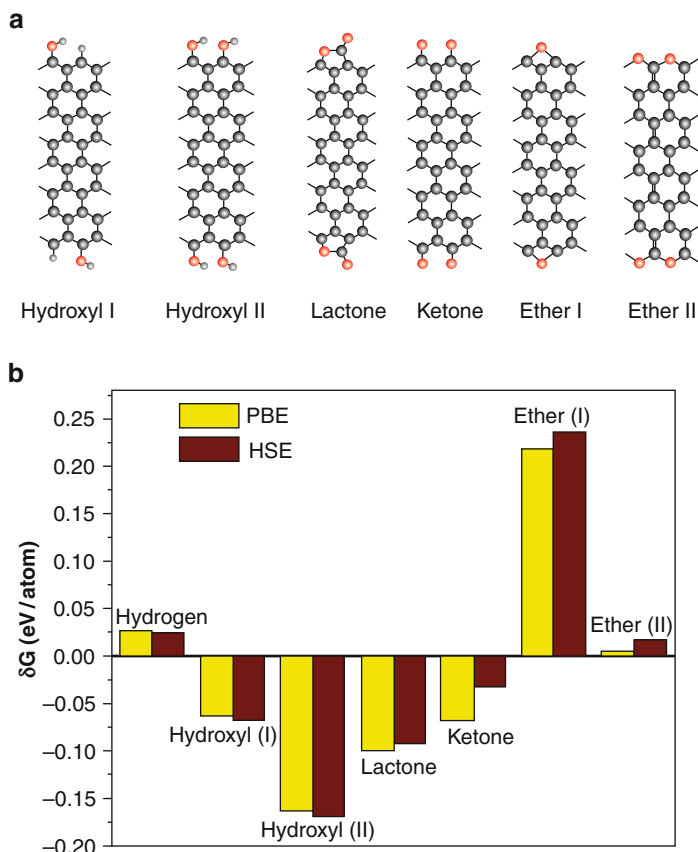


Fig. 24-9

(a) Scheme of the oxygen-containing groups considered. (b) Relative stability of the different chemical groups at the edges as calculated using the enthalpy of formation with respect to molecular oxygen and hydrogen, and graphene as shown in Hod et al. (2007a) (Reprinted (Adapted) with permission from Hod et al. (2007a). © (2007) American Chemical Society)

their work gives electronic states a few eV away from the Fermi level in armchair ribbons and does not significantly affect their bandgap. Lee and Cho (2009) presented calculations based on the local spin density approximation and found that edge-oxidated ZGNRs present a metallic behavior. This was rationalized in terms of the electronegativity of O with respect to C. However, it needs to be stressed that while LSDA or PBE calculations might yield a metallic solution, hybrid functionals still predict all oxidation schemes to be semiconducting (Hod et al. 2007a).

Chemical functionalization of rectangular graphene nanodots has been studied in detail using the DFT-B3LYP approach (Zheng and Duley 2008). This study shows that edge chemical modifications in finite ribbons significantly alter their electronic structure. Finite size effects in this type of dots will be further discussed in the next section.

It is interesting to note that besides chemical functionalization at the edges of graphene it is possible to introduce adatoms on the graphene surface. Usually, this type of interaction is



governed by a charge transfer mechanism. Rigo et al. (2009) presented DFT calculations on Ni adsorption on graphene nanoribbons. The adsorption takes place preferentially along the edges of zigzag nanoribbons and the interaction of the adatom with the carbon backbone quenches the magnetization of the latter in the neighborhood of the adsorption site. Other transition metal atoms adsorbed on GNRs were studied using DFT (Sevincli et al. 2008). Interestingly, Fe or Ti adsorption makes certain armchair GNRs half-metallic with a 100% spin polarization at the Fermi level. These results indicate that the properties of graphene nanoribbons can be strongly modified through the adsorption of  $3d$  transition metal atoms. Alkaline and alkali metal adsorption on graphene nanoribbons were found to exhibit a strong site-dependent interaction (Choi and Jhi 2008). Similar results have been obtained by Uthaisar et al. (2009) when considering the interaction of Li adatoms and graphene nanoribbons. The strength of the interaction is much larger in zigzag GNRs than in armchairs and occurs preferentially along the edges. This enhancement is rationalized in terms of the larger number of electron acceptor states in ZGNRs compared to AGNRs. Energy barriers for Li migration also present important characteristics along the edges which can result in faster kinetics than in regular graphene (Uthaisar and Barone 2010). In addition, recent computational studies suggest lithium doping as a possible route for bandgap engineering of graphitic systems (Krepel and Hod 2011).

## Finite Size Effects in Low-Dimensional Graphitic Materials

---

Finite size effects play a central role in dictating the electronic properties of materials at the nanoscale. Due to their unique electronic structure, quasi-zero-dimensional (quantum dots) graphitic structures may exhibit fascinating physical phenomena, which are absent in their quasi-one-dimensional (nanowires, nanotubes, and nanoribbons) counterparts. Many factors govern the effect of reduced dimensions on the electronic properties of nanoscale materials. Here we focus on two such important factors, which are strongly manifested in the electronic characteristics of graphitic materials, namely, quantum confinement and edge effects:

1. Quantum confinement is related to the boundary conditions enforced on the electronic wave function by the finite size of the system. When the typical de-Broglie wavelength associated with the Fermi electrons becomes comparable to the dimensions of the system, its electronic and optical properties deviate substantially from those of the bulk system. As the confining dimension decreases and reaches this limit (which is typically within the nanometer regime) the energy spectrum turns discrete and the energy gap becomes size dependent.
2. Edge effects in graphitic materials are dominated by localized states, which are physically located at the boundaries of the system and energetically positioned in the vicinity of the Fermi energy. These states influence not only the electronic properties of these systems but also their chemical reactivity.

## Quantum Confinement in Graphitic Systems

---

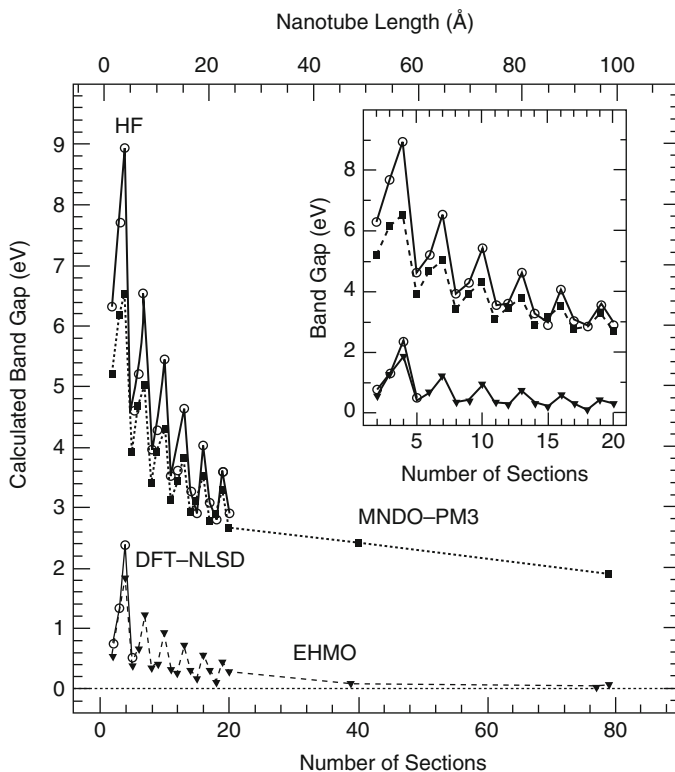
As shown in previous sections, combining the unique electronic structure of the two-dimensional graphene sheet with the quantum confinement in quasi-one-dimensional graphene derivatives, results in unique electronic properties, which are governed by the specific

geometry and dimensions of the relevant system. In [Section “Structure–Property Relations in Single-Walled Carbon Nanotubes and Graphene Nanoribbons,”](#) it was shown that one of the most notable examples of such effects is found in the strong dependence of the electronic character of carbon nanotubes on their specific diameter and chirality. This diversity in the electronic structure obtained from a single material just by changing its spatial symmetry, is one of the most promising characteristics of carbon nanotubes for applications as basic components in future nanoscale electronic devices.

Recent experimental procedures have allowed the production of ultra-short carbon nanotubes (Chen et al. 2006a, b; Gu et al. 2002; Javey et al. 2004; Khabashesku et al. 2002; Mickelson et al. 1998; Nakamura et al. 2003). The electronic structure of these quasi-zero-dimensional systems is expected to be considerably different from their elongated counterparts, since the reduction of dimensionality implies additional confinement restrictions which may result in the emergence of new and interesting physical phenomena. Several theoretical investigations have addressed the importance of quantum confinement on the electronic properties of finite carbon nanotubes (Baldoni et al. 2007; Li et al. 2002; Liu et al. 2001; Rochefort et al. 1999b). Using a variety of methods including the HF approximation, semiempirical calculations, and the GGA, Rochefort et al. (1999b) have investigated the change in bandgap, density of states, and binding energies as a function of the length of armchair carbon nanotubes. In contrast with the metallic character of the infinite tubes, finite segments shorter than 10 nm are predicted to present a considerable bandgap, which vanishes as the length of the tube increases. Interestingly, the convergence to the infinite metallic system is non-monotonic, and pronounced threefold bandgap oscillations occur as the length of the tube is extended (see [Fig. 24-10](#)). These bandgap oscillations were associated with the periodic changes in the bonding characteristics of the HOMO (highest occupied molecular orbital) and LUMO (lowest unoccupied molecular orbital), which are a direct consequence of the quantum confinement of the  $\pi$  electrons along the tube axis.

As one may expect, the calculated bandgaps strongly depend on the specific computational method, where the HF and semiempirical approximations predict bandgap values which are four to six times larger than those obtained by the generalized gradient DFT and extended Huckel calculations. Nevertheless, the general characteristics of the bandgap behavior and the existence of the bandgap oscillations are predicted by all methods. Similar results have been obtained using the hybrid B3LYP functional for open-ended and capped finite nanotube sections (Li et al. 2002). Expanding the study to the case of zigzag and chiral nanotubes, Liu et al. (2001) have used extended Huckel calculations to show the dependence of the bandgap oscillations on the chirality of the finite nanotube segment. As shown in [Fig. 24-11](#), as the chirality of the tube changes gradually from armchair to zigzag, the amplitude of the oscillations reduces, and almost vanishes for the case of (12,0) zigzag nanotube segments. This leads to the interesting conclusion that the metallic character of the infinite armchair nanotubes is replaced by HOMO–LUMO gap oscillations for finite armchair nanotube segments, while the oscillatory bandgap nature of infinite zigzag nanotubes is replaced by a vanishing HOMO–LUMO gap for the finite zigzag nanotube segments. An interesting interpretation of the behavior of the HOMO and LUMO levels of finite carbon nanotube segments as a function of their length was recently given using Clar sextet theory (Baldoni et al. 2007).

As discussed above, when an infinite graphene sheet is cut to form a quasi-one-dimensional graphene nanoribbon with a finite width and infinite length, the  $\pi$ -electrons wave function is confined along the direction perpendicular to the axis of the ribbon and is forced to vanish at large distances along this direction. These “particle in a box” like boundary conditions induce

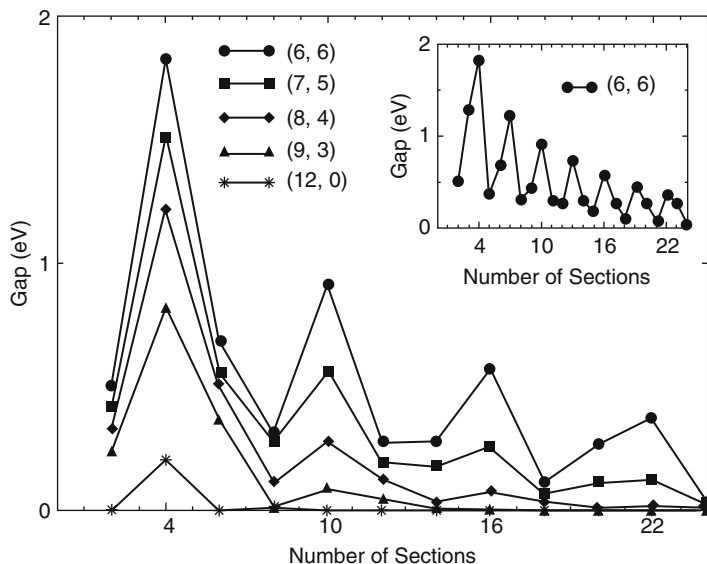


■ Fig. 24-10

Variation of the band gap of a (6,6) nanotube as a function of its length determined using different computational techniques (Reprinted (Adapted) with permission from Rochefort et al. (1999b). © (1999) American Chemical Society)

discretization of the two-dimensional dispersion relation into a set of one-dimensional bands. This discretization induces bandgap dependence on the width of the obtained ribbons.

The dimensionality of these systems may be further reduced to form graphene nanodots, which can be viewed as molecular derivatives of graphene. This extra confinement has been recently shown to strongly impact the electronic structure of these systems (Hod et al. 2008; Shemella et al. 2007). ● Figure 24-12 presents the HOMO-LUMO gaps as a function of the length and width of a large number of graphene quantum dots calculated using the local density approximation (upper left panel), the PBE flavor of the generalized gradient correction (upper right panel), and the screened-exchange hybrid HSE functional (lower left panel). The studied graphene derivatives are rectangular in shape and denoted by  $N \times M$  where  $N$  and  $M$  are the number of hydrogen atoms passivating the armchair and zigzag edge, respectively. As in the case of infinite armchair graphene nanoribbons, an oscillatory behavior of the energy gap as a function of the length of the ribbon is observed. The periodicity of these oscillations appears to be somewhat different than the threefold period obtained for the infinitely long counterparts. This, however, is a result of the fact that in order to prevent dangling carbon bonds, the width step taken for the finite systems is twice as large than the one taken in the infinitely long armchair



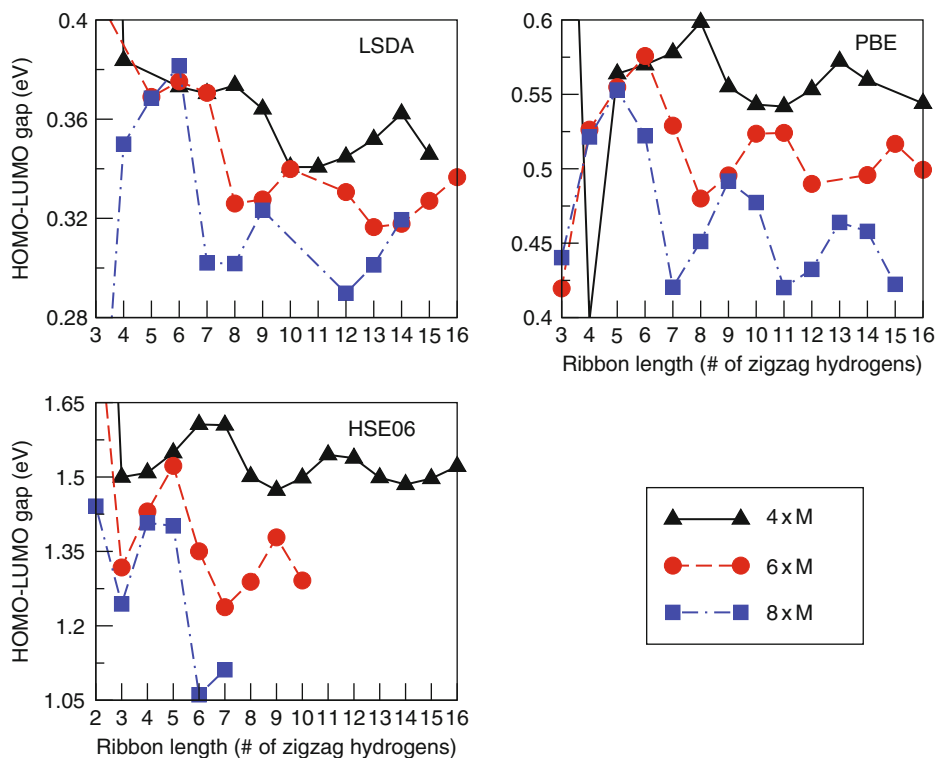
■ Fig. 24-11

The bandgap as a function of the (even) number of SWNTs sections (Reprinted with permission from Liu et al. (2001). © (2001) by the American Physical Society)

ribbon calculations. The amplitude of the oscillations is found to be considerably damped due to the finite size of the ribbons. As expected, when the length of the armchair edge ( $N$ ) is increased, the oscillation amplitude increases as well. It is interesting to note that, in general, the HOMO–LUMO gap is inversely proportional to the width ( $N$ ) and the length ( $M$ ) of the finite GNR in accordance with the semimetallic graphene sheet limit. Therefore, in order to obtain energy gap tailoring capability, one will have to consider GNRs with long armchair edges (large  $N$  values) and short zigzag edges (small  $M$  values). This will increase the amplitude of the energy gap oscillations while maintaining overall higher gap values.

## Edge Effects in Graphitic Systems

The effects of localized edge states on the electronic properties of quasi-one-dimensional systems have been discussed in previous sections. The question arises of whether similar effects can be observed in quasi-zero-dimensional systems. It is well established that small molecular derivatives of graphene, such as different types of polyaromatic hydrocarbons, have a closed shell nonmagnetic ground state. On the other hand, infinite ZGNRs present a spin-polarized ground state. This suggests that there exists a critical size at which molecular graphene derivatives become spin polarized. One of the earliest studies addressing this issue dates back to more than two decades ago (Stein and Brown 1987). Using Huckel theory it was found that finite graphene flakes exhibit electronic edge states along the zigzag edges. More recently, several studies, based on DFT calculations have investigated this question in detail. As a first step for obtaining quasi-zero-dimensional

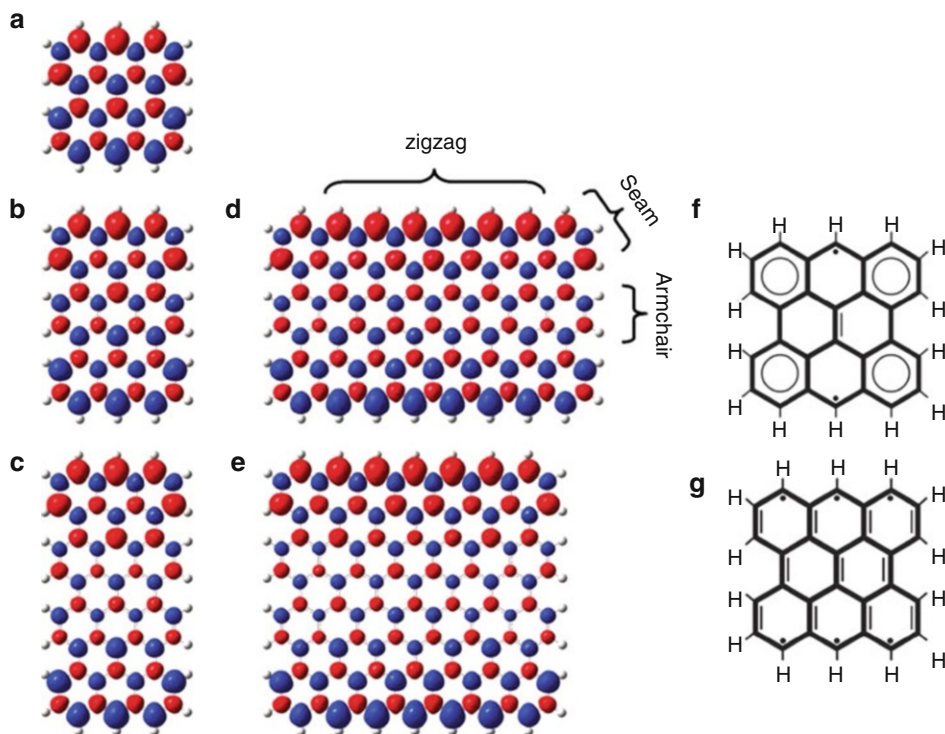


■ Fig. 24-12

HOMO–LUMO gap values for three sets of graphene nanodots, as calculated by the local spin density approximation (*upper left panel*), PBE functional (*upper right panel*), and the HSE functional (*lower left panel*) (Reprinted with permission from Hod et al. (2008). © (2008) by the American Physical Society)

graphene derivatives, it is convenient to consider truncated graphene nanoribbons in the form of rectangular nanodots (Hod et al. 2008; Jiang et al. 2007; Kan et al. 2007; Rudberg et al. 2007; Shemella et al. 2007). Surprisingly, it was found that even molecular scale graphene derivatives, such as the bisanthrene (phenanthro[1,10,9,8-opqra]perylene) isomer of the  $C_{28}H_{14}$  molecule and  $C_{36}H_{16}$  (tetrabenzo[bc,ef,kl,no]coronene), are predicted to present a spin polarized ground state as shown in Fig. 24-13 (Hod et al. 2008; Jiang et al. 2007; Kan et al. 2007). For the smaller molecules, this was further verified using a complete active space self-consistent field many-body-wave function approach (Jiang et al. 2007). Furthermore, the application of an in-plane electric field perpendicular to the zigzag edge was found to turn the finite systems into molecular scale half-metals (Hod et al. 2008; Kan et al. 2007), similar to the case of infinite ZGNRs.

When considering more complicated graphene derivatives such as triangular graphene flakes (Ezawa 2007; Fernandez-Rossier and Palacios 2007), the combination of the local anti-ferromagnetic spin ordering on adjacent carbon sites and the edge geometry of the triangular structure results in spin frustration. This leads to a metallic ground state with an overall ferromagnetic character and a finite magnetic moment. The results of tight-binding Ising model



■ Fig. 24-13

(a)–(e) Isosurface spin densities of the antiferromagnetic ground state of several molecular graphene derivatives as obtained using the HSE functional and the 6-31G\*\* basis set. (f) and (g) represent diradical and hexaradical Clar structures of bisanthrene (Reprinted with permission from Hod et al. (2008). © (2008) by the American Physical Society)

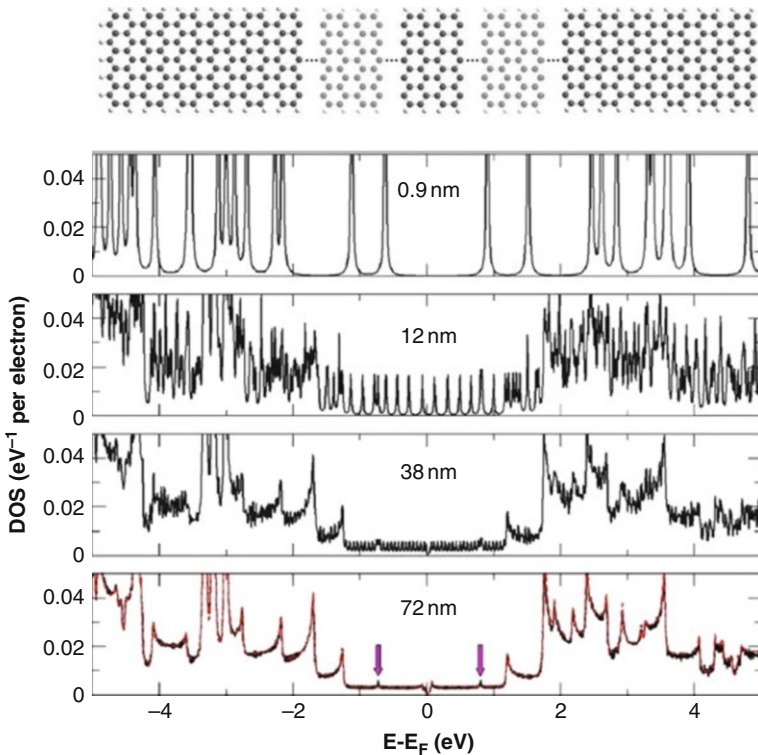
(Ezawa 2007) and Hubbard model (Fernandez-Rossier and Palacios 2007) Hamiltonians are consistent with the predictions of DFT (Fernandez-Rossier and Palacios 2007). These can be further rationalized by Lieb's theorem (Lieb 1989) regarding the total spin  $S$  of the exact ground state of the Hubbard model in bipartite lattices. The honeycomb lattice of graphene is formed by two triangular interpenetrating sublattices,  $A$  and  $B$ . Since triangular nanostructures have more atoms in one sublattice,  $N_A > N_B$  the total spin  $S$  of the ground state is  $2S = N_A - N_B > 0$ . Here, the main contribution to the magnetic moment comes from edge states around the zigzag edges of the triangular structure. Such molecular graphene derivatives were suggested to function as permanent magnets in future nanoscale memory devices.

Naturally, the effect of edge states reduces as the surface to edge ratio becomes larger. An interesting question to address is at what length would the effect of the edges disappear and the electronic structure of the system becomes essentially identical to that of the infinite system? In a recent study, this question was addressed using a divide-and-conquer (D&C) DFT approach, which enables the efficient and accurate calculation of the electronic properties and charge transport through finite elongated systems (Hod et al. 2006). Within this approach, the Hamiltonian  $\mathbf{H}$  is given in a localized basis set representation by a block-tridiagonal matrix,

where the first and last diagonal blocks correspond to the two terminating units of the ribbon (see upper panel of [Fig. 24-14](#)). The remaining diagonal blocks correspond to the central part of the GNR which is composed of a replicated unit cell. The terminating units and the replicated central part unit cell are chosen to be long enough such that the block-tridiagonal representation of  $\mathbf{H}$  (and the overlap matrix  $\mathbf{S}$ ) is valid. The terminating unit diagonal Hamiltonian blocks and their coupling to the central part are evaluated via a molecular calculation involving the two terminating units and one unit cell cut out of the central part. The replicated unit cell blocks of the central part and the coupling between two such adjacent blocks are approximated to be constant along the GNR and obtained from a periodic boundary conditions calculation. The resulting block-tridiagonal matrix  $ES - \mathbf{H}$  is then partially inverted for each value of the energy  $E$  using an efficient algorithm, to obtain the relevant Green's function blocks needed for the DOS and transport calculations using the following formula

$$\rho(E) = -\frac{1}{\pi} \text{Im} \{ \text{Tr} [ G^r(E) \mathbf{S} ] \}, \quad (24.2)$$

where  $G^r(E) = [ES - \mathbf{H}]^{-1}$ . A detailed account of the D&C method can be found in Hod et al. (2006).



■ Fig. 24-14

*Upper panel:* A finite elongated graphene nanoribbon. *Lower panels:* DOS of the finite GNR at different lengths. The red curve in the lowermost panel is the DOS of the infinite system (Reprinted with permission from Hod et al. (2007b). © (2006) by the American Physical Society)



To study these edge effects in graphene, three graphene nanoribbons with consecutive widths were considered and their DOS as a function of the ribbons' length were calculated using this D&C approach (Hod et al. 2007b). As an example, Fig. 24-14 presents the DOS of a finite graphene nanoribbon of different lengths. It can be seen that for graphene nanodots up to 12 nm in length, the DOS resembles that of a finite molecular system characterized by a discrete set of energy levels. When the ribbon is further elongated to 38 nm, a constant DOS around the Fermi energy of the infinite system arises and typical Van Hove singularities start to build up. For this specific system, at a length of 72 nm most of the features that are related to the edge states disappear, and the DOS almost perfectly matches that of an infinite armchair graphene nanoribbon. The rate of convergence of the electronic properties of finite systems to those of the infinite counterparts will depend on the type of the system and the specific interactions that govern its electronic character. Therefore, the divide-and-conquer method allows the quantitative estimation of this rate based on state-of-the-art DFT approximations.

We now turn back to the case of carbon nanotubes. When a zigzag nanotube is cut into finite segments, the zigzag edges are exposed. We have shown in the previous section that quantum confinement effects may play an important role in determining the electronic character of such structures. Similar to the case of graphene nanoribbons, these effects are now accompanied by the formation of spin-polarized edges states which put their own fingerprints on the electronic structures of the system (see Fig. 24-15). There has been a debate in the literature regarding the energetic stability of these edge states, and whether they would appear for all finite zigzag nanotubes regardless of their diameter (Higuchi et al. 2004; Kim et al. 2003; Okada and Oshiyama 2003). It is now well accepted that all finite zigzag SWNT segments are expected to present a spin-polarized ground state (Hod and Scuseria 2008; Kim et al. 2003; Mananes et al. 2008). Furthermore, as for ZGNRs, the application of an axial electric field will drive

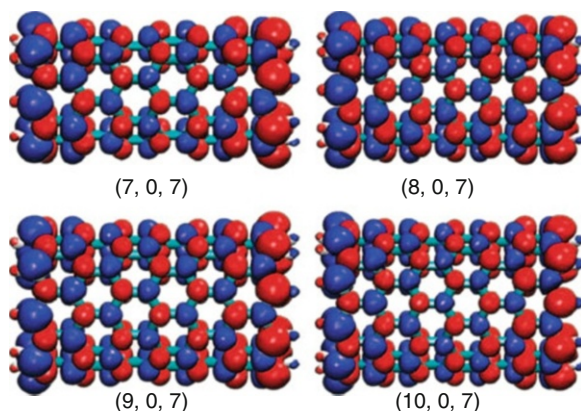


Fig. 24-15

Antiferromagnetic-type ground state spin density maps of the (7,0) (upper left panel), (8,0) (upper right panel), (9,0) (lower left panel), (10,0) (lower right panel) finite zigzag SWNT segments as obtained using the HSE functional with the 6-31G\*\* basis set. Red and blue isosurfaces indicate the two spin flavors with an isovalue of  $0.0015 \text{ a}_0^{-3}$  (Reprinted (Adapted) with permission from Hod and Scuseria (2008). © (2008) American Chemical Society)



the system into a half-metallic state, thus forming a perfect spin filter. If one now eliminates only one zigzag edge of the tube by capping it with a half-fullerene, spin frustration results in a spin-polarized ferromagnetic ground state (Kim et al. 2003), which resembles the case of triangular graphene derivatives discussed above and forms a molecular magnet bearing a permanent magnetic moment.

Two-dimensional graphene and its lower dimensional derivatives present a diversity of electronic behaviors, making them particularly attractive as building blocks for future nano-devices. Simplified model Hamiltonian approaches may give important insights on the general physical trends in these systems. Nevertheless, density functional theory in general, and the screen exchange hybrid functional approximation, in particular, seem to be excellent tools to quantitatively study the structure–function relations in these systems and the effects of external perturbations such as chemical substitutions and electric and magnetic fields.


## Electromechanical Properties of One-Dimensional Graphitic Structures

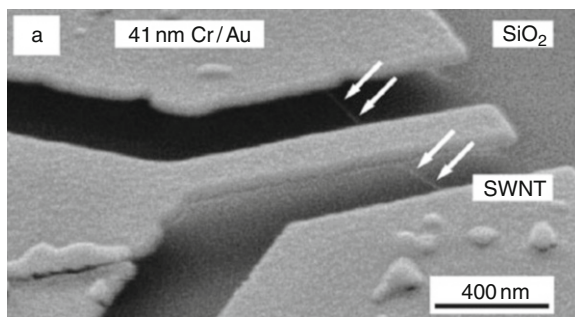
---

Electromechanical devices are based on systems for which the mechanical properties can be controlled via the application of external electric potentials and/or the electronic properties may be altered via induced mechanical deformations. Such devices can be scaled down to form microelectromechanical systems (MEMS), which are small integrated devices or systems that combine electrical and mechanical components. Their dimensions may vary from the submicron level up to a few millimeters. By fabricating miniature mechanical elements such as beams, gears, diaphragms, and springs MEMS enabled the realization of diverse applications including ink-jet-printer cartridges, accelerometers, miniature robots, microengines, locks, inertial sensors, microtransmissions, micromirrors, micro actuators, optical scanners, fluid pumps, transducers, and chemical, pressure, and flow sensors. Nanoelectromechanical (NEMS) systems present the ultimate miniaturization of such devices, scaling them further down to the molecular level. Apart from the reduced dimensions, these systems are characterized by lower energy consumption and increased sensitivity toward external perturbations. Furthermore, due to their quantum-mechanical nature, molecular-sized NEMS may present unique physical properties that cannot be obtained from their microscopic and macroscopic counterparts. The unique electronic and mechanical properties of carbon nanotubes have marked them as promising candidates for key components in NEMS. In recent years, several theoretical investigations as well as experimental realization of NEMS have been presented (Cao et al. 2003; Cohen-Karni et al. 2006; Fennimore et al. 2003; Gomez-Navarro et al. 2004; Hall et al. 2007; Maiti 2003; Minot et al. 2003; Nagapriya et al. 2008; Paulson et al. 1999; Rueckes et al. 2000; Sazonova et al. 2004; Semet et al. 2005; Stampfer et al. 2006; Tomblor et al. 2000).

## Carbon Nanotubes in NEMS Applications

---

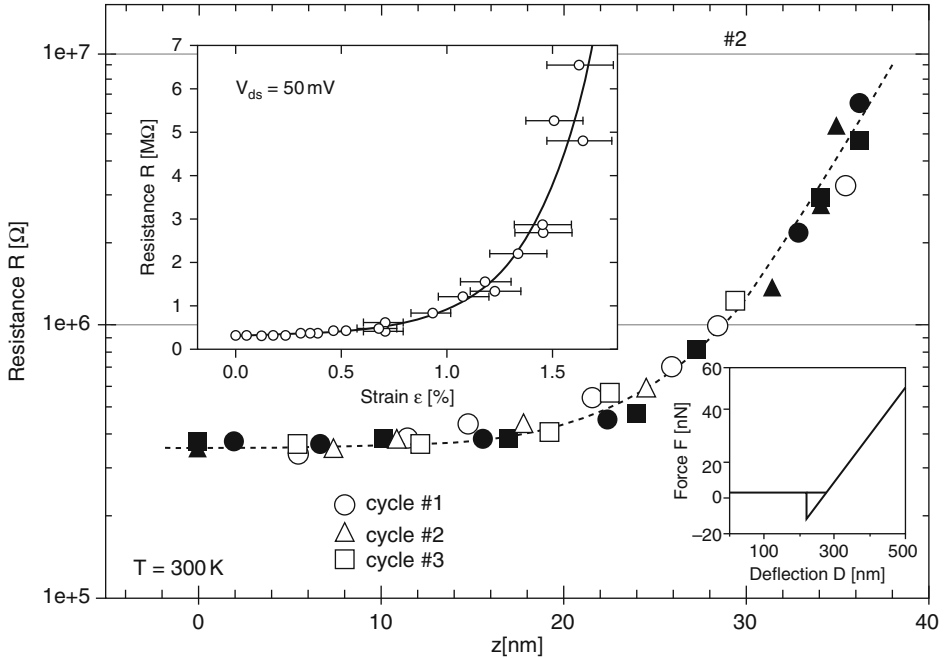
The key components in most of the suggested setups are suspended carbon nanotubes bridging the gap between two conducting electrodes without making contact with the underlying surface (see  Fig. 24-16). One may then induce mechanical deformations via manipulation of an external nanoscale tip while simultaneously measuring the changes in the conductance of



■ Fig. 24-16

SEM image of a cantilever-SWNT-based NEMS sensing device. The white arrows indicate the location of the suspended SWNT (Reprinted (Adapted) with permission from Stampfer et al. (2006). © (2006) American Chemical Society)

the system. Strong reversible electromechanical response of carbon nanotubes under combined bending and stretching deformations have been recorded by several experimental groups (Cao et al. 2003; Maiti 2003; Minot et al. 2003; Semet et al. 2005; Stampfer et al. 2006; Tomblér et al. 2000). In **▶ Fig. 24-17**, the change in the SWNT's resistance as a function of the depression applied to the top cantilever (**▶ Fig. 24-16**) is plotted. The resistance of the system increases by more than an order of magnitude over a depression range of less than 4 nm, suggesting that such setups may be used for highly sensitive and reliable displacement sensors. A similar setup, where a floating pedal is attached to a suspended multi-walled nanotube, has enabled the investigation of the electromechanical response of single (Hall et al. 2007) and multi-walled (Cohen-Karni et al. 2006) nanotubes under the application of torsional deformations. In this setup, an atomic force microscope (AFM) tip presses down on the floating pedal. Since the SWNT is fixed at both edges to the conducting electrodes, the central section experiences torsion. This change in helicity of the system induces considerable variations in the electronic conductance. Interestingly, pronounced bandgap oscillations are observed as a function of the deflection angle of the pedal. The origin of these oscillations has been associated with the distortion of the first Brillouin zone (fBZ), which results in the shifting of the Dirac points (Cohen-Karni et al. 2006; Nagapriya et al. 2008). As the Dirac points shift within the fBZ they may approach an allowed electronic band thus increasing the conductance of the system. Once the Dirac point crosses the allowed band the conductance reaches a maximum value. Further deformation results in shifting the Dirac points away from the allowed band and thus a decrease in the conductance. This process is repeated anytime the Dirac point crosses one of the many parallel allowed bands. Other prototype devices such as nanotube actuators (Fennimore et al. 2003; Gomez-Navarro et al. 2004), and nonvolatile memory components based on SWNTs junctions (Rueckes et al. 2000) have been successfully fabricated as well, demonstrating the potential of SWNTs as nanoscale electromechanical devices. Aiming to obtain a microscopic understanding of these experimental observations and to guide further experiments with carbon nanotubes under various mechanical deformation modes, many theoretical investigations have been performed (Maiti 2009). Due to the complexity of the deformed systems, most of the computational treatments were based on semiempirical or DFT-based TB calculations.



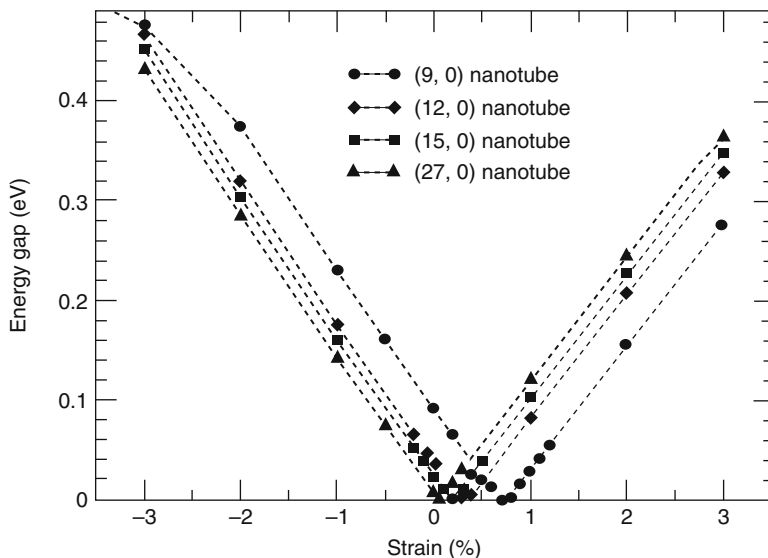
■ Fig. 24-17

Electromechanical measurements of an electromechanical device based on a metallic SWNT (► Fig. 24-16). The *upper insert* shows the resistance plotted as a function of strain. The *lower insert* shows a force versus deflection measurement performed on the cantilever-SWNT contact point (Reprinted (Adapted) with permission from Stampfer et al. (2006). © (2006) American Chemical Society)

The effects of axial stretching (Heyd et al. 1997; Jiang et al. 2004; Kane and Mele 1997; Kleiner and Eggert 2001; Yang et al. 1999), bending (Kane and Mele 1997; Liu et al. 2000; Nardelli 1999; Nardelli and Bernholc 1999; Rochefort et al. 1998, 1999a; Yang and Han 2000), torsion (Jiang et al. 2004; Kleiner and Eggert 2001; Rochefort et al. 1999a; Yang and Han 2000; Yang et al. 1999; Zhang et al. 2009), and radial compression (Lammert et al. 2000; Lu et al. 2003; Peng and Cho 2002; Svizhenko et al. 2005) were studied extensively showing high sensitivity of the electronic properties and transport characteristics of the deformed nanotubes to the applied deformations.

Several DFT calculations were conducted to study the effect of axial strain (Guo et al. 2005), bending (Maiti 2001; Maiti et al. 2002), radial compression (Mehrez et al. 2005; Wu et al. 2004), and torsional deformations in carbon nanotubes (Nagapriya et al. 2008):

1. *Axial strain*: While isolating the effect of axial stretching and compression is a challenging experimental task (Cao et al. 2003), pure axial deformations are easy to study using modern computational tools (Guo et al. 2005). Bandgap variations due to axial compression and stretching were studied using the local density approximation. As it can be seen in ► Fig. 24-18 for strains up to 3%, linear variations in the bandgap are predicted. The slope of the bandgap response depends on the tube type and on the sign of the axial deformation.



■ Fig. 24-18

Calculated bandgap variation of zigzag (9,0), (12,0), (15,0), and (27,0) SWNTs as a function of axial strain (Reprinted with permission from Guo et al. (2005). © (2005) American Institute of Physics)


For all systems studied, the relative changes in bandgap are of the order of 0.5 eV and are definitely measurable in experimental conditions.



2. *Bending*: The effect of pure bending and AFM tip-induced bending was studied using the Harris functional approximation (Maiti 2001; Maiti et al. 2002). It was shown that both pure bending and tip-induced compression maintain the hexagonal  $sp^2$  lattice structure up to relatively high bending angles. Armchair tubes remain significantly conducting even at large deformations. However, metallic zigzag tubes display a dramatic drop in conductance, in particular under tip-induced deformations.
3. *Compression*: Radial compression was studied via a combined molecular dynamics and density functional theory-based nonequilibrium Green's function approach (Wu et al. 2004). Reversible pressure-induced metal-to-semiconductor transitions of armchair SWNTs were predicted suggesting that SWNTs may be used as miniature sensitive pressure detectors (Mehrez et al. 2005; Wu et al. 2004).
4. *Torsion*: While the torsional electromechanical response was successfully explained via the deformation of the Brillouin zone, another possible explanation for the bandgap oscillations may be the periodic formation of Moire patterns due to registry mismatch between the different walls of the multi-walled tubes, which have a different curvature. In order to rule out this possibility, DFT calculations within the LSDA were used to show that the interlayer coupling is weak and the electronic structure of the individual walls resembles that of single-walled nanotubes for different intertube orientations (Nagapriya et al. 2008).

As can be seen from all of the examples given above, the study of the physical properties of nanotubes in general and their electromechanical behavior in particular requires

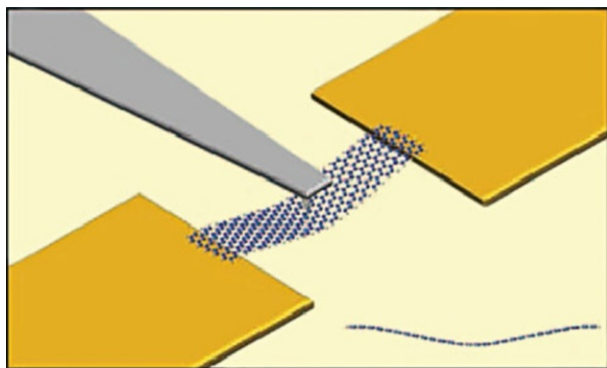
an intimate relation between theory and experiment, where the theoretical tools enable an atomic scale understanding of the experimental observations and provide guidelines for the design of new experiments. As we have seen above, when considering finite size effects and chemical functionalization, DFT presents new insights that are not captured within the simple TB approximations. When considering the electromechanical response of SWNTs to different mechanical deformations, TB calculations seem to give a reliable description. Nevertheless, calculations based on DFT are required for comparison and validation purposes.

## Graphene Nanoribbons in NEMS Applications

Soon after the successful isolation of a single graphene sheet (Novoselov et al. 2004) the first experimental realization of an electromechanical device based on graphene nanoribbons was presented (Bunch et al. 2007). In this setup, atomic thick layers of graphene were suspended above predesigned trenches carved in the underlying silicon oxide surface while bridging the gap between gold electrodes. Both optical and electrical actuation procedures were demonstrated resulting in vibrational frequencies in the MHz regime. High charge sensitivities suggested the possibility of using similar devices as ultrasensitive mass and force detection (Bunch et al. 2007). Following this novel experimental fabrication and manipulation of graphene nanoribbons as nanoelectromechanical components, several other studies have explored the mechanical (Frank et al. 2007; Poot and van der Zant 2008) and electromechanical response of these systems (Milaninia et al. 2009). The effects of uniaxial strains in isolated graphene nanoribbons were recently studied in details using the generalized gradient approximation of the exchange correlation functional within the framework of DFT (Faccio et al. 2009; Sun et al. 2008). It was found that the electronic properties of zigzag GNRs are not sensitive to uniaxial strain, while the energy gap of armchair nanoribbons displays an oscillatory pattern as a function of the applied strain. By comparison to TB calculations, it was deduced that the nearest-neighbor hopping terms between atomic sites within the carbon hexagonal lattice are responsible for the observed electromechanical response. To simulate the effects of bending and torsional deformations in suspended graphene nanoribbons, DFT calculations utilizing the screened-exchange HSE density functional were performed (Hod and Scuseria 2009). A large set of short armchair graphene nanoribbons was considered, where narrow strips of atoms close to the zigzag edges of the ribbon were fixed to simulate a doubly clamped suspended nanoribbon (see  Fig. 24-19).

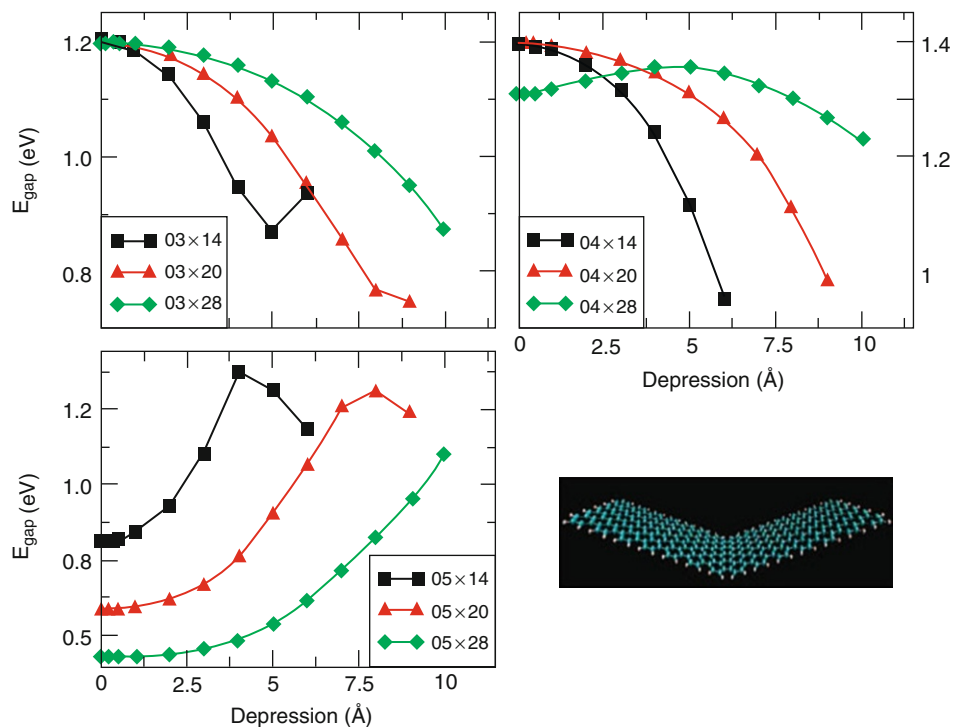
The effect of a driven deformation due to an external tip were simulated by constraining a strip of hexagons at the central part of the ribbon to be either depressed or rotated with respect to the fixed edge atoms. Extreme mechanical deformations, way beyond the linear response regime, were applied to the full set of nanoribbons studied. Most of the nanoribbons considered stayed stable under depressions of 1 nm as well as torsional angles of  $90^\circ$  maintaining their spin-polarized ground state character. As it can be seen in  Fig. 24-20, pronounced electromechanical responses for both bending and torsion (torsion not presented in  Fig. 24-20) have been obtained including evidence of dimension-dependent bandgap oscillations similar to the case of SWNTs (Cohen-Karni et al. 2006; Nagapriya et al. 2008).

Apart from indicating the promise that graphene nanoribbons hold from an electromechanical perspective, such calculations based on state-of-the-art density functional theory approaches, enhance the molecular scale understanding of the physical processes governing



■ Fig. 24-19

An artist view of an electromechanical device based on graphene nanoribbons. An external tip may induce bending and torsion of the nanoribbon (Reprinted (Adapted) with permission from Hod and Scuseria (2009). © (2009) American Chemical Society)



■ Fig. 24-20

HOMO-LUMO gap variations as a function of the depression applied to the central region of a doubly clamped GNR. Different panels and line colors represent results for GNRs of different widths and lengths, respectively (Reprinted (Adapted) with permission from Hod and Scuseria (2009). © (2009) American Chemical Society)

the behavior of these intriguing materials. Furthermore, theory and computations may guide future experiments to pursue promising scientific and technological routes toward which efforts and resources should be directed.

## Concluding Remarks

---

In this chapter, we have given several examples of how theoretical investigations can be applied to elucidate the behavior of carbon nanostructures with emphasis on the understanding of the basic physical mechanisms that take place at the molecular level. In particular, we have shown that density functional theory is a powerful tool to this end, and we have provided several examples where density functional theory has been utilized to investigate electronic and structural properties of graphene nanoribbons, carbon nanotubes, and other low-dimensional graphitic materials. We hope that this chapter will furnish the reader with an ample background on this growing field and that it will serve as a starting point for readers interested in pursuing research in this exciting field.

## Acknowledgments

---

VB acknowledges the donors of The American Chemical Society Petroleum Research Fund for support through the award ACS PRF#49427-UNI6. OH acknowledges the support of the Israel Science Foundation (Grant 1313/08), the Center for Nanoscience and Nanotechnology at Tel-Aviv University, the Lise Meitner-Minerva Center for Computational Quantum Chemistry, and the European Community's Seventh Framework Programme FP7/2007-2013 under grant agreement no. 249225. JEP acknowledges support from NSF DMR Award #DMR-0906617.

## References

---

- Adamo, C., & Barone, V. (1999). Toward reliable density functional methods without adjustable parameters: The PBE0 model. *The Journal of Chemical Physics*, *110*, 6158–6170.
- Adamson, R., Dombroski, J., & Gill, P. (1996). Chemistry without Coulomb tails. *Chemical Physics Letters*, *254*, 329–336.
- Adamson, R., Dombroski, J., & Gill, P. (1999). Efficient calculation of short-range Coulomb energies. *Journal of Computational Chemistry*, *20*, 921–927.
- Bachilo, S. M., Strano, M. S., Kittrell, C., Hauge, R. H., Smalley, R. E., & Weisman, R. B. (2002). Structure-assigned optical spectra of single-walled carbon nanotubes. *Science*, *298*, 2361–2366.
- Balaban, A. T., & Klein, D. J. (2009). Claromatic carbon nanostructures. *Journal of Physical Chemistry C*, *113*, 19123–19133.
- Baldoni, M., Sgamellotti, A., & Mercuri, F. (2007). Finite-length models of carbon nanotubes based on clar sextet theory. *Organic Letters*, *9*, 4267–4270.
- Baldoni, M., Sgamellotti, A., & Mercuri, F. (2008). Electronic properties and stability of graphene nanoribbons: An interpretation based on Clar sextet theory. *Chemical Physics Letters*, *464*, 202–207.
- Barone, V., & Scuseria, G. E. (2004). Theoretical study of the electronic properties of narrow single-walled carbon nanotubes: Beyond the local density approximation. *The Journal of Chemical Physics*, *121*, 10376–10379.
- Barone, V., Peralta, J. E., & Scuseria, G. E. (2005a). Optical transitions in metallic single-walled carbon nanotubes. *Nano Letters*, *5*, 1830–1833.
- Barone, V., Peralta, J. E., Wert, M., Heyd, J., & Scuseria, G. E. (2005b). Density functional theory

- study of optical transitions in semiconducting single-walled carbon nanotubes. *Nano Letters*, 5, 1621–1624.
- Barone, V., Hod, O., & Scuseria, G. E. (2006). Electronic structure and stability of semiconducting graphene nanoribbons. *Nano Letters*, 6, 2748–2754.
- Batista, E. R., Heyd, J., Hennig, R. G., Uberuaga, B. P., Martin, R. L., Scuseria, G. E., Umrigar, C. J., & Wilkins, J. W. (2006). Comparison of screened hybrid density functional theory to diffusion Monte Carlo in calculations of total energies of silicon phases and defects. *Physical Review B*, 74, 121102.
- Becke, A. D. (1993). Density-functional thermochemistry. III. The role of exact exchange. *The Journal of Chemical Physics*, 98, 5648–5652.
- Berger, C., Song, Z., Li, X., Wu, X., Brown, N., Naud, C., Mayou, D., Li, T., Hass, J., Marchenkov, A. N., Conrad, E. H., First, P. N., & de Heer, W. A. (2006). Electronic confinement and coherence in patterned epitaxial graphene. *Science*, 312, 1191.
- Bhardwaj, T., Antic, A., Pavan, B., Barone, V., & Fahlman, B. D. (2010). Enhanced electrochemical lithium storage by graphene nanoribbons. *Journal of the American Chemical Society*, 132, 12556–12559.
- Blase, X., Benedict, L. X., Shirley, E. L., & Louie, S. G. (1994). Hybridization effects and metallicity in small radius carbon nanotubes. *Physical Review Letters*, 72, 1878–1881.
- Brothers, E. N., Izmaylov, A. F., Normand, J. O., Barone, V., & Scuseria, G. E. (2008). Accurate solid-state band gaps via screened hybrid electronic structure calculations. *The Journal of Chemical Physics*, 129, 011102.
- Bunch, J. S., van der Zande, A. M., Verbridge, S. S., Frank, I. W., Tanenbaum, D. M., Parpia, J. M., Craighead, H. G., & McEuen, P. L. (2007). Electromechanical resonators from graphene sheets. *Science*, 315, 490–493.
- Cabria, I., Mintmire, J. W., & White, C. T. (2003). Metallic and semiconducting narrow carbon nanotubes. *Physical Review B*, 67, 121406.
- Cai, J., Ruffieux, P., Jaafar, R., Bieri, M., Braun, T., Blankenburg, S., Muoth, M., Seitsonen, A. P., Saleh, M., Feng, X., Müllen, K., & Fasel, R. (2010). Atomically precise bottom-up fabrication of graphene nanoribbons. *Nature*, 466, 470–473.
- Cao, J., Wang, Q., & Dai, H. (2003). Electromechanical properties of metallic, quasicrystalline, and semiconducting carbon nanotubes under stretching. *Physical Review Letters*, 90, 157601.
- Cervantes-Sodi, F., Csányi, G., Piscanec, S., & Ferrari, A. C. (2008a). Edge-functionalized and substitutionally doped graphene nanoribbons: Electronic and spin properties. *Physical Review B*, 77, 165427.
- Cervantes-Sodi, F., Csányi, G., Piscanec, S., & Ferrari, A. C. (2008b). Electronic properties of chemically modified graphene ribbons. *Physica Status Solidi B*, 245, 2068–2071.
- Chen, Z., Kobashi, K., Rauwald, U., Booker, R., Fan, H., Hwang, W.-F., & Tour, J. M. (2006a). Soluble ultra-short single-walled carbon nanotubes. *Journal of the American Chemical Society*, 128, 10568–10571.
- Chen, Z., Ziegler, K., Shaver, J., Hauge, R., & Smalley, R. (2006b). Cutting of single-walled carbon nanotubes by ozonolysis. *Journal of Physical Chemistry B*, 110, 11624–11627.
- Chen, Z., Lin, Y.-M., Rooks, M. J., & Avouris, P. (2007). Graphene nano-ribbon electronics. *Physica E*, 40, 228–232.
- Choi, S.-M., & Jhi, S.-H. (2008). Self-assembled metal atom chains on graphene nanoribbons. *Physical Review Letters*, 101, 266105.
- Cohen-Karni, T., Segev, L., Srur-Lavi, O., Cohen, S. R., & Joselevich, E. (2006). Torsional electromechanical quantum oscillations in carbon nanotubes. *Nature Nanotechnology*, 1, 36–41.
- Deslippe, J., Spataru, C. D., Prendergast, D., & Louie, S. G. (2007). Bound excitons in metallic single-walled carbon nanotubes. *Nano Letters*, 7, 1626–1630.
- Ernzerhof, M., & Scuseria, G. E. (1999). Assessment of the Perdew-Burke-Ernzerhof exchange-correlation functional. *The Journal of Chemical Physics*, 110, 5029–5036.
- Ezawa, M. (2006). Peculiar width dependence of the electronic properties of carbon nanoribbons. *Physical Review B*, 73, 045432.
- Ezawa, M. (2007). Metallic graphene nanodisks: Electronic and magnetic properties. *Physical Review B*, 76, 245415.
- Faccio, R., Denis, P. A., Pardo, H., Goyenola, C., & Momburu, A. W. (2009). Mechanical properties of graphene nanoribbons. *Journal of Physics Condensed Matter*, 21, 285304.
- Fantini, C., Jorio, A., Souza, M., Strano, M. S., Dresselhaus, M. S., & Pimenta, M. A. (2004). Optical transition energies for carbon nanotubes from resonant Raman spectroscopy: Environment and temperature effects. *Physical Review Letters*, 93, 147406.
- Feller, D. (1996). The role of databases in support of computational chemistry calculations. *Journal of Computational Chemistry*, 17, 1571–1586.



- Feller, D. (2007). *Basis set exchange: v1.2.2*. <https://bse.pnl.gov/bse/portal>.
- Fennimore, A., Yuzvinsky, T., Han, W., Fuhrer, M., Cumings, J., & Zettl, A. (2003). Rotational actuators based on carbon nanotubes. *Nature*, *424*, 408–410.
- Fernandez-Rossier, J., & Palacios, J. J. (2007). Magnetism in graphene nanoislands. *Physical Review Letters*, *99*, 177204.
- Frank, I. W., Tanenbaum, D. M., Van der Zande, A. M., & McEuen, P. L. (2007). Mechanical properties of suspended graphene sheets. *Journal of Vacuum Science & Technology B*, *25*, 2558–2561.
- Frey, J. T., & Doren, D. J. (2005). *TubeGen Online - Version 3.3 - Web-Accessible nanotube structure generator*. <http://turin.nss.udel.edu/research/tubegenonline.html>.
- Frisch, M. J., Trucks, G. W., Schlegel, H. B., Scuseria, G. E., Robb, M. A., Cheeseman, J. R., Scalmani, G., Barone, V., Mennucci, B., Petersson, G. A., Nakatsuji, H., Caricato, M., Li, X., Hratchian, H. P., Izmaylov, A. F., Bloino, J., Zheng, G., Sonnenberg, J. L., Hada, M., Ehara, M., Toyota, K., Fukuda, R., Hasegawa, J., Ishida, M., Nakajima, T., Honda, Y., Kitao, O., Nakai, H., Vreven, T., Montgomery, Jr., J. A., Peralta, J. E., Ogliaro, F., Bearpark, M., Heyd, J. J., Brothers, E., Kudin, K. N., Staroverov, V. N., Kobayashi, R., Normand, J., Raghavachari, K., Rendell, A., Burant, J. C., Iyengar, S. S., Tomasi, J., Cossi, M., Rega, N., Millam, N. J., Klene, M., Knox, J. E., Cross, J. B., Bakken, V., Adamo, C., Jaramillo, J., Gomperts, R., Stratmann, R. E., Yazyev, O., Austin, A. J., Cammi, R., Pomelli, C., Ochterski, J. W., Martin, R. L., Morokuma, K., Zakrzewski, V. G., Voth, G. A., Salvador, P., Dannenberg, J. J., Dapprich, S., Daniels, A. D., Farkas, Ö., Foresman, J. B., Ortiz, J. V., Cioslowski, J., & Fox, D. J. (2006). *GAUSSIAN development version*, revision f.02. Wallingford CT: Gaussian Inc. 2009.
- Fujita, M., Wakabayashi, K., Nakada, K., & Kusakabe, K. (1996). Peculiar localized state at zigzag graphite edge. *Journal of the Physical Society of Japan*, *65*, 1920–1923.
- Gomez-Navarro, C., de Pablo, P., & Gomez-Herrero, J. (2004). Radial electromechanical properties of carbon nanotubes. *Advanced Materials*, *16*, 549.
- Gruneich, A., & Hess, B. (1998). Choosing GTO basis sets for periodic HF calculations. *Theoretical Chemistry Accounts*, *100*, 253–263.
- Gu, Z., Peng, H., Hauge, R., Smalley, R., & Margrave, J. (2002). Cutting single-wall carbon nanotubes through fluorination. *Nano Letters*, *2*, 1009–1013.
- Gülseren, O., Yildirim, T., & Ciraci, S. (2002). Systematic ab initio study of curvature effects in carbon nanotubes. *Physical Review B*, *65*, 153405.
- Gunlycke, D., Li, J., Mintmire, J., & White, C. (2007). Altering low-bias transport in zigzag-edge graphene nanostrips with edge chemistry. *Applied Physics Letters*, *91*, 112108.
- Guo, G., Liu, L., Chu, K., Jayanthi, C., & Wu, S. (2005). Electromechanical responses of single-walled carbon nanotubes: Interplay between the strain-induced energy-gap opening and the pinning of the Fermi level. *Journal of Applied Physics Letters*, *98*, 044311.
- Hall, A. R., Falvo, M. R., Superfine, R., & Washburn, S. (2007). Electromechanical response of single-walled carbon nanotubes to torsional strain in a self-contained device. *Nature Nanotechnology*, *2*, 413–416.
- Hamada, N., Sawada, S., & Oshiyama, A. (1992). New one-dimensional conductors – Graphitic micro-tubules. *Physical Review Letters*, *68*, 1579.
- Han, M. Y., Oezylmaz, B., Zhang, Y., & Kim, P. (2007). Energy band-gap engineering of graphene nanoribbons. *Physical Review Letters*, *98*, 206805.
- Heyd, J., & Scuseria, G. E. (2004). Efficient hybrid density functional calculations in solids: Assessment of the Heyd-Scuseria-Ernzerhof screened Coulomb hybrid functional. *The Journal of Chemical Physics*, *121*, 1187–1192.
- Heyd, R., Charlier, A., & McRae, E. (1997). Uniaxial-stress effects on the electronic properties of carbon nanotubes. *Physical Review B*, *55*(11), 6820–6824.
- Heyd, J., Scuseria, G. E., & Ernzerhof, M. (2003). Hybrid functionals based on a screened Coulomb potential. *The Journal of Chemical Physics*, *118*, 8207–8215.
- Heyd, J., Peralta, J., Scuseria, G., & Martin, R. (2005). Energy band gaps and lattice parameters evaluated with the Heyd-Scuseria-Ernzerhof screened hybrid functional. *The Journal of Chemical Physics*, *123*, 174101.
- Heyd, J., Scuseria, G. E., & Ernzerhof, M. (2006). Erratum: Hybrid functionals based on a screened Coulomb potential [*The Journal of Chemical Physics*, *118*, 8207 (2003)]. *The Journal of Chemical Physics*, *124*, 219906.
- Higuchi, Y., Kusakabe, K., Suzuki, N., Tsuneyuki, S., Yamauchi, J., Akagi, K., & Yoshimoto, Y. (2004). Nanotube-based molecular magnets with spin-polarized edge states. *Journal of Physics Condensed Matter*, *16*, S5689–S5692.
- Hod, O., & Scuseria, G. E. (2008). Half-metallic-zigzag carbon nanotube dots. *ACS Nano*, *2*, 2243–2249.
- Hod, O., & Scuseria, G. E. (2009). Electromechanical properties of suspended graphene nanoribbons. *Nano Letters*, *9*, 2619–2622.

- Hod, O., Peralta, J. E., & Scuseria, G. E. (2006). First-principles electronic transport calculations in finite elongated systems: A divide and conquer approach. *The Journal of Chemical Physics*, *125*, 114704.
- Hod, O., Barone, V., Peralta, J. E., & Scuseria, G. E. (2007a). Enhanced half-metallicity in edge-oxidized zigzag graphene nanoribbons. *Nano Letters*, *7*, 2295–2299.
- Hod, O., Peralta, J. E., & Scuseria, G. E. (2007b). Edge effects in finite elongated graphene nanoribbons. *Physical Review B*, *76*, 233401.
- Hod, O., Barone, V., & Scuseria, G. E. (2008). Half-metallic graphene nanodots: A comprehensive first-principles theoretical study. *Physical Review B*, *77*, 035411.
- Iijima, S. (1991). Helical microtubules of graphitic carbon. *Nature*, *354*, 58–56.
- Javey, A., Qi, P., Wang, Q., & Dai, H. (2004). Ten- to 50-nm-long quasi-ballistic carbon nanotube devices obtained without complex lithography. *Proceedings of the National Academy of Sciences of the United States of America*, *101*, 13408–13410.
- Jiang, H., Bu, W., Jiang, J., & Dong, J. (2004). Electronic structure in finite-length deformed metallic carbon nanotubes. *The European Physical Journal B*, *42*, 503–508.
- Jiang, D. E., Sumpter, B. G., & Dai, S. (2007). First principles study of magnetism in nanographenes. *The Journal of Chemical Physics*, *127*, 124703.
- Kan, E. J., Li, Z., Yang, J., & Hou, J. G. (2007). Will zigzag graphene nanoribbon turn to half metal under electric field? *Applied Physics Letters*, *91*, 243116.
- Kane, C. L., & Mele, E. J. (1997). Size, shape, and low energy electronic structure of carbon nanotubes. *Physical Review Letters*, *78*(10), 1932–1935.
- Kataura, H., Kumazawa, Y., Maniwa, Y., Umez, I., Suzuki, S., Ohtsuka, Y., & Achiba, Y. (1999). Optical properties of single-wall carbon nanotubes. *Synthetic Metals*, *103*, 2555–2558.
- Khabashesku, V., Billups, W., & Margrave, J. (2002). Fluorination of single-wall carbon nanotubes and subsequent derivatization reactions. *Accounts of Chemical Research*, *35*, 1087–1095.
- Kim, Y., Choi, J., Chang, K., & Tomanek, D. (2003). Defective fullerenes and nanotubes as molecular magnets: An ab initio study. *Physical Review B*, *68*, 125420.
- Klein, D. (1994). Graphitic polymer strips with edge states. *Chemical Physics Letters*, *217*, 261–265.
- Kleiner, A., & Eggert, S. (2001). Band gaps of primary metallic carbon nanotubes. *Physical Review B*, *63*(7), 073408.
- Kobayashi, K. (1993). Electronic-structure of a stepped graphite surface. *Physical Review B*, *48*, 1757–1760.
- Kobayashi, Y., Fukui, K., Enoki, T., Kusakabe, K., & Kaburagi, Y. (2005). Observation of zigzag and armchair edges of graphite using scanning tunneling microscopy and spectroscopy. *Physical Review B*, *71*, 193406.
- Kobayashi, Y., Fukui, K., Enoki, T., Kusakabe, K., & Kaburagi, Y. (2006). Edge state on hydrogen-terminated graphite edges investigated by scanning tunneling microscopy. *Physical Review B*, *73*, 125415.
- Krepel, D., & Hod, O. (2011). Lithium adsorption on armchair graphene nanoribbons. *Surface Science*, *605*, 1633–1642.
- Kroto, H., Heath, J., Obrien, S., Curl, R., & Smalley, R. (1985). C-60 – Buckminsterfullerene. *Nature*, *318*(6042), 162–163.
- Kudin, K. N. (2008). Zigzag graphene nanoribbons with saturated edges. *ACS Nano*, *2*, 516–522.
- Kümmel, S., & Kronik, L. (2008). Orbital-dependent density functionals: Theory and applications. *Reviews of Modern Physics*, *80*, 3–60.
- Kusakabe, K., & Maruyama, M. (2003). Magnetic nanographite. *Physical Review B*, *67*, 092406.
- Lammert, P. E., Zhang, P., & Crespi, V. H. (2000). Gapping by squashing: Metal-insulator and insulator-metal transitions in collapsed carbon nanotubes. *Physical Review Letters*, *84*(11), 2453–2456.
- Lee, G., & Cho, K. (2009). Electronic structures of zigzag graphene nanoribbons with edge hydrogenation and oxidation. *Physical Review B*, *79*, 165440.
- Li, Z., Tang, Z., Liu, H., Wang, N., Chan, C., Saito, R., Okada, S., Li, G., Chen, J., Nagasawa, N., & Tsuda, S. (2001). Polarized absorption spectra of single-walled 4 angstrom carbon nanotubes aligned in channels of an AlPO<sub>4-5</sub> single crystal. *Physical Review Letters*, *87*, 127401.
- Li, J., Zhang, Y., & Zhang, M. (2002). The electronic structure and its theoretical simulation of carbon nanotube with finited length. Part I: The frontier orbitals and its properties of short armchair nanotubes. *Chemical Physics Letters*, *364*, 328–337.
- Lieb, E. (1989). 2 theorems on the Hubbard-model. *Physical Review Letters*, *62*, 1201–1204.
- Liu, H. J., & Chan, C. T. (2002). Properties of 4 angstrom carbon nanotubes from first-principles calculations. *Physical Review B*, *66*, 115416.
- Liu, L., Jayanthi, C. S., Tang, M., Wu, S. Y., Tomblor, T. W., Zhou, C., Alexseyev, L., Kong, J., & Dai, H. (2000). Controllable reversibility of an *sp*<sup>2</sup> to

- sp*<sup>3</sup> transition of a single wall nanotube under the manipulation of an afm tip: A nanoscale electromechanical switch? *Physical Review Letters*, 84(21), 4950–4953.
- Liu, L., Jayanthi, C., Guo, H., & Wu, S. (2001). Broken symmetry, boundary conditions, and band-gap oscillations in finite single-wall carbon nanotubes. *Physical Review B*, 64, 033414.
- Lu, J.-Q., Wu, J., Duan, W., Liu, F., Zhu, B.-F., & Gu, B.-L. (2003). Metal-to-semiconductor transition in squashed armchair carbon nanotubes. *Physical Review Letters*, 90(15), 156601.
- Machón, M., Reich, S., Thomsen, C., Sánchez-Portal, D., & Ordejón, P. (2002). Ab initio calculations of the optical properties of 4-angstrom-diameter single-walled nanotubes. *Physical Review B*, 66, 155410.
- Maiti, A. (2001). Application of carbon nanotubes as electromechanical sensors – Results from first-principles simulations. *Physica Status Solidi*, 226, 87–93.
- Maiti, A. (2003). Carbon nanotubes – Bandgap engineering with strain. *Nature Materials*, 2, 440–442.
- Maiti, A. (2009). *Integrated analytical systems, computational methods for sensor material selection*. New York: Springer.
- Maiti, A., Svizhenko, A., & Anantram, M. (2002). Electronic transport through carbon nanotubes: Effects of structural deformation and tube chirality. *Physical Review Letters*, 88, 126805.
- Mananes, A., Duque, F., Ayuela, A., Lopez, M. J., & Alonso, J. A. (2008). Half-metallic finite zigzag single-walled carbon nanotubes from first principles. *Physical Review B*, 78, 035432.
- Mehrez, H., Svizhenko, A., Anantram, M., Elstner, M., & Frauenheim, T. (2005). Analysis of band-gap formation in squashed armchair carbon nanotubes. *Physical Review B*, 71, 155421.
- Mickelson, E., Huffman, C., Rinzler, A., Smalley, R., Hauge, R., & Margrave, J. (1998). Fluorination of single-wall carbon nanotubes. *Chemical Physics Letters*, 296, 188–194.
- Milaninia, K. M., Baldo, M. A., Reina, A., & Kong, J. (2009). All graphene electromechanical switch fabricated by chemical vapor deposition. *Applied Physics Letters*, 95, 183105.
- Minot, E., Yaish, Y., Sazonova, V., Park, J., Brink, M., & McEuen, P. (2003). Tuning carbon nanotube band gaps with strain. *Physical Review Letters*, 90, 156401.
- Mintmire, J., Dunlap, B., & White, C. (1992). Are fullerene tubules metallic? *Physical Review Letters*, 68, 631.
- Nagapriya, K. S., Berber, S., Cohen-Karni, T., Segev, L., Srur-Lavi, O., Tomanek, D., & Joselevich, E. (2008). Origin of torsion-induced conductance oscillations in carbon nanotubes. *Physical Review B*, 78, 165417.
- Nakada, K., Fujita, M., Dresselhaus, G., & Dresselhaus, M. S. (1996). Edge state in graphene ribbons: Nanometer size effect and edge shape dependence. *Physical Review B*, 54, 17954–17961.
- Nakamura, E., Tahara, K., Matsuo, Y., & Sawamura, M. (2003). Synthesis, structure, and aromaticity of a hoop-shaped cyclic benzenoid [10]cyclophenacene. *Journal of the American Chemical Society*, 125, 2834–2835.
- Nardelli, M. B. (1999). Electronic transport in extended systems: Application to carbon nanotubes. *Physical Review B*, 60(11), 7828–7833.
- Nardelli, M. B., & Bernholc, J. (1999). Mechanical deformations and coherent transport in carbon nanotubes. *Physical Review B*, 60(24), R16338–R16341.
- Niimi, Y., Matsui, T., Kambara, H., Tagami, K., Tsukada, M., & Fukuyama, H. (2005). Scanning tunneling microscopy and spectroscopy studies of graphite edges. *Applied Surface Science*, 241, 43–48.
- Novoselov, K. S., Geim, A. K., Morozov, S. V., Jiang, D., Zhang, Y., Dubonos, S. V., Grigorieva, I. V., & Firsov, A. A. (2004). Electric field effect in atomically thin carbon films. *Science*, 306, 666–669.
- Okada, S., & Oshiyama, A. (2003). Nanometer-scale ferromagnet: Carbon nanotubes with finite length. *Journal of the Physical Society of Japan*, 72, 1510–1515.
- Onida, G., Reining, L., & Rubio, A. (2002). Electronic excitations: Density-functional versus many-body Green's-function approaches. *Reviews of Modern Physics*, 74, 601–659.
- Paier, J., Marsman, M., & Kresse, G. (2007). Why does the B3LYP hybrid functional fail for metals? *The Journal of Chemical Physics*, 127, 024103.
- Paulson, S., Falvo, M., Snider, N., Helser, A., Hudson, T., Seeger, A., Taylor, R., Superfine, R., & Washburn, S. (1999). In situ resistance measurements of strained carbon nanotubes. *Applied Physics Letters*, 75, 2936–2938.
- Peng, S., & Cho, K. (2002). Nano electro mechanics of semiconducting carbon nanotube. *Journal of Applied Mechanics*, 69, 451.
- Peralta, J. E., Heyd, J., Scuseria, G. E., & Martin, R. L. (2006). Spin-orbit splittings and energy band gaps calculated with the Heyd-Scuseria-Ernzerhof screened hybrid functional. *Physical Review B*, 74, 073101.
- Perdew, J. P., Burke, K., & Ernzerhof, M. (1996). Generalized gradient approximation made simple. *Physical Review Letters*, 77, 3865–3868.

- Perdew, J. P., Ernzerhof, M., & Burke, K. (1997). Rationale for mixing exact exchange with density functional approximations. *The Journal of Chemical Physics*, 105, 9982–9985.
- Pimenta, M., Gomes, A., Fantini, C., Cancado, L., Araujo, P., Maciel, I., Santos, A., Furtado, C., Peressinotto, V., Plentz, F., & Jorio, A. (2007). Optical studies of carbon nanotubes and nanographites. *Physica E*, 37, 88–92.
- Poot, M. & van der Zant, H. S. J. (2008). Nanomechanical properties of few-layer graphene membranes. *Applied Physics Letters*, 92, 063111.
- Prezzi, D., Varsano, D., Ruini, A., Marini, A., & Molinari, E. (2008). Optical properties of graphene nanoribbons: The role of many-body effects. *Physical Review B*, 77, 041477.
- Radovic, L. R., & Bockrath, B. (2005). On the chemical nature of graphene edges: Origin of stability and potential for magnetism in carbon materials. *Journal of the American Chemical Society*, 127, 5917–5927.
- Reich, S., Thomsen, C., & Ordejón, P. (2002). Systematic ab initio study of curvature effects in carbon nanotubes. *Physical Review B*, 65, 153405.
- Rigo, V. A., Martins, T. B., da Silva, A. J. R., Fazzio, A., & Miwa, R. H. (2009). Electronic, structural, and transport properties of Ni-doped graphene nanoribbons. *Physical Review B*, 79, 075435.
- Ritter, K. A., & Lyding, J. W. (2009). The influence of edge structure on the electronic properties of graphene quantum dots and nanoribbons. *Nature Materials*, 8, 235–242.
- Rochefort, A., Salahub, D. R., & Avouris, P. (1998). The effect of structural distortions on the electronic structure of carbon nanotubes. *Chemical Physics Letters*, 297, 45–50.
- Rochefort, A., Avouris, P., Lesage, F., & Salahub, D. R. (1999a). Electrical and mechanical properties of distorted carbon nanotubes. *Physical Review B*, 60(19), 13824–13830.
- Rochefort, A., Salahub, D., & Avouris, P. (1999b). Effects of finite length on the electronic structure of carbon nanotubes. *Journal of Physical Chemistry B*, 103, 641–646.
- Rudberg, E., Salek, P., & Luo, Y. (2007). Nonlocal exchange interaction removes half-metallicity in graphene nanoribbons. *Nano Letters*, 7, 2211–2213.
- Rueckes, T., Kim, K., Joselevich, E., Tseng, G., Cheung, C., & Lieber, C. (2000). Carbon nanotube-based nonvolatile random access memory for molecular computing. *Science*, 289, 94–97.
- Runge, E., & Gross, E. (1984). Density-functional theory for time-dependent systems. *Physical Review Letters*, 52, 997–1000.
- Saito, R., Fujita, M., Dresselhaus, G., & Dresselhaus, M. (1992). Electronic structure of graphene tubules based on  $C_{60}$ . *Physical Review B*, 46, 1804–1811.
- Saito, R., Dresselhaus, G., & Dresselhaus, M. S. (1998). *Physical properties of carbon nanotubes*. London: Imperial College Press.
- Sazonova, V., Yaish, Y., Ustunel, H., Roundy, D., Arias, T., & McEuen, P. (2004). A tunable carbon nanotube electromechanical oscillator. *Nature*, 431, 284–287.
- Semet, V., Binh, V., Guillot, D., Teo, K., Chhowalla, M., Amaratunga, G., Milne, W., Legagneux, P., & Pribat, D. (2005). Reversible electromechanical characteristics of individual multiwall carbon nanotubes. *Applied Physics Letters*, 87, 223103.
- Sevincli, H., Topsakal, M., Durgun, E., & Ciraci, S. (2008). Electronic and magnetic properties of 3d transition-metal atom adsorbed graphene and graphene nanoribbons. *Physical Review B*, 77, 195434.
- Sfeir, M. Y., Beetz, T., Wang, F., Huang, L. M., Huang, X. M. H., Huang, M. Y., Hone, J., O'Brien, S., Misewich, J. A., Heinz, T. F., Wu, L. J., Zhu, Y. M., & Brus, L. E. (2006). Optical spectroscopy of individual single-walled carbon nanotubes of defined chiral structure. *Science*, 312, 554–556.
- Shaver, J., Kono, J., Portugall, O., Krstic, V., Rikken, G. L. J. A., Miyauchi, Y., Maruyama, S., & Perebeinos, V. (2007). Magnetic brightening of carbon nanotube photoluminescence through symmetry breaking. *Nano Letters*, 7, 1851–1855.
- Shemella, P., Zhang, Y., Mailman, M., Ajayan, P. M., & Nayak, S. K. (2007). Energy gaps in zero-dimensional graphene nanoribbons. *Applied Physics Letters*, 91, 042101.
- Son, Y.-W., Cohen, M. L., & Louie, S. G. (2006a). Energy gaps in graphene nanoribbons. *Physical Review Letters*, 97, 216803.
- Son, Y.-W., Cohen, M. L., & Louie, S. G. (2006b). Half-metallic graphene nanoribbons. *Nature*, 444, 347–349.
- Spataru, C. D., Ismael-Beigi, S., Benedict, L. X., & Louie, S. G. (2004). Excitonic effects and optical spectra of single-walled carbon nanotubes. *Physical Review Letters*, 92, 077402.
- Spataru, C. D., Ismael-Beigi, S., Capaz, R. B., & Louie, S. G. (2008). Quasiparticle and excitonic effects in the optical response of nanotubes and nanoribbons. *Topics in Applied Physics*, 111, 195–227.
- Springborg, M., & Satpathy, S. (1994). Density-functional calculations of electronic and structural properties of small fullerene tubules. *Chemical Physics Letters*, 255, 454–461.

- Stampfer, C., Jungen, A., Linderman, R., Obergfell, D., Roth, S., & Hierold, C. (2006). Nano-electromechanical displacement sensing based on single-walled carbon nanotubes. *Nano Letters*, 6, 1449–1453.
- Stein, S., & Brown, R. (1987). Pi-electron properties of large condensed polyaromatic hydrocarbons. *Journal of the American Chemical Society*, 109, 3721–3729.
- Sun, L., Li, Q., Ren, H., Su, H., Shi, Q. W., & Yang, J. (2008). Strain effect on electronic structures of graphene nanoribbons: A first-principles study. *Journal of Chemical Physics*, 129, 074704.
- Svizhenko, A., Mehrez, H., Anantram, A. M. P., & Maiti, A. (2005). Sensing mechanical deformation in carbon nanotubes by electrical response: a computational study. *Proceedings of SPIE*, 5593, 416–428.
- Tanaka, K., Yamashita, S., Yamabe, H., & Yamabe, T. (1987). Electronic-properties of one-dimensional graphite family. *Synthetic Metals*, 17, 143–148.
- Tang, Z. K., Sun, H. D., Wang, J., Chen, J., & Li, G. (1998). Mono-sized single-wall carbon nanotubes formed in channels of  $\text{AlPO}_{4-5}$  single crystal. *Applied Physics Letters*, 73, 2287–2289.
- Tao, J., Perdew, J. P., Staroverov, V. N., & Scuseria, G. E. (2003). Climbing the density functional ladder: Nonempirical meta-generalized gradient approximation designed for molecules and solids. *Physical Review Letters*, 91, 146401.
- Telg, H., Maultzsch, J., Reich, S., Hennrich, F., & Thomsen, C. (2004). Chirality distribution and transition energies of carbon nanotubes. *Physical Review Letters*, 93, 177401.
- Tomblar, T., Zhou, C., Alexseyev, L., Kong, J., Dai, H., Lei, L., Jayanthi, C., Tang, M., & Wu, S. (2000). Reversible electromechanical characteristics of carbon nanotubes under local-probe manipulation. *Nature*, 405, 769–772.
- Tsukada, M., Adachi, H., & Satoko, C. (1983). Theory of electronic-structure of oxide surfaces. *Progress in Surface Science*, 14, 113–173.
- Uthaisar, C., & Barone, V. (2010). Edge effects on the characteristics of li diffusion in graphene. *Nano Letters*, 10, 2838–2842.
- Uthaisar, C., Barone, V., & Peralta, J. E. (2009). Lithium adsorption on zigzag graphene nanoribbons. *Journal of Applied Physics*, 106, 113715.
- Vanderbilt, D. (1990). Soft self-consistent pseudopotentials in a generalized eigenvalue formalism. *Physical Review B*, 41, 7892–7895.
- Vosko, S. H., Wilk, L., & Nusair, M. (1980). Accurate spin-dependent electron liquid correlation energies for local spin-density calculations – A critical analysis. *Canadian Journal of Physics*, 58, 1200–1211.
- Wakabayashi, K., Fujita, M., Ajiki, H., & Sigrist, M. (1999). Electronic and magnetic properties of nanographite ribbons. *Physical Review B*, 59, 8271–8282.
- Wang, F., Dukovic, G., Brus, L. E., & Heinz, T. F. (2005). The optical resonances in carbon nanotubes arise from excitons. *Science*, 308, 838–841.
- Wang, X., Ouyang, Y., Li, X., Wang, H., Guo, J., & Dai, H. (2008). Room-temperature all-semiconducting sub-10-nm graphene nanoribbon field-effect transistors. *Physical Review Letters*, 100, 206803.
- Wassmann, T., Seitsonen, A. P., Saitta, A. M., Lazzeri, M., & Mauri, F. (2008). Structure, stability, edge states, and aromaticity of graphene ribbons. *Physical Review Letters*, 101, 096402.
- Weisman, R. B., & Bachilo, S. M. (2003). *Nano Letters*, 3, 1235–1238.
- Wu, J., Zang, J., Larade, B., Guo, H., Gong, X., & Liu, F. (2004). Computational design of carbon nanotube electromechanical pressure sensors. *Physical Review B*, 69, 153406.
- Yang, L., & Han, J. (2000). Electronic structure of deformed carbon nanotubes. *Physical Review Letters*, 85(1), 154–157.
- Yang, L., Anantram, M. P., Han, J., & Lu, J. P. (1999). Band-gap change of carbon nanotubes: Effect of small uniaxial and torsional strain. *Physical Review B*, 60(19), 13874–13878.
- Yang, L., Cohen, M. L., & Louie, S. G. (2007). Excitonic effects in the optical spectra of graphene nanoribbons. *Nano Letters*, 10, 3112–3115.
- Yang, X., Dou, X., Rouhanipour, A., Zhi, L., Rader, H. J., & Müllen, K. (2008). Two-dimensional graphene nanoribbons. *Journal of the American Chemical Society*, 130, 4216.
- Zhang, D.-B., James, R. D., & Dumitrica, T. (2009). Electromechanical characterization of carbon nanotubes in torsion via symmetry adapted tight-binding objective molecular dynamics. *Physical Review B*, 80(11), 115418.
- Zhao, X., Liu, Y., Inoue, S., Suzuki, T., Jones, R. O., & Ando, Y. (2004). Smallest carbon nanotube is 3 angstrom in diameter. *Physical Review Letters*, 92, 125502.
- Zheng, H., & Duley, W. (2008). First-principles study of edge chemical modifications in graphene nanotubes. *Physical Review B*, 78, 045421.

# 25 Variation of the Surface to Bulk Contribution to Cluster Properties

*Antonis N. Andriotis<sup>1</sup> · Zacharias G. Fthenakis<sup>1</sup> · Madhu Menon<sup>2</sup>*

<sup>1</sup>Institute of Electronic Structure and Laser, FORTH, Heraklio, Crete, Greece

<sup>2</sup>Department of Physics and Astronomy and Center for Computational Sciences, University of Kentucky, Lexington, KY, USA

<i>Introduction</i> .....	940
<i>The Model</i> .....	942
Tight-Binding Molecular Dynamics Methodology .....	942
Collinear Magnetic Effects .....	943
Step 1: Inclusion of Randomness in the Direction of the Atomic Magnetic Moments ...	944
Step 2: Inclusion of Spin-Orbit Interaction .....	944
Evaluation of the TB representation of the SO-interaction .....	945
Step 3: Inclusion of Temperature Effects .....	946
<i>Computational Approach</i> .....	947
<i>Results and Discussion</i> .....	948
<i>Conclusion</i> .....	952
<i>Acknowledgments</i> .....	953
<i>References</i> .....	953

**Abstract:** Recent computer simulations have indicated that there is a linear relationship between the melting and the Curie temperatures for  $Ni_n$  ( $n \leq 201$ ) clusters. In this chapter, it is argued that this result is a consequence of the fact that the surface and the core (bulk) contributions to the cluster properties vary with the cluster size in an analogous way. The universal aspect of this result is also discussed. Among the many interesting consequences resulting from this relationship is the intriguing possibility of the coexistence of melting and magnetization. As demonstrated, these conclusions have as their origin the major contribution coming from the melting/magnetization ratio arising from surface effects and appear to overshadow all other contributions. As a result, this can be quantified with approximate methods which are suitable for describing any major surface contribution to a cluster property.

## Introduction

As the cluster size increases, the cluster properties evolve toward their bulk counterparts. The understanding of this evolution is of fundamental importance not only from the perspective of basic science but also from the technological viewpoint. At a very approximate level, one can claim that the cluster properties can be described in terms of their surface and core (bulk) contributions and due to the fact that the surface to bulk ratio gets smaller as the cluster size increases. Consequently, it is natural to expect that the cluster properties will evolve to their corresponding bulk-phase ones for large cluster sizes.

As one particular example, we mention the melting temperature of large clusters. According to the proposed model, the following functional relationship for the variation of the melting temperature,  $T_{melt,N}^{cl}$ , of a cluster as the number  $N$  of its atoms increases has been suggested:

$$T_{melt,N}^{cl} = T_{melt}^{bulk} - \delta_{melt} N^{-1/3}, \quad (25.1)$$

where  $T_{melt}^{bulk}$  is the melting temperature of the corresponding bulk phase and  $\delta_{melt}$  is a constant that depends on  $N$  (Garcia-Rodeja et al. 1994; Gunes et al. 2000; Lee et al. 2001; Nayak et al. 1998; Qi et al. 2001; Rey et al. 1993; Sun and Gong 1998). Correction terms in  $N^{-2/3}$  and  $N^{-1}$  powers to the above expression have also been suggested (Doye and Calvo 2001). The term proportional to  $N^{-1/3}$  in  $\blacklozenge$  Eq. 25.1 reflects the surface to bulk contribution to the melting temperature.

$\blacklozenge$  Equation 25.1 was found to describe reasonably well the experimental findings in the large-size regime ( $N > 500$ ). However, for clusters of smaller size, (especially for clusters with number of atoms  $N \leq 50$ ),  $\blacklozenge$  Eq. 25.1 does not ensure a quantitative description of the variation of  $T_{melt,N}^{cl}$  with the cluster size (see, e.g., Baletto and Ferrando 2005; Lee et al. 2001; Nayak et al. 1998; Qi et al. 2001). This is because for small clusters, (1) the surface-to-volume contribution to  $T_{melt,N}^{cl}$  is very large and (2) is very sensitive to the variations of the surface structure and the cluster geometry (symmetry), as both of these characteristics get altered as the cluster size changes.

Another property that has attracted much interest recently is the one pertaining to the evolution of the magnetic features of the magnetic clusters as the cluster size and temperature increase. This is mainly because of the potential applications of the magnetic grains in fabricating new materials for advanced magnetic storage devices and other applications (Bansman et al. 2005).

Recently, the results of our computer simulations led us to the conclusion that the Curie,  $T_{C,N}^{cl}$ , and the melting,  $T_{melt,N}^{cl}$ , temperature of  $Ni_N$  clusters consisting of  $N$  atoms are linearly



related over a large range of cluster sizes ( $N \leq 201$ ), and this relationship is quantified by the following equation (Andriotis et al. 2007) :

$$T_{melt,N}^{cl} = \alpha T_{C,N}^{cl} + \beta, \quad (25.2)$$

where  $\alpha$  and  $\beta$  are constants. Least square fitting of our results leads to  $\alpha = 0.5414$  and  $\beta = 443.82^\circ\text{K}$ . This relationship was suggested to be related to the ratio of the surface to bulk contributions to the cluster melting as well as to the average magnetic moment per cluster atom,  $\bar{\mu}_{i,N}(T)$   $i = 1, \dots, N$ . It was then claimed that this relationship could be justified within the mean field theory applied separately to the surface and core regions of the cluster (Andriotis et al. 2007).

A cursory thought seems to suggest that any type of direct relationship between  $T_{melt,N}^{cl}$  and  $T_{C,N}^{cl}$  to be fortuitous since melting and magnetic order seem to reflect completely different aspects of the crystal potential. Therefore,  $\blacklozenge$  Eq. 25.2 cannot be considered as one which reestablishes a valid physical relationship between these two cluster properties.

Furthermore, the variation of both  $T_{melt,N}^{cl}$  and  $T_{C,N}^{cl}$  with the cluster size constitute separate distinct and complicated projects for both theory and experiment. This is because significant contributions to both of these physical quantities have their origin in surface as well as cluster-core (bulk) effects which, at first look, affect  $T_{melt,N}^{cl}$  and  $T_{C,N}^{cl}$  differently. These contributions include: the effects of the cohesive energy, the shape (symmetry), the size, the surface to bulk ratio, the surface tension, the temperature of the cluster, etc.

In early reports, it was found that  $T_{melt,N}^{cl}$  is usually smaller than the corresponding bulk value. Of interest is the result applied for large enough spherical clusters of radius  $R$ :

$$T_{melt,N}^{cl}/T_{melt}^{bulk} = 1 - k_m/R \quad (25.3)$$

where  $k_m$  is a material-dependent constant (see, e.g., Buffat and Borel 1976 and references therein). A similar expression describing the variation of the Curie temperature with the cluster size was also found within the phenomenological Landau–Ginsburg–Devonshire theory (Huang et al. 2000), i.e.,

$$T_{C,N}^{cl}/T_C^{bulk} = 1 - k_c/R \quad (25.4)$$

Use of  $\blacklozenge$  Eqs. 25.3 and  $\blacklozenge$  25.4 gives the following values for  $\alpha$  and  $\beta$  in  $\blacklozenge$  Eq. 25.2:

$$\alpha = \frac{k_c}{k_m} \frac{T_C^{bulk}}{T_{melt}^{bulk}} \quad (25.5)$$

and

$$\beta = T_C^{bulk} - \alpha T_{melt}^{bulk} = \left(1 - \frac{k_c}{k_m}\right) T_C^{bulk}. \quad (25.6)$$

Diep and collaborators (Diep et al. 1989) using Monte Carlo simulations studied the effect of the magnetic interactions on the melting temperature of a cluster. Although their investigation was limited to very small clusters  $M_N$ , ( $N \in [7,17]$ ) of transition metals  $M$ , however, the conclusions they arrived at are very important. In particular, among others, they have found that the incorporation of the magnetic interactions leaves the cluster structure unchanged. However, magnetic interactions lead to sharper peaks in the specific heat (and, therefore, to more precise determination of melting and Curie temperatures), a slight increase in the melting temperature, and a slight cluster-volume contraction (magnetostriction). After examining more carefully the results of Diep et al. (1989) (included in their Fig. 12), we find that the relation of  $T_{melt,N}^{cl}$  and  $T_{C,N}^{cl}$  is more or less linear with the exception of the data of the very small clusters, i.e., for



$N \in [7,8,9]$ . The linear relationship between  $T_{melt,N}^{cl}$  and  $T_{C,N}^{cl}$  was also suggested recently on the basis of semiempirical and approximate phenomenological model descriptions (see Yang and Jiang 2005 and references therein).

All these descriptions support our findings (i.e.,  $\blacktriangleright$  Eq. 25.2), which are based on a firm quantum mechanical model procedure as outlined in the following. In this work, we investigate the implications of such a relationship which seems to specify a universal aspect of the surface contribution to the cluster properties.

## The Model

---

The investigation of clusters of medium and intermediate sizes consisting of transition metal atoms poses a severe challenge in terms of computer capacities and computer time. For this reason, approximate schemes have been employed with most pronounced being those based on empirical classical potentials. However, these models have limited applicability when there is a need to understand more about the electronic structure of these systems and follow its changes as the cluster size increases and approaches the bulk phase. It is thus necessary to use methods with firm ab initio footing while at the same time not sacrificing computational efficiency. One such method is based on the Tight-Binding approximation which we have adopted in our work.

In this section, we discuss briefly the implementation of this approach in order to model the temperature and magnetic features of transition metal clusters. We will firstly give a brief overview of our TB computational scheme that we used for systems at zero temperature. In the following sections, we will describe the generalization of our method enabling the inclusion of magnetic and temperature effects.

## Tight-Binding Molecular Dynamics Methodology

---

The details of our Generalized Tight-Binding Molecular Dynamics (GTBMD) scheme can be found in Andriotis and Menon (1998) and Menon et al. (1997). The GTBMD method makes explicit use of the nonorthogonality of the orbitals resulting in a transferable scheme that works well in the range all the way from a few atoms to the condensed solid. The scheme also includes *d*-electron interactions enabling dynamic treatment of magnetic effects in transition metal systems. Here, we give a brief overview.

The total energy  $U$  is written in its general form as a sum of several terms (Andriotis and Menon 1998),

$$U = U_{el} + U_{rep} + U_0, \quad (25.7)$$

where  $U_{el}$  is the sum of the one-electron energies  $E_n$  for the occupied states:

$$U_{el} = \sum_n^{occ} E_n. \quad (25.8)$$

In the tight-binding scheme,  $E_n$  is obtained by solving the characteristic equation:

$$(\mathbf{H} - E_n \mathbf{S}) \mathbf{C}^n = 0, \quad (25.9)$$

where  $\mathbf{H}$  is the Hamiltonian of the system and  $\mathbf{S}$  the overlap matrix.

The Hellmann–Feynman theorem for obtaining the electronic part of the force is given by Menon et al. (1997),

$$\frac{\partial E_n}{\partial x} = \frac{\mathbf{C}^{n\dagger} \left( \frac{\partial \mathbf{H}}{\partial x} - E_n \frac{\partial \mathbf{S}}{\partial x} \right) \mathbf{C}^n}{\mathbf{C}^{n\dagger} \mathbf{S} \mathbf{C}^n}. \quad (25.10)$$

The total energy expression also derives contributions from ion–ion repulsion interactions. This is approximated by a sum of pairwise repulsive terms and included in  $U_{\text{rep}}$ . This sum also contains the corrections arising from the double counting of electron–electron interactions in  $U_{\text{el}}$  (Andriotis and Menon 1998).  $U_0$  is a constant that merely shifts the zero of energy. The contribution to the total force from  $U_{\text{rep}}$  is rather straightforward. One can then easily do molecular dynamics simulations by numerically solving Newton’s equation,

$$m \frac{d^2 x}{dt^2} = F_x = - \frac{\partial U}{\partial x} \quad (25.11)$$

to obtain  $x$  as a function of time.

Our TBMD scheme for a binary system consisting of elements A and B is based on a minimal set of five adjustable parameters for each pair (A,A), (B,B), and (A,B). These parameters are determined by fitting to experimental data for quantities such as the bond length, the vibrational frequency, and the binding energy of the dimers  $A_2$ ,  $B_2$ , AB; the cohesive energy of the corresponding bulk states of the A, B, AB materials; and the energy level spacing of the lowest magnetic states of the dimer and trimer binary clusters consisting of atoms of A and B type. In the absence of experimental data, we fit to data of small clusters obtained using ab initio methods as described in the following subsection. It is apparent that only five parameters are required in the case of a single species system. The generalization to a system containing more than two kind of atoms is also plausible within this approach.

The fixed set of TB parameters are obtained from the universal scheme proposed by Harrison (1980) suitably scaled with respect to the interatomic distance (Andriotis and Menon 1998).

## Collinear Magnetic Effects

In order to calculate the Curie temperature of a magnetic cluster, it is necessary to include non-collinear magnetic effects in our model description. These are introduced by extending our zero temperature (ZT) Tight-Binding Molecular Dynamics (TBMD) approach at the Hubbard-U level of approximation (Andriotis and Menon 1998) which we used to study magnetic clusters in the collinear magnetic approximation. According to this collinear model, an exchange-splitting parameter  $s_0^{(i)}$  is introduced which is proportional to the intra-site Coulomb interaction  $U$ . This specifies the energy splitting between spin-up and spin-down electrons in the  $i$ th-atom in accordance with results obtained by ab initio methods. Thus, within this model, a site-diagonal spin-dependent Hamiltonian term  $\mathbf{V}_{spin}^{(i)}$  is introduced which has the form:

$$\mathbf{V}_{spin}^{(i)} = \begin{pmatrix} s_0^{(i)} & 0 \\ 0 & -s_0^{(i)} \end{pmatrix} \quad (25.12)$$

In this model, it is assumed that all atomic magnetic moments (MMs) (of the cluster atoms) are collinear to the  $z$ -axis of a local  $xyz$ -system assigned to the  $i$ th cluster-atom.

The generalization of this model to include non-collinear effects is achieved in three steps. In the first step, we include the randomness in the directions of the atomic MMs. In the second, we include the spin-orbit interaction, and in the third, we include the temperature effects. For the sake of completeness, we briefly discuss this generalization in the following.

## Step 1: Inclusion of Randomness in the Direction of the Atomic Magnetic Moments

In the first step, it is assumed that the deviation of the direction of the MM,  $\boldsymbol{\mu}_i$ , of the  $i$ th cluster-atom from the Z-axis of the global coordinate system XYZ is specified by the polar angles  $(\theta_i, \phi_i)$  defined with respect to this XYZ system. As a result, the potential  $\mathbf{V}_{spin}^{(i)}$ , originally defined in the local coordinate system xyz of the  $i$ th atom, is transformed to its expression  $\mathbf{V}_{spin}^{(i),global}$  in the global system XYZ as follows (Anderson and Hasegawa 1955; Uhl et al. 1994):

$$\mathbf{V}_{spin}^{(i),global} = \Xi^\dagger(\theta_i, \phi_i) \mathbf{V}_{spin}^{(i)} \Xi(\theta_i, \phi_i), \quad (25.13)$$

where  $\Xi(\theta_i, \phi_i)$  is the standard spin-1/2-rotation matrix :

$$\Xi(\theta_i, \phi_i) = \begin{pmatrix} e^{i\phi_i/2} \cos \theta_i/2 & e^{-i\phi_i/2} \sin \theta_i/2 \\ -e^{i\phi_i/2} \sin \theta_i/2 & e^{-i\phi_i/2} \cos \theta_i/2 \end{pmatrix} \quad (25.14)$$

It is assumed that the Z-axis of the global system can be arbitrarily chosen, and a usual choice is to take Z in alignment with the easy axis of the system.

## Step 2: Inclusion of Spin-Orbit Interaction

In the second step, we introduce the Spin-Orbit (SO) interaction,  $\mathbf{V}_{SO}^{(i)}$ , in the  $i$ th-atom within the L-S coupling scheme, i.e.,  $\mathbf{V}_{SO}^{(i)} = -\lambda^{(i)} \mathbf{L}^{(i)} \cdot \mathbf{S}^{(i)}$  where,  $\lambda^{(i)}$  is the spin-orbit coupling constant for the  $i$ th-atom,  $\mathbf{L}^{(i)}$  its orbital angular momentum along the Z-axis, and  $\mathbf{S}^{(i)}$  its total spin in the direction of  $\boldsymbol{\mu}_i$ .

Details of the implementation of the Spin-Orbit interaction within our TBMD method have been reported elsewhere (Andriotis and Menon 2004).

In the presence of a magnetic field,  $\mathbf{B}$  (assumed to be along the direction specified by the polar angles  $(\theta_0, \phi_0)$  with respect to XYZ-system), the atomic MMs of the cluster-atoms tend to become parallel to the direction of  $\mathbf{B}$ . The average projection of the MMs of the cluster-atoms,  $\mu_{cl}$ , along the direction of  $\mathbf{B}$  (which is the experimentally measured quantity) is,

$$\mu_{cl} = \frac{1}{N_{cl}} \left| \sum_i^{N_{cl}} \mu_i \cos \gamma_i \right|, \quad (25.15)$$

where  $N_{cl}$  is the number of cluster-atoms and  $\cos \gamma_i = \cos \theta_0 \cos \theta_i + \sin \theta_0 \sin \theta_i \cos(\phi_0 - \phi_i)$ .

In a different formulation within the Hubbard-U model approximation to the  $e$ - $e$  correlations, the spin-mixing interaction may be derived from a Coulomb-type Hamiltonian term of the form (Kato and Kokubo 1994; Ojeda et al. 1999):  $\mathbf{V}_{smix} = -U \sum_{l\sigma} \rho_{l\sigma, l\bar{\sigma}} c_{l\bar{\sigma}}^\dagger c_{l\sigma}$ , where  $c_{l\sigma}^\dagger$  ( $c_{l\sigma}$ ) is the creation (annihilation) operator for an electron with spin  $\sigma$  at site  $l$  and  $\rho_{l\bar{\sigma}, l\sigma}$  denote

the electron density matrix elements, i.e.,  $\rho_{l\sigma,l\bar{\sigma}} = \langle c_{l\bar{\sigma}}^\dagger c_{l\sigma} \rangle$ . It can be easily verified that the Hamiltonian term  $V_{smix}$  is equivalent to that given by  $\blacktriangleright$  Eq. 25.13, i.e.,  $\mathbf{V}_{spin}^{(i),global}$ .

## Evaluation of the TB representation of the SO-interaction

In order to proceed with the evaluation of the TB matrix elements of the SO-interaction, we write the SO-term as

$$\mathbf{S} \cdot \mathbf{L} = L_x S_x + L_y S_y + L_z S_z \quad (25.16)$$

and compute the matrix elements with respect to the basis set. We are using a basis set of atomic orbitals  $y_{ilm\sigma}(\mathbf{r})$ , where the index  $i$  specifies the atom on which the atomic orbital (AO) is centered,  $l$  specifies the angular momentum,  $m$  is used to count the various  $d$ -orbitals (i.e.,  $d_{xy}$ ,  $d_{xz}$ ,  $d_{yz}$ ,  $d_{x^2-y^2}$ ,  $d_{z^2}$ ), and  $\sigma$  denotes the spin. In terms of a linear superposition of these basis functions, the single electron wave functions take the form

$$\Psi_{i\sigma}(\mathbf{r}) = \sum_{l,m} C_{ilm\sigma} y_{ilm\sigma}(\mathbf{r}), \quad (25.17)$$

where  $C_{ilm\sigma}$  denote the coefficients which are to be determined from the diagonalization of the Hamiltonian.

The spin operators of  $\blacktriangleright$  Eq. 25.16 refer to the global system and care has to be exercised as they act on the local spin states, the latter related with the former according to  $\blacktriangleright$  Eqs. 25.13 and  $\blacktriangleright$  25.14. For example,

$$\langle \uparrow'_i | S_x | \downarrow'_i \rangle = \frac{1}{2} \cos \phi_i \sin \theta_i, \quad (25.18)$$

where the prime indicates the local functions and  $\uparrow, \downarrow$  indicate spin-up and spin-down states, respectively.

The matrix elements of the orbital angular momentum operators are obtained by operating on the angular part of the wave functions which, in our TBMD formalism are described by the Cubic harmonics. As an example, we write down the expression of the average value of the  $z$ -component of the orbital magnetic moment,  $L_z$ , in terms of its matrix elements :

$$\langle L_z \rangle = \sum_{i\sigma} \int d\mathbf{r} \Psi_{i\sigma}^*(\mathbf{r}) L_z \Psi_{i\sigma}(\mathbf{r}) \quad (25.19)$$

or

$$\langle L_z \rangle = \sum_{\sigma} \sum_i^{occ} \sum_{l,m} \sum_{l',m'} C_{ilm\sigma}^* C_{il'm'\sigma} \int d\mathbf{r} y_{ilm\sigma}^*(\mathbf{r}) L_z y_{il'm'\sigma}(\mathbf{r}) \quad (25.20)$$

Assuming orthogonality of AOs centered at different atoms, and orthonormal basis functions centered at one particular atom, we finally obtain the following expression for the  $d$ -orbital contribution to the orbital magnetic moment  $\langle L_z^d \rangle$  :

$$\langle L_z^d \rangle = \sum_{\sigma} \sum_i^{occ} \sum_{l=2} \sum_{mm'} \Delta_{mm'}^{il} C_{ilm\sigma}^* C_{il'm'\sigma} \quad (25.21)$$

where  $\Delta_{mm'}^{il}$  are constants easily calculated by applying the relation:

$$L_z Y_{lm} = m Y_{lm} \quad (25.22)$$

where  $Y_{lm}$  are the spherical harmonics. For example, a straightforward calculation of the constants  $\Delta_{mm'}^{il}$  shows that the only nonzero matrix elements of  $L_z$  are the following:

$$\langle d_{x^2-y^2} | L_z | d_{xy} \rangle = -2i \quad (25.23)$$

and

$$\langle yz | L_z | zx \rangle = -i \quad (25.24)$$

Combining the above, we construct the spin-dependent TB-representation of the SO-interaction term and add this to the other Hamiltonian terms.

### Step 3: Inclusion of Temperature Effects

In the third step, our ZT-TBMD method has been extended by incorporating the *Nose*-bath (Nose 1984) and the Multiple Histogram approximations (Fanourgakis et al. 1997), so as to be applicable to cluster studies at finite temperatures in an efficient way (Andriotis et al. 2006, 2007; Fthenakis et al. 2003). This generalization allows one to calculate the caloric curve for the cluster and use this to study the effect of temperature on the structural, electronic, and magnetic properties of transition metal clusters and binary systems containing transition metal and semiconductor atoms. The method has been used to study the variation of structural and magnetic properties with temperature as well as to obtain the caloric curves of the Ni-clusters (Andriotis et al. 2006, 2007; Fthenakis et al. 2003).

Upon thermalization at temperature  $T$ , a cluster can be described by the canonical probability distribution function of total energy,  $P_T(E)$ , which specifies the probability that the system will be found in the energy interval  $[E, E + \Delta E]$  at the specified temperature  $T$ . The distribution function corresponding to this temperature, within the canonical ensemble description, is (see Fanourgakis et al. 1997; Schmidt et al. 1997 and references therein):

$$P_T(E) = \frac{n_T(E)}{N_T} = \frac{[\Delta\Gamma(E)] e^{-E/k_B T}}{Z_T}, \quad (25.25)$$

where  $n_T(E)$  is the number of states in the energy interval  $[E, E + \Delta E]$ ,  $N_T$  is the total number of accessible states,  $k_B$  is Boltzmann's constant,  $\Delta\Gamma(E)$  the number of all the different states with energy in the interval  $[E, E + \Delta E]$  (i.e., given by  $Z_T = \sum_{E_i} \exp(-\beta E_i) = \sum_i \Delta\Gamma(E_i) \exp(-\beta E_i)$ ) and  $Z_T$  the partition function at temperature  $T$ .

A molecular dynamics (MD) simulation at a given temperature  $T$  provides numerical values for  $n_T(E)$  at every accessible energy  $E$ . Having obtained these, we make use of the proposed Multiple Histogram Method (MHM) (Weerasinghe and Amar 1993), and obtain the partition functions  $Z_{T_j}$  for a finite set of temperatures  $T_j$ ,  $j = 1, \dots, M$  ( $M \approx 200$ ) and the entropy terms  $S(E_i) = k_B \ln [\Delta\Gamma(E_i)]$  (within an additive constant) for a much larger set of energy values  $E_i$ ,  $i = 1, \dots, N$  ( $N \approx 6,000$ ) (Weerasinghe and Amar 1993).

Having obtained the quantities  $n_T(E)$ ,  $Z_T(E)$  and  $S_T(E)$ , we can then describe all the thermodynamic properties of the clusters and, in particular, the variation with temperature of their structural, electronic, and magnetic properties.

## Computational Approach

The computation of the magnetic features of the clusters is performed within the above described non-collinear TBMD scheme as this allows for a full quantum MD relaxation of systems containing several hundred transition metal atoms while incorporating magnetic effects dynamically. More specifically, it includes: (1) *e-e* correlation effects at the Hubbard-U approximation (Andriotis and Menon 1998), (2) the spin-orbit interaction (in the  $\mathbf{L} \cdot \mathbf{S}$  approximation), and (3) non-collinear magnetic effects (Andriotis and Menon 1998, 2004). Furthermore, the effect of temperature (Andriotis et al. 2006; Fthenakis et al. 2003) is included in the formalism while making use of the full *s, p, d* basis set and contains many unique features that make it ideally suited for the treatment of transition metal (TM) and semiconducting materials. For large-scale simulations we have developed a parallel algorithm that enables molecular dynamics simulations of systems containing atoms in excess of a thousand. This method is more accurate than the order-N methods that are being used at present to treat systems of these sizes. The successful application of our collinear TB scheme (see, e.g., Andriotis et al. 1998, 1999, 2000; Lathiotakis et al. 1996) guarantees similar success for the present generalization as well. Finally, we also mention that this approach has been suitably adapted in order for exclusive use in studying the transport properties (based on our computational codes as described in Andriotis and Menon 2001; Andriotis et al. 2002).

While the TBMD computational approach generalized in such a way is suitable for calculating the magnetic properties of the clusters (of a specific geometry), its use for relaxing the structure of particularly large clusters at nonzero temperatures has been found inefficient due to the extreme computational complexity. This is because the thermodynamic equilibration of a crystal requires sufficiently long MD relaxation time (of the order of 2–6 nanoseconds which is translated into 10–40 million MD steps with each step being of the order of a femtosecond).

In order to make our computations feasible, we firstly reach the thermodynamic equilibrium at each temperature using the classical Sutton–Chen interatomic potential (Sutton and Chen 1990) appropriately fitted to the TBMD results (Fthenakis et al.). It should be noted that for Ni, the classical Sutton–Chen potential (Sutton and Chen 1990) was found to give results closer in agreement with our TBMD method than any other classical potentials in use for Ni (Erkos 2001; Fthenakis et al.). While reaching the thermodynamic equilibrium, we apply our generalized TB formalism every 100 time-steps in order to calculate the MM of the cluster. In the MM calculation, the structure of the cluster is assumed frozen (as obtained within the classical potential approach at that particular time step), and the calculation of the MM of the cluster is repeated for a large number,  $N_{ran}^{(i)}$ , of atomic *spin configurations* taken randomly over the *i*th-structural configuration ( $N_{ran}^{(i)} \approx 120\text{--}300$  for every *i*-time step in the present calculations).

In view of these results,  $\blacktriangleright$  Eq. 25.15 is generalized as follows:

$$\mu_{cl} = \frac{1}{KN_{cl}} \left[ \sum_i^{N_{cl}} \sum_j^{N_{ran}^{(i)}} \mu_i^j \cos \gamma_i^j e^{-(E_i^j - E_0)/k_B T} \right], \quad (25.26)$$

under the assumption that each spin configuration contributes to the magnetic state of the *i*th geometric configuration with probability  $P_M(E_i^j) = \frac{1}{K} e^{-(E_i^j - E_0)/k_B T}$  where,

$$K = \sum_j^{N_{ran}^{(i)}} e^{-(E_i^j - E_0)/k_B T}. \quad (25.27)$$

The index  $j$  in  $\blacklozenge$  Eqs. 25.26–25.27 denotes quantities evaluated at the particular  $j$ th random atomic spin configuration of the  $i$ th structural configuration of the cluster.  $E_0$  is taken to be the energy of the ferromagnetically aligned atomic-spin configuration. In this way, we take the average over the low-lying spin configurations of the cluster of a particular (frozen) geometric structure (i.e., as calculated at the specific time step). Finally, the thermodynamic average of  $\mu_{cl}$  given by  $\blacklozenge$  Eq. 25.26 over the various cluster geometric structures (i.e., time-steps) is obtained with the help of the probability  $P_T(E)$  as given by  $\blacklozenge$  Eq. 25.25.

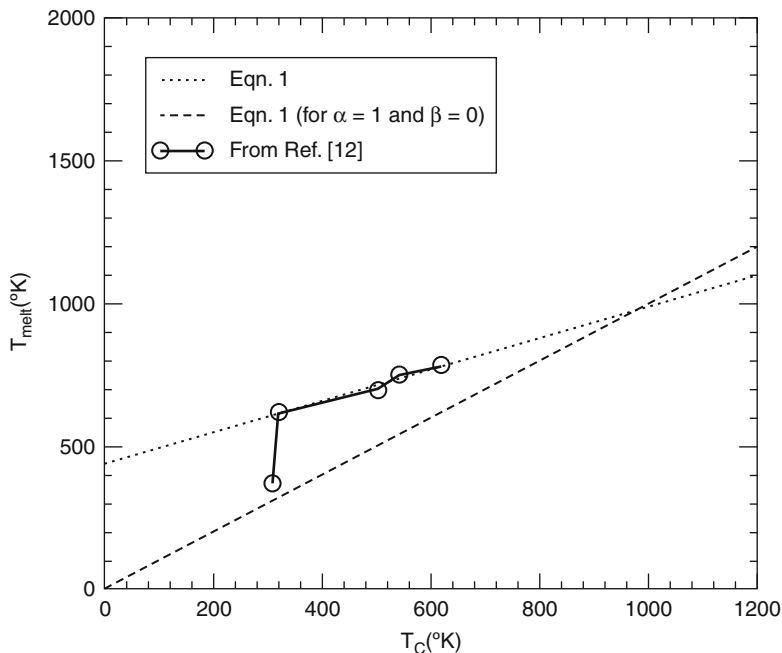
Having obtained the temperature dependence of the average magnetic moment  $\mu_{cl}(T)$  per cluster atom, we proceed with the calculation of the temperature dependence of the specific heat of each cluster by taking the derivative  $d\{\mu_{cl}(T)\}^2/dT$  of the corresponding  $\mu_{cl}(T)$  curves. Following Gerion et al. (2000), we obtain the Curie temperature  $T_{C,N}^{cl}$  for each cluster by locating the maximum of the magnetic contribution to  $C_V$ . This is repeated for a number of clusters of various sizes.

## Results and Discussion

In the present work, our focus is on the properties of the magnetic transition metal clusters and, in particular, on Ni clusters for which experimental data are available for comparison. Using the procedures discussed above, we have calculated the melting,  $T_{melt,N}^{cl}$ , and the Curie,  $T_{C,N}^{cl}$ , temperatures of the  $Ni_N$  clusters for  $N \leq 201$ . These results were discussed recently in Andriotis et al. (2007). The melting temperature  $T_{melt,N}^{cl}$  has been derived on the basis of the Lindemann index using the caloric curve as obtained from the classical potential MD simulations. The Curie temperature  $T_{C,N}^{cl}$  has been derived according to the quantum mechanical procedure discussed above. Both were found to increase with the cluster size tending to their corresponding bulk values as the size of the clusters increases, in good agreement with the existing experimental data (Andriotis et al. 2007).

The correlation between  $T_{melt,N}^{cl}$  and  $T_{C,N}^{cl}$  obtained from our results is shown in  $\blacklozenge$  Fig. 25-1 by the black solid line. This demonstrates and supports the validity of  $\blacklozenge$  Eq. 25.2. We discuss the universal aspect of this correlation and the conclusions that can be derived from in the following.

Firstly, it should be noted that the conclusions one can arrive at from the obtained relationship between melting and Curie temperatures of magnetic clusters depend crucially on the accuracy with which cluster melting temperatures are determined. This is a major issue as it has been extensively discussed in the literature (see, e.g., Baletto and Ferrando (2005); Qi et al. (2001); Sun and Gong (1998) and references therein). This is because surface melting of small particles occurs in a continuous manner over a broad temperature range in contradistinction to the melting of the solid-core (bulk-like) which occurs at a specific critical temperature (Garrigos et al. 1989). For this reason, it has been proposed that in order for  $T_{melt,N}^{cl}$  to be described quantitatively, the surface effects are usually treated separately from the core effects by introducing the *surface thickness*,  $t_0$ , as a free parameter and calculate  $T_{melt,N}^{cl}$  by expressing firstly the heat of the cluster fusion in terms of  $t_0$  and the cluster radius (see, e.g., Lai et al. 1996). A more commonly used approach for determining  $T_{melt,N}^{cl}$  is by employing the Lindemann's criterion, an approach followed in the present work (Fthenakis et al. 2003). Such a calculation is subject to the limitations and the accuracy of this method. In particular, the so derived melting temperatures depend strongly on the choice of the classical potential used (Andriotis et al. (2007); Fthenakis



■ Fig. 25-1

Plot of  $T_{melt,N}^{cl}$  as a function of  $T_{C,N}^{cl}$  for the  $Ni_N$  clusters studied in the present work,  $N = 43, 80, 147, 177, 201$  (solid line). The dotted black line denoted  $\blacktriangleright$  Eq. 25.2 while and dashed black line describes  $\blacktriangleright$  Eq. 25.2 setting  $\alpha = 1$  and  $\beta = 0$ . Points above (below) the dashed line have  $T_{melt} > T_C$  ( $T_{melt} < T_C$ ) respectively

et al. (2003)). This explains why the reported values for the melting temperature of Ni clusters cover a wide range. Nevertheless, the Sutton–Chen classical potential, employed in the present work for Ni, leads to accurate values for surface energies, vacancy energy, stacking fault energies, and bulk melting temperature in very good agreement with experiment (Qi et al. 2001).

The accuracy of Lindemann's criterion depends also on the steepness of its variation with temperature at phase transition and on the specification of its percentage increase which should be adequate to discriminate surface (partial) from all-cluster melting. In the present case, we assign  $T_{melt,N}^{cl}$  to the temperature at which Lindemann's index starts increasing. This allows us to obtain the onset of cluster melting and to derive the melting temperature corresponding to a cluster phase in which unmolten parts with a possible magnetic order are still present.

Similarly, the determination of  $T_{C,N}^{cl}$  depends crucially on the accurate location of the maximum of the heat capacity variation with temperature. This was demonstrated in our previous report (Andriotis et al. 2007) when discussing the  $T_{melt,N}^{cl}$  and  $T_{C,N}^{cl}$  results of  $Ni_{43}$  and their deviation from the prediction of  $\blacktriangleright$  Eq. 25.2. Additionally, the surface energy contribution to the free energy of the cluster may be another reason that small cluster temperatures cannot be extrapolated to bulk phase values (Qi et al. 2001).

Following these clarifications, we next discuss some obvious and hidden consequences of  $\blacktriangleright$  Eq. 25.2. One of the first conclusion that can be deduced from these results is that the Curie



temperature,  $T_{C,N}^{cl}$ , of a magnetic cluster has to follow a size-dependence relationship analogous to that of  $T_{melt,N}^{cl}$ . That is, if  $T_{melt,N}^{cl}$  is given by  $\blacktriangleright$  Eq. 25.1, then  $T_{C,N}^{cl}$  has to follow the following equation:

$$T_{C,N}^{cl} = T_C^{bulk} - \delta_C N^{-1/3}, \quad (25.28)$$

where  $\delta_C$  is a constant that may have an N-dependence as  $\delta_{melt}$ . In fact, assuming the validity of  $\blacktriangleright$  Eqs. 25.1 and  $\blacktriangleright$  25.28 and taking the ratio between  $\blacktriangleright$  Eq. 25.1 and  $\blacktriangleright$  Eq. 25.28 by parts, we obtain:

$$\frac{T_{C,N}^{cl} - T_C^{bulk}}{T_{melt,N}^{cl} - T_{melt}^{bulk}} = \frac{\delta_C}{\delta_{melt}} = \delta_0, \quad (25.29)$$

where  $\delta_0$  is a constant which is expected to depend on N. It is apparent that  $\blacktriangleright$  Eq. 25.29 has exactly the form of our  $\blacktriangleright$  Eq. 25.2, suggesting that the N-dependence of the constant  $\delta_0$  is very weak.

It is worth noting that the numerical justification of  $\blacktriangleright$  Eq. 25.29 by our results as expressed by  $\blacktriangleright$  Eq. 25.2 cannot ensure that the trends described by  $\blacktriangleright$  Eqs. 25.1 and  $\blacktriangleright$  25.28 and which are possibly valid for large clusters can be extrapolated to small clusters as well. The conclusion that comes from  $\blacktriangleright$  Eq. 25.2 is that whatever the functional relationship between the melting temperature of a cluster and its size (not necessarily limited to that of  $\blacktriangleright$  Eq. 25.1) is, the functional relationship followed by  $T_{melt,N}^{cl}$  should dictate the relationship between the Curie temperature with its size as well. This hypothesis is supported by the results of Diep and collaborators (Diep et al. 1989) who found that the incorporation of the magnetic interactions leaves the cluster structure unchanged, thereby justifying our computational procedure.

One may argue that the use of two noncomparable methods, i.e., that of a classical potential MD simulation for calculating the melting temperature and a quantum mechanical approximation for calculating the magnetic moments and the Curie temperature of a cluster, cannot lead to results that can be correlated. We addressed this issue by fitting the classical Sutton–Chen potential to the data for small clusters in such a way that resulted in TBMD and fitted Sutton–Chen potential simulations giving the same structural properties for small Ni clusters. Obtaining similar structural results by both methods appears to confirm the validity of the classical potential MD simulations for our present purpose.

Furthermore, in order to resolve any reservations and ambiguities about the consistency of our conclusions derived from the use of mutually inconsistent methods in calculating the melting and Curie temperatures, it is demonstrated in the following that a calculation of the melting temperatures within our TBMD approximation is in excellent agreement with the results of the classical potential approximation used in the derivation of  $\blacktriangleright$  Eq. 25.2.

Following exactly the same procedure as the one we used to calculate the average magnetic moment per cluster atom (and from this the Curie temperature) (Andriotis et al. 2007), we calculate the average total energy,  $\langle E_T \rangle$ , of each cluster at its thermodynamic equilibrium at a series of temperatures T. An average over  $N_{ran}$  random spin configurations over the cluster atoms is taken at each  $k$ th time step for  $N_{cl}$  time steps ( $N_{ran}$  is taken approximately between 100 and 200). Finally, these spin-averaged values are averaged over time. That is,

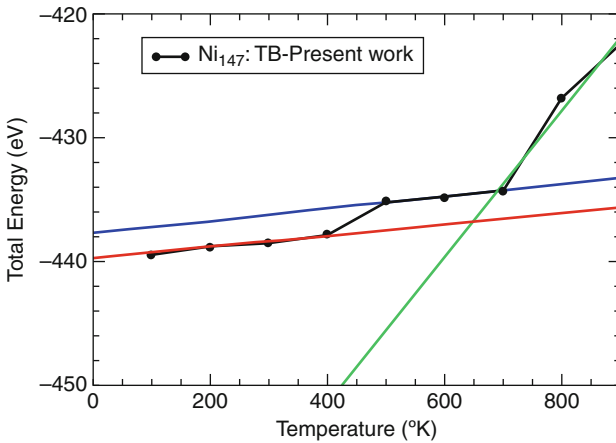
$$\langle E_T \rangle = \frac{1}{N_{cl}} \sum_{k=1}^{N_{cl}} \frac{1}{N_{ran}} \frac{\sum_{i=1}^{N_{ran}} E_i^k e^{-(E_i^k - E_0)/k_B T}}{\sum_{i=1}^{N_{ran}} e^{-(E_i^k - E_0)/k_B T}}. \quad (25.30)$$

where  $E_0$  is a reference energy (Andriotis et al. 2007). For completeness, it is recalled that

$$E_i^k = \sum_{j\sigma} \epsilon_{j\sigma}^{i,k} + E_{rep}^{i,k} \quad (25.31)$$

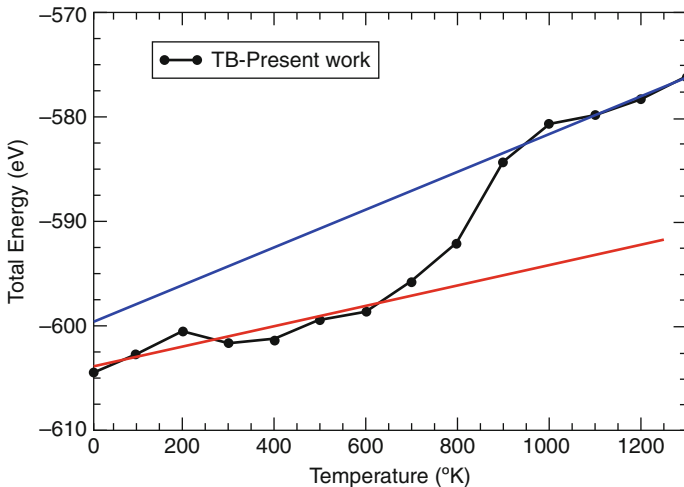
where  $\varepsilon_{j\sigma}^{i,k}$  denote the eigenvalues of the TB cluster Hamiltonian and  $E_{rep}^{i,k}$ , the sum of the repulsive interactions (Andriotis and Menon 1998) of the cluster at the  $i$ th random spin configuration and the  $k$ th time step. As in the case of the calculation of the Curie temperatures, the averaging process over time in  $\blacktriangleright$  Eq. 25.30 is performed while reaching the thermodynamic equilibrium every 100 time-steps.

In  $\blacktriangleright$  Figs. 25-2 and  $\blacktriangleright$  25-3, we present our TB results for the variation with temperature of  $\langle E_T \rangle$  for the  $\text{Ni}_{147}$  and  $\text{Ni}_{201}$  clusters. For  $\text{Ni}_{147}$ , it is observed that the onset of a phase change appears at  $\approx 450^\circ\text{K}$  while the melting starts at  $\approx 700^\circ\text{K}$ . For  $\text{Ni}_{201}$ , the melting takes place



■ Fig. 25-2

Numerical results obtained within the TBMD method for the variation with temperature of the average total energy of the  $\text{Ni}_{147}$  cluster. Straight lines are least square fits to portions of the numerical data



■ Fig. 25-3

The same as in  $\blacktriangleright$  Fig. 25-2 but for the  $\text{Ni}_{201}$  cluster

at  $\approx 800^\circ\text{K}$  (taken to be the midpoint of the “parallel” shift of the two linear parts of the thermodynamic curve). The so obtained melting temperatures appear to be in excellent agreement with the results found using the classical potential method and the Lindemann criterion according to which  $T_{\text{melt},N=147}^{\text{cl}} = 700^\circ\text{K}$  and  $T_{\text{melt},N=201}^{\text{cl}} = 780^\circ\text{K}$ .

Further headway can be made if  $\blacktriangleright$  Eq. 25.2 is taken to be the zeroth-order approximation of a *piece-wise function* of  $N$  in analogy to similar findings (Gunes et al. 2000; Qi et al. 2001) for the expression for  $T_{\text{melt},N}^{\text{cl}}$  given by  $\blacktriangleright$  Eq. 25.1. In this view, the results of Diep et al. (1989) (see Fig. 12 of their work) in the extreme case of very small clusters ( $N \in [7,17]$ ) can lend support to our results and conclusions.

The appearance of the nonzero constant term at the right-hand side of  $\blacktriangleright$  Eq. 25.2 indicates that there is a possibility for  $T_{C,N}^{\text{cl}}$  to be greater than  $T_{\text{melt},N}^{\text{cl}}$ . In particular,  $\blacktriangleright$  Eq. 25.2 predicts that  $T_{C,N}^{\text{cl}}$  could be greater than  $T_{\text{melt},N}^{\text{cl}}$  if

$$T_C^{\text{bulk}} > T_{C,N}^{\text{cl}} > \frac{\beta}{1-\alpha}. \quad (25.32)$$

However, according to our results, the above inequality does not hold for the Ni clusters since  $\beta/(1-\alpha) \approx 968^\circ\text{K}$ , a value much greater than  $T_C^{\text{bulk}} = 631^\circ\text{K}$ . This is demonstrated in  $\blacktriangleright$  Fig. 25-1 with the indicated crossing of the dotted and dashed black lines with the former describing  $\blacktriangleright$  Eq. 25.2 and the latter describing the same equation taking  $\alpha = 1$  and  $\beta = 0$  (i.e., corresponding to the  $T_{C,N}^{\text{cl}} = T_{\text{melt},N}^{\text{cl}}$  case). This incompatibility can be taken as an indication that the functional forms dictated by  $\blacktriangleright$  Eqs. 25.1 and  $\blacktriangleright$  25.28 are not valid for the entire range of the cluster sizes.

The nonzero value of the constant  $\beta$  has another consequence; it predicts that the ratio  $\frac{T_{\text{melt},N}^{\text{cl}}}{T_{C,N}^{\text{cl}}}$  depends on the cluster size and, in fact, increases as the cluster size decreases. If the variation of  $T_{\text{melt},N}^{\text{cl}}$  is assumed as given by  $\blacktriangleright$  Eq. 25.1, the predictions of  $\blacktriangleright$  Eq. 25.2 lead to the conclusion that  $T_{C,N}^{\text{cl}}$  decreases at a slower rate than  $T_{\text{melt},N}^{\text{cl}}$  as the cluster size decreases and, therefore, the “melting temperatures” of *partially molten clusters* can be found to be lower than the Curie temperatures as  $\blacktriangleright$  Eq. 25.2 implies. However, such a conclusion has to be taken with care as the validity of  $\blacktriangleright$  Eq. 25.1 over the entire range of cluster sizes is not valid.

## Conclusion

We have presented results for the variation with the cluster size of the melting and Curie temperatures of  $\text{Ni}_n$ ,  $n \leq 201$ , clusters. Two complimentary methods were used, i.e., the classical MD employing the Sutton–Chen potential and the TBMD for obtaining the melting and the Curie temperatures of the clusters. We have demonstrated that by fitting the classical potential to the results of the TB description in the case of small clusters, we can achieve excellent agreement between the results of the two methods referring to the structural properties and the estimation of the melting temperatures of the clusters.

Our results demonstrate without any ambiguity that the variation of the cluster properties with the cluster size exhibits strong dependence on the ratio of the surface to bulk (core) contributions, the latter appearing to have the same functional dependence on the cluster size for both  $T_{C,N}^{\text{cl}}$  and  $T_{\text{melt},N}^{\text{cl}}$ .

In view of the established dependence of the melting temperature of a cluster on its surface to volume contribution (as, for example,  $\blacktriangleright$  Eq. 25.1), our conclusion can be interpreted as an

indication of a universal aspect of the surface to volume contribution to the cluster properties. This justifies previous findings based on approximate and semiempirical approximations.

## Acknowledgments

The present work is supported by grants from US-DOE (DE-FG02-00ER45817 and DE-FG02-07ER46375).

## References

- Anderson, P. W., & Hasegawa, H. (1955). Considerations on double exchange. *Physical Review*, *100*, 675.
- Andriotis, A. N., Fthenakis, Z., & Menon, M. (2006). Theoretical study of the effect of temperature on the magnetism of transition metal clusters. *Europhysics Letters*, *76*, 1088.
- Andriotis, A. N., Fthenakis, Z. G., & Menon, M. (2007). Correlated variation of melting and curie temperatures of nickel clusters. *Physical Review B*, *75*, 073413.
- Andriotis, A. N., & Menon, M. (1998). Tight-binding molecular-dynamics study of ferromagnetic clusters. *Physical Review B*, *57*, 10069.
- Andriotis, A. N., & Menon, M. (2001). Greens function embedding approach to quantum conductivity of single wall carbon nanotubes. *Journal of Chemical Physics*, *115*, 2737.
- Andriotis, A. N., & Menon, M. (2004). Orbital magnetism: Pros and cons for enhancing the cluster magnetism. *Physical Review Letters*, *93*, 026402.
- Andriotis, A. N., Menon, M., Froudakis, G. E., Fthenakis, Z., & Lowther, J. E. (1998). A tight-binding molecular dynamics study of ni(m)si(n) binary clusters. *Chemical Physics Letters*, *292*, 487.
- Andriotis, A. N., Menon, M., Froudakis, G. E., & Lowther, J. E. (1999). Tight-binding molecular dynamics study of transition metal carbide clusters. *Chemical Physics Letters*, *301*, 503.
- Andriotis, A. N., Menon, M., & Froudakis, G. E. (2000). Contrasting bonding behaviors of 3-d transition metal atoms with graphite and c60. *Physical Review B*, *62*, 9867.
- Andriotis, A. N., Menon, M., & Srivastava, D. (2002). Transfer matrix approach to quantum conductivity calculations in single wall carbon nanotubes. *Journal of Chemical Physics*, *117*, 2836.
- Baletto, F., & Ferrando, R. (2005). Structural properties of nanoclusters: Energetic, thermodynamic and kinetic effects. *Reviews of Modern Physics*, *77*, 371.
- Bansman, J., Baker, S. H., Binns, C., Blackman, J. A., Bucher, J. P., Dorantes-Davila, J., Dupuis, V., Favre, L., Kechrakos, D., Kleibert, A., Meiwes-Broer, K. H., Pastor, G. M., Perez, A., Toulemonde, O., Trohidou, K. N., Tuaille, J., & Xie, Y. (2005). Magnetic and structural properties of isolated and assembled clusters. *Surface Science Reports*, *56*, 189.
- Buffat, P., & Borel, J. P. (1976). Size effect on the melting temperature of gold particles. *Physical Review A*, *13*, 2287.
- Diep, H. T., Sawada, S., & Sugano, S. (1989). Melting and magnetic ordering in transition-metal microclusters. *Physical Review B*, *39*, 9252.
- Doye, J. P. K., & Calvo, F. (2001). Entropic effects on the size dependence of cluster structures. *Physical Review Letters*, *86*, 3570.
- Erkos, S. (2001). In D. Stauffer (Ed.), *Annual reviews of computational physics* (Vol. IX). World Scientific Publ.
- Fanourgakis, G. S., Farantos, S. C., Parneix, P., & Brechignac, P. (1997). An effective transition state for a complex cluster isomerization process: Comparison between anharmonic and harmonic models for  $mg^+ ar_{12}$ . *Journal of Chemical Physics*, *106*, 4954.
- Fthenakis, Z., Andriotis, A. N., & Menon, M. (unpublished).
- Fthenakis, Z., Andriotis, A. N., & Menon, M. (2003). Temperature evolution of structural and magnetic properties of transition metal clusters. *Journal of Chemical Physics*, *119*, 10911.
- Fthenakis, Z., Andriotis, A. N., & Menon, M. (2003). Understanding the structure of metal encapsulated si cages and nanotubes. *Journal of Chemical Physics*, *119*, 10911.

- Garcia-Rodeja, J., Rey, C., Gallego, L. J., & Alonso, J. A. (1994). Molecular-dynamics study of the structures, binding energies, and melting of clusters of fcc transition and noble metals using the voter and chen version of the embedded-atom model. *Physical Review B*, 49, 8495.
- Garrigos, R., Cheyssac, P., & Kofman, R. (1989). Melting for lead particles of very small sizes: Influence of surface phenomena. *Zeitschrift für Physik D*, 12, 497.
- Gerion, D., Hirt, A., Billas, I. M. L., Chatelain, A., & de Heer, W. A. (2000). Experimental specific heat of iron, cobalt, and nickel clusters studied in a molecular beam. *Physical Review B*, 62, 7491.
- Gunes, B., & Erkoc, S. (2000). Melting and fragmentation of nickel nanoparticles: Molecular-dynamics simulations. *International Journal of Modern Physics*, 11, 1567.
- Harrison, W. (1980). *Electronic structure and properties of solids*. San Francisco: W. H. Freeman.
- Huang, H., Sun, C. Q., & Hing, P. (2000). Surface bond contraction and its effect on the nanometric sized lead zirconate titanate. *Journal of Physics: Condensed Matter*, 12, L127.
- Kato, M., & Kokubo, F. (1994). Partially antiferromagnetic state in the triangular hubbard model. *Physical Review B*, 49, 8864.
- Lai, S. L., Guo, J. Y., Petrova, V., Ramanath, G., & Allen, L. H. (1996). Size-dependent melting properties of small tin particles: Nanocalorimetric measurements. *Physical Review Letters*, 77, 99.
- Lathiotakis, N. N., Andriotis, A. N., Menon, M., & Connolly, J. (1996). Tight binding molecular dynamics study of ni clusters. *Journal of Chemical Physics*, 104, 992.
- Lee, Y. J., Lee, E. K., Kim, S., & Nieminen, R. M. (2001). Effect of potential energy distribution on the melting of clusters. *Physical Review Letters*, 86, 999.
- Menon, M., & Subbaswamy, K. R. (1997). Nonorthogonal tight-binding molecular-dynamics scheme for silicon with improved transferability. *Physical Review B*, 55, 9231.
- Nayak, S. K., Khanna, S. N., Rao, B. K., & Jena, P. (1998). Thermodynamics of small nickel clusters. *Journal of Physics Condensed Matter*, 10, 10853.
- Nose, S. (1984). A unified formulation of the constant temperature molecular dynamics methods. *Journal of Chemical Physics*, 81, 511.
- Ojeda, M. A., Dorantes-Davila, J., & Pastor, G. (1999). Noncollinear cluster magnetism in the framework of the hubbard model. *Physical Review B*, 60, 6121.
- Qi, Y., Cagin, T., Johnson, W. L., & Goddard, W. A. (2001). Melting and crystallization in nanoclusters: The mesoscale regime. *Journal of Chemical Physics*, 115, 385.
- Rey, C., Gallego, L. J., Garcia-Rodeja, J., Alonso, J. A., & Iniguez, M. P. (1993). Molecular-dynamics study of the binding energy and melting of transition-metal clusters. *Physical Review B*, 48, 8253.
- Schmidt, M., Kusche, R., Kronmüller, W., von Issendorff, B., & Haberland, H. (1997). Experimental determination of the melting point and heat capacity for a free cluster of 139 sodium atoms. *Physical Review Letters*, 79, 99.
- Sun, D. Y., & Gong, X. G. (1998). Structural properties and glass transition in  $a_n$  clusters. *Physical Review B*, 57, 4730.
- Sutton, A. P., & Chen, J. (1990). Long-range finnisinclair potentials. *Philosophical Magazine Letters*, 61, 139.
- Uhl, M., Sanrdatkii, L. M., & Kubler, J. (1994). Spin fluctuations in  $\gamma$ -fe and in  $fe_3pt$  invar from local-density-functional calculations. *Physical Review B*, 50, 291.
- Weerasinghe, S., & Amar, F. G. (1993). Absolute classical densities of states for very anharmonic systems and applications to the evaporation of rare gas clusters. *Journal of Chemical Physics*, 98, 4967.
- Yang, C. C., & Jiang, Q. (2005). Size and interface effects on critical temperatures of ferromagnetic, ferroelectric and superconductive nanocrystals. *Acta Materialia*, 53, 3305.

# 26 Theoretical Studies of Structural and Electronic Properties of Clusters

*Michael Springborg*

Physical and Theoretical Chemistry, University of Saarland, Saarbrücken, Germany

<i>Introduction</i> .....	956
<i>Basics</i> .....	959
<i>Only Nuclei</i> .....	961
Methods .....	961
Ni Clusters .....	964
Bimetallic Clusters .....	970
Clusters on Surfaces .....	972
<i>Only Electrons</i> .....	974
<i>Both Nuclei and Electrons</i> .....	974
Methods .....	974
Na and Au Clusters .....	976
HAIO Clusters .....	979
AB Semiconductor Clusters .....	984
Metcars .....	986
<i>Conclusions</i> .....	989
<i>Acknowledgment</i> .....	990
<i>References</i> .....	990

**Abstract:** Clusters contain more than just some few atoms but not so many that they can be considered as being infinite. By varying their size, their properties can often be varied in a more or less controllable way. Often, however, the precise relation between size and property is largely unknown: The sizes of the systems are below the thermodynamic limit so that simple scaling laws do not apply. Theoretical studies of such systems can provide relevant information, although in many cases idealized systems have to be treated. The challenge of such calculations is the combination of the relatively large size of the systems together with an often unknown structure.

In this presentation, different theoretical methods for circumventing these problems shall be discussed. They shall be illustrated through applications on various types of clusters. These include isolated metal clusters with one or two types of atoms, metal clusters deposited on a surface, nanostructured HAIO, semiconductor nanoparticles, and metallocarbohedrenes. Special emphasis is put on the construction of descriptors that can be used in identifying general trends.

## Introduction


---

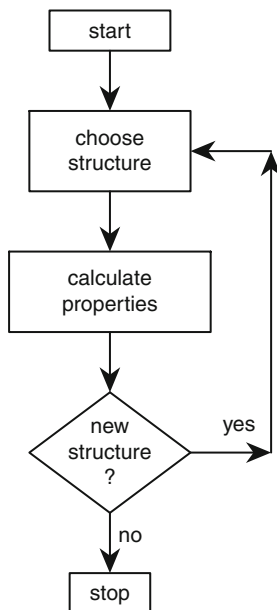
Nanostructures are materials whose spatial extension in 1, 2, or 3 dimensions is roughly of the order of at most some 100 nm. Thereby materials properties different from those of the macroscopic materials we know from our daily life emerge. According to the simplest description of the properties of some given material we may apply scaling laws so that, e.g., the electrical resistance scales with the inverse cross section and linearly with the length of the system. With such scaling laws it is indirectly assumed that the materials form some homogeneous continua and, accordingly, that the fact can be ignored that on the atomic length scale the materials are not at all homogeneous. However, since typical interatomic bond lengths are of the order of some tenths of a nanometer, a proper description of the materials properties of nanostructures often cannot be based on the above assumption that the materials are homogeneous. Thus, for nanomaterials one can no longer apply the above-mentioned scaling laws, i.e., the systems of interest have sizes far from the thermodynamic limit and one has left the scaling regime so that “every single atom counts.” Indeed, the fact that the materials properties depend, in some cases even strongly, on the size of the system for nanostructures is the reason for the large interest in such systems. Here, both the prospects related to possible practical applications of these materials as well as the wish to understand in detail the size-property relations are motivations behind this interest.

The present chapter is devoted to the results of our theoretical studies of clusters, i.e., nanostructures that are finite in all three spatial dimensions. Therefore, their number of surface atoms relative to their total number of atoms is large and, of the same reason, finite-size effects show up. In addition, they most often contain just one or, at most, a few types of atoms, with the possible existence of surfactants as an exception. The surfactants are radicals that are used in saturating dangling bonds at the surfaces and, thus, in stabilizing the materials. For theoretical studies it is important to notice that these systems are fairly large, but not so large that they can be considered as being infinite and periodic, and that, consequently, they may have quite a low symmetry so that in a theoretical calculation chemically identical atoms may have to be treated as being different since they have different surroundings.

In experimental studies, such clusters/colloids are often produced and studied in a solution or on the surface of some substrate. Moreover, as mentioned above, they are often stabilized through ligands. In total, this means that the systems often are interacting with other systems, this being the solvent, the substrate, or the ligands. This is contrasted by theoretical studies that often consider isolated nanoparticles in gas phase that, in addition, often are naked (i.e., without ligands). Another difference between experiment and theory is that the precise size of the experimentally studied systems often is only approximately known, whereas, per construction, theoretical studies consider well-defined systems, although for those one often assumes a certain structure that may or may not be realistic. Thus, experimental and theoretical studies are rarely competing but instead complementing each other.

When attempting to use electronic-structure methods in studying the properties of clusters, in particular the size dependence of those where one, accordingly, will consider a larger range of sizes, one very fast encounters some fundamental properties related to theoretical calculations. We shall here briefly outline those.

In a typical electronic-structure calculation the number and types of the atoms for the system that shall be studied are known. Then (cf.  Fig. 26-1), some initial structure is chosen and various properties for this structure are calculated. These properties are first of all the total energy but may also be others like the forces acting on the nuclei (i.e., the derivatives of the total energy with respect to the nuclear coordinates). Also available experimental information may be sought calculated. Subsequently, one may ask whether a new structure shall be studied. The reasons for doing so could be that the calculated forces are not approximately vanishing, that the calculated properties differ significantly from those obtained in experiment, or that one simply wants to explore further parts of the structure space.

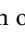


■ Fig. 26-1  
A flow chart for a typical electronic-structure calculation



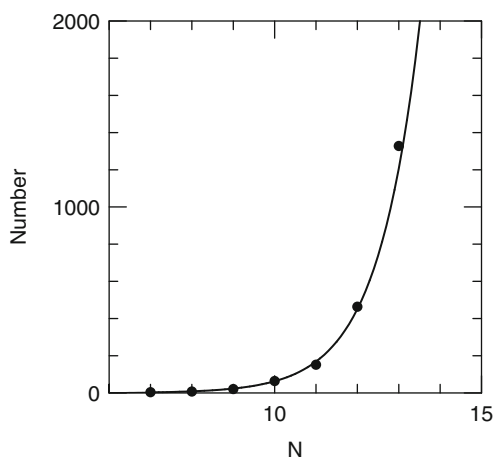
For larger systems this approach is related with two serious problems. First, if the system of interest contains  $N$  nuclei and  $M$  electrons, the computational costs for calculating the properties for one single structure scale as the size of the system to some power, i.e., like  $M^k$  or  $N^k$ , where  $k$  is some power from 2 upward. For some of the most popular approaches, like density-functional and Hartree–Fock methods (see, e.g., Springborg 2000),  $k$  is typically 3, but for more advanced methods  $k$  may be larger than 7. Thus, in this case it should be obvious that for just intermediately large systems the calculation of the properties for just one single geometry may become computationally very costly.

Independently of the scaling of the computational needs as a function of the size of the system, another, complementary, problem causes additional complications. This problem is related to the fact that the number of nonequivalent minima on the total-energy surface as a function of structure grows very fast with the size of the system. In fact, it has been shown (Wille and Vennik 1985) that the number of local total-energy minima grows faster than any polynomial in  $N$  or, alternatively expressed, that the determination of the global total-energy minimum is a so-called NP-hard problem.

A model system that is so simple that detailed studies can be performed is that of a cluster of identical atoms for which it is assumed that the total energy can be written as a sum of pair potentials, each one being a simple Lennard–Jones potential. This system was studied by Tsai and Jordan (1993), who found a rapidly increasing number of nonequivalent metastable structures as a function of size. In  Fig. 26-2 their results have been fitted with an exponential,  $a \cdot \exp(bN)$ , and it is seen that the fit follows the calculated results fairly close. The fit gave  $a = 0.00341$  and  $b = 0.983$ , which in turn means that for  $N = 55$  the fit predicts that of the order of  $10^{21}$  nonequivalent minima exist.

This result points directly to a central issue of this presentation, i.e., how can we determine the structure for a system with at least some tens of atoms and for which no, or only very limited, information on the structure can be used.

The ground-state *structure* is obtained by minimizing the total energy. Employing the Born–Oppenheimer approximation, the nuclei are treated as classical and not quantum



■ Fig. 26-2

A schematic representation of the number of nonequivalent local total-energy minima for Lennard–Jones clusters (*the black circles*) together with a fit with an exponential (*the full curve*)

particles, and there is no variational principle that can be used in systematically getting arbitrarily close to the true ground-state structure, even when assuming that the total energy can be calculated accurately for any structure. Instead, most often one has to change the structure “by hand” until one feels confident that the structure of the lowest total energy has been identified. But it shall be stressed that there is absolutely no approach that with absolute certainty can guarantee that precisely that structure has been found. Trying to prove so would require complete knowledge about the total-energy surface as a function of all internal degrees of freedom. This information is beyond whatever will be available, even if the computers keep on becoming more and more powerful, and the programs more and more efficient.

That this information will never become available can be seen by, e.g., considering the largest possible computer, i.e., the complete universe. Lloyd (2002) estimated that the complete universe, viewed as an enormous quantum computer that has been operating since the Big Bang, could have performed of the order of  $10^{120}$  binary operations. Although this number is very large, it is also finite. Therefore, it means that considering, e.g., a system of 42 atoms, assuming that a total-energy calculation for this system and a given structure is just one single binary operation, and considering just ten different values for each internal structural degree of freedom, exactly  $10^{120}$  calculations are needed for obtaining this, relatively crude, total-energy hypersurface. Thus, the calculations would have required the use of the complete universe since the Big Bang!

In total, it is obvious that for any but the absolutely smallest systems it is not possible to explore anything but very limited parts of the total-energy hyper-surface, and, moreover, that it is never possible to be absolutely sure that the true global total-energy minimum has been found. Any total-energy minimum may provide a total energy that is close to that of the global minimum, although the structures of the two may be markedly different, simply due to the very large number of local total-energy minima. It is also obvious that any attempt to identify the global total-energy minimum has to be based on some kind of qualified search in the multidimensional structure space.

It is one of the purposes of this presentation to discuss some of the approaches that we are using in searching for the global total-energy minimum in the structure space. Another purpose is to present various descriptors/tools that we have derived in order to extract chemical or physical information from the calculated properties. We emphasize that we shall concentrate on the results of our own studies. For more general reviews the reader is referred to, e.g., Baletto and Ferrando (2005), Ferrando et al. (2008), and Springborg (2009).

## Basics

In the most general case, our goal is to calculate the properties of a system containing  $N$  nuclei and  $M$  electrons. We shall denote the positions  $\vec{R}_1, \vec{R}_2, \dots, \vec{R}_N$  and those of the electrons  $\vec{r}_1, \vec{r}_2, \dots, \vec{r}_M$ . Moreover, we use Hartree atomic units and set accordingly  $m_e = |e| = 4\pi\epsilon_0 = \hbar \equiv 1$ . The mass and charge of the  $k$ th nucleus is then  $M_k$  and  $Z_k$ , respectively. The combined coordinate  $\vec{x}_i$  denotes the position and spin coordinate of the  $i$ th electron. In the absence of external interactions and relativistic effects, the Hamilton operator for this system can then be written as a sum of five terms,

$$\hat{H} = \hat{H}_{kn} + \hat{H}_{ke} + \hat{H}_{nn} + \hat{H}_{ee} + \hat{H}_{en}, \quad (26.1)$$

with

$$\begin{aligned}
 \hat{H}_{kn} &= - \sum_{k=1}^N \frac{1}{2M_k} \nabla_{\vec{R}_k}^2 \\
 \hat{H}_{ke} &= - \sum_{i=1}^M \frac{1}{2} \nabla_{\vec{r}_i}^2 \\
 \hat{H}_{nn} &= \frac{1}{2} \sum_{k \neq l=1}^N \frac{Z_k Z_l}{|\vec{R}_k - \vec{R}_l|} \\
 \hat{H}_{ee} &= \frac{1}{2} \sum_{i \neq j=1}^M \frac{1}{|\vec{r}_i - \vec{r}_j|} \\
 \hat{H}_{en} &= - \sum_{k=1}^N \sum_{i=1}^M \frac{Z_k}{|\vec{R}_k - \vec{r}_i|}, \tag{26.2}
 \end{aligned}$$

i.e., the kinetic-energy operator for the nuclei, that for the electrons, and the three potential-energy operators for the nucleus–nucleus, the electron–electron, and the electron–nucleus interactions, respectively.

The time-independent Schrödinger equation becomes then

$$\hat{H}\Psi(\vec{x}_1, \vec{x}_2, \dots, \vec{x}_M, \vec{R}_1, \vec{R}_2, \dots, \vec{R}_N) = E \cdot \Psi(\vec{x}_1, \vec{x}_2, \dots, \vec{x}_M, \vec{R}_1, \vec{R}_2, \dots, \vec{R}_N). \tag{26.3}$$

As indicated above, we shall assume that the Born–Oppenheimer approximation is accurate. Then,  $\hat{H}_{kn}$  is ignored and, furthermore, the wavefunction  $\Psi$  that depends functionally on both electronic and nuclear coordinates is written as a product of two functions,

$$\Psi(\vec{x}_1, \vec{x}_2, \dots, \vec{x}_M, \vec{R}_1, \vec{R}_2, \dots, \vec{R}_N) = \Psi_n(\vec{R}_1, \vec{R}_2, \dots, \vec{R}_N) \cdot \Psi_e(\vec{R}_1, \vec{R}_2, \dots, \vec{R}_N; \vec{x}_1, \vec{x}_2, \dots, \vec{x}_M). \tag{26.4}$$

Here,  $\Psi_n$  is the wavefunction for the nuclei (which for the present study is irrelevant) and  $\Psi_e$  is the electronic wavefunction.  $\Psi_e$  depends functionally on the electronic coordinates but also parametrically on the nuclear coordinates (implying that different structures have different electronic wavefunctions).  $\Psi_e$  is calculated from the electronic Schrödinger equation

$$\hat{H}_e \Psi_e = E_e \Psi_e \tag{26.5}$$

with

$$\hat{H}_e = \hat{H}_{ke} + \hat{H}_{ee} + \hat{H}_{en}. \tag{26.6}$$

Moreover, the total energy is

$$E = E_e + \hat{H}_{nn} = E(\vec{R}_1, \vec{R}_2, \dots, \vec{R}_N), \tag{26.7}$$

i.e., a function of the structure of the system.

Although the Born–Oppenheimer approximation does lead to some computational simplifications, solving the resulting equations is still computational demanding, so that when aiming at studying *many* structures for *larger* systems (as is the goal of the present work), it can easily become necessary to invoke additional approximations. Then, the type of approximation will depend on the system and scientific issue at hand, as we shall illustrate below.

## Only Nuclei

### Methods

Ultimately, the goal is to study the total energy,  $E$ , as a function of structure, i.e.,  $E(\vec{R}_1, \vec{R}_2, \dots, \vec{R}_N)$ . The determination of the electronic orbitals, their energies, and the total electronic energy,  $E_e$ , provides thereby additional information that may be highly relevant for other purposes, but may also be considered as a complication that might be circumvented. The use of approximate expressions (i.e., force fields) of the form

$$E(\vec{R}_1, \vec{R}_2, \dots, \vec{R}_N) \simeq \sum_i E_{t(i)}^{(1)} + \sum_{ij} E_{t(i),t(j)}^{(2)}(\vec{R}_i, \vec{R}_j) + \sum_{ijk} E_{t(i),t(j),t(k)}^{(3)}(\vec{R}_i, \vec{R}_j, \vec{R}_k) + \dots \quad (26.8)$$

represents one possibility. Here,  $t(i)$  is the atom type of the  $i$ th atom, and the total energy has been split into atomic parts as well as 2-, 3-, ... body interactions. The various functions  $E^{(i)}$  are then represented in some approximate, analytical or numerical, form.

Such approximations are very useful for the study of the structural properties of a larger number of larger systems, but may, of course, suffer from inaccuracies due to the approximate nature of the total-energy expression. The Lennard–Jones clusters discussed above represents one such expression, where only 1- and 2-body terms are included. Some further examples are discussed by Springborg (2006).

When applying such approaches to clusters, it is important to choose the method according to the chemical bonding of the system of interest. In metallic systems the electrons are considered as being delocalized and packing effects are often the main driving force for the structure. On the other hand, for many semiconductors and insulators the bonds between the atoms are partly covalent and partly ionic, so that directional bonding as well as electron transfers are important, i.e., a precise description of the electronic degrees of freedom is important. Yet other types of systems include, e.g., molecular crystals with weak interactions between the molecules, but here we are concerned with the first two types of systems.

One approach that we have been using for clusters of metal atoms is based on the embedded-atom method (EAM) of Daw, Baskes, and Foiles (Daw and Baskes 1983, 1984; Daw et al. 1993; Foiles et al. 1986). According to this method, the total energy of the system is written as a sum over atomic energies,

$$E_{\text{tot}} = \sum_{i=1}^N E_i \quad (26.9)$$

with

$$E_i = F_i(\rho_i^h) + \frac{1}{2} \sum_{i \neq j=1}^N \phi_{ij}(|\vec{R}_i - \vec{R}_j|) \quad (26.10)$$

being the energy of the  $i$ th atom.

In  $\blacktriangleright$  Eq. 26.10 the first term is the so-called embedding energy, which is obtained by considering each atom as an impurity embedded into a host provided by the rest of the atoms.

The second term describes electron–electron interactions and is represented in terms of short-ranged pair potentials. The local density at site  $i$  is assumed being a superposition of atomic electron densities,

$$\rho_i^h = \sum_{j(\neq i)} \rho_j^a(|\vec{R}_i - \vec{R}_j|) \quad (26.11)$$

where  $\rho_j^a(r)$  is the spherically averaged atomic electron density provided by atom  $j$  at the distance  $r$ .

With the EAM, the total-energy expression of  $\bullet$  Eq. 26.8 contains also contributions from  $P$ -body interactions with  $P$  being the number of nearest neighbors of the atoms of the system of interest. Other potentials that also include many-body interactions are the Gupta, Murrell–Mottram, Sutton–Chen, and Cleri–Rosato potentials. Since we have used the Gupta, Sutton–Chen, and Cleri–Rosato potentials in some studies we shall here discuss these briefly.

With the Gupta potential (Gupta 1981), the total energy is written in terms of repulsive and attractive many-body terms,

$$E_{\text{tot}} = \sum_{i=1}^N [V^r(i) - V^m(i)] \quad (26.12)$$

where

$$V^r(i) = \sum_{j=1(\neq i)}^N A(a, b) \exp \left[ -p(a, b) \left( \frac{|\vec{R}_i - \vec{R}_j|}{r_0(a, b)} - 1 \right) \right] \quad (26.13)$$

and

$$V^m(i) = \left\{ \sum_{j=1(\neq i)}^N \zeta^2(a, b) \exp \left[ -2q(a, b) \left( \frac{|\vec{R}_i - \vec{R}_j|}{r_0(a, b)} - 1 \right) \right] \right\}^{\frac{1}{2}}. \quad (26.14)$$

The summations run over all ( $N$ ) atoms of the system of interest. Furthermore,  $A$ ,  $r_0$ ,  $\zeta$ ,  $p$ , and  $q$  are fitted to experimental values of the cohesive energy, lattice parameters, and elastic constants for the crystal at 0 K. Finally,  $a = t(i)$  and  $b = t(j)$ .

The Sutton–Chen potentials are based on the empirical  $N$ -body potentials that have been developed by Finnis and Sinclair (1984) for the description of cohesion in metals. With these potentials, the total internal energy is represented by a cohesive functional of pair interactions and a predominantly repulsive pair potential. The main difference of such a potential to a pair potential is that using only pair potentials, the calculated force exerted by one atom on another depends on the interatomic distance only, whereas in the present case it depends on all neighbors of both atoms. Finnis–Sinclair potentials are of relatively short range and extend only to third neighbors in fcc crystals. The long-range modification constitutes the Sutton–Chen potential. This potential has an extra  $\frac{1}{r^\sigma}$  van der Waals tail and, accordingly, the following form

$$E = \varepsilon \left[ \frac{1}{2} \sum_i \sum_{j \neq i} V(|\vec{R}_i - \vec{R}_j|) - c \sum_i \sqrt{\rho_i} \right] \quad (26.15)$$

with

$$V(|\vec{R}_i - \vec{R}_j|) = \left( \frac{a}{|\vec{R}_i - \vec{R}_j|} \right)^n$$

$$\rho_i = \sum_{j \neq i} \left( \frac{a}{|\vec{R}_i - \vec{R}_j|} \right)^m. \quad (26.16)$$

With the empirical many-body potential given by Cleri and Rosato (1993) the cohesive energy of the system is written as

$$E_c = \sum_i (E_R^i + E_B^i), \quad (26.17)$$

where

$$E_R^i = \sum_j A e^{-p \left( \frac{|\bar{R}_i - \bar{R}_j|}{r_0} - 1 \right)}$$

$$E_B^i = - \left\{ \sum_j \xi^2 e^{-2q \left( \frac{|\bar{R}_i - \bar{R}_j|}{r_0} - 1 \right)} \right\}^{\frac{1}{2}}. \quad (26.18)$$

As for the Gupta potential, the values of the parameters that enter the Sutton–Chen and Cleri–Rosato potentials are determined from experimental information.

In a series of studies we have studied the properties of various metal clusters for which the total energy was approximated using one of those methods just mentioned. These include Ni (Grigoryan et al. 2006; Grigoryan and Springborg 2001, 2003, 2004), Al (Joswig and Springborg 2003), Ti (Joswig and Springborg 2007), Cu (Grigoryan et al. 2006), Au (Alamanova et al. 2006; Grigoryan et al. 2006), Ag (Alamanova et al. 2007), Ni–Cu (Hristova et al. 2008b), and K–Cs and Rb–Cs (Hristova et al. 2008a, 2009a) clusters.

In all cases the total-energy methods were combined with unbiased global optimization methods. For the studies we shall report below in this section, we used the Aufbau/Abbau method that was developed earlier by us (Grigoryan and Springborg 2003, 2004) and which consists of the following steps:

1. We assume that we have obtained the structures of the global total-energy minima for the clusters with up to  $N$  atoms.
2. In addition, we consider clusters with  $N + K$  atoms with  $K \simeq 5$ –10. For each of those sizes (i.e.,  $N$  and  $N + K$ ) we randomly generate and relax a large set of structures, from which the one with the lowest total energy is selected.
3. This leaves us with two “source” clusters with  $N$  and  $N + K$  atoms. For the cluster with  $N$  atoms we add at a random position a single atom and the structure is relaxed. This is repeated many hundred times. In parallel, we consider the  $N + K$  structures of  $N + K - 1$  atoms that can be obtained by removing one of the atoms from the cluster with  $N + K$  atoms and relaxing the structure. The structure of the lowest total energy is kept.
4. The procedure of step (3) is repeated  $K - 1$  times until we have obtained two sequences of cluster structures with  $N, N + 1, \dots, N + K - 1$ , and  $N + K$  atoms. From these two sets the structures of the lowest total energies are chosen.
5. Steps (3) and (4) are repeated with the new sets of structures, until no lower total energies are found. Then it is assumed that the global total-energy minima for this size range have been identified and we proceed to the next set of sizes.

By keeping track of not only the single energetically lowest isomer, but more of those, we also obtain information about the energetic distribution of different isomers of the same cluster sizes.

In some studies we used instead the basin-hopping method (Li and Scheraga 1987; Wales and Doey 1997) to determine the structures of total-energy minima. This method is closely related to the Monte Carlo methods, but considers a transformed total-energy surface. Thus,

for each structure,  $\vec{R} \equiv (\vec{R}_1, \vec{R}_2, \dots, \vec{R}_N)$ , instead of considering the true total energy  $E$  at that structure, one considers the total energy  $\tilde{E}$  that the structure would have after having relaxed to its closest total-energy minimum,


$$\tilde{E}(\vec{R}) = \min\{E(\vec{R})\}, \quad (26.19)$$

where it is indicated that  $\tilde{E}(\vec{R})$  is the lowest total energy that is obtained when starting from the structure  $\vec{R}$  but letting it locally relax. Ultimately, this leads to a transformed total-energy surface. The transformed energy surface  $\tilde{E}$  is much less structured than  $E$ , although the energies at the global and local total-energy minima are identical. The simpler shape of the transformed structure makes it significantly easier to identify the global total-energy minimum, without biasing the calculation in any way. In a practical calculation, instead of changing the structure according to the Monte Carlo steps directly, the structure is first locally relaxed using standard methods.

## Ni Clusters

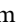

As a single example of isolated monatomic metal clusters, we shall in this subsection discuss some of our results for isolated  $\text{Ni}_N$  clusters (Grigoryan et al. 2006; Grigoryan and Springborg 2001, 2003, 2004).


The calculations outlined in the previous subsection give essentially nothing but a listing of the total energies and the nuclear coordinates for a set of clusters. Thus, in our study on the  $\text{Ni}_N$  clusters we considered the four energetically lowest isomers up to  $N = 150$  and obtained, accordingly, roughly 45,000 numbers. A large challenge is, consequently, to extract physical and chemical data from this information.

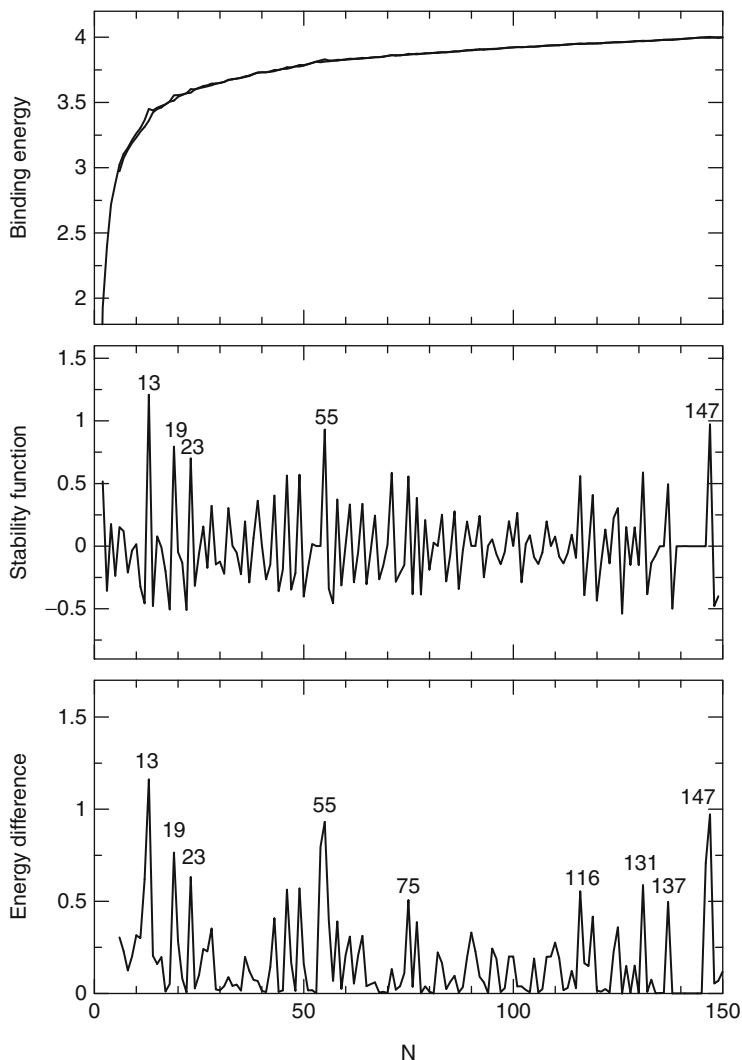
In  Fig. 26-3 we show in the upper panel the binding energy per atom. A careful inspection of the figure reveals that there are two curves very close in energy, since the results are given for the two energetically lowest isomers. Nevertheless, the curves are rather structureless which is a result of the fact that any cluster  $\text{Ni}_N$  cluster is stabler than any two noninteracting subparts  $\text{Ni}_{N-K}$  and  $\text{Ni}_K$  for all  $K > 0$ .

More information can be obtained from the so-called stability function:

$$\Delta_2 E(N) = E_{\text{tot}}(N-1, 1) + E_{\text{tot}}(N+1, 1) - 2E_{\text{tot}}(N, 1) \quad (26.20)$$

with  $E_{\text{tot}}(N, j)$  being the total energy for the energetically  $j$ th lowest isomer of the  $\text{Ni}_N$  cluster.  $\Delta_2 E(N)$  possesses peaks for clusters that are particularly stable compared to those with one atom more or less. As seen in the middle panel in  Fig. 26-3, this is the case for clusters with  $N = 13, 19, 23, 55,$  and  $147$ . These, so-called magic numbers, correspond to clusters with a particularly high-symmetric structure as can be seen from a more careful inspection of the structures. As examples we show in  Fig. 26-4 the structures of the  $\text{Ni}_N$  clusters with  $N = 13, 19, 55,$  and  $78$ .

Alternatively, one may compare the total energies for the energetically two lowest isomers of the same cluster size, i.e.,  $E_{\text{tot}}(N, 2) - E_{\text{tot}}(N, 1)$ . This has peaks for clusters that are particularly stable compared to the next isomer of the same cluster size. As seen in  Fig. 26-3, many of the magic-numbered clusters are also particularly stable according to this second criterion. This suggests that the characterization of certain clusters to be particularly stable is very robust.



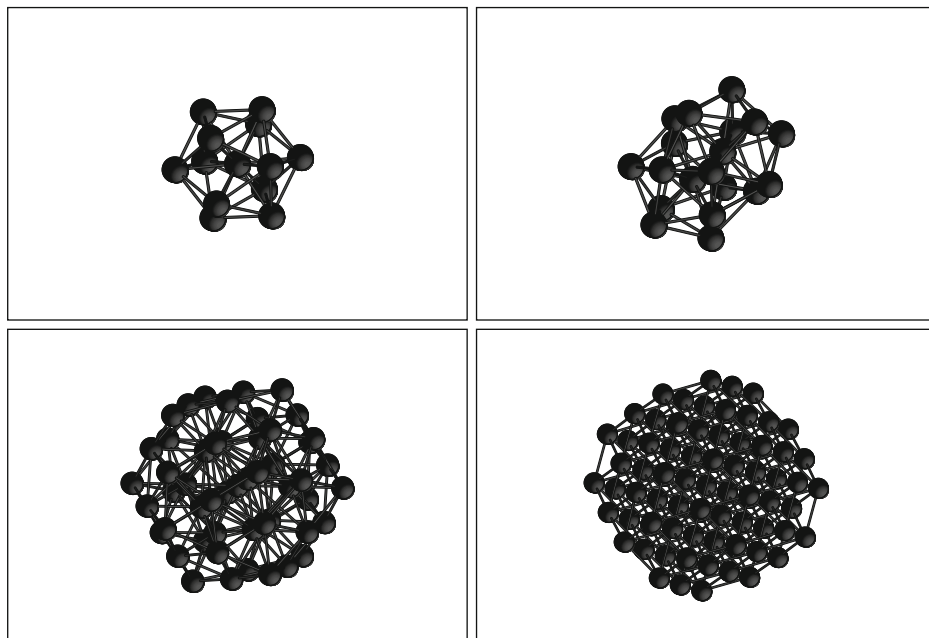
■ Fig. 26-3

The binding energy per atom for the energetically two lowest isomers (*upper part*), the stability function (*middle part*), and the total-energy difference for the two energetically lowest isomers (*lowest part*) for  $Ni_N$  clusters as functions of  $N$ . All energies are given in eV

In order to obtain information about the overall shape of the clusters we consider the  $3 \times 3$  matrix containing the elements

$$I_{st} = \frac{1}{u_l^2} \sum_{n=1}^N (R_{n,s} - R_{0,s})(R_{n,t} - R_{0,t}) \quad (26.21)$$





■ Fig. 26-4

The structures of the  $\text{Ni}_N$  clusters with (top, left)  $N = 13$ , (top, right) 19, (bottom, left) 55, and (bottom, right) 78

with  $u_l = 1 \text{ \AA}$  being a length unit,  $s$  and  $t$  being  $x$ ,  $y$ , and  $z$ ,

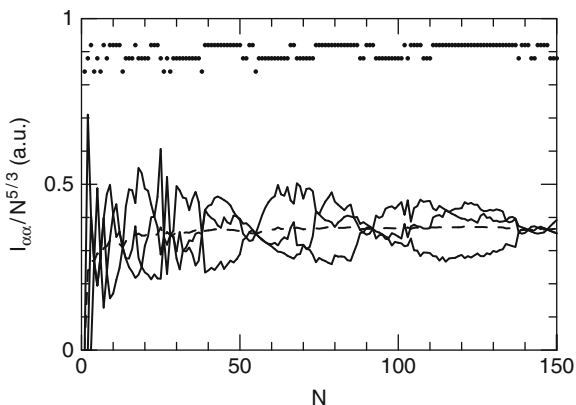
$$\vec{R}_0 = \frac{1}{N} \sum_{n=1}^N \vec{R}_n \quad (26.22)$$

being the center of the cluster, and  $\vec{R}_n$  being the position of the  $n$ th atom. The three eigenvalues of this matrix,  $I_{\alpha\alpha}$ , can be used in separating the clusters into being overall spherical (all eigenvalues are identical), more cigar-like shaped (one eigenvalue is large, the other two are small), or more lens-shaped (two large and one small eigenvalue). Moreover, the average of the three eigenvalues,  $\langle I_{\alpha\alpha} \rangle$ , is a measure of the overall extension of the cluster. Finally, the sum of any two of those three eigenvalues gives a moment of inertia that is relevant for rotational properties of the clusters.

For a homogeneous, spherical cluster with  $N$  atoms, the eigenvalues are proportional to  $N^{5/3}$ . Therefore, in  $\blacklozenge$  Fig. 26-5 we scale the eigenvalues by  $N^{-5/3}$ . This figure shows that the overall shape changes many times for clusters with  $N$  up to somewhat above 50. After that, the shape is more constant, with some few exceptions that in some cases are due to the fact that the three eigenvalues all are very close so that only small atomic displacements would change the shape classification.

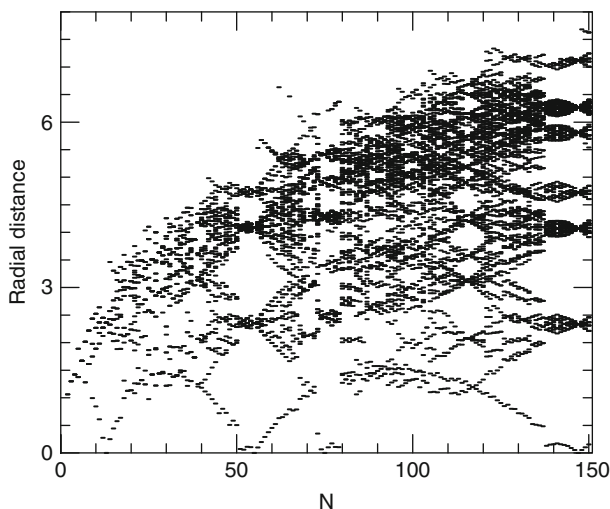
In order to obtain further information on the structure of the clusters we introduce the concept of radial distances. For each atom, its radial distance is defined as

$$r_n = |\vec{R}_n - \vec{R}_0|. \quad (26.23)$$



■ Fig. 26-5

The normalized eigenvalues of the matrix containing the elements of [Eq. 26.21](#) as functions of  $N$ . The three solid curves give the eigenvalues, and the dashed curve their average. In the upper part of the figure a simple estimate of the overall shape of the clusters is given: either being spherical (marked with points in the *lowest row*), cigar-shaped (points in the *middle row*), or lens-shaped (points in the *uppermost row*)



■ Fig. 26-6

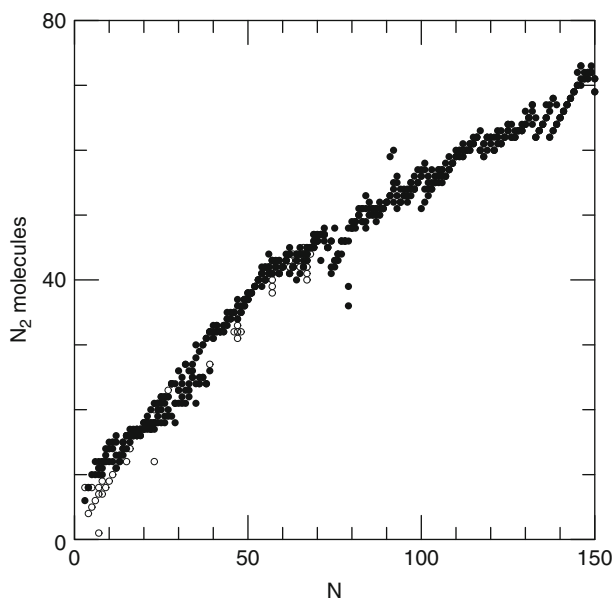
The radial distances (in Å) as a function of cluster size, i.e., each small line represents (at least) one atom with that radial distance

By plotting various properties as functions of the radial distances we can obtain further insight into the cluster properties. At first we show the radial distances themselves, cf. [Fig. 26-6](#). This figure shows that the overall size of the cluster (using the largest radial distance as a measure) in general increases with size of the cluster, although not monotonically. Moreover, for certain size ranges, like slightly above 50 and 140 atoms, the radial distances tend to form

different groups. This implies that those clusters have an onion-like structure with different, essentially concentric, shells of atoms. For other sizes, the clusters tend to have a much more irregular structure.

Riley and coworkers (Parks et al. 1997, 1998, 2001) have presented experimental results of so-called chemical-probe experiments on  $Ni_N$  clusters. By measuring the mass of the clusters before and after exposure to (in this case) an  $N_2$  atmosphere, the number of  $N_2$  molecules that are adsorbed on the surface of the cluster can be determined, which in turn gives information on the surface of the cluster. Thereby, Riley et al. make use of some simple empirical rules for the adsorption: Nickel atoms with a coordination of 4 or less will bind two molecules; for a coordination between 5 and 8 they will bind one molecule; for a coordination of 9 there may be one molecule bonded; and for larger coordinations there will be no molecule bonded. Using the same rules we calculated the number of  $N_2$  molecules that could be adsorbed on the structures we have determined for the four energetically lowest isomers and show the results, in comparison with the experiment, in [Fig. 26-7](#). It is here remarkable that there is a very good agreement between theory and experiment and, moreover, that the overall shape of the size dependence of this number appears to change slope for clusters with some 60–70 atoms. Unfortunately, the experimental studies do not allow for analyzing this prediction.

For the study of growth processes as well as for analyzing the size for which the clusters obtain structures that resemble small parts of the macroscopic crystalline material, we have found the concept of similarity functions useful. In order to compare two structures consisting of  $N_1$  and  $N_2$  atoms we shall, for each, calculate either the interatomic distances or the radial distances, subsequently sort these, and, finally, define a so-called similarity function through




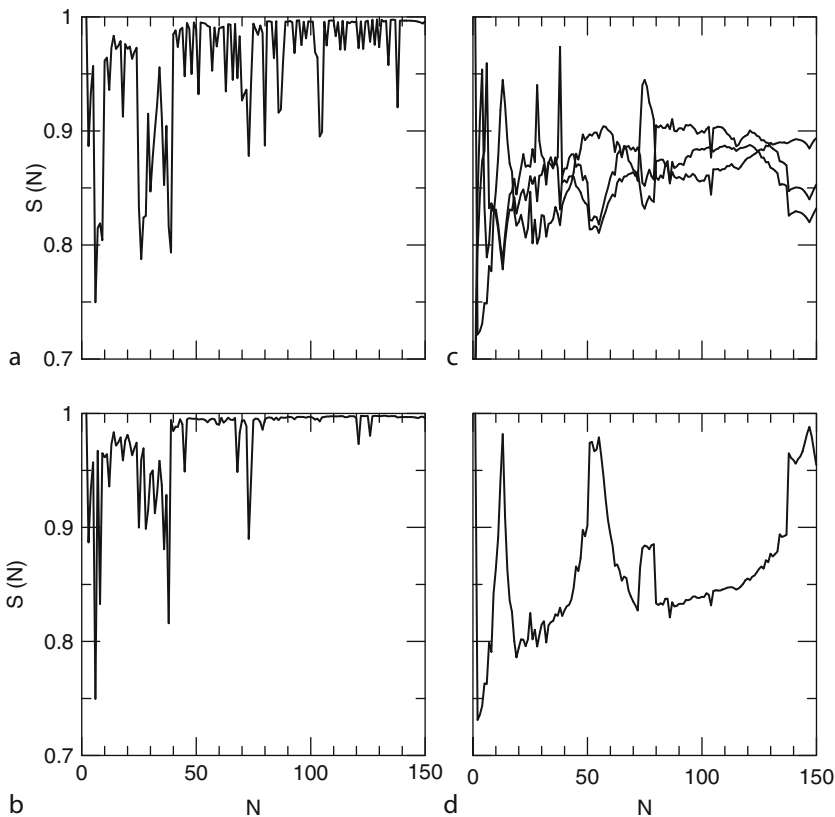
■ Fig. 26-7


The (*open circles*) experimentally determined number of  $N_2$  binding sites for  $Ni_N$  clusters as function of  $N$  in comparison with theoretical calculated numbers (*closed circles*)

$$S = \left\{ 1 + \left[ \frac{1}{M} \sum_{i=1}^M (d_i - d'_i)^2 \right]^{1/2} / u_i \right\}^{-1}. \quad (26.24)$$

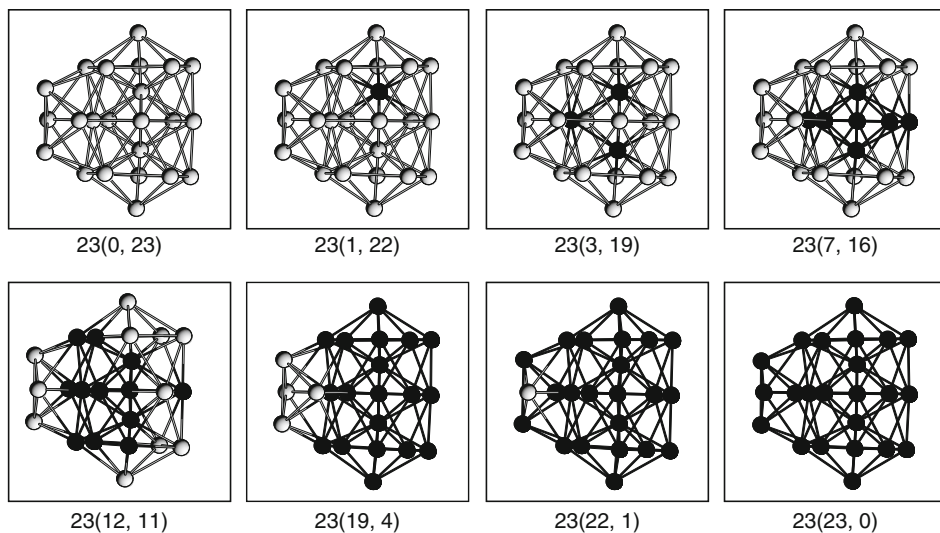
Here,  $u_i = 1 \text{ \AA}$ . Moreover  $\{d_i\}$  and  $\{d'_i\}$  are the sorted radial or interatomic distances for the two structures, and  $M$  is their total number (being either  $N$  or  $N(N-1)/2$  with  $N$  the smallest of  $N_1$  and  $N_2$ ). The two structures are very similar (different) if  $S$  approaches 1 (0). We add that our experience has shown that qualitatively the same results are obtained independently of whether the radial or the interatomic distances are used. Another result of our experience is that  $S$  below roughly 0.7–0.8 usually indicates that the structures are quite different.

At first, we shall use the similarity functions in studying whether the structure with  $N$  atoms can be considered similar to the one with  $N-1$  atoms plus an extra atom. To this end we consider each of the  $N$  structures that can be obtained by removing one of the atoms from the  $N$  atom cluster and keeping the positions of the remaining  $N-1$  atoms. Then, we compare this  $N-1$  atom fragment with the cluster with  $N-1$  atoms, using the similarity function. Ultimately, the largest of these  $N$  values for  $S$  is used.  *Figure 26-8a* shows the results when comparing the



 **Fig. 26-8**

The similarity functions for comparing the structure of the  $\text{Ni}_N$  cluster with (a) the energetically lowest cluster with  $N-1$  atoms, (b) the four energetically lowest clusters with  $N-1$  atoms. (c) a fragment of the fcc crystal, and; (d) an icosahedron. For details, see the text



■ Fig. 26-9

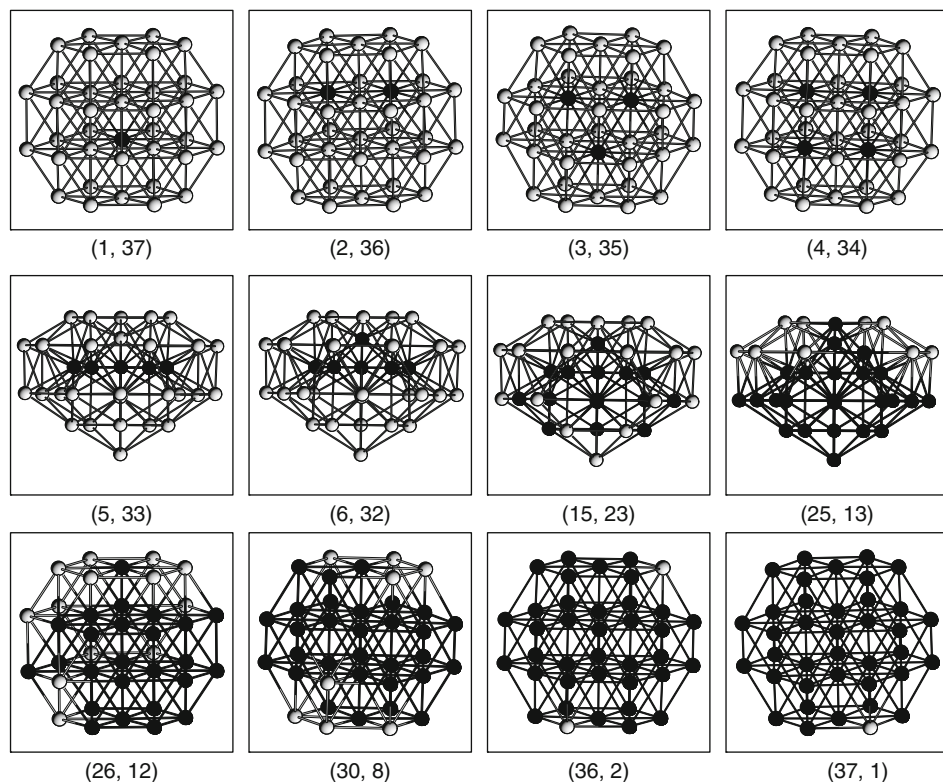
The structures of  $Ni_nCu_m$  clusters for a fixed value of  $N = n + m = 23$  and different values of  $(n, m)$ . The dark atoms mark the Ni atoms

energetically lowest isomers of the two clusters with  $N-1$  and  $N$  atoms. Also for this property we see many dips in the function for cluster sizes up to around 50 atoms after which  $S$  gets much more regular. This effect becomes even more pronounced when comparing the  $Ni_N$  cluster of the lowest energy with the four energetically lowest isomers with  $N-1$  atoms. Then (cf. ► Fig. 26-8b),  $S$  approaches 1 for almost all  $N > 50$ , suggesting that more different isomers are active in the growth processes: The most stable  $Ni_N$  cluster has a structure that may be derived from that of an energetically higher structure of the  $Ni_{N-1}$  cluster.

Finally, we show in ► Fig. 26-8 also the similarity function that is obtained when comparing the cluster structures with fragments of the crystal or with an icosahedron. In this case the similarity function is based on the radial distances, and for the crystal we have considered three different spherical fragments with different definitions of the center. It is immediately seen that for some ranges of  $N$  (e.g.,  $N$  around 75) the structures resemble fragments of the fcc crystal, but also that for even larger sizes (around 145 atoms) as well as for  $N \approx 55$  there is a considerably larger structural similarity with an icosahedron. Thus even clusters with around 150 atoms are too small to approach the macroscopic crystalline limit.

## Bimetallic Clusters

For binary clusters (i.e., clusters with two types of atoms) the additional existence of so-called homotops (Jellinek and Krissinel 1996; Lloyd et al. 2004) increases the computational demands enormously. Homotops for, e.g.,  $A_pB_q$  clusters are defined as clusters with the same size, composition, and geometric arrangement but differing in the way in which A- and B-type atoms are arranged. Their number for the  $A_pB_q$  cluster equals  $\frac{(p+q)!}{p!q!}$ .

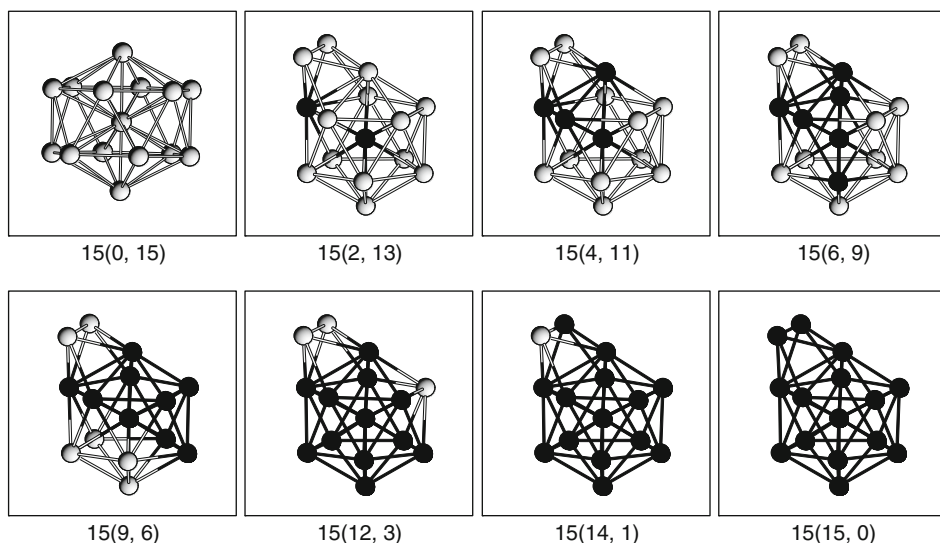


■ Fig. 26-10

The structures of  $\text{Ni}_n\text{Cu}_m$  clusters for a fixed value of  $N = n + m = 38$  and different values of  $(n, m)$ . The dark atoms mark the Ni atoms

As a single example we shall here discuss the results of our study on bimetallic  $\text{Ni}_n\text{Cu}_m$  clusters (Hristova et al. 2008a). In this case we used the basin-hopping method for optimizing the structure in combination with the EAM for the calculation of the total energy of a given structure. The EAM (as many other methods that do not include electronic/orbital degrees of freedom explicitly) has a preference for close-packed structures so that in many cases the EAM method predicts very similar structures for pure clusters with just one element. Therefore, often only one or two types of structures were found for different  $\text{Ni}_n\text{Cu}_m$  clusters with the same total number of atoms,  $N = n + m$ . The less obvious issue is accordingly, how the two types of atoms are distributed within the cluster and, if more than one overall structure exists, which structure is found for which stoichiometry.

For the  $\text{Ni}_n\text{Cu}_m$  clusters we found only three different types of scenarios. Either all clusters for a given  $N = n + m$  have the same structure, which is the case for  $N = 13$  and 23, for instance. ▶ Figure 26-9 shows the results for  $N = 23$ . Alternatively, for  $N = 38$ , the two pure clusters have the same structure, whereas for  $n = 5$ –25 another structure is found as shown in ▶ Fig. 26-10. Or, finally, for  $N = 15$  the two pure clusters have different structures, and the transition from the structure of the pure Cu cluster to that of the pure Ni cluster takes place for just 2 Ni atoms (cf. ▶ Fig. 26-11). In all cases, the Ni atoms tend to occupy inner positions,



■ Fig. 26-11

The structures of  $Ni_nCu_m$  clusters for a fixed value of  $N = n + m = 15$  and different values of  $(n, m)$ . The dark atoms mark the Ni atoms

whereas the Cu atoms more often are found on the surface. This difference can be understood when comparing the cohesive energy of the two metals: The larger value for Ni suggests that this type of atom has a stronger preference for high coordination than Cu has.

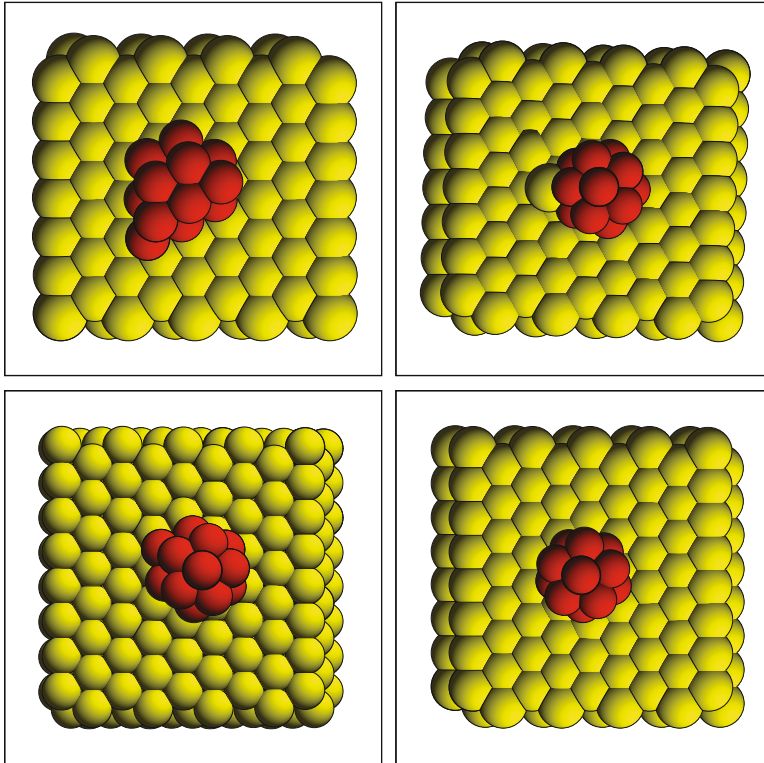
## Clusters on Surfaces

As mentioned in the introduction, [section “Introduction”](#), experimental studies of clusters often consider clusters on some surface. Both clusters that have been deposited on the surfaces and clusters that are grown directly on the surfaces have been studied. Since theoretical studies often consider clusters in the gas phase a highly relevant question is whether the latter have anything to do with clusters on a surface. In some few studies we have addressed this issue.

Using molecular-dynamics simulations and the EAM we studied the deposition of the particularly stable  $Ni_{13}$  and  $Cu_{13}$  clusters (cf. [section “Ni Clusters”](#)) on the (111) surfaces of crystalline Ni and Cu (Kasabova et al. 2007) as well as more different Cu clusters deposited on the Cu(111) surface (Alamanova et al. 2008). The deposition energies, 0–1 eV/atom, imply according to experimental classifications that the depositions are to be considered as being soft. Nevertheless, the depositions even at the smallest possible deposition energies (cf. [Fig. 26-12](#)) led to clusters that were highly deformed compared to the gas-phase structures. To some extent, Ni clusters deposited on the Cu surface were partly intact, which may be understood through the higher cohesive energy and bulk modulus of Ni compared with Cu. Thus, in this respect Ni and Cu can be classified as being hard and soft, respectively.

Alternatively, one may suggest that when clusters and surfaces are made of the same metal, the cluster atoms will lead to an epitaxial growth of the substrate. To quantify this suggestion,





■ Fig. 26-12

Top view of the final structures obtained when depositing  $A_{13}$  clusters on the B(111) surface with 0 eV/atom deposition energy. A and B are (top, left) Ni and Cu, (top, right) Cu and Ni, (bottom, left) Cu and Cu, and (bottom, right) Ni and Ni. The dark atoms are those of the clusters

we introduced a so-called index of epitaxy (Alamanova et al. 2008),  $I$ , through

$$q = \sum_i^N |\vec{R}_i - \vec{R}_c|^2$$

$$I = \frac{1}{1 + q/u_i^2}, \quad (26.25)$$

where  $|\vec{R}_i - \vec{R}_c|$  is the distance between the positions of the  $i$ th atom and the closest-lying fictitious atom in the infinite, periodic crystal that is obtained by continuing the structure of the substrate periodically.  $I = 1$  if perfect epitaxy is obtained. Our calculations indicated, however, very little epitaxy.

In another study we consider the structures that result when a cluster is grown directly on the substrate (Hristova et al. 2009b). We considered  $Ag_N$  clusters grown on Ag(111) and Ni(111) surfaces. Since the (111) surfaces are close packed and since the EAM (as mentioned above) has a strong (and, for the present systems, realistic) preference for structures with high-coordinated atoms, the growth of Ag clusters on the Ag(111) surface led to planar structures that moreover were roughly spherical. Thereby, the highest coordination for the cluster atoms could be obtained and since substrate and cluster are of the same material there is no strain involved.



This is different for Ag clusters on the Ni(111) surface. In this case, the lattice mismatch between Ag and Ni leads to some strain in the clusters grown epitaxially on the surface and, accordingly, the Ag clusters tend to get a somewhat elongated structure.

## Only Electrons

---

The approaches we have discussed in the preceding section were based on the rationale that for metal clusters, there is no directional bonding and, instead, the electrons are delocalized over the complete system. Thereby, particularly stable clusters (i.e., magic numbers) occur for clusters for which the atoms can form a particularly compact, close-packed geometrical structure. The electronic effects were at most indirectly included so that, e.g., stability due to electronic shell effects is not taken into account.

This is, on the other hand, the main effect that is included in the jellium model. Within the jellium model it is assumed that the system of interest forms a compact, close-packed structure and that the valence electrons are delocalized over the complete system. Due to the delocalization of the electrons they do hardly feel the precise arrangement of the nuclei and core electrons so that the effects of those can be approximated as being those of a homogeneous charge density with the same average density as for the true system. The valence electrons move then in the electrostatic potential created by this jellium.

The jellium model has been used intensively for the studies of clusters of metals (see, e.g., Brack 1993; de Heer 1993). In fact, one of the first papers in more recent times that treated the special properties of clusters was a combined experimental and theoretical study on  $\text{Na}_N$  clusters (Knight et al. 1984). Sodium can be considered the prototype of metal clusters for which the unidirectional bonding due to the 3s valence electrons suggests that the arguments above provide a good starting point for rationalizing the properties of Na clusters. Thus, packing effects, that can be modeled accurately with a simple potential that does not include electronic orbitals, will be responsible for the (essentially spherical) structures, and the particularly stable structures can be identified with a jellium model for delocalized electrons. In their study, Knight et al. assumed that the jellium was spherical and calculated, subsequently, the orbitals for the electrons moving in this jellium and under the influence of each other. Comparing with experimental mass abundance spectra they could explain the experimental observation of certain cluster sizes that showed up particularly often as related to these clusters' high stability. The latter was, in turn, due to the closing of shells of electronic orbitals; equivalent to what explains the inertness of the inert gases He, Ne, etc., in the periodic table.

In some more recent studies we have used the spherical jellium model to analyze the properties of  $\text{Cs}_N$  clusters (Springborg 1999) and of a  $\text{C}_{60}$  molecule coated with alkali metals (Springborg et al. 1996). We shall here, however, not discuss these studies further but below address the accuracy of this jellium model.

## Both Nuclei and Electrons

---

### Methods

---

When including both electrons and nuclei in the calculations, the calculations may become so demanding that the number of structures and/or the size of the systems have to be limited. It is

then often very useful to augment calculations with less accurate methods with more accurate ones on selected structures in order to access the accuracy of the approximate methods. In some cases we have done so, too, using density-functional methods (see, e.g., Springborg 2000 for a description of such methods).

As a compromise between accuracy and computational demands we have often used the so-called DFTB (density-functional tight-binding) method of Seifert and coworkers (Porezag et al. 1995; Seifert et al. 1996; Seifert and Schmidt 1992). The DFTB method is based on the density-functional theory (DFT) of Hohenberg and Kohn (1964) in the formulation of Kohn and Sham (1965). For more details we refer the reader to the original works or to Springborg (2000). Within the DFTB approach, the total energy relative to the non-interacting atoms is given as

$$E_{\text{tot}} \simeq \sum_i^{\text{occ}} \varepsilon_i - \sum_j \sum_m \varepsilon_{jm} + \frac{1}{2} \sum_{j \neq k} U_{jk} (|\vec{R}_j - \vec{R}_k|), \quad (26.26)$$

where  $\varepsilon_i$  is the energy of the  $i$ th orbital for the system of interest and  $\varepsilon_{jm}$  is the energy of the  $j$ th orbital for the isolated  $m$ th atom. Moreover,  $U_{jk}$  is a short-range pair potential between atoms  $j$  and  $k$  that is adjusted so that results from parameter-free density-functional calculations on two-atomic systems as a function of the interatomic distance are accurately reproduced. Finally, only the valence electrons are explicitly included in the calculations, whereas the other orbitals are treated within a frozen-core approximation.

The elements of the Hamilton and overlap matrices, i.e.,  $\langle \chi_{m_1 n_1} | \hat{H} | \chi_{m_2 n_2} \rangle$  and  $\langle \chi_{m_1 n_1} | \chi_{m_2 n_2} \rangle$  with  $\chi_{mn}$  being the  $n$ th atomic orbital of the  $m$ th atom, are obtained from calculations on diatomic molecules. The Hamilton operator contains the kinetic-energy operator as well as the potential. The latter is approximated as a superposition of the potentials of the isolated atoms,

$$V(\vec{r}) = \sum_m V_m (|\vec{r} - \vec{R}_m|), \quad (26.27)$$

and we assume that the matrix element  $\langle \chi_{m_1 n_1} | V_m | \chi_{m_2 n_2} \rangle$  vanishes unless at least one of the atoms  $m_1$  and  $m_2$  equals  $m$ .

Thus, within this approach all information that enters the calculations are extracted from the properties of diatomic molecules. These can, in turn, be determined from accurate, density-functional calculations. In order to access the accuracy of the approach we perform additional calculations on the infinite, periodic systems. If these provide accurate results, we assume that the results are accurate for the intermediate, finite clusters as well.

For an unbiased structure determination we combine the DFTB method with genetic algorithms. The genetic algorithms are based on the principles of natural evolution and are, therefore, also called evolutionary algorithms (Goldberg 1989; Holland 1975) and have been found to provide an efficient tool for global geometry optimizations. One version of the genetic algorithms that we are using is as follows.

A population of  $P$  initial structures is chosen randomly (these clusters are called parents) and each structure is relaxed to the nearest total energy minimum. By cutting each parent randomly into two parts a next set of  $P$  structures is obtained by interchanging (“mating”) these two parts and allowing the resulting “children” to relax too. Comparing the energies of the  $2P$  clusters of both sets, those  $P$  with the lowest total energies are chosen to form the set of parents for the next generation. This procedure is repeated for many hundred generations until the lowest total energy is unchanged for a large number of generations.

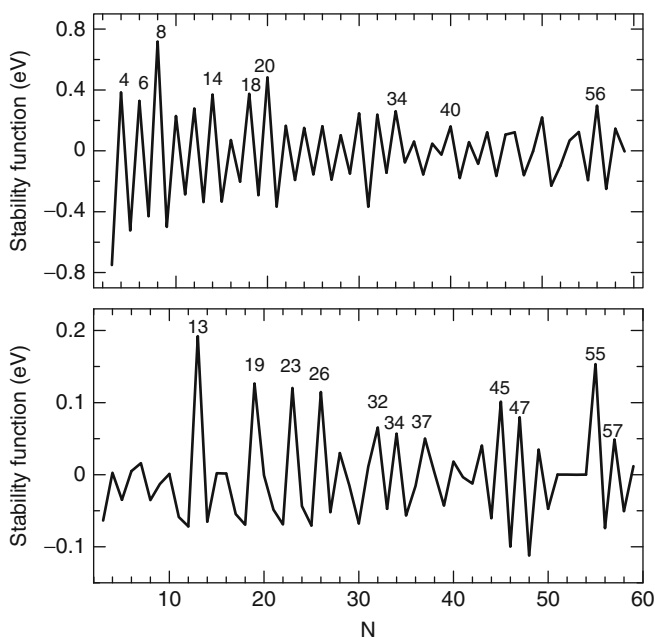
Alternatively, this “two-parents” method may be replaced by a “single-parent” method where the two parts of one cluster simply are interchanged. The advantage of this latter approach

is that for systems with more than one type of atom stoichiometry is automatically conserved. Moreover, in some cases we found that the latter is faster than the former.

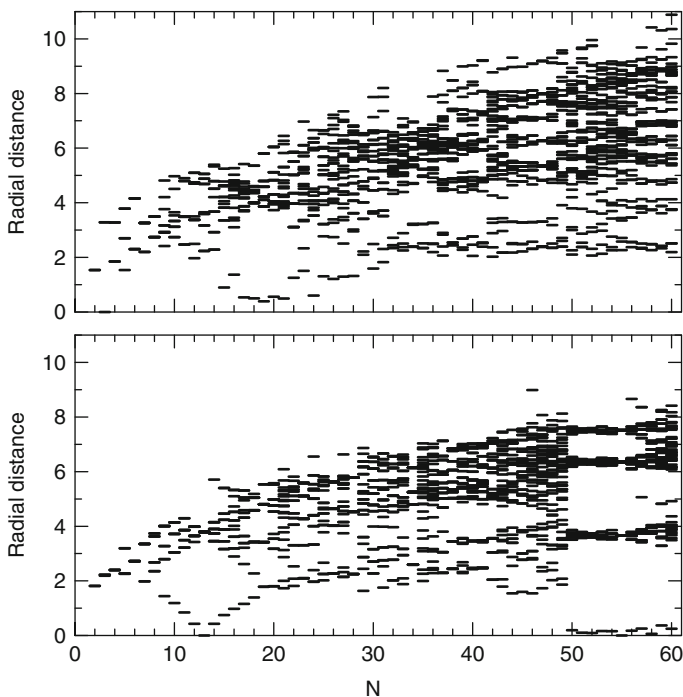
## Na and Au Clusters

As discussed in [▶ section “Only Electrons”](#), Na clusters may be considered as being the prototype for which the jellium model provides a good starting point. Therefore, it seems to be highly appropriate to start our discussion with considering this system but applying other theoretical approaches. Accordingly, we have studied the properties of  $\text{Na}_N$  clusters both using the EAM method of [▶ section “Only Nuclei”](#) and the DFTB method. In both cases, the total-energy methods were combined with unbiased structure-optimization methods (Tevekeliyska et al. 2010).

In [▶ Fig. 26-13](#) we show the resulting stability function and in [▶ Fig. 26-14](#) the radial distances of the atoms. The stability functions show only a marginal similarity and only the DFTB calculations find particularly stable clusters for sizes that agree with those of the mass abundance experiments and the jellium calculations (2, 8, 18, 20, 34, 40, 58, ...) (Knight et al. 1984). On the other hand, the radial distances indicate that the structures found in the EAM calculations are somewhat more symmetric than are those of the DFTB calculations. In fact, based on a shape analysis (not shown), we find that none of the DFTB structures can be considered as being roughly spherical, in marked contrast to the inherent assumptions behind the jellium calculations.



**■ Fig. 26-13**  
Stability function (in eV) as function of the size of the clusters from the DFTB (*upper part*) and the EAM (*lower part*) calculations

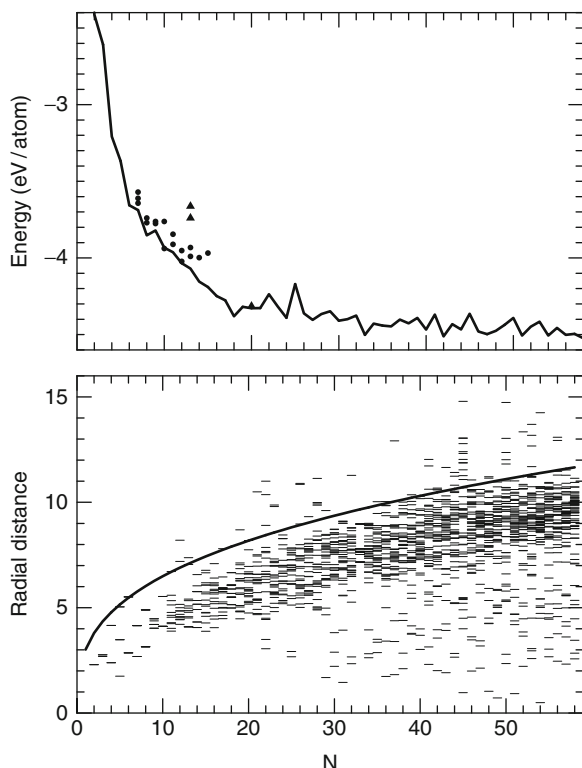


■ Fig. 26-14

Radial distances (in Å) for sodium clusters obtained with DFTB (*lower part*) and EAM (*upper part*) as a function of the number of atoms  $N$ . In each panel, a small horizontal line for a given  $N$  marks that at least one atom has that distance to the center of the cluster

Although gold often is considered as being a normal metal, it has remarkable bonding properties that manifest themselves clearly in nanosystems (see, e.g., Springborg 2009). Thus, gold is often found in situations with low coordinations. This is attributed to effects related to the electronic orbitals (although the precise role of various effects like  $sd$  hybridization, relativistic effects, the range of the atomic potential, etc., has not yet been clarified unambiguously) that are absent in the EAM. Therefore, that EAM calculations for gold clusters (Alamanova et al. 2006) led to too compact structures may not surprise.

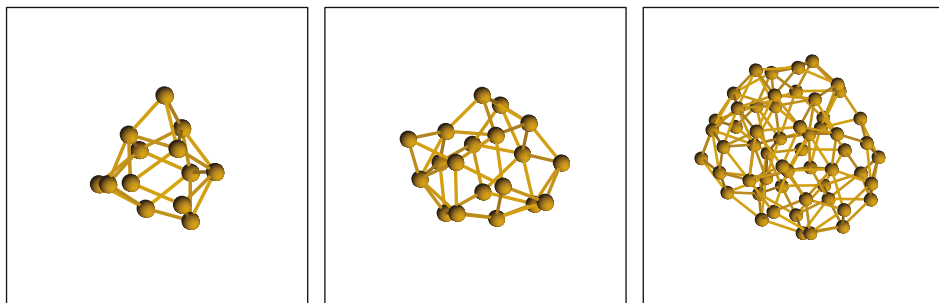
Instead, we used the DFTB method in combination with the genetic algorithms to study the properties of  $\text{Au}_N$  clusters with  $N$  up to 58 (Dong and Springborg 2007). The main findings are reproduced in ● Fig. 26-15. The total energy per atom is seen to have a strong size dependence until around 20 atoms after which it depends much weaker on the cluster size. It is known that small, neutral  $\text{Au}_N$  clusters are planar up to  $N$  somewhat above 10 (see, e.g., the discussion in Dong and Springborg 2007), although this is not found in the present calculations. On the other hand, as seen in the figure, the difference in the total energy between the planar and our nonplanar structures is small. This difference can be taken as an estimate of the accuracy of the present DFTB approach. Moreover, also the experimentally observed tetragonal  $\text{Au}_{20}$  structure is not found in our calculations, although it has a total energy that is very close to that of our optimized structure. On the other hand, as all other electronic-structure studies on  $\text{Au}_{13}$ , our calculations do not find the icosahedron to be the most stable structure.



■ Fig. 26-15

The upper part shows the variation in the total energy per atom (relative to that of the isolated atom) for the optimized  $Au_N$  clusters (solid curve) together with those of planar structures (dark circles) and those of icosahedral  $Au_{13}$  and tetragonal  $Au_{20}$  clusters (dark triangles). The lower part shows the radial distances as a function of cluster size, i.e., each small line represents (at least) one atom with that radial distance. The curve shows the radius of the spherical jellium with a density as in the crystal

From the radial distances of the  $Au_N$  clusters we see that they all are low symmetric. This can also be seen when comparing the (high-symmetric) structures of  $Ni_N$  clusters with those of  $Au_N$  clusters with the same number of atoms, i.e., when comparing [Figs. 26-4](#) and [26-16](#). Moreover, for  $10 \leq N \leq 20$  no atom has a small value for its radial distance, implying that these structures are shell-like (see also [Fig. 26-16](#)). Indeed the finding of such “golden cages” is in agreement with other studies. Finally, we add that when analyzing the coordination of the individual atoms we found that no atom has a coordination larger than 11, i.e., the value of 12 of crystalline fcc gold is not found even for the fairly large clusters of this study. This may be considered a further confirmation of the ability of gold atoms to exist in low-coordinated situations.



■ Fig. 26-16

The structures of the  $Au_N$  clusters with (from left to right)  $N = 13, 19,$  and  $55$

## HAIO Clusters

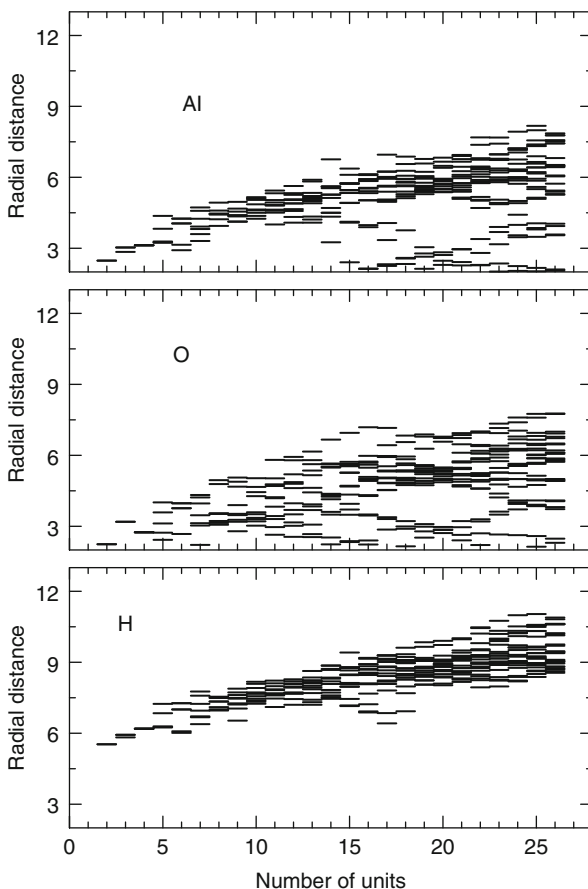
HAIO is a nanostructured material that can be used as substrate for deposition of other materials. However, little is known about the material itself, except that it is stoichiometric (i.e., it contains 1:1:1 mole fractions of H, Al, and O). From nuclear resonance and vibrational spectroscopy experiment some information can be obtained about the short-range arrangements of the atoms.

In a collaboration with members of one of the groups that synthesize this material we studied its properties using different theoretical methods (Dong et al. 2005). Genetic algorithms together with the DFTB method were used in an unbiased determination of isolated  $(HAIO)_n$  clusters with  $n \leq 26$ . Moreover, since the material is macroscopic and contains interacting nanostructures, we also studied the interactions between two of those optimized clusters using the DFTB approach. Finally, the predictions of the calculations were supported by parameter-free density-functional calculations on selected structures for clusters with  $n \leq 6$ .

At first, we show in ► Fig. 26-17 the radial distances for each atom type as a function of  $n$ . It is evident from this figure that the clusters consist of a core of aluminum and oxygen atoms covered by a shell of hydrogen atoms. A more careful inspection of the structures (not shown) reveals that for the Al-O core only heteroatomic (i.e., Al-O) and not homoatomic (Al-Al or O-O) bonds exist.

The results of the parameter-free density-functionals are in support for these structural findings. We considered in total 50 isomers of  $(HAIO)_n$  with  $n = 1, 2, 3, 4,$  and  $6$ . When analyzing the structures of those we found that none possessed O-O or H-H nearest neighbors and that it was relatively easy to identify Al-H, Al-O, and O-H bonds as being pairs with an interatomic distance smaller than 2.2, 2.5, and 1.5 Å, respectively. The Al-Al interatomic distances, on the other hand, showed a large spread and it was not possible readily to identify a cutoff distance below which the Al atoms could be considered as being bonded. In the subsequent analysis we, therefore, considered two extreme values, 2.5 and 4.1 Å.

Next we studied the total energy per unit as a function of number of A-B bonds per unit, with A and B being H, Al, and O. The results are shown in ► Fig. 26-18. The results are very scattered but it is possible to identify certain trends. First, the total energy decreases as the number of Al-O bonds increases. Second, a similar, but much weaker, trend can be identified for the number of Al-Al bonds (here we have used 4.1 Å as our cutoff value, but 2.5 Å gives very



■ Fig. 26-17

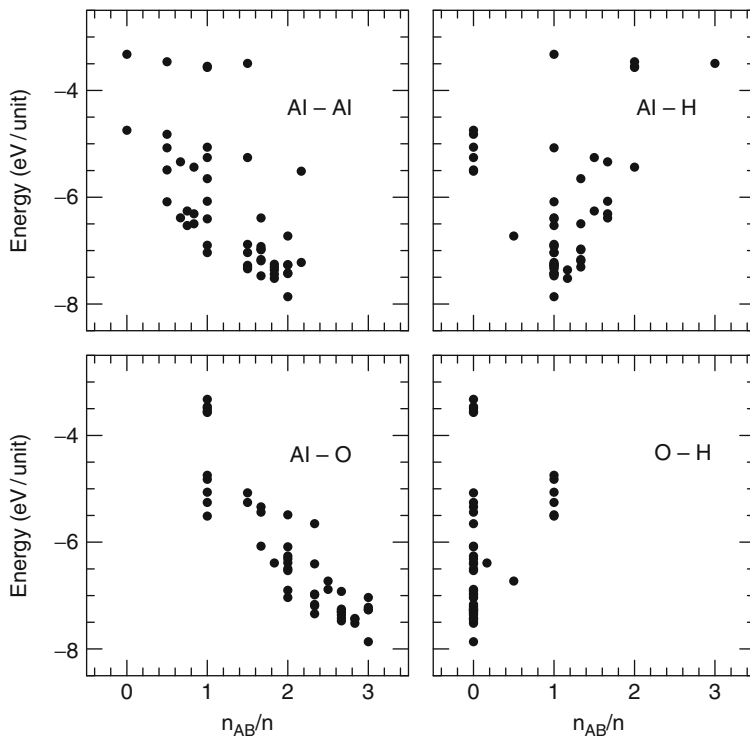
The radial distances (in a.u.) for Al, O, and H atoms, separately, as a function of the size of the cluster  $n$  for  $(\text{HAIO})_n$  clusters. In each panel, a small horizontal line shows that at least one atom of the corresponding type has that distance to the center of the cluster for a given value of  $n$

similar results). Third, there is a clear preference for structures with one Al–H bond per unit. These observations can be quantified by approximating the total energy of the various  $(\text{HAIO})_n$  isomers as

$$E_{\text{tot}} \simeq n \cdot E_0 + n_{\text{AlAl}} \cdot E_{\text{AlAl}} + n_{\text{AlO}} \cdot E_{\text{AlO}} + n_{\text{AlH}} \cdot E_{\text{AlH}} + n_{\text{OH}} \cdot E_{\text{OH}}. \quad (26.28)$$

A least-squares fit gave  $E_{\text{AlAl}} = -0.175 \text{ eV}$  ( $-0.122 \text{ eV}$ ),  $E_{\text{AlO}} = -1.000 \text{ eV}$  ( $-1.170 \text{ eV}$ ),  $E_{\text{AlH}} = 0.750 \text{ eV}$  ( $0.678 \text{ eV}$ ), and  $E_{\text{OH}} = 1.119 \text{ eV}$  ( $0.798 \text{ eV}$ ), when using  $4.1 \text{ \AA}$  ( $2.5 \text{ \AA}$ ) as cutoff distance for Al–Al bonds. These numbers show that Al–O bonds are strongly preferred and that when choosing between adding H to either Al or O, it is energetically preferred to create Al–H bonds.

Our theoretical findings that the H atoms prefer to stay outside an AlO core, which for larger clusters becomes increasingly difficult when requiring that the material is stoichiometric, suggest that stable structures of HAIO may occur for layers of HAIO. In order to study

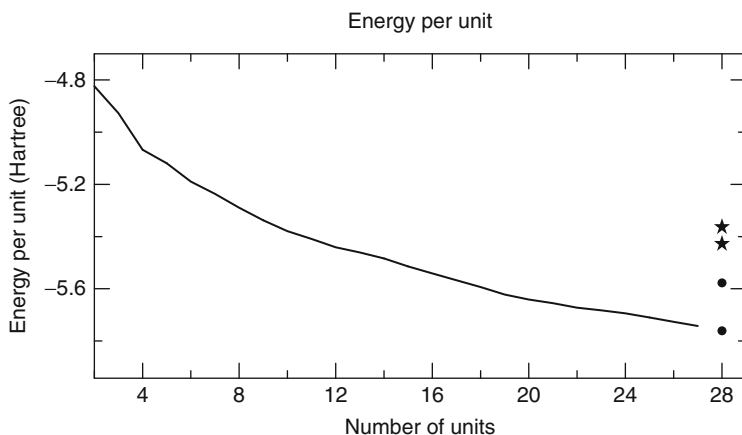


■ Fig. 26-18

Variation in the total energy per unit as function of the number of A-B bonds per unit. The results are from the parameter-free density-functional calculations for the  $(\text{HAIO})_n$  clusters with  $n = 1, 2, 3, 4, 6$  and the meaning of A and B is given in the panels

this proposal further we considered theoretically extended HAIO systems consisting of either one or two layers of HAIO. We add that these calculations ignore interlayer interactions that can be very important and that, therefore, may modify our conclusions significantly, when included. For a single layer of HAIO, one can imagine two highly symmetric cases, i.e., one where all H atoms are on the one side of the layer, and one where every second H atom is above and every second H atom below the AlO layer. For the case that all H atoms are on the same side of the layer, the Al and O atoms form a layer with bond lengths of 3.33 a.u. = 1.76 Å and 3.34 a.u. = 1.77 Å. Moreover, the hydrogen atoms are sitting on the outside of the layer bonded to the Al atoms with Al-H bond lengths of 3.21 a.u. = 1.70 Å. The Al-O-Al bond angles are 85–86° and 147–152°. Remarkably different things occur when the H atoms are sitting alternating on the two sides of the single AlO layer. Then we found that the layer split into several small parts all with the same kind of structure, i.e., the H atoms are binding to the Al atoms with Al-H bond lengths around 3.08 a.u. = 1.63 Å, whereas the Al-O bond lengths are around 3.40 a.u. = 1.80 Å. For the case of two layers of HAIO we studied two cases, i.e., either the Al atoms of one layer were placed on top of the O atoms of the other layer, or they were placed on top of the Al atoms of the other layer. It turned out that the first situation was much more stable than the second one, which may not surprise, and in the second case we found that the system breaks into small parts.



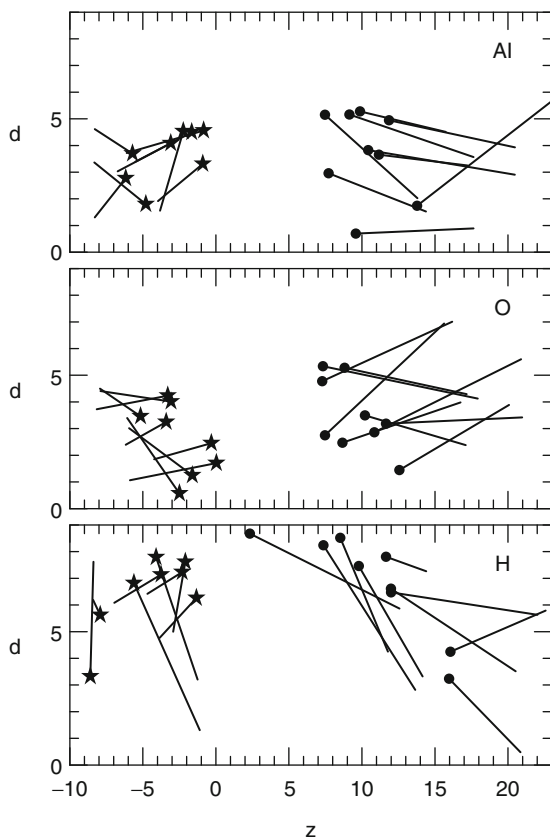


■ Fig. 26-19

Variation in energy per unit for isolated clusters and for the layers of HAIO. The results for the layers are shown to the right with the one-layer results marked with stars (here, the lowest total energy is for the case that the H atoms are on the same side, whereas they are alternating on the two different sides in the other case) and the two-layer results marked with circles (here, the lowest total energy is for the case that Al–O bonds form the bonds between the layers). The energy is given in Hartrees (1 Hartree  $\approx$  27.21 eV)

Finally, in [Fig. 26-19](#) we show the energy per unit for the finite clusters in comparison with that for the layers. It is remarkable that the two-layer structure is not significantly more stable than the finite clusters. We believe that the systems prefer to have H atoms on some surface. However, since the surface area scales as  $n^{2/3}$ , the available area per H atom scales like  $n^{-1/3}$ , meaning that above a certain critical size, the finite  $(\text{HAIO})_n$  clusters will be less stable simply due to too little space for the H atoms on the surface. This effect is not found for the layers that per construction are infinite. But it suggests that there is a competition between clusters of HAIO and layers of HAIO, which may explain why different synthesis routes lead to different materials. It is not possible to determine directly the critical size of the finite  $(\text{HAIO})_n$  clusters above which they become unstable, but our results suggest that this size may be comparable to the largest clusters of the present study.

As mentioned above, HAIO is a nanostructured material, so that the individual clusters may interact with each other. In this context it is an interesting issue whether the H atoms will try to remain outside a central part, as we have observed for the individual, isolated clusters. We decided, therefore, to study the interaction between two clusters by putting two of the previously optimized clusters together. This was done as follows. We placed two clusters of  $n_1$  and  $n_2$  units so close to each other that they would interact. The initial structures were those of the isolated  $(\text{HAIO})_{n_1}$  and  $(\text{HAIO})_{n_2}$  clusters, and we considered very many relative orientations of the two clusters out of which we chose the one that led to the lowest total energy after structural relaxation. For the case that the two clusters were brought so close that they interact, before the combined cluster was relaxed, it was found that the hydrogen atoms are placed between the two cores of AlO, but after the combined cluster was relaxed, the hydrogen atoms are only sitting on the surface of the combined cluster. This supports our consensus that clusters with hydrogen sitting on the surface of the clusters are most stable.



■ Fig. 26-20

A graphical illustration of the structural relaxations of bringing the  $n_1 = 8$  (left part) and  $n_2 = 9$  (right part) HAIO clusters together. Shown are the relaxations in a cylindrical coordinate system with  $z$  and  $d$  being the position along the cylindrical axis and distance from it, respectively, both in a.u. The three panels show the displacements of the Al, O, and H atoms, individually. For details about the presentation, see the text

This is illustrated in [Fig. 26-20](#) that has been obtained as follows. We consider the case of  $n_1 = 8$  and  $n_2 = 9$  units before and after relaxation. In each case (i.e., before and after relaxation) we calculate the center of the two parts according to [Eq. 26.22](#). The line joining these two centers defines the  $z$  axis in a cylindrical coordinate system with  $z = 0$  being the midpoint between the two centers. Subsequently, we superpose the two coordinate systems in one figure and show the initial and final values of  $z$  and the distance to the  $z$  axis (denoted  $d$ ) for each atom separately by joining these points with a straight line. Finally, we depict these lines for each type of atom individually. The stars mark the final positions of the  $n_1 = 8$  system whereas the closed circles mark the final positions of the  $n_2 = 9$  system. In particular the H atoms tend to increase  $d$  upon relaxation, i.e., to move away from the region between the two clusters. On the other hand, first of all the O atoms but also to a lesser extent the Al atoms are seeking to fill out the space between the two clusters when they are combined.

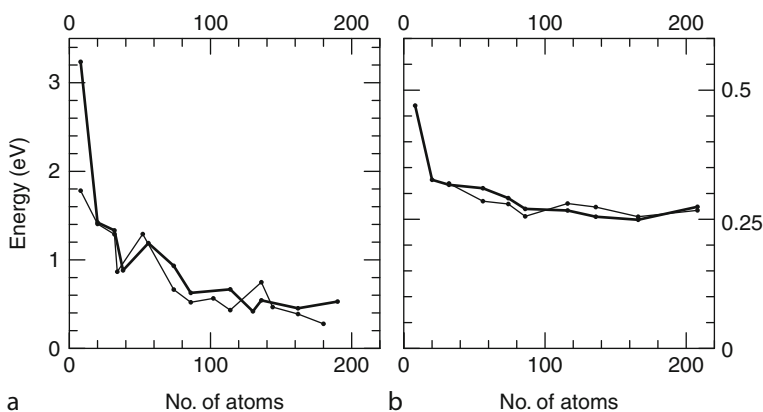
## AB Semiconductor Clusters

Semiconductors are interesting materials first of all because of their electronic properties. By modifying the material it is partly possible to vary these properties in a controllable way, and further possibilities are obtained by considering semiconductor nanoparticles. When the spatial extension of the clusters becomes comparable with that of an exciton, the electronic and optical properties of the semiconductor will depend markedly on the cluster size.

An important class of semiconductors are the II–VI and III–V semiconductors. For those an additional, relevant (and interesting) issue is that the macroscopic, crystalline material may exist in (at least) two structures that are energetically very close, i.e., the zincblende and the wurtzite structure (Yeh et al. 1992a, b). Accordingly, it is likely that for the finite-sized clusters, the energetic ordering of those two structures may change. To access this issue we have studied finite clusters of a larger range of II–VI and III–V semiconductor nanoparticles (Asaduzzaman and Springborg 2006; Goswami et al. 2006; Joswig et al. 2000, 2002, 2003; Roy and Springborg 2003, 2005; Sarkar and Springborg 2003; Sarkar et al. 2005; ur Rehman et al. 2011). We have used the DFTB method that includes electronic degrees of freedom and not attempted to optimize the structure completely. Instead, starting from the infinite, periodic crystals we have cut out a spherical part that subsequently was allowed to relax to the structure of the closest local total-energy minimum. In most cases we considered stoichiometric clusters that were obtained by placing the center of the above-mentioned sphere on the midpoint of a nearest-neighbor bond.

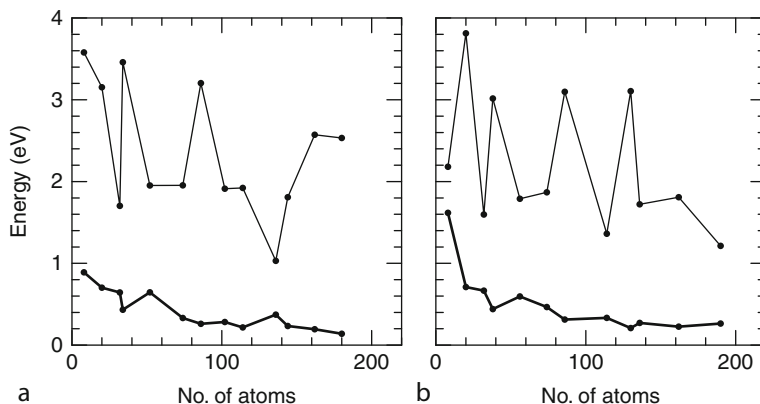
In **Fig. 26-21** we show representative examples for the relative total energy of clusters derived from the two different crystal structures. It is clear that the relative total energy depends critically both on size and on the material of the clusters. This is in agreement with experimental observations for nanoparticles of the same material but different sizes (see, e.g., Weller and Eychemüller 1996). Moreover, although the total energy does show an overall decreasing behavior as a function of size of the cluster, it is also structured.

There is an interesting correlation between the variation of the total energy and the energy gap between the highest occupied (HOMO) and lowest unoccupied (LUMO) molecular orbital.



**Fig. 26-21**

The variation in total energy per atom pair for stoichiometric (a) CdS and; (b) CdSe clusters for (*thick curves*) zincblende- and (*thin curves*) wurtzite-derived clusters



■ Fig. 26-22

Variation in the total energy per atom pair (*thick curves*) and band gap (*thin curves*) for CdS clusters with (a) zincblende- and; (b) wurtzite-derived structures as a function of the total number of atoms in the cluster

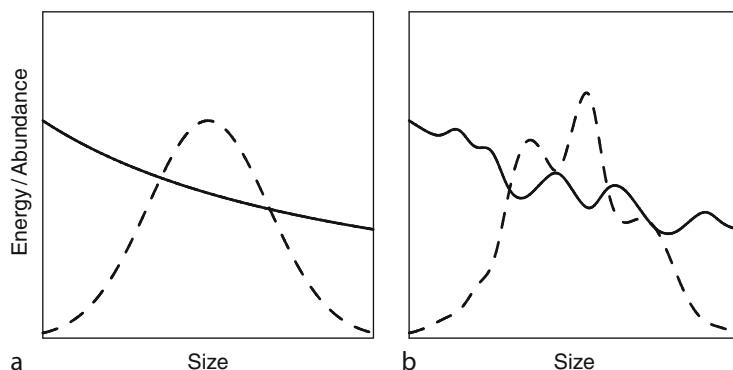
In ► Fig. 26-22 we illustrate this for a single example, i.e., CdS clusters. Similar results are obtained for the other systems. The figure demonstrates that high stability coincides with a high energy gap, which may be interpreted in terms of the so-called hard-and-soft-acids-and-bases (HSAB) principle (Pearson 1997). Moreover, a more detailed analysis of the frontier orbitals gives that for the less stable structures, i.e., the ones with a small HOMO–LUMO gap, at least one of the HOMO and LUMO orbitals is localized to the surface region. Because of these surface states, less stable clusters are particularly reactive.

From these results we obtain also an example of how strongly and irregularly the properties can depend on the size of the clusters. For  $\text{Cd}_n\text{S}_n$  clusters we find a HOMO–LUMO gap of around 1.6 eV for  $n = 16$ , which increases to 3.2 eV for  $n = 17$  (Joswig et al. 2003). When analyzing the structures of those two, this difference can be explained: for  $n = 16$  the cluster contains a number of single-coordinated atoms, making it less stable, whereas no such atoms are found for  $n = 17$ .

Finally, the fact that at least one of the frontier orbitals is localized to the surface is in agreement with experimental studies of the recombination of holes and electrons in such clusters (Lifshitz et al. 1998).

The results above have two important implications. First, in experimental studies it is often assumed (cf. ► Fig. 26-23) that one obtains a more or less narrow size distribution that is very regular as a function of size. Moreover, the size of the clusters is often estimated through the energy of the optical transition that is assumed to be a monotonous function of size. However, our results give that the total energy is structured as a function of size, suggesting that the size distribution also will be structured, and also that the energy for optical transitions is less regular as a function of cluster size, although a general decrease as a function of increasing cluster size can be identified.

Secondly, since the stability of the clusters is strongly dependent on the presence/absence of low-coordinated atoms on the surface, it should be possible to stabilize the clusters through properly chosen surfactants or by modifying the surface in other ways (Frenzel et al. 2005). For our stoichiometric AB clusters, the outermost atoms are formed to equal parts by A and by B atoms. Considering nonstoichiometric clusters constructed, e.g., as a spherical cut-out of



■ Fig. 26-23

Schematic presentation of the variation in the total energy per atom (*solid curve*) as a function of size of the cluster together with the size distribution (*dashed curve*) (a) as it usually is assumed together with; (b) a modification as it may be in reality. The solid curve may also represent the optical absorption threshold as a function of cluster size

the crystal with the center at an atomic position, the surface will contain exclusively one type of atoms. In one study, on InP clusters (Roy and Springborg 2003), we considered this case and did indeed observe a strong dependence of the properties on the surface, although the properties did not only depend on the type of the outermost atoms. A further study (Roy and Springborg 2005) demonstrated that surfactants could modify the electronic properties of the clusters, leading in most, but not all, cases to a larger HOMO–LUMO gap.

Alternatively, one may obtain more stable structures by considering the so-called core/shell nanoparticles, which are systems containing a core of one material coated by a shell of another. We studied such systems with the two materials being either CdS and CdSe or Si and Ge (Asaduzzaman and Springborg 2006; Sarkar et al. 2005) and found, besides a saturation of dangling bonds on the core part of the nanoparticle, that new properties may emerge from such systems. This includes that in some few cases the HOMO and LUMO are localized to the two different materials, making a charge separation upon optical excitation possible. Furthermore, the more stable systems were obtained when the shell material was the one with the lowest surface energy.

## Metcars




With the last example of this presentation we shall discuss the systems that initially led us to start the theoretical work on unbiased structure optimization for nanoparticles.

In the beginning of the 1990s, the group around Castleman in Pennsylvania produced metal-containing carbon clusters  $M_mC_n$ . In mass abundance spectra with M being Ti they observed a peak for  $(m, n) = (8, 12)$  (Guo et al. 1992), suggesting that this cluster was particularly stable. They proposed a cage-like structure of cubic  $T_h$  symmetry with 12 five-membered rings, each containing two metal and three carbon atoms. Thus, the topology is as that of the smallest possible fullerene molecule  $C_{20}$  but containing metal atoms. An alternative description of the structure is to consider it as formed by a cube of the eight metal atoms. The 12 carbon atoms

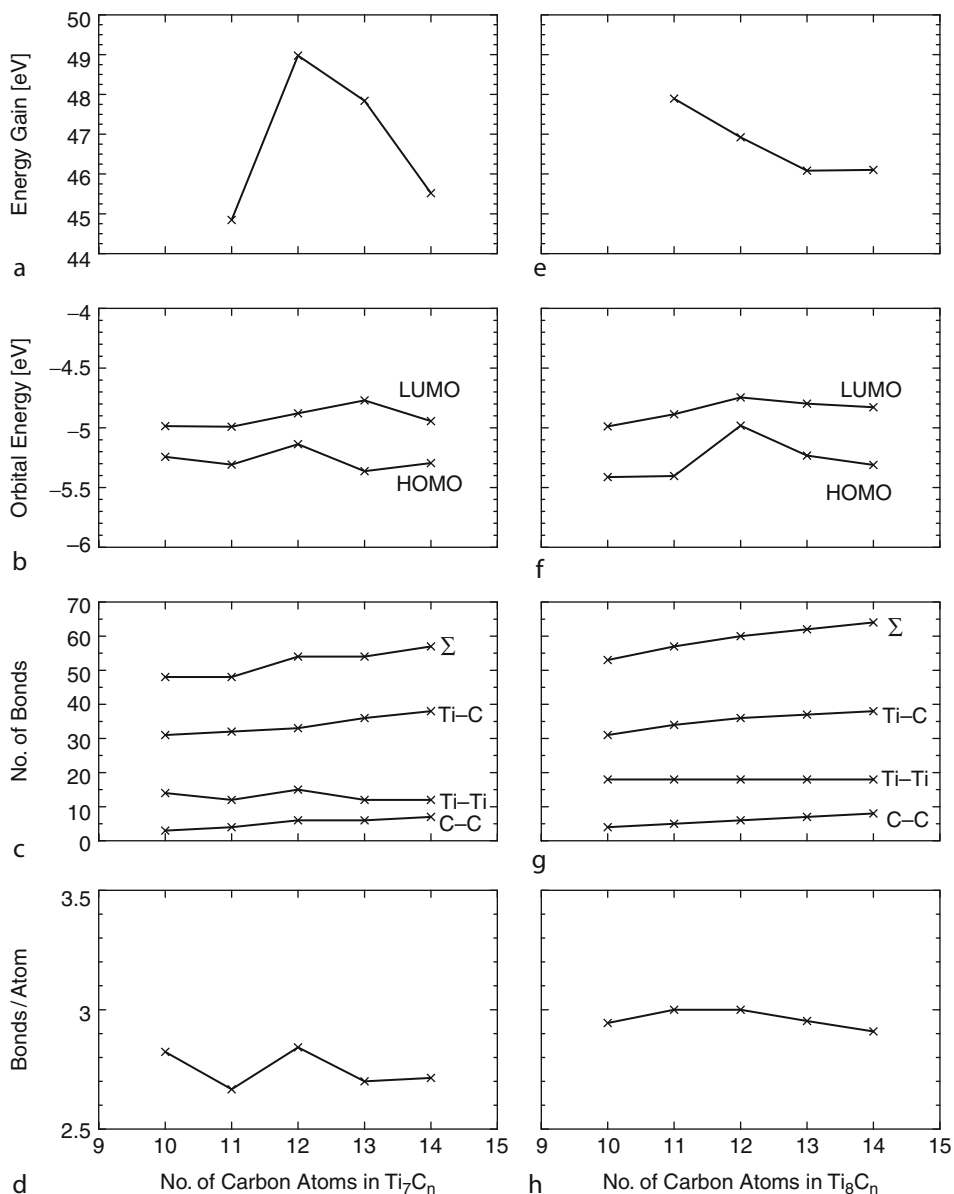
form six  $C_2$  units that are placed symmetrically above the sides of the cube with the C–C bonds parallel to the edges. Later, theoretical studies – first of all by Dance (1992) – suggested that the structure instead had tetragonal  $T_d$  symmetry. Compared with the  $T_h$  symmetry, the  $C_2$  dimers are for the  $T_d$  symmetry lying parallel to the diagonals of the six sides of the cube of the eight metal atoms and, in addition, the cube becomes somewhat distorted. First recently, theoretical and experimental studies agree that the tetragonal structure is the correct one (see, e.g., Rohmer et al. 2000). In the meantime it has been found that for other metals also (e.g., Hf, Zr, V) those so-called metallocarbohedrenes or metcars can be formed, and even metcars with more different types of metals have been produced. However, whether they occur in significant amounts depend strongly on the experimental conditions, suggesting that kinetic effects play a significant role in their production.

In order to study the properties of these Ti-based clusters further, the group around Ganteför in Konstanz, Germany, decided to study a whole class of  $Ti_mC_n$  clusters with different values of  $(m, n)$  centered around  $(m, n) = (8, 12)$  (Blessing 1998). Using two different sources, Ti and C atoms were produced that subsequently were allowed to form the clusters mentioned above. After ionization, a magnetic field could be used to mass-separate the clusters and, finally, photoelectron spectra could be recorded for these mass-selected clusters. Accompanying theoretical studies would then be very useful as a support for the interpretation of the experimental results.

As one of the clusters of the experiments, let us choose  $Ti_6C_{10}$ , i.e.,  $(m, n) = (6, 10)$ , whose structure is absolutely unknown. One suggestion could be to assume that it has a structure that can be formed by removing two carbon and two titanium atoms from the larger  $(m, n) = (8, 12)$  cluster, but the first question is then: which four atoms shall be removed? Starting with the two proposed structures (i.e., those of  $T_h$  and  $T_d$  symmetry) for the  $(m, n) = (8, 12)$  cluster mentioned above we tried this strategy but obtained a new structure in each attempt. The simplest approach would then be to choose the structure of the lowest total energy. However, it has to be remembered that the experiment is performed in a completely different way: instead of starting with the larger  $(m, n) = (8, 12)$  cluster and from that removing some atoms, the  $(m, n) = (6, 10)$  cluster is formed from essentially isolated atoms and, therefore, it is not at all given that its structure has any resemblance to that of the  $(m, n) = (8, 12)$  cluster.

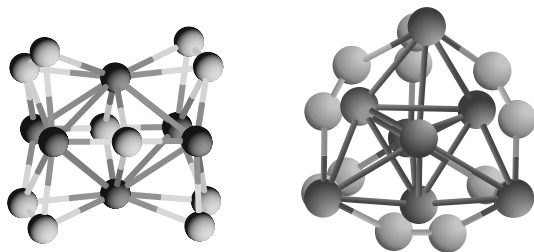
Therefore, in order to obtain unbiased information on the structures of the different  $Ti_mC_n$  clusters we started applying the genetic algorithms that were discussed earlier in this section together with the DFTB method and applied the approach to the metcars (Joswig and Springborg 2008; Joswig et al. 2001). In  Fig. 26-24 some of the results are summarized. This figure shows the total energies for two series of  $Ti_mC_n$  metcars, i.e., with  $m = 7, 8$  and  $n = 10-14$ . We have defined an energy gain, for clusters with same  $m$ , as the difference in the total energy of  $Ti_mC_{n-1}$  and  $Ti_mC_n$ . For  $m = 8$ , experiments found the  $Ti_8C_{12}$  metcar to be a particularly stable cluster. However, our calculations do not find a specially high energy gain for this cluster, although they do for the  $Ti_7C_{12}$  cluster. Also the HOMO-LUMO gap does not indicate a high stability for the  $Ti_8C_{12}$  metcar. Actually, it has the smallest gap in the  $m = 8$  series (cf.  Fig. 26-24f). Furthermore, there is no evidence that the number of bonds is related to the stability of the clusters, as also indicated by the results in  Fig. 26-24. In total, the structural properties give no hints to the experimentally observed special stability of the  $Ti_8C_{12}$  metcar.

Instead, one may suggest that effects (for instance, kinetic effects) that are beyond the calculational approach are important. An experimental support for this suggestion can be found in the work of van Heijnsbergen et al. (1999). These authors found that the mass abundance spectra depend critically on experimental parameters so that in one experiment the  $Ti_8C_{12}$



■ Fig. 26-24

(a), (e) Energy gain; (b), (f) HOMO and LUMO orbital energies; (c), (g) number of C-C, Ti-Ti, Ti-C bonds and their total number, and; (d), (h) total number of bonds divided by total number of atoms for (left)  $Ti_7C_n$  and (right)  $Ti_8C_n$  as functions of  $n$



■ Fig. 26-25

Optimized structure of (right)  $\text{Ti}_6\text{C}_{10}$  and (left)  $\text{Ti}_8\text{C}_{12}$ . Light (dark) spheres represent C (Ti) atoms

metcar showed a large abundance, whereas in another it hardly occurred whereas a  $\text{Ti}_{14}\text{C}_{13}$  cluster (that has a structure similar to a part of the rocksalt crystal, cf. Joswig and Springborg 2008) was found in large abundance.

Finally, we mention that exactly the  $\text{Ti}_6\text{C}_{10}$  metcar that we discussed above was found in our calculations to be particularly stable and of special, high symmetry, see [Fig. 26-25](#). However, so far it has not been discussed in detail in connection with experimental studies.

## Conclusions

---

In this overview we have presented various, typical results from our theoretical studies on structural and electronic properties of clusters and colloids. We have put the main emphasis on presenting the principles behind our approaches and less on the discussion of the different systems, separately. It shall be added that there are many other, related studies by others, but that we have here chosen to focus on our own work.

The major challenge related to studies as those we have presented here is the complexity of the calculations due to the fairly large size combined with an often low symmetry. In addition, when aiming at extracting trends, as we have been, one needs to study not only one cluster size of a given material but a whole range, adding to the computational demands.

Moreover, the fact that there is no standard method that can be used in identifying unambiguously the structure of the lowest total energy for a given system means that one has to apply more or less intelligent methods in the structure optimization and, furthermore, that there never will be any guarantee that the structure of the lowest total energy indeed is identified. Experience has shown that specially developed methods for unbiased structure optimization are the most efficient ones, whereas others, e.g., molecular-dynamics simulations and random searches, often perform considerably worse. In this overview we have presented a few intelligent methods, including genetic algorithms, basin-hopping methods, and our own Aufbau/Abbau method. Alternatively, one may also consider only certain types of structures when aiming at studying special effects. The latter we illustrated through our study on AB semiconductor particles for which an interesting issue is the relative stability of cluster structures that can be derived from two different crystal structures (in this case, the zinblende and wurtzite structures).

But even when applying such intelligent structure-optimization methods one often has to perform maybe even several millions of total-energy calculations for a given cluster. Therefore, it is often necessary to use approximate total-energy methods, that then shall be chosen carefully according to the properties of the system of interest. In this presentation we have discussed



embedded-atom methods and Gupta potentials and similar approaches as useful methods for metallic systems with delocalized electrons, the DFTB method for systems with directional, covalent bonds, and the jellium model, also for metallic systems with delocalized electrons. Due to the approximations inherent in such approaches it is always important to access their accuracy through comparison with results of more accurate calculations or with other studies on similar systems.

Finally, we placed much emphasis in presenting various descriptors that we have developed in order to be able to extract general chemical or physical information from the, often enormous amount of, information from the calculations. This included descriptors for analyzing stability, shape, spatial distribution of atoms and orbitals, and structural similarity.

## Acknowledgment

The work that has been presented in this overview would not have been possible without the active participation of a number of persons, including (in alphabetic order) Denitsa Alamanova, Abu Asaduzzaman, Markus Burkhard, Yi Dong, Valeri G. Grigoryan, Elisaveta Hristova (née Kasabova), Jan-Ole Joswig, Sudip Roy, Pranab Sarkar, Sashi Satpathy, Gotthard Seifert, Violina Spurk (née Tevekeliyska), and Michael Veith. Moreover, we have benefited from financial support through the German Research Council (DFG).

## References

- Alamanova, D., Grigoryan, V. G., & Springborg, M. (2006). Theoretical study of structure and energetics of gold clusters with the EAM method. *Zeitschrift für Physikalische Chemie*, 220, 811–829.
- Alamanova, D., Springborg, M., & Grigoryan, V. G. (2007). Theoretical study of the structure and energetics of silver clusters. *The Journal of Physical Chemistry C*, 111, 12577–12587.
- Alamanova, D., Grigoryan, V. G., & Springborg, M. (2008). Deposition of copper clusters on the Cu(111) surface. *Surface Science*, 602, 1413–1422.
- Asaduzzaman, A. Md., & Springborg, M. (2006). Structural and electronic properties of Si/Ge nanoparticles. *Physical Review B*, 74, 165406.
- Baletto, F., & Ferrando, R. (2005). Structural properties of nanoclusters: Energetics, thermodynamic, and kinetic effects. *Reviews of Modern Physics*, 77, 371–423.
- Blessing, N. (1998). *Diplomarbeit*. University of Konstanz.
- Brack, M. (1993). The physics of simple metal clusters: Self-consistent jellium model and semiclassical approaches. *Reviews of Modern Physics*, 65, 677–732.
- Cleri, F., & Rosato, V. (1993). Tight-binding potentials for transition metals and alloys. *Physical Review B*, 48, 22–33.
- Dance, I. G. (1992). Geometric and electronic structures of [Ti<sub>8</sub>C<sub>12</sub>]: Analogies with C<sub>60</sub>. *Journal of the Chemical Society, Chemical Communications*, 1992, 1779–1780.
- Daw, M. S., & Baskes, M. I. (1983). Semiempirical, quantum mechanical calculation of Hydrogen embrittlement in metals. *Physical Review Letters*, 50, 1285–1288.
- Daw, M. S., & Baskes, M. I. (1984). Embedded-atom method: Derivation and application to impurities, surfaces, and other defects in metals. *Physical Review B*, 29, 6443–6453.
- Daw, M. S., Foiles, S. M., & Baskes, M. I. (1993). The embedded-atom method: A review of theory and applications. *Materials Science Reports*, 9, 251–310.
- de Heer, W. A. (1993). The physics of simple metal clusters: Experimental aspects and simple models. *Reviews of Modern Physics*, 65, 611–676.
- Dong, Y., Burkhardt, M., Veith, M., & Springborg, M. (2005). Electronic and structural properties of nanostructured HAIO. *The Journal of Physical Chemistry B*, 109, 22820–22829.

- Dong, Y., & Springborg, M. (2007). Unbiased determination of structural and electronic properties of gold clusters with up to 58 atoms. *The Journal of Physical Chemistry C*, 111, 12528–12535.
- Ferrando, R., Jellinek, J., & Johnston, R. L. (2008). Nanoalloys: From theory to applications of alloy clusters and nanoparticles. *Chemical Reviews*, 108, 846–910.
- Finnis, M. W., & Sinclair, J. E. (1984). A simple empirical  $N$ -body potential for transition metals. *Philosophical Magazine A*, 50, 45–55.
- Foiles, S. M., Daw, M. S., & Baskes, M. I. (1986). Embedded-atom-method functions for the fcc metals Cu, Ag, Au, Ni, Pd, Pt, and their alloys. *Physical Review B*, 33, 7983–7991.
- Frenzel, J., Joswig, J.-O., Sarkar, P., Seifert, G., & Springborg, M. (2005). The effects of organisation, embedding and surfactants on the properties of Cadmium Chalcogenide (CdS, CdSe and CdS/CdSe) semiconductor nanoparticles. *European Journal of Inorganic Chemistry*, 2005, 3585–3596.
- Goldberg, D. E. (1989). Genetic algorithms in search, optimization and machine learning. Reading: Addison-Wesley.
- Goswami, B., Pal, S., Sarkar, P., Seifert, G., & Springborg, M. (2006). Study of structural, electronic, and optical properties of  $Zn_mSe_n$  clusters. *Physical Review B*, 73, 205312.
- Grigoryan, V. G., Alamanova, D., & Springborg, M. (2006). Structure and energetics of  $Cu_N$  clusters with ( $2 \leq N \leq 150$ ): An embedded-atom-method study. *Physical Review B*, 73, 115415.
- Grigoryan, V. G., & Springborg, M. (2001). A theoretical study of the structure of Ni clusters ( $Ni_N$ ). *Physical Chemistry Chemical Physics*, 3, 5125–5129.
- Grigoryan, V. G., & Springborg, M. (2003). Structure and energetics of Ni clusters with up to 150 Atoms. *Chemical Physics Letters*, 375, 219–226.
- Grigoryan, V. G., & Springborg, M. (2004). Structural and energetic properties of nickel clusters:  $2 \leq N \leq 150$ . *Physical Review B*, 70, 205415.
- Guo, B. C., Kearns, K. P., & Castleman, A. W., Jr. (1992).  $Ti_8C_{12}^+$ -metallo-carbohedrenes: A new class of molecular clusters? *Science*, 255, 1411–1413.
- Gupta, R. P. (1981). Lattice relaxation at a metal surface. *Physical Review B*, 23, 6265–6270.
- Holland, J. H. (1975). *Adaption in natural algorithms and artificial systems*. Ann Arbor: University of Michigan Press.
- Hohenberg, P., & Kohn, W. (1964). Inhomogeneous electron gas. *Physical Review*, 136, B864–B871.
- Hristova, E., Dong, Y., Grigoryan, V. G., & Springborg, M. (2008a). Structural and energetic properties of Ni-Cu bimetallic clusters. *The Journal of Physical Chemistry A*, 112, 7905–7915.
- Hristova, E., Grigoryan, V. G., & Springborg, M. (2008b). Structure and energetics of equiatomic K-Cs and Rb-Cs binary clusters. *Journal of Chemical Physics*, 128, 244513.
- Hristova, E., Grigoryan, V. G., & Springborg, M. (2009a). Theoretical study on the structural properties of Alkali-metal heteroclusters. *The European Physical Journal D*, 52, 35–38.
- Hristova, E., Grigoryan, V. G., & Springborg, M. (2009b). Structure and stability of Ag clusters on Ag (111) and Ni (111) surfaces. *Surface Science*, 603, 3339–3345.
- Jellinek, J., & Krissinel, E. B. (1996).  $Ni_nAl_m$  alloy clusters: Analysis of structural forms and their energy ordering. *Chemical Physics Letters*, 258, 283–292.
- Joswig, J.-O., & Springborg, M. (2003). A genetic-algorithms search for global minima of aluminum clusters using a Sutton-Chen potential. *Physical Review B*, 68, 085408.
- Joswig, J.-O., & Springborg, M. (2007). Size-dependent structural and electronic properties of  $Ti_n$  clusters ( $n \leq 100$ ). *Journal of Physics: Condensed Matter*, 19, 106207.
- Joswig, J.-O., & Springborg, M. (2008). The influence of  $C_2$  dimers on the stability of  $Ti_mC_n$  metcar clusters. *Journal of Chemical Physics*, 129, 134311.
- Joswig, J.-O., Springborg, M., & Seifert, G. (2000). Structural and electronic properties of Cadmium Sulfide clusters. *The Journal of Physical Chemistry B*, 104, 2617–2622.
- Joswig, J.-O., Springborg, M., & Seifert, G. (2001). Structural and electronic properties of small Titanium-Carbon clusters (metcars). *Physical Chemistry Chemical Physics*, 3, 5130–5134.
- Joswig, J.-O., Roy, S., Sarkar, P., & Springborg, M. (2002). Stability and band gap of semiconductor clusters. *Chemical Physics Letters*, 365, 75–81.
- Joswig, J.-O., Seifert, G., Niehaus, T. A., & Springborg, M. (2003). Optical properties of Cadmium Sulfide clusters. *The Journal of Physical Chemistry B*, 107, 2897–2902.
- Kasabova, E., Alamanova, D., Springborg, M., & Grigoryan, V. G. (2007). Deposition of  $Ni_{13}$  and  $Cu_{13}$  clusters on Ni(111) and Cu(111) surfaces. *The European Physical Journal D*, 19, 425–431.
- Knight, W. D., Clemenger, K., de Heer, W. A., Saunders, W. A., Chou, M. Y., & Cohen, M. L. (1984). Electronic shell structure and abundances of Sodium clusters. *Physical Review Letters*, 52, 2141–2143.

- Kohn, W., & Sham, L. J. (1965). Self-consistent equations including exchange and correlation effects. *Physical Review*, *140*, A1133–A1138.
- Li, Z., & Scheraga, H. A. (1987). Monte Carlo-minimization approach to the multiple-minima problem in protein folding. *Proceedings of the National Academy of Sciences of the United States of America*, *84*, 6611–6615.
- Lifshitz, E., Dag, I., Litvin, I., Hodes, G., Gorer, S., Reisfeld, R., Zelner, M., Minti, H. (1998). Optical properties of CdSe nanoparticle films prepared by chemical deposition and Sol-Gel methods. *Chemical Physics Letters*, *288*, 188–196.
- Lloyd, S. (2002). Computational capacity of the universe. *Physical Review Letters*, *88*, 237901.
- Lloyd, L. D., Johnston, R. L., Salhi, S., & Wilson, N. T. (2004). Theoretical investigation of isomer stability in Platinum-Palladium nanoalloy clusters. *Journal of Materials Chemistry*, *14*, 1691–1704.
- Parks, E. K., Nieman, G. C., Kerns, K. P., & Riley, S. J. (1997). Reactions of Ni<sub>38</sub> with N<sub>2</sub>, H<sub>2</sub>, and CO: cluster structure and adsorbate binding sites. *Journal of Chemical Physics*, *107*, 1861–1871.
- Parks, E. K., Kerns, K. P., & Riley, S. J. (1998). The structure of Ni<sub>39</sub>. *Journal of Chemical Physics*, *109*, 10207–10216.
- Parks, E. K., Kerns, K. P., & Riley, S. J. (2001). The structure of Ni<sub>46</sub>, Ni<sub>47</sub>, and Ni<sub>48</sub>. *Journal of Chemical Physics*, *114*, 2228–2236.
- Pearson, R. G. (1997). *Chemical hardness*. Weinheim: Wiley-VCH.
- Porezag, D., Frauenheim, Th., Köhler, Th., Seifert, G., & Kaschner, R. (1995). Construction of tight-binding-like potentials on the basis of density-functional theory. *Physical Review B*, *51*, 12947–12957.
- Rohmer, M. M., Bénard, M., & Poblet, J. M. (2000). Structure, reactivity, and growth pathways of metallocarbohedrenes M<sub>8</sub>C<sub>12</sub> and transition metal/carbon clusters and nanocrystals: A challenge to computational chemistry. *Chemical Reviews*, *100*, 495–541.
- Roy, S., & Springborg, M. (2003). A theoretical study of structural and electronic properties of naked stoichiometric and non-stoichiometric Indium Phosphide clusters. *The Journal of Physical Chemistry B*, *107*, 2771–2779.
- Roy, S., & Springborg, M. (2005). Theoretical investigation of the influence of ligands on structural and electronic properties of Indium Phosphide clusters. *The Journal of Physical Chemistry A*, *109*, 1324–1329.
- Sarkar P., & Springborg, M. (2003). Density-functional study of size-dependent properties of Cd<sub>m</sub>Se<sub>n</sub> clusters. *Physical Review B*, *68*, 235409.
- Sarkar, P., Springborg, M., & Seifert, G. (2005). A theoretical study of the structural and electronic properties of Cd/Se and CdS/CdSe core/shell nanoparticles. *Chemical Physics Letters*, *405*, 103–107.
- Seifert, G., Porezag, D., & Frauenheim, Th. (1996). Calculations of molecules, clusters, and solids with a simplified LCAO-DFT-LDA scheme. *International Journal of Quantum Chemistry*, *58*, 185–192.
- Seifert, G., & Schmidt, R. (1992). Molecular dynamics and trajectory calculations: The application of an LCAO-LDA scheme for simulations of cluster-cluster collisions. *New Journal of Chemistry*, *16*, 1145–1147.
- Springborg, M. (1999). Electronic properties, stability, and length scales of Cs<sub>N</sub> clusters. *Journal of Physics: Condensed Matter*, *11*, 1–18.
- Springborg, M. (2000). *Methods of electronic-structure calculations*. Chichester: Wiley.
- Springborg, M. (2006). Determination of structure in electronic structure calculations. In A. Hinchliffe (Ed.), *Specialist periodical reports: Chemical modelling, applications and theory* (Vol. 4, pp. 249–323). Cambridge, MA: Royal Society of Chemistry.
- Springborg, M. (2009). Nanostructures. In M. Springborg (Ed.), *Specialist periodical reports: Chemical modelling, applications and theory* (Vol. 6, pp. 510–574). Cambridge: Royal Society of Chemistry.
- Springborg, M., Satpathy, S., Malinowski, N., Zimmermann, U., & Martin, T. P. (1996). Electronic shell structure and relative abundances in Alkali-coated C<sub>60</sub>. *Physical Review Letters*, *77*, 1127–1130.
- Tevekelyiska, V., Dong, Y., Springborg, M., & Grigoryan, V. G. (2010) Using theory in determining the properties of metal clusters: Sodium as a case study. In P. K. Chattaraj (Ed.), *Aromaticity and metal clusters* (pp. 161–185). Boca Raton: Taylor & Francis.
- Tsai, C. J., & Jordan, K. D. (1993). Use of an Eigenmode method to locate the stationary points on the potential energy surfaces of selected argon and water clusters. *The Journal of Physical Chemistry*, *97*, 11227–11237.
- ur Rehman, H., Springborg, M., & Dong, Y. (2011). Structural and electronic properties of Si<sub>n</sub>, Ge<sub>n</sub>, and Si<sub>n</sub>Ge<sub>n</sub> clusters. *The Journal of Physical Chemistry A*, *115*(10), 2005–2015.
- van Heijnsbergen, D., von Helden, G., Duncan, M. A., van Roij, A. J. A., & Meijer, M. (1999). Vibrational Spectroscopy of gas-phase metal-carbide clusters and nanocrystals. *Physical Review Letters*, *83*, 4983–4986.

- Wales, D. J., & Doye, J. P. K. (1997). Global optimization by basin-hopping and the lowest energy structures of Lennard-Jones clusters containing up to 110 atoms. *The Journal of Physical Chemistry A*, *101*, 5111–5116.
- Weller, H., & Eychmüller, A. (1996). Preparation and characterization of semiconductor nanoparticles. In P. V. Kamat & D. Meisel (Eds.), *Semiconductor nanoclusters* (pp. 5–22). Amsterdam: Elsevier.
- Wille, L. T., & Vennik, J. (1985). Computational complexity of the ground-state determination of atomic clusters. *Journal of Physics A*, *18*, L419–L422.
- Yeh, C.-Y., Lu, Z. W., Froyen, S., & Zunger, A. (1992a). Predictions and systematization of the Zinc-blende-wurtzite structural energies in binary Octet compounds. *Physical Review B*, *45*, 12130–12133.
- Yeh, C.-Y., Lu, Z. W., Froyen, S., & Zunger, A. (1992b). Zinc-blende-wurtzite polytypism in semiconductors. *Physical Review B*, *46*, 10086–10097.



# 27 Modeling of Nanostructures

Hande Toffoli<sup>1</sup> · Sakir Erkoç<sup>1</sup> · Daniele Toffoli<sup>2</sup>

<sup>1</sup>Department of Physics, Middle East Technical University, Ankara,  
Turkey

<sup>2</sup>Department of Chemistry, Middle East Technical University, Ankara,  
Turkey

<b>Introduction</b> .....	<b>996</b>
Hierarchy of Methods .....	996
<b>0D Structures: Nanoparticles</b> .....	<b>996</b>
Global Optimization with Empirical Potentials .....	999
Local Optimization with Higher Accuracy Methods .....	1001
<b>1D Structures: Nanotubes, Nanowires, Nanorods</b> .....	<b>1009</b>
Elastic and Structural Properties .....	1010
Structural Properties .....	1013
Electronic, Magnetic and Optical Properties .....	1014
<b>2D Structures: Graphene and Derivatives</b> .....	<b>1017</b>
Graphene, Nanosheets, Nanoribbons, Nanobelts, Nanostrips .....	1019
Electronic and Mechanical Properties .....	1024
Magnetic and Optical Properties .....	1032
Adsorption Phenomena .....	1035
<b>References</b> .....	<b>1036</b>


**Abstract:** Materials properties show a dependence on the dimensionality of the systems studied. Due to the increased importance of surfaces and edges, lower-dimensional systems display behavior that may be widely different from their bulk counterparts. As a means to complement the newly developed experimental methods to study these reduced dimensional systems, a large fraction of the theoretical effort in the field continues to be channeled towards computer simulations. This chapter reviews briefly the computational methods used for the low dimensional materials and presents how the materials properties change with dimensionality. Low dimensional systems investigated are classified into a few broad classes: 0D nanoparticles, 1D nanotubes, nanowires, nanorods, and 2D graphene and derivatives. A comprehensive literature will guide the readers' interest in computational materials sciences.

## Introduction

---

### Hierarchy of Methods

---

Methods for materials modeling are based on the particular length and time scales used for the investigation of various materials properties that operate only over those scales. This has led to basically four independent methodological streams, which may be categorized as ab-initio density functional theory, molecular dynamics, statistical methods based on Monte Carlo algorithms, and continuum mechanics (see  Fig. 27-1 for the ranges of them). Each of these is computationally intensive within its own range. However, the expanding capabilities of computational methods due to the increasing power of computers and continuing development of efficient algorithms, together with advances in the synthesis, analysis, and visualization of materials at increasingly finer spatial and temporal resolutions, have spawned a huge effort in the modeling of materials phenomena.

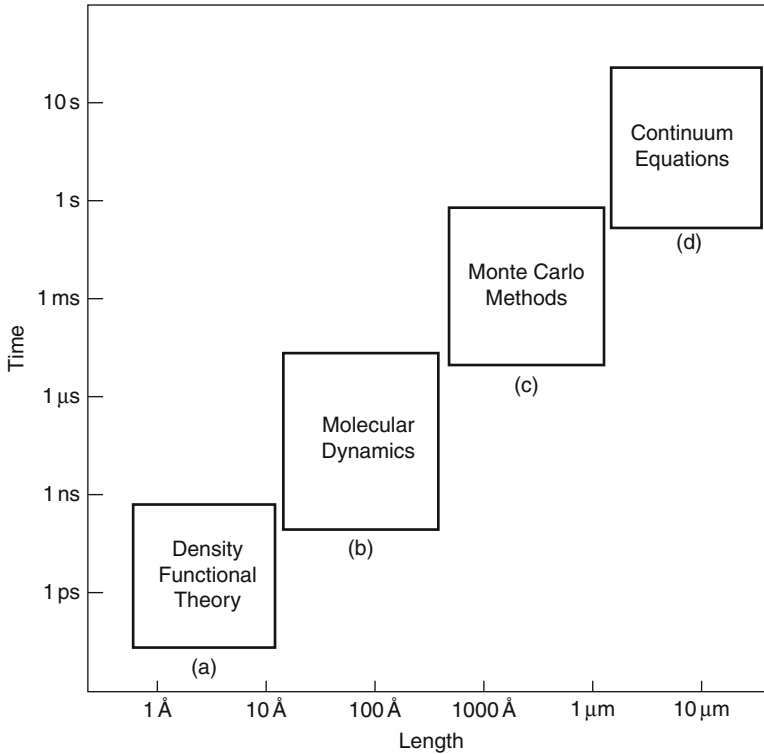
Since the materials properties are directly related with the dimensionality of materials, particularly at the nanoscale, it would be better to classify the methods of modeling of nanostructures with respect to the dimensionality, such as zero-dimensional (0D), one-dimensional (1D), two-dimensional (2D), and three-dimensional (3D) materials. At the nanoscale the first three dimensionalities (0D, 1D, 2D) are commonly used, but the 3D materials are usually considered as macroscopic systems; therefore those materials are not the subject of this chapter.

### 0D Structures: Nanoparticles

---

The class of nanomaterials that may be termed *zero-dimensional* comprise systems that are confined within up to several hundreds of nanometers in all three dimensions. Although there exists no clear-cut size threshold at which a system switches from a zero-dimensional system to bulk, there is a rather well-defined class of systems that fit the above definition with unique and intriguing properties. The most commonly studied zero-dimensional systems are *quantum dots*, *nanoparticles* (or *clusters*), and *cage-like structures*. In this section, we shall begin with an overview of methods used to study such materials.

After the 1980s, the field of nanoparticles has seen increasing activity. The results of these studies and their applications have been collected in several reviews (Balasubramanian 1990; Baletto and Ferrando 2005; Bonacic-Koutecky et al. 1991; Brack 1993; de Heer 1993; Halicioglu



■ Fig. 27-1

Ranges of scales used for different methods in materials properties (Adapted from Vvedensky 2004)

and Bauschlicher 1988; Morse 1986; Ustunel and Erkoç 2007; Weltner and Van Zee 1984). Studies on clusters have been concentrated on such diverse applications as catalysis, chemisorption and substrate adsorption, laser applications, magnetism, nucleation, photographic processes, and reactivity.

The term *cluster* may, in the broadest sense, be defined as an aggregate of atoms or molecules that form a size regime between molecules and bulk materials. It is far from a straightforward task to define the range of number of atoms which constitute a cluster. In contrast to their bulk counterparts, structural and electronic properties of clusters display a rather strong dependence on size and geometric configuration due to their large surface-to-volume ratio. Thus in order to understand the properties of clusters a careful determination of the equilibrium structure is crucial. In general, the equilibrium geometry is determined by locating the global minimum of the *potential energy surface* (PES) of a cluster, which in principle can be mapped out by calculating the total energy as a function of all possible locations of the atoms. Unfortunately even the smallest clusters often have extremely complicated potential energy surfaces with practically countless local minima. This requires a thorough search over the entire PES for a realistic determination of the equilibrium structure.

An added complication to the difficulty of determining the global minima is that clusters with different but similar sizes of the same material may present PESs that are entirely different. It is likely then that the equilibrium shape of a cluster of a given material and size is



significantly different from a different size cluster of the same material. Fortunately, some similarities may be found in the vast number of possible structures. Mass spectroscopy of clusters reveal that certain sizes of clusters are preferred over others, indicated by the high abundance detected (Martin 1996). The number of atoms or molecules in a preferred cluster is commonly referred to as a *magic number*. The origin of a magic number may be the completion of a *geometric* or an *electronic* shell of the cluster. The particular geometric or electronic shell being completed obviously depends upon the constituents of the clusters and the bonding between them. For instance, noble gases are found in polyhedral form whereas metallic clusters prefer cubic or prolate structures (Johnston 2002). The search for magic numbers has been the subject of a very large number of works (Anagnostatos 1987; Balasubramanian 1990; Bonacic-Koutecky et al. 1991; Haberland 1994; Jarrold and Constant 1991; Moraga 1993; Yang et al. 2006).

In order to map out the energy landscape of nanoparticles an adequate model for the interatomic interactions within the cluster needs to be employed. Empirical potentials, the tight-binding approximation, and density-functional theory whose brief description has been given in previous sections are the most commonly used methods in literature. While empirical potentials (Erkoc 1997, 2001) offer an efficient means of exploring the PES and determining the equilibrium structure of large clusters, calculations based on the tight-binding approximation and density functional theory are preferred for more accurate and detailed description of geometrical and electronic properties of small to medium sized clusters.

Once the method of choice is determined for interatomic interactions, the corresponding potential energy surface may be explored using *global search algorithms* to determine the lowest lying minima. A concise review of global optimization methods are given in the reviews (Baletto and Ferrando 2005; Dugan and Erkoc 2009; Wales and Doye 1997). Here, we shall briefly describe a few of them.

*The basin hopping algorithm* (Wales and Doye 1997) belongs to a class of optimization methods called *hypersurface deformation methods*. These methods aim to simplify the PES by applying a map that smooths it out. The global minimum of the simplified PES is then mapped back to that of the real PES assuming that it leads back to the global minimum of the real PES. In the basin hopping algorithm, the original, complicated PES,  $U(\vec{r})$ , is transformed onto a step-like function  $\tilde{U}(\vec{r})$  according to the rule (Baletto and Ferrando 2005; Wales and Doye 1997)

$$\tilde{U}(\vec{r}) = \min[U(\vec{r})], \quad (27.1)$$

where the min function implies that a local minimization is to be applied such as the conjugate gradients algorithm (Hestenes and Stiefel 1952).

In many of the cluster applications using basin hopping (Bromley and Flikkema 2005; Doye and Wales 1999; Hsu and Lai 2006; Wales and Doye 1997), this transformed PES is sampled with a Monte Carlo algorithm, sometimes with a fixed acceptance (Wales and Doye 1997).

The second method we shall mention is *the simulated annealing method* (Kirkpatrick et al. 1983), in which the system is evolved at high temperature and then gradually cooled down. Assuming that the system does not get trapped in a basin of attraction which is not the minimum, it reaches the state of lowest energy during the cooling process. Attempts to use simulated annealing to find the global energy minimum in larger systems is frustrated by high-energy barriers that trap the system in metastable configurations (Ma and Wang 2006).

Finally, we briefly describe a class of algorithms that has recently gained popularity, namely, *genetic algorithms*. Genetic algorithms (GAs) are based on ideas borrowed from natural evolution. As explained in Darby and coworkers (2002), they employ operators that are analogues of

the evolutionary processes of genetic crossover, mutation, and natural selection. A GA can be applied to any problem where the variables to be optimized can be encoded to form a string, each string representing a trial solution to the system. In cluster terminology each *string* is a list of coordinates of a cluster. An initial number of clusters are chosen according to some generation scheme (usually random) and locally minimized.

After the creation of the initial generation of strings, each member of this generation is assigned a *fitness parameter* based on a fitness function. In Darby and coworkers (2002), for example, this function was chosen to be the negative exponent of the deviation of the total energy of each cluster from the cluster with minimum energy.

Once a fitness parameter is assigned to each member of the population, a new generation is created: Two *parents* are chosen from members with high fitness parameter for each *offspring* (member of the new generation) and then subjected to the *crossover* operation. A crossover operation for clusters consists of a particular rearrangement and combination of the atomic coordinates in the parent clusters. For an example, see Darby and coworkers (2002). After each new cluster is generated a local minimization is performed. Mating continues in this way until the desired number of offsprings are generated. New fitness parameters are assigned to each offspring. In order to maintain diversity, new genetic material is introduced into the population by means of the *mutation* operator. After mutation in a cluster population, clusters are once again locally minimized.

Finally the next generation is completed by applying *natural selection*. The previous generation and the new generation are ranked in order of fitness and the best  $N$  individuals (clusters) are chosen, where  $N$  is the population of the original population. These  $N$  individuals constitute the new generation, and mating is performed again.

The process of mating, mutation, and selection is repeated for a predetermined number of generations or until a given criterion is reached. This criterion could be, for example, the convergence of the highest fitness to a plateau so that consecutive generations do not produce better results.

Other global search algorithms include parallel random tunneling, conformational space annealing, greedy search method, simulated annealing, quantum annealing, smoothing and hypersurface deformation techniques, lattice methods, growth sequence analysis, and replica exchange method.

## Global Optimization with Empirical Potentials

---

In spite of the wealth of information they provide, global search algorithms ordinarily fail to identify all the minima of a given cluster. The best explored potential surface for clusters belong to possibly the simplest empirical potential, namely, the Lennard-Jones potential. The Lennard-Jones potential is a simple model that captures the long- and short-range behavior of atoms and molecules. It was proposed in 1931 by J. E. Lennard-Jones (1931) and has been used in innumerable studies ever since. It has the following simple form

$$V(r) = 4\epsilon \left[ \left( \frac{\sigma}{r} \right)^{12} - \left( \frac{\sigma}{r} \right)^6 \right], \quad (27.2)$$

where  $\epsilon$  and  $\sigma$  are parameters that determine the depth and the width of the potential well, respectively, and  $r$  is the interatomic distance between atom pairs.

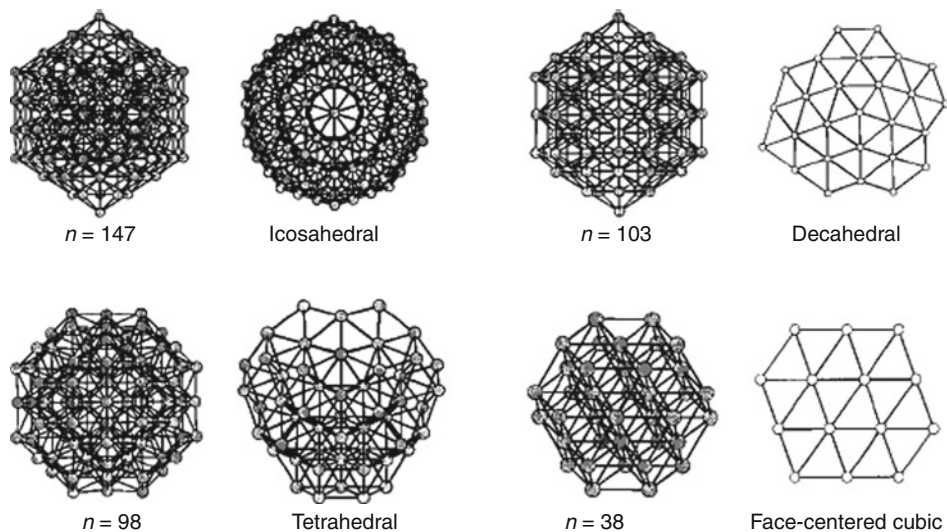
The four known structural forms for the LJ potential are (Hartke 2002) as seen in **Fig. 27-2**:

1. Icosahedral: formed by starting from the pentagonal bipyramid and adding a further layer of atoms.
2. Decahedral: icosahedral core surrounded by fcc stacks.
3. Tetrahedral: tetrahedron of atoms in the innermost core.
4. Face-centered cubic : sections of the fcc bulk structure.

For  $N < 1,000$ , Lennard-Jones clusters follow an icosahedral pattern growth with magic numbers corresponding to *Mackay icosahedra* (Mackay 1962) for  $N = 13, 55, 147, 309$ , etc. In between these magic numbers, most of the structures are Mackay-like with incomplete outer layers. Exceptions occur when there are alternative structures with complete shells. These are mostly Marks decahedra (Doye 2003) but there are instances of an fcc truncated octahedron and a Leary tetrahedron (Noya and Doye 2006). The preference for icosahedral structures of Lennard-Jones clusters at small sizes is thought to be due to a trade-off between optimal bond distance and strain (Hartke 2002; Krainyukova 2006).

In spite of its simplicity, the Lennard-Jones potential may not be used for accurate description of cluster properties with the possible exception of noble gas clusters. Often empirical potentials that involve a larger number of parameters than the two-parameter Lennard-Jones potential are employed for structural determination.

To understand their behavior at finite temperature, Wu and coworkers studied Zn clusters using the Gupta potential by means of molecular dynamics (Wu et al. 2005). Zn clusters are found to display peculiar structures that are very different from other *sp*-type metal clusters. The  $N = 13$  cluster, for instance, has a disordered structure instead of the icosahedral structure found in most metals of the same size. The  $C_v$  curve also differs in that it has a double



**Fig. 27-2**

The four basic structures of Lennard-Jones clusters (Reprinted with permission from Hartke (2002). © (2002) by Wiley-VCH Verlag GmbH & Co. KGaA)

peak structure, whereas icosahedral structures display a single peak. The  $\Delta E_2$  study in Wu et al. (2005) reveals that magic structures are found at  $N = 6, 13, 29, 33, 36, 42, 49,$  and  $53$ .

In a study by Rey and coworkers (1993), several transition metal clusters (Ni, Pd, Au, and Ag) were studied using different model potentials. Three different *embedded atom models* (EAM) and two different parameterizations of an N-body analytical potential were considered. For Ni clusters, although the binding energies provided by the various models showed differences, the peak stability was obtained for all the models at  $N = 13$  (icosahedron) and  $N = 19$  (double icosahedron). In this work (Rey et al. 1993), earlier experiments on large Ni clusters ( $N = 49$ – $2300$ ) are also quoted where icosahedral growth was observed. For Ni the EAM that was fitted to bulk values (EAM1) gave poorer results than the one fitted to diatomic values. For Pd, Au, and Ag, only EAM1 and one of parameterizations of the analytical potential (TBM1) were compared. EAM1 failed to yield enhanced stability for  $N = 13$  and  $N = 19$ , while TBM1 mostly gave icosahedral structures for both sizes. This shows the importance of parameterization for the accuracy of the model potentials.

In a recent study by Doye (2006), results for Pb clusters were calculated and compared for the Gupta potential and a glue potential in combination with a basin-hopping algorithm. Within the Gupta potential framework, Pb clusters, in contrast to Si, Ge, and Sn, do not show any tendency to form prolate or oblate structures. Their structures are mostly spherical with decahedra being the most favored structure followed by close-packed. This study also presents an interesting comparison between the Gupta potential and the glue potential, which reveals that there is virtually no agreement between the two potentials neither in the magic numbers nor in the resulting structures. This sharp discrepancy demonstrates that one should be very careful while comparing results from different methods. More disordered structures are favored for the glue potential than the Gupta potential because the embedding term dominates for the latter.

An interesting result from the work of Doye (2006) is that for the Gupta potential the uncentered Mackay icosahedron with  $N = 54$  is more stable than the complete  $N = 55$  Mackay icosahedron. This is because of the strain applied by the external atoms on the center, making it unfavorable to be occupied.

As a final remark on empirical potentials, we note that the particular parameterization of the potential plays a crucial role in correctly identifying structural properties, and caution should therefore be used in interpreting results for empirical potentials. For instance, according to (Michaelian et al. 1999), the global minima of Au clusters are difficult to localize because of the short range of the Au potential. As the range of a potential decreases, the number of global minima associated with the potential increases. As a result of this, different studies have identified different global minima for Au clusters. In addition different potential models for the metal yield different ordering of the lowest lying minima.

## Local Optimization with Higher Accuracy Methods

---

Outside of the domain of simple empirical potentials, identifying the global minima of cluster PESs becomes a prohibitively demanding task. Therefore, most studies on the theoretical determination of cluster minima employ methods that either focus on local minima obtained through an adequate initial guess or a mixture of global search algorithms with simple potentials to reduce the number of minima followed by local minimization techniques that are more accurate.

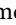
The majority of elements, regardless of whether they prefer atomic shells or electronic shells form clusters that are more or less spherical. The only elements that deviate from this behavior is the group IVA elements. This is especially remarkable in carbon, which goes from linear chains all the way to fullerenes. Clusters of Si and Ge first grow in one dimension and then abruptly change to form spherical clusters (Shvartsburg and Jarrold 1999). Some similarities exist between the growth patterns of Si and Ge cluster but major differences also occur especially concerning the size at which transition to bulk-like structures takes place (Shvartsburg and Jarrold 1999).

Because Si clusters undergo such a drastic change in cross section, an excellent experimental technique exists for studying the structure as a function of size. This technique (Jarrold and Constant 1991) is based upon the difference in the mobility of cluster ions that have different shapes. The ion mobility of a cluster depends on its rotationally averaged collision cross section, which depends on its size. Prolate and oblate geometries have a larger cross section and therefore smaller mobilities (Sieck et al. 2003). Mobility studies indicate that  $\text{Si}_n$  clusters undergo a phase transition at about  $n = 24\text{--}34$  from elongated to spherical whereas for the Ge clusters this transition size is between  $n = 64$  and  $n = 74$  (Jarrold and Constant 1991; Shvartsburg and Jarrold 1999).

The growth sequence of Si is realized by adding on small building blocks to smaller structures. In particular,  $\text{Si}_9$  (Shvartsburg and Jarrold 1999) and  $\text{Si}_{10}$  (Baletto and Ferrando 2005) have enhanced stability and, therefore, act as the fundamental building blocks. On the other hand, medium-sized Si clusters are quasispherical but not crystalline. Crystallinity does not become apparent until  $N$  gets as large as a few hundred atoms (Baletto and Ferrando 2005).

In the simulated annealing and DFT-based tight-binding work by Sieck and coworkers (2003), a *prolateness parameter* is defined as follows

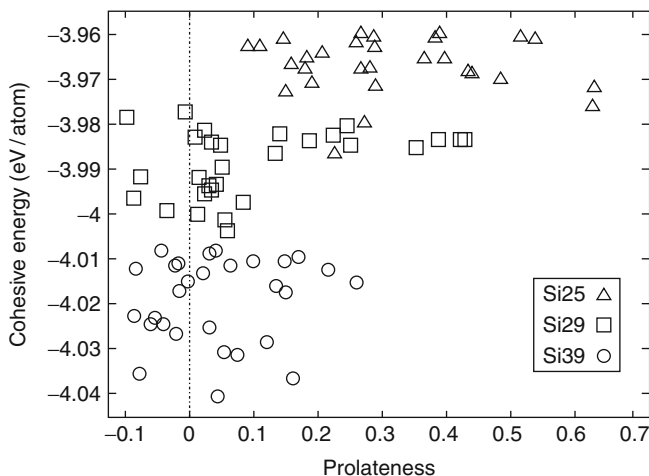
$$p = \sum_{j=1}^3 (I_j - \hat{I}) = -\frac{I_1}{2} + I_2 - \frac{I_3}{2}, \quad (27.3)$$

where  $0 < I_1 \leq I_3$  and  $\hat{I} = (I_1 + I_3)/2$ . For an oblate structure  $p < 0$ , for a prolate structure  $p > 0$ , and for a spherical structure  $p = 0$ . Sieck and coworkers (2003) studied various different isomers corresponding to three fixed sizes, namely,  $N = 25, 29$ , and  $35$ . In  Fig. 27-3, the cohesive energy versus the prolateness parameter for the low-lying isomers is displayed. An investigation into the most stable structures clearly indicate the tendency to go from elongated to spherical structures as the clusters grow in size.

An important point is noted by Sieck and coworkers (2003), which is that different methods, even different flavors of the same method (LDA/GGA in DFT) may disagree about the exact energetic ordering of clusters, however, usually the lowest energy structures are local minima in all of them.

As an example to the multiscale methods mentioned above Bulusu and coworkers (2005) used a basin-hopping algorithm combined with DFT to explore low-lying minima for  $\text{Ge}_{12\text{--}20}$ . Global minima for the Ge clusters in this size range is compared to minima of Si clusters. Various checks were performed to make sure different starting points yield the same global minima, such as different seeding patterns. Unlike most studies in the literature, zero-point motion is taken into account while calculating the binding energies.

In the same work (Bulusu et al. 2005) of Si and Ge clusters in the size range 12–20 were compared and clusters of both Si and Ge were shown to have prolate geometries. However, their growth patterns were found to diverge at  $N = 13$ . The global minima for Ge clusters of



■ Fig. 27-3

Cohesive energy versus prolateness parameter defined in Eq. 27.3 for 30 lowest lying isomers of  $\text{Si}_{25}$ ,  $\text{Si}_{29}$ , and  $\text{Si}_{35a}$  (Reprinted with permission from Sieck et al. (2003). © (2003) by Wiley-VCH)

size 12–16 are obtained by adding atoms to the  $\text{Ge}_9$  tetrapped trigonal prism (TTP) structure familiar from Si clusters (Bulusu et al. 2005). For low energy Si clusters TTP-to-six-fold puckered ring(six/six) transition occurs at  $N = 16$  and clusters with higher number of atoms all contain the six/six pattern. In contrast, TTP-to-six/six pattern may occur at  $N = 19$  for Ge clusters and at  $N = 20$ , the magic number cluster  $\text{Ge}_{10}$  appears to be the preferred structural motif.

According to Shvartsburg and Jarrold (1999), clusters of Sn up to  $n \approx 35$  follow the trend of germanium and prolate silicon clusters (Shvartsburg and Jarrold 1999). For  $N > 20$ , the mobility of Sn clusters show larger fluctuations than either Si or Ge. This might indicate the presence of multiple isomers of Sn clusters in this size range (Shvartsburg and Jarrold 1999). Even though the  $\alpha \Rightarrow \beta$  transition occurs between 286 K and  $\approx 310$  K in the bulk, Sn clusters do not undergo such a transition even at higher temperatures. In fact, mobility measurements show that Sn clusters do not show significant changes in structure for a very broad temperature range. Transition from prolate to spherical growth in Sn clusters is not abrupt like the transition in Si and Ge clusters but occurs in steps. Clusters of  $N \leq 35$  adopt a stacked prolate morphology much like Si and Ge clusters. This is unexpected because these highly noncompact structures are suitable for covalent materials whereas bulk Sn under ambient conditions is a metal. In a sense, the covalent-to-metal transition that occurs between the fourth and fifth row of the periodic table for the carbon series in the bulk fail to occur in their clusters. Shvartsburg and Jarrold (2000) also find that  $\text{Pb}_n^-$  and  $\text{Pb}_n^+$  clusters display different magic numbers.

Going down the group IV in the periodic table a comprehensive set of data is given by Shvartsburg and Jarrold (2000). Their findings reveal that Pb clusters are structurally different from Si, Ge, and Sn cluster for  $N < 25$ . While the latter clusters have low mobilities in this size range indicating a prolate structure, Pb clusters exhibit much higher mobilities meaning they are quasispherical in shape. For  $N > 25$ , Si clusters also display mobilities in accord with a spherical shape. However, their mobilities are considerably smaller than the Pb clusters in the



same size range. This is attributed to the densely-packed nature of the Pb clusters in contrast with the open, cage-like arrangement of the Si clusters.

Transition metals form the largest group of elements considered in this section. Even as bulk materials, they exhibit very interesting and diverse properties, in particular magnetism. Interesting questions therefore arise concerning whether such properties as magnetism are maintained or altered in clusters (Briere et al. 2002; Kabir et al. 2006). Appearance of magnetism in the clusters of  $4d$  elements (such as Ru, Rh, and Pd) is a very interesting phenomenon as these elements are nonmagnetic in the bulk. Clusters of  $3d$  elements (such as Fe, Co, and Ni), which are already magnetic in the bulk, exhibit enhanced magnetic moments in the cluster form due to narrower band widths and the increased localization of the electrons (Kumar and Kawazoe 2002; Pawluk et al. 2005). Indeed, a recent Stern–Gerlach experiment revealed that Mn clusters in the range  $N = 11$ –99 display ferromagnetic ordering even though no such ordering is observed in the bulk phase (Knickelbein 2001). These results reveal PES minima at  $N = 13$  and  $N = 19$  and PES maxima at  $N = 15$  and  $N = 23$ –25.

We should mention here that most of the magnetism studies mentioned in this section take into account only the electronic spin contribution to the magnetic moment. This can be done only in the cases where the spin-orbit coupling can be neglected.


In the work by Rodríguez-López and coworkers (2003), Co clusters in the range  $N = 4$ –60 were studied by means of an evolutive algorithm based on the Gupta potential and tight-binding. Experiments reveal that much like the Cr clusters (Payne et al. 2006), different isomers of Co clusters coexist with distinct magnetic moments. In this work two sets of isomers are identified for each size – the lowest and the second-lowest lying. For the lowest-lying isomers an icosahedral growth is observed with structures derived by adding atoms to the main icosahedral sizes at  $N = 7, 13, 19, 23, 26, 34, 43,$  and  $55$ . For the second isomers no particular growth pattern was identified. The stability of these sizes were also confirmed by the second energy difference  $\Delta E_2$  in addition to other, intermediate icosahedral structures.

Relative thermodynamic populations of the lowest-energy isomers were used to simulate possible experimental conditions. Isomers coexist particularly evenly between sizes of enhanced stability. This is due to the influence of the entropic contribution of the low-frequency normal modes of the isomers to the free energy. For both the global minimum and the second isomer, a nonmonotonic decrease is observed with increasing size. The greatest difference between the two sets of clusters arises in the range  $N = 20$ –40, which corresponds to the range where the average interatomic distance and average coordination of the two sets show significant difference. In this size range, two effects seem to compete for determining the magnetization of the two sets of configurations. On the one hand, the average coordination is higher for the global minima, which should result in lower magnetic moments for the global minima. On the other hand, the average nearest-neighbor distance is higher for the global minima, which should yield higher magnetic moments. The results indicate that the average coordination number effect dominates.

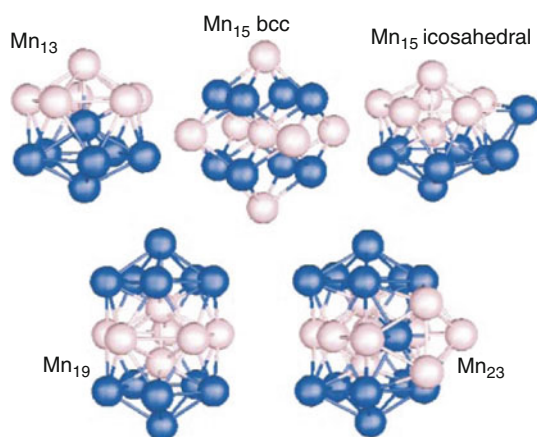
For noble and transition metals, the interactions between atoms are not pairwise and simple empirical potentials are inappropriate (Barreateau et al. 2000). Therefore incorporating many-body effects into the potentials is essential. Moreover, for magnetism studies, ab initio methods need to be employed, which render global optimization efforts extremely computation-intensive. Therefore, most results we shall quote here will be based on restricted searches of the potential energy surface.


In the work by Barreateau and coworkers (2000), for instance, the relative stability of cuboctahedra and Mackay icosahedra is determined for Rh and Pd clusters for  $N = 13, 55, 147, 309,$  and

561 using a tight-binding method. Since both structures have an identical sequence of magic numbers it is interesting to determine the transition size. A continuous transition is possible from the Mackay icosahedron to the cuboctahedron, and for the Rh and Pd clusters, this pathway is explored. An analysis of the Mackay transition from the cuboctahedron to the icosahedron reveals that for  $N = 13$ , the cuboctahedron is unstable for both Rh and Pd, becoming metastable for larger sizes with an increasing activation barrier with size. The magnetic moment of rhodium was found to disappear for sizes more than 100 atoms, and palladium clusters were found to be hardly magnetic.

In Mn clusters, on the other hand, magnetism plays an important role in determining the ground state structures. As mentioned in the work by Briere and coworkers (2002), many spin isomers can lie close in energy. In this work, a few local geometric configurations of  $N = 13$ , 15, 19, and 23 were studied using spin-polarized calculations. At all sizes except  $N = 15$ , the structure with the lowest energy was found to be icosahedral. For  $N = 15$ , a bcc configuration was found to be favorable. In terms of spin, all the structures were found to be ferrimagnetic with alternating domains of different spin configurations (see  Fig. 27-4). Except for  $N = 15$ , the mean value of the integrated spin density was found to decrease with increasing size.

In the DFT work by Kabir and Mookerjee (2006), the ground state structure for  $Mn_{13}$  was found to be the icosahedron with the two pentagonal rings that are coupled antiferromagnetically. Therefore, the resulting magnetization is small, namely,  $0.23\mu_B/\text{atom}$ . This magnetization is considerably smaller than the neighboring sizes 12 and 14. The  $N = 14$  structure differs from the  $N = 13$  structure by a single capping atom. However, the presence of this atom changes the magnetization arrangement considerably. In this case the pentagonal rings are ferromagnetically coupled and the magnetization is  $1.29\mu_B/\text{atom}$ . The case of  $Mn_{15}$  is worth mentioning because of the discrepancy between two DFT studies by Briere and coworkers (2002) and Kabir and Mookerjee (2006). In the latter, the ground state structure was found to be icosahedral with a magnetic moment of  $0.87\mu_B/\text{atom}$  whereas Briere et al. (2002) found a bcc



 Fig. 27-4

Lowest energy structures of some Mn clusters. Relative spin alignments are marked with dark for spin up and light for spin down (Reprinted with permission from Briere et al. (2002). © (2002) by the American Physical Society)



structure with  $0.20\mu_B/\text{atom}$ . For  $N = 19$ , a double icosahedron was observed, which again has a smaller magnetic moment,  $1.10\mu_B/\text{atom}$ , than its neighboring clusters. The central pentagonal ring is AFM coupled to the neighboring pentagonal rings. This behavior is persistent in the  $N = 20$  cluster, which has a magnetic moment of  $1.50\mu_B/\text{atom}$ . In the range  $N = 11 - 20$ , spin segregation is observed, where like spins tend to cluster. The binding energy is observed to increase monotonically with increasing size. This is due to the increased  $sp$  bonding. However, when compared with other transition metals, Mn clusters remain weakly bound.

An interesting property of Ta clusters were demonstrated in a recent study (Fa et al. 2006), where ferroelectricity and ferromagnetism was proven to coexist. Initial structures were obtained by simulated annealing using an empirical potential. These structures were later reoptimized with DFT calculations. The magic numbers for Ta clusters were found to be 4, 7, 10, 15, and 22. It was therefore deduced that Ta clusters do not prefer icosahedral growth. For  $N = 13$ , for instance, the lowest energy structure among those studied was found to be a distorted five-capped hexagonal bipyramid. For  $N = 19$ , the most stable structure is decahedral in contrast with the double icosahedron, which was found to be stable for many other clusters. No perfectly symmetric structures were found indicating that Jahn-Teller distortions play an important role in determining the ground state structures of Ta clusters. In the size range studied in this work (Fa et al. 2006), the atomic packing shows differences such that each size behaves like an individual system rather than steps of a continuous growth sequence. In addition, electronic dipole moment and magnetic moment were also calculated. The electronic dipole moment was found to have the same trend as the *inverse coordination number*, which is a parameter that reflects the asymmetry of the cluster. This agreement is attributed to the strong correlation between the structure and the electronic dipole moment of the clusters. Odd- $N$  Ta clusters also display a magnetic moment of about  $1\mu_B$ , which suggests the possibility of the coexistence of ferroelectricity and ferromagnetism. The growth pattern of Ta was found to be very similar to that of Nb. However, when compared with vanadium clusters, this similarity is absent (Fa et al. 2006).

In a similar work by Fa and coworkers (2005), Nb clusters were also found to display ferroelectricity supported by a recent experimental study. This is an important discovery because ferroelectricity was never observed in single element bulk materials. For  $N \geq 38$ , the electric dipole moment exhibits even-odd oscillations. This suggests that there is a strong correlation between the structure and the ferroelectricity.

In the work by Pawluk and coworkers (2005), the structure and stability of several Ir clusters were studied using DFT. Rather than using a global optimization algorithm, possible configurations both truncated from bulk and built independently were relaxed locally. The results indicate that Ir clusters mostly prefer cube-like structures up to  $N = 13$ , except for  $N = 11$ , which assumes an elongated structure. At  $N = 13$ , the lowest structure among the ones studied is the icosahedron. This is in contrast with Ru and Pt, which prefer simple cubic structures. When compared to clusters cut from the fcc bulk, simple cubic structures turn out to be more stable up to a size of  $N = 48$ . This transition occurs near  $N = 40$  in Ru and  $N = 13$  for Pt. Another interesting property studied in this work is the fluidity of clusters. The results indicate that while the Pt clusters exhibit a more fluidlike character and will thus easily coalesce with other clusters, Ir clusters are more rigid and have less tendency toward coalescence.


An interesting experimental result concerning Pt clusters was reported by Liu and coworkers (2006), who found that  $\text{Pt}_{13}$  clusters exhibit substantial magnetism (about  $0.65\mu_B/\text{atom}$ ) even though bulk Pt is not magnetic.

Although for such clusters as Ni and Au the icosahedral structure is calculated to be metastable with stability decreasing with size, experiment reveals that icosahedral structures are found in clusters containing several thousands of atoms. This means that kinetic effects are also very important in determining the structure of a cluster (Gafner et al. 2004). In order to simulate these kinetic effects, a 555 Ni cluster was studied using tight-binding by Gafner and coworkers in (2004). The cluster was heated to 1,800 K ( $T_{melt} = 1,145$  K) and subsequently cooled to 300 K. The melting and crystallization curves are determined from a sudden change in the potential energy as a function of temperature. They found that slow cooling results in an fcc structure whereas fast cooling results in the formation of a metastable icosahedral structure.

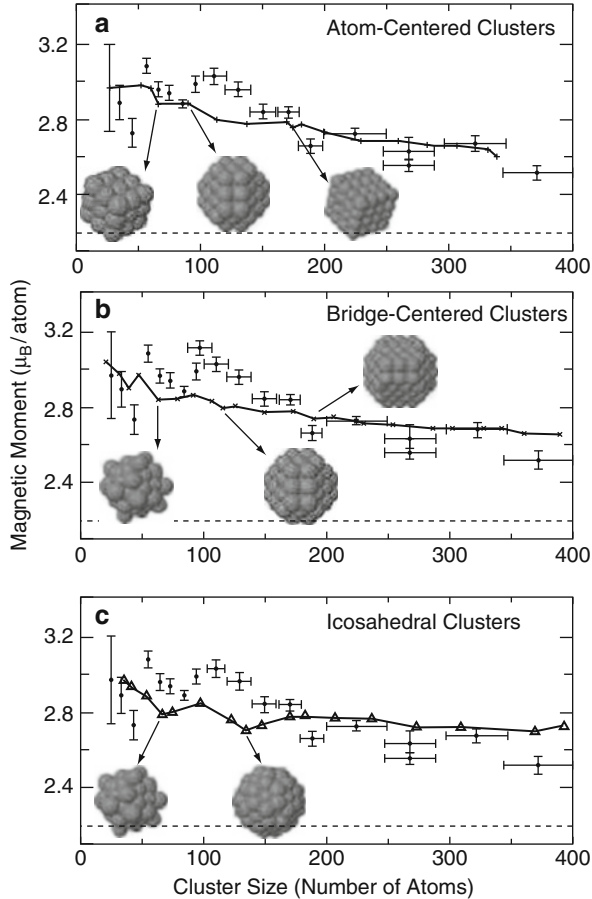
In the study by Köhler and coworkers (2006), the potential surface of a few sizes ( $N = 13, 53-57$ ) of Fe clusters were mapped out with respect to magnetization and volume change using a DFT-based tight-binding scheme. Icosahedra were found to be the most stable structures for the magic numbers  $N = 13$  and  $N = 55$ . Two local minima were observed for the  $N = 13$  icosahedron, one ferromagnetic and one antiferromagnetic. The PESs for clusters with  $N = 53-57$  were mapped out using a genetic algorithm-based procedure. Derivatives of the  $N = 55$  structure were considered for  $N = 53, 54, 56, \text{ and } 57$ . Generally icosahedra and icosahedron-derived structures have relatively small magnetic moments. The structures without apparent symmetry show higher magnetic moment than icosahedra. No ferromagnetic ordering was found for the  $\text{Fe}_{55}$  cluster.

Tiago and coworkers provide a very comprehensive explanation of the origin of magnetism in small Fe clusters in their article (Tiago et al. 2006). In the Fe atom, the magnetic moment is a result of exchange splitting. The  $3d_{\uparrow}$  states are occupied by 5 electrons, while the  $3d_{\downarrow}$  states are occupied by a single electron, which results in a rather high magnetic moment of  $4\mu_B$ . When the atoms come together to form a crystal, hybridization of the large 4s bands and the 3d bands reduce the magnetism down to  $2.2\mu_B$ . In clusters, hybridization is not so strong because of the reduced coordination numbers of the surface atoms. Because this hybridization depends on orientation, clusters with faceted surfaces are expected to have different magnetic properties than those with irregular faces. According to Tiago and coworkers (2006), this effect is the likely cause of the nonmonotonic suppression of magnetic moment as a function of size. Two classes of Fe clusters were considered in this work: faceted and nonfaceted. Nonfaceted structures are nearly spherical in shape and faceted structures are built using the conventional layer-by-layer growth model. The magnetic moment was calculated as the expectation value of the total angular momentum,

$$M = \frac{\mu_B}{\hbar} [g_s \langle S_z \rangle + \langle L_z \rangle], \quad (27.4)$$

where  $g_s = 2$  is the gyromagnetic ratio of the electron. The magnetic moments of the clusters as a function of size is displayed in  Fig. 27-5 for all classes of clusters considered. Suppression of the magnetic moment with increasing size is observed, in good agreement with experiment. Clusters with faceted surfaces indeed have a lower magnetic moment due to more efficient hybridization although the correlation of shape and magnetic moment is not always well defined. Icosahedral structures are predicted to have magnetic moments lower than bcc clusters.

Another good example of disagreement between different methods is given in Krüger and coworkers where Pd clusters having several high-symmetry structures including icosahedra, octahedra, and cuboctahedra were optimized using both the LDA and GGA in the DFT framework. GGA yields larger bond lengths in accord with the general expectation. But the difference is almost independent of size. Icosahedral structures tend to yield larger bond lengths



■ Fig. 27-5

Magnetic moments of faceted and nonfaceted Fe clusters in the icosahedral and bcc configurations: (a) atom-centered bcc, (b) bridge-centered bcc, and (c) icosahedral. Experimental data is displayed as black diamonds for comparison (Reprinted with permission from Tiago et al. (2006).

© (2002) by the American Physical Society)

than octahedral and cuboctahedral structures, also displaying a flatter variation with increasing coordination number. The accuracy of this *breathing mode* relaxation was confirmed by comparing to a full relaxation of the Pd<sub>55</sub> cluster.

The Pd<sub>13</sub> cluster was found in the work of Kumar and Kawazoe (2002) to have an icosahedral structure with a  $0.62\mu_B/\text{atom}$  magnetic moment. This result agrees with some of the earlier studies and disagrees with some others. The central atom in the cluster is found to have a smaller magnetic moment than the surface atom only by a very small amount unlike the large difference in the Mn<sub>13</sub> study of Kabir and coworkers (2006). For  $N = 14$  and 15 icosahedron-derived structures are favored over other high-symmetry structures. The magnetic moments for both sizes remain around  $0.5\mu_B/\text{atom}$ . Going from  $N = 16$  to the double icosahedron at  $N = 19$ , the magnetic moment decreases from  $0.38\mu_B/\text{atom}$  to  $0.32\mu_B/\text{atom}$ . As the cluster sizes increase

there is a decrease in local (atomic) magnetic moments. For  $N = 55$  and  $N = 147$ , the lowest-lying state was found to be the Mackay icosahedra. Cubic and decahedral structures were found to have the next highest energies, with  $0.29\mu_B/\text{atom}$  and  $0.41\mu_B/\text{atom}$  respectively. For the  $\text{Pd}_{55}$  cluster, structures with smaller magnetization lie very close to the ground state and would therefore be accessible at room temperature. So magnetic order can be easily lost under experimental conditions. In contrast to the results for Mn (Kabir et al. 2006), the icosahedral structures have a higher magnetic moment than other high-symmetry structures.

In work of Nava and coworkers (2003), Pd clusters were studied using the spin-polarized DFT method in the range  $N = 2\text{--}309$ . The  $N = 13$  cluster was found to have an icosahedral structure with a high spin state. It is seen to undergo a very slight Jahn-Teller distortion, which increases the cohesive energy only by 0.01 eV. The truncated decahedron and the cuboctahedron are found to be less stable.

Yao and coworkers (2007) utilized results from simulated annealing of Ni clusters using an empirical potential as starting configurations to further optimize them using a DFT code. This is another technique often used in cluster literature. In this work, Ni clusters with  $N = 10\text{--}27$  atoms were found to attain icosahedron-like structures with the  $N = 13$  cluster being a perfect icosahedron and  $N = 19$  the double icosahedron. Clusters in the range  $N = 28\text{--}40$  have very complicated structures because they are in the transition region between the  $N = 13$  icosahedron and the  $N = 55$  icosahedron. Around  $N = 19$  and  $N = 55$ , clusters are mostly formed by adding or removing a few atoms from the corresponding perfect icosahedra. Dips are observed in the magnetic moment for  $N = 13$  and 55 as expected from the compact structure of these clusters.

While all of the studies mentioned above deal with collinear spin, which singles out one direction along which the magnetic moment may be oriented, a very important class of clusters with high magnetic moments display noncollinear spin. In these clusters, the magnetic moment is allowed point in an arbitrary direction and thus present a new degree of freedom. A good example for the investigation of this effect is presented in the work by Du et al. (2010) where 6-atom clusters of Co and Mn atoms with several different compositions but always in the octahedral geometry were investigated within the DFT theory including the noncollinear spin formalism. Low-lying isomers with up to more than  $40^\circ$  of average degree of noncollinearity were identified. For certain compositions and geometries different tendencies for magnetic coupling (AFM vs FM) is also found to cause a certain degree of spin frustration.

In the work by Zhang and coworkers (2004), Mo clusters were studied within the DFT framework. An interesting result was that the initial icosahedral structure for the  $N = 13$  cluster was found to undergo a very large distortion. This distortion was explained by the tendency of Mo clusters to form Mo dimers. The strength of the bonds in  $\text{Mo}_{13}$  is covalent, therefore, at this size, the cluster shows nonmetallicity. At  $N = 55$ , the icosahedral structure is found to again undergo a large distortion. However in contrast to  $N = 13$ , the alternate  $O_h$  structure was not found to be much more stable than the distorted icosahedron. This was explained by the decrease of nonmetallicity with size.

## 1D Structures: Nanotubes, Nanowires, Nanorods

---

In nanoscience literature, the name *one-dimensional* was coined to describe systems where one of the dimensions is several orders of magnitude larger than the other two dimensions. Much like the zero-dimensional case, the border between one- and two-dimensional systems is

ill-defined and system-dependent. For this reason, two-dimensional systems exhibit the same richness in structural and electronic properties as in the zero-dimensional case unlike their bulk counterparts.

One, dimensional structures may, in the broadest classification, be divided into nanotubes, nanowires, and nanoribbons. *Nanotubes* are simply described as two-dimensional materials (such as graphene, BN sheets, TiO<sub>2</sub> sheets and many others) seamlessly rolled into a hollow cylinder although the actual fabrication usually follows a much more involved procedure. Nanotubes may be regarded as a unique subset of one-dimensional structures that do not have a surface and are thus devoid of surface effects. In this respect they are analogous to the fullerenes in the zero-dimensional case. *Nanowires* on the other hand are extremely thin wires that are grown or extracted along well-defined crystal directions and may have widely different surfaces. The surfaces, however, rarely remain in their bulk configuration and often reconstruct to reduce strain or saturate broken bonds. This procedure is highly size- and material-specific, and nanowires therefore display a large variety of strongly surface-dependent properties. Finally, *nanoribbons* are thin strips of two-dimensional materials such as graphene. The edges may reconstruct or be saturated with different species to modify their properties.

In addition to structural and electronic properties that are explored in zero-dimensional materials, one-dimensional materials also exhibit rather interesting elastic properties. We shall begin this section with a brief review of elastic considerations regarding one-dimensional nanomaterials and afterward move onto structural and electronic properties.

## Elastic and Structural Properties

---

In nanowire applications such as AFM tips, NEMS, and MEMS, which make use of mechanical properties, it is crucial to have a good understanding of the evolution of elastic properties all the way down to the nanoscale. Elastic properties that are ordinarily under investigation include elastic moduli, plasticity, crack propagation, buckling, and breaking points.

There are numerous examples of experimental determination of elastic properties of nanowires in the literature. A recent study by Barth and coworkers (2009) determines the Young's modulus of SnO<sub>2</sub> nanowires by anchoring and bending them with the help of an AFM tip. By mapping the bending amplitude to the Young's modulus through classical elasticity formulae the Young's modulus is estimated at around 110 GPa for the samples studied.

Contrary to the macroscopic scale, the elastic properties of nanoscale one-dimensional systems are often seen to depend on their physical dimensions. This intriguing fact brings forth the necessity of studying, among others, the elastic properties of such systems as a function of their size. In fact, the theoretical literature is very rich in examples of such studies. Empirical potentials are particularly suitable for studies of size dependence since systems with large numbers of atoms may be handled with relative ease, allowing the determination of convergence of elastic properties of nanomaterials to those of their bulk counterparts. A related question to this fact is to what extent the laws of continuum elasticity can be applied to nanoscale systems, which has received much attention both theoretically and experimentally. A recent study by Rudd and coworkers (2008) opens with this very same question, where the Young's modulus of Ta (001) and Si(001) nanowires has been determined using a Finnis-Sinclair (1984) and Stillinger-Weber (1985) potential respectively in a molecular dynamics simulation. Nanowire radii were explored up to approximately 10 nm and both materials were found to display a

strong dependence on the wire width eventually converging to the bulk value. Interestingly, the convergence trends are opposite where the Young's modulus of the Si nanowires increases while that of Ta nanowires decreases with radius. In the same study, DFT calculations were also performed on Si nanowires, partially confirming the outcome of the Stillinger-Weber calculations. However, the match with continuum theory was found to be much better for the DFT results.

Size-dependence is also demonstrated in a study by Hu and coworkers (2008) on ZnO nanowires and nanotubes where they use an exp-6 type empirical potential including Coulomb interaction for Young's modulus calculations. The Young's moduli of nanowires and nanotubes show a very strong dependence on the radius and wall thickness respectively.

Due to the extremely high surface-to-volume ratio in nanowires, the particular surfaces that are exposed at the outer edges of the nanowires play a crucial effect in the determination of their elastic properties. Recent evidence for this fact was demonstrated by Wang and Li (2008) in their DFT-parameterized model study of Ag, Au, and ZnO nanowires with different surface terminations. Their results show discernible albeit small differences in the size dependence of the Young's modulus for different surface terminations of the nanowires in question.

Nanotubes have also received a great deal of attention from researchers due to their extraordinary elastic properties. They have been shown to possess an unusually high axial stiffness in addition to very high reversibility under large distortions. In addition to the large body of literature on experiments probing the elastic properties of nanotubes, many theoretical studies have also been conducted. Due to their varying radii and chirality, nanotubes present endless possibilities for the investigation of their elastic properties. Liang and Upmanyu (2006), for instance, have studied the radius (or equivalently curvature) and chirality dependence of the torsion induced by applied axial strength of the nanotubes. Their studies, which utilize the widely used second-generation reactive empirical bond-order potential (Brenner 1989), revealed a torsional response of up to  $0.75^\circ$  nm, which varied remarkably for different radii and chiral angles. Conversely, as reported in several early studies on nanotubes employing DFT calculations, Young's modulus is known to be largely independent of the chirality.

Elastic properties of nanotubes of many materials other than C have also been theoretically explored. In an exhaustive work, Baumeier and coworkers (2007) used DFT calculations to survey such properties as strain energy and Young's modulus of SiC, BN, and BeO nanotubes. Baumeier and coworkers observe that being composed of two atomic species instead of one as in carbon nanotubes, the nanotubes made out of these materials exhibit a different relaxation pattern for the relevant anions and cations, suggesting possible different behavior than carbon nanotubes. Nevertheless, the results show that at least for  $(n, n)$  and  $(n, 0)$  nanotubes of similar radii the behavior is similar. All three materials display a decreasing Young's modulus as a function of radius converging to the sheet value for large radii. Among the three materials, BN nanotubes display a significantly high Young's modulus, followed by SiC and finally by BeO nanotubes.

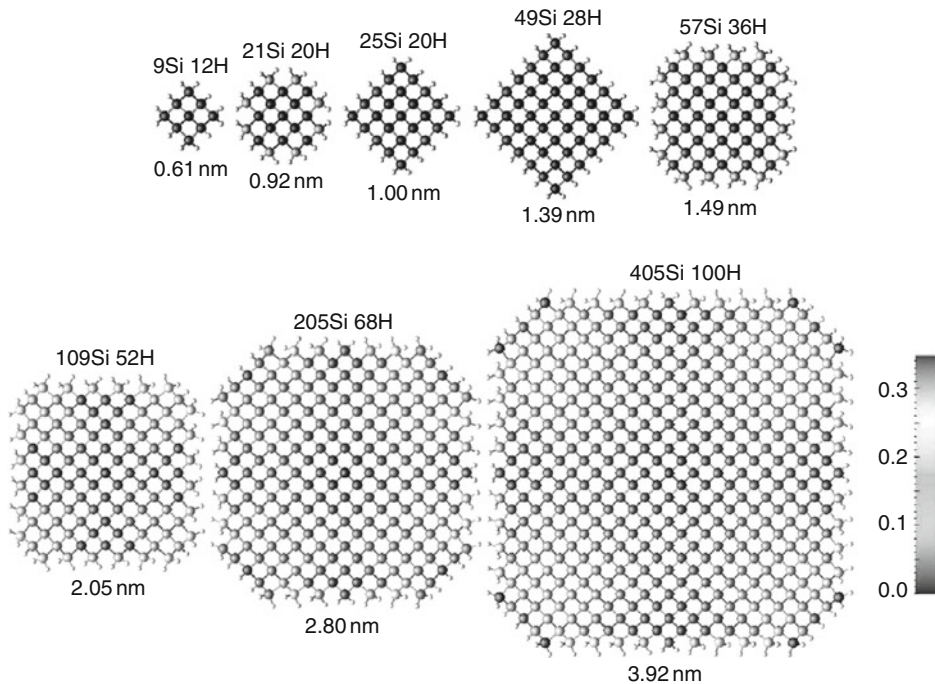
The interwall attraction in multi-walled nanotubes opens up another possible avenue for the study of elastic properties. Zhang (2008) and coworkers have studied the Young's modulus, Poisson ratio and the buckling point of multi-walled nanotubes using a combination of second-generation reactive bond-order potential to model intralayer bonding and a Lennard-Jones potential for the interlayer interaction. The multi-walled nanotubes studied were divided into two sets, the first formed by embedding increasingly smaller  $(n, n)$  tubes into a large  $(20, 20)$  nanotube (up to four walls) and the second by placing a  $(5, 5)$  tube into increasingly larger  $(n, n)$  tubes (again up to four walls). A molecular dynamics algorithm was used during their



calculation and the dependence of the moduli in addition to the buckled morphologies were presented. Young's modulus and Poisson's ratio turn out to follow a different trend for the two sets considered. While the set that grows inward display increasing (decreasing) Young's modulus (Poisson ratio) for increasing number of walls, the set that grows outward follow the opposite trend.

As mentioned in the introduction to this section, one way to saturate the surface bonds of nanowires is through passivation by different species. The elastic behavior of passivated versus unpassivated nanowires raises an interesting question. Lee and his coworkers (2007) studied several elastic properties of H-passivated nanowires of a large range of radii varying between 0.61 nm and 3.92 nm (see ► Fig. 27-6) using DFT. As expected, the Young moduli of H-passivated Si nanowires mostly follow predictions from continuum models regardless of the varying proportions of  $\langle 100 \rangle$  and  $\langle 110 \rangle$  surfaces exposed. This is attributed to the fact that the bulk-like covalent bonding character at the surfaces is preserved when H is used to passivate the dangling bonds at the surface.

Although microscopic modeling is of utmost importance in the understanding of nanoscale materials, there are a number of experimental situations of interest that cannot be handled by these time-intensive methods due to their large size. For large enough systems (such as large portions of nanotubes suspended over a trench) continuum methods may be employed (Ustunel et al. 2005). However, complete coarse-graining is also not always a viable choice since one then loses detailed information on locally nonhomogeneous regions of the system such as defects



■ Fig. 27-6

H-passivated Si nanowires of different sizes studied by Lee et al (Reprinted with permission from Lee and Rudd (2007). © (2007) by the American Physical Society)

and local deformations. In such cases, *multiscale methods* which apply different methods at different scales of the system are the methods of choice. An illustrative example was studied by Maiti (2008) where a micromechanical sensor made out of a nanotube was deformed by a Li needle. The bent but undeformed portions of the nanotube were modeled by a coarse-grained *molecular mechanics* simulation, while the highly deformed midsection (enclosed in a box) was modeled using a quantum mechanical method. The two methods were then matched at the interface of the two regions.

## Structural Properties

The novel electronic properties of nanotubes, nanowires, and nanobelts are inextricably linked to their structural properties. This is largely due to their high surface-to-volume ratio, where the bonding on the surface structure determines the electronic states which in turn determines such properties of the system as conductivity and magnetism.

As mentioned in the introductory section, nanowires nowadays may be manufactured from a great variety of materials. As fabricated, it is experimentally difficult, if not impossible, to intuitively infer their surface structure. Simulations on the other hand provide an inexpensive yet accurate way of studying this relation between structure and electronic properties.

The methods of preference in nanowire modeling is generally tight-binding and to a larger extent DFT, since electronic properties depend sensitively on the structure requiring accurate calculations. Once a material (or combination of materials) is chosen the important parameters of nanowire modeling are the particular surfaces surrounding the nanowire and passivation, that is, the saturation of the bonds at the surfaces. Two of the most commonly studied surface terminations are surface reconstruction and H-passivation.

Due to the axial periodicity of one-dimensional nanomaterials, plane wave-based methods which are traditionally used for crystals are very often employed. In the work of Arantes and Fazio (2007), where they study free and passivated Ge nanowires, the band gap of passivated and unpassivated nanowires were determined using a plane wave-based GGA-DFT method. The nanowires were grown in the  $\langle 110 \rangle$  and  $\langle 111 \rangle$  directions and their band gaps were calculated as a function of nanowire diameter. In spite of the well-known underestimation of the band gap by LDA and GGA methods, a trend can be obtained rather reliably. The band gaps are seen to vary with respect to direction and size.

Though not often encountered global search algorithms are also used for determining the structure of nanowires. Especially in the case of nanowires with smaller radii, the structure may be so different from bulk as to prevent any *a priori* prediction. Chan and coworkers (2006) conducted a genetic algorithm search based on the formation energy of H-terminated Si NWs where the formation energy is defined as

$$f = (E - \mu_H n_H) / n - \mu, \quad (27.5)$$

where  $E$  is the total energy of the NW in question,  $\mu_H$  and  $\mu$  are the chemical potentials of H and Si respectively, and  $n$  is the number of Si atoms. The genetic algorithm was conducted in two stages. In the first stage a long evolution through several generations was conducted using an empirical potential (of the Hansel-Vogel type). In the second stage the outcome structures of the evolution for each size were relaxed using a DFT algorithm. The result, reminiscent of cluster structures, is that certain sizes of Si NWs are preferred over other sizes. These structures are once again termed *magic sizes*. In general, structures with even number of Si atoms are preferred over



those with an odd number. The most stable structures are observed either in a *plate-like* form where chains of Si hexagons join together to form flat structures, or a *hexagon-shaped* cross section.

One of the most important parameters in determining the geometric and therefore the electronic structure of nanowires is surface termination. The high-energy dangling bonds at the surface may either be saturated by a rearrangement and rebonding of the surface atoms or by attaching electropositive species (such as H). In general, while the reconstruction may significantly alter the structural and electronic properties of the material, passivation by other species leaves these properties relatively unaltered. In the recent work of Migas and Borisenko (2008),  $\langle 001 \rangle$  oriented Si nanowires were passivated by O, F and H and the structural and a large number of different sizes and geometries were studied using DFT. Under different combinations and coverages by these elements, the band gap of the Si nanowires considered (only nanowires with rhombic cross sections were considered) were found to vary between 1.20 and 1.96 eV, which shows that termination can be used as a means to control the electronic properties.

Countless other studies in understanding the structure of experimentally relevant one-dimensional structures have been done. Bi nanowires (Qi et al. 2008), CdSe nanorods with hexagonal and triangular cross sections (Sadowski and Ramprasad 2007), and Te nanowires (Ghosh et al. 2007) are some studies that may be mentioned. In addition to materials that have already been manufactured, researchers have also been interested in the possible existence and properties of nanoscale systems that have not yet been experimentally realized. Rathi and Ray (2008), for instance, have examined the possibility of SiGe nanotubes, while Qi (2008) and coworkers investigated Bi nanotubes and hollow Bi rods. Recently it was demonstrated by model calculations that the stable carbon nanotube structure might be possible with non-graphene like form (Erkoc 2004). Furthermore, nanorod structures constructed from benzene rings only (called as *benzorods*) may also be possible. Their structural and electronic properties were investigated by performing model calculations (Erkoc 2003; Malcioglu and Erkoc 2004).

## Electronic, Magnetic and Optical Properties


---

As a result of the immense variation in structural properties of one-dimensional structures, one observes an equally diverse spectra of electronic properties. Perhaps the most intriguing property of one- and two-dimensional nanoscale systems is that after the required geometrical deformations in order to reach their equilibrium, one might observe a stark difference between the newly formed system and its bulk counterpart. A material which is an insulator in bulk may become a conductor when taken to the nanoscale. Similarly one- or two-dimensional nanostructures of a nonmagnetic material may have a nonzero magnetic moment. These differences usually stem from the new states introduced into the electronic structure of the material by terminating structures such as surfaces, steps, edges, and corners. The interest in these emergent properties is due to the possibilities of integrating these small-scale materials into technological applications and controlling their properties by controlling the structure.

Due to the ease of interfacing with current technology, Si nanowires have perhaps been the most intensely studied system. Rurali and Lorente (2005), for instance, explored a large range of surface reconstructions for  $\langle 100 \rangle$  Si nanowires with a small radius of about 1.5 nm. They discovered that for certain reconstructions the nanowires develop conducting states in their band gap, while for others the semiconducting behavior is retained. This is a prime example of effects of confinement on the electronic structure of a system.

Another parameter that has a strong effect on the electronic properties of nanowires is surface termination. As demonstrated by Rurali (2005) that both Si and C-terminated H-passivated SiC nanowires have a larger band gap than that of bulk SiC. As discussed by Rurali, this is purely a confinement effect since passivation prevents reconstruction and the related introduction of gap states. However, when the nanowires are allowed to reconstruct, both species of SiC nanowires are seen to become conducting due to the surface states introduced into the band gap.

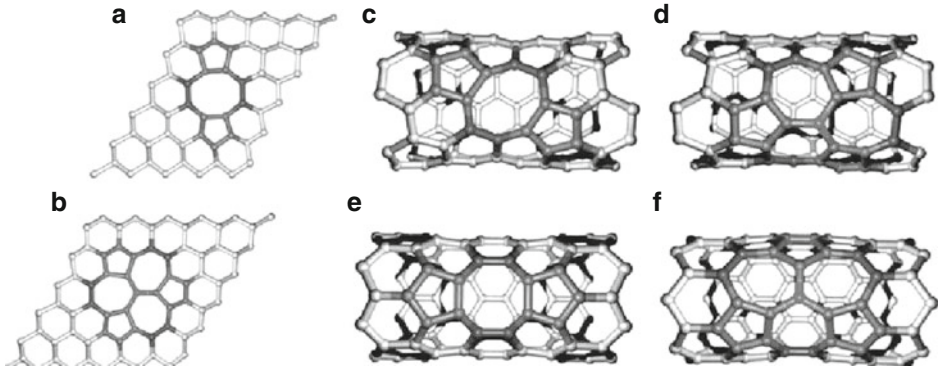
In addition to the conventional carbon nanotubes, several other materials were investigated as viable candidates for nanotube structures. BN (Chopra et al. 1995) and more recently (Sun et al. 2002) SiC nanotubes are two such materials which have been successfully synthesized in the nanotube form. Following their synthesis Gao and coworkers (2008) conducted a DFT-PAW study of undoped and N-doped SiC nanotubes of varying sizes. For each size the nanotubes were doped initially with 2 and 4 N atoms and their structural and electronic properties were studied. For each doping level, several possibilities were investigated and the most stable structure was identified. As an extreme case, the case in which all the C atoms were replaced with N atoms, in other words SiN nanotubes, was considered. These nanotubes, instead of being circular were found to have a staggered or star-like cross section. In all the cases considered the nanotubes were found to be semiconducting with an indirect band gap. Recent model calculations on binary compounds BN (Erkoc 2001), GaN (Erkoc et al. 2004), InP (Erkoc 2004), ZnO (Erkoc and Kokten 2005) nanotubes give reasonable results comparable with experimental findings.

Although by nature rather free of defects, the few existing defects in graphene and nanotubes change the electronic structure of their host material drastically (Pekoz and Erkoc 2008). In spite of the several experimental methods that have been developed to locate and study the properties of such defects, theoretical methods are an indispensable tool for creating isolated defects of the desired nature and studying their effects on electronic properties. A particularly interesting question is the stability of well-characterized graphene defects in nanotubes of varying radius and chirality. Since a graphene sheet can be viewed as a nanotube with an infinitely large radius, the formation energy of any nanotube defect should tend to the equivalent defect on a graphene sheet. Amorim et al. (2007) demonstrated an example of this behavior by studying the so-called 555777 defect, which is a combination of three pentagons and three heptagons. This defect is formed in two steps. In the first step two divacancies coalesce to form a new defect (585) composed of two pentagons and an octagon. This step is followed by a further structural change, which yields the 555777 defect, see  Fig. 27-7.

In graphene the 555777 defect is found to be more stable than the 585 defect by 0.8 eV. The same defects were then created in zigzag and armchair nanotubes of radius in the range of 7–15 Å. As in the graphene case the 555777 defect is found to be more stable in all the nanotubes studied. The formation energy is, however, lower than in the graphene case. The expected tendency toward the corresponding graphene values is seen in both cases and convergence is estimated to occur around a radius of 40 Å.

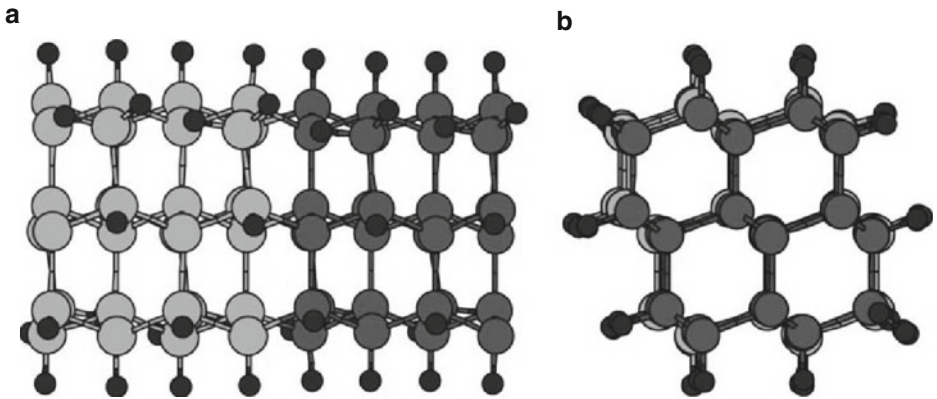
The effect of defects on the electronic properties of their host substance is illustrated in this work by the conductance graph calculated using the Green's function density functional theory. The results indicate that the presence of both the 585 and 555777 reduce the conductance considerably while at the same time displaying different voltage dependence.

Another investigation of defects in nanotubes for the purpose of application as a gas sensor was conducted by Andzelm and coworkers (2006). The particular question at hand is the binding of NH<sub>3</sub> molecule to nanotubes and whether or not binding is enhanced by defects. Three defects are considered: a Stone-Wales defect (a defect formed by rotating a given bond by 90°



■ Fig. 27-7

585 (a) and 555777 (b) defects in graphene and 585 (c,e) and 555777 (d,f) defects in a nanotube in different orientations (Reprinted with permission from Amorim et al. (2007). © (2007) by the American Chemical Society)



■ Fig. 27-8

A Si-Ge interface shaped into a nanotube. (a) Side view, (b) cross view (Adapted from Kagimura et al. 2007)

resulting in the formation of two pentagons and two heptagons), a monovacancy and an interstitial C atom placed on top of a bridge. In addition, the case of an  $O_2$  molecule dissociated on a SW defect was also considered to mimic the environmental effects. Two different orientations, straight and chiral, for the SW defect were considered. All-electron DFT calculations reveal that the monovacancy is the most stable. Calculation of reaction barriers also reveal that defects with preabsorbed O dissociate  $NH_3$  into  $NH_2$  and H.

The heterostructure problem, which has been widely studied in the bulk form, is becoming an increasingly popular topic also in the one-dimensional systems. The band alignment problem has been addressed recently in a DFT study conducted by Kagimura and coworkers (2007) where a Si-Ge interface was studied. The model for such a system is shown in ► Fig. 27-8. The band states contributed by the surface dangling bonds were investigated as possible candidates for the induction of a potential well.

The search for nanoscale materials that exhibit spontaneous magnetization has become an increasingly rich field in the past decade. Several materials such as doped nanotubes and nanowires, defective graphene and nanoribbons of two-dimensional materials can be itemized as candidates considered in these studies. In order to identify the suitability of a material for spontaneous magnetization, electron density in the two spin channels,  $n^\uparrow(\vec{r})$  and  $n^\downarrow(\vec{r})$  are compared. If there is a significant difference in this distribution, the material is nominated for use in magnetic applications. If in addition the density of states in the two spin channels show different characteristics at the Fermi level such that in one channel there is a significantly larger number of states than the other, then the material provides promise also in *spintronics* applications.

One such candidate material for magnetic applications is BN sheets and nanotubes doped with several different elements. In a recent example, Li and coworkers (2008a), in their DFT study on BN nanotubes with one, two, and three H atoms adsorbed at different locations, observed that some of the configurations considered may give rise to a magnetic moment of up to 2.0. The origin of this magnetic moment is evident from the band structures where the contribution of band gap states are due to only one of the spin channels. The states that are seen in the gap are also shown visually and their origin is unambiguously identified as due to the adsorbed hydrogen.

A rather novel and intriguing application of nanomaterials and its investigation using theoretical modeling is the subject of a recent work by Santos de Oliveira and Mina (2009). Their study discusses a phenomenon called *self-purification* of nanomaterials, namely, the expulsion of foreign species from the surface. Self-purification is attributed to the fact that nanoscale materials have a lower incorporation rate of impurities compared to their bulk counterpart. In this work SiC nanowires are studied as another potential example of self-purifying materials. B and N impurities were planted at different positions inside and on the surface of three SiC nanowire configurations ( $\langle 100 \rangle$  Si-coated,  $\langle 100 \rangle$  C coated and  $\langle 111 \rangle$  Si and C coated) at locations ranging from the center to the surface. The formation energies of the configurations thus formed were then calculated and compared. As a result, the self-purification process was found to be favorable for B-doped SiC nanowires irrespective of their orientation. The B atom was found to segregate favorably to the surface and thus expelled. The N impurities, however, were found to prefer the sites in the core of the nanowires, and therefore, N-doped SiC nanowires were found to fail as self-purifying materials.

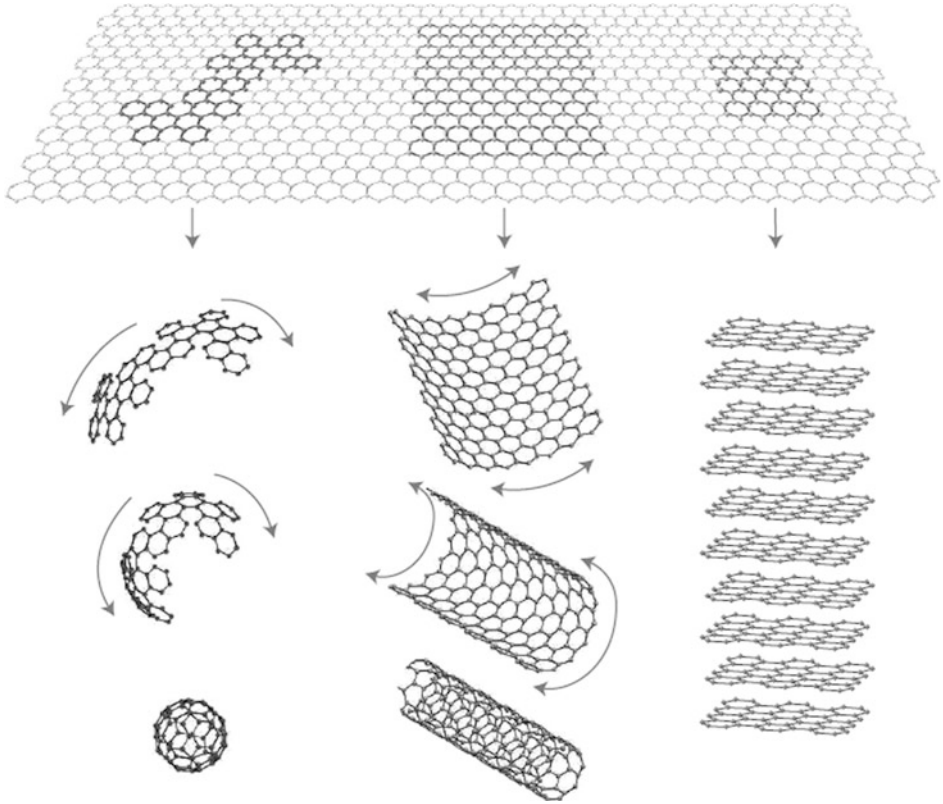
One-dimensional systems are actively sought after also for their optical properties. Using the GW method, which is an accurate method for studying excited states, Bruno and coworkers (2007) demonstrated that optical properties of Si and Ge nanowires depend not only on the nanowire diameter but also on the orientation.

## 2D Structures: Graphene and Derivatives

---

Due to the remarkable ability of carbon to exist in different hybridization states, carbon-based materials display an unusually rich variety. Diamond, graphene, cage-like molecules and perhaps most notably carbon nanotubes are examples of the large selection of possibilities.

Graphene, which is a single layer of graphite, may be thought of as the building block of most of the allotropes listed above (► Fig. 27-9). Nanotubes are geometrically rolled up versions of graphene, and fullerenes can be formed by introducing topological defects (heptagons



■ Fig. 27-9

Graphene is a 2D building material for carbon materials of all other dimensionalities. It can be wrapped up into 0D buckyballs, rolled into 1D nanotubes, or stacked into 3D graphite (Reprinted with permission from Geim and Novoselov (2007). © (2007) by Nature Publishing Group)

and pentagons) into the perfect honeycomb lattice structure of graphene in order to introduce positive and negative curvature (Freitag 2008; Peres et al. 2006).

Regardless of the immense attention that graphene received in the theoretical literature, it wasn't until 2004 (Novoselov et al. 2004) that a single layer of graphene was isolated experimentally. Since two-dimensional crystals were proven to be unstable theoretically (Landau and Lifshitz 1980; Mermin 1968), the discovery of free-standing graphene came as a surprise (Meyer et al. 2007). This apparent discrepancy, however, was lifted when upon closer inspection, the isolated graphene sheets were not perfectly flat but had corrugations reaching up to 1 nm in size.

Since the discovery and isolation of graphene was achieved, many other materials were found to form two-dimensional structures. In this chapter, we give an overview of carbon-based two-dimensional materials including graphene, graphene nanoribbons, nanobelts, and strips in addition to two-dimensional structures of several other materials.

## Graphene, Nanosheets, Nanoribbons, Nanobelts, Nanostrips

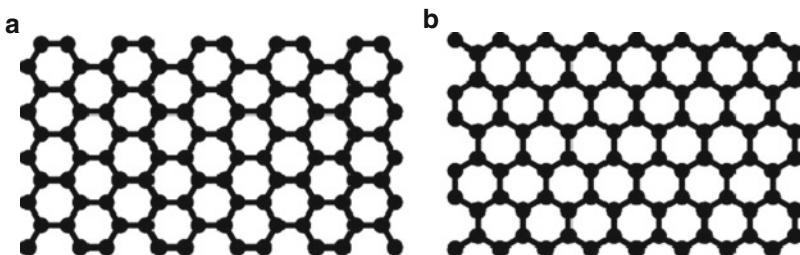
With the advent of several sophisticated experimental techniques, the two-dimensional confinement of graphene layers were further extended to one-dimensional in the form of *nanoribbons*. Nanoribbons are narrow strips of graphene that may exhibit quasi-metallic or semiconducting behavior depending on the geometry of their edges. Much like nanotubes, graphene nanoribbons (GNRs) are also termed *zigzag* or *armchair* based on the directionality of the bonds with respect to the long axis (see ► Fig. 27-10). Due to the dependence of their electronic properties on their geometry, it is important to control the morphology and crystallinity of these edges for practical purposes. It has been experimentally shown that (Jia et al. 2009) controlled formation of sharp zigzag and armchair edges in graphitic nanoribbons are possible by Joule heating. During Joule heating and electron beam irradiation, carbon atoms are vaporized, and subsequently sharp edges and step-edge arrays are stabilized, mostly with either zigzag- or armchair-edge configurations.

In addition to the edge geometry, the electronic properties, in particular the band gap, of nanoribbons also depend on their width (Han et al. 2007; Wu and Zeng 2008). The magnetic properties may also be severely altered upon reduction of size to a graphene fragment (Wang et al. 2008) which results in the emergence of giant spin moments.

Another path for controlling the electronic properties of nanoribbons is by an application of an external electric field or by chemical doping of the pristine samples. Half-metallicity, for instance, which has several applications in spintronics (Wu and Zeng 2008) may be introduced through functionalization with such species as H, COOH, OH, NO<sub>2</sub>, NH<sub>3</sub>, and CH<sub>3</sub> (Son et al. 2006).

Straight GNRs with zigzag, armchair, or mixed edges are proven to be semiconducting by the experiment. In addition, GNRs can be sculpted by attaching two segments together that are manufactured to make a 120 degree angle with each other thereby forming a *sawtooth-like* nanoribbon (► Fig. 27-11). The structure of a sawtooth-like GNR can be characterized by two integers ( $w, l$ ). The first integer denotes the width of the nanoribbon, while the second integer describes its periodic length (Wu and Zeng 2008).

Stability is an important issue for a material which is intended to be used as a building block of device applications. Even though perfect two-dimensional crystals are proven to be unstable, graphene is found to be stabilized by corrugations in the third dimension. Understanding the effect of GNR width on the stability is therefore also a central issue for possible applications. Molecular dynamics computer simulations using empirical interatomic potentials predict that



■ Fig. 27-10

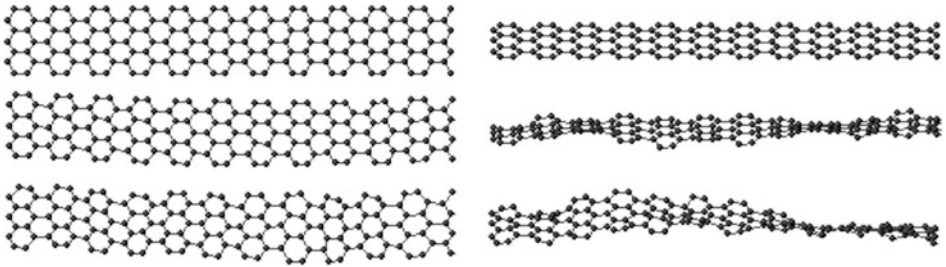
(a) Armchair graphene ribbon model. (b) Zigzag graphene ribbon model





■ Fig. 27-11

The model structure of a sawtooth-like GNR (Adapted from Wu and Zeng 2008)



■ Fig. 27-12

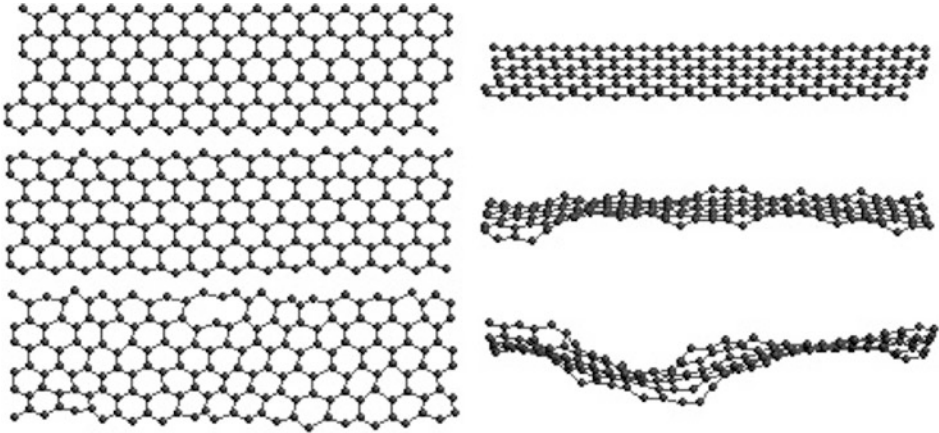
Armchair edged GNRs. *Left* column shows *top* view and *right* column shows tilted view. GNRs of width five hexagonal rings are shown. 1 K, 300 K, and final temperature images are given (Adapted from Dugan and Erkoc 2008)

structural stability of graphene nanoribbons show dependence on size (width) and edge orientation (Dugan and Erkoc 2008). ● *Figures 27-12* and ● *Fig. 27-13* show respectively the relaxed structures of armchair and zigzag edged GNRs with various widths.

In the recent nanoscale literature, a wealth of materials other than C have been identified, both theoretically and experimentally, as viable candidates for future use as two-dimensional devices.

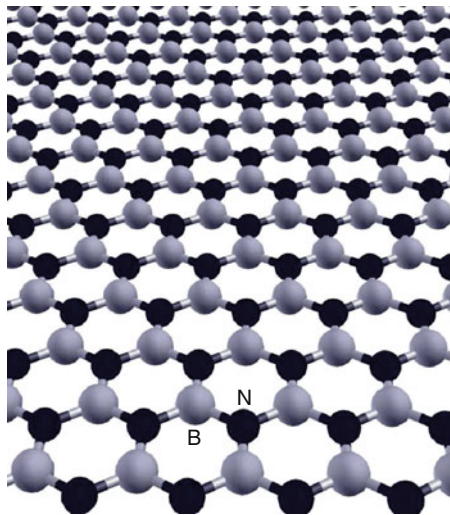
Boron nitride, for instance, having electronic properties that resemble carbon can exist in a hexagonal structure *h*-BN similar to the graphite layered geometry. Much like graphene sheets, BN sheets can be grown on more or less lattice-matched transition metal surfaces (Corso et al. 2004; Huda and Kleinman 2006). A model BN sheet is shown in ● *Fig. 27-14*.

BN, being a member of the III-V semiconductor family indicates the possibility of nanoribbons or nanobelts made of other semiconductor families. Indeed, several oxide and other II-VI family nanobelts have been discovered and reported (Pan et al. 2001) (ZnO, SnO<sub>2</sub>, CdO, Ga<sub>2</sub>O<sub>3</sub>, PbO<sub>2</sub>, ZnS, CdSe, and ZnSe). Some of the oxides in this family such as ZnO and SnO<sub>2</sub>, owing to their polarity and crystal structure, deform in novel morphologies such as rings, springs, and spirals in order to bring together the positive and negative charges, counteracting the charge imbalance (Yang and Wang 2006). These structures comprise a versatile set of nanomaterials that are promising candidates for various applications such as sensors, resonators, and transducers.



■ Fig. 27-13

Zigzag edged GNRs. *Left column shows top view and right column shows tilted view. Ribbons of width five hexagonal rings are shown. 1 K, 300 K, and final temperature images are given (Adapted from Dugan and Erkoç 2008)*



■ Fig. 27-14

The geometric structure of BN sheet (Adapted from Venkataraman et al. 2009)

*Nanobelts*, a term coined by researchers working on these structures (Wang 2004), are described as nanowires with not only a well-defined growth direction but also well-defined top, bottom and side edges and cross-section. The nanobelt structures are usually obtained from functional oxides, which are semiconductor materials, such as ZnO, Ga<sub>2</sub>O<sub>3</sub>, t-SnO<sub>2</sub>, o-SnO<sub>2</sub>, In<sub>2</sub>O<sub>3</sub>, CdO, and PbO<sub>2</sub>. Pure metal nanobelt structures are also possible, Zn is one of the metals that form fine nanobelt structures (Wang 2004). ZnO, being one of the most versatile materials in nanoscale research alongside with carbon and BN, has once again been investigated at

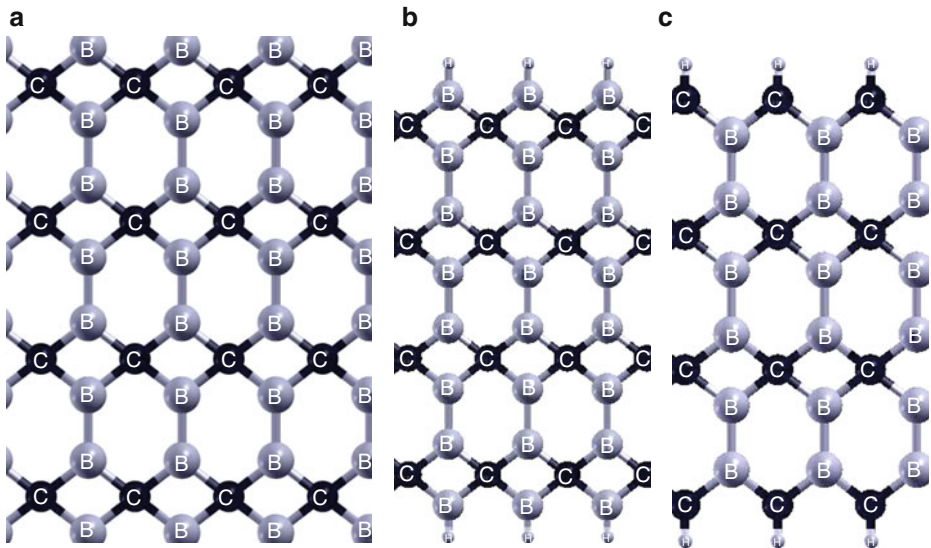


great depth in the context of nanobelts (Kulkarni et al. 2005; Wang 2004). Molecular dynamics computer simulations using empirical interatomic potentials (Kulkarni et al. 2005) reveal that ZnO nanobelts display properties that depend on their size and orientation. Depending on the growth direction, ZnO nanobelts may exhibit an interesting shell structure or a simple surface reconstruction.

Nanostrips are similar to nanobelts, they are used with the same meaning with nanobelts. All these nanostructures (ribbons, belts, strips) are ideal materials for building nano-sized devices and sensors (Lin et al. 2009).

In addition to the materials mentioned above, recent theoretical studies have proposed a wealth of two-dimensional structures that are composed of less common materials. One such example is the recently proposed  $B_2C$  graphene (Wu et al. 2009). The optimized  $B_2C$  graphene structure is displayed in **Fig. 27-15**. Two neighboring  $CB_4$  motifs share two common boron atoms, giving rise to a hexagon and a rhombus. The mean B–C and B–B bond length is 1.557 and 1.685 Å, respectively. The sheet is slightly corrugated with a distance of only  $\sim 0.085$  Å. The corrugation is a result of an excess of 2p electrons normal to the sheet relative to the gas-phase  $CB_4$  molecule.

The quasi-one-dimensional  $B_2C$  nanoribbons are finite-size graphene with parallel edges. The width of the  $B_2C$  nanoribbon is defined by the number of C atoms normal to the long-axis of the ribbon. As shown in **Fig. 27-15**, type I and II  $B_2C$  nanoribbons are displayed. The dangling bonds at the edges of  $B_2C$  nanoribbons can be passivated by either H atoms or CH groups.

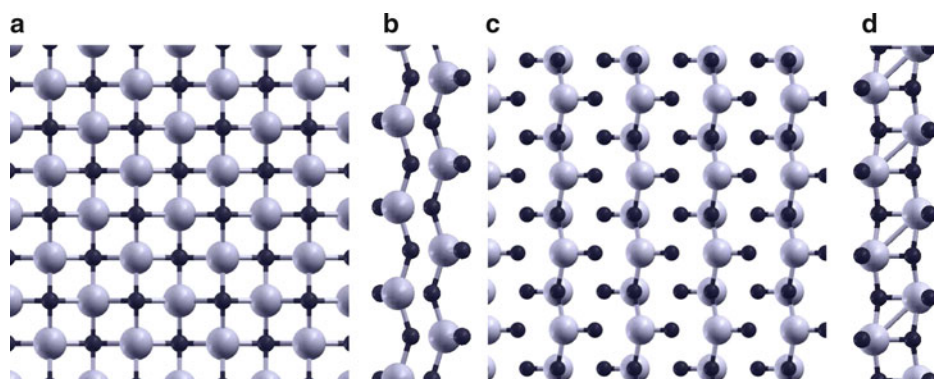


**Fig. 27-15**

(a) A  $C_{2V}$ - $CB_4$  motif structure. Each carbon atom is bonded with four boron atoms. Optimized structures of two types  $B_2C$  nanoribbons with two different edge configurations, referred as type I (b) and type II (c) (Adapted from Wu et al. 2009)

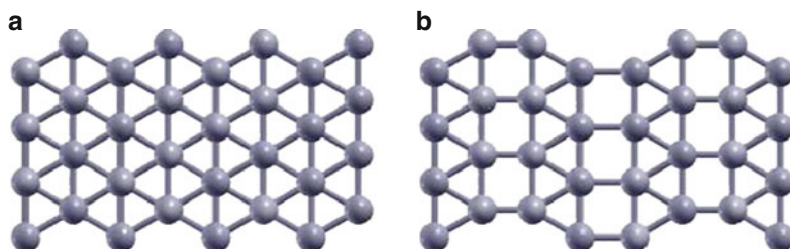
TiO<sub>2</sub> with its uses in solar cell applications and surface catalysis has received much attention both theoretically and experimentally. Its nanostructures are of equal interest to technology due to their chemical inertness, endurance, strong oxidizing power, large surface area, high photocatalytic activity, non-toxicity, and low production cost. The titania nanostructures are constructed by “cutting” of TiO<sub>2</sub> monolayers into nanostrips and by rolling them into cylindrical nanotubes or nanorolls (Enyashin and Seifert 2005). There are two different topological nanostrip models constructed from titania. One model is obtained from (101) surface of titania, called as anatase layer, and the second model is obtained from (010) surface of titania, called as lepidocrocite layer. A view of the structures of (101) and (010) TiO<sub>2</sub> layers are shown in ► Fig. 27-16. By rolling of these strips various nanostructures can be generated, such as nanotubes and nanospirals (nanorolls) (Enyashin and Seifert 2005).

Non-carbon elemental sheet structures have also been investigated. Lau et al. (2006) proposed four possible configuration models for the boron sheet. According to this study, the flat form, denoted {1212}, seen in ► Fig. 27-17 is a triangular network, while the buckled {1212}<sup>b</sup> and pair-buckled {1212}<sup>pb</sup> configurations include chain-wise and pair-wise out-of-plane displacements. Finally, a reconstructed {1221} configuration is investigated with inversion symmetry in the unit cell. It can be considered as a triangular-square-triangular unit network.



■ Fig. 27-16

Monolayers of TiO<sub>2</sub> in anatase (*top* (a) and *side* (b)) and lepidocrocite polymorphs (*top* (c) and *side* (d))




■ Fig. 27-17


Idealized 1212 (a) and reconstructed 1221. (b) Boron sheets

The DFT calculations reveal (Lau et al. 2006) that the reconstructed  $\{1221\}$  configuration is the most stable configuration by 0.23 eV/atom relative to the idealized  $\{1212\}$  configuration. Both the  $\{1212\}^b$  and  $\{1212\}^{bb}$  configurations tend to converge to the idealized  $\{1212\}$  configuration when relaxed during the geometry optimization.

## Electronic and Mechanical Properties

Graphene has a unique and curious band structure which can be approximated by a double cone close to the six Fermi points at the corners of the Brillouin zone (see  Fig. 27-18). Commonly referred to as Dirac electrons, the conduction electrons follow a linear energy-momentum dispersion and have a rather large velocity.

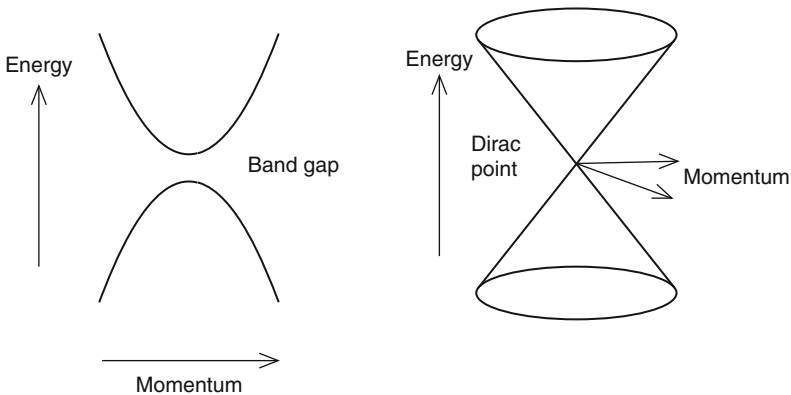
The conduction in graphene is enabled by the delocalized  $\pi$ -electrons above and below the plane. Due to their relative detachment from the tightly-knit planar network these electrons are free to move along the graphene sheet with rather high mobility. This is of course a rather desirable property for devices used in electronics (Li et al. 2008b).


A good yet simple method for understanding the band structure of graphene is the tight-binding formalism (Neto et al. 2009). Graphene is made out of carbon atoms arranged in hexagonal structure, as shown in  Fig. 27-19. The structure can be seen as a triangular lattice with a basis of two atoms per unit cell. The lattice vectors can be written as

$$\mathbf{a}_1 = \frac{a}{2}(3, \sqrt{3}), \quad \mathbf{a}_2 = \frac{a}{2}(3, -\sqrt{3}),$$

where  $a \sim 1.42 \text{ \AA}$ , is the carbon-carbon distance. The reciprocal-lattice vectors are given by

$$\mathbf{b}_1 = \frac{2\pi}{3a}(1, \sqrt{3}), \quad \mathbf{b}_2 = \frac{2\pi}{3a}(1, -\sqrt{3}),$$



 Fig. 27-18

The band structure of a representative three-dimensional solid (*left*) is parabolic, with a band gap between the lower-energy valence band and the higher-energy conduction band. The energy bands of 2D graphene (*right*) are smooth-sided cones, which meet at the Dirac point

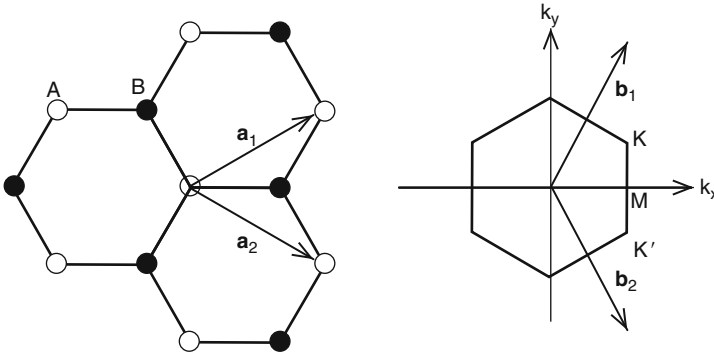


Fig. 27-19

Graphene lattice and its Brillouin zone. *Left:* lattice structure of graphene, made out of two interpenetrating triangular lattices ( $a_1$  and  $a_2$  are the lattice unit vectors). *Right:* corresponding Brillouin zone. The Dirac cones are located at the  $K$  and  $K'$  points

The two points  $K$  and  $K'$  at the corners of the graphene Brillouin zone (BZ) are named Dirac points. Their positions in momentum space are given by

$$\mathbf{K} = \left( \frac{2\pi}{3a}, \frac{2\pi}{3\sqrt{3}a} \right), \quad \mathbf{K}' = \left( \frac{2\pi}{3a}, -\frac{2\pi}{3\sqrt{3}a} \right).$$

The tight-binding Hamiltonian for electrons in graphene, considering that electrons can hop to both nearest- and next-nearest-neighbor atoms, has the form (in units  $\hbar = 1$ )

$$H = -t \sum_{\langle i,j \rangle, \sigma} (a_{\sigma,i}^\dagger b_{\sigma,j} + H.c.) - t' \sum_{\langle\langle i,j \rangle\rangle, \sigma} (a_{\sigma,i}^\dagger a_{\sigma,j} + b_{\sigma,i}^\dagger b_{\sigma,j} + H.c.), \quad (27.6)$$

where  $a_{i,\sigma}$  ( $a_{i,\sigma}^\dagger$ ) annihilates (creates) an electron with spin  $\sigma$  ( $\sigma = \uparrow, \downarrow$ ) on site  $\mathbf{R}_i$  on sublattice A (an equivalent definition is used for sublattice B),  $t$  ( $\sim 2.8$  eV) is the nearest-neighbor hopping energy (hopping between different sublattices), and  $t'$  ( $\sim 0.1$  eV) is the next nearest-neighbor hopping energy (hopping in the same sublattice). The Hamiltonian in Eq. 27.7 is solved at various momenta and the energy bands are obtained as follows:

$$E_{\pm}(\mathbf{k}) = \pm t \sqrt{3 + f(\mathbf{k})} - t' f(\mathbf{k}) \quad (27.7)$$

with

$$f(\mathbf{k}) = 2 \cos(\sqrt{3}k_y a) + 4 \cos\left(\frac{\sqrt{3}}{2}k_y a\right) \cos\left(\frac{3}{2}k_x a\right), \quad (27.8)$$

where the plus sign applies to the upper ( $\pi^*$ ) and the minus sign the lower ( $\pi$ ) band.


As illustrated by this simple model, graphene is a semimetal or a zero-gap semiconductor. At low temperatures it does not possess superconducting properties; however, as demonstrated by Pathak et al. (2008) using variational Monte Carlo, there is a possibility that doped graphene may superconduct.

The graphene nanoribbons (GNRs) discussed in the previous sections may also be modeled rather easily using the tight-binding formalism taking as the basis the usual Schrödinger's

equation (Ezawa 2006) or the massless particle Dirac equation (Sasaki et al. 2006). These models predict that armchair GNRs can be either metallic or semiconducting depending on their widths, and that zigzag GNRs with zigzag shaped edges are metallic regardless of the width.

The edges of GNRs are also suitable sites for chemical functionalization (Wang et al. 2007). Due to the existence of dangling bonds at the edges, the electronic properties of GNRs may be controlled by modifying these bonds by addition of other species.

The results of first-principle calculations using linear combination of atomic orbital density functional theory (DFT) method predict that the electronic band structures and band gaps of the GNRs show a dependence on the edge structure of the nanoribbons (Wu and Zeng 2008). Clearly, the electronic band structures are sensitive to the edge structure of the nanoribbons. All straight GNRs are semiconducting. Two distinct features can be seen concerning the band gap. The band gap of GNR with zigzag edges slightly decreases with increasing the width  $w$ , while that of GNR with armchair edges varies periodically as a function of  $w$ .

Like the straight GNRs, the calculated electronic band structures of the sawtooth-like GNRs (see  Fig. 27-20) also show semiconducting characteristics with direct band gap. More interestingly, even though the sawtooth-like GNRs have zigzag edges, their band gaps show similar oscillatory behavior as those of straight GNRs with armchair edges, which depend on the width  $w$ . However, for most nanoribbons, their band gap reduces monotonically with increasing periodic length  $l$ . The band gaps of nanoribbons with  $w = 1, 2, \text{ or } 4$  reduce much rapidly, whereas those of nanoribbons with  $w = 3 \text{ or } 5$  reduce gradually.

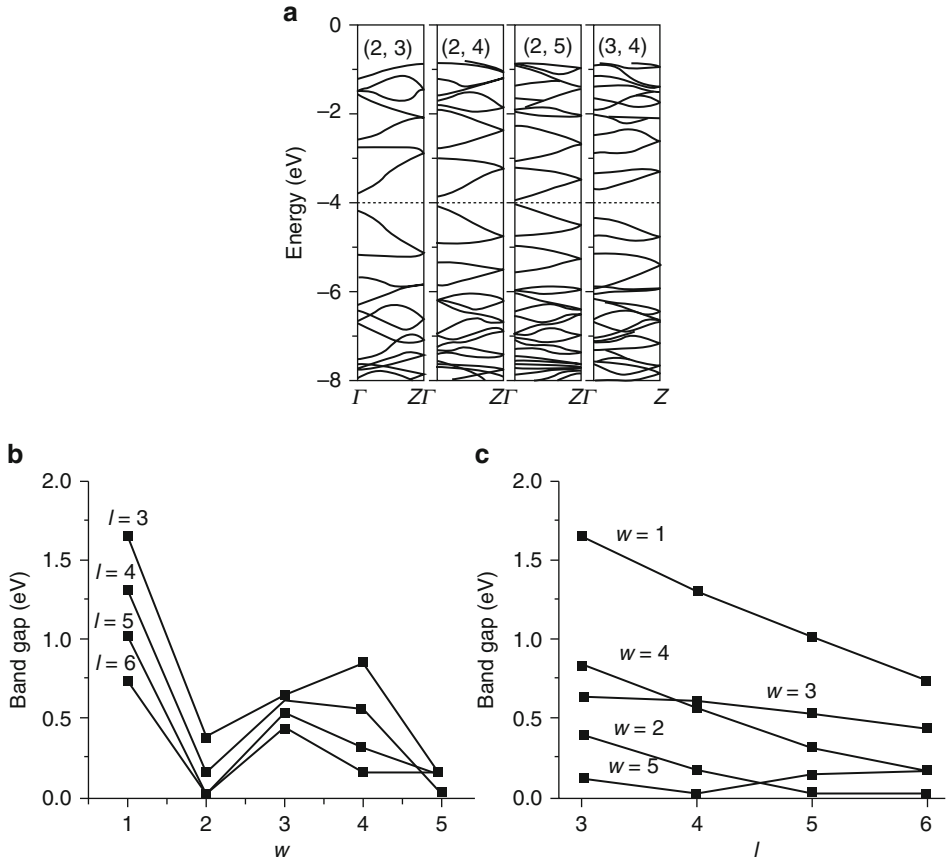
For  $(2, l)$  sawtooth-like nanoribbons, the band gap approaches zero rapidly as the  $l$  increases (Wu and Zeng 2008). These results show that the band gaps of the sawtooth-like GNRs are much more sensitive to their geometric structures, which is an opportunity for tuning the band gap.

Quantization of electric conductance under the action of an external magnetic field displays a rather interesting trend for GNRs. In the exhaustive tight-binding study conducted by Peres et al. (2006), the number of plateaus in the quantized conductance was found to be even in armchair GNTs while the same number is odd for the zigzag edge.

Rosales et al. (2008) investigated theoretically the effects of side-attached one-dimensional chains of hexagons pinned at the edges of the GNRs. These one-dimensional chains could be useful to simulate, qualitatively, the effects on the electronic transport of GNRs when benzene-based organic molecules are attached to the edges of the ribbons. They propose a simple scheme to reveal the main electronic properties and the changes in the conductance of such decorated planar structures. For simplicity, they consider armchair and zigzag nanoribbons and linear poly-aromatic hydrocarbons (LPHC) and poly(paraphenylene), as the organic molecules. The attached molecules are simulated by simple one-dimensional carbon hexagonal structures connected to the GNRs.

These nanostructures are described using a single-band tight-binding Hamiltonian and their electronic conductance and density of states are calculated within the Green's function formalism based on real-space renormalization techniques (Rosales et al. 2008).

As revealed by the theoretical analysis conducted by Nakabayashi et al., GNRs are a solution to the difficulty of producing an effective graphene switch for turning off the current. Zigzag nanotubes due to their peculiar band structures may be utilized for better current control rather than graphene. A single layer of graphene has no bandgap, which makes it difficult to control current. However, Nakabayashi et al. (2009) found that when a sheet of graphene was in the form of nanoribbons just a few nanometers wide, its electronic structure changed so that currents could be controlled in radically different ways in comparison to conventional semiconductor devices. Nakabayashi et al. (2009) showed that when a nanoribbon was cut so that

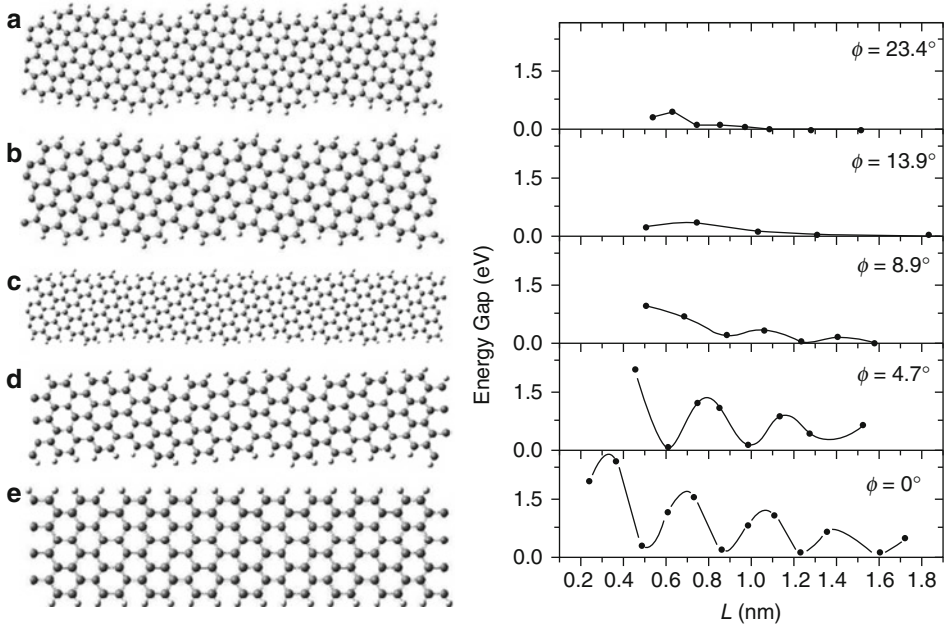


■ Fig. 27-20

(a) The electronic band structures of several sawtooth-like GNRs with various  $w$  and  $l$ . The band gaps versus (b) the width  $w$  and (c) the periodic length  $l$  (Reprinted with permission from Wu and Zeng (2008). © (2008) by Springer)

its edges formed a zigzag structure with an even number of zigzag chains across its width, and an electrostatic barrier potential applied along part of its length, then it behaved as a so-called band-selective filter, preferentially scattering charges into either even or odd numbered bands of its electronic structure depending on the potential. And when two such filters with different potentials were connected in series, they showed it should be possible to completely shut off the flow of current through the nanoribbons.

Tight-binding studies have revealed countless interesting electronic properties regarding GNRs. GNRs, much like single-walled carbon nanotubes, can display metallic or semiconducting properties depending on their orientation and width. Similar to armchair nanotubes, zigzag ribbons are all metallic and may have magnetic properties. Bare and H-terminated ribbons, as studied by Barone et al. may show such effects as gap oscillations which make them a viable choice for possible band structure engineering applications. The results of this study, which is a careful investigation of GNRs of several orientations, widths and terminations are displayed



■ Fig. 27-21

*Left:* A representative set of semiconducting hydrogen-terminated GNRs, created by “unfolding” and “cutting” different types of CNTs. (a) A GNR with a chiral angle of  $\phi = 23.4^\circ$  created by unfolding and cutting a C(6,4). (b) A GNR with a chiral angle of  $\phi = 13.9^\circ$  created by unfolding and cutting a C(6,2). (c) A GNR with a chiral angle of  $\phi = 8.9^\circ$  created by unfolding and cutting a C(20,4). (d) A GNR with a chiral angle of  $\phi = 4.7^\circ$  created by unfolding and cutting a C(10,1). (e) An armchair GNR ( $\phi = 0^\circ$ ) created by unfolding and cutting a zigzag CNT. *Right:* Dependence of the band gap on the width of hydrogen passivated chiral GNRs. The different panels correspond to the different CNRs presented in Left. (Reprinted with permission from Barone et al. (2006). © (2006) by the American Chemical Society)

in ● Fig. 27-21 along with the details of the models used and the band gap profiles of the corresponding models.

GNRs have localized edge states located near the Fermi level. By terminating the edges with different species, one can change the character of these states and consequently the properties of GNRs. In fact, a first-principles calculation within spin-unrestricted local-density functional formalism on zigzag-edge graphene nanostrips terminated with hydrogen and oxygen atoms as well as hydroxyl and imine groups show that these different species have a significant impact on the electronic structure of these strips near the Fermi level (Gunlycke et al. 2007). Zigzag-edge nanostrips terminated with hydrogen atoms or hydroxyl groups exhibit spin polarization, while the nanostrips terminated with oxygen or imine groups are unpolarized. These differences of course result in very different conductance characteristics for these systems.

In further support of the aforementioned evidence Zhang and Yang (2009) confirmed in their linear combination of atomic orbitals (LCAO) tight-binding study that H-terminated armchair GNTs exhibit size dependence in their conductance properties.



On the other hand, ZnO nanoribbons show different characteristics from that of carbon nanoribbons. ZnO nanoribbons grown along the [0001] direction can form two different planar monolayer, zigzag and armchair ribbons. First principles calculations of zinc oxide nanoribbons show that the stability of armchair edge structures is greater than the zigzag edge configurations. Furthermore, single layered armchair ribbons are semiconductors, whereas the zigzag counterparts are metallic (Botello-Mendez et al. 2007). An effect that is not present in purely carbon-based systems is the presence of two differently charged species offering different edge configurations. For the zigzag ZnO ribbons, for instance, the exposed atoms are oxygen atoms while the hidden are zinc. The opposite edge has the inverse structure. The armchair ribbons are characterized by a Zn-O pair at the outer edge and another pair at the inner edge. After relaxation, the far edge oxygen ions tend to shift outward on both sides of the ribbon. As in the case of graphene materials, understanding the effects of edge-dimensional variation on band gap energies will provide the new insights into the fundamental principle of architecture design of nanodevices fabricated with ZnO nanostructured materials. A simple tight-binding model can be used to investigate the electronic properties of nonpolar ZnO nanobelts following the procedure described below.

Consider a simplified unit cell model (see Fig. 27-22) along the nanobelt growth z direction with Zn and O in the xy plane. This is the actual case for the ultrathin ZnO film oriented along the [001] direction.

In this case, the tight-binding Hamiltonian is given by (Yang and Wang 2006):

$$H = \sum_{r \in A} \epsilon_r a_r^\dagger a_r + \sum_{r \in B} \epsilon_r b_r^\dagger b_r + \sum_{r \in A, B} \sum_{i=1,2,\dots} (\tau_{r,i} a_r^\dagger b_{r+S_i} + \tau_{i,r}^* b_r^\dagger a_{r+S_i}),$$

where operators  $a_r^\dagger$  ( $a_r$ ) and  $b_r^\dagger$  ( $b_r$ ) create (annihilate) a state at sites A (for Zn) and B (for O) at their coordinates  $r$ , respectively.  $\epsilon$  denotes the on-site self-interaction energy, whereas  $\tau$  is the interatomic coupling term. Similarly, the wave functions for Zn and O at their respective lattice sites can be written as a linear combination of Bloch waves along the  $z$  direction and standing waves along  $x$  and  $y$  as the following (Yang and Wang 2006),

$$|Zn, k_x, k_y \rangle = \sum_{m_x=1}^{M_x} \sum_{m_y=1}^{M_y} \sum_{z_m} c_p e^{ik_z z_m} \sin(k_x m_x a) \sin(k_y m_y b) a_{m_x m_y}^\dagger |0 \rangle$$

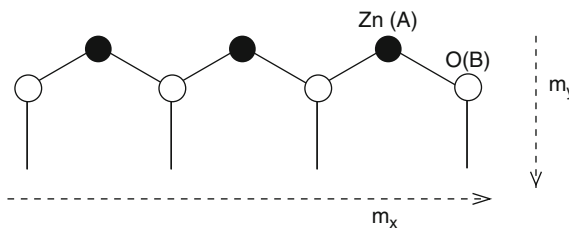


Fig. 27-22 Schematic illustration showing a tight binding unit cell for a ZnO nanobelt (Adapted from Yang and Wang 2006)



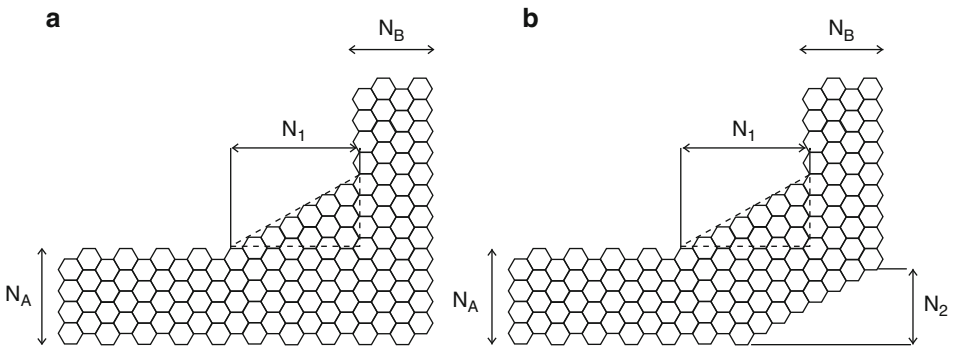
$$|O, k_x, k_y \rangle = \sum_{n_x=1}^{N_x} \sum_{n_y=1}^{N_y} \sum_{z_n} c_p e^{ik_z z_n} \sin(k_x n_x a) \sin(k_y n_y b) a_{n_x n_y}^+ |0 \rangle$$

in which lattice vectors  $a$  and  $b$  are as defined in [Fig. 27-19](#) and  $c_p$  and  $c_q$  are coefficients.

To simplify the model, one may consider only the coupling term between the nearest neighboring sites. In this case, on the same  $xy$  plane, the O-sites take the following coordinates around a Zn center:  $n_x = m_x - 1, m_x$  and  $m_x + 1$ ; with  $n_y = m_y - 1, m_y$  and  $m_y + 1$  in correspondence. Along the  $yz$  plane, there exist two O atoms that directly interact with the center Zn with  $z_n = z_m \pm c$ , respectively (Yang and Wang 2006).

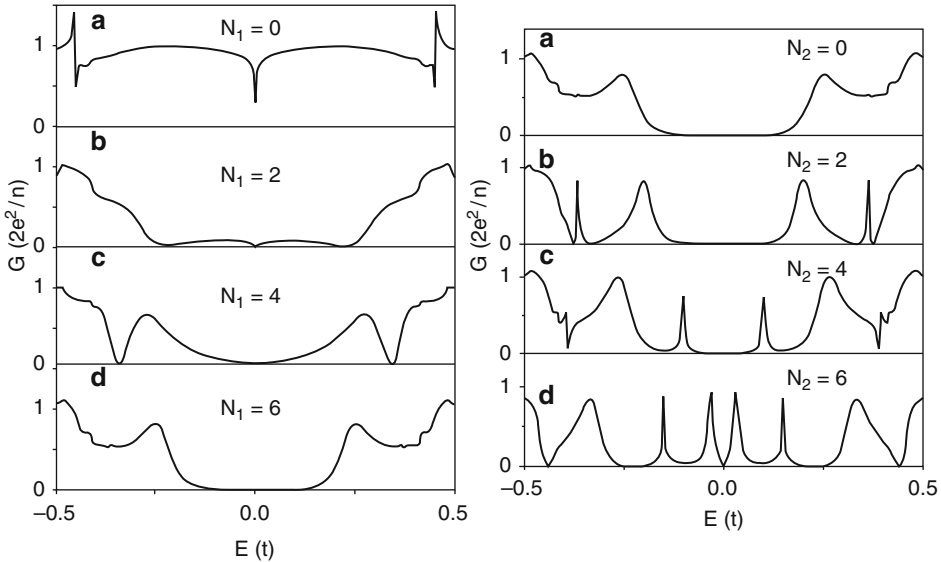
In addition to the conventional strip-like geometry, other configurations based on GNRs have also been proposed as a part of a search for favorable transport properties. Various graphene nanojunctions based on the GNRs have been studied, such as L-shaped, Z-shaped, and T-shaped GRN junctions (Areshkin et al. 2007; Chen et al. 2008; Jayasekera and Mintmire 2007). Of particular interest is the hybrid junctions which are mixtures of armchair and zigzag GNRs. Some studies have shown that the transport properties of these hybrid GNR junctions are very sensitive to the details of the junction region (Xie et al. 2009). A model calculation based on tight-binding and Green's function methods for L-shaped GNRs show that the corner geometry of the L-shaped junction has great influence on the electron transport around the Fermi energy (Xie et al. 2009). The L-shaped GNR models considered are shown in [Fig. 27-23](#). The calculated conductance plots as a function of electron energy are shown in [Fig. 27-24](#). Interestingly the results reveal that the corner is the decisive factor for the electronic properties of these junctions. As more carbon atoms are added to the inner side of the corner the junction moves from being metal to a semiconductor, developing a band gap.

Carbon nanoribbons have also interesting mechanical properties. For instance, Raman spectra show a remarkable dependence on ribbon width ( $W$ ) (Zhou and Dong 2008). For the



**Fig. 27-23**

(a) A deformed LGNR (called LGNR1) where a triangle graphene flake (in the dashed-line triangle) is connected to the inside corner of a standard right-angle LGNR. (b) A deformed LGNR (called LGNR2) in which a triangle graphene flake is cut from the outside corner of LGNR1 in (a).  $N_A$  and  $N_Z$  represent the widths of the semi-infinite AGNR and ZGNR, respectively;  $N_1$  represents the side length of added triangle flake, while  $N_2$  represents the side length of cut triangle flake (Adapted from Xie et al. 2009)



■ Fig. 27-24

**Left:** The conductance as a function of electron energy for the LGNR1 in [Fig. 27-23a](#) with different  $N_1$ . Other parameters are  $N_A = 11$  and  $N_Z = 7$ . **Right:** The conductance as a function of electron energy for the LGNR2 in [Fig. 27-23b](#) with  $N_1 = 6$  and different  $N_2$ . Other parameters are  $N_A = 11$  and  $N_Z = 7$  (Reprinted with permission from Xie et al. (2009). © (2009) by Elsevier)

GNRs whose widths are larger than  $25 \text{ \AA}$ , the radial breathing-like mode (RBLM) frequencies follow the  $1/W$  rule:

$$\omega = 3086.97 \times \frac{1}{W} + 1.08 \text{ in } 1/\text{cm}.$$

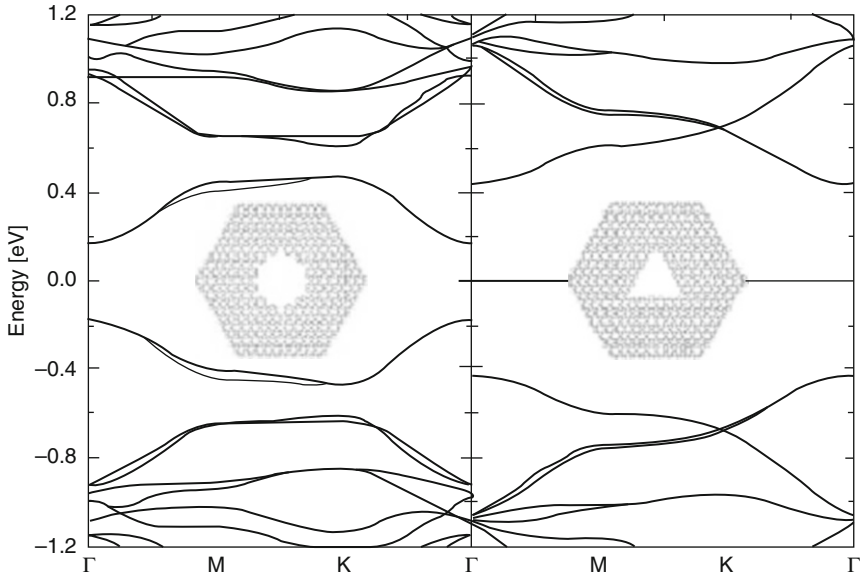
But for the narrow GNRs whose widths are less than  $25 \text{ \AA}$ , their RBLM frequencies follow the  $1/\sqrt{W}$  rule:

$$\omega = 1407.81 \times \frac{1}{\sqrt{W}} + 164.38 \text{ in } 1/\text{cm}.$$

A unified fitting function has been proposed (Zhou and Dong 2008), which can be suitable for all the GNRs:

$$\omega = 1584.24 \times \frac{1}{W} + 351.98 \times \frac{1}{\sqrt{W}} - 10.0 \text{ in } 1/\text{cm}.$$

Another interesting application of graphene is the antidot lattices. Antidot lattices are triangular arrangements of holes in an otherwise perfect graphene sheet. In each hexagonal unit cell of the lattice, a circular hole is introduced whose radius  $R$  can be adjusted along with the length of the hexagonal unit cell,  $L$ . Previously known applications of antidot lattices involve semiconductor lattices, while in a recent publication the possibility of creating antidot structures on graphene using e-beam lithography has been reported (Pedersen et al. 2008). The antidot lattice causes graphene to become a semiconductor, introducing a tuning parameter which is the dot size and shape. In addition spin qubit states can be formed in the antidot lattice by manipulating the antidot arrangement. Pedersen et al. (2008) demonstrated that the hole shape plays a



■ Fig. 27-25

Band structures of a  $\{10, 3\}$  antidot lattice and similar structure having a triangular hole with zigzag edges. Note the dispersion less band at 0 eV in the triangular case (Reprinted with permission from Pedersen et al. (2008). © (2008) by the American Physical Society)

crucial role in determining the electronic structure. A triangular hole instead of a circular hole results in the appearance of a metallic state at the Fermi level. The different band structures are illustrated in ● Fig. 27-25.

## Magnetic and Optical Properties

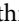
Lower-dimensional systems are expected to show electronic, magnetic, and optical properties that are not observed in their bulk counterparts. In two-dimensional structures, the inherent or emergent magnetic properties depend on many factors including shape, size, and the interaction between subregions (Jensen and Pastor 2003).

GNRs are a typical example of emergent and controllable magnetic systems. Spin-polarized first-principles calculations by Gorjizadeh et al. (2008) have shown that doping GNRs with 3d transition metals result in the appearance of FM or AFM states. In particular Cr and Co provide a large magnetic moment and doping with Fe or Mn at low densities yields half-metallic ribbons.

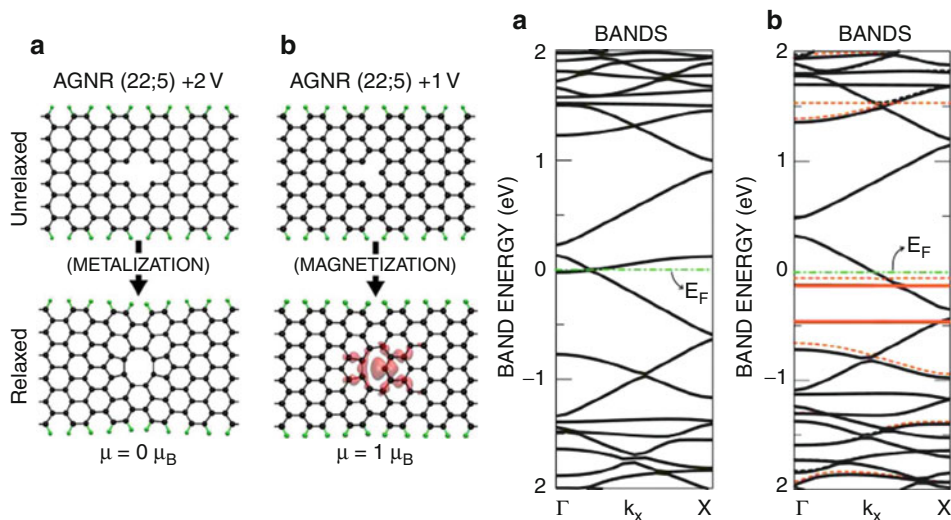
As discussed in the work by Enoki and Takai, as the dimension of the system decreases, the contribution coming from the edge states increases in proportion (Enoki and Takai 2009). The localized edge states in GNR, which are dispersionless states that appear at the Fermi level give rise to interesting magnetic properties.


From the applications point of view the magnetic properties of graphene nanoribbons are more interesting and studied both experimentally and theoretically. Particularly quasi 1D GNRs have magnetic properties depending on their size and symmetry. These are edge states

of nanoribbons with opposite spin polarization and band gaps varying with the width of the ribbon (Topsakal et al. 2008).

Using first-principles plane wave calculations within the DFT method Topsakal et al. (2008) predict that in addition to edge states electronic and magnetic properties of graphene nanoribbons can also be affected by defect-induced states. In particular, when H-saturated holes are introduced into the GNT, the band structure is modified dramatically altering in return the electronic and magnetic properties. Similarly, vacancies and divacancies induce metallization and magnetization in non-magnetic semiconducting nanoribbons due to the spin-polarization of local defect states. Antiferromagnetic ground state of semiconducting zigzag ribbons can change to ferrimagnetic state upon creation of vacancy defects. In this study, the changes in electronic properties are studied as a function of the location and the geometry of the vacancies in different types of armchair GNRs. Due to the spin polarization of localized states and their interaction with edge states, magnetization may be introduced into the GNRs. Some of the representative results of this work are displayed in  Fig. 27-26.

Not only armchair, but also zigzag nanoribbons are strongly affected by defects due to single and multiple vacancies (Topsakal et al. 2008). When coupled with the magnetic edge states of the zigzag nanoribbons the vacancy defect brings about additional changes. The magnetic state and energy band structure of these ribbons depend on the type and geometry of the defects. In a ZGNR(14;8) a single vacancy formation energy is lowered by 0.53 eV when the defect is situated at the edge rather than at the center of the ribbon. Furthermore, two defects associated



 Fig. 27-26

(a) Metallization of the semiconducting AGNR(22) by the formation of divacancies with repeat period of  $l = 5$ . (b) Magnetization of the non-magnetic AGNR(22) by a defect due to the single carbon atom vacancy with the same repeat periodicity. Iso-surfaces around the vacancy correspond to the difference of the total charge density of different spin directions. Solid (blue) and dashed (red) lines are for spin-up and spin-down bands; solid (black) lines are nonmagnetic bands (Reprinted with permission from Topsakal et al. (2008). © (2008) by the American Physical Society)

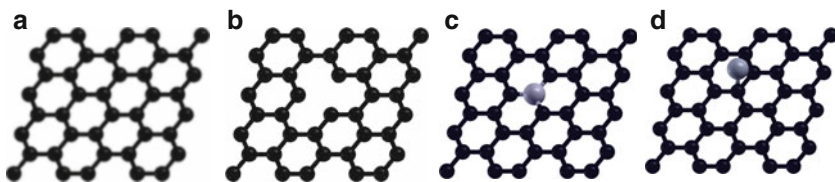
with two separated vacancy and a defect associated with a relaxed divacancy exhibit similar behavior (Topsakal et al. 2008).

On the other hand, Pisani et al. (2007) investigated theoretically the electronic and magnetic properties of zigzag graphene nanoribbons by performing first principles calculations within DFT formalism. They predict that the electronic structure of graphene ribbons with zigzag edges is unstable with respect to magnetic polarization of the edge states.

As can be seen from the model calculations of Topsakal et al. (2008, 2007), the energy band gaps and magnetic states of graphene nanoribbons can be modified by defects due to single or multiple vacancies. Electronic and magnetic properties of finite length graphene nanoribbons also show similar behavior as infinite length nanoribbons. Finite length ribbons are usually referred to as *graphene quantum dots* (GQD). Tang et al. (2008) investigated theoretically the electronic and magnetic properties of a square graphene quantum dot. Electronic eigen-states of a GQD terminated by both zigzag and armchair edges are derived in the theoretical framework of the Dirac equation. They find that the Dirac equation can determine the eigen-energy spectrum of a GQD with good accuracy. By using the Hartree-Fock mean field approach, they studied the size dependence of the magnetic properties of GQDs. They find that there exists a critical width between the two zigzag edges for the onset of the stable magnetic ordering. On the other hand, when such a width increases further, the magnetic ground state energy of a charge neutral GQD tends to a saturated value (Tang et al. 2008).

Magnetic properties of graphene show a sensitive dependence on single atom defects; defect concentration and packing play an important role in magnetism. Singh and Kroll (2009) investigated the magnetism in graphene due to single-atom defects by using spin-polarized density functional theory calculations. Interestingly, they find that while the magnetic moment per defect due to substitutional atoms and vacancies depend on the defect density, it is independent of defect density for adatoms. The graphene sheet with B adatoms is found to be nonmagnetic, but with C and N adatoms it is magnetic. The adatom defects cause a distortion of the graphene sheet in their vicinity. The distortion in graphene due to C and N adatoms is significant, while the distortion due to B adatoms is very small. The vacancy and substitutional atom (B, N) defects in graphene are planar in the sense that there is in-plane displacement of C atoms near the vacancy and substitutional defects. Upon relaxation the displacement of C atoms and the formation of pentagons near the vacancy site due to Jahn–Teller distortion depends upon the density and packing geometry of vacancies (Singh and Kroll 2009). The defect models considered by Singh and Kroll are shown in [Fig. 27-27](#).

The optical absorption coefficient is one of the most important quantities in solids and is closely related to the electronic band structure. The Kubo formula-based calculations of



■ Fig. 27-27

The model samples of (a) ideal graphene, (b) graphene with one atom vacancy, (c) graphene with one substitutional atom and (d) graphene with one adatom defect (Adapted from Singh and Kroll 2009)

Zhang et al. indicate that at high frequencies, the optical spectrum of graphene is highly anisotropic (Zhang et al. 2008). It has also been shown that the weak optical response in graphene nanoribbons can be significantly enhanced in an applied magnetic field (Liu et al. 2008).

Another effect important for determining the optical properties of graphene-related materials is spin-orbit coupling. Although spin-orbit coupling is negligible at high frequencies, it is found to have a significant enhancing effect on the optical absorption at lower frequencies as shown in a direct solution of the spin-orbit Hamiltonian in the effective mass approximation by Wright et al. (2009).

## Adsorption Phenomena

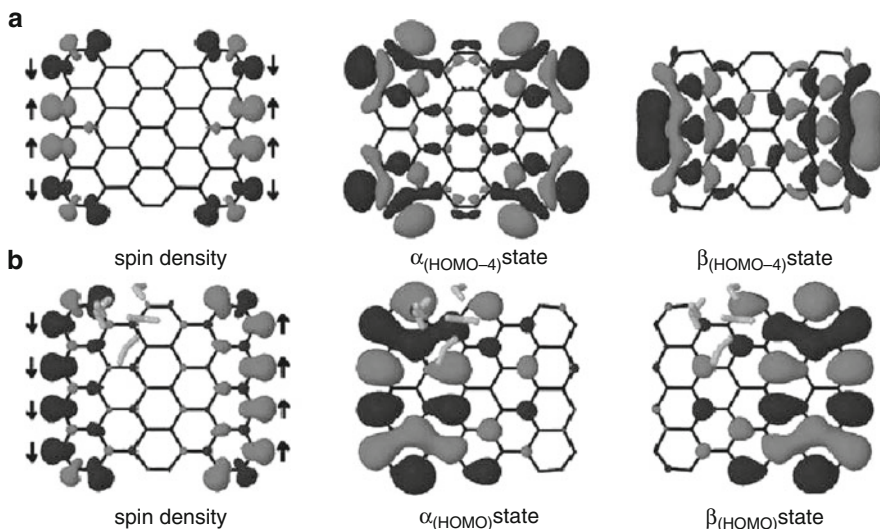
---

Adsorption of adatoms on graphene and/or graphene nanoribbons play an important role in functionalizing graphene materials for various device applications, such as gas sensors and spin-valves. Transition metal (TM) atom decorated graphene shows different magnetic properties depending on the concentration and the species of TM atoms. There are several coverage models, such as one TM atom adsorbed on either  $(2 \times 2)$  or  $(4 \times 4)$  unit cells on only one side as well as on both sides, namely, above and below the graphene. Sevincli et al. (2008) investigated the possible adsorption sites of TM atoms on graphene and GNR. The geometrical configurations of the structures they considered include bridge (over a C–C bond), atop (on top of a C atom) and on center (over the center of a hexagon) adsorption sites for both perfect graphene and for AGNR of various widths  $N_a$ .

In relation to another very important application, doping of transition elements was found to increase the hydrogen storage properties of materials (Shevlin and Guo 2006). Especially nickel and rhodium are widely used in the hydrogenation reaction and also in the synthesis of BN sheets. Considering the potential application of Ni and Rh nanoparticles in hydrogen storage and in catalysis, Venkataramanan et al. (2009) investigated the interaction of Ni and Rh atom on the BN sheets through first-principles calculations. They also analyzed the interaction between hydrogen molecules and the metal atoms adsorbed on the BN sheets, which might be useful to maximize the hydrogen storage capacity.

Hydrogen adsorption studies over the metal doped BN sheets shows that both Ni and Rh atoms can hold three hydrogen molecules. In the case of Ni doped BN sheet all three hydrogen molecules are chemically bound and are intact. In the case of Rh doped BN sheets, the first hydrogen molecule dissociates and the remaining hydrogen molecules are bound to the metal atom. The absorption energy for the first hydrogen was found to have a larger value for the Rh-doped BN sheet, whereas for the second and third hydrogen molecules, the absorption energies were higher for the Ni doped BN sheets. Upon addition of a fourth hydrogen molecule to the Ni doped BN sheets, the fourth hydrogen molecule moved to a distance of 3.855 Å. In the case of Rh-doped BN sheet, the Rh atom detached and acted in a similar way to a cluster. Thus Ni atoms are more stable on BN sheets, and have higher absorption energy compared to the Rh doped BN sheets (Venkataramanan et al. 2009).

Metallized graphene can be a potential high-capacity hydrogen storage medium. Graphene is metallized through charge donation by adsorbed Li atoms to its  $\pi^*$ -bands. Each positively charged Li ion can bind up to four  $H_2$  by polarizing these molecules. The storage capacity up to the gravimetric density of 12.8 wt % is possible with a favorable average  $H_2$  binding energy of 0.21 eV (Ataca et al. 2008).



■ Fig. 27-28

Plots of the spin density and electron density for the  $\alpha$ -spin (up) and  $\beta$ -spin (down) states in nanoscale graphene. For the spin density, different colors indicate the  $\alpha$ - and  $\beta$ -states, while for the electron density distribution ( $\alpha$ - and  $\beta$ -states) the different colors correspond to different signs of the molecular orbital lobes. (a) The electron density distribution in pure graphene. (b) The electron density distribution for graphene with adsorbed water (Reprinted with permission from Berashevich and Chakraborty (2009). © (2009) by the American Physical Society)

Water and gas molecules adsorbed on nanoscale graphene play the role of defects which facilitate the tunability of the bandgap and allow one to control the magnetic ordering of localized states at the edges (Berashevich and Chakraborty 2009). The adsorbed molecules push the  $\alpha$ -spin (up) and  $\beta$ -spin (down) states of graphene to the opposite (zigzag) edges such that the  $\alpha$ - and  $\beta$ -spin states are localized at different zigzag edges. This breaks the symmetry that results in the opening of a large gap. The efficiency of the wavefunction displacement depends strongly on the type of molecules adsorbed on graphene (Berashevich and Chakraborty 2009). The influence of adsorption of water on the electronic and magnetic properties of graphene is based on calculation of the spin-polarized density functional theory and the results of the calculations are depicted in ► Fig. 27-28.

## References

- Amorim, R. G., Fazzio, A., Antonelli, A., Novaes, F. D., & da Silva, A. J. R. (2007). Divacancies in graphene and carbon nanotubes. *Nano Letters*, 7, 2459.
- Anagnostatos, G. S. (1987). Magic numbers in small clusters of rare-gas and alkali atoms. *Physics Letters A*, 124, 85.
- Andzelm, J., Govind, N., & Maiti, A. (2006). Nanotube-based gas sensors — Role of structural defects. *Chemical Physics Letters*, 421, 58.
- Arantes, J. T., & Fazzio, A. (2007). Theoretical investigations of Ge nanowires grown along the [110] and [111] directions. *Nanotechnology*, 18, 295706.



- Areshkin, D. A., Gunlycke, D., & White, C. T. (2007). Ballistic transport in graphene nanostrips in the presence of disorder: importance of edge effects. *Nano Letters*, 7, 204.
- Ataca, C., Akturk, E., Ciraci, S., & Ustunel, H. (2008). High-capacity hydrogen storage by metallized graphene. *Applied Physics Letters*, 93, 043123.
- Balasubramanian, K. (1990). Spectroscopic constants and potential-energy curves of heavy p-block dimers and trimers. *Chemical Reviews*, 90, 93.
- Baletto, F., & Ferrando, R. (2005). Structural properties of nanoclusters: energetic, thermodynamic, and kinetic effects. *Reviews of Modern Physics*, 77, 371.
- Barone, V., Hod, O., & Scuseria, G. E. (2006). Electronic structure and stability of semiconducting graphene nanoribbons. *Nano Letters*, 6, 2748.
- Barreteau, C., Desjonqueres, M. C., & Spanjaard, D. (2000). Theoretical study of the icosahedral to cuboctahedral structural transition in Rh and Pd clusters. *European Physical Journal D*, 11, 395.
- Barth, S., Harnagea, C., Mathur, S., & Rosei, F. (2009). The elastic moduli of oriented tin oxide nanowires. *Nanotechnology*, 20, 115705.
- Baumeier, B., Kruger, P., & Pollmann, J. (2007). Structural, elastic, and electronic properties of SiC, BN, and BeO nanotubes. *Physical Review B*, 76, 085407.
- Berashevich, J., & Chakraborty, T. (2009). Tunable bandgap and magnetic ordering by adsorption of molecules on graphene. *Physical Review B*, 80, 033404.
- Bonacic-Koutecky, V., Fantucci, P., & Koutecky, J. (1991). Quantum chemistry of small clusters of elements of Groups Ia, Ib, and IIa: fundamental concepts, predictions, and interpretation of experiments. *Chemical Reviews*, 91, 1035.
- Botello-Mendez, A. R., Martinez-Martinez, M. T., Lopez-Urias, F., Terrones, M., & Terrones, H. (2007). Metallic edges in zinc oxide nanoribbons. *Chemical Physics Letters*, 448, 258.
- Brack, M. (1993). The physics of simple metal clusters: self-consistent jellium model and semiclassical approaches. *Reviews of Modern Physics*, 65, 677.
- Brenner, D. (1989). Relationship between the embedded-atom method and Tersoff potentials. *Physical Review Letters*, 63, 1022.
- Briere, T. M., Sluiter, M. H., Kumar, V., & Kawazoe, Y. (2002). Atomic structures and magnetic behavior of Mn clusters. *Physical Review B*, 66, 064412.
- Bromley, S. T., & Flikkema, E. (2005). Columnar-to-disk structural transition in nanoscale (SiO<sub>2</sub>)<sub>N</sub> Clusters. *Physical Review Letters*, 95, 185505.
- Bruno, M., Palumbo, M., Ossicini, S., & del Sole, E. (2007). First-principles optical properties of silicon and germanium nanowires. *Surface Science*, 601, 2707.
- Bulusu, S., Yoo, S., & Zeng, X. C. (2005). Search for global minimum geometries for medium sized germanium clusters: Ge<sub>12</sub>-Ge<sub>20</sub>. *Journal of Chemical Physics*, 122, 164305.
- Chan, T.-L., Ciobanu, C. V., Chuang, F.-C., Lu, N., Wang, C.-Z., & Ho, K.-M. (2006). Magic structures of H-Passivated (110) silicon nanowires. *Nano Letters*, 6, 277.
- Chen, Y. P., Xie, Y. E., & Yan, X. H. (2008). Electron transport of L-shaped graphene nanoribbons. *Journal of Applied Physics*, 103, 063711.
- Chopra, N. G., Luyken, R. J., Cherrey, K., Crespi, V. H., Cohen, M. L., Louie, S. G., & Zettl, A. (1995). Boron-nitride nanotubes. *Science*, 269, 966.
- Corso, M., Auwarter, W., Muntwiler, M., Tamai, A., Greber, T., & Osterwalder, J. (2004). Boron nitride nanomesh. *Science*, 303, 217.
- Darby, S., Mortimer-Jones, T. V., Johnston, R. L., & Roberts, C. (2002). Theoretical study of Cu-Au nanoalloy clusters using a genetic algorithm. *Journal of Chemical Physics*, 116, 1536.
- de Heer, W. A. (1993). The physics of simple metal clusters: experimental aspects and simple models. *Reviews of Modern Physics*, 65, 611.
- de Oliveira, I. S. S., & Miwa, R. H. (2009). Boron and nitrogen impurities in SiC nanowires. *Physical Review B*, 79, 085427.
- Doye, J. P. K. (2003). Identifying structural patterns in disordered metal clusters. *Physical Review B*, 68, 195418.
- Doye, J. P. K. (2006). Lead clusters: Different potentials, different structures. *Computational Materials Science*, 35, 227.
- Doye, J. P. K., & Wales, D. J. (1999). Structural transitions and global minima of sodium chloride clusters. *Physical Review B*, 59, 2292.
- Du, J., Shen, N., Zhu, L., & Wang, J. (2010). Emergence of noncollinear magnetic ordering in bimetallic Co<sub>6-n</sub>Mn<sub>n</sub> clusters. *Journal of Physics D*, 43, 015006.
- Dugan, N., & Erkoc, S. (2008). Stability analysis of graphene nanoribbons by molecular dynamics simulations. *Physica Status Solidi (B)*, 245, 695.
- Dugan, N., & Erkoc, S. (2009). Genetic algorithms in aication to the geometry optimization of nanoparticles. *Algorithms*, 2, 410.
- Enoki, T., & Takai, K. (2009). The edge state of nanographene and the magnetism of the



- edge-state spins. *Solid State Communications*, 149, 1144.
- Enyashin, A. N., & Seifert, G. (2005). Structure, stability and electronic properties of TiO<sub>2</sub> nanostructures. *Physica Status Solidi (B)*, 242, 1361.
- Erkoc, S. (1997). Empirical many-body potential energy function used in computer simulations Of condensed matter properties. *Physics Reports*, 278, 79.
- Erkoc, S. (2001). Empirical potential energy functions used in the simulations of materials properties. In D. Stauffer (Ed.), *Annual review of computational physics* (Vol. IX, pp. 1–103). Singapore: World Scientific.
- Erkoc, S. (2001). Structural and electronic properties of single-wall BN nanotubes. *Journal of Molecular Structure (THEOCHEM)*, 542, 89.
- Erkoc, S. (2003). Structural and electronic properties of “benzorods”. *Journal of Molecular Structure (THEOCHEM)*, 639, 157.
- Erkoc, S. (2004). Does tubular structure of carbon form only from graphine sheet? *Physica E*, 25, 69.
- Erkoc, S. (2004). Semi-empirical SCF-MO calculations for the structural and electronic properties of single-wall InP nanotubes. *Journal of Molecular Structure (THEOCHEM)*, 676, 109.
- Erkoc, S., & Kokten, H. (2005). Structural and electronic properties of single-wall ZnO nanotubes. *Physica E*, 28, 162.
- Erkoc, S., Malcioglu, O. B., & Tasci, E. (2004). Structural and electronic properties of single-wall GaN nanotubes: semi-empirical SCF-MO calculations. *Journal of Molecular Structure (THEOCHEM)*, 674, 1.
- Ezawa, M. (2006). Peculiar width dependence of the electronic properties of carbon nanoribbons. *Physical Review B*, 73, 045432.
- Fa, W., Luo, C., & Dong, J. (2005). Structure-dependent ferroelectricity of niobium clusters (Nb<sub>N</sub>, N = 2 – 52). *Physical Review B*, 71, 245415.
- Fa, W., Luo, C., & Dong, J. (2006). Coexistence of ferroelectricity and ferromagnetism in tantalum clusters. *Journal of Chemical Physics*, 125, 114305.
- Finnis, M. W., & Sinclair, J. E. (1984). A simple empirical n-body potential for transition metals. *Philosophical Magazine A*, 50, 45.
- Freitag, M. (2008). Nanoelectronics goes flat out. *Nature Nanotechnology*, 3, 455.
- Gafner, Y. Y., Gafner, S. L., & Entel, P. (2004). Formation of an icosahedral structure during crystallization of nickel nanoclusters. *Physical Solid State*, 46, 1327.
- Gao, G., & Kang, H. S. (2008). First-principles study of silicon nitride nanotubes. *Physical Review B*, 78, 165425.
- Geim, A. K., & Novoselov, K. S. (2007). The rise of graphene. *Nature Materials*, 6, 183.
- Ghosh, P., Kahaly, M. U., & Waghmare, U. V. (2007). Atomic and electronic structures, elastic properties, and optical conductivity of bulk Te and Te nanowires: a first-principles study. *Physical Review B*, 75, 245437.
- Gorjizadeh, N., Farajian, A. A., Esfarjani, K., & Kawazoe, Y. (2008). Spin and band-gap engineering in doped graphene nanoribbons. *Physical Review B*, 78, 155427.
- Gunlycke, D., Li, J., Mintmire, J. W., & White, C. T. (2007). Altering low-bias transport in zigzag-edge graphene nanostrips with edge chemistry. *Applied Physics Letters*, 91, 112108.
- Haberland, H. (1994). *Clusters of atoms and molecules*. Berlin: Springer.
- Halicioglu, T., & Bauschlicher, C. W. (1988). Physics of microclusters. *Reports on Progress in Physics*, 51, 883.
- Han, M. Y., Ozyilmaz, B., Zhang, Y. B., & Kim, P. (2007). Energy band-gap engineering of graphene nanoribbons. *Physical Review Letters*, 98, 206805.
- Hartke, B. (2002). Structural transitions in clusters. *Angewandte Chemie (International Ed. in English)*, 41, 1468.
- Hestenes, M. R., & Stiefel, E. (1952). Methods of conjugate gradients for solving linear systems. *Journal of research of the National Bureau of Standards*, 49, 409.
- Hsu, P. J., & Lai, S. K. (2006). Structures of bimetallic clusters. *Journal of Chemical Physics*, 124, 044711.
- Hu, J., Liu, X. W., & Pan, B. C. (2008). A study of the size-dependent elastic properties of ZnO nanowires and nanotubes. *Nanotechnology*, 19, 285710.
- Huda, M. N., & Kleinman, L. (2006). h-BN monolayer adsorption on the Ni(111) surface: a density functional study. *Physical Review B*, 74, 075418.
- Jarrold, M. F. & Constant, V. A. (1991). Silicon cluster ions: evidence for a structural transition. *Physical Review Letters*, 67, 2994.
- Jayasekera, T., & Mintmire, J. W. (2007). Transport in multiterminal graphene nanodevices. *Nanotechnology*, 18, 424033.
- Jensen, P. J., & Pastor, G. M. (2003). Low-energy properties of two-dimensional magnetic nanostructures: interparticle interactions and disorder effects. *New Journal of Physics*, 5, 68.
- Jia, X., Hofmann, M., Meunier, V., Sumpter, B. G., Campos-Delgado, J., Romo-Herrera, J. M., Son, H.,

- Hsieh, Y.-P., Reina, A., Kong, J., Terrones, M., & Dresselhaus, M. S. (2009). Controlled formation of Sharp Zigzag and Armchair Edges in Graphitic Nanoribbons. *Science*, 323, 1701.
- Johnston, R. L. (2002). *Atomic and molecular clusters*. London: Taylor & Francis.
- Kabir, M., Mookerjee, A., & Kanhere, D. G. (2006). Structure, electronic properties, and magnetic transition in manganese clusters. *Physical Review B*, 73, 224439.
- Kagimura, R., Nunes, R. W., & Chacham, H. (2007). Surface dangling-bond states and band Line-ups in Hydrogen-Terminated Si, Ge, and Ge/Si nanowires. *Physical Review Letters*, 98, 026801.
- Kirkpatrick, S., Gelatt, C. D., & Vecchi, M. P. (1983). Optimization by simulated annealing. *Science*, 220, 671.
- Knickelbein, M. B. (2001). Experimental observation of superparamagnetism in manganese clusters. *Physical Review Letters*, 86, 5255.
- Kohler, C., Seifer, G., & Fraueheim, T. (2006). Magnetism and the potential energy hypersurfaces of Fe<sub>53</sub> to Fe<sub>57</sub>. *Computational Materials Science*, 35, 297.
- Krainyukova, N. V. (2006). The crystal structure problem in noble gas nanoclusters. *Thin Solid Films*, 515, 1658.
- Kulkarni, A. J., Zhou, M., & Ke, F. J. (2005). Orientation and size dependence of the elastic properties of zinc oxide nanobelts. *Nanotechnology*, 16, 2749.
- Kumar, V., & Kawazoe, Y. (2002). Icosahedral growth, magnetic behavior, and adsorbate-induced metal-nonmetal transition in palladium clusters. *Physical Review B*, 66, 144413.
- Landau, L. D., & Lifshitz, E. M. (1980). *Statistical physics, Part I, sections 137 and 138*. Oxford: Pergamon.
- Lau, K. C., Pati, R., Pandey, R., & Pineda, A. C. (2006). First-principles study of the stability and electronic properties of sheets and nanotubes of elemental boron. *Chemical Physics Letters*, 418, 549.
- Lee, B., & Rudd, R. E. (2007). First-principles calculation of mechanical properties of Si<001> nanowires and comparison to nanomechanical theory. *Physical Review B*, 75, 195328.
- Lennard-Jones, J. E. (1931). Cohesion. *Proceedings of the Physical Society*, 43, 461.
- Li, F., Zhu, Z., Zhao, M., & Xia, Y. (2008a). Ab initio calculations on the magnetic properties of hydrogenated boron nitride nanotubes. *Journal of Physical Chemistry C*, 112, 16231.
- Li, Z. Q., Henriksen, E. A., Jiang, Z., Hao, Z., Martin, M. C., Kim, P., Stormer, H. L., & Basov, D. N. (2008b). Dirac charge dynamics in graphene by infrared spectroscopy. *Nature Physics*, 4, 532.
- Liang, H., & Upmanyu, M. (2006). Axial-strain-induced torsion in single-walled carbon nanotubes. *Physical Review Letters*, 96, 165501.
- Lin, Y.-M., Jenkins, K. A., Valdes-Garcia, A., Small, J. P., Farmer, D. B., & Avouris, P. (2009). Operation of graphene transistors at gigahertz frequencies. *Nano Letters*, 9, 422.
- Liu, J. F., Wright, A. R., Zhang, C., & Ma, Z. S. (2008). Strong terahertz conductance of graphene nanoribbons under a magnetic field. *A Physical Letters*, 93, 041106.
- Liu, X., Bauer, M., Bertagnolli, H., Roduner, E., van Slagere, J., & Philli F. (2006). Structure and magnetization of small monodisperse platinum clusters. *Physical Review Letters*, 97, 253401.
- Ma, S., & Wang, G. (2006). Structures of medium size germanium clusters. *Journal of Molecular Structure (THEOCHEM)*, 767, 75.
- Mackay, A. L. (1962). A dense non-crystallographic packing of equal spheres. *Acta Crystallographica*, 15, 916.
- Maiti, A. (2008). Multiscale modeling with carbon nanotubes. *Microelectronics Journal*, 39, 208.
- Malcioğlu, O. B., & Erkoc, S. (2004). Stability of C<sub>60</sub> chains: Molecular Dynamics Simulations. *Journal of Molecular Graphics and Modelling*, 23, 367.
- Martin, T. P. (1996). Shells of atom. *Physics Reports*, 273, 199.
- Mermin, N. D. (1968). Crystalline order in two dimensions. *Physical Review*, 176, 250.
- Meyer, J. C., Geim, A. K., Katsnelson, M. I., Novoselov, K. S., Booth, T. J., & Roth, S. (2007). The structure of suspended graphene sheets. *Nature*, 446, 60.
- Michaelian, K., Rendon, N., & Garzon, I. L. (1999). Structure and energetics of Ni, Ag, and Au nanoclusters. *Physical Review B*, 60, 2000.
- Migas, D. B., & Borisenko, V. E. (2008). Effects of oxygen, fluorine, and hydroxyl passivation on electronic properties of (001)-oriented silicon nanowires. *Journal of Applied Physics*, 104, 024314.
- Moraga, G. G. (1993). *Cluster chemistry*. Berlin: Springer
- Morse, M. D. (1986). Clusters of transition-metal atoms. *Chemical Reviews*, 86, 1049.
- Nakabayashi, J., Yamamoto, D., & Kurihara, S. (2009). Band-selective filter in a zigzag graphene nanoribbon. *Physical Review Letters*, 102, 066803.
- Nava, P., Seierka, M., & Ahlrichs, R. (2003). Density functional study of palladium clusters. *Physical Chemistry Chemical Physics*, 5, 3372.

- Neto, A. H. C., Guinea, F., Peres, N. M. R., Novoselov, K. S., & Geim, A. K. (2009). The electronic properties of graphene. *Reviews of Modern Physics*, *81*, 109.
- Novoselov, K. S., Geim, A. K., Morozov, S. V., Jiang, D., Zhang, Y., Dubonos, S. V., Grigorieva, I. V., & Firsov, A. A. (2004). Electric field effect in atomically thin carbon films. *Science*, *306*, 666.
- Noya, E. G., & Doye, J. P. K. (2006). Structural transitions in the 309-atom magic number Lennard-Jones cluster. *Journal of Physical Chemistry*, *124*, 104503.
- Pan, Z. W., Dai, Z. R., & Wang, Z. L. (2001). Nanobelts of semiconducting oxides. *Science*, *291*, 1947.
- Pathak, S., Shenoy, V. B., & Baskaran, G. (2008). Possibility of High Tc Superconductivity in doped Graphene, arXiv:0809.0244v1 [cond-mat.suprcon] 1 Sep 2008.
- Pawluk, T., Hirata, Y., & Wang, L. (2005). Studies of iridium nanoparticles using density functional theory calculations. *Journal of Physical Chemistry B*, *109*, 20817.
- Payne, F. W., Jiang, W., & Bloomfield, L. A. (2006). Magnetism and magnetic isomers in free chromium clusters. *Physical Review Letters*, *97*, 193401.
- Pedersen, T. G., Flindt, C., Pedersen, J., Jauho, A.-P., Mortensen, N. A., & Pedersen, K. (2008). Optical properties of graphene antidot lattices. *Physical Review B*, *77*, 245431.
- Pedersen, T. G., Flindt, C., Pedersen, J., Mortensen, N. A., Jauho, A.-P., & Pedersen, K. (2008). Graphene antidot lattices: Designed defects and spin qubits. *Physical Review Letters*, *100*, 136804.
- Pekoz, R., & Erkoc, S. (2008). Quantum chemical treatment of Li/Li<sup>+</sup> doped defected carbon nanocapsules. *Physica E*, *40*, 2752.
- Peres, N., Castro, A., & Guinea, F. (2006). Conductance quantization in mesoscopic graphene. *Physical Review B*, *73*, 195411.
- Peres, N. M. R., Guinea, F., & Neto, A. H. C. (2006). Electronic properties of two-dimensional carbon. *Annals of Physics*, *321*, 1559.
- Pisani, L., Chan, J. A., Montanari, B., & Harrison, N. M. (2007). Electronic structure and magnetic properties of graphitic ribbons. *Physical Review B*, *75*, 064418.
- Qi, J., Shi, D., Zhao, J., & Jiang, X. (2008). Stable structures and electronic properties of the oriented Bi Nanowires and Nanotubes from first-principle calculations. *Journal of Physical Chemistry C*, *112*, 10745.
- Rathi, S. J., & Ray, A. K. (2008). On the existence and stability of single walled SiGe nanotubes. *Chemical Physics Letters*, *466*, 79.
- Rey, C., Gallego, L. J., Garcia-Rodeja, J., Alonso, J. A., & Iniguez, M. P. (1993). Molecular-dynamics study of the binding energy and melting of transition-metal clusters. *Physical Review B*, *48*, 8253.
- Rodriguez-Lopez, J. L., Aguilera-Granja, F., Michaelian, K., & Vega, A. (2003). Structure and magnetism of cobalt clusters. *Physical Review B*, *67*, 174413.
- Rosales, L., Pacheco, M., Barticevic, Z., Latge, A., & Orellana, P. A. (2008). Transport properties of graphene nanoribbons with side-attached organic molecules. *Nanotechnology*, *19*, 065402.
- Rudd, R. E., & Lee, B. (2008). Mechanics of silicon nanowires: size-dependent elasticity from first principles. *Molecular Simulation*, *34*, 1.
- Rurali, R. (2005). Electronic and structural properties of silicon carbide nanowires. *Physical Review B*, *71*, 205405.
- Rurali, R., & Lorente, N. (2005). Metallic and semimetallic silicon (100) nanowires. *Physical Review Letters*, *94*, 026805.
- Sadowski, T., & Ramprasad, R. (2007). Stability and electronic structure of CdSe nanorods from first principles. *Physical Review B*, *76*, 235310.
- Sasaki, K. I., Murakami, S., & Saito, R. (2006). Gauge field for edge state in graphene. *Journal of the Physical Society of Japan*, *75*, 074713.
- Sevincli, H., Topsakal, M., Durgun, E., & Ciraci, S. (2008). Electronic and magnetic properties of 3d transition-metal atom adsorbed graphene and graphene nanoribbons. *Physical Review B*, *77*, 195434.
- Shevlin, S. A., & Guo, Z. X. (2006). Transition-metal-doping-enhanced hydrogen storage in boron nitride systems. *Applied Physics Letters*, *89*, 153104.
- Shvartsburg, A. A., & Jarrold, M. F. (1999). Tin clusters adopt prolate geometries. *Physical Review A*, *60*, 1235.
- Shvartsburg, A. A., & Jarrold, M. F. (2000). Transition from covalent to metallic behavior in group-14 clusters. *Chemical Physics Letters*, *317*, 615.
- Sieck, A., Frauenheim, T., & Jackson, K. A. (2003). Shape transition of medium-sized neutral silicon clusters. *Physica Status Solidi B*, *240*, 537.
- Singh, R., & Kroll, P. (2009). Magnetism in graphene due to single-atom defects: dependence on the concentration and packing geometry of defects. *Journal of Physics: Condensed Matter*, *21*, 196002.
- Son, Y. W., Cohen, M. L., & Louie, S. G. (2006). Half-metallic graphene nanoribbons. *Nature*, *444*, 347.
- Stillinger, F. H., & Weber, T. A. (1985). Computer simulation of local order in condensed phases of silicon. *Physical Review B*, *31*, 5262.

- Sun, X. H., Li, C. P., Wong, W. K., Wong, N. B., Lee, C. S., Lee, S. T., & Teo, B. K. (2002). Formation of silicon carbide nanotubes and nanowires via reaction of silicon (from disproportionation of silicon monoxide) with carbon nanotubes. *Journal of the American Chemical Society*, *124*, 14464.
- Tang, C., Yan, W., Zheng, Y., Li, G., & Li, L. (2008). Dirac equation description on the electronic states and magnetic properties of a square graphene quantum dot, arXiv:0811.4312v1 [cond-mat.str-el] 26 Nov 2008.
- Tiago, M. L., Zhou, Y., Alemany, M. M. G., Saad, Y., & Chelikowski, J. R. (2006). Evolution of magnetism in iron from the atom to the bulk. *Physical Review Letters*, *97*, 147201.
- Topsakal, M., Akturk, E., Sevincli, H., and Ciraci, S. (2008). First-principles approach to monitoring the band gap and magnetic state of a graphene nanoribbon via its vacancies. *Physical Review B*, *78*, 235435.
- Ustunel, H., & Erkoc, S. (2007). Structural properties and stability of nanoclusters. *Journal of Computational and Theoretical Nanoscience*, *4*, 928.
- Ustunel, H., Roundy, D., & Arias, T. A. (2005). Modelling a suspended nanotube oscillator. *Nano Letters*, *5*, 523.
- Venkataramanan, N. J., Khazaei, M., Sahara, R., Mizuseki, H., & Kawazoe, Y. (2009). First-principles study of hydrogen storage over Ni and Rh doped BN sheets. *Chemical Physics*, *359*, 173.
- Vvedensky, D. D. (2004). Multiscale modelling of nanostructures. *Journal of Physics: Condensed Matter*, *16*, R1537.
- Wales, D. J. & Doye, J. P. K. (1997). Global optimization by basin-hopping and the lowest energy structures of Lennard-Jones clusters containing up to 110 atoms. *Journal of Physical Chemistry A*, *101*, 5111.
- Wang, G., & Li, X. (2008). Predicting Young's modulus of nanowires from first-principles calculations on their surface and bulk materials. *Journal of Applied Physics*, *104*, 113517.
- Wang, W. L., Meng, S., & Kaxiras, E. (2008). Graphene nanoflakes with large spin. *Nano Letters*, *8*, 241.
- Wang, Z. F., Li, Q., Zheng, H., Ren, H., Su, H., Shi, Q. W., & Chen, J. (2007). Tuning the electronic structure of graphene nanoribbons through chemical edge modification: a theoretical study. *Physical Review B*, *75*, 113406.
- Wang, Z. L. (2004). Functional oxide nanobelts: materials, properties and potential applications in nanosystems and biotechnology. *Annual Review of Physical Chemistry*, *55*, 159.
- Weltner, W. J., & Van Zee, R. J. (1984). Transition metal molecules. *Annual Review of Physical Chemistry*, *35*, 291.
- Wright, A. R., Wang, G. X., Xu, W., Zeng, Z., & Zhang, C. (2009). The spin-orbit interaction enhanced terahertz absorption in graphene around the K point. *Microelectronics Journal*, *40*, 857.
- Wu, K. L., Lai, S. K., & Lin, S. D. (2005). Finite temperature properties for zinc nanoclusters. *Molecular Simulation*, *31*, 399.
- Wu, X., & Zeng, X. C. (2008). Sawtooth-like graphene nanoribbon. *Nano Research*, *1*, 40.
- Wu, X., Pei, Y., & Zeng, X. C. (2009). B<sub>2</sub>C graphene, nanotubes, and nanoribbons. *Nano Letters*. doi: 10.1021/nl803758s.
- Xie, Y. E., Chen, Y. P., Sun, L. Z., Zhang, K. W., & Zhong, J. X. (2009). The effect of corner form on electron transport of L-shaped graphene nanoribbons. *Physica B*, *404*, 1771.
- Yang, M., Jackson, K. A., Koehler, C., Frauenheim, T., & Jellinek, J. (2006). Structure and shape variations in intermediate-size cor clusters. *Journal of Chemical Physics*, *124*, 024308.
- Yang, R., & Wang, Z. L. (2006). Springs, rings, and spirals of rutile-structured tin oxide nanobelts. *Journal of the American Chemical Society*, *128*, 1466.
- Yao, Y. H., Gu, X., Ji, M., Gong, X. G., & Wang, D.-S. (2007). Structures and magnetic moments of Ni<sub>n</sub> ( $n = 10 - 60$ ) clusters. *Physics Letters A*, *360*, 629.
- Zhang, C., Chen, L., & Ma, Z. S. (2008). Orientation dependence of the optical spectra in graphene at high frequencies. *Physical Review B*, *77*, 241402.
- Zhang, W., Ran, X., Zhao, H., & Wang, L. (2004). The nonmetallicity of molybdenum clusters. *Journal of Chemical Physics*, *121*, 7717.
- Zhang, X. W., & Yang, G. W. (2009). Novel band structures and transport properties from graphene nanoribbons with armchair edges. *Journal of Physical Chemistry C*, *113*, 4662.
- Zhang, Y. Y., Wang, C. M., & Tan, V. B. C. (2008). Examining the effects of wall numbers on buckling behavior and mechanical properties of multiwalled carbon nanotubes via molecular dynamics simulations. *Journal of Applied Physics*, *103*, 053505.
- Zhou, J., & Dong, J. (2008). Radial breathing-like mode of wide carbon nanoribbon. *Physics Letters A*. doi: 10.1016/j.physleta.2008.10.059.



# 28 Quantum Cluster Theory for the Polarizable Continuum Model (PCM)

Roberto Cammi<sup>1</sup> · Jacopo Tomasi<sup>2</sup>

<sup>1</sup>Dipartimento di Chimica G.I.A.F, Università di Parma, Parma, Italy

<sup>2</sup>Dipartimento di Chimica e Chimica Industriale, Università di Pisa, Pisa, Italy

<i>Introduction: Quantum Cluster Theory and Solvation</i> .....	1044
<i>The Coupled-Cluster Theory for the Polarizable Continuum Model</i> .....	1048
<i>PCM-CCSD Analytical Gradients</i> .....	1055
<i>The Equation-of-Motion Coupled-Cluster Theory for the Polarizable Continuum Model</i> .....	1058
<i>PCM-EOM-CCSD Analytical Gradients</i> .....	1061
<i>Conclusions</i> .....	1063
<i>Appendix A: The Solute-Solvent PCM Operator</i> .....	1063
<i>References</i> .....	1064

**Abstract:** Recent extensions of the coupled-cluster (CC) theory to molecular solutes described with the Polarizable Continuum Model (PCM) are summarized. The recent advances covered in this review regard: (1) the analytical gradients for the PCM-CC theory at the single and double excitation level and (2) the analytical gradients for the PCM-EOM-CC theory at the single and double excitation level for the descriptions of the excited state properties of molecular solutes. As coupled-cluster is the top level that quantum mechanical (QM) calculations on molecules can presently be performed, and the PCM model gives an effective description of the solute-solvent interaction, these computational advances can be profitably used to study molecular processes in condensed phase, where both the accuracy of the QM descriptions and the influence of the environment play a critical role.

## Introduction: Quantum Cluster Theory and Solvation

---

In this chapter we present some aspects of our recent work on the extension of computing methods connected to the Polarizable Continuum Model (PCM). Our persevering attention to PCM can be in some sense immediately justified, as we proposed this method years ago and have since continued to develop it. In another sense, a justification is required, and may be expressed in the form of a question: why implement PCM with sophisticated procedures such as those given by the coupled-cluster (CC) theory?

Coupled-cluster is the top level at which quantum mechanical (QM) calculations on molecules can now be performed. PCM is characterized by a drastic simplification of the material system by replacing the degrees of freedom of the solvent molecules with a two body integral operator. Apparently, the two methods are operating at very different scales of accuracy, but actually they can be profitably coupled. To show it we will examine some features of PCM. The rapid examination of some technical aspects of the methods used in PCM will be also useful as an introductory section to our exposition.

The methodology on which PCM is based is that of an effective Hamiltonian expressed in terms of interaction integral operators depending on the solution of a non-linear Schrödinger equation. The method is powerful and versatile, allowing applications of very different natures. A good number of such applications have been elaborated over the years by our group and by others, and an undetermined, but large, number of new applications look promising. Many among them are beyond the field of dilute solutions, others address the description of solvent effects under special conditions, and a few regard higher levels of the QM theory.

We here consider an application of this last type. The features of PCM we have to examine are limited to the developments of the QM *ab initio* version of the procedures (other versions regard semiempirical and semiclassical descriptions).

PCM was born as a method to describe electrostatic solvation effects on the electronic distribution of a molecule (Miertuš et al. 1981). The method was conceived for *ab initio* QM calculations, using a technique to solve the electrostatic problem never used before in molecular sciences, a technique based on the use of the concept of apparent charges. The integral interaction operator is thus reduced to the Coulomb interaction with a charge distribution spread on the surface of the solute, and represented by a set of point charges.

Solute-solvent interactions are not limited to the electrostatic one. The non-electrostatic terms have been introduced in PCM with the aid of a phenomenological (and effective) Hamiltonian (Bonaccorsi et al. 1982). Each term of the interaction has a different physical meaning but

a similar formal expression, given by an integral operator with kernel  $Q_X(r, r')$ , where  $X$  stays for one of the contribution to the interaction energy: electrostatic, repulsion, dispersion, cavity formation. The effective Hamiltonian mixes quantum and classical components. In particular, the medium that appears in the kernel of the  $Q_X(r, r')$  operators, has to be precisely defined, in agreement with the physical conditions established for the experiments the computational model has to describe.

The formal elaboration of the physical components of the model has to be followed by the elaboration of the corresponding mathematical procedures. In this step several “concepts” of quantum and classical origin have to be introduced: examples are the molecular surface and the notion of charging process.

We shall use here the concept of charging process as a guide in our exposition. Charging processes are of general use in physics, but rarely mentioned in molecular quantum mechanics; more explicit is its use in statistical thermodynamics to which our model is connected.

The basic task in molecular QM, that of computing energy and charge distribution of an isolated molecule at a clamped nuclear geometry, corresponds to a charging process. The analogous process in solution with an effective continuum Hamiltonian presents, however, important differences. The medium defining the liquid portion of the material systems is changed (polarized) by charging processes. A portion of the energy gained in a reversible charging process is thus lost. The remaining portion of the energy is the free energy of the system, measured from a reference state composed by the unperturbed medium and by the appropriate assembly of non-interacting nuclei and electrons giving origin to the solute molecule. This process has a classical counterpart, and can be derived on QM grounds without invoking physical arguments (a derivation is based on the variational theorem with an effective Hamiltonian linearly dependent on the solution) (Tomasi and Persico 1994).

The picture of the charging process can be used for the phenomenological partition we have introduced earlier. This is a practice used in statistical thermodynamics.

The contributions can be described in an ordered sequence of charging processes; at the end of each process the medium is modified (polarized) and the so polarized medium is the starting point for the following charging process. The selected order of charging influences the result, because couplings in this procedure are neglected and they change according the ordering, but with an appropriate selection of the sequence the results of the solvation energy are well reproduced with a computational cost decidedly lower that of the full calculation (Tomasi et al. 2003).

The option of decoupling the non-electrostatic part from the main calculation also has another practical advantage, which we shall exploit in the rest of this chapter, namely, of provisionally discarding the non-electrostatic terms during the elaboration of a new electrostatic procedure. The non-electrostatic contributions to the energy are numerically large, but feebly coupled with the electrostatic one. We stress, however, that decoupling and simplified descriptions of single components are not strictly necessary: *ab initio* procedures computing everything in a unique calculation exists (Curutchet et al. 2006).

We have so far examined some points of the original PCM procedure. Other elements of interest for the present paper, drawn from the numerous procedures implemented and tested later (Tomasi et al. 2005), will be here considered. These points regard the improvements in the description of the solute's electronic wave function, and the description of excited states, including non-equilibrium solvent effects.

Improvements in the quantum description of a solute mostly regard the electron correlation effects. There are, in principle, no problems to introduce in the formal framework of



our effective Hamiltonian any version of QM methods describing electron correlation. Calculations including a description of correlation at a low level are nowadays routinely performed, but for calculations at high levels the convenience of keeping low computational cost becomes a necessity. There are features in the effective Hamiltonians for continuum solvation promising substantial reductions in some specific versions of post Hartree-Fock calculations. In the present chapter we will make use of a decoupling of the QM charging process elaborated years ago to better study the behavior of the many body perturbation scheme in continuum solution and later adopted to simplify calculations in the series of MPn calculations (del Valle and Tomasi 1991). The perturbation series may be expanded on the electronic configurations of the molecular solute's electron distribution computed in vacuo and then used for the calculation of solvent reaction potential and solvation free energy; this approximation is called PTD, being a version of the perturbation theory based on the electronic density. Another scheme is based on the expansion of the molecular solute's electron distribution computed with PCM at the Hartree-Fock level, and used to compute solvent reaction potential and energy; this approximation is called PTE. The comparison of the results obtained with the two schemes gave insights on the relative importance of the decoupled electron correlation and solvation potential effects on the solute. A more complete procedure couples the two effects into a single iterative computational scheme, with the correlated electronic density used to make the solvent field self-consistent; the procedure is called PTDE. We shall examine in a later section the PTE and PTDE version for the coupled cluster method.

In this chapter we will also consider the first basic aspects of the dynamical, i.e., non-equilibrium, behavior of liquid media. The subject embraces a very large variety of phenomena, requiring different formulation of the continuum models. We cite here an aspect, relatively simple, related to a phenomenon occurring in a span of time relatively short with respect to the characteristic relaxation times (CRT) of the solvent: the vertical electronic transitions in solutes (Basilevsky and Chudinov 1990; Kim and Hynes 1990; Marcus 1992).

Electronic transitions are very fast and the solvent molecules have no time to rearrange themselves during this phenomenon, save for the electronic component of the solvent polarization that has a CRT of the same order of magnitude of the vertical electronic transition. This effect means that the energy of the vertical transition (a free energy) has a component due to the solvent interaction limited to changes in the fast electronic polarization. The effects of the electronic transition continue in time, but these do not regard the vertical process and have to be described with a different formulation of the continuum method.

For the sake of completeness, we note that there are two theoretical models, respectively named Marcus and Pekar partitions, that describe this simple process, differing in the intermediate stages of the elaboration of the problem, but arriving at the same result when the correct expression for the non-equilibrium free energy functional is used. The PCM versions of the two models have been presented by Aguilar et al. (1993) and by Cammi and Tomasi (1995b); for a comment also see Aguilar (2001). A detailed comparison of the formulas of two models has been reported in Sect. 5.1 of Tomasi et al. (2005). The Pekar partition will be used in the following sections of this chapter; the Marcus partition is in this case less convenient.

Quantum models in condensed systems often present alternative computational routes merging into a unique form when the effects of the medium are neglected. In coding the formulas for problems, great attention must be paid to the proper inclusion of the corrections to satisfy the free energy requirements.

This last remark also holds for the topic we shall consider now: the calculation of the electronic excitation energies. Two approaches are generally used to obtain the excitation energies:

a version based on the CI approach or a version based on the response theory. Both approaches have in condensed media problems not present in the corresponding calculations in vacuo.

The roots of a CI calculation give in vacuo the energies of the various states; in solution these values have to be corrected for the effect of the solvent electronic polarization. Also the corresponding description of the so-defined electronic states has to be modified (with an iterative procedure), because mutual polarization effects occur at the same time. This operation of polarization has to be separately performed for each electronic state, being the effective Hamiltonian of each excited state different from the others. The method is said “state specific” (SS) and it constitutes the main way for the study of excited state potential surfaces. Note that the states so obtained are not rigorously orthogonal to each other. Also, in CI calculations for correlation in a given state (e.g., the ground state) of the solute there is no need for a SS procedure.

The second approach is based on a Hamiltonian with explicit time dependence, provided with an opportune form of the of the time-dependent variation principle (the Frenkel principle is generally used (Cammi et al. 1996)). From this starting point linear and non linear response functions are derived.

The linear response functions (LR) nowadays are amply used both in gas phase and in solution for the characterization of excited states and of molecular properties. The complete equivalence between SS and LR results for the excitation energies was universally accepted, but recently it was shown (Cammi et al. 2005; Corni et al. 2005; Kongsted et al. 2002) that this equivalence is valid only in vacuo, and that LR results can be seriously in error in solution. A computational strategy to reduce this error was proposed (Caricato et al. 2006; Improta et al. 2006), efficient enough to allow the exploitation of the less expensive LR scheme.

It is convenient to mention here another aspect of the continuum solvation theory that will be used in the following pages: the calculation of analytical derivatives.

It is essential for computational methods addressing chemical problems the availability of analytic expressions for derivatives. The variety of derivatives appearing in molecular calculations is quite large, but we limit ourselves to considering derivatives of the energy with respect to nuclear coordinates.

There is an important difference between these derivatives in vacuo and in solution. In solution it is compelling to compute derivatives taking into account partial derivation with respect to cavity parameters. An accurate description of the cavity shape is compulsory: examples of bad results due to inaccurate descriptions of the cavity are present in every field of application: from the determination of the molecular structure, to the equilibria among conformers, to spectroscopic properties. Spherical cavities have to be used only as first-order approximation; more subtle are the errors with cavities badly defined or treated in a simplified way during the calculations. The problems of accurate handling of the derivatives of the cavity parameters become more complex and computing expensive with the increase of the order of the derivative and of the computational level. The problem of the numerical stability of the second derivatives obliged us in the past to change the definition of the cavity elements. The analytical expressions of the first and second derivatives with respect to nuclear coordinates have been elaborated for the present version, but we shall use in the second part of this chapter the first derivatives only.

The methodological and computational bases of PCM have been elaborated more extensively than shown in this exposition, but what has been stated would be sufficient to show the care necessary to develop a reliable version of CC for PCM. Nothing has been said about the numerical accuracy of PCM results. The definition of the accuracy for a method allowing numerous different application is a problem; it is almost compulsory to separately consider different classes of phenomena. The largest number of applications of solvent methods regards

the solvation energy. Actually, there is no need for this property of an accurate description of the electronic distribution, and in fact many methods are based on semiclassical approximations. There are, however, difficult cases in which there is the need for an accurate description of geometry and electronic charge distribution: in these cases *ab initio* method of sufficient accuracy are necessary. There are several methods satisfying this criterion, and all perform well. A recent comparison (Cramer and Truhlar 2008; Klamt et al. 2009) gives some indications, even if the really difficult cases were not abundant in the these comparisons. Another point to remark is that the best fitting with experimental data were obtained using “calibrated parameters.” We have not discussed in the preceding pages the empirical calibration of parameters over experimental data, because we have not used this procedure in the elaboration of PCM methods (and we are not using it in this chapter). Calibration of parameters is necessary for explicitly declared semiempirical methods, but it is risky for methods aspiring to generality because *ad hoc* parameterizations are limited to one (or few) properties, and performed over a single specific definition of the computational parameters (QM method, basis set, etc.). Nevertheless, versions of PCM parameterized for solvation energies exist, and they behave very well.

More interesting is the consideration of accuracy for more complex problems of spectroscopic type, which actually constitute the direct motivation of this work. PCM is among the best methods in this field, with features not present in other methods, but the need to have a description of the electronic structure of the chromophore more accurate than those currently used in these studies is, in our opinion, quite manifest. There was a previous attempt, several years ago, with the use of a CC wavefunction modified by continuum solvent effects, just for the calculation of molecular properties. The proposal was made by Mikkelsen and coworkers (Christiansen and Mikkelsen 1999a) using a spherical cavity with a multipolar expansion of the solvent reaction potential. This attempt was bold and interesting, but the continuum model was forcibly simple, with the perspective of giving, when applied to more complex chromophores, results in which a gain in the description of the solute is accompanied by a poorer description of the solvent effect. Time was not yet ripe for efficient applications of the approach to systems of real spectroscopic interest. This is the answer to the question posed at the beginning of this introduction. There is the need for some specific scopes of molecular calculations more accurate than those currently available, and the more convenient way to arrive at this level of accuracy apparently is given by an accurate (in the formulation and in the execution) *ab initio* continuum code coupled to an efficient procedure of the coupled cluster family. First principles molecular dynamics at so high a level of quantum description is not feasible. The use of computer simulations at a lower level accompanied by a final calculation at the CC level is a risky procedure, requiring extensive validation.

In this introduction we have not examined the details of the coupled-cluster procedures because we have used in the implementation standard aspects of it, on which particular comments were not necessary (Bartlett and Musial 2007). Details and comments will be necessary when an extension of the present study is published.

---

## The Coupled-Cluster Theory for the Polarizable Continuum Model

---

The coupled-cluster (CC) theory for a molecular solute described within the PCM model exploits the concept of the coupled-cluster energy functional. For isolated molecules this energy functional corresponds to the coupled-cluster “expectation value” of the molecular hamiltonian operator (Bartlett and Musial 2007). The corresponding functional for molecular solute has an

important difference with respect to this case, because of its thermodynamical status of a free energy of the whole solute-solvent system, as we have already said in the Introduction. As a consequence, the coupled-cluster free energy functional is no more given as “expectation” value of the molecular (effective) hamiltonian operator (Cammi 2009; Christiansen and Mikkelsen 1999a).

In the following section we review both the formal PCM-CC equations, and their evaluation at the single and double excitation levels (PCM-CCSD). The use of the variational properties of the PCM-CC energy functional to obtain analytical expressions of the energy derivative, will be described in section “PCM-CCSD Analytical Gradients.” For reasons of length, the exposition will be limited to the analytical first derivatives only. The interested reader may find the analytical second derivatives expressions in Cammi (2009).

## The PCM-CC Reference State and the PCM-CC Energy Functional

The ket CC wavefunction of the molecular solute is written as exponential ansatz

$$|\text{CC}\rangle = e^T |\text{HF}\rangle, \quad (28.1)$$

where  $|\text{HF}\rangle$  is the reference state given by the Hartree-Fock ground state of the solvated molecule, and the cluster operator  $T$  is given as a sum of all possible excitation operators over the  $N$  electrons,

$$T = T_1 + T_2 + \dots + T_N, \quad (28.2)$$

$$T_n = \frac{1}{(n!)^2} \sum_{aibj\dots} t_{ij\dots}^{ab\dots} a_a^\dagger a_i a_b^\dagger a_j \dots,$$

weighted by the amplitudes  $t_i^a$ ,  $t_{ij}^{ab}$ , etc. The excitation operators are here represented as products of second quantization electron creation ( $a_i^\dagger$ ,  $a_b^\dagger$ ) and annihilation operators ( $a_i$ ,  $a_b$ ). As usual, indexes ( $i, j, k, \dots$ ) and ( $a, b, c, \dots$ ) denote, respectively, occupied and vacant spin orbitals MO, while ( $p, q, r, \dots$ ) denote general spin orbitals.

### The PCM Hartree-Fock Reference State

The Hartree-Fock reference state  $|\text{HF}\rangle$  is obtained by the stationarity condition of Hartree-Fock free energy functional  $\mathcal{G}_{\text{HF}}$ : (Cammi and Tomasi 1995a)

$$\mathcal{G}_{\text{HF}} = \langle \text{HF} | H^o + \frac{1}{2} \langle \text{HF} | \hat{\mathbf{Q}} | \text{HF} \rangle \cdot \mathbf{V} | \text{HF} \rangle, \quad (28.3)$$

where  $H^o$  is the Hamiltonian of the isolated solute, and  $\langle \text{HF} | \hat{\mathbf{Q}} | \text{HF} \rangle \cdot \hat{\mathbf{V}}$  is the solute-solvent interaction term, being  $\langle \text{HF} | \hat{\mathbf{Q}} | \text{HF} \rangle$  the solvent polarization charges computed with the Hartree-Fock state reference state  $|\text{HF}\rangle$ , and  $\hat{\mathbf{V}}$  the molecular electrostatic potential operator of the solute (see Appendix A); the one-half factor in front of the solute-solvent potential term is due to the energy loss during the process of polarization of the dielectric representing the solvent, as already noted in the introduction.

In an  $N$ -electron system with spin-orbitals expanded over a set of atomic orbitals (AO)  $\{\chi_\mu, \chi_\nu, \dots\}$ ,  $\mathcal{G}^{\text{HF}}$  may be written as:

$$\mathcal{G}^{\text{HF}} = \sum_{\mu\nu} P_{\mu\nu}^{\text{HF}} (h_{\mu\nu} + j_{\mu\nu}) + \frac{1}{2} \sum_{\mu\nu\lambda\sigma} P_{\mu\nu}^{\text{HF}} P_{\lambda\sigma}^{\text{HF}} [\langle \mu\lambda || \nu\sigma \rangle + \mathcal{B}_{\mu\nu,\lambda\sigma}] + \tilde{V}_{\text{NN}}, \quad (28.4)$$

where  $h_{\mu\nu}$  are the matrix elements, in the AO basis, of the one-electron core operator,  $\langle \mu\lambda || \nu\sigma \rangle$  are the antisymmetrized combination of regular two-electron repulsion integrals (ERIs) and  $P_{\mu\nu}^{\text{HF}}$  indicates the elements of the Hartree-Fock density matrix. The one-electron matrix elements  $j_{\mu\nu}$ , and the pseudo two-electron integrals  $\mathcal{B}_{\mu\nu,\lambda\sigma}$  describe the solute-solvent interactions within the PCM-Fock operator. The one-particle AO integrals  $j_{\mu\nu}$  and the pseudo two-electron integrals  $\mathcal{B}_{\mu\nu,\lambda\sigma}$  represent, respectively, the interactions with the nuclear and with the electronic components of the ASC charges. The solvent integrals  $j_{\mu\nu}$ ,  $\mathcal{B}_{\mu\nu,\lambda\sigma}$  may be expressed in the following form:

$$j_{\mu\nu} = \mathbf{v}_{\mu\nu} \cdot \mathbf{q}_{\text{Nuc}}, \quad (28.5)$$

$$\mathcal{B}_{\mu\nu,\lambda\sigma} = \mathbf{v}_{\mu\nu} \cdot \mathbf{q}_{\lambda\sigma}, \quad (28.6)$$

where  $\mathbf{v}_{\mu\nu}$  is a vector collecting the AO integrals of the electrostatic potential operator evaluated at the positions  $\mathbf{s}_k$  of the ASC charges;  $\mathbf{q}_{\text{Nuc}}$  is a vector collecting the ASC charges produced by the nuclear charge distribution;  $\mathbf{q}_{\lambda\sigma}$  is a vector collecting the apparent charges produced by the elementary charge distribution  $\chi_\lambda^*(\mathbf{r})\chi_\sigma(\mathbf{r})$ . The apparent surface charges may be obtained in terms of the electrostatic potential of the solute charge distributions by using the integral equation formalism of the PCM (Cances et al. 1997).

The last term of  $\blacklozenge$  Eq. 28.4,  $\tilde{V}_{\text{NN}}$  represents the interaction between the nuclei and the nuclear component of the apparent surface charges,  $\tilde{V}_{\text{NN}} = (1/2)\mathbf{v}_{\text{Nuc}} \cdot \mathbf{q}_{\text{Nuc}}$ .

Requiring that  $\mathcal{G}_{\text{HF}}$  be stationary with respect the variation of MO expansion coefficients we obtain the PCM-HF equations:

$$\sum_{\nu} (f_{\mu\nu}^{\text{PCM}} - \epsilon_p S_{\mu\nu}) c_{\nu p} = 0, \quad (28.7)$$

where  $S_{\mu\nu}$  and  $f_{\mu\nu}^{\text{PCM}}$  are, respectively, the matrix elements of the overlap matrix and of the PCM Fock matrix, in the AO basis, and  $\epsilon_p$  and  $c_{\nu p}$  are, respectively, the orbital energy and the expansion coefficients of the  $p$  MO. The PCM Fock matrix elements are given by:

$$f_{\mu\nu}^{\text{PCM}} = (h_{\mu\nu} + j_{\mu\nu}) + G_{\mu\nu}(\mathbf{P}^{\text{HF}}) + X_{\mu\nu}(\mathbf{P}^{\text{HF}}), \quad (28.8)$$

where  $G_{\mu\nu}(\mathbf{P}^{\text{HF}})$  are the matrix elements of the effective Coulomb-exchange two-electron operator, while  $X_{\mu\nu}(\mathbf{P}^{\text{HF}})$  are the matrix elements of the solvent operator representing an effective Coulomb two-electron mediated by the polarization of the solvent.

## The Coupled-Cluster PCM Free Energy Functional

To define the PCM free energy functional we introduce the bra coupled-cluster wavefunction:

$$\langle \tilde{\text{CC}} | = \langle \text{HF} | (1 + \Lambda) e^{-T}, \quad (28.9)$$

where  $\Lambda$  is a de-excitation operator,

$$\Lambda = \Lambda_1 + \Lambda_2 + \dots \Lambda_n = \frac{1}{(n!)^2} \sum_{ijkabc\dots} \lambda_{abc\dots}^{ijk\dots} a_i^\dagger a_a a_j^\dagger a_b a_k^\dagger a_c \dots, \quad (28.10)$$

and  $\lambda_a^i, \lambda_{ab}^{ij}, \dots$  are the de-excitation amplitudes.

In terms of the bra and ket wavefunctions the coupled-cluster free energy functional may be written as Christiansen and Mikkelsen (1999a) and Cammi (2009):

$$G_{CC}(\Lambda, T) = \langle \text{HF} | (1 + \Lambda) e^{-T} H_0 e^T | \text{HF} \rangle + \frac{1}{2} \bar{\mathbf{Q}}(T, \Lambda) \cdot \bar{\mathbf{V}}(T, \Lambda), \quad (28.11)$$

where  $\langle \text{HF} | (1 + \Lambda) e^{-T} H_0 e^T | \text{HF} \rangle$  is the energy functional for the isolated molecules and  $\bar{\mathbf{V}}$  and  $\bar{\mathbf{Q}}$  are, respectively, the coupled-cluster expectation value of the PCM operators  $\hat{\mathbf{Q}}$  and  $\hat{\mathbf{V}}$  (Bartlett and Musial 2007):

$$\bar{\mathbf{Q}}(T, \Lambda) = \langle \text{HF} | (1 + \Lambda) e^{-T} \mathbf{Q} e^T | \text{HF} \rangle, \quad (28.12)$$

$$\bar{\mathbf{V}}(T, \Lambda) = \langle \text{HF} | (1 + \Lambda) e^{-T} \mathbf{V} e^T | \text{HF} \rangle. \quad (28.13)$$

We note that arguments of the expectation values (● Eqs. 28.12 and ● 28.13) denote an explicit functional dependence on the  $T$  and  $\Lambda$  amplitudes. These amplitudes, which define completely the coupled-cluster wavefunction of the molecular solute, can be determined imposing the stationary conditions on the energy functional  $G_{CC}(\Lambda, T)$ .

## The PTDE and the PTE Coupled Cluster Schemes

To develop a coupled-cluster theory within the PTE and PTDE schemes described in the Introduction, the free energy functional  $G_{CC}(\Lambda, T)$  of ● Eq. 28.11 is partitioned into a Hartree-Fock component  $\mathcal{G}_{\text{HF}}$  and into a coupled-cluster component  $\Delta G_{CC}(\Lambda, T)$ :

$$G_{CC}(\Lambda, T) = \Delta G_{CC}(\Lambda, T) + \mathcal{G}_{\text{HF}}, \quad (28.14)$$

where  $\mathcal{G}_{\text{HF}}$  is the HF contribution, defined in ● Eq. 28.3, and  $\Delta G_{CC}(\Lambda T)$  denotes the correlative CC contribution:

$$\Delta G_{CC}(\Lambda, T) = \langle \text{HF} | (1 + \Lambda) e^{-T} \left[ H(0)_N + \frac{1}{2} \bar{\mathbf{Q}}_N(\Lambda, T) \cdot \mathbf{V}_N \right] e^T | \text{HF} \rangle. \quad (28.15)$$

The partition of ● Eq. 28.14 is based on the so-called normal ordered operators  $H(0)_N, \mathbf{V}_N$  and,  $\mathbf{Q}_N$  (Cammi 2009). Specifically,  $\bar{\mathbf{Q}}_N(\Lambda, T) \cdot \mathbf{V}_N$  is the component of the solvent reaction potential due to the correlation CC electronic density, and  $H(0)_N$  is the normal ordered form of Hamiltonian of the solute in presence of the frozen Hartree-Fock reaction field  $\bar{\mathbf{Q}}_{\text{HF}}$ .

## The Coupled-Cluster PTDE Scheme

Within the PTDE scheme the coupled-cluster electronic density is used to make the solvent reaction field self-consistent. This corresponds to making the free energy functional  $\Delta G_{CC}(\Lambda, T)$  stationary with respect to the  $\Lambda$  and the  $T$  amplitudes.

The stationarity with respect to the  $\Lambda$  amplitudes gives the equation for the self-consistent  $T$  amplitudes

$$\frac{\partial \Delta G_{CC}}{\partial \lambda_{ab..}^{ij..}} = \langle \text{HF} | \{ i^\dagger a j^\dagger b.. \} e^{-T} H(\Lambda, T)_N e^T | \text{HF} \rangle = 0. \quad (28.16)$$

In turn, the stationarity with respect to the  $T$  amplitudes gives the equation for the self-consistent  $\Lambda$  parameters:

$$\frac{\partial \Delta G_{CC}}{\partial t_{ij..}^{ab..}} = \langle \text{HF} | (1 + \Lambda) e^{-T} [H(\Lambda, T)_N, \{ a^\dagger i a^\dagger j.. \}] e^T | \text{HF} \rangle = 0. \quad (28.17)$$

In  $\blacktriangleright$  Eqs. 28.16 and  $\blacktriangleright$  28.17,  $H(\Lambda, T)_N$  is the Hamiltonian of the molecular solute in the PTDE scheme:

$$H(\Lambda, T)_N = H(0)_N + \tilde{\mathbf{Q}}_N(\Lambda, T) \cdot \mathbf{V}_N, \quad (28.18)$$

where  $H(0)_N$  is the normal ordered form of Hamiltonian of the solute in presence of the frozen HF reaction field, and  $\tilde{\mathbf{Q}}_N(\Lambda, T) \cdot \mathbf{V}_N$  is the coupled-cluster component of the solvent reaction potential, as described above.

The equation for the  $T$  amplitudes has a clear physical meaning: it corresponds to projection in the manifold spanned by all the orthonormal excitations to  $|\text{HF}\rangle$  of the coupled-cluster Schrödinger equation for the molecular solute,

$$[H(0)_N + \tilde{\mathbf{Q}}_N(\Lambda, T) \cdot \mathbf{V}_N] e^T | \text{HF} \rangle = \Delta E_{CC} e^T | \text{HF} \rangle, \quad (28.19)$$

where  $\Delta E_{CC}$  is given by

$$\Delta E_{CC} = \langle \text{HF} | (1 + \Lambda) e^{-T} H(\Lambda, T)_N e^T | \text{HF} \rangle. \quad (28.20)$$

The coupled-cluster eigenvalue  $\Delta E_{CC}$  differs from the free-energy functional  $\Delta G_{CC}(\Lambda, T)$  by the work spent during the charging process of the coupled-cluster reaction field, i.e.:

$$\Delta G_{CC} = \Delta E_{CC} - \frac{1}{2} \tilde{\mathbf{Q}}_N(\Lambda, T) \cdot \tilde{\mathbf{V}}_N(\Lambda, T), \quad (28.21)$$

where  $\tilde{\mathbf{V}}_N(\Lambda, T)$  is the coupled cluster expectation value of the electrostatic potential.

Being the Hamiltonian  $H(\Lambda, T)_N$  dependent on both  $T$  and  $\Lambda$  parameters, the corresponding PTDE equations ( $\blacktriangleright$  Eqs. 28.16 and  $\blacktriangleright$  28.17), are coupled, and they must be solved in an iterative and self-consistent way.

## The Coupled-Cluster PTE Scheme

In the PTE coupled-cluster approximation the electronic distribution is computed with PCM at the Hartree-Fock level. This approximation is easily obtained from the above PTDE equations by neglecting all the contributions related to the coupled-cluster solvent operator  $\tilde{\mathbf{Q}}_N(\Lambda, T) \cdot \mathbf{V}_N$ . Specifically, the PTE Hamiltonian is the Hamiltonian  $H(0)_N$ , which contains the fixed reaction potential of the solute at the HF level, and the free energy functional is given by

$$\Delta G_{CC}^{\text{PTE}} = \Delta E_{CC}^{\text{PTE}} = \langle \text{HF} | (1 + \Lambda) e^{-T} H(0)_N e^T | \text{HF} \rangle. \quad (28.22)$$

The stationary condition of  $\Delta G_{CC}^{\text{PTE}}$  leads to the following  $T$  equations:

$$\frac{\partial \Delta G_{CC}^{\text{PTE}}}{\partial \lambda_{ab..}^{ij..}} = \langle \text{HF} | \{ i^\dagger a j^\dagger b.. \} e^{-T} H(0)_N e^T | \text{HF} \rangle = 0, \quad (28.23)$$

and of the  $\Lambda$  equations

$$\frac{\Delta \partial G_{CC}}{\partial t_{ij..}^{ab..}} = \langle \text{HF} | (1 + \Lambda) e^{-T} H(0)_N, \{ a^\dagger i a^\dagger j \dots \} \rangle e^T | \text{HF} \rangle = 0. \quad (28.24)$$

Within the PTE approximation the PCM coupled-cluster equations (► Eqs. 28.16 and ► 28.17) have the same structure as the coupled-cluster equations of the isolated molecules and the  $T$ , and  $\Lambda$  amplitudes equations are not more coupled. As a consequence, we don't need to solve the  $\Lambda$  equations to compute the energy functional  $\Delta G_{CC}^{\text{PTE}}$ .

In the next section we describe how the basic PTDE and PTE equations lead to explicit expressions suitable for the implementation in quantum chemistry computational codes.

## The Explicit PCM-CCSD Equations

The explicit form of the PCM-CC equations (► Eqs. 28.16–28.24) has been recently presented (Cammi 2009) for the coupled-cluster single and double (CCSD) level, which restricts the  $T$  and  $\Lambda$  operators to excitation operators  $T_1, T_2$  and to the de-excitation operators  $\Lambda_1, \Lambda_2$ , respectively.

The key entities are the similarity transformed PTE Hamiltonian  $\mathcal{H}(0) = e^{-T} H(0)_N e^T$  and the similarity transformed molecular electrostatic potential operators  $\mathcal{V} = e^{-T} \hat{\mathbf{V}}_N e^T$ . Both operators can be expressed as a terminated Backer-Campbell-Hausdorff expansion. Specifically,  $\mathcal{H}(0)$  terminates at the four-fold commutator, because it has at most two-particle interactions:

$$\begin{aligned} \mathcal{H}(0) &= \hat{H}(0)_N + [\hat{H}(0)_N, T] + \frac{1}{2} [[\hat{H}(0)_N, T], T] \\ &\quad + \left[ \left[ \left[ \frac{1}{3!} \hat{H}(0)_N, T \right], T \right], T \right] + \frac{1}{4!} \left[ \left[ \left[ \left[ \hat{H}(0)_N, T \right], T \right], T \right], T \right] \\ &= (H(0)_N \exp(T))_C, \end{aligned} \quad (28.25)$$

while  $\mathcal{V}$  terminates at the two-fold commutator as it has at most one-particle interactions:

$$\mathcal{V} = \hat{\mathbf{V}}_N + [\hat{\mathbf{V}}_N, T] + \frac{1}{2} [[\hat{\mathbf{V}}_N, T], T] = (\mathbf{V}_N \exp(T))_C. \quad (28.26)$$

In ► Eqs. 28.25 and ► 28.26 the subscript  $C$  indicates that only the so-called connected terms are considered, when the operators are expressed in terms of normal ordered product of second-quantization creation and annihilation operators (Bartlett and Musial 2007).

The similarly transformed coupled-cluster PTDE-PCM Hamiltonian can then be written in the connected form,

$$\mathcal{H}(\Lambda, T) = (H(0)_N \exp(T))_C + (\mathbf{V}_N \exp(T))_C, \quad (28.27)$$

and the explicit PCM-CC equations may be obtained by substitution into ► Eqs. 28.16–28.21. The corresponding integrals may be obtained by an algebraic approach, which exploits the Wick theorem (Bartlett and Musial 2007) for normal product operators with  $H(T, \Lambda)_N$  written in the second quantized form,

$$H(T, \Lambda)_N = \sum_{p,q} \left( f_{p,q}^{\text{PCM}} + \hat{\mathbf{Q}}_N(\Lambda, T)_{\mathbf{v}pq} \right) \{ p^\dagger q \} + \frac{1}{4} \sum_{p,q,r,s} \langle pq || rs \rangle \{ p^\dagger q^\dagger sr \}. \quad (28.28)$$



The explicit equation for the correlation energy  $\Delta E_{CC}$  is obtained as

$$\Delta E_{CC} = \langle \text{HF} | \hat{H}(T, \Lambda)_N (T_2 + T_1 + \frac{1}{2}) T_1^2 | \text{HF} \rangle, \quad (28.29)$$

with the corresponding algebraic form given by

$$\Delta E_{CC} = \tilde{\mathbf{Q}}_N(\Lambda, T) \cdot \mathbf{v}_{ia} t_i^a + \frac{1}{4} \langle ij || ab \rangle \tau_{ij}^{ab}, \quad (28.30)$$

where  $\tau_{ij}^{ab} = t_{ij}^{ab} + t_i^a t_j^b - t_i^b t_j^a$ .

The explicit expressions for the  $T_1, T_2$  equations are given by

$$\begin{aligned} 0 &= \langle i^a | \hat{H}(T, \Lambda)_N (1 + T_2 + T_1 + T_1 T_2 + \frac{1}{2} T_1^2 + \frac{1}{3!} T_1^3) | \text{HF} \rangle_c \\ &= \langle i^a | f_N^{\text{PCM}} (1 + T_1 + T_2 + \frac{1}{2!} T_1^2) \\ &\quad + \tilde{\mathbf{Q}}_N(\Lambda, T) \cdot \mathbf{V}_N (1 + T_1 + T_2 + \frac{1}{2!} T_1^2) \\ &\quad W_N (T_1 + T_2 + \frac{1}{2!} T_1^2 + T_1 T_2 + \frac{1}{3!} T_1^3) | \text{HF} \rangle, \end{aligned} \quad (28.31)$$

$$\begin{aligned} 0 &= \langle ij^{ab} | \hat{H}(T, \Lambda)_N (1 + T_2 + T_1 + T_1 T_2 + \frac{1}{2} T_1^2 + \frac{1}{2!} T_2^2 + \frac{1}{2} T_1^2 T_2 \\ &\quad + \frac{1}{3!} T_1^3 + \frac{1}{4!} T_1^4) | \text{HF} \rangle_c \\ &= \langle ij^{ab} | f_N^{\text{PCM}} (T_2 + T_1 T_2) + \tilde{\mathbf{Q}}_N(\Lambda, T) \cdot \mathbf{V}_N (T_2 + T_1 T_2) \\ &\quad + W_N (T_2 + \frac{1}{2!} T_1^2 + T_1 T_2 + \frac{1}{3!} T_1^3 + \frac{1}{2!} T_2^2 + \frac{1}{2!} T_1^2 T_2 + \frac{1}{4!} T_1^4) | \text{HF} \rangle_c, \end{aligned} \quad (28.32)$$

where  $\langle ij^{ab} | \cdot \rangle = \langle \text{HF} | \{ i^\dagger a j^\dagger b \dots \} \rangle$ .

The explicit  $\Lambda_1, \Lambda_2$  equations are obtained as:

$$0 = \langle \text{HF} | \hat{H}(T, \Lambda)_N e^T | i^a \rangle_c + \langle \text{HF} | (\Lambda_1 + \Lambda_2) (\hat{H}(T, \Lambda)_N e^T) | i^a \rangle_c, \quad (28.33)$$

and

$$\begin{aligned} 0 &= \langle \text{HF} | \hat{H}(T, \Lambda)_N e^T | ij^{ab} \rangle_c + \langle \text{HF} | (\Lambda_1 + \Lambda_2) (\hat{H}(T, \Lambda)_N e^T) | ij^{ab} \rangle_c \\ &\quad + \sum_{c=a,b; k=i,j} \langle \text{HF} | \hat{H}(T, \Lambda)_N e^T | k^c \rangle \langle k^c | \Lambda_1 + \Lambda_2 | ij^{ab} \rangle. \end{aligned} \quad (28.34)$$

The algebraic forms for the  $T_1, T_2$  and  $\Lambda_1, \Lambda_2$  equations are reported elsewhere (Cammi 2009).

The above PTDE PCM-CC explicit equations can be easily implemented in any computational quantum code. However, the PTDE coupled-cluster procedure is different with respect to a calculation on isolate molecules, as anticipated above. The electron correlation component of the reaction field  $\tilde{\mathbf{Q}}_N(\Lambda, T) \cdot \mathbf{v}_{me}$  enters, as an effective one-body contribution, both in the  $T$  and in the  $\Lambda$  equations, which must be solved simultaneously by using a recursive procedure. The coupling between the  $T, \Lambda$  equations has obvious computational consequences, with an increase of computational cost with respect to a coupled-cluster calculation for isolated molecules. In fact, in this case it is not necessary to solve the  $\Lambda$  equation to obtain the CC energy and wavefunction.

The explicit equations for the PCM-CC-PTE approximation can be easily obtained from the PTDE equations by neglecting all terms involving the coupled-cluster components of the solvent reaction potential. This makes the computational cost of the PTE approximation similar to a coupled-cluster calculation for isolated molecules.

## PCM-CCSD Analytical Gradients

The differentiation with respect to a perturbational parameter  $\alpha$ , of the stationary PCM-CC functional  $\Delta G_{CC}$  leads to an expression that avoids the first derivative of the  $T$ ,  $\Lambda$  amplitudes. The first derivative  $\partial\Delta G_{CC}/\partial\alpha = \Delta G_{CC}^\alpha$  can be expressed in the following form:

$$\begin{aligned}\Delta G_{CC}^\alpha &= \langle \text{HF} | (1 + \Lambda) | e^{-T} [H(0)_N^\alpha e^T | \text{HF} \rangle \\ &+ \frac{1}{2} \langle \text{HF} | (1 + \Lambda) | e^{-T} \mathbf{Q}_N^\alpha e^T | \text{HF} \rangle \cdot \tilde{\mathbf{V}}_N(\Lambda, T) \\ &+ \frac{1}{2} \tilde{\mathbf{Q}}_N(\Lambda, T) \cdot \langle \text{HF} | (1 + \Lambda) | e^{-T} \mathbf{V}_N^\alpha e^T | \text{HF} \rangle, \end{aligned} \quad (28.35)$$

where the superscript  $\alpha$  of the various normal ordered operators denotes the total derivative of their second-quantization form.

The differentiated Hamiltonian  $H(0)_N^\alpha$  in the second quantized form is given by

$$H(0)_N^\alpha = \sum_{pq} f_{pq}^{\text{PCM},\alpha} \{p^\dagger q\} + \frac{1}{4} \sum_{pqrs} \langle pq || rs \rangle^\alpha \{p^\dagger q^\dagger sr\}, \quad (28.36)$$

where  $f_{p,q}^{\text{PCM},\alpha}$  and  $\langle pq || rs \rangle^\alpha$  denote, respectively, the total first derivatives of the PCM-Fock matrix elements and of the usual two-electron integrals, both in the MO basis.

The derivate matrix elements  $f_{p,q}^{\text{PCM},\alpha}$  may be written in terms of the derivatives of the constituting MO integrals

$$f_{pq}^{\text{PCM},\alpha} = h_{pq}^\alpha + j_{pq}^\alpha + \sum_j^{\text{occ}} (\langle pj || qj \rangle^\alpha + \mathcal{B}_{jj,pq}^\alpha), \quad (28.37)$$

where the derivatives of the solvent integrals  $j_{pq}^\alpha$  and  $\mathcal{B}_{jj,pq}^\alpha$  are given by

$$j_{pq}^\alpha = \mathbf{v}_{pq}^\alpha \cdot \mathbf{q}_{\text{Nuc}} + \mathbf{v}_{pq} \cdot \mathbf{q}_{\text{Nuc}}^\alpha, \quad (28.38)$$

$$\mathcal{B}_{pq,rs}^\alpha = \mathbf{v}_{\mu\nu}^\alpha \cdot \mathbf{q}_{rs} + \mathbf{v}_{\mu\nu} \cdot \mathbf{q}_{rs}^\alpha, \quad (28.39)$$

where  $\mathbf{q}_{p,q}^\alpha$   $\mathbf{v}_{p,q}^\alpha$  are, respectively, the differentiated apparent charges integrals and the differentiated electrostatic potential integrals (Cammi and Tomasi 1994).

The differentiated operators  $\mathbf{Q}_N^\alpha$  and  $\mathbf{V}_N^\alpha$  of [Eq. 28.35](#) are given by:

$$\mathbf{Q}_N^\alpha = \sum_{pq} \mathbf{q}_{pq}^\alpha \{p^\dagger q\}, \quad (28.40)$$

$$\mathbf{V}_N^\alpha = \sum_{pq} \mathbf{v}_{pq}^\alpha \{p^\dagger q\}. \quad (28.41)$$

Introducing  $\bullet$  Eqs. 28.36–28.41, the analytical gradients  $\Delta G_{CC}^\alpha$  can be written in the following explicit form:

$$\begin{aligned} \Delta G_{CC}^\alpha = & \sum_{ab} f_{ab}^{\text{PCM},\alpha} \gamma_{ab}^{\text{CC-resp}} + \sum_{ij} f_{ij}^{\text{PCM},\alpha} \gamma_{ij}^{\text{CC-resp}} \\ & + \sum_{ai} f_{ai}^{\text{PCM},\alpha} \gamma_{ai}^{\text{CC-resp}} + \sum_{ia} f_{ia}^{\text{PCM},\alpha} \gamma_{ia}^{\text{CC-resp}} \\ & + \frac{1}{2} \sum_{pqrs} \mathcal{B}_{pq,rs}^\alpha \gamma_{pq}^{\text{CC-resp}} \gamma_{rs}^{\text{CC-resp}} + \frac{1}{4} \sum_{pqrs} \langle pq||rs \rangle^\alpha \Gamma_{rs pq}, \end{aligned} \quad (28.42)$$

where  $\Gamma_{rs pq}$  are elements of the effective two-particle density matrix  $\Gamma$  (Bartlett and Musial 2007).

$\bullet$  Equation 28.42 is the most general form of  $\Delta G_{CC}^\alpha$  from which we can obtain explicit computational expressions. To proceed further, as in the case of isolated molecules, we have to consider two alternative forms of the PCM-CCSD analytical derivatives: the so-called non-relaxed MO form, which neglects the orbital relaxation effects, and the so-called relaxed MO form, which includes these effects (Gauss 1999). Which of the two forms must be used is a controversial issue in the CC properties calculations of isolated molecules. The use of unrelaxed derivatives has been advocated by Koch et al. (Koch and Jørgensen 1990) for the calculation of electrical properties. On the other hand, the use of the orbital relaxation effect is mandatory in all cases where perturbation-dependent basis functions are employed. For geometrical derivatives, only the MO relaxed derivatives provide a correct description of the potential energy surface. In the following subsection we present the orbital relaxed form the gradients  $\Delta G_{CC}^\alpha$ . The interested reader may find the corresponding formulation for the unrelaxed MO gradients in Cammi (2009).

## PCM-CCSD Analytical Gradients with Relaxed MO

When the MO are allowed to relax under the perturbation, the occupied-virtual block of the derivative of the PCM-Fock matrix,  $f_{a,i}^{\text{PCM},\alpha}$ , vanishes by virtue of the Brillouin's theorem. Therefore, the contribution to the gradients  $\Delta G_{CC}^\alpha$  of  $\bullet$  Eq. 28.42 due to the derivative PCM-Fock matrix consists only of occupied-occupied and virtual-virtual blocks:

$$\begin{aligned} \Delta G_{CC}^\alpha = & \sum_{ab} f_{ab}^{\text{PCM},\alpha} \gamma_{ab}^{\text{CC-resp}} + \sum_{ij} f_{ij}^{\text{PCM},\alpha} \gamma_{ij}^{\text{CC-resp}} \\ & + \frac{1}{2} \sum_{pqrs} (\mathbf{q}_{pq}^\alpha \cdot \mathbf{v}_{rs} + \mathbf{q}_{pq} \cdot \mathbf{v}_{rs}^\alpha) \gamma_{pq}^{\text{CC-resp}} \gamma_{rs}^{\text{CC-resp}} \\ & + \frac{1}{4} \sum_{pqrs} \langle pq||rs \rangle^\alpha \Gamma_{rs pq}. \end{aligned} \quad (28.43)$$

For the evaluation of the PCM-CC gradient the first derivatives of the PCM-Fock matrix and of the other one- and two-electron MO integrals are needed. These derivatives lead to terms involving the skeleton derivatives of the MO integrals, i.e., integrals that involve the derivative of the corresponding AO integrals, and also lead to terms involving the derivative of the MO

coefficients. Then, the gradients  $\Delta G_{CC}^\alpha$  may be written as:

$$\begin{aligned} \Delta G_{CC}^\alpha &= \sum_{ab} \gamma_{ab}^{CC\text{-resp}} f_{ab}^{\text{PCM},[\alpha]} + \sum_{ij} \gamma_{ij}^{CC\text{-resp}} f_{ij}^{\text{PCM},[\alpha]} \\ &+ \frac{1}{2} \sum_{rs} \gamma_{rs}^{CC\text{-resp}} \left[ \mathbf{q}_{rs}^{[\alpha]} \cdot \tilde{\mathbf{V}}_N + \tilde{\mathbf{Q}}_N \cdot \mathbf{v}_{rs}^{[\alpha]} \right] \\ &+ \sum_{pqrs} \Gamma_{pq,rs} \langle pq||rs \rangle^{[\alpha]} + \sum_{pq} I'_{pq} U_{pq}^\alpha, \end{aligned} \quad (28.44)$$

where the superscript  $[\alpha]$  denotes skeleton derivatives of the MO integrals,  $U_{mi}^a$  are the derivatives of the MO coefficients  $c_{\mu p}$ , in the MO basis, and  $I'_{pq}$  are auxiliary matrix elements whose expressions are given in Cammi (2009).

The explicit evaluation of the  $U_{mi}^a$  derivatives may be avoided by using the orthonormality constraints of the MO and by using the interchange (Z-vector) method of Handy and Schaefer properly extended to the PCM framework (Cammi et al. 1999).

The resulting PCM-CCSD gradients may be written as

$$\begin{aligned} \Delta G_{CC}^\alpha &= \sum_{ab} \gamma_{ab}^{CC\text{-resp}} f_{ab}^{\text{PCM},[\alpha]} + \sum_{ij} \gamma_{ij}^{CC\text{-resp}} f_{ij}^{\text{PCM},[\alpha]} \\ &+ \sum_{ij} \gamma_{ai}^{\text{MO-resp}} f_{ai}^{\text{PCM},[\alpha]} + \frac{1}{2} \sum_{rs} \gamma_{rs}^{CC\text{-resp}} \left[ \mathbf{q}_{rs}^{[\alpha]} \cdot \tilde{\mathbf{V}}_N + \tilde{\mathbf{Q}}_N \cdot \mathbf{v}_{rs}^{[\alpha]} \right] \\ &+ \sum_{pqrs} \Gamma_{pq,rs} \langle pq||rs \rangle^{[\alpha]} + \sum_{ij} I'_{ij} S_{ij}^{[\alpha]} + \sum_{ab} I_{ab} S_{ab}^{[\alpha]} - 2 \sum_{ai} I'_{ia} S_{ai}^{[\alpha]}, \end{aligned} \quad (28.45)$$

where the matrix elements  $\gamma_{ai}^{\text{MO-resp}}$  are obtained as solution of the PCM-Z vector equation, and  $I'_{ia} = I_{ia} - \gamma_{ai}^{\text{MO-resp}} f_{ii}^{\text{PCM}}$ , and  $I'_{ij}$  are given by

$$I'_{ij} = I_{ij} - \sum_{em} \gamma_{em}^{\text{MO-resp}} (\langle ei||mj \rangle + \langle im||je \rangle + 2\mathcal{B}_{em,ij}).$$

Finally, the expression of the PCM-CCSD gradients can be reverted from the MO to the AO representation, for an efficient computational implementation. The corresponding AO form is

$$\begin{aligned} \Delta G_{CC}^\alpha &= \sum_{\mu\nu} \gamma_{\mu\nu}^{CC\text{-MO}} (h_{\mu\nu}^\alpha + f_{\mu\nu}^\alpha) + \sum_{\mu\nu} I'_{\mu\nu} S_{\mu\nu}^\alpha \\ &+ \sum_{\mu\nu\rho\sigma} (\gamma_{\mu\nu}^{CC\text{-MO}} P_{\sigma\rho}^{\text{HF}} + \frac{1}{2} \gamma_{\mu\nu}^{CC\text{-resp}} \gamma_{\sigma\rho}^{CC\text{-resp}}) \mathcal{B}_{\mu\nu\sigma\rho}^\alpha \\ &+ \sum_{\mu\nu\sigma\rho} \Gamma'_{\mu\nu,\sigma\rho} \langle \mu\sigma||\rho\sigma \rangle^\alpha, \end{aligned} \quad (28.46)$$

where  $\Gamma'_{\mu\nu,\sigma\rho} = \Gamma_{\mu\nu,\sigma\rho} + \gamma_{\mu\nu}^{CC\text{-MO}} P_{\sigma\rho}^{\text{HF}}$ .

► Equation 28.46 refers to the PCM-CCSD analytical gradients within the PTDE scheme, as it contains terms involving coupled-cluster contribution to the solvent reaction field. By neglecting these contributions we obtain the corresponding analytical gradients within the PTE approximated scheme.

## The Equation-of-Motion Coupled-Cluster Theory for the Polarizable Continuum Model

In the previous sections we have shown how it is possible to obtain a coherent generalization of the coupled-cluster theory to the description of the ground state properties of molecular solutes. In this section we will show how a similar generalization can be obtained for the EOM-coupled cluster theory, for the description of the excited states properties of solvated molecules.

The problem of the description of the excited states within the Polarizable Continuum Model leads to two non-equivalent approaches, the approach based on the linear response (LR) approach, and the state specific (SS) approach, as already said in the Introduction. Each approach has advantages and disadvantages. The LR approach is computationally more convenient, as it gives the whole spectrum of the excited states of interest in a single calculation, but is physically biased. In fact, in the LR approach the solute-solvent interaction contains a term related to the one-particle transition densities of the solute connecting the reference state adopted in the LR calculation, which usually corresponds to the electronic ground state, to the excited electronic state. The SS approach is computationally more expensive, as it requires a separate calculation for each of the excited states of interest, but is physically un-biased. In fact, in the SS approach the solute-solvent interaction is determined by the effective one-particle electron density of the excited state.

An EOM-CC method for continuum solvation models has been developed by Mikkelsen and co-worker (Christiansen and Mikkelsen 1999a), based on the LR approach. In this chapter we will present a EOM-CC state specific (SS) method for the PCM. As already discussed in the Introduction, we limit ourselves to a formulation of the PCM-EOM-CC to describe vertical absorption processes (the emission processes require a slightly different formulation), and in particular of absorption processes from the electronic ground state to a generic excited state. For this processes we can give two versions: a first version in which the solvent is in equilibrium polarization with both states (state 0 and state K) and a second version in which the polarization of the K-th state is in non-equilibrium for the reasons discussed in the Introduction. The formulation that we report here refers to the equilibrium formulation. For the non-equilibrium formulation there are two versions: the formulation corresponding to the version II (Pekar) can be directly obtained from the equilibrium case by substituting the polarization charges of the solvent that appear in the following [Eq. 28.52](#) for the equilibrium case, with those corresponding to the non-equilibrium case (Tomasi et al. 2005). The version I of the non-equilibrium case requires a slightly more elaborated formulation.

### The PCM-EOM-CC Wavefunctions

In the PCM-EOM-CC approximation the excited electronic states are represented by a linear (CI-like) expansion build-up on the coupled-cluster wavefunction for the ground state. The corresponding expansion coefficients are then determined by solving a non-linear eigenvalue problem. The eigenvalue equations are determined by a variational procedure involving the PCM-EOM-CC free energy functional.

The EOM-CC ket wavefunction (Nakatsuji and Hirao 1978; Stanton and Bartlett 1993) for the K-th state is defined as

$$|\Psi_K\rangle = \mathcal{R}_K e^T |\text{HF}\rangle, \quad (28.47)$$

where  $e^T|\text{HF}\rangle$  is the coupled-cluster state obtained by solving the PCM-PTE equation (see [Eq. 28.23](#) in [section “The Coupled-Cluster PTE Scheme”](#)), and  $\mathcal{R}_K$  is a quasi-particle excitation operator

$$\begin{aligned}\mathcal{R}_K &= \mathcal{R}_{K,0} + \mathcal{R}_{K,1} + \mathcal{R}_{K,2} + \dots, \\ \mathcal{R}_{K,n} &= \frac{1}{n!^2} \sum_{ijkl\dots abc\dots} r_{ijkl\dots abc\dots}^{abc\dots}(K) a_a^\dagger a_i a_b^\dagger a_j a_c^\dagger a_k \dots.\end{aligned}\quad (28.48)$$

The corresponding EOM-CC bra wavefunction is given by

$$\langle \tilde{\Psi}_K | = \langle \text{HF} | \mathcal{L}_K e^{-T}, \quad (28.49)$$

where  $\mathcal{L}_K$  is a de-excitation operator

$$\begin{aligned}\mathcal{L}_K &= \mathcal{L}_{K,0} + \mathcal{L}_{K,1} + \mathcal{L}_{K,2} + \dots, \\ \mathcal{L}_{K,n} &= \frac{1}{n!^2} \sum_{ijkl\dots abc\dots} l_{ijkl\dots abc\dots}^{abc\dots}(K) a_i^\dagger a_a a_j^\dagger a_b a_k^\dagger a_c \dots.\end{aligned}\quad (28.50)$$

The set ket and bra wavefunctions  $\mathcal{L}_K$  and  $\mathcal{R}_K$  satisfy the property of bi-orthogonality many-body systems

$$\langle \tilde{\Psi}_K | \Psi_L \rangle = \langle \mathcal{L}_K | \mathcal{R}_L \rangle = \delta_{KL}. \quad (28.51)$$

The variational PCM-EOM-CC free energy functional for the state of interest,  $\Delta G_K^{\text{EOM}}$  may be written as:

$$\begin{aligned}\Delta G_K^{\text{EOM}} &= \frac{\langle \text{HF} | \mathcal{L}_K e^{-T} H_N(0) e^T \mathcal{R}_K | \text{HF} \rangle}{\langle \mathcal{L}_K | \mathcal{R}_K \rangle} \\ &+ \frac{1}{2} \tilde{\mathbf{Q}}_K^{\text{EOM}} \cdot \tilde{\mathbf{V}}_K^{\text{EOM}} + \langle \text{HF} | \mathcal{Z} e^{-T} H_N(0) \exp(T) | \text{HF} \rangle.\end{aligned}\quad (28.52)$$

Here the first term on the right side represents the EOM-CC energy of the state on interest in presence of the fixed HF reaction potential, while the second term  $\tilde{\mathbf{Q}}_K^{\text{EOM}} \cdot \tilde{\mathbf{V}}_K^{\text{EOM}}$  is the EOM-CC solute-solvent interaction contribution. Specifically,  $\tilde{\mathbf{Q}}_K^{\text{EOM}}$  and  $\tilde{\mathbf{V}}_K^{\text{EOM}}$  are the EOM-CC expectation value, respectively, of the polarization charges and of the electrostatic potential for the K-th state:

$$\begin{aligned}\tilde{\mathbf{Q}}_K^{\text{EOM}} &= \frac{\langle \text{HF} | \mathcal{L}_K e^{-T} \hat{\mathbf{V}}_N e^T \mathcal{R}_K | \text{HF} \rangle}{\langle \mathcal{L}_K | \mathcal{R}_K \rangle}, \\ \tilde{\mathbf{V}}_K^{\text{EOM}} &= \frac{\langle \text{HF} | \mathcal{L}_K e^{-T} \hat{\mathbf{Q}}_N e^T \mathcal{R}_K | \text{HF} \rangle}{\langle \mathcal{L}_K | \mathcal{R}_K \rangle}.\end{aligned}$$

The last term of  $\Delta G_K^{\text{EOM}}$  in [Eq. 28.52](#) introduces the constraint for the ground state coupled-cluster wavefunction, and contains the de-excitation operator  $\mathcal{Z}$  given by

$$\begin{aligned}\mathcal{Z} &= \mathcal{Z}_1 + \mathcal{Z}_2 + \dots, \\ \mathcal{Z}_n &= \frac{1}{n!^2} \sum_{ijkl\dots abc\dots} \xi_{ijkl\dots abc\dots}^{abc\dots} a_i^\dagger a_a a_j^\dagger a_b a_k^\dagger a_c \dots.\end{aligned}\quad (28.53)$$

The presence of the coupled-cluster constraint term is only relevant for the evaluation of analytical gradient of the PCM-EOM-CC energy functional.

## The PCM-EOM-CC Eigenvalue Equations

Imposing that  $\Delta G_{\text{PCM}}^{\text{EOM}}$  be stationary with respect to the  $\mathcal{R}_K$  and  $\mathcal{L}_K$  amplitudes, we obtain a right-hand and a left-hand eigenvalue equation:

$$\mathcal{H}_K^{\text{EOM}} \mathcal{R}_K | \text{HF} \rangle = \Delta E_K^{\text{EOM}} \mathcal{R}_K | \text{HF} \rangle, \quad (28.54)$$

$$\langle \text{HF} | \mathcal{L}_K \Delta E_K^{\text{EOM}} = \langle \text{HF} | \mathcal{L}_K \mathcal{H}_K^{\text{EOM}}, \quad (28.55)$$

where  $\mathcal{H}_K^{\text{EOM}}$  is the similarity-transformed state-specific PCM-EOM-CC Hamiltonian:

$$\mathcal{H}_K^{\text{EOM}} = e^{-T} H_N^{\text{EOM}}(K) e^T = H_N^{\text{EOM}}(K), \quad (28.56)$$

with

$$H_N^{\text{EOM}}(K) = H_N(0) + \bar{\mathbf{Q}}_K^{\text{EOM}} \cdot \mathbf{V}_N, \quad (28.57)$$

where the first term of state-specific Hamiltonian describes the solute in presence of the fixed HF polarization charges, while the second term,  $\bar{\mathbf{Q}}_K^{\text{EOM}} \cdot \mathbf{V}_N$ , represents the interaction of the solute with the polarization charges produced by the solute in the excited state K-th.

The left and right eigenvalues and the EOM-CC energy can be obtained from the matrix representing the non-Hermitian Hamiltonian  $\mathcal{H}_K^{\text{EOM}}$  in a suitable functional space. We limit ourselves to consider the case of the functional space associated to the coupled-cluster reference function at the CCSD level.

The EOM-CCSD the electronic states are associated with the diagonal representation of  $\mathcal{H}_K^{\text{EOM}}$  in the subspace  $|\mathbf{p}\rangle$ , spanned by the  $|\text{HF}\rangle$  determinant and by its single  $|i^a\rangle$  and double  $|ij^{ab}\rangle$  excited determinants (i.e.,  $|\mathbf{p}\rangle = |\text{HF}\rangle \oplus |i^a\rangle \oplus |ij^{ab}\rangle$ ). The  $\blacktriangleright$  Eqs. 28.54 and  $\blacktriangleright$  28.55 can be converted to a non-Hermitian CI-like eigenvalue problem

$$\tilde{\mathbf{H}}_K^{\text{EOM}} \mathbf{R}_K = \Delta E_K^{\text{EOM}} \mathbf{R}_K, \quad (28.58)$$

$$\mathbf{L}_L \tilde{\mathbf{H}}_K^{\text{EOM}} = \mathbf{L}_K \Delta E_K^{\text{EOM}}, \quad (28.59)$$

where  $\mathbf{R}_k$  and  $\mathbf{L}_k$  represent the vectors of coefficients for the chosen excited state, and  $\tilde{\mathbf{H}}_K^{\text{EOM}}$  is the PCM-EOM matrix Hamiltonian. The elements of matrix  $\tilde{\mathbf{H}}_K^{\text{EOM}}$  can be evaluated by standard methods. Details are given elsewhere (Cammi 2010a; Cammi et al. 2010b).

The manifold of the eigenvectors of matrix  $\tilde{\mathbf{H}}_K^{\text{EOM}}$  can be determined using a non-Hermitian modification of Davidson's method (Hirao and Nakatsuji 1982). From this manifold we can extract the  $\mathbf{R}_K$  and  $\mathbf{L}_K$  eigenvectors and the corresponding eigenvalue  $\Delta E_K^{\text{EOM}}$ . The remaining eigenvectors of the manifold are not of interest for the topics treated in this chapter.

Finally, the free energy functional value for the state of interest may be obtained in terms of the EOM-CC eigenvalue  $\Delta E_K^{\text{EOM}}$  as

$$\Delta G_K^{\text{EOM}} = \Delta E_K^{\text{EOM}} - \frac{1}{2} \mathbf{V}_K^{\text{EOM}} \cdot \mathbf{Q}_K^{\text{EOM}}. \quad (28.60)$$

We have thus completed the first step of the PCM-EOM-CC procedure, leading to the complete determination of the EOM-CC eigenfunctions and free energy for the target state K. We note that in this first step we have only exploited the stationarity condition of  $\Delta G_K^{\text{EOM}}$  with respect to the left and right eigenvectors. As already said, the stationary conditions on the  $\mathcal{Z}$  and  $T$  amplitude are not necessary at this stage, but they are instead necessary to obtain analytical derivatives of the  $\Delta G_K^{\text{EOM}}$  functional.

## PCM-EOM-CCSD Analytical Gradients

The analytical first derivative of the free energy PCM-EOM functional  $\Delta G^{\text{EOM}}$  may be easily obtained introducing the stationarity with respect to the  $\mathcal{Z}$  and the  $T$  amplitudes. This avoids the evaluation of the first derivative of these parameters with respect to the external perturbations.

### The PCM-EOM-CCSD Equations for the $\mathcal{Z}$ Amplitudes

The stationary condition for the  $\mathcal{Z}$  amplitudes leads to the PTE coupled-cluster equations for the reference ground state, which are assumed to be satisfied (see [Eq. 28.23](#)); the stationary condition for the  $T$  amplitudes gives in turn the equations for the  $\mathcal{Z}$  amplitudes.

The derivative of  $\Delta G^{\text{EOM}}$  with respect to the  $T$  amplitudes may be written as

$$\frac{\partial \Delta G_K^{\text{EOM}}}{\partial t_\tau} = \langle \text{HF} | \mathcal{L} [\mathcal{H}_K^{\text{EOM}}, \hat{\tau}] \mathcal{R} | \text{HF} \rangle + \langle \text{HF} | \mathcal{Z} [\mathcal{H}(0), \hat{\tau}] | \text{HF} \rangle = 0, \quad (28.61)$$

where  $\hat{\tau}$  is the excitation operator associated to the amplitude coefficient  $t_\tau$ ,  $\mathcal{H}_K^{\text{EOM}}$  is the similarity-transformed EOM Hamiltonian, and  $\mathcal{H}(0)$  is the PTE similarity-transformed Hamiltonian of [Eq. 28.25](#); the square brackets denote a commutator operator.

[Eq. 28.61](#) can be rewritten as an explicit linear system of equation for the  $\mathcal{Z}$  amplitudes:

$$\frac{\partial \Delta G_{\text{PCM}}^{\text{EOM}}}{\partial t_\tau} = \langle \text{HF} | \mathcal{Z} | \mathbf{g} \rangle \langle \mathbf{g} | \tilde{\mathcal{H}}(0) | \mathbf{g} \rangle - \langle \text{HF} | \Xi | \mathbf{g} \rangle = 0, \quad (28.62)$$

or

$$\langle \text{HF} | \mathcal{Z} | \mathbf{g} \rangle = -\langle \text{HF} | \Xi | \mathbf{g} \rangle \langle \mathbf{g} | \tilde{\mathcal{H}}(0) | \mathbf{g} \rangle^{-1}, \quad (28.63)$$

where  $|\mathbf{g}\rangle$  denotes the subspace of the single and double excited Slater determinants,  $|\mathbf{g}\rangle = |i^a\rangle \oplus |ij^{ab}\rangle$ ,  $\tilde{\mathcal{H}}(0)$  is defined as  $\tilde{\mathcal{H}}(0) = \mathcal{H}(0) - \langle 0 | \mathcal{H}(0) | 0 \rangle$ , and  $\Xi$  denotes the de-excitation operator

$$\Xi = \Xi_{11} + \Xi_2 + \dots, \quad (28.64)$$

$$\Xi_n = \frac{1}{n!^2} \sum_{ijkl\dots abc\dots} \xi_{ijk\dots}^{abc\dots} a_i^\dagger a_a a_j^\dagger a_b a_k^\dagger a_c \dots, \quad (28.65)$$

whose amplitudes  $\Xi_n$  are given as matrix elements of the operator  $\mathcal{R} \mathcal{H}_K^{\text{EOM}} | \mathbf{q} \rangle \langle \mathbf{q} | \mathcal{R}$  between  $\langle \text{HF} |$  and  $|\mathbf{g}\rangle = |i^a\rangle \oplus |ij^{ab}\rangle$

$$\langle \text{HF} | \Xi | \mathbf{g} \rangle = \langle \text{HF} | \mathcal{R} \mathcal{H}_K^{\text{EOM}} | \mathbf{q} \rangle \langle \mathbf{q} | \mathcal{R} | \mathbf{g} \rangle. \quad (28.66)$$

The explicit equation of the amplitudes  $\xi_n$  contains explicit PCM contributions that are given elsewhere (Cammi [2010a](#)).



## The Analytical Gradients of the PCM-EOM-CCSD Free Energy Functional $\Delta G_K^{\text{EOM}}$

The derivatives of free energy functional  $\Delta G_K^{\text{EOM}}$  may then be written as:

$$\begin{aligned} \frac{\partial \Delta G_K^{\text{EOM}}}{\partial \alpha} &= \langle \text{HF} | (\mathcal{L}_K + \mathcal{Z}) e^{-T} H_N(0) e^T \mathcal{R}_K | \text{HF} \rangle \\ &+ \frac{1}{2} \langle \text{HF} | \mathcal{L}_K e^{-T} \mathbf{V}_N^\alpha e^T \mathcal{R}_K | \text{HF} \rangle \cdot \mathbf{Q}_K^{\text{EOM}} \\ &+ \frac{1}{2} \langle \text{HF} | \mathcal{L}_K e^{-T} \mathbf{Q}_N^\alpha e^T \mathcal{R}_K | \text{HF} \rangle \cdot \mathbf{V}_K^{\text{EOM}}. \end{aligned} \quad (28.67)$$

This expression can be recast in a form that involves contractions between effective one- and two-particle EOM-CCSD density matrices and differentiated one- and two-electron MO integrals as:

$$\begin{aligned} \frac{\partial \Delta G_K^{\text{EOM}}}{\partial \alpha} &= \sum_{pq} J_{pq}^{\text{PCM},\alpha} \gamma_{pq}^{\text{EOM}}(K) \\ &+ \frac{1}{2} \sum_{pqrs} \mathcal{B}_{pq,rs}^\alpha \gamma_{pq}^{\text{EOM-NR}} \gamma_{rs}^{\text{EOM-NR}}(K) \\ &+ \frac{1}{4} \sum_{pqrs} \langle pq || rs \rangle^\alpha \Gamma_{\text{EOM}}(K), \end{aligned} \quad (28.68)$$

where the Einstein summation convention is followed. The density matrices,  $\gamma^{\text{EOM-NR}}$ ,  $\gamma^{\text{EOM}}$  and  $\Gamma^{\text{EOM}}$  are defined by Stanton (1993):

$$\begin{aligned} \gamma_{pq}^{\text{EOM-NR}}(K) &= \langle \text{HF} | \mathcal{L} [p^\dagger q \exp(T)]_c \mathcal{R} | \text{HF} \rangle, \\ \gamma_{pq}^{\text{EOM}}(K) &= \gamma_{pq}^{\text{EOM-NR}} + \langle \text{HF} | \mathcal{Z} [p^\dagger q \exp(T)]_c | \text{HF} \rangle, \\ \Gamma_{pqrs}^{\text{EOM}}(K) &= \langle \text{HF} | \mathcal{L} [p^\dagger q^\dagger sr \exp(T)]_c \mathcal{R} | \text{HF} \rangle + \langle \text{HF} | \mathcal{Z} [p^\dagger q^\dagger sr \exp(T)]_c | \text{HF} \rangle, \end{aligned} \quad (28.69)$$

where the subscript  $c$  denotes a limitation to connected diagrams. The effective density  $\gamma^{\text{EOM-NR}}$  is the usual reduced one-particle density (expectation value of  $p^\dagger q$ ), while the effective density matrices  $\gamma^{\text{EOM}}$  and  $\Gamma^{\text{EOM}}$  also contain correction terms that involve the  $\xi$  amplitude to account for the response of  $T$  to the perturbation.

The PCM-EOM-CCSD analytical gradients (🔗 Eq. 28.68) have the same form of PCM-CCSD analytical gradients (🔗 Eq. 28.42). Then, following the same procedure described for the PCM-CCSD gradients it is easy to show that the differentiation of the MO integrals in 🔗 Eq. 28.68 leads to terms involving the derivatives of the MO coefficients. In turn, the perturbative MO coefficients can be avoided using exploiting the PCM Z-vector technique (Cammi et al. 1999) to obtain a perturbation independent one-particle  $\gamma_{\mu\nu}^{\text{MO-resp}}$ . The corresponding expression of the PCM-EOM analytical gradients in the AO basis is given by

$$\begin{aligned} \frac{\partial \Delta G_K^{\text{EOM}}}{\partial \alpha} &= \sum_{\mu\nu} \gamma_{\mu\nu}^{\text{EOM-MO}}(K) (h_{\mu\nu}^\alpha + j_{\mu\nu}^\alpha) + \sum_{\mu\nu} I'_{\mu\nu} S_{\mu\nu}^\alpha \\ &+ \sum_{\mu\nu\rho\sigma} (\gamma_{\mu\nu}^{\text{EOM-MO}} P_{\sigma\rho}^{\text{HF}} + \frac{1}{2} \gamma_{\mu\nu}^{\text{EOM-NR}} \gamma_{\sigma\rho}^{\text{EOM-NR}}) \mathcal{B}_{\mu\nu\sigma\rho}^\alpha \\ &+ \sum_{\mu\nu\sigma\rho} \Gamma'_{\mu\nu,\sigma\rho} \langle \mu\sigma || \rho\sigma \rangle^\alpha, \end{aligned} \quad (28.70)$$

where the additional one-particle density matrix  $\gamma_{\mu\nu}^{\text{EOM-MO}}$  is defined as  $\gamma_{\mu\nu}^{\text{EOM-MO}} = \gamma_{\mu\nu}^{\text{EOM}} + \gamma_{\mu\nu}^{\text{MO-resp}}$ .

The equation of the PCM-EOM-CC analytical gradients contains additional one-electron MO derivative integrals with respect to the corresponding gradients for isolated molecules (Stanton 1993). As these solvation terms can be evaluated with a small effort, the PCM-EOM-CC analytical gradients can be performed for all the molecular systems for which the EOM-CCSD gradient calculations are feasible in gas phase.

## Conclusions

We have presented a short review of very recent progresses toward the description at the coupled-cluster level of the electronic structure and properties of molecular solutes with the Polarizable Continuum Model framework (Cammi 2009). Specifically, we have presented: (1) the detailed expression for the evaluation of the analytical gradients for the PCM-CC theory at the single and double excitation level, for the ground states; (2) the expression of the analytical gradients for the PCM-EOM-CC theory at the single and double excitation level for the descriptions of the excited state properties of molecular solute.

Several implementations of the PCM-CC theories have been presented. Caricato et al. (2010) have presented an implementation of the PCM-CC analytical gradients for the ground state of molecular solutes within the Gaussian suite of programs (Frisch et al. 2009). Cammi et al. (2010b) have presented an implementation of the PCM-CC and PCM-EOM-CC analytical derivatives methods within the framework of SAC/SACCI methods. We hope that these computational advances can be profitably used to study molecular processes in condensed phase, where both the accuracy of the QM descriptions and the influence of the environment play a critical role, as in photo-ionization processes, electronic transitions, and charge transfer reactions.

## Appendix A: The Solute-Solvent PCM Operator

In the Polarizable Continuum Model for solvation, the molecular solute is hosted in a cavity of a polarizable dielectric medium representing the solvent. The cavity is accurately modeled on the shape of the molecular solute (Miertuš et al. 1981), and the dielectric medium is characterized by the dielectric permittivity  $\epsilon$  of the bulk solvent. The physics of the model is very simple. The solute charge distribution polarizes the dielectric medium, which in turn acts back on the solute, in a process of mutual polarization that continues until self-consistence is reached. The polarization of the solvent is represented by an apparent charge distribution (ASC) spread on the cavity surface. In computational practice the ASC is discretized to a set of NTS point charges and the solute-solvent interaction is expressed as in terms of the interaction between these and the charge distribution of the molecular solute.

In this framework, the PCM solute-solvent interaction operator (see  $\blacktriangleright$  Eq. 28.3) can be defined in terms of molecular electrostatic operators  $\mathbf{V}$  and of a charges operator  $\mathbf{Q}$  describing the PCM solute-solvent interaction operator (Cammi et al. 2002, 2005).  $\mathbf{V}$  is a vector collecting the molecular electrostatic potential operator, evaluated at the positions of the ASC charges:

$$(\mathbf{V})_j = v_{el}(\mathbf{s}_j) + v_{\text{nuc}}(\mathbf{s}_j), \quad (28.71)$$

where  $v_{el}(\mathbf{s}_j)$  and  $v_{nuc}(\mathbf{s}_j)$  are the electrostatic potential of the electrons and of the nuclei, respectively, evaluated at the position  $\mathbf{s}_j$  of the  $j$ -th ASC point charge. In particular,

$$v_{el}(\mathbf{s}_j) = \sum_i^N \frac{-1}{|\mathbf{r}_i - \mathbf{s}_j|}, \quad (28.72)$$

where  $N$  is the number of electrons of the molecular solute and  $\mathbf{r}_i$  is the vector position of the  $i$ -th electron. A similar expression holds for the nuclei contribution  $\hat{v}_{nuc}(\mathbf{s}_j)$ .

The apparent charges vector operator  $\mathbf{Q}$  can be formally defined in different way, depending on the different version of the BEM. In the Integral Equation Formalism (IEF) version of the PCM (Cances et al. 1997), which is here adopted,  $\mathbf{Q}$  may be expressed as a linear transformation of the vector operator  $\mathbf{V}$ :

$$(\mathbf{Q})_j = \sum_l^{NTS} T_{jl}(\hat{\mathbf{V}})_l, \quad (28.73)$$

where the summation is over the NTS point charges, and  $T_{jl}$  are elements of the BEM square matrix. The matrix is dimensioned as the ASC charges and it depends on the geometry of surface cavity and on the dielectric permittivity of the medium. The expectation value of the  $\hat{\mathbf{Q}}$  operator,  $(\langle \Psi | \mathbf{Q} | \Psi \rangle)$  is a vector collecting the actual ASC charges induced by the molecular solute described by the wave function  $\Psi$ .

The solute-solvent interaction operator  $(\langle \Psi | \hat{\mathbf{Q}} | \Psi \rangle) \cdot \hat{\mathbf{V}}$  of [Eq. 28.3](#) of the text is then the inner product between the expectation values of the ASC,  $(\langle \Psi | \hat{\mathbf{Q}} | \Psi \rangle)$ , and the molecular electrostatic operator  $\mathbf{V}$ :

$$\langle \Psi | \mathbf{Q} | \Psi \rangle \cdot \mathbf{V} = \sum_j^{NTS} \langle \Psi | (\hat{\mathbf{Q}})_j | \Psi \rangle (\hat{\mathbf{V}})_j, \quad (28.74)$$

where  $\langle \Psi | (\mathbf{Q})_j | \Psi \rangle$  denotes the expectation value of the  $j$ -th apparent surface charge.

## References

- Aguilar, M. (2001). Separation of the electric polarization into fast and slow components: A comparison of two partition schemes. *The Journal of Physical Chemistry A*, 105, 10393.
- Aguilar, M., del Valle, F. J. O., & Tomasi, J. (1993). Nonequilibrium solvation: An ab initio quantum-mechanical method in the continuum cavity model approximation. *Journal of Chemical Physics*, 98, 7375.
- Bartlett, R. J., & Musial, M. (2007). Coupled-cluster theory in quantum chemistry. *Reviews of Modern Physics*, 79, 291.
- Basilevsky, M. V., & Chudinov, G. E. (1990). Application of generalized transition state theory for calculation of the rate constant of a chemical reaction with charge transfer in a polar solvent. *Chemical Physics*, 144, 155.
- Bonaccorsi, R., Ghio, G., & Tomasi, J. (1982). The effect of the solvent on electronic transition and other properties of molecular solutes. In R. Carbó (Ed.), *Current aspects of quantum chemistry* (p. 407). Amsterdam: Elsevier.
- Cammi, R. (2009). Quantum cluster theory for the polarizable continuum model. I. The CCSD level with analytical first and second derivatives. *Journal of Chemical Physics*, 131, 164104.
- Cammi, R., & Tomasi, J. (1994). Analytical derivatives for molecular solutes. I. Hartree-Fock energy first derivatives with respect to external parameters in the polarizable continuum model. *Journal of Chemical Physics*, 100, 7495.
- Cammi, R., & Tomasi, J. (1995a). Remarks in the use of the apparent surface charges (ASC) methods in solvation problems: Iterative versus

where  $e^T|\text{HF}\rangle$  is the coupled-cluster state obtained by solving the PCM-PTE equation (see [Eq. 28.23](#) in [section “The Coupled-Cluster PTE Scheme”](#)), and  $\mathcal{R}_K$  is a quasi-particle excitation operator

$$\begin{aligned}\mathcal{R}_K &= \mathcal{R}_{K,0} + \mathcal{R}_{K,1} + \mathcal{R}_{K,2} + \dots, \\ \mathcal{R}_{K,n} &= \frac{1}{n!^2} \sum_{ijkl\dots abc\dots} r_{ijkl\dots abc\dots}^{abc\dots}(K) a_a^\dagger a_i a_b^\dagger a_j a_c^\dagger a_k \dots.\end{aligned}\quad (28.48)$$

The corresponding EOM-CC bra wavefunction is given by

$$\langle \tilde{\Psi}_K | = \langle \text{HF} | \mathcal{L}_K e^{-T}, \quad (28.49)$$

where  $\mathcal{L}_K$  is a de-excitation operator

$$\begin{aligned}\mathcal{L}_K &= \mathcal{L}_{K,0} + \mathcal{L}_{K,1} + \mathcal{L}_{K,2} + \dots, \\ \mathcal{L}_{K,n} &= \frac{1}{n!^2} \sum_{ijkl\dots abc\dots} l_{ijkl\dots abc\dots}^{abc\dots}(K) a_i^\dagger a_a a_j^\dagger a_b a_k^\dagger a_c \dots.\end{aligned}\quad (28.50)$$

The set ket and bra wavefunctions  $\mathcal{L}_K$  and  $\mathcal{R}_K$  satisfy the property of bi-orthogonality many-body systems

$$\langle \tilde{\Psi}_K | \Psi_L \rangle = \langle \mathcal{L}_K | \mathcal{R}_L \rangle = \delta_{KL}. \quad (28.51)$$

The variational PCM-EOM-CC free energy functional for the state of interest,  $\Delta G_K^{\text{EOM}}$  may be written as:

$$\begin{aligned}\Delta G_K^{\text{EOM}} &= \frac{\langle \text{HF} | \mathcal{L}_K e^{-T} H_N(0) e^T \mathcal{R}_K | \text{HF} \rangle}{\langle \mathcal{L}_K | \mathcal{R}_K \rangle} \\ &+ \frac{1}{2} \tilde{\mathbf{Q}}_K^{\text{EOM}} \cdot \tilde{\mathbf{V}}_K^{\text{EOM}} + \langle \text{HF} | \mathcal{Z} e^{-T} H_N(0) \exp(T) | \text{HF} \rangle.\end{aligned}\quad (28.52)$$

Here the first term on the right side represents the EOM-CC energy of the state on interest in presence of the fixed HF reaction potential, while the second term  $\tilde{\mathbf{Q}}_K^{\text{EOM}} \cdot \tilde{\mathbf{V}}_K^{\text{EOM}}$  is the EOM-CC solute-solvent interaction contribution. Specifically,  $\tilde{\mathbf{Q}}_K^{\text{EOM}}$  and  $\tilde{\mathbf{V}}_K^{\text{EOM}}$  are the EOM-CC expectation value, respectively, of the polarization charges and of the electrostatic potential for the K-th state:

$$\begin{aligned}\tilde{\mathbf{Q}}_K^{\text{EOM}} &= \frac{\langle \text{HF} | \mathcal{L}_K e^{-T} \hat{\mathbf{V}}_N e^T \mathcal{R}_K | \text{HF} \rangle}{\langle \mathcal{L}_K | \mathcal{R}_K \rangle}, \\ \tilde{\mathbf{V}}_K^{\text{EOM}} &= \frac{\langle \text{HF} | \mathcal{L}_K e^{-T} \hat{\mathbf{Q}}_N e^T \mathcal{R}_K | \text{HF} \rangle}{\langle \mathcal{L}_K | \mathcal{R}_K \rangle}.\end{aligned}$$

The last term of  $\Delta G_K^{\text{EOM}}$  in [Eq. 28.52](#) introduces the constraint for the ground state coupled-cluster wavefunction, and contains the de-excitation operator  $\mathcal{Z}$  given by

$$\begin{aligned}\mathcal{Z} &= \mathcal{Z}_1 + \mathcal{Z}_2 + \dots, \\ \mathcal{Z}_n &= \frac{1}{n!^2} \sum_{ijkl\dots abc\dots} \zeta_{ijkl\dots abc\dots}^{abc\dots} a_i^\dagger a_a a_j^\dagger a_b a_k^\dagger a_c \dots.\end{aligned}\quad (28.53)$$

The presence of the coupled-cluster constraint term is only relevant for the evaluation of analytical gradient of the PCM-EOM-CC energy functional.

- Gauss, J. (1999). Coupled-cluster theory. In P. v. R. Schleyer (Ed.), *Encyclopedia of computational chemistry* (Vol. I, pp. 617–636). New York: Wiley.
- Hirao, K., & Nakatsuji, H. (1982). A generalization of the Davidson's method to large nonsymmetric eigenvalue problems. *Journal of Computational Physics*, 45, 246.
- Improta, R., Barone, V., Scalmani, G., & Frisch, M. J. (2006). A state-specific polarizable continuum model time dependent density functional theory method for excited state calculations in solution. *Journal of Chemical Physics*, 126, 054103.
- Kim, H. J., & Hynes, J. T. (1990). Equilibrium and nonequilibrium solvation and solute electronic structure. I. Formulation. *Journal of Chemical Physics*, 93, 5194.
- Klamt, A., Mennucci, B., Tomasi, J., Barone, V., Curutchet, C., Orozco, M., & Luque, F. J. (2009). On the performance of continuum solvation methods. A comment on "Universal Approaches to Solvation Modeling." *Accounts of Chemical Research*, 42, 489.
- Koch, H., & Jørgensen, P. (1990). Coupled cluster response functions. *Journal of Chemical Physics*, 93, 3333.
- Kongsted, J., Mikkelsen, K. V., & Christiansen, O. (2002). The QM/MM approach for wavefunctions, energies and response functions within self-consistent field and coupled cluster theories. *Molecular Physics*, 100, 1813.
- Marcus, R. A. (1992). Schrödinger equation for strongly interacting electron-transfer systems. *The Journal of Physical Chemistry*, 96, 1753.
- Miertuš, S., Scrocco, E., & Tomasi, J. (1981). Electrostatic interaction of a solute with a continuum. A direct utilization of *ab initio* molecular potentials for the prevision of solvent effects. *Chemical Physics*, 55, 117.
- Nakatsuji, H., & Hirao, K. (1978). Cluster expansion of the wavefunction. Pseudo-orbital theory based on the SAC expansion and its application to the spin density of open-shell systems. *Journal of Chemical Physics*, 68, 4279.
- Stanton, J. F. (1993). Many-body methods for excited state potential energy surfaces. I. General theory of energy gradients for the equation-of-motion coupled-cluster method. *Journal of Chemical Physics*, 99, 8840.
- Stanton, J. F., & Bartlett, R. J. (1993). The equation of motion coupled-cluster method. A systematic biorthogonal approach to molecular excitation energies, transition probabilities, and excited state properties. *Journal of Chemical Physics*, 98, 7029.
- Tomasi, J., & Persico, M. (1994). Molecular interactions in solution: An overview of methods based on continuous distributions of the solvent. *Chemical Review*, 94, 2027.
- Tomasi, J., Mennucci, B., & Cammi, R. (2003). Molecules in solution. In S. Wilson (Ed.), *Handbook of molecular physics and quantum chemistry* (Vol. 3, pp. 299–328). New York: Wiley.
- Tomasi, J., Mennucci, B., & Cammi, R. (2005). Quantum mechanical continuum solvation models. *Chemical Review*, 105, 2999.

# 29 Spin-Orbit Coupling in Enzymatic Reactions and the Role of Spin in Biochemistry

B. F. Minaev<sup>1,2</sup> · V. O. Minaeva<sup>2</sup> · Hans Ågren<sup>1</sup>

<sup>1</sup>Theoretical Chemistry, School of Biotechnology, Royal Institute of Technology, Stockholm, Sweden

<sup>2</sup>Bogdam Khmel'nitskii National University, Cherkassy, Ukraine

<i>Introduction</i> .....	1068
<i>O<sub>2</sub> Interaction with Heme, FAD, and Oxidases</i> .....	1069
<i>Definition of Spin and the Angular Momentum Conservation</i> .....	1071
<i>Molecular Oxygen Structure and Spectra</i> .....	1072
<i>Spin-Prohibition of Dioxygen Reactions</i> .....	1074
<i>Cytochrome Oxidases and Related Heme-Containing Enzymes</i> .....	1075
<i>Dioxygen Reaction with Glucose Oxidase</i> .....	1077
<i>Dioxygen Binding to Heme</i> .....	1079
<i>Spin-Orbit Coupling in O<sub>2</sub>-Heme Interaction</i> .....	1082
<i>The Role of Spin in Biochemistry</i> .....	1085
External Magnetic Field Effects in Biochemistry .....	1085
Spin Neuroscience .....	1087
<i>Conclusions</i> .....	1088
<i>Acknowledgment</i> .....	1090
<i>References</i> .....	1090

**Abstract:** We review the general concept of nonadiabatic quantum spin transitions in biochemistry. A few important examples are highlighted to illustrate the concept: the role of spin effects in oxidases, cytochromes, in dioxygen binding to heme, in photosynthesis, and in tentative models of consciousness. The most thoroughly studied of these effects are connected with dioxygen activation by enzymes. Discussion on the mechanisms of overcoming spin prohibitions in dioxygen reactions with flavin-dependent oxygenases and with hemoglobin and myoglobin is presented in some detail. We consider spin-orbit coupling (SOC) between the starting triplet state from the entrance channel of the O<sub>2</sub> binding to glucose oxidase, to ferrous heme, and the final singlet open-shell state in these intermediates. Both triplet (T) and singlet (S) states in these examples are dominated by the radical-pair structures D<sup>+</sup>-O<sub>2</sub><sup>-</sup> induced by charge transfer; the peculiarities of their orbital configurations are essential for the SOC analysis. An account of specific SOC in the open π<sub>g</sub>-shell of dioxygen helps to explain the probability of T-S transitions in the active site near the transition state. Simulated potential energy surface cross-sections along the reaction coordinates for these multiplets, calculated by density functional theory, agree with the notion of a relatively strong SOC induced inside the oxygen moiety by an orbital angular momentum change in the π<sub>g</sub>-shell during the T-S transition. The SOC model explains well the efficient spin inversion during the O<sub>2</sub> binding with heme and glucose oxidase, which constitutes a key mechanism for understanding metabolism. Other examples of nontrivial roles of spin effects in biochemistry are briefly discussed.

## Introduction

---

Many enzymes, for example, those that contain copper or iron-heme active sites (cytochromes, peroxidases), are paramagnetic and undergo spin transitions depending on the change of the metal site oxidation (Franzen 2002; Jensen and Ryde 2004; Prabhakar et al. 2003; Shaik et al. 2002; Shikama 2006; Sigfridsson and Ryde 2002; Stryer 1995). Oxygen molecules contain two unpaired valence electrons (Sawyer 1991) and are therefore also paramagnetic because of the nonzero total electron spin. The complete oxidation of organic materials by dioxygen in order to transfer them into CO<sub>2</sub> and water is highly exothermic (Sawyer 1991), but the kinetic barriers preclude, fortunately, this spontaneous combustion of living matter at normal conditions in the open air because of the spin selection rules (Prabhakar et al. 2003). Like mass and charge, spin is an integral property of the electron, however, spin reveals itself through the relativistic quantum equation as a pure quantum process associated with the structure of space-time, thus it is more fundamental. The role of this fundamental quantum feature of the electron in biochemistry could be extremely important, especially with respect to the mystery of the brain, the nature of consciousness (Penrose 1994), and oxygen activation by enzymes (Franzen 2002; Jensen and Ryde 2004; Prabhakar et al. 2003; Sawyer 1991; Shaik et al. 2002; Shikama 2006; Sigfridsson and Ryde 2002; Stryer 1995).

When O<sub>2</sub> reaches a red blood cell in the *alveoli of the lung*, where the gas exchange of *carbon dioxide* and *oxygen* takes place, the hemoglobin binds O<sub>2</sub> in such a strange way that the total electron spin of the whole heme-O<sub>2</sub> system is not conserved (Sigfridsson and Ryde 2002). In ordinary chemistry the spin conservation rule is usually fulfilled (Sawyer 1991; Shikama 2006; Stryer 1995), which is in agreement with the general conservation law of physics (Sawyer 1991). But the change of the electron spin is a rather common case in biochemistry of enzymes, in the respiration cycle and in other processes connected with dioxygen consumption

(Blomberg et al. 2005; Friedman and Campbell 1987; Lane 2002; Minaev 2007; Minaev et al. 2007; Silva and Ramos 2008; Strickland and Harwey 2007). The spin change has to be compensated by an orbital angular momentum change in order to follow the general conservation law of the total angular momentum. The present review will show that this requirement is fulfilled in a number of enzymatic processes that play key roles in biochemistry; this is accomplished by an analysis of spin-orbit coupling perturbations.

With the appearance of photosynthesis on the primitive earth, a dramatic change in life occurred when living cells adapted themselves from anaerobic life to the aerobic form (Shikama 2006). Anaerobic glycolysis represented a successful attempt to extract some of the chemical energy from glucose. In contrast, the complete oxidation of glucose to CO<sub>2</sub> and H<sub>2</sub>O by utilizing oxygen molecules was the most significant and crucial advancement in cellular metabolism. It thus allowed organisms to enhance their ability to utilize the chemical energy of sugar for a most effective consumption. In light of the high efficiency of energy conservation, this dramatic change from anaerobic to aerobic systems was designated as an “oxygen revolution” (Lane 2002; Penrose 1994; Shikama 2006; Stryer 1995). The most essential feature of this revolution was the involvement of spin-catalysis and quantum spin effects in ordinary chemistry (Minaev 2007). In fact, both processes, photosynthesis and respiration, are spin-forbidden; from one side we have diamagnetic reactants and the paramagnetic species from the other side

$6\text{CO}_2 + 6\text{H}_2\text{O} + \Delta E \xrightleftharpoons{\text{chlorophyll}} \text{C}_6\text{H}_{12}\text{O}_6 + 6\text{O}_2$ . In order to synthesize O<sub>2</sub> with chlorophyll from green plants beneath the sun and to use oxygen for glucose oxidation, nature has designed very smart chemical manipulations that allow spin prohibition in dioxygen activation to be overcome (Minaev 2007). With this revolution a large number of important enzymes that are based on spin-catalysis principles (Blomberg et al. 2000a; Jensen et al. 2005; Lane 2002; Minaev 2002, 2004, 2007, 2010; Minaev et al. 2007; Petrich et al. 1988; Prabhakar et al. 2002, 2004; Silva and Ramos 2008) have been developed and spread (Blomberg et al. 2000b; Klinman 2001; Minaev and Lunell 1993; Sheldon 1993).

## O<sub>2</sub> Interaction with Heme, FAD, and Oxidases

Some oxidases include flavin adenine dinucleotide (FAD), which can activate O<sub>2</sub> to produce diamagnetic products without radical chain reaction steps (Minaev 2002; Stryer 1995). For example, glucose oxidase (GO) is a well-known enzyme that can bind dioxygen directly from air and produce hydrogen peroxide in the metabolic cycle (Prabhakar et al. 2003). An X-ray structure of GO from *Aspergillus niger* is available (Klinman 2001) and used for simulation of the active site in theoretical modeling (Prabhakar et al. 2002). The histidine residue has been assigned an important role in the substrate oxidation by the GO active site.

In the heme biosynthesis pathway a deficient activity of the enzymes often leads to excessive excretion of porphyrins (Silva and Ramos 2008). These toxic products can induce porphyria diseases due to decreased activity of coproporphyrinogen III oxidase (CPO), which catalyzes the oxidative decarboxylation of propionic acid chains. This oxidase is similar to GO in that they both activate dioxygen without using metals and reducing agents. However, mechanisms by which these two oxidases produce diamagnetic peroxides from paramagnetic dioxygen are not properly understood on experimental grounds (Klinman 2001; Prabhakar et al. 2002; Silva and Ramos 2008), while some theoretical predictions seem to shed light on the specific quantum nature of such chemical transformations (Minaev 2007; Minaev et al. 2007;



Prabhakar et al. 2003; Silva and Ramos 2008). Density functional theory (DFT) calculations (Prabhakar et al. 2002, 2003; Silva and Ramos 2008) indicate the common feature of spin transitions in these oxidases' mechanisms.

Hemoglobin and myoglobin are important globular proteins that reversibly bind the O<sub>2</sub> molecule. Both proteins contain ferrous iron of a heme group, which is usually simulated by Fe(II) porphyrin, where the iron ion is tetra-coordinated to the nitrogen atoms of the tetrapyrrole rings (Franzen 2002; Jensen and Ryde 2004; Shikama 2006; Sigfridsson and Ryde 2002). The proximal histidine residue from the protein side chain is also bound to the Fe(II) ion leaving one empty position in the octahedral coordination sphere around the ferrous iron. Hemoglobin and myoglobin bind several small gaseous molecules (CO and NO) besides dioxygen (Sigfridsson and Ryde 2002). The binding of these diatomic ligands to heme has been studied in biochemistry for over a 100 years (Shikama 2006). Dissociation of CO, NO, and O<sub>2</sub> from the iron of heme occurs by both photolysis and thermolysis. In the former case, the fate of the diatomic ligands depends on the competition between geminate recombination and protein relaxation. Binding to heme occurs by the reverse of the thermal process (Franzen 2002).

It is well established that the structure of surrounding protein affects the ligand binding ability of the heme group; carbon monoxide binds to free heme in solution 10<sup>3</sup> times more effectively than dioxygen, but in myoglobin this ratio is strongly reduced (Franzen 2002). Thus, myoglobin seems to favor O<sub>2</sub> binding compared to CO (Franzen 2002; Jensen and Ryde 2004; Shikama 2006; Sigfridsson and Ryde 2002). Such discrimination is of vital importance: otherwise we would suffocate from CO produced in our body during metabolism. The reason for the discrimination has been connected with different geometric parameters of O<sub>2</sub> and CO binding to the heme iron: the Fe–C–O bond is linear, whereas the Fe–O–O bond is bent (Franzen 2002). Both hemoglobin and myoglobin have another, distal, histidine ligand (His-64) positioned above the Fe(II) ion, but too far away to coordinate directly to the iron. His-64 is in the right position to affect the Fe–CO group and to produce a tension. This idea was supported by early crystal structures, showing an Fe–C–O angle of 120–130° (Shikama 2006), an idea that has penetrated into the textbooks (Shikama 2006; Stryer 1995). Some newer X-ray measurements, IR spectra, and DFT calculations indicate that the Fe–C–O angle is nearly linear in the heme models; thus one finds the idea of a strongly bent Fe–C–O unit as the reason for the discrimination but which nowadays is agreed to be incorrect (Sigfridsson and Ryde 2002). Recent DFT calculations show that the FeO<sub>2</sub> group is much more polar than the FeCO group in heme models (Franzen 2002; Jensen and Ryde 2004; Shikama 2006; Sigfridsson and Ryde 2002). The electronic structure of the FeP complex with dioxygen is close to that of a superoxide anion bound to a ferric ion, and this charge-transfer complex is in the singlet spin state (Franzen 2002; Jensen and Ryde 2004; Shikama 2006; Sigfridsson and Ryde 2002). Thus, electrostatic interaction between the distal histidine and the Fe(III)–O–O<sup>−</sup> group is stronger than that for the Fe–CO group; therefore, the protein discriminates between O<sub>2</sub> and CO by hydrogen bonding and electrostatic interaction in myoglobin (Franzen 2002; Jensen and Ryde 2004; Sigfridsson and Ryde 2002).

Another important factor in such discrimination is determined by electron spin (Franzen 2002; Jensen and Ryde 2004; Minaev 2010; Shikama 2006; Sigfridsson and Ryde 2002; Stryer 1995). The O<sub>2</sub> binding to heme is highly non-exponential at ambient temperature with a rapid phase of 3 ps, a longer phase of similar geminate recombination (20–200 ps), and a slow bimolecular process of 1 ms; all phases are spin-dependent processes (Franzen 2002; Jensen and Ryde 2004; Petrich et al. 1988; Shikama 2006). At this point we need to consider it in more detail.

## Definition of Spin and the Angular Momentum Conservation

Spin is derived from the Dirac equation and is a general intrinsic quantum property of electrons (Esposito 1999; Hagan et al. 2002; Hameroff and Penrose 1996; Hu and Wu 2004; Penrose 1960). Spin is an angular momentum with a length of the momentum vector  $\sqrt{\hat{S}^2} = \sqrt{S(S+1)}\hbar = (\sqrt{3}/2)\hbar$ , where the spin quantum number for one electron is equal to  $S = 1/2$  and two projection  $M_S = \pm(1/2)\hbar$  described by  $\alpha$  and  $\beta$  wave functions exist (the doublet state) (Esposito 1999). The role of electron spin in chemistry is rationalized in terms of spin-valence concept: a covalent chemical bond is formed when atomic orbitals of two electrons with opposite spins overlap each other (Stryer 1995). This spin wave function ( $\alpha\beta - \beta\alpha$ ) is antisymmetric with respect to permutation of two electrons. The total spin of such pair is zero ( $S = 0$ ) and the state is singlet (only one state; no spin, no intrinsic magnetic moment, the molecule is diamagnetic). When spins are parallel the total spin has a quantum number  $S = 1$  in the equation for the length of the total spin angular momentum  $\sqrt{\hat{S}^2} = \sqrt{S(S+1)}\hbar = \sqrt{2}\hbar$  and there are three spin states ( $\alpha\alpha$ ,  $\beta\beta$ , and  $\alpha\beta + \beta\alpha$ ) with different projections on z-axis  $M_S = \pm\hbar$ , 0 (triplet state) (Penrose 1960). For a simple covalent  $\sigma$ -bond the triplet state is unstable and such simple molecule can exist only in the singlet state with two opposite spins. That is why almost all stable organic molecules contain an even number of electrons, which can be divided into  $\alpha$  and  $\beta$  pairs. They are diamagnetic, have paired spins and are in the singlet ground state.

Such diamagnetic substances usually do not change zero spin during chemical reactions (Blomberg et al. 2000a, 2005; Friedman and Campbell 1987; Jensen et al. 2005; Klinman 2001; Lane 2002; Minaev 2002, 2007, 2010; Minaev et al. 2007; Petrich et al. 1988; Prabhakar et al. 2002, 2004; Sawyer 1991; Silva and Ramos 2008; Strickland and Harwey 2007). The absence of the total electronic spin in stable molecules leads to the illusion that spin is not important in organic chemistry and biochemistry. In fact, the total electronic spin is the main regulating factor in many metabolic processes catalyzed by metal-organic enzymes, such as cytochromes (Blomberg et al. 2005; Minaev 2007; Minaev et al. 2007; Shaik et al. 2002; Stryer 1995), copper-aminoxidase (Prabhakar et al. 2003, 2004), and even in metal-free glucose oxidase (Minaev 2002; Prabhakar et al. 2002, 2003). Spin inversion is especially important in many dioxygen reactions, binding to heme (Jensen and Ryde 2004), combustion, and respiration (Minaev 2007). One can propose that the importance of spin inversion is also reflected in the Perutz model of the hemoglobin cooperativity (Franzen 2002; Minaev et al. 2007).

Dioxygen molecule is a well-known exception to the general rule: unlike many chemically stable organic compounds, the  $O_2$  molecule has the triplet ground state (Sawyer 1991). According to Hund's rule, two unpaired electrons in two degenerate  $\pi_{g,x}$ - and  $\pi_{g,y}$ -orbitals have a lower repulsive energy in the triplet state compared to the singlet one. Because of this, oxygen is paramagnetic, it has intrinsic magnetic moment due to spins of two unpaired electrons and its addition to organic compounds is spin forbidden: starting reactants have the total spin  $S = 1$  (from the  $O_2$ ), whereas the oxidation products are diamagnetic ( $S = 0$ ). This is the reason why organic matter may exist in the oxygen-rich atmosphere (Sawyer 1991). Because of the spin prohibition, combustion of organic fuels requires activation in the form of high-temperature ignition stage (Prabhakar et al. 2002; Sawyer 1991), i.e., generation of primary radicals. Reaction of radical R (the triplet,  $S = 1/2$ , doublet state) with  $O_2$  molecule is spin-allowed, since the starting reactants ( $O_2 + R$ ) and product ( $RO_2$ ) both have the doublet states (reactants also possess quartet state,  $S = 3/2$ , being non-reactive),



which provide the radical chain character of the combustion reactions (Minaev 2007).

The quantum cell  $[\uparrow]$  denotes (Eq. 29.1) a molecular orbital (MO) with  $\alpha$  spin; double brackets embrace one molecule. The radical  $\text{RO}_2^\cdot$  can decompose into radical  $\text{RO}^\cdot$  and biradical  $^\cdot\text{O}$  thus providing a branching chain reaction. In radical chain combustion the energy is released in the form of heat and light without any specific control (until fuel exhaustion). Clearly, such mechanism of oxidation by molecular oxygen cannot be realized in living cells. Cells meet their energy needs in the course of metabolic processes using strictly controlled energy of oxidation of organic compounds in their reactions with dioxygen, overcoming spin prohibition without high-temperature ignition step of a radical chain (Minaev 2007). An aerobic life evolved due to quantum kinetic prohibitions to reactions of paramagnetic oxygen with diamagnetic organic substances. The main reason for sluggish  $\text{O}_2$  reactivity at the ambient conditions is the spin prohibition, namely, the starting reagents have two unpaired spins (from  $\text{O}_2$  molecule), while in diamagnetic oxidation products ( $\text{CO}_2$ ,  $\text{H}_2\text{O}$ ,  $\text{N}_2$ ) all spins are always paired. Overcoming this prohibition by generating radicals to interact with dioxygen (like in combustion) is not possible in living matter. Since the cells cannot resist large temperature gradients, they have to transform the energy released through oxidation to some kind of chemical energy prior to dissipation in the form of heat. This occurs by combining oxidation with ATP synthesis. All versatile energy-supplying metabolic processes and reactions occur under subtle enzymatic regulation, which is often spin-dependent (Blomberg et al. 2000a; Jensen et al. 2005; Minaev 2002, 2007, 2010; Petrich et al. 1988; Prabhakar et al. 2002, 2004).

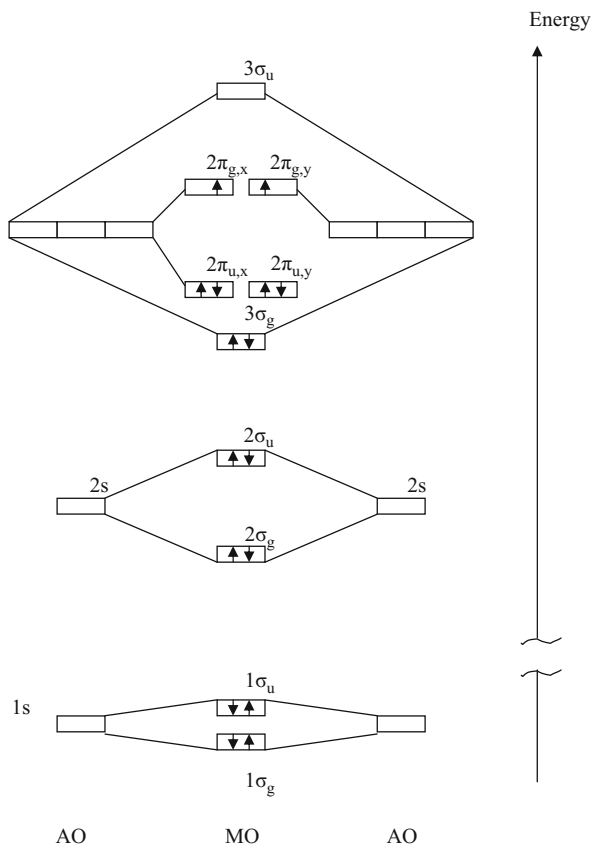
## Molecular Oxygen Structure and Spectra

The  $\text{O}_2$  molecule in the triplet ground state has the following electronic configuration (Sawyer 1991)  $(1\sigma_g)^2 (1\sigma_u)^2 (2\sigma_g)^2 (2\sigma_u)^2 (3\sigma_g)^2 (1\pi_u)^4 (1\pi_g)^2$  (Fig. 29-1). The two outer electrons in two degenerate  $1\pi_g$ -MO's provide the lowest triplet state of the type  $[\uparrow][\uparrow]$ , where the quantum cells  $[[\ ]]$  denote the degenerate  $\pi_g$ -orbitals. These two unpaired electrons in antibonding  $\pi_g$ -MOs (Fig. 29-1) are responsible for the specific character of the dioxygen interaction with radicals (combustion) and chemically stable diamagnetic compounds (slow oxidation), as outlined above. Two antibonding  $\pi_g$ -vacancies make it possible to transform dioxygen into  $\text{O}_2^-$  and  $\text{O}_2^{2-}$  anions, the formation of the latter being strongly dependent on the presence of electron donors (enzymes) and magnetic perturbations that affect the spin prohibition.

There are four possible quantum states (Eq. 29.2) for the electronic configuration mentioned above. For the imaginary form of two degenerate  $1\pi_g$ -MO's:  $1\pi_g^\pm = \psi(r, \theta) e^{\pm i\phi}$ , where  $\theta$  is an angle between the radius vector ( $r$ ) and the molecular axis ( $z$ ),  $\phi$  is the rotation angle of the radius vector about the  $z$  axis, the quantum states are represented by the scheme (Minaev 2007):

$$[\uparrow][\uparrow] \quad [\uparrow\downarrow][\ ] \quad [\ ][\uparrow\downarrow] \quad [\uparrow][\downarrow] \quad (29.2) \\ |^3\Sigma_g^- \rangle > |^1\Delta_g \rangle > |^1\Delta_g \rangle > |^1\Sigma_g^+ \rangle .$$

Exchange interaction stabilizes the triplet state  $|^3\Sigma_g^- \rangle$ , while the degenerate singlet state  $|^1\Delta_g \rangle$  is higher in energy by 22 kcal/mol, and the  $|^1\Sigma_g^+ \rangle$  state is the uppermost one (37 kcal/mol



■ Fig. 29-1  
Molecular orbital configuration of dioxygen

above the ground triplet  ${}^3\Sigma_g^-$  state). Interelectronic repulsion between the two electrons in the two closely space-distributed  $1\pi_g$ -MO's, expressed through exchange integrals, is relatively high. This is an additional reason for a barrier in the  $\text{O}_2({}^3\Sigma_g^-)$  reactions with the closed shell molecules.

The  ${}^3\Sigma_g^-$  and  ${}^1\Sigma_g^+$  states are mixed by weak internal magnetic perturbation, the so-called spin-orbit coupling (SOC) (Minaev 2007; Minaev and Lunell 1993). Some small admixture of one state (about 1.3%) is present in the other state, when SOC is additionally accounted for in the nonrelativistic Schrödinger equation. Such a small correction is very important because it makes the forbidden S-T transitions become allowed and can explain large difference in intensities of the atmospheric oxygen bands  ${}^3\Sigma_g^- - {}^1\Delta_g$  (1270 nm) and  ${}^3\Sigma_g^- - {}^1\Sigma_g^+$  (754 nm) (Minaev 1980, 1989, 2007; Minaev and Agren 1995, 1996; Minaev and Ågren 1997; Minaev and Minaeva 2001; Minaev et al. 1993, 1997, 1996, 2008; Ogilby 1999; Paterson et al. 2006; Schweitzer and Schmidt 2003). In the following analysis we want to understand the spin-dependent mechanism of the  $\text{O}_2$  binding step once dioxygen has moved from the solvent through the protein chains and reached either the myoglobin distal cavity near the ferrous-heme

cofactor or the flavin moiety in the active site of the GO enzyme. In both cases a similar SOC effect of the S-T states mixing is responsible for the biochemically important oxygen activation (Minaev 2002, 2007; Minaev and Agren 1995; Prabhakar et al. 2002).

The heme-O<sub>2</sub> binding step has been extensively studied after flash-photolysis (Franzen 2002; Jensen and Ryde 2004; Shikama 2006; Sigfridsson and Ryde 2002), which shows interesting kinetic features, like non-homogeneous decay, recombination barriers, etc., and indicates complicated spin-dependence (especially in comparison with NO and CO binding to myoglobin). Kinetics of dioxygen reaction with GO has been investigated by studies of deuterium isotope effect during oxidation half reaction (Klinman 2001; Prabhakar et al. 2002). Explanation of such spin-dependence is the main purpose of the present review. In the beginning we want to consider some general features of spin-effect manifestation in chemistry and in dioxygen activation.

## Spin-Prohibition of Dioxygen Reactions

Spins can undergo “depairing” when exposed to light; in (Eq. 29.3) an electron goes from a doubly occupied orbital [ $\uparrow\downarrow$ ] of the ground singlet state to a vacant MO [] with the simultaneous spin flip to produce the triplet excited state (Minaev 2007):



According to the Pauli principle, both spins can be parallel (total spin  $S = 1$ ) in such an excited state when two electrons occupy two different MOs. This triplet state has three possible orientations of the total spin vector, thus the singlet  $\rightarrow$  triplet excitation includes three possible transitions to three spin sublevels. All of them are spin-forbidden. This is a very strict prohibition, since it can be removed only by influence of magnetic interactions that are much weaker in general than the electric interactions. The latter determine the energetics of chemical bonding, electronic “depairing” excitation and the pathways of chemical reactions. The spin influences the energy through exchange interaction (Minaev 2007). A weak SOC slightly mixes the singlet and triplet states of molecules, which provides a non-zero rate for the T $\rightarrow$ S transitions. The late are observed in the form of phosphorescence and are well known as important quenching processes in photochemistry (Minaev 2004, 2007; Minaev and Minaev 2005). The nonradiative T-S transitions also play an important role in dark reactions, in particular, in catalysis (Metz and Solomon 2001; Minaev 2002). Weak SOC acts as a “key” needed to open a “heavy door”: that is, the system chooses a pathway of chemical reaction with low activation barrier in the triplet state instead of overcoming a high activation barrier in the singlet state. We remind that the exchange integral appears with different signs in the energy expression for the S and T states, namely, two radicals form a chemical bond in the S state and repel each other in the T-state (Friedman and Campbell 1987). The different behavior of the S and T states is important not only for radical reactions, but also for many chemical transformations that include spin “depairing” during bond scission or proceed through biradical intermediates. This often occurs in catalysis by transition metal compounds (Minaev et al. 2007; Prabhakar et al. 2004; Sheldon 1993), especially in hemoproteins (Franzen 2002; Jensen and Ryde 2004; Shikama 2006; Sigfridsson and Ryde 2002; Stryer 1995).

The complete occupation of the degenerate-shell,  $\blacktriangleright$  Eq. 29.2, requires adding two additional electrons in order to become diamagnetic species, like usual chemical substance. Therefore, the oxygen molecule has a very strong tendency to take electrons from other substances and to make the complete electron-pairing in its unoccupied orbitals. This leads to the sequential formation of highly reactive or toxic oxygen species such as the superoxide anion  $O_2^-$ , peroxide anion  $O_2^{2-}$ , as by-products of many normal cellular metabolisms. Consequently, the development of enzymes to protect cells against such “oxidant stress” was of great urgency to aerobic organisms. This resulted in the ubiquitous occurrence of superoxide dismutase, catalase, peroxidase, and so on (Shikama 2006).

## Cytochrome Oxidases and Related Heme-Containing Enzymes

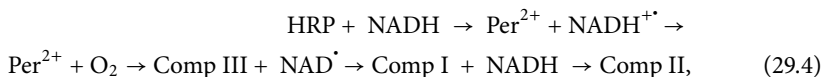
---

Many heme-containing enzymes share the same active-species of the iron-ion types, but at the same time they exhibit significant differences in biochemical properties and reactivity with complicated spin-dependent kinetics (Burnold and Solomon 1999; de Winter and Boxer 2003; Kumar et al. 2005; Metz and Solomon 2001; Orlova et al. 2003; Shaik et al. 1998, 2002, 2005). Some of these heme-containing enzymes, cytochrome P450, cytochrome c oxidase, and horseradish peroxidase (HRP), are utilized as the active site of a high-valent oxo-iron heme species, called compound I (Shaik et al. 2002). Shaik et al. (Kumar et al. 2005; Shaik et al. 2002, 2005) proposed that the diverse reactions catalyzed by cytochrome P450 could be explained in terms of the difference in reactivity between the high-spin and low-spin states of the compound I. Their proposed two-state reactivity concept (Kumar et al. 2005; Shaik et al. 2002, 2005) has been widely used for the cytochrome P450 family and based on spin conversion transition between these states during reactions.

HRP, being similar to cytochrome P450 by crystal structure of the active site, differs in axial (proximal) ligand bound to the iron; P450 has a thiolate ligand of a cysteinyl side chain, whereas HRP binds an imidazole group of a histidine residue side chain (Kumar et al. 2005). Although HRP functions predominantly as an electron sink (Kumar et al. 2005), it is also known to perform oxygen-transfer reactions (Afanasyeva et al. 2006; Chalkias et al. 2008; Shaik et al. 2002). Generally, however, the reactivity of HRP enzymes is sluggish compared with the P450 enzymes family; sulfoxidation is the most efficient while C-H hydroxylation is rather sluggish. This originates mainly in the much smaller substrate-binding pocket in HRP (Afanasyeva et al. 2006; Shaik et al. 2002). The recent DFT study of sulfoxidation by HRP and by cytochrome P450 reveals a spin-state selection dependency on the proximal ligand: for thiolate ligand the reaction prefers the high-spin quartet state path while for the imidazole ligand the reaction mechanism involves a two-state reactivity (Kumar et al. 2005). This spin pattern also obeys orbital-selection rules, which are derived from the MO involvement of the ligands into the key oxo-iron porphyrin orbitals (Kumar et al. 2005; Shaik et al. 2005). In the case of the two-state reactivity the SOC-induced spin-transitions between the high-spin and low-spin reaction pathways could be magnetic-field dependent, if the viscosity of the media is sufficiently high (Afanasyeva et al. 2006; Buchachenko and Kouznetsov 2008; Buchachenko et al. 2005; Chalkias et al. 2008; Grissom 1995; Minaev 1983; Minaev and Lunell 1993; Serebrennikov and Minaev 1987). This is because SOC in the active sites is highly anisotropic and provides different rate constants for different spin-sublevels in zero field (Minaev 2002; Minaev and

Lunell 1993), which become modified in the external field making the reaction to be magnetic-field dependent (Buchachenko and Kouznetsov 2008; Serebrennikov and Minaev 1987).

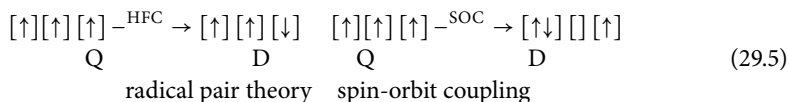
Such a dependence is found for the HRP-catalyzed oxidation of NADH, which can be presented by the schemes (Afanasyeva et al. 2006):



where compound II represents the Fe(IV)=O group connected with the porphyrin ring, compound I represents Fe(IV)=O connected with the radical cation of porphyrin, and compound III represents the porphyrin-containing Fe(IV)-OOH group. Here porphyrin denotes the protoporphyrin IX linked with protein chain by the histidine residue. The scheme (Eq. 29.4) is compatible with the magnetic-field dependence of the rate constants measured by stop-flow spectroscopy (Afanasyeva et al. 2006). The catalytic cycle starts with electron transfer from NADH to native HRP ( $\text{Per}^{3+}$ ) to produce  $\text{NADH}^{\cdot+}$  radical and the ferropoxidase intermediate ( $\text{Per}^{2+}$ ); ( $\text{Per}^{3+}$ ) actually means here the ferric porphyrin-Fe(III).

Interconversion of NADH to form  $\text{NAD}^+$  occurs by hydride transfer, in which the  $\text{H}^+$  ion and two electrons are transferred between the C(4) carbon atom of nicotinamide ring and substrate (Minaev et al. 1999). Catalytic cycle of NADH oxidation in the presence of hydrogen peroxide begins with a two-electron oxidation of the HRP enzyme to form  $\text{Fe}^{\text{IV}}$  and the porphyrin cation radical; this compound I is a highly reactive species that can accept one electron from NADH to form a  $\text{NADH}^{\cdot+}$  radical cation, which can undergo deprotonation to yield  $\text{NAD}^{\cdot}$  and compound II (Afanasyeva et al. 2006; Grissom 1995). The process is competitive with reverse electron transfer to regenerate NADH and Comp I, as shown by chemically induced dynamic nuclear polarization (CIDNP) of one of the C(4) protons in the NMR spectrum of NADH in presence of HRP (Afanasyeva et al. 2006). An alternative explanation of CIDNP is also possible (Minaev 2002; Serebrennikov and Minaev 1987), based on account of anisotropic SOC in compound I (Minaev 2010; Minaev and Lunell 1993; Minaev et al. 2007). The magnetic-field dependence of the enzymatic reaction helps to reveal electron spin correlation among the catalytic states. Paramagnetic intermediates in the HRP catalytic cycle are difficult to detect, since direct observation by the EPR method depends on trapping unstable kinetically relevant radicals that may be transient or present at insignificant concentrations. Compound I is illusive in the sense that it does not accumulate in the cycle. This transient radical was inferred by cryogenic EPR/ENDOR technique (Davydov et al. 2008). The cryoreduction of the EPR-silent compound II produces Fe(III) species retaining the structure of precursor  $[\text{Fe}(\text{IV})=\text{O}]^{2+}$  or  $[\text{Fe}(\text{IV})=\text{OH}]^{3+}$ ; thus the EPR spectra of cryoreduced HRP II provide evidence of the low-spin hydroxy-Fe(III) heme species (Davydov et al. 2008; Kumar et al. 2005).

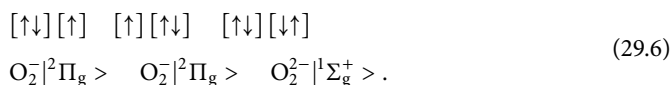
The first stage (Eq. 29.4) is thought to be magnitosensitive (Afanasyeva et al. 2006). Electron transfer from NADH to native HRP produces the quartet (Q) radical pair of  $\text{Per}^{2+}$  and  $\text{NADH}^{\cdot+}$ , which is unreactive toward recombination. The quartet – doublet (D) transition produces a radical pair that can recombine and quench the enzymatic process. It is claimed (Afanasyeva et al. 2006) that the Q-D transition is governed by isotropic hyperfine interaction and radical g-factors in terms of radical pair theory (Kumar et al. 2005). This Q-D transition is presented in the left part of the following scheme:





Here the set of three orbitals represents the triplet state of the  $\text{Per}^{2+}$  active site and one unpaired spin in the  $\text{NADH}^{+\cdot}$  radical. The ferro-porphyrin intermediate ( $\text{Per}^{2+}$ ) is known now to have a quintet ground state (Davydov et al. 2008) as follows from DFT calculations (Shaik et al. 2005). Thus, the main idea of the magnetic field mechanism (Afanasyeva et al. 2006) gives rise to some doubt. The most important objection is connected with the possible account of SOC, illustrated on the right side of the scheme (► Eq. 29.5). It is possible to construct a number of configurations that could be definitely admixed to the open shell ground states of the  $\text{Per}^{2+}$  active site, which provides a strong SOC between Q-D states of the radical pair (● Eq. 29.4). Such an SOC-induced mechanism could be applied to a number of magnetic field effects in metal-containing enzymes (Davydov et al. 2008; Engstrom et al. 1998, 2000; Gegear et al. 2008; Hoff 1986; Johnsen and Lohmann 2005; Maeda et al. 2008).

In the context of dioxygen activation we have to mention enzymes with binuclear metal centers, like cytochrome oxidase (Blomberg et al. 2000a, 2005), hemerythrin, and hemocyanin (Burnold and Solomon 1999; Metz and Solomon 2001). Generally speaking, the enzymes containing iron and copper active sites (Metz and Solomon 2001; Prabhakar et al. 2004) play key roles in dioxygen activation by generation of a peroxo intermediate; either  $\text{O}_2$  is reduced by two electrons, provided by a binuclear metal site, or one electron is provided by metal and a second electron by a cofactor (Prabhakar et al. 2004). Cytochrome oxidase catalyzes the four-electron reduction of oxygen molecule to water (Stryer 1995). No intermediates were detected in the reaction  $\text{O}_2 + 4\text{e}^- + 4\text{H}^+ = 2\text{H}_2\text{O}$ . However, many experimental measurements (Stryer 1995) have proved the formation of  $\text{O}_2^{2-}$ . The reaction center of cytochrome oxidase includes one heme ferrous ion and one copper ion (Blomberg et al. 2000a). The oxygen molecule binds to the heme  $\text{Fe}^{2+}$  cation and to the  $\text{Cu}^+$  ion that donates one electron each to form an  $\text{O}_2^{2-}$  anion. This provides a way to overcome the major obstacle to oxygen activation, that is, spin inversion (T-S transition). The  $\text{O}_2^-$  and  $\text{O}_2^{2-}$  species have the following ground state configurations (in addition to ● Fig. 29-1):



Since the  $\text{O}_2^{2-}$  dianion has a filled electron shell, the ground state of this species is totally symmetric and characterized by the term  $^1\Sigma_g^+$ . Transfer of two electrons causes the ground-state term,  $^3\Sigma_g^-$  of the  $\text{O}_2$  molecule (● Fig. 29-1), to transform smoothly to the term  $^1\Sigma_g^+$  of the dianion. The spin-orbit coupling between the states  $^3\Sigma_g^-$  and  $^1\Sigma_g^+$  is symmetry-allowed (Minaev 1980, 2007); therefore, the reduction  $\text{O}_2 \rightarrow \text{O}_2^{2-}$  is also symmetry allowed with inclusion of SOC. Transition of the active site of cytochrome oxidase to the singlet state removes spin prohibition for subsequent fast chemical reactions up to formation of stable diamagnetic products (Minaev 2010). The orbital doubly degenerate  $^2\Pi_g >$  ground state of the  $\text{O}_2^-$  ion is split by strong SOC (Minaev 2007), since it has a nonzero orbital angular momentum. This is an important key aspect of many enzymatic  $\text{O}_2$ -activation reactions, considered in the following sections.

## Dioxygen Reaction with Glucose Oxidase

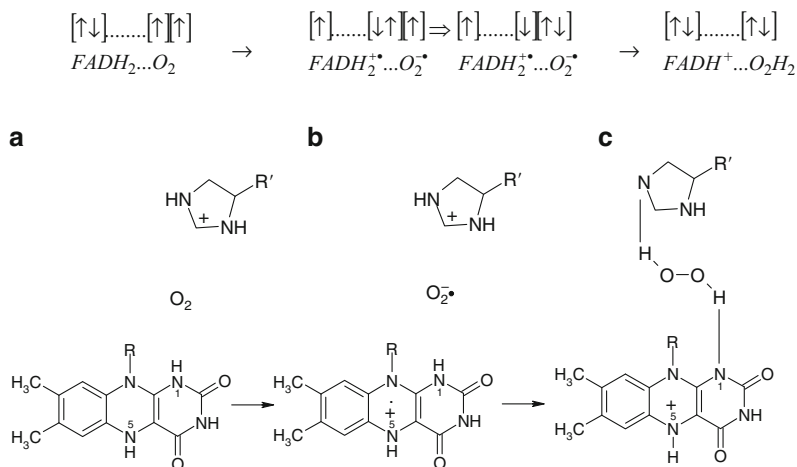
It is often assumed (Sawyer 1991; Shikama 2006; Stryer 1995) that one can overcome the spin prohibition to oxidation of organic substrates with atmospheric oxygen by successive addition



of single electrons and protons in the successive reduction of  $O_2$ . Further reactions of diamagnetic hydrogen peroxide, produced in such reduction, are spin allowed. It is assumed (Sawyer 1991; Sheldon 1993; Stryer 1995) that removal of spin prohibition in such reactions proceeds as in the case of radical-chain oxidation, where the spin prohibition can be removed upon formation of primary radicals. It is important to stress a fundamental difference between the enzymatic reactions involving radicals and the radical reactions in chain oxidation processes. In the latter case radicals go to the bulk of the gaseous plasma flame (or in the solution bulk) and no longer retain the “spin memory” about precursors. All participants of biochemical oxidation reactions, i.e., dioxygen and electron transfer agents, are confined within the same active site of enzyme. If an electron is transferred to the oxygen molecule from a diamagnetic enzyme  $M$ , i.e.,  $O_2 + M \rightarrow O_2^- + M^+$ , it produces a triplet radical ion-pair (triplet precursor), all spins remain correlated, the “spin memory” is retained, and the spin prohibition to subsequent reactions of the radical ion-pair thus generated is not removed and cannot lead to a singlet product.

For example, reaction of  $O_2$  with glucose oxidase (Klinman 2001; Minaev 2002; Prabhakar et al. 2002, 2003) involves flavin adenine dinucleotide (FAD) and includes two stages; namely, glucose oxidation to glucosolactone with reduction of FAD to  $FADH_2$  and the reverse cycle  $FADH_2 \rightarrow FAD$ , with reduction of  $O_2$  to  $H_2O_2$ . From the standpoint of dioxygen activation it is interesting to consider only the second stage (● Fig. 29-2). In this model the protonated histidine residue (His516) is included, which is in close proximity to FAD as follows from X-ray analysis (Klinman 2001).  $O_2$  can occupy the cavity between  $FADH_2$  and His516 (● Fig. 29-2a). DFT calculations indicate that an electron is transferred immediately from the reduced cofactor to dioxygen (● Fig. 29-2b); the electron transfer process is determined by low ionization potential of  $FADH_2$ , relatively high electron affinity of  $O_2$  (0.45 eV), and attraction of the  $O_2^-$  to the protonated histidine. After formation of a triplet radical pair,  $FADH_2 + O_2 \rightarrow FADH_2^{\cdot+} + O_2^{\cdot-}$ , the  $T \rightarrow S$  transition has to occur in order to provide the final diamagnetic products  $FAD + H_2O_2$ , to which the singlet-spin stage (● Fig. 29-2c) precedes.

After the  $T \rightarrow S$  transition in the ion-radical pair (● Fig. 29-2b), an ordinary chemical transformation on the singlet state PES occurs (● Fig. 29-2c). It involves abstraction of hydrogen atom from the N1 atom of  $FADH_2^{\cdot+}$  and a proton abstraction from the nearest histidine residue in order to create  $H_2O_2$  by reduction of the superoxide anion. This process, accompanied by the formation of hydrogen peroxide, can occur only in the singlet state. The final phase of the catalytic cycle (not shown in ● Fig. 29-2) consists of a subsequent proton transfer from  $FADH^+$  ion back to histidine across the system of H-bonds in water-protein chain (Prabhakar et al. 2003). This proton transfer does not change the number of active electrons and the closed-shell spin state. The  $T \rightarrow S$  transition has been explained (Prabhakar et al. 2003, 2004) by a relatively large SOC between the S and T states of the radical pairs (● Fig. 29-2b), which have different orbital structures inside the superoxide ion. As one can see in the orbital-configuration scheme (● Fig. 29-2), the  $T \rightarrow S$  transition includes an electron jump from one  $\pi_{g,x}$  molecular orbital of the dioxygen to another  $\pi_{g,y}$  orbital (Spin on the  $FADH_2^{\cdot+}$  moiety is non-active during the transition). Such transformation is equivalent to orbital rotation, or to a torque, which creates a transient magnetic field; finally this magnetic field induces a spin flip (Prabhakar et al. 2003, 2004). Thus, the reductive activation of dioxygen by GO is favored by an increased electron affinity of  $O_2$  due to the proximity of protonated His516-residue and a fast electron transfer followed by the  $T \rightarrow S$  transition induced by strong SOC in superoxide ion. This simple consideration is supported by direct quantum-mechanical calculations of the SOC integrals (Minaev 2010; Silva and Ramos 2008). Exactly the same mechanism of the  $T \rightarrow S$  transition is applied for explanation of activity of coproporphyrinogen III oxidase (CPO) in catalysis of the oxidative decarboxylation during the heme biosynthesis (Silva and Ramos 2008). Silva and Ramos have



■ Fig. 29-2

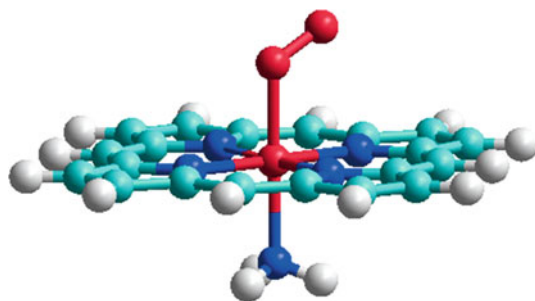
An active center of the glucosidase model. The first phase of the catalytic cycle (not shown) includes the FAD to FADH<sub>2</sub> reduction. (a) starting model of the dioxygen entrance to the active site; (b) electron transfer stage and spin transition in the radical pair; (c) hydrogen peroxide production. The final stage (not shown) includes the proton transfer from the N5 atom to the histidine residue along the hydrogen-bond network in peptide chain of the enzyme

supported the so-called Lash's model of CPO oxidation by dioxygen (Silva and Ramos 2008) and obtained the T-S crossing point that lies only 8 kcal/mol above the reactant state. They have calculated the SOC integral between T and S potential energy surfaces crossing to be equal to 77.45 cm<sup>-1</sup> in an excellent agreement with the earlier prediction for GO reaction (Minaev 2002; Prabhakar et al. 2002).

A similar mechanism of the SOC during the T → S transition has been used to explain bioluminescence induced by the luciferase enzyme (Orlova et al. 2003). Attachment of triplet dioxygen to the closed shell luciferin to yield a singlet state intermediate (which finally provides bioluminescence) is a spin-forbidden process (Orlova et al. 2003). It is important to the use of previous GO model (Minaev 2002; Prabhakar et al. 2002) that a critically significant protonated histidine residue resides in the proximity of the acidic group of luciferin (Orlova et al. 2003), quite similar to the GO active site (► Fig. 29-2). Photodestruction of this histidine inactivates luciferase completely, thus it is found plausible that the SOC-induced spin-flip in superoxide ion (Prabhakar et al. 2002) operates in the case of oxygenation by luciferase (Orlova et al. 2003). In the following we want to show that a similar mechanism of SOC enhancement by charge transfer can be applied for spin-dependent reaction of dioxygen binding to heme.

## Dioxygen Binding to Heme

The O<sub>2</sub> binding with myoglobin model was studied recently by DFT methods (Blomberg et al. 2005; Franzen 2002; Jensen and Ryde 2004; Jensen et al. 2005; Minaev 2007; Minaev et al. 1993, 2007; Sigfridsson and Ryde 2002; Strickland and Harwey 2007). Fully relaxed potential energy curves (PEC) were calculated for the seven lowest electronic states in Ref. Sigfridsson and Ryde (2002), Strickland and Harwey (2007), and Blomberg et al. (2005),



■ Fig. 29-3

**A simple model of Fe(II)-porphine-NH<sub>3</sub>-O<sub>2</sub> model of oxyhemoglobin (heme-cofactor coordinated with O<sub>2</sub>. Simulates the heme (with NH<sub>3</sub> as a model of a proximal histidine residue)**

while the PEC for spin states  $S = 0, 1, 2, 3$  at fixed geometry as a functions of the Fe–O<sub>2</sub> distances were presented in Ref. Franzen (2002). In this work we have recalculated some points of the fixed Fe–O distance (1.8, 2.0 and 2.5 Å) with full geometry optimization of all other parameters for all possible multiplets and accounting for different symmetries ( $A'$  and  $A''$ ) for the singlet and triplet states. The model of oxyheme is shown in ● Fig. 29-3, which includes Fe(II)-porphyrin coordinated with NH<sub>3</sub> as a model of proximal histidine residue. Its calculation gives the similar singlet ground state as for the simplified Fe(II)-Porphin-Imidazole-O<sub>2</sub>-model, which poses  $C_s$  symmetry (Sigfridsson and Ryde 2002). The simpler Fe(II)-Porphine-NH<sub>3</sub>-O<sub>2</sub> model (● Fig. 29-3) has been used in this work for DFT calculations in the vicinity of the equilibrium. The B3LYP/6-31G\* method (Frisch et al. 2003) has been employed and the results quite close to those presented in Ref. Sigfridsson and Ryde (2002) have been obtained. For the Fe(II)-Porphyrin-NH<sub>3</sub>-O<sub>2</sub> model, shown in ● Fig. 29-3, all vibrational frequencies and their intensity in the infrared and Raman spectra have been calculated. Many normal modes are similar to those calculated in Refs. Minaev et al. (2007) and Minaev (2002). An additional Fe–O<sub>2</sub> stretching vibrational frequency is calculated at 539 cm<sup>-1</sup>, which agrees qualitatively well with the resonance Raman band, observed at 567 cm<sup>-1</sup> for oxy-hemoglobin by Soret excitation (Potter et al. 1987). This indicates reliability of the chosen model and of the DFT method used in this work.

In the entrance channel of the O<sub>2</sub> binding reaction to heme we have a number of different multiplets. At the infinite separation the deoxyheme has a quintet ground state with the triplet state being very close in energy. This is in agreement with the experimental data (Shikama 2006), showing that the isolated deoxyheme is a high-spin quintet (Friedman and Campbell 1987). The optimized structure of this Fe(II)P complex with NH<sub>3</sub> at the fifth coordination position agrees with the X-ray analysis of the crystal structure of deoxymyoglobin. In this case the porphyrin Fe–N distances (2.08 Å) are larger than in the low-spin states of deoxymyoglobin (2.0 Å) and the iron ion is above the porphyrin ring plane by 0.3 Å in agreement with the X-ray data (0.36 Å) (Friedman and Campbell 1987; Sigfridsson and Ryde 2002). This illustrates the well-known fact that the high-spin iron ion Fe(II)(<sup>5</sup>D) is too large to fit into the porphyrin ring cavity (Jensen and Ryde 2004).

When this deoxyheme interacts with the triplet ground state dioxygen O<sub>2</sub>( $X^3\Sigma_g^-$ ), there are six unpaired electrons (two from O<sub>2</sub> plus 4 from heme). Their interaction can provide a variety of possible total spin states. The maximum spin corresponds to the septet ( $^7A''$ ,  $S = 5$ ) state, when both subsystems have parallel spins. If they are anti-parallel, the triplet state  $^3A''$  occurs. At long Fe–O distances ( $R > 2.5$  Å) these states are degenerate because of the absence

of exchange interactions between O<sub>2</sub> and heme. The intermediate quintet <sup>5</sup>A'' state is also degenerate together with the triplet and septet. The A'' symmetry is determined by the oxygen degenerate π<sub>g</sub> orbitals, which have the a' and a'' symmetry, respectively, with respect to the plane, which contains the O<sub>2</sub> and Fe–N bond in ammonia molecule.

In general, all spin states that occur at each random collision of heme and O<sub>2</sub> should lead to oxygen binding. But the rate constants would be spin-dependent and different for the triplet, quintet, and septet states (even for different spin sublevels of one multiplet). More detailed information about O<sub>2</sub> binding has been obtained in flash-photolysis studies of O<sub>2</sub> dissociation from heme, when the fate of dioxygen depends on the competition between intrinsic recombination rate constant and protein relaxation, as well as the O<sub>2</sub> escape from the protein (Shikama 2006). The greatly different recombination dynamics of O<sub>2</sub>, CO, and NO molecules with heme have been attributed to spin states of each ligand and to their possible combinations with the iron spin (Franzen 2002; Jensen and Ryde 2004; Shikama 2006; Sigfridsson and Ryde 2002). The observed recombination kinetics can be influenced by protein dynamics, if the intrinsic recombination rate constant is slower than this dynamics. By studies of viscosity and temperature dependence, the general averaged time scale for the recombination rate constant can be estimated (Friedman and Campbell 1987; Jensen and Ryde 2004; Shikama 2006).

It is interesting to compare O<sub>2</sub>, CO, and NO molecules in this respect (Blomberg et al. 2005; Friedman and Campbell 1987; Strickland and Harwey 2007). The CO recombination with heme is a single exponential process characterized by a slow rate constant ( $k \approx 10^6 \text{ s}^{-1}$ ) at the ambient temperature and a low solvent viscosity (below viscosity of globin). This intrinsic (geminate) recombination rate is slower than both protein relaxation and CO escape, thus the recombination yield is very small (0.04) (Shikama 2006). The rebinding of the NO stable radical (doublet ground state,  $S = 1/2$ ) is characterized by two-exponential kinetics with the rapid ( $k_1 \approx 10^8 \text{ s}^{-1}$ ) and slow ( $k_2 \approx 5 \cdot 10^6 \text{ s}^{-1}$ ) rate constants under ambient conditions (Friedman and Campbell 1987; Shikama 2006). Since the ground state heme has the quintet spin state ( $S = 2$ ), there are two starting states: ( $S = 2\frac{1}{2}$  and  $S = 1\frac{1}{2}$ ) depending on mutual spin orientation of two species, while the recombination NO-heme product has the doublet state ( $S = 1/2$ ) (Friedman and Campbell 1987; Strickland and Harwey 2007). Both types of geminate recombination require spin change. The slow process includes two-step spin-flip transformations ( $S = 2\frac{1}{2}$ ) → ( $S = 1\frac{1}{2}$ ) → ( $S = 1/2$ ), since spin-orbit coupling can mix states and induces spin transition with the selection rule  $\Delta S = 1$  (Minaev 2010). The rapid recombination occurs in one step ( $S = 1\frac{1}{2}$ ) → ( $S = 1/2$ ).

The CO molecule is diamagnetic; all spins are paired, the total spin is zero. The heme-CO adduct is also diamagnetic ( $S = 0$ ). Since the ground state heme has the quintet spin state ( $S = 2$ ), the geminate recombination reaction is doubly spin forbidden. First it should be a quintet-triplet transition, which needs to overcome an additional activation barrier (besides the spin flip, induced by SOC) and then a final triplet-singlet transition. This is the reason why the CO recombination with heme is so slow, in spite of the high binding energy (Franzen 2002; Jensen and Ryde 2004; Shikama 2006; Sigfridsson and Ryde 2002; Strickland and Harwey 2007).

It is interesting to make the comparison: inorganic ferric ion (Fe<sup>3+</sup>) has some catalytic activity for the decomposition of H<sub>2</sub>O<sub>2</sub> into water and oxygen. When the ion is incorporated into the porphyrin molecule to form heme, the molecule is about a thousand times more effective than Fe<sup>3+</sup> alone. If the protein component of the enzyme catalase then adds to the heme, the catalytic efficiency increases by a further factor of 10<sup>9</sup> times (Shikama 2006). This means that paramagnetic spin catalysis in combination with the SOC-induced spin-catalysis provide some kind of synergetic effect.

## Spin-Orbit Coupling in O<sub>2</sub>-Heme Interaction

In this review we shall consider dioxygen binding in more detail, since the O<sub>2</sub> molecule is the main subject of spin-dependent biochemical phenomena in a general context. The ground state of the oxyheme product is an open-shell singlet in agreement with EPR experiment and Mossbauer spectra (Friedman and Campbell 1987; Sigfridsson and Ryde 2002) (the closed-shell singlet has been obtained in a number of calculations (Jensen et al. 2005; Shikama 2006), however, this result has since been revised (Blomberg et al. 2005; Strickland and Harwey 2007)). Thus, the reaction of O<sub>2</sub> binding to heme is spin forbidden. At least the T-S transition has to occur (Franzen 2002). Such spin flip can be induced by spin-orbit coupling (SOC) between the T and S states. One has to calculate the matrix element of the SOC operator, which can be presented in the effective single-electron approximation as

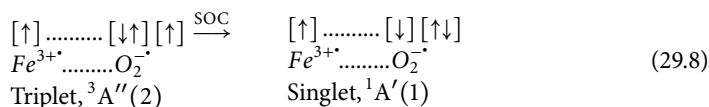
$${}^H\text{SO} = \sum_A \zeta_A \sum_i \vec{l}_{i,A} \cdot \vec{s}_i = \sum_i \vec{B}_i \cdot \vec{s}_i = \sum_i (B_{i,x}s_{i,x} + B_{i,y}s_{i,y} + B_{i,z}s_{i,z}). \quad (29.7)$$

In (Eq. 29.7)  $\zeta_A$  is a SOC constant for atom A ( $\zeta_0 = 153 \text{ cm}^{-1}$ ),  $\vec{l}_{i,A}$ ,  $\vec{s}_i$  – are the orbital and spin angular momentum operators for the  $i$ -th electron, respectively. This is the effective single-electron SOC approximation, which proved to be useful in many spectroscopic and chemical applications including oxygen spin-forbidden atmospheric bands (Minaev 1989; Minaev and Ågren 1997; Minaev et al. 1997, 1996, 2008; Ogilby 1999; Paterson et al. 2006; Schweitzer and Schmidt 2003) and spin-forbidden enzyme reactions (Minaev 2002, 2007, 2010; Minaev et al. 2007; Prabhakar et al. 2003, 2004).

Deoxyheme has a quintet ground state (four spins are unpaired,  $S = 2$ ) (Minaev et al. 2007; Sigfridsson and Ryde 2002) and the adduct with the triplet dioxygen (two unpaired spins) would be expected to have either six ( $4+2 = 6$ ) unpaired spins or two ( $4-2 = 2$ ) unpaired spins depending on ferromagnetic or antiferromagnetic relative orientation of the two magnetic moments of the deoxyheme and O<sub>2</sub>. An intermediate quintet spin state is also possible for the ground state species coupling. The triplet state of deoxyheme, being very close in energy, produces adducts with the triplet O<sub>2</sub>, which could be either quintet ( $S = 2$ ), triplet ( $S = 1$ ), or singlet ( $S = 0$ ) depending on if it is ferromagnetic or antiferromagnetic coupling of two species. Thus, only triplet deoxyheme could provide the ground singlet state product in the process of the antiferromagnetic coupling with the triplet O<sub>2</sub> in a spin-allowed oxyheme formation without spin flip. Spin transition from the ground quintet to the close-lying triplet deoxyheme can be induced by SOC in the third shell of the iron ion. In this case the primary electronic reorganization takes place in the ferrous ion at the equilibrium between the quintet and triplet states already before dioxygen approaches the deoxyheme (Franzen 2002; Jensen and Ryde 2004). All other recombination processes include spin flip induced during heme–O<sub>2</sub> interaction; they seem to be more important for dioxygen binding (Blomberg et al. 2005; Franzen 2002; Jensen and Ryde 2004; Minaev 2007; Minaev et al. 2007; Shikama 2006; Strickland and Harwey 2007). Such natural heme – O<sub>2</sub> reactions could start with the  ${}^3A''(2)$  state, which is repulsive at shorter distance ( $R < 2.5 \text{ \AA}$ ) or with the septet  ${}^7A''(1)$  state (Jensen and Ryde 2004) (both are the ground state of the entrance channel heme + O<sub>2</sub> and go in parallel with some other multiplets until the short distances limit ( $2.5\text{--}3 \text{ \AA}$ )). The energy gap is about 0.1 eV at these limits in agreement with Ref. Jensen and Ryde (2004). The optimized singlet ground state  ${}^1A'(1)$  in the reaction product is lower in energy than other multiplets at least by 0.4 eV; this oxyheme is an open-shell singlet of a complicated orbital and spin structure (Franzen 2002; Jensen and Ryde 2004; Sigfridsson

and Ryde 2002). It has a short Fe–O distance (1.81 Å) (Jensen and Ryde 2004) (reproduced in our DFT calculations, 1.84 Å) in contrast to the high-spin states (2–2.7 Å). Our result is close to the  $\text{Fe}^{3+}\text{-O}_2^-$  radical-pair structure in agreement with other DFT calculations and with Weiss' model (Franzen 2002; Jensen and Ryde 2004; Shikama 2006; Sigfridsson and Ryde 2002). The spin densities in oxyheme are equal to 0.94, –0.31, and –0.72 for the Fe–O–O chain, respectively, at the optimized bond angle of 118°. The O–O bond distance (1.36 Å) and vibration frequency (1110  $\text{cm}^{-1}$ ) correspond better to superoxide ion (Jensen and Ryde 2004; Minaev 2007).

Potential energy surfaces for  $\text{O}_2$  binding with the heme model (deoxy-Fe-porphyrin bound with imidazole) have been calculated by Jensen et al. (Jensen and Ryde 2004), who optimized by DFT method the  $C_s$  symmetry restricted reaction with fixed Fe–O bond length, which was systematically increased point by point. Jensen et al. (Jensen and Ryde 2004) found that the spin-change occurs easily due to a broad crossing region of five electronic states. Similar PES crossing are obtained in other studies (Franzen 2002; Minaev et al. 1993; Strickland and Harwey 2007). Accounts of our data and the results of Refs. Sigfridsson and Ryde (2002), Franzen (2002), Jensen and Ryde (2004), and Strickland and Harwey (2007) allow us to consider the following scenario of the  $\text{O}_2$  binding to myoglobin. At the intermediate distances 2.5–3 Å the starting  $^3A''(2)$  state from the entrance channel transfers to the triplet  $\text{Fe}^{3+}\text{-O}_2^-$  radical-pair. In this region there are few crossing points between S and T states, including the  $^3A''(2)$ – $^1A'(1)$  states crossing, where spin change could occur (Franzen 2002; Jensen and Ryde 2004; Sigfridsson and Ryde 2002). A simplified electronic structure of the  $^3A''(2)$  and  $^1A'(1)$  states near the crossing of the potential energy surfaces is presented in scheme (7). Outer electrons of the ground triplet state dioxygen in two degenerate  $\pi_g$ -MO's provide a scheme  $[\uparrow][\uparrow]$ ; electron transfer from  $\text{Fe}^{2+}$  to  $\text{O}_2$  in order to produce the radical pair  $\text{Fe}^{3+}\text{-O}_2^-$  (Eq. 29.8) can be accomplished by the occupation of either  $\pi_{g,x}$ - or  $\pi_{g,y}$ -orbitals. Both radical pairs could be in T and S states; all four states are almost degenerate at the intermediate distances. The most interesting spin states are those presented in scheme (Eq. 29.8), since they correspond to the desired T  $\rightarrow$  S transition and to the final product of the  $\text{O}_2$  binding by heme. The scheme (Eq. 29.8) is equivalent to the scheme (Eq. 29.5) and the same explanation for the high SOC matrix element (Minaev 2002; Prabhakar et al. 2002) is relevant.



In this model SOC perturbation occurs entirely in the oxygen moiety and the Fe(III) ion is magnetically silent. The starting triplet radical pair corresponds to a charge-transfer (CT) state described by  $^3A''(2)$  wave function  $^3\Psi_{CT_x} = \Re|(3d\alpha)(\pi_{g,x}\beta)(\pi_{g,x}\alpha)(\pi_{g,y}\alpha)|$ , that is, transfer of an electron to the  $\pi_{g,x}$ -orbital of  $\text{O}_2$  molecule, whereas the singlet radical pair corresponds to a CT state described by  $^1A'(1)$  wave function  $^1\Psi_{CT_y} = \Re|(3d\alpha)(\pi_{g,x}\beta)(\pi_{g,y}\alpha)(\pi_{g,y}\beta)|$  and a transfer of an electron to another degenerate orbital of oxygen,  $\pi_{g,y}$ . Here  $\Re$  means a proper anti-symmetrization of the wave function. Spin-orbit coupling between these CT states is the maximum possible for a system comprised of such light atoms like oxygen (Minaev 2002, 2004, 2007). The considered matrix element of the SOC operator (Eq. 29.7) is easily estimated to be equal:

$$\langle ^3A''(2) | H_{SO}^Z | ^1A'(1) \rangle = \langle ^3\Psi_{CT_x} | H_{SO}^Z | ^1\Psi_{CT_y} \rangle = \frac{1}{2} \langle \pi_{g,x} | B_z | \pi_{g,y} \rangle = \frac{i}{2} \zeta_O = 76.5 \text{ icm}^{-1} \quad (29.9)$$



The value is identical to those calculated for similar charge-transfer states including the GO (Minaev 2002; Prabhakar et al. 2002) and coproporphyrinogen III oxidase (Silva and Ramos 2008). This SOC matrix element (Eq. 29.9) is very close to a value of about  $80 \text{ cm}^{-1}$ , postulated in estimation of the Landau-Zener rate constant for T-S transitions in spin-dependent  $\text{O}_2$  and NO binding to heme (Franzen 2002; Friedman and Campbell 1987; Petrich et al. 1988). With such a proposal for the generally unknown SOC integral (Shaik et al. 2002) a quite reasonable estimation for the spin-dependent rate constants of the CO,  $\text{O}_2$ , and NO recombination in heme proteins are obtained (Franzen 2002; Petrich et al. 1988). For CO binding to heme a quintet-triplet-singlet step-wise transition is necessary, which explains the million times slower recombination rate in this case in comparison with the  $\text{O}_2$  and NO recombination in heme proteins (Franzen 2002; Shaik et al. 2002; Sigfridsson and Ryde 2002). The gradient difference at the location of crossing points that enters the denominator of the Landau-Zener expression of the rate constant for spin transition is quite small ( $0.1\text{--}0.2 \text{ eV/\AA}$ ) for  $\text{O}_2$  and NO binding to heme (Franzen 2002; Jensen and Ryde 2004), thus the topology of the binding curves supports a rapid recombination of both ligands to hemoglobin and myoglobin. The rapid NO rebinding to heme ( $k_1 \approx 10^8 \text{ s}^{-1}$ ) includes one-step quartet-doublet transition; since the NO radical has one outer electron at the degenerate  $\pi_x$  and  $\pi_y$  orbitals, a quite similar theory of SOC in quasi-degenerate charge transfer states, like that, presented in Eqs. 29.8 and 29.9, can be applied. The only difference is that the SOC integral (Eq. 29.9) now includes  $\pi_x$  and  $\pi_y$  orbitals of the NO molecule and thus is slightly smaller (about  $60 \text{ cm}^{-1}$ ). The rate constant of spin transition in the Landau-Zener model is determined by the square of the SOC integral. This explains that the rapid NO rebinding rate constant is about three times slower than the rapid rate constant of the  $\text{O}_2$  recombination in heme proteins (Franzen 2002; Jensen and Ryde 2004; Shikama 2006).

All previous analyses of SOC effects in hemoproteins were based on the assumption that the SOC integral in dioxygen binding to heme is determined by the iron ion and no attempt at direct calculation has been done (Blomberg et al. 2005; Franzen 2002; Jensen and Ryde 2004; Sigfridsson and Ryde 2002; Strickland and Harwey 2007). As follows from our simple analysis, the SOC integral (Eq. 29.9) is determined entirely by SOC in oxygen molecule and is connected with the degeneracy of the two  $\pi_{g,x}$ - and  $\pi_{g,y}$ -orbitals in the open-shell of dioxygen. This enhancement of SOC effect by inclusion of charge-transfer to  $\text{O}_2$  and involvement of superoxide-ion structure seems to be quite general in biochemistry (Minaev 2007, 2010); it is applied also to those enzymes that have no transition atoms, like glucose oxidase, or coproporphyrinogen III oxidase (Minaev 2007; Prabhakar et al. 2002; Silva and Ramos 2008). It is important to stress that the rapid T-S transition in  $\text{O}_2$  binding to heme is not only forbidden by spin, but also by orbital symmetry (it includes the  $A'' - A'$  symmetry change). Such double prohibition is necessary in order to make the spin change in chemical reaction to be effectively allowed (Minaev and Lunell 1993).

The iron ion can also contribute to the SOC integral in the  $\text{O}_2$  binding to heme. In general, contributions from different atoms can cancel each other in SOC calculations; it happens when orbital rotation for different atoms occurs in opposite directions along the same axis during the T-S transition (Minaev 2007; Minaev and Lunell 1993). This type of SOC suppression is known in the form of the destructive external heavy atom effect (Minaev 2010). However, such an effect cannot be applied for SOC analysis in heme- $\text{O}_2$  interaction. The main axis of the third-orbitals rotation in ferrous ion during the T-S transition is perpendicular to the porphyrin tetrapyrrole plane, while the SOC contribution from dioxygen is determined by the  $\pi_{g,x}$ - and  $\pi_{g,y}$ -orbitals' rotation around the O-O axis and the two axes do not coincide. The angle of  $118^\circ$  between these

axes excludes possibility of cancellation: only the sum of the squares of the x,y,z projections, of the type given by ► Eq. 29.9, contributes to the final SOC value, which determines the rate constant of the T-S transition in terms of the Landau-Zener approximation (Harvey 2004; Kondo and Yoshizawa 2003; Minaev 2002; Minaev and Agren 1995; Poli and Harvey 2003).

## The Role of Spin in Biochemistry

---

We can see that spin-dependent quantum effects and transformations are important in a number of biochemical processes (Afanasyeva et al. 2006; Blomberg et al. 2000a, 2005; Buchachenko 1977; Buchachenko and Kouznetsov 2008; Buchachenko et al. 2005; Burnold and Solomon 1999; Chalkias et al. 2008; Davydov et al. 2008; de Winter and Boxer 2003; Franzen 2002; Grissom 1995; Jensen and Ryde 2004; Jensen et al. 2005; Kumar et al. 2005; Lane 2002; Metz and Solomon 2001; Minaev 1983, 2002, 2007, 2010; Minaev et al. 1999, 2007; Orlova et al. 2003; Petrich et al. 1988; Prabhakar et al. 2002, 2003, 2004; Serebrennikov and Minaev 1987; Shaik et al. 1998, 2002, 2005; Sigfridsson and Ryde 2002; Silva and Ramos 2008; Strickland and Harwey 2007). Spin is a very fundamental quantum phenomenon associated with the structure of space-time (Esposito 1999; Hameroff and Penrose 1996; Hu and Wu 2004; Penrose 1960). Various models of elementary particles in modern physics and even space-time itself are built with spinors (Esposito 1999; Penrose 1960). Spin of the Dirac electron is qualitatively shown to be responsible for all known quantum effects and the quantum potential is a pure consequence of “internal motion” evidencing that the quantum behavior is a direct consequence of the fundamental existence of spin (Penrose 1960). These results have been expanded recently by deriving a spin-dependent gauge transformation between the Hamilton-Jacoby equation of classical mechanics and the time-dependent Schrödinger equation of quantum mechanics that is a function of the quantum potential in Bohm mechanics (Esposito 1999). It is quite natural that the most mysterious peculiarities of living matter, the neuron network machinery of brain, hemoglobin, cytochromes, and oxydases, cannot avoid utilizing such a fundamental property of electrons like spin and quantum behavior. The occurrence of non-zero electron spin in any bio-system indicates that we are at a level of the life science where classical concepts are insufficient for its proper description and understanding. Electron spin is much more important than nuclear spin since it determines the exchange interaction, the most significant part of chemical forces, which are finally responsible for the functions of cells and for metabolism processes.

## External Magnetic Field Effects in Biochemistry

---


Regardless of the comments above, we need to speak about nuclear spins, since they are everywhere (at least in the form of protons) and because they also can be connected with quantum effects in bio-systems. Recent experiments (Buchachenko and Kouznetsov 2008; Buchachenko et al. 2005) demonstrate that intramitochondrial nucleotide phosphorylation is a nuclear spin controlled process because the magnetic magnesium isotope  $^{25}\text{Mg(II)}$  increases the rate of mitochondrial ATP synthesis in comparison with the spinless nonmagnetic  $^{24}\text{Mg(II)}$ ,  $^{26}\text{Mg(II)}$  ions. Such nuclear spin isotope effect is usually interpreted in terms of radical pair theory for separated spins in solvent cage (Buchachenko 1977), but an alternative explanation based on



electronic spin-transition in the active center (Minaev 1983; Minaev and Agren 1995; Serebrennikov and Minaev 1987) is also possible. New developments in magnetic resonance imaging of the brain demonstrate that induced quantum coherences of proton spins separated by long distances ranging from thousands to millions of nanometers (from 1  $\mu\text{m}$  to 1 mm) are sustained for milliseconds and longer (Hu and Wu 2004). While these quantum couplings are not the type of quantum processes that are likely to prove useful in brain function (Hagan et al. 2002), they nonetheless show that biology can take advantage of mesoscopic quantum coherence in clever ways. These quantum modes are not the stable entangled superpositions required for quantum computations in brain, but the proton spins' coherence can indeed survive in DNA, peptides, and in the brain's milieu (Hameroff and Penrose 1996; Hu and Wu 2004). Some new theory of consciousness is based on an idea that spin is the "mind-pixel" (Hagan et al. 2002; Hameroff and Penrose 1996; Hu and Wu 2004); it postulates that consciousness is intrinsically connected to quantum spin, since the latter is the origin of quantum effects in Bohm formalism and a fundamental quantum process associated with the structure of space-time (Esposito 1999; Hagan et al. 2002; Hameroff and Penrose 1996; Hu and Wu 2004; Penrose 1960). Spin involvement in the theory of consciousness can be connected also with memory storage and magnetic perturbations.

External magnetic field effects (MFE) in biochemistry are well known (Afanasyeva et al. 2006; Buchachenko and Kouznetsov 2008; Buchachenko et al. 2005; Chalkias et al. 2008; Davydov et al. 2008; Engstrom et al. 1998, 2000; Grissom 1995; Hoff 1986; Minaev et al. 1999; Serebrennikov and Minaev 1987) and could be analyzed in terms of competition with the internal magnetic interactions including SOC as the most important one (Minaev 1983; Minaev and Agren 1995; Minaev and Lunell 1993) and hyperfine coupling (Burnold and Solomon 1999; Metz and Solomon 2001; Minaev 2004); the spin-dependent exchange interactions are also involved in the MFE theories as well as the whole spin-catalysis concept (Minaev and Agren 1996; Orlova et al. 2003). MFE on enzymatic reactions have been first interpreted (Grissom 1995) entirely in the context of RPT (Buchachenko 1977). It was clear since the 1980a that RPT cannot explain all variety of MFE in chemistry and biology and SOC effects could be taken into account (Minaev 1980, 1983). But only recently, a number of publications (Afanasyeva et al. 2006; Chalkias et al. 2008; Minaev 2002; Minaev and Agren 1995) examined the external MFE in terms of SOC effects on the kinetics of enzymatic reactions. Activity increase of horseradish peroxidase (HRP) in the presence of magnetic particles ( $\text{Fe}_3\text{O}_4$ ) (Chalkias et al. 2008) and external MFE in enzymatic oxidation of NADH by HRP (Afanasyeva et al. 2006) are the most interesting examples. Interconversion of NADH to form  $\text{NADH}^{+\cdot}$  and  $\text{NAD}^+$  occurs by hydride transfer, in which  $\text{H}^+$  ion and two electrons are transferred between the C(4) carbon atom of nicotineamide ring and substrate (Afanasyeva et al. 2006). Catalytic cycle of NADH oxidation in the presence of hydrogen peroxide begins with a two-electron oxidation of the HRP enzyme to form  $\text{Fe}^{\text{IV}}$  and the porphyrin cation radical; this compound I is a highly reactive species that can accept one electron from NADH to form  $\text{NADH}^{+\cdot}$  radical cation, which can undergo deprotonation to yield  $\text{NAD}^{\cdot}$  and compound II (Afanasyeva et al. 2006; Grissom 1995).

MFE on the photosynthetic light-harvesting reaction center in bacterium *Rhodospseudomonas sphaeroides* was the first successful observation and interpretation of spin-dependent intermediates in biology (Grissom 1995; Hoff 1986). The quantum yield of the triplet chromophore decreases by 50% at 0.05 T. As the applied magnetic field increases, the Zeeman interaction between  $M_S = \pm 1$  spin sublevels grows and causes a decrease of hyperfine coupling between triplet T( $\pm 1$ ) and singlet S states, thus only T(0)-S states can interconvert. At high magnetic fields greater than 0.5 T the quantum yield of the triplet chromophore begins to increase slowly and attains parity with the zero-field ( $B = 0$ ) value at  $B = 3$  Tesla. At higher fields a net

increase is detected, which is explained by T-S transitions via  $\Delta_g$  mechanism (Afanasyeva et al. 2006; Buchachenko 1977; Engstrom et al. 2000). Such biphasic MFE dependence on B is typical for many photochemical (Hoff 1986; Serebrennikov and Minaev 1987) and enzymatic (Afanasyeva et al. 2006; Grissom 1995) reactions that occur through the radical pair mechanism. No total MFE on the photosynthetic reaction center would be expected since the total quantum yield is composed of a series of coupled vectorial processes that create an irreversible free energy cascade and drive proton pumping (Grissom 1995; Hoff 1986). For similar reasons it is impossible to expect other MFE with biological relevance. For example, MFE is possible, in principle, for the spin inversion step in GO, if the rotation of reactants in the step shown on  Fig. 29-2b would be frozen. The T-S transitions for different  $M_S = \pm 1, 0$  spin sublevels are characterized by different rate constants even in zero field in the fixed molecular frame. But rotation at room temperature quenches all anisotropy of zero-field splitting and SOC-induced rate constants (Serebrennikov and Minaev 1987). That is why no MFE has been observed for glucose oxidase in vivo (Chalkias et al. 2008).

Many mammals, reptiles, birds, insects, and fish are known to use the Earth's magnetic field for orientation and navigation (Gegeer et al. 2008; Johnsen and Lohmann 2005; Maeda et al. 2008). Birds have been studied very intensively, but biophysics and neurobiology of their avian magnetoreception are still poorly understood (Grissom 1995; Johnsen and Lohmann 2005). Maeda et al. (2008) have recently proposed a carotenoid-porphyrin model system to demonstrate that the lifetime of a photochemically induced radical pair is changed by MFE with a low magnetic field of about 50  $\mu\text{T}$ , which is comparable with the Earth's magnetic field. Radiofrequency MFE can disrupt the ability of birds to orient and also has profound influence on radical pair reactions in vitro, which supports the RPT concept (Maeda et al. 2008). The recent DFT study of the electronic mechanisms of oxidative cleavage of the O–O bond by apocarotenoid oxygenase (ACO), which occurs in dark condition and includes a number of biradical and radical stages, is important additional support to the carotenoid-porphyrin model of Maeda et al. (2008).

In this context it is interesting to pay attention to molecular oxygen. Each  $\text{O}_2$  molecule contains two unpaired electron spins and is a paramagnetic species capable of producing a fluctuating magnetic field along its diffusing pathway. Thus,  $\text{O}_2$  serves as a natural contrast agent in magnetic resonance imaging (Hu and Wu 2004). The existence of unpaired electrons in stable molecules is very rare indeed. Dioxygen is the only paramagnetic species found in large quantities in the brain (besides the nitric oxide) and in other aerobic tissues. The singlet excited  $^1\Delta_g$  oxygen (Minaev 2007) is a metastable species with a relatively short lifetime (few microseconds in water) (Schweitzer and Schmidt 2003) and long diffusion path (Ogilby 1999); it could serve as a light signal transmitter or transfer other types of information along definite distance in tissue. Generation and quenching of the singlet  $^1\Delta_g$  oxygen are governed by SOC and other quantum perturbations (Minaev 1980, 1989, 2007; Minaev and Agren 1995, 1996; Minaev and Ågren 1997; Minaev and Minaev 2005; Minaev and Minaeva 2001; Minaev et al. 1993, 1997, 1996, 2008; Ogilby 1999; Paterson et al. 2006; Schweitzer and Schmidt 2003). But the ground state triplet  $^3\Sigma_g$  oxygen bound and transported by hemoglobin is a source of many other quantum effects besides those described above.

## Spin Neuroscience

Conventional neuroscience has been unable to provide a complete understanding of cognitive processes (Esposito 1999; Hagan et al. 2002; Hameroff and Penrose 1996; Hu and Wu 2004;

Penrose 1960). It has been accepted that the brain can be simulated as a neural network organized by the principles of classical physics (Hameroff and Penrose 1996; Shaik et al. 2002). Such an approach has delivered successful implementation of learning and memory and promoted optimism that a sufficiently complex artificial neural network would (in principle, at least) reproduce the full extent of brain processes involved in cognition and consciousness (Hagan et al. 2002). But the functioning of the nervous system lie outside the realm of classical mechanics; one finds ample support for this in analysis of sensory organs of vision, the operation of which is quantized at levels varying from the reception of individual photons by the retina to thousands of quanta in the auditory system (Hagan et al. 2002; Hameroff and Penrose 1996). It is also proposed that synaptic signal transmission has a quantum character (Hagan et al. 2002). The Penrose-Hameroff orchestrated objective reduction (OOR) model (Hameroff and Penrose 1996) of quantum computation in microtubules within neurons of the brain is compatible with modern physiology and can generate testable predictions. Coherent superpositions of tubulin proteins are unstable in the OOR model and subject to self-collapse under quantum criterion. The phase of quantum superposition/computation is a preconscious process and each self-collapse event corresponds to “moment of conscious experience.” An apparent shortcoming of the Penrose-Hameroff OOR model and other models of quantum processes relevant to consciousness is the question of environmental decoherence (Hagan et al. 2002).

The dioxygen utilization in living matter provides many interesting manifestations of spin-dependent quantum effects that are under a control by very weak relativistic perturbations (Minaev 2007). This illustrates a long-lived quantum coherence in O<sub>2</sub> binding to hemoglobin (Franzen 2002; Friedman and Campbell 1987; Shikama 2006). Spin coherence can occur in photosynthetic systems, in oxidases, and in cytochromes. It depends on hyperfine interactions and spin–spin coupling in the ensembles of paramagnetic complexes. The decoherence can be induced by spin-flip and this review illustrates how to calculate and interpret such phenomena. It seems promising that the SOC-induced spin effects connected with dioxygen activation in bio-systems could be useful in other areas of life science.

## Conclusions

---

In this review we consider spin effects in a number of biochemical processes with special attention to O<sub>2</sub> activation by heme, oxidases, and cytochromes. The universal role of the spin-orbit coupling (SOC) effect in such activations is stressed. Oxidation of organic materials by dioxygen, to give CO<sub>2</sub> and water, is very favorable (exothermic); fortunately, the unfavorable kinetics preclude this spontaneous combustion of living matter into “a puff of smoke” (Sheldon 1993). The reason for the sluggish O<sub>2</sub> reactivity is a spin barrier: the direct reaction of triplet dioxygen with singlet organic molecules to give stable diamagnetic products is a spin-forbidden process with a very low rate. The common way of circumventing this kinetic barrier via a free radical pathway (combustion) is impossible for living cells. The reaction of singlet (diamagnetic) molecules with <sup>3</sup>O<sub>2</sub> forming two radicals is a spin-allowed process. Usually it is highly endothermic; Sheldon provides as an example of such a reaction observed at moderate temperature the activation of <sup>3</sup>O<sub>2</sub> by flavin-dependent oxygenases (Sheldon 1993). He argues that it is possible only for very reactive substrates (flavins) that form resonance-stabilized free radicals, e.g., reduced flavins, like FADH<sup>+</sup>, and HO<sub>2</sub> as a counterpart. We have stressed that, even in this case, the complete oxidation in the enzyme (e.g., glucose oxidase) is spin-forbidden if the HO<sub>2</sub> radical

is not the final product that leaves the active center of enzyme and goes into the bulk of the cell, but still participates in further oxidative transformations (Minaev 2002). We have shown that flavin-dependent oxygenases provide a very efficient way to overcome the spin-prohibition by spin-orbit coupling perturbation at the stage of electron transfer (Eq. 29.4).

A second way to overcome the obstacle of spin conservation is for  $^3\text{O}_2$  to combine with a paramagnetic transition metal ion (Burnold and Solomon 1999; Metz and Solomon 2001; Prabhakar et al. 2003, 2004). Such reactions are spin-allowed and governed by exchange interactions (exchange-induced spin-catalysis) (Minaev 2007; Prabhakar et al. 2004). Peroxo-, dioxo-, and superoxo-complexes with metals in different oxidation degree are considered during the search of “dream reactions” for selective industrial catalysts (Sheldon 1993). The expectation that the resulting metal-dioxygen complexes may react selectively with organic substrates at moderate temperature forms a background for the extensive studies of metal-catalyzed oxidation during the last four decades (Prabhakar et al. 2002, 2004). In this respect the reactions of  $^3\text{O}_2$  with hemoglobin and myoglobin at moderate temperature are very peculiar, since they are still spin-forbidden and quite efficient (Franzen 2002; Jensen and Ryde 2004; Sigfridsson and Ryde 2002).

We have recalculated some potential energy surface cross-sections for different multiplets along the heme- $\text{O}_2$  binding reaction coordinate and obtained results in agreement with Refs. Sigfridsson and Ryde (2002), Franzen (2002), and Jensen and Ryde (2004). The Fe(II)porphine molecule coordinated with ammonia molecules (Fig. 29-3,  $\text{NH}_3$  as a model of the proximal histidine) are used as in other similar studies (Blomberg et al. 2005; Franzen 2002; Jensen et al. 2005; Sigfridsson and Ryde 2002; Strickland and Harwey 2007). The more realistic protoporphyrin IX model provides similar result for the ground state of the heme active site. Results of previous works (Blomberg et al. 2005; Franzen 2002; Jensen and Ryde 2004; Minaev 2007; Minaev et al. 2007; Sigfridsson and Ryde 2002; Strickland and Harwey 2007) indicate that the main reason for the facilitated binding of  $\text{O}_2$  to heme is a broad crossing region of the relevant spin states, which provides significant spin transition probabilities. They have shown that porphyrin is an ideal Fe(II) ligand for the spin-flip problem, because it tunes the spin states to be close in energy, giving parallel binding potential energy surfaces, small activation energies and large transition probabilities in terms of the Landau-Zener approach (Prabhakar et al. 2003). But none of these studies (Blomberg et al. 2005; Franzen 2002; Jensen and Ryde 2004; Jensen et al. 2005; Sigfridsson and Ryde 2002; Strickland and Harwey 2007) have considered the reason for relatively large spin-orbit coupling, which induces the necessary spin flip in the heme- $\text{O}_2$  binding reaction; a general assumption that the SOC integral at Fe(II) ion of about  $80\text{ cm}^{-1}$ , postulated in Ref. Petrich et al. (1988), has been put forward instead. We have shown that such SOC integral (Eq. 29.9) is determined entirely by SOC in the oxygen moiety and is connected with the two  $\pi_{g,x}$ - and  $\pi_{g,y}$ -orbitals in the open-shell of dioxygen. This is also connected with charge transfer (CT) and with the  $\text{Fe}^{3+}\text{-O}_2^-$  radical-pair structure of the ground state  $^1A'(1)$  and the close-lying  $^3A''(2)$  state near the crossing of the potential energy surfaces, see scheme (Eq. 29.8). This scheme indicates that the triplet and singlet states,  $^3A''(2)$  and  $^1A'(1)$ , differ by a single electron jump inside  $\text{O}_2$  from the  $\pi_{g,x}$  MO to the  $\pi_{g,y}$  orbital. Such transformation is equivalent to the electronic orbital rotation, i.e., a torque, which creates transient magnetic field during the T-S transition and this magnetic field is responsible for the spin flip. In this model the magnetic perturbation occurs entirely in the oxygen moiety and the iron ion is silent. Account of SOC in the third-shell of the metal has to increase the total SOC integral.

From a broader perspective, the non-zero electron spin and the concepts of quantum mechanics play a fundamental role in our understanding of the mystery of life. Spin of dioxygen

is a property of the ground state of the molecule and protects O<sub>2</sub> from its involvement in the realm of ordinary chemistry, where the brute force of activation energy just governs all spin-allowed biochemical transformations of diamagnetic species. Dioxygen is protected from brute force via the  $X^3\Sigma_g - a^1\Delta_g$  energy gap (22 kcal/mol) (Hagan et al. 2002) and via spin-prohibition; at the same time O<sub>2</sub> is extremely fragile and easily activated by the presence of small amount of radicals or by magnetic perturbations (Minaev 2007). Such quantum spin protection is very important for biological systems, which operate at room temperature and are extraordinary complex, diverse, noisy, and “wet.” The quantum spin protection of dioxygen reactivity and its dependence on weak internal and external magnetic perturbations is important in connection with a fundamental fact, namely that biological systems are open driven systems. Self-organization in such biosystems should involve additional and very common mechanisms of self control, like S-T transitions in the O<sub>2</sub> activating enzymes, cytochromes, heme, photosynthetic centers, and probably in neural networks.

A fundamental conclusion of this review is an assertion of the fact that the functioning of various enzymes is controlled by spin conversion determined by internal and external magnetic forces. The most important magnetic interaction is spin-orbit coupling and we indicate a simple physical origin of this perturbation as responsible for the functionality of enzymes like glucose oxidase, coproporphyrinogen oxidase, luciferase, and myoglobin, hemoglobin, and other hemoproteins.

## Acknowledgment

---

This work is supported by the State Foundation of Fundamental Investigations (DFFD) of Ukraine, the project F25.5/008, and by Visby project No = 01403/2007.

## References

---

- Afanasyeva, M. A., Taraban, M. B., Purtov, P. A., Leshina, T. V., & Grissom, C. B. (2006). Magnetic field effects in enzymatic reactions: Radical oxidation of NADH by horseradish peroxidase. *Journal of the American Chemical Society*, 128, 8651.
- Blomberg, M. R. A., Siegbahn, P. E. M., Babcock, G. T., & Wikstrom, M. (2000a). Modeling cytochrome oxidase: A quantum chemical study of the O–O bond cleavage mechanism. *Journal of the American Chemical Society*, 122, 12848.
- Blomberg, M. R. A., Siegbahn, P. E. M., Babcock, G. T., & Wikstrom, M. (2000b). O–O bond splitting mechanism in cytochrome oxidase. *Journal of Inorganic Biochemistry*, 80, 261.
- Blomberg, L. M., Blomberg, M. R. A., & Siegbahn, P. E. M. (2005). A theoretical study of the binding of O<sub>2</sub>, NO and CO to heme proteins. *Journal of Inorganic Biochemistry*, 99, 949.
- Buchachenko, A. L. (1977). Enrichment of magnetic isotopes—new method of investigation of chemical reaction mechanisms. *Russian Journal of Physical Chemistry*, 51, 2461.
- Buchachenko, A. L., & Kouznetsov, D. A. (2008). Magnetic field affects enzymatic ATP synthesis. *Journal of the American Chemical Society*, 130, 12868.
- Buchachenko, A. L., Kouznetsov, D. A., Orlova, M. A., & Markarian A. A. (2005). Spin biochemistry: Intramitochondrial nucleotide phosphorylation is a magnesium nuclear spin controlled process. *Mitochondrion*, 5, 67.
- Burnold, T. C., & Solomon, E. I. (1999). Reversible dioxygen binding to hemerythrin. *Journal of the American Chemical Society*, 121, 8288.
- Chalkias, N. G., Kahawong, P., & Giannelis E. P. (2008). Activity increase of horseradish peroxidase in the presence of magnetic particles. *Journal of the American Chemical Society*, 130, 2910.
- Davydov, R., Osborne, R. L., Kim, S. H., Dawson, J. H., & Hoffman, B. M. (2008). EPR

- and ENDOR studies of cryoreduced compound I. *Biochemistry*, 47, 5147.
- de Winter, A., & Boxer, S. G. (2003). Energetics of primary charge separation in bacterial photosynthetic reaction center mutants: Triplet decay in large magnetic field. *Journal of Physical Chemistry A*, 107, 3341.
- Engstrom, M., Minaev, B. F., Vahtras, O., & Agren, H. (1998). MCSCF linear response calculations of electronic g-factor and spin-rotational coupling constants for diatomics. *Chemical Physics Letters*, 237, 149.
- Engstrom, M., Himo, F., Graslund, A., Minaev, B. F., Vahtras, O., & Agren, H. (2000). H-bonding to the tyrosyl radical analyzed by ab initio g-tensor calculations. *Journal of Physical Chemistry A*, 104, 5149.
- Esposito, S. (1999). On the role of spin in quantum mechanics, *Foundations of Physics Letters*, 12, 165.
- Franzen, S. (2002). Spin-dependent mechanism for diatomic ligand binding to heme. *Proceedings of the National Academy of Sciences of the United States of America*, 99, 16754.
- Friedman, J., & Campbell, B. (1987). *Structural dynamics and reactivity in hemoglobin*. New York: Springer.
- Frisch, M. J., Trucks, G. W., Schlegel, H. B., et al. (2003). *Gaussian 03, Revision B. 03*. Pittsburg: Gaussian Inc.
- Gegear, R. J., Conelman, A., & Waddell, S. (2008). Cryptochrome mediates light-dependent magnetosensitivity in *Drosophila*. *Nature*, 454, 1014.
- Grissom, C. B. (1995). Magnetic field effects in biology: A survey of possible mechanisms with emphasis on radical-pair recombination. *Chemical Reviews*, 95, 3.
- Hagan, S., Hameroff, S. R., & Tuszyński, J. A. (2002). Quantum computation in brain microtubules. *Physical Review E*, 65, 061901.
- Hameroff, S., & Penrose, R. (1996). Conscious events as orchestrated space-time selections. *Journal of Consciousness Studies*, 3, 36.
- Harvey, J. N. (2004). Spin-forbidden CO ligand recombination in myoglobin. *Faraday Discussions*, 127, 165.
- Hoff, A. J. (1986). Magnetic interactions between photosynthetic reactants. *Photochemistry and Photobiology*, 43, 727.
- Hu, H. P., & Wu, M. X. (2004). Spin-mediated consciousness theory. *Medical Hypotheses*, 63, 633.
- Jensen, K. J., & Ryde, U. (2004). How O<sub>2</sub> binds to heme. *Journal of Biological Chemistry*, 279, 14561.
- Jensen, K. J., Ross, B. O., & Ryde, U. (2005). The CAS PT2 study of oxymyoglobin model. *Journal of Inorganic Biochemistry*, 99, 45.
- Johnsen S., & Lohmann, K. J. (2005). The physics and neurobiology of magnetoreception. *Nature Reviews Neuroscience*, 6, 703.
- Klinman, J. P. (2001). Life as aerobes: Are there simple rules for activation of dioxygen by enzymes? *Journal of Biological Inorganic Chemistry*, 6, 1.
- Kondo, M., & Yoshizawa, K. (2003). A theoretical study of spin-orbit coupling in an Fe(II) spin-crossover complex. Mechanism of the LIESST effect. *Chemical Physics Letters*, 372, 519.
- Kumar, D., de Viser, S. P., Sherma, P. K., Hirao, H., & Shaik, S. (2005). Sulfoxidation mechanisms catalyzed by cytochrome P450 and HRP models: Spin selection induced by the ligand. *Biochemistry*, 44, 8148.
- Lane, N. (2002). *Oxygen: The molecule that made the world*. Oxford: Oxford University Press.
- Maeda, K., Henbest, K. B., Cintolesi, F., Kuprov, I., Rodgers, C. T., Liddell, P. A., Gust, D., Timmel, C. R., & Hore, P. J. (2008). Chemical compass model of avian magnetoreception. *Nature*, 453, 387.
- Metz, M., & Solomon, E. I. (2001). Dioxygen binding to deoxyhemocyanin. *Journal of the American Chemical Society*, 123, 4938.
- Minaev, B. F. (1980). Intensities of spin-forbidden transitions in molecular oxygen. *International Journal of Quantum Chemistry*, 89, 367.
- Minaev, B. F. (1983). *Theoretical analysis and prognostication of spin-orbit coupling effects in molecular spectroscopy and chemical kinetics*. DrSc Dissertation, Institute of Chemical Physics, Moscow.
- Minaev, B. F. (1989). Solvent-induced emission of molecular a<sup>1</sup>Δ<sub>g</sub> oxygen. *Journal of Molecular Structure (Theochem)*, 183, 207.
- Minaev, B. F. (2002). Spin effects in reductive activation of O<sub>2</sub> by oxidase enzymes. *RIKEN Review*, 44, 147.
- Minaev, B. F. (2004). Ab initio study of the ground state properties of molecular oxygen. *Spectrochimica Acta Part A-Molecular and Biomolecular Spectroscopy*, 60, 1027.
- Minaev, B. F. (2007). Electronic mechanisms of molecular oxygen activation. *Russian Chemical Review*, 76, 1039.
- Minaev, B. F. (2010). Environment friendly spin-catalysis for dioxygen activation. *Chemistry & Chemical Technology*, 4, 1–16.
- Minaev, B. F., & Agren, H. (1995). Spin-orbit coupling induced chemical reactivity and spin-catalysis phenomena. *Collection of Czechoslovak Chemical Communications*, 60, 339.
- Minaev, B. F., & Agren, H. (1996). Spin-catalysis phenomena. *International Journal of Quantum Chemistry*, 57, 510.



- Minaev, B. F., & Ågren, H. (1997). Collision-induced  $b^1\Sigma_g-a^1\Delta_g$ ,  $X^3\Sigma_g-b^1\Sigma_g$ , and  $X^3\Sigma_g-a^1\Delta_g$  transition probabilities in molecular oxygen. *Journal of the Chemical Society-Faraday Transactions*, 93, 2231.
- Minaev, B. F., & Lunell, S. (1993). Classification of spin-orbit coupling effects in organic chemical reactions. *Zeitschrift Fur Physikalische Chemie-International Journal of Research in Physical Chemistry & Chemical Physics*, 182, 263.
- Minaev, B. F., & Minaeva, A. B. (2005). Calculation of the phosphorescence of porphyrins by the density functional method. *Optics and Spectroscopy*, 98, 214.
- Minaev, B. F., & Minaeva, V. A. (2001). MCSCF response calculations of the excited states properties of the O<sub>2</sub> molecule and a part of its spectrum. *Physical Chemistry Chemical Physics*, 3, 720.
- Minaev, B. F., Lunell, S., & Kobzev, G. I. (1993). The influence of intermolecular interaction on the forbidden near-IR transitions in molecular oxygen. *Journal of Molecular Structure (Theochem)*, 284, 1.
- Minaev, B. F., Mikkelsen, K. V., & Ågren, H. (1997). Collision-induced electronic transitions in complexes between benzene and molecular oxygen. *Chemical Physics*, 220, 79.
- Minaev, B. F., Vahtras, O., & Ågren, H. (1996). Magnetic phosphorescence of molecular oxygen. *Chemical Physics*, 208, 299.
- Minaev, B. F., Lyzhenkova, I. I., Minaeva, V. A., & Boiko, V. I. (1999). A quantum chemical approach to the mechanism of biochemical action of nicotinamide. *Theoretical and Experimental Chemistry*, 35, 258.
- Minaev, B. F., Minaeva, V. A., & Vasenko, O. M. (2007). Spin states of the Fe(II)-pporphin molecule: Quantum-chemical study by DFT method. *Ukrainica Bioorganica Acta*, 1, 24.
- Minaev, B. F., Minaeva, V. A., & Evtuhov, Y. V. (2008). Quantum-chemical study of the singlet oxygen emission. *International Journal of Quantum Chemistry*, 108, 500.
- Ogilby, P. R. (1999). Singlet oxygen. *Accounts of Chemical Research*, 32, 512.
- Orlova, G., Goddard, J. D., & Brovko, L. Y. (2003). Theoretical study of the amazing firefly bioluminescence. *Journal of the American Chemical Society*, 125, 6962.
- Paterson, M. J., Christiansen, O., Jensen, F., & Ogilby, P. R. (2006). Singlet oxygen. *Photochemistry and Photobiology*, 82, 1136.
- Penrose, R. (1960). A spinor approach to general relativity. *Annals of Physics*, 10, 171.
- Penrose, R. (1994). *Shadows of the mind*. Oxford: Oxford University Press.
- Petrich, J. W., Poyart, C., & Martin, J. L. (1988). Spin-forbidden binding of O<sub>2</sub> to hemoglobin. *Biochemistry*, 27, 4049.
- Poli, R., & Harvey, J. N. (2003). Spin-forbidden chemical reactions. *Chemical Society Reviews*, 32, 1.
- Potter, W. T., Ticker, M. P., & Caughey, W. S. (1987). Resonance Raman spectra of myoglobin. *Biochemistry*, 26, 4699.
- Prabhakar, R., Siegbahn, P. E. M., Minaev, B. F., & Ågren, H. (2002). Activation of triplet dioxygen by glucose oxidase: Spin-orbit coupling in the superoxide ion. *Journal of Physical Chemistry B*, 106, 3742.
- Prabhakar, R., Siegbahn, P. E. M., & Minaev, B. F. (2003). A theoretical study of the dioxygen activation by glucose oxidase and by copper amine oxidase. *Biochimica et Biophysica Acta*, 1647, 173.
- Prabhakar, R., Siegbahn, P. E. M., Minaev, B. F., & Ågren, H. (2004). Spin transition during H<sub>2</sub>O<sub>2</sub> formation in the oxidative half-reaction of copper amine oxidase. *Journal of Physical Chemistry B*, 108, 13882.
- Sawyer, D. T. (1991). *Oxygen chemistry*. New York: Oxford University.
- Schweitzer, C., & Schmidt, R. (2003). Physical mechanisms of generation and deactivation of singlet oxygen. *Chemical Reviews*, 103, 1685.
- Serebrennikov, Y. A., & Minaev, B. F. (1987). Magnetic field effects due to spin-orbit coupling in transient intermediates. *Chemical Physics*, 114, 359.
- Shaik, S., Filatov, M., Schroder, D., & Schwarz, H. (1998). Electronic structure makes a difference: Cytochrome P-450 mediated hydroxylation of hydrocarbons as a two-state reactivity paradigm. *Chemistry-A European Journal*, 4, 193.
- Shaik, S., Ogliaro, F., de Visser, S. P., Schwarz, H., & Schroeder, D. (2002). Two state reactivity mechanism of hydroxylation and epoxidation by cytochrome P450 revealed by theory. *Current Opinion in Chemical Biology*, 6, 556.
- Shaik, S., Kumar, D., de Visser, S. P., Altun, A., & Tiel, W. (2005). Theoretical perspective on the structure of cytochrome P450 enzymes. *Chemical Reviews*, 105, 2279.
- Sheldon, R. A. (1993). A history of oxygen activation. In D. Barton et al. (Eds.), *The Activation of dioxygen and homogeneous catalytic oxidation*. New York: Plenum.
- Shikama, K. (2006). Nature of the FeO<sub>2</sub> bonding in myoglobin and hemoglobin. A new molecular paradigm. *Progress in Biophysics and Molecular Biology*, 91, 83.

- Sigfridsson, E., & Ryde, U. (2002). Theoretical study of discrimination between O<sub>2</sub> and CO by myoglobin. *Journal of Inorganic Chemistry*, 91, 101.
- Silva, P. J., & Ramos, M. J. (2008). A comparative DFT study of the reaction mechanism of the O<sub>2</sub>-dependent coproporphyrinogen III oxidase. *Bioorganic Medical Chemistry*, 16, 2726.
- Strickland, N., & Harvey, J. N. (2007). Spin-forbidden ligand binding to the ferrous-heme group. *Journal of Physical Chemistry B*, 111, 841.
- Stryer, L. (1995). *Biochemistry* (4th ed., p. 152). New York: Freeman.





# 30 Protein Modeling

G. Náray-Szabó · A. Perczel · A. Láng

Laboratory of Structural Chemistry and Biology and Protein Modelling  
Group HAS-ELTE, Institute of Chemistry, Eötvös Loránd University,  
Budapest, Hungary

<b>Introduction</b> .....	<b>1096</b>
<b>Structure Determination</b> .....	<b>1096</b>
Experiment .....	1096
Protein Crystallography .....	1097
Nuclear Magnetic Resonance Spectroscopy .....	1099
Computer Modeling .....	1101
Molecular Mechanics .....	1102
Structure Prediction and Homology Modeling .....	1104
<b>Structure Representation</b> .....	<b>1105</b>
Molecular Graphics .....	1105
Electrostatics .....	1107
Solvent-Accessible Surface .....	1109
<b>Dynamics</b> .....	<b>1110</b>
Time Scales .....	1110
Dynamical Structures .....	1112
Dynamics of Interactions .....	1113
<b>Interactions</b> .....	<b>1113</b>
Protein Hydration .....	1114
Ligand Binding .....	1114
Protein–Protein Interactions .....	1116
<b>Enzyme Mechanisms</b> .....	<b>1119</b>
<b>Conclusion and Outlook</b> .....	<b>1121</b>
<b>Acknowledgments</b> .....	<b>1122</b>
<b>References</b> .....	<b>1122</b>

**Abstract:** Proteins play a crucial role in biological processes, therefore, understanding their structure and function is very important. In this chapter we give an overview on computer models of proteins. First we treat both major experimental structure determination methods, X-ray diffraction and NMR spectroscopy. In subsequent sections computer modeling techniques as well as their application to the construction of explicit models are discussed. An overview on molecular mechanics and structure prediction is followed by an overview of molecular graphics methods of structure representation. Protein electrostatics and the concept of the solvent-accessible surface are treated in detail. We devote a special section to dynamics, where time scales, structures, and interactions are discussed. Protein interactions are especially important, so protein hydration, ligand binding, and protein-protein interactions receive special attention. Finally, computer modeling of enzyme mechanisms is discussed. We try to demonstrate that protein representation by computers arrived to a very high degree of sophistication and reliability; therefore, even lots of experimental studies make use of such models. A list with 80 up-to-date bibliographic references helps the reader to get informed on further details.

## Introduction

---

In order to obtain versatile models we attribute a definite spatial structure and shape to molecules, which may, however, change in time. In the case of proteins the structure is too complicated and complex; thus the use of computer graphics is unavoidable. In this chapter we give an overview on the experimental and computational methods that provide information on protein structure and allow deriving its relation to function. Neither of the techniques currently available is able to yield full information. X-ray diffraction works only for crystalline samples; NMR techniques refer to restraints, which determine a manifold of related, but not identical structures, while modeling still lacks full reliability. Accordingly, in order to obtain thorough information on protein structure, various techniques should be combined, though in several cases even a single technique provides a model, which is adequate for some considerations. The present chapter should help in obtaining an overview on up-to-date techniques with reference to more detailed reviews on specific subjects.

## Structure Determination

---

Both experimental and modeling techniques are available for the determination of the three-dimensional structure of proteins. They vary in performance and neither of them offers a unique tool to be applied for any type of proteins and their complexes. In most cases publications refer to a single method only, structures are determined either by X-ray diffraction, nuclear magnetic resonance (NMR) spectroscopy, or, eventually, by computer modeling. In order to get a true, broad, and rather complete information on structural and dynamic properties of proteins, we need to compare data obtained by a variety of methods.

## Experiment

---

The first protein structures were determined by X-ray diffraction techniques; to date more than 60,000 structures are available in the Protein Data Bank (2011). Structure determination by

NMR spectroscopy is also rapidly growing; the number of deposited structures is more than 7,800 (Protein Data Bank 2011).

## Protein Crystallography

Protein structures can be visualized at the atomic level by working with X-rays. An appropriate crystal has to be irradiated, the obtained diffraction pattern recorded and analyzed by mathematical tools. The result is an electron density map with relative maxima at the position of atomic nuclei. Using classical chemical information the density map can be evaluated and the three-dimensional molecular model of the protein can be constructed. In order to determine the structure of a protein the following steps have to be performed (Brandén and Tooze 1999).

### Sample Preparation and Crystallization

Its goal is to produce a well-ordered crystal that is large enough to provide an appropriate diffraction pattern when irradiated with X-rays. It is inherently difficult because of the fragile nature of protein crystals. Proteins have irregularly shaped surfaces, which form large channels within the crystal. The non-covalent bonds that hold together the lattice must often be formed by flexible amino-acid residues of the protein surface. The success of crystallization of a protein depends on several factors, like purity, pH, concentration, temperature, and precipitants. In order to ensure sufficient homogeneity, the protein should be pure to at least 97%. It is necessary to screen a reasonable number of conditions; for that we need at least 200  $\mu\text{L}$  of material in a concentration of about 10 mg/mL. The most commonly used techniques for crystallization are the hanging and sitting drop methods (Horsefield and Neutze 2006) although alternative approaches have emerged, e.g., the micro-batch method (Luft et al. 2003). Recently, efficient high-throughput methods have been developed to speed up the process and to determine optimal crystallization conditions (Chayen 2007).

### Data Collection

Once we have an appropriate crystal, its symmetry, the unit cell parameters, and the resolution limit have to be determined. Then, it will be irradiated by an X-ray beam and continuously rotated by a small angle. Thus we can record the X-ray diffraction pattern containing relevant information on the position of scattering centers. For crystals of lower quality we may apply synchrotron radiation, where the beam intensity is greater, therefore data collection times are shorter, sometimes not more than 10 min. Synchrotron radiation is also the basis of time-resolved crystallography (Bourgeois and Royant 2005). The relatively slow reaction rates allow following changes in atomic positions during the enzymatic process.

### Structure Solution

The relationship between the scattering angle and the distance between planes passing through the atoms in the crystal is given by the Bragg's law. The electron density is related to the diffraction pattern by a mathematical function, the inverse Fourier transform. To compute this we need to know both the amplitude and the phase of the diffracted waves. Since we cannot measure the relative phase angles experimentally, we face the so-called phase-problem, often the most serious bottleneck in determining a new structure. A possible technique to solve this is the isomorphous replacement, i.e., to provide a crystal that is nearly identical to the one studied, except that a few atoms have been replaced or added. If these atoms have a large atomic number, they will strongly perturb the diffraction pattern and allow deducing possible values for the

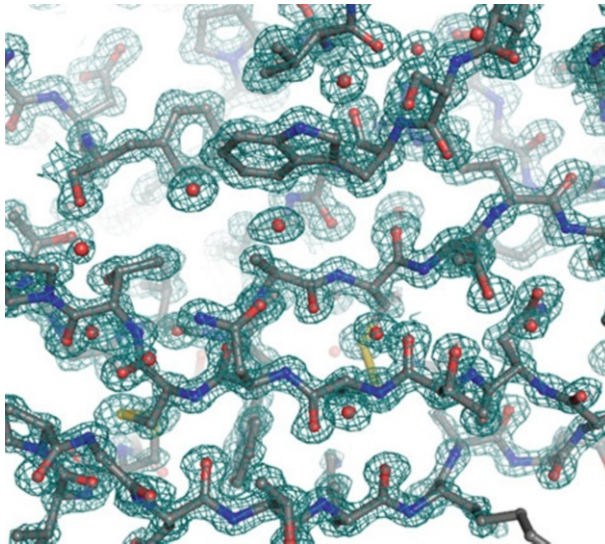
phase angles. A similar technique makes use of the multiple-wavelength anomalous dispersion (MAD). By changing the wavelength of the X-rays, the degree to which the anomalously scattering atoms perturb the diffraction pattern also changes. This gives the same kind of information as isomorphous replacement.

### Model Building

If the studied crystals were perfectly ordered, then all the atoms would scatter in phase and the electron density map would have peaks at each of the atomic positions. However, in electron density maps of most protein atoms are not resolved from each another; we need a model to be fitted to the electron density. Fitting models to density requires the use of computer graphics programs such as COOT (Emsley and Cowtan 2004) and as a result the electron density map is interpreted in terms of a set of atoms. In most cases the protein backbone is fitted first; then, if the resolution permits, the side-chain atoms are positioned. The result is dependent on the resolution and the quality of the phases (► Fig. 30-1). Often regions of high flexibility (e.g., surface lysine side chains) are not visible since the corresponding electron density is smeared.

### Refinement and Validation

An atomic model can be improved by refinement, in which it is adjusted to the measured diffraction data. Refinement improves the phases leading to clearer maps and better models. The quality of an atomic model can be judged by the so-called *R*-factor, which is the average fractional error in the calculated amplitude compared to the observed one. Since, in general, there are not enough diffraction data, these may be completed by restraints on geometry, which keep the bond lengths, angles, and close contacts within a reasonable range. Main-chain torsion



■ Fig. 30-1

Atomic (1.2 Å) resolution electron density map of a section of the complex between crayfish trypsin and an inhibitor from the desert locust *Schistocerca gregaria* (SGTI) (V. Harmat unpublished)

angles are difficult to restrain, but the distribution of these angles is strongly restricted, as shown by the Ramachandran plot (Hovmöller et al. 2002), which is thus an additional indicator of the quality of a structure. Neutron diffraction, a special method requiring high thermal-neutron fluxes, which can be obtained only from nuclear reactors, provides special information on proteins (Fitter et al. 2006). Hydrogen atoms can be precisely located, which is almost impossible by X-ray diffraction. A diffraction experiment can be performed on a crystal; the results can be evaluated similarly, as done for the X-ray technique.

## Nuclear Magnetic Resonance Spectroscopy

Nuclear magnetic resonance (NMR) spectroscopy is a versatile tool of modern structural biology, which allows determining protein structures, even in some cases where X-ray diffraction fails. It has become an independent method of routine structure determination for proteins with up to about 300 residues. Structure determination by NMR consists of multiple consecutive steps.

### Sample Preparation and Stability Testing

For successful NMR experiments a protein solution of high purity (>95%), stability (over a week), and appropriate concentration (0.1–1 mM) is needed; the total sample volume and mass should be 350–550  $\mu\text{L}$  and 3–30 mg, respectively. 2,2-Dimethyl-2-silapentane-5-sulfonic acid (DSS) rather than tetramethylsilane (TMS) is used as a reference compound. Although both natural and synthetic polypeptides and proteins can be used, most samples are expressed *via* a suitable prokaryotic or eukaryotic cellular or cell-free recombinant technique. The latter method eliminates most toxic effects attributed to the overproduction of recombinant proteins. Biotechnological approaches have the common advantage of large-scale protein production, specific or non-specific stable isotope labeling, and easy sequence variation.

### Data Acquisition

When placed in a magnetic field (10–20 T), magnetically active nuclei (e.g.,  $^1\text{H}$ ,  $^{13}\text{C}$ , or  $^{15}\text{N}$ ) absorb energy at a characteristic resonance frequency, which is detected in the form of a signal in the NMR spectrum (Schorn and Taylor 2004). The resonance frequencies, mostly between 500 and 950 MHz for  $^1\text{H}$  nuclei, referring to the energy of the absorption are proportional to the strength of the static magnetic field. Depending on the local chemical environment, nuclei of the same type in the same molecule resonate at slightly different frequencies. The relative shift from a reference (DSS for proteins in aqueous solution) resonance frequency is called the chemical shift. Peptides and proteins from natural sources are typically restricted to utilizing resonances based solely on protons, however, to get more information, further NMR active nuclei (mostly  $^{13}\text{C}$  and  $^{15}\text{N}$ ) have to be introduced or enriched in the molecule.

In ideal signal dispersion each magnetically active atom has its unique chemical shift by which it can be recognized and assigned. Assignment of each measured chemical shift to a single atom (or a group of atoms, e.g., a methyl group) is a mandatory step toward structure determination. Resonance frequency assignment is a very complicated and laborious procedure and often needs to introduce further “dimensions” into measurements, but provides useful information on protein structure, dynamics, interaction, and ligand binding. Beside the most common direct dimension, typically associated with  $^1\text{H}$ , experiments are run to generate additional dimensions to minimize spectral overlap. For structure determination, two

major types of NMR experiments are in everyday use: (1) the one based on coherence transfer between chemically connected atoms *via* indirect (through bond) coupling (e.g., COSY, TOCSY, HSQC, HNC0, HNCA, etc.) and (2) those relying on magnetization transfer between spatially close atoms (through space coupling; see below). The first set is for the identification of connected chemical shifts, while the second one is to localize related chemical shifts.

### Resonance Frequency Assignment

First, real and artificial (background) signals have to be distinguished; this provides the basis of the analysis of NMR-spectra. Then, one has to find out which chemical shift corresponds to which nuclei within the macromolecule. Several different protocols were invented to achieve this tedious goal, primarily depending on the type of isotope labeling introduced for proteins. Homonuclear techniques are used for unlabeled molecules by taking advantage of a series of specific experiments. Resonance assignment for proteins of medium size ( $5 < MW < 15$  kDa) relies on  $^{15}\text{N}$ -labeled samples by using suitable parameterized methods. Larger proteins require double ( $^{15}\text{N}$ -,  $^{13}\text{C}$ ) or triple ( $^2\text{H}$ -,  $^{15}\text{N}$ -,  $^{13}\text{C}$ ) labeling, enabling resonance assignment for both backbone and side-chain atoms. In principle, by filtering peaks, grouping of resonances, identifying spin-systems, and by grouping stretches of sequences into segments the full assignment procedure can be automated. Sophisticated software, like DYNASSIGN (Schmucki et al. 2009), ensures high completeness of the assignment procedure.

### Restraint Collection

Structure determination by NMR-spectroscopy depends on various structural restraints. Distance restraints are typically obtained from NOESY experiments, where cross peaks appear due to successful magnetization transfer events between spatially close nuclei. Once assigned, each of the cross peaks can be converted into the approximate internuclear distance. The success of a structure determination depends on several factors, such as the total number of Nuclear Overhauser Effect (NOE) defined hydrogen–hydrogen distance restraints, on their distribution within the molecule, accurate assignment, and on their proper calibration. Because of various limitations these distances cannot be determined precisely; rather they are sorted as short (1.8–2.7 Å), medium (1.8–3.5 Å), or large (1.8–6.0 Å) ones. Restraints on the backbone ( $\phi$  and  $\psi$ ) and side-chain ( $\chi_1$ ,  $\chi_2$  etc.) dihedral torsion angles can be obtained by measuring conformation sensitive indirect coupling constants. Various 2D- and 3D-methods have been developed for the accurate measurement of coupling constants by NMR both in solution and in solid state. By suitable measurements followed by careful calibrations these data can be converted into dihedral angle restraints. Orientation NMR restraints are commonly obtained for macromolecules. Dipolar couplings are averaged in solution because of fast molecular tumbling. However, due to slight overpopulation of one state, residual dipolar coupling (RDC) can be measured even in solution, if molecular tumbling is restricted by using suitable oriented media. Dipolar coupling is routinely used in solid state NMR and provides useful information about the relative orientation of bond vectors. Hydrogen bonds as structural restraints are typically determined by some sort of hydrogen/deuterium exchange experiment. H/D exchange can be quantitatively monitored by the isotope effect of deuterium on the chemical bond strength. The slower the NH exchanges to ND, the more the amide group is buried within the protein. For peptides and shorter proteins, the temperature dependence of NH chemical shifts can also be detected and used to estimate the involvement of the NH bond in an intramolecular H-bond. Various paramagnetic restraints can also be used for solution structure determination. Finally, order

parameters introduced as restraints reflect an advanced view on dynamic-structure of proteins. Raw data required typically involve Longitudinal  $R_1$  and transversal  $R_2$  relaxation rate constants,  $^{15}\text{N}$ - $\{^1\text{H}\}$ -NOE to determine order parameters beside the overall- and local-correlation times and chemical exchange rates. Recently, chemical shifts have been used to obtain preliminary models of protein structures (Cavalli et al. 2007).

### Structure Calculation and Refinement

Experimentally determined structural restraints are used as input for these structure elucidations. Computer programs, like XPLOR (Schwieters et al. 2006) combine as many restraints as possible in conjunction with general properties of proteins. These approaches convert the different structural restraints into target functions with general protein properties describing energy terms, all to be minimized at once. A bundle of structures will be obtained reflecting a selected molecular fold. Structure determination by NMR is yet a time consuming iterative process requiring well-trained and devoted specialists. The most time-consuming processes are the chemical shift and the NOE assignments. Automating and black-boxing the assignment to increase the throughput and to eliminate subjective decisions during structure elucidation is an important goal, yet partially achieved. Efforts are made to fully automate resonance assignment in conjunction with structure calculations in an integrated manner (Volk et al. 2008).

### Structure Validation

Structure Validation is strongly recommended by using special software [e.g., CheckShift (Ginzinger et al. 2007)] to check both the quality of the NMR experimental data and structural information before publication. In general these programs provide a means of validating both the geometry and restraint violations of an NMR driven protein structure bundle. The output provides both statistical summaries and visualizations on restraint violations, agreement with already deposited model parameters, quality of geometrical properties, etc.

Although NMR is a versatile tool for protein structure determination, it may have severe limitations such as spectral crowdedness, too fast relaxation, poor automation, etc. Traditionally, NMR has been used for proteins of small or medium size. Drawbacks and technical problems originate from the limited spectral resolution and signal overlap. Introducing multidimensional NMR spectroscopy, in conjunction with the different isotope labeling schemes, as well as the increase of the applied static magnetic field helped a lot in enhancing the power of NMR spectroscopy. An additional limitation is connected to spin relaxation; coherence and magnetization vanish quickly for larger macromolecules. This means that there is less and less time to acquire NMR signals, causing signal-broadening and weakening. Two techniques have been introduced lately to overcome this problem, a chemical one by the introduction of sample deuteration and a spectroscopic one, namely the transverse relaxation optimized spectroscopy (TROSY). Today, these technical novelties allow determining even structures of larger water soluble and membrane proteins (Wüthrich 2002).

## Computer Modeling

---

Modern computer hardware and software technology allows modeling of proteins at the atomic level quite precisely. Several computer methods are available for experiment-based structure determination, interpretation of structure-function relationships, as well as construction of explicit models of proteins from atomic or molecular fragments.



## Molecular Mechanics

Since proteins are very large, containing several thousand atoms, quantum mechanical calculations are not tractable for doing calculations on the whole system. Instead, the much simpler molecular mechanics (MM) or force field methods are applied, where a molecular system is treated as an ensemble of atoms connected by strings (bonds). A price for simplicity is that electrons are not treated explicitly and correctly. Forces acting between atoms are described by simple mathematical expressions, adapted from classical physics. A certain force field is composed by interaction terms describing different types of strain present in a molecule. The total energy of the system is typically calculated as the sum of the following terms:

$$E_{MM} = V_{\text{stretch}} + V_{\text{bend}} + V_{\text{torsion}} + V_{\text{outofplane}} + V_{\text{nonbonded}} \quad (30.1)$$

where stretching, bending, torsion, out-of-plane bending, van der Waals, and electrostatic terms, respectively, are defined as follows:

$$V_{\text{stretch}} = \sum_{\text{bonds}} K_{\text{stretch}} (r_{ij} - r_{ij}^0)^2 \quad (30.2)$$

$$V_{\text{bend}} = \sum_{\text{angles}} K_{\text{bend}} (\theta_{ijk} - \theta_{ijk}^0)^2 \quad (30.3)$$

$$V_{\text{torsion}} = \sum_{\text{dihedrals}} K_{\text{torsion}} [1 + \cos(n\phi - \delta)] \quad (30.4)$$

$$V_{\text{outofplane}} = \sum_{\text{impropers}} K_{\text{outofplane}} \chi_{ijk;l}^2 \quad (30.5)$$

$$V_{\text{nonbonded}} = \sum_{\text{non-bondedpairs}} [A_{\text{nonbonded}} (C_{12} r_{ij}^{-12} - C_6 r_{ij}^{-6}) + q_i q_j / D r_{ij}] \quad (30.6)$$

where  $r_{ij}$ ,  $r_{ij}^0$ ,  $\theta_{ijk}$ , and  $\theta_{ijk}^0$  are the actual and equilibrium bond lengths (interatomic distances) and bond angles, respectively,  $\phi$  is the dihedral angle and  $\delta$  is its phase shift,  $\chi_{ijk;l}$  is the angle between the bond  $jl$  and the plane  $ijk$ , where  $j$  is the central atom.  $K_{\text{stretch}}$ ,  $K_{\text{bend}}$ ,  $K_{\text{torsion}}$ , and  $K_{\text{outofplane}}$  refer to respective force constants;  $n$  is the multiplicity of the torsional function.  $A_{\text{nonbonded}}$ ,  $C_6$ , and  $C_{12}$  are adjustable parameters.  $q_i$  is the net charge on atom  $i$ ,  $D$  is the dielectric parameter. For review and comparison of various force fields see (Hu and Jiang 2009; MacKerell 2004; Wang et al. 2001).

Van der Waals and electrostatic parameters in [Eq. 30.7](#) are usually not calculated for atoms that are relatively close (at a distance of one or two bonds). In order to reduce computational efforts (e.g., methyl) groups of atoms may be considered as a single interacting unit. Force constants and other parameters in the energy expression are fitted to experimental or calculated data. Different parameters are used, e.g., for  $sp^3$ -,  $sp^2$ -, and  $sp$ -type atoms and additional ones for atoms in carbonyl or peptide groups or in aromatic systems. Accordingly, the total number of adjustable parameters may be quite large. As the number of atom pairs in  $V_{\text{nonbonded}}$  increases quadratically; in order to reduce computation time most programs use a cut-off value, beyond which the interactions are set to zero over an additional short distance. It has to be noticed that a certain set of parameters works only for a given force field, and a single parameter has no meaning in itself, it cannot be transferred to another force field.

Basically two ways of parametrization can be followed. Class I force fields like AMBER (Case et al. 2005) or GROMOS (2011), work with a simpler energy expression and their parametrization is based on experimental data. They find a wide application to proteins, nucleic acids, and carbohydrates, as well as their complexes. Class II force fields, e.g., the Merck Molecular Force Field (Halgren 1996) include higher order and cross terms, too; they are calibrated to

quantum mechanically calculated energies and gradients. This increases their transferability and reliability.

Various free or commercially available protein modeling software packages make use of different force fields. AMBER (Case et al. 2005) is a package of molecular simulation programs including both source code and demos. GROMACS (Van Der Spoel et al. 2005) is a highly optimized and fast program that supports several force fields and has an open source code. INSIGHT II from ACCELRY'S (<http://accelrys.com/>), SYBYL from TRIPOS (<http://www.tripos.com/>), CHARMM (<http://www.charmm.org>), and SCHRODINGER (<http://www.schrodinger.com/>) are licensed packages with many components, including force fields and programs for energy calculations.

A basic limitation to classical force fields is that they are valid only near local minima of the potential energy surface (PES) of a molecular system. Thus, they cannot be applied to, e.g., enzyme reactions, which pass through other regions of the PES, where the electronic distribution is strongly perturbed. In order to overcome this limitation, quantum mechanics, and molecular mechanics may be combined by partitioning large covalent systems in a quantum region, which is embedded in a classical one. The total energy in this approach (hybrid quantum mechanical/molecular mechanical, QM/MM) method (Gao and Truhlar 2002; Hu and Yang 2008), is as follows:

$$E = E_{\text{QM}} + E_{\text{MM}} + E_{\text{QM/MM}} \quad (30.7)$$

where  $E_{\text{QM}}$ ,  $E_{\text{MM}}$ , and  $E_{\text{QM/MM}}$  refer to the energies of the quantum and classical regions and their interaction, respectively.  $E_{\text{QM}} = \langle \Psi | \mathbf{H}_{\text{QM}} | \Psi \rangle$  is the expectation value of the Hamiltonian for the atoms in the quantum region, which is composed of kinetic, electron–electron, and electron–nucleus interaction energy terms

$$\mathbf{H}_{\text{QM}} = \sum \Delta_i + \sum 1/r_{ij} + \sum Z_a/r_{ia} \quad (30.8)$$

Here, subscripts “ $i$ ,” “ $j$ ,” and “ $a$ ” refer to electrons and nuclei of the quantum region.  $E_{\text{MM}}$  is calculated for atoms of the classical region as in [Eq. 30.1](#); the third term in [Eq. 30.7](#) refers to the interaction between atoms of the quantum and the classical region, respectively.  $E_{\text{QM/MM}} = \langle \Psi | \mathbf{H}_{\text{QM/MM}} | \Psi \rangle$  with

$$\mathbf{H}_{\text{QM/MM}} = \sum q_M/r_{iM} + \sum [Z_a q_M/r_{aM} + A_{\text{nonbonded}} (C_{12} r_{aM}^{-12} - C_6 r_{aM}^{-6})] \quad (30.9)$$

where  $M$  denotes an atom in the classical region.


For most QM/MM studies on proteins definition of the quantum region (mostly the active site) needs cutting covalent bonds, which requires special care in treating the boundary. This is very important to avoid artifacts and to ensure a relatively smooth variation of the energy and its gradient when passing from the quantum to the classical region, prerequisite for a successful molecular dynamics calculation. Two main approaches are available for the appropriate treatment of atoms at the boundary: the link atom and the localized orbital methods. In the first method an artificial link (dummy or hydrogen) atom is used to saturate the dangling bonds; the quantum calculation should be done for the saturated system. In the second method the bonds, connecting the quantum and classical regions are cut and represented by a set of strictly localized molecular orbitals, which are assumed to be transferable.

## Structure Prediction and Homology Modeling


Protein structures are very complicated, therefore their determination by energy minimization, like in case of small molecules, would need astronomical computational work. However, several methods are available for the prediction of such structures (Bujnicki 2009; Krieger et al. 2003; Xu et al. 2007). Below we discuss some of them.

### Homology Modeling


Proteins, derived from a common ancestor, are called homologous and their primary sequence overlaps to a certain extent. It has been observed that overlap in the sequences results in the partial conservation of three-dimensional structures. This allows constructing a model of an unknown protein on the basis of other, homologous ones, possessing some sequence similarity. Conservation of folds among homologues guides modeling, which follows four steps: fold recognition and template selection, target-template alignment, model building, and model assessment.

The first two steps are often performed together, as the most common methods of identifying templates rely on the production of sequence alignments. Selection of the correct template is of basic importance to the quality of the final model. Subsequent steps can be performed iteratively to improve the quality of the result. After the template was chosen on the basis of percentage of identities and similarities with the target protein it has to be corrected with respect to missing residues and improper bond lengths and mutated to the corresponding residues of the target protein. The gaps in the target sequence have to be excised; loops should be built and inserted by selecting anchoring residues (cf.  Fig. 30-2).

Loops satisfying the distance condition for connecting secondary structures can be located by a search in the Protein Data Bank. At last, using an appropriate force field the generated complete model has to be optimized.

Assessment of homology models can be performed with two main methods: statistical potentials or energy calculations. Both methods produce an estimate of the energy (or an analogous quantity) for the model being assessed. Unfortunately, neither of the two methods correlates very well with structural accuracy. Statistical potentials are computationally quite efficient and can be constructed empirically on the basis of observed residue–residue contact frequencies among proteins of known structure. Energy calculations are performed using a molecular mechanics force field (cf.  section “Molecular Mechanics”). The use of these methods is based on the hypothesis stating that a native structure of a protein refers to a minimum on the energy hypersurface, thus the lower the energy, the better the structure. Some methods employ implicit solvation, representing the solvent around a single protein molecule as a continuous dielectric medium. Quality of homology models decreases with decreasing sequence identity. At 70% and 25% identity the rms deviation between the matched C<sup>α</sup> atoms ranges between 1–2 and 2–4 Å, respectively. Several computer programs, like WHAT IF (Krieger

```
ARIFYDKGFQGHCKSEC-NLQP  
ARIFYDKG---RCYKSECPNLQP
```

 Fig. 30-2

Sequence alignment of template (*top*) and target (*bottom*) in homology modeling

et al. 2003), MODELLER (Fiser and Sali 2003), and SWISS-MODEL (2011) are available for homology modeling.

### Protein Threading

Protein Threading (fold recognition) is based on the observation that the number of different folds in nature is limited to approximately 1,000. Furthermore, 90% of the new structures submitted to the Protein Data Bank in the past few years have similar folds to the ones already stored. The method uses sequences, which have the same fold as some known structures but are not homologous with any of these. Prediction uses statistical relationships between structure and sequence. The prediction is made by aligning each amino acid in the target sequence to a given position in the template structure, and evaluating how well the target fits the template. After that the best-fit template is selected; the structural model of the sequence is built on the basis of the alignment with the chosen template.

### Ab Initio Methods

When structural analogues are not available, prediction has to be based on other information. Various types of potentials as well as evolutionary information may be used in generating spatial restraints or identifying local structural building blocks. A popular ab initio method is Rosetta@home (2011), where the conformations, specified by the non-hydrogen backbone and  $C^\beta$  atoms, observed for each short sequence segment in known protein structures are used as an approximation of the set of local conformers, which the same sequence segment would occupy in the modeled protein. The combination of local conformers, which has the lowest overall energy, is considered as the best model. Before its structure has been determined experimentally, ROSETTA provided a model for the protein T0283 having 112 residues. Comparison of this model to the experimental structure indicates an RMS deviation of 1.8 Å over 92 residues. Despite significant success, the enormous computer cost of the procedure is still prohibitive for routine use.

## Structure Representation

---

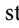
Protein structures contain typically thousands of atoms, therefore, their graphical representation, replacing old mechanical models, is essential for understanding structure, function, and their relationship. Modern computer technology provides an irreplaceable tool and allows insight into structural and functional details.

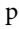
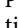
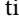
### Molecular Graphics

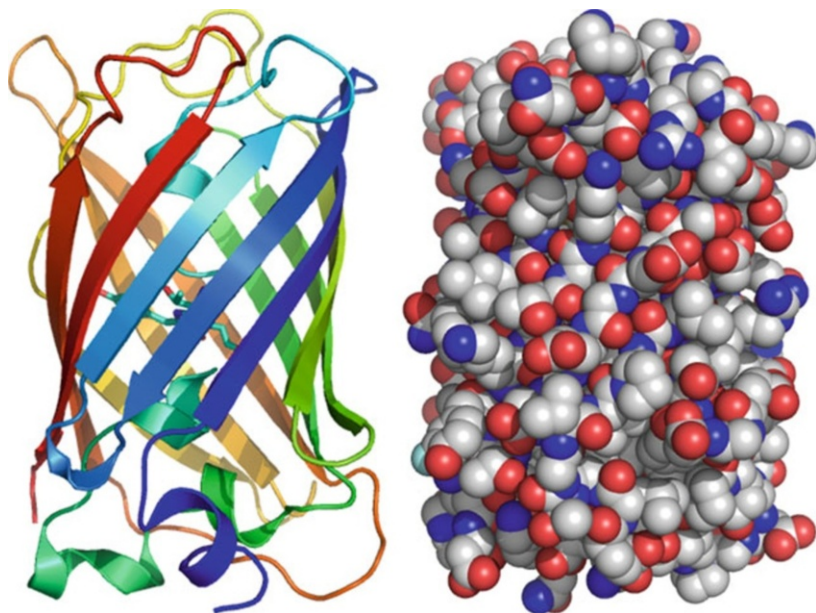
---


Three-dimensional structure of a molecule may be displayed on the computer screen in various representations (Lesk et al. 2008). The simplest is where the molecule is displayed as a chemical graph, in which vertices stand for atoms and edges for bonds. Usually this representation is not very useful for molecules as large as proteins, as the figure gets too crowded. However, for structures derived from X-ray data it is often used when mobility of various atoms is represented by spheres or ellipsoids centered at edges. In most cases evaluation of data from NMR

spectroscopy provides a bundle of structures, a superposition of those 10 or 20 ones that fit best to restraints extracted from the spectrum. In order to simplify the model a single structure, adopting the “average” conformation of the bundle, is often shown.

More sophisticated is the ball-and-stick model, displaying atoms as sticks connecting them. In space-filling, or CPK, representation atoms, represented by spheres with van der Waals radii, within which most of the electron density can be located, are drawn to suggest the amount of space they occupy. For proteins, ribbon diagrams offer a simple, yet powerful means to visualize special features of protein structure; they indicate whether the polypeptide chain is twisted, folded, or unfolded. They are generated by interpolating a smooth curve through the polypeptide backbone.  $\alpha$ -Helices are shown as coiled ribbons,  $\beta$ -strands as arrows, random coils as lines or thin tubes. As an example for the performance of ribbon diagrams we display a  $\beta$ -barrel, a bunch of large  $\beta$ -sheets that twist and coil to form a closed structure, on  Fig. 30-3. The ribbon representation allows easy recognition of backbone structural motifs, while the space-filling model refers to other steric aspects of the macromolecule, e.g., location and shape of crevices.

A special feature of molecular graphics is that it can generate various surfaces around the molecule, on which a variety of its properties can be displayed. For proteins the electrostatic potential (see  section “Electrostatics”), water accessibility, and hydrophobicity (see  section “Solvent-Accessible Surface”) patterns are most important. Commercial (see  section “Molecular Mechanics”) and open source code software, like PyMOL (<http://www.pymol.org/>) and Jmol (<http://jmol.sourceforge.net/>) is available for molecular graphics.



 Fig. 30-3

Ribbon (*left*) and space-filling (*right*) representation of green fluorescent protein (PDB code: 1RRX)

## Electrostatics

Since proteins have several polar or charged side chains, especially on their surface, electrostatics is a simple, yet quite reliable tool to study various processes involving proteins (Baker and McCammon 2009). Electrostatic interactions may play a role in protonation, ligand binding, enzymatic catalysis, redox processes, and electron–proton coupling (e.g., in photosynthesis).

The electrostatic potential generated by the electrons and the nuclei of a protein molecule in a given spatial point,  $\mathbf{r}_i$ , is calculated as follows:

$$V(\mathbf{r}_i) = \int \rho(\mathbf{r})/|\mathbf{r} - \mathbf{r}_i|d\mathbf{r} + \sum Z_a/|\mathbf{r}_i - \mathbf{R}_{ia}| \quad (30.10)$$

where  $\rho$  is the electron density of the protein, and  $Z_a$  is the nuclear charge of atom  $a$  located at the point  $\mathbf{R}_{ia}$ . Exact calculation of the electron density involves the quantum mechanically determined total wave function; for proteins this would need astronomical computer time. In order to reduce computational work the density can be approximated by a sum of quantum mechanically defined molecular fragments, classical atomic monopoles, or multipoles.

► Equation 30.10 refers to a protein molecule in vacuo, however, a realistic model should include explicit treatment of the surrounding biophase. This is done in the Poisson–Boltzmann approach, where the mobile ions around the protein are represented by a mean field approximation. A linearized equation can be derived, which combines the electron density of the protein and the charge represented by the mobile ions

$$\nabla[\varepsilon(\mathbf{r})\nabla V(\mathbf{r})] + 4\pi[-2IV(\mathbf{r})/kT + \rho(\mathbf{r})] = 0 \quad (30.11)$$

Here  $V(\mathbf{r})$ ,  $\varepsilon(\mathbf{r})$ , and  $\rho(\mathbf{r})$  are the electrostatic potential, the dielectric constant and the protein electron density in point  $\mathbf{r}$ , while  $I$  stands for the ionic strength. DelPhi, a versatile software package providing numerical solutions to the Poisson–Boltzmann equation, is widely used for the calculation and visualization of the protein electrostatic potential (DelPhi 2009).

An application of the Poisson–Boltzmann equation is the estimation of the effective  $\text{pK}_a$  of a given side-chain, which is related to the electrostatic potential generated by the whole protein near the protonated atom.  $\text{pK}$  shifts caused by, e.g., site-directed mutagenesis can be precisely calculated using electrostatics (Gilson and Honig 1987). In subtilisin mutants the calculated, ionic strength dependent  $\text{pK}$  shifts lie very close to the experimental values, the trend is correctly reflected for all but the lowest ionic strengths (cf. ► Table 30-1).

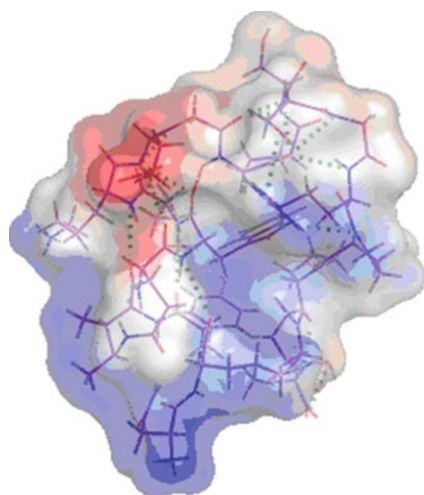
The electrostatic approach is quite useful in describing the binding of small ligands to proteins. ► Figure 30-4 shows a representation of the protein electrostatic potential on the surface, providing a simple means to roughly estimate position and binding strength of charged ligands. This point will be discussed in more detail in ► section “Protein Hydration.” Molecular recognition by proteins, as well as enzyme catalysis is also partly determined by electrostatics (cf. ► sections “Ligand Binding” and “Enzyme Mechanisms,” respectively).

Redox processes involve a change in the charge distribution of the participating protein fragments, therefore electrostatics may play here again a significant role. If a negative charge is located near the redox center, addition of an electron becomes more difficult, which lowers the redox potential. This effect is formally similar to the  $\text{pK}$  shift upon point mutation of a neutral side chain to a negative one. A specific advantage of the calculations is that contributions of various protein groups, the biophase, and ionized side chains can be treated separately. This information is very useful in the design of experiments, because probable effect of point mutations, ionic strength, and pH variation, respectively, can be predicted with a fair accuracy.

■ Table 30-1

Comparison of calculated and experimental (in parentheses)  $pK_a$  shifts in subtilisin mutants as a function of the ionic strength

$I$	D99S mutant	E156S mutant
0.500	0.10(0.09)	0.19(–)
0.100	0.18(0.23 – 0.29)	0.27(0.25)
0.025	0.25(0.36)	0.34(0.41)
0.010	0.29(0.42)	0.37(0.42)
0.005	0.31(0.38)	0.39(–)
0.001	0.34(–)	0.42(0.39)



■ Fig. 30-4

Electrostatic potential of the miniprotein Tc5b\_D9E mapped on the molecular surface (*red*: negative, *white*: neutral, *blue*: positive)

As an example, values of the one- and two-electron reduction potential of pheophytin-*a* were calculated in *N-N*-dimethylformamide by a combination of quantum mechanical, statistical mechanical, and polarizable continuum methods (Mehta and Datta 2008). Two different computational methods gave  $-0.92$  and  $-1.03$  V for the one-electron, while  $-1.34$  and  $-1.30$  V for the two-electron reduction potential values, respectively. The observed one- and two-electron potentials are  $-0.90$  and  $-1.25$  V, respectively. Solution of the Poisson-Boltzmann equation gave for the reduction potential of pheophytin-*a* within the thylakoid membrane  $-0.58$  V, which is in good agreement with the reported value of  $-0.61$  V.

Protonation-mediated modulation of electron transfer has been supposed to explain the location of the radical site in Compound I, an intermediate of the enzymatic reaction, of two related heme peroxidases (Menyhárd and Náray-Szabó 1999). Both molecular orbital and electrostatic potential calculations suggest that the spin distribution depends on the protonation state of the proximal His ... Asp ... Trp triad. If the transferable proton is shifted from the Trp side chain to Asp, the radical localizes on the indole group, while if it remains on the Trp the unpaired electron transfers to the heme group. Therefore, in cytochrome C peroxidase, Trp is

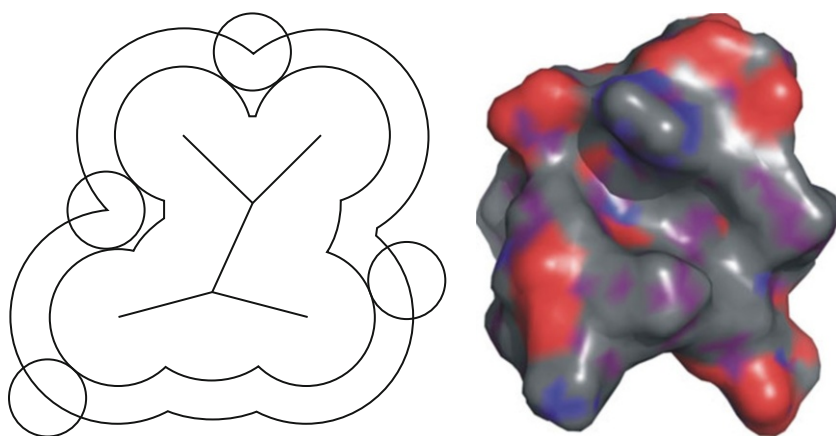


deprotonated in Compound I, while it is protonated and neutral in cytosolic ascorbate peroxidase. Protonation state of the proximal residues is influenced by the electrostatic effect of the protein environment that differs in these enzymes, especially in the immediate vicinity of the Asp side chain.

## Solvent-Accessible Surface

Protein surfaces are quite irregular; their analysis has application in structure-based drug design, since drugs bind in protein crevices. Since the hydrogen atom positions are generally not known, heavy atoms binding hydrogens are represented by a single sphere, whose van der Waals radius is increased by 0.1–0.3 Å. Several surfaces can be defined around proteins, maybe most important is the solvent (typically water) accessible surface (Connolly 1996). This is constructed using a probe sphere, representing the solvent molecule, which is rolled around the protein surface. A typical value of its radius is 1.4 Å, which corresponds to a water molecule. The contact surface is that part of the van der Waals surface that can be touched by the probe sphere; the solvent accessible surface is derived as the location of the center of the probe as it rolls over the van der Waals surface (see ► Fig. 30-5). The solvent-excluded volume of a protein is that volume of space where the probe sphere is in contact but does not collide with the atoms of the molecule.

The solvent accessible surface area (SASA) is often used as a descriptor in quantitative structure-activity relationships (Connolly 1996). For a wide variety of molecules there is an approximate linear relation between solvation free energies and SASA. However, theoretical considerations indicate that the SASA model is incapable of accurately describing non-polar solvation phenomena at length-scales comparable to the size of a water molecule. It is more useful at large length-scales when more extended hydrophobic surfaces are in contact with the solvent.



■ Fig. 30-5

*Left:* construction scheme of the solvent accessible surface from the van der Waals surface (inside, obtained as a union of van der Waals spheres representing protein atoms). *Right:* solvent accessible surface of the miniprotein Tc5b\_D9E



## Dynamics

---

Finding the optimum structure representation of a protein is often not easy, as for larger molecules even the simplest ball-and-stick models can be too cumbersome. Thus, any simplification (neglecting H-atoms, fold representation by ribbons, etc.) of the graphics (see above), especially on a paper plot is important. It can also be misleading to use rigid representations of a flexible macromolecule. Graphical representations are based on set(s) of congruent experimental or computational restraints, typically not shown in a figure. Clearly, it is inconvenient to display the electron density alone when reporting an X-ray structure, or plotting all collected NOE restraints, the source of structural models determined by NMR spectroscopy. However, the need to provide simple and easy-to-understand 3D structures of proteins drives scientists to neglect inherent dynamical properties of these molecules. For the very same reason, NMR spectroscopists tend to over-refine protein structures. Striving to obtain low RMSD values and to display an “X-ray-like,” static structure, the reported model can be biased. The static picture often provided fails to satisfactorily explain the results of associated biological assays, and is not fully compatible with ligand docking data. With the recent appearance of intrinsically unstructured proteins (IUPs) on stage, the importance of the inherent dynamics is unquestionable. In other words, the absurdity of reporting only a single mean conformer is becoming evident. The present chapter gives an account on the dynamics occurring on different timescales, ways of reporting and including them in protein representation and some hints on the relevance of dynamics to biology.

## Time Scales

---

Motions and events – especially when occurring periodically – are commonly characterized by their repetition rate, frequency, or by their time requirement. For example, our heart beats about once every second, so the heartbeat cycle, incorporating several steps such as the relaxation of the heart, opening of valves, etc., is occurring on the time scale of seconds. There are many slower events requiring more time than a second and thus, the introduction of minutes, hours, days, seasons, years, etc. is easily justified. In our everyday life we are experiencing motions happening simultaneously, but often on very different time scales. While going to work, which could take about an hour, our heart beats about 4,000 times and we repeat this daily routine nearly 300 times in a year. Proteins also have their “life,” which, after synthesis, starts with folding, an event that typically occurs on the millisecond time scale. As proteins are continually synthesized and degraded in all cells, the half-life time of a protein is about an hour, varying from a few minutes to several weeks. However, when we think of protein dynamics we are looking for much faster events such as secondary structure formation (e.g., winding and unwinding of an  $\alpha$ -helix) on the 10 ns–1 ms time scale, or opening and closing of loops and hairpins on the 10  $\mu$ s–1 ms time scale.

The rotational diffusion correlation time,  $\tau_C$ , is characteristic of any molecule as  $\tau_C^{-1}$  is the average frequency of molecular tumbling in solution. The *correlation time* for short, of a protein stands for the time that it takes for the molecule to reorient by 1 rad via tumbling in solution. Being dependent among others on molecular size, for proteins in aqueous solution at normal conditions  $\tau_C$  is in the range of 1–10 ns. However, there are additional interesting types of motions on an even faster timescale, such as protein backbone (1 ps–10 ns) and protein side-chain (0.1–10 ps) dynamics. Although even faster events may take place in proteins

(e.g., bond vibrations studied by Fourier transform infrared or vibrational circular dichroism spectroscopy), they are less characteristic of the whole and more complicated to interpret.

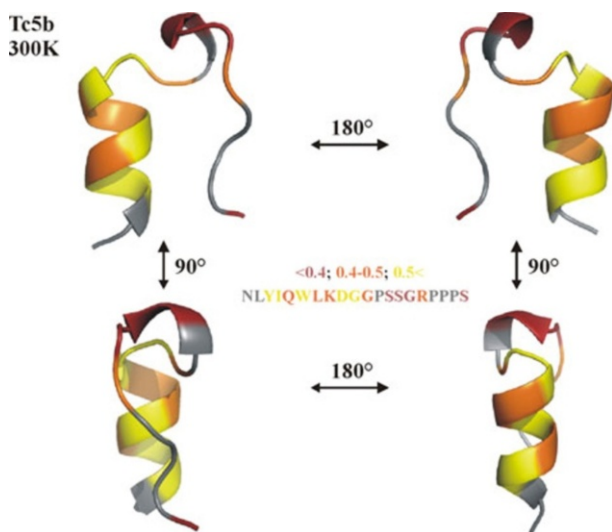
NMR has long been used to decipher dynamics of biopolymers, as the relaxation times and the line shapes of selected resonances are rather sensitive to chain motions. For proteins in solution, relaxation of the magnetically excited states occurs because of the above described very rapid and slower segmental motions. The somewhat localized motions are effective in causing relaxation in solution. As more than a single relaxation process characterizes the correlation function  $G(\tau)$ , often spanning a large time scale of motions (ps↔ms), it is advised to measure a number of different relaxation parameters at various magnetic fields and temperatures. During typical relaxation measurements, nuclear spins are excited by suitable radio frequency (RF) pulses, and then relaxation to equilibrium is monitored by heteronuclear single quantum coherence (HSQC) type 2D-experiments. Commonly measured relaxation parameters are longitudinal ( $R_1$ ) and transverse ( $R_2$ ) relaxation rate constants, constraints obtained on the basis of the heteronuclear Overhauser effect (hetNOE) and additional cross-correlated relaxation parameters (Jarymowycz and Stone 2006).

Today when routinely working with  $^{15}\text{N}$  and  $^{13}\text{C}$  labeled proteins it is common to estimate the degree of main-chain mobility by using  $^{15}\text{N}$  NMR relaxation. The associated experiments are straightforward to complete and the interpretation is relatively easy as it probes the reorientation of N–H bond vectors of protein amide bonds. Coupled primarily to fast (1 ps–10 ns) motion of the protein, heteronuclear NMR relaxation of backbone  $^{15}\text{N}$  atoms is usually interpreted in the “model-free” framework, where it is supposed that global ( $\tau_C$ ) and local ( $\tau_l$ ) motions are uncorrelated.  $R_1$ ,  $R_2$ , and  $^{15}\text{N}$ - $\{^1\text{H}\}$  NOE relaxation data of each  $^{15}\text{N}$  atom are measured and subsequently fitted to the model to reconstruct spectral density components,  $J(\omega_j)$ . Results are analyzed in terms of the lowest number of sufficient secondary parameters. Local N–H motions are quantified by the generalized order parameter,  $0 \leq S^2 \leq 1$ , reflecting the amplitude of N–H fluctuations with characteristic time constants (e.g., effective internal correlation time) (Cavanagh et al. 2007). A possible interpretation and graphical representation of the backbone dynamics is to map  $S^2$  values on the graphical representation of the structure (cf. [Fig. 30-6](#)). In case of the present example, conformation of the central Trp residue, forming the hydrophobic cluster of the protein, is most restricted.

Recent developments in molecular dynamics techniques allow consideration of  $S^2$  values and NOE restraints as an ensemble property (Lindorff-Larsen et al. 2005; Richter et al. 2007). The obtained ensembles represent a more realistic view of these flexible molecules in solution than those calculated with conventional NMR structure refinement methods. The dynamically restrained ensembles occupy a considerably larger conformational space than the conventionally calculated ones, and reproduce independent NMR parameters (e.g., chemical shifts) much better.

The model-free approach is not applicable for non-globular, highly asymmetric, and partially folded or fully unfolded proteins as they do not meet the criteria of separation of internal and overall motions. The reconstruction of spectral density components,  $J(\omega_j)$ , from  $R_1$ ,  $R_2$ , and  $^{15}\text{N}$ - $\{^1\text{H}\}$  NOE measurements is possible but more experiments are required (e.g., relaxation measurements at several  $B_0$  values). Nevertheless, IUPs can also be analyzed in terms of raw data as done recently, e.g., for the unstructured protease inhibitor calpastatin (Kiss et al. 2008).

Until now, we have discussed molecular motions 10 or 100 times faster than the rotational diffusion correlation time,  $\tau_C$ , of the protein. As mentioned above slower motions occurring on the microsecond-millisecond time scale are also of significance (loop fluctuations, secondary



■ Fig. 30-6

Residue-specific generalized order parameters,  $S^2$ , mapped on the Tc5b miniprotein represented by its ribbon structure. Mobility is color-coded: *brown* ( $S^2 < 0.4$ ) stands for high, while *yellow* ( $S^2 > 0.5$ ) for lower backbone NH mobility occurring on the 1 ps  $\leftrightarrow$  10 ns time scale of motion. *Orange* represents 0.4–0.5  $S^2$  values (Pohl et al. unpublished)

structure reorientations, etc.). Motions of this regime are accessible to spin relaxation arising from modulation of the isotropic chemical shift of  $^1\text{H}$ ,  $^{13}\text{C}$ , and  $^{15}\text{N}$  spins coupled to chemical exchange. NMR can also provide information on this much slower motional regime by recording  $^{13}\text{C}$  and  $^{15}\text{N}$  heteronuclear ZZ-exchange, NOESY-spectroscopy, or various relaxation data (Cavanagh et al. 2007). More recently, residual dipolar couplings (RDCs) are also used for assessing dynamics of supra- $\tau_C$  time scales (Lange et al. 2008). These techniques are sensitive to protein motions or chemical kinetic processes happening on microsecond time scales (Palmer et al. 2001). Beside conformational events such as protein folding, other biochemical processes, e.g., enzyme catalysis also occur on this time scale. It seems that information on the so-called slower dynamics could be of great use in the future when interconversion rates and populations of states, cooperative conformational transition(s), functional aspects of enzymes, enzyme dynamics, etc. are modeled.

## Dynamical Structures

Partially folded and molten globule states are of considerable interest and can be characterized by NMR and additional spectroscopic techniques. The molten globule state of a protein is folded to a given extent; it has native-like secondary structural elements and comprises a native-like 3D-structure. The main difference from the native state is the absence of important side-chain/side-chain interactions. This intermediate structure can be stabilized under selected conditions making it possible to obtain structural information. Proteins studied in their molten globule form are characterized as ensembles of a diverse set of interchanging conformers

(Gspöner et al. 2006). The study of molten globule states by X-ray diffraction is often impossible and can be difficult also if using NMR techniques. However, from simple line-shape and H/D exchange analysis obtained by NMR spectroscopy, measurement of the hydrodynamic radius, deciphering stable (or residual) secondary structural subunits (by, e.g., circular dichroism or fluorescence spectroscopy) molten globule states can be appropriately characterized (Redfield 2004). Thus, protein modeling can be possible even in the molten globule state.

## Dynamics of Interactions

---

Protein–protein and protein–ligand interactions have two apparently contradicting aspects. As these molecules are interacting 3D-objects coming in contact with each other, partners should have complementary shapes of considerable stiffness over time (cf. [▶](#) section “Ligand Binding”). However, several phenomena cannot be understood without considering the inherent flexibility and plasticity of proteins. Thus, the shape of a protein should be kept rigid to enhance selectivity, but it is also dynamically changing upon binding of a partner molecule. Thus, proteins should both have a well-defined shape and the ability to change it.

Although the rigid lock-and-key model has been revisited in the past decades, one of the last standing cases is that of the so-called canonical protease inhibitors. Proteases have the task to cut other proteins into pieces for various reasons, such as digestion, activation, degradation, etc. Thus, they should be under severe control both in space, time, and concentration, often manifested by fine tuned canonical inhibitors. Upon binding they are not expected to influence any conformational changes around the binding site of the protease, as they have to bind in a substrate-like manner to inhibit activity. Recently, fast (ps-ns) backbone dynamics of some canonical inhibitors was measured and found that, in contrast to the expectations, they are quite mobile. In fact these 35- to 40-residue-long inhibitor proteins, stabilized by three disulfide bonds, are as mobile as their protease binding region. Thus, even for canonical inhibitors, the classical lock-and-key model cannot remain valid. It was shown that the interaction cannot be properly described without taking into account the internal mobility of the partner proteins. Interestingly enough the presence of flexible rather than rigid keys removes the necessity of an entirely complementary shape of the interacting partners. In fact, “keys” can gently adapt to the locks, which are slightly different from case to case (Fodor et al. 2005). Moreover, conformational changes or flexibility of partners was found to be synchronized and also encoded (Szenthe et al. 2004). This might even mean that the lock-and-key concept, proven utterly useful in the early days of biochemistry, should be interpreted dynamically and replaced by the more general hand-and-a-glove analogy (cf. [▶](#) section “Ligand Binding”) (Goh et al. 2004).

## Interactions

---

Interaction of proteins with water, drugs, and other biological macromolecules plays an essential role in physiological processes. Owing to the very high number of atoms in a protein, in general, such interactions cannot be handled at the atomic level explicitly; simplified, still reliable models are needed.

## Protein Hydration

---

Hydration of proteins is especially important in determining their properties (Makarov et al. 2002). For example, protein activity is practically zero in the absence of hydrating water. The first hydration shell around proteins is ordered; surface water forms hydrogen-bonded patterns and positively charged surface side chains also take part in stabilization. The first hydration shell is denser by about 10–20% than bulk water and this is probably responsible for keeping the molecules sufficiently separated so that they remain in solution.

Proteins are flexible in solution, which involves a variety of hydration states, absent in the crystal or in non-aqueous environments. Hydration also affects redox potentials. The biological activity of proteins appears to depend on the formation of a hydrogen-bonded network connecting the protein surface and water clusters. Water molecules can form a bridge between the carbonyl oxygen atoms and amide protons of different peptide residues to stabilize protein–ligand and protein–protein complexes. Enzyme–substrate contact may be controlled by water molecules located in the protein environment, and one or more water molecules may be part of the catalytic machinery of enzymes. These water molecules act as proton donors or acceptors (or both) during reaction.

Computer modeling of protein hydration follows essentially two ways. One is to treat all water molecules in the hydration sphere explicitly and apply an appropriate force field (cf. [▶](#) section “[Molecular Mechanics](#)”) in molecular mechanics or molecular dynamics calculations. As an example, we present results of molecular dynamics calculations on aquaporin, a membrane protein facilitating the transport of water and other small solutes across biological membranes (Hub et al. 2009). Simulation was carried out with full electrostatics in a periodic simulation box containing the aquaglyceroporin tetramer, embedded within a lipid bilayer surrounded by water. The whole model consists of about 100,000 explicit atoms. The mechanism of water permeation through aquaporin was described, and it was found that protons are strictly excluded from the channel by a large electrostatic barrier. Both protein electrostatic field and desolvation contributes to this effect. Permeation of apolar molecules like carbon dioxide is hindered by a high energy barrier; therefore this process can only be expected to take place in membranes with low intrinsic gas permeability. Analysis of MD simulations indicated that a narrowing region, containing aromatic, and arginine side chains, filters uncharged solutes. Here, selectivity is controlled by the hydrophobic effect and steric restraints. As we see, simulation provides a specific tool to understand membrane permeation in atomic detail and to recognize its basic factors. No experimental means is available at present to provide such a detailed picture of the process.

Another way to consider protein hydration is to extend the concept of the solvent accessible surface (cf. [▶](#) section “[Solvent-Accessible Surface](#)”) applying continuum dielectrics models. For example, combination of the electrostatic and an appropriate hydrophobic potential, accounting for hydrophilic, and hydrophobic interactions, respectively, may be used as a solvation function, which considerably increases the reliability of protein structure predictions (Lin et al. 2007).

## Ligand Binding

---

Binding of small-molecule ligands, such as drugs, vitamins, flavors, or pheromones, takes place in crevices of the protein surface. In a broader sense ligand binding means the formation of a stable complex between a host and a guest [molecular recognition (Harmat and Náráy-Szabó

2009)], and it can be best understood in terms of the *lock-and-key* analogy. Under lock we mean here the protein crevice, while the key stands for a small molecule or a fragment of a larger one, fully, or partly embedded in the crevice. In general, we suppose that both lock and key are rigid, however, in many cases they are flexible and adopt their final shapes only upon binding. This process is best illustrated by the *hand-and-a-glove* analogy. If the macromolecular crevice undergoes conformational changes in order to provide the optimal shape for embedding the relatively rigid guest molecule, we speak about induced fit. Alternatively, the guest molecules may adopt different conformations, some of which are appropriate for binding. This alternative is called conformational selection.

Steric fit means that interacting atoms may not interpenetrate beyond their *van der Waals* spheres and, simultaneously, the host crevice should be filled as perfectly as possible reducing the empty space between host and guest atoms to a minimum. Electrostatic fit refers to the maximization of ionic, hydrogen-bonding, and other types of polar interaction, and is well accounted for by the molecular electrostatic potential provided by the host and acting on a charge distribution representing the guest. The term hydrophobic fit refers to the association trend between apolar groups in the biophase. This may be explained either in terms of density differences between water and the host, or macromolecular crowding, an entropy effect reducing water-accessible surfaces of dissolved molecules upon association, in order to avoid unfavorable perturbation of water structure around the separated solutes.

The accurate prediction of the binding mode and affinity of a small molecule to its putative receptor is crucial for successful drug design and optimization, therefore, a variety of computer methods has been developed for that. *Docking* is an optimization method, which predicts the preferred orientation of the ligand bound to the protein and forming a stable complex. It may be also used to predict the binding affinity using energy terms or an appropriately defined scoring function. Essentially three types of docking procedures are available (Mohan et al. 2005).

*Rigid body docking* assumes both the receptor and the small molecule to be rigid. *Flexible ligand docking* means that the receptor crevice is held fixed, but the ligand is treated as flexible (conformational selection, see above); this is the most commonly used method. In *flexible docking* both partners are considered to be able to change conformation easily. Following another classification, either a matching technique is used, which describes the protein crevice and the ligand as complementary surfaces, or the actual docking process is simulated and the ligand-protein interaction energies are calculated (Guvencs and MacKerrell 2009). Furthermore, modeling the role of the aqueous solvent in ligand-protein interactions is one of the key components. Three main computational techniques have been developed to model hydration: free energy methods, ligand-protein docking, and scoring, and the explicit inclusion of tightly bound water molecules in modeling (Mancera 2007).

Shape complementarity methods describe the protein and ligand in terms of complementary molecular surfaces. The host and guest protein surfaces are defined in terms of the SASA (cf. ● section “Solvent-Accessible Surface”) and the matching surface description, respectively. The complementarity between these two surfaces is defined as the shape matching, which may help finding the appropriate orientation of the ligand in the crevice. These methods are typically fast and robust; however, in general, they cannot model the dynamic changes in the conformation of the protein-ligand complex. They can scan through several thousand guest molecules in some seconds and figure out which of them can bind at the crevice.

Differences in binding energies of similar ligands, A and B, differing only by a few atoms, can be precisely calculated by the free-energy perturbation method (see ● Fig. 4.1). A thermodynamic cycle is constructed, where the horizontal free energies are determined experimentally,

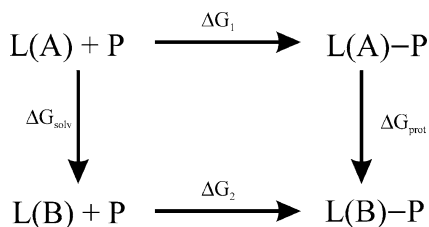
since they are difficult to calculate. The vertical free energies are calculated by simulation based on a force field or a continuum electrostatic model.  $\Delta G_{\text{solv}}$  corresponds to the hydration energy change mutating A into B in water, while  $\Delta G_{\text{prot}}$  is the binding energy change upon replacing A by B in the binding pocket. Since the thermodynamic cycle is closed and the free energy is a state function, we may write:  $\Delta\Delta G_{\text{bind}}(\text{A-B}) = \Delta G_2 - \Delta G_1 = \Delta G_{\text{prot}} - \Delta G_{\text{solv}}$ ; the difference can be obtained from calculated quantities. Instead of simulating the horizontal physical binding processes, which is quite uncertain, the non-physical transformations represented by the vertical reactions can be calculated relatively easily and precisely. An example for the successful application of the free-energy perturbation method is the calculation of the absolute binding free energy of benzamidine to trypsin, which is found to be  $-6.78 \text{ kcal mol}^{-1}$  (Jiao et al. 2008), while the experimental binding free energy ranges from 6.3 to 7.3  $\text{kcal mol}^{-1}$ . The calculated binding energy of a close analogue, diazamidine is weaker than that of benzamidine by  $1.21 \text{ kcal mol}^{-1}$ , agreeing well with the experimental value of  $1.59 \text{ kcal mol}^{-1}$  (► Fig. 30-7).

Docking by simulation is a much more complicated process. In this approach, the protein and the ligand are separated by a physical distance, and the guest finds its position in the crevice after a certain readjustment in the conformational space. This refers to translations, rotations, and conformational changes. Each of these induces an energy change of the system, which is calculated on the basis of a force field or a scoring function. Clearly, this method is much more sophisticated; it incorporates ligand-flexibility, which is, in general, absent from complementarity techniques (see Zsoldos et al. 2007 and references therein). A disadvantage is that it takes a much longer time to evaluate the optimal binding arrangement, since a rather large energy landscape has to be explored.

Docking is most commonly used in the field of drug design, to quickly screen large databases of potential drugs *in silico*, to identify molecules that are likely to bind to a certain protein target (virtual screening). In lead optimization docking may predict how a ligand binds to a protein crevice, information that may be used to design more potent and selective analogues. Several computer platforms are available for efficient and relatively fast docking, e.g., AUTODOCK (<http://autodock.scripps.edu/>).

## Protein–Protein Interactions

Proteins often exert their function through interaction with other ones, forming complexes, e.g., in the ribosome or in cell membranes, during immune response or enzyme catalysis. Complex



■ Fig. 30-7

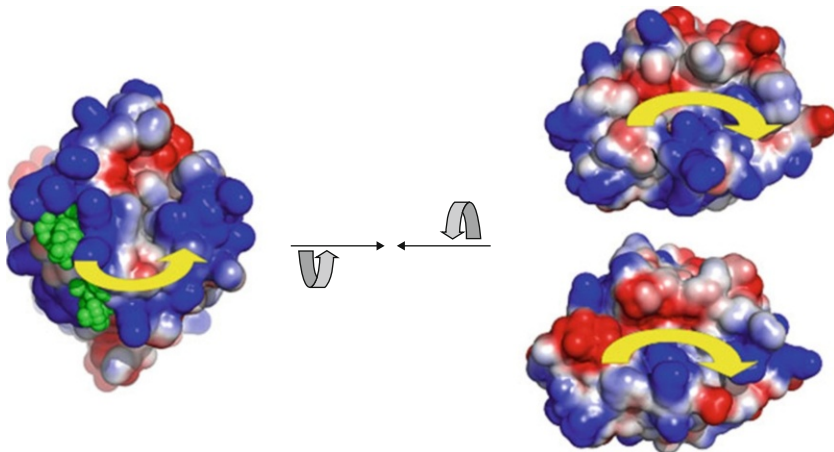
The thermodynamic cycle used to compute solvation (*left*) and protein binding (*right*) free energies. L: ligand with substituents A or B, P: protein



structures are essential in understanding action, therefore beyond experimental techniques, like X-ray diffraction, electron microscopy, or mass spectrometry, *in silico* methods also are of great interest. However, due to a number of practical difficulties, it seems unlikely that solving the structures of protein complexes will become routine in the near future. Hence, computational docking techniques play an important role (Ritchie 2008).

The simplest protein–protein docking methods are based on the complementarity principle and focus on the properties of the contact surface. To do this, interaction patterns, observed in protein–protein complexes of known structure, have to be analyzed. An example is based on shape and electrostatic complementarity (● Fig. 30-8), where spatial matching of surfaces with complementary electrostatic potential patterns can be observed (Harmat and Náráy-Szabó 2009). It can be supposed that much less improper orientations of the interacting partners would be obtained if one could first identify the interaction surfaces on them. For many (e.g., antibody-antigen or most enzyme-inhibitor) interactions, the binding site is known on one or more of the proteins to be docked. In other cases, a binding site may be strongly suggested by mutagenic or phylogenetic evidence.

Although the properties of protein–protein interfaces have been analyzed in considerable detail, it remains a significant challenge to reliably predict the locations of protein–protein interaction surfaces using computational techniques alone (Porollo and Meller 2007). Machine learning techniques are being used to develop automated protein–protein interface prediction software. These systems are typically trained using various combinations of, e.g., buried surface areas, desolvation, and electrostatic interaction energies, hydrophobicity scores, and residue conservation scores.



■ Fig. 30-8

Steric and electrostatic complementarity between C1 inhibitor (*left*, the docked heparin disaccharides are shown in *green*) and target proteases, factor XIa (*top right*) and C1s (*bottom right*). *Blue*, positive, *red*, negative electrostatic potential. *Yellow arrows* indicate the presumed position of the reactive center loop of C1 inhibitor in the complex. *Grey arrows* indicate that one of the interacting molecules must be rotated by 180° in order to get in the right position for overlap with the other at the contact surface (Figure by V. Harmat, Budapest)



Like in case of protein-ligand docking (cf. [●](#) section “[Ligand Binding](#)”), for protein–protein docking we have essentially two alternatives (Ehrlich and Wade 2001). In the rigid-body approach interacting partners do not relax; their structures remain unchanged during complex formation. Quite often substantial conformational change occurs within the components as a result of their interaction. In this case a soft docking technique has to be applied, where conformational relaxation is allowed.

Docking involves two main steps: (1) generating a set of reliable configurations and (2) distinguishing correct configurations from those not appropriate for complex formation. Docking algorithms may start with a rigid body representation of the protein, obtained by projecting interacting partners onto a three-dimensional grid, and by distinguishing grid cells according to whether they are near or intersect the protein surface, or are deeply buried within the core of the protein. A docking search is then performed by scoring the degree of overlap between pairs of grids in different relative orientations. After making exclusions based on experimental evidence or steric conflict, the remaining structures must be sampled by appropriately scoring each configuration. In the geometric hashing approach, each protein surface is first pre-processed to give a list of a few hundred critical points, which are then compared in a special algorithm to generate a relatively small number of trial docking orientations for grid scoring (Fischer et al. 1995).

An automated algorithm was developed to identify molecular surface complementarity (Katchalski-Katzir et al. 1992). It involves a digital representation of the molecules distinguishing between surface and interior, calculates a correlation function assessing the degree of surface overlap and penetration upon displacement using Fourier transformation, and scans relative orientations in three dimensions. The algorithm estimates the degree of geometric match between the surfaces of the interacting molecules. The procedure is equivalent to a six-dimensional search but it is much faster; the computation time depends only moderately on molecular size. Such methods can be used to evaluate very large numbers of configurations, however, this advantage is lost if conformational changes are also considered. Furthermore, it is possible to construct reasonable convolution-like scoring functions combining both steric and electrostatic fit.

Conformational changes can be considered in Monte Carlo methods, where an initial configuration is refined by taking random steps that are accepted or rejected based on their induced improvement in score, until a certain number of steps have been tried (Gray et al. 2003). It is assumed that convergence to the best structure should occur from a large class of initial configurations, only one of which needs to be accepted. Because of the difficulty of finding a scoring function that is highly discriminating and also converges to the correct configuration, various refinements have been proposed. Monte Carlo methods are not guaranteed to search exhaustively, so that the best configuration may be missed even using a scoring function which would in theory identify it.

To find a scoring function, which forms an appropriate basis for selecting the best configuration, studies should be carried out on a standard benchmark of protein–protein interaction cases. For example, a benchmark of several dozens of known protein–protein complexes has been developed for testing docking methods (Mintseris et al. 2005). The set is chosen to cover a wide range of interaction (e.g., enzyme-inhibitor, antigen-antibody) types and to avoid repetition. Scoring functions are assessed on the rank they assign to the best structure, and on the proportion of the benchmark cases for which they provide an acceptable result. Scores may be based on residue contacts, shape complementarity, interaction energies estimated by a force

field or on phylogenetic considerations. Often hybrid scores are created by combining one or more categories above.

Although solvation and desolvation effects are crucial in complex formation, most docking algorithms do not take into account the presence of water molecules near the protein–protein interface. An exception is the work by Van Dijk and Bonvin (2006).

## Enzyme Mechanisms

---

Catalysis is a molecular transformation where the rate of the chemical reaction increases through the interaction of the reacting partners with the catalyst without changing the equilibrium constant. Accordingly, the catalyst modifies the potential surface of the non-catalyzed reaction and reduces the activation barrier. In case of enzyme catalysis, the reference is the activation energy in aqueous solution, where the reaction mechanism may considerably differ from that in the enzyme. The enzymatic process is especially effective, since rate increase may be as large as  $10^{10}$ -fold in some cases. Protein modeling plays a crucial role in the understanding of the basis of enzymatic rate acceleration since experiments do not provide direct information on details, e.g., potential transition-state stabilization by the protein environment (Náray-Szabó et al. 1997).

Entropy effects may play an important role, though the actual advantage of their contribution to rate acceleration is still unresolved. This is partially due to the difficulties in obtaining estimates of entropic effects by modeling. Quite often it is argued that the binding of reacting partners to an enzyme active site freezes their motion reducing the entropy contributing to the activation energy. However, it has been shown that this effect is much smaller than thought, because many of the movements that are free in the initial state of the reference solution reaction are also free in the transition state of the enzymatic process. The binding to the enzyme does not completely freeze the motion of the reacting fragments so that the entropy change during reaction is limited. Furthermore, the binding entropy in the enzyme active site is not necessarily equal to the entropy change in the reference solution reaction (Warshel 2003).

Many enzymes make use of general acid or base catalysis, when a reaction step is modified and proton transfer is mediated by an acidic or basic side chain. This reduces the free energy of the proton transfer step and accelerates the reaction. For proton transfer, it may be supposed that rate acceleration is a consequence of the reduced distance between proton donor and proton acceptor, which is known to determine the activation energy. However, it has been shown that both in enzymes and the reference reaction in water H-bond distances are similar. General acid/base catalysis plays a role in enzymes by reducing the free energy of the proton transfer step using a different reaction path with different reactants, which is, however, not a true catalytic effect. Simulation studies have indicated that special effects such as desolvation, low-barrier hydrogen bonds, steric strain, or entropy traps do not account for the major part of the catalytic power of enzymes (Warshel 2003).

Molecular modeling and experiments provide more and more evidence for the crucial role of protein electrostatics in enzymatic rate acceleration. Enzymes, acting as a “supersolvent,” can strongly stabilize polar structures, like ion pairs or the  $(- + -)$  charge distribution located in their active sites. Stabilization in enzymes is stronger than in water, since preorganized and fixed protein dipoles are almost optimally oriented at the active site. The enzyme, therefore, provides a preoriented environment that stabilizes the transition state of the reaction. In contrary,

water dipoles are distributed randomly and have to reorient in order to stabilize transition states. Reduction of the reorganization free energy in the enzyme is due to its folding into its final configuration, which precedes the catalytic process and takes place independently, during protein synthesis.

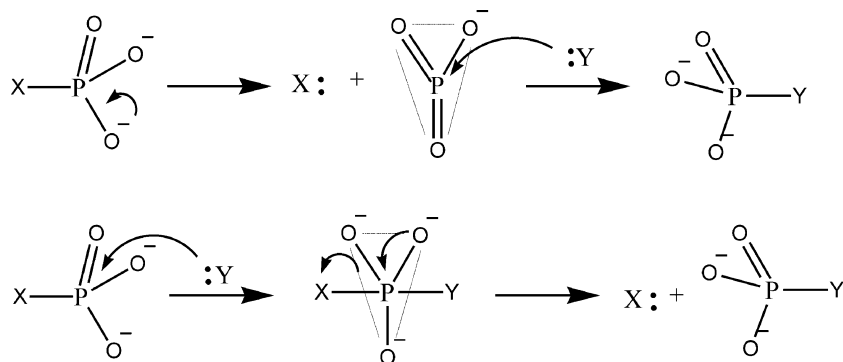
This contribution of the protein reorganization rather than the enzyme–substrate interaction is the most important factor in enzyme catalysis (Warshel 2003). In other words, enzymes have evolved to bind reacting groups in the correct position for reaction with a very high accuracy.

Because of the extreme importance of the protein environment in determining enzymatic reaction rates, the use of extended models and QM/MM computations methods is a must (cf. ► section “Molecular Mechanics”). Until now, a wide variety of QM/MM methods are available, which can be applied to the calculations on various enzyme reactions, it is therefore not easy to make a ranking. It seems, however, that basic features of most processes can be described by practically all types of methods, if a large enough number of protein atoms and surrounding water molecules is considered explicitly or if using a continuum approach combined with a relatively large model of the active site.

In the following we discuss a specific example, the catalytic mechanism of enzymatic phosphoryl transfer (Lasilla et al. 2011). This reaction plays a crucial role in most cellular functions, as DNA replication, signal transduction, metabolism, and transcription, it is involved in several enzymatic processes. Kinases catalyze the transfer of  $\gamma$ -phosphate from ATP to other molecules; mutases transfer phosphoryl groups between two atoms of the same molecule. Phosphatases accelerate the removal of phosphoryl groups, while polymerases catalyze the synthesis of nucleic acid polymers. Endonucleases are able to cleave the phosphodiester bond by transferring a phosphoryl group from a bridging oxygen atom to an activated water molecule.

It is generally claimed that phosphoryl transfer may follow basically two pathways (see ► Fig. 5.1). In the dissociative mechanism a trigonal metaphosphate intermediate is formed (Xu and Guo 2008), while the associative mechanism involves a relatively stable, trigonal bipyramidal intermediate (Lahiri et al. 2003). Note that an intermediate refers to a local energy minimum on the reaction path. However, a third option has to be mentioned, too, this is the classical  $S_N2$  mechanism with a trigonal bipyramidal transition state, referring to a maximum on the reaction path (Bernardi et al. 2002). The preferred pathway is determined by the nature of the phosphorus electrophile, the nucleophile, and the reaction medium (solvent or enzyme active site). Earlier computer simulations indicate that associative and dissociative mechanisms are similarly favored in the aqueous phase (Florián and Warshel 1998), and also calculations for different enzymes support either dissociative or associative pathways depending on a variety of factors (Klähn et al. 2006) (► Fig. 30-9).

It is not easy to propose a mechanism on the basis of experimental evidence alone, since measured data provide in most cases indirect information on the energy and structure of the transition-state complex. Mildvan (1997) evaluated possible mechanisms by using the distances between the attacking and leaving axial oxygen atoms and phosphorus in the trigonal bipyramidal state to decide between associative or dissociative character. These distances may be considered as a measure of the strength of the P–O bond. The Mildvan criterion may be presented as an example for the unclear information often inherent in experiment. Based on X-ray diffraction experiments, Lahiri et al. (2003) reported on a pentacovalent phosphorane intermediate in the phosphoryl transfer reaction catalyzed by  $\beta$ -phosphoglucomutase, which refers to an associative mechanism. However, the associative character, as calculated from experimental bond distances in the intermediate, is quite weak ( $\sim 0.2$ ), while for a truly associative reaction



■ Fig. 30-9

Two pathways of the phosphoryl transfer reaction. *Top*: dissociative, *bottom*: associative. X and Y denote an enzyme or some functional group

it should be near 1.0 (Berente et al. 2007). Another example for a trigonal bipyramidal intermediate, as observed by X-ray diffraction experiments, has been published by Barabás et al. (2004).

In general, the character of the TS changes from associative to dissociative upon decrease in the  $pK_a$  of the leaving group, but the potential surface is very flat; therefore, careful calculations have to be performed in each special case in order to get reliable information on the associative character of the reaction (Florián and Warshel 1998). Recently, calculations have been performed on a variety of enzyme reactions where the associative mechanism seems to be supported, see, e.g., Elsasser et al. (2009).

Enzymatic phosphoryl transfer reaction provides an example where quantum mechanical calculations are irreplaceable in the precise description of the mechanism. The process is very complicated, however, up-to-date methods are available for sophisticated studies and it can be anticipated that in the not too far future mechanistic studies will be considered even by experimentalists as very useful in understanding subtle details.

## Conclusion and Outlook

Molecules are not “seen” like macroscopic or microscopic objects, which provide a picture in our eyes by using visible light and human or artificial lens(es). As molecules are submicroscopic, they are too small to be visible even under the most powerful optical microscope. Although special optical microscopy allows seeing even cell cycles, the entire universe of atoms and molecules remains hidden for such a direct observation scheme. We may obtain “pictures” even on viruses having the size of 10–50 nm by transmission electron microscopy via electrons passing through an extensively prepared sample. Scanning tunneling microscopy and atomic force microscopy can improve resolution; however, neither of these techniques enable us to investigate molecules at an atomic level, especially not in solution. Accordingly, we must use indirect methods for visualization, by which we collect information on various physical properties related to the spatial position of atoms within a molecule. An ideal scenario is when a representation, or

in other words a model, of a molecule on the screen is extracted and subsequently reconstructed from a suitable set of experimental data typically processed and evaluated by the computer.

## Acknowledgments

We are indebted to our colleagues, Dr. Z. Gáspári, Dr. V. Harmat, and Ms. P. Rovó for important remarks on the manuscript and providing most of the figures.

## References

- Baker, N. A., & McCammon, J. A. (2009). Electrostatic interactions. In J. Gu & P. E. Bourne (Eds.), *Structural bioinformatics* (2nd ed., p. 575). Chichester: Wiley-Blackwell.
- Barabás, O., Pongrácz, V., Kovári, J., Wilmanns, M., & Vértessy, B. G. (2004). Structural insights into the catalytic mechanism of phosphate ester hydrolysis by dUTPase. *The Journal of Biological Chemistry*, *279*, 42907.
- Berente, I., Beke, T., & Náray-Szabó, G. (2007). Quantum mechanical studies on the existence of a trigonal bipyramidal phosphorane intermediate in enzymatic phosphate ester hydrolysis. *Theoretical Chemistry Accounts*, *118*, 129.
- Bernardi, F., Bottoni, A., De Vivo, M., Garavelli, M., Keserű, G. M., & Náray-Szabó, G. (2002). A hypothetical mechanism for HIV-1 integrase catalytic action: DFT modelling of a bio-mimetic environment. *Chemical Physics Letters*, *362*, 1.
- Bourgeois, D., & Royant, A. (2005). Advances in kinetic protein crystallography. *Current Opinion in Structural Biology*, *15*, 538.
- Brandén, C., & Tooze, J. (1999). *Introduction to protein structure*. New York: Garland.
- Bujnicki, J. M. (Ed.). (2009). *Prediction of protein structures, functions, and interactions*. Chichester: Wiley-Blackwell.
- Case, D. A., Cheatham, T. E., III, Darden, T., Gohlke, H., Luo, R., Merz, K. M., Jr., Onufriev, A., Simmerling, C., Wang, B., & Woods, R. (2005). The amber biomolecular simulation programs. *Journal of Computational Chemistry*, *26*, 1668.
- Cavalli, A., Salvatella, X., Dombson, C. M., & Vendruscolo, M. (2007). Protein structure determination from chemical shifts. *Proceedings of the National Academy of Sciences of the United States of America*, *104*, 9615.
- Cavanagh, J., Fairbrother, W. J., Palmer, A. G., III, Rance, M., & Skelton, N. J. (2007). *Protein NMR spectroscopy, principles and practice* (2nd ed.). Amsterdam: Elsevier.
- Chayen, N. E. (Ed.). (2007). *Protein crystallization strategies for structural genomics*. Biotechnology Series. La Jolla: International University Line.
- Connolly, M. L. (1996). *Molecular surfaces: A review*. <http://www.netsci.org/Science/Compchem/feature14.html>. Retrieved 7 Mar 2011.
- DelPhi. (2009). [http://wiki.c2b2.columbia.edu/honiglab\\_public/index.php/Software:DelPhi](http://wiki.c2b2.columbia.edu/honiglab_public/index.php/Software:DelPhi). Retrieved 10 Mar 2011.
- Ehrlich, L. P., & Wade, R. C. (2001). Protein-protein docking. *Reviews in Computational Chemistry*, *17*, 61.
- Elsasser, B., Valiev, M., & Weare, J. H. (2009). A dianionic phosphorane intermediate and transition states in an associative A(N)+D-N mechanism for the ribonucleaseA hydrolysis reaction. *Journal of the American Chemical Society*, *131*, 3869.
- Emsley, P., & Cowtan, K. (2004). Coot: Model-building tools for molecular graphics. *Acta Crystallographica*, *D60*, 2126.
- Fischer, D., Lin, S., Wolfson, H. L., & Nussinov, R. (1995). A geometry-based suite of molecular docking processes. *Journal of Molecular Biology*, *248*, 459.
- Fiser, A., & Sali, A. (2003). Modeller: Generation and refinement of homology-based protein structure models. *Methods in Enzymology*, *374*, 461.
- Fitter, J., Gutberlet, T., & Katsaras, J. (Eds.). (2006). *Neutron scattering in biology, techniques and applications*. Berlin: Springer.
- Florián, J., & Warshel, A. (1998). Phosphate ester hydrolysis in aqueous solution: Associative versus dissociative mechanisms. *The Journal of Physical Chemistry B*, *102*, 719.
- Fodor, K., Harmat, V., Kardos, J., Antal, J., Hetényi, C., Perczel, A., Szenthe, B., Gáspári, Z., Katona, G., & Gráf, L. (2005). Conformational adaptation of a canonical protease inhibitor

- upon its binding to the target protease increases specificity. *FEBS Journal*, 272, 167.
- Gao, J., & Truhlar, D. G. (2002). Quantum mechanical methods for enzyme kinetics. *Annual Review of Physical Chemistry*, 53, 467–505.
- Gilson, M. K., & Honig, B. (1987). Calculation of electrostatic potentials in an enzyme active site. *Nature*, 330, 84.
- Ginzinger, S. W., Gerick, F., Coles, M., & Heun, V. (2007). CheckShift: Automatic correction of inconsistent chemical shift referencing. *Journal of Biomolecular NMR*, 39, 223.
- Goh, C. S., Milburn, D., & Gerstein, M. (2004). Conformational changes associated with protein-protein interactions. *Current Opinion in Structural Biology*, 14, 104.
- Gray, J. J., Moughan, S. E., Wang, C., Schueler-Furman, O., Kuhlman, B., Rohl, C. A., & Baker, D. (2003). Protein-protein docking with simultaneous optimization of rigid-body displacement and side-chain conformations. *Journal of Molecular Biology*, 331, 281.
- GROMOS (2011). *Dynamic modelling of molecular systems*. <https://www1.ethz.ch/igc/GROMOS/>. Retrieved 10 Mar 2011.
- Gsponer, J., Hopearuoho, H., Whittaker, S. B. M., Spence, G. R., Moore, G. R., Paci, E., Radford, S. E., & Vendruscolo, M. (2006). Determination of an ensemble of structures representing the intermediate state of the bacterial immunity protein Im7. *Proceedings of the National Academy of Sciences of the United States of America*, 103, 99.
- Guvencs, O., & MacKerrell, A. D., Jr. (2009). Computational evaluation of protein-small molecule binding. *Current Opinion in Structural Biology*, 19, 56.
- Halgren, T. A. (1996). Merck molecular force field. 1–V. *Journal of Computational Chemistry*, 17, 490.
- Harmat, V., & Náray-Szabó, G. (2009). Theoretical aspects of molecular recognition. *Croatica Chemica Acta*, 82, 277.
- Horsefield, R., & Neutze, R. (2006). *Crystallization of lysozyme by the hanging drop method*. [http://www.csb.gu.se/rob/PDFs/Crystallisation\\_Course\\_2006\\_Part-I.pdf](http://www.csb.gu.se/rob/PDFs/Crystallisation_Course_2006_Part-I.pdf). Retrieved 10 Mar 2011.
- Hovmöller, S., Zhou, T., & Ohlson, T. (2002). Conformations of amino acids in proteins. *Acta Crystallographica*, D58, 768.
- Hu, H., & Yang, W. (2008). Free energies of chemical reactions in solution and in enzymes with ab initio quantum mechanics/molecular mechanics methods. *Annual Review of Physical Chemistry*, 59, 573.
- Hu, Z., & Jiang, J. (2009). Assessment of biomolecular force fields for molecular dynamics simulations in a protein crystal. *Journal of Computational Chemistry*. doi:10.1002/jcc.21330.
- Hub, J. S., Grubmüller, H., & de Groot, B. L. (2009). Dynamics and energetics of permeation through aquaporins. What do we learn from molecular dynamics simulations? In E. Beitz (Ed.), *Handbook of experimental pharmacology*, Aquaporins (Vol. 190, p. 57). Berlin: Springer.
- Jarymowycz, V. A., & Stone, M. J. (2006). Fast time scale dynamics of protein backbones: NMR relaxation methods, applications, and functional consequences. *Chemical Reviews*, 106, 1624.
- Jiao, D., Golubkov, P. A., Darden, T. A., & Ren, P. (2008). Calculation of protein–ligand binding free energy by using a polarizable potential. *Proceedings of the National Academy of Sciences of the United States of America*, 105, 6290.
- Katchalski-Katzir, E., Shariv, I., Eisenstein, M., Friesem, A. A., Aflalo, C., & Vakser, I. A. (1992). Molecular surface recognition: Determination of geometric fit between proteins and their ligands by correlation techniques. *Proceedings of the National Academy of Sciences of the United States of America*, 89, 2195.
- Kiss, R., Kovács, D., Tompa, P., & Perczel, A. (2008). Local structural preferences of calpastatin, the intrinsically unstructured protein inhibitor of calpain. *Biochemistry*, 47, 6936.
- Klähn, M., Rosta, E., & Warshel, A. (2006). On the mechanism of hydrolysis of phosphate monoesters dianions in solutions and proteins. *Journal of the American Chemical Society*, 128, 15310.
- Krieger, E., Nabuurs, S. B., & Vriend, G. (2003). Homology modeling. *Methods of Biochemical Analysis*, 44, 509.
- Lahiri, S. D., Zhang, G., Dunaway-Mariano, D., & Allen, K. N. (2003). The pentavalent phosphorus intermediate of a phosphoryl transfer reaction. *Science*, 299, 2067.
- Lange, O. F., Lakomek, N. A., Fares, C., Schroder, G. F., Walter, K. F. A., Becker, S., Meiler, J., Grubmüller, H., Griesinger, C., & de Groot, B. L. (2008). Recognition dynamics up to microseconds revealed from an RDC-derived ubiquitin ensemble in solution. *Science*, 320, 1471.
- Lasilla, J. K., Zalatan, J. G., & Herschlag, G. (2011). Biological phosphoryl transfer reactions: Understanding mechanism and catalysis. *Annual Review of Biochemistry*, 80. doi:10.1146/annurev-biochem-060409-092741.
- Lesk, A. M., Bernstein, H. J., & Bernstein, F. C. (2008). Molecular graphics in structural biology. In M. Peitsch & T. Schwede (Eds.), *Computational structural biology, methods and*

- applications* (p. 729). Singapore: World Scientific Publishing.
- Lin, M. S., Fawzi, N. L., & Head-Gordon, T. (2007). Hydrophobic potential of mean force as a solvation function for protein structure prediction. *Structure*, 15, 727.
- Lindorff-Larsen, K., Best, R. B., Depristo, M. A., Dobson, C. M., & Vendruscolo, M. (2005). Simultaneous determination of protein structure and dynamics. *Nature*, 433, 128.
- Luft, J. R., Collins, R. J., Fehrman, N. A., Lauricella, A. M., Veatch, C. K., & DeTitta, G. T. (2003). A deliberate approach to screening for initial crystallization conditions of biological macromolecules. *Journal of Structural Biology*, 142, 170.
- MacKerell, A. D., Jr. (2004). Empirical force fields for biological macromolecules: Overview and issues. *Journal of Computational Chemistry*, 25, 1584.
- Makarov, V., Pettitt, B. M., & Feig, M. (2002). Solvation and hydration of proteins and nucleic acids: A theoretical view of simulation and experiment. *Accounts of Chemical Research*, 35, 376.
- Mancera, R. L. (2007). Molecular modeling of hydration in drug design. *Current Opinion in Drug Discovery*, 10, 275.
- Mehta, N., & Datta, S. N. (2008). Theoretical investigation of redox species in condensed phase. *Journal of Chemical Sciences*, 119, 501.
- Menyhárd, D. K., & Náray-Szabó, G. (1999). Electrostatic effect on electron transfer at the active site of heme peroxidases: A comparative molecular orbital study on cytochrome C peroxidase and ascorbate peroxidase. *Journal of Physical Chemistry B*, 103, 227.
- Mildvan, A. S. (1997). Mechanisms of signaling and related enzymes. *Proteins: Structure, Function, and Genetics*, 29, 401.
- Mintseris, J., Wiehe, K., Pierce, B., Anderson, R., Chen, R., Janin, J., & Weng, Z. (2005). Protein-protein docking benchmark 2.0: An update. *Proteins: Structure, Function, and Bioinformatics*, 60, 214.
- Mohan, V., Gibbs, A. C., Cummings, M. D., Jaeger, E. P., & DesJarlais, R. L. (2005). Docking: Successes and challenges. *Current Pharmaceutical Design*, 11, 323.
- Náray-Szabó, G., Fuxreiter, M., & Warshel, A. (1997). Electrostatic basis of enzyme catalysis. In G. Náray-Szabó & A. Warshel (Eds.), *Computational approaches to biochemical reactivity*. Dordrecht: Kluwer.
- Palmer, A. G., III, Kroenke, C. D., & Loria, J. P. (2001). Nuclear magnetic resonance methods for quantifying microsecond-to-millisecond motions in biological macromolecules. *Methods Enzymology*, 339, 204.
- Porollo, A., & Meller, J. (2007). Prediction-based fingerprints of protein interactions. *Proteins: Structure Functional and Bioinformatics*, 66, 630.
- Protein Data Bank. (2011). *PDB current holdings breakdown*. <http://www.rcsb.org/pdb/statistics/holdings.do>. Retrieved 9 July 2011.
- Redfield, C. (2004). NMR studies of partially folded molten globule states. In A. K. Downing (Ed.), *Protein NMR techniques* (2nd ed.). Totowa: Humana Press Inc.
- Richter, B., Gsponer, J., Várnai, P., Salvatella, X., & Vendruscolo, M. (2007). The MUMO (Minimal Under-Restraining Minimal Over-Restraining) method for the determination of native state ensembles of proteins. *Journal of Biomolecular NMR*, 37, 117.
- Ritchie, D. W. (2008). Recent progress and future directions in protein-protein docking. *Current Protein and Peptide Science*, 9, 1.
- Rosetta@home. (2011). <http://boinc.bakerlab.org/rosetta/>. Retrieved 10 Mar 2011.
- Schmucki, R., Yokoyama, S., & Güntert, P. (2009). Automated assignment of NMR chemical shifts using peak-particle dynamics simulation with the DYNASSIGN algorithm. *Journal of Biomolecular NMR*, 43, 97.
- Schorn, C., & Taylor, B. J. (2004). *NMR-spectroscopy: Data acquisition* (2nd ed.). New York: Wiley.
- Schwieters, C. D., Kuszewski, J. J., & Clore, G. M. (2006). Using Xplor-NIH for NMR molecular structure determination. *Progress in Nuclear Magnetic Resonance Spectroscopy*, 48, 47.
- SWISS-MODEL. (2011). *A fully automated protein structure homology-modeling server*. <http://swissmodel.expasy.org/>. Retrieved 10 Mar 2011.
- Szentei, B., Gáspári, Z., Nagy, A., Perczel, A., & Gráf, L. (2004). Same fold with different mobility: Backbone dynamics of small protease inhibitors from the desert locust, *Schistocerca gregaria*. *Biochemistry*, 43, 3376.
- Van Der Spoel, D., Lindahl, E., Hess, B., Groenhof, G., Mark, A. E., & Berendsen, H. J. (2005). GROMACS: Fast, flexible, and free. *Journal of Computational Chemistry*, 26, 1701.
- Van Dijk, A. D. J., & Bonvin, A. M. J. J. (2006). Solvated docking: Introducing water into the modelling of biomolecular complexes. *Bioinformatics*, 22, 2340.
- Volk, J., Herrmann, T., & Wüthrich, K. (2008). Automated sequence-specific protein NMR assignment using the memetic algorithm MATCH. *Journal of Biomolecular NMR*, 41, 127.



- Wang, W., Donini, O., Reyes, C. M., & Kollman, P. A. (2001). Biomolecular simulations: Recent developments in force fields, simulations of enzyme catalysis, protein-ligand, protein-protein, and protein-nucleic acid noncovalent interactions. *Annual Review of Biophysics & Biomolecular Structure*, 30, 211.
- Warshel, A. (2003). Computer simulations of enzyme catalysis: Methods, progress, and insights. *Annual Review of Biophysics & Biomolecular Structure*, 32, 425.
- Wüthrich, K. (2002). *NMR studies of structure and function of biological macromolecules*. [http://nobelprize.org/nobel\\_prizes/chemistry/laureates/2002/wutrich-lecture.pdf](http://nobelprize.org/nobel_prizes/chemistry/laureates/2002/wutrich-lecture.pdf). Retrieved 10 Mar 2011.
- Xu, D., & Guo, H. (2008). Ab Initio QM/MM studies of the phosphoryl transfer reaction catalyzed by PEP mutase suggest a dissociative metaphosphate transition state. *Journal of Physical Chemistry B*, 112, 4102.
- Xu, Y., Xu, D., & Liang, J. (2007). *Computational methods for protein structure prediction and modeling* (Vols. 1–2). New York: Springer.
- Zsoldos, Z., Reida, D., Simona, A., Sadjada, S. B., & Johnson, A. P. (2007). eHiTS: A new fast, exhaustive flexible ligand docking system. *Journal of Molecular Graphics and Modelling*, 26, 198.





# 31 Applications of Computational Methods to Simulations of Proteins Dynamics

Wieslaw Nowak

Institute of Physics, Nicolaus Copernicus University in Torun,  
Torun, Poland

<i>Introduction</i> .....	1129
<i>Formalism of Molecular Mechanics and Molecular Dynamics Methods – A</i>	
<i>Short Presentation</i> .....	1130
Some History .....	1131
On the Origin of Potential Energy Surface (PES) Concept .....	1131
Force Fields .....	1133
Structure Optimization or Energy Minimization .....	1135
General Molecular Dynamics Scheme .....	1135
<i>Practical Aspects</i> .....	1137
MD Codes .....	1137
Visualization .....	1138
<i>Review of Reviews</i> .....	1138
<i>Selected Examples of Applications of MD to Study Proteins</i> .....	1140
Protein Folding Studies .....	1140
Protein-Drug Interactions and Docking .....	1141
Spectroscopy Experiments .....	1141
Functionally Important Motions (FIM) .....	1141
Molecular Machines .....	1142
The Mechanism of Enzymatic Activity .....	1142
Transport Phenomena in Proteins .....	1142
Structure and Dynamics of Ion Channels and Porins .....	1143
Charge Transfer in Protein Complexes .....	1143
Protein-DNA Interactions .....	1144
Origins of Molecular Diseases .....	1144
Simulations of Single Molecule AFM Experiments .....	1144

<i>Conclusions and Future Directions</i> .....	<b>1145</b>
<i>Acknowledgment</i> .....	<b>1145</b>
<i>References</i> .....	<b>1146</b>

**Abstract:** Advances in computer technology offer great opportunities for new explorations of protein structure and dynamics. Sound and well-established theoretical models may be successfully used for searching new biochemical phenomena, correlations, and protein properties. In this review the fast-growing field of computer simulations of protein dynamics is presented. The principles of currently used computational methods are outlined and representative examples of their recent advanced applications are given. In particular, protein folding studies, protein-drug interactions, transport phenomena, ion channels activity, molecular machines mechanics, origins of molecular diseases, and simulations of single molecule AFM experiments are addressed.

Experimentalists and management will not only become used to accepting the use of molecular modeling, but they will expect it. (Phillip R. Westmoreland)

WTEC Panel Report on Applications of Molecular and Materials Modeling, NIST 2002 (USA)

## Introduction

---

Proteins perform their functions through selective intermolecular interactions. These forces are exerted on external objects such as other proteins, inhibitors, nucleic acids, membranes, and signal molecules. The strength and temporal evolution of interactions depend on proteins' amino acid composition and a particular spatial arrangement of these basic building blocks. Non-native conformations usually prevent proteins from performing their "natural" tasks. The definition of "a protein conformation" is somewhat blurry, since proteins are flexible molecules. The energy landscapes of such large systems are very rich, complex, and highly multidimensional. In other words, one may expect that in its native, functional form a protein adopts not only one particular conformation but that rather numerous closely lying, related structures are present and all may participate in a given chemical or biological process. Quite often large-scale molecular motions are required for performing a given protein function (Bahar and Rader 2005; van Oijen 2007). For example, the enzyme helicase performs 50 revolutions per second during DNA replication and in RAS P21 protein conformational switch participate in signal transduction (Ma and Karplus 1997).

Capturing protein dynamical structures at work is not an easy task (Russel et al. 2009). Numerous experimental techniques have been developed throughout the twentieth century and in recent years: spectroscopy of all sorts, NMR, EPR, and even time-dependent X-ray crystallography. The advent of the computer era brought an excellent additional tool for studies of protein structures and dynamics. Since the pioneering application work by McCammon et al. (1977), empirical force fields have been used thousands of times to describe computationally proteins' dynamics and their interactions. Currently, quantum mechanics is the only physical theory having appropriate rigor for the description of molecular systems and their interactions. Unfortunately, *ab initio* (or force field-free) molecular dynamics (MD) simulations of proteins are still in their infancy and far from being widely available for research (Dal Peraro et al. 2007). On the other hand, a classical approximation, where individual atoms (or even groups of atoms) are replaced by model material points interacting through analytically predetermined potentials offers a very promising alternative for tedious, expensive, and difficult experimental studies of proteins. Computer modeling of protein structure and dynamics is currently a well-established, mature field of science (Karplus and McCammon 2002).

Why do we use computational molecular mechanics and/or molecular dynamics methods for studies of structure and protein dynamics? Here is a partial list of good reasons for their popularity and widespread applications:

1. Give material for mechanistic interpretation of protein functions.
2. Help to connect protein structure with its functions.
3. Provide time-resolved data on protein structures.
4. Provide visual models easy to manipulate (great pictures in papers!).
5. Promise to determine intra- and intermolecular interactions quantitatively.
6. Help to discover subtle functional differences in protein architectures.
7. Are useful in drug design (a great hope!).
8. Provide an easy tool to study mutants.
9. Allow for checking catalytic properties.
10. Are easy to verify, extend, or modify.
11. Bring information on thermodynamics.
12. Provide information on mechanical strength.
13. Quite often direct comparisons with experimental data such as NMR or x-ray structures, single molecule AFM spectroscopy are possible.
14. Cheap computers available everywhere.
15. Good quality, free software accessible via the Internet.
16. Relatively short “learning curve”.
17. Well-established field of computer modeling with many experts, conferences, and specialized journals.
18. Supercomputer power doubling every 18 months.
19. Strong support from industry and governments, biopharma sector, medical agencies, computer makers, etc.

And of course the last but not the least reason for the great popularity of computational modeling of proteins is just human curiosity and interest in solving interesting scientific problems. Solving the protein folding problem is the great challenge to scientific community. We know over 80 million protein sequences but only 70,000 3D structures are available in the Protein Data Bank (as of 2011). It is commonly believed that finding a realistic and sturdy method of converting a 1-D sequence into a 3-D structure should bring a Nobel Prize to the authors of such a discovery.

The purpose of this article is twofold: (a) we want to draw attention to major review papers and resources regarding studies of molecular dynamics of proteins and (b) we want to describe the most representative, modern applications of MD methods that have been published in recent years.

## **Formalism of Molecular Mechanics and Molecular Dynamics Methods – A Short Presentation**

---

In order to describe atomistic level chemical phenomena one has to use quantum mechanics (Dahl 2001). This theory applied to molecules brought “an explosion” of quantum chemistry and, together with the computer revolution, has changed the way the chemistry is done in the twentieth century. Despite great successes of quantum chemistry, this approach is now limited

to small or medium size systems, having 10–300 atoms. Proteins usually are composed of thousands of atoms; moreover their realistic models should take into account a substantial number of water molecules. Thus classical models of proteins are necessary. In such a simplified approach electrons are neglected, subtle quantum bonds are replaced by effective analytical potentials, and instead of atoms we have carefully designed model balls. The motion of atoms is treated in a classical way: validity of Newton equations of motion is assumed in the protein nanoworld. Structure of molecules may be optimized using classical force fields and methods of molecular modeling, the time evolution of a position of each individual atom may be followed for a reasonably long period of time using the molecular dynamics formalism, but a possibility of formation/breaking chemical bonds is basically lost. Thus, the real chemistry, based on chemical reactions, needs the full quantum theory. Nevertheless, the classical modeling provides so many useful hints into the nature of protein chemistry that computational modeling of protein structure and dynamics is a fundamental part of the research in all major laboratories.

## Some History

---

The Electronic Numerical Integrator And Computer (ENIAC) was completed at the University of Pennsylvania in Philadelphia in 1945. It weighed more than 27,000 kg (60,000 lb), and contained more than 18,000 vacuum tubes. It is regarded as the first successful digital computer. In 1955 E. Fermi, J. Pasta and S. Ulam calculated numerically the motions of a chain of coupled anharmonic oscillators. This is probably the first example that molecular dynamics simulation suggested an analytical solution for the problem studied. In 1957 Alder and Wainwright studied dynamics of a system of hard, two-dimensional discs (Alder and Wainwright 1957) Much later, in 1971, Rahman and Stillinger used a more realistic Lennard–Jones interaction potential to study motions in water (Rahman and Stillinger 1971). The duration of those simulations was about 10 ps.

The concept of interaction force field was applied to proteins by S. Lifson in 1969. This model was aimed at facilitating the refinement process of protein structure determination based on X-ray diffraction experiments (Levitt and Lifson 1969). Current force fields – sets of analytical formulas together with carefully chosen parameters – are based on infrared spectra, geometrical information from amide crystals, and quantum mechanical calculations. The famous paper published in 1977 by McCammon et al. (1977) on BPTI dynamics may be regarded as the first MD modeling of a protein. Interesting stories on the history and development of molecular dynamics simulations science may be found in the review published by Karplus (2003). At the beginning of 2011 in the PubMed bibliographical database nearly 9,000 papers were listed under the query “molecular dynamics simulation protein.” This area of computational chemistry and biology is very strong and is fast growing.

## On the Origin of Potential Energy Surface (PES) Concept

---

As we know, on the grounds of quantum mechanics, the complete information of the molecular system may be obtained from the wavefunction  $|\Phi\rangle$ , which is a solution of the Schrodinger equation:

$$\hat{H}|\Phi\rangle = \varepsilon|\Phi\rangle$$

where Hamiltonian  $\hat{H}$  contains both electron ( $i, j$ ) and nuclear (A,B) degrees of freedom (in atomic units):

$$\begin{aligned} \hbar &= 1 \\ "c &= 1"(137.) \\ m &= 1 \\ e &= 1 \end{aligned}$$

$$\begin{aligned} \hat{H} &= - \sum_{i=1}^N \frac{1}{2} \nabla_i^2 - \sum_{A=1}^M \frac{1}{2M_A} \nabla_A^2 \\ &\quad - \sum_{i=1}^N \sum_{A=1}^M \frac{Z_A}{r_{iA}} + \sum_{i=1}^N \sum_{i>j}^N \frac{1}{r_{ij}} + \\ &\quad + \sum_A^M \sum_{B>A}^M \frac{Z_A Z_B}{R_{AB}} \end{aligned}$$

If we adopt Born-Oppenheimer approximation, a separation of electronic and nuclear degrees of freedom is possible:

$$\hat{H}_{el} \Phi_{el} = \varepsilon_{el} \Phi_{el}$$

where electronic Hamiltonian is:

$$\hat{H}_{el} = \sum_{i=1}^N \frac{1}{2} \nabla_i^2 - \sum_{i=1}^N \sum_{A=1}^M \frac{Z_A}{r_{iA}} + \sum_{i=1}^N \sum_{i>j}^N \frac{1}{r_{ij}}$$

and electronic wavefunction  $\Phi_{el}$  depends in a parametric way on positions of all nuclei  $\{\vec{R}_A\}$ :

$$\begin{aligned} \Phi_{el} &= \Phi_{el}(\{\vec{r}_i\}; \{\vec{R}_A\}) \\ \varepsilon_{el} &= \varepsilon_{el}(\{\vec{R}_A\}) \end{aligned}$$

As one can see, the electronic energy  $\varepsilon_{el}$  depends on positions of nuclei as well. Thus, for each different arrangement of atoms  $\Phi_{el}$  is a different function of electron coordinates  $\vec{r}_i$ . For a fixed position of atoms (nuclei) the total energy reads:

$$\varepsilon_{tot}^{fixN} = \varepsilon_{el} + \sum_A^M \sum_{B>A}^M \frac{Z_A Z_B}{R_{AB}}$$

Such an approximation leads to the following nuclear Hamiltonian  $\hat{H}_{nucl}$ :

$$\begin{aligned} \hat{H}_{nucl} &= - \sum_{A=1}^M \frac{1}{2M_A} \nabla_A^2 + \langle \hat{H}_{nucl} \rangle_{\Phi_{el}} + \sum_A^M \sum_{B>A}^M \frac{Z_A Z_B}{R_{AB}} \\ &= - \sum_{A=1}^M \frac{1}{2M_A} \nabla_A^2 + \underbrace{\varepsilon_{el}(\{R_A\}) + \sum_A^M \sum_B^M \frac{Z_A Z_B}{R_{AB}}}_{\varepsilon_{tot}^{fixN}(\{R_A\})} \\ &= - \sum_{A=1}^M \frac{1}{2M_A} \nabla_A^2 + \varepsilon_{tot}^{fixN}(\{R_A\}). \end{aligned}$$

This total energy  $\epsilon_{\text{tot}}^{\text{fix}N}$  (with the fixed positions of atoms) provides a potential for nuclear motion. Such quantity is called Potential Energy Function (PES) and in molecular dynamics simulations is approximated by a force field. In terms of quantum mechanics solutions to the nuclear Schroedinger equation:

$$\hat{H}_{\text{nucl}}\Phi_{\text{nucl}} = \epsilon_{\text{nucl}}\Phi_{\text{nucl}}$$


provides information on vibrations, rotations and translations of the molecule. But the dynamics of a molecule (protein) may also be studied classically, provided that the realistic molecular PES is known.

## Force Fields

Classical force fields have a common assumption that the analytic potentials are a good approximation to the “real” PES. It is also assumed that parameters pertaining to particular atom types (or groups of atoms) are transferable from one model biomolecular system to similar ones.

The general expression for potential energy  $V$  is the following:

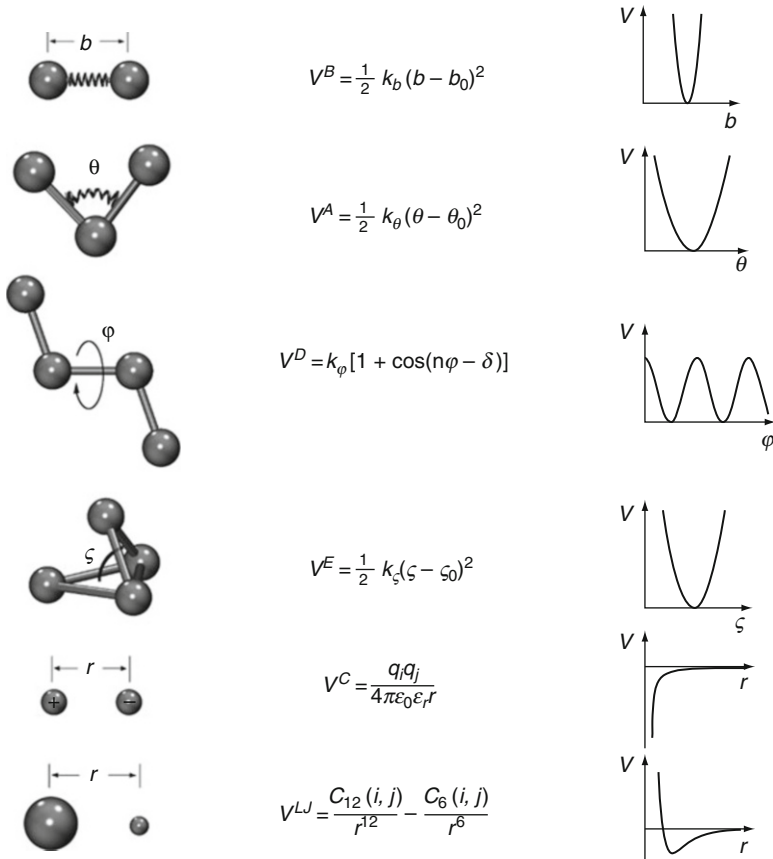
$$V = \sum_{\text{bonds } i} V_i^B + \sum_{\text{bond angles } j} V_j^A + \sum_{\text{torsional angles } k} V_k^D \\ + \sum_{\text{improper angles } l} V_l^E + \sum_{\text{atom pairs } (r,s)} (V_{r,s}^C + V_{r,s}^P + V_{r,s}^{VdW})$$

The physical meaning of each term is described in the legend to  Fig. 31-1. In general, an intuitive decomposition of energy is used in this equation. Additive components correspond to energies of chemical bonds ( $V_i^B$ ), energies related to angular deformation of the optimal molecular structure ( $V_j^A$ ,  $V_k^D$ ,  $V_l^E$ ) and pairwise interactions of all atoms present in the system related to Coulomb energy of a system of partially charged model atoms ( $V^C$ ) and so called Lennard–Jones (or Van der Waals) term ( $V^P + V^{VdW}$ ).

One should distinguish between all-atom and united-atom force fields. In this second type the groups of real atoms are used as a basic model “atoms,” for example, the methyl group  $\text{CH}_3$  may be treated as a special type of a united atom having molecular weight of 15. Such simplification saves some computer time and in certain cases does not affect the results of modeling. The drawback of the majority of force fields currently used is the lack of atomic polarization effects. Partial charges on atoms to some extent include polarization, but usually parameters remain fixed through the whole simulation. But the reality is different. Induced dipole moments may change dynamics of the molecule and may affect results of modeling. Charges are modified “on-the-fly.” Thus, it is expected, that the next generation of force fields will include atomic polarizability (Warshel et al. 2007).

There are tens of classical force fields designed for the description of protein structure and dynamics. Among the most popular ones are CHARMM (MacKerell et al. 1998), AMBER (Weiner et al. 1984), GROMOS05 (Christen et al. 2005), and OPLS (Jorgensen and Tiradorives 1988). Perhaps the best up-to-date account of various force fields and computer codes available for protein simulation is Wikipedia on the Internet. The problem of design of a potential energy function for proteins is discussed in Boas and Harbury (2007). Only very recently some papers concerning comparison of the quality of various force fields have appeared (Guvench and MacKerell 2008; Hornak et al. 2006). It is obvious that each force field was optimized for





■ Fig. 31-1

Interaction contributions to a typical force field. Bond stretch vibrations are described by a harmonic potential  $V^B$ , the minimum of which is at the equilibrium distance  $b_0$  between the two atoms connected by chemical bond  $i$  (the indices  $i, j$  etc. are not shown in the Figure). Bond angles and out-of-plane (improper) angles are also described by harmonic potential terms,  $V^A$  and  $V^E$ , where  $\theta_0$  and  $\zeta_0$  denote the respective equilibrium angles. Dihedral twists (torsional angles) are subjected to a periodic potential  $V^D$ ; the respective force constants are denoted by  $k$ 's with appropriate indices. Non-bonded forces are described by Coulomb interactions,  $V^C$ , and Lennard–Jones potentials,  $V^{LJ} = V^P + V^{vdW}$ , where the latter includes the Pauli repulsion,  $V^P \sim r^{-12}$  and the van der Waals interaction,  $V^{vdW} \sim -r^{-6}$ , respectively (based on: Grubmueller (2004). © 2004 by John von Neumann Institute for Computing)

a different set of systems and they were tuned to reproduce different properties, so it is not clear how a fair comparison should be performed. On the other hand, in the protein modeling community there is some tension and pressure that more effort should be devoted for careful scrutinizing of the force fields and for setting clear recommendations regarding “justified” error bars for results of computations (Aliev and Courtier-Murias 2010).

## Structure Optimization or Energy Minimization

The most standard problem of molecular mechanics applied to proteins is the following: what is the best (optimum) structure of the studied protein? The common assumption is that the minimization of the energy (or sometimes another thermodynamic function such as free energy) will give the answer. It is believed that such a structure is a good approximation to the native structure of the protein of interest.

There are numerous computational methods of finding local minima (Chou 2004; Klepeis et al. 2003; Kmiecik et al. 2007). Unfortunately, there is no general method known that might lead to the global minimum of PES of a given protein. Such techniques as simulated annealing (Kannan and Zacharias 2009) or replica exchange (Sugita 2009; Sugita and Okamoto 1999) supported by genetic algorithms, may help to sample the conformational space efficiently and may generate plausible “candidates” for the global minimum, but these approaches are heuristic recipes rather than rigorous procedures. Quite often the energetics of transition from a conformation A to a conformation B is of interest and should be calculated (Schlegel 2003). There are numerous methods of finding classical reaction paths appropriate for proteins, for example, the Self Penalty Walk (Nowak et al. 1991). It is worth noting the tricky and promising technique of milestoneing (Kuczera et al. 2009). The interested reader may find details of reaction paths calculations for large molecular systems in (Elber et al. 2002).

## General Molecular Dynamics Scheme

The basic physics behind a simple molecular dynamics scheme seems to be trivial. We want to solve simultaneously  $M$  Newton’s equation of motion for each individual atom  $i$  (or a grain of atoms):

$$a_i = \frac{1}{m_i} F_i, \quad i = 1, \dots, M$$

The force  $F_i$  acting on each atom may be calculated (locally) as gradient of the potential (PES):

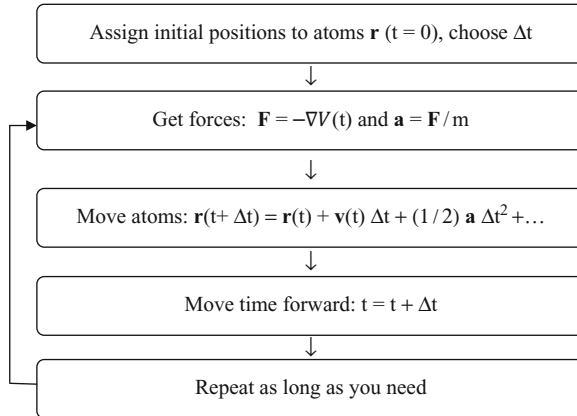
$$F_i = -\nabla V.$$

With forces, one can easily have accelerations acting on each atom. We assume that the molecular system is deterministic (not always the case) and we may predict the position of all atoms by integrating the acceleration (twice) with respect to time. There are many numerical algorithms suitable for solving these problems, but due to its simplicity and numerical stability the Verlet algorithm is perhaps the most frequently used in real simulations. Of course, one must assume the initial structure of the protein and plug in time into numerical algorithm. Time variable is discretized, the size of the time-step depends on the time scale of the fastest motions we want to study. For real proteins in ambient temperatures it is usually 1 fs ( $10^{-15}$  s).

► [Figure 31-2](#) shows the major steps in MD routines.

Here we present the typical steps in doing molecular dynamics simulations of proteins:

1. What is the scientific problem we want to solve?
2. Is classical MM/MD modeling an appropriate methodology for this type of the problem? Would these calculations help to understand nature? How might our results be verified experimentally?



■ Fig. 31-2

### A general scheme of generating MD trajectory

3. Do we have enough knowledge/experience/expertise or do we prefer a “black-box” approach? (“Let’s calculate something, and we will see ...”)?
4. What is the expected time of calculations required to obtain reasonable, publishable results? (Note: one trajectory usually is not enough)
5. Do we have sufficient resources (licensed codes, computer time, storage space, manpower, ...)?
6. Having answered points (1–5) we need to set up an initial model of the protein. Usually an experimental structure (X-ray or NMR) downloaded from the PDB [www.pdb.org](http://www.pdb.org) (Berman et al. 2000) is a good starting point.
7. We should check whether the structure is complete. Is the resolution of the structure adequate for our purposes? Does it contain all amino acids? Are there any missing atoms? Do we have force field parameters for prosthetic groups/ligands/metal ions/etc. and exotic stuff present in our favorite protein? One should always check the “biological unit” entry in PDB to avoid misunderstanding of the real structure of a protein of interest.
8. We need to decide in what particular environment simulation will proceed. Vacuum? Water? Continuum dielectric? Exotic solvent? pH? Should ions be added for charge neutralization?
9. In what conditions of temperature and pressure should we plan simulations? How will the temperature be maintained? Shall we switch to the Langevin dynamics?
10. Do we need the quasi-infinite model (Periodic Boundary Conditions, PBC)? What is an appropriate shape and size of the solvation box? Should we use the Ewald summation technique to properly calculate electrostatic interactions?
11. Let us assume we perform a standard 20 ns MD simulation of a protein having a reasonable initial structure. We will add a box of model water molecules at least 6 (or 9) Angström thick at each protein border region.
12. After these initial preparations, the first step will be an optimization of the protein structure. We may initially freeze the protein and allow for some steps of minimization of solvated water molecules (for example, 500 steps of the Steepest Descents (SD) method).
13. Next, we may allow for some MD simulations of the solvent (water). We may gradually increase the temperature of waters from 0 K (minimized structure in principle is not related

to any temperature), to 300 K, for a 500 ps period of time. The time step in MD is usually 1 fs, thus we will ask the MD code to perform 500,000 steps in integration of equations of motions.

14. We may relax constraints and “unfreeze” the protein. Some 500–3,000 SD steps should be sufficient to transfer the protein (+water) from the “experimental” minimum to a “local force field related” minimum.
15. We may increase the temperature in a stepwise manner from 0 to 300 K for the whole system. 1 ns of such heating phase is often more than enough.
16. If we perform  $T = \text{const.}$  simulation, we need to equilibrate the system well before useful data may be collected. The equilibration time  $t_{\text{eq}}$  depends on the system studied. In the current literature one can find  $t_{\text{eq}}$  from 1 to 5 ns. We should observe at least a few geometrical parameters of our protein. The RMS distance calculated for  $C_{\alpha}$  atoms from the minimized (or PDB) structure to the current one may help to estimate whether the model is fully equilibrated. The RMS plot versus time should be flat.
17. Now we may use the equilibrated system (protein + water) and launch a long production run (10–20) ns.
18. The structures at selected time point (frames) should be stored. These structures are further analyzed using computer graphics and specialized software analysis tools. One may store structures every 100 steps (fs) or even every 1,000 steps, depending on what data are needed.
19. In the theory we should set up modeling for infinite time in order to sample all configuration space of the protein studied. This is obviously not possible, thus we cross our fingers and believe in ergodicity of the trajectory obtained. Once calculated quantities do not depend on time of simulation, it is a reasonable signal that the longer calculation will not bring new information. Usually several shorter trajectories, with different initial conditions, will provide better understanding of the protein than one but very long trajectory.

One should note that solvation effects may be accounted for not only by including into the studied system explicit water molecules, but also via implicit solvents models (Chen and Brooks 2008; Chen et al. 2008). Changes in free energy upon solvation are often estimated using the generalized Born model (Bashford and Case 2000; Hou et al. 2011).

## Practical Aspects

---

Even the most sophisticated and advanced methods (Schwede and Peitsch 2008) need tools to perform practical computations. Both computer codes and hardware are required. The majority of papers published in this field utilized public domain codes to obtain data on protein dynamics. There are of course numerous advanced and elaborate commercial packages, such as Discovery Studio (Accelrys), HyperChem, Yassara, Desmond/Maestro (Schroedinger Inc.), popular in industry and certain research environments, but it seems that routine academic work is based on freely available software.

## MD Codes

---

One of the first codes was CHARMM (the commercial version is called CHARMM), originally developed at Harvard University. This suite of programs is very versatile and contains all major

computational methods. It is parallelized and allows also for QM/MM simulations (Brooks et al. 2009). The most recent, tenth, version of AMBER is heavily optimized with respect to performance and contains such advanced techniques as Locally Enhanced Sampling and SCC-DFTB QM/MM methods. AMBER force field is popularly used for modeling of nucleic acids, but thousands of simulations of proteins have been published as well (Case et al. 2005).

In Europe the GROMACS code has growing popularity due to its speed and good scaling on parallel clusters (Van Der Spoel et al. 2005). The methods of Essential Dynamics, Principal Component Analysis, and Flooding (Lange et al. 2006) are available here. Perhaps the recent GROMITA graphical interface to GROMACS 4.0 will increase further the number of users of this code (Hess et al. 2008; Sellis et al. 2009).


In our lab we are happy with the NAMD code (Phillips et al. 2005). It is well documented, relatively fast, well maintained, frequently updated and scales nicely. It has certain flexibility in selection of the force field (CHARMM, AMBER). The authors have implemented Locally Enhanced Sampling (LES), Implicit Ligand Sampling (ILS), Replica Exchange, and Steered Molecular Dynamics (SMD) schemes. New versions of NAMD will run on a GPU, and there are also some attempts to port this code to a computational grid environment.

This short presentation of major packages devoted to protein dynamics simulations is far from complete. Some Internet services, including Wikipedia, try to maintain the updated lists of available MD codes.

## Visualization

---

In the era of the Internet and efficient graphics cards we have tens of programs designed to visualize a protein structure. Each year brings new players in this competition. Many researchers prefer to pay a license fee and to use professional graphics for visualization of their structure and MD data: Accelrys, Maestro, HyperChem, Yassara, etc. A comprehensive list of modern molecular visualization codes may be found in the book by Gu and Bourne (2009).

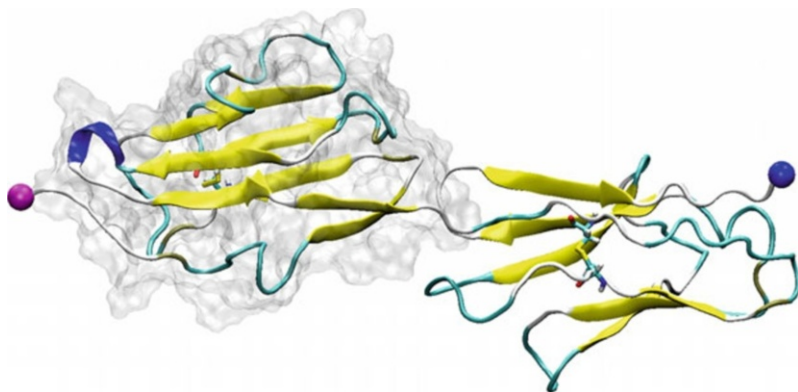
In recent years a very versatile, user friendly, and robust code evolved from the early Visual Molecular Dynamics (VMD) software, created by K. Schulten's group at UIUC in the US (Humphrey et al. 1996). There are thousands of users of this package. An example of VMD visualization of the gradual stretching of modular adhesive protein contactin is presented in  [Fig. 31-3](#). Preparation of a similar picture is not difficult if one uses a VMD guide (Hsin et al. 2008).

Caveat: It is interesting to note that an easy access to MD codes through a GUI is somewhat dangerous: without investing too much time an inexperienced user may obtain (by trial-and-error procedure) “reasonably” looking results that may be a completely wrong answer to the problem (Knapp and Schreiner 2009). Thus, in the MD simulations of proteins a good deal of time must be spent learning the theory and subtle features of this research method.

## Review of Reviews

---

Since the very first proceedings of CECAM workshop in France devoted to models for protein dynamics (Berendsen 1976), details of computer simulations of physical and biological systems have been described in many comprehensive books. For example, a good starting point may



■ Fig. 31-3

A fragment of modular adhesive protein contactin, present in neuronal connections, visualized using VMD code (Humphrey et al. 1996) (K. Mikulska, UMK, Poland)

be the book by Allen and Tildesley published in 1987 (Allen and Tildesley 1987). It is devoted mainly to simulations of liquids, but many methodological aspects of computational modeling of physical systems are well covered. Elementary details of molecular simulations are presented by Haile (1992). In a classical text by Rapaport (1995) explanations of basic software and algorithms may be found. The introductory book by Frenkel and Smit focuses on Monte Carlo and molecular dynamics methodologies. The authors analyze algorithms and present useful FORTRAN-based pseudocodes for basic algorithms (Frankel and Smit 2001). Broader aspects of molecular modeling are covered by Leach (2001). In this book, besides main algorithms and methods of computational chemistry and modeling methods of protein structure prediction, free energy calculations, solvation, and drug design applications are presented. The book co-authored by M. Karplus, one of the founding fathers of MD simulations of proteins, is a valuable source of information for everyone (Becker and Karplus 2006).

Excellent reviews on various aspects of biomolecular modeling are published quite often. Here only a very concise, subjective, and limited review of the recent (i.e., published in twenty-first century) reviews is presented, just to provide handy reference to further search for relevant information.

A large body of proteins perform catalytic functions. MD calculations of enzymatic mechanisms are a great challenge to theory and the best strategy for simulations is a matter of continuous debate. In reviews by Warshel (2002, 2003) the main aspects of proper understanding of catalysis are described. Modeling of chemical reactions requires a special approach – some possibilities are outlined in (van Speybroeck and Meier 2003) and a comprehensive review of computational enzymology, largely based on QM/MM methods, has recently appeared (Lonsdale et al. 2010). Yet another class of problems arise when protein-protein interactions are modeled (Elcock et al. 2001).

Basic methods and main applications of computer modeling of biosystems up to 2003 are presented in a comprehensive work by Schlick (2002), a review by Goodfellow et al. (Moraitakis et al. 2003), a paper by Hansson and van Gunsteren (2002), and in the review by Kremer (2003). Particularly interesting, but difficult due to special boundary conditions, are studies of membrane proteins (Ash et al. 2004; Gumbart et al. 2005). The progress in this particular field is

important, since receptor proteins are common and attractive drug targets. One can also find reviews dedicated to application of simulations in narrow subdisciplines, such as biotechnology (Aksimentiev et al. 2008).

A newer (2006) account on methods, problems, and goals of biomolecular simulations is given in a comprehensive article by Van Gunsteren (2006). Focused mainly on proteins, a very informative paper by Adcock and McCammon provides an excellent description of methods and key results from MD may be found. (Adcock and McCammon 2006). New methodological advances were also reviewed at the same time: Chu et al. popularize multiscale simulations (Chu et al. 2007), while Elber et al. comment on the current literature on long time simulation methods (Dal Peraro et al. 2005) and Liwo et al. on efficient methods of sampling of proteins' conformational space (Liwo et al. 2008).

A lot of effort has been put in elaborating reliable and practical methods of calculating changes in free energies (Christ et al. 2010; Kholmurodov et al. 2003; Meirovitch 2007; Pohorille et al. 2010). The term “computational alchemy” has even been coined for some counterintuitive but physically valid methods (Aleksandrov et al. 2010; Straatsma and McCammon 1992). Such data are required, for instance, in drug design (Galeazzi 2009; Morra et al. 2008).

One can find specialized reviews of MD approach to biological problems (Avila et al. 2011; Dodson et al. 2008) or to future nanotechnology applications of self-assembling systems (Klein and Shinoda 2008). Interestingly enough, with the largest computer system currently available, multimillion atom simulations are possible (Sanbonmatsu and Tung 2007). Prospects of the computational approach to chemistry and biology are outlined in a comprehensive review by Mulholland et al. (Van Der Kamp et al. 2008).

This field will surely profit from the use of the Internet. Some groups try to develop user-friendly and even charming portals to the simulation software (Miller et al. 2008). Other researchers, for example, the group of V. Daggett, invest in large-scale depositories of scientific data stemming from MD simulations (Simms et al. 2008). Sharing data, especially obtained using advanced computer resources, is always a good idea. Such an “ocean” of numbers deserves careful scrutiny. Hopefully, some scientific treasures will be fished-out in the near future.

## Selected Examples of Applications of MD to Study Proteins

---

It is not possible in this short chapter to describe all current applications of simulations for proteins dynamics studies. However, we point out selected, representative, widely discussed problems where the MD methods have been used.

### Protein Folding Studies

---

Proteins are synthesized as linear polymers, but for their function precise 3D structure is usually necessary. The process of folding to such native structure is vigorously studied using molecular dynamics simulations (Freddolino et al. 2010; Schaeffer et al. 2008; Zhang et al. 2009). The main obstacle in this research is still a very limited (10–100 ns) timescale accessible for standard modeling (Mayor et al. 2003; Scheraga et al. 2007). Only some benchmark, record calculations achieved microseconds (Piana et al. 2011), including studies for very small systems such as a

villin headpiece fragment, one of the most stable and fastest-folding naturally occurring proteins (Duan and Kollman 1998; Ensign et al. 2007; Freddolino and Schulten 2009). Simulations help to propose universal folding mechanisms and to determine intermediates, and to discover bias introduced by approximate nature of force fields (Freddolino et al. 2008, 2009). A lot of effort is devoted to finding an intelligent method of “ab initio” protein folding (Ekonomiuk et al. 2005; Shakhnovich 2006). The progress may be checked by following the worldwide folding competition CASP (Shi et al. 2009).

## Protein-Drug Interactions and Docking

---

The pharmaceutical industry badly needs reliable theoretical methods for calculating ligand binding affinities (Aqvist et al. 2002; Gallicchio and Levy 2011; Morra et al. 2010). The problem is not easy, since many factors, for example, multiple binding sites, protein flexibility, and solvent model, affect a small value of the free energy of binding (Deng and Roux 2009; Simonson et al. 2002; Spyraakis et al. 2011). The chance of getting wrong results is high. However, in the literature there are hundreds papers devoted to protein-drug interactions. The recent threat of a bird flu pandemic triggered studies of interactions of neuraminidases or influenza A peptides with antiviral drugs (Khurana et al. 2011; Le et al. 2009). The role of induced fit effects during ligand docking to steroid hormones binding receptors was analyzed by Cornell and Nam (2009). MD may be used in an anticancer drug development (Lauria et al. 2010; Rosales-Hernandez et al. 2009) or in studies of inhalation anesthetics interactions with proteins (Vemparala et al. 2010).

## Spectroscopy Experiments

---

Spectroscopy is an extremely useful analytical and diagnostic technique with wide applications in chemistry, physics, life sciences, industry, and medicine. Molecular dynamics helps to interpret experimental data. For example, Sen et al. used simulations to explain time-resolved Stokes-shift experiments with biopolymers (Sen et al. 2009). Fluorescent proteins, especially based on GFP, are often studied computationally. Recently Sun et al. applied QM/MM and MD to explain dependence of Red Fluorescent Protein on pH of the environment (Sun et al. 2010). Computational unfolding of Photoactive Yellow Protein may give useful hints for spectroscopic studies (Vreede et al. 2010) as well as the modeling of visual pigments (Wanko et al. 2006). Quite often the interpretation of NMR experiments profits from simulations, such as prediction of nitroxide hyperfine coupling constants in solution (Houriez et al. 2008) or evaluation of rotational diffusion constants from MD (Wong and Case 2008). On the other hand, the NMR spin relaxation data help to improve force fields (Showalter and Bruschweiler 2007).

## Functionally Important Motions (FIM)

---

Some motions of proteins are critical for their proper functioning (Henzler-Wildman and Kern 2007). MD simulations may identify such modes. Relation of protein's mechanics and function was reviewed in 2003 by Schulten (Tajkhorshid et al. 2003), but since that time this group studied new problems, for example, plant phototropism (Freddolino et al. 2006a) and complete



satellite Tobacco Mosaic Virus vibrations (Freddolino et al. 2006b). Other groups investigated large-scale motions in biosensors (Tatke et al. 2008), linker motions crucial for ligase (Liu and Nussinov 2010), or retinal release from opsin (Wang and Duan 2011). Extraction of information on FIM needs special methodology (Schuyler et al. 2009), such as Essential Dynamics (Amadei et al. 1993) or Metadynamics (Biarnes et al. 2011), thus new ways of MD data analysis are suggested (Hub and de Groot 2009).

## Molecular Machines

---

Having such powerful computers at hand, we are ready to study molecular machines – proteins or bio-complexes that perform some mechanical work during their activity cycle (Kolomeisky and Fisher 2007; Scheres 2010). Rotations of parts of ATPase were studied by Ma et al. in 2002, and molecular rotation in ATP synthase by Aksimentiev et al. in 2004. Solvent-induced lid opening in lipases was also analyzed computationally (Rehm et al. 2010). Later the whole cellular mechanics simulations were reviewed by Gao et al. (2006).

Mechanoselective ion channels may be considered as molecular machines, too, and ion gating is better understood now due to MD (Vasquez et al. 2008). Simulations were applied to the helicase motor (Dittrich and Schulten 2006; Flechsig and Mikhailov 2010; Yu et al. 2007) and perhaps to the most advanced (up to date) object: the ribosome (Becker et al. 2009; Romanowska et al. 2008; Trylska 2010).

## The Mechanism of Enzymatic Activity

---

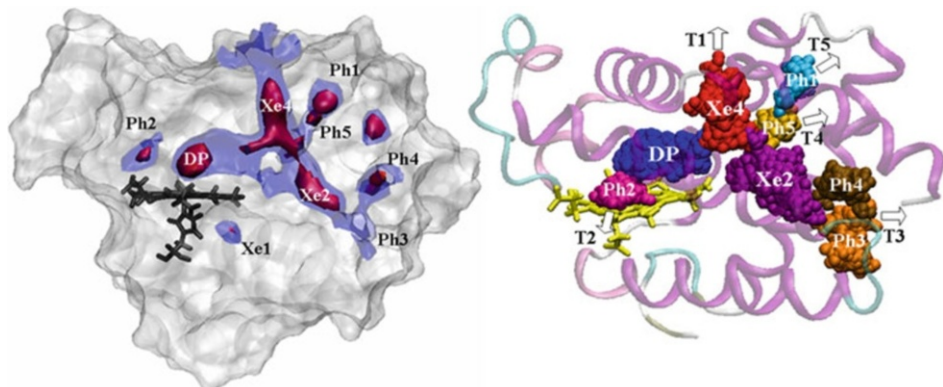
Recent progress in computational enzymology is described in Lonsdale et al. (2010). Numerous enzymes were studied using MD simulations, for example, Peplowski et al. used the steered MD method to enforce a ligand transport within the biotechnological enzyme nitrile hydratase (Peplowski et al. 2008). In that way residues that may change catalytic properties of this metalloprotein have been indicated. Carloni et al. recently used the MD approach to explain the mode of action of the famous group of signal G-proteins (Khafizov et al. 2009).

## Transport Phenomena in Proteins

---

Heme proteins are popular objects of MD simulations (Banci 2003; Bikiel et al. 2006), since transport processes of small gaseous ligands (O<sub>2</sub>, NO, CO) are important for physiology, and since they serve as a “test ground” for new methods. Myoglobin is even sometimes called a “hydrogen atom” of MD simulations. Recently, two new members of the hemoglobin family have been discovered, and studies of diffusion paths and free energy landscapes for neuroglobin (Orlowski and Nowak 2008) and cytoglobin were published (Orlowski and Nowak 2007). It seems that such systematic study allows for construction of a uniform picture of ligand migration pathways and the evolution of transport proteins structure (Cohen et al. 2008) (► Fig. 31-4).

Due to its versatile role, nitric oxide transport within proteins is particularly intensively studied (Marti et al. 2008).



■ Fig. 31-4

A comparison of low free energy regions (ILS/PMF maps, *left*) with oxygen diffusion paths in *Drosophila melanogaster* hemoglobin (*right*) calculated by MD simulations – 8 ns, CHARMM27 force field, NAMD code (Phillips et al. 2005), L. Dams, W. Nowak (unpublished results). Figure was prepared using the VMD code (Humphrey et al. 1996)

## Structure and Dynamics of Ion Channels and Porins

Dynamics and transport through ion channels and other pores in biological membranes is a subject of vigorous research. Among many papers, the work on channel gating by M. Sansom's group (Beckstein et al. 2003) is worth mentioning as well as by B. Roux et al. in computational studies of ion channels (Roux and Schulten 2004) and the paper on the ion conductance in a potassium channel (Boiteux et al. 2007).

References to numerous computational studies of aquaporins may be found in a review by Hub et al. (2009). Water transport in eye lenses has been recently investigated using large-scale simulations by D.E. Shaw's group (Ikeguchi 2009). At the same time, K. Schulten's team has watched carefully not only water transport phenomena (Zhu et al. 2004) but also nanomechanics of RNA in nanopores (Khalili-Araghi et al. 2009; Miao and Schulten 2009).

## Charge Transfer in Protein Complexes

Charge transfer (CT) and proton transport are very precisely tuned due to a protein structure. Such CT processes in photosynthetic complexes may be effectively modeled using both quantum and classical method (Buda 2009). Proton translocations in proteins are well followed by computer simulations (Cukier 2004). An application of the MD methods in studies of biomimetic complexes having some prospective usage in bionanotechnology has been published (Alvarez-Paggi et al. 2010).

## Protein-DNA Interactions

---

Transfer of information from DNA to proteins and its impact on the whole cell activity is determined by protein-DNA interactions. Such complexes are difficult to model due to their size and heterogeneity, but a good understanding of these systems is a key to genetics. MacKerell and Nilsson recently reviewed computational studies in this area (Mackerell and Nilsson 2008). Good examples of successful MD applications are studies of p53 protein binding modes to DNA quadruplexes (Ma and Levine 2007) or investigations that revealed fascinating details of the mechanism of Lac repression (Villa et al. 2005).

## Origins of Molecular Diseases

---

Applications of computer simulations in the areas related to medical problems are numerous and have been financed by both public and private sources. Many diseases have well-defined etiology, related to abnormalities in a protein structure, point mutations, etc. Such “molecular diseases” are popular objects of the theoretical modeling (Papaleo and Invernizzi 2011).

The epidemic of BSE spawned the great interest in the prion protein research. Early simulations of folding (Kupfer et al. 2009; Sakudo et al. 2010) evolved into studies of membrane bound complexes (DeMarco and Daggett 2009). Alzheimer’s disease is related to amyloid fiber formation in the brain, and this process has also been successfully modeled (Kassler et al. 2010; Straub and Thirumalai 2010; Urbanc et al. 2010). Less known are studies of transthyretin (TTR) fibril formation (Rodrigues et al. 2010), since mutations in this thyroid hormone transport protein are rare. However, the problem is serious, since the aggregation of TTR leads to a lethal illness. It is necessary to note some brilliant studies of HIV virus fragments (Carnevale et al. 2009), such as a flap opening of HIV-1 protease study by Tozzini et al. (2007). There are examples of computational research on proteins involved in eye diseases such as primary congenital glaucoma (Achary and Nagarajaram 2009), osteoporosis (Lee et al. 2011), and even on contactin – a less known protein related to the autism spectrum disorder (Strzelecki et al. 2009).

## Simulations of Single Molecule AFM Experiments

---

In the opinion of this author, computer modeling has excellent overlap with single molecule experiments performed by Atomic Force Microscope (AFM). (Nowak and Marszalek 2005). One of the first studies of ligand-antibody enforced dissociation was published in 2001 by Karplus et al. (Paci et al. 2001). Stretching of individual molecules by the AFM cantilever gives unique nanomechanical force spectroscopy (Rief and Grubmuller 2002) that may be confronted with MD simulations. Divergent time scales between experiments and modeling are still a problem, as the quantitative agreement between calculated and measured force maxima is concerned (Lee et al. 2004), but a good progress in this area is observed (Galera-Prat et al. 2010; Sotomayor and Schulten 2007) and discovery through a virtual (Nowak et al. 2007) or a computational microscope (Lee et al. 2009) is at hand.

## Conclusions and Future Directions

---

Computational chemistry is currently a well-established, fully functional branch of science. Easy access to computers and high-quality, specialized computer codes result in myriad of applications. There is a large, well-trained, and active community of computational chemists. Results of calculations are useful, but difficult to obtain without the theoretical and computational approach. Virtually all chemical and a large body of biological systems may be modeled using modern technologies.

It appears that computer simulations of proteins have a very bright future. There are numerous new and promising investigations. Better computational power offers a possibility of real-time calculations of dynamics. Haptic devices coupled to graphical workstations offer a true “hands-on” experience with interactive molecular dynamics of proteins’ models (Knoll and Mirzaei 2003). Electronic excited states of proteins are only a weakly explored area. The methodology of MD simulations of photoexcited states is not well established yet (Kubiak and Nowak 2008), but future applications for sure will include interactions of biological systems with light (Dittrich et al. 2005; Hayashi et al. 2009; Rossle and Frank 2009). Recently, good progress in understanding protonic gating in the popular Green Fluorescent Protein chromophore has been achieved through dynamical simulations (Olsen et al. 2010).

An interpretation of special experiments, such as high pressure studies (Paci 2002) or cryo electron microscopy (Trabuco et al. 2009), may be fruitfully augmented by an application of computational modeling. Computer scientists and physicists fight to enlarge the maximum size of the simulated system. The whole virus all-atom simulation is not a record study anymore (Sanbonmatsu and Tung 2007; Zink and Grubmuller 2009). It has been shown in Los Alamos NL that 320 million atom protein simulations are technically possible (2009). Large systems, such as big protein complexes in the living cell, will require coarse grained approaches (Clementi 2008). A lot of insight comes from such modeling of membrane proteins (Ayton et al. 2010; Sansom et al. 2008). Multiscale modeling is yet another line of methodological progress (Nielsen et al. 2010; Tozzini 2010). Such techniques expand the timescale accessible for MD studies beyond 1  $\mu$ s limit (Ayton et al. 2007; Chu et al. 2007; Sherwood et al. 2008). What is the best technological strategy for the optimum performance of MD simulations is a matter of fierce debate (Borell 2008). For example, D.E. Shaw has invested a lot of resources in order to develop dedicated chips with record performance for specialized tasks (Klepeis et al. 2009). Other groups, such as K. Schulten’s team, prefer improving algorithms and developing software for running calculations on very powerful, relatively inexpensive Graphical Processing Units, mass-produced for computer gaming (Hardy et al. 2009; Stone et al. 2007; see [http://www.nvidia.com/object/tesla\\_bio\\_workbench.html](http://www.nvidia.com/object/tesla_bio_workbench.html); Zhmurov et al. 2010).

Both approaches have difficulty with surpassing the grid computing idea. The “Folding@home” project created perhaps the most powerful computational device ever, and attracted many young people to science (Pande et al. 2003). Hopefully, all these computational chemistry modeling efforts will bring us a better understanding of nature and a better lives for all people.

## Acknowledgment

---

This work was supported in part by Polish Funds for Science (N N202 262038).

## References

- Achary, M. S., & Nagarajaram, H. A. (2009). Effects of disease causing mutations on the essential motions in proteins. *Journal of Biomolecular Structure and Dynamics*, 26, 609.
- Adcock, S. A., & McCammon, J. A. (2006). Molecular dynamics: Survey of methods for simulating the activity of proteins. *Chemical Reviews*, 106, 1589.
- Aksimentiev, A., Balabin, I. A., Fillingame, R. H., & Schulten, K. (2004). Insights into the molecular mechanism of rotation in the Fo sector of ATP synthase. *Biophysical Journal*, 86, 1332.
- Aksimentiev, A., Brunner, R., Cohen, J., Comer, J., Cruz-Chu, E., Hardy, D., et al. (2008). Computer modeling in biotechnology: A partner in development. *Methods in Molecular Biology*, 474, 181.
- Alder, B. J., & Wainwright, T. E. (1957). Phase transition for a hard sphere system. *Journal of Chemical Physics*, 27, 1208.
- Aleksandrov, A., Thompson, D., & Simonson, T. (2010). Alchemical free energy simulations for biological complexes: Powerful but temperamental. *Journal of Molecular Recognition*, 23, 117.
- Aliev, A. E., & Courtier-Murias, D. (2010). Experimental verification of force fields for molecular dynamics simulations using Gly-Pro-Gly-Gly. *The Journal of Physical Chemistry B*, 114, 12358.
- Allen, M. P., & Tildesley, D. J. (1987). *Computer simulation of liquids*. Oxford: Clarendon Press.
- Alvarez-Paggi, D., Martin, D. F., DeBiase, P. M., Hildebrandt, P., Marti, M. A., & Murgida, D. H. (2010). Molecular basis of coupled protein and electron transfer dynamics of cytochrome c in biomimetic complexes. *Journal of the American Chemical Society*, 132, 5769.
- Amadei, A., Linssen, A. B., & Berendsen, H. J. (1993). Essential dynamics of proteins. *Proteins*, 17, 412.
- Aqvist, J., Luzhkov, V. B., & Brandsdal, B. O. (2002). Ligand binding affinities from MD simulations. *Accounts of Chemical Research*, 35, 358.
- Ash, W. L., Zlomislic, M. R., Oloo, E. O., & Tieleman, D. P. (2004). Computer simulations of membrane proteins. *Biochimica et Biophysica Acta*, 1666, 158.
- Avila, C. L., Drechsel, N. J., Alcantara, R., & Ville-Freixa, J. (2011). Multiscale molecular dynamics of protein aggregation. *Current Protein & Peptide Science*, 12(3), 221–234.
- Ayton, G. S., Noid, W. G., & Voth, G. A. (2007). Multiscale modeling of biomolecular systems: In serial and in parallel. *Current Opinion in Structural Biology*, 17, 192.
- Ayton, G. S., Lyman, E., & Voth, G. A. (2010). Hierarchical coarse-graining strategy for protein-membrane systems to access mesoscopic scales. *Faraday Discuss*, 144, 347.
- Bahar, I., & Rader, A. J. (2005). Coarse-grained normal mode analysis in structural biology. *Current Opinion in Structural Biology*, 15, 586.
- Banci, L. (2003). Molecular dynamics simulations of metalloproteins. *Current Opinion in Chemical Biology*, 7, 143.
- Bashford, D., & Case, D. A. (2000). Generalized born models of macromolecular solvation effects. *Annual Review of Physical Chemistry*, 51, 129.
- Becker, O. M., & Karplus, M. (2006). *A guide to biomolecular simulations* (Vol. 4). Dordrecht: Springer.
- Becker, T., Bhushan, S., Jarasch, A., Armache, J. P., Funes, S., Jossinet, E., et al. (2009). Structure of monomeric yeast and mammalian Sec61 complexes interacting with the translating ribosome. *Science*, 326, 1369.
- Beckstein, O., Biggin, P. C., Bond, P., Bright, J. N., Domene, C., Grottesi, A., et al. (2003). Ion channel gating: Insights via molecular simulations. *FEBS Letters*, 555, 85.
- Berendsen, H. J. C. E. (1976). *Proceedings of the CECAM workshop on models for protein dynamics*. Orsay: University of Paris.
- Berman, H. M., Westbrook, J., Feng, Z., Gilliland, G., Bhat, T. N., Weissig, H., et al. (2000). The protein data bank. *Nucleic Acids Research*, 28, 235.
- Biarnes, X., Bongarzone, S., Vargiu, A. V., Carloni, P., & Ruggerone, P. (2011). Molecular motions in drug design: The coming age of the metadynamics method. *Journal of Computer-Aided Molecular Design*, 25, 395.
- Bikiel, D. E., Boechi, L., Capece, L., Crespo, A., De Biase, P. M., Di Lella, S., et al. (2006). Modeling heme proteins using atomistic simulations. *Physical Chemistry Chemical Physics*, 8, 5611.
- Boas, F. E., & Harbury, P. B. (2007). Potential energy functions for protein design. *Current Opinion in Structural Biology*, 17, 199.
- Boiteux, C., Kraszewski, S., Ramseyer, C., & Girardet, C. (2007). Ion conductance vs. pore gating and selectivity in KcsA channel: Modeling achievements and perspectives. *Journal of Molecular Modeling*, 13, 699.
- Borell, B. (2008). Chemistry: Power play. *Nature*, 451, 240.
- Brooks, B. R., Brooks, C. L., 3rd, Mackerell, A. D., Jr., Nilsson, L., Petrella, R. J., Roux, B., et al.

- (2009). CHARMM: The biomolecular simulation program. *Journal of Computational Chemistry*, 30, 1545.
- Buda, F. (2009). Introduction to theory/modeling methods in photosynthesis. *Photosynthesis Research*, 102(2–3), 437–441.
- Carnevale, V., Raugei, S., Neri, M., Pantano, S., Micheletti, C., & Carloni, P. (2009). Multi-scale modeling of HIV-1 proteins. *Journal of Molecular Structure-Theochem*, 898, 97.
- Case, D. A., Cheatham, T. E., 3rd, Darden, T., Gohlke, H., Luo, R., Merz, K. M., Jr., et al. (2005). The Amber biomolecular simulation programs. *Journal of Computational Chemistry*, 26, 1668.
- Chen, J., & Brooks, C. L., 3rd. (2008). Implicit modeling of nonpolar solvation for simulating protein folding and conformational transitions. *Physical Chemistry Chemical Physics*, 10, 471.
- Chen, J., Brooks, C. L., 3rd, & Khandogin, J. (2008). Recent advances in implicit solvent-based methods for biomolecular simulations. *Current Opinion in Structural Biology*, 18, 140.
- Chou, K. C. (2004). Structural bioinformatics and its impact to biomedical science. *Current Medicinal Chemistry*, 11, 2105.
- Christ, C. D., Mark, A. E., & van Gunsteren, W. F. (2010). Basic ingredients of free energy calculations: A review. *Journal of Computational Chemistry*, 31, 1569.
- Christen, M., Hunenberger, P. H., Bakowies, D., Baron, R., Burgi, R., Geerke, D. P., et al. (2005). The GROMOS software for biomolecular simulation: GROMOS05. *Journal of Computational Chemistry*, 26, 1719.
- Chu, J.-W., Ayton, G. S., Izvekov, S., & Voth, G. A. (2007). Emerging methods for multiscale simulation of biomolecular systems. *Molecular Physics*, 105, 167.
- Clementi, C. (2008). Coarse-grained models of protein folding: Toy models or predictive tools? *Current Opinion in Structural Biology*, 18, 10.
- Cohen, J., Olsen, K. W., & Schulten, K. (2008). Finding gas migration pathways in proteins using implicit ligand sampling. *Methods in Enzymology*, 437, 439.
- Cornell, W., & Nam, K. (2009). Steroid hormone binding receptors: Application of homology modeling, induced fit docking, and molecular dynamics to study structure-function relationships. *Current Topics in Medicinal Chemistry*, 9, 844.
- Cukier, R. I. (2004). Theory and simulation of proton-coupled electron transfer, hydrogen-atom transfer, and proton translocation in proteins. *Biochimica et Biophysica Acta*, 1655, 37.
- Dahl, J. P. (2001). *Introduction to the quantum world of atoms and molecules*. Singapore: World Scientific Publishing Co.
- Dal Peraro, M., Ruggione, P., Raugei, S., Gervasi, F., & Elber, R. (2005). Long-timescale simulation methods. *Current Opinion in Structural Biology*, 15, 151.
- Dal Peraro, M., Ruggione, P., Raugei, S., Gervasio, F. L., & Carloni, P. (2007). Investigating biological systems using first principles Car-Parrinello molecular dynamics simulations. *Current Opinion in Structural Biology*, 17, 149.
- DeMarco, M. L., & Daggett, V. (2009). Characterization of cell-surface prion protein relative to its recombinant analogue: Insights from molecular dynamics simulations of diglycosylated, membrane-bound human prion protein. *Journal of Neurochemistry*, 109, 60.
- Deng, Y., & Roux, B. (2009). Computations of standard binding free energies with molecular dynamics simulations. *The Journal of Physical Chemistry B*, 113, 2234.
- Dittrich, M., Freddolino, P. L., & Schulten, K. (2005). When light falls in LOV: A quantum mechanical/molecular mechanical study of photoexcitation in Phot-LOV1 of *Chlamydomonas reinhardtii*. *The Journal of Physical Chemistry B*, 109, 13006.
- Dittrich, M., & Schulten, K. (2006). PcrA helicase, a prototype ATP-driven molecular motor. *Structure*, 14, 1345.
- Dodson, G. G., Lane, D. P., & Verma, C. S. (2008). Molecular simulations of protein dynamics: New windows on mechanisms in biology. *EMBO Reports*, 9, 144.
- Duan, Y., & Kollman, P. A. (1998). Pathways to a protein folding intermediate observed in a 1-microsecond simulation in aqueous solution. *Science*, 282, 740.
- Ekonomiuk, D., Kielbasinski, M., & Kolinski, A. (2005). Protein modeling with reduced representation: Statistical potentials and protein folding mechanism. *Acta Biochimica Polonica*, 52, 741.
- Elber, R., Ghosh, A., & Cardenas, A. (2002). Long time dynamics of complex systems. *Accounts of Chemical Research*, 35, 396.
- Elcock, A. H., Sept, D., & McCammon, J. A. (2001). Computer simulation of protein-protein interactions. *The Journal of Physical Chemistry B*, 105, 1504.
- Ensign, D. L., Kasson, P. M., & Pande, V. S. (2007). Heterogeneity even at the speed limit of folding: Large-scale molecular dynamics study of a fast-folding variant of the villin headpiece. *Journal of Molecular Biology*, 374, 806.



- Flechsig, H., & Mikhailov, A. S. (2010). Tracing entire operation cycles of molecular motor hepatitis C virus helicase in structurally resolved dynamical simulations. *Proceedings of the National Academy of Sciences of the United States of America*, 107, 20875.
- Frankel, D., & Smit, B. (2001). *Understanding molecular simulation* (2nd ed.). San Diego: Academic.
- Freddolino, P. L., Arkhipov, A. S., Larson, S. B., McPherson, A., & Schulten, K. (2006a). Molecular dynamics simulations of the complete satellite tobacco mosaic virus. *Structure*, 14, 437.
- Freddolino, P. L., Ditttrich, M., & Schulten, K. (2006b). Dynamic switching mechanisms in LOV1 and LOV2 domains of plant phototropins. *Biophysical Journal*, 91, 3630.
- Freddolino, P. L., Liu, F., Gruebele, M., & Schulten, K. (2008). Ten-microsecond molecular dynamics simulation of a fast-folding WW domain. *Biophysical Journal*, 94, L75.
- Freddolino, P. L., Park, S., Roux, B., & Schulten, K. (2009). Force field bias in protein folding simulations. *Biophysical Journal*, 96, 3772.
- Freddolino, P. L., Harrison, C. B., Liu, Y., & Schulten, K. (2010). Challenges in protein folding simulations: Timescale, representation, and analysis. *Nature Physics*, 6, 751.
- Freddolino, P. L., & Schulten, K. (2009). Common structural transitions in explicit-solvent simulations of villin headpiece folding. *Biophysical Journal*, 97, 2338.
- Galeazzi, R. (2009). Molecular dynamics as a tool in rational drug design: Current status and some major applications. *Current Computer-Aided Drug Design*, 5, 225.
- Galera-Prat, A., Gomez-Sicilia, A., Oberhauser, A. F., Cieplak, M., & Carrion-Vazquez, M. (2010). Understanding biology by stretching proteins: Recent progress. *Current Opinion in Structural Biology*, 20, 63.
- Gallicchio, E., & Levy, R. M. (2011). Advances in all atom sampling methods for modeling protein-ligand binding affinities. *Current Opinion in Structural Biology*, 161, 161–166.
- Gao, M., Sotomayor, M., Villa, E., Lee, E. H., & Schulten, K. (2006). Molecular mechanisms of cellular mechanics. *Physical Chemistry Chemical Physics*, 8, 3692.
- Grubmueller, H. (2004). "Proteins as molecular machines: Force probe simulations" published in Computational soft matter: From synthetic polymers to proteins, lecture notes. In N. Attig, K. Binder, H. Grubmueller & K. Kremer (Eds.), *NIC series* (Vol. 23, pp. 401–422). Jülich: John von Neumann Institute for Computing. ISBN 3-00-012641-4.
- Gu, J., & Bourne, P. E. (Eds.). (2009). *Structural bioinformatics* (2nd ed.). Hoboken: Wiley-Blackwell.
- Gumbart, J., Wang, Y., Aksimentiev, A., Tajkhorshid, E., & Schulten, K. (2005). Molecular dynamics simulations of proteins in lipid bilayers. *Current Opinion in Structural Biology*, 15, 423.
- Guvench, O., & MacKerell, A. D., Jr. (2008). Comparison of protein force fields for molecular dynamics simulations. *Methods in Molecular Biology*, 443, 63.
- Haile, M. (1992). *Molecular dynamics simulation: Elementary methods*. New York: Wiley.
- Hansson, T. O. C., & van Gunsteren, W. (2002). Molecular dynamics simulations. *Current Opinion in Structural Biology*, 12, 190.
- Hardy, D. J., Stone, J. E., & Schulten, K. (2009). Multi-level summation of electrostatic potentials using graphics processing units. *Parallel Computing*, 35, 164.
- Hayashi, S., Tajkhorshid, E., & Schulten, K. (2009). Photochemical reaction dynamics of the primary event of vision studied by means of a hybrid molecular simulation. *Biophysical Journal*, 96, 403.
- Henzler-Wildman, K., & Kern, D. (2007). Dynamic personalities of proteins. *Nature*, 450, 964.
- Hess, B., Kutzner, C., van der Spoel, D., & Lindahl, E. (2008). GROMACS 4: Algorithms for highly efficient, load-balanced, and scalable molecular simulation. *Journal of Chemical Theory and Computation*, 4, 435.
- Hornak, V., Abel, R., Okur, A., Strockbine, B., Roitberg, A., & Simmerling, C. (2006). Comparison of multiple AMBER force fields and development of improved protein backbone parameters. *Proteins: Structure, Function, and Bioinformatics*, 65, 712.
- Hou, T., Wang, J., Li, Y., & Wang, W. (2011). Assessing the performance of the MM/PBSA and MM/GBSA methods. 1. The accuracy of binding free energy calculations based on molecular dynamics simulations. *Journal of Chemical Information and Modeling*, 51, 69.
- Houriez, C., Ferre, N., Masella, M., & Siri, D. (2008). Prediction of nitroxide hyperfine coupling constants in solution from combined nanosecond scale simulations and quantum computations. *Journal of Chemical Physics*, 128, 244504.
- Hsin, J., Arkhipov, A., Yin, Y., Stone, J. E., & Schulten, K. (2008). Using VMD: An introductory tutorial. *Current Protocols in Bioinformatics*, Chapter 5, p. Unit 5.7.
- Hub, J. S., & de Groot, B. L. (2009). Detection of functional modes in protein dynamics. *PLoS Computational Biology*, 5, e1000480.

- Hub, J. S., Grubmuller, H., & de Groot, B. L. (2009). Dynamics and energetics of permeation through aquaporins. What do we learn from molecular dynamics simulations? *Handbook of Experimental Pharmacology*, 190, 57.
- Humphrey, W., Dalke, A., & Schulten, K. (1996). VMD: Visual molecular dynamics. *Journal of Molecular Graphics*, 14, 33.
- Ikeguchi, M. (2009). Water transport in aquaporins: Molecular dynamics simulations. *Frontiers in Bioscience*, 14, 1283.
- Jorgensen, W. L., & Tiradorives, J. (1988). The OPLS potential functions for proteins – energy minimizations for crystals of cyclic-peptides and crambin. *Journal of the American Chemical Society*, 110, 1657.
- Kannan, S., & Zacharias, M. (2009). Simulated annealing coupled replica exchange molecular dynamics – an efficient conformational sampling method. *Journal of Structural Biology*, 166, 288.
- Karplus, M. (2003). Molecular dynamics of biological macromolecules: A brief history and perspective. *Biopolymers*, 68, 350.
- Karplus, M., & McCammon, J. A. (2002). Molecular dynamics simulations of biomolecules. *Nature Structural Biology*, 9, 646.
- Kassler, K., Horn, A. H. C., & Sticht, H. (2010). Effect of pathogenic mutations on the structure and dynamics of Alzheimer's A beta(42)-amyloid oligomers. *Journal of Molecular Modeling*, 16, 1011.
- Khafizov, K., Lattanzi, G., & Carloni, P. (2009). G protein inactive and active forms investigated by simulation methods. *Proteins-Structure Function and Bioinformatics*, 75, 919.
- Khalili-Araghi, F., Gumbart, J., Wen, P. C., Sotomayor, M., Tajkhorshid, E., & Schulten, K. (2009). Molecular dynamics simulations of membrane channels and transporters. *Current Opinion in Structural Biology*, 19, 128.
- Kholmurodov, K. T., Altaisky, M. V., Puzynin, I. V., Darden, T., & Filatov, F. P. (2003). Methods of molecular dynamics for simulation of physical and biological processes. *Physics of Particles and Nuclei*, 34, 244.
- Khurana, E., Devane, R. H., Dal Peraro, M., & Klein, M. L. (2011). Computational study of drug binding to the membrane-bound tetrameric M2 peptide bundle from influenza A virus. *Biochimica et Biophysica Acta*, 1808, 530.
- Klein, M. L., & Shinoda, W. (2008). Large-scale molecular dynamics simulations of self-assembling systems. *Science*, 321, 798.
- Klepeis, J. L., Pieja, M. J., & Floudas, C. A. (2003). Hybrid global optimization algorithms for protein structure prediction: Alternating hybrids. *Biophysical Journal*, 84, 869.
- Klepeis, J. L., Lindorff-Larsen, K., Dror, R. O., & Shaw, D. E. (2009). Long-timescale molecular dynamics simulations of protein structure and function. *Current Opinion in Structural Biology*, 19, 120.
- Kmiecik, S., Gront, D., & Kolinski, A. (2007). Towards the high-resolution protein structure prediction. Fast refinement of reduced models with all-atom force field. *BMC Structural Biology*, 7, 43.
- Knapp, B., & Schreiner, W. (2009). Graphical user interfaces for molecular dynamics-quo vadis? *Bioinformatics and Biology Insights*, 3, 103.
- Knoll, P., & Mirzaei, S. (2003). Development of an interactive molecular dynamics simulation software package. *Review of Scientific Instruments*, 74, 2483.
- Kolomeisky, A. B., & Fisher, M. E. (2007). Molecular motors: A theorist's perspective. *Annual Review of Physical Chemistry*, 58, 675.
- Kremer, K. (2003). Computer simulations for macromolecular science. *Macromolecular Chemistry and Physics*, 204, 257.
- Kubiak, K., & Nowak, W. (2008). Molecular dynamics simulations of the photoactive protein nitrile hydratase. *Biophysical Journal*, 94, 3824.
- Kuczera, K., Jas, G. S., & Elber, R. (2009). Kinetics of helix unfolding: Molecular dynamics simulations with milestoning. *The Journal of Physical Chemistry A*, 113, 7461.
- Kupfer, L., Hinrichs, W., & Groschup, M. H. (2009). Prion protein misfolding. *Current Molecular Medicine*, 9, 826.
- Lange, O. E., Schafer, L. V., & Grubmuller, H. (2006). Flooding in GROMACS: Accelerated barrier crossings in molecular dynamics. *Journal of Computational Chemistry*, 27, 1693.
- Lauria, A., Tutone, M., Ippolito, M., Pantano, L., & Almerico, A. M. (2010). Molecular modeling approaches in the discovery of new drugs for anti-cancer therapy: The investigation of p53-MDM2 interaction and its inhibition by small molecules. *Current Medicinal Chemistry*, 17, 3142.
- Le, L., Lee, E., Schulten, K., & Truong, T. N. (2009). Molecular modeling of swine influenza A/H1N1, Spanish H1N1, and avian H5N1 flu N1 neuraminidases bound to Tamiflu and Relenza. *PLoS Currents: Influenza*, 1, RRN1015.
- Leach, A. (2001). *Molecular modelling: Principles and applications* (2nd ed.). Harlow: Prentice Hall.
- Lee, E. H., Hsin, J., Sotomayor, M., Comellas, G., & Schulten, K. (2009). Discovery through the computational microscope. *Structure*, 17, 1295.



- Lee, G., Nowak, W., Jaroniec, J., Zhang, Q., & Marszalek, P. E. (2004). Nanomechanical control of glucopyranose rotamers. *Journal of the American Chemical Society*, 126, 6218.
- Lee, K. H., Kuczera, K., & Banaszak Holl, M. M. (2011). The severity of osteogenesis imperfecta: A comparison to the relative free energy differences of collagen model peptides. *Biopolymers*, 95, 182.
- Levitt, M., & Lifson, S. (1969). Refinement of protein conformation using a macromolecular energy minimization procedure. *Journal of Molecular Biology*, 46, 269.
- Liu, J., & Nussinov, R. (2010). Molecular dynamics reveal the essential role of Linker motions in the function of Cullin-RING E3 ligases. *Journal of Molecular Biology*, 396, 1508.
- Liwo, A., Czaplewski, C., Oldziej, S., & Scheraga, H. A. (2008). Computational techniques for efficient conformational sampling of proteins. *Current Opinion in Structural Biology*, 18, 134.
- Lonsdale, R., Ranaghan, K. E., & Mulholland, A. J. (2010). Computational enzymology. *Chemical Communications*, 46, 2354.
- Ma, J., Flynn, T. C., Cui, Q., Leslie, A. G., Walker, J. E., & Karplus, M. (2002). A dynamic analysis of the rotation mechanism for conformational change in F(1)-ATPase. *Structure*, 10, 921.
- Ma, J. P., & Karplus, M. (1997). Molecular switch in signal transduction: Reaction paths of the conformational changes in ras p21. *Proceedings of the National Academy of Sciences of the United States of America*, 94, 11905.
- Ma, B., & Levine, A. J. (2007). Probing potential binding modes of the p53 tetramer to DNA based on the symmetries encoded in p53 response elements. *Nucleic Acids Research*, 35, 7733.
- MacKerell, A. D., Bashford, D., Bellott, M., Dunbrack, R. L., Evanseck, J. D., Field, M. J., et al. (1998). All-atom empirical potential for molecular modeling and dynamics studies of proteins. *The Journal of Physical Chemistry B*, 102, 3586.
- Mackerell, A. D., Jr., & Nilsson, L. (2008). Molecular dynamics simulations of nucleic acid-protein complexes. *Current Opinion in Structural Biology*, 18, 194.
- Marti, M. A., Capece, L., Bidon-Chanal, A., Crespo, A., Guallar, V., Luque, F. J., & Estrin, D. A. (2008). Nitric oxide reactivity with globins as investigated through computer simulation. *Methods in Enzymology*, 437, 477.
- Mayor, U., Guydosh, N. R., Johnson, C. M., Grossmann, J. G., Sato, S., Jas, G. S., et al. (2003). The complete folding pathway of a protein from nanoseconds to microseconds. *Nature*, 421, 863.
- McCammon, J. A., Gelin, B. R., & Karplus, M. (1977). Dynamics of folded proteins. *Nature*, 267, 585.
- Meirovitch, H. (2007). Recent developments in methodologies for calculating the entropy and free energy of biological systems by computer simulation. *Current Opinion in Structural Biology*, 17, 181.
- Miao, L., & Schulten, K. (2009). Transport-related structures and processes of the nuclear pore complex studied through molecular dynamics. *Structure*, 17, 449.
- Miller, B. T., Singh, R. P., Klauda, J. B., Hodoscek, M., Brooks, B. R., & Woodcock, H. L. (2008). CHARMMing: A new, flexible web portal for CHARMM. *Journal of Chemical Information and Modeling*, 48, 1920.
- Moraitakis, G., Purkiss, A. G., & Goodfellow, J. M. (2003). Simulated dynamics and biological molecules. *Reports on Progress in Physics*, 66, 483.
- Morra, G., Meli, M., & Colombo, G. (2008). Molecular dynamics simulations of proteins and peptides: From folding to drug design. *Current Protein & Peptide Science*, 9, 181.
- Morra, G., Genoni, A., Neves, M. A., Merz, K. M., Jr., & Colombo, G. (2010). Molecular recognition and drug-lead identification: What can molecular simulations tell us? *Current Medicinal Chemistry*, 17, 25.
- Nielsen, S. O., Buló, R. E., Moore, P. B., & Ensing, B. (2010). Recent progress in adaptive multiscale molecular dynamics simulations of soft matter. *Physical Chemistry Chemical Physics*, 12, 12401.
- Nowak, W., Czerminski, R., & Elber, R. (1991). Reaction path study of ligand diffusion in proteins: Application of the self penalty walk (SPW) method to calculate reaction coordinates for the motion of CO through leghemoglobin. *Journal of the American Chemical Society*, 113, 5627.
- Nowak, W., & Marszalek, P. (2005). Molecular dynamics simulations of single molecule atomic force microscope experiments. In J. Leszczynski (Ed.), *Current trends in computational chemistry* (pp. 47–83). Singapore: World Scientific.
- Nowak, W., Wasilewski, S., & Peplowski, L. (2007). Steered molecular dynamics as a virtual atomic force microscope. In H. E. Ulrich, J. M. Hansmann, S. Mohanty & O. Zimmermann (Eds.), *From computational biophysics to systems biology (CBSB07), Proceedings of the NIC Workshop 2007* (p. 251). Jülich: John von Neumann Institute for Computing.
- Olsen, S., Lamothe, K., & Martinez, T. J. (2010). Protonic gating of excited-state twisting and charge localization in GFP chromophores:

- A mechanistic hypothesis for reversible photo-switching. *Journal of the American Chemical Society*, 132, 1192.
- Orlowski, S., & Nowak, W. (2007). Locally enhanced sampling molecular dynamics study of the dioxygen transport in human cytoglobin. *Journal of Molecular Modeling*, 13, 715.
- Orlowski, S., & Nowak, W. (2008). Topology and thermodynamics of gaseous ligands diffusion paths in human neuroglobin. *Biosystems*, 94, 263.
- Paci, E. (2002). High pressure simulations of biomolecules. *BBA-Protein Structure and Molecular Enzymology*, 1595, 185.
- Paci, E., Caffisch, A., Pluckthun, A., & Karplus, M. (2001). Forces and energetics of hapten-antibody dissociation: A biased molecular dynamics simulation study. *Journal of Molecular Biology*, 314, 589.
- Pande, V. S., Baker, I., Chapman, J., Elmer, S. P., Khaliq, S., Larson, S. M., et al. (2003). Atomistic protein folding simulations on the submillisecond time scale using worldwide distributed computing. *Biopolymers*, 68, 91.
- Papaleo, E., & Invernizzi, G. (2011). Conformational diseases: Structural studies of aggregation of polyglutamine proteins. *Current Computer-Aided Drug Design*, 7, 23.
- Peplowski, L., Kubiak, K., & Nowak, W. (2008). Mechanical aspects of nitrile hydratase enzymatic activity. Steered molecular dynamics simulations of *Pseudonocardia thermophila* JCM 3095. *Chemical Physics Letters*, 467, 144.
- Phillips, J. C., Braun, R., Wang, W., Gumbart, J., Tajkhorshid, E., Villa, E., et al. (2005). Scalable molecular dynamics with NAMD. *Journal of Computational Chemistry*, 26, 1781.
- Piana, S., Sarkar, K., Lindorff-Larsen, K., Guo, M., Gruebele, M., & Shaw, D. E. (2011). Computational design and experimental testing of the fastest-folding beta-sheet protein. *Journal of Molecular Biology*, 405, 43.
- Pohorille, A., Jarzynski, C., & Chipot, C. (2010). Good practices in free-energy calculations. *The Journal of Physical Chemistry B*, 114, 10235.
- Rahman, A., & Stillinger, F. H. (1971). Molecular dynamics study of liquid water. *Journal of Chemical Physics*, 55, 3336.
- Rapaport, D. C. (1995). *The art of molecular dynamics simulation*. Cambridge, MA: Cambridge University Press.
- Rehm, S., Trodler, P., & Pleiss, J. (2010). Solvent-induced lid opening in lipases: A molecular dynamics study. *Protein Science*, 19, 2122.
- Rief, M., & Grubmuller, H. (2002). Force spectroscopy of single biomolecules. *A European Journal of Chemical Physics and Physical Chemistry*, 3, 255.
- Rodrigues, J. R., Simoes, C. J. V., Silva, C. G., & Brito, R. M. M. (2010). Potentially amyloidogenic conformational intermediates populate the unfolding landscape of transthyretin: Insights from molecular dynamics simulations. *Protein Science*, 19, 202.
- Romanowska, J., Setny, P., & Trylska, J. (2008). Molecular dynamics study of the ribosomal A-site. *The Journal of Physical Chemistry B*, 112, 15227.
- Rosales-Hernandez, M. C., Bermudez-Lugo, J., Garcia, J., Trujillo-Ferrara, J., & Correa-Basurto, J. (2009). Molecular modeling applied to anti-cancer drug development. *Anti-Cancer Agents in Medicinal Chemistry*, 9, 230.
- Rossle, S. C., & Frank, I. (2009). First-principles simulation of photoreactions in biological systems. *Frontiers in Bioscience*, 14, 4862.
- Roux, B., & Schulten, K. (2004). Computational studies of membrane channels. *Structure*, 12, 1343.
- Russel, D., Lasker, K., Phillips, J., Schneidman-Duhovny, D., Velazquez-Muriel, J. A., & Sali, A. (2009). The structural dynamics of macromolecular processes. *Current Opinion in Cell Biology*, 21, 97.
- Sakudo, A., Xue, G. A., Kawashita, N., Ano, Y., Takagi, T., Shintani, H., et al. (2010). Structure of the prion protein and its gene: An analysis using bioinformatics and computer simulation. *Current Protein & Peptide Science*, 11, 166.
- Sanbonmatsu, K. Y., & Tung, C. S. (2007). High performance computing in biology: Multimillion atom simulations of nanoscale systems. *Journal of Structural Biology*, 157, 470.
- Sansom, M. S., Scott, K. A., & Bond, P. J. (2008). Coarse-grained simulation: A high-throughput computational approach to membrane proteins. *Biochemical Society Transactions*, 36, 27.
- Schaeffer, R. D., Fersht, A., & Daggett, V. (2008). Combining experiment and simulation in protein folding: Closing the gap for small model systems. *Current Opinion in Structural Biology*, 18, 4.
- Scheraga, H. A., Khalili, M., & Liwo, A. (2007). Protein-folding dynamics: Overview of molecular simulation techniques. *Annual Review of Physical Chemistry*, 58, 57.
- Scheres, S. H. (2010). Visualizing molecular machines in action: Single-particle analysis with structural variability. *Advances in Protein Chemistry and Structural Biology*, 81, 89.
- Schlegel, H. B. (2003). Exploring potential energy surfaces for chemical reactions: An overview of

- some practical methods. *Journal of Computational Chemistry*, 24, 1514.
- Schlick, T. (2002). *Molecular modeling and simulation – an interdisciplinary guide*. New York: Springer.
- Schuyler, A. D., Carlson, H. A., & Feldman, E. L. (2009). Computational methods for predicting sites of functionally important dynamics. *The Journal of Physical Chemistry B*, 113, 6613.
- Schwede, T., & Peitsch, M. C. (2008). *Computational structural biology: Methods and applications*. Hackensack, NJ: World Scientific.
- Sellis, D., Vlachakis, D., & Vlassi, M. (2009). Gromita: A fully integrated graphical user interface to Gromacs 4. *Bioinformatics and Biology Insights*, 3, 99.
- Sen, S., Andreatta, D., Ponomarev, S. Y., Beveridge, D. L., & Berg, M. A. (2009). Dynamics of water and ions near DNA: Comparison of simulation to time-resolved stokes-shift experiments. *Journal of the American Chemical Society*, 131, 1724.
- Shakhnovich, E. (2006). Protein folding thermodynamics and dynamics: Where physics, chemistry, and biology meet. *Chemical Reviews*, 106, 1559.
- Sherwood, P., Brooks, B. R., & Sansom, M. S. (2008). Multiscale methods for macromolecular simulations. *Current Opinion in Structural Biology*, 18, 630.
- Shi, S., Pei, J., Sadreyev, R. I., Kinch, L. N., Majumdar, I., Tong, J., et al. (2009). Analysis of CASP8 targets, predictions and assessment methods. *Database (Oxford)*, 2009, bap003.
- Showalter, S. A., & Bruschweiler, R. (2007). Validation of molecular dynamics simulations of biomolecules using NMR spin relaxation as benchmarks: Application to the AMBER99SB force field. *Journal of Chemical Theory and Computation*, 3, 961.
- Simms A. M., Toofanny R. D., Kehl C., Benson N. C., and Daggett, V. (2008). Dynamomics: Design of a computational lab workflow and scientific data repository for protein simulations. *Protein Engineering, Design and Selection*, 21, 369.
- Simonson, T., Archontis, G., & Karplus, M. (2002). Free energy simulations come of age: Protein-ligand recognition. *Accounts of Chemical Research*, 35, 430.
- Sotomayor, M., & Schulten, K. (2007). Single-molecule experiments in vitro and in silico. *Science*, 316, 1144.
- Spyrakakis, F., BidonChanal, A., Barril, X., & Luque, F. J. (2011). Protein flexibility and ligand recognition: Challenges for molecular modeling. *Current Topics in Medicinal Chemistry*, 11, 192.
- Stone, J. E., Phillips, J. C., Freddolino, P. L., Hardy, D. J., Trabuco, L. G., & Schulten, K. (2007). Accelerating molecular modeling applications with graphics processors. *Journal of Computational Chemistry*, 28, 2618.
- Straatsma, T. P., & McCammon, J. A. (1992). Computational alchemy. *Annual Review of Physical Chemistry*, 43, 407.
- Straub, J. E., & Thirumalai, D. (2010). Toward a molecular theory of early and late events in monomer to amyloid fibril formation. *Annual Review of Physical Chemistry*, 62, 437.
- Strzelecki, J., Mikulska, K., Lekka, M., Kulik, A., Balter, A., & Nowak, W. (2009). AFM force spectroscopy and steered molecular dynamics simulation of protein contactin 4. *Acta Physica Polonica A*, 116, S156.
- Sugita, Y. (2009). Free-energy landscapes of proteins in solution by generalized-ensemble simulations. *Frontiers in Bioscience*, 14, 1292.
- Sugita, Y., & Okamoto, Y. (1999). Replica-exchange molecular dynamics method for protein folding. *Chemical Physics Letters*, 314, 141.
- Sun, Q., Doerr, M., Li, Z., Smith, S. C., & Thiel, W. (2010). QM/MM studies of structural and energetic properties of the far-red fluorescent protein HcRed. *Physical Chemistry Chemical Physics*, 12, 2450.
- Tajkhorshid, E., Aksimentiev, A., Balabin, I., Gao, M., Isralewitz, B., Phillips, J. C., et al. (2003). Large scale simulation of protein mechanics and function. *Advances in Protein Chemistry*, 66, 195.
- Tatke, S. S., Loong, C. K., D'Souza, N., Schoepferster, R. T., & Prabhakaran, M. (2008). Large scale motions in a biosensor protein glucose oxidase: A combined approach by DENS, normal mode analysis, and molecular dynamics studies. *Biopolymers*, 89, 582.
- Tozzini, V. (2010). Multiscale modeling of proteins. *Accounts of Chemical Research*, 43, 220.
- Tozzini, V., Trylska, J., Chang, C. E., & McCammon, J. A. (2007). Flap opening dynamics in HIV-1 protease explored with a coarse-grained model. *Journal of Structural Biology*, 157, 606.
- Trabuco, L. G., Villa, E., Schreiner, E., Harrison, C. B., & Schulten, K. (2009). Molecular dynamics flexible fitting: A practical guide to combine cryo-electron microscopy and X-ray crystallography. *Methods*, 49, 174.
- Trylska, J. (2010). Coarse-grained models to study dynamics of nanoscale biomolecules and their applications to the ribosome. *Journal of Physics: Condensed Matter*, 22, 453101.
- Urbanc, B., Betnel, M., Cruz, L., Bitan, G., & Teplow, D. B. (2010). Elucidation of amyloid beta-protein oligomerization mechanisms: Discrete molecular dynamics study. *Journal of the American Chemical Society*, 132, 4266.

- Van Der Kamp, M. W., Shaw, K. E., Woods, C. J., & Mulholland, A. J. (2008). Biomolecular simulation and modelling: Status, progress and prospects. *Journal of the Royal Society Interface*, 5, 173.
- Van Der Spoel, D., Lindahl, E., Hess, B., Groenhof, G., Mark, A. E., & Berendsen, H. J. (2005). GROMACS: Fast, flexible, and free. *Journal of Computational Chemistry*, 26, 1701.
- Van Gunsteren, W. F., Bakowies, D., Baron, R., Chandrasekhar, I. C. M., Daura, X., Gee, P., et al. (2006). Biomolecular modeling: Goals, problems, perspectives. *Angewandte Chemie International Edition*, 45, 4064.
- van Oijen, A. M. (2007). Single-molecule studies of complex systems: The replisome. *Molecular BioSystems*, 3, 117.
- van Speybroeck, V., & Meier, R. J. (2003). A recent development in computational chemistry: Chemical reactions from first principles molecular dynamics simulations. *Chemical Society Reviews*, 32, 151.
- Vasquez, V., Sotomayor, M., Cordero-Morales, J., Schulten, K., & Perozo, E. (2008). A structural mechanism for MscS gating in lipid bilayers. *Science*, 321, 1210.
- Vemparala, S., Domene, C., & Klein, M. L. (2010). Computational studies on the interactions of inhalational anesthetics with proteins. *Accounts of Chemical Research*, 43, 103.
- Villa, E., Balaeff, A., & Schulten, K. (2005). Structural dynamics of the lac repressor-DNA complex revealed by a multiscale simulation. *Proceedings of the National Academy of Sciences of the United States of America*, 102, 6783.
- Vreede, J., Juraszek, J., & Bolhuis, P. G. (2010). Predicting the reaction coordinates of millisecond light-induced conformational changes in photoactive yellow protein. *Proceedings of the National Academy of Sciences of the United States of America*, 107, 2397.
- Wang, T., & Duan, Y. (2011). Retinal release from opsin in molecular dynamics simulations. *Journal of Molecular Recognition*, 24, 350.
- Wanko, M., Hoffmann, M., Frauenheim, T., & Elstner, M. (2006). Computational photochemistry of retinal proteins. *Journal of Computer-Aided Molecular Design*, 20, 511.
- Warshel, A. (2002). Molecular dynamics simulations of biological reactions. *Accounts of Chemical Research*, 35, 385.
- Warshel, A. (2003). Computer simulations of enzyme catalysis: Methods, progress, and insights. *Annual Review of Biophysics and Biomolecular Structure*, 32, 425.
- Warshel A., Kato M., & Pislakov A.V. (2007). Polarizable force fields: History, test cases, and prospects. *Journal of Chemical Theory and Computation*, 3, 2034.
- Weiner, S. J., Kollman, P. A., Case, D. A., Singh, U. C., Ghio, C., Alagona, G., Profeta, S., & Weiner, P. (1984). A new force-field for molecular mechanical simulation of nucleic-acids and proteins. *Journal of the American Chemical Society*, 106, 765.
- Wong, V., & Case, D. A. (2008). Evaluating rotational diffusion from protein MD simulations. *The Journal of Physical Chemistry B*, 112, 6013.
- Yu, J., Ha, T., & Schulten, K. (2007). How directional translocation is regulated in a DNA helicase motor. *Biophysical Journal*, 93, 3783.
- Zhang, J., Li, W., Wang, J., Qin, M., Wu, L., Yan, Z., et al. (2009). Protein folding simulations: From coarse-grained model to all-atom model. *IUBMB Life*, 61, 627.
- Zhmurov, A., Dima, R. I., Kholodov, Y., & Barsegov, V. (2010). SOP-GPU: Accelerating biomolecular simulations in the centisecond timescale using graphics processors. *Proteins*, 78, 2984.
- Zhu, F., Tajkhorshid, E., & Schulten, K. (2004). Theory and simulation of water permeation in aquaporin-1. *Biophysical Journal*, 86, 50.
- Zink, M., & Grubmuller, H. (2009). Mechanical properties of the icosahedral shell of Southern bean mosaic virus: A molecular dynamics study. *Biophysical Journal*, 96, 1350.



# 32 Molecular Dynamics and Advanced Sampling Simulations of Nucleic Acids

Jeremy Curuksu<sup>1</sup> · Srinivasaraghavan Kannan<sup>2,3</sup> · Martin Zacharias<sup>4</sup>

<sup>1</sup>Mathematics Department, Swiss Federal Institute of Technology, Lausanne (EPFL), Switzerland

<sup>2</sup>Martin-Luther-Universität Halle-Wittenberg, Institut für Pharmazie, Halle, Germany

<sup>3</sup>School of Engineering and Science, Jacobs University Bremen, Bremen, Germany

<sup>4</sup>Physik-Department T38, Technische Universität München, Garching, Germany

<b>Introduction</b> .....	<b>1156</b>
Molecular Dynamics Simulations of Nucleic Acids .....	1156
Induced Conformational Changes During Molecular Dynamics Simulations .....	1159
Replica-Exchange Molecular Dynamics Simulations .....	1161
<b>Combining Replica-Exchange and Umbrella Sampling Simulations</b> .....	<b>1163</b>
Simulation Studies on DNA Bending .....	1164
Conformational Transitions of Nucleic Acid Backbone States .....	1166
<b>Conclusions</b> .....	<b>1170</b>
<b>Acknowledgments</b> .....	<b>1170</b>
<b>References</b> .....	<b>1170</b>

**Abstract:** Molecular dynamics (MD) simulations based on a classical force field are increasingly being used to study the structure and dynamics of nucleic acids. Simulation studies are limited by the accuracy of the force field description and by the time scale accessible by current MD approaches. In the case of specific conformational transitions it is often possible to improve the sampling of possible states by adding a biasing or umbrella potential along some coordinate describing the conformational transition. It is also possible to extract the associated free energy change along the reaction coordinate. The development of advanced sampling methods such as the replica-exchange MD (REMD) approach allows significant enhancement of conformational sampling of nucleic acids. Recent applications of umbrella sampling and REMD simulation as well as combinations of both methodologies on nucleic acids will be presented. These approaches have the potential to tackle many open questions in structural biology such as the role of nucleic acid structure during recognition and packing and the function of nucleic acid fine structure and dynamics.

## Introduction

---

Nucleic acids have essential functions in a variety of biological processes, including storage of genetic information, replication of DNA, regulation of transcription, mRNA splicing, RNA interference, and protein synthesis. Most cellular DNA adopts primarily a double-stranded (B-form) helical structure and the interaction with proteins is mediated through major groove or minor groove recognition. The accessibility of DNA is also controlled by the condensation with nuclear proteins (histones) to compact structures (nucleosomes and chromatin in eukaryotes). Many cellular RNA molecules form more complex three-dimensional structures compared to DNA that consist only partially of double-stranded, base-paired regions frequently interrupted by extra-unmatched nucleotides, mismatched base pairs, bulge structures, or hair-pin loop structures that cap the end of helices (Al-Hashimi and Walter 2008; Leontis and Westhof 2003; Zacharias 2000).

In recent years, structural knowledge of RNA and RNA in complexes with proteins, small organic ligands, and ions has increased dramatically since many new structures have been solved by X-ray crystallography or Nuclear Magnetic Resonance (NMR) spectroscopy (Furtig et al. 2003; Hall 2008; Steitz 2008). The rapid increase of structural information has also helped to collect and better understand the types of interactions in folded nucleic acid structures and at nucleic acid–ligand interfaces (Al-Hashimi and Walter 2008; Hall 2008). Since RNA and DNA are of functional importance in many cellular structures, nucleic acids have also been increasingly recognized as possible drug targets. In addition, nucleic acids themselves may serve as drugs (DeJong et al. 2002; Wong et al. 2009; Zacharias 2003). However, the structural information on folded nucleic acid structures as well as complexes with ligands alone does not allow us to directly investigate the driving forces and energetic contributions to structure formation and association. In addition, experimental high-resolution structure determination methods have only a limited time resolution and allow only limited insights into the dynamics of nucleic acids and the process of structure formation and association.

## Molecular Dynamics Simulations of Nucleic Acids

---

For the theoretical investigation of nucleic acid structure and function the application of quantum mechanical approaches is currently limited by the large size and complexity of nucleic acids.

However, computer simulation studies based on classical molecular mechanics force fields that use the position of whole atoms as variables (instead of electrons and nuclei in case of quantum mechanics) are used frequently to study the dynamics of nucleic acids (Cheatham 2004; Mackerell and Nilsson 2008; McDowell et al. 2007; Orozco et al. 2008). Simulations can complement experimental studies if the timescales or the molecular properties of interest are difficult to access experimentally. In the current chapter we will focus on the application of advanced sampling molecular dynamics (MD) methods to follow the dynamics of biomolecules at high spatial and time resolution. These methods could be useful to study the driving forces of structure formation, provided that the force field to describe the molecular interactions is sufficiently accurate.

Typically, MD simulation studies include the nucleic acid molecule at atomic resolution. During the simulation Newton's equations of motion are solved numerical in small time steps of  $\sim 1\text{--}2$  fs ( $1\text{--}2 \cdot 10^{-15}$  s). The interatomic interactions are described using a classical molecular mechanics force field of the following form,

$$V_{\text{tot}} = \sum_{i=1}^{N_{\text{bonds}}} \frac{1}{2} k_{b_i} (b_i - b_{0i})^2 + \sum_{i=1}^{N_{\text{angles}}} \frac{1}{2} k_{\theta_i} (\theta_i - \theta_{0i})^2 \\ + \sum_{i=1}^{N_{\text{dihedral}}} \sum_{n=1}^{N_{\tau}} k_{\tau} (1 + \cos(n\tau_i + \delta_{ni})) \\ + \sum_{i \neq j}^{N_{\text{pairs}}} \left( A_{ij} / r_{ij}^{12} - B_{ij} / r_{ij}^6 + q_i q_j / r_{ij} \right)$$

The bonded terms (first three summations in the above equation) contain a sum over all chemical bonds, all bond angles, and dihedral angles of the nucleic acid structures. Usually, simple quadratic penalty terms with appropriate force constants ( $k_b$  and  $k_{\theta}$ , respectively) are used to control the bond length ( $b$ ) and bond angles ( $\theta$ ) variations of the molecules. A linear combination of periodic functions is typically employed to control dihedral torsion angles ( $\tau$ ). Additional non-bonded terms describe van der Waals and Coulomb interactions (as a double sum over all non-bonded pairs of atoms, the last two terms in the above equation). The form of the energy function allows a rapid evaluation of the potential energy of a molecule and calculation of gradients necessary for energy optimization and molecular dynamics simulations based on a numerical solution of the classical equations of motion.

Simulation studies on biomolecules require the inclusion of surrounding aqueous solvent and ions. However, the inclusion of a sufficiently large number of explicit water molecules significantly increases the computational demand. The possibility to implicitly account for solvent effects in molecular mechanics calculations is of great interest because it would allow longer simulation times and a better convergence of calculated thermodynamic averages. However, in the present review we will focus on simulation studies on nucleic acids with an explicit consideration of surrounding ions and water molecules. In order to account for long-range electrostatic interactions most simulations employ particle mesh Ewald (PME) methods where the long-range part of the electrostatic interaction is considered by an Ewald summation technique for periodic systems (Darden et al. 1993).

Several molecular mechanics force fields are available for simulation studies on nucleic acids. Among the most recent and best tested force fields are the Charmm27 (Foloppe and MacKerell 2000; MacKerell and Banavali 2000) and the Amber parmBsc0 (Perez et al. 2007a) force fields. In particular, the parmBsc0 force field has been tested during very long simulations starting from B-DNA (Perez et al. 2007b). The simulations gave good agreement



with the B-DNA starting structure for simulations that were extended to more than 1  $\mu$ s total simulation time.

More recently, force fields that account approximately for electronic polarization due to the strong electrostatic fields around nucleic acid molecules have become available (Babin et al. 2006). Additional terms often in the form of field-induced dipoles on atoms are used to approximately describe the deformation of the electron cloud due to an electrostatic field. It has been shown that such force field models can improve MD simulations of DNA resulting in overall better agreement with available experimental data than the standard force field form with fixed partial charges on atoms and no additional polarization term (Babin et al. 2006).

Efforts to systematically evaluate the accuracy of force fields and to study the fine structure of DNA on many different DNA sequences are underway (e.g., Lavery et al. 2009). Within these studies fairly long MD simulations (>50 ns) have been performed on several B-DNA duplex structures that contain all ten possible base pair steps and all possible sequential arrangements of four consecutive base pairs (Lavery et al. 2009). Starting from standard B-DNA these structures are equilibrated and simulated under identical conditions to allow direct comparison and extraction of sequence-dependent structural and dynamic features. This effort could eventually lead to a comprehensive description of the sequence dependent flexibility of DNA.

Nucleic acids are highly solvated systems and are surrounded by nonspecifically and specifically bound ions that stabilize the poly-electrolyte character of the nucleic acid molecule. A number of biophysical techniques allow the investigation of the effective charge of nucleic acids and high-resolution X-ray crystallography can provide detailed spatial information on specifically bound solvent molecules and ions. However, the dynamics of nucleic acid hydration and ion binding is difficult to study experimentally at high spatial and time resolution. MD simulation studies have been extensively used to characterize the distribution and life times of bound water molecules and ions in both DNA and RNA (reviewed in Hashem and Auffinger 2007).

In contrast to DNA, most RNA molecules are single stranded in a cell, which results in the possible formation of a variety of secondary and tertiary structures. Many larger functional biological assemblies contain not only proteins but also structured RNA components (e.g., ribosomes, spliceosomes, and editosomes). The flexibility of several RNA structural motifs that form building blocks for larger RNA containing biomolecules have been studied by MD simulations on the nano-second time scale. Simulations on such motifs start typically from experimentally determined structures and can give important insights into the dynamics and how it is coupled to the function of RNA structural motifs.

Unfortunately, the conformational sampling during conventional (c)MD simulations is strongly limited by the maximum simulation time that can currently be achieved. Even simulations of hundreds of nanoseconds or few microseconds that are currently possible are often too short to observe significant conformational transitions or the refolding of RNA or DNA structures. The poor sampling is due to kinetic trapping events in low-energy regions of the conformational free energy surface. The rugged nature of the energy hypersurface is in particular due to frequent atomic surface proximity inducing hard core van-der-Walls repulsion and due to a restricted allowable set of rotamers in the nucleic acid backbone dihedral angles. Thus, many interesting questions about non-equilibrium dynamics of biomolecules cannot be resolved by current equilibrium cMD simulations.

## Induced Conformational Changes During Molecular Dynamics Simulations

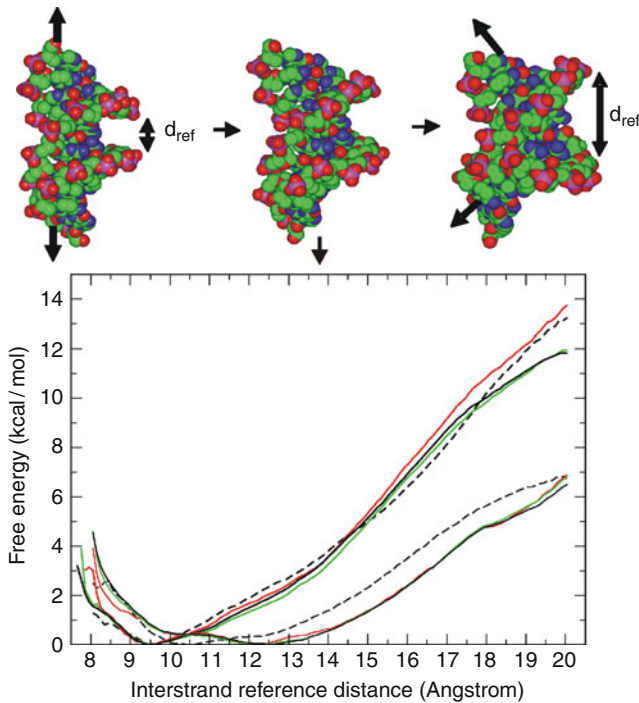
In cases where one is interested in specific conformational transitions it is possible to overcome the sampling problem by inducing a desired conformational change during a simulation. This is possible if one can associate a specific parameter (reaction coordinate) with the conformational change of interest. It is then possible to enforce structural transitions in MD simulations by adding a penalty potential (called umbrella potential) that biases the sampled conformations towards a desired state. The reaction coordinate can, for example, be the bending or stretching of a DNA molecule. Variants of this approach like targeted MD-simulations where one enforces movement of atoms towards a desired target structure have also been developed (Sanbonmatsu and Tung 2007).

Typically, in umbrella sampling simulations one adds a quadratic penalty term to the force field for keeping sampled states close to a desired interval along the reaction coordinate. This is then performed for many intervals (illustrated for the case of opening a DNA minor groove (Zacharias 2006) in [▶ Fig. 32-1](#)).

The consecutive sampling windows ensure a good probability of sampling along the generalized reaction coordinate. From the distributions of conformations within all the intervals along the reaction coordinate it is possible to extract the associated free energy change for the transition ([▶ Fig. 32-1](#)). Then an optimal unbiased probability density along the generalized coordinate can be recovered by statistical methods based on the analysis of weighted histograms (WHAM, see reference Kumar et al. 1992). The corrected probability density in turn equates the free energy along the generalized coordinate. The umbrella sampling methodology has been applied frequently to study structural transitions in nucleic acid molecules in recent years. Among these simulations are studies on the energetics of stacking and unstacking of nucleotides (Norberg and Nilsson 1995) and looping out single bases within a duplex DNA (Giudice and Lavery 2003; Giudice et al. 2003; Huang et al. 2003).

Nucleo-base looping out events are of significant biological importance because it forms the mechanistic basis for repairing mispaired or damaged bases by a number of DNA repair enzymes (Dalhus et al. 2009). In addition, many DNA-methylases induce looping out of nucleo-bases to perform sequence specific methylation (Cheng and Blumenthal 2008). Several umbrella sampling studies have been performed in order to calculate the free energy change associated with looping out a stacked and paired base in duplex DNA and RNA (Barthel and Zacharias 2006; Giudice and Lavery 2003; Giudice et al. 2003; Hart et al. 2005; Huang et al. 2003) and using either a pseudo angular or dihedral angle reaction coordinate. The calculated free energy in the range of 10–18 kcal mol<sup>-1</sup> indicates that looping out a paired base in DNA is unfavorable and corresponds to a rare event in case of free duplex DNA. In the case of looping out extra unmatched bases stacked between neighboring base-paired duplex RNA a significantly smaller barrier for looping out was found and it was possible to characterize stable conformational substates such as base triples that formed during the looping out process (Barthel and Zacharias 2006; Hart et al. 2005). The lower associated free energy of looping out extra unmatched bases indicates that such conformations can be significantly populated and are in equilibrium with stacked intra-helical states. In addition to localized structural transitions such as looping out bases, the umbrella sampling method has also been used to study global deformations of DNA and RNA molecules. This includes induced minor-groove opening and closing (Zacharias 2006) as well as over- and under-twisting of duplex DNA (Kannan et al. 2006). The opening of the minor groove is essential for the binding of several DNA-binding proteins among

them the prominent example of the TATA box binding transcription factors (Kim and Burley 1994; Nikolov et al. 1996). Simulation studies on duplexes with a central TATATA or AAATTT sequence motif showed significant differences in the calculated free energies associated with minor groove opening and a much smaller associated free energy change for the TATATA vs. AAATTT case (see [Fig. 32-1](#)). The calculations indicated that the free energy change associated with the deformation of DNA towards a form with an open minor groove (as seen in several protein-DNA complexes) can be significant and depends on the sequence. It also allows one to estimate the free energy contribution to the indirect readout of DNA due to differences in deformability.



■ Fig. 32-1

Illustration of umbrella sampling simulations on induced minor groove opening in two DNA sequences (according to reference 33). The reaction coordinate for this simulation was the distance between two groups of backbone atoms on opposite DNA strands (*double arrow*). The distance was harmonically restrained to various values close to the reference distance  $d_{\text{ref}}$  (*upper panel*). Conformational snapshots observed during different stages of the umbrella sampling simulation are shown as van der Waals representations (*upper panel*, atom color code) and the  $d_{\text{ref}}$  distance and the helical axis directions (*bold arrows*) are indicated. In the lower panel the calculated free energy changes vs. distance extracted from the umbrella sampling simulations for a self-complementary 5'-CGCGAAATTTGCG sequence (*upper set of curves*) and for the 5'-CGCGTATATACGCG sequence (smaller free energy changes) are indicated. The different line colors correspond to different simulation lengths (1 and 2 ns per simulation window and combined data) in the forward direction (increasing  $d_{\text{ref}}$ ) and the dashed line represents the result for a backward simulation starting from the DNA with the opened minor groove (further details in Zacharias 2006)

## Replica-Exchange Molecular Dynamics Simulations

The application of classical molecular dynamics (cMD) simulations for studying the dynamics of biomolecules is limited by the accuracy of current force fields and the simulation time scale. Biomolecules like peptides and nucleic acids can adopt a variety of locally stable conformations that are separated by large energy barriers. Standard MD simulation at room temperature may be kinetically trapped in one of these local minima and conformational transitions between stable states can therefore be rare events on currently accessible time scales. The replica exchange (parallel tempering) technique is a widely used method to enhance conformational sampling in Monte Carlo (MC) (Swendsen and Wang 1986) and MD simulations (Gnanakaran et al. 2003; Kaihsu 2004; Sugita and Okamoto 1999). In replica exchange simulations several copies (replicas) of the system are simulated independently and simultaneously using classical MD or MC methods at different simulation temperatures (or force fields: Hamiltonians). In standard REMD, copies or replicas of the system are simulated at different temperature ( $T_0, T_1, T_2, \dots, T_N$ ). Each replica evolves independently and after preset intervals (in the range of 500–1,000 MD-steps  $\sim 1$ –2 ps) an exchange of pairs of neighboring replica is attempted according to a Metropolis acceptance criterion.

$$\begin{aligned}w(x_i \rightarrow x_j) &= 1 && \text{for } \Delta \leq 0; \\w(x_i \rightarrow x_j) &= \exp(-\Delta) && \text{for } \Delta > 0\end{aligned}$$

where

$$\Delta = (\beta_i - \beta_j) [E(r_j) - E(r_i)]$$

with  $\beta = 1/RT$  ( $R$ : gas constant and  $T$ : temperature) and  $E(r)$  representing the potential energy of system for a given configuration.

The random walk in temperature allows conformations trapped in locally stable states (at a low simulation temperature) to escape by exchanging with replicas at higher simulation temperature. The REMD method has been successfully applied in folding simulations of several peptides and mini-proteins (Kaihsu 2004) and has more recently also being used for studying nucleic acids (Kannan and Zacharias 2007a, 2009; Garcia and Paschek 2008; Villa et al. 2008; Zhuang et al. 2007).

Recently, Kannan and Zacharias (2007a) applied the REMD method to study the folding process of a DNA hairpin structure. Hairpin loops with a central GNA trinucleotide motif (G, guanine; A, adenine; N, any nucleotide) have been found to form particularly stable structures (Yoshizawa et al. 1997). For example, the 5'-GCGCAGC sequence in DNA forms a stable tri-nucleotide hairpin loop (with a sheared G:A closing pair) flanked by a two base-pair stem helix. The thermodynamic stability of the GCA trinucleotide loop, the influence of loop expansion, the influence of closing and flanking sequences, and also the contribution of individual hydrogen bonds and other non-bonded contacts to the folding stability have been studied extensively (Moody and Bevilacqua 2003).

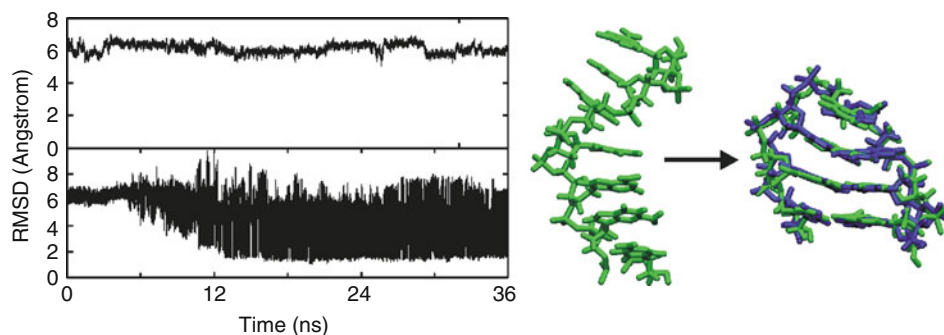
Temperature-based REMD with 16 replicas in explicit solvent was used to study the structure formations of the 5'-GCGCAGC motif in DNA (Kannan and Zacharias 2007a) starting from single-stranded DNA. After an equilibration phase at constant pressure and temperature the REMD simulations were conducted under constant volume using 16 replicas ranging in temperature from 315 to 425 K.

During REMD simulations (each 36 ns), conformations in very close agreement with the experimental hairpin structure appeared as dominant conformations during the final phase of the REMD simulations ( $\sim 35\%$  at the lowest temperature replica). During REMD simulations

already at a simulation time of 12 ns, conformations with an RMSD of  $\sim 2$  Å from experiment were sampled. After  $\sim 15$ – $20$  ns simulation time conformations as close as  $1.2$ – $1.6$  Å (heavy atoms) with respect to the reference hairpin conformation were sampled as the dominant conformational states (🔍 Fig. 32-2).

Simultaneous compaction and accumulation of folded structures was observed. Interestingly, at early stages of the simulations a variety of central loop conformations but also arrangements close to experiment were sampled before the fully folded structure appeared. The analysis of intermediates at or shortly before the occurrence of fully folded hairpin structures indicated the formation of near-native tri-nucleotide loop conformations (without fully formed stem). Most of these intermediates included a stacking of the  $C_2$  and  $G_3$  bases, which was further stabilized by hydrogen bonding to the  $A_5$  base. Folding to the native hairpin structure appeared to occur almost simultaneously or quickly after the formation of the near-native tri-nucleotide loop. The simulations suggest a folding mechanism where these intermediates can rapidly proceed towards the fully folded hairpin and emphasizes the importance of loop and stem nucleotide interactions for hairpin folding. In contrast to REMD, during cMD simulations starting from the same single-stranded DNA molecule no folding transitions to a structure close to the experimental hairpin loop conformation were observed (Kannan and Zacharias 2007a). The root mean square deviation (RMSD) from the reference hairpin structure (heavy atoms) remained around  $5$ – $8$  Å in cMD simulations over the entire simulation time (🔍 Fig. 32-2) and even during extended simulations of  $>75$  ns. More recently, the folding of a similar DNA-hairpin motif has been successfully achieved in very long continuous MD simulations (Portella and Orozco 2010).

The REMD methodology has also been used for simulation studies of an RNA hairpin and for the folding of an RNA tetraloop r(5'-GCUUCGGC) in explicit solvent starting from a fully extended conformation using 52 replicas (Garcia and Paschek 2008). Apart from the folding process, REMD simulations were used to study the effect of changing the loop sequence and the closing base pair on the conformational distribution and on the thermostability of two RNA hairpins that have similar structures (Villa et al. 2008). A variation of REMD, called serial



■ Fig. 32-2

(left panel) Heavy atom root mean square deviation (RMSD) of sampled DNA conformations (5'-GCGCAGC) from folded hairpin structure during a continuous MD simulation (upper graph) and a T-REMD simulation (lower graph) vs. simulation time. (Right panel) Single stranded start structure (left) and fully folded hairpin loop structure from the REMD simulation (green stick model, right side) superimposed on to the experimental hairpin structure (blue color)

replica exchange molecular dynamics (SREMD), has been employed to gain insight into the folding intermediates of another common the RNA tetraloop hairpin with a central GCAA loop sequence (Bowman et al. 2008).

Although the REMD methodology improves sampling in the above discussed cases a drawback of the conventional temperature (T-)REMD is the rapid increase of the number of replicas with increasing system size in order to cover a desired temperature range (Fukunishi et al. 2002). The ratio of the standard deviation of the system potential energy (a measure of the energy fluctuation) vs. average energy decreases with the square-root of the system size. Hence, to achieve sufficient overlap of the energy distributions between replica runs at different temperatures (required to achieve a reasonable exchange acceptance ratio) the temperature “spacing” between neighboring replicas is required to decrease with system size. Another drawback of large numbers of replicas is the need to run longer simulations (or more exchanges) to allow sufficient “travelling (diffusion)” or exchanges between high and low temperature replicas compared to a small number of replicas. Especially in case of simulations that include a large number of explicit water molecules the rapid increase of the number of replicas in T-REMD simulations limits the applicability to small bimolecular systems.

Instead of using the simulation temperature as a replica coordinate one can also use the force field or Hamiltonian of the system as a replica-coordinate (Affentranger et al. 2006; Fukunishi et al. 2002; Jang et al. 2003; Liu et al. 2005; Kannan and Zacharias 2007b; Zacharias 2008). In H-REMD simulations it is possible to modify only a part of the Hamiltonian along the replica simulations. The advantage is that then exchanges between replicas depend only on the part of the Hamiltonian that differs between replicas. Consequently, such approaches may require much fewer replicas for efficient sampling compared with T-REMD. Various H-REMD methods have been proposed mainly for peptides and proteins and demonstrated enhanced conformational sampling can be achieved with fewer replicas as compared to standard T-REMD (Affentranger et al. 2006; Kannan and Zacharias 2007b).

## Combining Replica-Exchange and Umbrella Sampling Simulations

---


Combining umbrella sampling with the replica exchanges is a variant of the H-REMD method (Curuksu and Zacharias 2009; Sugita et al. 2000) and consists of periodically swapping conformations between adjacent umbrella sampling windows  $i$  and  $j$ . The exchange criterion takes the form of an equation of micro-reversibility that takes into account the conformational probability density of the two windows  $i$  and  $j$ , i.e., Boltzmann factors based on the biased potential energy function of window  $i$  and window  $j$ . One advantage of coupling umbrella sampling with replica exchanges (REUS) is due to the fact that in general there is no obvious best possible coordinate for a given dynamical conformational transition (Sugita et al. 2000), especially when it involves many degrees of freedom (typically bending and folding of biomolecules). As a consequence it may not be possible to overcome all relevant barriers within the phase space associated to a given value of the generalised coordinate, i.e., within each umbrella window. The restriction of sampling only a narrow range along a reaction coordinate can cause conformational trapping of the sampled structures. Through periodic swaps between the sampling windows, the conformations trapped in a low energy region of the conformational landscape easily diffuse to neighboring windows with a different associated umbrella energy function. Hence, the neighbor replicas provide an enhanced variety of conformations accessible to every sampling window




in the limit of a high number of swaps between the windows. In the area of nucleic acids this methodology has been applied, for example, in a study of dinucleotide stacking in DNA (Norberg and Nilsson 1995) and in simulation studies on the free energy of bending of the kink turn motif in RNA (Curuksu et al. 2009a).

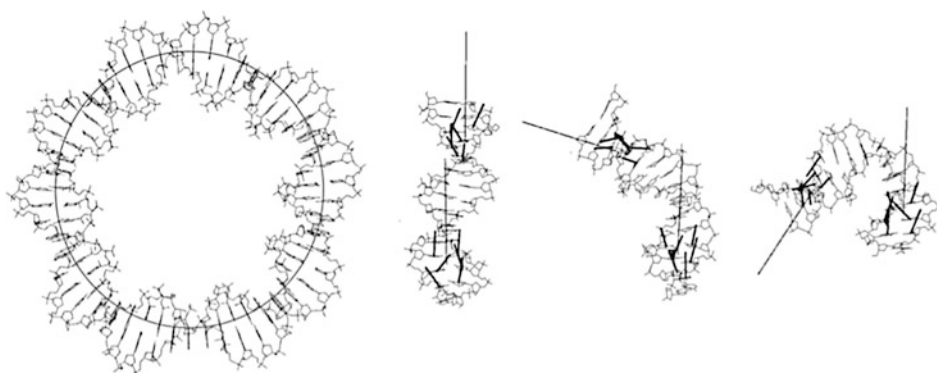
## Simulation Studies on DNA Bending

Bent (i.e., curved) conformational states of DNA over several base pairs can be seen in many protein-DNA complexes (Zacharias 2003), in nucleosomal organizations of eukaryotic genetic material (Ong et al. 2007), in the prokaryotic nucleoles (Travers and Muskhelishvili 2005), and in viral DNA packed in capsids (Garcia et al. 2007). Recent experimental studies employing cyclization assays (Cloutier and Widom 2004), molecular force sensors (Shroff et al. 2005), FRET (Fluorescence Resonance Energy Transfer) (Yuan et al. 2008), and AFM (Atomic Force Mechanics) (Wiggins et al. 2006) experiments indicate that strong DNA bending may result in base pair kinking and a smaller deformation energy than expected from simple elastic models. The occurrence of sharp kinks in MD simulations of short minicircles was reported in Lankas et al. (2006) with the same DNA sequences as studied experimentally in Cloutier and Widom (2004).

DNA bending during MD simulations can be imposed by an appropriate restrain between regions flanking the DNA region of interest (Curuksu and Zacharias 2009) or, alternatively, circularizing this DNA sequence into minicircles (Lankas et al. 2006;  Fig. 32-3). A full dynamical pathway of nucleic acids global bending can also be characterized by MD simulations combined with enhanced sampling (Curuksu et al. 2008, 2009b), such as the Umbrella Sampling and Replica Exchange (REUS) method introduced in the previous paragraph.

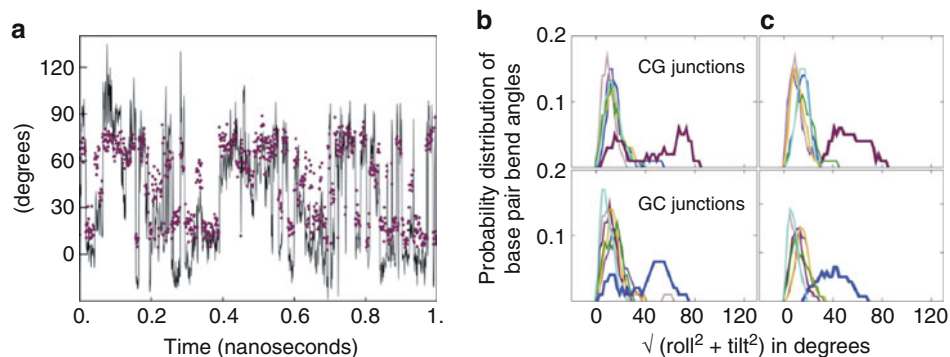
To gain insight into the full dynamical pathway of DNA global bending, our laboratory has carried out umbrella sampling by defining a generalized coordinate for bending short DNA oligomers (Curuksu et al. 2008, 2009b). The bend angle is defined as an angle between two screw axes of the double helical segments referred to as handles. To calculate each screw axis, internucleotide rotation vectors are calculated for several neighboring dinucleotide steps within a fragment of  $n$  base pairs. Each rotation vector is based on a rotation matrix that is the total transformation from one nucleotide-fixed axis system into the coordinate frame of its neighboring nucleotide. The sum of the rotation vectors defines a vector “handle” oriented as a function of  $(2n-2)$  specific inter-nucleotide rotations angles (Curuksu et al. 2008).

During the simulations described in ref. 106, four terminal base pairs at each end of a 15 basepair duplex DNA molecule were included to define two (terminal) handles. The global bend angle is given by the angle between the two handle vectors and a restraining potential of the form  $V(\theta) = k(\theta - \theta_{\text{ref}})^2$  was added to the force field ( $\theta$  corresponds to the angle between the two handles). Since the bend angle restraining potential depends on the position of many atoms (because each handle is influenced by all the atoms that define the local axis system) the restraining force is optimally distributed over all atoms that affect the bending angle. Simulation of several nanoseconds per umbrella sampling window and periodical swapping of conformations between adjacent windows was carried out at regular intervals (every 2 ps). The global bending angle can be smoothly restrained to values around  $0^\circ$  and up to  $150^\circ$  (the most extreme DNA bending regimes as observed in nucleosomes are on the order of  $90^\circ$  for a 15 bp duplex DNA).  Figure 32-4 illustrates the probability histograms of the rotation variable about the long base pair axis between two adjacent base pairs (helical “roll” variable) that characterizes kink motifs through which DNA fragments may relax the bending stress (Curuksu et al. 2009a;



■ Fig. 32-3

Geometrical methods to induce bending of nucleic acids molecules. (*Left panel*): “self bent” DNA mini-circle system. (*Right panels*): duplex DNA oligonucleotide bent by the load imposed at its two ends when restraining the angle between two vector-handles (Curuksu et al. 2008). The vector-handles (*local helical axis*) are indicated as *lines* and the local axis vectors as *short arrows*



■ Fig. 32-4

(a) Time series of roll angle for base pair step C7pG8 (*dots*) and propeller angle at base pair C7:G24 (*line*) in the regime of large induced bending angle ( $150^\circ$ ) during umbrella sampling *with* replica-exchange of the duplex  $d(\text{CGCGCGCGCGCGCG})_2$ . Roll values were averaged over four adjacent umbrella windows. Base pair kink density histogram observed for simulation windows with large DNA bending strain ( $135\text{--}150^\circ$ ) during umbrella sampling, with (b) and without replica exchanges between neighboring sampling windows (c). Upper set of plots corresponds to roll fluctuations for every pyrimidine–purine base pair steps (CG) and the second set of plots to every purine–pyrimidine base pair steps GC in the oligomer (unpublished results and Curuksu et al. 2009b)



Lankas et al. 2006). Reversible partial unstacking events associated with strong local bending kinks at central GC and CG steps were observed in several sampling windows of the REUS application (results for the 150° bending window are shown in **► Fig. 32-4a**) characterized by a roll angle >40°.

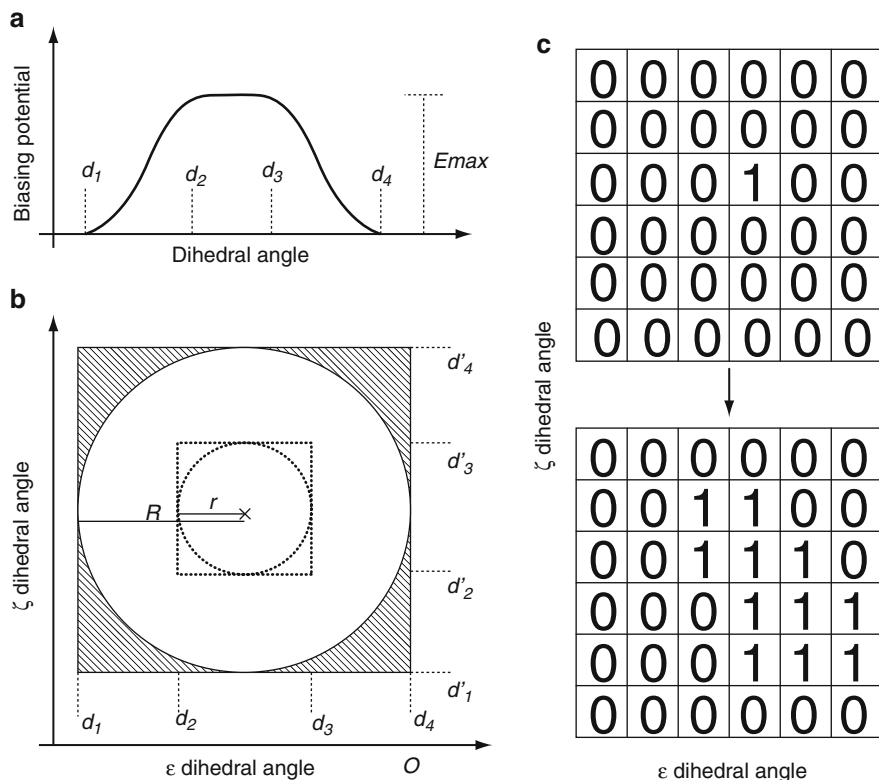
The base pair bend density histograms appeared as distributions with two maxima for the two junctions that form a kink (C7G8 in purple and G6C7 in blue), which is not the case in the umbrella sampling without replica exchange (**● Fig. 32-4b, c**). This means that these two neighboring junctions are both kinked during a significant part of the trajectory as in conventional umbrella sampling (Curuksu et al. 2009b) but can also adopt stacked conformations (no kink) during another significant part of the same trajectory. This is also indicated in **► Fig. 32-4a**, which illustrates the bend angle of the C7G8 junction and at the propeller twist of the base pair intermediate between G6C7 and C7G8 (C7:G24) as a function of simulation time. Propeller twist is the contra-rotation about the long base pair axis within one base pair and together with the roll deformations above were shown to characterize a specific kink motif called type II kink (Lankas et al. 2006). The time-series for roll (purple dots) indicates a number of transitions between large bend angles (~60°) and small bend angles (~15°) corresponding to the two sub-maxima on the density plot (**► Fig. 32-4b**) for the C7G8 step. Moreover, these transitions occur in concert with propeller transitions (black line) between values typical for B-form DNA and values specific to the type II kink. Thus, the simulations suggested that type II kink is an elastic reversible deformation, which could not have been deduced from a standard umbrella sampling (Curuksu and Zacharias 2009) where no exchange between the sampling windows took place. Clearly, type II kink appears as an important transient DNA motif at the regime of bending probed in the induced bending simulations (up to bend angles of 150°).

## Conformational Transitions of Nucleic Acid Backbone States

Various phosphodiester backbone substates can be found in X-ray crystal structures of free nucleic acids and in complexes with proteins (Djuranovic and Hartmann 2004; Varnai et al. 2002). In particular, the coupled  $\epsilon$  (rotation around C3'–O3' bond in C4'–C3'–O3'–P) and  $\zeta$  (rotation around O3'–P bond in C3'–O3'–P–O5') in gauche-/trans and in trans/gauche-regimes, termed B<sub>I</sub> and B<sub>II</sub> substates, respectively, are frequent in crystal structures of free DNA (Varnai et al. 2002).

Since conformational transitions in dsDNA or dsRNA often require transitions of backbone dihedral angles, a generalized coordinate defined as a set of dihedral angles can in principle promote more global transitions. For example, we have designed a replica exchange method that employs different levels of a specific biasing potential (illustrated in **► Fig. 32-5**) to induce coupled transitions of the nucleic acid backbone dihedral angles  $\epsilon/\zeta$  along the replicas (Curuksu and Zacharias 2009). The sampled conformations can exchange with a reference replica that is controlled by the original force field. The choice of biasing potentials in the replicas can be either fixed at the beginning of the simulation or optimized during an equilibration phase. The nucleic acid dihedral angle dependent biasing potential that destabilizes a given  $\epsilon/\zeta$  combination takes the following form (penalty term added to the original force field):

$$v_i(\epsilon, \zeta) = k \times \begin{cases} ((x-r)^2 - (R-r)^2)^2 & \text{if } r < x < R \\ (R-r)^4 & \text{if } x < r \\ 0 & \text{otherwise} \end{cases}$$

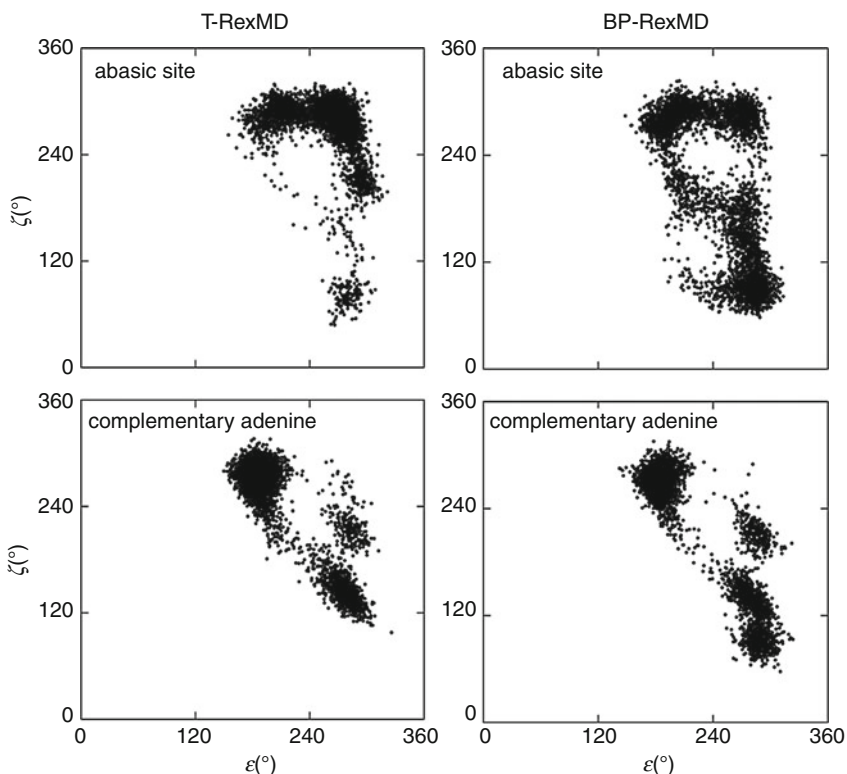


■ Fig. 32-5

(a) Shape of the dihedral angle biasing potential in one dimension. The potential is constant ( $E_{max}$ ) between  $d_2$  and  $d_3$  and decreases continuously to zero for dihedral angles in the interval  $d_2, d_1$  as well as  $d_3, d_4$ . Different levels of the BP were added to the force field to control replica runs during BP-REMD simulations. (b) Shape of the BP in two dimensions ( $\epsilon/\zeta$  dihedral angles). The potential is constant for  $\epsilon/\zeta$  dihedral combinations within radius  $r$  from the reference (marked by a cross) and decreases smoothly to zero within radius  $R$ . (c) The upper panel indicates the initial placement of the 2D biasing potential (bumps) illustrated in (b) on the complete 2D plane of possible  $\epsilon/\zeta$  dihedral angles during BP-REMD simulations (labeled 1). After an equilibration phase the placement of additional bumps is illustrated (labeled 1, non-biased regimes are labeled 0). The biasing level at all placements is scaled along the replica coordinate during BP-REMD simulations (see text for details)

where  $x = \sqrt{(\epsilon - \epsilon_r)^2 + (\zeta - \zeta_r)^2}$  is the coordinate in the two dimensional  $\epsilon/\zeta$  phase-space defined by taking the center of the ceiling ( $\epsilon_r, \zeta_r$ ) as origin (see ● Fig. 32-6).  $r$  is the radius of the ceiling and  $R$  the radius of the biasing potential. This function has the shape of a quasi-Gaussian with flat ceiling but does not use the computationally expensive exponential function. The width and height of the potential can be independently chosen and different levels of the potential (with different values of  $k$  or  $E_{max}$ ) were used along the replicas to destabilize some given  $\epsilon/\zeta$  substates.

In order to systematically cover the whole two dimensional plane of possible  $\epsilon/\zeta$  combinations, a set of 36 regularly spaced positions of biasing potentials can be used (spaced by  $60^\circ$  in

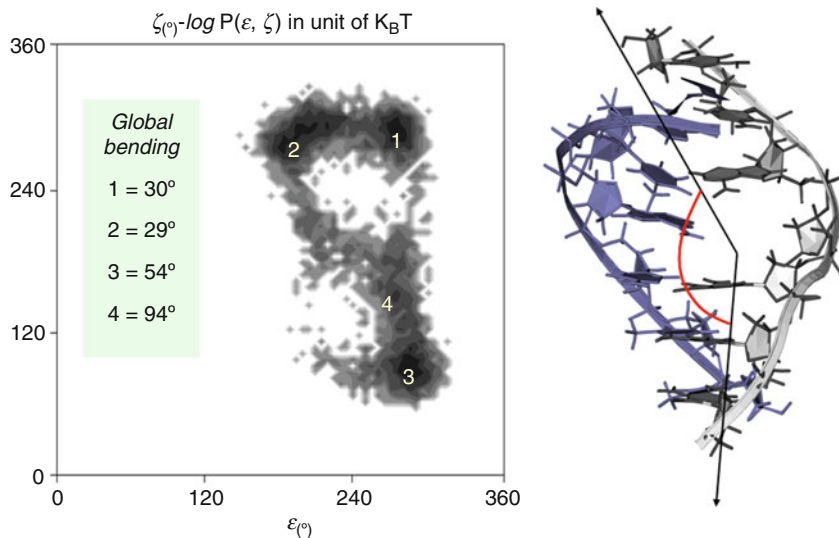


■ Fig. 32-6

Comparison of  $\epsilon/\zeta$  backbone dihedral angle sampling at the abasic site (*upper panels*) and the opposing adenine (*lower panels*) of the double stranded DNA with a central abasic site (Curuksu and Zacharias 2009). Each dot in the plots corresponds to an  $\epsilon/\zeta$  pair of a conformation sampled every 0.75 ps. The T-REMD simulations required 16 replicas and the BP-REMD was performed with 5 replicas (5 biasing levels). Only the sampling in the reference replica (at lowest temperature of 300 K in case of T-REMD and at the original force field in case of BP-REMD)

each of the two dihedral angles) (Curuksu and Zacharias 2009). In each dimension six different sets of the following biasing potential parameters ( $d_1, d_2, d_3, d_4$  as in [Fig. 32-5](#)) were possible: ( $0^\circ, 30^\circ, 60^\circ, 90^\circ$ ); ( $60^\circ, 90^\circ, 120^\circ, 150^\circ$ ); ( $120^\circ, 150^\circ, 180^\circ, 210^\circ$ ); ( $180^\circ, 210^\circ, 240^\circ, 270^\circ$ ); ( $240^\circ, 270^\circ, 300^\circ, 330^\circ$ ); and ( $300^\circ, 330^\circ, 360^\circ, 390^\circ$ ). In simulation studies described in reference 109, the width of each potential was  $90^\circ$  and the tail region of each potential was  $30^\circ$  (corresponding to the difference between  $d_1$  and  $d_2$  or  $d_3$  and  $d_4$ , respectively). The sampling of conformations within each of the 36 intervals could be monitored by collecting all  $\epsilon/\zeta$  pairs within each interval. The variance of the sampled states within an interval was used to decide on positioning a biasing potential at the corresponding  $\epsilon/\zeta$  location during an equilibrating simulation phase.

Test simulations on nucleic acid systems indicated that an  $E_{\max} = 10.0 \text{ kcal}\cdot\text{mol}^{-1}$  was necessary to allow for efficient nucleic acid backbone transitions and it was chosen as the highest biasing level. During replica exchange simulations five replicas with  $E_{\max}$  levels of 0 (reference replica without biasing), 1, 3, 6, and  $10 \text{ kcal}\cdot\text{mol}^{-1}$  were used, which resulted in an exchange




■ Fig. 32-7

**Coupling of sampled  $\epsilon/\zeta$  dihedral angle substates and global bending of the abasic site [109]. (left panel) Distribution of  $\epsilon/\zeta$  dihedral angles during BP-REMD (replica with the original force field) at the abasic site. The global bend angle of the DNA related to each  $\epsilon/\zeta$  dihedral angle regime is indicated. (right panel) Illustration of the global bend angle in the BP-REMD simulation of a DNA oligonucleotide with central abasic site**

acceptance rate of  $\sim 40\%$ . The method was applied (Curuksu and Zacharias 2009) to an experimental structure of an abasic site embedded in double strand DNA (seven central base pairs of a DNA abasic site deposited in the protein data bank: pdb-entry: 2HSS; Chen et al. 2007). An abasic site occurs notably when chemical or radiation damage of DNA result in the loss of a base in one strand leaving an unpaired base in the opposite strand (Dempfle and Harrison 1994). From conventional MD simulations it is known that abasic sites have significantly altered dynamics compared to regular DNA (Fujimoto et al. 2005).

The abasic site system was investigated using cMD simulation (5 ns, 300 K), a T-REMD simulation (16 replicas) and using a 5 ns Biasing Potential Replica Exchange MD with 5 replicas (in the following termed BP-REMD). The dihedral biasing potential (36 possible potentials) was only applied to  $\epsilon/\zeta$  dihedral angles at the abasic site itself and the adenine nucleotide on the opposite strand. All other nucleotides were only controlled by the original force field (in each replica). Thus, dihedral angle sampling was focused on the sampling at the abasic site and at the opposing adenine (► Fig. 32-6). The cMD simulation indicated sampling of the ( $\epsilon/\zeta$ )  $B_I$  region at the abasic site (with a dominant sampling of the (*-gauche*/*-gauche*) regime (90%) compared to the standard (*trans*/*-gauche*) state). For the opposing adenine nucleotide both  $B_I$  and  $B_{II}$  states were sampled during cMD (not shown). Both the temperature REMD as well as the BP-REMD showed much more extensive sampling of the possible ( $\epsilon/\zeta$ ) pairs compared to cMD on the same time scale (in the reference replica, ► Fig. 32-6). Both replica simulations predict an even ( $\sim 1:1$ ) distribution of the  $B_I$  substates = (*-gauche*/*-gauche*) versus (*trans*/*-gauche*) and

also sampled several additional states (e.g., in  $B_{II}$  region) both for the abasic site as well as for the opposing adenine (not sampled in the cMD simulations).

The observed difference in sampling of the four major ( $\epsilon/\zeta$ ) dihedral states demonstrated that cMD and T-REMD approaches undersampled (or did not sample at all) the (*-gauche/trans*) and (*-gauche/+ gauche*) regimes for the abasic site and the (*-gauche/- gauche*) and (*-gauche/+ gauche*) regime in the case of the opposing adenine. Application of the BP-REMD methodology to a DNA with a central abasic site significantly improved sampling of the  $\epsilon$  and  $\zeta$  dihedral angle substates compared to cMD simulations and also compared to T-REMD at smaller computational costs. The coupling of the global structure of the DNA with a central abasic site to the ( $\epsilon/\zeta$ ) dihedral substate sampling is illustrated in  Fig. 32-7. Each of the sampled substate regions at the abasic site correlated with a different global bending geometry of the DNA molecule. This coupling may have important consequences for the recognition process of damaged DNA by repair enzymes.

## Conclusions

---

The focus of this chapter was the description of REMD methods to improve umbrella sampling, in combination with a specific biasing potential to promote dihedral transitions in nucleic acid molecules. Replica exchanges between umbrella sampling windows avoid trapping of conformations due to the restraining of the system with respect to a selected regime along a reaction coordinate. This can significantly improve the free energy convergence of such calculations. The technique has a wide range of possible applications to investigate the deformability of DNA and RNA molecules and to better understand its coupling to recognition by proteins and other ligands.

The BP-REMD technique described here can help to better characterize available backbone dihedral angle substates of nucleic acids and may yield a better understanding of the relation between nucleic acid fine structure and how it is influenced by binding processes.

## Acknowledgments

---

This work was supported by a grant (I/80485) from the Volkswagen Foundation to M.Z.

## References

---

- Affentranger, R., Tavernelli, I., & Di Iorio, E. E. (2006). A novel Hamiltonian replica exchange MD protocol to enhance protein conformational space sampling. *Journal of Chemical Theory and Computation*, 2, 217.
- Al-Hashimi, H. M., & Walter, N. G. (2008). RNA dynamics: It is about time. *Current Opinion in Structural Biology*, 18, 321.
- Babin, V., Baucom, J., Darden, T. A., & Sagui, C. (2006). Molecular dynamics simulations of DNA with polarizable force fields: Convergence of an ideal B-DNA structure to the crystallographic structure. *The Journal of Physical Chemistry B*, 110, 11571.
- Barthel, A., & Zacharias, M. (2006). Conformational transitions in RNA single uridine and adenosine bulge structures: A molecular dynamics free energy simulation study. *Biophysical Journal*, 90, 2450.
- Bowman, G. R., Huang, X., Yao, Y., Sun, J., Carlsson, G., et al. (2008). Structural insight into RNA hairpin folding intermediates. *Journal of*

- the American Chemical Society*, 130, 9676
- Cheatham, T. E. (2004). Simulation and modeling of nucleic acid structure, dynamics and interactions. *Current Opinion in Structural Biology*, 14, 360.
- Chen, J., Dupradeau, F. Y., Case, D. A., Turner, C. J., & Stubbe, J. (2007). Nuclear magnetic resonance structural studies and molecular modeling of duplex DNA containing normal and 4'-oxidized abasic sites. *Biochemistry*, 46, 3096.
- Cheng, X., & Blumenthal, R. M. (2008). Mammalian DNA methyltransferases: A structural perspective. *Structure*, 16, 341.
- Cloutier, T. E., & Widom, J. (2004). Spontaneous sharp bending of double-stranded DNA. *Molecular Cell*, 14, 355.
- Curuksu, J., & Zacharias, M. (2009). Enhanced conformational sampling of nucleic acids by a new Hamiltonian replica exchange molecular dynamics approach. *Journal of Chemical Physics*, 130, 104110.
- Curuksu, J., Zakrzewska, K., & Zacharias, M. (2008). Magnitude and direction of DNA bending induced by screw-axis orientation: Influence of sequence, mismatches and abasic sites. *Nucleic Acids Research*, 36, 2268.
- Curuksu, J., Spomer, J., & Zacharias, M. (2009a). Elbow flexibility of the kt38 RNA kink-turn motif investigated by free-energy molecular dynamics simulations. *Biophysical Journal*, 97, 2004.
- Curuksu, J., Zacharias, M., Lavery, R., & Zakrzewska, K. (2009b). Local and global effects of strong DNA bending induced during molecular dynamics simulations. *Nucleic Acids Research*, 37, 3766.
- Dalhous, B., Laerdahl, J. K., Backe, P. H., & Bjoras, M. (2009). DNA base repair-recognition and initiation of catalysis. *FEMS Microbiology Reviews*, 33, 1044.
- Darden, T., York, D., & Pedersen, L. (1993). Particle mesh Ewald: An N-log(N) method for Ewald sums in large systems. *Search Results, Journal of Chemical Physics*, 98, 10089.
- DeJong, E. S., Luy, B., & Marino, J. P. (2002). RNA and RNA-protein complexes as targets for therapeutic intervention. *Current Topics in Medicinal Chemistry*, 2, 289.
- Demple, B., & Harrison, L. (1994). Repair of oxidative damage to DNA: Enzymology and biology. *Annual Review of Biochemistry*, 63, 915.
- Djuranovic, D., & Hartmann, B. (2004). DNA fine structure and dynamics in crystals and in solution: The impact of BI/BII backbone conformations. *Biopolymers*, 73, 356.
- Foloppe, N., & MacKerell, A. D., Jr. (2000). All-atom empirical force field for nucleic acids: I. parameter optimization based on small molecule and condensed phase macromolecular target data. *Journal of Computational Chemistry*, 21, 86.
- Fujimoto, H., Pinak, M., Nemoto, T., O'Neill, P., Kume, E., Saito, K., & Maekawa, H. (2005). Molecular dynamics simulation of clustered DNA damage sites containing 8-oxoguanine and abasic site. *Journal of Computational Chemistry*, 26, 788.
- Fukunishi, H., Watanabe, O., & Takada, S. (2002). On the Hamiltonian replica exchange method for efficient sampling of biomolecular systems: Application to protein structure prediction. *Journal of Chemical Physics*, 116, 9058.
- Furtig, B., Richter, C., Wöhnert, J., & Schwalbe, H. (2003). NMR spectroscopy of RNA. *European Journal of Chemical Biology*, 4, 936.
- Garcia, H. G., Grayson, P., Han, L., Inamdar, M., Kondev, J., Nelson, P. C., Phillips, R., Widom, J., & Wiggins, P. A. (2007). Biological consequences of tightly bent DNA: The other life of a macromolecular celebrity. *Biopolymers*, 85, 115.
- Garcia, A. E., & Paschek, D. (2008). Simulation of the pressure and temperature folding/unfolding equilibrium of a small RNA hairpin. *Journal of the American Chemical Society*, 130, 815.
- Giudice, E., & Lavery, R. (2003). Nucleic acid base pair dynamics: The impact of sequence and structure using free-energy calculations. *Journal of the American Chemical Society*, 125, 4998.
- Giudice, E., Várnai, P., & Lavery, R. (2003). Base pair opening within B-DNA: Free energy pathways for GC and AT pairs from umbrella sampling simulations. *Nucleic Acids Research*, 31, 1434.
- Gnanakaran, S., Nymeyer, H., Portman, J., Sanbonmatsu, K. Y., & Garcia, A. E. (2003). Peptide folding simulations. *Current Opinion in Structural Biology*, 15, 168.
- Hall, K. B. (2008). RNA in motion. *Current Opinion in Chemical Biology*, 12, 612.
- Hart, K., Nyström, B., Öhman, M., & Nilsson, L. (2005). Molecular dynamics simulations and free energy calculation of base flipping in dsRNA. *RNA*, 11, 609.
- Hashem, Y., & Auffinger, P. (2007). Nucleic solvation: From outside to insight. *Current Opinion in Structural Biology*, 17, 325.
- Huang, N., Banavali, N. K., & MacKerell, A. D., Jr. (2003). Protein facilitated base flipping in DNA by cytosine-5-methyltransferase. *Proceedings of the National Academy of Sciences of the United States of America*, 100, 68.
- Jang, S., Shin, S., & Pak, Y. (2003). Replica-exchange method using the generalized effective potential. *Physical Review Letters*, 91, 58305.

- Kaihsu T. (2004). Conformational sampling for the impatient. *Biophysical Chemistry*, 107, 213.
- Kannan, S., Kohlhoff, K., & Zacharias, M. (2006). B-DNA under stress: Over and un-twisting of DNA during molecular dynamics simulations. *Biophysical Journal*, 91, 2956.
- Kannan, S., & Zacharias, M. (2007a). Folding of a DNA Hairpin loop structure in explicit solvent using replica-exchange molecular dynamics simulations. *Biophysical Journal*, 93, 3218.
- Kannan, S., & Zacharias, M. (2007b). Enhanced sampling of peptide and protein conformations using replica exchange simulations with a peptide backbone biasing-potential. *Proteins*, 66, 697.
- Kannan, S., & Zacharias, M. (2009). Simulation of DNA double-strand dissociation and formation during replica-exchange molecular dynamics simulations. *Physical Chemistry Chemical Physics*, 11, 10589.
- Kim, J. L., & Burley, S. K. (1994). 1.9 Å resolution refined structure of TBP recognizing the minor groove of TATAAAAG. *Nature Structural & Molecular Biology*, 1, 638.
- Kumar, S. D., Bouzida, R., Swendsen, H., Kollman, P. A., & Rosenberg, J. M. (1992). The weighted histogram analysis method for free-energy calculations on biomolecules. I. The method. *Journal of Computational Chemistry*, 13, 1011.
- Lankas, F., Lavery, R., & Maddocks, J. H. (2006). Kinking occurs during molecular dynamics simulations of small DNA minicircles. *Structure*, 14, 1527.
- Lavery, R., et al. (2009). Molecular dynamics simulations of the 136 unique tetranucleotide sequences of DNA oligonucleotides. I. Research design and results on d(CpG) steps. *Biophysical Journal*, 87, 3799.
- Leontis, N. B., & Westhof, E. (2003). Analysis of RNA motifs. *Current Opinion in Structural Biology*, 13, 300.
- Liu, P., Kim, B., Friesner, R. A., & Berne, B. A. (2005). Replica exchange with solute tempering: A method for sampling biological systems in explicit water. *Proceedings of the National Academy of Sciences*, 102, 13749.
- MacKerell, A. D., Jr., & Banavali, N. (2000). All-atom empirical force field for nucleic acids: II. Application to molecular dynamics simulations of DNA and RNA in solution. *Journal of Computational Chemistry*, 21, 105.
- Mackerell, A. D., Jr., & Nilsson, L. (2008). Molecular dynamics simulations of nucleic acid-protein complexes. *Current Opinion in Structural Biology*, 18, 194.
- McDowell, S. E., Spacková, N., Sponer, J., & Walter, N. G. (2007). Molecular dynamics simulations of RNA: An in silico single molecule approach. *Biopolymers*, 85, 169.
- Moody, E. M., & Bevilacqua, P. C. (2003). Folding of a stable DNA motif involves a highly cooperative network of interactions. *Journal of the American Chemical Society*, 125, 16285.
- Nikolov, D. B., Chen, H., Halay, E. D., Hoffman, A., Roeder, R. G., & Burley, S. K. (1996). Crystal structure of a Human TATA box-binding protein/TATA element complex. *Proceedings of the National Academy of Sciences of the United States of America*, 93, 4862.
- Norberg, J., & Nilsson, L. (1995). Potential of mean force calculations of the stacking-unstacking process in single-stranded deoxyribonucleoside monophosphates. *Biophysical Journal*, 69, 2277.
- Ong, M. S., Richmond, T. J., & Davey, C. A. (2007). DNA stretching and extreme kinking in the nucleosome core. *Journal of Molecular Biology*, 368, 1067.
- Orozco, M., Noy, A., & Pérez, A. (2008). Recent advances in the study of nucleic acid flexibility by molecular dynamics. *Current Opinion in Structural Biology*, 18, 185.
- Perez, A., Marchan, I., Svozil, D., Sponer, J., Cheatham, T. E., III, Laughton, C. A., & Orozco, M. (2007a). Refinement of the AMBER force field for nucleic acids: Improving the description of conformers. *Biophysical Journal*, 92, 3817.
- Perez, A., Luque, F. J., & Orozco, M. (2007b). Dynamics of B-DNA on the microsecond time scale. *Journal of the American Chemical Society*, 129, 14739-14745.
- Portella, G., & Orozco, M. (2010). Multiple routes to characterize the folding of a small DNA Hairpin. *Angewandte Chemie International Edition England*, 49, 7673-7676.
- Sanbonmatsu, K. Y., & Tung, C. S. (2007). High performance computing in biology: Multimillion atom simulations of nanoscale systems. *Journal of Structural Biology*, 157, 470.
- Shroff, H., Reinhard, B. M., Siu, M., Agarwal, H., Spakowitz, A., & Liphardt, J. (2005). Biocompatible force sensor with optical readout and dimensions of 6 nm. *Nano Letters*, 5, 1509.
- Steitz, T. A. (2008). A structural understanding of the dynamic ribosome machine. *Nature Reviews Molecular Cell Biology*, 9, 242.
- Sugita, Y., & Okamoto, Y. (1999). Replica-exchange molecular dynamics method for protein folding. *Chemical Physics Letters*, 314, 141.



- Sugita Y., Kitao, A., & Okamoto, Y. (2000). Multi-dimensional replica-exchange method for free energy calculations. *Journal of Chemical Physics*, 113, 6042.
- Swendsen, R. H., & Wang, J. S. (1986). Replica Monte Carlo simulations of spin glasses. *Physical Review Letters*, 57, 2607.
- Travers, A., & Muskhelishvili, G. (2005). Bacterial chromatin. *Current Opinion in Genetics & Development*, 15, 507
- Varnai, P., Djuranovic, D., Lavery, R., & Hartmann, B. (2002). alpha/gamma Transitions in the B-DNA backbone. *Nucleic Acids Research*, 30, 5398.
- Villa, A., Widjajakusuma, E., & Stock, G. (2008). Molecular dynamics simulation of the structure, dynamics, and thermostability of the RNA Hairpins uCACGg and cUUCGg. *The Journal of Physical Chemistry B*, 112, 134.
- Wiggins, P. A., Van Der Heijden, T., Moreno-Herrero, F., Spakowitz, A., Phillips, R., Widom, J., Ceekers, C., & Nelson, P. C. (2006). High flexibility of DNA on short length scales probed by atomic force microscopy. *Nature Nanotechnology*, 1, 137.
- Wong, H. M., Payet, L., & Huppert, J. L. (2009). Function and targeting of G-quadruplexes. *Current Opinion in Molecular Therapeutics*, 11, 146.
- Yoshizawa, S., Kawai, G., Watanabe, K., Miura, K., & Hirao, I. (1997). GNA trinucleotide loop sequences producing extraordinarily stable DNA minihairpins. *Biochemistry*, 36, 4761.
- Yuan, C., Chen, H., Lou, X. W., & Archer, L. A. (2008). DNA bending stiffness on small length scales. *Physical Review Letters*, 100, 018102.
- Zacharias, M. (2000). Simulation of the structure and dynamics of nonhelical RNA motifs. *Current Opinion in Structural Biology*, 10, 307.
- Zacharias, M. (2003). Perspectives of drug design that targets RNA. *Current Medicinal Chemistry*, 2, 161.
- Zacharias, M. (2006). Minor groove deformability of DNA: A molecular dynamics free energy simulation study. *Biophysical Journal*, 91, 882.
- Zacharias, M. (2008). Combining elastic network analysis and molecular dynamics simulations by Hamiltonian replica exchange. *Journal of Chemical Theory and Computation*, 4, 477.
- Zakrzewska, K. (2003). DNA deformation energetics and protein binding. *Biopolymers*, 70, 414.
- Zhuang, Z., Jaeger, L., & Shea, J. E. (2007). Probing the structural hierarchy and energy landscape of an RNA T-loop Hairpin. *Nucleic Acids Research*, 35, 6995.





# 33 Model Systems for Dynamics of $\pi$ -Conjugated Biomolecules in Excited States

Mario Barbatti<sup>1,2</sup> · Matthias Ruckebauer<sup>1,3</sup> · Jaroslaw J Szymczak<sup>1</sup> · Bernhard Sellner<sup>1</sup> · Mario Vazdar<sup>4</sup> · Ivana Antol<sup>4</sup> · Mirjana Eckert-Maksić<sup>4</sup> · Hans Lischka<sup>1,5</sup>

<sup>1</sup>Institute for Theoretical Chemistry, University of Vienna, Vienna, Austria

<sup>2</sup>Max-Planck-Institut für Kohlenforschung, Mülheim an der Ruhr, Germany

<sup>3</sup>Research Lab Computational Technologies and Applications, University of Vienna, Vienna, Austria

<sup>4</sup>Laboratory for Physical-Organic Chemistry – Division of Organic Chemistry and Biochemistry, Rudjer Bošković Institute, Zagreb, Croatia

<sup>5</sup>Department of Chemistry and Biochemistry, Texas Tech University, Lubbock, Texas 79409-1061, USA

<b>Introduction</b> .....	<b>1177</b>
<b>Mixed Quantum-Classical Dynamics Simulations</b> .....	<b>1179</b>
<b>Protonated Schiff Base Chains and Retinal</b> .....	<b>1180</b>
The Primary Mechanism of Vision .....	1180
Model 1: PSB3 .....	1182
Model 2: PSB4 .....	1183
Current Status of the Field .....	1186
<b>Heteroaromatic Rings and Nucleic Acid Bases</b> .....	<b>1187</b>
Photostability of DNA and RNA .....	1187
Model 1: Aminopyrimidine .....	1189
Model 2: Pyrrole .....	1192
Current Status of the Field .....	1195
<b>Formamide and Peptide Bonds</b> .....	<b>1197</b>
Probing Photoexcitation of Proteins .....	1197
Model 1: Formamide .....	1198
Model 2: Protonated Formamide .....	1200
Current Status of the Field .....	1202

<i>Conclusions and Outlook</i> .....	1203
<i>Acknowledgments</i> .....	1204
<i>References</i> .....	1204

**Abstract:** Mixed-quantum classical dynamics simulations have recently become an important tool for investigations of time-dependent properties of electronically excited molecules, including non-adiabatic effects occurring during internal conversion processes. The high computational costs involved in such simulations have often led to simulation of model compounds instead of the full biochemical system. This chapter reviews recent dynamics results obtained for models of three classes of biologically relevant systems: protonated Schiff base chains as models for the chromophore of rhodopsin proteins; nucleobases and heteroaromatic rings as models for UV-excited nucleic acids; and formamide as a model for photoexcited peptide bonds.

**List of Abbreviations:** *BLA*, Bond length alternation; *BP*, Bicycle pedal; *bR*, Bacteriorhodopsin; *CAS*, Complete active space; *CASSCF*, CAS self-consistent field; *CASPT2*, CAS second-order perturbation theory; *DFT*, Density functional theory; *DFTB*, Density functional based tight binding; *ESI*, Electrospray ionization; *FT*, Folding table; *GVB,PP*, Generalized valence bond in the perfect pairing approximation; *HT*, Hula-twist; *LIIC*, Linear interpolation of internal coordinates; *MALDI*, Matrix-assisted, laser-desorption ionization; *MCSCF*, Multiconfigurational self-consistent field; *MCTDH*, Multiconfigurational time-dependent Hartree; *MRCI*, Multireference configuration interaction; *MR-CIS*, MRCI with single excitations; *MR-CISD*, MRCI with single and double excitations; *MXS*, Minimum on the crossing seam; *NRBP*, Non-rigid bicycle pedal; *OBF*, One bond flip; *OM2*, Orthogonalization model 2; *PSB*, Protonated Schiff base; *PSB<sub>n</sub>*, PSB with n double bonds; *QM/MM*, Quantum-mechanical/molecular-mechanical; *Rh*, Rhodopsin; *ROKS*, Restricted open-shell Kohn-Sham; *RPSB*, Retinal protonated Schiff base; *SA*, State average; *TDSE*, Time-dependent Schroedinger equation; *UV*, Ultraviolet; *WC*, Watson-Crick; *ZPE*, Zero point energy

## Introduction

---

Photoelectronic excitation of organic molecules may trigger complex series of chemical and physical events, which are activated not only by the excess of energy provided by the photon but also by the reactive nature of the excited-state potential energy surfaces. While electronic ground states normally present relatively high barriers for interconversion between minima and strong adiabatic character, excited-state potential energy surfaces tend to show much lower energy barriers and numerous crossings between adiabatic states. The low energy barriers allow the molecule to explore geometric conformations that challenges the chemical intuition. The state crossings bring the molecule to the limit of validity of the Born–Oppenheimer approximation.

Between the photoabsorption and the formation of the final products, the electronic energy excess may be converted into mechanical energy of molecular vibration, isomerization, and dissociation, it may be dissipated as heat into the environment, or it may be reemitted with a red-shifted wavenumber. A measure of how diverse and complex these processes are can be seen from the fact that, depending on the molecule and on the excitation wavelength, they span a range of more than ten orders of magnitude between a few tens of femtoseconds of a radiationless decay and the milliseconds of the phosphorescent decay (Zewail 2000). Besides their intrinsic interest in basic sciences, molecular photoactivated processes are relevant for

important natural phenomena and technological applications. In terms of the natural phenomena that will be discussed in this chapter, they constitute the first steps for the primary process of vision (Wald 1968) and the remarkable photostability of the five natural nucleic acid bases may have had important impact on life on Earth (Crespo-Hernandez et al. 2005).

In this chapter we will focus on dynamics simulations for photoexcited molecules and the understanding these simulations may provide. Naturally, dynamics simulations are tailored to answer questions related to time-dependent properties such as time constants of specific processes. In addition, dynamics simulations show which regions of the configuration space are explored and whether they are populated or not. For example, one may frequently find multiple reaction pathways departing from the Franck-Condon region that are all energetically accessible (Barbatti and Lischka 2008). While conventional static calculations with optimization of stationary structures can reveal such pathways but only give indirect information on the importance of each one based on relative energies, dynamics simulations can, in principle, tell much more precisely which one will be preferred and when it will be activated.

The applicability of excited-state dynamics simulations is still limited by its extreme computational demands. Different from ground-state dynamics simulations for which good force-fields and semi-empirical methods are available for computationally efficient simulations, the treatment of molecules in excited states depends very much on costly electronic structure calculations and on hybrid methods like QM/MM approaches. Moreover, when the molecule evolves into state-crossing regions of the configuration space, non-adiabatic corrections are required too (Worth and Cederbaum 2004). Despite several attempts to develop semiempirical and DFT-based methods to treat the molecule in such regions (Fabiano et al. 2008b; Granucci et al. 2001; Levine et al. 2006; Tapavicza et al. 2007), the most reliable approaches to date are based on the multiconfiguration self-consistent field (MCSCF) and multireference configuration interaction (MRCI) *ab initio* levels.

Currently, most of the dynamics simulations for systems of chemical or biological interest are performed with the on-the-fly approach, in which energy gradients and other properties are computed as needed during the dynamics propagation. This avoids the cumbersome work of building a multidimensional potential energy surface or being forced to make educated guesses about a few important degrees of freedom. The price to pay for the on-the-fly approach is the lack of non-local information during the dynamics. Thus, the use of the on-the-fly, excited-state dynamics simulation approach should be done with an awareness of the risk of improper description of the zero-point energy and phase space distribution (Santoro et al. 2007b). Luckily, as soon as medium- and large-sized molecules move out of the Franck-Condon region, hot species are formed and such quantum effects tend to be reduced.

In view of the computational costs of the on-the-fly, excited-state dynamics simulations, these calculations are currently limited to few picoseconds of a ten- to twenty-atom molecule. This is usually enough to investigate ultrafast internal conversion processes and will be the main topic of this chapter.

With the double aim of reducing computational costs as well as of understanding the most basic constituents in photodynamics processes, it has been common to investigate model systems, which are supposed to be the minimal unit that can still reproduce the photodynamics observed in the complete molecule. In the following sections, we shall review three classes of molecules and their model systems: (1) protonated Schiff bases, models for rhodopsin chromophores; (2) heteroaromatic rings, models for nucleic acid bases; and (3) formamide, model for peptide bonds.

## Mixed Quantum-Classical Dynamics Simulations

Mixed quantum-classical approaches (Tully 1998) are the most popular methods to perform on-the-fly, excited-state dynamics simulations including non-adiabatic effects. In these approaches, which include the multiple spawning (Ben-Nun et al. 2000), the surface hopping (Tully 1990), and the Ehrenfest (Li et al. 2005) methods, the nuclear time evolution is treated classically by means of Newton's equations, while the time evolution of the population of each electronic state is treated separately, within different degrees of approximation. In the surface hopping method, the time evolution of the population is obtained in two steps: first, a non-adiabatic transition probability between each pair of states is computed and a stochastic algorithm is applied to decide in which state the classical trajectory is propagated in the next time step. Second, statistics over a large set of independently computed trajectories allow acquisition of the fraction of trajectories (occupation) in each state as a function of time.

Several procedures have been proposed to compute non-adiabatic transition probabilities in the surface hopping approach, from the most simple one, which just assumes that the probability is the unity if the energy gap between two states is smaller than some threshold (Hayashi et al. 2009), to more sophisticated approaches that take into account the variation of wavefunction coefficients (Fabiano et al. 2008a) or compute the Landau-Zener transition probability (Lasser and Swart 2008). One of the most reliable procedures for computing the non-adiabatic transition probability is Tully's fewest switches algorithm (Tully 1990). In this approach, the time-dependent Schroedinger equation (TDSE) is integrated simultaneously to the classical trajectory (Ferretti et al. 1996). To cope with the lack of non-local information introduced by the on-the-fly approach, non-local terms in the TDSE are neglected and the nuclear wavefunction is supposed to be entirely localized at the classical position determined by Newton's equation. Integration of this semi-classical version of the TDSE gives the adiabatic population of the states, which are then used to compute the probability using the fewest switches formula.

The integration of the TDSE depends on non-adiabatic coupling terms connecting different states. If an adiabatic representation is used to expand the molecular wavefunction, non-adiabatic coupling vectors need to be computed. Alternatively, if a diabatic representation is used, non-diagonal Hamiltonian elements are required. Either way, the computation of the non-adiabatic coupling terms are the bottleneck in non-adiabatic dynamics approaches. These terms are usually not available for most of quantum chemical methods and, when they are, they are computationally expensive with the cost increasing with the square of the number of states (Pittner et al. 2009). These difficulties have motivated, on one hand, the search for approximated hopping algorithms as those mentioned above, and on the other hand the computation of the coupling terms based on wavefunction overlaps (Fabiano et al. 2008a; Granucci et al. 2001; Hammes-Schiffer and Tully 1994; Pittner et al. 2009; Tapavicza et al. 2007; Werner et al. 2008). We should also point out that the availability of analytical gradients and non-adiabatic coupling vectors procedures at MRCI and MCSCF levels has been of great importance for dynamics simulations (Dallos et al. 2004; Lischka et al. 2002, 2004; Shepard 1995; Shepard et al. 1992).

One consequence of the hyperlocalization of the nuclear wavefunction in this approach is that non-diagonal terms in the density matrix do not vanish with time as they should do (Granucci and Persico 2007; Zhu et al. 2004). Decoherence can be imposed by applying an ad hoc correction to the adiabatic population every time step (Granucci and Persico 2007), which forces the non-diagonal terms in the density matrix to be reduced to zero within a certain time constant.

When a hopping event between two states takes place, this usually happens at a finite energy gap. To keep the total energy constant in the subsequent trajectory, it is necessary to correct the kinetic energy, for example, by rescaling the momentum or by adding more momentum to the direction of the non-adiabatic coupling vector (Ferretti et al. 1996; Muller and Stock 1997). It may also happen that the stochastic algorithm attempts to make a hop from a lower to an upper state in a region where there is not enough energy to do so. Such cases have been usually treated by forbidding the hopping occurrence (Ferretti et al. 1996). The momentum can be kept or reversed afterwards. Another possibility is to take the time uncertainty principle to search for a geometry nearby where the hopping is allowed (Jasper et al. 2002).

Because of the stochastic nature of the fewest switches surface hopping approach, trajectories starting with the same initial conditions will give rise to different time development. Moreover, the initial conditions should reflect the initial phase space distribution. Therefore, the averages that define the state occupation should in principle be performed over this double ensemble of trajectories starting in different points of the phase space, several times in each one. Because of computational limitations, this procedure is usually reduced to a single ensemble of trajectories starting only once in different points of the phase space.

The ensemble of initial conditions can be generated in a diversity of ways. For instance, the simulation of an instantaneously excited wave packet into the Franck-Condon region may be achieved by selecting geometries and velocities obtained from a dynamics in the ground state, with this dynamics performed for a period long enough as to allow an adequate sampling of the phase space. Alternatively, each nuclear degree of freedom can be treated within the harmonic approximation and a Wigner distribution can be built. In most of the applications discussed here, the second alternative is used since it is expected to provide realistic initial conditions for single molecules.

Several applications will be reviewed and discussed in the following sections. Specific information about methods used will be given. Details can be found in the proper references. The simulations carried out by the present authors have been performed with the NEWTON-X program (Barbatti et al. 2007a, b) for mixed quantum-classical dynamics simulations, interfaced with the COLUMBUS program (Lischka et al. 1981, 2001, 2006) for MRCI and MCSCF electronic structure calculations.

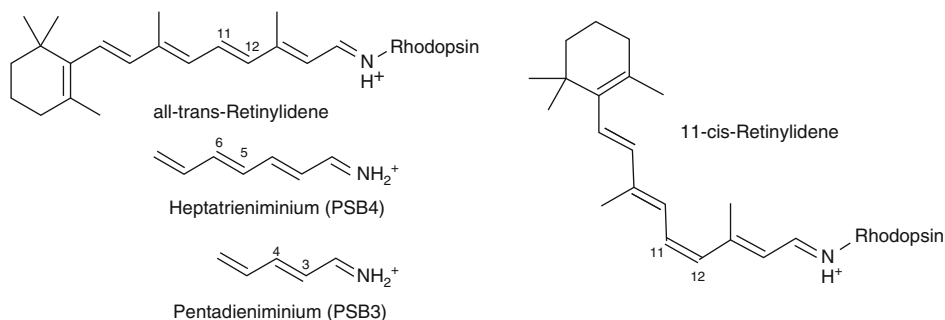
## Protonated Schiff Base Chains and Retinal

---

### The Primary Mechanism of Vision

---

Understanding the initial molecular mechanism of vision has been one of the most challenging subjects in the area of computational science during the last four decades (Andruniow et al. 2004; Ben-Nun et al. 1998; Birge 1981; Frutos et al. 2007; Garavelli et al. 1999b; González-Luque et al. 2000; Hayashi et al. 2009; Logunov et al. 1996; Polli et al. 2010; Rohrig et al. 2005; Saam et al. 2002; Send and Sundholm 2007; Szymczak et al. 2008, 2009; Wanko et al. 2005; Warshel 1976; Warshel and Barboy 1982; Warshel and Chu 2001; Weingart et al. 2007). The photoisomerization of the retinal protonated Schiff base (RPSB), the chromophore of the visual pigment rhodopsin (Rh) (Birge 1981, 1990; Palings et al. 1987; Schoenlein et al. 1991; Wang et al. 1994), followed by conformational changes in the protein is the primary event that initiates vision. This reaction, involving cis-trans isomerization of 11-cis RPSB (● Fig. 33-1) to its all-trans form



■ Fig. 33-1

### Retinylidene, the chromophore of the rhodopsin proteins, and the Protonated Schiff Base (PSB) models

belongs to the fastest photochemical reaction in nature (Birge 1990). Many theoretical studies have been dedicated to the exploration of the nature of this process, however, the question of the detailed mechanism and assignment of experimentally obtained lifetimes remains open, mostly due to the fact that the structures of intermediates are unknown to a large extent. The proper description of the mechanism requires involvement of a high-level theoretical treatment, which is especially challenging due to the large size of RPSB, the multireference character of the electronic wavefunction in regions of interest, and the need of dynamics simulations. Besides vision, photoisomerization in rhodopsin proteins is also important for proton pump processes in archae microorganisms (Birge 1981).

The photochemical properties of RPSB have been studied theoretically, mostly by simulation of model systems. Various mechanisms of the process were proposed in the literature, related strongly to the model used in investigations. In the last two decades, large effort has been dedicated to the theoretical modeling of the Rh photo-behavior in the single-torsion motion called one-bond flip (OBF) as the main isomerization mechanism. These predictions, however, were based mostly on calculations of the minimum energy path or dynamics of the short PSB3 model (Garavelli et al. 1997; Migani et al. 2003; Szymczak et al. 2008; Vreven et al. 1997; Weingart et al. 2004, 2006). On the other hand, investigations on longer PSB chains in earlier works by Warshel (Warshel 1976; Warshel and Barboy 1982) or in more recent investigations (Andruniow et al. 2004; Frutos et al. 2007; Hayashi et al. 2009; Ishida et al. 2009; Polli et al. 2010; Saam et al. 2002; Szymczak et al. 2009) indicate that double-torsion mechanisms like bicycle pedal and nonrigid or asynchronous bicycle pedal should be the main isomerization mechanisms. Also our recent results (Szymczak et al. 2009), based on ab initio dynamics simulations of PSB4 model (discussed below) strongly indicate that RPSB isomerizes in the excited state by performing two concerted twist motions, from which only one tends to be continued during the relaxation into the ground state. Torsional motions of similar character were observed in the recent works by Buss and co-workers (Schapiro et al. 2009; Weingart et al. 2007), whose studies were based on similar four double-bond models augmented by two additional methyl groups in the  $C_9$  and  $C_{13}$  positions. It is also worth mentioning that QM/MM simulations of full RPSB employing the restricted open-shell Kohn-Sham (ROKS) method (Rohrig et al. 2004) do not support double-torsions mechanism, pointing entirely to OBF as a way of performing photoisomerization in the Rh pocket. At the same time, QM/MM minimum energy path investigations



of the same system (Gascon and Batista 2004) report non negligible involvement of four additional torsions to the main torsion in the isomerization process. The uncertainty among the scientific community about the nature of mechanism of RPSB photoisomerization clearly shows the need for further investigations in this field.

## Model 1: PSB3

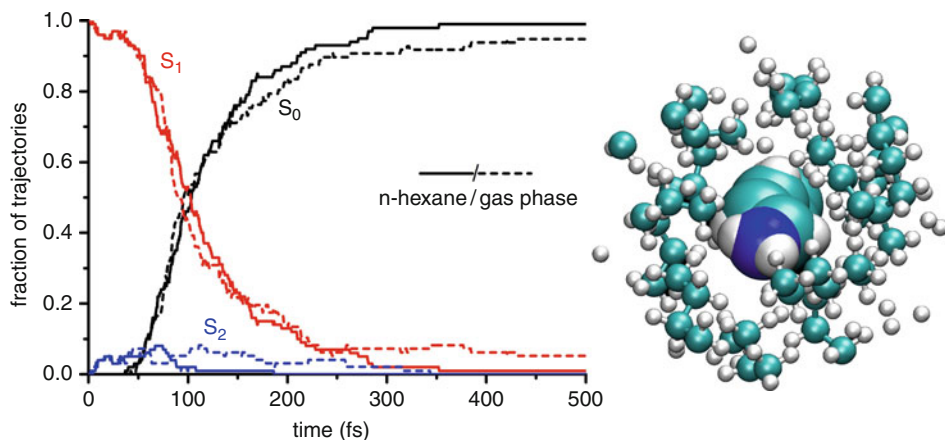
---

The penta-3,5-dieneiminium cation (PSB3) is the shortest of homologues that are investigated to understand the basic principles of the excited state behavior of retinal. It is the first molecule in the group reaching from methaniminium to retinal that features a double bond with further conjugated double bonds on both sides. At the same time the molecule is small enough to still be treated with high computational methods and medium-sized basis sets, even in dynamics. Therefore it has been subject of extensive theoretical investigations, especially by the groups of Robb, Buss, and Olivucci, which have contributed to the understanding of the excited state behavior and deactivation pathways of PSB3 in gas and solvated phases (Barbatti et al. 2007a, 2008; Garavelli et al. 1999a; Keal et al. 2009; Migani et al. 2003; Szymczak et al. 2008; Weingart et al. 2004, 2005).

Most dynamics investigations of PSB3 have been performed on a CASSCF level including all  $\pi$  orbitals in the active space with 6-31G/6-31G\* or similar basis sets. The gas phase dynamics of PSB3 can be explained in a two-state, two-mode model (Garavelli et al. 1997; González-Luque et al. 2000; Migani et al. 2003) involving the ground and the first excited ( $\pi\pi^*$ ) states and two dominating motions, a torsion around the central double bond, and the adjustment of the bond length alternation (BLA).

After vertical excitation into the first excited state the bond pattern adjusts to the changed electronic structure. The double/single bond distinction of the ground state is lifted and the BLA, being expressed as the difference between average single bond length and average double bond length, which is somewhat positive at the beginning, drops quickly to a larger negative value. This is accompanied by a shift of the highest occupied orbitals,  $\pi$  and  $\pi^*$ . They are separated from each other at the respective ends of the PSB3 molecule and, each occupied with one electron, induce a torsional motion around the central double bond of the molecule, in a mechanism known as *one-bond-flip* (Szymczak et al. 2008). This motion leads exactly to a conical intersection that is reached at a perpendicular orientation of the two halves of the molecule and small BLA. The excited state lifetime is about 100 fs. The high torsional momentum leads to a quantum yield of isomerization of PSB3 after photoexcitation of about 60%, regardless of the conformation the process started in, cis or trans. When restrictions are applied to the extremes of PSB3, another relaxation mechanism starts to compete with the one-bond-flip (Szymczak et al. 2008). This mechanism, named *folding table*, involves the torsion around the central bond occurring simultaneously to the semi-torsions around the other two formal double bonds.

Surface hopping dynamics simulations of PSB3 with the semiempirical OM2 method (Keal et al. 2009) show a picture very distinct from the CASSCF simulations. Depending on the choice of active space, the excited state relaxation shows a bi-exponential decay profile of the  $S_1$  population, with a fast sub-picosecond time constant and a picosecond time constant. Overall, the relaxation process is predicted to be larger than 600 fs, much slower than the 100 fs predicted by CASSCF. Similar multi-exponential decay has also been described in wave packet propagation on a two-dimensional surface model for RPSB (Santoro et al. 2007b).



■ Fig. 33-2

Average adiabatic populations of PSB3 in gas phase and n-hexane (left) and twisted PSB3 in n-hexane (right)

Inclusion of a solvent has the potential to change the dynamics drastically. A wide, space-requiring motion of a molecule would be hindered by collisions with the solvent molecules and different deactivation channels, which are normally not accessed, can become the primary path.

To assess the steric environmental effects on the photochemical deactivation of PSB3 it was embedded in a small sphere of n-hexane molecules at room temperature using a QM/MM scheme (Ruckebauer et al. 2010). The surface hopping dynamics simulations discussed here were computed at the MRCIS(4,5)/SA3CASSCF(6,6)/631G level, where 11 orbitals were frozen during the MR-CIS procedure. For solvation, the same quantum mechanical level was employed and 150 n-hexane molecules were introduced into the calculation using electrostatic embedding with the OPLSAA/TIP3P force field (Jorgensen and McDonald 1998).

The comparison of dynamics simulations in gas phase to simulations in n-hexane shows that the relaxation process is not too much affected by solvation. PSB3 is still too small a molecule to show steric hindering of the isomerization. Figure 33-2, right, shows a snapshot of one trajectory for the twisted PSB3 in n-hexane. It clearly demonstrates that PSB3 rotates in a quite volume conserving way, which minimizes the interactions with the solvent. As a consequence, the lifetime is roughly the same in gas phase and n-hexane (Fig. 33-2, left), in n-hexane slightly longer than in gas phase simulations, but the effect is limited to a difference of about 3 fs, which is statistically not significant.


## Model 2: PSB4

The recent progress in computer capacity and in computational methods made it possible to address by high-level ab initio dynamics more realistic models than the just-described PSB3. In one of our latest investigations (Szymczak et al. 2009), the photodynamics of the hepta-3,5,7-trieniminium cation (PSB4) is investigated by performing extended on-the-fly surface hopping dynamics calculations in vacuo. This compound exhibits a significantly enhanced

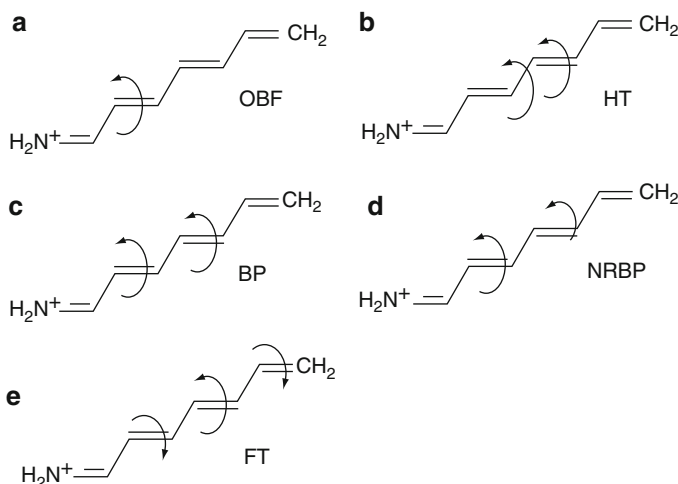
torsional variability while keeping the computational effort for the on-the-fly surface hopping calculations manageable so that good statistics within the framework of *ab initio* approaches can be achieved. Similar to our previous work on PSB3 (Szymczak et al. 2008), mechanical restrictions corresponding to the protein link on one PSB4 end and representing the remaining RPSB molecule on the other were applied by increasing masses of corresponding hydrogens to 1,000 amu. The constrained 5-*cis* isomer of PSB4 was investigated in order to model RPSB in the rhodopsin; dynamics results for doubly restricted PSB4 were then compared to time-dependent femtosecond-resolved experiments (Kochendoerfer and Mathies 1996; Kukura et al. 2005; Peteanu et al. 1993; Schoenlein et al. 1991).

Dynamic simulations were performed at CASSCF level. Eight electrons were included in the calculations within an active space consisting of eight orbitals (four  $\pi$  and the corresponding four  $\pi^*$  orbitals) and averaged over two states [SA-2-CASSCF(8,8)]. To validate the correctness of the method employed, calculations of the vertical excitation energies and conical intersections (MXS) were performed also at MRCI level. Additionally, calculations of LIIC paths from the  $S_1$  minimum to the MXSs give similar, very satisfactory accord between different methods. Thus, the applied theoretical level has been carefully chosen and verified to balance quality of the approach and the computational cost of few hundred thousands of quantum chemical calculations (energies, gradients, and non-adiabatic coupling vectors).

The photorelaxation of PSBn chains is well described by the two-state, two-mode model discussed in the previous section (Garavelli et al. 1997; González-Luque et al. 2000; Migani et al. 2003). After photoexcitation, in the initial stage of the dynamics the PSBn system relaxes by adjusting the bonds lengths, elongating the double bonds and shortening the single bonds. This phase, common to all currently studied PSBn systems, has been described in the previous section. After adjusting all bonds, PSBn proceeds to the second step of the dynamics. The crossing seam is reached by skeletal torsions around one or more bonds. When the molecular system switches from the excited state to the ground state it can either continue or reverse its motion that led to the crossing seam and further relax to the final product geometry.

The kind of torsional motion taking place in PSB4 was assigned to one of five main groups (see  Fig. 33-3): one-bond flip (OBF), bicycle pedal (BP) (Warshel 1976), non-rigid bicycle pedal (NRBP) (Warshel and Barboy 1982), hula-twist (HT) (Liu and Asato 1985), and the recently proposed folding table (FT) (Szymczak et al. 2008) mechanisms. A classification scheme was developed (Szymczak et al. 2008, 2009) facilitating the automatic assignment of these structures. It divides the analysis of the torsional dynamics into two stages: motions driving the system to the conical intersection and motions after decaying to the ground state, with independent possibility of investigation of the product formation. The advantage of the proposed scheme is that this classification algorithm is general enough to be applied for the massive amount of information coming from dynamics simulations. It can also be applied for investigations of longer PSBs and can even be further used to study behavior of complete RPSB.

The analysis of the first stage of the process, the mechanisms leading 5-*cis*-PSB4 to the seam of conical intersections, shows the coexistence of two groups of mechanisms. The first one includes OBF and FT mechanisms and proceeds as such to produce a complete torsion around only one bond, mostly around the one equivalent to the  $C_{11}C_{12}$  bond in RPSB. The other rotation proceeds around the  $C_{13}C_{14}$  bond, however, its importance is significantly smaller (less than 20% of cases featuring single torsion mechanism). All together, OBF and FT constitute around one third of motions driving 5-*cis*-PSB4 to the conical intersection. The second group, double-torsion mechanisms, is dominating and appears about twice as frequent as the single-torsion group. It includes BP and NRBP, which are characterized by performing concerted twists around



■ Fig. 33-3

Torsional motions involved in the main isomerization mechanisms: (a) OBF; (b) HT; (c) BP; (d) NRBP; (e) FT

two bonds. Within this group twice as many trajectories feature the NRBP than the BP mechanism. Not a single case of hula-twist motion was observed during the dynamics simulations of 5-cis-PSB4, no matter what was the degree of restrictions (Szymczak et al. 2009).

When returning to the ground state, the excess electronic energy is converted into mechanical energy. In this vibrationally hot ground state there will be freedom to move into different conformations, which in normal thermal situations are usually confined by high potential energy barriers. Since the transfer of the mechanical energy to the protein will take at least several picoseconds (Birge 1981), the motion in the hot ground state may be decisive for the actual quantum yields. The behavior of PSB4 after decaying to the ground state was analyzed from two points of view: firstly, whether the mechanism bringing PSB4 to the intersection seam is reversed or not after hopping; secondly, whether the initial motion results in the associated products or not. Here we concentrate only on the double-torsion mechanisms. The most abundant way of continuation of concerted double-torsion motions is not a complete continuation or reversion, but partial continuation. Interestingly, the second torsion involved in concerted motion is the one equivalent to the  $C_{13}C_{14}$  bond in RPSB. The same pattern was observed by Buss and co-workers (Schapiro et al. 2009; Weingart et al. 2007), whose studies were based on a similar four double-bond model PSB4 augmented by two additional methyl groups in the  $C_9$  and  $C_{13}$  positions. On the hand, available studies on complete RPSB (Hayashi et al. 2009; Ishida et al. 2009; Warshel 1976; Warshel and Barboy 1982) point to  $C_9C_{10}$  as the other torsion involved in the concerted twist mechanism. This difference may suggest that either the chain lengths of the systems studied is still too short for representing complete RPSB or that the methyl group at the  $C_{13}$  plays important role in blocking the given torsion in the protein pocket. The full continuation (rotation around both involved double-bonds) of double-torsion group of mechanisms appears only in 22% of NRBP cases and 10% of the BP cases. But even when full continuation is observed, the associated photoproduct is formed in half or less of the cases because of the hot ground state isomerization processes. The overall picture that can be

drawn from our simulations is the one in which 5-cis-PSB4 performs concerted twists around two double bonds to reach the region of conical intersection of which only one is continued after decaying to the ground state.

Although we expect that inclusion of at least one more double bond to PSB4 model may affect the relative importance of mechanisms or may even reveal new mechanisms, one can clearly see qualitative advance in comparison to the PSB3 case for revealing the role of multiple-bond torsional mechanisms. The next natural step in this sequence of models of Rh and bR chromophores investigations is to perform a full nonadiabatic dynamics for RPSB.

## Current Status of the Field

---

The large improvement of computational capabilities opened new possibilities in the field of studies of the excited state behavior of retinal and retinal model systems. Recent studies on the subject of dynamics are basically going in two directions. First, they combine more extended and complete models of retinal with use of higher theoretical levels. Second, they focus on studies of environmental influence on the electronic structure and excited state behavior. For the latter, two main features are of highest interest: the influence of charged groups on the spectral sensitivity of retinal and the change in the mechanism leading to the conical intersection when the molecule is restricted in a confined and restricted space. The problem of including environmental effects on the static and dynamic properties of retinal and its models is mostly addressed by using hybrid QM/MM methods. Other studies, as discussed in the previous section, simulated the mechanical constraints for the molecules by means of explicitly constraining the movement of single atoms or groups.

As was previously mentioned, recent work by Schapiro et al. (2009), who employed the PSB4 model augmented by two methyl groups, reports bicycle pedal mechanism involving the equivalent of  $C_{13}C_{14}$  bond as a second torsion. Although, these findings are in line with others based on PSB4 (Szymczak et al. 2009) and modified RPSB models (Ishida et al. 2009), simulations involving complete RPSB suggest that the  $C_9C_{10}$  should be the secondary bond performing concerted torsion with  $C_{11}C_{12}$ . Hayashi et al. (2009), have performed CASSCF QM/MM surface hopping dynamics for the complete retinal mechanically embedded in rhodopsin. Their analysis gave a picture in which isomerization around the  $C_{11}C_{12}$  double bond is accompanied by coupled torsions around  $C_9C_{10}$  and  $C_6C_7$ . It is concluded (Hayashi et al. 2009) that the excited state dynamics proceeds in such a way as to minimize interaction with the protein. On the other hand, scaled CASSCF QM/MM dynamics simulations of a single trajectory of retinal in bovine rhodopsin by Frutos et al. (2007) suggested the action of steric constraints for the torsion around  $C_9C_{10}$ . A quenching influence of protein was also proposed in the recent semiempirical QM/MM multiple spawning dynamics by Martinez and coworkers (Virshup et al. 2009). There, in contrast to RPSB simulations in vacuo, environmental effect was predicted to create highly directed dynamics leading to high yields of specific photoproducts. The same was concluded in simulations employing the ROKS method (Rohrig et al. 2004), which predict OBF as the only mechanism responsible for formation of all-trans RPSB.

As one can see in this brief review, despite important advances in the studies of retinal and its models based on dynamics simulation methods achieved in the last years, there is still an ongoing discussion about the mechanism of retinal isomerization in rhodopsin proteins, which calls for further investigations.

## Heteroaromatic Rings and Nucleic Acid Bases

### Photostability of DNA and RNA

The five natural nucleobases, adenine, guanine, cytosine, thymine, and uracil, absorb UV radiation in the range of 250–280 nm (UVC band) and at higher energies of about 200 nm (Abouaf et al. 2003; Clark and Tinoco 1965; Clark et al. 1965; Duggan et al. 1957; Middleton et al. 2009). This radiation, mainly the UVC, which is not blocked by the ozone in the air, causes DNA damage that, when not repaired by enzymatic mechanisms, may lead to mutagenesis and carcinogenesis (Cadet and Berger 1985).

The five nucleobases are non-fluorescent species (Longworth et al. 1966), which implies that the photo-energy is dissipated by means of ultrafast internal conversion. Time-resolved spectroscopy experiments have shown that either in gas phase or in solution the time constant for deactivation of the nucleobases excited at the 260 nm  $\pi\pi^* \leftarrow S_0$  band is in the range of 0.5–6 ps (Canuel et al. 2005; Crespo-Hernandez et al. 2004; Kang et al. 2002; Ullrich et al. 2004). This means that pathways to conical intersections where radiationless decay occurs are easily available from the Franck-Condon region.

The fact that nucleobases remain in reactive excited states only for a short time has been taken as an indication of enhanced photostability against UV irradiation (Middleton et al. 2009; Serrano-Andres and Merchan 2009). It may have happened that in the prebiotic era or in the early stages of evolution of the genetic code, nucleobases showing ultrafast decay had a competitive advantage against other chemical species more prone to undergo photochemical reactions. Indeed, one of the problems in understanding how life originated is to understand how chemical reactions not controlled by biogenetic mechanisms could lead to a few key substances instead of a multitude of chemicals, all of them with minor concentrations. It has been recently shown (Powner et al. 2009) that one possible route for prebiotic formation of nucleotides possesses as one of the steps an UV bath that could eliminate all but the nucleotides themselves, which reinforce the hypothesis that the intrinsic photostability of the nucleobases played an important role in the origin of life on Earth.

The mechanisms by which the nucleobases return to the ground state are subtly connected to the molecular structure of these bases. For instance, simple tautomerization of adenine into 2-aminopurine results in an increase of excited-state lifetime from 1.1 to 30 ps (Canuel et al. 2005). Methyl-substitution of cytosine or cytidine at C<sub>5</sub> position increases the lifetime in water solution by a factor of seven (Malone et al. 2003). Fluoro-substitution at the same site or acetyl-substitution at N<sub>4</sub> have even larger effects, increasing the lifetime from 1 ps to, respectively, 88 and 280 ps (Malone et al. 2003). Double methyl substitution in positions N<sub>1</sub> and N<sub>3</sub> of thymine increases its lifetime in gas phase from 5 ps (Canuel et al. 2005) to about 150 ps (He et al. 2003). Similar effects were also reported for single and double methyl substitutions in uracil (He et al. 2003).

Protonation and deprotonation of the bases depending on the environmental conditions has also influence on the excited-state lifetimes, although not so strong to make them fluorescent (Longworth et al. 1966). For cytosine, for example, the lifetime in water solution is raised from 1 to 13 ps when the pH is changed from 6.8 to 13 (Malone et al. 2003). For cytidine, the lifetime in water solution is reduced from 1 to 0.6 ps when the pH is changed from 6.8 to 0.08 (Malone et al. 2003). The excited-state lifetimes of nucleobases are dependent on the excitation wavenumber as well. For adenine, it increases from 1.1 ps to about 1.7 ps when the pump wavelength is changed

from 276 to 267 nm (Chin et al. 2007). For 1-3-dimethyl thymine, it increases from about 60 to 200 ps when the pump wavelength is changed from 240 to 280 nm (He et al. 2003).

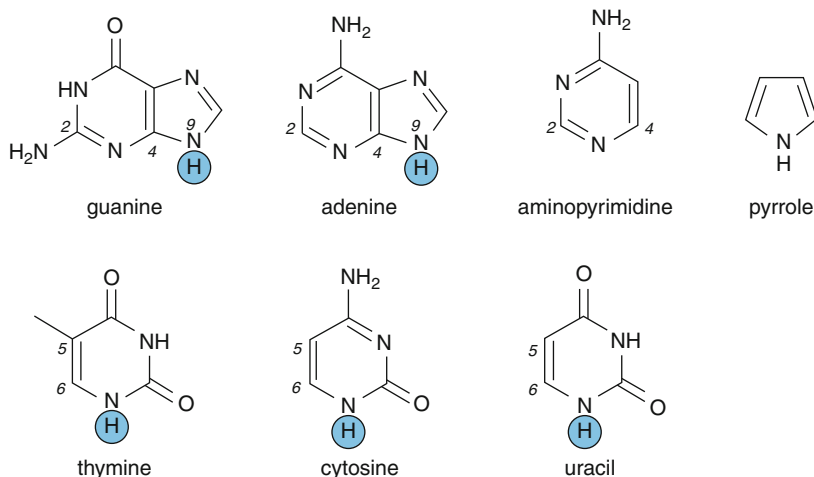
A great deal of theoretical work has been dedicated to nucleobases and their derivatives to identify conical intersections and reaction paths leading to them. In summary it has been found that these conical intersections can be formed by four different mechanisms:

1. Ring-puckering (Marian 2005; Perun et al. 2005a). In these conical intersections, the pyrimidine ring is deformed into conformations that produce twisted bonds (Barbatti et al. 2008). These conical intersections, which normally connect the  $\pi\pi^*$  to the ground state, have the same origin as the twisted conical intersection in the methaniminium cation or the twisted pyramidalized conical intersection in ethylene (Barbatti et al. 2008). They are usually connected to the  $\pi\pi^*$  state at the Franck-Condon region by barrierless pathways (Merchan et al. 2006). Out-of-plane amino and methyl deformations observed in conical intersections of adenine, cytosine, and thymine are caused by ring puckering as well.
2. Carbonyl out-of-plane deformation (Matsika 2004). In these conical intersections the ring remains planar, while the CO bond becomes almost perpendicular to the ring plane. The paths connecting the Franck-Condon region to them show an up-hill profile, which should decrease their efficiency for internal conversion (Zechmann and Barbatti 2008). This kind of conical intersection is analogous to formamide (Antol et al. 2007) and formaldehyde (Araujo et al. 2008) and connects the  $n_O\pi^*$  state to the ground state.
3. Ring-opening (Perun et al. 2005b). These conical intersections are caused by stretching of CN ring bonds and connect  $\pi\sigma_{CN}^*$  states to the ground state. Usually they appear in low-energy regions but are separated from the Franck Condon by high barriers. They are analogous to the stretched-pyramidalized conical intersection in the methaniminium cation (Barbatti et al. 2008).
4. NH stretching (Perun et al. 2005b). These conical intersections connect the  $\pi\sigma_{CH}^*$  and the ground states. They are accompanied by small barriers to the  $\pi\pi^*$  state in the Franck-Condon region. Several of such conical intersections are not available in the nucleotides because of the hydrogen substitution by the sugar linkage.

Internal conversion may take place not only at the conical intersections of isolated nucleobases but also at intersections formed along the hydrogen bonds connecting base pairs. It has been shown that a charge-transfer state crosses the ground state along the inter-pair hydrogen transfer (Schultz et al. 2004). When this mechanism is compared between guanine-cytosine Watson-Crick (WC) pair and other non-WC pairs formed by the same bases, it turns out that the WC pair possesses the lowest energy crossings (Sobolewski et al. 2005). This has been taken as an indication that inter-pairs internal-conversion may have constituted an evolutionary advantage for WC conformations. This hypothesis, however, has been disputed based on experiments showing that single and double stranded DNA decay follow a similar kinetics (Crespo-Hernandez et al. 2005). According to these experiments, initially excited state decays to an exciplex state in less than 1 ps. The exciplex state involves stacked nucleobases and lives for 10–100 ps before returning to the ground state via charge recombination. The stacking character of the exciplex state limits the damage to one single strand. The undamaged strand may then be used as a template for the repair mechanisms (Crespo-Hernandez et al. 2005; Middleton et al. 2009).

In the next sections we will focus on recent investigations of internal conversion in nucleobases and nucleobase models using dynamics simulations. First, we will explore aminopyrimidine (🔍 Fig. 33-4), a model system that can help to understand how pyrimidine rings deactivate





■ Fig. 33-4

The five nucleobases and the heterocycle models aminopyrimidine and pyrrole. The connections to the sugar in the nucleotides are indicated by the detached hydrogen atom

after UV excitation. Then, we will focus on pyrrole, to see how five-membered rings deactivate. Finally, in section “Current Status of the Field,” we will discuss dynamics simulations of the nucleobases themselves.

## Model 1: Aminopyrimidine

Pyrimidine rings are structural subunits of all five nucleobases. In fact, the strong UV absorption in the 260 nm band is due to the  $\pi\pi^*$  transition in the pyrimidine ring of both pyrimidine and purine nucleobases. For this reason, it is especially relevant to understand how internal conversion takes place in these systems.

Conical intersections in aminopyrimidine are very similar to those in the pyrimidine ring of adenine. The same is true for reaction paths connecting the Franck-Condon region to these conical intersections (Barbatti and Lischka 2008; Barbatti et al. 2008). As can be expected from simple inspection, main differences arise in the two carbon sites where the imidazole group connects with pyrimidine to form the purine structure (► Fig. 33-4). While in aminopyrimidine a low energy conical intersection is formed by puckering of the  $C_4$  atom, this kind of deformation is hindered in the  $C_4$  site of adenine. (Note that the numbering for aminopyrimidine indicated in ► Fig. 33-4 is not the conventional one, but that it is chosen to make the comparison to adenine straightforward.)

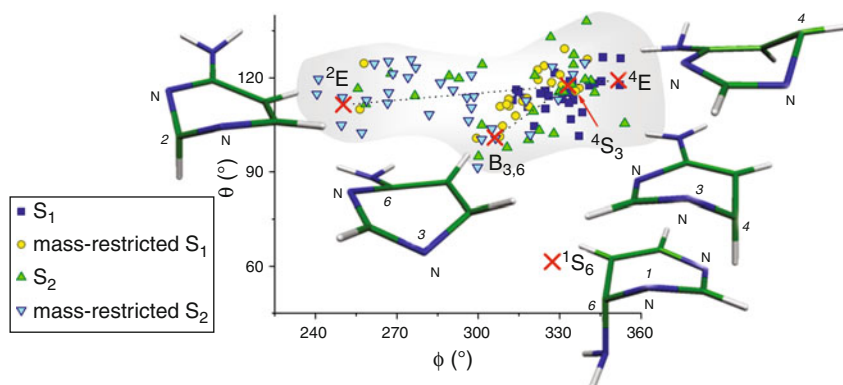
A series of investigations have focused on dynamics simulations for aminopyrimidine (Barbatti and Lischka 2007; Barbatti et al. 2008). As we discuss in this section, these results show that in spite of the strong similarities between the electronic excited states of adenine and aminopyrimidine, the restrictions imposed by the imidazole group make the dynamics of the two species essentially distinct.



Surface-hopping dynamics simulations was performed at SA-3-CASSCF(8,7)/6-31G\* level (Barbatti and Lischka 2007; Barbatti et al. 2008). First, 30 trajectories were started in the  $S_1$  state. The molecule returned to the ground state in 0.4 ps. A second batch of 30 trajectories was started in the  $S_2$  state. In this case, the  $S_2 \rightarrow S_1$  deactivation occurred in only 9 fs. The return to the ground state took place again in about 0.4 ps. These time constants are too fast compared to adenine, which has an excited-state lifetime of 1 ps (Canuel et al. 2005). In order to understand the reason for the difference, we can look at the nuclear conformation at the  $S_1 \rightarrow S_0$  hopping time. These conformations are shown for all trajectories in **Fig. 33-5** projected on the  $\theta - \phi$  Cremer–Pople space (Boeyens 1978; Cremer and Pople 1975). Each point in this space represents a different kind of puckering of a six-membered ring, constituting a very convenient way to describe puckered conformations in heterocycles. As we can see in the figure, both sets of trajectories (starting in  $S_1$  and starting in  $S_2$  states) return to the ground state preferentially at conical intersections showing ring deformation at  $N_3$  and  $C_4$  sites, mainly at the screw-boat conformation  ${}^4S_3$ . The hopping distribution is more broadly spread when the dynamics starts in  $S_2$ , which can be explained by the energy excess. In this case, we can observe trajectories returning to ground state at the boat conformation  $B_{3,6}$  and even a few of them at the envelope  ${}^2E$  conformation.

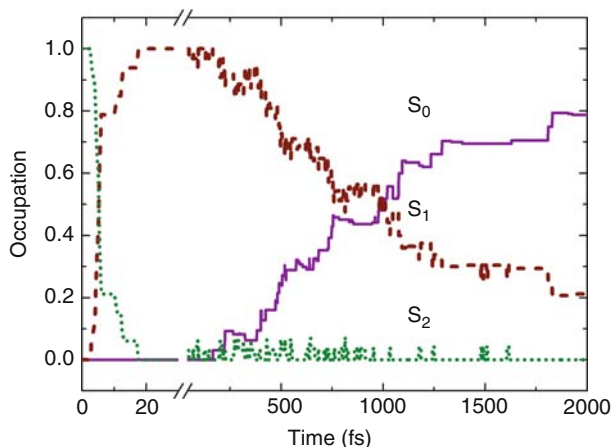
Since puckering at the  $C_4$  site is hindered in adenine by the imidazole group, the concentration of hopping events involving deformation of this site in aminopyrimidine explains the difference between the lifetimes of both species. Apparently, aminopyrimidine is decaying at conical intersections not available in adenine. This hypothesis can be tested by restricting puckering deformation at sites  $C_4$  and  $C_5$  of aminopyrimidine in a similar way as they are restricted in adenine (Barbatti and Lischka 2007). To do so, the mass of the hydrogen atoms at these sites is increased to 45 amu. as to emulate the moment of inertia imposed by an imidazole group. Two new sets of 30 trajectories were run. One set starting in the  $S_1$  state and another set starting in the  $S_2$  state. Results of this second set are shown for the first time in this work.

Mass-restricted trajectories starting in  $S_1$  returned to ground state in  $0.96 \pm 0.2$  ps (Barbatti et al. 2008). In spite of the good agreement with the 1 ps measured for adenine, the hopping conformations are still concentrated in  $N_3$  and  $C_4$  deformations (**Fig. 33-5**). This occurs



**Fig. 33-5**

$S_1 \rightarrow S_0$  hopping position in the  $\theta - \phi$  Cremer–Pople space for aminopyrimidine (Data from Barbatti and Lischka 2007; Barbatti et al. 2008)



■ Fig. 33-6  
State occupation of mass-restricted aminopyrimidine starting in the  $S_2$  state

because the mass restrictions at  $C_4$ -H and  $C_5$ -H are decoupled. This is different in adenine, where the ring imposes a strong correlation in the motion of these sites. The long lifetime of mass-restricted aminopyrimidine in comparison to the non-restricted case is due to the longer period that the molecule needs to tune the conical intersection coordinates. Figure 33-5 also shows that the hopping events of mass-restricted aminopyrimidine starting in the  $S_1$  state are displaced in the direction of  $B_{3,6}$  conformations.

Curiously, when mass-restricted dynamics is started in the  $S_2$  state, the lifetime is increased even more, to 1.4 ps (Figure 33-6). Hopping events occur along the whole region connecting the envelope  $^4E$  conformations to envelope  $^2E$  conformations indicating that a branch of crossing seam exists in this region. Different from the other three sets of dynamics simulations, a substantial amount of hopping events occurs at the  $^2E$  conformation, which, as we shall review in section “Current Status of the Field,” is the main conformation accessed for adenine deactivation (Barbatti and Lischka 2008). Note that two conditions were necessary to trigger internal conversion in this region of the crossing seam, first the restriction of the  $C_5$  and  $C_4$  sites and second the excess of energy of the  $S_2$  initial state.

Hopping events at  $^6S_1$  conical intersections, which are energetically accessible from the Franck-Condon region, were not observed in any of the four sets of trajectories (Figure 33-5). Characteristically,  $^6S_1$  conformations imply a strong out-of-plane deformation of the amino group. A plausible explanation for the lack of internal conversion in this region of the crossing seam is that trajectories are trapped in other regions of the  $S_1$  surface before the molecule has time to undergo this strong deformation. Results for aminopyrimidine starting in  $S_2$  state without mass-restriction, but increasing the active space from (8,7) to (10,8) by addition of one more  $n$  orbital to the active space show that a fraction of trajectories (about 15%) can access this conical intersection (Szymczak et al. 2011).

The effect of stacking interactions in DNA conformation has also been investigated in the dynamics of aminopyrimidine interacting with guanine nucleobases (Nachtigalova et al. 2010). The results show that the ring puckering process observed in gas phase is not restricted by the neighbor molecules.

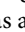
## Model 2: Pyrrole

Pyrrole cannot be directly regarded as a model for nucleobases. However, the understanding of its UV-excited dynamics may bring insights of the role of the imidazole ring in the pyrimidine bases adenine and guanine. Different from the pyrimidine subunit, which is responsible for the UV absorption in the near UV region, both pyrrole and imidazole absorb at much shorter wavelengths of about 200 nm (Daura et al. 1999; Devine et al. 2006). Because of this, it may be expected that purine bases absorbing in the far UV region may present an excited state dynamics similar to that of five-membered rings.

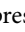
Pyrrole is a simple five-membered heterocyclic compound which undergoes a rapid non-adiabatic deactivation (Lippert et al. 2004) with very low quantum yields (Shin 2004). It has been proposed (Sobolewski and Domcke 2000) that deactivation occurs via a NH-stretching mechanism along a  ${}^1\pi\sigma^*$  excited state surface. Although it is certain that fast H fragments are formed through this mechanism, it cannot explain experimental findings of slow H atoms and other fragments such as HCN and  $C_3H_3$  (Blank et al. 1994; van den Brom et al. 2005; Wei et al. 2004). This means that another mechanism should occur in competition with the NH stretching, which was proposed to involve ring-puckering and ring-opening of the heterocyclic ring (Barbatti et al. 2006; Poterya et al. 2007).

Non-adiabatic dynamics simulations for the pyrrole radical cation and other five-membered rings were performed in reduced dimensionality by means of wave packet propagation using the multiconfigurational time-dependent Hartree approach (MCTDH) together with the linear vibronic model, allowing a good reproduction of spectral features (Köppel et al. 2004; Venkatesan et al. 2007). Wave packet dynamics simulations have also been performed focusing on the NH-stretching reaction coordinate (Lan and Domcke 2008; Vallet et al. 2004, 2005) revealing details of the reaction along this coordinate, especially of the dependence of the dissociation branching ratios and time scales on the initially excited modes. These simulations in reduced dimensionality predict a quantum yield for NH dissociation near to unity. Dynamics simulations of pyrrole in its full dimensionality have been performed using surface hopping approach (Vazdar et al. 2009), and, as we are going to discuss in more detail next, it revealed that other deactivation channels beyond the NH-stretching are activated. These channels involve strong ring deformation. The adiabatic dynamics in the vibrationally excited ground state, also discussed below (Sellner et al. 2009), showed that these ring deformation channels result in photochemical products consistent with the heavy fragments experimentally observed.

Excited-state non-adiabatic dynamics simulations were performed for 90 trajectories in a total simulation time of 200 fs with a time step of 0.5 fs (Vazdar et al. 2009). The dynamics simulations have been calculated at the MR-CISD/SA-5-CASSCF(4,5) level of theory including five electronic states (ground state, two  $\pi\pi^*$  states and two Rydberg  $\pi-3s(\sigma^*)$  states).

After excitation to the  $S_4$  state, pyrrole depopulates via a series of conical intersections between valence and Rydberg states in a very short time. The average adiabatic population of ground and excited states as a function of time is presented in  Fig. 33-7.

The analysis shows that the valence  $S_4$  state depopulates very quickly. After around 10 fs, the average population of  $S_4$  and  $S_3$  states is identical. After 50 fs, the  $S_4$  state is completely depopulated, while  $S_3$  and  $S_2$  state depopulate after ca 75 fs. The  $S_1$  state starts to depopulate after ca 100 fs. After 100 fs, the dynamics is basically a two-state dynamics between ground and first excited state. The complete population transfer to the ground state occurs within 200 fs.

The statistical analysis presented in  Fig. 33-8 reveals that 80% of trajectories follow the NH stretching mechanism for deactivation into the ground state. The remaining 13% of trajectories

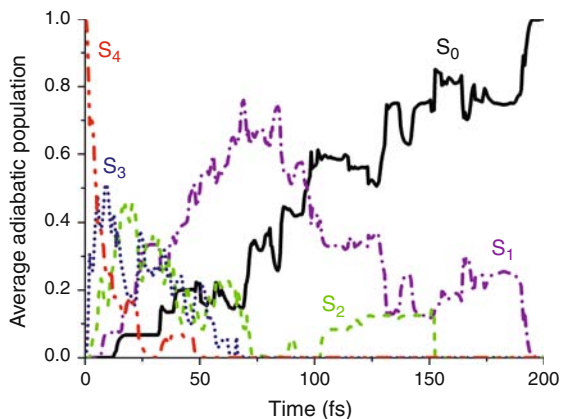


Fig. 33-7

Average adiabatic populations of trajectories for five states as a function of time after photoexcitation of pyrrole into the S<sub>4</sub> state (Data from Vazdar et al. 2009)

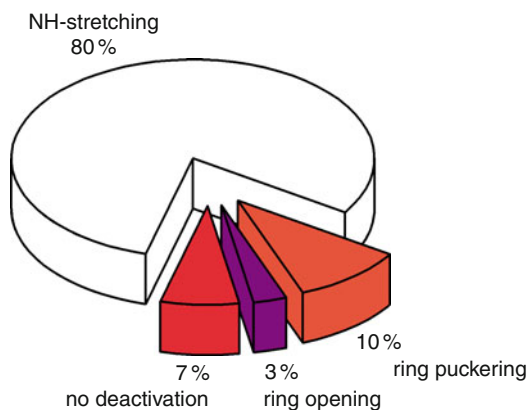


Fig. 33-8

Statistical analysis of different trajectory types in excited-state dynamics of pyrrole (Data from Vazdar et al. 2009)

undergo a ring deformation mechanism (10% is ring puckering and 3% is ring opening). Finally, 7% of trajectories do not deactivate during 200 fs of the dynamics simulation. Dynamics performed with TDDFT method showed a very similar distribution of mechanisms (Barbatti et al. 2010b).

The observation of the ring deformation deactivation mechanism for a substantial number of trajectories confirms that it can be the source of experimentally observed heavy fragments. To verify this hypothesis, dynamics in the ground state should be performed. This is a specially challenging task because after deactivating, the photoenergy is converted into vibrational energy. In this very hot vibrational ground state, pyrrole can reach strongly distorted geometries and dissociate through several channels. Most of conventional quantum chemical methods are not tailored to work under such extreme conditions.

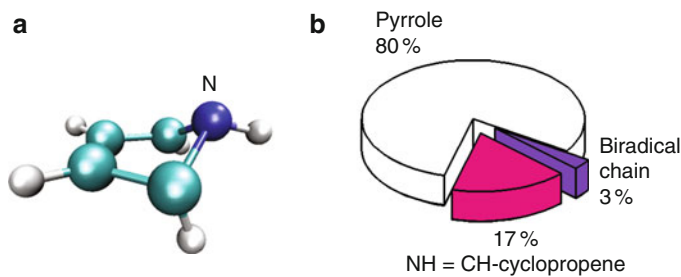


Fig. 33-9

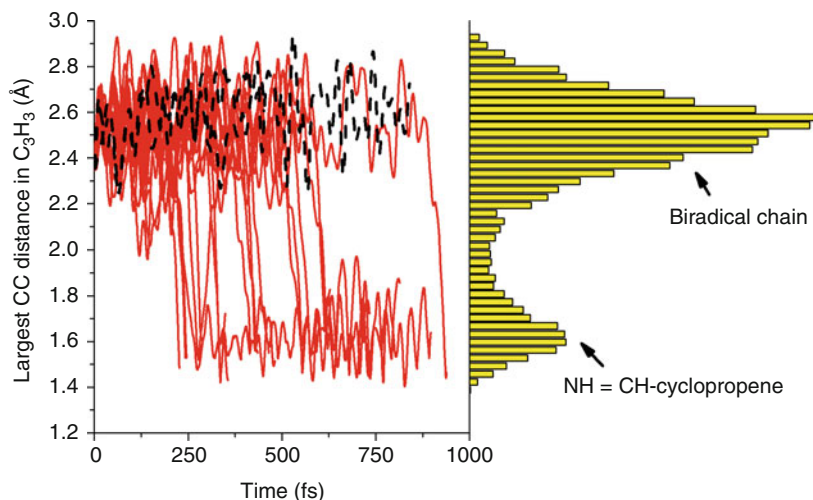
(a) Ring-puckered ring-opened  $S_0/S_1$  conical intersection (initial geometry of adiabatic ground state dynamics for pyrrole); and (b) quantum yield within 1 ps of simulation (Data from Sellner et al. 2009)

This problem has been addressed by starting the hot ground state dynamics at a ring-puckered ring-opened conical intersection (see Fig. 33-9a) using a wavefunction formed by a combination of the generalized valence bond method in the perfect pairing approximation (GVB-PP) and complete active space (CAS) (Sellner et al. 2009). The GVB-PP-CAS(6,5)/6-31G\* level applied to the gradient calculation for the dynamics has proven not only to be more reliable concerning photoproducts but also much more stable during dynamics compared to conventional SA-2-CAS(6,6) calculations. The results reported here have been calculated with this GVB-PP-CAS(6,5) space. A hundred trajectories have been propagated for a maximal time of 1 ps using a step size of 0.5 fs.

As the dynamics is started on a point in the crossing seam, special care has to be taken to generate initial velocities. Two approaches have been employed, sampling initial velocities only in the branching space and sampling random velocities in the complete space using weighted Gaussian random numbers, both showing good correlation. The results discussed here are based on the second approach. Translational and rotational contributions of these velocities were removed, which have been rescaled to an energy of 3.01 eV. This energy is the sum of half of the ZPE (2.24 eV) and the energy difference between the Frank Condon point and the MXS which is assumed to be converted from potential to kinetic energy.

The results show that besides pyrrole itself, two main photoproducts were obtained within the simulation time (see Fig. 33-9b). These are NH=CH-C<sub>3</sub>H<sub>3</sub> and a biradical chain (NH=CH-CH=CH). A detailed analysis of the trajectories ending at these photoproducts shows that the biradical chain is mainly a precursor to the substituted cyclopropene fragment. The cyclization starts after 200 fs and the new ring formation occurs in an average time of only 17 fs (see Fig. 33-10). Regarding the consequences on the experimentally observed (cyclo)propene fragment, this shows that the ring formation can not only happen before the dissociation into the HCN and C<sub>3</sub>H<sub>3</sub> fragments takes place, but seems to be the dominating process.

Dissociation into H<sub>x</sub>CN (x=1,2) and C<sub>3</sub>H<sub>3</sub> did not take place within the 1 ps simulation time and it should occur on a longer timescale. The systematic investigation of the average bond distances during the dynamics (Sellner et al. 2009), clearly reveals that cleavage of those bonds yielding the experimentally observed fragments are more likely to occur than the cleavage of bonds leading to non-observed fragments.



■ Fig. 33-10

Largest CC distance in  $C_3H_3$  as a function of time showing the dynamics of the formation of  $NH=CH$ -cyclopropene out of the biradical chain (Data from Sellner et al. 2009)

Summarizing, non-adiabatic excited state dynamics of pyrrole showed two main deactivation mechanisms, the first one being the  $NH$  stretching explaining the (fast) hydrogen atoms and the second one the ring deformation (including opening and puckering). Dynamics from the puckered conical intersection showed that the second pathway is responsible for  $NH=CH-C_3H_3$  and the biradical chain which can be seen as precursors to the experimentally observed heavier fragments regarding their electronic structure and bonding situation.

## Current Status of the Field

A relatively large number of investigations reporting dynamics simulations for nucleobases, nucleobase tautomers, nucleotides, derivatives, WC pairs and quartets in different solvation conditions has been published in the last years. Recent overviews of the field can be found in Refs. (Alexandrova et al. 2010; Barbatti et al. 2010a). In this section, we shortly review the dynamics of isolated bases focusing on which relaxation mechanism these works have proposed for each molecular system.

*Adenine*: In spite of a large number of different conical intersections that has been described for this nucleobase (see Barbatti and Lischka 2008 and references therein), theoretical analyses have converged to two main pathways, one involving puckering of the  $C_2$  atom (envelope  $E_2$ ) and another one involving puckering of the  $C_1$  and  $C_6$  atoms along with out-of-plane displacement of the amino group (screw-boat  $^1S_6$ ). Surface hopping dynamics simulations based on MR-CIS potential energy surfaces showed that adenine is trapped in envelope  $E_2$  geometries much before it can reach other reaction pathways (Barbatti and Lischka 2008). Nevertheless, a different result has been achieved by surface hopping simulations based on semiempirical methods, with most of trajectories following the  $^1S_6$  pathway (Alexandrova et al. 2010; Fabiano

and Thiel 2008). Dynamics simulations based on TD-DFTB surfaces indicated a intermediary situation with selective activation of the  $^1S_6$  and  $E_2$  pathways depending on the excitation energy (Lei et al. 2008) and very long lifetime (Mitric et al. 2009b).

*Guanine*: A series of investigations on guanine tautomers and derivatives in gas phase and water employing surface hopping based on ROKS potential energy surfaces have shown that out-of-plane distortions increase the non-adiabatic transition probability and induce the transition to the ground state in about 1 ps (see Santoro et al. 2007a and references therein). Surface hopping dynamics based on OM2 surfaces predicted a major role for processes involving  $C_2$  puckering, with a lifetime of about 0.2 fs. Similar process has been observed at the ab initio level (Barbatti et al. 2011b). In the particular case of the enol form of guanine, simulations predicted that OH dissociation channel is a major deactivation pathway (Langer et al. 2005).

*Cytosine*: Multiple spawning dynamics simulations based on CASSCF(2,2) surfaces predicted that deactivation of this nucleobase should occur in approximately 0.5 ps mainly through conical intersections involving out-of-plane distortions of the amino group (65%) and with minor contribution of the  $n_O\pi^*$  (15%) and of the ethylene (5%) pathways (Hudock and Martinez 2008). OM2-based surface hopping dynamics, on the other hand, predicts that the ethylene pathway should dominate the deactivation, which occurs in about 0.4 ps (Lan et al. 2009). Dynamics for this molecule computed with surface hopping at CASSCF surfaces predict dominance of the  $n_O\pi^*$  pathway (Barbatti et al. 2011a; González-Vázquez and González 2010).

*Thymine*: This nucleobase has the longest lifetime among the five naturally occurring bases (Canuel et al. 2005; Kang et al. 2002). Multiple spawning dynamics simulations based on CASSCF surfaces have revealed that the source of this feature may be a trapping of thymine in a minimum of the  $S_2$  state for a few picoseconds (Hudock et al. 2007). Surface hopping dynamics based on the OM2 method, however, predict a very short stay in the  $S_2$  state (0.02 ps) and an overall excited-state lifetime of 0.4 ps (Lan et al. 2009). In this latter case, the decay to  $S_0$  occurred mainly through the out-of-plane O conical intersection (82%) and pathways involving puckering at the  $C_5$  atom were observed in the other 12% of trajectories. Surface hopping dynamics based on CASSCF surfaces agree with the multiple spawning results and predicts that the  $n\pi^*$   $S_1$  state will be populated after 2.6 ps (Gustavsson et al. 2006). Surface hopping simulations also based on CASSCF surfaces, but starting at the transition state in the  $S_2$  state, predict that both the  $\pi\pi^*$   $S_1$  state (65%) and the  $n\pi^*$   $S_1$  state should be populated (Asturiol et al. 2009). While according to (Gustavsson et al. 2006) trajectories should remain in the  $n\pi^*$   $S_1$  state for additional few picoseconds, results of (Asturiol et al. 2009) indicated that, independently of the diabatic character, the  $S_1$  state should be depopulated in about 0.1 ps through conical intersections involving puckering at the  $C_5$  atom.

*Uracil*: Similarly to thymine, multiple spawning CASSCF dynamics predict a long stay of uracil in the  $S_2$  state (Hudock et al. 2007). Surface hopping OM2 dynamics, in contrast, predict a very fast decay to  $S_1$  and an overall lifetime of about 0.6 ps with trajectories following out-of-plane O pathways in 85% of the cases and puckering at  $C_5$  atom in the remaining 15% of the cases (Lan et al. 2009). Wave packet propagation in a 3-D model surface also predicts a very fast  $\pi\pi^* \rightarrow n\pi^*$  transition taking place in less than 0.1 ps (Improta et al. 2009). Surface hopping dynamics simulations on ROKS surfaces in gas phase and in water favor deactivation through the  $C_5$  puckering pathway (Nieber and Doltsinis 2008).

As we have seen, dynamics simulations carried out with different methods have often presented conflicting results. This may be mainly attributed to differences between quantum-chemical electronic structure methods used to compute the potential energy surface, rather



than to the different non-adiabatic dynamics methods. More about the limitation of the methods will be discussed in the conclusions for this chapter. For now, we may note that even though dynamics simulations have not achieved a degree of agreement that would allow assigning specific relaxation mechanisms for each nucleobase, they have been able to reduce the possibilities to a few mechanisms in each case.

## Formamide and Peptide Bonds

### Probing Photoexcitation of Proteins

The peptide linkage plays an important role in many biological processes and the knowledge of how it interacts with ultraviolet light is of fundamental importance for understanding biological activities in living organism. This holds in particular for interaction of peptides with 193 nm excimer ArF laser due to its proximity to the absorption maximum of peptide bonds (Gingell et al. 1997). This is an effect of considerable importance because ArF lasers are widely used clinically for laser surgery (Mulcahy et al. 2000). It is shown, for instance, that the peptide bond is the main target of irradiation in collagen and its scission is claimed to be the most important photochemical reaction taking place during photorefractive keratectomy (Torikai and Shibata 1999). Furthermore, the peptide group appears as the repeat unit in some industrially important polymeric materials (Greenberg et al. 2002) and knowledge about the mechanism of its interaction with ultraviolet light has implications for understanding crucial factors influencing their photostability. The smallest molecule of the peptide prototype is formamide (Fig. 33-11) and as such it has been frequently used as the simplest model for studying fundamental aspects of photochemical and photophysical processes taking place in peptides and proteins (Antol et al. 2007, 2008a, b; Back and Boden 1971; Kang and Kim 2006; Liu et al. 2000; Lundell et al. 1998). An overview of the recent studies related to the second topic will be presented in section “Model 1: Formamide” of this chapter.

Photoinduced fragmentation of charged small polypeptides has also been studied extensively in recent years due to their importance in “soft” ionization methods such as MALDI and ESI (Cui et al. 2005; Grégoire et al. 2007; Jeong et al. 2005, 2007; Kang et al. 2004; Nolting et al. 2006; Thompson et al. 2004, 2007). Photo-dissociation dynamics of small protonated peptides containing aromatic amino acids excited by 266 nm laser beams have been also

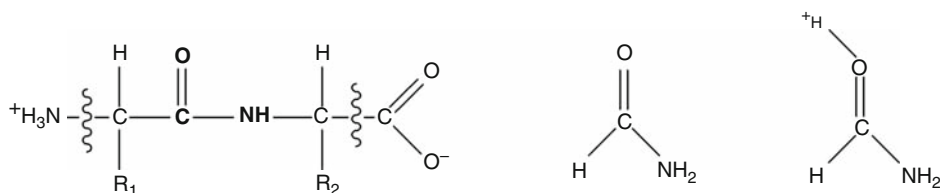


Fig. 33-11

Schematic presentation of a polypeptide chain with the peptide bond showed in bold (left), of formamide (center) and of oxygen-protonated formamide (right).  $R_1$  and  $R_2$  stand for the amino acid chains

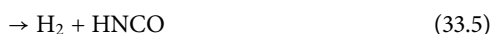
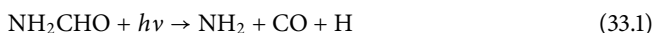


explored by pump/probe femtosecond measurements (Grégoire et al. 2006, 2007; Nolting et al. 2006). However, the deactivation mechanism of possible pathways could not be derived, neither experimentally nor theoretically due to the size and complexity of the explored systems. Concomitantly, several experimental and computational photoexcitation studies have been undertaken on gas-phase protonated amino acids (Cui et al. 2005; Thompson et al. 2007). This led to the proposition of a deactivation mechanism (Kang et al. 2005, 2004) compatible with experimental results obtained for small polypeptides containing aromatic amino acids (Grégoire et al. 2006, 2007; Nolting et al. 2006). A recent review on this topic is given in Grégoire et al. (2009). With the aim of exploring possible alternative pathways of photodissociation of polypeptides we recently examined impact of protonation on fragmentation of the peptide bond using protonated formamide as the model molecule (Antol et al. 2008b). The most salient results from this work will be described in [▶ section “Model 2: Protonated Formamide.”](#)

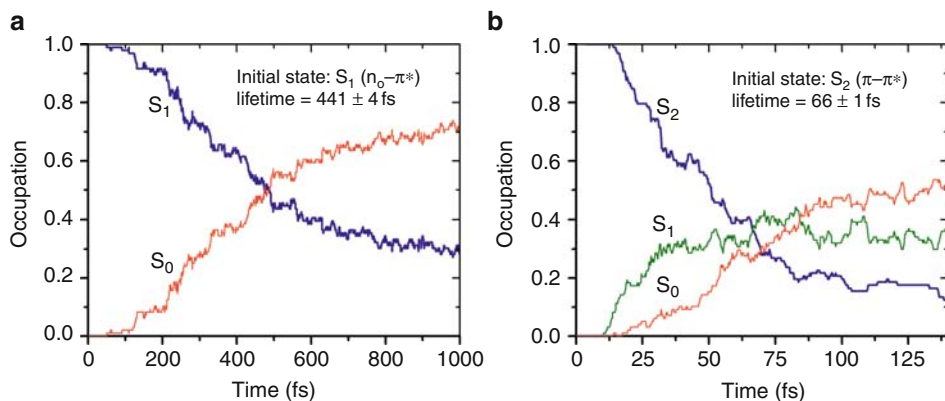
## Model 1: Formamide

Photodissociation of formamide has been studied in the gas phase (Back and Boden 1971), solution (Petersen et al. 2008) and in noble-gas matrices of argon and xenon (Lundell et al. 1998). In gas phase photolysis, CO, H<sub>2</sub> and NH<sub>3</sub> fragments with quantum yields of 0.8, 0.6, and 0.2, respectively, were detected (Boden and Back 1970). Their formation was rationalized by three major primary processes forming the products NH<sub>2</sub>+CO+H, HNCHO+H, and NH<sub>3</sub>+CO. Subsequently, Lundell et al. (1998) reported that photolysis of formamide in the argon matrix by 193 nm laser leads to formation of a weakly bound complex between NH<sub>3</sub> and CO. Its formation was ascribed to the breaking of the C–N bond in formamide followed by hydrogen atom transfer from the formyl radical HCO to the NH<sub>2</sub> radical. On the other hand, when the formamide was trapped into solid Xe matrix major photoproducts were H<sub>2</sub> and HNCO. The change in composition of the products was explained by intersystem crossing to the triplet state induced by a strong external heavy-atom effect in the Xe matrix.

The mechanism of photodissociation in the gas phase has been also studied computationally at various levels of theory (Back and Boden 1971; Liu et al. 2000; Lundell et al. 1998). For instance, Liu and co-workers (2000) considered the mechanism of formamide photodissociation in the S<sub>1</sub> and the T<sub>1</sub> excited states using the CASPT2/CASSCF method. They located transition structures for each of the paths presented by [▶ Eqs. 33.1–33.5](#) and found that the transition structure for C–N dissociation ([▶ Eq. 33.1](#)) has the lowest energy on the S<sub>1</sub> as well on the T<sub>1</sub> potential energy surfaces, indicating that this reaction path is the most probable one.



However, the full understanding of the photodeactivation process in addition to characterization of the energy minima of the reactants and products and the transition state structures, requires also knowledge about minima on the crossing seams between involved excited states and the ground state, as well as information about nuclear motion of atomic nuclei during the



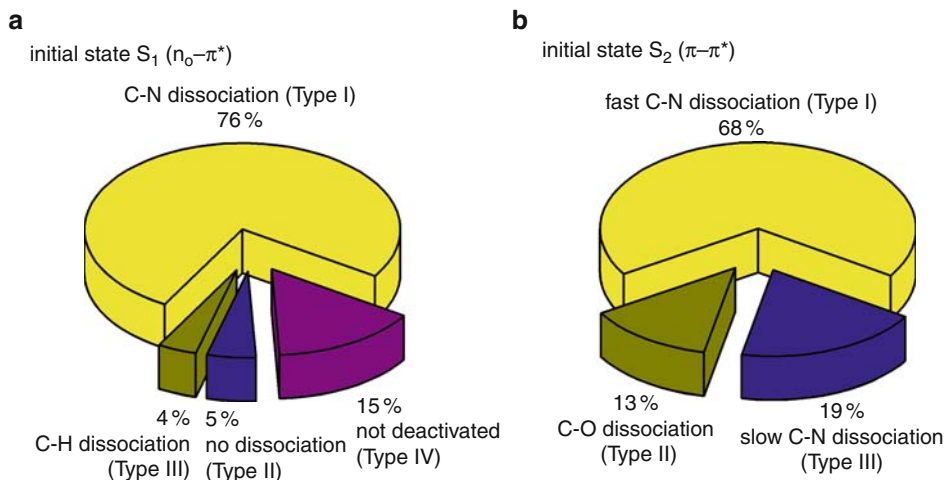
■ Fig. 33-12

Fraction of trajectories for each state as a function of time after photoexcitation into (a)  $S_1$  initial state; and (b)  $S_2$  initial state (Data from Antol et al. 2007)

process. Therefore, we recently reexamined the reaction paths considered by Liu and coworkers (2000) for the  $S_1$  state taking into account both of these requirements and at higher level of theory. In addition, photodissociation of formamide in the second excited singlet state was considered also. The details of computational methods are given in Antol et al. (2007). Following location of all critical points on the  $S_1$  and  $S_2$  surfaces, we turned to dynamic simulations, which were carried by the direct trajectory surface hopping method based on the state average SA-3-CASSCF(10,8)/6-31G(d) calculations. For each of the initial states, one hundred trajectories were propagated for 1 ps. The average occupations of the  $S_1$  and  $S_2$  states are shown in Fig. 33-12. It appears that the average occupation of the  $S_1$  state remains practically unchanged for about 43 fs. After this initial stage, its occupation starts to decay exponentially. The lifetime of the state was calculated to be  $441 \pm 4$  fs. On the other hand depopulation of the  $S_2$  state starts after only 12 fs and the overall estimated lifetime is  $66 \pm 1$  fs. After passing through the  $S_2/S_1$  conical intersection, formamide resides on the  $S_1$  surface only shortly and decays to the ground state.

Analysis of the trajectories (Fig. 33-13) revealed that after excitation into the  $S_1$  state about 75% of the examined trajectories followed the C–N dissociation channel. After reaching the ground state, the energy of the system is transferred to translational motion of the HCO and the  $\text{NH}_2$  radicals and to C–H dissociation from vibrationally hot CHO fragment, which finally results in formation of  $\text{NH}_3$  and CO.

In addition to this channel, three additional types of trajectories were observed, but their fraction was found to be much lower. In trajectories of type II, the molecules decay to the ground state either via the same C–N conical intersection as in the previous case, followed by back formation of formamide on the  $S_0$  PES or return to the ground state via a nondissociative MXS (Antol et al. 2007). In either case, no dissociation is observed within the simulation time. In trajectories of type III, hoppings to the ground state cause activation of the C–H vibrations and the molecule undergoes C–H bond stretching. Full C–H dissociation, however, was observed in only one trajectory. Finally, in 15% trajectories, formamide did not decay to the ground state and did not dissociate within the simulation time.



■ Fig. 33-13

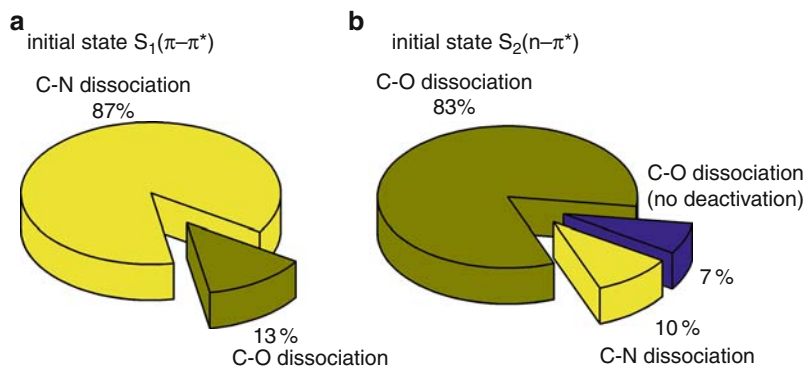
Photodeactivation paths observed during dynamics simulations of formamide starting at the (a)  $S_1$  ( $n_o\pi^*$ ) and at the; (b)  $S_2$  ( $\pi\pi^*$ ) states (Data from Antol et al. 2007)

Following excitation to the second excited state, three types of trajectories were observed. The dominant type, corresponding to 68% of the trajectories, is characterized by a very fast C–N bond cleavage starting immediately after photoexcitation and still taking place on the  $S_2$  surface. The deactivation to the  $S_1$  occurs in an average time of 31 fs. The system remains on the  $S_1$  surface only for a short time and then switches to the  $S_0$  state in an average time of 65 fs. Such fast  $S_1 \rightarrow S_0$  decay is opposite to the slow  $S_1 \rightarrow S_0$  decay observed when the initial state was  $S_1$ . This is ascribed to the cooperative action of the energy transferred from the  $S_2$  state, and the momentum acquired by the system along the C–N stretching coordinate during its motion from the Franck–Condon region to the  $S_2/S_1$  conical intersection. A similar process has been observed in the dynamics of protonated formamide (Antol et al. 2008b) and the  $\text{CH}_2\text{NH}_2^+$  cation (Barbatti et al. 2007a).

In addition to the C–N dissociation channel, two alternative types of trajectories, both of them involving the C=O stretching mode, were observed, but their fraction was found to be much lower. The first among them (trajectories of type II) is characterized by dissociation of the oxygen atom and concomitant merging of all three potential energy surfaces. It corresponds to 13% of all observed events. Finally, trajectories of type III (19%) are best described as combination of the trajectories of types I and II. In this case, initial motion involves the C–O stretching mode, but the C–O bond cleavage does not occur due to recombination of the molecule in the  $S_2$  followed by C–N bond dissociation.

## Model 2: Protonated Formamide

The most basic site of formamide in the ground, as well as in the excited state is the oxygen atom (Antol et al. 2008a). Therefore, in this section we shall restrict our discussion to the photofragmentation of the O-protonated species (► Fig. 33-11). The calculations were carried



■ Fig. 33-14

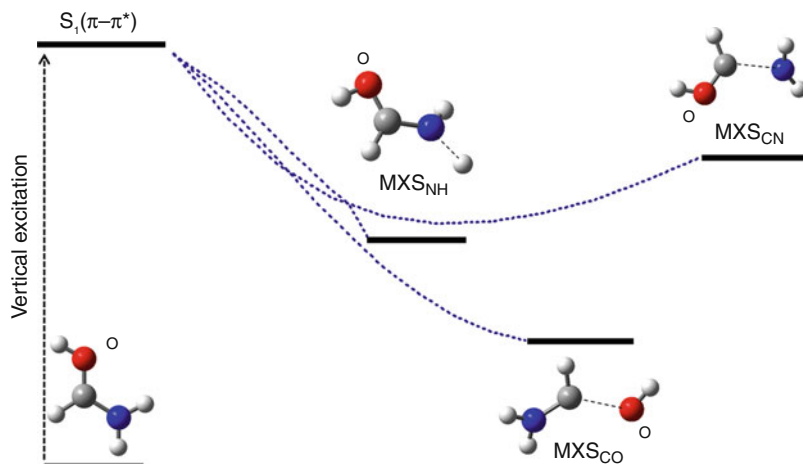
Photodeactivation paths observed during dynamics simulations of O-protonated formamide starting at the (a)  $S_1(\pi\pi^*)$  and at the; (b)  $S_2(n\pi^*)$  states (Data from Antol et al. 2008b)

out by means of the same computational approach used for the parent molecule, the SA-3-CASSCF(10,8)/6-31G(d) method. A summary of dynamics calculations results are presented in [Fig. 33-14](#). More detailed discussion, including dynamics simulations of photodissociation of N-protonated formamide, can be found in Antol et al. (2008b).

Examination of the results shows that dissociation of the O-protonated formamide from the  $S_1$  state strongly resembles the mechanism of dissociation observed from the second excited state in the neutral molecule, as expected, due to the fact that both states are of  $(\pi\pi^*)$  character. This is also reflected in considerable shortening of the calculated lifetime relative to that calculated for the  $S_1$  state in the neutral molecule ( $33 \pm 1$  fs vs.  $441 \pm 4$  fs).

In searching for possible deactivation paths, three minima on the crossing seam between  $S_1$  and  $S_0$  were found to be accessible without energy barrier indicating very fast dynamics. The other interesting feature is that, in contrast to the neutral molecule, the MXS for the C–N dissociation has the highest energy ([Fig. 33-15](#)). In spite of that, analysis of the calculated trajectories revealed that this is the major dissociation channel. The reason for that lies in the fact that this reaction path has the steepest “slope” in the Franck–Condon region ([Fig. 33-15](#)). In other words, as the molecule in the Franck–Condon region does not have information about energies of conical intersections, it selects the energetically most favorable reaction path and not one leading to the most stable minimum on the crossing seam. The predominance of non-adiabatic transitions near highest energy MXS has also been observed in photodissociation of aminopyrimidine (Barbatti and Lischka 2007). In protonated formamide this deactivation path is activated in 87% of trajectories. After reaching the ground state, the energy of the system is transferred to translational motion of the HCOH and  $\text{NH}_2$  fragments in 33% of trajectories, while in 47% of trajectories HCOH and  $\text{NH}_2$  recombine into the vibrationally excited starting structure. Furthermore, in 7% of trajectories the proton transfer from the HCOH radical cation to the  $\text{NH}_2$  radical occurs resulting in formation of the  $\text{NH}_3$  radical cation and HCO radical.

In addition to the C–N dissociation path, in 13% of trajectories the dissociation channel involving stretching of the C–O bond becomes activated. This dissociation path strongly resembles the C–O dissociation channel from the second excited state of the neutral molecule (trajectories of type II).



■ Fig. 33-15  
 Schematic presentation of reaction paths in photodissociation of oxygen protonated formamide.  $MXS_{NH}$ ,  $MXS_{CO}$ , and  $MXS_{CN}$  denote minima on the crossing seam for dissociation of N-H, C=O, and C-N bond, respectively. Geometries are optimized at the CASSCF(10,8)/6-31G(d) level (Data from Antol et al. 2008b)

Dissociation of the O-protonated formamide following excitation to the second excited state is also interesting. It triggers a very fast switch (10 fs) from the  $S_2$  to the  $S_1$  state via a highly pyramidalized non-dissociated MXS (Antol et al. 2008b), followed by activation of two dissociation processes (C–O and C–N) on the  $S_1$  surface, with the C–O dissociation path being observed in 83% of trajectories. It is interesting to note that the resulting branching ratio between C–O and C–N dissociation pathway differs considerably from that observed upon photodissociation from the  $n\pi^*$  state in the neutral molecules in which the C–N dissociation was the major photodissociation channel. The major reason for this behavior could be connected to the direction of the momentum along the C–O stretching coordinate inherited from the  $S_2/S_1$  conical intersection in the O-protonated formamide. Another point worth of noting concerns formation of the OH radical, indicating that protonated formamide might be a precursor in the photogeneration of potentially deleterious OH radical.

## Current Status of the Field

One point of particular relevance in the photodynamics studies of formamide and peptides that has not been considered in this section is the effect of the environment. Environmental effects are expected to change the relative position of the electronic states, the position, and the topology of the conical intersections (Burghardt and Hynes 2006). QM/MM dynamics simulations of photodissociation of formamide embedded in argon matrix showed strong impact on the outcome of the process. This was illustrated by formation of the 1:1 complex between ammonia and CO and prevention of full separation of the  $NH_2^\bullet$  and  $HCO^\bullet$  subunits in the  $NH_2^\bullet + HCO^\bullet$  radical pair. Also, the argon matrix influenced the lifetime of the  $S_1$  state, which increased by 211 fs relative to the gas phase (Eckert-Maksić et al. 2010b). Another important issue that deserves attention concerns the effect of substituents on the mechanism of photodissociation

of formamide. Some experimental, as well as computational studies, on the effect of methyl (Chen et al. 2003; Eckert-Maksić and Antol 2009; Liu 2002) and benzyl (Chen and Fang 2004; Pei et al. 2008) substituents related to this issue have been recently reviewed (Eckert-Maksić et al. 2010a). Finally, the possibility of intersystem crossing to the first triplet state has not been fully explored. This holds, in particular, for photodissociation of formamide in matrices, but also for photodissociation of higher analogues of formamide. This possibility, however, cannot be considered by dynamic simulations because it demands propagation times that are too long.

## Conclusions and Outlook

---

We have reviewed a series of investigations of  $\pi$ -conjugated molecules using mixed quantum-classical dynamics simulations. All these molecules have been chosen as models for biologically relevant systems. Dynamics simulations are able to provide information on time-dependent phenomena, which can only be obtained in a very indirect way by conventional static quantum-chemistry simulations. The main pieces of information brought by dynamics in excited states are the time constants for the relaxation processes following the photoexcitation and the relative importance of each available pathway.

In an effort to reduce computational demands, several levels of approximation are employed, starting with the dynamics methodology itself, which propagates the nuclear motion classically for all degrees of freedom, while partially recovering the quantum information of the non-adiabatic transitions between states. Although methodological progress has been achieved by the development of the multiple spawning (Ben-Nun et al. 2000; Hack et al. 2001; Levine et al. 2008) and MCTDH (Worth et al. 2003) approaches, the *everyday* method for tackling dynamics simulations in excited state is still the surface hopping approach, mainly due to its easy implementation and intuitive conceptual background.

At another level of approximation, simplified models have often been employed in substitution of the full biochemical system. In this chapter, we have discussed protonated Schiff base chains as models for the chromophore of rhodopsin proteins, heteroaromatic rings as models for UV-excited nucleic acids, and formamide as a model for photoexcited peptide bonds. With development of quantum chemical methods and computational resources, effective progress has been achieved by taking larger models at higher theoretical levels. This process, however, evolves very slowly and there are no perspectives of extending the quantum-mechanical treatment much beyond the chromophore region of the system. Instead, the development of hybrid methods, especially the quantum-mechanics/molecular-mechanics based approach, have been demonstrated to be of great utility in accounting for the effects of the molecular environment into the excited-state region of the molecule (Ciminelli et al. 2008; Hayashi et al. 2009; Levine et al. 2008; Lin and Truhlar 2007). Recently, methods for treating the excited-state evolution under the influence of an external electric field have been proposed (Jones et al. 2008; Mitric et al. 2009a; Yagi and Takatsuka 2005). They open the perspective of achieving a more complete treatment of the photo-excitation phenomena, by, for example, taking into account the effect of laser fields.

In a third level of approximations, the quantum chemical methods employed in dynamics simulations are naturally much lower than those employed at conventional quantum chemical calculations. As an example, dynamics simulations for molecules of biological interest are quite restricted to the use of double- $\zeta$  basis sets. Moreover, it is common to have a poor treatment of ionic states and non-adiabatic events, to neglect Rydberg states, and to neglect electron

dynamic correlation. Although all these approximations are usually carefully employed by extended comparisons to high-level benchmark data, dynamics results obtained under such approximations should be regarded only as semi-quantitative.

Even in view of all these limitations, excited-state non-adiabatic dynamics simulations based on mixed quantum-classical methods constitute a fascinating and active research field providing essential information on the nature of molecular phenomena.

## Acknowledgments

The authors gratefully acknowledge computer time at the Vienna Scientific Cluster (project nos. 70019 and 70151). This work was supported by the Austrian Science Fund within the framework of the Special Research Program F41 Vienna Computational Materials Laboratory (ViCoM). The work in Zagreb (M.E.-M., I.A., and M.V.) is supported by the Ministry of Science, Education and Sport of Croatia through the project. No. 098-0982933-2920. The support by the COST D37 action, WG0001-06 and the WTZ treaty between Austria and Croatia (Project No. HR17/2008) is also acknowledged. This work was also performed as part of research supported by the National Science Foundation Partnership in International Research and Education (PIRE) Grant No. OISE-0730114; support was also provided by the Robert A. Welch Foundation under Grant No. D-0005.

## References

- Abouaf, R., Pommier, J., & Dunet, H. (2003). Electronic and vibrational excitation in gas phase thymine and 5-bromouracil by electron impact. *Chemical Physics Letters*, 381(3–4), 486–494. doi:10.1016/j.cplett.2003.09.121.
- Alexandrova, A. N., Tully, J. C., & Granucci, G. (2010). Photochemistry of DNA fragments via semiclassical nonadiabatic dynamics. *The Journal of Physical Chemistry B*, 114(37), 12116–12128. doi:10.1021/jp103322c.
- Andruniow, T., Ferre, N., & Olivucci, M. (2004). Structure, initial excited-state relaxation, and energy storage of rhodopsin resolved at the multiconfigurational perturbation theory level. *Proceedings of the National Academy of Sciences of the United States of America*, 101(52), 17908–17913. doi:10.1073/pnas.0407997101.
- Antol, I., Eckert-Maksić, M., Barbatti, M., & Lischka, H. (2007). Simulation of the photodeactivation of formamide in the  $n_o\pi^*$  and  $\pi\pi^*$  states: An ab initio on-the-fly surface-hopping dynamics study. *Journal of Chemical Physics*, 127(23), 234303–234308. doi:10.1063/1.2804862.
- Antol, I., Barbatti, M., Eckert-Maksić, M., & Lischka, H. (2008a). Quantum chemical calculations of electronically excited states: Formamide, its protonated form and alkali cation complexes as case studies. *Monatshefte für Chemie/Chemical Monthly*, 139(4), 319–328. doi:10.1007/s00706-007-0803-2.
- Antol, I., Vazdar, M., Barbatti, M., & Eckert-Maksić, M. (2008b). The effect of protonation on the photodissociation processes in formamide – An ab initio surface hopping dynamics study. *Chemical Physics*, 349(1–3), 308–318. doi:10.1016/j.chemphys.2008.01.026.
- Araujo, M., Lasorne, B., Bearpark, M. J., & Robb, M. A. (2008). The photochemistry of formaldehyde: Internal conversion and molecular dissociation in a single step? *The Journal of Physical Chemistry A*, 112(33), 7489–7491.
- Asturiol, D., Lasorne, B., Robb, M. A., & Blancafort, L. (2009). Photophysics of the  $\pi\pi^*$  and  $n,\pi^*$  states of thymine: MS-CASPT2 minimum energy paths and CASSCF on-the-fly dynamics. *The Journal of Physical Chemistry A*, 113(38), 10211–10218. doi:10.1021/jp905303g.
- Back, R. A., & Boden, J. C. (1971). High-temperature photolysis and pyrolysis of formamide vapour, and thermal decomposition of carbamyl



- radical. *Transactions of the Faraday Society* 67(577), 88–96.
- Barbatti, M., & Lischka, H. (2007). Can the nonadiabatic photodynamics of aminopyrimidine be a model for the ultrafast deactivation of adenine? *The Journal of Physical Chemistry A*, 111(15), 2852–2858. doi:10.1021/jp070089w.
- Barbatti, M., & Lischka, H. (2008). Nonadiabatic deactivation of 9H-adenine: A comprehensive picture based on mixed quantum-classical dynamics. *Journal of the American Chemical Society*, 130(21), 6831–6839. doi:10.1021/ja800589p.
- Barbatti, M., Vazdar, M., Aquino, A. J. A., Eckert-Maksić, M., & Lischka, H. (2006). The nonadiabatic deactivation paths of pyrrole. *Journal of Chemical Physics*, 125(16), 164323. doi:10.1063/1.2363376.
- Barbatti, M., Granucci, G., Persico, M., Ruckebauer, M., Vazdar, M., Eckert-Maksić, M., & Lischka, H. (2007a). The on-the-fly surface-hopping program system Newton-X: Application to ab initio simulation of the nonadiabatic photodynamics of benchmark systems. *Journal of Photochemistry and Photobiology A*, 190(2–3), 228–240. doi:10.1016/j.jphotochem.2006.12.008.
- Barbatti, M., Granucci, G., Ruckebauer, M., Pittner, J., Persico, M., & Lischka, H. (2007b). NEWTON-X: A package for Newtonian dynamics close to the crossing seam. [www.newtonx.org](http://www.newtonx.org)
- Barbatti, M., Ruckebauer, M., Szymczak, J. J., Aquino, A. J. A., & Lischka, H. (2008). Nonadiabatic excited-state dynamics of polar p-systems and related model compounds of biological relevance. *Physical Chemistry Chemical Physics*, 10, 482. doi:10.1039/b709315m.
- Barbatti, M., Aquino, A. J. A., Szymczak, J. J., Nachtigallova, D., Hobza, P., & Lischka, H. (2010a). Relaxation mechanisms of UV-photoexcited DNA and RNA nucleobases. *Proceedings of the National Academy of Sciences of the United States of America*, 107(50), 21453–21458. doi:10.1073/pnas.1014982107.
- Barbatti, M., Pittner, J., Pederzoli, M., Werner, U., Mitric, R., Bonacic-Koutecký, V., & Lischka, H. (2010b). Non-adiabatic dynamics of pyrrole: Dependence of deactivation mechanisms on the excitation energy. *Chemical Physics*, 375(1), 26–34.
- Barbatti, M., Aquino, A. J. A., Szymczak, J. J., Nachtigallova, D., & Lischka, H. (2011a). Photodynamics simulations of cytosine: Characterization of the ultra fast bi-exponential UV deactivation. *Physical Chemistry Chemical Physics*, 13, 6145–6155. doi:10.1039/C1030CP02142C.
- Barbatti, M., Szymczak, J. J., Aquino, A. J. A., Nachtigallova, D., & Lischka, H. (2011b). The decay mechanism of photoexcited guanine – A nonadiabatic dynamics study. *Journal of Chemical Physics*, 134(1), 014304.
- Ben-Nun, M., Molnar, F., Lu, H., Phillips, J. C., Martinez, T. J., & Schulten, K. (1998). Quantum dynamics of the femtosecond photoisomerization of retinal in bacteriorhodopsin. *Faraday Discuss*, 110, 447–462.
- Ben-Nun, M., Quenneville, J., & Martinez, T. J. (2000). Ab initio multiple spawning: Photochemistry from first principles quantum molecular dynamics. *The Journal of Physical Chemistry A*, 104(22), 5161–5175.
- Birge, R. R. (1981). Photophysics of light transduction in rhodopsin and bacteriorhodopsin. *Annual Review of Biophysics & Bioengineering*, 10, 315–354.
- Birge, R. R. (1990). Nature of the primary photochemical events in rhodopsin and bacteriorhodopsin. *Biochimica et Biophysica Acta*, 1016(3), 293–327.
- Blank, D. A., North, S. W., & Lee, Y. T. (1994). The ultraviolet photodissociation dynamics of pyrrole. *Chemical Physics*, 187(1–2), 35–47.
- Boden, J. C., & Back, R. A. (1970). Photochemistry and free-radical reactions in formamide vapour. *Transactions of the Faraday Society* 66, 175–182.
- Boeyens, J. C. A. (1978). The conformation of six-membered rings. *Journal of Chemical Crystallography*, 8, 317–320.
- Burghardt, I., & Hynes, J. T. (2006). Excited-state charge transfer at a conical intersection: Effects of an environment. *The Journal of Physical Chemistry A*, 110(40), 11411–11423.
- Cadet, J., & Berger, M. (1985). Radiation-induced decomposition of the purine-bases within DNA and related model compounds. *International Journal of Radiation Biology*, 47(2), 127–143.
- Canuel, C., Mons, M., Piuze, F., Tardivel, B., Dimicoli, I., & Elhanine, M. (2005). Excited states dynamics of DNA and RNA bases: Characterization of a stepwise deactivation pathway in the gas phase. *Journal of Chemical Physics*, 122(7), 074316.



- Chen, X.-B., & Fang, W.-H. (2004). Insights into photodissociation dynamics of benzamide and formanilide from ab initio calculations. *Journal of the American Chemical Society*, *126*(29), 8976–8980.
- Chen, X.-B., Fang, W.-H., & Fang, D. C. (2003). An ab initio study toward understanding the mechanistic photochemistry of acetamide. *Journal of the American Chemical Society*, *125*(32), 9689–9698.
- Chin, C. H., Mebel, A. M., Kim, G. S., Baek, K. Y., Hayashi, M., Liang, K. K., & Lin, S. H. (2007). Theoretical investigations of spectroscopy and excited state dynamics of adenine. *Chemical Physics Letters*, *445*(4–6), 361–369.
- Ciminelli, C., Granucci, G., & Persico, M. (2008). The photoisomerization of a peptidic derivative of azobenzene: A nonadiabatic dynamics simulation of a supramolecular system. *Chemical Physics*, *349*(1–3), 325–333. doi:[10.1016/j.chemphys.2008.01.030](https://doi.org/10.1016/j.chemphys.2008.01.030).
- Clark, L. B., & Tinoco, I. (1965). Correlations in ultraviolet spectra of purine and pyrimidine bases. *Journal of the American Chemical Society*, *87*(1), 11.
- Clark, L. B., Peschel, G. G., & Tinoco, I. (1965). Vapor spectra and heats of vaporization of some purine and pyrimidine bases. *The Journal of Physical Chemistry*, *69*(10), 3615–3618.
- Cremer, D., & Pople, J. A. (1975). General definition of ring puckering coordinates. *Journal of the American Chemical Society*, *97*(6), 1354–1358.
- Crespo-Hernández, C. E., Cohen, B., Hare, P. M., & Kohler, B. (2004). Ultrafast excited-state dynamics in nucleic acids. *Chemical Reviews*, *104*(4), 1977–2019.
- Crespo-Hernandez, C. E., Cohen, B., & Kohler, B. (2005). Base stacking controls excited-state dynamics in A-T DNA. *Nature*, *436*(7054), 1141–1144. doi:[10.1038/Nature03933](https://doi.org/10.1038/Nature03933).
- Cui, W., Thompson, M. S., & Reilly, J. P. (2005). Pathways of peptide ion fragmentation induced by vacuum ultraviolet light. *Journal of The American Society for Mass Spectrometry*, *16*(8), 1384–1398.
- Dallos, M., Lischka, H., Shepard, R., Yarkony, D. R., & Szalay, P. G. (2004). Analytic evaluation of nonadiabatic coupling terms at the MR-CI level. II. Minima on the crossing seam: Formaldehyde and the photodimerization of ethylene. *Journal of Chemical Physics*, *120*(16), 7330–7339.
- Daura, X., Antes, I., van Gunsteren, W. F., Thiel, W., & Mark, A. E. (1999). The effect of motional averaging on the calculation of NMR-derived structural properties. *Proteins-Structure Function and Genetics*, *36*(4), 542–555.
- Devine, A. L., Cronin, B., Nix, M. G. D., & Ashfold, M. N. R. (2006). High resolution photofragment translational spectroscopy studies of the near ultraviolet photolysis of imidazole. *Journal of Chemical Physics*, *125*(18), 184302. doi:[Artn184302](https://doi.org/Artn184302), [10.1063/1.2364504](https://doi.org/10.1063/1.2364504).
- Duggan, D. E., Bowman, R. L., Brodie, B. B., & Udenfriend, S. (1957). A spectrophotofluorometric study of compounds of biological interest. *Archives of Biochemistry and Biophysics*, *68*(1), 1–14.
- Eckert-Maksić, M., & Antol, I. (2009). Study of the mechanism of the N-CO photodissociation in N,N-Dimethylformamide by direct trajectory surface hopping simulations. *The Journal of Physical Chemistry A*, *113*(45):12582–12590. doi:[10.1021/jp9046177](https://doi.org/10.1021/jp9046177).
- Eckert-Maksić, M., Antol, I., Vazdar, M., Barbatti, M., & Lischka, H. (2010a). Formamide as the model compound for photodissociation studies of the peptide bond. In P. Paneth & A. Dybala-Defratyka (Eds.), *Kinetics and dynamics: Challenges and advances in computational chemistry and physics* (pp. 77–106). Netherlands: Springer.
- Eckert-Maksić, M., Vazdar, M., Ruckebauer, M., Barbatti, M., Muller, T., & Lischka, H. (2010b). Matrix-controlled photofragmentation of formamide: Dynamics simulation in argon by nonadiabatic QM/MM method. *Physical Chemistry Chemical Physics*, *12*(39), 12719–12726.
- Fabiano, E., & Thiel, W. (2008). Nonradiative deexcitation dynamics of 9H-adenine: An OM2 surface hopping study. *The Journal of Physical Chemistry A*, *112*(30), 6859–6863. doi:[10.1021/Jp8033402](https://doi.org/10.1021/Jp8033402).
- Fabiano, E., Groenhof, G., & Thiel, W. (2008a). Approximate switching algorithms for trajectory surface hopping. *Chemical Physics*, *351*(1–3), 111–116.
- Fabiano, E., Keal, T. W., & Thiel, W. (2008b). Implementation of surface hopping molecular dynamics using semiempirical methods. *Chemical Physics*, *349*(1–3), 334–347. doi:[10.1016/j.chemphys.2008.01.044](https://doi.org/10.1016/j.chemphys.2008.01.044).
- Ferretti, A., Granucci, G., Lami, A., Persico, M., & Villani, G. (1996). Quantum mechanical and semiclassical dynamics at a conical intersection. *Journal of Chemical Physics*, *104*(14), 5517–5527.
- Frutos, L. M., Andruniow, T., Santoro, F., Ferre, N., & Olivucci, M. (2007). Tracking the excited-state time evolution of the visual pigment with multi-configurational quantum chemistry. *Proceedings of the National Academy of Sciences of the United States of America*, *104*(19), 7764–7769.
- Garavelli, M., Celani, P., Bernardi, F., Robb, M. A., & Olivucci, M. (1997). The C5H6NH2+ protonated Schiff base: An ab initio minimal

- model for retinal photoisomerization. *Journal of the American Chemical Society*, 119(29), 6891–6901.
- Garavelli, M., Bernardi, F., Robb, M. A., & Olivucci, M. (1999a). The short-chain acrolein-iminium and pentadieniminium cations: Towards a model for retinal photoisomerization. A CASSCF/PT2 study. *Journal of Molecular Structure: THEOCHEM*, 463(1–2), 59–64.
- Garavelli, M., Negri, F., & Olivucci, M. (1999b). Initial excited-state relaxation of the isolated 11-cis protonated Schiff base of retinal: Evidence for in-plane motion from ab initio quantum chemical simulation of the resonance Raman spectrum. *Journal of the American Chemical Society*, 121(5), 1023–1029.
- Gascon, J. A., & Batista, V. S. (2004). QM/MM study of energy storage and molecular rearrangements due to the primary event in vision. *Biophysical Journal*, 87(5), 2931–2941. doi:10.1529/biophysj.104.048264.
- Gingell, J. M., Mason, N. J., Zhao, H., Walker, I. C., & Siggel, M. R. F. (1997). VUV optical-absorption and electron-energy-loss spectroscopy of formamide. *Chemical Physics*, 220(1–2), 191–205.
- González-Luque, R., Garavelli, M., Bernardi, F., Merchán, M., Robb, M. A., & Olivucci, M. (2000). Computational evidence in favor of a two-state, two-mode model of the retinal chromophore photoisomerization. *Proceedings of the National Academy of Sciences of the United States of America*, 97(17), 9379–9384.
- González-Vázquez, J., & González, L. (2010). A time-dependent picture of the ultrafast deactivation of keto-cytosine including three-state conical intersections. *A European Journal of Chemical Physics and Physical Chemistry*, 11(17), 3617–3624.
- Granucci, G., & Persico, M. (2007). Critical appraisal of the fewest switches algorithm for surface hopping. *Journal of Chemical Physics*, 126(13), 134114–134111.
- Granucci, G., Persico, M., & Toniolo, A. (2001). Direct semiclassical simulation of photochemical processes with semiempirical wave functions. *Journal of Chemical Physics*, 114(24), 10608–10615.
- Grégoire, G., Lucas, B., Barat, M., Fayetteon, J. A., Dedonder-Lardeux, C. & Jouvét, C. (2009). UV photoinduced dynamics in protonated aromatic amino acid. *European Physical Journal D*, 51(1), 109–116.
- Grégoire, G., Dedonder-Lardeux, C., Jouvét, C., Desfrancois, C., & Fayetteon, J. A. (2007). Ultrafast excited state dynamics in protonated GWG and GYG tripeptides. *Physical Chemistry Chemical Physics*, 9(1), 78–82.
- Grégoire, G., Kang, H., Dedonder-Lardeux, C., Jouvét, C., Desfrancois, C., Onidas, D., Lepere, V., & Fayetteon, J. A. (2006). Statistical vs. non-statistical deactivation pathways in the UV photo-fragmentation of protonated tryptophan-leucine dipeptide. *Physical Chemistry Chemical Physics*, 8(1), 122–128.
- Greenberg, A., Breneman, C. M., & Liebman, J. F. (2002). *The amide linkage: Selected structural aspects in Chemistry, Biochemistry, and Materials Science. The amide linkage: Structural significance in Chemistry, Biochemistry, and Materials Science*. New York: Wiley
- Gustavsson, T., Sarkar, N., Lazzarotto, E., Markovitsi, D., & Improta, R. (2006). Singlet excited state dynamics of uracil and thymine derivatives: A femtosecond fluorescence upconversion study in acetonitrile. *Chemical Physics Letters*, 429(4–6), 551–557. doi:10.1016/j.cplett.2006.08.058.
- Hack, M. D., Wensmann, A. M., Truhlar, D. G., Ben-Nun, M., & Martínez, T. J. (2001). Comparison of full multiple spawning, trajectory surface hopping, and converged quantum mechanics for electronically nonadiabatic dynamics. *Journal of Chemical Physics*, 115(3), 1172–1186.
- Hammes-Schiffer, S., & Tully, J. C. (1994). Proton-transfer in solution—Molecular-dynamics with quantum transitions. *Journal of Chemical Physics*, 101(6), 4657–4667.
- Hayashi, S., Taikhorshid, E., & Schulten, K. (2009). Photochemical reaction dynamics of the primary event of vision studied by means of a hybrid molecular simulation. *Biophysical Journal*, 96(2), 403–416. doi:10.1016/j.bpj.2008.09.049.
- He, Y., Wu, C., & Kong, W. (2003). Decay pathways of thymine and methyl-substituted uracil and thymine in the gas phase. *The Journal of Physical Chemistry A*, 107(26), 5145–5148. doi:10.1021/jp034733s
- Hudock, H. R., & Martinez, T. J. (2008). Excited-state dynamics of cytosine reveal multiple intrinsic subpicosecond pathways. *A European Journal of Chemical Physics and Physical Chemistry*, 9(17), 2486–2490. doi:10.1002/cphc.200800649.
- Hudock, H. R., Levine, B. G., Thompson, A. L., Satzger, H., Townsend, D., Gador, N., Ullrich, S., Stolow, A., & Martinez, T. J. (2007). Ab initio molecular dynamics and time-resolved photoelectron spectroscopy of electronically excited uracil and thymine. *The Journal of Physical Chemistry A*, 111(34), 8500–8508.
- Improta, R., Barone, V., Lami, A., & Santoro, F. (2009). Quantum dynamics of the ultrafast

- $\pi\pi^*/n\pi^*$  population transfer in uracil and 5-fluoro-uracil in water and acetonitrile. *The Journal of Physical Chemistry B*, 113(43), 14491–14503
- Ishida, T., Nanbu, S., & Nakamura, H. (2009). Nonadiabatic ab initio dynamics of two models of schiff base retinal. *The Journal of Physical Chemistry A*, 113(16), 4356–4366. doi:10.1021/jp8110315.
- Jasper, A. W., Stechmann, S. N., & Truhlar, D. G. (2002). Fewest-switches with time uncertainty: A modified trajectory surface-hopping algorithm with better accuracy for classically forbidden electronic transitions. *Journal of Chemical Physics*, 116(13), 5424–5431.
- Jeong, H. M., Young, S. S., Hyun, J. C., & Myung, S. K. (2007). Photodissociation at 193 nm of some singly protonated peptides and proteins with m/z 2000–9000 using a tandem time-of-flight mass spectrometer equipped with a second source for delayed extraction/post-acceleration of product ions. *Rapid Communications in Mass Spectrometry*, 21(3), 359–368
- Jeong, H. M., So, H. Y., & Myung, S. K. (2005). Photodissociation of singly protonated peptides at 193 nm investigated with tandem time-of-flight mass spectrometry. *Rapid Communications in Mass Spectrometry*, 19(22), 3248–3252
- Jones, G. A., Acocella, A., & Zerbetto, F. (2008). On-the-fly, electric-field-driven, coupled electron-nuclear dynamics. *The Journal of Physical Chemistry A*, 112(40), 9650–9656. doi:10.1021/jp805360v.
- Jorgensen, W. L., & McDonald, N. A. (1998). Development of an all-atom force field for heterocycles. Properties of liquid pyridine and diazenes. *Journal of Molecular Structure: Theochem*, 424(1–2), 145–155.
- Kang, T. Y., & Kim, H. L. (2006). Photodissociation of formamide at 205 nm: The H atom channels. *Chemical Physics Letters*, 431(1–3), 24–27.
- Kang, H., Jouvét, C., Dedonder-Lardeux, C., Martrenchard, S., Grégoire, G., Desfrancois, C., Schermann, J. P., Barat, M., & Fayetteon, J. A. (2005). Ultrafast deactivation mechanisms of protonated aromatic amino acids following UV excitation. *Physical Chemistry Chemical Physics*, 7(2), 394–398.
- Kang, H., Dedonder-Lardeux, C., Jouvét, C., Martrenchard, S., Grégoire, G., Desfrancois, C., Schermann, J. P., Barat, M., & Fayetteon, J. A. (2004). Photo-induced dissociation of protonated tryptophan TrpH<sup>+</sup>: A direct states dissociation channel in the excited controls the hydrogen atom loss. *Physical Chemistry Chemical Physics*, 6(10), 2628–2632.
- Kang, H., Lee, K. T., Jung, B., Ko, Y. J., & Kim, S. K. (2002). Intrinsic lifetimes of the excited state of DNA and RNA bases. *Journal of the American Chemical Society*, 124(44), 12958–12959.
- Keal, T., Wanko, M., & Thiel, W. (2009). Assessment of semiempirical methods for the photoisomerisation of a protonated Schiff base. *Theoretical Chemistry Accounts: Theory, Computation, and Modeling (Theoretica Chimica Acta)*, 123(1), 145–156.
- Kochendoerfer, G. G., & Mathies, R. A. (1996). Spontaneous emission study of the femtosecond isomerization dynamics of rhodopsin. *The Journal of Physical Chemistry*, 100(34), 14526–14532.
- Köppel, H., Gromov, E. V., & Trofimov, A. B. (2004). Multi-mode-multi-state quantum dynamics of key five-membered heterocycles: Spectroscopy and ultrafast internal conversion. *Chemical Physics*, 304(1–2), 35–49.
- Kukura, P., McCamant, D. W., Yoon, S., Wandschneider, D. B., & Mathies, R. A. (2005). Structural observation of the primary isomerization in vision with femtosecond-stimulated Raman. *Science*, 310(5750), 1006–1009.
- Lan, Z., & Domcke, W. (2008). Role of vibrational energy relaxation in the photoinduced nonadiabatic dynamics of pyrrole at the  ${}^1\pi\sigma^* - S_0$  conical intersection. *Chemical Physics*, 350(1–3), 125–138.
- Lan, Z., Fabiano, E., & Thiel, W. (2009). Photoinduced nonadiabatic dynamics of pyrimidine nucleobases: On-the-fly surface-hopping study with semiempirical methods. *The Journal of Physical Chemistry B*, 113(11), 3548–3555. doi:10.1021/jp809085h.
- Langer, H., Doltsinis, N. L., & Marx, D. (2005). Excited-state dynamics and coupled proton-electron transfer of guanine. *A European Journal of Chemical Physics and Physical Chemistry*, 6(9), 1734–1737.
- Lasser, C., & Swart, T. (2008). Single switch surface hopping for a model of pyrazine. *Journal of Chemical Physics*, 129(3), 034302–034308.
- Lei, Y., Yuan, S., Dou, Y., Wang, Y., & Wen, Z. (2008). Detailed dynamics of the nonradiative deactivation of adenine: A semiclassical dynamics study. *The Journal of Physical Chemistry A*, 112(37), 8497–8504. doi:10.1021/jp802483b.
- Levine, B. G., Ko, C., Quenneville, J., & Martínez, T. J. (2006). Conical intersections and double excitations in time-dependent density functional theory. *Molecular Physics*, 104(5–7), 1039–1051.

- Levine, B. G., Coe, J. D., Virshup, A. M., & Martinez, T. J. (2008). Implementation of ab initio multiple spawning in the MOLPRO quantum chemistry package. *Chemical Physics*, 347(1–3), 3–16. doi:10.1016/j.chemphys.2008.01.014.
- Li, X. S., Tully, J. C., Schlegel, H. B., & Frisch, M. J. (2005). Ab initio Ehrenfest dynamics. *Journal of Chemical Physics*, 123(8), 084106.
- Lin, H., & Truhlar, D. G. (2007). QM/MM: What have we learned, where are we, and where do we go from here? *Theoretical Chemistry Accounts*, 117(2), 185–199.
- Lippert, H., Ritze, H. H., Hertel, I. V., & Radloff, W. (2004). Femtosecond time-resolved hydrogen-atom elimination from photoexcited pyrrole molecules. *A European Journal of Chemical Physics and Physical Chemistry*, 5(9), 1423–1427.
- Lischka, H., Shepard, R., Brown, F. B., & Shavitt, I. (1981). New implementation of the graphical unitary-group approach for multi-reference direct configuration-interaction calculations. *International Journal of Quantum Chemistry*, S.15, 91–100.
- Lischka, H., Shepard, R., Pitzer, R. M., Shavitt, I., Dallos, M., Müller, T., Szalay, P. G., Seth, M., Kedziora, G. S., Yabushita, S., & Zhang, Z. Y. (2001). High-level multireference methods in the quantum-chemistry program system COLUMBUS: Analytic MR-CISD and MR-AQCC gradients and MR-AQCC-LRT for excited states, GUGA spin-orbit CI and parallel CI density. *Physical Chemistry Chemical Physics*, 3(5), 664–673.
- Lischka, H., Dallos, M., & Shepard, R. (2002). Analytic MRCI gradient for excited states: Formalism and application to the  $n-\pi^*$  valence- and  $n-(3s,3p)$  Rydberg states of formaldehyde. *Molecular Physics*, 100(11), 1647–1658.
- Lischka, H., Dallos, M., Szalay, P. G., Yarkony, D. R., & Shepard, R. (2004). Analytic evaluation of nonadiabatic coupling terms at the MR-CI level. I. Formalism. *Journal of Chemical Physics*, 120(16), 7322–7329.
- Lischka, H., Shepard, R., Shavitt, I., Pitzer, R. M., Dallos, M., Mueller, T., Szalay, P. G., Brown, F. B., Ahlrichs, R., Boehm, H. J., Chang, A., Comeau, D. C., Gdanitz, R., Dachsel, H., Ehrhardt, C., Ernzerhof, M., Hoecht, P., Irl, S., Kedziora, G., Kovar, T., Parasuk, V., Pepper, M. J. M., Scharf, P., Schiffer, H., Schindler, M., Schueler, M., Seth, M., Stahlberg, E. A., Zhao, J.-G., Yabushita, S., Zhang, Z., Barbatti, M., Matsika, S., Schuurmann, M., Yarkony, D. R., Brozell, S. R., Beck, E. V., & Blaudeau, J.-P. (2006). COLUMBUS, an ab initio electronic structure program, release 5.9.1. [www.univie.ac.at/columbus](http://www.univie.ac.at/columbus)
- Liu, R. S. H., & Asato, A. E. (1985). Photochemistry of polyenes. 22. The primary process of vision and the structure of bathorhodopsin – A mechanism for photoisomerization of polyenes. *Proceedings of the National Academy of Sciences of the United States of America*, 82(2), 259–263.
- Liu, R. S. H. (2002). Introduction to the symposium-in-print: Photoisomerization pathways, torsional relaxation and the Hula Twist & para. *Photochemistry and Photobiology*, 76(6), 580–583.
- Liu, D., Fang, W. H., & Fu, X. Y. (2000). Ab initio molecular orbital study of the mechanism of photodissociation of formamide. *Chemical Physics Letters*, 318(4–5), 291–297.
- Logunov, I., & Schulten, K. (1996). Quantum chemistry: Molecular dynamics study of the dark-adaptation process in bacteriorhodopsin. *Journal of the American Chemical Society*, 118(40), 9727–9735.
- Longworth, J. W., Rahn, R. O., & Shulman, R. G. (1966). Luminescence of pyrimidines purines nucleosides and nucleotides at 77 degrees K. Effect of ionization and tautomerization. *Journal of Chemical Physics*, 45(8), 2930.
- Lundell, J., Krajewska, M., & Räsänen, M. (1998). Matrix isolation Fourier transform infrared and ab initio studies of the 193-nm-induced photodecomposition of formamide. *The Journal of Physical Chemistry A*, 102(33), 6643–6650.
- Malone, R. J., Miller, A. M., & Kohler, B. (2003). Singlet excited-state lifetimes of cytosine derivatives measured by femtosecond transient absorption. *Photochemistry and Photobiology*, 77(2), 158–164.
- Marian, C. M. (2005). A new pathway for the rapid decay of electronically excited adenine. *Journal of Chemical Physics*, 122(10), 104314.
- Matsika, S. (2004). Radiationless decay of excited states of uracil through conical intersections. *The Journal of Physical Chemistry A*, 108(37), 7584–7590.
- Merchan, M., Gonzalez-Luque, R., Climent, T., Serrano-Andres, L., Rodriaguez, E., Reguero, M., & Pelaez, D. (2006). Unified model for the ultrafast decay of pyrimidine nucleobases. *The Journal of Physical Chemistry B*, 110(51), 26471–26476. doi:10.1021/jp066874a.
- Middleton, C. T., de La Harpe, K., Su, C., Law, Y. K., Crespo-Hernandez, C. E., & Kohler, B. (2009). DNA excited-state dynamics: From single bases to the double helix. *Annual Review of Physical Chemistry*, 60(1), 217–239. doi:10.1146/annurev.physchem.59.032607.093719.

- Migani, A., Robb, M. A., & Olivucci, M. (2003). Relationship between photoisomerization path and intersection space in a retinal chromophore model. *Journal of the American Chemical Society*, 125(9), 2804–2808.
- Mitric, R., Petersen, J., & Bonacic-Koutecky, V. (2009a). Laser-field-induced surface-hopping method for the simulation and control of ultrafast photodynamics. *Physical Review A*, 79(5), 053416.
- Mitric, R., Werner, U., Wohlgemuth, M., Seifert, G., & Bonacic-Koutecky, V. (2009b). Nonadiabatic dynamics within time-dependent density functional tight binding method. *The Journal of Physical Chemistry A*, 113(45), 12700–12705. doi:10.1021/jp905600w.
- Mulcahy, M., McInerney, J. G., Nikogosyan, D. N., & Görner, H. (2000). 193 Nm photolysis of aromatic and aliphatic dipeptides in aqueous solution: Dependence of decomposition quantum yield on the amino acid sequence. *Biological Chemistry*, 381(12), 1259–1262.
- Muller, U., & Stock, G. (1997). Surface-hopping modeling of photoinduced relaxation dynamics on coupled potential-energy surfaces. *Journal of Chemical Physics*, 107(16), 6230–6245.
- Nachtigallova, D., Zeleny, T., Ruckebauer, M., Muller, T., Barbatti, M., Hobza, P., & Lischka, H. (2010). Does stacking restrain the photodynamics of individual nucleobases? *Journal of the American Chemical Society*, 132(24), 8261–8263. doi:10.1021/ja1029705.
- Nieber, H., & Doltsinis, N. L. (2008). Elucidating ultrafast nonradiative decay of photoexcited uracil in aqueous solution by ab initio molecular dynamics. *Chemical Physics*, 347(1–3), 405–412. doi:10.1016/j.chemphys.2007.09.056.
- Nolting, D., Schultz, T., Hertel, I. V., & Weinkauff, R. (2006). Excited state dynamics and fragmentation channels of the protonated dipeptide H2N-Leu-Trp-COOH. *Physical Chemistry Chemical Physics*, 8(44), 5247–5254. doi:10.1039/B609726.
- Palings, I., Pardoën, J. A., Vandenberg, E., Winkel, C., Lugtenburg, J., & Mathies, R. A. (1987). Assignment of fingerprint vibrations in the resonance Raman-spectra of rhodopsin, isorhodopsin, and bathorhodopsin – Implications for chromophore structure and environment. *Biochemistry (Mosc)*, 26(9), 2544–2556.
- Pei, K.-M., Ma, Y., & Zheng, X. (2008). Resonance Raman and theoretical investigation of the photodissociation dynamics of benzamide in  $S_3$  state. *The Journal of Chemical Physics*, 128(22), 224310–224310.
- Perun, S., Sobolewski, A. L., & Domcke, W. (2005a). Ab initio studies on the radiationless decay mechanisms of the lowest excited singlet states of 9H-adenine. *Journal of the American Chemical Society*, 127(17), 6257–6265.
- Perun, S., Sobolewski, A. L., & Domcke, W. (2005b). Photostability of 9H-adenine: Mechanisms of the radiationless deactivation of the lowest excited singlet states. *Chemical Physics*, 313(1–3), 107–112.
- Peteanu, L. A., Schoenlein, R. W., Wang, Q., Mathies, R. A., & Shank, C. V. (1993). The 1st Step in vision occurs in femtoseconds – Complete blue and red spectral studies. *Proceedings of the National Academy of Sciences of the United States of America*, 90(24), 11762–11766.
- Petersen, C., Dahl, N. H., Jensen, S. K., Poulsen, J. A., Thøgersen, J., & Keiding, S. R. (2008). Femtosecond Photolysis of Aqueous Formamide. *The Journal of Physical Chemistry A*, 112(15), 3339–3344.
- Pittner, J., Lischka, H., & Barbatti, M. (2009). Optimization of mixed quantum-classical dynamics: Time-derivative coupling terms and selected couplings. *Chemical Physics*, 356(1–3), 147–152. doi:10.1016/j.chemphys.2008.10.013.
- Polli, D., Altoe, P., Weingart, O., Spillane, K. M., Manzoni, C., Brida, D., Tomasello, G., Orlandi, G., Kukura, P., Mathies, R. A., Garavelli, M., & Cerullo, G. (2010). Conical intersection dynamics of the primary photoisomerization event in vision. *Nature*, 467(7314), 440–443. doi:10.1038/nature09346.
- Poterya, V., Profant, V., Farnik, M., Slavicek, P., & Buck, U. (2007). Experimental and theoretical study of the pyrrole cluster photochemistry: Closing the  $\pi\sigma^*$  dissociation pathway by complexation. *Journal of Chemical Physics*, 127(6), 064307. doi:10.1063/1.2754687.
- Powner, M. W., Gerland, B., & Sutherland, J. D. (2009). Synthesis of activated pyrimidine ribonucleotides in prebiotically plausible conditions. *Nature*, 459(7244), 239–242. doi:10.1038/Nature08013.
- Rohrig, U. F., Guidoni, L., Laio, A., Frank, I., & Rothlisberger, U. (2004). A molecular spring for vision. *Journal of the American Chemical Society*, 126(47), 15328–15329. doi:10.1021/ja048265r.
- Rohrig, U. F., Guidoni, L., & Rothlisberger, U. (2005). Solvent and protein effects on the structure and dynamics of the rhodopsin chromophore. *A European Journal of Chemical Physics and Physical Chemistry*, 6(9), 1836–1847. doi:10.1002/cphc.200500066.
- Ruckebauer, M., Barbatti, M., Muller, T., & Lischka, H. (2010). Nonadiabatic excited-state

- dynamics with hybrid ab initio quantum-mechanical/molecular-mechanical methods: Solvation of the pentadieniminium cation in Apolar media. *The Journal of Physical Chemistry A*, 114(25), 6757–6765. doi:10.1021/jp103101t.
- Saam, J., Tajkhorshid, E., Hayashi, S., & Schulten, K. (2002). Molecular dynamics investigation of primary photoinduced events in the activation of rhodopsin. *Biophysical Journal*, 83(6), 3097–3112.
- Santoro, F., Barone, V., & Improta, R. (2007a). Influence of base stacking on excited-state behavior of polyadenine in water, based on time-dependent density functional calculations. *Proceedings of the National Academy of Sciences of the United States of America*, 104(24), 9931–9936. doi:10.1073/pnas.0703298104.
- Santoro, F., Lami, A., & Olivucci, M. (2007b). Complex excited dynamics around a plateau on a retinal-like potential surface: Chaos, multi-exponential decays and quantum/classical differences. *Theoretical Chemistry Accounts*, 117(5–6), 1061–1072. doi:10.1007/s00214-006-0220-3.
- Shapiro, I., Weingart, O., & Buss, V. (2009). Bicycle-pedal isomerization in a rhodopsin chromophore model. *Journal of the American Chemical Society*, 131(1), 16. doi:10.1021/Ja805586z.
- Schoenlein, R. W., Peteanu, L. A., Mathies, R. A., & Shank, C. V. (1991). The 1st step in vision – Femtosecond isomerization of rhodopsin. *Science*, 254(5030), 412–415.
- Schultz, T., Samoylova, E., Radloff, W., Hertel, I. V., Sobolewski, A. L., & Domcke, W. (2004). Efficient deactivation of a model base pair via excited-state hydrogen transfer. *Science*, 306(5702), 1765–1768.
- Sellner, B., Barbatti, M., & Lischka, H. (2009). Dynamics starting at a conical intersection: Application to the photochemistry of pyrrole. *Journal of Chemical Physics*, 131(2), 024312. doi:10.1063/1.3175799.
- Send, R., & Sundholm, D. (2007). Stairway to the conical intersection: A computational study of the retinal isomerization. *The Journal of Physical Chemistry A*, 111(36), 8766–8773.
- Serrano-Andres, L., & Merchan, M. (2009). Are the five natural DNA/RNA base monomers a good choice from natural selection? A photochemical perspective. *Journal of Photochemistry and Photobiology C: Photochemistry Reviews*, 10(1), 21–32. doi:10.1016/j.jphotochemrev.2008.12.001.
- Shepard, R. (1995). The analytic gradient method for configuration interaction wave functions. In D. R. Yarkony (Ed.), *Modern electronic structure theory*. Advanced series in physical chemistry (Vol. 1, p. 345). Singapore: World Scientific.
- Shepard, R., Lischka, H., Szalay, P. G., Kovar, T., & Ernzerhof, M. (1992). A general multireference configuration-interaction gradient program. *Journal of Chemical Physics*, 96(3), 2085–2098.
- Shin, E. J. (2004). Photochemistry of anthrylethene derivatives containing heteroaromatic ring: Pyrrole and indole derivatives. *Bulletin of the Korean Chemical Society*, 25(6), 907–909.
- Sobolewski, A. L., & Domcke, W. (2000). Conical intersections induced by repulsive  $^1\pi\sigma^*$  states in planar organic molecules: Malonaldehyde, pyrrole and chlorobenzene as photochemical model systems. *Chemical Physics*, 259(2–3), 181–191.
- Sobolewski, A. L., Domcke, W., & Hättig, C. (2005). Tautomeric selectivity of the excited-state lifetime of guanine/cytosine base pairs: The role of electron-driven proton-transfer processes. *Proceedings of the National Academy of Sciences of the United States of America*, 102(50), 17903–17906.
- Szymczak, J. J., Barbatti, M., & Lischka, H. (2008). Mechanism of ultrafast photodecay in restricted motions in protonated Schiff bases: The pentadieniminium cation. *Journal of Chemical Theory and Computation*, 4(8), 1189–1199. doi:10.1021/Ct800148n.
- Szymczak, J. J., Barbatti, M., & Lischka, H. (2009). Is the photoinduced isomerization in retinal protonated schiff bases a single- or double-torsional process? *The Journal of Physical Chemistry A*, 113(43), 11907–11918. doi:10.1021/jp903329j.
- Szymczak, J. J., Barbatti, M., & Lischka, H. (2011). Influence of the active space on CASSCF nonadiabatic dynamics simulations. *International Journal of Quantum Chemistry*, 111(13), 3307–3315. doi:10.1002/qua.22978.
- Tapavicza, E., Tavernelli, I., & Rothlisberger, U. (2007). Trajectory surface hopping within linear response time-dependent density-functional theory. *Physical Review Letters*, 98(2), 023001.
- Thompson, M. S., Cui, W., & Reilly, J. P. (2007). Factors that impact the vacuum ultraviolet photofragmentation of peptide ions. *Journal of The American Society for Mass Spectrometry*, 18(8), 1439–1452.
- Thompson, M. S., Cui, W., & Reilly, J. P. (2004). Fragmentation of singly charged peptide ions by photodissociation at  $i\gg=$  157 nm. *Angewandte Chemie-International Edition*, 43(36), 4791–4794.
- Torikai, A., & Shibata, H. (1999) Effect of ultraviolet radiation on photodegradation of collagen. *Journal of Applied Polymer Science*, 73(7), 1259–1265.



- Tully, J. C. (1990). Molecular-dynamics with electronic-transitions. *Journal of Chemical Physics*, 93(2), 1061–1071.
- Tully, J. C. (1998). Mixed quantum-classical dynamics. *Faraday Discussions*, 110, 407–419.
- Ullrich, S., Schultz, T., Zgierski, M. Z., & Stolow, A. (2004). Electronic relaxation dynamics in DNA and RNA bases studied by time-resolved photoelectron spectroscopy. *Physical Chemistry Chemical Physics*, 6(10), 2796–2801.
- Vallet, V., Lan, Z. G., Mahapatra, S., Sobolewski, A. L., & Domcke, W. (2004). Time-dependent quantum wave-packet description of the  ${}^1\pi\sigma^*$  photochemistry of pyrrole. *Faraday Discussions*, 127, 283–293.
- Vallet, V., Lan, Z. G., Mahapatra, S., Sobolewski, A. L., & Domcke, W. (2005). Photochemistry of pyrrole: Time-dependent quantum wave-packet description of the dynamics at the  ${}^1\text{GREEK}(\text{ps})^* - S_0$  conical intersections. *Journal of Chemical Physics*, 123(14), 144307.
- van den Brom, A. J., Kapelios, M., Kitsopoulos, T. N., Nahler, N. H., Cronin, B., & Ashfold, M. N. R. (2005). Photodissociation and photoionization of pyrrole following the multiphoton excitation at 243 and 364.7 nm. *Physical Chemistry Chemical Physics*, 7(5), 892–899.
- Vazdar, M., Eckert-Maksić, M., Barbatti, M., & Lischka, H. (2009). Excited-state non-adiabatic dynamics simulations of pyrrole. *Molecular Physics*, 107(8), 845–854. doi:10.1080/00268970802665639.
- Venkatesan, T. S., Mahapatra, S., Meyer, H. D., Koppel, H., & Cederbaum, L. S. (2007). Multimode Jahn-Teller and pseudo-Jahn-Teller interactions in the cyclopropane radical cation: Complex vibronic spectra and nonradiative decay dynamics. *The Journal of Physical Chemistry A*, 111(10), 1746–1761.
- Virshup, A. M., Punwong, C., Pogorelov, T. V., Lindquist, B. A., Ko, C., & Martinez, T. J. (2009). Photodynamics in complex environments: Ab initio multiple spawning quantum mechanical/molecular mechanical dynamics. *The Journal of Physical Chemistry B*, 113(11), 3280–3291. doi:10.1021/jp8073464
- Vreven, T., Bernardi, F., Garavelli, M., Olivucci, M., Robb, M. A., & Schlegel, H. B. (1997). Ab initio photoisomerization dynamics of a simple retinal chromophore model. *Journal of the American Chemical Society*, 119(51), 12687–12688.
- Wald, G. (1968). Molecular basis of visual excitation. *Science*, 162(3850), 230.
- Wang, Q., Schoenlein, R. W., Peteanu, L. A., Mathies, R. A., & Shank, C. V. (1994). Vibrationally coherent photochemistry in the femtosecond primary event of vision. *Science*, 266(5184), 422–424.
- Wanko, M., Hoffmann, M., Strodet, P., Koslowski, A., Thiel, W., Neese, F., Frauenheim, T., & Elstner, M. (2005). Calculating absorption shifts for retinal proteins: Computational challenges. *The Journal of Physical Chemistry B*, 109(8), 3606–3615.
- Warshel, A. (1976). Bicycle-pedal model for 1st step in vision process. *Nature*, 260(5553), 679–683.
- Warshel, A., & Barboj, N. (1982). Energy-storage and reaction pathways in the 1st step of the vision process. *Journal of the American Chemical Society*, 104(6), 1469–1476.
- Warshel, A., & Chu, Z. T. (2001). Nature of the surface crossing process in bacteriorhodopsin: Computer simulations of the quantum dynamics of the primary photochemical event. *The Journal of Physical Chemistry B*, 105(40), 9857–9871.
- Wei, J., Riedel, J., Kuczmann, A., Renth, F., & Temps, F. (2004). Photodissociation dynamics of pyrrole: Evidence for mode specific dynamics from conical intersections. *Faraday Discussions*, 127, 267–282.
- Weingart, O., Buss, V., & Robb, M. A. (2005). Excited state molecular dynamics of retinal model chromophores. *Phase Transitions* 78(1–3), 17–24.
- Weingart, O., Migani, A., Olivucci, M., Robb, M. A., Buss, V., & Hunt, P. (2004). Probing the photochemical funnel of a retinal chromophore model via zero-point energy sampling semiclassical dynamics. *The Journal of Physical Chemistry A*, 108(21), 4685–4693.
- Weingart, O., Schapiro, I., & Buss, V. (2006). Bond torsion affects the product distribution in the photoreaction of retinal model chromophores. *Journal of Molecular Modeling*, 12(5), 713–721.
- Weingart, O., Schapiro, I., & Buss, V. (2007). Photochemistry of visual pigment chromophore models by ab initio molecular dynamics. *The Journal of Physical Chemistry B*, 111(14), 3782–3788.
- Werner, U., Mitric, R., Suzuki, T., & Bonacic-Koutecký, V. (2008). Nonadiabatic dynamics within the time dependent density functional theory: Ultrafast photodynamics in pyrazine. *Chemical Physics*, 349(1–3), 319–324.
- Worth, G. A., & Cederbaum, L. S. (2004). Beyond Born-Oppenheimer: Molecular dynamics through a conical intersection. *Annual Review of Physical Chemistry*, 55, 127–158.
- Worth, G. A., Hunt, P., & Robb, M. A. (2003). Nonadiabatic dynamics: A comparison of surface hopping direct dynamics with quantum wavepacket calculations. *The Journal of Physical Chemistry A*, 107(5), 621–631.

- Yagi, K., & Takatsuka, K. (2005). Nonadiabatic chemical dynamics in an intense laser field: Electronic wave packet coupled with classical nuclear motions. *Journal of Chemical Physics*, *123*(22), 224103. doi:[Artn224103](https://doi.org/10.1063/1.2130335). doi:[10.1063/1.2130335](https://doi.org/10.1063/1.2130335).
- Zechmann, G., & Barbatti, M. (2008). Photophysics and deactivation pathways of thymine. *The Journal of Physical Chemistry A*, *112*(36), 8273–8279. doi:[10.1021/jp804309x](https://doi.org/10.1021/jp804309x).
- Zewail, A. H. (2000). Femtochemistry: Atomic-scale dynamics of the chemical bond. *The Journal of Physical Chemistry A*, *104*(24), 5660–5694. doi:[10.1021/Jp001460h](https://doi.org/10.1021/Jp001460h).
- Zhu, C. Y., Nangia, S., Jasper, A. W., & Truhlar, D. G. (2004). Coherent switching with decay of mixing: An improved treatment of electronic coherence for non-Born-Oppenheimer trajectories. *Journal of Chemical Physics*, *121*(16), 7658–7670.





# 34 Low-Energy Electron (LEE)-Induced DNA Damage: Theoretical Approaches to Modeling Experiment

Anil Kumar · Michael D. Sevilla

Department of Chemistry, Oakland University, Rochester, MI, USA




<i>Introduction</i> .....	1216
<i>Proposed Mechanism of LEE Induced DNA Strand Breaks</i> .....	1219
<i>Electron–Molecule Interaction Events</i> .....	1220
<i>Resonance (TNI) Formation: A Molecular Orbital Approach</i> .....	1222
<i>Shape Resonances of DNA Bases</i> .....	1225
<i>Electron Attachment to DNA/RNA Bases in Gas-Phase</i> .....	1229
<i>Choice of the Basis Set</i> .....	1230
<i>Effect of Solvation (Condensed Media)</i> .....	1232
<i>Proposed Theoretical Models of DNA Damage</i> .....	1235
Excited States of TNI (Resonance Formation) .....	1240
LEE Induced Base Release .....	1244
Effect of Solvation on Strand Break Formation .....	1246
<i>Conclusions</i> .....	1249
<i>References</i> .....	1249

**Abstract:** Low-energy electrons (LEE) have been experimentally found to result in DNA damage such as base damage, base release, and strand breaks. This has engendered a considerable number of theoretical studies of the mechanisms involved in the DNA damage. In this chapter, we discuss the various pathways for LEE interaction with DNA and the theoretical treatments most suited to unravel these pathways. For example, inelastic electron scattering produces excitation, ionization, and transient negative ions (TNI) via shape, core-excited, and vibrational Feshbach resonances, which can all lead to DNA damage. Each of these pathways is distinguished and pertinent to the experimental results and theoretical approaches used to explain the results described. Shape resonances can be understood as interactions with the electron with unoccupied molecular orbitals of neutral molecule, while core-excited states involve excitation of inner shell electrons and can be treated with theoretical methods such as time-dependent density functional theory (TD-DFT) or CASSCF. In treating the electron–molecule interaction, special care is needed to distinguish between diffuse and valence states of the TNI. The role of the vertical and adiabatic states of the radical anion is important as the electron adds to the neutral molecular framework, and reactions induced likely occur before equilibration to the adiabatic state. The effect of solvation is critical to both energetics of the interaction and the nature of the TNI formed. For example, gas-phase calculations show diffuse dipole-bound character for adenine, guanine, and cytosine anion radicals, but each of these is found to be in a valence state in aqueous solution by experiment. DNA base anion radicals often show ground states that are diffuse in character and that collapse to valence states on solvation. Such processes are shown to be accounted for inclusion of the polarized continuum model (PCM) for solvation. TD-DFT excited-state calculations including solvation show that the diffuse states rise in energy on solvation as expected. For LEE in the aqueous phase, new energy states become available such as conduction band or presolvated electrons, which may have sufficient energy to cause DNA damage.

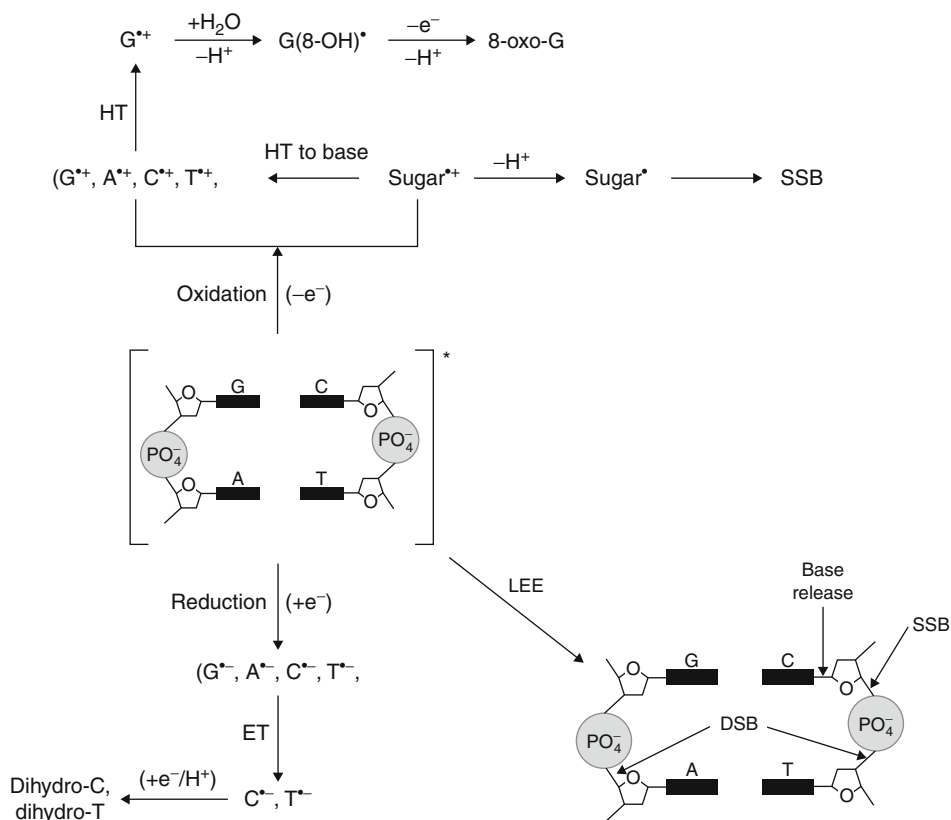
## Introduction

---

The DNA sequence contains the information necessary for the functioning of all cellular processes. Exposure of DNA to high-energy radiation leads to disruption of this sequence or actual strand cleavage that results in potential mutagenic or lethal damage (Becker and Sevilla 1993, 2008; Swarts et al. 1992; Becker et al. 2007, 2010; Li and Sevilla 2007; Swiderek 2006; Kumar and Sevilla 2008a, 2010a, b; Sevilla and Bernhard 2008; Sanche 2008; Yokoya et al. 2008; Denifl et al. 2007; von Sonntag 1991). In the early stage of the radiation-induced DNA damage, high-energy radiation ionizes and excites each component of DNA (i.e., base, sugar, and phosphate backbone) and the surrounding water molecules randomly and produces “holes,” secondary electrons, and excited states (Kumar and Sevilla 2008a, 2010a, b; Sevilla and Bernhard 2008; Sevilla et al. 1991). The hole (positive charge or radical cation), produced during ionization event in DNA, transfers to the site in DNA with the lowest ionization energy. Of the four DNA bases (adenine [A], guanine [G], cytosine [C], and thymine [T]), guanine is found to have the lowest ionization potential (Kumar and Sevilla 2008a; Hush and Cheung 1975; Orlov et al. 1976; Yang et al. 2004; Steenken and Jovanovic 1997) and acts as the locus for hole transfer in DNA (Becker and Sevilla 1993, 2008; Swarts et al. 1992; Becker et al. 2010; Li and Sevilla 2007; Kumar and Sevilla 2008a, 2010a, b; Sevilla and Bernhard 2008; Sevilla et al. 1991). The guanine radical cation ( $G^+$ ), formed on ionization, reacts further to produce oxidative DNA damage in

the form of 8-oxoG (Burrows and Muller 1998; Cadet et al. 2008). A hole created on the sugar phosphate backbone undergoes two competitive reactions: (a) formation of neutral sugar radical after deprotonation ( $-H^+$ ) from the specific sites of the sugar ring (Becker et al. 2003; Shukla et al. 2004, 2005; Adhikary et al. 2005, 2006a, b, 2007, 2008; Khanduri et al. 2008) and (b) hole transfer to the nearby base in DNA followed by *base-to-base* transfer to guanine (Adhikary et al. 2006b). Secondary electrons formed by the ionizing event lose their kinetic energy, thermalize, add to DNA, and transfer to the bases of highest electron affinities, i.e., the pyrimidines, T and C. This produces the anion radicals ( $T^{\cdot-}$  and  $C^{\cdot-}$ ) (Sevilla et al. 1991). Secondary electrons before thermalization possess substantial kinetic energy, which can lead to DNA damage. Such electrons with kinetic energies below 20 eV are known as *low-energy electrons* (LEE) (Sanche 2008; Pimblott et al. 1996; Pimblott and LaVerne 2007) and are produced in great numbers ( $\sim 4 \times 10^4$  electrons per MeV energy deposited) (International Commission on Radiation Units and Measurements 1979) along the tracks of the ionizing radiation. LEEs have been recognized as the potential significant contributor to DNA damage. Collisions of LEEs with the aqueous medium result in most being thermalized within  $10^{-12}$  s to become solvated electrons. Those LEEs produced in or near DNA are able to damage DNA via resonant absorption processes (Kumar and Sevilla 2010a). In their pioneering work, Sanche and coworkers (Boudaïffa et al. 2000; Huels et al. 2003; Sanche 2005; Zheng et al. 2005, 2006, 2008; Ptasińska and Sanche 2007a, b) established that LEEs are able to create single- and double-strand breaks (SSB and DSB) in plasmid DNA through a dissociative electron attachment (DEA) mechanism. This finding initiated several studies by a number of workers on the interaction of LEEs with DNA and its components (Baccarelli et al. 2007; Sulzer et al. 2006; Bald et al. 2006, 2008; König et al. 2006; Ptasińska et al. 2005a, 2006). A number of other recent reviews have focused on this important area of research (Li and Sevilla 2007; Swiderek 2006; Kumar and Sevilla 2008a, 2010a, b; Sanche 2008, 2009, 2010; Rak et al. 2008). The initial events induced in DNA by high-energy radiation discussed above are summarized in  Fig. 34-1. The events shown in  Fig. 34-1 follow the oxidative and reductive processes that are initiated by radiation to the dominant end products formed. When a number of the damage sites, shown in  Fig. 34-1, are formed in proximity, a multiple damage site (MDS) is formed. MDSs are often irreparable owing to the loss of DNA information and the inability of enzymatic repair processes to recognize individual damages. They therefore represent the most lethal type of damage.

Ionization, and to a lesser extent, excitation were in the past considered the primary causes of DNA radiation damage. However, results have strongly implicated the role of low-energy electrons in this damage, and their study has been of intense interest in recent times. In this chapter, we will be focusing on the interaction of LEE with DNA, which leads to a variety of physical and chemical changes in DNA. A number of efforts to elucidate the mechanisms of LEE-induced DNA damage have been made in recent years employing theory (Li and Sevilla 2007; Kumar and Sevilla 2008a, 2010a; Rak et al. 2008; Simons 2006) and experiments (Sanche 2005, 2008, 2009; Denifl et al. 2007; Boudaïffa et al. 2000; Huels et al. 2003; Zheng et al. 2005, 2006, 2008; Ptasińska and Sanche 2007a, b; Baccarelli et al. 2007; Sulzer et al. 2006; Bald et al. 2006, 2008; König et al. 2006; Ptasińska et al. 2005a, 2006; Rak et al. 2008). Recent efforts have implicated the role of vibrational and electronic excited states in LEE interactions with DNA. The advent of substantial computing power at low cost and the accessibility of computational resources at national centers (Baker et al. 2009) allow the use of rigorous ab initio quantum chemical methods such as density functional theory (DFT), Møller–Plesset perturbation theory (MP2), CCSD(T), and CASPT2 for DNA components. Such theoretical studies shed light on the underlying mechanisms of LEE-induced DNA damage. The applicability of MP2,



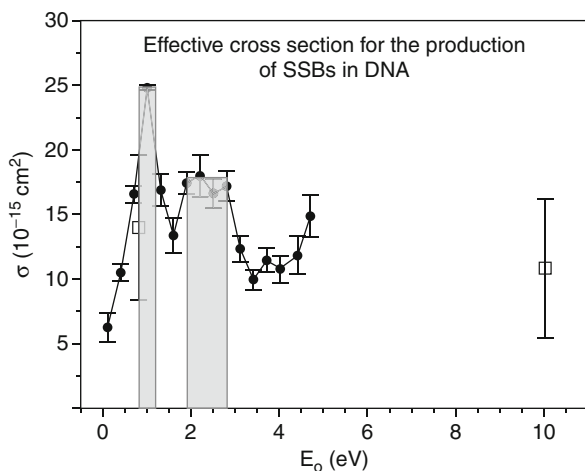
■ Fig. 34-1

Schematic diagram showing the overall processes (oxidation, reduction, and LEE-induced DNA damage) that occur during high-energy radiation interaction with DNA. *HT* hole transfer, *ET* electron transfer

CCSD(T), and CASPT2 methods are still limited to small-to-modest size molecules such as DNA base pairs. However, DFT can be applied to larger molecular systems having as many as a 1,000 atoms (Neese et al. 2009) and has been found suitable to handle electron-molecule interaction processes (Schwabe and Grimme 2008; Zhao and Truhlar 2008; Shao et al. 2006). In this chapter, we include a brief summary of the experimental findings and provide a detailed description of the recent applications of theory toward the understanding of the mechanisms of action of LEE-induced DNA damage. The chapter includes discussions of (1) shape and core-excited resonances, (2) valence and dipole-bound states of DNA bases and their associated electron affinities, (3) the best choice of the basis sets to tackle the valence and dipole-bound radical anions, (4) effects of condensed phase on dipole-bound states, (5) single-strand breaks formation in the ground state of the radical anion, (6) importance of the excited states of radical anions (resonances) for LEE-induced DNA single-strand breaks formation, (7) LEE-induced base release, and (8) the effect of solvation on the formation of LEE-induced strand breaks.

## Proposed Mechanism of LEE Induced DNA Strand Breaks

As briefly described in the introduction, low-energy electrons (LEE) are produced abundantly during high-radiation events and are increasingly being recognized as potent DNA-damaging agents. In fact, LEEs are found to be several times more damaging than photons that have similar energy. The pioneering series of experiments by Sanche and coworkers (Boudaïffa et al. 2000; Huels et al. 2003; Martin et al. 2004; Panajotovic et al. 2006; Brun et al. 2009; Li et al. 2008; Zheng et al. 2004; Abdoul-Carime et al. 2001), showed that LEEs in the 0–10 eV range produce single- and double-strand breaks in DNA. In their first report (Boudaïffa et al. 2000), the plasmid DNA (pGEM 3Zf(-)) was extracted from *E. coli* and hydrated to 2.5 water/base pair, and then irradiated with LEE beam with kinetic energies 3–20 eV. From these experiments, it was concluded that electrons having energy below the ionization limit of DNA (ca. 7.5–10 eV [Hush and Cheung 1975; Orlov et al. 1976; Yang et al. 2004; Colson et al. 1992]) were able to cause SSB and DSB. The corresponding yields of SSB and DSB were found to be  $8.2 \times 10^{-4}$  and  $2 \times 10^{-4}$  strand breaks per incident electron for 10 eV electrons. The yields of SSB and DSB in DNA depended on the energy of the interacting electron and have been suggested to be caused by the rapid fragmentation reactions of transient molecular resonances localized on DNA components, i.e., base, sugar, and phosphate back bone (Boudaïffa et al. 2000). In later experiments, Sanche and coworkers (Martin et al. 2004; Panajotovic et al. 2006) found that 0–4.7 eV electrons can effectively produce SSB in plasmid DNA with similar yields to those produced at far higher energies. (See **Fig. 34-2**, where it is evident that the cross section for SSB formation at 1 eV is actually greater than that found at 10 eV [Panajotovic et al. 2006].) They also found that 0.1–4.5 eV electrons induce only SSB (Martin et al. 2004) (see Fig. 1 in Martin et al. [2004]). Apparent resonances for inducing SSB are found at 0.8 and 2.2 eV, characterizing the formation of transient negative ion (TNI) at these energies (Martin et al. 2004). Due to low energies, these resonances were interpreted as shape resonances (Martin et al. 2004). The SSB yield at 0.8 and 2.2 eV, found



**Fig. 34-2**

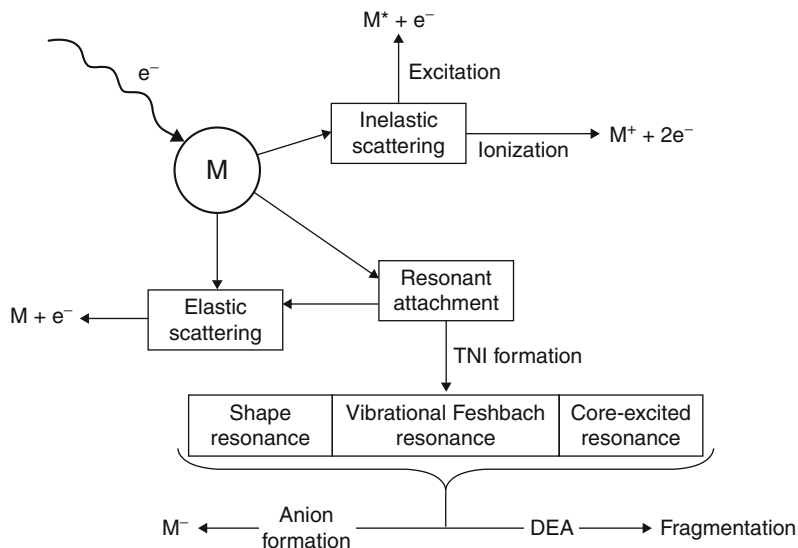
Effective cross sections ( $\sigma$ ) for the formation of SSB in plasmid DNA by 0.1–4.7 eV electrons. The peaks at 1 eV and around 2.5 eV (see shaded portion) correspond to shape resonances (Reprinted with permission from Panajotovic et al. [2006]. © (2006) Radiation Research Society)

in Sanche's work, were compared with electron capture cross sections of the DNA bases which were assigned to  $\pi^*$ -shape resonances. The vertical attachment energies of DNA bases were taken from electron transmission spectroscopy (ETS) (Aflatooni et al. 1998), and their peak magnitudes were scaled to reflect the inverse energy dependence of the electron capture cross sections. The lowest peak present at 0.39 eV in the modeled cross section was shifted by 0.41 eV to match the SSB yield at 0.8 eV (Martin et al. 2004). A good agreement between the experimental and simulated SSB yield between 0 and 4 eV certainly suggests the involvement of shape resonances in creating LEE-induced single-strand breaks. Indeed from their studies of strand breaks in plasmid DNA induced by 3–100 eV electrons (Huels et al. 2003; Martin et al. 2004; Panajotovic et al. 2006), it was concluded that below 5 eV LEE-induced SSB occurs through dissociative electron attachment (DEA) via shape resonances (Boudaïffa et al. 2000; Huels et al. 2003; Martin et al. 2004; Panajotovic et al. 2006; Brun et al. 2009), while between 5 and 15 eV, the core-excited resonances induce SSB and DSB similar to those produced at far higher energies such as 100 eV. More recently, Illenberger and coworkers (Baccarelli et al. 2007; Sulzer et al. 2006; Bald et al. 2006, 2008; König et al. 2006; Ptasińska et al. 2005a, b, 2006; Abdoul-Carime et al. 2004a, b; Hanel et al. 2003) have contributed to the understanding of these processes by showing that electron attachment directly to the phosphate moiety can lead to fragmentation (Bald et al. 2006). The involvement of shape resonances to create molecular fragmentation in DNA model compounds was also proposed in their work (Baccarelli et al. 2007; Sulzer et al. 2006; Bald et al. 2006, 2008; König et al. 2006; Ptasińska et al. 2005a, c, 2006). Recently, several groups used scattering theory to help elucidate the nature of LEE interactions resulting in DNA damage (Caron and Sanche 2003, 2004, 2005, 2006; Caron et al. 2008; Tonzani and Greene 2006b; Dora et al. 2009; Gianturco et al. 2008; Winstead and McKoy 2006) through resonances. The modeling of shape resonances, created during electron–molecule interaction, using theory is discussed in ► section “Resonance (TNI) Formation: A Molecular Orbital Approach”.

## Electron–Molecule Interaction Events

---

Electron–molecule interactions give rise to energetic species that result in physical and, subsequently, chemical changes in the parent molecule. The initial energy of the interacting electron is critical to the formation of such species. Understanding the physical and chemical changes induced requires an understanding of the underlying fundamental processes that govern the electron–molecule interaction. One of the most important of these interactions is dissociative electron attachment (DEA), which may result in DNA strand breaks discussed in ► section “Proposed Mechanism of LEE Induced DNA Strand Breaks”. A scheme that depicts the various paths available during electron–molecule interaction is shown in ► Fig. 34-3. The collision of an electron with molecule involves two types of interactions: (a) direct scattering and (b) resonant interactions. In nonresonance electron–molecule scattering (direct scattering), the electron interacts with the molecule for a very short time (typically less than ca.  $10^{-15}$  s), i.e., approximately the transit time for an electron through the dimensions of a molecular framework. A state with angular momentum such as a p state can extend the time of the resonance. Depending on the energy transferred from electron to the molecule during collision, the direct scattering is known as: (a) elastic, if no kinetic energy is transferred to the internal degrees of freedom (electronic, rotational, and vibrational) of the parent molecule, and (b) inelastic, if some part of the electron energy is transferred to the molecule and excites these internal



■ Fig. 34-3  
Schematic diagram showing the scattering and resonant attachment events taking place during electron–molecule interactions

degrees of freedom. In an elastic collision, only kinetic energy can be transferred through the conservation of momentum. However, no significant kinetic energy is transferred in an elastic collision owing to the small mass of the electron, which is negligible compared to the mass of the molecule. Inelastic scattering can result in ionization as well as vibrational and/or electronic excitation, as shown in [Fig. 34-3](#).

In resonant interactions, the electron–molecule interaction lasts for a longer time ( $\sim 10^{-12}$ – $10^{-15}$  s) and results in the formation of transient negative ions (TNI) of several types discussed in [section “Resonance \(TNI\) Formation: A Molecular Orbital Approach”](#). Once these resonances are formed, they may decay via: (a) autodetachment, in which the electron is emitted from the negative ion  $(M^-)^*$  resulting  $M^*$  and  $e^-$ ; (b) dissociative electron attachment (DEA), in which the negative ion  $(M^-)^*$  stabilizes by dissociating one of its chemical bonds to form anion and neutral fragments; and (c) radiative cooling, which means the negative ion  $(M^-)^*$  is stabilized by emission of one or more photons. This last process does not usually occur in the gas phase as the lifetimes are short owing to processes (a) and (b).

For the DEA process (b), the time needed to stretch a specific bond in its neutral potential energy surface (PES) so that it crosses the repulsive anion surface is usually less than the vibrational period of that bond. On the basis of the timescale, DEA and autodetachment are clearly in competition with each other. Such electron resonances are well described in the literature (Schulz 1973a, b; Lane 1980; Sanche 1995; Jordan and Burrow 1987; Simons and Jordan 1987; Simons 2008; Modelli and Martin 2002; Wetzal and Brauman 1987; Chen and Gallup 1990; McConkey et al. 2008; Hotop et al. 2003). Since the TNI formation can occur in the continuum, special care is needed to handle these problems in any theoretical treatment. Quantum chemical methods employing compact basis sets (Chen and Gallup 1990) have been used to study the nature and properties of TNIs/resonances by several groups such as Burrow (Jordan

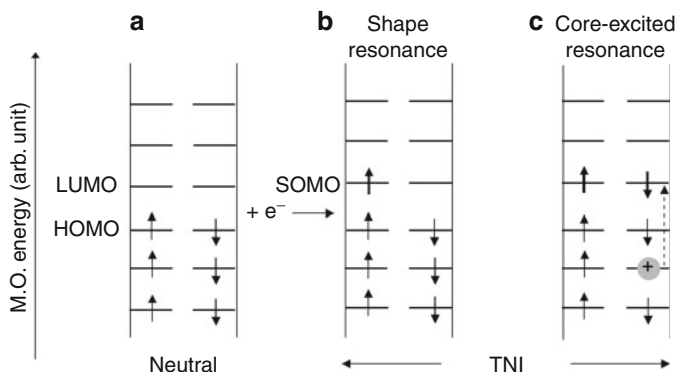


and Burrow 1987), Jordon (Jordan and Burrow 1987; Simons and Jordan 1987), Simons (Simons and Jordan 1987; Simons 2008), and Modelli (Modelli and Martin 2002). This method has been widely used and can give reasonable estimates of the energetics involved. However, the scattering phenomenon can only be approximated by such approaches. The present chapter elucidates the mechanism of DNA damage caused by resonant interaction events only.

## Resonance (TNI) Formation: A Molecular Orbital Approach

From the above discussion we see that electron–molecule interactions can lead to transient negative ion (TNI) formation and subsequently to a variety of chemical changes. On TNI formation, an extra electron is captured into the unoccupied molecular orbital (UMO) of the neutral molecule, and a shape or core-excited resonance results (see [Fig. 34-4](#)).

*Shape resonances:* In a shape resonance, an extra electron occupies a normally unoccupied (vacant) MO without perturbing the inner electronic configuration of the parent molecule. This results in the formation of a transient negative ion (TNI) (Schulz 1973a, b; Lane 1980; Sanche 1995) (see [Fig. 34-4b](#)). In a time-dependent picture, such TNIs (Schulz 1973a, b) are formed by an electron transition from the continuum ( $e + M$ ) to a quasi-discrete state of the transient molecular anion ( $M^-$ )\*. Because electron attachment is rapid with respect to nuclear motion, the negative ion ( $M^-$ )\* is formed at the geometry of the neutral molecule. Shape resonances are also known as “single-” or “one-particle, no-hole” resonances. Generally, they occur at low energies (0–4 eV) and have lifetimes in the range  $10^{-15}$  to  $10^{-10}$  s. Longer lifetimes may occur if attachment is followed by vibrational motion into portions of the nuclear potential surface



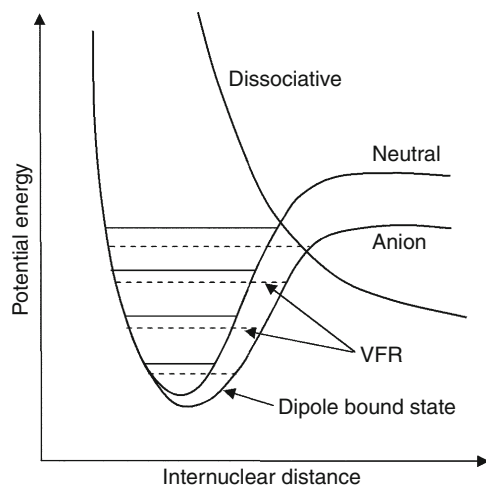
■ Fig. 34-4

Schematic diagram showing the electronic configuration of a neutral (a) and transient negative ion (TNI) (b, c). The interacting electron initially captures into the unoccupied MOs of the neutral molecule resulting in TNI formation via: (a) shape resonance or (c) core-excited resonance. For a shape resonance, the electron can interact with any unoccupied MO. The SOMO was the empty LUMO before the LEE interaction. In core-excited resonance, on electron interaction an electronic transition takes place from an inner shell to the vacant MOs creating a “hole” (+ charge) in the inner shell, shown by an arrow (c). The up and down arrows show the occupancy of the molecular orbitals (MOs) with electrons of  $\alpha$  and  $\beta$  spins. HOMO highest occupied molecular orbital, LUMO lowest unoccupied molecular orbital, SOMO singly occupied molecular orbital

lying below that of the neutral, where the electron cannot autodetach. Shape resonances may result in a dissociative electron attachment (DEA) process forming an anion fragment and a neutral fragment.

**Core-excited resonances:** A core-excited resonance is formed when an interacting electron excites one of the core electrons of the parent molecule, resulting in a hole in the inner filled MOs and two electrons, an extra electron and one from the core, in unoccupied MOs (see [Fig. 34-4c](#)). Such resonances are also known as “two-particle, one-hole” resonances. Core-excited resonances occur typically above 4 eV; those lying below the “parent” molecular excited state are known as “Feshbach resonances” and may have lifetimes comparable to vibrational periods. If they lie above the parent, they are called “core-excited shape resonances” (Schulz 1973a) and generally have much shorter lifetimes because of decay into the parent state. Thus, core-excited shape resonances exhibit a negative electron affinity, relative to the excited parent, whereas Feshbach resonances have a small positive electron affinity (Schulz 1973a). Core-excited resonances are highly energetic and have been suggested to play a role in double-strand breaks in DNA (Huels et al. 2003; Martin et al. 2004; Panajotovic et al. 2006; Brun et al. 2009).

**Vibrational Feshbach resonances (VFRs):** In a vibrational Feshbach resonance, the interaction of a slow electron takes the form of a virtual excitation of a vibrational level of the neutral molecule with capture of the electron (Hotop et al. 2003; Dessent et al. 2000). For the zero point vibration, the maximum probability of interaction of the electron with parent molecule occurs at zero energy. If the dipole moment of the neutral molecule exceeds the critical value of approximately 2 Debye, the impinging electron may be trapped into the diffuse bound state, which provides a much longer timescale for the electron to stay near the molecule (Hotop et al. 2003; Dessent et al. 2000; Illenberger 1992), and VFRs may appear as shown in [Fig. 34-5](#).

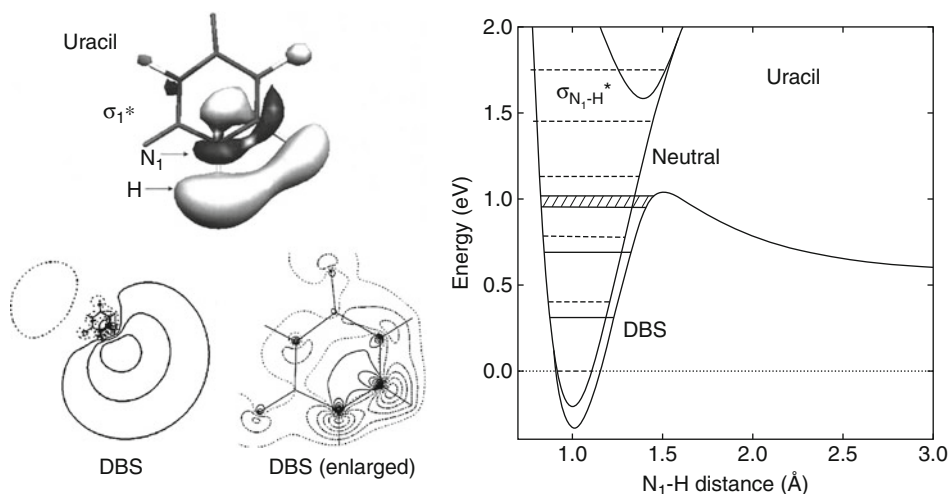


■ Fig. 34-5

Diabatic potential energy surfaces of neutral and dipole-bound anion showing the origin of the vibrational Feshbach resonances (VFRs). An extra electron attaching into the diffuse dipole-bound MO of the parent can excite the nearby vibrational levels of the parent molecule resulting in VFRs

Here, the PES of the anion lies close to, but below, the neutral surface, and the lowest vibrational levels of the dipole-bound anion are located just below the corresponding vibrational levels of the neutral. These long-lived VFRs appear as narrow features below the vibrational thresholds in elastic or vibrationally inelastic electron scattering cross sections (Hotop et al. 2003). VFRs may also decay through the dissociative electron attachment mechanism. For an excellent, detailed overview, see reviews by Schulz (1973a, b) and Hotop et al. (2003).

Recently, an excellent example of the synergy of vibrational Feshbach resonances with dipole-bound anion states of uracil and thymine in DEA of  $N_1$ -H bond has been reported by Burrow et al. (Burrow et al. 2006; Scheer et al. 2004). Sharp peaks ( $<3$  eV) in the dissociative electron attachment cross sections of uracil and thymine were assigned as vibrational Feshbach resonances (Burrow et al. 2006; Scheer et al. 2004). Methylation at  $N_1$  or  $N_3$  site of these bases selectively eliminates the hydrogen atom (H) loss at the site of methyl substitution and thus allows for site assignments of DEA yield with energy of the LEE. At 1 eV, the H loss occurred from the  $N_1$  site, while at 1.8 eV, the H loss occurred from the  $N_3$  site (Ptasińska et al. 2005a), indicating the involvement of two distinct DEA pathways (Ptasińska et al. 2005a; Burrow et al. 2006) for dissociation. Using quantum chemical calculations and very diffuse basis sets 6-311G(d) augmented with four Gaussian sets of (s,  $p_x$ ,  $p_y$ ,  $p_z$ ) orbitals with scale factors of 0.04, 0.004, 0.0004, and 0.00004, Burrow et al. (2006) showed that an excess electron is bound in the electric dipole potential field of the uracil molecule resulting a dipole-bound state (DBS), which lies below the neutral state of the uracil (see  $\blacktriangleright$  Fig. 34-6). From  $\blacktriangleright$  Fig. 34-6 (left), we see that the DBS and the  $\sigma^*$  ( $N_1$ -H) anion state can mix by symmetry, and this coupling allows LEEs to excite the  $N_1$ -H bond vibrations.



$\blacksquare$  Fig. 34-6

(Left) The valence  $\sigma_1^*$  orbitals and expanded view of the dipole-bound anion state (DBS) of uracil on the molecular frame. (Right) Potential energies of the neutral, dipole-bound state and valence  $\sigma^*$  anion state as a function of  $N_1$ -H separation (Reprinted with permission from Burrow et al. [2006]. © (2006) American Institute of Physics)

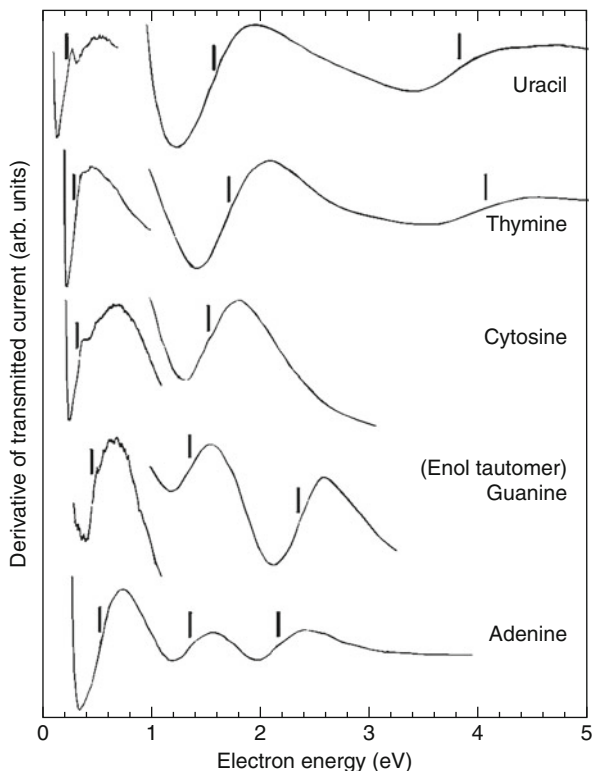
This results in H loss in uracil ( $(\text{U-H})^- + \text{H}^*$ ), (see Fig. 4 of Burrow et al. [2006]). LEE resonances at 0.69 and 1.01 eV were identified with the second and third vibrational levels for the  $\text{N}_1\text{-H}$  bond stretch (see [Fig. 34-6](#)).

## Shape Resonances of DNA Bases

As pointed out above, when LEEs are captured in the virtual (unfilled) orbitals of the parent (neutral) molecule, a transient negative ion formation results known as a “shape resonance.” These resonances are generally unstable with respect to the autodetachment and therefore possess negative electron affinity, i.e., the anion state lies above the neutral state of the molecule. In the gas phase, they are commonly studied by electron transmission spectroscopy (ETS). In ETS, a signal consisting of the derivative with respect to energy of the electron beam current transmitted through a gas cell is plotted as a function of electron kinetic energy. The energies of the resonances are termed as electron vertical attachment energies (VAEs) and are always found positive by ETS experiment (Aflatooni et al. 1998; Schulz 1973a, b; Jordan and Burrow 1987; Simons and Jordan 1987; Allan 1989). In this chapter, we will refer to such states as having negative vertical electron affinities. To our knowledge, there are no experimental available LEE scattering data for a complete DNA fragment (composing base, sugar, and phosphate). However, there are ETS results for the DNA/RNA bases, i.e., adenine, cytosine, thymine, uracil, and guanine reported by Aflatooni et al. (1998).

From ETS experiments (Aflatooni et al. 1998), Aflatooni et al. showed that energies required to attach an electron into the lowest empty valence molecular orbitals of all the bases are positive. This means that all the bases have negative valence vertical electron affinity ( $<0$ ). The vertically formed anions of pyrimidines bases (C, T, and U) were found to be more stable than the purines (G and A) by ca. 0.2 eV. The ETS spectra of U, T, C, G, and A are shown in [Fig. 34-7](#). The spectra in [Fig. 34-7](#) arise due to the occupation of the lowest empty  $\pi^*$ -MOs of the parent molecules by the electron. The vertical lines on the spectra ([Fig. 34-7](#)) show the position of the vertical attachment energies. For guanine anion, the ETS (shown in [Fig. 34-7](#)) was observed for its enol tautomer (for details see Aflatooni et al. [1998]). For each of these molecules, three VAEs, associated with the three lowest vacant  $\pi_1^*$ ,  $\pi_2^*$ , and  $\pi_3^*$  MOs, were determined. The VAEs 0.22, 1.58, and 3.83 eV for uracil; 0.29, 1.71, and 4.05 eV for thymine; 0.32, 1.53, and 4.50 eV for cytosine; 0.54, 1.36, and 2.17 eV for adenine; and 0.46, 1.37, and 2.36 eV for guanine(enol) tautomer were determined by ETS.

The VAEs of bases were also predicted using theoretical methods such as semiempirical Pariser–Parr–Pople (PPP) (Compton et al. 1980; Younkin et al. 1976) and ab initio methods (Sevilla et al. 1995). Since these anion states are metastable with respect to the autodetachment of the electron, special care was taken in the aforementioned theoretical approaches to handle these anion states by employing confined basis set, Koopmans’ theorem approximation, and empirical determination of parameters to scale the theoretical results to the experimentally measured anion state energies for other compounds. Sevilla et al. (1995) used calculated values for VAEs of benzene, naphthalene, pyridine, pyrimidines, and uracil, which have experimentally known values to scale theoretically calculated VAEs for the DNA bases. A comparison of the experimental VAEs of the bases to those predicted theoretically is presented in [Table 34-1](#). From [Table 34-1](#), we see that the calculated VAE values are in excellent agreement with experimental VAEs and the difference between theory and experiment lies in the range



■ Fig. 34-7

ETS spectra of uracil, thymine, cytosine, guanine, and adenine. The experimentally determined  $\pi^*$  anion state energies are indicated by vertical lines (Reprinted with permission from Aflatooni et al. [1998]. © (1998) American Chemical Society)

0.03–0.2 eV. The PPP method only shows a qualitative agreement with the experiment. Recently, the resonance energies of DNA/RNA bases, including deoxynucleosides and deoxynucleotides, were studied using scattering theory (Winstead and McKoy 2008; Gianturco and Lucchese 2004; Tonzani and Greene 2006a; Yalunin and Leble 2007). The calculated values (Gianturco and Lucchese 2004; Tonzani and Greene 2006a; Yalunin and Leble 2007) were found to be several electronvolts more than the experimental ETS values (Aflatooni et al. 1998); however, the first  $\pi_1^*$  resonance energies reported by Winstead and McKoy (2008) were in reasonable agreement with experiment (Aflatooni et al. 1998) for uracil, thymine, and cytosine.

Recently, we studied the vertical attachment energies of 5'-thymidine monophosphate (5'-dTMP) using the density function theory (DFT) B3LYP/6-31G\* method (Kumar and Sevilla 2007). A nucleotide such as 5'-dTMP represents the smallest fragment of DNA containing all three components: base, sugar, and phosphate. This study was carried out with a view to draw some fruitful insights about the nature and location of the “shape resonances” during transient negative ion (TNI) formation. In this study, the five lowest unoccupied molecular orbitals (LUMOs) along with the highest occupied molecular orbital (HOMO) of the neutral 5'-dTMPH were considered. The B3LYP/6-31G\* method predicted HOMO and the lowest two UMOs as  $\pi$ -type localizing on the thymine base, while the third, fourth, and fifth UMOs as

Table 34-1

Experimental (ETS) and theoretical vertical attachment energies (VAEs) in uracil and the DNA bases<sup>a,b</sup>

Compound	Vertical attachment energies (eV)				
	Assignment	Theory			
		Exp. (ETS)	PPP	Sevilla et al. (1995)	6-31G*/3-21G
Uracil	$\pi_1^*$	0.22	0.48	0.19	0.216
	$\pi_2^*$	1.58	1.50	–	1.609
	$\pi_3^*$	3.83	3.35	–	5.009
Thymine	$\pi_1^*$	0.29	–	0.32	0.364
	$\pi_2^*$	1.71	–	–	1.771
	$\pi_3^*$	4.05	–	–	4.057
Cytosine	$\pi_1^*$	0.32	–	0.4	0.524
	$\pi_2^*$	1.53	–	–	1.918
	$\pi_3^*$	4.50	–	–	5.235
Adenine	$\pi_1^*$	0.54	0.82	0.74	0.794
	$\pi_2^*$	1.36	1.43	–	1.379
	$\pi_3^*$	2.17	2.39	–	2.405
Guanine (keto)	$\pi_1^*$	–	0.94	1.23	1.191
	$\pi_2^*$	–	1.64	–	1.441
	$\pi_3^*$	–	2.55	–	2.575
Guanine (enol)	$\pi_1^*$	0.46	–	–	0.908
	$\pi_2^*$	1.37	–	–	1.662
	$\pi_3^*$	2.36	–	–	2.597

<sup>a</sup>See Aflatooni et al. (1998).

<sup>b</sup>Values correspond to negative electron affinities.

$\sigma$ -type localized on the phosphate ( $\text{PO}_4$ ) group, the sugar moiety, and on the sugar-phosphate group, respectively (see Fig. 34-8). The B3LYP/6-31G\* calculated orbital energies in eV of HOMO and the five LUMOs are  $-6.24(\pi)$ ,  $-0.84(\pi_1^*)$ ,  $0.43(\pi_2^*)$ ,  $0.73(\sigma_1^*)$ ,  $1.27(\sigma_2^*)$ , and  $1.78(\sigma_3^*)$ , respectively (see Fig. 34-8). From ETS and the theoretical calculations discussed above, it is evident that within Koopmans' theorem approximation, the vertical attachment energies (VAEs) are equivalent to the virtual orbital energies (VOEs). But these VOEs calculated at the Hartree-Fock or DFT(B3LYP) levels are appreciably overestimated by several electronvolts and thus need scaling to appropriately represent the measured VAEs (Aflatooni et al. 1998; Sevilla et al. 1995). Using this procedure, Modelli (2003) proposed an equation for appropriate scaling of B3LYP results for  $\pi^*$  resonances. Using Modelli's equation (Modelli 2003), the scaled VOEs of corresponding B3LYP/6-31G\* computed LUMOs of 5'-dTMPH are found to be  $0.53(\pi_1^*)$ ,  $1.56(\pi_2^*)$ ,  $1.80(\sigma_1^*)$ ,  $2.23(\sigma_2^*)$ , and  $2.64(\sigma_3^*)$  eV, respectively (Kumar and Sevilla 2007). The calculated lowest two VAEs  $0.53(\pi_1^*)$  and  $1.56(\pi_2^*)$  are in reasonable agreement with those reported by Aflatooni et al. (1998) using ETS of thymine, as shown in Table 34-1. This theoretical calculation predicts that for energies of less than 2 eV there are UMOs on base, sugar, and phosphate available to capture the LEE. The theoretical procedure of scaling of orbital energies of neutral LUMOs gives good estimates of the resonance energies; however, it has several drawbacks, e.g., (a) during TNI formation, the UMOs of the neutral molecule can be perturbed and can reorder the UMOs energies so they are not as in the neutral molecule and

MOs		Orbital Energy (eV)	Scaled VOE (eV)
LUMO + 4 ( $\sigma_3^*$ )		1.78	2.64
LUMO + 3 ( $\sigma_2^*$ )		1.27	2.23
LUMO + 2 ( $\sigma_1^*$ )		0.73	1.80
LUMO + 1 ( $\pi_2^*$ )		0.43	1.56 (1.71)
LUMO ( $\pi_1^*$ )		-0.84	0.53 (0.29)
HOMO ( $\pi$ )		-6.24	

■ Fig. 34-8

Molecular orbital plots of neural 5'-dTMPH, calculated using the B3LYP/6-31G\* method. B3LYP/6-31G\* calculated orbital energies along with scaled values are given in electronvolts. The experimental VOs of thymine (Aflatooni et al. 1998) are given in electronvolts (in parentheses) (Reprinted with permission from Kumar and Sevilla [2007]. © (2007) American Chemical Society)

(b) this procedure gives no information about core-excited resonances. In this context, the excited-state calculations for the TNI provide the only convenient means to rectify these drawbacks. This will be discussed in ► section “Excited States of TNI (Resonance Formation)”.

A summary of the semantics of electron molecular resonances occurring in the gas phase have been described by Schulz (1973a) (see ► Table 34-2) with relevance to the condense phase.

■ **Table 34-2**  
**Semantics of electron-molecular resonances<sup>a</sup>**

Resonance <sup>a</sup>		"Parent" <sup>a</sup>	Energy <i>vis-a-vis</i> parent <sup>a</sup>	Characteristics	
				Gas phase <sup>a</sup>	Condensed phase
Shape (1 particle, 0 hole)		Ground electronic state (GS)	Above parent (0–4 eV)	Yes	Yes
Core-excited (2 particles, 1 hole)	Feshbach	Mostly Rydberg ES	Below parent (ca. 0.5 eV)	Yes	No
	Shape	Valence ES	Above parent (0–2 eV)	Yes	Yes
Vibrational Feshbach <sup>b</sup> (VFR)		Vibrational level of GS	Below	Yes	No

<sup>a</sup>Terminology adapted from Schulz (1973a). *GS* ground electronic state, *ES* excited electronic state.

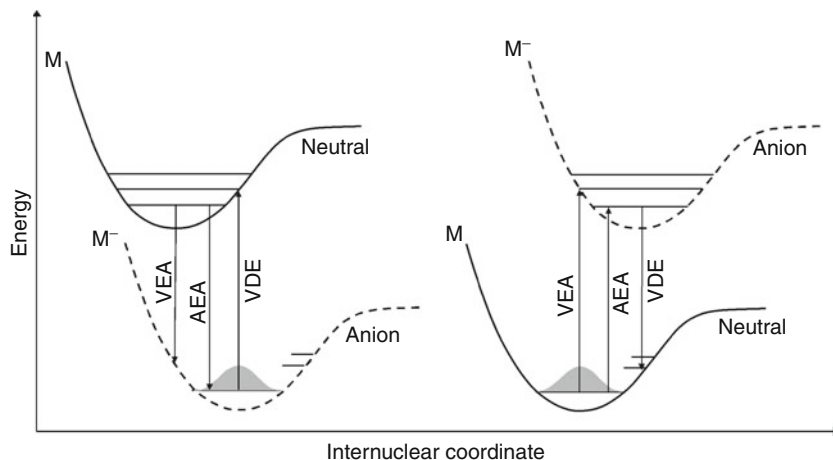
<sup>b</sup>Hotop et al. (2003).

## Electron Attachment to DNA/RNA Bases in Gas-Phase

The energy change on electron attachment to a molecule is described as the electron affinity of that molecule. Upon electron attachment to the neutral molecule (*M*), the geometry of the neutral molecule undergoes nuclear relaxation with adiabatic anion (*M*<sup>−</sup>) formation. Electron attachment to the neutral molecule without a nuclear relaxation gives vertical electron affinity (VEA), and on nuclear relaxation the overall energy change gives the adiabatic electron affinity (AEA). The energy needed to detach an electron from the adiabatic anion without relaxation of the resulting neutral molecule is termed as vertical detachment energy (VDE). Depending on the stability of the anion formation with respect to the neutral molecule, a molecule has positive or negative electron affinity (VEA and AEA) values (see ● Fig. 34-9). The various processes taking place during electron attachment to a molecule (*M*) are shown in ● Fig. 34-9.

From theory (Compton et al. 1980; Younkin et al. 1976; Sevilla et al. 1995; Winstead and McKoy 2008; Gianturco and Lucchese 2004; Tonzani and Greene 2006a; Yalunin and Leble 2007; Kumar and Sevilla 2007) and experiment (Aflatooni et al. 1998) it is well established that all the DNA/RNA bases have negative vertical electron affinity (VEA) values in gas phase. The adiabatic electron affinities (AEA) of these bases were also studied using anion photoelectron spectroscopy by Bowen (Hendricks et al. 1996, 1998) and Weinkauff (Schiedt et al. 1998), and Rydberg electron transfer (RET) experiments by Schermann (Desfancois et al. 1996, 1998) and their coworkers. These experiments showed the formation of stable dipole-bound anion of uracil, thymine, and cytosine having AEA in the range of 0.06–0.1 eV (see ● Table 34-3). The experimentally estimated dipole-bound AEA of uracil ~93 meV and thymine ~68 meV were found to be in excellent agreement with the theoretically predicted dipole-bound AEA values 86 and 88 meV of the corresponding bases by Oyler and Adamowicz (1993, 1994) using SCF and MP2 methods in combination with a very diffuse basis set. In recent years, density functional theory (DFT) and CCSD(T) methods were also applied to evaluate the electron affinities (EAs) of the bases (Li et al. 2002; Vera and Pierini 2004; Puiatti et al. 2009; Wesolowski et al. 2001; Bachorz et al. 2007). The DFT-calculated positive electron affinity values for the pyrimidines are overestimated by about 0.15 eV (see ● Table 34-3). From theory and experiment it is now





■ Fig. 34-9

Potential energy surfaces (PES) of an anion formation ( $M^-$ ) after electron ( $e^-$ ) attachment to the neutral molecule ( $M$ ). When the energy of an anion ( $M^-$ ) lies below the neutral molecule, positive electron affinity is observed (*left*); otherwise the molecule is said to have negative electron affinity (*right*). Energy changes shown for an electron attachment or detachment event are: (1) the vertical electron affinity (VEA), (2) the adiabatic electron affinity (AEA), and (3) the vertical detachment energy (VDE). The VDE and VEA impose the upper and lower bounds to AEA

well established that VEA of the bases are negative and the AEA of U, T, and C are near zero and still negative for A and G. The best estimated theoretical electron affinities of bases along with their experimental values are presented in ► [Table 34-3](#).

## Choice of the Basis Set

From the discussions in the preceding sections, it is clear from theory and experiment that vertical electron affinities of all the nucleic acid bases are negative while the adiabatic electron affinities of pyrimidines are near zero. This means that an electron is unbound with the bases in the vertical state (TNI formation) and very loosely bound into the diffuse orbital of the bases in the adiabatic state, and in both the cases the choice of the basis set is crucial in determining the electron attachment process. The extent of the electron density localization with respect to the molecular frame for “dipole-bound” and “valence-bound” states can only be treated by an appropriate selection of the basis set. Generally, the basis set needed in a calculation consists of valence and extended (double- and triple- $\zeta$ ) basis, which is further augmented with polarization and diffuse functions. While the polarization functions are important to study molecules with strained chemical bonds (Simons 2008), diffuse functions are necessary for dealing with anions or Rydberg type of species. In calculations for “dipole-bound” anions, the valence basis set must be augmented with very diffuse functions to successfully describe the system. Such basis sets were employed by Burrow et al. (2006) in the study of VFRs of thymine and uracil, and by Oyler and Adamowicz (1993, 1994) for estimating the dipole-bound adiabatic binding

■ Table 34-3

Selected theoretical and experimental gas-phase electron affinities of DNA/RNA bases (eV)

Bases	VEA		AEA		Valence		
	Experiment	Theory	DB(meV) <sup>a,b,c</sup>		Experiment	DFT	Ab initio
			Experiment	Theory			
U	-0.22 <sup>d</sup>	-0.27 <sup>e</sup>	93 ± 7 <sup>b</sup>	86 <sup>f</sup>	ca. 0 <sup>g</sup>	0.20 <sup>h</sup>	0.002 <sup>i</sup>
	-0.30 <sup>j</sup>	-	86 ± 8 <sup>c</sup>				0.040 <sup>k</sup>
T	-0.29 <sup>d</sup>	-0.30 <sup>e</sup>	69 ± 7 <sup>b</sup>	88 <sup>l</sup>	ca. 0 <sup>g</sup>	0.15 <sup>h</sup>	0.018 <sup>m</sup>
	-	-	62 ± 8 <sup>c</sup>			-	-
C	-0.32 <sup>d</sup>	-0.55 <sup>e</sup>	85 ± 8 <sup>c</sup>	-		-0.05 <sup>h</sup>	-0.13 <sup>i</sup>
	-0.55 <sup>j</sup>	-				-	
A	-0.54 <sup>d</sup>	-0.74 <sup>e</sup>	12 ± 5 <sup>a</sup>	-	-	-0.35 <sup>h</sup>	-
	-0.45 <sup>j</sup>	-				-	-
G	(-0.74) <sup>d</sup>	-1.25 <sup>n</sup>	-	-	-	-0.75 <sup>h</sup>	-0.52 <sup>o</sup>

<sup>a</sup>Dipole bound (DB) (Desfancois et al. 1996).

<sup>b</sup>Dipole-bound (DB) (Hendricks et al. 1996; Schiedt et al. 1998).

<sup>c</sup>Dipole-bound (DB) (Schiedt et al. 1998).

<sup>d</sup>Electron transmission spectroscopy (ETS) results due to Aflatooni et al. (1998). For G, VEA was estimated for keto tautomer from enol tautomer experimental value (-0.46 eV) plus the calculated difference in total energies between the two tautomers (0.28 eV).

<sup>e</sup>B3LYP/6-311G(2df,p) values due to Vera and Pierini (2004) and Wetmore et al. (2000).

<sup>f</sup>Oyler and Adamowicz (1993).

<sup>g</sup>Estimated from stable valence anion complexes, e.g.; U(Ar)<sup>-</sup> (Hendricks et al. 1998).

<sup>h</sup>Best estimates from DFT basis set dependence study due to Li et al. (2002). The DFT values are generally overestimated by 0.15 eV.

<sup>i</sup>Calculated using CBS-Q (Li et al. 2004).

<sup>j</sup>Rydberg electron transfer spectroscopy (RET) results due to Periquet et al. (2000).

<sup>k</sup>Bachorz et al. (2007).

<sup>l</sup>Oyler and Adamowicz (1994).

<sup>m</sup>CCSD(T) correction to MP2 complete basis set (CBS) limit including ZPE correction. See Svozil et al. (2005).

<sup>n</sup>Best estimates from B3LYP/D95V+(D) trends for other bases (Li et al. 2002).

<sup>o</sup>Haranczyk and Gutowski (2005).

energy of excess electrons to uracil and thymine. At times, the diffuseness of the basis functions is inadequate and the dipole-bound state mixes with the valence-bound state of the molecule (see Fig. 1 in Oyler and Adamowicz [1993]). If the energy of the dipole-bound and valence-bound states is equal, such a mixture could represent a proper solution for the molecular anion radical.

Diffuse functions are not a good choice for dealing with virtual “valence” states in TNIs or the available energies for shape resonances in the continuum. Any ab initio calculation employing the variational method with diffuse functions for a molecule with a negative electron affinity will fail and result in an unbound electron in the continuum at zero energy as the lowest energy state. Thus, the calculation of the negative electron affinity is not properly treated by a variational method. Nevertheless, virtual TNI states can be estimated with the use of compact basis sets such as 6-31G\* as these compact basis sets avoid mixing with dipole-bound states and the continuum. Calculations using compact basis sets, when scaled, can provide good estimates of the virtual “valence” states in reasonable agreement with experiment. Further, these calculations can provide insights into the nature of such intermediate states and mechanisms of action of

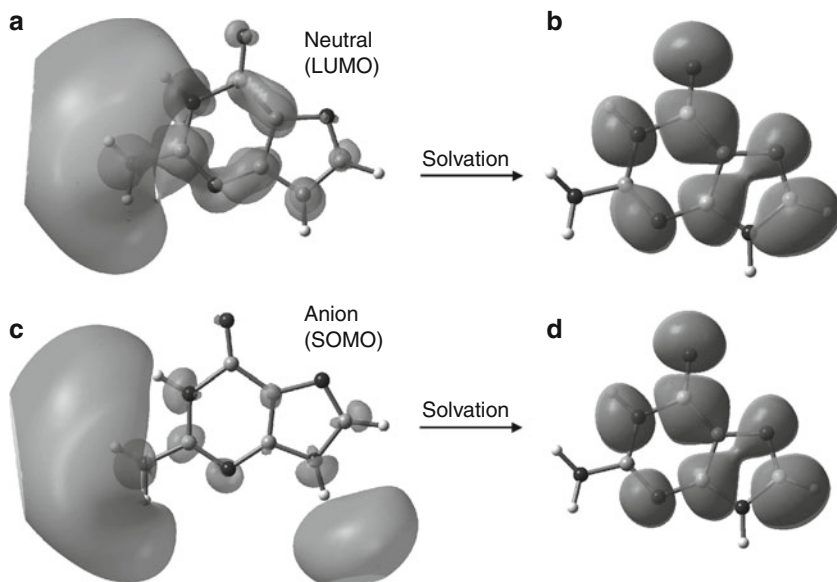
LEE in the induction of chemical change. The use of the compact basis set in the study of resonances (TNIs) is well documented in the literature (Jordan and Burrow 1987; Simons and Jordan 1987; Simons 2008; Modelli and Martin 2002; Staiey and Strnad 1994). Using compact 6-31G(d) to very diffuse 6-311++G(2d,p) basis sets, Li et al. (2002) calculated the negative valence electron affinities of the bases. Their calculated SOMO surfaces of the DNA bases demonstrated that while the compact basis set represents the valence type  $\pi^*$ -anions (the SOMO surfaces reside on the molecular frame) and give good estimates of negative electron affinities, the use of extended basis sets results in a collapse of the electron-binding energy to near zero, which is expected for the continuum and dipole-bound states. SOMO surfaces for extended basis sets show the characteristics of the dipole-bound state with the electron density residing away from the molecular frame. In the extreme of extension of the basis set, the electron would reside in the continuum, or if the molecule has a dipole, a weakly bound electron in a dipole-bound state.

## Effect of Solvation (Condensed Media)

---

The discussion above describes the events of electron–molecule interaction in the gas phase. However, in condensed aqueous media, the nature of these processes is significantly altered. For example, dipole-bound states are not likely to be present as they are suppressed by the surrounding medium, and this is confirmed from the photoelectron spectroscopy of the hydrated uracil, thymine, cytosine, and adenine (Schiedt et al. 1998; Eustis et al. 2007) as the photoelectron spectra are blue-shifted with the increase of the number of hydrated water molecules and show valence-bound anion formation. For a visual inspection of this phenomenon, we plotted the LUMO and SOMO surfaces of guanine in neutral and anion radical states, using the B3LYP/6-311++G(2d,p) method in gas phase, and in aqueous media using polarized continuum model (PCM). The LUMO and SOMO surfaces in the gas phase and in the solvated phase of guanine in neutral and in anion radical states are shown in [Fig. 34-10](#). From [Fig. 34-10](#), it is inferred that LUMO and SOMO represent a dipole-bound state (Li et al. 2002) in the gas phase (see [Fig. 34-10a, c](#)), which is destabilized under the influence of the full solvation and becomes the valence bound state (see [Fig. 34-10b, d](#)).

The solvent has a number of other effects on TNIs. First, relaxation of an excited TNI in the condensed media is rapid owing to the coupling with the high density of states in the matrix such as vibrational and phonon modes. Coupling to matrix energy levels quickly deactivates the excited vibrational states (within 1–10 ps). Further, the dielectric of the medium changes the energetics of the TNI first by the fast dielectric response, and as nuclear relaxation and reorientation takes place in the matrix, the full dielectric response ensues. The fast electronic response accounts for ca. 1 eV of stabilization and the slow dielectric response can account for several electronvolts. This stabilization can move the TNI (resonances) from the continuum into a valence-bound state. As a result, the autodissociation pathway is diminished or stopped altogether. In this context, it is worth considering the effect of secondary electrons generated by radiation damage to liquid water surrounding the DNA. It is found that on thermalization, the spatial extent of radiation-produced electrons in liquid water is in the range of 20–50 Å in what is considered the conduction band (Galduel et al. 1989; Crowell and Bartels 1996). In solution, the electron has several energy states (see [Table 34-4](#)), all lower than in the gas phase (see [Fig. 34-11](#)). The ground or the lowest energy state for the electron is the fully solvated electron ( $e_{aq}^-$ ), which is stabilized by several electronvolts of solvation energy. The electron



■ Fig. 34-10

B3LYP/6-311++G(2d,p)-calculated lowest unoccupied molecular orbital (LUMO) of neutral guanine in gas phase (a) and in solution (b). The singly occupied molecular orbital (SOMO) of guanine anion radical in gas phase (c) and in solution (d). The dipole-bound anion in (a, c) becomes a  $\pi^*$ -valence anion in (b, d). The effect of full solvation was considered through the use of polarized continuum model (PCM) considering the optimized gas-phase geometries

■ Table 34-4

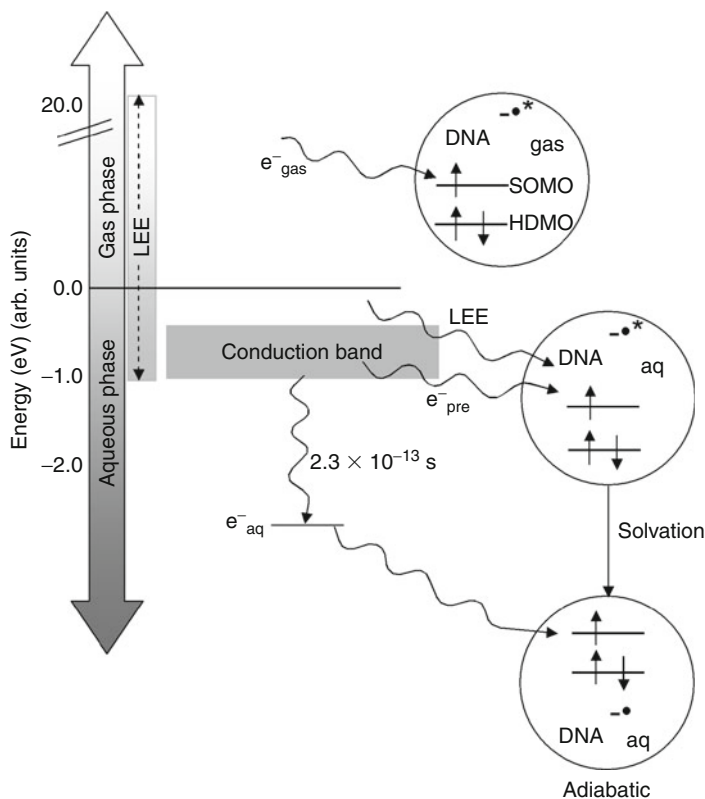
Electron type based on their energies in gas phase and in liquid water

Electron type	Medium	Energy (eV)
LEE	Gas phase	0 to 20
Thermalized electron	Gas phase	0.026 <sup>a</sup>
LEE	Water	-1 to 20
Thermalized electrons	Water	
Conduction band (presolvated electron [ $e_{pre}^-$ ])		-1
p-state (excited state of solvated electron)		-1
Solvated electron		-2.5

<sup>a</sup>Energy at 300 K.

can be excited to a p-state and a conduction band, which are 1–2 eV higher in energy. For the electron–molecule interaction the energy of the electron (see ► [Table 34-4](#)) makes for a number of possible interaction types.

The TNI of DNA stabilized in solution over a TNI of DNA in the gas phase is shown in ► [Fig. 34-11](#). Once formed in solution, the TNI will undergo solvent reorganization, which liberates additional solvation energy. This occurs within a hundred picoseconds and results in stabilization by several electronvolts. For a stable (adiabatic) anion radical to be formed, the



■ Fig. 34-11

Schematic diagram showing the addition of LEE to DNA in gas phase ( $e_{\text{gas}}^-$ ) and in liquid water via pre-hydrated electrons ( $e_{\text{pre}}^-$ ) from the conduction band and by LEE addition. In the gas phase, LEE ( $e_{\text{gas}}^-$ ) can be captured into one of the UMOs of DNA (shown as SOMO after the  $e_{\text{gas}}^-$  capture) creating the TNI ( $\text{DNA}_{\text{gas}}^{-*}$ ). A TNI formed in the liquid water ( $\text{DNA}_{\text{aq}}^{-*}$ ) is quickly solvated resulting in the adiabatic DNA radical anion ( $\text{DNA}_{\text{aq}}^-$ ). The energy of the solvated electron ( $e_{\text{aq}}^-$ ) must be below the energy of the solvated electron ( $e_{\text{aq}}^-$ ) to be stable to electron loss to water. For clarity, the MOs of DNA below the HDMO (highest doubly occupied MOs) and above the SOMO are not shown in the figure. (Figure based in part from Wang et al. 2009)

energy must be below the energy of the solvated electron ( $e_{\text{aq}}^-$ ), as shown in ► Fig. 34-11. The adiabatically solvated DNA radical anion ( $\text{DNA}^{\cdot-}$ ) can subsequently undergo protonation reactions on pyrimidines for further stabilization, but will not undergo a strand break. The reaction of the TNI to form a DNA strand break must take place before solvation to form the stable anion radical. This allows only a short time window for the reaction to take place.

Because of the importance of solvation to the reactivity of electrons, studies of electrons in water at various energy states are needed. A few recent studies (Wang et al. 2009; Orlando et al. 2008) have appeared. The first (Wang et al. 2009) reported the plasmid DNA damage by the prehydrated electron ( $e_{\text{pre}}^-$ ) (energy of the conduction band in ► Fig. 34-11). The electrons

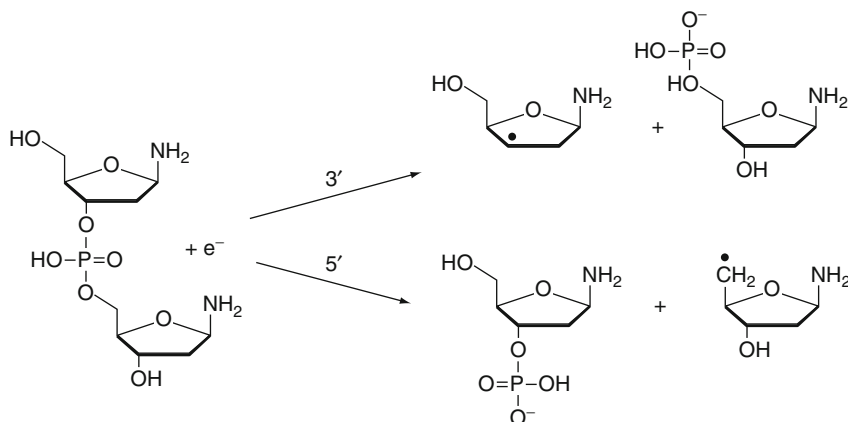
were generated by water excitation using two UV photon laser pulses. The TNI formation was reported to result in fast DEA processes, resulting in strand breaks. This work is the first to suggest conduction band electrons ( $e_{pre}^-$ ) would be reactive in this manner. The results appear problematic because the concentrations of the solutes may not have been high enough to scavenge sufficient extremely short lived (0.3 ps) prehydrated electrons. Confirmation experiments are needed to verify this very interesting result. LEE-induced damage in hydrated A- and B-DNA has also recently been studied by Orlando et al. (2008) using elastic scattering of 5–30 eV electrons. In this study, a featureless amplitude build up of elastic scattered electrons on the sugar and phosphate groups was observed for all energy ranges from 5 to 30 eV.

## Proposed Theoretical Models of DNA Damage

After the discovery that low energy (3–20 eV) electrons induced single- and double-strand breaks in plasmid DNA (Boudaiffa et al. 2000), a number of theoretical studies have attempted to elucidate the mechanism of LEE induction of DNA strand breaks. As the calculation of the entire DNA molecule at the *ab initio* or DFT levels is currently prohibitive; fragments of DNA structure usually including the base, sugar and phosphate attached at 3'- and 5'- ends of the sugar ring have been treated.

The first mechanism for LEE-induced SSBs was proposed by Simons and coworkers employing a Hartree–Fock (UHF) level of theory and 6-31+G\* basis set (Barrios et al. 2002). In their study, they considered 3'-cytidine mono phosphate (3'-dCMPH) as a model of DNA and studied the ground-state potential energy surfaces (PESs) of the C<sub>3'</sub>–O<sub>3'</sub> bond dissociation in the neutral and in radical anion states, and at each C<sub>3'</sub>–O<sub>3'</sub> bond increment the geometries were fully optimized. The calculations suggest a shape resonance, i.e., the initial attachment of the excess electron on the  $\pi^*$  virtual molecular orbital localized on the cytosine base. During the C<sub>3'</sub>–O<sub>3'</sub> bond elongation process on the PES of the anion radical, the excess electron, captured on the base, was found to be transferred to the C<sub>3'</sub>–O<sub>3'</sub> bond region (joining the sugar and phosphate groups) at the transition state. From the calculated energy profile of C<sub>3'</sub>–O<sub>3'</sub> bond dissociation, the energy barrier was estimated to be ca. 13 kcal/mol and the fragmentation process was found to be exothermic in nature. Based on this study, the authors proposed an *indirect mechanism* of SSB in which an electron transfers from base ( $\pi^*$ ) to break the remote ( $\sigma^*$ ) C–O bond. Here, we note that the statement “indirect mechanism” is not related to the terms direct and indirect effect of radiation-induced DNA damage. This first theoretical calculation clearly predicted that SSBs can occur below 3 eV as later found in LEE experiments (Martin et al. 2004; Panajotovic et al. 2006). While groundbreaking in nature, this study had several drawbacks: (a) it did not consider the higher energy shape resonances; (b) it considered the adiabatic state of the radical anion for the bond fragmentation, not the TNI, which is the initial state of the shape resonance formation as discussed in the [☛ section “Shape Resonances of DNA Bases”](#); and (c) it was not clear whether the proposed mechanism was pertinent to the actual DNA environment, where the bases are stacked over each other and the electron transfer process between the bases is likely preferred over the electron transfer process to the sugar phosphate region (Wagenknecht 2005).

Just after Simons's work (Barrios et al. 2002), Li, Sevilla, and Sanche (Xi et al. 2003) proposed that the direct attachment of the excess electron to the sugar phosphate backbone of the DNA



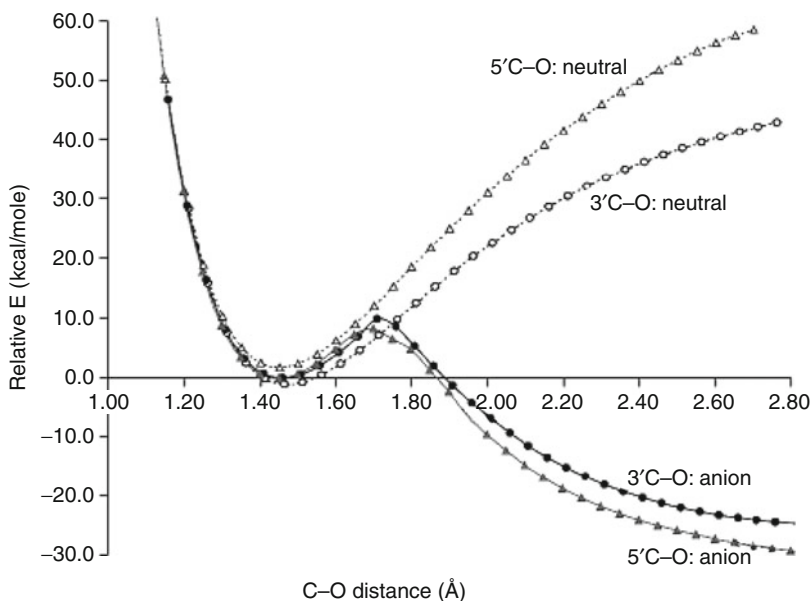
■ Fig. 34-12

**Sugar–phosphate–sugar (S-P-S) model representing a section of DNA backbone. Electron-induced bond dissociations at the 3′ and 5′-ends of the model are investigated. Figure modified according to the spin density distribution shown in Li and Sevilla (2007), which showed no valence state but a dipole-bound precursor (Reprinted with permission from Xi et al. [2003]. © (2003) American Chemical Society)**

may create the SSB. To investigate this process, they modeled the sugar–phosphate–sugar (S-P-S) backbone of the DNA without bases attached to the sugar ring (see ● Fig. 34-12). Because of the large size of the model, they used the ONIOM approach to optimize the geometry of the S-P-S model shown in ● Fig. 34-12. In the ONIOM treatment, B3LYP/6-31+G(d) level of theory was used for the critical bond cleavage atoms (higher layer), and the semiempirical AM1 method was used for the rest of the atoms (lower layer). In their treatment, they calculated the PESs of the  $C_{3′}-O_{3′}$  and  $C_{5′}-O_{5′}$  bonds dissociation of the S-P-S model in their neutral and anionic radical states. The study showed that in the radical anion state, the 3′- and 5′-C–O bonds cleavage occurred with a low activation barrier (ca. 10 kcal/mol) in comparison to the neutral state. The bond dissociation process for radical anion was found to be highly favorable thermodynamically (see ● Fig. 34-13). This work suggested that a vibrational excitation of the C–O bond could capture an electron and lead to a strand break. An important aspect about the nature of an excess electron association into the sugar phosphate region showed the formation of the dipole-bound anion state rather than the valence anion state, which is expected as only electronic excited states are expected to be available for electron capture in the sugar phosphate structure.

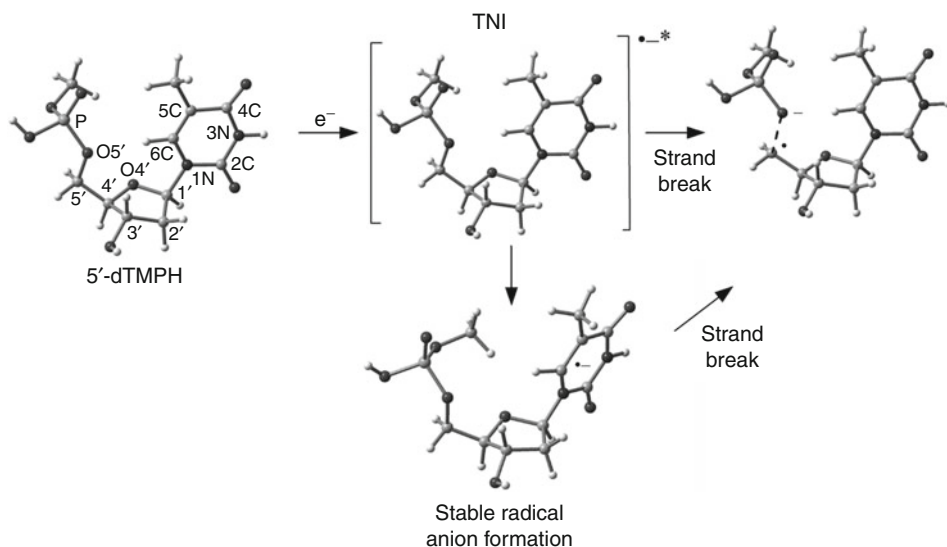
In a recent work (Kumar and Sevilla 2007), the interaction of LEE with a model for DNA (5′-dTMPH) was studied at the B3LYP level of theory considering both the vertical (TNI) and the adiabatic states of the radical anion. Since the TNI (shape resonance) formation has only a short life time of  $10^{-15}$  to  $10^{-10}$  s, the study was performed with the hypothesis that SSBs may occur before as well as after molecular relaxation, as shown in ● Scheme 34-1.

In this calculation, the potential energy surface (PES) for  $C_{5′}-O_{5′}$  bond dissociation of 5′-dTMPH in vertical and adiabatic states was calculated using both compact (6-31G\*) and diffuse (6-31++G\*\*) basis sets. At each step on the PES, the singly occupied molecular orbital (SOMO)



■ Fig. 34-13

Adiabatic potential energy surfaces for 3'C-O and 5'C-O bond rupture before and after electron addition to the S-P-S model. All energies are relative to the energies of the anions at equilibrium (Reprinted with permission from Xi et al. [2003]. © (2003) American Chemical Society)

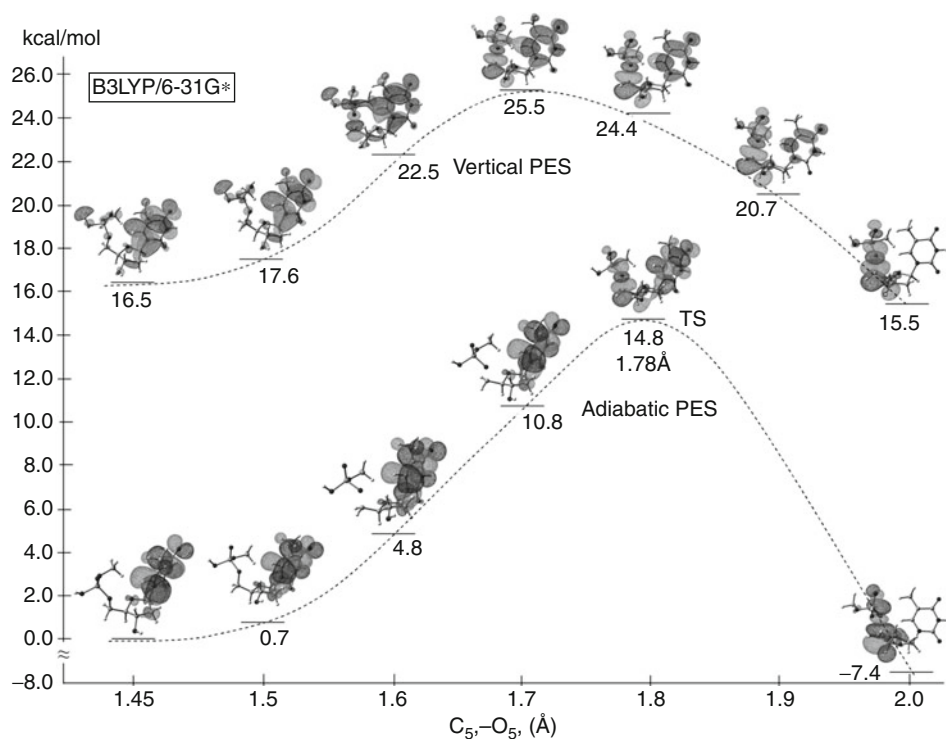


■ Scheme 34-1

Proposed mechanism of single-strand break (SSB) due to attachment of LEE with 5'-dTMPH molecule in vertical and adiabatic states (Reprinted with permission from Kumar and Sevilla [2007]. © (2007) American Chemical Society)

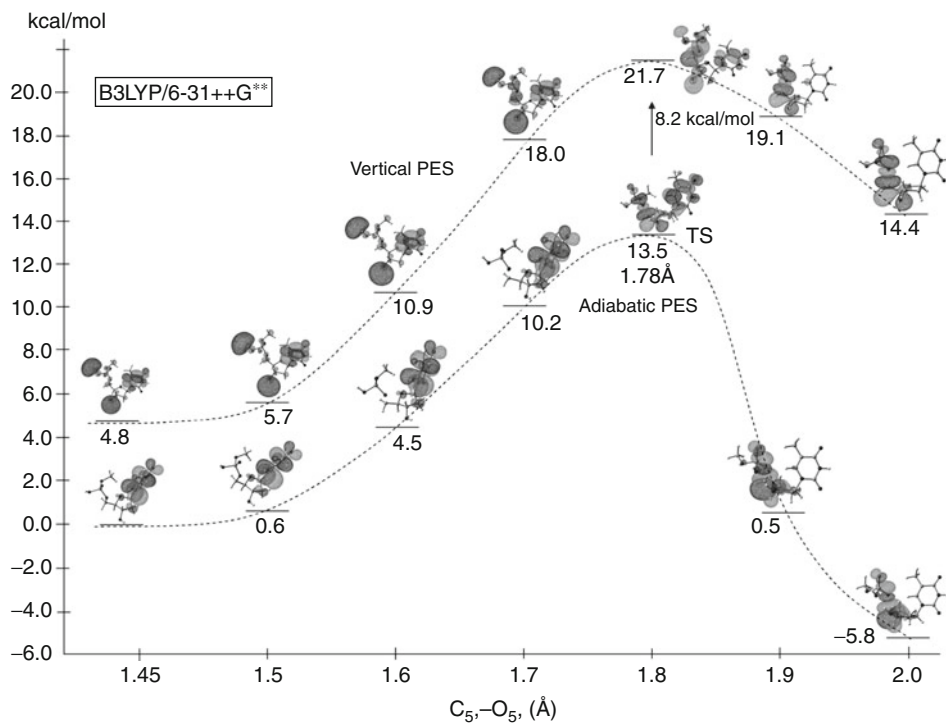


was plotted to observe the pattern of the excess electron localization on the molecular frame. To elucidate the mechanism of SSB, the PES was scanned by stretching the  $C_{5'}$ - $O_{5'}$  bond from the equilibrium bond length of the neutral and anion radical of 5'-dTMPH to 2 Å in the increments of 0.1 Å. On the vertical radical anion (TNI) PES, the  $C_{5'}$ - $O_{5'}$  bond was scanned by maintaining the remainder of the geometry in the neutral state; however, on the adiabatic state, the geometry was optimized at each step of the bond elongation on the PES. The B3LYP/6-31G\* and B3LYP/6-31++G\*\* calculated PESs of  $C_{5'}$ - $O_{5'}$  bond dissociation are shown in ▶ Figs. 34-14 and ▶ 34-15, respectively. On the adiabatic surface, both methods gave similar barrier heights, i.e., 14.8 and 13.5 kcal/mol for the  $C_{5'}$ - $O_{5'}$  bond dissociation. The SOMO, which is initially localized on the thymine as expected (Becker et al. 2010; Li and Sevilla 2007; Kumar and Sevilla 2008a), transfers to the  $C_{5'}$ - $O_{5'}$  bond region only after the transition state for the  $C_{5'}$ - $O_{5'}$  bond rupture. For the vertical PES, B3LYP/6-31G\* theory predicted the barrier height for  $C_{5'}$ - $O_{5'}$  bond dissociation as 9 kcal/mol, while the corresponding barrier was predicted to be 17 kcal/mol at the B3LYP/6-31++G\*\* level of theory. An important feature of this study is that in the vertical state excess electron begins transferring smoothly into the  $C_{5'}$ - $O_{5'}$  bond region before the TS during bond elongation process; however, in the adiabatic state



■ Fig. 34-14

B3LYP/6-31G\*-calculated adiabatic and vertical potential energy surfaces (PESs) of  $C_{5'}$ - $O_{5'}$  bond dissociation of 5'-dTMPH radical anion. Energies and distances are given in kcal/mol and angstroms (Å), respectively. The singly occupied molecular orbital (SOMO) is also shown (Reprinted with permission from Kumar and Sevilla [2007]. © (2007) American Chemical Society)



■ Fig. 34-15

B3LYP/6-31++G\*\*-calculated adiabatic and vertical potential energy surfaces (PESs) of  $C_{5'}-O_{5'}$  bond dissociation of 5'-dTMPH radical anion. Energies and distances are given in kcal/mol and angstroms (Å), respectively. The singly occupied molecular orbital (SOMO) is also shown (Reprinted with permission from Kumar and Sevilla [2007]. © (2007) American Chemical Society)

electron transfer takes place from base to  $C_{5'}-O_{5'}$  bond region after the TS (see SOMO plots in ► Figs. 34-14 and ► 34-15). The facile electron transfer from base to sugar in the vertical state supports the hypothesis that the transiently bound electron in the TNI (shape resonance) results in SSBs in DNA without the need for significant molecular relaxation. From this work, it was also inferred that TNI formation may excite some specific vibrational mode which has the lower barrier for the bond fragmentation, as already proposed by Burrow et al. (Afatooni et al. 1998; Jordan and Burrow 1987) and Sanche et al. (Levesque et al. 2003). It is also noted that on timescale appropriate for the transition state ( $<10^{-12}$  s) (Zewail 2000), specific vibrational motions may dominate. Therefore, on TNI formation a vibrational excitation of the  $C_{5'}-O_{5'}$  bond would need only a small or negligible barrier for the bond dissociation. In this model, the incoming LEE must vibrationally excite the  $C_{5'}-O_{5'}$  bond during the TNI (shape resonance) at thymine base. Since this mechanism seems improbable, alternatively, the LEE may directly attach into the phosphate group in an UMO and create such a vibrational excitation through resonance formation on phosphate. From the computed vertical attachment energies of 5'-dTMPH, shown in ► Fig. 34-8, it is evident that  $<2$  eV UMOs on phosphate group and base are available to capture LEEs (Kumar and Sevilla 2007). Thus, it is quite possible that on TNI formation these UMOs will excite the vibrational mode and result in SSBs.

## Excited States of TNI (Resonance Formation)

The theoretical model (Kumar and Sevilla 2007) of LEE attachment to the LUMO leading to strand break formation provides one pathway that TNI formation can lead to DNA strand breaks, but it ignores the role of shape resonances that are available at 1–2 eV and above (estimated from the vertical attachment energies of the UMOs of 5'-dTMPH, see [Fig. 34-8](#) and Kumar and Sevilla [2007]). It is well known that during electron–molecule interactions, a variety of excited states can be involved. Therefore, the study of excited states of the TNI, that model resonance states formed on the electron attachment to the parent molecule, can be pursued to better understand LEE interactions in DNA. With this in mind, we studied the excited states of anion radical of 5'-dTMPH (as a model of DNA) using time-dependent (TD) density functional theory (Kumar and Sevilla 2008b). The geometries of 5'-dTMPH in their neutral and anion radical state were fully optimized using the B3LYP/6-31G\* method. The lowest excited states of the TNI were calculated using TD-B3LYP and TD-BHandHLYP methods using the 6-31G\* basis set. In this study, a compact basis set (6-31G\*) was employed to avoid the mixing of the valence states with the dipole-bound states and continuum (Li et al. 2002). The assumption of this work is that the TNI (resonance) formation is equivalent to an excited state of the electron adduct of the parent molecule. Further, the applicability of both functionals was tested for a number of anion radicals for which experimental and theoretical values were available (for details see the supporting information of Kumar and Sevilla [2008b]). Also, the transition energies, calculated using both the methods, were compared with the available shape resonance energies of adenine, thymine, cytosine, and uracil, as determined from the ETS experiment (Aflatooni et al. 1998), and 5'-dTMPH with their scaled vertical attachment energies (see [Table 34-5](#)). From [Table 34-5](#), we see that both the methods provide reasonable estimates of shape resonance energies of the bases. However, for 5'-dTMPH radical anion, the B3LYP method was found to largely underestimate the transition energies, while the BHandHLYP method was found to give more realistic values. The problem with the B3LYP method in underestimating the long-range Coulomb interactions in charge transfer states is well documented in the literature, and this arises from the small contribution of the Hartree–Fock exchange (20%) in the B3LYP functional (Dreuw and Head-Gordon 2005). However, for this case, the charge transfer state is not created during the excitation because only the excess electron transfers between the nominally neutral portions of the molecule; this is another limitation of the B3LYP functional. In view of this, we employed the BHandHLYP/6-31G\* method to compute the excitation energies of 5'-dTMPH radical anion in the vertical and adiabatic states.

In this study, the ground- and excited-state potential energy surfaces were generated by scanning the C<sub>5'</sub>–O<sub>5'</sub> bond from their equilibrium bond length in neutral and anion radical state to 2 Å in the step size of 0.1 Å. At each fixed C<sub>5'</sub>–O<sub>5'</sub> bond length, the lowest excited states were calculated. The excited states of the TNI of 5'-dTMPH, calculated at the optimized geometry of the neutral 5'-dTMPH, are shown in [Fig. 34-16](#). The TD-BHandHLYP/6-31G\* calculated three lowest transition energies of TNI were found to be  $\pi(\text{T}) \rightarrow \sigma(\text{PO}_4)^*$ ,  $\pi(\text{T}) \rightarrow \pi(\text{T})^*$ , and  $\pi(\text{T}) \rightarrow \sigma(\text{S})^*$  in nature, and the corresponding transition energies are 1.42, 1.68, and 2.06 eV, respectively. The calculated  $\pi(\text{T}) \rightarrow \pi(\text{T})^*$  transition energy 1.68 eV is in good agreement with those calculated using ETS experiment of thymine (see [Table 34-5](#) and [Fig. 34-16](#)). From the ground-state surface, it is evident that SOMO is localized on the base as found from the ESR (electron spin resonance) experiments (Sevilla et al. 1991). From

Table 34-5

Vertical excitation energies ( $\Delta E$ , eV) of transient negative ion (TNI) of DNA/RNA bases calculated using TD-B3LYP/6-31G\* and TD-BHandHLYP/6-31G\* methods and their comparison with available experimental values<sup>a</sup>

Transition	Molecule	$\Delta E$		
		B3LYP	BHandHLYP	Exp <sup>b,c</sup>
–	Uracil	–	–	0.22 ( $\pi_1^*$ )
$\pi \rightarrow \pi^*$		1.33	1.85	1.58 ( $\pi_2^*$ )
$\pi \rightarrow \pi^*$		4.27	4.73	3.83 ( $\pi_3^*$ )
–	Thymine	–	–	0.29 ( $\pi_1^*$ )
$\pi \rightarrow \pi^*$		1.38	1.89	1.71 ( $\pi_2^*$ )
$\pi \rightarrow \pi^*$		3.86	4.46	4.05 ( $\pi_3^*$ )
–	Cytosine	–	–	0.32 ( $\pi_1^*$ )
$\pi \rightarrow \pi^*$		1.55	1.91	1.53 ( $\pi_2^*$ )
$\pi \rightarrow \pi^*$		4.47	5.06	4.50 ( $\pi_3^*$ )
–	Adenine	–	–	0.54 ( $\pi_1^*$ )
$\pi \rightarrow \pi^*$		0.88	1.0	1.36 ( $\pi_2^*$ )
$\pi \rightarrow \pi^*$		1.89	1.86	2.17 ( $\pi_3^*$ )
–	5'-dTMPH <sup>d</sup>	–	–	(0.53 T) <sup>d</sup>
$\pi \rightarrow \pi^*$		1.16	1.68	(1.56 T) <sup>d</sup>
$\pi \rightarrow \sigma^{*e}$		0.18	1.42	(1.80 PO <sub>4</sub> ) <sup>d</sup>
$\pi \rightarrow \sigma^{*e}$		0.70	2.06	(2.23 S) <sup>d</sup>

<sup>a</sup>Transition energies of radical anions were calculated at the optimized neutral geometry of the molecules.

<sup>b</sup>Energies of the shape resonances in the electron transmission spectroscopy (ETS) experiment (Afatooni et al. 1998).

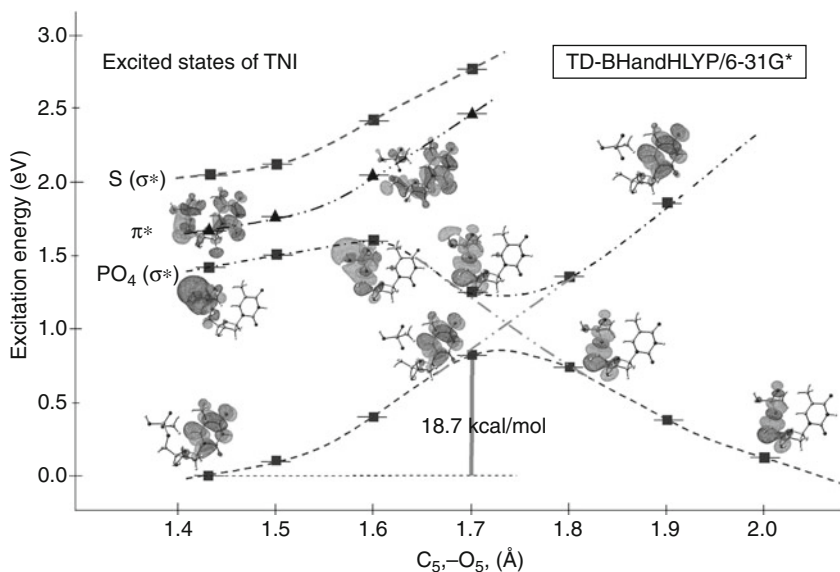
<sup>c</sup> $\pi_1^*$  corresponds to the energy of the singly occupied molecular orbital (SOMO) and its difference with  $\pi_2^*$  and  $\pi_3^*$  orbital energies gives the estimate of the transition energies.

<sup>d</sup>Scaled B3LYP orbital energies (VOE) (Kumar and Sevilla 2007).

<sup>e</sup>Electron transfers from thymine ( $\pi$ ) to PO<sub>4</sub> and sugar ( $\sigma$ ) part of 5'-dTMPH (Reprinted with permission from Kumar and Sevilla [2008b]. © (2008) American Chemical Society).

the nature of the PES in the ground state, we see that the ground state surface (lowest surface, in **Fig. 34-16**) shows the bound character and attains the transition state at 1.7 Å with a barrier height of 18.7 kcal/mol (see **Fig. 34-16**). The second and third surfaces corresponding to  $\pi(T) \rightarrow \pi(T)^*$  and  $\pi(T) \rightarrow \sigma(S)^*$  transitions also exhibit the bound character. However, the first surface, which is a  $\pi(T) \rightarrow \sigma(PO_4)^*$  type, shows a dissociative nature.

Such a dissociative nature of  $\pi \rightarrow \sigma^*$  transitions in excited states is well documented in the literature (Domcke and Sobolewski 2003; Sobolewski and Domcke 2002; Ashfold et al. 2006). The presence of  $\pi(T) \rightarrow \sigma(PO_4)^*$  transition <2 eV clearly indicates that LEEs with this energy can directly attach to the sugar-phosphate group during TNI formation and result in a prompt SSB formation in DNA. This transition is dark in nature and cannot be populated directly; however, it can be populated through vibronic coupling when the neighboring  $\pi(T) \rightarrow \pi(T)^*$  state lies at 1.68 eV. The coupling of  $\pi^*$  and  $\sigma^*$  surfaces leads to a facile strand break formation within picoseconds. Recently, Sanche and coworkers (Martin et al. 2004; Panajotovic et al. 2006) studied the yields of SSB and DSB induced by 0–4 eV electrons and found two peaks near  $0.8 \pm 0.3$  and 2.2 eV, respectively. Our calculated transitions at 1.4 and 1.7 eV are in reasonable agreement



■ Fig. 34-16

**Lower curve:** Potential energy surface (PES) of the 5'-dTMPH transient negative ion (TNI) calculated in the neutral optimized geometry of 5'-dTMPH with  $C_{5'}-O_{5'}$  bond elongation. SOMO is shown at selected points. **Upper curves:** calculated vertical excitation energies of the radical anion at each point along the PES; MOs involved in excitations are also shown. Energies and distances are given in electronvolts and angstroms, respectively. The lowest  $\pi\pi^*$  state (triangles) and lowest  $\pi\sigma^*$  states (square) are shown (Reprinted with permission from Kumar and Sevilla [2008b]. © (2008) American Chemical Society)

to the experimental observation. Further, the  $\sigma^*$  nature of shape resonance localized on the phosphate group in 5'-dTMPH radical anion is also supported from the recent experimental study carried out by Burrow et al. (2008) for the temporary anion states of trimethyl phosphate and several P=O groups containing compounds. The electron-scattering study of the A and B forms of DNA concluded that electrons with energies between 2 and 5 eV had the largest probability of electron capture on the phosphate group versus on the other components of the DNA (Caron and Sanche 2005). Experiments reported by Illenberger and coworkers (König et al. 2006) showed that C–O bond rupture is caused by LEE that directly attach to the phosphate group.

More recently, the above study was extended to radical anions of a series of nucleoside diphosphate: 2'-deoxyguanosine-3',5'-diphosphate(3',5'-dGDP); 2'-deoxyadenosine-3',5'-diphosphate (3',5'-dADP); 2'-deoxythymidine-3',5'-diphosphate(3',5'-dTDP); and 2'-deoxycytidine-3',5'-diphosphate (3',5'-dCDP). The excited states of these species in gas phase and in the condensed phase in their TNI and adiabatic states were calculated using the BHandHLYP/6-31G\* method (Kumar and Sevilla 2009). The geometries of each species (3',5'-dGDP, 3',5'-dADP, 3',5'-dTDP, and 3',5'-dCDP) in their neutral and radical anionic states, in the gas phase, and in the presence of two and three water molecules were fully optimized at the B3LYP/6-31G\* level of theory. In this work, the nature of the resonances under the influence of

the bulk solvent was modeled by the use of integral equation formalism-polarized continuum model (IEF-PCM) on the optimized hydrated geometries in the neutral and radical anion states. To the best of our information, this was the first study that showed that while in the gas phase the dissociative ( $\sigma^*$ ) state is accessible by LEEs, in solution these states are blue-shifted toward higher energy and are not accessible by LEEs having energy under 4 eV. This phenomenon is well understood from the photoelectron spectroscopy of the solvated anions. It is well known that under solvation, anions become energetically more stable (see discussion in [section “Effect of Solvation \(Condensed Media\)”](#)) and a higher detachment energy (VDE) is needed in solution in comparison to the gas phase. As a result, the photoelectron spectra of solvated anions have their peaks blue-shifted (Simons [2008](#); Schiedt et al. [1998](#); Eustis et al. [2007](#)) in comparison to their gas phase spectra.

In this work, the lowest vertical  $\pi \rightarrow \pi^*$ ,  $\pi \rightarrow \sigma^*$  excited states and core excitation of each of the molecules in gas phase and in solution were calculated. As an example, we present the excited states of TNI of 3', 5'-dADP in the gas phase and in solvation in [Fig. 34-17](#). In the gas phase, the lowest three transitions of 3', 5'-dADP are  $\pi(A) \rightarrow \pi(A)^*$ ,  $\pi(A) \rightarrow \sigma(3'-PO_4)^*$ , and  $\pi(A) \rightarrow \sigma(5'-PO_4)^*$  in nature and the corresponding transition energies are 0.99, 1.07, and 1.14 eV, respectively. The first transition,  $S_1$ , occurs from SOMO( $\pi$ )  $\rightarrow$  (121 $\alpha$  and 124 $\alpha$ ) MOs on the adenine base. The other two transitions,  $S_2$  and  $S_3$ , occur from SOMO( $\pi$ ) to 3'- and 5'-ends of the  $PO_4$  group. These transitions are singly dominant transitions and each has ca. 90% contribution. In [Fig. 34-17](#), we present the excited states of TNI of fully solvated 3', 5'-dADP + 3H<sub>2</sub>O. In this case, we found the two lowest transitions ( $S_1$  and  $S_2$ ) are  $\pi(A) \rightarrow \pi(A)^*$  in nature and the corresponding transition energies are 0.76 and 1.54 eV, respectively. Interestingly, the transitions  $\pi(A) \rightarrow \sigma(5'-PO_4)^*$  and  $\pi(A) \rightarrow \sigma(3'-PO_4)^*$  are blue-shifted under solvation toward high energy in comparison to their corresponding gas-phase values (see [Fig. 34-17](#)). This phenomenon is observed for all the cases studied here (for details see Kumar and Sevilla [[2009](#)]).

Since  $\pi \rightarrow \sigma^*$  states, localized on 5'- and 3'-ends of the  $PO_4$  group, are dissociative in nature, they are of particular interest. Therefore, we also calculated the variation of the transition energies of these states in: (1) gas-phase, (2) with discrete water molecules, and (3) and (4) in the presence of bulk solvent with two dielectric constant values  $\epsilon = 7.0$  and 78.4, respectively, for TNI and their adiabatic states. As an example, the plot of the variation of transition energies of  $\pi \rightarrow \sigma(5'-PO_4)^*$  with increasing solvation is shown in [Fig. 34-18](#). From [Fig. 34-18](#), it is evident that transition energies for the  $\pi \rightarrow \sigma^*$  states increase with increasing solvation and become less accessible by LEEs <4 eV. This conclusion is also supported by the earlier conclusion of Sevilla et al. ([1994](#)) that diffuse states are destabilized under the influence of the solvation. Therefore, from this work we conclude that  $\sigma^*$  states lie in the range of 1.1–1.7 eV (in the gas phase) and are in close agreement with the experimental threshold value of  $0.8 \pm 0.3$  eV for creating SSBs (Martin et al. [2004](#); Panajotovic et al. [2006](#)). However, the most important point we can draw from this work is that in solution these dissociative ( $\sigma^*$ ) states increase in energy by several electronvolts. This clearly suggests that solvation of DNA would reduce the direct cleavage of DNA by LEEs in the energy range of 0–4 eV.

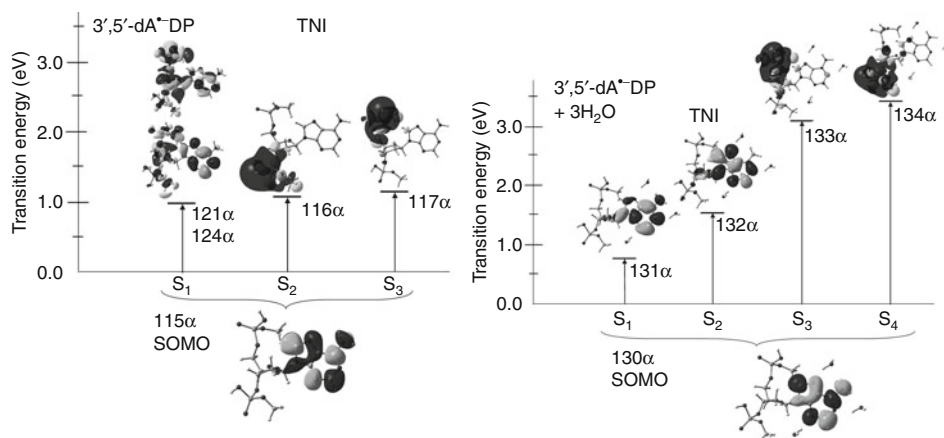
Recently, Leszczynski and coworkers (Bao et al. [2006](#); Gu et al. [2006](#)) used the B3LYP/DZP++ method to study the  $C_{5'}-O_{5'}$  and  $C_{3'}-O_{3'}$  bond cleavage in pyrimidine nucleotides anion radical in their adiabatic states. This work supported the mechanism suggested by Simons and coworkers (Barrios et al. [2002](#)). An alternative mechanism using the concept of electron-induced proton transfer mechanism was proposed by Dabkowska et al. ([2005](#)) considering a cytosine nucleotide as a model of DNA for creating SSBs in DNA. In this model,

two electrons and a proton add to the cytosine base, which then undergoes proton transfer from the sugar  $C_{2'}$  site to the base subsequently resulting in strand cleavage. Such a mechanism may be active in radiation damage regions where several excess electrons and protons are produced in a small spatial region, i.e., a spur. In addition to these works, a number of other studies related to the LEE-induced DNA damage have appeared over the last few years (Zhang et al. 2008; Xie et al. 2008; Takayanagi et al. 2009; Solomun et al. 2009; Solomun and Skalicky 2008).

## LEE Induced Base Release

In addition to LEE-induced SSBs and DSBs in DNA, glycosidic bond cleavage (base release) induced by LEE has also been experimentally observed by Sanche and coworkers (Zheng et al. 2004, 2005, 2008) as well as by Illenberger and coworkers (Ptańska et al. 2006; Abdoul-Carime et al. 2004b). LEEs with 4–15 eV energy were found to be effective in causing base release in thymidine, as well as in the DNA sequence 5'-TpTpT-3' (Zheng et al. 2004, 2008). The initial quantum yield for thymine release in thymidine was found to be  $3.2 \times 10^{-2}$  pre-incident electron (Zheng et al. 2004). The conversion of thymidine into thymine and sugar was proposed due to the localization of LEEs into the antibonding MOs of  $N_1-C_{1'}$  (glycosidic) bond which leads either to homolytic or heterolytic cleavage of the  $N_1-C_{1'}$  bond joining the thymine and sugar ring (Zheng et al. 2004).

Using the B3LYP/DZP++ method, Schaefer and coworkers (Gu et al. 2005), calculated the ground-state adiabatic PESs for the  $N_1-C_{1'}$  bond dissociation considering the radical anions of 2'-deoxyribothymidine (dT) and 2'-deoxyribocytidine (dC). Subsequently, a detailed analysis of the base release process in dC, dT, and deoxyadenosine in two conformations, i.e., dA1 (with internal hydrogen bonding) and dA2 (without hydrogen bond) was carried

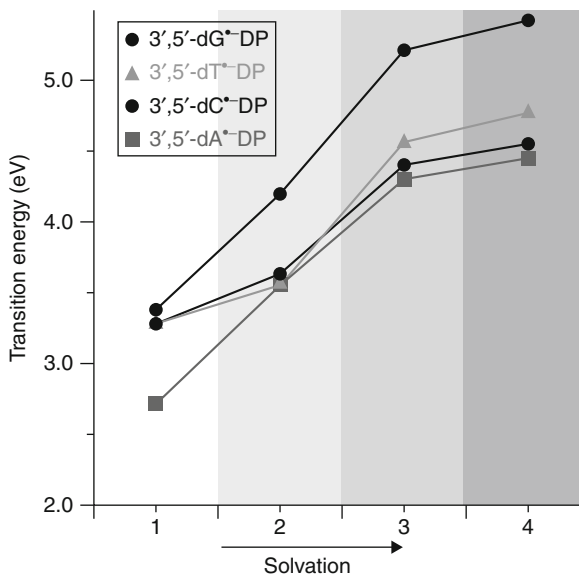


■ Fig. 34-17

TD-BHandHLYP/6-31G\* computed transition energies in TNI state of 3',5'-dADP in gas phase (*left*) and aqueous solution (*right*). The effect of bulk water solvent was considered using IEF-PCM model on the trihydrated 3',5'-dA $\cdot$ -DP system. Transition from SOMO to different MOs (*shape resonance*) are shown. Transition energies are given in electronvolts (Reprinted with permission from Kumar and Sevilla [2009]. © (2009) Wiley-VCH Verlag GmbH & Co. KGaA Weinheim)



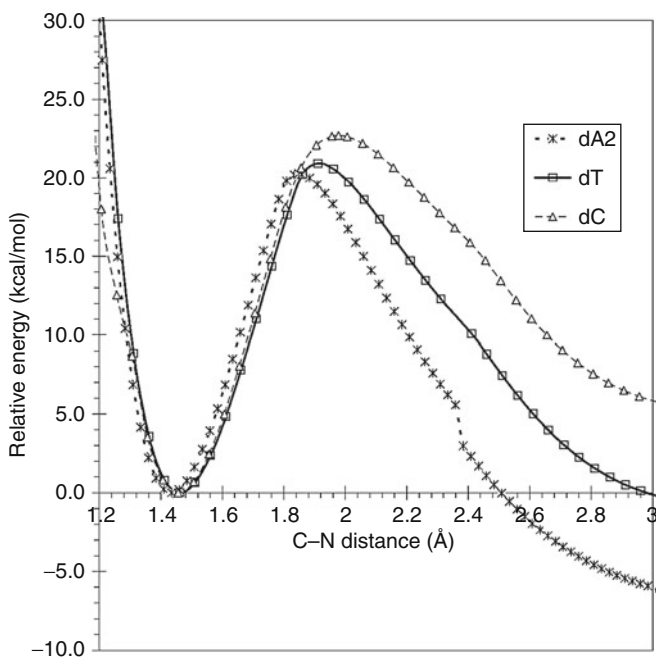
out by Li, Sanche, and Sevilla (Xi et al. 2006) using B3LYP/6-31+G(d) level of theory. This work provided some insight into the relative energies of  $N_1-C_{1'}$  (glycosidic) bond dissociation of these molecules in their neutral and anion radical states in gas phase as well as in the presence of bulk solvent via the PCM method. This study showed that LEEs in fact greatly weakened the  $N_1-C_{1'}$  bond strength of these molecules in comparison to their corresponding bond strength in neutral state. The bond dissociation energy of the  $N_1-C_{1'}$  bond in gas phase is found to be exergonic for dA ( $\Delta G = -14$  kcal/mol) and dT ( $\Delta G = -6$  kcal/mol), and is endergonic for dC ( $\Delta G = 1$  kcal/mol). The PESs for the  $N_1-C_{1'}$  bond dissociation of these molecules are shown in [Fig. 34-19](#). From [Fig. 34-19](#), it is clearly evident that the barrier for the  $N_1-C_{1'}$  bond dissociation is located between 19 and 23 kcal/mol for all the molecules. The experimental value for LEE-induced thymine release in dT of about 1 eV (ca. 23 kcal/mol) (Zheng et al. 2004, 2005, 2008; Ptasńska et al. 2006; Abdoul-Carime et al. 2004b) is in good agreement with the calculated value of barrier for thymine release in dT (19 kcal/mol) (see [Fig. 34-19](#)). From the SOMO, it was found that in adiabatic states all the molecules showed the valence bound  $\pi^*$  state. Also, on the PES as the  $N_1-C_{1'}$  bond extends from its equilibrium value, the  $\pi^*$  (valence state) crosses the antibonding  $\sigma^*$  dissociative state at transition state and excess electron localized on  $N_1-C_{1'}$  bond region creating a negative nitrogen site on the base and a free radical at  $C_{1'}$  site on the sugar ring.



■ Fig. 34-18

Variation of transition energies (eV) of the  $\pi \rightarrow \sigma^*(5'-PO_4)^*$  excited state of nucleotides in adiabatic state with increasing solvation. Different solvation levels labeled on X-axis are: 1 – gas phase, 2 – three discrete water molecules, 3 – three waters and a continuous dielectric ( $\epsilon = 7.0$ ) and 4 – three waters and a continuous dielectric ( $\epsilon = 78.4$ ) (Reprinted with permission from Kumar and Sevilla [2009]. © (2009) Wiley-VCH Verlag GmbH & Co. KGaA, Weinheim)





■ Fig. 34-19

Anionic N1-C potential energy surfaces of deoxyadenosine (dA2), thymidine (dT), and deoxycytidine (dC). dA1 has a similar profile to dA2 (Reprinted with permission from Xi et al. [2006]. © (2006) Radiation Research Society)

## Effect of Solvation on Strand Break Formation

In comparison to gas-phase investigations, studies concerning electron-induced strand breaks under the influence of solvation are few in number. From pulse radiolysis experiments, it is well known that solvated electrons do not cause strand breaks upon attachment to DNA in an aqueous environment (von Sonntag 1987; Nabben et al. 1982); this is discussed in detail in section “Effect of Solvation (Condensed Media)”. Most theoretical studies to date have assumed adiabatic systems and have attempted to explain the effect of solvation on strand breaks using polarized continuum model (Simons 2006; Barrios et al. 2002; Xi et al. 2003; Bao et al. 2006; Gu et al. 2006; Xi et al. 2006). Though the PCM model is adequate for bulk solvent effects, it neglects the specific local interactions and hydrogen-bonding energetics, which are substantial contributions to solvation energetics and are critical in determining reaction pathways. This level of sophistication is usually avoided owing to the increase in complexity of the treatment.

In order to gain an understanding of the influence of specific hydrogen-bonding effects in an aqueous environment on potential strand breaks, we considered (Kumar and Sevilla 2007) a 5'-dTMP that includes a solvation shell of 11 waters and a sodium counterion to neutralize the phosphate group. Using this hydrated (5'-dTMPNa + 11 H<sub>2</sub>O) model, we calculated the adiabatic PES of C<sub>5'</sub>-O<sub>5'</sub> bond dissociation in the neutral and radical anion states using the

B3LYP/6-31G\*\* level of theory. On the PES of radical anion state, we also plotted the SOMO at each step of the  $C_{5'}-O_{5'}$  bond elongation. This calculation showed that the solvent has a pronounced effect which would essentially eliminate strand break formation. The barrier for the  $C_{5'}-O_{5'}$  bond dissociation in the radical state was found to be 29 kcal/mol. This is in accord with the experimental finding that aqueous electrons do not cause strand breaks.

Very interestingly, we found that SOMO initially localized on the  $\pi^*$  MO on thymine was still localized on the thymine at the TS. However, in gas phase (see [▶ Figs. 34-14](#) and [▶ 34-15](#)), the SOMO transferred to the  $\sigma^*$   $C_{5'}-O_{5'}$  bond at the TS. The B3LYP/6-31G\*\* calculated AEA and VDE of 5'-dTMPNa + 11 H<sub>2</sub>O in full solvent using PCM was found to be 2.17 and 3.20 eV, respectively. This study confirmed that in comparison to the gas-phase, the vertical detachment energies (VDEs) of the 5'-dTMP radical anion in the solvated environment is enhanced appreciably (3.20 eV), which shows that the excess electron in the solvated anion radical is highly stable toward electron detachment. Recently, the 3'- and 5'-C-O bond rupture in cytosine monophosphate was studied by Schyman et al. (2008) in the aqueous environment using a molecular dynamics study. The authors also found a higher barrier for the 3'- and 5'-C-O bond rupture. In another study, Schyman and Laaksonen (2008) studied the  $C_{3'}/O_{3'}$  bond dissociation in guanine 3'-monophosphate (3'-GMPH) radical anion in gas phase as well as in the presence of 21 water molecules using the B3LYP/DZP++ method. In this calculation, the authors found dipole-bound state for gas phase, which was expected. Surprisingly they also reported dipole-bound state for the hydrated system. As has already been mentioned, in solution diffuse states such as dipole-bound states are destabilized relative to valence-bound states, which become lower in energy (see [▶ Fig. 34-10](#) and Li et al. [2002]). This is already well established experimentally from the photoelectron spectroscopy of nucleic acid bases (Schiedt et al. 1998) as well as from theoretical calculations (Li et al. 2002). Thus, the calculation of Schyman and Laaksonen (2008) for hydrated 3'-GMPH radical anion is considered to be problematic.

More recently, Loos et al. (2009) calculated the  $C_{3'}/O_{3'}$  bond cleavage of the radical anion of 2-deoxycytidine-3'-monophosphate moiety (3'-dCMPH) in single- and double-stranded DNA (5'-CCC-3' sequence) in gas phase using the QM/MM approach. The authors also reported the dipole-bound diffuse state localized near the phosphate group. They did not, however, report the initial attachment of the excess electron on the cytosine. Thus, the approach which may be applicable to the gas phase is not predictive for the condensed phase. A similar calculation was already done by Simons and coworkers (Anusiewicz et al. 2004) considering a single-strand CCC sequence. Due to the large size of the system, they considered the ONIOM approach. The central nucleotide was treated with the UHF method with a 6-311+G\* basis set; however, the two terminal nucleotides were treated at the lower level using a 4-31G\* basis set. In this calculation, the initial attachment of an excess electron was found to be localized on the  $\pi^*$  MOs of the middle cytosine showing valence-bound nature as expected from ESR experiments (Sevilla et al. 1991). A recent report by Kobyłeczka et al. (2008) also showed a valence-bound anion formation on thymine in the DNA  $\pi$ -stacked system using the MP2/aug-cc-pVDZ method.

Very recently, Park et al. (2011) investigated the DNA damage caused by LEE for nucleotides and short oligonucleotides in the solid state. The samples of TpTpT were irradiated with monoenergetic electrons of energy 10 eV and subsequently analyzed by high-performance liquid chromatography (HPLC) and mass spectrometry. The study showed that about 67% of the total damage was identified as 5,6-dihydrothymine and 33% damage involved the phosphodiester-sugar (C-O) bond and the N-glycosidic bond (CN) dissociation. However, in

a similar type of study (Li et al. 2010), the total damage (base release and C–O bond cleavage) was found to undergo a twofold decrease for the following trimer sequences in the order: TTT > TCT > TAT > TGT. The nonmodified base release was found to be 17–24% of the total damage and mainly occurred from the terminal sites of the trimers. The phosphodiester–sugar (C–O) bond cleavage was found to be only 9–20%. Both the studies certainly conclude that an excess electron initially attached to the base forms a stable radical anion, which protonates to form 5,6-dihydrothymine as observed in a variety of ESR experiments on hydrated DNA samples (Sevilla et al. 1991; Gregoli et al. 1989). Once localized to the base, no transfer to phosphodiester–sugar bond region is likely, as discussed in sections “Effect of Solvation (Condensed Media)” and “Proposed Theoretical Models of DNA Damage”. Thus, SSBs are not produced from the adiabatic base anion radicals by reductive cleavage.

Using B3LYP/DZP++ level of theory, Gu et al. (2010a, b) reported the  $C_{3'}-O_{3'}$ ,  $C_{5'}-O_{5'}$   $\sigma$  bond and N-glycosidic bond dissociation energies of anion radicals of 2'-deoxycytidine-3',5'-diphosphate (3',5'-dCMP), 2'-deoxythymidine-3',5'-diphosphate (3',5'-dTMP), and 2'-deoxyguanosine-3',5'-diphosphate (3',5'-dGMP) in gas phase and in aqueous media using the PCM model. For 3',5'-dCMP and 3',5'-dTMP, the order of bond dissociation energy was found to be  $C_{3'}-O_{3'} < C_{5'}-O_{5'} < \text{N-glycosidic bond}$ , and the calculated energies lie in the range ca. 6–29 kcal/mol for both gas phase and in aqueous solution. For 3',5'-dGMP, the energies for breaking the corresponding bonds in the gas phase were calculated to be 11–24 kcal/mol, while in aqueous solution, the energies decrease appreciably than their gas-phase values and lie in the range ca. 1–10 kcal/mol, which indicates that  $C_{5'}-O_{5'}$  bonds are more susceptible for cleavage than  $C_{3'}-O_{3'}$  bonds. However, these activated processes are unlikely in aqueous solutions since the faster protonation reactions of the anion radicals will outcompete such processes as pointed out above.

ESR work by Becker et al. (1996, 2003) has found evidence for both phosphodiester–sugar (C–O) bond cleavage and P–O bond cleavage (see Scheme 34-1). In these experiments, free radicals formed from 60 MeV/nucleon  $^{16}\text{O}^{8+}$  ion beam irradiation of DNA samples at 77 K were analyzed by the ESR and a new phosphorus-centered radical species was identified by its large  $^{31}\text{P}$  parallel hyperfine coupling of about 780 G (Becker et al. 1996). The radical was identified as a phosphoryl radical, which was produced by the direct dissociation of the P–O bond. However, the yield of this radical was found to be very small (0.1% of the total radicals). In other experiments, DNA samples were irradiated by  $^{36}\text{Ar}$  and  $^{40}\text{Ar}$  ion beams and these two types of radicals were again identified by ESR at 77 K (Becker et al. 2003). These radicals were produced from dissociation of the C–O and P–O bonds at the  $C_{3'}$  of the sugar moiety. The yield of the  $C_{3'}$ -dephos radical produced by C–O bond dissociation was estimated as 95%, while the  $\text{ROPO}_2^-$  produced by P–O bond dissociation was estimated to be 5%.

Very recently, a mechanism of SSB by P–O bond fragmentation in DNA was proposed by Rak et al. (2011) using B3LYP/6-31++G\*\* level of theory. In their model, the authors proposed that LEE initially attached to the thymine, which is subsequently protonated at the C5 position of the thymine to produce the dihydro-6'-thymyl radical. In the next event, intramolecular hydrogen atom transfer takes place from  $C_{3'}$  or  $C_{5'}$  sites of sugar ring to the C6 site of the thymine, and finally the P–O bond is broken. However, from the calculated kinetic and thermodynamic barriers related to the P–O bond fragmentation, the authors concluded that the proposed mechanism was not favorable over the LEE-induced C–O bond fragmentation. ESR studies in solution suggest protonation at C6 of the thymine anion radical is favored, and the most favored reaction path for the  $C_{5'}$  radical in aqueous media is by phosphate loss, i.e., C–O bond cleavage.

## Conclusions

---

Our understanding of the interaction of low-energy electrons with DNA has increased substantially over the past few years. From experiment it is clear that single- and double-strand breaks, base damage, and base release are all direct results of DEA. For strand breaks, addition of an electron to the base and the sugar phosphate backbone can lead to strand breaks from shape and core-excited resonances. From their higher energies and nature, core-excited resonances are those likely to be involved in double-strand breaks. Simple vibrational excitations have been shown to provide the necessary excitation when combined with an even 0 eV electron to result in strand cleavage. While much work presented in this chapter has focused on the DNA components without surroundings (“gas phase” calculations), these calculations often give diffuse states (dipole-bound electrons and continuum states) as ground states for the system. Theoretical treatments of DNA systems, relevant to biology, must include the aqueous phase, including specific water hydrogen bonding, as well as the base stacking and counterion placement. In such systems, diffuse states are greatly destabilized and valence-bound states dominate. Theoretical methods such as DFT with various solvation models are now able to treat more complex and more biologically relevant systems. In the future, improved techniques should provide a better understanding of the actions of LEEs with the DNA in a biological environment.

## Acknowledgments

---

This work was supported by the NIH NCI under Grant R01CA045424. The authors thank Prof. P.D. Burrow for helpful discussions and advice. The authors are also grateful to the Arctic Region Supercomputing Center (ARSC) for generously providing the computational time to perform some of these calculations. Computational studies were also supported by a computational facilities grant NSF CHE-0722689.

## References

---

- Abdoul-Carime, H., Huels, M. A., Illenberger, E., & Sanche, L. (2001). Sensitizing DNA to secondary electron damage: Resonant formation of oxidative radicals from 5-halouracils. *Journal of the American Chemical Society*, *123*, 5354.
- Abdoul-Carime, H., Gohlke, S., & Illenberger, E. (2004a). Site-specific dissociation of DNA bases by slow electrons at early stages of irradiation. *Physical Review Letters*, *92*, 168103.
- Abdoul-Carime, H., Gohlke, S., Fischbach, E., Scheike, J., & Illenberger, E. (2004b). Thymine excision from DNA by subexcitation electrons. *Chemical Physics Letters*, *387*, 267.
- Adhikary, A., Malkhasian, A. Y. S., Collins, S., Koppen, J., Becker, D., & Sevilla, M. D. (2005). UVA-visible photo-excitation of guanine radical cations produces sugar radicals in DNA and model structures. *Nucleic Acids Research*, *33*, 5553.
- Adhikary, A., Collins, S., Koppen, J., Becker, D., & Sevilla, M. D. (2006a). C5'- and C3'-sugar radicals produced via photo-excitation of one-electron oxidized adenine in 2'-deoxyadenosine and its derivatives. *Nucleic Acids Research*, *34*, 1501.
- Adhikary, A., Kumar, A., & Sevilla, M. D. (2006b). Photo-induced hole transfer from base to sugar in DNA: Relationship to primary radiation damage. *Radiation Research*, *165*, 479.
- Adhikary, A., Collins, S., Khanduri, D., & Sevilla, M. D. (2007). Sugar radicals formed by photoexcitation of guanine cation radical in oligonucleotides. *The Journal of Physical Chemistry B*, *111*, 7415.

- Adhikary, A., Khanduri, D., Kumar, A., & Sevilla, M. D. (2008). Photoexcitation of adenine cation radical [A<sup>+</sup>] in the near UV-vis region produces sugar radicals in adenosine and in its nucleotides. *The Journal of Physical Chemistry B*, *112*, 15844.
- Aflatooni, K., Gallup, G. A., & Burrow, P. D. (1998). Electron attachment energies of the DNA bases. *The Journal of Physical Chemistry A*, *102*, 6205.
- Allan, M. (1989). Study of triplet states and short-lived negative ions by means of electron impact spectroscopy. *Journal of Electron Spectroscopy and Related Phenomena*, *48*, 219.
- Anusiewicz, I., Berdys, J., Sobczyk, M., Skurski, P., & Simons, J. (2004). Effects of base  $\pi$ -stacking on damage to DNA by low-energy electrons. *The Journal of Physical Chemistry A*, *108*, 11381.
- Ashfold, M. N. R., Cronin, B., Devine, A. L., Dixon, R. N., & Nix, G. D. (2006). The role of pi sigma\* excited states in the photodissociation of heteroaromatic molecules. *Science*, *312*, 1637.
- Baccarelli, I., Gianturco, F. A., Grandi, A., Sanna, N., Lucchese, R. R., Bald, I., et al. (2007). Selective bond breaking in  $\beta$ -D-ribose by gas-phase electron attachment around 8 eV. *Journal of the American Chemical Society*, *129*, 6269.
- Bachorz, A. R., Klopper, W., & Gutowski, M. (2007). Coupled-cluster and explicitly correlated perturbation-theory calculations of the uracil anion. *The Journal of Chemical Physics*, *126*, 085101.
- Baker, J., Wolinski, K., Malagoli, M., Kinghorn, D., Wolinski, P., Magyarfalvi, G., et al. (2009). Quantum chemistry in parallel with PQS. *Journal of Computational Chemistry*, *30*, 317.
- Bald, I., Kopyra, J., & Illenberger, E. (2006). Selective excision of C5 from D-ribose in the gas phase by low-energy electrons (0–1 eV): Implications for the mechanism of DNA damage. *Angewandte Chemie International Edition*, *45*, 4851.
- Bald, I., Dąbkowska, I., & Illenberger, E. (2008). Probing biomolecules by laser-induced acoustic desorption: Electrons at near zero electron volts trigger sugar-phosphate cleavage. *Angewandte Chemie International Edition*, *47*, 8518.
- Bao, X., Wang, J., Gu, J., & Leszczynski, J. (2006). DNA strand breaks induced by near-zero-electron-volt electron attachment to pyrimidine nucleotides. *Proceedings of the National Academy of Sciences of the United States of America*, *103*, 5658.
- Barrios, R., Skurski, P., & Simons, J. (2002). Mechanism for damage to DNA by low-energy electrons. *The Journal of Physical Chemistry B*, *106*, 7991.
- Becker, D., & Sevilla, M. D. (1993). The chemical consequences of radiation damage to DNA. *Advances in Radiation Biology*, *17*, 121.
- Becker, D., & Sevilla, M. D. (2008). EPR studies of radiation damage to DNA and related molecules. *Electron Paramagnetic Resonance*, *21*, 33.
- Becker, D., Razskazovskii, Y., Callaghan, M. U., & Sevilla, M. D. (1996). Electron spin resonance of DNA irradiated with a heavy-ion beam (<sup>16</sup>O<sup>8+</sup>): Evidence for damage to the deoxyribose phosphate backbone. *Radiation Research*, *146*, 361.
- Becker, D., Bryant-Friedrich, A., Trzasko, C., & Sevilla, M. D. (2003). Electron spin resonance study of DNA irradiated with an argon-ion beam: Evidence for formation of sugar phosphate backbone radicals. *Radiation Research*, *160*, 174.
- Becker, D., Adhikary, A., & Sevilla, M. D. (2007). The role of charge and spin migration in DNA radiation damage. In T. Chakraborty (Ed.), *Charge migration in DNA* (p. 139). Berlin/Heidelberg: Springer.
- Becker, D., Adhikary, A., & Sevilla, M. D. (2010). Mechanisms of radiation-induced DNA damage: Direct effects. In B. S. M. Rao & J. Wishart (Eds.), *Recent trends in radiation chemistry* (p. 509). Singapore/New Jersey/London: World Scientific Publishing.
- Boudaïffa, B., Cloutier, P., Hunting, D., Huels, M. A., & Sanche, L. (2000). Resonant formation of DNA strand breaks by low-energy (3 to 20 eV) electrons. *Science*, *287*, 1658.
- Brun, E., Cloutier, P., Sicard-Roselli, C., Fromm, M., & Sanche, L. (2009). Damage induced to DNA by low-energy (0–30 eV) electrons under vacuum and atmospheric conditions. *The Journal of Physical Chemistry B*, *113*, 10008.
- Burrow, P. D., Gallup, G. A., Scheer, A. M., Deniff, S., Ptasńska, S., Märk, T., et al. (2006). Vibrational Feshbach resonances in uracil and thymine. *The Journal of Chemical Physics*, *124*, 124310.
- Burrow, P. D., Gallup, G. A., & Modelli, A. (2008). Are there  $\pi^*$  shape resonances in electron scattering from phosphate groups? *The Journal of Physical Chemistry A*, *112*, 4106.
- Burrows, C. J., & Muller, J. G. (1998). Oxidative nucleobase modifications leading to strand scission. *Chemical Reviews*, *98*, 1109.
- Cadet, J., Douki, T., & Ravanat, J. L. (2008). Oxidatively generated damage to the guanine moiety of DNA: Mechanistic aspects and formation in cells. *Accounts of Chemical Research*, *41*, 1075.
- Caron, L., & Sanche, L. (2003). Low-energy electron diffraction and resonances in DNA and other helical macromolecules. *Physical Review Letters*, *91*, 113201.

- Caron, L., & Sanche, L. (2004). Diffraction in resonant electron scattering from helical macromolecules: A- and B-type DNA. *Physical Review A*, 70, 032719.
- Caron, L., & Sanche, L. (2005). Diffraction in resonant electron scattering from helical macromolecules: Effects of the DNA backbone. *Physical Review A*, 72, 032726.
- Caron, L., & Sanche, L. (2006). Temporary electron localization and scattering in disordered single strands of DNA. *Physical Review A*, 73, 062707.
- Caron, L., Sanche, L., Tonzani, S., & Greene, C. H. (2008). Diffraction in low-energy electron scattering from DNA: Bridging gas-phase and solid-state theory. *Physical Review A*, 78, 042710.
- Chen, D., & Gallup, G. A. (1990). The relationship of the virtual orbitals of self-consistent-field theory of temporary negative ions in electron scattering from molecules. *The Journal of Chemical Physics*, 93, 8893.
- Colson, A. O., Besler, B., & Sevilla, M. D. (1992). Ab initio molecular orbital calculations on DNA base pair radical ions: Effect of base pairing on proton-transfer energies, electron affinities, and ionization potentials. *The Journal of Physical Chemistry*, 96, 9787.
- Compton, R. N., Yoshioka, Y., & Jordan, K. D. (1980). Comment on semi-empirical calculations of electron affinities. *Theoretica Chimica Acta*, 54, 259.
- Crowell, R. A., & Bartels, D. M. (1996). Multiphoton ionization of liquid water with 3.0–5.0 eV photons. *Journal of Physical Chemistry*, 100, 17940.
- Dabkowska, I., Rak, J., & Gutowski, M. (2005). DNA strand breaks induced by concerted interaction of H radicals and low-energy electrons – A computational study on the nucleotide of cytosine. *European Physical Journal D: Atomic, Molecular, Optical and Plasma Physics*, 35, 429.
- Denifl, S., Sulzer, P., Huber, D., Zappa, F., Probst, M., Märk, T. D., et al. (2007). Influence of functional groups on the site-selective dissociation of adenine upon low-energy electron attachment. *Angewandte Chemie International Edition*, 46, 5238.
- Desfancois, C., Abdoul-Carime, H., & Schermann, J. P. (1996). Electron attachment to isolated nucleic acid bases. *The Journal of Chemical Physics*, 104, 7792.
- Desfancois, C., Periquet, V., Bouteiller, Y., & Schermann, J. P. (1998). Valence and dipole binding of electrons to uracil. *The Journal of Physical Chemistry A*, 102, 1274.
- Dessent, C. E. H., Kim, J., Johnson, M. A. (2000). Spectroscopic observation of vibrational Feshbach resonances in near-threshold photoexcitation of  $X^- \cdot CH_3NO_2$  ( $X^- = I^-$  and  $Br^-$ ). *Faraday Discussion*, 115, 395.
- Domcke, W., & Sobolewski, A. L. (2003). Chemistry-unraveling the molecular mechanisms of photoacidity. *Science*, 302, 1693.
- Dora, A., Tennyson, J., Bryjko, L., & van Mourik, T. (2009). R-matrix calculation of low-energy electron collisions with uracil. *The Journal of Chemical Physics*, 130, 164307.
- Dreuw, A., & Head-Gordon, M. (2005). Single-reference ab Initio methods for the calculation of excited states of large molecules. *Chemical Reviews*, 105, 4009.
- Eustis, S., Wang, D., Lyapustina, S., & Bowen, K. H. (2007). Photoelectron spectroscopy of hydrated adenine anions. *The Journal of Chemical Physics*, 127, 224309.
- Galduel, Y., Pommeret, S., Migus, A., & Antonetti, A. (1989). Femtosecond dynamics of geminate pair recombination in pure liquid water. *The Journal of Physical Chemistry*, 93, 3880.
- Gianturco, F. A., & Lucchese, R. R. (2004). Radiation damage of biosystems mediated by secondary electrons: Resonant precursors for uracil molecules. *The Journal of Chemical Physics*, 120, 7446.
- Gianturco, F. A., Sebastianelli, F., Lucchese, R. R., Baccarelli, I., & Sanna, N. (2008). Ring-breaking electron attachment to uracil: Following bond dissociations via evolving resonances. *The Journal of Chemical Physics*, 128, 174302.
- Gregoli, S., Olast, M., & Bertinichamps, A. (1989). Radiolytic pathways in  $\gamma$ -irradiated DNA: Influence of chemical and conformational factors. *Radiation Research*, 89, 238.
- Gu, J., Xie, Y., & Schaefer, H. F. (2005). glycosidic bond cleavage of pyrimidine nucleosides by low-energy electrons: A theoretical rationale. *Journal of the American Chemical Society*, 127, 1053.
- Gu, J., Wang, J., & Leszczynski, J. (2006). Electron attachment-induced DNA single strand breaks:  $C_3-O_3'$   $\sigma$ -bond breaking of pyrimidine nucleotides predominates. *Journal of the American Chemical Society*, 128, 9322.
- Gu, J. D., Wang, J., & Leszczynski, J. (2010a). Electron attachment-induced DNA single-strand breaks at the pyrimidine sites. *Nucleic Acids Research*, 38, 5280.
- Gu, J., Wang, J., & Leszczynski, J. (2010b). Comprehensive analysis of DNA strand breaks at the guanosine site induced by low-energy electron attachment. *Chemphyschem*, 11, 175.



- Hanel, G., Gstir, B., Denifl, S., Scheier, P., Probst, M., Farizon, B., et al. (2003). Electron attachment to uracil: Effective destruction at subexcitation energies. *Physical Review Letters*, *90*, 188104.
- Haranczyk, M., & Gutowski, M. (2005). Valence and dipole-bound anions of the most stable tautomers of guanine. *Journal of the American Chemical Society*, *127*, 699.
- Hendricks, J. H., Lyapustina, S. A., de Clercq, H. L., Snodgrass, J. T., & Bowen, K. H. (1996). Dipole bound, nucleic acid base anions studied via negative ion photoelectron spectroscopy. *The Journal of Chemical Physics*, *104*, 7788.
- Hendricks, J. H., Lyapustina, S. A., de Clercq, H. L., & Bowen, K. H. (1998). The dipole bound-to-covalent anion transformation in uracil. *The Journal of Chemical Physics*, *108*, 8.
- Hotop, H., Ruf, M. W., Allan, M., & Fabrikant, I. I. (2003). Resonance and threshold phenomena in low-energy electron collisions with molecules and clusters. *Advances in Atomic, Molecular, and Optical Physics*, *49*, 85.
- Huels, M. A., Boudaïffa, B., Cloutier, P., Hunting, D., & Sanche, L. (2003). Single, double, and multiple double strand breaks induced in DNA by 3–100 eV electrons. *Journal of the American Chemical Society*, *125*, 4467.
- Hush, N. S., & Cheung, A. S. (1975). Ionization potentials and donor properties of nucleic acid bases and related compounds. *Chemical Physics Letters*, *34*, 11.
- Illenberger, E. (1992). Electron-attachment reactions in molecular clusters. *Chemical Reviews*, *92*, 1589.
- International Commission on Radiation Units and Measurements. (1979). ICRU Report No. 31. ICRU, Washington, DC.
- Jordan, K. D., & Burrow, P. D. (1987). Temporary anion states of polyatomic hydrocarbons. *Chemical Reviews*, *87*, 557.
- Khanduri, D., Collins, S., Kumar, A., Adhikary, A., & Sevilla, M. D. (2008). Formation of sugar radicals in RNA model systems and oligomers via excitation of guanine cation radical. *The Journal of Physical Chemistry B*, *112*, 2168.
- Kobylecka, M., Leszczynski, J., & Rak, J. (2008). Valence anion of thymine in the DNA  $\pi$ -stack. *Journal of the American Chemical Society*, *130*, 15683.
- König, C., Kopyra, J., Bald, I., & Illenberger, E. (2006). Dissociative electron attachment to phosphoric acid esters: The direct mechanism for single strand breaks in DNA. *Physical Review Letters*, *97*, 018105.
- Kumar, A., & Sevilla, M. D. (2007). Low-energy electron attachment to 5'-thymidine monophosphate: Modeling single strand breaks through dissociative electron attachment. *The Journal of Physical Chemistry B*, *111*, 5464.
- Kumar, A., & Sevilla, M. D. (2008a). Radiation effects on DNA: Theoretical investigations of electron, hole and excitation pathways to DNA damage. In M. K. Shukla, J. Leszczynski (Eds.), & J. Leszczynski (Series Ed.), *Radiation induced molecular phenomena in nucleic acids: Vol. 5. Challenges and advances in computational chemistry and physics* (p. 577). Amsterdam: Springer.
- Kumar, A., & Sevilla, M. D. (2008b). The role of  $\pi\sigma^*$  excited states in electron-induced DNA strand break formation: A time-dependent density functional theory study. *Journal of the American Chemical Society*, *130*, 2130.
- Kumar, A., & Sevilla, M. D. (2009). Role of excited states in low-energy electron (LEE) induced strand breaks in DNA model systems: Influence of aqueous environment. *ChemPhysChem*, *10*, 1426.
- Kumar, A., & Sevilla, M. D. (2010a). Proton-coupled electron transfer in DNA on formation of radiation-produced Ion radicals. *Chemical Reviews*, *110*, 7002.
- Kumar, A., & Sevilla, M. D. (2010b). Theoretical modeling of radiation-induced DNA damage. In M. Greenberg (Ed.), *Radical and radical ion reactivity in nucleic acid chemistry* (p. 1). Hoboken: Wiley, ISBN: 978-0-470-25558-2.
- Lane, N. F. (1980). The theory of electron-molecule collisions. *Reviews of Modern Physics*, *52*, 29.
- Levesque, P. L., Michaud, M., Sanche, L. (2003). Cross sections for low energy (1–12 eV) inelastic electron scattering from condensed thymine. *Nuclear Instruments and Methods in Physics Research B*, *208*, 225.
- Li, X. F., Cai, Z. L., & Sevilla, M. D. (2002). DFT calculations of the electron affinities of nucleic acid bases: Dealing with negative electron affinities. *The Journal of Physical Chemistry A*, *106*, 1596.
- Li, X. F., Sevilla, M. D., & Sanche, L. (2004). Hydrogen atom loss in pyrimidine DNA bases induced by low-energy electrons: Energetics predicted by theory. *The Journal of Physical Chemistry B*, *108*, 19013.
- Li, X., & Sevilla, M. D. (2007). DFT treatment of radiation produced radicals in DNA model systems. *Advances in Quantum Chemistry*, *52*, 59.
- Li, Z., Zheng, Y., Cloutier, P., Sanche, L., & Wagner, J. R. (2008). Low energy electron induced DNA damage: Effects of terminal phosphate and base moieties on the distribution of damage. *Journal of the American Chemical Society*, *130*, 5612.

- Li, Z., Cloutier, P., Sanche, L., & Wagner, J. R. (2010). Low-energy electron-induced DNA damage effect of base sequence in oligonucleotide trimers. *Journal of the American Chemical Society*, 132, 5422.
- Loos, P. F., Dumont, E., Laurent, A. D., & Assfeld, X. (2009). Important effects of neighbouring nucleotides on electron induced DNA single-strand breaks. *Chemical Physics Letters*, 475, 120.
- Martin, F., Burrow, P. D., Cai, Z., Cloutier, P., Hunting, D., & Sanche, L. (2004). DNA strand breaks induced by 0–4 eV electrons: The role of shape resonances. *Physical Review Letters*, 93, 068101.
- McConkey, J. W., Malone, C. P., Johnson, P. V., Winstead, C., McKoy, V., & Kanik, I. (2008). Electron impact dissociation of oxygen-containing molecules – A critical review. *Physics Reports*, 466, 1.
- Modelli, A. (2003). Electron attachment and intramolecular electron transfer in unsaturated chloroderivatives. *Physical Chemistry Chemical Physics*, 5, 2923.
- Modelli, A., & Martin, H. D. (2002). Temporary anions and empty level structure in cyclobutanediones: Through-space and through-bond interactions. *The Journal of Physical Chemistry A*, 106, 7271.
- Nabben, F. J., Karman, J. P., & Loman, H. (1982). Inactivation of biologically active DNA by hydrated electrons. *International Journal of Radiation Biology*, 42, 23.
- Neese, F., Hansen, A., Wennmohs, F., & Grimme, S. (2009). Accurate theoretical chemistry with coupled pair models. *Accounts of Chemical Research*, 42, 641.
- Orlando, T. M., Oh, D., Chen, Y., & Aleksandrov, A. B. (2008). Low-energy electron diffraction and induced damage in hydrated DNA. *The Journal of Chemical Physics*, 128, 195102.
- Orlov, V. M., Smirnov, A. N., & YaM, V. (1976). Ionization potentials and electron-donor ability of nucleic acid bases and their analogues. *Tetrahedron Letters*, 17, 4315.
- Oyler, N. A., & Adamowicz, L. (1993). Electron attachment to uracil. Theoretical *ab initio* study. *The Journal of Physical Chemistry*, 97, 11122.
- Oyler, N. A., & Adamowicz, L. (1994). Theoretical *ab initio* calculations of the electron affinity of thymine. *Chemical Physics Letters*, 219, 223.
- Panajotovic, R., Martin, F., Cloutier, P. C., Hunting, D., & Sanche, L. (2006). Effective cross sections for production of single-strand breaks in plasmid DNA by 0.1 to 4.7 eV electrons. *Radiation Research*, 165, 452.
- Park, Y., Li, Z., Cloutier, P., Sanche, L., & Wagner, J. R. (2011). DNA damage induced by low-energy electrons: Conversion of thymine to 5,6-dihydrothymine in the oligonucleotide trimer TpTpT. *Radiation Research*, 175, 240.
- Periquet, V., Moreau, A., Carles, S., Schermann, J. P., & Desfrancois, C. (2000). Cluster size effects upon anion solvation of N-heterocyclic molecules and nucleic acid bases. *Journal of Electron Spectroscopy and Related Phenomena*, 106, 141.
- Pimblott, S. M., & LaVerne, J. A. (2007). Production of low-energy electrons by ionizing radiation. *Radiation Physics and Chemistry*, 76, 1244.
- Pimblott, S. M., Laverne, J. A., & Mozumber, A. (1996). Monte Carlo simulation of range and energy deposition by electrons in gaseous and liquid water. *The Journal of Physical Chemistry*, 100, 8595.
- Ptasińska, S., & Sanche, L. (2007a). Dissociative electron attachment to a basic DNA. *Physical Chemistry Chemical Physics*, 9, 1730.
- Ptasińska, S., & Sanche, L. (2007b). Dissociative electron attachment to hydrated single DNA strands. *Physical Review E*, 75, 031915.
- Ptasińska, S., Denifl, S., Scheier, P., Illenberger, E., & Märk, T. D. (2005a). Bond- and site-selective loss of H atoms from nucleobases by very-low-energy electrons (<3 eV). *Angewandte Chemie International Edition*, 44, 6941.
- Ptasińska, S., Denifl, S., Grill, V., Märk, T. D., Illenberger, E., & Scheier, P. (2005b). Bond- and site-selective loss of H<sup>-</sup> from pyrimidine bases. *Physical Review Letters*, 95, 093201.
- Ptasińska, S., Denifl, S., Grill, V., Märk, T. D., Scheier, P., Gohlke, S., Huels, M. A., & Illenberger, E. (2005c). Bond-selective H<sup>-</sup> ion abstraction from thymine. *Angewandte Chemie International Edition*, 44, 1647.
- Ptasińska, S., Denifl, S., Gohlke, S., Scheier, P., Illenberger, E., & Märk, T. D. (2006). Decomposition of thymidine by low-energy electrons: Implications for the molecular mechanisms of single-strand breaks in DNA. *Angewandte Chemie International Edition*, 45, 1893.
- Puiatti, M., Vera, D. M. A., & Pierini, A. B. (2009). In search for an optimal methodology to calculate the valence electron affinities of temporary anions. *Physical Chemistry Chemical Physics*, 11, 9013.
- Rak, J., Mazurkiewicz, K., Koblecka, M., Storoniak, P., Haranczyk, M., Dąbkowska, I., Bachorz, R. A., Gutowski, M., Radisic, D., Stokes, S. T., Eustis, S. N., Wang, D., Li, X., Ko, Y. J., & Bowen, K. H. (2008). Stable valence anions of nucleic acid



- bases and DNA strand breaks induced by low energy electrons. In M. K. Shukla, J. Leszczynski (Eds.), & J. Leszczynski (Series Ed.) *Radiation induced molecular phenomena in nucleic acids: Vol. 5. Challenges and advances in computational chemistry and physics* (p. 619). Amsterdam: Springer.
- Rak, J., Kobyzicka, M., & Storoniak, P. (2011). Single strand break in DNA coupled to the O-P bond cleavage. A computational study. *The Journal of Physical Chemistry B*, 115, 1911.
- Sanche, L. (1995). Interactions of low-energy electrons with atomic and molecular-solids. *Scanning Microscopy*, 9, 619.
- Sanche, L. (2005). Low energy electron-driven damage in biomolecules. *European Physical Journal D: Atomic, Molecular, Optical and Plasma Physics*, 35, 367.
- Sanche, L. (2008). Low energy electron damage to DNA. In M. K. Shukla, J. Leszczynski (Eds.), & J. Leszczynski (Series Ed.), *Radiation induced molecular phenomena in nucleic acids: Vol. 5. Challenges and advances in computational chemistry and physics* (p. 531). Amsterdam: Springer.
- Sanche, L. (2009). Role of secondary low energy electrons in radiobiology and chemoradiation therapy of cancer. *Chemical Physics Letters*, 474, 1.
- Sanche, L. (2010). Low-energy electron interaction with DNA: Bond dissociation and formation of transient anions, radicals, and radical anions. In M. Greenberg (Ed.), *Radical and radical ion reactivity in nucleic acid chemistry* (p. 239). Hoboken: Wiley, ISBN: 978-0-470-25558-2.
- Scheer, A. M., Afatoon, K., Gallup, G. A., & Burrow, P. D. (2004). Bond breaking and temporary anion states in uracil and halouracils: Implications for the DNA bases. *Physical Review Letters*, 92, 068102.
- Schiedt, J., Weinkauff, R., Neumark, D. M., & Schlag, E. W. (1998). Anion spectroscopy of uracil, thymine and the amino-oxo and amino-hydroxy tautomers of cytosine and their water clusters. *Chemical Physics*, 239, 511.
- Schulz, G. J. (1973a). Resonances in electron impact on atoms. *Reviews of Modern Physics*, 45, 378.
- Schulz, G. J. (1973b). Resonances in electron impact on diatomic molecules. *Reviews of Modern Physics*, 45, 423.
- Schwabe, T., & Grimme, S. (2008). Theoretical thermodynamics for large molecules: Walking the thin line between accuracy and computational cost. *Accounts of Chemical Research*, 41, 569.
- Schyman, P., & Laaksonen, A. (2008). On the effect of low-energy electron induced DNA strand break in aqueous solution: A Theoretical study indicating guanine as a weak link in DNA. *Journal of the American Chemical Society*, 130, 12254.
- Schyman, P., Laaksonen, A., & Hugosson, H. W. (2008). Phosphodiester bond rupture in 5' and 3' cytosine monophosphate in aqueous environment and the effect of low-energy electron attachment: A Car-Parrinello QM/MM molecular dynamics study. *Chemical Physics Letters*, 462, 289.
- Sevilla, M. D., & Bernhard, W. A. (2008). Mechanisms of direct radiation damage to DNA. In M. Spothem-Maurizot, M. Mostafavi, T. Douki, & J. Belloni (Eds.), *Mechanisms of direct radiation damage to DNA. In radiation chemistry from basics to applications in material and life sciences* (p. 191). Cedex A, France: EDP Sciences.
- Sevilla, M. D., Becker, D., Yan, M., & Summerfield, S. R. (1991). Relative abundances of primary ion radicals in  $\gamma$ -irradiated DNA: Cytosine vs. thymine anions and guanine vs. adenine cations. *The Journal of Physical Chemistry*, 95, 3409.
- Sevilla, M. D., Besler, B., & Colson, A. O. (1994). Comment on "electron attachment to uracil. Theoretical *ab Initio* study." *The Journal of Physical Chemistry*, 98, 2215.
- Sevilla, M. D., Besler, B., & Colson, A. O. (1995). *Ab initio* molecular orbital calculations of DNA radical ions. 5. Scaling of calculated electron affinities and ionization potentials to experimental values. *The Journal of Physical Chemistry*, 99, 1060.
- Shao, Y., Molnar, L. F., Jung, Y., Kussmann, J., Ochsenfeld, C., Brown, S. T., et al. (2006). Advances in methods and algorithms in a modern quantum chemistry program package. *Physical Chemistry Chemical Physics*, 8, 3172.
- Shukla, L. I., Pazdro, R., Huang, J., DeVreugd, C., Becker, D., & Sevilla, M. D. (2004). The formation of DNA sugar radicals from photoexcitation of guanine cation radicals. *Radiation Research*, 161, 582.
- Shukla, L. I., Pazdro, R., Becker, D., & Sevilla, M. D. (2005). Sugar radicals in DNA: Isolation of neutral radicals in gamma-irradiated DNA by hole and electron scavenging. *Radiation Research*, 163, 591.
- Simons, J. (2006). How do low-energy (0. 1–2 eV) electrons cause DNA-strand breaks? *Accounts of Chemical Research*, 39, 772.
- Simons, J. (2008). Molecular anions. *The Journal of Physical Chemistry A*, 112, 6401.
- Simons, J., & Jordan, K. D. (1987). *Ab Initio* electronic structure of anions. *Chemical Reviews*, 87, 535.
- Sobolewski, A. L., & Domcke, W. (2002). On the mechanism of nonradiative decay of DNA

- bases: Ab initio and TDDFT results for the excited states of 9H-adenine. *European Physical Journal D: Atomic, Molecular, Optical and Plasma Physics*, 20, 369.
- Solomon, T., & Skalicky, T. (2008). The interaction of a protein–DNA surface complex with low-energy electrons. *Chemical Physics Letters*, 453, 101.
- Solomon, T., Seitz, H., & Sturm, H. (2009). DNA damage by low-energy electron impact: Dependence on guanine content. *The Journal of Physical Chemistry B*, 113, 11557.
- Staiey, S. W., & Strnad, J. T. (1994). Calculation of the energies of  $\pi^*$  negative ion resonance states by the use of Koopmans' theorem. *The Journal of Physical Chemistry*, 98, 116.
- Steenken, S., & Jovanovic, S. V. (1997). How easily oxidizable is DNA? One-electron reduction potentials of adenosine and guanosine radicals in aqueous solution. *Journal of the American Chemical Society*, 119, 617.
- Sulzer, P., Ptasińska, S., Zappa, F., Mielewska, B., Milosavljevic, A. R., Scheier, P., et al. (2006). Dissociative electron attachment to furan, tetrahydrofuran, and fructose. *The Journal of Chemical Physics*, 125, 044304.
- Svozil, D., Frigato, T., Havlas, Z., & Jungwirth, P. (2005). Ab initio electronic structure of thymine anions. *Physical Chemistry Chemical Physics*, 7, 840.
- Swarts, S. G., Sevilla, M. D., Becker, D., Tokar, C. J., & Wheeler, K. T. (1992). Radiation-induced DNA damage as a function of hydration. I. Release of unaltered bases. *Radiation Research*, 129, 333.
- Swiderek, P. (2006). Fundamental processes in radiation damage of DNA. *Angewandte Chemie International Edition*, 45, 4056.
- Takayanagi, T., Asakura, T., & Motegi, H. (2009). Theoretical study on the mechanism of low-energy dissociative electron attachment for uracil. *The Journal of Physical Chemistry A*, 113, 4795.
- Tonzani, S., & Greene, C. H. (2006a). Low-energy electron scattering from DNA and RNA bases: Shape resonances and radiation damage. *The Journal of Chemical Physics*, 124, 054312.
- Tonzani, S., & Greene, C. H. (2006b). Radiation damage to DNA: Electron scattering from the backbone subunits. *The Journal of Chemical Physics*, 125, 094504.
- Vera, D. M. A., & Pierini, A. B. (2004). Species with negative electron affinity and standard DFT methods. *Physical Chemistry Chemical Physics*, 6, 2899.
- von Sonntag, C. (1987). *The chemical basis of radiation biology*. London: Taylor and Francis.
- von Sonntag, C. (1991). The chemistry of free-radical-mediated DNA damage. In W. A. Glass & M. N. Varma (Eds.), *Physical and chemical mechanisms in molecular radiation biology* (p. 287). New York: Plenum.
- Wagenknecht, H. A. (Ed.) (2005). *Charge transfer in DNA. From mechanism to application*. New York: Wiley-VCH, Verlag GmbH.
- Wang, C. R., Nguyen, J., & Lu, Q. B. (2009). Bond breaks of nucleotides by dissociative electron transfer of nonequilibrium prehydrated electrons: A new molecular mechanism for reductive DNA damage. *Journal of the American Chemical Society*, 131, 11320.
- Wesolowski, S. S., Leininger, M. L., Pentchev, P. N., & Schaefer, H. F. (2001). Electron affinities of the DNA and RNA bases. *Journal of the American Chemical Society*, 123, 4023.
- Wetmore, S. D., Boyd, R. J., & Eriksson, L. A. (2000). Electron affinities and ionization potentials of nucleotide bases. *Chemical Physics Letters*, 322, 129.
- Wetzel, D. M., & Brauman, J. I. (1987). Electron photodetachment spectroscopy of trapped negative ions. *Chemical Reviews*, 87, 607.
- Winstead, C., & McKoy, V. (2006). Interaction of low-energy electrons with the purine bases, nucleosides, and nucleotides of DNA. *The Journal of Chemical Physics*, 125, 244302.
- Winstead, C., & McKoy, V. (2008). Resonant interactions of slow electrons with DNA constituents. *Radiation Physics and Chemistry*, 77, 1258.
- Xie, H. J., Wu, R. B., Xia, F., & Cao, Z. X. (2008). Effects of electron attachment on C-5'-O-5' and C-1'-N-1 bond cleavages of pyrimidine nucleotides: A theoretical study. *Journal of Computational Chemistry*, 29, 2025.
- Xi, L., Sevilla, M. D., & Sanche, L. (2003). Density functional theory studies of electron interaction with DNA: Can zero eV electrons induce strand breaks? *Journal of the American Chemical Society*, 125, 13668.
- Xi, L., Sanche, L., & Sevilla, M. D. (2006). Base release in nucleosides induced by low-energy electrons: A DFT study. *Radiation Research*, 165, 721.
- Yalunin, S., & Leble, S. B. (2007). Multiple-scattering and electron–uracil collisions at low energies. *European Physical Journal*, 144, 115.
- Yang, X., Wang, X. B., Vorpapel, E. R., & Wang, L. S. (2004). Direct experimental observation of the low ionization potentials of guanine in free oligonucleotides by using photoelectron

- spectroscopy. *Proceedings of the National Academy of Sciences of the United States of America*, *101*, 17588.
- Yokoya, A., Shikazono, N., Fujii, K., Urushibara, A., Akamatsu, K., & Watanabe, R. (2008). DNA damage induced by the direct effect of radiation. *Radiation Physics and Chemistry*, *77*, 1280.
- Younkin, J. M., Smith, L. J., & Compton, R. N. (1976). Semi-empirical calculations of p-electron affinities for some conjugated organic molecules. *Theoretica Chimica Acta*, *41*, 157.
- Zewail, A. H. (2000). Femtochemistry: Atomic-scale dynamics of the chemical bond. *The Journal of Physical Chemistry A*, *104*, 5660.
- Zhang, R. B., Zhang, K., & Eriksson, L. A. (2008). Theoretical studies of damage to 3'-uridine monophosphate induced by electron attachment. *Chemistry A European Journal*, *14*, 2850.
- Zhao, Y., & Truhlar, D. G. (2008). Density functionals with broad applicability in chemistry. *Accounts of Chemical Research*, *41*, 157.
- Zheng, Y., Cloutier, P., Hunting, D. J., Wagner, J. R., & Sanche, L. (2004). Glycosidic bond cleavage of thymidine by low-energy electrons. *Journal of the American Chemical Society*, *126*, 1002.
- Zheng, Y., Cloutier, P., Hunting, D. J., Sanche, L., & Wagner, J. R. (2005). Chemical basis of DNA sugar-phosphate cleavage by low-energy electrons. *Journal of the American Chemical Society*, *127*, 16592.
- Zheng, Y., Wagner, J. R., & Sanche, L. (2006). DNA damage induced by low-energy electrons: Electron transfer and diffraction. *Physical Review Letters*, *96*, 208101.
- Zheng, Y., Hunting, D. J., Ayotte, P., & Sanche, L. (2008). Role of secondary low-energy electrons in the concomitant chemoradiation therapy of cancer. *Physical Review Letters*, *100*, 198101.

# 35 Computational Modeling of DNA and RNA Fragments

Jiří Šponer<sup>1</sup> · Manoj K. Shukla<sup>2,3</sup> · Jerzy Leszczynski<sup>2</sup>

<sup>1</sup>Institute of Biophysics, Academy of Sciences of the Czech Republic, Brno, Czech Republic

<sup>2</sup>Department of Chemistry and Biochemistry, Interdisciplinary Center for Nanotoxicity, Jackson State University, Jackson, Mississippi, USA

<sup>3</sup>Environmental Laboratory, US Army Engineer Research and Development Center, Vicksburg, Mississippi, USA

<i>Introduction</i> .....	1258
<i>Hydrogen Bonding and Stacking Interactions in Nucleic Acids</i> .....	1262
Level of Computations .....	1263
Gold Standard .....	1264
Other Approaches .....	1265
<i>Geometries</i> .....	1266
<i>Interpreting the Computations</i> .....	1269
<i>Conclusion</i> .....	1271
<i>Acknowledgments</i> .....	1271
<i>References</i> .....	1271

**Abstract:** A comprehensive analysis of the benefits and pitfalls of quantum chemical methods used to determine the structures, properties, and functions of DNA and RNA fragments is presented. Main emphasis is given to the application of different *ab initio* quantum chemical methods. An overview of computations reveals that quantum chemical methods provide an important means to investigate structures and interactions in nucleic acids. However, judicious selection of computational approach is necessary, depending upon the nature of the problem under investigation.

## Introduction

---

Over the past several decades investigations of the structure and property of nucleic acids have been an important subject of scientific research. Such investigations have been motivated by the fundamental roles played by RNA and DNA in biology.

Deoxyribonucleic acid (DNA) has been considered to be the central biology molecule, being the depository of genetic information, where hereditary information (of higher-level life forms) is encoded in the form of specific sequences of hydrogen bonds formed between the purine (adenine and guanine) and complementary pyrimidine (thymine and cytosine) bases. Obviously, any permanent variation in the hydrogen bonding pattern may change the function and can even be lethal (especially when specific mutations accumulate). On the other hand all kinds of beneficial mutations, ranging from small-scale mutations (such as point mutations, insertions and deletions) to large-scale mutations (such as chromosomal translocations), are the driving force of evolution. This demands that the structural integrity of DNA be maintained for the identity of each and every organism. It is, however, notable that the biology of DNA does not depend only on the “digital” information of the base sequence. In reality, key aspects of DNA storage in the chromatin and all major aspects of DNA-based control of gene expression are regulated by the subtle sequence-dependent variability of conformational and physicochemical properties of DNA double helix, which is definitely everything else than just a regular double helix.

RNA was, until the 1980s, considered a boring and unimportant cousin of DNA. However, since earth-shaking discovery of RNA catalysis in 1982 (Guerrier-Takada et al. 1983; Kruger et al. 1982)(1989 Nobel Prize for chemistry, Cech and Altman), major RNA discoveries keep coming one after another. We now assume that the RNA molecule is likely the primary molecule of life, the first modern replicator, which in later stages of primary evolution created chemically more stable DNA for better coding and proteins for more diverse catalysis. Since the early stages of evolution, RNA has kept control over many key processes in cellular life while also acquiring new functions. Thus, in the last two decades in biology and biochemistry much of the research focus shifted from DNA to RNA (not reflected by adequate efforts in the field of computational chemistry), as exemplified, e.g., by the 2006 Nobel Prize in Physiology and Medicine awarded to Fire and Mello for their 1998 discovery of RNA interference (Fire et al. 1998) and 2009 Chemistry Nobel Prize to Ramakrishnan, Steitz and Yonath for solving (in 2000) the atomic-resolution structures of the most formidable molecular machine, the ribosome (Ban et al. 2000; Wimberly et al. 2000). A ribosome is a large RNA assembly that has been in the course of evolution supplemented by dozens of ribosomal proteins. It is now well established that while less than 2% of the genomic DNA codes protein sequences, over 80% of the genome is actually transcribed into RNA during the cellular life, most of it (obviously besides genes coding, e.g., ribosomal and

transfer RNAs) as non-coding RNA molecules of yet unknown function. In other words, what was not a long time ago considered as “junk” DNA with no obvious role has emerged as DNA template coding for critically important regulatory RNAs that probably affect every corner of gene expression and regulation. One example is the discovery of small RNA molecules (micro-RNA) that regulate gene expression at multiple levels. The structural versatility and complexity of RNA molecules is incomparably larger than the the variability of DNA.

Although the research related to nucleic acids has grown manifold, giving rise to various distinct research fields, the age-old question as to the origin of life on earth remains to be answered. We do not know if it was a spontaneous process which, over the period of time, evolved into the current form on earth or it was endowed from outer space. In fact, we still do not know all the species present on our planet. The existence of different simple molecules, which can be precursors of genetic monomers, such as water, carbon mono and dioxides, formaldehyde, nitrogen, hydrogen cyanide, hydrogen sulfide, and methane, have been shown in cometary comas (Mix 2006). The purine base adenine has been observed in asteroids and comets. The existence of significant amounts of HCN and HNC molecules in the interstellar space is well known (Ishii et al. 2006). Tennekes et al. (2006) have measured the distribution of these isomers (HCN and HNC) in the protostellar dust core. Smith et al. (2001) have discussed the formation of small HCN-oligomers in the interstellar clouds. It has been demonstrated experimentally that under certain conditions adenine can be formed from the pentamerization of HCN in the solid, liquid and gas phases (Miller and Urey 1959; Ponnampertuma et al. 1963). Based on the appearance of the brown-orange color as the consequence of impacts of comet P/Shoemaker-Levy 9 on the planet in 1994, the presence of HCN polymers has been speculated on Jupiter (Matthews 1997). The coloration of the Saturn has also been speculated to be due to the presence of HCN polymer. To understand prebiotic adenine synthesis, Glaser et al. (2007) recently performed theoretical calculations on the pyrimidine ring formation of monocyclic HCN-pentamers and found that the key steps proceed without any catalysts producing the purine ring under photolytic conditions and no activation barrier was involved.

It is a valid assumption to speculate that life on earth probably evolved under acute harsh environments including the presence of different kinds of irradiations. Therefore, it is expected that several structural transformations/refinements with respect to genetic code preservation must have taken place. Survival of the fittest prevailed over the period of time in evolution, thereby bringing the purine and pyrimidine bases as the genetic molecules. Further, since these molecules absorb ultraviolet (UV) irradiation, some sort of mechanism was needed to avoid the excited state photo reactions. This was probably achieved through the ultrashort excited state lifetimes of nucleic acid bases (Harpe and Kohler 2011; Middleton et al. 2009; Serrano-Andres and Merchan 2009; Shukla and Leszczynski 2007, 2008). Recent state-of-the-art investigations have suggested that such ultrafast excitation processes are achieved through internal conversion where excited and ground state potential energy surfaces conically intersect (Barbatti et al. 2010; Bisgaard et al. 2009; de Vries and Hobza 2007; Harpe and Kohler 2011; Kohler 2010; Middleton et al. 2009; Serrano-Andres and Merchan 2009; Shukla and Leszczynski 2007, 2008; Yamazaki et al. 2008). And thus, the absorbed energy is efficiently dissipated in the form of heat. Therefore, it is not unexpected that accurate structural determination of nucleic acids and their fragments have been one of the fundamental areas of research. Another obvious precondition that has to be fulfilled in the initial selection of a nucleobase is its inability to tautomerize in aqueous solution, as tautomers would bias any nucleobase-based genetic code as well as RNA folding; thus none of the native nucleobases tautomerize under biochemical conditions to any appreciable amount.

Computational quantum chemical techniques are fast becoming an attractive alternative to the expensive and time-consuming experimental methods in determining the structures and activities of molecular systems. Although we would like to state that modeling of the exact experimental environment, in particular the large biological systems *in vivo*, is not yet possible, computational methods can still provide reliable predictions and thus can be useful to experimentalists. Theoretical methods are especially attractive in the area where experimental measurements are still not possible, e.g., the determination of excited state geometries of complex molecular systems. For the smaller molecular species one can routinely apply a high level of electron correlated methods and large basis sets, however, for larger molecular systems one has to make a compromise between the level of theory and the basis set and thus with computational accuracy. Experimental determination of excited state geometries of complex molecules like nucleic acid bases is still not possible; only some limited information such as possibility of excited state nonplanarity can be deduced. On the other hand, quantitative information about the excited state geometries can be obtained using the reliable theoretical level, although one has to make a compromise between the theoretical method and the size of the system under investigation. Further, while there was some indication about the amino group nonplanarity in nucleic acid bases in the crystal environment (McMullan et al. 1980), quantitative prediction about amino group nonplanarity was obtained through the quantum mechanical calculations about a decade ago (Leszczynski 1992). It should be noted that such nonplanarity in the gas phase of molecules using experiment was obtained by Dong and Miller in 2002 (Dong and Miller 2002). However, we believe that theoretical and experimental methods are complementary to each other, and a judicious decision is needed for their efficient application. One of the classical examples would be the tautomerism in guanine.

It is well known that due to the lowest ionization energy among nucleic acid bases, guanine is the primary target for nucleic acid damage by ionizing irradiation (Crespo-Hernandez et al. 2004; Lin et al. 1980). Further, low-energy electrons can also cause the strand break (Boudaffa et al. 2000; Gu et al. 2007; Kumar and Sevilla 2007). A recent experimental study on single-strand DNA oligonucleotide suggests that there is a linear correlation between the low-energy electron-induced DNA damage and the presence of the guanine molecules in the sequence (Solomun et al. 2009). Further, guanine can potentially form the most diverse set of energetically accessible rare tautomers in non-polar environments. Initially, based upon the infra-red (IR) spectroscopic analysis of guanine in the argon matrix the presence of equal proportions of keto and enol forms was suggested (Sheina et al. 1987). But, the canonical form of guanine dominates in the polar solvent (Leszczynski 2000). Theoretical methods have generally predicted that the keto-N7H tautomer of guanine is the most stable in the gas phase, but the keto-N9H tautomer dominated in the water solution. At the MP2 and CCSD(T) levels along with several large basis sets, the four low-energy tautomers of guanine (keto-N9H, keto-N7H and cis- and trans- forms of enol-N9H) have been shown to be within 1 kcal/mol of energy (Gorb et al. 2005). The assignments of resonance-enhanced multiphoton ionization spectra of laser-desorbed, jet-cooled guanine have suggested the presence of four tautomers of guanine (Mons et al. 2002; Nir et al. 2001). Based upon the comparison of IR spectra of thermally vaporized guanine trapped in helium droplets with that of computed vibrational frequencies at the MP2 level with the 6-311++G(d,p) and aug-cc-pVDZ basis sets, Choi and Miller (2006) have assigned the presence of keto-N9H, keto-N7H, and cis- and trans-forms of enol-N9H tautomer of guanine. The results of guanine in helium droplets necessitated the reassignment of earlier R2PI data and accordingly, based upon the comparison of experimental and theoretical results, Mons et al. (2006), found the presence of enol-N9H-trans, enol-N7H and two rotamers of the keto-N7H-imino



tautomers of guanine in the supersonic jet-beam. Thus, in the new assigned R2PI spectra the stable keto-N9H and keto-N7H tautomers of guanine are not present. The high level of theoretical calculations (Chen and Li 2006; Marian 2007) on guanine tautomers also supported the reassignment of the R2PI spectra of guanine tautomers in the supersonic jet cooled beam and suggested the presence of efficient nonradiative deactivation channels as the reason for the missing of spectral origins of the stable tautomers in the R2PI experiments. Recently, Zhou et al. (2009) have performed a comprehensive investigation of guanine tautomers using the VUV photoionization technique, where the gas phase of guanine was obtained at the both the thermal vaporization and laser desorption methods. It was revealed that the method used to generate the gas phase sample of guanine has significant influence on the population of tautomers in the experiment. Consequently, it was found that in the thermal vaporization, a maximum of five most stable tautomers are populated and these results are in agreement with that obtained in the helium droplet experiment. On the other hand, when the laser desorption technique was used to make a gas phase sample of guanine, up to seven tautomers are populated. As noted above, however, guanine for obvious reasons does not tautomerize in biochemically relevant environments, as convincingly shown more than a decade ago also by advanced computational methods (Colominas et al. 1996). Eventual computations suggesting formation of tautomers of natural bases in water are to be dismissed and are at odds with all other experimental data.

Another unique feature of QM methods is their capability to reveal relation between molecular structures and molecular energies at the level of direct (contact, gas phase, electronic structures) interactions. This concerns mainly the two fundamental interactions, base stacking and base pairing. Stacking interactions play an important role in the biological structure, providing both thermodynamics stability and structuring of nucleic acids. For example, base stacking is assumed to be the primary determinant of sequence-dependence of B-DNA structure and flexibility, which is the single most important feature of DNA that enters all of DNAs molecular interactions, genetic material storage, replication and gene expression. The sequence dependence of DNA (and the role of base stacking) has been intensely studied. Despite this, all the experimental and theoretical research failed to provide clear rules allowing to predict the fine B-DNA structural variability from sequence (Calladine 1982; Dickerson and Drew 1981; Spomer and Kypr 1991; Suzuki et al. 1997; Wing et al. 1980; Yanagi et al. 1991). The research in this area has been stalled for some time and perhaps improved description of stacking with the help of modern QM methods could bring some new ideas.

Base pairing (extended beyond the base – base interactions) is especially interesting in large functional RNAs, where it determines their architectures and gives very strict constraints on RNA evolutionary patterns (Leontis et al. 2002; Spomer et al. 2010; Stombaugh et al. 2009; Zirbel et al. 2009). Large RNA molecules are organized as complex (and often very dynamical) jigsaw puzzles, where the exact shapes of the base pairs determine function and thus also allowable mutations (isostericity principle). Nevertheless, recent studies also indicate a non-negligible role of energy of molecular interactions supplementing the basic isostericity principle (Zirbel et al. 2009).

Although stacking interactions are important and high level *ab initio* methods are needed to account for such interactions, it is only possible to use these methods to model systems and very small fragments of large biomolecules, even using the large computational resources. Therefore, especially force field methods (and QM/MM method to certain extent) are mainly used to study larger biopolymers and other large biological systems. Nevertheless, QM calculations remain instrumental in reference studies on the nature and magnitude of molecular interactions in



nucleic acids and in verification of the other methods. Quantum chemical calculations provided the ultimate answer about the physico-chemical nature of base stacking and characterized many other features of nucleobase interactions (Hobza and Sponer 1999; Morgado et al. 2009; Svozil et al. 2010).

## Hydrogen Bonding and Stacking Interactions in Nucleic Acids

---

The most fundamental roles of nucleic acid bases (nucleobases) in biology and chemistry is their involvement in two qualitatively different mutual interactions: hydrogen bonding (base pairing) and aromatic base stacking.

The base pairing is utilizing the H-bond donor and acceptor capabilities of nucleobase exocyclic groups and ring nitrogen atoms. In RNA molecules, the base pairing also involves the sugar ribose which, in contrast to DNA deoxyribose, possesses hydroxyl group in the 2' position (Leontis et al. 2002; Sponer et al. 2005a, 2007, 2009, 2010; Stombaugh et al. 2009). The 2'-hydroxyl group is a powerful donor and acceptor of hydrogen bonds. In fact, key RNA base pair families utilize the 2'-OH group for base pairing and these extended base pairs are known as sugar-edge (SE) base pairs or interactions. Many important "SE" base pairs include no direct base to base H-bonds and yet they are crucially important for folding of complex functional non-coding RNA molecules and ribonucleoprotein particles. By non-coding RNAs we mean RNA molecules that are not translated to proteins via messenger RNA and perform different functions instead. Note that recent research highlighted that while less than 2% of the human genome directly codes for proteins, at least 80% of the genomic DNA is actually transcribed into RNA. Thus, majority of the genome encodes non-coding RNAs that play absolutely essential roles in life and evolution (many of the RNA functions have yet to be discovered but they are assumed to be key players in fine regulation of gene expression), which is a finding that has truly revolutionized biology in recent years. The largest non-coding RNAs are, obviously, ribosomal RNAs. The most important RNA tertiary interactions (A-minor and P-interactions) are base pairs, triads, and quartets mediated by base-sugar and sugar-sugar interactions (Sponer et al. 2007). Recently, the RNA base pairing classification was extended to include base-phosphate (BPh) interactions, after recognizing that ~12% of nucleotides in ribosome are involved with BPh interactions with other proximal or distal nucleotides while these interactions bring important evolutionary constraints (Zirbel et al. 2009).

Base stacking occurs between the aromatic faces of the nucleic acid bases and is at least equally as important as base pairing, for both thermodynamics stabilization and shaping of nucleic acids. Stacking is responsible for the local conformational variations and other sequence-dependent properties of B-DNA. Unambiguous classification of base stacking is missing. One of the reasons is flexibility of base stacking, as the stacked bases can always slide and twist over a range of mutual stacked geometries, being not fixed by the individual H-bonds (note, however, that many complex RNA base pairs also possesses complex conformational space with multiple competing conformations). While classification of base pairing could have been done purely by considering structural data (i.e., geometries seen in X-ray structures) classification of base stacking will likely require appropriate energy analyzes.

The ab initio QM technique can be used to determine optimal structures of molecular clusters and to calculate energies for any single geometry of the cluster. QM calculations provide molecular wave functions, which can be used to derive physicochemical properties, such

as vibrational spectra, dipole and higher multipole moments, polarizabilities, proton affinities, NMR parameters and others. Nevertheless, the main achievement of QM calculations was the description of the nature and energetics of nucleobase interactions. This is because the leading experimental approaches of structural biology, that is, mainly X-ray crystallography, provide purely structural data. Information about energetics of molecular interactions can be inferred only indirectly while the interpretation of structural data ignoring energetics of molecular interactions is often misleading.

QM calculations can help to understand the role of molecular interactions in nucleic acids because of their capability to give a direct link between structures and energies. Nevertheless, QM calculations are always done on small systems and typically in the gas phase, that is far from real environments and structural contexts. To make meaningful QM computations with biological relevance, we need to follow several rules (Svozil et al. 2010).

First, we need to make the strategic decision whether our computations aim to be indirectly or directly relevant to biology. By indirect relevance we mean for example the use of QM calculations for parameterization or validation of other methods (mainly the molecular mechanical force fields) or for basic understanding of the physical chemistry of interactions. By direct relevance we mean applications that range from calculations of some specific interaction patterns seen in structural studies (Sponer et al. 2003) through combined QM-bioinformatics studies aimed at classifying interactions (Sponer et al. 2003; Zirbel et al. 2009) up to QM/MM calculations of RNA catalysis (Banaš et al. 2009). Then, there are at least three tactical issues that need to be very carefully decided. We need to select the level of calculations, i.e., primarily the method and basis set. Equally important is the appropriate choice or preparation of geometries used in computations. Inappropriate geometries may easily blow up the whole effort and result in computations that are misleading (Svozil et al. 2010). Finally, the results should be properly interpreted. We also need to separately consider applications that deal with nucleic acid bases but are directed to other areas of science (basic physico-chemical experiments, origin of life studies, adsorption on surfaces, supramolecular assemblies, etc.)

## Level of Computations

---

Let us assume that we have a dimer of two nucleic acid bases, *A* and *B*, with a given geometry. For that geometry, the interaction energy between *A* and *B*,  $\Delta E^{A\dots B}$ , is the energy difference between the total electronic energy of the dimer  $E^{A\dots B}$  and the electronic energies  $E^A$  and  $E^B$  of isolated bases.

$$\Delta E^{AB} = E^{AB} - E^A - E^B \quad (35.1)$$

The interaction energy reflects a hypothetical dimerization process at 0 K and is not measurable. In order to be related to experimental dissociation energies  $D_0$  and enthalpies of formation, the deformation energy of monomers and the zero-point vibration energy must be included. The zero-point energies and enthalpy and entropy contributions at nonzero temperature are usually calculated in the harmonic approximation. Since base-pair complexes are weak, anharmonicity can play an important role, especially for stacked systems and particularly at higher temperatures. Nevertheless, except for direct comparison with gas phase experiment, interaction energy evaluation is the sufficient outcome of QM analysis.

Methods suitable for base stacking and base pairing calculations have been discussed many times (Morgado et al. 2009; Spöner et al. 2008; Svozil et al. 2010) and will thus be only briefly noted here. With modern computers, we have methods that are satisfactorily accurate.

Base stacking stabilization is dominated by the intermolecular electron correlation effects (i.e., the dispersion energy). Therefore, stacking calculations must be done with inclusion of electron correlation effects and with large basis sets of atomic orbitals. The dispersion energy is created in the space between the interacting monomers that are separated by  $\sim 3.3\text{--}3.4$  Å. This space needs to be covered by atomic orbitals, dictating the use of diffuse-polarized basis sets. H-bonded complexes are not dominated by the dispersion energy, albeit it is still a very significant contribution. Thus, HF calculations or computations with “dispersion-neglecting” DFT methods, while not being accurate, are not entirely incorrect. When including electron correlation, higher-angular momentum functions are important for base pairing, since the space between the interacting monomers is bridged by H-atoms so the requirement for the diffusivity of atomic orbitals is not as strict as for stacking.

The best accuracy is achieved by complete basis set (CBS) extrapolation methods, when two systematically improved basis sets are applied and the data is then extrapolated. The interaction energy computations, even with large basis sets, need to be corrected for basis set superposition error (BSSE). We oppose suggestions to ignore the BSSE correction or to attempt only its partial inclusion while assuming that the numbers can be correct due to error cancellation. This is a risky game. It is much better to provide BSSE-corrected numbers where a solid estimate of the underestimation of the interaction is typically possible. Fortunately, the CBS calculations are intrinsically BSSE-free. Similarly, computations with modern parameterized DFT-D methods (see below) do not require BSSE correction, since it is indirectly (effectively) included via parameterization.

H-bonded complexes are rather well described by the MP2 method while for aromatic stacking this method typically significantly overshoots the stabilization. Thus, for stacking higher-order electron correlations are quite important.

## Gold Standard

Within the variation (supramolecular) approach, definitely the method of choice for interaction energies would be the coupled cluster CCSD(T) method (in which the single and double excitations are evaluated iteratively while the triple excitations are included in a non-iterative way). The CCSD(T) method yields a significant portion of the correlation energy. The MP2 method, including the double electron excitations at the second order of perturbation theory, overestimates the correlation interaction energy for stacking, as noted above.

The determination of a CBS limit of CCSD(T) calculations is still difficult. Until recently, the CCSD(T) calculations for larger complexes were performed only with medium basis sets (e.g. 6-31G\*) and even these calculations were at the computer limits. Thus, the gold standard in base stacking and pairing calculations is the method sometimes abbreviated as CBS(T), which utilizes the similar basis set dependence of the CCSD(T) and MP2 energies. Thus, the difference between CCSD(T) and MP2 interaction energies ( $\Delta E^{\text{CCSD(T)}} - \Delta E^{\text{MP2}}$ ) exhibits small basis set dependence and the CCSD(T)/CBS interaction energy can be approximated as

$$\Delta E_{\text{CBS}}^{\text{CCSD(T)}} = \Delta E_{\text{CBS}}^{\text{MP2}} + (\Delta E^{\text{CCSD(T)}} - \Delta E^{\text{MP2}})|_{\text{medium basis set}}$$

which is abbreviated as CBS(T) to distinguish from full CCSD(T)/CBS computation (Sponer et al. 2006, 2008). Various extrapolation schemes have been suggested for the determination of the  $\Delta E^{\text{MP2}}_{\text{CBS}}$  term; the one proposed by Halkier et al. (1999) is the most widely used.

For aromatic stacking interactions the  $\Delta\text{CCSD(T)}$  correction term is systematically non-negligible (repulsive) and should never be omitted. For H-bonding interactions, the  $\Delta\text{CCSD(T)}$  correction term is typically very small (Sponer et al. 2004, 2006, 2008).

## Other Approaches

---

Earlier calculations on base stacking were done with the MP2 method utilizing the modified 6-31G\*(0.25) basis set (Hobza and Sponer 1999; Sponer et al. 1996b, 1997). The polarization d-functions of the standard 6-31G\* basis with an exponent of 0.8 were replaced by more diffuse ones with an exponent of 0.25, allowing inclusion of a major part of the dispersion energy. While the MP2/6-31G\*(0.25) method is now outdated, the main conclusions reached by the MP2/6-31G\*(0.25) studies remain valid.

DFT methods were for years not recommended for stacking calculations, because common DFT methods (based on the local density, its gradient, and the local kinetic-energy density) notoriously fail to capture the (non-local) dispersion energy (Hobza et al. 1995; Kristyán and Pulay 1994).

This is a common feature of all LDA and GGA functionals, not excluding even the most advanced meta-GGA functionals. Many recent DFT methods provide much better results for dispersion-controlled complexes (Zhao and Truhlar 2008).

Nevertheless, we still suggest use of caution (and testing) in their application to stacking complexes. An alternative (which can achieve, at least for now, better accuracy and major speed up) is based on augmenting the DFT energy by an empirical London dispersion energy term (Elstner et al. 2001; Grimme 2004; Jurecka et al. 2007).

To correct for the overlap effects the dispersion energy is damped by distance-dependent damping function. The dispersion energy, represented by the  $C_6/R^6$  formula, is calculated separately from the DFT calculation and is simply added to the DFT energy. The disadvantage of DFT-D methods is obviously the need to combine electronic structure calculations with classical “force field” correction term, which also affects the transferability of these methods. Thus these methods are expected to be surpassed in the future by “true” DFT-based dispersion-including methods; however for the moment it seems to us that DFT-D is more satisfactory for routine calculations of nucleobase interactions. One present difficulty is that we have so many new methods in the literature that is difficult to choose. This issue is beyond the scope of this chapter and we refer the reader to specialized literature (Banáš et al. 2009; Sponer et al. 2008). We hope that standard (optimal) wide-spectrum dispersion-including DFT methods will soon be identified.

Interaction energies can also be obtained by perturbation methods, as a sum of perturbation contributions. The Symmetry Adapted Perturbation Theory (SAPT) provides the interaction energy as a sum of first-, second- and higher-order perturbation terms (Heßelmann et al. 2005; Jeziorski et al. 1994). The first-order contribution contains the electrostatic and exchange energies while the second-order term includes induction and dispersion energies. The charge transfer energy is included in the second-order induction energy and higher-order contributions. SAPT (with extended basis sets) yields accurate values of the energy components and also

of the total interaction energies. The determination of the interaction energy is straightforward and is not biased by additional theoretical problems, such as the BSSE inherent to variational methods. The broad use of SAPT is, however, hampered by large computer requirements. A significant improvement was reached by the combination of SAPT and DFT theories (Jeziorski et al. 1994). The DFT-SAPT approach has been rather routinely used for base – base calculations. When making SAPT decompositions, it is extremely important to use well-defined geometries, as the SAPT components are exceptionally sensitive to inter-monomer separation, much more than the total interaction energies. SAPT decompositions can be spoiled by inappropriate choice of geometries (Sponer et al. 2008). Note also that from the biological point of view, what primarily matters are the interaction energies. Thus the usefulness of decompositions should not be over-interpreted (Sponer et al. 2008).

## Geometries

---

Quantum-chemical calculations can provide meaningful data only when the energies are derived at appropriate geometries.

The easiest systems to deal with are well-behaved base pairs where gradient optimization leads to relevant structures. Modern QM programs allow easy gradient optimizations of base pairs, where all coordinates (or parameters) are optimized. Standard optimizations are not corrected for BSSE. Some earlier studies where base pairs were optimized in a step-by-step manner are of historical interest only. Since the optimization itself is more computer-demanding than the subsequent interaction energy evaluation, very often a better level of theory (level X) is used for interaction energy calculation than for optimization (level Y). This is abbreviated as X/Y. For example, the abbreviation MP2/aug-cc-pVTZ//MP2/cc-pVDZ indicates that the optimized structure was obtained at the MP2/cc-pVDZ level while the energies were derived for this optimized geometry at the MP2/aug-cc-pVTZ level.

The gradient optimization is good for systems with well-defined local minima while the minima correspond to the biochemically relevant structures. Stacking patterns seen in nucleic acids do not correspond to minima on the potential energy surfaces of isolated stacked dimers and thus conformational scanning is preferred. Further, gradient optimizations of dispersion-controlled clusters are affected by enormous BSSE, unless a very large basis sets are used. With lower quality methods the structures are unstable and convert to H-bonded ones. In addition, gradient optimizations of stacked dimers lead to puckering of the aromatic ring (Hobza and Sponer 1998). This is usually not desirable since in real environments the nucleobases have some interactions at both their sides, probably preventing such puckering. Thus, stacking calculations are mostly carried out as a series of single points with fixed geometries and rigid monomers (Sponer et al. 1996b, 1997).

An attractive option is to take structures from experimental (X-ray) studies (Sponer et al. 1997). However, usual accuracy of these experiments does not guarantee their straightforward utilization in QM energy computations. First, it is not advisable to directly use monomer geometries from PDB files of NA X-ray structures. Due to limited resolution the monomer geometries carry limited experimental information about monomer geometries while the bases are often deformed after the refinement. Such deformed monomer geometries frustrate the electronic structure. It is necessary to replace (for example via overlay) the monomers from the PDB files via QM-optimized monomers.

In addition, intermolecular X-ray geometries may cause substantial errors in calculations. Especially drastic distortions of the calculated energies can be introduced by steric clashes in the refined crystal structures (Sponer and Kypr 1993). A real nightmare occurs when the X-ray base stacks are effectively vertically compressed or extended due to inaccurate determination of the interbase angles (propeller twist, base pair roll, etc). This requires a case-by-case judgment and some experience with crystallography. Note that a rather small error in the interbase distances (which may still be tolerable from the geometry point of view) can lead to a considerable energy artifact. This is when the geometry falls into a region of interatomic distances where the short-range repulsion starts to dominate. The calculated energy is a highly nonlinear function of the interatomic distance (Sponer et al. 2008).

Similarly, H-bonded base pairs are sensitive to experimental geometry errors due to the genuine close contact between H-bond partners. Besides data and refinement errors a bad geometry can result from the presence of two or more local substates. Substates cannot be distinguished except as having nominal resolution better than  $\sim 1$  Å. The refined geometry reflects an averaged geometry which may have very poor energy. Fiber diffraction models cannot be recommended for direct calculations (Svozil et al. 2010).

We would like to caution against using averaged (3D-bioinformatics) geometries, as they can represent unrealistic single structures from the energy point of view. It is always advisable to generate a range of structures around such geometries and to analyze the properties of the potential energy surfaces. Actually, an open question remains whether the base stacking can be characterized by some single representative geometry. Most likely stacking states correspond to a range of populated geometries, as evidenced, for example, by significant coordinate fluctuations seen for stacked bases in explicit solvent molecular dynamics simulations (Svozil et al. 2010).

We are interested in analyzes of specific interactions which are neither stacking nor H-bonding and are substantially affected by the overall topology of the studied systems. The best approach is to fix the intermolecular geometry of interest (typically using a set of three dihedrals and two valence angles plus one intermonomer distance per each dimer) and then relax the monomers intramolecularly (Sponer and Hobza 1994; Sponer et al. 2003; Vlieghe et al. 1999). This approach has been applied in studies of cross-strand close amino group contacts in B-DNA, DNA-drug interactions, bifurcated H-bonds, out-of-plane H-bonds and some other interactions. If a steric clash is suspected, then the intermonomer distance can again be varied (Sponer and Hobza 1994; Sponer et al. 2003; Vlieghe et al. 1999).

A specific problem is represented by the complex RNA base pairing patterns involving the sugar edges (Sponer et al. 2005a, b, 2007). Many of these base pairs have multiple minima. For many of them, the functional (observed) structures do not correspond to any intrinsic gas phase minimum energy structures, since they are constrained by other interactions and the overall RNA topology. Some base pairs can be intrinsically water-mediated. Huge problems in computations can be created by the sugar hydroxyl group in position 3', which normally is involved in the covalent backbone chain. One option is 3'-methylation. In some cases the phosphate groups participate in the interactions and need to be included in computations. This creates problems due to a strong ionic nature of the associated interactions which are, in real systems, obviously attenuated by solvent screening. Close to insurmountable electrostatic problems arise when more than one phosphate directly participates in the interaction. Thus, QM studies of RNA base pairs often require applications of sophisticated geometrical constraints which need to be implemented case by case. For non-neutral systems, even optimizations upon inclusion of continuum solvent could be a viable option. The situation is further complicated by very limited resolution of the experimental structures of folded RNAs (not mentioning ribosome) and their

dynamical nature. This can lead to large coordinate errors (including poorly refined *syn* vs. *anti* orientation of the bases or incorrect sugar puckers). Thus, studies of RNA base pairs are far from routine. Studies of geometries that are substantially rearranged compared to the experimental structures are of a little value, similar to studies neglecting the sugar rings for base pairs where the 2'-OH groups are directly involved in base pairing.

When gradient optimization is carried out, the monomer geometries are changed upon complexation. This is due to mutual adaptations of the monomers that improve the intermolecular interaction at the expense of the intramolecular energy terms. Some of the deformations can be directly related to the binding strength. However, for larger systems, some monomer rearrangements reflect rather long-range effects. For example, there could be a substantial re-orientation of the flexible sugar-phosphate backbone upon complex formation. Thus, real deformations consist of two contributions. Direct deformations (always present) reflect the strength of the binding and may be complemented by various indirect larger-scale conformational rearrangements. Besides real deformations, the BSSE contributes to the deformation when standard gradient optimization is applied. The BSSE contribution is obviously a computational artifact.

As explained above, the interaction energies of the optimized complexes should be a posteriori corrected for the BSSE using the geometry of the complex and dimer-centered basis set. Then we separately calculate the deformation energy using the monomer basis sets, as difference of monomer energies in the deformed (complex) and optimized (isolated) monomer geometries.

$$E_{\text{Def}}^A = E^{A(\text{dimer geometry})} - E^{A(\text{monomer geometry})}$$

Thus, the interaction energy of a dimer is defined in the following way:

$$\Delta E^{A\dots B} = E^{A\dots B} - (E^A + E^B) + E_{\text{Def}}^A + E_{\text{Def}}^B.$$

The first three energies are calculated in a dimer-centered basis set. The intramolecular deformation energy actually cancels a large part of the intermolecular energy improvement caused by mutual monomer adaptations.

In some of the literature, the authors include deformation energy formally as part of the BSSE correction. We consider this a weird option which may substantially spoil the interpretation of the results. Although it might look more sophisticated mathematically, this approach is misleading, mixing apples and oranges, and is especially unsuitable for larger systems such as base pairs and other fragments of biopolymers (Sponer et al. 2004). In fact, the integrated expression is, after formal rearrangements, *entirely identical* to the above definition, which in addition is older (Sponer et al. 1996a), i.e., the correction was commonly known before researchers started to include deformations into BSSE correction. Second, while BSSE is a mathematical artifact, monomer deformations are not. They correspond to fundamental properties of the studied clusters including their vibrational spectra and polarization/charge transfer effects. Thus, it is useful to evaluate the magnitude of the monomer deformations explicitly. For flexible systems with large indirect rearrangements (as explained above) any formal inclusion of the deformation term into the BSSE correction is meaningless. Thus, albeit widespread, for base pairs and larger systems of chemical and biological interest, this approach it is not appropriate (Szalewicz and Jeziorski 1998).

An alternative approach is to use counterpoise-corrected gradient optimization where the BSSE is removed in each gradient iteration, although with a substantial increase of the computer requirements. It eliminates the BSSE part of the deformation energies while true deformations persist.



In base pairing studies the deformation energy can be calculated either with respect to the planar monomers, thus neglecting the amino group nonplanarity, or with respect to nonplanar bases. These two numbers differ simply by the difference between energies of planar and nonplanar monomers and can be easily compared when needed (Sponer et al. 2004).

## Interpreting the Computations

---

QM calculations (on nucleobase dimers) reveal the binding energy between two bases in the gas phase, i.e., in *complete isolation*. They thus describe the *intrinsic* interactions of the systems with no perturbation by external effects such as solvent. The intrinsic intermolecular stabilities are directly linked to molecular structures and can be derived in any selected geometry. However, the gas phase interaction energies do *not* correspond to the stability of the interactions in nucleic acids, as measured by thermodynamics experiments. It is not possible to easily correlate the QM calculations with measured base pairing and stacking stabilities in nucleic acids. The apparent (measured) strength of the base-base interactions in nucleic acids in various experiments is determined by a complex interplay of many factors and the intrinsic base-base term is only one of them. Many researchers incorrectly believe that the experiments reflect the “true” stabilities of base-base interactions and vice versa.

A textbook example of complexity of molecular interactions is stacking of consecutive protonated cytosines. This is a highly repulsive interaction in the gas phase due to a charge-charge repulsion (Sponer et al. 1996c). Nevertheless, in intercalated i-DNA quadruplex, stacking of a set of consecutive closely spaced protonated cytosines occurs (Gehring et al. 1993). The i-DNA tetraplex is paired via cytosine – protonated (N3) cytosine base pairs, each possessing charge +1. Both cytosines are equivalent in X-ray and NMR experiments suggesting rather fast intra-basepair proton switches (Chen et al. 1994). Two duplexes intercalate to form the tetraplex. Stability of i-motif is due to this massive accumulation of closely spaced protonated base pairs. In i-DNA, the vertical repulsion between consecutive protonated base pairs is counterbalanced by solvent screening effects and possibly specific interactions with the anionic backbone (Spackova et al. 1998). Thus i-DNA indeed has, in contrast to other DNAs, *repulsive intrinsic stacking energy terms*. This example clearly demonstrates the actual magnitude of mutual compensation of molecular interactions in nucleic acids. The i-DNA stability contradicts the gas phase stacking energy calculations and demonstrates why we cannot use these calculations to directly predict DNA stability. However, the relation can be also reversed. It is not possible to unambiguously evaluate the *intrinsic* stacking energetics based on thermodynamics studies of nucleic acids. There is no unambiguous way to decompose the measured free energies into separate terms that would correspond to stacking, base pairing, etc. In other words, we cannot make straightforward extrapolation from gas phase to nucleic acids while, conversely, studies of nucleic acids bring no unambiguous information about the intrinsic base-base terms.

To show the full complexity of molecular interactions, let us underline that the screening is specific for i-DNA. Strikingly contrasting i-DNA is the behavior of consecutive protonated cytosines in C+-G.C triples of Pyr-Pur.Pyr triplexes. Consecutive protonated cytosines would be needed to recognize consecutive guanines in the second strand (Soliva et al. 1998). The vertical position of protonated cytosines in triplex would adopt arrangement closely resembling i-DNA and also planar H-bonding of the third-strand protonated cytosines to N7 of second-strand guanines resembles the i-DNA base pairing. However, this sharply destabilizes the DNA



triplex, and even two or three consecutive  $\text{CH}^+$  are not tolerated. This indicates that in triplex the screening of the vertical electrostatic repulsion by the backbone and solvent is less efficient than in i-DNA. Thus in this particular case of i-DNA and triplexes we cannot transfer experience concerning nucleobase interactions between two DNA forms. Each case should be studied separately. In other words, a given type of base pairing and base stacking may have entirely opposite roles in different nucleic acid forms. A given interaction may be a crucial stabilizing factor for one type of nucleic acid architecture (protonation of consecutive cytosines in the i-motif) while it may be even not tolerated in another architecture. This illustrates that there is no way to design some ultimate experiments to decide about the *common nature* of base stacking in nucleic acids. This simply is a wrong question. In order to understand the interactions in nucleic acids, we need to consider a wide range of systems and the gas phase data represent an important part of the overall picture.

It is nevertheless clear that proper inclusion of solvent screening could help in interpretation of the QM data. Unfortunately, accurate inclusion of solvent effects into QM calculations is difficult. One option is to extend the studied system by a finite set of explicit water molecules. Such calculations still deal with a gas phase molecular cluster and do not correspond to bulk hydration. The cluster hydration patterns differ from those in water where the first shell waters interact with the second shell, etc., and the whole system is dynamical, as evidenced by large-scale explicit solvent simulations of nucleic acids. In a small cluster, individual water molecules will form bridges and zippers between bases in order to maximize the number of H-bonds. The hydration picture in solution (MD data) and X-ray structures is different and reveals simple non-cooperative in-plane hydration of the polar nucleobase sites (the nitrogens and oxygens). Water binding sites in common hydration sites around nucleic acids have water binding times  $\sim 50$ – $500$  ps. In complex RNA molecules or in molecular complexes, some hydration sites may be occupied by tightly bound water molecules (Réblová et al. 2003). A substantial problem of cluster calculations is that the potential energy surface contains a large number of minima and, without an efficient sampling technique, it is virtually impossible to verify the true global minimum (Kabelác and Hobza 2001).

The other option is to include the solvent as a polarizable continuum. QM methods consider effects of the continuum on the electronic structure of the solute molecules, in contrast to classical continuum approaches. The outcomes are quite sensitive to the choice of parameters such as the atomic radii used to define the “solute” cavity; no universal accurate set of “true” radii can be established. The continuum calculations may be combined with cluster calculations, where the first hydration shell is treated explicitly. Even if QM continuum solvent calculation is properly performed, such calculations are not sufficient to achieve a direct correspondence with thermodynamics experiments. In practice we are neglecting, for example, the loss of degrees of freedom upon duplex formation, all effects associated with the presence of sugar-phosphate backbone including the only partial exposure of the bases to the solvent, etc. In addition, different base sequences are likely associated with different solute flexibilities (some base pair step sequences are stiff, others flexible) which will contribute to the free energy balance via solute entropy contributions. Reliable evaluation of these contributions is outside the applicability of available computational methods. Thus, the continuum solvent calculations should be considered just as rough estimates of the attenuation of the electrostatic contributions to the free energy upon solvation, which are still far from fully competent free energy computations.

All of the above-mentioned considerations explain why the QM calculations on base stacking and base pairing do not (and should not) correlate with the measured thermodynamics properties of nucleic acids. Therefore, QM calculations and intrinsic interaction energies should

never be interpreted as straightforward determinants of nucleic acid stabilities. This naive over-interpretation of otherwise very valuable computed data can discredit the computations. There is a plenty of evidence suggesting that the role of molecular interactions in thermodynamics stabilization of even the simplest duplex nucleic acids is more complex than usually assumed, and results from tiny, irregular, and case-specific interplays of all molecular forces, where literally a single specific hydration site or pocket can change the balance. Even simple base modifications and substitutions, as small as deletions of a single exocyclic group, may have complex and, at first sight, mutually contradicting context-dependent impacts on the measured thermodynamics stabilities that cannot be a priori predicted (Chen and Turner 2006; Siegfried et al. 2007).

We nevertheless suggest that this enormous complexity of molecular interactions defines new roles for modern computations, combing well-calibrated simulation approaches and accurate QM calculations. The calculations can provide key insights into the tricky games of molecular interactions that are shaping up the molecules with their associated free energies and that are not fully understandable based on purely experimental approaches (Kopitz et al. 2008; Yildirim and Turner 2005; Yildirim et al. 2009).

## Conclusion

---

QM calculations represent the leading tool to study intrinsic molecular interactions in nucleic acids, such as base stacking and base pairing. However, the QM data should not be over-interpreted and any extrapolation to nucleic acids requires proper consideration of the gas phase nature of QM calculations. In addition, in order to obtain meaningful QM data, basic methodological requirements must be fulfilled. These include, in addition to the obvious selection of appropriate level of calculations, very careful selection or determination of geometries, which is discussed in detail in this chapter.

## Acknowledgments

---

JS acknowledges the support from the Grant Agency of the Academy of Sciences of the Czech Republic grant IAA400040802, Grant Agency of the Czech Republic grant 203/09/1476, Ministry of Education of the Czech Republic LC06030 and Academy of Sciences of the Czech Republic, grants no. AV0Z50040507 and AV0Z50040702. MKS and JL are thankful for supports from NSF-CREST Grant No. HRD-0833178 and NSF EPSCoR Grant No. 362492-190200-01\NSFEPS-0903787 and computational support from Mississippi Center for Supercomputing Research (MCSR).

## References

---

- Ban, N., Nissen, P., Hansen, J., Moore, P. B., & Steitz, T. A. (2000). The complete atomic structure of the large ribosomal subunit at 2.4 Angstrom resolution. *Science*, 289, 905.
- Banáš, P., Jurecka, P., Walter, N. G., Šponer, J., & Otyepka, M. (2009). Theoretical studies of RNA catalysis: Hybrid QM/MM methods and their comparison with MD and QM. *Methods*, 49, 202.

- Barbatti, M., Aquino, A. J. A., Szymczak, J. J., Nachtigallova, D., Hobza, P., & Lischka, H. (2010). Relaxation mechanisms of UV-photoexcited DNA and RNA nucleobases. *Proceedings of the National Academy of Sciences of the United States of America*, *107*, 21453.
- Bisgaard, C. Z., Satzger, H., Ullrich, S., & Stolow, A. (2009). Excited-state dynamics of isolated DNA bases: A case study of adenine. *ChemPhysChem*, *10*, 101.
- Boudaffa, B., Cloutier, P., Haunting, D., Huels, M. A., & Sanche, L. (2000). Resonant formation of DNA strand breaks by low-energy (3 to 20 eV) electrons. *Science*, *287*, 1658.
- Calladine, C. R. (1982). Mechanics of sequence-dependent stacking of bases in B-DNA. *Journal of Molecular Biology*, *25*, 343.
- Chen, H., & Li, S. (2006). Theoretical study on the excitation energies of six tautomers of guanine: Evidence for the assignment of the rare tautomers. *The Journal of Physical Chemistry A*, *110*, 12360.
- Chen, G., & Turner, D. H. (2006). Consecutive GA pairs stabilize medium-size RNA internal loops. *Biochemistry*, *45*, 4025.
- Chen, L., Cai, L., Zhang, X., & Rich, A. (1994). Crystal structure of a four-stranded intercalated DNA: d(C4). *Biochemistry*, *33*, 13540.
- Choi, M. Y., & Miller, R. E. (2006). Four tautomers of isolated guanine from infrared laser spectroscopy in helium nanodroplets. *Journal of the American Chemical Society*, *128*, 7320.
- Colominas, C., Luque, F. J., & Orozco, M. (1996). Tautomerism and protonation of guanine and cytosine. Implications in the formation of hydrogen-bonded complexes. *Journal of the American Chemical Society*, *118*, 6811.
- Crespo-Hernandez, C. E., Arce, R., Ishikawa, Y., Gorb, L., Leszczynski, J., & Close, D. M. (2004). Ab initio ionization energy thresholds of DNA and RNA bases in gas phase and in aqueous solution. *The Journal of Physical Chemistry A*, *108*, 6373.
- de Vries, M. S., & Hobza, P. (2007). Gas-phase spectroscopy of molecular building blocks. *Annual Review of Physical Chemistry*, *58*, 585.
- Dickerson, R. E., & Drew, H. R. (1981). Structure of a B-DNA dodecamer. II. Influence of base sequence on helix structure. *Journal of Molecular Biology*, *15*, 761.
- Dong, F., & Miller, R. E. (2002). Vibrational transition moment angles in isolated biomolecules: A structural tool. *Science*, *298*, 1227.
- Elstner, M., Hobza, P., Frauenheim, T., Suhai, S., & Efthimos, K. (2001). Hydrogen bonding and stacking interactions of nucleic acid base pairs: A density-functional-theory based treatment. *Journal of Chemical Physics*, *114*, 5149.
- Fire, A., Xu, S. Q., Montgomery, M. K., Kostas, S. A., Driver, S. E., & Mello, C. C. (1998). Potent and specific genetic interference by double-stranded RNA in *Caenorhabditis elegans*. *Nature*, *391*, 806.
- Gehring, K., Leroy, J.-L., & Gueron, M. (1993). A tetrameric DNA structure with protonated cytosine-cytosine base pairs. *Nature*, *363*, 561.
- Glaser, R., Hodgen, B., Farrelly, D., & Mckee, E. (2007). Adenine synthesis in interstellar space: Mechanisms of prebiotic pyrimidine-ring formation of monocyclic HCN-pentamers. *Astrobiology*, *7*, 455.
- Gorb, L., Kaczmarek, A., Gorb, A., Sadlej, A. J., & Leszczynski, J. (2005). Thermodynamics and kinetics of intramolecular proton transfer in guanine. Post Hartree-Fock study. *Journal of Physical Chemistry B*, *109*, 13770.
- Grimme, S. (2004). Accurate description of van der Waals complexes by density functional theory including empirical corrections. *Journal of Computational Chemistry*, *25*, 1463.
- Gu, J., Wang, J., Rak, J., & Leszczynski, J. (2007). Findings on the electron-attachment-induced abasic site in a DNA double helix. *Angewandte Chemie*, *119*, 3549.
- Guerrier-Takada, C., Gardiner, K., Marsh, T., Pace, N., & Altman, S. (1983). The RNA moiety of ribonuclease P is the catalytic subunit of the enzyme. *Cell*, *35*, 849.
- Halkier, A., Helgaker, T., Jorgensen, P., Klopper, W., & Olsen, J. (1999). Basis-set convergence of the energy in molecular Hartree-Fock calculations. *Chemical Physics Letters*, *302*, 437.
- Harpe, K. de La & Kohler, B. (2011). Observation of long-lived excited states in DNA oligonucleotides with significant base sequence disorder. *The Journal of Physical Chemistry Letters*, *2*, 133.
- Heßelmann, A., Jansen, G., & Schütz, M. (2005). Density-functional theory-symmetry-adapted intermolecular perturbation theory with density fitting: A new efficient method to study intermolecular interaction energies. *Journal of Chemical Physics*, *122*, 014103.
- Hobza, P., & Sponer, J. (1998). Significant structural deformation of nucleic acid bases in stacked base pairs: An ab initio study beyond Hartree-Fock. *Chemical Physics Letters*, *288*, 7.
- Hobza, P., & Sponer, J. (1999). Structure, energetics, and dynamics of the nucleic acid base pairs: Nonempirical ab initio calculations. *Chemical Review*, *99*, 3247.

- Hobza, P., Šponer, J., & Reschel, T. (1995). Density-functional theory and molecular clusters. *Journal of Computational Chemistry*, 16, 1315.
- Ishii, K., Tajima, A., Taketsugu, T., & Yamashita, K. (2006). Theoretical elucidation of the unusually high [HNC]/[HCN] abundance ratio in interstellar space: Two-dimensional and two-state quantum wave packet dynamics study on the branching ratio of the dissociative recombination reaction  $\text{HCNH}^+ + e^- \rightarrow \text{HNC}/\text{HCN} + \text{H}$ . *The Astrophysical Journal*, 636, 927.
- Jeziorski, B., Moszynski, R., & Szalewicz, K. (1994). Perturbation theory approach to intermolecular potential energy surfaces of van der Waals complexes. *Chemical Review*, 94, 1887.
- Jurecka, P., Cerny, J., Hobza, P., & Salahub, D. R. (2007). Density functional theory augmented with an empirical dispersion term. Interaction energies and geometries of 80 noncovalent complexes compared with ab initio quantum mechanics calculations. *Journal of Computational Chemistry*, 28, 555.
- Kabelác, M., & Hobza, P. (2001). At nonzero temperatures, stacked structures of methylated nucleic acid base pairs and microhydrated nonmethylated nucleic acid base pairs are favored over planar hydrogen-bonded structures: A molecular dynamics simulations study. *Chemistry – A European Journal*, 7, 2067.
- Kohler, B. (2010). Nonradiative decay mechanisms in DNA model systems. *The Journal of Physical Chemistry Letters*, 1, 2047.
- Kopitz, H., Zivkovic, A., Engels, J. W., & Gohlke, H. (2008). Determinants of the unexpected stability of RNA fluorobenzene self pairs. *ChemBioChem*, 9, 2619.
- Kristyán, S., & Pulay, P. (1994). Can (semi)local density functional theory account for the London dispersion forces? *Chemical Physics Letters*, 229, 175.
- Kruger, K., Grabowski, P. J., Zaug, A. J., Sands, J., Gottschling, D. E., & Cech, T. R. (1982). Self-splicing RNA: Autoexcision and autocyclization of the ribosomal RNA intervening sequence of Tetrahymena. *Cell*, 31, 147.
- Kumar, A., & Sevilla, M. D. (2007). Low-energy electron attachment to 5'-thymidine monophosphate: Modeling single strand breaks through dissociative electron attachment. *Journal of Physical Chemistry B*, 111, 5464.
- Leontis, N. B., Stombaugh, J., & Westhof, E. (2002). The non-Watson-Crick base pairs and their associated isostericity matrices. *Nucleic Acid Research*, 30, 3497.
- Leszczynski, J. (1992). Are the amino groups in the nucleic acid bases coplanar with the molecular rings? Ab Initio HF/631G\* and MP2/631G\* Studies. *International Journal of Quantum Chemistry: Quantum Biology Symposium*, 19, 43.
- Leszczynski, J. (2000). Isolated, solvated, and complexed nucleic acid bases: Structures and properties. In M. Hargittai & I. Hargittai (Eds.), *Advances in molecular structure research* (Vol. 6, p. 209). Stamford, CT: JAI Press.
- Lin, J., Yu, C., Peng, S., Akiyama, I., Li, K., Lee, L. K., & LeBreton, P. R. (1980). Ultraviolet photoelectron studies of the ground-state electronic structure and gas-phase tautomerism of purine and adenine. *Journal of the American Chemical Society*, 102, 4627.
- Marian, C. M. (2007). The guanine tautomer puzzle: Quantum chemical investigation of ground and excited states. *The Journal of Physical Chemistry A*, 111, 1545.
- Matthews, C. N. (1997). Hydrogen cyanide polymers from the impact of Comet P/Shoemaker/Levy 9 on Jupiter. *Advance in Space Research*, 19, 1087.
- McMullan, R. K., Benci, P., & Craven, B. M. (1980). The neutron crystal structure of 9-methyladenine at 126 K. *Acta Crystallographica Section B*, 36, 1424.
- Middleton, C. T., de La Harpe, K., Su, C., Law, Y. K., Crespo-Hernandez, C. E., & Kohler, B. (2009). DNA excited-state dynamics: From single bases to the double helix. *Annual Review of Physical Chemistry*, 60, 217.
- Miller, S. L., & Urey, H. C. (1959). Organic compound synthesis on the primitive earth. *Science*, 130, 245.
- Mix, L. J. (2006). The astrobiology primer: An outline of general knowledge - version 1, 2006. *Astrobiology*, 6, 735.
- Mons, M., Dimicoli, I., Piuzzi, F., Tardivel, B., & Elhannine, M. (2002). Tautomerism of the DNA base guanine and its methylated derivatives as studied by gas-phase infrared and ultraviolet spectroscopy. *The Journal of Physical Chemistry A*, 106, 5088.
- Mons, M., Piuzzi, F., Dimicoli, I., Gorb, L., & Leszczynski, J. (2006). Near-UV resonant two-photon ionization spectroscopy of gas phase guanine: Evidence for the observation of three rare tautomers. *The Journal of Physical Chemistry A*, 110, 10921.
- Morgado, C. A., Jurecka, P., Svozil, D., Hobza, P., & Šponer, J. (2009). Balance of attraction and repulsion in nucleic-acid base stacking: CCSD(T)/complete-basis-set-limit calculations on uracil dimer and a comparison with the force-field description. *Journal of Chemical Theory and Computation*, 5, 1524.

- Nir, E., Janzen, Ch., Imhof, P., Kleinermanns, K., & de Vries, M. S. (2001). Guanine tautomerism revealed by UV-UV and IR-UV hole burning spectroscopy. *Journal of Chemical Physics*, *115*, 4604.
- Ponnamperuma, C., Lemmon, R. M., Mariner, R., & Calvin, M. (1963). Formation of adenine by electron irradiation of methane, ammonia, and water. *Proceedings of the National Academy of Sciences of the United States of America*, *49*, 7p. 37.
- Rébllová, K., Spackova, N., Štefl, R., Csaszar, K., Koča, J., Leontis, N. B., & Šponer, J. (2003). Non-Watson-Crick base pairing and hydration in RNA motifs: Molecular dynamics of 5S rRNA Loop E. *Biophysical Journal*, *84*, 3564.
- Serrano-Andres, L., & Merchán, M. (2009). Are the five natural DNA/RNA base monomers a good choice for natural selection? *Journal of Photochemistry and Photobiology C: Photochemistry Reviews*, *10*, 21.
- Sheina, G. G., Stepanian, S. G., Radchenko, E. D., & Blagoi, Yu. P. (1987). IR spectra of guanine and hypoxanthine isolated molecules. *Journal of Molecular Structure*, *158*, 275.
- Shukla, M. K., & Leszczynski, J. (2007). Electronic spectra, excited state structures and interactions of nucleic acid bases and base assemblies. *Journal of Biomolecular Structure & Dynamics*, *25*, 93.
- Shukla, M. K., & Leszczynski, J. (Eds.). (2008). In J. Leszczynski (Ed.), Computational study of UV-induced excitations of DNA fragments. *Radiation induced molecular phenomena in nucleic acids*, Challenges and advances in computational chemistry and physics (Vol. 5). Dordrecht: Springer Science+Business Media B.V.
- Siegfried, N. A., Metzger, S. L., & Bevilacqua, P. C. (2007). Folding cooperativity in RNA and DNA is dependent on position in the helix. *Biochemistry*, *46*, 172.
- Smith, I. W. M., Talbi, D., & Herbst, E. (2001). The production of HCN dimer and more complex oligomers in dense interstellar clouds. *Astronomy & Astrophysics*, *369*, 611.
- Soliva, R., Laughton, C. A., Luque, F. J., & Orozco, M. (1998). Molecular dynamics simulations in aqueous solution of triple helices containing d(G.C.C) trios. *Journal of the American Chemical Society*, *120*, 11226.
- Solomon, T., Seitz, H., & Sturm, H. (2009). DNA damage by low-energy electron impact: Dependence on guanine content. *Journal of Physical Chemistry B*, *113*, 11557.
- Spackova, N., Berger, I., Egli, M., & Šponer, J. (1998). Molecular dynamics of hemiprotonated intercalated four-stranded i-DNA: Stable trajectories on a nanosecond scale. *Journal of the American Chemical Society*, *120*, 6147.
- Šponer, J., & Hobza, P. (1994). Bifurcated hydrogen bonds in DNA crystal structures. An ab initio quantum chemical study. *Journal of the American Chemical Society*, *116*, 709.
- Šponer, J., & Kypr, J. (1991). Different intrastrand and interstrand contributions to stacking account for roll variations at the alternating purine-pyrimidine sequences in A-DNA and A-RNA. *Journal of Molecular Biology*, *221*, 761.
- Šponer, J., & Kypr, J. (1993). Theoretical analysis of the base stacking in DNA: choice of the force field and a comparison with the oligonucleotide crystal structures. *Journal of Biomolecular Structure & Dynamics*, *11*, 277.
- Šponer, J., Leszczynski, J., & Hobza, P. (1996a). Structures and energies of hydrogen-bonded DNA base pairs. A nonempirical study with inclusion of electron correlation. *The Journal of Physical Chemistry*, *100*, 1965.
- Šponer, J., Leszczynski, J., & Hobza, P. (1996b). On the nature of nucleic acid base stacking. Nonempirical ab initio and empirical potential characterization of 10 stacked base pairs. Comparison of stacked and H-bonded base pairs. *The Journal of Physical Chemistry*, *100*, 5590.
- Šponer, J., Leszczynski, J., Vetterl, V., & Hobza, P. (1996c). Base stacking and hydrogen bonding in protonated cytosine dimer: The role of molecular ion-dipole and induction interactions. *Journal of Biomolecular Structure & Dynamics*, *13*, 695.
- Šponer, J., Gabb, H. A., Leszczynski, J., & Hobza, P. (1997). Base-base and deoxyribose-base stacking interactions in B-DNA and Z-DNA. A quantum-chemical study. *Biophysical Journal*, *73*, 76.
- Šponer, J., Mokdad, A., Šponer, J. E., Spackova, N., Leszczynski, J., & Leontis, N. B. (2003). Unique tertiary and neighbor interactions determine conservation patterns of Cis Watson-Crick A/G base-pairs. *Journal of Molecular Biology*, *330*, 967.
- Šponer, J., Jurecka, P., & Hobza, P. (2004). Accurate interaction energies of hydrogen-bonded nucleic acid base pairs. *Journal of the American Chemical Society*, *126*, 10142.
- Šponer, J. E., Leszczynski, J., Sychrovský, V., & Šponer, J. (2005a). The sugar edge/sugar edge base pairs in RNA. Stabilities and structures from quantum chemical calculations. *Journal of Physical Chemistry B*, *109*, 18680.
- Šponer, J. E., Spackova, N., Leszczynski, J., & Šponer, J. (2005b). Principles of RNA base pairing: Structures and energies of the trans Watson-Crick/sugar edge base pairs. *Journal of Physical Chemistry B*, *109*, 11399.

- Sponer, J., Jurecka, P., Marchan, I., Luque, F. J., Orozco, M., & Hobza, P. (2006). Nature of base stacking. Reference quantum chemical stacking energies in ten unique B-DNA base pair steps. *Chemistry – A European Journal*, *12*, 2854.
- Sponer, J. E., Réblová, K., Mokdad, A., Sychrovský, V., Leszczynski, J., & Šponer, J. (2007). Leading RNA tertiary interactions: Structures, energies, and water insertion of A-minor and P-interactions. A quantum chemical view. *Journal of Physical Chemistry B*, *111*, 9153 and references cited therein.
- Sponer, J., Riley, K. E., & Hobza, P. (2008). Nature and magnitude of aromatic stacking of nucleic acid bases. *Physical Chemistry Chemical Physics*, *10*, 2595.
- Sponer, J., Zgarbova, M., Jurecka, P., Riley, K. E., Sponer, J. E., & Hobza, P. (2009). Reference quantum chemical calculations on RNA base pairs directly involving the 2'-OH group of ribose. *Journal of Chemical Theory and Computation*, *5*, 1166.
- Sponer, J., Sponer, J. E., Petrov, A. I., & Leontis, N. B. (2010). Quantum chemical studies of nucleic acids can we construct a bridge to the RNA structural biology and bioinformatics communities? *Journal of Physical Chemistry B*, *114*, 15723.
- Stombaugh, J., Zirbel, C. L., Westhof, E., & Leontis, N. B. (2009). Frequency and isostericity of RNA base pairs. *Nucleic Acid Research*, *37*, 2294.
- Suzuki, M., Amano, N., Kakinuma, J., & Tateno, M. (1997). Use of a 3D structure data base for understanding sequence-dependent conformational aspects of DNA. *Journal of Molecular Biology*, *274*, 421.
- Svozil, D., Hobza, P., & Sponer, J. (2010). Comparison of intrinsic stacking energies of ten unique dinucleotide steps in A-RNA and B-DNA duplexes. Can we determine correct order of stability by quantum-chemical calculations? *The Journal of Physical Chemistry B*, *114*, 1191.
- Szalewicz, K., & Jeziorski, B. (1998). Comment on "On the importance of the fragment relaxation energy terms in the estimation of the basis set superposition error correction to the intermolecular interaction energy" [*Journal of Chemical Physics*, *104*, 8821 (1996)]. *Journal of Chemical Physics*, *109*, 1198.
- Tennekes, P. P., Harju, J., Juvela, M., & Toth, L. V. (2006). HCN and HNC mapping of the protostellar core Chamaeleon-MMS1. *Astronomy & Astrophysics*, *456*, 1037.
- Vlieghe, D., Sponer, J., & Van Meervelt, L. (1999). Crystal structure of d(GGCCAATTGG) complexed with DAPI reveals novel binding mode. *Biochemistry*, *38*, 16443.
- Wimberly, B. T., Brodersen, D. E., Clemons, W. M., Jr., Morgan-Warren, R. J., Carter, A. P., Vornrhein, C., Hartsch, T., & Ramakrishnan, V. (2000). Structure of the 30S ribosomal subunit. *Nature*, *407*, 327.
- Wing, R., Drew, H., Takano, T., Broka, C., Tanaka, S., Itakura, K., & Dickerson, R. E. (1980). Crystal structure analysis of a complete turn of B-DNA. *Nature*, *287*, 755.
- Yamazaki, S., Domcke, W., & Sobolewski, A. (2008). Nonradiative decay mechanisms of the biologically relevant tautomer of guanine. *The Journal of Physical Chemistry A*, *112*, 11965.
- Yanagi, K., Prive, G. G., & Dickerson, R. E. (1991). Analysis of local helix geometry in three B-DNA decamers and eight dodecamers. *Journal of Molecular Biology*, *217*, 201.
- Yildirim, I., & Turner, D. H. (2005). RNA challenges for computational chemists. *Biochemistry*, *44*, 13225.
- Yildirim, I., Stern, H. A., Sponer, J., Spackova, N., & Turner, D. H. (2009). Effects of restrained sampling space and nonplanar amino groups on free-energy predictions for RNA with imino and sheared tandem GA base Pairs. Flanked by GC, CG, iGc or iCiG base pairs. *Journal of Chemical Theory and Computation*, *5*, 2088.
- Zhao, Y., & Truhlar, D. G. (2008). Density functionals with broad applicability in chemistry. *Accounts of Chemical Research*, *41*, 157.
- Zhou, J., Kostko, O., Nicolas, C., Tang, X., Belau, L., de Vries, M. S., & Ahmed, M. (2009). Experimental observation of guanine tautomers with VUV photoionization. *The Journal of Physical Chemistry A*, *113*, 4829.
- Zirbel, C. L., Sponer, J. E., Sponer, J., Stombaugh, J., & Leontis, N. B. (2009). Classification and energetics of the base-phosphate interactions in RNA. *Nucleic Acid Research*, *37*, 4898.



# 36 Metal Interactions with Nucleobases, Base Pairs, and Oligomer Sequences; Computational Approach

Jaroslav V. Burda<sup>1</sup> · Jiří Šponer<sup>2</sup> · Jerzy Leszczynski<sup>3</sup>

<sup>1</sup>Charles University in Prague, Prague 2, Czech Republic

<sup>2</sup>Institute of Biophysics, Academy of Sciences of the Czech Republic, Brno, Czech Republic

<sup>3</sup>Interdisciplinary Nanotoxicity Center, Department of Chemistry and Biochemistry, Jackson State University, Jackson, Mississippi, USA

<b>Introduction</b> .....	<b>1278</b>
<b>Properties of Metal Adducts with Nucleobases</b> .....	<b>1279</b>
Interaction of Bare Cations with Bases .....	1279
Metal Interactions in Implicit Solvent Model .....	1284
Interactions of Explicitly Hydrated Cations .....	1285
Hydrated Alkaline Earth and Zinc-Group Metal Cations .....	1285
Complexes of Hydrated Copper Cations with Guanine .....	1287
Interaction with Platinum Metal Complexes .....	1289
The Tautomeric Equilibrium of the Metalated Nucleobases .....	1290
Interaction of Nucleobases with Half-Sandwich Ru(II) Complexes .....	1291
<b>The Metal Coordination to Multiple Nucleobase Systems</b> .....	<b>1295</b>
Interaction with Base Pairs .....	1295
Metal Cations From Ia, Ib, IIa, and IIb Groups .....	1295
Enhancement of Base Pairing by Pt Complexes .....	1299
Interactions of Hydrated Cations with Nucleotides .....	1299
Metal Interactions with Stacked Bases .....	1301
Metal Adducts in Oligomeric Sequences .....	1302
<b>Conclusion</b> .....	<b>1303</b>
<b>Acknowledgment</b> .....	<b>1304</b>
<b>References</b> .....	<b>1304</b>



**Abstract:** This review summarizes computational studies devoted to interactions of metal cations with nucleobases, nucleotides, and short oligonucleotides considered as DNA/RNA models. Since this topic is complex, basically only the results obtained using *ab initio* and DFT methods are discussed. Part I focuses mainly on the interactions of the isolated bases with metal cations in bare, hydrated, and ligated forms. First, interactions of bare cations with nucleobases in gas phase approach are mentioned. Later, solvation effects using polarizable continuum models are analyzed and a comparison with explicitly hydrated ions is presented. In Part II, adducts of alkali metal, metal of alkaline earth, and zinc group metal cations with canonical base pairs are discussed. A separate section is devoted to platinum complexes related to anticancer treatment. Stacked bases and larger systems are discussed in last section. Here, semiempirical methods and molecular modeling are also discussed due to extensive size of studied complexes.

## Introduction

---

This chapter provides a brief overview of recent model calculations and simulations of metal interactions with nucleic acid (NA) bases, base pairs, and short oligomers. For historical reasons alkali metals and metals of alkaline earth are discussed first. All possible forms (or models) of the metal cations are considered, starting with bare cations, which have been studied mostly in earlier papers. In addition, complexes with hydrated or ligated cations investigated in more recent works are also reviewed. Despite the simplicity of bare cations and the fact that their bonding energies are overestimated due to an exaggerated contribution of Coulomb interaction, these models enable a clear insight into basic bonding characteristics and other electronic properties. Many studies have focused on transition metal complexes, motivated by known anticancer activity of cisplatin and related metallodrugs. While in the binding of alkali metals the electrostatic contribution dominates, the coordination covalent character is also an important term in the complexes of transition metals.

In general, the structure and function of DNA are dependent on metal ions. These ions can interact with many sites in DNA (Saenger 1983; Sigel 1993), including the phosphate groups, the sugar moiety, and the DNA bases. While metal cations usually interact with the phosphate group and, to a lesser extent, with the bases, cation–base interactions are expected to be involved in many important biophysical processes, such as different stabilization of DNA triple helices (Potaman and Soyfer 1994), stabilization of quadruple helices (Hud et al. 1996), and stabilization of the ribose-base stacking in Z-DNA (Egli and Gessner 1995). It is assumed that the interaction of a divalent cation with the base can cause significant polarization of the bases associated with stabilization of certain H-bonded DNA base pairs and other interactions (Anwander et al. 1990; Egli and Gessner 1995; Hud et al. 1996). However, the most ions do not interact with nucleic acids in a direct manner but rather contribute to an unspecific loose ion atmosphere around the nucleic acids (Chu et al. 2008). Note that while theoretical studies usually deal with binding of cations to DNA, the RNA cation binding is much more biochemically important and diverse. Many folded RNAs contain indispensable specific structural ions that may also be directly involved in RNA catalysis (Banas et al. 2009; Draper et al. 2005; Lilley and Eckstein 2008).

In the DNA double helix, the known sites for the cation coordination are mainly the N7 atoms of purines, while a simultaneous interaction with the O6 atom of guanine is also acknowledged. Some other sites, such as N3 of cytosine and N1 of adenine, are blocked by the hydrogen

bonding. It should be noted that the metal cation interactions are not restricted only to the DNA bases. The cation can simultaneously interact with the phosphate group and is usually surrounded by water molecules or by various ligands. The coordinated metal cations can interact with the DNA base directly (inner-sphere coordination) or a water molecule can link the DNA base with the metal cation (outer-sphere coordination) (Egli et al. 1991; Sigel 1993). Experimental studies on 5'-monophosphates revealed the following order of macrochelate coordination involving the N7 position of purines: GMP > IMP (I - inosine) > AMP (Sigel 1993). This order was explained as a result of different basicity of the N7 sites of guanosine, inosine, and adenine. It also correlates with the dipole moments of DNA bases.

## Properties of Metal Adducts with Nucleobases

### Interaction of Bare Cations with Bases

The first models investigated in connection with metal–nucleobases interactions employed bare cations. One of the pioneering studies on this topic was published in 1970 by Rozsnyai and Ladik (Rozsnyai and Ladik 1970), who considered the influence of water and divalent ions on base pairing. This paper was followed by del Bene's *ab initio* calculations (Del Bene 1984). She explored interactions of isolated Li<sup>+</sup> cation with all DNA bases. In this early work, all the basic features of modern quantum chemical calculations are already present – the structures were optimized at the HF/STO-3G level with single point calculations (SP) using the double-zeta basis set (6-31G). As the most stable adduct, the [Li-(Gua-O6,N7)]<sup>+</sup> chelate was established (with association energy of 78.4 kcal/mol) followed by cytosine complex [Li-(Cyt-O2,N3)]<sup>+</sup> (77.1 kcal/mol). The interaction energy of the most stable adenine conformer [Li-(Ade-N3)]<sup>+</sup> was estimated to be substantially lower – about 48.4 kcal/mol. These energies clearly demonstrate the dominant role of monopole (the cation)–dipole moment (the nucleobases) electrostatic interaction. In the study, both O2 and O4 thymine complexes were predicted to be more stable than the adenine adducts by about 10 kcal/mol. Soon after this keystone study, another work dealing with interactions of the A-T and G-C base pairs with the Li<sup>+</sup> cation appeared (Del Bene 1985). In the most stable Li<sup>+</sup>-A-T conformer, the Li cation was coordinated to the O2 site of thymine. In the G-C pair, the N3 position of guanine was preferred by 4 kcal/mol over O6, N7 chelate structure. We address here one important point: The numbers above, as well as most other numbers in this part, refer to gas phase interactions of metal cations with nucleic acids components. Such interactions are dominated by ionic electrostatic effects, which drastically become (almost completely) extinct in nucleic acids as well as in typical bioinorganic experiments. This must be kept in mind when interpreting the results. For more discussion of various aspects of the interplay between the gas phase interactions and real systems (see Burda et al. 2003; Petrov and Lamm 2005; Schmidt et al. 2002; Šponer et al. 2001).

Metal coordination sites in natural nucleotides are: (a) oxygen atoms of phosphate groups where cations neutralize the negative charge (these sites can be considered quite unspecific for any cation); (b) hydroxyl groups of sugar moiety usually chosen by alkali metals or metals of alkaline earth; (c) nitrogen atoms of heterocyclic bases – especially N1, N3, and N7 atoms of purine and N3 of pyrimidine bases, which exhibit large affinity to cations or generally electrophilic (in DNA/RNA oligomeric sequences only sites in minor or major grooves are accessible for interactions; this means that solely the N3 and N7 sites of purine bases are

■ **Table 36-1**

**Preferred sites for metalation and protonation**

Base	Coordination	Protonation
Adenine	N7 > N1	N1 > N7
Cytosine	N3	N3
Guanine	N7 > N1	N7 > N1
Thymine, uracil	O2 > O4	O4 > O2

available for the interactions); and (d) oxygens of keto-groups (O2 of cytosine, O6 of guanine and O2, O4 of thymine and uracil) as positions for binding of “hard” cations, e.g., alkali metals (and less frequently for transition metal).

Comparing cation coordination and protonation of these active sites, large similarities can be noticed in the case of guanine, cf. ● [Table 36-1](#). On the contrary, more remarkable differences are observed for adenine, uracil, or thymine.

Coordination of the  $Mg^{2+}$  cation to purine DNA bases was recently explored in many experimental as well as computational studies (e.g., Elmahdaoui and Tajmirrahi 1995; Sychrovsky et al. 2004), where bonding properties of selected mono- and divalent metal cations with N7 position of guanine and adenine were examined.

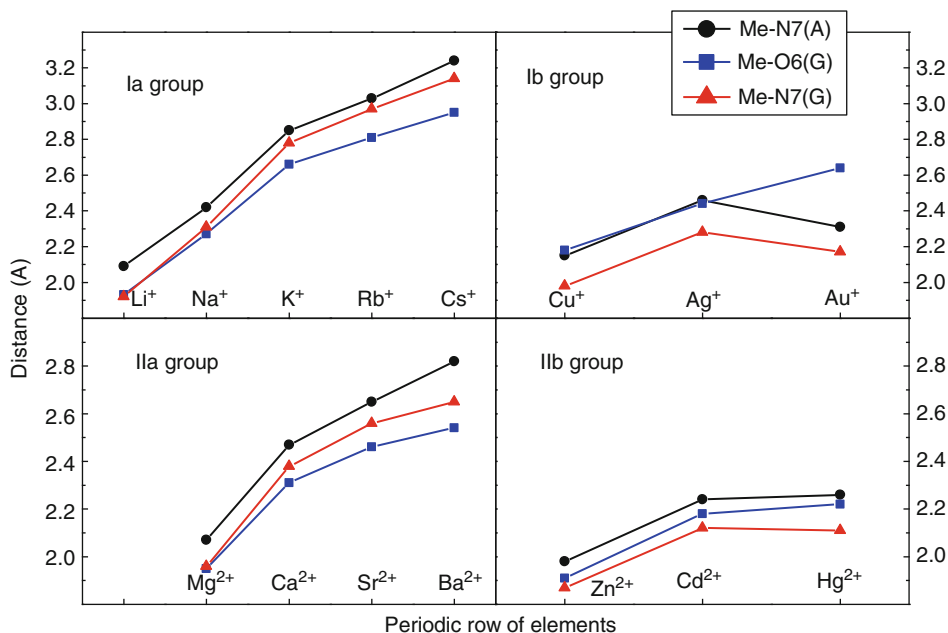
The interaction of bare monovalent (alkali metals and coinage metals) and divalent (alkaline earth and zinc group metals) cations with the N7 site of purine NA bases was examined in gas phase using MP2/6-31G(d,p)//HF/6-31G(d,p) level of theory (Burda et al. 1996). A graphical illustration of the dependence of the coordination distance on the atomic number of the cations is displayed in ● [Fig. 36-1](#). The intermolecular M-N7 distance monotonically increase with the atomic numbers for the alkali metals and metals of alkaline earths (cf. ● [Fig. 36-1](#)). This increase of the distances is more pronounced for the alkali metals where it exceeds 1 Å. The calculated M-N7 distances for both types of metals correlate well with the known ionic radii, e.g., Lide (1977). The influence of the relativity for the 5s and 5p electrons ( $Cs^+$ ,  $Ba^{2+}$ ) is not as pronounced as for the 5d electrons ( $Au^+$ ,  $Hg^{2+}$ ) (Pyykko 1988).

The stabilization energies of base...M complexes were determined according to the formula:

$$\Delta E^{Stab} = - \left[ E^{Complex} - \left( E_{BSSE}^{base} - E_{BSSE}^{metal} \right) \right] + \Delta E_{deform}^{base} \quad (36.1)$$

Here,  $E_{BSSE}^{base}$  represents total energy of the base (adenine or guanine) within the basis set superposition error (BSSE) scheme of Boys Bernardi (1970). The results are displayed in ● [Fig. 36-2](#), and it is evident that the values for guanine complexes are systematically larger than those of adenine. This is due to the larger dipole moment of guanine and the more favorable orientation of the ions and guanine dipole moment, as can be seen in ● [Fig. 36-3 a](#) and [c](#). The stabilization energies of the complexes with divalent ions are larger than those with monovalent ions and, as can be expected, the stabilization energies decrease with increasing atomic number of the metal ions. The only exception is revealed for the  $Au^+$  and  $Hg^{2+}$  complexes, where, due to the more pronounced relativistic effects, the respective stabilization energies are larger than the energies of the preceding cations ( $Ag^+$  and  $Cd^{2+}$ ).

In the coinage and zinc-group metal complexes, the bonding interaction is markedly stronger in comparison with coordination of the Ia and IIa metals. This is due to the presence of lower-energy vacant s-orbitals (compared with the same orbitals of the alkali metals), enabling to some extent the dative bonding into these orbitals from the occupied orbitals of the

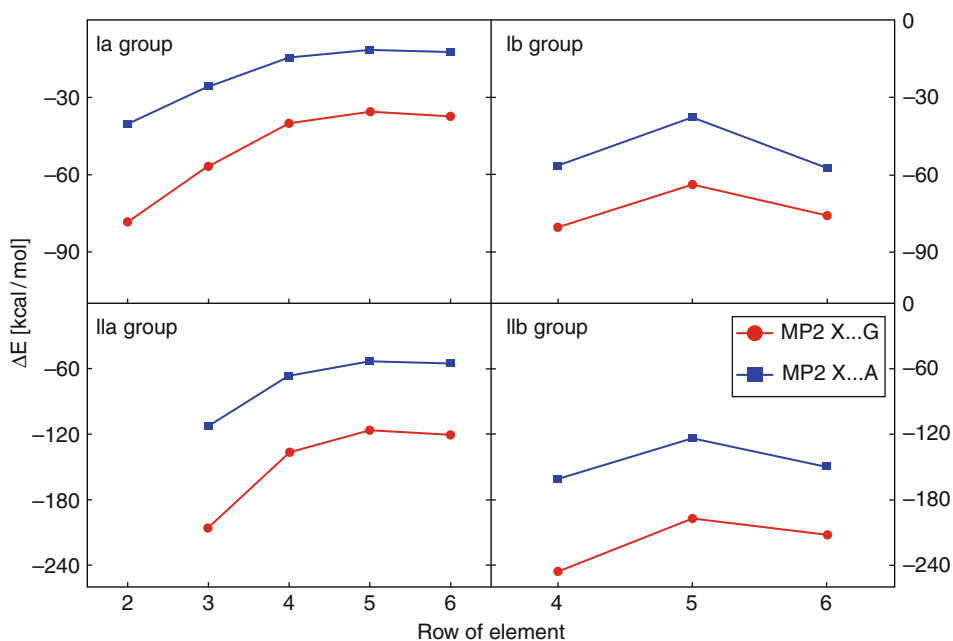


■ Fig. 36-1

Metal-base distances for Ia, Ib monovalent, and IIa and IIb divalent cations interacting with N7 (and O6) guanine and adenine sites

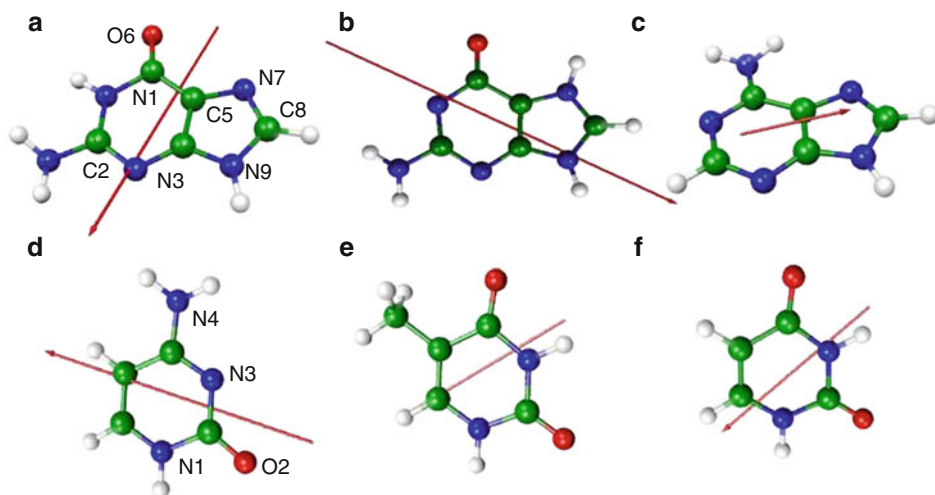
bases. This leads to the increase of covalent character of the interaction that explains the basic difference between coordination of K<sup>+</sup> and Cu<sup>+</sup> cations.

Complexes with a Li<sup>+</sup> bare cation were computationally explored in gas phase by Ruso et al. (2001) at the DFT(B3LYP) level within several basis sets. They found that the most stable complex of adenine and lithium is imino-tautomer with N6, N7 coordination. In this way, a five-membered chelate is formed where the Li<sup>+</sup>-N6 bond is 1.971 Å and Li<sup>+</sup>-N7 distance is 2.022 Å. The remaining explored (amino) structures, [Li-(Ade-N3,N9)]<sup>+</sup>, [Li-(Ade-N6,N7)]<sup>+</sup>, and [Li-(Ade-N3)]<sup>+</sup>, lie about 2, 10, and 15 kcal/mol higher on the potential energy surface. In the guanine adducts, the most stable structure is [Li-(Gua-O6,N7)]<sup>+</sup>, followed by chelate [Li-(Gua-N3,N9)]<sup>+</sup>, its enol form, and the enol form of the (O6,N7)-chelate, which are 11, 12, and 15 kcal/mol less stable. The interaction of lithium cation with uracil yields complexes with an energy difference lower than that revealed between corresponding isolated isomers but the stability order remains unchanged. The most stable complex with uracil is [Li-(Ura-O4)]<sup>+</sup> adduct (cf. ● Fig. 36-4). The chelate structures [Li-(Ura-O2,N3)]<sup>+</sup> and [Li-(Ura-O4,N3)]<sup>+</sup> lie about 3 and 7 kcal/mol above the global minimum and the [Li-(Ura-O2)]<sup>+</sup> adduct is about 5 kcal/mol above the O4-conformer. This fact clearly shows the electrostatic origin of the interaction when one considers the direction of the uracil dipole moment. In the case of thymine, a similar picture is revealed, only the differences are slightly smaller. The relative energy of two higher-lying tautomers with respect to [Li-(Thy-O4)]<sup>+</sup> adduct are 2 kcal/mol for (O2,N3)-chelate and 5 kcal/mol for (N3,O4)-chelate. In the cytosine complexes, the [Li-(Cyt-O2,N3)]<sup>+</sup> structure is the most stable minimum followed by enol tautomer of [Li-(Cyt-N1,O2)]<sup>+</sup>, and the enol form



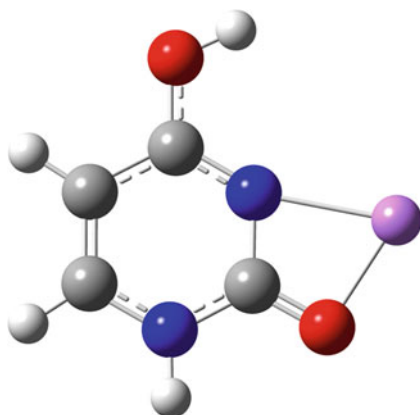
■ Fig. 36-2

Stabilization energies of metal-base complexes for la, lb, lla, and llb metal cations interacting in N7(O6) position of the base



■ Fig. 36-3

Orientation and size of the isolated NA bases: (a) guanine, (b) N7 protonated guanine tautomer, (c) adenine, (d) cytosine, (e) thymine, (f) uracil. Standard atom numbering is used (e.g., textbook of Saenger 1983)



■ Fig. 36-4  
Structure of the  $[\text{Li}-(\text{Ura-O2,N3})]^+$  cation (enol form of O2,N3-chelate)

of  $[\text{Li}-(\text{Cyt-O2,N3})]^+$  (where N1 proton is transferred to O2 site). These two complexes lie about 12 and 17 kcal/mol higher on the potential energy surface.

The coordination of divalent metal cations with the phosphate group of various nucleotides (GMP, AMP, UMP, and CMP) was studied by Varnali (Varnali and Tozumcalgan 1995). In her study a semiempirical PM3 method was used. From the results it follows that the most stable metal adducts are formed with the phosphate group of AMP, closely followed by CMP for all explored metals.

The calculations of the NMR spin-spin coupling constants and the NMR shifts of the direct and water-mediated binding of a divalent metal cations to guanine were performed by Sychrovský (Sychrovsky et al. 2004). The intermolecular coupling constants  $(1)J(X, O6)$  and  $(1)J(X, N7)$  ( $X = \text{Mg}^{2+}, \text{Zn}^{2+}$ ) were unambiguously assigned to the specific binding motif of the hydrated cation with O6 and N7 sites of guanine. The calculated coupling constants  $(1)J(\text{Mg}, O6)$  and  $(1)J(\text{Zn}, O6)$  were 6.2 and  $-17.5$  Hz for the inner-shell complex where the cation is directly interacting with the guanine O6 position. For the inner-shell coordination of the cation at nitrogen N7, the calculated coupling constants  $(1)J(\text{Mg}, N7)$  and  $(1)J(\text{Zn}, N7)$  were 5.6 and  $-36.5$  Hz, respectively. When the cation binding is water-mediated, the corresponding coupling constants are zero. The calculated NMR shifts  $\delta(N7) = -15.3$  and  $-12.2$  ppm upon the coordination of  $\text{Mg}^{2+}$  and  $\text{Zn}^{2+}$  ion are similar to the NMR shift of 19.6 ppm toward the high field measured by Tanaka (Tanaka et al. 2002) for the coordination of  $\text{Cd}^{2+}$  to the N7-guanine site.

The B3LYP/6-311+G(2df,2p) level was used to explore geometry of all possible adducts originating from the interaction of  $\text{Cu}^{2+}$  cation with the most stable tautomers of DNA and RNA free bases (Marino et al. 2004). Several attachment sites for both purine and pyrimidine bases have been taken into account for possible formation of both mono-adducts and chelates. The copper ion (II) has the highest affinity for the most stable tautomer of guanine base.


Also, a comparison of various divalent metal cation complexes ( $\text{Zn}^{2+}, \text{Cu}^{2+}, \text{Ni}^{2+}$ ) with hypoxanthine and uracil was performed by Matsubara (Matsubara and Hirao 2002). The B3LYP level stabilization energies of both M(II)-hypoxanthine and M(II)-uracil complexes reflect the strength of the M-N(base) interaction, giving the same sequence  $\text{Zn}^{2+} > \text{Cu}^{2+} > \text{Ni}^{2+}$  for both bases.

## Metal Interactions in Implicit Solvent Model

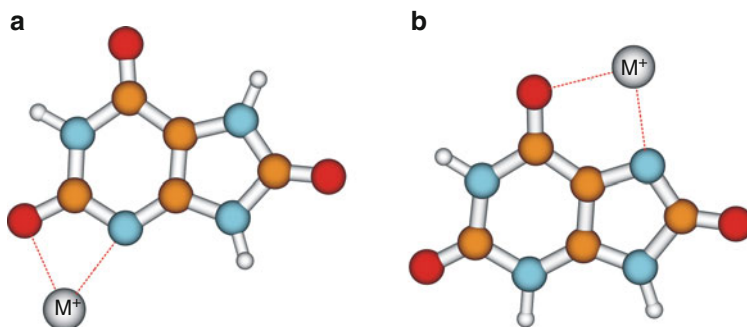
The calculated interaction energies of the bare cations with nucleobases reveal large overestimation of the electrostatic interaction in comparison with experimental samples. This overestimation is clearly due to the uncompensated charge of the bare cation since cations in water solution are surrounded by solvent molecules. In this way the charge of the cation is screened and the electrostatic part of the metal–base interaction is substantially reduced. The role of electrostatic contribution in the case of the Pt-base coordination will be demonstrated later. As the approach of PCM models is very popular there are a large number of such studies. Here only a few recent works will be mentioned.

In 2008 Ai published a study (Ai et al. 2008) on tautomer equilibrium of adenine in the presence of  $\text{Zn}^{2+}$  cation at the DFT level (B3LYP/6-311+G\*\*). It was found that the  $[\text{Zn}-(\text{Ade-N6,N7})]^{2+}$  imino complex is the most stable structure in accord with the gas phase calculations of Kabeláč (Kabeláč and Hobza 2006). The latter calculations explored tautomers of all DNA bases in the presence of  $\text{Na}^+$ ,  $\text{Mg}^{2+}$ , and  $\text{Zn}^{2+}$  bare cations evaluated at the RI-MP2/TZVPP level of theory.

Metal cation binding to deoxyguanosine monophosphate was examined by Bouř (Andrushchenko and Bouř 2009). Infrared spectra of complexes with  $\text{Na}^+$ ,  $\text{Mg}^{2+}$ ,  $\text{Ca}^{2+}$ ,  $\text{Ni}^{2+}$ ,  $\text{Cu}^{2+}$ ,  $\text{Zn}^{2+}$ , and  $\text{Cd}^{2+}$  cations were recorded and interpreted on the basis of density functional theory. The solvation effects were simulated by PCM and cluster models (combined explicit solvent and PCM). The coordination to the guanine N7 position was considered and obtained calculated spectra predict a blue-shift of the characteristic  $1,578\text{ cm}^{-1}$  frequency, in accord with experimental data. Binding to the phosphate group causes significant spectral changes in the sugar-phosphate vibration region but also notable frequency shifts of the carbonyl vibrations. The  $\text{Cu}^{2+}$  and  $\text{Zn}^{2+}$  cations induced the largest changes in measured vibrational absorption, which corresponds to the computationally determined strong interaction energies in the N7-complexes. The  $\text{Cu}^{2+}$  binding to guanine was revealed to be a two-step process, which was also confirmed by the microcalorimetry titration curve.

Another study on interaction of bare cations with metabolite of purine bases – uric acid should be mentioned (Allen et al. 2006). The geometries of the complexes of  $\text{Li}^+$ ,  $\text{Na}^+$ ,  $\text{K}^+$ ,  $\text{Be}^{2+}$ ,  $\text{Mg}^{2+}$ , and  $\text{Ca}^{2+}$  metal cations with various nucleophilic sites of uric acid were optimized at the B3LYP/6-311++G(d,p) level. Single point energy calculations were performed at the MP2/6-311++G(d,p) level. It was found that cations mainly form chelate structures with a bidentate coordination. In the gas phase, the most preferred position for the interaction of  $\text{Li}^+$ ,  $\text{Na}^+$ , and  $\text{K}^+$  monovalent cations is between the N3 and O2 sites, while all divalent cations prefer coordination between the N7 and O6 sites of the urate. The influence of aqueous solvent on the relative stability of various complexes was examined by PCM model. The BSSE corrected interaction energies were also determined. It was found that aqueous solution has a significant impact on the relative stability of complexes. The global minimum of urate with  $\text{Mg}^{2+}$  and  $\text{Ca}^{2+}$  cations is represented by the O2,N3-chelates in analogy with monovalent cations. Moreover, the relative energy differences are very small. Especially for the  $\text{Ca}^{2+}$  structures, practically energies of all conformers are in the range of 2 kcal/mol. The most stable structures are depicted in  Fig. 36-5.

The binding of first-row transition metal monocations ( $\text{Sc}^+ - \text{Cu}^+$ ) to N7 of guanine and N7 or N3 of adenine nucleobases was studied using the DFT approach with B3LYP functional. The electrostatic character of these interactions is mainly represented by metal-ligand repulsion.



■ Fig. 36-5

The optimized structures of the metal complexes with urate (a) (O2,N3)-chelate, (b) (O6,N7)-chelate

The  $M^+$ -guanine binding energies are about 18–27 kcal/mol larger than those of  $M^+$ -adenine, the differences decreasing along the row of these metal cations (Noguera et al. 2008).

## Interactions of Explicitly Hydrated Cations

Another approach to a more realistic description of metal cation interactions with nucleobases is represented by a model of the explicitly hydrated cations – usually up to hexacoordinated cations.

### Hydrated Alkaline Earth and Zinc-Group Metal Cations

One of the first studies on this topic was published by Šponer et al. (1998). In this study, pentaqua divalent cation adducts (of  $Mg^{2+}$ ,  $Ca^{2+}$ ,  $Sr^{2+}$ ,  $Ba^{2+}$ ,  $Zn^{2+}$ ,  $Cd^{2+}$ , and  $Hg^{2+}$ ) to the N7 position of guanine were explored at the MP2/6-31G\*\*/HF/6-31G\* level. Quasi-relativistic-pseudopotentials were used for the description of the cations. The interaction between hydrated cation and guanine is significantly reduced compared to the guanine-unsolvated cation model, cf. Table 36-2. The cations of IIb group together with  $Mg^{2+}$  are tightly bound to the N7 atom of guanine, whereas the O6 site is involved in H-bonding with the aqua ligands from the metal hydration shell. The cations with greater radius ( $Ca^{2+}$ ,  $Sr^{2+}$ , and  $Ba^{2+}$ ) prefer simultaneous coordination to the N7 and O6 atoms of the base. Also, the cation–guanine distance increases with the atomic number. The energy difference between the N7 and N7-O6 types of coordination is rather small. Relativistic effects are apparent in the case of  $Hg^{2+}$ , similar to the complexes with a bare cation, reported above (Burda et al. 1996). The  $Zn^{2+}$  and  $Mg^{2+}$  cations show different balance between the cation–base and cation–water interactions. While the  $Zn^{2+}$  cation is bound more tightly to the base (93 kcal/mol) and its water shell is more flexible (203 kcal/mol), a different situation (with stronger metal–water binding) was found in the  $Mg^{2+}$  complex. The binding energy of the  $Mg(H_2O)_5^{2+}$  cation with the N7 position of guanine in GC pair is approximately 89 and binding energy of five water molecules with  $Mg(GC)$  complex is about 220 kcal/mol. The different binding picture for  $Zn^{2+}$  and  $Mg^{2+}$  cations can be partly explained as a shift



■ Table 36-2

Interaction energies in the complexes of solvated cation (Mw)-(N7) purine (G/tG/A)

	$\Delta E_{Mw-G}$	$\Delta E_{Mw-tG}$	$\Delta E_{MG \text{ bare}}$	$\Delta E_{Mw-A}$	$\Delta E_{MA \text{ bare}}$
Mg <sup>2+</sup>	-89.3	-84.8	-198.7	-46.0	-107.9
Ca <sup>2+</sup>	-82.6	-80.1	-133.9	-33.5	-61.6
Sr <sup>2+</sup>	-76.0	-	-	28.9	-48.9
Ba <sup>2+</sup>	-71.2	-71.4	-118.3	-28.1	-54.4
Zn <sup>2+</sup>	-93.8	-90.1	-237.2	-53.7	-152.9
Cd <sup>2+</sup>	-87.9	-107.6	-192.6	-45.9	-116.6
Hg <sup>2+</sup>	-94.3	-149.2	-208.0	-55.3	-141.1

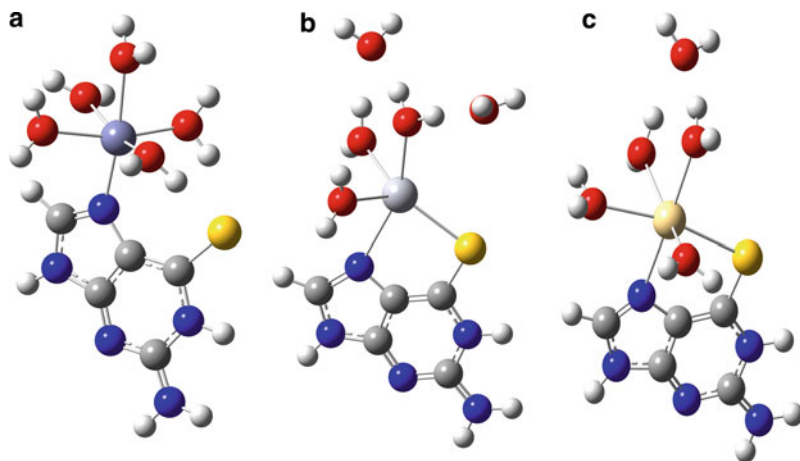
from the interaction between nucleobase and hydrated cation (Mg<sup>2+</sup>) toward the hydration of a metalated base (Zn).

From ▶ [Table 36-2](#) it follows that, despite the substantial reduction of the M-N7 interaction energy, the ratio of the energy values for guanine and adenine remains approximately two, similar to the results obtained in the study of the bare cations (Burda et al. 1996). This confirms the dominant role of the electrostatic term in these complexes. In platinum complexes a substantially higher covalent contribution is demonstrated in the limit of total charge going to zero (cf. ▶ [Figs. 36-9](#) and ▶ [Fig. 36-14](#), below).

The question, which coordination mode of hydrated Mg cation with DNA is dominant (direct metal-N7 coordination or indirect interaction by water molecule through the polarized H-bonding), was addressed by Bandyopadhyay (Bandyopadhyay and Bhattacharyya 2003). Based on HF and DFT calculations the authors show that both binding modes are of similar importance.


The tautomeric equilibrium and hydrogen bonding in nucleotide 2'-deoxyguanosine monophosphate in interaction with hydrated [Mg(H<sub>2</sub>O)<sub>4</sub>]<sup>2+</sup> cation were studied at the MP2/cc-pVDZ//B3LYP/cc-pVDZ and B3LYP/aug-cc-pVTZ//B3LYP/cc-pVDZ levels of theory by Kosenkov et al. (2008). The Mg<sup>2+</sup> ion forms two inner-shell contacts with the nucleotide, similar to small phosphorylated molecules under physiological conditions. The hydrated magnesium cation in the presence of the phosphate group can change the guanine tautomeric equilibrium in comparison to free guanine. The canonical O6-oxo form of guanine is more stable (by 6–8 kcal/mol) than the O6-hydroxo form in anti-conformation. The interaction with the Mg<sup>2+</sup> ion is capable of suppressing a spontaneous transient formation of the rare tautomer.

A very interesting case was revealed when a thioguanine base was explored (Šponer et al. 1999). In accord with the Pearson HSAB principle (Parr and Pearson 1983), a stronger interaction with the S6 site of thioguanine is observed for the heavier transition metal cations, as can be seen by comparing columns  $\Delta E_{Mw-G}$  and  $\Delta E_{Mw-tG}$  in ▶ [Table 36-2](#). While in the case of alkaline earth cations (Mg<sup>2+</sup>, Ca<sup>2+</sup>) even mild weakening of the bonding energy is visible, a very robust adduct is formed with the Hg<sup>2+</sup> cation. This very firm coordination is also partially the consequence of a smaller number of water molecules in the first hydration shell. Due to the strong Hg-S coordination two water molecules are pushed out from the hydration shell. The optimized (S6,N7)-chelate structure resembles the situation of bare cations, cf. ▶ [Fig. 36-6b](#). However, a shorter Hg-S distance (2.50 Å) was obtained comparing the Hg-N bond (2.57 Å). A similar chelate structure was also found in the Cd<sup>2+</sup> complex, despite the coordination with four water molecules, cf. ▶ [Fig. 36-6c](#). But a slightly longer Cd-S distance (2.67 Å) than





■ Fig. 36-6

Different cases of hydrated-metal coordination to thioguanine: (a)  $\text{Zn}^{2+}$ , (b)  $\text{Hg}^{2+}$ , and (c)  $\text{Cd}^{2+}$

$\text{Cd-N}$  (2.40 Å) was obtained in this structure. In the remaining complexes no direct metal-sulfur interaction was found at the HF/6-31G\* optimization level. Nevertheless, at the DFT level, a slightly different coordination pattern is revealed for Mg and Zn cations. The preferred structure contains six coordinated cation spheres, but only with four water molecules, similar to the chelate arrangement of the  $\text{Cd}^{2+}$  complex (Šponer et al. 1999) as shown in the  Fig. 36-6c.

Šponer et al. investigated possible binding of hydrated cations to nucleobases in a cation- $\pi$  manner but concluded that such interactions are very unlikely in nucleic acids as they are out-competed by conventional cation binding patterns. The suggestion of the existence of cation- $\pi$  interactions in DNA was shown to be a case of misinterpretation of structural data (Šponer et al. 2000).

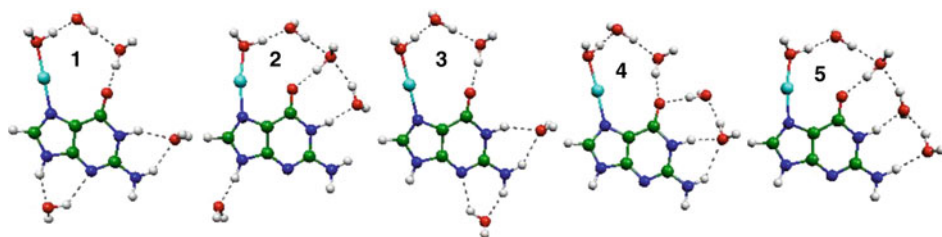
## Complexes of Hydrated Copper Cations with Guanine

Interaction of hydrated Cu(I)/Cu(II) cations with guanine represents another interesting system that has been explored. In this case, redox properties under hydration and complexation can be compared to copper complexes with water and ammonium ligands (Burda et al. 2005; Pavelka et al. 2008). One of the examined features of the copper complexes involves the number of coordinated ligands. While the Cu(I) complexes prefer two-coordinated structures, the geometry of Cu(II) complexes usually has the coordination number four or five, in accord with the small inorganic copper complexes studied previously (Pavelka and Burda 2005; Pavelka et al. 2006). Also, the affinity of various active sites of the metalated guanine for water molecules in comparison with a non-metalated (isolated) base was explored. The resulting preference for individual conformers determined at the B3LYP/6-311++G(2df,2pd) level can be seen in  Table 36-3, and the most stable structures are displayed in  Fig. 36-7. The affinity of the isolated base was explored by Poltev et al. (1996), who used empirical potentials. They found that in the case of hydration of guanine with a single water molecule, the global minimum structure has one water molecule between the O6 and N1 sites, followed by the N1-N2 water adduct. Unfortunately, the

■ Table 36-3

The relative differences of  $\Delta G$  and  $\Delta E^{Stab}$  and Cu–N7 and Cu–O binding energies for the selected conformers in kcal/mol

Conformer	$\Delta G$	$\Delta E^{Stab}$	$E(\text{Cu-N})$	$E(\text{Cu-O})$
1	0.0	–168.4	83.4	60.4
2	1.1	–167.9	81.0	59.9
3	2.6	–165.3	80.4	60.7
4	3.5	–166.5	74.4	60.6
5	3.6	–167.7	76.5	60.1



■ Fig. 36-7

The most stable conformers of  $[\text{Cu}(\text{H}_2\text{O})_5(\text{N7-guanine})]^+$  complex

N9 position was not considered. In another study (Colominas et al. 1996) various tautomeric forms of guanine and cytosine and their influence on Watson–Crick H-bonding were studied. From these results, it is clear that there is no substantial change due to the polarization effects of Cu(I) cation revealed by semiempirical methods, in comparison with the MP2 approach. Another comparison concerns metal–N7 bonding energies where our earlier works on metal coordination to purine DNA bases can be used (Burda et al. 1996, 1997). Despite the fact that in the earlier investigations only bare cations were considered at the MP2/6-31G(d)//HF/6-31G(d) level, the relative interaction energies are similar to the analogous energies of these hydrated structures.

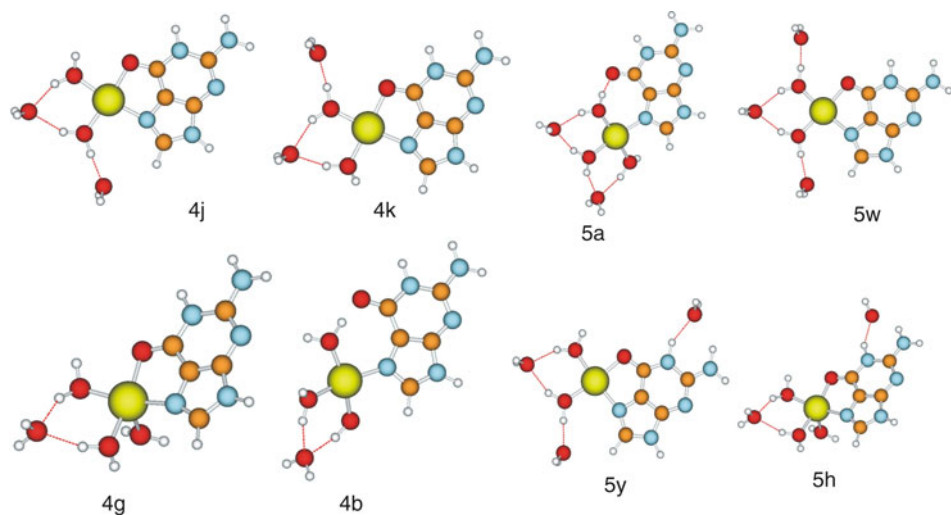
The adducts of the hydrated copper(II) cation with guanine were explored in the study of Pavelka (Pavelka et al. 2006). Various numbers of water molecules were considered in combination with the different coordination pattern of the  $\text{Cu}^{2+}$  cation. The most stable structures are summarized in ▶ Table 36-4 and displayed in ▶ Fig. 36-8. The full set of investigated structures can be viewed in the original paper (Pavelka et al. 2006).

From this study it follows that the penta-coordination of Cu(II) in these complexes is visibly less convenient than that in the case of the small inorganic complexes (for both purely aqua ligands (Burda et al. 2004) or mixed aqua-ammine ligands (Pavelka and Burda 2005)). The Cu(I) complexes do not create chelate structures since the linear mono-aqua-form with the remaining water molecules in the solvation shell is substantially more stable. In the mono-aqua Cu(I) and Cu(II) complexes, the strength of Cu–N7 bond (–81/–230 kcal/mol for Cu(I)/Cu(II)) and Cu–O(aq) bond (–35/46 kcal/mol) roughly follow a formal electrostatic relationship. Higher preference for N7 coordination in the Cu(II) complex is related to the possibility of the higher electron transfer of more polarizable nitrogen atom.

■ Table 36-4

Relative differences of Gibbs energies  $\Delta G$  and stabilization energies  $\Delta E^{stab}$  (in kcal/mol) with respect to global minima structure. Abbreviation *c.n.* corresponds to the type of coordination and *struct.* is used for identification of the optimized structure in ► Fig. 36-8

System	<i>c.n.</i>	<i>struct.</i>	$\Delta G^{total}$	$\Delta\Delta E^{stab}$
[CuG(H <sub>2</sub> O) <sub>4</sub> ] <sup>2+</sup>	4	4b	2.2	4.6
	4 <sup>chel</sup>	4j	0.0	0.0
	4 <sup>chel</sup>	4k	2.0	1.0
	5 <sup>chel</sup>	4g	4.3	4.9
CuG(H <sub>2</sub> O) <sub>5</sub> <sup>2+</sup>	4	5a	2.8	0.0
	4 <sup>chel</sup>	5w	0.0	1.7
	4 <sup>chel</sup>	5y	1.1	1.0
	5 <sup>chel</sup>	5h	6.4	5.4



■ Fig. 36-8

The most stable structures in complexes with four and five water molecules

## Interaction with Platinum Metal Complexes

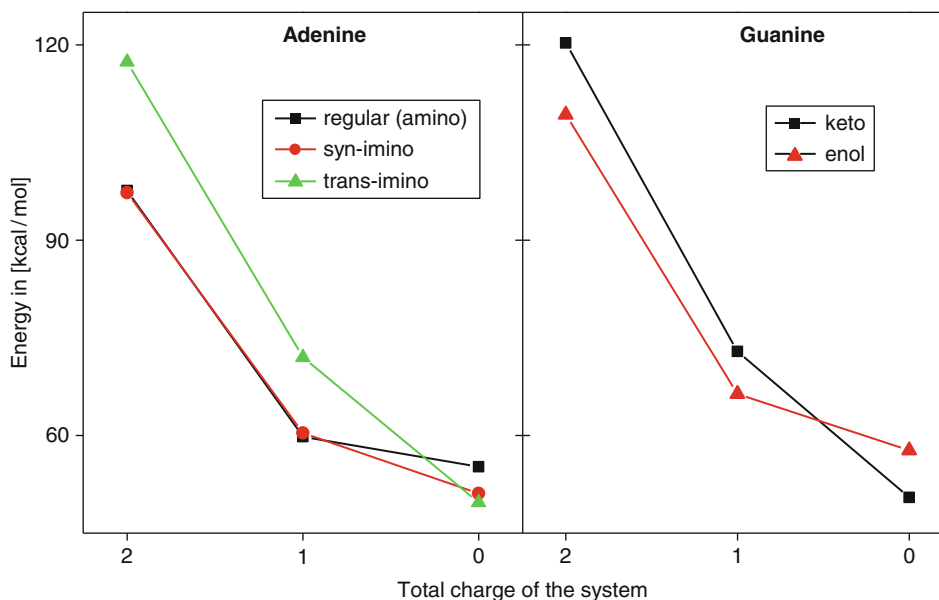
One of the most frequently studied metals in connection with nucleobases is platinum. Since the late 1960s, when B. Rosenberg published his series of studies on anticancer activity of cisplatin (Rosenberg et al. 1965, 1969) much effort has been devoted to this compound and its derivatives, as well as other transition metal complexes where similar activities can be expected. Early calculations were performed by Basch et al. (1986) and by Lipinski (1989). Since then a vast number of studies can be found in the literature on this topic. Many DFT and ab initio calculations were performed, especially on platinum interactions with nucleobases, nucleotides, and other DNA models. One of the important questions that had to be solved concerned tautomeric equilibria due to the possible point mutations. This topic was addressed in several studies considering various nucleobases. Because metallodrugs are generally expected to coordinate predominately in the major groove of genomic DNA, the discussion starts with the interaction in N7 position of purine bases.

## The Tautomeric Equilibrium of the Metalated Nucleobases

Several platinum complexes with varying total charge were explored at the B3LYP/6-31G(d) level (Burda et al. 2000): neutral trans-dichloro-diamine-platinum, +1 charged trans-triamine-chloro-platinum, and +2 charged tetraamine-platinum. Two tautomers of guanine were considered – keto and enol forms as well as N6-amino and syn- and anti-imino forms of adenine. In this way the role of electrostatic contribution could be elucidated. Despite the calculations were performed in gas phase, the bonding energy and tautomeric relations in solvent can be easily estimated (i.e., extrapolated). In [Fig. 36-9](#), the relative tautomeric stabilization energies are displayed.

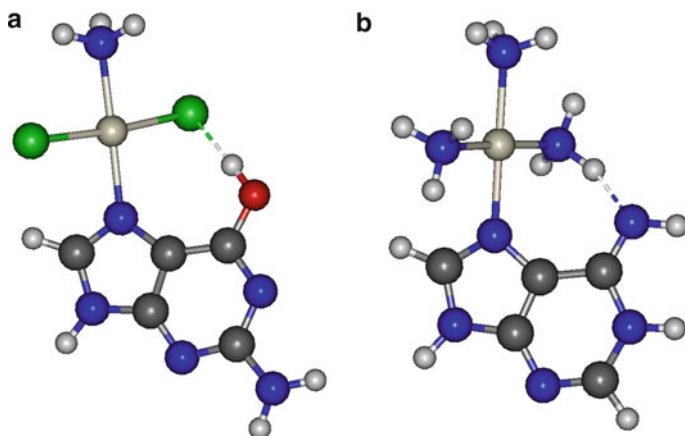
From this figure it follows that the trans-imino-tautomer of adenine is better stabilized under platination, which could lead to mispairing. In the case of guanine, the regular keto form is more stable in the case of charged complexes. Moreover, the enol preference in the electroneutral complex is caused by additional H-bonding stabilization between platinum ligand (aqua or chloro) with hydrogen from the enol group (cf. [Fig. 36-10a](#)), which may not be present in solvent due to competitive H-bonding interactions. This study in general suggests that the largest part of the tautomeric effects of the N7 platination is due to gas phase effects, which are assumed to be annihilated in real condensed phase conditions.

Šponer (Šponer et al. 1999) explored metalation of the exocyclic amino group of cytosine and adenine nucleobases by Pt(II) and Hg(II) complexes. Metalation induces protonation of the N3 site of cytosine and N1 atom of adenine. Hence, it causes a proton shift from an exocyclic to



■ Fig. 36-9

Stabilization energies of the platinum-base complexes in dependence on the total charge of the (a) adenine and (b) guanine complex



■ Fig. 36-10

Structure of platinum(II) complexes with (a) enol-tautomer of guanine and (b) trans-imino-tautomer of adenine

an endocyclic N atom (similar to situation in [Fig. 36-10b](#)). In this way the metal-assisted process can lead to the generation of rare nucleobase tautomers. The calculations demonstrate that metalation of the exocyclic amino group of nucleobases significantly increases the protonation energy of the aromatic rings of nucleobases by about 30–34 kcal/mol for the Pt(II) adduct and by about 10–14 kcal/mol for the Hg(II) adduct. This study demonstrates a tautomeric shift that is caused by changes of the electronic structure of nucleobases and is unrelated to electrostatic effects. Thus, the authors suggested separating purely electrostatic effects from non-electrostatic (molecular orbital) contributions. The former are expected to be unimportant in aqueous solution or x-ray crystallography experiments, where the systems are overall strictly neutral. The non-electrostatic contributions are assumed to remain insensitive to the environment and are fully expressed under usual experimental conditions.

Rare tautomers of 1-methyluracil (MeUH) and 1-methylthymine (MeTH) in coordination with Pt(II) complexes were explored by van der Wijst et al. (2009). Comparing the calculations in gas phase and water, the influence of the solvation effects can be estimated. These authors also showed that relative stabilization energies of the Pt(II) complexes with various tautomers of MeUH and 1-MeTH differ from the isolated tautomers. This leads to the conclusion that some rare tautomers may become favored under metalation.

### Interaction of Nucleobases with Half-Sandwich Ru(II) Complexes

Recently, computations on ruthenium complexes with nucleobases were published by Futera (Futera et al. 2009). In his comprehensive study interactions of piano-stool ruthenium metallodrug with nucleobases were investigated. In the same study the reaction profile of the chloro-ligand replacement by water molecule and the role of the arene-ring size were also explored. From the point of this review, an important part of Futera's study deals with interactions of Ru(II) with various sites of all the nucleobases in vacuum and under implicit solvent model. For the optimized structures, the bonding and stabilization energies were determined.

■ Table 36-5

Bonding and stabilization energies (in kcal/mol); for easier comparison of various adducts, total energies (in a.u.) are also presented (bz means benzene, cym means p-cymene ligand)

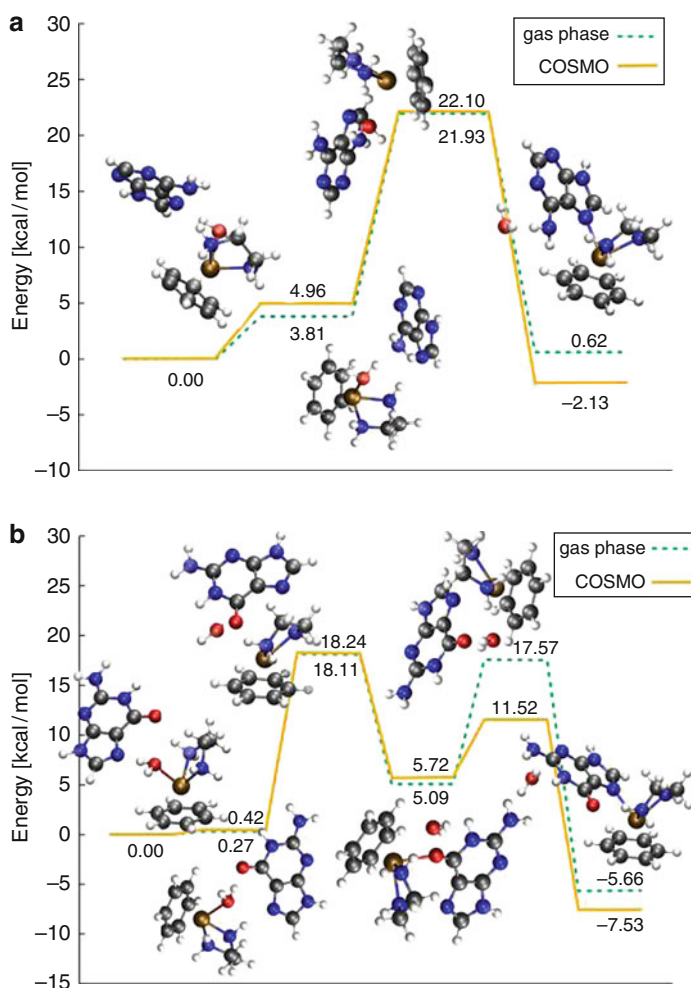
	Ru(bz)(Ade-N1)		Ru(bz)(Ade-N3)		Ru(bz)(Ade-N7)		Ru(cym)(Ade-N7)	
Adenine	in vacuo	COSMO	in vacuo	COSMO	in vacuo	COSMO	in vacuo	COSMO
$\Delta E^{BE}$ (ade)	-72.7	-48.7	-69.1	-47.7	-69.7	-50.3	-65.4	-50.2
$\Delta E^{Stab}$	431.1	389.2	426.9	387.9	426.2	390.0	441.4	396.5
$E^{Total} + 900$	-81.612	-81.880	-81.605	-81.879	-81.606	-81.881		
Guanine	Ru(bz)(Gua-N1)		Ru(bz)(Gua-N3)		Ru(bz)(Gua-N7)		Ru(cym)(Gua-N7)	
$\Delta E^{BE}$ (gua)	-103.9	-59.7	-56.4	-45.3	-90.7	-56.0	-86.1	-57.2
$\Delta E^{Stab}$	442.7	390.9	412.6	384.7	449.7	395.3	465.6	383.3
$E^{Total} + 1000$	-56.687	-56.944	-56.637	-56.939	-56.695	-56.955		
Cytosine	Ru(bz)(Cyt-N1)		Ru(bz)(Cyt-N3)		Ru(bz)(Cyt-O2)			
$\Delta E^{BE}$ (cyt)	-89.5	-56.0	-79.0	-52.8	-84.0	-45.9		
$\Delta E^{Stab}$	441.1	392.6	438.4	392.2	444.6	389.2		
$E^{Total} + 900$	-9.447	-9.710	-9.444	-9.709	-9.449	-9.701		
Thymine	Ru(bz)(Thy-N1)		Ru(bz)(Thy-N3)		Ru(bz)(Thy-O2)		Ru(bz)(Thy-O4)	
$\Delta E^{BE}$ (thy)	-65.0	-46.5	-82.8	-51.3	-53.9	-31.3	-60.0	-34.7
$\Delta E^{Stab}$	407.4	372.3	424.9	380.3	412.5	374.0	420.2	376.2
$E^{Total} + 900$	-68.436	-68.717	-68.467	-68.727	-68.440	-68.717	-68.454	-68.721
Uracil	Ru(bz)(Ura-N1)		Ru(bz)(Ura-N3)		Ru(bz)(Ura-O2)		Ru(cym)(Ura-O4)	
$\Delta E^{BE}$ (ura)	-61.6	-45.9	-79.8	-51.1	-50.8	-31.7	-59.1	-34.3
$\Delta E^{Stab}$	403.2	371.2	422.7	380.5	410.5	375.3	419.3	377.3
$E^{Total} + 900$	-29.240	-29.527	-29.274	-29.539	-29.247	-29.531	-29.262	-29.534

Characteristics of the most stable conformers are summarized in [Table 36-5](#). In order to make a comparison between various conformers easier, the total energies are also included. From [Table 36-5](#) it follows that, in the case of purine bases, the most stable adenine structure (Ru<sup>2+</sup>-(Ade-N1) conformer) differs from the most stable guanine complex (Ru<sup>2+</sup>-(Gua-N7) conformer), as revealed in the gas-phase calculations. Nevertheless, in the PCM model, the N7-conformer represents the most stable form of the both purine nucleobases. This change of adenine global minimum follows from the general reduction of the electrostatic forces, which are substantially screened in PCM approaches. In gas phase, the Ru<sup>2+</sup>-(Ade-N1) coordination is enhanced by favorable orientation of the adenine dipole moment of about 2.70 D (determined at the MP2/6-31++G(d,p), gas-phase level) aiming in the N1-C8 direction while the guanine dipole of 6.36 D points in the N7-N3 direction, as can be seen in [Fig. 36-3](#). An even larger dipole moment was predicted for the N1-guanine tautomer with proton transferred to N7 atom ( $\mu = 9.55$  D). This dipole value correlates with the fact that the Ru-(Gua-N1) adduct exhibits the highest  $\Delta E^{BE}$  (Ru-(base-N)) bonding energy among all the explored complexes (interestingly, in both gas phase and PCM approach). The effect of decreased electrostatic enhancement is responsible for the change in energy preference in the case of cytosine adducts. The Ru<sup>2+</sup>-(Cyt-O2) structure becomes the least stable in water (by more than 7 kcal/mol) and the most stable adduct is Ru<sup>2+</sup>-(Cyt-N1), closely followed by the Ru<sup>2+</sup>-(Cyt-N3) complex with practically the same stabilization and total electronic energies. The thymine and uracil bases favor the N3 coordination regardless the environment. This preference is in accord with different orientation of the dipole moment of uracil and thymine in comparison with cytosine (cf. [Fig. 36-3](#)). Another



computational study dealing with the interaction of different forms of ruthenium complexes with DNA bases was published in 2007 (Besker et al. 2007). Here, similar bonding energies (in comparison to Futera's work) were obtained for relevant structures in both gas phase and PCM.

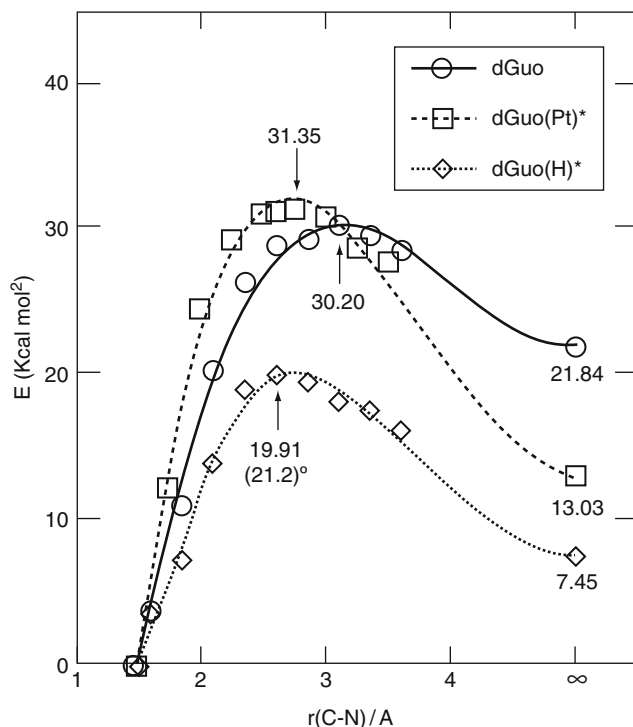
The molecular mechanism for the replacement of chloro-ligand by water and subsequently of aqua-ligand by nucleobase was also explored by Futera (Futera et al. 2009). Similar to the platination process, the hydration reaction is mildly endoergic ( $\Delta G = 2$  kcal/mol). Formation of the guanine adduct is exoergic by ca. 7 kcal/mol. Nevertheless, all these reactions are faster in the case of the ruthenium complex (in equimolar concentrations) since the activation barriers are lower, e.g., the values for replacement of both adenine and guanine are about 18 kcal/mol while in the cisplatin case analogous barriers are ca. 20 kcal/mol (cf. [Table 36-9](#)). Moreover, while a "simple" mechanism was found in the adenine reaction (as displayed in [Fig. 36-11a](#)), a two-step reaction mechanism was suggested for the guanine replacement ([Fig. 36-11b](#)).



■ Fig. 36-11

(a) Reaction coordinate for replacement of water by adenine and (b) guanine





■ Fig. 36-12

Reaction energy profile of the free energies for dissociation of N9–C1' glycoside bond of dGuo, dGuo(H)<sup>+</sup>, and dGuo(Pt)<sup>+</sup> in solvent

In these mechanisms, a lower activation barrier for adenine replacement corresponds to a higher rate constant (1.7 vs. 0.5 M.s<sup>-1</sup>). Nevertheless, since the minimum associated with the reaction coordination (“direct reactant”) is about 4 kcal/mol higher than the global minimum, it means the concentration of the form corresponding to this local minimum will be three orders of magnitude lower (according to the Boltzmann equilibrium law). A different situation occurs for analogous local minimum of guanine. Here the instant concentration (equilibrium occurrence) of the local reaction minimum is comparable to the global minimum and, therefore, the real reaction rate will actually be substantially higher for the process of guanine replacement.

Osmium complexes were also considered as possible metallodrugs. The hydrogenation energies of various nitrogen heterocycles in the presence of osmium tetroxide were investigated and published by Deubel (2003). While hydrogenation of pyrimidine bases is exothermic, the C4–C5 bond in purine bases does not have a tendency to hydrogenate.

An interesting study on the difference between protonation and metalation of the N7 position of deoxyguanosine was published by Baik et al. (2002). While under protonation the glycoside N9–C1' bond breaks, the Pt(II) adduct does not change the strength of the glycosidic bond substantially, as can be noticed from the ► Fig. 36-12.

## The Metal Coordination to Multiple Nucleobase Systems

### Interaction with Base Pairs

#### Metal Cations From Ia, Ib, IIa, and IIb Groups

The influence of metal coordination from the major groove on the enhancement of base pairing was explored by Burda et al. (1997). The energy decomposition for these systems requires, in addition to total stabilization and pair energies, the non-additive three-body contribution.

The studied complexes were partitioned into three subsystems: the two bases ( $B_1$ ,  $B_2$ ) and a metal cation ( $M$ ). The total stabilization energy ( $\Delta E^{Stab}$ ) is, within the BSSE counterpoise error, defined as:

$$\Delta E^{Stab} = -\{E(B_1, B_2, M) - [E(B_1, gB_2, gM) + E(gB_1, B_2, gM) + E(gB_1, gB_2, M)]\} \quad (36.2)$$

where  $E(B_1, B_2, M)$  represents total energy of the whole complex, and, e.g.,  $E(B_1, gB_2, gM)$  is a total energy of the base  $B_1$  in presence of the basis functions on ghost systems  $B_2$  and  $M$ . Alternatively, the total stabilization energy  $\Delta E$  can be expressed in terms of pair stabilization energies and the three-body contribution:

$$\Delta E^{Stab} = E(B_1 - B_2) + E(B_1 - M) + E(B_2 - M) + E(3) \quad (36.3)$$

where each pair-stabilization energy is calculated within the BSSE scheme. For example, the  $E(B_1 - B_2)$  energy can be determined from formula:

$$E(B_1 - B_2) = -\{E(B_1, B_2, gM) - [E(B_1, gB_2, gM) + E(gB_1, B_2, gM)]\} \quad (36.4)$$

In addition to these pairwise energies, interactions of one subsystem of the complex (metal or pyrimidine) with the remaining part were also evaluated. The interaction of thymine with a (metal + adenine) subsystem can be determined as:

$$E(MA - T) = -\{E(A, T, M) - [E(A, gT, M) + E(gA, T, gM)]\} \quad (36.5)$$

The whole system can be regarded as a composition of a strongly bonded metal cation–purine base part plus two weak interactions: metal cation–remote pyrimidine base and Watson–Crick H-bonded base pair. The latter two terms represent only a small perturbation of the first one, and their mutual influence is basically very small. Therefore, it is not surprising that similar geometry and energy parameters for metal coordination were obtained, comparing with the same characteristics found in ref. Burda et al. (1996). Also, the obtained geometries match well with the results reported by Anwander et al. (1990) for complexes with  $\text{Ca}^{2+}$ ,  $\text{Mg}^{2+}$ , and  $\text{Zn}^{2+}$ . Some small differences originate from the smaller basis set they used: e.g., too short distances between the purine base and the metal cation, especially for the  $\text{Zn}^{2+}$  complexes (our calculations predict 1.95 Å for the  $\text{Zn}^{2+}\text{GC}$  complex, while Anwander reported 1.72 Å).

The metal cation significantly influences the geometry of the base pair. The (C)O2...H–N2(G) H-bond lengths in the GC complexes are systematically reduced, in comparison with the isolated pair. This reduction is largest for bivalent ions (0.3 Å). The central H-bond N3–H...N1 remains practically unchanged, and the third N4–H...O6 H-bond, which is closest to the metal cation, is significantly lengthened in comparison with the isolated GC pair. The elongation is again the largest for bivalent ions (0.65 Å in  $\text{Zn}^{2+}\text{GC}$  and  $\text{Mg}^{2+}\text{GC}$ ). In the AT pair, the metal

cations affect the H-bonds in a different way. The (T)O4...H-N6(A) H-bond, which is closer to the metal-ion coordination site, shows substantial shortening (0.35 Å in complexes with Zn<sup>2+</sup> and Mg<sup>2+</sup>), while the other H-bond (N3-H...N1) is lengthened (by 0.18 Å in Zn<sup>2+</sup> AT complex). The geometric rearrangements of the pair structures can be regarded as the rotation around the center of the pyrimidine ring towards the metal cation in the case of the AT pair, and away from it in the case of the GC pair.

Basically, the same dependencies of the stabilization energies on increasing atomic numbers of metal cations are observed in metal-purine-pyrimidine complexes as in previously published metal-purine species (Burda et al. 1996). Stabilization energies of complexes with divalent ions are larger than those of monovalent ions, and M-GC stabilization energies are larger than those for M-AT complexes. Both conclusions reflect the dominant role of the ion-dipole electrostatic contribution to the stabilization energy of these complexes.

Compared with the study of Anwander (Anwander et al. 1990), very close agreement was obtained for complexes of Ca<sup>2+</sup> with base pairs (within 5 kcal/mol). However, larger differences were found in Mg<sup>2+</sup>-containing systems (≈20 kcal Mg<sup>2+</sup>-AT and ≈40 kcal Mg<sup>2+</sup>-GC; the values in Burda's work describe larger stabilization for both base pairs). However, the use of a minimal basis set (MBS) for zinc (all-electron calculations) nearly doubles the stability ( $\Delta E^{HF}(\text{MBS}:\text{Zn}^{2+}\text{-GC}) = 448$  kcal/mol versus Burda's  $\Delta E^{HF}(\text{AREP}:\text{Zn}^{2+}\text{-GC}) = 254$  kcal/mol and  $\Delta E^{HF}(\text{MBS}:\text{Zn}^{2+}\text{-AT}) = 328$  kcal/mol versus  $\Delta E^{HF}(\text{AREP}:\text{Zn}^{2+}\text{-AT}) = 158$  kcal/mol).

The H-bond WC interactions in the AT pair within the geometries of M-AT complexes are systematically weakened in comparison with the isolated optimized AT pair ( $\Delta E^{MP2} = 12.3$  kcal/mol). This weakening, which is larger for divalent ions amounts to about 4 kcal/mol, leads to AT pairing energy of ca. 8 kcal/mol. A similar weakening of H-bonds was expected to occur in the M-GC complexes. However, it was found that  $\Delta E^{MP2}$  of H-bonds in the GC pair within the M-GC complexes are a little stronger (with Ca<sup>2+</sup> – Ba<sup>2+</sup> exceptions) than those of the H-bonds in the isolated GC pair ( $\Delta E^{MP2} = -26.3$  kcal/mol). It can be shown that these changes correspond to the geometry deformation under the metal coordination. Nevertheless, from the energy decomposition it can be concluded that H-bond strength of GC or AT pair, calculated as a pairwise interaction energy within the optimized M-GC or M-AT complexes, is influenced only slightly by cations.

However, metal cations bound to the WC base pairs dramatically (directly or indirectly) change many characteristics of the base pairing. Actually, one should consider not pairwise energies of the G-C and A-T pairs but the MG-C and MA-T H-bonding energies, and these values are systematically higher – up to 24 kcal/mol for A-T and 48 kcal/mol for G-C H-bonding in the presence of the Zn<sup>2+</sup> cation. This amounts to nearly two times enhancement of the original base pairing energy (● Table 36-6).

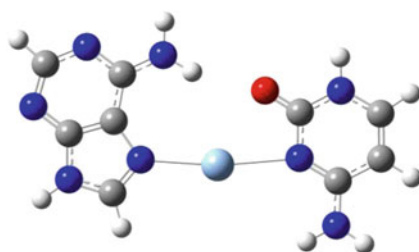
Similar conclusions are also reported in other studies on the metal-nucleobases interactions. Trimer base arrangement was explored using a similar computational model. The enhancement of G.GC(rH), G.GC(H), A.AT(rH), T.AT(H) and some other base interactions including reverse Hoogsteen pairs GG(rH) and AA(rH) was proved in the presence of Li<sup>+</sup> and Ca<sup>2+</sup> cations (Šponer et al. 1997). A study on the strength of H-bonding of WC base pairing under metalation at various active sites of bases concluded that the N3(Adenine) site available in the minor groove has higher chances for platination, in comparison with the N7-site of the base (Zhang and Huang 2007).

An interesting idea is related to a replacement of proton in H-bonding by metal. In this way the non-canonical A-C base pair was examined with the coinage metal cations (Cu<sup>+</sup>, Ag<sup>+</sup>,

■ Table 36-6

Enhancement of Watson-Crick base pairing energy under the metalation. (energies calculated at the MP2/6-31G\*\* level)

Metal	E(M-A)	E(A-T)	E(M-AT)	E(MA-T)	E(M-A-T)	E(M-G)	E(G-C)	E(M-GC)	E(MG-C)	E(M-G-C)
Cu <sup>+</sup>	-54.5	-12.0	-58.6	-16.1	-70.5	-79.9	-27.2	-86.1	-33.3	-113.3
Ag <sup>+</sup>	-36.0	-12.0	-40.0	-16.0	-52.0	-64.2	-27.0	-69.0	-31.8	-96.1
Au <sup>+</sup>	-55.0	-12.0	-59.1	-16.1	-71.1	-75.9	-27.0	-81.8	-32.9	-108.8
Zn <sup>2+</sup>	-152.9	-10.8	-165.9	-23.8	-176.7	-237.2	-26.1	-259.4	-48.2	-285.4
Cd <sup>2+</sup>	-116.6	-10.9	-129.3	-23.6	-140.2	-192.6	-25.9	-211.3	-44.6	-237.2
Hg <sup>2+</sup>	-141.1	-10.9	-153.8	-23.7	-164.7	-207.9	-25.9	-228.0	-45.9	-253.9
Mg <sup>2+</sup>	-107.9	-10.8	-120.7	-23.5	-131.5	-198.6	-25.9	-217.8	-45.1	-243.8
Ca <sup>2+</sup>	-61.6	-11.1	-73.1	-22.6	-84.2	-133.8	-25.7	-146.9	-38.8	-172.6
Sr <sup>2+</sup>	-48.9	-11.2	-59.8	-22.1	-71.0					
Ba <sup>2+</sup>	-51.4	-11.2	-62.3	-22.1	-73.5	-118.8	-25.6	-130.4	-37.2	-156.0



■ Fig. 36-13

Cytosine-M<sup>+</sup>-Adenine complexes, M = (Cu, Ag, Au)

and Au<sup>+</sup>) used as a bridge between both bases (Šponer et al. 1999), cf. ● Fig. 36-13. The possibility of additional water coordination to metal was also considered. In the original paper it is concluded that these metal-bridged complexes are substantially more stable than the original (protonated) base pair. The water coordination does not influence the strength of the metal bridge substantially, nevertheless, its presence has some impact on the geometry of the complexes. Comparing bonding properties of all three metal cations, it was found that the Ag cation coordinates relatively weakly, which is in good accord with previous results (Burda et al. 1996, 1997). The slightly shorter bond length of d(M-N7-Adenine) than d(M-N3-Cytosine) contradicts the estimated bonding energies since  $\Delta E^{M-A}$  is smaller than  $\Delta E^{M-C}$ . This can be explained by two facts: (a) the electrostatic contribution to the metal coordination is much smaller in the adenine case (see the size and orientation of the dipole moments of both bases in ● Fig. 36-3), and (b) the metal-cytosine interaction cannot be considered purely of the M-N3 character and simultaneously, the M-O2 contribution plays non-negligible role.

The results of investigation on Cu<sup>+</sup>/Cu<sup>2+</sup> interaction with AT and GC pairs were published by Sodupe's group (Noguera et al. 2004, 2007). The influence of metal cations coordinated to N7 position of guanine on the intermolecular proton-transfer reaction in the guanine-cytosine base pair was studied with the B3LYP density functional. Gas phase metal cation interaction stabilizes the ion pair structure derived from the N1(G) → N3(C) single-proton-transfer reaction, the effects being more pronounced for the divalent cation than for the monovalent one.

For  $\text{Cu}^{2+}$ -GC, the reaction is largely favored due to both electrostatic and oxidative effects. Hydration of the metal cation reverts this trend due to the screening of electrostatic effects.

In the section on interaction of hydrated metal complexes, the Šponer study (Šponer et al. 1998) was mentioned where, in addition, to purine nucleobases the GC, AT, and AA base pairs were also considered. Since the metal–purine base interaction is not substantially influenced by the remote pyrimidine base, we will focus on base pair enhancement and some changes observed in comparison with the study on bare metal cations complexes (Burda et al. 1997). The strength of the guanine-cytosine Watson-Crick base pair is enhanced by ca. 20–30% due to the coordination of the hydrated cation, while in the case of bare cations this enhancement was about 60–90%. From Table 36-7 it follows that the bare cations deform the base pair geometry more noticeably than the hydrated cations. Only in the  $\text{Ba}^{2+}$  case, the hydration sphere is H-bonded to the O6 site more strongly than in other cations, decreasing the GC base pairing energy.

In addition, an interesting comparison of  $\text{Zn}^{2+}$  and  $\text{Mg}^{2+}$  hydrated cations in Pu-Pu-Py triplexes was carried out (Šponer et al. 1999), where a hydrated metal is coordinated to the N7 position of purine base attached to the Watson-Crick base pair. Using this model, metal-assisted triplex stabilization was studied. It was shown that in both A.A and G.G the Hoogsteen pairing is strengthened under metalation. A substantially stronger enhancement of (MG).G pairing was revealed (19.8 and 20.4 kcal/mol for  $\text{Mg}^{2+}$  and  $\text{Zn}^{2+}$  cations, respectively), in comparison with similar adenine structures where practically no additional stabilization was detected (only about 2.7 kcal/mol for both metal cations). In another study (Šponer et al. 1999), a more extended set of divalent metal cations ( $\text{Mg}^{2+}$ ,  $\text{Ca}^{2+}$ ,  $\text{Sr}^{2+}$ ,  $\text{Ba}^{2+}$ ,  $\text{Zn}^{2+}$ ,  $\text{Cd}^{2+}$ , and  $\text{Hg}^{2+}$ ) hydrated by five water molecules was explored with rAA and AT base pairs interacting with the N7 site of adenine, confirming the previously obtained results.

Schreiber et al. (Schreiber and Gonzalez 2007) explored the Ag(I) adducts with DNA base and the influence of Ag(I) coordination for adenine-cytosine mispairing. Their calculations showed that in gas phase the canonical form of cytosine is stabilized upon metalation, whereas the lowest energy structure of Ag-adenine corresponds to the imino tautomer. The most stable metalated adenine-cytosine mispair was formed from the canonical cytosine and adenine tautomers. Other types of A–C pairs (e.g., reverse Wobble) were found much less stable. The same authors also performed an interesting study dealing with the role of the Ag(I) cation on electronic spectra of the A–C pairs using a very accurate MS-CASPT2 approach (Schreiber and Gonzalez 2007).

Interestingly, possibilities of so-called M-DNA crosslink stabilization of GC base pairs by divalent zinc have been investigated by Fuentes-Cabrera et al. (2007).

Table 36-7

Difference in base-pair energies under the metalation (in kcal/mol)

	$\Delta E_{GC}$ (hydr)	$\Delta E_{GC}$ (bare)
$\text{Mg}^{2+}$	-26.4	-26.0
$\text{Ca}^{2+}$	-26.3	-25.8
$\text{Sr}^{2+}$	-25.8	-
$\text{Ba}^{2+}$	-23.2	-25.6
$\text{Zn}^{2+}$	-26.4	-26.1
$\text{Cd}^{2+}$	-26.3	-26.0
$\text{Hg}^{2+}$	-26.2	-25.9



## Enhancement of Base Pairing by Pt Complexes

Several interesting studies related to platinum metal interactions with base pairs and the influence of metal complexes on the strength of pairing should be mentioned.

Molecular structures of several Pt complexes with the Watson-Crick AT and GC base pairs were optimized using the B3LYP method. The interaction energies were analyzed using B3LYP, and MP2 approaches (Burda et al. 2001). Platination causes some distortion in the H-bond arrangement of the base pairs. The pyrimidine bases rotate around their center of mass under the influence of the charged Pt entities. This effect is quite general and was already discussed above (Burda et al. 1997; Šponer et al. 1998, 1999). The metal-binding affects the strength of individual H-bonds involved in the base pairing.

It was concluded that ligands attached to the Pt(II) cation form strong intramolecular H-bonds with the X6 exocyclic site of purine bases. The adenine amino group adopts a pronounced pyramidal geometry and its nitrogen serves as H-bond acceptor for the ammine ligands of cisplatin.

The Pt-binding has a comparable effect on the base pairing stability as binding of hydrated metals of IIa and IIb groups. In the electroneutral form, the Pt-adduct does not influence the base pair stability. Charged Pt adducts substantially strengthen the stability of G.C base pair via polarization effects. The influence of the +2 charged Pt-adduct is even larger compared with hydrated metals of IIa and IIb groups. No such polarization effects have been revealed for the A.T base pair. However, gas phase stability of this pair is effectively enhanced by long-range electrostatic interaction between the charged metal group and thymine.

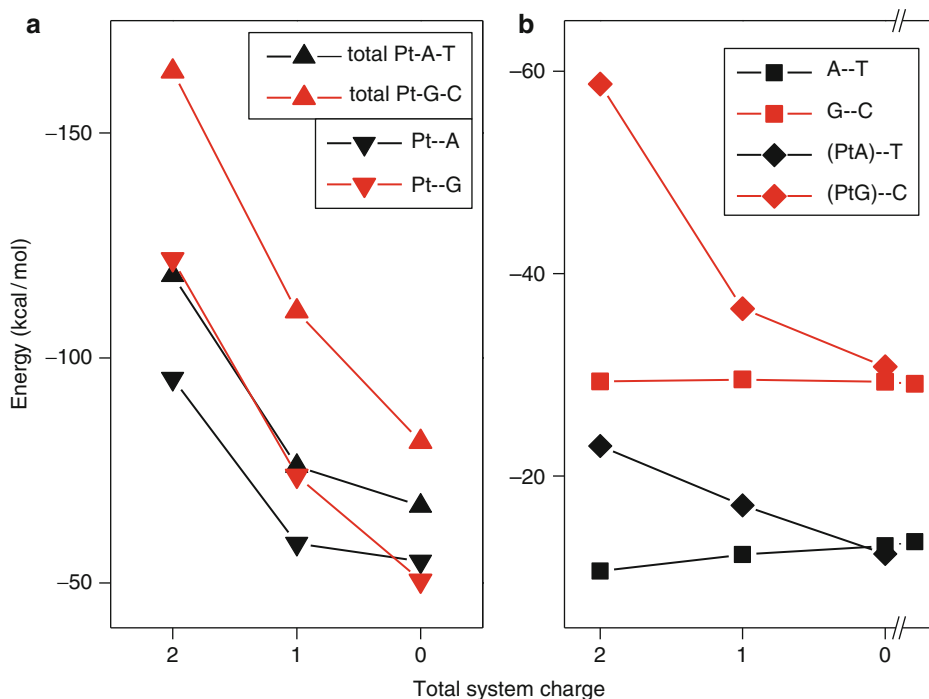
The dependence of the stabilization and Pt-N7 bonding energies on the total charge of the complex is displayed in  Fig. 36-14a. Here, the role of electrostatic contributions is clearly demonstrated for both kinds of energies. Interestingly, in electroneutral complexes, the Pt-N7 bonding energies are similar in guanine and adenine structures ( $\approx 50$  kcal/mol). In  Fig. 36-14b, the base pairing energies are drawn showing that the geometry deformations do not influence these values. Nevertheless, the interaction of metalated purine base with pyrimidine base is substantially strengthened, especially in charged complexes (e.g., in complexes of hydrated cisplatin).

It is important to point out that the effect of base pair stabilization enhancement due to cation binding has been confirmed experimentally by Sigel and Lippert (1999).

Zilberberg et al. reported the influence of chelated cisplatin complex with guanine(O6,N7) on Watson-Crick base pairing (Zilberberg et al. 1997). In such chelate structures, more distinct perturbation of base pairing was revealed. However, such chelate binding pattern is unlikely to be relevant to real ds-DNA conditions.

## Interactions of Hydrated Cations with Nucleotides

Šponer et al. (2000) studied the coordination of hydrated zinc and magnesium group divalent cations to the N7 position of purine nucleotides. They showed that the sugar-phosphate backbone provides significant screening of the charge of the metal, while the backbone geometry is affected by the cation. Polarized water molecules of the cation hydration shell form very strong hydrogen bridges between the cation and the anionic oxygen atoms of the phosphate group. Weaker hydrogen bonds are formed between the cation hydration shell and the exocyclic purine X6 atoms. The cation binding to N7 of adenosine monophosphate forces the adenine amino group to adopt non-planar conformation. Its nitrogen atom serves as an H-acceptor



■ Fig. 36-14

(a) The stabilization and metalation M–N7 energies; (b) enhancement of the Watson-Crick pairing energies for AT and GC base pairs

for a water molecule from the cation hydration shell. Cation binding to N7 does not lead to any major changes in the geometry of the base pairing. However, the stability of the base pairing can be increased by polarization of the purine base by the cation and by long-range electrostatic attraction between the hydrated cation and the other nucleobase. The stability of guanine-cytosine Watson-Crick base pairing is enhanced by the polarization mechanism while the stability of the adenine-thymine Watson-Crick base pair is amplified by the electrostatic effects as shown in the case of base pairs model discussed previously (Burda et al. 1997). Also, the guanine-guanine reverse-Hoogsteen base pairing is stabilized by both contributions while the adenine-adenine reverse-Hoogsteen system is not influenced by the cation. Binding of a cation to the N7 of guanine promotes transfer of its H1 proton to the N3 acceptor site of cytosine. However, the negatively charged backbone exerts a significant screening effect on this potentially mutagenic process, and the probability of such a proton transfer in DNA should be only moderately enhanced by a cation binding.

A comprehensive study dealing with a coordination of hydrated cations Zn(II) and Mg(II) to guanosine 5' monophosphate was performed by Gresh (Gresh et al. 2003) in order to obtain parameters for polarizable molecular mechanics for metal – DNA and RNA simulations.

Inner-shell binding of selected hydrated metal ions ( $\text{Mg}^{2+}$ ,  $\text{Cu}^{2+}$ ,  $\text{Zn}^{2+}$ , and  $\text{Cd}^{2+}$ ) to the guanine N7 position was investigated in relation to outer- and inner-shell binding to an anionic phosphate group (Rulíšek and Šponer 2003). The study was focused on the mutual

interplay between the metal-phosphate and metal-nucleobase binding and the role of non-electrostatic effects in the metal binding. The analysis of the equilibrium structures and the energy decompositions reveal that these effects substantially contribute to the differences in the coordination behavior of the studied metal ions. The  $\text{Zn}^{2+}$  and  $\text{Cd}^{2+}$  cations show a clear preference (compared to  $\text{Mg}^{2+}$ ) to bind to N7 of guanine. The selectivity amounts to approximately 3–4 kcal/mol. This energy difference is sufficient to provide enough binding selectivity in the condensed phase where the dominant pair electrostatic terms (ion–ion, molecule–ion) are attenuated.  $\text{Cu}^{2+}$  shows even stronger relative preference for N7 binding and it also has different coordination requirements. The nucleobase's N7 metal binding causes approximately 20–30 kcal/mol destabilization of the metal-phosphate outer-shell binding, due to non-electrostatic effects.

## Metal Interactions with Stacked Bases

Cisplatin bridges between two consequent bases (1,2-GpG) are believed to be the key structure for triggering the apoptotic process. Recently, several studies on these cross-linked structures have been published. The properties of Pt-bridges were explored (Burda and Leszczynski 2003; Zeizinger et al. 2004) showing that relatively strong Pt–N7 coordination is formed. The process of aqua ligand replacement by nucleobase is mildly exoergic in both steps forming: (a) a mono-functional adduct and, consequently, (b) the cross-linked structure. Stabilization energies of the Pt–GG, Pt–GA, and Pt–AA bridges are given in [Table 36-8](#). The relative amount of these values correlates well with the relative abundance of individual structures in real samples, assuming the gas phase calculations require some additional rescaling in correspondence to the reduced electrostatic interactions in solvent.

The influence of the sugar phosphate backbone on the strength of Pt-bridge was also examined (Zeizinger et al. 2004). Some additional stabilization of the Pt cross-linked structures appeared as a result of the interaction between negatively charged phosphate group and the Pt cation.

One of the first papers studying transition states of the replacement aqua ligand by nucleobase was published by Chval (Chval and Sip 2003). His model was based on the gas phase calculations, and the estimated activation barrier is too low in comparison with experimental value. This situation was improved in studies of Raber (Raber et al. 2005) and Baik (Baik et al. 2003). They have taken into account the hydration effects employing an implicit solvent model. Raber's results in particular are in fairly good accord with experimental data. Activation barriers of mono-aqua and diaqua Pt(II) complexes are summarized in [Table 36-9](#) for both guanine and adenine replacement of the first and second leaving (aqua) ligand.

■ Table 36-8

Stabilization energies of the Pt-cross-linked structures (in kcal/mol)

	$\Delta E^{stab}$ (MP2)
Pt- $a_2A_2$	491.5
Pt- $a_2AG$	514.6
Pt- $a_2G_2$	528.3



■ Table 36-9

Substitution energies for the aqua ligand replacement by purine base (in kcal/mol)

	chloro-aqua	Diaqua
1st step		
Guanine	21.4 <sup>a</sup>	19.5 <sup>a</sup>
	25.6 <sup>b</sup>	21.8 <sup>b</sup>
	14 <sup>c</sup>	17.9 <sup>c</sup>
		18.3 <sup>d</sup>
Adenine	24.0 <sup>a</sup>	24.8 <sup>a</sup>
	37.6 <sup>b</sup>	34.5 <sup>b</sup>
	14.5 <sup>c</sup>	14.5 <sup>c</sup>
2nd step		
GG hh		22.5 <sup>a</sup>
		23.4 <sup>e</sup>
GA hh		28.6 <sup>a</sup>

<sup>a</sup>Ref. Raber et al. 2005

<sup>b</sup>Ref. Baik et al. 2003

<sup>c</sup>Ref. Chval and Sip 2003

<sup>d</sup>Ref. Arpalahti and Lippert 1990, and

<sup>e</sup>Ref. Bancroft et al. 1990

## Metal Adducts in Oligomeric Sequences

The infrared (IR) and vibrational circular dichroism (VCD) spectra of guanosine-5'-hydrazide have been measured and analyzed on the basis of ab initio modeling (Setnicka et al. 2008). The B3LYP/6-31G(d,p) calculations predict that guanine, forming a clear solution in deuterated DMSO, is present in monomeric form in this solvent, whereas strong gelation in a phosphate buffer is due to the formation of a guanine-quartet structure. Here, the four bases are linked by hydrogen-bonded guanine moieties and stabilized by an alkali metal cation. The DFT prediction of the IR and VCD spectra are based on the nearly planar quartet structure, which is slightly distorted from the  $C_{4h}$  symmetry. The guanine bases interact via four Hoogsteen-type hydrogen bonds and a sodium cation is positioned in the middle of the guanine quartet. The obtained results are in very good agreement with the experimental spectra, indicating that calculated structure is the highly probable in the gel state.

The guanine quartets were also examined by Gu and Leszczynski (2000). The normal four-stranded Hoogsteen-bonded G-quartet structures were optimized in the gas-phase with monovalent cations obtaining the stability order  $Li^+ > Na^+ > K^+$ . However, after the correction on solvent effects, the stability sequence of the monovalent cation-guanine-tetrad complexes follows the opposite trend  $K^+ > Na^+ > Li^+$ . The preferential binding of potassium over sodium and lithium in water solutions reproduces the experimental ion selectivity of the guanine quadruplex. Moreover, weak stabilization energy of the  $K^+$ -G-quartet in the coplanar form corresponds with the fact that the potassium cation tends to locate between two successive quartets. These results are in accord with the study of Hud et al. (1998) on the ion selectivity of the guanine quartets in water solutions, which are governed by the relative free energies of hydration. The experimental data on the cation-oxygen distances in the sodium ion complex are  $2.34 \pm 0.02$  Å. This value matches the HF value of 2.33 Å. The slightly shorter  $Na^+-O6$  distance

was predicted by the DFT approach together with a significant shortening of the hydrogen bonds suggesting an overestimation of the H-bonding in the guanine quartets at the DFT level. A comprehensive study on metal–quartet interactions was published by Meyer et al. (2001). It should be noted, however, that, in principle, accurate studies of quadruplex–ion interactions would require inclusion of the whole solvated quadruplex fragment, due to the unique balance of molecular interactions in this important noncanonical DNA (Šponer and Spackova 2007).

A similar topic was examined by Ida (Ida and Wu 2008). In this study, molecular dynamics was employed exploring G-quadruplex stabilized by Na and Rb cations, which were found to be tightly bound to a quadruplex structure. Moreover, in d(G(4)T(4)G(4)) sequences the Na<sup>+</sup> ions are found to be located in the diagonal T-4 loop region of the G-quadruplex, which is formed by two strands of d(G4T4G4) sequence. The authors proposed that the loop Na<sup>+</sup> ion is located above the terminal G-quartet, coordinating to four guanine O6 atoms from the terminal G-quartet and one O2 atom from a loop thymine base and one water molecule. The Na<sup>+</sup> coordination was also supported by quantum chemical calculations on <sup>23</sup>Na chemical shifts.

Larger systems like metal adducts to oligomer sequences or metal interactions with a higher number ( $n > 5$ ) of nucleobases are difficult to treat using standard quantum chemical tools. Therefore, most of these studies are performed with combined QM/MM or classical MM and MD simulations.

Montrel et al. (1998) compared experimentally observed coordination of metal ions to DNA oligonucleotides using electrostatic potential (EP) along the helix. Their calculations have been performed for three different models of the oligonucleotide duplex [d(CGCGAATTCGCG)2] using several variants of EP calculations, including a solution of non-linear Poisson–Boltzmann equation (NPBE). The N7 atom of guanine adjacent to the adenine base was recognized as the most negative site in the major groove.

The influence of sodium cations and chain length on the structure and dynamics of single strand DNA of polythymidylate was studied using molecular dynamics simulations (Martinez et al. 2001). The base stacking interaction increases with the length of the oligomeric chain of the strand. Sodium ions interact with the phosphate groups as well as with keto oxygens of the thymine bases. Formation of simultaneous phosphate and keto complexes were observed for one of the sodium ions with lifetimes around 1 ns.

The Poisson–Boltzmann solvent model was used for examination of polynucleotides (Korolev et al. 2002) in the presence of K<sup>+</sup>, Na<sup>+</sup> and Mg<sup>2+</sup> cations. The stability of rare tautomers for N4 metalated cytosine in environments with various dielectric constant from gas phase ( $\epsilon = 0$ ) to implicit water model ( $\epsilon = 78$ ) is revealed in the study of Monajjemi et al. (2004).

## Conclusion

---

In this review the results of recent investigations on metal interactions with nucleobases, base pairs, and some larger models (including base stacking or oligomer sequences) are summarized.

The studies dealing with metal cations (in naked, hydrated, and ligated forms) provide various details on their interactions with nucleobases, however, such models are in many cases oversimplified. Despite the fact that some sites on the isolated nucleobase (especially in adenine) exhibit higher affinity to metal cations, in a DNA helix not all of them are available for interactions since they are involved in H-bonding (purine N1 site) or in the glycosidic bond (N9 site).

All forms of metal cations enhance the Watson-Crick base pairing interaction if their positive charge is not fully compensated. The different mechanism for the A.T and G.C adducts was revealed. While in A.T the direct electrostatic link between remote thymine (negatively charged O4) and metal cation exists, in the G.C pair the non-additive, three-body term is important since the positively charged NH<sub>2</sub> exo-group is in the proximity of the metal cation.

Clearly, metalation at the N7 position leads to many new, exceptional properties of the studied systems that are dependent on characteristics of involved metals. Some of them are discussed in detail in this text.

## Acknowledgment

The study was supported by projects MSM 0021620835, Grant Agency of the Czech Republic (GAČR) No P205/10/0228 (JVB) and GAČR No. 203/09/1476 (JS). The work in the USA was supported by the NSF CREST Grant No. 9805465. The authors thank the Meta-Centers in Prague (Charles University and Czech Technical University), Brno (Masaryk University), and Pilsen (University of West Bohemia) for the generous support of the computational resources.

## References

- Ai, H. Q., Yang, A. B., & Li, Y. G. (2008). Theoretical study on the interactions between Zn<sup>2+</sup> and adenine isomers in aqueous phase. *Acta Physico-Chimica Sinica*, 24, 1047.
- Allen, R. N., Shukla, M. K., Burda, J. V., & Leszczynski, J. (2006). Theoretical study of interaction of urate with Li<sup>+</sup>, Na<sup>+</sup>, K<sup>+</sup>, Be<sup>2+</sup>, Mg<sup>2+</sup>, and Ca<sup>2+</sup> metal cations. *The Journal of Physical Chemistry A*, 110, 6139.
- Andrushchenko, V., & Bouř, P. (2009). Infrared absorption detection of metal ion-deoxyguanosine monophosphate binding: Experimental and theoretical study. *The Journal of Physical Chemistry B*, 113, 283.
- Anwander, E. H. S., Probst, M. M., & Rode, B. M. (1990). The influence of Li<sup>+</sup>, Na<sup>+</sup>, Mg<sup>2+</sup>, Ca<sup>2+</sup>, and Zn<sup>2+</sup> ions on the hydrogen bonds of the Watson-Crick base pair. *Biopolymers*, 29, 757.
- Arpalahti, J., & Lippert, B. (1990). Coordination of Aqueated *cis*-Pt(II) Diamines to purine nucleosides. Kinetics of complex formation. *Inorganic Chemistry*, 29, 104.
- Baik, M.-H., Friesner, R. A., & Lippard, S. J. (2002). Theoretical study on the stability of N-glycosyl bonds: Why does N7-platination not promote depurination? *Journal of the American Chemical Society*, 124, 4495.
- Baik, M. H., Friesner, R. A., & Lippard, S. J. (2003). Theoretical study of cisplatin binding to purine bases: Why does cisplatin prefer guanine over adenine? *Journal of the American Chemical Society*, 125, 14082.
- Banas, P., Jurecka, P., Walter, N. G., Sponer, J., & Otyepka, M. (2009). Theoretical studies of RNA catalysis: Hybrid QM/MM methods and their comparison with MD and QM. *Methods*, 49, 202.
- Bancroft, D. P., Lepre, C. A., & Lippard, S. J. (1990). *Journal of the American Chemical Society*, 112, 6860.
- Bandyopadhyay, D., & Bhattacharyya, D. (2003). Different modes of interaction between hydrated magnesium ion and DNA functional groups: Database analysis and ab initio studies. *Journal of Biomolecular Structure and Dynamics*, 21, 447.
- Basch, H., Krauss, M., Stevens, W. J., & Cohen, D. (1986). Binding of Pt(NH<sub>3</sub>)<sub>3</sub><sup>2+</sup> to nucleic acid bases. *Inorganic Chemistry*, 25, 684.
- Besker, N., Coletti, C., Marrone, A., & Re, N. (2007). Binding of antitumor ruthenium complexes to DNA and proteins: A theoretical approach. *The Journal of Physical Chemistry B*, 111, 9955.
- Boys, S. F., & Bernardi, F. (1970). The calculation of small molecular interactions by the differences of separate total energies. Some procedures with reduced errors. *Molecular Physics*, 19, 553.
- Burda, J. V., & Leszczynski, J. (2003). How strong can the bend be on a DNA helix from cisplatin? DFT and MP2 quantum chemical calculations of

- cisplatin-bridged DNA purine bases. *Inorganic Chemistry*, 42, 7162.
- Burda, J. V., Sponer, J., & Hobza, P. (1996). Ab initio study of the interaction of guanine and adenine with various mono- and bivalent metal cations (Li+, Na+, K+, Rb+, Cs+; Cu+, Ag+, Au+; Mg2+, Ca2+, Sr2+, Ba2+; Zn2+, Cd2+, and Hg2+). *Journal of Physical Chemistry*, 100, 7250.
- Burda, J. V., Sponer, J., Leszczynski, J., & Hobza, P. (1997). Interaction of DNA base pairs with various metal cations (Mg2+, Ca2+, Sr2+, Ba2+, Cu+, Ag+, Au+, Zn2+, Cd2+, and Hg2+): Nonempirical ab initio calculations on structures, energies, and nonadditivity of the interaction. *The Journal of Physical Chemistry B*, 101, 9670.
- Burda, J. V., Sponer, J., & Leszczynski, J. (2000). The interactions of square platinum(II) complexes with guanine and adenine: A quantum-chemical ab initio study of metalated tautomeric forms. *Journal of Biological Inorganic Chemistry*, 5, 178.
- Burda, J. V., Sponer, J., & Leszczynski, J. (2001). The influence of square planar platinum complexes on DNA base pairing. An ab initio DFT study. *Physical Chemistry Chemical Physics*, 3, 4404.
- Burda, J. V., Sponer, J., Hrabadkova, J., Zeizinger, M., & Leszczynski, J. (2003). The influence of N-7 guanine modifications on the strength of Watson-Crick base pairing and guanine N-1 acidity: Comparison of gas-phase and condensed-phase trends. *The Journal of Physical Chemistry B*, 107, 5349.
- Burda, J. V., Pavelka, M., & Simanek, M. (2004). Theoretical model of copper Cu(I)/Cu(II) hydration. DFT and ab initio quantum chemical study. *Journal of Molecular Structure-Theochem*, 683, 183.
- Burda, J. V., Shukla, M. K., & Leszczynski, J. (2005). Theoretical model of the aqua-copper [Cu(H2O)(5)](+) cation interactions with guanine. *Journal of Molecular Modeling*, 11, 362.
- Chu, V. B., Bai, Y., Lipfert, J., Herschlag, D., & Doniach, S. (2008). A repulsive field: advances in the electrostatics of the ion atmosphere. *Current Opinion in Chemical Biology*, 12, 619–625.
- Chval, Z., & Sip, M. (2003). Transition states of cisplatin binding to guanine and adenine: Ab initio reactivity study. *Collection of Czechoslovak Chemical Communications*, 68, 1105.
- Colominas, C., Luque, F. J., & Orozco, M. (1996). Tautomerism and protonation of guanine and cytosine. Implications in the formation of hydrogen-bonded complexes. *Journal of the American Chemical Society*, 118, 6811.
- Del Bene, J. E. (1984). Molecular orbital study of the Li+ complexes of the DNA bases. *Journal of Physical Chemistry*, 88, 5927.
- Del Bene, J. E. (1985). Molecular orbital theory of the hydrogen bond. *Journal of Molecular Structure*, 124, 201.
- Deubel, D. V. (2003). Reactivity of osmium tetraoxide towards nitrogen heterocycles: Implications for the molecular recognition of DNA mismatch. *Angewandte Chemie International Edition*, 42, 1974.
- Draper, D. E., Grilley, D., & Soto, A. M. (2005). *Annual Review of Biophysics and Biomolecular Structure*, 34, 221.
- Egli, M., & Gessner, R. V. (1995). Stereoelectronic effects of deoxyribose O4' on DNA conformation. *Proceedings of the National Academy of Sciences of the United States of America*, 92, 180.
- Egli, M., Williams, L. D., Frederick, C. A. & Rich, A. (1991). DNA-Nogalamycin Interactions, *Biochemistry*, 30, 1364–1372.
- Elmahdaoui, L., & Tajmirriahi, H. (1995). A Comparative-study Of Atp and Gtp complexation with trivalent Al, Ga and Fe cations - Determination of cation-binding site and nucleotide conformation by FTIR difference spectroscopy. *Journal of Biomolecular Structure and Dynamics*, 13, 69.
- Fuentes-Cabrera, M., Sumpter, B. G., & Sponer, J. E. (2007). Theoretical study on the structure, stability, and electronic properties of the guanine-Zn-cytosine base pair in M-DNA. *The Journal of Physical Chemistry B*, 111, 870.
- Futera, Z., Klenko, J., Sponer, J. E., Sponer, J., & Burda, J. V. (2009). Interactions of the “piano-stool” ruthenium(II)(eta(6)-arene)(en)Cl (+) complexes with water and nucleobases; ab initio and DFT study. *Journal of Computational Chemistry*, 30, 1758.
- Gresh, N., Sponer, J. E., Špaková, N., Leszczynski J., & Šponer, J. (2003). Theoretical study of binding of hydrated cations Zn(II) and Mg(II) to guanosine 5' monophosphate. Towards polarizable molecular mechanics for DNA and RNA. *The Journal of Physical Chemistry B*, 107, 8669.
- Gu, J. D., & Leszczynski, J. (2000). A remarkable alteration in the bonding pattern: An HF and DFT study of the interactions between the metal cations and the Hoogsteen hydrogen-bonded G-tetrad. *The Journal of Physical Chemistry A*, 104, 6308.
- Hud, N. V., Smith, F. W., Anet, F. A. L., & Feigon, J. (1996). The selectivity for K+ versus Na+ in DNA quadruplexes is dominated by relative free energies of hydration: A thermodynamic analysis by 1H NMR. *Biochemistry*, 35, 15383.
- Hud, N. V., Schultze, P., & Feigon, J. (1998). *Journal of the American Chemical Society*, 120, 6403.

- Ida, R., & Wu, G. (2008). Direct NMR detection of alkali metal ions bound to G-quadruplex DNA. *Journal of the American Chemical Society*, *130*, 3590.
- Kabeláč, M., & Hobza, P. (2006). Na<sup>+</sup>, Mg<sup>2+</sup>, and Zn<sup>2+</sup> binding to all tautomers of adenine, cytosine, and thymine and the eight most stable keto/enol tautomers of guanine: A correlated ab initio quantum chemical study. *The Journal of Physical Chemistry B*, *110*, 14515.
- Korolev, N., Lyubartsev, A. P., & Nordenskiöld, L. (2002). Application of the Poisson Boltzmann polyelectrolyte model for analysis of equilibria between single-, double-, and triple-stranded polynucleotides in the presence of K<sup>+</sup>, Na<sup>+</sup>, and Mg<sup>2+</sup> ions. *Journal of Biomolecular Structure and Dynamics*, *20*, 275.
- Kosenkov, D., Gorb, L., Shishkin, O. V., Spöner, J., & Leszczynski, J. (2008). Tautomeric equilibrium, stability, and hydrogen bonding in 2'-deoxyguanosine monophosphate complexed with Mg<sup>2+</sup>. *The Journal of Physical Chemistry B*, *112*, 150.
- Lide, D. R. (1977). *CRC Handbook of chemistry and physics*. Cleveland: CRC.
- Lilley, D. M. J., & Eckstein, F. (2008). *Ribozymes and RNA catalysis*. Cambridge: Royal Society of Chemistry.
- Lipinski, J. (1989). Electronic structure of platinum(II) antitumor complexes and their interactions with nucleic acid bases. Part ii. *Journal of Molecular Structure (Theochem)*, *201*, 295.
- Marino, T., Toscano, M., Russo, N., & Grand, A., (2004). Gas-phase interaction between DNA and RNA bases and copper(II) ion: A density functional study. *International Journal of Quantum Chemistry*, *98*, 347.
- Martinez, J. M., Elmroth, S. K. C., & Kloo, L. (2001). Influence of sodium ions on the dynamics and structure of single-stranded DNA oligomers: A molecular dynamics study. *Journal of the American Chemical Society*, *123*, 12279.
- Matsubara, T., & Hirao, K. (2002). Density functional study of the binding of the cyclen-coordinated M(II) (M = Zn, Cu, Ni) complexes to the DNA base. Why is Zn better to bind? *Journal of Molecular Structure-Theochem*, *581*, 203.
- Meyer, M., Steinke, T., & Brandl, M. (2001). Density functional study of guanine and uracil quartets and of guanine quartet/metal ion complexes. *Journal of Computational Chemistry*, *22*, 109.
- Monajjemi, M., Ghiasi, R., Ketabi, S., Passdar, H., & Mollaamin, F. (2004). A theoretical study of metal-stabilised rare tautomers stability: N4 metalated cytosine (M=Be<sup>2+</sup>, Mg<sup>2+</sup>, Ca<sup>2+</sup>, Sr<sup>2+</sup> and Ba<sup>2+</sup>) in gas phase and different solvents. *Journal of Chemical Research-S*, *2004*(1), 11. <http://stl.publisher.ingentaconnect.com/content/stl/jcr>
- Montrel, M., Chuprina, V. P., Poltev, V. I., Nerdal, W., & Sletten, E. (1998). Sequence-dependent binding of metal ion to DNA oligomers. A comparison of molecular electrostatic potentials with NMR data. *Journal of Biomolecular Structure and Dynamics*, *16*, 631.
- Noguera, M., Bertran, J., & Sodupe, M. (2004). A quantum chemical study of Cu<sup>2+</sup> interacting with guanine-cytosine base pair. Electrostatic and oxidative effects on intermolecular proton-transfer processes. *The Journal of Physical Chemistry A*, *108*, 333.
- Noguera, M., Branchadell, V., Constantino, E., Rios-Font, R., Sodupe, M., & Rodriguez-Santiago, L. (2007). On the bonding of first-row transition metal cations to guanine and adenine nucleobases. *The Journal of Physical Chemistry A*, *111*, 9823.
- Noguera, M., Bertran, J., & Sodupe, M. (2008). Cu<sup>2+</sup>/+ cation coordination to adenine-thymine base pair. Effects on intermolecular proton-transfer processes. *The Journal of Physical Chemistry B*, *112*, 4817.
- Parr, R. G., & Pearson, R. G. (1983). Absolute hardness: Companion parameter to absolute electronegativity. *Journal of the American Chemical Society*, *105*, 7512.
- Pavelka, M., & Burda, J. V. (2005). Theoretical description of copper Cu(I)/Cu(II) complexes in mixed ammine-aqua environment. DFT and ab initio quantum chemical study. *Chemical Physics*, *312*, 193.
- Pavelka, M., Šimánek, M., Šponer, J., & Burda, J. V. (2006). Copper cation interactions with biologically essential types of ligands: A computational DFT study. *The Journal of Physical Chemistry A*, *110*, 4795.
- Pavelka, M., Shukla, M. K., Leszczynski, J., & Burda, J. V. (2008). Theoretical study of hydrated copper(II) interactions with guanine: A computational density functional theory study. *The Journal of Physical Chemistry A*, *112*, 256.
- Petrov, A. S., Lamm, G., & Pack, G. R. (2005). Calculation of the binding free energy for magnesium - RNA interactions. *Biopolymers*, *77*, 137.
- Poltev, V. I., Malenkov, G. G., Gonzales, E. J., Teplukhin, A. V., Rein, R., Shibata, M., & Miller, J. H. (1996). Modeling DNA hydration: Comparison of calculated and experimental hydration properties of nucleic acid bases. *Journal of Biomolecular Structure and Dynamics*, *13*, 717.

- Potaman, V. N., & Soyfer, V. N. (1994). Divalent metal cations upon coordination to the N7 of purines differentially stabilize the PyPuPu DNA triplex due to unequal Hoogsteen-type hydrogen bond enhancement. *Journal of biomolecular structure and dynamics*, *11*, 1035.
- Pyykko, P. (1988). Relativistic effects in structural chemistry. *Chemical Reviews*, *88*, 563.
- Raber, J., Zhu, C., & Eriksson, L. A. (2005). Theoretical study of cisplatin binding to DNA: The importance of initial complex stabilisation. *Journal of Physical Chemistry*, *109*, 11006.
- Rosenberg, B., Van Camp, L., & Krigas, T. (1965). Inhibition of cell division in *Escherichia coli* by electrolysis products from a platinum electrode. *Nature*, *205*, 698.
- Rosenberg, B., Van Camp, L., Trosko, J. L., & Mansour, V. H. (1969). Platinum drugs; a new class of potent antitumor agents. *Nature*, *222*, 385.
- Rozsnyai, F., & Ladik, J. (1970). Calculation of effects of hydration and divalent metal ions on DNA base pairs. *Bulletin of the American Physical Society*, *15*, 325.
- Rulišek, L., & Šponer, J. (2003). Outer-shell and inner-shell coordination of phosphate group to hydrated metal ions (Mg<sup>2+</sup>, Cu<sup>2+</sup>, Zn<sup>2+</sup>, Cd<sup>2+</sup>) in the presence and absence of nucleobase. The role of nonelectrostatic effects. *The Journal of Physical Chemistry B*, *107*, 1913.
- Russo, N., Toscano, M., & Grand, A. (2001). Bond energies and attachments sites of sodium and potassium cations to ONA and RNA nucleic acid bases in the gas phase. *Journal of the American Chemical Society*, *123*, 10272.
- Saenger, W. (1983). *Principles of nucleic acid structure*. New York: Springer.
- Schmidt, K. S., Reedijk, J., Weisz, K., Basilio Janke, E. M., Sponer, J. E., Sponer, J., & Lippert, B. (2002). Loss of Hoogsteen pairing ability upon N1 adenine platinum binding. *Inorganic Chemistry*, *41*, 2855.
- Schreiber, M., & Gonzalez, L. (2007). Structure and bonding of Ag(I)-DNA base complexes and Ag(I)-adenine-cytosine mismatches: An ab initio study. *Journal of Computational Chemistry*, *28*, 2299.
- Schreiber, M., & Gonzalez, L. (2007). The role of Ag(I) ions in the electronic spectroscopy of adenine-cytosine mismatches: A MS-CASPT2 theoretical study. *Journal of Photochemistry and Photobiology A: Chemistry*, *190*, 301.
- Setnicka, V., Novy, J., Bohm, S., Sreenivasachary, N., Urbanova, M., & Volka, K. (2008). Molecular structure of guanine-quartet supramolecular assemblies in a gel-state based on a DFT calculation of infrared and vibrational circular dichroism spectra. *Langmuir*, *24*, 7520.
- Sigel, H. (1993). Interactions of metal ions with nucleotides and nucleic acids and their constituents. *Chemical Society Reviews*, *22*(4), 255.
- Sigel, R. K. O., & Lippert, B. (1999). Pt<sup>II</sup> coordination to guanine-N7: Enhancement of the stability of the Watson-Crick base pair with cytosine. *Chemical Communications*, *21*(1999), 2167.
- Šponer, J., & Spackova, N. (2007). Molecular dynamics simulations and their application to four-stranded DNA. *Methods*, *43*, 278.
- Šponer, J., Burda, J. V., Mejzlik, P., Leszczynski, J., & Hobza, P. (1997). Hydrogen-bonded trimers of DNA bases and their interaction with metal cations: Ab initio quantum-chemical and empirical potential study. *Journal of Biomolecular Structure and Dynamics*, *14*, 613.
- Šponer, J., Burda, J. V., Sabat, M., Leszczynski, J., & Hobza, P. (1998). Interaction between the guanine-cytosine Watson-Crick DNA base pair and hydrated group IIa (Mg<sup>2+</sup>, Ca<sup>2+</sup>, Sr<sup>2+</sup>, Ba<sup>2+</sup>) and group IIb (Zn<sup>2+</sup>, Cd<sup>2+</sup>, Hg<sup>2+</sup>) metal cations. *The Journal of Physical Chemistry A*, *102*, 5951.
- Šponer, J., Burda, J., Leszczynski, J., & Hobza, P. (1999). Interactions of hydrated IIa and IIb group metal cations with thio-adenine-cytosine DNA base pair: Ab initio and density functional theory investigation of polarization effects, differences among cations, and flexibility of the cation hydration shell. *Journal of Biomolecular Structure and Dynamics*, *17*, 631.
- Šponer, J., Sabat, M., Burda, J. V., Leszczynski, J., & Hobza, P. (1999). Interaction of the adenine-thymine Watson-Crick and adenine-adenine reverse-Hoogsteen DNA base pairs with hydrated group IIa (Mg<sup>2+</sup>, Ca<sup>2+</sup>, Sr<sup>2+</sup>, Ba<sup>2+</sup>) and IIb (Zn<sup>2+</sup>, Cd<sup>2+</sup>, Hg<sup>2+</sup>) metal cations: Absence of the base pair stabilization by metal-induced polarization effects. *The Journal of Physical Chemistry B*, *103*, 2528.
- Šponer, J., Sabat, M., Burda, J. V., Leszczynski, J., Hobza, P., & Lippert, B. (1999). Metal ions in non-complementary DNA base pairs: An ab initio study of Cu(I), Ag(I), and Au(I) complexes with the cytosine-adenine base pair. *Journal of Biological Inorganic Chemistry*, *4*, 537.
- Šponer, J., Sponer, J. E., Gorb, L., Leszczynski, J., & Lippert, B. (1999). Metal-stabilized rare tautomers and mismatches of DNA bases: N6-metallated adenine and N4-metallated cytosine, theoretical and experimental views. *The Journal of Physical Chemistry A*, *103*, 11406.

- Šponer, J., Sabat, M., Gorb, L., Leszczynski, J., Lippert, B., & Hobza, P. (2000). The effect of metal binding to the N7 site of purine nucleotides on their structure, energy, and involvement in base pairing. *The Journal of Physical Chemistry B*, 104, 7535.
- Šponer, J., Šponer, J. E., & Leszczynski, J. (2000). Cation - pi and amino-acceptor interactions between hydrated metal cations and DNA bases. A quantum-chemical view. *Journal of Biomolecular Structure and Dynamics*, 17, 1087.
- Šponer, J. E., Leszczynski, J., Glahe, F., Lippert, B., & Šponer, J. (2001). Protonation of platinated adenine nucleobases. Gas phase vs condensed phase picture. *Inorganic Chemistry*, 40, 3269.
- Sychrovsky, V., Sponer, J., & Hobza, P. (2004). Theoretical calculation of the NMR spin-spin coupling constants and the NMR shifts allow distinguishability between the specific direct and the water-mediated binding of a divalent metal cation to guanine. *Journal of the American Chemical Society*, 126, 663.
- Tanaka, Y., Kojima, C., Morita, E. H., Kasai, Y., Yamasaki, K., Ono, A., Kainosho, M., & Taira, K. (2002). Identification of the metal Ion binding site on an RNA motif from hammerhead ribozymes using 15N NMR spectroscopy. *Journal of the American Chemical Society*, 124, 4595.
- van der Wijst, T., Guerra, C. F., Swart, M., Bickelhaupt, F. M., & Lippert, B. (2009). Rare tautomers of 1-Methyluracil and 1-Methylthymine: Tuning relative stabilities through coordination to Pt-II complexes. *Chemistry - A European Journal*, 15, 209.
- Varnali, T., & Tozumcalgan, D. (1995). Interaction of divalent metal-cations and nucleotides - A computational study. *The Journal of Structural Chemistry*, 6, 343.
- Zeizinger, M., Burda, J. V., & Leszczynski, J. (2004). The influence of a sugar-phosphate backbone on the cisplatin-bridged BpB' models of DNA purine bases. Quantum chemical calculations of Pt(II) bonding characteristics. *Physical Chemistry Chemical Physics*, 6, 3585.
- Zhang, Y., & Huang, K. X. (2007). The influence of the hydrated metal cations binding to adenine-N7 or adenine-N3 on the hydrogen bonding in adenine-thymine base pair: A comparative study. *Journal of Molecular Structure: Theochem*, 822, 57.
- Zilberberg, I. L., Avdeev, V. I., & Zhidomirov, G. M. (1997). Effect of cisplatin binding on guanine in nucleic acid: An ab initio study. *Journal of Molecular Structure (Theochem)*, 418, 73-81.



# 37 Predictive QSAR Modeling: Methods and Applications in Drug Discovery and Chemical Risk Assessment

Alexander Golbraikh<sup>1</sup> · Xiang Simon Wang<sup>1</sup> · Hao Zhu<sup>1</sup> ·  
Alexander Tropsha<sup>2</sup>

<sup>1</sup>Laboratory for Molecular Modeling and Carolina Center for Exploratory Cheminformatics Research, Division of Medicinal Chemistry and Natural Products, UNC Eshelman School of Pharmacy, University of North Carolina, Chapel Hill, North Carolina, USA

<sup>2</sup>Division of Medicinal Chemistry and Natural Products, UNC Eshelman School of Pharmacy, University of North Carolina, Chapel Hill, North Carolina, USA

## **QSAR Methodology: Summary of Approaches for Model**

<b><i>Building and Validation</i></b> .....	<b>1311</b>
Data Preparation .....	1311
The Problem of Outliers .....	1315
QSAR Model Development .....	1315
QSAR Methods .....	1316
Target Functions .....	1318
Continuous QSAR Models .....	1319
Target Functions and Validation Criteria for Classification QSAR Models .....	1319
Target Functions and Validation Criteria for Category QSAR Models .....	1320
Applicability Domains .....	1321
Y-randomization .....	1322
External Validation .....	1323

## ***“Good Practices” in QSAR Modeling: Examples of Models and Their Application to Virtual Screening and Lead Identification*** .....

<b><i>Virtual Screening and Lead Identification</i></b> .....	<b>1323</b>
QSAR-Aided Discovery of Novel Anticonvulsant Compounds .....	1324
QSAR-Enabled Discovery of Novel Anticancer Agents .....	1326
QSAR Enabled Discovery of Novel Geranylgeranyltransferase I Inhibitors(GGTIs) ..	1326

## ***“Good Practices” in QSAR Model Development: Applications to Toxicity Modeling*** ... **1328**

Quantitative Structure In Vitro–In Vivo Relationship Modeling .....	1329
Using “Hybrid” Descriptors for QSIIR Modeling of Rodent Carcinogenicity .....	1330
Using “Hybrid” Descriptors for the QSIIR Modeling of Rodent Acute Toxicity .....	1331



Collaborative and Consensus Modeling of Aquatic Toxicity .....	1332
Universal Statistical Figures of Merit for All Models .....	1333
Consensus QSAR Models of Aquatic Toxicity; comparison Between Methods and Models .....	1334
<i>Conclusions: Emerging Chemical/Biological Data and QSAR Research Strategies</i> . . . .	<b>1335</b>
<i>References</i> .....	<b>1336</b>

**Abstract:** Quantitative structure–activity relationship (QSAR) modeling is the major cheminformatics approach to exploring and exploiting the dependency of chemical, biological, toxicological, or other types of activities or properties on their molecular features. QSAR modeling has been traditionally used as a lead optimization approach in drug discovery research. However, in recent years QSAR modeling found broader applications in hit and lead discovery by the means of virtual screening as well as in the area of drug-like property prediction, and chemical risk assessment. These developments have been enabled by the improved protocols for model development and most importantly, model validation that focus on developing models with independently validated external prediction power. This chapter reviews the predictive QSAR modeling workflow developed in this laboratory that incorporates rigorous procedures for QSAR model development, validation, and application to virtual screening. It also provides several examples of the workflow application to the identification of experimentally confirmed hit compounds as well as to chemical toxicity modeling. We believe that methods and applications considered in this chapter will be of interest and value to researchers working in the field of computational drug discovery and environmental chemical risk assessment.

## QSAR Methodology: Summary of Approaches for Model Building and Validation

---

In order to find new leads in the process of drug design and discovery, there is a need for efficient and robust computational procedures that can be used to screen chemical databases and virtual libraries against molecules with known activities or properties. For this purpose, quantitative structure–activity relationship (QSAR) analysis is widely used. QSAR modeling provides an effective way for establishing and exploiting the relationship between chemical structures and their biological actions toward the development of novel drug candidates. Theoretically, QSAR analysis is the application of mathematical and statistical methods for the development of models for the prediction of biological activities or properties of compounds. Formally, a QSAR model can be expressed in the following generic format:

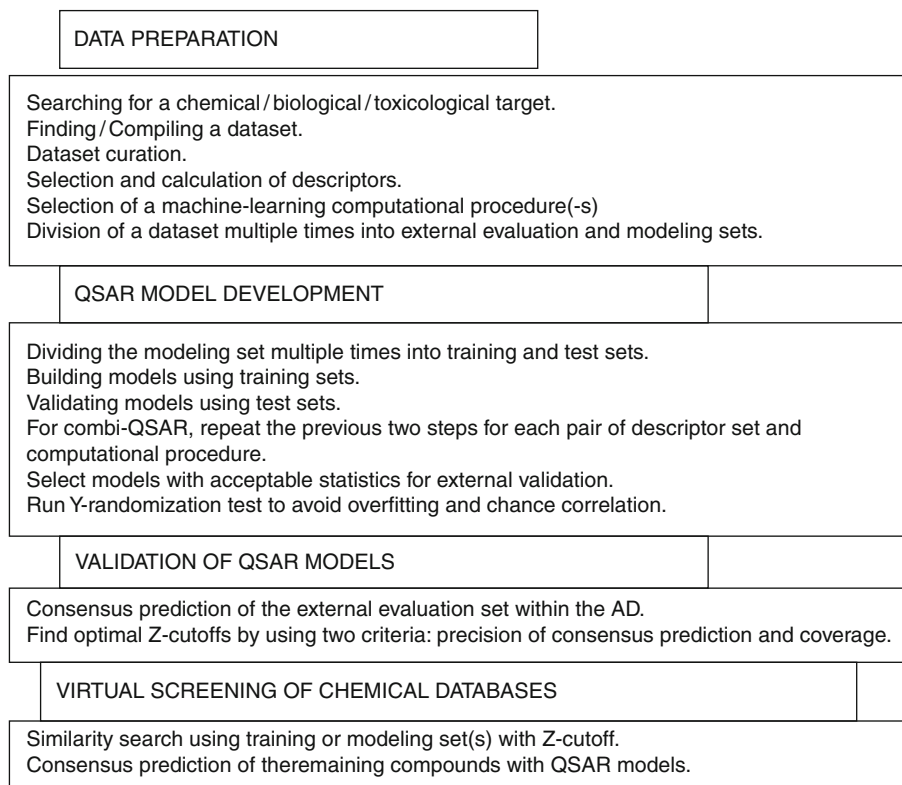
$$\text{Predicted Biological Activity} = \text{Function}(\text{Chemical Structure}) \quad (37.1)$$

A QSAR procedure tries to minimize the error of prediction, for example, in the form of the sum of squares between predicted and observed activities. The process of QSAR model development can be divided into three parts: data preparation, data analysis, and model validation (🔍 Fig. 37-1). Model validation should include establishment of model applicability domain (AD). Recently, the European Organization for Economic Co-operation and Development (OECD) developed a set of principles for the development and validation of QSAR models, which, in particular, requires “appropriate measures of goodness-of-fit, robustness, and predictivity” (Organisation 2008). The OECD guidance document especially emphasizes that QSAR models should be rigorously validated using external sets of compounds that were not used in the model development.

## Data Preparation

---

The first part of QSAR analysis includes selection of a molecular dataset for QSAR studies, acquiring or calculation of molecular descriptors (quantities characterizing molecular



■ Fig. 37-1

### Major steps of QSAR modeling

structures), and selection of a QSAR (statistical analysis and correlation) method. Datasets for QSAR studies can be found in research papers or electronic databases available either publicly (PubChem 2010; BindingDB (Liu et al. 2007); ChEMBL 2010; DSSTox 2008; NIMH Psychoactive Drug Screening (PDSP) 2010) or commercially (e.g., Wombat (Olah et al. 2007) or MDDR 2009); more examples are given in a recent review (Oprea and Tropsha 2006). The dataset should include biological activity values for all compounds (e.g., binding energies to a receptor, or inhibition constants  $IC_{50}$ , or in case of toxicity modeling, lethal concentration in water  $LC_{50}$ , or lethal dose  $LD_{50}$ , etc.) preferably measured in the same lab using the same experimental method. If these experimental data are not available from one lab or one source, and the correlation between measurements made in different labs or by different methods cannot be established, they may not be used directly in QSAR studies. Instead, compounds in the dataset should be given a rank or assigned to categories of activities: for example, a compound can be very active, moderately active, or inactive. In the majority of such cases, binary classification is used, in which a compound is classified as either active or inactive. Another situation may arise, when compounds in the dataset naturally belong to different classes, for example, they are ligands to different receptors. In this case, the types of ligand specificity for a target can be considered as classes of compound activities, and the goal of QSAR analysis becomes to achieve accurate prediction of the target specificity for a new compound.

According to the nature of the activity data, QSAR studies can be divided into continuous (activities, i.e., response variable, takes many different values from within some interval), category (activities are represented by ranks or ordinal numbers), and classification (activities are different types of biological properties which cannot be rank ordered) approaches.

Prior to QSAR modeling, a dataset should be curated, that is, all structures should be verified with respect to their correct representation in the dataset; structures containing atoms, for which there are no parameters for descriptor calculation should be removed; structures consisting of several disconnected parts should be removed; salts should be removed; a problem of isomerism should be addressed; and duplicate structures should be removed. There are different tools available for dataset curation. For example, Molecular Operating Environment (MOE) (2008) includes DatabaseWash tool. It allows changing molecules' names, adding or removing hydrogen atoms, removing salts and heavy atoms, even if they are covalently connected to the rest of the molecule, and changing or generating the tautomers and protomers (cf. the MOE manual for more details). Various database curation tools are included in ChemAxon (2008) as well. If commercial software tools such as MOE are unavailable (notably, ChemAxon software is free to academic investigators), one can use standard UNIX/LINUX tools to perform some of the dataset cleaning tasks (Tropsha and Golbraikh 2010). It is important to have some freely available molecular format converters such as OpenBabel (2010) or MolConverter from ChemAxon (2008). Major procedures for database curation are discussed in our recent paper (Fourches et al. 2010).

After the dataset is selected and curated, the next task is the acquisition or calculation of descriptors. According to an excellent monograph titled *Handbook of Molecular Descriptors* by Roberto Todeschini and Vivian Consonni (2000) molecular descriptors can be grouped into zero-dimensional [0D] (sometimes referred to as constitutional descriptors), one-dimensional [1D] (e.g., counts of different molecular groups, physicochemical properties of compounds, etc), two-dimensional [2D] (invariants of molecular graphs, e.g., connectivity indices, information indices, counts of paths and walks, etc.), three-dimensional [3D], which are based on geometrical spatial properties of molecules [e.g., Comparative Molecular Field Analysis (CoMFA) descriptors (Tripos 2010) which are values of steric and electrostatic fields around aligned molecules, and different CoMFA-like descriptors (Klebe 1998; Kubinyi et al. 1998; Robinson et al. 1999)], and some other descriptors. Some descriptors can be experimental or calculated physicochemical properties of molecules such as molecular weight, molar refraction, energies of HOMO and LUMO, normal boiling point, octanol/water partition coefficient, molecular surface, molecular volume, etc.

Herein, we will not discuss different types of descriptors in detail but mention briefly major descriptor software. Most of descriptors included in the *Handbook of Molecular Descriptors* (Todeschini and Consonni 2000) can be calculated by the Dragon software (Dragon 2007). Molconn-Z (2007) is another widely used descriptor calculation software which calculates more than 800 descriptors. A relatively small, but diverse set of molecular descriptors can be calculated by the MOE (2008) software. Chirality molecular topological descriptors (CMTDs) developed in our laboratory append 2D descriptors by conformation-independent chirality and ZE-isomerism topological indices (Golbraikh and Tropsha 2003; Golbraikh et al. 2001, 2002). Another group of descriptors frequently used in our laboratory is atom-pair (AP) descriptors (Carhart et al. 1985). Each descriptor is defined as a count of pairs of atoms of certain types being away from each other on a certain topological distance (2D AP descriptors) or a Euclidean distance within certain intervals (3D AP descriptors); chirality AP descriptors can be calculated as well (Kovatcheva et al. 2005).

Many descriptors calculated from the knowledge of 3D structure of molecules (3D descriptors) have been developed and published as well. Although these are inherently more rigorous, one should keep in mind that their calculation is much more time and resource consuming. In many QSAR applications, the calculation of 3D descriptors should be preceded by conformational search and 3D structure alignment. However, even for rigid compounds, it is not generally known whether the alignment corresponds to real positions of molecules in the receptor binding site (Cherkasov 2008). There are different conformational analysis and pharmacophore modeling tools included in molecular modeling packages such as MOE (2008), Sybyl (there are LINUX and MS Windows versions) (Tripos 2010), Discovery Studio (2010), LigandScout (2010), etc. It has been demonstrated that in many cases QSAR models based on 2D descriptors have comparable (or even superior) predictivity than models based on 3D descriptors (Bures and Martin 1998; Golbraikh et al. 2001; Hoffman et al. 1999; Zheng and Tropsha 2000). Thus when 3D QSAR studies are necessary, if possible, 3D alignment of molecules should be preferably obtained by docking studies. VolSurf (Crivori et al. 2000; Cruciani et al. 2000) and GRIND (Pastor et al. 2000) descriptors are examples of alignment-free 3D descriptors. But their calculation still requires extensive conformational analysis of molecules. Both VolSurf and GRIND descriptors are available in Sybyl (VolSurf and Almond modules) (Tripos 2010). Various types of descriptors can be calculated by different modules of Schrodinger software (2010). Virtually, any molecular modeling software package contains sets of its own descriptors and there are many other descriptors not mentioned here that can be found in the specialized literature.

There are sets of descriptors that take values of zero or one depending on the presence or absence of certain predefined molecular features (or fragments) such as oxygen atoms, aromatic rings, rings, double bonds, triple bonds, halogens, and so on. These sets of descriptors are called molecular fingerprints or structural keys. Such descriptors can be represented by bit strings and many are found in popular software packages. For instance, several different sets of such descriptors are included in MOE (2008), Sybyl (Tripos 2010), and others, and examples of their use can be found in the published literature (McGregor and Pallai 1997; Waller 2004). Molecular holograms are similar to fingerprints; however, they use counts of features rather than their presence or absence. For example, holograms are included in the Sybyl HQSAR module (Tripos 2010). There are also more recent approaches when molecular features are not predefined a priori (as fingerprints discussed above) but are identified for each specific dataset. For example, frequent subgraph mining approaches developed independently at the University of North Carolina (Huan et al. 2006) and at the Louis Pasteur University in Strasbourg (Horvath et al. 2007) can find all frequent closed subgraphs (i.e., subgraph descriptors) for given datasets of compounds described as chemical graphs. A large and diverse set of 2D descriptors can be generated by MOLD2 software (Hong et al. 2008) available from FDA. A wide variety of descriptors are included in ADRIANA software (Gasteiger 2006).

Prior to QSAR studies, processing of descriptors is required. It includes: exclusion of descriptors having the same value for all compounds in the dataset as well as duplicate descriptors. To avoid higher influence on QSAR models of descriptors with higher variance, all descriptors are usually normalized (in most cases, range scaling or autoscaling is used). Molecular holograms or AP descriptors do not need to be normalized. Molecular field values around molecules are also not normalized. Preferably, descriptors with low variance and one of the highly correlated pair of descriptors should be excluded as well.

Finally, data for QSAR model development can be represented in a form of a table (see ► [Table 37-1](#)), in which each compound is a row and each descriptor as well as activity is a column.

■ Table 37-1  
QSAR table

Compound	Descriptor 1	Descriptor 2	...	Descriptor N	Activity
1	$X_{11}$	$X_{12}$	...	$X_{1N}$	$Y_1$
2	$X_{21}$	$X_{22}$	...	$X_{2N}$	$Y_2$
...	...	...	...	...	...
M	$X_{M1}$	$X_{M2}$	...	$X_{MN}$	$Y_M$

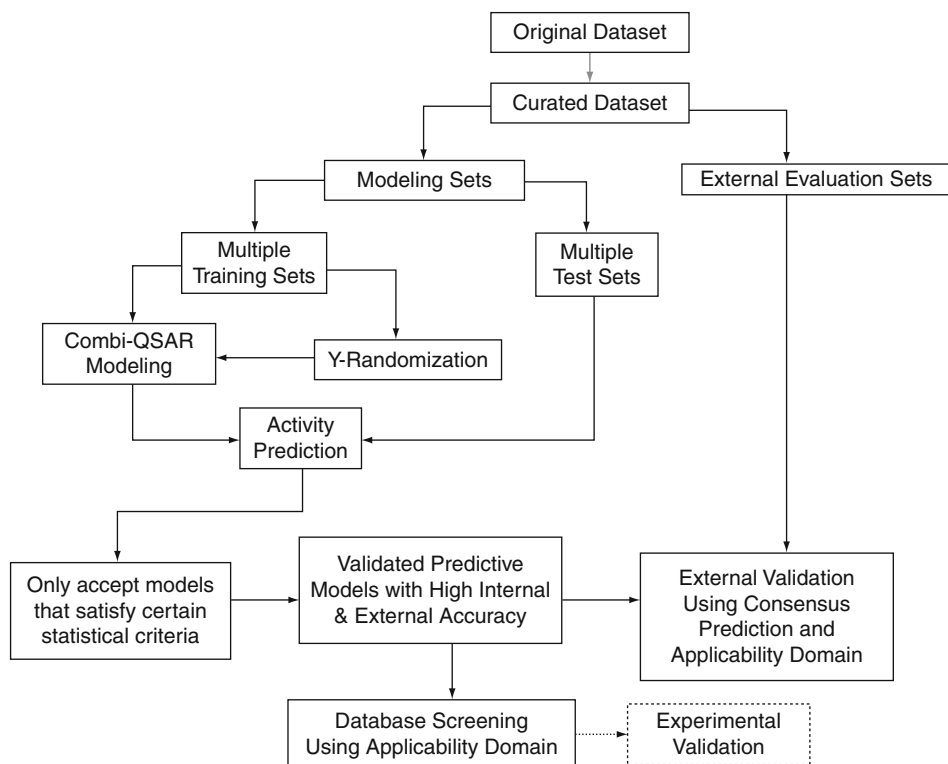
## The Problem of Outliers

Success of QSAR modeling depends on the appropriate selection of a dataset for QSAR studies. In a recent editorial of the *Journal of Chemical Information and Modeling*, Maggiora (2006) noticed that one of the main deficiencies of many chemical datasets is that they do not fully satisfy the main hypothesis underlying all QSAR studies: Similar compounds are expected to have similar biological activities or properties. Maggiora defines the “cliffs” in the descriptor space where the properties change so rapidly, that, in fact adding or deleting one small chemical group can lead to a dramatic change in the compound’s property. In other words, small changes of descriptor values can lead to large changes in molecular properties. Generally, in this case there could be not just one outlier, but a subset of compounds properties of which are different from those on the other “side” of the cliff. In other words, cliffs are areas where the main QSAR hypothesis does not hold. So cliff detection remains a major QSAR problem that has not been adequately addressed in most of the reported studies.

There are two types of outliers we must be aware of: *leverage* (or structural) outliers and *activity* outliers. In case of activity outliers the problem of “cliffs” should be addressed as well. Recently, different approaches to find activity outliers have been published (Bajorath et al. 2009; Guha and Van Drie 2008a,b; Sisay et al. 2009). We have suggested that Grubb’s (Environmental Protection Agency 1992) and Dixon’s (Fallon et al. 1997) statistical tests can be used to find activity outliers (Tropsha and Golbraikh 2010). Structural outliers can be defined as compounds that are largely dissimilar to all other compounds in the descriptor space. The methods of finding them are similar to finding compounds out of QSAR model applicability domains (Tropsha and Golbraikh 2010) that is discussed below.

## QSAR Model Development

The ultimate goal of QSAR analysis is the development of validated models for accurate and precise prediction of biological activities of compounds which could be potential leads in the process of drug discovery. Eventually, predictions should be confirmed by experimental validation. The general QSAR modeling workflow is represented in ● Fig. 37-2. Following the data curation step, we start by randomly selecting a fraction of compounds (typically, 10–20%) as an external evaluation set. The Sphere Exclusion protocol implemented in our laboratory (Golbraikh and Tropsha 2002; Golbraikh et al. 2003) is then used to rationally divide the remaining subset of compounds (the modeling set) multiple times into pairs of training and test sets that are used for model development and validation, respectively. We employ multiple QSAR techniques based on the combinatorial exploration of all possible pairs of descriptor sets and various

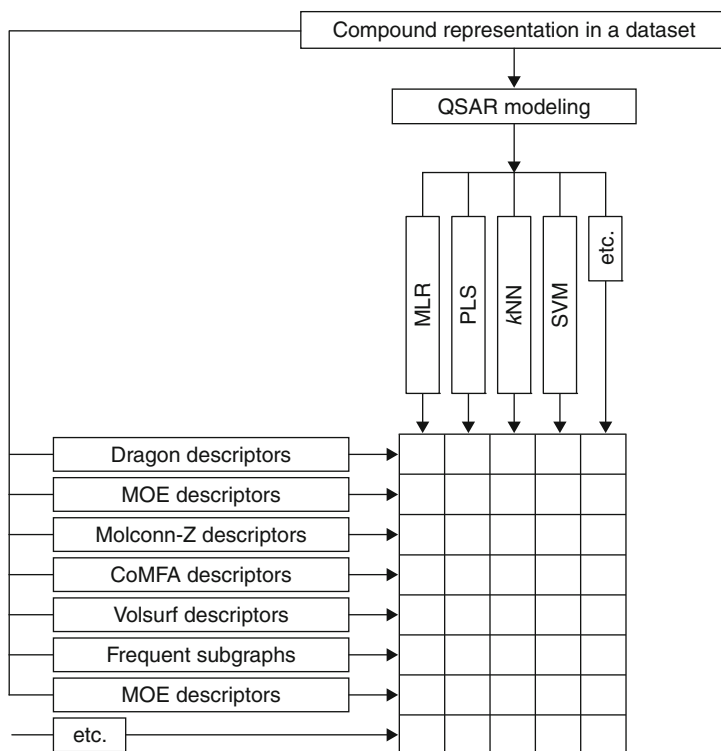


■ Fig. 37-2  
Predictive QSAR modeling workflow

supervised data analysis techniques (combi-QSAR) (► Fig. 37-3) and select models characterized by high accuracy in predicting both training and test sets data. Validated models are finally tested using the external evaluation set. The critical step of the external validation is the use of applicability domains (ADs). If external validation demonstrates the significant predictive power of the models, we employ them for virtual screening of available chemical databases (e.g., ZINC (Irwin and Shoichet 2005)) to identify putative active compounds and work with collaborators who could validate such hits experimentally. The entire approach is described in detail in several recent papers and reviews (Tropsha 2005; Tropsha and Golbraikh 2007).

## QSAR Methods

QSAR modeling techniques employ various methods of multidimensional data analysis as well as supervised machine learning used in different areas of research in natural and social sciences such as biological sciences, geography, psychology, medicine, economics, signal processing, speech recognition, forensic studies, etc. Herein, it is impossible to discuss all the methods used in QSAR analysis. Instead, we will name only some of them. All these methods can be classified into linear and nonlinear approaches. Linear methods include simple and



■ Fig. 37-3  
Combinatorial QSAR modeling

multiple linear regression (MLR), principal component regression (PCR), partial least squares (PLS), etc. The main distinctive characteristic of these methods is the linearity of the function approximating the biological activity (see Eq. 37.1) of their arguments (which are molecular descriptors). In linear discriminant analysis (LDA), linear combinations of descriptors are built, which define hyperplanes that separate representative points of different classes of compounds in the multidimensional descriptor space.

Nonlinear methods can be based derived from linear or based on more complex approaches that predict compound activities from their descriptors by the means of nonlinear relationships. For example, if nonlinear terms (like squares, products, or logarithms of some descriptors) are added to a linear regression, it becomes nonlinear regression. Many nonlinear methods are derived from linear methods via transforming them by a so-called kernel trick. Calculations are executed in a so-called feature space where linear methods are applied. The advantage of these methods is that there is no need to directly calculate the transformation functions. Examples of such methods include non-linear support vector machines (SVMs) and support vector regression (SVR) methods (Berk 2008; Vapnik 2000), nonlinear discriminant analysis, kernel-PCA, kernel-PLS, etc. In the multidimensional feature space, SVM builds a soft margin hyperplane, which separates points belonging to two different classes, or more hyperplanes to separate points of larger number of classes. In contrast, SVR builds a hyperplane such that



as many points as possible are within the margin. Good SVM tutorial was written by Burges (1998), and SVR tutorial by Smola and Schoelkopf (2004). Other non-linear methods include  $k$ -nearest neighbors QSAR, in which the activity of a compound is predicted as a (weighted) average of activities of its nearest neighbors.  $k$ -nearest neighbor methods can include stochastic (Zheng and Tropsha 2000) or stepwise variable (descriptor) selection (Ajmani et al. 2006).

Another large group of generally nonlinear methods are artificial neural networks (ANNs) (Neural Networks 1996; Salt et al. 2006; Zupan and Gasteiger 1999). Ensembles of ANNs can make use of bagging and boosting approaches (Agrafiotis et al. 2002). ANNs consist of groups of artificial neurons. In feed-forward back-propagation neural networks (Neural Networks 2010), neurons are organized in input, hidden, and output layers. Input layer neurons receive descriptor values of compounds, which are passed with different weights to the hidden layer neurons. A neuron activation function is then applied at each neuron to the sum of weighted inputs, and the results are passed to the output layer neurons, which calculate predicted activities of compounds. During training process, parameters of neuron functions and weights are adjusted so that the total error of predictions is minimized. There are network architectures with multiple hidden layers.

Recursive partitioning (RP) methods build decision trees in order to precisely assign compounds to their classes. The tree consists of one root node containing all objects (compounds), intermediate (or decision), and leaf (terminal) nodes. A measure of node purity is introduced; for example, it could be the ratio of counts of compounds belonging to majority and minority class in a node. At each node, the procedure tries to partition the data to increase the purity measure, that is, to make the difference between sum of child node purities and parent node purity as higher as possible. Analysis is based on descriptor value distributions between classes at the node. If such a partition at the node is impossible, it becomes a leaf node. Additional criteria may be imposed on the minimum number of compounds in a leaf node, etc. Compounds in each node satisfy certain descriptor criteria. After growing, some leaves are consecutively removed based on the improvement of classification at them (so-called pruning of a tree). Without pruning, the tree could be overfitted. Prediction process consists of moving a query compound up the tree (based on its descriptor values) until it reaches a leaf node. Predicted class of a compound is defined as that of the majority class in this node. There are also RP regression methods which are used, if response variable is continuous. There are several RP algorithms widely used such as Classification and Regression Trees (CART (Berk 2008)), C4.5 (Quinlan 1993), C5.0 (2008), etc.

Random Forest methods (Breiman 2001; Random Forests 2001) construct ensembles of trees based on multiple random selections of subsets of descriptors and bootstrapping of compounds. The compounds not selected in a particular bootstrapping are considered as a so-called out of bag set, and used as the test set. The trees are not pruned. Best trees in the forest are chosen for consensus prediction of external compounds. The method can include bagging (Berk 2008; Breiman 1996) and boosting (Berk 2008; Breiman 1998) approaches.

## Target Functions

---

Based on the nature of the response variable, QSAR approaches can be grouped into classification, category, or continuous QSAR (*vide infra*). Classes are different from categories in a sense that the former cannot be ordered in any scientifically meaningful way, while the latter can be rank ordered.

## Continuous QSAR Models

We suggested that the following validation criteria should be used for continuous QSAR models (Tropsha and Golbraikh 2010): (1) leave-one-out (LOO) cross-validated  $q^2$  (which is also used as the target function, that is, it is optimized by the QSAR modeling procedure) (2) square of the correlation coefficient  $R$  ( $R^2$ ) between the predicted and observed activities of the test set; (3) coefficients of determination (predicted versus observed activities  $R_0^2$ , and observed versus predicted activities  $R_0'^2$  for the test set) for regressions through the origin; (4) slopes  $k$  and  $k'$  of regression lines through the origin (predicted versus observed activities, and observed versus predicted activities for the test set). In our studies, we consider models acceptable, if they have (1)  $q^2 > 0.5$ ; (2)  $R^2 > 0.6$ ; (3)  $(R^2 - R_0^2)/R^2 < 0.1$  and  $0.85 \leq k \leq 1.15$  or  $(R^2 - R_0'^2)/R^2 < 0.1$  and  $0.85 \leq k' \leq 1.15$ ; (4)  $|R_0^2 - R_0'^2| < 0.3$ . Sometimes, stricter criteria are used (Tropsha and Golbraikh 2010).

In some papers, other criteria are used. For example, sometimes standard error of prediction is used instead of (or together with)  $R^2$ . Standard error of prediction itself makes no sense until we compare it with the standard deviation for activities of the test set, which brings us back to the correlation coefficients. If used, mean absolute error (MAE) should be compared with the mean absolute deviation from the mean. Sometimes,  $F$ -ratio is calculated, which is the variance explained by the model divided by the unexplained variance. It is believed that the higher is the  $F$ -ratio, the better is the model. We suppose that when  $F$ -ratio is used, it must be always accompanied by the corresponding  $p$ -value.

Frequently, especially for linear models such as developed with multiple linear regression (MLR) or partial least squares (PLS) the adjusted  $R^2$  is used:

$$R_{adj}^2 = 1 - (1 - R^2) \frac{n - 1}{n - c - 1}, \quad (37.2)$$

where  $n$  is the number of compounds in the dataset, and  $c$  is the number of variables (descriptors or principal components) included in the regression equation. It should be recognized that  $R_{adj}^2 \leq R^2$ . The higher the number of explanatory variables  $c$  is, the lower  $R_{adj}^2$  is.  $R_{adj}^2$  is particularly important for linear QSAR models developed with variable selection.  $R_{adj}^2$  is not a good criterion for variable selection  $k$ NN QSAR models, since contrary to regression methods, in the  $k$ NN algorithm descriptors are just selected or not selected, that is, their weights are either zero or one. As a result, much larger set of descriptors is selected by the  $k$ NN procedure than, for example, by stepwise regression.

## Target Functions and Validation Criteria for Classification QSAR Models

We consider a classification QSAR model predictive, if the prediction accuracy characterized by the correct classification rate (CCR) for each class is sufficiently large:

$$CCR_{\text{class}} = \frac{N_{\text{class}}^{\text{corr}}}{N_{\text{class}}^{\text{total}}} \quad (37.3)$$

and the  $p$ -value for each  $CCR_{\text{class}}$  value is not higher than a predefined threshold (in case of two classes, the  $CCR_{\text{class}}$  threshold should not be lower than 0.65–0.70, and generally, for any number of classes,  $p$ -value should not be higher than 0.05 for each class).

For the classification QSAR with  $K$  classes, we shall use the following criterion

$$\text{CCR} = \frac{1}{K} \sum_{i=1}^K \text{CCR}_i = \frac{1}{K} \sum_{i=1}^K \frac{N_i^{\text{corr}}}{N_i^{\text{total}}} \quad (37.4)$$

along with the correct classification rate for each class (see [Eq. 37.2](#)). Criterion [\(37.4\)](#) is correct for both balanced and imbalanced (biased) datasets (i.e., when the number of compounds of each class is different). For imbalanced datasets, formula  $N(\text{corr})/N(\text{total})$ , where  $N(\text{corr})$  and  $N(\text{total})$  are the number of compounds predicted correctly and the total number of compounds in the dataset) is incorrect. QSAR procedure should maximize the CCR value calculated according to [Eq. 37.4](#), and at the same time it should be penalized by too high differences between CCR values for different classes.

### Target Functions and Validation Criteria for Category QSAR Models

Category QSAR with more than two classes should use target functions and validation criteria other than those used in classification QSAR. These target functions and validation criteria should consider errors as differences between predicted and observed categories, or increasing functions of these differences. The total error of prediction over all compounds is the sum of all errors of predictions for individual compounds. Let  $n_{ij}$  be the number of compounds of category  $i$  assigned by a model to category  $j$  ( $i, j = 1, \dots, K$ ). Then the total error is calculated as follows:

$$E = \sum_{i=1}^K \sum_{j=1}^K n_{ij} f(|i - j|). \quad (37.5)$$

where  $f(|i - j|)$  is the increasing function of errors. In case of biased datasets, it would be important to normalize the errors for compounds of category  $i$  on the number of compounds in this category:

$$E = \sum_{i=1}^K \frac{1}{N_i} \sum_{j=1}^K n_{ij} f(|i - j|). \quad (37.6)$$

where  $N_i$  is the number of compounds of category  $i$ . QSAR procedure should minimize the total error of prediction calculated with [Eqs. 37.5](#) or [37.6](#). In practice, the accuracy can be defined as  $A = 1 - E/E_{\text{exp}}$ , where  $E_{\text{exp}}$  is the expected total error. Thus, QSAR procedure should maximize the target function  $A$  penalized by too high differences between CCR values for different classes.

More detailed consideration of target functions and validation criteria as well as different aspects of cost-sensitive learning, weighting, penalties, as well as threshold moving in QSAR studies are discussed in our recent review (Tropsha and Golbraikh 2010). General aspects of cost-sensitive learning are discussed by Elkan (The Foundations 2001) and Chen et al. (2004). Oversampling of the minority class, that is, inclusion of compounds of the minority class in the dataset more than once, is considered by Yen and Lee (2006), and Kubat and Matwin (1997). The opposite approach, called undersampling, that is, removing part of the majority class from the dataset, is considered by Japkowicz (2000). Using moving threshold for dividing compounds into active and inactive classes when continuous property values are available but one desires to use classification modeling approaches is considered by Zhou and Liu (2006). In QSAR studies, threshold is usually moved toward the larger class, which is easier to predict correctly.

## Applicability Domains

Here we are approaching an extremely important problem of QSAR studies: model applicability domain (AD). Formally, a QSAR model can predict the target property for any compound for which chemical descriptors can be calculated. However, if a compound is highly dissimilar from all compounds of the modeling set, reliable prediction of its activity is unlikely to be realized. A concept of AD was developed and used to avoid such an unjustified extrapolation in activity prediction. Applicability domains are one of the areas of intensive research. Different methods of defining AD exist. Among others, the following definitions are considered by Jaworska and colleagues (2005, 2008).

*Descriptor-range-based AD.* AD is defined as a hyperparallelepiped in the descriptor space in which representative points are distributed (Netzeva et al. 2006; Nikolova-Jeliazkova and Jaworska 2005; Saliner et al. 2006). Dimensionality of the hyperparallelepiped is equal to the number of descriptors, and the size of each dimension is defined by the minimum and maximum values of the corresponding descriptor or it stretches beyond these limits to some extent up to predefined thresholds.

*Geometric Methods: Convex Hull AD.* AD is defined as a convex hull of points in the multidimensional descriptor space (Fechner et al. 2008).

The drawbacks of these definitions are as follows. Generally, the representative points are distributed not in the entire hyperparallelepiped or convex hull, but only in a small part of it. Another drawback is that structural outliers in the dataset can enormously increase the size of the hyperparallelepiped, and the area around the outlier will contain no other points. Consequently, for many compounds within the hyperparallelepiped or convex hull, prediction will be unreliable. Besides, if the number of linearly independent descriptors exceeds the number of compounds, the convex hull is not unique.

*Leverage-based AD.* Leverage for a compound is defined as the corresponding diagonal element of the hat matrix (Afantitis et al. 2006). A compound is defined as outside of the AD, if its leverage  $L$  is higher than  $3K/N$ , where  $K$  is the number of descriptors and  $N$  is the number of compounds. The drawbacks of the leverage-based AD are as follows. (a) for each external compound, it is necessary to recalculate leverage; (b) if there are cavities in the representative point distribution area, a query compound the representative point of which is in this area will be considered to be within the AD, while in fact it is far from all other compounds (Tropsha and Golbraikh 2010).

*Distance-based AD.* In our studies, the AD is defined as the Euclidean distance threshold  $DT$  between a query compound and its closest  $k$ -nearest neighbors of the training set. It is calculated as follows:

$$DT = \bar{y} + Z\sigma \quad (37.7)$$

Here,  $\bar{y}$  is the average Euclidean distance between each compound and its  $k$ -nearest neighbors in the training set  $k$  is optimized in the course of QSAR modeling, and the distances are calculated using descriptors selected by the optimized (model only),  $\sigma$  is the standard deviation of these Euclidean distances, and  $Z$  is an arbitrary cutoff parameter defined by a user (de Cerqueira et al. 2006; Hsieh et al. 2008; Kovatcheva et al. 2005; Zhang et al. 2008). We set the default value of this parameter  $Z$  at 0.5, which formally places the allowed distance threshold at the mean plus one-half of the standard deviation. We also define the AD in the entire

descriptor space. In this case, the same  $\blacklozenge$  Eq. 37.7 is used,  $k = 1$ ,  $Z = 0.5$ , and Euclidean distances are calculated using all descriptors. Thus, if the distance of the external compound from its nearest neighbor in the training set within either the entire descriptor space or the selected descriptor space exceeds these thresholds, the prediction is not made. We have also investigated changes of predictive power by changing the values of  $Z$ -cutoff. We have found that in general, starting from some  $Z$ -cutoff value, predictive power decreases while  $Z$ -cutoff value increases (Zhu et al. 2009), as expected. Instead of Euclidean distances, other distances and similarity measures can be used.

*Consensus Prediction AD.* The predicted activity of a query compound by an ensemble of QSAR models is calculated as the average over all predicted values. In binary QSAR modeling, each model will predict the compound category as either 0 (inactive) or 1 (active); however, different models used in an ensemble may yield inconsistent predictions. Consequently, the averaged predicted activity value for an external compound resulting from the use of an ensemble of models may fall anywhere within the [0;1] range. For classification and category QSAR, the average predicted value is rounded to the closest integer (which is a class or category number); in the case of imbalanced datasets, rounding can be done using the moving threshold (*vide supra*). Predicted average classes or categories (before rounding) that are closer to the nearest integers are considered more reliable since such value indicates higher concordance between different models. For example, before rounding, one compound has the predicted value of 0.2, but the other has 0.4. Hence, both compounds are predicted to belong to class 0 but the prediction for the first compound is considered more reliable. Using these prediction values, additional constraint on the AD can be defined by a threshold of the absolute difference between the predicted and the rounded predicted activity. There are several other definitions of AD (Jaworska and Nikolova-Jeliazkova 2008; Tetko et al. 2006) based on probability density distributions, distances to models, etc.

## Y-randomization

To establish model robustness, Y-randomization (randomization of the response variable) test should be used. This test consists of repeating all the calculations with scrambled activities of the training set. Ideally, calculations should be repeated at least five (better, more) times. The goal of this procedure is to establish whether models built with real activities of the training set have good statistics not due to overfitting or chance correlation. If predictive power for the training or the test set of all models built with randomized activities of the training set is significantly lower than that of models built with real activities of the training set, the latter ones are considered reliable. Using different parameters of the model development procedure, multiple QSAR models are built which have acceptable statistics. Suppose, the number of these models is  $m$ . Y-randomization test can also give  $n$  models with acceptable statistics. For acceptance of models developed with real activities of the training set, the condition  $n \ll m$  should be satisfied. In (Kovatcheva et al. 2005) and (de Cerqueira et al. 2006), we have introduced the measure of robustness  $R = 1 - n/m$ . If  $R > 0.9$ , the models are considered robust and their high predictive accuracy cannot be explained by the chance correlation or overfitting. Y-randomization test is particularly important for small datasets. Unfortunately, in many publications on QSAR studies, Y-randomization test is not carried out but all QSAR practitioners must be strongly encouraged to use this simple procedure.

## External Validation

Our previous experience suggests that the consensus prediction, which is the average of predicted activities over all predictive models, always provides the most stable results (Zhang et al. 2008; Zhu et al. 2008), and thus naturally avoids the need for (the best) model selection based on the statistics for the training and test sets. The consensus prediction of biological activity for an external compound on the basis of several QSAR models is more reliable and provides better justification for the experimental exploration of hits.

External evaluation set compounds are predicted by models that have passed all validation criteria described above. Each compound is predicted by models for which the compound is within the AD. Actually, each external compound should be within the AD of the training set within the entire descriptor space as well (*vide supra*). A useful parameter for consensus prediction is the minimum number (or percentage) of models for which a compound is within the AD; it is defined by the user. If the compound is found within the AD of a lower number of models, it is considered to be outside of the AD. Prediction value is the average of predictions by all models. If a compound is predicted by more than one model, standard deviation of all predictions by these models is also calculated. For classification and category QSAR, the average prediction value is rounded to the closest integer (which is a class or category number); in case of imbalanced datasets, rounding can be done using the moving threshold.

Predicted average classes or categories (before rounding), which are closer to the nearest integers are considered more reliable (Zhang et al. 2008). Using these prediction values, AD can be defined by a threshold of the absolute difference between predicted and rounded predicted activity. For classification and category QSAR, the same prediction accuracy criteria are used as for the training and test sets. The situation is more complex for the continuous QSAR. In this case, if the range of activities of the external evaluation set is comparable to that for the modeling set, criteria (1)–(4) are used (see [section “Target Functions”](#)). Sometimes, however, the external evaluation set may have a much smaller range of activities than the modeling set, so it could be impossible to obtain sufficiently large  $R^2$  value (and other acceptable statistical characteristics) for it. In this case, we recommend using the mean absolute error (MAE) or the standard error of prediction (SEP) as discussed in one of our previous publications (Tropsha and Golbraikh 2010).

We have used consensus prediction in many studies (de Cerqueira et al. 2006; Kovatcheva et al. 2005; Shen et al. 2004; Votano et al. 2004; Zhang et al. 2007, 2008; Zhu et al. 2008) and have shown that in most cases it gives better prediction and coverage than most of the individual predictive models. Thus, we recommend using consensus prediction for virtual screening of chemical databases and combinatorial libraries for finding new lead compounds for drug discovery.

## “Good Practices” in QSAR Modeling: Examples of Models and Their Application to Virtual Screening and Lead Identification

---

As discussed above, our experience in QSAR model development and validation has led us to establishing a complex but straightforward workflow summarized in [Fig. 37-2](#). The last critical component of this workflow is the use of models to identify tentative active hits that

should be validated in experimental laboratories, and we strongly encourage every computational scientist to use this ultimate model validation strategy. We note that this approach shifts the emphasis from ensuring good (best) statistics for the model that fits known experimental data toward generating testable hypotheses about purported bioactive compounds. Thus, the output of the modeling has exactly same format as the input, that is, chemical structures and (predicted) activities making model interpretation and utilization completely seamless for medicinal chemists. In our recent studies, we have been fortunate to recruit experimental collaborators who have validated computational hits identified through our modeling of anti-convulsants (Shen et al. 2004), HIV-1 reverse transcriptase inhibitors (Medina-Franco et al. 2005), D1 antagonists (Oloff et al. 2005), antitumor compounds (Zhang et al. 2007), beta-lactamase inhibitors (Hsieh et al. 2008), geranylgeranyltransferase inhibitors (Peterson et al. 2009), and others. The discovery of novel bioactive chemical entities is the primary goal of computational drug discovery, and the development of validated and predictive QSAR models is critical to achieve this goal. We note that such studies could only be done if there is sufficient data available for a series of tested compounds such that robust validated models could be developed using the workflow described in [Fig. 37-2](#). We present several examples of these studies below to illustrate the use of QSAR models as virtual screening tools for lead identification.


## QSAR-Aided Discovery of Novel Anticonvulsant Compounds

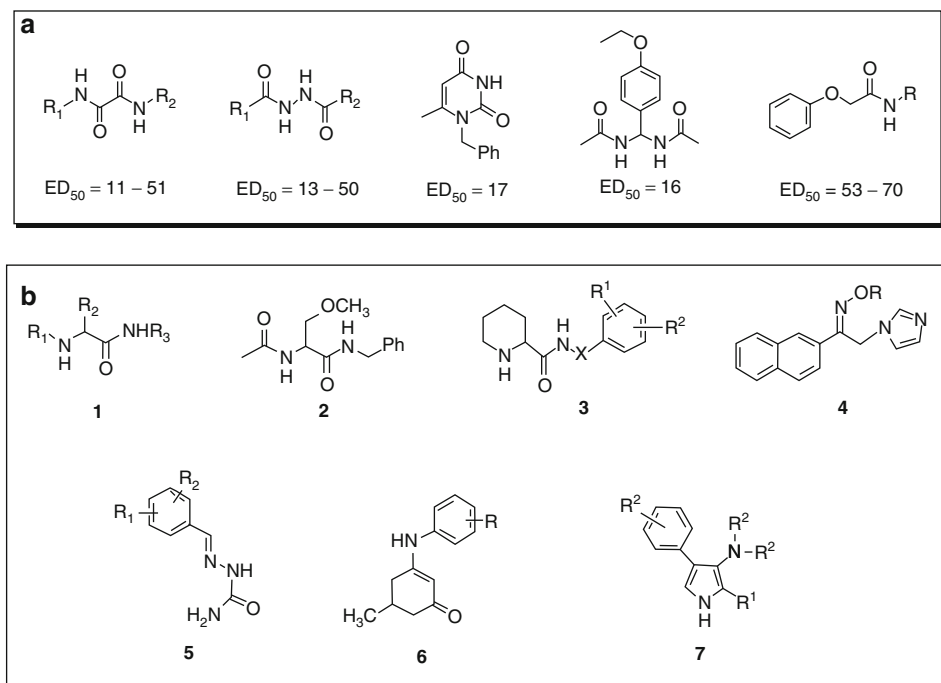
We have applied kNN (Zheng and Tropsha 2000) and simulated annealing – partial least squares (SA-PLS) (Cho et al. 1998) QSAR approaches to a dataset of 48 chemically diverse functionalized amino acids (FAAs) with anticonvulsant activity that were synthesized previously, and successful QSAR models of FAA anticonvulsants have been developed (Shen et al. 2002). Both methods utilized multiple descriptors such as molecular connectivity indices or atom-pair descriptors, which are derived from two-dimensional molecular topology. QSAR models with high internal accuracy were generated, with leave-one-out cross-validated  $R^2$  ( $q^2$ ) values ranging between 0.6 and 0.8. The  $q^2$  values for the actual dataset were significantly higher than those obtained for the same dataset with randomly shuffled activity values, indicating that models were statistically significant. The original dataset was further divided into several training and test sets, and highly predictive models providing  $q^2$  values for the training sets greater than 0.5 and  $R^2$  values for the test sets greater than 0.6.


In the second phase of modeling, we have applied the validated QSAR models to mining available chemical databases for new lead FAA anticonvulsant agents. Two databases have been explored: the National Cancer Institute (nci 2007) and Maybridge (2005) databases, including (at the time of that study) 237,771 and 55,273 chemical structures, respectively. Database mining was performed independently using ten individual QSAR models that have been extensively validated using several criteria of robustness and accuracy. Each individual model selected some number of hits as a result of independent database mining, and the consensus hits (i.e., those selected by all models) were further explored experimentally for their anticonvulsant activity. As a result of computational screening of the NCI database, 27 compounds were selected as potential anticonvulsant agents and submitted to our experimental collaborators. Of these 27 compounds, our collaborators chose two for synthesis and evaluation; their choice was based on the ease of synthesis and the fact that these two compounds had structural features that would not be expected to be found in active compounds based on prior experience. Several



additional compounds, which were close analogs of these two were either taken from the literature or designed in our collaborator's laboratory. In total, seven compounds were resynthesized and sent to the NIH for the Maximum Electroshock (MES) test (a standard test for the anticonvulsant activity, which was used for the training set compounds as well). The biological results indicated that upon initial and secondary screening, five out of seven compounds tested showed anticonvulsant activity with  $ED_{50}$  less than 100 mg/kg, which is considered promising. Interestingly, all seven compounds were also found to be very active in the same tests performed on rats (a complete set of experimental data on rats for the training set were not available, and therefore no QSAR models for rats were built).

Mining of the Maybridge database yielded two additional promising compounds that were synthesized and sent to the NIH for the MES anticonvulsant test. One of the compounds showed moderate anticonvulsant activity of  $ED_{50}$  between 30 and 100 mg/kg (in mice), while the other was found to be a *very* potent anticonvulsant agent with  $ED_{50}$  of 18 mg/kg in mice (ip). In summary, both compounds were found to be very active in both mice and rats.  Figure 37-4 shows chemical structures of experimentally confirmed hits that were identified by using validated QSAR models for virtual screening as applied to the anticonvulsant dataset. It is important to note that *none* of the compounds identified in external databases as potent anticonvulsants and validated experimentally belong to the same class of FAA molecules as the training set. This observation was very stimulating because it underscored the power of our methodology



 Fig. 37-4

Uniqueness of scaffolds for QSAR-based experimentally confirmed virtual screening hits (a) as compared to training set compounds; (b) for the anticonvulsant dataset



to identify potent anticonvulsants of novel chemical classes as compared to the training set compounds, which is one of the most important goals of virtual screening.

## QSAR-Enabled Discovery of Novel Anticancer Agents

---

A combined approach of validated QSAR modeling and virtual screening was successfully applied to the discovery of novel tylophorine derivatives as anticancer agents (Zhang et al. 2007). QSAR models have been initially developed for 52 chemically diverse phenathrene-based tylophorine derivatives (PBTs) with known experimental  $EC_{50}$  using chemical topological descriptors (calculated with the Molconn-Z program) and variable selection  $k$ -nearest neighbor (kNN) method. Several validation protocols have been applied to achieve robust QSAR models. The original dataset was divided into multiple training and test sets, and the models were considered acceptable only if the leave-one-out cross-validated  $R^2(q^2)$  values were greater than 0.5 for the training sets and the correlation coefficient  $R^2$  values were greater than 0.6 for the test sets. Furthermore, the  $q^2$  values for the actual dataset were shown to be significantly higher than those obtained for the same dataset with randomized target properties ( $Y$ -randomization test), indicating that models were statistically significant. Ten best models were then employed to mine a commercially available ChemDiv Database (ca. 500 K compounds) resulting in 34 consensus hits with moderate to high predicted activities. Ten structurally diverse hits were experimentally tested and eight were confirmed active with the highest experimental  $EC_{50}$  of  $1.8 \mu M$  implying an exceptionally high hit rate (80%). The same ten models were further applied to predict  $EC_{50}$  for four new PBTs, and the correlation coefficient ( $R^2$ ) between the experimental and predicted  $EC_{50}$  for these compounds plus eight active consensus hits was shown to be as high as 0.57.

## QSAR Enabled Discovery of Novel Geranylgeranyltransferase I Inhibitors (GGTIs)

---

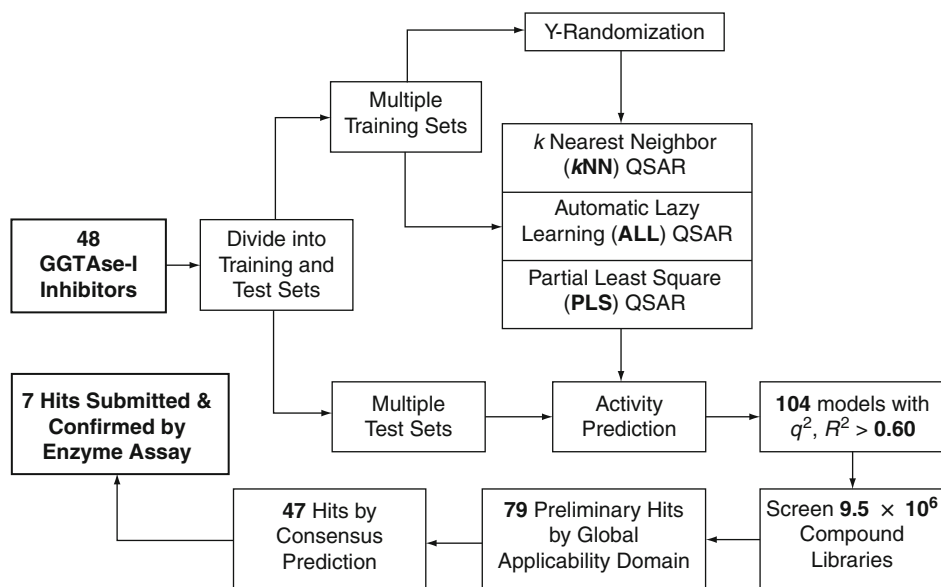
The proper functioning of proteins often relies on posttranslational modification of the polypeptide leading to changes in chemical characteristics. Found at the extreme carboxyl terminus of the protein, one posttranslational “program” utilized for over 140 proteins is the so-called CaaX box, where “C” is a cysteine, “aa” is any aliphatic dipeptide, and “X” is the terminal residue that directs which of two prenyl groups is added (Cox and Der 2002; Zhang and Casey 1996). Protein geranylgeranyltransferase type I (GGTase-I) transfers the 20-carbon geranylgeranyl group to proteins including critical signaling molecules from many classes, for example, the Ras superfamily (including K-Ras, Rho, Rap, Cdc42, and Rac), several G-protein gamma subunits, protein kinases (rhodopsin kinase, phosphorylase kinase, and GRK7), and protein phosphatases (Casey and Seabra 1996; Sebti and Hamilton 2000). Several GGTIs have been developed that inhibit C20 lipid modification of GGTase-I substrates. GGTIs have been primarily developed for use as cancer therapeutics, particularly in cancers that have high levels, or activating mutations of geranylgeranylated proteins (Sebti and Hamilton 2000; Winter-Vann and Casey 2005).

The pharmacological data for 48 GGTIs reported in (Peterson et al. 2009) were generated as part of an iterative drug discovery program that led to GGTI-DU40 (Peterson et al. 2006). The structure of GGTI-DU40 can be discussed in the context of the CaaL peptide framework.

There is a free amide group, a spacer domain relating to the dialiphatic motif, and critical sulfur as found in the requisite cysteine residue of GGTase-I's substrates. Four additional GGTIs included in the data set were peptidomimetics as well. Importantly, the modeling set included compounds with different (chemical scaffolds), which in theory (and as we have established in our study, in practice) should have enabled the identification of chemically diverse hits from virtual screening.

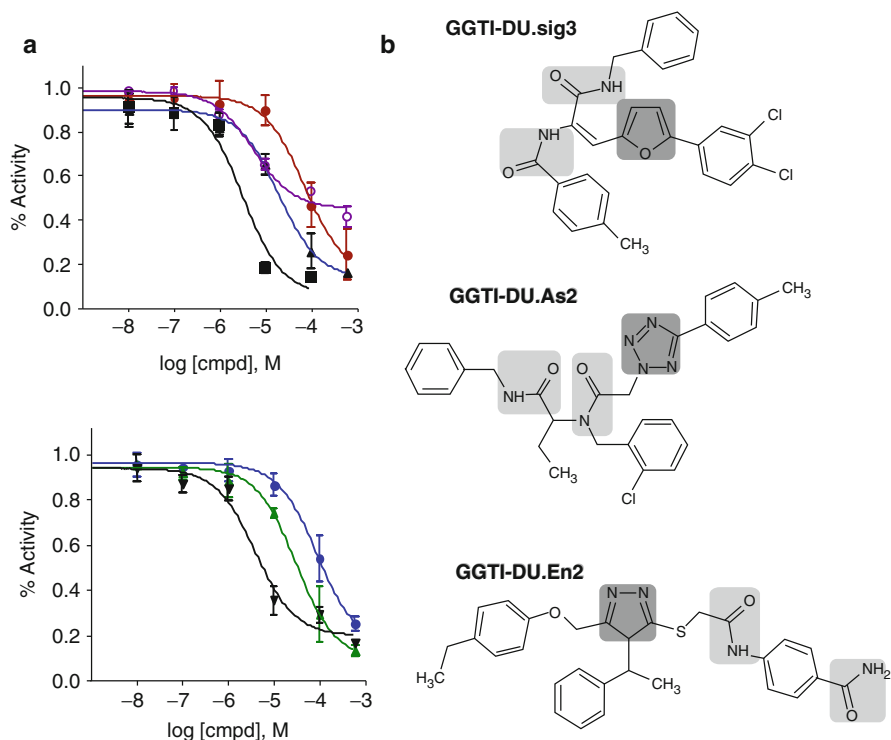
Three different modeling techniques have been used to model GGTIs following our general combi-QSAR strategy (► Fig. 37-3); the specific workflow as applied to the GGTI dataset is shown in ► Fig. 37-5. As the first step of our QSAR-based virtual screening, the preliminary filtering of the 9.5 million compounds in our screening library yielded 79 initial hits. This was done by using the global applicability domain of all 48 GGTIs in the modeling set. After consensus predictions by 104 validated *k*NN models, their predicted activities (*pIC*<sub>50</sub>) were found ranging from 4.51 to 5.96. Only 47 hits, including two pairs of stereoisomers, showed high predicted activity (*pIC*<sub>50</sub> > 5.50) as well as high model coverage and were designated as the final hits. Concurrently, two additional QSAR models were employed to reevaluate those 79 hits in order to identify the consensus hits among all three methods. In the end, seven compounds were prioritized for experimental validation based on high predicted activity, uniqueness of structure, and availability.

Using purified recombinant GGTase-I as an enzyme source and GGpp and Ras-CVLL as substrates, seven hit compounds were tested in vitro as a matter of the experimental validation. The selection was based on high predicted activity, availability, and structural uniqueness. All tested compounds showed inhibition of GGTase-I with the *pIC*<sub>50</sub> ranging from 3.63 to 5.44 (cf. ► Fig. 37-6).



■ Fig. 37-5

The predictive QSAR modeling workflow illustrated for GGTIs



■ Fig. 37-6

Experimental validations of computational GGTI hits using GGTase-I in vitro activity assay. (a) Inhibition curves; (b) Chemical structures of three representative confirmed hits; the novel scaffolds in the structures are highlighted

The unexpected result was to identify several predicted actives that did not have a common ring feature in their structure. In fact, seven highly ranked hits had no apparent relationship with any of the training set molecules. They had furan, triazole, tetrazole, and pyridine cores in their scaffolds while all non-peptidomimetic compounds of the training set were based on a pyrazole core. Therefore, the seven hit compounds appeared to be the structurally novel hits.

► [Figure 37-6b](#) shows chemical structures of the three representative confirmed hits with novel scaffolds highlighted. This study reconfirmed the observation that we already emphasized earlier with anticonvulsant compounds that contrary to the common belief, QSAR-based virtual screening is capable of identifying experimentally confirmed hit compounds with novel scaffolds.

## “Good Practices” in QSAR Model Development: Applications to Toxicity Modeling

Many compounds entering clinical studies do not survive as a good pharmacological lead to become a marketed drug. Chemical toxicity and safety have been regarded as the major reason

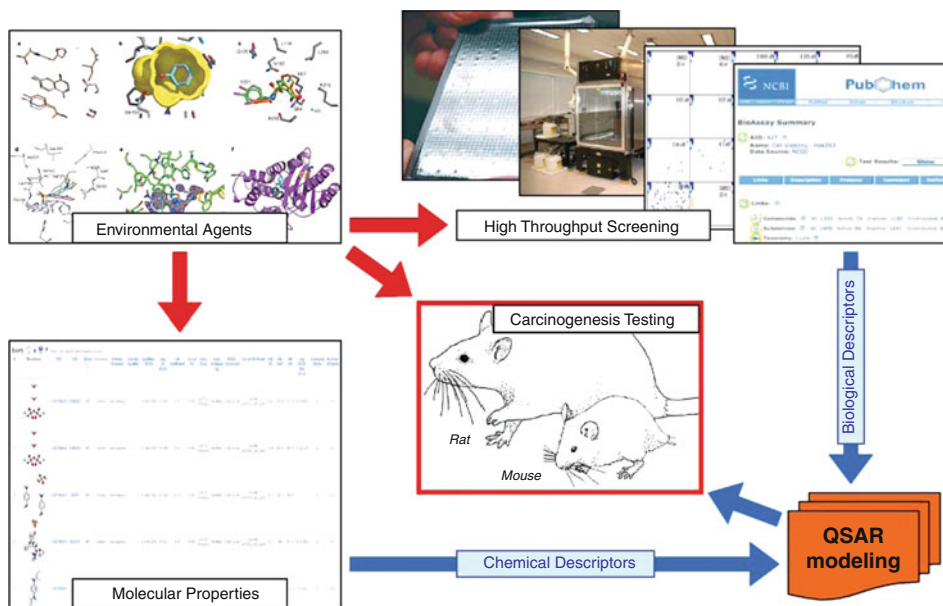
for attrition in the past decades (Kola and Landis 2004). However, evaluation of chemical toxicity and safety *in vivo* at the early stage of drug discovery process is expensive and time consuming. To replace the traditional animal toxicity testing and to understand the relevant toxicological mechanisms, many *in vitro* toxicity screens and computational toxicity models have been developed and implemented by academic institutes and pharmaceutical companies (Cheeseman 2005; Dash et al. 2009; Dix et al. 2007; Inglese et al. 2006; Park et al. 2009; Riley and Kenna 2004; Valerio 2009; Yang et al. 2009). In the past 15 years, innovative technologies that enable rapid synthesis and high throughput screening of large libraries of compounds have been adopted for toxicity studies. As a result, there has been a huge increase in the number of compounds and the associated testing data in different *in vitro* screens. With this data, it becomes feasible to reveal the relationship between the high throughput *in vitro* toxicity testing results and the low throughput *in vivo* low dose toxicity evaluation for the same set of compounds. Understanding these relationships could help us delineate the mechanisms underlying animal toxicity of chemicals as well as potentially improve our ability to predict chemical toxicity using short-term bioassays.

The unique advantage of using a computational toxicity model in risk analysis is that a chemical could be evaluated for its toxicity potential even before it is synthesized. The computational toxicity tools based on QSAR models have been used to assist in predictive toxicological profiling of pharmaceutical substances for understanding drug safety liabilities (Durham and Pearl 2001; Jacobson-Kram and Contrera 2007; Muster et al. 2008; Valerio 2009), supporting regulatory decision making on chemical safety and risk of toxicity (Bailey et al. 2005), and are effectively enhancing an already rigorous US regulatory safety review of pharmaceutical substances (Valerio 2008). Predictive QSAR models of chemical toxicity are beginning to be used to evaluate compounds' safety in the pharmaceutical industry and environmental agencies (Durham and Pearl 2001; Snyder 2009). However, it has been reported that most QSAR models do not work well for evaluating *in vivo* toxicity, especially for external compounds (Zvinavashe et al. 2008, 2009). Several reviews were published recently that challenge the feasibility and reliability of QSAR models of chemical toxicity (Johnson 2008; Stouch et al. 2003). At the same time, experimental data resulting from short-term high throughput screening assays are emerging prompting the development of novel modeling approaches that can combine short-term assay data and conventional chemical descriptors of molecules to develop enhanced QSAR models of animal toxicity. We briefly review these emerging approaches and applications below.

## Quantitative Structure In Vitro–In Vivo Relationship Modeling

---

To stress a broad appeal of the conventional QSAR approach, it should be made clear that from the statistical viewpoint QSAR modeling is a special case of general statistical data mining and data modeling where the data is formatted to represent objects described by multiple descriptors and the robust correlation between descriptors and a target property (e.g., chemical toxicity *in vivo*) is sought. In previous computational toxicology studies, additional physicochemical properties, such as water partition coefficient ( $\log P$ ) (Klopman et al. 2003), water solubility (Stoner et al. 2004), and melting point (Mayer and Reichenberg 2006) were used successfully to augment computed chemical descriptors and improve the predictive power of QSAR models. These studies suggest that using experimental results as descriptors in QSAR modeling could prove beneficial. The already available and rapidly growing HTS data for large and diverse chemical libraries makes it possible to extend the scope of the conventional QSAR in toxicity studies



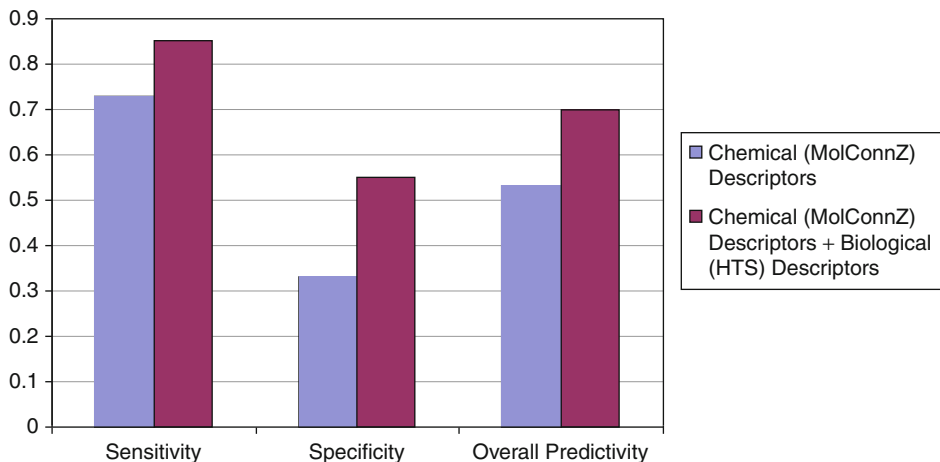
■ Fig. 37-7

Combining chemical and biological profiles as descriptors in QSIIR modeling of chemical carcinogenicity

by using *in vitro* testing results as additional biological descriptors. Therefore, in some of the most recent toxicology studies, the relationships between various *in vitro* and *in vivo* toxicity testing results were generated (Forsby and Blaauboer 2007; Piersma et al. 2008; Schirmer et al. 2008; Sjostrom et al. 2008). Based on these reports, we proposed a new modeling workflow called Quantitative Structure *In vitro*–*In vivo* Relationship (QSIIR) and used it in animal toxicity modeling studies (Zhu et al. 2008, 2009). The target properties of QSIIR modeling were still biological activities, such as different toxicity end points, but the content and interpretation of “descriptors” and the resulting models is different. This focus on the prediction of the same target property from different (chemical, biological, and genomic) characteristics of environmental agents affords an opportunity to most fully explore the source-to-outcome continuum of the modern experimental toxicology using cheminformatics approaches. ▶ *Figure 37-7* provides visual illustration of the integrated QSIIR approach to *in vivo* toxicity modeling.

### Using “Hybrid” Descriptors for QSIIR Modeling of Rodent Carcinogenicity

To explore efficient approaches for rapid evaluation of chemical toxicity and human health risk of environmental compounds, the National Toxicology Program (NTP), in collaboration with the National Center for Chemical Genomics (NCGC) has initiated an HTS Project (Inglese et al. 2006; Thomas et al. 2009). The first batch of HTS results for a set of 1,408 compounds tested in six human cell lines was released via PubChem. We have explored this data in terms of their



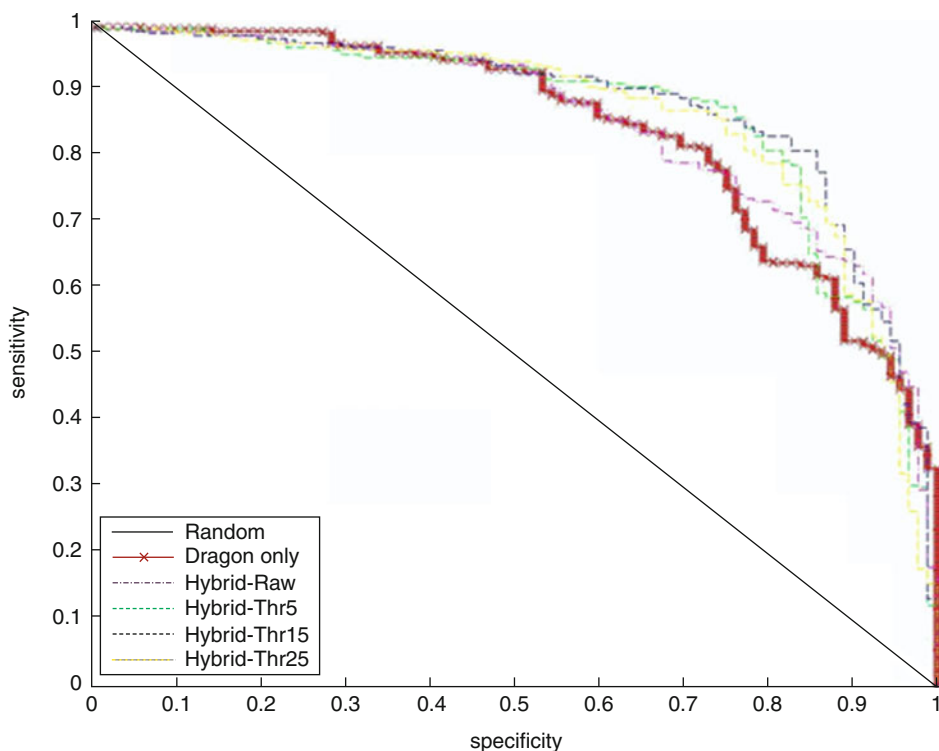
■ Fig. 37-8

**Comparison of the prediction power of QSTR models of chemical carcinogenicity for the independent validation set using conventional versus hybrid descriptors**

utility for predicting adverse health effects of the environmental agents (Zhu et al. 2008). Initially, the classification  $k$ -nearest neighbor (kNN) QSAR modeling method was applied to the HTS data only for the curated dataset of 384 compounds. The resulting models had prediction accuracies for training, test (containing 275 compounds together), and external validation (109 compounds) sets as high as 89%, 71%, and 74%, respectively. We then asked if HTS results could be of value in predicting rodent carcinogenicities. We identified 383 compounds for which data were available from both the Berkeley Carcinogenic Potency Database and NTP-HTS studies. We found that compounds classified by HTS as “actives” in at least one cell line were likely to be rodent carcinogens (sensitivity 77%); however, HTS “inactives” were far less informative (specificity 46%). Using chemical descriptors only, kNN QSAR modeling resulted in the overall external prediction accuracy of 62% for rodent carcinogenicity. Importantly, the prediction accuracy of the model was significantly improved (to 73%) when chemical descriptors were augmented by the HTS data, which were regarded as biological descriptors (● Fig. 37-8). Thus, our studies suggested, for the first time, that combining HTS profiles with conventional chemical descriptors could considerably improve the predictive power of computational approaches in chemical toxicology.

### Using “Hybrid” Descriptors for the QSIR Modeling of Rodent Acute Toxicity

We used the cell viability qHTS data from NCGC as mentioned in the above section for the same 1,408 compounds but in 13 cell lines (Xia et al. 2008). Besides the carcinogenicity, we asked if HTS results could be of value in predicting rodent acute toxicity (Sedykh et al. in press). For this purpose, we have identified 690 of these compounds, for which rodent acute toxicity data (i.e., toxic or nontoxic) was also available. The classification  $k$ NN QSAR modeling method was applied to these compounds using either chemical descriptors alone or as a combination of chemical and qHTS biological (hybrid) descriptors as compound features. The



■ Fig. 37-9

Acute toxicity modeling. The ROC curves for conventional QSAR model (*bold line*) and different hybrid models for the same external compounds.

external prediction accuracy of models built with chemical descriptors only was 76%. In contrast, the prediction accuracy was significantly improved to 85% when using hybrid descriptors. The receiver operating characteristic (ROC) curves of conventional QSAR models and different hybrid models are shown in [Fig. 37-9](#). The sensitivities and specificities of hybrid models are clearly better than for conventional QSAR model for predicting the same external compounds. Furthermore, the prediction coverage increased from 76% when using chemical descriptors only to 93% when qHTS biological descriptors were also included. Our studies suggest that combining HTS profiles, especially the dose-response qHTS results, with conventional chemical descriptors could considerably improve the predictive power of computational approaches for rodent acute toxicity assessment.

## Collaborative and Consensus Modeling of Aquatic Toxicity

We discuss below the results of a recent important study of aquatic toxicity (Zhu et al. 2008). In our opinion, this particular study may serve as a useful example to illustrate the complexity and power of modern QSAR modeling approaches and highlight the importance of collaborative and consensual model development.

The combinational QSAR modeling approach has been applied to a diverse series of organic compounds tested for aquatic toxicity in *Tetrahymena pyriformis* in the same laboratory over nearly a decade (Aptula et al. 2005; Netzeva and Schultz 2005; Schultz 1999; Schultz and Netzeva 2004; Schultz et al. 2001, 2002, 2003, 2005a, b). The unique aspect of this research was that it was conducted in collaboration between six academic groups specializing in cheminformatics and computational toxicology. The common goals for our virtual collaboratory were to explore the relative strengths of various QSAR approaches in their ability to develop robust and externally predictive models of this particular toxicity end point. We have endeavored to develop the most statistically robust, validated, and *externally* predictive QSAR models of aquatic toxicity. The members of our collaboratory included scientists from the University of North Carolina at Chapel Hill in the United States (UNC); University of Louis Pasteur (ULP) in France; University of Insubria (UI) in Italy; University of Kalmar (UK) in Sweden; Virtual Computational Chemistry Laboratory (VCCLAB) in Germany; and the University of British Columbia (UBC) in Canada. Each group relied on its own QSAR modeling approaches to develop toxicity models using the same modeling set, and we agreed to evaluate the realistic model performance using the same external validation set(s).

The *T. pyriformis* toxicity dataset used in this study was compiled from several publications of the Schultz group as well as from data available at the Tetratox database Web site of (<http://www.vet.utk.edu/TETRATOX/>). After deleting duplicates as well as several compounds with conflicting test results and correcting several chemical structures in the original data sources, our final dataset included 983 unique compounds. The dataset was randomly divided into two parts: (1) the modeling set of 644 compounds; (2) the validation set including 339 compounds. The former set was used for model development by each participating group and the latter set was used to estimate the external prediction power of each model as a universal metric of model performance. In addition, when this project was already well underway, a new dataset had become available from the most recent publication by the Schultz group (Schultz et al. 2007). It provided us with an additional *external* set to evaluate the predictive power and reliability of all QSAR models. Among compounds reported in (Schultz et al. 2007) 110 were unique, that is, not present among the original set of 983 compounds; thus, these 110 compounds formed the second independent validation set for our study.

## Universal Statistical Figures of Merit for All Models

Different groups have employed different techniques and (sometimes) different statistical parameters to evaluate the performance of models developed independently for the modeling set (described below). To harmonize the results of this study, the same standard parameters were chosen to describe each model's performance as applied to the modeling and external test set predictions. Thus, we have employed  $Q_{abs}^2$  (squared leave-one-out cross-validation correlation coefficient) for the modeling set,  $R_{abs}^2$  (frequently described as coefficient of determination) for the external validations sets, and MAE (mean absolute error) for the linear correlation between predicted ( $Y_{pred}$ ) and experimental ( $Y_{exp}$ ) data (here,  $Y = pIGC_{50}$ ); these parameters are defined as follows:

$$Q_{abs}^2 = 1 - \frac{\sum_Y (Y_{exp} - Y_{LOO})^2}{\sum_Y (Y_{exp} - \langle Y \rangle_{exp})^2} \quad (37.8)$$



$$R_{abs}^2 = 1 - \frac{\sum_Y (Y_{exp} - Y_{pred})^2}{\sum_Y (Y_{exp} - \langle Y \rangle_{exp})^2} \quad (37.9)$$

$$MAE = \frac{\sum_Y |Y - Y_{pred}|}{n} \quad (37.10)$$

Many other statistical characteristics can be used to evaluate model performance; however, we restricted ourselves to these three parameters that provide minimal but sufficient information concerning any model's ability to reproduce both the trends in experimental data for the test sets as well as mean accuracy of predicting all experimental values. The models were considered acceptable if  $R_{abs}^2$  exceeded 0.5.

## Consensus QSAR Models of Aquatic Toxicity; comparison Between Methods and Models

The objective of this study from methodological prospective was to explore the suitability of different QSAR modeling tools for the analysis of a dataset with an important toxicological end point. Typically, such datasets are analyzed with one (or several) modeling techniques, with a great emphasis on the (high value of) statistical parameters of the training set models. In this study, we went well beyond the modeling studies reported in the original publications in several respects. First, we have compiled all reported data on chemical toxicity against *T. pyriformis* in a single large dataset and attempted to develop global QSAR models for the entire set. Second, we have employed multiple QSAR modeling techniques thanks to the engagement of six collaborating groups. Third, we have focused on defining model performance criteria not only using training set data but most importantly using external validation sets that were not used in model development in *any* way (unlike any common *cross-validation* procedure) (Gramatica 2007). This focus afforded us the opportunity to evaluate and compare all models using simple and objective universal criteria of *external* predictive accuracy, which in our opinion is the most important single figure of merit for a QSAR model that is of practical significance for experimental toxicologists. Fourth, we have explored the significance of applicability domains and the power of consensus modeling in maximizing the accuracy of external predictivity of our models.

We believe that results of our analysis lend a strong support for our strategy. Indeed, all models performed quite well for the training set with even the lowest  $Q_{abs}^2$  among them as high as 0.72. However, there was much greater variation between these models when looking at their (universal and objective) performance criteria as applied to the validation sets.

Of 15 QSAR approaches used in this study, nine implemented method-specific applicability domains. Models that did not define the AD showed a reduced predictive accuracy for the validation set II even though they yielded reasonable results for the validation set I. On average, the use of applicability domains improved the performance of individual models although the improvement came at the expense of the lower chemistry space coverage.

For the most part all models succeeded in achieving reasonable accuracy of external prediction especially when using the AD. It then appeared natural to bring all models together to explore the power of *consensus prediction*. Thus, the *consensus model* was constructed by averaging all available predicted values taking into account the applicability domain of each individual model. In this case, we could use only 9 of 15 models that had the AD defined. Since each model had its unique way of defining the AD, each external compound could be found within the AD

of anywhere between one and nine models so for averaging we only used models covering the compound. The advantage of this data treatment is that the overall coverage of the prediction is still high because it was rare to have an external compound outside of the ADs of all available models. The results showed that the prediction accuracy for both the modeling set and the validation sets was the best compared to any individual model. The same observation could be made for the correlation coefficient  $R_{abs}^2$ . The coverage of this consensus model II was 100% for all three data sets. This observation suggests that consensus models afford both high space coverage and high accuracy of prediction

In summary, this study presents an example of a fruitful international collaboration between researchers that use different techniques and approaches but share general principles of QSAR model development and validation. Significantly, we did not make any assumptions about the purported mechanisms of aquatic toxicity yet were able to develop statistically significant models for all experimentally tested compounds. In this regard it is relevant to cite an opinion expressed in an earlier publication by T. Schultz that “models that accurately predict acute toxicity without first identifying toxic mechanisms are highly desirable” (Schultz 1999). However, the most significant single result of our studies is the demonstrated superior performance of the *consensus modeling* approach when all models are used concurrently and predictions from individual models are averaged. We have shown that both the predictive accuracy and coverage of the final consensus QSAR models were superior as compared to these parameters for individual models. The consensus models appeared robust in terms of being insensitive to both incorporating individual models with low prediction accuracy and the inclusion or exclusion of the AD. Another important result of this study is the power of addressing complex problems in QSAR modeling by forming a virtual collaboratory of independent research groups leading to the formulation and empirical testing of *best modeling practices*. This latter endeavor is especially critical in light of the growing interest of regulatory agencies to developing most reliable and predictive models for environmental risk assessment (Yang et al. 2006) and placing such models in the public domain.

## Conclusions: Emerging Chemical/Biological Data and QSAR Research Strategies

---

In the past 15 years, innovative technologies that enable rapid synthesis and high throughput screening of large libraries of compounds have been adopted in almost all major pharmaceutical and biotech companies. As a result, there has been a huge increase in the number of compounds available on a routine basis to quickly screen for novel drug candidates against new targets or pathways. In contrast, such technologies have rarely become available to the academic research community, thus limiting its ability to conduct large-scale chemical genetics or chemical genomics research. The NIH Molecular Libraries Roadmap Initiative has changed this situation by forming the national Molecular Library Screening Centers Network (MLSCN) (Austin et al. 2004) with the results of screening assays made publicly available via PubChem (2010). These efforts have already led to the unprecedented growth of *available* databases of biologically tested compounds [cf. our recent review where we list about 20 available databases of compounds with known bioactivity (Oprea and Tropsha 2006)].

This growth creates new challenges for QSAR modeling such as developing novel approaches for the analysis and visualization of large databases of screening data, novel biologically relevant chemical diversity or similarity measures, and novel tools for virtual screening of compound libraries to ensure high expected hit rates. Application studies discussed in this chapter have established that QSAR models could be used successfully as virtual screening tools to discover compounds with the desired biological activity in chemical databases or virtual libraries (Hsieh et al. 2008; Oloff et al. 2005; Shen et al. 2004; Tropsha 2005; Tropsha and Zheng 2001; Zhang et al. 2007). The discovery of novel bioactive chemical entities is the primary goal of computational drug discovery, and the development of validated and predictive QSAR models is critical to achieve this goal. Due to the significant recent increase in publicly available datasets of biologically active compounds and the critical need to improve the hit rate of experimental compound screening there is a strong need in developing widely accessible and reliable computational QSAR modeling techniques and specific end-point predictors.

## Acknowledgments

---

The studies described in this chapter were supported in parts by the NIH research grants R01GM066940 and R21GM076059 and EPA grants EPA (RD832720 and RD833825).

## References

---

- (1997). *Addressing the curse of imbalanced training sets: One sided selection*. San Francisco: Morgan Kaufmann.
- Afantitis, A., Melagraki, G., Sarimveis, H., Koutentis, P. A., Markopoulos, J., & Igglessi-Markopoulou, O. (2006). A novel QSAR model for predicting induction of apoptosis by 4-aryl-4H-chromenes. *Bioorganic & Medicinal Chemistry*, 14, 6686.
- Agrafiotis, D. K., Cedeno, W., & Lobanov, V. S. (2002). On the use of neural network ensembles in QSAR and QSPR. *The Journal of Chemical Information and Computer Science*, 42, 903.
- Ajmani, S., Jadhav, K., & Kulkarni, S. A. (2006). Three-dimensional QSAR using the k-nearest neighbor method and its interpretation. *The Journal of Chemical Information and Modeling*, 46, 24.
- Aptula, A. O., Roberts, D. W., Cronin, M. T. D., & Schultz, T. W. (2005). Chemistry-toxicity relationships for the effects of Di- and trihydroxy-benzenes to *Tetrahymena pyriformis*. *Chemical Research in Toxicology*, 18, 844.
- Austin, C. P., Brady, L. S., Insel, T. R., & Collins, F. S. (2004). NIH molecular libraries initiative. *Science*, 306, 1138.
- Bailey, A. B., Chanderbhan, R., Collazo-Braier, N., Cheeseman, M. A., & Twaroski, M. L. (2005). The use of structure-activity relationship analysis in the food contact notification program. *Regulatory Toxicology and Pharmacology*, 42, 225.
- Bajorath, J., Peltason, L., Wawer, M., Guha, R., Lajiness, M. S., & Van Drie, J. H. (2009). Navigating structure-activity landscapes. *Drug Discovery Today*, 14, 698.
- Berk, R. A. (2008). *Classification and Regression Trees (CART). Statistical learning from a regression perspective*. New York: Springer.
- Breiman, L. (1996). Bagging predictors. *Machine Learning*, 24, 123.
- Breiman, L. (1998). Arcing classifiers. *The Annals of Statistics*, 26, 801.
- Breiman, L. (2001). Random forests. *Machine Learning*, 45, 5.
- Bures, M. G., & Martin, Y. C. (1998). Computational methods in molecular diversity and combinatorial chemistry. *Current Opinion in Chemical Biology*, 2, 376.
- Burges, J. C. (1998). Tutorial on support vector machines for pattern recognition. *Data Mining and Knowledge Discovery*, 2, 121.
- C5.0. (2008).

- Carhart, R. E., Smith, D. H., & Venkataraghavan, R. (1985). Atom pairs as molecular features in structure-activity studies: Definition and applications. *The Journal of Chemical Information and Computer Science*, 25, 64.
- Casey, P. J., & Seabra, M. C. (1996). Protein prenyl-transferases. *The Journal of Biological Chemistry*, 271, 5289.
- Cheeseman, M. A. (2005). Thresholds as a unifying theme in regulatory toxicology. *Food Additives & Contaminants*, 22, 900.
- ChemAxon. (2008). <http://www.chemaxon.com>.
- ChEMBL Database. (2010). <http://www.ebi.ac.uk/chembl/db/>.
- Chen, C., Liaw, A., & Breiman, L. (2004). *Using random forest to learn imbalanced data*. 666. Berkeley: Department of Statistics, University of California.
- Cherkasov, A. (2008). An updated steroid benchmark set and its application in the discovery of novel nanomolar ligands of sex hormone-binding globulin. *Journal of Medicinal Chemistry*, 51, 2047.
- Cho, S. J., Zheng, W., & Tropsha, A. (1998). Rational combinatorial library design. 2. Rational design of targeted combinatorial peptide libraries using chemical similarity probe and the inverse QSAR approaches. *The Journal of Chemical Information and Computer Science*, 38, 259.
- Cox, A. D., & Der, C. J. (2002). Farnesyltransferase inhibitors: Promises and realities. *Current Opinion in Pharmacology*, 2, 388.
- Crivori, P., Cruciani, G., Carrupt, P. A., & Testa, B. (2000). Predicting blood-brain barrier permeation from three-dimensional molecular structure. *The Journal of Medicinal Chemistry*, 43, 2204.
- Cruciani, G., Pastor, M., & Guba, W. (2000). VolSurf: A new tool for the pharmacokinetic optimization of lead compounds. *The European Journal of Pharmaceutical Sciences*, 11(Suppl 2), S29-S39.
- Dash, A., Inman, W., Hoffmaster, K., Sevidal, S., Kelly, J., Obach, R.S., et al. (2009). Liver tissue engineering in the evaluation of drug safety. *Expert Opinion on Drug Metabolism & Toxicology*, 5, 1159.
- de Cerqueira, L. P., Golbraikh, A., Oloff, S., Xiao, Y., & Tropsha, A. (2006). Combinatorial QSAR modeling of P-Glycoprotein substrates. *The Journal of Chemical Information and Modeling*, 46, 1245.
- Discovery Studio. (2010).
- Dix, D. J., Houck, K. A., Martin, M. T., Richard, A. M., Setzer, R. W., & Kavlock, R. J. (2007). The ToxCast program for prioritizing toxicity testing of environmental chemicals. *Toxicological Sciences*, 95, 5.
- Dragon. (2007). [http://www.taletе.mi.it/help/dragon\\_help/index.html?IntroducingDRAGON](http://www.taletе.mi.it/help/dragon_help/index.html?IntroducingDRAGON).
- DSSTox. (2008). <http://www.epa.gov/nheerl/dsstox/About.html>.
- Durham, S. K., & Pearl, G. M. (2001). Computational methods to predict drug safety liabilities. *Current Opinion in Drug Discovery & Development*, 4, 110.
- Environmental Protection Agency. (1992). *Statistical training course for ground-water monitoring data analysis EPA/530-R-93-003*. Washington: Office of Solid Waste.
- Fallon, A., Spada, C., & Gallagher, D. (1997). Detection and Accommodation of Outliers in Normally Distributed Data Sets. <http://ewr.cce.vt.edu/environmental/teach/smprimer/outlier/outlier.html>. Accessed 25 April 2005.
- Fechner, N., Hinselmann, G., Schmiedl, C., & Zell, A. (2008). Estimating the applicability domain of kernel-based QSPR models using classical descriptor vectors. *pdf. Chemistry Central Journal*, 2(Suppl.1), P2.
- Forsby, A., & Blaauboer, B. (2007). Integration of in vitro neurotoxicity data with biokinetic modelling for the estimation of in vivo neurotoxicity. *Human & Experimental Toxicology*, 26, 333.
- Fourches, D., Muratov, E., & Tropsha, A. (2010). Trust, but verify: On the importance of chemical structure curation in cheminformatics and QSAR modeling research. *The Journal of Chemical Information and Modeling*, 50, 1189-1204.
- Gasteiger, J. (2006). Of molecules and humans. *The Journal of Medicinal Chemistry*, 49, 6429.
- Golbraikh, A., & Tropsha, A. (2002). Predictive QSAR modeling based on diversity sampling of experimental datasets for the training and test set selection. *The Journal of Computer-Aided Molecular Design*, 16, 357.
- Golbraikh, A., & Tropsha, A. (2003). QSAR modeling using chirality descriptors derived from molecular topology. *The Journal of Chemical Information and Computer Science*, 43, 144.
- Golbraikh, A., Bonchev, D., & Tropsha, A. (2001). Novel chirality descriptors derived from molecular topology. *The Journal of Chemical Information and Computer Science*, 41, 147.
- Golbraikh, A., Bonchev, D., & Tropsha, A. (2002). Novel ZE-isomerism descriptors derived from molecular topology and their application to QSAR analysis. *The Journal of Chemical Information and Computer Science*, 42, 769.
- Golbraikh, A., Shen, M., Xiao, Z., Xiao, Y. D., Lee, K. H., & Tropsha, A. (2003). Rational

- selection of training and test sets for the development of validated QSAR models. *The Journal of Computer-Aided Molecular Design*, 17, 241.
- Gramatica, P. (2007). Principles of QSAR models validation: Internal and external. *Qsar & Combinatorial Science*, 26, 694.
- Guha, R., & Van Drie, J. H. (2008a). Structure-activity landscape index: Identifying and quantifying activity cliffs. *The Journal of Chemical Information and Modeling*, 48, 646.
- Guha, R., & Van Drie, J. H. (2008b). Assessing how well a modeling protocol captures a structure-activity landscape. *The Journal of Chemical Information and Modeling*, 48, 1716.
- Hoffman, B., Cho, S. J., Zheng, W., Wyrick, S., Nichols, D. E., Mailman, R. B., et al. (1999). Quantitative structure-activity relationship modeling of dopamine D(1) antagonists using comparative molecular field analysis, genetic algorithms-partial least-squares, and K nearest neighbor methods. *The Journal of Medicinal Chemistry*, 42, 3217.
- Hong, H., Xie, Q., Ge, W., Qian, F., Fang, H., Shi, L., et al. (2008). Mold(2), molecular descriptors from 2D structures for chemoinformatics and toxicoinformatics. *The Journal of Chemical Information and Modeling*, 48, 1337.
- Horvath, D., Bonachera, F., Solov'ev, V., Gaudin, C., & Varnek, A. (2007). Stochastic versus stepwise strategies for quantitative structure-activity relationship generation—how much effort may the mining for successful QSAR models take? *The Journal of Chemical Information and Modeling*, 47, 927.
- Hsieh, J. H., Wang, X. S., Teotico, D., Golbraikh, A., & Tropsha, A. (2008). Differentiation of AmpC beta-lactamase binders vs. decoys using classification kNN QSAR modeling and application of the QSAR classifier to virtual screening. *The Journal of Computer-Aided Molecular Design*, 22, 593.
- Huan, J., Bandyopadhyay, D., Prins, J., Snoeyink, J., Tropsha, A., & Wang, W. (2006). Distance-based identification of structure motifs in proteins using constrained frequent subgraph mining. *Computational Systems Bioinformatics Conference*, 227.
- Inglese, J., Auld, D. S., Jadhav, A., Johnson, R. L., Simeonov, A., Yasgar, A., et al. (2006). Quantitative high-throughput screening: A titration-based approach that efficiently identifies biological activities in large chemical libraries. *Proceedings of the National Academy of Sciences of the United States of America*, 103, 11473.
- Irwin, J. J., & Shoichet, B. K. (2005). ZINC—a free database of commercially available compounds for virtual screening. *The Journal of Chemical Information and Modeling*, 45, 177.
- Jacobson-Kram, D., & Contrera, J. F. (2007). Genetic toxicity assessment: Employing the best science for human safety evaluation. Part I: Early screening for potential human mutagens. *Toxicological Sciences*, 96, 16.
- Jaworska, J., & Nikolova-Jeliazkova, N. (2008). Review of methods to assess a QSAR Applicability Domain. [http://ambit.acad.bg/nina/publications/2004/AppDomain\\_qsar04.ppt](http://ambit.acad.bg/nina/publications/2004/AppDomain_qsar04.ppt).
- Jaworska, J., Nikolova-Jeliazkova, N., & Aldenberg, T. (2005). QSAR applicability domain estimation by projection of the training set descriptor space: A review. *Alternatives to Laboratory Animals*, 33, 445.
- Johnson, S. R. (2008). The trouble with QSAR (or how I learned to stop worrying and embrace fallacy). *The Journal of Chemical Information and Modeling*, 48, 25.
- Klebe, G. (1998). Comparative molecular similarity indices: CoMSI. In H. Kubinyi, G. Folkers, & Y. Martin (Eds.), *3D QSAR in drug design* (pp. 87–104). Great Britain: Kluwer.
- Klopman, G., Zhu, H., Ecker, G., & Chiba, P. (2003). MCASE study of the multidrug resistance reversal activity of propafenone analogs. *The Journal of Computer-Aided Molecular Design*, 17, 291.
- Kola, I., & Landis, J. (2004). Can the pharmaceutical industry reduce attrition rates? *Nature Reviews Drug Discovery*, 3, 711.
- Kovatcheva, A., Golbraikh, A., Oloff, S., Feng, J., Zheng, W., & Tropsha, A. (2005). QSAR modeling of datasets with enantioselective compounds using chirality sensitive molecular descriptors. *SAR and QSAR in Environmental Research*, 16, 93.
- Kubinyi, H., Hamprecht, F. A., & Mietzner, T. (1998). Three-dimensional quantitative similarity-activity relationships (3D QSIAR) from SEAL similarity matrices. *The Journal of Medicinal Chemistry*, 41, 2553.
- (2000). *Learning from imbalanced datasets: A comparison of various strategies*. AAAI Workshop. Menlo Park: AAAI Press.
- LigandScout. (2010).
- Liu, T., Lin, Y., Wen, X., Jorissen, R. N., & Gilson, M. K. (2007). BindingDB: A web-accessible database of experimentally determined protein-ligand binding affinities. *Nucleic Acids Research*, 35, D198–D201.
- Maggiora, G. M. (2006). On outliers and activity cliffs—why QSAR often disappoints. *The Journal of Medicinal Chemistry*, 46, 1535.

- Maybridge. (2005). <http://www.daylight.com/products/databases/Maybridge.html>.
- Mayer, P., & Reichenberg, F. (2006). Can highly hydrophobic organic substances cause aquatic baseline toxicity and can they contribute to mixture toxicity? *Environmental Toxicology & Chemistry*, 25, 2639.
- McGregor, M. J., & Pallai, P. V. (1997). Clustering of large databases of compounds: Using the MDL "Keys" as structural descriptors. *The Journal of Chemical Information and Computer Science*, 37, 443.
- MDDR.SYMYX technologies. (2009). [http://www.mdl.com/products/knowledge/drug\\_data\\_report/index.jsp](http://www.mdl.com/products/knowledge/drug_data_report/index.jsp).
- Medina-Franco, J. L., Golbraikh, A., Oloff, S., Castillo, R., & Tropsha, A. (2005). Quantitative structure-activity relationship analysis of pyridinone HIV-1 reverse transcriptase inhibitors using the k nearest neighbor method and QSAR-based database mining. *The Journal of Computer-Aided Molecular Design*, 19, 229.
- Molconn-Z. (2007). <http://www.edusoft-lc.com/>.
- Molecular Operating Environment (MOE). (2008). <http://www.chemcomp.com/>.
- Muster, W., Breidenbach, A., Fischer, H., Kirchner, S., Muller, L., & Pahler, A. (2008). Computational toxicology in drug development. *Drug Discovery Today*, 13, 303.
- nci. (2007). [http://dtp.nci.nih.gov/docs/3d\\_database/structural\\_information/smiles\\_strings.html](http://dtp.nci.nih.gov/docs/3d_database/structural_information/smiles_strings.html).
- Netzeva, T. I., Gallegos, S. A., & Worth, A. P. (2006). Comparison of the applicability domain of a quantitative structure-activity relationship for estrogenicity with a large chemical inventory. *Environmental Toxicology & Chemistry*, 25, 1223.
- Netzeva, T. I., & Schultz, T. W. (2005). QSARs for the aquatic toxicity of aromatic aldehydes from Tetrahymena data. *Chemosphere*, 61, 1632.
- (1996). *Neural networks in QSAR and drug design*. San Diego: Academic.
- Neural Networks. (2010). <http://www.learnartificialneuralnetworks.com/>.
- Nikolova-Jeliazkova, N., & Jaworska, J. (2005). An approach to determining applicability domains for QSAR group contribution models: An analysis of SRC KOWWIN. *Alternatives to Laboratory Animals*, 33, 461.
- Olah, M., Rad, R., Ostopovici, L., Bora, A., Hadaruga, N., Hadaruga, D., et al. (2007). WOMBAT and WOMBAT-PK: Bioactivity databases for lead and drug discovery. In S. L. Schreiber, T. M. Kapoor, & G. Weiss (Eds.), *Chemical biology: From small molecules to systems biology and drug design* (pp. 760–786). Weinheim: Wiley-VCH.
- Oloff, S., Mailman, R. B., & Tropsha, A. (2005). Application of validated QSAR models of D1 dopaminergic antagonists for database mining. *The Journal of Medicinal Chemistry*, 48, 7322.
- (2010). OpenBabel: The OpenSource Chemistry Toolbox. [Openbabel.org](http://openbabel.org). 2-1-2010.
- Oprea, T., & Tropsha, A. (2006). Target, chemical and bioactivity databases – integration is key. *Drug Discovery Today*, 3, 357–365.
- Organisation for Economic and Co-operation Development. (2008). OECD Quantitative Structure-Activity Relationships [(Q)SARs] Project. [http://www.oecd.org/document/23/0,3343,en\\_2649\\_34365\\_33957015\\_1\\_1\\_1\\_1,00.html](http://www.oecd.org/document/23/0,3343,en_2649_34365_33957015_1_1_1_1,00.html).
- Park, M. V., Lankveld, D. P., van, L. H., & de Jong, W. H. (2009). The status of in vitro toxicity studies in the risk assessment of nanomaterials. *Nanomedicine (Lond)*, 4, 669.
- Pastor, M., Cruciani, G., McLay, I., Pickett, S., & Clementi, S. (2000). GRIND-INdependent descriptors (GRIND): A novel class of alignment-independent three-dimensional molecular descriptors. *The Journal of Medicinal Chemistry*, 43, 3233.
- PDSP. (2010). PDSP. <http://pdsp.med.unc.edu>.
- Peterson, Y. K., Kelly, P., Weinbaum, C. A., & Casey, P. J. (2006). A novel protein geranylgeranyltransferase-I inhibitor with high potency, selectivity, and cellular activity. *The Journal of Biological Chemistry*, 281, 12445.
- Peterson, Y. K., Wang, X. S., Casey, P. J., & Tropsha, A. (2009). Discovery of geranylgeranyltransferase-I inhibitors with novel scaffolds by the means of quantitative structure-activity relationship modeling, virtual screening, and experimental validation. *The Journal of Medicinal Chemistry*, 52, 4210.
- Piersma, A. H., Janer, G., Wolterink, G., Bessems, J. G., Hakkert, B. C., & Slob, W. (2008). Quantitative extrapolation of in vitro whole embryo culture embryotoxicity data to developmental toxicity in vivo using the benchmark dose approach. *Toxicological Sciences*, 101, 91.
- PubChem. (2010). <http://pubchem.ncbi.nlm.nih.gov/>.
- Quinlan, J. R. (1993). *C4.5: Programs for machine learning*. San Mateo: Morgan Kaufmann.
- Random Forests. (2001).
- Riley, R. J., & Kenna, J. G. (2004). Cellular models for ADMET predictions and evaluation of drug-drug interactions. *Current Opinion in Drug Discovery & Development*, 7, 86.
- Robinson, D. D., Winn, P. J., Lyne, P. D., & Richards, W. G. (1999). Self-organizing molecular field



- analysis: A tool for structure-activity studies. *The Journal of Medicinal Chemistry*, 42, 573.
- Saliner, A. G., Netzeva, T. I., & Worth, A. P. (2006). Prediction of estrogenicity: Validation of a classification model. *SAR and QSAR in Environmental Research*, 17, 195.
- Salt, D. V., Yildiz, N., Livingstone, D. J., & Tinsley, C. J. (2006). The use of artificial neural networks in QSAR. *Pesticide Science*, 36, 161.
- Schirmer, K., Tanneberger, K., Kramer, N. I., Volker, D., Scholz, S., Hafner, C., et al. (2008). Developing a list of reference chemicals for testing alternatives to whole fish toxicity tests. *Aquatic Toxicology*, 90, 128.
- Schrodinger Software. (2010).
- Schultz, T. W. (1999). Structure-toxicity relationships for benzenes evaluated with *Tetrahymena pyriformis*. *Chemical Research in Toxicology*, 12, 1262.
- Schultz, T. W., & Netzeva, T. I. (2004). Development and evaluation of QSARs for ecotoxic endpoints: The benzene response-surface model for *Tetrahymena* toxicity. In M. T. D. Cronin & D. J. Livingstone (Eds.), *Modeling environmental fate and toxicity* (pp. 265–284). Boca Raton: CRC Press.
- Schultz, T. W., Cronin, M. T., Netzeva, T. I., & Aptula, A. O. (2002). Structure-toxicity relationships for aliphatic chemicals evaluated with *Tetrahymena pyriformis*. *Chemical Research in Toxicology*, 15, 1602.
- Schultz, T. W., Hewitt, M., Netzeva, T. I., & Cronin, M. T. D. (2007). Assessing applicability domains of toxicological QSARs: Definition, confidence in predicted values, and the role of mechanisms of action. *QSAR & Combinatorial Science*, 26, 238.
- Schultz, T. W., Netzeva, T. I., & Cronin, M. T. (2003). Selection of data sets for QSARs: Analyses of *Tetrahymena* toxicity from aromatic compounds. *SAR and QSAR in Environmental Research*, 14, 59.
- Schultz, T. W., Netzeva, T. I., Roberts, D. W., & Cronin, M. T. (2005a). Structure-toxicity relationships for the effects to *Tetrahymena pyriformis* of aliphatic, carbonyl-containing, alpha,beta-unsaturated chemicals. *Chemical Research in Toxicology*, 18, 330.
- Schultz, T. W., Yarbrough, J. W., & Woldemeskel, M. (2005b). Toxicity to *Tetrahymena* and abiotic thiol reactivity of aromatic isothiocyanates. *Cell Biology and Toxicology*, 21, 181.
- Schultz, T. W., Sinks, G. D., & Miller, L. A. (2001). Population growth impairment of sulfur-containing compounds to *Tetrahymena pyriformis*. *Environmental Toxicology*, 16, 543.
- Sebti, S. M., & Hamilton, A. D. (2000). Farnesyltransferase and geranylgeranyltransferase I inhibitors in cancer therapy: Important mechanistic and bench to bedside issues. *Expert Opinion on Investigational Drugs*, 9, 2767.
- Sedykh, A., Zhu, H., Tang, H., Zhang, L., Rusyn, I., Richard, A., et al. The use of dose-response qHTS data as biological descriptors improves the prediction accuracy of QSAR models of acute rat toxicity. *Environmental Health Perspect*, In press.
- Shen, M., Beguin, C., Golbraikh, A., Stables, J. P., Kohn, H., & Tropsha, A. (2004). Application of predictive QSAR models to database mining: Identification and experimental validation of novel anticonvulsant compounds. *Journal of Medicinal Chemistry*, 47, 2356.
- Shen, M., LeTiran, A., Xiao, Y., Golbraikh, A., Kohn, H., & Tropsha, A. (2002). Quantitative structure-activity relationship analysis of functionalized amino acid anticonvulsant agents using k nearest neighbor and simulated annealing PLS methods. *The Journal of Medicinal Chemistry*, 45, 2811.
- Sisay, M. T., Peltason, L., Bajorath, J. (2009). Structural interpretation of activity cliffs revealed by systematic analysis of structure-activity relationships in analog series. *The Journal of Chemical Information and Modeling*, 49, 2179.
- Sjostrom, M., Kolman, A., Clemedson, C., & Clothier, R. (2008). Estimation of human blood LC50 values for use in modeling of in vitro-in vivo data of the ACuteTox project. *Toxicology In Vitro*, 22, 1405.
- Smola, A. J., & Schoelkopf, B. A. (2004). *Tutorial on support vector regression*. Tuebingen: Max Planck Society - eDocument Server (Germany).
- Snyder, R. D. (2009). An update on the genotoxicity and carcinogenicity of marketed pharmaceuticals with reference to in silico predictivity. *Environmental and Molecular Mutagenesis*, 50, 435.
- Stoner, C. L., Gifford, E., Stankovic, C., Lepsey, C. S., Brodfuehrer, J., Prasad, J. V. N. V., et al. (2004). Implementation of an ADME enabling selection and visualization tool for drug discovery. *Journal of Pharmaceutical Sciences*, 93, 1131.
- Stouch, T. R., Kenyon, J. R., Johnson, S. R., Chen, X. Q., Doweyko, A., & Li, Y. (2003). In silico ADME/Tox: why models fail. *The Journal of Computer-Aided Molecular Design*, 17, 83.
- Tetko, I. V., Bruneau, P., Mewes, H. W., Rohrer, D. C., & Poda, G. I. (2006). Can we estimate the accuracy of ADME-Tox predictions? *Drug Discovery Today*, 11, 700.
- The Foundations of Cost-sensitive Learning. (2001).

- Thomas, C. J., Auld, D. S., Huang, R., Huang, W., Jadhav, A., Johnson, R. L., et al. (2009). The pilot phase of the NIH chemical genomics center. *Current Topics in Medicinal Chemistry*, 9, 1181.
- Todeschini, R., & Consonni, V. (2000). *Handbook of molecular descriptors*. Weinheim: Wiley-VCH.
- Tropsha, A. (2010). Sybyl-X 1.0.
- Tropsha, A. (2005). Application of predictive QSAR models to database mining. In T. Oprea (Eds.), *Cheminformatics in drug discovery* (pp. 437–455). Wiley-VCH.
- Tropsha, A., & Golbraikh, A. (2007). Predictive QSAR modeling workflow, model applicability domains, and virtual screening. *Current Pharmaceutical Design*, 13, 3494.
- Tropsha, A., & Golbraikh, A. (2010). Predictive quantitative structure–activity relationships modeling: Development and validation of QSAR models. In J.-L. Faulon & A. Bender (Eds.), *Handbook of chemoinformatics algorithms*. The Netherlands: Leiden University, Chapman and Hall/CRC.
- Tropsha, A., & Golbraikh, A. (2010). Predictive quantitative structure–activity relationships modeling. *Data Preparation and the General Modeling Workflow*. In J.-L. Faulon & A. Bender (Eds.), *Handbook of chemoinformatics algorithms* (pp. 175–214). The Netherlands: Leiden University, Chapman and Hall/CRC.
- Tropsha, A., & Zheng, W. (2001). Identification of the descriptor pharmacophores using variable selection QSAR: Applications to database mining. *Current Pharmaceutical Design*, 7, 599.
- Valerio, L., Jr. (2008). Tools for evidence-based toxicology: Computational-based strategies as a viable modality for decision support in chemical safety evaluation and risk assessment. *Human & Experimental Toxicology*, 27, 757.
- Valerio, L. G., Jr. (2009). In silico toxicology for the pharmaceutical sciences. *Toxicology and Applied Pharmacology*, 241, 356.
- Vapnik, V. (2000). *Nature of statistical learning theory*. New York: Springer.
- Votano, J. R., Parham, M., Hall, L. H., Kier, L. B., Oloff, S., Tropsha, A., et al. (2004). Three new consensus QSAR models for the prediction of Ames genotoxicity. *Mutagenesis*, 19, 365.
- Waller, C. L. (2004). A comparative QSAR study using CoMFA, HQSAR, and FRED/SKEYS paradigms for estrogen receptor binding affinities of structurally diverse compounds. *The Journal of Chemical Information and Computer Science*, 44, 758.
- Winter-Vann, A. M., & Casey, P. J. (2005). Post-prenylation-processing enzymes as new targets in oncogenesis. *Nature Reviews Cancer*, 5, 405.
- Xia, M., Huang, R., Witt, K. L., Southall, N., Fostel, J., Cho, M. H., et al. (2008). Compound cytotoxicity profiling using quantitative high-throughput screening. *Environmental Health Perspect*, 116, 284.
- Yang, C., Richard, A. M., & Cross, K. P. (2006). The art of data mining the minefields of toxicity databases to link chemistry to biology. *Current Computer-Aided Drug Design*, 2, 135.
- Yang, C., Valerio, L. G., Jr., & Arvidson, K. B. (2009). Computational toxicology approaches at the US food and drug administration. *Alternatives to Laboratory Animals*, 37, 523.
- Yen, S.-J., Lee, Y.-S. (2006). Under-sampling approaches for improving prediction of the minority class in an imbalanced dataset. *Lecture Notes in Control and Information Sciences*, 344, 731.
- Zhang, F. L., & Casey, P. J. (1996). Protein prenylation: Molecular mechanisms and functional consequences. *Annual Review of Biochemistry*, 65, 241.
- Zhang, S., Wei, L., Bastow, K., Zheng, W., Brossi, A., Lee, K. H., et al. (2007). Antitumor agents 252. Application of validated QSAR models to database mining: Discovery of novel tylophorine derivatives as potential anticancer agents. *Journal of Computer-Aided Molecular Design*, 21, 97.
- Zhang, L., Zhu, H., Oprea, T. I., Golbraikh, A., & Tropsha, A. (2008). QSAR modeling of the blood-brain barrier permeability for diverse organic compounds. *Pharmaceutical Research*, 25, 1902.
- Zheng, W., & Tropsha, A. (2000). Novel variable selection quantitative structure–property relationship approach based on the k-nearest-neighbor principle. *The Journal of Chemical Information and Computer Science*, 40, 185.
- Zhou, Z. H., & Liu, X.-Y. (2006). Training cost-sensitive neural networks with methods addressing the class imbalance problem. *IEEE Transactions on Knowledge and Data Engineering*, 18, 63.
- Zhu, H., Rusyn, I., Richard, A. M., & Tropsha, A. (2008). Use of cell viability assay data improves the prediction accuracy of conventional quantitative structure–activity relationship models of animal carcinogenicity. *Environmental Health Perspect*, 116, 506.
- Zhu, H., Tropsha, A., Fourches, D., Varnek, A., Papa, E., Gramatica, P., et al. (2008). Combinatorial QSAR modeling of chemical toxicants tested against tetrahymena pyriformis. *Journal of Chemical Information and Modeling*, 48, 766.
- Zhu, H., Tropsha, A., Fourches, D., Varnek, A., Papa, E., Gramatica, P., et al. (2008). Combinatorial



- QSAR modeling of chemical toxicants tested against *tetrahymena pyriformis*. *The Journal of Chemical Information and Modeling*.
- Zhu, H., Ye, L., Golbraikh, A., & Tropsha, A. (2009). QSAR studies of chemical aquatic acute toxicity using k Nearest Neighbor (kNN) Methodology.
- Zhu, H., Ye, L., Richard, A., Golbraikh, A., Wright, F. A., Rusyn, I., et al. (2009). A novel two-step hierarchical quantitative structure-activity relationship modeling work flow for predicting acute toxicity of chemicals in rodents. *Environmental Health Perspect*, 117, 1257.
- Zupan, J., & Gasteiger, J. (1999). *Neural networks in chemistry and drug design*. Weinheim: Wiley-VCH.
- Zvinavashe, E., Murk, A. J., & Rietjens, I. M. (2008). Promises and pitfalls of quantitative structure-activity relationship approaches for predicting metabolism and toxicity. *Chemical Research in Toxicology*.
- Zvinavashe, E., Murk, A. J., & Rietjens, I. M. (2009). On the number of EINECS compounds that can be covered by (Q)SAR models for acute toxicity. *Toxicology Letters*, 184, 67.

# 38 Quantitative Structure–Activity Relationships of Antimicrobial Compounds

F. P. Maguna<sup>1</sup> · N. B. Okulik<sup>1</sup> · Eduardo A. Castro<sup>2</sup>

<sup>1</sup> Facultad de Agroindustrias, Universidad Nacional del Nordeste, Chaco, Argentina

<sup>2</sup> INIFTA, División Química Teórica, Departamento de Química, Facultad de Ciencias Exactas, UNLP Diag. 113 y 64, La Plata, Buenos Aires, Argentina

<i>Introduction</i> .....	1344
<i>General Overview of Methods Used in QSAR of Antimicrobial Compounds</i> .....	1345
Antimicrobial Activity Determination .....	1345
Quantitative Structure–Activity Relationship (QSAR) .....	1345
Generation of Molecular Descriptors from Structure .....	1346
Selection of Relevant Molecular Descriptors .....	1346
Mapping the Descriptors to Activity .....	1346
Descriptors Used in Antimicrobial Activity Studies .....	1347
<i>QSAR Studies of Antimicrobial Compounds</i> .....	1347
Coumarins .....	1347
Benzamides .....	1348
Cinnamic Acid .....	1349
Flavanones .....	1349
Phenolic Compounds .....	1350
<i>Furan Derivatives</i> .....	1350
<i>mt-QSAR Studies</i> .....	1351
<i>Conclusions</i> .....	1352
<i>References</i> .....	1353

**Abstract:** A thorough antimicrobial review of an increasing number of reports reveals a broad spectrum of research activity in the development practices that are used to treat a variety of diseases. The quantitative relationship between chemical structure and biological activity has received considerable attention in recent years because it allows one to predict theoretically bioactivity without an inordinate amount of experimental time and effort. In this chapter we collect and discuss critically published results concerning the QSAR research on antimicrobial compounds. Finally, we present an updated perspective about the future trends in this area.

## Introduction

---

Antimicrobial drugs are drugs designed to kill, or prevent the growth of microorganisms (bacteria, fungi, and viruses). The development of antimicrobial agents for clinical use has brought unquestionable benefit to individuals and society. Infectious diseases that were formerly often fatal became curable (Lerner 1998). However, antibiotics ultimately have lost their original effectiveness as they have been used over time and resistant strains of bacteria have been developed and there is thus an urgent need to identify novel, active chemotypes as leads for better drug development (Cragg et al. 1997; Hall 2004; Mcdermott et al. 2003).

The versatility of bacterial populations to adapt to environmental toxicity and associated facilities for transferring genetic material show that the antibiotic resistance a biological phenomenon is inevitable and will continue to be a chronic medical condition. The appropriate employment of antimicrobials in use and the continued development of new ones are vital to protect the health of men and animals from pathogens (Mcdermott et al. 2003).

Natural products could play a crucial role in meeting this demand (Cragg and Newman 2001). The use of natural products for the treatment of human diseases is a practice that has been used for a long time. It is estimated that 40% of medicines available for the current treatment of diseases have been developed from natural sources (Cragg and Newman 2001; Shu 1998). The knowledge generated as a result of the use of natural product derivatives of the higher plants, microorganisms, and toxins animals was essential in the discovery of new drugs for modern medical treatment.

In medicine, natural products provide high number of drugs useful in case of complex chemical synthesis and can also serve as basic compound models of synthetic drugs or suitable modifications that reduce its toxicity (Demain 1999).

The quantitative relationship between chemical structure and biological activity has received considerable attention in recent years because it allows one to predict theoretically bioactivity without an inordinate amount of experimental time and demanding efforts.

Computational methods for predicting compounds with specific pharmacodynamic, pharmacokinetic, or toxicological properties are useful for facilitating drug discovery and drug safety evaluation. The quantitative structure-activity relationship (QSAR) and quantitative structure–property relationship (QSPR) methods are the most successfully used statistical learning methods for predicting compounds with specific properties.

More recently, other statistical learning methods such as neural networks and support vector machines have been explored for predicting compounds of higher structural diversity than those covered by QSAR and QSPR approaches. These methods have shown promising potential in a number of studies. Many attempts have been made to elucidate the QSAR of antimicrobials by using different physicochemical parameters.

This chapter is intended to review some of the strategies and current progresses in using statistical learning methods for predicting compounds with specific desired properties in antimicrobial activity.

## General Overview of Methods Used in QSAR of Antimicrobial Compounds

---

### Antimicrobial Activity Determination

---

As microbiological methods incorporate viable test microorganisms, predictability of the outcome is not always clear and subject to many environmental influences that may impact on a given response. Hence, it is of the utmost importance that parameters such as plant collection, validation of laboratory equipment, chemical analysis, and various intricacies of antimicrobial investigations be carefully defined.

Although several methods are used to assess antimicrobial activity, the two most common methods used are disk diffusion and minimum inhibitory concentration (MIC) assays. Generally disk diffusion studies are the method of choice due to their simplicity and capacity to analyze a large number of test samples. Even though disk diffusion methodology is a quick simple means of screening for antimicrobial activity, it is a qualitative assay because it shows if there is antimicrobial activity or not. The MIC measurement to determine antimicrobial activity is a quantitative method based on the principle of contact of a test organism to a series of dilutions of test substance. Assays involving MIC methodology are widely used and an accepted criterion for measuring the susceptibility of organisms to inhibitors (Lambert and Pearson 2000).

### Quantitative Structure–Activity Relationship (QSAR)

---

Quantitative structure–activity relationship (QSAR) analysis is in constant development since the works of Hansch (Hansch and Fujita 1964) in early 1960s. The QSAR methodology focuses on finding a model, which allows one for correlating the activity to structure within a family of compounds. QSAR studies can reduce the costly failures of drug candidates in clinical trials by filtering the combinatorial libraries. Virtual filtering can eliminate compounds with predicted toxic or poor pharmacokinetic properties (Hodgson 2001; van de Waterbeemd and Gifford 2003) early in the pipeline.

Considering activity optimization, building target-specific structure-activity models based on identified hits can guide high throughput screening (HTS), a recent technological improvement in drug discovery pipeline, by rapidly screening the library for most promising candidates (Dudek et al. 2006). Such focused screening can reduce the number of experiments and allows for use of more complex and low throughput assays (Bajorath 2002). Interpretation of created models gives insight into the chemical space in proximity of the hit compound. Feedback loops of high-throughput and virtual screening, resulting in sequential screening approach (Lewis 2005), allow therefore for more rational progress toward high quality lead compounds. Later in the drug discovery pipeline, accurate QSAR models constructed on the basis of the lead series can assist in optimizing the lead (Prado-Prado et al. 2008).

Main stages of a QSAR study can be divided into three groups, i.e., extracting descriptors from molecular structure, choosing those informative in the context of the analyzed activity, and, finally, using the values of the descriptors as independent variables to define a mapping that correlates them with the activity in question (Dudek et al. 2006).

## Generation of Molecular Descriptors from Structure

Compounds are defined by their structure, encoded as a set of atoms and covalent bonds between them. However, the structure cannot be directly used for creating structure-activity mappings because it does not usually contain in an explicit form the information that relates to activity. Molecular descriptors accentuate different chemical properties implicit in the structure of the molecule and so those properties may correlate more directly with the activity. Such properties range from physicochemical and quantum-chemical to geometrical and topological features.

On the other hand, most methods of statistical data analysis employed to predict the activity require as input numerical vectors of features of uniform length for all molecules. Chemical structures of compounds are diverse in size and nature and as such do not fit into this model directly. Molecular descriptors convert the structure to the form of well-defined sets of numerical values.

## Selection of Relevant Molecular Descriptors

Although it is possible to generate hundreds or thousands of different molecular descriptors, only some of them are significantly correlated with the activity. Furthermore, many of the descriptors are intercorrelated. This has negative effects on several aspects of QSAR analysis. Some statistical methods require that the number of compounds is significantly greater than the number of descriptors and using large descriptor sets would require large datasets. Other methods, while capable of handling datasets with large descriptors to compounds ratios, nonetheless suffer from loss of accuracy. Large number of descriptors also affect interpretability of the final model. To tackle these problems, a wide range of methods for automated narrowing of the set of descriptors to the most informative ones is used in QSAR analysis.

## Mapping the Descriptors to Activity

Once the relevant molecular descriptors are computed and selected, the final task of creating a function between their values and the analyzed activity can be carried out. The value quantifying the activity is expressed as a function of the values of the descriptors. The most accurate mapping function from some wide family of functions is usually fitted based on the information available in the training set, i.e., compounds for which the activity is known. A wide range of mapping function families can be used, including linear or nonlinear ones, and many methods for carrying out the training to obtain the optimal function can be employed.

## Descriptors Used in Antimicrobial Activity Studies

The QSAR techniques involve correlating the logarithm of the reciprocal molar concentration of a bioactive compounds required for a specific biological response such as  $ED_{50}$  (dose of a drug that is pharmacologically effective for 50% of the population exposed to the drug or a 50% response in a biological system that is exposed to the drug) or  $LD_{50}$  (Lethal Dose 50%, dose that kills half population tested) values with linear free energy constants such as the Hammett constant  $\sigma$ , a measure of aromatic substituent electronic effects; Taft polar constant  $\sigma^*$ , a measure of substituent polar effects; the logarithm of the 1-octanol/water partition coefficient ( $\log P$ ), a measure of hydrophobic-hydrophilic effects; and the Taft steric constant  $E_s$ , a measure of substituent steric effects, etc.

A very important role may be played by computer aided drug design techniques based on multi-target quantitative structure–activity relationships (mt-QSAR) studies. It means that they are models connecting the structure of drugs with the biological activity against different targets (microbial species in the case of antimicrobial drugs) (Prado-Prado et al. 2008, 2009). This kind of study may also help in a multi objective optimization (MOOP) of desired properties or activity of drugs against different targets; see for instance the recent works carried out by Cruz-Monteagudo in the topic (Cruz-Monteagudo et al. 2008a, b). In principle, up to date there are over 1,500 molecular descriptors that may be generalized and used to solve the former problem (González et al. 2004; Kubinyi 1990; Marrero-Ponce et al. 2005; Todeschini and Consonni 2002).

Many of these indices are known as topological indices (TIs) or simply invariants of a molecular graph, whose vertices are atoms weighed with physicochemical properties (mass, polarity, electro negativity, or charge) (Estrada and Molina 2001).

## QSAR Studies of Antimicrobial Compounds

### Coumarins

As a result of the continuously growing interest for antimicrobial activity of coumarins (Al-Haiza et al. 2003; Althaus et al. 1988; Galm et al. 2004; Hoult and Paya 1996; Kulkarni and Patil 1981, 1983; Laurin et al. 1999; Reusser and Dolak 1986; Rodighiero and Antonello 1958; Vieira et al. 2001), a few coumarin antibiotics became candidates for human and veterinary medicine applications. The most important representative is the 3-aminocoumarin derivative novobiocin, the antibiotic that has been relatively recently approved for medical use in the USA for SA infection treatment (Schmutz et al. 2003). Besides novobiocin, other coumarin derivatives like eskuletin, umbelliferon, and related compounds possess antibacterial properties as well (Heinrich et al. 2004). Antifungal activity has been attributed to some of the coumarin derivatives, including coumarin (1,2-benzopyranone) itself (Mares 1987). Antimicrobial activity of 3-nitrocoumarins and related compounds against *Candida albicans* and *Staphylococcus aureus* has been shown recently (Tisi et al. 2001).

Debeljak et al. (2007) studied 3-nitrocoumarins and related compounds, in order to explore their activity and molecular properties that determine their antimicrobial effects. QSAR models involved most of the 64 descriptors extracted from semiempirical and density functional theory (DFT) founded calculations have been proposed. For the study, literature data containing results

of microbiological activity screening of 33 coumarin derivatives against selected clinical isolates of *Candida albicans* and *Staphylococcus aureus* were selected. Candidate molecules were checked by cross-validated models, and selected derivatives were synthesized. Their antimicrobial activities were compared to antimicrobial activities of the representative derivatives from the original set in terms of minimal inhibitory concentration (MIC). High ranking of descriptors consistent with the degree of hydrolytic instability of selected compounds is common to models of antimicrobial activity against both microorganisms. However, descriptor ranking indicates different antimicrobial mechanisms of action of chosen coumarin derivatives against selected microbial species.

A set of 68 coumarins and coumarin derivatives with already reported antifungal activities was selected and eleven attributes were generated in order to represent a relationship between the physicochemical properties and their biological activities. The descriptors were used to perform artificial neural network (ANN) and to build a model for predicting effectiveness of the new ones. With good correlation between the experimental and the predicted MIC values pertaining to all the coumarins, the study paves the way for further researches about antifungal activity of coumarins, and offers a powerful tool in modeling and prediction of their bioactivities (Soltani et al. 2009).

A series of new coumarin derivatives has been synthesized and the in vitro antimicrobial activity against thirteen strains of bacteria and three fungal/yeast strains were screened. They were shown to possess a wide range of activities from almost completely inactive compounds to medium active ones (Dekić et al. 2010).

## Benzamides

---

Benzamides are an important class of compounds that show various types of biological activities (Itaru et al. 1973; Mrozik et al. 1969). Oxyclozanide was reported as an antihelmintic agent effective against *Fasciola hepatica* for the treatment of liver fluke infection (Mrozik et al. 1969). The synthesis of some *N*-(*o*-hydroxyphenyl) benzamides and phenylacetamides as possible metabolites of antimicrobial active benzoxazoles has been reported (Sener et al. 2000).

A series of substituted benzamides were synthesized by (Kumar et al. 2007). The synthesized compounds were evaluated for in vitro antibacterial activity against Gram-positive *Staphylococcus aureus*, *Bacillus subtilis* and Gram-negative *Escherichia coli*, and in vitro antifungal activity against *Aspergillus ficcum* and *Aspergillus parasiticus*. In antibacterial assay minimum inhibitory concentrations (MIC) were determined, and the antifungal activity against the fungal species was determined by serial dilution method. The structural characteristics governing antibacterial activities of substituted benzamides were studied using QSAR methodology. The results obtained indicate that the benzamides are effective against the microbial species tested, and that the *N*-(2-hydroxyphenyl)-3-methoxy-2-nitrobenzamide and *N*-(2-hydroxy-6-carbomethoxyphenyl)-2-benzoyloxybenzamide are the most effective ones. A general trend showed that the presence of electron-withdrawing groups (NO<sub>2</sub>, Cl) leads to an increase in the activity in comparison to the presence of electron releasing group. The results showed that the antimicrobial activity could be modeled using the topological descriptors, molecular connectivity indices (<sup>2</sup>χ<sup>v</sup> and <sup>2</sup>χ), and Kiers shape index (κ<sub>α1</sub>). The low residual activity and high cross-validated *r*<sup>2</sup> values (*r*<sub>cv</sub><sup>2</sup>) observed indicated the predictive ability of the developed QSAR models.

## Cinnamic Acid

---

Cinnamic acid plays an important role for the antimicrobial activity (Ahluwalia et al. 1986; Christine et al. 1984; Cremllyn et al. 1984, 1986). Derivatives of cinnamic acid, displaying a broad spectrum of biological activity and low toxicity, are of interest for the purposes of creating new effective drugs based on them (Simonyan 1993). There are several studies on cinnamic acid derivatives with antibacterial and antifungal activity (Ahmed et al. 1995; Lee and Ahn 1998; Ovale et al. 1996; Ramanan and Rao 1987; Srivastava et al. 1999; Tawata et al. 1996). Potential antimicrobial activity of sorbic, cinnamic, and ricinoleic acid derivatives was reported some time ago (Narasimhan et al. 2003). The synthesis and the correlation between physicochemical properties and biological activity were carried out. Later, the evaluation of the in vitro antimicrobial activity of over 30 compounds belonging to a series of esters, substituted derivatives, and amides of cinnamic acid was performed by Narasimhan et al. and the investigation of the relationship between their physicochemical properties and microbiological effects have been widely discussed (Narasimhan et al. 2004). Quantitative structure–activity relationship investigation with multiple linear regression analysis was applied to find a correlation between different calculated physicochemical parameters of the compounds and biological activity. All the compounds showed a good antibacterial activity against Gram-negative *Escherichia coli* than Gram-positive *Staphylococcus aureus* and *Bacillus subtilis*. The chemical structure of each compound was described by three groups of parameters: steric, electronic and hydrophobic which were selected due to their encouraging effect in describing antimicrobial activity (Narasimhan et al. 2003). The quantitative models relating the structural features of cinnamic acid derivatives and their antimicrobial activity showed that Gram-negative *Escherichia coli* and *Candida albicans* (fungus) were the most sensitive microorganisms. The regression equations obtained for the bacterial species showed the importance of constitutional parameter unsaturation index ( $U_i$ ), global topological charge index (JGT), and the lipophilic parameter  $\log P$  in contribution to antibacterial activity.

## Flavanones

---

Among the drugs approved between 1983 and 1994 by either the United States Food and Drug Administration (FDA) or comparable entities in other countries, drugs of natural origin predominated (78%) in the area of antibacterials (Cragg and Newman 2001). A large number of homoisoflavanones have been isolated from several hyacinthaceous genera including *Eucomis* L'Hér., *Merwillia* Speta, *Ledebouria* Roth, *Veltheimia* Gled. and *Drimiopsis* Lindl. and Paxton (Pohl et al. 2000). Homoisoflavanones belong to a small homogeneous group of naturally occurring oxygen heterocycles which, within the *Hyacinthaceae*, are largely but not exclusively restricted to the subfamily *Hyacinthoideae*. The few reports on the biological activity of homoisoflavanones describe anti-inflammatory, antibacterial, antihistaminic, antimutagenic, and angioprotective properties, and potent phosphodiesterase inhibition (Amschler et al. 1996; Della Loggia et al. 1989; Heller and Tamm 1981).

Du Toit et al. (2007) determined the antibacterial activity of thirteen homoisoflavanones isolated from six Hyacinthaceae species against *Staphylococcus aureus*. They also developed a set of physicochemical parameters that would describe antibacterial activity for these and future compounds. Stepwise multiple linear regression analysis of the data yielded a statistically significant two-component model ( $R^2 = 0.81$ ,  $p < 0.003$ ).



## Phenolic Compounds

---

Natural and synthetic phenolic compounds were evaluated against oral bacteria. Thus, many antimicrobial agents have been developed for the inhibition of halitosis bacteria and thus for the treatment of oral malodor (Giertsen 2004; Greenstein et al. 1997; Hayashi et al. 2007; Loesche 1979). Antibacterial compounds such as chlorhexidine, cetylpyridinium chloride, triclosan, and chlorine dioxide have been tested either alone or in different combinations. However, most compounds have been known to induce undesired side effects (Rule et al. 2005).

Greenberg et al. performed a systematic evaluation of various phenolic compounds to develop a quantitative structure-active relationship (QSAR) (Greenberg et al. 2007). They observed that a number of phenolic compounds in natural botanic extracts and flavors demonstrated antimicrobial activity. Among them, eugenol, magnolol, honokiol, thymol, and xanthorrhizol showed strong activity against oral bacteria. Magnolia bark extract, a traditional Chinese medicine isolated from the stem bark of *Magnolia officinalis*, consists primarily of magnolol and honokiol, the two phenolic isomers, and has a strong germ-kill activity against oral bacteria.

In the QSAR approach applied for a range of about 20 phenolic compounds the lipophilicity and steric effects were found to be two key factors in determining germ-kill activity (Greenberg et al. 2008). The optimum lipophilicity, measured by the logarithm of the octanol/water partition coefficient, or log *P*, was found to be 5.5 for *Fusobacterium nucleatum*, a Gram-negative type of oral bacteria that causes bad breath. The optimum log *P* was found to be 7.9 for *Streptococcus mutans*, a Gram-positive type of oral bacteria that causes tooth decay.

The steric effect of substituents ortho to the phenolic group was found to be critical in reducing antibacterial activity despite having increased lipid solubility approaching the optimum lipophilicity value. The antibacterial activity of phenolic compounds is likely exerted by multiple functions, primarily comes from its capability to act as a nonionic surface-active agent therefore disrupting the lipid–protein interface.

## Furan Derivatives

---

Furan derivatives, both obtained from synthetic and natural sources, have much interest due to the wide range of pharmaceutical applications they have shown (Hofnung et al. 2002; Khan et al. 2005; Kupchan et al. 1971; Shevchenko 1999). A series of synthetic nitrofuranyl amides showed good in vitro inhibitory activity against *Mycobacterium tuberculosis* (Tangallapally et al. 2006; Tomlin 1994) especially 5-nitro-furan-2-carboxylic acid *N*-[4-(4-benzylpiperazin-1-yl)-benzyl]-5-nitrofuran-2-carboxamide and 2-methyl-*N*-phenylfuran-3-carboxamide.

Preparation of furan-3-carboxylic acid and derivatives and their assessment against a panel of microorganisms including yeast-like fungi, bacteria, and algae were reported (Zanatta et al. 2004). Because some of the furan-3-carboxamides exhibited significant in vitro antimicrobial activity, the synthesis and characterization of an extended and planned series of new furan-3-carboxamides was carried out (Zanatta et al. 2007). The obtained furan-3-carboxamides were assessed against a panel of microorganisms including yeast, filamentous fungi, bacteria, and algae. Preliminary antimicrobial activity assays of some of the furan-3-carboxamides exhibited significant in vitro antimicrobial activity. QSAR investigation was applied to find

a correlation between the different physicochemical parameters of the compounds studied and their biological activity. Yeasts showed a negative correlation with the indicator variables  $I_R$ , but *Saccharomyces cerevisiae* showed a better correlation with the steric and polarity descriptors, Gram-positive and Gram-negative bacteria correlate with the increase of the steric volume and the polarizability parameter and negatively correlated with hardness, and filamentous fungi correlate with the increase of the steric volume and the polarity of groups.

An interesting QSAR study of diacyl-hydrazine derivatives containing furan rings was conducted and compared with the DFT method and AM1-MOPAC method (Zhang et al. 2010). The DFT-optimized conformations and ESP-fitting charges of the target compounds were also used for 3D-QSAR analysis, including CoMFA and CoMSIA. The QSAR results were consistent with the 3D-QSAR results, indicating that the electrostatic and hydrophobic properties of the target compounds were significant to the biological activity.

## mt-QSAR Studies

---

One limitation of almost QSAR models is that they predict the biological activity of drugs against only one species of fungi, virus, bacteria or parasite species. Consequently, the development of multitasking QSAR models (mt-QSAR) to predict drugs activity against different species of antimicrobial agents is of vital importance. These mt-QSARs offer also a good opportunity to construct drug–drug Complex Networks (CNs) that can be used to explore large and complex drug-viral species databases. In very large CNs it is possible to use the Giant Component (GC) as a representative sub-set of nodes (drugs) and but the drug–drug similarity function selected may strongly determines the final network obtained. Several mt-QSAR models were reported to predict the antimicrobial activity against different fungi (González-Díaz et al. 2006), bacteria (Prado-Prado et al. 2007), parasite (Prado-Prado et al. 2008), and virus species (Prado-Prado et al. 2009) and to calculate the parameters for RNAs of both parasites and hosts (González-Díaz et al. 2011).

For example, the most important limitation of antifungal QSAR models is that they predict the biological activity of drugs against only one fungal species due the fact that most of the up-to-date reported molecular descriptors encode only information about the molecular structure. Prado-Prado et al. calculated, within a unifying framework, the probabilities of antifungal action of drugs against many different species based on spectral moment's analysis (Prado-Prado et al. 2009). They calculated new multi-target spectral moments to fit a QSAR model that predicts the antifungal activity of more than 280 drugs against 90 fungi species. Linear discriminant analysis was used to classify drugs into two classes as active or non-active against the different tested fungal species. Moreover, it was developed one single unified equation explaining the antifungal activity of structurally heterogeneous series of compounds against as many fungus species as possible (González-Díaz and Prado-Prado 2008; González-Díaz et al. 2006).

In fact, other mt-QSAR approaches, with demonstrated usefulness, have been introduced recently in medicinal chemistry (González-Díaz et al. 2006; Marrero-Ponce et al. 2004; Molina et al. 2004). A Markov Model encoding molecular backbones information was introduced in the method named the MARCH-INSIDE, MARKovian CHEmicals IN Silico DEsign (González-Díaz et al.). This method allows one to introduce matrix invariants such as stochastic entropies,

potentials, and spectral moments for the study of molecular properties (González-Díaz et al. 2005; Ramos de Armas et al. 2004) and they have been largely used for small molecule mt-QSAR problems including the design of flucicidal, anticancer, and antihypertensive drugs (Prado-Prado et al. 2007). Applications to macromolecules have been restricted to the field of RNA without applications to proteins (González-Díaz and Uriarte 2005; González-Díaz et al. 2003, 2007; Saiz-Urra et al. 2005).

The QSAR models based on different MARCH-INSIDE indices may be very useful to optimize important aspects such as activity, toxicity, or pharmacokinetics using one single model in many bioorganic and medicinal chemistry problems such as estimation of anticoccidial activity, modeling the interaction between drugs and HIV-packaging-region RNA, and predicting proteins and virus activity (González-Díaz et al. 2004, 2006). In recent studies, the MARCH-INSIDE method has been extended to encompass molecular environment, interesting information in addition to molecular structure data (Cruz-Monteaugudo et al. 2007).

Multiple applications of MARCH-INSIDE to classic QSAR, macromolecular QSAR, and specially mt-QSAR were discussed (González-Díaz et al. 2007, 2008a, b; Mahiwal et al. 2010).

Finally, with the mt-QSAR methodology it is possible to predict the biological activity of drugs in more general situations than with the traditional QSAR models, whose greatest limitation is predicting the biological activity of drugs against only one microbial species. Then, this methodology improves models and allows one to predict biological activity of many organic compounds against a very large diversity of pathogens microorganisms.

## Conclusions

---

During the last decade an increasing number of reports describe the antimicrobial activity of several compounds. A review of the literature reveals the existence of a broad-spectrum of research activity in the development practices that are used to treat a variety of diseases and significant current progresses in using statistical learning methods for predicting compounds of specific property in antimicrobial activity.

The quantitative relationship between chemical structure and biological activity allows one to predict theoretically bioactivity without resorting to an inordinate amount of time and effort making the experimental determinations. Many attempts have been performed to elucidate the QSAR of antimicrobials by using different physicochemical parameters.

In this review we have discussed published results concerning the QSAR research on antimicrobial properties of synthetic and natural compounds. Antifungal and antimicrobial activity of some coumarin derivatives, various types of biological activities of benzamides, several studies on cinnamic acid derivatives with antibacterial and antifungal activity, reports on the biological activity of homoisoflavanones and phenolic compounds, as well as pharmaceutical applications of furan derivatives have been shown.

The actual capabilities of multitasking QSAR methodology and mt-QSAR models to predict drugs activity against different species of antimicrobial agents have also been revised.

It was been demonstrated that with the mt-QSAR methodology it is possible to predict the biological activity of drugs in more general situations than with the traditional QSAR models, predicting biological activity of many organic compounds against a very large diversity of pathogens microorganisms.

## References

- Ahluwalia, V. K., Kaila, N., & Bala, S. (1986). *Indian Journal of Chemistry Section-B*, 25, 663.
- Ahmed, S. P., Ahmad, M., Kazmi, S. U., Shahid, M., & Ahmed, S. I. (1995). Studies on the antibacterial and HPFC activity of a phenylpropanoid glycoside. *Pakistan Journal of Pharmacology*, 12(2), 31.
- Al-Haiza, M. A., Mostafa, M. S., & El-Kady, M. Y. (2003). Synthesis and biological evaluation of some new coumarin derivatives. *Molecules*, 8, 275.
- Althaus, I. W., Dolak, L., & Reusser, F. (1988). Coumarins as inhibitors of bacterial DNA Gyrase. *The Journal of Antibiotics*, 41, 373.
- Amschler, G., Frahm, A. W., Hatzelmann, A., Kilian, U., Muller-Doblies, D., & Muller-Doblies, U. (1996). Spirocyclic nortriterpenes from the bulbs of *Veltheimia viridifolia*. *Planta Medica*, 62, 534.
- Bajorath, J. (2002). Integration of virtual and high-throughput screening. *Nature Reviews Drug Discovery*, 1, 882.
- Christine, S. V., Rohan, K. G., & Ian, B. R. (1984). The effect of food preservatives on pH homeostasis in *Escherichia coli*. *Journal of General Microbiology*, 130, 2845.
- Cragg, G. M., & Newman, D. J. (2001). Natural product drug discovery in the next millennium. *Pharmaceutical Biology*, 39, 8.
- Cragg, G. M., Newman, D. J., & Snader, K. M. (1997). Natural products in drug discovery and development. *Journal of Natural Products*, 60, 52.
- Cremlyn, R. J., Thandi, K., & Wilson, R. (1984). *Indian Journal of Chemistry Section-B*, 23, 94.
- Cremlyn, R. J., Obioran, O., & Singh, G. (1986). *Indian Journal of Chemistry Section-B*, 25, 559.
- Cruz-Monteaugudo, M., González-Díaz, H., Agüero-Chapin, G., Santana, L., Borges, F., Domínguez, R. E., Podda, G., & Uriarte E. (2007). Computational chemistry development of a unified free energy Markov model for the distribution of 1,300 chemicals to 38 different environmental or biological systems. *Journal of Computational Chemistry*, 28, 1909.
- Cruz-Monteaugudo, M., Borges, F., Cordeiro, M. N., Cagide Fajin, J. L., Morell, C., & Ruiz, R. M. (2008a). Desirability-based methods of multiobjective optimization and ranking for global QSAR studies. Filtering safe and potent drug candidates from combinatorial libraries. *Journal of Combinatorial Chemistry*, 10, 897.
- Cruz-Monteaugudo, M., Borges, F., & Cordeiro, M. N. (2008b). Desirability-based multiobjective optimization for global QSAR studies: application to the design of novel NSAIDs with improved analgesic, antiinflammatory, and ulcerogenic profiles. *Journal of Computational Chemistry*, 29, 2445.
- Debeljak, Ž., Šykrbo, A., Jasprica, I., Mornar, A., Plecko, V., Banjanac, M., & Medic-Šarić, M. (2007). QSAR study of antimicrobial activity of some 3-Nitrocoumarins and related compounds. *Journal of Chemical Information and Modeling*, 7, 918.
- Dekić, B., Dekić, V., Radulović, N., Vukićević, R., & Palić, R. (2010). Synthesis of new antimicrobial 4-aminosubstituted 3-nitrocoumarins. *Chemical Papers*, 64(3), 354–359.
- Della Loggia, R., Del Negro, P., Tubaro, A., Barone, G., & Parrilli, M. (1989). Homoisoflavonones as anti-inflammatory principles. *Planta Medica*, 55, 587.
- Demain, A. L. (1999). Metabolites, primary and secondary. In M. C. Flickinger & S. C. Drew (Eds.), *Encyclopedia of bioprocess technology: Fermentation*. New York: Wiley.
- Du Toit, K., Elgorashi, E. E., Malan, S. F., Mulholland, D. A., Drewes, S. E., & Van Staden, J. (2007). Antibacterial activity and QSAR of homoisoflavonones isolated from six *Hyacinthaceae* species. *South African Journal of Botany*, 73, 236.
- Dudek, A. Z., Arodzb, T., & Gálvez, J. (2006). Computational methods in developing quantitative structure-activity relationships (QSAR): a review. *Combinatorial Chemistry & High Throughput Screening*, 9, 213.
- Estrada, E., & Molina, E. (2001). 3D connectivity indices in QSPR/QSAR studies. *Journal of Chemical Information and Computer sciences*, 41, 791.
- Galm, U., Dessoy, M. A., Schmidt, J., Wessjohann, L. A., & Heide, L. (2004). In vitro and in vivo production of new aminocoumarins by a combined biochemical, genetic and synthetic approach. *Chemistry & Biology*, 11, 173.
- Giersten, E. (2004). Effects of mouthrinses with triclosan, zinc ions, copolymer, and sodium lauryl sulphate combined with fluoride on acid formation by dental plaque in vivo. *Caries Research*, 38, 430.
- González-Díaz, H., & Prado-Prado, F. (2008). Unified QSAR and network-based computational chemistry approach to antimicrobials, part I: multispecies activity models for antifungals. *Journal of Computational Chemistry*, 29, 656.
- González-Díaz, H., & Uriarte, E. (2005). Proteins QSAR with Markov average electrostatic potentials. *Bioorganic & Medicinal Chemistry Letters*, 15, 5088.

- González-Díaz, H., Gia, O., Uriarte, E., Hernández, I., Ramos, R., & Chaviano, M. (2003). Markovian chemicals “in silico” design (MARCH-INSIDE), a promising approach for computer-aided molecular design I: discovery of anticancer compounds. *Journal of Molecular Modeling*, 9, 395.
- González-Díaz, H., Molina, R., & Uriarte, E. (2004). Markov entropy backbone electrostatic descriptors for predicting proteins biological activity. *Bioorganic & Medicinal Chemistry Letters*, 14, 4691.
- González-Díaz, H., Molina-Ruiz, V., & Hernández, I. (2007). MARCH-INSIDE v3.0 (MARKOV CHAINS INVARIANTS FOR SIMULATION & DESIGN). Cuba.
- González, M. P., Morales, A. H., & González-Díaz, H. (2004). A TOPS-MODE approach to predict permeability coefficients. *Polymer*, 45, 2073.
- González-Díaz, H., Aguero, G., Cabrera, M. A., Molina, R., Santana, L., Uriarte, E., Delogo, G., & Castañedo, N. (2005). Unified Markov thermodynamics based on stochastic forms to classify drugs considering molecular structure, partition system, and biological species: distribution of the antimicrobial G1 on rat tissues. *Bioorganic & Medicinal Chemistry Letters*, 15, 551.
- González-Díaz, H., Perez-Bello, A., Uriarte, E., & González-Díaz, Y. (2006). QSAR study for mycobacterial promoters with low sequence homology. *Bioorganic & Medicinal Chemistry Letters*, 16, 547.
- González-Díaz, H., Prado-Prado, F. J., Santana, L., & Uriarte, E. (2006). Unify QSAR approach to antimicrobials. Part I: predicting antifungal activity against different species. *Bioorganic & Medicinal Chemistry*, 14, 5973.
- González-Díaz, H., Sanchez-Gonzalez, A., & González-Díaz, Y. (2006). 3D-QSAR study for DNA cleavage proteins with a potential antitumor ATCUN-like motif. *Journal of Inorganic Biochemistry*, 100, 1290.
- González-Díaz, H., Saiz-Urra, L., Molina, R., Santana, L., & Uriarte, E. (2007). A model for the recognition of protein kinases based on the entropy of 3D van der Waals interactions. *Journal of Proteome Research*, 6, 904.
- González-Díaz, H., Vilar, S., Santana, L., & Uriarte, E. (2007). Medicinal chemistry and bioinformatics—current trends in drugs discovery with networks topological indices. *Current Topics in Medicinal Chemistry*, 7, 1015.
- González-Díaz, H., González-Díaz, Y., Santana, L., Ubeira, F. M., & Uriarte, E. (2008a). Proteomics, networks and connectivity indices. *Proteomics*, 8, 750.
- González-Díaz, H., Prado-Prado, F., Ubeira, F. M. (2008b). Predicting antimicrobial drugs and targets with the MARCH-INSIDE approach. *Current Topics in Medicinal Chemistry*, 8, 1676.
- González-Díaz, H., Vilar, S., & Pérez-Montoto, L. G. (2011). 6. Predicting parasite-host networks with Markov Entropy measures for secondary structures of RNA phylogenetic biomarkers. In H. González-Díaz, F. J. Prado-Prado, & X. García-Mera, (Eds.), *Complex network entropy: from molecules to biology, parasitology, technology, social, legal, and neurosciences*. Kerala, India: Transworld Research Network.
- Greenberg, M., Urnezis, P., & Tian, M. (2007). Compressed mints and chewing gum containing magnolia bark are effective against bacteria that are response for oral malodor. *Journal of Agricultural and Food Chemistry*, 55, 9465.
- Greenberg, M., Dodds, M., & Tian, M. (2008). Naturally occurring phenolic antibacterial compounds show effectiveness against oral bacteria by a quantitative structure-activity relationship study. *Journal of Agricultural and Food Chemistry*, 56, 11151.
- Greenstein, R. B.-N., Goldberg, S., Marku-Cohen, S., Sterer, N., & Rosenberg, M. (1997). Reduction of oral malodor by oxidizing lozenges. *Journal of Periodontology*, 68, 1176.
- Hall, B. G. (2004). Predicting the evolution of antibiotic resistance genes. *Nature Reviews Microbiology*, 2, 430.
- Hansch, C., & Fujita, T. (1964).  $\rho$ - $\sigma$ - $\pi$  analysis. A method for the correlation of biological activity and chemical structure. *Journal of the American Chemical Society*, 86, 1616.
- Hayashi, Y., Ohara, N., Ganno, T., Yamaguchi, K., Ishizaki, T., Nakamura, T., & Sato, M. (2007). Chewing chitosan-containing gum effectively inhibits the growth of cariogenic bacteria. *Archives of Oral Biology*, 52, 290.
- Heinrich, M., Barnes, J., Gibbons, S., & Williamson, E. M. (2004). *Fundamentals of pharmacognosy and phytotherapy*. Edinburgh: Churchill Livingstone.
- Heller, W., & Tamm, C. (1981). Homoisoflavanones and biogenetically related compounds. *Fortschritte der Chemie Organischer Naturstoffe*, 40, 106.
- Hodgson, J. (2001). ADMET-turning chemicals into drugs. *Nature Biotechnology*, 19, 722.
- Hofnung, M., Quillardet, V. M., & Touati, E. (2002). Genotoxicity of 2-nitro-7-methoxynaphtho[2,1-b]furan (R7000): a case study with some considerations on nitrofurantoin and nifuroxazide. *Research in Microbiology*, 153, 427.

- Hoult, J. R. S., & Paya, M. (1996). Pharmacological and biochemical actions of simple coumarins: natural products with therapeutic potential. *General Pharmacology*, 27, 713.
- Itaru, S., Seizo, M., & Takashi, K. (1973). Japan Patent, 73, 37, p. 819.
- Khan, M. W., Alam, M. J., Rashid, M. A., & Chowdhury, R. (2005). A new structural alternative in benzo[b]furans for antimicrobial activity. *Bioorganic & Medicinal Chemistry*, 13, 4796, and references therein.
- Kubinyi, H. J. (1990). Quantitative structure-activity relationships (QSAR) and molecular modeling in cancer research. *Journal of Cancer Research and Clinical Oncology*, 116, 529.
- Kulkarni, M. V., & Patil, V. D. (1981). Studies on coumarins I. *Archives of Pharmacology*, 314, 708.
- Kulkarni, M. V., & Patil, V. D. (1983). Studies on coumarins II. *Archives of Pharmacology*, 316, 15.
- Kumar, A., Narasimhan, B., & Kumar, D. (2007). Synthesis, antimicrobial, and QSAR studies of substituted benzamides. *Bioorganic & Medicinal Chemistry*, 15, 4113.
- Kupchan, S. M., Eakin, M. A., & Thomas, A. M. (1971). Tumor inhibitors. 69. Structure-cytotoxicity relationships among the sesquiterpene lactones. *The Journal of Medicinal Chemistry*, 111, 1147.
- Lambert, R. J. W., & Pearson, J. (2000). Susceptibility testing: accurate and reproducible minimum inhibitory concentration (MIC) and non-inhibitory concentration (NIC) values. *Journal of Applied Microbiology*, 88, 784.
- Laurin, P., Ferroud, D., Klich, M., Dupuis-Hamelin, C., Mauvais, P., Lassaingne, P., Bonnefoy, A., & Musicki, B. (1999). Synthesis and *In Vitro* evaluation of novel highly potent coumarin inhibitors of Gyrase B. *Bioorganic & Medicinal Chemistry Letters*, 9, 2079.
- Lee, H. S., & Ahn, Y. J. (1998). Growth-inhibiting effects of *Cinnamomum cassia* bark-derived materials on human intestinal bacteria. *Journal of Agricultural and Food Chemistry*, 46, 8.
- Lerner, S. A. (1998). Clinical impact of antibiotic resistance. In B. P. Rosen & S. Mobashery (Eds.), *Resolving the antibiotic paradox. Progress in understanding drug resistance and development of new antibiotics*. New York: Plenum Publishers.
- Lewis, R. A. (2005). A general method for exploiting QSAR models in lead optimization. *Journal of Medicinal Chemistry*, 48, 1638.
- Loesche, W. (1979). Clinical and microbiological aspects of chemotherapeutic agents used according to specific plaque hypothesis. *Journal of Dental Research*, 58, 2404.
- Mahiwal, K., Kumar, P., & Narasimhan, B. (2010). Synthesis, antimicrobial evaluation, ot-QSAR and mt-QSAR studies of 2-amino benzoic acid derivatives. *Medicinal Chemistry Research*, 1 <https://springerlink3.metapress.com/content/v8rr537t3g832716/resource-secured/?target=fulltext.pdf&sid=hgvns0moaos2mq3vea5ali2b&sh=www.springerlink.com>
- Mares, D. (1987). Antimicrobial activity of protoanemonin, a lactone from Ranunculaceae Plants. *Mycopathologia*, 98, 133.
- Marrero-Ponce, Y., Díaz, H. G., Zaldívar, F., Torrens, V. R., & Castro, E. A. (2004). 3D-Chiral quadratic indices of the 'molecular pseudograph's atom adjacency matrix' and their application to central chirality codification: classification of ACE inhibitors and prediction of  $\sigma$ -receptor antagonist activities. *Bioorganic & Medicinal Chemistry*, 12, 5331.
- Marrero-Ponce, Y., Marrero, R. M., Torrens, F., Martínez, Y., Bernal, M. G., & Zaldívar, V. R. (2005). Non-stochastic and stochastic linear indices of the molecular pseudograph's atom-adjacency matrix: a novel approach for computational in silico screening and "rational" selection of new lead antibacterial agents. *Journal of Molecular Modeling (Online)*, 1. 12(3), 255–271.
- Mcdermott, P. F., Walker, R. D., & White, D. G. (2003). Antimicrobials: modes of action and mechanisms of resistance. *International Journal of Toxicology*, 22(2), 135.
- Molina, E., González-Díaz, H., González, M. P., Rodríguez, E., & Uriarte, E. (2004). Designing antibacterial compounds through a topological substructural approach. *Journal of Chemical Information and Computer Science*, 44, 515.
- Mrozik, H., Jones, H., Frieddman, J., Schwartzkopf, G., Schardt, R. A., Patchett, A. A., Hoff, D. R., Yaktis, J. J., Riek, R. F., Ostlind, D. A., Plishker, G. A., Butler, R. W., Cuckler, A. C., & Campbell, W. C. (1969). A new agent for the treatment of liver fluke infection (fascioliasis). *Experientia*, 25, 883.
- Narasimhan, B., Belsare, D., Pharande, D., Mourya, V., & Dhake, A. (2004). Esters, amides and substituted derivatives of cinnamic acid: synthesis, antimicrobial activity and QSAR investigations. *European Journal of Medicinal Chemistry*, 39, 827.
- Narasimhan, B., Kothawade, U. R., Pharande, D. S., Mourya, V. K., & Dhake, A. S. (2003). Syntheses and QSAR studies of sorbic, cinnamic and ricinoleic acid derivatives as potential antibacterial agents. *Indian Journal of Chemistry*, 42(B), 2828.
- Ovale, J. M., Landman, D., Zaman, M. M., Burney, S., & Sathe, S. S. (1996). In vitro activity of



- Cinnamomum zeylanicum. *American Journal of Chinese Medicine*, 24, 103.
- Pohl, T. S., Crouch, N. R., & Mulholland, D. A. (2000). Southern African Hyacinthaceae: chemistry, bioactivity and ethnobotany. *Current Organic Chemistry*, 4, 1287.
- Prado-Prado, F. J., González-Díaz, H., Santana, L., & Uriarte E. (2007). Unified QSAR approach to antimicrobials. Part 2: predicting activity against more than 90 different species in order to halt antibacterial resistance. *Bioorganic & Medicinal Chemistry*, 15, 897.
- Prado-Prado, F. J., González-Díaz, H., de la Vega, O. M., Ubeira, F. M., & Chou, K. C. (2008). Unified QSAR approach to antimicrobials. Part 3: first multi-tasking QSAR model for input-coded prediction, structural back-projection, and complex networks clustering of antiprotozoal compounds. *Bioorganic & Medicinal Chemistry*, 16, 5871.
- Prado-Prado, F. J., Borges, F., Perez-Montoto, L. G., & González-Díaz, H. (2009). Multi-target spectral moment: QSAR for antifungal drugs vs. different fungi species. *European Journal of Medicinal Chemistry*, 44, 4051.
- Prado-Prado, F. J., de la Vega, O. M., Uriarte, E., Ubeira, F. M., Chou, K.C., & González-Díaz, H. (2009). Unified QSAR approach to antimicrobials. 4. Multi-target QSAR modeling and comparative multi-distance study of the giant components of antiviral drug-drug complex networks. *Bioorganic & Medicinal Chemistry*, 17, 569.
- Ramanan, P. N., & Rao, M. N. (1987). Antimicrobial activity of cinnamic acid derivatives. *Indian Journal of Experimental Biology*, 25, 42.
- Ramos de Armas, R., González-Díaz, H., Molina, R., Pérez González, M., Uriarte, E. (2004). Stochastic-based descriptors studying peptides biological properties: modeling the bitter tasting threshold of dipeptides. *Bioorganic & Medicinal Chemistry*, 12, 4815.
- Reusser, F., & Dolak, L. A. (1986). Novenamamine is the active moiety in novobiocine. *The Journal of Antibiotics*, 39, 272.
- Rodighiero, G., & Antonello, C. (1958). Sintesi di Alcuni Derivati 3-Ammino Cumarinici e Prime Notizie Sulle Loro Proprieta' Antibatteriche. *Bollettino Chimico Farmaceutico*, 97, 592.
- Rule, K. L., Ebbett, V. R., & Vikes, P. J. (2005). Formation of chloroform and chlorinated organics by free-chlorine-mediated oxidation of triclosan. *Environmental Science and Technology*, 39, 3176.
- Saiz-Urra, L., González-Díaz, H., & Uriarte, E. (2005). Proteins Markovian 3D-QSAR with spherically-truncated average electrostatic potentials. *Bioorganic & Medicinal Chemistry*, 13, 3641.
- Schmutz, E., Mühlenweg, A., Li, S., & Heide, L. (2003). Resistance genes of aminocoumarin producers: two type II topoisomerase genes confer resistance against coumermycin A1 and clorobiocin. *Antimicrobial Agents and Chemotherapy*, 47, 869.
- Sener, E. A., Bingol, K. K., Oren, I., Arpaci, O. T., Yalcin, I., & Altanlar, N. (2000). Synthesis and microbiological activity of some *N*-(*o*-hydroxyphenyl)benzamides and phenylacetamides as the possible metabolites of antimicrobial active benzoxazoles: part II. *Il Farmaco*, 55, 469.
- Shevchenko, N. E. (1999). Synthesis of 3-substituted furylethylamines. *Chemistry of Heterocyclic Compounds*, 35, 164.
- Shu, Y. Z. (1998). Recent natural products based drug development: a pharmaceutical industry perspective. *Journal of Natural Products*, 61, 1053.
- Simonyan, A. V. (1993). Activity of cinnamic acid derivatives and new methods for their synthesis (review). *Pharmaceutical Chemistry Journal*, 27(2), 92.
- Soltani, S., Dianat, S., & Sardari, S. (2009). Forward modeling of the coumarin antifungals; SPR/SAR based perspective avicenna. *Journal of Medical Biotechnology*, 1(2), 95.
- Srivastava, A., Shukla, Y. N., & Kumar, S. (1999). Phytotoxic and antimicrobial constituents of *Argyrea speciosa* and *Oenothera biennis*. *Journal of Ethnopharmacology*, 67, 241.
- Tangallapally, R. P., Lee, R. E. B., Lenaerts, A. J. M., & Lee, R. E. (2006). Synthesis of new and potent analogues of anti-tuberculosis agent 5-nitro-furan-2-carboxylic acid 4-(4-benzyl-piperazin-1-yl)-benzylamide with improved bioavailability. *Bioorganic & Medicinal Chemistry Letters*, 16, 2584.
- Tawata, S., Taira, S., Kobamoto, N., Zhu, J., Ishihara, M., & Toyama, S. (1996). Synthesis and antifungal activity of cinnamic and esters. *Bioscience Biotechnology & Biochemistry*, 60, 909.
- Tisi, R., Cocchetti, P., Banfi, S., & Martegani, E. (2001). 3-Nitrocoumarin is an efficient inhibitor of budding yeast phospholipase-C. *Cell Biochemistry and Function*, 19, 229.
- Todeschini, R., & Consonni, V. (2002). *Handbook of molecular descriptors*. Bicocca: Wiley-VCH.
- Tomlin, C. (1994). *The pesticide manual* (10th ed.). UK: British Crop Protection Council and Royal Society of Chemistry.
- van de Waterbeemd, H., & Gifford, E. (2003). ADMET in silico modelling: towards prediction paradise? *Nature Reviews Drug Discovery*, 2, 192.

- Vieira, P. C., Mafezoli, J., Pupo, M. T., Fernandes, J. B., da Silva, M. F. G. F., de Albuquerque, S., & Pavao, F. (2001). Strategies for the isolation and identification of trypanocidal compounds from the Rutales. *Pure and Applied Chemistry*, *73*, 617.
- Zanatta, N., Faoro, D., Silva, S. C., Bonacorso, H. G., & Martins, M. A. P. (2004). Convenient synthesis of furan-3-carboxylic acid and derivatives. *Tetrahedron Letters*, *45*, 5689.
- Zanatta, N., Alves, S. H., Coelho, H. S., Borchardt, D. M., Machado, P., Flores, K. M., da Silva, F. M., Spader, T. B., Santurio, J. M., Bonacorso, H. G., & Martins, M. A. P. (2007). Synthesis, antimicrobial activity, and QSAR studies of furan-3-carboxamides. *Bioorganic & Medicinal Chemistry*, *15*, 1947.
- Zhang, L., Cui, Z., Yin, B., Yang, G., Ling, Y., & Yang, X. (2010). QSAR and 3D-QSAR studies of the diacyl-hydrazine derivatives containing furan rings based on the density functional theory. *Science China. Chemistry*, *53*(6), 1322.





# 39 Ab Initio Investigation of Photochemical Reaction Mechanisms: From Isolated Molecules to Complex Environments

Igor Schapiro<sup>1</sup> · Patrick Zakhia El-Khoury<sup>1</sup> · Massimo Olivucci<sup>1,2</sup>

<sup>1</sup>Chemistry Department, Bowling Green State University, Bowling Green, OH, USA

<sup>2</sup>Dipartimento di Chimica, Università di Siena, Italy

<b>Introduction</b> .....	<b>1360</b>
<b>Methods in Computational Photochemistry</b> .....	<b>1364</b>
Multiconfigurational Quantum Chemistry .....	1364
QM/MM Methodology .....	1368
<b>Case Studies of Isolated Chromophores</b> .....	<b>1371</b>
Photoisomerization in a Rhodopsin Chromophore Model .....	1371
Photofragmentation Through a Conical Intersection: The Photodenitrogenation of a Bicyclic Azoalkane .....	1377
Charge Transfer and Intermolecular Hydrogen Transfer Mediated by a Conical Intersection: Quenching the Fluorescence of Bicyclic Azoalkanes .....	1379
<b>Case Studies of Chromophores Embedded in a Molecular Environment</b> .....	<b>1385</b>
Green Fluorescent Proteins (GFP) .....	1385
Understanding the Spectral Tuning in Retinal Proteins .....	1387
Deactivation Mechanism in Cytosine-Guanine DNA Base Pair .....	1392
Absorption Spectra of a Coumarin in Solution .....	1394
<b>Excited State Molecular Dynamics</b> .....	<b>1396</b>
Tracking the Photoisomerization of Retinal in Different Environments .....	1396
<b>Conclusion</b> .....	<b>1398</b>
<b>References</b> .....	<b>1398</b>

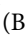
**Abstract:** This chapter focuses on the computational investigations of light-induced chemical reactions in different systems ranging from organic molecules in vacuo to chromophores in complex protein environments. The aim is to show how the methods of computational photochemistry can be used to attain a molecular-level understanding of the mechanisms of photochemical and photophysical transformations. Following a brief introduction to the field, the most frequently used quantum chemical methods for mapping excited state potential energy surfaces and for studying the mechanism of photochemical reactions in isolated molecules are outlined. In the following sections, such methods and concepts are further developed to allow the investigation of photo-induced reactions in solution and in the protein environment.

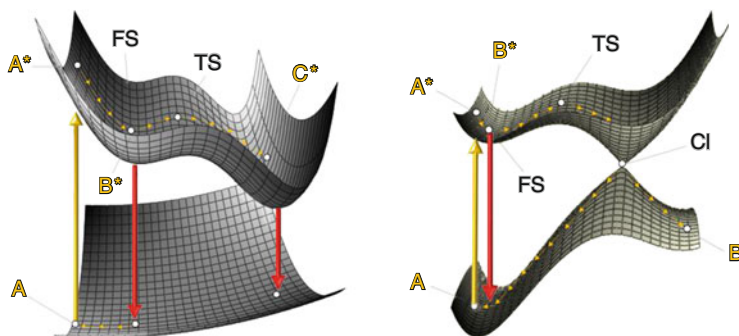
## Introduction

---

Since the early 1990s, quantum chemical methods based on *ab initio* multiconfigurational wavefunctions have been used to investigate the mechanisms of photochemical organic reactions and have led to the development of the field of computational photochemistry (Bernardi et al. 1996b). As a consequence it is now possible, using available program packages (examples of which include Molcas (Andersson et al. 2009; Aquilante et al. 2009), Gaussian (Frisch et al. 2009), Gamess-US (Gordon et al. 2005; Schmidt et al. 1993), Columbus (Lischka et al. 2006), Molpro (Werner et al. 2008), and Q-Chem (Adams et al. 2009; Shao et al. 2006)), to locate excited state equilibrium structures, conical intersections, or singlet/triplet crossings, and map ground or excited state minimum energy paths at a level of accuracy that often allows for comparison with spectral data (Kutateladze 2005; Olivucci and Sinicropi 2005). This offers chemists a powerful tool to rationalize and predict such complex processes as the light-induced response of a molecule.

There are two events that may happen when light energy is absorbed by a molecule: wastage or exploitation. Some technological application may require molecules whose structures are unaffected by light absorption, those that efficiently dispose of the excess electronic energy (e.g., through light emission and internal conversion). Other applications may require molecules that exploit light to drive specific chemical, conformational and electronic changes (e.g., through photochemical reactions or light-induced energy or electron transfer). It can be easily recognized that nature provides many examples of effective light energy wastage and exploitation. Therefore, the understanding of these events can be considered a basic requirement for the rational design of efficient photochemical reactions, artificial photosynthetic systems, and molecular-level devices and machines. Below, we will present case studies from small molecules in the gas phase to molecules in complex environments such as biological photoreceptors.

The computational investigation of a light-induced reactive process requires the construction of the associated photochemical reaction path (Olivucci and Sinicropi 2005). In its simplest form, this is defined by a branched minimum energy path that connects the Franck–Condon (FC) point  $A^*$  on the potential energy surface of the light-absorbing state with one (or more) primary photoproduct (B) or original reactant (A). As illustrated in  Fig. 39-1 left, if the relaxation of  $A^*$  leads to a stable excited state equilibrium species (structure  $B^*$ ) this may form a luminescent state, for instance a fluorescent state (FS), thus leading to radiative deactivation. High fluorescence quantum yields require long excited state lifetimes that, among other



■ Fig. 39-1

Schematic structure of the photochemical reaction path. *Left*: general structure of the excited state energy surface in the vicinity of the Franck–Condon point.  $A^*$  is geometrically identical to the minimum on the ground state, but has the electronic wave function of the excited state. The species  $B^*$  is a relaxed form of  $A^*$  that may emit fluorescence and/or evolve towards a different region of the excited state potential energy surface through the transition state (TS), producing a different emitting or reactive species  $C^*$ . *Right*: intersecting ground and excited state potential energy surfaces. The arrows indicate the direction of the minimum energy path connecting  $A^*$  to the conical intersection (CI) and then to the photoproduct B or original reactant A

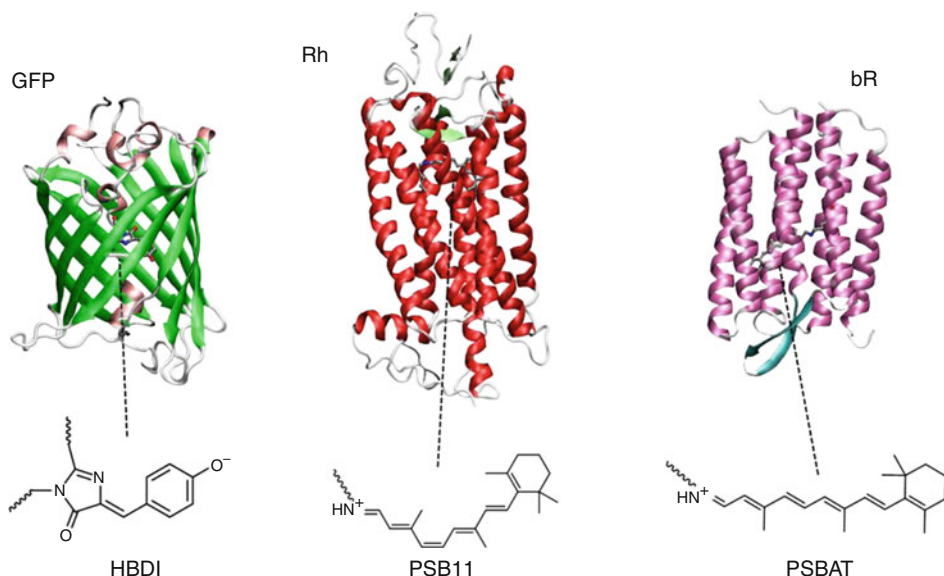
factors, could be imposed by high energy barriers restraining further evolution of  $B^*$ . If this is not the case,  $B^*$  can evolve beyond a transition state (TS), to produce a different excited state species ( $C^*$ ) that may also decay radiationally. If this is the case, one has an excited state conformational or chemical change that might lead to a different fluorescence emission. One of the most prominent examples of this so-called dual fluorescence is that produced by 4-(*N,N*-dimethylamino)benzonitrile in polar solvents (Grabowski et al. 2003). Alternatively (see ● Fig. 39-1 right), the excited state transition structure could connect  $B^*$  to a point where efficient radiationless decay (internal conversion) takes place. In the limiting case of a negligible or non-existent barrier,  $A^*$  may promptly reach such point on a picoseconds time-scale. For internal conversion, this process is usually associated with regions where there is a limited gap between ground and excited states, a large overlap between a low lying vibrational state of the photoexcited molecule and a suitable ground state vibrational mode (Simons 1983). These conditions are satisfied in the regions surrounding a conical intersection (CI). Therefore, evolution towards a CI leads to an efficient decay to the ground state (decay is common in the whole region surrounding the CI). When the relaxation following decay results exclusively in reactant back-formation (CI→A stream of arrows) one has internal conversion. In contrast, when the ground state relaxation produces a novel species B (a primary photoproduct) by following a different relaxation path, one has a photochemical event (left to right stream of arrows).

CIs provide a common key mechanistic entity for the description of a photochemical reaction and ultrafast internal conversion (Turro et al. 2009). The potential energy surface region surrounding each CI point can be seen as an efficient radiationless deactivation channel (Bernardi et al. 1996a; Migani and Olivucci 2004; Robb et al. 1995) that, in photochemistry, is

called a funnel. A photochemical funnel (Braslavsky 2007) corresponds to a molecular structure in the vicinity of a CI that would decay within one half of a vibrational period. For this reason computer simulations appear to be the only “direct” source of information about the structure of a molecule in a funnel. Notice that one has a CI only when the ground and the excited state have the same spin. If this is not the case and the electronic states have different spins the process is called intersystem crossing (Simons 1983; Turro et al. 2009).

In ► *Fig. 39-1* we show that the entire “photochemical reaction path” is defined and computed in terms of a set of connected minimum energy paths (MEP) corresponding to steepest descent lines. In particular, the path starting at  $A^*$  on the spectroscopic state and ending at the photoproduct energy minimum B on the ground state energy surface is constructed by joining two MEPs. A first MEP connects FC point to the CI. A second MEP connects the CI to the photoproduct B. A third MEP can be computed that starts at CI and describes the reactant reconstitution process responsible for partial return of the photoexcited species to the original ground state minimum (i.e., internal conversion). The mapping of the excited state potential energy surface of chemically different organic chromophores, strongly supports the idea that the mechanistic scenario described above (i.e., involving decay at a CI), is common. This was first realized after the development of CASSCF gradients (Schlegel and Robb 1982) in the early 1980s, and through a systematic computational research effort carried out in the 1990s (Bernardi et al. 1990, 2006). Also a number of algorithms were developed in order to locate the conical intersections and characterize the associated geometries (Anglada and Bofill 1997; Bearpark et al. 1994; De Vico et al. 2005; Farazdel and Dupuis 1991; Koga and Morokuma 1985; Levine et al. 2006; Ragazos et al. 1992; Yarkony 1993). Since the conical intersections are high-dimensional entities and not single points, the algorithms minimize the energy along the intersection seam. The points with the lowest energy of the seam are referred to as minimum energy conical intersections (MECI). The decay processes that are mediated by conical intersection are ultrafast and therefore too fast to allow the molecule to travel along the seam to reach the MECI. Thus transitions can occur at intersections which are higher in energy than MECI. This idea prompted the development of advanced methods to optimize stationary points along the multidimensional seam of intersection and determine the structure of more extended segments of the crossing (Laino and Passerone 2004; Sicilia et al. 2007, 2008). A better way of defining the conical intersection point during the decay is to perform molecular dynamics simulation, which considers the kinetic energy of the molecule and can explore different regions of the excited state surface provided a number of different initial conditions. The methods solve the classical equations of motions and use forces from electronic structure methods to move on a single potential energy surface. In order to account for non-adiabatic transitions, a variety of approaches have been produced. Trajectory surface hopping algorithms are widely used to accomplish this task. They have in common that a transition is induced, i.e., a hop between surfaces, when the non-adiabatic coupling becomes strong. There are several examples where this surface hopping algorithm has been successfully applied to study photochemical events (Barbatti and Lischka 2008; Barbatti et al. 2008; Groenhof et al. 2004, 2008; Schaefer et al. 2007; Schapiro et al. 2009; Virshup et al. 2009; Weingart 2007; Weingart et al. 2004). A more sophisticated approach that treats both electrons and nuclei quantum mechanically was implemented by Martinez and co-workers (Ben-Nun and Martinez 1998; Levine et al. 2006). Herein an additional basis function describing the nuclei is created or spawned (therefore the name “multiple-spawning”) when strong non-adiabatic coupling between different states arises.

Below we discuss selected case studies of a series of processes investigated by means of computational photochemistry. We begin with isolated molecules in vacuum and conclude with



■ Fig. 39-2

**Cartoon representation of the three-dimensional structures of three different photoresponsive proteins. Left: GFP with its HBDI anionic chromophore. Center the bovine visual pigment rhodopsin together with the cationic PSB11 chromophore. Right: bacteriorhodopsin and its PSBAT chromophore**


chromophores in complex environments. The first case study focuses on reduced models of the retinal chromophore of visual photoreceptors. Subsequently the photodenitrogenation, intermolecular charge transfer and hydrogen transfer in azoalkanes are described. The following section deals with chromophores in complex environments. An overview will be given starting with GFP and asFP595 which is a GFP-like protein (▶ Fig. 39-2) whose fluorescence can be switched on by *Z/E* photoisomerization. This is followed by an extensive discussion of a simulation of the photoisomerization of rhodopsin, a membrane protein characterized by seven  $\alpha$ -helices (▶ Fig. 39-2). The cationic Rh chromophore is the 11-*cis* stereoisomer of the protonated Schiff base of retinal (PSB11), and is connected through one covalent bond to the Lys296 residue. Upon absorption of visible light, PSB11 undergoes a *Z/E* photoisomerization and produces (stereoselectively) the corresponding all-*trans* chromophore (PSBAT), which ultimately triggers the Rh activity (Kandori et al. 2001; Mathies and Lugtenburg 2000; Palczewski et al. 2000; Teller et al. 2001). Computational studies of bR, an archaeal rhodopsin with a red-shifted absorption maximum ( $\lambda_{\text{max}}^a$ ) relative to Rh, and with a PSBAT chromophore, rather than PSB11, are described. Another class of molecules that have been excessively studied by tools of computational photochemistry are the deoxyribonucleic acids (DNA). We will illustrate how quantum chemistry is applied to unveil a mechanism of photodeactivation in a cytosine-guanine base pair. In the next case study the calculation of absorption spectra, including solvent effects and a novel method for taking vibrational contributions into account, is applied to coumarin C153. Finally, we highlight molecular dynamics simulations used to understand the isomerization mechanism in retinal containing proteins (Rh and bR).

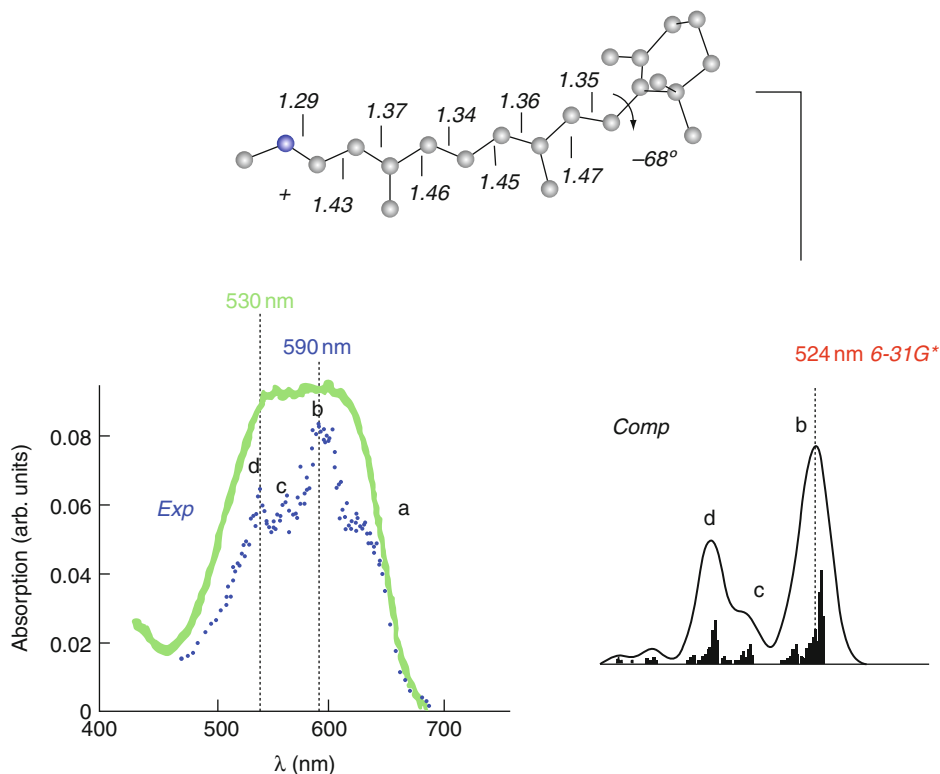
## Methods in Computational Photochemistry

### Multiconfigurational Quantum Chemistry

Among the possible quantum chemical methodologies (e.g., semi-empirical or *ab initio*) used to model excited state species, below we mainly deal with *ab initio* (i.e., from first principles of quantum mechanics) approaches. In particular, to describe the evolution of intermediates and species whose geometries are far from equilibrium, one employs *ab initio* multiconfigurational methods. These methods are based on the multideterminant configuration interaction ansatz (i.e., where the electronic wavefunction is represented by a linear combination of determinants rather than by a single determinant) being the methods of choice when, in a photochemical process, a molecule rapidly changes its electronic structure and enters regions of crossing between different potential energy surfaces. The favorable properties of these methods are: (1) the accuracy can be systematically improved until they provide the exact solution of the non-relativistic Schrödinger equation (when a full-configuration interaction wavefunction and basis set close to the Hartree limit are used), (2) they are unbiased in the sense that they do not contain empirical parameters, and (3) they are suitable for dealing with potential energy surface crossings between electronic states of the same or different spin-multiplicity (e.g., when the wavefunction is written in terms of Slater determinants) and there is a rapid change of electronic structure. The drawback is that these types of calculations are computationally expensive even though, nowadays, progress is being made to extend their applicability (Aquilante et al. 2009).

The *ab initio* complete-active-space self-consistent-field (CASSCF) method (Roos 1987) is a multiconfigurational method that offers maximum flexibility for an unbiased description of the electronic and geometrical features of molecules in their ground and excited electronic states. This is a particularly powerful method because the orbital coefficients are optimized together with the weights of a linear combination of all possible configurations constructed from a selected set of electrons and orbitals (Roos and Taylor 1980; Schmidt and Gordon 1998; Siegbahn et al. 1981). Furthermore, the CASSCF wavefunction can be used for subsequent second-order perturbation theory computations (CASPT2) of the dynamic correlation energy, (Andersson et al. 1990) ultimately allowing for a quantitative simulation and prediction of excitation energies.

In order to illustrate the accuracy that one can reach by a CASPT2//CASSCF protocol (the ‘//’ sign indicates that the molecular structure is determined (optimized) at the CASSCF level but that the energy is computed at the CASPT2 level), we report the results of the simulation of the observed gas-phase spectra of PSBAT in  Fig. 39-3 (Andruniw and Olivucci). The spectrum was simulated according to the procedure described in ref. Andruniw and Pawlikowski (1998). The  $S_0 \rightarrow S_1$  electronic excitation is found to be 524 nm at the CASPT2//CASSCF/6-31G\* level of theory (the 6-31G\* Pople-type acronym refers to the specific atomic basis set used in the calculation). In 2006 the experimental spectrum of PSBAT was measured by Andersen and co-workers showing several overlapping bands that were initially attributed to the vibrational excitations in  $S_1$  (Nielsen et al. 2006). The most intense peak was at 590–600 nm meaning the error of the CASPT2//CASSCF protocol is nearly  $6 \text{ kcal} \cdot \text{mol}^{-1}$ . However, very recently the same group has repeated the gas phase measurement finding a remarkably broad absorption with a flat top ranging from 530 to 610 nm (Rajput et al. 2010). By probing different retinal PSB analogues it was shown that the broadness of the band is due to a highly flexible C5–C6–C7–C8 dihedral angle. The C6–C7 bond connects the polyene chain with the  $\beta$ -ionone ring and has either a 6s-*cis* or 6s-*trans* conformation. The shorter wavelength of 530 nm was assigned



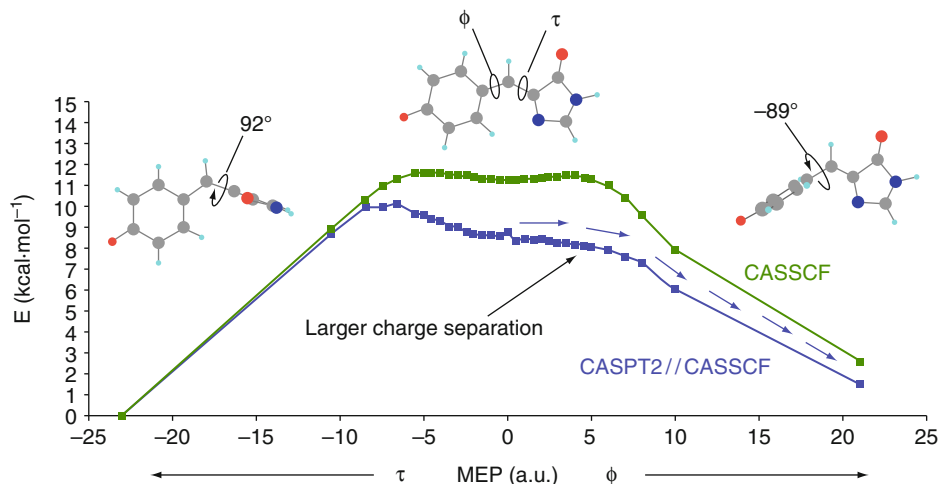
■ Fig. 39-3

The  $S_0 \rightarrow S_1$  absorption band of gas-phase PSBAT computed on the basis of excited state CASSCF frequency calculations (the frequencies have been scaled using a 10% factor). *Top*: the equilibrium geometry of the PSBAT is computed at the CASSCF/6-31G\* level of theory with a 12 electrons in 12 orbitals active space. *Left*: experimental absorption spectra recorded by Andersen and co-workers (Nielsen et al. 2006; Rajput et al. 2010). *Right*: simulation of the first order line spectra and of the spectral band by Lorentzian fitting. The maximum "b" is assigned to the vertical transition and it is <600 nm (~590 nm). The vertical excitation energy resulting in the predicted  $\lambda_{\max}^a$  value is computed by single-point CASPT2/6-31G\* calculation on the CASSCF equilibrium geometry. Normal modes involving mixed  $\beta$ -ionone ring and chain torsion and bending, as well as C-CH<sub>3</sub> motion in simulated spectrum are difficult to assign because of overlapping bands

to the 6s-cis-conformer and the longer wavelength of 610 nm to the 6s-trans-conformer. Compared to the new absorption maximum the CASPT2//CASSCF value is in very good agreement (0.6 kcal · mol<sup>-1</sup>).

The general assumption underlying the validity of the CASPT2//CASSCF protocol is that the CASSCF level of theory is accurate enough to provide qualitatively correct ground and excited state equilibrium structures, and in particular, MEPS. Currently this is of practical importance since only the CASSCF energy gradient can be evaluated analytically while the analytical CASPT2 gradients are not available for molecules of the size of interest in photobiology.





■ Fig. 39-4

CASSCF (green squares) and CASPT2 (blue squares) energy profiles for the electronic  $S_1$  state for the torsional relaxation. The stream of arrows indicates the energetically favored relaxation path. A change in shape of the reaction energy profiles after dynamic electron correlation correction (i.e., passing from CASSCF to CASPT2) has also been documented in other systems. See a discussion in ref. Sinicropi et al. (2003) (Redrawn with permission from ref. Martin et al. 2004)

This approximation is still awaiting a thorough evaluation. However, in certain cases, the equilibrium structures on a CASPT2 potential energy surface may differ significantly from the same structure calculated at the CASSCF level. In order to illustrate this point, the energy profile along a CASPT2//CASSCF minimum energy path computed for a simplified HBDI chromophore in the excited state is compared to the CASSCF energy profile in Fig. 39-4 (Martin et al. 2004).

Recently (Valsson and Filippi 2010) reported the photoisomerization of retinal models using high-level quantum chemical methods, among others CASPT2, which include dynamic electron correlation. The two and three double bond truncated retinal models optimized at the CASPT2 level and numerical gradients. It was found that all bonds were equally lengthened and therefore the rotation around several bonds became possible. However, not all of the rotations lead to radiationless decay to the ground state. Some of the pathways on the excited state involved single bond rotation up to  $45^\circ$  and ended up in energy wells on the excited state (see Fig. 39-1 left). This finding is in contrast with the widely accepted reaction coordinate established at the CASSCF level which is driven subsequently by two uncoupled modes. The first mode is responsible for the inversion of the bond length alternation in the excited state whereas the second mode is mainly the rotation of the central double bond. It is shown that this path also exists in the CASPT2 potential energy surface but it is reached rather from relaxing directly out of the Franck–Condon point. These controversial results on retinal chromophore *in vacuo* outline the importance of the dynamic electron correlation and the choice of the QM method that need to be verified for more realistic models. The size of the chromophore models should be extended towards the full retinal. However, the lack of the analytical gradients for CASPT2 makes these calculations extremely computationally demanding.

The difference between the CASPT2 and CASSCF geometries has also been investigated for both ground and excited state models of the PSB11 chromophore. The main difference in the results between these treatments is found in the ground state equilibrium geometry, where one finds a bond length alternation (BLA) pattern along the polyene chain which is less pronounced at the CASPT2 level (indicating a more extended delocalization) than at the CASSCF level (Page and Olivucci 2003). However, these studies were carried out with limited basis sets. Recently, different quantum chemical studies of the  $\lambda_{\max}^a$  of biological chromophores have employed density functional theory (DFT) rather than CASSCF ground state equilibrium geometries. For PSB11 and PSBAT these levels yield significantly different BLA values. Blomgren et al. (Blomgren and Larsson 2005) have proposed that this difference originates from the dynamic electron correlation which is (partially) included in DFT functionals. The changes in the BLA computed for PSB11 are also reflected in the magnitude of the twisting of the C6–C7 single bond with respect to the backbone (see [Fig. 39-2](#)) and consequently in the conformation of the  $\beta$ -ionone ring. The ring is nearly planar in the DFT geometry but highly twisted in the CASSCF geometry as reported by Bravaya et al. (2007). Using the PBE0/cc-pVDZ calculations these authors find that PSB11 has two conformers featuring a  $-39^\circ$  and  $+170^\circ$  twisting of the C5–C6–C7–C8 dihedral angle corresponding to *s-cis* and *s-trans* isomers of the  $\beta$ -ionone ring, respectively. These results can be compared with the CASSCF/6-31G\* data presented by Cembran et al. (2005) for the same chromophore. The CASSCF/6-31G\* level of theory yields a single highly twisted PSBAT conformer with a  $-69^\circ$  C5–C6–C7–C8 dihedral angle.

The gas-phase  $\lambda_{\max}^a$  (i.e., the corresponding vertical excitation energy) of PSB11 has been computed with different protocols that are also a matter of debate. Using a modified multiconfiguration quasi-degenerate perturbation theory aug-MCQDPT2 for excitation energies and DFT optimized geometry at PBE0/cc-pVDZ level for PSB11 (Bravaya et al. 2007) yields a 599 nm  $\lambda_{\max}^a$ , which appeared to be a very good estimate of the experimentally observed value for the gas-phase PSB11 ( $\sim 610$  nm) (Nielsen et al. 2006). In the light of the refined experimental absorption maximum at 530 nm (Rajput et al. 2010) the deviation is  $7 \text{ kcal} \cdot \text{mol}^{-1}$ . The use of a computationally consistent (i.e., with geometry and energy computed using the same method) TDDFT//DFT protocol (TD-B3LYP/6-31+G\*\*//B3LYP/6-31G) yields a 537 nm  $\lambda_{\max}^a$  (Wanko et al. 2005) and therefore performs better than mixed wavefunction-based/density-functional approaches. Also the CASPT2/ANO//MP2/6-31G\*\* calculated result is far off (606 nm) which is based on a protonated PSB11 model rather than an alkylated (*N*-dimethyl) like in the aug-MCQDPT2//PBE0 study, which is more consistent with the measured chromophore. In contrast the CASPT2//CASSCF/6-31G\* method yields 524 nm (Andruniw and Olivucci) which appears to be close to the recent experimental excitation energy of 530 nm (Rajput et al. 2010). TDDFT is a method that has much promise in studying excited states, but currently has limitations. It has been shown to be effective when used to compute valence-excited states (Dreuw and Head-Gordon 2005). However, when the excited state being studied has charge transfer (CT) character (either intermolecular or intramolecular) or if the molecule has an extended  $\pi$  system, TDDFT cannot reliably predict excitation energies. It has failed to accurately describe the CT states of several biologically relevant molecules, some of which include porphyrin complexes (Dreuw and Head-Gordon 2005). The failure is extensive. Not only is the energy gap inaccurate but also the topography of the excited state potential energy surface. This can be seen from the results of a study conducted in our laboratory (Fantacci et al. 2004), the results of which are displayed in [Fig. 39-5](#). A MEP was calculated for a truncated model of the retinal chromophore (only three conjugated double bonds were included) with CASSCF. Energies were then recalculated

at geometries along the path using CASPT2//CASSCF and various density functionals using TDDFT//CASSCF. Near the FC point, where the wavefunction changes rapidly, a potential energy well and maximum were found using TDDFT. These are features of an excited state energy surface that would not be expected to be exhibited by a molecule that undergoes an ultrafast femtosecond-scale photochemical reaction, so it is presumed that they are artifacts resulting from the use of TDDFT. The CASPT2//CASSCF surface is more accurate, exhibiting a plateau, with only a minuscule potential energy well. Another benchmark study came to similar conclusions, finding that the use of TDDFT led to a qualitatively incorrect description of the excited state potential at geometries distant from the FC point when the method was used on model retinal chromophores (Wanko et al. 2004). The source of the problem can be attributed to the CT nature of retinal's first excited state.

Problems with TDDFT can be found at all points of a photochemical reaction path, from the FC point to the CI. At the CI the quality of the immediately surrounding ground and excited state potential energy surface (PES) is inaccurate (Levine et al. 2006). A CI must have two branching directions (i.e., there must be two different motions that the molecule can undergo that will cause the energies of the states to separate). TDDFT, in contrast, describes a CI where only one branching direction lifts the degeneracy of states. An additional problem is that near the CI the slope of the PES along the single degeneracy-lifting coordinate is much steeper than that obtained with more reliable methods, as shown in the case of butadiene (Levine et al. 2006).

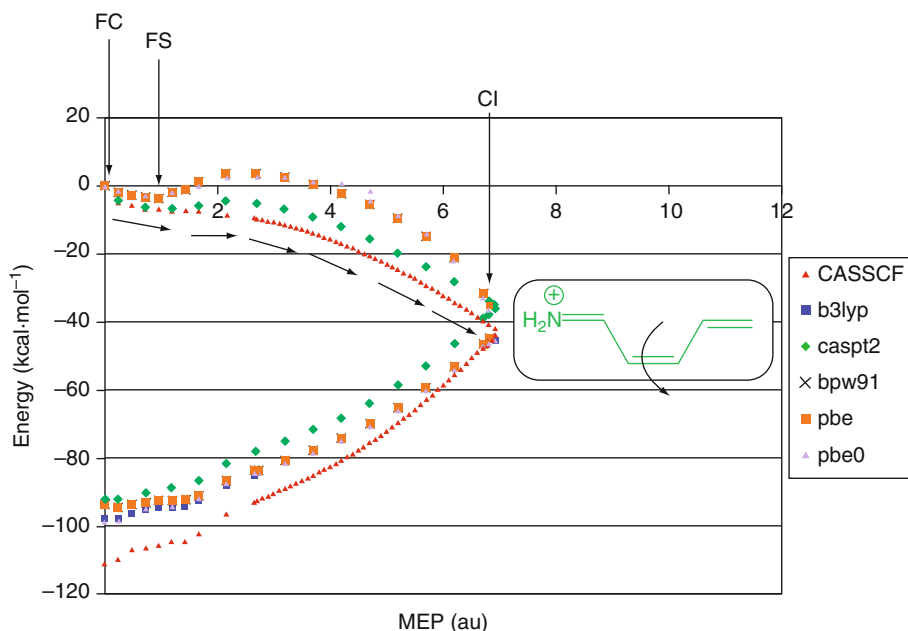
There are many reasons why TDDFT is not appropriate to study excited states, especially when double excitation or CT states are involved. For further reading we recommend the review by Dreuw et al. (Dreuw and Head-Gordon 2005). CASPT2 is much more reliable, in terms of accuracy, but cannot be used for optimizations, unless the molecule being studied is very small, in which case numerical gradients can be calculated with CASPT2. In the majority of cases, though, the best compromise will be CASPT2//CASSCF.

## QM/MM Methodology

---

The quantum mechanical methods described above are limited in the application by the size of the molecule. In 1976 Warshel (Warshel and Levitt 1976) proposed a hybrid treatment, which allowed to treat biological macromolecules such as proteins that are too large for quantum chemical calculations. The idea is to divide the macromolecule into two or more subsystems which have different sizes and functions. The smaller subsystem, where a change of electronic structure or a chemical reaction occurs, is described by a quantum mechanical (QM) approach (i.e., by a suitable quantum chemical method), whereas the larger residual subsystem is treated using a molecular mechanics (MM) force field. Fortunately, because photochemical reactions are localized only to a specific area (i.e., the chromophore) electronic structure methods can be applied to this significantly smaller region, and the remaining part can be treated on a lower level such as a classical force field. This approach allows the study of large systems but also introduces new problems, the most important of which regards the treatment of the frontier between the two subsystems. In the past three decades much work has been done to solve this problem and for a comprehensive outline the reader is referred to the review by Senn and Thiel (2009).

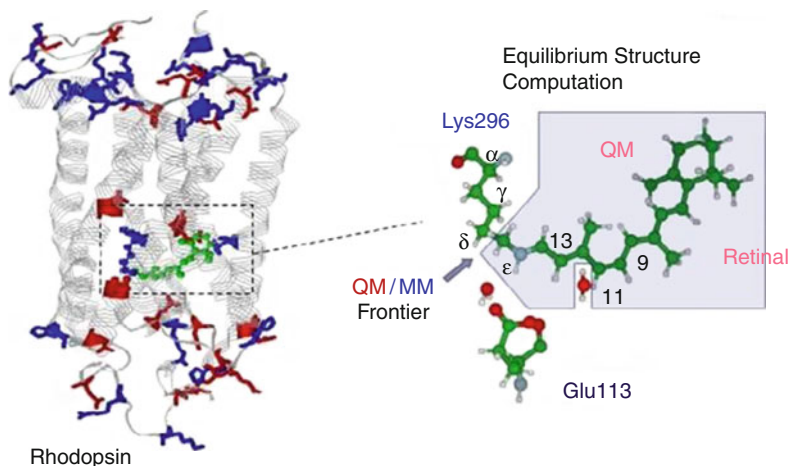
Using the multiconfigurational approach combined with classical or molecular mechanics treatment of the environment a CASPT2//CASSCF/MM protocol was established (the // separator has the same meaning as above). Thus geometry optimization and molecular dynamics simulations are carried out at the CASSCF/MM level (this notation indicates that



■ Fig. 39-5

Energy profiles along the  $S_1$  photoisomerization coordinate of a simplified PSB11 model computed at the CASPT2//CASSCF/6-31G\* level. The energy at the Franck–Condon point is taken as the reference for the comparison. The fluorescent state (FS) corresponds to the local minimum along the TDDFT curve. The local maximum of the TDDFT curve corresponds to a model structure whose dihedral angle around the central isomerizing double bond measures  $15^\circ$ . There is no maximum or energy well along the CASSCF energy profile and these features are much less distinct along the CASPT2//CASSCF energy profile. In the PSB11 chromophore the value of the C5–C6–C7–C8 dihedral angle strongly affects the vertical excitation energy of the gas-phase retinal chromophore. By changing it one can change the excitation energy by up to 0.7 eV. The PBE0/cc-pVDZ bond alternation value is close to the value found for N-methyl-11-*cis* PSBR obtained by Sekharan et al. (2006) with the MP2 method. As suggested by Wanko et al. (2005) the hybrid exchange–correlation functionals like the PBE0 used in the aforementioned work, should provide BLA values very close to those computed at the CASPT2 level of theory. Also the similarity of MP2/6-31G\* and CASPT2/6-31G\* equilibrium geometry was directly demonstrated for short retinal chromophore models (i.e., the pentadieniminium cation) (Page and Olivucci 2003). Of course, no CASPT2 optimization of the full retinal chromophore with adequate (e.g., large ANO) basis sets has been reported up to now and in our view the issue regarding the correct ground state geometry of the retinal chromophore has still to be settled (Redrawn with permission from ref. Fantacci et al. 2004)

the QM part of the molecule is described at the CASSCF level while the rest is described with an MM force field such as AMBER (Case et al. 2002; Ponder and Case 2001), CHARMM, (Brooks et al. 1983) or OPLS (Jorgensen and Tirado-Rives 1988)). Of course, the application of this methodology requires the construction of a suitable protein model. In order to study the Rh pigment, a CASPT2//CASSCF/AMBER protocol based on the QM/MM link-atom



■ Fig. 39-6

Main parts of a QM/MM model for Rh. The protein structure is usually obtained from the Protein Data Bank (Berman et al. 2000). The QM part corresponds to the chromophore plus a part of the side-chain of the amino acid that is linked to it. The QM/MM frontier region usually corresponds to a weakly polarized C–C bond that, for Rh, is chosen to correspond to the C<sub>δ</sub>–C<sub>ε</sub> bond of the Lys296 side chain in Rh. In this bond the QM atom (C<sub>ε</sub>) is capped with an H link-atom and the MM atom (C<sub>δ</sub>) is held in place by MM potentials that are specifically parameterized for this region. This MM parameterization of the QM/MM frontier region is specific to the chromophore and the side chain

electrostatic-embedding scheme (Senn and Thiel 2009) (see ● Fig. 39-6) has been implemented and successfully applied for the first time in our laboratory (Ferré and Olivucci 2003a, b; Ferré et al. 2004).

A meaningful calculation of the spectroscopic parameters can be achieved by running a long time ground state QM/MM trajectory simulation and computing CASPT2 vertical excitation energies at regular time intervals. In this way the  $\lambda_{\max}^a$ , fluorescence maximum ( $\lambda_{\max}^f$ ) or phosphorescence maximum could be obtained by averaging these results (for an application of this concept using other quantum chemical methods see refs Hoffmann et al. (2006) and Pistolesi et al. (2009)). However, because of the cost of CASPT2//CASSCF calculations this strategy appears to be unpractical. The calculation of quantities such as the  $\lambda_{\max}^a$  and  $\lambda_{\max}^f$  cannot be systematically carried out using this approach. Yet, as explicitly mentioned above, the CASPT2//CASSCF level of QM treatment is required if one wants an unbiased and rigorous quantitative description of the electronic excited state of an organic chromophore/fluorophore. One possible solution to this problem is to prepare a model of the system that provides a sufficiently accurate representation of the time-averaged configuration of the chromophore/fluorophore and its environment. Using this model the chromophore would effectively feel the average steric and electrostatic field imposed by the protein.

The case studies given in ● section “Case Studies of Chromophores Embedded in a Molecular Environment” show that within certain accuracy QM/MM models are viable for different proteins. Indeed, we have shown that models based on the experimental crystallographic

structure (i.e., where the protein is not fully relaxed or equilibrated) allow the prediction of the spectroscopic parameters with an accuracy of a few  $\text{kcal} \cdot \text{mol}^{-1}$  for systems that differ in protein structure and in the chemical nature of the chromophore/fluorophore.

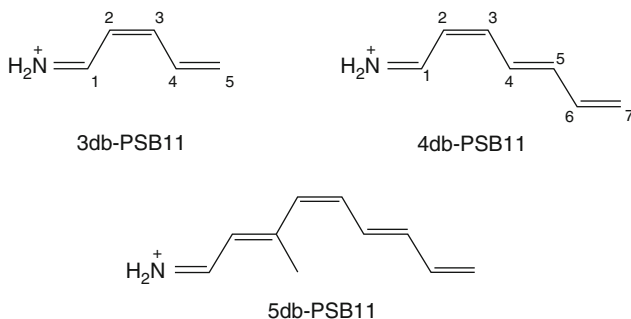
## Case Studies of Isolated Chromophores

### Photoisomerization in a Rhodopsin Chromophore Model

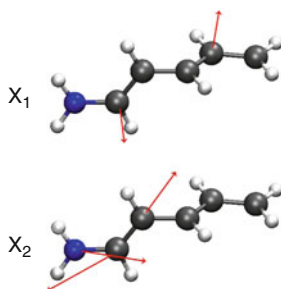
The protonated Schiff base of 11-*cis*-retinal (PSB11) is the chromophore in the visual receptor rhodopsin. A light-induced *cis/trans* isomerization of the chromophore triggers the primary event in vision, which is a series of conformational changes of the protein. This photoreaction is considered as the archetype of a chemical reaction optimized by nature to achieve a specific molecular response. Hence, it was in focus of numerous computational and experimental investigations.

The first detailed structure of the excited and ground state potential energy surfaces of the rhodopsin chromophore model was obtained for the three double-truncated 11-*cis*-retinal (3db-PSB11). In particular the structure of the excited and ground state reaction path branches has been fully elucidated. Furthermore the reduced dimension of the model (● Scheme 39-1) has allowed for the computations of ab-initio CASSCF semi-classical trajectories and the evaluation of the excited state lifetime and time scale of the photochemical isomerization (Weingart et al. 2004). The results demonstrated that 3db-PSB11 provides a reasonable model for more realistic structures. In particular, the two-state, two-mode nature of the reaction coordinate computed and observed (both in solution and in the protein) is maintained in the minimal model and the computed ultrafast excited state dynamics is still characterized by two different timescales corresponding to a the initial stretching relaxation (i.e., an inversion of the single bond/double bond length alternation) and to the following torsional deformation (about the central  $\text{C}_2\text{-C}_3$  bond), respectively.

In ● Fig. 39-7 we plot the branching plane vectors ( $\mathbf{X}_1$  and  $\mathbf{X}_2$ ) at the conical intersection of 3db-PSB11 model. The conical intersection structure features one highly twisted double bond (about  $92^\circ$ ) and involves two electronic configurations, an ionic and a covalent state, that differ for the transfer of one electron between the  $\text{C}_5\text{-C}_4\text{-C}_3\text{-}$  and  $\text{-C}_2\text{-C}_1\text{-N}$  fragments.

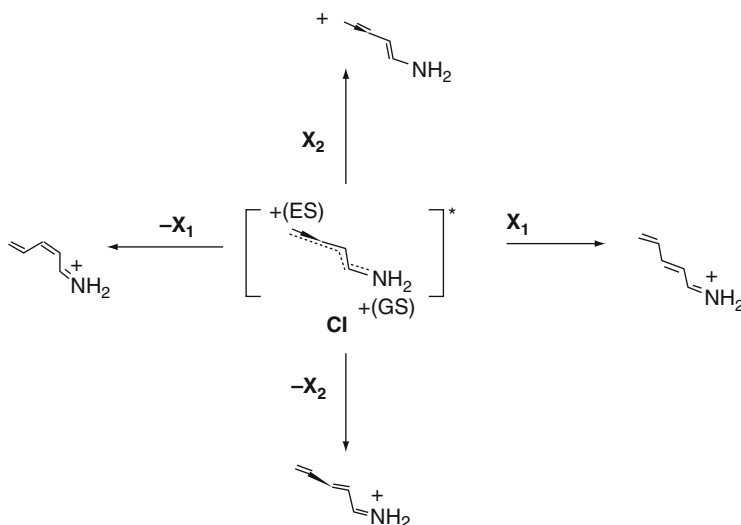


■ Scheme 39-1  
Reduced models of PSB11



■ Fig. 39-7

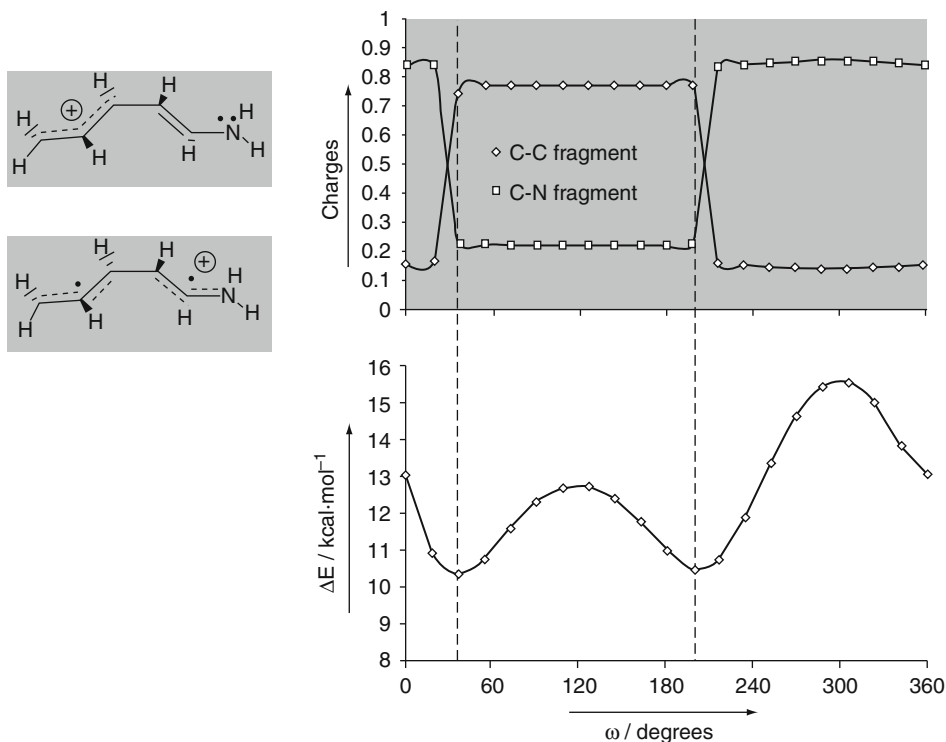
Branching (or g,h) plane vectors for the CI structure of 3db-PSB11. The  $X_1$  and  $X_2$  vectors correspond to the derivative coupling (or non-adiabatic coupling) and gradient difference vectors between the  $S_1$  and  $S_0$  states (Redrawn with permission from ref. Migani and Olivucci 2004)



■ Scheme 39-2

Deformation of the CI geometry of 3db-PSB11 along the branching plane vectors  $X_1$  and  $X_2$

From the structure of the branching plane it is apparent that in this molecule  $X_1$  and  $X_2$  describe two types of processes. As shown in [Scheme 39-2](#), motion along the  $X_1$  corresponds to a coupled pyramidalization (wagging) modes at the  $C_1$  and  $C_4$  centers of the  $\pi$ -chain. This motion allows for a widening of the  $C_4-C_3-C_2-C_1$  dihedral angle leading to a  $\pi$ -bond breaking process. The  $X_2$  mode is characterized by a stretching deformation (a double bond expansion and single bond contraction mode) of the  $N=C_1-C_2=C_3-C_4=C_5$  chain segment. Thus, motion along the  $X_2$  direction would ultimately yield two structures that be represented by (resonance) formulas with inverted single and double bonds and with the positive charge shifted from the N-terminal to the  $C_5$ -terminal. These two  $92^\circ$  twisted structures will be less stable than those generated by displacement along the wagging mode since the deformation along  $X_1$  allows for reconstitution of the central double bond providing strong coupling with



### ■ Scheme 39-3

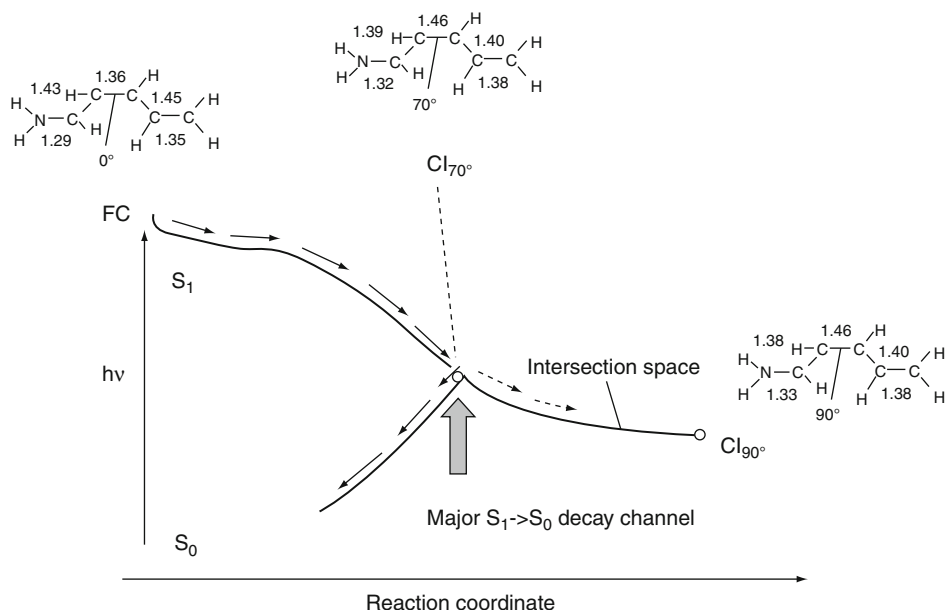
**Characterization of the topology around the CI of 3db-PSB11 by charge distribution of the model chromophore and the energy profile**

the Z/E double bond isomerization coordinate. Thus, structural analysis of the branching plane suggests that upon decay from **CI** the molecule will generate the Z and E stereoisomers.

The analysis of the wavefunction, taken together with the analysis of the branching plane, provides the basis for the rationalization of the electronic structure of the ground state energy surface comprising the reactant and product valleys (and, eventually, the transition structures connecting them). The result of such an analysis for chromophore model 3db-PSB11 is shown in **Scheme 39-3**, where the wavefunction is analyzed in terms of point charges of the C<sub>5</sub>-C<sub>4</sub>-C<sub>3</sub>- and -C<sub>2</sub>-C<sub>1</sub>-N fragments along a loop centered on the **CI** (angle ω) and lying on the plane defined by the X<sub>1</sub> and X<sub>2</sub> modes. The charge distribution of the system demonstrates the existence of two different regions. The first region 0° < ω < 30°, 200° < ω < 360° is characterized by a structure where the charge is mainly localized on the N-terminal part of the molecule. The second region 30° < ω < 200° is characterized by a structure where the positive charge is mainly located on the C-terminal part of the molecule. The border between the two regions corresponds to the electron transfer events between the two fragments. Notice that the wavefunction changes are associated with the two minima in the energy gap diagram.

As we have previously underlined, the low-lying conical intersections could be only provided through the computation of the photochemical minimum energy path (MEP). However, some cases have been documented where excited state reaction path does not necessarily hit the lowest energy point belonging to the intersection space (**IS**) and the decay may not occur in this region. One of these cases concerns the excited state relaxation path of the 3db-PSB11





■ Fig. 39-8

The excited state reaction path of the cation 3db-PSB11 intercepts the conical intersection point  $CI_{70^\circ}$  located ca.  $5 \text{ kcal} \cdot \text{mol}^{-1}$  above the minimum energy conical intersection  $CI_{90^\circ}$ . The values of the relevant structural parameters are given in Å and degrees (Redrawn with permission from ref. Migani and Olivucci 2004)

chromophore. Indeed, the mapping of the low-lying segments of the IS for this chromophore (see Fig. 39-8), by means of constrained MEP computations, demonstrated that it ends at a conical intersection with a ca.  $70^\circ$  ( $CI_{70^\circ}$ ) twisted structure. The intersection space remains then coincident with the reaction path up to the lowest energy intersection ( $CI_{92^\circ}$ ) that has a  $92^\circ$  twisted structure (Migani et al. 2003). Notice that in this situation the main locus of excited state ( $S_1$ ) decay is predicted to be  $CI_{70^\circ}$ .

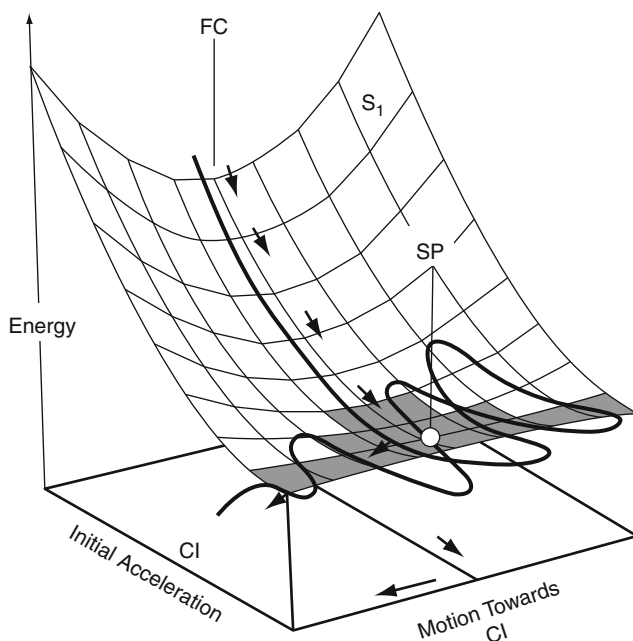
In the follow-up study an extended model with four double bonds (4db-PSB11 in Scheme 39-1) confirmed the topological features found in 3db-PSB11 (Migani et al. 2004). But it also shows expansion of the intersection space segment because of an increased number of double bonds. In the 4db-PSB11 model there are two central double bonds. Twisting each of them at a time and both simultaneously on the excited state can lead to CIs. One can expect a topology of the IS space where these singly twisted CIs are connected by the doubly twisted conical intersections. Indeed, two singly twisted CIs could be identified via IS steepest descent path (ISDP) calculations starting from the doubly twisted CI-geometry T,T-CI (Fig. 39-9). For nomenclature of these structures, the first letter describes the C2–C3 and the second the C4–C5 double bond conformation, with T being a nearly  $90^\circ$  twisted dihedral. It shows that one can smoothly change the amount of twisting about the C2–C3 and C4–C5 bonds without leaving the IS.

In principle, two additional paths should also connect the complementary isomers of the singly-twisted geometries with the doubly twisted structure. Starting at the same T,T-CI point



along the C10–C11–C12–C13 torsion from  $80^\circ$  to  $110^\circ$ . It should be noticed that certain substituents or a suitably designed molecular environment can change the energy profile favoring one isomerization channel over the other or even stabilizing the central part of it.

A more realistic chromophore model including all five double bonds of the polyene chain of retinal (5db-PSB11 in [Scheme 39-1](#)) was studied by Gonzalez Luque et al. (2000). A minimum energy path (MEP) was computed at the CASSCF level of theory. Ten  $\pi$ -electrons included in  $\pi$ -type orbitals with 6-31G\* basis set were employed. It should provide an unambiguous *cis/trans* photoisomerization coordinate for PSB11 (and PSBT) under isolated conditions. This coordinate suggests the dynamic behavior illustrated in [Fig. 39-11](#), where a metastable species performs many skeletal oscillations along an energy plateau before the reactive torsional modes get fully populated. The plateau may be assigned to the picosecond “fluorescent state” observed in solution and therefore drastically reduces the efficiency of the photoisomerization compared to the protein environment. A second basic feature of the computed path is the positive-charge translocation along the chromophore framework. The positive charge was found to shift partially from the N end to the C end of the models upon  $S_0 \rightarrow S_1$  photoexcitation and  $S_1$  in-plane relaxation. The following twisting deformation leads to a complete translocation of the charge that localizes on the fragment containing the C end as already demonstrated for the smaller model 3db-PSB11.



■ Fig. 39-11  
Shape of the FC → SP region of the S<sub>1</sub> energy surface of 5db-pSB11 model

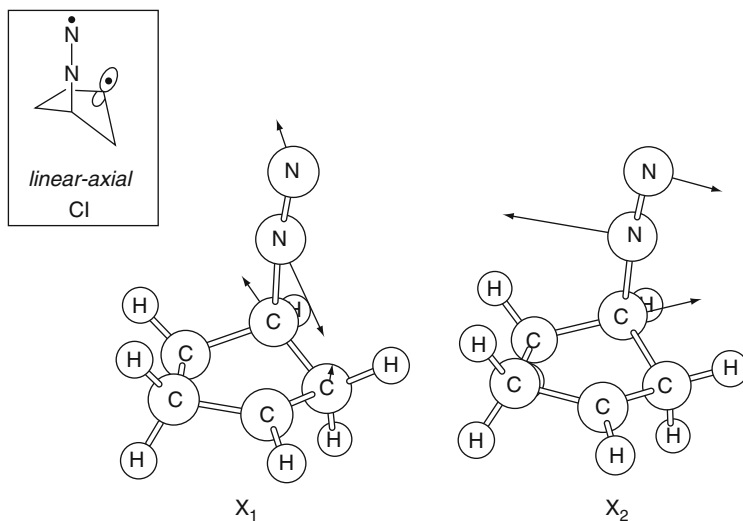
## Photofragmentation Through a Conical Intersection: The Photodenitrogenation of a Bicyclic Azoalkane

Photo-induced denitrogenation of 2,3-diazabicyclo[2.2.1]hept-2-ene (DBH) has been the subject of debate ever since it was first reported by Solomon et al. (1968). The observed stereoselectivity in the nitrogen extrusion and housane formation processes was of particular interest. The conical intersection structure which mediates the C–N  $\alpha$ -cleavage is characterized by a linear-axial arrangement at the NNC moiety where one of the two CN bonds is still intact (1.48 Å) (Page and Olivucci 2003; Yamamoto et al. 1998). The branching plane vectors  $X_1$  and  $X_2$  correspond to two orthogonal bending motions of the NNC angle, as illustrated in **Fig. 39-12**.

When the CI structure is displaced along  $X_1$  and  $X_2$ , the CNN bending motions prompt the formation of the ground state diazenyl diradical ( $^1DZ$  in the **Scheme 39-4**) either in the exo, endo, or endo-exo forms, as illustrated in **Scheme 39-5**.

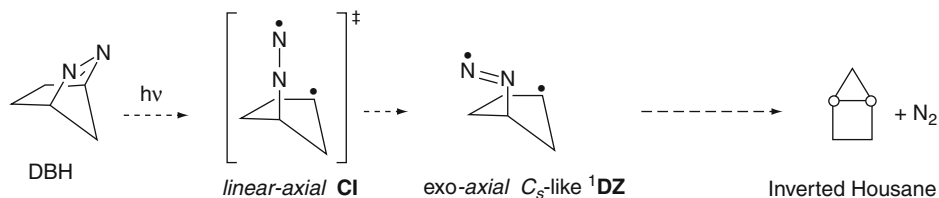
The electronic structure of the intersecting states of the  $\alpha$ -CN bond cleavage of DBH is illustrated in **Scheme 39-6**. The electronic configuration of the  $S_1$  state of the azoalkane corresponds to a tetraradical configuration where two electrons are localized in each  $\alpha$ -CN  $\sigma$ -orbital, one electron in the excited nitrogen lone pair, and one electron residing in the p-orbital nitrogen bound to the  $\alpha$ -C. On the other hand, the electronic configuration of the ground state azoalkane consists of a biradical in which the two  $\alpha$ -CN  $\sigma$ -orbitals are singly occupied.

Reaction path calculations explain the observed inversion of stereoselectivity. It is ascribed to an impulsive population of a vibrational mode that triggers axial-to-equatorial ring inversion. This idea is supported by classical molecular dynamics simulations. **Figure 39-13** reveals that



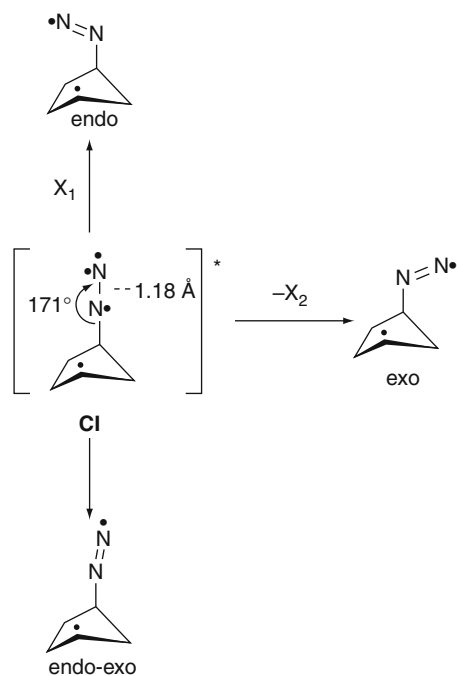
**Fig. 39-12**

Gradient difference ( $X_1$ ) and derivative coupling ( $X_2$ ) vectors for the CI structure of DBH (illustrated schematically in the inset). The vectors correspond to two orthogonal bending motions of the NNC angle (Redrawn with permission from ref. Sinicropi et al. 2003)



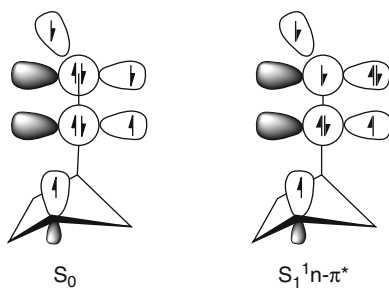
■ Scheme 39-4

Photofragmentation of DBH to the Inverted Housane



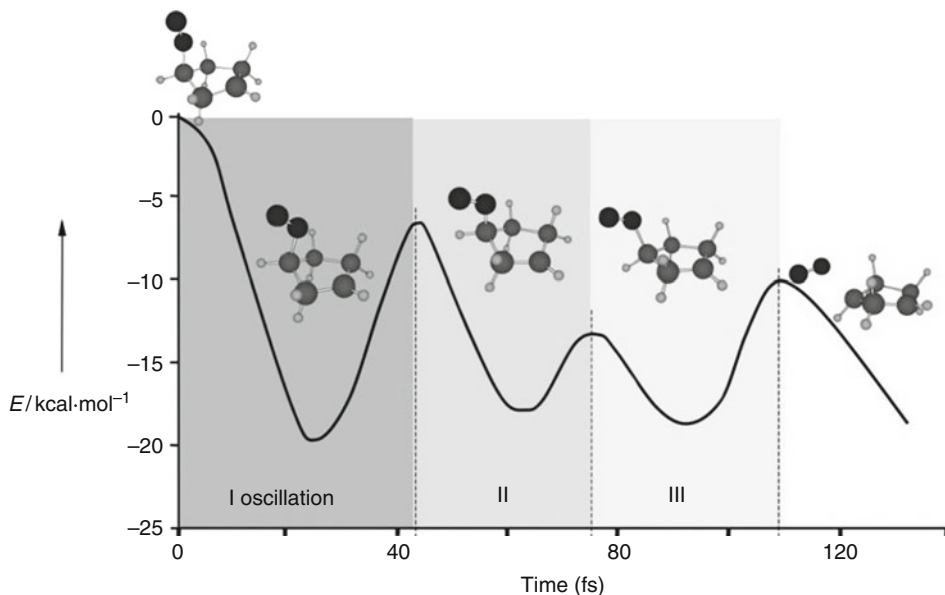
■ Scheme 39-5

Formation of different isomers starting from the diradical CI structure



■ Scheme 39-6

Electronic structure of the  $S_0$  and  $S_1$  state




■ Fig. 39-13

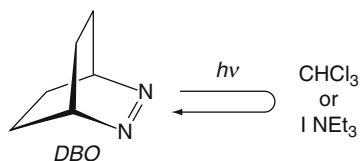
Triplet DFT energy profiles along the molecular dynamics simulations started in the vicinity of the CI structure of DBH. The snapshots demonstrate the molecular changes along the trajectory (This figure is redrawn with permission from ref. Sinicropi et al. 2003)

after a single oscillation (on a 40 fs timescale) in the direction of a transient bicyclic intermediate, the molecule reaches a strained structure that it can only relax following the initial direction of motion. After 60 fs, the *exo-axial*<sup>1</sup>DZ configuration is reached, followed by the axial to equatorial transition structure on an 80 fs timescale. Within 100 fs, the inverted configuration is observed.

## Charge Transfer and Intermolecular Hydrogen Transfer Mediated by a Conical Intersection: Quenching the Fluorescence of Bicyclic Azoalkanes

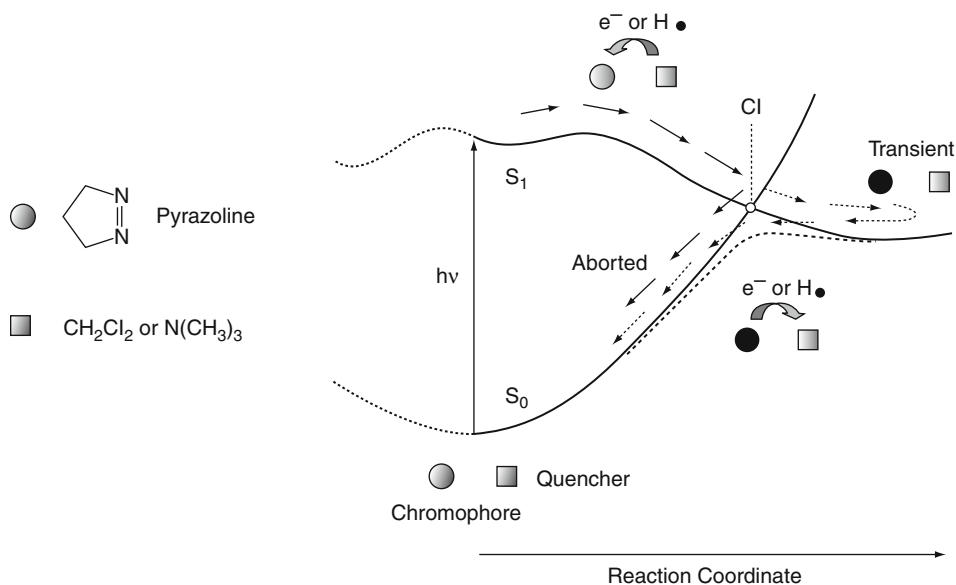
In contrast to DBH, the so-called “reluctant” azoalkanes are inert to photochemical denitrogenation. One representative system is the *2,3-diazabicyclo[2.2.2]oct-2-ene* (DBO,  Scheme 39-7). DBO exhibits a long-lived excited  $n,\pi^*$ -singlet state (on the order of  $\mu$ s).

Using the *1,2-diazacyclopent-1-ene* (pyrazoline) as a model of DBO allows the use of accurate yet computationally demanding (expensive) methods. In combination with experimental evidence, two mechanisms for quenching  $^1n,\pi^*$  states were proposed (Sinicropi 2002; Sinicropi et al. 2000, 2001, 2002). DBO is efficiently quenched by hydrogen donors (for instance by solvents such as chloroform, methanol, and benzene) either via a concerted or a stepwise process. DBO luminescence can be quenched by electron donors (e.g., with triethylamine),



■ Scheme 39-7

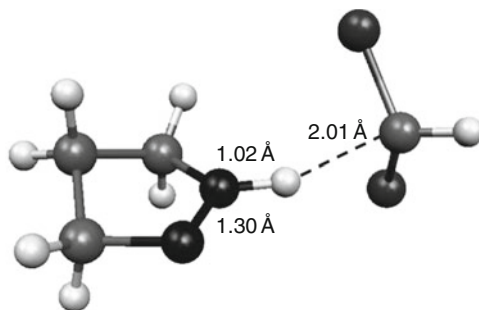
Internal conversion of DBO



■ Fig. 39-14

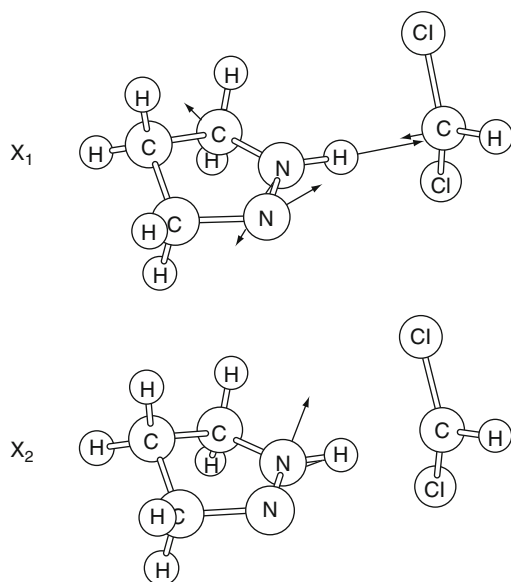
Potential energy diagram showing the interplay between ground ( $S_0$ ) and excited ( $S_1$ ) state surfaces in the fluorescence quenching of  $^1n,\pi^*$  state chromophores due to an hydrogen donor or electron donor species. The full and light arrows describe the concerted and stepwise energy wastage route

however, only through a concerted process. Calculations have been carried out using CH2Cl2 and methanol to model hydrogen donors, and trimethylamine/dimethyl ether as strong/weak electron donor solvents on the other hand. As shown in [Fig. 39-14](#), both quenching routes involve bimolecular photochemical reactions. Deactivation occurs through an  $S_1/S_0$  CI, located halfway along the reaction coordinate, and prompting bifurcation. The first branch (represented by full arrows) resembles a photophysical transformation and has been termed an “aborted” photochemical transformation. The second branch (represented by light arrows) is associated with production of a transient species that reverts to the original starting reactants by passage through a low-lying transition state located on the ground state reaction coordinate (depicted by a dashed curve). Thus, both routes correspond to a photochemical transformation, which was initiated but never achieved.



■ Fig. 39-15

The molecular structure of the characterized conical intersection that mediates hydrogen abstraction in the presence of  $\text{CH}_2\text{Cl}_2$



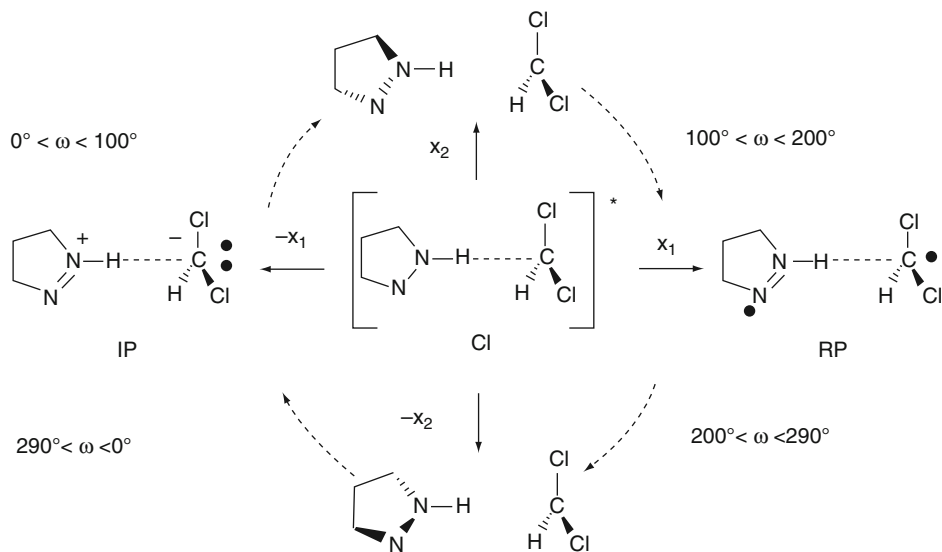
■ Fig. 39-16

$X_1$  and  $X_2$  vectors for the CI structure of pyrazoline +  $\text{CH}_2\text{Cl}_2$  involved in the hydrogen abstraction mechanism (Redrawn with permission from ref. Olivucci and Sinicropi 2005)

The conical intersection for the hydrogen abstraction mechanism (in the presence of  $\text{CH}_2\text{Cl}_2$ ) is characterized, with respect to the reactant pair, by shortening the H–N distance (from 2.22 to 1.02 Å) and simultaneously lengthening the C–H distance (from 1.07 to 2.01 Å). The structure on the conical intersection for this bimolecular reaction is given in [Fig. 39-15](#), whereas the degeneracy-lifting vectors are illustrated in [Fig. 39-16](#).

Motion along  $X_1$  stretches the intermolecular N–H distance whereas displacement along  $X_2$  causes an out-of-plane pyrazoline ring distortion, both translations lifting the degeneracy between the two states. Structural evolution along both displacements is illustrated in [Scheme 39-8](#). Translation along  $X_1$  leads to the radical pair (RP) while displacement





■ Scheme 39-8

**Characterization of the topology around the CI of associated pyrazoline–dichloromethane model pair**

along  $-X_1$  leads to production of an unstable ion pair (IP). Evolution in the  $X_2$  and  $-X_2$  directions leads to two equivalent ground state transition structures, featuring a distorted pyrazoline ring.

An analysis of the wavefunction indicates that the  $n,\pi^*$ -excited state correlates with the radical pair structure (derived from a complete *hydrogen atom* abstraction), whereas the ground state correlates with the ion pair (derived from *proton* abstraction), see ● Fig. 39-17a. Although this case study deals with bimolecular photochemical processes, it is in a sense similar to the retinal PSB models as the electronic configurations describing the intersecting states are interchanged by charge transfer. The charge distribution of the system along a circular cross section – spanning the plane defined by the  $X_1$  and  $X_2$  vectors and centered around CI – is displayed in ● Fig. 39-17b with  $\omega$  expressing the rotation. It reveals the existence of two distinct regions. The first region ( $0^\circ < \omega < 100^\circ$  and  $290^\circ < \omega < 360^\circ$ ) is characterized by an ion pair structure where the charge on the pyrazoline is positive while it is negative on  $\text{CHCl}_2$ . The second region  $100^\circ < \omega < 290^\circ$  is characterized by a covalent structure. The border between the two regions corresponds to two sudden electron transfer events, one from the  $\text{CHCl}_2$  anion to the pyrazoline cation yielding the RP configuration ( $\omega = 90^\circ$ ) and the second in opposite direction ( $\omega = 270^\circ$ ).

The molecular structure of the conical intersection along with the degeneracy-lifting vectors of the branching plane for the charge transfer process is given in ● Fig. 39-18. Notice that  $X_1$  is dominated by an out of plane deformation of the pyrazoline ring whereas  $X_2$  is dominated by the interfragment distance. The computed photochemical reaction path demonstrates that the excited state branch of the photochemical reaction path is dominated by an decrease in the distance between the pyrazoline and  $\text{N}(\text{CH}_3)_3$  fragments. After a low-lying excited state barrier, the evolution along the path leads to the formation of an exciplex located in the vicinity

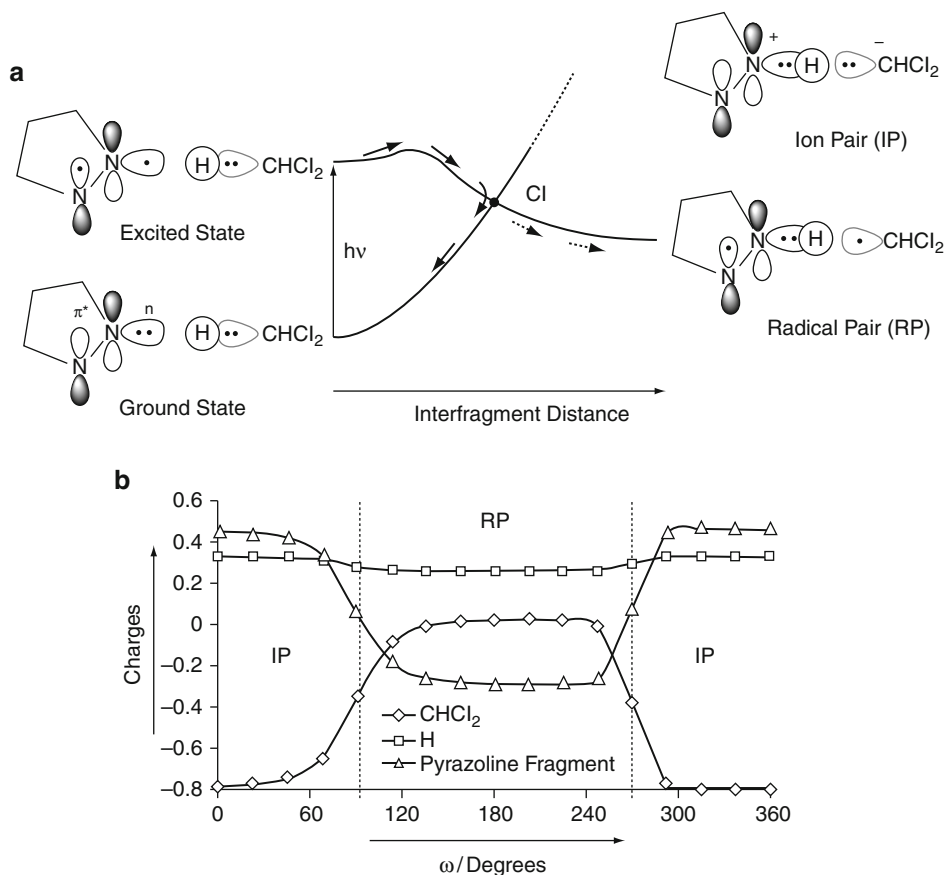
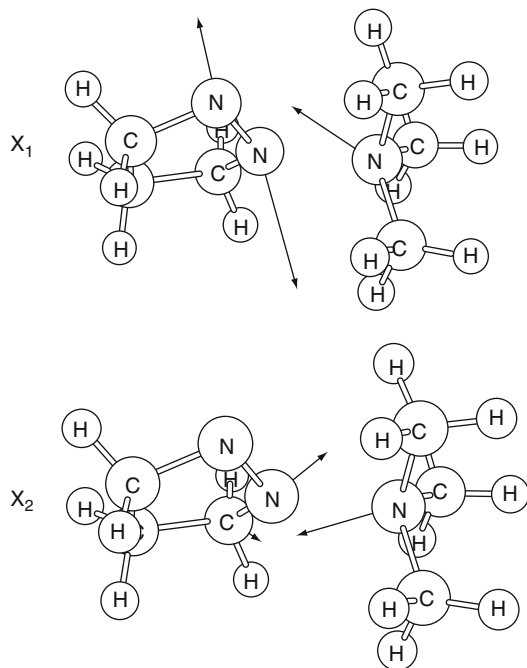


Fig. 39-17

(a) Modified state correlation diagram of the  $n, \pi^*$ -excited state (ES) of pyrazoline +  $\text{CH}_2\text{Cl}_2$  correlating with the radical pair (RP) derived from hydrogen atom abstraction and the ground state (GS) correlating with the ion pair (IP) derived from proton abstraction. (b)  $S_0$  fragment charges [au] along a circular cross section centered at Cl and spanning the branching plane (pyrazoline fragment, open triangles; hydrogen atom, open squares;  $\text{CHCl}_2$  fragment, open circles) (Redrawn with permission from ref. Sinicropi et al. 2001)

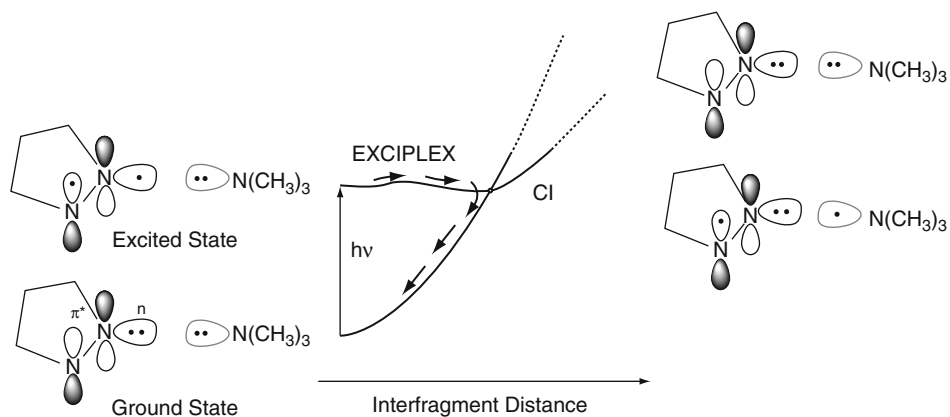
of a conical intersection. The intersection is accessed when the distance between the pyrazoline and nitrogen atoms of the amine is ca. 2 Å. In the exciplex, the computed amount of charge transfer from the trimethylamine lone pair to the excited state half-vacant nonbonding orbital of one pyrazoline nitrogen atom is about 0.3 electrons.

The exciplex N...N two-orbital/three-electron bond can be viewed as a mixture of a covalent ( $\text{N} = \text{N}^\bullet \cdots \text{NMe}_3$ ) and an ionic ( $\text{N} = \text{N}^{\bullet-} \cdots {}^+\text{NMe}_3$ ) electronic configurations. A steep rise of the ground state energy surface towards the conical intersection is due to a destabilizing two-orbital/four-electron repulsive interaction ( $\text{N} = \text{N} : \cdots : \text{NMe}_3$ ) (see Fig. 39-19).



■ Fig. 39-18

$X_1$  and  $X_2$  vectors for the CI structure of pyrazoline + trimethylamine involved in the charge transfer process (Redrawn with permission from ref. Olivucci and Sinicropi 2005)




■ Fig. 39-19

Modified correlation diagram for the interaction of the  $n,\pi^*$ -excited state of pyrazoline with an electron donor such as the trimethylamine reflecting the occurrence of an exciplexes and a conical intersection along the reaction pathway (Redrawn with permission from ref. Sinicropi et al. 2000)


## Case Studies of Chromophores Embedded in a Molecular Environment

### Green Fluorescent Proteins (GFP)

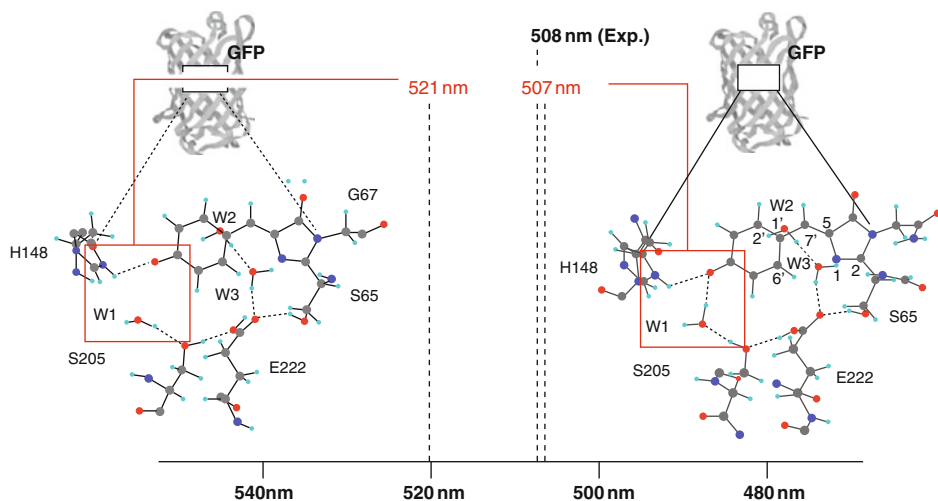
In 1961 the Green Fluorescent Protein (GFP) was discovered in the jellyfish *Aequorea Victoria* and became the first representative of the same named protein family (Shimomura 2009). Its chromophore is p-hydroxybenzylideneimidazolinone (HBDI), enclosed in a  $\beta$ -barrel structure. It emits a green fluorescence light if exposed to blue light. The corresponding fluorescence spectrum shows a single peak at 508 nm attributed to the anionic form of the chromophore. In contrast, in water solution the HBDI anion shows a blue-shifted fluorescence that has a very short lifetime.

The GFP chromophore has been studied extensively, both by means of experimental and theoretical methods. Sinicropi et al. (2005) performed the first QM/MM simulation of GFP suitable for the quantitative evaluation of  $\lambda_{\max}^a$  and  $\lambda_{\max}^f$ . Calculations were done at the CASPT2//CASSCF/CHARMM level of theory with the 6-31G\* basis set because a previous study (Martin et al. 2004) suggested that dynamic electron correlation is important to reproduce the observed quantities. The  $\lambda_{\max}^a$  was evaluated for the anionic ground state form in the emitting state (state I) and in a modified I state with a disrupted hydrogen bond between the chromophore and the closest water molecule (see  Fig. 39-20).

For the full protein model of the I state the calculated peaks for absorption and emission are 468 and 507 nm, respectively, compared with the experimental values of 495 and 508 nm (Brejc et al. 1997; Chattoraj et al. 1996) resulting in an error of less than 4 kcal · mol<sup>-1</sup>. A somewhat better agreement with experimental data is achieved by Altoe et al. (2007) using a similar computational protocol. The calculations were performed at the CASPT2//CASSCF/AMBER level for the chromophore with the same basis set. Prior the QM/MM excited state calculation the model was equilibrated by MD simulation. The authors calculated the absorption of 504 nm for the I state (experimentally 495 nm).

The GFP model (Sinicropi et al. 2005) shows that there is a charge translocation towards the imidazolinone moiety in the I state, indicating that the excited state is a charge transfer state. It is shown that the hydrogen bond between the proximal water molecule and the phenoxy oxygen of the chromophore localizes the negative charge on that oxygen atom. In fact, as reported in  Fig. 39-20, removing that water molecule has a great effect on structure and energy, which leads to a less stable structure (20 kcal · mol<sup>-1</sup> higher in energy). A different effect is found when comparing a protein model with the positively charged counter-ion Arg96 to a protein model without it: the protein environment balances the counter-ion effect to the same extent in S<sub>0</sub> and S<sub>1</sub>. A similar quenching effect is also observed for Rh (Strambi et al. 2007) (see below) despite its very different protein and chromophore structure.

Another member of the GFP protein family is asFP595, which was discovered in *Anemonia sulcata* (Quillin et al. 2005). It fluoresces brightly at 595 nm after intense illumination at 568 nm at room temperature. The X-ray crystal structure was obtained in 2005 for the dark state at 1.38 Å resolution. The chromophore was discovered to be the same as in GFP, and the initial hypothesis for explaining the fluorescence was a Z/E photoisomerization because the chromophore cavity can easily accommodate both the isomers, as was seen from the crystal structure. The first QM/MM study on asFP595 was carried out by Grigorenko et al. (2006). The ground state equilibrium structure was determined at the RHF/6-31G\*\* and B3LYP/6-31+G\* level while the



■ Fig. 39-20

**Right:** Chromophore cavity of the model for the GFP fluorescent state I displaying the hydrogen bond network and the values of the computed  $\lambda_{\max}^f$  value. **Left:** The change in the hydrogen bond network by disruption of the W1–chromophore bond leads to a red shift in the predicted  $\lambda_{\max}^f$

excited state properties were studied at the CASSCF/AMBER level with the 6-31+G\* basis set (with a 10 electron/10 orbital active space). The QM region included the chromophore unit and the sidechains of the His197, Glu215, and Arg92 residues, all of which are involved in the hydrogen bonding to the chromophore. For the HBDI moiety three options were considered: the *E* anion, the *Z* anion, and the *E* zwitterion. The protein environment was shown to stabilize the zwitterion with respect to the gas phase, which confirmed the importance of evaluating the role of the protein matrix. The CASSCF vertical transition energies give support to the experimentally based hypothesis that the dark state features an anionic or zwitterionic *E* conformation, while the emitting state features an anionic *Z*-isomer formed upon light absorption by the *E* ground state. However, it is known that the CASSCF vertical excitation energies are far from being quantitative and may change dramatically for transitions to charge transfer states upon CASPT2 correction.

A 2007 study by Schäfer and coworkers (Schaefer et al. 2007) shed light on the photochemical reaction path in asFP595, finding many similarities with GFP. They used TDDFT to establish the general features of the photocycle: after photon absorption the zwitterionic *E* dark state chromophore is converted into the anionic *Z* form by proton transfer from the imidazolinone ring to the Glu215 side chain and *E*→*Z* isomerization. A proton wire connects the chromophore cavity to the external solution in order to achieve protonation of the phenolate oxygen, which leads to the neutral *Z* form. Another proton wire is able to release protons from His197 to the solution along five residues and a buried water molecule. The proton transfer seems to be important in preventing the reverse photochemical reaction that would result from absorption of a second photon. Photoisomerization leading to changes in protonation states seems to be a general principle exploited by evolution: both bR and PYP rely on the same mechanism. Subsequently, the CASSCF method (Schaefer et al. 2008) was employed to gain

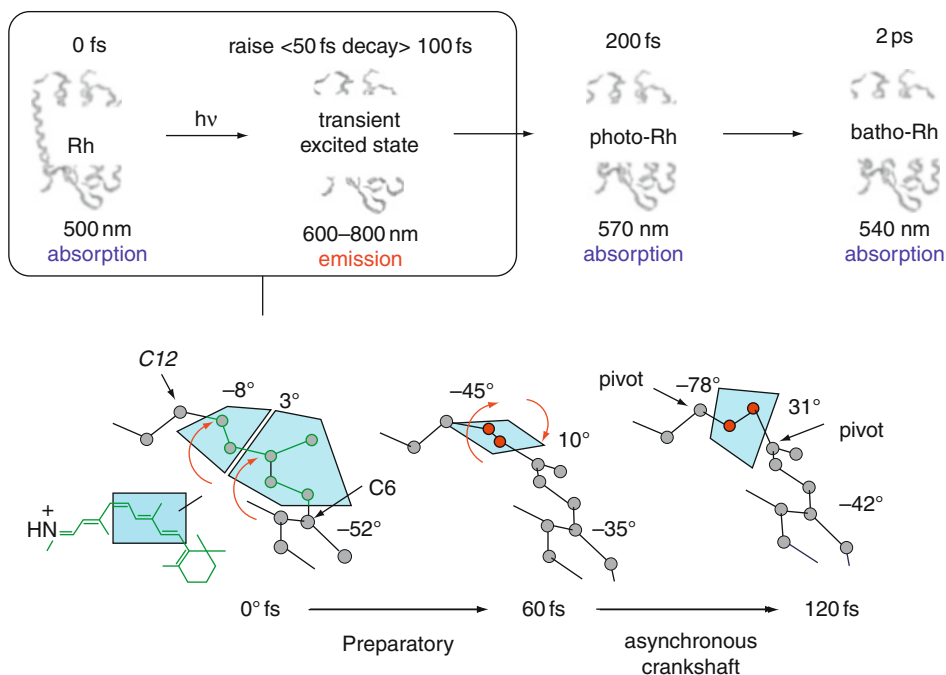
deeper insight into the mechanism and its features at the atomic level. A QM/MM MD simulation was performed, evaluating energies and forces of  $S_1$  and  $S_0$  at the CASSCF/3-21G level with a six electron/six orbital active space to reduce the computational cost. The QM region included only the chromophore, and the OPLS force field was used for the rest of the system. The results confirmed the conclusions of the previous paper in a more detailed way: the proton distribution in the active site controls the possible photochemical pathways of the protein-embedded chromophore. There are six different states, arising from the combination of *E* and *Z* conformations with a neutral, anionic, or zwitterionic chromophore. To switch from the non-fluorescent to the fluorescent state an *E* → *Z* isomerization is required. It has been observed to happen only for the neutral chromophore which is poorly populated. The fluorescent state is the zwitterionic *Z* form reached upon protonation of Glu215, but this state is also sparsely populated. These two findings are in agreement with the observed low overall photoisomerization quantum yield of asFP595. Moreover, excitation of the neutral *E* chromophore should be performed with green light otherwise the blue-shifted *Z* photoproduct would isomerize back. The neutral *Z* state is more populated than the other *Z* forms, so the efficiency of the back reaction, i.e., the switching off, is very high.

## Understanding the Spectral Tuning in Retinal Proteins

Rhodopsin, the dim-light photoreceptor in vertebrate retina, belongs to the G-protein-coupled receptor family. The 11-*cis*-retinal (PSB11) that is covalently bound to Lysine 296 via a Schiff-Base link serves as the chromophore (► Fig. 39-2). Upon light absorption PSB11 undergoes a stereoselective *Z/E* isomerization to the all-*trans* isomer, which leads to a protein-wide conformational change that initiates light perception. As summarized in ► Fig. 39-21, this is an ultrafast photochemical reaction featuring a ~100 fs lifetime of the excited state and a 200 fs appearance-time of the vibrationally hot intermediate photorhodopsin (photo-Rh). The first isolable intermediate, bathorhodopsin (batho-Rh), is detected on a 2 ps time scale. Below we review the results of recent research efforts to investigate the mechanism of the excited state isomerization in Rh using a QM/MM model.

More than 30 years ago Warshel proposed, on the basis of semiempirical simulations, an isomerization mechanism that could explain how this process can occur in the restricted space of the Rh binding pocket (Warshel 1976). Since two adjacent double bonds were found to isomerize simultaneously the mechanism reveal a so-called bicycle pedal motion. Due to the concerted rotation of two double bonds in opposite directions the overall conformational change is minimized and hence this mechanism was found to be space-saving. The empirical valence bond (EVB) method (Warshel and Levitt 1976) was used to compute the excited state potential energy surface of the chromophore during a trajectory calculation where the steric effects of the protein matrix were modeled by specific restraints on the retinal atoms. Since then, Warshel and his coworkers have improved the model employing better structural data and new computational developments (Warshel and Barboy 1982; Warshel and Chu 2001; Warshel et al. 1991). The main refinement of the bicycle pedal mechanism was that the simultaneous rotation of the adjacent double bonds is aborted at a twist of 40° and leads to the isomerization of only one bond (Warshel and Barboy 1982).

Since the crystal structure of the rhodopsin protein became available in 2000, a more accurate description of the protein environment was available for computational investigation and for the interpretation of the experimental data. In 2003 Ferré and co-workers performed the



■ Fig. 39-21

**Top:** Observed  $\lambda_{\text{max}}^a$  values and excited state lifetimes associated with the initial steps of the photoisomerization of Rh. **Bottom:** Schematic representation of the excited state isomerization motion of PSB11 dominated by an asynchronous crankshaft structure deformation (Frutos et al. 2007) and documented for a CASSCF/AMBER model of Rh

first QM/MM simulations using the *ab initio* CASPT2//CASSCF/AMBER protocol applied to the protein-embedded retinal chromophore in the excited state (Ferré and Olivucci 2003b). In this study the authors have truncated the retinal chromophore at the QM level to make the calculation feasible. The authors used a five double-bond N to C6 retinal fragment. The CASSCF level of theory was used to determine the ground state equilibrium structure with all 10  $\pi$ -electrons in 10  $\pi$ -type orbitals comprising the active space. The protein was modeled with the AMBER force field.

Starting from the 1HZX (Palczewski et al. 2000) crystallographic structure, it was shown that the CASPT2//CASSCF/AMBER protocol can be used to construct a Rh model featuring the full retinal chromophore treated at the QM level. This model could reproduce the stationary spectroscopic features (see ► Fig. 39-22 top left for a comparison of the observed and computed values, given in italics and plain text, respectively) with an error similar to the one found for GFP systems described above. For instance, the  $\lambda_{\text{max}}^a$  is reproduced with only 3 kcal · mol<sup>-1</sup> error (476 nm versus 498 nm). But also the computation of the corresponding  $\lambda_{\text{max}}^a$  in solution employing the same methodology led to an error within 2 kcal · mol<sup>-1</sup> of the so-called opsin-shift (the 445 nm  $\lambda_{\text{max}}$  observed for PSB11 in methanol is red-shifted to 498 nm in Rh).

Furthermore we have been able to investigate the effect of water relocation inside the Rh cavity (Strambi et al. 2007). A second water (W2) had to be placed into the protein binding

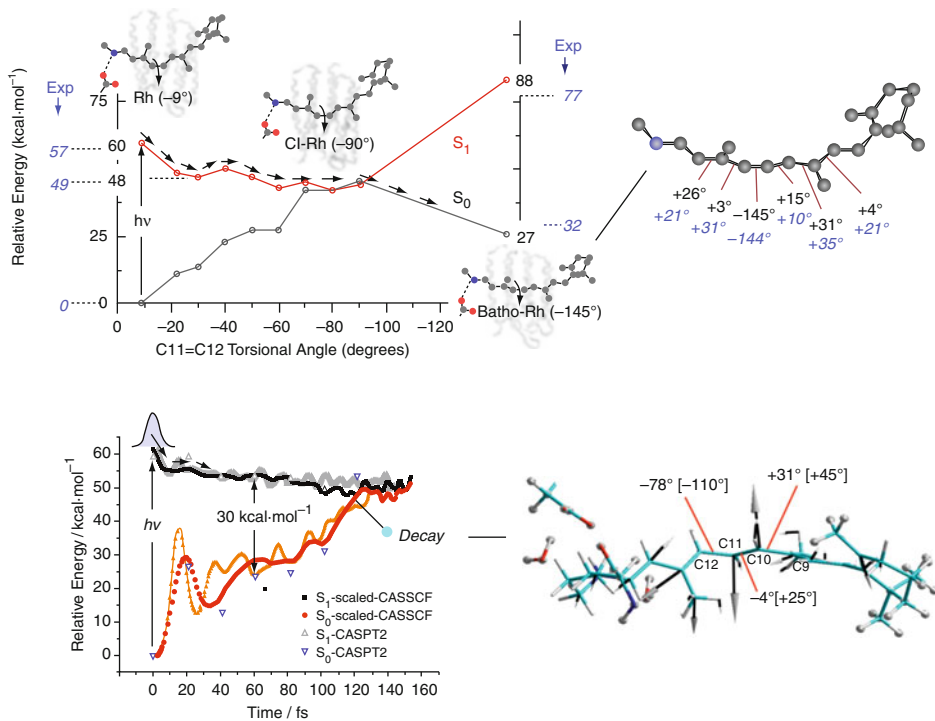


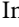

Fig. 39-22


**Top left:** Energy profiles along the  $S_1$  photoisomerization coordinate of Rh computed at the CASPT2//CASSCF/AMBER level. The PSB11 structure on the right corresponds to the first isolable intermediate batho-Rh. The values in italics correspond to observed values (See ref. Kukura et al. 2005). **Bottom:** Scaled-CASSCF  $S_1$  and  $S_0$  energy profiles and CASPT2 points along the  $S_1$  trajectory of Rh. The  $S_1$  and  $S_0$  energy profiles are reported for two Rh models based on the 1HZX (red and black lines) and 1U19 (orange and grey lines) crystallographic structures (M. M. Huntress, M. Olivucci, unpublished data). The structure on the right represents the point of decay (conical intersection structure) reached after  $\sim 120$  fs time evolution. The vectors represent the velocities at the decay point and clearly show a crankshaft-like motion at the center of the PSB11 backbone

pocket according to qualitative space filling and electrostatic considerations since the original 1HZX crystallographic structure only showed the presence of one water molecule (W1). However, the more recent and better resolved crystallographic structure (PDB Code: 1U19) (Okada et al. 2004) points to a different location and different hydrogen bonding for W2. The sensitivity of  $S_0 \rightarrow S_1$  excitation energies with respect to the position of W2 has been investigated by constructing a new Rh model with the revised water placement. The results from the refined structure indicate a fairly low sensitivity of the  $\lambda_{\max}^a$  to the significant geometrical change of the salt bridge region, which suggests that there is a compensation mechanism that counteracts the effects of this change on the  $\lambda_{\max}^a$ . Our analysis points to a displacement of the chromophore to a cavity region with a larger positive electrostatic potential as a means to offset the effect of the decrease in NH(+)-OI(-) salt bridge distance. We have also compared the effect of a



reduction of the full opsin model to a model with only the 27 amino acids of Palczewski's cavity (Palczewski et al. 2000), those that surround the retinal. It was found that the value predicted for the  $S_0 \rightarrow S_1$  excitation energy is substantially the same indicating that for Rh the charges of distant residues are of minor importance for the optical absorption features of PSB11. Of course, we do not expect this to be a general result. Highly truncated protein models should always be applied carefully until a systematic analysis is carried out to determine their limitations and reliability.

In  Fig. 39-22 top left, we report the  $S_1$  branch of the photochemical reaction path of Rh computed in terms of a relaxed scan driven by the torsional deformation of the reacting bond. Using this data we have located and assigned the  $S_1$  structure that corresponds to transient fluorescent state I. We then located the structure of the lowest lying  $S_1/S_0$  CI (CI-Rh) that also corresponds to the local  $S_1$  minimum. This structure displays a  $\sim 90^\circ$  twisted C11–C12 bond. Starting from the CI-Rh geometry, using standard optimization, the first stable ground state intermediate bathorhodopsin (batho-Rh) has been located. It exhibits absorption at 540 nm and features an all-*trans*-like chromophore structure ( $\sim 150^\circ$  dihedral angle around the C11–C12 double bond). The computed structure of batho-Rh can be compared with the structure that was experimentally derived by Mathies and coworkers (Kukura et al. 2005) by femtosecond resolved resonance Raman spectroscopy (see  Fig. 39-22 top right). The comparison indicates that it is possible to predict the structure of an intermediate. Concerning the photon energy of  $\sim 32 \text{ kcal} \cdot \text{mol}^{-1}$  that is efficiently stored in batho-Rh, the results of our CASPT2//CASSCF/AMBER energy profile show that we reproduce this quantity with an error of  $5 \text{ kcal} \cdot \text{mol}^{-1}$ .

A mechanistic picture of the space-saving isomerization mechanism is derived from the reaction path of the Rh QM/MM model and the associated structural deformation. The predominant change in the retinal geometry that occurs immediately after excitation leading to the fluorescent state I is a bond length alteration (BLA) in the  $-C9 = C10 - C11 = C12 - C13 = C14-$  moiety. A complete inversion between single and double bonds is found at the geometry characterizing the state I. The CI-Rh displays a highly helical structure compared with Rh and FS-Rh and is mainly characterized by a large structural change in the  $-C9 = C10 - C11 = C12 - C13 = C14-$  moiety. Thus, the motion driving the  $S_1 \rightarrow S_0$  decay is mainly torsional with a rotation of  $\sim 68^\circ$  ( $22^\circ \rightarrow 90^\circ$ ) around the C11 = C12 bond, and  $37^\circ$  and  $15^\circ$  twisting around the C9 = C10 and C13 = C14 bonds, respectively. Therefore, from a general point of view, during photoisomerization the structural changes do not occur exclusively at the central double bond but also involve the other two adjacent double bonds, which lead to a global change in the helicity of the chromophore. A mechanism can be derived considering the largest changes. These involve the torsion about the reactive bond C11 = C12 and about the adjacent C9 = C10 bond. As highlighted in  Fig. 39-21 (bottom) these twisting deformations occur in opposite directions and results in the rotation of the  $-CH-CH-$  moiety with respect to the remaining framework. The mechanism confirms that the space-saving motion imposed by the tight Rh cavity is of the crankshaft type. However, since the progression about the C9 = C10 bond is more limited, we can talk of an asynchronous crankshaft mechanism (Frutos et al. 2007). Furthermore, a comparison of the CI-Rh structure with the batho-Rh structure establishes (consistent with the experimental data) that the less twisted C9 = C10 reverts to its original stereochemistry after ground state relaxation, so we can talk of an aborted asynchronous crankshaft mechanism.

Another widely studied retinal protein is bacteriorhodopsin (bR), a light-driven ion pump discovered in *Halobacterium salinarum* in 1971 (Oesterhelt and Stoeckenius 1971). It is a membrane protein, which upon illumination generates and maintains a proton gradient across the

cell membrane (Oesterhelt and Stoeckenius 1973). The gradient can be used as a source of energy, for example, by adenosine triphosphate synthase. bR shares some similarities with the visual rhodopsin: seven transmembrane  $\alpha$ -helices and a protonated Schiff base with lysine-bound retinal as the chromophore. The X-ray crystal structure was first obtained at 3.50 Å resolution in 1996 (Grigorieff et al. 1996). By 1999, the resolution had improved to 1.55 Å (Luecke et al. 1999). The bR photocycle consists of several intermediates labeled K, L, M, N, and O, which were characterized by spectroscopy and trapped at low temperature in order to be studied by crystallography (Balashov and Ebrey 2001; Lanyi 2000). Light absorption triggers the *Z/E* isomerization of the C13 = C14 double bond of the PSBAT chromophore. The bond isomerization is completed at the K intermediate, yielding a 13-*cis* chromophore (PSB13); the following thermal relaxation leads to Schiff base proton transfer to the Asp85 counter-ion, in the L and M steps. The proton flux is completed during the remaining part of the photocycle, along with other accompanying proton transfers and protein structural changes.

The first *ab initio* QM/MM calculation on bR was reported by Hayashi et al. using multi-configurational methods to evaluate the excited state properties (Hayashi and Ohmine 2000). The protein model was based on the crystal structure determined by Luecke et al. (1999) where the missing residues were taken from the PDB structures 2BRD (Grigorieff et al. 1996), 1C3W, (Luecke et al. 1999) and 1QHJ (Belrhali et al. 1999). The geometry was optimized at the HF level, using DZV and 3-21G basis sets with polarization functions on oxygen atoms. CASSCF(12,9) was employed to calculate retinal excitation energies. Five different models were built, each with different atoms included in the QM region. The results demonstrated that the protein environment affects the absorption properties of the chromophore. The side chains and the water molecules in the binding pocket affect the geometry of the retinal, forcing a twisting of the C13 = C14 double bond. The protein environment is anionic near the Schiff base, which stabilizes the ground state with respect to the excited state, causing a blue shift of the  $S_0 \rightarrow S_1$  excitation energy.

Later the Schulten group (Hayashi et al. 2001) performed a further analysis to elucidate the physical mechanisms of the observed spectroscopic tuning in the rhodopsin family. A comparison between bR and the sensory rhodopsin II (sRII) was done to understand the origin of the change in  $\lambda_{\max}^a$  from 568 nm in bR to 497 nm in sRII. This difference was observed experimentally, in spite of the same chromophore in both proteins and the similar protein environments. As in the previous work, a QM/MM methodology was employed, with AMBER as the MM force field. The equilibrium geometries of the QM regions were computed at the HF/DZV level. The excitation energies were evaluated with a CASSCF(10,11) wave function. The QM region included the retinal, the retinal-bound lysine (starting from C $\gamma$ ), and parts of the binding pocket: two aspartic acid residues (starting from C $\beta$ ) and three water molecules. The comparison between bR and sRII was performed by calculating the contributions to the  $S_0$ – $S_1$  excitation energy: the total energy was rewritten as a sum of the energy of the isolated chromophore, the electronic reorganization energy arising from the modification of the wave function in the presence of the protein, and the electrostatic interaction energy between protein and chromophore. The results showed that the main contribution is electronic reorganization in the retinal and a closer inspection of the structures showed a reduced counter-ion–Schiff base distance in sRII compared with bR. This is the reason for the blue shift, consistent with the picture given in a previous paper (Hayashi et al. 2001).

Another spectroscopic feature of the bR photocycle was addressed by the same group in 2002 (Hayashi et al. 2002). The early K and L intermediate models were built using MD and refined with QM/MM optimization, following the same method as described above. The

geometry optimization showed an increased chromophore distortion on passing from the ground state to the K intermediate. Moreover, the local hydrogen bond network is perturbed: a water molecule is displaced and the hydrogen bond between Thr89 and Asp85 is broken because the latter group undergoes a conformational change. Another result of that change is the reduction of the distance between the Asp85 carboxyl group and the Schiff base, which is thought to prompt the proton transfer in the following L-to-M process. Regarding the optical properties, K and L intermediates are red-shifted with respect to the initial absorption of bR. The excitation energies were evaluated at the CASSCF(12,11)//HF level, with a three state averaged calculation followed by state specific computation for  $S_0$  and  $S_1$ . The theoretical results are in good agreement with the experimental red shift, even though the absolute values are quite different and the spectroscopic shifts are overestimated. The reason for the shortcomings of the computational theory in this case is the failure of the CASSCF method to account for dynamic correlation. An analysis of the individual contributions to the total excitation energy allows one to pinpoint the main factors affecting the spectroscopic shift. Chromophore distortion around the C15 = N and C13 = C14 double bonds was found to be the main factor. It destabilizes  $S_0$  more than  $S_1$ , therefore reducing the energy gap. Another factor is the reduced electrostatic interaction between protein and chromophore, which increases the  $S_0$  energy without affecting  $S_1$ , where the charge is more delocalized towards the  $\beta$ -ionone ring. Nevertheless the geometry is optimized at the HF level, which is known to overestimate bonding character, compared with post-SCF methods, which leads to a likely underestimation of bond torsion in the chromophore.

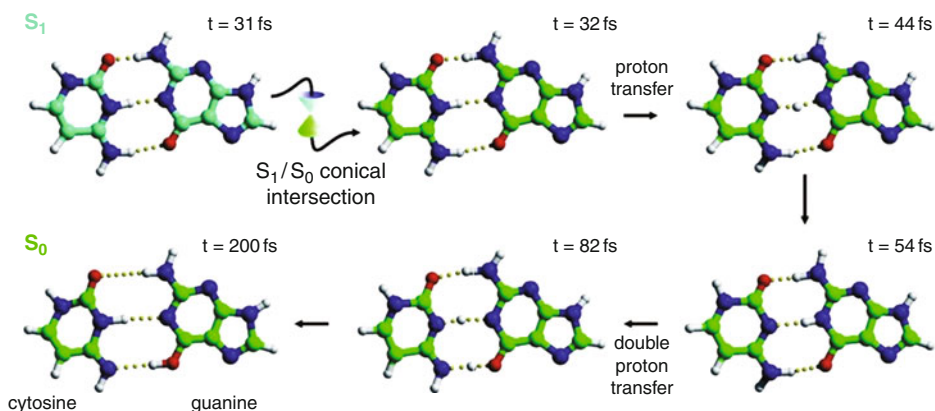
## Deactivation Mechanism in Cytosine-Guanine DNA Base Pair

Deoxyribonucleic acid (DNA) is a common biomolecule in all living organisms that contains the genetic information used for their development and functioning. It is composed of nucleotides, with backbones made of sugars and phosphate groups joined by ester bonds, forming long polymer chains. Attached to each sugar is one of only four bases: adenine (A), cytosine (C), guanine (G), and thymine (T). These bases belong to two types of organic molecules – adenine and guanine are purines that are fused five- and six-membered heterocyclic compounds, while cytosine and thymine are pyrimidines, which are six-membered rings. A pair of strands is usually arranged in the shape of a double helix by strong hydrogen bonds between the bases that stack upon each other. Due to the aromatic character of the nucleotide bases DNA absorbs in the harmful ultraviolet (UV) region of the spectrum. Hence, UV irradiation is one sort of mutagen that can damage DNA and subsequently lead to cancer. It is not surprising that DNA and its building blocks have been extensively investigated by computational quantum chemistry. The full coverage of the applications goes beyond the scope of this book chapter. Instead we are reporting an investigation using multiconfigurational *ab initio* calculations combined with AMBER force field in a QM/MM approach to study ultrafast radiationless deactivation mechanism of cytosine-guanine inter-strand base pair (Groenhof et al. 2007).

Groenhof et al. (2007) used a multiconfigurational approach as part of the QM/MM setup to study the inter-strand excited state proton transfer. One of the fastest deactivation processes in DNA was related to the cytosine-guanine base pair occurring on sub-picosecond time-scale. Therefore excited state molecular dynamics were employed to track this reaction. CASSCF with a reduced active space of eight electrons in eight orbitals and a 3-21G basis set was employed to model the molecular dynamics of the photoactivated C–G base pair. A surface hopping algorithm was used to detect a transition from the excited to the ground state.

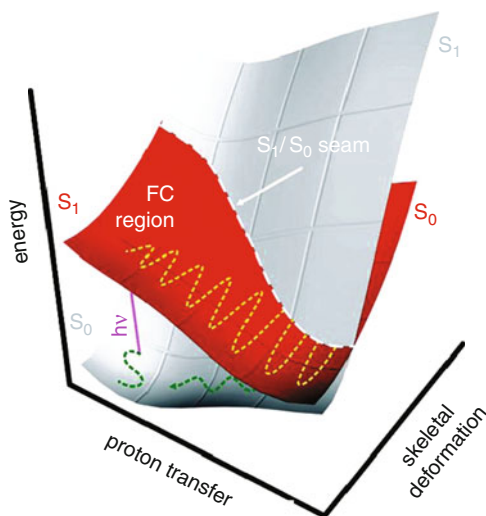
The crystal structure of the human DNA/topoisomerase I complex provided the initial coordinates for the QM/MM simulations. In total, 22 base pairs of B-DNA molecule were used. The partitioning of the system was done in a way that the cytosine-guanine base pair in the center of the molecule was described at the QM level. The remainder of the system was modeled with AMBER force field (Case et al. 2002). The chemical bonds between the bases and the deoxyribose sugar rings connecting the QM and the MM subsystems were replaced by constraints and the QM part was capped with two hydrogen link atoms. To equilibrate the DNA and the solvent prior to the QM/MM simulations, the system was equilibrated classically for 1,000 ps. The initial conditions for the excited-state simulations were obtained by taking 20 frames at equal time intervals from an additional 2 ps ground state trajectory at the CASSCF(8,8) level. In the excited state MD simulations, a time step of 0.5 fs was used.

In consequence, the ultrafast photodeactivation mechanism of the cytosine-guanine base pair was uncovered by the molecular dynamics simulations (see **Fig. 39-23**). The excitation to the charge transfer state induces a transfer of a proton from guanine to cytosine within a few femtoseconds. After the proton transfer, the system approaches the conical intersection seam and returns to the ground state. However, within a few femtoseconds the seam is closed again, and a second hop takes the system back to  $S_1$  where it stays until another hop occurs. Most trajectories showed several hopping events between the  $S_1$  and  $S_0$  surfaces, with an average excited state lifetime of 200 fs for the entire process. This can be rationalized by the topology of the  $S_1$ - $S_0$  intersection space (see **Fig. 39-24**). The proton transfer coordinate in the vicinity of the  $S_1$  minimum is parallel to the extended hyperline and allows multiple transitions between the crossing states.



**Fig. 39-23**

Sequence of events after the excitation. A proton is abstracted from guanine and accepted by cytosine. After the decay to the ground state via a conical intersection the proton returns to the guanine base. The excess thermal energy that is released upon returning to  $S_0$  is responsible for spontaneous double proton transfer (at 82 fs) which leads to the formation of a different tautomeric state of the base pair (200 fs) (Redrawn with permission from ref. Groenhof et al. 2007)



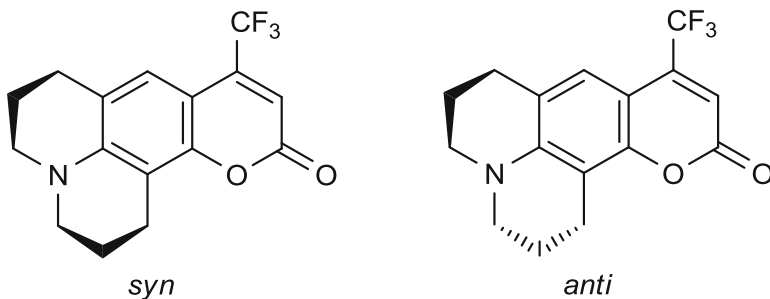
■ Fig. 39-24

Excited and ground state potential energy surface crossing of the cytosine-guanine base pair. The two reaction coordinates are proton transfer and skeletal deformation of the bonds. The *dashed yellow* and *green lines* schematically represent a path sampled in a typical trajectory on the  $S_1$  and the  $S_0$  potential, respectively. Along the proton-transfer coordinate the system moves out of Franck–Condon region to the minimum of the excited state. Due to the oscillations of the second reaction coordinate the trajectory hits the seam more than once (Redrawn with permission from ref. Groenhof et al. 2007)

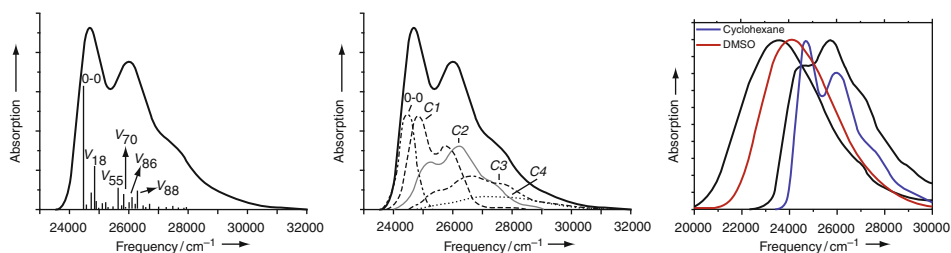
## Absorption Spectra of a Coumarin in Solution

The calculation of absorption spectra is of great interest to chemists, since these spectra provide a wealth of information about the molecule, its environment and its properties. As a result of solvent effects and solute-solvent interactions the spectra can be quite complex. In addition, some of the information can be convoluted under the broad bands. Nowadays, computational photochemistry serves as a standard tool for spectroscopists, used to assign the experimental spectra. Until recently the calculations yield simple stick absorption spectra, which show the excitation energies and their relative intensities, without taking environmental effects into account. Recent advances in quantum chemistry allow researchers to treat solvents and to calculate vibrational contributions to the spectra. Here we present a case study of coumarin C153 (► [Scheme 39-9](#)) computed by TD-DFT including solvent effects considered by polarized continuum model (PCM). Improta, Barone, and Santoro have studied the spectra in two different solvents: cyclohexane and dimethylsulfoxide (DMSO) (Improta et al. 2007). Coumarin C153 was selected to evaluate this novel methodology because it exhibits significantly different polarizabilities on its ground and electronically excited states. Therefore solvents with different polarities lead to large solvatochromic shifts that ought to be accounted for by the simulations.

The calculated stick absorption spectrum of the *anti* isomer of coumarin at 0 K in cyclohexane is shown in ► [Fig. 39-25 left](#). The authors employ an algorithm for automatic selection of transitions between vibrational states since the full set is too computationally demanding. After harmonic analysis the algorithm was used to select  $27 \cdot 10^6$  transitions out of a total of  $10^{36}$



■ Scheme 39-9



■ Fig. 39-25

Calculated spectra of C153 in cyclohexane. *Left*: 0 K stick spectrum and its assignment including transitions with one quantum in a single oscillator. *Middle*: A decomposition of the spectrum (*thick line*) in its components, where  $C_n$  dominates collection of transitions to vibrational states with the same number  $n$  of simultaneously excited oscillators. *Right*: Calculated spectra in cyclohexane (*blue*) and DMSO (*red*) compared to the experimental spectra (*black*) (Redrawn with permission from ref. Improta et al. 2007)

states. For the convolution of the spectrum the full width at half maximum of a Gaussian was chosen to match the main experimental bands. The spectrum was found to be unaltered when calculated for 300 K and also to be practically indistinguishable for the *anti* and *syn* isomers. The line shapes of the calculated spectrum resemble its experimental counterpart as shown for *anti* coumarin in cyclohexane (▶ Fig. 39-25 middle). The two-peak structure with a spacing of  $1,400\text{ cm}^{-1}$  is qualitatively reproduced. The first band is mainly due to the 0–0 transition and a contribution from transitions to the single vibrationally excited state (C1). However, the computed spectrum is found to be blue-shifted by  $400\text{ cm}^{-1}$ . The second band is composed of contributions from transitions to the first (C1), second (C2), and third (C3) vibrational states. The only deviation from the experimental spectrum is manifested in the relative height of these two bands.

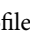
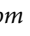
In DMSO the spectrum consisting of an asymmetric broad band, extended towards the blue wing of the maximum, is correctly reproduced by the simulation (▶ Fig. 39-25 right). This proves the reliability of the calculated vibrational progression hidden within the band. However, similar to the case of cyclohexane, the spectrum is found to be red-shifted by  $400\text{ cm}^{-1}$ . The authors ascribe the latter to the effect of dynamic solvent fluctuations which are much more pronounced in polar solvents. Finally, the DMSO→cyclohexane solvatochromic shift is estimated to be only  $150\text{ cm}^{-1}$  smaller than its experimental counterpart.


Using this novel protocol Improta, Barone, and Santoro were able to simulate the spectrum of coumarin C153 in different solution environments with a high degree of accuracy. Complex band structures were reproduced for solvents of varying polarities with a computational procedure feasible for large molecular systems.

## Excited State Molecular Dynamics

### Tracking the Photoisomerization of Retinal in Different Environments

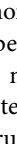
The first attempts to study the photoisomerization of the retinal chromophore by using *ab initio* excited state molecular dynamics were reported by Robb and coworkers (Vreven et al. 1997; Weingart et al. 2004) focusing on a model chromophore in the gas phase at the CASSCF level of theory. A more recent work by Weingart, again for an isolated retinal model, has shown that the quantum yield of the photoisomerization process depends critically on the initial retinal configuration (Weingart 2007). In the resting state of bovine rhodopsin, the chromophore deviates from planarity (Okada et al. 2004; Palczewski et al. 2000). By taking this retinal structure as a starting point for a series of excited state CASSCF semi-classical trajectories the author found that 70% of the trajectories ended at the all-*trans* photoproduct. This result suggests that selectivity and quantum efficiency might originate from strain imposed by steric interactions between the chromophore and the protein before photon absorption.

Recently we have reported the first  $S_1$  trajectory computation for Rh carried out with a scaled CASSCF force field that reproduces the static and transient spectroscopic parameters (Frutos et al. 2007). Because of the immense cost of the CASPT2 gradients, their application in trajectory computation is impossible for the retinal chromophore even if such a calculation is limited to a few hundred femtoseconds. However, CASSCF energies not only fail to reproduce the observed spectroscopic properties of Rh but also yield an energy profile that is too steep. In order to overcome this problem and evaluate a realistic trajectory we noticed that scaling the CASSCF isomerization energy profile along the  $S_1$  branch of the reaction path of  Fig. 39-22 top left, yields a curve overlapping with the corresponding CASPT2 curve (Frutos et al. 2007). As displayed in  Fig. 39-22 bottom left, the results show that this potential drives the chromophore to the CI on a 120 fs time scale. This time scale is in line with the observed excited state Rh lifetimes, which confirms the suitability of the scaled force field.

The assertion that a scaled CASSCF potential can approximate CASPT2 accuracy has been assessed by single point CASPT2//CASSCF/AMBER calculations along the trajectory. In  Fig. 39-22 bottom-left we report the  $S_1$  potential energy along the computed trajectory. Seven single point CASPT2/6-31G\*/AMBER computations have been performed to validate the scaled energy profile and to compute the correct  $S_1-S_0$  energy gap. The scaled CASSCF energies remain close to the CASPT2 energies all along the trajectory supporting the accuracy of our procedure.

Within 10 fs the  $S_1$  system undergoes a  $\sim 8 \text{ kcal} \cdot \text{mol}^{-1}$  energy decrease. Following this event the potential energy decreases slowly and monotonically until, after 110 fs, a region of degeneracy located  $\sim 15 \text{ kcal} \cdot \text{mol}^{-1}$  below the Franck-Condon point is reached. Since the initial motion is dominated by simultaneous double bond expansion and single bond contraction,  $8 \text{ kcal} \cdot \text{mol}^{-1}$  of vibrational energy must be initially located along this mode, which leads



to complete inversion of the double bond/single bond character centered in the  $-C9=C10-C11=C12-C13=C14-$  moiety. The analysis of the entire 140 fs  $S_1$  trajectory together with the resulting backbone deformation depicted in  Fig. 39-22, points to a space saving isomerization mechanism that includes the previously proposed bicycle pedal or crankshaft coordinate. The  $-C7=C8-C9=C10-C11=C12-$  segment of PSB11 twists with respect to the two remaining fragments, namely the  $-NH=C15-C14=C13-C12-$  and the  $\beta$ -ionone ring, during the first 60–70 fs. Such a motion is mainly characterized by a negative twist of the reactive  $-C11=C12-$  bond and a positive twist of the  $-C6-C7-$  bond. At the critical 60 fs mark the nature of the motion changes. The  $-C6-C7-$  twist stops and the  $-C9=C10$  bond adjacent to the reactive  $-C11=C12-$  bond starts to twist in the positive direction. In other words, the  $=C10-C11=$  fragment rotates with respect to the backbone, leading to an  $80^\circ$  twisted  $-C11=C12-$  bond and to a moderately twisted ( $\sim 30^\circ$ )  $-C9=C10-$  bond after 110 fs. The nature of this motion is confirmed by plotting the linear momentum vectors in the 65–110 fs region. Further studies have revealed that this motion may be an intrinsic property of the retinal chromophore (Schapiro et al. 2009).

A more recent CASSCF/AMBER trajectory study of the photoisomerization of Rh was reported by Hayashi et al. (2009). The protein model was constructed based on the 1U19 crystal structure. It was equilibrated using classical MD and provided, after a 2 ns equilibration, a sample of 14 different starting points for the trajectory calculations. The polyene chain of the retinal, including the double bond of the  $\beta$ -ionone ring, was treated at the CASSCF level using a DZV basis set. The active space was composed of 12  $\pi$ -electrons and 12  $\pi$ -type orbitals. The first two roots were averaged in the CASSCF wave function. In order to describe the interaction between the QM part and the MM part, mechanical embedding was employed. This is an important difference from the excited state trajectory presented above (Frutos et al. 2007) that uses electrostatic embedding instead. In mechanical embedding the interaction between the QM and the MM region is treated at the MM level, which is less accurate. However, the transition from the excited to the ground state was initiated using the energy difference as criterion, namely when it was less than  $7.5 \text{ kcal} \cdot \text{mol}^{-1}$ . In addition, a trajectory of isolated retinal was calculated using a structure taken from the equilibrated rhodopsin.

It was found that all 14 CASSCF/AMBER trajectories decayed to the ground state within 100 fs (the shorter time could be attributed to a lack of scaling and the unrealistically steep CASSCF energy surface), which is of the same order of magnitude as the trajectory by Frutos et al. (2007). Batho-Rh is formed in 13 cases and in one case a 9-*cis* isomer (isorhodopsin) is produced by a bicycle pedal isomerization of C9–C10 and C11–C12 bond. However, an accompanying rotation of  $60^\circ$ , on average, is found around C9–C10 in the 13 trajectories showing a crankshaft or aborted bicycle pedal-type mechanism, which is consistent with the previous findings.

The first QM/MM trajectory computation describing the photoisomerization of bR was reported by Hayashi et al. (2003). However, the selected QM part corresponded to a highly reduced PSBAT chromophore featuring only three double bonds. This was described by a three state averaged CASSCF wave function with 6  $\pi$ -electrons in a 6  $\pi$ -type orbitals active space with a DZV basis set. The MM part was described using AMBER for the protein and the TIP3P model for the water molecules. An ensemble of starting conditions was generated by a classical MD simulation of the resting state of bR at constant temperature (300 K). To compare the effect of the protein on the photoisomerization, trajectories of the same retinal model were calculated under vacuum. In total, 11 trajectories were performed to see if the high selectivity of the isomerization could be reproduced in the absence of the protein environment. It was found that the initial stretching relaxation is followed by a selective isomerization exclusively around



the C13–C14 bond. It should be mentioned that this double bond is the central one in the investigated model. Hence, its preference for rotation compared with the terminal bonds is expected. The analysis of the isomerization dynamics of the six isolated chromophore trajectories shows that four trajectories isomerize around C13–C14 and two around the terminal C15–N16 bond. The authors concluded that the high selectivity in bR is a result of the protein environment.

## Conclusion

---

In this chapter we have presented a few selected computational photochemistry case studies of model systems with increasing complexity, starting from isolated molecules that served as models in early works. The photochemical reaction paths of these systems were examined in mechanistic investigations, resulting in a general understanding of light-induced processes. Towards the end of the chapter we have given more recent examples of steady state spectra, minimum energy path calculations, and molecular dynamics simulations in different environments. More realistic models and rigorous simulation not only provided an explanation for the photochemical events, but also allowed a comparison with experimental data: the shape of spectra in solution can be convoluted, *ab initio* dynamics can predict excited state lifetimes and quantum yields, and conical intersections of chromophores in proteins can be located. All this reveals that the current stage of the tools of computational photochemistry are already providing results with accuracy comparable to experimental observables.

Nevertheless, we have also shown that some questions remain open, needing more accurate treatments which are still not feasible to date. Therefore further breakthroughs in computational photochemistry are anticipated. On one hand the development of quantum chemical methods and algorithms for effective computations is expected in the near future, whereas an increase of computational resources and computing power on the other hand ought to lead to another bloom in this research field.

## References

---

- Adams, T. R., Adamson, R. D., Austin, B., Baker, J., Bell, A. T., Beran, G. J. O., Baer, R., Besley, N. A., Brooks, B., Brown, S. T., Byrd, E. C., Casanova, D., Challacombe, M., Chai, J., Chakraborty, A. K., Cheng, C., Chien, S., Chipman, D. M., Cramer, C., Crittenden, D., Dachselt, H., Jr., R. A. D., Doerksen, R. J., Dombroski, J. P., Dreuw, A., Dunietz, B. D., Dutoi, A. D., Florian, J., Furlani, T. R., Epifanovsky, E., Gan, Z., Ghysels, A., Gilbert, A. T. B., Gill, P. M. W., Head-Gordon, M., Gwaltney, S. R., Hawkins, G., Hehre, W. J., Herbert, J. M., Heyden, A., Hohenstein, E. G., Hirata, S., Hsu, C., Ishikawa, N., Johnson, B. G., Jung, Y., Kedziora, G., Keil, F. J., Kelly, C., Khal-ullin, R. Z., Klunzinger, P., Korambath, P. P., Krylov, A. I., Kurlancheek, W., Kong, J., Kussmann, J., Lee, A. M., Lee, M., Levchenko, S. V., Liang, W., Lin, C. Y., Liotard, D., Livshits, E., Lochan, R. C., Lotan, I., Manohar, P., Marenich, A., Maslen, P. E., Maurice, D. R., Fusti-Molnar, L., Nair, N., Oana, M., O'Neill, D. P., Neuhauser, D., Ochsenfeld, C., Olson, R., Oumi, M., Peters, B., Pieniazek, P. A., Proynov, E. I., Rassolov, V. A., Rhee, Y., Ritchie, J. P., Rohrdanz, M. A., Rosta, E., Schaefer, H. F., III, Shao, Y., Sherrill, C. D., Schultz, N. E., Simmonett, A. C., Slipchenko, L. V., Sodt, A., Steele, R. P., Subotnik, J. E., Thanthiriwatt, K., Thom, A. J. W., Truhlar, D. G., Vanovschi, V., Voorhis, T. V., Wang, T., Warshel, A., White, C., Williams, C. E., Lee Woodcock, H., Wu, Q., You, Z., Zhang, W., & Zhao, Y. (2009). *Q-Chem* (3.2 ed.). Pittsburgh: Q-Chem, Inc.
- Altoe, P., Stenta, M., & Garavelli, M. (2007). Rhodopsin and GFP chromophores: QM/MM absorption spectra in solvent and protein. *AIP Conference Proceedings*, 963(2), 689–692.

- Andersson, K., Aquilante, F., Barysz, M., Bednarz, E., Bernhardsson, A., Blomberg, M. R. A., Carissan, Y., Cooper, D. L., Cossi, M., Devarajan, A., Vico, L. D., Ferré, N., Fülcher, M. P., Gaenko, A., Gagliardi, L., Ghigo, G., de Graaf, C., Hess, B. A., Hagberg, D., Holt, A., Karlström, G., Krogh, J. W., Lindh, R., Malmqvist, P.-Å., Nakajima, T., Neogrady, P., Olsen, J., Pedersen, T. B., Raab, J., Reiher, M., Roos, B. O., Ryde, U., Schimmelpfennig, B., Schütz, M., Seijo, L., Serrano-Andrés, L., Siegbahn, P. E. M., Stålring, J., Thorsteinsson, T., Varyazov, V., Widmark, P.-O., & Wolf, A. (2009). *MOLCAS* (Version 7.4. ed.). Lund: University of Lund.
- Andersson, K., Malmqvist, P. A., Roos, B. O., Sadlej, A. J., & Wolinski, K. (1990). 2nd Order perturbation-theory with a CASSCF reference function. *Journal of Physical Chemistry*, *94*(14), 5483–5488.
- Andruniow, T., & Olivucci, M. PSBAT absorption spectra in vacuo [Unpublished results].
- Andruniow, T., & Pawlikowski, M. (1998). On the Franck-Condon effects in the absorption spectrum of ClO<sub>8</sub> anion. The analysis based on the *ab initio* MCSCF method. *Acta Physica Polonica A*, *93*, 707–715.
- Anglada, J. M., & Bofill, J. M. (1997). A reduced-restricted-quasi-Newton-Raphson method for locating and optimizing energy crossing points between two potential energy surfaces. *Journal of Computational Chemistry*, *18*(8), 992–1003.
- Aquilante, F., De Vico, L., Ferré, N., Ghigo, G., Malmqvist, P.-Å., Neogrady, P., Pedersen, T. B., Pitoák, M., Reiher, M., Roos, B. O., Serrano-Andrés, L., Urban, M., Varyazov, V., & Lindh, R. (2009). *MOLCAS 7: The next generation*. *Journal of Computational Chemistry*, *31*(1), 224–247. doi:10.1002/jcc.21318.
- Balashov, S. P., & Ebrey, T. G. (2001). Trapping and spectroscopic identification of the photointermediates of bacteriorhodopsin at low temperatures. *Photochem Photobiol*, *73*(5), 453–462.
- Barbatti, M., & Lischka, H. (2008). Nonadiabatic deactivation of 9H-adenine: A comprehensive picture based on mixed quantum-classical dynamics. *Journal of the American Chemical Society*, *130*(21), 6831–6839. doi:10.1021/ja800589p.
- Barbatti, M., Ruckebauer, M., Szymczak, J. J., Aquino, A. J. A., & Lischka, H. (2008). Nonadiabatic excited-state dynamics of polar pi-systems and related model compounds of biological relevance. *Physical Chemistry Chemical Physics*, *10*(4), 482–494. doi:10.1039/b709315m.
- Bearpark, M. J., Robb, M. A., & Schlegel, H. B. (1994). A direct method for the location of the lowest energy point on a potential surface crossing. *Chemical Physics Letters*, *223*(3), 269–274.
- Belrhali, H., Nollert, P., Royant, A., Menzel, C., Rosenbusch, J. P., Landau, E. M., & Pebay-Peyroula, E. (1999). Protein, lipid and water organization in bacteriorhodopsin crystals: A molecular view of the purple membrane at 1.9 Å resolution. *Structure (London, England : 1993)*, *7*(8), 909–917.
- Ben-Nun, M., & Martinez, T. J. (1998). Nonadiabatic molecular dynamics: Validation of the multiple spawning method for a multidimensional problem. *Journal of Chemical Physics*, *108*(17), 7244–7257.
- Berman, H. M., Westbrook, J., Feng, Z., Gilliland, G., Bhat, T. N., Weissig, H., Shindyalov, I. N., & Bourne, P. E. (2000). The protein data bank. *Nucleic Acids Research*, *28*(1), 235–242.
- Bernardi, F., De, S., Olivucci, M., & Robb, M. A. (1990). The mechanism of ground-state-forbidden photochemical pericyclic reactions: Evidence for real conical intersections. *Journal of the American Chemical Society*, *112*(5), 1737–1744.
- Bernardi, F., Olivucci, M., Michl, J., & Robb, M. A. (1996a). Conical intersections in the theory of organic singlet photochemistry. *The Spectrum*, *9*, 1–6.
- Bernardi, F., Olivucci, M., & Robb, M. A. (1996b). Potential energy surface crossings in organic photochemistry. *Chemical Society Reviews*, *25*(5), 321–328.
- Bernardi, F., Olivucci, M., & Schlegel, H. B. (2006). Michael Alfred Robb: A short biography. *Molecular Physics*, *104*(5), 655–659. doi:10.1080/00268970600595129.
- Blomgren, F., & Larsson, S. (2005). Exploring the potential energy surface of retinal, a comparison of the performance of different methods. *Journal of Computational Chemistry*, *26*(7), 738–742.
- Braslavsky, S. E. (2007). Glossary of terms used in photochemistry, 3rd edition. *Pure and Applied Chemistry*, *79*, 293–465.
- Bravaya, K., Bochenkova, A., Granovsky, A., & Nemukhin, A. (2007). An opsin shift in rhodopsin: Retinal S0-S1 excitation in protein, in solution, and in the gas phase. *Journal of the American Chemical Society*, *129*(43), 13035–13042. doi:10.1021/ja0732126.
- Brejč, K., Sixma, T. K., Kitts, P. A., Kain, S. R., Tsien, R. Y., Ormó, M., & Remington, S. J. (1997). Structural basis for dual excitation and photoisomerization of the *Aequorea victoria* green fluorescent protein. *Proceedings of the National Academy of*

- Sciences of the United States of America*, 94(6), 2306–2311.
- Brooks, R., Bruccoleri, R. E., Olafson, B. D., States, D. J., Swaminathan, S., & Karplus, M. (1983). CHARMM: A program for macromolecular energy, minimization, and dynamics calculations. *Journal of Computational Chemistry*, 4, 187–217.
- Case, D. A., Pearlman, D. A., Caldwell, J. W., Cheatham, T. E., III, Wang, J., Ross, W. S., Simmerling, C. L., Darden, T. A., Merz, K. M., Stanton, R. V., Cheng, A. L., Vincent, J. J., Crowley, M., Tsui, V., Gohlke, H., Radmer, R. J., Duan, Y., Pitera, J., Massova, I., Seibel, G. L., Singh, U. C., Weiner, P. K., & Kollman, P. A. (2002). *AMBER* (7th ed.). San Francisco: University of California.
- Cembran, A., Bernardi, F., Olivucci, M., & Garavelli, M. (2005). The retinal chromophore/chloride ion pair: Structure of the photoisomerization path and interplay of charge transfer and covalent states. *Proceedings of the National Academy of Sciences of the United States of America*, 102(18), 6255–6260. doi:10.1073/pnas.0408723102.
- Chattoraj, M., King, B. A., Bublit, G. U., & Boxer, S. G. (1996). Ultra-fast excited state dynamics in green fluorescent protein: Multiple states and proton transfer. *Proceedings of the National Academy of Sciences of the United States of America*, 93(16), 8362–8367.
- De Vico, L., Olivucci, M., & Lindh, R. (2005). New general tools for constrained geometry optimizations. *Journal of Chemical Theory and Computation*, 1(5), 1029–1037. doi:10.1021/ct0500949.
- Dreuw, A., & Head-Gordon, M. (2005). Single-reference *ab initio* methods for the calculation of excited states of large molecules. *Chemical Reviews*, 105(11), 4009–4037.
- Fantacci, S., Migani, A., & Olivucci, M. (2004). CASPT2//CASSCF and TDDFT//CASSCF mapping of the excited state isomerization path of a minimal model of the retinal chromophore. *The Journal of Physical Chemistry B*, 108(7), 1208–1213. doi:10.1021/jp0362335.
- Farazdel, A., & Dupuis, M. (1991). On the determination of the minimum on the crossing seam of two potential energy surfaces. *Journal of Computational Chemistry*, 12(2), 276–282.
- Ferré, N., & Olivucci, M. (2003a). The amide bond: Pitfalls and drawbacks of the link atom scheme. *Theochem-Journal of Molecular Structure*, 632, 71–82. doi:10.1016/s0166-1280(03)00289-6.
- Ferré, N., & Olivucci, M. (2003b). Probing the rhodopsin cavity with reduced retinal models at the CASPT2//CASSCF//AMBER level of theory. *Journal of the American Chemical Society*, 125(23), 6868–6869. doi:10.1021/ja035087d.
- Ferré, N., Cembran, A., Garavelli, M., & Olivucci, M. (2004). Complete-active-space self-consistent-field/Amber parameterization of the Lys296-retinal-Glu113 rhodopsin chromophore-counterion system. *Theoretical Chemistry Accounts*, 112(4), 335–341. doi:10.1007/s00214-004-0593-0
- Frisch, M. J., Trucks, G. W., Schlegel, H. B., Scuseria, G. E., Robb, M. A., Cheeseman, J. R., Scalmani, G., Barone, V., Mennucci, B., Petersson, G. A., Nakatsuji, H., Caricato, M., Li, X., Hratchian, H. P., Izmaylov, A. F., Bloino, J., Zheng, G., Sonnenberg, J. L., Hada, M., Ehara, M., Toyota, K., Fukuda, R., Hasegawa, J., Ishida, M., Nakajima, T., Honda, Y., Kitao, O., Nakai, H., Vreven, T., Montgomery, J., Jr., Peralta, J. E., Ogliaro, F., Bearpark, M., Heyd, J. J., Brothers, E., Kudin, K. N., Staroverov, V. N., Kobayashi, R., Normand, J., Raghavachari, K., Rendell, A., Burant, J. C., Iyengar, S. S., Tomasi, J., Cossi, M., Rega, N., Millam, J. M., Klene, M., Knox, J. E., Cross, J. B., Bakken, V., Adamo, C., Jaramillo, J., Gomperts, R., Stratmann, R. E., Yazyev, O., Austin, A. J., Cammi, R., Pomelli, C., Ochterski, J. W., Martin, R. L., Morokuma, K., Zakrzewski, V. G., Voth, G. A., Salvador, P., Dannenberg, J. J., Dapprich, S., Daniels, A. D., Farkas, O., Foresman, J. B., Ortiz, J. V., Cioslowski, J., & Fox, D. J. (2009). *GAUSSIAN 09* (Vol. Revision A.1). Wallingford CT: Gaussian Inc.
- Frutos, L. M., Andruniów, T., Santoro, F., Ferré, N., & Olivucci, M. (2007). Tracking the excited-state time evolution of the visual pigment with multi-configurational quantum chemistry. *Proceedings of the National Academy of Sciences of the United States of America*, 104(19), 7764–7769. doi:10.1073/pnas.0701732104.
- Gonzalez-Luque, R., Garavelli, M., Bernardi, F., Merchan, M., Robb, M. A., & Olivucci, M. (2000). Computational evidence in favor of a two-state, two-mode model of the retinal chromophore photoisomerization. *Proceedings of the National Academy of Sciences of the United States of America*, 97(17), 9379–9384.
- Gordon, M. S., Schmidt, M. W., Frenking, G., Kim, K. S., & Scuseria, G. E. (2005). Advances in electronic structure theory: GAMESS a decade later. In C. Dykstra, G. Frenking, K. S. Kim, & G. E. Scuseria (Eds.), *Theory and applications of computational chemistry: The first forty years* (pp. 1167–1189). Amsterdam: Elsevier.
- Grabowski, Z. R., Rotkiewicz, K., & Rettig, W. (2003). Structural changes accompanying

- intramolecular electron transfer: Focus on twisted intramolecular charge-transfer states and structures. *Chemical Reviews*, 103(10), 3899–4032. doi:10.1021/cr9407451.
- Grigorenko, B., Savitsky, A., Topol, I., Burt, S., & Nemukhin, A. (2006). Ground-state structures and vertical excitations for the kindling fluorescent protein asFP595. *The Journal of Physical Chemistry B*, 110(37), 18635–18640.
- Grigorieff, N., Ceska, T. A., Downing, K. H., Baldwin, J. M., & Henderson, R. (1996). Electron-crystallographic refinement of the structure of bacteriorhodopsin. *Journal of Molecular Biology*, 259, 393–241.
- Groenhof, G., Bouxin-Cademartory, M., Hess, B., deVisser, S. P., Berendsen, H. J. C., Olivucci, M., Mark, A. E., & Robb, M. A. (2004). Photoactivation of the photoactive yellow protein: Why photon absorption triggers a trans-to-cis isomerization of the chromophore in the protein. *Journal of the American Chemical Society*, 126(13), 4228–4233.
- Groenhof, G., Schäfer, L. V., Boggio-Pasqua, M., Goette, M., Grubmuller, H., & Robb, M. A. (2007). Ultrafast deactivation of an excited cytosine-guanine base pair in DNA. *Journal of the American Chemical Society*, 129(21), 6812–6819. doi:10.1021/ja069176c.
- Groenhof, G., Schäfer, L. V., Boggio-Pasqua, M., Grubmuller, H., & Robb, M. A. (2008). Arginine52 controls the photoisomerization process in photoactive yellow protein. *Journal of the American Chemical Society*, 130, 3250–3251.
- Hayashi, S., & Ohmine, I. (2000). Proton transfer in bacteriorhodopsin: Structure, excitation, IR spectra, and potential energy surface analyses by an *ab initio* QM/MM method. *The Journal of Physical Chemistry B*, 104(45), 10678–10691.
- Hayashi, S., Tajkhorshid, E., Pebay-Peyroula, E., Royant, A., Landau, E. M., Navarro, J., & Schulten, K. (2001). Structural determinants of spectral tuning in retinal proteins-bacteriorhodopsin vs sensory rhodopsin II. *The Journal of Physical Chemistry B*, 105(41), 10124–10131.
- Hayashi, S., Tajkhorshid, E., & Schulten, K. (2002). Structural changes during the formation of early intermediates in the bacteriorhodopsin photocycle. *Biophysical Journal*, 83(3), 1281–1297.
- Hayashi, S., Tajkhorshid, E., & Schulten, K. (2003). Molecular dynamics simulation of bacteriorhodopsin's photoisomerization using *ab initio* forces for the excited chromophore. *Biophysical Journal*, 85(3), 1440–1449.
- Hayashi, S., Tajkhorshid, E., & Schulten, K. (2009). Photochemical reaction dynamics of the primary event of vision studied by means of a hybrid molecular simulation. *Biophysical Journal*, 96(2), 403–416.
- Hoffmann, M., Wanko, M., Strodel, P., König, P. H., Frauenheim, T., Schulten, K., Thiel, W., Tajkhorshid, E., & Elstner, M. (2006). Color tuning in rhodopsins: The mechanism for the spectral shift between bacteriorhodopsin and sensory rhodopsin II. *Journal of the American Chemical Society*, 128(33), 10808–10818.
- Improta, R., Barone, V., & Santoro, F. (2007). *Ab initio* calculations of absorption spectra of large molecules in solution: Coumarin C15313. *Angewandte Chemie International Edition*, 46(3), 405–408.
- Jorgensen, W. L., & Tirado-Rives, J. (1988). The OPLS [optimized potentials for liquid simulations] potential functions for proteins, energy minimizations for crystals of cyclic peptides and crambin. *Journal of the American Chemical Society*, 110(6), 1657–1666. doi:10.1021/ja00214a001.
- Kandori, H., Schichida, Y., & Yoshisawa, T. (2001). Photoisomerization in rhodopsin. *Biochemistry-Moscow*, 66, 1197–1209.
- Koga, N., & Morokuma, K. (1985). Determination of the lowest energy point on the crossing seam between two potential surfaces using the energy gradient. *Chemical Physics Letters*, 119(5), 371–374.
- Kukura, P., McCamant, D. W., Yoon, S., Wandschneider, D. B., & Mathies, R. A. (2005). Structural observation of the primary isomerization in vision with femtosecond-stimulated Raman. *Science*, 310(5750), 1006–1009. doi:10.1126/science.1118379
- Kutateladze, A. G. (2005). *Computational methods in photochemistry*. Boca Raton: Taylor & Francis.
- Laino, T., & Passerone, D. (2004). Pseudo-dynamics and band optimizations: Shedding light into conical intersection seams. *Chemical Physics Letters*, 389(1–3), 1–6. doi:10.1016/j.cplett.2004.02.110.
- Lanyi, J. K. (2000). Molecular mechanism of ion transport in bacteriorhodopsin: Insights from crystallographic, spectroscopic, kinetic, and mutational studies. *The Journal of Physical Chemistry B*, 104, 11441–11448.
- Levine, B. G., Ko, C., Quenneville, J., & Martinez, T. J. (2006). Conical intersections and double excitations in time-dependent density functional theory. *Molecular Physics*, 104(5–7), 1039–1051. doi:10.1080/00268970500417762
- Lischka, H., Shepard, R., Shavitt, I., Pitzer, R. M., Dallos, M., Müller, T., Szalay, P. G., Brown, F. B., Ahlrichs, R., Böhm, H. J., Chang, A., Comeau, D. C., Gdanitz, R., Dachsel, H., Ehrhardt, C.,

- Ernzerhof, M., Höchtl, P., Irlé, S., Kedziora, G., Kovar, T., Parasuk, V., Pepper, M. J. M., Scharf, P., Schiffer, H., Schindler, M., Schüler, M., Seth, M., Stahlberg, E. A., Zhao, J.-G., Yabushita, S., Zhang, Z., Barbatti, M., Matsika, S., Schuurmann, M., Yarkony, D. R., Brozell, S. R., Beck, E. V., & Blaudeau, J.-P. (2006). *COLUMBUS, an ab initio electronic structure program*. (release 5.9.1 ed.). Vienna: University of Vienna.
- Luecke, H., Schobert, B., Richter, H. T., Cartailler, J. P., & Lanyi, J. K. (1999). Structure of bacteriorhodopsin at 1.55 Ångstrom resolution. *Journal of Molecular Biology*, 291, 899–911.
- Martin, M. E., Negri, F., & Olivucci, M. (2004). Origin, nature, and fate of the fluorescent state of the green fluorescent protein chromophore at the CASPT2/CASSCF resolution. *Journal of the American Chemical Society*, 126(17), 5452–5464.
- Mathies, R. A., & Lugtenburg, J. (2000). The primary photoreaction of rhodopsin. In D. G. de Stavenga, W. J. & Grip, E. N. Pugh (Eds.), *Handbook of biological physics* (Vol. 3, pp. 55–90). Amsterdam: Elsevier Science Press.
- Migani, A., & Olivucci, M. (2004). A computational strategy for organic photochemistry. In W. Domcke, D. R. Yarkony, H. Köppel (Eds.), *Conical intersections: Electronic structure, dynamics and spectroscopy* (pp. 271–320). Singapore: World Scientific.
- Migani, A., Robb, M. A., & Olivucci, M. (2003). Relationship between photoisomerization path and intersection space in a retinal chromophore model. *Journal of the American Chemical Society*, 125, 2804–2808.
- Migani, A., Sinicropi, A., Ferré, N., Cembran, A., Garavelli, M., & Olivucci, M. (2004). Structure of the intersection space associated with Z/E photoisomerization of retinal in rhodopsin proteins. *Faraday Discussion*, 127, 179–191.
- Nielsen, I. B., Lammich, L., & Andersen, L. H. (2006). S-1 and S-2 excited states of gas-phase schiff-base retinal chromophores. *Physical Review Letters*, 96(1), 18304–18304.
- Oesterhelt, D., & Stoekenius, W. (1971). Rhodopsin-like protein from the purple membrane of halobacterium halobium. *Nature New Biology*, 233, 149–152.
- Oesterhelt, D., & Stoekenius, W. (1973). Functions of a new photoreceptor membrane. *Proceedings of the National Academy of Sciences of the United States of America*, 70, 2853–2857.
- Okada, T., Sugihara, M., Bondar, A.-N., Elstner, M., Entel, P., & Buss, V. (2004). The retinal conformation and its environment in rhodopsin in light of a new 2.2 Å crystal structure. *Journal of Molecular Biology*, 342, 571–583.
- Olivucci, M., & Sinicropi, A. (2005). Computational photochemistry. In M. Olivucci (Ed.), *Computational photochemistry. Theoretical and computational chemistry* (Vol. 16, pp. 1–33). Amsterdam: Elsevier.
- Page, C. S., & Olivucci, M. (2003). Ground and excited state CASPT2 geometry optimizations of small organic molecules. *Journal of Computational Chemistry*, 24(3), 298–309. doi:10.1002/jcc.10145.
- Palczewski, K., Kumasaka, T., Hori, T., Behnke, C. A., Motoshima, H., Fox, B. A., Trong, I. L., Teller, D. C., Okada, T., Stenkamp, R. E., Yamamoto, M., & Miyano, M. (2000). Crystal structure of rhodopsin: A G protein-coupled receptor. *Science*, 289, 739.
- Pistolesi, S., Sinicropi, A., Pogni, R., Basosi, R., Ferré, N., & Olivucci, M. (2009). Modeling the fluorescence of protein-embedded tryptophans with *ab initio* multiconfigurational quantum chemistry: The limiting cases of parvalbumin and monellin. *The Journal of Physical Chemistry B*, 113(49), 16082–16090.
- Ponder, J. W., & Case, D. A. (2001). Force fields for protein simulations. *Advances in Protein Chemistry*, 66, 27–85.
- Quillin, M. L., Anstrom, D. A., Shu, X. K., O’Leary, S., Kallio, K., Chudakov, D. A., & Remington, S. J. (2005). Kindling fluorescent protein from *Anemonia sulcata*: Dark-state structure at 1.38 Ångstrom resolution. *Biochemistry-US*, 44(15), 5774–5787.
- Ragazos, I. N., Robb, M. A., Bernardi, F., & Olivucci, M. (1992). Optimization and characterization of the lowest energy point on a conical intersection using an MC-SCF Lagrangian. *Chemical Physics Letters*, 197(3), 217–223.
- Rajput, J., Rahbek, D. B., Andersen, L. H., Hirshfeld, A., Sheves, M., Altoe, P., Orlandi, G., & Garavelli, M. (2010). Probing and modeling the absorption of retinal protein chromophores in vacuo. *Angewandte Chemie International Edition*, 49(10), 1790–1793. doi:10.1002/anie.200905061.
- Robb, M. A., Bernardi, F., & Olivucci, M. (1995). Conical intersection as a mechanistic feature of organic-photochemistry. *Pure and Applied Chemistry*, 67(5), 783–789.
- Roos, B. O. (1987). The complete active space self-consistent field method and its applications in electronic structure calculations. In K. P. Lawley (Ed.), *Advances in chemical physics; Ab initio methods in quantum chemistry - II* (pp. 399–445). Chincester: Wiley.

- Roos, B. O., & Taylor, P. R. (1980). A complete active space SCF (CASSCF) method using a density-matrix formulated super-CI approach. *Chemical Physics*, 48(2), 157–173.
- Schäfer, L. V., Groenhof, G., Klingen, A. R., Ullmann, G. M., Boggio-Pasqua, M., Robb, M. A., & Grubmueller, H. (2007). Photoswitching of the fluorescent protein asFP595: Mechanism, proton pathways, and absorption spectra. *Angewandte Chemie International Edition*, 46(4), 530–536.
- Schäfer, L. V., Groenhof, G., Boggio-Pasqua, M., Robb, M. A., & Grubmueller, H. (2008). Chromophore protonation state controls photo-switching of the fluoroprotein asFP595. *PLoS Computational Biology*, 4(3), e1000034.
- Schapiro, I., Weingart, O., & Buss, V. (2009). Bicycle-pedal isomerization in a rhodopsin chromophore model. *Journal of the American Chemical Society*, 131(1), 16–17. doi:10.1021/ja805586z.
- Schlegel, H. B., & Robb, M. A. (1982). MC SCF gradient optimization of the  $\text{H}_2\text{CO} \rightarrow \text{H}_2 + \text{CO}$  transition structure. *Chemical Physics Letters*, 93, 43–46.
- Schmidt, M. W., & Gordon, M. S. (1998). The construction and interpretation of MCSCF wavefunctions. *Annual Review of Physical Chemistry*, 49, 233–266.
- Schmidt, M. W., Baldridge, K. K., Boatz, J. A., Elbert, S. T., Gordon, M. S., Jensen, J. H., Koseki, S., Matsunaga, N., Nguyen, K. A., Su, S. J., Windus, T. L., Dupuis, M., & Montgomery, J. A. (1993). General atomic and molecular electronic-structure system. *Journal of Computational Chemistry*, 14(11), 1347–1363.
- Sekharan, S., Weingart, O., & Buss, V. (2006). Ground and excited states of retinal Schiff base chromophores by multiconfigurational perturbation theory. *Biophysical Journal*, 91(1), L7–L9.
- Senn, H. M., & Thiel, W. (2009). QM/MM methods for biomolecular systems. *Angewandte Chemie International Edition*, 48(7), 1198–1229.
- Shao, Y., Molnar, L. F., Jung, Y., Kussmann, J., Ochsenfeld, C., Brown, S. T., Gilbert, A. T. B., Slipchenko, L. V., Levchenko, S. V., O'Neill, D. P., DiStasio, R. A., Lochan, R. C., Wang, T., Beran, G. J. O., Besley, N. A., Herbert, J. M., Lin, C. Y., Van Voorhis, T., Chien, S. H., Sodt, A., Steele, R. P., Rassolov, V. A., Maslen, P. E., Korambath, P. P., Adamson, R. D., Austin, B., Baker, J., Byrd, E. F. C., Dachsel, H., Doerksen, R. J., Dreuw, A., Dunietz, B. D., Dutoi, A. D., Furlani, T. R., Gwaltney, S. R., Heyden, A., Hirata, S., Hsu, C. P., Kedziora, G., Khalliulin, R. Z., Klunzinger, P., Lee, A. M., Lee, M. S., Liang, W., Lotan, I., Nair, N., Peters, B., Proynov, E. I., Pieniazek, P. A., Rhee, Y. M., Ritchie, J., Rosta, E., Sherrill, C. D., Simmonett, A. C., Subotnik, J. E., Woodcock, H. L., Zhang, W., Bell, A. T., Chakraborty, A. K., Chipman, D. M., Keil, F. J., Warshel, A., Hehre, W. J., Schaefer, H. F., Kong, J., Krylov, A. I., Gill, P. M. W., & Head-Gordon, M. (2006). Advances in methods and algorithms in a modern quantum chemistry program package. *Physical Chemistry Chemical Physics*, 8(27), 3172–3191.
- Shimomura, O. (2009). Discovery of green fluorescent protein (GFP) (nobel lecture). *Angewandte Chemie International Edition*, 48(31), 5590–5602. doi:10.1002/anie.200902240.
- Sicilia, F., Blancafort, L., Bearpark, M. J., & Robb, M. A. (2007). Quadratic description of conical intersections: Characterization of critical points on the extended seam. *The Journal of Physical Chemistry A*, 111(11), 2182–2192. doi:10.1021/jp067614w.
- Sicilia, F., Blancafort, L., Bearpark, M. J., & Robb, M. A. (2008). New algorithms for optimizing and linking conical intersection points. *Journal of Chemical Theory and Computation*, 4(2), 257–266. doi:10.1021/ct7002435.
- Siegbahn, P. E. M., Almlof, J., Heiberg, A., & Roos, B. O. (1981). The complete active space SCF (CASSCF) method in a Newton-Raphson formulation with application to the  $\text{HNO}$  molecule. *Journal of Chemical Physics*, 74(4), 2384–2396.
- Simons, J. (1983). *Energetic principles of chemical reactions*. Boston: Jones and Bartlett.
- Sinicropi, A. (2002). *The mechanism of light energy wastage and exploitation in  $\text{In}, \text{p}^*$  chromophores*. Ph.D., University of Siena, Siena.
- Sinicropi, A., Pischel, U., Basosi, R., Nau, W. M., & Olivucci, M. (2000). Conical intersections in charge-transfer induced quenching. *Angewandte Chemie International Edition*, 39(39), 4582–4586.
- Sinicropi, A., Pogni, R., Basosi, R., Robb, M. A., Gramlich, G., Nau, W. M., & Olivucci, M. (2001). Fluorescence quenching via sequential hydrogen, electron, and proton transfer in the proximity of a conical intersection. *Angewandte Chemie International Edition*, 40(22), 4185–4189.
- Sinicropi, A., Nau, W. M., & Olivucci, M. (2002). Excited state quenching via “unsuccessful” chemical reactions. *Photochemical and Photobiological Sciences*, 1(8), 537–546.
- Sinicropi, A., Page, C. S., Adam, W., & Olivucci, M. (2003). Computational study on the origin of the stereoselectivity for the photochemical denitrogenation of diazabicycloheptene. *Journal of the American Chemical Society*, 125(36), 10947–10959. doi:10.1021/ja0263137.



- Sinicropi, A., Andruniow, T., Ferre, N., Basosi, R., & Olivucci, M. (2005). Properties of the emitting state of the green fluorescent protein resolved at the CASPT2//CASSCF/CHARMM level. *Journal of the American Chemical Society*, 127(33), 11534–11535.
- Solomon, B. S., Thomas, T. F., & Steel, C. (1968). Primary processes in the photochemistry of bicyclic azo compounds. *Journal of the American Chemical Society*, 90, 2249–2258.
- Strambi, A., Coto, P. B., Ferré, N., & Olivucci, M. (2007). Effects of water re-location and cavity trimming on the CASPT2//CASSCF/AMBER excitation energy of rhodopsin. *Theoretical Chemistry Accounts*, 118(1), 185–191. doi:10.1007/s00214-007-0273-y.
- Teller, D. C., Okada, T., Behnke, C. A., Palczewski, K., & Stenkamp, R. E. (2001). Advances in determination of a high-resolution three-dimensional structure of rhodopsin, a model of G-protein-coupled receptors (GPCRs). *Biochemistry-US*, 40, 7761–7772.
- Turro, N. J., Ramamurthy, V., & Scaiano, J. C. (2009). *Principles of molecular photochemistry: An introduction*. Sausalito: University Science Books.
- Valsson, O., & Filippi, C. (2010). Photoisomerization of model retinal chromophores: Insight from quantum monte carlo and multiconfigurational perturbation theory. *Journal of Chemical Theory and Computation*, 6(4), 1275–1292. doi:10.1021/ct900692y.
- Virshup, A. M., Punwong, C., Pogorelov, T. V., Lindquist, B. A., Ko, C., & Martinez, T. J. (2009). Photodynamics in complex environments: Ab initio multiple spawning quantum mechanical/molecular mechanical dynamics. *The Journal of Physical Chemistry B*, 113(11), 3280–3291. doi:10.1021/jp8073464.
- Vreven, T., Bernardi, F., Garavelli, M., Olivucci, M., Robb, M. A., & Schlegel, H. B. (1997). Ab initio photoisomerization dynamics of a simple retinal chromophore model. *Journal of the American Chemical Society*, 119(51), 12687–12688.
- Wanko, M., Garavelli, M., Bernardi, F., Niehaus, T. A., Frauenheim, T., & Elstner, M. (2004). A global investigation of excited state surfaces within time-dependent density-functional response theory. *Journal of Chemical Physics*, 120(4), 1674–1692.
- Wanko, M., Hoffmann, M., Strodel, P., Koslowski, A., Thiel, W., Neese, F., Frauenheim, T., Elstner, M. (2005). Calculating absorption shifts for retinal proteins: Computational challenges. *The Journal of Physical Chemistry B*, 109(8), 3606–3615. doi:10.1021/jp0463060.
- Warshel, A. (1976). Bicycle-pedal model for the first step in the vision process. *Nature*, 260(5553), 679–683.
- Warshel, A., & Barboy, N. (1982). Energy storage and reaction pathways in the first step of the vision process. *Journal of the American Chemical Society*, 104(6), 1469–1476.
- Warshel, A., & Chu, Z. T. (2001). Nature of the Surface Crossing Process in bacteriorhodopsin: Computer simulations of the quantum dynamics of the primary photochemical event. *The Journal of Physical Chemistry B*, 105, 9857–9871.
- Warshel, A., & Levitt, M. (1976). Theoretical studies of enzymic reactions: Dielectric, electrostatic and steric stabilization of the carbonium ion in the reaction of lysozyme. *Journal of Molecular Biology*, 103(2), 227–249.
- Warshel, A., Chu, Z. T., & Hwang, J.-K. (1991). The dynamics of the primary event in rhodopsins revisited. *Chemical Physics*, 158 303–314.
- Weingart, O. (2007) The twisted C11 = C12 bond of the rhodopsin chromophore—a photochemical hot spot. *Journal of the American Chemical Society*, 129(35), 10618–10619. doi:10.1021/ja071793t.
- Weingart, O., Migani, A., Olivucci, M., Robb, M. A., Buss, V., & Hunt, P. (2004). Probing the photochemical funnel of a retinal chromophore model via zero-point energy sampling semiclassical dynamics. *The Journal of Physical Chemistry A*, 108(21), 4685–4693. doi:10.1021/jp049140b.
- Werner, H.-J., Knowles, P. J., Lindh, R., Manby, F. R., Schuetz, M., Celani, P., Korona, T., Mitrushenkov, A., Rauhut, G., Adler, T. B., Amos, R. D., Bernhardtsson, A., Berning, A., Cooper, D. L., Deegan, M. J. O., Dobbyn, A. J., Eckert, F., Goll, E., Hampel, C., Hetzer, G., Hrenar, T., Knizia, G., Koepl, C., Liu, Y., Lloyd, A. W., Mata, R. A., May, A. J., McNicholas, S. J., Meyer, W., Mura, M. E., Nicklass, A., Palmieri, P., Pflueger, K., Pitzer, R., Reiher, M., Schumann, U., Stoll, H., Stone, A. J., Tarroni, R., Thorsteinsson, T., Wang, M., & Wolf, A. (2008). *MOLPRO, a package of ab initio programs* (Version 2008.3 ed.). Cardiff: University of Cardiff.
- Yamamoto, N., Olivucci, M., Celani, P., Bernardi, F., & Robb, M. A. (1998). An MC-SCF/MP2 study of the photochemistry of 2,3-diazabicyclo [2.2.1] hept-2-ene: Production and fate of diazenyl and hydrazone biradicals. *Journal of the American Chemical Society*, 120(10), 2391–2407.
- Yarkony, D. R. (1993). Systematic determination of intersections of potential energy surfaces using a Lagrange multiplier constrained procedure. *Journal of Physical Chemistry*, 97(17), 4407–4412.

# Index

## A

- Ab initio, 818, 819, 1279, 1289, 1302
  - methods, 943, 1178, 1183
  - accuracy, 453, 459
  - p-benzoquinone, 525
  - CCSD(T), 450, 459
  - DFT, 459
  - intermolecular interaction, 449
  - programms, 620
  - molecular dynamics, 200–201
- Absorption, 334–336, 389, 392–393, 405
  - p-benzoquinone, 527
  - differential, 404, 405
  - DNA, 513, 544, 545
  - energy, 1035
  - Franck–Condon principle, 489, 517
  - one-photon, 374, 389–392, 487, 489, 505, 527
  - psoralen, 512–517, 549
  - spectrum, 488, 513, 516, 527, 544, 549
  - theory vs. experiment, 515, 517
  - three-photon, 374, 393
  - thymine, 531, 532
  - two-photon, 392–393, 405
  - UV-light, 547, 548
  - vertical, 488–490, 517
- Accuracy, 327, 343, 354
  - basis set, 472
  - CASPT2, 505, 516, 517, 530, 556
  - CC3, 505
  - CCSD(T), 474
  - chemical, 471, 473, 476–479, 481, 575, 603
  - coupled cluster, 494, 501, 505, 511, 517
  - DFT, 599
  - DFT/MRCI, 506
  - electronic energy, 470
  - EOM-CC(T), 517
  - multiconfigurational methods, 502, 505, 506, 511, 517, 556
  - multireference methods, 502, 505
  - TD-DFT, 511, 517
- ACES II, 511
  - features, 623
- ACES III, features, 623
- Ad-dimer defect, 798
- 1,2-Addition, 697, 698, 701, 704, 706, 707
- 1,4-Addition, 697, 698, 702, 704, 707
- Additivity, 262, 265, 275, 286
- Adenine (A), 1187–1192, 1195–1196, 1216, 1225–1227, 1232, 1240, 1241, 1243, 1258, 1259, 1278–1282, 1284–1286, 1290–1303
- ADF, 511, 575
- ADFT. *See* Auxiliary density functional theory
- Adiabatic, 2, 3, 6, 10
  - band origin, 488–489, 517, 532
  - divergence, 22
  - electron affinity, 526, 528–531
  - energy difference, 517–518
  - reaction, 490
  - transition, 488
- Adjacent pentagons, 672, 674, 690, 695
- ADPT. *See* Auxiliary density perturbation theory
- Adsorption transition
- Advanced sampling, 1156–1170
- AFM. *See* Atomic force microscope; Atomic force microscopy
- Ag clusters, 973, 974
- AGNR. *See* Armchair graphene nanoribbons
- AlAs, 748
- Al clusters, 963, 979
- Alkali metals, 1278–1280, 1302
- AlP, 725, 747, 748
- AMI, 455, 461, 615, 617
- AMBER. *See* Assisted model building with energy refinement
- AMI-D, 455
- Aminopyrimidine, 1188–1191, 1201
- Ampac, web page, 625
- Angle
  - bending, 262, 266, 272, 278, 285, 286
  - bending interactions, 208, 212
  - bond, 262, 269, 272, 279, 280
  - potential, 208
  - torsion, 262, 269, 270, 280
  - valence, 262–264, 270, 272, 275
- Angular momentum, 370, 372, 397, 420, 421, 1007
  - electronic, 23, 25–28
  - nuclear, 25–27, 29
- Anharmonicity, 8, 334, 1263
- Anion
  - basis set, 503, 525–528, 530, 556
  - p-benzoquinone, 524–527
  - dipole-bound states, 512, 525, 526, 528
  - valence-bound states, 525–528
- Anomalous dispersion, 143
- Antibiotics, 1344, 1347
- Antibonding, 1244, 1245
- Antimicrobial, 1343–1352
- Antioxidant, 851
- Antisymmetry, 6, 8, 9, 21, 42, 66, 72, 99, 495, 497, 500



- Approximation, 2–10, 363, 365, 367, 368, 374, 375, 378, 384, 390, 392, 397, 404, 415, 416, 418, 420, 422–425  
   –adiabatic, 265  
   –dipole, 273, 274  
   –monopol, 273, 274  
 Aquaporins, 1143  
 Aqueous electrons, 1247  
 Armchair, 813, 814, 816, 818, 819, 821, 822, 835–842, 844–850  
   –edge, 1019, 1020, 1026, 1029, 1034  
   –GNR, 1026, 1028, 1033  
 Armchair graphene nanoribbons (AGNR), 906, 908, 909, 915, 918, 920, 925, 930  
 Aromaticity, 804, 835  
 Artificial neural network (ANN), 1348  
 Assisted model building with energy refinement (AMBER), 279–285, 455, 1133, 1138, 1369, 1386, 1388–1393, 1396, 1397  
 Assumption, 260–262, 265, 268, 286  
 Asymmetry, 388, 399, 414  
 Atom  
   –approach, 268, 274, 282, 286  
   –scheme, 268, 274  
   –term, 263, 271, 275  
   –type, 262, 264, 268, 279, 283  
   –united, 271, 281, 282, 284–286  
 Atom–atom potentials, 183–185  
   –polarizable potentials, 186  
 Atomic, 453, 454, 456  
   –charge, 686–688  
   –orbitals, 456  
   –partitioning scheme, 352  
 Atomic force microscope (AFM), 1130, 1144  
 Atomic force microscope (AFM) tip, 1010  
 Atomic force microscopy (AFM), 330, 798, 853  
 Atoms-in-molecules, 6  
 Au clusters, 976–979  
 Aufbau/Abbau method, 963, 989  
 Auger recombination, 891–896  
 Autocorrelation function, 229  
 Auxiliary density functional theory (ADFT), 575–603  
 Auxiliary density perturbation theory (ADPT), 576, 584–585, 603  
 Axial, 400  
 Axial strain, 928–929  
 Azoalkanes, 1363, 1377–1384
- B**  
 Bacteriorhodopsin, 1363, 1390  
 Bader analysis, 8  
 Badgers rule, 30
- Band  
   –area, 527  
   –gap, 813, 815, 821, 822, 836, 842, 851, 903–906, 909–912, 916–920, 927–930, 1013–1015, 1017, 1019, 1024, 1026–1033, 1034  
   –half-width, 341  
   –intensity, 335, 347  
   –maximum, 489, 515, 527, 554  
   –origin, 488, 489, 514–518, 532  
   –shape, 518–519  
   –width, 341  
 Base pair, 1261–1264, 1266–1271  
 Base pair enhancement, 1295–1299, 1304  
 Base release, 1216, 1218, 1244–1246, 1248, 1249  
 Basin hopping algorithm, 998, 1001, 1002  
 Basin hopping method, 963, 971, 989  
 Basis functions, 15, 19, 28, 31, 32, 41, 42, 45  
 Basis set, 294, 326, 329, 342, 374, 375, 377–379, 383, 384, 389–391, 393–398, 402, 403, 408, 417, 418, 422, 423, 430, 431, 448, 450, 455–457, 459, 461, 462, 566, 818, 819, 824, 827, 828, 845, 1218, 1221, 1224, 1225, 1229–1232, 1235, 1236, 1240, 1247, 1279, 1281, 1295, 1296  
   –Ahlich, 456  
   –anion, 503, 525–528, 530, 556  
   –ANO, 503, 504, 509–511, 513, 527, 530, 543, 555  
   –auxiliary, 108, 110, 456, 462, 580  
   –BSSE, 545–547, 552–557  
   –cage effect, 525, 526  
   –calculations, 408, 417, 418  
   –complete, 60, 497–499  
   –contraction, 502, 503  
   –convergence, 394, 395, 398, 403, 408, 417, 423  
   –correlation-consistent, 118, 475–476, 479, 503, 511  
   –diffuse functions, 377, 383, 473, 503, 523, 524, 526–528  
   –double- $\zeta$ , 502  
   –Dunning, 118, 119, 123, 475, 511  
   –electron correlation, 509  
   –exponent, 354  
   –extrapolation, 476–479  
   –finite, 498, 499, 553  
   –Gaussian function, 354  
   –Gaussian type orbitals, 4, 108, 123  
   –minimal, 84, 499, 501, 502  
   –perturbation-dependent, 584, 585  
   –plane waves, 566  
   –polarization functions, 472, 473, 475, 503  
   –Pople, 112, 468, 473–475, 503  
   –Rydberg states, 503, 509, 521–525, 527, 556  
   –Slater type orbitals, 4, 123  
   –split-valence, 502  
   –superposition error, 122  
   –thermochemistry, 469  
   –triple- $\zeta$ , 502, 504

- Basis set superposition error (BSSE), 164, 450, 456, 457, 461, 602, 765–766, 827, 1264, 1266, 1268, 1280, 1284, 1295  
–counterpoise correction, 73, 83, 84, 545, 555  
–excited states, 553–555
- B-DNA, 1261, 1262, 1267
- Becke–Lee–Yang–Parr (BLYP), 804
- Beeman’s algorithm, 252–254
- Benchmark sets, 453, 457–459, 461
- Bending, 927–929, 931
- Benzamides, 1348, 1352
- Benzene ring, 698–701, 706
- Benzonitrile, 1361
- Benzorod, 1014
- Berendsen barostat, 224
- Berendsen thermostat, 222–224, 253, 254
- BFGS. *See* Broyden–Fletcher–Goldfarb–Shannon
- Biasing potential replica exchange molecular dynamics (BP-REMD), 1167–1170
- Bicycle pedal mechanism, 1387
- Bioactive compound, 1347
- Biomolecules, 269, 281, 283
- Bionanotechnology, 1143
- Biopolymer, 240–256
- Biopolymer structure, 260
- Birefringence  
–axial, 400  
–Buckingham, 378, 400, 406, 407, 409, 410, 422  
–circular, 400, 406, 409  
–Cotton–Mouton effect, 407–408  
–EFG induced, 409–410  
–electric-field-induced optical, 400  
–field-induced, 407  
–flexible molecules, 402–404  
–Jones, 400  
–Kerr (electro-optical) effect, 400  
–linear, 399  
–magnetochiral, 400  
–magneto-electric, 400  
–optical activity, 400  
–optically induced, 401
- Bloch theorem, 873, 880, 883, 885, 893
- Blue-shift, 1232, 1243
- BLYP. *See* Becke–Lee–Yang–Parr
- B3LYP, 825
- BN sheet, 1010, 1017, 1020, 1021, 1035
- Bofill, 301, 324
- Bofill formula, 324
- Boltzmann average, 153, 154, 403
- Boltzmann distribution, 309
- Bond dissociation, 1235, 1236, 1238, 1239, 1244–1248
- Bonded interactions, 208, 212
- Bond length, 262, 264, 266, 268–270, 272, 275, 279, 280, 282
- Bond length alternation (BLA), 1366, 1367, 1369, 1371, 1390
- Bond-order potential, 1011
- Born–Mayer–Huggins potential, 211
- Born–Oppenheimer approximation, 3, 5, 6, 8, 10, 17, 21, 28–30, 64, 99, 197, 199–200, 205, 208, 295, 327, 333, 397, 420, 424, 485–487, 490, 492, 498, 519, 566, 958, 960  
–beyond, 200  
–molecular dynamics, 201
- Boundary atoms, 206
- BP-REMD. *See* Biasing potential replica exchange molecular dynamics
- Branching plane vector, 1371, 1372, 1377
- Breaking point, 1010
- Brillouin theorem, 82, 86
- Brillouin zone, 1024, 1025
- Brønsted acid, 591, 598
- Broyden–Fletcher–Goldfarb–Shannon (BFGS), 300, 301, 307, 308, 313, 314, 316, 317
- BSSE. *See* Basis set superposition error
- Buckingham potential, 210, 211
- Buckling, 1010, 1011
- Buckminsterfullerene, 796, 797, 800, 801, 807, 810, 811, 831, 832
- Buckyball, 795, 796
- ## C
- C20, 803–805, 807, 818, 828, 829, 831
- C60, 795–797, 800–802, 804–807, 810, 818, 825, 828–835
- C70, 796, 800, 801, 803–807, 825
- C140, 801
- C260, 801
- C540, 796, 803, 827, 829
- Cadmium sulfide clusters, 749
- Cage structures, 996, 1017
- Calculation, 260–279, 281–283, 285
- Canonical probability distribution, 946
- Carbon nanostructures, 795, 797, 818, 819, 852, 854
- Carbon nanotube, 796, 797, 813, 904–906, 912–916, 919, 925–928, 932
- Car–Parrinello, 566, 567
- Car–Parrinello molecular dynamics, 201
- Cartesian, internal, 616
- Casimir–Polderformul, 388
- CASPT2  
–accuracy, 505, 516, 517, 530, 556  
–p-benzoquinone, 526, 527  
–cytosine dimer, 545–547, 554  
–electron correlation, 539  
–ethene, 523, 524  
–ethylene dimer, 542, 543  
–guanine, 530, 539, 540, 543, 544  
–level-shift, 509, 513  
–LiF, 541, 542  
–multi-state, 510, 524, 541, 542

- NABs, 530
- psoralen, 513, 514, 517, 538, 550
- size-extensivity, 500
- thymine, 530, 532, 534, 539, 543, 547
- water, 513, 514, 521, 522, 532
- CASSCF, 616, 620, 621
  - accuracy, 508, 510, 530, 539
  - active space, 508–510, 513, 519, 521, 526, 530, 543
  - p-benzoquinone, 525–527
  - electron correlation, 539
  - ethene, 524, 532
  - guanine, 530, 539, 543, 544
  - NABs, 530
  - psoralen, 513, 517, 550
  - size-extensivity, 506
  - state average, 506–507, 510, 513, 524
  - thymine, 530, 543
  - valence-Rydberg mixing, 521, 523, 524
  - water, 513, 521
- CASSI, 508, 513
- CASVB, 508
- Cauchy moments, 381, 386–387, 408
- CC. *See* Correlation-consistent
- CCD. *See* Coupled cluster
- CCSD, 818
- CCSD(T), 819
- C<sub>3</sub>-dephos radical, 1248
- CdnTen, 739
- CdS, 725, 737, 738, 747, 748, 751
- CdSe, 725, 737, 738, 747, 748, 750, 751
- Center-of-mass
  - coordinates, 18, 19
  - translation, 17–19
- Centrosymmetric structures, 744
- CFOUR, features, 623–624
- Chair conformer, 822
- Charge
  - control, 126
  - distribution, 6, 126
  - transfer, 124, 1363, 1367, 1379–1386, 1393
  - transfer states, 1084
- CHARMM. *See* Chemistry at HARvard Macromolecular Mechanics
- Chemical bond, 261–263, 272, 286
- Chemical functionalization, 916, 917, 930, 1026
- Chemical potential, 229
- Chemical-probe experiments, 968
- Chemical shift, 418, 826, 835, 1099–1101, 1111, 1112
- Cheminformatics, 1330, 1333
- Chemisorption, 818, 820, 823, 824, 839–842
- Chemistry at HARvard Macromolecular Mechanics (CHARMM), 282–285, 1133, 1137, 1138, 1143, 1369, 1385
- Chiral, 812–814, 819, 842, 843
  - Chirality, 335, 399, 405, 812, 813, 839
  - molecules, 399, 400, 402, 403
- Cholesky decomposition, 580, 581
- Cinnamic acid, 1349, 1352
- Circular, 379, 392, 399, 409
- Circular dichroism, 374, 382, 401, 402, 404–406, 410–411
  - electronic, 401, 402, 404
  - magnetic, 382, 406, 410–411
  - rotational strength, 336
  - two-photon, 405–406
  - vibrational, 294, 335
- Cisplatin, 1278, 1289, 1293, 1299, 1301
- cis/trans photoisomerization, 1376
- Clamped-nuclei approximation, 2, 14–27, 37
- Clar, 835–837, 842
- Classical force fields, 762, 763
- Classical molecular dynamics, 200–204, 226
- Classical reaction paths, 1135
- Clathrate hydrate structure I lattice, 782
- Clausius–Mossotti relation, 746
- Clebsch–Jordan coefficient, 45
- Cleri–Rosato potential, 962, 963
- Cluster approach model, 632
- Cluster growth, 968, 970, 972, 973
- Clusters, 996–1009
- Coarse graining, 241
- Coarse grain molecular dynamics, 197, 198, 1145
- Coil-globule transition<sub>2</sub>, 244
- Coinage metal, 1280, 1296
- Columbus, 539, 1360
  - features, 623–624
- Cometary comas, 1259
- Commutator, 32, 40
- Complementarity, 1115–1118
- Complete active space self-consistent field (CASSCF), 1362, 1364–1376, 1385–1393, 1396, 1397
- Complete active space with second order perturbation theory (CASPT2), 1366, 1369, 1389
- Complete basis set (CBS), 1264
- Complete basis set (CBS) limit, 456, 457, 765–767, 780
- Complex, 105, 109–111, 114, 116–118, 121–125
- Components, 447, 461
- Compression, 928, 929
- Computational drug discovery, 1324, 1336
- Computational enzymology, 1139, 1142
- Computational toxicology, 1329, 1333
- Computer modeling, 1129, 1130, 1139, 1144, 1145
- Condensed phase, 1218, 1242, 1247
- Condon approximation, 489
- Conduction-band electron, 871, 885
- Conductor-like screening model (CSMO), 613
- Configuration, 263–265, 275, 277

- Configuration interaction (CI), 375, 613–616, 619–621, 624
- CIS, 504, 556
  - DCI, 499, 501
  - DFT/MRCI, 506
  - FCI, 499, 501, 506, 508
  - multireference, 495, 500–502, 504–506, 510, 539, 541, 556
  - Rydberg states, 503, 510, 521, 523, 524
  - SDCI, 499, 501, 507
  - size-extensivity, 499, 500
- Configuration-state functions (CSFs), 424, 504, 506
- Confinement effect, 525, 526, 591
- Conformation, 6, 261, 264–273, 275, 279–282, 284
- Conformational sampling, 1158, 1161, 1163
- Conformational space annealing, 999
- Conformational transitions, 1158, 1159, 1161, 1163, 1166–1170
- Conical intersection, 1182, 1184, 1186–1192, 1194–1196, 1199–1202, 1360–1362, 1371, 1373, 1374, 1377–1384, 1389, 1393, 1398
- Conjugated systems, 384
- Conjugate gradient method, 220
- Conjugate gradients algorithm, 998
- Consistent valence force field (CVFF), 632, 641, 657
- Contact contributions, 413, 416, 419, 422
- Continuous transformation of the origin of the current density (CTOCD), 415
- Continuum, 1216, 1221, 1222, 1231–1233, 1240, 1243, 1246, 1249
- Continuum model, 241–244
- Convergence
- basis set, 475
  - coordinates, 302, 303
  - criteria, 308, 317, 324, 581
  - optimizations, 309
  - perturbation series, 30, 509
  - SCF, 306, 579, 581, 582
- Coordinates, 615–620
- branching and intersection space, 491, 492
  - Cartesian, 302, 303, 308–310, 313, 319, 323, 327, 329–331, 333, 343
  - Cartesian redundant, 19
  - center-of-mass, 18, 19
  - cluster, 329, 330
  - Coriolis coupling, 28
  - frozen, 536
  - internal, 25, 28, 29, 302, 303, 308–323, 325, 329, 330, 343, 536
    - delocalized, 303, 309–311, 313–315, 318–321, 329
    - natural, 302, 303, 309, 343
    - redundant, 303, 312, 329, 343
  - internal redundant, 593, 599
  - mass-weighted, 492, 531
  - nuclear, 489, 490
  - performance, 309
  - reaction, 325, 536, 543
  - spherical polar, 22, 25
  - vibrational, 332
  - X-ray diffraction, 327
  - Z-matrix, 302, 303, 308
- Coordination number, 1004, 1006–1008
- Copper-aminoxidase, 1071
- Corannulene, 802
- Core-electron spectroscopy, 576
- Core-excited resonance, 1220–1223, 1228, 1249
- Core-excited shape resonances, 1223
- Core/shell particles, 986
- Correlation
- effects, 342, 352, 354, 450, 453, 1045
    - basis sets, 475–476, 504
    - core, 476
    - dynamic, 504, 506, 508, 513, 521, 545
    - energy, 498, 499, 501–504, 510, 513, 516, 523, 540, 553
    - exchange, 497, 499
    - Fermi, 497, 499
    - HF, 342
    - large-range, 501
    - left-right, 498
    - long-range, 539
    - nondynamic, 501, 506
    - Rydberg states, 503, 521, 523, 524
    - short-range, 501, 508, 539
    - static, 506, 540
  - energy, 93
  - hole, 9, 102, 103
  - time, 1101
- Correlation-consistent (CC), 456
- COSMO. *See* Conductor-like screening model
- Cotton-Mouton effect (CME), 400, 407–408
- Coulomb, 449, 453, 455
- coefficient, 583
  - correlation, 449
  - coupling matrix, 585
  - energy, 493, 577, 593, 599
  - hole, 2, 9, 103, 493, 497
  - integrals, 453
  - interaction, 2, 9, 14–18, 24, 28, 30, 53, 99, 103
  - matrix, 580–581
  - norm, 580
  - potential, 497, 579, 582
  - vector, 580
- Coulomb's law, 212
- Coumarin C153, 1363, 1394–1396
- Coumarins, 1347–1348, 1352
- Counterpoise correction (CP), 122, 164, 165, 450, 457, 461, 545, 554, 555

- Coupled cluster (CCD), 447, 449  
 –accuracy, 449, 474, 494, 501, 505, 511, 517  
 –CC3, 375, 390, 391  
 –CCSD, 375, 390, 494, 501, 516, 517, 528–530, 539  
 –CCSD(T), 375, 418  
 –cross section, 392  
 –EOM-CC, 505, 517, 613, 614, 1058–1063  
 –heat of formation, 479  
 –NABs, 530  
 –non-variational, 375  
 –nuclear coupling constant, 389  
 –PCM, 1049, 1053–1056, 1063  
 –PCM-CC, 1049, 1053–1056, 1063
- Coupling coefficient, 45, 48
- Covalent bond, 8
- Covalent functionalization, 820, 837
- Crack propagation, 1010
- Critical exponents, 245–246
- Critical phenomena, 245–246, 248
- Critical point, 8
- Crossover operation, 999
- Cross section, 492
- Crystal  
 –calculation, 272  
 –energy, 267, 268, 272–274, 276–278  
 –molecular, 266–268, 274  
 –structure, 6, 267, 268, 279–281
- Crystallization, 1097
- Crystallographic database, 215
- Crystallography, 1097–1099
- Cu clusters, 970–972
- Curie temperature, 941, 943, 948, 950–952
- Curvature effects, 906, 929
- CVFF. *See* Consistent valence force field
- Cytochromes, 1068, 1071, 1075–1077, 1085, 1088, 1090
- Cytosine (C), 1187–1189, 1196, 1216, 1225–1227, 1229, 1232, 1235, 1240, 1241, 1243, 1244, 1247, 1258, 1269, 1270, 1278–1282, 1288, 1290, 1292, 1297, 1298, 1300, 1303  
 –dimer, 544–548, 554
- Cytosine-guanine base pair, 1363, 1392–1394
- D**
- DALTON, 511  
 –features, 618
- Damping function, 172–174, 176
- Darwin term, 367, 382
- Data analysis, 197, 227–230
- DBIPs. *See* Double bonds in pentagons
- DCACP. *See* Dispersion-corrected atom-centered potential
- Dc-optical rectification, 383
- Dc-pockels effect, 383
- Dc-shg, 385
- Decahedral, 1000, 1006, 1009
- 585 Defect, 1015, 1016
- 555777 Defect, 1015, 1016
- Deformation, 7, 10  
 –energy, 1263, 1268
- Degenerate four wave mixing (DFWM), 385
- Degrees of freedom, 296, 299, 301, 310, 311, 315, 318, 322, 325, 331, 333, 364  
 –vibrational, 531
- DeMon, 575, 576, 579–583, 588, 591–593, 599, 600, 603
- Density, 48, 52  
 –fitting, 108, 168–169, 171, 177, 178, 450, 456  
 –functional, 52  
 –matrix elements, 48
- Density-functional based tight-binding method (DFTB), 455, 673, 677, 678, 680–683, 701
- Density-functional methods, 975
- Density functional theory (DFT), 159, 165, 201, 213, 294, 352–355, 468, 469, 472–474, 477, 478, 575, 576, 579, 582, 586, 588, 598, 599, 612, 617–620, 622, 633, 634, 638, 639, 657, 659, 660, 673, 804, 818, 819, 821, 826, 827, 839, 844, 845, 903–932, 1284, 1367, 1379  
 –accuracy, 494, 502, 506, 511, 530  
 –asymptotic behaviour, 390  
 –auxiliary, 575–603  
 – $\pi$ – $\pi$  stacking, 122, 123  
 –conjugated systems, 383  
 –correlation effects, 386  
 –Coulomb, 103  
 –DCACP, 454  
 –DFT-D, 447, 452–455, 460, 461, 1264, 1265  
 –DFT-D3, 453  
 –DFT/MRCI, 506, 537  
 –dispersion, 122  
 –dispersion interaction, 451  
 –excited states, 502, 505, 506, 511, 516, 530  
 –fullerenes, 576, 598–602  
 –functional, 352–355, 385, 423, 432, 433  
 –functional choice, 462  
 –functional total energy, 597  
 –generalized gradient approximation, 451  
 –H-bond, 121  
 –hybrid-GGA, 451  
 –hyperfine coupling constants, 432  
 –hyperfine interaction, 416, 431  
 –hyperpolarizability, 383, 385  
 –interaction, 102, 103, 111, 122  
 –Jacob’s ladder, 451, 459  
 –Kohn-Sham, 576–578  
 –LCGTO-DFT, 579, 588  
 –local density approximation (LDA), 451, 588, 599  
 –magnetizability, 393–396  
 –method, 453, 1009, 1013, 1026  
 –nuclear shielding constant, 416

- nuclear Zeeman interaction, 427
- polarizability, 588
- self-interaction, 579
- sodium cluster, 576, 586–589
- spin-orbit coupling constant, 425
- time-dependent, 505, 511, 517, 520, 523, 556, 613
- time-dependent-DFT (TD-DFT), 576
- van der Waals, 122, 123
- weak, 111, 122–123
- Density-functional tight-binding method (DFTB), 975–977, 979, 984, 987, 990
- Density matrix, 503, 1050, 1056, 1063
  - perturbed, 584, 585
- Deoxynucleosides and deoxynucleotides, 1226
- Deoxyribonucleic acid (DNA), 269, 272, 273, 275, 282, 284, 1258–1271, 1363, 1392–1394
  - bases, 1216, 1218, 1220, 1225–1229, 1232, 1235
  - bending, 1164–1166
  - damage, 1216–1249
  - hairpin, 1161, 1162
- Dependence, 379, 395, 402, 409, 411, 414, 415, 431
- Depolarization ratio, 335, 341, 347
- Deposition, 972, 973, 979
- Descriptors, 1346–1348, 1351
- DFT. *See* Density functional theory
- DFTB. *See* Density-functional tight-binding method
- DGAUSS, 575, 582
- Diamagnetic, 370, 394, 408
  - contribution, 394, 395, 408, 414
  - hypermagnetizability, 408
  - magnetizability, 370, 394, 408
  - shielding, 370, 371
  - spin-orbit, 370, 371, 422
    - contribution, 422
    - operator, 370, 371
- Diamagnetism, 394
- Diamond, 795, 796, 821, 828
- 2,3-Diazabicyclo[2.2.1]hept-2-ene (DBH), 1377–1379
- 2,3-Diazabicyclo[2.2.2]oct-2-ene (DBO), 1379, 1380
- Dielectric constant, 376, 382, 564, 565, 1303
- Dielectric properties, 746
- Diels–Alder reaction, 324, 818
- Diffraction limit, 870
- Diffuse functions, 456, 473–476
- Diffuse states, 1216, 1243, 1247, 1249
- Diffusion coefficient, 229
- 5,6-Dihydrothymine, 1247, 1248
- DIIS. *See* Direct inversion of the iterative subspace
- Dimensionality of materials, 996
- Dioxygen activation by enzymes, 1069, 1077
- Dioxygen consumption, 1069, 1074, 1077, 1078, 1088
- Dipole, 451, 458
  - approximation, 392, 548, 549
  - bound, 1216, 1218, 1223, 1224, 1229–1233, 1236, 1240, 1247, 1249
  - CO, 501
  - derivative, 341
  - electric, 335, 336, 368, 376, 380, 387, 400–402, 407–409
  - excited state, 489, 490, 501, 505, 511–514, 518, 519, 525–528, 549, 555
  - IR spectrum, 334, 335
  - magnetic, 335, 336
  - moment, 6, 53, 334–336, 377–380, 382, 384, 399, 408, 410, 412, 451, 490, 501, 505, 512–514, 518, 519, 525, 527, 555, 564, 1279–1281, 1292, 1297
  - nitromethane, 527
  - oscillating, 549
  - psoralen, 512, 514, 518, 519, 548, 549
- Dipole bound anion state (DBS), 1224, 1236
- Dipole-dipole interaction, 371, 376, 388, 411, 429
- Dirac, 100
  - delta function, 366, 371
  - electron, 1024
  - equation, 1071
  - notation, 59, 873
  - point, 1024, 1025
  - theory, 2
- Dirac–Hartree–Fock method, 418, 420
- Directed walk, 245, 246
- Direct inversion of the iterative subspace (DIIS), 26–27, 306, 307
- Dispersion, 1264–1266
  - DCACP, 454
  - DFT-D, 452–453
  - force field, 453
  - HFD, 451
  - interaction, 119, 123, 451
  - MP2, 452
- Dispersion-corrected atom-centered potential (DCACP), 454
- Dispersion interaction, 564
- Dispersionless state, 1032
- Displacement, 298, 306, 308–310, 312–317, 319–323, 331, 332, 341
- Dissociation, 296, 297, 334, 471, 479, 481, 488–502, 504, 536, 541
- Dissociative electron attachment (DEA), 1217, 1220, 1221, 1223, 1224, 1235, 1249
- Distributed multipoles, 176–177
- Distributed polarizabilities, 173, 175, 177, 178
- Distribution methods
  - distributed multipole analysis (DMA), 176, 186
  - Williams–Stone–Misquitta (WSM) method, 159, 177–178
- Divacancy, 1034
- DKn, 613
- DMOL, 575
- DNA. *See* Deoxyribonucleic acid
- Docking, 1110, 1115–1119, 1141
- Double bonds in pentagons (DBIPs), 697, 698, 700

- Double helix, 1268  
 Double hybrid functionals, 452, 453, 462  
 Double-strand breaks (DSB), 1217, 1219, 1220, 1223, 1235, 1242, 1244, 1249  
 Drug design, 445  
 Drugs, 1344, 1345, 1347, 1349, 1351, 1352  
 0D structures, 996–1009  
 1D structures, 996, 1009–1017  
 2D structures, 1017–1036  
 Dummy atom, 302  
 Dunning, 456  
 Dynamic electron correlation, 1366, 1367, 1385  
 Dynamics, 1099, 1101, 1103, 1110–1114  
 Dynamics simulations, 1178–1186, 1188–1193, 1195–1197, 1199–1204
- E**
- ECEPP. *See* Empirical conformational energy program for peptides  
 ECP. *See* Effective core potential  
 Edge states, 908, 910, 916, 921, 923, 925  
 Effective core potential (ECP), 454, 613, 614, 618, 619, 623  
 Effective ESR, 426–428  
 Effective Hamiltonian, 411, 412, 424, 426, 428  
 EFG. *See* Electric field gradient  
 EFISH. *See* Electric field induced second harmonic  
 Eigenfunction
  - angular momentum, 25, 27, 28, 30
  - Fock operator, 84, 497, 498
  - Hamiltonian, 15, 19, 21, 25, 27, 28, 30–53, 59–62, 66, 71, 84, 493, 495
  - level shift, 509
  - reduced density matrix, 503
  - spin, 21, 30, 32, 36, 47, 48, 51, 497, 498, 504
  - $S_z$ , 30, 47
- Eigenvalue, 2, 8, 125, 411, 428, 429
  - angular momentum, 23
  - eigenvector following algorithm, 304, 305
  - equation, 16, 56, 58, 63
  - FCI, 499
  - Hamiltonian, 15, 16, 20, 23, 31, 49, 52, 53, 59, 60, 62, 63, 66, 67, 70, 86, 87, 493, 495, 509
  - Hessian, 299–301, 304, 305, 310, 312–314, 316, 320–322, 324
  - level shift, 509
  - negative, 299–301, 304, 305, 324, 326
  - positive, 299, 300
  - problem, 15, 20, 52, 141, 142, 151
  - Roothaan's equations, 498, 499
  - shift parameter, 304
  - spin, 31, 49
- Einstein coefficients, 490  
 Einstein relation, 229  
 Einstein summation convention, 364, 1062
- Elastic moduli, 1010  
 Elastic properties, 1010–1012  
 Electric dipole, 368, 376, 379–383, 387, 400–402, 404, 406–409
  - electric quadrupole, 402, 404, 409
  - magnetic dipole, 376, 401, 402, 404
- Electric field, 10  
 Electric field gradient (EFG), 368, 377, 388–389, 409, 411, 412, 428  
 Electric field induced second harmonic (EFISH), 385  
 Electric quadrupole, 368, 376, 378, 389, 405, 409, 417  
 Electric second harmonic generation (ESHG), 385, 386  
 Electromagnetic interference, 851  
 Electromechanical properties, 926–932  
 Electron, 295, 296, 327, 333, 336, 342, 350, 353, 354
  - adiabatic, 515, 529
  - affinity, 525, 526, 528, 529, 1223, 1225, 1229–1231
  - correlation, 9, 74, 99, 378, 383, 384, 386, 391, 395, 398, 399, 403, 418
  - density, 327, 371, 397, 403, 502, 514, 515, 685–687, 1017, 1036
    - ground state, 576, 577
    - normalization, 578
    - polarizability, 586
  - diffraction, 800, 801, 813
  - distribution, 445, 566
  - plots, 514
  - vertical, 529
- Electronic properties, 997, 998, 1010, 1013–1015, 1019, 1020, 1026, 1027, 1029, 1030, 1033  
 Electronic shell, 998, 1002  
 Electronic structure, 200, 205, 213, 215  
 Electron-molecule interaction, 1216, 1218, 1220–1222, 1232, 1233, 1240  
 Electron spin resonance (ESR), 1240, 1247, 1248  
 Electron spin-Zeeman interaction, 414, 427  
 Electron transmission spectroscopy (ETS), 1220, 1225–1227, 1231, 1240, 1241  
 Electro-optic effect, 749  
 Electro-optic Pockels effect (EOPE), 383, 387  
 Electrostatic interactions, 205, 208, 212, 1279, 1284, 1299, 1301  
 Electrostatics, 1106–1109, 1114, 1119  
 Embedded atom method, 15, 211, 961, 990  
 Embedded atom models, 1001  
 Embedding, 205, 211  
 Emission
  - cytosine dimer, 544
  - DNA, 545
  - psoralen, 512–516
  - spectrum, 549
  - thymine, 532
  - vertical, 489, 515, 518, 545, 554, 555

- Empirical conformational energy program for peptides (ECEPP), 272, 279–281
- Empirical potential, 998–1001, 1004, 1006, 1009–1011, 1013
- ENDOR spectroscopy, 426
- Energy
- basis set, 470
  - bottom-of-the-well, 469
  - correlated method, 474
  - DFT, 474
  - electronic, 470, 472
  - expansion, 375–377
  - function, 264, 272, 280
  - minimum, 263
  - nonbonded, 261
  - potential, 260, 261, 263, 266, 267, 272, 280
  - psoralen, 516
  - rotational, 469
  - sublimation, 279
  - term, 261, 262, 264, 265, 268, 272, 279, 282
  - torsion, 262
  - total, 265, 267, 272, 284
  - transfer, 487, 531, 1200
  - translational, 469
  - vibrational, 469
- Enthalpy, 340, 341, 345
- of formation, 477, 480
  - molar, 469
  - standard, 469, 477
- Entropy, 340, 341, 345, 468, 1115, 1119
- Enzyme, 1103, 1107, 1114, 1119, 1120
- EOM-CC. *See* Equations-of-motion coupled cluster
- Equation-of-motion, 494, 504, 505
- Equations-of-motion coupled cluster (EOM-CC), 375, 613, 614, 623
- Equilibrium constant, 468
- ESHG. *See* Electric second harmonic generation
- ESR
- effective spin, 426–428
  - spectrum, 427, 430
- Ethene, 523, 524, 532, 534, 535
- Euler equation, 577
- Ewald sum, 212
- Exact enumeration technique, 240, 248–249, 254, 256
- Exchange, 497, 499, 549
- correlation, 352, 354, 383, 385, 390, 396, 431, 432
    - auxiliary functions, 582
    - coefficient, 583, 584
    - derivative, 581, 583
    - energy, 352, 354, 452, 577, 579, 581–583, 599
    - functional, 451, 577
    - kernel, 584
    - PBE, 596
    - potential, 578, 582, 583, 593, 599
    - energy, 579
    - hole, 9, 102
    - potential, 497
- Excimer, 544–547, 554
- cytosine dimer, 544, 547, 554
- Exciplex, 545
- Excitation, 9, 295, 334, 335, 1046, 1047, 1049, 1051–1053, 1059, 1061, 1063
- accuracy, 502, 505, 517–518, 556, 557
  - CIS, 504
  - energy, 124–126, 141–143, 380, 387–390, 426, 504, 505, 508–510, 513, 515, 517–519, 527, 535, 549, 557, 1240–1242
  - level-shift, 509, 513
  - psoralen, 514, 515
  - Rydberg, 124, 523
  - in solute, 1061
  - valence, 111, 124
  - vertical, 489, 514, 517, 527, 1058
- Excited states, 138, 140–143, 147, 151, 152, 334, 335, 380, 384, 387, 390–393, 396, 422, 430, 1177–1204, 1216–1218, 1223, 1228, 1233, 1236, 1240–1245
- anion, 503, 524–526
  - basis set, 502–504, 510, 519, 525, 553–555
  - BSSE, 553–555
  - calculations, 483–557
  - charge transfer, 505
  - cytosine dimer, 544–548
  - environmental effects, 496, 519
  - multiconfigurational, 486, 494–495, 504–506, 511–513, 519–520, 556
  - nomenclature, 488
  - programs, 511, 518
  - psoralen, 512–516, 548–553
  - Rydberg, 511, 512, 520–525, 556
  - thymine, 531–535
  - valence, 503, 506, 511, 521, 525
- Exciton, 984
- Excitonic polariton, 870, 871
- Exciton longitudinal-transverse splitting, 881
- Excluded volume effect, 242–244
- Exclusion principle, 9, 99
- Expansion, 367, 377, 380, 381, 388, 389, 407, 412, 430
- Exp-6 potential, 1011
- Extinction coefficient, 389
- Extrapolation, 456, 457, 461, 470, 475–477, 479–481
- ## F
- Face centered cubic (fcc), 801
- lattice, 872, 884
  - truncated octahedron, 1000
- Faceted surface, 1007



- FAD. *See* Flavin adenine dinucleotide
- Faraday effect, 410
- Fast Fourier transform, 212
- FCI. *See* Full configuration-interaction
- FCP. *See* Function counterpoise method
- Femtosecond processes, 1177
- Fe-porphyrin, 1083
- Fermi
- contact, 371, 413, 416, 419, 422, 423, 430
  - correlation, 497, 499
  - golden rule, 489, 549, 552
  - hole, 9, 103, 497
- Ferroelectricity, 1006
- Feshbach resonances, 1216, 1223, 1224
- FIM. *See* Functionally important motions
- Fine structure constant, 365
- Finite field technique, 382, 385
- drawbacks, 378
- Finite size effects, 917–926, 930
- Finnis–Sinclair potential, 1010
- Firefly features, 616
- First hyperpolarizability, 741
- First principles methods, 197, 200, 201, 213, 215
- Fitness function, 999
- Fitness parameter, 999
- Flash vacuum pyrolysis (FVP), 802, 808
- Flavanones, 1350
- Flavin adenine dinucleotide (FAD), 1069–1070, 1078, 1079, 1085
- Fluorescence, 487, 490, 514–516, 518, 531, 532, 536, 544, 545, 549, 555, 1360, 1361, 1363, 1370, 1379–1385
- excimer, 544
- Fock, 294, 306, 329, 342, 355, 356
- corrected, 451
  - effects, 449
  - eigenfunction, 497, 498
  - matrix, 306, 329
  - matrix representation, 497, 498
  - operator, 449, 497, 498
- Fold, 1101, 1104–1106, 1110–1112, 1119, 1120
- Force, 470
- AMBER, 455
  - constant, 300, 332, 333, 340, 342, 343, 345, 356
  - dispersion, 448, 455
  - electrostatic, 447
  - external, 330, 331
  - field, 307, 342, 343, 453, 455, 457
  - geometry optimization, 331
  - GROMOS, 455
  - Hessian matrix, 300
  - Hooke's law, 332
  - intermolecular, 329
  - intramolecular, 329
  - scaling, 343
- Force-extension curve, 241, 243, 244, 254
- Force field, 197, 198, 200, 204, 205, 207–210, 213, 217–219, 225, 260–272, 274–286, 566, 567, 596, 961, 1129, 1131, 1133–1134, 1136–1138, 1141, 1143, 1157–1159, 1161, 1163, 1164, 1166–1169, 1368, 1369, 1387, 1388, 1391–1393, 1396
- Force intermolecular, 376, 388, 396
- Force spectroscopy, 1144
- Force-temperature diagram, 254
- Formamide, 1178, 1188, 1197–1203
- Formation energy, 819, 821, 822, 844, 845, 847, 848, 850
- FORS. *See* Full orbital reaction space
- Fourier amplitudes, 380
- Fourier transform, 334
- Fragment deformation energy, 766
- Franck Condon (FC)
- factors, 489
  - geometry, 490, 491, 513, 523, 553
  - point, 1360, 1361, 1366, 1369, 1396
  - principle, 489, 517
  - rule, 651
  - transition, 488
- Free-energy perturbation method, 1115, 1116
- Freely jointed chain, 241, 242
- Frenkel principle, 1047
- Frequencies, 111, 115–117
- Frequency-dependent, 375, 376, 379–381, 385, 387, 398, 407–409
- Frequency-dependent density susceptibility (FDDS), 166
- Frequency(time)-independent, 374
- Frozen localized orbitals, 206
- Fukui functions, 585
- Full configuration-interaction (FCI), 375
- Fullerene, 576, 598–602, 725, 738, 795–798, 800–812, 817–833, 835–837, 852, 1002, 1010, 1017
- bromofullerene, 702
  - dimetallofullerene, 684, 687, 693
  - endohedral metallofullerene, 668, 669, 680, 684–692, 694, 695
  - fluorofullerene, 700
  - fullerene derivative, 672, 676, 696–698, 700, 701
  - higher fullerene, 668, 673, 676, 677, 679–683, 706–710
  - hydrofullerene, 700
  - “insoluble” fullerene, 677, 679, 680
  - isomers, 802, 804, 809, 810, 818, 824–827

- LCGTO-DFT, 599
  - non-IPR fullerene, 690, 695, 696
  - Full orbital reaction space (FORS), 613
  - Function, 364, 373–375, 382, 388, 390–395, 398, 403, 408, 410, 417, 422, 424–426, 429, 431
  - Functional
    - BB95, 114, 116, 121
    - BBIK, 118–120
    - BHandH, 452
    - BH&HLYP, 114
    - BHLYP, 506
    - BLYP, 108, 109, 112, 113, 115, 118, 120, 121, 125, 129, 396, 431, 452, 462, 472–476
    - B1LYP, 109, 118, 120, 125
    - B<sub>3</sub>LYP, 108, 294, 296, 309, 326–329, 331, 336, 342, 344–347, 350, 351, 354, 355, 385, 396, 402, 403, 431, 472–478, 502
    - BMK, 124
    - B3P86, 108
    - BP86, 108
    - B2PLYP, 462
    - B3PW91, 108, 477, 478
    - B<sub>3</sub>PW<sub>91</sub>, 327
    - BPW91, 108
    - CAMB3LYP, 125
    - CAM-B3LYP, 385, 517
    - derivative, 578, 583
    - Dirac, 588, 599
    - double hybrid, 452, 453, 462
    - exchange-correlation, 451, 588, 593, 596
    - GGA, 97, 105–106, 451, 462
    - gradient-corrected, 585
    - HFLYP, 125
    - HMGGA, 111, 114, 116, 118–123
    - HTCH, 113
    - hybrid, 575
    - hybrid-GGA, 451, 462
    - hyper-GGA, 106
    - Jacob's ladder, 104–107, 129
    - kinetic energy, 577
    - LDA, 100, 451
    - magnetic properties, 369, 393, 396, 415
    - meta-GGA, 106
    - MHGGA, 117
    - MPWB1K, 119, 120, 122, 123
    - MPW1K, 114, 119, 120, 122, 123
    - MPW1KCIS, 114, 116, 119, 121
    - MPWPBE, 119, 121
    - MPWPW91, 119, 121
    - OBLYP, 125
    - OLYP, 113, 119, 124
    - OPBE, 124, 125
    - PBE, 108, 109, 113, 118–125, 129, 452, 453, 462, 588
    - PBEKCIS, 118
    - PBELYP, 109, 119
    - PBEPBE, 111, 113, 114, 116, 119–122, 124, 125
    - PW91, 114, 116, 121, 122
    - PW6B95, 123
    - PW6BK, 120, 123
    - PWB6K, 123
    - PW91LYP, 119
    - range-separated hybrid, 453
    - theory, 97–129
    - total energy, 498, 597
    - TPSS, 108–111, 113–116, 119–121, 462
    - TPSSh, 111, 113–116, 119–121, 124
    - TPSSKCIS, 119
    - VWN, 600, 602
    - XB1K, 119
  - Functionalization, 1019, 1026
  - Functionally important motions (FIM), 1141–1142
  - Function counterpoise method (FCP), 766
  - Furan derivatives, 1350–1352
  - Furocoumarins, 512, 537, 549, 551, 553
  - FVP. *See* Flash vacuum pyrolysis
- ## G
- Ga<sub>1</sub>As<sub>5</sub>, 735
  - Ga<sub>2</sub>As<sub>4</sub>, 734, 735
  - Ga<sub>3</sub>As<sub>3</sub>, 735, 747–749
  - Ga<sub>4</sub>As<sub>1</sub>, 735
  - Ga<sub>5</sub>As<sub>5</sub>, 735, 747
  - GaAs clusters, 736, 737, 743, 748
  - GAMESS, 511
  - GAMESS-UK
    - features, 616–617
  - GAMESS-US, 1360
    - features, 614–615
  - GanAsn, 734, 737
  - Gap state, 1015, 1017
  - Gauge
    - correction, 429
    - Coulomb, 368, 369
    - dependence, 369
    - gauge invariance, 149–151, 155
    - invariance, 390
    - length, 390, 403–405
    - length gauge, 149–151
    - modified velocity gauge, 151
    - origin, 369, 394, 395, 402, 403, 408, 414, 415, 417, 421, 422, 429
    - velocity, 390, 403, 405
    - velocity gauge, 149–151

- Gauge invariant atomic orbitals (GIAOs), 336, 395, 418
- Gauge origin, 369, 394, 395, 402, 403, 408, 414, 415, 417, 421, 422, 429
- Gaussian, 500, 502, 511, 1360, 1395  
 –chain, 241–244  
 –function, 3, 4, 49, 50, 108, 111  
 –web page, 624
- Gaussian-type functions, 423  
 –contracted, 500, 502  
 –four-center integrals, 502  
 –LCGTO, 578–582, 599  
 –primitive, 500, 502
- GDIIS, 306–307
- General conservation law, 1069
- Generalized gradient approximation (GGA), 214, 451, 462, 639, 1265
- Generalized valence bond method, 612
- Generating function technique, 246–247
- Genetic algorithm, 975, 977, 979, 987, 989, 998, 1007, 1013
- Geometric mixing, 210
- Geometric shell, 998
- Geometry  
 –constrained, 301, 308, 325  
 –1,2-dichloroethane, 336–352  
 –enforced, 331  
 –experimental, 378, 402, 423  
 –external force, 330–336  
 –formaldehyde, 615  
 –molecular clusters, 329–330  
 –optimization, 5, 110, 294, 297, 299–311, 313–315, 317–326, 329–331, 333, 340, 344, 353, 470, 564, 575, 576, 581, 592, 593  
 –fullerene, 599  
 –modernite, 591  
 –output, 310, 317  
 –symmetry, 307  
 –transition state, 307
- GGA. *See* Generalized gradient approximation
- Giant fullerenes, 801, 803, 827–828
- GIAOs. *See* Gauge invariant atomic orbitals
- Gibbs free energy, 468
- Global minimum, 998, 1004
- Global optimization, 998–1001, 1004, 1006
- Global search algorithms, 998, 999, 1001, 1013
- Glucose oxidase (GO), 1069, 1071, 1077–1079, 1084, 1087, 1088, 1090
- Glue potential, 1001
- Glycosidic bond, 1294, 1303
- Golden cages, 978
- GPU, 1138
- Gradient, 294, 297, 298, 300, 302, 303, 306–308, 310, 312–320, 322–324, 336, 352–354, 470, 491, 492, 510, 513, 516, 538, 543, 582, 584, 588, 593, 599, 612, 614–622, 624
- Graphane, 821, 822, 851
- Graphene, 795, 797–799, 812, 814, 817, 819–821, 823, 824, 828–830, 839, 840, 847–852, 996, 1010, 1014–1026, 1028–1036  
 –nanodots, 917, 920, 922, 925  
 –nanoribbons, 905–916, 918–920, 922, 925, 930–932
- Graphene nanoribbon (GNR), 1018–1020, 1025, 1026, 1028, 1030, 1032–1035
- Graphite, 795–797, 811, 812, 845
- Greedy search method, 999
- Green-fluorescent protein (GFP), 1363, 1385–1388
- Green's function formalism, 1026
- Green's functions, 504
- GRN junction, 1030
- GROMACS. *See* GRONing Machine for Chemical Simulation
- GROMOS. *See* GRONing Molecular Simulation package
- GRONing Machine for Chemical Simulation (GROMACS), 284, 285, 1138
- GRONing Molecular Simulation package (GROMOS), 284–286
- Ground state, 3, 5, 6, 23, 51, 98–102, 112, 123, 126, 127, 295, 296, 331, 334, 386, 394, 424, 456, 485–492, 494, 495, 497, 499, 501, 503, 505, 506, 509–514, 516–519, 521–529, 531–535, 537, 539, 541, 543–547, 549, 551, 554–557, 576, 577, 601  
 –energy, 66, 67, 70, 78, 86, 87  
 –Hamiltonian, 63, 66, 67, 69, 78, 86  
 –structure, 725–728, 730–735, 739, 745
- Group theory, 488, 518
- Growth sequence analysis, 999
- Guanine(G), 528, 530, 531, 533, 535, 543, 544, 1187–1189, 1191, 1192, 1196, 1216, 1217, 1225–1227, 1232, 1233, 1247, 1258, 1260, 1261, 1269, 1278–1294, 1297–1303  
 –MEP, 539, 540
- Gupta potential, 962, 963, 990, 1000, 1001, 1004
- Gyromagnetic ratio, 1007
- ## H
- Half-metallic behavior, 910, 916
- HAIO, 979–983
- Halogen bond, 187
- Hamilton, 364
- Hamiltonian, 2, 98, 102, 364–369, 371, 377, 394, 411–414, 419–421, 424, 425, 428–430, 469, 612, 613, 615, 617, 740, 742, 744, 1132  
 –Breit–Pauli, 364–367, 419, 420, 425, 429  
 –clamped nuclei, 14–53  
 –Coulomb, 14–18, 24, 28, 30, 53  
 –diagonalization, 510, 524  
 –diatomic, 17, 21–28, 49

- Dirac, 365
- eigenvalue problem, 15, 20, 52
- electronic, 14–53, 65–67, 70, 71, 77
- expectation value, 495, 497
- hardness, 584
- matrix, 495, 498, 543, 579
- matrix elements, 49, 74
- multistate effective, 541
- nuclear, 16, 19–30, 32, 39, 52, 53
- PCM, 1044
- perturbation theory, 493, 495, 508
- semi-empirical, 454–455
- spherical polar coordinates, 22, 25
- Hamiltonian replica exchange molecular dynamics (H-REMD), 1163
- Hammond postulate, 318
- Hanging drop method, 1097
- Hansel-Vogel potential, 1013
- Hard-and-soft-acids-and-base (HSAB) principle, 985
- Hardness, 584
- Hard-sphere, 269
- Harmonic oscillator, 332–334, 469
  - potential energy, 332
- Hartree, 3–5, 9, 42, 52
  - approximation, 101
  - product, 99
- Hartree-Fock (HF) method, 9, 42, 99, 110, 116, 123–126, 374, 383, 389, 395, 396, 399, 418, 420, 451, 472, 579, 599, 818
  - accuracy, 327, 343, 354, 390
  - dispersion corrected, 451
  - dissociation, 498
  - equations, 77, 84, 100
  - exchange, 104, 110, 114, 116, 123–125, 451, 904
  - limit, 395, 396, 498
  - method, 294, 329, 342, 355, 356, 420, 496, 612, 613
  - orbitals, 126
  - restricted, 374, 612, 622, 624
  - restricted open-shell, 499, 612
  - restricted, RHF, 498
  - time-dependent, 390
  - unrestricted, 499, 612, 613, 624
  - wave function, 74–78
- H-bond, 121, 122
- Heat of formation
  - calculations, 471
  - FO, 477, 478
  - F<sub>2</sub>O, 477, 478
  - H<sub>2</sub>SO<sub>2</sub>, 479–481
  - natural orbitals, 477
  - perturbation theory, 472
  - potential energy surface, 468
  - reaction, 468
- Heisenberg, 427
- Heisenberg Hamiltonian, 427
- Helium atom, 417
- Helium droplet, 1260, 1261
- Hellman-Feynman theorem, 8, 374, 378, 744
- Heme-O<sub>2</sub> system, 1068
- Heme proteins, 1142
- Hemoglobin, 1068, 1070, 1071, 1084, 1085, 1087–1090
- Herzberg-Teller expansion, 489
- Hessian, 517, 519, 527
  - approximate, 306, 340
  - diagonalization, 298
  - eigenvalue, 299, 301, 304, 305, 310, 313, 314, 316, 319–321
    - negative, 299, 301, 304
    - positive, 299, 300
  - eigenvector, 298, 303–305, 307, 310, 324, 333
  - mass-weighted, 333, 340
  - matrix, 8
  - positive-definite, 300, 305, 307
  - update
    - BFGS, 300, 307, 314, 316, 317
    - Bofill, 301, 324
    - Murtagh-Sargeant, 319, 321, 322
    - Powell, 320–322
    - weight derivative, 353, 354
- Heterofullerenes, 806
- Hexaanion, 680, 689–691
- Hexagonal close packed, 801
- Hexagonal index, 675
- Hexadecapole, 740
- HgnTen, 739
- Hierarchy of methods, 996
- Highest occupied molecular orbital (HOMO), 7, 1222, 1226–1228
- High performance liquid chromatography (HPLC), 808
- High-resolution transmission electron microscopy (HRTEM), 798, 799, 816, 817
- Histidine ligand, 1070
- Hohenberg-Kohn theorem, 101, 502, 576, 577
- Homodesmotic, 471
- Homology modelling, 1104–1105
- HOMO-LUMO gap, 804, 824–830, 834–836, 838, 842, 845
- Homotops, 970
- Honeycomb lattice, 1018
- Hooke's law, 332
- Hopping energy, 1025
- Host-guest, 445, 632–636, 641, 654–657, 660
- HPLC. *See* High performance liquid chromatography
- H-REMD. *See* Hamiltonian replica exchange molecular dynamics

- HRTEM. *See* High-resolution transmission electron microscopy
- HSAB principle. *See* Hard-and-soft-acids-and-base (HSAB) principle
- Hubbard-U, 943, 944, 947
- Huckel theory, 835
- Hybrid descriptors, 1330–1332
- Hybrid functionals, 215, 904, 905, 912, 914, 917
- Hybrid GNR junction, 1030
- Hybridization, 797, 821, 842
- Hydrated cation, 1283, 1285–1289, 1298–1301
- Hydration, 281, 1107, 1114–1116
- Hydrocarbon, 260, 264, 266, 268, 271, 275, 276
- Hydrogenation, 821–824, 842–845
- Hydrogen bond, 21, 111, 121–122, 162, 163, 176, 183, 184, 187, 263, 269, 272, 273, 1258, 1262–1266
- intermolecular interactions, 446
  - length, 446
  - weak, 446
- Hydrogen storage, 1035
- Hydrogen-transfer, 1363, 1379–1384
- 4-Hydroxybenzylidene-1,2-dimethylimidazoline (HBDI), 1363, 1366, 1385, 1386
- HyperChem web page, 625
- Hyperfine coupling constants, 431, 432
- Hyperfine coupling tensors, 416, 430–432
- Hyperpolarizability, 576, 659–661, 741, 745, 748–750
- Hypersurface deformation methods, 998
- Hypersurface deformation technique, 999
- Hypervirial relationship, 390
- I**
- Icosahedral, 1000, 1001, 1004–1009
- Icosahedron, 800, 801, 803
- i-DNA, 1269, 1270
- III-V semiconductors, 984
- II-VI semiconductors, 984
- Impact ionization, 891–896
- Implicit solvent, 1284–1285, 1291, 1301
- In<sub>2</sub>As<sub>2</sub>, 750
- Index of epitaxy, 973
- Individual gauge for localized orbitals (IGLO), 415
- Infrared, 800, 801, 810
- Infrared (IR) intensity, 633
- InP, 725, 748, 749
- In-solvent, 563
- Intensity-dependent refractive index (IDRI), 385
- Interaction, 364, 366, 369, 388, 399, 401, 411, 412, 424, 425, 427, 430
- atom-atom, 268
  - Coulomb, 2, 9, 14, 277, 283
  - electrostatic, 271, 274, 276, 281, 283
  - energy, 160–166, 168, 169, 171, 172, 174–176, 186, 187, 1263–1266, 1268
  - intermolecular, 263, 267, 268, 273, 277
  - intramolecular, 263, 267–269
  - potentials, 197, 200, 208
  - resonance, 273
  - site, 277, 281
  - torsion, 262, 263
  - van der Waals, 263, 264, 274, 282
- Interaction energy components
- charge-transfer, 170–171
  - deformation energy, 160
  - dispersion, 160–163
  - electrostatic, 161, 163
  - exchange-repulsion, 160, 162, 163
  - induction, 160–163
  - van der Waals, 163
- Interaction-induced effects, 363
- $\pi$ – $\pi$  Interactions, 819
- Interatomic interactions, 998
- Intermolecular interactions, 363, 418, 563, 577, 591, 597, 762–764, 783
- dispersion interaction, 591
  - electrostatic, 520, 525
  - electrostatic interaction, 595
  - van der Waals, 591
- Internal conversion, 487, 488, 491, 531, 536, 537, 552, 553, 1269, 1360–1362, 1380
- Intersystem crossing, 425, 487, 488, 491, 531, 533–538, 552, 553
- intramolecular interactions, 425
- Intramolecular
- charge transfer, 512
  - dispersion effects, 453
  - force, 329
  - H-bond, 1299
  - hydrogen bond, 446
  - interaction, 461
  - vibrational relaxation, 487
- Intruder states, 509, 513
- Inverse coordination number, 1006
- Ion channel, 1142, 1143
- Ionic bonding, 686
- Ionization energy, 1260
- Ionization potential, 520, 526, 528, 1260
- Ion mobility, 1002
- IPR. *See* Isolated pentagon rule
- Irreducible representation, 341, 507, 513, 518, 521
- IR spectrum
- combination bands, 348
  - 1,2-dichloroethane, 336–352
  - FT-IR, 345, 348
  - hot bands, 334
  - intensity, 341, 349, 489
  - overtone bands, 334

- scaling, 342, 343, 345, 347–349
- selection rule, 334
- Isodesmic, 471, 477, 478, 481
- Isogyric, 471
- Isolated pentagon rule (IPR), 668, 671–677, 679, 680, 682, 683, 689–692, 695–696, 800, 806–810, 824–826, 829–831, 851
- Isomerism, 684, 687–695
- Isomorphous replacement, 1097, 1098
- Isotropic, 377, 382, 383, 385, 392, 393, 395, 396, 399, 400, 402, 410–412, 414, 422, 427, 430, 431
- Isotropic average, 382, 385
- IS steepest descent path (ISDP), 1374, 1375

## J

- Jablonski diagram, 487
- Jacobian, 26, 29, 46
- Jacob's ladder, 451, 459
- Jaguar web page, 625
- Jahn–Teller distortion, 1006, 1009, 1034
- Jellium model, 586, 589, 974, 976, 990
- Justification, 260, 265, 268, 275

## K

- K–Cs clusters, 963
- Kekule, 835–837, 842
- Kerr (electro-optical) effect, 382, 385, 386, 401
- Kleinman's symmetry, 384
- Kohn–Sham (KS), 201, 213–217, 220, 431, 506, 638, 639
  - equations, 108
  - exchange-correlation potential, 102, 108
  - LCAO MO, 108
  - one-electron approximation, 101, 126
  - orbitals, 101, 107, 125–127
  - theory, 125
- Kohn–Sham approximation
  - canonical, 578
  - coupled-perturbed, 581, 585
  - energy, 579
  - equations, 577, 578
  - matrix, 581, 582, 584
  - orbitals, 577–579, 581, 583
  - perturbed, 584, 585
  - potential, 577
- Koopmans's theorem, 9, 526, 1225, 1227
- Kuhn length, 241, 243

## L

- Lagrange multiplier, 306, 325, 577, 578, 581
- Langevin–Born theory, 407, 409
- Langevin thermostat, 253

- Laplacian, 36–38
- Lattice model, 241, 248
- LCAO MO, 42, 49, 52
- LCGTO. *See* Linear combination of Gaussian-type orbitals
- LDA. *See* Local density approximation
- Leap-frog algorithm, 203, 251
- Leap-frog Verlet, 203
- Leary tetrahedron, 1000
- Length-velocity gauge, 390
- Lennard–Jones cluster, 958, 961, 1000
- Lennard–Jones potential, 210, 999–1011
- LES. *See* Locally enhanced sampling
- Lifetime, 1181–1183, 1187, 1190, 1191, 1196, 1199, 1201, 1202, 1259
- LiF molecule, 541
- Ligand binding, 1099, 1107, 1113–1116, 1118
- Light emission, 1360
- Linear combination of atomic orbitals (LCAO), 455, 495, 523
- Linear combination of Gaussian-type orbitals (LCGTO), 578
  - kernel, 585
  - LCGTO- $X\alpha$ , 575
- Linear dependency, 369
- Linear momentum, 364, 369
- Linear response model in the framework of the linear combination of atomic orbitals (LR-LCAO), 828
- Link atoms, 204–206
- Local density approximation (LDA), 214, 451, 638, 659, 804, 819, 846–848, 1365
- Local field, 661, 662
- Localized basis functions, 903
- Localized edge state, 1028, 1032
- Locally enhanced sampling (LES), 1138
- Local methods, 450
- Local minimum, 997, 998, 1004
- Lock-and-key model, 1113, 1115
- London, 394, 395, 398, 402, 408, 419, 422, 429
- Long-range dispersion, 387–388
- Longuet–Higgins approach, 29
- Lorentz–Berthelot mixing, 210
- Lorentzian line broadening, 391
- Low energy electrons (LEE), 1216–1249
- Lowest unoccupied molecular orbitals (LUMO), 7, 1222, 1226–1228, 1232, 1233, 1240

## M

- Mackay icosahedra, 1000, 1004, 1009
- MAD. *See* Multiple-wavelength anomalous dispersion

- Magic numbers, 964, 974, 998, 1000, 1001, 1003, 1005–1007
- Magic structure, 1001
- Magnetic, 361–433
- anisotropy, 396, 400, 406
  - calculations, 364, 369, 395, 396, 398, 402, 404, 408, 410, 415, 417–419, 429, 431
  - contributions, 366, 376, 412, 416, 428
  - diamagnetic, 370, 371, 394, 395, 408, 414, 417, 421, 422
  - dipole, 376, 397, 402, 406, 408, 412, 417, 428, 429
  - divergence, 368, 369
  - electronic, 416
  - field induction, 366–371, 396, 398, 400, 406–409, 413–417, 419, 427
  - induced, 369–371, 393, 394, 396–398, 406, 420, 421
  - magnetizability, 370
  - moment, 364, 366, 369–372, 393, 394, 396–398, 411–416, 419–421, 427, 430, 941, 943–945, 948, 950, 1004–1009, 1014, 1017, 1034
  - nuclear, 363, 366, 369–371, 397, 411, 412, 414–420, 427, 430
  - order, 941, 949
  - properties, 1007, 1019, 1027, 1032–1036
  - vector potential, 366–370, 394, 395, 411, 430
- Magnetic optical rotatory dispersion (MORD), 406
- Magnetizability contributions, 394, 395
- Magnetization, 1004, 1005, 1007, 1009, 1017, 1033
- Magnetogyric ratio, 366, 370, 396, 421
- Many-body expansion, 449
- 2-body interaction energy, 160–164
  - three-body correction, 160, 175
- Mapping function, 1346
- Marks decahedra, 1000
- Mass abundance experiment, 976
- Massively parallel quantum chemistry (MPQC), 624
- Mass spectroscopy, 800, 804
- Mass-velocity term, 367, 382
- Materials modeling, 996
- Maxwell–Garnett nanocomposite, 635
- Maxwell–Garnett theory, 882, 888
- MCSCF. *See* Multi-configurational self-consistent-field
- MD codes, 1137–1138
- Mean square displacement, 229, 230
- Mechanical properties, 1010, 1024–1032
- Mechano-chemistry, 330
- MEG. *See* Multiple exciton generation
- Merck molecular force field (MMFF), 279, 282
- Metal-cage bonding, 684–687
- Metal cation, 1278–1280, 1282–1287, 1295–1298, 1302–1304
- Metallic, 805, 813, 835, 844, 848, 850, 851
- Metallization, 1033
- Metallo-carbohedrenes, 956, 987
- Metallo-drug, 1278, 1289, 1291, 1294
- Metal-nitride cluster, 668, 687
- Metals of alkaline earths, 1278–1280, 1285–1287
- Metcars, 986–989
- Metropolis method, 249
- Microorganisms, 1344, 1345, 1348–1350, 1352
- Minimum energy conical intersection (MECI), 1362
- Minimum energy path (MEP), 1360–1362, 1365–1367, 1373, 1374, 1376, 1398
- Minimum inhibitory concentration, 1345, 1348
- Mixed, 376, 390, 401, 402, 404, 409, 410
- Mixed quantum-classical methods, 1179, 1204
- MMFF. *See* Merck molecular force field
- MNDO. *See* Modified neglect of differential overlap
- Model, 1344–1349, 1351, 1352
- Modified neglect of differential overlap (MNDO), 613, 615, 617
- Molcas, 508, 511, 518, 520, 1360
- web page, 625
- Molecular, 99, 102, 103, 105, 111–126
- clusters, 329–330
  - confinement, 256
  - crowding, 256
  - diseases, 1144
  - dynamics (MD), 250, 252, 254, 263, 279, 283, 285, 286, 566, 567, 632, 634, 638, 640–641, 656–659, 818, 819, 942–943, 946, 947, 972, 989, 996, 1000, 1010, 1011, 1019, 1022, 1129–1137, 1139–1141, 1145, 1156–1170, 1362, 1363, 1368, 1377, 1379, 1392, 1393, 1396–1398
    - Born–Oppenheimer, 576, 588, 603
    - electrostatic potential, 590, 592, 595
  - graphics, 1105–1106
  - junctions, 815, 817
  - machines, 1142
  - mechanics (MM), 260–286, 297, 302, 307, 455, 494, 818, 826, 1013, 1102–1104, 1106, 1114, 1120
  - modeling, 261, 1131, 1139
  - properties, 363–365, 367, 375, 376, 382, 411, 432
    - multipoles, 171
    - polarizability, 177
- Møller–Plesset perturbation theory (MPPT), 449–450, 501, 506
- Molpro, 511, 1360
- web page, 625
- Molten globule, 1112, 1113
- Momentum, 366, 367, 370
- Monte Carlo, 820, 941
- algorithm, 996, 998
  - simulation, 249, 254
- Moore’s Law, 870
- Mordenite, 592–598
- MP2, 452, 726, 731, 732, 737, 743, 744, 750, 804, 818, 819
- MP3, 744
- MP4, 743

- MPn, 462, 1046  
 MPQC. *See* Massively parallel quantum chemistry  
 MPWPW91, 119, 121  
 MRCC, 495, 502, 505, 556  
 MRCI, 495, 500, 502, 504, 506, 510, 537, 539, 541, 556  
 MRPT, 495, 556  
 Multiconfigurational methods, 88  
 –active electrons, 506  
 –active space, 519–520  
 –psoralen, 513  
 –Rydberg states, 511, 512  
 Multi-configurational self-consistent-field (MCSCF), 374, 424, 429, 431, 494–495, 501, 506  
 –features, 623–624  
 Multiconfiguration quasi-degenerate perturbation theory (aug-MCQDPT2), 1367  
 Multiple exciton generation (MEG), 891, 895, 896  
 Multiple histogram, 946  
 Multiple photon excitation, 89–891  
 Multiple-spawning, 1362  
 Multiple vacancy, 1033, 1034  
 Multiple-wavelength anomalous dispersion (MAD), 1098  
 Multiplicity, 191, 296, 426, 427, 429, 487, 488  
 Multipole expansion, 171–174, 178, 377, 378, 387  
 –distributed multipole expansion, 173  
 Multipole moments, 375–379, 400, 401, 1263  
 Multireference, 429  
 Multireference approach, 424, 429  
 Multireference CI (MRCI), 429  
 Multi-reference methods, 1178  
 Multiscale methods, 1002, 1013  
 Multiscale simulations, 1140  
 Multi target quantitative structure–activity relationships (mt-QSARs), 1347, 1351–1352  
 Multi-walled carbon nanotubes (MWCNT), 811–813, 815, 819, 852  
 Multi-walled nanotube, 1011  
 Murrell–Mottram potential, 962  
 Mutation, 1258, 1261  
 Mutation operator, 999  
 MWCNT. *See* Multi-walled carbon nanotubes  
 Myoglobin, 1070, 1073, 1074, 1079, 1080, 1083, 1084, 1089, 1090  
 Mystery of brain, 1068
- N**  
 Na clusters, 974, 976–979  
 NAMD, 1138, 1143  
 Nanobelt, 1013, 1018–1024, 1029  
 Nanobud, 795  
 Nano-capsules, 805–806  
 Nanocomposite, 632–663  
 Nanocup, 795  
 Nanoelectromechanical systems (NEMS), 851  
 Nanohorn, 795  
 Nanomechanics, 1143  
 Nano-onion, 795  
 Nanoparticles, 996–1009, 1035  
 Nanoribbons, 821, 822, 851, 1010, 1017–1027, 1029, 1030, 1032–1035  
 Nanoscience, 724, 813, 817, 854  
 Nanotechnology, 797, 803, 811, 813, 852, 854  
 Nanotori, 795  
 Nanotube, 996, 1009–1019, 1023, 1026  
 Nanowire, 996, 1009–1017, 1021  
 Natural orbitals, 503, 513  
 Natural products, 1344  
 Nature of consciousness, 1068  
 Near-degeneracy, 509, 510  
 NEMS. *See* Nanoelectromechanical systems  
 Neutron diffraction, 1099  
 Newton–Raphson method, 297–299, 303, 304, 306, 317, 333  
 –shift parameter, 303–305  
 Ni clusters, 964–972  
 NICS. *See* Nucleus independent chemical shift  
 Ni–Cu clusters, 963  
 Nitromethane, 527  
 NMR spectrum, 327, 336, 411, 413–415, 576  
 –anisotropy, 382, 396, 400, 401, 405–407, 409, 414, 422  
 –basis set, 374, 375, 377–379, 383, 384, 389–391, 393–398, 402, 403, 408, 417, 418, 422, 423, 430, 431  
 –chemical shift, 336, 417, 418  
 –contact contributions, 413, 416  
 –diamagnetic contribution, 394, 395, 408, 414  
 –diamagnetic spin-orbit, 370–371, 422  
 –Fermi-contact, 371, 413, 416, 419, 422, 423, 430  
 –isotropy, 377, 382, 383, 385, 392, 393, 395, 396, 400, 402, 412, 414, 422, 427, 430, 431  
 –non-adiabatic effects, 397  
 –one-electron, 367, 390, 425  
 –one-photon absorption, 374, 389–392  
 –paramagnetic contribution, 394, 395, 414–416  
 –paramagnetic spin-orbit, 370, 422  
 –polarizability, 376, 378–384, 388, 400–402, 404, 406–409, 419  
 –spectrum shielding, constant, 389, 411–420, 422, 425, 428, 430, 432  
 –spin-dipolar term, 419  
 –spin-orbit approximation, 425  
 –spin-orbit interaction, 425  
 –spin-spin coupling constant, 389, 411–413  
 –transition moment, 374, 389–393, 426  
 Noble gas clusters, 1000  
 NOE. *See* Nuclear Overhauser effect  
 Non-additive contribution, 1295



- Non-adiabatic coupling, 1362, 1372  
 Non-adiabatic effects, 397  
   –reactions, 486, 493  
 Nonbonded interactions, 208–210  
 Non-collinear, 943, 944, 947  
 Nondynamic, 450  
 Nonmetallicity, 1009  
 Normalization, 24  
 Normal mode, 333, 335, 337, 341, 343, 344,  
   347, 489  
 Normal model, 593  
 Normconserving pseudopotentials,  
   216–217  
 Nose-bath, 946  
 Nose–Hoover barostat, 224–225  
 Nose–Hoover thermostat, 223–225,  
   253, 254  
 Nose–Hoover thermostat chain, 588  
 Notation, 31, 34, 45, 49  
 NP-hard problem, 958  
 Nuclear coupling constant, 389, 428  
 Nuclear magnetic, 366, 369, 371, 412, 415,  
   417–419, 430  
 Nuclear magnetic resonance (NMR), 801, 808, 809,  
   819, 824, 826  
   –effective spin, 411, 421  
 Nuclear magnetic resonance (NMR) spectroscopy,  
   672, 679, 682, 699, 700, 705, 710, 1096, 1097,  
   1099–1101, 1110, 1113  
 Nuclear Overhauser effect (NOE), 1100, 1101,  
   1110, 1111  
 Nuclear quadrupole moments, 389  
 Nucleic acid, 260, 269, 272–275, 281–286, 1156–1170,  
   1258–1271  
 Nucleic acid bases, 451, 528  
 Nucleobase, 1187–1189, 1191, 1192, 1195–1197,  
   1277–1304  
 Nucleus independent chemical shift (NICS),  
   835, 837  
 Numerical integration, 353, 354, 575, 579,  
   582, 583  
 NWCHEM, 511  
   –features, 619–620
- O**  
 Octupole, 740  
 Oligomer, 1277–1304  
 OMx, AM1-D, PM3-D, 455  
 One-electron, 100, 102,  
   108, 126  
   –approximation, 21, 23, 42, 70–74  
   –basis set, 498, 502, 504, 506, 521, 525, 530, 556  
   –effective potential, 497  
   –operator, 498  
   –wave function, 495, 500
- One-photon  
   –absorption, 505  
   –probability, 489  
   –transition, 489, 518  
 ONIOM, 818, 839  
 Open-shell system, 416, 424, 427–429, 499  
 Operator  
   –angular momentum, 370, 372, 420, 421  
   –core-Hamiltonian, 497, 498  
   –Coulomb, 497  
   –diamagnetic magnetizability, 370, 394, 408  
   –diamagnetic shielding, 370, 371  
   –diamagnetic spin-orbit, 370–371  
   –electric dipole, 335, 368, 387  
   –electric field gradient, 368, 388–389,  
     409–412, 428  
   –electric quadrupole, 368, 378, 405  
   –exchange, 497  
   –Fermi contact, 371, 416, 419, 430  
   –Fock, 449, 497, 498  
   –Hamilton, 364, 493, 497  
   –kinetic energy, 493, 498  
   –linear momentum, 364, 369  
   –magnetic dipole, 335, 370, 393, 394, 396–398,  
     402, 414, 428, 429  
   –momentum, 364, 367–369, 372  
   –NMR effective spin, 411–413, 421  
   –optical rectification, 383, 385  
   –paramagnetic spin-orbit, 370, 422  
   –potential energy, 493  
   –spin-dipole, 371, 416, 422, 430  
   –spin-orbit interaction, 425  
   –spin-Zeeman, 367, 370, 371, 427–430
- OPLS. *See* Optimized potentials for liquid  
 simulations  
 Opsin shift, 1388  
 Optical  
   –activity, 400, 433  
   –basis set, 383–385, 402, 403  
   –dispersion, 400, 402, 406  
   –electron correlation, 383, 384, 386, 403  
   –flexible molecules, 402–404, 432  
   –properties, 1014–1017, 1032–1035  
   –rectification, 383, 385  
   –rotation, 401–404, 406  
   –transitions, 912, 914, 915  
 Optimization algorithms, 219  
 Optimized potentials for liquid simulations (OPLS),  
   284, 285, 1369, 1387  
 $\pi$ -Orbital axis vector (POAV), 828–831  
   –analysis, 674  
   –pyramidalization angle, 676  
 $\pi$ -Orbital misalignment, 830, 837, 839  
 Orbitals  
   –active, 506, 507, 513  
   –antibonding, 295, 296

- atomic, 3, 4, 8, 21, 32, 42, 43, 49, 99–101, 107, 108, 295, 336, 456, 496, 502, 578, 579, 592
- bonding, 295
- canonical, 578
- delocalized, 496
- energy, 9, 32, 52, 78, 83, 88
- frozen, 526
- Hartree-Fock, 126, 497, 506
- HOMO, 296
- hydrogen, 32, 42
- inactive, 506
- Kohn-Sham, 107, 125, 126, 577–579, 581, 583
- localized, 496
- London, 375, 394–398, 408, 422
- lone-pair, 513, 520
- LUMO, 296
- MC-SCF, 88, 89
- molecular, 32, 42, 44, 99, 125, 126, 455, 485, 494, 496, 498, 506, 511, 530, 581, 584, 585
- nonbonding, 512
- occupied, 512, 521, 577, 581, 584
- orthonormality, 583
- relaxation, 375
- Rydberg, 521, 522, 524
- secondary, 506
- spin-orbital, 9, 10, 21, 32, 42, 47–51, 76–79, 82, 83, 87, 88
- valence, 456, 521
- virtual, 503, 512, 522, 525
- ORCA features, 620–621
- Organic crystals, 183–185, 187
  - polarization in organic crystals, 183–184
- Origin dependence, 395, 402, 414, 429
- Oscillating, 384, 406
- Oscillator strength
  - calculations, 390
  - Rydberg states, 523, 524
- Overlap
  - integral, 49, 63, 72–74
  - matrix, 49, 63, 80
- Oxidation, 1218
  
- P**
- Pairwise energy, 1295, 1296
- Parallel random tunneling, 999
- Parallel tempering, 1161
- Paramagnetic contribution, 394, 395, 414–416
- Paramagnetic spin-orbit, 370, 422
- Paramagnetism, 394
- Parameters, 260–286
- Parametric Method 3 (PM3), 308, 309, 318, 613, 615, 617, 640, 642, 649
- Parametric Method 6 (PM6), 460, 613, 617
- Parametrization, 450
- Partition function, 247, 248, 255, 256
  
- Passivated nanowire, 1012, 1013
- Path integral MD, 197
- Pauli exclusion principle, 495
- Pauli principle, 9, 31, 32, 100, 103
- PBE1PBE, 818
- PC. *See* Polycarbonate
- PCM. *See* Polarizable continuum model
- PCM-CC, reference state, 1049
- PCM-HF equations, 1050
- Peapod, 795
- Penrose-Hameroff model, 1088
- Peptide bond, 1197–1203
- Perfluoroalkylation, 672, 682, 683, 701–706
- Performance, 459–461
- Periodic boundary condition, 819, 821, 847
- Persistence length, 243
- Perturbation, 9
  - dependent, 417, 418
  - expansion, 70, 73, 138
  - Møller-Plesset, 78–83
  - theory, 48, 65, 71, 73, 74, 78–83, 88, 159–174, 187, 448, 449, 452
    - auxiliary density, 576, 584–585
    - polarization expansion, 161, 162, 174
    - self-consistent, 584
    - series convergence, 509
    - supermolecular approach, 175, 181
- PES. *See* Potential energy surface
- Phase problem, 1097
- Phase space, 250
- Phase transition, 1002
- Phenolic compounds, 1350–1352
- Phosphorescence, 374, 426
  - decay time, 514
  - radiative lifetime, 426, 514
- Phosphoryl transfer, 1120, 1121
- Photochemistry, 1181, 1183, 1187, 1192, 1197
- Photodeactivation path, 1200, 1201, 1363, 1393
- Photodenitrogenation, 1363, 1377–1379
- Photodissociation, 1197, 1198
- Photoelectron spectra, 804
- Photoelectron spectroscopy, 576
- Photoexcitation, 1197–1198
- Photoexcited states, 1145
- Photoisomerization, 808, 1180–1182
- Photoluminescence (PL), 633, 634, 645, 647–654, 663
- Photoreceptor, 1360, 1363, 1387
- Photosensitizers, 851
- Photostability, 1187–1189
- Physisorption, 824
- Piano-stool complex, 1291
- PL. *See* Photoluminescence
- Plane-wave basis set, 819, 821
- Plane waves, 206, 215, 216, 219, 220, 226

- Plasticity, 1010
- PM3-D, 455
- PMMA. *See* Poly(methyl methacrylate)
- Pockels effect, 632, 654–655
- Poisson–Boltzmann equation, 1107, 1108, 1303
- Polarizability(ies), 335, 336, 341, 376, 378–384, 388, 400–402, 404, 406–409, 419, 505, 640, 642, 659, 661, 663, 731, 740–751, 828, 829
- ADFT, 588
  - anisotropy, 382, 396, 400, 401, 405–407, 409, 414, 422
  - basis set, 374, 375, 377–379, 383, 384, 389–391, 393–398, 402, 403, 408, 417, 418, 422, 423, 430, 431
  - calculations, 363, 364, 369, 378, 380, 383, 389–391, 395, 396, 398, 402–404, 408, 410, 415, 417–419, 423, 425, 429, 431–433
  - Casimir–Polder formula, 388
  - DFT, 371, 383, 385, 388, 390, 396, 402, 403, 423, 431
  - electric dipole, 368, 376, 379–383, 387, 400–402, 404, 406–409
    - electric quadrupole, 402, 404, 409
    - magnetic dipole, 376, 401, 402, 404
  - electron correlation, 378, 383, 384, 386, 391, 395, 398, 399, 403, 418
  - expansion, 388
  - frequency-dependent, 375, 376, 379–381, 385, 387, 398, 407–409
  - helium atom, 417
  - isotropic average, 382, 385
  - sodium clusters, 586
  - static, 360, 376, 377, 385, 386, 400, 401, 403, 419
- Polarizable continuum model (PCM), 564, 565, 613, 615, 1216, 1232, 1233, 1243–1248
- accuracy, 1047, 1048
  - EOM-CC, 1058–1061
  - equations, 1051
  - excited state, 1045
  - PCM-CC, 1044
- Polarization functions, 450, 456
- Poly(methyl methacrylate) (PMMA), 636, 654, 656–663
- Polycarbonate (PC), 636, 654, 656–658, 661–663
- Polymer, 240–248, 254
- Poly-N-vinylcarbazole (PVK), 636, 654, 656–663
- Polypeptide, 264, 269–272
- Pople, 456
- Pople–Nesbet equations, 499
- Positive and negative dielectric constant, 887
- Post Hartree–Fock methods, 294, 306, 342, 355, 356, 494, 499, 502, 503, 613, 1046
- Postprocessing, 227–229
- Potential
  - empirical, 277
  - energy, 260, 261, 263, 266, 267, 280
    - energy surface, 24, 29, 30
    - function, 267, 268, 270, 272, 277, 280, 281
    - Lennard–Jones, 263, 265, 278
    - nonbonded, 268, 272
    - rotation, 15, 22, 24–27, 29
- Potential energy surface (PES), 2, 490, 554, 564, 601, 602, 1131–1133, 1361, 1362, 1364, 1366–1368, 1371, 1387, 1394
- local, 295, 309
  - minimum, 307–310
  - scan, 296
- Potential of mean force, 229
- PQS, web page, 625
- Pressure, 7, 10
- Prolateness parameter, 1002, 1003
- Propagator approach, 504, 505
- Property, 1344, 1352
  - optimized, 417
- Protein, 260, 261, 264, 269–286, 1096–1122
  - conformation, 1129
- Protein-DNA interactions, 1144
- Protein folding, 1130, 1140–1141
- Protein-protein interaction, 1116–1119
- Protonated formamide, 1200–1202
- Protonated Schiff base, 1177, 1178, 1180–1186, 1203
- Protonation, 1107–1109
- Pseudopotentials, 206, 215–217
- PSI3, features, 621–622
- Psoralen, 512–520, 536–538, 544, 548–553
- Pt-bridge, 1301
- Pt cross-link, 1301
- PVK. *See* Poly-N-vinylcarbazole
- Pyraclyene, 810
- Pyramidalization, 676
  - angle, 828–831, 836, 837, 839, 842, 844–846
- Pyrrole, 1192–1195
- ## Q
- QCFF/PI, 672, 673, 676, 680, 681, 683, 688
- Q-Chem, 1360
  - web page, 625
- qHTS, 1331, 1332
- QMC. *See* Quantum Monte Carlo
- QM/MM method, 204–206, 576, 1103, 1120, 1261, 1263, 1271, 1368–1371, 1385, 1387, 1388, 1390–1393, 1397
- QM/QM', 576
- QTAIM. *See* Quantum theory of atoms in molecules
- Quadrature
  - grid points, 354
  - weight, 354
- Quadruplex, 1302, 1303
- Quadrupole, 740
  - moment, 377, 398, 409
    - electric, 376, 389, 405, 409, 417

- induced, 376
  - nuclear, 368, 377, 389, 426
  - Quantitative structure-activity relationship (QSAR), 1343-1352
  - Quantum, 817-820, 826, 831, 833, 839
    - annealing, 999
    - chemistry, 1130, 1179, 1184, 1193, 1196, 1203
    - confinement effect, 632, 635
  - Quantum dots, 996, 1034
    - nano-composite material, 870-897
  - Quantum mechanical/Molecular mechanical (QM/MM), 562, 566-568
  - Quantum mechanics, 260, 264, 265, 270, 273, 277, 282-286, 1129-1131, 1133
  - Quantum Monte Carlo (QMC), 449
  - Quantum potential models, 763
  - Quantum theory of atoms in molecules (QTAIM), 686-688
  - Quantum yield, 1360, 1387, 1396, 1398
  - Quasispherical, 1002, 1003
  - Quasi static equilibrium, 240
- R**
- Radial breathing mode (RBM), 813
  - Radial distance, 966-968, 970, 976-980
  - Radial distribution function, 228
  - Raman
    - depolarization ratio, 341
    - intensity, 341, 345, 347, 349, 642, 644-646
    - scattering, 335
      - anti-Stokes, 335
      - stokes, 335, 341, 349
    - selection rules, 334
    - spectrum
      - band intensity, 341
      - 1,2-dichloroethane, 336-352
  - Random walk, 244
  - Range-separated hybrid (RSH+MP2), 453
  - Rational functional optimization (RFO), 304, 305, 310, 312-316, 324
  - Rayleigh scattering, 335, 382
  - Rb-Cs clusters, 963
  - RBM. *See* Radial breathing mode
  - Reaction
    - coordinate, 240, 301, 302, 325, 1293, 1294
    - Diels-Alder, 324-326
    - HCN ↔ HNC, 318, 323, 324
    - path, 295, 301, 307
  - Reactive bond-order potential, 1011
  - Reciprocal space, 872
  - Recommendations, 461-462
  - Rectification, 383, 385
  - Reduction, 1218
  - Reference interaction site model (RISM), 567-568
  - Refractive index, 376, 382, 385, 399, 400
  - Relative energy, 673, 677, 691, 693, 702, 704, 709
  - Relativistic effects, 364, 367, 419, 420, 425, 428, 431, 432
  - Relativistic mass correction, 428
  - Relaxation, 375, 389, 412, 414, 1101, 1110-1112, 1118
  - REMD. *See* Replica exchange molecular dynamics
  - Replica exchange method, 999
  - Replica exchange molecular dynamics (REMD), 1161-1163, 1169, 1170
  - Replica exchange umbrella sampling (REUS), 1163-1164, 1166
  - Resolution-of-the-identity (RI), 110, 111, 452-453, 456
  - Resonance, 1096, 1099-1101, 1111, 1218-1229, 1231, 1232, 1235, 1236, 1239-1244, 1249
  - Response
    - equations
      - iterative procedure, 140
      - residual vector, 140
      - tolerance, 140, 142
    - function, 1047
      - conjugation relations, 145, 146
      - cubic, 373, 374, 385, 387, 392, 393, 408
      - damped, 143, 144, 155
      - frequency-dependent, 137-140, 142, 147
      - frequency(time)-independent, 374
      - Kleinman symmetry, 146
      - linear, 140-147, 149-151, 373, 381, 394, 397, 398, 401, 414, 419, 421, 425
      - permutation relations, 145, 146
      - poles, 141, 142, 152
      - properties, 365, 371, 374, 376, 387, 393, 411
      - quadratic, 145-148, 150, 373, 374, 383, 384, 392, 406, 408, 410, 419, 426
      - residue, 373, 374, 391, 392, 404, 410, 425, 426
      - residues, 142, 145-147, 149
      - static, 138, 147-148, 152, 155
      - theory, 372-376
    - theory, 136-155
      - damped, 143, 144, 155
  - Restraint, 1096, 1098, 1100-1101, 1105, 1106, 1110, 1111, 1114
  - Retinal model, 1177, 1180-1186
  - Retinal protonated Schiff Base (RPSB), 1363, 1371, 1391
  - REUS. *See* Replica exchange umbrella sampling
  - R-factor, 1098
  - Rhodopsin, 1363, 1371-1376, 1387, 1391, 1396, 1397
  - Ribosome, 1258, 1262, 1267
  - Rigid-body motion, 331
  - Rigid-rotor model, 469
  - Ring puckering, 1188, 1194
  - RISM. *See* Reference interaction site model
  - RM<sub>BH</sub>, 455

- RMS distance, 1137  
 RNA, 1258–1271  
 Rotational  
 –effect, 397  
 –fine structure, 388, 389  
 –*g*-tensor, 395–401  
 –rotatory strength, 404  
 –two-photon, 405  
 –spectrum, 389, 411, 420, 421  
 –spin-rotation constants, 415  
 –strength, 335, 336, 341, 350, 401, 404  
 –translation, 333, 336, 340, 341  
 Rotatory strength, 145, 404, 405  
 Rugby ball, 801  
 Rydberg state, 390
- S**
- SAPT. *See* Symmetry adapted perturbation theory  
 SASAWs. *See* Self attracting-self avoiding walk  
 Sawtooth-like GNR, 1019, 1020, 1026, 1027  
 Sawtooth-like nanoribbon, 1019, 1026  
 Scalar electrostatic potential, 366, 367  
 Scaled quantum mechanical (SQM), 343, 345–350, 355  
 Scattering, 1216, 1220–1222, 1224–1226, 1235, 1242  
 –elastic, 335  
 –inelastic, 335  
 –Raman, 335  
 –anti-Stokes, 335  
 –stokes, 335  
 –Rayleigh, 335  
 SCC-DFTB, 455  
 Schlegel diagram, 784, 804, 807  
 Schrödinger equation, 16, 24, 37, 48, 53, 56, 58, 70, 98, 360, 364, 411, 412, 1044, 1052  
 –time-dependent, 2, 3, 5, 7, 8, 53  
 SCRF. *See* Self-consistent reaction field  
 SCS-MP2, 447, 450, 461  
 SCSN-MP2, 450  
 Second derivative, 294, 297–299, 301, 302, 307, 354, 356  
 Second harmonic generation, 383, 385, 387  
 Second quantization, 1049, 1053, 1055  
 Secular problem, 48–51  
 Selection rules, 9, 46  
 –IR, 334  
 –Raman, 334  
 –symmetry, 334  
 Self attracting-self avoiding walk (SASAWs), 244  
 Self avoiding walk, 244–246, 249, 254  
 Self-consistent, 578  
 –convergence, 579, 581, 582  
 –field, 585, 603  
 –convergence, 306  
 –energy, 310, 323  
 Self-consistent perturbation theory, 584  
 Self-consistent reaction field (SCRF), 564, 613, 615, 618  
 Self purification, 1017  
 Semi-Ab initio, 818  
 Semi-classical methods, 1179  
 Semiconductor, 812, 813, 821, 844, 850, 851  
 –clusters, 724–751  
 Semiempirical methods, 214, 444, 449, 452, 633, 638, 640–642, 649, 673, 680, 681, 683, 701, 818, 824, 826, 832, 1048, 1283, 1288  
 Sensors, 819, 851, 852  
 Shape analysis, 976  
 Shape resonance, 1216, 1219, 1220, 1222, 1223, 1225–1229, 1231, 1235, 1236, 1239–1242, 1244  
 Shielding, 370, 411–422, 430, 432  
 Shift parameter, 303–305, 310, 317, 324  
 Si<sub>6</sub>, 730  
 SiC. *See* Silicon carbide  
 Silicon carbide (SiC), 633–637, 642–644, 646–663  
 Silicon clusters, 724, 729–734, 746, 749  
 Similarity function, 968–970  
 Simplification, 265, 271  
 Simulated annealing, 801, 998, 999, 1002, 1006, 1009  
 Simulation, 260, 263, 269, 271, 272, 276, 278, 280, 283–286  
 –Monte Carlo (MC), 263, 277, 278, 281, 284, 285  
 Si nanowire, 1011, 1012, 1014  
 Single-centre technique, 352  
 Single-point calculations, 468, 470  
 Single-strand breaks (SSB), 1217–1220, 1235–1239, 1241, 1243, 1244, 1248  
 Singlet/triplet crossing, 1360. *See also* Intersystem crossing  
 Single-walled carbon nanotubes (SWNTs), 806, 811–821, 828–830, 835–853, 904–907, 910, 912–914, 916, 921, 925, 927–930  
 Singly occupied molecular orbital (SOMO), 1222, 1232–1234, 1236, 1238–1245, 1247  
 Singular value decomposition (SVD), 581  
 Skew pentagonal pyramid (SPP) motif, 700, 702  
 Slater, 99–101, 108, 123  
 –determinant, 3, 21, 32, 47–51, 73–75, 79, 99, 101, 125  
 –eigenvalue, 49  
 –functions, 4, 73–75, 79, 82, 83, 86, 99  
 –rules, 49, 82, 83, 86  
 –spin, 21, 32, 47–50, 74, 75, 79, 82, 83  
 –spin-orbital, 21, 32, 42, 47–49  
 Slater determinant, 424, 577, 1061  
 Slater-type functions, 395, 455  
 Small-gap materials, 185  
 SMD. *See* Steered molecular dynamics

- Smoothing technique, 999
- SMx models, 565
- Sodium, 974, 977
- cluster
  - polarizability, 586
  - symmetry, 592
- Solute-solvent, 562–565, 568
- intermolecular interactions, 1044, 1058, 1059, 1063
- Solvation, 282–285, 1216, 1218, 1232–1235, 1243, 1245–1249
- effects, 1137, 1183, 1284, 1291
- Solvent-accessible surface, 1106, 1109, 1114, 1115
- Solvent effects
- accuracy, 1044, 1047, 1048
  - Born formula, 564
  - cavity, 563–565, 1045, 1047, 1048
  - charging process, 1045, 1046
  - continuum models, 563–566, 568
  - COSMO, 565, 613, 615, 619
  - C-PCM, 565
  - electron correlation, 1045, 1046
  - electrostatic contribution, 564, 565
  - excited state, 1045, 1047
  - free energy of solvation, 564, 565, 568
  - generalized Born model, 565
  - Hamiltonian, 566
  - Kirkwood model, 564
  - Langevin dipole model, 568
  - Marcus partition, 1046
  - molecular dynamics, 566, 567
  - multipole expansion, 564
  - non-electrostatic contribution, 565
  - non-electrostatic terms, 1044, 1045
  - non-equilibrium, 1045, 1046
  - Onsager model, 564, 565
  - PCM, 613, 615, 1044–1048
  - Pekar partition, 1046
  - PTD approach, 1046
  - PTDE approach, 1046
  - PTE approach, 1046
  - QM/MM approach, 562, 566
  - reference state, 1045
  - RISM, 567–568
  - shape, 564, 565
  - volume, 564, 565
- SOPPA, 375
- SOS-MP2, 450
- Spartan, web page, 625
- Spatial distribution function, 227–229
- Spectral tuning, 1387–1392
- Spectroscopy, 1129, 1130, 1141, 1144
- Spherical cluster, 1002
- Spin, 8, 9
- contamination, 296, 424, 432
  - density, 1005, 1036
  - DFT, 111, 112, 123–124
  - dipolar term, 419
  - dipole operators, 371, 416, 419
  - isomer, 1005
  - moment, 1019
  - orbit/orbital, 71, 72, 74–92, 944, 947
  - polarized, 1005, 1009, 1032, 1034, 1036
  - states, 112, 123–124
  - transition, 123
- Spin-orbit approximation, 425
- Spin-orbit coupling, 1068–1090
- Spin-orbit interaction, 367, 370, 372, 416, 419, 425, 430
- diamagnetic, 370–371
  - operator, 419, 426, 428–431
  - paramagnetic, 370
- Spin-spin coupling, 423
- Spintronic, 1017, 1019
- Spin-Zeeman contribution, 367, 370, 371, 427–430
- Spin-Zeeman operator, 371, 428
- Spiral algorithm, 670, 671
- Split-valence, 456
- Spontaneous magnetization, 1017
- SQM. *See* Scaled quantum mechanical
- Stability function, 964, 965, 976
- Stabilization energy, 444, 1280, 1282, 1283, 1289–1292, 1295, 1296, 1301, 1302
- Stacked bases, 1301, 1302
- Stacking interaction, 1261–1266
- $\pi$ - $\pi$  Stacking, 122, 123, 446–447, 458
- Standard state, 469, 479
- State, 16, 22, 24, 26–28, 31, 36, 48, 51, 53, 97–102, 107, 112, 119, 120, 123–127, 129
- Static properties, 375
- Stationary point, 294, 297, 299, 300, 303, 304, 309, 324
- Steepest descent, 219–220, 298, 300
- Steered molecular dynamics (SMD), 1138
- Steric strain, 673–676, 692
- Stillinger-Weber potential, 211, 1010–1011
- Stone-Wales defect, 821, 832, 1015
- Structural properties, 1001, 1010–1014
- Structural stability, 1020
- Structure, 1344–1347, 1349, 1351, 1352
- factor, 228
  - optimization, 1135
- Sugar-edge, 1262
- Sumanene, 802
- Sum-over-states, 141–143, 152, 373, 380, 422, 430
- expansion, 430
- Supercapacitor, 851
- Supermolecular approach, 448, 457, 461
- Supermolecule, 562–563
- Superoxide anion, 1070, 1075, 1078
- Surface hopping, 1182, 1190, 1195, 1196
- Surface reconstruction, 1013, 1014, 1022

- Surface-to-volume ratio, 997, 1011, 1013  
Sutton–Chen potential, 962, 963  
SVD. *See* Singular value decomposition  
SWNTs. *See* Single-walled carbon nanotubes  
Symmetry, 296, 307, 309, 310, 324, 335, 336, 341, 345, 347, 364, 374, 378, 384, 386, 388, 399, 400, 403, 414, 417, 422–425, 470  
Symmetry adapted perturbation theory (SAPT), 159, 165–168, 187, 441, 448, 461, 1265, 1266  
–based on density functional theory (SAPT(DFT)), 166–168
- T**
- Tautomers, 1260, 1261, 1281, 1283, 1284, 1290, 1291, 1298, 1303  
Taylor series, 60  
TBMD. *See* Tight-binding molecular dynamics  
TDDFT. *See* Time dependent density functional theory  
Temperature Replica Exchange Molecular Dynamics (T-REMD), 1162, 1163, 1168–1170  
Tersoff potential, 17  
Tetrahedral, 1000  
Tetraradical configuration, 1377  
Theory, 364, 367, 370, 374, 387, 390, 396, 407, 418–421, 424, 428, 429, 431, 432  
Thermal de Broglie wavelength, 229  
Thermodynamics, 336, 340, 341, 344, 468  
Thermostats, 221–225, 227  
Thioguanine, 1286, 1287  
Third harmonic generation, 385  
THJ. *See* Triple hexagon junction  
Thole-type model for water (TTM2-F, TTM3-F), 764  
Thomas–Reiche–Kuhn sum rule, 390  
Three-body contribution, 1295  
Three-photon absorption, 393  
5'-Thymidine mono-phosphate (5'-dTMP), 1226–1228, 1236–1242, 1246–1248  
Thymine (T), 1187–1189, 1196, 1216, 1224–1232, 1238–1241, 1244, 1245, 1247, 1248, 1258, 1279–1282, 1292, 1295, 1299, 1300, 1303, 1304  
Ti clusters, 963, 986, 987  
Tight-binding approximation, 998  
Tight-binding Hamiltonian, 1025, 1026, 1029  
Tight-binding molecular dynamics (TBMD), 818, 942–944, 946, 947, 950, 952  
Time correlation function, 221, 229  
Time-dependent, 613, 619  
Time dependent density functional theory (TD-DFT), 659, 660, 804, 819, 1367–1369, 1388, 1394  
Time-dependent Hartree–Fock (TDHF), 390, 391  
Time evolution, 137, 138  
Time scale, 1110–1112  
Timestep, 201–204, 222, 224–226  
Topological descriptors, 1348  
Topological ring defect, 846–850  
Torsion, 927–931  
Torsional interactions, 213  
TPSS, 462  
Trajectory surface hopping algorithm, 1362  
Transferability, 262, 286  
Transient negative ions (TNI), 1216, 1219–1228, 1230–1244  
Transition  
–allowed, 46  
–amplitudes, 375, 380  
–forbidden, 46  
–metals, 941, 942  
–moment, 335, 363, 374, 389, 391–393, 426  
–one-photon, 374  
–phosphorescence, 374  
–state, 53, 562, 566, 576, 591, 1361, 1375, 1380  
–Diels–Alder reaction, 324  
–LST approach, 301  
–PES scan, 302  
–QST approach, 301  
–strength, 392  
–three-photon, 374, 393  
–two-photon, 374, 392, 405, 410  
Translation, center-of-mass, 17–20, 23  
Transmission electron microscope (TEM), 795, 798, 815, 821, 853  
Transthyterin (TTR), 1144  
T-REMD. *See* Temperature replica exchange molecular dynamics  
Triple  
–BSSE, 457  
–CC, 457  
Triple hexagon junction (THJ), 707, 709, 710  
Triplet instability, 425  
Triplet-singlet transition, 1081  
TTR. *See* Transthyterin  
TurboMole, web page, 625  
Two-photon absorption, 392–393  
–cross section, 392  
Two state, 240
- U**
- Ultrafast process, 1178, 1187  
Ultrasoft pseudopotentials, 217  
Umbrella sampling, 1159, 1160, 1163–1170  
Unitary transformation, 298  
Unpassivated nanowire, 1012, 1013  
UNRES, 281  
Uracil (U), 1187, 1189, 1196, 1224–1227, 1229–1232, 1240, 1241  
UV absorption, 1189, 1192  
UV spectra, 819

**V**

- Vacancy, 1016, 1033, 1034
  - defect, 799, 816, 824, 848
- Valence, 42
  - bond theory, 42
  - excitation, 124
- Valence-band hole, 895
- Valence bound, 1230–1232, 1245, 1247, 1249
- Vanderbilt pseudopotentials, 217
- van der Waals
  - coefficient, 584
  - interaction, 447, 455
  - interactions, 205, 208, 591
- van der Waals density functional (vdW-DF), 453
- Variationality, 42, 69, 92, 98, 101
- Variational principle, 65–67, 73, 101, 374
- VASP. *See* Vienna ab initio simulation package
- VDOS. *See* Vibrational density of states
- vdW-DF. *See* van der Waals density functional
- Vector, 16, 21, 22, 25, 26, 28, 30, 34, 37, 41, 45
  - coupling coefficient, 45
- Velocity rescaling, 222
- Velocity Verlet algorithm, 203–204, 251, 252
- Verdet constant, 406, 410
- Verlet algorithm, 202–204, 226, 251, 252
- Vertical attachment energies (VAEs), 1220, 1225–1227, 1229, 1230, 1239, 1240, 1243, 1247
- Vibration, 24
  - analysis, 8, 110
  - anharmonicity, 8, 342
  - assigning bands, 334, 347, 348
  - centre of mass, 331–333
  - correction
    - temperature-dependent, 153
    - zero-point, 146, 153, 154
  - excited state, 24
  - frequencies, 11, 115–117
  - frequency, 334, 336, 345, 612
    - scaling, 343
  - frequency weight derivative, 353, 354
  - fundamental frequency, 332
  - harmonic, 354, 355
  - linear molecule, 332
  - mode
    - antisymmetric, 347
    - symmetric, 335, 341
  - normal mode, 333–335, 337, 341, 343, 344, 347
  - scaling factor
    - global, 343
  - SQM, 348
- Vibrational density of states (VDOS), 633, 635, 644–650, 663
- Vibrational Feshbach resonances (VFR), 1216, 1223, 1224, 1229
- Vibration frequency, 468, 470, 472, 584

- Vibration-rotation spectra, 334
- Vienna ab initio simulation package (VASP), 819, 821
- Virtual orbital energies (VOEs), 1227, 1241
- Virtual screening, 1316, 1323–1328, 1336
- Visualization, 197, 230, 231, 1138
- Visual molecular dynamics (VMD), 1138, 1143
- VMD. *See* Visual molecular dynamics

**W**

- Water
  - model, 278, 283
  - molecule, 271, 277, 283
- Water cages
  - pentagonal dodecahedron (H<sub>2</sub>O)<sub>20</sub>, 782–785
  - tetraakis-decahedron (H<sub>2</sub>O)<sub>24</sub>, 785–786
- Water clusters (H<sub>2</sub>O)<sub>n</sub>
  - n=2, 767–771
  - n=3, 767–771
  - n=4, 767–771
  - n=5, 767–771
  - n=6, 767–771
  - n=7, 767–771
  - n=8, 767–771
  - n=9, 767–771
  - n=10, 767–771
  - 11 ≤ n ≤ 16, 771–775
  - n=12, 769, 772, 774, 776
  - n=14, 769, 772, 773
  - n=15, 769, 772, 776
  - n=16, 769, 772, 773
  - n=17, 769, 772, 775–776
    - interior & all-surface minima, 776, 777
    - vibrational spectra, 780–781
  - n=20 isomers, 769
    - vibrational spectra, 780–781
- Watson–Crick pair, 1288, 1295, 1297–1300, 1304
- Wave function, 56–93, 98–102, 125, 364, 390, 391, 393, 424, 425, 429, 431, 564, 613–615, 617–621
  - antisymmetry, 6, 8, 9, 31, 35, 42
  - many-particle, 31
  - multireference, 429
  - normalization, 24
  - nuclear, 16, 24
  - one-electron, 100
  - one-particle, 19, 30, 31, 36, 42
  - open-shell, 424
  - restricted, 296, 431
  - theory, 97, 98, 125
  - unrestricted, 431
- Wavepacket dynamics, 197
- Weight derivative, 352–355



- Weighted histogram analysis method  
(WHAM), 1159
- Weyl tableaux, 51
- WHAM. *See* Weighted histogram analysis method
- Wigner, 45  
-3-j symbol, 45
- Worm like chain, 241, 243
- X**
- X-ray diffraction, 800, 801, 1096, 1097, 1099, 1113, 1117, 1120, 1121
- Y**
- Young diagram, 34, 35, 51
- Young's modulus, 819, 820, 851, 1010–1012
- Z**
- ZAPT. *See* Z-averaged perturbation theory
- Z-averaged perturbation theory (ZAPT), 613
- Zeeman interaction, 414, 415, 427  
-rotational effect, 397
- ZEKE. *See* Zero electron kinetic energy
- Zeolite, 576, 590–592, 594–596, 598, 603
- Z/E photoisomerization, 1363, 1376, 1385. *See also* cis/trans photoisomerization
- Zerner's modification of the intermediate neglect of differential overlap approach (ZINDO), 613
- Zero electron kinetic energy (ZEKE), 576
- Zero-field splitting, 427, 429–430  
-basis, 430  
-contributions, 429–430
- Zero-point vibration energy, 327, 1263
- ZGNR. *See* Zigzag graphene nanoribbons
- Zig-zag, 813, 814, 819, 821–823, 837, 839, 840, 842, 844, 846, 848, 850
- Zigzag edge, 1020, 1021, 1026, 1028, 1029, 1032, 1034, 1036
- Zigzag graphene nanoribbons (ZGNR), 906, 908, 910, 917, 918, 921, 922, 925, 930, 1026, 1030
- Zinblende lattice, 872
- ZINDO. *See* Zerner's modification of the intermediate neglect of differential overlap approach
- Z-matrix, 302, 303, 308, 309